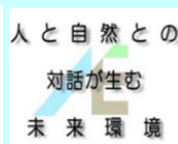




Md. Zakaria Hossain and Bujang B.K. Huat — Editors



GEOMATE 2012 Kuala Lumpur
GEOTECHNIQUE, CONSTRUCTION MATERIALS AND ENVIRONMENT

PROCEEDINGS OF SECOND INTERNATIONAL CONFERENCE – GEOMATE 2012
GEOTECHNIQUE, CONSTRUCTION MATERIALS AND ENVIRONMENT KUALA LUMPUR,
MALAYSIA 14-16 NOVEMBER, 2012

Geotechnique, Construction Materials and Environment

Edited by

Md. Zakaria Hossain
*Graduate School of Bioresources
Mie University*

Bujang B.K. Huat
*School of Graduate Studies
Universiti Putra Malaysia*



THE GEOMATE INTERNATIONAL SOCIETY

Copyright @ 2012 by The GEOMATE International Society

All rights reserved. In principle, no part of this publication or the information contained herein may be reproduced in any form or by any means, translated in any language, stored in any data base or retrieval system, or transmitted in any form or by any means without prior permission in writing from the publisher.

Disclaimer: The editors and the publisher have tried their best effort to ensure the integrity and the quality of this publication and information herein. However, they give no warranty of any kind, expressed or implied with regard to the material contained in this book, and will not be liable in any event for the consequences of its use.

Published by:
The GEOMATE International Society
Tsu city, Mie, Japan
E-mail: geomate@gi-j.com
www.gi-j.com

ISBN Number: 978-4-9905958-1-4 C3051

Table of Contents

Preface	x
Organization	xi

ID *Keynote Papers*

1	Use of microbial technology in geotechnical engineering <i>Jian Chu, Volodymyr Ivanov, Jia He and Viktor Stabnikov</i>	1-4
2	A study on slow moving slopes <i>L G Tham and Xu Kai</i>	5-11
3	Bearing capacity and settlement behaviour of shallow foundations in unsaturated sands <i>Sai K. Vanapalli and Fathi M. O. Mohamed</i>	12-21
4	Development of Piled Geo-wall <i>Hara, T., Tsuji, S., Yoshida, M. and Sawada, K.</i>	22-29
5	Measurement of strain distribution along precast driven pile during full scale pile load test <i>Faisal Ali and Lee Sieng Kai</i>	30-39
6	Unique grouting material composed of calcium phosphate compounds <i>S. Kawasaki and M. Akiyama</i>	40-46
7	Stiffness Anisotropy and Resilient Modulus of an Unsaturated Soil under Static and Cyclic loads <i>Charles W.W. Ng, C. Zhou and J. Xu</i>	47-62
8	Nanoparticles for Geotechnical Engineering <i>Mohd Raihan Taha</i>	63-68

Technical Papers

	<i>Geotechnique</i>	69
24	Damage Assessment and Strengthening of R/C Building Constructed on Expansive Soils <i>Osama M. A. Daoud</i>	70-75

29	Gravitational Sphere Packing Method To Find The Porosity Of The Soil Particles With The Identical Size in cylindrical container <i>Mohammad Mahdi Roozbahani , Bujang B. K. Huat, Afshin Asadi</i>	76-78
34	Parametric Study of Piled Raft Foundations to improve the Design Method <i>Tohidi A., MH .Sadagiani</i>	79-84
39	Experimental Study of Suction-Monitored CBR test on Sand-Kaolin Clay Mixture <i>Purwana, Y.M., Nikraz H., and Jitsangiam P.</i>	85-90
41	Foundation Strengthening of Historic Buildings by Micropiles <i>Azza M. Elleboudy</i>	91-96
44	Group effects of piles due to lateral soil movement <i>Hongyu Qin1 and Wei Dong Guo</i>	97-102
45	Collapse-Settlement Calculations for Embankments Based on a Collapsible Soil Subgrade <i>Moshe Livneh</i>	103-108
46	The influence of trench soil properties on the accuracy of pressure cell measurements in an earthfill dam <i>D. Elmi, A. A. Mirghasemi</i>	109-112
50	Studying the effects of considering dilation angle over the performance of geotechnical elements using numerical methods <i>Salman Hanifi, Amin Naeimabadi , Mohammad Reza Atrchian</i>	113-117
50a	Comparing the excavating effect of single and twin tunnels on the earth surface settlement by numerical methods <i>Amin Naeimabadi, Salman Hanifi , Mohammad Reza Atrchian</i>	118-124
107	Excess Pore Pressure Characteristics of Sand Mat using Dredged Soil <i>M.S LEE, K. ODA</i>	125-130
110	Effect of clays fraction to california bearing ratio laboratory test value with and without soaked <i>Soewignjo Agus NUGROHO, Syawal Satibi and Ferry Fatnanta</i>	131-136
111	Compressibility Characteristics of Residual Soil Subjected to Microbial Treatment <i>Lee Min Lee, Ng Wei Soon, and Yasuo Tanaka</i>	137-140
115	Strength and aging of cement treated low plastic soils <i>Fabien Szymkiewicz, Antoine Guimond-Barrett, Alain Le Kouby</i>	141-145
119	Performance Of Cantilever Sheet Pile Supporting Excavation Adjacent To Strip Footing <i>Yousry M. Mowafe, Ahmed M. Eltohamy and Ahmed A. Mohamed</i>	146-153
119a	Enhancing Stability of Slopes with Cement Kilin Dust Sand Mixture Layer <i>Al Serif M. Abd Alazez1, Ahmed M. Eltohamy and Ahmed Rusdy Towfek</i>	154-161
122	The effect of confining stress on the analysis of excavations with adjacent existing buildings <i>Sabzi Zahra, Fakher Ali</i>	162-166
125	Bored Pile Socket in Erratic Phyllite of Tuang Formation <i>D.E.L. Ong</i>	167-171

133	Swelling deformation of the bentonite mixed with silica fume or sodium carbonate in calcium hydroxide solution <i>Yuki YOKOYAMA and Kenichiro Nakarai</i>	172-175
136	A Combined Probabilistic Method for Engineering Failure analyses and Applications in Typical Geotechnical Structures <i>Duruo Huang</i>	176-181
137	Parametric Study of Crossing Tunnels at Different Level <i>A. Tohidi, MH.Sadagiani</i>	182-189
143	Use of post-floatation copper tailings in the construction of dump dams <i>Tschuschke W., Wierzbicki J.</i>	190-195
150	Effects of Slope Inclination on the Rain-induced Instability of Embankment Slopes <i>Chaminda Gallage, Shiran Jayakody and Taro Uchimura</i>	196-201
225	Extension of an integrated AHP and TOPSIS approach in the earth dam site selection <i>Minatour Yasser, Khazaie Jahangir</i>	202-208
227	Using Geogrid Boxes as a New Approach for Reinforcement of Rock Slopes <i>Ahmad Fahimifar, Arvin Abdolmaleki</i>	209-214
228	Volume Change Characteristics of Clay Mixes with Different Bentonite Percentages <i>J. M. Kate, Sunil Kumar, M. P. Bhorkar</i>	215-218
236	FE Analysis for Settlement of Peat Ground under Embankment Loading <i>Satoshi Nishimoto and Hirochika Hayashi</i>	219-224
237	Seismic behavior of pile group in soil slopes: 1g shake table tests <i>H. Elahi, M. Moradi, A. Ghalandarzadeh and A. Elahi</i>	225-229
239	Electrophoresis of Bacteria and Electro-Biogrouting <i>Hamed A. Keykha, Bujang B. K. Huat, Afshin Asadi, Satoru Kawasaki</i>	230-232
240	Consideration concerning reasonable modified form of Floating-type Improved Ground <i>Hijiri Hashimoto, Satoshi Nishimoto and Hirochika Hayashi</i>	233-236
241	Numerical Study Effect of Nail Angle Change on Stability and Displacement of Excavation Wall in Cohesive and Cemented Non-Cohesive Soils <i>Navid Shahnazi, Jahangir Khazaie, Mohamad Sharifipour and Kiarash Ashtari</i>	237-241
242	An investigation on behavior of geogrid reinforced soil retaining walls applying finite difference method (F.D.M) <i>Jahangir Khazaie and Alireza Sadeghabadi</i>	242-252
243	Effects of humic acid and salt additives on the behaviour of lime-stabilised organic clay. <i>N.Z. Mohd Yunus, D. Wanatowski, and L.R. Stace</i>	253-256
244	Sodium Tripolyphosphate For Stabilizing Of Contaminated Soil <i>Amin Falamaki, Hossein Tavallali and Shahrbanoo Rezanejad Farahmand</i>	257-260
246	Evaluation of Soil Water Characteristic Curves for Sand-Expansive Clay Mixture <i>T. Y. Elkady, M. A. Dafalla, A. M. Al-Mahbashi and Mosleh Al Shamrani</i>	261-265

247	Coastal soils improvement <i>Mohammad reza Atrchian, Morteza Ala, Amin Naeimabadi</i>	266-269
248	A Hybrid Intelligent System of Fuzzy C-Mean Clustering and Neural Networks to Predict the Compaction Characteristics of Fine Grained Soils <i>Iman Ashayeri, Mahnoosh Biglari</i>	270-273
249	Equivalent linear seismic ground response analysis of unsaturated soil deposits <i>Mahnoosh Biglari, Iman Ashayeri</i>	274-278
251	The Correction of Shallow Foundation Settlement Equations by Finite Element Method <i>Mohammad Arab Ameri, Hakime Rabbanifar and Mehdi Arab Ameri</i>	279-284
255	Numerical study of earthquake hazards of liquefaction occurring on the site and sustainable transport pipes <i>Hamed Bavanpouri, Jahangir Khazaie, Dr.Hasan Sharafi</i>	285-288
266	Analysis of geogrid reinforced soil retaining walls with limit equilibrium and finite difference method <i>Alireza Sadeghabadi, Jahangir Khazaie and Mostafa Yousefi Rad</i>	289-293
270	Recent Development in Electrokinetic Stabilization of Soft Soil, A review <i>Hossein Moayed, Sina Kazemian, and Bujang B. K. Huat</i>	294-298
275	Application of ion-exchange solution soil stabilizer in increasing CBR values of clayey soils <i>Reza Ziaie Moayed, Seyed Ali Hashemi and Farzad Allahyari</i>	299-302
276	Assessment of Low Strain Wave Attenuation for Piles Cast in Very Dense Granular Soil <i>Ramli Nazir and Osman El Hussien</i>	303-307
279	Dynamic Soil-Structure Interaction Considering Pore-Water Pressure Coupling <i>Qutayba Nazar Al-Saffar, P Akram Y. Al-Sa'aty, Mohamad T. Al-Layla</i>	308-325
281	Analysis and design of tunnel lining in alluvial soil deposits <i>Nuri al-Mohamadi</i>	326-330
285	Effect of silt content on the anisotropic behaviour of silt-sand mixtures <i>Navid Khayat, Abbas Ghalandarzadeh</i>	331-337
288	Optimizing the twin tunnels position for reduction the surface ground movements <i>Mehdi Mokhberi, Seyed Ali Farjam</i>	338-344
290	Evaluation of pile lateral capacity in clay applying evolutionary approach <i>Alkroosh I., Nikraz H</i>	345-348
293	Effect of Reservoir Drawdown Rate on Phreatic Line Recession in Homogeneous Earth Dams <i>R. Ziaie Moayed, V. Rashidian</i>	349-352
294	The effect of lime-microsilica stabilization on California Bearing Ratio of silty soils <i>R. Ziaie Moayed, Y. Daghighi, B. Pourhadi and N. Sahebzamani</i>	353-356
295	Effect of elastic modulus varieties in depth on modulus of subgrade reaction on granular soils <i>Reza Ziaie Moayed, Mahdi Ali Bolandi</i>	357-360

296	Flexural Buckling Behavior of Steel Pile with Vertical Load in Liquefied Soil <i>Yoshihiro Kimura and Koichi Onohara</i>	361-365
305	Two-dimensional finite difference pseudo-static deep-seated slope stability analysis of embankments over stone column-improved soft clay <i>Farshad Fayyaz Jahani, Mohammad Sharifipour</i>	366-371
308	Parametric study of Geo-grid soil reinforced retaining walls under dynamic loading by ABAQUS software <i>Atrechian mohammad reza, Daghighi younes, Ghanbari namin hamed</i>	372-380
2010	Sensitivity analysis in soil nail wall for Tehran-Tabriz railway by considering the coefficient of variation for effective parameters in stability analysis <i>Mohammad Moghadaripour, Ardalan Akbari Hamed, Ali Ghozat</i>	381-384
2012	Evaluation of Strength Parameters of Improved Collapsible Soils with Current Additives (Case study: Atrak zone, Iran) <i>Mohammad Arab Ameri, Samaneh Kargar and Mehdi Arab Ameri</i>	385-390
2100	Influences of soil material parameters in compaction simulation with soil/water/air coupled F.E. code <i>S. Sakamoto, K. Kawai, V. Phommachanh and A. Iizuka</i>	391-396
2105	Lower bound limit analysis of strip footings resting on cohesive soils <i>S.M. Binesh, A. Gholampour</i>	397-402
2106	Upper bound limit analysis of strip footings resting on cohesive soils <i>S.M. Binesh, S. Raei</i>	403-408
2108	Evaluating and optimizing different methods of treating and cleaning contaminated soil <i>Mohammad Reza Atrechian, Seyed Salman Musavi Khosro Ebrahimkhani</i>	409-412
2112	Experimental study concerning impact characteristics by collision of weight on sand cushion over steel beam <i>Tam Sy Ho, Hiroshi Masuya and Naoto Takashita</i>	413-419
2114	Landslides in Tea Plantation Fields in Shizuoka, Japan <i>Jun Sugawara</i>	420-425
2115	Natural base isolation system for earthquake protection <i>Srijit Bandyopadhyay, Aniruddha Sengupta and G.R. Reddy</i>	426-431
2116	Comparison of Effect of Percent of Compaction, Sand and Cement on The Amount and Time of Swelling of Bentonite <i>Mohammad S. Pakbaz and B. Rafiee</i>	432-435
2118	Prediction of the Axial Bearing Capacity of Piles by SPT-based and Numerical Design Methods <i>Issa Shooshpasha, Ali Hasanzadeh and Abbasali Taghavi</i>	436-439
2120	Application of recently developed mechanistic-empirical methods for the design of heavily loaded pavement structures <i>John N. Mukabi</i>	440-447
2121	Design of support system for excavation in black cotton soils in Guntur, India <i>D. Neelima Satyam, Akhila Manne</i>	448-451
2127	Numerical modeling of pullout capacity of a pile in sand under oblique load <i>Md. Iftekharuzzaman and Dr. Bipul Hawlader</i>	452-457

2130	Slope Failure in Residual Soils of Peru <i>A. Carrillo-Gil</i>	458-461
2131	Back-analysis of Frictional Jacking Forces Based on Shear Box Testing of Excavated Spoils <i>Choo Chung Siung and Dominic Ong E. L.</i>	462-467
2132	Lime Stabilization of Tropical Soft Soils <i>Dygku Salma Awg Ismail, Tan Jui Siang and Siti Noor Linda Taib</i>	468-471
2138	Increase Of Piles Bundle Capacity By Making A Base Joining Them <i>Jan Jaremski</i>	472-478
2139	The Effects of soil-Pile Interaction on Seismic Parameters of Superstructure <i>Mahdy KhariI, Khairul Anuar Bin Kassim, Azlan Bin Adnan</i>	479-484
2140	Investigation on Finite Element Modeling of Group of Stone Columns <i>M. Mirshekari, C. Behnia and S. Fakhretaha</i>	485-488
2147	Suction Controlled Triaxial Apparatus for Saturated-Unsaturated Soil Test <i>Luky Handoko, Noriyuki Yasufuku, Kiyoshi Oomine, Hemanta Hazarika</i>	489-493
2154	Monitoring Program and Dilapidation Survey for Grouting of Karst Cavities <i>Hasan A. Kamal and Hassan J. Karam</i>	494-497
2156	Numerical Analysis of Soil Nail Walls under Seismic Condition in 3D Form Excavations <i>Siavash Zamiran, Hamidreza Saba</i>	498-501
2159	Shear strength improvement of fibrous peat due to consolidation pressure <i>Vivi Anggraini, Nurly Gofar and Bujang bin Kim Huat</i>	502-506
2164	Factors affecting the stability analysis of earth dam slopes subjected to reservoir drawdown <i>T. Souliyavong, C. Gallage, P. Egodawatta and B. Maher</i>	507-512
2165	Lateral stress induced due root-water-uptake in unsaturated soils <i>Mu'azu Mohammed Abdullahi and Nazri Bin Ali</i>	513-517
2166	The effect of pre-tensioned rock bolts on seismic behavior of urban tunnels <i>Farshad Fayyaz Jahani, Mohammad Sharifipour</i>	518-523
2170	Effect of silt content on the anisotropic behaviour of silt-sand mixtures <i>Navid Khayat, Abbas Ghalandarzadeh</i>	524-530

Construction Materials

24b	Production and Properties of High Strength Concrete for Concrete Dam Heightening Project in Sudan <i>Osama M. A. Daoud and, H. S. Sagady</i>	531-537
27	Effect of openings locations of quadratic folded plate roofing systems on their static and dynamic behavior <i>Ahmed Hassan</i>	538-544

48	Improving concrete compression strength using natural additive <i>Abdoulallah Namdar, Ideris Bin Zakaria and Nurmunira Binti Muhammad Atan</i>	545-548
53	DEM simulations and laboratory experiments on physical and mechanical properties of sand-gravel mixtures <i>Janaka J. Kumara, Kimitoshi Hayano, Yuuki Shigekuni and Kota Sasaki</i>	549-554
120	Rock slope stability problems in Gold Coast area in Australia <i>Shokouhi Ali, Gratchev Ivan, Charrismanagara Arry</i>	555-558
121	Techno-commercial development of pre-fabricated structures using geopolymer concrete <i>J. Santhosh, R.Sanjeev, P.Sethu Raja, A. Rajendra Prasad, A. Abdul Rahman</i>	559-563
124	Mechanical Properties of Recycled Steel Fibre Reinforced Concrete <i>A.S.M. Abdul Awal, Lim Lion Yee, M. Dianah1 and M. Zakaria Hossain</i>	564-569
134	Effects of Gradation of Various Sand Deposits of Pakistan on Strength of Hardened Concrete <i>Gauhar Sabih , S. Muhammad Jamil and Kamran Akhtar</i>	570-574
203	Assessment of recycled concrete aggregates for road base and sub-base <i>S. Jayakody, C. Gallage, A.Kumar</i>	575-579
232	Estimation of consolidation properties of Holocene clays with artificial neural network <i>Kazuhiro ODA , Minsun Lee and Shotaro Kitamura</i>	580-585
250	Measurement of The Crack Displacement Using Digital Photogrammetry for Evaluation of The Soundness of Tunnels <i>A. Kanazawa, S.Nishiyama, T.Yano, T.Kikuchi</i>	586-592
259	Numerical modelling of a small scale shallow foundation reinforced by Soil-Mixing <i>Anna GRZYB, Mahmoud Dhaybi and Frederic Pellet</i>	593-598
262	Physical modelling of a small scale shallow foundation reinforced by Soil-Mixing <i>Mahmoud Dhaybi and Frederic Pellet</i>	599-604
282	Prediction compressive strength of concretes containing silica fume and styrene-butadiene rubber (SBR) with a mathematical model <i>A.Haghollahi, M.Shafieyzadeh</i>	605-610
283	Sliding stability of dry masonry block retaining structure with a resistance plate <i>Akihiro Hashimoto, Noriyuki Yasufuku, Yoshio Suematsu, Kazuo Fujita1 and Toshimitsu Komatsu</i>	611-616
287	Evaluation and Prediction Method on Neutralization of Supplied Long-term Hydraulic Concrete Structure <i>Man-Kwon Choi , Yuki Hasegawa, Shinsuke Matsumoto, Shushi Sato and Tsuguhiro Nonaka</i>	617-621
297	Measurement of tensile properties of geogrids <i>Raid R. Al-Omariand Mohammed K. Fekheraldin</i>	622-631
306	Modeling the Swelling strain and pressure of Weak Rock using Adaptive Network-Based Fuzzy Inference System <i>Ramin Doostmohammadi</i>	632-636
309	Centrifuge Modeling Of Reinforced Embankments On Soft Foundation <i>Ali Sobhanmanesh, Nurly Gofar</i>	637-642

2102	Centrifuge model tests and finite element analyses on the seismic behavior of the quay walls backfilled with cement treated granulate soils <i>Hayano, K., Morikawa, Y., Fukawa, H., Takehana, K. and Tanaka, S.</i>	643-650
2109	Response of Piered Retaining Walls to Lateral Soil Movement Based on Numerical Modeling using Matlab <i>Siamak Pahlevanzadeh</i>	651-654
2122	Evaluation of Thermal Response Tests in Energy Piles <i>Seung-Rae Lee, Seok Yoon, Hyun-Ku Park, Gi-Dae Oh</i>	655-659
2134	Experimental Study on Mechanical Characteristics of Soil-Geosynthetic Interface <i>Md. Bellal Hossain, Md. Zakaria Hossain and Toshinori Sakai</i>	660-665
2136	An Interpretation of Mechanical Properties of Bentonite as a Non-linear Elastic Material <i>Y. Takayama, S. Tsurumi, A. Iizuka, K. Kawai</i>	666-671
2149	Effect of carbonation on strength of cement treated sand <i>Kenichiro Nakarai and Tomomi Yoshida</i>	672-675
2167	Application of PML to Analysis of Nonlinear Soil-Structure-Fluid Problem using mixed element <i>Pahaiti Rehemani, Hiroo Shiojiri</i>	676-681
<i>Environment</i>		64
28	Recycled Bassanite as a Stabilizing Agent for Cohesion-less Soil <i>Aly Ahmed and Keizo Ugai</i>	682-687
31	The effects of environmental on today construction industry <i>Mahdy Khari1, Khairul Anuar Bin Kassim, Azlan Bin Adnan</i>	688-692
33	A Case History of Quay Wall Failure and Remedial Design <i>C. S. Chen</i>	693-696
37	Environmental economical efficiency in treatment/reutilization of construction sludges considering delay in process flow <i>Shinya Inazumi, Hiroyasu Ohtsu and Takayuki Isoda</i>	697-702
42	Evaluation and validation of elastic-fragile damage modeling for unsaturated porous media in θ -stock <i>B. Gatmiri, M. Fathalikhani</i>	703-708
43	Estimation of the Landslide Dam Sustainability in the Gigantic Seimareh Landslide Using the Rate of Sedimentation <i>Zieaoddin Shoaie</i>	709-7012
47	Influence of soil and rock mineralogy and geomorphology on Landslides Occurrence and soil erosion in the Merek Catchment, Iran <i>Mosayeb Heshmati, Nik Muhamad Majid, J. Shamshuddin, Arifin Abdu and Muhamad Ghaituri</i>	713-719
112	The effect of historical land use on landslide initiation <i>Gholamreza Shoaie</i>	720-723
114	Integrated Environmental Management for Sustained Development <i>J.Rajaraman and K.Thiruvengatasamy</i>	724-729

114a	Lowland Environmental Geotechnology of Seismosediments of Kandla Port In India <i>J.Rajaraman and K.Thiruvengatasamy</i>	730-735
123	Single step extraction to find out soluble lead in soil <i>Masahiko Katoh, Satoshi Masaki, Takeshi Sato</i>	736-741
127	Biogas Production from Tannery Sludge <i>A.Rajendra Prasad, A.Dhanalakshmi, S.Usha and A.Abdul Rahman</i>	742-746
131	Water Harvesting and Salinization Prevention by Capillary Barrier of Soil <i>Toshihiro Morii, Mitsuhiro Inoue, Kaoru Kobayashi, Tetsuya Suzuki and Takayuki Kawai</i>	747-752
204	Study of the Performance of anaerobic digestion of greasy skim as a renewable energy source <i>Salam J. Bash Al-Maliky</i>	753-756
209	Seismic evaluation of NARGES soil nailed wall under Cyclic loading and Pseudo Static forces <i>Ardalan Akbari Hamed , Mohammad Moghadaripour , Ali Ghazat</i>	757-761
229	Purification System of Ocean Sludge by and Using Coagulants and then Activating Microorganisms <i>Kyoichi Okamoto and Kenji Hotta</i>	762-767
233	Mechanical properties of volcanic products mixed with industrial wastes <i>K. Yamamoto, T. Negami2, M. Hira, N. Aramaki and Y. Hayashi</i>	768-771
235	Measurement of Hydraulic Conductivity for Peat Ground Using CPTU <i>Hirochika Hayashi and Satoshi Nishimoto</i>	772-775
252	Extraction of temporal and spatial properties on habitat of snail by means of statistical approach <i>Masaaki KONDO and Takamitsu KAJISA</i>	776-781
265	The use of Nano Zero Valent Iron to remediation of contaminated soil and groundwater <i>Taghizadeh Maryam , Yousefi Kebria Daryoush and Gholamreza Darvishi</i>	782-785
267	A Multi-parameter Water Quality Analysis by onsite filtered 2mL Sample to Monitor Urban River Eutrophication <i>Akira Kikuchi, Nor Eman Ismail, Narges Janalizadeh, Musa Mutah and Muhamad Faiz</i>	786-790
268	The intelligent performance installations in energy efficiency in green buildings <i>Hooman Abadi, Rouzbeh Abadi, Poona Abadi</i>	791-796
271	Study the Effect of Polyvinyl Chloride (PVC) Addition on the Permeability of Anbar Soils <i>Ahmed H. Abdul Kareem & Omar Mustafa</i>	797-802
274	Monitoring deforestation and rangeland destruction through land use alteration during 1955- 2002, using GIS and RS in Merek sub-basin, west Iran <i>Mohammad Gheitury, Mosayeb Heshmati, Mohammad Ahmadi and Nik Muhamad Majid</i>	803-807
280	The comparison of phytoremediation and electrokinetic methods in remediation of petroleum hydrocarbons contaminated soil <i>Gholami Meade, Yousefi Kebria Daryoush</i>	808-811
286	Using Metacognitive Strategies On Listening Comprehension <i>Mahshid Mirzaaghaee</i>	812-822

298	Evaluation of Run-Off Supply Projects in Hamedan Province(Iran) <i>N. Rostam Afshar, M. Abdoli</i>	823-827
299	Protective measures of the monumental pine in Rikuzentakada with soil-water-air-solved material coupled model <i>Y. Sugiyama, S. Nomura, K. Kawai and A. Iizuka</i>	828-833
304	Effects of Biosurfactants in Electrokinetic Remediation of contaminated soils <i>Bour Moslem and Yousefi kebria Daryoush</i>	834-838
2117	Change in structure of ground-beetle assemblage on river areas after construction of biotopes using the technique, “Nature oriented river works” <i>Michko Masuda, Takaaki Tsukada and Fumitake Nishimura</i>	839-844
2123	Dense granular-fluid mixture: the effects of the natural grains characteristics and the interstitial fluid viscosity <i>Anna Maria Pellegrino and Leonardo Schippa</i>	845-850
2131	Back-analysis of Frictional Jacking Forces Based on Shear Box Testing of Excavated Spoils <i>Choo Chung Siung and Dominic Ong E. L.</i>	851-856
2137	An idea of multi-functional reservoirs in mountain regions <i>Jan Jaremski</i>	857-862
2141	Estimation Method of Amount of Tsunami Disaster Wastes during the 2011 off the Pacific Coast of Tohoku Earthquake <i>Minoru Yamanaka, Naoya Toyota, and Shuichi Hasegawa, Atsuko Nonomura</i>	863-866
2143	Assessment of Runoff in the High Humid Foot-hill Areas of Arunachal Himalayas Using Thornthwaite Equation <i>Md. Eahya Al Huda and Surendra Singh</i>	867-871
2161	Natural Radiation level in Groundwater from Katsina, a Semi Arid Region of Northern Nigeria <i>B.G. Muhammad and M.S. Jaafar</i>	872-876
2163	Cost-Performance Studies of Abandoned Shell Husks (ASH) for Soil Reinforcement Applications <i>Md. Toriqul Islam, Md. Zakaria Hossain, Masaaki Ishida, Md. Bellal Hossain and Md, Jamal Uddin</i>	877-880
2171	Cyclones Path and Severities: Effect on Flood Height and Damages of Land and Embankments in Bangladesh <i>Musahaq Ali, Zakaria Hossain and Shigeko Haruyama</i>	881-884
	Author index	885

Preface

The Second International Conference on Geotechnique, Construction Materials and Environment GEOMATE2012, held at the Istana Hotel, Kuala Lumpur, Malaysia, was organized by the School of Graduate Studies, Universiti Putra Malaysia, in collaboration with the GEOMATE International Society, AOI-Engineering, the Useful Plant Spread Society, HOJUN and Glorious International. Its aim was to provide scholars the space and opportunity to share common interests on geo-engineering, construction materials, environmental issues, water resources, and earthquake and tsunami disasters. The key objective of this conference was to promote interdisciplinary research from different regions across the globe.

On Friday 11 March 2011, at 14:46 Japan Standard Time, the north east of Japan was struck and severely damaged by a series of powerful earthquakes which also caused a major tsunami. This conference was dedicated to the tragic victims of the Tohoku-Kanto earthquake and tsunami disasters. This was the second event after the first international conference that was successfully held in Tsu city, Mie, Japan, with more than 150 participants.

The conference had three major themes with 17 specific themes including:

- Advances in Composite Materials
- Computational Mechanics
- Foundation and Retaining Walls
- Slope Stability
- Soil Dynamics
- Soil-Structure Interaction
- Pavement Technology
- Tunnels and Anchors
- Site Investigation and Rehabilitation
- Ecology and Land Development
- Water Resources Planning
- Environmental Management
- Public Health and Rehabilitation
- Earthquake and Tsunami Issues
- Safety and Reliability
- Geo-Hazard Mitigation
- Case History and Practical Experience

The proceedings from this conference contain eight keynote papers along with 145 technical papers from 25 countries. The technical papers were selected from the vast number of contributions submitted, after a review of the abstracts. The final papers selected to be included in the proceedings have been peer reviewed rigorously and revised as necessary by the authors. We are especially grateful to the authors for their resourcefulness and their help in maintaining the high standard of the collection, as well as their co-operation in complying with the requirements of the editor and the reviewers. We wish to express our sincere thanks to the Organizing Committee Members, the National Advisory Committee Members and the International Advisory Committee Members for their invaluable support. We would also like to acknowledge the support of the School of Graduate Studies, Universiti Putra Malaysia, the GEOMATE International Society, AOI-Engineering, the Useful Plant Spread Society, HOJUN and Glorious International.



Prof. Dr. Bujang B.K. Huat
Conference Chairman



Dr. Md. Zakaria Hossain
Conference Secretary

Organization

Scientific Committees:

Conference Chairman: Prof. Dr. Bujang B.K. Huat, Universiti Putra Malaysia, Malaysia
Conference Honorary Chairman: Emeritus Prof. Dr. Sohji Inoue, Mie University, Japan

Conference Organizing Committee:

Prof. Faisal Ali, Universiti Pertahanan Nasional Malaysia
Prof. Mohd Raihan, Taha Universiti Kebangsaan Malaysia
Prof. Roslan Hashim, Universiti Malaya
Prof. Thamer A. Mohamed, Universiti Putra Malaysia
Prof. Dato' Ismail Bakar, Universiti Tun Hussein Onn Malaysia

National Advisory Committee:

Prof. Dr. A.S.M. Abdul Awal, Universiti Teknologi Malaysia, Malaysia
Prof. Dr. Ideris Bin Zakaria, Univ. Malaysia Pahang, Malaysia
Prof. Dr. Muhammad Ibn Ibrahimy, International Islamic University, Malaysia
A/Prof. Dr. Zunaidi Bin Ibrahim, Deputy Rector, Kolej Universiti TATI, Malaysia
A/Prof. Dr. Abdoullah Namdar, Universiti Malaysia Pahang, Malaysia
Prof. Dr. Suleyman Aremu Muyibi, International Islamic University, Malaysia
Prof. Dr. Shahjahan Mridha, International Islamic Univ., Malaysia
Prof. Dr. Faisal HJ Ali, National Defense University of Malaysia

International Advisory Committee:

Prof. Dr. Fumio Tatsuoka, Tokyo University of Science, Japan
Prof. Sai Vanapalli, University of Ottawa, Canada
Prof. Dr. Nemy Banthia, University of British Columbia, Canada
Prof. Dr. Ian Jefferson, University of Birmingham, UK
Prof. Dr. John Bolander, University of California, USA
Prof. Dr. Shamsul Chowdhury, Roosevelt University, USA
Prof. Dr. Isabel Pinto, University of Coimbra, Portugal
A/Prof. Mark Jaksa, University of Adelaide, Australia
A/Prof. Dr. William Sebudde Kaggwa, University of Adelaide, Australia
Dr. John N. Mukabi, President of Kenya Geotechnical Society, Kenya
Prof. Dr. Jing-Cai Jiang, University of Tokushima, Japan
A/Prof. Dr. Kingshuk Roy, Nihon University, Japan
A/Prof. Dr. Md. Shahin Hossain, Nagoya Institute of Technology, Japan
Prof. Dr. Mounir Bouassida, National School of Engineering of Tunis
Prof. Dr. Lilia Robles Austriaco, Angeles University Foundation, Philippines
Prof. Dr. Zahurul Islam, Bangladesh University of Engineering and Technology, Bangladesh

Conference Secretariat:

Dr. Zakaria Hossain, Associate Professor
Division of Environmental Science and Technology
Graduate School of Bioresources
Mie University, 1577 Kurima Machiya-cho
Tsu-city, Mie 514-8507, Japan
E-mail: zakaria@bio.mie-u.ac.jp
Tel: +81-59-231-9578、 Fax: +81-59-231-9591

Editorial Committee:

Md. Zakaria Hossain
Prof. Dr. Bujang B.K. Huat

Executive Committee:

Bujang B.K. Huat
Md. Zakaria Hossain
Muhammad Ibn Ibrahimy
Md. Bellal Hossain
Afshin Asadi

Use of Microbial Technology in Geotechnical Engineering

Jian Chu^{1,2}, Volodymyr Ivanov², Jia He² and Viktor Stabnikov²

1 Department of Civil, Construction & Environmental Engineering, Iowa State University, USA

2 School of Civil and Environmental Engineering, Nanyang Technological University, Singapore

ABSTRACT

The recent development and principles of the application of microbiology in geotechnical engineering are briefly introduced. The microbial approach has several advantages over the conventional soil improvement methods. It is more cost effective, energy saving, environmentally friendly, and simpler to implement. Three types of applications that have been studied recently are introduced. The first is improvement of shear strength of soils by introducing crystallizations or slimes using the microbial process. The second is mitigation of liquefaction potential of soils by forming uniformly distributed and stable gas bubbles in liquefiable soil layers using bacteria. The third is seepage and erosion control by forming a hard layer of calcite crust on the soil surface using the microbial urea hydrolyzing process.

Keywords: geotechnical engineering, grouting, microbiology, soil improvement

1. INTRODUCTION

When there are constructions over soft ground, the soft soil needs to be treated. There are a number of ways to strengthen soft or weak soil. One of the common approaches is to use cement or chemicals to increase the load bearing capacity or the so-called shear strength of soil. The same process can be used to reduce the water conductivity of soil or the rate of water flow in soil. This is necessary when there is a need to prevent water from flowing in the ground, for example, for cutting off contaminated groundwater flow. In the above cases, cement or chemicals are used as a binder to mix with soil to either increase the shear strength or reduce the water conductivity of soil. However, the use of cement or chemicals for construction or soil improvement is not sustainable in the long run as cement or chemicals require a considerable amount of natural resource (for example limestone) and energy to produce. The production process also generates carbon dioxide, dust and possibly other toxic substances and thus is not environmentally friendly. The use of cement or chemicals for soil improvement is also expensive and time consuming. There is an urgent need to develop new and sustainable construction materials that can reduce the use of cement or chemicals for geotechnical applications.

Using the latest microbial biotechnology, a new type of construction material, biocement, has been developed as an alternative to cement or chemicals [1], [2]. Biocement is made of naturally occurring microorganisms at ambient temperature and thus requires much less energy to produce. It is sustainable as microorganisms are abundant in nature and can be reproduced easily at low cost. The microorganisms that are suitable for making biocement are non-pathogenic and environmentally friendly. Furthermore, unlike the use of cement, soils can even be treated or improved without disturbing the ground or environment as microorganisms can

penetrate and reproduce themselves in soil. Harnessing this natural, unexhausted resource may result in an entirely new approach to geotechnical or environmental engineering problems and bring in enormous economic benefit to construction industries. The application of microbial biotechnology to construction will also simplify some of the existing construction processes. For example, the biocement can be in either solid or liquid form. In liquid form, the biogrout has much lower viscosity and can flow like water. Thus, the delivery of biocement into soil is much easier compared with that of cement or chemicals. Furthermore, when cement is used, one has to wait for 28 days for the full strength to be developed, whereas when biocement is used, the reaction time can be much reduced if required.

2. PRINCIPLES

The principles of microbial treatment are to use the microbially-induced calcium carbonate precipitation or other approaches to produce bonding and cementation in soil so as to increase the strength and reduce the water conductivity of soil. A number of studies have been carried out in recent years [2]-[5]. Much of the work still stays at the experimental stage. However, the scale of treatment has increased rapidly with time and has reached 100 m³ in the recent years [5].

The microbiological processes induce calcium carbonate crystals, other minerals or slimes as illustrated by examples shown by Van der Ruyt and van der Zon (2009) [4], Van Paassen et al. (2010) [5] and Chu et al. (2012) [6]. Those minerals or slimes act as cementing agencies between sand grains to increase the shear strength of soil and/or to fill in the pores in soil to reduce the water conductivity as illustrated schematically in Fig. 1. The two processes to increase strength and reduce conductivity have been called biocementation and bioclogging respectively [2]. The process

to deliver the biocement in-situ to achieve biocementation or bioclogging is called biogrouting. As the viscosity of biogrout is low, it is possible to pump in the biogrout into the ground without mixing for sandy soil. This will enable the construction process to be simplified. The existing study so far shows that the biocement method is effective in both increasing the shear strength and reducing the water conductivity of soil.

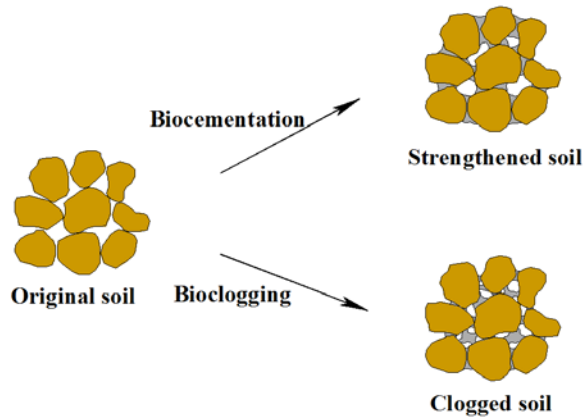


Fig. 1. Schematic Illustration of biocementation and bioclogging process



Fig. 2. Sand column treated by biocement

3. POTENTIAL APPLICATIONS OF BIOCEMENT

3.1 Enhancing Shear Strength of Sand

By using the microbially-induced calcium carbonate precipitation method, the shear strength of soil can be increased. We know from our childhood experience in castle building on the beach that dry sand will not stand. However, when dry sand is treated by biocement, a sand column not only can stand, but also can sustain a lot of weight as shown in

Fig. 2 as an example. When cement or chemicals are used to treat soil, the amount of improvement in the shear strength of soil is dependent on the amount of cement or chemical used. Similarly, when biocement is used, the shear strength of soil is affected by the amount of metal precipitation. One way to measure the shear strength of soil is by simply compressing a soil column in between of two rigid plates, the so-called uniaxial compression test. The shear strength measured by this method is called the uniaxial compressive strength (UCS). In one study by Van der Ruyt and van der Zon (2009) [4], the UCS of biocement treated sand was measured for specimens having different calcium carbonate contents. The results are shown in Fig. 3. It can be seen that the UCS strength increases with increasing calcium carbonate content. The highest UCS obtained is 27 MPa. For normal applications, the UCS strength required is less than 3 MPa. This will only require a calcium content of 100 to 200 kg/m³. To achieve the same UCS strength for sand using cement grouting, the amount of cement used would be between 250 to 300 kg/m³. As the production of biocement can be cheaper as discussed by Ivanov and Chu (2008) [2], the overall cost for biogrouting can be potentially lower. Another advantage is that when cement grouting, it takes 28 days for the UCS to reach the targeted value. However, when biocement is used, full strength can be gained in a much shorter time if required.

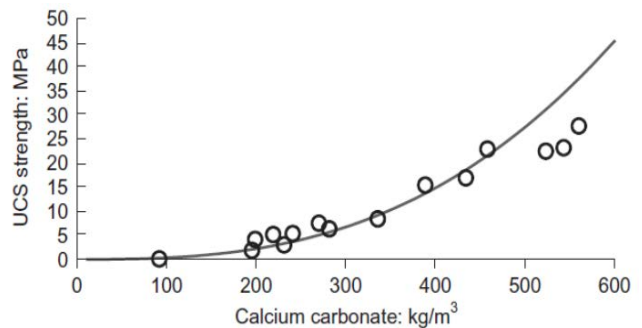


Fig. 3. The unconfined compression strength (UCS) versus calcium carbonate content relationship for biocement treated sand (after Van der Ruyt and van der Zon, 2009)

3.2 Mitigation of Soil Liquefaction by Biogas

Soil liquefaction refers to a phenomenon in which a soil is transformed into a substance that acts like a liquid in response to an external action such as earthquake. When liquefaction occurs, the ground loses completely its bearing capacity and undergoes large deformation. Soil liquefaction normally occurs in saturated sand deposits during earthquake. The ground shaking will cause the water pressure in soil or the so-called pore water pressure to build up. When the pore water pressure has increased to a certain point, soil liquefaction will occur. Soil liquefaction has been one of the major causes for serious damages and earthquake related disasters. More recently liquefaction was largely responsible for extensive damage to residential properties in the eastern suburbs and satellite townships of Christchurch, New Zealand during the 2010 Canterbury earthquake and more extensively again following the Christchurch earthquakes that followed in early and middle 2011.

The common methods that can be adopted for mitigation of soil liquefaction include densification and ground modification using cement or chemicals. A new approach that is being developed is the so-called biogas method. In this method, tinny gas bubbles are generated in-situ in saturated sand at where liquefaction may occur. When saturated sand is made slightly unsaturated by the inclusion of gas bubbles, the amount of reduction in the pore water pressure generated in sand under a dynamic load will be greatly reduced. Based on our research, if we replace only about 5% of water by gas by volume, we will be able to increase the liquefaction resistance of loose sand by more than 2 times.

It is not easy to introduce gas into ground. Pumping can be used. Fig. 4 shows a schematic illustration of how to carry out air pumping for liquefaction mitigation. However, the distribution of gas bubbles introduced by pumping will not be even. Furthermore, the gas pumped into ground tends to present in the form aggregated gas pockets rather than individual bubbles. As a result, the gas tends to escape from the ground. One of the most effective ways to introduce tinny gas bubbles in-situ is to use microorganisms. This method has the following three advantages over the existing methods: (1) Biocement is like water in the liquid form and flow easily in sand. Gases can be generated easily by bacteria anywhere underground by consuming only a small amount of energy. Thus the biogas method will be much more cost-effective than any other methods. As the scale of treatment for liquefaction is normally very large, the potential economic benefit is significant; (2) The gas bubbles generated by bacteria can be distributed more evenly than other means. This is because biocement can be delivered by water flow in sand and the gas bubbles are generated in-situ rather than pumped; (3) The gas bubbles generated by bacteria can be much smaller. It is necessary for the gas bubbles to be tinnier so the gas bubbles are less prone to escaping from the ground.

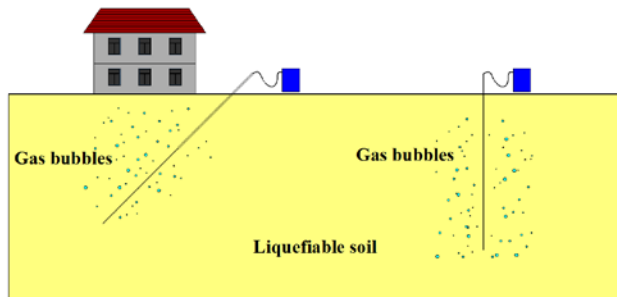


Fig. 4. Mitigation of soil liquefaction by air injection

Some model tests using a laminate box and a shake table to generate ground motion were carried out. A comparison of ground settlement for a fully saturated sand layer and a sand layer treated with biogas is made in Fig. 5. The settlement is expressed as a settlement ratio with the settlement for fully saturated sand as 100%. It can be seen from Fig. 5 that with only 5% of gas replacement, the ground settlement generated under ground shaking with an acceleration of 1.5 m/s^2 can be reduced by more than 90%. Thus, the biogas method is effective in preventing the occurrence of soil liquefaction or reducing the damage caused by liquefaction.

Compared with conventional soil liquefaction mitigation methods, the biogas method has some significant advantages. Conventional methods, such as compaction, cementation, lowering ground water table, and pore pressure relief using vertical drains, etc., are usually expensive when applied to large areas, or need high maintenance. However, the biogas method is rather cost effective. One reason is that density of gas is very small, about three orders of magnitude smaller than solid and liquid, so relatively small amount of solid or liquid substrates can produce relatively large volume of gas. The other reason is that the operation is easy, because the liquid phase substrates can easily spread throughout the sand layer, thus the construction fee can be largely reduced. Other advantages of the biogas method include environmentally friendly, energy saving, and time saving. These advantages make the biogas method a very promising way to solve liquefaction-related problems in large areas, such as lateral spreading.

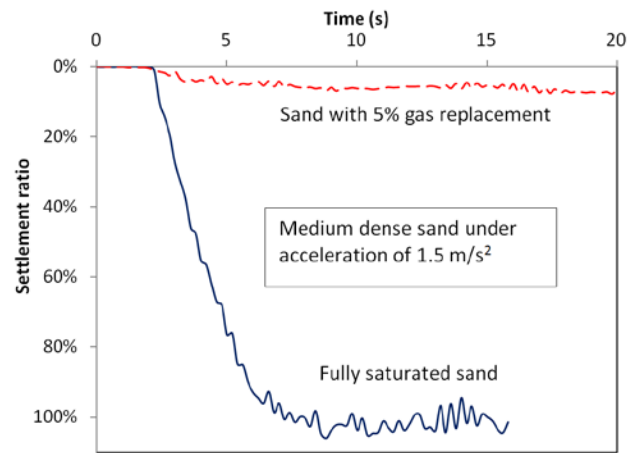


Fig. 5. Comparison of ground settlement induced by ground shaking under an acceleration of 1.5 m/s^2 for a saturated sand layer and a sand layer with 5% gas replacement.

3.3 Seepage and Erosion Control

Biocement can also be used to reduce the water conductivity of sand through the so-called bioclogging mechanism as shown in Fig. 1. One of the methods that has been developed by our research group is to use urea reducing bacteria to precipitate a layer of calcium carbonate on top of sand as shown in Fig. 6. This hard layer of crust has a water conductivity of less than 10^{-7} m/s and thus can be used as an impervious layer for water storage or for erosion control of beach or riverbank. As the layer of treatment is rather thin, the amount of biogrout used is small. Thus the method can be more economical than conventional methods. The detail of this method is described in Chu et al. (2012) [6].

4. CONCLUSIONS

The recent development in the application of microbiology in geotechnical engineering was briefly reviewed in this paper. The biogrout method has a number of advantages over the conventional grouting methods. Several potential

applications were discussed. These include enhancing the shear strength of sand, mitigation of liquefaction of sand using biogas and control of seepage and erosion of sand by bioclogging. The biogrout method paves a more cost-effective, sustainable and environmentally friendly solution to ground improvement. However, a lot of research studies are still required to be carried out before this new approach can be developed into a common practice.



(a)



(b)

Fig. 6. Formation of (a) a thin impervious layer on top of sand using a biogrouting method and (b) a water pond model in sand using this method

5. REFERENCES

- [1] Whiffin VS, "Microbial CaCO_3 precipitation for the production of biocement", Ph.D. Thesis, Murdoch University, 2004.
- [2] Ivanov V and Chu J, "Applications of microorganisms to geotechnical engineering for bioclogging and biocementation of soil in situ." *Reviews in Environmental Science and Biotechnology* vol. 7(2), 2008, 139-153.
- [3] Mitchell JK and Santamarina JC, "Biological considerations in geotechnical engineering." *ASCE Journal of Geotechnical and Geoenvironmental Engineering*, vol. 131(19), 2005, 1222-1233.
- [4] van der Ruyt M, & Van der Zon W, "Biological in situ reinforcement of sand in near-shore areas." *Geotechnical Engineering*, vol. 162(1), 2009, 81-83.
- [5] van Paassen LA, Ghose R, van der Linden TJM, van der Star WRL and van Loosdrecht MCM, "Quantifying

biomediated ground improvement by ureolysis: Large-scale biogrout experiment" *ASCE Journal of Geotechnical & Geoenvironmental Engineering*, vol. 136(12), 2010, 1721-1728.

- [6] Chu J, Stabnikov V and Ivanov V, "Microbially induced calcium carbonate precipitation on surface or in the bulk of soil", *Geomicrobiology Journal*, vol. 29, 2012, 544-549.

A study on slow moving slopes

L G Tham and Xu Kai

Department of Civil Engineering, The University of Hong Kong

ABSTRACT

This paper investigates the mechanism of slow moving slopes by carrying out full scaled field monitoring. Two typical slopes, representing engineered as well as natural slopes, were studied. In the field monitoring, the variation of pore water pressure, soil moisture content, deformations were measured for more than a year so that one can establish the behaviour of the slopes for both the wet and dry seasons. Based on the monitored results of the hydrogeological responses, hydrogeological models were proposed. The subsurface deformations recorded were analyzed and the deformation mode was also discussed. Furthermore, laboratory tests were carried out to determine the soil properties (strength, stiffness, permeability and soil water characteristics curve) for the subsequent numerical modelling, which was based on a coupled seepage and deformation finite element model. The numerical results were compared with the field monitored data. The study finds that the deformation of the slopes is closely associated with the change in the groundwater table : the slopes will move downhill during rain but they may rebound during the dry period after rain. The re-bounce could be considerable during the dry season. Nevertheless, the net movement is still downhill annually.

Keywords: Slope, movement, numerical simulation, rainfall

1. INTRODUCTION

Rainfall is reckoned as one of the main triggering factors of landslides. Rainfall infiltration into unsaturated soil slopes (e.g., Li et al [1]; Zhan et al [2]; Olivares and Damiano [3]), and the influence of infiltrated water on soil suction and shear strength (e.g., Melinda et al [4]; Farooq et al [5]; Collins and Znidarcic [6]; Zhang et al [7]) have been investigated by experimental or numerical approaches. Take and Bolton [8] conducted centrifuge tests on an over-consolidated clay embankment subjected to seasonal weather cycles. They reported seasonal fluctuation in pore water pressure initiated progressive failure. During the wet seasons, the reduction in soil suction induced down-slope movements but the rate was greatly reduced during the subsequent dry seasons. Some of the downhill deformation was seen to have been recovered, though not fully. On the other hand, the results obtained by Hudacsek and Bransby [9] indicated that the rate of downslope deformation reduced greatly during drying but it did not show any significant recovery. The tests were carried out under condition similar to that of Take and Bolton [7]. Field studies had also been carried out (e.g., Lim et al [10]; Springman et al [11], Li et al [12]) with the focus mainly on the mechanisms of rainfall infiltration and their influence on slope stability in various ground conditions. Studies had further shown that the slopes exhibit seasonally fluctuation and the downslope movements accumulates (Malet [13]; Coe[14]; Malet [15]; van Asch [16]; van Asch [17]; Glastonbury [18]; van Asch [19]). Cheuk et al [20] monitored a high slope (height of 17m) having a slope angle of 25° in Tai Lam Chung, Hong Kong. The geology comprises layer of colluvium (1-2m thick) overlying completely decomposed volcanoclastic and tuffaceous sediments (approximately 30m thick). As reported by Cheuk et al [20] :

- *The monitored results indicate that the slope apparently exhibits continuous cycles of uphill and downhill surface movements. For this site, the rate of net surface downhill movement is approximately 1.5 mm/year. The movements are more pronounced within the colluvium layer and completely decomposed tuff (CDT) layers (i.e. the top 2 m to 4 m), and are above a set of pre-existing slip surfaces that were identified by ground investigations in 2001.*
- *The piezometer records reveal that the main groundwater table is located at about 10 m to 12 m below ground surface. Seasonal fluctuations caused the water level to vary within ± 5 m. The Halcrow bucket measurements indicate that the perched groundwater level may be at times as high as 0.5 m below ground surface.*

In general, the slope body will move downslope. However, it is inconclusive whether the slope will rebound during dry season or not. In order to have a better understanding on the slow moving slopes under the influence of seasonal wetting-drying cycles, two slopes (Kwong and Leung [21,22] and Xu [23]) were investigated by carrying out field monitoring and numerical simulation. This paper will highlight the findings of the study.

2. CASE ONE (Kwong and Leung [21,22])

Figs. 1 and 2 present the plan of the site and the geological feature at a typical section. The bed rock is moderately strong to strong yellowish brown to brownish grey, coarse ash tuff. The rockhead is highest, about 40–45 mPD at the crest of the slope and dips in a southwest direction. Hence, the rockhead is dipping parallel with that of the cut slope. The rock, depending on its depth below the surface, has been decomposed to various stages and can be categorised into three layers: colluvium layer, completely decomposed volcanic (CDV) layer and highly decomposed volcanic (HDV) layer. The CDV soil is characterized by higher

percentage of soil particles having smaller grain size, whilst relatively more coarse particles are contained in the HDV soil.

One can also note that the upper part of the slope was formed by cutting into the natural ground and the lower part is a crib wall retaining compacted backfill. The crib wall is about 5 m high. A closer examination of the rockhead level in the area around shows that there is a localized depression of the rockhead level.

As the slope was subjected to severe deformation in the form of surface cracks and local failures during the previous rainy seasons, sensors, including piezometers and inclinometers, was installed to monitor the slope. Daily rainfall during the period was also monitored by raingauges.

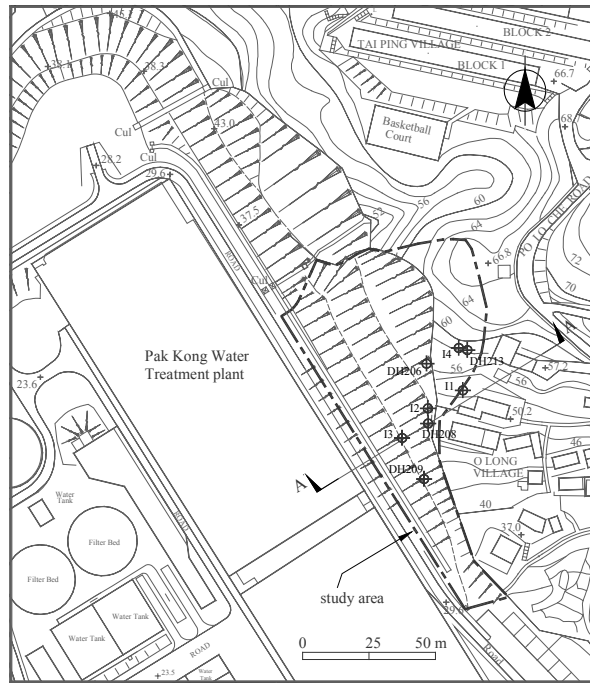


Fig. 1 Plan of the slope

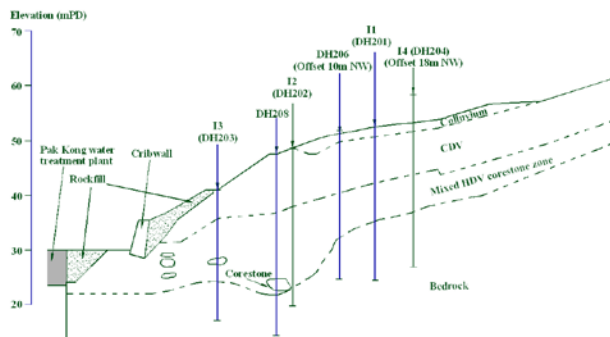


Fig 2 Typical geological cross section of the slope

2.1 Monitored results

Fig. 3 presents the variations of groundwater level measured by piezometers between 15 December 1992 and 31 May 1995.

The daily rainfall records in the same period are also given in the figure. As expected, the groundwater table rose in the wet season and dropped in the dry season. The largest fluctuation of groundwater level was about 9 m and it was recorded at DH213.

In Fig. 4, the variations of slope movement at an inclinometer (I2) with time are plotted. One can easily note the strong correlation between the slope movement and the groundwater level. The slope moved in the downhill direction progressively as the groundwater level rose during the rainy seasons. On the other hand, there were considerable rebound movements during the dry seasons when the groundwater level dropped. Fig. 5 depicts the variations of horizontal downslope displacements with depth for the inclinometer. Note that the corresponding records at the start of the dry season (1 October) in 1992 were taken as the reference.

During the first dry period (October 1992 to April 1993), the inclinometer readings rebound. In particular, there was an overall upslope movement for the upper portion of the soil. The peak rebound displacement was 17 mm, at a depth of 3 m underneath the ground surface.

During the first wet period (May 1993 to September 1993), one can note that significant downhill displacements were mobilized in the slope by the rainfall.

The measurements at other inclinometers showed quite similar trend with larger displacement mobilized at shallow depth [24].

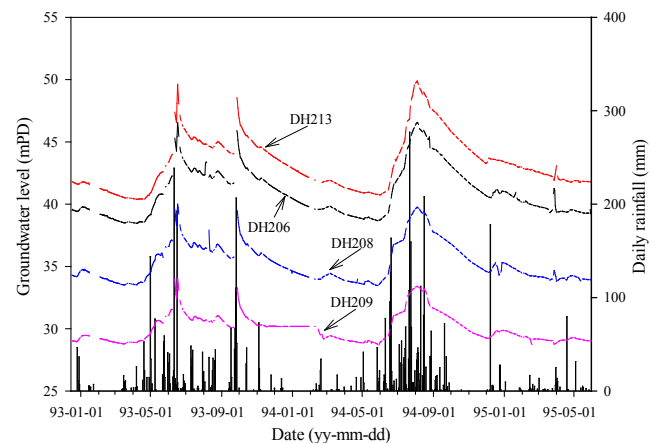


Fig. 3 Time variation of groundwater levels at different drillhole locations in relation to the daily rainfall records

In the subsequent dry periods (October 1993 to April 1994 and October 1994 to April 1995), the inclinometer readings indicate that the slope bounced backwards after the preceding wet periods (April to October in 1993 and 1994).

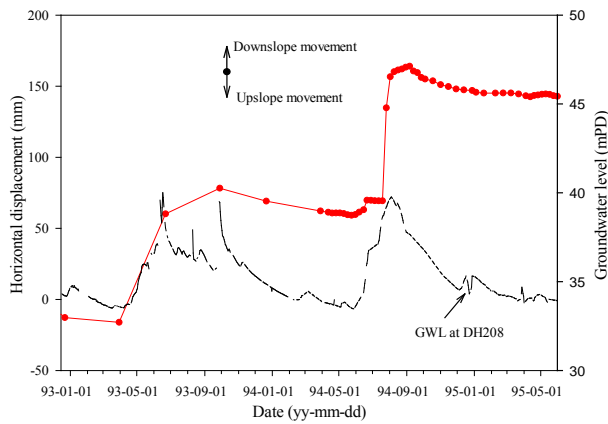


Fig. 4 Time variation horizontal displacements at a depth of 0.5m below the ground surface in relation to the change of groundwater level (I2)

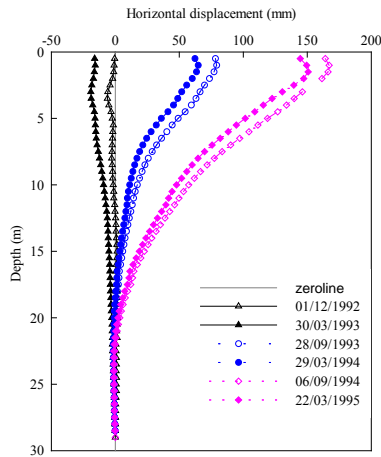


Fig. 5 Distribution of horizontal downslope displacement with respect to depth during the monitored period (The readings at 01/10/1992 are taken as the reference) (I2)

2.2 Numerical simulation

The finite element mesh for the simulation is shown in Fig. 6. The four-node bilinear plane strain element was used in the model. Each node of the soil elements consisted of three degrees of freedom (one for pore water pressure and two for displacements). On the other hand, only deformation degrees of freedom were considered in the elements for modelling the cribwall, the rockfill, and the bedrock layer, as the redistribution of pore water within these layers should be negligible. During the hydraulic analysis for a steady state solution of the pore water pressure field, the groundwater level distribution at the corresponding stage in the slope was defined in the numerical model (Fig. 7). With the calculated pore water pressure distribution, a mechanical analysis was conducted subsequently to determine the slope deformation with the displacement boundary conditions given in Fig. 6. For the cribwall and rockfill materials, as well as the bedrock layer underneath the HDV layer, the deformation was small enough during the monitored period. Hence, they were modelled by a linear elastic model with the parameters can be found in Table 1 of Reference [21]. The behaviour of the soil

layers was modelled by a nonlinear hypoelastic-perfectly plastic model with a non-associated flow rule. Readers can refer to Zhou et al [24] for the details of the adopted constitutive relationships.

Fig. 8 presents the variation of relative rebound displacements due to drying with depth predicted by the numerical model. The corresponding field results are also shown in the same figure for comparison. As mentioned in the previous section, the horizontal displacement on 06 September 1994 (start date) was taken as the reference for the determination of the relative rebound movement.

On 01 November 1994, the simulation results show considerable rebound movements in response to the change of pore water pressure redistribution induced by a drop of groundwater level of about 2.5 m. The predictions give similar distribution pattern along the depth direction as the corresponding field measurements, with a slight over-prediction. Furthermore, both the predictions and field measurements illustrate that the affected range of soil layers representing rebound feature greatly exceeds the thickness of the unsaturated zone.

With the drying progressed from November 1994 to March 1995, both the field and numerical results (Fig. 8) present a significant increase of rebound deformation. It has to be pointed out that the change of the groundwater level in this stage was about twice as large as that during the previous stage. However, the predictions and field monitoring data demonstrate that only about 60% increase in the incremental rebound displacements is induced by the redistribution of pore water pressure.

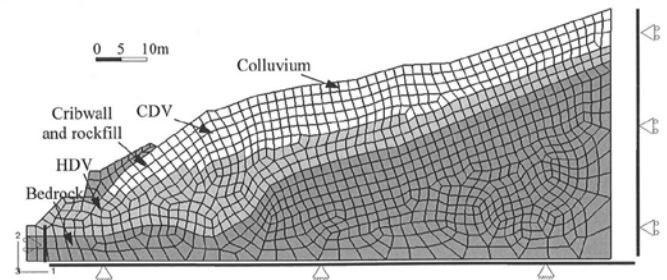


Fig. 6 Finite element model of Section A-A of the study slope

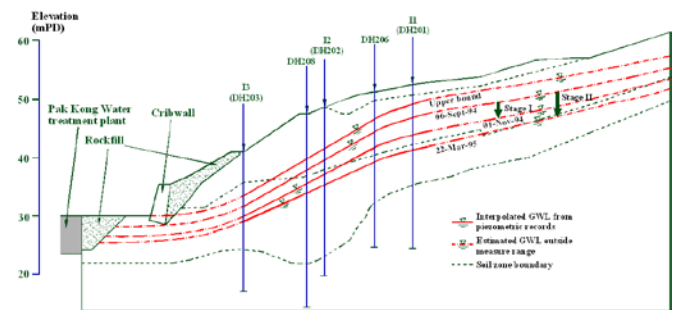


Fig 7 Groundwater level distributions

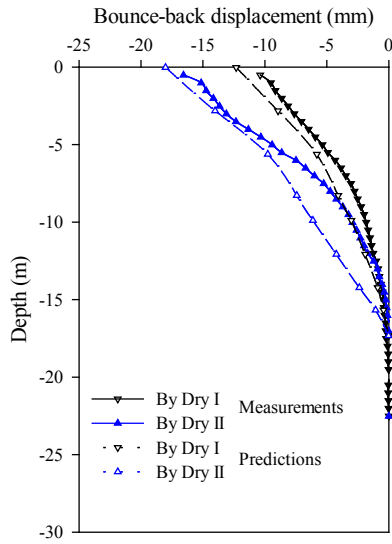


Fig 8 Comparison of the predictions and the monitored horizontal bounce-back movements (The results on 06/09/1994 are taken as the reference)

It can also be observed that some discrepancy exists between the numerical predictions and the field measurements, and it could be attributed to the two-dimensional plane strain simplification in the numerical model. It should also be noted that as only limited piezometric data were obtained from field monitoring (Fig. 6), differences may exist between the prescribed groundwater distributions in the numerical model and the actual conditions.

3. CASE TWO (Xu [23])

The second case involves a relict old landslide resting on a V-shaped valley. The typical section is shown in Fig. 9. It is much steeper in the upstream than the downstream (the slope angle is approximately 20°). The top stratum is a thin layer of colluvium. The typical thickness of colluvium is from 1.3m to 5.7m; the average thickness is approximately 3m. Under the colluvium layer is the highly sheared and altered completely decomposed andesite which has a depth of around 20m. The bottom stratum is bedrock which consists of moderately decomposed Andesite and slightly decomposed andesite.

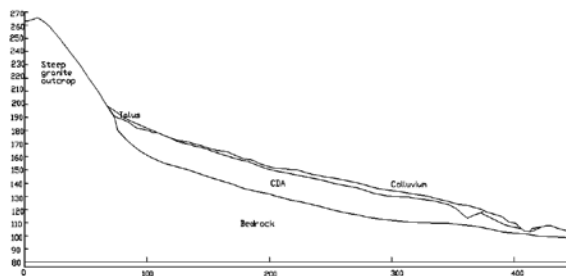


Fig. 9 Typical Geological Section

Past record (Fig. 10) indicates that the slope was moving slowly downhill and the occurrence of landslides was not infrequent. The movement is believed to be occurring along the weak interface between colluvium and completely decomposed andesite or within the completely decomposed andesite layer.

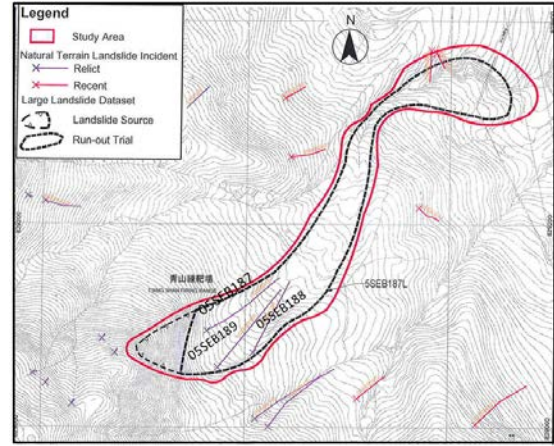


Fig. 10 Landslide History

3.1 Monitored results

To closely monitor the slope, “real-time” monitoring was conducted. The instrumentations include piezometers, inclinometers, moisture probe, tensiometers and rain gauges. The layout for the inclinometers is shown in Fig. 11 and that for other instruments can be found in Xu [23].

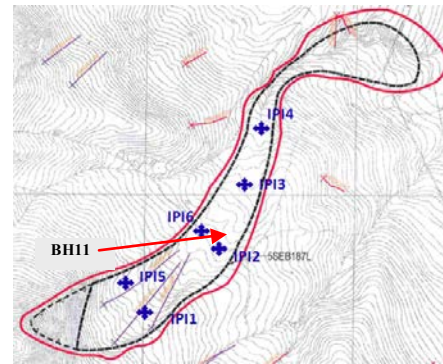


Fig. 11 Layout Plan of In-place Inclinometers

Fig. 12 shows the variation of the groundwater table at mid-slope (BH11) from 2008-2009. At the beginning of the wet season, the groundwater level was about 136mPD. One can note the groundwater rose rapidly in response to the rainfall and it could have nearly reached the ground surface after prolong period of heavy rain during the wet season. On the other hand, the groundwater table dropped in the dry season gradually and it could have almost dropped back to the level at the beginning of the wet season. The groundwater table along the slope is depicted in Fig. 13.

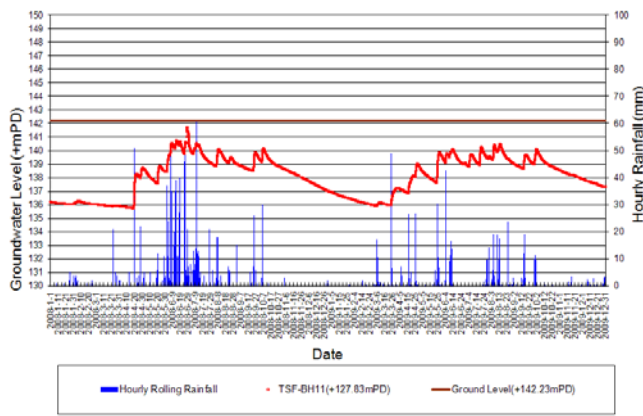


Fig. 12 Groundwater Levels Monitored at BH11

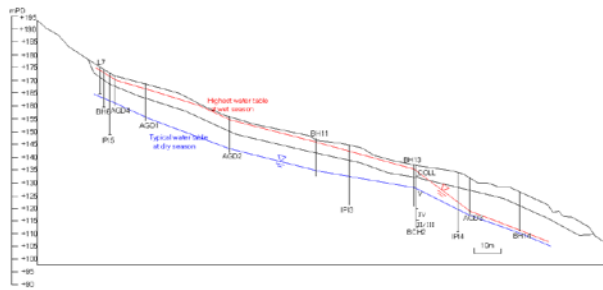


Fig.13 Groundwater distribution

The deformations at IPI3 (Figs. 14 and 15) also indicate that the slope deformation is closely correlated to the rainfall and the groundwater level. The slope moved downhill during the wet season, though the magnitudes depended on the depth below the slope surface : most of the movement was restricted to the top 3-4m. The movement also indicates that the slope rebound after rain and the uphill movement continued during the dry seasons. However, the movement was not fully recovered. Similar movement pattern was observed in other locations, though the magnitude of the downhill and uphill movements could be different. The general direction of the movement is shown in Fig. 16 and one can note that the slope is moving downhill along the valley.

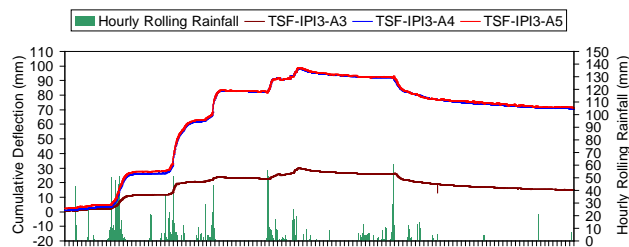


Fig.14 Downslope Cumulative Deformation Monitored (IPI3)

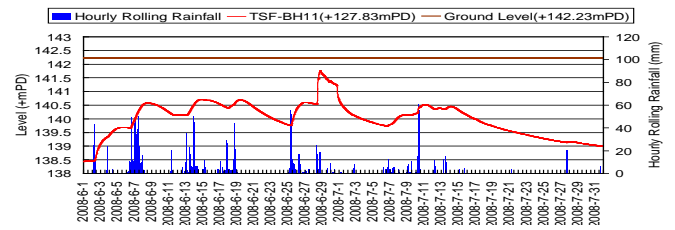


Fig.15 Groundwater table (IPI3)

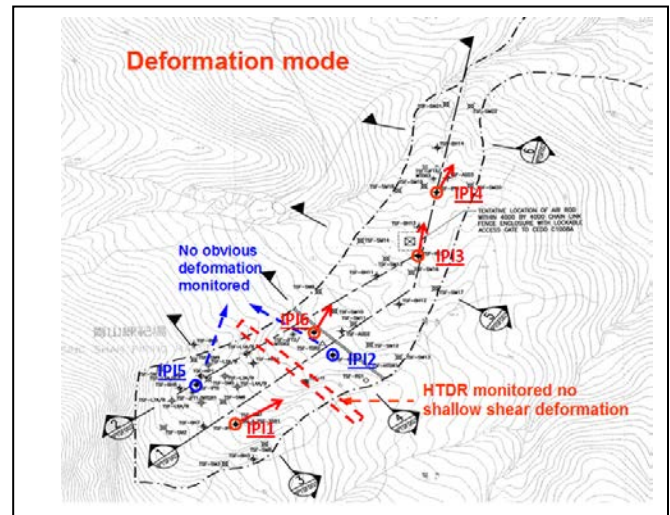


Fig.16 Schematic Deformation Mode

3.2 Numerical simulation

A 2-D finite element mesh was also built up according to the geometry of typical section of the slope for numerical analyses. The length of the model was 450 m, and the height of the model was 150m; there were typically three layers: colluvium (including talus at slope head), completely decomposed andesite (CDA) and bedrock. The slope was modelled using a finite element mesh consisting of 3122 nodes and 2784 plane-strain four-node bilinear elements. Again, each node for the soils has three dofs (degree of freedom): one was for pore water pressure and the other two were for displacements. The controlling sections and points are shown in Fig. 17. In the analyses, various boundary conditions and rainfall patterns were considered and interested readers can refer to Xu [23] for the full details. The present paper will focus on the movement and pore pressure at Section E.

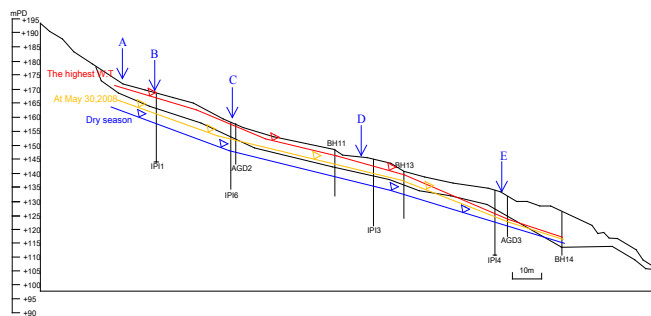


Fig.17 Monitored Groundwater Distribution Illustration at Typical Section S1-S1

The comparisons of the simulated and measured pore water pressure and horizontal displacement are shown in Figs. 18 and 19, respectively. Though there are discrepancies in the magnitude for both parameters, the simulation can provide quite a reasonable prediction of their variation qualitatively. It appears that some fine tuning of the input parameters can improve the prediction, however, matching of the results is not the objective of the present study.

4. CONCLUSIONS

This paper presents a study on the rebound behaviour observed in two slopes. Field measurements of deformation, groundwater level as well as the rainfall intensity were presented, and the monitoring data indicated that considerable bound-back deformation in the uphill direction were mobilized in the slope during the dry seasons. Simulations, based on two-dimensional finite element model, were carried out and typical wetting-drying processes had been analyzed to investigate the mechanism of the drying induced rebound movements. Through comparison with the corresponding field measurements, it is found that the volume contractive behaviour, as a result of the suction increase within the unsaturated soil zones and the pore pressure reduction in the saturated soil zones is the main factor contributing to such rebound movements.

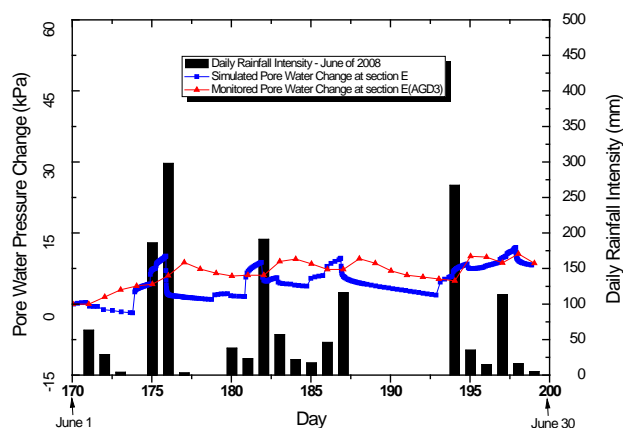


Fig.18 Comparison between Simulated and Monitored Pore Water Change of Case T3 at Section E

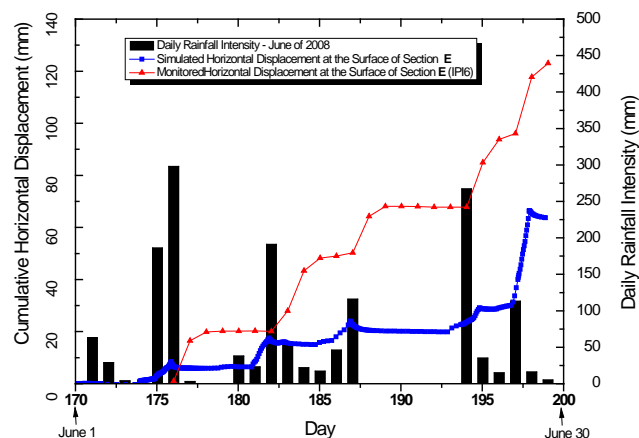


Fig.19 Comparison between Simulated and Monitored Horizontal Displacement of Case T3 at Section E

5. ACKNOWLEDGMENT

The authors would like to acknowledge the contribution of Professor Zhou Yuande of Tsinghua University, China and Dr AKL Kwong of MTRC, HK.

6. REFERENCES

- [1] Li AG, Yue ZQ, Tham LG, Lee CF, Law KT, "Field-monitored variations of soil moisture and matric suction in a saprolite slope," Canadian Geotechnical Journal, vol 42(1), 2005, pp 13-26.
- [2] Zhan TLT, Ng CWW, Fredlund DG, "Field study of rainfall infiltration into a grassed unsaturated expansive soil slope," Canadian Geotechnical Journal, vol 44(4), 2007, pp 392-408.
- [3] Olivares L, Damiano E, "Postfailure mechanics of landslides: Laboratory investigation of flowslides in pyroclastic soils," Journal of Geotechnical and Geoenvironmental Engineering, vol 133(1), 2007, pp 51-62.
- [4] Melinda F, Rahardjo H, Han KK, Leong EC, "Shear strength of compacted soil under infiltration condition," Journal of Geotechnical and Geoenvironmental Engineering, vol 130(8), 2004, pp 807-817.
- [5] Farooq K, Orense R, Towhata I, "Response of unsaturated sandy soils under constant shear stress drained condition," Soils and Foundations, vol 44(2), 2004, pp 1-13.
- [6] Collins BD, Znidarcic D, "Stability analyses of rainfall induced landslides," Journal of Geotechnical and Geoenvironmental Engineering, vol 130(4), 2004, pp 362-372.
- [7] Zhang LL, Fredlund DG, Zhang LM, Tang WH, "Numerical study of soil conditions under which

- matric suction can be maintained,” *Canadian Geotechnical Journal*, vol 41(4), 2004, pp 569-582.
- [8] Take WA, Bolton MD, “Identification of seasonal slope behaviour mechanisms from centrifuge case studies,” *Advances in Geotechnical Engineering: The Skempton Conference*, London, Thomas Telford, vol. 2, vol 2004, pp 992-1004.
- [9] Hudacsek P, Bransby MF, “Centrifuge modelling of embankments subject to seasonal moisture changes,” *Proceedings of the First ISSMGE International Conference on Transportation Geotechnics*, Nottingham, UK, September, 2008.
- [10] Lim TT, Rahardjo H, Chang MF, Fredlund DG, “Effect of rainfall on matric suctions in a residual soil slope,” *Canadian Geotechnical Journal*, vol 33(4), 1996, pp 618-628.
- [11] Springman SM, Jommi C, Teyssie P, “Instabilities on moraine slopes induced by loss of suction: A case history,” *Geotechnique*, vol 53(1), 2003, pp 3-10.
- [12] Li J, Tham LG, Junaideen SM, Yue Zq, Lee CF, “Loose fill slope stabilization with soil nails: full-scale test,” *Journal of Geotechnical and Geoenvironmental Engineering*, vol 134(3), 2008, pp 277-288.
- [13] Malet JP, Maquaire O, Calais E, “The use of global positioning system techniques for the continuous monitoring of landslides: application to Super-Sauze earthflow (Alpes-de-Haute-Provence, France),” *Geomorphology*, vol. 43, 2002, pp. 33-54.
- [14] Coe JA, Ellis WL, Godt JW, Savage WZ, Savage JE, Michael JA, Kiblet JD, Powers PS, Lidke DJ, Debray S, “Seasonal movement of the Slumgullion landslide determined from global positioning system surveys and field instrumentation, July 1998-March 2002,” *Engineering Geology*, vol. 68, 2003, pp. 67-101.
- [15] Malet JP, Laigle D, Remaitre A, Maquarie O, “Triggering conditions and mobility of debris flows associated to complex earthflows,” *Geomorphology*, vol. 66, 2005, pp. 215-235.
- [16] van Asch TWJ, “Modelling the hysteresis in the velocity pattern of slow-moving earth flows: the role of excess pore pressure,” *Earth Surface Processes and Landform*, vol. 30, 2005, pp 403-411.
- [17] van Asch Th W J, Van Beek L P H, Bogaard, “Problems in predicting the mobility of slow-moving landslides,” *Engineering Geology*, vol 91, 2007, pp 46-55.
- [18] Glastonbury J, Fell R, “Geotechnical characteristics of large slow, very slow, and extremely slow landslides,” *Canadian Geotechnical J*, vol 45, 2008, pp 984-1005.
- [19] van Asch Th W J, Malet J P, Bogaard, “The effect of groundwater fluctuations on the velocity pattern of slow-moving landslides,” *Nat. Hazards and Earth System Sciences*, vol 9, 2009, pp 739-749.
- [20] Cheuk J, Ng A, Endicott J, Ho K, “Progressive slope movement due to seasonal wetting and drying,” *The State-of-the-art Technology and Experience on Geotechnical Engineering in Malaysia and Hong Kong* Wednesday, 25 February 2009, pp 105-114.
- [21] Kwong AKL, Leung RHT, “Back analyzing the failure mechanism of a slope experienced large movements from 1986 to 1997,” *International Conference on Slope Engineering*, Hong Kong, edited by CF Lee and LG Tham, 2003, pp 796-802.
- [22] Kwong AKL, Leung RHT, “Constructional aspects of remedial works for slope above Pak Kong water treatment works,” *International Conference on Slope Engineering*, Hong Kong, edited by CF Lee and LG Tham, 2003, pp 803-809.
- [23] Xu K, “Study on a Slow Moving Slope in Hong Kong,” PhD Thesis, Department of Civil Engineering, The University of Hong Kong, 2011.
- [24] Zhou Y D, Tham L G, Kwong A K L, Tang X W, “Mechanism of drying induced rebound movements in a soil slope in Sai Kung, Hong Kong,” *Engineering Geology*, vol 116(1-2), 86-94, 2010.

Bearing Capacity and Settlement of Footings in Unsaturated Sands

Sai K. Vanapalli¹ and Fathi M. O. Mohamed²

^{1,2}Department of Civil Engineering, University of Ottawa, K1N 6N5, Canada

ABSTRACT

The focus of the study presented in this paper is towards understanding the influence of three parameters; namely, (i) matric suction, (ii) overburden stress, and (iii) dilation, on the bearing capacity and settlement behaviour of surface and embedded footings in saturated and unsaturated sands. The results show that the bearing capacity and settlement behaviour of unsaturated sands are significantly influenced by all the three parameters. In addition, comparisons are provided between the measured and estimated bearing capacity and settlement using the proposed modified Terzaghi's equation and modified Schmertmann's CPT-based method, respectively. There is a good comparison between the measured and estimated values for both the laboratory and field tests using the modified methods.

Keywords: Bearing capacity; settlement; matric suction; sand; PLT; CPT.

1. INTRODUCTION

The two key properties required in the design of shallow foundations are the bearing capacity (i.e., q_u) and settlement (i.e., Δ) behaviour of soils. Structures such as silos, antenna towers, bridges, power plants, and housing subdivisions can be constructed on shallow foundations (e.g., spread footings near the ground surface) in sandy soils assuring a safe and economical design. The shallow footings are typically designed to transfer the loads safely from the superstructure to the supporting soil such that the settlements are in acceptable limits as per the design and construction codes. The bearing capacity of shallow foundations is estimated using the approaches originally presented by [1] and [2] assuming the soil is in a state of saturated condition. Typically, shallow foundations are placed above the ground water table and the variation of stress with respect to depth associated with the loads from the superstructure is distributed through the substructure (i.e., shallow foundations) predominantly in the vadose zone (i.e., the zone in which soil is in a state of unsaturated condition). This is true in many regions and especially for semi-arid and arid regions. A framework for interpreting the bearing capacity and settlement behaviour from experimental and modelling studies for unsaturated sands is recently evolving ([3], [4], [5], [6], and [7]).

Comprehensive data for interpreting the bearing capacity and settlement behaviour of footings in unsaturated sands taking account of influence of the capillary stresses (i.e., matric suction), overburden stress (i.e., confinement) and dilation is however are not available in the literature. Due to these reasons, an extensive experimental program is undertaken to study the bearing capacity and settlement behaviour of sandy soil from model footings in specially designed equipment.

In addition, comparisons are provided between the measured and estimated values of the bearing capacity and settlement behaviour of model footings respectively using the approaches provided by investigators [3] and [7] for sands modifying the original contributions of Terzaghi's equation [1] and Schmertmann's equation [8], respectively. The study shows that there is a good comparison between the measured and estimated values of the bearing capacity and settlement behaviour using the proposed modified equations.

2. BACKGROUND

2.1 Bearing Capacity of Soils

Terzaghi and others [1], [2], [9] studies were directed towards understanding the bearing capacity of shallow foundations in saturated or dry conditions using conventional soil mechanics. However, soils are typically found in a state of unsaturated condition in semi-arid and arid regions. Therefore, estimation of the bearing capacity of shallow foundations using conventional soil mechanics for these regions may underestimate the bearing capacity values and lead to conservative and costly foundation designs.

Several researchers carried out investigations to study the bearing capacity of unsaturated soils ([10], [11], [12], [13], [14], [3], [15]). Investigators [16] designed special equipment and conducted studies to understand the bearing capacity of surface model footing in a sandy soil. These studies have shown that the matric suction values in the range of 2 to 6 kPa contribute to 5 to 7 times higher than the bearing capacity values in comparison to saturated condition. A framework was provided by [3] to predict the variation of bearing capacity of a soil with respect to matric suction using the saturated shear strength parameters (c' and ϕ') and the Soil-Water Characteristic Curve (SWCC).

2.2 Settlement of Shallow Footings

The shallow footings are typically designed in sandy soils such that the settlement is less than 25 mm. In addition, applied loads from the superstructure need to be safely carried to the soil below the footing with a factor of safety recommended by the design and construction codes. Elastic or immediate settlements in sandy soils are assumed to occur instantaneously when static loads are applied. Several empirical equations are proposed in the literature that can be used in the estimation of the settlement of footings in sands based on cone penetration tests (CPT) results ([17], [9], and [8]). The presently available methods in the literature overestimate the settlements leading to an overly conservative footing design ([18], and [7]). This can be attributed to ignoring the influence of matric suction below the foundations. In many scenarios such an assumption is not valid, particularly where the soils are typically in a state of unsaturated condition.

Simple relationships are proposed by [7] modifying the Schmertmann's method [8] that is conventionally used in practice for settlement estimations from the CPT results. The modified method was successfully used in the estimation of the settlement behaviour of model footing tests and full-scale footings tested in-situ under both saturated and unsaturated conditions in sandy soils.

The focus of the present study is to understand the influence of the capillary stresses (i.e., matric suction), overburden stress (i.e., confinement) and dilation on the variation of the bearing capacity and settlement behaviour of both surface and embedded footings in unsaturated sand. In the present study, the same sand used by investigators [3] is tested.

3. THE TESTED SOIL

3.1 Soil Properties

Table 1 summarizes the properties of the sand used in this study. The soil can be classified according to the USCS as poorly graded coarse-grained sand.

Table 1. Properties of the tested soil

Soil properties	Value
Coefficient of uniformity, C_u	1.83
Coefficient of curvature, C_c	1.23
Specific gravity, G_s	2.65
Average dry unit weight, γ_d , kN/m ³	16.02
Min. dry unit weight, $\gamma_{d(\min)}$, kN/m ³	14.23
Max. dry unit weight, $\gamma_{d(\max)}$, kN/m ³	17.25
Average relative density, %	65.0
Optimum moisture content, OMC , %	14.6
Void ratio, e (after compaction)	0.62 – 0.64
Effective cohesion, c' , kN/m ²	0.6
Effective friction angle, ϕ' (°)	35.3

Dilation in Sandy Soils

The effective cohesion, c' and the angle of internal friction, ϕ' were measured from the direct shear test (i.e., CD test) results. Several studies suggest the overburden effective stress (i.e., confinement) and soil density influence the

dilatancy behaviour of sands ([9], [19], and [20]). The dilatancy angle, ψ , is always based on the studies by [21]. The dilation behaviour of sand can be attributed to the soil particles rolling on top of each other without crushing during the shearing stage. Experiments (using steel shots that do not break down during shearing) conducted by researcher [22] have shown that an increase in confinement leads to a decrease in the dilatancy angle. ψ decreases with an increase in the effective overburden stress [23]. Therefore, in the analysis of surface model footing results of the present study, bearing capacity and settlement behaviour of shallow footings were interpreted taking into account of the influence of dilation angle, ψ , on the effective friction angle, ϕ' of the sand.

4. EQUIPMENT AND METHODOLOGY

Fig. 1 shows the details of the modified University of Ottawa Bearing Capacity Equipment (modified UOBCE). Schematic of a sectional view of the equipment is shown in Fig. 2. The modified UOBCE is designed to determine the variation of bearing capacity and settlement of sands with respect to matric suction using model footings which are interpreted similar to plate load tests (i.e., PLTs). In the remainder of the paper, model footing tests are referred to as model PLTs for brevity. The equipment setup consists of a rigid-steel frame made of rectangular section pipes with thickness of 6 mm and a box of 1500 mm (length) \times 1200 mm (width) \times 1060 mm (depth). The test box can hold up to 3 tons of soil and the capacity of the loading machine (i.e., Model 244 Hydraulic Actuator with stroke length of 250 mm) is 28.5 kN. The model PLTs were performed using different strain rates of 1.2 mm/min and 2.5 mm/min. The results suggest that the load carrying capacity of the sand is not influenced by the two different strain rates used in the present study.

The equipment used in the present study (see Fig. 1) in terms of test box size and its loading capacity is twice in comparison to the UOBCE used by [16]. The equipment in the present study has special provisions to achieve different degrees of saturation conditions below the model footings similar to the original UOBCE. The variation of matric suction with respect to depth in the unsaturated zone of the test box can be measured using commercial Tensiometers.

5. LABORATORY PLT AND CPT TESTS

Several tests were conducted to determine the bearing capacity of the sand with different values of matric suction using surface PLTs (i.e., model footing depth, $D_f = 0$ mm), embedded PLTs (i.e., $D_f = 150$ mm) and CPTs (i.e., cone penetration tests). A minimum of three tests were conducted and average values are reported in this paper.

5.1 Surface Plate Load Tests

Model PLTs of 150 mm \times 150 mm (i.e., surface footings) were conducted by researchers [16] using the UOBCE (see sectional view in Fig. 2) which consists of a rigid-steel tank of 900 mm (length) \times 900 mm (width) \times 750 mm (depth). Applied stress versus settlement relationships for surface

model footing of 150 mm × 150 mm from that study are summarized in Fig. 4.

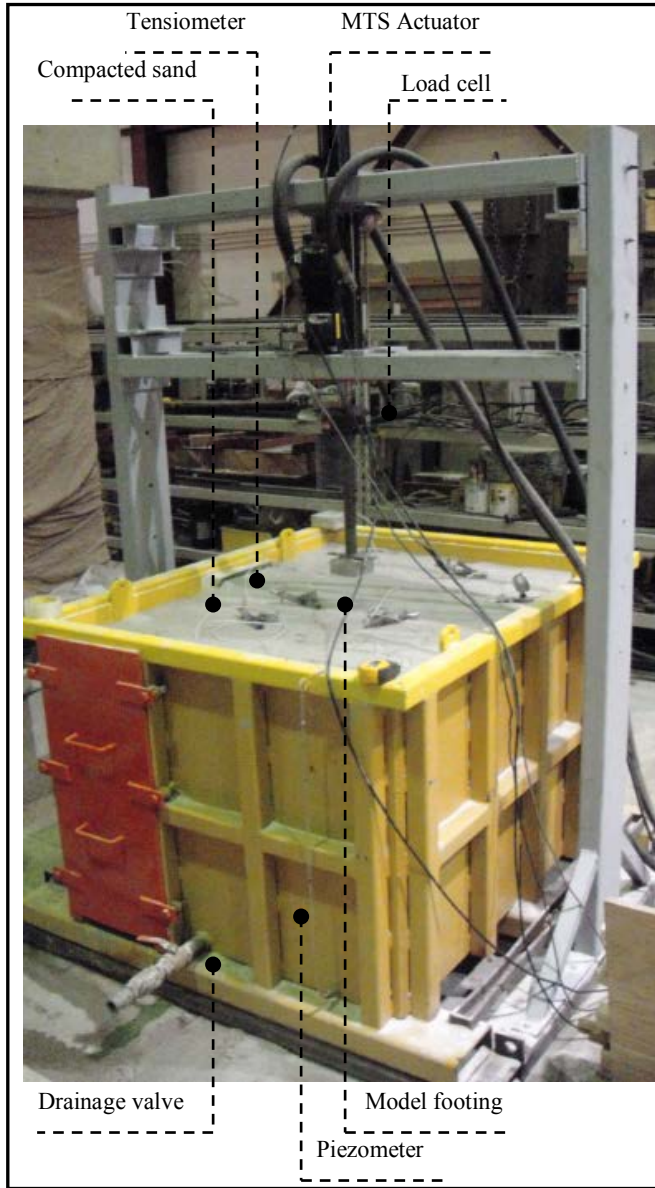


Fig. 1. Modified University of Ottawa bearing capacity equipment (modified UOBCE)

5.2 Embedded Plate Load Tests

The model footings embedded in the modified UOBCE test box are analyzed considering the influence of average matric suction value in the proximity of the stress bulb zone which is equal to depth $1.5B$. Fig. 3 provides details of the procedure used in the estimation the average matric suction value. The depth $1.5B$ considered is the zone in which stresses are predominant due to the loading of shallow square footings with $D_f/B \leq 1.0$ ([24], [3], and [5]).

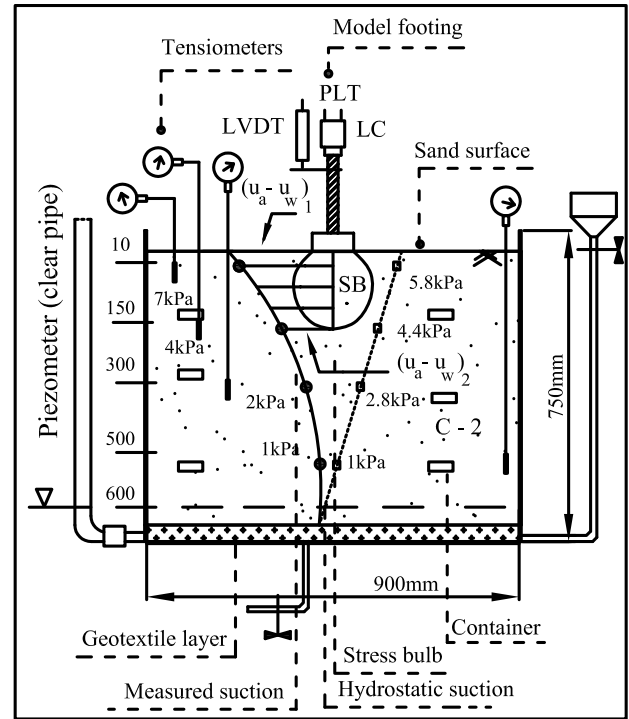


Fig. 2. Schematic to illustrate the test setup and the procedure used for estimating the average matric suction of 6 kPa within the stress bulb (SB) zone of the surface footing using UOBCE

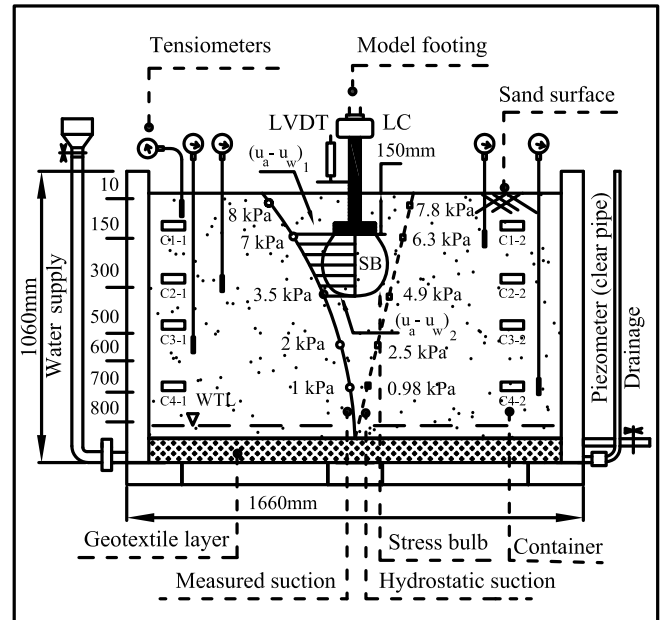


Fig. 3. Schematic to illustrate the test setup and the procedure used for estimating the average matric suction of 6 kPa within the stress bulb (SB) zone of the embedded footing using modified UOBCE

In this series of tests, the model footing of 150 mm × 150 mm size is placed at a depth of 150 mm below the soil surface to investigate the effect of the overburden stress. The tests were

conducted with different average matric suction values below the footing (i.e., 0 kPa, 2 kPa and 6 kPa). Equilibrium conditions with respect to matric suction in the test box were typically achieved in a period of 48 hrs in the test box shown in Fig. 3. Table 2 summarizes a typical set of results in which the average matric suction in the vicinity of the footing base is 6 kPa (see Fig. 3).

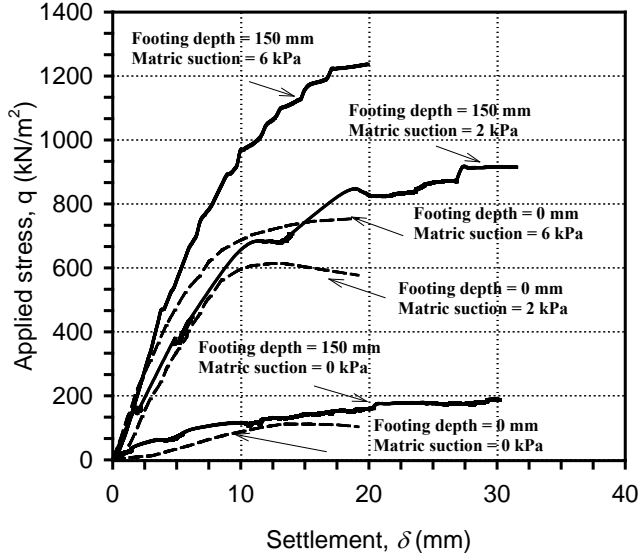


Fig. 4. Relationship between the applied stress versus settlement behaviour of surface and embedded model footing tests (PLTs) of 150 mm × 150 mm using the UOBCE and the modified UOBCE respectively

Table 2. Typical data from the test box for AVR matric suction of 6 kPa in the stress bulb zone (i.e., 1.5B)

D^* (mm)	\square (kN/m ³)	\square_b (kN/m ³)	w (%)	S (%)	$(u_a - u_w)_{AVR}$ (kPa)
12	18.16	16.20	12.10	53	8.0
150	19.00	16.24	17.00	75	7.0
355	19.20	16.13	19.00	82	5.0
500	19.50	16.12	21.00	91	2.0
700	19.74	16.03	23.11	98	1.0
800	19.75	15.95	23.81	100	0.0

* Depth of a Tensiometer from the soil surface

The measured water content and matric suction values from the test box of the modified UOBCE are similar to the corresponding water content and matric suction values in both measured and predicted SWCC of the tested sand. This observation provides credence to measurements using the Tensiometers. The air-entry value for the sand was found to be between 2.5 kPa and 3 kPa. Details of the SWCC for the tested sand are available in an investigation conducted by researchers in [16].

The measured bearing capacity of the compacted unsaturated sand for both surface and embedded footings were in the range of 5 to 7 times higher than the saturated bearing capacity values.

5.3 Cone Penetration Tests

Researchers [25] conducted several CPTs in a laboratory

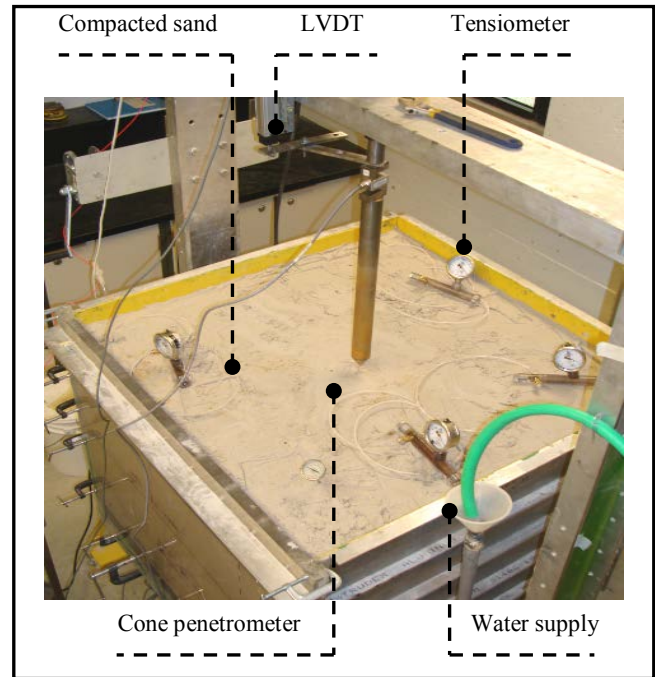


Fig. 5. Top view of the test tank showing the penetrometer (CPT) using the UOBCE

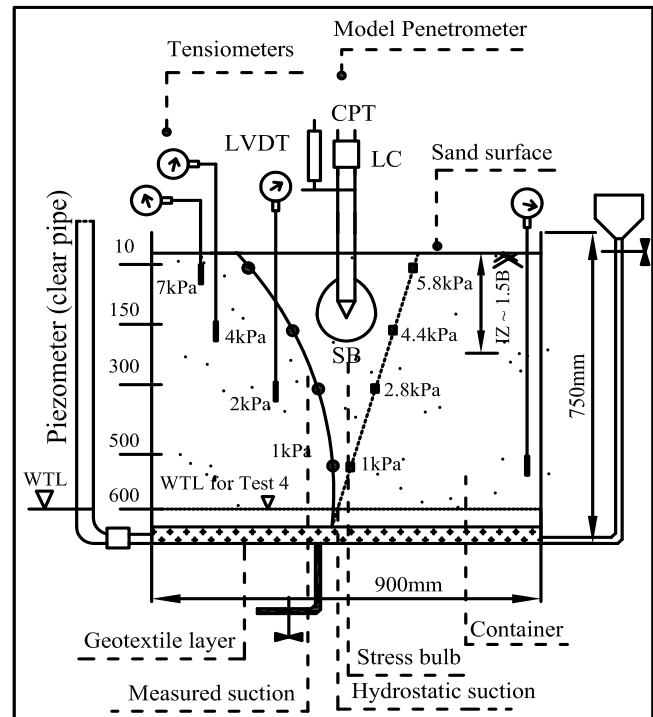


Fig. 6. Schematic to illustrate the test setup and the procedure used for estimating the average matric suction of 6 kPa within the influence zone (IZ) using the model penetrometer (CPT) using the UOBCE

environment in a compacted sand ($D_r = 65\%$) in the UOBCE under both saturated and unsaturated conditions (i.e., 0 kPa, 1 kPa, 2 kPa and 6 kPa). The setup, experimental results and analyses of the variation of cone resistance, q_c with penetration depth were presented in [25]. Fig. 5 and Fig. 6 show details of the sectional view of the test box used to carry out the CPTs respectively. The measured settlement results of the studies described in section 8.2 are used to check the validity of the proposed modified Schmertmann's relationships based on the CPTs results in a later section to estimate the settlement of shallow footings in sand under both saturated and unsaturated conditions.

6. BEARING CAPACITY OF UNSATURATED SOILS

Terzaghi [1] suggested Eq. (1) to estimate the ultimate bearing capacity, q_u of saturated soils assuming general shear failure conditions:

$$q_u = c' N_c + \gamma D_f N_q + 0.5 \gamma B N_\gamma \quad (1)$$

where:

q_u = ultimate bearing capacity, kN/m²
 c' = effective cohesion, kPa
 γ = unit weight, kN/m³
 D_f = footing base level, m
 B = footing width, m
 N_c, N_q, N_γ = bearing capacity factors which are function of effective friction angle, ϕ' .

A semi-empirical equation (i.e., Eq. (2)) was suggested by [3] to predict the variation of bearing capacity with respect to matric suction for surface footings on unsaturated soils using the effective shear strength parameters (i.e. c' and ϕ') and the SWCC as below:

$$q_u = [c' + (u_a - u_w)_b (\tan \phi' - S^{\psi_{BC}} \tan \phi')] + (u_a - u_w)_{AVR} S^{\psi_{BC}} \tan \phi' N_c \zeta_c + 0.5 \gamma B N_\gamma \zeta_\gamma \quad (2)$$

where:

$(u_a - u_w)_b$ = air entry value from SWCC, kPa
 $(u_a - u_w)_{AVR}$ = average matric suction value, kPa (Fig. 2; Fig. 3)
 ϕ' = effective friction angle, °
 S = degree of saturation, %
 ψ_{BC} = bearing capacity fitting parameter
 ζ_c, ζ_γ = shape factors

There is a smooth transition between the bearing capacity equation proposed by [3] for unsaturated soils and the conventional Terzaghi's bearing capacity equation for saturated soils. In other words, the equation (i.e., Eq. (2) proposed by [3]) will be the same as Terzaghi's bearing capacity equation when the matric suction value is set equal to zero.

The general form of equation to estimate the bearing capacity of unsaturated soils is shown in Eq. (3). This equation takes

into account of the influence of overburden stress and the shape factors.

$$q_u = [c' + (u_a - u_w)_b (\tan \phi' - S^{\psi_{BC}} \tan \phi')] + (u_a - u_w)_{AVR} S^{\psi_{BC}} \tan \phi' N_c \zeta_c F_c + \gamma D_f N_q \zeta_q F_q + 0.5 \gamma B N_\gamma \zeta_\gamma F_\gamma \quad (3)$$

where:

F_c, F_q, F_γ = depth factor
 $\zeta_c, \zeta_q, \zeta_\gamma$ = shape factor

The bearing capacity fitting parameter, ψ_{BC} along with the effective shear strength properties (c' and ϕ') and the SWCC are required for predicting the variation of bearing capacity with respect to matric suction assuming drained loading conditions. The bearing capacity fitting parameter, ψ_{BC} can be estimated from relationship provided by researchers [3] in Eq. (4) given below:

$$\psi_{BC} = 1.0 + 0.34(I_p) - 0.0031(I_p)^2 \quad (4)$$

Several investigators provided bearing capacity factors for cohesion, N_c ; surcharge, N_q and unit weight, N_γ ([1], [2], [26], and [26]). The values for bearing capacity factors of N_c and N_q provided by various investigators are approximately the same. For this reason, the bearing capacity factors, N_c and N_q originally proposed by Terzaghi [1] were used in the analysis. The N_γ values suggested by [26] have been more widely used in recent years. For this reason, the bearing capacity factor, N_γ values proposed by [26] are used in this study.

7. COMPARISON BETWEEN MEASURED AND PREDICTED BEARING CAPACITY

7.1 Measured and Predicted B.C. for Surface PLTs

The bearing capacity values of surface model footings of 150 mm × 150 mm were measured using the UOBCE [16] under both saturated and unsaturated conditions. Both the bearing capacity under saturated and unsaturated conditions was interpreted taking into account of influence on the dilatancy angle, ψ for sand.

Table 3. B.C. factors, shape factors and depth factors used in the analysis for the surface PLT

Effective friction angle, $\phi' = 35.3^\circ$								
Estimated dilatancy angle, $\psi = 3.53^\circ$								
Modified friction angle, $\phi'_m = (\phi' + \psi) \approx 39^\circ$								
B.C. Factors ¹			Shape Factors ²			Depth Factors ³		
N_c	N_q	N_γ	ζ_c	ζ_q	ζ_γ	F_c	F_q	F_γ
86	70	95	1.8	1.8	0.6	1.0	1.0	1.0

¹ from [1]; ² from [36]; ³ from [27]

The dilatancy angle, ψ was not measured in this study but was approximated for typical sand based on the information reported in the literature. The dilatancy angle, ψ value assumed to be equal to 10 % of effective friction angle, $\phi'/10$

35.3 is equal to 35.3° following [28] (i.e., DS 415. 1984). In other words, the modified friction angle, ϕ'_m is 38.53° or approximately 39° . Summary of the values of the bearing capacity factors, shape factors and depth factors for the surface model footings with a modified friction angle of $\phi'_m = 39^\circ$ are presented in Table 3.

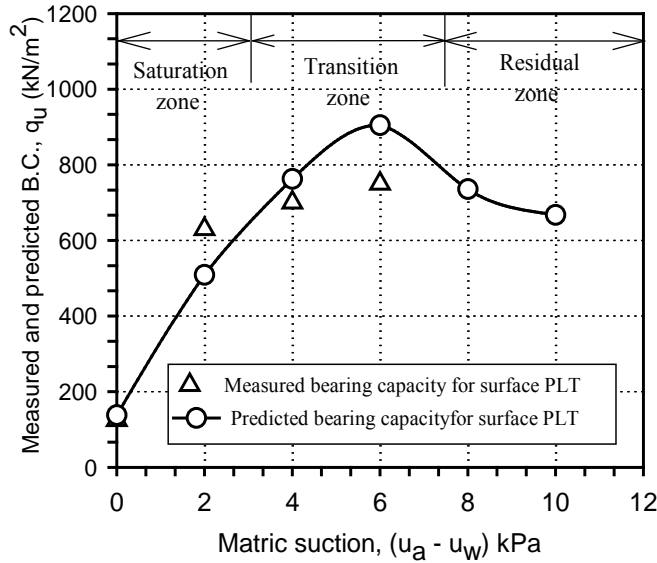


Fig. 7. Measured and predicted B.C. for surface model footing (PLT) of 150 mm × 150 mm using the UOBCE

The same approach has been extended for analyzing surface model footing results of another three sands tested by researcher [11]. Similar to the test results of sand used in the present study, good comparison was observed between the measured and predicted bearing capacity values for these three sands considering a dilatancy angle value equal to 10 % of effective friction angle. Summary of these discussions are available in [29]. More recently, [5] have undertaken numerical modeling studies to predict the variation of bearing capacity with respect to matric suction. These modeling results also show that reasonably good comparisons were possible between the measured and modeled bearing capacity values using a dilatancy angle, λ as shown in Fig. 7.

7.2 Measured and Predicted B.C. for Embedded PLTs

The bearing capacity of 150 mm × 150 mm embedded model footing (sandy soils in both saturated and unsaturated conditions) was measured using the modified UOBCE (see Fig. 1). The model footing of 150 mm × 150 mm is located at a depth, D_f of 150 mm below the soil surface simulating an overburden stress which also acts as a confinement all around the footing.

Equation (3) is used in the interpretation of the bearing capacity results of embedded footings in saturated and unsaturated sandy soils taking account of the influence of the overburden stress and the shape factors. However, the influence of dilatancy angle, λ was not considered

Table 4. B.C. factors, shape factors and depth factors used in the analysis for the embedded PLT

Effective friction angle, $\phi' = 35.3^\circ$								
Estimated dilatancy angle, $\lambda = 0^\circ$								
B.C. Factors ¹			Shape Factors ²			Depth Factors ³		
N_c	N_q	$N_{\phi'}$	ϕ'	ϕ'_q	$\phi'_{\phi'}$	F_c	F_q	$F_{\phi'}$
58	41	45	1.7	1.7	0.6	1.4	1.2	1.0

¹ from [1]; ² from [36]; ³ from [27]

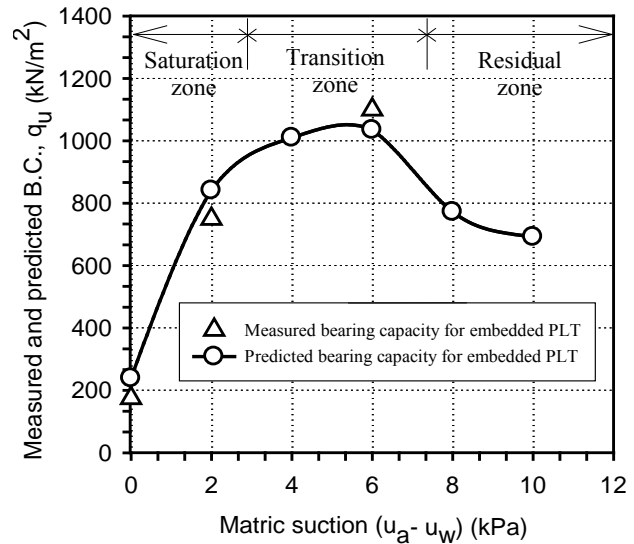


Fig. 8. Measured and predicted B.C. for embedded model footing (PLT) of 150 mm × 150 mm using the modified UOBCE

In other words, the bearing capacity factors, shape factors and depth factors were obtained using the effective friction angle, $\phi' = 35.3^\circ$ (see Table 4). There is a good comparison between the measured and estimated bearing capacity values for interpreting the embedded model footing results without taking account of the influence of dilatancy angle, λ as shown in Fig. 8. Such a behavior can be attributed to the influence of the confinement with a depth which is equal to the width, B of the foundation ($D_f = 150$ mm; as illustrated in Fig. 4). These results are also consistent with the studies of several investigators who have shown that the influence of dilation in the sand decreases with an increase in overburden effective stress or confinement ([19], [23], and [30]).

8. CORRELATIONS BETWEEN THE CONE RESISTANCE AND THE SETTLEMENT OF FOOTINGS IN SAND

8.1 Proposed Technique

The modulus of elasticity, E_s typically increases with depth in sandy soils and the stresses associated with the applied load decrease with an increase in depth. In other words, settlement will be less in deeper layers in comparison to shallow layers. Schmertmann [8] suggested equation (i.e., Eq. (5)) by extending this philosophy for the estimation of footing

settlement in sands using average cone penetration resistance, q_{ci} over a depth of $2B$ from the bottom of the footing.

$$\delta = C_1 C_2 (q_a - \sigma'_{z,d}) \sum_{i=0}^{2B} \left(\frac{I_{zi} \Delta z_i}{E_s} \right) \quad (5)$$

where:

$$C_1 = 1 - 0.5[\sigma'_{z,d} / (q_a - \sigma'_{z,d})] ; \quad C_2 = 1 - 0.21 \log[t / 0.1]$$

δ = settlement, C_1 = depth factor, C_2 = time factor, q_a = footing pressure; $\sigma'_{z,d}$ = vertical effective stress at footing base level; $E_s = f \times q_{ci}$ (i.e., elastic modulus of soil); I_{zi} = influence factor, B = footing width; q_{ci} = resistance of each layer; f = coefficient; Δz_i = thickness of each layer; and t = time.

This method is widely used in geotechnical engineering practice. One of the key limitations of this method is that it does not take into account the influence of capillary stress or matric suction and is used for sands both in saturated and unsaturated conditions.

Investigators [7] suggested two empirical relationships that can be used in the Schmertmann's equation [8] to estimate the settlements in sands. These empirical relations are useful in estimating the modulus of elasticity, E_s of sands in saturated and unsaturated conditions. The relationships are proposed based on the analysis from the PLT and CPT results.

Equation (6) is suggested to estimate the modulus of elasticity, E_s for saturated sands (i.e., $(u_a - u_w) = 0$ kPa) as given below:

$$E_{s(sat)} = f_1 \times q_{c sat} \quad (6)$$

where: $E_{s(sat)}$ = modulus of elasticity for saturated homogenous sand, $f_1 = 1.5 \times ((D_r/100)^2 + 3)$ (i.e. f_1 is a correlation factor and D_r is the relative density in %), $q_{c(sat)}$ = average cone resistance under saturated sands condition (e.g. within an influence zone, IZ equal to $1.5B$ from the footing base level) and B = footing width.

Equation (7) is suggested to estimate the modulus of elasticity, E_s for unsaturated sands (i.e., $(u_a - u_w) > 0$ kPa):

$$E_{s(unsat)} = f_2 \times q_{c unsat} \quad (7)$$

where: $E_{s(unsat)}$ = modulus of elasticity for unsaturated homogenous sands, $f_2 = 1.2 \times ((D_r/100)^2 + 3.75)$ for sands with $D_r < 50\%$ or $f_2 = 1.7 \times ((D_r/100)^2 + 3.75)$ for sands with $D_r \geq 50\%$, (i.e. f_2 is a correlation factor and D_r is the relative density in %), $q_{c(unsat)}$ = average cone resistance under unsaturated sands conditions (e.g., within influence zone, IZ equal to $1.5B$ from the footing base level) and B = footing width.

Fig. 9 summarizes various steps detailed earlier in the form of a flow chart. The modulus of elasticity, E_s from Eq. (6) or Eq. (7) can be substituted into Schmertmann's equation (i.e., Eq. (5)) [8] to estimate the immediate settlement.

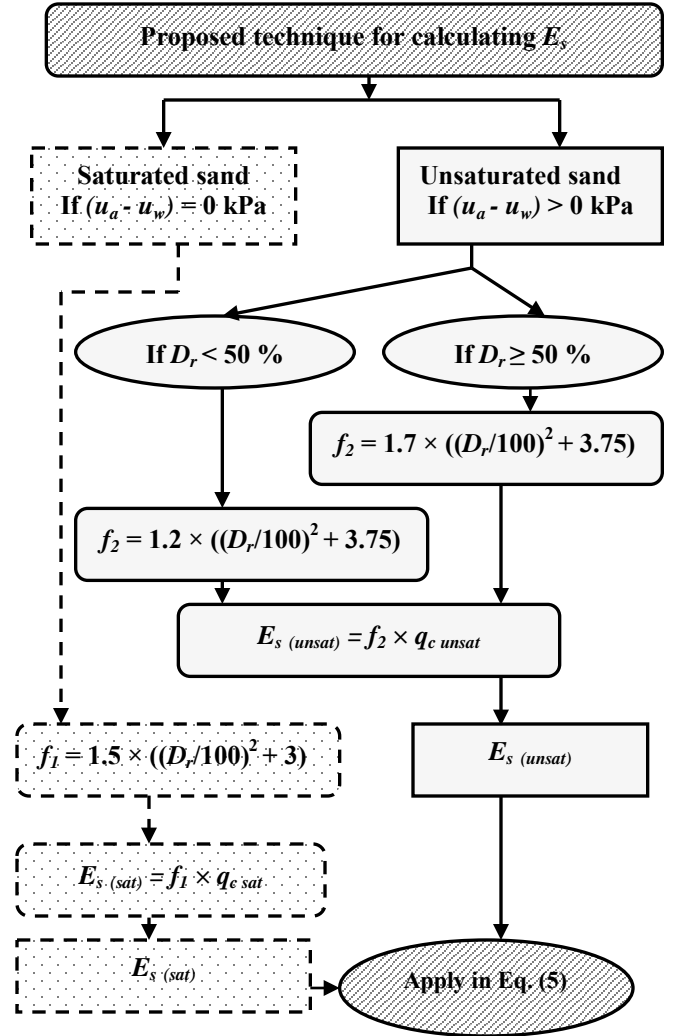


Fig. 9. Flow-chart to illustrate the proposed technique used for calculating the modulus of elasticity, $E_{s(sat)}$ and $E_{s(unsat)}$

Fig. 10 and Fig. 11 provide comparisons between the estimated and measured settlement values for both surface and embedded respectively of $150 \text{ mm} \times 150 \text{ mm}$ model PLTs in the tested sand with different average matric suction values (i.e., 0 kPa, 2 kPa and 6 kPa) using the proposed relationships into the Schmertmann's equation [8]. The footing settlements decrease with an increase in the matric suction and the overburden stress.

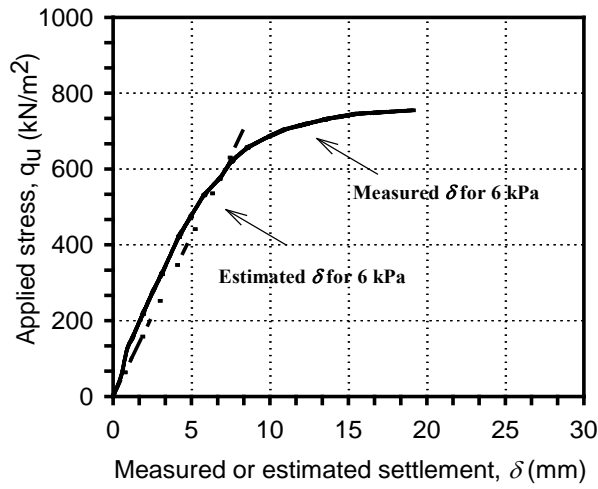


Fig. 10. Comparison between the measured and estimated settlements using the modified Schmertmann's equation for a surface PLT of 150 mm \times 150 mm (UOBCE)

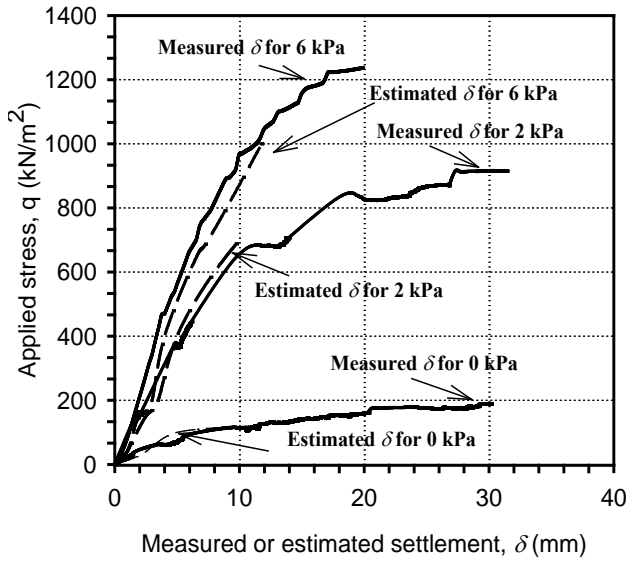


Fig. 11. Comparison between the measured and estimated settlements using the modified Schmertmann's [8] equation for embedded PLTs of 150 mm \times 150 mm (modified UOBCE)

8.1 Validation of the Proposed Technique

Comparisons are provided between the estimated settlement (from the proposed technique) and measured settlement (from in-situ FLT tests conducted by [35]) values for both saturated and unsaturated sands to validate the proposed technique. More details of the analysis and comparisons between the measured and estimated settlement values using the proposed relationships in Eq. (5) and measured settlement values for both saturated and unsaturated sands using four in-situ footing load tests (FLT) are provided. The results summarized in Fig. 12 show the settlement values estimated using the proposed technique for a typical full-scale footing in

unsaturated sand from in-situ presented in [35]. It can be seen that the proposed technique provides reasonable settlement estimations in comparison to the measured values. This can be attributed to the use of different correlations (i.e., f_1 and f_2) between the cone resistance, q_c and modulus of elasticity, E_s in the new relationships which are better in representing the settlement behaviour of sands. Furthermore, the selection of these correlations are not only functions of the CPTs results but also are based on the soil condition (e.g., saturated or unsaturated) and the relative density, D_r .

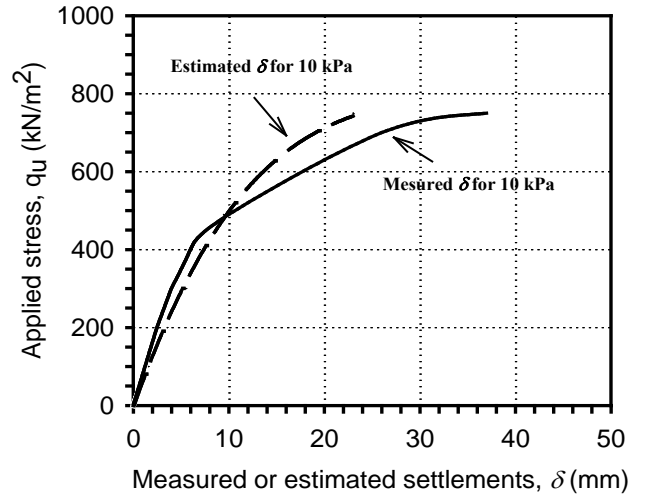


Fig. 12. Comparison between the measured and estimated settlements using the modified Schmertmann's equation for a FLT of 1500 mm \times 1500 mm (FLT from [35])

9 DISCUSSION OF RESULTS

The correlation factor, f_1 value for estimating reliable settlement behaviour of shallow footings in sands under saturated condition is typically in the range of 4.5 to 5.0. On the other hand, the correlation factor, f_2 value for estimating the settlement of unsaturated sands falls between 4.5 and 7.5 for the sands evaluated. The need for using such a wide range of f_2 values (i.e., 4.5 to 7.5) can be attributed to the influence of matric suction on the cone resistance, q_c values which contributes to a reduction of the settlement, δ of sands under unsaturated conditions (i.e., $(u_a - u_w) > 0$ kPa).

It should be noted that the factors, f_1 and f_2 values for saturated and unsaturated sand conditions respectively are dependent on the relative density, D_r . In both cases, the correlation factor increases proportionally with an increase in the relative density, D_r . These observations are consistent with the conclusions drawn by researchers [34]. Estimated and measured settlement values of large-scale footings (four FLT) from a reported in-situ case study presented in [35] are compared in this study as shown in Fig. 13.

Because of the limited depth of the test box of both the UOBCE and the modified UOBCE in the laboratory, the maximum average matric suction value (i.e., $(u_a - u_w)_{AVR}$) simulated in the tank was 6 kPa. The proposed technique was developed based on test results using average matric suction

values ≤ 6 kPa; however, it provides good comparisons for footings constructed in sands for higher matric suction values (i.e., 10 kPa) for the FLT's. The average matric suction value $(u_a - u_w)_{AVR}$ for the FLT's in sand using [35] results was determined assuming a constant matric suction distribution as the depth of groundwater table is at 4.9 m and the natural water content over this depth was constant.

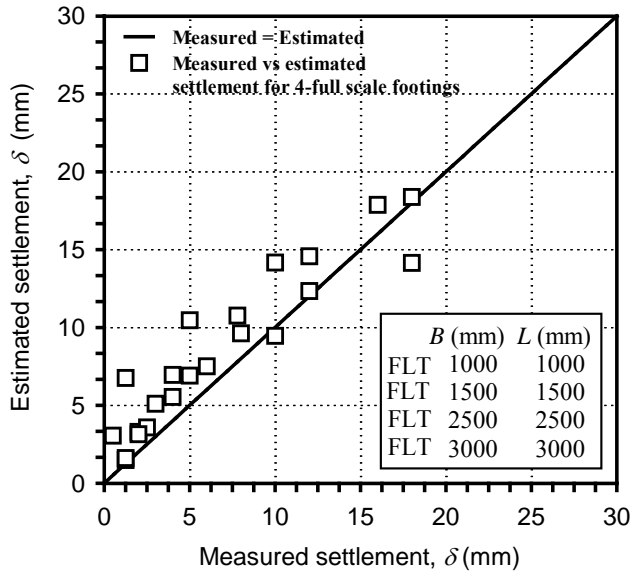


Fig. 13. Comparison between estimated and measured settlements of four full-scale footings (FLT's from [35]) in unsaturated sands corresponding to different applied stresses

10 SUMMARY AND CONCLUSIONS

The bearing capacity and settlement behaviour of sandy soil under saturated and unsaturated conditions using surface and embedded model footings tests are studied in this research program. The bearing capacity values are underestimated for surface model footings (i.e., the depth of the model footing is equal to zero) when calculations are based on effective friction angle, $\phi' = 35.3^\circ$ for the tested sand both in saturated and unsaturated conditions. Typical value of dilatancy angle for sands is equal to 10 % of effective friction angle, $\phi' / 10$ (see Table 3). Reasonably good comparisons were observed between measured bearing capacity and predicted values using Eq. (2) particularly when the influence of the dilatancy angle, $\phi' / 10$ is taken in

There is no need to increase the effective friction angle, ϕ' by 10% to obtain reasonable comparison between the measured and estimated bearing capacity values (see Table 4) for embedded footings. In other words, the dilatancy angle, $\phi' / 10 = 0$ for shallow foundations whose $D_f / B \approx 1$. Such a contrasting behavior between surface and embedded footings may be attributed to the contribution of the overburden stress which eliminates the influence of dilation. These observations are consistent with the conclusions drawn in ([19], [23] and [31]) with respect to dilation effects in sandy soils.

The bearing capacity of unsaturated sands increases with matric suction in a linear fashion up to the air-entry value (saturation zone). There is a non-linear increase in the bearing capacity in the transition zone (i.e., from air-entry to the residual suction value). The bearing capacity however decreases in residual zone of unsaturation. Fig. 4 shows a set of typical results and behaviour of variation of bearing capacity with respect to matric suction. The behaviour of bearing capacity of unsaturated soils is consistent with the shear strength behaviour of unsaturated sands ([32], [33]). Schmertmann's equation [8] (i.e., Eq. (5)) with proposed relationships for modulus of elasticity, E_s for saturated and unsaturated conditions (i.e., Eq. (6) and Eq. (7)) provide reasonably good comparisons between measured and estimated settlements for both model PLTs and in-situ FLT's (see Figs. 10, 11, 12 and 13).

The modified Terzaghi and modified Schmertmann's procedures for predicting the bearing capacity and settlement behavior of sandy soils, respectively for both saturated and unsaturated conditions are promising and can be used by practicing engineers.

11 ACKNOWLEDGMENTS

Funding received from Natural Sciences and Engineering Research Council (NSERC) of Canada for this project is acknowledged. The second author thanks the Ministry of Higher Education and Scientific Research in Libya (M.H.E.S.R) for the financial support. The authors thank Jean Claude Celestin, technical officer of the Geotechnical Laboratory, University of Ottawa for his assistance.

12 REFERENCES

- [1] Terzaghi K, "Theoretical Soil Mechanics," John Wiley and Sons. New York, NY, USA, 1943.
- [2] Meyerhof GG, "The ultimate bearing capacity of foundations," *Géotechnique*, 1951, (2), 301 – 332.
- [3] Vanapalli SK and Mohamed FMO, "Bearing capacity of model footings in unsaturated soils," In *Experimental Unsaturated Soil Mechanics*, Springer Proc. in Physics. Springer-Verlag Berlin Heidelberg, 2007, 112, 483 – 493.
- [4] Vanapalli SK, "Shear strength of unsaturated soils and its applications in geotechnical engineering practice," Keynote Address. Proc. 4th Asia-Pacific Conf. on Unsaturated Soils. New Castle, Australia, Edited by O. Buzzi, S. Fityus and D. Sheng. 2010 Taylor & Francis Group, London, ISBN 978-0-415-80480-6, 2009, 579 – 598.
- [5] Oh WT and Vanapalli SK, "Modeling the stress versus settlement behavior of model footings in saturated and unsaturated sandy soils," *Canadian Geotechnical J.*, 2011, 48, 425 – 438.
- [6] Oh WT and Vanapalli SK, "Modelling the settlement behaviour of shallow foundations in unsaturated sands," In *Proc. of GeoCongress*, Oakland, 2012, 2542 – 2551.
- [7] Mohamed FMO, Vanapalli SK and Saatcioglu M, "Settlement estimation of shallow footings in saturated and unsaturated sands using cone penetration test (CPT)

- results,” 2011 CSCE Annual Conf. – Engineers Advocates for Future Policy, 2011.
- [8] Schmertmann JH, Hartman JP and Brown P, “Improved strain influence factor diagrams,” *J. of Geotechnical Eng. Division, ASCE*, 1978, 104 (8), 1131 – 1135.
 - [9] DeBeer E, “Bearing capacity and settlement of shallow foundations on sand,” *Proc. of Symposium on Bearing Capacity and Settlement of Foundations*, Durham, NC, 1965, 15 – 33.
 - [10] Broms BB, “The effect of degree of saturation on the bearing capacity of flexible pavements,” *Highway Research Record*, 1963, 71, 1 – 14.
 - [11] Steensen-Bach JO, Foged N and Steenfelt JS, “Capillary induced stresses – fact or fiction?,” 9th ECSMFE, *Groundwater Effects in Geotechnical Engineering*, Dublin, 1987, 83 – 89.
 - [12] Fredlund DG and Rahardjo H, “Soil mechanics for unsaturated soils,” 1st ed., Wiley, New York, 1993.
 - [13] Costa YD, Cintra JC and Zornberg JG, “Influence of matric suction on the results of plate load tests performed on a lateritic soil deposit,” *Geotechnical Testing J.*, 2003, 26(2), 219 – 226.
 - [14] Oloo SY, Fredlund DG and Gan JK M, “Bearing capacity of unpaved roads,” *Canadian Geotechnical J.*, 1997, 34, 398 – 407.
 - [15] Vanapalli SK and Oh WT, “Mechanics of unsaturated soils for the design of foundation structures,” Plenary Address. *Proc. 3rd WSEAS International Conference on Engineering Mechanics, Structures, Engineering Geology*, Corfu Island, Greece, 2010, 363 – 377.
 - [16] Mohamed FMO and Vanapalli SK, “Laboratory investigations for the measurement of the bearing capacity of an unsaturated coarse-grained soil,” *Proceedings of the 59th Canadian Geotechnical Conf.*, Vancouver, B.C, 2006, 219 – 226.
 - [17] Meyerhof GG, “Penetration tests and bearing capacity of cohesionless soils,” *J. of Soil Mechanics and Foundation Division, ASCE*, 1956, 82 (1), 1 – 19.
 - [18] Das B and Sivakugan N, “Settlement of shallow foundations on granular soil – an Overview,” *Int. J. of Geotechnical Eng.*, 2007, 1, 19 – 29.
 - [19] Bolton MD, “The strength and dilatancy of sands,” *Géotechnique*, 1986, 36 (1), 65 – 78.
 - [20] Sfriso A, “The friction angle and critical state void ratio of sands,” *Proc. of 17th Int. Conf. of Soil Mechanics and Geotechnical Eng.*, ICSMGE, Alexandria, Egypt, 2009, 433 – 435.
 - [21] Vermeer PA and DeBorst R, “Non-associated plastic for soils, concrete and rock,” *Heron*, 1984, 5 – 64.
 - [22] Bishop AW, “Shear strength parameters for undisturbed and remoulded soils specimens,” *In stress strain behaviour of soils*. Foulis, London, 1972, 3 – 58.
 - [23] Chakraborty T and Salgado R, “Dilatancy and shear strength of sand at low confining pressure,” *J. of Geotechnical and Geo-environmental Eng.*, 2010, 136, 527 – 32.
 - [24] Poulos H and Davis E, “Elastic solutions for soil and rock mechanics,” John Wiley and Sons, NY, USA, 1974.
 - [25] Mohamed FMO and Vanapalli SK, “An experimental investigation of the bearing capacity of an unsaturated sand using cone penetration tests,” *Proc. 62nd Canadian Geotechnical Conf.*, Halifax, NS, 2009, 205 – 213.
 - [26] Kumbhokjar AS, “Numerical evaluation of Terzaghi’s N_{\square} ,” *J. of Geotechnical Eng.*, American Society of Civil Engineers, 1993, (3), 598 – 607.
 - [27] Hansen BJ, “A revised and extended formula for bearing capacity,” *Bulletin No. 28*, Danish Geotechnical Institute, Copenhagen, Denmark, 1970, 5 – 11.
 - [28] DS 415, “The Danish code of practice for foundation engineering,” Danish Society of Civil Engineering, 1984.
 - [29] Mohamed FMO, “A semi-empirical approach for the interpretation of the bearing capacity of unsaturated soils,” Master’s Thesis, University of Ottawa, Ottawa, ON, Canada, 2006.
 - [30] Liao HJ and Hsu ST, “Uplift behavior of blade-underreamed anchors in silty sand,” *J. of Geotechnical and Geoenvironmental Eng.*, 2003, 560 – 568.
 - [31] Vesić AS and Clough GW, “Behaviour of granular materials under high stresses,” *J. of Soil Mechanics and Foundation Division. ASCE* 94, 1968, SM3, 661 – 688.
 - [32] Vanapalli SK, Fredlund DG, Pufahl DE and Clifton AW, “Model for the prediction of shear strength with respect to soil suction,” *Canadian Geotechnical J.*, 1996, 33 (3), 379 – 392.
 - [33] Vanapalli SK and Lacasse F, “Comparison between the measured and predicted shear strength behavior of four unsaturated sands,” *Proc. of the 4th Asia-Pacific Conf. on Unsaturated Soils*. New Castle, Australia. Edited by O. Buzzi, S. Fityus and D. Sheng. 2010 Taylor & Francis Group, London, ISBN 978-0-415-80480-6, 2009, 121 – 127.
 - [34] Lee J and Salgado R, “Estimation of footing settlement in sand,” *The Int. J. of Geomechanics*, 2002, 1 (2), 1 – 28.
 - [35] Giddens R and Briaud J, “Load tests on five large spread footings on sand and evaluation of prediction methods,” *Federal Highway Administration Department of Civil Engineering*, A&M University, TX., USA, 1994.
 - [36] Vesić AS, “Analysis of ultimate loads of shallow foundations,” *J. of the Soil Mechanics and Foundation Division, ASCE* 99, (SM1), 1973, 45 – 73.

Development of Piled Geo-wall (New type reinforced soil wall)

Hara, T., Tsuji, S., Yoshida, M. and Sawada, K.
Gifu University, Japan

ABSTRACT

This study aims to achieve a new type of independent reinforced soil wall (Piled Geo-wall) that can be substitute for one made up of concrete with similar scale, and to contribute to sustainable development. In order to confirm the practicability of the novel structure, three experimental studies with static and impact loading tests and a dynamic centrifuge model test were carried out in the past years, which were reported on the 1st GEOMATE conference. Simple design methods of the novel structure, which can reproduce the results of the experiments, are introduced in this paper.

Keywords: Reinforced soil wall, Pile foundation, Earth-retaining wall, Rock-fall protection wall

1. INTRODUCTION

The high ductility of soil structure reinforced by geogrid is well known, as is the possibility of building independent soil wall. The independent reinforced soil wall has been applied to such diverse structures as rock-fall protection walls, mud and snow avalanche protection walls and the suchlike. Since it can be built using existing soil at the construction site if it is compactable one, they are being used ever more frequently as one of economic and CO2 reducible structures. At present, however, the adoption of the spread foundation for the independent reinforced soil wall makes the design too wide for application to narrow construction sites, such as beside mountainous road. If a narrow independent reinforced soil wall as like as RC wall with pile foundation is achieved, it could be widely applied. And it can also be substitute for concrete ones and contribute sustainable development.

Therefore, a new type of independent reinforced soil wall with inserting piles into the Geo-wall body, as shown in Fig. 1, which is referred to “Piled Geo-wall or PGW” in this paper, has been developed. The practicability of Piled Geo-wall to diverse structures has been already confirmed from three experimental studies with full-scale static and impact loading tests and a dynamic centrifuge model test (25G) were carried out in the past years [1], [2]. Recognizing the practicability, a study on simple design method to apply Piled Geo-wall to earth-retaining walls, rock-fall protection walls, and seismic countermeasure walls of road embankment in order to reduce deformation of road surface, has been conducted. In this paper, because of paper limitation, simple external stability verification methods of Piled Geo-wall as well as the reproducibility of the experiments’ results by using the proposed verification methods are introduced.

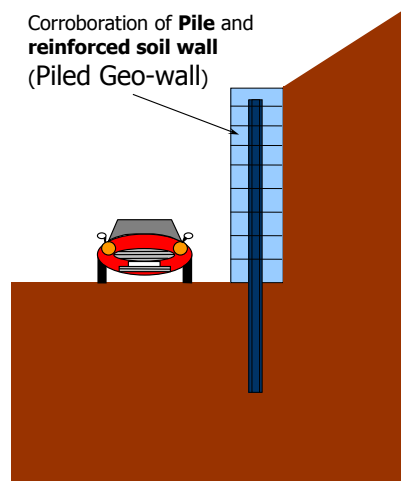


Fig. 1. Image of Piled Geo-wall (PGW).

2. FUNDAMENTAL EXTERNAL STABILITY MODEL

Piled Geo-wall was devised from an assumption regarding the interaction between pile and Geo-wall body, which the Geo-wall body with high ductility is possible to transmit lateral forces to the piles despite large relative displacement between the pile and the Geo-wall body as shown in Fig.2. Hence, in the design, the responses of the pile and the Geo-wall body have to be estimated respectively. Fig. 3 shows the proposed simple estimation model of the responses of the pile and the Geo-wall body of Piled Geo-wall.

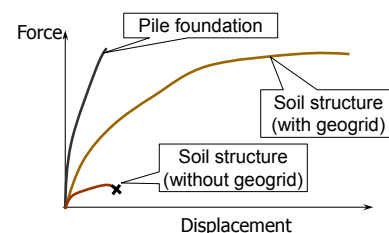
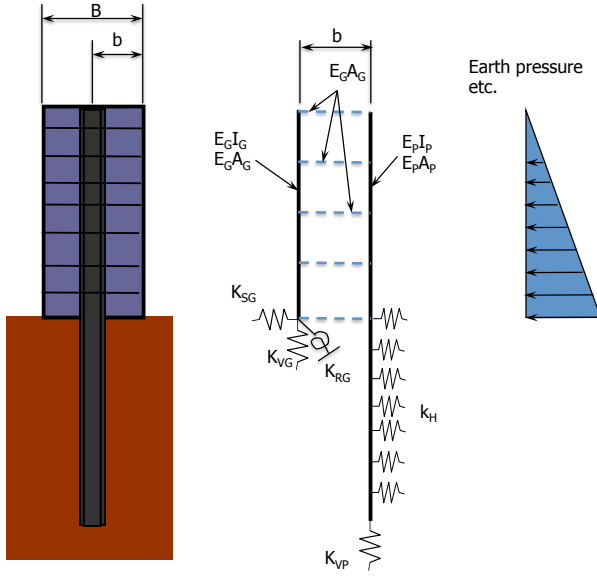
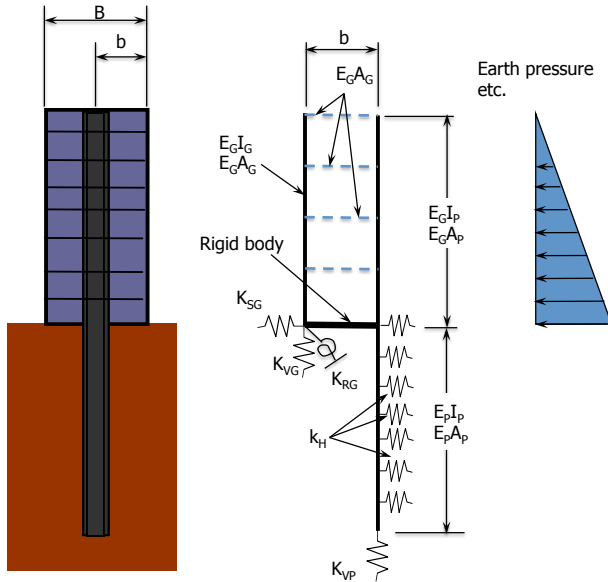


Fig. 2. Interaction image between pile and Geo-wall body.



(a) Estimation model for pile response



(b) Estimation model for Geo-wall body response

Fig. 3. Fundamental external stability model.

Where, $E_P I_P$, $E_G I_G$: flexural stiffness of pile and Geo-wall (kNm^2/m), $E_P A_P$, $E_G A_G$: compressional stiffness of pile and Geo-wall (kNm^2/m), $E_G I_P$: extent without considering flexural stiffness of pile, k_H : elasto-perfectly plastic spring constant of horizontal subgrade reaction (kN/m) set from Eq. (1), the limited value of k_H is passive earth pressure, K_{VG} : elasto-perfectly plastic spring constant of vertical subgrade reaction beneath the Geo-wall body (kN/m) set from Eq. (2), the limited value of K_{VG} is ultimate bearing capacity, K_{SG} : elasto-perfectly plastic spring constant of horizontal shear reaction beneath the Geo-wall body (kN/m) set from Eq. (3), the limited value of K_{SG} , S_{\max} , is set from Eq. (4), K_{RG} : elasto-plastic rotation spring constant beneath the Geo-wall body (kN/rad) set from Eq. (5), the limited value of K_{RG} is determined by the ultimate bearing capacity, K_{VP} : elasto-

perfectly plastic vertical spring constant beneath the pile (kN/m) set from Eq. (6), the limited value of K_{VP} is the ultimate bearing capacity of pile, k_h and k_v : coefficients of horizontal and vertical subgrade reaction (kN/m^3) in normal time or seismic situation, which are estimated from Specifications for Highway Bridges (Part IV) [3], D : pile diameter (m), d_u : unit depth, namely 1.0m, A_G and A_P : cross section areas of the Geo-wall body and the pile (m^2), c and ϕ : cohesion and shear resistance angle of foundation ground (kPa and rad).

$$K_H = k_h \cdot D \cdot d_u \quad (1)$$

$$K_{VG} = k_v \cdot A_G \quad (2)$$

$$K_{SG} = 1/3 \cdot k_v \cdot A_G \quad (3)$$

$$S_{\max} = c \cdot A_G + \sigma \cdot \tan \phi \quad (4)$$

$$K_{RG} = k_v \cdot b \quad (5)$$

$$K_{VP} = k_v \cdot A_P \quad (6)$$

3. PRACTICABILITY OF THE MODEL TO DESIGN

3.1 Earth retaining wall in normal time design situation

The summary of the static loading test of Piled Geo-wall [1], which is targeted for verification of the practicability of the proposed external stability model to the design of earth retaining wall in normal time situation, is shown in Fig. 4.

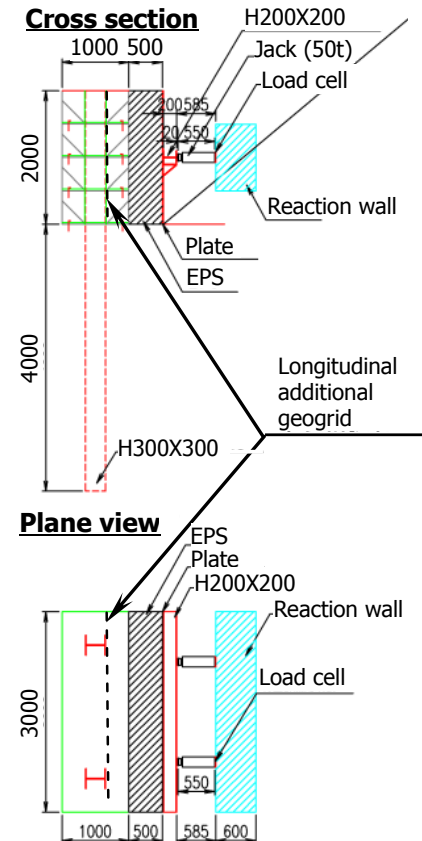


Fig. 4. Summary of target static loading test.

Fig.5 shows the results of dynamic penetration tests converted to N value of standard penetration test (SPT) as the ground condition of the test. In this verification, the results of PD-2 obtained at the vicinity point of the target Piled Geo-wall was referred.

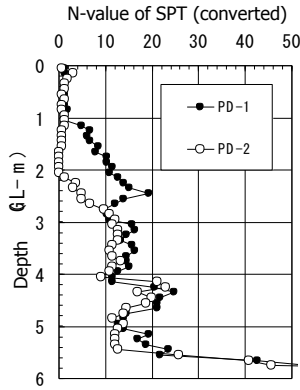


Fig. 5. Ground condition.

Fig. 6 shows the analysis results of the relationship between static load and displacement of Piled Geo-wall, top of the pile and Geo-wall body, which are compared with measured value from the test.

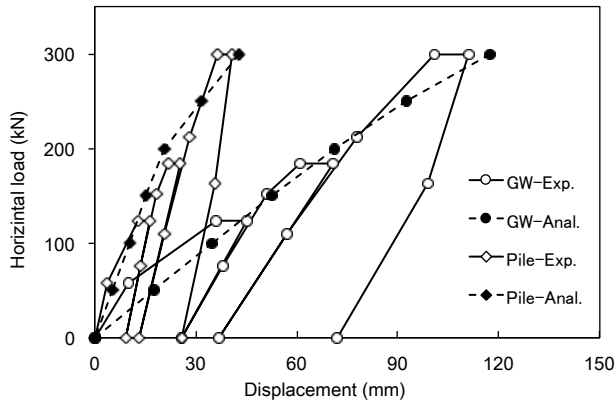


Fig. 6. Relative displacement between pile and Geo-wall.

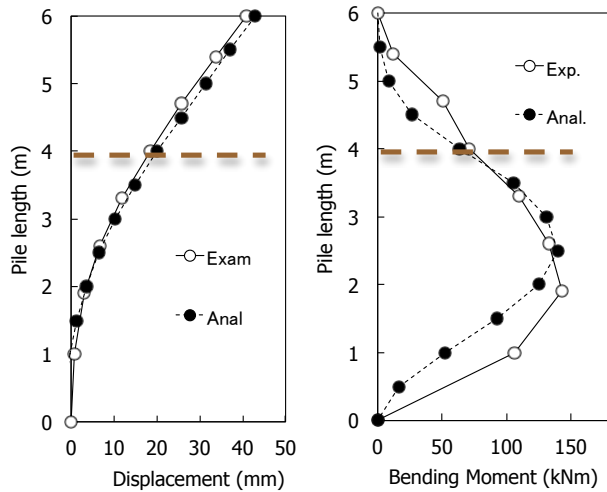


Fig. 7. Maximum response of pile.

And Fig. 7 shows comparisons with the analysis results of maximum response of pile and measured ones from the test. According to the results, it is confirmed that the proposed model can reproduce the response of Piled Geo-wall and relative displacement between pile and Geo-wall body.

3.2 Earth retaining wall in seismic design situation

Fig. 8 shows the transverse section of the model adopted in the dynamic centrifuge test (25G) [2], which is targeted for verification of the practicability of the proposed external stability model to the design of earth retaining wall in seismic situation. In this test, Piled Geo-wall was adopted as a seismic countermeasure for prevention of large deformation of the road embankment built on a slope. Slope ground was made up of cement-stabilized soil and, the soil of the embankment and the Geo-wall body was compacted with density control. Geotechnical and structural parameters converted to actual scale are presented on Table.1 and 2, respectively. Fig. 9 shows the input earthquake wave converted to actual scale.

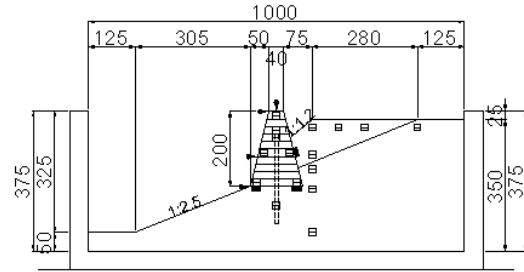


Fig. 8. Model of dynamic centrifuge test (25G).

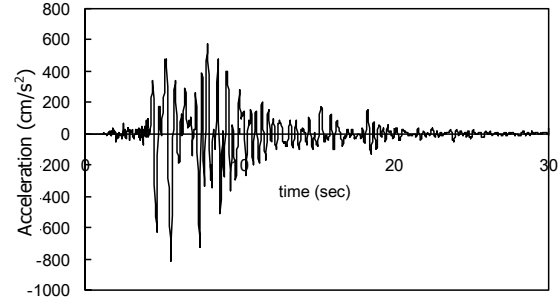


Fig. 9. Input earthquake.

Table. 1. Geotechnical parameter.

	E_0 (kPa)	c (kPa)	ϕ (deg)
Slope	3.26×10^5	55	0
Embankment	3.0×10^4	0	40
Geo-wall	3.0×10^4	0	40

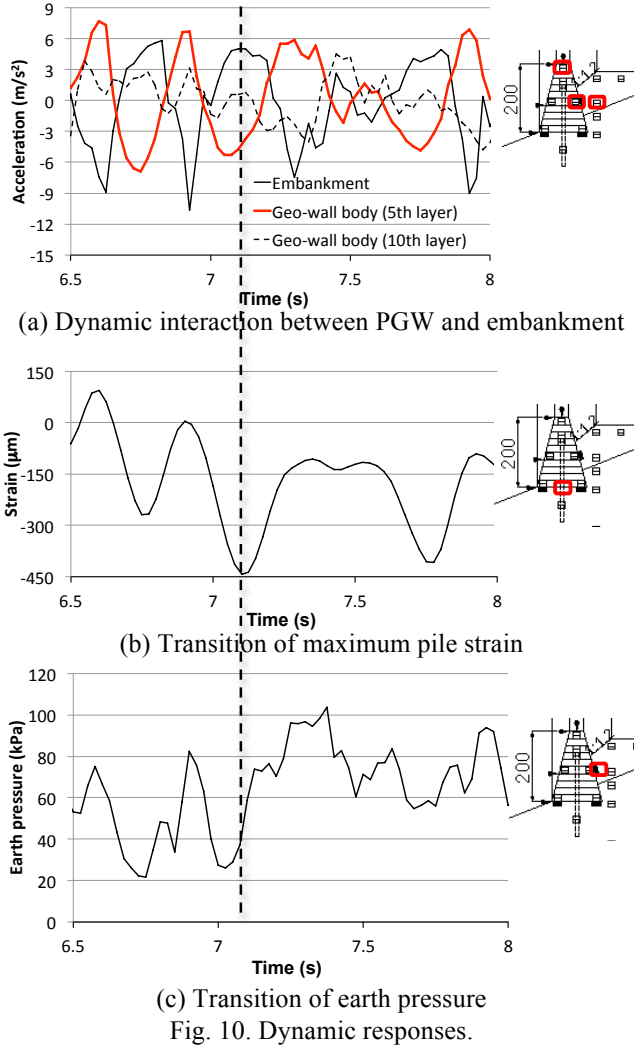
E_0 : deformation modulus, c : cohesion, ϕ : shear resistance angle

Table. 2. Structural parameter.

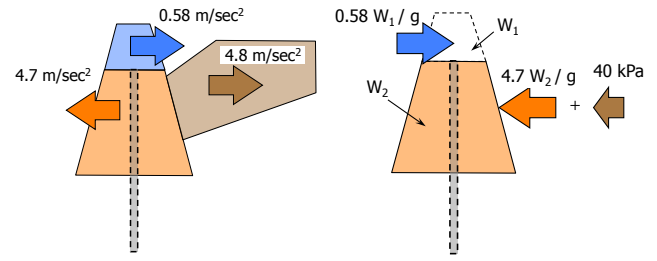
	E (kPa)	A (m ² /m)	I (m ⁴)
Pile	2.0×10^8	4.79×10^{-3}	2.04×10^{-4}
Geogrid	8.0×10^5	1.0×10^{-3}	-

E : Young modulus, A : sectional area, I : moment of inertia

Because recognizing of dynamic interaction between structure and surrounding ground is necessary in order to design the structure by static analysis, dynamic interaction between the Piled Geo-wall and the embankment, transition of pile response and earth pressure at the embankment side of the Piled Geo-wall at the time that the maximum pile response was obtained are shown in Fig. 10.



According to the results, the antiphase between the response of Geo-wall body at 5th layer (the part with inserting pile) and ones of embankment and Geo-wall body at 10th layer (the part without inserting pile) is confirmed. And the states of inertia forces and earth pressure acting on the embankment side of Piled Geo-wall body at the time that the maximum pile response was obtained were confirmed as shown in Fig. 11. Fig.12 shows comparisons of the maximum response of the pile, which analyzed one by the confirmed load states and obtained one from the experiment. From this result, it could be confirmed that the proposed estimation model can reproduce well the actual response of the pile of the Piled Geo-wall.



(a) Dynamic interaction (b) Load situation
Fig. 11. Design situation.

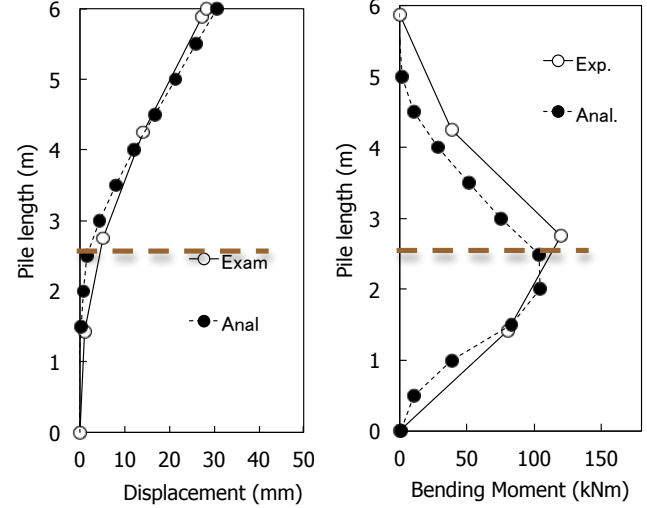


Fig. 12. Maximum response of pile.

In practical design, however, considering real dynamic interaction and load situation on the design stage is difficult. The inertia forces are estimated from design horizontal seismic coefficient of 0.8 in the experimental ground condition and the earthquake level and the earth pressure with the coefficient of earth pressure predicted by Eq. (7) is considered in Japan [4]. Large load situation is assumed in the design as the result as shown in Fig. 13.

Fig. 14 shows the maximum pile response analyzed by proposed model with the design load situation shown in Fig. 13. An abnormal bending moment is occurred at the upper part of the pile as well as larger response than real one is obtained. This is caused by the considering of excessive inertia force, about 14 times of real one, at the upper part of the Geo-wall body (the part without inserting pile). From the following viewpoints, however, it is considered that the proposed model can be applied to practical design.

- In the design executed on the stage that the real dynamic interaction and the real load situation, overestimating the response of the target structure is practical rather than the reproduction of actual one. It is the practical design.
- From specifying that the piles have to be inserted to the top of Geo-wall body, occurrence of abnormal bending moment at upper part of the pile can be prevented.

$$K_{EA} = 0.26 + 0.97 \cdot kh \quad (7)$$

Where, K_{EA} : coefficient of active earth pressure during

earthquake, k_h : design horizontal seismic coefficient

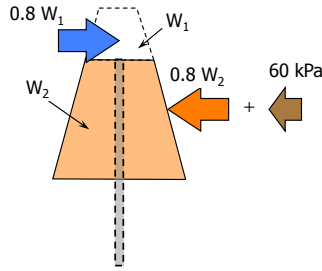


Fig. 13. Design load situation.

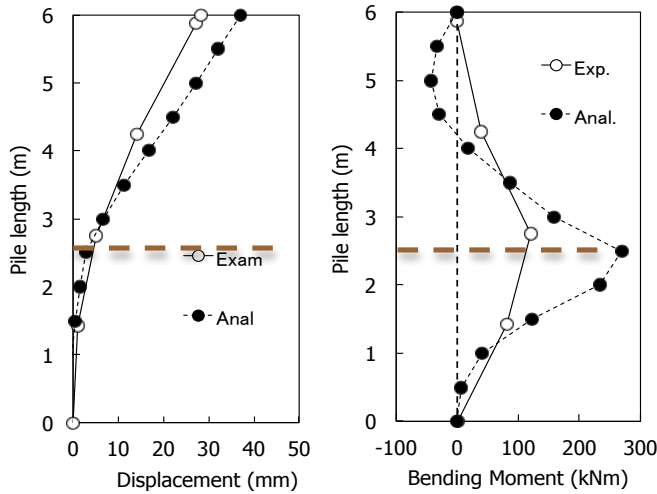


Fig. 14. Maximum response of pile.

Fig. 15 shows the comparison with the analysis result of the maximum response of Geo-wall body and measured one from the experiment. According to the results, it is confirmed that the proposed model can reproduce the real response of the Geo-wall body.

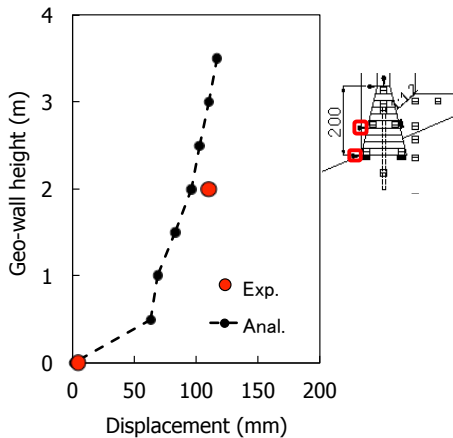


Fig. 15 Maximum response of Geo-wall body.

3.3 Seismic countermeasure wall for road embankment

The practicability of proposed model to the design on seismic countermeasure wall for prevention of large deformation of road embankment is confirmed from comparison with analyzed road surface deformation depending on maximum response of Piled Geo-wall

estimated by the proposed model and ones obtained from the dynamic centrifuge model test (25G) shown in Fig.8. The measured points of the road surface deformation in the experiment are shown in Fig. 16.

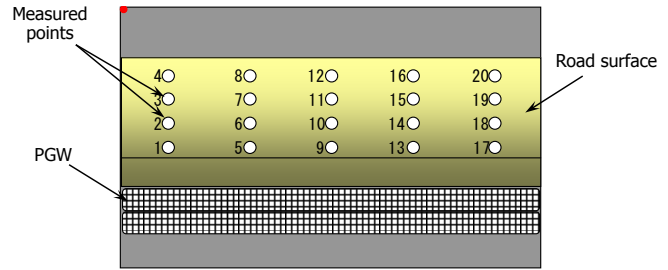


Fig. 16 Measured points of the road surface deformation.

The road surface deformation depending on maximum response of Piled Geo-wall estimated by the proposed model is analyzed by using simple two-dimensional static elastic FEM as shown in Fig. 17. In this analysis, road surface deformation is analyzed by inputting estimated maximum Geo-wall response from the proposed model as an imposed deformation.

Fig. 18 and 19 show the entire deformation results obtained from FEM and the comparison with analyzed road surface deformation by FEM and measured one from the experiment. According to the results, the analyzed deformation reproduces measured one comparatively well, hence it can be confirmed that the proposed model can apply to the verification of seismic performance of road embankment with Piled Geo-wall as a seismic countermeasure.

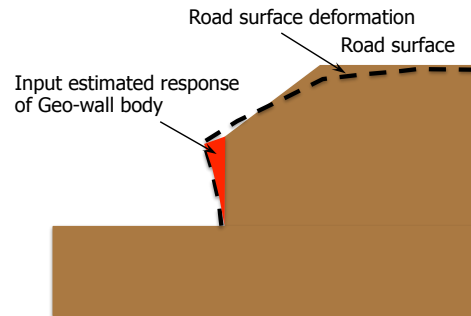


Fig. 17. Analysis of road surface deformation.

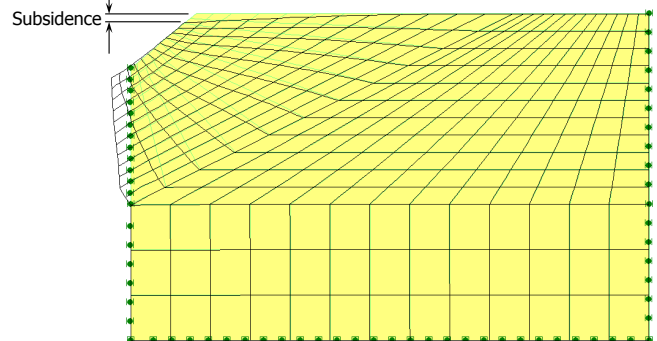


Fig. 18. Entire deformation obtained from FEM.

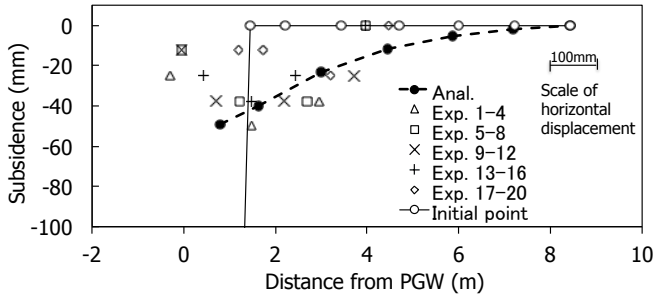


Fig. 19. Road surface deformation.

3.4 Rock-fall protection wall

The impact-loading test of Piled Geo-walls [1], which is targeted for verification of the practicability of the proposed external stability model to the design of rock-fall protection wall, is shown in Fig. 20. In this verification, the results of two impact-loading tests to actual scale models, one is adopted in the static loading test (PGW-1) shown in Fig.4 and another is a new one (PGW-2), are targeted. The piles of PGW-2 are installed at outside of Geo-wall as shown in Fig. 21, are adopted.

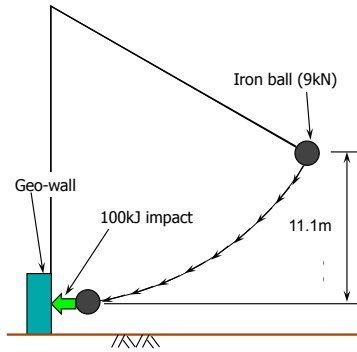


Fig. 20. Impact-loading test.

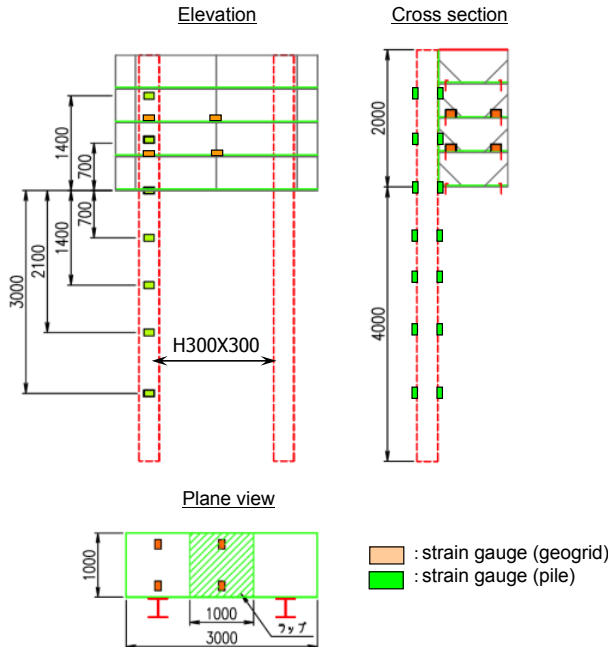


Fig. 21. Structural condition and measurements of PGW-2.

Fig. 22 shows proposed conversion procedure of design static load from impact-load in this study.

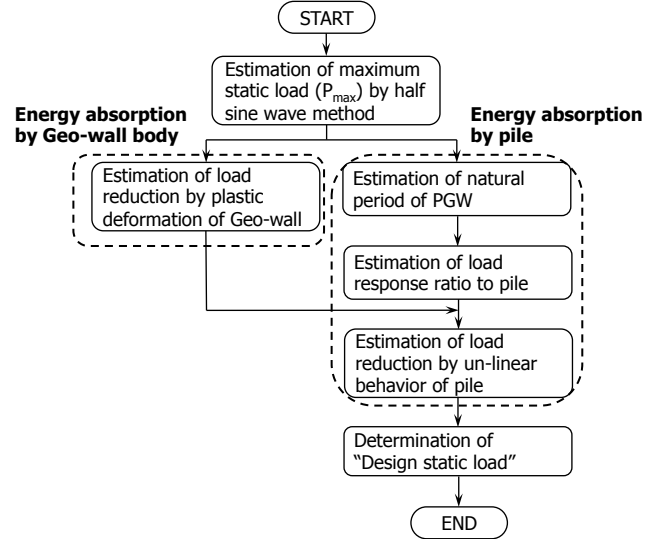


Fig. 22. Conversion procedure of design static load.

Where, the maximum static load (P_{max}) based on half sine wave method is estimated by Eq. 8. In this equation, m is mass, V_0 is initial velocity (m/sec) at the time of the rock-fall impact to the Geo-wall body, which is predicted by Eq. 9, T is sustaining period (sec) of the impact by PGW, which is assumed as 0.07sec from the experiments, g is G-force, h is falling height of the rock fall.

$$P_{max} = \frac{\pi \cdot m \cdot V_0}{T} \quad (8)$$

$$V_0 = \sqrt{2 \cdot g \cdot h} \quad (9)$$

Energy absorption by Geo-wall body was assumed as follows;

- The displacement-time relationship of the iron ball and the pile obtained from the experiment is converted to the load reduction-time relationship as shown in Fig. 23. The maximum load reduction is the maximum static load estimated by Eq. 8. Load reduction by pile is assumed from inverse analysis with using proposed external stability model, because high reproducibility of the static loaded pile displacement by using the proposed model was confirmed at the section "3.1".

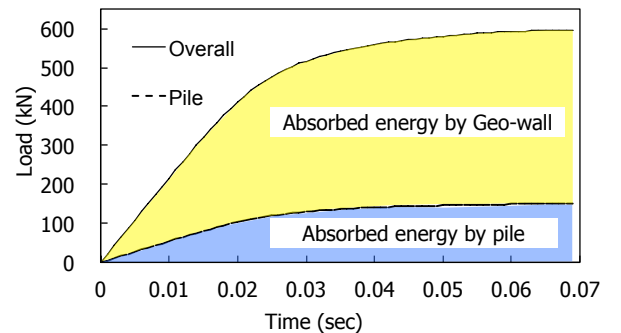


Fig. 23. Load reduction-time relationship

- b. The iron ball displacement expresses entire energy absorption, thus the difference of entire load reduction and one of pile was assumed as the reduction load by plastic deformation of Geo-wall body.
- c. From the abovementioned result, the relationship between load reduction ratio and plastic displacement of Geo-wall body was assumed as Eq. 10.

$$c_{RP} = 9.8 \cdot \delta \cdot (\delta - 0.144) \quad (0.15 \leq \delta) \quad (10)$$

$$\delta = P_{\max} / K_s \quad (11)$$

$$P_{R\max} = P_{\max} \cdot (1 - c_{RP}) \quad (12)$$

Where, c_{RP} : load reduction ratio caused by plastic deformation of Geo-wall body, δ : plastic deformation of Geo-wall body (m) estimated by Eq. 11, K_s : equivalent plastic spring constant with respect to inserting rock-fall into Geo-wall body (kN/m), which is assumed as 1650kN/m from the experiments, $P_{R\max}$: reduced static load with considering energy absorption by Geo-wall.

The values of the impact period (T) and the equivalent plastic spring constant (K_s) are considered as variables depending on stiffness of the Geo-wall body and so on, but because the stiffness would not be so large different one if it is similar scale PGW with experiment one, it is considered that the values can be applied to small type of PGW.

Load response ratio to pile expresses reduction (or amplification) effect of transmitting load to pile. It is well known that the response reduces if the structure with long natural period receives the impact load with short impact period; in contrast, the response amplifies if the structure with short natural period receives the impact load with comparative long impact period. Therefore, the coefficient considered the characteristics in case of using load estimated from half sine curve method was proposed, as Eq.13, from the past study [5]. According to the past study, the border of reduction and amplification of the response is said to be the case that the ratio of impact period of road and natural period of structure is about 0.26.

$$c_{res} = -4 \cdot r_t \cdot (0.6 \cdot r_t - 1.1) \quad (13)$$

$$r_t = T/t \quad (14)$$

$$P_{RES} = P_{R\max} \cdot c_{res} \quad (15)$$

Where, c_{res} : load response ratio to pile, r_t : the ratio of impact period of road and natural period of pile, as Eq.14, t : natural period of pile (sec), P_{RES} : load transmitting to pile (kN).

And finally, the design static load (P_D) is determined from the load reduction, which is estimated by equivalent energy method [6] of both elastic and elasto-plastic analyses with using the proposed external stability model. Fig. 24 shows an example of equivalent energy method applied to PGW design.

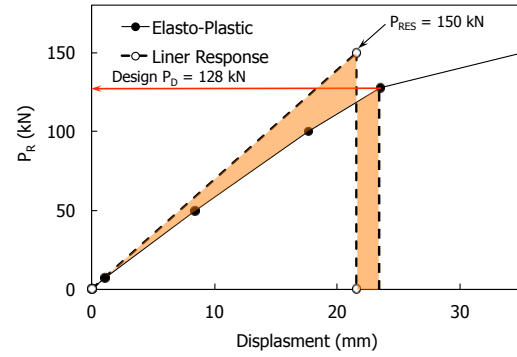


Fig. 24. An example of equivalent energy method.

Fig.25 and 26 show the maximum pile responses of PGW-1 and 2, respectively. According to the results, it can be confirmed that the proposed external stability model reproduces well ones obtained from the experiments. Where, although it is no wonder that analyzed pile top displacements match up to obtained ones because the energy absorption of Geo-wall body was determined from inverse analysis of pile, the reproducibility can be confirmed from the distribution in depth of the displacement and the bending moment of piles.

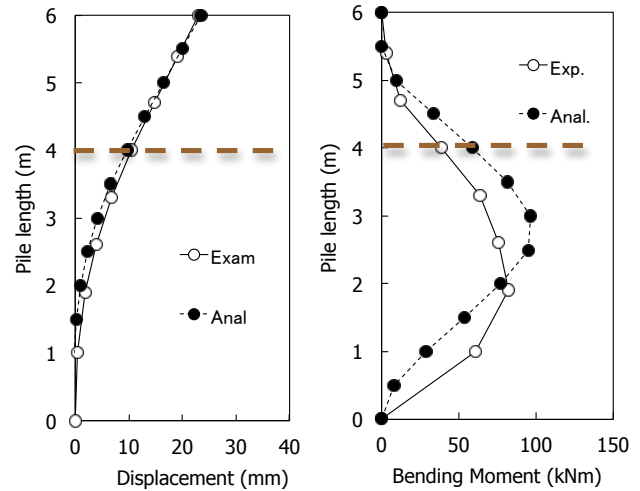


Fig. 25. Maximum pile response (PGW-1).

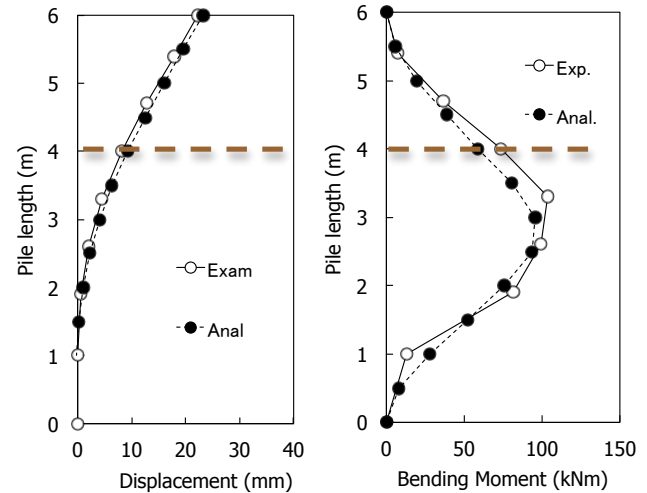


Fig. 26. Maximum pile response (PGW-2).

4. CONCLUSIONS

The contents of this paper are concluded as follows;

- Simple external stability model of Piled Geo-wall for practical design was proposed.
- The practicability of the proposed design model was confirmed from good reproducibility of real response obtained from full-scale static and impact loading tests, and a dynamic centrifuge model test.
- In the design on Piled Geo-wall in static load situation, high reproducibility of interaction between pile and Geo-wall body as well as one of pile response were confirmed.
- In the design on Piled Geo-wall in seismic situation, it was confirmed that safety design can be executed in case with design load situation as well as high reproducibility of the pile response in case with real load situation.
- In the design on Piled Geo-wall for rock-fall protection, conversion procedure of design static load from impact one was also proposed and its practicability was confirmed from good reproducibility of pile response by using the proposed procedure.

The following issues, however, have to be conducted to apply the proposed model to more wide condition of Piled Geo-wall.

- Application of the method to design on large scale (width, height) Piled Geo-wall.
- Application of steel-pipe pile and multiple rows' piles to Piled Geo-wall.
- Improvement of static load conversion procedure from impact one as being able to apply to diverse conditions of Piled Geo-wall.

Meanwhile, simple internal stability model has been also studied; it will be presented after more verification of validity.

REFERENCES

- [1] Hara T, Tsuji S, Yoshida M, Ito S and Sawada K, "Experimental development of new type reinforced soil wall," Int. J. of GEOMATE, June 2012, Vol. 2, No.2 (Sl. No.4), pp.213-218
- [2] Hara T, Tsuji S, Yashima A and Sawada K, "Independent reinforced soil structure with pile foundation," J. of SOILS AND FOUNDATIOS, Vol.50, No.5, 2010, pp. 565-571.
- [3] Japan Road Association (JRA), "Specifications of highway bridges (Part IV: Substructures), Mar. 2002
- [4] Japan Road Association (JRA), "Specifications of highway bridges (Part V: Seismic design), Mar. 2002
- [5] Clough RW and Penzien J, "Dynamics of structures," McGraw-Hill, 1975, p.80.
- [6] Newmark NM and Veletson AS, "Effect of inelastic behavior on the response of simple systems to earthquake motions," Proc. of 2nd WCEE, 1960, pp.895-912

Measurement of Strain Distribution Along Precast Driven Pile During Full Scale Pile Load Test.

Faisal Ali and Lee Sieng Kai
Department of Civil Engineering, National Defense University of Malaysia

ABSTRACT

One of the basic parameters required for forecasting pile deformation under loads is the characteristics and profile of the shaft load transfer from the pile to the surrounding soil. This parameter can be obtained by measuring the strain distribution along the pile during full-scale pile load test. For cast-in situ bored pile the strain measurement can be easily done by fixing the sensors to the reinforcement cage before pouring the concrete. For precast driven / jack-in piles, the application of instrumented full-scale static load tests is far more challenging than their bored pile counterparts due to significant difference in method of pile installation. Due to practical shortcoming of conventional instrumentation method instrumented full-scale static load tests are in fact rarely used in driven pile application in this region. For hollow precast spun concrete piles attempts have been made by geotechnical engineers to measure the strain distribution by installing either an instrumented reinforcement cage or instrumented pipe into the hollow core of spun piles followed by cement grout. However in this method, known as approximate method, the measured characteristics cannot be considered to represent the working piles because the presence of reinforcement/pipe and the grout would alter the stiffness of the test pile. In this paper a method to measure the strain distribution along the installed precast spun concrete pile during full-scale pile load test is described. The method utilizes the hollow core of the spun pile without changing the physical properties e.g. stiffness, of the pile. The main advantages of this method are: the measurement can be done at any location along the pile, the sensors can be retrieved and the measured characteristics are representative of those of the working piles.

Keywords: pile, ultimate capacity, instrumentation, spring-loaded transducer

1. INTRODUCTION

The high strength prestressed spun concrete piles, commonly driven with hydraulic impact hammers or preferably installed with jacked-in rigs when considering the stricter regulations with respect to noise and vibrations in more urban areas, often offer a competitive choice of foundation system for projects with medium and high loadings. They are widely used in foundations for schools, high-rise buildings, factories, ports, bridges and power plants in this region.

In early years, the main construction control for driven piles was mostly based on the measurement of set of each pile coupled with a selected small number of non-instrumented static load tests to verify the specified load-settlement requirements.

In recent years, with critical evolution in the understanding of the load transfer and bearing behaviour of piles mainly through analysis of instrumented full-scale load tests (particularly for bored cast-in-place piles), many engineers can now appreciate that the pile performance is not simply a matter of ultimate load value alone. According to Fleming [1][2] some of the basic parameters required for forecasting pile deformation under loads include (a) Ultimate shaft load and its characteristics of transformation to the ground; (b) Ultimate base load; (c) Stiffness of the soil below the pile

base; (d) Pile dimensions; and (e) Stiffness of the pile material.

This recent development in the understanding of the load transfer and bearing behaviour of piles in fact exerted a significant and positive influence on the evolution of codes of practice and design methods for foundations in some countries. For example, the revised Singapore Standard on Code of Practice for Foundations CP4: 2003[3], recommends that the static load test on preliminary test pile be instrumented to measure the transfer of load from the pile shaft and pile toe to the soil. The Code also recommends that for driven piles (similar to bored cast-in-place piles), the axial load capacity can be evaluated empirically from correlation with standard penetration tests SPT N-values (which are widely used in this region) using modified Meyerhof Equation, where the ultimate bearing capacity of a pile in compression is given by:

$$Q_u = K_s * N_s * A_s + K_b * (40 N_b) * A_b \quad (1)$$

where:

Q_u = ultimate bearing capacity of the pile, kN,

K_s = empirical design factor relating ultimate shaft load to SPT values, kN/ m² per SPT blow,

N_s = SPT value for the pile shaft, blows/300mm,

A_s = perimeter area of the shaft, m²,

K_b = empirical design factor relating ultimate end bearing load to SPT values, kN/m^2 per SPT blow,
 N_b = SPT value for the pile base, blows/300mm, and
 A_b = cross-sectional area of the pile base, m^2 .

For bored piles, instrumentation using sacrificial cast-in vibrating wire strain gauges and mechanical tell-tales which permit for monitoring of axial loads and movements at various levels down the pile shaft including the pile toe level had been practiced successfully within limits of accuracy posed by constraints inherent of the installation method, in this region for many decades, allowing insight evaluation of K_s and K_b factors, including well documented history of “The Design of Foundations for Suntec City, Singapore” [4][5]. Recent use of Global Strain Extensometers (Glostrex) Method for bored piles in this region [6][7] also provides an excellent alternative means for similar purpose, but with the capability of producing a more reliable performance and accurate results. For precast driven piles, the application of instrumented full-scale static load tests is far more challenging than their bored pile counterparts due to significant difference in method of pile installation. Due to practical shortcoming of conventional instrumentation method and the lack of innovation in this area, instrumented full-scale static load tests are in fact rarely used in driven pile application in this region. Therefore, the far lacking driven pile industry is long due for a better technology to revolutionize the methodology in the acquisition of design data in a more accurate and reliable way, to catch up with the evolution in the design methods.

2. CURRENT METHODS OF PILE INSTRUMENTATION

2.1 Conventional Instrumentation Method

A conventional instrumentation scheme for spun pile static load testing is shown in Fig. 1. The method involves incorporating high temperature-resistant strain gauges into the heat-cured production process of prestressed spun concrete piles.

This method is extremely unpopular and difficult to be routinely applied in project sites due to the following constraints:

- High cost of these temperature-resistant strain gauges;
- Tremendous difficulties involved in coordinating the installation of the strain gauges into pile segments;
- Long lead-time is normally required for instrumentation works, as the instruments have to be pre-assembled and installed onto the high strength prestressing bar cage prior to heat-cured ‘spin-cast’ production process of the piles; and
- Great uncertainty over the ability of the delicate instruments to withstand the stresses arising from pile production and driving processes.

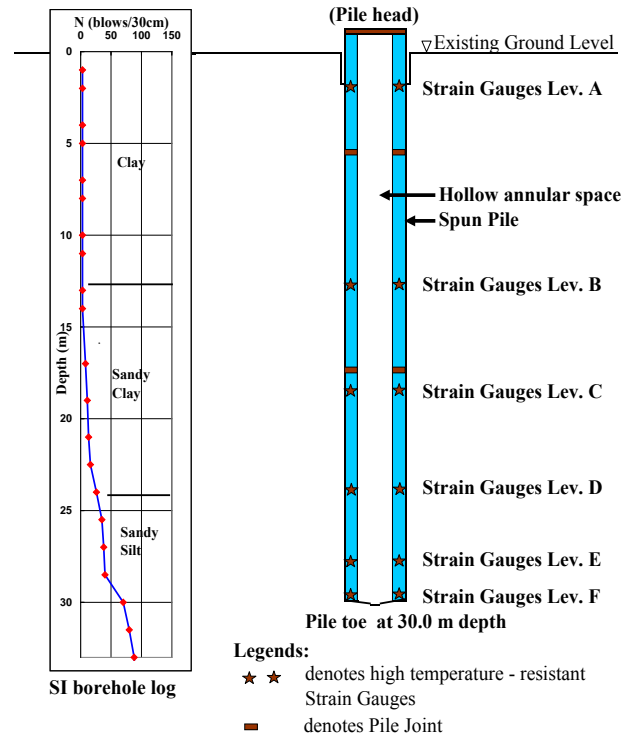


Fig. 1 - Diagrammatic illustration of conventional spun pile instrumentation scheme

2.2 Approximate Instrumentation Method

Due to the difficulties of using the conventional method, the engineering community for spun pile industry has been using an approximate instrumentation method for the past few decades, by installing either an instrumented reinforcement cage or an instrumented pipe, into the hollow core of spun piles followed by cement grout infilling (Fig. 2(a)).

As this approximate method is comparatively more “convenient” to be implemented than the conventional method, it was widely practiced in this region for the past few decades. Some contract specifications also ask for the inclusion of conventional sleeved rod extensometers (depending on the space available) to monitor the pile shortening reading during the static load tests. Either using an instrumented reinforcement cage or an instrumented pipe, with or without the added-in sleeved rod extensometers, the end product after the cement grout infilling is more towards a solid pile, as shown in Fig. 2(b).

Therefore the obvious shortcomings of this approximate method include:

- The infilling of cement grout substantially alters the structural properties of the piles, thus rendering them significantly different from the actual working spun piles, which are usually not grouted internally;
- The presence of the grout would change the overall stiffness of the pile and therefore the measured load distribution along the pile would be different under the applied loading.

- (c) Structural shortening measurement of the test piles are not representative of the actual working piles;
- (d) Structural integrity of the original pile cannot be reliably ascertained, particularly performance of pile joints, during the static load test as the stiffness of the pile has been altered; and
- (e) Significant time loss due to grout infilling and curing process, beside the environmental unfriendly nature of this method.

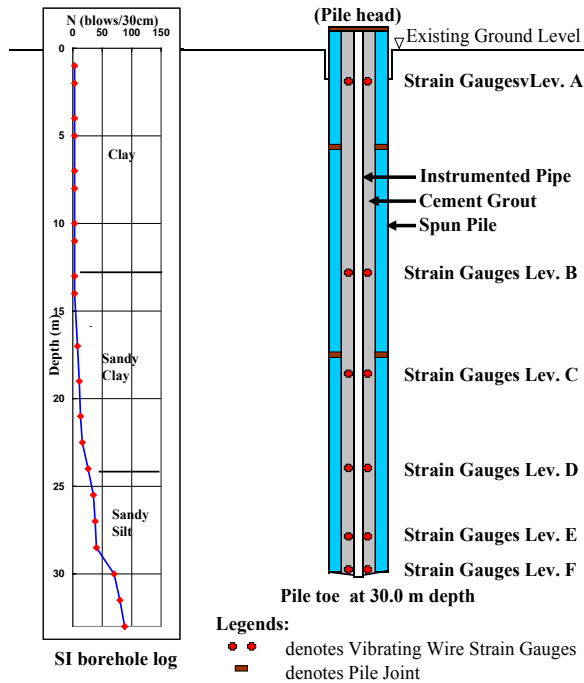


Fig. 2(a) - Diagrammatic illustration of approximate spun pile instrumentation method

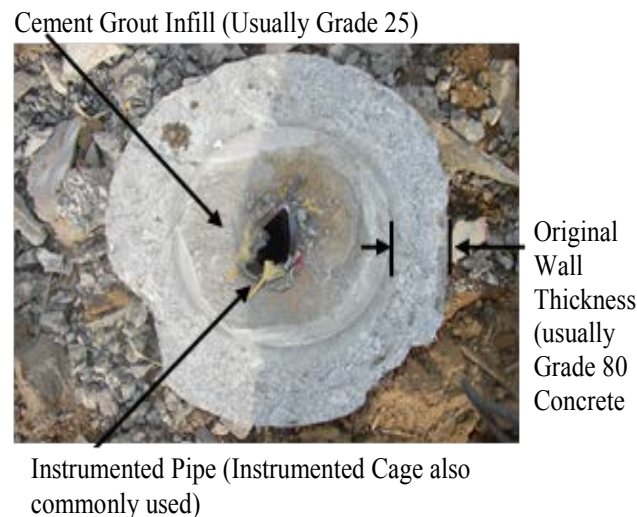


Fig. 2(b) - Section of instrumented spun pile after cement grout infilling in Approximate Method

3. RECENTLY DEVELOPED INSTRUMENTATION

To address the challenges and difficulties posed by the conventional and approximate methods, Global Strain Extensometer technology for spun piles had been developed, improved and field tested.

In order to meet the requirements for practical instrumentation application on spun piles, the desired characteristics for the retrievable pneumatically anchored extensometer system were identified as follow:

- (i) To utilize the hollow core of spun piles (or cylinder concrete piles) as an ideal recess means for instrumentation purpose, generally the system shall be designed for clamping to internal side wall of spun piles;
- (ii) In use, the system shall be able to be pneumatically actuated and control remotely above the ground and the series of anchors in access hole shall be able to be connected by means of interconnecting rods.
- (iii) The system shall be designed to be retrievable from the access hole, with allowance for eight retractable pistons per anchor.
- (iv) The anchor shall be able to be clamped to the side wall by at least 300 psi pressure.
- (v) Materials : Stainless steel or copper.
- (vi) The series of anchors in access hole shall have allowance for connecting to precision transducer sensor by means of fittings that grip the interconnecting rods.

The concept of using hollow core of spun piles (or cylinder concrete piles) as recess means for retrievable instrumentation approach was then reviewed and re-examined, leading to suggested ideal arrangement of retrievable instrumentation approach as shown in Figures 3(a),(b) , (c) & (d).

3.1 Description of the State-of-the-Art Global Strain Extensometer technology

The technology consists of a deformation monitoring system that uses advanced pneumatically-or hydraulically-anchored extensometers coupled with high-precision spring-loaded transducers, and a novel analytical technique to monitor loads and displacements down the shaft and at the toe of foundation piles. This method is particularly useful for monitoring pile performance and optimizing pile foundation design.

To appreciate the innovation contained in the technology, the basic deformation measurement in the pile by strain gauges and tell-tale extensometers are reviewed. Normally, strain gauges (typically short gauge length) are used for strain measurement at a particular level or spot, while tell-tale extensometers (typically long sleeved rod length) are used purely for shortening measurement over an interval (over a length between two levels). From a 'strain measurement' point of view, the strain gauge gives strain measurement over a very short gauge length while the tell-tale extensometer gives strain measurement over a very long gauge length! Tell-tale extensometer that measure strain over a very long gauge length may be viewed as a very large strain gauge or

simply called Global Strain Extensometer. With recent advancement in the manufacturing of high-precision spring-loaded vibrating-wire sensors, it is now possible to measure strain deformation over the entire length of piles in segments with ease during static load testing.

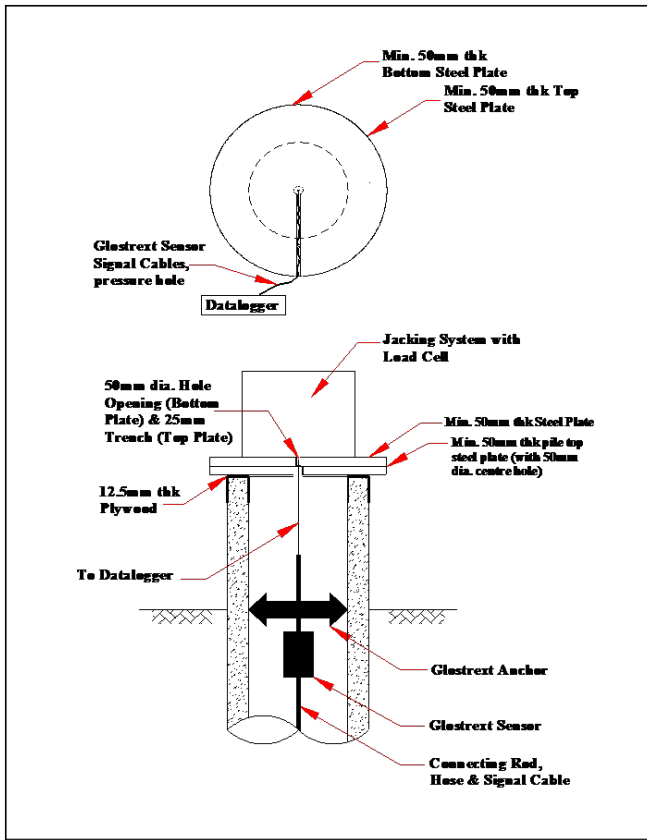


Fig.3(a) Arrangement of retrievable instrumentation approach for typical spun pile instrumentation application.



Fig. 3(c) Completed improved prototype for application



Fig. 3 (d) Actual Global Strain Extensometer system for spun pile application

Fig. 3(b) Design for retrievable pneumatic extensometer anchors and transducer system

Fig. 4 shows a schematic spun pile instrumentation diagram using Global Strain Extensometer technology. This system is equivalent to the conventional method of using 24 no. strain gauges and 6 no. sleeved rod extensometers, which might not be possible to be installed satisfactorily due to congestion in the spun piles.

For the analysis of test data for spun piles using Global Strain Extensometer technology, the load distribution can be computed from the measured changes in global strain gauge readings and pile properties (cross-section area of spun pile and concrete modulus). Load transferred (P_{ave}) at mid-point of each anchored interval can be calculated as:

$$P_{ave} = \epsilon(E_c A_c) \quad (2)$$

where,

ϵ = average change in global strain gauge readings;

A_c = cross-sectional area of spun pile section;

E_c = concrete secant modulus in pile section.

With the instrumentation set-up as described in Fig. 4, the

state-of-the-art Global Strain Extensometers system is able to measure shortening and strains over an entire section of the test pile during each loading steps of a typical static pile load test, thus it integrates the strain over a larger and more representative sample.

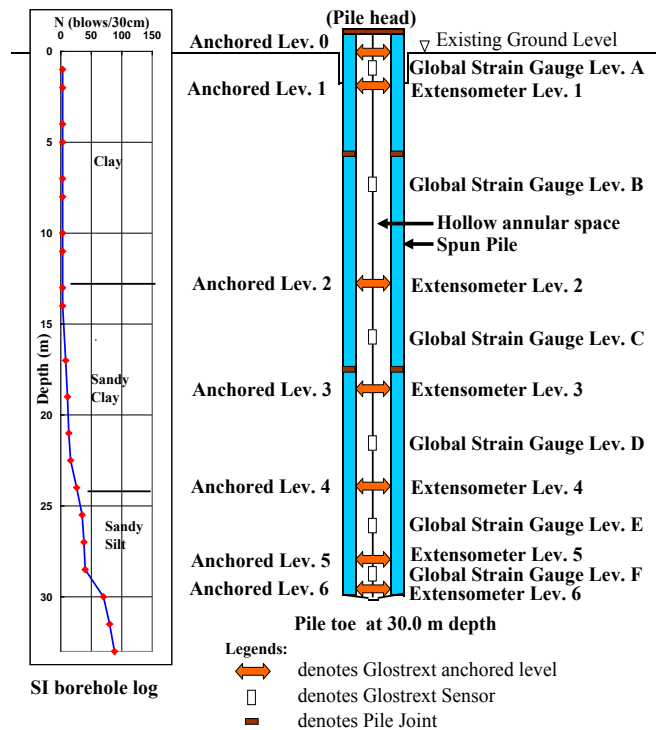


Fig. 4 - Schematic diagram of typical instrumented spun pile using Global Strain Extensometer technology

3.2 Verification of the Global Strain Extensometer System

For the purpose of verification of the Global Strain Extensometer system, a special and detailed laboratory testing programme consisting of a series of full-scale tests on spun pile sections of various sizes has been implemented. The tests were carried out and completed in the laboratory, incorporating Global Strain Extensometer instrumentation technique alongside with and against well proven vibrating wire strain gauges systems in the test sections.

The instrumented spun pile sections were tested by the normal Maintained Load (ML) Method, using hydraulic jack and high strength stress bar system. In the typical set-up used, the test loads were applied using 1 no. hydraulic jack (1,000 tonnes capacity) acting against the main beam connected by high strength stress bar system. The jack was operated by an electric pump. The applied loads were indicated by calibrated Vibrating Wire Load Cell. To obtain good quality data, all instruments readings were logged automatic using Micro-10x datalogger, at 1 to 2 minutes interval for close monitoring during loading and unloading steps. The detailed test set-up, pile instrumentation comparison schemes adopted (using Global Strain Extensometer technique and strain gauges

systems) and test data acquisition systems for verification load testing programmes are as shown in Figure 5.

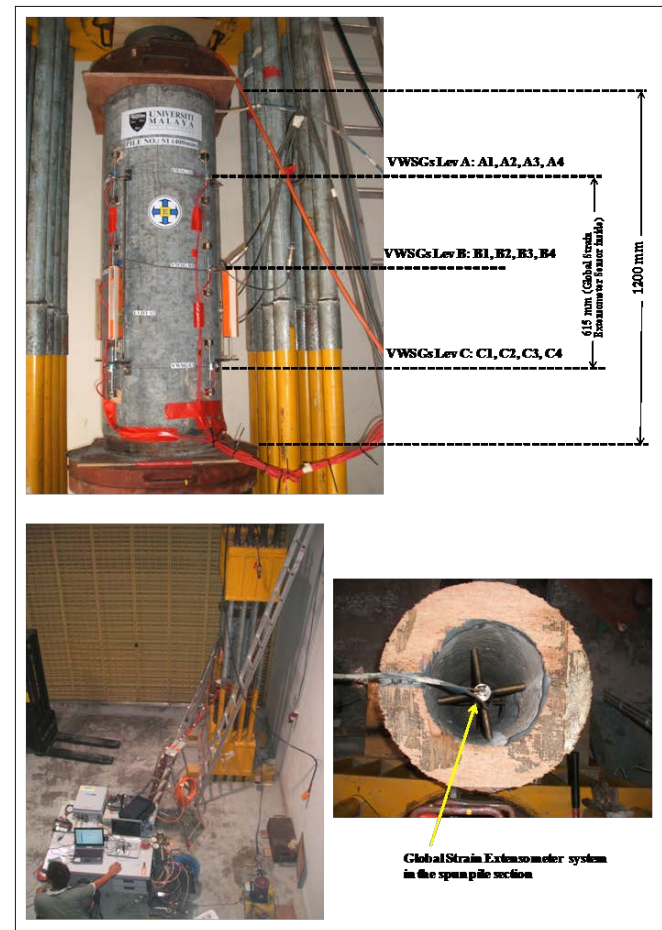


Fig. 5 Instrumentation Details and Test Setup.

For a typical spun pile section, the test results for Pile Top Loads Versus Change in Strain measured by both Global Strain Extensometer Technology and Average of 12 no. Vibrating Wire Strain Gauges at Levels A, B and C are shown in Figure 6 and , plot of Pile Top Load & Change in Strain Versus Time for both Global Strain Extensometer Technology and Average of 12 no. Vibrating Wire Strain Gauges at Levels A, B and C are shown in Figure 7.

Based on the results obtained from the laboratory tests it can be concluded that the axial strains measured by the two independent systems (conventional vibrating wire strain gauges and Global Strain Extensometers technique) show very similar characteristics and therefore in good agreement. The Global Strain Extensometers measure strains over an entire segment of the pile samples, thus it integrates the strains over a larger and more representative sample than the conventional strain gauges.

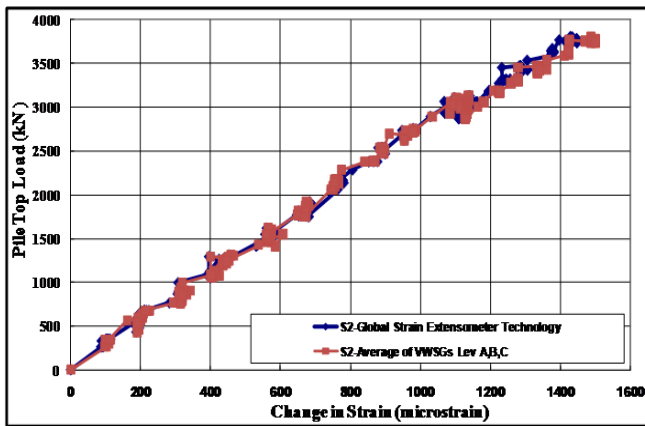


Fig. 6. Plot of Pile Top Loads (kN) Vs Change in Strain (μ s)

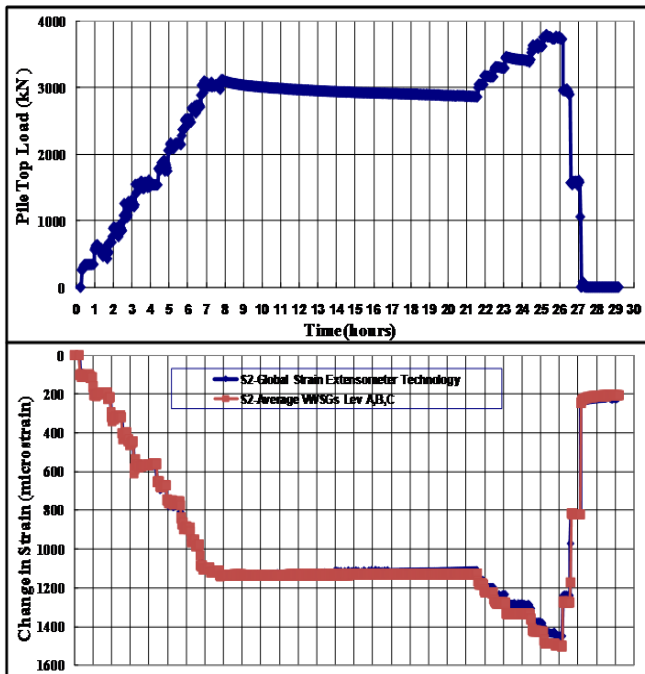


Fig. 7. Plot of Pile Top Loads (kN) & Change in Strain (μ s) Vs Time (hours) for Spun Pile Section

4.0 FIELD TESTING ON INSTRUMENTED SPUN PILES.

The unique Global Strain Extensometer technology developed has been used to fully instrument 10 nos. of static axial compression load tests on driven prestressed spun concrete pile for a project site in the state of Johor, Malaysia. The structural properties and installation details (including drop height and final set record taken) for each test pile are given in Table 1 below.[8]

The high strength prestressed spun concrete piles are driven with hydraulic impact hammers at the site. The test piles STP3, STP4R and STP7 were installed with a 9-ton BSP hydraulic impact hammer, STP5, STP6, STP8R2, STP10R and STP1 were also installed with a 9-ton BSP hydraulic impact hammer, while test piles STP2 and STP9R2 were installed with a 16-ton Twinwood hydraulic impact hammer,

over a period of approximately two months.

A typical pile instrumentation schemes adopted (using Global Strain Extensometer technique) for load testing programme, along with nearby borehole SPT N-values plot and subsurface exploration results from soil investigation are graphically represented in Figure 8.

Table 1. Test Piles Structural Properties and Installation Details for Driven Piles

Test Pile No.	Nominal Diameter (mm)	Wall Thickness (mm)	9mm Ø Pre-stressing Bar Reinforcement	Driven Pile Length (m)	Hydraulic Hammer Weight (tons)	Drop Height (mm)	Final Set (mm)
STP3	450	80	8 no.	47.25	9	400	3
STP4R	450	80	8 no.	38.5	9	500	10
STP7	450	80	8 no.	36.75	9	700	44
STP5	600	100	14 no.	38.0	9	900	20
STP6	600	100	14 no.	38.0	9	800	14
STP8R2	600	100	14 no.	39.75	9	800	20
STP10R	600	100	14 no.	37.75	9	600	10
STP1	700	110	20 no.	47.9	9	800	4
STP2	700	110	20 no.	36.4	16	800	36
STP9R2	700	110	20 no.	47.0	16	700	12

Instrumentation levels for Instrumented Test Spun Pile STP6 (600 mm Ø) (with 100mm wall thickness)
Driven Pile length = 38.0m from Platform Level of RL 5.78 mCD

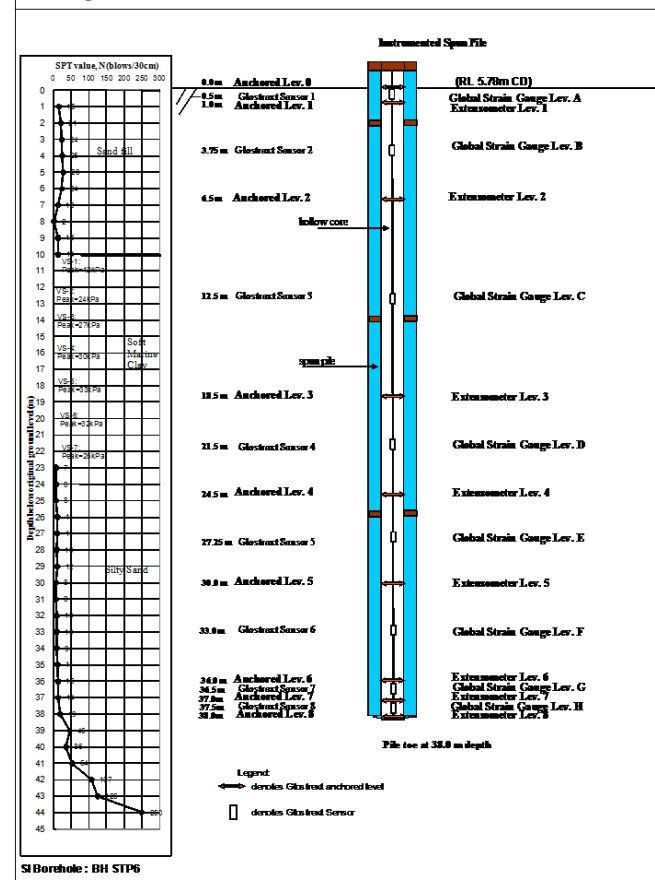


Fig. 8. Pile instrumentation schemes adopted (using Global Strain Extensometer technique)

Test results acquired from Global Strain Extensometer technology on all tested piles appeared to be consistent, and the typical test results are reproduced here to highlight the capability of this technique (See Figures 9(a) to (f)). From highly consistent measurements of the structural elongation of the entire length of piles using Global Strain Extensometers the pile toe displacement behaviour can be reliably established by subtracting the structural elongation from the pile head displacement .

Similarly, Global Strain Extensometer technology also enable pile displacement under load at any depth along the shaft to be accurately derived, based on its ability to make segmental or global shortening/elongation measurement along the whole pile independent of any external reference and free of common errors associated with the conventional sleeved rod extensometers. This enables the movement and strains at various levels down the pile shaft to be accurately determined, thus permitting a significantly improved means for the acquisition of load transfer data.

The technology not only enables ease of the assessment of modulus-strain relationship and load transfer study it also significantly improves the reliability of the measurement of movement of pile between deeper soil strata, as illustrated in the characteristic curves of mobilized unit shaft friction .

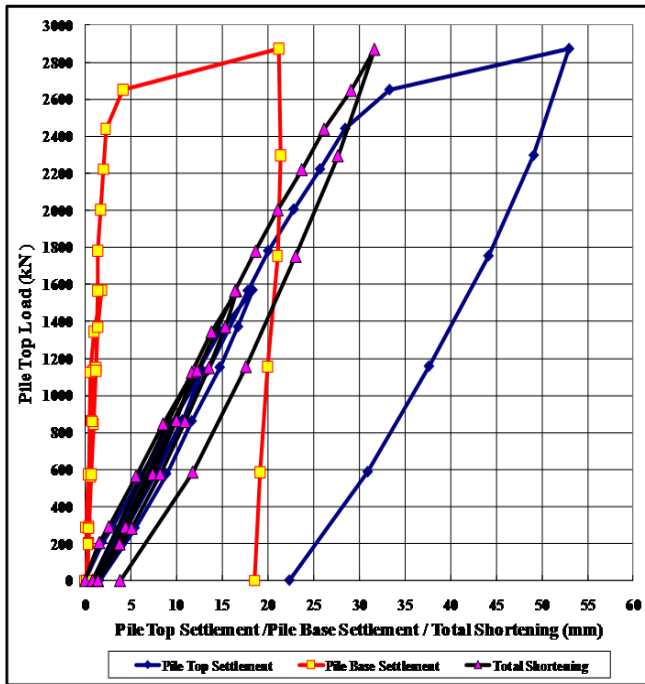


Fig. 9(a). Plot of pile top load versus pile top settlement, pile base settlement and total shortening

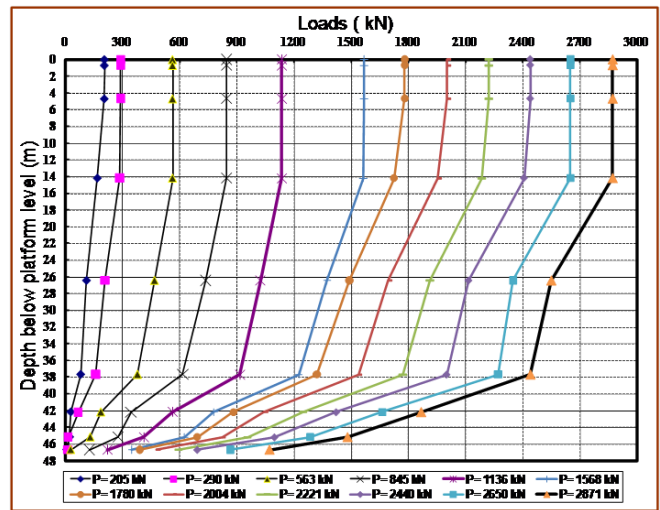


Fig. 9(b). Load Distribution Curve

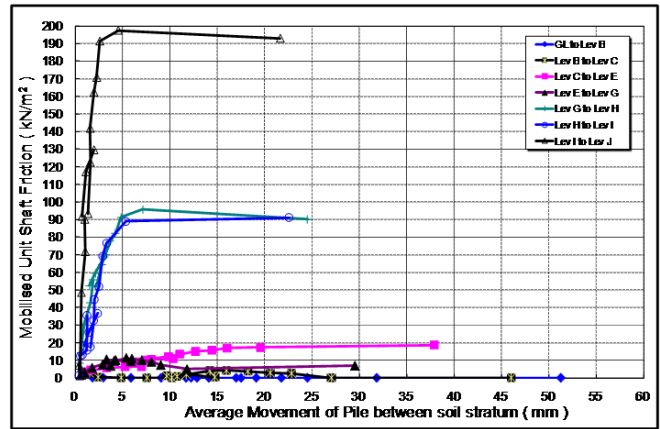


Fig. 9(c). Load Transfer Characteristics during Loading stages

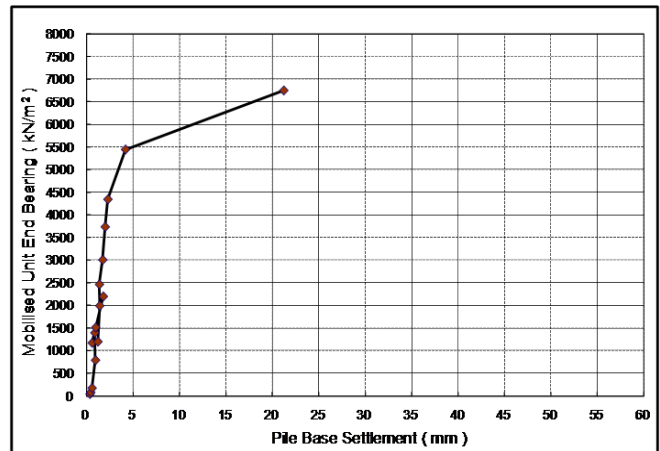


Fig. 9(d). Plot of Mobilised Unit End Bearing versus Pile Base Settlement

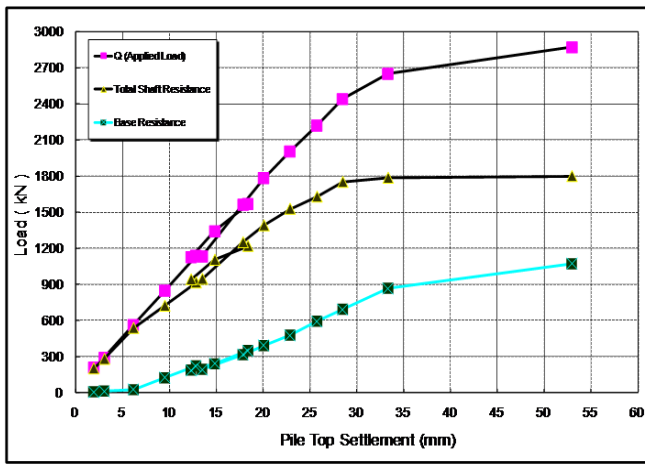


Fig. 9(e). Plot of Applied Pile Top Load, Total Shaft Resistance and Base Resistance versus Pile Top Settlement

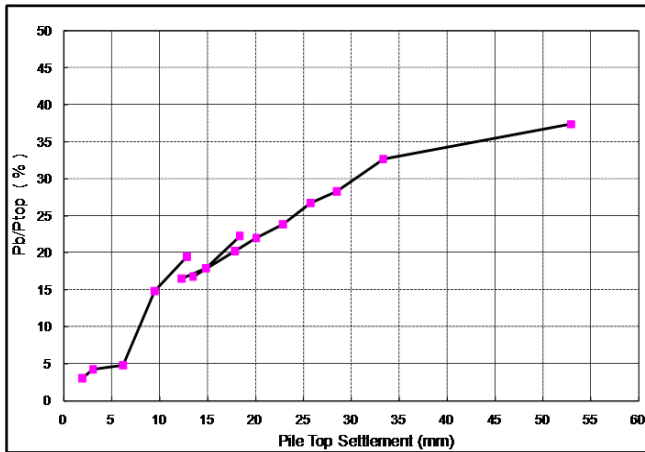


Fig. 9(f). Plot of Pile Base Load over Applied Pile Top Load versus Pile Top Settlement

4.1 Correlation between SPT N-Value and Pile Design Parameters for Driven Spun Piles Test Results

With critical evolution in the understanding of the load transfer and bearing behaviour of piles in recent years mainly through analysis of instrumented full-scale load tests, it is common that for driven piles, the axial load capacity can be evaluated empirically from correlation with standard penetration tests SPT N-values (which are widely used in this region) using modified Meyerhof Equation, where the ultimate bearing capacity of a pile in compression is given by equation (1)

As the instrumented full-scale static load tests for driven piles are rarely being carried out in this region due to lack of innovation in this area, there is strong need for the evaluation of K_s and K_b factors for driven piles to be carried out more routinely for the improvement of empirical method of designing piles based on the results of full-scale instrumented load tests, to catch up with the evolution in the design

methods.

For driven spun piles test results analyzed in this study, the results of the load transfer parameters for silty sand layer are summarized in the corresponding correlation of SPT-N values versus Maximum Mobilised Unit Shaft Resistance for driven spun piles under this study as shown in Figure 10. The results of the end bearing parameters for driven spun piles are summarized in the plot of SPT-N values versus Maximum Mobilised Unit End Bearing Resistance under this study as shown in Figure 11

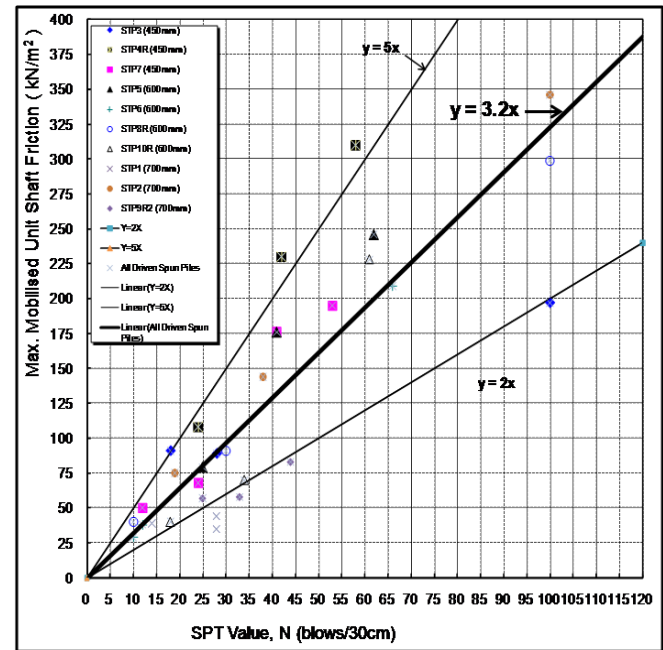


Fig. 10 Correlation of SPT value versus maximum mobilized unit shaft friction in silty sand layer for driven spun piles.

Fig. 11 Correlation of SPT value versus max. mobilized unit end bearing in silty sand layer for driven spun piles.

The comments on correlation for driven spun piles test results are as follow:

- a) The silty sand layer for pile founding depth is generally overlain by 7m to 10m hydraulic sand fill followed by compressible weak marine clay layer from approximately 10m to 26m depth, and the silty sand layer that underlies the sand fill and marine clay extends to depths beyond the toe of all driven spun piles;
- b) The SPT N-value in this silty sand layer generally varies between 10 and 100. The maximum mobilized unit shaft friction from the test results is generally between 29 kpa to 346 kpa;
- c) Correlation results for driven spun piles yield shaft resistance factor, $K_s = 3.2$ in the shaft resistance empirical relationship of $f_s = K_s \cdot N_s$, where f_s is the ultimate unit shaft resistance, K_s is the empirical design factor relating ultimate shaft load to SPT N-value, kN/m² per SPT blow and N_s is the average SPT value for the pile shaft, blows/300mm.
- d) Correlation results for driven spun piles yield end bearing resistance factor, $K_b = 1.3$ in the end bearing resistance empirical relationship of $q_b = K_b \cdot (40N_b)$, where q_b is the ultimate unit end bearing resistance, K_b is the empirical design factor relating ultimate end bearing load to SPT N-value, kN/m² per SPT blow, N_b is the SPT value for the pile base, blows/300mm.
- e) It is worth to note that Singapore Standard (SS) CP4: 2003 code of practice for foundations' recommendation for K_s is between 2 to 5 for driven piles shaft resistance factor, subject to a limit of $f_s = 200$ kpa, and K_b is between 6 to 9 for driven piles end bearing resistance factor, subject to a limit of $q_b = 18,000$ kpa.
- f) Normally the critical shaft displacement is relatively small to fully mobilize the shaft resistance compared to the big movement that is needed to fully mobilize the end bearing. Therefore $K_s = 3.2$ from this study is able to serve as a useful initial design guide for shaft resistance factor in silty sand materials, while $K_b = 1.3$ represent a conservative approach for end bearing resistance factor in silty sand materials, as the majority of the piles are not tested to full failure.

4.2 Advantages of using the Global Strain Extensometer Technology

Due to the significant difference in the methodology evolution, from conventional sacrificial cast-in method to a new retrievable post-install approach, the Global Strain Extensometer technology has been proven via full-scale load tests to be a reliable and powerful pile load testing and data

interpretation tool, capable of leading the spun pile instrumentation industry to a revolutionary improvement not seen in the past.

Some of the obvious benefits of using Global Strain Extensometer technology are as follow:

- (i) The technology enables installation of instrumentation after pile-driving and thus virtually eliminates the risk of instrument damage during pile production and installation;
- (ii) The post-install nature of the method empowers engineers to select instrumentation levels along the as-built depth of foundation piles using pile driving/installation records and site investigation data as guides;
- (iii) The technology reliably measures segmental shortening/elongation and strain over an entire section of the test pile during each loading step of a typical static load test. Unlike the conventional strain gauges that make just localized strain measurements, the new technology integrates individual measurements over a larger and more representative sample;
- (iv) Significant cost and time saving, as the additional cage and cement grout infilling are not required;
- (v) The technology is extremely environmental friendly, as the sensors are retrievable, and no messing around with cement grouts; and

5. CONCLUSIONS.

The successful driven field testing programmes using the unique Global Strain Extensometer pile instrumentation technique have clearly demonstrated that the novel Global Strain Extensometer instrumentation technique provides high quality, reliable and consistent results. Three distinct features of this method would especially appeal to engineers:

- The method enables installation of instrumentation after pile-driving and thus virtually eliminates the risk of instrument damage during pile production and installation.
- The post-install nature of the method enables engineers to select instrumentation levels along the as-built depth of driven piles using pile driving records and site investigation data as guides.
- The method reliably measures segmental shortening and strains over an entire section of the test pile during each loading step of a typical static load test and unlike conventional strain gauges that make just localized strain measurements, integrates individual measurements over a larger and more representative sample, thus making the test results more informative.

Pile instrumentation using the Global Strain Extensometer technique developed enables acquisition of design data in a more accurate and reliable way for shaft friction and end bearing parameters to be obtained for driven piles and subsequently help to optimize pile design. It also helps to

derive correlation of shaft friction and end bearing parameters with the standard penetration tests commonly used locally.

5 REFERENCES.

- [1] Fleming, K., 1992, "A New Method For Single Pile Settlement Prediction and Analysis," *Geotechnique* 42, No.3, 411-425.
- [2] Fleming, K., 1996, Talking Point: Ken Fleming Assesses the Present Major Issues in the Pile Testing Industry, Page 3. *Ground Engineering*, October 1996.
- [3] Singapore Standard on Code of Practice for Foundations, CP4:2003
- [4] Chan, S.F. & Lee, P.C.S., 1990, "The Design of Foundations for Suntec City, Singapore," *Proceedings of Conference on Deep Foundation Practice*, Singapore.
- [5] Chan, S.F., 2004, "Special Lecture, Design and Construction of Foundations for Suntec City, Singapore," *Proceedings of the Malaysian Geotechnical Conference*, Malaysia, pp 21-43.
- [6] Aziz, H.M. A. & Lee, S.K., 2005, Innovation in Instrumented Test Piles in Malaysia: Application of Global Strain Extensometer (GLOSTREXT) Method for Instrumented Bored Piles in Malaysia, *Bulletin of the Institution of Engineers, Malaysia*, October 2005 issue. pp 10-19.
- [7] Aziz, H.M. A. & Lee, S.K., 2006, "Application of Global Strain Extensometer (GLOSTREXT) Method for Instrumented Bored Piles in Malaysia," *Proceedings of 10th International Conference on Piling and Deep Foundations*, Amsterdam, pp 669-767
- [8] Lee, S.K., 2011, "Development and Application of a New Instrumentation Technique for Spun Concrete Piles" Ph.D Thesis, University of Malaya.

Unique Grouting Material Composed of Calcium Phosphate Compounds

S. Kawasaki¹ and M. Akiyama²

¹ Hokkaido University, Japan

² Geoscience Research Laboratory Co., Ltd., Japan

ABSTRACT

To employ calcium phosphate compounds (CPCs) in ground improvement measures such as the reinforcement of soil and rock, we examined suitable conditions for CPC precipitation and performed unconfined compressive strength (UCS) tests of sand test pieces cemented by CPC. Two types of phosphate stock solution and two types of calcium stock solution were used to prepare the reaction mixtures and CPC precipitation was confirmed in all reaction mixtures. The volume of CPC precipitation in the mixture increased as the pH rose from strongly acidic to around neutral. The UCS of sand test pieces cemented by 1.5 M diammonium phosphate and 0.75 M calcium acetate tended to increase with time, reaching a maximum of 87.6 kPa. The results indicate the practical feasibility of using unique and new CPC grouts as chemical grouts because of their self-setting property and as biogrouts because of the pH dependence of precipitation.

Keywords: calcium phosphate compound, grout material, unconfined compressive strength, self-setting property

1. INTRODUCTION

Novel grout materials have been developed to reinforce the ground and/or to control ground permeability with bacterially produced cement material [1]–[6]. These grout materials are called biogrouts. Three mechanisms of mineral formation have mainly been considered for biogrouts. The first mechanism is the precipitation of calcium carbonate by in situ microorganisms and/or added yeasts [2]. In this process, calcium carbonate is precipitated by the binding of carbonate ions released from microorganisms and calcium ions from the grout, which includes calcium and glucose. The second mechanism was reported by Whiffin et al. [3], who used urea instead of glucose and ureolytic *Sporosarcina pasteurii* instead of yeast and other in situ microorganisms; the decomposition of urea by *S. pasteurii* produced carbon dioxide, which supplied the carbonate ions. In both cases, additional pH buffers or ammonium ions play the role of pH adjusters for effective precipitation. The third mechanism is based on the pH dependence of the extension speed of the siloxane bond; this mechanism was reported by Terajima et al. [5], who utilized the carbon dioxide produced by yeast to neutralize the alkaline active silica solution because the siloxane bond rapidly extends and gels in the middle range of pH.

Soil and rock vary infinitely in their physical and chemical properties. This fact orients the development of biogrout along two main directions: one, to develop a highly general-purpose biogrout, and the other, to develop a specialized biogrout for a specific type of soil or rock. To

apply biogrout to various soils and rocks, it is very important to increase the number of mechanisms available for the precipitation of cement materials.

In engineering as well as in science, it is essential to learn from nature. In nature, various minerals, such as calcium carbonate, calcium sulfate, calcium phosphate, calcium oxalate, silicate, and iron oxide are precipitated by living organisms. These biominerals are promising as engineering materials because they have considerable strength and low environmental impact. In this study, we carried out a fundamental examination on novel grout materials composed of calcium phosphate compounds (CPCs) (Fig. 1). CPCs exist as phosphate rocks (e.g., fluorapatite) in the natural environment and also as an important inorganic substance (e.g., hydroxyapatite, HA) in living organisms [7]. As shown in Table 1, there are 11 known CPCs with various calcium-to-phosphate (Ca/P) molar ratios in the ternary system $\text{Ca}(\text{OH})_2\text{--H}_3\text{PO}_4\text{--H}_2\text{O}$. Research and development of materials composed of CPCs are currently in progress, especially in the fields of medicine and dentistry.

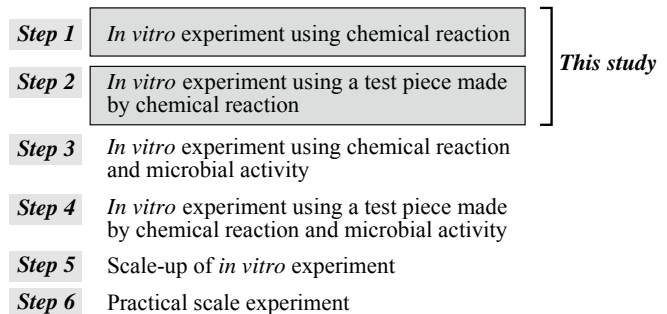


Fig. 1 Flowchart of the study. The steps carried out in this study are highlighted in gray.

Table 1 Properties of biologically relevant calcium orthophosphates. The table is adapted from Dorozhkin and Epple [7].

Ca/P ratio	Compound	Abbreviation	Formula
0.5	Monocalcium phosphate monohydrate	MCPM (MCP)	$\text{Ca}(\text{H}_2\text{PO}_4)_2 \cdot \text{H}_2\text{O}$
0.5	Monocalcium phosphate anhydrite	MCPA (MCP)	$\text{Ca}(\text{H}_2\text{PO}_4)_2$
1.0	Dicalcium phosphate dihydrate	DCPD (DCP)	$\text{CaHPO}_4 \cdot 2\text{H}_2\text{O}$
1.0	Dicalcium phosphate anhydrite	DCPA (DCP)	CaHPO_4
1.33	Octacalcium phosphate	OCP	$\text{Ca}_8(\text{HPO}_4)_2(\text{PO}_4)_4 \cdot 5\text{H}_2\text{O}$
1.5	α -tricalcium phosphate	α -TCP	$\alpha\text{-Ca}_3(\text{PO}_4)_2$
1.5	β -tricalcium phosphate	β -TCP	$\beta\text{-Ca}_3(\text{PO}_4)_2$
1.2-2.2	Amorphous calcium phosphate	ACP	$\text{Ca}_x(\text{PO}_4)_y \cdot n\text{H}_2\text{O}$
1.5-1.67	Calcium-deficient hydroxyapatite	CDHA	$\text{Ca}_{10-x}(\text{HPO}_4)_x(\text{PO}_4)_{6-x}(\text{OH})_{2-x} \quad (0 < x < 1)$
1.67	Hydroxyapatite	HA	$\text{Ca}_{10}(\text{PO}_4)_6(\text{OH})_2$
2.0	Tetracalcium phosphate	TTCP	$\text{Ca}_4(\text{PO}_4)_2\text{O}$

Medical CPC paste, however, is extremely expensive and has high viscosity, which makes it unfeasible for engineering applications. Therefore, we considered CPC use from an engineering viewpoint and aimed to develop a grout material that could be precipitated under normal temperature and pressure through microbial activity by using materials that can be easily handled. To the best of our knowledge, no existing grout material makes use of the self-setting mechanism of CPC alone or employs microbial pH adjustment activity for CPC precipitation. CPCs have unique physical and chemical properties. Their numerous advantages as a grout material include the following:

- (1) Gel-like or amorphous CPCs change into HA over time (Fig. 2 [8]). Therefore, CPC hardens after injection into soil and rock because of the self-setting mechanism.
- (2) The solubility of CPCs depends on the pH of the surrounding environment (Figs. 3 [8] and 4). This makes it possible to utilize the mechanisms of pH adjustment by microorganisms, which are used in known biogROUT methods to control CPC precipitation.
- (3) Phosphate and calcium stock solutions can be made from fertilizers, and calcium and phosphate can also be extracted from the bones of livestock and the shells of aquatic animals, respectively.
- (4) CPCs that precipitate after grout injection are non-toxic.
- (5) Unlike concrete, re-excavated muck that consists of soil, rock, and CPC grout is recyclable as agricultural fertilizer.

We begin by focusing on the development of a novel grout material intended for soil materials (sand, in this study). We then extend our approach to control the strength and permeability of rock materials. This work can contribute to

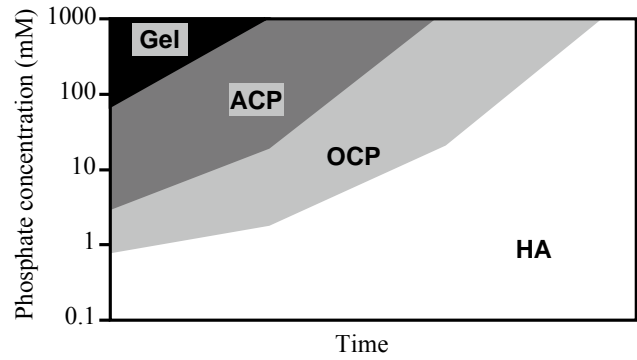


Fig. 2 Formation, stability, and hydrolysis of calcium phosphates as a function of phosphate concentration ($\log(\text{P})$) in solutions of amorphous calcium phosphate (ACP) at neutral pH. OCP, octacalcium phosphate; HA, hydroxyapatite. The figure is adapted from Tung [8].

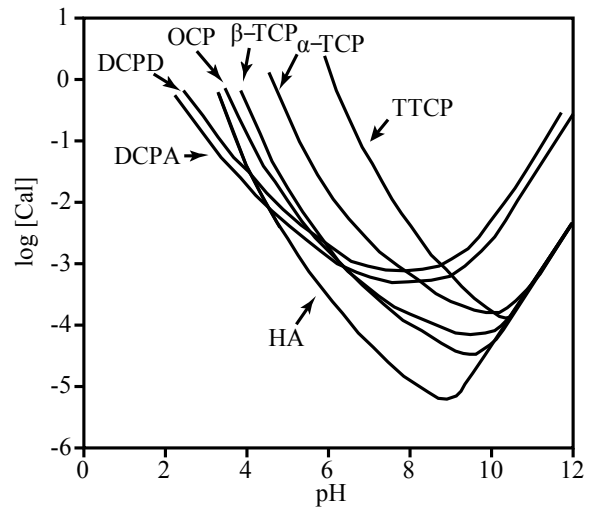


Fig. 3 Solubility phase diagrams for the ternary system, $\text{Ca}(\text{OH})_2\text{-H}_3\text{PO}_4\text{-H}_2\text{O}$, at 25 °C, showing the solubility isotherms of CaHPO_4 (DCPA), $\text{CaHPO}_4 \cdot 2\text{H}_2\text{O}$ (DCPD), $\text{Ca}_8\text{H}_2(\text{PO}_4)_6 \cdot 5\text{H}_2\text{O}$ (OCP), $\alpha\text{-Ca}_3(\text{PO}_4)_2$ (α -TCP), $\beta\text{-Ca}_3(\text{PO}_4)_2$ (β -TCP), $\text{Ca}_4(\text{PO}_4)_2\text{O}$ (TTCP), and $\text{Ca}_{10}(\text{PO}_4)_6 \cdot (\text{OH})_2$ (HA). The figure is adapted from Tung [8].

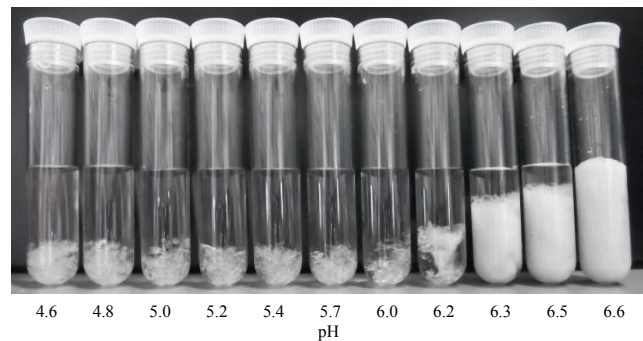


Fig. 4 Effect of pH on the precipitation volume of CPC. countermeasures for liquefaction in alluvial plains and reclaimed land, and to measures for preventing the failure of natural and/or artificial slopes.

In this study, the most suitable conditions for CPC precipitation were determined in an in vitro examination by using phosphate and calcium stock solutions (Step 1 in Fig. 1). Subsequently, test pieces composed of sand cemented by CPC were subjected to unconfined compressive strength (UCS) tests and observed by scanning electron microscopy (SEM) (Step 2 in Fig. 1). Our aim was to evaluate the feasibility of using the unique and novel grout as both a chemical and a microbiological grout by exploiting the self-setting property of CPC and the microbial pH adjustment activity in CPC precipitation, respectively.

2. MATERIALS AND METHODS

2.1 CPC Precipitation Test

Reagents with relatively high solubility were chosen for convenient handling in a practical application. Monoammonium phosphate (MAP, pH 4.2) and diammonium phosphate (DAP, pH 8.0) were used as the components of the phosphate stock solution—a type of agricultural fertilizer that can be prepared easily. For the calcium stock solution, calcium nitrate (CN) or calcium acetate (CA) was used. All reagents were of special grade.

The reaction mixtures were prepared by mixing the ammonium phosphate (AP) solution and one of the two calcium solutions at a 1:1 volume ratio (2 mL each); consequently, the final concentrations of the AP and calcium stock solutions were half the initial concentrations. The initial concentrations of the AP and CN solutions were 0.2, 1.0, 2.0, and 3.0 M (the final concentrations were 0.1, 0.5, 1.0, and 1.5 M). A 3.0 M MAP solution could not be prepared because the water solubility of MAP at 20 °C is 27.2 g/100 g. The solubility of calcium acetate is 25.8 g/100 g water (20 °C). Because we could not prepare a 2 M solution of calcium acetate, the concentrations of the CA stock solution were set at 0.2, 1.0, and 1.5 M (the final concentrations were 0.1, 0.5, and 0.75 M). The in vitro precipitation tests were conducted for the entire set of combinations of AP stock solutions and CN or CA stock solutions.

Subsequently, the reaction mixtures were left standing at 20 °C for 3 months to monitor their precipitation status; a period of 3 months was chosen because changes in this status can appear with time depending on the properties of the CPC. To observe the precipitation status, the proportion of the CPC precipitation volume to the reaction mixture volume (PPV) was measured during this time (the maximum PPV was 1.0). Simultaneously, the pH of the reaction mixture was measured by using a pH Spear, a device designed for measuring the pH of solids and semisolids, including gels.

2.2 UCS Test of Sand Test Pieces Cemented by CPC

Reaction mixtures (sets of each stock solution) for the UCS test (Fig. 5) were selected according to three criteria, based on

the results of the in vitro CPC precipitation test.

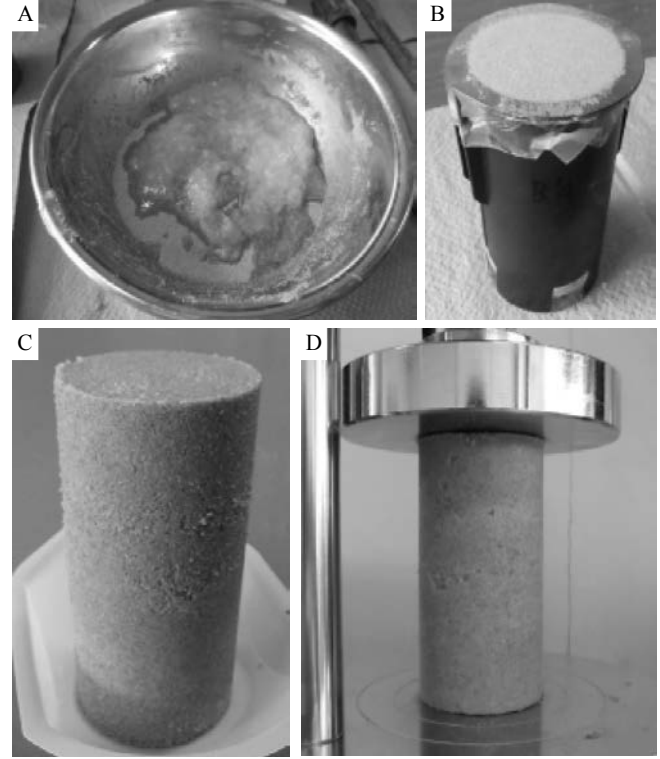


Fig. 5 Toyoura sand test pieces cemented by CPC. A, mixing stock solutions and Toyoura sand; B, a test piece covered with Parafilm; C, a self-standing test piece cemented by CPC; D, UCS test.

Table 2 Physical characteristics of Toyoura sand.

Soil particle density, ρ_s (g/cm ³)	2.64
Minimum density, ρ_{dmin} (g/cm ³)	1.335±0.005
Maximum density, ρ_{dmax} (g/cm ³)	1.645±0.010
Maximum void ratio, e_{max}	0.973
Minimum void ratio, e_{min}	0.609
Mean grain size, D_{50} (mm)	0.17
10% diameter on grain size diagram, D_{10} (mm)	0.11
Fine fraction content, F_c (%)	0

Criterion 1: Set of stock solutions with the minimum concentration among reaction mixtures that showed a PPV of 1.0 (DAP/CN = 1.0 M:0.5 M, DAP/CA = 1.0 M:0.5 M).

Criterion 2: Set of stock solutions with the maximum PPV among those with the maximum concentration (DAP/CN = 1.5 M:1.5 M, DAP/CA = 1.5 M:0.75 M).

Criterion 3: Set of stock solutions with a concentration that is closest to average of the concentrations discussed in criteria 1 and 2 (DAP/CN = 1.0 M:1.0 M, DAP/CA = 1.0 M:0.75 M).

Table 2 lists the physical properties of the Toyoura sand used as a soil material in this study. To avoid the destruction of the test pieces during their removal from the mold, the inner wall of the mold container ($\phi = 5$ cm, $h = 10$ cm) was covered with a 0.01-cm-thick overhead projector (OHP) sheet. The volumes of the test pieces made by the mold container

and maximum volume of the reaction mixture injected into the voids between the Toyoura sand particles were 194.59 cm³ and 73.3 mL, respectively. Considering these values, 36.7 mL each of the DAP and calcium stock solutions were mixed, making their final concentrations half of their initial concentrations. Immediately after the reaction mixture was prepared, it was uniformly mixed with weighted Toyoura sand in a stainless-steel ball for 2 min. This mixture was divided into quarters, each of which was placed into a mold with an OHP sheet. The sand in the mold container was tamped down 30 times by a hand rammer after each of the four quarters was placed in the mold. Finally, the edge surface of the test piece was molded flat and covered with Parafilm M to avoid desiccation. The test pieces were cured in an airtight container at a high humidity for 1, 7, 14, and 84 days at 20 °C. The UCS of the test pieces removed from the mold container after curing was measured at an axial strain rate of 1 %/min by employing a UCS apparatus. For each curing time, two test pieces were used to perform the UCS test.

2.3 SEM Observation of Sand Test Pieces Cemented by CPC

Segments of UCS test pieces cemented by the reaction mixture with the maximum PPV value among the sets of AP and calcium stock solutions with the maximum concentration were observed by SEM. The segment of the test piece was allowed to dry naturally at 20 °C for a few days and was then carbon-coated by a carbon coater. SEM observations were carried out at an accelerating voltage of 15 kV and at $\times 2000$ magnification. Simultaneously, elemental analyses of test piece segments were performed by using an energy dispersive X-ray fluorescence spectrometer (EDX) with SEM.

3 RESULTS

3.1 CPC Precipitation Test

CPC precipitation was observed in all reaction mixtures (Fig. 6). The pH of the reaction mixture ranged from 1.6 to 7.5 for CN and from 4.6 to 7.9 for CA. The pH showed the highest values among all combinations of AP and CN or CA when DAP was used as AP. The PPV showed a tendency to increase with the pH.

3.2 UCS Test of Sand Test Pieces Cemented by CPC

Toyouira sand test pieces cemented by six reaction mixture sets were selected based on the results of an in vitro precipitation test (Fig. 7). The measured UCS in this study ranged from 10.2 to 87.6 kPa. The maximum value was measured when the DPA/CA ratio was 1.5 M:0.75 M (Fig. 7 (F)). The UCS tended to increase with the curing time. Test pieces with a DAP/CA ratio of 1 M:0.5 M showed a UCS of over 20 kPa without any tendency to increase with curing time. The UCS values of the other four reaction mixtures were below 20 kPa and showed neither increasing nor decreasing trends as a function of the curing time.

3.3 SEM Observation of Sand Test Pieces Cemented by CPC

Segments of UCS test pieces cemented by the reaction

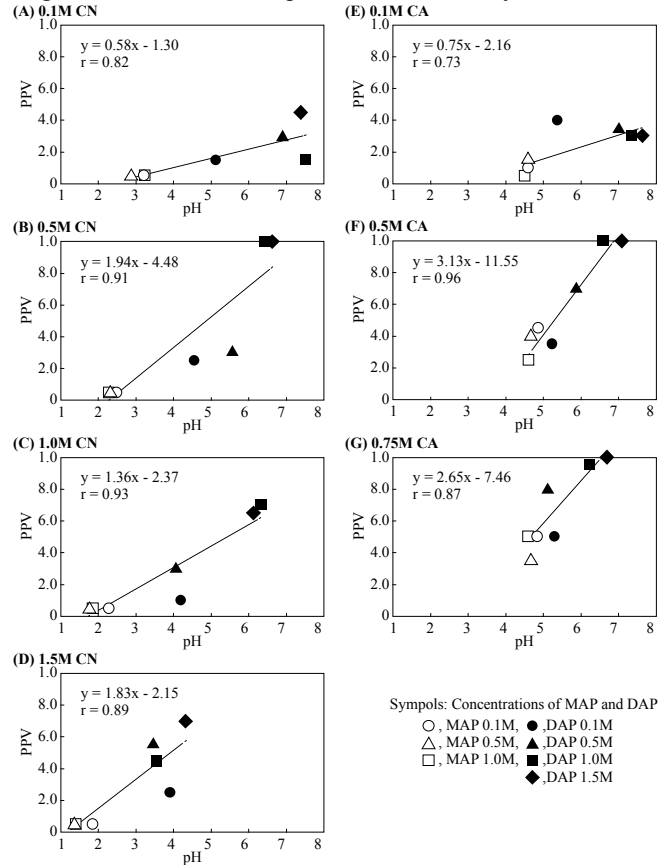


Fig. 6 Relationship between the proportion of CPC precipitation volume of reaction mixture (PPV) and pH for calcium nitrate (CN) and calcium acetate (CA). The value is represented as the proportion of the precipitation volume to the entire volume of the reaction mixture (4 mL). In vitro precipitation test was carried out by mixing equal volumes of ammonium phosphate and calcium nitrate or calcium acetate solutions.

mixture with the maximum PPV among the sets of AP and calcium stock solutions with the maximum concentration were observed by SEM (Figs. 7 (C) and (F)). In images captured at $\times 76$ magnification, particles of Toyoura sand were covered with precipitation in both the CN and CA stock solutions (Figs. 8 (A) and (D)). In images captured at $\times 600$ magnification, bridges built between particles of Toyoura sand by precipitation were observed (Figs. 8 (B) and (E)). At $\times 2000$ magnification, plate-like crystals with diameters of ~ 10 μ m were observed in the segment cemented by CN stock solution (Fig. 8 (C)). In contrast, a collection of whisker-like precipitations was formed in the segment cemented by the CA stock solution (Fig. 8 (F)). Through elemental analysis, it was found that the distributions of phosphorous and calcium overlapped and corresponded to the distribution of precipitation in the SEM images.

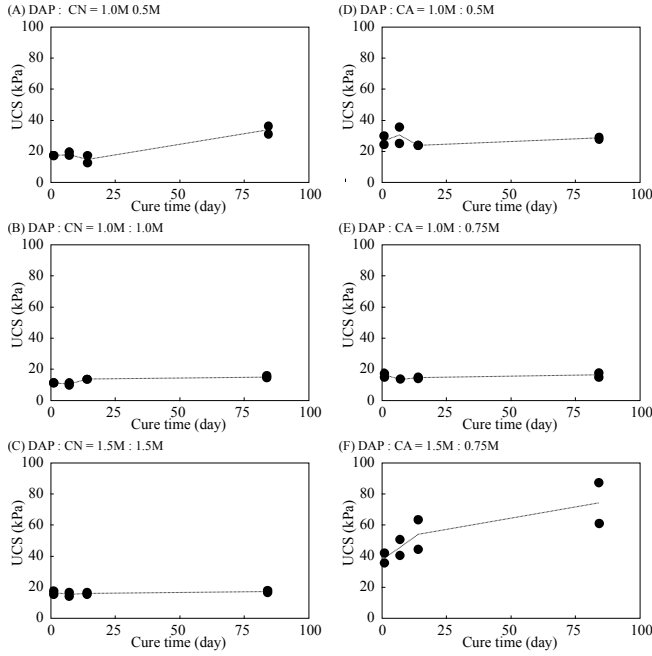


Fig. 7 Temporal variations in unconfined compressive strength (UCS) of Toyoura sand test pieces cemented by CPCs. Mixing concentrations of diammonium phosphate (DAP) and calcium solutions (calcium nitrate (CN) and calcium acetate (CA)) for mixture of each grout: (A), 1.0 M:0.5 M; (B), 1.0 M:1.0 M; (C), 1.5 M:1.5 M; (D), 1.0 M:0.5 M; (E), 1.0 M:0.75 M; (F), 1.5 M:0.75 M. The dashed line represents the change in the average of two measurements.

4 DISCUSSION

4.1 Relationship between CPC Precipitation and pH of Reaction Mixture

The results of an in vitro CPC precipitation test showed that the PPV tended to increase as the pH increased from strongly acidic to around neutral. Apparently, this is why the solubility of the CPC decreased at around neutrality and in a weakly alkaline region [8]. The Ca/P molar ratios in all reaction mixtures of each set were constant, regardless of pH. This indicates the possibility that pH-increasing actions, including microbial activity, e.g., urea hydrolysis of *S. pasteurii* [3], can effectively promote crystallization of CPC after the injection of an acidic reaction mixture with little precipitation into soil and rock.

In the case of 1.5 M CN (Fig. 6 (D)), the pH of the reaction mixture was below 4, even at the maximum PPV. This shows that if calcium is saturated, CPC can be precipitated in acidic conditions under which the solubility of CPC is higher. Some types of peat soils, which typically form a poor ground surface, show acidic properties due to the presence of humic acid [9]. The above results demonstrate the suitability of applying the CPC grout to such a soil. Because the solubility of CPC is also higher in alkaline regions around pH 12, a high

concentration of calcium can be achieved in such alkaline conditions [10]. The mechanism proposed by Kawasaki et al. [2] of utilizing acidification by carbon dioxide from yeasts

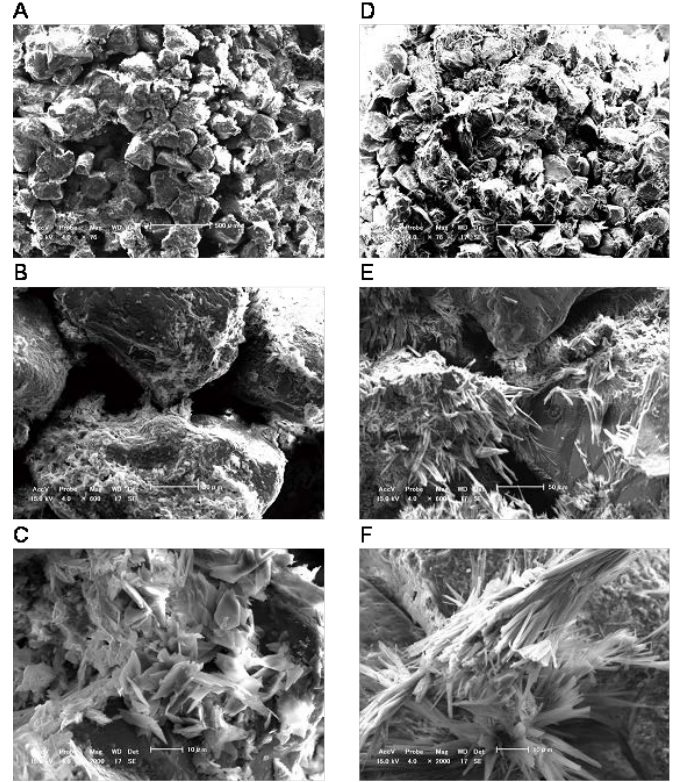


Fig. 8 Scanning electron microscope (SEM) images of Toyoura sand test pieces cemented by diammonium phosphate and calcium nitrate (A, B, and C) or calcium acetate (D, E, and F). A and D, $\times 76$; B and E, $\times 600$; and C and F, $\times 2000$. An accelerating voltage of 15 kV was used for the observations. Bars represent 500, 50, and 10 μm in A and D, B and E, and C and F, respectively.

may precipitate a large amount of CPC if an alkaline stock solution is initially used. In this case, it is necessary to study the utilization and activation of alkali-tolerant yeasts and bacteria.

4.2 UCS Improved by CPC

The most suitable combination of AP and calcium stock solution concentrations for improving the strength of the UCS test piece was a DAP/CA ratio of 1.5 M:0.75 M (Fig. 7 (F)), for which the UCS reached a maximum of 87.6 kPa. In contrast, all UCS values of the test pieces subjected to CN treatment were below 20 kPa and showed no significant trends (Figs. 7 (A)–(C)). SEM images of test pieces subjected to CA treatment showed whisker-like crystal formation among particles of Toyoura sand (Fig. 8). It has been reported that HA whiskers are formed by adding an acetic acid solution to amorphous calcium phosphate [11]. In Portland cement, the formation of ettringite, which shows whisker-like crystals, promotes solidification and increases strength [12]. These results suggest that the strength of the test pieces subjected to CA treatment in this study might increase if

whisker-like HA crystals are formed within them. In addition, they show that CA would be a potent candidate calcium stock solution in applications of CPC grout. In contrast, plate-like crystals were formed in test pieces treated with CN (Fig. 8). Zhang et al. [13] reported that plate-like HA formed in cases where CN was used as the calcium stock solution. There are a few CPCs, e.g., octacalcium phosphate (OCP) [14] and dicalcium phosphate (DCP) [11], whose precipitation leads to plate-like crystals. Non-HA CPC ultimately changes into HA [8]. Thus, the crystal form in test pieces treated with CN may change after a long curing period, thereby increasing the strength of the test pieces.

Whiffin et al. [3] reported that the precipitation of at least 60 kg/m³ of calcium carbonate is required to achieve a measurable strength improvement in a sand test piece (porosity, 37.8%) by using biogROUT. Assuming that HA (Ca/PO₄/OH molar ratio of 5:3:1) precipitates maximally in the most porous of the Toyoura sand test pieces, the theoretical value of CPC precipitation in 73.3 mL of the reaction mixture was 5.5 g in the test piece shown in Fig. 7 (F) (porosity, 37.7%). The details of this piece, which is cemented with a DAP/CA ratio of 1.5 M:0.75 M, are as follows:

- (1) 0.75 M Ca corresponds to ~2.2 g of Ca mass
- (2) 0.45 M PO₄ corresponds to ~3.1 g of PO₄ mass
- (3) 0.15 M OH corresponds to ~0.2 g of OH mass

The volume of the Toyoura sand test piece was 194.59 cm³; therefore, the proportionate CPC precipitation mass for a volume of 1 m³ is 28.3 kg. This means that the CPC grout attained a UCS of 87.6 kPa by a relatively low amount of CPC precipitation. A surplus of phosphate may exist in the pore water of the test pieces treated with CA because HA has a calcium-phosphorus molar ratio of 1.67 (Table 1). This suggests that multiple injections of calcium stock solution increase HA precipitation and induce the strengthening of test pieces, as described previously [6].

In this study, we begin by focusing on the development of novel grout material intended for soil materials (sand, in this study) and assume that the phosphate solution and calcium solution are mixed just before injection or that they are mixed in the ground after being sequentially injected. The procedure for mixing them might be formulated based on the viscosity of the reaction mixture, the PPV of CPC precipitation, and the precipitation status over time for a particular combination of stock solutions. It is also necessary to conduct a detailed evaluation of the relationship between the UCS and the rate of stiffening because temporal variation in the UCS over the long term may prove to be one of the most important parameters in determining the applicability of CPC.

4.3 Application of Knowledge in and Collaboration with Medical and Dental Sciences

The feasibility of improving the UCS was examined by forming CPC with only solutions that can be conveniently handled during practical application. Chow [15] reported that the utilization of CPC seed crystal caused the strengthening of HA in CPC solution. In particular, Chow [15] pointed out that utilization of a powder mixture of TTCP (tetracalcium

phosphate) and DCP led to a stronger HA with the greatest purity. The pastes also possessed the properties of self-setting and biocompatibility.

Research on CPC paste has established that a maximum compressive strength of 56 MPa can be obtained with a mixture of DCP and α -TCP (α -tricalcium phosphate) pastes and a seed crystal of calcium carbonate; this is substantially larger than the compressive strength of 35 MPa obtained without the seed [16]. This observation shows that the presence of the calcium carbonate seed crystal can supplement the effect of strength reinforcement, as is the case for the CPC grout studied here. Co-existing ions (e.g., magnesium ions) with in situ pore water change the form of the CPC crystal [17], and the compressive strength of HA is increased by the co-existence of bone marrow cells and CPC [18]. These observations suggest that the effective utilization of ionic and/or organic materials can be an important method for strength reinforcement in the geotechnical field.

Nowadays, clinical breakthroughs are made daily in the medical and dental sciences; these include the enhancement of the injectable [19], biocompatibility, and self-setting properties of CPC paste by organic matter [20] as well as the development of novel apatite blocks [21]. The injectability of CPC grout is also one of the most important factors in its application to natural soils and rocks with minute cracks. The medical and dental sciences have accrued an extensive amount of fundamental knowledge regarding CPC.

5 CONCLUSION

In this study, we examined the feasibility of a new grout material composed of CPC. A candidate cement type that increased the UCS of the sand test piece with time was identified by evaluating the effect of pH, the type of phosphate and calcium stock solutions, and the component ratios of the phosphate stock solution on the PPV of CPC. Although only chemical reactions for CPC precipitation were examined, the results of this study showed that CPCs have sufficient potential for use as (1) chemical grouts, because of their self-setting property, and (2) biogROUTs, because of their crystal structure and the pH dependence of precipitation.

Changes in the concentration of the reaction mixture were not reflected proportionally in the strength of the sand test pieces. In the future, additional tests aimed at determining the improvement in the strength by CPC are needed to understand more clearly the underlying mechanical processes and to facilitate practical application. The relationship between the strength and the various CPC precipitation parameters (concentration and pH of reaction mixture, curing time, etc.) should be examined in further detail, as continued research is needed to identify the process or processes that link crystal precipitation to the increase in strength. Furthermore, shearing and permeability tests using pieces cemented by CPC should be conducted to evaluate the applicability of CPCs for purposes such as permeability control and reinforcement of soil and rock.

6 REFERENCES

- [1] DeJong JT, Fritzges MB, Nusslein K, "Microbial induced cementation to control sand response to undrained shear," *Journal of Geotechnical and Geoenvironmental Engineering*, Vol. 132, 2006, pp. 1381–1392.
- [2] Kawasaki S, Murao A, Hiroyoshi N, Tsunekawa M, Kaneko K, "Fundamental study on novel grout cementing due to microbial metabolism," *Journal of the Japan Society of Engineering Geology*, Vol. 47, 2006, pp. 2–12 (in Japanese with English abstract).
- [3] Whiffin VS, Van Paassen LA, Harkes MP, "Microbial carbonate precipitation as a soil improvement technique," *Geomicrobiology Journal*, Vol. 24, 2007, pp. 417–423.
- [4] Ivanov V, Chu J, "Applications of microorganisms to geotechnical engineering for bioclogging and biocementation of soil in situ," *Reviews in Environmental Science and Biotechnology*, Vol. 7, 2008, pp. 139–153.
- [5] Terajima R, Shimada S, Oyama T, Kawasaki S, "Fundamental study of siliceous biogROUT for eco-friendly soil improvement," *JSCE Journal of Geotechnical and Geoenvironmental Engineering*, Vol. 65, 2009, pp. 120–130 (in Japanese with English abstract).
- [6] Van Paassen LA, Ghose R, Van der Linden TJM, Van der Star WRL, Van Loosdrecht, MCM, "Quantifying biomediated ground improvement by ureolysis: Large-scale biogROUT experiment," *Journal of Geotechnical and Geoenvironmental Engineering*, Vol. 136, 2010, pp. 1721–1728.
- [7] Dorozhkin SV, Epple M, "Biological and medical significance of calcium phosphates," *Angewandte Chemie International Edition*, Vol. 41, 2002, pp. 3130–3146.
- [8] Tung MS, "Calcium phosphates: structure, composition, solubility, and stability," in Zahid A (Ed), *Calcium Phosphates in Biological and Industrial Systems*, Kluwer Academic Publishers, Norwell, 1998, pp. 1–19.
- [9] Reddy KR, DeLaune RD, "Biogeochemistry of Wetlands: Science and Applications," CRC Press, Boca Raton, 2008, pp. 38–40.
- [10] Takagi S, Chow LC, Ishikawa K, "Formation of hydroxyapatite in new calcium phosphate cements," *Biomaterials*, Vol. 19, 1998, pp. 1593–1599.
- [11] Toyama T, Ohshima A, Yasue T, "Hydrothermal synthesis of hydroxyapatite whisker from amorphous calcium phosphate and effect of carboxylic acid," *Journal of the Ceramic Society of Japan*, Vol. 109, 2001, pp. 232–237 (in Japanese with English abstract).
- [12] Sakai E, Nikaido Y, Itoh T, Daimon M, "Ettringite formation and microstructure of rapid hardening cement," *Cement and Concrete Research*, Vol. 34, 2004, pp. 1669–1673.
- [13] Zhang, H-B, Zhou K-C, Li Z-Y, Huang S-P, "Plate-like hydroxyapatite nanoparticles synthesized by the hydrothermal method," *Journal of Physics and Chemistry of Solids*, Vol. 70, 2009, pp. 243–248.
- [14] Wang J, Layrolle P, Stigter M, De Groot K, "Biomimetic and electrolytic calcium phosphate coatings on titanium alloy: physicochemical characteristics and cell attachment," *Biomaterials*, Vol. 25, 2004, pp. 583–592.
- [15] Chow LC, "Development of self-setting calcium phosphate cements," *The Centennial Memorial Issue of the Ceramic Society of Japan*, Vol. 99, 1991, pp. 954–964.
- [16] Fernández E, Gil FJ, Best SM, Ginebra MP, Driessens FCM, Planell JA, "Improvement of the mechanical properties of new calcium phosphate bone cements in the CaHPO_4 - α - $\text{Ca}_2(\text{PO}_4)_2$ system: compressive strength and microstructural development," *Journal of Biomedical Materials Research*, Vol. 41, 1998, pp. 560–567.
- [17] Cheng P-T, Pritzker KPH, "Solution Ca/P ratio affects calcium phosphate crystal phases," *Calcified Tissue International*, Vol. 35, 1983, pp. 596–601.
- [18] Vuola J, Taurio R, Göransson H, Asko-sljavaara S, "Compressive strength of calcium carbonate and hydroxyapatite implants after bone-marrow-induced osteogenesis," *Biomaterials*, Vol. 19, 1998, pp. 223–227.
- [19] Böhner M, Baroud G, "Injectability of calcium phosphate pastes," *Biomaterials*, Vol. 26, 2005, pp. 1553–1563.
- [20] Maruyama M, Ito M, "In vitro properties of a chitosan-bonded self-hardening paste with hydroxyapatite granules," *Journal of Biomedical Materials Research*, Vol. 32, 1996, pp. 527–532.
- [21] Tas AC, "Preparation of porous apatite granules from calcium phosphate cement," *Journal of Materials Science: Materials in Medicine*, Vol. 19, 2008, pp. 2231–2239.

Shear Stiffness of Unsaturated Soil under Static and Cyclic Loads

C. W. W. Ng, C. Zhou and J. Xu

Department of Civil and Environmental Engineering, the Hong Kong University of Science and Technology, Clear Water Bay, Kowloon, Hong Kong Special Administrative Region

ABSTRACT

Shear stiffness of soil is one of the most important geotechnical parameters for predicting ground movements and dynamic responses of many earth structures. In this study, a suction-controlled triaxial apparatus is newly modified to investigate anisotropic shear stiffness of an unsaturated soil either subjected to static or cyclic loads. This new apparatus is equipped with three pairs of bender elements and local Hall-effect transducers. Measured results of anisotropic shear modulus at very small strains, shear modulus degradation curve at small strains and resilient modulus of an unsaturated soil under both static and cyclic loading-unloading are reported. Semi-empirical state-dependent equations predicting anisotropic shear modulus and resilient modulus of unsaturated soil are proposed and verified using experimental results.

Keywords: unsaturated soil, anisotropic stiffness, shear modulus degradation curve, resilient modulus

1. INTRODUCTION

Soils are natural and environmentally friendly materials and they can be very economical for constructing fill slopes, landfill covers, pavements and various earth structures including retaining walls, dams and foundations. Under proper design, they can be very robust. Accurate measurements of soil stiffness at very small strains (0.001% or less) and small strains (between 0.001% and 1%) is essential for correctly predicting ground movements and dynamic responses of many earth structures at working conditions (Burland, 1989; Atkinson and Sallfors, 1991; Mair, 1993; Ng and Lings, 1995; Brown, 1996; Malone et al., 1997; Atkinson, 2000; Mancuso et al., 2002; Ng and Menzies, 2007; Ng and Yung, 2008; Clayton, 2011; Ng and Xu, 2012). Up to now, small-strain stiffness of saturated soils has been studied by many researchers (Atkinson and Sallfors, 1991; Atkinson, 2000; Clayton, 2011). It is found that shear stiffness of saturated soil depends on many factors such as effective stress, strain level and recent stress history.

In many parts of the world, soils at and near the Earth's surface are often unsaturated and they are subjected to seasonal variations of moisture content (i.e., soil suction). Previous experimental studies revealed that shear modulus G_0 at very small strains of an unsaturated soil is significantly affected by soil suction (Mancuso et al. 2002). This study is limited to the measurement of a single G_0 value from each specimen. The degree of stiffness anisotropy of unsaturated soil is rarely reported, with the exceptions of Ng and Yung (2008) and Ng et al. (2009). The former investigated the degree of stiffness anisotropy of recompacted completely decomposed tuff (CDT) under both saturated and unsaturated

conditions, whereas the latter studied the effects of wetting-drying and stress ratio on anisotropic shear stiffness of CDT at very small strains. Ng and Xu (2012) explored the effects of suction history, which refers to current suction ratio and recent suction history, on both very small strain shear modulus and shear modulus reduction curve of an unsaturated soil.

For pavements, subgrade soils are often unsaturated and they are subjected to seasonal variations of moisture and cyclic traffic loads. Resilient modulus M_R , defined by Seed (1962) as the ratio of repeated deviator stress to recoverable axial strain in a cyclic triaxial test, is commonly used to determine soil stiffness under cyclic loads. By testing soil specimens compacted at different water contents, previous researchers reported that M_R of an unsaturated soil is significantly dependent on water content (Seed et al., 1962; Jin et al., 1994; Lekarp et al., 2000; Kim and Kim, 2007). However, soil suction was rarely measured or controlled in previous resilient modulus tests.

By using a newly modified suction-controlled triaxial apparatus equipped with three pairs of bender elements and local Hall-effect transducers, measurements of anisotropic shear modulus at very small strains and shear modulus degradation curve of an unsaturated weathered soil (completely decomposed tuff, CDT) at small strains are described and discussed in this paper. Moreover, resilient modulus of CDT under cyclic loads is investigated. Semi-empirical state-dependent equations are proposed to describe and predict anisotropic shear modulus and resilient modulus of the unsaturated CDT. It should be noted that the contents of this keynote paper are mainly based on Ng and Yung (2008), Ng et al. (2009) and Ng and Xu (2012) and Ng et al. (2012).

2. THEORETICAL CONSIDERATIONS

2.1 State-dependent anisotropic shear modulus at very small strains

Previous researchers (Roesler, 1979; Stokoe et al., 1995; Jamiolkowski et al., 1995; Bellotti et al., 1996) found that the velocity of a shear wave propagating in a completely dry or saturated soil depends on the principal stresses in the plane of shear (i.e., stresses in the directions of wave propagation and particle motion), but it is independent of the stress normal to the plane of shear. Effects of the two principal stresses in the plane of shear on shear wave velocity are found to be similar (Bellotti et al., 1996). In addition to principal stresses, void ratio also has an effect on shear wave velocity. Based on these findings, Ng and Leung (2007) proposed a semi-empirical equation for the relationship between shear wave velocity and the state of a saturated soil:

$$v_{s(ij)} = C_{ij} f(e) p_r^{-n} (\sigma_i' \times \sigma_j')^{n/2} \quad (1)$$

where C_{ij} is a constant reflecting the inherent soil properties in the ij plane, with dimension m/s; $f(e)$ is a void ratio function relating shear wave velocity to void ratio; p_r is a reference pressure, taken as 1 kPa for simplicity in this study; n is an empirical stress exponent; σ_i' and σ_j' are effective principal stresses in the direction of wave propagation and particle motion, respectively.

With the development of unsaturated soil mechanics since the 1950s, various stress state variables have been proposed to describe the behaviour of unsaturated soils (Bishop, 1959; Jennings and Burland, 1962; Fredlund and Morgenstern, 1977; Alonso et al., 1990; Wheeler and Sivakumar, 1995; Houslsby, 1997; Gens, 2010). Based on thermodynamic theory, Houslsby (1997) showed that a complete description of unsaturated soil behaviour requires at least two stress state variables. Keeping the interpretation of experimental data rigorous yet simple, this study adopts the most commonly used two independent stress state variables (Jennings and Burland, 1962), namely net normal stress ($\sigma - u_a$) and matric suction ($u_a - u_w$), where σ , u_a , u_w are total normal stress, pore air pressure and pore water pressure, respectively. Based on these two independent stress state variables, Ng and Yung (2008) proposed the following expression to capture velocity of shear waves travelling in unsaturated soil:

$$v_{s(ij)} = C_{ij} f(e) \left[\frac{(\sigma_i - u_a)}{p_r} \times \frac{(\sigma_j - u_a)}{p_r} \right]^{\frac{n}{2}} \left[1 + \frac{(u_a - u_w)}{p_r} \right]^b \quad (2)$$

where b is an empirical exponent reflecting the influence of matric suction on shear wave velocity. This equation allows a smooth transition between unsaturated and saturated states. When soil is saturated (i.e., $u_a - u_w = 0$), Eq. (2) reduces to Eq. (1).

The shear wave velocity for a homogeneous cross-anisotropic elastic continuum with a symmetrical vertical axis subjected to principal stresses in the horizontal and vertical directions is expressed by the following equation (Mavko et al., 1998):

$$v_{s(ij)} = \sqrt{G_{0(ij)} / \rho} \quad (3)$$

where ρ is bulk density of the medium and $G_{0(ij)}$ is elastic shear modulus in the ij plane. If a specimen is homogeneous and cross-anisotropic, shear modulus of an unsaturated soil, $G_{0(ij)}$, can be obtained from Eq.s (2) and (3) and expressed as follows (Ng and Yung, 2008):

$$G_{0(ij)} = C_{ij}^2 F(e) \left[\frac{(\sigma_i - u_a)}{p_r} \times \frac{(\sigma_j - u_a)}{p_r} \right]^n \left[1 + \frac{(u_a - u_w)}{p_r} \right]^{2b} \quad (4)$$

where $F(e)$ is void ratio function relating shear modulus to void ratio, given by

$$F(e) = \frac{[f(e)]^2 (G_s + S_r e)}{1 + e} \rho_w \quad (5)$$

where e is void ratio; G_s is specific gravity of soil; ρ_w is water density and S_r is degree of saturation, which is 1 for saturated soil.

2.2 Degree of stiffness anisotropy

If the degree of stiffness anisotropy of a soil is expressed in terms of the ratio of shear modulus in the horizontal plane ($G_{0(hh)}$) to that in the vertical plane ($G_{0(hv)}$), by making use of Eq. (4), degree of stiffness anisotropy of an unsaturated soil can be expressed as follows (Ng and Yung, 2008):

$$\frac{G_{0(hh)}}{G_{0(hv)}} = \left(\frac{v_{s(hh)}}{v_{s(hv)}} \right)^2 = \frac{C_{hh}^2}{C_{hv}^2} \left[\frac{(\sigma_h - u_a)}{(\sigma_v - u_a)} \right]^n \quad (6)$$

It can be seen from Eq. (6) that the degree of stiffness anisotropy of an unsaturated soil depends on inherent material properties, C_{hh}^2/C_{hv}^2 , and the ratio of net normal stresses in the horizontal and vertical directions, $(\sigma_h - u_a)/(\sigma_v - u_a)$. However, the degree of stiffness anisotropy appears to be independent of matric suction. If a soil is subjected to isotropic stress condition, this equation can be further simplified:

$$\frac{G_{0(hh)}}{G_{0(hv)}} = \left(\frac{v_{s(hh)}}{v_{s(hv)}} \right)^2 = \frac{C_{hh}^2}{C_{hv}^2} \quad (7)$$

Equation (7) suggests that under isotropic stress state, degree of stiffness anisotropy expressed in terms of $G_{0(hh)}/G_{0(hv)}$ only depends on inherent anisotropic material properties.

2.3 Resilient modulus under cyclic loads

Many equations have been proposed to predict M_R . One of the most widely used formulations in pavement engineering is as follows (Uzan, 1985):

$$M_R = a_r \left(\frac{\sigma_1 + \sigma_2 + \sigma_3}{p_{atm}} \right)^{b_r} \left(\frac{q_{cyc}}{p_{atm}} \right)^{c_r} \quad (8)$$

where σ_1 , σ_2 and σ_3 are principal total stresses; q_{cyc} is cyclic shear stress, defined as the amplitude of change in deviator stress during cyclic loading-unloading; p_{atm} is atmospheric pressure and parameters a_r , b_r and c_r are regression coefficients. Clearly, Eq. (8) cannot completely describe M_R of an unsaturated soil since it does not consider the effects of matric suction on soil behaviour explicitly.

Following its definition, M_R can be considered to be equivalent to secant Young's modulus of a material (Brown et al., 1987). For an isotropic elastic material, Young's modulus is linked to shear modulus G by the formulation of $E = 2G(1+\nu)$, where ν is Poisson's ratio. It may be reasonable to assume that suction affects shear modulus and resilient modulus in a similar manner qualitatively. Referring to Eq. (4), it is logical to propose and revise Eq. (8) for M_R of an unsaturated soil as follows:

$$M_R = M_0 \left(\frac{p}{p_r} \right)^{k_1} \left(\frac{q_{cyc}}{p_r} \right)^{k_2} \left(1 + \frac{u_a - u_w}{p} \right)^{k_3} \quad (9)$$

where p is net mean stress, defined as $((\sigma_1 + \sigma_2 + \sigma_3)/3 - u_a)$. Parameters k_1 , k_2 and k_3 are regression exponents. The term M_0 denotes the resilient modulus at the reference stress state when $p - u_a = p_r$, $q_{cyc} = p_r$ and $u_a - u_w = 0$. It empirically incorporates the effects of a number of factors such as microstructure and void ratio on M_0 , which is equivalent to C_{ij} and $F(e)$ in Eq. (4). The term $(p/p_r)^{k_1}$ quantifies the influence of net mean stress on M_R . The term $(q_{cyc}/p_r)^{k_2}$ reflects the variations of M_R with cyclic stress. The term $(1 + (u_a - u_w)/p)^{k_3}$ accounts for the influence of matric suction on M_R .

When q_{cyc} approaches 0 (i.e., at very small strains), $q_{cyc}^{k_2}$ approaches infinite because the power k_2 is negative. Therefore, M_R predicted by Eq. (9) approaches infinity when q_{cyc} approaches 0. This prediction contradicts experimental observations that soil stiffness at very small strain levels is finite (Mancuso et al., 2002; Ng and Yung 2008). The limitation of this equation may be overcome by replacing the term (q_{cyc}/p_r) by $(1 + q_{cyc}/p_r)$. Then, this equation can be rewritten as:

$$M_R = M_0 \left(\frac{p}{p_r} \right)^{k_1} \left(1 + \frac{q_{cyc}}{p_r} \right)^{k_2} \left(1 + \frac{u_a - u_w}{p} \right)^{k_3} \quad (10)$$

In this paper, Eq. (10) is proposed to predict stress-dependent M_R of an unsaturated soil.

The validity of the above state-dependent equations, for predicting anisotropic shear modulus at very small strains (Eq. (4)), degree of stiffness anisotropy (Eq. (7)) and resilient modulus (Eq. (10)) of an unsaturated soil, are verified experimentally later.

3. MODIFIED SUCTION-CONTROLLED TRIAXIAL APPARATUS

Fig. 1 shows the schematic diagram of a modified triaxial system for testing saturated and unsaturated soils (Ng and

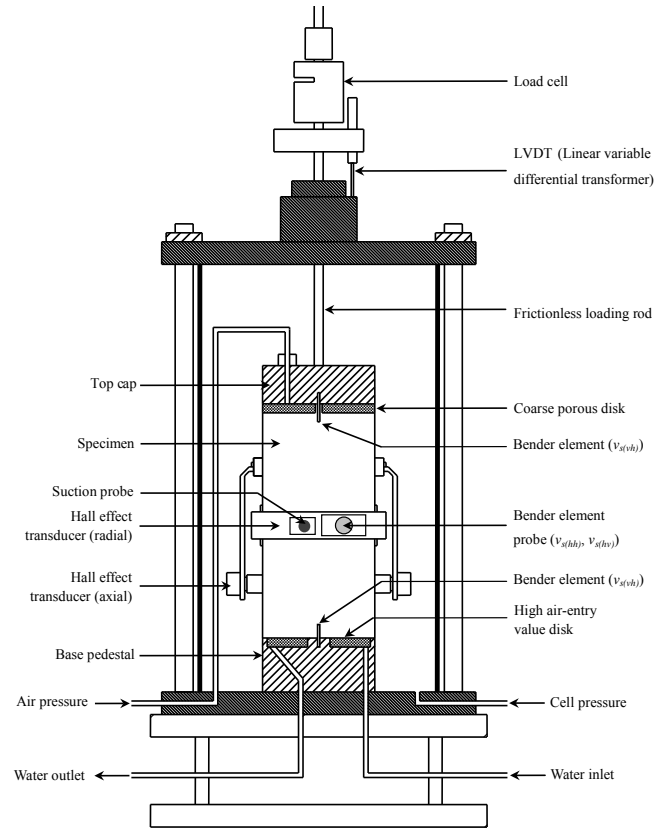


Fig. 1. Modified suction-controlled triaxial apparatus for testing unsaturated soil (modified from Ng and Yung, 2008)

Yung, 2008; Ng et al., 2012). The system consists of a triaxial cell, four independent pressure controllers, five transducers and a computer. The four pressure controllers are capable of controlling axial stress (σ_a), cell pressure (σ_r), pore air pressure (u_a) and pore water pressure (u_w) independently. The five transducers consist of an external load cell for measuring axial force, a linear variable differential transformer (LVDT) for measuring axial displacement externally and three pressure transducers for monitoring cell pressure (σ_r), pore air pressure (u_a) and pore water pressure (u_w). This triaxial system is controlled by a closed-loop feedback scheme. It can be used to apply both static and cyclic loads. To measure water volume change of a soil specimen, a vertical tube is connected to the pedestal to determine the amount of water flowing in or out of the soil specimen. This is achieved by measuring the height of the water column by a sensitive differential pressure transducer inside the tube. In addition, this triaxial apparatus is equipped with a shear-wave velocity measurement system, a set of local Hall-effect strain transducers and a high capacity suction probe.

To control matric suction ($u_a - u_w$) during a test, the axis-translation technique (Hilf, 1956) is adopted to control ($u_a - u_w$) of each specimen by applying u_a and u_w independently. u_a was controlled through a coarse low air-entry value (AEV) corundum disk placed on top of a soil specimen, whereas u_w was controlled through a saturated high AEV (300 kPa) ceramic disk sealed to the base pedestal of the triaxial apparatus. The conventional pedestal of the

triaxial cell was modified to incorporate both a high-entry value ceramic disk and a bender element. In addition, a spiral-shaped drainage groove of 3 mm wide and 3 mm deep connected to the water drainage system was carved in the base pedestal. It serves as a water channel for flushing air bubbles that may be trapped or accumulated beneath the ceramic disk as a result of air diffusion during long periods of unsaturated soil testing. Diffused air was removed by flushing de-aerated water along the spiral-shaped drainage groove beneath the ceramic disk once every 24 hours throughout a test.

3.1 Shear wave velocity measurement system

The shear wave velocity measurement system consists of bender elements, a function generator, a power amplifier, a multi-channel filter, an oscilloscope and a computer. The arrangement of bender elements on each specimen are shown in Fig. 2(a). Three pairs of bender elements are installed on each specimen to measure shear wave velocities in different planes. Thus, very small strain shear moduli in different planes can be determined. A pair of bender elements was inserted into the top and bottom platens to measure the velocity of vertically transmitted shear wave with horizontal polarization, $v_{s(vh)}$. A pair of bender element probes was developed and inserted into the mid-height of each specimen to measure velocities of horizontally transmitted shear waves with vertical and horizontal polarization, $v_{s(hv)}$ and $v_{s(hh)}$. Each bender element probe consists of two pieces of bender elements, 9 mm in length and 6 mm in width, in a T-shaped assembly, as shown in Fig. 2(b). More details of the bender elements probe are given by Ng et al. (2004).

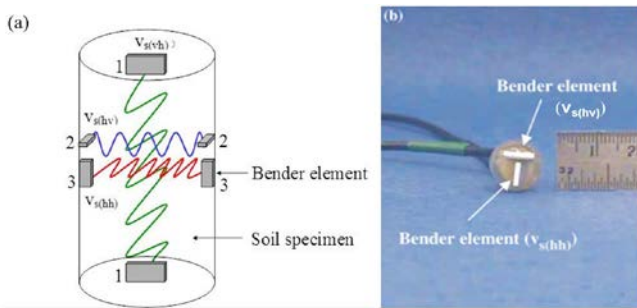


Fig. 2. Details of bender element (Ng et al., 2004) (a) Arrangement of bender elements; (b) Details of horizontal bender element probe at the mid-height of soil specimen

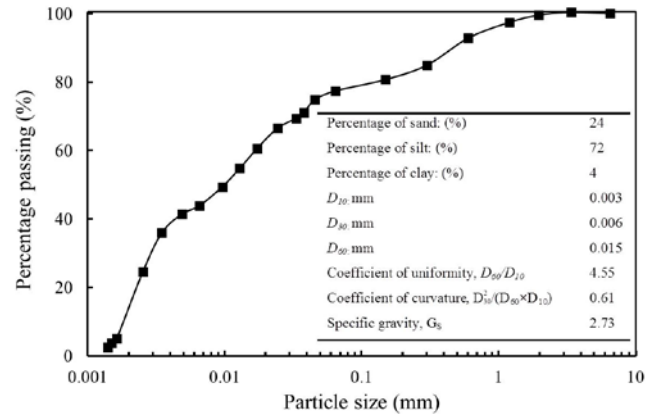


Fig. 3. Particle size distribution of completely decomposed tuff (CDT) (data from Ng and Yung, 2008)

The input signal consists of a single sinusoidal pulse with a frequency of 2 to 15 kHz. The range of frequency was selected to obtain a clear signal and to minimize the near field effect (Sanchez-Salinero et al., 1986). The velocity of a shear wave propagating in soils in the direction of the wave propagation, i , and particle motion, j , can be calculated from the following equation:

$$v_{s(ij)} = \frac{L_i}{t_{ij}} \quad (11)$$

where L_i is current travel distance and t_{ij} is travelling time of the shear wave propagating over the distance L_i . In this study, L_i is determined as the tip-to-tip distance between transmitter and receiver bender elements (Dyvik and Madshus, 1985; Viggiani and Atkinson, 1995b). t_{ij} is determined by measuring time shift between characteristic points of the transmitted and received signals (Pennington et al., 2001; Lee and Santamarina, 2005).

3.2 Hall-effect local strain transducers

In order to avoid possible errors in the conventional external measurements of axial strain using a LVDT, such as seating, alignment, bedding and compliance errors (Scholey et al., 1995), Hall-effect transducers (Clayton et al., 1989) are adopted to measure local strains at center portion of each soil specimen. As shown in Fig. 1, the triaxial apparatus is equipped with two axial and one radial Hall-effect transducers for measuring local axial and radial deformations of a specimen. After calibration by a micrometer, the resolution and accuracy of each Hall-effect transducer is about 1 and 3 μm , respectively. In the axial strain measurement, 3 μm corresponds to a strain of about 0.004% in this study.

3.3 High capacity suction probe

A high capacity suction probe is developed and used in this study for measuring pore water pressure at the mid-height of soil specimen. It is used to provide a guideline for the termination of suction equalisation stage. When suction equalisation is reached, u_w measured using suction probe is equal to u_w applied from the base pedestal. The suction probe

Table 1. Index properties of CDT (Ng and Yung, 2008)

Index test	Measured value
Standard compaction tests	
Maximum dry density: (kg/m ³)	1760
Optimum water content: (%)	16.3
Atterberg limits (grain size < 425 μ m)	
Liquid limit: (%)	43
Plastic limit: (%)	29
Plasticity index: (%)	14

was modified from Druck PDCR 81 miniature pore water pressure transducer, which mainly consists of a ceramic tip, a small water reservoir and a diaphragm. The original low air-entry value ceramic tip was replaced by a ceramic tip with a higher air-entry value (500 kPa). It is able to measure a negative pore water pressure of up to 480 kPa, close to the AEV of the ceramic tip used in the probe, as verified in free evaporation tests. More details of its development, saturation procedures and performance can be referred to Ng and Xu (2012).

4. TEST MATERIAL AND SPECIMEN PREPARATION

The material investigated in this study is yellowish-brown completely decomposed coarse ash tuff (CDT) (Geotechnical Engineering Office, 1988). CDT is weathered saprolite, commonly found in Hong Kong and often used as construction materials. Fig. 3 shows the particle size distribution of CDT as determined by sieve and hydrometer analyses (British Standards Institution, 1990). The physical properties of CDT are summarized in Table 1. Following the Unified Soil Classification System, CDT is classified as silt (ML) (ASTM, 2006).

Fig. 4 shows two stress-dependent soil-water characteristic curves (SDSWCCs) of CDT. The SDSWCCs were measured using a triaxial pressure plate system (Ng et al., 2011). Two identically prepared compacted triaxial specimens were subjected to a drying and wetting cycle under net mean stresses of 100 and 200 kPa. Total volume change and water volume changes of each specimen were measured by a double-cell measurement system and a ballast tube, respectively. It can be seen from this figure that soil-water characteristic curve is dependent on stress level. The specimen subjected to a higher net mean stress tends to possess a higher AEV. The AEVs are estimated to be 60 and 90 kPa at net mean stresses of 100 and 200 kPa, respectively. In addition, the specimen subjected to net mean stress of 200 kPa shows a slightly lower desorption rate than the one under net mean stress of 100 kPa. The above observations are probably because that soil specimen under higher net mean stress has a smaller average pore-size distribution and thus a better water retention ability (Ng and Pang, 2000).

Each triaxial specimen, 76 mm in diameter and 152 mm in height, is compacted at initial water content of about 16.3% and dry density of about 1760 kg/m³. In order to produce a uniform specimen, the specimen is compacted in 10 layers. After the completion of compaction, the height and diameter

dimensions of the specimen are measured by a caliper (readable to 0.01 mm) and a PI tape (readable to 0.01 mm), respectively. The average initial suction of the specimens after compaction is 95 kPa as measured by a high capacity suction probe. The variations of measured initial suction among different height of each specimen and the variations of measured initial suction among different specimens are all less than ± 2 kPa.

5. TEST PROGRAM AND PROCEDURES

Four series of tests were carried out on compacted CDT specimens at unsaturated state. Two of them were conducted to study anisotropic shear modulus at very small strains. The third series of tests were carried out to study shear modulus degradation curve at small strains. The purpose of the fourth series of tests was to study resilient modulus under cyclic loading-unloading.

5.1 Series A tests: isotropic compression test under constant matric suction

In order to study anisotropic shear modulus of unsaturated CDT under isotropic stress state and to verify Eq.s (4) and (7), four isotropic compression tests (series A) were carried out at different suctions (Ng and Yung, 2008). The stress path of each test is illustrated in Fig. 5. The four specimens (iso-s0, iso-s50, iso-s100 and iso-s200) were firstly subjected to net mean stress of 110 kPa and matric suction of 0, 50, 100 and 200 kPa, respectively. Then each specimen was left for suction equalisation. The purpose of applying a suction equalisation state is to ensure that soil moisture has reached its equilibrium state, when pore air pressure and pore water pressure are equal to predefined values throughout a specimen. This stage was considered to be completed when the rate of water content change was less than 0.04% per day (Sivakumar, 1993), which corresponded to a water flow of about 0.5 cm³ per day in this study. This equalisation criterion was used in all series of tests in this study. Once a specimen was equalised at its predefined stress and suction level, it was isotropically compressed to each required net mean stress at constant matric suction. The cell pressure was ramped up at a rate of 3 kPa per hour to each target value, while maintaining constant pore air and pore water pressures. This compression rate was reported by Ng and Chiu (2001) to be slow enough to

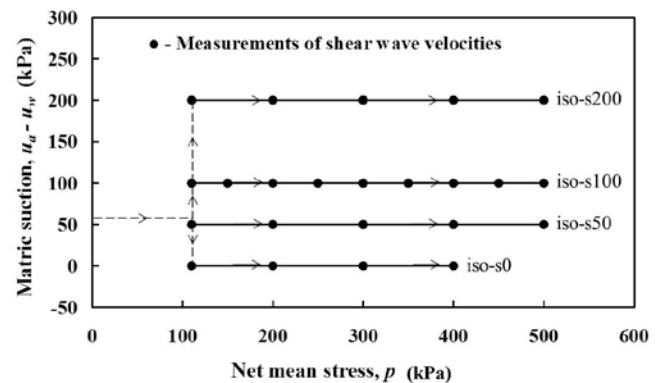


Fig. 5. Stress path of isotropic compression tests at different matric suction

ensure fully drained condition by monitoring both changes in water flow and volume change in a soil specimen at the end of each compression stage. Shear wave velocities ($v_{s(vh)}$, $v_{s(hv)}$ and $v_{s(hh)}$) were measured at each predefined net mean stress, as shown by dots in the figure. More details of this series of tests were given by Ng and Yung (2008).

5.2 Series B tests: dying-wetting test under constant isotropic net stress

Two dying-wetting tests (series B) were conducted under two different constant isotropic net stresses to study the effects of wetting-drying cycle on anisotropic shear modulus at very small strains. Fig. 6 shows the stress paths of the two tests. Desired net mean stresses of 110 and 300 kPa were first applied to specimens (dw-p100 and dw-p300), which were then brought to zero matric suction at constant net mean stress for equalisation. Shear wave velocities ($v_{s(vh)}$, $v_{s(hv)}$ and $v_{s(hh)}$) were measured at the end of the equalisation stage, and then matric suction was increased to the next desired value. Upon completion of the drying phase at a matric suction of 250 kPa, wetting phase began. When matric suction was decreased to zero, the wetting phase was completed. The drying-wetting tests consisted of a sequence of equalisation stages. Shear wave velocities ($v_{s(vh)}$, $v_{s(hv)}$ and $v_{s(hh)}$) were measured at the end of each equalisation stage, as shown by dots in the figure. More details of this series of tests were given by Ng et al. (2009).

5.3 Series C tests: suction-controlled constant p triaxial compression test

Two suction-controlled constant p triaxial compression tests (series C) were carried out on two CDT specimens (tc-s150 and tc-s300) to study effects of matric suction on shear modulus degradation curve of unsaturated soil. The stress paths in (p : q : s) space for series C tests are shown in Fig. 7. Desired net mean stress (100 kPa) and matric suctions (150 and 300 kPa) were first applied to the two soil specimens for equalisation. After the equalisation stage, deviator stress was increased at a rate of 3 kPa per hour while the net mean stress and matric suction were kept constant. The shearing rate was confirmed by the measurement of the suction probe to be slow enough that the excess pore water pressure generated during shearing stage was negligible (less than ± 2 kPa). The use of a constant p stress path was to eliminate the coupling effects on shear modulus due to a change in the net mean stress (Atkinson and Sallfors, 1991; Ng et al., 2000). More details of this series of tests were given by Ng and Xu (2012).

5.4 Series D tests: suction-controlled cyclic triaxial test

Six cyclic triaxial tests (series D) were carried out to investigate resilient modulus of unsaturated soil under cyclic loads. Fig. 8 shows the stress path of each test in this series. Three specimens (cyc-s60, cyc-s30 and cyc-s0) were wetted from initial suction (i.e., 95 kPa) to 60, 30 and 0 kPa at net mean pressure of 30 kPa, respectively. After suction equalisation, each specimen was subjected to cyclic loading-unloading to determine M_R . Measured resilient moduli of these three specimens were compared to investigate effects of matric suction on M_R along a wetting path. Similarly, the other three specimens (cyc-s100,

cyc-s150 and cyc-s250) were dried to matric suctions of 100, 150 and 250 kPa, respectively. Measured resilient moduli were compared to study suction effects on M_R along a drying path.

During cyclic loading-unloading, net confining pressure was maintained constant at 30 kPa while applied axial stress

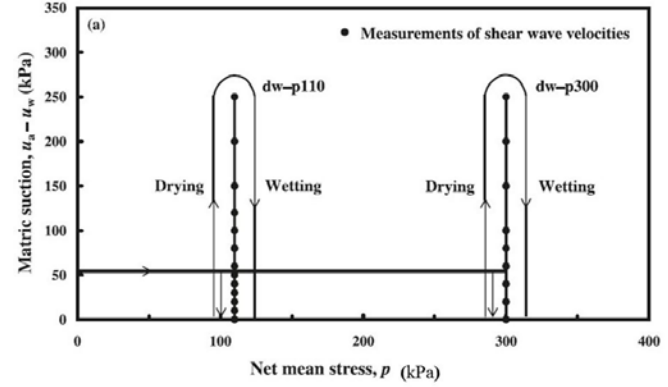


Fig. 6. Stress paths of dying-wetting tests at different isotropic net stresses

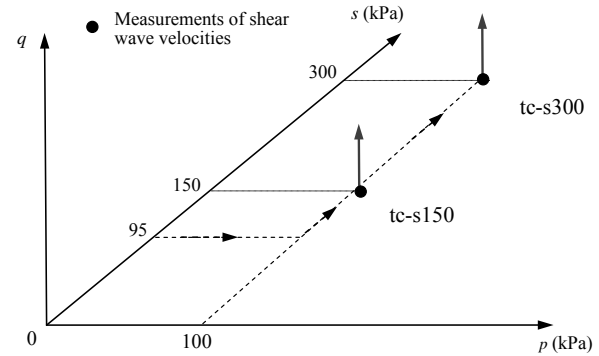


Fig. 7. Stress paths of constant p compression tests at different matric suctions

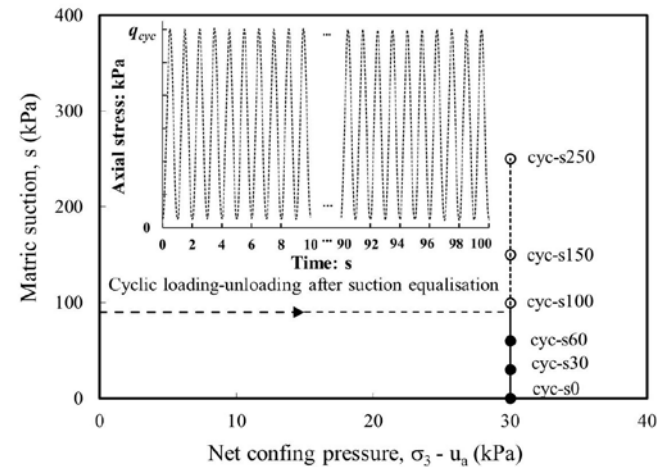


Fig. 8. Stress paths of cyclic triaxial tests at different matric suctions

was varied with time following a haversine form. For clarity, variations of axial stress during the first and last 10 cycles are shown in an insert in the figure. According to AASHTO (2003) standard for a resilient modulus test, four levels of cyclic stress (i.e., 30, 40, 55 and 70 kPa) were considered and applied to each specimen in succession. At each level of cyclic stress (q_{cyc}), 100 cycles of loading-unloading were applied at 1 Hz. It should be pointed out that constant water content condition was simulated under cyclic loads because the dissipation rate of excess pore water pressure is low compared to the rate of repeated traffic loads in the field. Excess pore water pressure was monitored by a suction probe at mid-plane of each specimen. More details of this series of tests were given by Ng et al. (2012).

6. INTERPRETATIONS OF EXPERIMENTAL RESULTS

6.1 Anisotropic shear modulus at very small strains

Fig. 9 shows variations of measured very small strain shear moduli ($G_{0(vh)}$, $G_{0(hv)}$ and $G_{0(hh)}$) with net mean stress at different matric suctions (0, 50, 100 and 200 kPa) (obtained from series A tests). At any suction level, measured shear moduli, $G_{0(vh)}$, $G_{0(hv)}$ and $G_{0(hh)}$, increase with increasing net mean stress. As given in Eq. (4), shear modulus is proportional to p^{2n} . As reported by Ng and Yung (2008), n is 0.17 for the CDT. With this positive exponent, the form of the proposed Eq. (4) is consistent with measured data shown in the figure. Moreover, the rates of increase in shear moduli with increasing net mean stress are slightly higher when matric suction is lower, but the differences become less pronounced at high suctions ranging from 50 to 200 kPa. For instances, measured $G_{0(vh)}$, $G_{0(hv)}$ and $G_{0(hh)}$ at zero suction (saturated state) increase by 144%, 140% and 144%, respectively, as net mean stress increases from 110 to 400 kPa. While at a suction of 100 kPa, measured $G_{0(vh)}$, $G_{0(hv)}$ and $G_{0(hh)}$ increase by 96%, 89% and 94%, respectively, for the same net mean stress change. Thus, the rate of increase in shear modulus with increasing net mean stress also depends on matric suction.

It can be seen from the figure that measured shear moduli, $G_{0(vh)}$, $G_{0(hv)}$ and $G_{0(hh)}$, increase with increasing matric suction at a given net mean stress. The observed increase in shear moduli with an increase in matric suction is explained by the term, $[1+(u_a-u_w)/p_r]^{2b}$, in Eq. (4). As reported by Ng and Yung (2008), the b value is 0.045 for the CDT specimens. Thus, shear modulus is proportional to $[1+(u_a-u_w)/p_r]^{0.09}$. Similar results that G_0 of unsaturated soil increases with increasing matric suction have been reported by Cabarkapa et al. (1999) and Mancuso et al. (2000) in their measurements of single G_0 values. The beneficial effects of matric suction on very small strain shear modulus arise from at least two possible reasons. Firstly, when a soil specimen becomes unsaturated, voids are partly filled with water and partly occupied by air, resulting in an air-water interface in each void. When there is an increase in matric suction, the radius of an air-water interface decreases and hence induces a larger normal inter-particle contact force (Fish, 1926; Mancuso et

al., 2002; Wheeler et al., 2003; Ng and Yung, 2008). This normal inter-particle

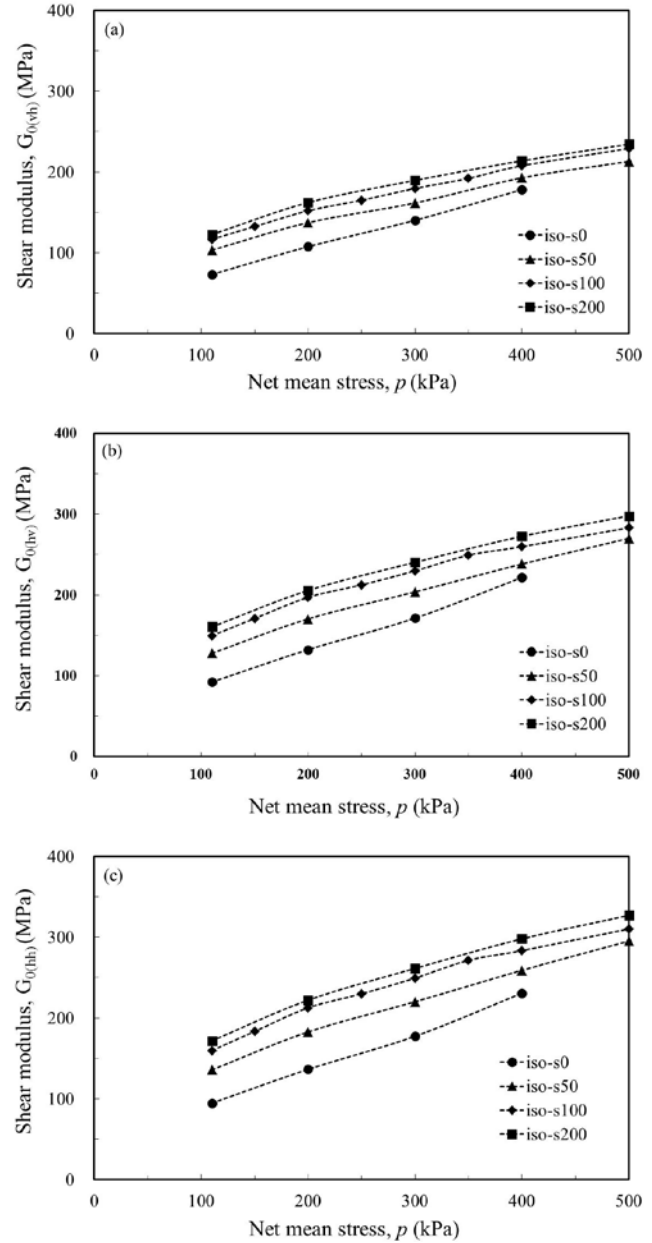


Fig. 9. Variations of (a) $G_{0(vh)}$, (b) $G_{0(hv)}$, (c) $G_{0(hh)}$ with net mean stress during isotropic compression tests (Ng and Yung, 2008)

contact force provides a stabilizing effect on an unsaturated soil by inhibiting slippage at particle contacts and enhancing the shear resistance of the unsaturated soil (Wheeler et al., 2003). Secondly, an increase in matric suction induces the volume shrinkage of soil specimen (Ng and Pang, 2000). Due to stronger inter-normal force between particles and higher density, shear modulus measured at higher matric suctions is larger.

It is also revealed in the figure that measured shear moduli ($G_{0(vh)}$, $G_{0(hv)}$ and $G_{0(hh)}$) increase significantly as matric suction increases from 0 to 50 kPa at a given net stress. Beyond a suction of 50 kPa, measured shear moduli continue to increase but at a reduced rate. Based on the test data given

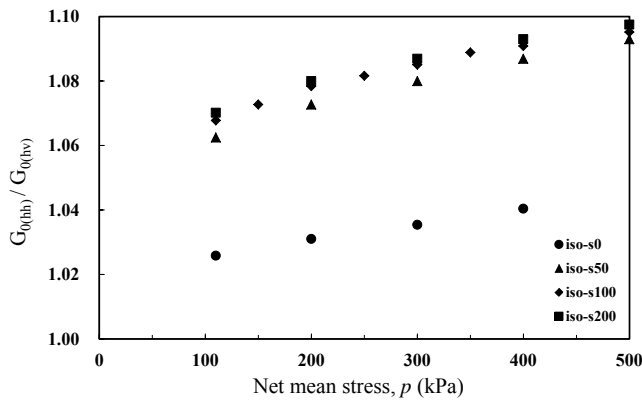


Fig. 10. The influence of net mean stress on $G_{0(hh)}/G_{0(hv)}$ during isotropic compression tests (Ng and Yung, 2008)

in Fig. 4, the AEV of the two specimens are estimated to be 60 and 90 kPa at net mean stresses of 110 and 300 kPa, respectively. Soil specimen subjected to a higher net mean stress tends to possess a higher air-entry value. Since the net mean stresses applied in this series of tests are 110 kPa or even higher, the AEV of specimens in this series should be equal to or larger than 60 kPa. The observed significant increase in shear moduli when matric suction increases from 0 to 50 kPa (less than AEV of test material) may be because each specimen remains essentially saturated at any matric suction less than AEV and so bulk water effects dominate soil responses (Mancuso et al., 2002). Any increase in matric suction is practically equivalent to an increase in effective mean stress, resulting in a smaller void ratio and a much stiffer soil. On the other hand, as matric suction increases above the AEV, each soil specimen starts to desaturate, resulting in the formation of an air-water interface at the contact points of soil particles. Although the meniscus water causes an increase in the normal forces which “hold” soil particles together and hence lead to higher shear moduli, this beneficial holding effects could not increase infinitely. This is because of progressive degradation in meniscus radius when matric suction increases above AEV of a soil specimen (Mancuso et al., 2002; Ng and Yung, 2008).

6.2 Degree of stiffness anisotropy at very small strains

The degree of stiffness anisotropy is expressed in terms of the ratio of shear modulus in the horizontal plane ($G_{0(hh)}$) to that in the vertical plane ($G_{0(hv)}$ or $G_{0(vh)}$) in this study. In a homogeneous cross-anisotropic elastic continuum, $G_{0(vh)}$ should be equal to $G_{0(hv)}$. However, a discrepancy between measured $G_{0(vh)}$ and $G_{0(hv)}$ is observed, as illustrated in Figs 9(a) and 9(b). This discrepancy may be attributed to the following four reasons (Ng et al., 2009). Firstly, soil specimen was actually not a homogeneous cross-anisotropic elastic continuum. Due to the preferred orientation of particles in the horizontal direction, a horizontally transmitted shear wave travels through fewer particle contacts per unit distance than does a vertically transmitted shear wave and this results in $v_{s(hv)}$ being higher than $v_{s(vh)}$ (Jardine et al., 1999). Secondly, transmitting frequencies used by the horizontally mounted bender element probes ($v_{s(hh)}$ and $v_{s(hv)}$) were higher than those used by the platen-mounted bender elements

($v_{s(vh)}$) (Pennington et al., 2001). Thirdly, bender element embedded in the base pedestal probably deflected more than the horizontally mounted bender elements did inside the probe and hence resulted in a lower $v_{s(vh)}$ (Pennington et al., 2001). Fourthly, platen end effects on stiffness measurements (Germine and Ladd, 1988; Lacasse and Berre, 1988) could be another cause of the discrepancy. To eliminate the differences in frequency and boundary effects, $G_{0(hh)}$ and $G_{0(hv)}$ reported in Fig. 9 were chosen for calculating degree of stiffness anisotropy. This is because that $G_{0(hh)}$ and $G_{0(hv)}$ were generated by the same bender element probe and they had the same frequency, travelling path and boundary conditions (Pennington et al., 2001; Ng et al., 2004).

Fig. 10 shows the relationship between degree of stiffness anisotropy ($G_{0(hh)}/G_{0(hv)}$) and net mean stress at different matric suctions (0, 50, 100 and 200 kPa). When matric suction is zero, $G_{0(hh)}$ is about 2.5% to 4% higher than $G_{0(hv)}$ for net mean stress range from 110 to 400 kPa. According to Eq. (7), this observed stiffness anisotropy should be attributed to the inherent anisotropy (C_2^{hh}/C_2^{hv}) induced in the tested material during specimen preparation (Ng and Yung, 2008). However, this observed stiffness anisotropy may not be solely caused by the inherent anisotropy induced during specimen preparation. This is because the specimens have undergone isotropic compression and suction equalisation, as illustrated in Fig. 5. The ratio ($G_{0(hh)}/G_{0(hv)}$) changes during the isotropic compression and suction equalisation. When matric suction increases from 0 to 50 kPa, the degree of stiffness anisotropy ($G_{0(hh)}/G_{0(hv)}$) increases by a ratio of 3.6%, 4.2%, 4.5% and 5.1% at 0, 50, 100 and 200 kPa, respectively. On the other hand, there is only a very small increase (less than 1%) in the stiffness ratio when matric suction is increased from 50 to 200 kPa. The differences in measured results at different suction ranges seem to suggest that bulk water effects dominate soil behaviour when matric suction is lower than AEV of soil specimen and meniscus water effects dominate soil behaviour when matric suction above the AEV. Although the magnitudes of increase in $G_{0(hh)}/G_{0(hv)}$ are not large, there is a clear trend showing that $G_{0(hh)}/G_{0(hv)}$ of CDT increases with an increase in matric suction but at a reducing rate at a given net mean stress. The measured results seem to be consistent with theoretical and experimental work by Li (2003) and Mui (2005) who demonstrated that variations of matric suction could induce anisotropic strains under isotropic stresses.

There is a 1% to 3% increase in $G_{0(hh)}/G_{0(hv)}$ when net mean stress increases from 110 to 500 kPa at matric suctions ranging from 50 to 200 kPa. Although it is generally recognized that shear modulus will increase with an increase in net mean stress, it is somewhat surprising that the stiffness ratio also increases with an increase in net mean stress. This observed behaviour may be attributed to the coupling effects between the hydraulic and mechanical behaviour of unsaturated soils (Wheeler et al., 2003). As net mean stress increases at a given matric suction, specific void volume of a soil specimen decreases and water flows out of the specimen to maintain constant suction. This may provide an opportunity for re-distribution bulk water and meniscus water throughout soil specimen. As a consequence of water redistribution, different mechanical behaviour including

shear stiffness response is expected even if the values of net mean stress, matric suction and specific volume were identical (Wheeler et al., 2003).

Test results shown in Fig. 10 cannot be explained by Eq. (7) fully. This may be attributed to two reasons: firstly, the proposed equation does not consider any possible coupling effects between the hydraulic and mechanical characteristics of unsaturated soils, i.e., possible re-distributions of bulk water and meniscus water of soil specimens; secondly, measurements of shear wave velocity are not accurate enough to differentiate such small degree of stiffness anisotropy. The estimated measurement error in shear modulus ($G_{0(ij)}$) is about $\pm 5\%$ (Ng and Yung, 2008).

6.3 Effects of drying-wetting on anisotropic shear modulus at very small strains

Fig. 11 shows variations of $G_{0(vh)}$, $G_{0(hv)}$ and $G_{0(hh)}$ with matric suction during two drying-wetting tests (obtained from series B tests). It can be seen that $G_{0(vh)}$, $G_{0(hv)}$ and $G_{0(hh)}$ increase with increasing matric suction following a similar trend during a drying path. This is consistent with the observation from series A tests. After drying to the maximum suction of 250 kPa, soil suction is reduced by wetting the soil specimen. Similar to SDSWCCs (see Fig. 4), there is a hysteresis between the drying and wetting stiffness curves showing variations of shear moduli with matric suction. At any given suction, the shear moduli measured during wetting are consistently higher than those obtained during drying. Since the induced axial and radial strains of each soil specimen are relatively small (less than $\pm 0.3\%$), total volume change is not significant. The shear modulus hysteresis may be because that the water content on the adsorption curve is lower than that on the desorption curve at the same suction.

Fig. 12 shows the relationship between degree of stiffness anisotropy, $G_{0(hh)}/G_{0(hv)}$, and matric suction for the two drying-wetting tests. At net mean stresses of 110 and 300 kPa, variations of degree of stiffness anisotropy with matric suction follow a similar trend. Although the magnitudes of the increase in $G_{0(hh)}/G_{0(hv)}$ with an increase in matric suction are very small, there is a clear trend showing that the degree of stiffness anisotropy increases with increasing matric suction. Moreover, $G_{0(hh)}/G_{0(hv)}$ value at net mean stress of 300 kPa is consistently higher than that at net mean stress of 110 kPa. These observations are consistent with Fig. 10,

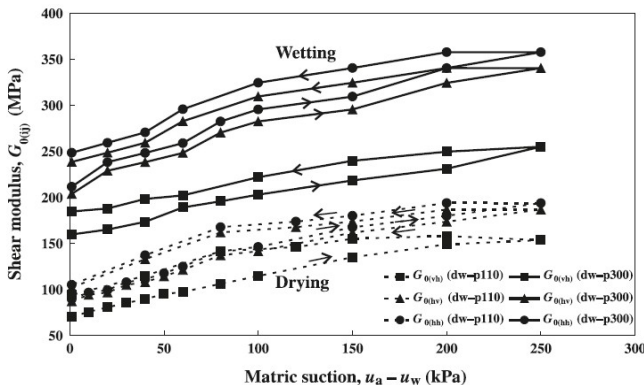


Fig. 11. Variations of shear moduli with matric suction during drying-wetting tests (Ng et al., 2009)

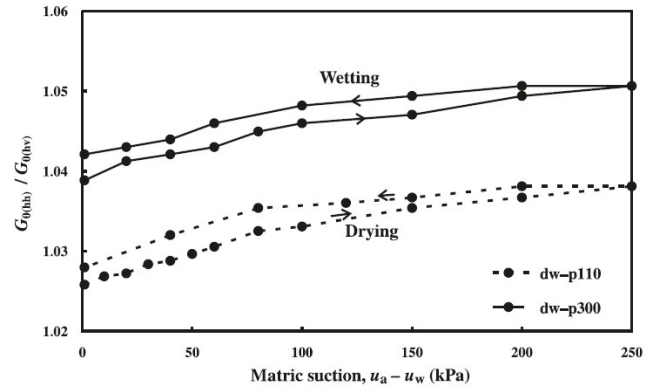


Fig. 12. The relationship between degree of stiffness anisotropy and matric suction during drying-wetting tests (Ng et al., 2009)

illustrating that stiffness anisotropy is more significant at higher matric suction and higher net mean stress. There is a hysteresis between the drying and wetting stiffness curves showing the variations of stiffness anisotropy with matric suction. The changing rates of $G_{0(hh)}/G_{0(hv)}$ and the sizes of hysteresis loops at two different net mean stresses are almost the same.

6.4 Shear modulus degradation curve at small strains

The shear modulus degradation curves at small strains are studied by constant p triaxial compression tests. Fig. 13(a) shows measured stress-strain relationship at matric suctions of 150 and 300 kPa (obtained from series C tests). When deviator stress increases, shear strain of each specimen increases non-linearly at an increasing rate. Under the same deviator stress, soil specimen tested at a matric suction of 300 kPa produces consistently smaller shear strain than that at matric suction of 150 kPa under the same deviator stress. This is because the fact that shear stiffness of unsaturated soil increases with increasing suction level, as illustrated in Figs 9 and 11. It is shown in Fig. 13(a) that secant shear modulus (G_{sec}) of each specimen at small strains can be obtained from the slope of a deviator stress-shear strain curve. Theoretically, G_0 may be determined from the initial slope of the stress-strain curve. Due to the limited accuracy of Hall-effect transducers, G_0 cannot be determined from the stress-strain curve reliably in this study. Therefore, G_0 measured by bender elements is adopted to represent shear stiffness at very small strain level. As illustrated in Fig. 10, measured $G_{0(hh)}$ is slightly larger than $G_{0(hv)}$, meaning that CDT is stiffer in the horizontal direction. Yimsiri and Soga (2002) proposed a micromechanics model and demonstrated that the shear modulus evaluated from triaxial tests is closer to the shear modulus in the vertical plane ($G_{0(vh)}$ or $G_{0(hv)}$) when the soil is stiffer in the horizontal direction. Besides, $G_{0(hv)}$ is believed to be more reliable than $G_{0(vh)}$ as discussed in section 6.2. Therefore, measured $G_{0(hv)}$ is selected for comparison with G_{sec} at different shear strains obtained from constant p triaxial compression tests.

Fig. 13(b) shows the influence of shear strain on G_{sec} in a semi-logarithmic scale at matric suctions of 150 and 300 kPa. $G_{0(hv)}$ measured by bender elements before constant p compression is also shown for comparison. The

corresponding shear strain for G_0 is assumed to be 0.001% in this study (Dyvik and Madhus, 1985). The measured $G_{0(hv)}$ at matric suctions of 150 and 300 kPa are 164 and 220 MPa, respectively. $G_{0(hv)}$ increases by 34% when matric suction increases from 150 to 300 kPa. Suction effects on G_0 have been explained in section 6.1. Due to the limited accuracy of Hall-effect local strain transducers, strain less than 0.003% cannot be measured accurately. Thus, there is no reliable data in the strain range from 0.001% to 0.003% shown in this figure. When shear strain increases from 0.003% to 1%, G_{sec} of the two specimens both reduces significantly but at different rates. The G_{sec} measured at a matric suction of 300 kPa is consistently higher than that obtained at a matric suction of 150 kPa.

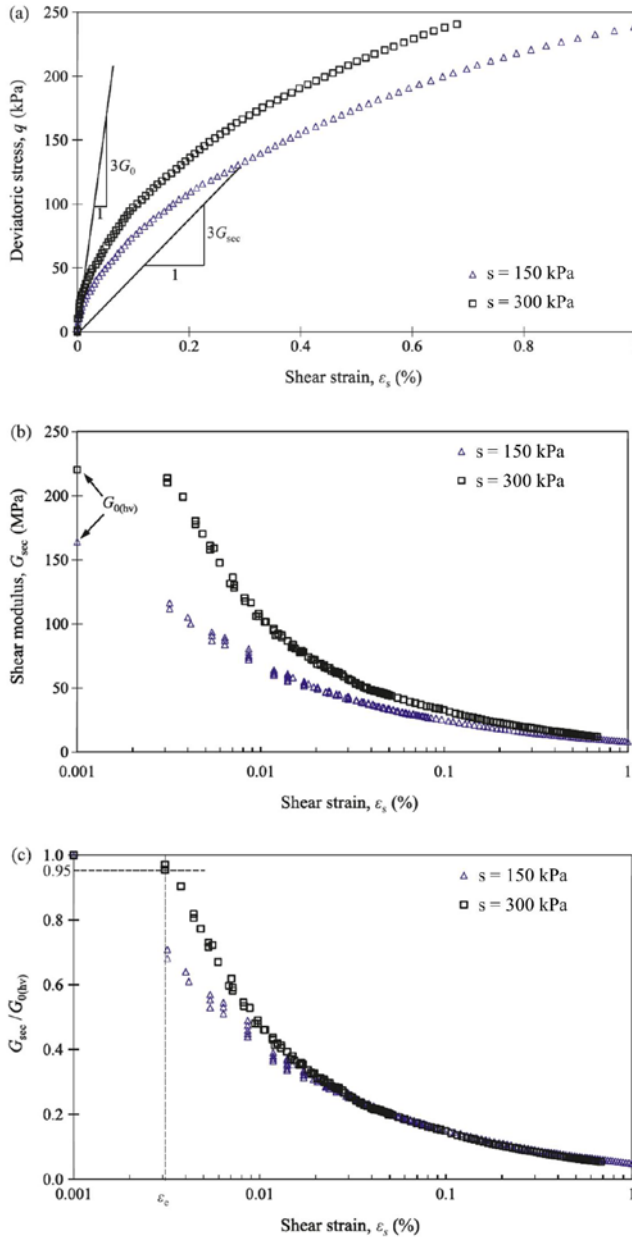


Fig. 13. Effects of matric suction on (a) stress - strain relationship; (b) shear modulus degradation curve; (c)

normalized shear modulus degradation curve during constant p compression tests (Ng and Xu, 2012)

Fig. 13(c) shows secant shear modulus degradation curve normalized by $G_{0(hv)}$. The stiffness could be roughly constant if the soil behaves elastically as straining proceeds (Simpson, 1992). The shear strain corresponding to the limit of the elastic proportion is generally described as elastic threshold shear strain (ϵ_e). Stokoe et al. (1995) reported that ϵ_e of sand is about 0.001% while ϵ_e of clay is much larger (in the order of 0.005%). In order to avoid subjective assessment, ϵ_e in this study is quantified as the shear strain corresponding to $G_{sec}/G_{0(hv)} = 0.95$ (similar to Clayton and Heymann, 2001). As illustrated in the figure, the ϵ_e of the specimen tested at a matric suction of 300 kPa is about 0.003%. For the specimen tested at a matric suction of 150 kPa, although there is no reliable data shown in the strain range from 0.001% to 0.003%, from the trend it can be seen that the ϵ_e is very likely smaller than 0.003%. The elastic “proportion” of a soil specimen might represent the proportion of the contacts between soil particles which are still intact and have not started to slide (Simpson, 1992). For soil specimen at a higher matric suction and lower degree of saturation, more meniscus water exists in the specimen. Meniscus water causes an increase in the normal force holding the soil particles together and resisting the slippage between soil particles. Therefore, the specimen at a higher suction has a larger ϵ_e . Beyond the ϵ_e , normalized shear modulus reduces significantly with shear strain, as shown in the figure. The rate of degradation is higher for the specimen at higher matric suction. When the shear strain is larger than about 0.02%, the two normalized shear modulus degradation curves overlap with each other. This means that the effects of suction on normalized shear modulus degradation curve become negligible when the shear strain is larger than 0.02%.

6.5 Effects of number of load applications on resilient modulus

In series D tests, there are 100 cycles of loading-unloading at each stress and suction level. To investigate the influence of number of load applications on resilient modulus, resilient modulus from the N th cycle (M_r^N) is normalised by resilient modulus from the first cycle (M_r^1).

Fig. 14(a) shows variations of normalised resilient modulus (M_r^N/M_r^1) with number of load applications (N) after wetting to zero matric suction (obtained from test cyc-s0 in Fig. 8). It can be seen that M_r^N/M_r^1 increases with an increase in N at each cyclic stress (30, 40, 55 and 70 kPa). This is a consequence of progressive densification resulting from that the application of repeated cyclic stress (Dehlen, 1969). In this study, volume change was determined from axial and radial strains measured using Hall-effect transducers. At zero matric suction, contractive volumetric strains measured after 100 cycles of loading-unloading are 0.03%, 0.04%, 0.09% and 0.25%, corresponding to cyclic stresses of 30, 40, 55 and 70 kPa, respectively. The decreasing volume and hence increasing dry density of each specimen results in an increase in M_r^N/M_r^1 with increasing N .

Fig. 14(a) also reveals that the rate of increase in M_r^N/M_r^1 with increasing N is dependent on cyclic stress. When cyclic

stress is 30 and 40 kPa, M_r^N/M_r^1 increases by about 10% during the first 20 cycles of loading-unloading. After the first

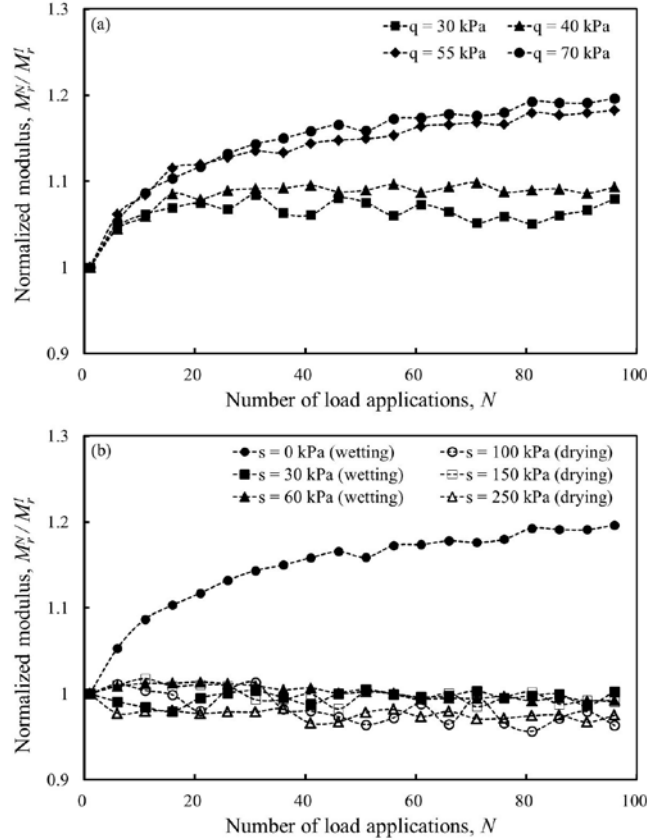


Fig. 14. Relationship between normalized resilient modulus and cyclic number at (a) zero suction; (b) cyclic stress of 70 kPa during cyclic triaxial tests (Ng et al., 2012)

20 cycles, there is no obvious variation of M_r^N/M_r^1 . For the case of cyclic stress of 55 and 70 kPa, M_r^N/M_r^1 increases continuously during the 100 cycles of loading-unloading, but at a decreasing rate after the first 20 cycles. Thus, the influence of N on M_r^N/M_r^1 is more significant at higher cyclic stress. This is because that accumulated contractive volumetric strain during cyclic loading-unloading increases with an increase in cyclic stress at an increasing rate. The measured contractive volumetric strain is only 0.03% and 0.04% at cyclic stresses of 30 and 40 kPa, but increases to 0.09% and 0.25% under cyclic stress of 55 and 70 kPa. Due to larger contractive volumetric strain, densification effect on M_R is more significant at a higher cyclic stress.

Fig. 14(b) shows the relationship between M_r^N/M_r^1 and N at cyclic stress of 70 kPa but different matric suctions (0, 30, 60, 100, 150 and 250 kPa). This figure clearly reveals two types of soil response. At zero matric suction, M_r^N/M_r^1 increases continuously with increasing N . The total increase during the 100 cycles of loading-unloading is up to 20%. On the other hand, when matric suction is equal to or larger than 30 kPa ($s = 30, 60, 100, 150$ and 250 kPa), M_r^N/M_r^1 varies only slightly with N . One reason is that contractive volumetric strain under cyclic loads is much smaller when matric suction is equal to or larger than 30 kPa. For example, contractive volumetric strain under cyclic loading-unloading measured at cyclic

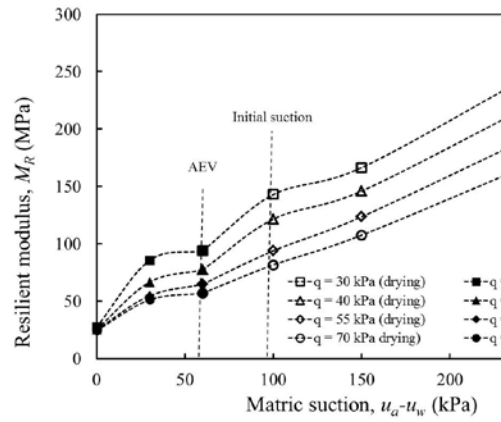


Fig. 15. Influence of matric suction on resilient modulus during cyclic triaxial tests (Ng et al., 2012)

stress of 70 kPa decreases from 0.25% to 0.03% when matric suction increases from 0 to 30 kPa. Given such a small volumetric strain, the variation of M_r^N/M_r^1 with N becomes insignificant. At higher matric suction such as 100 kPa, there is even a slight degradation in M_r^N/M_r^1 with N . This is because that soil dilation rather than contraction occurs under cyclic loads because of suction induced dilatancy (Ng and Zhou, 2005). Dilative volumetric strain of -0.03% is measured during cyclic loading-unloading at cyclic stress of 70 kPa and matric suction of 100 kPa. Due to the occurrence of dilation, soil density and hence resilient modulus decreases with an increase in number of load applications. Suction effects on soil behavior under cyclic loads are further discussed in the next subsection.

Fig. 14 suggest that the variation of M_r^N/M_r^1 is negligible when number of load applications is larger than 20, except when cyclic stress is larger than 55 kPa at zero matric suction. An unsaturated CDT specimen generally achieves a stable resilient modulus within 100 loading-unloading cycles.

6.6 Effects of stress and suction level on resilient modulus

Fig. 15 shows the relationship between M_R and s at different cyclic stresses (30, 40, 55 and 70 kPa) (obtained from series D tests). M_R is the average resilient modulus of the last five cycles at each stress state (i.e., $N = 96-100$). Irrespective of whether it is along a drying or a wetting path, M_R increases with increasing s significantly. At cyclic stress of 30 kPa, M_R increases by eight times when s increases from 0 to 250 kPa. The suction effects on soil stiffness have been well illustrated in Figs 9, 11 and 13(b) and explained in the section 6.1. The influence of s on M_R is captured by the term $(1+s/p)^{k_3}$ in Eq. (10). Since M_R increases with an increase in s , the parameter k_3 should be positive.

Further inspection of this figure reveals that the relationship between M_R and s is highly nonlinear along a wetting path, along which soil suction is smaller than initial suction. Given the same increase in s , the percentage of increase in M_R is much larger in the lower suction range. At a cyclic stress of 30 kPa, M_R doubles when s increases from 0 to 30 kPa, while only increases by 10% when s increases from 30 to 60 kPa. Along a drying path, the increase rate of M_R with increasing s is almost constant. The different results observed in different suction ranges are likely related with

AEV of a soil specimen, as illustrated in Fig. 10. The different results observed in different suction ranges are probably because the bulk water effects dominate soil behaviour when matric suction is lower than AEV of soil specimen (here about 60 kPa, see Fig. 4) and meniscus water effects dominate soil behaviour when matric suction exceeds AEV (Ng and Yung, 2008).

It is revealed in Fig. 15 that M_R decreases significantly with increasing q_{cyc} at all matric suctions except $s = 0$. For instance, M_R decreases by about 40 % when q_{cyc} increases from 30 kPa to 70 kPa at a matric suction of 30 kPa. The observed decrease of M_R with an increase in q_{cyc} is due to the non-linearity of soil stress-strain relationship (Atkinson, 2000). Fig. 13 shows that soil stiffness is high at very small strains but it decays with an increase in strain level. In resilient modulus tests, strain level increases with an increase in q_{cyc} , hence measured M_R decreases with an increase in q_{cyc} . The non-linearity of soil stress-strain behaviour is captured by the term $(1+q_{cyc}/p_r)^{k_2}$ in Eq. (10). Since M_R decreases with increasing q_{cyc} , the parameter k_2 should be negative. For a soil specimen with a larger degree of non-linearity, the degradation of M_R with q_{cyc} should be more significant and parameter k_2 should be smaller.

6.7 Verification of proposed equations

6.7.1 Verification of proposed state-dependent equation for very small strain shear modulus

As predicted by Eq. (4), G_0 of an unsaturated soil depends on void ratio, net normal stress and matric suction. Assuming that the void ratio function takes the form of a power function in e^a , where a is an empirical void ratio exponent. For isotropic stress condition, Eq. (4) can be rewritten as

$$G_{0(ij)} = C_{ij}^2 \rho e^{2a} p^{2n} [1 + (u_a - u_w)]^{2b} \quad (12)$$

Taking the logarithm of each side gives

$$\ln G_{0(ij)} = 2 \ln C_{ij} + \ln \rho + 2a \ln e + 2n \ln p + 2b \ln [1 + (u_a - u_w)] \quad (13)$$

Equation (13) is applied to fit very small strain shear moduli of CDT measured in series A tests (Ng and Yung, 2008). The parameters C_{ij} , a , n , and b in Eq. (13) can be determined by the least squares method using a multiple linear regression model. The fitted parameters are listed in Table 2. Shear

Table 2. Fitted parameters for shear wave propagating in different polarization planes (Ng and Yung, 2008)

Shear wave, $v_{s(ij)}$	C_{ij}	a	n	b	R^2
$G_{0(hh)}$	65.5	-0.77	0.17	0.045	0.94
$G_{0(hv)}$	63.2	-0.77	0.17	0.045	0.94
$G_{0(vh)}$	57.7	-0.77	0.17	0.045	0.99

modulus can be calculated based on Eq. (12) with the fitted parameters. The coefficient of determination, R^2 , for the calculated and measured shear modulus in each polarization plane are also summarised in this table. The average value of R^2 is about 0.96, suggesting very strong correlations between the calculated and measured shear wave velocities. Thus, it is clear that Eq. (12) describes the test results well.

6.7.2 Verification of proposed equations for resilient modulus

In order to verify the validity of Eq. (10) for representing resilient modulus of an unsaturated soil, the measured resilient modulus of four different fine-grained soils are fitted, including CDT and Keuper Marl, Gault clay and London clay. M_R of CDT is measured in series D tests in this study and that of the other three soils is reported by Brown et al. (1987). According to AASHTO classification (2000), Gault clay and London clay are classified as A-7-5 soil, whereas CDT and Keuper Marl are classified as A-7-6 soil. Equation (10) was firstly applied to fit resilient modulus of CDT measured in series D tests. Four parameters in the equation (M_0 , k_1 , k_2 and k_3) are determined by curve fitting using least square method. This set of parameters except M_0 was applied to fit resilient modulus of Keuper Marl. The parameter M_0 , which incorporates the density effect on M_R , is determined using the least square error method. Similarly, Eqn (10) was used to fit resilient modulus of two A-7-5 soils. The values of soil parameters except M_0 were determined from resilient modulus of Gault clay. Then this set of parameters was applied to fit measured resilient modulus of London clay. The basic soil properties and parameter values are summarised in Table 3.

It should be pointed out that this study does not focus on the influence of net mean stress on resilient modulus. No cyclic triaxial test is conducted for calibrating k_1 , which is

Table 3. Fitted parameters for resilient modulus of four different soils (Ng et al., 2012)

Material	AASHTO classification	Specific gravity	Plastic limit	Liquid limit	Plasticity index	M_0	k_1	k_2	k_3	R^2	Se/Sy
CDT	A-7-6	2.73	29	43	14	8.32	1.00	-0.65	1.01	0.98	0.14
Keuper Marl	A-7-6	2.69	18	37	19	6.32	1.00	-0.65	1.01	0.66	0.60
Gault clay	A-7-5	2.69	25	61	36	0	1.00	-0.36	1.31	0.98	0.14
London clay	A-7-5	2.73	23	71	48	0.53	1.00	-0.36	1.31	0.96	0.21

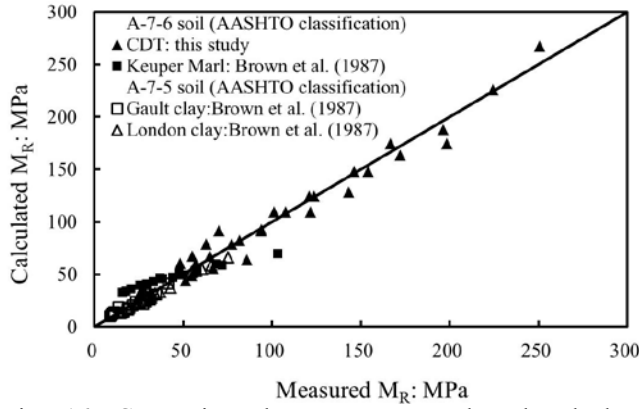


Fig. 16. Comparison between measured and calculated resilient modulus of four different soils using newly proposed semi-empirical equation (Ng et al., 2012)

determined based on previous theoretical and experimental studies. According to the well-known modified Cam-clay model, M_R (i.e., the axial Young's modulus during unloading) is proportional to effective mean stress p' (Muir Wood, 1990). Viggiani and Atkinson (1995a) also performed triaxial compression tests to study the relationship between shear modulus and p' , where n is regression coefficient. They observed that n is 0.72 at very small strain levels and increases to 1.0 at a strain level of 0.5%. In this study, the total axial strain, including both permanent plastic strain and recoverable resilient strain, is generally between 0.1% and 1%. Therefore, it may be reasonable to assume that M_R increases linearly with an increase in $(p - u_a)$ (i.e., $k_1 = 1$) for simplicity.

Fig. 16 compares the calculated and measured resilient modulus of these four fine-grained soils. It is well illustrated that the proposed Eq. (10) is able to capture the variation of resilient modulus of different soils with stress and suction level. It should be pointed out that two underlying assumptions are made to keep this equation simple. Firstly, parameters k_1 , k_2 and k_3 are assumed to be constant, independent of stress level and stress history. Secondly, density effect on M_R is incorporated in M_0 . If this equation is used to describe M_R of soil specimens with different initial densities, a single value for M_0 may be not sufficient.

7. SUMMARY AND CONCLUSIONS

Shear stiffness of an unsaturated soil is one of the most important geotechnical parameters for predicting ground movements and dynamic responses of many earth structures. In this study, a suction-controlled triaxial apparatus was newly modified to measure shear stiffness of an unsaturated weathered soil subjected to both static and cyclic loading conditions. This apparatus is equipped with three pairs of bender elements and Hall-effect transducers. Semi-empirical state-dependent equations were proposed to capture effects of net mean stress, matric suction and void ratio on anisotropic shear moduli at very small strains and resilient modulus under cyclic loading-unloading. The validity of these equations was verified by experimental study. Based on derived equations

and experimental measurements, some key conclusions are summarised.

From isotropic compression test on compacted soil specimens at different matric suctions, measured very small strain shear moduli, $G_{0(vh)}$, $G_{0(hv)}$ and $G_{0(hh)}$ consistently increase with an increase in net mean stresses. They also show significant increases with increasing matric suction at a given net stress. Moreover, the shear moduli increase more significantly below air-entry value (60 kPa). The effects of bulk water appear to be dominating when matric suction is smaller than the air-entry value whereas the influence of meniscus water prevails when matric suction exceeds the air-entry value.

Measured $G_{0(hh)}$ was about 2.5% to 4% higher than $G_{0(hv)}$ at zero matric suction for net mean stress varying from 110 to 500 kPa. When matric suction was increased from 0 to 50 kPa, $G_{0(hh)}/G_{0(hv)}$ increased by 3.6% to 5.1%. No further significant increase in suction-induced stiffness anisotropy was observed at matric suctions higher than the air-entry value. Moreover, a small increase (less than 3%) in the shear modulus ratio, $G_{0(hh)}/G_{0(hv)}$ was observed when the isotropic net mean stress increased from 110 to 500 kPa at a constant matric suction ranging from 0 to 200 kPa. This may be attributed to the coupling effects of hydraulic and mechanical characteristics of the unsaturated soil or to sample preparation.

From wetting and drying tests, it was found that there is a hysteresis between the drying and wetting stiffness curves showing the variations of very small strain shear moduli with matric suction. At the same suction, the shear moduli measured during wetting are consistently higher than those obtained during drying. The shear modulus hysteresis is possibly because water content on the adsorption curve is lower than that on the desorption curve at the same suction.

There is a clear trend showing that the degree of stiffness anisotropy increases with an increase in matric suction. There is also a hysteresis between the drying and wetting stiffness curves showing variations of stiffness anisotropy with matric suction. Although the size of hysteresis loop is very small, the trend is clear. The changing rates of $G_{0(hh)}/G_{0(hv)}$ and the sizes of hysteresis loops at two different net mean stresses (110 and 300 kPa) are almost the same.

From constant p triaxial compression test, shear modulus of unsaturated soil is consistently larger at higher matric suction in the shear strain range of 0.001% to 1%. However, the effects of suction on normalized shear modulus degradation curve become negligible when shear strain is larger than 0.02%. G_0 , elastic threshold strain (ϵ_e) and the rate of stiffness degradation all increase with an increase in suction magnitude. This may be attributed to the stabilisation effect arising from meniscus water when the degree of saturation and water content decrease.

For a contractive soil, measured M_R of unsaturated soil increases with the number of load applications under cyclic loads. On the contrary, M_R decreases slightly with increasing number of load applications in dilative soil. An unsaturated CDT specimen generally achieves a steady resilient response within 100 cycles of loading-unloading.

Measured M_R is highly dependent on stress state. M_R decreases with an increase in cyclic stress due to the

non-linearity of soil stress-strain behaviour, whereas it increases significantly with an increase in matric suction. When matric suction is increased from 0 to 250 kPa at a cyclic stress of 30 kPa, M_R increases by up to one order of magnitude. This may be attributed to a larger induced inter-particle normal force resulting from an increase in matric suction.

8. ACKNOWLEDGEMENTS

The research grant 2012CB719805 of 2012CB719800 provided by the Ministry of Science and Technology of the People's Republic of China through the National Basic Research Program (973 project) is gratefully acknowledged. In addition, the authors would like to thank the Research Grants Council of the Hong Kong Special Administrative Region (HKSAR) for supporting the research grant HKUST9/CRF/09.

9. REFERENCES

- AASHTO 2000. Classification of soil and soil-aggregate. American Association of State Highway and State Highway Officials, Washington, D.C.
- AASHTO 2003. AASHTO guide for the design of pavement structures. American Association of State Highway and State Highway Officials, Washington, D.C.
- Alonso, E.E., Gens, A. and Josa, A. 1990. A constitutive model for partly saturated soils. *Géotechnique*, 40(3): 405–430.
- ASTM 2006. Standard practice for classification of soils for engineering purpose (Unified Soil Classification System). American Society of Testing and Materials, West Conshohocken.
- Atkinson, J.H. 2000. Non-linear soil stiffness in routine design. *Géotechnique*, 50(5): 487–508.
- Atkinson, J.H. and Sallfors, G. 1991. Experimental determination of stress-strain-time characteristics in laboratory and in-situ tests. Proc. 10th Eur. Conf. Soil Mech. and Found. Engrg., Balkema, Vol.3: 915–956.
- Bellotti, R., Jamiolkowski, M., Lo Presti, D.C.F., and O'Neill, D.A. 1996. Anisotropy of small strain stiffness in Ticino sand. *Géotechnique*, 46(1): 115–131.
- Bishop, A.W. 1959. The principal of effective stress. Lecture delivered in Oslo, Norway, 1955, Technisk Ukeblad, 106(39): 859–863.
- BSI. 1990. British standard methods of test for soils for civil engineering purposes. Part 2. British Standards Institution, London.
- Brown, S.F. 1996. Soil mechanics in pavement engineering. *Géotechnique*, 46(3): 383–426.
- Brown, S.F., Loach, S.C. and O'Reilly, M.P. 1987. Repeated loading of fine grained soils. Contractor Report, 72, Transportation Research Laboratory.
- Burland, J.B. 1989. Small is beautiful – the stiffness of soils at small strains. *Canadian Geotechnical Journal*, 26(4): 499–516.
- Cabarkapa, Z., Cuccovillo and Gunn, M. 1999. Some aspects of the pre-failure behaviour of unsaturated soil. In Jamiolkowski, Lancellotta and Lo Presti (eds.), Proceedings of II Int. Symp. On Prefailure Deformation Characteristics of Geomaterials, Torino, Balkema, Vol.1: 159–165.
- Clayton, C.R.I. 2011. Stiffness at small strain: research and practice. *Géotechnique*, 61(1): 5–37.
- Clayton, C.R.I. and Heymann, G. 2001. Stiffness of geomaterials at very small strains. *Géotechnique*, 51(3): 245–255.
- Clayton, C.R.I., Khatrush, S.A., Bica, A.V.D. and Siddique, A. 1989. The use of Hall Effect Semiconductors in Geotechnical Engineering. *Geotech. Test. J., ASTM*, 12(1): 69–76.
- Dehlen, G.L. 1969. The effect of non-linear material response on the behaviour of pavements subjected to traffic loads. PhD thesis, University of California, Berkeley.
- Dyvik, R. and Madhus, C. 1985. Laboratory measurement of G_{max} using bender elements. Proceedings of ASCE Annual convention: Advances in the Art of Testing Soils under Cyclic Condition, Detroit: 186–196.
- Fisher, R.A. 1926. On the capillary forces in an ideal soil; correction of formulas by W.B. Haines. *J. Agric. Sci.*, 16: 492–505.
- Fredlund, D.G. and Morgenstern, N.R. 1977. Stress state variables for unsaturated soils. *Journal of the Geotechnical Engineering Division, ASCE*, 103(5): 447–466.
- Gens, A. 2010. Soil-environment interactions in geotechnical engineering. *Géotechnique*, 60(1): 3 – 74.
- Geotechnical Engineering Office 1988. Guide to rock and soil descriptions: Geoguide 3. Geotechnical Engineering Office, Civil Engineering Department, the Government of the Hong Kong SAR.
- Germine, J.T. and Ladd, C.C. 1988. Triaxial testing of saturated cohesive soils. In Donaghe, Chaney and Silver (eds.), Advanced Triaxial Testing of Soil and Rock, ASTM STP 977, American Society for Testing and Materials, Philadelphia: 421–459.
- Hilf, J.W. 1956. An investigation of pore-water pressure in compacted cohesive soils. PhD Dissertation, Tech. Memo. No.654, U.S. Dep. Of the Interior, Bureau of Reclamation, Design and Construction Div., Denver, CO.
- Houlsby, G.T. 1997. The work input to an unsaturated granular material. *Géotechnique*, 47(1): 193–196.
- Jamiolkowski, M., Lancellotta, R. and Lo Presti, D.C.F. 1995. Remarks on the stiffness at small strains of six Italian clays. In S. Shibuya, T. Mitachi and S. Muira (eds.), Proceedings of International Symposium on Pre-failure Deformation of Geomaterials, Vol.2: 817–836.
- Jardine, R.J., Kuwano, R., Zdravkovic, L. and Thornton, C. 1999. Some fundamental aspects of the pre-failure behaviour of granular soils. Proc. Int. Symp. on Pre-failure Deformation of Geomaterials, Vol.2: 1077–1111.
- Jennings, J. E. and Burland, J.B. 1962. Limitations to the use of effective stresses in partly saturated soils. *Géotechnique*, 12 (2): 125–144.

- Jin, M.S., Lee, W. and Kovacs W.D. 1994. Seasonal variations of resilient modulus of subgrade soils. *Journal of Transportation Engineering*, ASCE, 124(4): 603–615.
- Kim, D. and Kim, J.R. 2007. Resilient behaviour of compacted subgrade soils under the repeated triaxial test. *Construction and Building Material*, 21: 1470-1479.
- Lacasse, S. and Berre, T. 1988. Triaxial testing methods for soils. In Donaghe, Chaney and Silver (eds.), *Advanced Triaxial Testing of Soil and Rock*, ASTM STP 977, American Society for Testing and Materials, Philadelphia: 264-289.
- Lekarp, F., Isacsson, U. and Dawson, A. 2000. State of the art: resilient response of unbound aggregates. *Journal of Transportation Engineering*, 126(1): 66-75.
- Lee, J.S. and Santamarina, J.C. 2005. Bender elements: performance and signal interpretation. *Journal of Geotechnical and Geoenvironmental Engineering*, ASCE, 131(9): 1063-1070.
- Li, X.S. 2003. Effective stress in unsaturated soil: a microstructural analysis. *Géotechnique*, 53(2): 273-277.
- Mair, R.J. 1993. Developments in geotechnical engineering research: application to tunnels and deep excavations. *Proceedings of the Institution of Civil Engineers and Civil Engineering*: 27-41.
- Malone, A., Ng, C.W.W. and Pappin, J. 1997. Invited paper: Displacements around deep excavations in completely decomposed granite. *Proc. 14th Int. Conf. Soil Mech. and Fdn. Engng.*, Hamburg. Vol.4: 2325-2328.
- Mancuso, C., Vassallo, R. and d'Onofrio, A. 2000. Soil behaviour in suction controlled cyclic and dynamic torsional shear tests. *Proc. of 1st Asian Regional Conference on Unsaturated Soils*, Singapore: 539-544.
- Mancuso, C., Vassallo, R. and d'Onofrio, A. 2002. Small strain behavior of a silty sand in controlled-suction resonant column–torsional shear tests. *Canadian Geotechnical Journal*, 39(1): 22-31.
- Mavko, G. M., Mukerji, T., and Dvorkin, J. 1998. *The Rock Physics Handbook*. New York: Cambridge University Press.
- Mui, T.S. 2005. The shearing effect of suction. MPhil thesis, Hong Kong University of Science and Technology.
- Muir Wood, D. 1990. *Soil behaviour and critical state soil mechanics*. Cam-bridge University Press, Cambridge, London.
- Ng, C.W.W. and Chiu, C.F. 2001. Behaviour of a loosely compacted unsaturated volcanic soil. *Journal of Geotechnical and Geoenvironmental Engineering*, ASCE, 127(12): 1027-1036.
- Ng, C.W.W., Lai, C.H. and Chiu, C.F. 2011. A modified triaxial apparatus for measuring the stress-path dependent water retention curve. *Geotechnical Testing Journal*, ASTM, 35(3): 490-495.
- Ng, C.W.W. and Leung, E.H.Y. 2007. Determination of shear wave velocities and shear moduli of completely decomposed tuff. *Journal of Geotechnical and Geoenvironmental Engineering*, ASCE, 133(6): 630-640.
- Ng, C.W.W., Leung, E.H.Y., and Lau, C.K. 2004. Inherent anisotropic stiffness of weathered geomaterial and its influence on ground deformations around deep excavations. *Canadian Geotechnical Journal*, 41(1): 12-24.
- Ng, C.W.W. and Lings, M.L. 1995. Effects of modelling soil non-linearity and wall installation on the back-analysis of a deep excavation in stiff clay. *Journal of Geotechnical Engineering*, ASCE, 121(10): 687-695.
- Ng, C.W.W. and Menzies, B. 2007. *Unsaturated Soil Mechanics and Engineering*. Taylor and Francis, UK and USA.
- Ng, C.W.W. and Pang, Y.W. 2000. Experimental investigations of soil-water characteristics of a volcanic soil. *Canadian Geotechnical Journal*, 37(6): 1252-1264.
- Ng, C.W.W., Pun, W.K. and Pang, R.P.L. 2000. Small strain stiffness of natural granitic saprolite in Hong Kong. *Journal of Geotechnical and Geoenvironmental Engineering*, ASCE, 126(9): 819-833.
- Ng, C.W.W. and Xu, J. 2012. Effects of current suction ratio and recent suction history on small-strain behaviour of an unsaturated soil. *Canadian Geotechnical Journal*, 49(1): 226-243.
- Ng, C.W.W., Xu, J. and Yung, S.Y. 2009. Effects of wetting-drying and stress ratio on anisotropic stiffness of an unsaturated soil at very small strains. *Canadian Geotechnical Journal*, 46(9): 1062-1076.
- Ng, C.W.W. and Yung, S.Y. 2008. Determination of the anisotropic shear stiffness of an unsaturated decomposed soil. *Géotechnique*, 58(1): 23-35.
- Ng, C.W.W. and Zhou, R.Z.B. 2005. Effects of soil suction on dilatancy of an unsaturated soil. *Proc. 16th Int. Conf. Soil Mech. and Geotech. Engrg.* Osaka, Japan, 2: 559–562.
- Ng, C.W.W., Zhou, C., Yuan, Q. and Xu, J. (2012). Resilient modulus of unsaturated subgrade soil: experimental and theoretical investigations. *Canadian Geotechnical Journal*. Under re-review.
- Pennington, D.S., Nash, D.F.T., and Lings, M.L. 2001. Horizontally mounted bender elements for measuring anisotropic shear moduli in triaxial clay specimen., *Geotechnical Testing Journal*, ASTM, 24(2): 133-144.
- Roesler, S. K. 1979. Anisotropic shear modulus due to stress anisotropy. *J. Geotech. Eng.*, ASCE. 105(7): 871-880.
- Scholey, G.K., Frost, J.D., Lo Presti, D.C.F. and Jamiolkowski, M. 1995. A review of instrumentation for measuring small strains during triaxial testing of soil specimens. *Geotechnical Testing Journal*, ASTM, 18(2): 137-156.
- Sánchez-Salinero, I., Roesset, J.M. and Stokoe, K.H. 1986. Analytical studies of body wave propagation and attenuation. Report GR 86-15, University of Texas, Austin.
- Seed, H.B., Chan, C.K. and Lee, C.E. 1962. Resilience characteristics of subgrade soils and their relation to fatigue failures, *Proc. Int. Conf. Structural Design of Asphalt Pavements*, Ann Arbor, Michigan: 611-636.
- Simpson, B. 1992. Retaining structures – displacement and design. *Géotechnique*, 42(4): 539-576.
- Sivakumar, V. 1993. A critical state framework for unsaturated soils. PhD Thesis, University of Sheffield.

- Stokoe, K.H. II, Hwang, S.K., Lee, J.N.K., and Andrus, R.D. 1995. Effects of various parameters on the stiffness and damping of soils at small to medium strains. In S. Shibuya et al. (eds.), Proc., Int. Symp. on Pre-failure Deformation of Geomaterials, Vol.2: 785-816.
- Uzan, J. 1985. Characterization of granular material. *Transportation Research Record*, 1022: 52-59.
- Viggiani, G. and Atkinson, J.H. 1995a. Stiffness of fine-grained soil at very small strains. *Géotechnique*, 45(2): 249-265.
- Viggiani, G. and Atkinson, J.H. 1995b. Interpretation of bender element tests. *Géotechnique*, 45(1): 149-154.
- Wheeler, S.J., Sharma, R.S. and Buisson, M.S.R. 2003. Coupling of hydraulic hysteresis and stress-strain behaviour in unsaturated soil. *Géotechnique*, 53(1): 41-54.
- Wheeler, S. J. and Sivakumar, V. 1995. An elasto-plastic critical state framework for unsaturated soil. *Géotechnique*, 45(1): 35-53.
- Yimsiri, S. and Soga, K. 2002. Application of micromechanics model to study anisotropy of soils at very small strains. *Soils and Foundations*, 42(5): 15-26.

Nanoparticles for Geotechnical Engineering

Mohd Raihan Taha
Dept of Civil & Structural Engineering, Universiti Kebangsaan Malaysia

ABSTRACT

Nanoparticles, one of the results of nanotechnology are very fine materials with wide range of applications. In fields such as electronics, manufacturing, energy, and medicine its application is well established. However, geotechnical engineers have not ventured well into nanotechnology although they have understood the importance of nano level concepts for many-many years. Nevertheless, geotechnical engineers have done research and published on common nanotechnology topics such as molecular dynamics, nanomechanics, nanoindentation, atomic force microscopy, etc. Some of these contributions are summarized in this paper. Conventional soil improvement studies using nanoparticles are also included to show that nanoparticles such as nano-soil, nano-clay, carbon nanotubes, nanoalumina have characteristics that can be of advantage to geotechnical engineers.

Keywords: Nanoparticle, nano-soil, geotechnical engineering, soil improvement, geoengineering

1. INTRODUCTION

Developments in nanotechnology particularly over the past 10 years have been fully tapped for its advantage by all fields of knowledge. On the other hand, this cannot be much said for geotechnical engineering. By its own right, geotechnical engineering should be at the forefront of nanotechnology as it is one of the biggest users of materials. In addition, geotechnical engineers are amongst the earliest “nanotechnologist” in which in the past they have dealt with materials at nano sizes and phenomenon that operates at nano scale [1]. Geoenvironmental engineers are the only group of geotechnical/soil engineers that are well into applying nanomaterials in their work, especially for environmental remediation.

This purpose of this paper is to provide some background on “nano” related research works in geotechnical engineering. In addition, some results on the use of nanomaterials such as carbon nanotubes, nano-soil, nano-clay, nanoalumina, etc for soil improvement will be covered. As previously mentioned, geotechnical engineers as one of the major user of materials, thus should exploit this technology/material to our advantage and provide efficient use of materials for clients/society.

2. REVIEW OF RELATED “NANO” STUDIES IN GEOTECHNICAL ENGINEERING

Many phenomena that are part of basic geotechnical knowledge such as soil moisture, water molecule characteristics, diffuse double layer systems, soil mineralogy are processes and materials that operates at nano level [1] & [2]. The following provides some other examples of research works in order to show geotechnical engineers involvement in nano related studies.

3.1 Clay Structure

Based on the fundamental definition of nanomaterial, it is not difficult to envisage that a clay particle is a nanomaterial. Furthermore, geotechnical engineers have long recognized the “nano” dimensions related clay structures. Only previously, these dimensions were provided in unit of angstrom (Å) in which 1 Å is 0.1 nm [3].

Molecular issues related to the properties of nano-meso-microscale montmorillonite clay particulate systems were studied by Katti et al.[4]. It was shown (first using a controlled uniaxial device then electron microscopic and Fourier transform infrared spectroscopic) that the addition of solvents causes breakdown of large particles to smaller nano and meso scale particles with increased water incorporation in the interlayers causing swelling. In addition, using micro-attenuated total reflectance (ATR) spectroscopy they found that the increased swelling is related to increased misorientation of the montmorillonite platelets. Thus, these investigation, observation and behavior can be used to develop novel nanocomposite systems based on montmorillonite with tailored properties.

Understanding the nanostructure of clays has lead to the synthesis of many clay products of various uses. For example, Chen et al. [5] produced nanostructure nano-clay multi layers for potential applications such as coatings and membranes for MEMS/NEMS (micro/nano electrical-mechanical systems) and sensors. Nanostructured composite consisting of zirconia and nano-clays is chemically inert, high thermal resistance, high hardness and the presence of platy nano-clay layer within the structure increases fracture toughness by deflecting cracks, rendering even higher hardness of themultilayers. In geotechnical and geoenvironmental engineering, these properties may be useful for liners and caps of nuclear waste containment systems. Thus, with the

knowledge now available, it is possible to produce any nanomaterial to suits our needs.

3.2 Molecular Dynamics Simulation

Molecular dynamics (MD) refers to numerical methods of solving classical equations of motion (particle dynamics) for multiparticle systems with known interatomic potentials [7]. Further computer processing and visualization simulations of results are commonly known as molecular dynamics simulations. This approach is particularly popular amongst nanoscientist in their study of particle interactions in nanosystems.

In general, the classical Newton's Law for motion of particles is given by

$$F_i = m_i \frac{d^2 r_i}{dt^2} \quad (1)$$

where F_i is the force acting on particle i , m is the mass of the particle, r is the distance of the particle i from a datum, t is time. The force acting on the particle calculated from the interatomic potential function U_{ij} , may be written as

$$F_i = \sum_{i \neq j} F_{ij}, \quad F_{ij} = -\nabla U_{ij} \quad (2)$$

The potential function can be obtained classically using Hooke's Law. However, in MD simulations, nanoscientist commonly used the Lennard-Jones (L-J) potential function which gives the total van der Waals force and written as follows [6]

$$U(x) = 4\varepsilon_{LJ} \left(\frac{\sigma^{12}}{r^{12}} - \frac{\sigma^6}{r^6} \right) \quad (3)$$

In Eq. (3), ε_{LJ} is the dislocation energy, and σ is the collision diameter, i.e. the distance in which $U = 0$. Another common model involving short-range pair-wise interaction is the Morse potential. A host of other potentials may also be used. For example, a general 3-D interatomic function also involving the long range Coulomb, van der Waals interaction, etc. was described by Gutierrez [7]

Skipper [8], used MD simulations of clay nano-structure to study the influence of pore-fluid interaction. The interlayer region of the stacked clay nano-structure was looked into to provide insight into the molecular mechanisms underlying clay swelling.

The influence of applied load on the interlayer of pyrophyllite was studied by Katti et al.[9]. Using steered MD simulations (SMD), where external forces were applied to individual atoms, they found that deformation largely occurred in the interlayer with the clay layer show relatively little deformation. In another studies [10], [11], & [12], Katti and his co-workers used SMD to study the load-deformation behavior of the interlayer water and nature of water in the interlayer.

3.3 Nanomechanics

Nanomechanics (nanoscale mechanics) also include molecular dynamics and its applications in geotechnical engineering were specifically mentioned by Voyiadjis and Song [13]. It is based on quantum and molecular mechanics and thus it deals with the equilibrium states of atomic and molecular forces. Bridging nano-, micro- and macro scales can be achieved by combination of molecular mechanics, particular mechanics and continuum mechanics based on the hierarchical approach [14].

However, there are some advantages and disadvantages of using nanomechanics in geotechnical engineering. Advantages include input parameters physical quantities, such as electron charge, dihedral angle, electron permittivity, etc. are known and well established [13]. Thus, nanomechanics provide a new insight into soil behavior particularly at atomic level. Amongst the disadvantages is the amount of computational time required to arrive at the overall solution. However, recent developments have reduced this time to a reasonable period especially with the aid of many up-to-date softwares now available in the market. Many of theories are also unfamiliar to many geotechnical engineers. Therefore, most geotechnical engineers will not have the motivation or capacity to learn and apply them.

Nanoindentation and atomic force microscope (AFM) are the two main equipment which have found much use in the study of nanomaterials. Developed in the early 70's, nanoindentation was initially designed for testing of small volume materials. It is simply a device with nano size indenter providing stress-strain behavior at relatively minute loadings and displacements. Two main properties as a result nanoindentation testing are Young's modulus and hardness. It is now commonly equipped with a microscope so that the load target area/aim is known. It can also provide "signature" responses of materials even for materials with very similar crystal structures [15].

For geotechnical applications, Zhang et al. [16] wrote that understanding the macroscopic behavior of geomaterials requires an insight into the micro/nano scale behavior of individual particles. Advances in understanding the Young's modulus and hardness of individual soil particles can contribute significantly to micro/nano mechanics and multiscale modeling of geomaterials.

A schematic diagram of the nanoindentation processes and load- displacement curve is shown in Fig. 1. For the load displacement curve, in conventional loading apparatus for soils (and other materials), the resulting curve is different in which load reduces with increasing displacement. In addition, the resulting plot shows that the behavior of materials is non-linear even at very-very small loadings.

The AFM is mainly used to study the surface morphology of materials. In addition, it can be used to measure friction and almost all surface forces. Using a tip (a mechanical probe) which is made of diamond, or silicon or CNT, etc. the probe moves up and down according to the nature of the surface during scanning (Fig. 2).

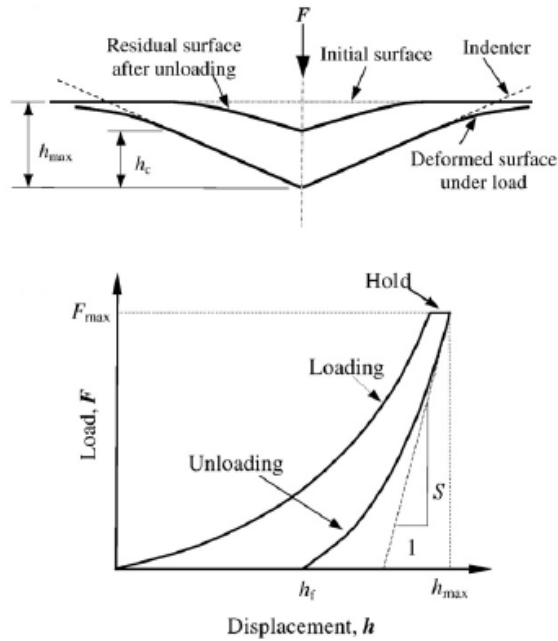


Figure 1: Nanoindentation processes and typical load-displacement curve [16].

A 3-D image may also be obtained through this imaging process which can reach down to sub-nanometer range, which is smaller than the capacity of SEM (scanning electron microscope). Because it uses a probe, it is possible for the user to manipulate atoms on materials surfaces. In one investigation on the pore structure of wet clay [17], there was a linear decay of pore structure when the water content was increased. This was postulated due to the reduction in the diffuse double layer and more extensive hydrogen bonds between clay particles and bipolar water molecules. Microfabric of clay was studied quantitatively using AFM by Sachan [18]. The quantification was done by developing the criteria for average and maximum values of angle of particle orientation using empirical equations for intermediate and extreme microfabrics. Dispersed or flocculated clay structures were able to be identified for kaolin with varying content of dispersing agent.

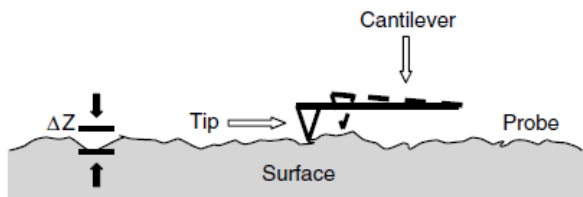


Figure 2: AFM scanning probe and its interaction with a surface [19].

4 SOIL IMPROVEMENT WITH NANOPARTICLES

In this section, some results on the applications of nanomaterials for improving the properties of soil will be

presented and discussed.

4.1 Nano-soil

The nano-soil was obtained by grinding a local soil (metasedimentary residual soil within the campus of Universiti Kebangsaan Malaysia, UKM). After the disturbed soil was dug and taken to the laboratory, it was first cleared of all roots and stones, dried in an oven, and sieved. Soil samples passing through 425 mm sieve was then pulverized in a planetary mono mill. In this mill, 20 small diameter (5 mm diameter) balls made of sintered corundum move in a fast planetary/cyclonic fashion to pulverize the soil. The time of pulverization was about 10-13 hours in which during this period, distilled water was added to provide over heating. SEM images of the soil sample before and after milling showed that there was much more soil in the nano range (i.e. 50-60 nm) in the soils after milling[20]. The specific surface of the soil obtained from EGME (ethylene glycol monoethyl ether) method improve from 2.4 m²/g to 3.9 m²/g. Milling of kaolinite and montmorillonite samples show similar observation.

In order to evaluate its potential for improving soil properties, a soil-cement mix was prepared and the nano-soil was added to the mix. The amount of nano-soil added was 1 and 2 % by weight of the UKM soil. Thus, the overall mixture is 94% UKM original soil, 6 % Portland cement, and nano-soil.

The results of compression test on 50 mm³ samples are shown in Fig. 3 [21]. It shows significant improvement in the strength of the nano-soil mixtures over the control test albeit the amount of nano soil added was rather quite low. The strength of the soil-cement mixture almost doubled when 1 % UKM nano-soil was added compared to samples without nano-soil. In addition, the mixture which is usually termed as cement-modified soil in geotechnical engineering will have lower tendency of volume change and PI in addition to increase in load bearing capacity [21]. This study have demonstrated that even a small addition of nanoparticles will show marked enhancement in soil behavior. It is also possible to engineer nanoparticles to improve behavior of soils to suit design and practice requirements.

4.1 Carbon Nanotube (CNT)

Carbon nanotube is considered as the first generation nanomaterial in that it is one of the earliest nanoparticles that were produced. Carbon nanotube is so popular and interesting because it has many “super” properties, especially for those working in electronics and superconducting industries. It has high unparalleled strength, high electrical and thermal conductivities, making it ideal for wide range applications [22] & [23]. Thus, it is sometime termed as the “king of nanomaterial” and also “a solution waiting for problem”. In order to study the behavior of soil-CNT mix, kaolinite was used as the soil material. The CNT is a multi-walled nanotube (MWNT) and was purchased from Arkema, France under product name Graphistrength C100.

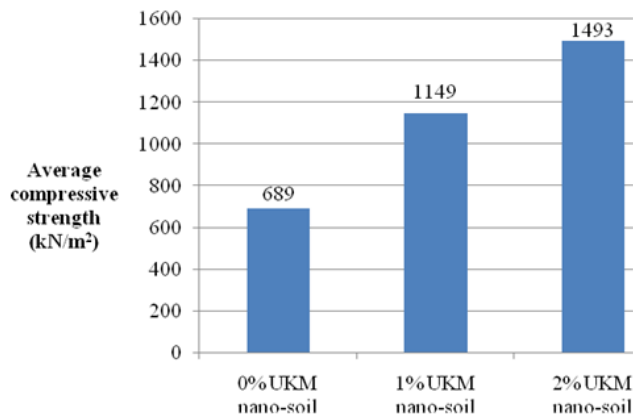


Figure 3: Compressive strength of soil-cement and nano-soil mix.

The black powder CNT material used in this study have a bulk density ranging between 50-400 kg/m³. The results of Atterberg limit tests are shown in Fig. 4 [25]. It is shown that even with small amount of CNT, the changes in basic characteristics are measurable. Increase in CNT led to increase in LL, PL and plasticity index (PI=LL-PL). In these tests, the addition of the fine CNT particles certainly increases the overall specific surface of the mixture. As a result, the need for water, is greater and thus this is indirectly shown by an increase in LL.

The increase in PI is due to the fact that the increase in PL is not as dramatic as the increase in LL. It was also found that the values of G_s , in general, also decrease upon addition of CNT due to the low density of CNT.

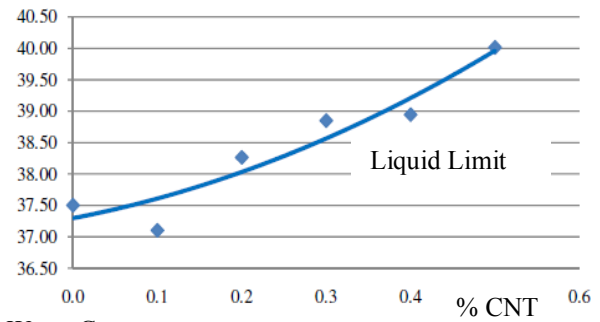
These results have important significance in geotechnical engineering. In terms of mechanical properties, increase in LL (and increase in surface area) means the soil will have higher capacity for water thus decreasing its strength and increasing its consolidation/compressibility (settlement). However, increase in PI will generally mean a decrease in its hydraulic conductivity. For geotechnical structures (such as foundations and retaining walls) in which strength and compressibility are the main criteria, the use of CNT may not be advantageous. In the case of landfill liners and caps, in which low hydraulic conductivity is very important, its use may thus be considered.

4.2 Nano-clay

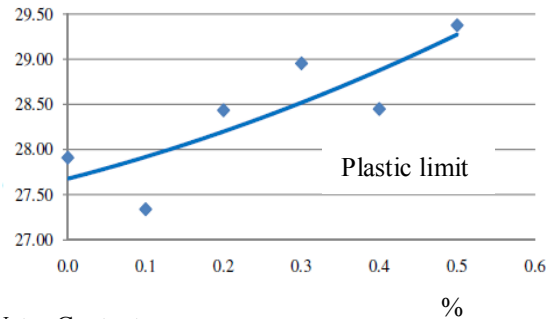
The performance of nanoparticle in arresting volume change of compacted residual soil (UKM metasedimentary residual soil) mixed with a natural montmorillonite was studied using nano-clay. The nano-clay material was supplied by Southern Clay Products Inc, Gonzales, Texas, USA under the product name Cloisite®Na⁺. The size of the particle is 5-15 nm in thickness and 20 nm to 10 µm in diameter.

It was observed that the increase in nano-clay causes small increase in the plasticity index and linear shrinkage of the soil. This happened because the nano-clay material is an expansive clay.

Water Content



Water Content



Water Content

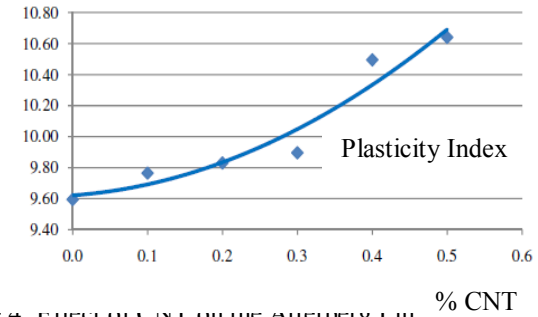


Figure 4. Effect of CNT on the Atterberg Limit.

It was also found that the increase in nano-clay gives a decrease in hydraulic conductivity (Fig. 5) due to increase in the smaller size of particles. The nano-clay particles probably diffuse between the large sedimentary soil particles, closing or minimizing the pores which lead to a decrease in the flow of water in the soil mixtures. This is a very significant results because one of the common materials tested to reduce the shrinkage strain is fiber. Mixing the soil with fiber can reduce the shrinkage strain up to 90% but the fiber cause an increase in the hydraulic conductivity up to 50 times [26].

4.3 Nanoalumina

The tests with nanoalumina follow that of nano-clay as discussed in the previous section. The soil used is the UKM residual soil mixed with various percentages of montmorillonite to produce soil mix with different plasticity index. Nanoalumina was then added to these soil mixes and its plasticity, shrinkage and hydraulic conductivity was studied.

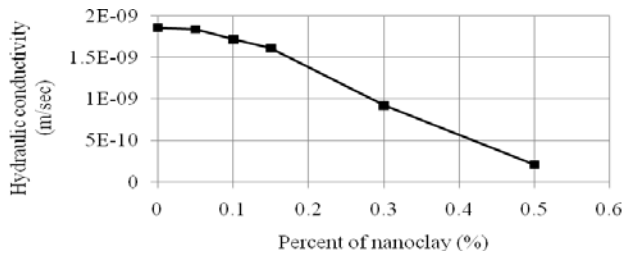


Figure 5: Influence of nano- clay on the hydraulic conductivity

The nanoalumina used was purchased from Infamat Advanced Materials, Manchester, CT, USA. It has a chemical formula Al_2O_3 , particle density of 3.6 g/cm^3 , surface area of $> 150 \text{ m}^2/\text{g}$, and a transitional gamma crystal structure [27].

The physical properties of the soil mix are shown in Table 1. Adding nanoalumina within 0.1-0.3% (by weight) causes a slight decrease in the plasticity index of the soil mix (Fig. 6). Maintaining this basic property is important in soil improvement process as the enhancement of other more important properties are sought.

Table 1: Physical characteristics of the soil mix.

Characteristics	Values and descriptions			
	S1 (0)*	S2(5)	S3(15)	S4(20)
G_s	2.607	2.609	2.612	2.617
PI (%)	16.96	28.26	36.18	69.01
Passing No. 200 sieve (%)	47.16	49.80	52.44	57.72
Clay % ($< 2 \mu\text{m}$)	18	22.9	28.5	38.5
USCS classification	CL	CL	CH	CH
Compaction properties				
w_{opt} (%)	14.29	16.01	18.63	20.3
γ_{max} (kN/m^3)	18.05	17.70	16.93	16.12

*The number in the parenthesis indicate the percentage of montmorillonite.

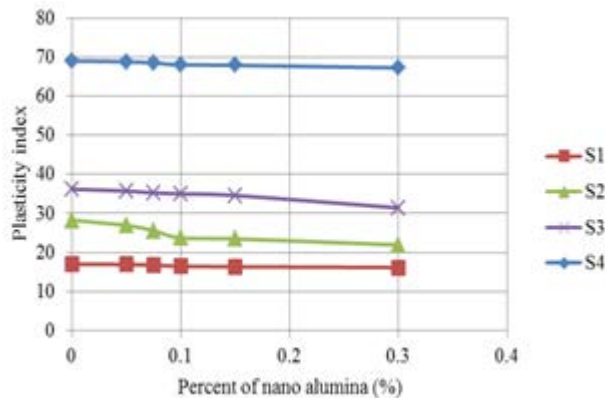


Figure 6: Effect of nanoalumina on plasticity index.

Apparently with regard to total volumetric strain, it was found that that minimum volume change occurs between 0.05 % to 0.1 % nanoalumina content. For high plasticity soils, i.e. S3 and S4, the crack intensity factor (CIF [26]), is minimum at 0.1 % (Fig. 7). Furthermore, the hydraulic conductivity measurements showed that adding nanoalumina will cause a slight decrease in its value (Table 2). Thus, using nanoalumina for dessication crack control does not cause detrimental effects on the hydraulic behavior of the soil.

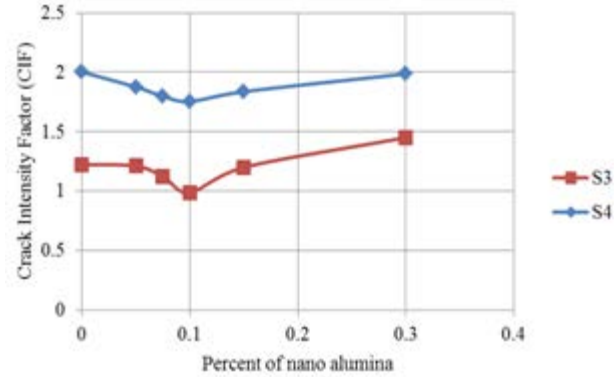


Figure 7: Effect of nanoalumina on crack intensity factor.

Table 2: Hydraulic conductivity values for various nanoalumina mix.

Soil type	Nanoalumina content (%)	Hydraulic conductivity (m/s)
S1	0	1.86E-09
S1	0.05	1.81E-09
S2	0	1.24E-11
S2	0.075	1.30E-11
S3	0	1.00E-11
S3	0.1	5.40E-12
S4	0	4.56E-12
S4	0.1	1.59E-12

5 CONCLUSION

Some general nano level concepts, contributions of geotechnical engineers in nanotechnology and use of nanomaterials for soil improvement are described in this paper. Concepts such as moisture around a soil particle, dipolar characteristic of water molecule, diffuse double layer, and clay structure are some examples of phenomena that operate at nano level. They have been known and researched by geotechnical engineers for quite sometime. These serve to show that geotechnical engineers have long been making contributions in the field of nanotechnology. The application of nanomaterials described in this paper is mainly used for soil improvement. For example, a small amount of nano-soil when added to soil-cement mix causes considerable increase in its compressive strength. The addition of nano-clay and

nanoalumina for dessication crack control of soils results in soils with minimal change in plasticity and reduced hydraulic conductivity. Thus, nanomaterials could offer varieties of soil behavior which may be advantageous for many geotechnical applications.

6 REFERENCES

- [1] Taha, M.R., Ismail, E., & Chik, Z., Some nano aspects and concepts in geotechnology, 2nd Intl Symp on Nanotechnology in Construction, 2005, pp. 373-381.
- [2] Taha, M.R., Nanotechnology in Geoenvironmental Engineering, Sabbatical Report, Universiti Kebangsaan Malaysia, 2007, 33 p.
- [3] Grim, R.E., Clay Mineralogy, 2nd Ed., New York:McGraw-Hill, 1968, 600 p.
- [4] Katti, D.R., Katti, K.S., & Shanmugasundaram, V., Role of clay-solvent inter and intraparticle interactions on swelling characteristics of montmorillonite nano-meso-micro scale particulate systems, MRS Proceedings, 2001, 704:W9.14.1, 6 p.
- [5] Chen, H., Zhang, G., Richardson, K., & Luo, J., Synthesis of nanostructured nanoclay-zirconia multilayers: A feasibility study, Journal of Nanomaterials, 2008, 8 p.
- [6] Liu, W.K., Karpov, E.G., & Park, H.S., Nano Mechanics and Materials: Theory, Multiscale Methods and Applications, Chichester, UK: John Wiley & Sons Ltd, 2006, 320 p.
- [7] Gutierrez, M., Nanogeomechanics:Potential applications of nano-mechanics in geotechnical engineering, International Workshop on Micro-Geomechanics Across Multiple Strain Scales, Cambridge, UK, March 20-23, 2005, 12 p.
- [8] Skipper, N.T., Influence of pore fluid composition on clay behavior: Molecular dynamics simulations of nano-structure, in Chemo-Mechanical Coupling in Clays:From Nano-Scale to Engineering Applications, DiMaio, C.D., Huckel, T., & Loret, B. (eds), 2002, Lisse: Swets & Zeitlinger BV, 2002, pp.65-73.
- [9] Katti, D.R., Schmidt, S., Ghosh, P., & Katti, K.S., Modeling response of pyrophyllite clay interlayer to applied stress using steered molecular dynamics, Clays and Clay Minerals, 52(2), 2005, pp.171-178.
- [10] Schmidt, S., Katti, D., Ghosh, P., & Katti, K., Evolution of mechanical response of sodium montmorillonite interlayer with increasing hydration, Langmuir, 21, August, 2005, pp. 8069-8076.
- [11] Katti, D.R., Schmidt, S., Ghosh, P., & Katti, K.S., Steered molecular dynamics simulations of dry and hydrated sodium montmorillonite interlayer, Canadian Geotech J., 44, 2007, 425-435.
- [12] Katti, D.R., Katti, K.S., Amarasinghe, P., & Pradhan, S., Interlayer fluid flow and the role of clay-fluid molecular interactions on the swelling behavior of montmorillonite clays, Poromechanics IV, Lanchester, Pennsylvania:DEStech Publications Inc., 2009, pp.836-841.
- [13] Voyiadjis, G. Z. & Song, C.R., Coupled Theory of Mixtures in Geomechanics with Application, Berlin:Springer, 2006, 438p.
- [14] Song, C.R., Cho, H., Jung, Y.H., Cheng, A.H.D., & Alostaz, A., Bridging molecular, particulate, and continuum mechanics for geomechanics application, Advances in Measurement and Modeling of Soil Behavior (GSP 173), Reston:ASCE, 2007, pp.
- [15] Varughese, S., Kiran, M.S.R.N., Solanko, K.A., Bond, A.D., Ramamurty, U., & Desiraju, G.R., Interaction anisotropy and shear instability of aspirin polymorphs established by nanoindentation, Chem. Sci., 2011,2, 2236-2242
- [16] Zhang, G., Wei, Z., & Ferrel, R.E., Elastic modulus and hardness of muscovite and rectorite determined by nanoindentation, Applied Clay Science, 4, 2009, pp.271-281.
- [17] Selvam, A., See, C.H., Barkdoll, B., Prasad, S., & O'Haver, J., Use of atomic force microscopy for examining wet clay, Clays and Clay minerals, Vol. 54, No.1, 2006, pp. 25-28.
- [18] Sachan, A., Use of atomic force microscopy (AFM) for microfabric study of cohesive soils, Journal of Microscopy, Vol. 232, Pt 3, 2008, pp 422-431.
- [19] Nguyen, C.V., Applications in scanning probe microscopy, in Carbon Nanotubes – Science and Applications, Meyyappan, M. eds, Boca Raton:CRC Press, 2005, pp. 137-161.
- [20] Taha, M.R., Lim, S.Y., & Chik, Z., Ciri-ciri asas beberapa tanah yang dikisar (Basic properties of milled soils), Jurnal Kejuruteraan, UKM, Vol 21, 2009, pp.1-10.
- [21] Taha, M.R., Geotechnical properties of soil-ball milled soil mixtures, Nanotechnology in Construction, Proc NICOM3, Berlin Heidelberg:Springer-Verlag, 2009, pp. 377-382.
- [22] Ozin, G.A., & Arsenault, A.C., Nanochemistry: A Chemical Approach to Nanomaterials, Cambridge, UK:RSC Publishing, 2005, 628 p.
- [23] Marx, W., & Barth, A., Carbon n nanotubes-A scientometric study, in Carbon Nanotube, Marulanda, J.M. eds, Intech Publishers, 2010, pp. 1-18.
- [24] Taha, M.R., & Ting, Y., Effect of carbon nanotube on kaolinite: Basic geotechnical behavior, The Eighteenth Annual Intl Conf. on COMPOSITES/ NANO ENGINEERING (ICCE - 18) Anchorage Alaska, USA, Int Community for Composites Engineering, 2010, pp. 721-722.
- [25] Taha, O.M.E., & Taha, M.R. Experimental study on the expansive-shrinkage behavior of residual soil mix with nano-clay, Proc 5th Jordanian International Civil Engineering Conference, Jordan Engineers Association, 2012, pp. 417-423.
- [26] Taha, M.R., & Taha, O.M.E., Hydraulic conductivity and dessication crack behavior of compacted soil-nanolaumina mixture, in NICOM4-Nanotechnology in Construction-4 Intl Symposium, Konsta-Gdoutos, M.S., ed., ACI, 2012, 9 p.

Damage Assessment and Strengthening of R/C Building Constructed on Expansive Soils

Osama M. A. Daoud

Building and Road Research Institute, University of Khartoum, Sudan
General Manager of ESCAD Consultancy Co. Ltd.

ABSTRACT

This paper presents an experience in assessment and strengthening of a R/C building carried out in Sudan during the last year. A four-story R/C framed hospital building was constructed five years ago in the middle of Sudan, by the White Nile River. Due to differential upheaval movement of the underneath expansive clay soils (15-25cm), the building had experienced serious instability problems and severe structural cracks. A comprehensive assessment of the building skeleton including geotechnical investigation, DT and NDT methods revealed the need of five different strengthening and retrofitting techniques; there are, transformation of foundation system from isolated footings to strap foundation to increase the stiffness and rigidity of footings, concrete jacketing of basement floor columns, metal jacketing of the second floor columns, construction of shear walls to enhance the stability of the building and finally CFRP laminates for strengthening of basement floor cover slab. The building had been monitored during and after completion of strengthening and retrofitting works to measure any movements during the last year rainy season. Measurements revealed the efficiency of implemented strengthening and retrofitting techniques.

1. INTRODUCTION

Kosti Military Hospital is a four-story R/C framed building constructed five years ago in Kosti city in the middle of Sudan, by the White Nile River (Fig. 1). The building was designed and constructed over an area of 1350 sq. m to provide advanced medical services for the citizens of the White Nile state. Because of inadequate geotechnical investigation prior to construction, the building was constructed in an area of highly potential expansive soils, without any special considerations for this type of soil.

The building is a R/C frame type building, the frame is a column-flat slab type, supported on isolated footings. All parts of the building are used as rooms for doctors and hospital wards for patients.

As reported by the local governmental authorities, a few years after completion of construction of the hospital, the building started to suffer from cracks and visible movements of the expansion joints. Lack of routine inspection and maintenance and poor previous rehabilitation works had led to continuous and fast development of cracks and movements.



Figure 1. Location of Kosti Military Hospital (Google Earth).

2. LITERATURE REVIEW

Expansive soils are soils that have potential for swelling and shrinkage under changing moisture conditions. The volume change resulting from swelling and shrinking causes damages to structures founded on them. The expansive soil area includes nearly all the agricultural schemes and most of the development projects in Sudan and covers about 40% of the total area of Sudan (Osman and Charlie 1983).

Damages of structures caused by expansive soils have been reported from different locations in the clay plain (Lates et al 1983). The damages include buildings, roads, factories, hydraulic structures etc., and were attributed to lack of proper identification and classification of expansive soils and improper design of the foundations of the damaged structures (Elsharief, 2009).

3. ASSESSMENT PROGRAM AND RESULTS

A comprehensive structural-geotechnical assessment program was designed and implemented. The following sections discuss the steps and findings of this program.

3.1 Visual inspection & excavations

A careful visual inspection was performed for the structural members of the building, it was clear from the inspection that the building was unstable since expansion joints were undergone excessive rotations (Fig. 2) and severe structural cracks were seen in some columns. The maximum opening of the expansion joints at the top of the building was about 13cm which indicates that the building had undergone a total rotation of 0.67 degrees. Fortunately, foundations were not affected by these movements. A number of internal and external footings were excavated for visual inspection and measurements. Excavation has been done on some of the foundations with great difficulty because of the saturation

of the clay soil, and in some cases, water gushed profusely about the footings (Fig.3). Because of the upheaval movement of the soils, and probably due to the weakness of concretes some of the basement columns were buckled and crushed (Fig. 4). All sanitation systems of the building were damaged. Leakage and accumulation of waste water and chemicals (waste of hospital's laboratories) around the columns and in contact with the basement cover slab had caused deterioration and corrosion of reinforcement of columns and slabs (Fig. 5).



Figure 2. Opening at expansion joint.



Figure 3. Dewatering during excavation.



Figure 4. One of buckled basement columns



Figure 5. Corrosion of reinforcement of basement slab and columns

3.2 Detailed geotechnical investigation

3.2.1 Drilling of Boreholes

Three boreholes were drilled, two of them to about 10.0m and the third one to 15.0m depth, in different locations around the building. The boreholes were drilled using a rotary soil mechanics drilling rig. Disturbed soil samples were collected at 1-m meter intervals for visual inspection and classification tests. Undisturbed samples were taken at 1.5-m intervals from the cohesive soil. The standard Penetration Test (SPT) was performed in silt or sand layers or whenever there was difficulty in getting undisturbed soil samples. The SPT was performed by driving an open tube sampler (50mm O.D.) by the blows of a standard automatic hammer weighing 64kg and falling freely from a height of 760mm. The number of blows required to give tube penetration of 300mm was taken as SPT-N value.

3.2.2 Excavation of Test Pits

Three test pits were excavated manually to about 4.0m at different locations around the building. The disturbed soil samples were collected at each meter interval for visual inspection and laboratory testing.

3.2.3 Groundwater

No groundwater was observed during the drilling of boreholes in this site. It is expected to be far below the effective zone of the foundations.

3.3.4 Soil Conditions

The soil profile for the two boreholes and test pits is shown in Appendix (A). The three boreholes showed relatively similar soil stratification consisted of dark brown silty clay of high plasticity (CH) and dark brown to yellowish greyish very loose to medium dense clayey sand (SC) at the top 4.0m to 5.5m. Below this alternative layers of very stiff brown low plastic silty clay (CL) and very stiff brown low plastic silt (ML) and very stiff dark to light brown highly plastic silty clay (CH) were encountered down to the bottom of boreholes at 10.0m and 15.0m depths.

Test pits soil profile showed one layer of dark to light brown silty clay of high plasticity (CH) extending down to the bottom of test pits at 4.0m depth.

3.2.5 Laboratory Testing

Laboratory tests were performed on a number of disturbed and undisturbed soil samples. The tests included Atterberg limits, grain size analysis, natural moisture content, UU triaxial test, consolidation test, swelling pressure test and chemical tests. The procedures followed were in general conformance with those recommended in the British Standard BS 1377 (1990). Soils were classified according to the Unified Soil Classification System (USCS).

3.2.5.1 Classification Tests

The objective of these tests was to reveal soil types encountered at different depths of the boreholes. Tests carried out included Atterberg limits, grain size analysis and natural moisture content. These classification tests confirmed the soil profile described in subsection 3.5.

3.2.5.2 Atterberg Limits

The tests were carried out on clayey soil samples taken from different depths. The results gave liquid limit values ranging between 29% to 85% and plasticity index values between 11% to 60%. This indicated high swell potential for the clayey soil at the present site.

3.2.5.3 Grain Size Distribution

The grain size distribution of the soil samples was determined in the laboratory. The results of this test with combination of Atterberg limits test results were used to assess the soil types according to the Unified Soil Classification System (USCS).

3.2.5.4 Natural Moisture Content

The natural moisture content was determined from undisturbed samples and by weighting the disturbed samples obtained from SPT sampler in the field and then the test was continued in the laboratory.

3.2.5.5 UU-Triaxial Test

The undrained unconsolidated (UU) triaxial test was conducted to measure the shear strength parameters of the soil. The average measured shear parameters (ϕ & c) were 9.33° and 45.93 kPa respectively.

3.2.5.6 Consolidation Tests

Consolidation tests provide information for use in evaluating the compressibility of the soils and estimating the settlement of foundations established on these soils. The consolidation tests were performed on undisturbed clayey samples. First, the swelling pressure test was conducted on the samples. Then the samples were loaded beyond the swelling pressure to allow consolidation to proceed.

3.2.5.7 Swelling Pressure Test

The swelling pressure tests were conducted on undisturbed soil samples. The volume of the soil was kept constant in an oedometer cell, while the soil was saturated with water during the test. The results are shown in Table 1 below. The results reflected low swelling pressures. This is due to high moisture content of these samples, usually high swelling pressures depend on high moisture content deficiency. Also the soil samples may be subjected to some disturbance during mobilization.

Table 1: Swelling Pressure Test Results

B.H. No.	Depth (m)	Swelling Pressure (kN/m ²)	Initial Moisture Content (%)	Final Moisture Content (%)	Soil Type According to USCS
1	1.5	0	29.05	33.68	CH
1	3.0	20	19.05	23.23	SC
2	3.0	20	21.92	24.80	SC
3	3.0	20	23.70	24.52	CH

3.2.5.8 Chemical Tests

Chemical tests were performed according to BS 1377,1990-2 on two soil samples and one water sample to determine chloride content, sulphate content and the pH value. The results are shown in Table 2 below. The results indicated alkaline soil and water of low contents of chloride and sulphate. Therefore, the building foundations are not expected to be affected by these low contents of chemical salts.

Table 2: Chemical Test Results

Sample No.	Sample Type	Location	Depth (m)	Chloride (%)	Sulphate (%)	pH
1	Soil	B.H. 2	2.0	0.2142	0.2513	5.27
2	Soil	B.H. 3	2.0	0.2213	0.1642	4.34
3	Water	-	-	0.2057	0.2043	5.10

3.2.6 Analysis of geotechnical results

It is evident from the soil profile that the top 4.0 to 5.5m layer of highly plastic silty clay (CH) and very loose to medium dense clayey sand (SC) was encountered. This is underlain by alternative layers of very stiff low plastic silty clay (CL) and very stiff low plastic silt (ML) and very stiff highly plastic silty clay (CH) extending down to the end of boreholes. No groundwater was encountered in boreholes during this investigation; it is expected to be far below the effective zone of the foundations. Although low values of

swelling pressures were measured in the laboratory, the index properties of the investigated soil indicated high swelling potential for the clayey layers. The SPT N-values generally indicated soft to very stiff clays and very loose to medium dense sands, which reflects low to medium shear strength for the soil at the present site. The chemical test results showed acidic soils of high contents of harmful chemical salts. The building was constructed on isolated footing foundations placed at about 2.9-m depth below the ground surface level. At this depth the bearing capacity of the soil recommended to be 140 kN/m².

The bearing capacity determination was based on soil classification and SPT results. Use SPT-N average value below the foundation level and maximum footing width of 4.5m for permissible settlement of 25mm at (Terzaghi and Peck Chart, Bowles, 1994).

3.3 Field and Lab. Testing of concretes

A combination of destructive core tests, ultrasonic pulse velocity and rebound hammer tests was performed to find the compressive strength and to assess the quality and uniformity of the concretes of the building.

3.3.1 Core test results

Six core specimens were extracted from the foundations and floor slabs using an electrical type core cutting machine. All core specimens were thoroughly inspected and prepared for the compression test. Visual inspection of the core specimens before compression tests revealed the following:

- Entrapped air voids were noticed in the core specimens which indicated that the concretes of different structural elements of the building were not properly vibrated and compacted.
- The concrete mix was found to be over sanded (i.e. the amount of cement was less than required).
- Many decayed aggregate particles were noticed in the mix. Also the maximum size of aggregate found was less than 15mm and the grading observed was not uniform.
- After visual inspection the specimens were prepared and tested under uniaxial compression load, the average value of the strength results was 14N/mm².

3.3.2 Ultrasonic pulse velocity tests results

Ultrasound pulse velocity was performed to assess the quality of concretes of columns and to evaluate the degree of compaction.

Ultrasonic pulse velocity test is usually performed for assessing the quality and integrity of concrete by passing ultrasound waves through the specimen or reinforced concrete member under test, This test can also be used to determine the presence of honeycombs, voids, cracks etc. The main strength of the method is in finding general changes in condition such as areas of weak concrete in a generally sound concrete. At the same time, the UPV technique is not always

practicable in testing sound concrete. Especially in investigation of crack depth, it is ineffective if the crack is water filled. The performance is also often poor in very rough surfaces. Sometimes good contact requires the use of a coupling gel between the transducers and the structure. Sound energy above the audible frequency of 16,000 Hz is designated as ultrasonic (Song & Sarthawathy, 2007). The instrument consists of transmitter and receiver (two probes). The time of travel for the wave to pass from the transmitter to the receiver when kept opposite to each other is recorded in the ultrasonic instrument. The distance between the two probes (path length) can be physically measured. Hence ultrasonic pulse velocity = path length/time. This velocity in concrete can be related to its compressive strength. Different approaches have been published for classification of concrete quality based on the pulse velocity. In this study the Whitehurst (5) classification method was adopted. According to the Whitehurst classification method, the quality of concretes of the columns of different floors was found to be varying between poor (pulse velocity < 3Km/sec.) and doubtful (pulse velocity < 3.5 km/sec.), whereas some points were found to indicate very poor quality (pulse velocity < 2.5km/sec.).

3.3.3 Rebound hammer test results

This test is basically a surface hardness test and should be used only where the surface has not carbonated as the results tend to be very high and unrealistic on carbonated surfaces. It is also possible to evaluate the degree of uniformity of concrete through statistical analysis of test results (ACI, 1195).

The building under consideration was constructed four years ago so little carbonation effect is possible. Rebound hammer values obtained from different columns at different floor levels showed low surface hardness (average rebound number 14) and high variability (standard deviation of rebound number 12.5) in the properties of concretes of columns.

3.4 Structural analysis

A structural analysis of the concrete frame was performed based on the actual dimensions of the building and main findings of field and laboratory tests results. The structural analysis showed that all the basement columns, second floor columns and the basement cover slab were stressed beyond the ultimate limits. While the bearing capacity of foundations were found to far less than the applied axial and bending forces of basement columns, the uplift pressures of soil didn't affect the punching shear strength of foundations.

4. SUGGESTED STRENGTHENING METHODS

After a comparative socio-economic feasibility study of the two options of demolishing and strengthening, it was decided by the different consultancies and authorities involved to strengthen the building. Time was critical since the hospital building had to be restored to provide medical services. Based

on the findings of the assessment program, it was clear that the building required faster major and minor strengthening and retrofitting. It was also critical for building and strengthening works to be implemented before the rainy season, so as to prevent any moisture variation in soils and to stop any further movement of the building skeleton. Five different major structural strengthening techniques were suggested and implemented.

4.1 Modification of foundation system

It was suggested that the isolated footings of the foundation to be strengthened and connected using reinforced concrete beams fixed on top of footings. This will increase the stiffness and tightness of the foundation; hence redistribute the bearing stresses and the non-uniform uplift soil pressures. Also this will eliminate any stress concentrations and prevent any further increase in differential movement of underneath soils (Fig.6). This was performed after restoring the affected footings to their initial levels. Soils beneath the footings affected by the uplift pressures were removed and the footings were allowed to restore gradually to the initial levels under the existing dead loads. Wherever needed, additional surcharge loads were applied to push the footings down to their initial levels. For damaged short columns, shoring of upper floors was sometimes needed to reduce the applied loads, strengthen the columns and restore the footings.



Figure 6. Modification of foundation and concrete jacketing of short columns

4.2 Concrete jacketing of short columns

Strengthening of basement columns using concrete jacketing was apparent since the load carrying capacities of these columns were much less than the applied axial forces and bending moments. Shear connectors were first inserted and fixed in the old concrete columns using a carefully selected epoxy binder. The surfaces of the old concrete columns were roughened and a suitable epoxy binder was distributed before the additional reinforcement was placed (Hollaway and Leeming, 2005). After that additional flexure and shear

reinforcements were fixed around the columns before final concreting.

4.3 Metal jacketing of columns

In order to increase the load carrying capacity of the second floor columns while maintaining the same cross-section, metal jacketing was the best solution. The columns were strengthened using four channel sections at the four corners along the columns, connected via horizontal steel strips at a suitable spacing (Fig. 7). The gaps between the concrete and the added steel frame were filled with a suitable epoxy mortar.



Figure 7. Metal jacketing of second floor columns

4.4 CFRP for basement cover slabs

The basement cover slab (total area 1350 sq.m) was strengthened using carbon fiber reinforced polymer laminates fixed at the soffit of the concrete slab using selected epoxy resin (Bank, 2006). This technique was the best solution to remedy the two deficiencies of the slab; structural cracks due to foundation movements and corrosion of reinforcements due to chemical attack (Fig. 8).



Figure 8. CFRP for basement cover slabs

4.5 Shear wall installation

To enhance the stability of the building and to rectify the openings at the expansion joints caused by the differential movement of the foundations, concrete shear walls were installed at both sides of each expansion joint along the total height of the building (Fig. 9).



Figure 9. Installation of shear walls at expansion joints

5. CONCLUDING REMARKS

This case study highlights the following facts:

- Clever combination between different strengthening and retrofitting techniques can save a lot of money and time.
- When considering the strengthening and rehabilitation of structures, it is essential to establish the nature of the problems, extent, severity and exact causes. If this is not done the symptoms could be treated rather than the causes.
- There is no substitute for following sound design and construction principles when constructing structures on expansive soils.
- Careful and continuous monitoring during and after installation of strengthening and retrofitting works is vital to evaluate the efficiency of such works.

6. REFERENCES

- [1] Mohammed A. Osman & W. A. Charlie, (1984). "Engineering Properties of Expansive Soils in Sudan" 5th International Conference on Expansive Soils, Adelaide, South Australia, 21-23 May 1984, pages 311-315.
- [2] Lates E. M., Elmonshid B. E. F. and Abbo S. H., (1983) "Review of Problems Generated by Expansive Soils in Sudan" Proc. of Seminar on Expansive Clay Soils Problems in Sudan, Wad Medani, January 1983, Hydraulic Research Station, HRS.
- [3] El-sharief A. M., (2009). "Foundations on Expansive Soils Sudan Experience" Proc. Of First Conference of Postgraduate Studies and Scientific Research, University of Khartoum, Sudan.
- [4] Joseph E. Bowles, (1994) Foundation Analysis and Design, Fifth Edition.
- [5] Ha-Won Song & Velu Sarthawathy (2007), "Corrosion Monitoring of Concrete Structures- A Review", Int. Journal of Elect. Chemical Science, 2(2007) 1-28.
- [6] American Concrete Institute, (1995), "In Place Methods to Estimate Concrete Strength", Reported by ACI Committee 228.
- [7] L.C. Hollaway & M. B. Leeming (2005), "Strengthening of Reinforced Concrete Structures", CRC Press, Woodhead Publishing Limited, England.
- [8] Lawrence C. Bank (2006). "Composites for Construction-Structural Design with FRP Materials", John Wiley & Sons, INC.

Gravitational Sphere Packing Method to Find the Porosity of the Soil Particles with the Identical Size inside the Cylindrical Container

Mohammad Mahdi Roozbahani , Bujang B. K. Huat, Afshin Asadi

Universiti Putra Malaysia

mahdi_roozbeh@yahoo.com, bujang@eng.upm.edu.my, afshin.asadi@yahoo.com,
Civil Engineering Department, Faculty of Engineering, Universiti Putra Malaysia, 43400 UPM-Serdang,
Malaysia

ABSTRACT

The present article demonstrates new gravitational sphere packing with geometrical method within the cylindrical container. Wall effects are considered for this container to simulate the reality conditions in the laboratory works. It is shown that the porosity is reduced by increasing in the volume size of the container, and the same results of the porosity have been achieved for both mathematical and geometrical methods.

Keywords: Porosity, wall effects, sphere packing, cylindrical container, gravitational sphere packing

1. INTRODUCTION

Sphere packing is a method which has been used in many fields such as geotechnical and chemical engineering, physic, ceramics, powder technology, and biology [1]-[2]-[3]-[4]-[5]-[6]-[7]-[8]-[9]. Porosity calculation of the soil is important from the aspect view of finding the void fraction of the particles, permeability computation, and interaction between the particles.

There are two types of sphere packing which are 1: loose or gravitational sphere packing, and 2: close sphere packing. The former one simulates the conditions of the unconsolidated soil particles with loosely interior structure, whereas the latter one simulates the conditions of consolidated soil particles with fully compacted particulate materials. The model structures of two sphere packing are quite different with each other. In the first one, the method of the drop and roll from specified height is applied, while for the second one, providing the most compacted packed bed is the striking aim which should be met.

In the current paper, authors utilized the loose or gravitational sphere packing which can simulate layering of the soil particles without any compaction called unconsolidated porosity value. Tory was the inventor of this method, whilst the other researchers have promoted the work of him [10]-[11]-[12]. Loose sphere packing can employ equal-sized spheres from nano- till coarse-sized particles, hence wide variety applications of this method would be very helpful in the field of soil particles interaction.

Variations of container size have positive correlation with the final porosity results. However, some researchers

have expressed periodic boundary condition to eliminate the wall effects and provide the raw data of porosity [12]. Periodic boundary condition is a computational box which is repeated infinitely in x and y direction. In fact, periodic boundary condition checks on the spheres which are exited from the wall, and those spheres enter inside the container from opposite side.

In some cases, the containers are not eliminated to simulate the reality condition of the interaction of the particles with each other, thus the resulted porosity would have higher value in comparison with the manner without the effect of wall. The higher porosity results will be achieved without wall effects because of the partial ordering of soil particles near the wall. Consequently, the most porous regions of a container are near the walls, but it should be mentioned that shape of the containers have some effects in partial ordering.

The most common containers are cylindrical and square container. Of these, cylindrical container is more popular because of the having same shape with the equipments in laboratory.

Mathematical [13] and geometrical [10] are the most common ways to simulate the sphere packing. There are pros and cons for the both way. In the former one, the porosity can be calculated by mathematical formulas analytically, whereas it is not able to depict the spheres and interaction of them. In the latter one, the speed of packing process will decrease by increasing the number of elements. The macro and micro structures of particles, however, can be defined minutely. The geometrical approaches are applied for this present paper, therefore different geometrical methods are employed to create the structure of loose sphere packing. Apollonius 3D has been implemented for equations of tangents controlling treatments of soil particles.

2. Computational method

The Tory's method has been applied for the current work. However, pure geometrical approaches have been employed rather than vectors manipulations. The base of the work of Tory can be summarized as follows:

1: The initial co-ordinates of spheres are chosen based on the random number generator on which the Monte-Carlo method is implemented.

2: The first height of every sphere is chosen based on the previously settled particles, hence the upmost height of pre-settled spheres is chosen, and the first height of incoming sphere is defined according to the upmost height.

3: The incoming sphere may collide with other fixed spheres. In this case, the stability conditions have to be controlled for the incoming sphere. If there have been three spheres underneath of the incoming sphere, the sphere is determined as a stable sphere; otherwise that sphere rolls down on the other spheres to find the stability condition which is usually called reaching the minimum potential point. Subsequently, there are two stability methods. The first one is being stable on the top of the other spheres and the second one is being stable by hitting the floor [10]-[11]-[14].

Apollonius 3D governs the equations of the contacting an incoming sphere with one, two, and three spheres. The formulas for contacting with three spheres are as follows:

Take for example:

The fixed spheres have been determined with 1, 2 and 3 subscripts and incoming sphere is determined by "s" subscript.

$$(X_s - X_1)^2 + (Y_s - Y_1)^2 + (Z_s - Z_1)^2 = (R_s + R_1)^2 \quad (1)$$

$$(X_s - X_2)^2 + (Y_s - Y_2)^2 + (Z_s - Z_2)^2 = (R_s + R_2)^2 \quad (2)$$

$$(X_s - X_3)^2 + (Y_s - Y_3)^2 + (Z_s - Z_3)^2 = (R_s + R_3)^2 \quad (3)$$

3. Results and discussion

The simulated sphere packing is verified with the literature, and the verification has been done with the mathematical method [15], which can explore that the results of the mathematical and geometrical are same intrinsically. The results are shown in Table 1.

Table 1 Comparison of porosity between geometrical and mathematical method.

N ¹	Container size(radius, mm)	Height of the container, mm)	Porosity ² (%)	Porosity ³ (%)
50	3.5	10.6177	54.7885	54.15
60	3.5	12.6174	53.3936	53.7
80	4.5	9.6620	52.9012	52.63
100	4.5	11.9555	51.5812	51.31
125	4.5	14.7689	50.9920	50.15

1: N is the number of the spheres as to the literature.

2: Porosity results of present work.

3: Porosity results in literature.

Stoyan found the porosity values of loosely packed spheres by the means of "greedy algorithm".

The porosity results are decreased by increasing the diameter and the height of the container, and the reason is interpreted by the effects of the container volume on the results.

One sample of sphere packing is shown in Fig. 1, 2, and 3 which are the 3D and 2D view of packed spheres. Container shape is not completely shown in order to better observation of the identical size of the soil particles, and interaction with them.

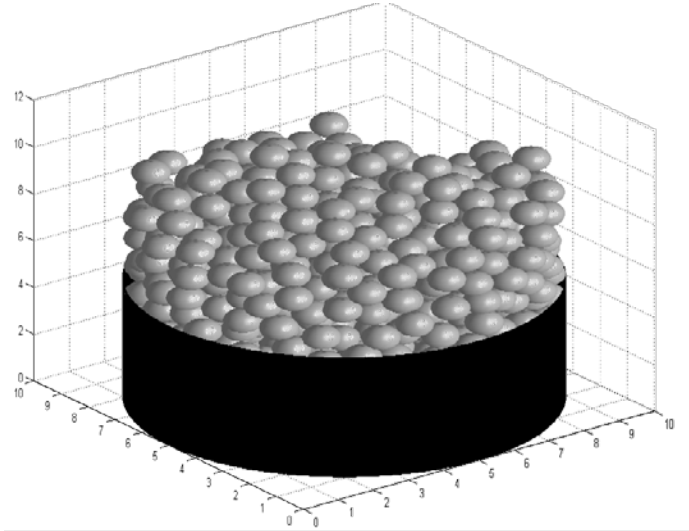


Figure 1. Three dimensional view of the sphere packing model

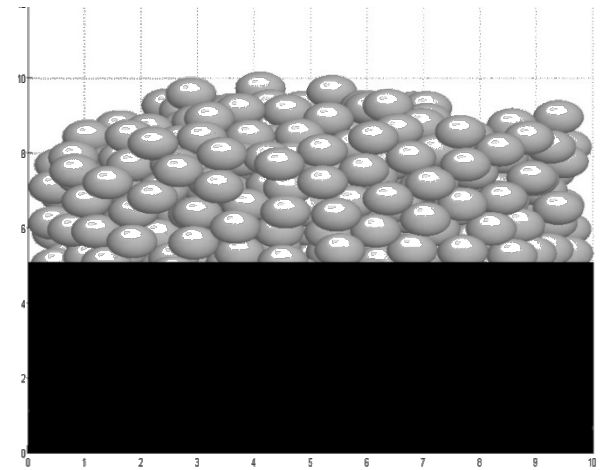


Figure 2. Cross section sample of the sphere packing

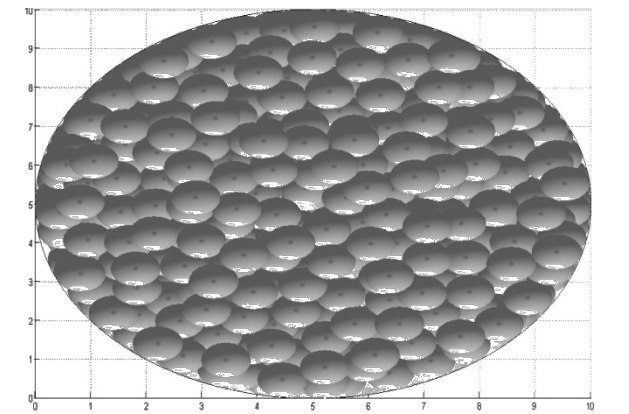


Figure 3. Plane view of the sphere packing

4. ACKNOWLEDGMENT

Support for this work by the University of Putra Malaysia Research Board is grate-fully acknowledged.

5. CONCLUSION

It is shown that the values of porosities for the both geometrical and mathematical methods are very close to each other.

It is construed that with increasing in the volume of the container, the porosity will be decreased subsequently. Because, there are more porous regions near the wall of the container, and increasing the volume size of the container will diminish these effects drastically.

6. REFERENCES

- [1] K. Sobolev, A. Amirjanov, Application of genetic algorithm for modeling of dense packing of concrete aggregates, *Construction and Building Materials*. 24 (2010) 1449-1455.
- [2] A.V. Kyrlyuk, A. Wouterse, A.P. Philipse, Random Packings Of Rod-Sphere Mixtures Simulated By Mechanical Contraction, *Physics*. (2009) 211-214.
- [3] G. a Georgalli, M. a Reuter, A particle packing algorithm for pellet design with a predetermined size distribution, *Powder Technology*. 173 (2007) 189-199.
- [4] L.T. To, Z.H. Stachurski, Random close packing of spheres in a round cell, *Journal of Non-Crystalline Solids*. 333 (2004) 161-171.
- [5] C.R. a Abreu, R. Macias-Salinas, F.W. Tavares, M. Castier, A Monte Carlo simulation of the packing and segregation of spheres in cylinders, *Brazilian Journal of Chemical Engineering*. 16 (1999) 1-12.
- [6] a Galakhov, V. Shevchenko, Analysis of two-dimensional packings, *Ceramics International*. 18 (1992) 213-221.
- [7] A.N.E.W. Algorithm, F.O.R. Close, R. Packing, Computer simulation of close random packing of equal spheres', *Physical Review A*. 32 (1985) 2347-2351.
- [8] T. Quickenden, Random packing in two dimensions and the structure of monolayers, *Journal of Colloid and Interface Science*. 48 (1974) 382-393.
- [9] D. Haughey, Local voidage variation in a randomly packed bed of equal-sized spheres, *Chemical Engineering Science*. 21 (1966) 905-915.
- [10] E.M. Tory, B.H. Church, M.K. Tam, M. Ratner, Simulated random packing of equal spheres, *The Canadian Journal of Chemical Engineering*. 51 (1973) 484-493.
- [11] W.S. Jodrey, E.M. Tory, Simulation of random packing of spheres, *Simulation*. 32 (1979) 1-12.
- [12] Y. Shi, Y. Zhang, Simulation of random packing of spherical particles with different size distributions, *Applied Physics A*. 92 (2008) 621-626.
- [13] Y.G. Stoyan, G.N. Yaskov, Packing identical spheres into a cylinder, *International Transactions in Operational Research*. 17 (2009) 51-70.
- [14] W.S. Jodrey, Computer Simulation of Equal Spheres of Isotropic , Homogeneous , Dense Random Packing, 30 (1981) 111 - 118.
- [15] Stoyan, Yu.G, Mathematical methods for geometric design, *Proceedings of International Conference PROLAMAT* 82. (1983) 67-86.

Parametric Study of Piled Raft Foundations to Improve the Design Method

Abbasali Taghavi, Asskar Janalizade Choobbasti
Babol Noshirvani Institute of Technology, Iran

ABSTRACT

The piled raft Foundation is a geotechnical composite construction, consisting of pile, raft and soil elements, which is applied for the foundation of tall buildings in an increasing number. Conventionally, there are two main design methodologies for this kind of foundation. The first design method is based on reducing raft foundation settlement by adding a certain number of piles. Another design method assumes that all structure loads to be transferred to piles without considering contribution of load taken by the raft. In this paper a parametric study of piled raft foundations, taking account of their components interaction, accomplished by Finite Element Method (FEM). The results show that conventional methods of design are based upon relatively conservative assumptions and using of numerical methods considering interaction between the piled raft components, might give an economic design approach.

Keywords: Piled raft foundation; Settlement – based design; Finite element method; Soil – Structure Interaction

1. INTRODUCTION

In the past decade, piled raft foundations have been widely used in practice to support heavy and high - rise buildings and extensive studies have been done about their design methods. The piled raft foundation is a combination of a raft foundation with piles. Taking into account the design requirements and bearing capacity, piles in piled rafts are designed. In soft soils where a raft alone may not provide the bearing capacity, connected piles to enhance the performance of the raft or unconnected piles to reinforce the supporting soil are usually added. The most effective application of piled rafts occurs when the raft can provide adequate load capacity, but the settlement or differential settlement of the raft alone exceeds the allowable values. In this situation, piles are used as settlement reducer and designed to have small size and number in comparison with conventional pile groups.

Piled raft foundation consists of three carrying elements: soil, raft and pile, which the interaction between the elements may cause some complexity in prediction of this composite foundation.

One of the Technical Committees of the International Society for Soil Mechanics and Foundation Engineering (ISSMFE) focused its efforts in the period 1994 - 7 towards piled raft foundations, collected considerable information on case histories and methods of analysis and design, and produced comprehensive reports on these activities including O'Neill et al. [1]; van Impe & Lungu [2]. The concept of piled raft foundations is by no means new, and has been described by several authors, including Zeevaert [3], Davis & Poulos [4], Hooper [5], Burland et al. [6], Sommer et al. [7] and Franke [8], among many others.

Poulos [9] developed a program GARP which employs an approximation method for the analysis of piled raft with the consideration interaction effects between the piles and raft.

Allowances were made for the piles to reach their ultimate capacities and local bearing failure of the raft. Russo [10] employed a similar method where the piles and soil were modelled by linear or non-linear interacting springs. The soil displacements were calculated using Boussinesq's solution thus yielding a closed form solution. The non-linear behaviour of the piles was modelled by the assumption of a hyperbolic load-settlement curve for a single pile. Brown and Wiesner [11] used the Boundary Element Method to analyse a strip footing supported by equally spaced identical piles embedded in an isotropic homogenous elastic half space. Application of Mindlin's solution was used to determine the interaction relationships due to the interface forces. Poulos [12] extended a method of BEM to incorporate the effect of free-field soil movement, load cutoffs for the pile - soil and raft – soil interfaces to examine the interaction mechanism between the piled raft and a soil subjected to externally imposed vertical movement. The analysis is implemented via a computer program PRAWN. Hooper [5] used Finite Element Method to analyze a piled raft and considered the stiffening effect of the superstructure on the behaviour of the piled raft by introducing an equivalent raft thickness. Liu and Novak [13] employed the finite element method to examine the behaviour of a raft supported by a single pile at the centre. Mapped infinite elements are used to model the far - field soil medium to simulate an unbounded domain. A weak zone around the pile with lower strength and modulus was introduced to account for the slip at the pile-soil interface. Reul and Randolph [14] presented a three-dimensional elasto-plastic finite element method using program ABAQUS for the analysis of piled raft foundations in overconsolidated clay. Oh et al [15] used finite element program PLAXIS for the analysis of piled rafts on Australian sand.

Combined Boundary and Finite Element Method as well as Combined Finite Element and Finite Layer Method are used to reduce the calculation time by some authors including Mandolin and Viggiani [16] and Zhang. In this paper finite element is employed to perform parametric studies.

2. DESIGN CONCEPTS

As with any foundation system, the design of a piled raft foundation requires the consideration of a number of issues, including: ultimate load capacity for vertical, lateral and moment loadings, maximum settlement, differential settlement, raft moments and shears for the structural design of the raft, pile loads and moments, for the structural design of the piles.

In much of the available literature, emphasis has been placed on the bearing capacity and settlement under vertical loads. While this is a critical aspect, and is considered in detail herein, the other issues must also be addressed. In some cases, the pile requirements may be governed by the overturning moments applied by wind loading, rather than the vertical dead and live loads.

2.1 Alternative Design Philosophies

Randolph [17] has defined clearly three different design philosophies with respect to piled rafts:

(a) The “conventional approach”, in which the piles are designed as a group to carry the major part of the load, while making some allowance for the contribution of the raft, primarily to ultimate load capacity

(b) “Creep piling”, in which the piles are designed to operate at a working load at which significant creep starts to occur, typically 70 - 80% of the ultimate load capacity; sufficient piles are included to reduce the net contact pressure between the raft and the soil to below the preconsolidation pressure of the soil.

(c) Differential settlement control, in which the piles are located strategically in order to reduce the differential settlements, rather than to reduce the overall average settlement substantially.

2.2 The Design Process

Poulos [18] has suggested that a rational design process for piled rafts involves three main stages:

(a) A preliminary stage to assess the feasibility of using a piled raft, and the required number of piles to satisfy design requirements

In the preliminary stage, it is necessary first to assess the performance of a raft foundation without piles. Estimates of vertical and lateral bearing capacity, settlement and differential settlement may be made via conventional techniques.

(b) A second stage to assess where piles are required and the general characteristics of the piles

Much of the existing literature does not consider the detailed pattern of loading applied to the foundation, but assumes uniformly distributed loading over the raft area. While this may be adequate for the preliminary stage described above, it is not adequate for considering in more detail where the piles should be located when column loadings are present. Assessment of the maximum column loadings for this control is the subject of second stage.

(c) A final detailed design stage to obtain the optimum number, location and configuration of the piles, and to

compute the detailed distributions of settlement, bending moment and shear in the raft, and the pile loads and moments. The first and second stages involve relatively simple calculations, which can usually be performed without a complex computer program. The detailed stage will generally demand the use of a suitable computer program that accounts in a rational manner for the interaction among the soil, raft and piles and may be the effect of the superstructure. In order to do this stage carefully, there are many approaches including “strip on springs” approach, “plate on springs” approach, boundary and element method and etc. In this paper we employ mentioned design process and philosophies to perform a suitable design.

3. FINITE ELEMENT MODELING

3.1 Finite Element Mesh and Boundary Condition

The behavior of the piled raft was investigated by carrying out 3D numerical analyses. The geotechnical finite element code PLAXIS (Vermeer and Brinkgreve [19]) was used for this purpose and 15-node triangular elements were used. Fig.1 shows a typical finite element mesh used for parametric study. This parametric study has been done for different raft and pile sizes and different number of piles. Material properties of soil and piled raft are shown in Table I.

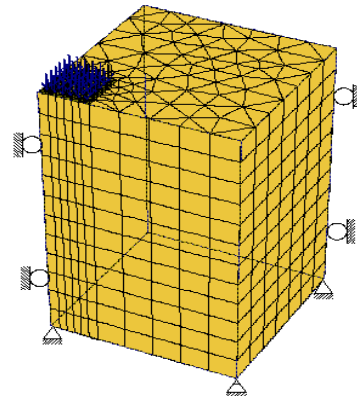


Fig1. Typical Finite Element mesh used for numerical method

Table I. Material properties used for analysis

	E (MPa)	ν	γ (kN/m ³)	C (kPa)	ϕ
Soil	14	0.18	18	5	30
Pile	25000	0.20	24	-	-
Raft	25000	0.20	24	-	-

The pile head was connected to the raft rigidly. Special interface element was used at the soil – pile and raft – pile interface. A relatively fine mesh was used near the interfaces while a coarser mesh was used further from the pile and raft. Vertical boundaries are assumed to be on rollers to allow downward movement of the soil layers and the beneath of the model is fixed in three orthogonal directions. For the far-field boundaries, the distance of the boundary from the edge of the raft was greater than the pile length since the observed influence zone based on the finite element analysis including interface is there [20]. This limit prevents the effects of

boundaries and works as infinite elements to simulate half space. After initial equilibrium, the vertical loading was applied on the top of the raft surface. Since modeling of the entire pile installation process is rather complicated, the pile was assumed to be in a stress-free state at the start of the analysis.

3.2 Constitutive Modeling

Based on the materials, it is preferable to use the Mohr-Coulomb model for relatively quick and simple and first analysis of any problem considered. To simplify the analysis process, average values of material parameters (as mentioned in Table I) were adopted for the soil layer. The raft and piles has great Young's modulus in comparison with the soil and remain in elastic area, so they were modeled with a linear elastic model.

The modeling techniques used for the pile - soil interface are generally divided into two types: slip element and thin layer element. The former was used by Jeong et al. [20] and Lee et al. [21], in which the slip behavior could be considered. The latter was used by Reul and Randolph [14] and de Sanctis and Mandolini [22]. In this paper thin layer elements with a thickness of 0.1d (d, pile diameter) is used.

4. VALIDATION

The validation of the present model was done by a comparison with a centrifuge model test for a circular piled raft on stiff clay, which was carried out by Horikoshi and Randolph [23]. The total number of piles was nine (a 3×3 array with a pile spacing of 2.5 m) with a length of 15 m and diameter of 0.32 m, which were located under a 14 m diameter circular raft with a thickness of 0.05 m. A soil depth of 25 m was taken into account. Eq.1 describes the average settlement. Also a comparison of the results with a numerical method proposed by Prakoso and Kulhawy [24] has been done. The results are shown in Fig.2 and Table II.

$$S_{average} \approx \frac{1}{3}(2S_{center} + S_{corner}) \quad (1)$$

where S_{corner} is the settlement of the raft corner and S_{center} is the displacement of the raft center of piled raft system.

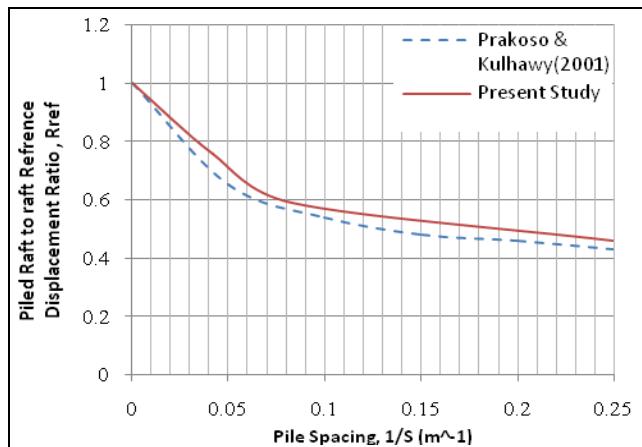


Fig2. Comparison between present method and a numerical method

Table II. Comparison of the results with the test data

	Average Settlement, Savg (mm)	Load taken by piles (%)
Horikoshi and Randolph	22	19
Present Study	21.67	23.55

5. PARAMETRIC STUDY

Table III lists soil, raft and pile configurations, different sizes and distances and number of piles used in the raft only and piled raft analyses.

Table III. System configuration for parametric study

Pile	Length	40 m – combined 20 and 40 m
	Diameter	0.5 m
	Distance	s/d= 4 , 6
	Arrangement	Center- Uniform
Raft	Thickness	0.5, 1, 2 m
	Width	26 by 26
Load	Uniform	150 , 200 kN/m ²
	Concentrated	Equal to uniform load (on piles)

Fig.3 shows different arrangements used for parametric study. Arrangements have 16, 25, 36, 81 and 169 piles, respectively. Arrangement 3 and 5 have s/d=4 and others have s/d=6.

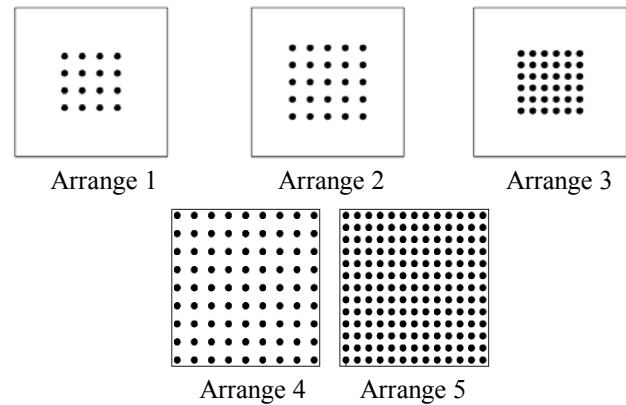


Fig3. Different arrangement used for parametric study

In order to consider more detailed design stage, as mentioned, uniform loading results (preliminary stage) are compared with the nonuniform and concentrated loading one. For a concentrated load, the load was applied at the center of the raft, but the equivalent magnitude of the load in the two different loads was the same. The vertical loading was applied on the top of the raft surface after initial equilibrium. All analyses were carried out under drained conditions. Thus, hydrostatic water pressure distribution was assumed in a drained condition with the ground water table located on the top of the soil layer.

6. COMPUTED RESULTS AND DISSCUSION

As mentioned before, maximum settlement, differential settlement, raft moments and pile loads are the main

parameters in the assessment of the piled raft behaviour. Also concentrated and local loading is used to consider the design stages proposed by poulos in addition to uniform loading. Fig.4 shows the variation of the normalized average settlement with the square root of the number of piles, $\sqrt{n_p}$.

Each value of this parameter also introduces an arrangement. The average settlement is calculated using Eq.1 and normalized respect to average settlement of the raft only.

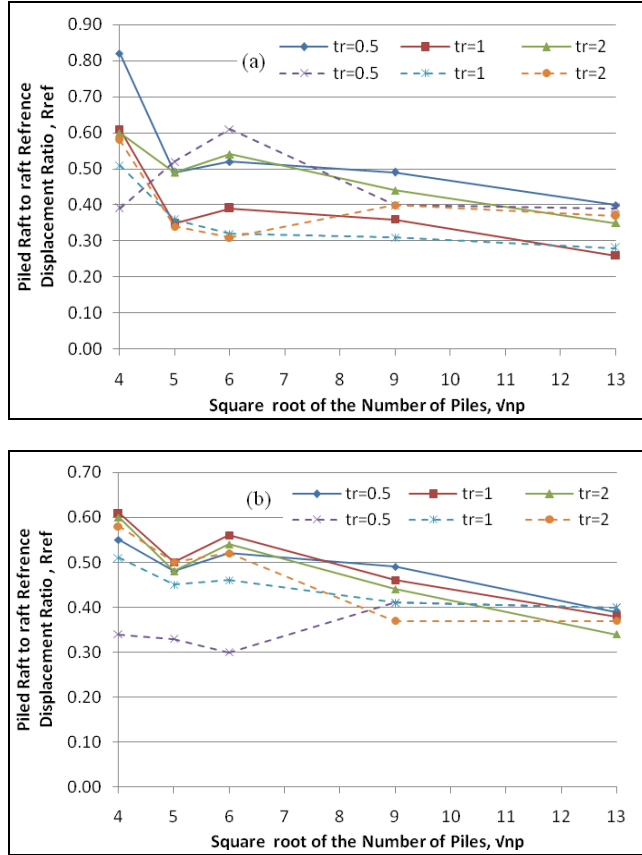


Fig4. Variation of normalized average settlement with the square root of the number of piles (a) Load: 150 kPa (b) Load: 200 kPa

The average settlement is reduced with increasing the number of piles. Arrangement 3 shows satisfactory performance for both loads and beyond that the reduction procedure continued at a slow rate. The average settlement due to uniform loading (solid line) is less than the average settlement caused by concentrated loading (dashed line) in most cases. Because in the piled raft under uniform loading there are regions without loading and the settlement in this regions is not considerable. Therefore, the resultant of average settlement in this case in comparison with the concentrated loading becomes less.

Another point that realized from Fig.4 is that increasing in raft thickness may lead to reduction of average settlement, but this reduction is not remarkable and with the increase in load level the lines are approaching. The raft thickness of 1 meter shows acceptable performance between different thicknesses. Concentrated loading has unfavorable effect that is obvious in differential settlement. Fig.5 shows the variation of the

normalized average settlement with the square root of the number of piles, $\sqrt{n_p}$. The normalized differential settlement, S_d , is calculated from Eq.2.

$$S_d = \frac{\Delta w_{c-e} E_s}{q \cdot B_r} \quad (2)$$

where Δw_{c-e} is the differential settlement, E_s is the modulus of elasticity for the soil, q is the applied load and B_r is raft breadth.

In this case, arrangement 3 does not act so well and shows significant differential settlement especially under concentrated loading. As expected, when the load applied in certain point (on the piles), significant local displacement occurs and make remarkable differential settlement.

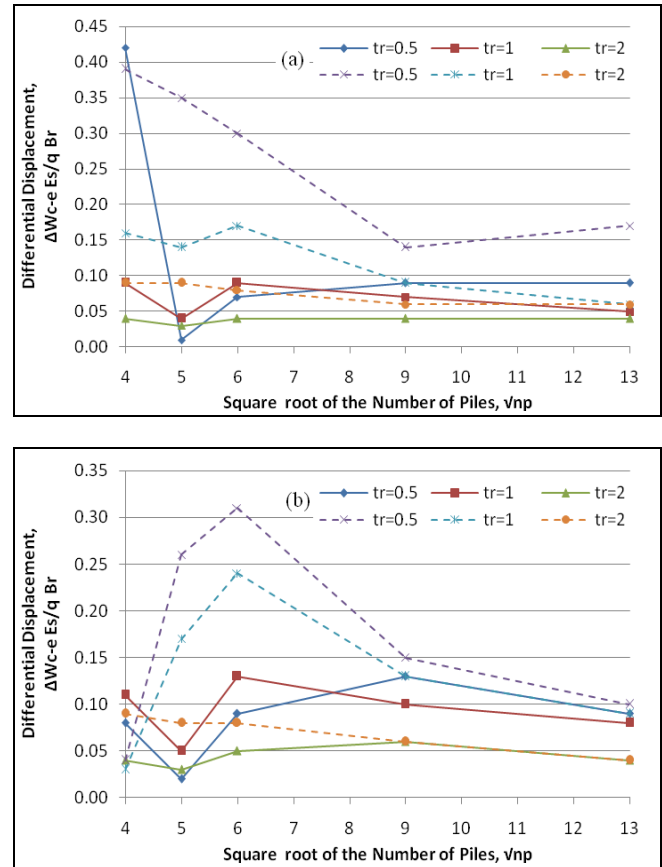


Fig5. Variation of normalized differential settlement with the square root of the number of piles (a) Load: 150 kPa (b) Load: 200 kPa

For piled raft under uniform loading a decrease of normalized differential settlement with increasing load level can be observed. This is due to the plastic deformation under the edge being larger than those under center of the raft. According to this figure, at arrangement 4, foundation shows good performance. After the arrangement 4 ($n_p=81$), reduction procedure continued at a very slow rate and modifying the pile number and arrangement is not required. As previously mentioned by Horikoshi and Randolph [14], raft thickness describes the piled raft foundation stiffness

when raft width and soil configurations are constant. Thus, it can be mentioned that the differential settlement increases with decreasing foundation stiffness. Using thin raft ($t_r=0.5$) is less favorable, because it makes two or three times further differential settlement than other conditions. On the other hand, Using thick raft ($t_r=2$) just to decrease the differential settlement is not an economic plan. Raft thickness of 1 meter shows satisfactory performance except at one case (concentrated load: 200 kPa).

Another unfavorable aspect of using thick raft is exceeding maximum raft moment from the acceptable limits in design procedure. Fig.6 clearly indicates rapid increase in maximum raft bending moment when using larger value of raft thickness.

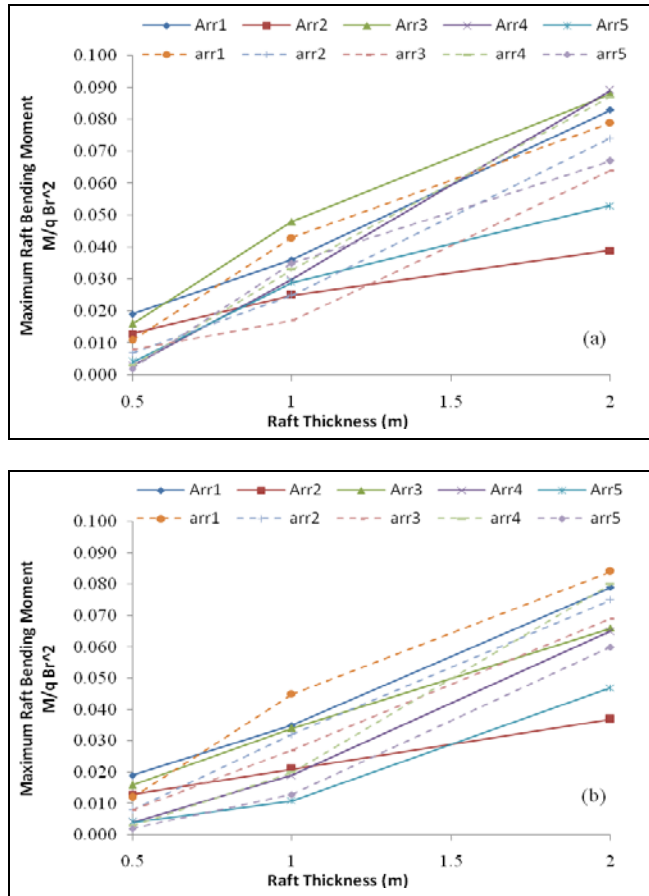


Fig6. Normalized maximum bending moment in raft for different raft thicknesses (a) Load: 150 kPa (b) Load: 200 kPa

As mentioned above, raft thickness of 1 meter in this case is admitted. Load type and magnitude has not had any considerable on the normalized bending moment and both types can be placed at a certain limit. At $t_r=1$ arrangement 5 shows the best performance and indicates that using uniform distributed arrangement of piles may cause reduction in raft bending moment and so the optimized design can be achieved.

Fig.7 shows the ratio of load taken by the piles. In some instances piles take more than 90 percent of applied load. In the scope of acceptable and economic design it is not

admitted. However, the limit of 70 percent of applied load as an average seems good. In this case, arrangements 2 and 3 at raft thickness of 1 meter shows reasonable design alternative.

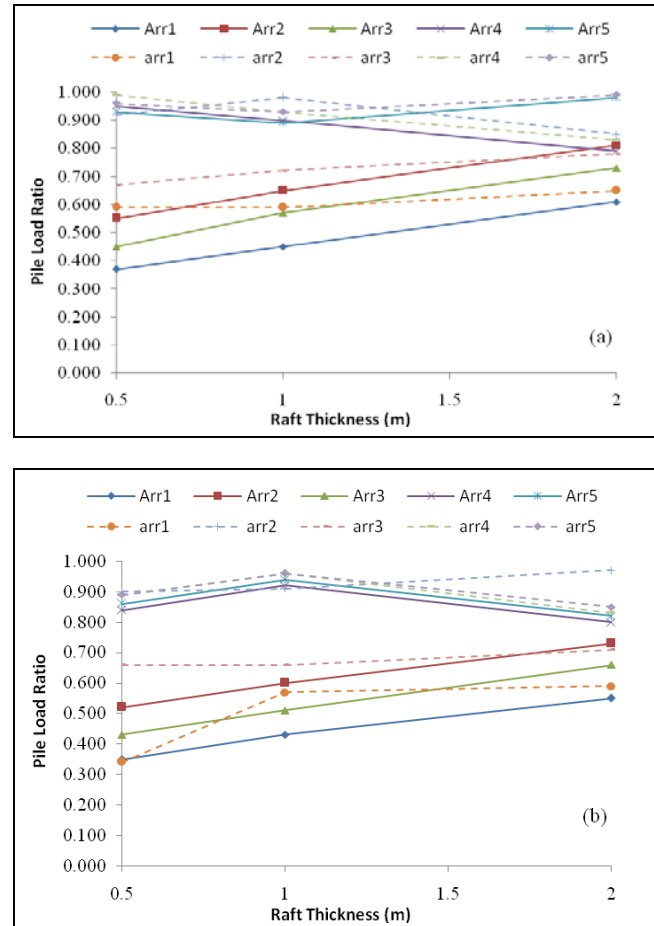


Fig7. Pile load ratio for different raft thicknesses (a) Load: 150 kPa (b) Load: 200 kPa

Therefore, assumption of two mentioned conventional method about giving all loads to raft or to piles is not acceptable and each of these elements play different role in the foundation behaviour.

7. AN EXAMPLE OF OPTIMIZED DESIGN

In Table IV two arrangement of the parametric study is compared with an example of optimized design for $t_r=1$ m and load = 150 kPa. As suggested by Reul and Randolph [14], the piles under the core 25% of the raft area have the same length (40 m) and others constructed shorter. In this example other piles have 20 m length. According to the table, reduction of the total pile length up to 30 percent makes little increase in the average and differential settlements. Also, the magnitude of maximum absolute bending moment of the raft becomes little larger and in some cases decreases in comparison with the studied ones. Therefore, in the optimum design such cases should be considered to achieve the best design alternative.

Table IV. Comparison of the foundation behaviour by equal piles and combined piles

		S_{avg} (cm)	Δw_{c-e} (cm)	Raft moment (kN.m)
Arrange3 (Uniform)	Equal piles	4.4	1.2	2435
	Combined piles	6.17	2	1610
Arrange3 (concentrated)	Equal piles	4	3.8	1855
	Combined piles	6.2	3.9	2625
Arrange5 (Uniform)	Equal piles	3.7	1	1500
	Combined piles	5.6	1.8	1690
Arrange5 (concentrated)	Equal piles	3.8	1.3	1650
	Combined piles	5.6	2.5	1670

8. CONCLUSION

In this paper a parametric studies on the piled raft foundation behaviour has been done by accurate analysis and design method (FEM) and it is understood that two mentioned conventional design method are conservative. Because it has been seen that for some cases, pile groups undergo just 40 or 50 percent of applied load and installation of the acceptable raft above that can improve the design process. On the other hand, using of piles as settlement reducer is not an economic option and the design of raft in order to carry all superstructure loads makes difficulties in this element performance like exceeding bending moment. Therefore, using more accurate analysis and design procedures help us to consider different aspects of design and lead to choice of the best option.

9. REFERENCES

- [1] O'Neill MW, Caputo V, De Cock F, Hartikainen J. and Mets M, "Case histories of pile-supported rafts," Report for ISSMFE Technical Committee TC18. Houston, TX: University of Houston, 1996.
- [2] Van Impe W F and Lungu I, "Methods of analysis of piled raft foundations," A Report Prepared on Behalf of Technical Committee TC18 on Piled Foundations, 2001.
- [3] Zeevaert L, "Compensated friction-pile foundation to reduce the settlement of buildings on highly compressible volcanic clay of Mexico City," Proc. 4th Int. Conf. Soil Mech. Found. Engng, London 2, 1957.
- [4] Davis EH and Poulos HG, "The analysis of piled raft systems," Aust. Geomech. J, vol. 2, 1972, pp. 21-27.
- [5] Hooper JA, "Observations on the behaviour of a piled-raft foundation on London Clay," Proc. Inst. Civ. Engrs 55, No. 2, 1973, pp. 855-877.
- [6] Burland JB, Broms BB and De Mello VFB, "Behaviour of foundations and structures," Proc. 9th Int. Conf. Soil Mech. Found. Engng, Tokyo 2, 1977, pp. 495-546.
- [7] Sommer H, Wittman P and Ripper P, "Piled raft foundation of a tall building in Frankfurt Clay," Proc. 11th Conf. Soil Mech. Found. Engng, San Francisco 4, 1985, pp. 2253-2257.
- [8] Franke E, "Measurements beneath piled rafts," ENPC Conference, Paris, 1991, pp. 1-28.
- [9] Poulos HG, "An Approximate Numerical Analysis of Pile-raft Interaction," Int. J. for Numerical and Analytical Methods in Geomechanics, Vol. 20, 1994, pp. 57-72.
- [10] Russo G, "Numerical Analysis of Piled rafts," Int J. for Numerical and Analytical Methods in Geomechanics, Vol. 22, No. 6, 1998, pp. 477-493.
- [11] Brown PT and Wiesner T J, "The Behaviour of Uniformly Loaded Piled Strip Footings," Soils and Foundations, Vol. 15, No. 4, 1975, pp. 13-21.
- [12] Poulos HG, "Piled Rafts in Swelling or Consolidating Soils," J. Geotech. Engng, ASCE, Vol. 119, No. 2, 1993, pp. 374-380.
- [13] Liu W and Novak M, "Soil-pile-cap Static Interaction Analysis by Finite and Infinite Elements," Canadian Geotechnical J., Vol. 28, 1991, pp. 771-783.
- [14] Reul O and Randolph MF, "Design Strategies for Piled Rafts Subjected to Nonuniform Vertical Loading," J. of Geotec and GeoEnv Engng, Vol. 130, 2004, pp. 1-10.
- [15] Oh EYN, Huang M, Surarak C, Adamec R and Balasurbamaniam AS, "Finite Element Modeling for Piled raft Foundation in Sand", EASEC-11, Taiwan, 2008.
- [16] Mandolini A and Viggiani C, "Settlement of Piled Foundations," Géotechnique, Vol. 47, 1997, pp. 791-816.
- [17] Randolph MF, "Design methods for pile groups and piled rafts," state-of-the-art report. Proc. 13th Int. Conf. Soil Mech. Found. Engng, New Delhi 5, 1994, pp. 61-82.
- [18] Poulos HG, "Piled raft foundations: design and applications," Geotechnique, Vol. 51, 2001, pp. 95-113.
- [19] Brinkgreve RBJ, Broere W. Plaxis 3D Foundation, Version 1.6. User manual, Delft University of Technology & plaxis bv, The Netherlands, 2006.
- [20] Jeon SS, Lee JH and Lee CJ, "Slip effect at the pile-soil interface on dragload," Computers and Geotechnics 2004 Vol. 31 pp.115-26.
- [21] Lee J, Kim Y, Sangseom J, "Three-dimensional analysis of bearing behavior of piled raft on soft clay," Computers and Geotechnics, Vol. 37, 2010, pp. 103-114.
- [22] De Sanctis L, Mandolini A. "Bearing capacity of piled rafts on soft clay soils," JI of Geotec & Geoenv Engng (ASCE), Vol. 132(12), 2006, pp. 1600-10.
- [23] Horikoshi K, and Randolph MF, "A Contribution to the Optimum Design of Piled Rafts," Géotechnique, Vol. 48, No. 2, 1998, pp. 301-317.
- [24] Prakoso W A and Kulhawy FH, "Contribution to Piled Raft Foundation Design," JI. of Geotechnical and GeoEnvironmental Engineering, Vol. 127, No. 1, 2001, pp.17-24.

Experimental Study of Suction-Monitored CBR Test on Sand-Kaolin Clay Mixture

Purwana, Y.M., Nikraz H., and Jitsangiam P.
Curtin University, Australia

ABSTRACT

Conventional laboratory CBR test has been widely used for predicting bearing capacity of subgrade layer for pavement design. In unsaturated soil, suction is one of the key parameters for understanding the soil behavior. The analysis of CBR is commonly presented in CBR-water content relation. The information of CBR based on soil suction is very rare and more study is still required. This paper presents a laboratory experiment of CBR test with direct suction measurement. Suction-monitored CBR test is introduced by attaching tensiometers on CBR mold and its surcharge. The standard compacted test on various proportions of sand-kaolin clay mixtures starting from 0% (pure sand), 5%, 10%, and 20% of clay were used. The tests were performed with different value of water content in both soaked and unsoaked conditions. The results indicated that the CBR versus matric suction forms a bi-linear curve. The discussion is presented in term of CBR-water content and CBR-matric suction relation.

Keywords: Bi-linear curve, CBR, matric suction, sand-kaolin mixture

1. INTRODUCTION

The California Bearing Ratio (CBR) has been used as a semi empirical approach for predicting bearing capacity of subgrade for pavement design. The method was firstly used in 1920's in the California State Highway Department and was adapted by US Corp of Engineer in the 1940's for military airfield. After the Second World War, the CBR was also used in UK and has spread to European countries [1]-[2]. Due to its simplicity and relatively low cost, this method has been widely used around the world for flexible pavement design. The CBR test is performed by penetrating a plunger with constant penetration rate of 1.27 in/min on compacted specimen on rigid mould with diameter of 152.4 mm and a height of 177.8 mm as describe in ASTM D 1883-07. There are 2 types of CBR test associated with the treatment of the sample: unsoaked and soaked. The unsoaked CBR test is performed to simulate the natural condition whereas the soaked one is performed to replicate the worst condition such as high water table in the field, in which the soil layer is considered to be in saturated or nearly saturated condition. The intensive study of the CBR and its relationship with water content and dry density has been studied by Davis [3] using a relatively wide range variation of soils from heavy clay to sandy gravel. The relation was presented in semi logarithm diagram, showing that the log CBR value was affected by water content, dry density and structure of soil particle. As water content increased, the CBR value went down linearly for plastic soil, whereas for non-plastic soils the relation was non-linear. The non-plastic the soil exhibited increasing in CBR at initial range of water content, and decreasing as the water content increased. This non linearity

was believed as the effect of compaction on the soil structure of the soil.

Black [4] carried out the study to estimate the CBR value of cohesive soil indirectly using the soil plasticity and its moisture content. Firstly, soil suction and true angle of friction were predicted using soil suction-water content and true angle of friction-plasticity index curves respectively. From this, the predicted suction and the true angle of friction were used to calculate bearing capacity, and finally the CBR was estimated using the calculated bearing capacity.

Paraire [5] carried out the study for predicting CBR in unsaturated condition indirectly using bearing capacity approach. He performed the bearing capacity test using a small cone with an angle of 30° and 2.03 cm in diameter penetrated on the surface of silt and quartz sand specimen with similar dimension of CBR mould. During the test, suction was generated using suction plate apparatus and water content was also measured. The CBR was indirectly obtained from the large number of suction-bearing capacity data. The result indicated that there was a non-linear suction-CBR relation in which the increase in suction caused the increase in CBR.

The non-linearity of CBR with respect to matric suction was also resulted from the study carried out by Sivakumar and Tan [6]. They investigated the effect of compacted water content on CBR of tills, while matric suction was taken into consideration using a pressure plate. The effect of matric suction was presented indirectly by water content, and indicated that water content has a significant effect on CBR. The result also indicated that the rate increase in CBR at wet side of optimum water content was lower than that at dry side. The effect of matric suction on CBR value has also been studied by Ampadu [7] on decomposed granite. He focused on the effect of drying and wetting of remolded specimen on

CBR value. The result indicated that from the OMC the CBR tends to increase rapidly as water content decreased. The CBR was drop as water content increased due to soaking. In his study, matric suction was obtained indirectly from SWCC using filter paper method.

The aforementioned studies indicated that many more investigations regarding the effect of matric suction on CBR were still required. This paper presents the experimental study of CBR on various proportion of sand-kaolin mixtures with direct measurement of matric suction using tensiometer.

2. SUCTION-MONITORED CBR DEVICE

The suction-monitored CBR is the device for CBR test in which matric suction is monitored during the test. It is made by a modification of conventional CBR by attaching 1-bar miniature tensiometers on its mold and surcharge weight. The set-up and configuration of the test is shown in Fig. 1. The tensiometers were connected to the data logger or readout unit so that the suction measurement together with the loading and displacement can be recorded continuously during the test.

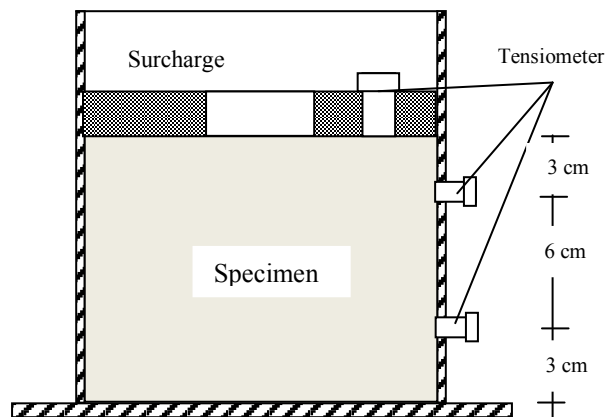


Fig. 1: The setup of modified CBR test (not to scale)

3. TESTING PROGRAM

3.1 Preparation

Sand-kaolin mixture with different proportion of 100% sand, 95:5, 90:10, 80:20 dry weight were investigated. The sand was taken from Baldvis sand pit, Western Australia, and has the specific gravity of 2.63. Grain size analysis indicated that it consists of 99.74 % fine and medium size of sand and 0.26 % of fines. According to the ASTM D 2487, this material is classified as poorly-graded sand (SP). The trade mark of kaolin clay was obtained from the UNIMIN Australia Ltd., and has the liquid limit and plasticity index of 48.1 and 17.4 respectively. The dry sand and kaolin clay were then mixed with the pure water according to the desired proportion and put in a sealed plastic bag for at least 72 hours for curing and water content equilibration. The compaction test was performed following the Proctor compaction procedure as

described in ASTM D 698. The grain size distribution curves of all mixtures are shown in Fig. 2.

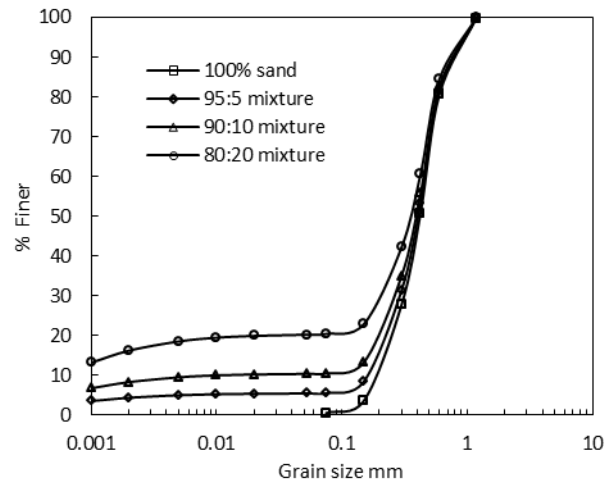


Fig. 2. Grain size distribution curves

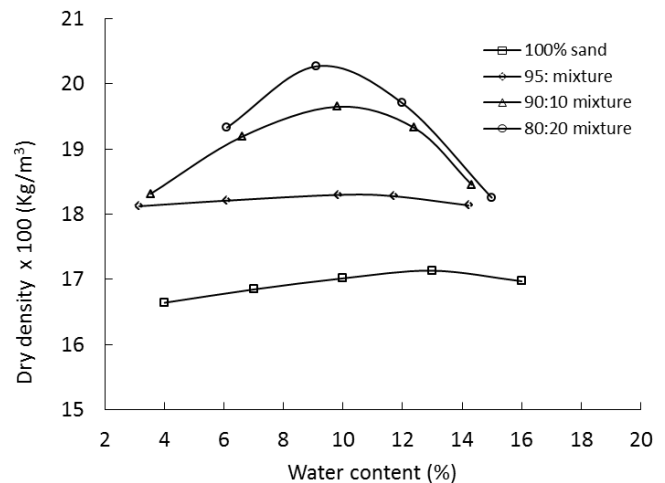


Fig. 3. Compaction curves

Fig. 3 and Table 1 show the compaction curves and compaction characteristic respectively. During compaction, the small particles of kaolin clay fill the voids causing the increase in MDD and the decrease in void ratio. This result has a good agreement with the result of Mullins and Panayiotopoulos [8] and Chiu and Shackelford [9]. The optimum water content (OWC) and maximum dry density (MDD) were two referenced parameters for the compaction of CBR specimens. The relatively high water content in 100% sand was caused by the high portion of fine size of sand (> 50%).

Table 1. Compaction characteristic of the sand-kaolin mixture

Sand-kaolin clay mixture	MDD (kg/m ³)	OWC (%)	Void ratio (e)
100% sand	1700	13	0.55
95:5	1830	11	0.45
90:10	1970	9.8	0.35
80:20	2030	9.1	0.31

Prior to the CBR compaction, the orifices prepared for attaching the tensiometers on the mold were blocked tightly with electrical tape. This was done to avoid the specimen coming out from the mold through these holes during compaction. The CBR tests were performed on both “saturated” and unsaturated conditions, represented by soaked and unsoaked specimen respectively.

It is essential to ensure that before and during matric suction measurement, the tensiometers were completely free of air bubbles. The presence even a small air bubble would have affected the performance of the tensiometer by increasing the response time. The saturation of tensiometers was then required. It was performed by immersing its ceramic disk and reservoir in the distilled water and then was vacuumed using a desiccator and a vacuum pump for around 2-3 hours.

3.2 Testing Program

Prior to plunger penetration, the tensiometers were installed through the orifices on the CBR mold and its surcharge in such a way that its high air entry disk (HAED) of tensiometers has a good contact with the specimen. High quality removable adhesive and clamping set were utilized to hold the tensiometers in their position. Pneumatic machine was utilized to penetrate the CBR plunger on the specimen with a constant rate of 1 mm/min. A load-penetration curve produced from the test was utilized for determining the CBR value. By definition, the CBR value is the magnitude of stress at which the specimen has been penetrated at 1 in (2.54 mm) compared to a standard stress of 6.9 MPa. During the test, the matric suction of the bottom and upper layers of the specimen were recorded. After the CBR test, the water content of the bottom, middle and top layer of specimen were determined. In this study, various water contents were obtained by air-drying for different time periods from unsoaked specimens.

4. RESULTS

4.1 The Effect of Clay Content and Air Drying Period on CBR

Fig. 4 shows the effect of kaolin clay content on CBR for various periods of time. The CBR of 100% sand (0% kaolin clay content) are not significantly affected by the water content, as the CBR values remain around 15-20% at any water content. The increase of kaolin clay content up to 5% causes the decrease in CBR in both soaked and unsoaked condition, but it causes a slight increase in CBR when the specimens were dried up for 1 or 2.5 day. The significant increase in CBR is shown by 10% kaolin clay content (90:10 mixture) when the specimen was dried up. The mixture of 90:10 exhibits the best proportion in term of CBR (even though according to compaction curves, the highest MDD was resulted from 80:20 mixture). The CBR of 90:10 mixture increases from 18.6% in soaked condition to 28.3% in unsoaked condition. Again, the CBR increases to 41.3% and 48.5%, when the sample was dried up for 1 and 2.5 days respectively. Beyond 10% kaolin clay content, the CBR decreases even though the samples were air-dried.

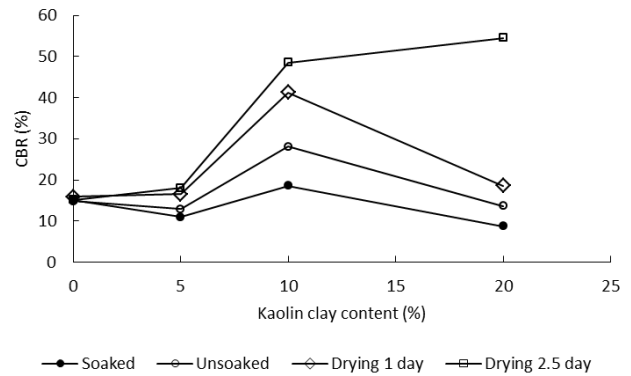


Fig. 4. The effect of kaolin clay content on CBR

4.2 The Effect of Water Content and Matric Suction on CBR

Fig. 5 quantifies the effect of the decrease in water content due to air-drying on CBR. The CBR-water content relation forms a non-linear curve. Until its water content reaches the OWC, the CBR increases slightly as the water content decreases, and a significant increase rate in CBR occurs when the water content is less than OWC. The result has a good agreement with the result of Ampadu [6]. In general, the longer the air-drying period, the lower the specimen water content and the higher the CBR value.

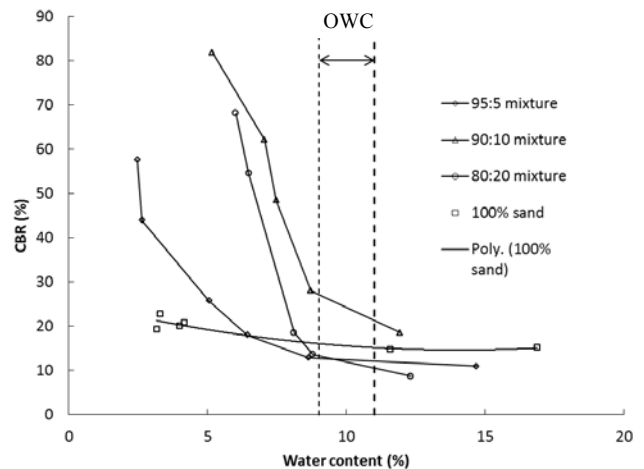


Fig. 5. The effect of water content on CBR

The effect of water content and matric suction on the strength of compacted sand-kaolin mixtures has been investigated as part of the author’s study. The result indicated that to some extent the presence of kaolin clay affected the shear strength through the increase of effective cohesion and the decrease of effective internal friction angle. However, the cohesion itself was affected by the amount of water in the mixture. Accordingly, it may be deduced that the CBR of compacted sand-kaolin clay mixture is affected by the combination effect of kaolin clay and water content altogether.

It has been recognized that the decrease in water content leads to the increase in matric suction. The effect of the increased matric suction on the CBR is presented in Fig. 6. This result

may be explained as the decrease in water content due to drying causes the increase in water tension amongst the soil particles causing the increase in matric suction, and as a consequence, causing the increase in strength.

It can be observed from the figure that the relation between CBR and matric suction forms a bi-linear curve. The first part of the curve starts from near zero matric suction (soaked sample) to 5-7 kPa, at which the CBR increases sharply, and the second part starts from 5-7 kPa with a relatively slower increase in CBR. It also can be seen that the matric suction has never attained zero even though the sample was soaked for 4 days. The soaked CBR test was not performed in the fully saturated condition. The reason is that the test was performed 15 minutes after removing the mold from the bath. Some of the water in the specimen may infiltrate through the base, and some of them may evaporate.

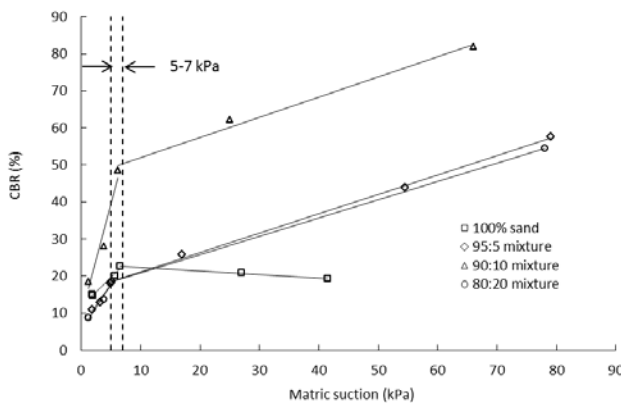


Fig. 6. Bi-linear curve of CBR versus matric suction relation

5. SUMMARY AND CONCLUSION

Based on the laboratory testing on CBR with suction measurement, it can be concluded:

1. Suction-monitored CBR is modification of conventional CBR by attaching tensiometers on its mould and surcharge weight.
2. The CBR test was performed on sand-kaolin clay mixtures of 100% sand, 95:5, 90:10, and 80:20 dry weight proportion, combined with the variation of water content and matric suction using air-drying method.
3. The CBR value of each mixture was presented in respect to water content and matric suction. The decrease in water content leads to the increase in matric suction, and the increase in matric suction leads to the increase in CBR.
4. The relation between CBR versus water content and also the CBR versus matric suction are non-linear. Until the water content reaches the OWC, the CBR increases slightly as the water content decreases. A significant increase rate in CBR value occurs when the specimen water content is less than its OWC.
5. In this study, the non-linearity of CBR in respect to matric suction forms a bi-linear curve for all mixtures. The first part of the curve at which the CBR increases

sharply is started at near zero matric suction (soaked sample) until 5-7 kPa, continued by a relatively slower increase in CBR at the second part of the curve. For 100% sand, the second part of the curve exhibits the decrease in CBR even though the matric suction is increased.

6. Further study is required using the device with higher matric suction capacity such as suction probe, and also using the wider range of soil types.

6. ACKNOWLEDGEMENTS

The first author gratefully acknowledges the Indonesian Ministry of Education for providing funds through the DIKTI Scholarship Project.

7. REFERENCES

- [1] Croney, D. and Croney, P., *The Design and Performance of Road Pavements*, 2nd edition, Mc-Graw Hill Book Company, 1991, Part 3, pp. 159.
- [2] Asworth, R. 'Highway Engineering', Heinemann Education Books, London, 1972, Chapter 11, pp. 190.
- [3] Davis, E.H. 'The California Bearing Ratio Method for the Design of Flexible Roads and Runway', *Geotechnique*, Vol. 1, No. 4, 1946, pp. 249-263.
- [4] Black, W.P.M. 'A Method of Estimating the California Bearing Ratio of Cohesive Soils from Plasticity Data', *Geotechnique*, Vol. 12, No. 4, 1962, 271-282.
- [5] Paraire J., 'Suction Tests on CBR-Diameter Specimens. The Bearing Capacity-Suction Relation', Transport and Road Research Lab. (TRRL), 1987.
- [6] Sivakumar, V. and W.C Tan, W.C., 'CBR, Undrained Strength and Yielding Characteristics of Compacted Tills', *Unsaturated Soils: Proc. of the Third International Conference on Unsaturated Soils*, 2002, pp. 657-661.
- [7] Ampadu, S., 'A Laboratory Investigation into the Effect of Water Content on the CBR of a Subgrade Soil', *Experimental Unsaturated Soil Mechanics*, Springer Berlin Heidelberg, 2007, pp. 137-144.
- [8] Mullins, C.E. and Panayiotopoulos, K.P., 'Compaction and Shrinkage of sands and sands-kaolin mixture', *Soil and Tillage Research*, 4, 1984, pp. 191-198.
- [9] Chiu, T.F. and Shackelford, C.D., 'Unsaturated Hydraulic Conductivity of Compacted Sand-Kaolin Mixture', *J. of Geotechnical and Geoenvironmental Engineering*, Vol. 124, No.2, 1998, pp. 160-170.

{The person who says it can not be
done should not interrupt the person
doing it-Chinese Proverb}

Foundation Strengthening of Historic Buildings by Micropiles

Professor Dr. Azza M. Elleboudy
Benha University, Egypt

ABSTRACT

Cairo contains a treasure of historical buildings and monuments. Several magnificent monuments have deteriorated over the years due to environmental changes. The restoration schemes of two important monuments are the subject of this paper. Damage caused by rise of ground water table and a recent earthquake resulted in cracks in their walls, facades, columns and arches. Restoration started with strengthening the bearing soil strata and the foundations with micropiles to transfer a part of the loads to deep granular soil layer below the weak heterogeneous fill. They were reinforced by steel pipes, and injected with cement grout under different pressures. Micropiles have provided not only an excellent structural support but also a system that minimized settlement, and allowed their execution under the existing restricted access conditions with minimal disturbance of the buildings during underpinning.

Keywords: Micropiles, Foundations, Monuments, Restoration

1 INTRODUCTION

Cairo and its environs preserved and contained a parade of historical buildings and monuments famous for their precious value and fascinating design. Several Islamic and Christian monuments have suffered from severe environmental attack over the years and showed serious signs of distress. Structural cracks caused by differential settlement of the foundations were noted in walls, facades, columns and arches of these invaluable buildings. These phenomena called for a comprehensive geotechnical investigation to outline the causes of the problem and suggest the proper strengthening and rehabilitation schemes. Micropiles were a rather successful means in the restoration process of these important structures [1].

Micropiles were first installed in Italy in the 1950s and were utilized as a method to underpin historic buildings and monuments. In the 1970s, this new technique was introduced in the U.S. In the late 1980s, it gained a wide acceptance as a means for strengthening and underpinning foundations of ancient buildings and existing structures as well in the construction of new civil projects in many countries. Micropiles were successfully used in Turkey [2], Spain [3], France [4], Japan [5], Canada [6] and Australia [7] as well as many other countries around the world.

Micropiles were used in Egypt for the first time in 1993 in the restoration of Sultan El-Ghoury Mosque in Cairo. Since then, they have been utilized in the rehabilitation of many historic structures [8] such as Al-Azhar Mosque, and the Hanging Church, the subject of this paper. Al-Azhar Mosque is one of the most important mosques in Cairo, built in the Fatimid era in year 970. The Hanging Church is the most famous

Coptic Christian church in Cairo. It was built in the 7th century.

2 MICROPILES

Micropiles are drilled, cast-in-place, and grouted piles with small diameter, normally between 125 and 250 mm. They have the capability of sustaining high loads. The main advantage of employing micropiles in the renovation of the historic buildings is their suitability for headroom restricted access, their suitability for wide range of soil conditions and their ability to penetrate obstructions. Furthermore, micropiles can be constructed with minimal noise, vibration and disturbance of the structure and the surrounding buildings, at any angle below horizontal.

Micropiles are mainly used for:

- a. Foundation rehabilitation with underpinning, upgrading foundation capacity, and seizing the foundation movement
- b. Soil reinforcement as in landslide stabilization, soil strengthening, and settlement reduction
- c. Resisting dynamic loads
- d. Excavation support
- e. Resisting uplift forces

Micropiles are installed mainly by two methods; Replacement and Displacement methods. Piles, when driven, are defined as "Displacement Piles" because their installation methods laterally displace the soils through which they are installed. The most commonly used in ancient buildings are the "Replacement Piles" which are formed by drilling and grouting. The load is mainly carried by the micropiles reinforcement and transferred through the grout to the surrounding soils by high values of interfacial friction. The majority of micropiles are between 100 and 250 mm in diameter, 15 to 30 m in length and 250 to 1000 kN in compressive or tensile service load [9].

2.1 Design Aspects

Several design procedures were suggested by many researchers [10]. The design methods are intended to provide an axial capacity for initial design which should be checked with results of load tests. Locally, the methods widely adopted are the Empirical Methods described as follows.

2.1.1 Anchor System

Based on field experience [11], the design method for anchors grouted under pressures of less than 1.0 MPa can be used to calculate the capacity of the micropile, Q_u , obtained by side friction.

$$Q_u = L \times n \times t \times \tan \phi' \quad (\text{kN}) \quad (1)$$

where,

L : pile bond length in meter

ϕ' : effective angle of shearing resistance

n : factor in kN/m, affected by the drilling technique, depth of overburden pressure in the range 30 to 1000 kPa, in situ stress field, and dilation characteristics of the soil.

Table I gives the values of “ n ” for a given soil type based on field experience. They were obtained for normally consolidated materials for borehole anchor diameters of approximately 0.1 m. If the drilling diameter changes significantly, n should be proportionally modified.

Table I. Values of factor n (kN/m)

Type of Soil	Permeability (m/sec)	n
Coarse sand & Gravel	$> 10^{-4}$	400 to 600
Medium to fine sand	10^{-4} to 10^{-6}	130 to 165

2.1.2 Lizzi's Method

Lizzi proposed a simple empirical formula to evaluate the ultimate load of the micropile [12], which is:

$$Q_{ult} = D \times L \times K \times I \quad (2)$$

Where,

D : nominal diameter of the micropile in cm (drilling diameter)

L : length of the pile in cm

K : pile-soil adherence coefficient, Table II

I : dimensionless coefficient depends on the micropile nominal diameter (drilling diameter), Table III

Table II. Values of K

Soil Type	K (kg/cm ²)
Soft soil	0.5
Loose soil	1.0
Soil of average compactness	1.5
Very stiff soil, gravels, sands	2.0

Table III. Values of I

Pile Diameter	I
10 cm	1.00
15 cm	0.90
20 cm	0.85
25 cm	0.80

The empirical design method proposed by Lizzi, developed basically for root piles with relatively low grouting pressures.

It mostly yielded very low computed capacities compared to the observed capacities, showing that this method is not appropriate for compaction grouted piles.

2.2 Method of Construction

2.2.1 Placing the casing into the ground

To place the casing into the ground, drilling is used because the placing can be done in almost every ground conditions. If the casing is drilled properly, it does not cause significant disturbance to adjacent structures or to the structure being underpinned. Where, a casing is rotated with a "drilling bit" at the bottom to cut the soil and fluid circulates through the casing to flush the soil cuttings through the space between the casing and the ground.

2.2.2 Placing the steel reinforcement

Reinforcement is placed in the casing. It can be a single rebar, cage of reinforcement bars or a steel pipe. If the reinforcement is a steel pipe, it can be provided with sleeves and packers. The grouting can be performed through the steel pipe at specific horizons. If the reinforcement is not a pipe, either a plastic pipe for grouting may be placed near the reinforcement or grouting is done directly through the casing.

2.2.3 Injecting the grout

The typical grout used in micropile practice is a mixture of water and cement with a water/cement ratio between 0.40 and 0.55. Sand is sometimes added to decrease the cost of the mixture.

In many cases and before injecting the grout, the casing is filled with grout placed by tremie to push the drilling fluid out of the casing. Reinforcement is sometimes installed after tremie grouting. The subsequent pressure injection of the grout can be done in different ways; through the casing as it is removed, or through the steel pipe used for reinforcement, or through a plastic pipe placed near the reinforcement.

Repeated pressure grouting is used in some cases. It costs more than the single injection, but the capacity of the micropile increases due to the better grout-soil bond obtained. Typical dimensions and grouting pressures reported by various authors [9], [13] and [14] from the state-of-the-practice are summarized in Table IV.

Table IV. Typical characteristics of a micropile

Reference	Boring Diameter (mm)	Length (m)	Grouting Pressure (MPa)	Service Load
[9]	100-250	Up to 40	Low: 0.2-0.5 High: 1.0-2.0	150-600 kN
[13]	100-250	20-30	Up to 8 MPa	300-1000 kN
[14]	67-89	4-4.9	Up to 9 MPa	Ultimate 99-140 kips

3 AL-AZHAR MOSQUE

It is one of the most important mosques in Cairo, Egypt (Fig. 1). Al-MuizzliDinAllah, the Fatimid Caliphate commissioned its construction for the newly established capital city in year 970. After its dedication in 972, and with the hiring by

mosque authorities of 35 scholars in 989, the mosque slowly developed into what is today the second oldest continuously run university in the world, Al-Azhar University, which has long been regarded as the foremost institution in the Islamic world [15].



Fig. 1. Al-Azhar Mosque interior yard

The Mosque has drawn the attention to its precious value and fascinating design features with their clever and inspired craftsmanship (Fig. 2 and 3). Over the course of a millennium-long history, the mosque has been alternately neglected and highly regarded by Egypt's rulers, and numerous expansions and renovations took place. Recently, Egypt showed differing degrees of deference to the mosque. Today, Al-Azhar remains a deeply influential institution in Egyptian society and a symbol of Islamic Egypt.



Fig. 2. Al-Azhar Mihrab

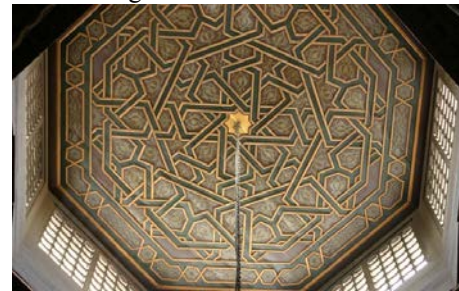


Fig. 2. Artistic details in the ceiling

3.1 The Problem

The mosque recent area is about 12000m². It has 3 gates, 5 minarets, and 380 columns. It included several parts built in different eras starting with the Fatimid epoch in 972 to Mamluki and Othmani periods. In the recent time, which starts in 1936, the main façade was built in 1970. Therefore, every edition was built on a different foundation at various foundation level, size and material.

The walls, arches and footings of Al-Azhar Mosque were made of masonry (bricks & stones) and clay-lime mortar. Its walls and columns were supported by strip footings built on heterogeneous fill that extended to a considerable depth. After the 1992 strong earthquake that hit Cairo, wide and deep cracks spread in the arches and walls of the mosque, and inclination was noticed in many columns.

3.2 Rehabilitation Plan

An engineering committee including geotechnical and structural engineers, as well as architects studied these phenomena to outline the causes. A restoration and renovation program was initiated. It started with a foundation investigation. Test pits were executed to inspect the foundations. They revealed that the bearing walls were resting on weak lime stone footings 25cm wider than the wall, at depth varied from 1,40m to 2.40m below the floor level, and at depth of 0.90m under the columns. The grade

beams, when existed, were built with old red bricks where the mortar consisted of lime and clay, and they were much deteriorated. In some places, there were no foundations under some walls and columns which aggravated the problem. The deep borings executed at the site indicated that the soil is generally formed of a heterogeneous fill layer started from the mosque floor to a depth varied between 3 and 7m followed by a silty clay layer contained limestone fragments to a depth around 9m. The bottom layer consisted of graded sand with traces of silt and clay.

The geotechnical engineers recommended the use of micropiles to reinforce the existing foundation. The footings were underpinned using micropiles 15 cm in diameter, 12-15m in depth, reinforcement was high tensile steel pipe of 9 cm outer diameter and 1.0 cm thick. Grouting was carried out using cement grout under pressure (low pressure of 0.2 - 0.5 MPa & high pressure of 1-2 MPa) [8].

Micropiles were connected together by a reinforced concrete continuous cap. Caps were built on the sides of walls or columns at the same level under the floor. The cap was connected to the masonry strip footing by means of shear connectors. Figure 4 illustrates the method of underpinning the masonry footings supporting columns and walls.

Parts of the walls and columns located upper the level of pile cap must be strong or strengthened by grouting. The masonry walls and columns were repaired by jet grouting under low pressure of 0.1 MPa.

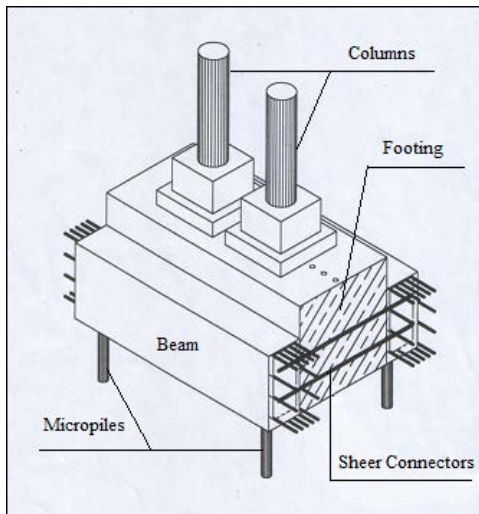


Fig. 4. Underpinning foundations with micropiles

4 THE HANGING CHURCH

The Hanging Church is the most famous Coptic Christian church in Cairo (Fig.5). The Saint Virgin Mary's Coptic Orthodox Church which known as the Hanging or the Suspended Church is one of the oldest churches in Egypt. It is located in a religious compound in Old Cairo, adjacent to the Amr Ibn Al-Ass Mosque, Ben Ezra Synagogue and a collection of churches. The Hanging is named for its location above a gatehouse of Babylon Fortress [15].

4.1 Historical Background

The Hanging Church was built in the 7th century, probably on the site of a 3rd or 4th century church for the soldiers of the bastion. It has been rebuilt several times since then, including a major rebuild under Patriarch Abraham in the 10th century. By the 11th century, it became the official residence of the Coptic patriarchs of Alexandria and several Coptic synods were held in the church. The main furnishings and the pulpit and screens date from the 13th century. The church was largely rebuilt by the Pope Abraham (975-78) and has seen many restorations over the years including the very recent one finished in 2009.

4.2 Building Description

Since the Hanging Church stands with its Basilica-style architecture on top of the Roman Fortress of Babylon in Old Cairo, its nave is suspended over a passage. The land surface has risen by some 6 meters since the Roman period so that the Roman tower is mostly buried below ground, reducing the visual impact of the church's elevated position.



Fig. 5. The Hanging Church entrance

The entrance to the Hanging Church is via a beautifully decorated gate under a pointed stone arch. The nineteenth century facade with twin bell towers is then seen beyond a narrow courtyard decorated with modern art biblical designs. This leads into an open courtyard, flanked by mosaics, from which there are 29 steps to the church. At the top of the stairs are three wooden doors decorated with geometric patterns, framed with decorative carvings in the stone wall (Fig. 5). Up the steps and through the entrance is a further small courtyard leading to the eleventh century outer porch. Inside, only the

section to the right of the sanctuary, above the southern bastion, is considered original. Nevertheless, the Hanging Church remains one of the most impressive churches in the city, remarkable for its marble pulpit, inlaid screens, icons and murals. The timber roof of the nave recalls Noah's Ark (Fig. 7).



Fig. 6. Detail of decoration over the door-arch



Fig.7. Hanging Church barrel-vaulted aisle-ceiling

4.3 Damage Assessment

The Hanging Church, like other monuments located in heavily populated areas, was suffering from environmental hazards including air pollution, a high subsoil water level, a high rate of humidity, leakage of water from the outdated and decayed sewage system installed 100 years ago.

The environmental impact on this magnificent monument resulted in a serious static crisis. The main reason for such damage and deterioration is attributed to human abuse. The increase of the population and economic activities around the building, rapid urbanization in the whole area, and consequently, the rise of the ground water table led to hazardous environmental changes that damaged the integrity of the church [16]. Above that, the adverse effects of the 1992's strong earthquake increased the number of cracks all over the church's walls, barrel-vaulted aisle-wooden ceiling and door arches. Ground water had flooded the Babylon fortress, which supports the church and leaked through to the church. The ground in front of the Hanging Church had caved in. The church priests thought that the church was on the brink of destruction.

4.4 Restoration Project

In 1997 the Supreme Council of Antiquities (SCA) launched a comprehensive restoration project to preserve Egypt's Coptic shrine and return such a distinguished church to its original splendor. The restoration project of the Hanging Church in Old Cairo was started in 1997 and completed in 2009. The restoration process was indeed very complex because it is a comprehensive project that deals with underground water; the most pressing problem facing Islamic and Coptic antiquities since 120 years, besides the reinforcement and repair of most structural elements and architectural features of the monuments.

There were many important parameters and considerations in the selection of the appropriate restoration schemes. Saving the monument should start with preventing the main cause of the problem. It was important to lower the ground water table and stop the leaking water. Monitoring the water table in this area called for an overall dewatering project to be implemented in old Cairo without causing any excessive settlement to the existing buildings.

The aim of restoration, which was carried out in phases, was mainly to reduce the water leakage into the church and strengthen the church's foundations and the Babylon fortress in order to protect them from future settlements and relative movement that causes further damage.

4.4.1 Lowering the groundwater level

The first stage included reducing the level of the water in the fortress. Deep wells were dug in the area around the fortress to trap any excess water. Two additional wells were dug in front of the fortress, and in front of the newly revealed door to the adjacent Mosque of Amr. The water gathered in the wells was siphoned out via pipes to the main sewage system. Then, a comprehensive dewatering project was carried out in the whole area of old Cairo to lower the ground water table and stabilize it at a reasonable depth below the foundations of the Church and the surrounding monuments.

4.4.2 Strengthening the foundations

A geotechnical investigation was carried out at the church site which revealed that soil layers are mainly composed of thick layer of heterogeneous fill that extended to 8m below the ground surface in some spots at the site. This layer was followed by sand interlayered with silty clay and extending at least to a depth of 10m; the end of borings. The walls were rested on deteriorated lime stone strip footings. The proposed foundation rehabilitation was to transfer at least half of the loads carried by the masonry bearing walls to a deeper stronger subsoil layer by means of micropiles. The micropiles were the most suitable means for foundation reinforcement to ensure the least disturbance for the old monument and to manage its installation in locations with low headroom, and narrow and restricted access. The load transfer from the old footings to the piles were made by constructing reinforced concrete beams as pile caps, transversally connected to the existing footings by shear connectors as illustrated in Fig. 8. Following that the re-enhancement of the old masonry footings took place.

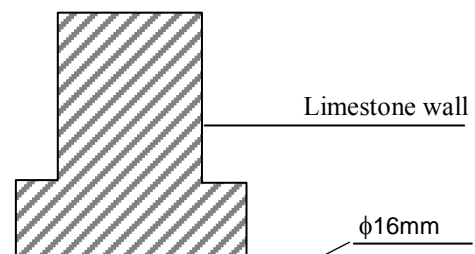


Fig. 8. Construction detail of micropiles

4.4.3 Repairing the super structural elements

The walls and the columns that hold the church also needed reinforcement as well as ceilings of the church. Injection of the church supporting walls with a filler material of the same type used in the original construction, to replace the original filler materials lost as a result of the variance in ground water levels. Repair of all wall cracks. Masonry stitching of the walls of the Church was carried out. The walls were reinforced, missing and decayed stones were replaced, and masonry was cleaned and desalinated.

4.4.4 Dovetailing the stones of the Babylon Fortress

The walls and the ceiling of the fortress were restored as well as the artwork throughout the fortress (Fig. 9).

4.4.5 Repair of all the fine detailed works

The decorations and icons of the church were also subjected to fine restoration and new lighting and ventilation systems have been installed. Every effort was made to ensure that all the original architectural features were retained.

Moreover, the restoration work had been extended beyond the church's walls to reach its neighboring monuments and the streets surrounding it, and the entire neighborhood was being revived and upgraded.



Fig. 9. Babylon Fortress

5 CONCLUSIONS

Micropiles have been utilized for underpinning of historic buildings and monuments since they were successfully used for this purpose in Italy during the seventies. This technique

gained a wide acceptance as a means for strengthening and underpinning foundations of ancient buildings and existing structures as well as construction of new civil projects in many countries.

Since 1993 up to 2001, micropiles have been used to strengthen 12 Egyptian historic buildings, 11 of them are in Cairo. These micropiles were mostly vertical with working load ranged between 15 to 45 tons and reached to 80 tons in few cases. Diameters of micropiles were between 14 to 20 cm and their lengths ranged between 12 to 23.5 m. The outer steel diameters of micropiles varied between 88.9 to 127 mm, and both high and low pressures were used in their grouting.

This paper discussed the use of micropiles to strengthen the bearing soils and the foundations of two significant historic buildings in Cairo, Egypt, namely, Al-Azhar Mosque and the Hanging Church. Both of them are masonry structures with bearing walls founded on continuous stone brick footings supported by heterogeneous fill. The recent severe deterioration was due to rise of water table and the strong 1992 earthquake. Micropiles were the essential factor in the rehabilitation and restoration process. They were successfully installed to transfer a good part of the load to deeper subsoil and to strengthen the foundations. Then, a whole renovation of all the structural members, architectural features and artistic details took place to reserve the monuments' glory and reopen them to worshippers and tourists.

6 REFERENCES

- [1] Elleboudy A and Hamdy G, "Strengthening and repair of a monument in Cairo," Proc. 1st European Workshop on Structural Health Monitoring, Paris, 2002, pp. 1235-1242.
- [2] Togrol E, "Ground improvement and piling," Proc. 14th ICSMFE, Hamburg, Vol.2, 1997, pp. 907-910.
- [3] Babu G et al., "Bearing capacity improvement using micropiles: a case study," Civil Engineering, ASCE, Vol. 73, No.10, 2004, pp. 92-99.
- [4] Maleki K and Frank R, "an approach for the analysis of axially loaded micropile groups," Proc. 14th ICSMFE, Hamburg, Vol. 2, 1997, pp. 1107-1110.
- [5] Kamon M, "Case studies of reinforced ground with micropiling and other improvement techniques," Proc. Symp. on Prediction versus Performance in Geotechnical Engineering, Bangkok, Thailand, 1992, pp. 115-125.
- [6] To P and Watts B, "Tension/compression load testing of a minipile," Proc. 13th Conf. ICSMFE, New Delhi, India, Vol. 3, 1994, pp. 1219-1222.
- [7] Makarchian M and Poulos H G, "Underpinning by piles: a numerical study," Proc. 13th Conf. ICSMFE, New Delhi, India, Vol. 4, 1994, pp. 1467-1470.
- [8] Yusef A, "Foundation repair for Al-Azhar Mosque," Technical Report, ACTI, Egypt, 1998, pp.1-25.
- [9] Egyptian Code of Practice for Soil Mechanics and Design and Construction of Foundations, Vol. 4, Deep Foundations, 2005.

- [10] Micropile Design and Construction Guidelines, Implementation Manual. FHWA – SA-97-070, 2000.
- [11] Schwarz H, et al., “Special use of micropiles and permanent anchors,” J. of Geotechnical Engineering, ASCE, Vol. 128, No. 11, 2003, pp. 945-957.
- [12] Lizzi F, The Static Restoration of Monuments. Genoa, Italy: Sagep Publisher, 1988.
- [13] Bruce D, et al., “A primer on micropiles”, Civil Engineering, ASCE, Vol. 65, No. 12, 1995, pp.51-54.
- [14] “Evaluation of Compaction Grouted Minipiles,” the Northwestern University National Geotechnical Experimentation Site, 1993, pp. 1-62.
- [15] Koraim S, Cairo: A City of 5000 Years. Cairo: Egyptian Book Authority, 1995.
- [16] Elleboudy A and El-Sohby M, “Environmental effects on the groundwater in Greater Cairo,” Proc. Int. Symp. on Environmental Geotechnology, Allentown, Pennsylvania, USA. Vol. 1, 1995, pp. 167-180.

Group Effects of Piles Due To Lateral Soil Movement

Hongyu Qin¹ and Wei Dong Guo²

¹School of Engineering, Griffith University, Gold Coast, QLD 4222 Australia

²School of Civil, Mining and Environmental Engineering, University of Wollongong, NSW 2522, Australia

ABSTRACT

Laboratory model tests have been conducted to investigate the responses of piles subjected to lateral soil movement. The results of a single pile test and four tests on two piles arranged in a row perpendicular to the direction of soil movement are presented. The development of maximum bending moment, maximum shear force, and pile deflection with soil movement and the largest pile response profiles for the single pile and pile groups are compared. Group effect was evaluated using group factor which is defined in terms of the measured maximum bending moment. The major findings are (1) the pile head conditions (free or capped) are insignificant on piles subjected to lateral soil movement when arranged in a row, (2) the group factor decreases as the pile spacing reduces, (3) a linear relationship exists between the maximum bending moment and maximum shear force for both the pile groups and single pile.

Keywords: Piles, Group Effect, Lateral Soil Movement

1. INTRODUCTION

Structures built on piles are vulnerable to lateral forces caused by soil movements, which may be seen when they are used in slope stabilization, to support bridge abutments, and as foundations of tall buildings adjacent to tunnelling and excavation or lateral spreading in liquefied sand during earthquake. Lateral loads generated by soil movements induce additional deflections and bending moments in piles or pile groups, which may undermine the structural integrity of the piles or groups and leads to serviceability or even failure of the piles. Although this characterization has been extensively studied through centrifuge modeling and 1g small scale model tests in [1]-[9], field tests in [10]-[11] and theoretical and numerical analysis in [12]-[16], the pile soil interaction mechanism is still not clearly understood. For instance, the recent numerical studies in [12]-[13] assumes a fixed depth of moving soil, in which the movement of soil is simultaneously mobilized along the pile. However, in a practical scenario, soil movement may be gradually mobilized to a deep layer. The effect of progressive soil movement on the response of piles has not been completely investigated, particularly, when it is coupled with axial load. With an experimental apparatus developed, extensive tests have been undertaken for piles and pile groups in sand to investigate the responses of piles under combined vertical load and lateral soil movement. Reference [5] presents simple solutions for piles in moving sand from the results of 14 typical 1g model pile tests. References [7]-[8] further verified the solutions and findings by investigating the pile responses due to effective soil movement and impact of a uniform and triangular soil movement profile.

This paper investigates the group effects of piles due to lateral

soil movement. Four tests on a group of two piles in a row with the pile head capped and a single pile of free head were conducted. Typical pile responses are presented. Group factors are used to quantify the group effect and compared with previous experimental and numerical analysis results.

2. APPARATUS AND TEST PROCEDURES

For brevity, detailed information regarding the apparatus, test preparation, data acquisition and measurement system, and data process program are omitted. Only the relevant parts are briefly introduced herein.

2.1 Shear Box and Loading System

A schematic cross section of the shear box and the loading system is shown in Fig. 1. The internal dimensions of the shear box are 1 m by 1 m, and 0.8 m in height. The upper part of the shear box is made of a series of 25 mm thick square laminar steel frames. The frames, which are allowed to slide, contain the “moving layer of soil” of thickness L_m . The lower section of the shear box comprises a 400 mm high fixed timber box and the desired number of frames to achieve a “stable layer of soil” of thickness L_s (≥ 400 mm). A loading block is used to apply lateral force on the laminar frames, which is made into arc, rectangular, and triangular shape to impose varying soil movement profiles. In this paper, an arc loading block was used. The rate of movement of the upper shear box (thus the soil) is controlled by a hydraulic pump (lateral jack), and a flow control valve. A vertical jack is used to install the pile into the shear box.

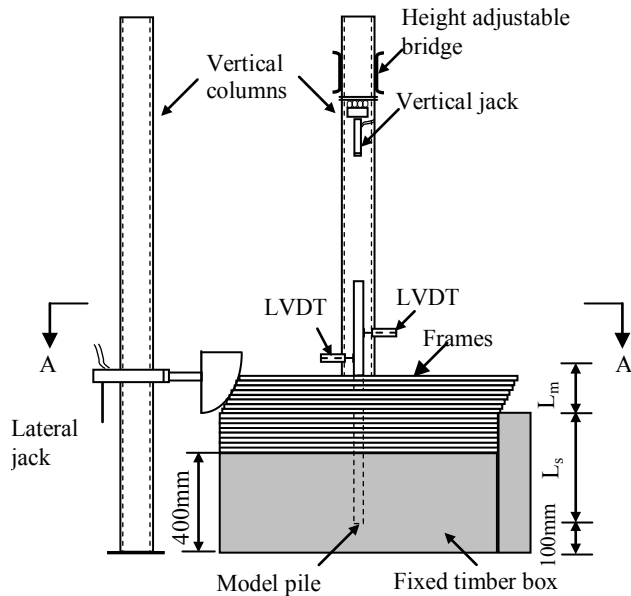
2.2 Model Piles

Fig. 2 shows a schematic diagram of the model pipe pile under testing. The aluminum pile has a length of 1200mm, outer diameter of 32mm and wall thickness of 1.5mm. The pile was instrumented with 10 pairs of strain gauges at an

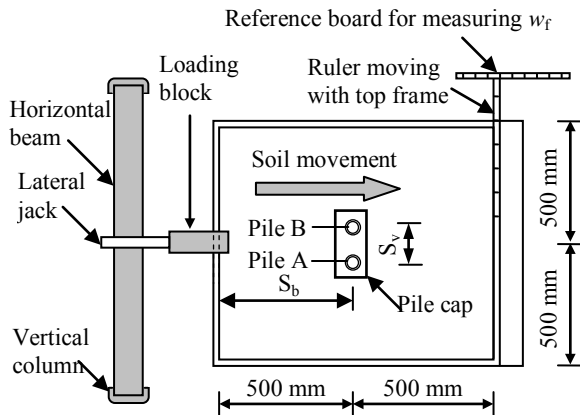
interval of 100mm. Prior to the testing, the strain gauges were calibrated by exerting a transverse load in the middle of the pile that was clamped at both ends. Given various magnitudes of the load, measured strains were compared with those calculated for each gauge, so that a calibration factor was obtained, which in turn allows a measured strain to be converted to an actual strain. To protect from damage, the gauges were covered with 1mm epoxy and wrapped by tapes.

2.3 Sand Properties

The sand used in this study was oven dried medium grained quartz, sand with a uniformity coefficient C_u of 2.92 and a coefficient of curvature of C_c of 1.15. The sand was discharged into the shear box through a rainer hanging over the box to achieve a reasonably uniform density of the sand within the shear box. The falling height of sand was chosen as 600 mm, which gave a uniform relative density of about 89%, and a unit weight of 16.27kN/m^3 . Angle of internal friction was 38° as evaluated from direct shear tests.



(a) Elevation view



(b) Initial plan view (A-A)

Figure 1. Schematic of shear box

2.4 Test Procedures

The model tests were conducted using an arc loading block as shown in Fig. 2. The instrumented pile was installed at a distance, S_b of 500mm from the loading side (see Fig. 1(b)) to an embedded depth, L of 700 mm in the shear box. The predetermined final sliding depth, L_m and stable layer depth, L_s was maintained as 200mm and 500mm. After pile installation, a pile cap fabricated from solid aluminum was used to secure the piles in the pile cap. Weights were put on the pile cap to apply axial load. The strain gauges were connected to a data acquisition system and measurement system established. During testing, the frame movement, w_f was measured from a reference board using a ruler moving with the top frame (see Fig. 1(b)) and up to 120mm. Each test is denoted by a combination of letters and numbers, e.g. AS32-0 or AG32-3d-294, where 'AS' or 'AG' signifies Single pile or pile Group test using an Arc loading block; '32' indicates 32 mm in diameter, '3d' denotes the pile center to center spacing, $S_v=3d$, '0' or '294' represents an axial load of 294N or 30kg per pile.

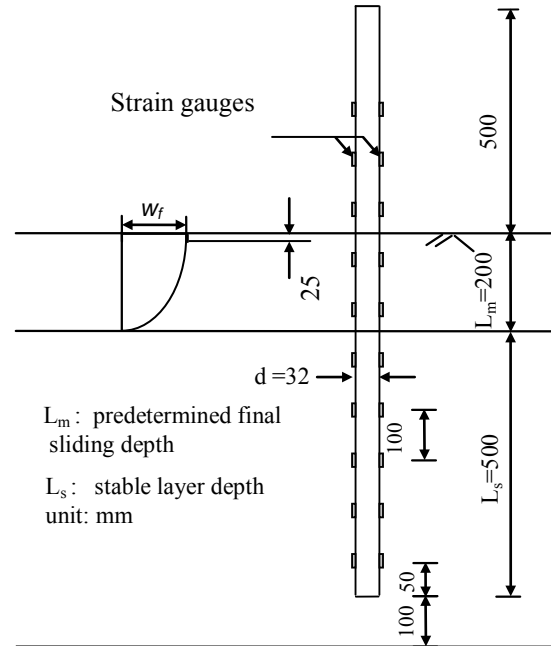


Figure 2. Schematic of a tested pile

3 TEST RESULTS

The pile deflection profiles were derived from double numerical integration of the bending moment profiles, using the measured pile deflection and rotation at ground surface as input boundary conditions. The shear force profiles were deduced by single numerical differentiation of the bending moment profiles. It is noted that both piles A and B (Fig. 1(b)) were instrumented with strain gauges. The pile responses obtained from the two piles are similar, therefore only the data collected from pile A were used. These profiles were plotted at every 10mm frame movement, w_f for all the tests. Due to space limitation, only the profiles in tests AS32-0 and

AG32-3d-0 were presented. The development of maximum bending moment, M_{max} , shear force, T_{max} and pile deflection at ground line, y_0 are plotted against the frame movement, w_f for all the tests. Table 1 summaries these values at $w_f = 120\text{mm}$.

3.1 Test AS32-0

Test AS32-0 was conducted without axial load. Similar to the tests using a triangular loading block described in [5], the arc loading block induces an increasing soil movement both horizontally and vertically with the progressive mobilization of the frames. Fig. 3 shows the pile response profiles for a frame movement, w_f up to 120 mm. The bending moment profile is of parabolic shape when $w_f \geq 90\text{mm}$. The bending moment increases significantly at a frame movement $w_f \geq 80\text{mm}$ and has not reached the ultimate value even at $w_f = 120\text{mm}$. The measured maximum bending moment occurs at about the same depth of 350 mm, which is about half of the pile's embedded length. At $w_f = 120\text{mm}$, two local largest shear forces of -137.2N and 122.4N was deduced from the bending moment profile. The pile rotated around the pile tip with a pile deflection of 4.2mm.

3.2 Test AG32-3d-0

Test AG32-3d-0 was conducted with the pile arranged in a row ($S_v = 3d$) perpendicular to the direction of soil movement and pile head capped as shown in Fig. 1. Presented in Fig. 4 are the five response profiles. A very similar trend to those observed in the single pile test TS32-0 was noted. At $w_f = 120\text{mm}$, the maximum bending moment, M_{max} , is 23.5 kNmm, occurring at a depth of 350 mm. Again, two largest shear forces, T_{max} of -96.2N and 88.8N occur in the sliding and stable layers, respectively. The pile deflected by rotation, with a magnitude of about 3.6mm at the ground level.

3.3 Response of M_{max} , T_{max} and y_0 versus w_f

The development of the maximum bending moment, M_{max} shear force, T_{max} and pile deflection at ground level, y_0 for the five tests are plotted in Figs. 5(a), 5(b) and 5(c) against the frame movement, w_f . These figures demonstrate:

- The initial frame movement w_i of 40mm caused negligible or little M_{max} , T_{max} and y_0 for the pile group tests and single pile test using the arc loading block. At $w_f = 40\sim 80\text{mm}$, the three critical responses for the single pile are generally less than those of the piles in a group, but overall the pile responses are still very small. Afterwards, the single pile responses surpass those of the pile groups, showing greater rigidity of the pile groups with the pile head capped at larger soil movement.
- The development pattern of M_{max} , T_{max} and y_0 with w_f for the pile groups and single pile are similar, revealing that the pile cap and pile-soil-pile interaction have insignificant impact on the performance of the two piles in a row.
- Imposing the axial load of 588 N on the pile cap, i.e. 294 N per pile, and the pile spacing of 3d and 5d have little

impact on the development pattern of M_{max} , T_{max} and y_0 with w_f .

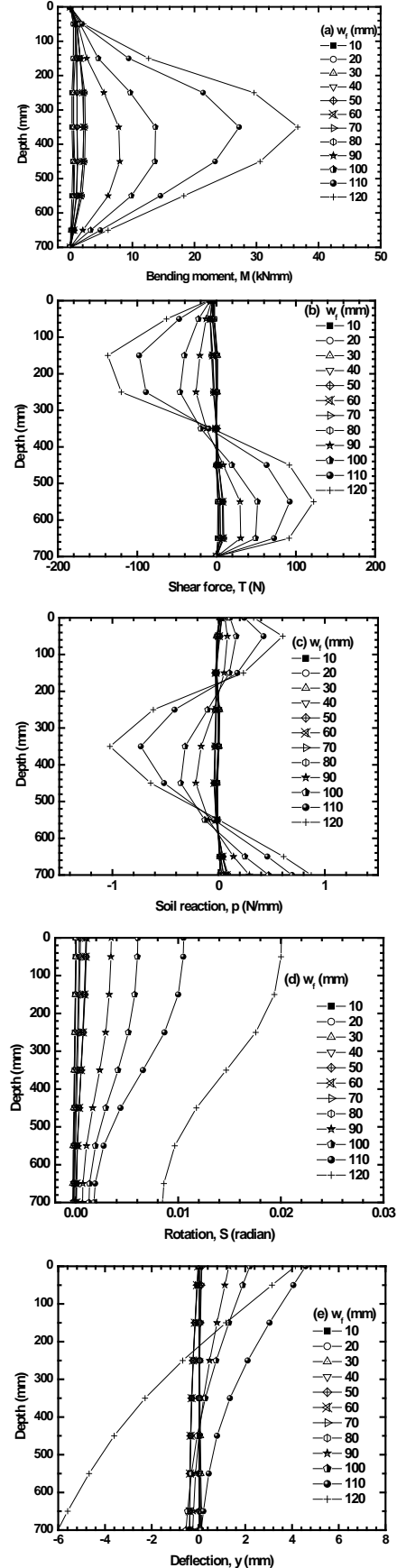


Figure 3. Response of pile during AS32-0

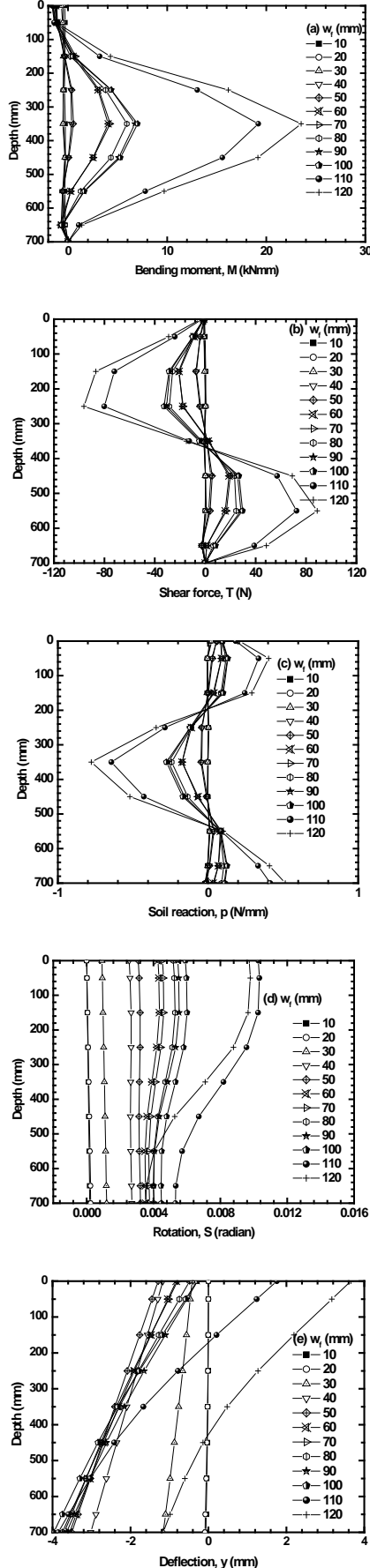


Figure 4. Response of pile during AG32-3d-0

3.4 Maximum Pile Response Profiles

The largest bending moment, shear force and pile deflection profiles with depth for the five tests at $w_f=120\text{mm}$ are plotted in Figs. 6(a), 6(b) and 6(c). These figures show that

- The bending moment profiles of the pile group tests and single pile test are similar amongst themselves and analogous to parabolic. The maximum bending moment occurs at a depth of 350mm below the ground surface, which is 0.5 times of the pile embedded length.
- The shear force profiles are also of similar shape. Two local largest shear forces of approximately equal magnitude but of opposite signs are deduced from the bending moment profiles.
- The bending moment and shear force profiles of the single pile encompass those of the pile group tests.
- The axial load of 588N and pile spacing of 3d and 5d have little impact on bending moment and shear force profiles, except that very small bending moment of 1.67kNm and 4.0kNm was measured at the ground level in tests AG32-3d-294 and AG32-5d-294.
- Pile deflects mainly by rotation about the pile tip or a depth near the pile tip.

4 DISCUSSIONS

4.1 M_{\max} versus T_{\max}

The deduced T_{\max} in Fig. 5(b) are plotted in Fig. 7 against the corresponding measured M_{\max} in Fig. 5(a) for the five tests. This figure shows a remarkably good linear relationship between T_{\max} and M_{\max} under any w_f and independent of the pile head restraint conditions and pile spacing.

Reference [5] presents equivalent elastic solutions for piles subjected to moving sand, giving

$$M_{\max} = T_{\max} L / m \quad (1)$$

where $L(=0.7\text{m})$ is the embedded length of the pile and m is a non-dimensional constant. The value of m is estimated as 2.8 with a variation of $\pm 5\%$ for the best curve fitting between T_{\max} and M_{\max} for the 32mm diameter pile tests using a triangular loading block. The current test results corroborate this linear relationship as shown in Fig. 7. This equation may be used in the estimation of the lateral thrust (shear force), which is required in the design of reinforcing piles to increase slope stability in [15].

4.2 Group effect

In order to assess the group effect and investigate the pile-soil interaction behavior of piles subjected to lateral soil movement, the critical pile responses of a pile within a group, such as the maximum bending moment, pile head deflection and limiting soil pressure are compared with those of a single pile. Investigation on group effect on the behavior of piles subjected to lateral soil movement has been carried out both numerically and experimentally on piles with various pile head fixity conditions in sand and weathered soil in [2],[4],[16]. Reference [4] demonstrates that the group effect

quantified in terms of measured maximum bending moment may be more reliable and consistent

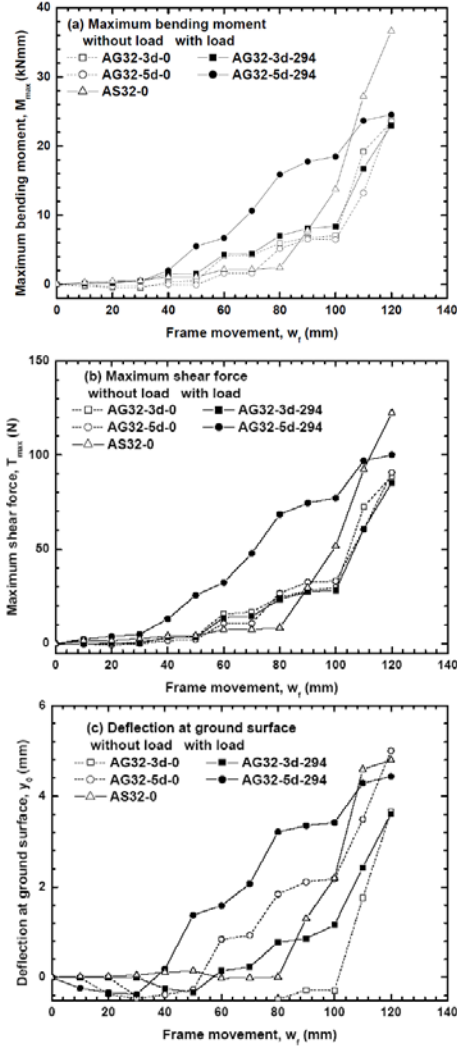


Figure 5. Response of pile during AS32-0

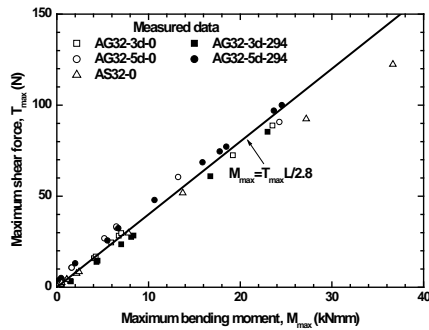


Figure 7. Measured M_{max} versus T_{max}

In this study, the group effect was evaluated by a group factor, F_m based on the measured M_{max} .

$$F_m = \frac{M_{gmax}}{M_{smax}} \quad (2)$$

in which M_{gmax} is the maximum bending moment for a pile in a group at a frame movement, M_{smax} is the maximum bending moment from the single pile at the same frame movement. Table 1 summarize the group factors, F_m at $w_f=120$ mm and

those obtained from the previous studies on capped-piles in sand. The current test results indicate that for the capped-piles

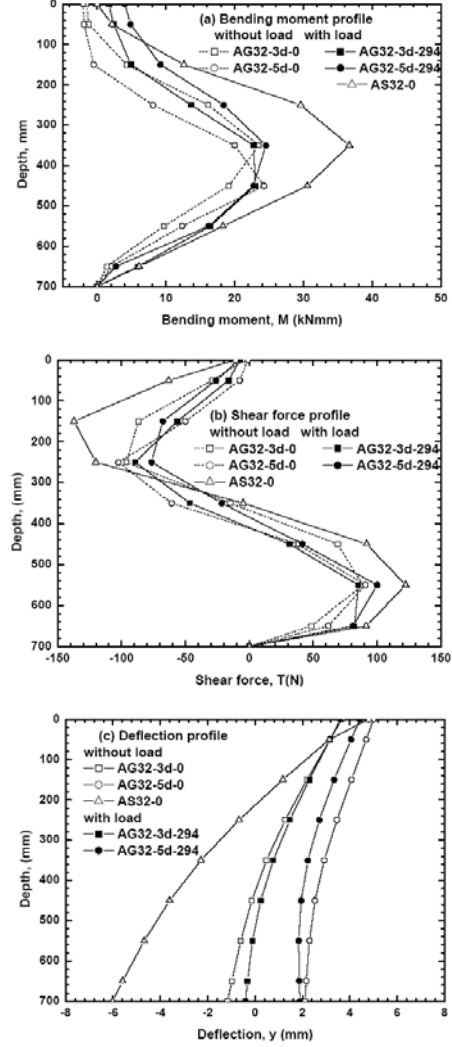


Figure 6. Response of pile during AS32-0

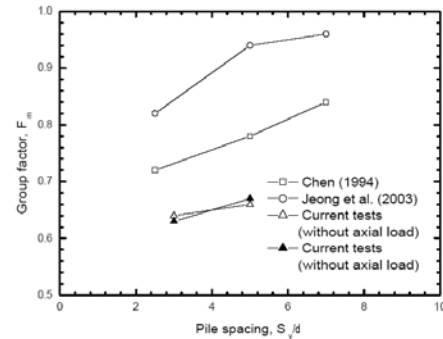


Figure 8. Variation of F_m with pile spacing S_v/d

in a row, the group factor F_m for the group with a spacing of 3d is less than those of 5d. The axial load of 294 N per pile has virtually very limited impact on the group factors. The group factors are plot in Fig. 8 against the normalized pile pacing. It is found that the group factors are less than unit in the investigated pile spacing of (2.5~7)d and decrease as the pile spacing decreases. Nevertheless, the group factors from the current results are 17% and 30% less than those presented in

[2][16] on average. This may be attributed to the pile positions in the shear box discussed below.

Table 1 Summary of test results at $w_f=120\text{mm}$

Test	M_{max} (kNmm)	T_{max} (N)	y_0 (mm)
AS32-0	36.6	122.4	3.6
AS32-3d-0	23.5	88.8	5.0
AS32-5d-0	24.3	90.7	3.6
AS32-3d-294	22.9	85.3	4.4
AS32-5d-294	24.5	100.0	4.8

Table 2 Summary of group factor F_m

Spacing	2.5	3	5	7
Current (without load)		0.64	0.66	
Current (with load)		0.63	0.67	
Reference [16]	0.82		0.94	0.96
Reference [4]	0.72		0.78	0.84

The experimental results from three series of nine tests on a 25mm and 32mm pile using a triangular and rectangular loading block [5]-[7] show that the M_{max} decreases with increasing distance S_b between the pile location and the loading side where free soil movement is generated. The experimental investigation on two piles in a row subjected to soil movement induced by a triangular loading block in [6] further reveals that the group factor F_m decreases with increasing S_b for both free and capped pile head fixity conditions.

5 CONCLUSIONS

Laboratory model tests were conducted to investigate the responses of piles due to lateral soil movement. The results of a single pile test and four group tests on two piles in a row with pile head capped were presented. These tests were carried out using an arc loading block, which induces progressive soil movement. The group effect was assessed by using group factors. The key findings from the studies are summarized as follows:

1. The bending moment, shear force and deflection profiles for a pile in the two piles in a row group tests are very similar to the shape of those in a single pile test, including the position of the maximum bending moment, but their magnitudes are generally smaller, showing group effect.
2. The development pattern of M_{max} , T_{max} and y_0 with w_f for the pile groups and single pile are similar, revealing that the pile cap and pile-soil-pile interaction have insignificant impact on the performance of the two piles in a row.
3. The axial load of 588N on the pile cap, i.e. 294N per pile, has little impact on the responses of the piles in a row.
4. A linearly relationship exists between the M_{max} and the T_{max} , which can be described by Eq. (1) with $m=2.8$.
5. The group factors, F_m are less than unit in the investigated pile spacing of (2.5~7)d and decrease as the pile spacing decreases.

6. The group factors, F_m from current experimental investigation are 17% and 30% less than those obtained in [2],[16].

6 REFERENCES

- [1] Steward DP, Jewell RJ, Randolph, MF, "Design of piled bridge abutment on soft clay for loading from lateral soil movement," Geotechnique, vol. 44, no. 2, pp. 277-296.
- [2] Chen LT, "The effects of lateral soil movements on pile foundations," Ph D Thesis, University of Sydney, Australia, 1994
- [3] Poulos HG, Chen LT, Hull TS, "Model tests on single piles subjected to lateral soil movement", Soils Found., vol.35, no.4, Dec. 1995, pp.85-92.
- [4] Chen LT, Poulos HG, Hull TS, "Model tests on pile groups subjected to lateral soil movement", Soils Found., vol.37, no.1, Mar. 1997, pp.1-12.
- [5] Guo WD, Qin HY, "Thrust and bending moment for rigid piles subjected to moving soil," Can. Geotech. J., vol.47, no.2, Feb 2010, pp.180-196.
- [6] Qin HY, "Response of pile foundations due to lateral force and soil movements," Ph D thesis, Griffith University, Australia, 2010.
- [7] Qin HY, Guo WD, "Pile response due to lateral soil movement of uniform and triangular profiles," in GeoFlorida2010, 2010, pp. 1515-1522.
- [8] Qin HY, Guo WD, "Pile response subjected to effective soil movement," in Proc. 7th Int. Conf. on Physical Modelling in Geomechanics (ICPMG) 2010, pp. 823-828.
- [9] White DJ, Thompson MJ, Suleiman MT, Schaefer VR, "Behavior of slender piles subjected to free-field lateral soil movement", J.Geotech. Geoenviron. Eng., vol. 134, no. 4, Apr. 2008, pp.428-436.
- [10] Frank R, Pouget, P, "Experimental pile subjected to long duration thrusts owing to a moving slope," Geotechnique, vol. 58, no. 8, Aug. 2008, pp. 645-658.
- [11] Smethurst JA, Powrie W, "Monitoring and analysis of the bending behavior of discrete piles used to stabilize a railway embankment," Geotechnique, vol. 57, no. 8, Aug. 2007, pp. 663-677.
- [12] Kourkoulis R, Gelagoti F, Anastasopoulos I, Gazetas G, "Slope stabilizing piles and pile-groups: parametric study and design insights," J.Geotech. Geoenviron. Eng., vol. 137, no. 7, July 2011, pp.663-677.
- [13] Kanagasbai S, Smethurst JA, Powrie W, "Three-dimensional numerical modeling of discrete piles used to stabilize landslides", Can. Geotech. J., vol.48, no. 11, July 2011, pp.1393-1411.
- [14] Guo WD, "p_u based solutions for slope stabilizing piles," Int. J. Geomech., 2011, to be published.
- [15] Poulos HG, "Design of reinforcing piles to increase slope stability", Can. Geotech. J., vol.32, no.5, May 1995, pp.808-818.
- [16] Jeong S, Kim B, Won J, Lee J, "Uncoupled analysis of stabilizing piles in weathered slopes," Comput. Geotech. vol. 30, Aug. 2003, pp. 671-682.

- [17] Viggiani C, "Ultimate lateral load on piles used to stabilize landslide," in Proc. 10th Int. Conf. on SMFE, 1981, 555-560.

Collapse-Settlement Calculations for Embankments Based on a Collapsible Soil Subgrade

Moshe Livneh, Technion-Israel Institute of Technology, Haifa, Israel
Noam A. Livneh, Noam Livneh Engineering Ltd., Haifa, Israel

ABSTRACT

Collapsible soil deposits are found extensively in many arid and semi-arid regions of the world. These soils are conventionally considered problematic, since they exhibit a high potential for collapse under loading. Upon loading, all soils settle, the amount of settlement varying from soil to soil and dependent on load-induced stresses; but such settlement will eventually cease after a certain period of time. However, under certain conditions, subsequent wetting may cause additional settlement, known as collapse. Evaluation of the collapse potential is, thus, required for settlement calculations relating to the base of embankments placed on a collapsible soil subgrade. The evaluation conducted here leads to the conclusion that collapse potential is dependent upon the following parameters: (a) liquid limit, (b) plasticity index, (c) in-situ dry density, (d) in-situ moisture content, and (e) applied pressure at wetting in the single-odometer test. Knowledge of these parameters, together with that of the water-penetration depth into the subgrade stratum and the effect of partial saturation on a reduction of the full collapse potential, is shown to enable a calculation of the amount of collapse-settlement.

Keywords: Collapse, Embankment, Settlement, Silty-characteristics

1. INTRODUCTION

Collapsible soil deposits are found extensively in many arid and semi-arid regions of the world [1]. These soils are conventionally considered problematic, since they exhibit a high potential for collapse under loading. Upon loading, all soils settle, but the amount of settlement varies from soil to soil and is dependent on load-induced stresses. Although such settlement will eventually cease after a certain period of time, subsequent wetting under certain conditions may cause additional settlement, known as collapse. An evaluation of a soil's collapse potential should, thus, be included in all settlement calculations. In this paper, the base of embankments placed on a collapsible soil subgrade provides the objective of these calculations.

According to [2], soils subject to collapse have a honeycombed structure of bulky shaped particles or grains held in place by a bonding material or by capillary-tension forces. Common bonding agents include soluble compounds, such as calcareous or ferrous cementation, that can be weakened or partly dissolved by water, especially acidic water. Removal of the supporting material or force occurs when *water is added*, enabling the soil grains to slide or shear and move into voids.

Two methods currently exist to determine the amount of collapse in the laboratory, the single-odometer test and the double-odometer test. This paper refers only to the single-odometer test, known also as ASTM D 5333 collapse testing. In this test, an undisturbed or remolded specimen is first driven into the odometer ring and then subjected to increasing vertical load. The specimen is permitted to attain

equilibrium deformation at each level of pressure. It is then inundated at a prescribed applied pressure, and the deformation is measured. The deformation induced by the addition of water, divided by the initial height of the specimen, expressed in percentage terms, defines the collapse potential, which this paper also terms vertical collapse.

Now, a prediction of the settlement of the base of an embankment as a result of added water, and thus as a result of subgrade collapse, necessitates knowledge of the collapse-pressure characteristics (curves) of the silty strata under consideration. These curves, which are usually obtained from laboratory tests on undisturbed and remolded silty samples, are in general terms dependent on the following parameters: (a) liquid limit, (b) in-situ moisture content, (c) in-situ dry density, and (d) coefficient of uniformity.

In light of all these introductory notes, the objectives of this paper are as follows:

- Developing the collapse model for a given data of laboratory collapse tests conducted on silty undisturbed and remolded specimens.
- Formulating the effect of partial saturation on collapse potential and evaluating the in-situ saturation distribution from wetting.
- Outlining the suggested collapse-calculation procedures for any given site conditions.

Finally, through an Excel spreadsheet, the paper offers a practical example of how the suggested collapse calculation can be applied with any given set of data.

2. VERTICAL COLLAPSE MODEL

As mentioned previously, predicting the settlement of an

embankment-base surface as a result of subgrade collapse necessitates knowledge of the collapse-pressure characteristics (curves of the collapse model) of the silty strata under consideration, and these are usually obtained from laboratory tests on undisturbed silty samples. This prediction model denotes a statistical relationship between the vertical collapse (C_p), in percentage, that is due to applied vertical pressure (P_p) in kPa, and the following parameters characterizing the silty specimens under examination: moisture content (W) in percentage, in-situ dry density (D) in kN/m^3 and dry density at liquid limit (D_{LL}) in kN/m^3 as defined by Eq. (2). For 73 local specimens extracted from a silty subgrade situated in the southern part of the country, for which the plasticity data are given in Figure 1, the best formulation of this model is as follows:

$$C_p = 28.5354 - 27.0305 \times (D/D_{LL})^{0.9825} + 0.0001196 \times [\log(P_p)]^{11.3741} / (W/PL)^{1.4908} \quad (1)$$

$$D_{LL} = 9.807 \times 100 / (100/G + LL) \quad (2)$$

In Eq. (2), G denotes the solid specific gravity of the silty specimen, and LL denotes its liquid limit in percentage. Here it should be noted that Eq. (1) has been derived with the aid of the Excel Solver command.

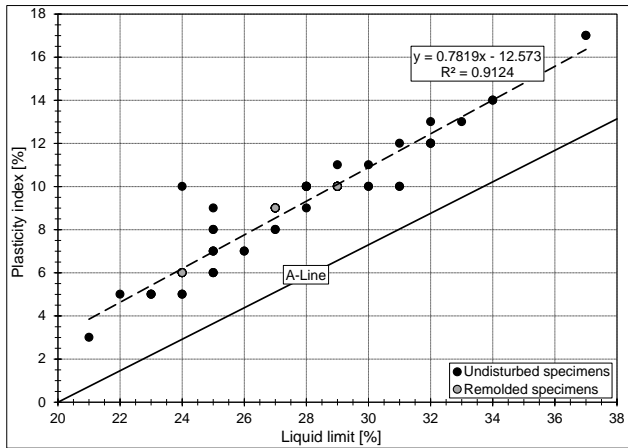


Figure 1: Plasticity data from 73 silty specimens (65 undisturbed and 8 remolded)

As shown in Fig. 2, the R^2 (coefficient of determination) value obtained for the collapse model of Eq. (1) is 0.535. In addition, the accompanying SE (standard error) value obtained is 4.206%, and the SE/SY (ratio of standard error to standard deviation of the measured vertical collapse values) is 0.707. In other words, 68 percent of all predictions from Eq. (1) may be expected to be accurate within $\pm 4.206\%$, and 95 percent to be accurate within $\pm 8.412\%$.

Here, it should be mentioned that Eq. (1) was formulated to yield the highest R^2 value from among all possibilities that (a) include the independent variables of the soil's plasticity and (b) yield true physical behavior as clearly described in [3] (i.e., an increase in C_p with increasing P_p , and a decrease in C_p with increasing W , D and LL). The D/D_{LL} variable of Eq. (1) exactly follows this finding as given in [4] or indirectly as given by a similar finding in [5].

It is interesting to compare all the statistics given above with those in Table 1. This table contains the statistical criterion for goodness of fit (SE/SY) and validity of correlation (R^2) as taken from [6] for five states of correlation: excellent, good, fair, poor and very poor. The comparison leads to the conclusion that the Excel Solver analysis of the 65 specimens given in Fig. 1 can be categorized as leading to a fair state of correlation for Eq. (1) together with Eq. (2).

Table 1: Statistical criterion for goodness-of-fit statistic (SE/SY) and validity-of-correlation statistic (R^2), after [6]

Criteria for Correlation	R^2	SE/SY
Excellent	≥ 0.90	≤ 0.35
Good	0.70-0.89	0.36-0.55
Fair	0.40-0.69	0.56-0.75
Poor	0.20-0.39	0.76-0.90
Very Poor	≤ 0.19	≥ 0.91

In addition, Fig. 3 depicts Eq. (1) graphically for the silty material. For comparison purposes, this figure also includes the collapse results obtained from the laboratory testing of the 73 specimens of Fig. 1.

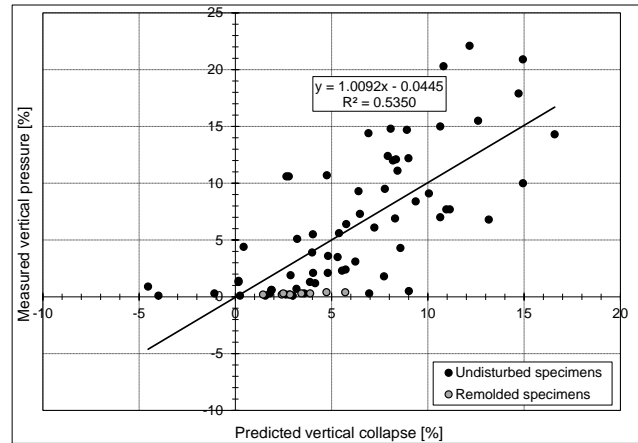


Figure 2: Measured vertical collapse versus predicted vertical collapse from Eq. (1) for the experimental data shown in Fig. 1

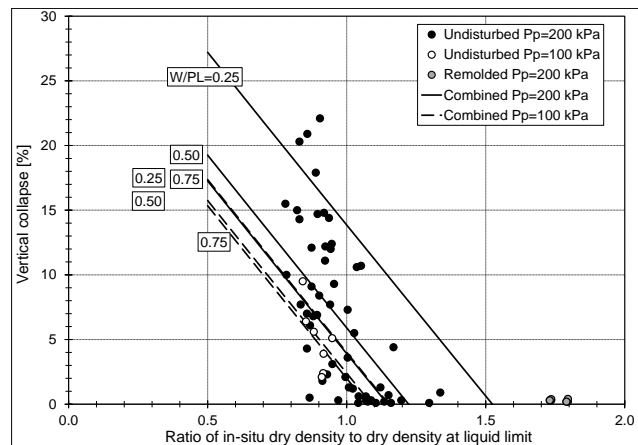


Figure 3: Vertical collapse versus density ratio (D/D_{LL}) for vertical pressures of 100 kPa and 200 kPa as derived from Eq. (1) for the experimental data shown in Fig. 1

Finally, in order to illustrate that Eq. (1) yields the highest R^2 value obtained from among various regression formulations, the following equation may be offered for comparison reasons:

$$C_p = 1,009.1849 - 944.1516 \times (W/PL)^{0.004543} - 95.0980 \times (D/D_{LL})^{0.8239} + 16.6917 \times [\log(P_p)]^{0.8239} \quad (3)$$

For this equation, the R^2 value obtained is lower, 0.510. In addition, the accompanying SE obtained is higher, 4.318%, as is the SE/SY obtained, 0.726.

3. ALTERNATIVE COLLAPSE MODEL

In connection with Eq. (1) and Eq. (3), another multiple linear regression equation can be derived for the data of Fig. 1. This equation, although it yields a somewhat higher value for R^2 , 0.595 (see Fig. 4), and a somewhat lower value for SE, 4.049%, as well as a somewhat lower value for SE/SY, 0.650, contains only two independent variables:

$$C_p = 26.8201 - 0.5065 \times W - 2.6995 \times D + 10.9653 \times \log(P_p) \quad (4)$$

The outputs of Eq. (4) are shown in Fig. 4 and Fig. 5. The latter figure indicates that its predicted C_p values are somewhat lower than those given in Fig. 3. It should be noted that Eq. (4) follows the general pattern of Eq. (5), reproduced from [7]. For this latter equation, the R^2 value obtained for its experimental data (138 remolded specimens) was much higher than the preceding two R^2 values, 0.94. Furthermore, the SE value was much lower than the preceding two values, 1.94%. Finally the formulation of this equation is as follows:

$$C_p = 48.496 + 0.102 \times C_u - 0.457 \times W - 3.533 \times D + 6.447 \times \log(P_p) \quad (5)$$

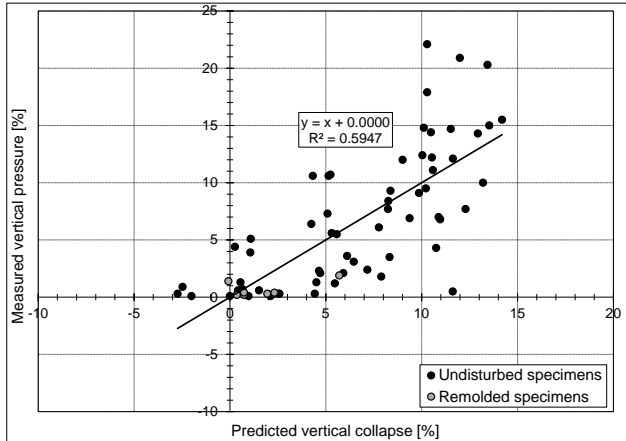


Figure 4: Measured vertical collapse versus predicted vertical collapse from Eq. (4) for the experimental data shown in Fig. 1

Compared with Eq. (4), Eq. (5) contains an additional independent variable, C_u , which denotes the coefficient of uniformity of the prescribed silt. For the case of $C_u=80$, which represents the average C_u value for the 73 specimens of Fig. 1, Eq. (4) yields higher C_p values than those of Eq. (5) by about a ratio of 2.1-3.9 for the W range of 5-15%, $D=13 \text{ kN/m}^3$ and $P_p=200 \text{ kPa}$. For the $P_p=100 \text{ kPa}$ case, this range of ratio values increases to 2.2-13.6. These differences in the

predicted C_p values might result from the fact that most of the specimens for Eq. (4) are of the undisturbed type and all of them for Eq. (5) are of the remolded type. For lower values of C_u , the percentage values change to a lower range of ratio values.

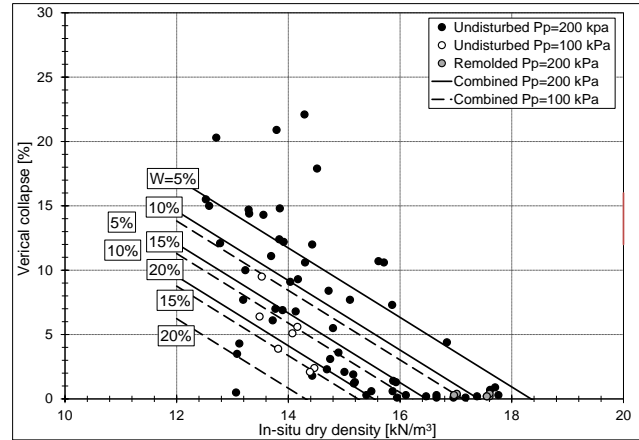


Figure 5: Vertical collapse versus dry density ratio for vertical pressures of 100 kPa and 200 kPa as derived from Eq. (4) for the experimental data shown in the Fig. 1

Following Eq. (4), the results obtained for additional multiple linear regressions conducted with (a) the X_1 , X_2 and X_3 independent variables are shown in Table 2 and (b) the X_4 independent variable, which as always is equal to $\log(P_p)$.

Table 2: Summary of statistic-values of four multiple linear regression analyses conducted on vertical collapse testing data for 73 specimens

X_1	X_2	X_3	SE [%]	SY/SE	R^2
W	D	LL	3.806	0.640	0.614
W/PL	D/D_{LL}	LL	3.809	0.640	0.613
$W^{(1)}$	$D^{(1)}$	---	3.869	0.650	0.595
W/PL	D/D_{LL}	---	4.327	0.727	0.493

⁽¹⁾ This row represents the outputs for Eq. (4).

Table 2 indicates that the best statistical results are associated with the equation in the first row below the heading row; i.e., Eq. (4) modified by adding the LL variable). However, this equation cannot be regarded as applicable, as it leads to increased collapse values with increasing LL values. The same applies to the equation in the second row below the heading row. In other words, these findings lead to the conclusion that the plasticity inputs in the regression analysis should be eliminated.

This conclusion is compatible with [8], who suggests eliminating the use of LL or PI in these regression analyses and, instead, including the gradation characteristics, such as the percentage difference between gravel and fines, and the percentage difference between sand and fines. This suggestion is of similar magnitude to that given in [7, 9], who include sand percentage, silt content and clay percentage in their regression analyses. All these findings lead to the conclusion that the regressions of Table 2 with the LL variable should be eliminated; as a result, Eq. (4) is seen to be

the most favorable of the four equations given in the table.

4. FINAL COLLAPSE MODEL

Finally, a determination needs to be made of the regression equation--the collapse model--that is more preferable to employ, Eq. (1) or Eq. (4). To do so, it is advisable first to check the differences in the predicted vertical collapse values between these two equations. Figure 6 depicts the predicted vertical collapse value of Eq. (4) for the given 65 specimens compared to Eq. (1). As this figure indicates, the results of these two equations are, on the average, similar. Yet, as Eq. (4) does not contain any independent variable to represent the plasticity of the specimens examined, it seems that Eq. (1) is preferable one, but only if the findings of [4] and [5] on plasticity influence are to be adopted.

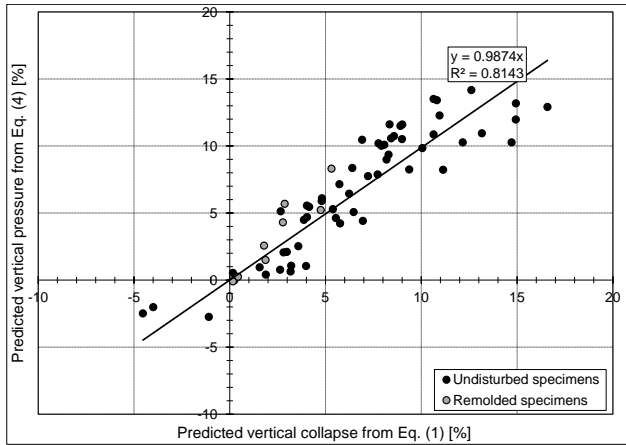


Figure 6: Predicted vertical collapse from Eq. (4) versus predicted vertical collapse from Eq. (1) for the data of the 73 specimens of Fig. 1

5. EFFECT OF PARTIAL WETTING

Partial wetting of the specimens in the single-odometer test results in only a proportion of the total collapse value that is compatible with the case of total specimen inundation. The study conducted in [10] indicates that full collapse essentially occurs for degrees of saturation of 65%-70% and above. However, for degrees of saturation of 50%, only about 85% of the full collapse occurs.

Fig. 7, reproduced from Fig. 14 in [10], enables formulation of the aforementioned collapse reduction resulting from partial saturation. The equations obtained are the following:

$$Ro = -6.95 \times (\Delta So)^3 + 7.20 \times (\Delta So)^2 - 0.20 \times (\Delta So) - 0.004151 \quad (6)$$

$$\Delta So = (S_F - S_I) / (100 - S_I) \quad (7)$$

In Eq. (6), Ro denotes the collapse reduction; i.e., the ratio of vertical collapse resulting from a partially saturated state to the full vertical collapse resulting from a fully saturated state. ΔSo denotes the ratio increase in the degree of saturation from wetting as defined by Eq. (7). In the latter equation, S_I denotes the initial degree of saturation (prior to wetting) in percentage and S_F denotes the final degree of saturation (after wetting) in percentage.

The calculation of collapse for field conditions should obviously take into consideration the distribution of the degree of saturation with depth after wetting. According to [11], the depth of a change in moisture content occurring in the silty subgrade of an unpaved shoulder in a semi-arid zone resulting from a cumulative total of 300 mm rainfall per year extends down to 2,000 mm only. Fig. 8 depicts this moisture distribution as reported in [11]. An analysis of this distribution with the aid of Eq. (8) and Eq. (9) leads to the conclusion that a good correspondence exists between the amount of effective rainfall that has penetrated into the silty subgrade and the characteristics of the moisture distribution shown in the figure.

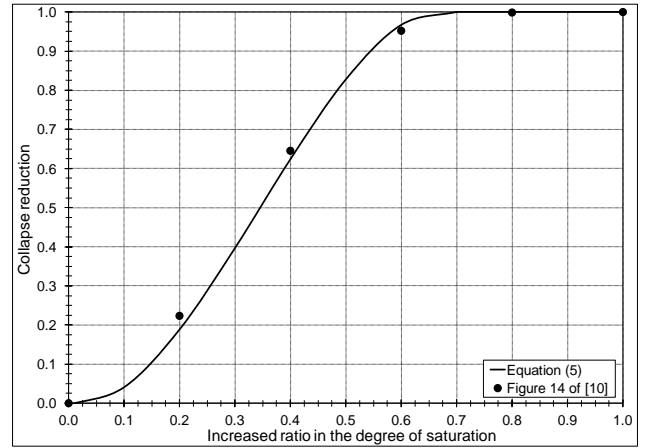


Figure 7: Collapse reduction (Ro) versus increased ratio in the degree of saturation (ΔSo)

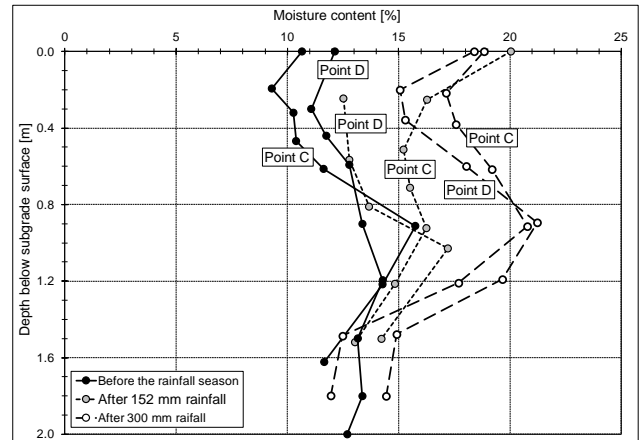


Figure 8: Moisture-content versus depth as measured in a silty subgrade from an unpaved shoulder of a flexible pavement, after [11]

The same pattern of moisture-content or degree of saturation distribution is reported in [8]. This reference deals with a full-scale test in which artificial wetting (by ponding the site) is applied to cause settlement collapse in a silty stratum possessing a single concrete footing on its surface. For this test, the degrees of saturation monitored before and after wetting are given in Fig. 9, in which the degree of saturation distribution, as suggested by this paper for design purposes, is also included.

In addition, the data in [10] also includes in-situ moisture-content distribution before and after artificial wetting. Figs 9-11 in this reference indicate that the general pattern of moisture-content distribution or the degree of saturation distribution in Fig. 8 or Fig. 9 also exists in these figures.

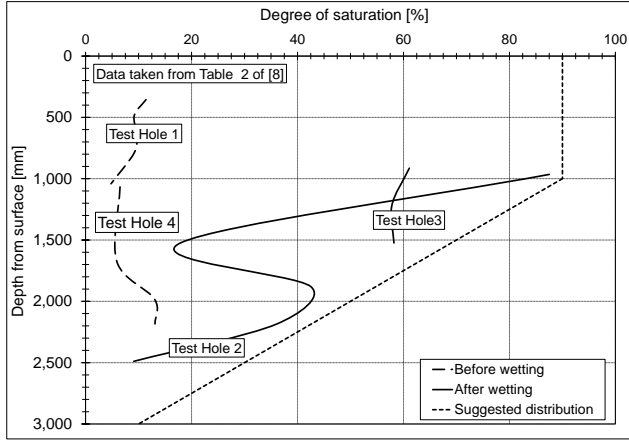


Figure 9: Degree of saturation versus depth as measured in the collapse field test of [12]

6. SETTLEMENT CALCULATIONS

The first step in calculating the settlement of an embankment base constructed on silty subgrade is to evaluate S_F and ΔS_o from the rainfall quantity together with the final moisture distribution as described in Fig. 9. This calculation is performed with the aid of the following equations:

$$W_{FM} = 100 \times H_W / (Z_F \times D_1 / 9.807) \quad (8)$$

$$W_{FT} = 2 \times Z_F \times W_{FM} / (Z_C + Z_F) \quad (9)$$

$$S_1 = 100 \times W_1 / (100 \times 9.807 / D_1 - 100 / G) \quad (10)$$

$$S_{FT} = 100 \times W_{FT} / (100 \times 9.807 / D_F - 100 / G) \quad (11)$$

In these equations, W_1 denotes the initial moisture content in percentage, W_{FM} denotes the average final moisture content along the wetted zone in percentage, W_{FT} denotes the final moisture content at the top of the subgrade in percentage, Z_F denotes the depth of active (wetting) zone in mm (i.e., usually 3,000 mm; see Fig. 9), Z_C denotes the depth of the constant wetting region measured from the surface of the subgrade in mm (i.e., usually 1,000 mm; again see Fig. 9), H_W denotes the effective rainfall quantity that penetrates into the subgrade in mm, D_1 denotes the dry density of the silt before wetting in kN/m^3 , D_F denotes the dry density of the silt after wetting in kN/m^3 , G denotes the solid specific gravity of the silt, S_1 denotes the initial degree of saturation (prior to wetting) in percentage, and S_{FT} denotes the final degree of saturation (after wetting) at the top of the subgrade in percentage. Note that these equations refer to a homogeneous silty stratum in regard to in-situ water content and dry density. Similar equations, however, can be developed for a heterogeneous silty stratum.

Now, for the subgrade depth range of 0 to Z_C mm, the increased ratio in the degree of saturation that is due to

wetting is:

$$\Delta S_{OZ} = \Delta S_{OT} \times (Z_R - Z) / (Z_R - Z_C) \quad (13)$$

The development of Equations (12) and (13) enables a computation of settlement resulting from rain water penetration into the silty stratum for any given in-situ data. This computation is performed by dividing the silty stratum into horizontal strips down to a depth of Z_F (i.e., usually, again, 3,000 mm). The final computed settlement (δ) for a homogeneous silty stratum is derived from the following equation:

$$\delta = \sum (Roi \times Cpi \times di) / 100 \quad (14)$$

Where: d_i denotes the thickness of the horizontal strip of the silty stratum under consideration (usually, a constant value of 500 mm, thus 6 strips in all for the case of $Z_F = 3,000 \text{ mm}$); Roi denotes the collapse reduction for the middle depth of the i^{th} strip; and Cpi denotes the vertical collapse in percentage, again for the middle depth of the i^{th} strip, for which the vertical pressure (P_{pi}) is given by the following equation:

$$P_{pi} = H_E \times D_E + H_P \times D_P + Z_i \times D_1 \times (1 + W_1 / 100) \quad (15)$$

Where: H_E denotes the height of the given embankment in mm, D_E denotes the wet in-situ density of the embankment in kN/m^3 , H_P denotes the thickness of the given pavement in mm, D_P denotes the wet in-situ density of the pavement in kN/m^3 , Z_i denotes the depth to the middle thickness of the i^{th} strip, and P_{pi} denotes the vertical pressure acting at the middle thickness of the i^{th} strip in kPa.

Base-Settlement Calculations					
Spreadsheet for Embankments & Homogeneous Strata					
Design Input for the Silty Stratum			Design Input for the Embankment		
Liquid Limit [%]	30		Height of Embankment [mm]	12,000	
Plasticity Limit [%]	20		Thickness of Pavement [mm]	600	
In-Situ Moisture Content [%]	10.0		Wet Density of fill material [kN/m^3]	18.7	
In-Situ Dry Density [kN/m^3]	14.7		Wet Density of Pavement [kN/m^3]	22.7	
Thickness of Compaction [mm]	600		Rainfall & Moisture Data per Season		
Collapse Model Coefficients			Effective Rainfall per Year [mm]	150	
Calculated Intercept Value	1.64		Depth of Active Zone [mm]	3,000	
Calculated Slope Value	0.0003		Depth of Uniform Moisture [mm]	1,000	
			Cal' Increase in Top Saturation [%]	0.25	
Calculations					
Depth from Surface of Subgrade to Middle Depth of Horizontal Strip	Vertical Pressure on Middle of Horizontal Strip	Full Vertical Collapse	Calculated Ratio Increase in Saturation	Final Partial Vertical Collapse	Amount of Predicted Settlement
[mm]	kN/m^3	[%]	[/]	[%]	[mm]
300	242.9	0.0	0.2	0.0	0
850	251.8	8.8	0.2	2.4	12
1,350	259.8	9.2	0.2	1.8	9
1,850	267.9	9.7	0.1	0.9	4
2,350	276.0	10.2	0.1	0.2	1
2,850	284.1	10.8	0.0	0.0	0
3,350	292.2	11.3	0.0	0.0	0
3,850	300.3	11.8	0.0	0.0	0
4,350	308.4	12.4	0.0	0.0	0
4,850	316.4	12.9	0.0	0.0	0
Sum of Predicted Settlements [mm]					27

Figure 10: An Excel spreadsheet demonstrating a settlement computation for the data given in the figure

The best way to demonstrate the settlement computation is by

presenting a specific illustrative example. This was done with the aid of the Excel spreadsheet shown in Fig. 10 (located in the previous page) for the data given in the uncolored cells of the figure and for the collapse model formulated by Eq. (1). To emphasize, the computations given in Fig. 10 assume these distribution inputs for the rainfall and moisture: $H_w=150$ mm, $Z_c=1,000$ mm and $Z_r=3,000$ mm. The final settlement result is 27 mm, which is an acceptable value for withstanding the collapse event. For the same Fig. 10 data, the use of Eq. (4) instead of Eq. (1) leads to a lower total settlement value: 25 mm. Thus, the use of Eq. (1) seems to be preferable in order to enhance the factor of safety.

7. SUMMARY AND CONCLUSIONS

This paper dealt with the issue of calculating collapse settlement, specifically that of the base of an embankment constructed on collapsible silty subgrade. An essential input for this type of calculation, in addition to such routine characteristics as liquid limit, plasticity limit, in-situ moisture content and in-situ dry density, is an evaluation of the collapsing characteristics of the silty stratum; that is, the vertical collapse percentage.

It was shown that for a given set of experimental results on undisturbed and remolded silty specimens, Eq. (1) constitutes the best available collapse model of all models analyzed, utilizing both the Excel solver command technique and the multiple linear regression technique. This equation includes plasticity inputs, whereas such inputs were found to be inadequate in the multiple linear regression analysis.

The accuracy of all collapse models examined was found to be only fair: i.e., more than a poor state but less than a good state. This is a frequent finding, however, in similar analyses offered in the technical analysis literature [10].

In addition, it should be recalled that the collapse model is based on experimental results obtained from ASTM D 5333 collapse testing (also known as single-odometer testing). Therefore, this model is compatible only with a final wetting state of full saturation. However, it was shown that only a final state of partial saturation is reached. The influence of this partial final site condition state on vertical collapse values is very significant as shown in Fig. 7 taken from [10]. Thus, the formulation of the curve given in this figure yields an important input for the settlement calculations discussed.

In order to utilize the reduced vertical collapse resulting from partial saturation, the depth of the wetting zone and the degree of saturation distribution along this zone should be evaluated. This was done in this paper by analyzing three different site tests reported in the technical literature [10, 11 and 12]. Moreover, it was found that the amount of effective rainfall that penetrates into the subgrade governs the characteristics of this distribution.

The final conclusion is that all the above findings can serve as a proper tool for calculating the collapse settlement of the base of an embankment constructed on a collapsible silty subgrade. This is illustrated in this paper by utilizing an Excel

spreadsheet for a given practical example.

8. ACKNOWLEDGEMENT

The paper is based on engineering studies conducted for Olizki Earthworks, Roads & Development Ltd. under assignment by Israel Railways Ltd., and thanks are therefore due them.

9. REFERENCES

- [1] Wiseman, G., and Lavie, G., "Arid Zone Subsurface Exploration and Loading Tests," Proc. of the 7th Asian Regional Conf. on Soil Mechanics and Foundation Engineering, Vol. 1, 1983, Haifa, pp. 98-104.
- [2] U.S. Army Corps of Engineers, "Application with Unstable Foundation Soils," Chapter 5 in Engineering and Design Settlement Analysis, EM 1110-1-1904, 1990, pp. 5-1 to 5-18.
- [3] Lawton, E.C., Frigaszy, R.J., and Hardcastle, J.H., "Collapse of Compacted Clayey Sand," Journal of Geotechnical Engineering, Vol. 115, No. 9, 1989, pp. 1,252-1,267.
- [4] Zur, A., and Wiseman, G., "A Study of Collapse Phenomena of an Undisturbed Loess," Proc. of the 7th Int. Conf. on Soil Mechanics and Foundation Engineering, Vol. 2.2, 1973, Moscow, Russia, pp. 265-269.
- [5] Austerlitz, G., Ishai, I., and Komornik, A., "Prediction of Collapse Potential in Israeli Loess Subgrade," Proc. of the 7th Asian Regional Conf. on Soil Mechanics and Foundation Engineering, Vol. 1, Haifa, 1983, pp. 106-111.
- [6] Dongré, R., Leslie, M., D'Angelo, J., Paugh, C., and Gudimetlla, J. "Field Evaluation of Witczak and Hirsch Models for Predicting Dynamic Modulus of Hot-Mix Asphalt," Journal of the Association of Asphalt Paving Technologists, Vol. 74, 2005, pp. 381-442.
- [7] Basma, A.A., and Tuncer, E.R., "Evaluation and Control of Collapsing Soils," Journal of Geotechnical Engineering, Vol. 118, No. 10, 1992, pp. 1,491-1,504.
- [8] Junk, C.H., and Elton, D.J., "Predicting Collapse Potential with Neural Networks," Transportation Research Record 1582, 1997, pp. 22-28.
- [9] Basma, A.A., and Kallas, N., "Modeling Soil Collapse by Artificial Neural Networks," Geotechnical and Geological Engineering, 22, 2004, pp. 427-438.
- [10] El-Ehwany, M., and Houston, S.L., "Settlement and Moisture Movement in Collapsible Soils," Journal of Geotechnical Engineering, Vol. 116, No. 10, 1990, pp. 1521-1534.
- [11] Livneh, M., and Shklarsky, E., "Saturation Criteria in Pavement Design for Semi-Arid Zones," Proc. of the Int. Conf. on Moisture Equilibria and Moisture Changes in Soils beneath Covered Areas, 1965, pp. 237-247.
- [12] Houston, S.L., Houston, W.N., and Spadola, D.J., "Prediction of Field Collapse of Soils Due to Wetting," Journal of Geotechnical Engineering, Vol. 114, No. 1, 1988, pp. 40-58.

Study on the influence of soil mechanical properties of earth pressure cell installation trench on stress measurement and local arching in earthfill dam to calibrate total stress registered by earth pressure cell

D. Elmi¹, A. A. Mirghasemi²

School of Civil Engineering, College of Engineering, University of Tehran, Tehran, Iran

ABSTRACT

An understanding of the total stress distribution in an earthfill dam plays a key role in monitoring and guaranteeing dam safety. The registered total stress by earth pressure cell is not enough satisfactory and many factors such as installation method complicate its performance. To avoid damage of pressure cell, it is recommended to backfill the installation trench with fine grained and light compacted soil. This nonconformity in soil mechanical properties of the trench results in local arching between the core and trench. The presence of installation trench changes total stress distribution, and the registered pressure in presence of trench becomes less than the pressure in its absence. In design calculation, this registered stress must be calibrated. This paper studies the changes of local arching by increasing the elevation of dam construction to find methods for stress calibration.

Keywords: Arching, Earthfill dam, Earth pressure cell, Stress measurement

1 INTRODUCTION

Geotechnical monitoring of earthfill dam during construction and operation is critical to control static and dynamic stability of dam. For this purpose different instruments are used in a dam. Earth pressure cells are installed within earthfill dams to monitor stress in different directions. The accuracy of their measurements is important for anticipating destructive phenomena like hydraulic fracture in an earthfill dam. Earth pressure cells are difficult to monitor accurate total stress due to various reasons such as installation method. Dunncliff and Green (1988) have expressed their concerns on factors affecting earth pressure cell readings such as cell dimension, stiffness ratio, aspect ratio and placement effects [1].

A report by the International Society for Rock Mechanics (ISRM, 1981c) includes detailed recommendations for installation of embedment earth pressure cells [2]. The report recommends excavating a trench with a compacted and level base. Then, cells should be installed in small pockets at the base of excavation and protruding stones should be removed since earth pressure cells are prone to damage due to heavy loads. Although it is ideal that the soil within the trench have a density similar to that of the core, it should be backfilled using stone-free soil and compacted by hand-operated equipment.

Although the above procedure prevents damage of cells but many studies have been done to increase the accuracy of measurements. Matsui et al. (2008), quantitatively evaluated measurement errors caused by embedding method and the trench geometry for earth pressure cells to be installed in the central core-type rock-fill dam [3]. Ahangari and Noorzad (2010) carried out laboratory tests, using a casing material for the cell to improve the accuracy of the results. Their study shows that when the casing material is softer than surrounding soil, the pressure cell underestimates the stress [4]. Shabbazian and Fakharian

(2007) indicated that measurement of total stress is not only affected by the inclusion made by the pressure cell, but the trench geometry and installation procedure also contributes to nonconformities in the medium. They concluded that the main dominating parameter in installation is over/under compaction of a backfill material [5].

The accuracy of stress measurement is evaluated by arching ratio, which is the proportion of registered stress to theoretical normal stress:

$$ArchingRatio = \frac{\sigma_v}{\gamma \cdot z} \quad (1)$$

Where σ_v is total vertical stress registered by pressure cell, γ is soil unit weight and z is earthfill height above the pressure cell.

In an ideal measurement, when the stiffness of medium is equal with the surrounding, arching ratio is near to unity. Conversely, smaller arching ratio means the stress is transmitted from flexible zone to stiffer one.

Three types of arching are probable in an earthfill dam: First, transversal arching which happens between different zones (shell, core, filter,...) of an embankment dam. Second, longitudinal arching which is caused by steep slope of valley, usually V shape. This occurs between body and dam abutments. Third, local arching that is possible when the fill around pressure cells has different material compared to surrounding medium.

Presence of pressure cell installation trench with different material affects natural stress distribution. Total stress transmits from the trench to the core and pressure cell registers less stress at this location. This inaccuracy of field readings should not be considered in designing program. This paper, studies on changing of local arching during construction steps to calibrate total stress data of pressure cell.

2 NUMERICAL MODEL

In this study the installation trench is modeled within an earth fill dam in ABAQUS which uses finite element method to analyze the problem. Fig. 1 shows a 2D model of the non-homogeneous earthfill dam in which dam height, core width and shell slopes are assumed to be 128m, 66m and 1:2.5 respectively. The trench is situated 4 meters above the bed. To simulate a real model with reliable results, dam sides are assumed to be 600m and bed depth is two times of dam height.

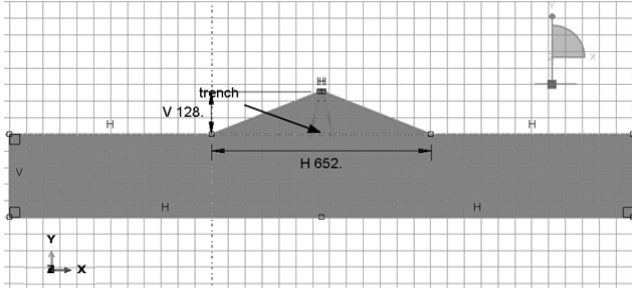


Fig. 1 The view of dam-foundation model

Soil is assumed to be 100% saturated with Mohr Columb behavior. Table 1 presents soil mechanical properties of dam in different zones. To mesh the model, 4-node bilinear plane stress element (CPS4) is used. Fig. 2 shows the grid mesh zone for the dam.

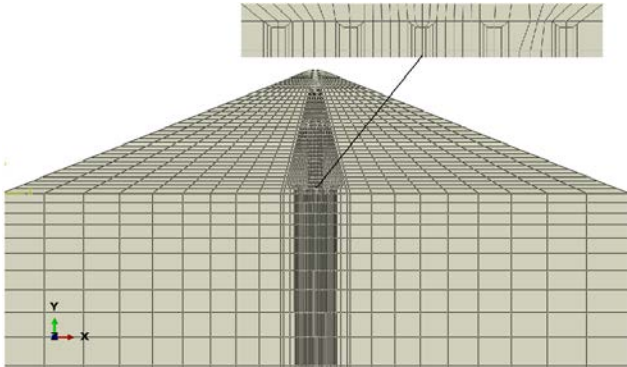


Fig. 2 Quadratic mesh for different regions

Table I. Material properties of earthfill dam

	Trench	Core	Transition zone	shell	bed
Density (kg/cm³)	1740	1740	1950	2050	2100
Young's Modulus (MPa)	35	35	70	102	900
Poisson's Ratio	0.35	0.35	0.27	0.25	0.25
Permeability (m/s)	K _x =1e-8 K _y =1e-9	K _x =1e-8 K _y =1e-9	1e-5	1e-6	1e-10

Bulk mod of fluid (GPa)	2	2	-	-	2
Friction angle (deg)	20	20	35	39	39.4
Dilation angle (deg)	0	0	3	5	9
Cohesion (kg/cm²)	0.3	0.3	0	0	0.85
Void ratio	0.35	0.35	0.45	0.3	0.4

A basic concept in ABAQUS is the division of the problem history into steps. As depicted in Fig.3 dam is constructed in 46 layers within 2 years. Layers are generally 4 meters at except at upper elevations and near to the crest. In construction steps the load changes linearly from one magnitude to another.

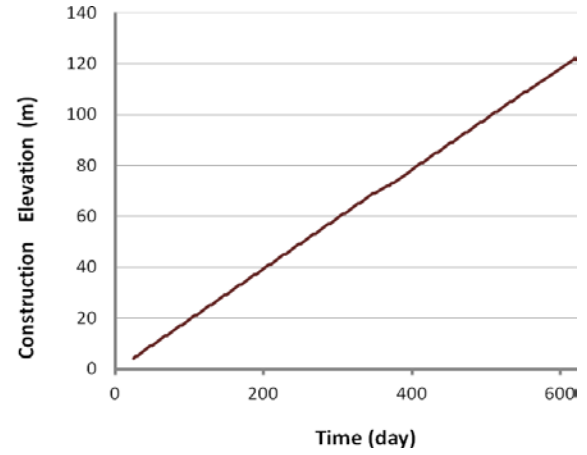


Fig. 3 dam construction time

The choice of initial time step is important in consolidation analysis in ABAQUS. Due to the coupling of spatial and temporal scales, it follows that no useful information is provided by solutions generated with time steps smaller than the mesh and material-dependent characteristic time. This issue is discussed by Vermeer and Verruijt (1981) [6], who propose the criterion:

$$\Delta t \geq \frac{\gamma_w \Delta h^2}{6E.k} \quad (1)$$

Where Δh is the distance between nodes of the finite element mesh near the boundary condition change, E is the elastic modulus of the soil skeleton, k is the soil permeability, and γ_w is the specific weight of water.

To verify that the geostatic stress field is in equilibrium with the applied loads and boundary conditions on the model, initial stress condition of bed is considered. In this case, the loads and initial stresses equilibrate and produce zero deformations. Zero-valued boundary conditions are imposed on displacements to constrain the movement of the selected degrees of freedom of bed to zero. To specify the zero pore pressure at the surface of each layer during

construction, pore pressure boundary conditions are imposed in each step.

3 ANALYSES RESULTS

To clarify the influence of mechanical properties on local arching, the proportion of trench to core was set to 1/2, 1/5, 1/10, 1/20, 1/35, 1/50 and 1/100.

In non-homogeneous earth fill dam, transversal arching happens between various zones due to nonconformity of material. By completing the construction steps core settlement increases and more stress transmits from flexible zone (core) to stiffer one (shell). During initial steps of construction up to 10-15 m backfilling, the influence of transversal arching is negligible and just local arching happens between the core and the trench due to different material. By increasing dam elevation, registered total stress by pressure cell will be affected by local and transversal arching. Fig. 4 represents total stress distribution along a horizontal path in dam section at pressure cell elevation in different steps. It is clear that at the end of construction stress is significantly transmitted from core to the shell, while it is more slightly at stages of 9 and 13m of backfilling.

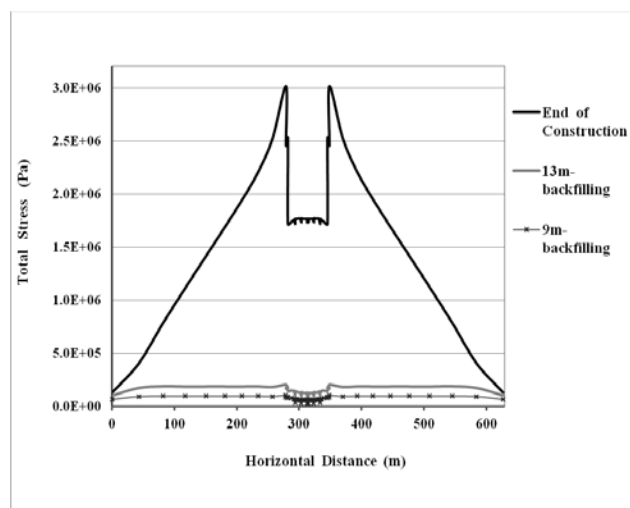


Fig. 4 Total stress distributions along a horizontal path in construction steps

Evaluation of stress and transversal arching is critical to guarantee safety of embankment dam; however, presence of trench changes the natural stress field. To reach the natural field of stress in presence of trench, calibration should be done on pressure cell data for designing procedure.

A study was taken on local arching ratio during construction steps to express total stress calibration. For this, the stiffness of trench material set equal to stiffness of the core. Thus, registered stress by pressure cell (S1) was affected by transversal arching. In other analyses, the proportion of elastic modulus of trench to core material set to 1/2, 1/5, 1/10, 1/20, 1/35, 1/50 and 1/100 and stress distribution plotted for trench center with respect to construction level (S2). In this case, measured stress at center of the trench was affected by local and transversal

arching. In other step S1 subtracted from S2 to evaluate intensity of local arch action (ΔS_L).

The proportion of measured stress to theoretical stress (ΔS_L /Theoretical Stress) presented for the center of trench, in different stiffness, during the construction procedure to specify arching ratio changing. Fig. 5 shows local arching ratio (ΔS_L /Theoretical Stress) for the trench in 7 modes of stiffness.

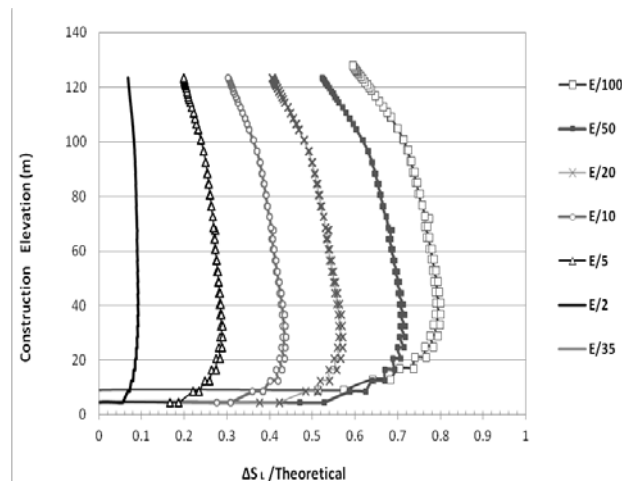


Fig. 5 Local arching ratio at the trench center, during construction

As it is shown in Fig. 5, when the elastic modulus of the trench was half of the surrounding medium, the transmitted stress to the core is about 5% of the normal pressure above the cell ($\gamma \cdot h$) during backfilling. Analyses show that local arching remains approximately constant during construction procedure. In this case, it is possible to subtract local arch action from field readings of pressure cell to calibrate data and reach the natural field of stress in dam body.

3 CONCLUSION

Earth pressure measurements are carried out in order to determine stress redistribution occurring within the dam. The reliability of these measurements is significantly reduced, however, by many factors such as presence of installation trench with material different from the core. Therefore, local arching changes the natural stress field and transmits total stress from trench to stiffer zone (core). This paper studied on local arching trend by increasing the construction elevation. The study concluded that the stress which was transmitted to the core, due to stiffness nonconformity, remained approximately stable during construction steps. Moreover, subtraction of pressure cell field readings from analytical stress in absence of trench material is a constant percent of normal stress ($\gamma \cdot h$). Therefore, local arching can be divided from field readings to reach to natural stress in absence of the trench.

4 REFERENCES

- [1] Dunnicliff, J. and Green, G. E. "Geotechnical instrumentation for monitoring field performance,"

John Wiley and Sons Inc. New York. 1988, ISBN-0-471-09614-8, pp 165-177

- [2] ISRM (1981c), "Suggested Methods for Pressure Monitoring Using Hydraulic Cells," Rock Characterization Testing and Monitoring, ISRM Suggested Methods, Pergamon Press, Oxford, 1981, pp. 201-211
- [3] Matsuu, M. Takashi, A. Uchita, Y. and Ohta, H. "Improvement of earth pressure measuring method in rock-fill dams," International commission on large dams 76th annual meeting, 2-6 June 2008, Sofia, Bulgaria.
- [4] Ahangari, K. and Noorzad, A. "Use of casing and its effect on pressure cells," Mining Science and Technology, 20(2010) 0384-0390.
- [5] Shahbazian, H. and Fakharian, K. "Numerical investigation of trench geometry and soil property effects on the accuracy of embedded pressure cell measurements," OttawaGeo2007: The Diamond Jubilee Conference, 2007, Ottawa.
- [6] Vermeer, P. A. and Verruijt, A. "An Accuracy Condition for Consolidation by Finite Elements," International Journal for Numerical and Analytical Methods in Geomechanics, Vol. 5, 1981, pp. 1-14.

Studying the effects of considering dilation angle over the performance of geotechnical elements using numerical methods

Salman hanifi¹, Amin naeimabadi², Mohammad reza atrchian³
Islamic Azad University Of Zanzan, Iran

ABSTRACT

Applying geo textile and nail elements adjacent to structures like: shallow foundations, dams, tunnels, slopes, retaining walls, etc is a very important and inevitable case in most geotechnical projects. In other hand, installing these elements truly and precisely, needs the distinction of geological and geotechnical condition in project site. Among the countless mechanical soil parameters, dilation angle is one the most effective and also controversial parameters, so that any highly over/under estimation of this parameter could result to irrecoverable structural and economical consequences. In this paper the effects of considering the dilation angle over performance of above elements in soil are studied, using the finite element code FLAC.2D. Also further to considering a great variation of quantities for dilation angle and gaining a reasonable trend, comprehensive results are acquired. It is observed that variation of dilation angle between $\phi/3$ up to $\phi/2$ (ϕ is the soil internal friction angle) has a great effect on geo textile elements, so that increasing of dilation angle leads to a more stable condition in geotechnical structures containing elements like geo textiles or nails.

Keywords: Dilation angle, Geo textile, Nailing, FLAC 2.D

1. INTRODUCTION

If the adjacent soil of a geotechnical structure does not have proper condition and durability/ resistance, various ways such as inserting geo synthetic layers, soil stabilization, and nailing can be used. In addition, among the geo synthetics, geo textiles are the best and most useful ones. These plates are similar to fabric layers which instead of cotton, wool and silk, synthetic materials are used in their textures. At least 80 specific uses are defined for geo textiles, but their basic application can be summarized in five cases: Separation, reinforcing, filtration, drainage and sealing membrane[1]. By entering geo synthetics to geotechnic engineering, a lot of research was done by researchers such as Seki (1986), Korner (1994), Basarest (1998), sheen and Das (1998). They studied different kinds of geotechnical structure buried in reinforced soil by geo textile material. Furthermore in recent years other studies about geo synthetic behavior available in shallow were done by shookla and yeen (2006), Chang and kasekant(2007) and Sawav(2007).

Three decades ago, nailing was introduced as a technique for trench stability and protection of excavation, wall nailing means reinforcing existing soil in the form of in situ and installing adjacent steel bars in a sloppy area or dug in ground. In this way the bars usually are put in to holes created in soil walls and are controlled in their own place by cement grout. This process has passive performance and applies its effect by soil-bar interaction. The issue of soil interaction with reinforced elements has been in the focus of many researchers. Clearly, true understanding of this problem necessitates information about soil mechanic parameters and their effect on interaction between soil and elements. One of

the most important parameters is dilation angle. As we know, in general, five parameters are needed in Mohr-Coulomb behavioral model which are as follows: Young modules, void ratio, friction angle, cohesion and dilation Angle. Dilation angle has a unit of degree. For heavily-over consolidated clay, the dilation angle is counted zero. On the other hand the amount of dilation in sands depends on compaction and friction angle. for quartz sand is approximately $\phi-30$ and for $\phi < 30$ it's amount can be considered zero. Additionally negative amount of ψ can only be applied for very loose sands. By using finite element program Afena, Vafaiean[2] calculated bearing capacity coefficients of shallow foundations in wide spectrum of parameters including dilation angle. Fahimifar and Javaheri[3], examined shear behavior and dilation of two sliding surfaces on each other by modeling direct shear test. Rabi'ee & Shahkarami[4] by examining the effect of various parameters on bearing capacity of foundation on the slope, found that by increasing dilation angle from zero to ϕ , the amount of bearing capacity increased such that they recorded the effect of dilation angle on less slope, in a clearer and better way. Fredman and Burd(1997)[5] examined the changes of bearing capacity coefficients (N_γ) for dilation angle between zero to ϕ in the smooth and rough foundations and came to the conclusion that in smooth foundations and for internal friction angle under 35° , changing the dilation angle, significant difference is not observed in N_γ amount, but for amount of friction angle plus 35° and change of dilation angle between 0.0 to ϕ significant changes is observed in bearing capacity coefficient N_γ . Shahbarkhordar & et.al)[6] examined the sensitivity of bearing capacity coefficients N_γ toward changes of dilation angle and by using finite element method. By calculating bearing capacity coefficients, Griffiths [7] observed that in the case of dilation angle equal zero,

Significant instability is created in calculation process (trends). Owlaapour & Fakhradini [8] worked on the effects of various parameters such as dilation angle and emphasized numerical analyses the effect of clay layer on bearing capacity of sandy soil by using finite element program PLAXIS. Amir Hossein & Ali shaffie[9], also calculated bearing capacity coefficient of a shallow strip foundation for wide variety of changes in dilation angle. In the present paper, modeling and examining the performance of geo technical elements, geo textile and nailing operation by using finite difference program (FLAC.2D) was emphasized. The performance of these two geo technical elements is calculated for different amounts of soil dilation angle and by following a reasonable trend, general results are achieved.

2. Introducing FLAC.2D software

Flac is a two-dimensional finite difference program that is exclusively used for geotechnical calculations. by using this software, we can model the behavior and performance of any construction (structure) on soil , stone or any building materials which may undergo a kind of plastic flow during the yield limit. in a general view, materials are defined in FLAC by help (means) of elements or Zones, And by forming a network, the geology shape of the object or structure to be modeled, is formulated. Both elements in this software are defined based on a linear or non-linear stress-strain rule and react against applied boundary conditions. Another feature of FLAC is yielding and flowing of materials in parallel to changes in network form in the case of large-strain mode. Accurate calculation of Langrage along with techniques based on definition of behavioral zones and availability of wide variety of materials in this software, makes the modeling of failure and flowing more exact (accurate). On the other hand, since no matrix will be formed in FLAC, it is possible to do two-dimensional calculations without the need for extra memory. Also formulating (existing limitation in the given time to run the problem or definition of needed damping) have been lifted in this virtual space especially by automatic scaling inertia capability and defining automatic damping (this problem has no effect on failure situation). Although FLAC has exclusively been designed to solve geo technical and mining engineering problems, it has also great capability in analyzing complex mechanical problems. Such that by means of various defined behavioral models in it we can model and simulate many of geologic non-linear and irreversible behaviors.

3. statement of the problem

3.1. soil (ground) space

The target soil in the problem site, was mono layer sand and had the following specifications:

Table 1: constant parameters used in the modeling trend of soil space.

Resistance cohesion (C) kPa	Internal friction angle(ϕ)	Bulk modulus kPa	Shear modulus kPa	Unit weight KN/m ³
0.0	35	2×10^8	1×10^8	10

We know that, introducing the parameter of dilation angle in the position of internal friction angle which is greater than or equals 30 is meaningless and can be ignored. Therefore in order to have a realistic modeling the degree of internal friction angle of target sandy soil in this study is 30 to 40 and to be more exact it is 35. It must be noted that the target failure criterion in this modeling was Mohr-Coulomb criteria.

3.2. Geo textile Element

In order to have a much better and effective geo textile element, two parameters should be taken into account. First, the question of flexibility of texture of geo textile and second, the question of the interaction of inserted geo textile with its own upper and lower soil surface. Performing this task in finite difference program FLAC.2D, is possible through connecting beam element to its upper and lower network lines. In this way by putting moment of inertia of modeled beam to zero in the FLAC.2D consider its performance as equal to geo textile elements. furthermore, one of the major problem of soil profiles reinforced with geo textile element, is the possibility of sliding on both sides of installed geo textile plates and consequently is the happening of pull out and eventually paying the way for large strain.

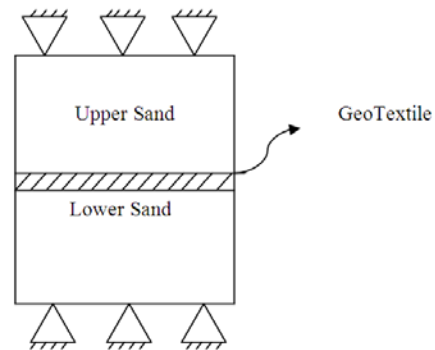


Fig 1: schematic drawing of investigated geo textile model

According to fig(1) the used numerical model is a rectangle network in the dimensions of 5(m)*7(m) [5 meter width 2 & 7 meter depth). The boundary conditions on this model are regarded in such a way That the bottom and the upper part of the model is supported in both directions, and its left and right ends are free in both directions. The reason for leaving free support conditions in both ends, as to facilitate the modeling of sliding phenomenon. In this way by inserting geo textile element in the center of target profile, It is possible to observe the effect of pull out happening on it Directly. In order to apply loading in the case of strain control, the load has been introduced as application of velocity vectors. The amount of these velocity vectors in vertical loading equals

0.5×10^{-4} and the case of loading it is regarded 1×10^{-4} m for each step of loading. The amount of velocity vector in both states, is considered in such a way that, it prevents an initial shock to system and to neutralize and modify the initial and temporary effect of the loading.

3. 3. Nailing Operation

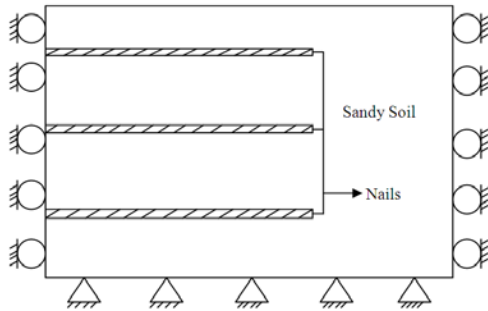


Fig 2: schematic drawing of nailing model.

Modeling of nailing operation in ELAC.2D has been done by cable element. According to figure (2), the applied model is a rectangle network with the dimensions of $11\text{m} \times 11\text{m}$ (11 meter width * 11 meter depth). In this model border lines are considered in such a way that model bottom is supported in both directions but its left and right end(s) has reactions only in horizontal direction or (X axis). In this situation three layers of nailing are predicted for protection of a vertical deposit. In this case the behavior and reaction of nail elements are analyzed against the force of deposit weight. In order to make real the modeling of nail elements, we can show the effects of grout injection around the nails by considering a friction resistance among the nail and sand soil. This resistance force is regarded as a friction angle between nail and soil and its amount, is determined 20 according to reference[10]. On the other hand, by regarding support conditions by maintaining more consistency in nail performance, the effect of shotcrete performance has been taken into account.

4. Modeling and analyzing the results

4.1 geo textile element

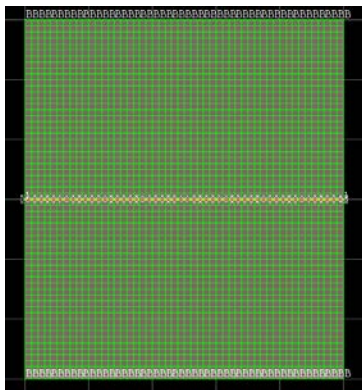


Fig 3. Element network of geo textile problem in FLAC.2D

Element network for geo textile modeling is based on fig 3. Having done the modeling, the problem for dilation angles equals Zero, $\phi/30$ (5 degree), $\phi/3$ (about 12 degree), $\phi/2$ (about 18 degree) and ϕ (equals 35 degree), is solved. It should be noted that the assumption of equality between amounts of dilation and internal friction means that soil follows an associated flow rule which is not a correct assumption. But in the present article, to compare with the result of other targeted amounts, for dilation angle and examining the effect of increasing the amount of ψ , we have taken this assumption. Based on Table 2 and Fig 4, we can see that by increasing dilation angle, the amount of bearable axial force on part of geo textile element is increasing, in other words its bearing capacity is rising.

Table 2: The amount of axial force applied on geo textile on the moment of failure

35	$\phi/2 \approx 18$	$\phi/3 \approx 12$	5.0	0.0	$^\circ\psi$
103547	84954	59237	48657	42358	Fa(N)

In table (2) the amount ψ dilation angle is based on degree, and F_a is the amount of axial Force on geo textile element in terms of Newton at the moment of failure. As mentioned before, by increasing dilation angle, the bearing capacity of geo textile element is also increased. According to figures 4 and 5, The greatest amount of the increase has been recorded in ψ equals to 12 to 18 degrees.

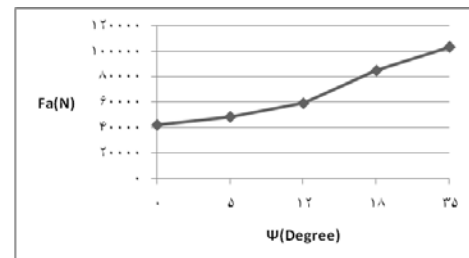


Fig 4: Changes of amounts of axial force according to dilation angle.

Table 3: The resultant increasing amounts in axial bearing capacity according to increasing the dilation angle

18-35	12-18	5-12	0.0-5	Ψ°
22	43	22	15	$\Delta(\%)$

In table 3, Δ is increasing in amount of axial bearing capacity of geo textile element in term of percentage. As it can be seen, the greatest amount of this increase is in ψ within 12 to 18 degree which record in $\psi/3$ to $\psi/2$. Additionally It was seen that by increasing dilation angle, the depth of shear failure mechanism is also increased. In fig 5 and 6 we can easily see the progress of shear failure mechanism, particularly under inserted geo textile layers.

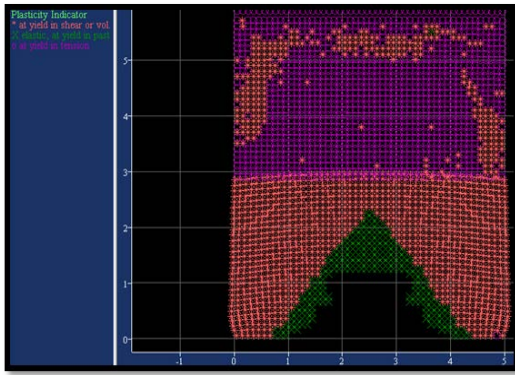


Fig 5: Shear failure areas (zones) under geo textile regarding $\psi=12^\circ$

Based on fig 5 and 6, It can be seen that the depth of shear failure mechanism in dilation angle equals 12 degrees, is less than the situation in which dilation angle is 18 degrees. In other words in $\psi=18^\circ$, bearing threshold of system is evaluated much greater than $\psi=12$ degrees, such that by forming greater failure zones, the system undergoes instability and failure.

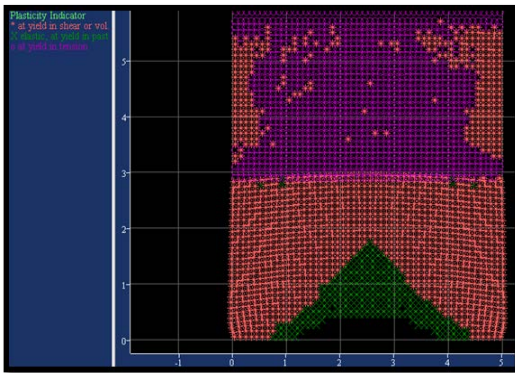


Fig 6: Shear failure zones under geo textile regarding $\psi=18^\circ$

4.2. Nailing operation

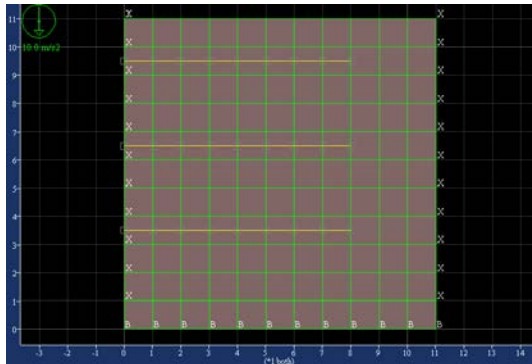


Fig 7: Element network for nailing problem in FLAC.2D

The applied element network for modeling of nailing operation is given in fig 7. After modeling, just like what was done before, the problem is solved regarding dilation angles equal to Zero, $\phi-30$ (5 degrees), $\phi/3$ (about 12 degrees), $\phi/2$ (about 18 degrees) and ϕ (35 degrees). It must be noted once again that the assumption of equality the amounts of dilation

angles and internal friction implies that soil acts as associated flow rule, which is not a true assumption, but in this paper it is accounted to compare with results of other targeted amount of dilation angle and assessing the effect of increasing the amount of ψ .

According to table 4 and fig 8, we can see that by increasing dilation angle, the amount of bearable axial force is increased on part of each of the nails.

Table 4: Resultant increasing amounts of axial bearing capacity of nails regarding to increasing the dilation angle

35	18	12	5	0.0	Ψ°	Fa (N)
21687	18553	14924	11761	9439	Cable 1	
27379	22491	18325	15587	12325	Cable 2	
29953	23284	20136	17693	16554	Cable 3	

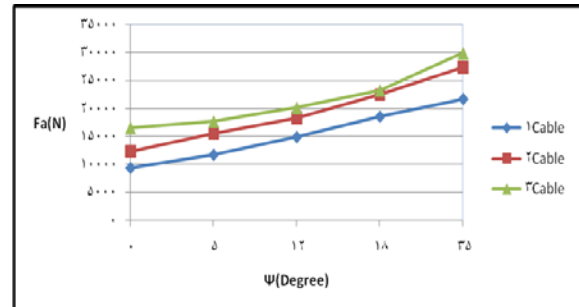


Fig 8: Variation in amounts of axial force of nails according to dilation angle

According to Table 4, the amount of increase in bearing capacity, has directly relationship with increasing dilation angle and the depth of buried nail element, such that nail or cable number 3 with the greatest amount of depth regarding dilation angle of 35 degrees experiences (bears) the greatest amount of axial force. [The nail are put in order of 1, 2 and 3 from top to bottom]. According to Table 5, by increasing buried depth, the increase in bearing axial capacity of nails in ψ between $\phi/2$ to ϕ is very conspicuous. put simply, the more the amount of surcharge soil is increased, the greater amount of dilation angle (with in $\phi/2$ to ϕ) will have more effect on enhancing axial bearing capacity of nails. It is noted again that in Table 5, Δ is increasing in axial bearing capacity in each of nails in terms of percentage.

Table 5: Resultant increasing amount in axial bearing capacity regarding to increasing the dilation angle

18-35	12-18	5-12	0.0-5	Ψ°	$\Delta(\%)$
17	24	27	25	Cable 1	
22	23	18	25	Cable 2	
28	16	14	7	Cable3	

However for lower amount of dilation angle, increasing of buried depth, not only did not cause the increase of bearing capacity of nails (relative to upper nail) but also bring about decreasing bearing capacity of nail elements in comparison with its upper elements.

5. CONCLUSION

In this paper the effect of dilation angle on the performance or function of geo technical elements like geo textiles and nailing operation was examined. Modeling of these two cases was done by finite difference code FLAC.2D and in the condition of Mohr-Coulomb criteria. Generally it was seen that by increasing dilation angle, the axial bearing capacity of geo textile and nails is also enhanced. In other words, by increasing dilation angle, the threshold of system failure and the width (extension) of shear failure zones are increased; meaning that by accounting greater amounts for dilation angle, the necessary condition for instability in system is forming and joining more failure zones. Furthermore, in modeling geo textile element, the greatest amount in bearing capacity occurs in dilation angle within $\phi/2$ to $\phi/3$. However the problem of increasing amount of bearing capacity in modeling the operation of nailing does not follow a specific rule or order. We come to conclusion that due to greater amount of dilation angle (within $\phi/2$ to ϕ) as the amount of surcharge soil increases, the axial bearing capacity is also intensified.

6. REFERENCES

1. Designing with geosynthetics. Robert.M.Koerner .
2. VaFaaiean Mahmoud: Determining bearing capacity coefficient of soil by means of finite element and based on Mohr-coloumb elastic model, esteghlal publication, year:22, No 1, 2003.
3. Fahimifar, Ahmad, Amin Javaheri, Amir Reza, Modeling direct shear experiment for study the behavior of fissures around tunnel. transportation research Quarterly 8th year second Vol 2011.
4. Rabi'ee, Meysam, Amir Shaakarami, A, Examining the effect of Various parameters on bearing capacity of foundation over a slope.
5. Frydman, S., and Burd, H., "Numerical studies of bearing-capacity factor N_γ ", Journal of geotechnical and geo environmental engineering., vol 123, No 1, pp. 20-28, 1997.
6. shahbarkhordar, S.H, Roshanzamir, M.A, Hashem Alhoseyni.H, Calculating the coefficient of N_γ in bearing capacity by using finite element method, The first national civil engineering congress April 2004. San'ati Sharif university, article code 83-1193.
7. Griffiths, D. V .,"Computation of bearing capacity factors using finite elements", Geotechnique. 32. No. 3, pp.195-202, 1982.
8. Owlapoor, M. Fakhradini, M. Numerical Analysis of the effect of clay layer on bearing capacity of sand soil 4th international geotechnical engineering&soil mechanic, 2-3 November 2010 Tehran, Iran. Article Code: 432 (BATOLA)
9. Shafi'ee, Amir Hossein, Shafi'ee, Ali, "Computation of bearing capacity factors using finite element method", 8th International Congress on Civil Engineering, May 11-13 2009, Shiraz University, Shiraz, Iran.
10. FLAC.2D manual, Itasca Consulting Group, Inc. Minneapolis, Minnesota, USA.
11. Feyzabadi, Mohiyadin, shahnazari, Habib, Numerical Modeling of shallow foundation next to a slope 4th international geotechnical engineering and soil mechanic, 2-3 November 2010 Tehran, Iran, Code, and number of article: 678 (MANFEY).

Comparing the excavating effect of single and twin tunnels on the earth surface settlement by numerical methods

Amin Naeimabadi, Salman Hanifi, Mohammad reza Atrchian

Department of Geotechnic Engineering, Faculty of civil engineering, Islamic Azad University, Zanjan Branch, Zanjan, Iran

ABSTRACT

Nowadays due to increasing rate of urbanization, population compaction and construction in Iran, the issue of construction of underground tunnels become the center of attentions, due to it's capability to obviate the problems regarding transportation, water transmission and subsurface structures. In this way, studying about the right placement, procedure of excavating tunnels and it's possible effects on superstructures specially an ancient buildings are very important and vital. In this research, the settlement of a single tunnel excavated in the depths of Isfahan city (Cultural capital of Islam world) in Iran has was studied, using the finite element program PLAXIS, then the results of this numerical analyze was compared with the data obtained from field instrumentations, Finally these results were generalized to twin tunnels. In the next stage, after studying the effect of spacing between twin tunnels over these settlements, those quantities, which are greater than the allowable settlement and their situation were recognized. It is obvious that this problem will highlight the importance of Following a good and reliable design process.

Keywords: Settlement, Twin Tunnels, Numerical Method, PLAXIS

1. INTRODUCTION

The approach to growing use of tunnels to facilitate transportation in busy and crowded parts of cities has brought about deflection in soil mass and eventually in ground surface. Among the features of urban tunnels, their less surcharge depth, loose ground of towns, large span of these areas and the buildings on the stations are important, All of them make the control of shallow settlement and maintaining stability in the underground spaces very difficult. Settlements due to tunnel excavation, can cause serious damages to the neighboring structures.

In this study, we examined single tunnels by numerical method and twin tunnels by computer modeling and accurate instrumentations. The researches on comparing the effect of single tunnel and twin tunnels on settlement of ground surface has been limited. In Iran, after the growing trend of subway tunnel excavation, in urban regions, irreparable damage of ground surface settlement on building and ancient monuments particularly in Isfahan and Siyo-Se-poul, are noticeable [Fig 1].

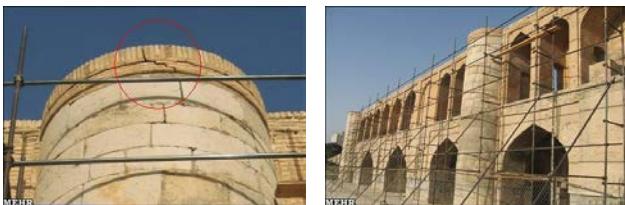


Fig 1: Damage to Siyo-Se-Poul, a worldly recorded monument due to settlement of ground surface.

Perhaps Terzaghi's report[1] is among the first reports that show the effect of soil type in transferring settlement to ground surface. Regarding coarse-grained soil, he believed that all ground displacement in tunnel site owing to dilation gradually disappear to ground surface. However in clay layer, this effect is less clear mostly due to lack of volume change and soil layer which are influenced by cohesion.

Peck(1969) presented a comprehensive report containing general collection of executive operation of tunnel in soft ground. In his detailed examination, he divided settle able ground into four categories. Then for each of soils mentioned, measurements for tunnels situated in these soils[12]. He showed that the cure of ground surface settlement to tunnel excavation has normal distribution and presented a relation for the profile of settlement as follows:

$$S(x) = S_{\max} \times \exp\left(-\frac{x^2}{2i}\right) \quad (1)$$

This equation has no theoretical foundation and chosen because of its similarity to experimental form of settlement. In i and S_{\max} were determinant and a lot of research was done to determine them amounts and many suggestions were made to calculate them. Most of the studies are to modify determine i . Another important parameter is S_{\max} [Fig2]. To achieve a relationship to calculate the amount of this parameter, a parameter called ground loss is defined ,which is in fact equals to contraction of tunnel span. In clay soils, the condition of undrained is governed during tunnel excavation, Therefore the contracted volume at tunnel's span, equals to volume of clay soil on ground surface. The amount of name it, V_L follows as eq.(2)

$$V_L = \frac{4V_s}{HD^2} \quad (2)$$

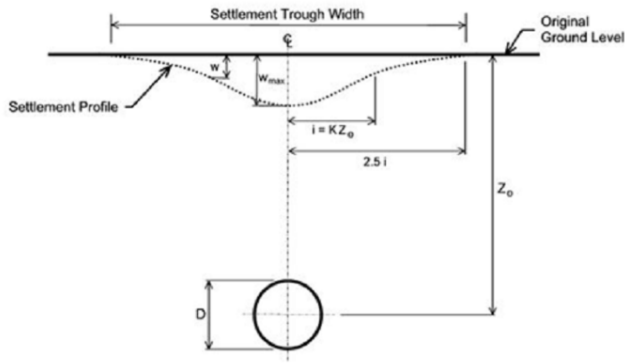


Fig 2: Curve of ground surface settlement due to tunnel excavation [12]

Where D is diameter of tunnel and V_L is reduction of ground volume relative to excavation. V_L was calculated as a percentage of settlement of volume in ground surface to tunnel volume per unit of length. V_s is the total volume of ground surface settlement and is determined by integrating the relationship eq.(1) as in eq.(3):

$$V_s = \sqrt{2\pi \times IS_{\max}} \quad (3)$$

By combining eqs.(2) and (3) and by regarding $i = KZ$, S_{\max}

$$S_{\max} = \frac{0.313VL^2}{KZ_o} \quad (4)$$

In this equation, S_{\max} is the maximum ground settlement above tunnel axis, S_x ground surface settlement to the distance of x relative to tunnel symmetry axis and i is the landmark of the curve.

Although this equation has no theoretical foundation, it has been chosen due to its similarity to experimented values of settlement. As it was seen, i is an important parameter in showing curve width[12].

Sagaseta(1987) [15] presented a solution to determine stress-strain behavior in an isotropic homogeneous environment while the incompact able soil and excavation is near ground surface. The relation which he proposed for settlement shape in plain strain state, in equations (5) and (6):

$$s_{xo} = -\frac{(a^2 x)}{(x^2 + h^2)} \quad (5)$$

Horizontal displacement at ground surface

$$s_{xo} = -\frac{(a^2 h)}{(x^2 + h^2)} \quad (6)$$

Settlement at ground surface

In this equations (a) is tunnel's radius, and (h) is the depth of tunnel's axis. Because of incompatibility of soil the Poisson coefficient is 0.5 presented a linear elastic analysis for a tunnel in an isotropic environment. They use elasticity theory and approximate method of Sagaseta [15] which is even usable for compactable soils with arbitrary amounts of Poisson coefficient. Their solution that is the generalized method Sagaseta, considers oval deflection of tunnel section [16].

Another factor that is defined in different condition of ground settlement is ground loss parameter that is the percentage of the ratio of settlement volume at ground surface to tunnel volume per unit of length. Based on ground loss, gap parameter is defined as follows:

$$g = GP + U_{3D} + \omega \quad (7)$$

In which the difference between maximum internal diameter of excavated tunnel and external diameter of tunnel lining is for circular tunnel. Equivalent 3D Deflections are, in form of elastic-plastic at the front of the tunnel and determinant of excavation quality and operation of the tunnel.

2. TUNNEL GEOMETRY

Fig 3 shows complete sections of twin tunnel of Isfahan subway. It is a two-arc tunnel that .

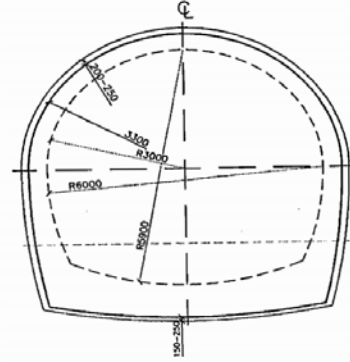


Fig 3. Sample section of the tunnel: (Center of documentation of urban trains, Isfahan (2003))

Based on the first stage research, urban train of Isfahan was designed in the form two dimensional and horse-shoe section, 7m in the middle part and its axis to axis distance is 14m.

Fig 5. is a part of target vertical section in the direction of tunnel excavation. This section was built in the width of Chahar Bagh street. Due to symmetry of boundary and environmental condition of these two tunnels, only half of geometry of target section, regarding environmental condition and loading shallow adjacent to tunnel is shown [10].

This street has two driving lines and 7m of its middle section is occupied by landscaping. The street width is assumed to be 90m in which 22.5m from each direction, is allocated to the buildings. Loading system of building is accounted 20 kPa in two ways and loading of middle part (traffic loading) is supposed to be 10 KP [11].

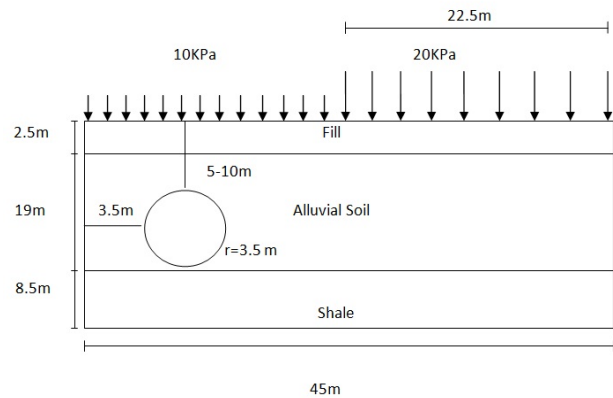


Fig 4: Vertical section of the symmetrical geometry of the tunnels and the region under study

So in the first stage, regarding the present situation, the geometry of modeled section is made in the form of two dimensional by PLAXIS software and based on Fig 5.

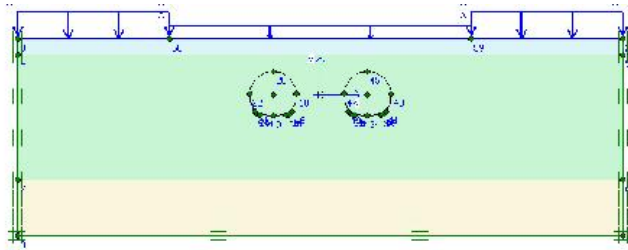


Fig 5: Modeled geometry of tunnels in software space for 5 meter depth [10]

3. DETERMINING THE SPECIFIC FEATURES OF GEO TECHNICAL MODEL

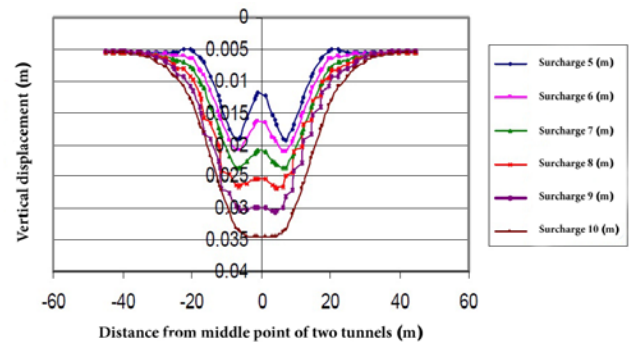
Based on present reality and environmental condition, in this model, geology layers and behavioral model of soil are assumed horizontal and coarse-grained respectively. These layers are defined in three different parts and in the form of fill materials, alluvial and silt from up to down. Geotechnical parameters given in Table 1.

Table 1: Behavioral model and geotechnical specification of soil [11]

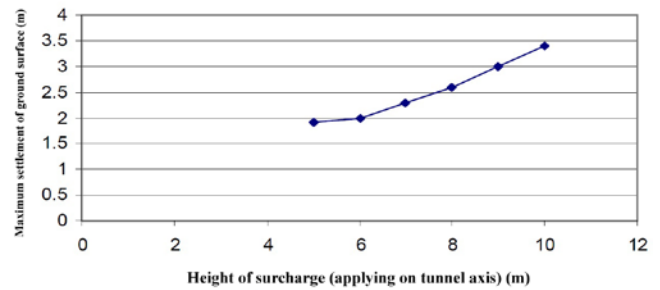
Fill Material	Alluvial	Shale	Unit	Symbol	Parameter
0-2.5	2.5-21.5	21.5-30	m	H	Depth
18	21.5	26	kN/m ³	γ_d	Unit Weight
5×10^{-7}	2.5×10^{-7}	5×10^{-6}	m/s	K_h	Permeability
1×10^{-6}	2.5×10^{-4}	1×10^{-6}	m/s	K_v	Permeability
1.5×10^4	8×10^4	1.7×10^6	kN/m ³	E	Young Modulus
0.35	0.3	0.3	-	ν	Poisson Ratio
15	50	0.8	kN/m ³	C	Cohesion
23	35	26	Degree	ϕ	Internal Friction Angle

4. ANALYSIS OF OUTPUT DATA

Based on carried out modeling in four different and subsequent phases, the results for shallow settlement, for six different states at tunnel depth are achieved. According to these results, it is clear that maximum settlement in ground surface is occurred around the tunnel axis in all states, and by increasing the surcharge of the tunnel, the interference of settlement depth of two tunnels is also increasing to the point that in surcharge state of 10m , a ditch of settlement is seen completely. The varying trend of maximum settlement relative to excavation depth of tunnel is shown in Fig 6. It is obvious that by increasing the depth of tunnel excavation, the amount of maximum settlement is significant [10].



(a)



(b)

Fig6: Comparison of shallow settlement profile for six states of tunnel depth (a) - The varying trend of maximum settlement relative to excavation depth (b)[10]

The results show that:

- In different states of surcharges(5 up to 10 meters), settlement in neighborhood of buildings in both sides of street is within the allowable of 1.0 centimeter.
- Maximum settlement at ground surface happened at neighboring points of axis of tunnel.
- By increasing the height of rock load on tunnels, the interaction of ditches of resulted settlement us increased.
- the amount and area of settlement of ground surface, has direct relationship with depth of tunnel excavation.
- It must be noted that the modeling can be done by examining three-dimensional effects of front of activities on shallow settlement amounts in neighborhood of tunnels and assess the results [10]

5. EFFECTS OF THE DISTANCE BETWEEN PARALLEL TUNNELS ON SETTLEMENT LEVEL

Instrumentation studies show that if center to centre distance of two underground space is more than three times or much as diameter, the excavation of these two spaces will not affect each other, and can be considered separately. In this section we will address this issue by numerical method and examining a tunnel.

First, the settlement from a tunnel excavation in an urban environment is modeled, and then the effect of excavating another tunnel in its neighborhood on the settlement is considered. A tunnel with 4.5m diameter and 10m depth is excavated. Before tunnel excavation the present stress in environment is in the horizontal form. It should be kept in mind that the best and optional distance for neighboring borders is the amount that, stresses at borders, has not changed just before and after the excavation and disturbance in stress contour doesn't happen[fig7][Fig8][Fig9] .

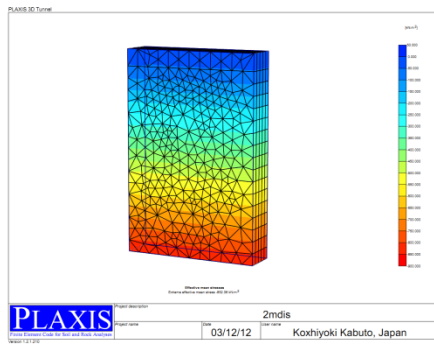


Fig7: Initial stresses before excavating the tunnel

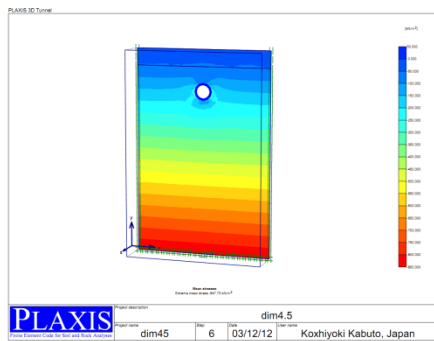


Fig8: Stress state after excavating 10m of the tunnel

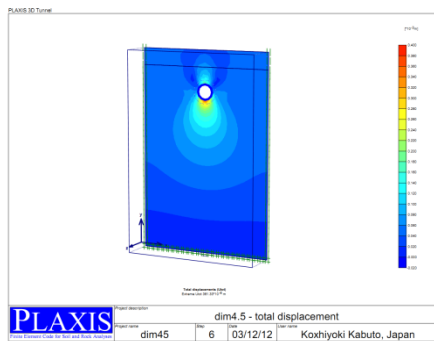


Fig9: Single tunnel total displacement

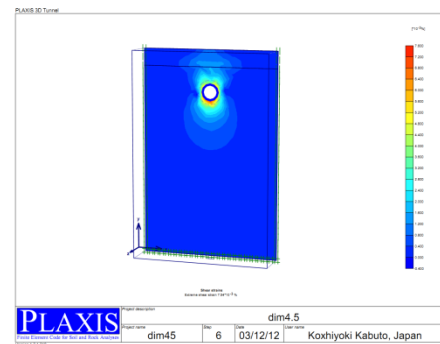


Fig10: Total strain - single tunnel

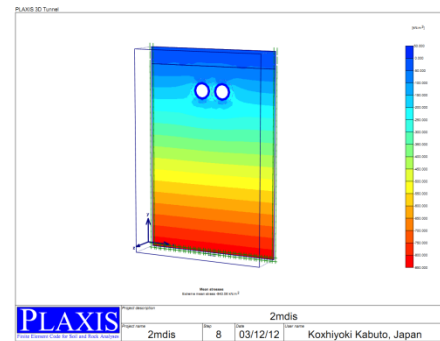


Fig11: Total stress - twin tunnel with 2m distance

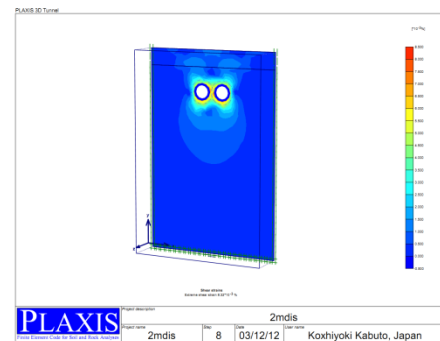


Fig12: Total strain - twin tunnel with 2m distance

After that the effect of neighboring tunnel excavation is considered with the same characteristic and in different distances. To do this, 5 states have been regarded. The distance we mean in this study is the ledge to ledge distance of two neighboring tunnels. The purpose of examining several cases (states) is obtaining optimal distance between two neighboring tunnels. At first neighboring (adjacent) tunnel is put in two meters distance from the first tunnel [Fig 10][Fig11][Fig12] .

As it can be seen, stress contours have overlap and do not act independently so that stress contour of twin tunnel is not similar to that of single tunnel, and this is also true for soil displacement around the tunnel. In the following situation tunnels are placed in 4 meter distance. In this case, although the interaction of stress and displacements contours in two tunnels are decreasing, but they still influence on each other.

In another situation, two tunnels are put in 8m distance from each other. It may be said that behavior of two tunnels is partially independent and have the least effect on each other [Fig13][Fig14] .

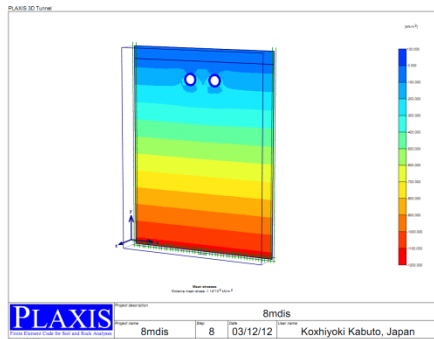


Fig 13: Total strain twin tunnel with 8m distance

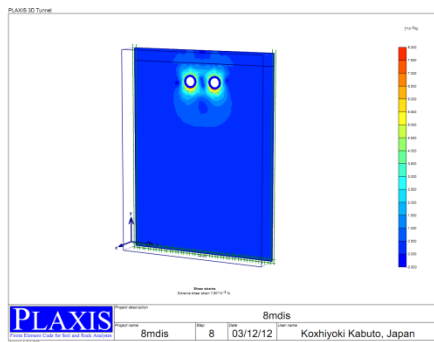


Fig 14: Total stress with tunnel with 8m distance

In another situation two tunnels are put in 10m distance and as expected, by increasing this distance and keeping the tunnels away from each other, their behavior becomes more separate [Fig15][Fig16] .

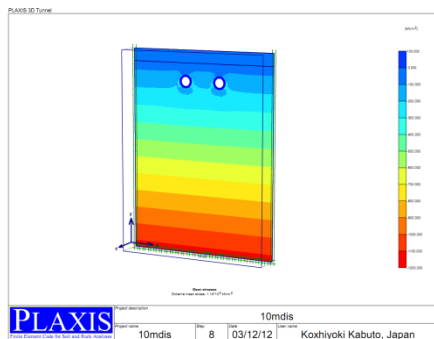


Fig 15: Total stress- twin tunnel with 10m distance

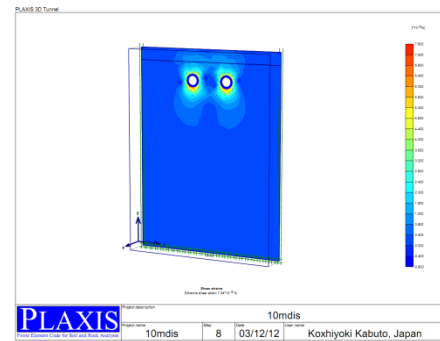


Fig16: Total strain- twin tunnel with 10 m distance

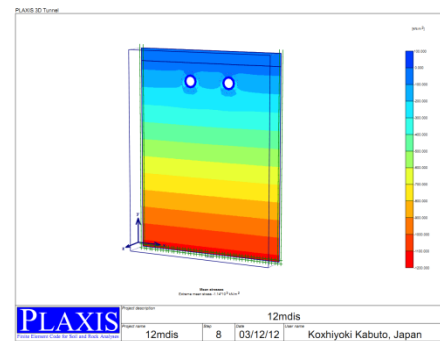


Fig 17: Total stress- twin tunnel with 12m distance

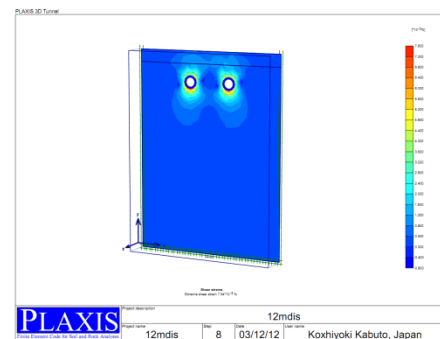


Fig 18: Total strain -twin tunnel with 12m distance

In the next situation two tunnels are put in 12m distance. As it was seen from the distance of 10m or more, stress contours and displacement around each tunnel are just alike single tunnel and next tunnel excavation has no effect on displacement and applied stresses on neighboring tunnel so that to simplify and reduce the calculation, we can examine them independently (separately) [Fig17][Fig18] .

6. COMPARING OF SINGLE TUNNEL BEHAVIOR WITH PARALLEL TUNNEL (WITH EQUAL EFFICIENCY)

In this part a tunnel with 9 m diameter (two times as much diameter as former tunnel) is excavated and studied at the same environment and condition. The purpose of this study is

to examine settlement from tunnel excavation with larger diameter and its comparison with settlement from two tunnels, each one with a diameter equals to the radius of larger tunnel (with different distance from each other) [Fig19][Fig20] .

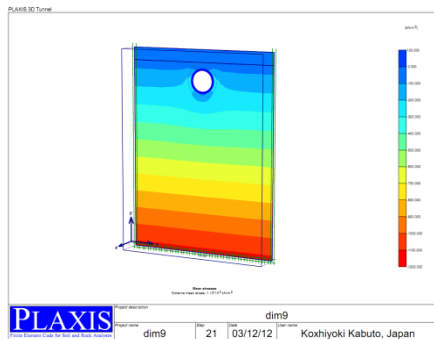


Fig 19: Total stress-single tunnel d=9m

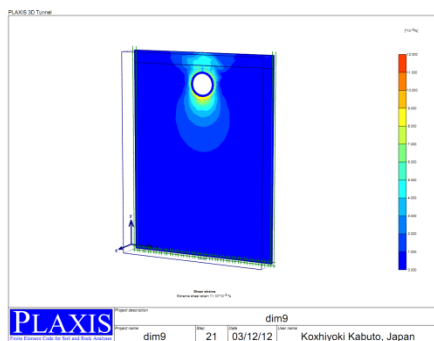


Fig 20: Total strains-single tunnel d=9m

As it was seen in comparing the displacement from excavation of two neighboring tunnels (with smaller diameter) and larger tunnel, it would be better to excavate two tunnels separately so that their distance should be in allowable level and has not much effect on displacement and settlement of ground surface.

7. CONCLUSION

In this study first the situation (condition) of urban train tunnels is studied in Isfahan and then a comprehensive review of literature is discussed about created deflections on an underground excavation and their settlement. Then general overview of stability analysis approaches are considered and regarding the use of PLAXIS software some brief description is provided. Two cross sections of subway tunnel of Isfahan were studied in which the settlement of ground surface and tunnel crown were measured by instrumentation equipments and was modeled by PLAXIS 3D. The outputs of software were adapted with measured data in above supposed stations. Furthermore, in order to examine the effect of important parameters of soil (such as cohesion, Poisson coefficient, elasticity modulus and unit weight) different diagrams of

settlement were drawn and the result of created effect on the settlement of ground surface and tunnel crown was studied due to increasing or reduction of each of the mentioned parameters. Finally by modeling a tunnel with 9m diameter on one hand and two neighboring tunnels, each one with 4.5m on the other hand, and putting them in different distance from each other and observing created changes in stress contour and displacement as to using or not using two tunnel with smaller diameter instead of a tunnel with larger diameter in urban regions were explained. Regarding above –mentioned materials, following results are concluded:

1. The result from in situ measurement indicates that maximum settlement from excavation of subway tunnel in Isfahan in monitored regions is less than amount of allowable settlement (0.5 under the building as 1 inch at street level).
2. based on done research on stress contours and length displacement of 9 m diameter, and its comparison with stress contours and displacement of a twin tunnel-each with 4.5 m diameter at different distance from each other and with similar and same condition of a larger tunnel, we may say that in situations where tunnel construction is in urban regions or other sensitive places(areas), naturally any increase will have some important consequences. Using twin tunnels with smaller diameter seems reasonable and justified if the allowable distance for each of the tunnels-instead of excavating a tunnel with larger diameter- is observed.
3. In cases where the distance of two neighboring tunnels are equal or more than allowable level, we can model one of two tunnels and use results for another tunnel and generalize its result(s) to another tunnel.

8. REFERENCES

- [1]- Terzaghi,k. Rock defects and loads on yunnel supports . in: Rock tunneling with steel supports.editors r.v.proctor and t.white . Published by commercial shearing and stamping co . , Youngstown,1946,pages 15-99
- [2]- Shariatmadari,N, Farzaneh, (2001), investing settlement of ground surface due to tunnel excavation in Tehran. p.p 265-277 the proceedings of 5th conference of Iran's tunnel Tehran's Technical- Department of Tehran University
- [3]- Vafa'eeyan, M (2001): the characteristics of ground settlement owing to shallow tunnel excavation p.p 313-321
- [4]- Proceeding of 5th conference on Iran:Tunnel Tehran Technical engineer Department of Tehran University The collection of reports of document center of subway organization of Isfahan and neighbor hood (2003), Report of analysis and design of maintenance system and installing program of exact instrument and of first section.
- [5]- The collection of documentation center reports of subway organization of Isfahan and neighborhood (2008): monthly report of instrumentation of subway tunnel of Isfahan, southern piece (part).
- [6]- The company of consulting engineers of Zamin Fan Avaran (2005). Final report of geo technical studies southern part of Isfahan metro subway.

- [7]- Collections of reports of documentation center of subway organization of Isfahan and neighborhood (2001) potentiality of fast and dense transportation of Isfahan
- [8]-Raftari, P. (2011) Analysis of stress and deflections of the tunnel of Isfahan subway by using the results of instrumentation and its adaption with results gained by PLAXIS 3D tunnel software, M.Sc thesis Azad University of Zanjan Engineering Department.
- [9]- Khosrotash Mehran, Taskindoust, kashfi mojtaba (2007). Detailed report of Behavior Assessment tunnel, first section 2nd line karaj and neighborhood subway consulting engineers of Rad Tunnel No 4.
- [10]- Majid Nourian bidgoli, (2009): Studying the settlement of ground surface due to excavation of twin tunnels in urban areas 8th conference of Tunnel. Tarbiat Modares, Tehran(2004)
- [11]-Consultant engineers of Saazbon porozhe, reports of first stage study of geology and geotechnical of Isfahan subway within the Shariati-Azadi Station subway organization of Isfahan and neighborhood, (2004).
- [12]- Peck, R. B. (1969). "Deep excavation and tunneling in soft ground." Proceeding of 7th int. Conf. on soil mechanic, Mexico: state of the art, pp. 225-290.
- [13]- new& O'Reilly. (1982) "Representing Settlement for Soft Ground Tunnleing" Journal of Geotechnical and Geoenvironmental Eng., Vol. 124, No.9, pp. 846-856.
- [14]- Mair, R. J., Tailor, R. N., and Bracegirdle, A. (1987). "Surface settlement profiles above tunnels in clay." Journal of Geotechnique, Vol. 37, No. 3, pp. 301-330.
- [15]- Sagaseta, C. (1987). "Analysis of underground soil deformation due to ground loss". Journal of Geotechnique, Vol. 37, No. 3, pp. 301-330.
- [16]- Verruijt, A. and Booker, J. R. (1996). "Surface settlement due to deformation of a tunnel in an elastic half plane." Journal of Geotechnique, Vol. 46, No. 4, pp. 753-756.
- [17]- Rowe, R. K. and Kack, G. J. (1983). "A theoretical examination of the settlement induced by tunneling." Canadian Geotechnical Journal., Vol. 29, pp. 299-314.
- [18]- Lee, K. N., Rowe, R. K. and Lo, K. Y. (1992). "Subsidence owing to tunneling, Estimation the gap parameter." Canadia Geotechnical Journal., Vol. 29, pp. 929-940.
- [19]- Najjar, Y. and, M. (1993). "Surface subsidence prediction by non-linear finite element analysis." Journal of Geotechnical Eng., Vol. 119, No. 11, pp. 1790-1804.
- [20]- Selby, A. R. (1999). "Tunnelling in soil-ground movements and damage to building in Workington, UK. "Geotechnicl and Geological Engineering, Vol. 17, pp. 351-371.
- [21]- Wang, Z. W., Sampaco, K. L., Fischer, G. R., Kuchker, M. S., Godlewski, P. M. and Robinson, R. A. (2000). Models for predicting surface settlements due to soft ground tunneling. Boston: Proceeding of North American Tunnelling, pp. 645-652.

Excess Pore Pressure Characteristics of Sand Mat using Dredged Soil

M.S LEE, K. ODA

Department of Civil Engineering, Graduate School of Engineering, Osaka University, Japan

ABSTRACT

The design of sand mat should be reviewed by behavior of excess pore pressure which is obtained by combining characteristics of soft ground with the permeability of sand mat. In this paper, in order to investigate the distribution of hydraulic gradient of sand mat, a banking model test was performed using dredged sand as materials of sand mat, and these results were compared by the numerical analysis results utilizing Terzaghi's consolidation equation. As the results, it shows that the pore pressure was influenced by the settlement increasing in the center area of sand mat as the height of embankment increases, and uprising speed of excess pore pressure due to residing water pressure is delayed comparing with the results of numerical analysis. Finally, the construction of sand mat should be laid to reduce the increased hydraulic gradient at the center area of embankment.

Keywords: Dredged Soil, Sand Mat, Model Test, Hydraulic gradient, Pressure Head

1. INTRODUCTION

Sand mat is used as a horizontal drainage method during embankment to facilitate the initial consolidated settlement due to the weakness of the surface layer of dredged and reclaimed sites, and this construction method is applied in general areas of soft soil ground. In particular, due to the insufficient amount of sand in dredged and reclaimed areas and areas of soft soil ground, there is a desperate need to procure alternative materials, which has increased the need for research on using quality dredged soil as a sand mat.

Thus, in order to determine whether dredged soil is a suitable material to be used as a sand mat, a large sample was collected for physical properties analysis and permeability testing. Based on the results, the representative dredged soil (of the samples with permeability coefficients that fit the criteria for sand mat, the sample with the worst particle size as it contains the most amount of fine powder) was selected and a model test was conducted to determine its applicability as a sand mat in advance. The distribution of pore water pressure and the drainage of the sand mat, which is necessary in the improvement of soft soil ground, were identified and the amount of consolidated settlement according to the embankment load was measured in order to perform a finite-element analysis and predict its behavior. After the consolidation was completed by the final load, a discharge test was performed and the effect of the permeability was observed. The aim of this study is to apply the theoretical review to the design by proposing a testing technique that can be utilized on sand mat, and improving the technology of utilizing alternative materials for sand mat based on the results.

2. THEORETICAL WATER PRESSURE DISTRIBUTION IN SAND MAT

The pore water pressure of sand mat laid on the soft clay ground generally increases in proportion to the amount of settlement in the clay layer according to Terzaghi's theory of one-dimensional consolidation (Terzaghi, 1943, Terzaghi, et al., 1967). The increased excess pore water pressure is quickly drained out from the embankment body due to the permeability of the sand mat. However, as shown in Fig. 1, if the permeability of the sand mat is low or there is large settlement of the soft clay ground, drainage is delayed in the central part of the embankment, which increases the pressure head. In Fig. 1, it is assumed that the amount of consolidated settlement in the saturated clay layer generated by the embankment load undergoes a one-dimensional change and the pore water from consolidation is completely drained out from the embankment body in a horizontal direction through the saturated sand mat. Thus, for saturated clay ground, the consolidated settlement of the clay layer can be represented as a function of the average degree of consolidation (U) and time (t) according to Terzaghi's consolidation equation. The pressure head (H) occurring at the horizontal distance (x) of the sand mat can be presented as Eq (1) according to Terzaghi's one-dimensional consolidation equation.

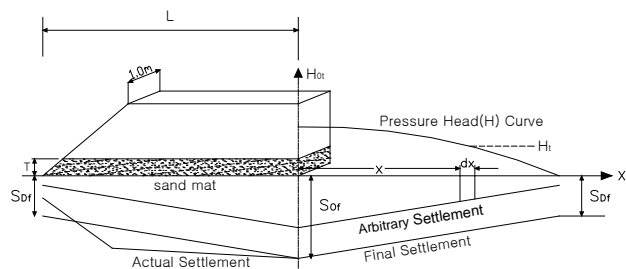


Fig. 1 Distribution of pressure head of sand mat

$$H = \frac{\gamma_w}{2k \cdot T} \cdot \frac{dU(t)}{dt} \cdot \left(S_{0f} \cdot x - \frac{S_{0f} - S_{Df}}{2L} \cdot x^2 \right) dx \quad (1)$$

where $dU(t)/dt$ is the settlement rate of the clay layer, S_{0f} is the final amount of settlement in the center of the embankment, S_{Df} is the final amount of settlement in the sides of the embankment, T is the thickness of the sand mat, k is the permeability coefficient of the sand mat, $2L$ is the full width of the sand mat, and γ_w is the unit weight of water. Because Eq (1) assumes a one-dimensional, horizontal flow of the pore water from the sand mat, the pressure head is zero ($H=0$) at the sand mat boundary ($x=L$). Thus, when the maximum pressure head at the center of the embankment is set as H_{0t} and the average pressure head in the transverse distribution is indicated as H_t , the pressure heads can be presented as follow in Eq (2) and Eq (3).

$$H_{0t} = \frac{\gamma_w}{2k \cdot H} \left(\frac{S_{0f}}{3} + \frac{S_{Df}}{6} \right) L^2 \cdot \frac{dU(t)}{dt} \quad (2)$$

$$H_t = \frac{\int_0^L h \cdot dx}{L} = \frac{\gamma_w \cdot L^2}{2k \cdot T} \left(\frac{5S_{0f}}{24} + \frac{S_{Df}}{8} \right) \frac{dU(t)}{dt} \quad (3)$$

In Eq (2) and Eq (3), the pressure heads of the sand mat vary depending on the settlement rate, final amount of settlement, sand mat thickness, permeability coefficient, and the width of the embankment. Here, the settlement rate can be obtained from the approximation formula of the relationship between the degree of consolidation (U) and time factor (T_v) in Terzaghi's one-dimensional consolidation equation and the measured settlement as follow in Eq (4) and Eq (5).

$$S_f = \frac{C_c}{1 + e_0} \times H \times \log \frac{P_0 + \Delta p}{P_0} \quad (4)$$

$$U(\%) = \sqrt{\frac{4}{\pi} T_v} = \sqrt{\frac{4}{\pi} \times \frac{C_v \cdot t}{H^2}} = \frac{S_t}{S_f} \times 100 \quad (5)$$

In Eq (4) and Eq (5), S_f is the final amount of settlement, whereas S_t is the amount of settlement at an arbitrary time and the other coefficients have the same symbols as those in Terzaghi's one-dimensional consolidation equation.

3. MODEL TEST ON BEHAVIOR OF PORE WATER PRESSURE IN SAND MAT

3.1 Experimental Apparatus and Method

For the model test, head devices were designed to be placed on both sides of the soil tank (dimensions: 300cm × 70cm × 70cm) to maintain the groundwater inside the sand mat at a constant level, and 4 pore water pressure cells, 3 settlement plates and 2 earth pressure cells were installed to measure the amount of settlement of the clay layer and sand mat and the pore water pressure during embankment loading. The soft clay in the bottom of the sand mat was sufficiently stirred with distilled water using an electric agitator in a simple soil tank, and the slurry was inserted up to a height of 30cm. Then, saturated water was supplied for approximately a week by the head devices until a steady state was reached. Later, a sheet was laid, upon which dredged soil was spread to a height of 20cm in place of the sand mat. The drainage valves on the left and right sides (Fig. 2) were closed and saturated water was supplied for a day. Then, spreading and loading were performed up to the third level using weathered soil.

3.2 Physical and Mechanical Properties of Sand Mat and Clay

The physical properties and particle distribution of dredged soil used in this experiment are shown in Table 1 and Fig. 3. Fig. 3 also contains information on the general particle distribution of sand mat applied in general soft soil ground designs. The dredged soil used in this experiment is slightly poor compared to quality sand as it is close to the lower limit of the fine materials used for sand mat, but it is deemed to have a good alternative to other materials for sand mat. In order to examine the consolidation characteristics of the lower clay used in this experiment, overconsolidated clay was turned in a slurry form using an agitator. Then, the consolidation sample was produced using a consolidation device. The standard consolidation characteristics of the test sample and the input moisture content (w_n), etc., of the slurry form inserted into the model soil tank are shown in Table 2.

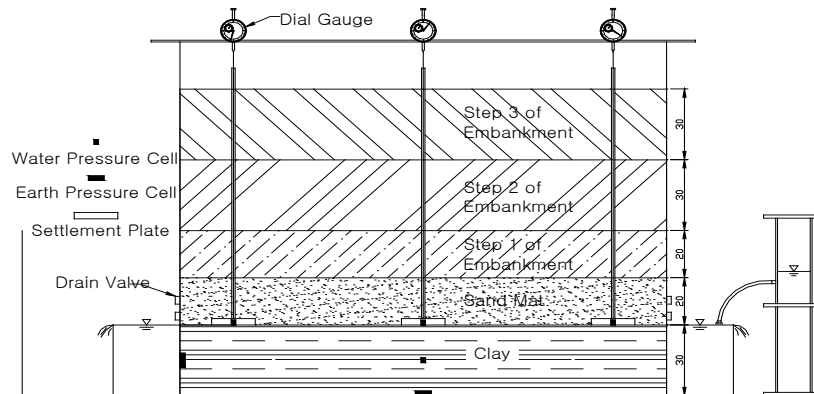


Fig.2 Model test on hydraulic gradient of sand mat (unit: cm)

Table.1 Physical properties of sand mat used in experiment

Water Content (%)	17.6
Plasticity Index (I_p)	NP
Specific Gravity (G_s)	2.60
Passing 75 μ m sieve (%)	9.5~13.3
Coefficient of Permeability (cm/sec)	1.34×10^{-3}
USCS	SM

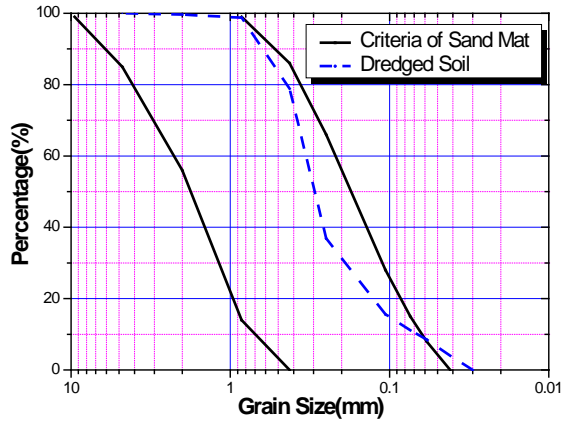


Fig.3 Distribution of the pressure head of a sand mat

Table.2 Physical and mechanical properties of remolded clay

Water Content (w_n , %)		54.5
Unit Weight (γ_t , kN/m ³)		16.6
Specific Gravity (G_s)		2.60
Consolidation	e_0	1.26
	C_c	0.380
	C_s	0.159
	C_v (cm ² /sec)	1.56×10^{-4}
	P_c (kPa)	10
USCS		CL

3.3 Settlement Characteristics According to Embankment

For the embankment, the degree of consolidation was confirmed to be over 90% using the hyperbolic method (Tan, et al., 1991) and loading was performed in 3 steps up to a height of 100cm over the course of 11 days. The degree of consolidation according to the settlement of the clay ground was assessed using the ratio of the amount of settlement actually measured through the model test and the final amount of settlement calculated using the specifications of the consolidation test. The final amount of settlement was calculated based on the initial void ratio according to the input moisture content and the ground stress (Δp) measured using the earth pressure cell at the bottom of the clay layer. The measured values (Δp) of the earth pressure cell at the center, the amount of settlement (S_{of} and S_{Df}) measured using the dial gauge at the center and the left and right fore-ends in the model test device (Fig. 2) during the embankment are shown in Table 3.

Table.3 Amount of settlement and ground stress measured during embankment

		S_{Df} (cm)	S_{of} (cm)	Δp (kPa)
Sand Mat		0.89	1.33	3.4
Embankment	Step 1	1.35	1.87	3.6
	Step 2	1.76	2.32	5.1
	Step 3	2.04	2.62	5.1

4 NUMERICAL ANALYSIS OF PORE WATER PRESSURE OF SAND MAT

4.1 Pore Water Pressure According to Permeability Coefficient and Thickness of Sand Mat

The settlement rate ($dU(t)/dt$) for the initial consolidation degree (U) of 3%, obtained when the clay layer thickness of 30cm and consolidation coefficient in Table 2, are substituted into Eq (5) and the amount of settlement at the center of the embankment (S_{of}) and the amount of settlement in the outer part of the embankment (S_{Df}) measured at step 3 of embankment, and the spread thickness (T) of 20cm, were substituted into Eq (2). When the permeability, k , changed up to $10^{-4} \sim 10^{-2}$ (cm/sec), the pressure head, H_t , was calculated according to the horizontal distance of the sand mat, and the results are shown in Fig. 4. As shown in the figure, the lower the permeability coefficient of the sand mat, the higher the hydraulic gradient at the center of the embankment, which in turn increases the pressure head. In particular, there is a significant increase in the pressure head when the permeability coefficient of the sand mat is below 10^{-4} (cm/sec) as it causes a delay in the draining of pore water. Also, the settlement rate calculated when the degree of consolidation was 3% using Eq (2), the amount of settlement at the center of the embankment (S_{of}) and the amount of settlement in the outer part of the embankment (S_{Df}) measured at step 3 as shown in Table 3 were substituted into the equation, with the permeability coefficient, k , maintained at a constant of 10^{-3} (cm/sec). Then the thickness of the sand mat (T) was varied in the range of 5 to 30cm to analyze the resulting value of the pressure head, the results of which are shown in Fig. 5. The figure shows that with an increase in the thickness of the sand mat, the pressure head decreased, and the change in the pressure head was small in the outer part of embankment as it is less affected by the hydraulic gradient.

4.2 Pore Water Pressure of Sand Mat Based on Coefficient of Consolidation in Clay Layer

In order to analyze the pressure head of the sand mat according to the settlement rate of clay in the bottom, the coefficient of consolidation (C_v) was selected as a factor affecting the settlement rate in the clay layer. when the consolidation coefficient (C_v) of the clay layer is changed up to the range of $10^{-5} \sim 10^{-3}$ (cm²/sec) with the initial degree of consolidation (U) at 3%, the consolidation time (t) for the arbitrary consolidation coefficient can be calculated using Eq (5) and thus, the settlement rate ($dU(t)/dt$) with respect to the degree of consolidation can be obtained.

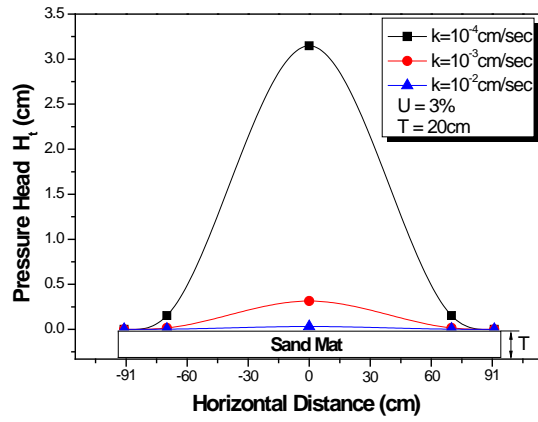


Fig.4 Pressure head according to changes in permeability coefficient

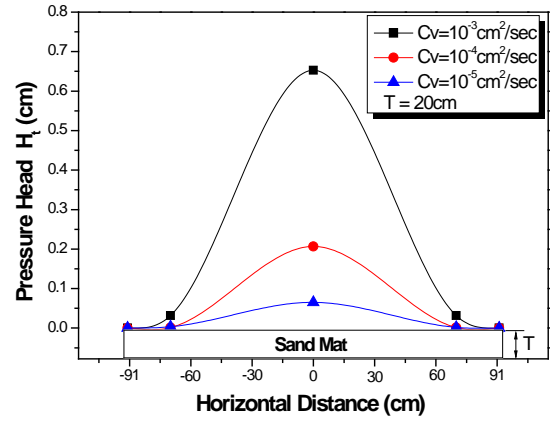


Fig.6 Pressure head according to changes in consolidation coefficient

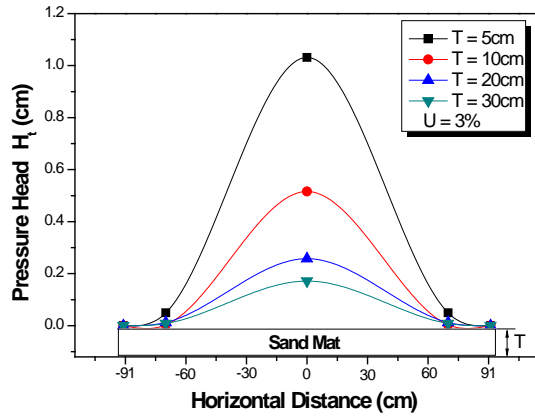


Fig.5 Pressure head according to changes in thickness of sand mat

Thus, the amount of settlement at the center of the embankment (S_{0f}) and the amount of settlement in the outer part of the embankment (S_{Dr}) measured at step 3 as shown in Table 3 and the permeability coefficient, k , a constant of 10^{-3} (cm/sec), were substituted into Eq (2) to obtain the pore water pressure in the sand mat. The results are shown in Fig 6, which shows a positive correlation between the consolidation coefficient of the clay layer and the pressure head at the center of the embankment. This is due to the increase in the amount of consolidation drainage resulting from the increased settlement rate of the clay layer caused by increased stress at the center of the embankment.

5 ANALYSIS AND DISCUSSION OF RESULTS

5.1 Pore Water Pressure of Sand Mat According to Height of Embankment

The top of Fig 7 shows the results of the FEM analysis conducted based on the modified cam-clay model (Snadhu, et al., 1969, Mayhe, 1980, Gens, 1988) of the settlement, measured in the settlement gauges installed in the left, central and right parts of the sand mat layer, according to the elapsed time during embankment. The bottom of the figure shows the measurements of the pore water pressure cells installed inside the sand mat layer and at the center of the clay layer.

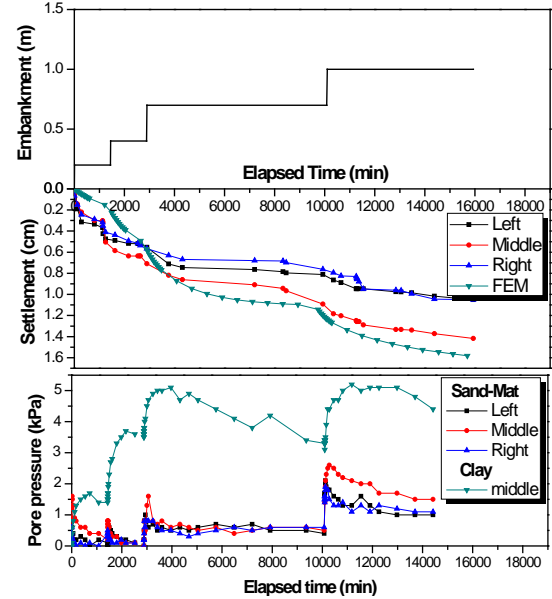


Fig.7 Pore water pressure of sand mat and settlement and pore water pressure of clay ground

As the height of the embankment increased, there was a higher amount of settlement in the central part of the clay layer compared to the left side. Because of the soft surface and the low shear strength, there was a immediate settlement during the laying of the sand mat and the primary embankment, and the actual measurement of the settlement was higher than the settlement calculated based on FEM analysis. Afterward, the measured settlement and the result of the FEM analysis tended to be similar, but the actual settlement was slightly smaller due to the buoyancy effect caused by inhibited drainage during the experiment. Also, a comparison of the pore water pressure in the clay layer and sand mat layer during embankment showed a significant increase of pore water pressure in the clay layer, whereas such increase was prominent at the center and low in the left and right sides of the sand mat layer. This is due to the increased hydraulic gradient caused by an increase in the residual pore water pressure resulting from the concentrated stress in the central part of the clay layer.

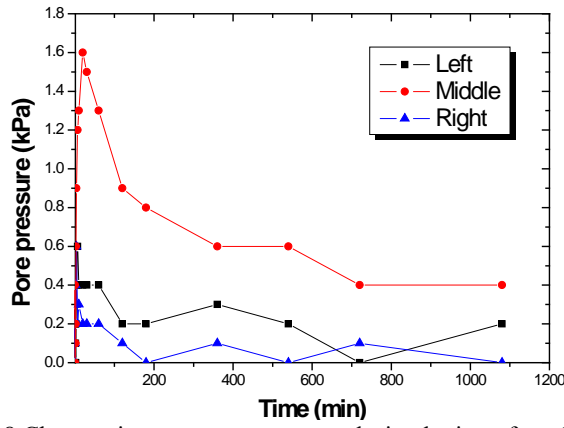


Fig. 8 Changes in pore water pressure during laying of sand mat

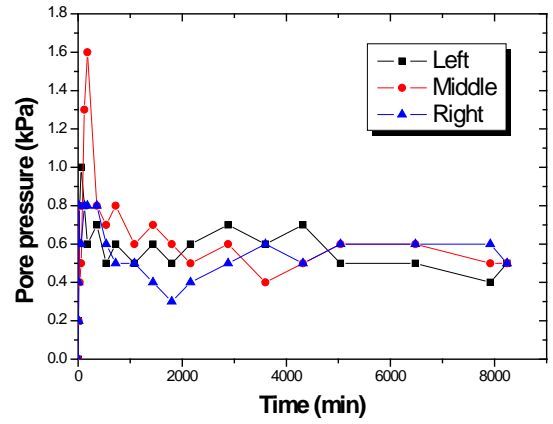


Fig. 10 Changes in pore water pressure during step 2 of embankment

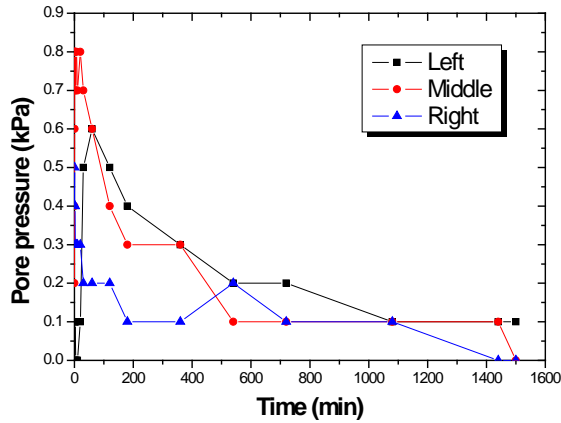


Fig. 9 Changes in pore water pressure during step 1 of embankment

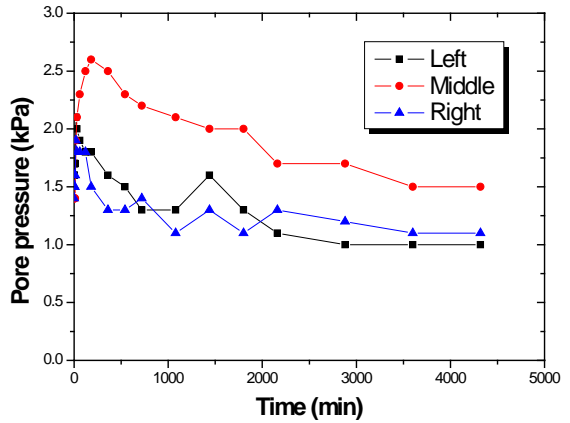


Fig. 11 Changes in pore water pressure during step 3 of embankment

Fig. 8 to 11 show the results of the pore water pressure measured using the pore water pressure cells installed in the sand mat and the clay layer according to the embankment during the model test. Fig. 8 shows a rapid increase of pore water pressure caused by soil disturbance and the groundwater level remaining at the top of the saturated soft clay layer. The pore water pressure increased up to 1.6 kPa at the center of the sand mat, and gradually decreased over time until it reached 0.6~0.4 kPa after 400 min. Fig. 9 shows the result of the pore water pressure measured during the primary embankment, which slightly increased at the center to a maximum of 0.8 kPa and greatly increased in the left and right sides to a maximum of 0.6 kPa in comparison with the loading of the sand mat. Fig. 10 shows the pore water pressure measured during the step 2 of embankment. The pore water pressure at the center increased up to 1.6 kPa at initial loading before decreasing to approximately 0.5 kPa over time. The bottom clay foundation subsided uniformly until the step 2 of embankment, which showed that the sand mat has maintained the horizontal function. The changes in the pore water pressure of the sand mat at the time of final embankment shown in Fig. 11 revealed that there was a significant increase of pore water pressure in the central part of up to 2.6 kPa and in the left and right sides of up to 2 kPa during initial loading compared to the step 2 of loading.

Over time, the pore water pressure in the central part of the sand mat was observed to be higher than the left and right sides, with a constant slope. There was an increase of settlement at the center of the embankment and the sand mat formed a concave shape, which caused the pore water to form a pool as it could not be drained out.

5.2 Pressure Head of Sand Mat According to Degree of Consolidation in Clay Layer

In order to compare and identify the tendency of the water head of the sand mat according to the degree of consolidation in the clay layer during the embankment based on theory and experiment, the pressure head measured using the pore water pressure cells installed in the sand mat and the pressure head predicted using Eq (2) are indicated in Fig 12 and 13. The thickness and consolidation coefficient of the clay layer in the experiment were substituted into Eq (5) to obtain the settlement rate ($dU(t)/dt$) with respect to the predetermined degree of consolidation, which was then substituted into Eq (2) to calculate the pressure head. Then, the degree of consolidation of the clay ground was obtained using the ratio of the amount of settlement (S_t) measured through the model test and the final amount of settlement (S_f) calculated using Eq (4). The pore water pressures of the laboratory clay ground corresponding to the predetermined degree of consolidation are indicated in Fig 12 and 13.

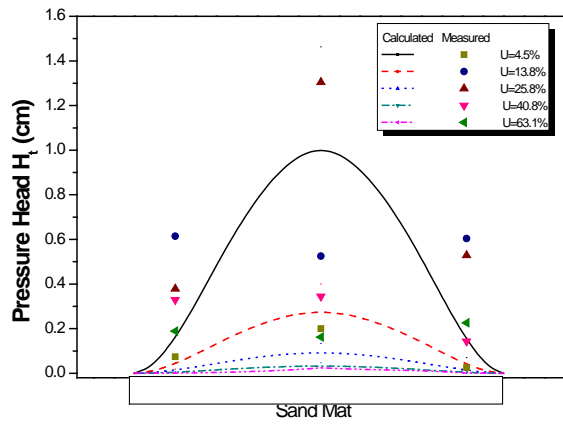


Fig.12 Comparison of results and numerical analysis of pore water pressure according to degree of consolidation during step 2 of embankment

An analysis of the step 2 and step 3 of embankment, which caused a significant increase in the pore water pressure, showed that the pore water pressure of the sand mat measured during the step 2 of embankment in the model test was generally higher due to the increase in the degree of consolidation compared to the result of the numerical analysis. The measured pore water pressure was at its maximum at the center when the degree of consolidation was 26% and at the left and right sides when the degree of consolidation was 14%. On the other hand, the result of the numerical analysis revealed that the maximum pore water pressure was reached when the degree of consolidation was 5%. Fig. 13 shows that the pore water pressure was measured to be at its maximum at the center during the step 3 of embankment when the degree of consolidation was 14% and at the left and right sides when the degree of consolidation was 5% and 14%. On the other hand, the result of the numerical analysis revealed that the maximum pore water pressure was reached when the degree of consolidation was 5%, just as with the step 2 of embankment. In the case of step 3 of embankment where the height of the embankment is greater, the pore water pressures measured in the left and right sides were higher compared to the values measured during the step 2 of embankment, and with an increase in the degree of consolidation, the measured values for the left and right sides of the sand mat were greater than the results of the numerical analysis. As the embankment grew taller, there was an increase of settlement in the central part of the sand mat, causing a deformation, which inhibited drainage. Thus,

6 CONCLUSION

In this study, the pressure head distribution of a sand mat laid on a clay layer was analyzed based on Terzaghi's one-dimensional consolidation, which takes into consideration the settlement characteristics of the bottom clay layer. Also, the effect of the settlement characteristics of the soft clay layer on the pore water pressure distribution of the upper sand mat layer was reviewed based on the model loading test. The findings of this study can be summarized as follows:

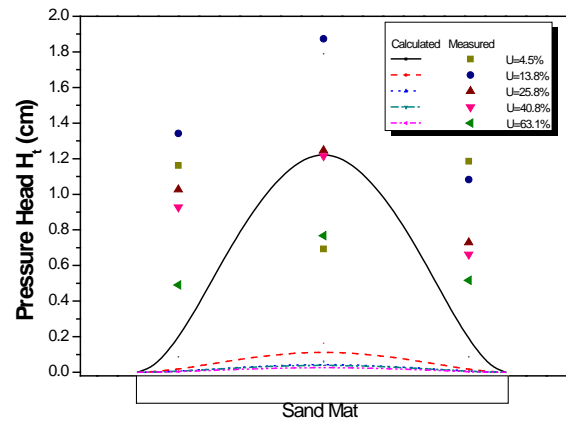


Fig.13 Comparison of results and numerical analysis of pore water pressure according to degree of consolidation during step 3 of embankment

- (1) Terzaghi's one-dimensional consolidation equation, which takes into account the rate of consolidated settlement in the clay layer and the settlement level, is highly influenced by the permeability coefficient and thickness of the sand mat and the consolidation coefficient of the clay layer.
- (2) Because the settlement level of the embankment center increases pressure head, it reduces the horizontal drainage of sand mat.
- (3) The reason for the delay in the drainage of the pressure head measured during the test compared to the result of the numerical analysis is the increased hydraulic gradient occurring because the increased settlement in the central part is transferred to the left and right sides.
- (4) The amount of settlement in the central, left and right sides should be predicted prior to the laying of the sand mat in order to reduce the hydraulic gradient and the horizontal water head resistance in the sand mat.

7 REFERENCES

- [1] Terzaghi, K, "Theoretical Soil Mechanics," New York: John Wiley and Sons, 1943.
- [2] Terzaghi, K. & R. B. Peck, "Soil mechanics in engineering practice," 2nd ed. New York: John Wiley and Sons, 1967
- [3] Tan T. S., Inoue. T., Lee. S. L, "Hyperbolic method for consolidation analysis," Journal of Geotechnical Engineering, vol. 117, No.11, 1991, pp.1723-1737.
- [4] Snadhu, R, S. & E. L. Wilson, "Finite Element Analysis of Seepage in Elastic Media," J. Engrg. Mech. Division ASCE, Vol.95, No. EM3. 1969, pp.641-651.
- [5] Mayhe, PW, "Cam-Clay predictions of undrained strength," Journal of the geotechnical and geoenvironmental engineering, ASCE, Vol.106, No. GT11, 1980, pp.1219-1242.
- [6] A. Gens, D.M. Potts, "Critical state models in computational geomechanics," Engineering Computations, Vol. 5 Iss: 3, 1988, pp.178 - 197.

Effect Of Clays Fraction To California Bearing Ratio Laboratory Test Value With And Without Soaked

Soewignjo Agus NUGROHO, Syawal SATIBI and Ferry FATNANTA
Civil Engineering Department, Riau University, Indonesia

ABSTRACT

In design of highway, soil bearing capacity is very affecting the thickness of pavement. One of the methods to determine the soil bearing capacity in Indonesia is CBR (California Bearing Ratio) test. The field soil conditions are soaked (saturated) and un-soaked, considering these conditions, conducted CBR testing in the laboratory on soaked and un-soaked conditions.

This research aims to make comparisons between CBR soaked test results for CBR un-soaked in some variation of clay content and make simple comparisons between CBR soaked for CBR un-soaked by considering the soil properties whereas can be predicted the CBR soaked value based on the CBR un-soaked test results.

The results showed that there was a linear correlation between the CBR soaked and CBR un-soaked also influenced by the nature of the index (the properties of the soil). The maximum value of CBR ranges of 30-40 percent clay content.

Keywords : California Bearing Ratio, Soaked and un-soaked, correlation

1. INTRODUCTION

Sub-Grade soil bearing capacity plays very important role for the design of highway structure. It determines design thickness of the pavement. High bearing capacity of sub-grade soils reduces the required thickness of pavement. The bearing capacity of sub-grade (base soil) is mostly influenced by the type of soil, water content and its density. Several methods are available to determine base soil bearing capacity such as California Bearing Ratio (CBR) test, Plate Bearing test (to determine modulus of sub-grade reaction and modulus of resilient), Dynamic Cone Penetrometer (DCP) test, Machintosh Probe and Hand Cone Penetrometer (HCP) test, which is also known as Proving Ring Penetrometer [1]

It is common in Indonesia that the base soil bearing capacity for highway pavement design is determined by CBR test measurement. This can be from the laboratory CBR test or directly from field CBR test. However, base soil bearing capacity can also be determined using field tests such as DCP, HCP, and Machintosh Probe [6]. These tests are much simpler and faster to perform. Correlation between the result of DCP test and CBR value, CBR test and HCP test are available whereas the prediction between the result of CBR laboratory soaked test and CBR laboratory soaked value is hardly found. Moreover, this prediction should be determined locally based on common local experience.

This research is aimed to obtain a local correlation between the results of CBR laboratory test without soaked and CBR soaked value. The correlation is based on the comparison CBR un-soaked test results and CBR soaked value which has the same fraction of sand and clay in soil

2. LITERATURE REVIEW

Proctor Compaction Test

The Proctor compaction test is a laboratory method of experimentally determining the optimal moisture content at which a given soil type will become most dense and achieve its maximum dry density. These laboratory tests generally consist of compacting soil at known moisture content into a cylindrical mould of standard dimensions using a compactive effort of controlled magnitude. The soil is usually compacted into the mould to a certain amount of equal layers, each receiving a number blows from a standard weighted hammer at a specified height. This process is then repeated for various moisture contents and the dry densities are determined for each. The graphical relationship of the dry density to moisture content is then plotted to establish the compaction curve. The maximum dry density is finally obtained from the peak point of the compaction curve and its corresponding moisture content, also known as the optimal moisture content (OMC).

The testing described is generally consistent with the American Society for Testing and Materials (ASTM) standards, and are similar to the American Association of State Highway and Transportation Officials (AASHTO)

standards. Currently, the procedures and equipment details for the standard Proctor compaction test is designated by ASTM D698 and AASHTO T99. Also, the modified Proctor compaction test is designated by ASTM D1557 and AASHTO T180 [2].

2.1 California Bearing Ratio (CBR) test

The equipment for determining CBR value is a piston having an area of three square-inches. The piston is moved in vertical direction on a soil sample with a speed of 0.05 inch/minute. A Proving ring with dial gauge is attached to the piston to measure the load at certain penetration. The CBR value is the comparison between applied piston loads on a soil sample and the standard loads, which value is expressed in percentage [2]).

Basically, the CBR value describes the strength soil compared to the standard material. Indirectly, it also describes the relative density of the soil. Several correlations between CBR values and the results of other field measurements exist such as to results of Dynamic Cone Penetrometer (DCP) test [3], [4], [5]. This has been used in practice.

A comparative study of HCP and CBR field tests has been performed by Nugroho et al. [6] on peat, sand, clayey sand and clays soil. The study was aimed to indirectly relate the value of CBR un-soaked to CBR soaked value through the comparison of the results of HCP to CBR field tests. From the point of view of testing mechanism, CBR field test and CBR laboratory test procedures are the same. CBR field test uses static penetration whereas HCP is also uses quasi-static penetration test. Compared to CBR un-soaked test, which is also a quasi-static penetration test, CBR laboratory is a closer method. Hence, direct correlation between CBR un-soaked tests results to CBR soaked value seems to be more relevant. This correlation can be based on the same soil mixture. This study aims to obtain direct local correlation between the two latest two tests.

3. MATERIALS AND METHODS

In order to obtain the correlation between CBR soaked test and CBR un-soaked test results, comparison of two kind CBR test condition of several mixture soil samples from Pekanbaru were performed. The CBR tests of two condition tests were performed for each mix-soil sample from each variation. Thus, the density before and after soaked of the soil for both tests is the same for each soil from each condition. There were 45 CBR soaked tests and 45 CBR un-soaked tests

performed at nine conditions of sand and clay mixture soil within the city of Pekanbaru, Indonesia. The result of index properties can be seen in Table 1. For index properties, soil can be classification for sand poorly graded (SP) to clay with low plasticity (CL) [7], [8]

Table 1 Properties of Materials

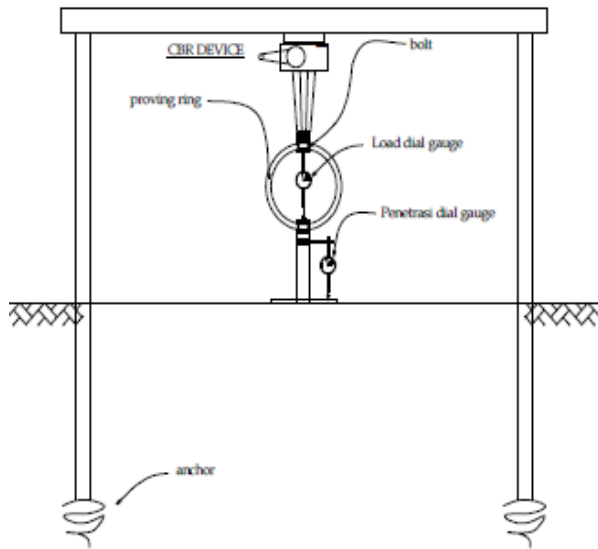
Clays	LL (%)	PL (%)	Gs	USCS
0	NP	NP	2,671	SP
30	13,58	2,43	2,677	SM
40	16,87	5,56	2,679	SM-SC
45	19,16	6,86	2,681	SM-SC
50	20,36	7,84	2,684	SC
55	20,54	7,96	2,688	CL
60	23,81	9,86	2,704	CL
70	25,63	8,32	2,699	CL
100	37,73	16,19	2,75	CL

3.1 Materials

Materials required for field tests are a set field CBR tools and a CBR mould. The CBR mould was used to obtain undisturbed sample for determination of physical and mechanical properties of the soil in laboratory and CBR mould uses to determine CBR value after soaked in the Laboratory for 7 (seven) days. Along mould containing specimen soaked, swelling of the specimen should be noted to know swelling potential of the soil from different location. Figure 1 shows the layout of CBR test in the field (un-soaked) and in the Laboratory (soaked)



a. CBR Laboratory



b. Field CBR equipment

Figure 1 Testing Equipment

3.2 Methods

Surcharge weights of 2.5kg are placed on top surface of soil. The penetration plunger is brought in contact with the soil and a load of 4kg (seating load) is applied so that contact between soil and plunger is established. Then dial readings are adjusted to zero. Load is applied such that penetration rate is approximately 1.25mm per minute. Load at penetration of 0.5, 1, 1.5, 2, 2.5, 3, 4, 5, 7.5, 10 and 12.5 mm are noted.

The CBR soaked (CBR tested in laboratory) tests were performed simply. After mould containing specimen soaked about 7 days, mould containing specimen is placed in position on the testing machine, by pressing the piston into the mould containing specimen from different locations. After that, load is applied such that penetration rate is 1.25mm per minute and then the tests were performed. For the determination of the physical and mechanical properties of the soils, undisturbed samples were taken from each location and the tests were done in laboratory.

4. RESULTS AND DISCUSSION

The results of this research are presented in three parts. First, the results of the all performed tests are described. After that regression analysis between CBR test results and filed CBR values as well as regression of fraction clay with G_s , Atterberg limits, unit weight density of the soils are shown. In the final part, the correlation between CBR soaked tests results and CBR un-soaked test results are put forward

4.1 Physical and Mechanical Properties of Test Samples

The test results of physical and mechanical properties of the samples can be divided into four categories based on the type of soils as seen in Table 2 and Table 3.

Table 2: Physical and Mechanical Properties of CBR unsoaked Test Samples

Sand (%)	Clay (%)	w (%)	γ_d (kN/m ³)	CBR (%)
100	0	7.5	16.24	12.710
70	30	10.70	20.50	34.005
60	40	11.75	20.09	14.433
55	45	12.60	19.75	14.738
50	50	12.80	19.65	13.927
45	55	12.85	19.18	13.509
40	60	14.00	19.12	13.411
30	70	14.75	18.68	13.786
0	0	14.85	16.31	4.739

Table 3: Physical and Mechanical Properties of CBR soaked Test Samples

Sand (%)	Clay (%)	w (%)	γ_d (kN/m ³)	CBR (%)
100	0	9.379	16.05	9.573
70	30	10.276	19.13	21.286
60	40	12.648	18.18	8.910
55	45	13.726	18.25	4.976
50	50	13.889	18.61	4.979
45	55	14.223	18.16	3.862
40	60	15.510	17.98	3.507
30	70	19.153	17.05	1.625
0	0	24.805	15.71	2.795

For the soils which are considered as in-organic soils (Sand, Clay, Sand-Clay mixture), in general, they have water content, w_n between 7.50–14.85%, dry unit weight, γ_d between 16.24–20.50 kN/m³. in field (un-soaked) and have water content between 9.379–24.805%, dry unit weight between 15.71–19.13kN/m³ (after soaked in laboratory). Furthermore, It was recorded that the values of CBR un-soaked tests on those soils are between 4.739–34.005% and CBR soaked values between 2.795–21.286% (see Table 2 and Table 3). It is shown that the range of the physical and mechanical properties the soils varies considerably.

As also can be seen in Table 2 and Table 3, for sand soil (sand poorly graded, SP), its properties (water content, dry unit weight, CBR value) are not different compared between soaked and un-soaked condition showing that it has a significant characteristic compared to the other samples. The

soils with clay fraction 70% and sand fraction 30% of sample CBR value is far above the maximum CBR value of all soils. The values of its dry unit weight, CBR soaked, and CBR un-soaked are far below the values of the other soils.

4.2 Regression Analysis of CBR, index properties and unit weight density

Figure 2 to Figure 4 show the results of regression analyses between clay fraction, index properties and unit weight density tests results as well as regression results between CBR un-soaked and CBR soaked test results. The regression analyses are made for each clay fraction of soils which are 0% clay, 0% sand, clay and sand and clay mixture.

It can be seen that regression using linear function suits the relation between water content and clay fraction relatively accurately whereas for the relation between Atterberg limits and clay fraction, second order polynomial function shows relatively accurate approximation. The two regression analyses will be combined later using Pearson's correlation method to find the correlation between CBR test results and Atterberg limit with unit weight density.

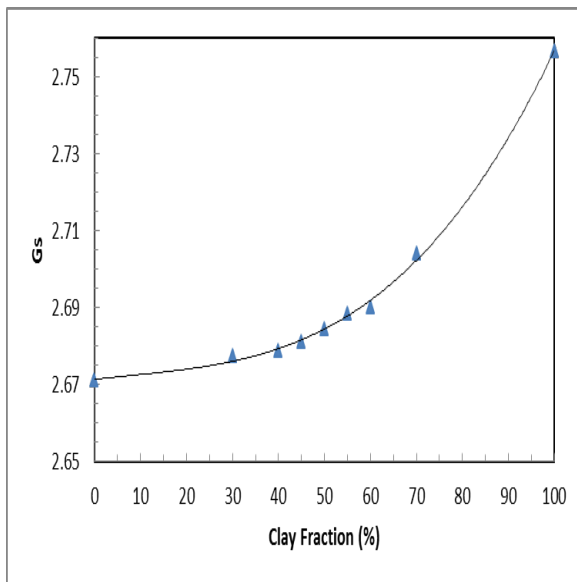


Figure 2 Regression results for Specific Gravity

Figure 3 shows that the value of liquid limit and plastic limit of soils increased with increasing clay fraction in the soil. Gradient increasing of liquid limit higher than plastic limit of soil. So, plasticity index of soils increases in proportion to the increase in soil clay fraction. Figure 3 also shows that optimum moisture content, determined from compaction test, same as with value of plastic limit at clay fraction between 30% and 70%. It means that for sand clay soils with for 30% to 70% clay fraction, water content for CBR test can be approximated by the value of the soil plastic limit.

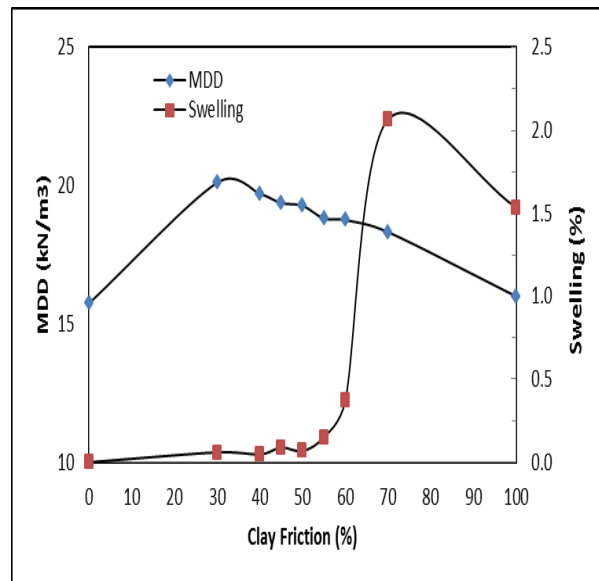
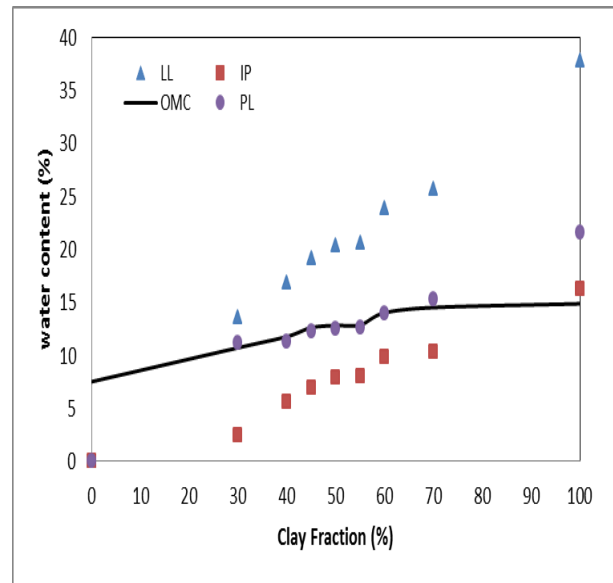


Figure 4: Regression Results for Clay

It can be seen from Figure 4 that for the clay fraction smaller than 70%, swelling is relatively smaller. Therefore, potential swelling for soil containing fine grain smaller than 70% is relatively small.

Figure 4 shows that maximum density is on a combination of 30% clay and 70% sand. In other words, it is the best composition to obtain the optimal value of CBR is in the range of 30-70% clay fraction. Fraction of clay between 30% and 70%, soil density is more than 90% of the value of density of 30% clay and 70% sand.

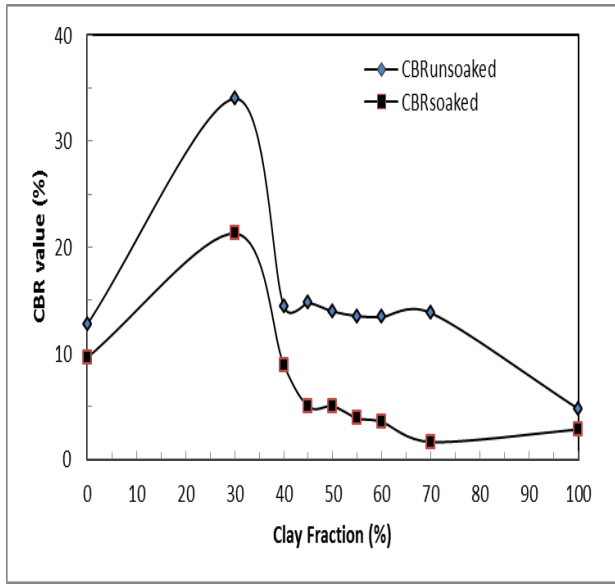


Figure 5: Regression Results for Sand-Clay Mixture

Figure 5 shows that the difference of the results of the CBR un-soaked and the CBR soaked are increase for 0% to 30% fraction of clay and then decreases again up to 45% fraction of clay. For clay fraction more than 45% difference between the CBR un-soaked and CBR soaked tend to a constant.

4.3 Correlation CBR Test Results

In the previous section, relations between Clay Fraction and index properties as well as between clay fraction and soil density have been obtained. In order to correlate the CBR un-soaked test results to CBR soaked CBR value, Pearson's correlation method is applied to both obtained power and polynomial functions for each type of soils.

On using soil index properties (liquid limit, index plasticity) and the value of unit weight density (OMC, MDD) test as variables, the following linear equation can be applied to find simple correlation between CBR soaked and CBR un-soaked on the basis of the same clay fraction value of (Nugroho, 2011)

$$\Delta Y = b_0 + b_1 X_1 + b_2 X_2 + b_3 X_3 + b_4 X_4 \quad (1)$$

with

b_0, b_1, b_2, b_3, b_4 = constants

ΔY = value of CBR un-soaked – CBR soaked (%)

X_1 = clay fraction (%)

X_2 = value of liquid limit (%)

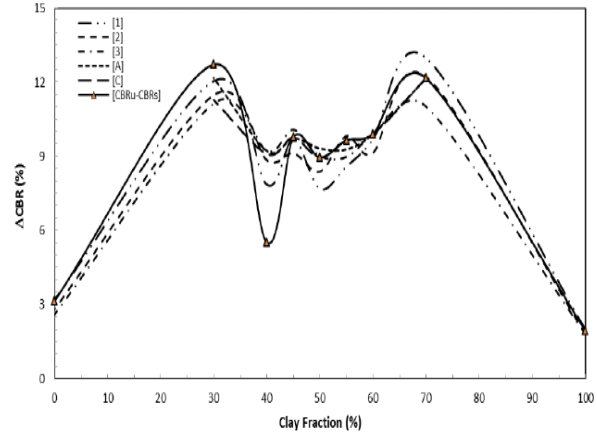
X_3 = value of plasticity index (%)

X_4 = value of optimum water content (%)

The values of the constants b_0, b_1, b_2, b_3, b_4 can be solved using SPSS software which is based on the solution of the following matrix

$$\begin{bmatrix} 9 & \sum X_1 & \sum X_2 & \sum X_3 & \sum X_4 \\ \sum X_1 & \sum X_1 X_1 & \sum X_1 X_2 & \sum X_1 X_3 & \sum X_1 X_4 \\ \sum X_2 & \sum X_2 X_1 & \sum X_2 X_2 & \sum X_2 X_3 & \sum X_2 X_4 \\ \sum X_3 & \sum X_3 X_1 & \sum X_3 X_2 & \sum X_3 X_3 & \sum X_3 X_4 \\ \sum X_4 & \sum X_4 X_1 & \sum X_4 X_2 & \sum X_4 X_3 & \sum X_4 X_4 \end{bmatrix} \begin{bmatrix} b_0 \\ b_1 \\ b_2 \\ b_3 \\ b_4 \end{bmatrix} = \begin{bmatrix} \sum \Delta Y \\ \sum X_1 \Delta Y \\ \sum X_2 \Delta Y \\ \sum X_3 \Delta Y \\ \sum X_4 \Delta Y \end{bmatrix} \quad (2)$$

It was found that value for b_0, b_1, b_2, b_3 and b_4 are -25.28, 0.168, -0.064, -2.356 and 3.562 respectively for all soils. However, for the value of a_3 , there is no unique solution for all soils



The correlation formula obtained from the correlation analyses can be written as follow:

$$\Delta CBR_{[1]} = 10.78 + 0.01C + 0.01LL - 4.41IP + 6.37OMC - 2.15MD \quad (3)$$

$$\Delta CBR_{[2]} = -25.75 + 0.34C - 0.53LL - 2.63IP + 3.81OMC \quad (4)$$

$$\Delta CBR_{[3]} = -25.91 + 0.09LL - 0.98IP + 3.80OMC \quad (5)$$

$$\Delta CBR_{[A]} = -2.25 + 2.19LL - 2.98IP - 0.76OMC \quad (6)$$

$$\Delta CBR_{[C]} = -25.28 + 0.17C - 0.06LL - 2.35IP + 3.56MC \quad (7)$$

It is found that the value of b_0 of -25, suits for equation (4), (5) and (7), clay and sand-clay mixture (in-organic soils) whereas for the solution of b_0 is for minus 25 to minus 26. The final correlation formula can be written as follow:

$$\Delta CBR = -25 + C_1 C + C_2 LL + C_3 IP + 3.5 OMC \quad (8)$$

Where C_1, C_2 and C_3 is 0.34; -0.53 and -2.63 for sand, clay and sand-clay mixture (in-organic soils). ΔCBR is the value of CBR un-soaked-CBR soaked.

For soils containing clay between 30 and 70%, the value of C_2 need to be further tested and the C_3 value is 2.35. The formula can be rewritten below.

$$\Delta CBR = -25 + 0.168 C - 0.064 LL - 2.356 IP + 3.5 OMC \quad (9)$$

4.4 Validation of the Correlation Formula

For the validation of Equation (9), several prediction tests have been performed. Figure 7a to figure 7b show the comparison between predicted values of field CBR and measured field CBR values for different soil types and soil densities.

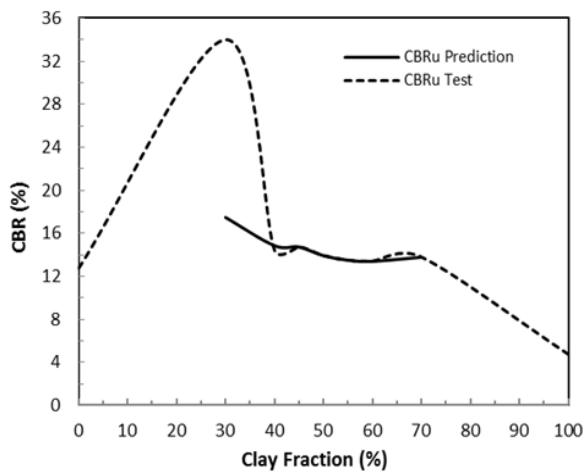


Figure 6 Predicted and Tested CBR un-soaked (30-70%)

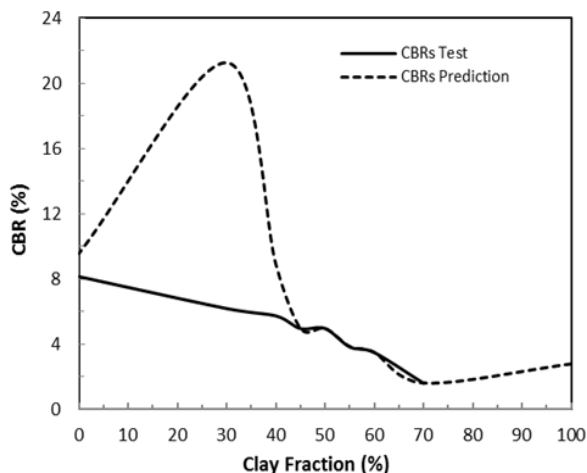


Figure 7 Predicted and Tested CBR soaked (0-70%)

It can be seen from Figure 6 to figure 7; the predicted field CBR values give significant agreements with the measured field CBR from the tests for soils that containing clay between 30% and 70%. On the other hand, very poor agreements were found for soils contain clay less than 30% and more than 70%. Hence, the local correlation formula is only valid for in-clayey sand or sandy clay.

5. CONCLUSIONS

This research has been performed to find local correlation between CBR un-soaked test results and CBR soaked values. A linear correlation has been put forward for the local correlation between the two values. Verification of the formula shows that the correlation can be used relatively accurately for predicting the difference CBR values from the

CBR with and without soaked test for in-organic soils (sand, clay and sand-clay mixture). The formula needs to be modified and further research need to be done for peat soils.

REFERENCES

- [2] Annual Book of ASTM Standards, 1997, Standard Test Method for CBR (California Bearing Ratio) of Laboratory-Compacted Soils, ASTM D1883, West Conshohocken, PA
- [9] Anonyms, 2007, In Situ Testing and Soil properties Correlation, International Conference on In Situ Measurement of Soil Properties and Case Histories, Bali, Indonesia
- [7] CRAIG, R., F., 2004, Soil Mechanic, 7th Edition, Taylor & Francis e-library, McGraw-Hill 270 Madison Ave, New York, USA.
- [8] DAS, Braja, M., 2008, Advanced Soils Mechanic, 3rd Edition, Taylor & Francis Group, McGraw-Hill 270 Madison Ave, New York, USA
- [1] FARRSHAD A, 2003, Potential Applications of dynamic and Static Cone Penetrometer in MDOT Pavement Design and application, Final Report, Department of Civil Engineering Jackson State University, Corporate Department of Transportation and US Department of Transportation Federal Highway Administration, Mississippi
- [4] KLIMOCHKO, Dennis, 1991, the Application of the Dynamic Cone Penetrometer Test in Determining In Situ Sub-grade CBR. Paper submitted for the 44th Annual Conference, Saskatoon, Western Association of Canadian Officials, Geotechnical and Materials Branch, Saskatchewan Highways and Transportation, Regina, Saskatchewan, Canada.
- [5] SMITH, R.B., and PRATT, D.N., 1983, *A Field Study of In Situ California Bearing Ratio and Dynamic Cone Penetrometer Testing for Road Design Investigations*, Australian Road Research, pp. 285-294,
- [3] VAN VUUREN, 1969, *Rapid Determination of CBR with the Portable Dynamic Cone Penetrometer*,. Reprint from "The Rhodesian Engineer".

Compressibility Characteristics of Residual Soil Subjected to Microbial Treatment

Lee Min Lee¹, Ng Wei Soon¹, and Yasuo Tanaka¹

¹Faculty of Engineering and Science, Universiti Tunku Abdul Rahman, Malaysia

ABSTRACT

Microbially induced calcite precipitation (MICP) has recently emerged as a new sustainable technique for soil improvement. The technique utilizes bio-activity to generate cement compounds into soils, and hence to improve their inherent engineering properties. This paper investigates the effectiveness of the MICP technique in improving the compressibility characteristics of a typical tropical residual soil (sandy silt). A species of *Bacillus* group bacteria, namely *B. megaterium* was used to trigger the calcite precipitation. The soil specimens were treated for three durations, i.e. 24, 48, and 72 hours. The experimental results showed that the recompression index (C_r), preconsolidation stress (p_c), and total consolidation settlement (S_c) reduced with the increased amount of calcite precipitated / MICP treatment duration. The total consolidation settlements (S_c) of the MICP treated soils were reduced by about 2-21%. The MICP treatment, however, has minimal effects on the compression index (C_c) and the coefficient of compressibility (C_v) under a high applied stress. This was probably caused by the breaking of the calcite inter-particle bonds when the soil subjected to high stresses.

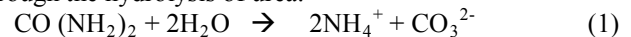
Keywords: Consolidation; microbial treatment; residual soil; calcite precipitation

1. INTRODUCTION

Microbially induced calcite precipitation (MICP) has recently emerged as a new sustainable technique for soil improvement. The calcites precipitated from bio-activity are used for cementing and clogging soil particles, and hence to improve the overall engineering performances of the soils. This technique has also shown promising applications in other construction materials, i.e. improvements of concrete strength, concrete durability [1], [2], and brick durability [3]. Despite being a relatively young technology, studies pertaining to the soil improvement through MICP had been reported by numerous researchers. DeJong et al. [4] provided an overview of potential applications of this new technique in improving the engineering properties of soil. Various microscopy techniques were used to quantitatively assess the distribution of calcite during the soil improvement. Qian et al. [5] used three types of bacteria to consolidate and cement sand grains. They found that the precipitation program was essential for obtaining an effective cementation in the sand body. Qabany et al. [6] investigated the potential factors affecting the MICP. They concluded that high chemical efficiency of MICP can be achieved by supplying a low input rate (less than 0.042 mole/liter/hr) of urea and calcium chloride. Recently, Martinez et al. [7] attempted to upscale the bio-mediated treatment process for in situ implementations. They concluded that continued research must address several challenges associated with the field implementations such as soil and pore fluid interactions,

bioaugmentation versus biostimulation of microbial communities, controlled distribution of mediated calcite precipitation, and permanence of the cementation.

Most of the current studies on MICP used microbially catalyzed hydrolysis of urea to produce calcite [8]. The bacteria suitable for this type of biological processes are of urease positive type i.e. genera *Bacillus*, *Sporosarcina*, *Spolactobacillus*, *Clostridium* and *Desulfotomaculum* [9]. The urease enzyme produced from the urease positive bacteria is responsible for decomposing urea ($\text{CO}(\text{NH}_2)_2$) through the hydrolysis of urea:



The release of ammonium (NH_4^+) increases pH, and eventually creates an ideal environment for calcite precipitation with the presence of calcium ion (Ca^{2+}) from the supplied calcium chloride:



The calcite (CaCO_3) precipitated is responsible for improving the inherent properties of soil through biocementation and bioclogging. Biocementation is defined as an improvement of soil strength by the production of particle-binding materials through microbial means, while bioclogging is the reduction of hydraulic conductivity of soil or porous rock by pore-filling materials generated by microbial processes [10]. From the foregoing, it can be concluded that most of the previous studies had focused on the biocementation and bioclogging of sand grains [4] - [6], [8]. Attempts on other types of soils i.e. silty or clayey soils are still very limited. Besides, the efficiencies of MICP soil improvements were usually quantified by the measurements of calcite precipitated, shear wave velocity, or direct measurements of unconfined compressive strength and permeability. The effect of MICP on other engineering properties of soil such as

compressibility characteristics had never been reported in the previous studies. To address these research gaps, this paper attempts to investigate the compressibility behaviours of a MICP treated silty residual soil through one-dimensional consolidation tests.

2. MATERIALS & METHODS

2.1 Type of Bacteria

The urease-producing bacterium used in this study was *B. megaterium* ATCC 14581. The bacterium has a diameter of about 2 - 5 μm .

2.2 Cementation Reagents

Cementation reagents serve as important ingredients for promoting calcite precipitation. As shown in the equations (1) and (2), the ammonium (NH_4^+) and calcium (Ca^{2+}) ions are decomposed from urea ($\text{CO}(\text{NH}_2)_2$) and calcium chloride (CaCl_2), respectively. It is thus important to supply sufficient amounts of urea and calcium chloride into the soil to promote effective MICP. In the present study, the concentration of cementation reagents was fixed at 0.5 M [6]. The cementation reagents also contained 3 g nutrient broth, 10 g NH_4Cl , and 2.12 g NaHCO_3 per litre of deionized water [11].

2.3 Soil Materials

The soil specimens used in the present study was a typical silty residual soil retrieved from a site in Kuala Lumpur, Malaysia. The soil has particle sizes ranging from clay fraction to 2 mm. Rebata-Landa [12] suggested that the most optimum range of grain size for the bio-cementation process is between 50 and 400 μm as bacterial activity cannot take place in very fine soils, while large amounts of calcites are required to promote effective improvements in the very coarse soil. In the present study, 32% of the residual soil particles fall within the range of 50-400 μm . Table 1 tabulates the physical properties of the soil.

2.4 Apparatus Setup

Fig. 1a shows the schematic diagram of the apparatus setup for the MICP treatments. The apparatus consisted of a steel mould of 50 mm in diameter and 170 mm in length (Fig. 1b), an air compressor, a pressure tank, and an effluent collector. The air compressor and pressure tank was used to control the flow pressure of the cementation reagents at approximately 1 bar.

2.5 MICP Treatment Procedures

To perform the MICP soil improvement, the bacteria were first cultivated in nutrient broth to a concentration of 1×10^8 cfu/ml (optical density of 3.3). The bacteria were then mixed with soil specimens and compacted into the prefabricated steel mould at a dry density of about 1519 kg/m^3 (90% of maximum dry density). The treatment commenced by supplying the cementation reagents into the soil specimen at room temperatures (ranging from 25 to 30 $^\circ$). Upon the completion of the treatment, the soil was extruded from the steel mould, and was fitted into the standard oedometer ring of same diameter. The consolidation test was then carried out in accordance to the British Standard (BS1377-Part 5).

2.6 Experimental Variables

The main variable in this study was treatment duration. Three treatment durations were adopted, i.e. 24, 48, and 72 hours. It was hypothesized that longer treatment duration would promote more calcite precipitations, and thus the compressibility characteristics of the soil for different amounts of calcite can be assessed.

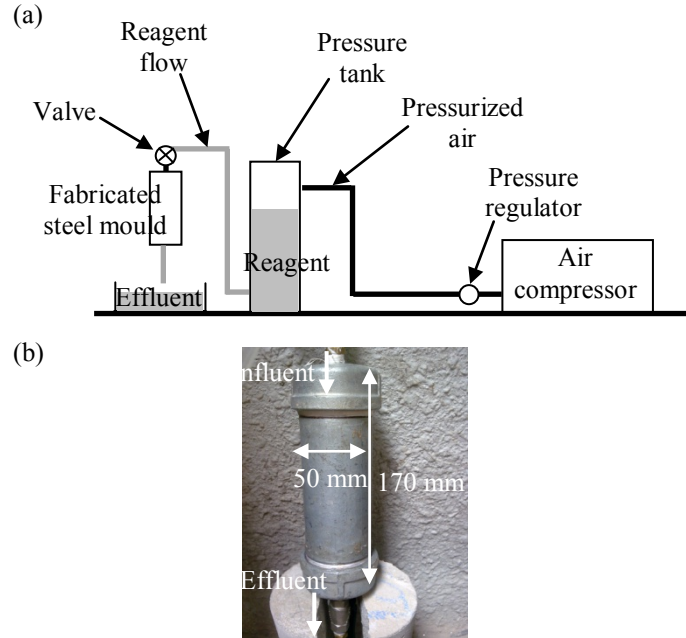


Fig. 1(a) Schematic diagram of the apparatus setup; (b) Photograph of the fabricated mould

Table 1 Original Soil properties

Properties	Indices
Grain size	0% Gravel, 38% Sand, 43% Silt, 19% Clay
Liquid limit	40.4%
Plastic limit	24.9%
Maximum dry density	1688.5 kg/m^3

3. RESULTS AND DISCUSSIONS

3.1 Calcite contents

Fig. 2 shows the correlations between treatment duration and calcite precipitated. Acid-treatment weight loss technique was employed to determine the carbonate content in the soil specimens. The carbonate content that existed naturally in the original soil was 0.67%. The increment in the carbonate contents upon the MICP treatments can be safely assumed to be caused by the calcite (Calcium carbonate) precipitation. The calcite content was found to increase proportionally with the treatment duration up to 48 hours. Beyond this duration, the amount of calcite precipitated was negligible. A plausible explanation to this observation is that the pore throats might be clogged by the calcite precipitated resulting in lesser cementation reagents flowing through the soil column. The cementation reagents also contained nutrients for the bacteria.

The lack of nutrient supplies may create an unfavorable environment for the bacteria to sustain the calcite precipitation.

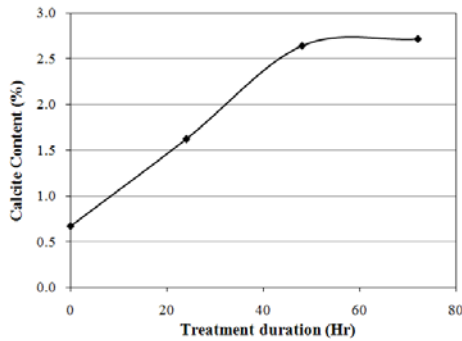


Fig. 2 Correlation between treatment duration and amount of calcite precipitated

3.2 Compressibility Characteristics of Soils

The compressibility characteristics of the soils were evaluated through the following four parameters: (1) compression index (C_c) and recompression index (C_r) that explains the relation between applied stress and amount of consolidation, (2) preconsolidation stress (p_c) that explains the consolidation status of soil, (3) total consolidation settlement (S_c) that indicates the absolute value of settlement, and (4) coefficient of consolidation (C_v) which explains the time rate of consolidation.

Fig. 3 shows the plotting of void ratio (e) versus stress in logarithm scale ($\log p$) for the residual soils subject to various MICP treatment durations. The values of all the compressibility characteristics are summarized in Table 2. The results showed that there was no consistent relationship between the C_c values and the amounts of calcite precipitated / treatment duration. The C_c values were in the range of 0.175 – 0.195, indicating that the effect of MICP treatment on the C_c value was of minimal. On the contrary, the C_r values were significantly reduced (from 0.130 to 0.076) by the MICP treatments. The higher the amounts of calcite precipitated, the lower the C_r value. Similar trends were observed for the p_c and S_c values. These observations can be explained by the calcite bonding between the soil particles. Upon the MICP treatment, the stiffness of soil was enhanced through the formations of calcite bonds. As the result, the amount of consolidation was reduced when the soil was subjected to a low stress (lower than p_c), and hence yielded a lower C_r value. However, the calcite bonds were insufficiently strong to resist a high stress (higher than p_c). Consequently, the breaking of the calcite bonds caused the soil to behave like its original untreated state. This explained the minimal effect of the MICP treatment on the C_c value. The total consolidation settlement, S_c of the MICP treated soils were reduced by about 2 – 21% compared to the original soil. The reductions in the S_c were mainly attributed to the reductions in the C_r values.

To evaluate the coefficient of consolidation (C_v), the deformation of soil (δ) was plotted against square root of time (\sqrt{t}) under a stress lower than p_c (i.e. 25 kPa), and a stress higher than p_c (i.e. 400 kPa), as shown in Fig. 4a and 4b, respectively. The coefficient of consolidation (C_v) of soil was

estimated using the Taylor's square root of time method [13]. Under the stress condition of lower than p_c , the dissipation rate of excess pore-water pressure in the MICP treated soils were faster than that of the original soil. The coefficient of consolidation (C_v) increased with the increased amounts of calcite precipitated / treatment durations. This phenomenon can be attributed to the higher stiffness of the MICP treated soils compared to the original soil [14]. It is worth noting that the permeability of the MICP treated soils might be reduced through bioclogging, and eventually causes a reduction in the dissipation rate of the excess pore-water pressure. However, it is believed that the significant increment in the soil stiffness associated to the formations of calcite bonds has outperformed the factor of reduced permeability. Under the stress condition of higher than p_c , the improvements in the C_v values were negligible. These observations can again be explained by the breaking of the calcite bonds under the high applied stresses.

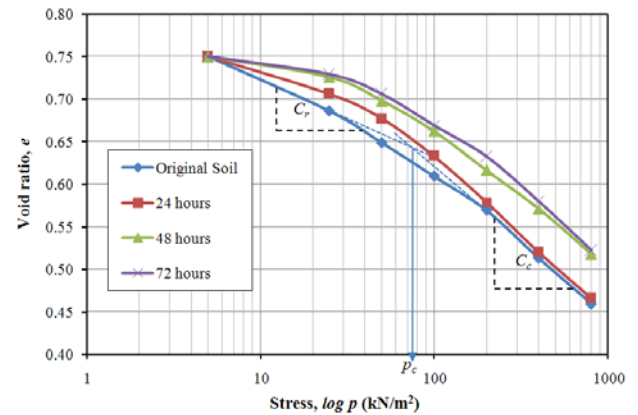


Fig. 3 Void ratio (e) versus stress in logarithm scale ($\log p$)

Table 2 Compressibility characteristics of soils

Compressibility characteristics	Treatment Conditions			
	Original	24 hrs	48 hrs	72 hrs
Compression index, C_c	0.187	0.195	0.175	0.182
Recompression index, C_r	0.130	0.098	0.079	0.076
Preconsolidation stress, p_c (kN/m ²)	72	52	42	42
Total consolidation settlement, S_c (mm)	3.22	3.15	2.60	2.55
Coefficient of consolidation, C_v (mm ² /min):				
@ 25 kPa	85	133	236	236
@ 400 kPa	85	105	94	94

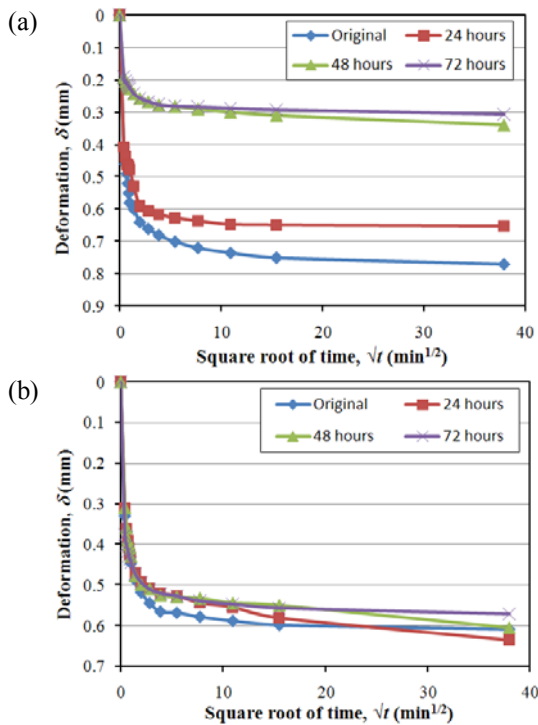


Fig. 4 Deformation versus square root of time under the applied stresses of (a) 25 kPa, (b) 400 kPa

4. CONCLUSION

This paper presents experimental works to investigate the effectiveness of MICP treatment in improving the compressibility characteristics of a typical residual soil. The following conclusions can be drawn from this study:

- i) The calcite content increases proportionally with the treatment duration up to 48 hours. Beyond this duration, the amount of calcite precipitated is negligible. This can be attributed to the lack of cementation reagents and nutrients flowing through the soil column due to bioclogging.
- ii) The recompression index (C_r), preconsolidation stress (p_c), and total consolidation settlement (S_c) reduce with the increased amounts of calcite precipitated / treatment durations. The total consolidation settlements (S_c) of the MICP treated soils are reduced by about 2-21%.
- iii) Under a low applied stress (lower than p_c), the coefficient of consolidation (C_v) increased significantly with the increased amounts of calcite precipitated / treatment durations. This can be explained by the enhanced stiffness of the MICP treated soils.
- iv) The effects of MICP treatments on the compression index (C_c) and the coefficient of consolidation (C_v) under a high applied stress are negligible. This is probably caused by the breaking of the calcite bonds under high stresses.
- v) Future studies may be carried out by applying unloading and reloading cycles to further investigate the effect of cementation on the soil compressibility after large loading. Comparisons may also be made between the compressibility behaviours of the MICP treated soils and the natural aged clay.

5. ACKNOWLEDGMENT

This work is financially supported by the Ministry of Higher Education, Malaysia under Fundamental Research Grant Scheme, FRGS.

6. REFERENCES

- [1] De Muynck W, Debrouwer D, De Belie N & Verstraete W, "Bacterial carbonate precipitation improves the durability of cementitious materials," *Cem. Concr. Res.*, vol. 38, 2008, pp. 1005-1014.
- [2] Achal V, Pan X & Özyurt N, "Improved strength and durability of fly ash-amended concrete by microbial calcite precipitation," *Ecol. Eng.*, vol. 37, 2011, pp. 554-559.
- [3] Sarda D, Choonia H, Sarode D & Lele S, "Biocalcification by *Bacillus pasteurii* urease: a novel application," *J. Ind. Microbiol. Biotechnol.*, vol. 36, 2009, pp. 1111-1115.
- [4] Dejong JT, Mortensen BM, Martinez BC & Nelson DC, "Bio-mediated soil improvement," *Ecol. Eng.*, vol. 36, no. 2, 2010, pp. 197-210.
- [5] Qian C, Pan Q & Wang R, "Cementation of sand grains based on carbonate precipitation induced by microorganism," *Sci. China Technol. Sci.*, vol. 53, 2010, pp. 2198-2206.
- [6] Al Qabany A, Soga K & Santamarina JC, "Factors affecting efficiency of microbially induced calcite precipitation", *ASCE Journal of Geotechnical and Geoenvironmental Engineering*, In Press, 2012.
- [7] Martinez BC, Barkouki TH, DeJong JT & Ginn TR, "Upscaling of microbial induced calcite precipitation in 0.5m columns experimental and modeling results," *Geo-Frontiers*, 2011, pp. 4049-4059.
- [8] van Paassen LA, Daza CM, Staal M, Sorokin DY, van der Zon W & van Loosdrecht Mark CM, "Potential soil reinforcement by biological denitrification," *Ecol. Eng.*, vol. 36, 2010, pp. 168-175.
- [9] Kucharski ES, Cord-ruwisch R, Whiffin V & Al-thawadi SM, "Microbial biocementation," *United States Patent*, 2008.
- [10] Ivanov V & Chu J, "Applications of microorganisms to geotechnical engineering for bioclogging and biocementation of soil in situ," *Rev. Environ. Sci. Biotechnol.*, vol. 7, 2008, pp. 139-153.
- [11] Al Qabany A, Mortensen B, Martinez BC, Soga K & DeJong JT, "Microbial carbonate precipitation correlation of S-wave velocity with calcite precipitation," *Geo-Frontiers*, 2011, pp. 3993-4001.
- [12] Rebata-Landa V & Santamarina, JC, "Mechanical limits to microbial activity in deep sediments," *Geochemistry, Geophysics, Geosystems*, vol. 7, no. 11, 2006, pp. 1-12.
- [13] Taylor DW, *Fundamentals of soil mechanics*. New York: John Wiley & Sons Inc., 1948.
- [14] Yin JH & Fang Z, "Discussion on Physical modeling of consolidation behavior of a composite foundation consisting of a cement-mixed soil column and untreated soft marine clay," *Geotechnique*, vol. 56, No. 8, 2006, pp. 579-582.

Strength and aging of cement treated low plastic soils

Fabien Szymkiewicz¹, Antoine Guimond-Barrett², Alain Le Kouby¹, Philippe Reiffsteck¹, and Sonia Fanelli¹

¹IFSTTAR / Université Paris-Est, France

²IFSTTAR / Université du Havre, France

ABSTRACT

Deep mixing is a method frequently used for various applications ranging from ground improvement and confinement to foundations. With the increase of the use of deep mixing for foundations, it is imperative to better define the mechanical behaviour and ageing of the material, which depends on the cement content and grain size distribution. This study aims to quantify the impact of these parameters as well as the percentage of fines on the mechanical behaviour of the mixed material. A number of unconfined compression tests were carried out. The results showed that it was possible to predict the strength of the mixed material after seven and 28 days of curing, based on the cement content and the percentage of fines.

Keywords: deep soil mixing, unconfined compression tests; mechanical behaviour; sand, cement

1. INTRODUCTION

Initially, the main purpose of deep soil mixing was to improve the stability and reduce settlements of structures such as embankments on soft soils of low shear strength or very high moisture contents [1]. These days, improving the strength and deformation properties as well as the permeability of very soft soils by deep soil mixing is a frequently used stabilization method, and the interest in the use of this technique not only for soft soils stabilization but also to construct temporary foundation/structural (load bearing) elements [2] and excavation retaining walls is increasing, as the execution is easier and less costly than traditional methods.

Deep mixing is an all-purpose term for a large number of techniques in which binding agents are mechanically dispersed within the soil in slurry form. The amount of cement used in soil stabilization is usually much lower than the amounts used for the construction of structural elements. Consequently, the cement content varies largely from one application to another, ranging from 50 to 500 kg per cubic meter of soil. However, no binder content methodology has yet been accepted, even if a large number of studies using cement as well as industrial by-products such as wastepaper sludge ash, pulverised fuel ash, etc. have been carried out ([3]; [4]; [5]).

Sandy soils, that simplify the distribution of cement [6], are the most suitable for new applications of deep mixing, as the created material can be compared to a mortar, although with a higher water content. However, grain size distribution influences the unconfined compression strength as it seems that the smallest 25% to 40% of particle size controls the mechanical behaviour of soils ([7]; [8]; [9]).

Furthermore, even if laboratory tests are the usual tests

carried out in feasibility studies for soil mixing projects and if a large number of factors (such as the binder and soil nature as well as the mixing and curing conditions) are known to influence the strength and deformation properties of the treated soils [10], no international standard exists for the preparation of treated soil specimens in the laboratory [11]. It is therefore difficult to compare results from differences sources of the literature.

This communication focuses on the mechanical properties of non-plastic sandy soils stabilized with cement to create self-compacting mixes simulating the deep mixing process. The objectives of this research were to evaluate and compare the effects of time, cement content and grain size distribution on strength of sandy soils when mixed in the laboratory with portland blastfurnace cement. Correlations and mathematical relations between different parameters such as strength, cement and fine content are presented, enabling the final design strength to be predicted, depending on the cement content and the grain size distribution.

2. EXPERIMENTAL PROGRAM

2.1 Materials

The soils used in the testing were obtained from different regions of France, depending on the availability of test sites: Fontainebleau sand, which is a French reference sand, comes from the south of Paris. Triel sand comes from the west of Paris and Fréjus sand comes from the south of France, where in situ soil-mixing tests were carried out [2].

Fontainebleau sand is a sub-rounded silicate sand which has a uniform grain size distribution with no fines. Silica flour is an artificial soil created by crushing Fontainebleau sand, and was used in this research to study the influence of high fine content on the strength of the soil mixing material, by using it pure and also mixing it with Fontainebleau sand. Triel and

Fréjus sands, which are also silicate sands, show distributions that are more widely spread and contain 3% and 10% of fines respectively. Grain size distributions of all the soils are shown in Fig 1.

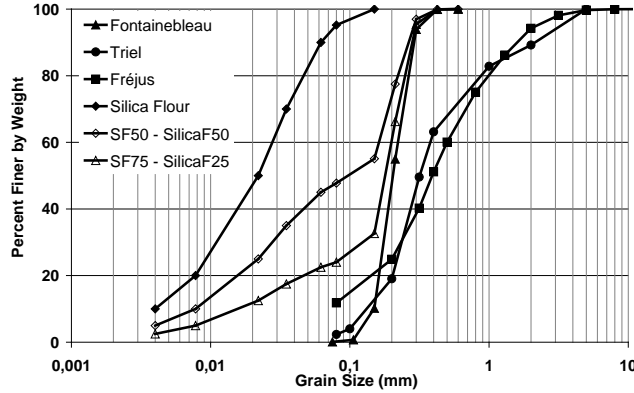


Fig. 1: Grain size distribution of the soils

These soils present Methylene Blue Values ranging from 0 (Fontainebleau sand) to 0.2 (Fréjus), showing the low content of clay particles.

The cement used for this experimental program is a Portland blastfurnace cement containing 85% ground granulated blast furnace slag, with the rest Portland clinker and a little gypsum (European classification: CEM III/C 32,5 N CE PM-ES NF 'HRC') [12].

2.2 Mixing, moulding and storage procedure

The cement content C was chosen to cover the complete range of French soil mixing applications (from ground improvement to structural elements), i.e. from 70 to 400 kg/m³. Cement contents and equivalences are presented in Table 1.

Table 1: Cement equivalences

C (kg/m ³)	C (%)
70	4.2
140	8.4
210	12.7
265	16
320	19.4
400	24.2

The water content w was chosen to attain a sufficient workability, i.e. to ensure that the material was fluid enough to be poured in the moulds and be self-compacting.

The preparation and conservation method of the specimens is described in a few words here. More details can be found in [13]. Soil and cement were first thoroughly dry-mixed manually, in order to obtain a uniform consistency. This premix was then put in the Hobart mixer and water was added. The amount of water was calculated based on the target water content of the mixes, i.e. 19% for the pure sands. After waiting three minutes to ensure complete wetting of the materials, the mixing process could now begin: five minutes in the mixer with constant intervention of the operator. The mix was then poured into cylindrical moulds of 52 mm

diameter, and, to avoid air bubbles in the specimens, were rodded and tapped. References [14] and [15] showed this moulding method gives the best homogeneity and continuity (and hence compression strength) to the samples. The moulds were capped, and sealed in a hermetic bag containing a high relative humidity. These were stored at a temperature of $20 \pm 3^\circ\text{C}$ until their testing day (7, 14, 21, 28, 56 and 90 days).

2.3 Unconfined compression tests

The samples were taken out of the moulds the day of the test. They were then cut and smoothed to create plan and parallel end surfaces. They were measured and weighed, then tested for their unconfined compressive strength (q_u). Three specimens were tested at each curing time. The mean value of these tests is presented in this paper. In cases of clearly deviating results, an additional specimen was tested.

3 RESULTS AND ANALYSES

It has been observed that as expected the cement content has a great effect on the strength of these sand–cement mixtures. A small difference in cement content has a significant impact on the performance of the soil–cement mixing.

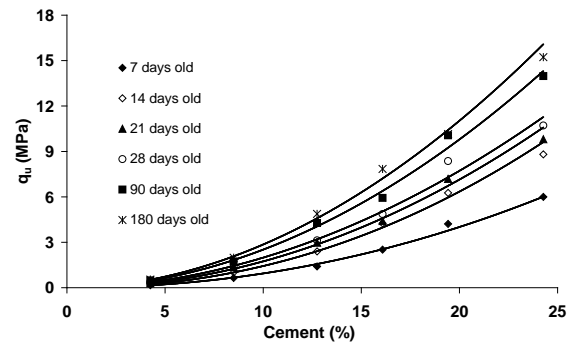
Reference [16] proposed a power function, defined by Eq. (1), as the most adapted to fit the experimental relation between the unconfined compression strength (q_u) and the cement content (C).

$$q_u = a \times C^b \quad (1)$$

where a is a parameter expressed in kPa and b a dimensionless parameter. Both are experimental parameters.

Fig. 2a and 2b show the relationships between q_u and C for Fontainebleau sand and the Silica Flour. Again, the best fit curves follow a power function. However, the curvature is not the same, depending on the type of sand and age. The results show the same pattern for the Fréjus and Triel sands.

The power function is the best fit for the range of cement contents tested (up to 25%, which is close to the maximum cement content used for deep mixing applications). However, it is clear that should C increase drastically, a plateau would be reached, then a decrease of strength would appear, meaning that the power function would no longer be the best fit.



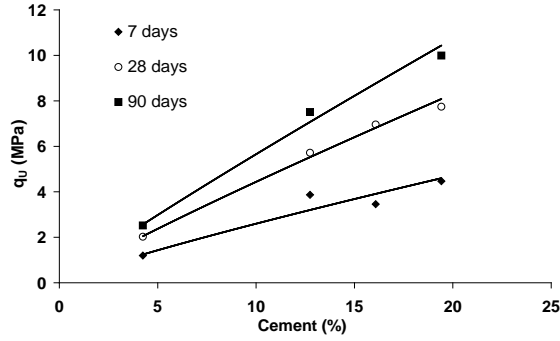


Fig. 2: Evolution of the q_u -C relationship with time for (a) Fontainebleau sand and (b) silica flour

Whereas the mixtures made with pure Fontainebleau sand do not show a noticeable change of the values of parameters a and b (with a increasing from 7 to 28 and b decreasing from 2.15 to 1.96 between 7 and 90 days of curing), comparatively, the Triel and Fréjus mixtures show a significant variation for those two parameters with time, with a increasing from 30 for both sands to 1144 for Triel and to 210 for Fréjus, and with b decreasing from 1.8 to 0.9 and from 1.5 to 1.17 for Triel and Fréjus respectively. For the mixtures containing silica flour, a increases significantly with time, whereas b is relatively stable.

The decrease of b with time means that the effect of the cement content decreases for older ages.

A clear linear relation in a semi logarithmic plan between the parameters a and b exists after 7 days of curing (Fig. 3). Eq. (2) describes the relationship between a and b after seven days of curing.

$$b_7 = -0.3145 \ln a_7 + 2.7097 \quad (2)$$

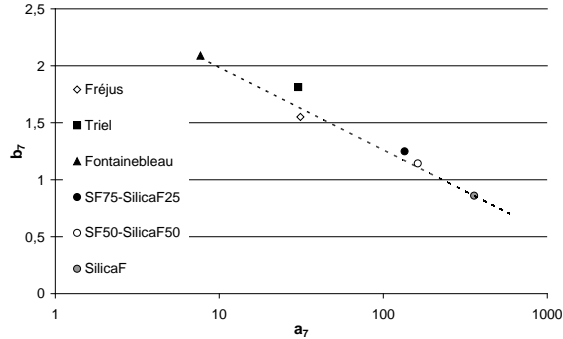


Fig. 3: Parameter b_7 as a function of parameter a_7

Therefore, it is possible to produce a formula (Eq. (3)) linking q_u to C with only b_7 as an experimental parameter:

$$q_u = e^{8.616} \times e^{b_7(\ln C - 3.18)} \quad (3)$$

Introducing the fines content C_{63} (63 μ m is a common threshold extensively used in earthworks to separate fine from coarse particles [17], it is possible to find a relation between b_7 and the percentage of fines (Eq. (4)).

$$b_7 = -0.1711 \times \ln C_{63} + 1.7767 \quad (4)$$

Fig. 4 shows the relationship between b_7 and the percentage of fines C_{63} .

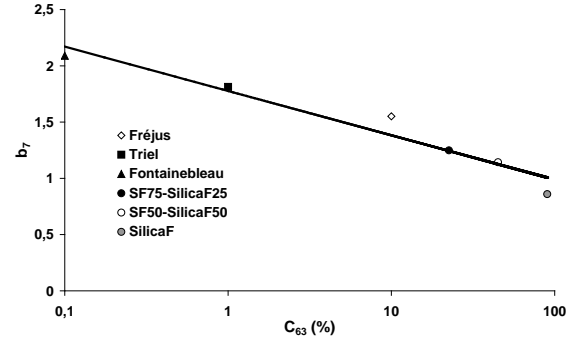


Fig. 4: Relation between C_{63} and b_7

It is therefore possible to propose a formula allowing the designer to estimate the strength of stabilised granular soils based on the cement content and the percentage of fines (Eq. (5)).

$$q_{u7} = 19.428 \times C^{1.777 - 0.171 \ln C_{63}} \times C_{63}^{0.544} \quad (5)$$

This formula gives compression strength after 7 days of curing. Fig. 5 and Eq. (6) show the good correlation between the laboratory results and the values given by Eq. (5).

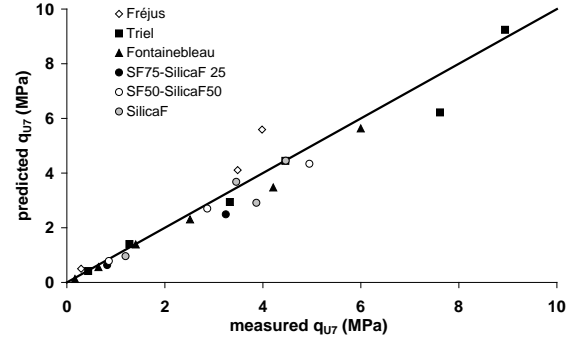


Fig. 5: Predicted q_{u7} versus measured q_{u7}

$$q_{u7 \text{ predicted}} = 0.96 \times q_{u7 \text{ measured}} \quad (6)$$

We have established that it is possible to predict the strength after 7 days of curing for a non-plastic granular soil, depending on the content of cement and fines. This is valuable as contractors have a need to determine the strength of the material as quickly as possible (so as to be able to readjust the cement content for example). However, for design purposes, it is often the unconfined compression strength at 28 days that is taken into account; therefore it is important to be able to predict this strength.

Reference [18] showed that q_{u28} is by no means the highest achievable strength, and that it depends from the grain size distribution of the soil. Therefore, considering q_{u28} equal to 2 times q_{u7} for purpose design as estimated by [6] can be dangerous. In our case, doing so leads to an overestimation of q_{u28} by almost 10%. On the contrary, it was shown by [18] that the highest achievable strength is at least equal to 2 times q_{u7} , for treated sandy soils.

Looking closer to the shape of the typical curves presenting the strength as a function of time, we observe that the relation linking these parameters follows a logarithmic function (Eq. 7)

$$q_{u_i} = g \times \ln(t) - h \quad (7)$$

Where g and h (in kPa) are experimental parameters. Reference [19] showed that the values of these parameters are in general close to each other, and directly related to q_{u7} . We can then propose the following formula (Eq. 8)

$$q_{u_i} = \beta \times q_{u7} \times (\ln(t) - 1) \quad (8)$$

With β an experimental coefficient to be determined, and implicitly taking into account the water and cement content. During the curing process, the only known variable value is the water content, which decreases. Reference [20] proposed a formula enabling us to estimate the final water content of the mix (Eq. 9).

$$w_f = \frac{\rho_{soil} \times \frac{w_n}{w_n + 1} - k \times \frac{C}{1000}}{\rho_{soil} \times \frac{1}{w_n + 1} + (1 + k) \times \frac{C}{1000}} \quad (9)$$

Where w_n is the initial water content and k the non evaporable water content, equal to 0.23. Considering that the parameter β is equal to the ratio final water content w_f on initial water content w_i , we have the following formula (Eq. 10).

$$q_{u_i} = \frac{w_f}{w_i} \times q_{u7} \times (\ln(t) - 1) \quad (10)$$

Finally, Fig. 6 shows the comparison between the strength measured after 28 days of curing and the strength at 28 days calculated from the Eq. 11, which combines Eq. 5 and Eq. 10: the precision is very good ($R^2 = 0.88$) with an underestimation of the laboratory results of about 6 %.

$$q_{u_i} = \frac{w_f}{w_i} \times 19.428 \times C^{1.777 - 0.171 \ln C_{63}} \times C_{63}^{0.544} \times (\ln(t) - 1) \quad (11)$$

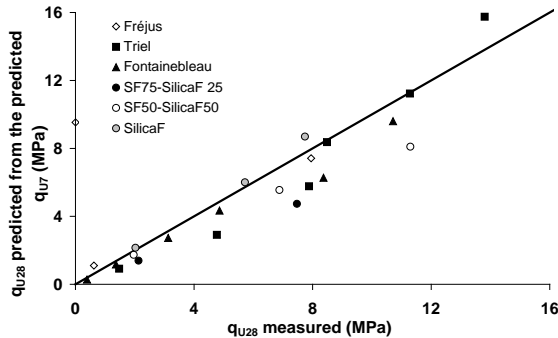


Fig. 6: q_{u28} predicted with Eq. (5) and (10) versus q_{u28} measured in the laboratory

It is then possible to predict the strength of the Deep Mixing material made of a non-plastic sandy soil and cement, knowing only the fine content C_{63} of the soil, the target cement content C (%), and the initial and final water contents w_i and w_f of the Deep Mixing material.

4 CONCLUSIONS

This communication focused on granular materials to study the influence of fines and cement content on the mechanical

strength of the cement mixed materials.

This study has shown that the mix strength depends on the cement content, following a power relationship. In addition, the exponent depends directly on the soil fines content: the cleaner the sand, the higher the value. It seems that the upper limit of the value of this parameter is around 2.1 and the lower limit is 0.8.

By studying six granular soils, we have proposed a formula to predict a cement treated granular soil q_{u7} solely from the cement content and the parameter C_{63} .

Finally, a formula to predict 28-day strength is proposed, based on strength after seven days of curing, with very satisfactory accuracy. We are therefore able to predict 28-day strength of a granular soil treated with cement knowing only soil particles size and the cement content used. The results were not compared to other authors' results due to differences in the preparation method. In particular, compaction is a big issue. However, the relationship linking q_u to C is always a power function for the range of applications concerned. Therefore, the formula simply needs to be reviewed for compacted Soil Mixing applications, taking into account the compaction energy.

This formula needs now to be tested in situ. However, it should not be a big issue to transpose it for on sites mixes, as the sandy soils are the easiest soils to mixes, with a smaller number of inclusions [18] and a ratio in situ / laboratory with a value near one [20]. Hence, this is a real advance for practitioners, when encountering non to low plastic soils. It is now important to study the influence of plastic fines on strength and aging.

5 ACKNOWLEDGMENT

The authors would like to thank Soletanche-Bachy for funding this research.

6 REFERENCES

- [1] CDIT. The Deep Mixing Method – Principle, Design and Construction. The Netherlands. 2002. A.A. Balkema Publishers.
- [2] Rocher-Lacoste, F., Le Kouby, A., Szymkiewicz, F., Lechevallier, S., & Fraysse, B. "The soil-cement column, an alternative foundation and soil improvement method: static load tests". 11th International Conference. Geotechnical Challenges (ICGC) in Urban Regeneration, DFI 2010.
- [3] Ahnberg, H., & Johanson, S.-E. "Increase in strength with time in soils stabilised with different types of binder in relation to the type and amount of reaction products". Deep Mixing '05, 2005 pp. 195–202.
- [4] Bujulu, P.M., & Grimstad, G. "An innovative binder study and constitutive model for deep-mix stabilized quick clay". Deep Mixing '09, 2009.
- [5] Jegandan, S., Liska, M., Osman, A.A.-M., & Al-Tabbaa, A. "Sustainable binders for soil stabilization". Journal of Ground Improvement, 163, 2010, pp 53–61.

- [6] Topolnicki, M. "Chapter 9: In situ soil mixing". Ground Improvement M.P.M.K. Kirsch (Ed.), Abingdon, UK: Spon Press, 2004, pp. 331–423.
- [7] Kawasaki, T., Niina, A., Saitoh, S., Suzuki, Y., & Honjo, Y. "Deep mixing method using cement hardening agent". 10th International Conference on Soil Mechanics and Foundation Engineering, 1981, pp. 721–724.
- [8] Lade, P.V., Liggio, C.D., & Yamamuro, J.A., "Effects of non-plastic fines on minimum and maximum void ratio of sand". Geotechnical Testing Journal, 21, 1998, pp 336–347.
- [9] Reiffsteck, P. "Influence de la répartition granulométrique sur le comportement mécanique d'un sol". Bulletin de liaison des laboratoires routiers des Ponts et Chaussées, 268–269, 2007, pp 83–103.
- [10] Terashi, M. "Theme lecture: deep mixing method – brief state of the art". 14th International Conference on Soil Mechanics and Foundation Engineering, 1997, pp. 2475–2478.
- [11] Kitazume, M., Nishimura, S., Terashi, M., & Ohishi, K. "International collaborative study task 1: investigation into practice of laboratory mix tests as means of QC/QA for deep mixing method". Deep Mixing '09, 2009.
- [12] CEN. "Cement – Part 1: Composition, specifications and conformity criteria for common cements". EN 197–1, 2005.
- [13] Szymkiewicz, F., Le Kouby, A., Reiffsteck, P., & Fanelli, S. "Influence de la granulométrie sur la résistance à la compression d'un sol-ciment: comparaisons entre deux sols". AUGC, 2010, pp. 82–92.
- [14] Ahnberg, H., & Holm, G. "Influence of laboratory procedures on properties of stabilized soil specimens". Deep Mixing '09, 2009.
- [15] Kitazume, M., & Nishimura, S. "Influence of specimen preparation and curing conditions on unconfined compression behaviour of cement-treated clay". Deep Mixing '09, 2009.
- [16] Consoli, N.C., Caberlon Cruz, R., Floss, M.F., & Festugato, L. "Parameters controlling tensile and compressive strength of artificially cemented sand". Journal of Geotechnical and Geoenvironmental Engineering, 136, 2010, pp 759–763.
- [17] AFNOR. "Geotechnical investigation and testing – Identification and classification of soil Part 1: identification and description". NF EN ISO 14688–1, 2003.
- [18] Szymkiewicz, F. "Evaluation des propriétés mécaniques du matériau Soil-Mixing" (PhD Thesis). 2011.
- [19] Guimond-Barrett, A., Szymkiewicz, F., Reiffsteck, P., Pantet, A, Le Kouby & A., Guédon, S. "On the strength and durability of cement-stabilised sands". International Symposium on Recent Research, Advances & Execution Aspects of Ground Improvement Works, 2012, Volume II, pp 345-354.
- [20] Ahnberg, H., Johanson, S.-E., Pihl, H., & Carlsson, T. "Stabilising effects of different binders in some Swedish soils". Ground Improvement, 7, 2003, pp 9–23.
- [21] PWRC. "Technical manual of deep mixing with special reference to on land applications". Public Works Research Center [in Japanese], 1999.

Performance Of Cantilever Sheet Pile Supporting Excavation Adjacent To Strip Footing

Yousry M. Mowafe 1, Ahmed M. Eltohamy 2 and Ahmed A. Mohamed 3

1 Professor of Geotechnical Eng., Faculty of Engineering, Azhar Univ., Egypt.

2 Associate Professor of Geotechnical Eng., Faculty of Engineering, Beni Suafe Univ., Egypt.

3 Assistant Professor of Geotechnical Eng., Faculty of Engineering, Azhar Univ., Egypt.

ABSTRACT

Ground movements induced from excavations are a major cause of deformation and damage to the adjacent foundations and utilities. A numerical prototype model has been verified by analyzing the results of an experimental model. The influence of foundation depth and distance from the excavation on straining actions and deformation of sheet pile and strip foundation were investigated. The lateral deformation of the cantilever retaining sheet pile wall and the accompanied vertical settlement of adjacent foundation nearly vanished as the excavation was shifted far away from the foundation by a distance equal to or more than 1.5 times excavation depth in both medium and dense sand. As the ratio between adjacent foundation depth to excavation depth increases a corresponding decrease in straining actions on retaining sheet pile and settlement of foundation occurs. Differential settlement of strip foundation adjacent to excavation vanished when distance of the footing reached 1.5 times excavation depth. Empirical formulae have been presented to express head deflection of cantilever sheet pile retaining wall, maximum bending moment and ratio of adjacent strip footing maximum settlement to corresponding values in the case of no adjacent footing or in case of footing before excavation cases.

Keywords: Braced excavation, Sheet pile, Lateral deformation, Straining actions.

1. INTRODUCTION

Space of construction activities is usually limited due to the proximity of adjacent structures. A major concern for projects involving deep excavation is the impact of such excavation on adjacent ground and structures [1]. Deformations of the excavation support system, adjacent ground and structures are influenced by a number of factors including stiffness of the excavation support system, installation procedures of the system, soil conditions, excavation procedures, type of foundation, distance of foundation from excavation, and orientation of foundation with respect to the excavation [2-4]. Wall pressures and deformation increase with the decrease in adhesion between sheet pile wall and soil [5]. The deformation behind flexible retaining walls anchored at the top was studied analytically through performing a number of model tests with dense sand [6]. Using a series of numerical nonlinear finite element analyses of experiments the effects of wall embedment depth, support conditions, and stress history profile on the undrained deformations around a braced diaphragm wall in a deep clay deposit were studied [7]. The results were presented in the form of design charts for estimating ground movements as functions of the excavation depth, supporting conditions. Braced excavation was observed to inevitably result in deformation of the adjacent ground and settlement of adjacent buildings behind the wall. Building settlement is believed to exceed the amount of associated ground settlement by 500% of the settlement under building weight before excavation [8]. This is due to the

decrease in stiffness of the foundation soil that is caused by lateral movement of the excavation face. It was also observed that additional settlement substantially decreased as the foundation level reached a depth equal to or more than 0.5 of excavation depth. To quantify the amount of building settlement, a model testing was conducted to determine the magnitude of the additional settlement of the structure and the effect of varying the building's depth and of its distance away from the excavation wall. Bearing walls oriented in a direction perpendicular to an excavation wall tend to become distorted with shear strain and lateral strain at the foundation level [9]. When ground movement initially impinged on the front of the building, the building is primarily subjected to shear distortion and lateral strain at the base. For deep excavations in stiff clays, residual soils, and sands, the average normalized lateral wall movement divided by excavation height " ζ_{Hmax}/H " nearly equaled 0.2%, and increases to 0.5% for poor construction conditions [10-12]. Other researchers specified a range of "0.1-0.5%" for " ζ_{Hmax}/H ", [13-14]. " ζ_{Hmax}/H " is affected by relative density of soil. For loose and dense sand, it was observed to range from "0.2% - 0.4%" and "0.1% - 0.2%", respectively, [15]. Adjacent foundation settlement was observed to depend on footing load level and relative density of sand. Excavation effect nearly vanished as the foundation was shifted away three times the foundation width [16]. There are two ways of modeling the interaction between the soil and the structure including a method based on a modified Winkler model in which the soil reaction is expressed by a number of elasto-plastic supports. The other method models the soil reaction as continuous elasto-plastic media. The first method

underestimates forces in struts and anchors, as well as bending moments in walls [17].

The present study aims to investigate different aspects of the behavior of excavations in soil and the response of structures located near these excavations. The main objectives for this research are:-

- I. Establishing an analytical model to represent realistic behavior for the excavation and the adjacent strip footing.
- II. Studying the parameters affecting the behavior of the chosen model such as distance between the foundation and excavation and foundation depth.
- III. Expressing maximum deformation and straining actions of sheet pile and settlement of foundation adjacent to retained excavation in terms of corresponding values of before excavation.

2. MODEL TEST SETUP, MATERIALS AND PROCEDURE

A schematic drawing of the test setup used in this study is shown in Fig. 1. The model test box was made of 2 mm thick steel sheets, 500 mm wide, 1000 mm high, and 1700 mm long. The excavation wall was made of a 1 mm thick steel sheet. The model strip footing was made of 500 mm firm wooden block. An automatic IOtech DaqBoard/2005 data acquisition system with LabView software was used to continuously monitor and record data during all stages of the tests. Multiplexing Isolated Analog Input DBK207 with 16 channel capacity was used to monitor the output voltages from instruments.

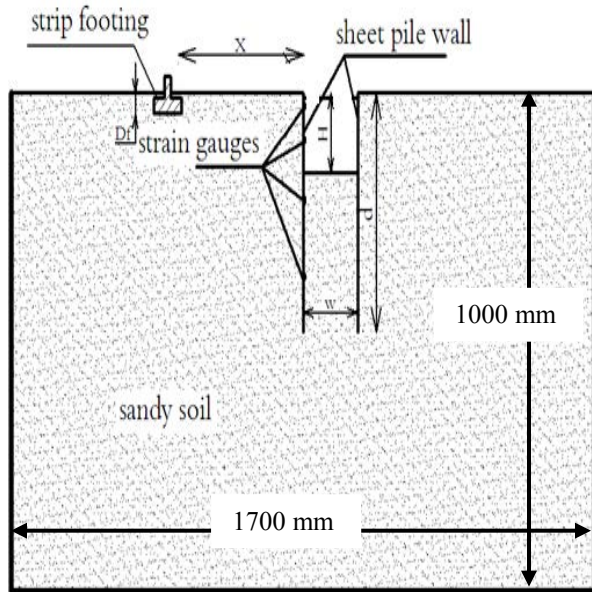


Fig. 1 Model of excavation, adjacent area and footing.

The data acquisition system was connected to a PC Pentium IV processor, as shown in Fig. 2. The footing was stiffened by a vertical tapered wooden plate 500 mm wide extending from strip footing top level to the level arm loading rod. The dimensions of different model items are as follows:

- Width of excavation (w) = 16 cm,

- Depth of excavation = (H) cm,
- Total height of sheet pile wall = (d) cm,
- Building distance from excavation = (x) cm,
- Foundation depth = (D_f) cm.

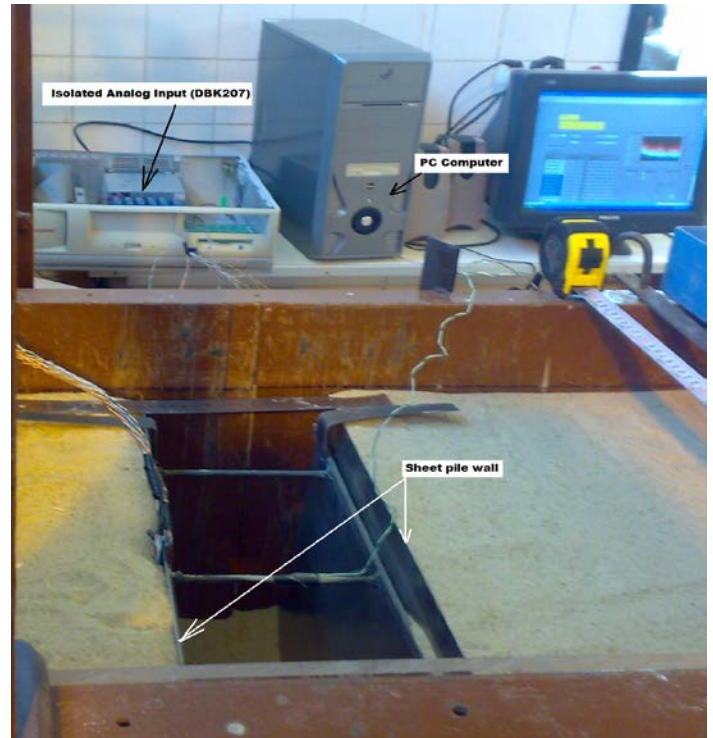


Fig. 2. Sheet pile wall supporting excavation and Data Acquisition system.

The undrained shearing resistance of the sand compacted to a dry unit weight of 17 kN/m^3 was determined using triaxial tests and found to be 36° . The gradation curve is shown in Fig. 3. According to the Unified soil classification system, sand can be classified as SP. More detailed information regarding the experimental setup may be found in reference No. [18].

3. NUMERICAL MODELING AND SELECTION OF PARAMETERS

Soil code Finite Element Program Plaxis 8.0 [19] was used in numerical modeling. In order to determine the appropriate numerical modeling meshing coarseness and refinement that are most suitable in modeling the studied geotechnical application a number of program runs were carried out to analyze the experimental model studied cases with different mesh configuration. The configuration that results in similar performance and close values of dependent parameter upon variation of independent investigated parameters will be

adopted for extension of the study with prototype dimensions.

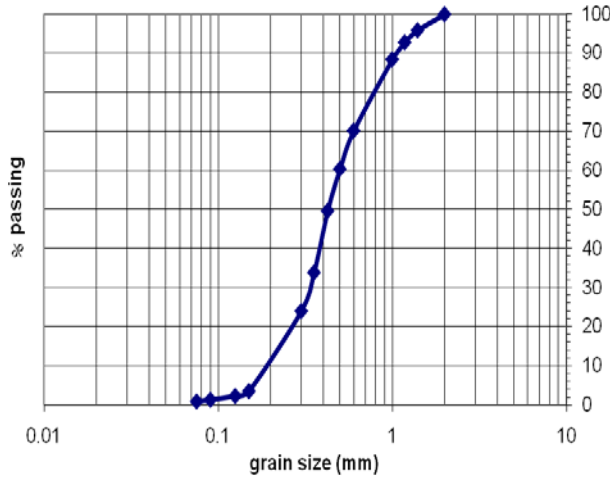


Fig. 3. Particle size distribution of tested soil.

3.1 Material Model of Sandy Soil

In order to make realistic predictions of the stability and deformations of excavation and adjacent strip footing, the hardening soil model in PLAXIS program was used for sand idealization. Material properties are presented in Table 1 for medium and dense sand. The sand is modeled by 15-node triangular elements in the analysis using an elastic perfectly plastic hardening model. The value of relative density is 0.53 for medium sand and 0.76 for dense sand.

Table 1. Input Physical And Mechanical Properties of Sand.

Parameter	Medium sand	Dense sand
Soil dry unit weight (γ_d) (kN/m ³)	17	18
Soil wet unit weight (γ_{wet}) (kN/m ³)	20	20
Secant stiffness in drained Triaxial test (E_{50}^{ref}) (kN/m ²)	14925	29850
Tangent stiffness for odometer loading (E_{oed}^{ref}) (kN/m ²)	10447	20894
Unloading / reloading stiffness (E_{ur}^{ref}) (kN/m ²)	44775	89550
Poisson's ratio for unloading-reloading (ν_{ur})	0.25	0.25
Cohesion (c) (kN/m ²)	10	10
Friction angle (ϕ) (degree)	36	42
Dilatancy angle (ψ) (degree)	6	12
Interface reduction factor (R)	0.8	0.8
Power for stress-level dependency of stiffness (m)	0.5	0.5
Reference stress for stiffness (p^{ref}) (kN/m ²)	100	100

3.2 Sheet Pile Wall

The sheet pile wall "S.P.W." is modeled as a beam element. The parameters for sheet pile wall are presented in Table 2. The interaction between the wall and the soil is modeled at both sides by means of interface elements.

The interfaces allow for the specification of a reduced wall friction compared to the friction in the soil.

Table 2. Material properties of sheet pile.

Parameter	Value
Normal stiffness (EA) (kN/m)	2.68×10^6
Flexural rigidity (EI) (kN/m ² /m)	9.68×10^3
Equivalent thickness (d) (m)	0.208
Weight (w) (kN/m)	1.2
Poisson's ratio (ν)	0.3

3.3 Strip Footing

Strip footing can be simulated as a beam element taking the modulus of elasticity for concrete "E" as follows:

$$E = 4400 \sqrt{F_{cu}} \text{ (N/mm}^2\text{)} \quad (1)$$

Where

F_{cu} : characteristic strength (25N/mm²)

The footing is loaded with distributed load 100 kN/m², the properties of footing are given in Table 3.

Table 3. Material properties for strip footing.

Parameter	Value
Axial stiffness (EA) (kN/m)	3.811E+07
Flexural rigidity (EI) (kN.m ² /m)	3.175E+06
Equivalent thickness (EI) (m)	1.00
Weight (w) (kN/m)	25.00
Poisson's ratio (ν)	0.2

3.4 Verification of Numerical Modeling

The mesh coarseness and refinement that results in similar performance of experimental and numerical small-scale model analysis is the very fine mesh coarseness and refinement along "S.P.W." line. Figures 4 and 5 illustrate experimental and numerical bending moment "B.M." distribution along "S.P.W." for $R_x = (x/H)$ equals 0.5 and 1, respectively, for medium sand. As can be observed the general trend of "B.M." distribution along "S.P.W." for both experimental and numerical analysis was similar. Maximum "B.M." of experimental and numerical curves occurs at one third "S.P.W." height measured from its top level. The maximum experimental "B.M." values were observed to be higher than corresponding numerical values by nearly 16%. The previously presented observations regarding "B.M." distribution and maximum "B.M." value applies when the strip footing was shifted away from the "S.P.W." with the cases of $R_x = 1.5$ and 2.0. The reduction of maximum "B.M." value due to the increase of R_x compared to the closest case of $R_x = 0.5$ are 68, 90 and 94% for $R_x = 1.0, 1.5$ and 2.0, respectively, for the experimental investigation. The corresponding values recorded for the numerical investigation are 65, 90 and 93%.

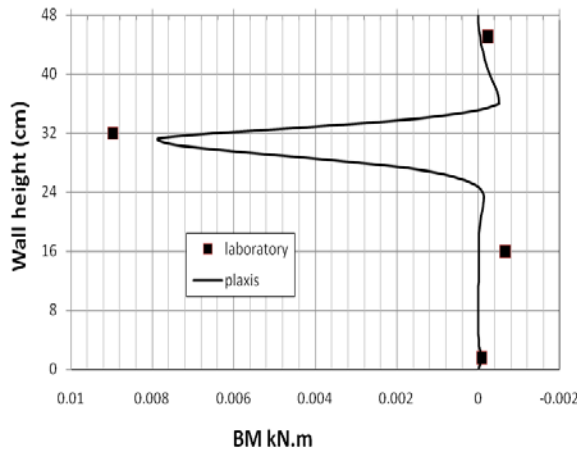


Fig. 4. Variation of the sheet pile wall bending moment for $x=8\text{cm}$ and $H=16\text{cm}$.

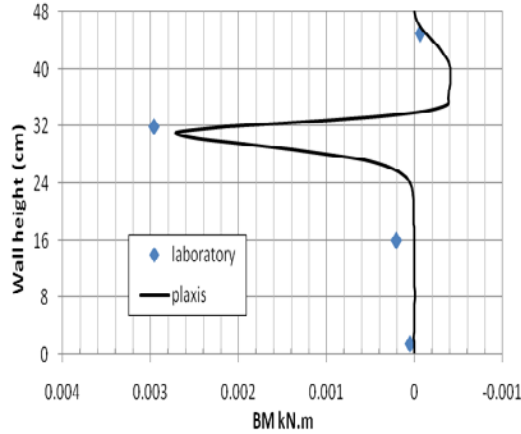


Fig. 5. Variation of the sheet pile wall bending moment for $x=16\text{cm}$ and $H=16\text{cm}$.

Comparing these ratios, it can be concluded that variation of “B.M.” values corresponding to variation of the independent variable R_x recorded close values in both experimental and numerical analysis. Hence it can be concluded that the adopted mesh coarseness and refinement results in a similar “B.M.” distribution profiles and relatively close “B.M.” maximum values. The variation in maximum “B.M.” values resulting due to corresponding variation of the independent parameter R_x has close values in both experimental and numerical analysis. Hence the mesh configuration will be adopted for the prototype scale model investigation of the tested parameters.

4. NUMERICAL INVESTIGATION WITH PROTOTYPE DIMENSIONS

The general layout of the physical model is shown in Fig. 6. The adopted finite element mesh was illustrated in Fig. 7. The independent parameters taken into consideration are the distance of strip footing “ x ” and the depth of foundation “ D_f ”. Table 4 presents the cases of studied parameters including relative depth “ $R_d=D_f/H$ ” and the ratio of strip footing distance to depth of excavation “ $R_x=X/H$ ”. The resulting straining actions and deformations due to excavation are

presented in terms of “ $R_x = 0.5, 1, 1.5$ and 2 ” and R_d having the values of “ 0.25 and 0.5 ”.

Table 4. Cases analyzed in the numerical study.

Case No.	1	2	3	4	5	6	7	8
	medium							
$R_d = D_f/H$	0.25				0.50			
$R_x = X/H$	0.50	1.00	1.50	2.00	0.50	1.00	1.50	2.00
Case No.	9	10	11	12	13	14	15	16
	Dense							
$R_d = D_f/H$	0.25				0.50			
$R_x = X/H$	0.50	1.00	1.50	2.00	0.50	1.00	1.50	2.00

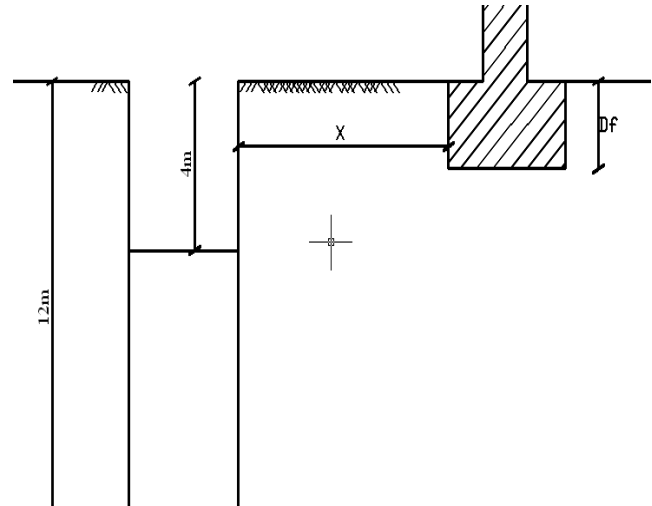


Fig. 6. Model of excavation, adjacent area and strip footing.

5. ANALYSIS AND RESULTS

5.1 Lateral Deformation of Sheet Pile

Figure 8 illustrates the lateral deformation profile of “S.P.W.” due to retained excavation in medium sand and the adjacent strip footing loading with varying distances from “S.P.W.” of $R_x = 0.5, 1.0, 1.5$ and 2.0 , and $R_d = 0.25$. As may be expected the maximum lateral deformation “ ζ_{Hmax} ” was recorded at The head of the wall lateral deformation was sharply reduced with depth until the mid height level of “S.P.W.”. Lateral deformation at this level reaches a value less than 50.0 % of deformation at head level without an adjacent strip footing case. The reduction ratio reaches a value of nearly 20% for R_x values of $2.0, 1.5$ and 1.0 , while it reaches 10% for $R_x = 0.5$. Lateral deformation gradually reduces from mid height level until approaching nearly zero value at tip level of “S.P.W.”.

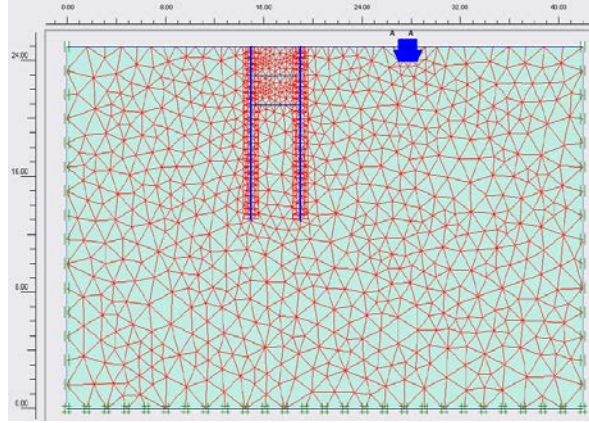


Fig. 7. Finite element mesh for the model of deep excavation and adjacent area.

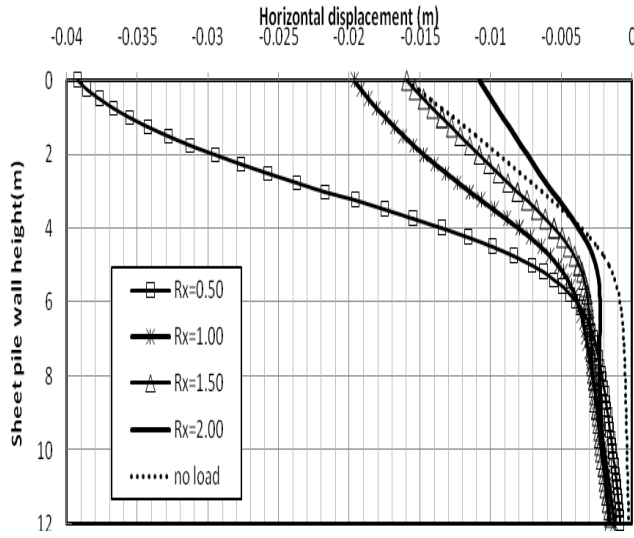


Fig. 8. Variation of the lateral deformation of sheet pile wall for different values of R_x and " $R_d = 0.25$ " for medium sand.

Figure 9 illustrates the lateral deformation profile for excavation in medium sand for different R_x values with $R_d = 0.5$. Figures 10 and 11 illustrate the same profile for excavation in dense sand for $R_d = 0.25$ and 0.5 , respectively. As can be concluded from these figures the lateral deformation profile remains unchanged from that previously described. Figure 12 illustrates the head deformation " ζ_{Hmax} " values for the previously mentioned different cases. It can be concluded that the values of " ζ_{Hmax} " of "S.P.W." excavated in dense sand are nearly 50% of the corresponding values recorded in case of medium sand. Other researchers observed a reduction in head deformation of "S.P.W." excavated in dense sand equaling one half of the corresponding value when excavating in loose sand [15]. It can be also observed that the existence of strip footing in case of close excavation of $R_x = 0.5$ produces increase in head deflection of 2.4 and 3.0 times the non strip footing case for excavation in medium and dense sand, respectively. As the footing was shifted away from the "S.P.W.", a reduction occurs in head deflection by

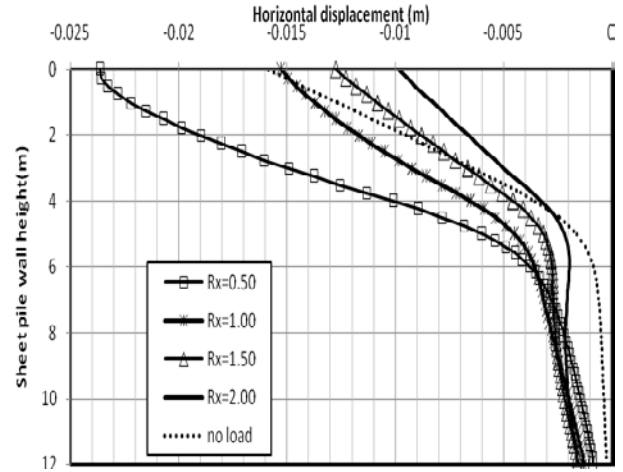


Fig. 9. Variation of the lateral deformation of sheet pile wall for different values of R_x and " $R_d = 0.50$ " for medium sand.

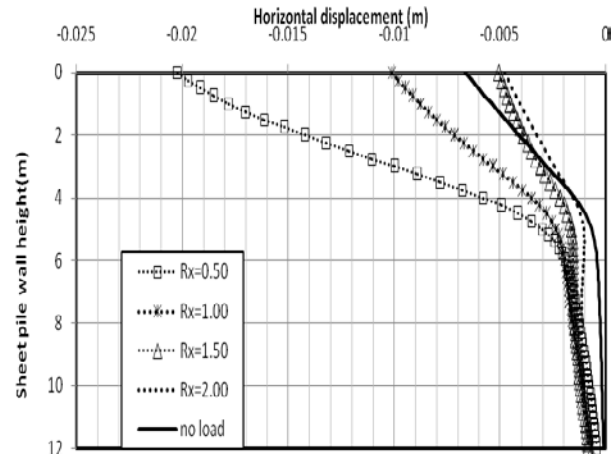


Fig. 10. Variation of the lateral deformation of sheet pile wall for different values of R_x and " $R_d = 0.25$ " for dense sand.

50, 40 and 30% for both medium and dense sand for $R_x = 1.0$, 1.5 and 2.0, respectively. The reduction in head deflection " ζ_{Hmax} " that occurs due to increasing foundation relative depth of the footing from R_d of 0.25 to 0.5 for both medium and dense sand is 38, 25 and 20% for R_x of 0.5, 1.0 and 1.5, respectively. This may be attributed to the following. As the strip footing gets deeper the increase in vertical stress and the accompanying increase in lateral horizontal stress is shifted downwards and the rotation is reduced resulting in less head deflection. The effect of foundation depth vanishes as the footing is located relatively far away from the "S.P.W." with R_x reaching 1.5. As for "S.P.W." head deflection to excavation depth ratio " ζ_{Hmax}/H " the recorded values for different R_x and R_d values as illustrated in Table 5. As can be observed from Table 5, " ζ_{Hmax}/H " values coincide with values cited in the previous work [15], for $R_x \geq 1.5$. For strip footing loading closer to "S.P.W." ($R_x = 0.5$ and 1.0) the recorded values of " ζ_{Hmax}/H " were higher than the corresponding values recorded in previous work [15].

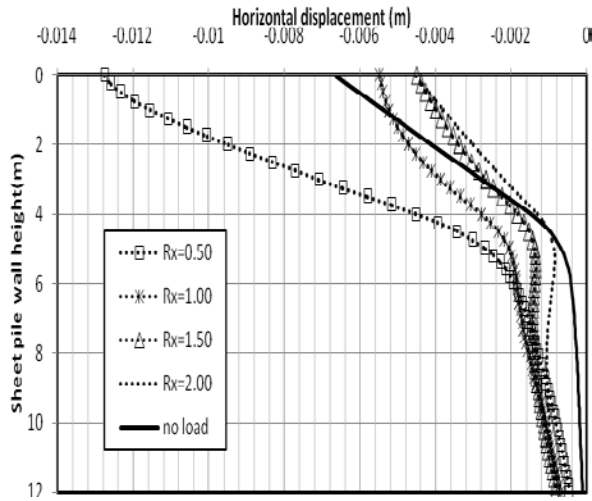


Fig. 11. Variation of the lateral deformation of sheet pile wall for different values of R_x “ $R_d = 0.50$ ” for dense sand.

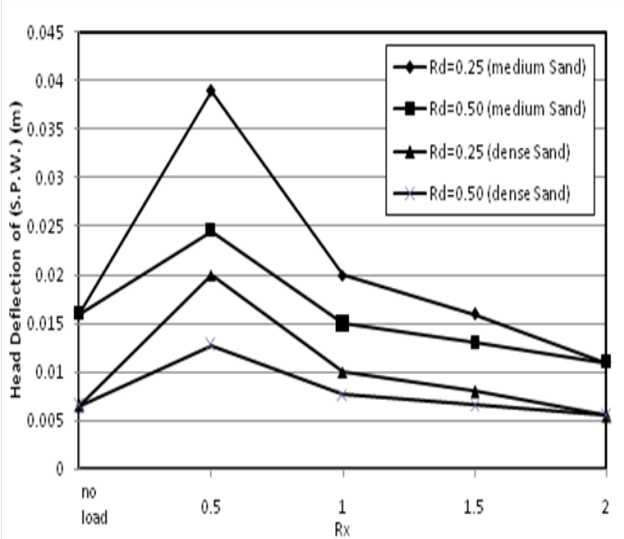


Fig. 12. Variation of the lateral head deformation of sheet pile wall for different values of R_x and R_d .

The effect of strip footing loading adjacent to “S.P.W.” excavation may be expressed in terms of “ ζ_{Hmax}/H ” value in the case of a strip footing loading adjacent to the corresponding value without an adjacent strip footing “for sheet pile embedment depth to excavation depth ratio equaling 2.0” may be expressed as follows:
For medium sand:

Table 5. Head deflection to excavation depth ratio “ ζ_{Hmax}/H ” for different R_x and R_d .

		Medium Sand		Dense Sand	
$R_x \backslash R_d$		0.25	0.5	0.25	0.5
Non strip footing		0.4	0.375	0.163	0.165
0.5		0.9	0.613	0.5	0.32
1.0		0.5	0.375	0.25	0.138
1.5		0.4	0.325	0.125	0.11
2.0		0.275	0.25	0.125	0.11

$$(\zeta H \max / H) \text{ ratio} = \frac{(\zeta H \max / H)_{S.F.}}{(\zeta H \max / H)} = (1.6 - 1.22 R_d) R_x^{(1.2 R_d - 1.2)} \quad (2)$$

For dense sand:

$$(\zeta H \max / H) \text{ ratio} = \frac{(\zeta H \max / H)_{S.F.}}{(\zeta H \max / H)} = (2.0 - 1.47 R_d) R_x^{(1.2 R_d - 1.2)} \quad (3)$$

Where

$(\zeta H \max / H)_{S.F.}$: Head deflection of “S.P.W.” in case of an adjacent strip footing.

$(\zeta H \max / H)$: Head deflection of “S.P.W.” in case of without an adjacent strip footing.

5.2 Bending Moment along Sheet Pile

Figure 13 illustrates bending moment “B.M.” distribution along “S.P.W.” due to retained excavation and adjacent strip footing loading for medium sand with $R_d = 0.25$ and different R_x values. As can be observed from this figure, “B.M.” increases from head level recording a maximum value at 0.38 of “S.P.W.” height from top level. Then “B.M.” decreases downwards until vanishing at 0.67 of “S.P.W.” height measured from its top. This profile was observed also for the case of $R_d = 0.5$ for medium sand and $R_d = 0.25$ and 0.5 for dense sand. Figure 14 illustrates maximum “B.M.” values with different R_x , R_d and sand density. As can be observed from this figure, maximum “B.M.” value with the case of excavation in medium sand was nearly 1.5 times the corresponding value recorded with dense sand. It can be also observed that placing a strip footing close to a retaining “S.P.W.” with $R_x = 0.5$ results in increasing maximum “B.M.” value by 2.6 and 2.8 for $R_d = 0.25$ for excavation in medium and dense sand, respectively. Relatively smaller increasing ratios, of 2.0 and 1.8 were recorded for deeper foundation level of $R_d = 0.5$ due to shifting of increase of lateral pressure downwards. The matter results in increasing the fixation effect of embedment length of “S.P.W.” and hence results in reduction of “B.M.”. Shifting of strip footing away from “S.P.W.” results in reducing maximum “B.M.” values by 0.55, 0.45 and 0.35 for $R_x = 1.0, 1.5$ and 2.0 , respectively for excavation in medium sand. Corresponding values for excavation in dense sand are 0.6, 0.57 and 0.51, respectively. It can also be observed that as the strip footing is shifted 2.0 times excavation depth from excavation the footing existence does not result in additional straining actions along sheet pile compared to the non strip footing case. The ratio between maximum “B.M.” values in the case of an adjacent strip footing to those in the case of no strip footing “for sheet pile embedment depth to excavation depth ratio equaling 2.0” may be expressed as follows:

For medium sand:

$$\text{Max.}(B.M.) \text{ ratio} = \frac{\text{Max.}(B.M.)_{S.F.}}{\text{Max.}(B.M.)} = (1.76 - 1.0 R_d) R_x^{(R_d - 1.0)} \quad (4)$$

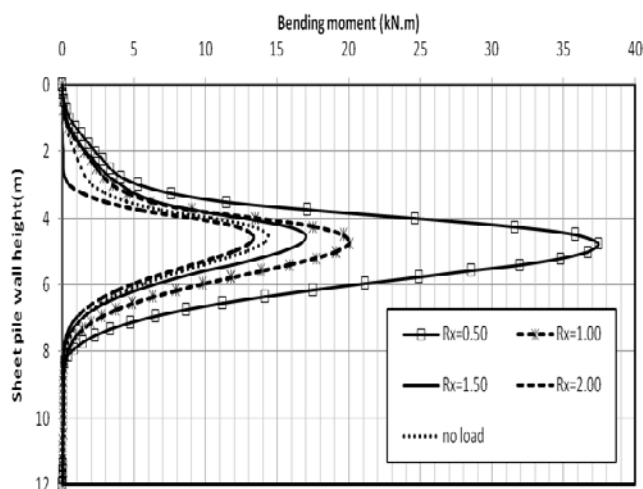


Fig. 13. Variation of the sheet pile wall bending moment for different values of R_x and " $R_d = 0.25$ " for medium sand.

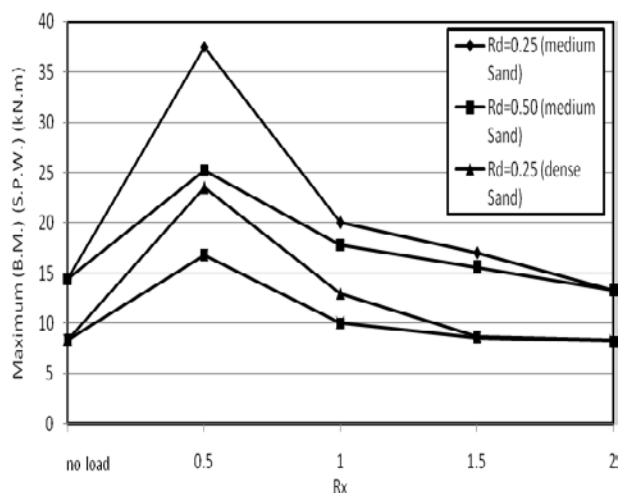


Fig. 14. Variation of maximum bending moment values on sheet pile wall for different values of R_x and R_d .

For dense sand:

$$\text{Max. (B.M.) ratio} = \frac{\text{Max. (B.M.)}_{S.F.}}{\text{Max. (B.M.)}} = (1.88 - 1.25R_d) R_x^{(R_d-1.0)} \quad (5)$$

Where:

$\text{Max. (B.M.)}_{S.F.}$: Maximum "B.M." value with an adjacent strip footing.

Max. (B.M.) : Maximum "B.M." value without an adjacent strip footing.

5.3 Settlement of Strip Footing

Figure 15 illustrates variation of strip footing settlement for different R_x and " $R_d=0.25$ " for medium sand. It can be observed that the footing settlement increases as the footing is closer to the retaining "S.P.W.". The settlement of strip footing towards excavation side was recorded to be 1.6 and 1.2 times corresponding settlement in the case of no adjacent excavation for $R_x=0.5$ and 1.0, respectively. Longer distance

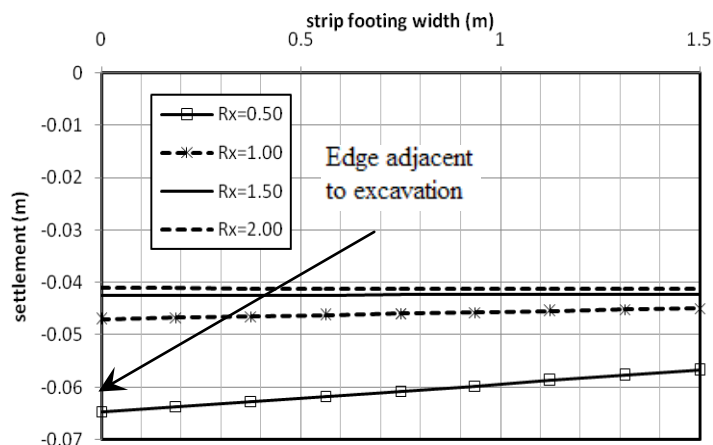


Fig. (15): Variation of raft settlement for different values of R_x and " $R_d = 0.25$ " for medium sand.

Table 6. Differential Settlement for different R_x and R_d values.

		R_x				
			0.5	1.0	1.5	2.0
Medium	R_d	0.25	4.67×10^{-3}	2.0×10^{-3}	0.0	0.0
		0.50	4.0×10^{-3}	2.0×10^{-3}	0.0	0.0
Dense	R_d	0.25	2.71×10^{-3}	0.67×10^{-3}	0.0	0.0
		0.50	1.33×10^{-3}	0.8×10^{-3}	0.0	0.0

was between strip footing and excavation (cases of $R_x=1.5$ and 2.0), the settlement value remains nearly unchanged compared to the corresponding value before excavation. Table 6 illustrates recorded values of differential settlement for different R_x and R_d values. As can be observed from this table differential settlement of strip footing exceeding 1/500 was recorded in the case of medium sand for $R_x = 0.5$ and 1.0 for both foundation level values of $R_d= 0.25$ and 0.5. This was also recorded in the case of dense sand for relatively close footing having $R_x=0.5$ and a relatively shallow foundation level of $R_d=0.25$. No differential settlement was recorded for strip footing having $R_x=1.0$ and 1.5 for both studied foundation levels and sand densities. For different R_x and R_d values, it can be observed that the maximum settlement value was nearly reduced to one half its value with the case of excavation in dense sand compared to the medium sand case. It also can be observed that executing retained excavation near the strip footing results in increasing its maximum settlement value by nearly 60% and 30% for $R_d = 0.25$ and 0.5, respectively. Maximum settlement value reduces as the footing was shifted away from the "S.P.W." until nearly reaching the value corresponding to that before excavation case as R_x reaches 2.0. The ratio of maximum settlement value in the case of an adjacent excavation of a varying distance from strip footing R_x to the corresponding value without excavation (Max. (S) ratio) for sheet pile embedment depth to excavation depth ratio equaling 2.0" may be expressed as follows:

For medium sand:

$$Max.(S) ratio = \frac{Max(S) S.F.}{Max(S)} = (1.37 - 0.4Rd) Rx^{(0.5Rd-0.5)} \quad (6)$$

For dense sand:

$$Max.(S) ratio = \frac{Max(S) S.F.}{Max(S)} = (1.29 - 0.3Rd) Rx^{(0.5Rd-0.5)} \quad (7)$$

Where:

Max. (S) S.F.: Maximum settlement value in case of an adjacent strip footing.

Max. (S): Maximum settlement value in case of without an adjacent strip footing.

6. CONCLUSIONS

In the present numerical analysis study the effect of retained excavation on adjacent strip foundation was investigated. The effect of strip footing relative distance and foundation depth related to cantilever sheet pile wall retained excavation on straining actions along sheet pile and deformation of foundation was studied. Analyzing the investigation results it may be concluded that the lateral deformation of the cantilever retaining sheet pile wall and the accompanying vertical settlement of adjacent foundation nearly vanishes as the excavation was shifted far away from the foundation by a distance equaling or more than 1.5 times excavation depth in both medium and dense sand. As the ratio between adjacent foundation depth to excavation depth increases a corresponding decrease in straining actions on retaining sheet pile and settlement of foundation occurs. Differential settlement of strip foundation adjacent to excavation vanishes when the distance between excavation and the footing reaches 1.5 times excavation depth. Empirical formulae have been presented to express head deflection of cantilever sheet pile retaining wall, maximum bending moment and adjacent strip footing maximum settlement to corresponding values in case of no adjacent footing or before excavation cases for sheet pile embedment depth to excavation depth ratio equaling 2.0.

7. REFERENCES

- [1] Bryson, L. S., "Performance of Stiff Excavation Support System In Soft Clay and the Response of an Adjacent Building", Ph.D. Dissertation, Northwest University, 2002.
- [2] Boscardin, M. D., and Cording, E. J., "Building Response to Excavation Induced Settlement" J. of Geotechnical Eng., Vol. 115, No. 1, , 1989 pp. 1-20.
- [3] Boone, S. J., "Ground-Movement-Related Building [Damage]" J. of Geotechnical Eng., Vol. 122, No. 11, 1996, pp. 886-896.
- [4] Moormann, A., "Analysis of Wall and Ground Movements due to Deep Excavations in Soft Soil Based on a New Worldwide Database", Soils and Foundations, Vol. 44, No. 1, 2004, pp. 87-98.
- [5] Kishnani, S. S., and Borja, R. I., "Seepage and Soil-Structure Interaction Effects in Braced Excavations" J. of Geotechnical Eng., ASCE, Vol. 119, No. 5, 1993, pp. 912-928.
- [6] Milligan, G. W. E., "Soil Deformations near anchored sheet-pile Walls," Geotechnique J., Vol. 33, No. 1, 1983, pp. 41-55.
- [7] Hashash, Y.M.A., and Whittle, A.J., "Ground Movement Prediction for Deep Excavations in Soft Clay", J. of Geotechnical Eng., Vol. 122, No. 6, 1996, pp. 474-486.
- [8] Seok, J. W., Kim, O. Y., Chung, C. K., and Kim, M. M., "Evaluation of Ground and Building Settlement Near Braced Excavation Sites by Model Testing", Canadian Geotechnical J., 2001, Vol. 38.
- [9] Son, M., and Cording, E. J., "Estimation of Building Damage due to Excavation-Induced Ground Movements", J. of Geotechnical and Geo-Environmental Eng., ASCE, 2005 pp. 162-177.
- [10] Peck, R.B., "Deep Excavation and Tunneling in Soft Ground", In Proc. of the 7th Int. Conf. on Soil Mechanics and Foundation Eng., Vol. 1, 1969, pp. 225-290.
- [11] Clough, G.W., and O'Rourke, T.D., "Construction Induced Movements of in Situ Walls. In Design and Performance of Earth Retaining Structures", Edited by P.C. Lambe and L.A. Hansen, American Society of Civil Engineers, Geotechnical Special Publication, No. 25, 1990, pp. 869-884.
- [12] Goldberg, H., "Lateral Support Systems and Underpinning, Construction Methods", Rep. FHWA-RD-75-128, 129 and 130, Federal Highway Administration, Washington, D.C., 1976.
- [13] Hsing, B.-C. B., "A Case Study on the Behaviour of a Deep Excavation in Sand", Computers and Geotechnics, Vol. 36, 2009, pp. 665-675.
- [14] Brahana, P.E., William, M., Tanner, E.I., and Larry, D. "Deflection and Earth Pressure Measurements of an Anchored Concrete Shoring Wall", 7th Int. Symp. on Field Measurements in Geomechanics, 2007.
- [15] Jalla, R., "Basement Wall Design for Geotechnical Aspects" J. of Architectural Eng., 1999, pp. 89-91.
- [16] El Swafe, M., and Nazir, A. K., "The Effect of Deep Excavation-Induced Lateral Soil Movement on Behavior of Strip Footing Supported on Reinforced Sand", J. of Advanced Research of Cairo University, Egypt. 2011.
- [17] Krasinski, A., and Urban, M., "The results of analysis of deep excavation walls Using Two Different Methods of Calculations", Archives of Civil Eng., Vol. LVII, 2011, No. 1.
- [18] Mohamed, A. A., "The Effect of Ground Movement Induced by Retained Excavation on Adjacent Structures", PhD. Thesis Submitted for Examination, Civil Eng. Dept., Al-Azhar University, Egypt 2011.
- [19] PLAXIS Version 8.0 Material Models Manual, "Finite Element Code for Soil and Rock Analysis", 1998.

Enhancing Stability of Slopes with Cement Kiln Dust Sand Mixture Layer

Al Serif M. Abd Alazez¹, Ahmed M. Eltohamy² and Ahmed Rusdy Towfek³

¹ Professor of Geotechnical Eng., Faculty of Engineering, Assuit Univ., Egypt.

² Associate Professor of Geotechnical Eng., Faculty of Engineering, Beni Suafe Univ., Egypt.

³ Assistant Professor of Geotechnical Eng., Faculty of Engineering, Azhar Univ., Egypt.

ABSTRACT

Cement kiln dust, CKD is a by-product produced at relatively high rates at cement manufacturing plants. In many Egyptian cement plants CKD is completely land filled at nearby valleys causing economical and environmental problems. A numerical prototype dimensions model has been experimentally verified and investigated to examine the effectiveness of stabilizing sand slopes by a surface layer of sand-(CKD) mixture. It was concluded that addition of (CKD) to sand improves compaction properties, compressive strength and shear strength. A numerical prototype dimensions model has been experimentally verified and investigated to examine the effectiveness of stabilizing sand slopes by a surface layer of sand-(CKD) mixture. It was concluded that covering the sand slope with a layer of sand-(CKD) mixture effectively improves the carrying capacity of strip footing loading on slope crust level. The improvement increases with increase of (CKD) addition ratio and soil density.

Keywords: Cement kiln dust; Enhancing slope stability

1. INTRODUCTION

Cement Kiln Dust (CKD) is one of the byproducts of cement industry that is produced in relatively large quantities. (CKD) is a finally divided, dry practice material drained from cement kiln by exhaust gases and captured by the kilns' air pollution filtering system, [1]. The raw input material of cement industry includes limestone shale, sand and iron. Ratios and type of these materials together with manufacturing technology, required product specifications, kiln type and fuel type which determine the chemical composition and physical properties of the byproduct [2]–[6]. Appropriate disposal of (CKD) is a challenging problem in cement industry due to environmental concerns. Although modern advances in cement manufacturing technology resulted in considerable reduction of the produced quantities of (CKD), however production rates may still be considered as an industry byproduct being produced in relatively large quantities. The majority of Egyptian cement manufacturing plants transport (CKD) to land filling areas with considerable transportation costs, environmental pollution problems and certainly in an uneconomical way of dealing with this problem, [7]. The composition of (CKD) is similar to that of cement, consisting of alumina, silica, calcium oxide, alkalis and sulfates. The high alkalinity and fine particle size, in addition to its cementitious properties make this material usable for several applications, [8]. There are a number of studies that indicated the effectiveness of using (CKD) in a number of geotechnical, civil, structural and agricultural applications, [9]–[21].

The effectiveness of using (CKD) as a stabilizer of granular soil was studied experimentally by a number of researchers, [22] and [23]. It was concluded that the unconfined compressive strength of sand-(CKD) mixtures increases as (CKD) in addition ratio increases up to 75-100% by total dry weight. In other cases peak unconfined strength that mixture was achieved at 15% of (CKD) by total weight, [24]. It was also found that the compressive strength increased with the increase of curing time, [22]. Maximum dry unit weight (MDUW) and optimum moisture content (OMC) are affected with (CKD) addition to granular soil. This was attributed to the ability of (CKD) to absorb water and alter soil structure through the pozzolonic and cation exchange reactions, [25]. In a number of previous studies (MDUW) decreased while (OMC) increased as (CKD) ratio by dry weight increased, [26]–[28]. Other studies observed a reverse trend, [23] and [24]. The effect of salts in calcareous soils on long term performance of soil stabilizers such as (CKD), may be eliminated by using asphalt coating and wrapping techniques, [30].

As can be concluded from the previously presented review of research work, one of the challenging problems that the cement industry faces is to either reduce (CKD) or to explore additional ways for beneficial uses of the by-product. The relatively high lime, alkaline content and high fineness of (CKD) make it a potential candidate for stabilizing soils. In Egyptian cement manufacturing plants the main production rate of (CKD) is nearly 2% of the amount of produced cement. This relatively high (CKD) production rate motivated the researcher to examine the effectiveness of using (CKD) in stabilizing slopes with a covering layer of (CKD) sand mixture.

2. MATERIALS AND EQUIPMENTS

2.1 Sand

Washed, air dried siliceous yellow sand was used in the model test. The sand was sieved through sieve No.4 with opening size of 4.75 mm. The specific gravity of soil particles was determined by the gas jar method. The main value determined from 3 tests was 2.66. The maximum and minimum dry unit weight of the sand was 18.22 and 15.45 kN/m³, respectively. The grain size distribution was determined using dry sieve method and the results are shown in Fig 1. From the grain size curve it was concluded that, D₁₀, D₃₀ and D₆₀ were 0.3, 0.6 and 1.0 mm. Uniformity coefficient, C_u and coefficient of curvature, C_c were 3.3 and 1.14, respectively.

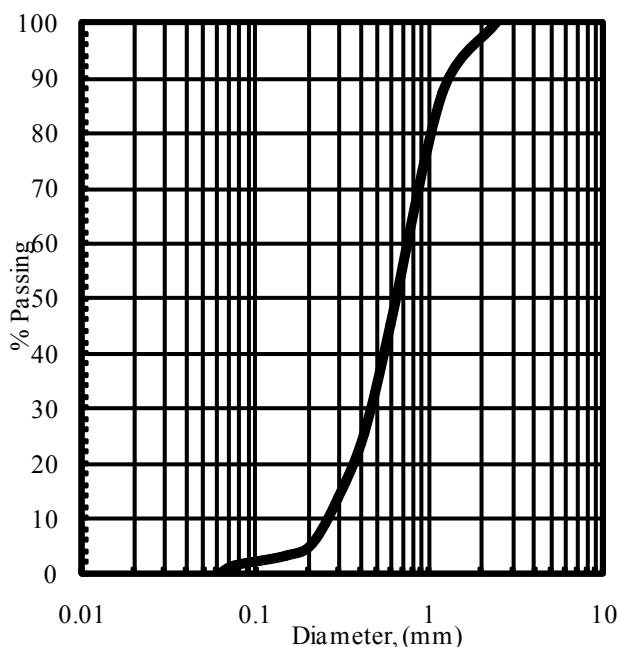


Fig.1 Particle size distribution of sand.

The sand can be described as coarse to medium sand and according to unified soil classification system sand can be classified as (SW). The shear strength parameters of sand were determined by drained triaxial compression test with three different confining pressures under vertical movement rate of 1 m m/min. Table 1 illustrates unit weight, strain and shear strength parameters of sand compacted to different relative densities of 60, 70 and 82%.

2.2 Cement kiln dust

Table 2 illustrates ratios of oxides composition of CKD collected along a production day at "CEMAX" Cement production company, Assuit, Egypt. As can be indicated from the table (CKD) has relatively high free lime oxide (CaO) of 41.57% and sulphate oxide (SO₃) of 18.08%. Thus the production of cementitious compounds on hydration of (CKD) was expected. A fresh sample of (CKD) was put in a plastic bag and brought to the geotechnical laboratory. Grain size

distribution analysis was carried out on the sample. From this analysis it can be concluded that, effective diameter D₁₀=4.0 Mm. D₃₀=7.0Mm, D₆₀=8.0 Mm, Uniformity coefficient C_u=2.0 and coefficient of gradation C_c=1.53.

Table (1) Physical properties of sand

Parameter	Relative density		
	60%	70%	80%
Unit weight γ (kN/m ³)	17	17.4	17.9
Youngs' modulus E (kN/m ²)	8000	10000	12000
Poissons' ratio ν	0.35	0.3	0.27
Friction angle ϕ (°)	36	37	41

Table (2) Oxides composition of tested (CKD)

Oxide	Mean ratio %
SiO ₂	10.12
Al ₂ O ₃	2.0
Fe ₂ O ₃	4.03
CaO	41.57
MgO	0.57
SO ₃	18.08
NaO	2.51
K ₂ O	7.94
Cl	7.19
LOI	5.26

2.3 Sand-(CKD) mixture

2.3.1 Compaction properties of mixture

Standard compaction tests were carried out to determine compaction properties of sand-(CKD) mixture. Fig. 2 illustrates the relation between moisture content and dry density of pure sand and sand-(CKD) mixture for different addition ratios of 10, 20 and 30%. The optimum moisture content (OMC) can be observed to increase almost linearly with the increase of (CKD) ratio. The recorded values are 7.7, 9, 10.5 and 11.5% for pure sand, (CKD) ratios of 10, 20 and 30%, respectively. The maximum dry densities (MDUW) corresponding to (CKD) addition ratios are 19.32, 19.56 and 18.8 kN/m³, respectively. Comparing the maximum dry density of mixtures and that of pure sand an increase in maximum dry density of 10, 11.6 and 7.6% compared to pure sand case for 10, 20 and 30 addition ratios, respectively. This general trend of the variation of (OMC) and (MDUW) with increase of (CKD) ratio agrees with previous research work as in [26] - [28].

2.3.2 Compressive Strength:

Sand-(CKD) mixture was compacted at maximum dry density in cubes 100x100x100 mm to measure compressive strength of cubes with varying (CKD) ratios and curing time of 3, 7, 14, 28 and 56 day. Different mixes Mix (1), Mix(2) and Mix (3) with (CKD) ratio of 10, 20 and 30% were

investigated. Fig.3 illustrates the average value of compressive strength of three specimens prepared of different (CKD) ratios, and curing time. It can be observed that increasing (CKD) ratio up to 20 and 30% results in increasing compressive strength of mixture by 16 and 42% as the corresponding value recorded with (CKD) ratio of 10%. It

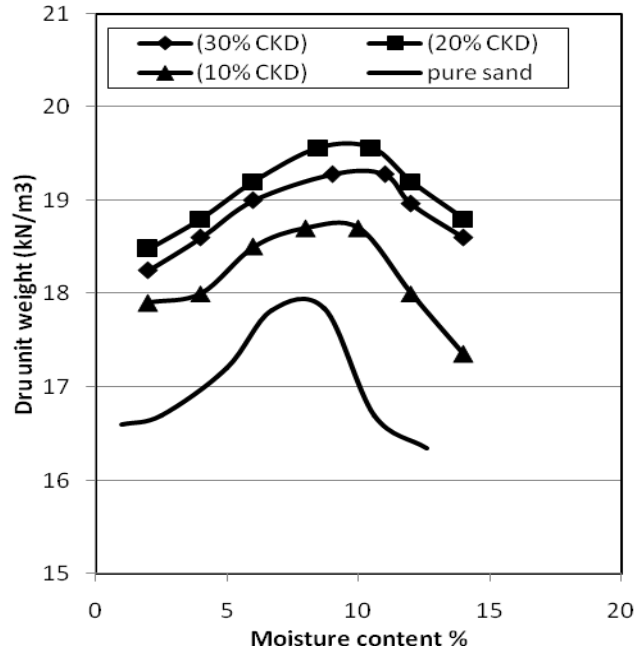


Fig. 2 Relation between moisture content and dry density for different (CKD) ratios of 10, 20 and 30%.

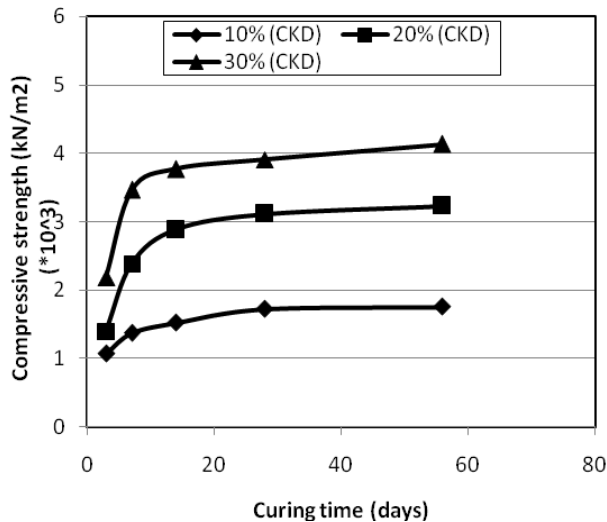


Fig. 3 Relation between curing time and compressive strength of sand-(CKD) mixture of different addition ratios of 10, 20 and 30%.

can be observed that the compressive strength of mixture increases as curing time increases with a relatively high rate up to 28 days. The increasing ratios were 30, 72 and 114% for curing time of 7, 14 and 28 days, respectively compared to the corresponding value at 3 days for different (CKD) ratios of

10, 20 and 30%. For a larger curing period up to 56 days the recorded compressive strength was 2.7% only of the corresponding value at 28 days for different (CKD) ratios.

2.3.3 Shear Strength and Stress Strain parameters:

Drained triaxial test was carried out on different adopted mixtures Mix (1), Mix(2) and Mix (3) to determine stress strain parameters. Direct shear test was also carried out on mixtures to determine shear strength parameters. Table (3) illustrates measured parameters of different mixtures.

Table (3) stress – strain and shear parameters of different mixtures:

Parameter	Mix (1) (CKD)10%	Mix (2) (CKD)20%	Mix (3) (CKD)30%
Unit weight & (K _N /m ³)	19.3	19.6	18.8
Young's modulus E (K _N /m ²)	31000	40000	52000
Passions ratio	0.26	0.24	0.22
Friction angle (°)	26	20	19
Cohesion C (K _N /m ²)	8	25	40

2.4 Sand Container

The sand container mounted under the loading frame is illustrated in Fig. 4. The tank dimensions are 500 * 1200mm with a depth of 1000mm. One side of the tank is made of Perspex 10mm in thickness, while the other three sides together with the base made from steel sheets 3mm in thickness. The steel sheets were stiffened by steel angles. A manual loading screw jack was used to apply vertical load to the strip model footing 100mm in width, 50mm depth and 500mm in length hollow steel section was used. The load was applied at two points separated by 250mm. The bottom and sides of the footing was covered by a sand paper to mobilize sufficiently the interface between footing and sand. The manual screw jack was mounted to the bottom flange of the loading frame which was fabricated from a steel beam (BF1B No.20).

3.0 EXPERIMENTAL PROCEDURES AND TESTING PROGRAM

To examine the effectiveness enhancing stability of sand slopes by a covering layer of sand-(CKD) mixture the following experimental testing program was adopted. Fig 5 illustrates strip footing slope system in the plain strain experimental model before and after improvement with a covering sand-(CKD) mixture layer. The parameters adopted for the testing program are:



Fig. 4 Sand container mounted under loading frame

- i. relative density of sand (D_r)=60, 70 and 82%.
- ii. addition ratios of (CKD) in sand-(CKD) mixture of 10, 20 and 30%.
- iii. distance of strip footing from slope $b/B = 0, 1$ and 2.

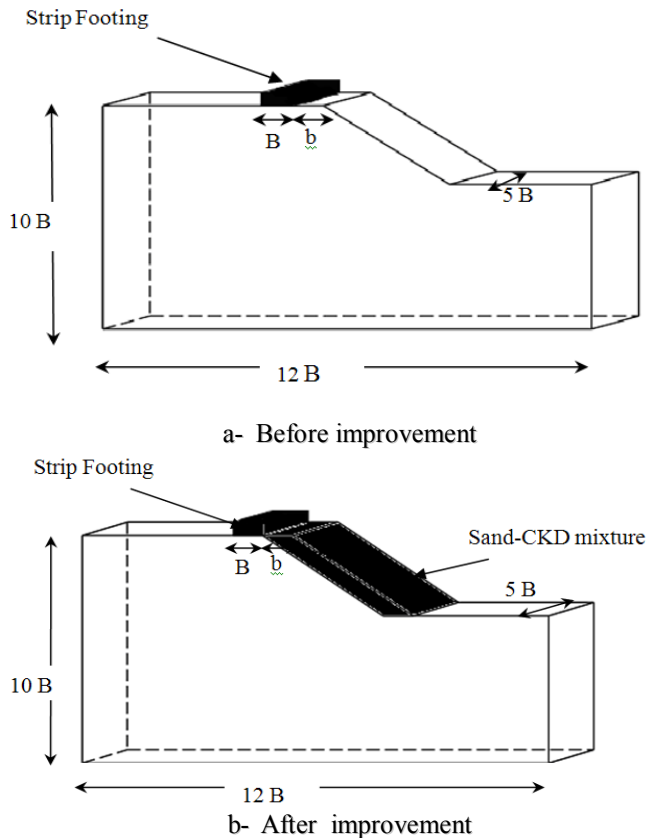


Fig. 5 Strip footing slope system before and after improvement with sand-(CKD) mixture layer.

4.0 FINITE ELEMENT ANALYSIS:

4.1 Conditions analyzed:

A series of two dimensional finite element analysis (FEA) of footing slope system model were performed on the sand slope model before and after adding the covering stabilizing (CKD) sand mixture. The (FEA) will serve to assess the laboratory model tests and find out deformation trends on soil body. Finite element code for soil and rock analysis plaxis [29] computer soft ware was used in the analysis. The initial conditions include initial ground water conditions, initial geometry configuration and initial effective stress state. As the sand used in the laboratory model was dry the ground water table was chosen to be at the bottom level of the model as the default of the program for dry soil condition. The initial stress condition of the slope was first generated by applying the gravity force due to soil weight.

4.2 Finite element modeling:

The software program enables automatic generation of 15 mode triangle plain strain elements for the soil and the footing. Displacements are presented in the form of a fourth order interpolation function. The element stiffness matrix is evaluated by numerical titration using twelve stress points. The nonlinear Mohr Column criteria were adopted to model the soil. The geometry of typical finite element model verified for the analysis is shown in Fig.6. The parameters used in the (FEA) were determined from experimental tests carried on sand and) sand-(CKD) mixture as previously presented. Different finite element mesh coarseness were investigated to decide which to give the results most close to the experimental model.

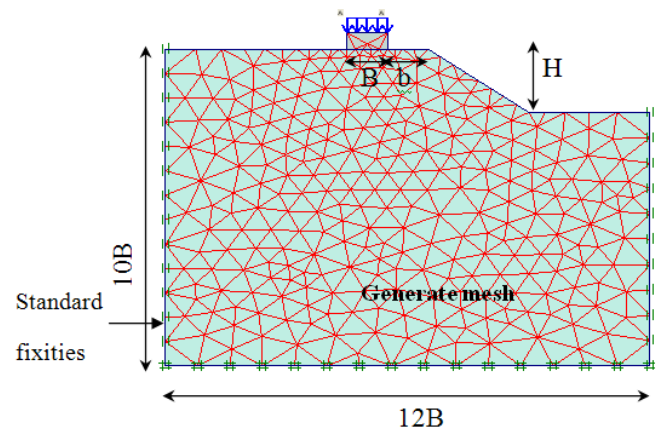


Fig. 6 Geometry of finite element model verified for the analysis.

A refined mesh was adopted to eliminate the mesh coarseness dependency of the finite element modeling for cases of unstabilized and stabilized slopes. Since the ground surface of the slope is not horizontal. A prediscrised footing load was then applied in increments with iterative analysis up to failure. To model the boundary conditions of the

experimental testing program, the vertical boundary is free vertically and constrained horizontally while the bottom boundary is fully fixed. After comparing the results of the experimental model and the (FEA) study on model scale, the computer program soft ware PLAXIS was used to investigate the affection of selected parameters on prototype scale numerical model.

5.0 RESULTS AND DISCUSSION:

5.1 Verification of numerical model:

Bearing capacity settlement curves were sketched for different (b/B) ratios and different soil relative densities for experimental and numerical models. Fig. 7 illustrates bearing capacity settlement curves for $(b/B=1.0)$ for medium soil density soil as an example to examine the adopted numerical modeling.

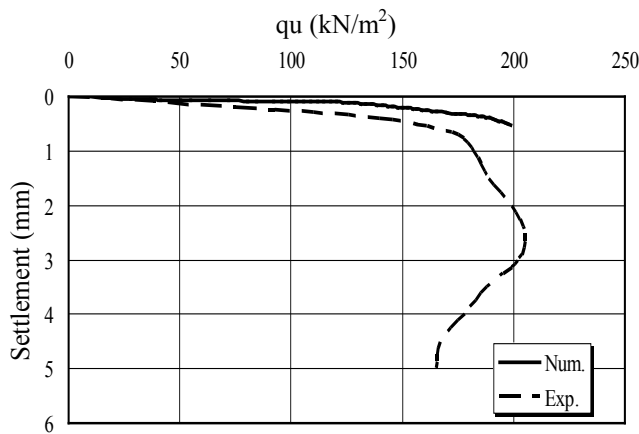


Fig. 7 Bearing capacity settlement relation for medium sand ($b/B= 1$).

As can be observed from this figure the bearing capacity settlement curves for experimental analysis can be divided to three stages. The first stage is approximately a straight line, where the soil behavior is mainly elastic. This stage ends at bearing capacity equaling 0.4 of ultimate value (q_u) and settlement equaling 0.2 of ultimate settlement (S_u). The second stage is of a curved trend where soil starts to plastify. In this stage bearing capacity increases with the increase of settlement up to the ultimate load at which the tangent to the curve becomes horizontal, this corresponds to settlement equaling 5% of footing breadth. In the third stage load decreases rapidly in a non linear trend with the increase of settlement with a plastic soil performance. The marked peak value indicated with experimental curves indicates occurrence of general shear failure for different soil densities due to existence of slope. The previously described trend was in good agreement with the previous studies, [30], [31] and [32]. Curves corresponding to numerical investigation reflected a close trend to experimental curves at the initial stage with slight increase of modulus of elasticity of soil. In spite of the relative close ultimate bearing capacity of experimental and numerical curves no marked peak value was

indicated. Similar trends have been indicated for other cases of $(b/B) = 0$ and 2, however curves corresponding to such cases will not be presented for abbreviation. Fig. 8 indicates bearing capacity settlement curves for the stabilized slope case with sand-(CKD) mixture of 10% addition ratio of medium sand.

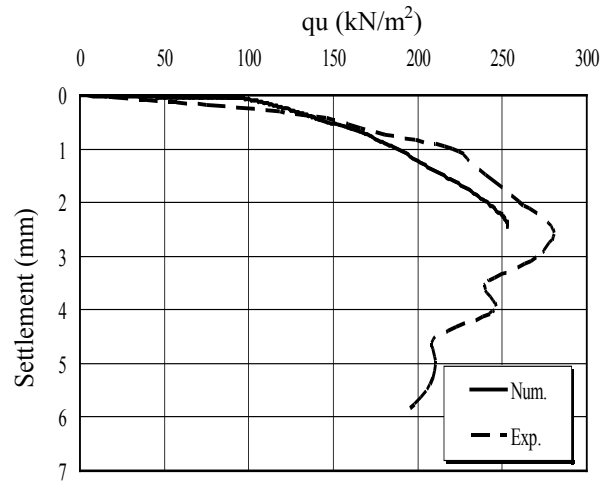


Fig. 7 Bearing capacity settlement relation for medium sand ($b/B= 1$) for stabilized slope case (CKD) = 10%.

medium and loose sand cases, respectively. As can be indicated from these figures curves corresponding for the stabilized slope case preserved the same trend for both experimental and numerical cases as that of unstabilized slope. The same trend has been also observed with other cases including $(b/B= 0.2)$ and different (CKD) addition ratios of 10 and 30%. The ultimate bearing capacity of experimental analysis overestimated that of numerical analysis by average percentage ratios of 0.05 and 0.15% for unstabilized and stabilized slopes, respectively. Hence, it can be concluded that numerical analysis, with the adopted mesh coarseness and conditions results in a fairly good agreement of stress strain behavior of footing resting stabilized and unstabilized slope. This applies also for the relatively close ultimate bearing capacity values. The deformed soil profile underneath the strip footing at failure is illustrated in Fig. 9.

5.2 Prototype scale numerical model:

Figs. 10, 11 and 12 illustrate the relation between the bearing capacity of the strip footing and the addition ratio of the (CKD) stabilizer with different densities of loose, medium and dense sand for relative footing distance (b/B) of 0, 1 and 2, respectively. For the case of the strip footing located at the crust of slope, stabilizing the slope surface layer with (CKD) of 10, 20 and 30% addition ratio results in enhancing bearing capacity by 22, 46 and 67%, respectively for dense sand case. For medium sand the recorded ratios were 24, 34 and 48, respectively.



Fig. 9 Deformed shape profile of soil under the footing at failure.

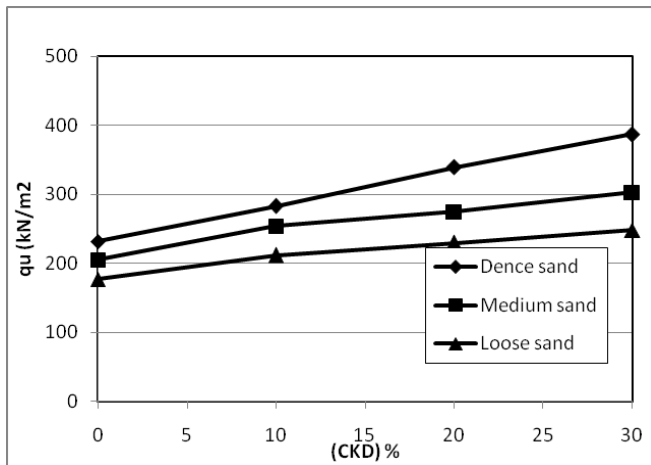


Fig. 9 Effect of (CKD) addition ratio on bearing capacity of footing for different soil density for (b/B=0).

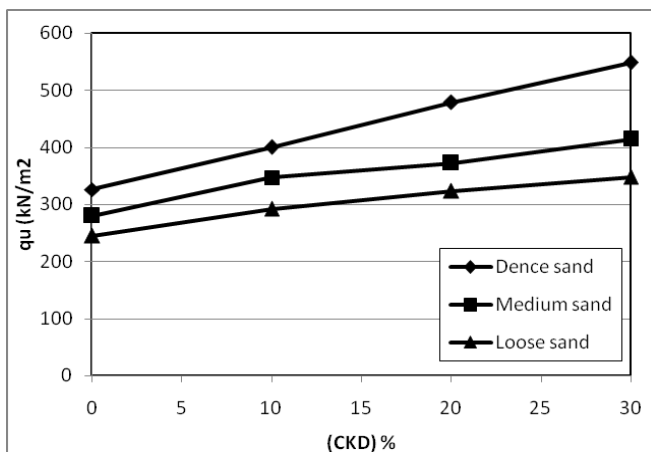


Fig. 10 Effect of (CKD) addition ratio on bearing capacity of footing for different soil density for (b/B=1).

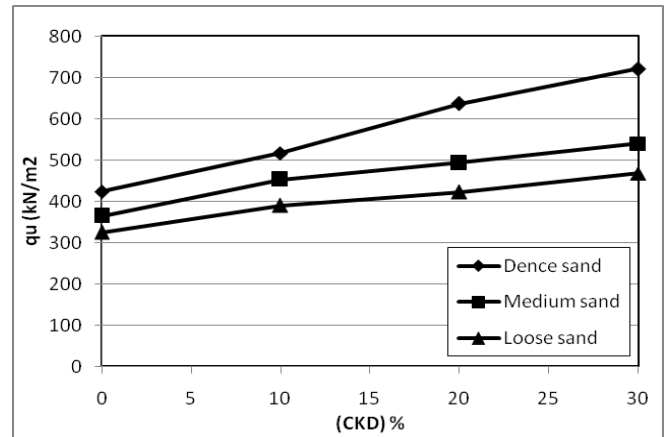


Fig. 11 Effect of (CKD) addition ratio on bearing capacity of footing for different soil density for (b/B=2).

Stabilizing the surface layer for the case of loose sand appeared to have a smaller effect as the enhancement ratios were 20, 30 and 40%, respectively. Slightly higher enhancement ratios have been observed with the strip footing shifted away from the slope crust, (b/B=1). Enhancement ratios for dense sand were 37, 47 and 69% for 10, 20 and 30% (CKD) addition ratios, respectively. Further shifting of the strip footing from slope crust (b/B=2) does not result in increasing bearing capacity compared to the more close case of (b/B=1.0). Hence it may be stated that the suggested technique appears to be more effective in enhancing the carrying capacity of strip footing for the case of footing distance from crust of more than footing breadth. Slightly lower enhancement in carrying capacity has been recorded as the footing is more close to the slope crust. Figs. 12 and 13 indicate total displacement at failure of a slope loaded with strip footing before and after stabilization with sand-(CKD) mixture, respectively. As can be indicated from these figures the enhancement of carrying capacity of a strip footing may be attributed to that the stabilized layer with relatively higher unit weight and enhanced engineering properties results in directing the lateral component of the foundation soil settlement under the strip footing to the downward direction, the matter that results in not affecting the stability of the slope and hence increasing the caring capacity of the footing compared to the unstabilized slope. For the relatively close strip footing to the slope for the foundation soil to deform and hence the footing to settle down, the deforming soil has to lift up and push beside the stabilized soil layer. The relatively high unit weight of stabilized layer will hence resist the deformation of soil and settlement of foundation.

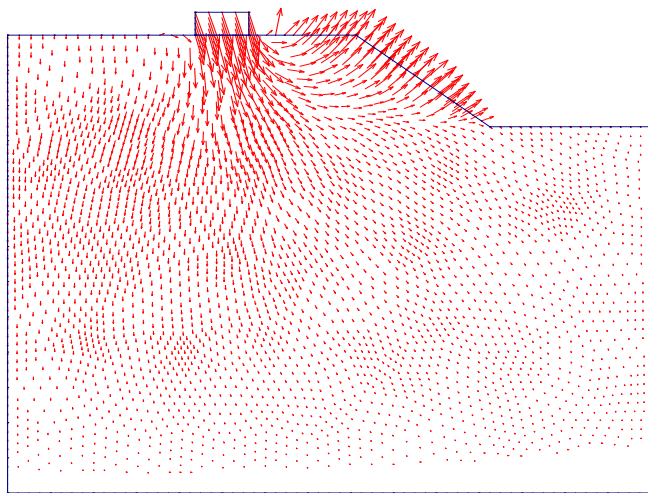


Fig. (12) Deformed numerical soil profile of unstabilized slope for ($b/B = 1$).

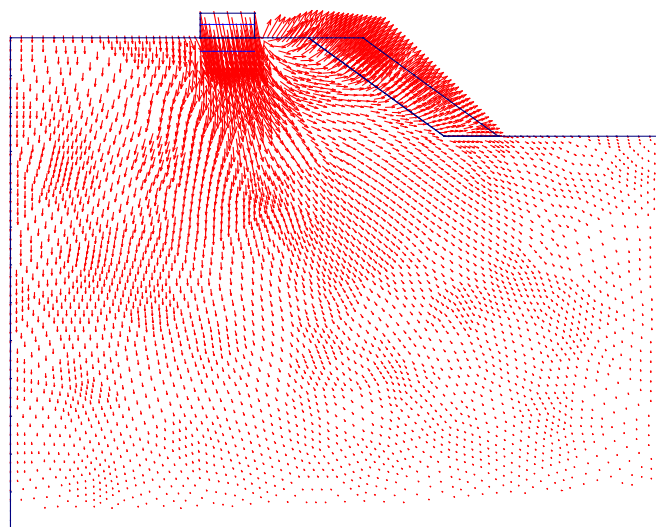


Fig. (13) Deformed numerical soil profile of (CKD) surface layer stabilized slope for ($b/B = 1$).

6.0 CONCLUSIONS

Cement Kiln Dust (CKD) is one of the byproducts of cement industry that is produced in relatively large quantities. In Egyptian cement manufacturing plants the main production rate of (CKD) is nearly 2% of the amount of produced cement. The produced (CKD) has high lime, alkaline content and high finesses which make it a potential candidate for stabilizing soils. It was concluded that addition of (CKD) to sand improves compaction properties, compressive strength and shear strength. A numerical prototype dimensions model has been experimentally verified and investigated to examine the effectiveness of stabilizing sand slopes by a surface layer of sand-(CKD) mixture. It was concluded that covering the sand slope with a layer of sand-(CKD) mixture effectively improves the carrying capacity of strip footing loading on slope crust level. The improvement increases with increase of

(CKD) addition ratio and soil density. The suggested technique appears to be more effective in enhancing the carrying capacity strip footing for the case of footing distance from crust was more than footing breadth. Slightly lower enhancement in carrying capacity has been recorded as the footing is more close to the slope crust.

7. REFERENCES

- [1] Peethamparan S, Olek J, and Lovell J. Influence of chemical and physical characteristics of cement kiln dusts (CKDs) on their hydration behavior and potential suitability for soil stabilization ELSEVIER. Cement and Concrete Research, 2008; 38: 803-815. Author H, A Book. New York: Publisher, Yr, ch. 3.
- [2] Sreekrishnavilasam A, Rahardja S, Kmetz R, and Santagata M. Soil treatment using fresh and land filed cement kiln dust. ELSEVIER, Constructional Building Materials, 2007; 21: 318-327.
- [3] Aheln D L, Hastings R J, Sexhreiber R J, Yonleg C. Detailed illustration of contingent management for cement kiln dust. In: Research and development bulletin, SPIIST. Skokie (IL): Portland cement Association; 1993.
- [4] Dyer T D, Halliday J E, Dhir R K. An investigation of the hydration chemistry of ternary blends containing cement kiln dust. J Mater Sci 1999; 34 (20): 4975-4985.
- [5] Hawkins, G. J., Bhatta, J. I., and O'Hare, A. T., "Cement kiln dust production, management and disposal", R & D Serial No.2327, Portland Cement Association, Skokie, Illinois, (2003).
- [6] Schreiber, R. J, "An Overview of CKD Generation", In PCA's Cement Technical Support Library DVD020.01©2005, Portland Cement Association, Skokie, Illinois, (1995).
- [7] El-Tuhami, A. M., "Utilization of cement kiln dust for stabilizing clayey soil", Journal of Al-Azhar University Engineering sector", Vol. 4, No. 11, Ciara, Egypt, April 2009.
- [8] Bhatta, M. S. Y., "Properties of blended cement made with portland cement, cement kiln dust, fly ash and slag," Proceedings of the 8 th International Congress on the Chemistry of Cement, Rio de Janeiro, Brazil, 1986 pp. 118-127.
- [9] Connor, J. R., Cotton, S., and Lear, P. P., "Chemical Stabilization of Contaminated Soils and Sludges Using Cement and Cement by Products," Proceedings of the Cement Industry Solutions to Waste Management, Calgary, Alberta, Canada, Oct. 7-9, 1992, pp.73-97.
- [10] McKay, M., and Emery, J., "Stabilization/Solidification of Contaminated Soils and Sludges Using Cementitious Systems," Proceedings of the Cement Industry Solutions to Waste Management, Calgary, Alberta, Canada, Oct. 7-9, 1992, pp. 135-151.
- [11] Bhatta, J. I., Bhattacharja, S., and Todres, H. A., "Use of cement kiln dust in stabilizing clay soils", PCA serial

- No.2035, Portland Cement Association, Skokie, Illinois, 1996.
- [12] Wang, M. L., and Ramakrishnan, V., "Evaluation of blended cement, mortar and concrete made from type III cement and kiln dust," *Construction and Building Materials*, 4(2), 1990, pp. 78-97.
 - [13] Detwiler, R. J., Bhatta, J. I., and Bhattacharja, S., "Supplementary Cementitious Materials for Use in Blended Cements", R&D Bulletin, RD112, Skokie, Portland Cement Association, Illinois, 1996.
 - [14] Udoeyo, F. F., and Hyee, A., "Strength of Cement Kiln Dust Concrete," *ASCE Journal of materials in civil engineering*, Nov./Dec., 2002, pp. 524-526.
 - [15] Al-Harthy, A.S., Taha, R., and Al-Maamary, F., "Effect of cement kiln dust (CKD) on mortar and concrete mixtures", *Construction and Building Materials*, 17, 2003, pp. 353-360.
 - [16] Hawkins, G. J., Bhatta, J. I., and O'Hare, A. T., "Cement kiln dust production, management and disposal", R & D serial No.2327, Portland Cement Association, Skokie, Illinois, 2003.
 - [17] Detwiler, R. J., Bhatta, J. I., and Bhattacharja, S., "Supplementary Cementitious Materials for Use in Blended Cements", R&D Bulletin, RD112, Skokie, Portland Cement Association, Illinois, 1996.
 - [18] Preston, M. L., "Use of cement kiln dust as an agricultural lime and fertilizer," *Emerging Technologies Symposium On Cement and Concrete in the Global Environment*, Chicago, March 10-11, 1993, In PCA's Cement Technical Support Library DVD020.01©2005, Portland Cement Association, Skokie, Illinois, 1993.
 - [19] Pierce, C. E., Tripathi, H., and Brown, T. W., "Cement Kiln Dust in Controlled Low-strength Materials," *ACI Materials Journal*, 100(6), pp. 455-462, (2003).
 - [20] Katz, A., and Kovler, K., "Utilization of Industrial by Product for the Production of Controlled Low Strength Materials (CLSM)," *Waste Management*, 24, 2004, pp. 501-512.
 - [21] Santagata, M. C., and Bobet, A. "The use of Cement Kiln Dust (CKD) for Subgrade Stabilization/Modification" (No. SPR 2575), Purdue University, West Lafayette, Indiana, USA, 2002.
 - [22] Baghdadi, Z. A., Fatani, M. N., and Sabban, N. A., "Soil Modification by Cement Kiln Dust", *Journal of Materials in Civil Engineering*, Nov. 1995, pp. 218-222.
 - [23] Baghdadi, Z. A., and Rahman, M. A., "Potential of Cement kiln dust for the stabilization of dune sand in highway construction", *Building and Environment*, 25(4), 1990, pp. 285-289.
 - [24] Taha, R., "Evaluation of Cement Kiln Dust-Stabilized Reclaimed Asphalt Pavement Aggregate Systems in Road Bases", *Transportation Research Record, Journal of the Transportation Research Board*, TRB Record 1819, Washington D.C., USA, 2003, pp. 11-17.
 - [25] Bhatta, J. I., "Alternative Uses of Cement Kiln Dust, PCA R&D 327, Portland Cement" Association, Skokie, Illinois, 2003.
 - [26] Zaman, M., Laguros, J.G., Sayah, A. "Soil Stabilization Using Cement Kiln Dust", *Proceedings 7th International Conference on Expansive Soils*. Dallas, Texas, 1992, pp. 347-351.
 - [27] Miller, G.A. and Azad, S., "Influence of Soil Type on Stabilization With Cement Kiln Dust", *Construction and Building Materials*, 14(2), pp. 2000, 89-97.
 - [28] Sreekrishnavilasam, A.; Rahardja, R.; Kmetz, R., and Santagata, M., "Soil Treatment Using Fresh and Landfilled Cement Kiln Dust", *Construction and Building Materials*, Vol. 21, 2007, pp. 318-327.
 - [29] Bringkgreve, R.B.J, Vemeer, P.A., PLAXIS – finite element code for soil and rock analysis, version 7.0, PLAXIS B.V., 1998, The Netherland.
 - [30] Zadroga, B "Bearing capacity of shallow foundation on noncohesive soils", *Journal of Geotechnical Eng., ASCE*, vol.120, No.11, 1994, pp. 1991-2007.
 - [31] Ahmed, M. M., "Effect of geosynthetic reinforced sand cohesion on the soil-structure interaction", M.Sc. Thesis, Assuit Univ. Assuit, Egypt, 2002.
 - [32] Yoo, R.B., " Laboratory investigation of bearing capacity of strip footing on geogrid-reinforced sand slope" *Geotextile and Geomembrane*, 19, 2001, pp. 279-298.

The effect of confining stress on the analysis of excavations adjacent to existing buildings

Sabzi Zahra¹, Fakhre Ali².

1: PhD student; School of Civil Engineering; Faculty of Engineering; University of Tehran; Iran

2: Associate Professor, School of Civil Engineering; Faculty of Engineering; University of Tehran; Iran

ABSTRACT

In the design of urban excavations controlling soil and adjacent buildings' displacement are important. The accurate prediction of displacements is difficult because they are influenced by several parameters. Soil stiffness is an important parameter in design and it is often assumed as a constant value, but stress distribution in the soil changes during the excavation and consequently changes the stiffness.

A vast zone of Tehran is composed of coarse-grained cemented sediments and its stiffness is highly influenced by confining pressure. In this article, a verified FE analysis has been performed to investigate Tehran soil behavior in excavation. The used soil model is a nonlinear elastic-plastic model in which the effect of confining pressure on stiffness has been indicated using *Janbu* model that was calibrated for Tehran soil.

Results show that assuming stiffness as previously mentioned, influences the estimation of wall displacement, ground settlement and also the type of ground support.

Keywords: excavation, displacement, Tehran soil, stiffness, confining stress.

1. INTRODUCTION

In urban areas, the design of new buildings often necessitates the construction of braced excavations. During excavation, the state of stress in soil changes. These changes in stress are typically expressed in the form of lateral movement and settlement of the ground which can have damaging effects on adjacent buildings.

Shoring and underpinning are methods used as supports in excavations. Shoring is a form of temporary support which can be tie to existing buildings adjacent to excavation to avoid damages. Underpinning is a temporary support that its main function is to transfer the load carried by a foundation from its existing bearing level to a new level at a lower depth. [1] Similarly, one type of shoring method, called "Inclined Strut", is widely used in different areas of Iran and is considered a traditional method in Tehran (Fig1). Inclined Strut can be considered as shoring or underpinning.

In the design of braced excavation the target is to minimize the cost of the support system while ensuring that the support is not so flexible that it causes additional soil displacement that damage adjacent buildings. The design of braced excavations is a complicated soil-structure interaction problem. Usage of the numerical modeling to analyze these soil-structure interaction problems by engineers is increasing. Many investigators [2], [3], [4], [5] have verified the reliability of FEM method in analyses of excavations.

In addition to reasonably modeling the actual construction sequences, selecting an appropriate soil model and the corresponding soil parameters is an essential step in the FEM analysis of excavation problems. Soil stiffness is an important

parameter that is often assumed as a constant value but actually during excavation, soil stiffness changes. Previous studies [6] have demonstrated that the soil stiffness in Tehran at small-strain can be higher than stiffness of most gravelly soils reported in technical literature.

In this paper, a verified FEM analysis has been conducted to investigate Tehran soil behavior, considering the effects stiffness changes based on *Janbu* model.[7]

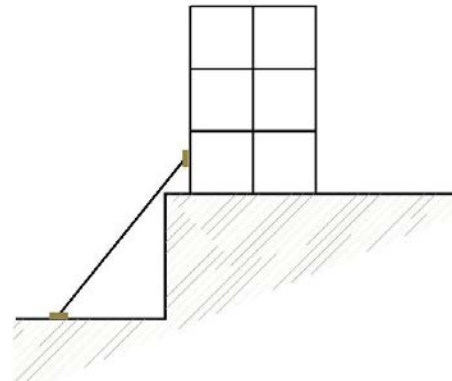


Fig 1: schematic traditional shoring method

2. EFFECT OF CONFINING STRESS ON SOIL BEHAVIOR

Elastic stress-strain relations are introduced with two constants which can be bulk modulus K and shear modulus G .

In nonlinear elastic models, when stress state changes, elastic parameters K , G change too. Comprehensive description of a model requires presenting changes of K , G in relation to changes in stress states. [6]

Constitutive models indicate stress-strain relationships. The key to a successful design is to use appropriate

parameters of soil models, which are able to present real behavior of soils. Description of nonlinear stress-strain behavior is necessary in excavation analysis. Many models have been presented, in which, soils have taken nonlinear elastic materials. Stiffness is one of the important soil parameters and is a variable that relates axial or shear stress increments to axial or shear strain increments. Stiffness varies with strain increase in which it has the most value when strain is small and decreases when strain increases. So assuming stiffness as a constant value is wrong. Nonlinear models of soils include two separate questions. One is determining stiffness in small strains and the other is ascertaining relationship between maximum stiffness and stiffness in larger strains [7]. Nonlinear stress strain curve can be determined by several methods. Some of these methods proposed by Duncan J.M. and Chang C.Y. [9], Fahey and Carter [8], Lehane B. and Fahey M. [10], Ramberg-Osgood, Seed and Idriss [11] and Janbu N [7]. In this article Janbu model used to simulate behavior soil of Tehran.

Janbu model:

In nonlinear models stiffness can be considered dependent on confining pressure. The effect of confining pressure on stiffness can be shown using Janbu model (Janbu N, 1963):

$$G = K_G P_a \left(\frac{\sigma'_m}{P_a} \right)^n \quad (1)$$

In this equation (Eq. (1)), G is stiffness, σ'_m is average of effective stress, P_a is reference stress to normalize the equation (usually $P_a=100$ kPa) and n and K_G are equation parameters.

3. GEOLOGY AND CHARACTERIZATION OF TEHRAN SOIL

Alluvial deposits of Tehran have been studied by many researchers during recent years. Numerous classifications of these deposits have been proposed. Observations of Tehran alluvia have shown that grain size and shape, sedimentary age, cementation, grain contact type, faults, fractures and weathering affect the geotechnical properties of these coarse-grained materials [12]. The effects of these factors have been discussed by Fakher [13]. Rieben [14] divided the Tehran alluvia into four categories based on geological factors, and identified them as A, B, C and D alluvia. The A alluvium is the oldest and D alluvium is the youngest. The grain sizes of the alluvia are variable and some are naturally cemented. The cementation grades vary from strongly cemented to noncemented depending mainly on the nature of the cementitious material. Strongly cemented Tehran alluvium is usually seen in A alluvium and is a secondary development resulting from the recrystallization of previously dissolved calcite carbonate of the source rock. Moderately cemented Tehran alluvium is usually seen in C alluvium and is clayey. The B alluvium presents weak and variable cementation, and D alluvium, being the youngest, has no cementation. A unique trend was observed in increase of soil stiffness with in relation to depth or confining pressure at

several points of Tehran. By review of other coarse-grained soils stiffness, it was observed that the behavior of gravelly soils with high percentage of gravel, over consolidated coarse-grained soils, pre-strained coarse-grained soils and cemented soils are similar to Tehran soil. The specific behavior of Tehran soil and its dissimilarity to other coarse-grained soils is relevant to its cementation and over consolidation [6].

The investigations on Tehran soil has been done by Sangtarashha et al, then Janbu model has been applied supposing soil behavior [6]. Taking undisturbed samples for triaxial tests or using self-boring pressuremeter was not possible at coarse-grained soils of Tehran. Therefore, Pressuremeter test has been performed with stress control according to method A of ASTM D4719-1994 and parameter of Janbu model obtain for some points of Tehran and some of that results used here are shown in table I.

Table I: Janbu models parameter obtained for Tehran sediments

Deposit Type	K_G	n	γ (kg/m ³)
A	16500	0.6	2200
B	7120	0.5	1850
C	4870	0.6	2000

Studies about Tehran soil indicate that stiffness increase with depth has similar trend in different points of Tehran and Janbu model can estimate it well. Coefficient n in this Eq.(1) varies between 0.5 and 0.6 for Tehran soil and in most points is about 0.6. [6]

4. NUMERICAL MODELING

In this research, we performed two-dimensional total stress elasto-plastic FEM analysis to examine ground movement and stress in the ground after installation of inclined struts in excavation.

Two-dimensional numerical simulations were carried out using a FEM analysis code. Fig. 2 shows the FEM mesh. A large zone was selected to avoid any measurable effects from the boundary in the final results. In this research, we use rectangular elements for two-dimensional analysis. These elements have four nodes and four integration points, and the Gaussian integration method was applied to them. The inclined struts and neighboring building were modeled using beam elements. The analyzed soil has 861 nodes and 800 elements in total. Mohr-Coulomb constitutive model was chosen for soil elements. Dimensions and soil parameters of hypothetical excavation case are shown in Table II. To minimize boundary effects, the vertical boundary at the far ends was set almost as 3 times of excavation's width from the center of excavation. Therefore, it was assumed to be free in vertical direction and restricted in horizontal direction. The bottom horizontal boundary was restricted in both horizontal and vertical directions. The boundary condition of model is shown in Fig.2 too.

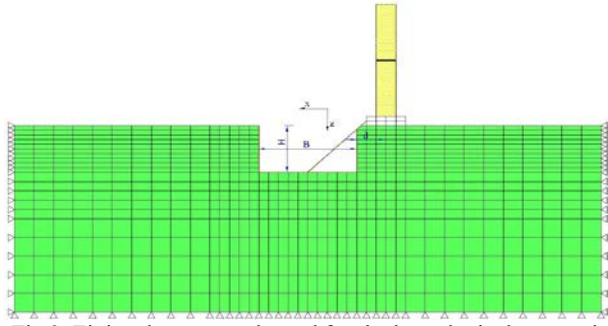


Fig.2. Finite element mesh used for the hypothetical excavation case.

In modeling stages, firstly, the in-situ horizontal and vertical stresses were generated. Initial in-situ horizontal and vertical stresses are as follows.

$$\sigma_z = \gamma h$$

$$\sigma_x = K_0 \sigma_z$$

Which γ is the soil density, K_0 is the coefficient of earth pressure at-rest, and σ_z , σ_x are the vertical and horizontal initial stresses at depth of h respectively. Then, it was assumed that the building was located next to the excavation and applied to model and excavation stages are modeled according to common excavation procedures. Finally inclined strut added to model as a support system.

Table II: The parameters of soil and struts used in numerical modeling

Parameter	C (kN/m ²)	ϕ (degree)	H (m)	B (m)	E steel	E concrete
amount	75	30	5	10	2.0E+8	2.0E+7

A series of numerical analysis was performed to investigate the effect of confining stress on selecting the stiffness of soil and consequently on the deformation caused by excavation. Fakher et al have been done the studies to determine geotechnical properties based on geological features. Their proposed stiffness parameter for A, B and C alluvia are shows in Table 3.[13] Linear analyses have been done on the A, B and C alluvia with parameters presented in

Table III: Geotechnical parameter obtained for Tehran sediments

Deposit Type	E (MPa)
A	200
B	100
C	50

Variation of stiffness with confining stress based on *Janbu* relation are shown in Fig.3 for A, B and C alluvia using the parameters presented in Table 1. To investigate the effect of confining stress on the stiffness, *Janbu* model applied to constitutive relations and soil stiffness considered as a solution dependent parameter. Calculating the confining stress in each step, related stiffness calculated and applied to analysis.

Results of analyses are illustrated in Fig.4-Fig.6

Fig 4, 5 and 6. show the comparison between the results of analysis with considering stiffness as a constant value and the results of analysis with considering variation of stiffness with confining stress. Results show that the wall deflection and surface settlement obtained from nonlinear analysis (stiffness is solution dependent) are significantly more than obtained from linear analysis (stiffness is a constant value).

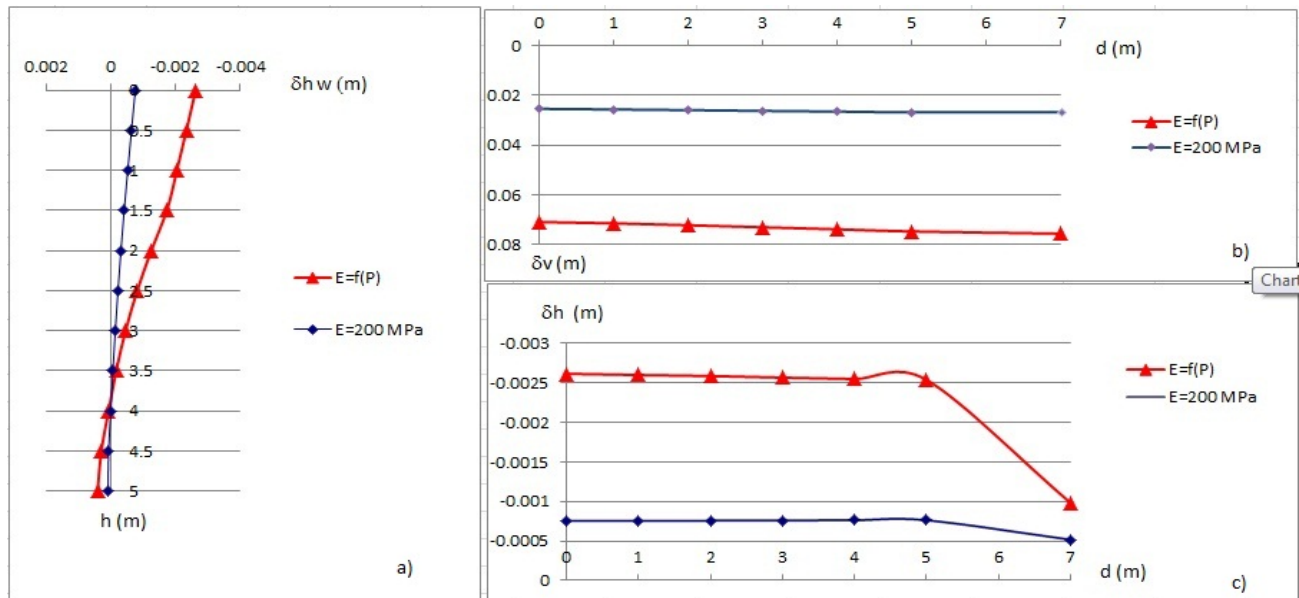


Fig 4. a) Deformation of excavation wall. b) Ground surface settlement. c) Ground surface lateral displacement for soil A

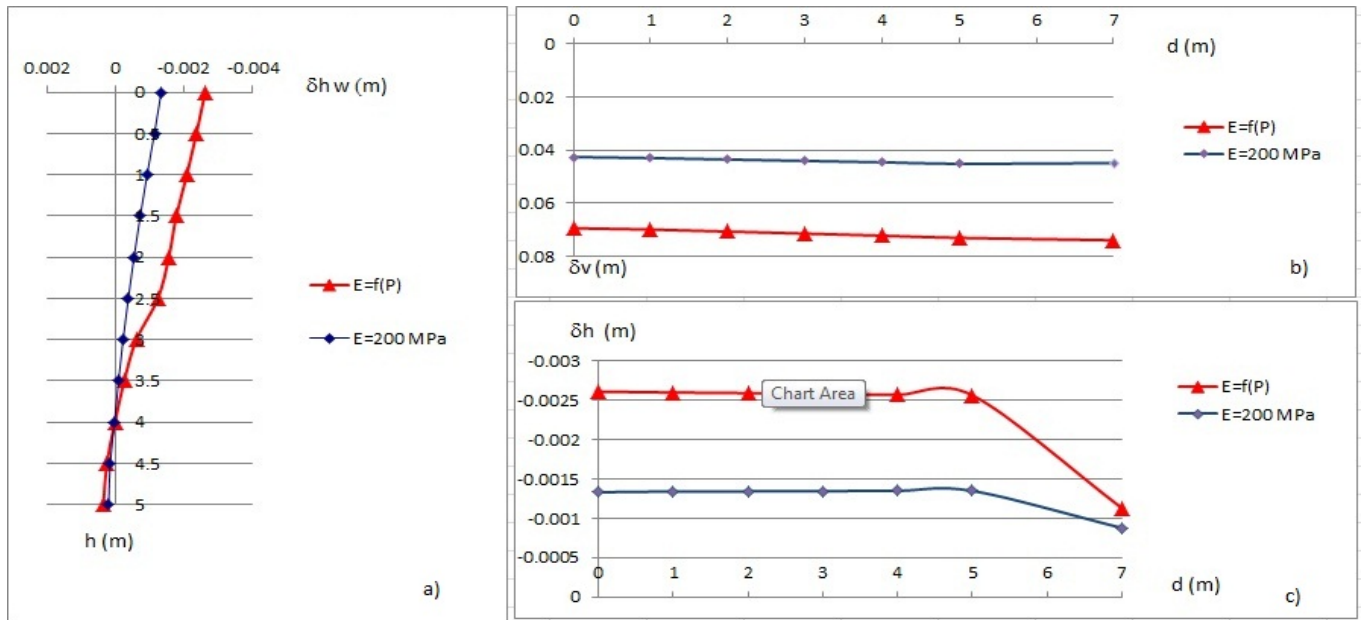


Fig 5. a) Deformation of excavation wall. b) Ground surface settlement. c) Ground surface lateral displacement for soil B

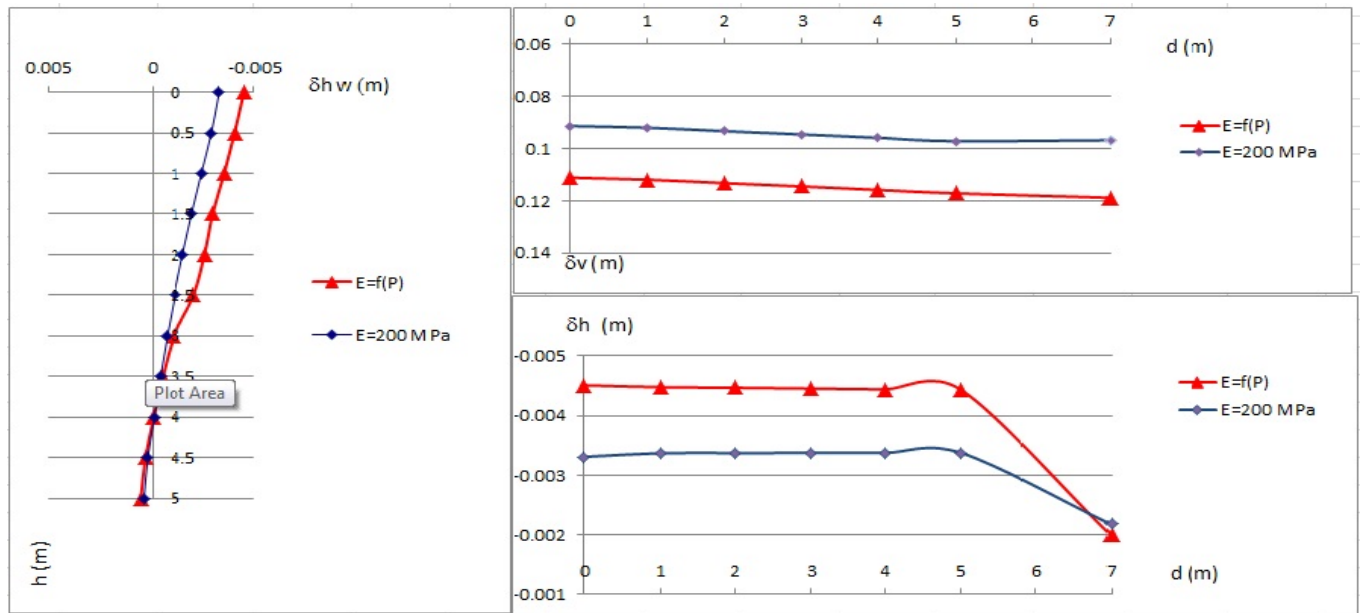


Fig 6. a) Deformation of excavation wall. b) Ground surface settlement. c) Ground surface lateral displacement for soil C

Excavation leads to reduction in lateral pressure in some elements and consequently confining stress decrease and relative stiffness decrease too and if only a constant modulus of elasticity is considered i.e., the degradation of stiffness due to excavation is ignored, the displacements are obviously underestimated.

Results show that loads in inclined strut obtained from linear analysis is less than obtained from nonlinear analysis. Considering stiffness as a constant parameter cause to underestimate the strut loads and then lead to underestimate the design loads and consequently cross section of support system.

5. CONCLUSIONS

1. Stiffness of soil of Tehran increases with depth and confining stress and significantly decreases with excavation.
2. In order to reasonably modeling the excavation and to understanding the actual soil behavior, selecting an appropriate soil parameters is an essential step in the analysis. Considering variation of stiffness with variation of confining stress can rationally model the excavations.

3. The results of the analysis with constant stiffness of soil show that the excavation-induced deformation can be underestimated and serious damage can occur in real behavior of soil.
4. These result show that considering soil with greater stiffness than real stiffness cause to underestimate the loads in inclined strut.

6. REFERENCES

- [1] Sadeghian S, Fakher A, "An Investigation into a Shoring Method to Support Buildings Adjacent to Excavations" The 17th Southeast Asian Geotechnical Conference proceeding., (2010)
- [2] Boone, S. J., "Design of Deep Excavation in Urban Environments", Ph.D. thesis, Univ. of Toronto. (2003).
- [3] Kung, G. T. C., Juang, C. H, Ou, C. Y., (2009), "Modeling Small-Strain Behavior of Taipei Clays for Finite Element Analysis of Braced Excavations", *Computers and Geotechnics*, Vol 36 (2009), pp 304–319.
- [4] Hsiao, C. L., "Wall and Ground Movements in a Braced Excavation in Clays and Serviceability Reliability of Adjacent Buildings", (2007). Ph.D. thesis, Clemson University.
- [5] Tang, Y.G. and Kung, G. T.C. "Investigating the Effect of Soil Models on Deformations Caused by Braced Excavations through an Inverse-Analysis Technique", *Computers and Geotechnics*, Vol 37 (2010) pp769–780.
- [6] Sangtarashha K. Fakher A. Pahlevan B. "Variation of stiffness of Tehran coarse-grained soil with depth and strain"
- [7] Janbu N, "soil compressibility as determined by oedometer and triaxial tests." *Proc. European Conf. on Soil Mech. Fndn. Engng., Weisbaden1(1963).*, pp. 19-24
- [8] Fahey M. and Carter J.P., "a finite element study of the pressuremeter test in sand using a nonlinear elastic plastic model." *Canadian Geotechnical Journal*, (1993). vol. 30, pp. 348-362
- [9] Duncan J.M. and Chang C.Y., "nonlinear analysis of stress and strain in soils." *Journal of the Soil Mechanics and Foundations Division, ASCE*, vol.96 SM5, (1970). pp. 1629-1653
- [10] Lehan B. and Fahey M. "a simplified nonlinear settlement prediction model for foundations on sand." *Canadian Geotechnical Journal*, , (2002). vol.39, pp. 293-303.
- [11] Seed H.B. and Idriss I.M. "soil moduli and damping factors for dynamic response analysis." *Earthquake engineering research center, University of California, Berkeley*, (1970). report EERC 70-10.
- [12] A. Cheshomi, A. Fakher and C.J.F.P. Jones. "A correlation between friction angle and particle shape metrics in Quaternary coarse alluvia Quarterly" *Journal of Engineering Geology and Hydrogeology* 2009; v. 42; p. 145-155
- [13] Fakher, A., Cheshomi, A. & Khamechian, M. "The addition of geotechnical properties to a geological classification" of coarse grain alluvium in a pediment zone. *Quarterly Journal of Engineering Geology and Hydrogeology*, 2007. 40, 163–174.
- [14] Reiban, E.H. "Geological Observation on Alluvial Deposits in Northern Iran". Geological Organization of Iran, 1966. Report, 2 [in French].

Bored Pile Socket in Erratic Phyllite of Tuang Formation

D.E.L. Ong¹

¹Swinburne University of Technology (Sarawak Campus), Malaysia

ABSTRACT

This paper highlights a case study where about 950 nos. of cast in-situ bored piles were used as a deep foundation system to support a large manufacturing plant in suburban Kuching, Sarawak, Malaysia. Localised moderately-strong metamorphic metagreywacke and extrusive igneous andesite are found occurring together with the more dominant but erratic, metamorphic phyllite due to regional metamorphism. Such combination of geology requires stringent quality control during construction to ensure sufficient bored pile socketing lengths into the mostly erratic phyllite. For this very reason, 33 nos. of Pile Dynamic Analyzer (PDA) and 4 nos. of Maintained Load tests were carried out to determine the ultimate static capacities of the installed bored piles. The PDA and Maintained Load test results show that all the tested piles meet the pre-determined design working loads.

Keywords: phyllite, socket, Tuang formation, point load test

1 INTRODUCTION

The project location has been found to be influenced by contrasting geology that consists of the Padawan (mainly sedimentary), Tuang (mainly metamorphic) and Quaternary formations. Localised moderately-strong metamorphic metagreywacke and extrusive igneous andesite are found occurring together with the more dominant but erratic metamorphic phyllite due to regional metamorphism. The Tuang formation has been noted to be most prominent during construction, evidenced by the abundant encounters with the friable and erratic phyllite. The construction of the large manufacturing plant required thorough understanding of the underlying geology. A cast in-situ deep foundation system was recommended for the plant due to heavy imposed loads and limited tolerance to differential settlement. For the foundation system to be effective, sufficient socketing length is required into the erratic phyllite. This paper is an extension of Ong & Choo (2011) [1].

2 SITE GEOLOGY

The proposed deep foundation system was socketed in geology comprising mostly of moderately weathered phyllite, and flanked at the site boundaries with intrusions of moderately to completely weathered shale and strong moderately weathered andesite. These geological conditions are synonymous with the Tuang Formation, and to a lesser extent the Padawan and Quaternary formations. The manifestation of the metamorphic phyllite rock in the Tuang Formation is characterised by semi-schistose features, further evidenced by the parallel arrangements of distinct cleavages and grains, occasionally interbedded with discrete bands of quartz and calcite.

Recovered cores of phyllite mostly revealed RQD values of 0%, up to a maximum of 75%. Fig. 1 shows phyllite cores with Total Core Recovery (TCR) of 100% but having Rock Quality Designation (RQD) of 0%. This observation is consistent with indications reported in Tan (1993) [2]. If RQD is used as a measure of rock strength for design purpose, then literally phyllite has zero strength! However, as a homogenous rock mass underground, it is impossible that phyllite has no strength!



Fig. 1. Discontinuous and highly fractured cores of phyllite

3 BEHAVIOUR OF ERRATIC PHYLLITE

An overview of RQD and the Unconfined Compressive Strength (UCS) tests on the phyllite rock cores is presented in Fig. 2. Due to the relatively low RQD values, it was only possible to conduct UCS tests on 14 of the 194 core runs extracted (12.4%). A conservative approach for the design of deep foundations in rock considers that the pile capacity is attributed only to the rock strength. Hence, it is critical to determine the socketing length required for piled foundation systems. The requirements of the manufacturing plant also

warranted the use of a piled foundation system to mitigate serviceability issues, such as differential settlement and pile movements. Given such conditions, the erratic phyllite behaviour provides serious challenges to designers.

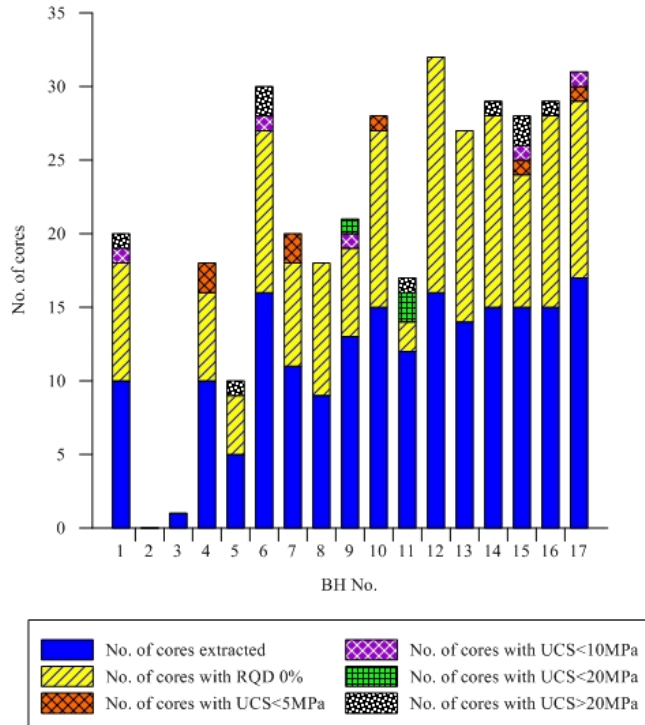


Fig. 2. Overview of RQD and UCS tests on phyllite cores (per 1m run)

3.1 Point load test on site

The outcome of the soil investigation works signalled expected difficulties in verification of socketing material during the construction of the deep foundation system. The occurrence of phyllite as well as its RQD values has been observed to be very low, most likely due to its friability. As such, point load testing was suggested to be used as a complementary index test to help correlate the UCS values tested on the limited and unpredictable solid cores of phyllite.

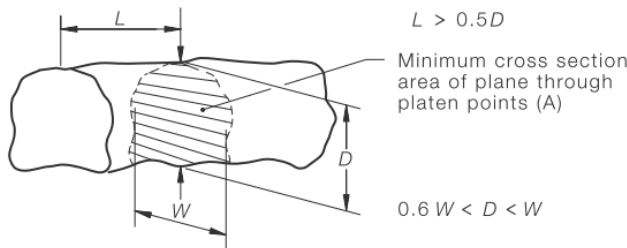


Fig. 3. Shape proportion for point load testing on irregular lumps (AS 4133.4.1-2007).

The point load testing apparatus was deemed suitable for field use due to its simple operation. The procedures outlined in AS 4133.4.1-2007 [3] were preferred for carrying out point load testing due to the allowances for tests to be carried out on

irregular lumps. Requirements for sample size restricted testing to be performed on lumps with aspect ratios illustrated in Fig. 3. Irregularly-shaped test samples for verification purposes were collected from spoils during boring. Fig. 4 shows rock samples collected from various coring depths, which were subsequently collected for point load testings on site.



Fig. 4. Excavation spoils collected from various boring depths.

3.2 Review of test results

Table 1 shows the summary of results for 3 types of tests carried out as an attempt to characterise phyllite, namely (i) Point Load Index test on lump samples, (ii) Point Load Index test on rock core (axial direction) and (iii) Unconfined Compression Strength (UCS) test. It can be seen that the average Point Load Index, I_{s50} value for lump samples within depths of 10.0m-11.9m, 12.0m-13.9m, 14.0m-15.9m and 16.0-17.9m are 3.094MPa, 3.749MPa, 3.866MPa and 3.654MPa, respectively. No lump samples were available for depths exceeding 18m as the preliminary design did not warrant any bored pile socket length greater than 18m. Despite the consistency of the average values over the various depths as reported, the standard deviations are rather poor i.e. at 2.033MPa, 2.838MPa, 2.696MPa and 2.510MPa, respectively. In other words, if assumed on a normal distribution probability density function, the probability of getting the average I_{s50} value of 3.753MPa over the 374 samples is only about 15.1%.

Table 1 further shows the difficulty of obtaining intact core samples (minimum 14.1mm in length) for Point Load test (axial direction) between depths 10m and 14m due to the friability of the phyllite at the upper depths. Between depths of 14.0m-15.9m, 16.0-17.9m and 20.0m-21.9m, the average I_{s50} values for intact cores tested on axial direction are 0.745MPa, 1.235MPa and 1.256MPa, respectively. The standard deviations recorded are 0.120MPa, 0.12MPa and 0.730MPa, respectively. If interpreted on a normal distribution probability density function, the probability of getting the average I_{s50} value of 1.138MPa over the limited number of 9 samples is about 43%.

Since UCS test requires intact rock core of at least 94mm in length, relatively competent phyllite is only available from 16m depth as shown in Table 1. At depths of 16m-17.9m, 18m-19.9m, 20-21.9m, 22m-23.9m and 26m-27.9m the average UCS values obtained are 9.53MPa, 4.45MPa, 5.2MPa, 9.33MPa and 12.06MPa, respectively. The standard deviations recorded are 2.051MPa, 3.286MPa, 4.030MPa, 5.629MPa and 17.519MPa, respectively. If interpreted on a normal distribution probability density function, the probability of getting the average UCS value of 8.259MPa over the 14 samples is only about 4%.

Therefore, surprisingly as a summary on testing in this study, it seems that the most reliable way of statistically measuring the phyllite rock strength is via the Point Load (axial core) as compared to Point Load lump and UCS testing methods.

suggested by Williams et al. (1980) [4] and recommended for use by Ting and Fuad (2003) [5] for metamorphosed sedimentary rocks comprising a sequence of slate and phyllite intercalated rhythmically with greywacke sandstone found at the Batang Rajang Bridge site in Sarawak. In the absence of a more systematic design procedure for phyllite, Ting & Fuad (2003) [5] suggestion is hence adopted for use in this study as it is perhaps the closest empirical representation to phyllite for this case study.

During the design stage when only UCS and I_{s50} (axial core) values were available, based on judgment and literature review of Basu & Kamran (2010) [6] and Ting & Fuad (2003) [5], a preliminary design USC value of 7.4MPa is assumed and this value must be verified through pile load tests performed on sacrificial piles on site. A factor of safety of 2.0 has been used in the design of the bored piles.

Table 1. Summary of test results based on UCS and Point Load test on phyllite

	Information available only during design stage						Information available only during construction stage		
	PLT (axial core)			UCS			PLT (lump sample)		
Depths where phyllite are tested	No. of samples	Ave. I_{s50} (axial core) (MPa)	Std dev (axial core) (MPa)	No. of samples	Ave. UCS (MPa)	Std dev on UCS (MPa)	No. of samples Lump for I_{s50}	Ave. I_{s50} (lump sample) (MPa)	Std dev (lump sample) (MPa)
Depth 10m-11.9m	0	N/A	N/A	0	N/A	N/A	23	3.094	2.033
Depth 12m-13.9m	0	N/A	N/A	0	N/A	N/A	77	3.749	2.838
Depth 14m-15.9m	2	0.745	0.120	0	N/A	N/A	166	3.866	2.696
Depth 16m-17.9m	2	1.235	0.120	2	9.53	2.051	81	3.654	2.510
Depth 18m-19.9m	0	N/A	N/A	2	4.45	3.286	0	N/A	N/A
Depth 20m-21.9m	5	1.256	0.730	3	5.20	4.030	0	N/A	N/A
Depth 22m-23.9m	0	N/A	N/A	0	N/A	N/A	0	N/A	N/A
Depth 24m-25.9m	0	N/A	N/A	2	9.33	5.629	0	N/A	N/A
Depth 26m-28.0m	0	N/A	N/A	5	12.06	17.519	0	N/A	N/A
Over entire depths 10m-28m	9	1.138	0.476	14	8.259	9.975	347	3.753	2.637

4 BORED PILE DESIGN

It is common practice to determine the unit shaft and unit base resistances based on UCS or q_u values of intact rock core samples, for example, Williams et al. (1980) [3] states that:

$$f_s = 0.05q_u \text{ (MN/m}^2\text{)} \quad (1)$$

$$f_b = 0.5q_u \text{ (MN/m}^2\text{)} \quad (2)$$

Typical limiting resistance values (ultimate), but may vary subject to load test results. The analyses carried out in the subsequent sections are based on the empirical equations

5 PILE LOAD TEST

In order to improve the confidence level of the designer in view of the difficulty of determining a feasible rock strength value for phyllite during the preliminary design stage, pile load tests during the construction stage become very important. The field testing result would then provide data for back-analysis purpose and to subsequently firm up the design value for phyllite. As a procedure to ensure that the bored pile can perform satisfactorily at its allowable load limit and to verify the preliminary design UCS value of 7.4MPa, 33 sets

of Pile Dynamic Analyzer (PDA) tests as well as 4 sets of Constant Rate Penetration (CRP) and Maintained Load Test (MLT) tests were performed on site.

Table 2. shows the results of the 33 Nos. of PDA tests performed on site. Based on the field test results, the average factors of safety provided for the 600mm diameter bored pile Types 1 and 2, as well as 750mm, 1000mm and 1200mm diameter bored piles are 2.23, 2.17, 2.06, 2.37 and 2.26, respectively. These values are in general comparable to the factor of safety of 2 used in the preliminary design stage.

Table 2. Summary of pile PDA test results

Bored pile diameter	Rock socket length in phyllite	Test pile ID	Measured PDA ult. static resistance	Design working load (WL)	FOS
(mm)	(m)	(-)	(kN)	(kN)	(-)
600 (Type 1) WL=1540kN	2.0	23	3,258	1,540	2.12
		39	3,541	1,540	2.30
		91	3,310	1,540	2.15
		106	4,197	1,540	2.73
		496	3,411	1,540	2.21
		505	3,277	1,540	2.13
		511	3,359	1,540	2.18
		515	3,502	1,540	2.27
		621	3,257	1,540	2.11
		779	3,380	1,540	2.19
600 (Type 2) WL=2500kN	2.1	620	5,398	2,500	2.16
		622	5,607	2,500	2.24
		624	5,183	2,500	2.07
		626	5,738	2,500	2.30
		629	5,349	2,500	2.14
		633	5,475	2,500	2.19
		704	5,390	2,500	2.16
		705	5,283	2,500	2.11
		735	5,135	2,500	2.05
		798	5,223	2,500	2.09
		TP1	5,875	2,500	2.35
750 WL=3250kN	2.2	5	6,676	3,250	2.05
		11	6,891	3,250	2.12
		13	6,588	3,250	2.03
		780	6,657	3,250	2.05
1000 WL=4500kN	2.3	56	9,257	4,500	2.06
		508	10,553	4,500	2.35
		508	10,553	4,500	2.35
		520	11,976	4,500	2.66
		778	10,988	4,500	2.44
		56	9,257	4,500	2.06
1200 WL=5800kN	2.5	436	13,605	5,800	2.35
		470	12,554	5,800	2.16

From the Maintained Load Test results as shown in Table 3, the magnitudes of the settlements that govern the serviceability limit state design are all less than the limit of 12.5mm, 38.0mm and 6.5mm at Working Load, twice Working Load and residual conditions, respectively. This means the design UCS ultimate value of 7.4MPa for phyllite is thus broadly verified in terms of strength and serviceability. Once sufficient confidence had been achieved on site after performing the CRP and MLT tests, mass installation of bored piles commenced.

Table 3. Summary of measured pile head settlement

Pile head sett	Criteria - Not exceeding (mm)	Bored pile diameter (mm)			
		600 Type 2	750	1000	1200
1xWL	12.5	5.32	4.06	5.59	4.45
2xWL	38.0	12.85	9.39	10.67	7.37
Residual	6.5	1.35	1.33	0.14	1.00

WL=working load

6 IMPORTANT OBSERVATION OF STRENGTH OF PHYLLITE

An important observation made is that despite the very low RQD obtained for the phyllite rock cores between 10m-18m depths (actual range of pile socketing depths as installed on site) and hence very limited UCS test was possible, however, from the back-analysis of the load test results the interpreted UCS ultimate value of 7.4MPa for phyllite seems to be very encouraging. It is therefore believed that phyllite, despite being friable, actually does have a reasonable good in-situ strength as a mass, which is often neglected because most, if not all the time, rock coring was carried out and hence RQD is usually used to interpret the rock strength.

It is believed that the main reason for obtaining a relatively high UCS of 7.4MPa for phyllite is due to the relatively large overburden pressure of 10m-18m overlying the rock layer. This provides a reliable confining stress to the phyllite layer. The metamorphic phyllite may be well-known to have small-scale slip-faults, intense shearing and faulting, but if it is kept largely under a confining pressure (compression in nature) with minimal disturbances, the in-situ strength will mostly be preserved. For this very reason, if external mechanical stresses are introduced to a mass of phyllite during rock coring, phyllite will tend to be disintegrated and when the core is retrieved the logging of phyllite as 'friable' in borehole logsheets is inevitable, hence the injustice of a misconception that by default phyllite should have a low strength value.

From this study, the following relationships on phyllite can be developed based on the successful pile socketing depths of between 10m and 18m on site (considering average values with respect to their respective standard deviations):

Unconfined Compressive Strength Test in cored samples

$$UCS = 7.48 - 11.58 \text{ MPa} \quad (3)$$

Point Load Test in axial direction on cored samples

$$UCS = k_A * I_{s50}$$

(4)

where $k_A = 5.5 - 12.0$ and I_{s50} is the point load index in MPa

Point Load Test using lump samples

$$UCS = k_L * I_{s50}$$

(5)

where $k_L = 0.9 - 6.6$ and I_{s50} is the point load index in MPa

Coincidentally, the preliminary design UCS value of 7.4MPa seems to coincide with the lower bound value of the UCS test within the depths of 10m-18m, noting that the I_{s50} lump results during design stage was still unknown. The coefficients k_A and k_L are applicable to Point Load test on samples in axial direction and Point Load test on lump samples, respectively.

Nonetheless, to increase the confidence level of utilising a relatively higher UCS design value for phyllite, more data is to be collected and interpreted in the future. In-situ testing, for example, pressuremeter test is definitely a recommended method to obtain a more reliable UCS value for use in design. The main advantage in using the pressuremeter test is that no extraction of phyllite sample is required and as such the in-situ strength of the rock mass is preserved and hence can be reliably tested.

7 CONCLUSIONS

This paper has documented the difficulties in quantifying rock strengths and designing for geological conditions with high degrees of fracturing, i.e. RQD of 0%, typical of the metamorphic phyllite of the Tuang Formation. Recovery of cores for testing is only sporadic at best, requiring the sinking of more boreholes for the extraction of intact rock cores.

Efforts to correlate UCS with the point load index require further studies, in particular the lower bound results which would govern the conservative design of piles socketed in rock.

Further research could realise the great potential in applying the in-situ pressuremeter test to obtain values of phyllite rock strength for the design of bored piles. The main advantage in proposing the pressuremeter test is that no extraction of sample is required and as such the in-situ strength of the strong mass is preserved and hence reliably tested.

It is important for engineers to be able to interpret the magnitude of phyllite rock strength as this would ultimately impact the design and costs of bored piles to be installed.

8 ACKNOWLEDGMENT

The authors would like to acknowledge Jurutera Jasa (Sarawak) Sdn. Bhd. for their kind co-operation in making this paper a reality.

9 REFERENCES

- [1] Ong, D.E.L. and Choo, C.S. Sustainable Bored Pile Construction in Erratic Phyllite. ASEAN-Australian Engineering Congress. CD proceeding (ISBN 978-967-10485) July 2011.
- [2] Tan, D.N.K. Geology of the Kuching Area, West Sarawak, Malaysia. Report 16, Geological Survey of Malaysia, Kuching, 1993.
- [3] Australian Standard AS 4133.4.1-2007: Methods of testing rocks for engineering purposes - Rock strength tests - Determination of point load strength index. Sydney, NSW, Australia, Standards Australia Limited.
- [4] Williams, A.F., Johnston, I.W. & Donald, I.B. The design of socketed piles in weak rock. Proc. of International Conference On Structural Foundation On Rock, Sydney, 1980, pp. 327-347.
- [5] Ting, W.H. and Fuad, N. Pile Socket Capacity and Rock Mass Classification. Journal of the Southeast Asian Geotechnical Society, April 2003.
- [6] Basu, A. and Kamran, M. Point load test on schistose rocks and its applicability in predicting uniaxial compressive strength. International Journal of Rock Mechanics and Mining Sciences, 47, 2010, pp. 823-828.

Swelling deformation of the bentonite mixed with silica fume or sodium carbonate in calcium hydroxide solution

Yuki YOKOYAMA¹ and Kenichiro NAKARAI²

¹Graduate School of Engineering, Gunma University, Japan

²Graduate School of Engineering, Hiroshima University, Japan

ABSTRACT

From these experimental results, it was found that the mixing of small amount of silica fume or sodium carbonate to bentonite can reduce the deterioration of the bentonite in alkaline water from the viewpoint of swelling performance. Swelling performance of the bentonite specimen was measured using a one-dimensional swelling-deformation test under constant vertical pressure. In this paper, we propose a method to solve this problem by the mixing of silica fume or sodium carbonate. These materials are expected to react with the leached calcium ions from the cement-based materials and reduce the deterioration of the bentonite. It decreases swelling performance of the bentonite. However, during the tens of thousands of years, bentonite can be deteriorated and dissolved by alkaline water with the leached ions from the surrounding cement-based materials. In radioactive waste disposal facility, sodium-type bentonite will be used as an artificial barrier material.

Keywords: artificial barrier, bentonite, silica fume, sodium carbonate, swelling deformation

1. INTRODUCTION

In radioactive waste disposal facilities, sodium bentonite having high swelling capacity will be used as an artificial barrier material. It is expected to delay the infiltration of groundwater and to fill cracks of the surrounding host rock. However, during tens of thousands of years, the bentonite can be deteriorated by the alkaline water with the leached ions from the surrounding cement-based materials. It decreases swelling capacity of the bentonite [1]. To reduce the decrease in the swelling capacity by the alkaline water, the authors have proposed two kinds of admixtures. One is the mixing of pozzolanic materials such as silica fume and fly ash to the sodium bentonite [2]. These pozzolanic materials are expected to consume the leached calcium ions from the cement-based materials and to reduce the deterioration of the bentonite. Experimental results in the previous research [2] showed that the mixing of the pozzolanic materials can reduce the decrease in the swelling capacity. In the experiment, the one-dimensional vertical swelling deformation was measured by using the swelling-deformation tests proposed by Komine and Ogata [4], [5]. Especially, the mixing of 1 mass% of silica fume was the most effective to reduce the deterioration by calcium hydroxide solution. But, the detailed investigation should be added because the range of experimental conditions was limited.

The other proposal is the mixing of sodium carbonate to the bentonite. Here, calcite precipitation between the bentonite-based materials and cement-based materials was expected. The previous experimental results conducted by Nakarai et al [3] showed the calcite precipitation can reduce the deterioration of the bentonite due to calcium leaching from the cement paste. Here, the immersion tests of the composite specimens consisting of the cement paste and the

bentonite were performed. Then, the effect of the mixing of the sodium carbonate was investigated from the distribution of calcium measured by Electron Probe Micro Analysis (EPMA). But, the swelling characteristics of the sodium carbonate mixed bentonite haven't been studied.

In this study, we investigated the effect of the mixing of silica fume or sodium carbonate to bentonite on the swelling characteristics of the bentonite. To investigate the swelling characteristics, we also used swelling-deformation tests proposed by Komine and Ogata [4], [5]. Then, we measured swelling deformation of the compacted bentonites which were immersed in the distilled water or the saturated aqueous solution of calcium hydroxide. As preliminary experiments, we also studied the influence of the experimental condition such as means of water supply and concentration of calcium hydroxide solution. Then, we decided the condition to appropriately measure the swelling deformation of the bentonite specimens in this study.

2. OUTLINE OF EXPERIMENTS

2.1 Materials for specimens

Table.1 shows the outline of specimens. In this study, we used silica fume or sodium carbonate as an admixture. Then, we prepared three kinds of specimens; pure bentonite without admixtures, bentonite mixed with silica fume, and bentonite mixed with sodium carbonate. This study used commercial bentonite, called Kunigel-V1, extracted from the Tsukinuno Mine in Japan. This study also used silica fume. The 94.9% of silica fume was SiO₂ and its specific surface area was 17.5 m²/g. This study also used commercial sodium carbonate. Its content of sodium carbonate was 99.8%. The mixing ratios of silica fume to dry bentonite were 0.5, 1.0, 2.0, 5.0, 8.0 mass% while the mixing ratios of sodium carbonate were 1.0, 4.0 mass%. The water content of bentonite was set to 21 % by considering the planned value in the design of a subsurface

radioactive waste repository for low level wastes in Japan. In this paper, the names of specimens indicated the composition of the materials, the mixing ratio of admixture, the type of solution (W: distilled water, CHs: saturated calcium hydroxide solution, CHp: saturated calcium hydroxide solution with calcium hydroxide powder) and supply of solution (1: one side, 2: two sides). The supplying method will be discussed only in chapter 3.

2.2 Mixing of materials

The mixing process is as follows. First, air-dried bentonite and admixture were mixed at low speed for 30 seconds using an Omni mixer. During the mixing, water contents of these mixtures were also adjusted. Here, we sprayed distilled water. After that, they were mixed at high-speed for 60 seconds. And they were kept in a polyethylene bag for 24 hours. Next day, these mixtures were mixed at high-speed for 60 seconds again, and we measured water contents of these mixtures.

2.3 Specimens

In this study, cylindrical specimens having diameters of 60mm and heights of 5mm were prepared. The height of the specimens became small to save time for water absorption because the compacted bentonite specimens have low conductivities. The dry density was set to $1.3\text{g}/\text{cm}^3$ to easily assess deterioration. The sample was statically compacted by vertical pressure for several hours until the height of specimens became 5mm.

2.4 Swelling-deformation test

Fig. 2.1 shows the test apparatus. Swelling characteristics of the bentonite specimens were evaluated by using the one-dimensional swelling-deformation test under a constant vertical pressure proposed by Komine and Ogata [4], [5]. Iron plate was fixed to the top of the piston applying the constant vertical pressure. We used a filter paper, of which the diameter is 60mm and the thickness is 0.19mm, and a porous metal, with 60mm diameter and 5mm thickness, as filter. The filters were placed below the top cap and on the pedestal. They were used for mitigating the outflow of bentonite particles from specimens.

After applying the prescribed vertical pressure (10kPa) to the specimen, aqueous solutions were supplied to the specimen. Then, the relationship between the axial swelling deformation and the time required from the start of water supply was measured.

The solutions supplied to the specimens were three kinds of aqueous solutions. The first solution was the distilled water to measure basic performance. The second and third solutions were the saturated aqueous solutions of calcium hydroxide to discuss the effects of calcium ions leached from cement-based materials. The third solution included additional calcium hydroxide powders to keep saturated concentration, while the second solution without additional calcium hydroxide allowed decrease in the concentration during experiments.

In the cases of specimens of the pure bentonite without admixtures and the bentonite mixed with silica fume, the temperature during the experiments was set to 40°C in order

Table1. 1 Outline of specimen

Names of specimens	Material composition [mass%]			Type of solution	Supply of solution
	Be	SF	Na_2CO_3		
Be-W	100.0	0.0	0.0	distilled water	one side
BeSF-0.5-W	99.5	0.5	0.0		
BeSF-2-W	98.0	2.0	0.0		
BeSF-3-W	97.0	3.0	0.0		
BeSF-5-W	95.0	5.0	0.0		
BeSF-8-W	92.0	8.0	0.0		
Be-CHs	100.0	0.0	0.0	saturated calcium hydroxide solution	one side or two sides
Be-CHp	100.0	0.0	0.0	saturated calcium hydroxide solution with calcium hydroxide powder	one side
BeSF-0.5-CHp	99.5	0.5	0.0		
BeSF-1-CHp	99.0	1.0	0.0		
BeSF-2-CHp	98.0	2.0	0.0		
BeSF-5-CHp	95.0	5.0	0.0		
BeSF-8-CHp	92.0	8.0	0.0		
Be Na_2CO_3 -1-CHp	99.0	0.0	1.0		
Be Na_2CO_3 -4-CHp	96.0	0.0	4.0		

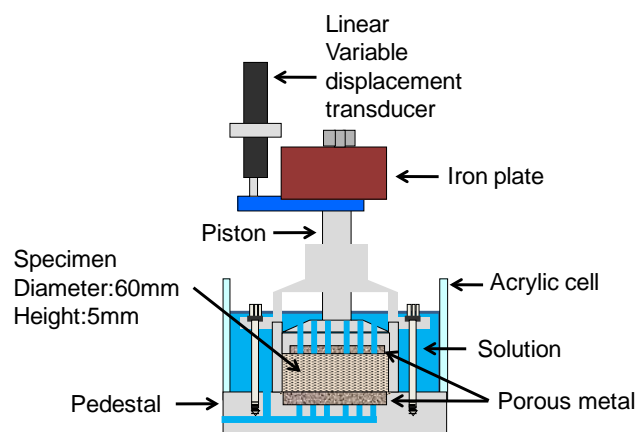


Fig. 2.1 Schematic drawing of test apparatus

to promote pozzolanic reaction of silica fume. In the case of specimens of the bentonite mixed with sodium carbonate, the temperature was set to 20°C . They were determined by considering the experimental condition in the previous studies [2], [3].

The solution was supplied from one side of specimens in this study. Although the water supply from two sides could save time for measurements, the condition in this study was decided to be same as the previous study [2] to easily compare the results. The validity of this water supplying condition was investigated by the preliminary experiments.

Measurement period was also investigated by the preliminary experiments. Then, it was decided to be 7 days. It was longer than the previous study conducted by Nakarai and Shimakura [2] to improve the accuracy of data.

2.5 Evaluation method

The swelling strain (%) is defined by

$$\varepsilon_s = \frac{\Delta S}{H_0} \times 100 \quad (1)$$

where ε_s is swelling strain (%), ΔS is swelling deformation, and H_0 is initial specimen height.

It is known that the curves of swelling strain versus time can be approximated by the hyperbola in Eq.(2) [4], [5]. The maximum swelling strain ε_{smax} (%) is obtained from the asymptotic line of the hyperbola, and can be calculated by Eq.(3)

$$\varepsilon_s(\text{time}) = \frac{\text{time}}{a + b \text{time}} [\%] \quad (2)$$

$$\varepsilon_{smax} = \lim_{\text{time} \rightarrow \infty} \varepsilon_s(\text{time}) = \frac{1}{b} [\%] \quad (3)$$

where “time” is the duration (in day) from the start of water supply, $\varepsilon_s(\text{time})$ is swelling strain at “time”, and a and b are constants determined by fitting procedures.

3 RESULTS OF PRELIMINARY EXPERIMENT

This chapter describes the results of the preliminary experiment to decide the experimental conditions of the swelling-deformation test.

3.1 Influence of additional calcium hydroxide powder

Fig.3.1 shows the results of the swelling-deformation tests investigating the influence of additional calcium hydroxide powder. They show the relation between the curve of swelling strain versus time and the calculated maximum swelling strain. The swelling strain of Be-CHs-1 was greater than that of Be-CHp-1. We supposed that the reduction of the deterioration of the bentonite in the case of Be-CHs-1 without additional calcium hydroxide powders was caused by the decrease in the concentration of calcium ions in the solution. Deterioration of the bentonite in the case of Be-CHp-1 including additional calcium hydroxide powders is progressed because the solution kept saturated concentration. To keep saturated concentration is necessary to correctly evaluate swelling performance of the bentonite.

Therefore, we used the solution included additional calcium hydroxide powders in the experiment described in the next chapter.

3.2 Influence of supplying method of solution

We studied influence of the supply of the solution to swelling strain of specimen. Fig.3.1 shows the results of the swelling-deformation tests on the influence of the supply of solution. The swelling deformation rate of Be-CHs-2 was relatively fast and the swelling was almost converged in three days. On the other hand, the swelling deformation rate of Be-CHs-1 was relatively slow and the swelling deformation was gradually increased until 7 days (the end of measurement). In the specimen of Be-CHs-2, the rate of the supply was faster than that in Be-CHs-1 because the saturated

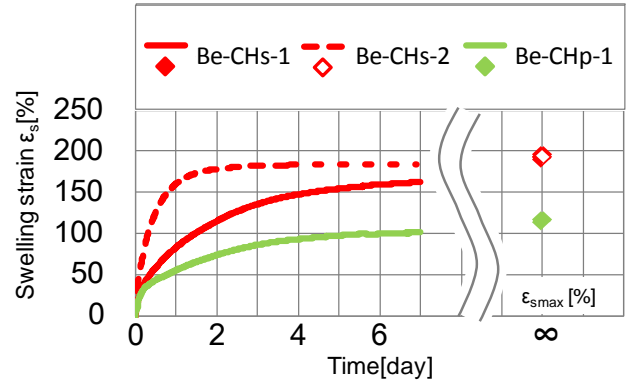


Fig.3.1 Curves of swelling strain versus time and the maximum swelling strain

calcium hydroxide solution was supplied from the bottom and top of the specimen. This increase in the solution supply rate caused the increase in the swelling deformation. The results of the maximum swelling strain of Be-CHs-1 and Be-CHs-2 are approximately same. It means that the supplying method of the solution doesn't affect the maximum swelling strain.

4 RESULTS AND DISCUSSIONS

Fig.3.2 shows the results of the swelling-deformation tests investigating the swelling deformation when the distilled water (W) was supplied to the specimens which were mixed with silica fume. Fig.3.3 shows the results of the swelling-deformation tests when the saturated calcium hydroxide solution with additional powders (CHp) was supplied to specimens which were mixed with silica fume. Fig.3.4 shows the relationship between the calculated maximum swelling strain and the mixing ratio of silica fume. Here, the solid and broken lines in the figure show the predicted maximum swelling strain in W and CHp, respectively. They were predicted from the maximum swelling strain of the pure bentonite specimens and the mixing ratio. Fig.3.5 shows the change in the measured swelling strain with time and the calculated maximum swelling strain.

4.1 Effect of silica fume as an admixture

According to Fig.3.4, in the case of W, the maximum swelling strain of specimen was smaller than the predicted maximum swelling strain indicated by the solid line. Therefore, it was found that the maximum swelling strain was decreased by the mixing of silica fume when W was supplied. We suppose that it was caused by solidification with the pozzolanic reaction of silica fume in the water. In the case of CHp, it was found that the maximum swelling strain of specimens mixed with silica fume (0.5 ~ 5 mass %) became larger than the predicted maximum swelling strain indicated by the solid line. It means that the mixing of silica fume can reduce the deterioration of bentonite by alkali. Especially, the mixing of 1mass% of silica fume was most effective to suppress the deterioration. When we mixed silica fume more than 1mass%, the maximum swelling strain gently decreased as mixing ratio of silica fume increase. It was caused by the decrease in the bentonite proportion in the specimen and

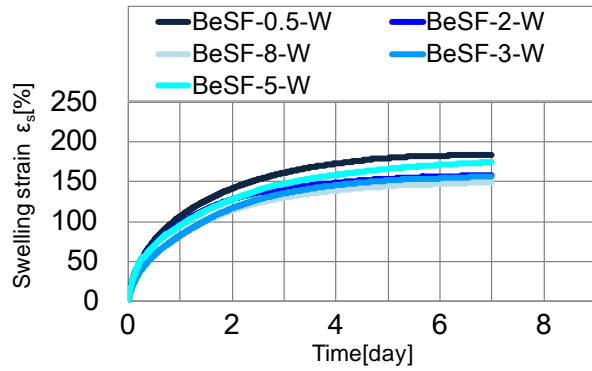


Fig.3.2 Curves of swelling strain versus time

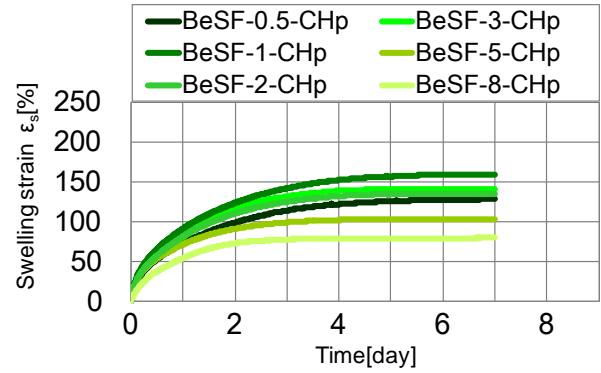


Fig.3.3 Curves of swelling strain versus time

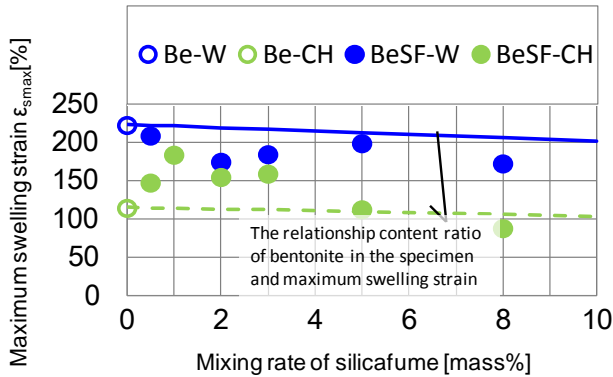


Fig.3.4 Relationship between maximum swelling strain and mixing rate of silica fume

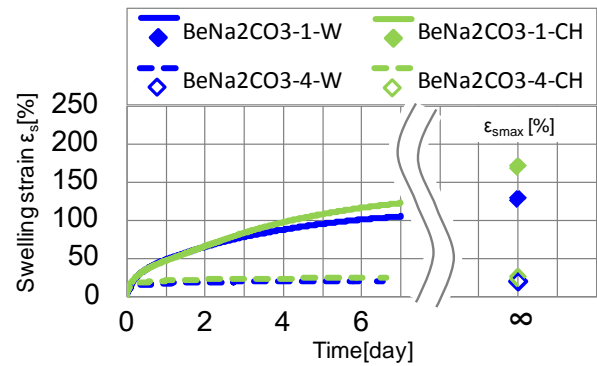


Fig.3.5 Relationship between maximum swelling strain and curves of swelling strain versus time

solidification associated with the pozzolanic reaction of silica fume in the water.

4.2 Effect of sodium carbonate as an admixture

According to Fig.3.5, in the case of the mixing of 4 mass% of sodium carbonate, the specimens both in W and CHp showed similar swelling behaviors. It means that the mixing of 4 mass% of sodium carbonate did not reduce the degradation of bentonite. In the case that mixing ratio of sodium carbonate was 1mass%, there were no differences in the swelling behaviors until 2 days. But, after 2days, it was found that the swelling strain of BeNa₂CO₃-1-CHp was greater than that of BeNa₂CO₃-1-W. It was supposed to be caused by the decrease in the ionic strength of the pore water in the particles associated with the precipitation of calcite.

5 CONCLUSIONS

In this study, we investigated the effect of admixtures such as silica fume and sodium carbonate in order to develop new materials suppressing the deterioration by alkali from the viewpoint of swelling performance. The performance was evaluated based on the swelling deformation of specimens measured in the distilled water and the saturated calcium hydroxide solution. Then, the following conclusions were drawn from the results of the experiments.

- (1) The mixing of small amount of silica fume can reduce the deterioration of the bentonite in alkaline water.
- (2) The mixing of 1 mass% of sodium carbonate can reduce the deterioration of the bentonite in alkaline water.

6 REFERENCES

- [1] Japan Society of Civil Engineers, "The method for setting nuclide migration assessment parameter used in groundwater migration scenario in safety assessment of sub-surface disposal," 2008. (in Japanese)
- [2] Nakarai K., and Shimakura C., "Swelling deformation of the bentonite mixed with pozzolanic materials in calcium hydroxide solution," Proceedings of 46th Conference of the Japanese Geotechnical Society, 2011, pp.2089-2090. (in Japanese)
- [3] K. Nakarai, M. Watanabe, H. Ishii, K. Koibuchi: Reduce the deterioration between cement and bentonite mixed with Na₂CO₃, Proceedings of the 66th Annual Conference of the Japan Society of Civil Engineers, pp.99-100, 2011.
- [4] H. Komine, H. Ogata: Experimental study on swelling characteristics of compacted bentonite, Canadian Geotechnical Journal, Vol.31, No.4, pp.478-490, 1994.
- [5] H. Komine, H. Ogata: Experimental study on swelling characteristics of sand-bentonite mixture for nuclear waste disposal, Soils and Foundations, Vol.39, No.2, pp.83-97, 1999.

An Interpretation of Mechanical Properties of Bentonite as a Non-linear Elastic Material

Y.TAKAYAMA, S.TSURUMI, A.IIZUKA, K.KAWAI
KOBE UNIVERSITY, JAPAN
S.OHNO
KAJIMA CORPORATION, JAPAN

ABSTRACT

Due to its low permeability and remarkable expansion characteristics, bentonite is an excellent candidate with potential use as a buffer in the disposal of nuclear waste. In order to examine long term safety of bentonite buffer in the disposal of nuclear waste, constitutive modeling of bentonite materials and numerical simulations into which its constitutive modeling is incorporated have been actively developed in recent years. The bentonite materials are usually modeled as a geo-material composed by elasto-plastic isotropic compression/expansion and plastic dilatancy characteristics. However, based on recent experimental data, the authors have begun to think that such usual treatment of constitutive modeling for geo-materials may not be applicable to the bentonite materials. In this paper, fundamental considerations in elasto-plastic constitutive modeling for fully saturated bentonite materials are made. According to uniaxial compression test data by Sasakura et al (2003) in which lateral earth pressure was measured, it is found that the hysteresis response between loading and unloading processes does not appear. It suggests that the bentonite is elastic materials in which the swelling line corresponds with the normally consolidation line in the e - $\log p'$ relationship. Also, according to triaxial CU test results of bentonite materials, it can be seen that the effective mean stress is almost unchanged during shearing. This implies that the bentonite does not have dilatancy characteristics based on the critical state theory. Similar interpretation can be derived from the experimental results obtained from a series of triaxial CD tests by Cui et al (2006).

1. INTRODUCTION

Bentonite is known to be a material that has remarkable expansion characteristics and very low permeability. Therefore, the bentonite material is expected to use as a buffer in the geological disposal of nuclear waste facility and its mechanical and mineralogical properties have been investigated. In the nuclear disposal site, the role to prevent leaking of radioactive polluted water by self-seal ability and performance to mitigate stresses generated due to creep of base rock are expected for the bentonite as a buffer. Also, the stability and safety for an extremely long period of time are required for the geological disposal of nuclear facility. In order to address such problems, it is necessary to predict the long term behavior of the geological disposal of nuclear waste facility and reliable numerical simulation technique that enables it is required. The constitutive modeling of a material which describes the mechanical properties is an essential key technique in the numerical simulation. As for the constitutive modeling of bentonite materials, it has been formulated phenomenologically based on the elasto-plastic response under the loading and unloading processes and dilatancy characteristics during shearing like other clayey materials. However, in case of bentonite materials, the authors think that explicit experimental supports to such constitutive modeling are not sufficient. Remarkable expansion characteristics on water absorption and very low permeability of the bentonite make it difficult to interpret their fundamental mechanical behavior. The aim of this paper is to reconsider the

based on recent experimental data and to discuss the theoretical formulation of constitutive modeling for the bentonite materials.

2. Isotropic compression and swelling characteristics of saturated bentonite materials

Usually, isotropic compression and swelling characteristics are discussed based on the experimental data obtained from triaxial tests under the drained condition. However, in the case of bentonite materials, there is not sufficient reliable data on the compression and swelling characteristics obtained from triaxial tests under the drained condition. Many oedometer test data have been reported instead. Compression and swelling behavior of the bentonite materials obtained from the oedometer tests is not directly available in discussing compression and swelling characteristics under isotropic confining pressure, because the lateral stress cannot be measured in the oedometer tests. If the lateral stress can be reliably estimated, more intensive discussion and more strict interpretation on the compression and swelling characteristics of the bentonite materials is thought to be made possible. In this paper, the authors cite the experimental data of measuring the lateral stress with a special oedometer test apparatus for the bentonite materials by Sasakura et al. (2003) and discuss the compression and swelling characteristics of the bentonite materials under isotropic confining pressure, which are fundamental mechanical properties for constitutive modeling.

(1) K_0 compression and swelling test

Sasakura et al. (2003) carried out one dimensional compression and swelling tests for Kunigel V-1, which is a typical material of sodium bentonite and is planned to be used in the nuclear waste disposal site, Japan. And they tried to measure the lateral stress under one dimensional loading and unloading processes with a special oedometer test apparatus. Their experimental results are shown in Fig.1. It is found that the coefficient of earth pressure at rest, K_0 , is almost kept 1.0 under the normally compression process and then increases with OCR under the unloaded swelling process. The relationship between K_0 value and OCR is indicated in Fig.2. In this figure, experimental data by Sasakura et al. (2003) are indicated by white circles and the following empirical relation, Eq.(1), between K_0 -value and OCR with the evaluation parameter, m , is compared,

$$K_{0-NC} = K_{0-OC} OCR^m \quad (1)$$

in which K_{0-NC} : the coefficient of earth pressure at rest under the normally compression process, K_{0-OC} : the coefficient of earth pressure at rest under the unloaded swelling process, OCR : over-consolidation ratio defined by σ'_{v0}/σ'_v , σ'_{v0} : pre-consolidation vertical stress, σ'_v : current vertical stress, m : evaluation constant. According to Fig.2, Eq.(1) with

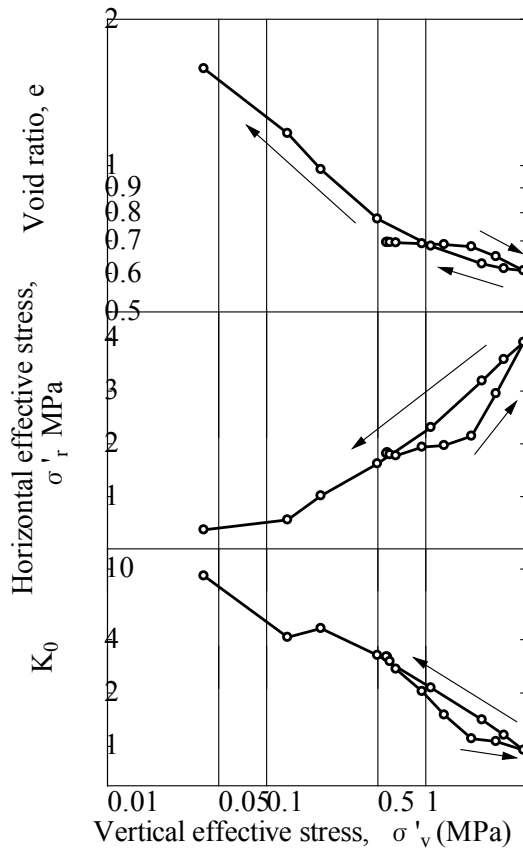


Fig.1 K_0 compression and swelling test result

m of 0.6 seems to well explain experimental results of the bentonite, Kunigel V-1. If it is allowed to employ Eq.(1) with

m of 0.6 in converting the vertical stress into the isotropic confining pressure, fundamental mechanical properties on compression and swelling characteristics under the isotropic confining pressure can be discussed using experimental data obtained from the oedometer test.

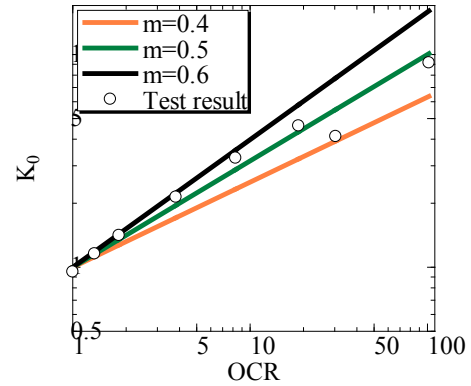


Fig.2 The relationship between K_0 value and OCR

(2) Isotropic deformation characteristics

Fig.3 shows one dimensional compression (consolidation) characteristics of Kunigel V1 obtained from the oedometer tests by Sasakura et al. (2002) and Ishikawa et al. (1997). Normally consolidation lines by Sasakura et al.(2002) and Ishikawa et al.(1997) does not correspond each other. This would be because the nature of the bentonite slightly differs depending on the year when the bentonite is produced and the content of the montmorillonite is slightly different even though the same bentonite.

According to Kobayashi et al. (2007), one dimensional normally consolidation characteristics of the bentonite under

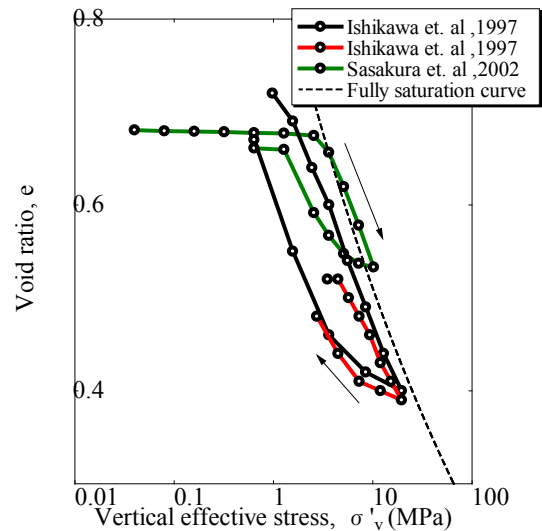
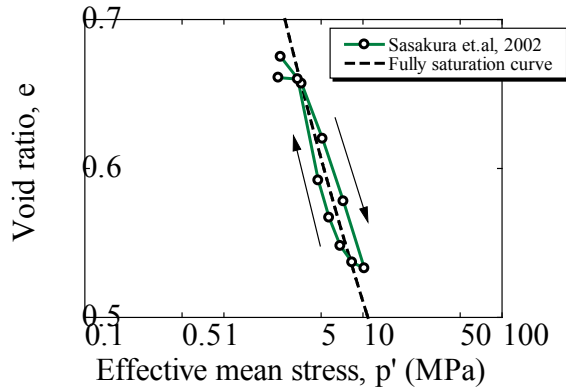


Fig.3 One dimensional compression (consolidation) characteristics of Kunigel V1

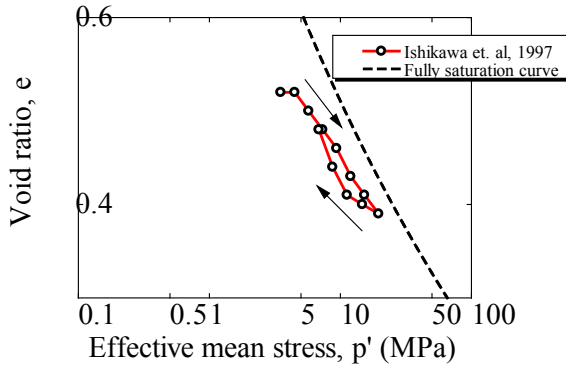
fully saturated state is uniquely expressed as,

$$e = \lambda_\rho \ln \frac{\sigma'_{v\max}}{\sigma'_v} \left/ \left(G_s - \lambda_\rho \ln \frac{\sigma'_{v\max}}{\sigma'_v} \right) \right. \quad (2)$$

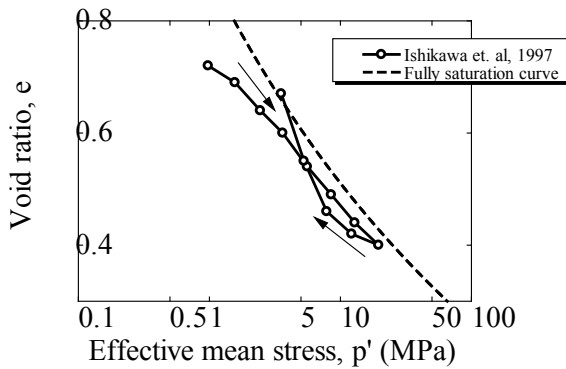
in which λ_ρ : material constant, G_s : specific gravity of soil particle, $\sigma'_{v\max}$: reference and maximum vertical stress corresponding to the void ratio vanishing. This curve is called as fully saturation curve. In the case of data by Sasakura et al. (2002), $\lambda_\rho = 0.156$, $G_s = 2.733$,



(A)



(B)



(C)

Fig.4 Isotropic compression and swelling characteristics of saturated bentonite materials

$$\sigma'_{v\max} = 3.73 \text{ GPa} .$$

Then, the effective vertical stress can be converted into the effective mean stress using Eq.(1) as,

$$p' = \frac{\sigma'_v + 2K_0\sigma'_v}{3} \quad (3)$$

in which p' : effective mean stress, σ'_v : effective vertical stress, K_0 : coefficient of earth pressure at rest. All data in Fig.3 are converted in terms of effective mean stress using Eq.(3) and are depicted in Fig.4 as a relation between the void ratio and the effective mean stress, in which $K_{0-NC} = 1$ and $m=0.6$ are employed. It is found that the hysteresis loop between loading and unloading processes disappears and the swelling line corresponds with the compression line in Fig.4. If the compression and swelling responses in Fig.4 can be interpreted as isotropic compression and swelling characteristics of the bentonite, the bentonite can be regarded as a material having no plastic deformation. Namely it can be said that the bentonite is a non-linear elastic material.

3. Dilatancy characteristics of saturated bentonite materials

In this section, we examine the dilatancy characteristics of bentonite. Usually, dilatancy characteristics are examined conducting triaxial CD test in which the principal mean effective stress is maintained constant. However, in the case of bentonite materials, there is not sufficient reliable data obtained from this test. Therefore, we examine dilatancy characteristic using the results of triaxial CU test on bentonite.

(1) Triaxial CU test

Results of triaxial CU test on some kind of bentonite are shown in Fig.5-8. These figures show the relationship between effective mean stress and

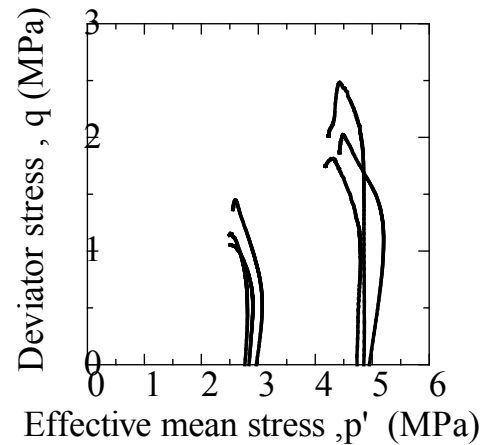


Fig.5 Triaxial CU test result on Sodium type of Bentonite conducted by Sasakura et al. (2002)

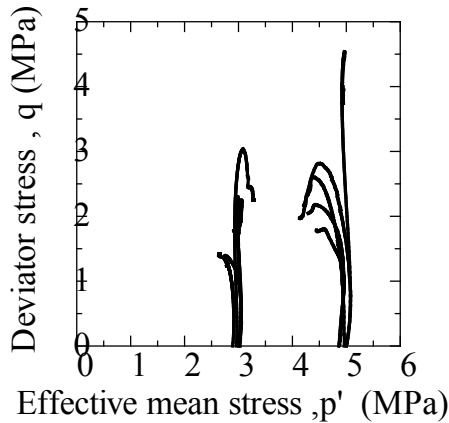


Fig.6 Triaxial CU test result on Calcium type of Bentonite conducted by Sasakura et al. (2002,2003)

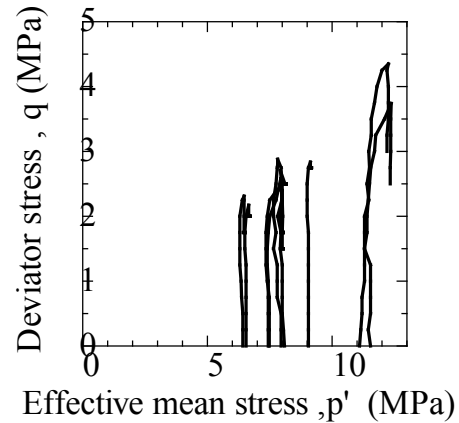


Fig.8 Triaxial CU test result on MX-80 conducted by Ann et al. (2010)

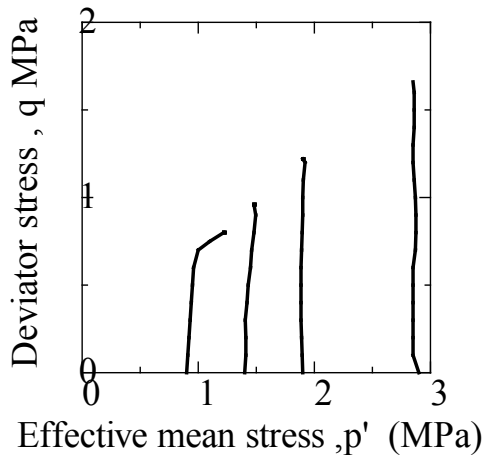


Fig.7 Triaxial CU test result on OT-9607 conducted by Takaji et al. (1999)

deviator stress. According to these test results, it can be seen that the effective mean stress is almost unchanged during shearing. Usually, the effective mean stress decreases with increasing shear stress because of negative dilatancy when triaxial CU test on normally consolidated clay is conducted. Therefore, it is implied that the bentonite does not have dilatancy characteristics based on the critical state theory.

4. Swelling characteristic of saturated Bentonite

As one of important mechanical properties of bentonite, there are swelling characteristic that is found in process from unsaturated to saturated. We have two tests, swelling deformation test and swelling pressure test, as a way of measuring of swelling characteristic. Swelling deformation test teaches us deformation when the bentonite suck the water under controlling the stress, and the swelling pressure test teach us swelling pressure when the bentonite suck the water

under uniforming the volume. Typically, these result is arranged as connection between pressure at saturation to dry density. However, the relationship between these test's results and full saturation line is not elucidated perfectly. Saturated bentonite is the elastic body, so its condition is always on full saturation line. Because of this, we estimate that the final value of these swelling test get to full saturation line. Now, we examine relationship between swelling characteristic and full saturation line, based on the result of these swelling test.

(1)bentonite's swelling deformation test

Cui(2006) conducted swelling deformation test and isotropic unloading test with controlling principal stress. This test was performed on the sample of compacted Kunigel V-1/Toyourasa mixture with Kunigel V-1 content of 50% in dry mass. In this test, they set the initial dry density three patterns, 1.69, 1.54, 1.2g/m³, and then did water absorption test with hydrostatic stress, based on the condition that the test keep mean principal stress settled. We show the sample's initial value, initial dry density and initial water content ratio, and the value of mean effective principal stress which the sample suck the water on the table-1.

In addition, they did isotropic unloading test which reduce the load under 49kPa after the sample suck the water with mean principal stress set 392kPa. Fig-9 show these result, relationship between mean effective principal stress and void ratio at the finish of retting and swelling, of these three case of initial dry density and relationship between mean principal stress and void ratio when the test goes on isotropic unloading. In the case that it gave the sample some water in same mean stress, Fig-9 shows that the void ratio takes same value regardless of initial dry density. Furthermore, the value of unloading pass at isotropic unloading shows the almost same result with the swelling deformation test. Now, we take the three words, full saturated line/normal consolidation line/isotropic unloading line, as the same meaning. Based on these result, we can find that the value in case of swelling test is on full saturated line at saturated condition. Next, they conducted swelling test with the different stress ratio

$R(= \sigma_a / \sigma_r)$ in which the principal mean stress and principal stress ratio are maintained constant. The initial value of the sample takes 1.69g/m^3 as dry density and 18.7% as initial water content ratio. We show the relationship between void ratio and mean principal stress at the end of soaking in Fig-10. Fig-10 teaches us that void ratio and mean stress are relationship of one to one regardless of principal stress ratio. So, our examination that saturated bentonite is nonlinearly elastic material without characteristic of dilatancy coincides with the result of Cui's test.

ρ_{d0} (g/cm^3)	w_0 (%)	p (kPa)
1.69	18.7	49,98,147,196
1.54	18.7	19.6,49,88,196,294,392
1.2	19	49,98,196,392

Table-1 initial value

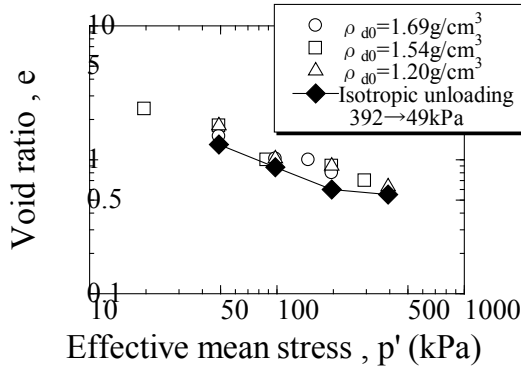


Fig.9 the result of amount of swelling test

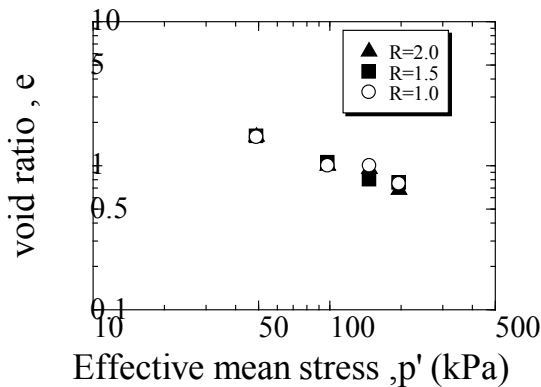


Fig.10 the result of swelling test

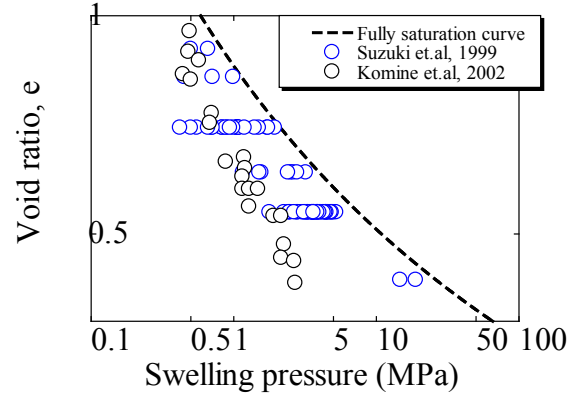


Fig.11 the result of swelling pressure test

(2) Swelling pressure test of bentonite

Swelling pressure test, using the equipment similar to one-dimensional consolidation equipment, is the test which can measure counter force of vertical direction caused by vertical soaking under settled volume. Fig-11 shows the result of swelling pressure test of Kunigel V-1, and shows relationship between void ratio and vertical swelling pressure at saturated. This figure teaches us that void ratio is smaller, then swelling pressure is larger and swelling pressure takes apart value in the same void ratio, but the value doesn't exceed the full saturated line. But, considering the result so far obtained, these apart value results from measuring only vertical swelling pressure. So, if we take account of lateral stress and reconsider by the use of mean stress, and we consider that the value is all on the full saturated line.

5. Conclusion

This study examines the mechanical characteristics of bentonite based on recent experimental data. The conclusions are summarized as follows.

- (1) The swelling line at $S_r = 1.0$ corresponds with the Normal Consolidation line. And saturated bentonite does not have dilatancy characteristics. Therefore, saturated bentonite is a non-linear elastic material.
- (2) When water is supplied from unsaturated state to saturated state, the final or saturation points reach on the fully saturation curve.

In Fig. 12, the schematics of relationship between void ratio and the principal mean stress during loading, unloading and swelling are summarized.

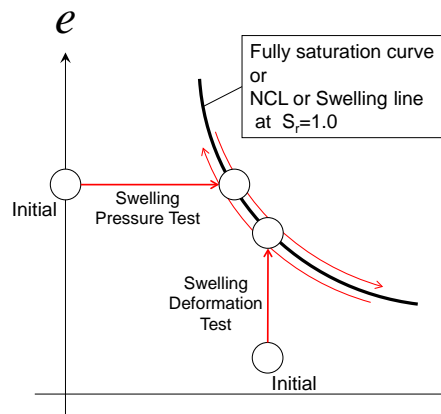


Fig. 12 Schematics of relationship between void ratio and the principal mean stress

REFERENCES

- [1] SASAKURA,T., KUROYANAGI,M., KOBAYSHI,I., OKAMOTO,M. "Studies on mechanical behavior of bentonite for development of the constitutive model II", 2003 ,JNC TJ8400 2003-048. (in Japanese)
- [2] SASAKURA,T., KUROYANAGI,M., OKAMOTO,M., "Studies on mechanical behavior of bentonite for development of the constitutive model", 2002, JNC TJ8400-2002-025. (in Japanese)
- [3] ISHIKAWA,H., ISHIGURO,K., NAMIKAWA,T., SUGANO,T., "Consolidation Properties of Buffer Material" 1997, PNC TN8410 97-051 . (in Japanese)
- [4] KOBAYSHI,I., TOIDA,M., SASAKURA,T. and OHTA,H., "Interpretation of compression/swelling behavior of compacted bentonite using constant water-content line and constant degree-ofsaturation line", 2007,JSCE Journal of Geotechnical Engineering, 63(4):1065-1078. (in Japanese)
- [5] TAKAJI,K., SUZUKI,H. "Static Mechanical Properties of Buffer Material" 1999, JNC TN8400 99-041 (in Japanese)
- [6] Ann Dueck, Lennart Börgesson, Lars-Erik Johannesson, "Stress-strain relation of bentonite at undrained shear" 2010, SKB Technical Report TR-10-32
- [7] Hongbin CUI, De'an SUN, MATSUOKA,H., "Swelling characteristics of Sand-Bentonite mixtures under isotropic and anisotropic stress States" 2006, JSCE Journal of Geotechnical Engineering, 62(3): 657-666. (in Japanese)
- [8] SUZUKI,H. and FUJITA,T, "Swelling Characteristics of Buffer Material" 1999, JNC TN8400 99-038. (in Japanese)
- [9] KOMINE,H. and OGATA,N., "Swelling characteristics of sand-bentonite mixture and various kinds of bentonite", 2002, JSCE Journal of Geotechnical Engineering, 701(III-58):373-385. (in Japanese)

Parametric Study of Crossing Tunnels at Different Level

A. Tohidi^{*} MH.Sadagiani
School of Civil Engineering, Sharif University of Technology, Iran,

ABSTRACT

Tunnel construction in congested urban areas is an essential part of transportation system development. In this study a parametric Analysis was conduct to study the effect of tunneling on the existing support system (i.e. shotcrete lining) of a shallow tunnel and Surface Settlement. The parameters which can be studied are Soil characteristics, construction procedure and angle of intersection. Finite element method with Mohr-coloumb constitutive model was applied for numerical simulation of excavation process.

Parametric analysis shows notable importance for each parameter and we are able to minimize the Surface Settlement with some suitable considerations.

boring of shallow tunnel firstly, soil improvement in concerned area and selection of a perpendicular angle in intersection region are some instances that will decrease Surface Settlement.

Keywords: Crossing tunnels at different level, Numerical modeling, parametric analysis

1. Introduction

There are different applications for underground structures in metropolitan area including transportation, lifeline utilities and etc. These various applications show the importance and necessity of using underground spaces. Underground metro lines and underground facilities are a suitable solution for traffic problems; therefore, probability of locating a new tunnel nearby other existing underground structures incredibly increases. In these cases, the influence of new tunnel construction on increasing the ground surface settlement and bending moment of existing structure should be investigated. Generally, there are four approaches for predicting the surface settlement and bending moment in different steps of tunneling, including laboratory, experimental, analytical and numerical methods. In this article, 3D numerical simulation has been applied by Abaqus finite element software. The constitutive models which

represent soil and tunnel lining behavior are mohr-coloumb and linear elastic, respectively.

The effect of Important parameters such as construction procedure, intersection angle and soil improvement are Studied. In conclusion, it has been shown that the proper selection of these parameters minimizes the effect of new tunnel construction on surface settlement or bending moment of existing tunnel.

As before mentioned there are three main methods to study the interaction of nearby tunnels containing: field observation [1], physical model tests [2] and numerical simulation methods [3, 4, 5]. Liu (2009) presented a good summary about studies conducted until know.

In general Most of the numerical modeling is 2D and in 3D model a brief study about the influence of parameter like angle of intersection.

2. Geometry and mesh of the model

The dimensions of whole model according to figure 2-1 is 111 x 111 x 70m, also tunnels with polycentric section have been considered according to figure 2-2. The depth of shallow tunnel is 10 m and the depth of deep tunnel is 22 m the distance between the floor of shallow tunnel and crest of deep tunnel is 3.5 m. the properties of soil and initial lining have been shown in table I. try and error in modeling, showed that for tunnel area and around it, the use of Wedge elements is more convenient than Structure(cube)elements, so the Wedge elements have been used around the shallow and deep tunnels, and the eight-node isoparametric hexahedral elements with reduced integration (C3D8R) used in rest cases.

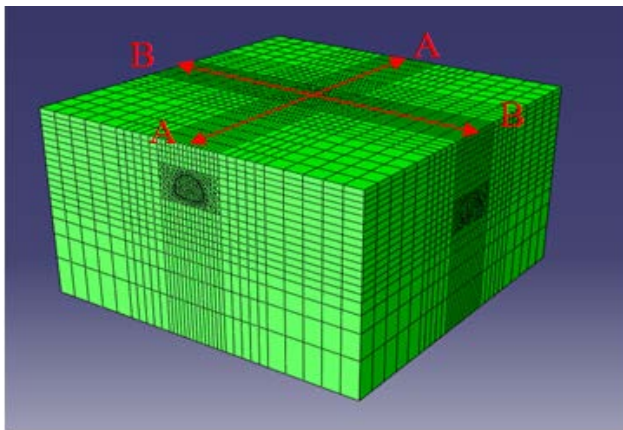


Fig 2-1.The Geometry, Mesh and Monitored Paths

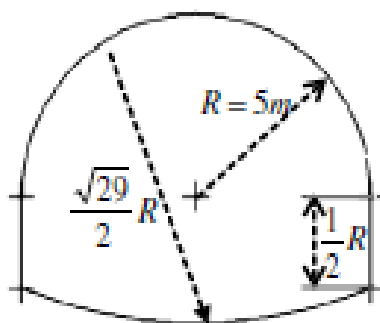


Fig 2-2. section of excavated tunnel

27480 elements used in soil area and 7104 element used for initial lining. In simulation of lining, the four-node shell elements with reduced integration (S4R) have been used. The way of mesh modeling is such that whatever we go away from tunnels, the mesh density proceeds to attenuate. The numbers

of excavation stages in base model are 53 stages, in stage 1 the gravity load applied and stage 2 to 27 is related to excavation of shallow tunnel and from stage 28 to 53 deep tunnel excavated. For the stability of analysis the 6m at the begin and end of the tunnel weren't excavated.

This technique caused more reasonable result than when the excavation starts at the boundary condition.

Unsupported span length is 1.5 m at 12 m before and after the intersection point and 3m at the rest.

In one stage the soil element is inactive and in next stage the lining element will be active.

All parameters that study are presented in table II.

3. Results

For gaining the influence of interaction, we must study at first what happen in boring the shallow tunnel and deep tunnel alone and then compare the result when both of them excavated. Thus in figure 3.1, the surface settlement of shallow tunnel alone and both tunnels have been shown and in figure 3.2, the surface settlement of deep tunnel alone and both tunnels have been shown. In figure 3.3, the diagram of bending moment in shallow tunnel crest during the shallow tunnel and deep tunnel excavation have been shown.

Table I- specifications of base model

Parameters	Soil: Mohr-Colomb - $K_0=0.5$	Initial lining: 30 cm - linear elastic
Internal friction Angle	30°	-
Cohesion (kPa)	50	-
Poisson coefficient	0.3	0.15
Elastic module (MPa)	50	30000
Density (kg/m ³)	2000	2400

Table II – parameters that study

Parameters	Descriptions																				
Construction Procedure	<div>1. first the shallow tunnel then deep tunnel excavated</div> <div>2. first the deep tunnel then shallow Tunnel excavated</div> <div>3.The shallow and deep tunnels excavated simultaneously</div>																				
Soil Characteristics	<table><tr><th>Type of soil</th><th>Cohesion (Kpa)</th><th>Friction Angle</th><th>Young’s Modulus (Mpa)</th></tr><tr><td>One</td><td>65</td><td>40°</td><td>100</td></tr><tr><td>Two</td><td>55</td><td>35°</td><td>75</td></tr><tr><td>Three (base)</td><td>50</td><td>30°</td><td>50</td></tr><tr><td>Four (Improved)</td><td>100</td><td>30°</td><td>200</td></tr></table>	Type of soil	Cohesion (Kpa)	Friction Angle	Young’s Modulus (Mpa)	One	65	40°	100	Two	55	35°	75	Three (base)	50	30°	50	Four (Improved)	100	30°	200
Type of soil	Cohesion (Kpa)	Friction Angle	Young’s Modulus (Mpa)																		
One	65	40°	100																		
Two	55	35°	75																		
Three (base)	50	30°	50																		
Four (Improved)	100	30°	200																		
Intersection Angle	<div>Three models with intersection angle</div> <div>0° , 60°, 90°</div>																				

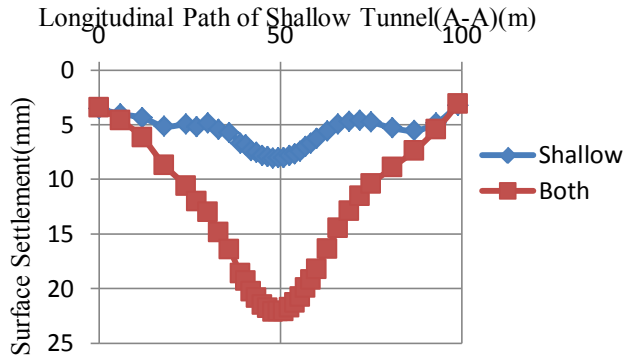


Fig3.1. surface settlement of shallow tunnel alone and crossing tunnels in path A-A

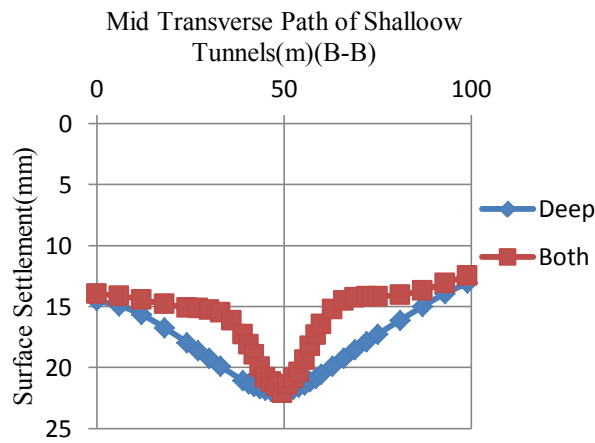


Fig3.2. surface settlement of deep tunnel alone and crossing tunnels in Path B-B

The first matter we get from longitudinal settlement of shallow and deep tunnels(alone) is that the variation of longitudinal settlement in distance 45 to 55 m ($4.5D - 5.5D$) very close to each other which describe the plane strain conditions in model and this result could be used for determining the minimum length of base model. However this above condition is not valid in crossing tunnels and the necessity of three dimensional simulations is clear. With consideration to figures 3.1 and 3.2, we understand that use of linear superposition for estimating the total settlement of two tunnels construction is not true. In other word to gain the maximum settlement, algebraic sum of maximum settlement of shallow and deep tunnel construction, cause incorrect outcomes.

A notable point from figure 3.2 that settlement of both tunnel smaller than the settlement of deep tunnel only! Because of

same module of elasticity in loading and unloading for mohr-columb model, when a shallow tunnel excavated heave occurred. But in this article we study the effect of parameters in settlement ratio and there is no significant error in our analysis.

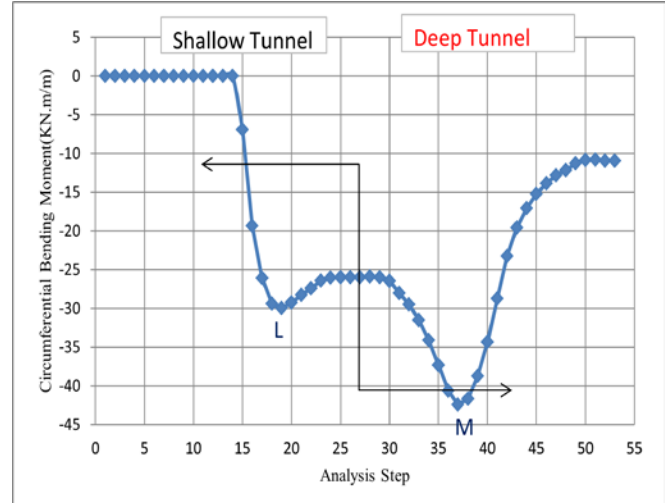


Fig 3.3. Bending moment in shallow tunnel crest during the excavation process

As we observe from Fig 3.3. before excavation and lining installation, the bending moment is zero in intersection points but after activation of lining, suddenly this moment reaches to -30KN.m/m (L point) and in following process, this quantity reduces because of lining installation in following process to reach a constant value, after starting the deep tunnel excavation, increasing of moment continues until the deep tunnel approaches to intersection point then the bending moment gradually increases and reaches to maximum value -42.6KN.m/m when deep tunnel crosses beneath the shallow tunnel (M point). In other words when deep tunnel excavate the increase of 36% in crest of bending moment in shallow tunnel is observed. After crossing the deep tunnel beneath the shallow ones, the negative bending moment gradually reduces until to reach the -11KN.m/m at the end of excavation. The interesting object that bending moment reaches a maximum value during the construction and the necessity of stage construction analysis in soil structure interaction observed.

With consideration to fig 3.1 and 3.2,we observed that the settlement in initial and final 6 m of shallow or deep tunnel

alone is equal to settlement of two tunnels. Also in diagram 3.3 it is observed that immediately after excavation of deep tunnel (stage 28) the moment doesn't change in shallow tunnel crest but approximately after crossing the 6 m of deep tunnel excavation, it increases gradually in shallow tunnel crest. From these result we can conclude that if we far from intersection point about 4.5D the influence of deep tunnel on shallow one can be ignore.

This conclusion is important when you want to determine the area of influence.

In the future we study the influence of parameter on interaction between tunnels.

3.1. Construction procedure

The first model is the base model which at first the shallow tunnel and then the deep tunnel had been excavated. In second model, two tunnels were excavated simultaneously thus, when 3 m of shallow tunnel was excavated, in the following process instead of next 3 m excavation, 3 m of deep tunnel excavated and in the third model the deep tunnel excavated initially and then shallow tunnel excavated. For comparing these three models, surface settlement in shallow tunnel width (path B-B in figure 2-1) have been shown in figure 3.4.

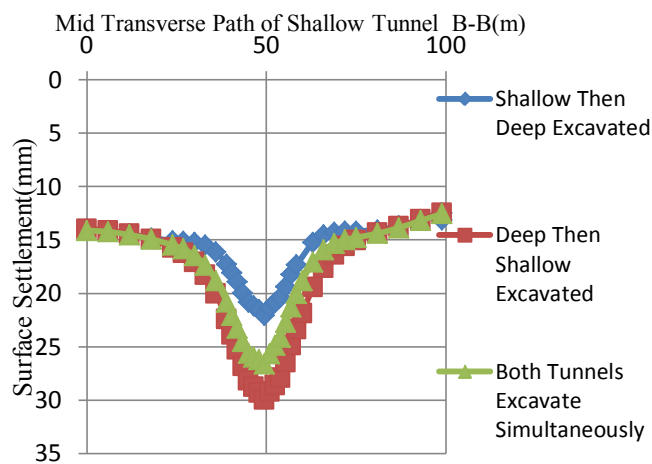


Fig3.4. influence of tunnels construction procedure on surface settlement of shallow tunnel

We get from figure 3.4 when at first the shallow tunnel and then deep ones is excavated, the maximum of surface settlement is 22.1 mm and during the tunnels simultaneous

excavation the quantity of settlement is equal to 26.6 mm that shows the 20% increase in maximum settlement. But when at first the deep tunnel and then the shallow ones is excavated, the produced maximum settlement is 30 mm in relation to previous condition we have 12% increasing in settlement. This approves that when settlement is at first importance, the shallow tunnel should be excavated first and then the deep ones to produce the less Total settlement. In figure 3.5 bending moment in shallow tunnel crest has been shown by three construction procedures.

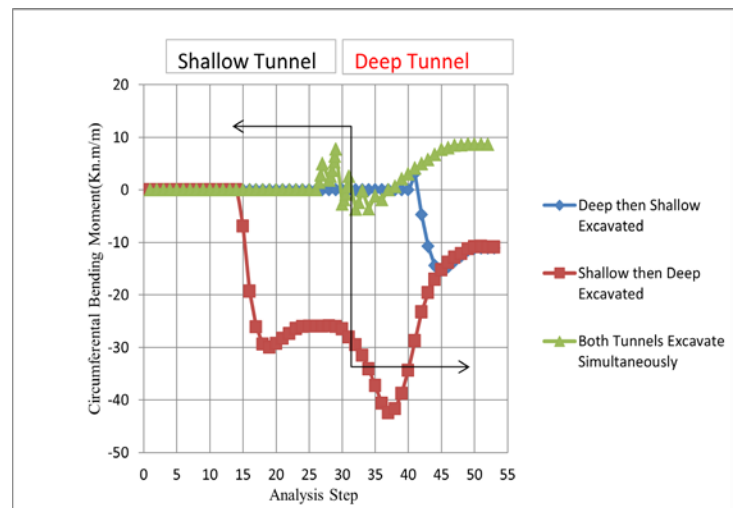


Figure 3.5. Bending moment of shallow tunnel crest in three construction procedures

With consideration to figure 3.5 the minimum moment occurs in simultaneous excavation of two tunnels, but the direction of this moment changes alternatively (because of alternative excavation of shallow and deep tunnel) afterwards the deep tunnel excavation and then shallow ones give less bending moment than shallow tunnel excavation then deep ones. Thus the parameter of construction procedure acts differently in settlement and moment. For example initial excavation of shallow tunnel results in producing the less surface settlement but creates more bending moment in shallow tunnel crest. The incremental ratio of bending moment ($\frac{M_M - M_L}{M_L}$) in condition of shallow tunnel excavation and then deep ones 63% increase, and in deep tunnel excavation and then shallow ones 400% increase which shows the immense influence of construction procedure on bending moment alterations.

3.2. Soil characteristic

In this part according to table II, the influence of soil type on surface settlement and bending moment of shallow tunnel crest was investigated. So four models were produced with various soil type. In case four, soil is improved with grouting that increase cohesion. With consideration to figure 3.6 and 3.7, the maximum settlement in first type soil during the shallow tunnel excavation is equal to 3.8 mm and when the deep tunnel is excavated reaches to 10.5 mm, that indicate maximum relative surface settlement 175% increase. Also the maximum settlement in second type soil during the shallow tunnel excavation is 5 mm which this settlement after deep tunnel excavation reaches to 14.1 mm that shows 180% relative surface settlement increase. In third type during the shallow tunnel excavation, the maximum settlement reaches to 8 mm that after deep tunnel excavation underneath the shallow tunnel this quantity raise to 22.1 we understand the 175% relative surface settlement increase in intersection point. In fourth type soil which is improved, settlement in shallow tunnel excavation is 1.6 mm which during the deep tunnel excavation reaches to 4.9 mm and shows a 212% increase of maximum settlement during the shallow tunnel excavation. So we cannot anticipate a distinct rule to compare the interaction effect between soil type.

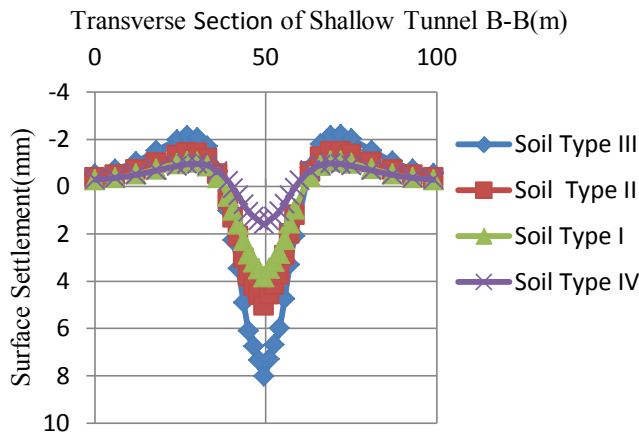


Fig 3.6. Surface linear settlement during the shallow tunnel excavation in different types of soils

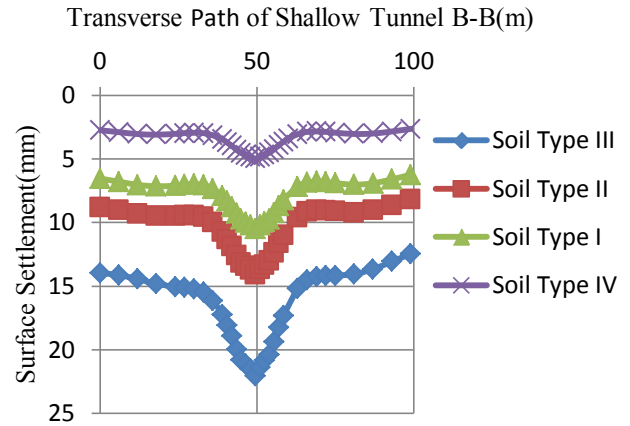


Fig 3.7. Surface linear settlement during the deep tunnel excavation in different types of soils

According to figures 3.6 and 3.7 in shallow tunnel excavation from first type soil to second type and from first type soil to third type results in 32 and 111 percent increase of settlement respectively. In intersection tunnels from first type to second type and from first type to third type soil results in 34 and 110 percent increasing of settlement. In other words the Soil improvement in intersections area can result in settlement reducing. When the soil is improved (fourth type soil) in relation to first type in shallow tunnel excavation, the maximum settlement decreases to 58% and during the deep tunnel excavation the maximum settlement decreases to 52%. In figure 3-6, the alterations of bending moment in shallow tunnel crest during the excavation of this tunnel and deep ones have been shown.

With consideration to figure 3-6, in first type soil the moment changes from -17KN.m/m(L point) to -28.KN.m/m(M point) which shows 68% increasing in maximum bending moment. For second type soil, the bending moment changes from -20KN.m/m to -35KN.m/m which shows 75% increasing in bending moment during the excavation. Also for third type soil, the moment changes from -26KN.m/m to 42.4KN.m/m which shows 63% increasing in scale of bending moment. In improved soil (fourth type) the moment reaches from -5KN.m/m to -10KN.m/m which shows 50% increasing. A noticeable point is that in the case of the soil improvement the relative bending moment decrease to a minimum value compare to other soil type. The other important point we

realize here is that the soil improvement in intersection area not only causes the settlement decrease but also is a reason for decreasing the bending moment in lining tunnel, in contrast with other parameters that each of them if decrease the surface settlement increase the bending moment and vice versa. But soil improvement decrease both of the surface settlement and bending moment because in this case the improved soil carry more load than other soil type.

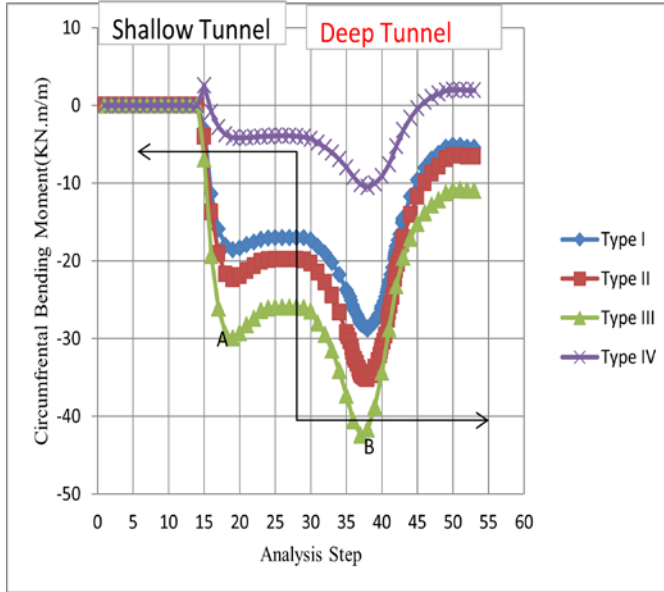


Fig 3.8. Produced bending moment in shallow tunnel crest in different types of soils

3.3. Intersection angle

In order to clarify the influence of intersection angle between two tunnels in surface settlement and bending moment, three models with angles of 60° , 90° , 0° have been made. The surface settlement in length of shallow tunnel for three 60° , 90° , 0° has been shown in figure 3-7. With consideration to figure 3-7, the minimum settlement has been presented for intersection angle of 90° , the produced maximum settlement for intersection angle of 0° hasn't much difference with other settlement curves but this maximum settlement occurs in all lengths of tunnel. As it described before the reason of difference in settlement in 24 m initial and final of tunnel for 0° is, this length was excavated with 3m Unsupported length and others with 1.5 m Also in angle of 0° we could observe the plane strain conditions for parallel tunnels and the two

dimensional simulation can be used instead of three dimensional. In figure 3-8, the bending moment has been shown in shallow tunnel crest. The noticeable point is that produced bending moment in shallow tunnel crest in 90° intersection angle has the most quantity and in intersection angle of 60° , this is approximately identical. So, a parameter not only causes decrease in settlement but also increase in bending moment.

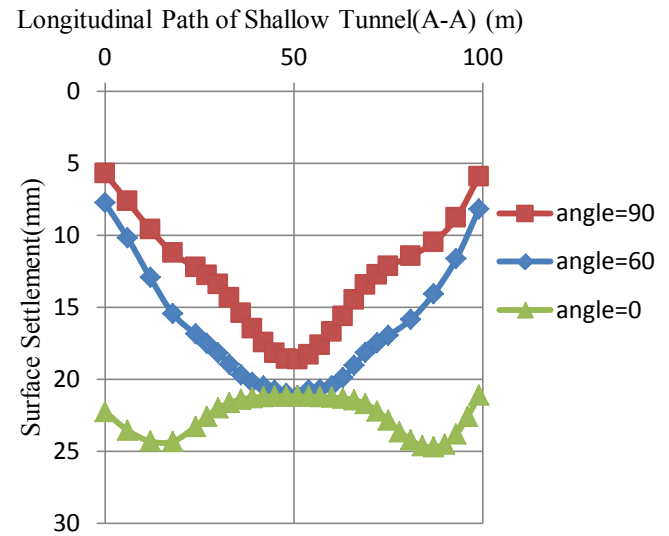


Fig 3.9. Surface settlement for three different intersection angles

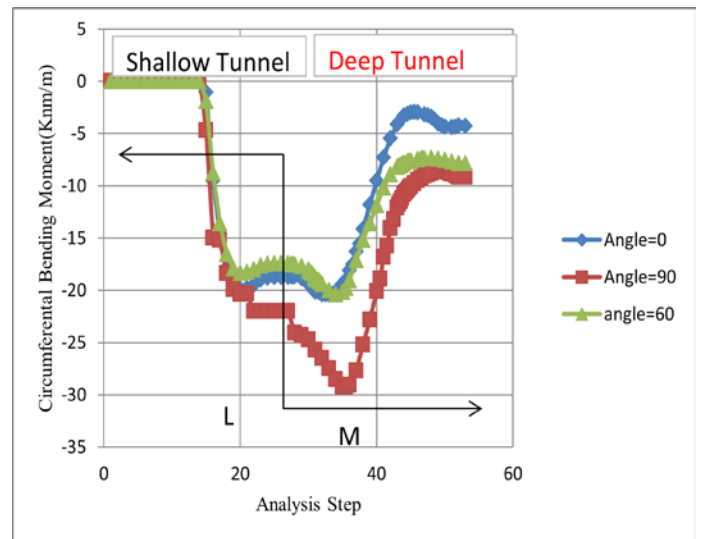


Fig 3.10. Bending moment in shallow tunnel crest for three intersection angles

4-Conclusion

Totally we can say if we go 4.5D farther from two tunnels intersection point, the influences of interaction between two tunnels can be negligible.

Also with consideration to bending moment in presented tunnel crest, the most bending moment occurs during the construction and when deep tunnel crossing beneath the shallow ones.

If a parameters cause to decrease the settlement, results in bending moment growth or vice versa but in soil improvement, the improvement of soil transfers load to soil and cause decrease in both settlement and moment. In general the parameters change is more efficient in decreasing and increasing of bending moment in proportion to decreasing or increasing of surface settlement. Some parameters such as unsupported length despite of increasing the relative settlement decrease the total settlement.

5 - REFERENCES

- [1] Asano T, Ishihara M, Kiyota Y, Kurosawa H, Ebisu S. An observational excavation control method for adjacent mountain tunnels. Tunnel UndergrSpace Technology 2003; 18(2–3):291–301
- [2] Kim SH., 1996. Model testing and analysis of interactions between tunnels in clay. PhD thesis, Department of Engineering Science, University of Oxford.
- [3] Liu HY, Small JC, Carter JP. Full 3D modeling for effects of tunneling on existing support systems in the Sydney region. Tunnel Underground Space Technology 2008; 23:399–420
- [4] Liu HY, Small JC, Carter JP, Williams. Effects of tunneling on existing support systems of perpendicularly crossing tunnels. Computers and Geotechnics 2009; 36:880-894.

Use of post-flotation copper tailings in the construction of dump dams

Tschuschke W., Wierzbicki J.

Department of Geotechnics, Poznań University of Life Sciences, Poland

ABSTRACT

Considerable amounts of mine tailings are produced by the mining industry every day. Post-flotation tailings in the mining of copper ores in Poland constitute 95% excavated mine run and are deposited in dumps. Constructional elements of a dump include outer dams surrounding the object. Durability and stability of these building structures determines safe operation of the entire object. Selection of adequate quality soils for the construction of dams is a crucial factor limiting the risk of a potential disaster. Very large dumps require adequately large amounts of soil for the construction of dams. An alternative for this classical approach may be provided by the use of deposited tailings as the structural material. In this solution the amount of mine waste deposited in the dump is reduced, there is no need to exploit deposits of natural soils and the potential capacity of the dump is increased.

The paper presents principles of the construction technology of hydraulic fill dams, criteria for grain size distribution and physical properties of sediments to be used in the construction of dams, principles of quality control for earth work and methodology of control tests. The paper comments on the effect of the applied technology on the condition of the natural environment.

Keywords: mine tailings, dump construction

1. INTRODUCTION

Competent waste management in accordance with legal regulations at the site of their deposition is a priority for properly managed and exploited dumps. This problem becomes particularly significant when deposited waste products may be economically re-used. Such a situation occurs e.g. in case of wastes classified as neutral to the environment. The category of such wastes frequently includes also mining wastes, distinguished by two indicators: varied composition, dependent on the site and technology of produced tailings, and their considerable volume.

In open pit mines it is most typically overburden removed from the layers over the deposit, while in deep mines it is landings coming from the construction of the mine and exploitation of the subsurface deposit. Thus formally the suitability of the run of mine as engineering construction material should be similar to that of natural soils. However, in practice the input material comprises the run of mine after processing, differing in terms of its strength from the material deposited on the dump. A key element of the change results from the fact that the rock material of continuous structure changes after crumbling and is transformed into ground material with a three-phase structure. A very good example of such material is provided by post-flotation tailings from copper ore treatment. The utilization of post-flotation tailings as a construction material suitable for earthen structures requires first of all the determination of physico-mechanical properties required in case of a construction material, while secondly we need to identify the use, type and parameters of the structure, where the material is to be used.

2. THE OBJECT

Poland is a world leading producer of copper and silver, exploiting non-ferrous metal ores located on the south-western part of the country. In that region the entire copper ore mining and processing industry is found. The winnings from all (solely deep) mines are subjected in the process line to mechanical treatment and flotation processes and - after the isolation of copper headings - it constitutes post-flotation tailings, which need to be properly managed. In the global scale post-flotation tailings constitute approx. 95% excavated deposit, which due to the volume of production, results in the need to manage approx. 25 million Mg waste annually. Starting from the year 1997 all post-flotation tailings are transported to one dump, which recently has been officially named the Żelazny Most mining refuse neutralisation facility (OWOU). The amount of waste deposited over the years of dump operation has resulted in the construction of a hydroengineering mega-structure, second (after the Chinese Great Wall) engineering structure seen from space.

The size of the object is indicated by its parameters: the amount of deposited tailings – over 500 million m³, dump area – 14 km², the capacity of the tailings pond - 7 million m³, the length of dams surrounding the dump – 14.3 km, the height of the highest dams – over 60 m (Fig. 1). Post-flotation tailings are transported to the dump by hydraulic method, first under the pressure and then by gravity, in the form of a mixture with process water from the mines, at mixture density of 1.11÷1.15 Mg/m³. Refuse is discharged to the dump from pipelines located in the crown of external dams surrounding the dump (Fig. 2). After discharge tailings particles are sedimented on the dump beach, while water flows to the pond

located in the central part of the dump, where after clearing in flow towers it is directed to the secondary technological cycle. Guidelines for the safe operation of the dump require the maintenance of the water line at a minimum distance of 200 m from the dam crown, which determines beach slope, naturally oscillating around 1%.



Fig. 1. The general view of the OUOW Żelazny Most [KGHM Polska Miedź S.A.].

The dump is expanded by the upstream construction of the dam superstructure on hydraulically filled beaches. The superstructure above the crown of star dams is constructed from tailings deposited on the beach [1]. In all cases the height of the superstructure is 2.5 m and it is adapted to the rotation system of feeder pipelines. Annual increment in dump height is on average 1.3 m.



Fig. 2. Observed plunge pool at discharge point at the Żelazny Most dump [3].

3. CHARACTERISTICS OF DEPOSITED TAILINGS

Post-flotation tailings produced from ores genetically connected with dolomites and copper shales are characterized by considerable grain angularity, while that from sandstones have a milder morphology or even a preserved original grain

shape in deposits with a weaker binder. The basic component of the fraction of less than 0.06 mm comprises chips of carbonate rocks, while in the coarser fraction quartz is the dominant material, found in considerable amounts in the fraction of 0.25÷0.1 mm. Shale content decreases with a reduction of grain diameter. Characteristics of tailings connected with their original geomorphology determine mechanical properties of the material to be used in the construction of earth dams.

Tailings gravitationally silted up on the beach are subjected to the natural process of sedimentation segregation, as a result of which coarser fractions are deposited in the vicinity of tailings discharge sites, while finer fractions flow with water over the surface of the beach towards the pond. The finest tailings (carbonate-clay tailings) are excluded from the ring silting process, as they may not be used in dam superstructures. These wastes are discharged directly inside the dump to seal the pond bottom. Hydraulic filling by tailings is a cyclical process, in which a fragment of the beach is elevated by several dozen centimeters at a time. Then the beach drying stage occurs, lasting up to 2 months, followed by another hydraulic fill process. The technology of tailings hydraulic transport and beach hydraulic filling, the process of drainage, drying and beach formation cause significant effects, i.e. spatial heterogeneity of sediment consolidation and a specific macrostructure, characterized by horizontal laminations. The number and thickness of laminations with the smallest grain size increases with the distance from the tailings discharge site, limiting the range of the sedimentation zone for deposits suitable for dam superstructure. Sediments deposited in that zone as a construction material have to meet specific compactability criteria, and as a consequence - also bearing capacity, since additionally they constitute the subsoil for dam superstructures constructed by the upstream method. A diagram for the dump section with an arbitrary division into zones is presented in Fig. 3.

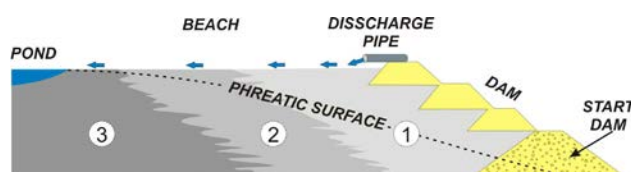


Fig. 3. Diagrammatic cross-section of dump: 1 – coarse tailings (fine sand), 2 – intermediate zone (sandy silt), 3 – slimes (predominate silt and clay fraction) [3].

4. CRITERIA FOR THE SELECTION OF MATERIAL FOR DAM CONSTRUCTION

Due to the necessity to regularly increase the dump capacity, the processes of engineering design, tailings deposition and dam superstructures constructed are realized in parallel. The adopted method of upstream superstructure development results in a situation when only the start dams made from natural soils are founded on the subsoil. Successive stages of superstructure development, proceeding as the dump is being

filled, are realized from drained sediments deposited on beaches. Design of the dump development requires geotechnical identification of deposited sediments. Geotechnical parameters of sediments change with the distance from the discharge site, while they also depend on the type of rock from which they originate, applied processing, disposal technology, filtration and consolidation processes. Only some of the deposited sediments may be used as a construction material in the creation of dam superstructure. Extremely fine silty deposits exhibit properties of a plastic material with limited shear strength. Sandy deposits have the characteristics of a non-cohesive material with a much greater rigidity and shear strength, while indexes referring to compactability are best suited to describe sediment behavior. Assuming the strength criterion as the starting point for the determination of suitability of deposits for construction purposes, a series of tests was performed in a direct shear apparatus at deposit compaction corresponding to maximum dry density from the Proctor test (Fig. 4). Samples of deposits were differentiated in terms of their grain size distribution, as identified by SFR (ratio of sand to fines <0,074mm) [2]. The correlation identified on the basis of model tests between internal friction angle and a grain size parameter SFR was used in the determination of the physical criterion of sediment suitability (Fig. 5).

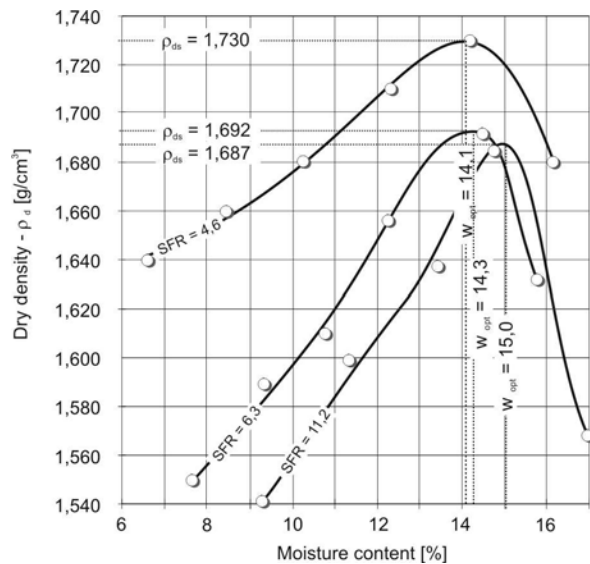


Fig. 4. Standard Proctor test results for the Želazny Most mine tailings (ρ_{ds} – maximum dry density, w_{opt} – optimum moisture content).

Relatively high values of the internal friction angles result from angularity of sediment grains. On the basis of an analysis of stability it may be assumed that sediments embedded in dams, in order to meet the strength criterion ($\phi > 35^\circ$) at the required compaction, should have $SFR > 2$, which corresponds to a limitation of the silt content in the sediments to 30%. The area of grain size variability in sediments classified as suitable for dam construction is presented in Fig. 6.

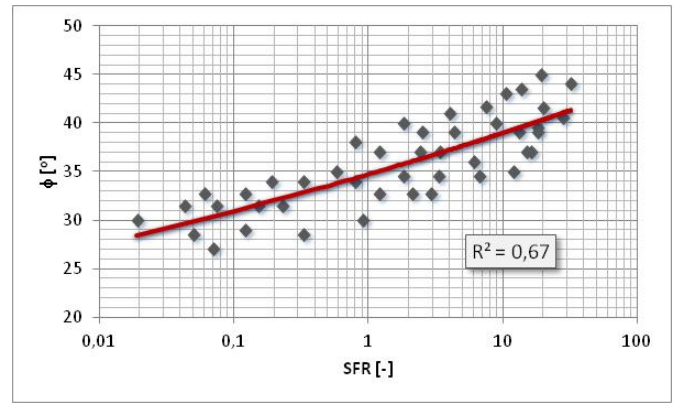


Fig. 5. Correlation between internal friction angle (ϕ) and SFR coefficient for compacted tailings within the range of natural moisture content equal $\pm 5\%$ of optimum moisture content.

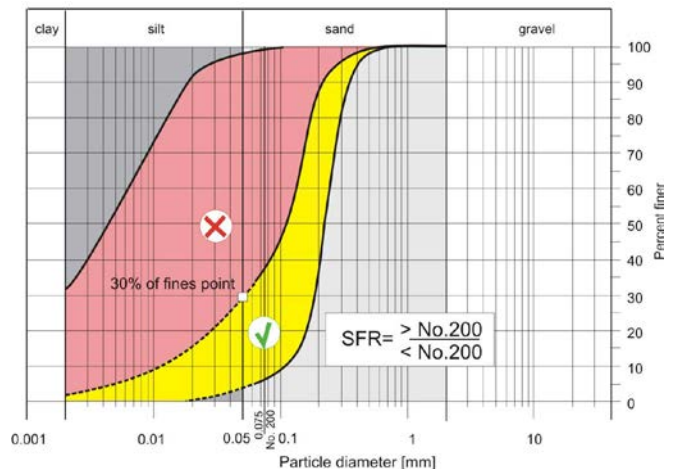


Fig. 6. Grading envelopes for the Želazny Most mine tailings.

The identification of the distribution and potential prediction of changes in sediment grain size in the beach profile and cross-section constitutes the basic information in the technology of sediment collection from the beach for the construction of dams and for the determination of geotechnical parameters of sediments for the needs of the analysis of object stability. The process of sediment deposition results in a situation when the hydraulically filled beach is a heterogeneous medium of random character. Identification of deposit grain size, being a function of the location in space, may be considered as a deterministic problem for a heterogeneous medium [3]. Probability of occurrence of sediments with varying grain size at a specific distance from the dam may be investigated by clustering sediments into groups with similar grain size or by the so-called continuous distribution method for one of the adopted measures of the grain size curve (Fig. 7) [3], [4], [5]. It results from the analysis of Fig. 7 that the previously determined criterion of granularity ($f_p > 70\%$) is met by sediments deposited in the belt of the beach adjacent to the dam at a distance up to 70 m from the discharge site [3]. This

fragment of the beach was assumed as the potential zone of earth work, from which collected sediments may be used for dam superstructures. An advantage of the earth work in the identified zone of the beach is connected with the mixing of sediments with different grain sizes, together with the elimination of laminations of cohesive deposits formed in the course of hydraulic filling and compaction of the subsoil for the future dam superstructures.

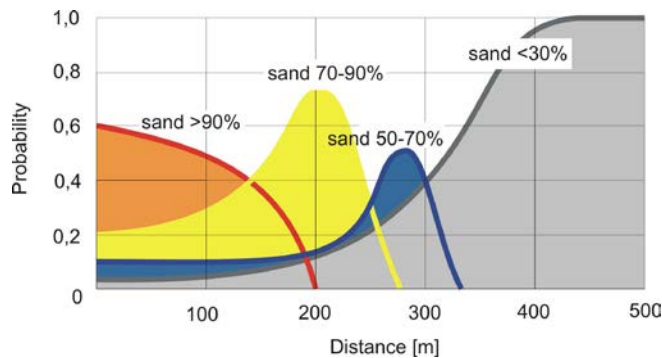


Fig. 7. The probability of tailings grain size distribution with the distance from the dam [3].

The conditions specified above for the construction of dam superstructures from the material deposited in the dump, i.e. mine tailings, constituted the basis for the development of a procedure defining the manner and sequence of operations:

- Hydraulic filling of a specified fragment of the beach with post-flotation tailings,
- Drainage and drying of deposited sediments in the beach to a moisture content corresponding to optimal moisture content,
- Using bulldozers, collection of hydraulically deposited sediments from a beach section of 70 m in width (at this stage the beach was further compacted for the successive stages of dam superstructure construction) (Fig. 8),

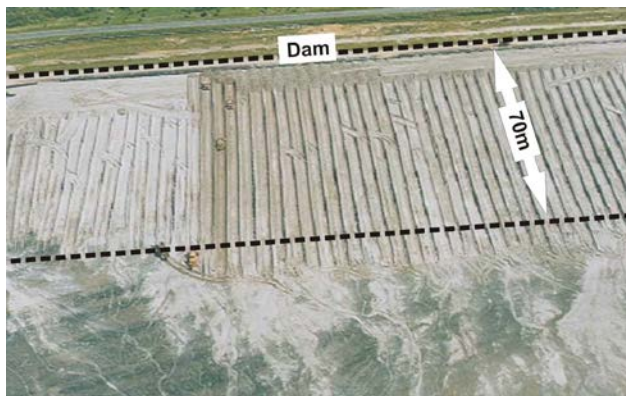


Fig. 8. The view of the zone of tailings used for dam construction [3].

- Formation of a dam superstructure with a layer of up to 0.5 m in thickness,

- Compaction of the formed layer using a vibrating roll until the required compaction criterion is met,
- Quality control testing of performed earth work.

A repetition of the entire cycle until the complete module of dam superstructure, 2.5 m in thickness, is obtained, together with the final geotechnical acceptance test.

5. QUALITY CONTROL OF PERFORMED EARTH WORKS

The structures of high, hydraulically filled dams from post-flotation tailings surrounding the object, which role is to accumulate these wastes, requires strict adherence to the technological regime and particularly thorough quality control tests of the performed earth work.

Meeting the criteria of grain size distribution and compaction of the material incorporated in the dam is a necessary pre-condition for the safe operation of the object, guaranteeing its stability and durability. Within the framework of control tests, testing is performed on an on-going basis by the surface method after the formation and compaction of a successive layer of 0.5 m in thickness and the final verification tests by the depth penetration test after the completion of the construction stage of the dam superstructure with a thickness of 2.5 m. Surface tests are based on standard methods, i.e. isotope and volumetric tests (Fig. 9) [6].



Fig. 9. Troxler gauge and hand CPT equipment during testing tailings [6].

The former determines moisture content and density of deposits in the controlled layer and as a consequence - its relative compaction – R (dry density – ρ_d to maximum dry density – ρ_{ds}) (Fig. 4). In the latter laboratory analyses of physical parameters are performed on the collected sediment samples, which results - in relation to the Proctor test - make it possible to determine the relative compaction and additionally verify the grain size criterion. An original solution in this respect is provided by the depth testing method based on the standard cone penetration test CPT [3], [7]. In this method penetration characteristics are recorded, i.e. cone resistance – q_c and friction ratio – R_f , which are

indicators for the assessment of relative density – D_r and grain size in sediments over the entire analyzed profile. Sediments embedded in the dams meet the compaction criterion when the condition described by equation 1 is met.

for $D_r > 70\%$:

$$q_c > \exp((36.81 \cdot \ln(\sigma_{v0}) + 733) / (17 \cdot \sigma_{v0}^{0.0876})) \quad (1)$$

where: σ_{v0} – overburden stress.

To verify measures of sediment compaction it is possible to evaluate the relative compaction - R by relative density – D_r on the basis of a correlation dependence expressed by equation 2.

$$R = 0,855 + 0,165 \cdot D_r \quad (2)$$

The required criterion for sediment grain size ($f_{\pi} < 30\%$) expressed by CPT parameters is determined by condition $R_f < 1.3\%$ [3].

An example of an interpretation of CPT testing in order to identify grain size and compaction of sediments in the dam superstructure profile is presented in Fig. 10.

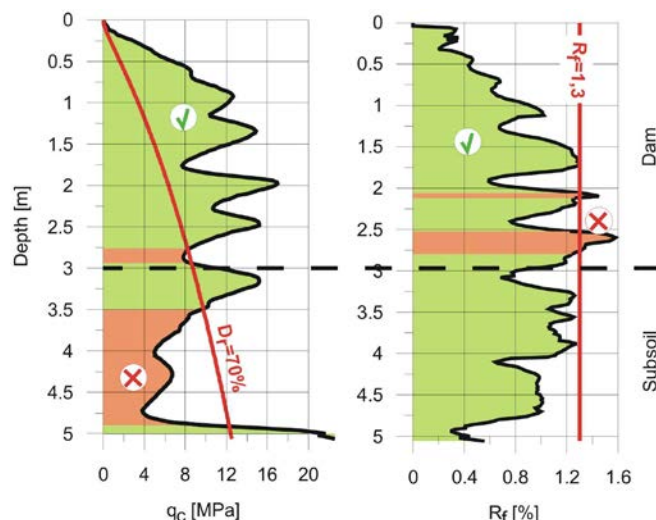


Fig. 10. CPT results at the background of quality criterion.

6. THE EFFECT OF DAM SUPERSTRUCTURE TECHNOLOGY ON THE CONDITION OF THE NATURAL ENVIRONMENT

In order to assure environmentally safe operation of the Żelazny Most mining refuse neutralization facility we need to mention the following crucial problems [1]:

- Assurance of object stability,
- Limitation of migration of contaminated process waters from the dump to groundwaters,
- Limitation of dusting.

The applied technology of gradual stage dam superstructure construction from post-flotation tailings previously deposited in the dump, in case of the first two problems does not generally differ from the conventional method of dam construction. In case of a risk of stability loss in the threatened sections of the dam the vent embankment of the

dam is loaded. Limitation of process water migration from the dump to the subsoil is provided by the construction of ring drainage at successive layers of the dump, girdling ditches around the dump as well as the barrier of deep wells at the dump forefield. In contrast to the previous aspects, the hazard connected with dusting is a specific characteristic of the Żelazny Most facility. Post-flotation tailings deposited on the dump beach and used in dam construction are characterized by the capacity to dry rapidly. Dry sediments, free of the binding force, are exposed to the action of wind and are easily transported outside the dump area, forming fine dust suspended in the air. The impact of dust on the environment is so intense that as a counter-measure the surface of the beach and dams is covered with air-sprayed bituminous emulsion.

7. CONCLUDING REMARKS

The presented technology of gradual stage construction of dam superstructure, performed in the course of the operation of the wet waste disposal site from selected material, i.e. post-flotation tailings deposited in that dump, has at least one spectacular economic advantage. The use of wastes for the formation of dams on the one hand reduces the amount of wastes deposited in the dump, while on the other hand it eliminates the need to exploit deposits of natural soils and transport them to the crown of the constructed dam superstructure. In case of a huge object such as the Żelazny Most facility, in which the annual dam superstructure requires approx. 300 thousand m^3 soil, savings connected with the applied technology covering two basic cost components, i.e. elimination of fees for the disposal of sediments embedded in the dams and no need to extract and transport natural soils for dam construction, reach over 2 million US dollars annually. We also need to mention another advantage, i.e. the fact that as a result of crushing of run of mine the resulting post-flotation tailings have the characteristics of fine-grained broken aggregate, easily compacted and with advantageous shear strength parameters, provided that the strict technological regime of the dam superstructure construction is maintained. A problem which may be perceived as a drawback of this technology is the adverse environmental impact connected with increased dusting of dried sediments embedded in the dams. This may be solved by the application of appropriate counter-measures reducing dust emissions to areas adjacent to the dump.

8. REFERENCES

- [1] Wolski W. "Tailings dams – selected question", Proc. of 13th European Conference on Soil Mechanics and Geotechnical Engineering, Prague, Vol. 3, Vanicek et al. (eds.), pp. 167-176.
- [2] Lipiński M.J., Wolski W., Fioravante V., Jamiolkowski M.B., "Preliminary evaluation of hazard due to liquefaction for Żelazny Most tailings pond", Proc. of 14th International Conference on Soil Mechanics and Foundation Engineering, Vol. 3, Hamburg 1997, pp. 1843-1846.
- [3] Tschuschke W., "Cone penetration tests in-post flotation sediments", Silesian University of

Technology, Civil Engineering (110), Gliwice, Poland 2006, p. 266.

- [4] Pordzik P., Tschuschke W., Wierzbicki J., "Statistical evaluation of tailings grain size distribution of the Żelazny Most Reservoir dams", Proc. of 12th Polish National Conference on Soil Mechanics and Foundation Engineering, Szczecin-Międzyzdroje, Poland 2001, Vol. 1b, pp. 181-191.
- [5] Gołębiewska A., Lipiński M.J., "Measures for characterization of grain size distribution of post floatation tailings", Proc. of 12th Polish National Conference on Soil Mechanics and Foundation Engineering, Szczecin-Międzyzdroje, Poland 2001, Vol. 1a, pp. 211-219.
- [6] Wierzbicki J., Niedzielski A., Waliński M., Wołyński W., "The quality control of postfloatation reservoir dam by determination of relative compaction index in various methods", Geotechnical and Geophysical Site Characterization Viiana da Fonseca & Mayne (eds.). Millpress, Rotterdam 2004, ISBN 90 5966 009 9, pp. 1371-1375.
- [7] Młynarek W., Tschuschke W., Welling E., "Control of strength parameters of tailings used for construction of reservoir dams", Proc. of the 5th International Conference on Tailings and Mine Waste, Fort Collins, Colorado, USA 1998, pp. 213-221.

Effects of Slope Inclination on the Rain-induced Instability of Embankment Slopes

Chaminda Gallage¹, Shiran Jayakody¹ and Taro Uchimura²

¹Queensland University of Technology, Brisbane, Australia

²The University of Tokyo, Tokyo, Japan .

ABSTRACT

Rainfall has been identified as one of the main causes for embankment failures in areas where high annual rainfall is experienced. The inclination of the embankment slope is important for its stability during rainfall. In this study, instrumented model embankments were subjected to artificial rainfalls to investigate the effects of the slope inclination on their stability. The results of the study suggested that when the slope inclination is greater than the friction angle of the soil, the failure is initiated by the loss of soil suction and when it is smaller than the friction angle of the soil, the failure is initiated by the positive pore water pressure developed at the toe of the slope. Further, slopes become more susceptible to sudden collapse during rainfall as the slope angle increases.

Keywords: Embankment model tests, instrumentation, soil suction, transient seepage, rain-induced slope failures

1. INTRODUCTION

Embankments are very useful geo-engineering structures that are widely used to support roads and rails. They are constructed by shaping the natural slope or by compacting the imported soils. Failure of these embankment slopes can cause for human casualties as well as negative impacts on a country's economy. Most embankment slopes are initially unsaturated prior to any rainfall. In addition to triggering by earthquakes, rainfall has caused the failure of many embankment slopes, worldwide [1]-[4].

Reference [5] performed a series of parametric studies to understand the significance of hydrological and geotechnical parameters of a slope on its rain-induced instability. The study revealed that rainfall, rainfall intensity, soil properties, location of the ground water table, and the slope geometry (angle, height) play a significant role in the rain-induced instability of a slope. Angle and height of an embankment are two key geometrical parameters that control the extent of the area covered by the embankment slope and its stability. In developed/developing area areas, there is a great demand to reduce the area covered by the embankment slopes and hence the embankments are constructed with steeper slopes and in some occasions geo-reinforced embankments are constructed with vertical slopes [6].

Unsaturated embankment slopes can be stable with very steep slope angle until it is exposed to rainfall. The mechanism of slope failure induced by rainfall can vary depending on the slope angle. It is important to understand the mechanism and initiation of failure of an embankment slope to provide better countermeasures against the failure. This paper presents the results of the embankment model tests conducted to investigate the effects of slope angle on the mechanism and the initiation of the failure the of embankment slope subjected

to rainfall. Two instrumented model embankment slopes with two different slope angles (e.g. 30° and 60°) were subjected to artificial rainfall until the failure.

2. TESTING MATERIALS

Edosaki soil procured from a natural slope in Ibaraki prefecture in Japan was employed in the experimental work of this study. Wet sieving and hydrometer analyses were performed on this material as it contains fines (particles finer than 0.075 mm) content of 17.1 %. The grain-size distribution curve of the test material is shown in Figure 1. The specific gravity, maximum void ratio, and minimum void ratio of the soil were measured as 2.75, 1.59, and 1.01, respectively. The soil was found to be non-plastic. The optimum gravimetric water content and the maximum dry density of the sand obtained from the standard proctor compaction test were 16.5% and 1.725 g/cm³ respectively. According to the Unified Soil Classification System, the soil can be classified as silty sand

2.1 Soil Water Characteristic Curves (SWCCs)

Figure 2 depicts the soil-water characteristic curve (SWCC) for Edosaki sand obtained in the laboratory using a Tempe pressure cell. Both the drying and the wetting SWCCs were obtained for the test material using a sample with dry density of 1.22 g/cm³. Model slopes were constructed using Edosaki sand to achieve dry density of 1.22 g/cm³. Since the air-entry value of the ceramic disk used in Tempe pressure cell is 300 kPa, the measured SWCCs were restricted to the maximum suction of 200 kPa. More details about SWCC measurement using Tempe pressure cell is given in [7]. As shown Figure 2, the laboratory measured SWCC data were fitted using the equation proposed by Fredlund and Xing [8].

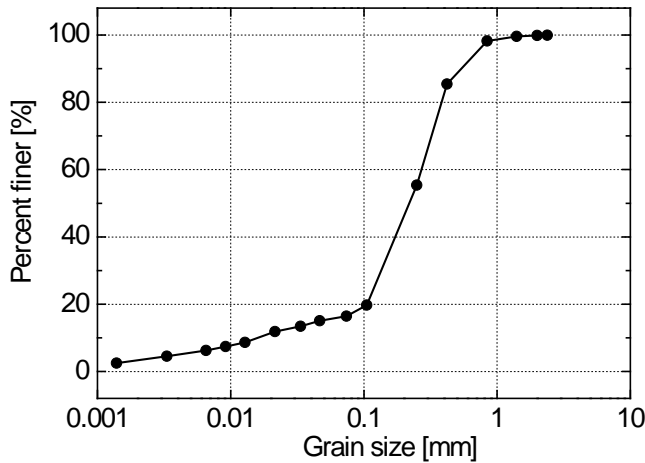


Figure 1. Grain size distribution curve of Edosaki soil

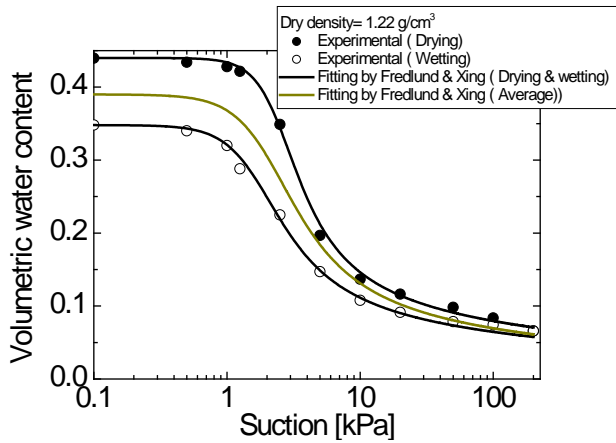


Figure 2. SWCCs of test material

2.2 Unsaturated Permeability

Permeability function of unsaturated soils was measured using a laboratory developed permeameter based on steady-state method [9]. Figure 3 shows the variation of measured coefficient of permeability with suction following the drying path of the SWCC. The test was conducted on the dry density of 1.22 g/cm^3 of Edosaki sand. Figure 3 also compares the laboratory measured permeability function with the predictions using the methods proposed by Fredlund [10], Green & Corey [11], and Van Genuchten [12] (all three methods are included in SEEP/W -2004).

2.3 Unsaturated Shear Strength

A conventional direct shear apparatus was modified to measure unsaturated shear strength under controlled suction. Figure 4 (a) depicts the variation of the ϕ' with the suction. The ϕ' was obtained from both saturated and unsaturated consolidated drained tests employing the modified direct shear device. The results suggested that the effects of suction on the ϕ' is not significant. However, as shown in Figure 4 (b), the apparent cohesion (c) increases with the suction in a decreasing rate.

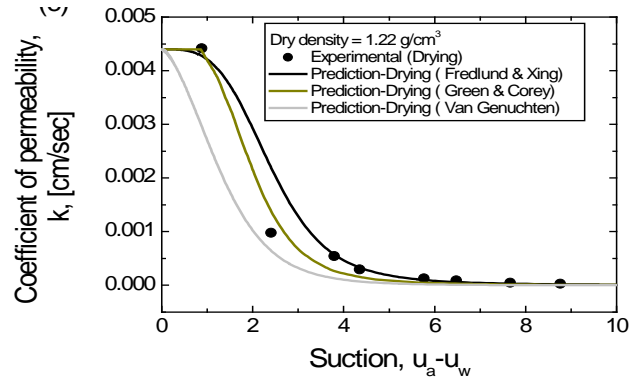


Figure 3. Measured and predicted permeability function of test material

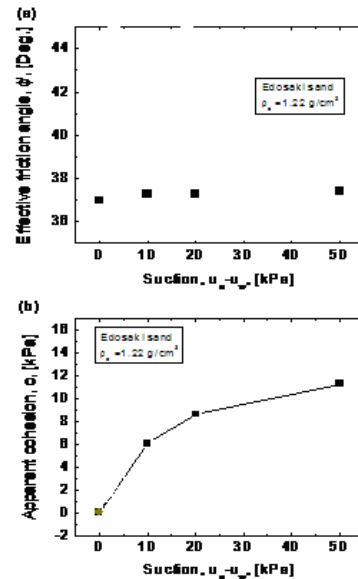


Figure 4. Measured unsaturated shear strength properties of test material

3. MODEL TESTS

In order to examine the effects of slope inclination on the mechanism of rain-induced slope (embankment) failures, two instrumented model tests with two different slope inclinations (i.e. 30° and 60°) were subjected to an artificial rainfall until the failure of the slope. Pore-water pressures, volumetric water contents, soil displacements were monitored continuously at different locations on and in the slope during the construction of the slope and the application of the rainfall.

3.1 Instruments Used

The tank (Figure 5) used in model test has a length of 2.0 m, width of 0.8 m, and a height of 1.0 m. The walls of the tank are made up of steel plates, except for the front side which is made of acrylic glass for easy observation of deformation processes.

ADR (Amplitude Domain Reflectometry) and ECHO types soil moisture sensors were used in the model tests to measure

soil moisture content during water infiltration. In order to measure both positive and negative water pressures, KYOWA 05 PMG pressure sensors were modified with a ceramic cup of 100 kPa air-entry value. Figure 6 shows the types of sensors used in the model tests. LVDTs were used to measure the local displacements on the slope surface. Inclinoimeters installed in the soil measured the sub-soil displacements. Evaflow side spray irrigation tube (hole size, 0.1 mm) was used to simulate rainfall as shown in Figure 5.

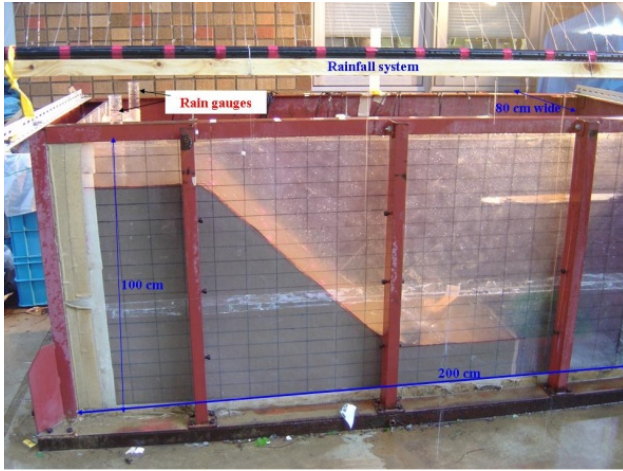


Figure 5. Tank used for model tests

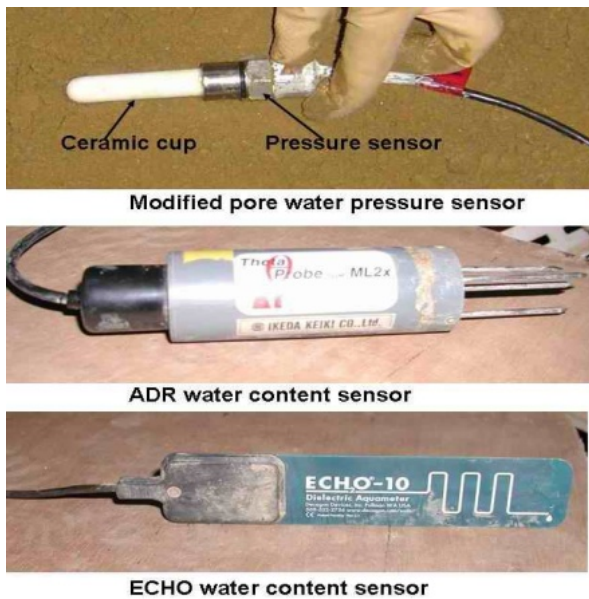


Figure 6. Sensors used in model tests

3.2 Model Preparation

Two model embankments with different slope inclinations (e.g. 30° , 60°) were constructed by compacting Edosaki sand with the initial gravimetric water content of 13.5 %. The compaction was performed in order to achieve the dry density of 1.22 g/cm^3 . 15 pore-water pressure sensors, 15 water content sensors, three inclinometers, and two LVDTs were installed in each model embankment. All the sensors were connected to a data acquisition system for continuous logging of data during the construction of the slope and as well as

during rainfall application.

3.3 Rainfall Simulation

Approximately 24 hours after the completion of the construction of the slope, the slope was subjected to a rainfall with an approximate intensity of 40 mm/hr. During the rainfall application, it was set to log data for every 2 seconds from all the sensors connected with the logging system. Evaflow side spray irrigation tube system used in this experiment was able to provide a relatively uniform constant rainfall between 20 mm/hr and 50 mm/hr. It was able to control the rainfall intensity by regulating the pressure of the water supplied to the system. This rainfall system was calibrated to give different rainfall intensities with supplied water pressure. Four measuring cylinders (rain gauges) were used to measure intensity of rainfall; two of them were positioned near the toe and the other two were placed on the top of the embankment. The rainfall intensity mentioned in this study was calculated by averaging the measured rainfall over the entire duration of rainfall and the numbers of measuring points. To minimize the possible fluctuation of rainfall intensity with time and space (due to wind), the rainfall was applied in the morning (e.g., 5.30 a.m) in most tests.

4. RESULTS AND DISCUSSIONS

Figure 07 shows the locations of the different transducers (pore-water pressure, water content, and horizontal displacement) installed in the model slope which has an inclination of 30° . At the beginning of the artificial rainfall of 40 mm/hr, the slope was in unsaturated conditions with the suction of 6 ~ 12 kPa (Figure 8(a)) and corresponding volumetric water content 0.2 ~ 0.15 (Figure 8(c)). As the rainfall progressed, the water contents and the pore-water pressures at the different locations in the slope increased as shown in Figure 8(b) and (a), respectively. The lower part of the slope became saturated first forming a water table below the toe area of the slope. As shown in Figure 8(c), the horizontal deformation of the slope started when the toe of the slope was saturated (P8 registered positive value by the time the deformation started) at about 5000 sec after the beginning of rainfall. The deformation seemed to be progressive (Figure 9) with the rise of water table. The rate of horizontal slope displacement was measured to be 3.4 ~ 7.9 mm/hr.

A slope with an inclination of 60° was constructed and instrumented as shown in Figure 10. Once the slope was subjected to an artificial rainfall of 45 mm/hr, as shown in Figure 11(c), the horizontal deformation of the slope (D1, D2, and surface at inclination 3 (Incli.3)) began with a rate of about 14.4 mm/hr even before the water table rose up to the level of P10 and P8 (Figures 11(a) & (b)). Cracks appeared at the top (crest) of the slope with the start of deformation (at about 2000 sec after the beginning of rainfall). Within 1000 sec after the cracks appearance at the top, the entire slope collapsed as shown in Figure 12. It was interesting to observe that the most part of the slope was unsaturated (the water front

did not reach some areas) by the time the entire slope collapse. It seemed that this failure was initiated by the decrease in the shear strength of the slope due to the loss of soil suction. An unsaturated slope with the inclination greater than the friction angle of the soil can be stable until the suction is decreased by the rain water infiltration into the slope.

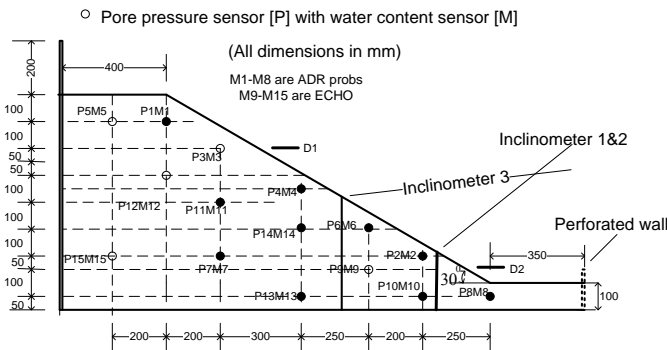


Figure 7. Sensor locations in model test with 30° inclination

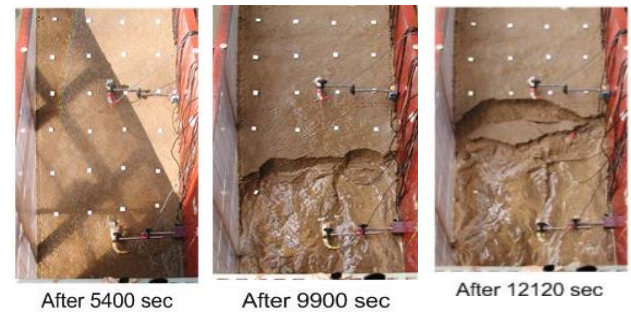


Figure 9. The progress of the failure of the slope with 30° inclination

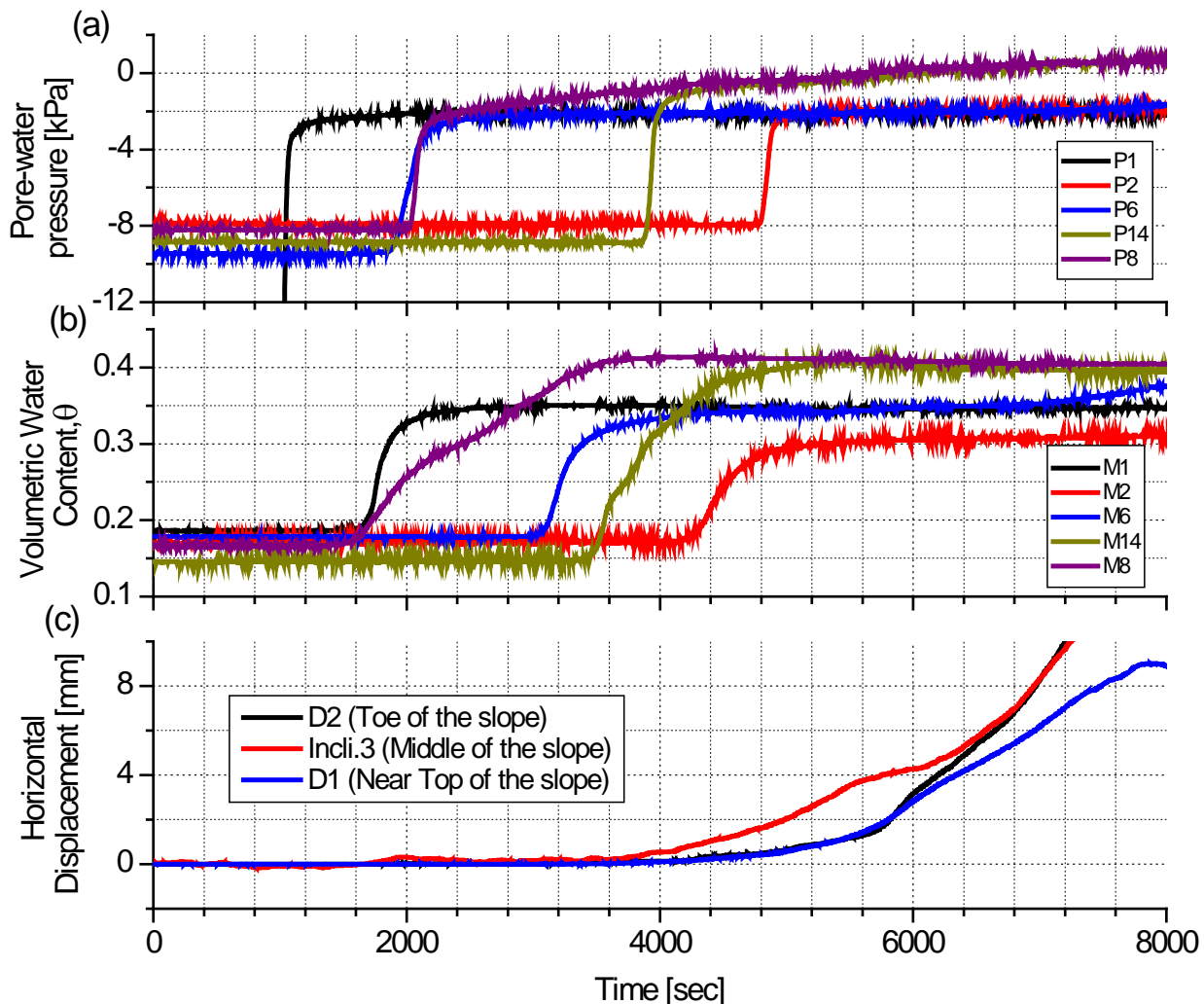


Figure 8. Time histories of: (a) pore-water pressure; (b) volumetric water content; and (c) displacement at various locations of the slope with 30° inclination

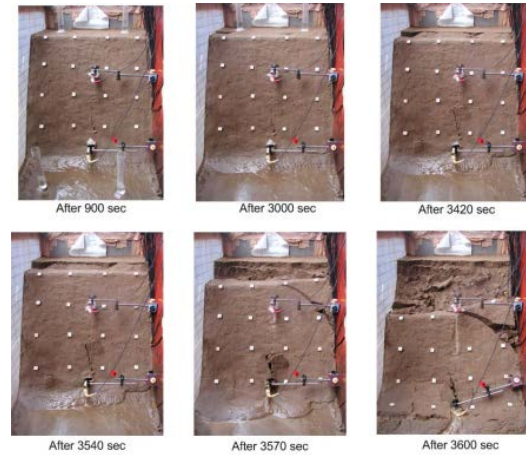
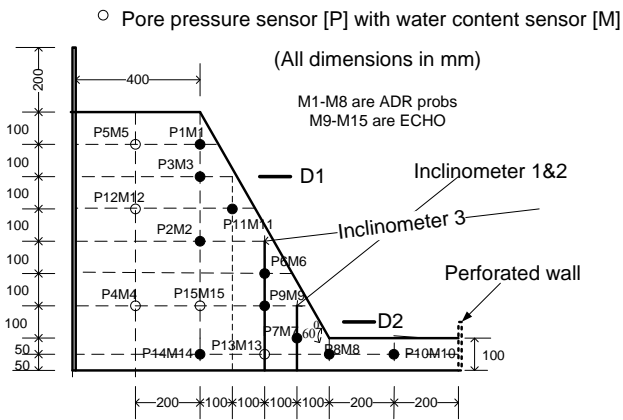


Figure 10. Sensor locations in model slope with 60° Inclination

Figure 12. The progress of the failure of the slope with 60° inclination

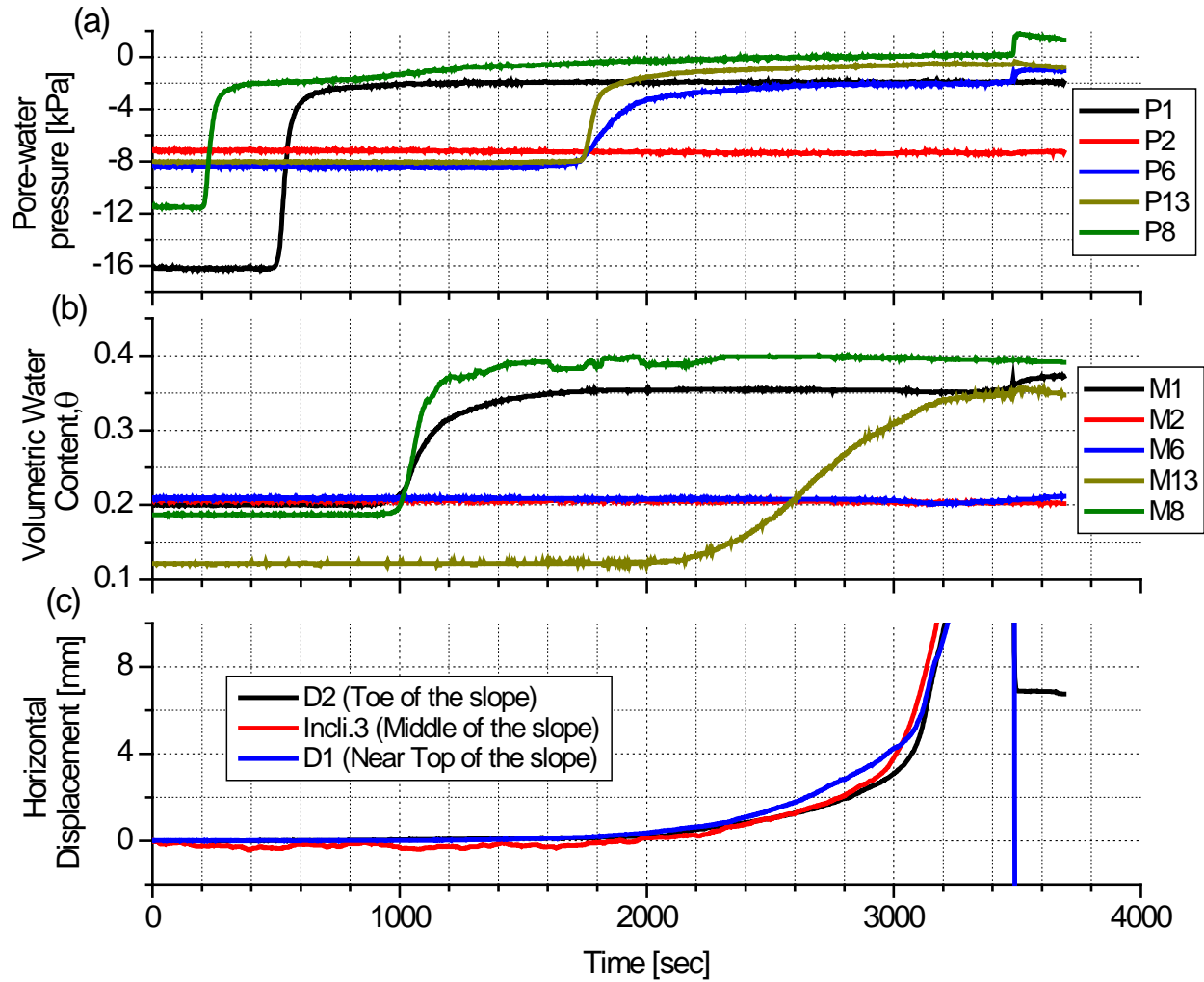


Figure 11. Time histories of: (a) pore-water pressure; (b) volumetric water content; and (c) displacement at various locations of the slope with 60° inclination

5. CONCLUSIONS

The following conclusions can be drawn from this experimental investigation:

- Slopes become more vulnerable to sudden collapse with the increase in their inclinations.
- Failures of gently slopes are initiated by the development of positive pore-water pressure near the toe and the failure is relatively slow and progressive.
- In the case of steep slopes (especially when slope inclination is greater than the soil's friction angle), the decrease in suction is a predominant factor for the failure initiation.

REFERENCES

- [1] Kunio, K. and Hiroakai, S. (1989). "Embankment design in mountainous area with heavy rainfall." *Soils and Foundations*, 29(4), 35 – 48.
- [2] Okada, K. and Sugiyama, T. (1994). "A risk estimation method of railway embankment collapse due to heavy rainfall." *Structural Safety*, 14(2), 131-150
- [3] Aleotti, P. (2004). "A warning system for rainfall-induced shallow failures." *Engineering Geology*, 73(4), 247 – 257.
- [4] Ng, C.W.W. and Zhan, L.T. (2007). "Comparative study of rainfall infiltration into a bare and a grassed unsaturated expansive soil slope." *Soils and Foundations*, 47(2), 207–217.
- [5] Rahardjo, H., Ong, T. H., Rezaur, R. B., and Leong, E. C. (2007). "Factors controlling instability of homogeneous soil slopes under rainfall." *Journal of Geotechnical and Geoenvironmental Engineering*, 133 (12), 1532–1543.
- [6] Tatsuoka, F. (2011). "Developments of geosynthetic-reinforced soil technology in Japan: Retaining walls and bridge abutments". *Proceeding of First International Conference on Geotechnique, Construction Materials, and Environment*, Mie, Japan.
- [7] Gallage, C. P. K., and Uchimura, T. (2010). "Effect of dry density and grain size distribution of soil-water characteristic curve of sandy soils." *Soils and Foundations*, 50(1), 161-172.
- [8] Fredlund, D. G., and Xing, A. (1994). "Equation for the soil-water characteristic curve." *Canadian Geotechnical Journal*, 31, 521-532.
- [9] Klute, A. (1965). "Laboratory measurement of hydraulic conductivity of Unsaturated soil." *In methods of soil analysis*, Mono. 9, Part 1, Amer. Soc. Of Agronomy, Madison, WI, 253-261.
- [10] Fredlund, D. G., Xing, A., and Huang, S. 1994. Prediction of the permeability function for unsaturated soils using the soil-water characteristic curve, *Canadian Geotechnical Journal*, 31: 533-546.
- [11] Green, R. E., and Corey, J. C. (1971). "Calculation of hydraulic conductivity: A further evaluation of some predictive methods." *Soil Science Society of America Proceedings*, 35, 3-8.
- [12] Van Genuchten, M. T. (1980). "A closed-form equation for predicting the hydraulic conductivity of unsaturated soils." *Soil Science Society of American Journal*, 44: 892-898.

Extension of an integrated AHP and TOPSIS approach in the earth dam site selection

Minatour Yasser¹, Khazaie Jahangir^{2,*}

1. M.Sc. Student of Water Eng., Dept. of Civil Eng., Razi Univ., Kermanshah, Iran

2. Assist. Prof. of Civil Eng., Dept. of Civil Eng., Razi Univ., Kermanshah, Iran
J.khazaie@razi.ac.ir

ABSTRACT

Optimal locating the dam site is one of problems associated with water resources management and it depends on a set of qualitative and quantitative criteria. Therefore, such problems can be resolved by multi-criteria decision making (MCDM) approach. This study aims to develop MCDM approach to locate the dam site, for this purpose an integrated AHP (Analytic Hierarchy Process) and TOPSIS (Technique for Order Performance by Similarity to Ideal Solution) approach was applied in the Harsin earth dam site selection at the western part of Iran. To do this, firstly the influential criteria for locating the earth dam site were determined using comprehensive literature review and the experts' opinions. Then, some watersheds in the surrounding areas of Iran's Harsin city were studied and four feasible sites proposed. In the final stage, these sites in order to construct a multi-purpose earth dam were prioritized using this integrated approach, and the most optimal site was selected. AHP was used to determine the relative weight of criteria and TOPSIS was used to rank the alternatives.

Keywords: AHP; Earth dam; Multi-Criteria Decision Making (MCDM); TOPSIS, Site selection.

1 INTRODUCTION

Water resources management because of the water crisis and depending on various factors is one of the most important and complex problems in different countries. The dam site selection is one of problems associated with water resources management. In addition, dam construction inflicts high costs and it should be constructed in a site with higher potential to compensate the costs. In this situation in order to locate the optimal dam site, various studies must be conducted. As this issue is related to different qualitative and quantitative criteria, decision making in this area is complex act. Therefore, in order to solve this problem, multi-criteria decision making (MCDM) methods could be used. MCDM is one of the branches of operation research which investigates the decision making problems under some decision making criteria. This kind of decision making utilizes a number of criteria instead of solely one optimal assessment criterion. MCDM is categorized into two main groups of multi-objective decision making (MODM) and multi-attribute decision making (MADM) (Pohekar and Ramachandran 2004). The aim of the MODM problems is the simultaneous optimization of a number of target functions under a series of limitations. Generally, MODM techniques are applied to design and optimization problems. The MADM methods are used for selecting the best alternative amongst various alternatives and obtaining a ranking for the alternatives. different methods have been presented for MADM, including: compromise programming [2]; elimination et choice translating reality I (ELECTRE I)

[3,4], ELECTRE II [5], and ELECTRE III [6]; analytic hierarchy process (AHP) [7]; simple additive weighting (SAW) [8]; technique for order preference by simulation of ideal solution (TOPSIS) [8]; preference ranking organization method for enrichment evaluations (PROMETHEE) [9]; gray relational analysis [10]; the weighted sum method (WSM) [11]; visekriterijumska optimizacija i kompromisno resenje (VIKOR) [12,13]; and data development analysis [14].

MADM methods have been used in the various fields of water engineering [15-30]. But, the application of these methods to locating the earth dam site has not been reported yet. In this study, an integrated AHP and TOPSIS technique were used to locate the earth dam site.

2. METHODOLOGY

In this study, the AHP introduced by saaty (1980) was used to determine the weight of criteria and TOPSIS first developed by Hwang and Yoon (1981) was used to rank the alternatives. Decision making using this model involves two essential stages: applying the AHP to determine the weight of criteria, applying the TOPSIS method to rank alternatives.

2.1. Applying the AHP to determine the weight of criteria

The AHP is one of the most powerful and simplest techniques for solving MADM problems. The working principle of this technique is based on the judgment of the user and pair-wise comparisons. Weight of criteria using this method is calculated in two steps as follows:

2.1.1 Construction of pair-wise comparison matrix

In the first step, pair-wise comparison matrix of criteria is constructed as:

$$A = \begin{bmatrix} \frac{w_1}{w_1} & \frac{w_1}{w_2} & \dots & \frac{w_1}{w_n} \\ \frac{w_2}{w_1} & \frac{w_2}{w_2} & \dots & \frac{w_2}{w_n} \\ \vdots & \vdots & \ddots & \vdots \\ \frac{w_n}{w_1} & \frac{w_n}{w_2} & \dots & \frac{w_n}{w_n} \end{bmatrix} \quad (1)$$

Where A is the comparison pair-wise matrix of criteria; w_1 the weight of criterion 1; w_2 the weight of criterion 2 and w_n is the weight of criterion n .

To determine the relative preference for two criteria of the hierarchy in matrix A an underlying semantic scale is employed having values from 1 to 9 according to Table 1.

Table 1 Saaty's scale of preferences in the pair-wise comparison process [7]

Intensity of Importance	Definition
1	Equal importance
3	Weak importance of one over Another
5	Essential or strong importance
7	Demonstrated importance
9	Absolute importance
2, 4, 6, 8	Intermediate values between adjacent scale values

2.1.2 Calculation of relative weights

In AHP, the eigenvector method uses for calculating the relative weights. In this method, firstly, by using Eq. 2 the eigenvalues of matrix A are calculated. Then, the relative weights of matrix A (the relative weights of criteria) are obtained with simultaneous solution of Eqs. 3 and 5:

$$AW = \lambda W \quad (2)$$

$$(A - \lambda_{\max} I)W = 0 \quad (3)$$

$$W = (w_1, w_2, w_3, \dots, w_j, \dots, w_n) \quad (4)$$

$$\sum_{j=1}^n w_j = 1 \quad (5)$$

Where λ_{\max} is the biggest eigenvalue of matrix A , W the weight vector, w_j weight of criterion j and I is the unit matrix.

2.2 Applying the TOPSIS method to rank alternatives

Among the MCDM methods, TOPSIS is a practical and useful technique for ranking and selecting a number of possible alternatives via measuring Euclidean distances. The working principle of TOPSIS is based on the fact that the

chosen alternative should have the shortest distance from the Positive Ideal Solution (PIS) and the farthest from the Negative Ideal Solution (NIS) for solving MCDM problems. In short, the PIS is composed of all the best indices, whereas the NIS is made up of all the worst attainable indices. Assume a MCDM problem has m alternatives (A_1, A_2, \dots, A_m), and n decision criteria (C_1, C_2, \dots, C_n). Each alternative is assessed with respect to the n criteria. All the values allocated to the alternatives with respect to each criterion form a decision matrix shown by $X = (x_{ij})_{m \times n}$. Let $W = (w_1, w_2, \dots, w_n)$ be the relative weight vector of the criteria, satisfying $\sum_{j=1}^n w_j = 1$. The procedure of TOPSIS can be expressed in a series of steps [31-34]:

2.2.1 Calculate the normalized decision matrix

The normalized value n_{ij} is calculated as:

$$n_{ij} = \frac{x_{ij}}{\sqrt{\sum_{i=1}^m x_{ij}^2}}, \quad i = 1, 2, 3, \dots, m; \quad j = 1, 2, 3, \dots, n \quad (6)$$

2.2.2. Calculate the weighted normalized decision matrix

The weighted normalized value v_{ij} is calculated as:

$$v_{ij} = w_j n_{ij}, \quad i = 1, 2, 3, \dots, m; \quad j = 1, 2, 3, \dots, n \quad (7)$$

Where, w_j is the weight of the j th criterion.

2.2.3 Determine PIS and NIS

The PIS indicates the most preferable alternative, and the NIS indicates the least preferable alternative. So determine PIS and NIS as follows:

$$A^+ = \{v_1^+, \dots, v_n^+\} = \left\{ \left(\max_j v_{ij} \mid i \in E \right), \left(\min_j v_{ij} \mid i \in F \right) \right\} \quad (8)$$

$$A^- = \{v_1^-, \dots, v_n^-\} = \left\{ \left(\min_j v_{ij} \mid i \in E \right), \left(\max_j v_{ij} \mid i \in F \right) \right\} \quad (9)$$

Where, A^+ and A^- are PIS and NIS, respectively. E is associated with benefit criteria (+), and F is associated with cost criteria (-).

2.2.4 Calculate the distance from PIS and NIS.

The Euclidean distance of each alternative from the PIS is obtained as:

$$d_i^+ = \sqrt{\sum_{j=1}^n (v_{ij} - v_j^+)^2}, \quad i = 1, 2, 3, \dots, m \quad (10)$$

Similarly, the Euclidean distance of each alternative from the NIS is given as:

$$d_i^- = \sqrt{\sum_{j=1}^n (v_{ij} - v_j^-)^2}, \quad i = 1, 2, 3, \dots, m \quad (11)$$

2.2.5 Calculate the relative closeness of each alternative to the PIS

The relative closeness of the alternative A_i with respect to A^+ is defined as CC_i :

$$CC_i = \frac{d_i^-}{d_i^+ + d_i^-}, \quad i = 1, 2, 3, \dots, m \quad (12)$$

2.2.6. Determine the overall ranking

The overall ranking of alternatives is obtained using the relative closeness to the PIS. Each alternative with higher the CC_i has the higher priority.

3 CRITERIA

In order to determine effective criteria in selecting an appropriate earth dam site, comprehensive literature review were conducted and the most important criteria was selected. A brief explanation about the criteria is presented:

3.1 Health dam site (C_1)

The dam site must be located in a place where seams and tracks and the possibility of tectonic activities such as an earthquake, landslide, subsidence, etc., are minimal and abutments are more stable. Also, with lesser permeability and liquefaction properties of soil and natural materials in the dam site, better results will be achieved. In addition, soil mechanical properties of the region (compaction, consolidation, etc.) and kind of region geological layers in terms of influence on reservoir water quality (for instance, it must not be limestone), construction of dam reservoir and foundation, stability in the condition of rapid discharge of the reservoir, etc., should be considered.

3.2 Overall cost (C_2)

The overall cost for the construction of the dam is another important criterion in selecting the earth dam site. This overall cost includes: construction of the dam body and reservoir, water diversion during construction, water transfer to the consumption location, energy supply, site preparation, land use, and other costs associated with the dam projects.

3.3 Annual yield (C_3)

The annual volume of the water that passes through the cross section of the river in the dam site is called the annual yield, which plays important roles in locating the dam site.

3.4 Topographic conditions (C_4)

The existence of the secondary valley or stone abutments with suitable topography around the main river for constructing dam spillway is important. Also, when the main river is U or S shaped, it makes the length of tunnel, channel, and other water transfer systems short to divert or transfer water from upstream to downstream at the time of the dam construction and after that. In general, with regard to dam reservoir and its body, the best site for the dam is a place where a wide valley with high walls leads to a narrow canyon with tenacious walls.

3.5 Access to materials and facilities (C_5)

Access to materials (borrow sources, cement, etc.) and facilities (the power transmission lines, oil and gas distribution pipelines, road, etc.) is important.

3.6 Economic Development (C_6)

The effect of dam construction on agriculture and industrial development, power generation, fishery, job creation, etc., which are related to economic development, are regarded as important attributes for selecting the dam site.

3.7 Water quality (C_7)

The quality of water stored in reservoirs used for drinking and agriculture is important. Therefore, the dam site must be selected in a place where the quality of the water entering the reservoir is better. Also, factors that may reduce water quality (such as salt mine, gypsum, lime, etc.) should be considered.

3.8 Damage of dam body and reservoir (C_8)

The damages caused by the construction of the dam body and reservoir, including: environmental damages, destroying mines, historical monuments, agricultural lands and residential areas; displacement of roads, Railway and power lines, change the route of oil and gas pipelines, telecommunication facilities, etc. should be considered.

3.9 Volume of reservoir (C_9)

When the reservoir created after dam construction has more volume, the surface area of the reservoir water is increased, and it has more impact on the climate, but evaporation and water pollution potential increase. On the other hand, if the dam is to be constructed in a site where by increasing the volume of reservoir water the surface area of the reservoir water will not significantly be altered (the slope of the valley is high), the height and water hydrostatic pressure will be increased, and it is beneficial in terms of energy generation and water transfer downstream. But, more power would be imposed on the dam's body, and the structure should be built higher and stronger. Therefore, the dam should be constructed where the reservoir capacity based on the above-mentioned items, leakage, and other losses are optimal.

3.10 River flow regime (C_{10})

Permanent or seasonal flow regime of the river at the dam site is important. The seasonal rivers have more sediment transport and less water quality, and also, the management of water resources is harder due to the lack of accurate discharge of water entering the reservoir. Therefore, a permanent flow regime is recommended.

3.11 Water diversion and transfer (C_{11})

Dam site must be selected in a place where the costs of water diversion during construction and water transfer to consumption location are lesser. Also the costs of maintenance of water diversion and transfer systems (such as: channel, tunnel, pipe, etc) and other costs and damages (such

as: environmental, displacement of roads, railway and power lines, change at the route of oil pipelines, gas, telecommunication facilities, etc) are lesser.

3.12 Annual volume of sediment (C_{12})

When the annual volume of sediment entering the reservoir is lesser, the volume of the reservoir during its useful life, water quality, and the efficiency of the dam are higher.

3.13 Probable dam break (C_{13})

Material and moral damages caused by a probable dam break are among the important attributes for locating the dam site, and the dam should be constructed in a place where the amount of damages due to its probable break is low.

3.14 Probable maximum flood (C_{14})

The maximum volume of water caused by thawing snow and ice or other atmospheric precipitation occurring probably in rivers is called probable maximum flood.

3.15 Average annual evaporation (C_{15})

Regarding the annual average temperature difference in Iran's different regions, evaporation from the dam reservoir in different areas is different. And this affects the retention time of water in the reservoir (in terms of volume) and consequently the efficiency of the dam.

3.16 Environmental impacts (C_{16})

Changing weather conditions, vegetation, and wildlife are other factors that play significant roles in locating the dam site.

3.17 Social impacts (C_{17})

The The social impacts of population center displacement and the integration of different ethnic cultures due to the destruction of residential places for dam construction, reservoir dewatering, and also the utilization of the dam water downstream should be considered.

3.18 Political impacts (C_{18})

The dam construction goals for reducing political tensions including water supply of a city, preventing grievances and immigration of residents of a border city, etc., are among the attributes that should also be considered.

4 CASE STUDY

This study aims to develop an integrated AHP and TOPSIS approach to locate the dam site, in this section, presented methodology was applied in the optimal selection of the Harsin earth dam site. The purpose of this dam is development of agriculture and Industrial, drinking water supply, power generation, fishery, etc. in Harsin city at the western part of Iran. This city is located 16 km east of Kermanshah city (the capital of Kermanshah province, Iran). Its location is $34^{\circ} 16'$ longitude and $45^{\circ} 35'$ latitude. Fig. 1 shows the location of Harsin city in Kermanshah province, Iran.

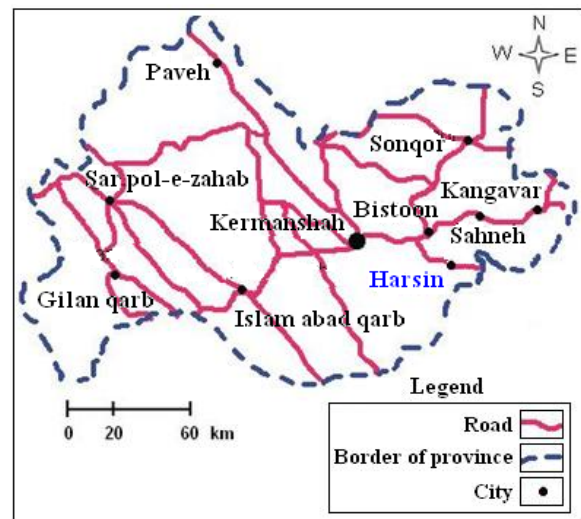


Fig. 1 Location of Harsin city in Kermanshah province, Iran

Then, according to the effective criteria in the dam site selection (mentioned in the previous part) and using the experiences and opinions of experts and existing information and data, four feasible alternatives in the surrounding areas of Harsin city were proposed, which are known as letters 'A', 'B', 'C' and 'D'. Fig. 2 shows the location of these proposed alternatives in studied field.

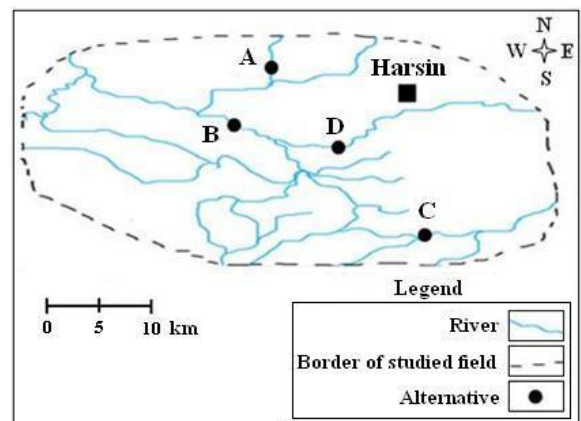


Fig. 2 Location of the proposed alternatives in studied field

After selecting criteria for locating the earth dam site and proposed alternatives (see Fig. 2), integrated AHP and TOPSIS approach was applied to select the optimal alternative for the Harsin earth dam site. To do this, firstly, pair wise comparison matrix of criteria was constructed by using the experts' opinions based on saaty's scale (see Eq. 1). Then the relative weights of criteria were obtained via Eqs. 2-5, the results are given in Table 2.

Table 2 Relative weights of criteria

Criterion	Definition	Relative weight
C ₁ (+)	Health dam site	0.161
C ₂ (-)	Overall cost	0.155
C ₃ (+)	Annual yield	0.075
C ₄ (+)	Topographical conditions	0.074
C ₅ (+)	Access to materials and facilities	0.045
C ₆ (+)	Economic development	0.120
C ₇ (+)	Water quality	0.077
C ₈ (-)	Damage of dam body and Reservoir	0.053
C ₉ (+)	Volume of reservoir	0.038
C ₁₀ (+)	River flow regime	0.015
C ₁₁ (-)	Water diversion and transfer	0.046
C ₁₂ (-)	Annual volume of sediment	0.033
C ₁₃ (-)	Probable dam break	0.020
C ₁₄ (-)	Probable maximum flood	0.020
C ₁₅ (-)	Average annual evaporation	0.016
C ₁₆ (+)	Environmental impacts	0.028
C ₁₇ (+)	Social impacts	0.017
C ₁₈ (+)	Political impacts	0.008

In the second stage, the TOPSIS method was applied to rank alternatives as follows:

The normalized decision matrix is obtained via Eq. 6. Obtaining matrix is shown in Table 3. Then, by using Eq. 7, the normalized weighted fuzzy decision matrix is calculated and the result is presented in Table 4.

Table 3 Normalized fuzzy decision matrix

Criterion	Alternative			
	A	B	C	D
C ₁ (+)	0.000210	0.000210	0.000030	0.000270
C ₂ (-)	0.008606	0.008216	0.008006	0.007196
C ₃ (+)	0.017091	0.016612	0.005397	0.003598
C ₄ (+)	0.000150	0.000210	0.000270	0.000270
C ₅ (+)	0.000090	0.000150	0.000210	0.000270
C ₆ (+)	0.000150	0.000150	0.000210	0.000210
C ₇ (+)	0.000270	0.000210	0.000150	0.000150
C ₈ (-)	0.000150	0.000150	0.000210	0.000210
C ₉ (+)	0.000150	0.000150	0.000090	0.000090
C ₁₀ (+)	0.005397	0.004888	0.006957	0.006597
C ₁₁ (-)	0.000150	0.000090	0.000150	0.000270
C ₁₂ (-)	0.000660	0.000690	0.000750	0.000810
C ₁₃ (-)	0.000150	0.000030	0.000270	0.000090
C ₁₄ (-)	0.709743	0.639278	0.226686	0.151124
C ₁₅ (-)	0.047976	0.053973	0.062339	0.056971
C ₁₆ (+)	0.000150	0.000270	0.000150	0.000270
C ₁₇ (+)	0.000090	0.000150	0.000150	0.000090
C ₁₈ (+)	0.000150	0.000210	0.000150	0.000150

Table 4 Normalized weighted fuzzy decision matrix

Criterion	Alternative			
	A	B	C	D
C ₁ (+)	0.000034	0.000034	0.000005	0.000043
C ₂ (-)	0.001334	0.001273	0.001241	0.001115
C ₃ (+)	0.001282	0.001246	0.000405	0.000270
C ₄ (+)	0.000011	0.000016	0.000020	0.000020
C ₅ (+)	0.000004	0.000007	0.000009	0.000012
C ₆ (+)	0.000018	0.000018	0.000025	0.000025
C ₇ (+)	0.000021	0.000016	0.000012	0.000012
C ₈ (-)	0.000008	0.000008	0.000011	0.000011
C ₉ (+)	0.000006	0.000006	0.000003	0.000003
C ₁₀ (+)	0.000081	0.000073	0.000104	0.000099
C ₁₁ (-)	0.000007	0.000004	0.000007	0.000012
C ₁₂ (-)	0.000022	0.000023	0.000025	0.000027
C ₁₃ (-)	0.000003	0.000001	0.000005	0.000002
C ₁₄ (-)	0.014195	0.012786	0.004534	0.003022
C ₁₅ (-)	0.000768	0.000864	0.000997	0.000912
C ₁₆ (+)	0.000004	0.000008	0.000004	0.000008
C ₁₇ (+)	0.000002	0.000003	0.000003	0.000002
C ₁₈ (+)	0.000001	0.000002	0.000001	0.000001

The PIS (A^+) and the NIS (A^-) were determined as follows (see Eqs. 8 and 9):

$A^+ = (0.0000434, 0.0011154, 0.0012819, 0.0000200, 0.0000121, 0.0000252, 0.0000208, 0.0000079, 0.0000057, 0.0001043, 0.0000041, 0.0000218, 0.0000006, 0.0030225, 0.0007676, 0.0000076, 0.0000025, 0.0000017)$

$A^- = (0.0000048, 0.0013339, 0.0002699, 0.0000111, 0.0000040, 0.0000180, 0.0000115, 0.0000111, 0.0000034, 0.0000733, 0.0000124, 0.0000267, 0.0000054, 0.0141949, 0.0009974, 0.0000042, 0.0000015, 0.0000012)$

The distance of each alternative from PIS and NIS solutions was obtained by using Eqs. 10 and 11 as:

$$d_A^+ = 0.011, \quad d_A^- = 0.001$$

$$d_B^+ = 0.010, \quad d_B^- = 0.002$$

$$d_C^+ = 0.002, \quad d_C^- = 0.010$$

$$d_D^+ = 0.001, \quad d_D^- = 0.011$$

Consequently, the relative closeness of the alternative A_i with respect to the PIS can be calculated as shown below (see Eq. 12):

$$CC_A = \frac{0.001}{0.011 + 0.001} = 0.085$$

$$CC_B = \frac{0.002}{0.010 + 0.002} = 0.150$$

$$CC_C = \frac{0.010}{0.002 + 0.010} = 0.845$$

$$CC_D = \frac{0.011}{0.001 + 0.011} = 0.916$$

The relative closeness to the PIS clearly shows the rating of alternatives. Based on these values (CC_i), four proposed

alternatives were ranked “D”, “C”, “B” and “A”, respectively. This means that, the alternative ‘D’ is the optimal alternative for the Harsin earth dam site. Fig. 3 shows the Front view of this alternative.

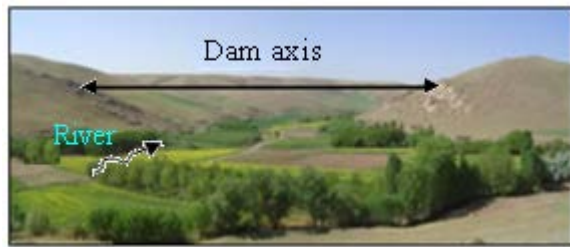


Fig. 3 Front view of the optimal site (alternative D)

5 CONCLUSION

The dam site selection is related to many factors. Therefore, multi-criteria decision making could be used to solve this problem. In this study, AHP and TOPSIS, which are two of the most powerful and flexible methods for use in solving multiple criteria problems were used in an integrated approach for locating the optimal earth dam site, this approach was applied to locate the Harsin earth dam site at the west of Iran. For this purpose, four alternatives A, B, C and D, were evaluated with regard to the most effective criteria. After applying this integrated approach, alternative D was identified as the optimal site for the Harsin earth dam. The Merit of this site (Alternative D) was also approved by experts involved in this project. Therefore, this approach could be used in selecting the optimal site in other dams.

6 ACKNOWLEDGMENT

The authors would like to appreciate Kermanshah Regional Water Company and Pandam Consulting Engineers Company for providing required information and data.

7 REFERENCES

- [1] Pohekar SD, Ramachandran M, “Application of multi-criteria decision making to sustainable energy planning—A review”, *Renew. Sust. Enrg. Rev.*, vol. 8, 2004, pp. 365-381.
- [2] Charnes A, Cooper WW, *Management Models and Industrial Applications of Linear Programming*. New York: Wiley, 1961.
- [3] Benayoun R, Roy B, Sussman, N, *Manual de reference du programme electre. Note De Synthese et Formaton*, Paris: Direction Scientifique SEMA, 1966.
- [4] Roy B, “Classement et choix en presence de points de vue multiples: La methode ELECTRE”, *RIRO*, vol. 8, 1968, pp. 57-75.
- [5] Roy B, Bertier P, “La methode Electre II: Une application au media-planing”, In: M. Ross (ed.), *VIIeme Conference Internationale de Recherche Operationnelle*, 1973, pp. 291-302.
- [6] Roy B, “ELECTRE III: un algorithme de classement fondé sur une représentation floue des préférences en présence de critères multiples”, *Cahiers du CERO*, vol. 20, 1978, pp. 3-24.
- [7] Saaty TL, *The analytic hierarchy process*. New York: McGraw-Hill, 1980.
- [8] Hwang CL, Yoon K, *Multiple attribute decision making*. Berlin: Springer-Verlag, 1981.
- [9] Brans JP, Vincke P, Mareschal B, “How to select and how to rank projects: the PROMETHEE method”, *Eur. J. Oper. Res.*, vol. 24, 1986, pp. 228-238.
- [10] Deng JL, “Introduction to grey system theory”, *The Journal of Grey System*, vol. 1, 1989, pp. 1-24.
- [11] Janssen R, *Multiobjective Decision Support for Environmental Management*. Netherlands: Kluwer Academic Publishers, 1996.
- [12] Opricovic S, *Multi-criteria optimization of civil engineering systems*. Belgrade: Faculty of Civil Engineering, 1998.
- [13] Opricovic S, Tzeng GH, “Multicriteria planning of post earthquake sustainable reconstruction”, *Comput-Aided. Civil. Infrastruct. Eng.*, vol. 17, 2002, pp. 211-220.
- [14] Cooper WW, Sieford LM, Tone K, “*Data Envelopment Analysis: A Comprehensive Text with Models, Applications, References and DEA-Solver Software*”, Boston: Kluwer Academic Publishers, 2000.
- [15] Anand Raj PA, Kumar DN, “Ranking of river basin alternatives using ELECTRE”, *Hydrolog. Sci. J.*, vol. 41, 1996, pp. 697-713.
- [16] Despic O, Simonovic SP, “Aggregation operators for soft decision making in water resources”, *Fuzzy Sets Syst.*, vol. 115, 2000, pp. 11-33.
- [17] Choi DJ, Park H, “Analysis of water privatization scenarios in Korea with multicriteria decision making techniques”, *J. Water Supply Res. T.-AQUA*, vol. 50, 2001, pp. 335-352.
- [18] Kheireldin K, Fahmy H, “Multi-criteria approach for evaluating long term water strategies”, *Water Int.*, vol. 26, 2001, pp. 527-535.
- [19] Ahmed SA, Tewfik SR, Talaa HA, “Development and verification of a decision support system for the selection of optimum water reuse schemes”, *Desalination*, vol. 152, 2002, pp. 339-352.
- [20] Chuntian C, Chau KW, “Decision aiding three-person multi-objective conflict decision in reservoir flood control”, *Eur. J. Oper. Res.*, vol. 142, 2002, pp. 625-631.
- [21] Cai X, Lasdon L, Michelsen AM, “Group Decision Making in Water Resources Planning Using Multiple Objective Analysis”, *J. Water Res. Pl.-ASCE*, vol. 130, 2006, pp. 4-14.
- [22] Abrishamchi A, Ebrahimian A, Tajrishi M, “Case Study: Application of Multicriteria Decision Making to Urban Water Supply”, *J. Water Res. Pl.-ASCE*, vol. 131, 2005, pp. 326-335.

- [23] Limon GA, Martinez Y, "Multi-criteria modeling of irrigation water market at basin level: A Spanish case study", *Eur. J. Oper. Res.*, vol. 173, 2006, pp. 313-336.
- [24] Bojan S, "Linking analytic hierarchy process and social choice methods to support group decision-making in water management", *Decis. Support Syst.*, vol. 42, 2007, 2261–2273.
- [25] Montazar A, Behbahani SM, "Development of an optimized irrigation system selection model using analytical hierarchy process", *Biosystems Eng.*, vol. 98, 2007, pp. 155–165.
- [26] Stefan H, Andrew H, "A comparison of multiple criteria analysis techniques for water resource management" *Eur. J. Oper. Res.*, vol. 184, 2008, pp. 255-265.
- [27] Montazar A, Zadbagher E, "An analytical hierarchy model for assessing global water productivity of irrigation networks in Iran", *Water Resour. Manag.* vol. 24, 2010, pp. 2817-2832.
- [28] Weng SQ, Huang GH, Li YP, "An integrated scenario-based multi-criteria decision support system for water resources anagement and planning – A case study in the Haihe River Basin", *Expert. Syst. Appl.*, vol. 37, 2010, pp. 8242-8254.
- [29] Marianna G, Laia F-M, Alessandra B, Simona T, "Multi-criteria analysis for improving strategic environmental assessment of water programmes. A case study in semi-arid region of Brazil", *J. Environ. Manage.*, vol. 92, 2011, pp. 665-675.
- [30] Nitirach S, Vilas N, "Strategic decision making for urban water reuse application: A case from Thailand", *Desalination*, vol. 268, 2011, pp. 141-149.
- [31] Jahanshahloo GR, Lotfi FH, Izadikhah M, "Extension of the TOPSIS method for decision-making problems with fuzzy data", *Appl. Math. Comput.*, vol. 181, 2006, pp. 1544-1551.
- [32] Olson DL, "Comparison of weights in TOPSIS models", *Math. Comput. Model.*, vol. 40, 2004, pp. 721-727.
- [33] Sen P, Yang JB, *Multiple criteria decision support in engineering design*. London: Springer-Verlag London Limited, 1998.
- [34] Yang T, Hung CC, "Multiple-attribute decision making methods for plant layout design problem", *Robt. Cim.-Int. Maunf.*, vol. 23, 2007, pp.126–137.

Using Geogrid Boxes as a New Approach for Reinforcement of Rock Slopes

Ahmad Fahimifar ^a, Arvin Abdolmaleki ^b

^aDepartment of Civil Engineering, Amirkabir University of Technology, Tehran, Iran.

^bDepartment of Civil Engineering, Tafresh University, Tafresh, Iran.

ABSTRACT

Use of geosynthetic reinforcement in structures such as soil slopes, paved or unpaved roads and runways, has been the subject of wealth of research works. However, there is no published work that encompasses the scope of stabilization of rock slopes using geogrid boxes. The main objective of this research is to introduce the geogrid box reinforcement method as a new approach to reinforce rock slopes and investigate whether the new approach can be a satisfactory alternative for the other conventional slope stabilization methods. The limit equilibrium (LE) and finite element (FE) analysis were conducted to predict the response of the slope to a broad range of possible conditions, namely dry, half-saturated and saturated states; as well as, static, quasi-static and dynamic conditions. Results confirmed that installing geogrid box can be used as a satisfactory alternative for the rock bolt system method.

Keywords: Rock slope stability, geogrid box, rock bolt, limit equilibrium analysis, finite element analysis.

1. INTRODUCTION

Geosynthetics have become well established construction materials for geotechnical and environmental applications. In the last two decades the use of geosynthetic materials for reinforcing slopes and retaining walls in fill has increased extensively throughout the world. In slope and wall applications the function of the geosynthetic layers is to offer resistance to driving forces or moments caused by the self-weight of the soil and applied surcharges [1], [2]. Wealth of research have been carried out on reinforcement of soil slopes by geosynthetics, most of which highlight the advantages of using this method over other reinforcement methods [1]-[3]. San and his associates [1] indicated that FE and LE methods could consistently determine the locations of critical slip surfaces and required tensile strength of reinforcement in geosynthetic-reinforced slopes. Despite extensive research on geogrid-reinforced soil slopes, we know of hardly any published work that covers the scope of stabilization of rock slopes using geogrid boxes. Therefore our objectives at the present work are to introduce this method as a new approach to reinforce rock slopes and

compare this method with other conventional slope stabilization methods.

2. EXPERIMENTAL PROCEDURE AND CASE STUDY

The study area is located approximately along km 11+060 of Mianeh-Ardabil railway track. This section is problematic due to the existence of lithological units with variable character. The Engineering geological properties of the rocks exposed in the case study slopes and technical specifications of geogrid are presented in Table I. Fig. 1 depicts the profile of site.

Three design methodologies were presented to investigate the effect of height and width of geogrid boxes on the factor of safety. The factor of safety for slope stability analysis is defined as the ratio of the ultimate shear strength divided by the mobilized shear stress at incipient failure.

Table I. Required parameters for stability analysis and geogrid parameters

Parameter	Symbol	Unit	Rock type	Value
Cohesion	C	kPa	R-I	570
			R-II	50
			R-III	390
			R-used in geogrid box	140
Internal friction angle	φ	degree	R-I	60
			R-II	25
			R-III	55
			R-used in geogrid box	40
Unit weight	γ	KN/m ³	R-I	26.5
			R-II	24.5
			R-III	25
			R-used in geogrid box	26.5
Elasticity modulus	E	KN/m ²	R-I	6.067 e + 09
			R-II	3.77 e + 07
			R-III	2.42 e + 09
			R-used in geogrid box	6.06 e + 08
Poisson's ratio	ν	--	R-I	0.25
			R-II	0.32
			R-III	0.27
			R-used in geogrid box	0.25
Horizontal earthquake acceleration in quasi-static analysis	K _h	m/s ²	--	0.1g
Geogrid parameters	Tensile Strength	N _p	KN/m	--
	Cohesion	C	KN/m ²	200
	Friction angle	φ	degree	5
	Equivalent axial stiffness	EA	KN/m	--
				40
				1.71 e + 04

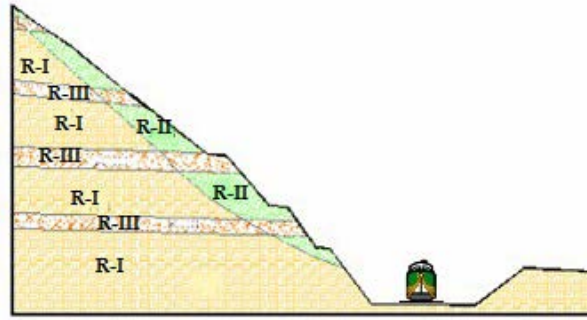


Fig. 1 Profile of the slope

3. RESULTS AND DISCUSSIONS

3.1. Stability analysis of the excavated slope

The safety factors obtained for the excavated slope in different conditions are shown in Table II. The results indicate that excavation of the slope has considerably

decreased the factor of safety. For the LE analysis we adopted the Spencer method which assumes a constant relationship between the magnitude of the interslice shear and normal forces [4]. This method satisfies both the moment equilibrium and force equilibrium. The only limitation of this method is the need to a software program to conduct the complicated calculations.

Table II. Factor of safety for excavated slope in Plaxis and Slide

	Factor of safety (FE based software)			Factor of safety (LE based software)	
	Static	Quasi-static	Dynamic	Static	Quasi-static
Dry	1.13	1.00	1.05	1.28	1.13
Half-saturated	1.19	0.94	0.98	1.24	1.07
Saturated	1.08	0.91	0.94	1.07	0.94

The different safety factors obtained can be attributed to the analysis mode performed by PLAXIS and SLIDE. PLAXIS performs numerical analysis in which no pre-defined slip surface or inter-slice forces are required. Furthermore, the possible slip in FE method takes place in a zone. On the other hand, in LE based software SLIDE, the shape and position of slip surface have to be priori defined and the slide surface is considered to be a narrow curve. Considering above, the outputs of numerical methods seem to be more valid than that of limit equilibrium methods [5]-[10].

The calculations were carried out for the different conditions with a maximum height of 8 m for each bench by selecting a thickness of 1 m for every reinforcement layer. At the beginning of each bench the width of geogrid box is 10 m. The width of the upper box is 9.5 m and the 0.5 m reduction in box width will be continued so that the box width at the end of each bench reaches 6.5 m. Fig. 2 depicts the schematic of Plan 1. The results of stability analysis are presented in Table III. As is observed, the factor of safety has increased to a considerable extent.

3.2. Plan 1

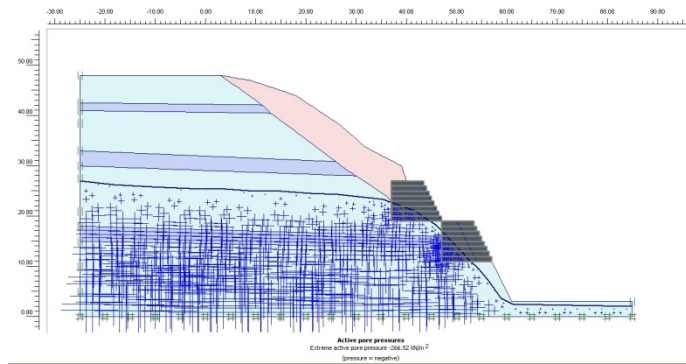


Fig. 2. Schematic of geogrid boxes installation in plan 1

Table III. Factor of safety for plan 1 in Plaxis and Slide

	Factor of safety (FE based software)			Factor of safety (LE based software)	
	Static	Quasi-static	Dynamic	Static	Quasi-static
Dry	1.70	1.44	1.52	1.75	1.53
Half-saturated	1.64	1.39	1.48	1.72	1.50
Saturated	1.40	1.30	1.39	1.66	1.37

3.3. Plan 2

In this plan, at the beginning of each bench the width of geogrid box is 15 m. The width of the upper box is 14.5 m and the 0.5 m reduction in box width will be continued so that the box width at the end of each bench reaches 11.5 m. All the boxes are 1 m in height.

The results of stability analysis are presented in Table IV. As is observed, in comparison with plan 1 the factor of safety decreases. Further increase in box width requires larger amount of excavation, as a result of which, the incline of upper eroded slope increases, and hence the factor of safety decreases.

Table IV. Factor of safety for plan 2 in Plaxis and Slide

	Factor of safety (FE based software)			Factor of safety (LE based software)	
	Static	Quasi-static	Dynamic	Static	Quasi-static
Dry	1.42	1.22	1.31	1.66	1.44
Half-saturated	1.41	1.20	1.28	1.63	1.41
Saturated	1.40	1.18	1.27	1.54	1.32

3.3. Plan 3

In this plan at the beginning of each bench the width of geogrid box is 5 m. The width of the upper box is 4.5 m and the 0.5 m reduction in box width will be continued so that

the box width at the end of each bench reaches 1.5 m. All the boxes are 1 m in height.

The results of stability analysis are presented in Table V. As is observed, the factors of safety obtained are lower than those obtained in plans 2 and 3. Referring to Tables III-V

and regarding the amount of consumed geogrid, plan 1 is selected for reinforcement of the rock slope and comparison with rock bolt system method.

Table V. Factor of safety for plan 3 in Plaxis and Slide

	Factor of safety (FE based software)			Factor of safety (LE based software)	
	Static	Quasi-static	Dynamic	Static	Quasi-static
Dry	1.40	1.15	1.24	1.49	1.12
Half-saturated	1.36	1.13	1.22	1.48	1.11
Saturated	1.29	0.85	0.94	1.42	1.09

3.4. Rock bolt system

Based upon available information, the ribbed bolts were installed using 3×3 staggered pattern [11]. A hex nut and bearing plate are used to distribute the tensile load from the bolt to the rock mass. Both surface and subsurface drains were installed to decrease the pore pressure acts on the rock mass and hence increasing the factor of safety. Subsequent stabilization measures were also implemented including adding shotcrete. To increase tensile strength and structural support, the shotcrete was used with welded wire mesh.

The results of stability analysis using rock bolt system are shown in Table VI. Considering above plan 1 enjoys the maximum factor of safety. In comparison with rock bolt system, implementing plan 1 causes cost reduction due to decrease in amount of excavation, allowing the slope to stand at steeper angles, reduction in labor, increasing the factor of safety, omitting some of the machinery and utilizing the existence material in the place, as well as reduction in construction time. This method also can be satisfactorily used to meet a variety of geological conditions and various support requirements.

Table VI. Factor of safety for rock bolt system in PLAXIS and SLIDE

	Factor of safety (FE based software)			Factor of safety (LE based software)	
	Static	Quasi-static	Dynamic	Static	Quasi-static
Dry	1.38	1.27	1.31	1.40	1.33
Half-saturated	1.32	1.20	1.23	1.31	1.25
Saturated	1.23	1.12	1.12	1.12	1.05

4. CONCLUSION

Stability analyses are routinely performed in order to assess the safe and functional design of an excavated slope. The analysis technique chosen depends on both site conditions and the potential mode of failure, with careful consideration being given to the varying strengths, weaknesses and limitations inherent in each methodology. The limit equilibrium (LE) and finite element (FE) analysis were conducted to predict the response of rock slopes to a broad range of possible scenarios, namely dry, half-saturated and saturated states; as well as, static, quasi-static and dynamic

conditions. The results indicate that the factors of safety obtained through the geogrid box method are higher than those obtained through rock bolt system method.

5. REFERENCES

- [1] San, K.C., D. Leshchinsky, and T. Matsui, "Geosynthetic Reinforced Slopes: limit equilibrium and finite element analysis," Soil and Foundations, 1994. 34: p. 79-85.
- [2] Chen, H.T., et al., "Centrifuge Modeling Test of a Geotextile-reinforced Wall with a Very Wet Clayey

- Backfill," *Geotextiles and Geomembranes*, 2007. 25(6): p. 346-359.
- [3] Ahn, T.B., S.D. Cho, and S.C. Yang, "Stabilization of Soil Slope Using Geosynthetic Mulching Mat," *Geotextiles and Geomembranes*, 2002. 20: p. 135-146.
- [4] Hryciw, R.D. and K. Haji-Ahmad, Design of Anchored Geosynthetic Systems for Slope Stabilization, in *Stability and Performance of Slopes and Embankments* 1994: Berkeley
- [5] Viswanadham, B.V.S. and D. Konig, "Centrifuge Modeling of Geotextile-Reinforced Slopes Subjected to Differential Settlements," *Geotextiles and Geomembranes*, 2009. 27: p. 77-88.
- [6] Spencer, E., "A Method of Analysis of the stability of Embankments Assuming Parallel Interslice Forces," *Geotechnique*, 1967. 17: p. 11-26.
- [7] Mahboubi, A., M. Aminpour, and A. Noorzad, Conventional and Advanced Numerical Methods of Rock Slope Stability Analysis, A Comparison Study, Gotvand Dam Right Abutment (Iran) Case Study, in the "12th International Conference of International Association for Computer Methods and Advances in Geomechanics (IACMAG)2008" Goa, India
- [8] Huang, M. and C.Q. Jia, "Strength Reduction FEM in Stability Analysis of Soil Slopes Subjected to Transient Unsaturated Seepage," *Computers and Geotechnics*, 2003. 36: p. 93-101.
- [9] Gurocak, Z., S. Alemdag, and M.M. Zaman, "Rock Slope Stability and Excavatability Assessment of Rocks at the Kapikaya Dam Site, Turkey," *Engineering Geology*, 2008. 96: p. 17-27.
- [10] Alkasawneh, W., et al., "A Comparative Study of Various Commercially Available Programs in Slope Stability Analysis," *Computers and Geotechnics*, 2008. 35: p. 428-435.
- [11] Abramson, L.W., et al., *Slope Stability and Stabilization Methods*. 2 ed. 2002: John Wiley and Sons.

Volume Change Characteristics of Bentonite Kaolinite Mixes

J. M. Kate

Datta Meghe Institute of
Engineering, Technology & Research,
Wardha - 442004, India

Sunil Kumar

Former M. Tech student,
Indian Institute of Technology
Delhi, New Delhi- 110016, India

M. P. Bhorkar

Datta Meghe Institute of
Engineering, Technology & Research,
Wardha - 442004, India

ABSTRACT

The fat clay commercially known as 'Bentonite' has extensive utilities in construction industries. The present experimental study has been undertaken to understand swelling pressure and volume change behavior of bentonite and kaolinite (kaoline clay) mixed in different proportions by weight. Mathematical equations correlating bentonite percentages with swelling, swelling pressure and related index properties have been developed. The studies clearly indicate considerable influence of bentonite on volume change behavior and related properties of clay mixes. The findings of the present study and the recommendations given may prove to be useful in construction industry where bentonite is extensively used as a single material or mixed with other clays.

Keywords: Bentonite, Free Swell Index, Kaolinite, Swelling Pressure, Volume Change

1. INTRODUCTION

Extremely fine grained fat clay commercially known as 'Bentonite' is composed of montmorillonite as its predominant mineral constituent. The properties such as very high volume change (swelling and shrinking), swelling pressure, high cohesion, extremely low permeability, thixotropy, etc. possessed by bentonite clays make it extremely useful material in construction industry especially for specific civil engineering construction, exploration and ground improvement practices. Just to list a few of utilities, it is extensively used during the construction of diaphragm wall, also used in slurry forms as bore hole stabilizer, fine clay grout, drilling mud, etc. Processed bentonite clay is invariably adopted as a sealing / lining material for industrial waste repositories and landfills to prevent percolation of liquid pollutants in to the surroundings. It is used as a single material only or in combination with other clays mostly on economy considerations. Processed kaoline clay having kaolinite as its predominant mineral constituent, is chosen for this investigation as it possesses negligible swelling and related properties.

In view of numerous utilities and related specification requirements, the present experimental study has been conducted to understand the volume change, swelling pressure behavior of clay mixes of bentonite and kaoline clay in different proportions. Here in an attempt has been made to develop mathematical equations to correlate bentonite percentages with volume change (swelling), swelling pressure. The findings have been discussed in the light of industrial applications of this study. The recommendations pertaining to suitability of clay mixes for particular job have been given.

2. LITERATURE REVIEW

2.1 Overview

The swelling phenomenon in clays is attributed mainly to the presence of montmorillonite clay mineral in them. Bentonite clay contains sodium montmorillonite as its predominant mineral constituent. The governing property of bentonite to satisfy specification requirements is different in different utility jobs. However, all such properties are directly related with degree of expansivity & swelling potential, e.g. in its use as a sealing material in underground subsurface waste repositories, the governing property/ criterion is its extremely low permeability. The clays with higher degree of expansivity exhibit lower permeability [1]. Similarly all other governing properties/ criteria can be assessed/ predicted from swelling/ volume change behaviour of expansive clays.

2.2 Engineering behaviour of expansive clays

Experimental investigation was carried out by Kate [1] on two extreme (low and high) grades of Indian bentonites to assess their suitabilities for utilities in civil engineering construction works. The relevant properties determined were mineralogy, chemical compositions, swelling, swelling pressure and coefficient of permeability. The bentonite slurry behaviour was assessed through viscosity, shear strength, pH, sedimentation and electrical conductivity. He reported that even without any additive both these extreme grade bentonites satisfy minimum specification requirements for their uses in almost all Civil engineering construction works. Based on synthesis of data available in literature Sridharan and Prakash [2] summarized broad guidelines to predict degree of expansivity of clays from routine tests. Accordingly, from the magnitudes of liquid limit, plasticity index, colloidal clay contents, shrinkage limit, free swell index, etc. the

degree of expansivity (low, medium, high or very high) can be predicted. The synthesis and analysis of available data from literature on swelling, swelling pressure and other relevant engineering characteristics of expansive clays were carried out by Sunil Kumar [3]. He reported good correlations between free swell index, maximum percentage swell and corresponding swelling pressure of such clays.

3. EXPERIMENTAL PROGRAMME

3.1 Clays & clay mixes

Commercially available processed bentonite clay and kaoline clay (Kaolinite) passing through 425-micron sieve have been used for the present study. Representative clay mixes were prepared by thoroughly mixing absolutely dry (zero moisture content) bentonite and kaolinite in desired proportions by weight. The proportions of bentonite and kaolinite adopted were 100:0, 80:20, 70:30, 50:50 and 30:70, which for brevity are referred in the text as clay mix A, B, C, D and E respectively.

3.2 Tests Conducted

Both the clays (bentonite, kaolinite) and clay mixes have been tested for their basic physical and engineering properties following the procedure as per Indian standard codes of practice for various laboratory tests. These tests include specific gravity, specific surface, hydrometer analysis and Standard Proctor test (for maximum dry unit weight and OMC). Chemical analysis of bentonite and kaolinite has also been carried out. Atterberg's limits such as liquid limit, plastic limit, plasticity index and shrinkage limit of all these clays & mixes were determined. Free Swell Index tests on clay mixes were conducted adopting the procedure suggested in IS: 2720, part 40 [4].

The maximum percentage swell and swelling pressure were determined as per the procedure given in International standard TC-6 [5]. Accordingly, the maximum percentage swell is the ratio of heave (under applied stress of 5kPa) to the initial thickness of clay sample in Oedometer. The percent swell has been obtained under each applied stress followed by determination of swelling pressure (which corresponds to magnitude of applied stress at zero percent swell) from the plot of percent swell versus applied stress (on log 10 scale). Swell and swelling pressure tests have been conducted on all these clay samples remoulded at initial compaction unit weight of 12.6 kN/m³, which corresponds to Standard Proctor maximum dry unit weight of bentonite. The initial moisture content for all clay mixes was maintained at zero percent as it provides maximum value of swelling pressure corresponding to chosen compaction dry unit weight.

The procedure adopted to compact the samples was that, calculated quantity (weight) of clay mix corresponding to initial unit weight of 12.6 kN/m³ and zero moisture content was placed in Oedometer ring attached with collar. This mix

was then compressed upto desired thickness in the ring using plunger plate (of same diameter as ring) and hydraulic jack. These clay samples in the ring were subjected to full water saturation under desired applied stresses during which changes in their thicknesses were recorded.

4. RESULTS AND DISCUSSION

4.1 Engineering properties and chemical composition

The physical and engineering properties of clays and their mixes are illustrated in Table I.

Table I Physical and Engineering properties of clays

Property	Clay Samples					Kaolinite
	A	B	C	D	E	
Specific gravity	2.71	2.71	2.70	2.68	2.65	2.63
Specific surface (m ² /g)	135	-	-	-	-	14
Maximum dry unit weight (kN/m ³)	12.6	13.2	14.0	14.9	15.1	16.9
OMC (%)	41	26	24	23	21	20
Silt (%) (0.075mm-0.002mm)	22	26	28	35	39	46
Clay (%) (<0.002mm)	78	74	72	65	61	54
Colloidal clay (%) (<0.001mm)	47	41	37	35	31	24
Classification	CH	CH	CH	CH	CH	CH

A-100*:0⁺ B-80*:20⁺ C-70*:30⁺ D-50*:50⁺ E-30*:70⁺
 *Bentonite Clay (%), ⁺ Kaolinite Clay (%)

The Table clearly shows distinct trend of changes in all the properties brought due to decreasing percentage of bentonite. For example, the maximum dry unit weight continuously increases from 12.6 kN/m³ for 100% bentonite (Sample A) to 16.9 for 0% bentonite (100% Kaolinite). Such trends of either continuous decrease or increase in magnitudes of property with decrease in bentonite percentage are distinctly noticeable.

The percentages of colloidal clay (<0.001 mm) in these mixes >27% indicate that, they possess very high degree of expansivity [2]. All the clays and clay mixes are classified ('A' line classification) as CH i.e. clays with high plasticity. The chemical composition of bentonite and kaolinite is presented in Table II, which shows SiO₂ is their predominant constituent followed by Al₂O₃.

Table II Chemical composition of clays

Chemical Composition (%)	Clay	
	Bentonite	Kaolinite
SiO ₂	60.23	53.06
Al ₂ O ₃	15.16	28.98
Fe ₂ O ₃	8.39	2.03
CaO	4.78	0.84
MgO	2.18	0.12
Na ₂ O	2.57	0.17
K ₂ O	0.83	2.66
SO ₃	0.25	0.11
Others	1.23	2.97
Loss on Ignition	4.38	9.06

4.2 Atterberg's limits and Index properties

The variation of liquid limit (LL), plastic limit (PL) and plasticity index (PI) with bentonite percentages present in clay mixes is illustrated in Fig. 1. It shows all increases exponentially with increase in bentonite percentages.

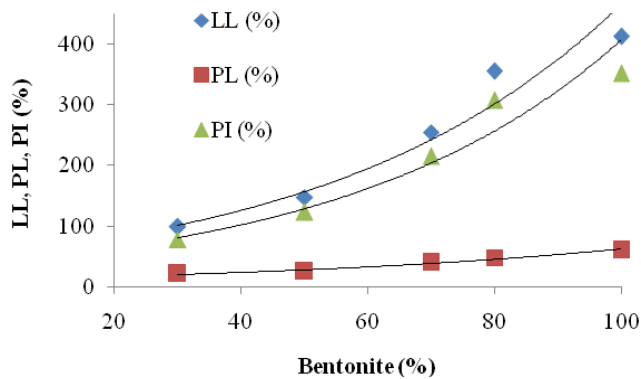


Fig. 1. Variation of Atterberg limits with bentonite percentages

The magnitudes of LL (>60%) and PI (>32%) exhibited by clay mixes demonstrate very high degree of their expansivity [2]. The regression analysis of the data provides the correlations expressed by Equations (1), (2) and (3)

$$LL = 52.74e^{0.022(B)} \quad (R^2 = 0.988) \quad (1)$$

$$PL = 0.0033(B)^2 + 0.16(B) + 12.14 \quad (R^2 = 0.915) \quad (2)$$

$$PI = 0.783(B)^{1.331} \quad (R^2 = 0.878) \quad (3)$$

Wherein, B denotes bentonite percentage and R^2 is coefficient of correlation

Free Swell Index (FSI) and shrinkage limit (SL) as a function of bentonite percentage in these clay mixes is shown in Fig. 2.

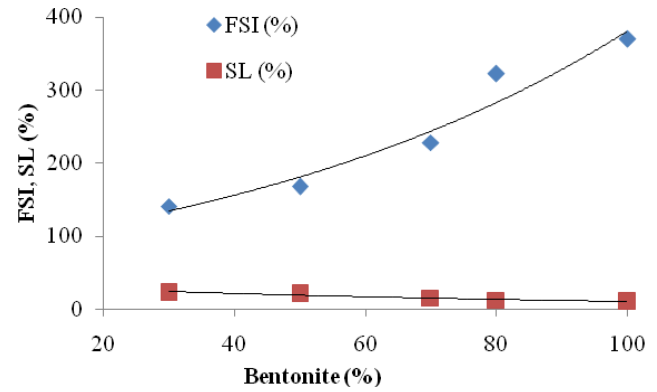


Fig. 2. FSI and SL as a function of bentonite percentage

It is seen from this figure that with increase in bentonite percentage the FSI increases exponentially, whereas SL decreases. The values of FSI (>200%) exhibited by clay mixes with bentonite percentage of 70 and above fall in very high expansivity, whereas the remaining clay mixes belongs only to high expansivity category as per [2].

4.3 Maximum swell and swelling pressure

The plots of swell versus applied stress for these clay mixes are shown in Fig. 3. The swell decrease with increasing applied stress as represented by variational curves in Fig. 3. The magnitudes of swelling pressure have been obtained from these curves.

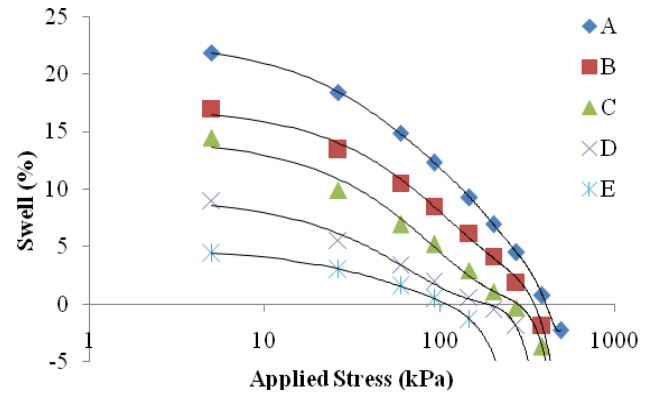


Fig. 3. Effect of applied stress on swell for clay mixes

The swelling pressure exhibited by clay mix A, B, C, D and E are 425, 340, 255, 175 and 106 kPa respectively and the corresponding maximum swells are 21.86, 17.02, 14.45, 9.00 and 4.83 percents. These values of swelling pressures as well as maximum swell (%) fall under very high for A, B & C and high/ moderate categories for D & E.

The swelling pressure as well as maximum swell as a function of bentonite percentage demonstrates that both increases with increase in bentonite as illustrated by curves in Fig. 4.

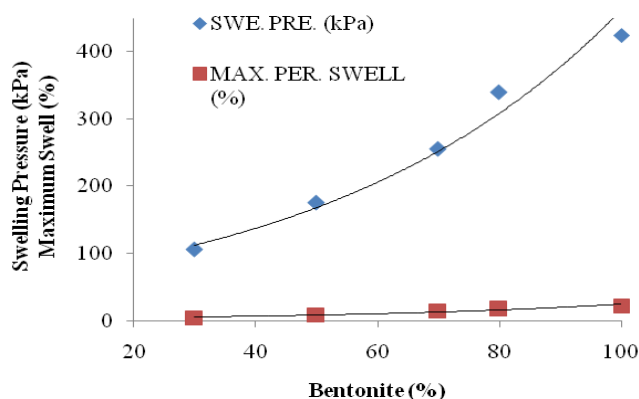


Fig. 4. Swelling pressure and maximum swell as a function of bentonite percentage

The relationship between swelling pressure (P_{sw}) and bentonite percentage is expressed by Eq. (4).

$$P_{sw} = 0.018(B)^2 + 2.37(B) + 16.06 \quad (R^2 = 0.855) \quad (4)$$

4.4 FSI and Swelling Pressure

A synthesis of available data on FSI and corresponding swelling pressure for various expansive clays extracted from most recent literature has been carried out in the present study. Various points on the plot of FSI versus swelling pressure shown in Fig. 5 correspond to such data from several investigators [3].

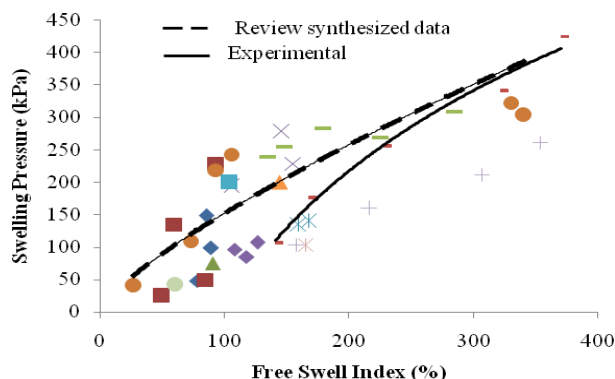


Fig. 5. Synthesized and experimental data of swelling pressure versus FSI

The curve in this figure has been derived as a best fit representing the entire data, and its regression analysis provides the correlation expressed by Eq. (5).

$$P_{sw} = 4.46 (FSI)^{0.725} \quad (R^2 = 0.921) \quad (5)$$

The experimental results of the above expansive properties obtained in this study are also illustrated in Fig. 5. The experimental values of swelling pressure of these clay mixes correlates with FSI as given in Eq. (6).

$$P_{sw} = 4.1 (FSI)^{0.76} \quad (R^2 = 0.953) \quad (6)$$

It is seen in Fig. 5 that both the curves exhibit nearly the same trend of power law relationships. It is interesting to note that these curves show significant deviations at lower values of swelling pressures, which tends to reduce with increasing values and beyond swelling pressure of 250 kPa both these curves overlap. This reflects on the distinct behaviour of bentonite and its mixes as compared to other expansive clays. The synthesized data from the literature corresponds mostly to clays having combination of montmorillonite and illite as their mineral constituents.

5. CONCLUSIONS

The findings of the present experimental study lead to the following conclusions .

- (i) The degree of expansivity as predicted from semi-direct criteria such as colloidal clay contents and Atterberg's limits, most of the clay mixes fall in the category of very high expansivity.
- (ii) The prediction through direct criteria i.e. FSI, percent swell and swelling pressure, the clay mixes with 70% and above bentonite fall in very high expansivity category & the remaining mixes (50% and 30% bentonite) between high to moderate category.
- (iii) The synthesized data from literature and present experimental data demonstrate a power law relationship between FSI and swelling pressure covering a very wide range of their magnitudes.

6. RECOMMENDATIONS

The clay mix (with comparable quality of bentonite and kaolinite) having 70% and above bentonite is recommended for its use in construction of diaphragm wall, sealing/ lining for industrial waste repositories, etc. Further, it is recommended to use clay mixes having 50% or only 30% bentonite for the work where used in slurry form e.g. fine clay grouts, borehole stabilizer, drilling mud, etc.

7. REFERENCES

- [1] Kate J M, "Mineralogical and Engineering Behaviour of Indian Bentonites", Proc. 2nd World Congress on Non-metallic Minerals, Beijing, China, Oct. 1989, pp. 393-398.
- [2] Sridharan A and Praksh K, "Classification Procedures for expansive Soils", J. of Institution of Civil Engineers, Geotechnical Engineering, vol. 143, 2000, pp. 235-239.
- [3] Sunil Kumar, "An Experimental Study on the Behaviour of Expansive Clays treated with different Fly Ashes", Unpublished M. Tech. Thesis CE Deptt., IIT Delhi, May 2007, pp.1-158.
- [4] Indian Standard IS: 2720, Part 40, "Determination of Free Swelling Index of Soils", Bureau of Indian Standards, New Delhi, 1997, pp. 1-17.
- [5] Technical Committee TC- 6, "Evaluation of Swelling Pressure and corresponding Heave of Expansive Soils by constructing Swell percentage versus applied total stress

diagram”, Report of Technical Committee (ISSMGE) on expansive soils, 1993, CBIP, New Delhi, pp. 1-26.

FE Analysis for Settlement of Peat Ground under Embankment Loading

Satoshi Nishimoto and Hirochika Hayashi
Civil Engineering Research Institute for Cold Region, Japan

ABSTRACT

Peaty ground commonly found in Hokkaido, Japan, is an extremely soft ground, which is highly organic and has special engineering properties. Finite element analysis (FE analysis) with consideration of the overlay pavement load as a measure against residual settlement was thus conducted concerning the long-term settlement of a road on peaty soft ground, and the relationship between the residual settlement and repair cost was studied. It was found that FE analysis using the Sekiguchi-Ohta model can express the long-term settlement of peaty soft ground. It was also revealed that the amount of residual settlement greatly affects the repair cost.

Keywords: peat, FE analysis, monitoring, settlement, life cycle cost, expressway embankment

1. INTRODUCTION

Peaty ground distributed widely in Hokkaido, Japan, is an extremely soft ground, which is highly organic and has special engineering properties. Roads on peaty ground are usually designed to allow for a certain degree of settlement and are repaired and maintained during their service, since considerable settlement occurs over a long period of time in such roads. The Manual for Peaty Soft Ground Countermeasures [1] stipulates the allowable residual settlement as between 10 to 30 cm in three years after an expressway is placed in service. These values were, however, determined empirically and should be reconsidered for the minimization of the life cycle cost (LCC).

FE analysis with consideration to the overlay pavement load as a measure against residual settlement was thus conducted concerning the long-term settlement of a road on peaty soft ground, and the relationship between the residual settlement and repair cost was studied.

2. SETTLEMENT BEHAVIOR OF PEATY GROUND AND THE CONCEPT OF THE LIFE CYCLE COST

Figure 1 is a conceptual diagram of the settlement of peaty ground. A characteristic of the settlement of peaty ground is the long-term settlement called secondary consolidation, which occurs linearly to the logarithm of time and causes continuous settlement after the placement of roads in service. The type of ground, where soft clay layers often accumulate at the bottom of peat, is called peaty soft ground. In addition to the peculiarity of peat, the existence of thick clay layers makes the problem of long-term settlement even more complex.

The standard method in the Peaty Soft Ground

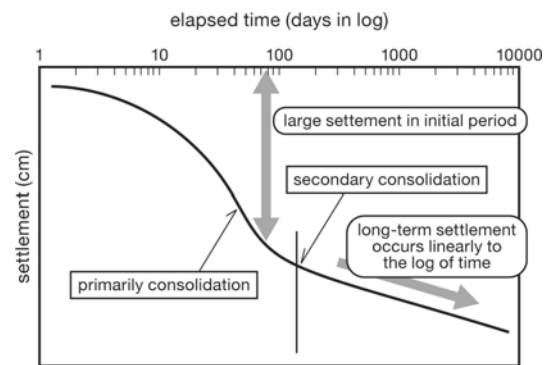


Figure 1. A typical settlement curve of peaty ground

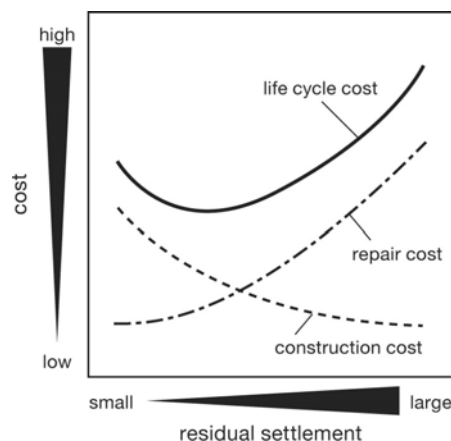


Figure 2. The concept of the life cycle cost

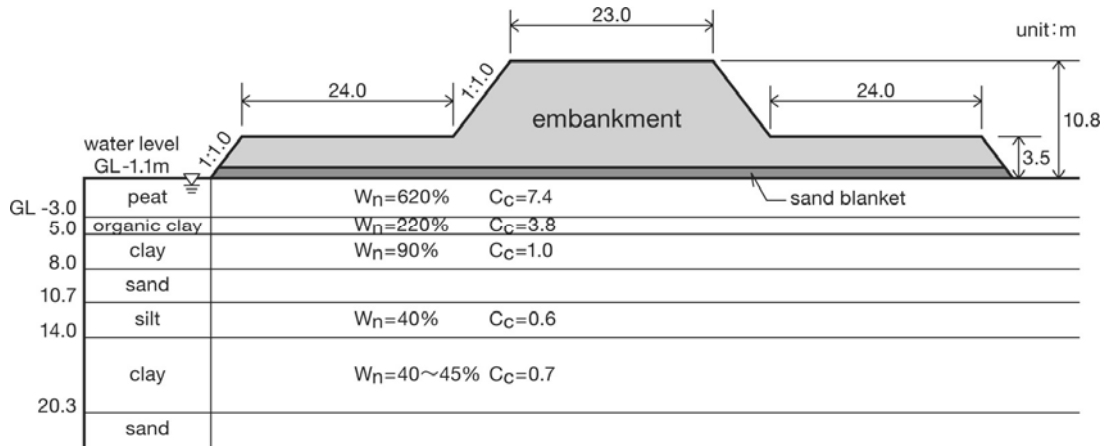


Figure 3. The cross section of the embankment

Countermeasures Manual for the construction of a road embankment on peaty soft ground is the method of allowing for a certain degree of residual settlement after the placement of the road in service and conducting maintenance and repair works during its service life. This method is used for reducing road construction costs, as well as for ensuring the flatness of the road surface and controlling road repair costs depending on the importance level of the road. It means that the concept of LCC shown in Figure 2 has been introduced. There are, however, some problems that must be solved for rationalization, such as the empirical setting of allowable residual settlement.

3. OVERVIEW OF FE ANALYSIS

3.1 Overview of the section of analyzed

The subject of the analysis, Mihara Bypass (1.4 km long), is an expressway on the outskirts of Sapporo, which is the largest city in Hokkaido. It is a two-lane road constructed on peaty soft ground. To ensure stability and reduce residual settlement, the preload method was adopted in combination with the counterweight fill method, which is the use of loading berms at the sides of the main embankment (Figure 3). Measurements of settlement have been continued since this expressway was placed in service in March 2005.

3.2 Analysis conditions

FE analysis was conducted using the Sekiguchi-Ohta model [2], which can express long-term settlement. Table 1 presents the analysis cases. A comparison between measured settlement and analysis results was first made as a preliminary study, and the applicability of the constitutive model and validity of parameters were verified.

Next, in the main study, virtual simulation was conducted for three cases with different amounts of residual settlement three years after their placement in service. At that time, the ground and other conditions were assumed to be uniform and the specific amounts of settlement were set by varying the period of waiting time for decreasing settlement. Concerning the bumps caused by settlement, it was assumed that repairs (overlay pavement) were repeated whenever

Table 1. Analysis cases and conditions

case	analysis conditions	
	overlay pavement load	residual settlement (cm)
preliminary case	no loading	—
main case	1 loading	30
	2 loading	20
	3 loading	10

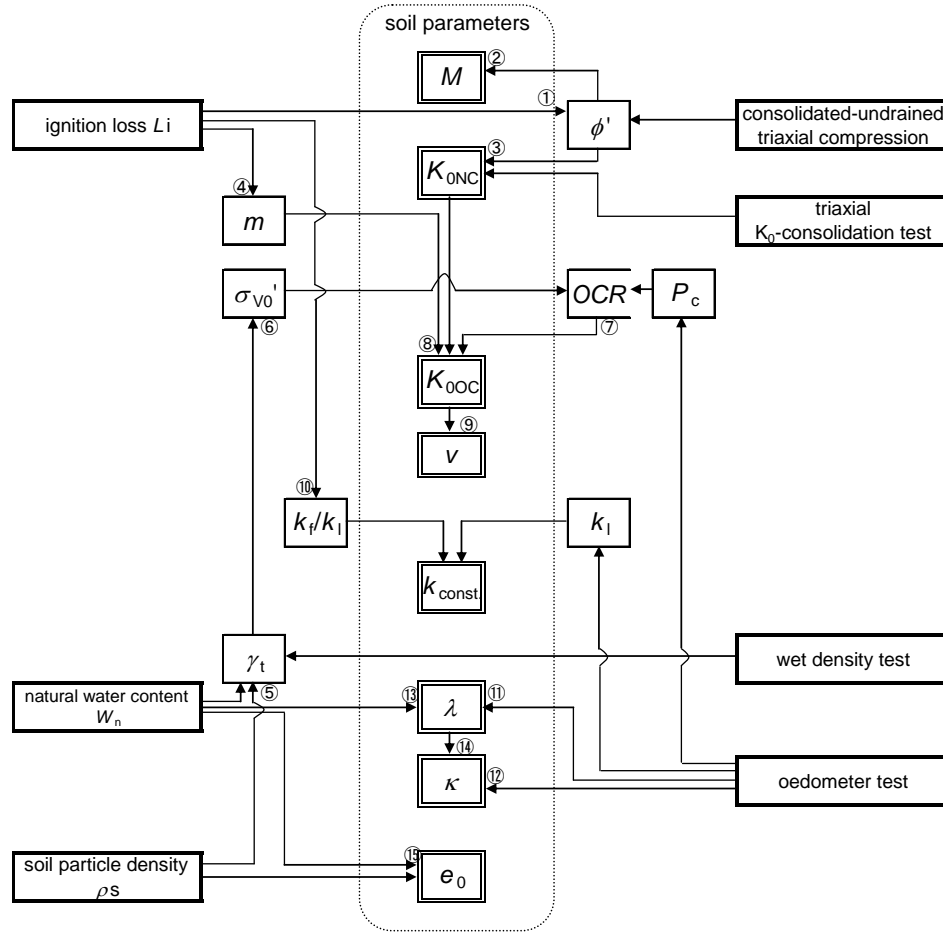
settlement reached 10 cm, based on the results of the fact-finding survey of repairs conducted by Nishimoto and Hayashi [3]. As the loading condition at that time, the load of the pavement thickness of 10 cm was uniformly distributed over the embankment crest, thus causing a slight increase in load from the embankment at this point. The traffic load generated by vehicles passing over the bumps was not taken into account because the embankment was high.

3.3 Determination of soil parameters

When analyzing the long-term settlement of peat, it is important to determine the coefficient of permeability and coefficient of secondary consolidation. Hayashi et al. [4] have revealed that the coefficient of permeability of peat decreases considerably with consolidation and that the actual coefficient of permeability is 10 to 30 times as large as the values found by the oedometer test. These are engineering properties peculiar to peat. In this analysis, therefore, the initial coefficient of permeability was determined by Eqs. (1) and (2). The changes in the coefficient of permeability associated with consolidation were given by Eq. (3). Where, k_{oed} is the coefficient of permeability found by the oedometer test (cm/s), C_v is the coefficient of consolidation (cm^2/day), m_v is the coefficient of volume compressibility (m^2/kN), γ_w is the unit weight of water ($=9.81\text{kN}/\text{m}^3$), k_0 is the initial coefficient of permeability (cm/s), $k_{\text{oed-p0}}$ is the coefficient of permeability at the time of effective overburden pressure

convenient method

detailed method



- ① $\phi' = 0.19Li (\%) + 32$
- ② $M = 6\sin\phi' / (3 - \sin\phi')$
- ③ $K_{0NC} = 1 - \sin\phi'$ Jaky (1948)
- ④ $m = 0.005Li (\%) + 0.45$
- ⑤ $\gamma_t = ((\rho_s - \rho_w)/(1 + e))g_n$
- ⑥ $\sigma_{v0}' = \gamma_t h - P_w$
- ⑦ $OCR = P_c / \sigma_{v0}'$
- ⑧ $K_{0OC} = K_{0NC} OCR^m$
- ⑨ $v = k_0 / (1 + k_0)$
- ⑩ $k_t/k_I = 0.33Li (\%)$
- ⑪ $\lambda = C_c/2.3$
- ⑫ $\kappa = C_s/2.3$
- ⑬ $C_c = 0.01W_n(\%)$
- ⑭ $C_s = 0.1C_c$
- ⑮ $e_0 = \rho_s/\rho_w W_n(\%)$

Figure 4. Determination procedures of soil parameters for FE analysis of peat and organic clay (Hayashi et al, 2007b)

Table 2. The list of soil parameters used

soil layer	coefficient of dilatancy D	irreversibility ratio λ	critical state parameter M	compression index λ	initial void ratio e_0	coefficient of secondary consolidation α	initial volumetric strain rate V_0 (day/1)	Pissov's ratio v	coefficient of in-situ earth pressure at rest K_{0OC}	coefficient of earth pressure at rest K_0	coefficient of permeability		
											horizontal k_H (m/day)	Vertical k_V (m/day)	change with void ratio λ_k
peat	0.10	0.92	1.94	2.69	12.36	0.03	2.2×10^{-5}	0.21	0.30	0.26	8.6×10^{-2}	1.7×10^{-2}	1.16
organic clay	0.15	0.90	1.48	1.62	5.44	0.02	3.3×10^{-5}	0.30	0.43	0.43	2.6×10^{-2}	5.2×10^{-3}	0.84
clay	0.11	0.80	1.08	0.39	1.63	0.01	2.9×10^{-6}	0.37	0.78	0.58	8.6×10^{-4}	8.6×10^{-4}	0.43
silt	0.07	0.82	1.16	0.20	0.91	0.01	2.3×10^{-5}	0.35	0.71	0.54	1.6×10^{-3}	1.6×10^{-3}	0.24
clay	0.09	0.86	1.10	0.24	1.06	0.01	1.4×10^{-6}	0.36	0.59	0.57	9.9×10^{-4}	9.9×10^{-4}	0.31

found by the oedometer test (cm/s), e is the void ratio at the end of consolidation and e_0 is the initial void ratio. The constant C_k in Eq. (3) was determined from the relationship between the void ratio and the coefficient of permeability

found by the oedometer test.

$$k_{\text{oed}} = C_v m_v \gamma_w / (8.64 \times 10^6) \quad (1)$$

$$k_0 = 10_{k_{\text{oed-P0}}} \quad (2)$$

$$k = k_0 \exp((e - e_0) / C_k) \quad (3)$$

Noto [5] related the coefficient of the secondary consolidation C_s (%) of peat with the natural water content W_n and expressed the relation by Eq. (4). The coefficient of secondary consolidation in this analysis was determined using Eq. (4).

$$C_s (\%) = 3.3 + 0.0043 W_n (\%) \quad (4)$$

Other soil parameters of peat were determined from the results of laboratory soil tests using the flow chart (Figure 4) proposed by Hayashi et al. [6]. The parameters of clay were determined using the method of Iizuka and Ohta [7]. Table 2 lists the soil parameters used for analysis.

4. RESULTS OF PRELIMINARY STUDY

Figure 5 displays the changes in measured and analyzed ground surface settlement at the center of the embankment with the passage of time. The embankment constructed at the section was 10.8 m in thickness, and the measured settlement at the start of service was approximately 4 m, indicating the high compressibility of the ground. Measured values have been obtained for 2,075 days (684 days in service) so far, and almost correspond with the analysis results. This means that FE analysis using the Sekiguchi-Ohta model is effective in the examination of the long-term settlement of peaty ground. It also shows that the procedure to determine soil parameter presented in this paper was valid.

5. RESULTS OF THE MAIN STUDY

Figure 6 presents the analysis results of Case 1 (30cm residual settlement in three years after placement in service). According to the analysis results, settlement will continue after placement in service and the residual settlement in 50 years is expected to be approximately 92 cm only in the case with the embankment load and 114 cm in the case where the overlay load is also taken into account. While the overlay load is rarely considered in normal settlement analysis, it is worth noting that, in the analysis results of this study, the amount of residual settlement was 22 cm greater with the overlay load than in the case with only the embankment load. Considering that residual settlement is often discussed on the order of around 10 cm, the overlay factor can be regarded as an important factor in the examination of residual settlement.

Analysis was conducted for other two cases using the above method, and the schedule and number of overlay repairs for respective cases were found (Figure 7). In the case where residual settlement was 30 cm three years after placement in service, six repairs were necessary in 10 years. In the first four years, in particular, repairs had to be

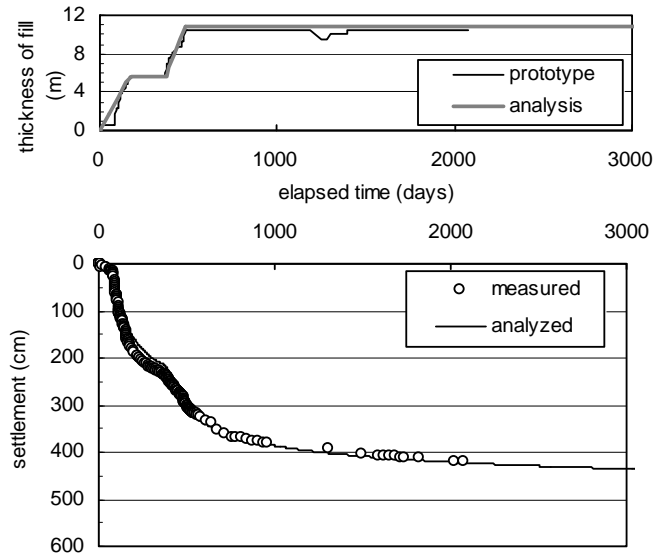


Figure 5. The changes in measured and analyzed ground surface settlement at the center of the embankment

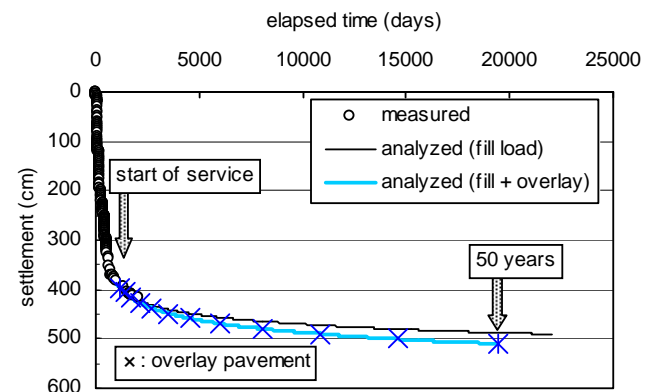


Figure 6. The effect of additional overlay pavement from repairs in increasing embankment load and settlement

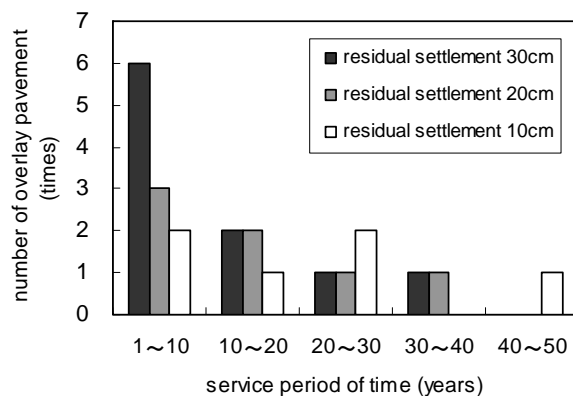


Figure 7. The number of overlay pavement repairs for respective cases

conducted every year. In the cases where residual settlement was 10 and 20 cm, however, the number of repairs was half or less. In the case of a two-lane road, closure is necessary even for a simple repair like overlaying. It is considered difficult to gain the understanding of users and related organizations if repairs requiring road closure must be made frequently soon after the opening of the road.

On the Mihara Bypass (1.4 km long), box culverts are placed at average intervals of 170 m. On the assumption that residual settlement would cause bumps before and after these culverts, the relationship between residual settlement and the overlay repair cost for the length of 1.4 km in 50 years was estimated (Figure 8). The conditions for the estimation were set using the actual repair cost found by Nishimoto and Hayashi [3] as a reference. Compared with the case of 30 cm residual settlement, the repair cost was approximately 72 and 59% in the cases of 20 and 10 cm settlement, respectively. It can be seen that the setting of the amount of residual settlement greatly affects the repair cost.

6. CONCLUSION

It was found that FE analysis using the Sekiguchi-Ohta model can express the long-term settlement of peaty soft ground. It was also revealed that the amount of residual settlement greatly affects the repair cost.

The authors intend to conduct further studies using the method applied in this study as an analysis tool and present the rational amount of residual settlement, repair schedule and other guidelines.

REFERENCES

- [1] Civil Engineering Research Institute of Hokkaido, Manual for Countermeasure against Peat Soft Ground, pp.42-44, 2002. (in Japanese)
- [2] Sekiguti, H. and Ohta, H., Induced anisotropy and time dependency in clays. Proceedings of the 9th ICSMFE, pp.229-239, 1977.
- [3] Nishimoto S. and Hayashi, H., A Case Study on The Long-term Settlement and Life Cycle Cost of A Road on Peaty Ground, Proceedings of 1st International Conference on Transportation Geotechnics, pp.397-400, 2008.
- [4] Hayashi, H., Mitachi, T. and Nishimoto S., Permeability Characteristics of Peaty Ground, Technical reports of Hokkaido branch, JGS, Vol. 46, pp.31-36, 2007a. (in Japanese)
- [5] Noto, S., Revised Formula for Prediction of Settlement on Soft Peaty Deposits. Monthly Report of Civil Engineering Research Institute, No. 446, pp.2-9, 1990. (in Japanese)
- [6] Hayashi, H., Mitachi, T. and Nishimoto S, Determination Procedure of Soil Parameters for Elasto-plastic FE Analysis of Peat Ground, Proceedings of the 13th Asian Regional Conference on SMFE, pp.145-148, 2007b.

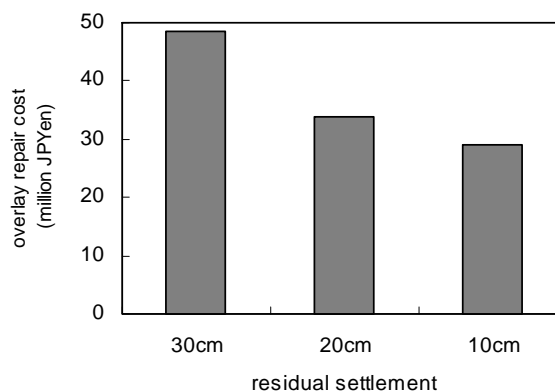


Figure 8. The relationship between residual settlement and the overlay repair cost

- [7] Iizuka, A. and Ohta, H., A determination procedure of input parameters in elasto-viscoplastic finite element analysis, Soils and Foundations, 27(3), pp.71-87, 1987.

Seismic behavior of pile group in soil slopes: 1g shake table tests

H. Elahi¹, M. Morad², A. Ghalandarzadeh³ and A. Elahi⁴
^{1,4}SPT Co, Tehran, Iran, ^{2,3}Tehran University, Tehran, Iran

ABSTRACT

A number of 16 physical model tests were conducted using a 1g shake table in order to investigate the seismic behavior of pile group in a soil slope. The instrumented physical models were exposed to sinusoidal motions of constant amplitudes. The parameters of the amplitude of the incoming motion, the number and spacing of piles in the group were altered. Single pile and group piles of 2×1 and 2×2 configuration with pile spacing to diameter ratios of 3, 5.4 and 7.8 were considered. Some observation and conceptual results about piles and pile cap displacements as well as lateral soil pressure on rear and front piles in group. The most essential result of these set of tests was to support the concept of utilizing the Newmark sliding block theory in the analysis of group pile within a slope. As the results of these tests, the preliminary diagrams for estimation of yield acceleration of pile group in the slope and its reliance upon group parameters are presented.

Keywords: pile group, seismic, slope, shake table, Newmark method

1. Introduction

For many years seismic behavior of pile group is attended from researchers around the world. Against of wide investigations, complexity of their behavior in soil makes many ambiguities in this field of foundation engineering. In earthquake loading and presence of nonlinear soil-pile-structure interaction, make this issue more sensible. Furthermore when the piles located in slope the complex behavior of these geotechnical structures is increased. Often pile group seat on soil slope such as foundation of structures in slopes, foundation and/or abutment of bridges pile supported wharves and some roads or pipelines on slopes. According to above mentioned complexities, there is not any simple and reliable analytical method in these conditions. Due to unknown behavior, numerical methods are not reliable too and their results may not be explained suitable. Therefore attempting on exploring seismic behavior of pile group in soil slope can be an important and applicable issue for investigation. Present work is done as an initiative research in this field beneath performing some shake table model tests.

2. Shake table model tests

2.1. Shake table specifications

Used equipment has several parts such as a table with dimension 180*120 cm², hydraulic actuator, power unit,

measuring and control system. The model box is constructed with Plexiglas which has dimension of 180*80 cm² in plan and 120 cm height (Fig. 1).

Many sensors such as accelerometers, electrical strain gauges, displacement gauges (LVDT) are used for instrumentation which all of them have dynamic sampling ability. Two dynamic data logger instruments with 20 channels are applied to gathering required data related with piles, pile cap and soil parameters (Fig. 1).

2.2. Dimensional analysis and scaling laws

Reference [2] presented the non-dimensional parameters for modeling of lateral pile behavior in shake table as following equation:

$$\frac{y}{d} = K \left(\frac{L_p}{u_0}, \frac{\rho_p}{\rho_s}, \frac{E_p I_p}{G_s u_0^4}, \frac{\omega^2 u_0}{g}, \frac{m_c}{\rho_s u_0^3} \right) \quad (1)$$

In which, y: Lateral dynamic deflection of pile, d: pile diameter, L_p: pile length, u₀: displacement amplitude of input motion, ρ_p: pile density, ρ_s: soil density, E_pI_p: pile flexural stiffness, G_s: shear modulus of soil, ω: frequency of input motion, m₀: mass of pile cap. Piles spacing to diameter ratio (s/d) is an additional non-dimension parameter which considered pile group effects. Therefore the scale factors for pile group shake table models can be presented as table 1.

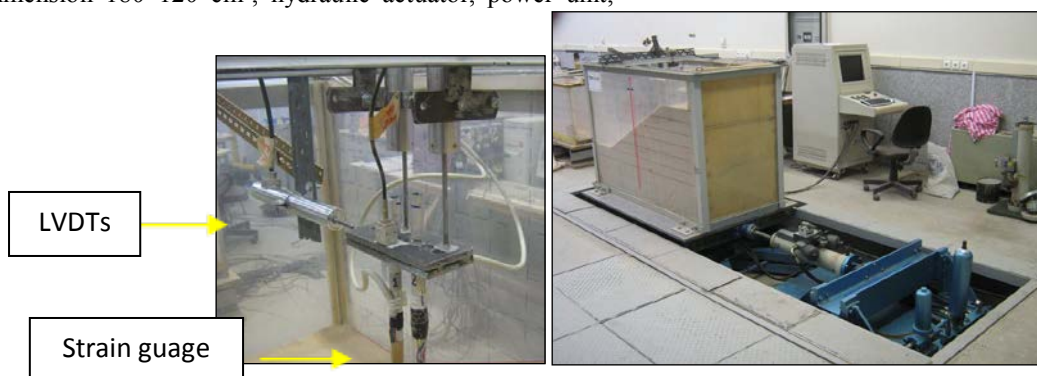


Fig. 1. Schematics of physical models and testing instrument

Table 1. Scale factors for mechanical parameter in 1g model of pile group

Parameter	Lp	EpIp	m _c	a ₀	F	s/d
Scale Factor	n	n ^{6.5}	n ^{4.6}	1	1/n ^{0.75}	1

2.3. Geometry of model

Geometry of models is shown in Fig. 2(a). All models are constructed with 9 layers and total height of 90 cm. Piles length are 90 cm and the height of slope foundation is 40 cm.

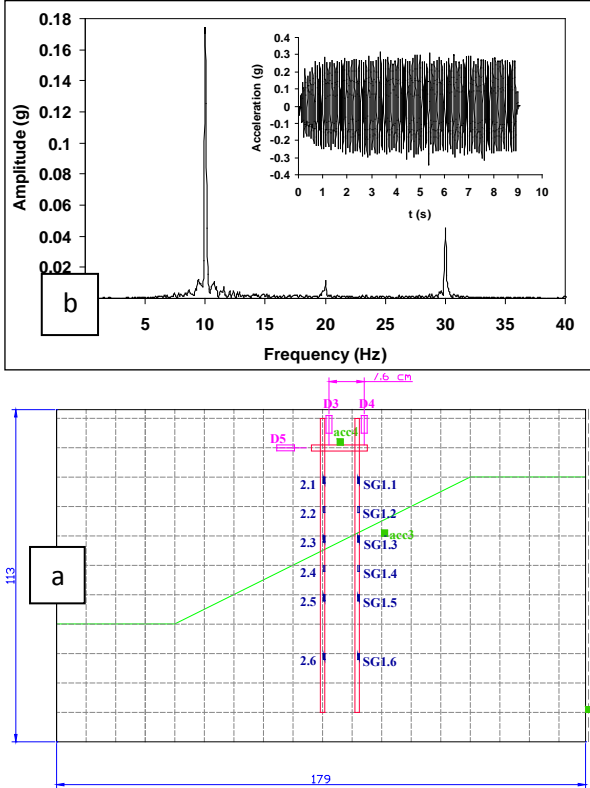


Fig. 2. a) Geometry of physical models (dimensions are in cm), b) a sample of time history of input motion with Fourier spectrum

2.4. Materials

a. sandy soil: Firouzkouh (No. 161) siliceous sand is used for model tests. This kind of sand has uniform aggregation and in the current study it has relative density of about 60%. Some specification of used soil is presented in table 2. b- Pile and pile cap: model piles made from Aluminum pipe with 15 mm external diameter and 1 mm thickness. Piles tip are conic with 30 degree angle. In each 2*2 group 2 piles are instrumented with 6 strain gauges. Pile cap is made from steel plate which contains 3 sets of 4 number of 16 mm diameters holes that covered pile spacing to diameter ratios included 3, 5.4 and 7.8.

2.5. Input motions

Base input motions are harmonic with fixed amplitude and frequency of 10 Hz. Each of physical models was tested with 2 different motions until reach to large deformations. At first a weaker motion with maximum acceleration of about 0.15g exerted to model and then a stronger input motion with maximum acceleration of about 0.3g were applied (Fig. 2(b)). There is a useful dynamic parameter that used in previous researches for considering both

amplitude and frequency content of the motion [2]. RMS acceleration is defined as following:

$$a_{RMS} = \sqrt{\frac{1}{T_d} \int_0^{T_d} a^2(t) dt} \quad (2)$$

In which, T_d : input motion duration, $a(t)$: acceleration. Because of less dependency of a_{RMS} to large accelerations and frequencies and existence of motion duration in it, it is a good parameters for research and engineering applications [3]. a_{RMS} is used in the current study as representative acceleration parameter.

2.6. Tests plan

Some of model parameters such as number and arrange of piles in group, piles spacing to diameter ratio, slope angle and input motion specifications such as maximum acceleration are changed to study seismic behavior of pile group in slope. Plan of tests is illustrated in table 3.

2.7. Construction procedure of the models

Construction of the physical model has four important parts; making a pile group, making a slope with sand rain, installing the piles in the slope and completing the instrumentation. Fig. 3 shows above mentioned sequences.

3. Tests results

Piles bending moment, displacement and acceleration of pile cap are recorded and analyzed. A sample of recorded data is presented in fig. 4.

3.1. Pile cap behavior

Seismic response of pile cap and acceleration of pile cap are imparted as basic parameters of pile cap response.

A. Pile cap acceleration: Based on try and error with several examinations on various parameters,

$a_{RMS, cap} / n.s.f^2$ was selected in which a_{cap} is pile cap acceleration, n is number of piles in group, s is piles spacing in group and f is input motion frequency. Fig. 5(a) shows relation between these parameters and base input acceleration.

B. Lateral displacement of pile cap: Residual and cyclic displacement are two component of cap displacement at each time (Fig. 5(b)). To understanding some basic components of behavior two hybrid parameter including

$n.Disp(Res)/s$ and $(n \cdot \frac{Disp(Res)}{Disp(Cyc)}) / (\frac{s}{d})$ versus

$a_{RMS, base} / s.f^2$ is shown in Fig. 6.

Shape of cap residual displacement in Fig. 5 (b) shows it may be possible to estimate cap residual displacement using Newmark sliding rigid block analysis [4]. Try and error analyses were conducted to estimate yield acceleration (a_y) for each test via comparison between measured and calculated displacement of pile cap (i.e. Fig. 7 for tests 2-3-2 and 1-1-2). Relationship between calculated a_y and some parameters such as base acceleration (a_{base}), cap acceleration (a_{cap}), cap inertial force (ma_{cap}), number of piles in group (n) and s/d was evaluated through try and error progress with various non-dimensional hybrid parameters. Results show that a_y is dependent to s/d , a_{base} and a_{cap} (Fig. 8). As seen, a_y and $(ma_{RMS, cap}) / (n.s/d)$ parameter have the best correlation (Fig. 9).

Table 2. Specification of FIRUZKUH 161 sand

USCS Name	D ₁₀ (mm)	D ₃₀ (mm)	D ₅₀ (mm)	D ₆₀ (mm)	Passing #200 %	Sand %	Cu	Cc	φ degree	e _{max}	e _{min}
SP	0.16	0.21	0.27	0.3	1	99	1.87	0.88	40 ⁰	0.874	0.548

Table 3. Parameters and specifications of physical models

No.	Test Name	a _{max} (g)	a _{RMS} (g)	Slope	s/d	Group Configuration
1	1-1-1	0.22	0.08	1:2	0	single
2	1-1-2	0.48	0.22	1:2	0	single
3	2-1-1	0.15	0.04	1:2	5.4	2*1
4	2-1-2	0.46	0.20	1:2	5.4	2*1
5	2-2-1	0.22	0.08	1:2	7.8	2*1
6	2-2-2	0.46	0.23	1:2	7.8	2*1
7	2-3-1	0.11	0.09	1:2	3	2*1
8	2-3-2	0.39	0.20	1:2	3	2*1
9	3-1-1	0.16	0.07	1:2	3	2*2
10	3-1-2	0.44	0.21	1:2	3	2*2
11	3-2-1	0.20	0.08	1:2	5.4	2*2
12	3-2-2	0.43	0.21	1:2	5.4	2*2
13	3-3-1	0.18	0.06	1:2	7.8	2*2
14	3-3-2	0.43	0.16	1:2	7.8	2*2
15	3-4-1	0.17	0.06	horizontal	7.8	2*2
16	3-4-2	0.50	0.23	horizontal	7.8	2*2



Fig. 3. Construction of Models

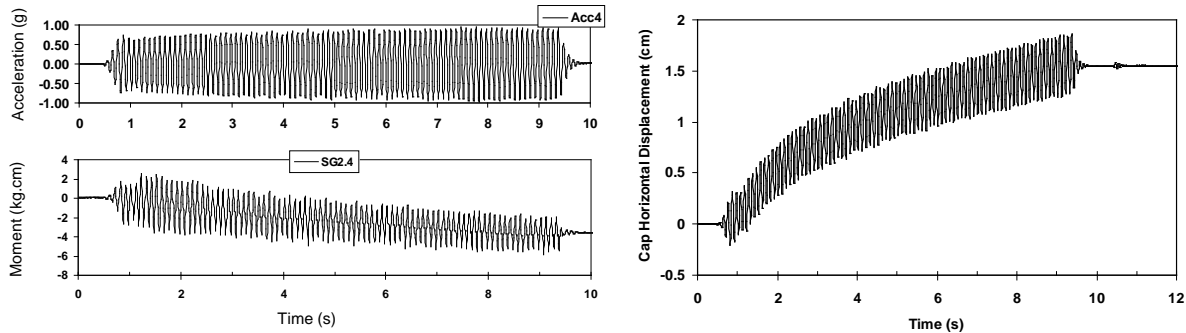


Fig. 4. Sample of recorded acceleration, pile bending moment and horizontal displacement of pile cap (test 2-3-2)

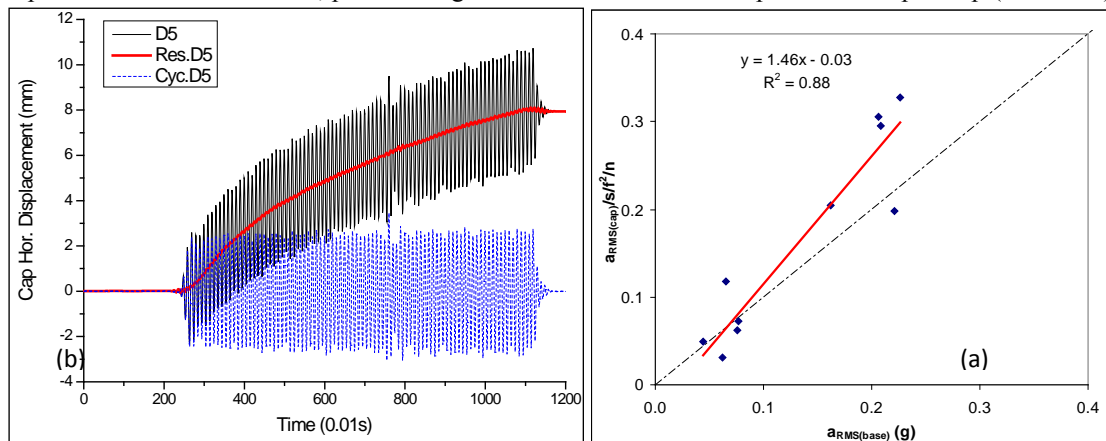


Fig. 5. a) Cap versus base acceleration, b) components of cap displacement in test no. 3-1-2

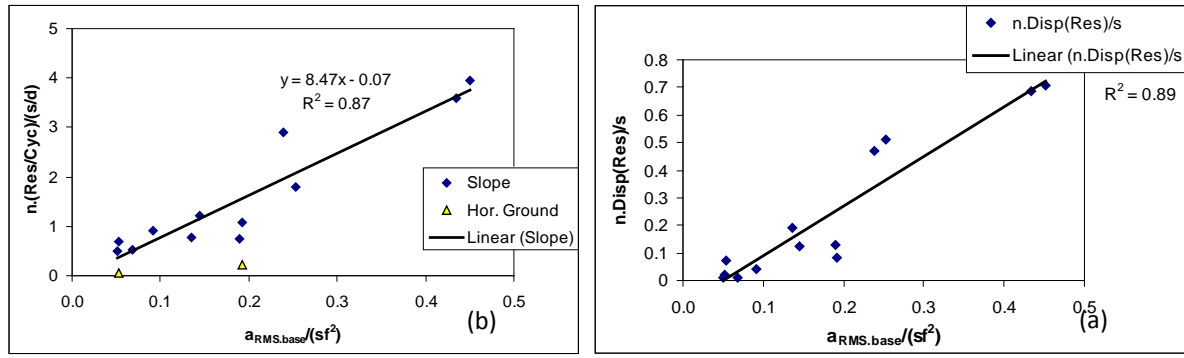


Fig. 6. a) Variation of n.Disp(Res)/s versus base acceleration, b) variation of cap displacement components versus base acceleration

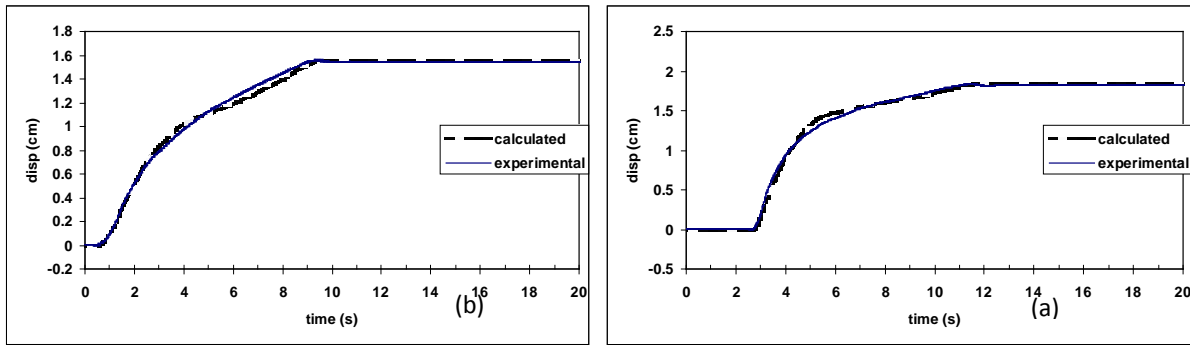


Fig. 7. Back calculating of yield acceleration (a_y) for a) test 1-1-2, b) test 2-3-2

3.2. Pile Behavior

Pile deflection, moment and shear as well as lateral soil pressure on piles are known as pile seismic response. According to importance of lateral soil pressure on front and rear piles (Fig. 10a) and its unknown aspects, test results on this parameter are presented in the current paper. Discussion on other mentioned parameters is presented in

4. Conclusion

16 1g shake table model tests on 2*1 and 2*2 pile group in soil slope were performed and the following results about seismic behavior of pile group in soil slope are seen and presented:

- Pile cap motion in slope has 2 components: residual and cyclic.
- With increasing the base acceleration, $a_{RMS.cap}/(n.s.f^2)$ which is composed of pile cap acceleration ($a_{RMS.cap}$), numbers (n) and piles spacing (s) and input motion frequency (f), increased.
- With raising the base acceleration hybrid parameter ($a_{RMS.base}/sf^2$), another hybrid parameters of horizontal motion of pile cap [$n \cdot \frac{Disp(Res)}{Disp(Cyc)} \cdot \frac{s}{d}$ and $n \cdot Disp(Res)/s$ and $Disp(Cyc)/s$] are increased.

[5]. In the current study maximum lateral soil pressure is normalized by dividing to pressure coefficient (K). Comparison of lateral soil pressure coefficient of rear and front piles is shown in fig. 10b in which variation of K_{rear}/K_{front} is presented versus a hybrid parameter related with base acceleration and group geometry ($a_{RMS(base)} \cdot (s/d)$).

Soil pressure on rear pile, is 1 to 2 times of pressure on front pile. The ratio of coefficients of lateral pressure on rear and front pile (K_{rear}/K_{front}) is decreased when a hybrid parameter based on input motion acceleration and group geometry [$a_{RMS(base)} \cdot (s/d)$] is increased.

Results of present tests, confirm the applicability of Newmark sliding block method in simulation of grouped piles located in slopes.

Yield acceleration for application of Newmark method for pile group in slopes is different with common yield acceleration in slopes. Meanwhile, yield acceleration of pile group in slope (a_y), is increased with raising the hybrid variable ($ma_{RMS.cap}/(n.s/d)$) included pile cap inertial force, number of pile in group and piles spacing to diameter ratio.

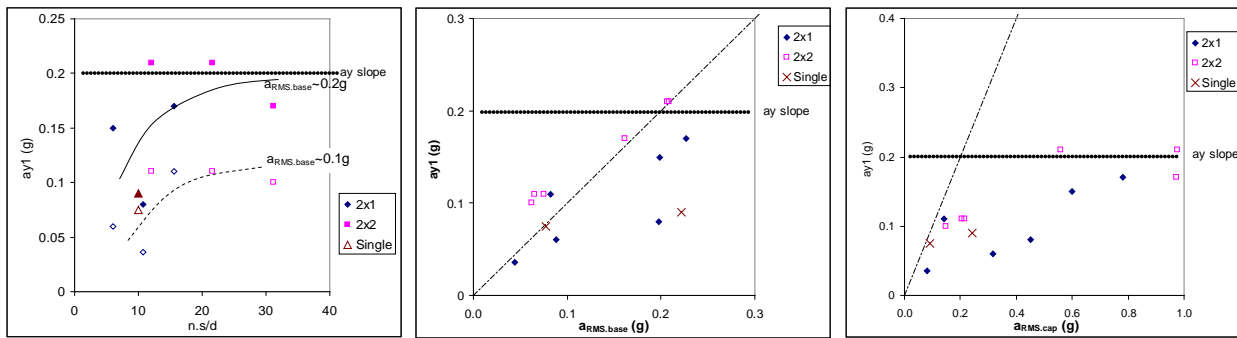


Fig. 8. Relationship between a_y and base and cap acceleration, n.s/d in model tests

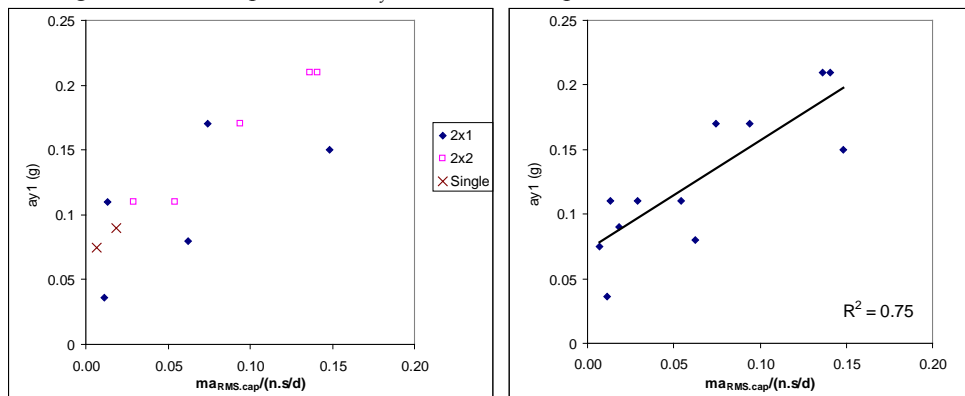


Fig. 9. Dependency of a_y to group parameters

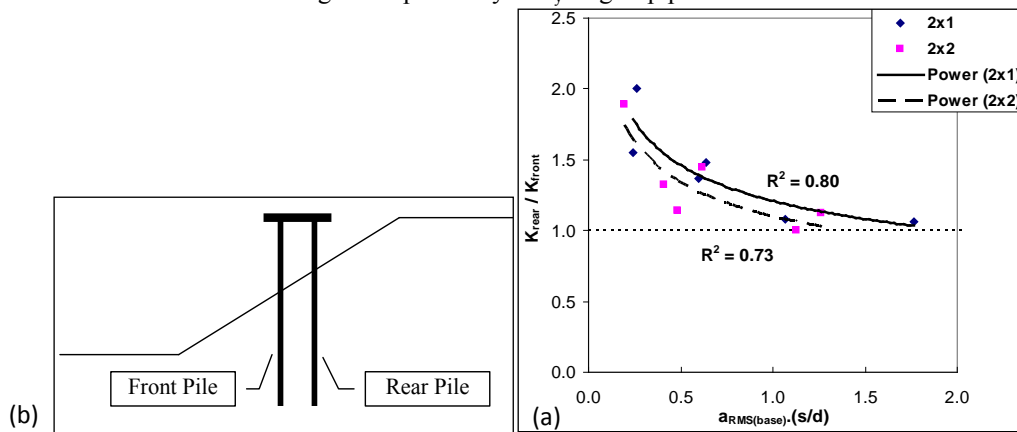


Fig. 10. a) Rear and front pile definition, b) relationship between the ratio of lateral soil pressure coefficient of rear and front piles and a hybrid parameter includes base acceleration and s/d

References

- [1] Gohl, W., (1991), "Response of Pile Foundations to Simulated Earthquake Loading", Ph.D Thesis;
- [2] Sabermahani, M., (2008), "A study on seismic displacement of reinforced soil walls", Ph.D thesis, Tehran university, Tehran, Iran;
- [3] Kramer, S. L., (1996), "Geotechnical Earthquake Engineering", Prentice Hall, USA.
- [4] Newmark, N.M., (1965), "Effects of Earthquakes on Dams and Embankments", Geotechnique, 15 (2), pp. 139-159.
- [5] Elahi, h., (2009), "Seismic behavior of pile group in soil slope", Ph.D thesis, Tehran university, Tehran, Iran.

Effect of Acid Rain on Soil Consistency

Zeinab Bakhshipour⁽¹⁾, Bujang Kim Huat⁽¹⁾, Afshin Asadi⁽¹⁾, Shaharin Ibrahim⁽²⁾, Majid Mirzaei⁽¹⁾
Civil Engineering Department, Faculty of Engineering, University Putra Malaysia,
43400 Serdang, Selangor, Malaysia⁽¹⁾
Environmental Sciences Department, Faculty of Environmental, University Putra Malaysia,
43400 Serdang, Selangor, Malaysia⁽²⁾

ABSTRACT

Acidic deposit that fall to Earth from the atmosphere is named acid rain. Acidic rainfall as an environmental factor has a potential to effect of consistency parameter of soil. This paper describes the degree of difference in the properties of consistency soils in Malaysia of acid rain equivalent to 0.005N of H_2SO_4 or HNO_3 . The sampling of soil from two locations that are Batu Cave (BC) as clay soil and Taman Ukay Perdana (TUP) as weathering granite soil having different plasticity were composed and distinctly preserved with acid sulfuric (H_2SO_4) and acid nitric (HNO_3) to examine the outcome of acid rain on their texture. The amounts of deviation in the engineering properties are experiential to be more distinct in soils with low plasticity than those with high plasticity.

Keywords: Acid rain, Soil, Consistency, H_2SO_4 , HNO_3 .

1. INTRODUCTION

Environmental Geotechnology is developing as an interdisciplinary discipline, directing at predicting, analyzing and solving the geotechnical problems linking the influence of environmental factors [1].

With rapid and developed industrialization of world, so have become an increase acid rain and an environmental concern. Mutilation to the natural environment, mainly the bio-sphere, such as alterations in the chemistry of surface water, reduction in the population of aquatic fauna and flora, and a growth in the outflow of heavy metals in industrial country have been blamed on acid rain [2], [3], [4] and [5]. Malaysia is also not safe acid rain phenomenon. Anthropogenic emissions have increased over the year as the level of pollutant suspended in the atmosphere is increasing.

Acidification of rain is produced by air pollutants comparable sulfur dioxide and oxides of nitrogen, which decreases its pH as low as 5.2. The process of effect of acid rain on soil properties is the H^+ content of acid rain falling for a short duration is very low compared to cation argument capacity of soil. This will definitely increase the rate of leaching of cations from the soil. Fascination of H^+ , SO_4^{2-} , NO_3^- and CO_3^{2-} by the soil particle is effect on change physical, chemical and engineering properties [6].

One of the greatest important environmental factors, directly affect of acid rain on soil properties. Objective of this study was to find degree variation of

acid rain on soil consistency with different pH 3.6, 4.2, 5.2 and 6.7 in tow kind of soil. Two kind of soil Clay and granite having different plasticity were collected and separately acidified with acid rain equivalent to 0.005N of H_2SO_4 and HNO_3 . In this paper some of the results obtained are discussed.

2. METHODOLOGY

The soil samples used in this study were obtained from Batu Cave (BC) as clay soil and Taman Ukay Perdana (TUP). All soil samples were oven dried and sieved BS. The sample of sieve material was used for additional experimental work. The consistencies of the samples were determined for the soil fraction passing 425 μm sieve. The results are summarized in Table 1.

Table 1. Characteristics of original soil samples of clay (BC) and granite (TUP)

characteristic	Soil sample	
	BC	TUP
Liquid limit (W_L) %	52.56	46.50
Plastic limit (W_p) %	55.57	28.58
Shrinkage limit %	10.71	2.14

2.1 EXPERIMENTAL METHODS

1 kg of each soil sample BC and UTP was separately shaken for 8 hours with 1 liter of 0.005N H_2SO_4 and HNO_3 . The H_2SO_4 treated samples (BCS, UTPS) and the HNO_3 treated samples (BCN and UTPN) were then filtered and air dried. These samples were then used to find their consistency as per British Standard [7].

3. RESULT AND DISCUSSIONS

3.1 CONSISTENCY CHARACTERISTIC

Values of Liquid limit (W_L), Plastic limit (W_P) and Shrinkage limit for the soil samples with different pH before and after acid treatment are presented in Figure 1, 2 and 3. The results show that on treatment with the acids the value of W_L , W_P and SL got reduced while that of pH decreased.

The degree of variation with liquid limit of BCS, BCN, TUPS and TUPN was found to be maximum W_L in pH 6.7 (H_2SO_4) with value of 64.61% while the least in pH 3.6 with value of 46.79%. The degree of variation in pH 3.6 (H_2SO_4) was shown with value of 31.24% (Figure 1).

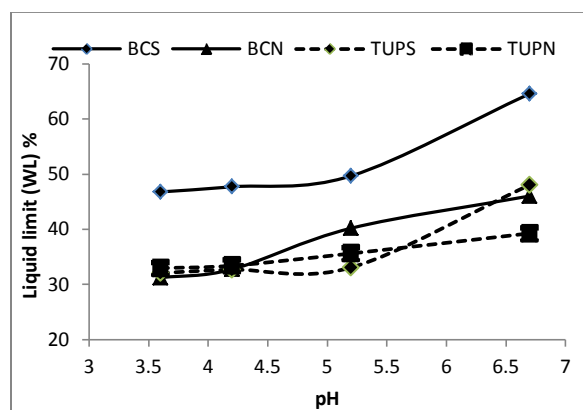


Figure 1. Characterization of liquid limit in clay and granite in different pH with H_2SO_4 and HNO_3

The degree of variation with plastic limit of BCS, BCN, TUPS and TUPN was found to be maximum W_P in pH 6.7 (H_2SO_4) with value of 39.44% while the least in pH 3.6 with value of 21.29%. The degree of variation in pH 3.6 (H_2SO_4) was shown with value of 31.24% (Figure 2).

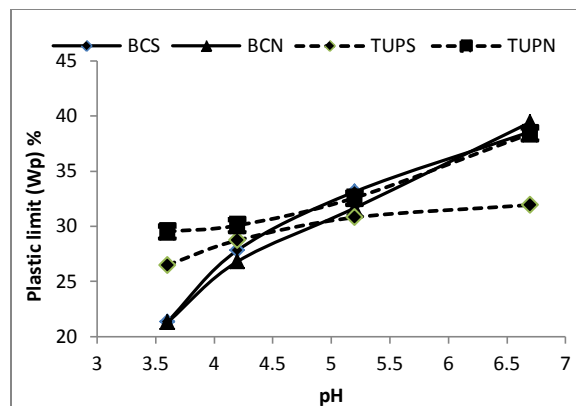


Figure 2. Characterization of plastic limit in clay and granite in different pH with H_2SO_4 and HNO_3

In figure 3 shows the degree of variation of shrinkage limit (SL) in BCS, BCN, TUPS and TUPN with maximum LS in pH 3.6 (H_2SO_4) with value of 10.28% and the least value in pH 6.7 is 1.07%.

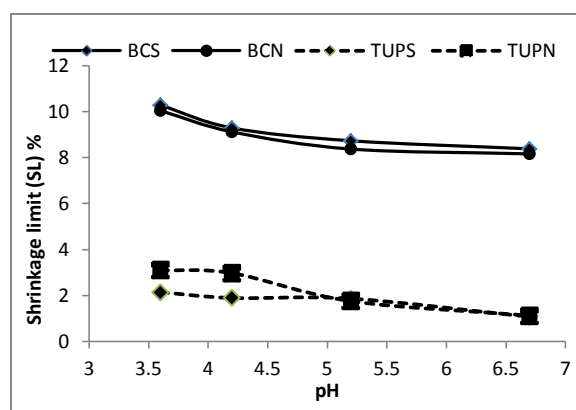


Figure 3. Characterization of shrinkage limit in clay and granite in different pH with H_2SO_4 and HNO_3

The degree of variation in the consistency characteristics of the soil depends on factors like type of soil, electrical charge of exchangeable cation absorbed by soil particles and concentration of cation in soil water [6].

4. CONCLUSIONS

Acid rain results in deviations in physico-chemical characteristics of soil. pH of the soil reductions while the concentration of captivated H^+ and SO_4^{2-} rises. The grain size of soil distribution will move near finer sections when subjected to acid rain. Acid rain affects on consistency properties of different soils with different pH. The data found through the experiments is useful in evaluating the compensations to the soil that could occur due to the

acid rain in future. However the greatness of the decline will depend on determination and strength of acid rain. In further research need to study in effect and strength of acid rain on different types of soils is for an improved evaluation of difference in its physicochemical, consistency and engineering properties.

5. ACKNOWLEDGEMENTS

The authors extend their sincere thanks to Professor Dr. Bujang Kim Huat, Dr. Afshin Asadi, and Associate professor Dr. Shaharin Ibrahim. Also extend our sincere gratitude to all the authors whose publications provided us directional information from time to time.

6. REFERENCES

- [1] Manassero M and Deangeli C, "Education in Environmental Geotechnics", Proceedings of Indian Geotechnical Conference, Vol. 2, Allahabad, India, 2002, pp. 840–848.
- [2] Hileman, B., "Acid rain: A rapidly shifting sence," Environ. Sci. Technol., Vol. 17, No. 9, 1983, pp. 401-405.
- [3] Havas, M., "Red herrings in acid rain research," Environ. Sci. Technol., Vol. 18, No. 6, 1984, pp. 176-185.
- [4] Elzerman, A., "Acidification of southern Appalachian lakes," Environ. Sci. Technol., Vol. 19, No. 6, 1985, pp. 552-557.
- [5] Henriksen, A., "Sulfate deposition to surface waters," Environ. Sci. Technol., Vol. 22, No. 1, 1988, pp.8-14.
- [6] Kamon Masashi, Ying Changyun and Katsumi Takeshi, "Effect of acid rain on physico-chemical and engineering properties of soils", Japanese Geotechnical Society, 37 (4), 1997, PP. 23-32
- [7] British Standard, 1377-2:1990.

Consideration concerning reasonable modified form of Floating-type Improved Ground

Hijiri HASHIMOTO¹, Satoshi NISHIMOTO¹ and Hirochika HAYASHI¹
Civil Engineering Research Institute for Cold Region, PWRI, JAPAN

ABSTRACT

In this study, centrifugal model tests were conducted to clarify the rational improvement width (B) and improvement depth (H) at which embankment stability as well as a deformation prevention effect for the surrounding ground can be achieved when rectangular floating-type improved ground is created at the toe of an embankment slope.

The results produced the following findings: the creation of floating-type improved ground (FTIG) helps to stabilize embankments; FTIG can be expected to help prevent deformation of the surrounding ground; and the failure of improved soil does not have a substantial impact on embankment stability. Even if the B/H ratio of improved soil is the same, unless it is placed (hereinafter, “embedded”) deeper than the sliding line, it does not contribute to displacement prevention in the surrounding ground.

Keywords: Four or Five Keywords

1. INTRODUCTION

Most stabilization measures for embankments to be constructed on soft terrain involve the improvement of ground down to the bottom of the solid bearing layer. Regarding the form of improved soil, the recommended ratio of the improvement width (B) to the improvement depth (H) (hereinafter, “the B/H ratio”) is set to at least 0.5 to 1.0 to prevent the action of excessive bending stress on the improved soil. As the B/H ratio increases, a greater improvement effect can be expected, but there also tends to be a corresponding increase in construction costs.

In view of this, the creation of improved ground that does not involve treating soil down to the bearing layer (hereinafter, “floating-type improved ground”) is considered to be more effective. However, the extent to which the method stabilizes embankments and prevents displacement of the surrounding ground is unclear. Against this background, centrifugal loading model tests were conducted in this study to review whether greater B/H ratios in floating-type improved ground or differences in the improvement type used help to prevent displacement of the toe of embankment slopes and the surrounding ground.

2. PURPOSE AND DETAILS OF THE CENTRIFUGAL LOADING MODEL TESTS

The purpose of the centrifugal loading model tests was to verify whether floating-type improved ground is effective in stabilizing embankments and preventing displacement of the surrounding ground.

Table 1 lists the experimental cases and study items. The experiments included a case in which no improved soil was present at the toe of the embankment slope (case 1) and four

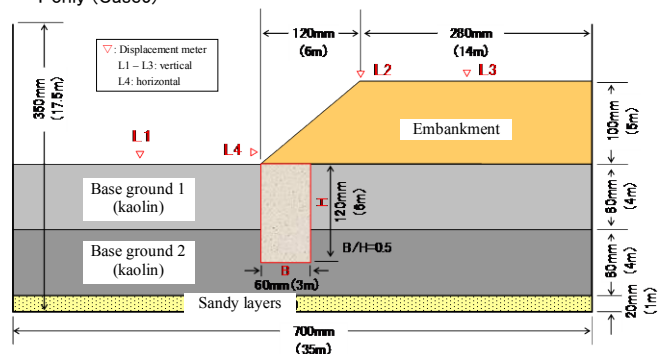
in which floating-type improved ground was present at the toe (cases 2 to 5). In these cases, observation was performed to verify whether differences in the B/H ratio (i.e., variations in the improvement width and/or improvement depth with the same improved area) would affect the failure conditions of the improved soil and the deformation conditions of the surrounding ground. The models had a scale of 1/50 of the actual size, and the tests were conducted in centrifugal acceleration fields of 10 to 50 G (G: gravitational acceleration). Paper size 210mm × 297mm of A4 paper.

Table 1 Experimental cases and study items

Case	1	2	3	4	5
Improvement Condition	Improvement width B(m)				
	0	1	2	3	
Improvement depth H(m)	0	No Improvement	Case2, 3 and 4		
		B/H=0.17	Improvement width		
	6		B/H=0.33		
	4	Case3, 5		B/H=0.5	B/H=0.75

※Sizes corresponded to actual scale (50G)

※Improvement down to base ground 2(case2,3,4) and down to base ground 1 only (Case5)



* Figures in parentheses indicate full-scale values.

Fig. 1 Model ground and measurement positions (case 3)

Please save to MS Word templates directory. Times New Roman, Font size 10, normal. Try to avoid Underline or Bold within texts.

Table 2 Properties of base ground, improved soil and embankment

	Item	Value	
Base ground	Material	Kaolin clay	
	Natural water content (%)	62.2 ($W_L \times 1.5$)	
	Density of soil particles (g/cm ³)	2.738	
	Grain size	Fragment (%)	0
		Sand (%)	0
		Silt (%)	45.1
		Clay (%)	54.9
		Maximum grain diameter (mm)	0.075
Single-axis compression	Base ground 1 (kN/m ²)	12.5	
	Base ground 2 (kN/m ²)	28.5	
Improved soil	Material	Kaolin clay + ordinary Portland cement	
	Cement content (kg/m ³)	220	
	Water cement ratio (W/C)	1	
	Single-axis compression (kN/m ²)	360 (3-day curing)	
Embankment	Material	Toyoura standard sand:kaolin = 8:2	
	Compaction (%)	85	
	Density of soil particles (g/cm ³)	2.665	
	Maximum dry density (g/cm ³)	1.88	
	Optimal water content (%)	10.2	
	Adhesion (kN/m ²)	3.2	
	Angle of shear resistance (°)	31.9	

2.1 Model ground

Figure 1 shows a cross section of the completed model ground, while Table 2 lists the properties of the base ground, the improved soil and the embankment materials. The method of construction for each type of ground and the experimental earth tank installation technique are described below.

(1) Base ground 1 and base ground 2 (clay layer)

The base ground was made by adding water to kaolin clay (in a dry powder condition) to adjust the water content to 1.5 times the liquid limit, i.e., 62%.

One-dimensional consolidation was then carried out using an auto-load controller. The final consolidation pressure on base ground 1 was $p = 30 \text{ kN/m}^2$, and for base ground 2 the corresponding values were $p = 60 \text{ kN/m}^2$.

The reason for introducing a difference in the pressure loads on base ground 1 and base ground 2 was to provide a sliding surface at the boundary between the two layers.

(2) Improved ground

Ground was improved by adding ordinary Portland cement (amount: $W = 220 \text{ kg/m}^3$) to kaolin clay with a water content of 1.5 times the liquid limit and agitating it with a mixer.

(3) Embankment

Embankment materials were made by mixing Toyoura sand and kaolin at a dry-weight ratio of 8:2 and a water content w of 10%. The constituents were stirred using a vacuum mixer for 40 minutes, and were then cured for a day or longer.

The embankment materials were used after being passed through a 2-mm sieve to give them a uniform consistency. Each layer was compacted to a finishing thickness of 1 cm using a small rammer.

2.2 Measurement device

Ground level upheaval, horizontal displacement of the embankment slope toe, and settlement of the embankment crown were measured with a laser displacement meters (L1 – L4 in Fig. 1).

Silver line noodles were also installed on the visual surface to support determination of the soft ground and embankment deformation mode.

2.3 Centrifugal acceleration

The completed model was mounted on centrifugal loading equipment, and measuring devices were installed. Centrifugal acceleration was increased gradually to 10, 20, 30, 40 and then 50 G. The centrifugal acceleration retention time was two minutes at 10 G, four minutes at 20, 30 and 40 G, and five minutes at the final stage (50 G). Each period of retention lasted until the deformation of base ground 1 and base ground 2 returned to normal after centrifugal acceleration was increased to the next step.

3 TEST RESULTS AND REVIEW

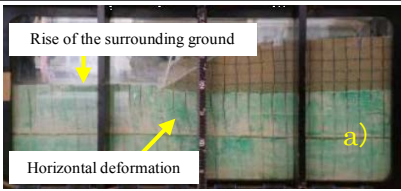
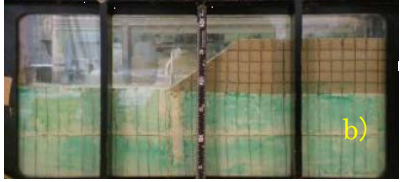
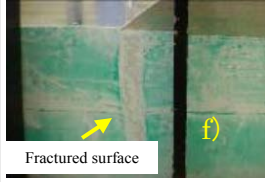










3.1 Improved ground and ground deformation

Table 3 shows transverse and longitudinal sectional views of improved soil at the time when embankment loading was completed (i.e., after loading of 50 G). The transverse and longitudinal cross sections were photographed after completion of the test (1-G field).

In the deformation of the base ground and embankment when a 50-G load was applied in case 1, no sliding failure occurred. However, base ground 1 horizontally deformed, and the whole of the surrounding ground rose as a result (Table 3 a).

Conversely, the deformation modes of the base ground and embankment for loads of under 50 G in cases 2 to 5 were small (Table 3 b). In the transverse and longitudinal cross sections, it can be seen that the improved soil curved at the boundary surface between base ground 1 and base ground 2 in case 2 (Table 3 f). Likewise, the longitudinal cross section shows the occurrence of cracking in the improved soil (Table 3 j). As this cracking was located at the boundary surface between base ground 1 and base ground 2, it can be inferred that the sliding soil mass acted on the boundary surface with a strength differential between the base ground layers as the

Table 3 Base ground deformation and improved soil in each case

Case	Embankment height	B/H	After 50-G loading	Transverse cross section of improved soil	Longitudinal cross section of improved soil
1	5	—	 a)	—	—
2	5	0.17	 b)	 f)	 j)
3	5	0.33	 c)	 g)	 k)
4	5	0.5	 d)	 h)	 l)
5	5	0.75	 e)	 i)	 m)

embankment load increased. This may have caused fracturing of the improved soil.

In the longitudinal cross section of the improved soil in cases 3 and 4, none of the cracking seen with the improved soil in case 2 was found (Tables 3 g, h, k, l). This is because horizontal soil pressure acted on the improved soil. However, the improvement was wide, with B/H values of 0.33 and 0.5, respectively. It is presumed that strong resistance of the improved soil prevented its failure. There was no cracking in the improved soil of case 5, and its condition was as sound as those in cases 2 to 4 (Table 3 m), but the surrounding ground rose (Table 3 e). This was because the improved soil did not reach (i.e., it was not embedded in) base ground 2. The improved soil may have entered a sliding mode in which the sliding of the soil mass could be prevented.

3.2 Impact on the surrounding ground

(1) Surface displacement gauge values

Figure 2 shows the relationship between the embankment height and surface displacement gauge values, with positive numbers indicating a rise. The gauge values on the 5-m-high

embankment in cases 2 to 4 were about 30 to 50% smaller than that in case 1. This indicates that floating-type improved ground is effective in preventing deformation of the surrounding ground. However, there was no evident difference in the displacement prevention effect regardless of the improvement width (i.e., the B/H ratio). Conversely, the surface displacement gauge values in case 5 were about the same as those in case 1. This was because little sliding soil mass prevention effect was achieved without improved soil embedded in base ground 2.

Next, cases 3 and 5 with the same improved cross section were compared. The results suggested that the surface displacement gauge value was reduced in case 3, which involved improvement deeper than the sliding line (on the boundary surface between base ground 1 and base ground 2).

(2) Slope toe horizontal displacement gauge values

Figure 3 shows the relationship between embankment height and the horizontal position of the embankment slope toe. Comparison of the horizontal displacement gauge values in cases 2 to 5 and that in case 1 showed a reduction by about half in the former. It was thus confirmed that floating-type

ground improvement is effective in reducing slope toe horizontal displacement gauge values.

The displacement gauge values in cases 2 and 5 were slightly larger than those in cases 3 and 4. This was because: 1) the improved width in case 2 was smaller ($B/H = 0.17$), which reduced the resistance by which soil mass sliding could be prevented; this in turn caused cracking in the improved soil, and displacement could not be prevented; 2) in case 5, soil mass sliding acted on the improved soil, but this improved soil was embedded in base ground 2. As a result, soil mass sliding was not prevented in the improved soil.

Accordingly, it was confirmed that floating-type improved ground would not be able to fully prevent horizontal displacement of embankment slope toes and/or rising of the surrounding ground, although it is effective for such prevention to some extent. Particularly, in case 2 ($B/H = 0.17$), the sliding safety factor (F_s) for circular slippage was calculated as less than 1 ($F_s < 1$) for an embankment height of 5 m (Figure 4). Although the improved soil fractured in a centrifugal loading model test, the impact on the surrounding ground was almost the same as in cases 3 and 4, in which the improved soil was sound. This suggests that failure of improved soil will not affect embankment stability or displacement of the surrounding ground. It is also clear that

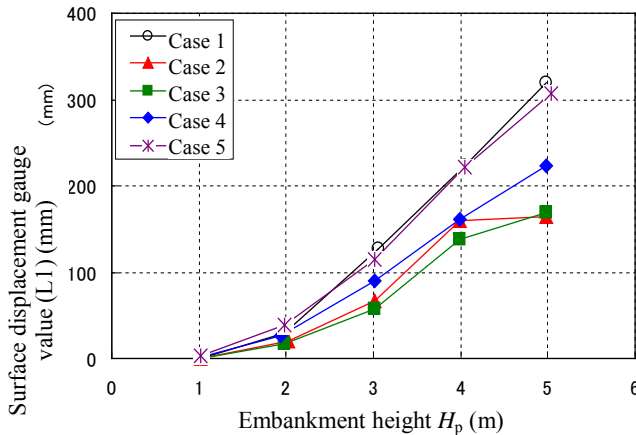


Fig. 2 Improvement effect on surface displacement gauge values: measurement position (L1)

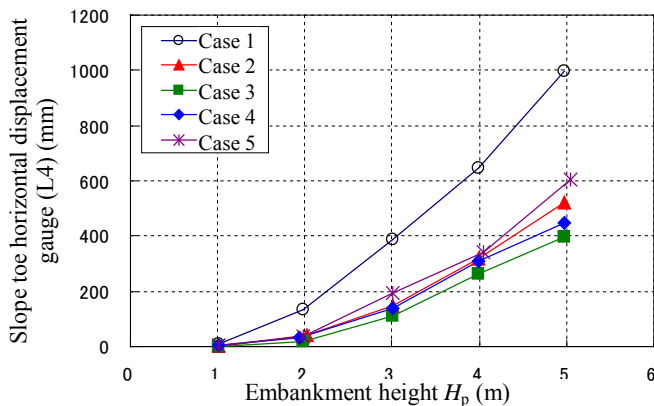


Fig. 3 Improvement of slope toe horizontal displacement gauge: measurement position (L4)

even with the same B/H ratio, non-embedded soil will not contribute to the prevention of such displacement.

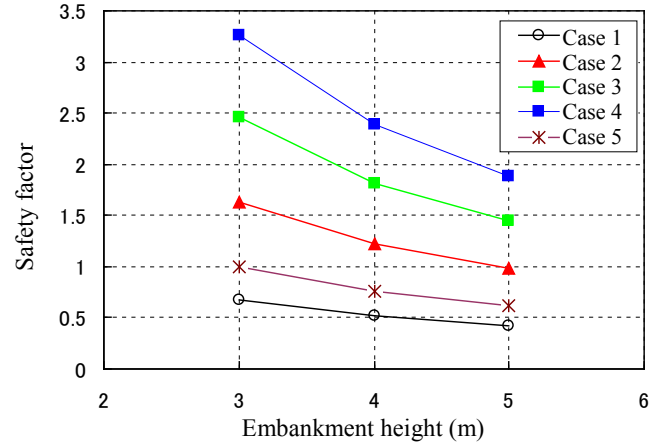


Fig. 4 Embankment height and sliding safety factor

4 CONCLUSION

The conclusions drawn from the centrifugal loading model tests can be summarized as follows:

- 1) Floating-type improved ground can be used for embankment stabilization.
- 2) The method also helps to prevent displacement in the surrounding ground.
- 3) It was found that improvement soil failure does not greatly impact embankment stability.
- 4) Even if the B/H ratio of improved soil is the same, unless the improved soil is embedded deeper than the sliding line, it does not contribute to displacement prevention in the surrounding ground.

In practical terms, floating-type improved ground is not suitable for sites where displacement of the surrounding ground must be avoided. However, if some displacement is permissible outside the roadway, its application may be appropriate.

5 REFERENCES

- [1] S. Kuga, T. Hattori, M. Kamimura, N. Sagawa, "Study on a test embankment on stabilized soft ground," Japan Society of Civil Engineers 54th Annual Academic Conference, pp. 466 – 467, 1999.
- [2] K. Tsubota, H. Nakajima, M. Nishigaki, "Study on measures against settlement of surrounding areas on soft ground by embankment construction," papers of the Japan Society of Civil Engineers, Vol. 63, No. 3, pp. 323 – 334, 2007.
- [3] Public Works Research Center: Design and implementation of the deep mixing method for work on land, revised edition, 2004.
- [4] H. Hashimoto, S. Nishimoto, H. Hayashi, S. Kajitori, "A rational form of floating-type improved ground," Japan Society of Civil Engineers 67th Annual Academic Conference, 2012.

Numerical Study Effect of Nail Angle Change on Stability and Displacement of Excavation Wall in Cohesive and Cemented Non-Cohesive Soils

Navid Shahnazi¹, Jahangir Khazaie², Mohamad Sharifipour³ and Kiarash Ashtari⁴
Tehran, Iran

ABSTRACT

Increasing population growth and the need for buildings of greater height, and condensation of urban texture, construction of underpasses in highways intersections with height difference, demolition of old buildings and construction of new and high buildings next to each other involve vertical deep excavation. In the meantime, soil consistency of the excavated walls is considered as one of the crucial issues in geo-technique engineering.

Installation angle of reinforcement member (element) in excavation wall and soil shearing strength effects on nail angle is among the parameters which affects design, installation and execution methods as well as execution costs. Since parameters of soil shearing strength are amongst the effective elements in obtaining the nail's optimum angle, and with change of these parameters, the nail's optimum angle will change, in this research, it has been tried by numerical modeling and problem analysis using Plaxis software to design 10-meter excavation with specific parameters of cohesive and cemented non-cohesive soils, and in the next step, it has been tried to investigate effect of changes in soil's shearing strength parameter in the 2 states on nail angle as well as on displacement and confidence coefficient of excavation wall in this type of soils.

Keywords: stabilization, vertical slope wall, nail angle, soil shearing resistance parameters

1. INTRODUCTION

Soil nailing is one of the suitable methods for the stabilization of earth walls which its execution way is from up to down contrary to other soil stabilization methods.

Reinforcement angle is one of the effective parameters in the stability of nailed walls. Reinforcement angle (nailing) plays an important role in improving nail resistance, for this reason also in practical cases nails should be placed with deviation toward horizontal axis. In this paper the effect of changing the various parameters of soil shear resistance on nail angle will be considered by using Limited Parts Software to specify how the optimum nail angle varies in granular soils and cohesive ones. In vitro studies done by (Satyendra Mittal, 2006) showed that Factor of Safety will decrease with the increase of reinforcement angle (nailing) to more than 15 degrees.

(Chai- Cheng Fan, Jiun-Hung Luo, 2008) in a numerical study regarding the optimum arrangement of soil nailing for the stability of excavation concluded that the optimum angle of nail decreases with the increase of slope angle so that zero-degree angle has been introduced as optimum nail angle for vertical slope.

(w.B.wei, y.m.cheng, 2010) by studying on different slopes represented that with the increase of nail angle, first Factor of Safety goes up gradually and then down.

(TohidAhklaghi, Hassan Panahpoor, 2011) in considering the effective factors in the optimum plan of nailed walls by using Plaxis Software propounded that in case of using horizontal nails, changing horizontal shapes in excavation have less amounts and also the increase of nails angles to 15 degrees causes the safety factor of excavation to increase.

2- Analytical Model

In this paper numerical modeling is done by use of Plaxis Software. This software is able to do non-linear analysis and also calculate movement and the safety factor of excavation wall. For assurance of done modeling primary model has been calibrated with the existing model in Plaxis Manual and then the planned model is done. Studied vertical slope is 10 meters deep and 15 meters wide and the effect of load in the movement of excavation wall has been waived. In the contemplated plan, 2 first nails are 7 and 3 middle nails are 6 and 2 last nails are

5meters long. Also 6 first excavations are 1.5 meter and last excavation is 1 meter deep.

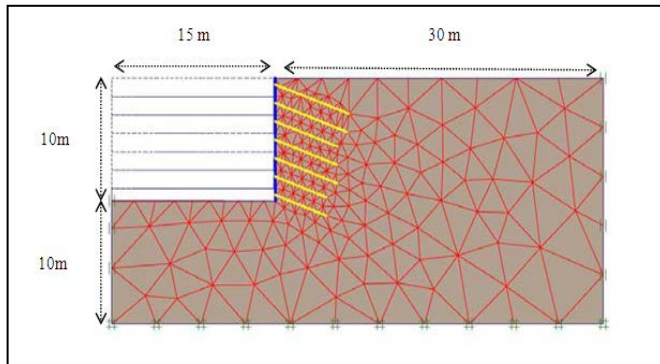


Figure 1- The Analytical Model of the Studied Area and Meshing the Nailed Wall

1-2- Boundary and Meshing Conditions

In this study the dimensions of the analytical model have been considered in a way that any location change in borders is zero and just 2 sides of the model will be able to move in vertical direction. 15-node triangular meshes are also used for meshing. The general mesh of atmosphere is Coarse and just nails are refined line twice.

2-2- The Specifications of Materials and Related Parameters

Average specifications related to the soil of the considered location are presented in Table 1 that soil is sandy with average cementation. Also Mohr-Coulomb Standard is used for modeling soils.

γ_{sat}	18.6 KN/m^3
γ_{dry}	18.6 KN/m^3
c	4 Kpa
ϕ	30
E	$3 \times 10^4 \text{ KN/m}^2$
ν	0.28

Table 1- The Specifications of the Used Soil in Analysis

The specifications relative to nail are also presented in Table 2. The effects of subterranean water are waived as nailed walls are generally drained before shotcrete. Meanwhile nails are modeled in an elastic way.

Nailing Method	Injection
Nail Length	Variable
EA	$1.58 \times 10^5 \text{ KN/m}$

Table 2- The Specifications of the Used Nails in Analysis

3-2- How to Model Nailing

The modeling of the excavation wall is done in Plain Strain way and 15-node triangular element has been used. Nails are made of ribbed bar $\Phi 32$ and with yield stress 400 Mpa. The excavation diameter of bore is 10 cm and nails are modeled by use of Geogrid element that the shear and flexural capacities of the nails are waived in design. This performance will be toward assurance. The below relations are also used for obtaining the equivalent elasticity modulus and axial stiffness of nail.

(Equivalent Elasticity Modulus)

$$E_{eq} = E_n \left(\frac{A_n}{A} \right) + E_g \left(\frac{A_g}{A} \right)$$

(Axial Stiffness)

$$EA = \frac{E_{eq}}{S_h} \left(\frac{\pi D_{BH}^2}{4} \right)$$

Plate element is used for the modeling of the shotcrete cover. The cover juncture to soil is rigid and modeled in elastic way. The cover specifications are presented in Table 3.

EA	$4.38 \times 10^6 \text{ KN/m}$
EI	$1.46 \times 10^4 \text{ KNm}^2/\text{m}$
d	0.2 m

Table 3- The Specifications Relative to the Shotcrete Cover

Reduction analysis is also used for obtaining Factor of Safety. In this method the resistance parameters of the soil heap decrease gradually and finally break happens, in fact Factor of Resistance Decrease in break time is the same safety factor of slope.

For considering production stages and its effect on the model, phasing has been accomplished in 7 steps and in each stage, according to the execution of the nailed wall, one-level excavation is done and the nail and shotcrete cover of that stage becomes active.

3-The Results of Parametric Study on the Analytical Model

First the effect of the nail angle changes in stability and horizontal movement of the excavation has been considered in granular soil.

Then we make the internal friction angle of soil fixed ($\phi = 30$) and change soil cohesion and proceed to consider Factor of Safety and the horizontal movement of the excavation in different nail angles in order to get the optimum reinforcement angle.

1-3- Considering the effect of cohesion on the optimum reinforcement angle (nail) in soils with low cohesion

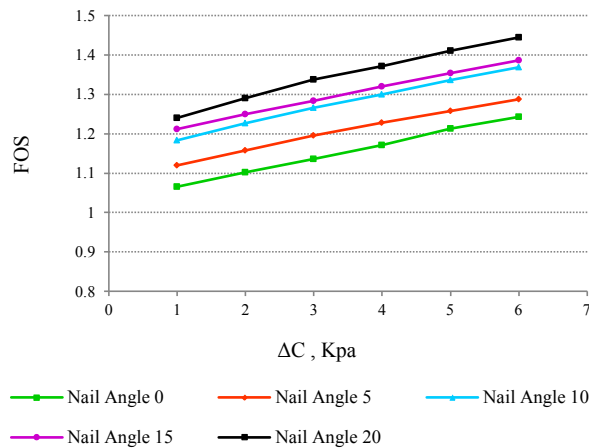


Figure 2-The Effect of Cohesion Change on NailAngleWith Respect to Factor of Safety

As regarded in Figure 2, with the slight increase in cohesion amount, the safety factor of the excavation wall will have the greatest amount in return for 20- degree nailing angle and this process is increasing.

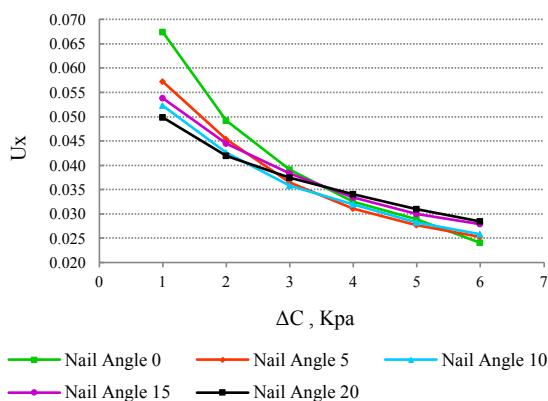


Figure 3-The Effect of Cohesion Change on NailAnglewith regard to the Horizontal Movementof the Excavation Wall- the Internal FrictionAngle of Soil ($\phi=30$) degree

As observed in Figure 3, the horizontal movement of the excavation wall will decrease with the slight increase in the cohesion amount of soil. Meanwhile it is considered that the greatest reduction of the horizontal movement of the excavation wall occurs in the little nailing angles and with the increase of the nailing angle, the horizontal

movement changes of the excavation wall will decrease toward the increase of soil cohesion.

2-3- Considering the effect of friction angle on the optimum reinforcement angle (nail) in soils with low cohesion

At this stage we consider soil cohesion fixed ($C=4$ KPA) and change the internal friction angle of soil and proceed to consider Factor of Safety and the horizontal movement of the excavation under different nailing angles.

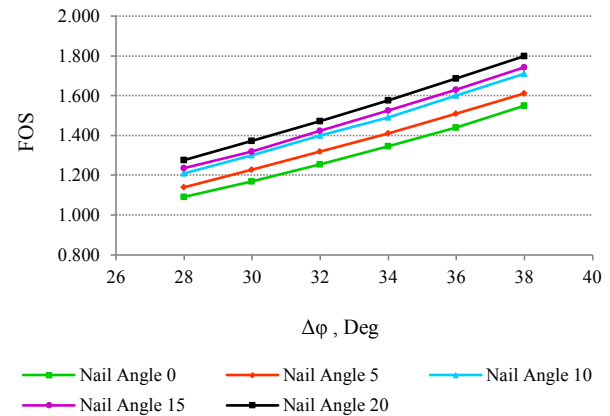


Figure 4-The Effect of Changing the Internal Friction Angle of Soil on Nail Angle with regard toFactor of Safety –Soil Cohesion ($C=4$ KPA)

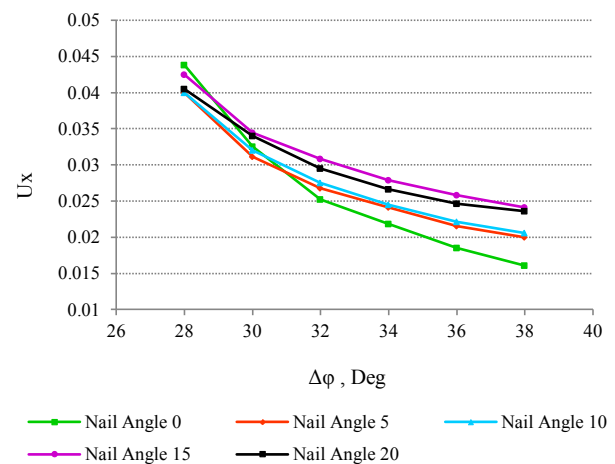


Figure 5-The Effect of Changing the Internal Friction Angle of Soil on Nail Angle with regard tothe Horizontal Movementof the Excavation Wall–Soil Cohesion ($C=4$ KPA)

As observed, the optimum nail angle decreases with the increase of friction angle in soils with a little cohesion so that the optimum nailing angle is ever zero degree at friction angle about 35 degrees and more. Furthermore the optimum nail angle will increase with the reduction of the

internal friction angle of soil so that the optimum angle is about 20 degrees.

3-3- Considering the effect of cohesion on the optimum reinforcement angle (nail) in cohesive soils

In this section, the internal friction angle of soil is fixed and equal to ($\phi = 30$) and soil cohesion will change from $C = 15$ KPA to $C = 25$ KPA.

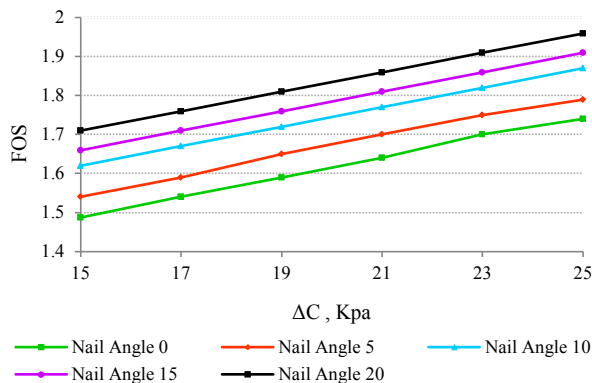


Figure 6 -The Effect of Cohesion Change on Nail Angle with regard to Factor of Safety the Internal Friction Angle of Soil ($\phi = 30$) degree

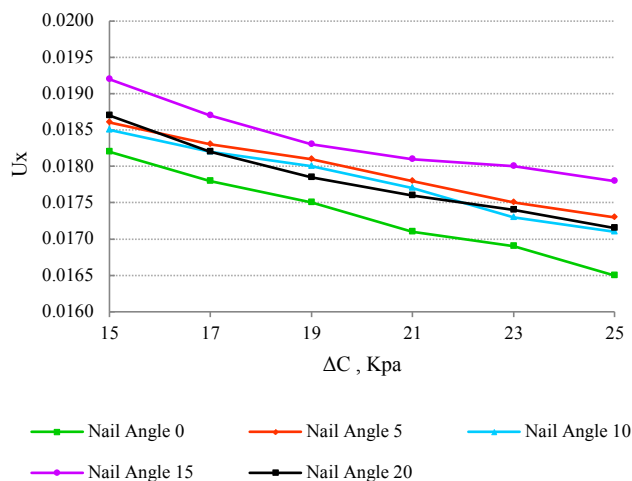


Figure 7 -The Effect of Cohesion Change on Nail Angle with regard to the Horizontal Movement of the Excavation Wall – The Internal Friction Angle of Soil ($\phi = 30$) degree

As considered in figure 6, 7, the optimum nail angle decreases in cohesive soils with considering the horizontal movement of the excavation wall so that zero degree is the best amount and the optimum nail angle has the best amount at 20 degrees with respect to Factor of Safety.

At the end it is necessary to remind that the horizontal and vertical distances and lengths of the nails have been considered fixed in all the above stages. In the meantime all the soil specifications are constant such as Elasticity

Modulus, Factor of Poisson, Special Weight of Soil and Shotcrete Features and just the shear resistance parameters (the friction angle of soil and cohesion) have changed.

4- Conclusion and Totaling

- 1- The least movement occurs at zero degree in cohesive soils but in granular soils with paltry cohesion the least movement is not at zero-degree angle.
- 2- Contrary to what is indicated in the papers (Chia-Cheng Fan, Jiun-Hung Luo, 2008) and (Tohid Ahklaghi, Hassan panahpoor, 2011), zero-degree angle has the least horizontal movement, this matter has no meaning for granular soils with paltry cohesion.
- 3- In granular soils and cohesive ones, zero-degree angle has the least factor of safety and 20-degree angle has the greatest factor of safety.
- 4- According to the control standard regarding restricting the movement of the excavation wall (the maximum horizontal break in amount of $0.005 H$) is observed in granular soils that the above standard is gratified for the studied friction angle and cohesion interval just at 20-degree nailing angle.
- 5- In granular soil, the effect of the friction angle increase in the increase of the excavation safety factor is more than the cohesion increase so that nailing in condensed granular soils can be done in desirably.
- 6- Based on the obtained results from this research, 15-degree nail angle which is often used by contractors and consultants in designs, in any of granular and cohesive soils does not have preference to other angles.

References

- [1] Byrne RJ, Cotton D, Porterfield J, Wolschlag C, Ueblacker G. Manual for design and construction monitoring of soil nail walls. Federal Highway Administration (FHWA) Report No. FHWA-SA-96-069, Washington, DC, USA; 1996.
- [2] PLAXIS BV. User's manual of PLAXIS. Published by A.A. Balkema Publishers; 2002.
- [3] Sivakumar Babu GL, Srinivasa Murthy BR, Srinivas A. Analysis of construction factors influencing the behaviour of soil-nailed earth retaining walls. Ground Improv 2002;6(3):137–43.

- [4] Fan CC. Effect of geometric layout of soil nails on stability of soil nailed slopes. In: Proceedings of 15th Southeast Asia geotechnical conference, Bangkok, Thailand; 2004. p. 309–14.
- [5] S. Mittal, R.P. Gupta and N. Mittal . Housing Construction On Inclined Cuts Asian Journal Of Civil Engineering (BUILDING AND HOUSING) VOL. 6, NO. 4 (2005) PAGES 331-346
- [6] Satyendra mittal. Soil nailing application in erosion control – an experimental study Geotechnical and Geological Engineering (2006) 24: 675–688
- [7] Liew S.S and Khoo C.M., “Performance of Soil Nail Stabilisation Works for a 14.5m Deep Excavation in Uncontrolled Fill Ground, Proceeding of 16th Southeast Asian Geotechnical Conference, Subang Jaya, Malaysia, 8 - 11 May 2007, pp. 827-837
- [8] Chia-cheng Fan,JIUN-HUNG Luo.Numerical Study on the optimum layout of soil-nailed slopes. computer and Geotechnics (2008).
- [9] G.L. Sivakumar Babu and Vikas Pratap Singh Numerical Analysis of performance of soil nail walls in seismic conditions. ISET Journal of Earthquake Technology, Paper No. 496, Vol. 45, No. 1-2, March-June 2008, pp. 31–40
- [10] Vikas Pratap Singh . G. L. Sivakumar Babu. 2D Numerical Simulations of Soil Nail Walls. Geotech Geol Eng (2009).
- [11] W.B. Wei, Y.M. Cheng Soil nailed slope by strength reduction and limit equilibrium methods Computers and Geotechnics 37 (2010) 602–618

An Investigation On Behavior Of Geogrid Reinforced Soil Retaining Walls Applying Finite Difference Method (F.D.M)

Jahangir Khazaie¹ and Alireza Sadeghabadi²

¹Assist. Prof. of Civil Eng., Dept. of Civil Eng., Univ. of Razi, Kermanshah, Iran; Tel: +98-9123271926;

Fax: +988314283264; Email: j.khazaie@razi.ac.ir

²M.Sc. Student of civil Eng., Dept. of Civil Eng., Science & Research Branch., Islamic Azad University, central Branch(Markazi), Iran;

Tel: +98-9122070810; Fax: +988314283264; Email: alireza_sadeghi56@yahoo.com

ABSTRACT

Due to increasing usage of polymeric reinforced retaining walls in civil projects, researches on the behavior of these types of walls are further essential. So in this paper the behavior of geogrid reinforced retaining walls is surveying by numerical method (F.D.M). For this purpose FLAC^{2D} (Fast Lagrangian Analysis of Continua) software is applied to represent numerical model that experimental results are available. Then the software capability is assessed in wall deformation, reinforcement tension forces and vertical displacement of reinforced soil layers. As a result of this research, way of polymeric materials arrangements is specified according to their strength parameters.

Keywords: *Geosynthetic, geogrid, finite difference method "FDM", Plasticity model, Polymeric reinforced soil retaining walls, FLAC^{2D} software, Numerical modeling.*

1. Introduction

According to worldwide application of retaining walls in many projects, specially urban construction projects, further study is felt in this case. In this reason, the geosynthetic reinforced soil as a polymeric composite material and an updated reinforcing method has caused a revolution in geotechnical engineering for its simple usage, cost-saving and ability to improve the visual appearance. Many field and laboratory studies are performed on different reinforced retaining walls, such as full scale and small-scale model and also centrifuged decreased models.

Researches in this field- specially bearing capacity of reinforced retaining wall-were proposed in 1960 by "Vidal" for the first time and were being continued till present.

In 1998 "Reda M. Bakeera, Sayed M. Sayeda, Peter Catesa, Rajesh Subramania" studied about Pullout and shear tests on geogrid reinforced lightweight aggregate. Their researches

Contains the results of laboratory tests conducted on a lightweight aggregate reinforced with a geogrid. The large-size shear tests included direct simple shear tests on the aggregate, shear tests on the aggregate reinforced with a uniaxial geogrid, and geogrid pullout tests. All tests were performed on air-dried material samples. Each type of test was repeated using three different confining pressures representing different

heights of fill. The angle of internal friction (ϕ) of the lightweight aggregate material and its interface friction angle (δ) with the geogrid were found to be 52° and 48° , respectively. These values represent an efficiency of friction angle mobilization (E_ϕ) of about 87%. Some crushing occurred in the material under a higher confining pressure specifically near the front edge and center of the shear box.

In 2006, Nicola Moraci, Domenico Gioffrè had a research on, "A simple method to evaluate the pullout resistance of extruded geogrids embedded in a compacted granular soil"

In 1994 Mr. porbaha performed laboratory study on a "centrifuge modeling of geotextile reinforced cohesive soil retaining walls". He had made a .51m height .61m width and 1.12m length model of soil reinforced soil with 8 geogrid layer embedded on sandy foundation .

And in 2011, by Kerry Rowe & Graeme D, A numerical examination of the behavior of an 8 m high geosynthetic reinforced soil wall constructed on a layered foundation stratum is described. The foundation consists of a 0.8 m hard crust, underlain by 2.95 m of soft loam (sandy/silty) and then 1.3 m of stiff clay. Below the clay is 1.75 m of fine sand underlain by a layer of clayey/fine sand extending to a depth below 10 m. The wall was constructed with 16 segmented concrete facing blocks, a sandy backfill material with 30% fines and 11 layers of geogrid reinforcement 6 m long. Five additional, one meter long layers of reinforcement were used between the 6 m long layers within the upper 5 m of the wall to improve the local stability of the facing blocks. The analysis examines the effect of uncertainty regarding the drained and undrained strength of the loam foundation material, its stiffness, the thickness of this soft layer and its position with respect to the bottom of the wall on the calculated behavior and compares the calculated and observed behavior.

2. Model specifications

In a modular block or shotcrete wall, the geosynthetic layers are placed between the concrete blocks at regular vertical spacing. The blocks or shotcrete are used to retain the backfill. The dead weight of modular blocks contributes to the global stability of the GPSRW. The contribution of the facing was neglected in early designs; then, Bathurst and Simac (1994) and Ieshchinsky (1993) proposed limit equilibrium design to account for the modular blocks.

Here, we consider a geogrid reinforced retaining wall. This model is made in Federal Highway administration (U.S. Department of transportation-FHWA) in 1996. The wall has a length of 420cm & 600cm height. The reinforcements with full length have been laid in horizontal direction in 10 layers of soil. A linear surcharge pressure $q_y (=75 \text{ KN/m}^2)$ acts on the top of the wall by the length of 1.5m. The facing of this wall is placed in a depth of 6cm into the dense sand soil foundation. The rigid rock dimension is about $33.4 \times 19.5\text{m}$, as the wall is placed in length of 13.7m inside it. (Figure 1)

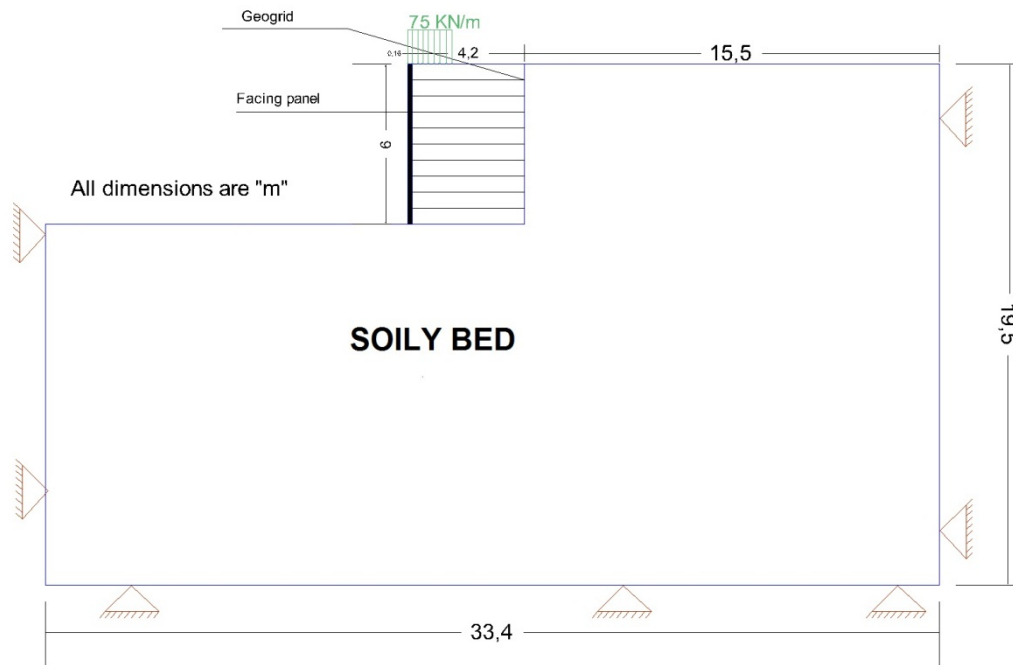


Figure 1) Schematic model of Geogrid reinforced soil retaining wall.

3. Numerical modeling of Full scale Model

The model form is shown in Figure 2. Dimension of 67×34 meshes are variable. Dense sand foundation modeled as a homogeneous shape in order to minimize eventual errors.

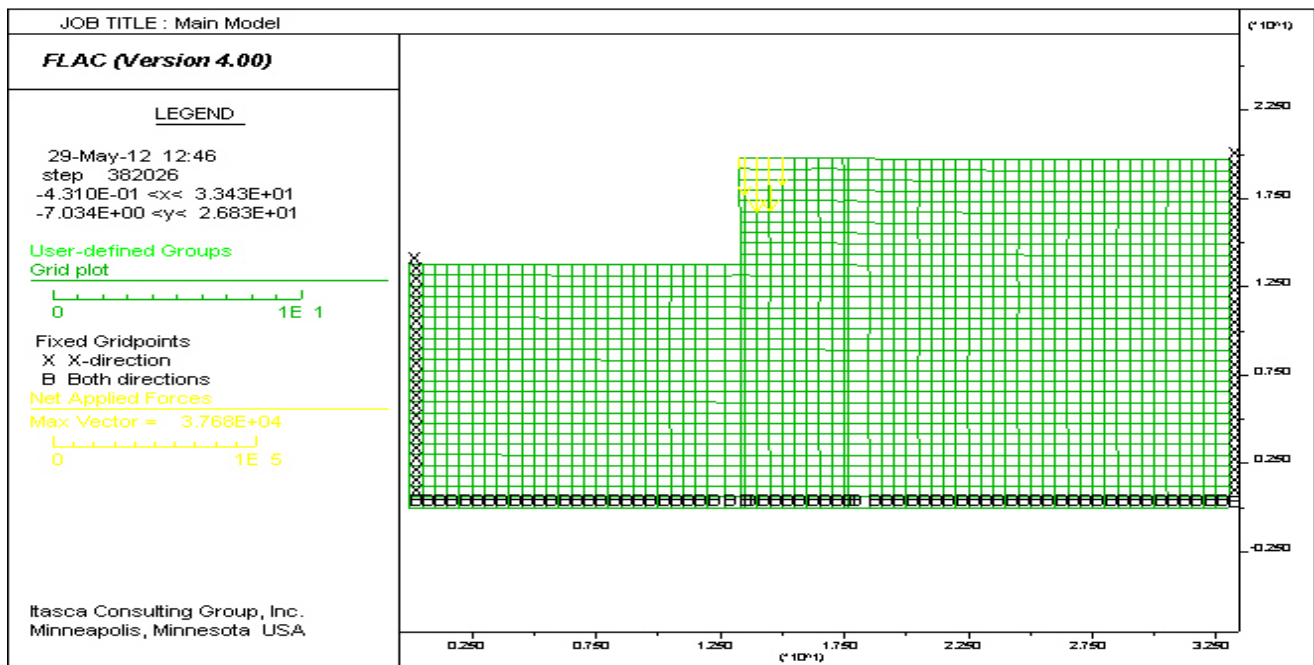


Figure 2) model of reinforced soil retaining wall in the software

In this episode, the full scale reinforced FHWA model collaborates by applying FLAC^{2D} and experimental results. The soil is a “Mohr-coulomb” plasticity model.

Modeling follows a construction stages. At first, in this method embankment is done in one layer .and then polymer mesh embeds on the soil layer and this period repeats at 8 stages.

It should be noted that the facing panel modeled in two methods, one is applying an elasticity model and the other one is applying a beam structure. Modeling methods are shown in table1 as a summary.

Material	Model	type	
soil	Mohr-coloumb	-----	
Facing panel	Elastic	-----	
	Elastic	Beam structure	
Polymer(geogrid)	Elastic	Cable structure	

Table1) Modeling of different properties in FLAC^{2D}

4. Material properties

4.1. Reinforced backfill soil properties

- (1) Young modulus (E): 15000 k.pa
- (2) Dry density (γ): 17.6 KN/m²
- (3) Poisson (ν): 0.3
- (4) Cohesion (C): 18.5 KN/m²
- (5) Internal friction angle (ϕ): 36

4.2. Facing panel properties:

- (1) Young modulus (E): 300 GPa
- (2) equivalent thickness: 17 cm
- (3) Yielding stress (for structural elements): 2400 KN/m²

4.3. "Geogrid" properties:

- (1) Young modulus (E): 160 M.pa
- (2) Ultimate strength tensile: 54 k.pa

4.4. Foundation bed:

- (1) Young modulus (E): 25000 k.pa
- (2) Dry density (γ): 17.6 KN/m²
- (3) Poisson (ν): 0.3
- (4) Cohesion (C): 19.5 KN/m²

4. Verifying numerical results:

To validate the developed numerical model, as noted in above, a physical model was constructed. The developed numerical model was used to predict the behavior of the reinforced soil structure in the model test under applied load. The results of the model performed by this numerical method were compared with those measured in the experimental test (FHWA-A0).

Diagrams printed in figures 3a, 3b show respectively the horizontal displacement of the facing and vertical settlement on the top of this wall predicted by the numerical analysis, finite difference analysis, together

with those measured in the experimental model test. Comparison of the results shows that numerical results predicted by F.D.M are in a good agreement with the experimental results.

As the diagram shows in these figures, when the panel is predicted as a structural element, beam, results are closer to reality special in deformation of the panel prediction in F.D.M.

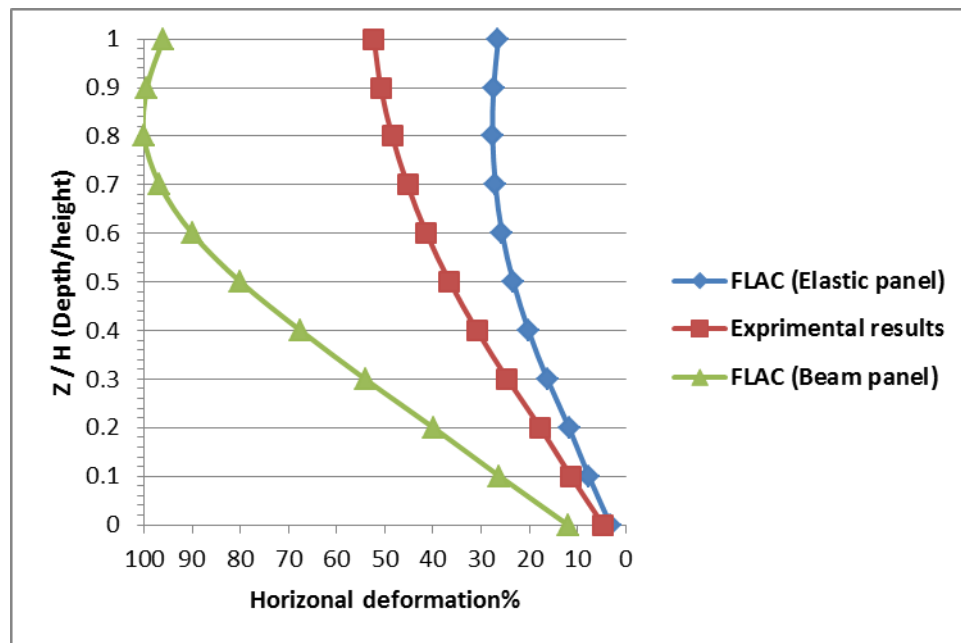


Figure 3) Panel deformation in different levels of the wall.

5. A Numerical study in GPSRW

5.1. Displacement:

The maximum settlements occur in the central region (core) of the wall in an specified Hyperbolic limitation.

Moving away from this area to the regions lead to staddle and upper surfaces, settlement contours decrease. But in opposite direction to upper regions end up to the external surface of the wall adjacent to loading area, displacements in Y-direction increases again. (Figure 4-b)

In general, settlements in upper reinforcement layers is bigger than lower ones because failure wedges occur in a surface with slope angle $(45+\Phi/2)$. The maximum amount for displacement contours in X direction

into the wall occurs in the zones near facing panels and upper layers. Excessive distribution of displacement contours in the zones near the facing panel and interfaces with foundation is beheld. (Figure 4-b)

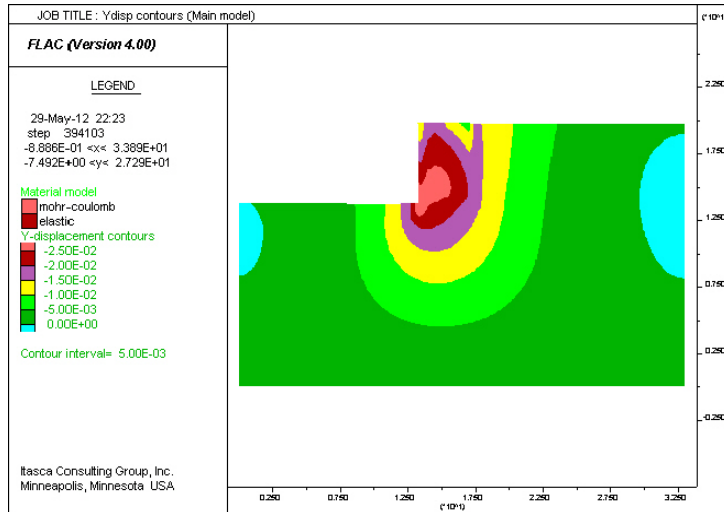


Figure 4-b) Settlement contours distribution

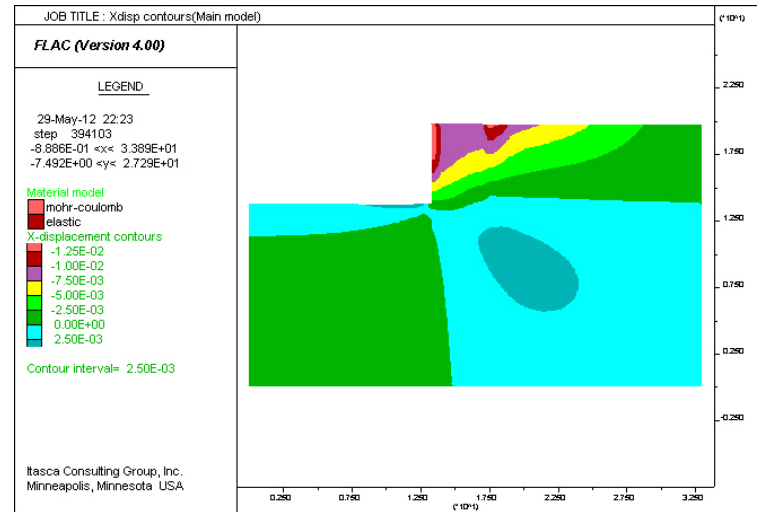


Figure4-b) X-displacement contours distribution

5.2. Stresses contours:

Design of a geosynthetic reinforced embankment should basically verify the strain compatibility between the soil and the reinforcements and ensure that the anticipated displacements are consistent with performance criteria of the structure. Total horizontal stresses, shows their values in backfills. As shown in figure 5-a, " S_{xx} " is concentrated adjacent to linear loading with minimum amounts. In other zones, contours distributes as pressure with a moderate incremental trend.

Compressive stresses under linear load indicate that moderate stresses placed within failure wedge, Hence application of low compressive strength geogrids is recommended in this region. Also, total vertical stresses occur in a parabolic limitation, consist of the soil wall and the foundation precisely placed under it.

As shown in figure 5-b, maximum compressive stresses start from a central region and contours spread with reduction proceedings. It's noted that there're maximum tensile stresses adjacent to linear loading region, again.

Additionally, the basic formulation for Finite Difference Method" (FLAC) is for a two dimensional plane-strain model. This condition is associated with long structures or excavations with constant cross section and acted on by loads in the plane of the cross section.

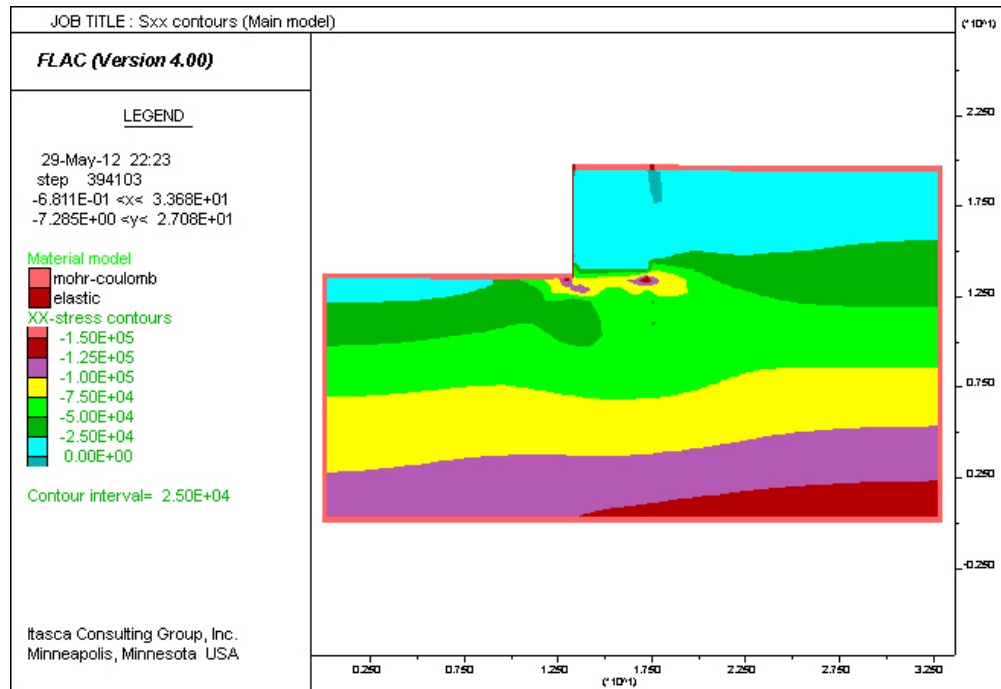


Figure 5-a) stress distribution within geosynthetic reinforced soil retaining wall (σ_x , F.D.M)

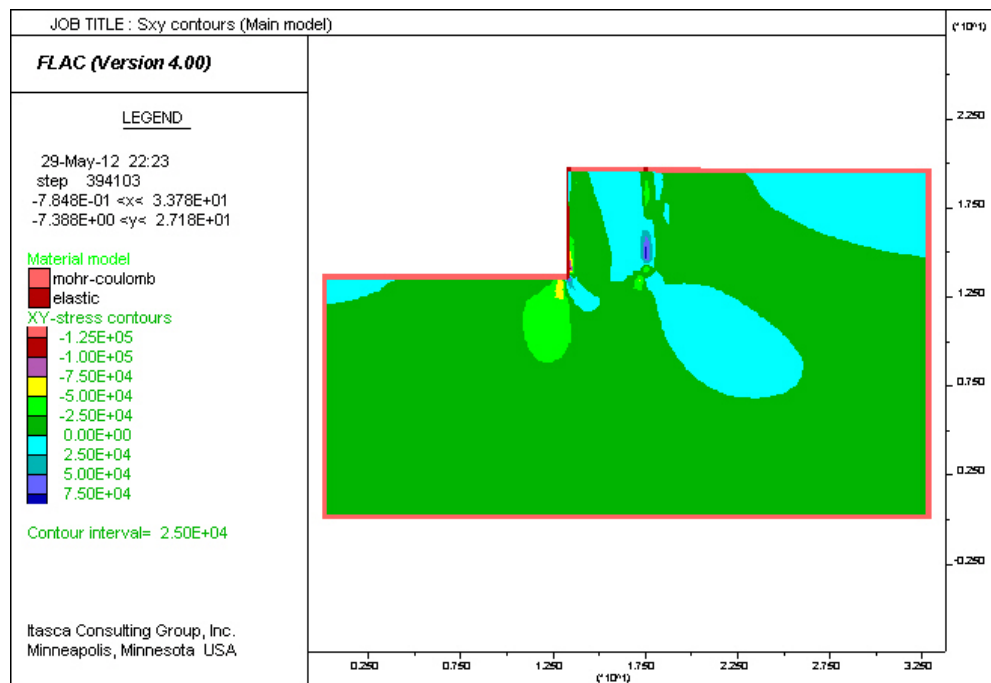


Figure 5-b) stress distribution within geosynthetic reinforced soil retaining wall (σ_y , F.D.M)

5.3. Displacement of reinforcements:

Diagrams printed in Figure 7 show vertical displacement of reinforcements in "mm". These displacement curves are decreasing from the upper layers to lower ones.

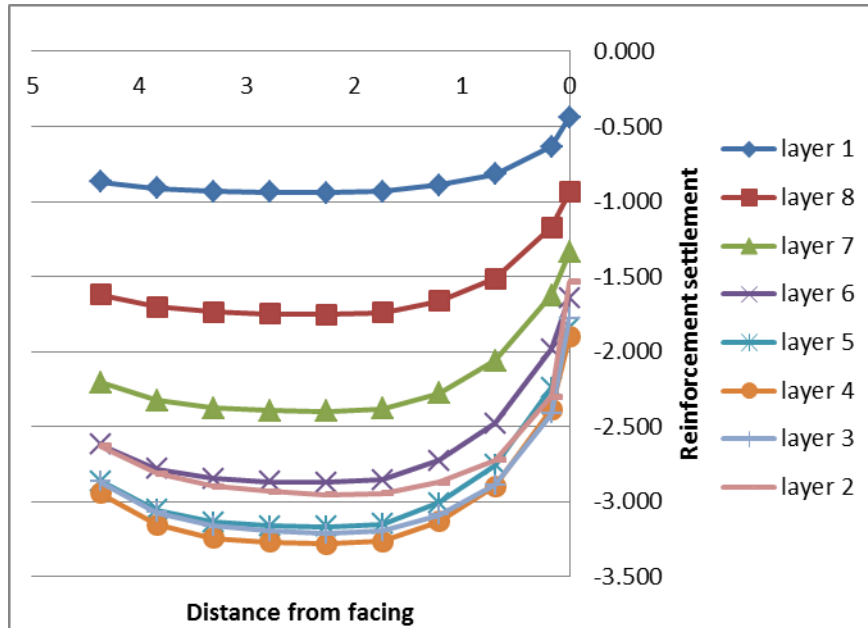


Figure 6) vertical displacement of reinforcements as result of Finite Difference Method

5.4. Forces in reinforcements:

Numerical results Finite Difference Analysis for tension forces in polymeric reinforcements was being printed in a diagram. As shown in this diagram, tension in these types of geogrids increases from base of the soil wall to the surface. As regards, tension is further adjacent to elastic panel (figure 8).

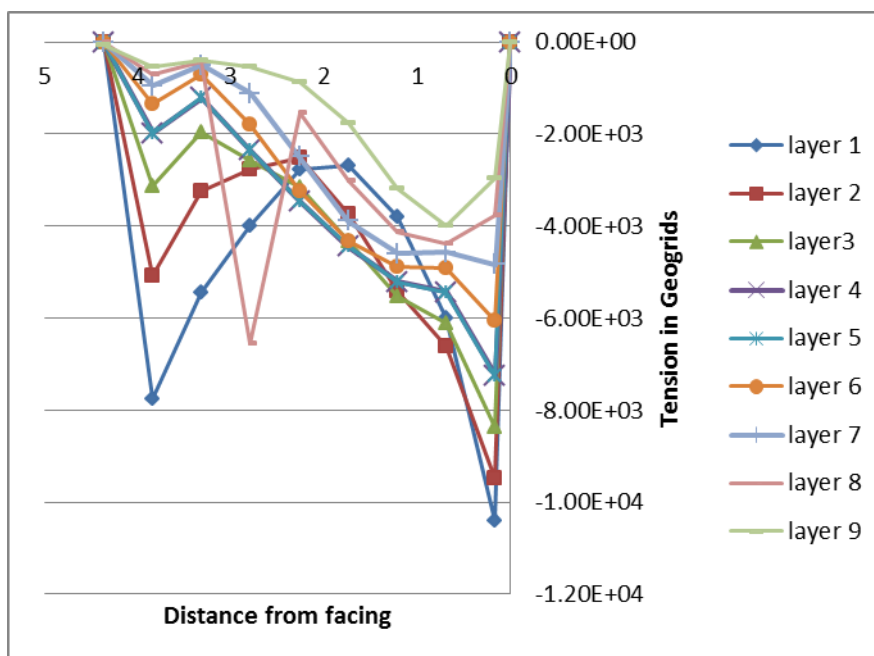


Figure 7) Tension in reinforcements diagrams by distance from panel as result of FLAC^{2D}.

5.5. Reinforced soil elasticity modals:

Normalized maximum axial forces in Geogrids for different values of Elasticity modulus by the different height of the reinforced wall are shown in figure 8.

As shown in this figure the values of normalized maximum axial forces reduce with increasing Elasticity modulus. Also, with increasing Elasticity values modulus from 10 M.Pa. to 70 M.Pa normalized axial tensions reduced to 30%. However, with increasing values of “E” from 70 M.Pa. to upper values normalized axial tensions decrease with a reduction rate.

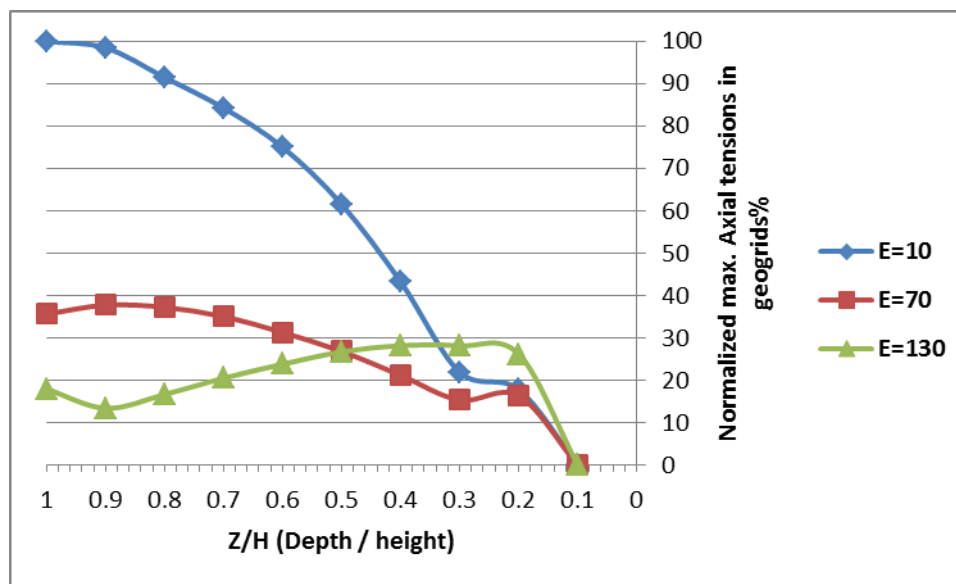


Figure 8) Normalized maximum axial tensions by different height of the wall with variable Elasticity modulus.

6. Conclusion

1-Finite Difference analysis were conducted to simulate the construction response of a geosynthetic reinforced soil retaining wall with a concrete block or shotcrete facing.

2-Comparison between measured and predicted behavior are presented for the wall deformation, vertical and lateral stresses in geogrid layers.

3- This study presented a Finite Difference analytical model, based on the theory of plasticity which can be used in analysis of geogrid reinforced soil structures.

4- Axial Tension forces in these type of geogrids increase from base of soil wall to the surface, so the upper layer reinforced layers sustain greater tensions.

- 5- Polymeric materials manufactured by "Tenser" company are convenient to reinforced soil walls.
- 6- Linear loading along the wall surface affects larger settlements in the layers near the surface.
- 7- "FLAC^{2D}" software (based on F.D.M) is verified by collaborating with experimental results.
- 8- The values of normalized maximum axial forces reduce with increasing Elasticity modulus of the reinforced system.

References

- 1. FHWA (2001), mechanically stabilized Earth walls and reinforced soil slopes. Design and construction Guidelines, FHWA-NHI-00-043, Federal Highway Administration, U.S. Department of Transportation. Washington D.C.
- 2. Rowe, R.K. and skinner, G.D .(2001) Numerical analysis of geosynthetic reinforced retaining wall constructed on a layered soil foundation, Geotextile and Geo-membranes, 19(7), 387-412.
- 3. FLAC's Manual, Itasca Consulting Group, Inc. Minneapolis, Minnesota (version 4.0)
- 4. FHWA,(1998)"Geosynthetic Design and construction guideline" publication No, FHWA-HI-95-038,National Highway Institute.
- 5. Bathurst, R.J., Walters, D.,vlachopoulos N.,burgess, P., and Allen T.M.,(2000),"Full scale Testing of Geosynthetic reinforced walls", ASCE special publication, proceeding of GeoDenver, PP.201-217
- 6. Bowels, Joseph E. Foundation Analysis and Design-5th ed. McGraw-Hill, New York,1996.

Effects of humic acid and salt additives on the behaviour of lime-stabilised organic clay.

1. N.Z. Mohd Yunus, *Department of Geotechnics and Transportation, Universiti Teknologi Malaysia, Skudai.*
2. D. Wanatowski, and L.R. Stace, *Faculty of Engineering, University of Nottingham, United Kingdom.*

ABSTRACT

The presence of organic matter, in particular humic acid, is one of the most important factors affecting the effectiveness of lime stabilisation of clays. In this paper, an investigation on the effects of humic acid content on the strength of lime-stabilised organic clay is presented. Artificial organic clay with different humic acid contents of 0.5%, 1.5% and 3.0% was used. The organic clay was stabilised with 5%, 10% and 15% of hydrated lime. The strength of the lime-treated organic clay was analysed using the Unconfined Compression Strength (UCS) tests at different curing periods of 7, 28 and 90 days. A microstructure analysis of selected specimens was also carried out using a Scanning Electron Microscope (SEM). The results showed that a significant strength loss was obtained beyond 1.5% humic acid content and the strength was diminished at longer curing periods. However, it was found that the behaviour of lime-treated specimen with 1.5% humic acid content can be successfully improved by addition of 0.5% chloride salts. Furthermore, the shear strength of the specimens increased with increasing curing period. Therefore, there is a real potential for the use of chloride salts to improve the lime stabilisation process of organic clay in geotechnical practice.

Keywords: organic clay, lime stabilisation, salt additives, shear strength, laboratory tests

1. INTRODUCTION

Lime as a chemical stabiliser has been proved successful with regards to its ability to alter the properties of weak soils, especially those of a cohesive nature [1], [2], [3] and [4]. In contrast, lime stabilisation of organic clay has always faced a complex outcome in the long term due to the presence of high concentrations of organic matter in clay soil [5], [6], [7] and [8]. Specifically, among the constituents of organic matters, humic acid is believed to be the most disruptive to the lime stabilisation process. In fact, it has been reported that more than 1% humic acid content in clay may render the lime stabilisation process ineffective [9], [10], and [11]. Therefore for organic soils, lime alone may not be effective or even sufficient as a stabiliser.

One way of mitigating the adverse effects of humic acid is by introducing a small amount of chloride salts (i.e. CaCl_2 and NaCl) to lime-treated organic clay. The idea of adding admixture to lime-treated clay is to provide additional cations (i.e. Ca^{2+} and Na^+) to promote ion exchange activity and dissolution of clay minerals such as silica and alumina for pozzolanic reactions. These reactions are thought to enable the greater development in shear strength of organic clay, especially in the long term [9], [12], [13].

This paper presents an experimental study on the behaviour of lime-treated organic clay with various humic acid contents. In addition, the influence of 0.5% CaCl_2 and 0.5% NaCl on the behavior of lime-treated organic clay is investigated. Changes in the soil structure due to the addition of chloride salts were also examined using the Scanning Electron Microscope (SEM).

2. MATERIALS

Artificial organic clay used in this study was prepared by mixing commercial kaolin with commercial humic acid contents of 0%, 0.5%, 1.5% and 3.0% according to the dry mass of kaolin. The chemical elements present in each soil mixture are given in Table 1. In general, the effect of humic acid on the chemical elements can be detected from the increase in carbon and oxide ions. As a result, the increase in amounts of carbon and oxide ions and the decrease in silica and alumina contents can be observed with increasing humic acid content, as shown in Table 1.

Table 1. Chemical elements in the tested soils.

Element	Weight %		
	0.5% humic acid	1.5% humic acid	3% humic acid
C	2.8	2.74	20.16
O	50.45	54.54	48.97
Na	0.36	0.41	0.81
Mg	0.65	0.64	0.56
Al	16.94	18.47	12.8
Si	24.74	21.52	14.07
P	0.18	0.28	0.16
S	0.05	0.12	0.42
Cl	0	0.01	0.19
K	3.42	0.79	0.59
Ca	0.02	0.04	0.33
Ti	0	0.02	0.18
V	0	0.01	0.01
Fe	0.39	0.4	0.74

The results of index testing carried out on inorganic and organic clays are summarized in Table 2. All of the tested soils were suitable to be stabilized by lime as the plasticity index (PI) is more than 10.

Table 2. Physical properties of clay with different humic acid contents.

Property	Humic acid content (%)			
	0	0.5	1.5	3
Liquid limit (%)	65.4	64.4	63.6	61.0
Plastic limit (%)	30.4	33.0	33.8	34.5
Plasticity index (%)	35	31.4	29.5	26.5
Specific gravity	2.61	2.53	2.51	2.47
pH	5.52	5.34	5.16	5.07
OMC (%)	30.6	30.9	30.6	33.4
MDD (kg/m ³)	1440	1429	1425	1404

3. SPECIMEN PREPARATION

Specimens tested in this study were prepared using procedures described in the ASTM standard D5102. Initially, the specimens were oven-dried at 60°C until the constant weight was obtained. Clay with different amounts of humic acid was prepared by mixing relevant amounts of dry kaolin with 0.5%, 1.5%, and 3% of humic acid by dry mass of kaolin. Mixing of dry materials was continued until a uniform appearance of the kaolin-humic acid mixture was obtained. Distilled water was then added and further mixing was performed until a homogeneous appearance of the soil paste was achieved. This paste was then used for plasticity and compaction tests. The specimens (76 mm in height and 38 mm in diameter) were compacted into the mould, extruded from it and wrapped in cling film to preserve the water content and to keep them free from carbon dioxide (CO₂). The specimens were then cured in a desiccator at 20°C and with humidity of more than 90% for 7, 28, and 90 days, respectively.

4. RESULTS AND DISCUSSIONS

The results of a short term strength assessment of lime-treated clay with different humic acid contents (0%, 0.5%, 1.5%, 3%) and lime contents (5%, 8%, 10%, 15%) are shown in Fig. 1.

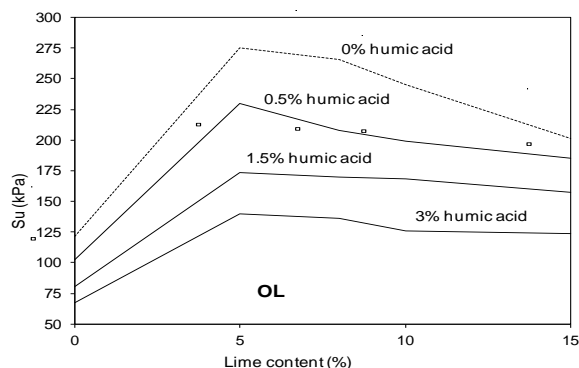


Figure 1. Effect of lime content on the undrained shear strength of clay with different humic acid contents after 7 days curing.

All the specimens were cured for 7 days. It can be seen from Fig. 1 that the undrained shear strength (S_u) of the specimens with 5% lime content increases significantly compared to the strength of untreated clay (i.e. 0% lime). However, the shear strength of specimens with higher than 5% lime content reduces gradually with increasing lime content regardless of the humic acid content in the clay. Therefore, 5% was taken as the optimum lime content (OLC) for each type of organic clay. Fig. 1 also shows that the shear strength of organic clay decreases with increasing humic acid content, which proves that the presence of humic acid in organic clay diminishes its shear strength.

In a further assessment of the effect of humic acid on lime stabilisation, samples were tested at 0, 7, 28, and 90 days to ascertain the duration of the stabilisation process. Since the OLC of each specimen was identical, investigation of the development of the lime-clay reaction with time was conducted only at 5% lime content. Fig. 2 illustrates the development of the shear strength of the lime-treated specimens at 0, 7, 28 and 90 days. It appears that with the exception of the inorganic clay (0% humic acid) the undrained strength of the lime-treated clays comprising 0.5%, 1.5% and 3.0% humic acid decreased over the 90 day curing period. A slight loss in the strength is observed for organic clay with 0.5% humic acid, while substantial loss in strength is evident where the humic acid content is equal to or greater than 1.5%. The results demonstrate that lime stabilization of organic clay with high humic acid content is not very efficient in the long term. Similar observations were reported by other researchers [8], [9], [10] and [11]. It should be noted that despite exhibiting a loss in strength in the long term, the undrained strengths of lime-treated samples at 90 days were still higher than those of untreated specimens (see Fig. 1 for 0% lime). However, for practical purposes, it is not reasonable to consider lime stabilisation as successful when long term strength is uncertain.

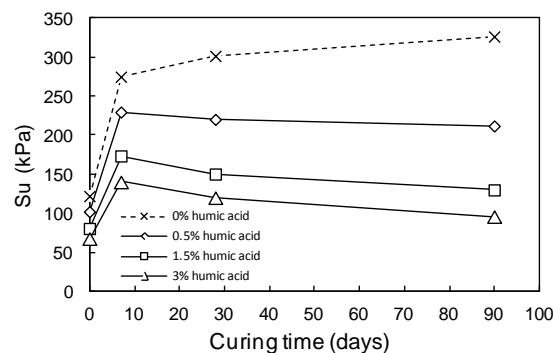


Figure 2. Effect of curing period on the undrained shear strength of lime-treated clay.

The impedance in the formation and development of cementitious products with increasing humic acid content over longer curing periods may be due to various reasons.

Firstly, the reduction in pH value at longer curing periods may be one of the reasons that decreased the shear strength value. Fig. 3 shows the pH value of various humic acid contents treated at OLC = 5% for different curing periods. It

can be seen that, except for inorganic clay, the pH values of organic clays decreased with increasing curing period. After 28 days, specimens which consist of 1.5% and 3.0% humic acid contents had a pH lower than 12.40, which is the minimum value required for the successful production of cementing materials [14].

Secondly, bearing in mind that the dissolution of clay minerals is highly dependent on pH value, it is thought that the presence of a certain amount of humic acid made it difficult for the solution to recover from its acidified condition. The humic acid may have coated the clay particles, thereby preventing the lime from coming into contact with clay minerals during the pozzolanic reaction. Consequently, the dissolution of clay minerals becomes insufficient, thus limiting the production of cementitious materials.

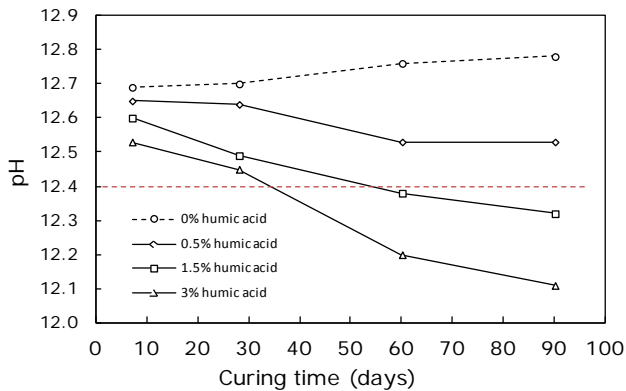


Figure 3. Effect of curing period on pH value of lime-treated organic clay with different humic acid contents.

The findings obtained from the experiments on lime-treated organic clay revealed that lime may not be suitable for stabilising organic clay with more than 1.5% humic acid content [15]. Therefore, two chloride salts (calcium chloride (CaCl_2) and sodium chloride (NaCl)) were considered as potential additives that could improve the effectiveness of lime stabilisation in organic clay. The analysis was carried out for the clay with 1.5% humic acid content stabilised with 5% of lime.

Fig. 4 shows development of the undrained strength with increasing salt (CaCl_2 and NaCl) content for different curing periods. The salts-treated specimens are also compared to those treated by lime alone (i.e. 0% salt content) at corresponding curing periods. A clear increase in the strength can be noted for both types of salt as the curing period increases from 7 to 90 days. Overall, the strengths recorded for the lime- CaCl_2 mixtures were higher than those of the lime- NaCl mixtures [13]. A similar finding was reported by [12]. It may be because of the dual function of Ca^{2+} ions promoting better ion exchange and contributing towards the formation of cementing products (i.e. calcium silicate hydrate, CSH and calcium aluminate hydrate, CAH). The Na^+ ions, on the other hand are only believed to accelerate silica dissolution [9], [12] and [13].

Changes in soil structure and chemical compositions were analysed using a Scanning Electron Microscope (SEM). Fig. 5 shows the image of a lime-treated specimen with 1.5%

humic acid content without the addition of salt. The changes in soil structure due to lime stabilisation were hardly visible. The microstructure of the specimen was very similar to that of a specimen without lime [21].

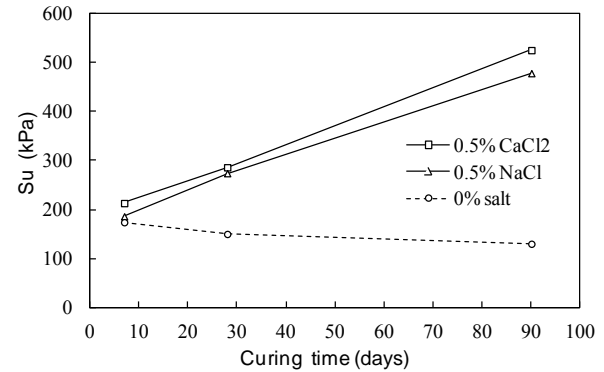


Figure 4. Effect of the chloride salts on the shear strength of lime-treated clay at different curing periods.

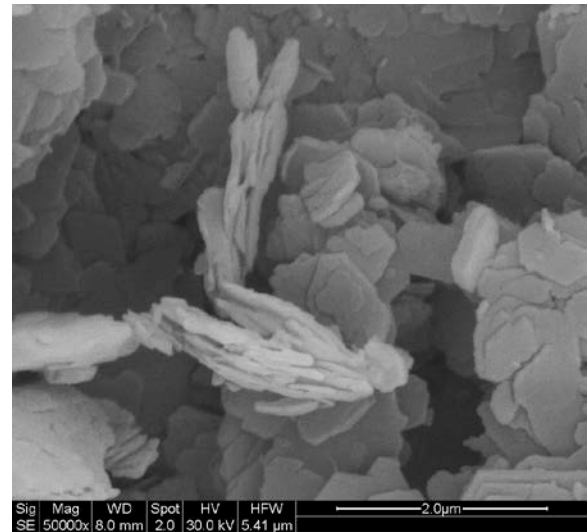


Figure 5. SEM image of lime-treated clay with 1.5% humic acid and without the addition of salt.

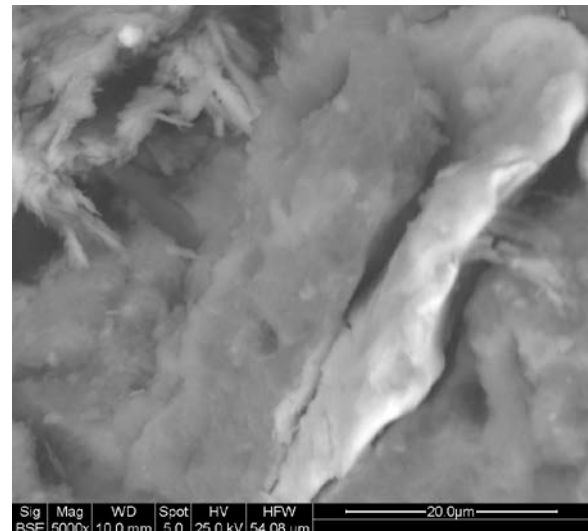


Figure 6. SEM image of lime-treated clay with the addition of 0.5% CaCl_2 at 28 days of curing.

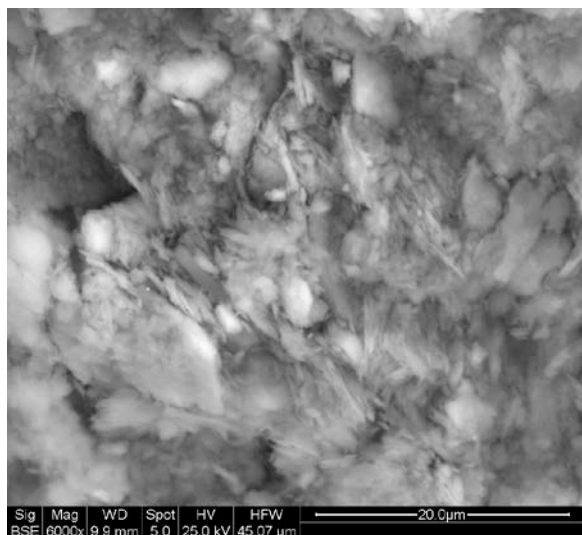


Figure 7. SEM image of lime-treated clay with the addition of 0.5% NaCl at 28 days of curing.

Fig. 6 and Fig. 7 show the SEM images of lime-treated organic clay with the addition of 0.5% chloride salts. The micrographs were taken from UCS test samples after 28 curing days. The flaky and plate-like structure present in the lime-treated organic specimen (Fig. 5) has almost completely disappeared. A clear cemented structure, mainly calcium silicate hydrate (CSH) was identified by a fine tubular shape and well knit structure (needle-like form) that bridge the aggregates [13], [15]. The presence of cementing structures in specimens with the addition of salts explains the improvement in the strength obtained from UCS tests.

5. CONCLUSIONS

In this paper, the effectiveness of lime stabilisation of organic clay was investigated. In addition, a preliminary investigation on the effect of salts on the strength of lime-treated organic clay was analysed. Based on the experimental results obtained in the study, the following conclusions can be made.

1. The shear strength of lime-treated organic clay reduces when the lime content exceeds 5%. Thus, 5% of lime is identified as the optimum lime content (OLC) for the organic clay tested in this study.
2. The shear strength of the lime-treated organic clay reduces at longer curing periods. A slight loss in strength is observed for organic clay with 0.5% humic acid, while a substantial loss in strength is evident where the humic acid content is equal to or greater than 1.5%. These results show that the presence of more than 1.5% humic acid in the organic clay tested in this study reduces significantly the efficiency of the lime stabilisation process.
3. The results obtained from the UCS tests carried out on specimens with 1.5% of humic acid treated with 5% lime show that the strength of lime-treated organic clay can be successfully improved with addition of 0.5% chloride salts. Therefore, there is a potential for the use of chloride salts in lime stabilisation of organic clay in geotechnical practice.

4. The SEM images of lime-treated organic clay show the flocculated and aggregated structure, without appearance of cementation. In contrast, a clear evidence of cemented structure is observed when lime-treated organic samples are stabilised by addition of 0.5% CaCl_2 and 0.5% NaCl.

6. REFERENCES

- [1] Bell FG, "Lime stabilization of clay minerals and soils," *Engineering Geology*, 1996, vol. 42, no. 4, pp. 223-237.
- [2] Rajasekaran G and Rao N, "The microstructure of lime-stabilized marine clay," *Ocean Engineering*, 1997, vol. 24, no. 9, pp. 867-875.
- [3] James R, Kamruzzaman AHM, Haque A, Wilkinson A, "Behaviour of lime-slag-treated clay," *Proc. the ICE, Ground Improvement*, 2008, vol. 161, no. 4, pp. 207-216.
- [4] Consoli NC, da Silva Lopes Jr L, and Heineck KS, "Key parameters for the strength control of lime stabilized soils," *J. of Materials in Civil Engineering*, 2009, vol. 21, no. 5, pp. 210-216.
- [5] Kuno G, Kutara K and Miki H, "Chemical stabilization on soft soils containing humic acid," *Proc. 12th International Conference Soil Mechanics Foundation Engineering*, 1989, Rio de Janeiro, vol. 2, pp. 1381-1384.
- [6] Hebib S. and Farrell ER, "Some experiences on the stabilization of Irish peats," *Canadian Geotechnical J.*, 2003, vol. 40, pp. 107-120.
- [7] Chen D, Si Z and Saribudak M, "Roadway heaving caused by high organic matter," *J. of Performance of Constructed Facilities*, 2009, vol. 23, no. 2, pp. 100-108.
- [8] Huat BB, Maail KS and Ahmed Mohamed T, "Effect of chemical admixtures on the engineering properties of tropical peat soils," *American J. of Applied Sciences*, 2005, vol. 2, no. 7, pp. 1113-1120.
- [9] Koslanant S, Onitsuka K and Negami T, "Influence of salt additive in lime stabilization on organic clay," *Geotechnical Engineering*, 2006, vol. 39, pp.95-101.
- [10] Harris P, Harvey O, Sebesta S, Chikyala SR, Puppala A, and Saride S, "Mitigating the effects of organics in stabilized soil," *Technical Report No. 0-5540-1*, 2009, Texas Transportation Institute, USA.
- [11] Zhu W, Chiu CF, Zhang CL and Zeng K, "Effect of humic acid on the behaviour of solidified dredged material," *Canadian Geotechnical J.*, 2009, vol. 46, pp. 1093-1099.
- [12] Modmoltin C and Voottipruex P, "Influence of salts on strength of cement-treated clays," *Proc. the ICE, Ground Improvement*, 2009, vol. 162, no. 1, pp. 15-26.
- [13] Danmarks B and Allan Haliburton T, "Effects of sodium chloride and sodium chloride-lime admixtures on cohesive Oklahoma soils," *Highway Research Record*, Washington, 1999, vol. 315, pp.102-111.
- [14] Mohd Yunus NZ, Wanatowski D, and Stace LR, "Effect of humic acid on physical and engineering properties of lime-treated organic clay," *Proc. World Academy of Science Engineering and Technology*, 2011, Issue 59, Part XV, 1820-1825.
- [15] Mohd Yunus NZ, *Behaviour of lime-stabilised organic clay*. PhD Thesis, 2011, University of Nottingham, UK.

Sodium Tripolyphosphate For Stabilizing Of Contaminated Soil

Amin Falamaki¹, Hossein Tavallali² and Shahrbanoo Rezanejad Farahmand³
^{1,2,3} Payame Noor University, PO BOX 19395-3697 Tehran, Iran

ABSTRACT

The objective of this study is to stabilize the polluted soil using sodium tripolyphosphate (STPP). In this study a series of leachate column tests were conducted to find out the effect of STPP on Pb polluted soil. In addition, to understand the concentration of STPP on the efficiency of the method, different samples with different polluted soils were tested. STPP with 0.1, 0.2 and 0.5 mg/kg dry soil were added to the polluted soil and the samples were kept for 1 month. The results show that STPP may stabilize Pb in the soil. Increasing the concentration of STPP, decreases the concentration of metals in the effluent, means more stabilized metals in the soils. The results also show that 0.2 mg/kg dry soil of STPP is enough to stabilize the metals from the first stages of the tests.

Keywords: Lead Stabilization, Phosphate amendment, Contaminated soil.

1. INTRODUCTION

Today in developing countries, unfortunately, due to lack of advanced technologies, disposal of contaminated soils with heavy metals and radioactive in the environment, causes spread of contaminants in groundwater. In addition, methods for decontamination of the soil are very expensive and require advanced technology. Therefore, disposal of mining waste and industrial soil waste using an inexpensive method that prevents from spreading pollution of soil is very important.

Solidification/stabilization technique is relatively a simple and inexpensive method for removing contaminants from the soil. In this method one stabilizer is used to immobilize pollutants in soil and prevent them from spreading over. This technique is especially useful for urgent disposal of contaminated soils in the environment.

Lee et al., (2009) stated different amendments that used in situ stabilization of heavy metals in soils, including agricultural products, such as lime, phosphate, and organic matter, as well as various industrial products, such as zeolites and red-mud. [1]

Falamaki et al., (2009) declared the phosphate based binders have many applications in geotechnical and geoenvironmental engineering such as: improvement and stabilization of tailing dams, rehabilitation of old landfills, construction of new clay liners, containment and permeable barriers, etc. [2]

Mignardi et al., (2011) showed, The reaction mechanisms for metal immobilization by phosphate minerals which includes: (a) ion exchange process, (b) surface complexation, (c) dissolution of the original phosphate minerals and precipitation of new metal phosphates, and (d) substitution of Ca in phosphate by other metals during recrystallization (coprecipitation). [3]

Orthophosphate (PO_4^{3-}) is one of metals stabilization

agents that have many applications to stabilize a variety of hazardous and industrial wastes. This agent combines with metals to form phosphate minerals, and reducing solubility metals through absorption or precipitation and immobilize them. [4]

Laperche et al., (1996) declared The use of phosphate to immobilize metals has been advocated for lead-contaminated soils. [5]

The purpose of this research, is stabilization of lead (Pb) in contaminated soil, using STPP in three stabilizer / soil ratio (0.5/100, 0.2/100, 0.1/100 w/w) as a chemical immobilization agent, using leachate column test described in ASTM D 4874- 95. The optimum amount of STPP is also investigated in this paper.

2. MATERIALS AND METHODS

2.1 Soil description

A fine silty sand from Shiraz sand mines (Fars Province, Iran) was used in this study. The amount of soil moisture content is equal to 0/94%. Soil pH is 7. The aggregation analysis using sieve showed that 57.4% was sand.

2.2 STPP characterization

One of the phosphate compounds that used in this study is sodium tripolyphosphate, STPP, A white powder, which is inexpensive. This detergent mater forms complexes with water ions, such as calcium and magnesium. The other uses of STPP are emulsifier of oil and grease, peptizing agent, deflocculating agent in oil well and sequester in cotton boiling (Tavallali et al., 2010)

2.3 Leachate column test

Apparatus that used in this study were Sens AA flame atomic absorption spectrometer. Standard solution of (lead (II) nitrate) and stabilizer (sodium tripolyphosphate) obtained from Merck as analytical materials and were used without further purification. All dilute solutions were prepared from

double distilled water.

Experimental program is based on soil column experiment. Soil samples are prepared according to leachate column test. This is a standard method described in ASTM D 4874-95 is fully. In order to achieve the research objectives, soil samples were dried by oven at temperature= 150° C for 24 hours. The spiked dry soil sample was prepared by mixing the soil with $Pb(NO_3)_2$ solution at a concentration of 500 mg Pb/kg dry soil, and were cured for one month to prevent loss of moisture. More investigations should be accomplished to determine the

optimum and/or most economical content for the different purposes such as contaminant stabilization. The ratios of the STPP/dry soil are chosen as 0.1, 0.2, and 0.5 % in this study. STPP -dry soil mixtures were kept for 2 week. After 2 weeks, then the leachate column tests were conducted. Also measurements were done at pH≈5, (using HCl 0.1M), and room temperature

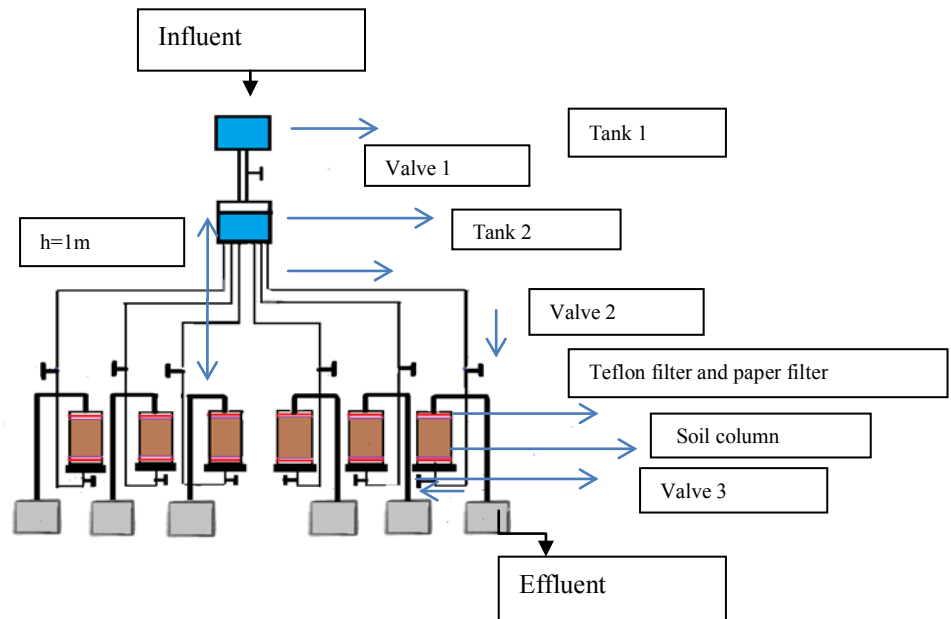


Fig. 1. Schematic diagram of the apparatus

The leachate column test is a standard method described in ASTM D 4874-95 is fully. The Leachate column test was carried out by passing the leachate through a bed of dry soil or soil-contaminant (Pb) mixtures or soil- contaminant (Pb)-stabilizer mixtures contained in a column. Passing the leachate is conducted in an up-flow mode. Column (56.4mm in diameter and 74.6 mm in height), was uniformly packed with soil samples. Maximum amount of soil poured and compacted in each cell was 280 gr.

Figure 1 illustrates a schematic diagram of the apparatus which is designed for this study. Comparison of data obtained from the latex output using atomic absorption spectroscopy apparatus was used to evaluate the efficiency of the method.

2.4 EXPERIMENTAL PROGRAM

To achieve the objectives of this research an experimental program is scheduled as given in Table 2.

Table 2.EXPERIMENTAL PROGRAM

Row	Experiment	STPP/soil ratio	pollution and stabilizer	Storage time for polluted sample	curing time for polluted sample and stabilizer
1	T0 - No additive- No pollute	-	-	-	-
2	T1- No additive- Add pollute	0/100	Only pollution	1 month	-
3	T2-Additive-contaminated soil	0.1/100	pollution then stabilizer	1 month	2 week
4	T3-Additive-contaminated soil	0.2/100	pollution then stabilizer	1 month	2 week
5	T4-Additive-contaminated soil	0.5/100	pollution then stabilizer	1 month	2 week

Void ratio (e) for columns with varied stabilizer / soil ratios calculated and results are shown in Table. 3. In this method

for evolution of efficiency of columns with varied stabilizer / comparability of the samples.
soil,all columns are similar in void ratio to provide

Table 3. Properties of samples

Samples	STPP/soil ratio	Dry soil weight (g)	γ_d	e	n	pore volume
T0 until T7	0/100,0.1/100,0.2 /100and 0/5/100	280	1.50	0.76	0.431	80.25

3. Results and Discussion

To interpret the leachate column test results break through curves for each test in Table. 2 were plotted. As depicted in Table. 2 a control test (T0) was conducted to show that the

amount of the Pb is negligible in the soil. Results obtained from T0 in Fig. 2 shows that soil sample is clean and without any contaminant.

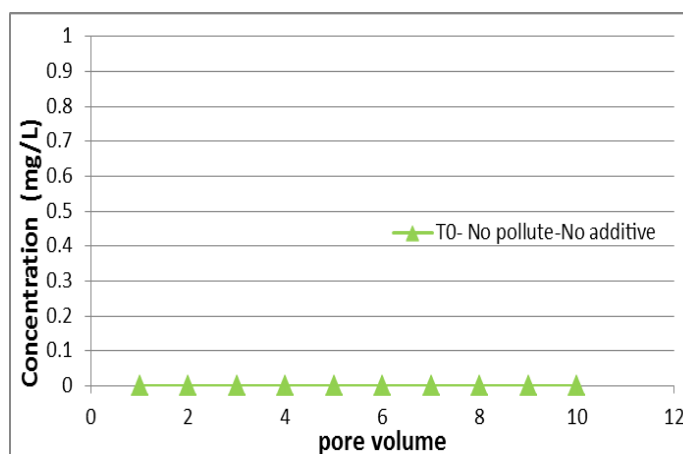


Fig.2. Control test (T0), soil sample with no pollutant and additive

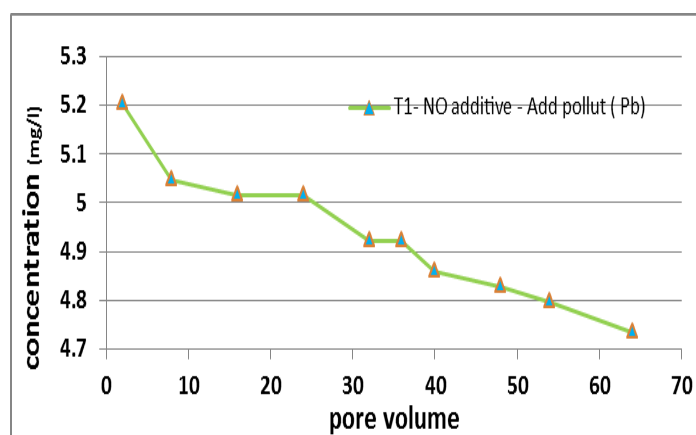


Fig.3..Pb contaminated soil sample (T1) with no additive

After polluting the soil with Pb, the concentration of contaminant in the effluent vs pore volume was plotted in Fig. 3 and it is seen that as the clean water passes through the soil, Pb leachates continually by water. Fig. 4 shows the effect of STPP stabilizer on the polluted soil. According to this figure, adding

STPP to the polluted soils decreases the extracted Pb in the effluent water. Increasing the amount of STPP, decreases the extracted Pb, this means more immobilization of Pb. However, the optimum amount of STPP seems to be 0.2% by weight for this soil condition.

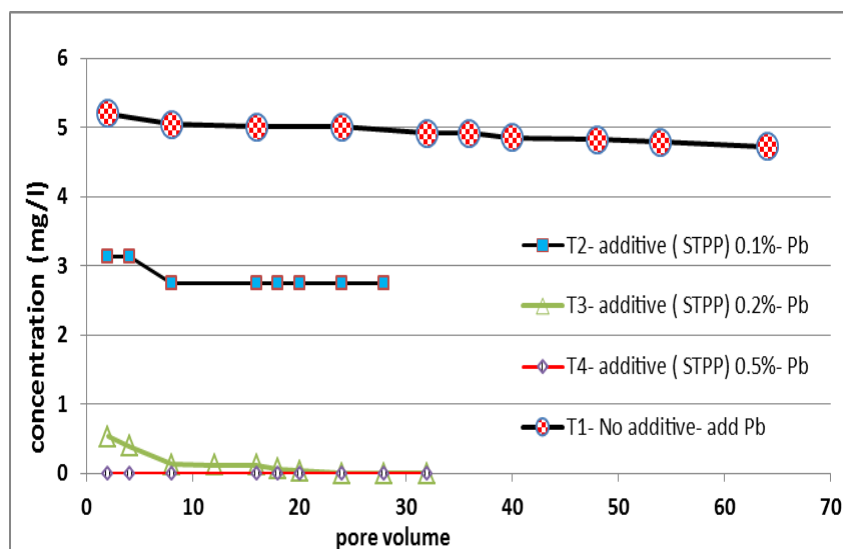


Fig.4.effect of STPP stabilizer on the polluted soil

4. Conclusion

This study investigated the effectiveness of STPP in immobilization Pb in fine silty sand.

All results showed that complexation reaction and stabilization process occur in any ratio of STPP.

Increasing the concentration of STPP, decreases the concentration of metals in the effluent, means more stabilized metals in the soils. The results also show that 0.2 mg/kg dry soil of STPP is enough to stabilize the metals from the first stages of the tests.

5. REFERENCES

- [1] Lee S.H, Lee J.S, Choi Y.J, Kim J.G, "In situ stabilization of cadmium, lead, and zinc-contaminated soil using various amendments," J. Chemosphere 77 Aug. 2009, pp. 1.
- [2] Falamaki a, Shariatmadari N, Noorzad A, "Strength Properties of Hexametaphosphate Treated Soils," J. of GEOTECHNICAL AND GEOENVIRONMENTAL ENGINEERING Aug. 2008, pp. 1. ,ASCE. 1090-0241.
- [3] Mignardi S, Corami A, Ferrini V, "Evaluation of the effectiveness of phosphate treatment for the remediation of mine waste soils contaminated with Cd, Cu, Pb, and Zn," Aug. 2011, pp. 1.

- [4] Tavallali H, Falamaki A, Salehi H, 2010. "Stabilization of Metal contaminants in Municipal Waste Leachate using Metal precipitant additives," J. of Chemtech Aug. 2010, pp. 1-2

- [5] Laperche, V., Traina, S.J., Gaddam, P., Logan, T.J. "Chemical mineralogical characterization of Pb in a contaminated soil: reactions with synthetic apatite." Environ. Sci. Technol. 1996, 30, 3321–3326.

Evaluation of Soil Water Characteristic Curves of Sand-Clay Mixtures

T. Y. Elkady¹, M. A. Dafalla¹, A. M. Al-Mahbashi¹ and Mosleh Al Shamrani¹
¹King Saud University, Saudi Arabia

ABSTRACT

This paper presents an experimental investigation performed to evaluate the soil water characteristic curves of sand-Al-Qatif clay mixtures. Al-Qatif clay is natural expansive clay widely spread in the eastern province of Saudi Arabia. Detailed mineralogical and physical tests were performed on Al-Qatif clay for the characterization. Mixtures of sand and Al-Qatif clay were prepared with sand being the base material and with different clay contents (0%, 5%, 10% and 15%). Test results indicate that the shape of SWCC curves changes from the unimodal to the bimodal form of soil water characteristic curve with the increase in clay content indicative of changes in sand/clay mixture micro-and macro-pores.

Keywords: Soil Water Characteristic Curves, Sand- clay mixture, soil suction

1. INTRODUCTION

Hydraulic barriers are integral components of various engineering systems such as waste containment facilities, earth dam, and water conservation practices. The purpose of these barriers is to preclude the migration of water or leachate. Compacted sand-bentonite barriers have proven to be a suitable material for hydraulic barriers. Several researchers [1]-[6] reported that the amendment of sand with bentonite (ranging between 4 and 20 percent) yielded hydraulic conductivity values acceptable to engineering standards. In addition, sand mixed with bentonite yielded a composite material with satisfactory characteristics in regards to shear strength, susceptibility to desiccation cracking, and ease of construction.

The Kingdom of Saudi Arabia (KSA) is one of the countries which have considerable areas of expansive soil formations. These formations cover vast area of KSA estimated to be about 800,000 km² [7] (Fig. 1). This study evaluates the hydraulic characteristics of compacted sand/Al-Qatif expansive clay hydraulic barriers. Al-Qatif clay represents a natural expansive clay that is abundant in the Arabian Gulf coastal region (Fig.1). This over-consolidated clay is extremely fissured in the natural unsaturated state and exhibits significant volume changes when water content is altered. The volume change potential is due to the high amount of expansive clay minerals such as smectite and illite [8].

The hydraulic characteristics and proper simulation of water flow through compacted sand-clay barriers require consideration of unsaturated liquid flow principles. One of the main unsaturated soil parameters required for modeling is the soil water characteristic curve (SWCC). SWCC is defined as the relationship between soil suction and water content (whether gravimetric, volumetric).

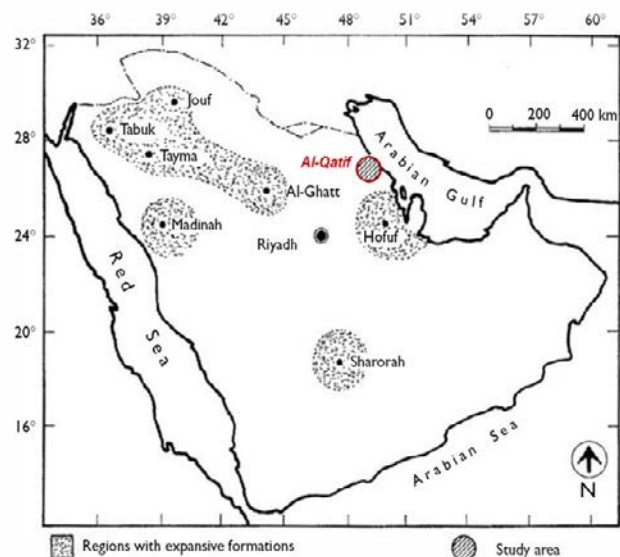


Fig. 1 Distribution of expansive soil formations in Saudi Arabia [7].

Previous studies [9]-[11] focused on the evaluation of SWCC of compacted sand-bentonite mixtures. Results of these studies revealed that the retention capacity increased with increase in bentonite content. Reference [9] indicated that the SWCC possessed a hysteresis effect depending on the wetting and drying paths. In addition, the initial density had a markable effect on the air entry value of SWCC.

Review of technical literature showed a possible trend regarding the shape of SWCCs of sand-bentonite mixtures. SWCCs with unimodal shape were reported for sand-bentonite mixtures with high bentonite content (greater than 30%) [10]-[12]. However, SWCC with bimodal form were observed in case of low bentonite content-sand mixtures. References [13], [14] reported that the SWCC of sand-bentonite mixture with 8% bentonite content revealed a bimodal shape (i.e., curve with four bending curves). This

was attributed to pore water trapped between both the larger, interaggregate pores between the sand particles and bentonite platelets and the smaller, intra-aggregate pores.

This paper presents aims at performed evaluating the effect of Al-Qatif clay percentage on the SWCCs of sand/Al-Qatif clay mixtures. Clay content considered were 0%, 5%, 10%, and 15% per dry mass mix. This was achieved by measuring the soil water characteristic curves over a range that captures the main features of the curves.

2. MATERIAL AND METHODS

This section describes the material used for the compacted sand-Al-Qatif expansive clay mixtures. Initially, the geotechnical properties of each of the sand and clay material are presented. Finally, the effect of clay content on the geotechnical characteristics of sand clay mixture is highlighted.

2.1 Soil Used

The expansive clay used in this study was obtained from the city of Al-Qatif located on the Arabian Gulf shoreline at a distance of 400 km from Riyadh the capital of Saudi Arabia. Several researchers investigated the swelling characteristics of Al-Qatif expansive clay [8], [15], [16]. Based on these investigations, Al-Qatif clay was characterized as highly expansive soil due to the presence of high montmorillonite mineral content.

Soil samples were obtained from open pits excavated to a depth of 1.5 - 3.0 m below ground surface. Samples were transferred to laboratory and complete mineralogical and geotechnical characterization was performed. A summary of geotechnical characterization results is presented in Table 1.

Table 1. Soil Characterization Data for Al-Qatif Soil

Test	Value
Specific Gravity, G_s	2.70
Liquid Limit, w_L (%)	137 %
Plastic Limit, w_p (%)	60 %
Shrinkage Limit, w_{sh} (%)	12 %
% passing Sieve No. 200	99 %
Unified soil classification	CH
Standard Proctor Compaction Test	
Maximum dry unit weight (kN/m^3)	12 kN/m^3
Optimum water content (%)	40 %
Swelling potential (ASTM D4546)	16-18%
Swelling pressure (ASTM D4546)	550-600 kN/m^2

Mineralogical characterization of Al-Qatif soil was performed using Bruker D8 Advance system. Samples were scanned from 2° to 60° (2θ) using 2.2kW Cu anode long fine focus ceramic X-ray tube at a scanning rate of 1 degree per minute. The X-Ray diffraction analysis shown in Figure. 1

depicts that Al-Qatif clay consist of montmorillonite and palygorsite which are typical swelling minerals.

Uniform sand was used in this study with grain size ranging from 0.6 to 0.1 mm. The grain size distribution of sand used is shown in Figure 2. According to unified soil classification system, the sand was classified as poorly graded sand (SP).

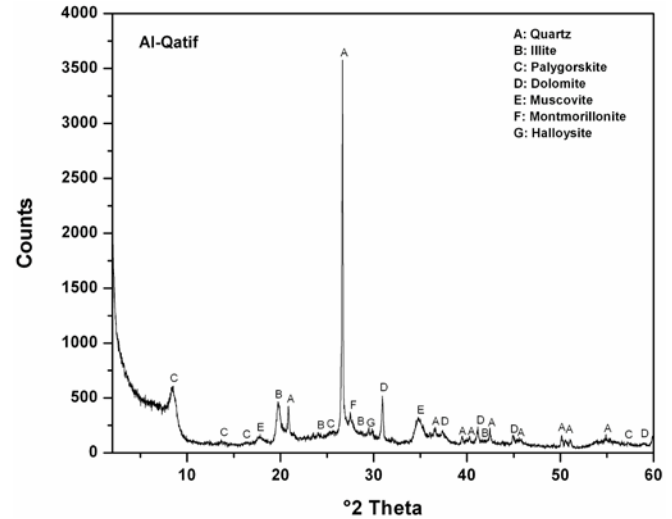


Fig. 1. X-Ray diffraction analysis.

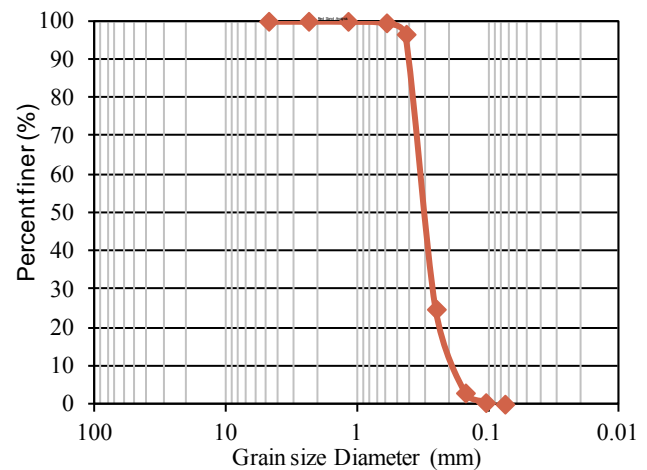


Fig. 2 Grain size distribution of sand.

2.2 Compaction Curves of Sand-Clay Mixtures:

Standard compaction tests were performed in accordance with ASTM D 698 [17] to evaluate the compaction characteristics of sand-clay mixtures. The results of the tests are presented in Fig. 3 where it is observed that maximum unit weight increased with increase of clay content, while the optimum water content increased with increase in clay content.

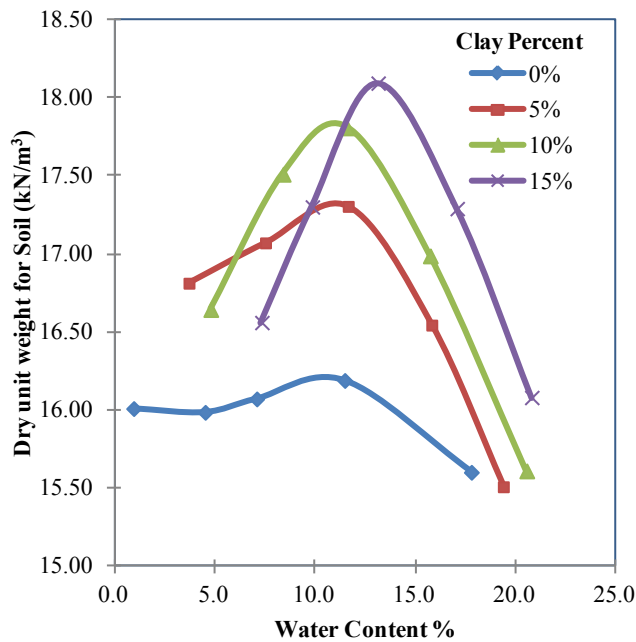


Fig. 3 Compaction curves for sand-clay mixtures with different clay contents

2.3 Sample Preparation

Samples of Al-Qatif expansive clay obtained from the field were air dried, pulverized and sieved using sieve No. 40. The sand and clay content were mixed thoroughly and then optimum water content corresponding to each mix was added and stored in plastic bags for 24 hours to mellow. Compacted samples of sand- AlQatif clay mixtures were prepared for the determination of the soil water characteristic curves. Samples were statically compacted in a stainless steel ring to maximum unit weight corresponding to that presented in Fig. 3. All samples were 50 mm in diameter and 20 mm thick.

3 EXPERIMENTAL PROGRAM

2.2 Soil water characteristic Curves

The drying curve of the SWCCs of sand- AlQatif clay mixtures were evaluated using pressure plate test and hanging column technique. Pressure plate extraction apparatus is based on the principle of axis translation technique [18] and was used to apply suction ranging from 5 kPa to 1500 kPa. The hanging column technique was used to evaluate the SWCC for the suction levels less than 5 kPa. All tests were performed according to ASTM D6836 [19].

For the pressure plate extractor test, samples were placed in confined compartment with a ceramic disc base of air entry value of 5 or 15 bars. Prior to the test, the ceramic disk was saturated by soaking it in water of 24 hours. Suction on samples was applied in increments and water exiting from the compartment below the ceramic disc was monitored. Equilibrium under each suction level was assumed to be attained when no water egress was observed. After equilibrium under each suction level, the amount of water lost from tests samples was determined by weighing the samples

using a balance with a 0.0001 resolution. At the end of the test, the final water content of the sample was calculated using gravimetric methods. The water content at each suction level was back-calculated based on the final water content and the amount of water loss recorded at each suction level. The hanging column apparatus comprise of a glass Buchner funnel with a porous plate and two graduated burette system connected to the outflow end of the funnel as shown in Fig. 4. The purpose of these burettes is to apply suction and measure water outflow during the test. The "suction application" burette contains a valve to seal the top of burette from the atmosphere. Suction was applied by raising the Buchner funnel such that base of the sample is above the water level in the suction application burette when the valve is closed. Suction is calculated as the difference between water level multiplied by unit weight of water. The "water outflow" burette was used to monitor and record the amount of water expelled or entered during the test. Equilibrium was attained when no change in water level was observed. Water content at each suction level was calculated based on final water content of sample and amount of water expelled at each suction level.

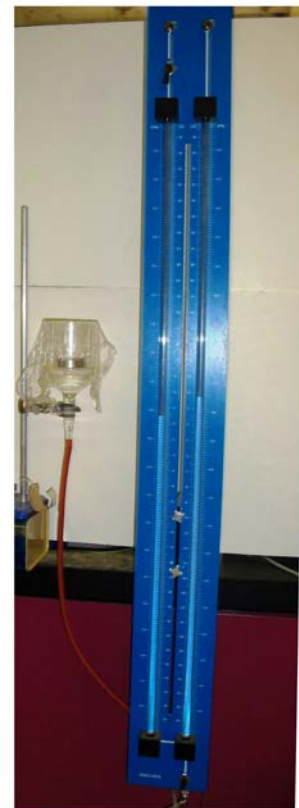


Fig. 4 Hanging column apparatus

4 RESULTS AND DISCUSSIONS

The SWCCs for sand-expansive clay mixtures under different clay contents are depicted in Fig. 5. In Fig. 5, a gradual transition from a unimodal SWCC to a bimodal SWCC was observed as clay content increases. The unimodal SWCC is

characterized by having two bends in the curve defining the air entry value and residual water content (Fig. 5). The air entry value is defined as the matric suction above which air commence to enter the soil pores. The residual water content is defined as the water content beyond which no significant decrease in water content occurs. The bimodal SWCC is characterized by having four distinct bendings: two air entry values and two residual water contents. For clay content equal to or less than 5 percent, the SWCC show a unimodal form of SWCC. With the increase of clay content greater than 5%, the SWCC show a bimodal form.

It is further observed from Fig. 5 that the residual water content increases with the increase of the clay content. In addition, the air entry value increases with the increase in clay content. These observations are attributed to the presence of smaller pore size developed as a result of clay particles filling the voids between sand particles.

Bimodal SWCC are generally observed for gap-grade grain size distribution soils [20] as well as soils that includes two levels of pore sizes defined as macropores and micropores [21]. Therefore, it can be inferred that the increase of clay content resulted in the formation of mesopores/micropores within the compacted sand-clay mixtures. The portion of the soil water characteristic curves that represent macropore size ranges from matric suction 0.1 to 100 kPa. Whereas, the portion of the SWCC representing mesopores/micropore sizes lies between matric suction 200 and 1500 kPa.

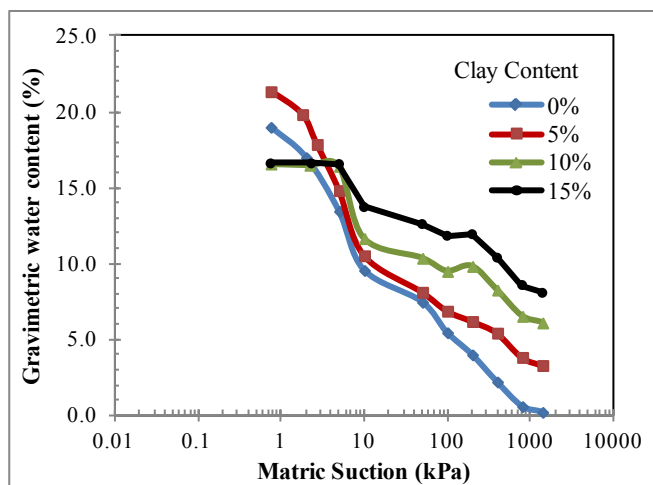


Fig. 5 Soil water characteristic curves of sand Clay Mixtures

5 SUMMARY AND CONCLUSIONS

In this study, the effect of clay content on the soil water characteristic curves of compacted sand-AlQatif clay mixtures were evaluated. Clay contents considered include 0%, 5%, 10%, 15%. Results from this study indicated that, as the clay content increased, the shape of the SWCC of sand-clay mixtures transforms from a unimodal form to a bimodal form.

Furthermore, the residual water content was observed to increase with increase in clay content signifying increase in

water retention capacity increases with increase in clay content.

The bimodal form of the SWCC indicates the presence of two levels of pore sizes; namely macropores and mesopores/micropores. For 10% and 15% clay content, the macropores are considered the dominant pore size covering a broad range of the SWCC from 0.1 kPa to 100 kPa. Therefore, it is inferred that the SWCC of compacted sand-clay mixtures are strongly related to the texture and pore size distribution of the sand-clay mixture which in turn, has a significant impact on its hydraulic characteristics.

6 ACKNOWLEDGMENT

This paper is a part of a research project supported through NPST program by King Saud University, Project No. ENV 1183. The authors thank the staff of Bugshan Research Chair in Expansive Soils and especially Eng. Abdulla Shaker for his works in constructing the soil compaction curves for sand clay mixtures.

7 REFERENCES

- [1] Cho, WJ, Lee, JO, and Kang, CH, "Hydraulic conductivity of compacted soil-bentonite mixture for a liner material in landfill facilities," Korea Society of Environmental Engineers, Environ.Eng. Res. Vol. 7. No. 3, 2002, pp. 121-127.
- [2] Komine, H, "Simplified evaluation on hydraulic conductivities of sand-bentonite mixture backfill," Applied Clay Science, vol. 26, 2004, pp. 13- 19
- [3] Chalermyanont, T. and Arrykul, S, "Compacted sand-bentonite mixtures for hydraulic containment liners," J. Sci. Technololgy, Vol. 27, No.2, Mar - Apr 2005.
- [4] Ameta, NK and Abhay, S W, "Effect of bentonite on permeability of dune sand," EJGE, Vol 13, (2008).
- [5] Akgün, H, "Geotechnical characterization and performance assessment of bentonite/sand mixtures for underground waste repository sealing," Applied Clay Science, Vol. 49, 2010, pp. 394-399.
- [6] Gueddouda, MK, Lamara, MNA, and Taibi, S, "Hydraulic conductivity and shear strength of compacted dune sand - bentonite mixtures," ICCBT, 2008.
- [7] Ruwaih, IA, "Experiences with Expansive Soils in Saudi Arabia," in Proc. 6th Int. Conf. on Expansive Soils, New Delhi, India, 1987, pp.317-322.
- [8] Azam, S, "Influence of mineralogy on swelling and consolidation of soils in eastern Saudi Arabia," Canadian Geotechnical Journal, Vol.40, No. 5, 2003, pp. 964-975.
- [9] Montanez, JEC. "Suction and volume changes of compacted sand-bentonite mixtures," Ph.D. Dissertation, Imperial College of Science, 2002
- [10] Agus, SS and Schanz, T, "wetting, drying, suction characteristic curves of bentonite sand," Proceedings of the Fourth International Conference on Unsaturated Soils, April 2-6, 2006, Carefree, AZ, pp. 1405-1414.

- [11] Pei-yong, L and Qing, Y, "Test study on soil-water characteristic curve of bentonite-sand mixtures," EJGE, Vol. 14, 2009, pp. 1-8
- [12] Sun, D et al, "Hydro-mechanical behaviors of highly compacted sand-bentonite mixture," Journal of Rock Mechanics and Geotechnical Engineering, Vol. 2, No. 1, 2010, pp. 79–85.
- [13] Stoicescu, J T, " Soil water characteristics and pore size distribution of a sand-bentonite mixture," In Proc. 49th Canadian Geotechnical Conference, St. John's Newfoundland, September 23-25, Vol 2, 1996, pp. 721-728.
- [14] Stoicescu, JT et al., "Soil water characteristics of sand-bentonite mixtures used for liners and covers," Second International Conference of Unsaturated Soils, Beijing, China, August 27-30, Vol 1, 1998, pp. 143-148.
- [15] Abduljuawad, SN, Hameed, RA, Al-Sulaimani, GJ, Basunbal, IA, Safar, MM, "Expansive soils in Eastern Province of Saudi Arabia," Proceedings of 7th International Conference on Expansive Soils, Dallas, TX, vol. 1, 1992, pp. 426-431.
- [16] Azam, S, Abduljauwad, SN, Al-Shayea, NA, Al-Amoudi, OSB, "Expansive characteristics of gypsiferous/anhydritic formations," Engineering Geology, Vol. 51, 1998, pp. 89-107.
- [17] ASTM D698 - 02 Standard Test Methods Standard Test Methods for Laboratory Compaction Characteristics of Soil Using Standard Effort (12 400 ft lbf/ft³ (600 kN m/m³), Vol. 15.09, Annual book of ASTM Standards, West Conshohocken, PA.
- [18] Hilf, JW, "An investigation of pore-water pressure in compacted cohesive soils," Ph.D. Thesis, Tech. Memo No. 654, U.S. Dept. of interior Bureau of Reclamation, Design and Construction Div., Denver, Colorado, 1956
- [19] ASTM D6836 - 02 Standard Test Methods for Determination of the Soil Water Characteristic Curve for Desorption Using a Hanging Column, Pressure Extractor, Chilled Mirror Hygrometer, and/or Centrifuge, Vol. 15.09, Annual book of ASTM Standards, West Conshohocken, PA.
- [20] Durner, W, "Hydraulic conductivity estimation for soils with heterogeneous Pore Structure," Water Resources Research, Vol. 30, No. 2, 1994, pp. 211-223.
- [21] Burger, CA and Shackelford, CD, "Soil-Water Characteristic Curves And Dual Porosity of Sand–Diatomaceous Earth Mixtures. Journal Of Geotechnical And Geoenvironmental Engineering, Vol. 127 No. 9, September 2001, pp. 790-800

Coastal soils improvement

Mohammad reza Atrchian¹, Morteza Ala², Amin Naeimabadi³
Islamic Azad University Of Zanzan, Iran

ABSTRACT

with an ever-increasing population growth, the development of industries and the deficit problem of land for establishing the required constructions have been caused that people use the lands with lower engineering qualification. But for establishing a suitable construction the qualification of soil should be improved by a technique respect to engineering parameters. In this condition it has a suitable operation in effect of involving forces. Soil improvement techniques can be classified in different points of view. These methods are divided in to three general groups: Compaction, Solidification and Stabilization. With regard to this point that coastal soils have the capability of liquefaction and they are clayey soils, in this article, first of all we will inspect these soils and the problems that they are caused and then their characteristics improvement techniques based on geotechnical methods such as placing trenches for limited land, sand wills for liquefiable, saturated and clayey soil ;stone columns for clayey soil that have bearing capacity problem and dual purpose micro pile and compaction will be surveyed. Outdoor investigations and their findings show that the soils with SPT lower than 12 in each depth are problematic surely and should improved.

Keywords: soils improvement, liquefaction, stone column, micropiles, compaction

1. INTRODUCTION

Soil structure (construction) can be considered as an ideal and suitable place by engineers to have 4 features. 1. Having enough shear strength and bearing capacity of the soil. 2. having low degree of immediate settlement and consolidation caused by the load. 3. Acceptable changes of volume expansion of the soil (for instance, swelling caused by unloading or humidity rise in clay soil) or volume contraction of the soil (caused by decreased humidity) so that the construction effacing won't be conflict. 4. Not having any serious problem in construction place.

Houseman (1990) has basically classified soil improvement goals as the following.

Soil bearing capacity increase, soil settlement decrease, void decrease and soil density increase, regularizing of the features of changeable materials. Improvement requires not only

consideration of pre-acting construction but also of reword and the meantime construction. There are some major methods like compression and micropile, but according to the modern technology, new ways of biotechnology has been founded that can prepare the life condition for underground animate to fill up the holes of the sand that prevents water pressure while earthquake and finally there won't be soil liquefaction. Or for the soil dams the haies can be filled by bacteria injection and rising them instead of providing the required amount of water at the centre.

2-Based on boring log there are two kinds of problematic soil

One kind is soft clay soils and the other kind is susceptible liquefaction soils. In deeper areas there are smaller sands that are susceptible for liquefaction, but coast line sands are more average & bigger. The more stickiness the more resistance of the sand against liquefaction.

2-1. Liquefaction is a phenomenon that is resulted of a decrease in hardness & resistance of the soil caused by earthquake and quick loading. This phenomenon and its consequences mode huge damages in recent years around the world. Which usually happens in saturated soils. Existing water in soil particles gets soil particles under pressure and this event causes strong compression of the soil. Before the earthquake water pressure in not considerable, but after starting it water pressure increases that the result is soil particle movement. However the mentioned factor can be reason for the liquefaction phenomenon. There are also ether reasons like constructing activating such as explosion and basically any changes in the ground by loading and unloading.

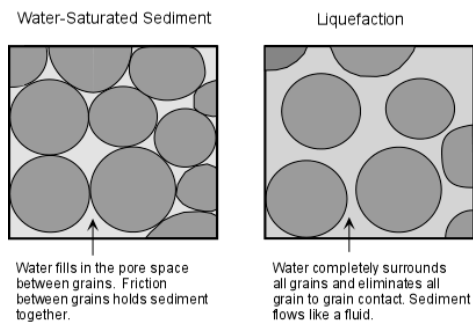


Fig 1 : water ,saturated sediment – liquefaction

Liquefaction consequences: boiling of sand ground settlement, decrease in soil resistance and strength for keeping the buildings and bridges up, side ground expansion .



Fig 2 : Liquefaction damage

2-2. According to the experiments on the coastal soil consequences (13, 14 and 15 SPT) there is a doubt of the being liquefiable soil, but SPT lower than 12 in any depth will certainly be problematic. Capable liquefaction soil can be built by silt rather than fine grained sand but remember that the mixture of silt an fine grained sands is really qualified for liquefaction that the cleaner and through water path.

3-geotechnical improvement method based on the coast line areas:

3-1: trenches: in small land where we have just 2 or 3 meter soil for improving, if we want to protect our own building, well do trenches around the land. For a 30 cm thick sealing in the case of using bentonite with 4% cement, there will be a time of 3years for water to pass just 1cm. so for passing about 30 cm around 90 years will be needed.

3-2. Compaction methods:

In rural areas and around the built building we can't roller on the other hand the action of compaction can't be used in coastal area sands more than 30 - 40 cm. dynamic compaction method will be suitable for liquefiable soil and loose grain that have the problem of bearing capacity and fine grain soil. Disadvantages of this method are noise pollution not being able to use in residential areas and 30 - 40 m vibration produced by it.



Fig 3 : compaction methods

3-3. Stone Column method: this method can be used to improve soil bearing capacity and decrease the basement

settlement which is based on the 45 – 35 percent changes of the compaction of unqualified soil by digging wills with specific thickness, depth and distance of compaction in vertical Columns. Then the materials will be spread in several layers into the digger will and vibrate and compact by special machines. The most significant use of vertical Columns is in soft clay that bearing issue appears. While liquefiable soils don't have this problem.

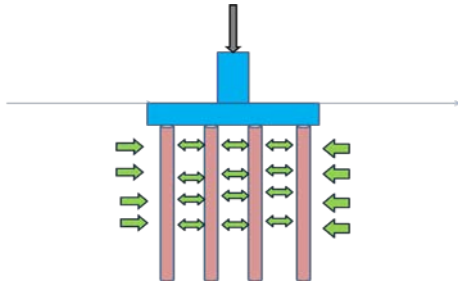


Fig 4 : How Stress distribution

3-4. Soil wills (pressure-breaking wills): the method will work for liquefiable and soft clay soils. In this procedure at first wedding, if underground existing water was problem well cover the soil after that the inside must be filled with sand, while filling up the cover need to break until the drainage be done well. After digging for the wills we put layers on it. The efficiency of this way against earthquake will be remarkable; its action is easy and can be done in any depth. Like filter designing method in liquefiable soils that has the role of pressure breaking of water. The between centers should be 1.5–2 meter. With triangle like models. The distance is more important rather than the thickness.



Fig 5 : With triangle like models

3-5. Grouting method by micropile:

This method should be done before the foundation stage. Micropile is considered to do two factions, for liquefaction

decrease and ground bearing strengthening in coastal areas. If we have used micro pile in loose layer, their ending must reach to the resistant layer.

According to the received results which are analyses in an article by sarang sirafian. About sand soil the following conclusions can be achieved.

1. In grouting foundation became of the hitting empty metal frame and also under pressure grout, soil parameters have been improved and the weal sand level will change to a suitable and reliable level for bearing of the loaded and accrued settlement.

2. Considering of some factor such as material expenses, human force and security beside it, high speed of practical operation, sumultaniouy actions of different working groups of the project and reasonable required machines, using of micropile foundations in constructing of 15 or less floors would be logical and better economically.

3. High buildings constructing, buildings more than 15 floors in sand soils due to construction heaviness, micropile distribution under level, the foundation will become more compacted and the distances in micropile will decrease and then individual micropile act like a group micropile finally this procedure will decrease micropile bearing capacity and won't be reasonable.

Conclusions:

1. In some cases soil improvement is the most reasonable method for solving geotechnical matters.

2. There's usually or doubt for being liquefiable SPT of 13 – 14 and 15, but lower than 12 in any depth soil improvement is required.

3. For soil improvement of liquefiable soil, methods of compaction sands will and micropile are being used.

4. We use stone Columns and sand wills methods for soft clay soil.

6. REFERENCES

1. Design and construction of Stone- Colum (2009), dr mahmood ghazavi,iran .
2. FHWA,(2000) " micropile design and construction guidelines", US Department of Transportation, Federal Highway Administration, NO. - SA - 97 - 070, June,
3. Hausmann, M.R. (1990), "Engineering Principle of Ground Modifications, Mc-GrawHill Publishing Company, New York.
- 4.barksdale, R.D ,and bachus, R.C, design and construction of stone colum vol FHWA /RD-DECEMBER-1983

A Hybrid Intelligent System of Fuzzy C-Mean Clustering and Neural Networks to Predict the Compaction Characteristics of Fine Grained Soils

Iman Ashayeri, Mahnoosh Biglari
Civil Engineering Dept., School of Engineering, Razi University, Iran

ABSTRACT

One of the most usual processes in geotechnical applications is the compaction of loose fine grained soils to the desired density. The results of compaction tests on about 220 plastic soils are collected for this study. The liquid limit and plasticity index of the soils range from 15.5% and 2.1% to 170% and 110% respectively. The aim of this study is to present a flexible hybrid intelligent system of fuzzy C-mean clustering and neural networks which works with this database to predict the optimum water content and maximum dry unit weight of soils under standard Proctor effort. The system does not use a fixed amount of data to train the neural network, but uses the fuzzy C-mean clustering method to determine the most familiar cases with the unknown data for training the neural network. While, each input question is treated individually a more reliable measure of the performance of the system is obtained.

Keywords: Fuzzy C-mean, Neural Networks, Soil Compaction, Fine Grained Soils

1. INTRODUCTION

In the recent years several investigations were focused on the applications of intelligent systems in the field of soil mechanics and geotechnical engineering. Among them the applications of artificial neural networks on the modeling and prediction of soil behavior or characteristic indices are numerous. A comprehensive overview on the recent advances for artificial neural systems in geotechnical engineering applications can be found in [1]. Most of these applications are based on the available experimental or field observations and measurements. The complex, irregular and nonlinear behavior of soil is aimed to be dug out of available data. Although in the most of the applications the performance of the system was satisfactory, some important questions still stay and should be considered in future investigations.

What is the appropriate set of the data to be trained?

How reliable is the system? And how different is the reliability of the system for different inputs?

One of the most usual processes in geotechnical applications is the compaction of loose fine grained soils to the desired density to pass criteria of shear strength, permeability and etc. The compaction characteristics of fine grained soils are known by the compaction curves from standard and modified Proctor tests as the optimum water content and the maximum dry unit weight. The results of compaction tests on about 220 plastic soils are collected from literature for this study. The aim of this study is to present a flexible hybrid intelligent system of fuzzy C-mean clustering and neural networks which works with this database to predict the optimum water content and maximum dry unit weight of soils under standard Proctor effort. The system does not use a fixed amount of data to train the neural network, but uses the fuzzy C-mean clustering method to determine the most familiar cases with the unknown data for training the neural network. In other

words, not an identical neural network is trained and used to predict the optimum water content or maximum dry unit weight of questioned inputs. While, each input question is treated individually and the most related known patterns are used to answer it, a more reliable measure of the performance and generalization power of the system is obtained.

2. BACKGROUND OF THE STUDY

Due to the importance of the compaction characteristics of fine grained soils in many geotechnical engineering problems several investigators have attempted to model the optimum water content and the maximum dry unit weight of the soil at different compaction efforts. Among them [2]-[7] can be categorized in traditional mathematical methods used to predict optimum water content and/or maximum dry unit weight in terms of index properties and compaction effort. In addition to the traditional methods some investigators utilized artificial neural networks to predict the compaction characteristics [8]-[12]. Although the approaches differ in each study they resulted in acceptable performance of the system within the range of the data used for correlating the empirical equations or training the artificial neural networks.

Furthermore, Shahin et al. [13] proposed using fuzzy C-mean clustering in selection of sets of data to train, validate and test artificial neural networks. Fuzzy C-mean (FCM) clustering uses fuzzy logic in clustering data so that each data pattern belongs to each cluster with a membership value. The method was first developed by Dunn [14] and improved by Bezdek [15]. The FCM clustering gives back the membership value of each data pattern to each cluster as well as the centers for the clusters.

3. CHARACTERISTICS OF DATABASE

The database required for this study was collected from high quality research articles previously published by several investigators across the globe. Table 1 presents the

range of index properties of the soils available in this database.

Table 1. Range of index properties of soils in database

Index	CSF (%)	FC (%)	Gs	LL (%)	PI (%)
Min	2	18.6	2.46	15.5	2.1
Max	98	100	2.90	170	110
CSF: clay size fraction, FC: fine contents					

Fig. 1 plots the plasticity index of the soils versus their liquid limits in the Casagrande chart. Furthermore, the values of optimum water content (OWC), and maximum dry unit weight (MDUW), of the soils at standard Proctor (SP) compaction effort are plotted against liquid limit as in Figs. 2 and 3 respectively. It is clear from the Table 1 and Figs. 1 to 3 that the variety of data range plus the inherent complex influence of the indices on OWC and MDUW of soils will make it inaccurate to postulate a unique model for prediction of OWC and MDUW, which works in the whole data range in the database. One may ask the first question mentioned in the introduction of what the most similar data patterns are to specific unknown? Furthermore, the accuracy and reliability of a unique model trained for all data range in the database is variable with respect to the input record. Therefore, one concludes that if only the most similar patterns to the unknown record are trained to the model then the answer of the trained model would be more reliable, which addresses the second question mentioned in the introduction. These two main concepts are dealt with the selection of most similar patterns to the input question using FCM. The performance of this hybrid application of FCM and ANN is validated by two question records in the following sections.

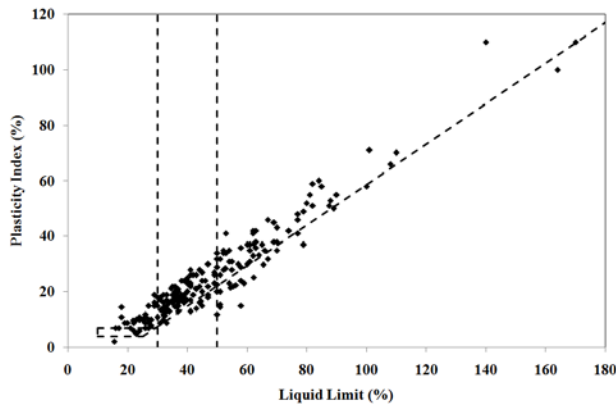


Fig. 1 LL and PI of soils in the database

4. VALIDATION OF THE PERFORMANCE OF FCM AND ANN COMBINATION

Two question records of low plastic (LPS), and high plastic (HPS), soils are selected to validate the application of the hybrid FCM and ANN model. Table 2 summarizes the index properties as well as OWC and MDUW of them.

Table 2. Index and compaction characteristics of validation set

Index	Silt (%)	CSF (%)	Gs	LL (%)	PI (%)	OWC (%)	MDUW (KN/m ³)
LPS	60	18	2.65	29	12	15.4	17.4
HPS	45	25	2.49	52	31	19.3	16.6

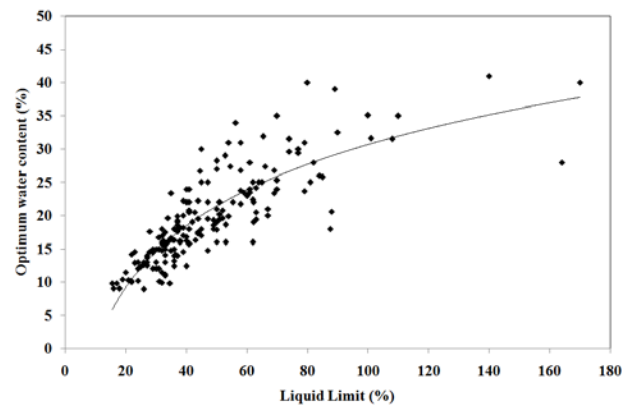


Fig. 2 OWC vs. LL of soils in database

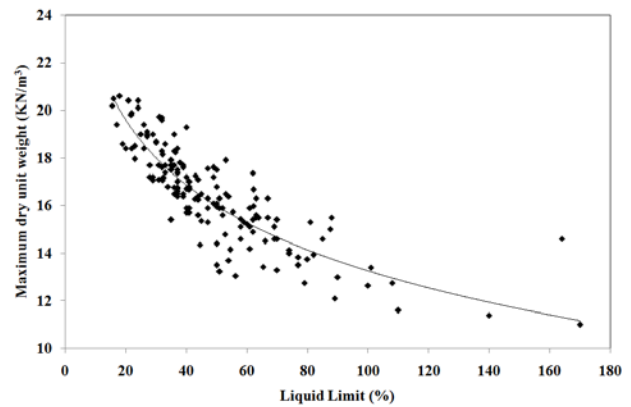


Fig. 2 MDUW vs. LL of soils in database

To seek simplicity and avoid inclusion of the effects of the ANN architecture on their performance, the architecture of the ANNs are kept similar that is a single hidden layer feedforward error backpropagation network with 6 input neurons corresponding to the 6 index parameters of Silt content, CSF, FC, Gs, LL and PI, with two neurons in the only intermediate layer and finally one neuron for the output, which is OWC or MDUW.

With respect to the contribution of A. Casagrande on the classification of plastic soils based of their LL and PI, these two variables are used to classify the patterns in the database by FCM. Each question record is classified with the whole database several times considering the number of clusters is variable from 3 to 6. A computer program was prepared in the MatLab environment to give the training set of ANN corresponding to each question record. The ANN is trained and the performance of the training phase is evaluated by the average of training absolute error (ATerr), as well as the standard deviation of the training absolute error (SDTErr). Afterward, the question record is recalled and the predicted value by the model is compared by the actual output quantity given as in Table 2 by calculating the absolute error. This process is repeated for each question record at the other number of clusters. For instance, Fig. 4 presents the selected training set for the LPS when the number of clusters is 5 and Fig. 5 presents the selected training set for HPS when the number of clusters is 4 in the Casagrande chart with the position of the LPS and HPS as well as the centers of the clusters. Tables 3 and 4 summarize the statistical quantities identified above for LPS and HPS at all combination of cases respectively.

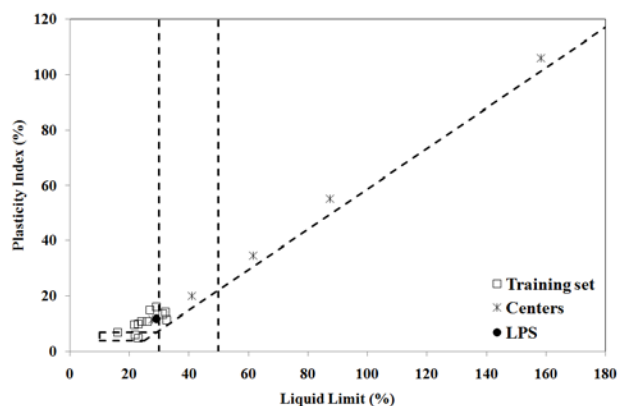


Fig. 4 Selected training set for LPS with 5 clusters

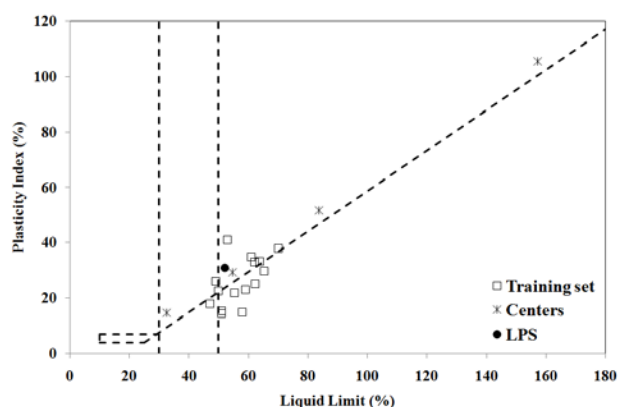


Fig. 5 Selected training set for HPS with 4 clusters

Table 3. Summary of statistical quantities of models for LPS

Model	No. of clusters	No. of training patterns	ATerr (%)	SDTerr (%)	MMV of LPS	Err LPS (%)
OWC	3	29	9.6	8.1	0.97	6.8
	4	25	9.5	8.3	0.97	7.2
	5	12	6.4	3.6	0.99	1.8
	6	24	9.3	7.3	0.79	4.2
MDUW	3	30	3.8	2.4	0.97	2.7
	4	24	2.3	1.7	0.975	2.2
	5	12	1.7	0.9	0.98	0.2
	6	23	1.8	1.2	0.74	0.5

Table 4. Summary of statistical quantities of models for HPS

Model	No. of clusters	No. of training patterns	ATerr (%)	SDTerr (%)	MMV of LPS	Err LPS (%)
OWC	3	17	10.0	7.0	0.84	26.3
	4	15	5.8	3.9	0.98	2.5
	5	19	6.5	4.9	0.63	17.2
MDUW	3	45	3.9	2.4	0.65	4.1
	4	15	1.7	1.8	0.98	3.5
	5	19	2.7	2.2	0.59	6.0
	6	18	2.6	2.0	0.80	7.4

In addition to statistical quantities for training and testing of the neural networks the maximum membership value (MMV), of the question records (LPS or HPS) are given in Tables 3 and 4 for each case. As the number of the clusters increases the higher MMV indicates that the question record is closer to the center of the cluster. The analysis on the results is presented in the following section.

5. CONCLUDING REMARKS

The performance of the ANN models at training phase is evaluated by the ATerr and SDterr values so that the smaller values are more preferred. It can be found from the Tables 3 and 4 that the smaller values of ATerr and SDterr correspond to the cases with the largest MMV. Looking to the number of training patterns reveals that in all cases this higher performance level for the ANN models was achieved by smaller size of the training set. In other words, the corresponding training set with smaller ATerr and SDterr contains the most correlated patterns in the database required to train the ANN.

One measure for the reliability of the performance of the ANN is the smaller error at testing set. However, this is not known when actually an unknown record is answered by the model. This shortcoming can be fulfilled by a quantity which expresses the correlation between the training set and the unknown record in terms of their known input parameters. In this study this correlation is expressed by the MMV. Comparing the MMV and Err of each ANN model for question records in Tables 3 and 4 reveal that the smaller error in predicted values of OWC and MDUW also corresponds to the largest MMV. It can be concluded that the combination of the statistical measures from training phase with the quantity obtained from FCM analysis can present a suitable criterion of the performance and reliability of the ANN. It should be noted that analysis performed in this study reveals that increasing the number of training patterns does not increase the performance and reliability of the system. However, the more appropriate and coherent training set with the question record results in more reliable answers and this study shows that such coherency and appropriateness can be expressed and determined by Fuzzy C-mean clustering technique.

6. ACKNOWLEDGMENT

The authors wish to acknowledge the support of Razi University by funding this research project.

7. REFERENCES

- [1] Shahin M A, Jaksa M B, and Maier H R, "Recent Advances and Future Challenges for Artificial Neural Systems in Geotechnical Engineering Applications" *Advances in Artificial Neural Systems*, 2009, doi:10.1155/2009/308239
- [2] Jumikis A, "Geology and Soils of the Newark (N.J.) Metropolitan Area" *J. Soil Mech. And Found. Div.*, vol. 94, 1958.
- [3] Hilf J, "A Rapid Method of Construction Control for Embankments of Cohesive Soil" *Engrg Monograph*, vol. 26, 1956.
- [4] Ring G, Sallberg J, and Collins W, "Correlation of Compaction and Classification Test Data" *Hwy. Res. Bull.* 1962, pp. 55-75.
- [5] Ramiah B, Viswanath V, and Krishnamurthy H, "Interrelationship of Compaction and Index Properties" in *Proc. 2nd Southeast Asian Conf. on Soil Engrg.*, 1970, pp. 577-587.

- [6] Wang M, and Huang C, "Soil Compaction and Permeability Prediction Models" J. Envir. Engrg., vol. 110, 1984, pp. 1063-1083.
- [7] Blotz LR, Benson CH, and Boutwell GP, "Estimating Optimum Water Content and Maximum dry Unit Weight for Compacted Clays" J. Geotech. Geoenvir. Engrg., vol. 124, 1998, pp. 907-912.
- [8] Basheer IA, "Empirical Modeling of the Compaction Curve of Cohesive Soils" Can. Geotech. J., vol. 38, 2001, pp. 29-45.
- [9] Yasrebi SS, and Ashayeri I, "Predicting Optimum Water Content and Dry Unit Weight of Clay Soils Using Neural Networks" in Proc. 56th Canadian Geotechnical Conference, 2003.
- [10] Sinha SK, and Wang MC, "Artificial Neural Network Prediction Models for Soil Compaction and Permeability", Geotechnical and Geological Engineering, vol. 26, 2008, pp. 47-64.
- [11] Adel-Rahman AH, "Predicting Compaction of Cohesionless Soils Using ANN", Ground Improvement, vol. 161, 2008, pp. 3-8.
- [12] Sivrikaya O, Soykan TY, "Estimation of Compaction Parameters of Fine-grained Soils in terms of Compaction Energy Using Artificial Neural Networks", Int. J. Numer. Anal. Meth. Geomech., vol. 35, Dec. 2011, pp. 1830-1841.
- [13] Shahin MA, Maier HR, and Jaksa MB, "Data Division for Developing Neural Networks Applied to geotechnical Engineering", J. Computing in Civil Engrg, vol. 18, 2004, pp. 105-114.
- [14] Dunn JC, "A Fuzzy relative of the ISODATA Process and Its Use in Detecting Compact Well-separated Clusters", J. of Cybernatics, vol. 3, 1973, pp. 32-57.
- [15] Bezdek JC, "Pattern Recognition with Fuzzy Objective Function Algorithms", Plenum Press, 1981.

Equivalent Linear Seismic Ground Response Analysis of Unsaturated Soil Deposits

Mahnoosh Biglari, Iman Ashayeri
Civil Engineering Dept., School of Engineering, Razi University, Iran

ABSTRACT

Seismic ground motion is profoundly affected by geometrical and mechanical properties of soil deposits overlaying bedrock. Seismic ground response of saturated soil deposits was studied in literature by applying the effects of soil stress state and index properties on the strain-dependent normalized shear modulus reduction and damping ratio curves in an equivalent linear analysis. Recent experimental investigations revealed that, G_0 , G/G_0 , and D of unsaturated soils are influenced by stress state as well as suction. This study presents the results of linear and equivalent linear seismic ground response analysis of unsaturated soil deposits with considering suction effects on G/G_0 and D curves. Analysis was done by the computer program EERA for two sets of soil profiles, which include in saturated, constant and linearly variable suction deposits. Results show that natural frequency of the soil profile increases as the suction increases.

Keywords: soil, soil dynamics, equivalent-linear, seismic ground response analysis

1. INTRODUCTION

The local soil conditions have a profound influence on the ground response during earthquakes, which is modelled through direct non-linear elasto-plastic [1] or equivalent-linear elastic ground response analysis [2] and [3]. In spite of its theoretical shortcomings, the latter has become the major tool in practical engineering applications due to its simplicity. The equivalent-linear analysis consists of modifying normalized shear modulus G/G_0 , and damping ratio D , of a visco-elastic soil model with shear strain level, γ . Regularly, the strain-dependent normalized shear modulus reduction ($G/G_0-\gamma$), damping ratio ($D-\gamma$) curves are obtained by laboratory tests. However, mathematical functions were presented for ($G/G_0-\gamma$) and ($D-\gamma$) in terms of stress state and index properties of saturated soils based on enormous experiments by various investigators [4]-[6].

Experimental investigations revealed that, the initial shear modulus G_0 , of unsaturated soils is influenced by stress state as well as suction [7]-[12]. Furthermore, recent investigation on the measurements of shear modulus of an unsaturated soil at wider shear strain range by suction-controlled cyclic tri-axial apparatus show that $G-\gamma$ and $D-\gamma$ curves are influenced by the suction levels too [13]. On the basis of this experimental evidence, Biglari and Ashayeri [14] modified the empirical equation proposed by [6] for $G/G_0-\gamma$ and $D-\gamma$ to take into the account the influence of the suction level as well as stress state and index properties for unsaturated soils. d'Onza et al. [15] investigated the effects of unsaturated soil suction on the seismic ground response by means of linear analysis which takes into the account the influence of suction on the shear wave velocity or initial shear modulus of the unsaturated soil deposits. They have presented the results in

terms of amplification ratio of surface motion in the frequency domain and concluded that the natural frequency of soil deposit significantly increases with suction increase and the maximum amplification ratio is substantially reduced. This study presents the results of linear and one dimensional equivalent linear seismic ground response analysis of unsaturated soil deposit not only considering the effects of suction variation on the shear wave velocity (or G_0), but also taking into the account the dependency of $G/G_0-\gamma$ and $D-\gamma$ on the suction level based on the developed empirical model for $G-\gamma$ and $D-\gamma$ [14]. Seismic ground response analysis was done with the computer program "Equivalent-linear Earthquake site Response Analyses" (EERA) [3], for five soil suction profiles and three time histories of acceleration. The results are discussed in terms of comparison between the acceleration time history at surface and bedrock, the amplification ratio and natural frequency of soil deposits as well as spectral acceleration of the ground motion at surface and bedrock.

2. SOIL PROFILES

Five soil profiles were considered in this study within two sets of analysis. The first set compares two soil profiles P1 and P2 of lean clay deposit 24 meters deep overlaying the bedrock. Table 1 presents the variation of suction, shear wave velocity, and total unit weight of different layers of the soil profiles P1 and P2. Soil profile P1 is formed of a two meters of saturated soil layer over the bedrock that is overlaid by 22 meters of unsaturated soil with variable suctions. The unsaturated soil deposit of P1 was divided into 6 layers of constant suction varying from zero to 250 kPa. On the other hand, soil profile P2 is formed of 24 meters of the saturated soil deposit overlaying the bedrock that is divided into 7 layers of variable shear wave velocity and unit weight.

The second set of analysis compares three soil profiles P3, P4,

and P5 of the same deposit 24 meters deep overlaying the bedrock. Table 2 presents the variation of suction, shear wave velocity, and total unit weight of the different layers of the soil profiles P3, P4, and P5. Soil profile P3 is formed of 24 meters of the saturated soil deposit overlaying the bedrock that is divided into 6 layers with variable shear wave velocity and unit weight. Soil profile P4 is formed of 24 meters of the unsaturated soil deposit with constant suction of 150 kPa overlaying the bedrock and is divided into 6 layers with variable shear wave velocity and unit weight. Soil profile P5 is formed of 24 meters of the unsaturated soil deposit with constant suction of 300 kPa overlaying the bedrock and again is divided into 6 layers with variable shear wave velocity and unit weight.

Table 1. Description of soil profiles of the first set of analysis

Layer	Thickness (m)	Profile					
		P1			P2		
		s^1 (kPa)	V_s^2 (m/s)	γ^3 (KN/m ³)	s (kPa)	V_s (m/s)	γ (KN/m ³)
1	4	250	159	13.43	0	125	19.30
2	4	200	159	13.63	0	125	19.30
3	4	150	170	14.18	0	130	19.38
4	4	100	187	15.15	0	142	19.57
5	4	50	201	16.19	0	154	19.61
6	2	0	195	19.86	0	164	19.65
7	2	0	200	19.95	0	172	19.77
8	bedrock		1219	22.02		1219	22.02

¹Suction, ²Shear wave velocity, ³Unit weight

Table 2. Description of soil profiles of the second set of analysis

Layer	Thickness (m)	Profile					
		P3 (s=0)		P4 (s=150)		P5 (s=300)	
		V_s (m/s)	γ (KN/m ³)	V_s (m/s)	γ (KN/m ³)	V_s (m/s)	γ (KN/m ³)
1	4	125	19.30	159	13.70	176	13.50
2	4	125	19.30	159	13.70	176	13.50
3	4	130	19.38	170	14.20	185	13.80
4	4	142	19.57	188	14.60	203	14.30
5	4	154	19.61	203	15.10	219	14.50
6	4	168	19.71	219	15.30	233	14.70
7	bed	1219	22.02	1219	22.02	1219	22.02

The shear wave velocities of the soil layers of all the five profiles were calculated from the model for initial shear modulus of unsaturated soils calibrated for the current material, which was presented by [11] and [12].

3. MODULUS REDUCTION AND DAMPING CURVES

In order to generate the modulus reduction and damping curves, the empirical models presented by [14] were used with considering the soil plasticity index ($PI = 12\%$), and appropriate suction and confining pressure of each layer of the soil profiles. Figs. 1 to 5 present the generated G/G_0 - γ and D - γ for layers of soil profiles P1 to P5, respectively.

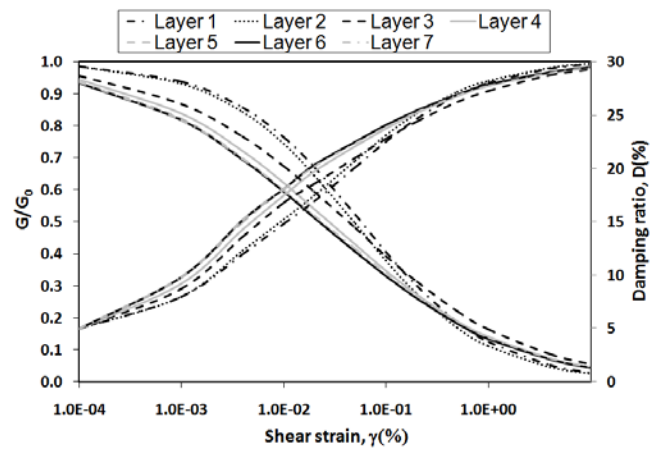


Fig. 1 G/G_0 - γ and D - γ curves of layers of P1

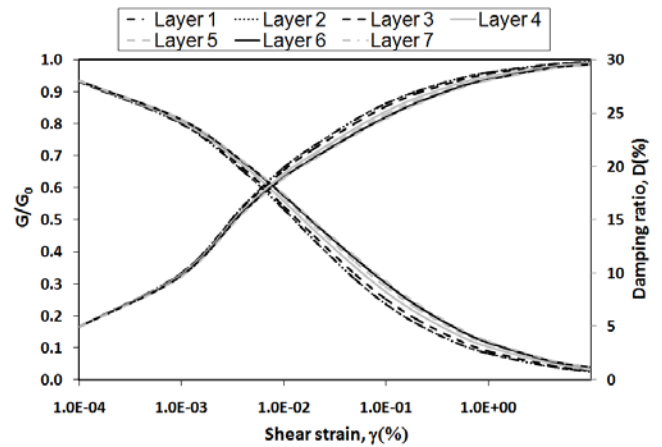


Fig. 2 G/G_0 - γ and D - γ curves of layers of P2

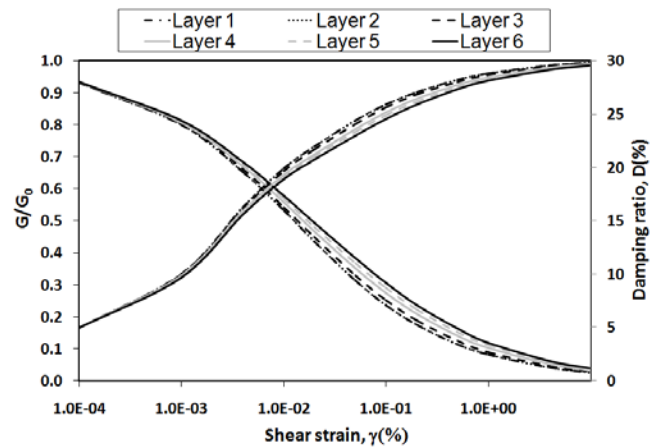


Fig. 3 G/G_0 - γ and D - γ curves of layers of P3

4. GROUND RESPONSE ANALYSIS

Seismic ground response analysis was done with the computer program EERA [3] for the five soil profiles P1 to P5. EERA is a modern implementation of the well-known concepts of equivalent linear earthquake site response analysis applied in SHAKE [16]. The soil profiles are subjected to the input ground motion from the bedrock that is specified as an out-crop motion. To avoid dependency of the ground response to the input motion, three earthquakes were

used in the analysis. These three input motions are the acceleration time history of Loma Prieta 1989, Kobe 1995, and Chichi 1999 earth-quakes (Records P0782, P1043 & P1116 at <http://peer.berkeley.edu/smcat/>). The ground motions are normalized to a target peak acceleration of 0.1g. The comparisons between Peak Ground Acceleration (PGA) at surface, amplification factor, and first natural frequency of each soil profile are presented in Table 3 for the three ground motions. The first natural frequency increases from 0.8 Hz for P2 to 1.4 Hz for P1 and it varies from 0.8 Hz for P3 to 1.6 Hz for P5 by increasing suction. The PGA of the motion at surface of the all profiles is larger than the bedrock motion and this is more significant at the unsaturated profiles.

Figure 6 shows amplification between the surface motion and the base motion at varying frequencies for P1 and P2 for Loma Prieta earthquake. The increase in the natural frequency with suction increase reasonably can be assigned to the in-crease of shear modulus by suction. However, the variation of amplification factor is related to the admittance ratio between the soil and the bedrock, which resulted into increasing amplification factor by increasing suction. To provide comparison of the effects of non-linearity, series of linear analyses were performed for P3 to P5 which, the results are presented in figures 7 to 9. It is clear that non-linearity has influenced the results significantly in terms of both amplification factor and natural frequency.

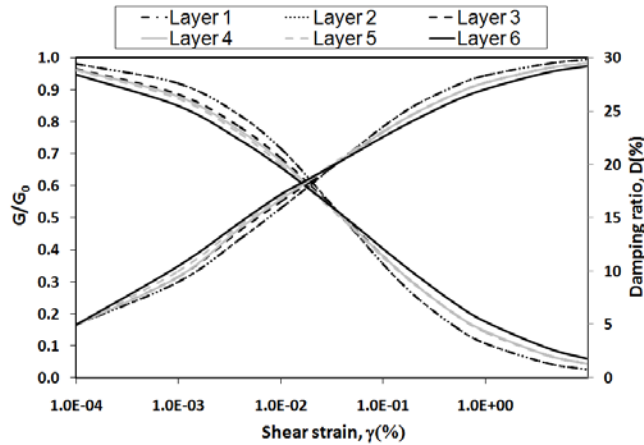


Fig. 4 G/G_0 - γ and D - γ curves of layers of P4

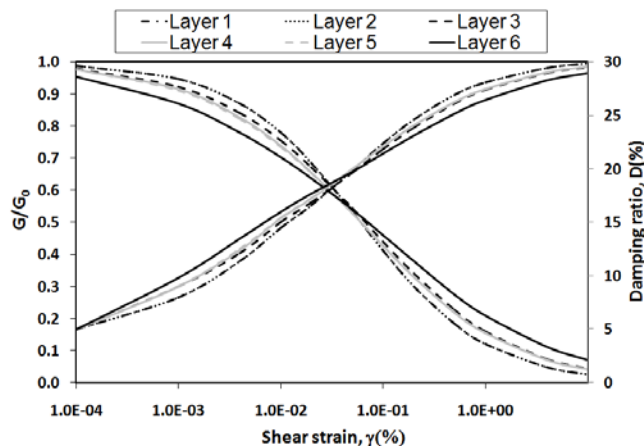


Fig. 5 G/G_0 - γ and D - γ curves of layers of P5

Table 3. Comparison between PGA values of bed rock and surface of the all profiles

Profile	PGA (g), Amplification factor, 1 st natural frequency (Hz)		
	Loma Prieta	Kobe	ChiChi
P1	0.146, 2.25, 1.4		
P2	0.113, 2.29, 0.8		
P3	0.113, 2.29, 0.8	0.117, 2.30, 0.8	0.104, 2.19, 0.8
P4	0.148, 2.61, 1.4	0.155, 2.56, 1.4	0.154, 2.59, 1.4
P5	0.146, 2.71, 1.6	0.154, 2.69, 1.6	0.175, 2.69, 1.6

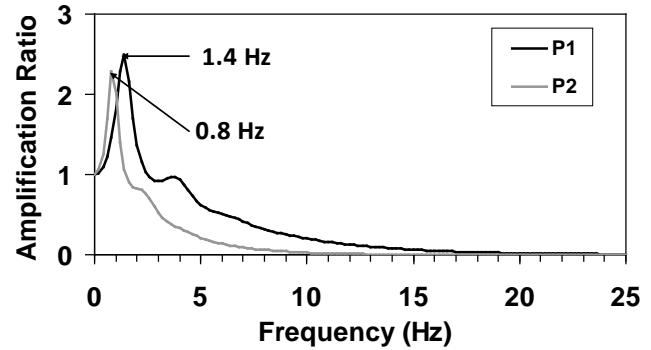


Fig. 6 Amplification functions of P1 and P2.

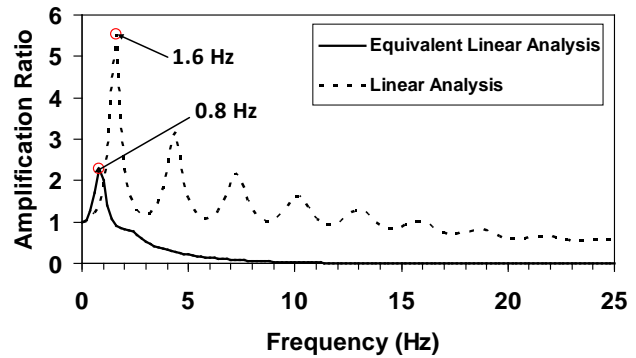


Fig. 7 Amplification functions of P3 in different analysis.

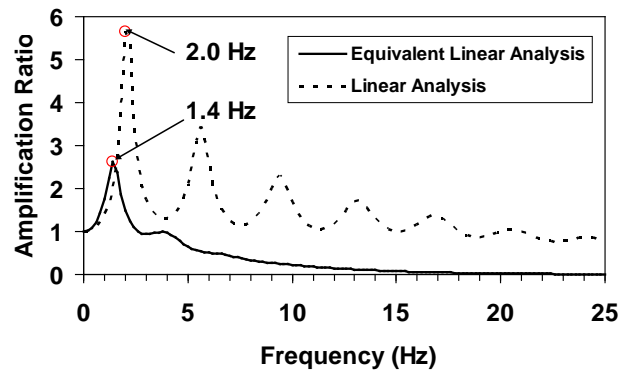


Fig. 8 Amplification functions of P4 in different analysis.

Another index to seismic hazard of buildings and structures is response spectral acceleration curve. Spectral acceleration S_a , is the maximum acceleration of a single degree of freedom oscillator with different natural frequencies but unique damping. Figures 10 to 13 compare the S_a with 5% damping

ratio at the ground surface of the profiles with the one at bedrock for the two sets of analysis. Shift of S_a to the lower frequencies (higher periods) at the surface of the saturated profiles (P2 and P3) is observed. However, S_a of the surface ground motion of unsaturated profiles (P1, P4, and P5) is considerably different with the ones of saturated profiles (P2 and P3) and the bed rock. The results show that the S_a increases by suction increase for high frequencies (periods less than 1 sec). This is very important and should be noticed in seismic design of structures on the un-saturated soil deposits particularly for short buildings with high natural frequency.

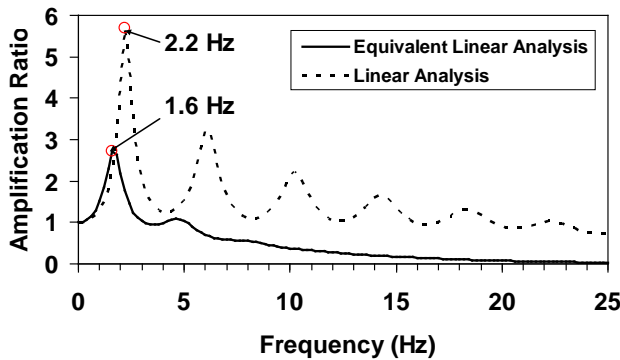


Fig. 9 Amplification functions of P5 in different analysis.

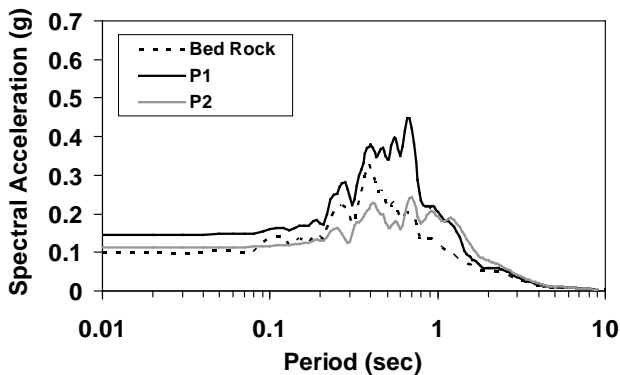


Fig. 10 S_a of P1 and P2 for Loma Prieta.

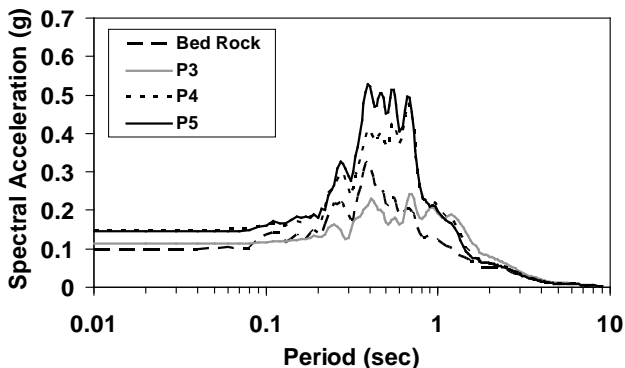


Fig. 11 S_a of P3, P4, and P5 for Loma Prieta.

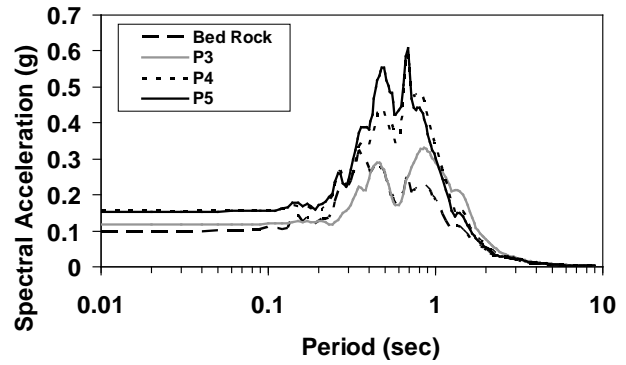


Fig. 12 S_a of P3, P4, and P5 for Kobe.

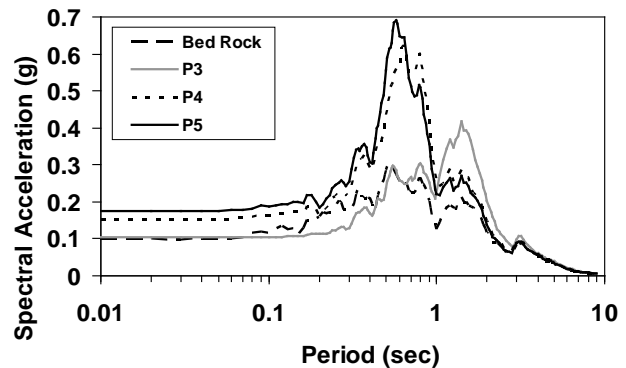


Fig. 13 S_a of P3, P4, and P5 for Chichi.

5. SUMMARY AND CONCLUSIONS

The aim of this study was to perform 1D equivalent linear site response analysis by considering the influence of suction on the shear wave velocity, shear modulus reduction and damping ratio curves. Two sets of analysis compare the response of three unsaturated soil profiles with the saturated ones due to three earthquakes. It came out with the following conclusions for the selected soil profiles.

- The natural frequency of the soil profile increases as the suction increases. This will attract the attentions to the suitable natural frequency of the buildings on the unsaturated soil deposits.
- The ground motions were amplified at the surface for all of the saturated (P2 and P3) and unsaturated profiles (P1, P4 & P5). However, the combined conditions considered in the soil profiles showed that the amplification ratio is slightly larger at unsaturated soils that may not to be a general behaviour.
- Response spectral accelerations calculated for damping of 5%, show that the response of the structures on the unsaturated soil profiles are more severe than saturated ones, particularly at higher frequencies.

6. ACKNOWLEDGMENT

The authors wish to acknowledge the support of the Razi University through research grant Code: 36471.

7. REFERENCES

- [1] Hashash Y M A, and Park D, "Non-linear one-dimensional seismic ground motion propagation in the Mississippi embayment", *Engineering Geology*, vol. 62, 2001, pp.185-206.
- [2] Idriss I M, and Seed H B, "Seismic Response of Horizontal Soil Layers", *J. Soil Mech. Found. Div.*, vol. 94, 1968, pp.1003-1031.
- [3] Bardet JP, Ichii K, and Lin CH, "EERA, A computer program for Equivalent linear Earth-quake site Response Analysis of layered soils deposits", *Software Manual*, University of Southern California, Los Angeles, 2000.
- [4] Seed HB, Wong RT, Idriss IM, and Tokimatsu K "Moduli and damping factors for dynamic analyses of cohesionless soils", *J. Geotech. Engrg.*, vol. 112, 1986, pp.1016-1032.
- [5] Vucetic M, and Dobry R, "Effect of soil plasticity on cyclic response", *J. Geotech. Engrg.*, vol. 117, 1991, pp.89-107.
- [6] Ishibashi I, and Zhang X, "Unified dynamic shear moduli and damping ratios of sands and clays", *Soils and Foundations*, vol. 33, 1993, pp.182-191.
- [7] Mancuso C, Vassallo R, and d'Onofrio A, "Small strain behavior of a silty sand in controlled-suction resonant column – torsional shear tests", *Can. Geotech. J.*, vol. 39, 2002, pp.22– 31.
- [8] Vassallo R, Mancuso C, and Vinale F, "Effects of net stress and suction history on the small strain stiffness of a compacted clayey silt", *Can. Geotech. J.*, vol. 44, 2007, pp. 447- 462.
- [9] Vassallo R, Mancuso C, and Vinale F, "Modelling the influence of stress–strain history on the initial shear stiffness of an unsaturated compacted silt", *Can. Geotech J.*, vol. 44, 2007, pp.463- 472.
- [10] Ng CWW, and Yung SY, "Determination of the anisotropic shear stiffness of an unsaturated decomposed soil", *Géotechnique*, vol. 58, 2008, pp.23–35.
- [11] Biglari M, d'Onofrio A, Claudio M, Jafari MK, and Shafiee A, "Small strain stiffness of Zenoz kaolin in unsaturated conditions", *Can. Geotech. J.*, vol. 49, 2012, pp.311-322.
- [12] Biglari M, Mancuso C, d'Onofrio A, Jafari MK, and Shafiee A, "Modelling the initial shear stiffness of unsaturated soils as a function of the coupled effects of the void ratio and the degree of saturation", *Computers and Geotechnics*, vol. 36, 2011, pp.709-720.
- [13] Biglari M, Jafari MK, Shafiee A, Mancuso C, and d'Onofrio A, "Shear Modulus and Damping Ratio of Unsaturated Kaolin Measured by New Suction-Controlled Cyclic Triaxial Device", *Geotechnical Testing J.*, vol. 34, 2011, pp.525-536.
- [14] Biglari M, and Ashayeri I, "An empirical model for shear modulus and damping ratio of unsaturated soils", in *Proc. 5th Asia-Pacific Conf. on Unsaturated Soils*, 2011, pp.591-596.
- [15] d'Onza F, d'Onofrio A, and Mancuso C, "Effects of unsaturated soil state on the local seismic response of soil deposits", in *Proc. 1st European Conf. on Unsaturated Soils*, 2008, pp.531-536.
- [16] Schnabel PB, Lysmer J, and Seed HB, "SHAKE: A Computer Program for Earthquake Response Analysis of Horizontally Layered Sites", Report No. UCB/EERC-72/12, Earthquake Engineering Research Center, University of California, Berkeley, December 1972, 102p.

The Correction of Shallow Foundation Settlement Equations by Finite Element Method

Mohammad Arab Ameri¹, Hakime Rabbanifar² and Mehdi Arab Ameri³

¹MSc, earthquake engineering, Iran

²MSc, geotechnique engineering, Iran

³MSc, geotechnique engineering, Iran

ABSTRACT

Since Hough (1959) showed that foundation settlement calculations must be done after foundation bearing capacity calculations, several methods have been suggested to determine settlement of shallow foundations. These methods have several limitations such as hypothesis of vertical strain creation due to foundation loading, one-dimensional (vertical) excess pore water pressure dissipation and irrespective of horizontal drainage of the pore water. Also these methods do not account for the effect of soil type on amount of excess pore water pressure beneath the footing and effect of plastic deformations in soil structure. In this study the effective elements in settlement of shallow foundations have been investigated and with the aid of PLAXIS software, the effect of elastic strains, plastic strain related to local collapse, anisotropy in soil deformation parameters and secondary strains have been considered in modeling the settlement of shallow foundations with footing dimension and soils with different overconsolidation ratio. Then the results have been introduced as modification coefficients.

Keywords: Settlement, Shallow Foundations, Correction Coefficient, Relative Pressure, Secondary Consolidation

1. INTRODUCTION

Nowadays the fact that the settlement of shallow foundations is an important factor in their design is widely accepted. This factor earned its situation in design of these foundations not earlier than 1960. Prior practical engineers thought that if a foundation is approved against the bearing capacity issue it will have enough safety factor against the settlement issue. It was 1959 when Hough indicated that the estimation of settlement in shallow foundations should be followed right after the consideration of bearing capacity of such foundations. Since then, several methods for this estimation are introduced.

The first point of view for estimation of settlement in shallow foundations is related to Terzaghi (1925) who adopted the parameters of his model from one-dimensional oedometer test. Despite its widespread usage, the method worked with some limitations. In this theory, it was assumed that: The foundation pressure produces only vertical strains in subsoil, all the induced settlement is one-dimensional and that relating to the shear strain is neglected, the dissipation of excess pore water pressure takes place only in vertical direction and the lateral dissipation is ignored and finally the excess pore water pressure is equal for all types of subsoil and is not dependant to the soil type.

Above-mentioned limitations of Terzaghi method is somewhat revised at the method introduced by Skempton and Bjerrum (1957). They presented the settlement of a shallow foundation as a resultant of two phenomena: Immediate and consolidation settlement along with a correction coefficient which is known as Skempton and Bjerrum coefficient. Similar to the Terzaghi method, their work has several limitations, for instance: Skempton and Bjerrum limited their

studies on strip and circular foundations and other shape of foundations like rectangular foundations were not put into consideration, they assumed no specific distinction between rigid and flexible foundations and finally the plastic deformations of soil mass was neglected and all the settlement assumed to be elastic where as in coarse-grained soils, the secondary plastic settlement may become several times greater than elastic one. Regarding these limitations, introducing a new method with revisions on these limitations seems to be unavoidable.

Studies of Davis and Poulos (1968) indicated that for overconsolidated and soft clays, one-dimensional consolidation analysis represents a good approximation for total settlement and this approximation is valid for soils with drained Poisson's ratio less than 0.35. Increasing the value of this parameter and thickness of the subsoil strata, make the method to under predict the actual settlement value.

Most of the commonly-used methods of settlement analysis, assume the soil to behave elastically. Since the nonlinearity in soil behavior is considered in other ones and normally and overconsolidation states is distinguishable in them by employing different values of compressibility for these two states, the consideration of local yielding arising from the foundation pressure is not noticeable in these methods (Poulos, 2000). Burland et al. (1977) showed that for normally consolidated soils neglecting the local yielding and plastic deformation phenomena make the settlement analysis to be unreliable in most of the cases.

Davis and Poulos (1968) indicated that applied pressure at which local yielding commences is a function of safety factor against the bearing capacity issue and initial stress state. D'Appolonia (1971) extended this idea and presented a correction factor for consideration the influence of local yielding. It is important to notice that the effect of local yielding on consolidation is not put into consideration since the

studies of Carter et al. (1979) show that local yielding has no meaningful effect on consolidation settlement and elastic theory introduces appropriate approximation in this issue. The existence of creep and secondary consolidation, have strict influence on the rate and magnitude of settlement of foundations on clay soil. Most of the practical methods which regard the creep in the settlement analysis are related to studies done by Buisman (1936). In these studies, a linear relation between the magnitude of settlement and the logarithm of time is assumed. The gradient of this relationship is known as the coefficient of secondary consolidation, c_α .

$$c_\alpha = \frac{\Delta E}{\Delta(\text{Log} t)} \quad (1)$$

Mesri and Godlewski (1977) found that c_α is nearly dependant to the consolidation coefficient, c_c and the ratio of c_α/c_c has a narrow range of variation. The rate of secondary consolidation for an overconsolidated soil is much less than the normally consolidation state of that soil.

The difficulty of employing c_c in settlement analysis arises from this fact that the time at which the creep commences is not well definable. Since some researchers believe that creep takes place after the consolidation (Mesri et al. 1994) others assume a simultaneous occurrence of creep and initial consolidation (Leroueil, 1996).

Since different values of secondary consolidation coefficients are seen in the literature (Gibson and Lo 1961, Garlanger 1972), employing appropriate parameters for including the creep in the settlement analysis at least in its simplest and one-dimensional model are difficult and unusual. It seems that, among the different aspects of settlement theory, creep and secondary consolidation have the least development and need for extra considerations.

The above mentioned considerations approve that, in the new methods for settlement analysis, the influence of both elastic and plastic strains should be considered, where the hardening soil model which is employed in the PLAXIS software competently has this ability.

2. Present Study

Nowadays the finite element theory and softwares using it have an important part in the analysis of stress and strain inside a soil mass. The output parameters of such softwares have a good approximation with the monitored parameters. At present study, with the aid of PLAXIS software and employing Hardening Soil model, the settlement of shallow foundations which are assumed to be rigid are estimated and the results are compared with those obtained from elastic solutions and sets of correction factors are introduced for elastic settlement analysis. In this study, the modeled foundations have three different widths and are embedded on four clays with different overconsolidation ratios.

The Hardening Soil Model has no constant yield surface and can expand due to plastic strain. Two types of hardening are distinguishable in this model, namely shear hardening and

compression hardening. Shear hardening and Compression hardening are used to model irreversible strains due to respectively primary deviatoric loading and primary compression in oedometer and isotropic loadings.

This model is an advanced model for simulating the behaviour of different types of soil, both soft and stiff soils, (Schanz, 1998).

When a soil is subjected to initial deviatoric stress, indicates a simultaneous decrease in its hardness and occurrence of irreversible plastic strain. For example, for drained triaxial test, the relation between axial strain and deviatoric stress can be described by:

$$-\varepsilon_1 = \frac{1}{E_i} \frac{q}{1 - q/q_a} \quad (2)$$

Where ε_1 is vertical strain, q is the deviatoric stress; q_a is the asymptotic value of the shear strength and E_i the initial stiffness.

Such relationship first formulated by Konder (1963) and is employed at hyperbolic model (Duncan and Chang, 1970). The Hardening Soil model, however, supersedes the hyperbolic one firstly by using the theory of plasticity rather than the elastic one. Secondly by including soil dilatancy and thirdly by introducing a yield cap.

Some of the specifications of this model are: the dependence of hardness to the stress with a power law, the dependence of plastic strains to initial deviatoric loading and primary compression, elastic unloading / reloading and finally failure according to the Mohr-Coulomb model.

The basic feature of this model is its dependency on the stress level. For instance, for oedometric stress and strain condition the model introduces an equation as:

$$E_{oed} = E_{oed}^{ref} \left(-\sigma'_1 / p^{ref} \right)^m \quad (3)$$

Where E_{oed} is oedometer modulus, p^{ref} is a reference pressure, E_{oed}^{ref} is oedometer modulus measured at reference pressure, σ'_1 is the major principal stress and m the power in stress-dependent stiffness relation.

3. The Employed Model

The geometry of the model used in this study is presented in fig. 1. The aspect ratios are assumed to be constant as $H/B=5$ and $L/B=9$. For considering the influence of the foundation width in the analysis, three values of 1, 1.5 and 2 are assumed for this parameter and since the effect of foundation flexibility is neglected and is relegated to future studies, a high value of bending

modulus is assumed for the foundation to demonstrate a rigid behavior.

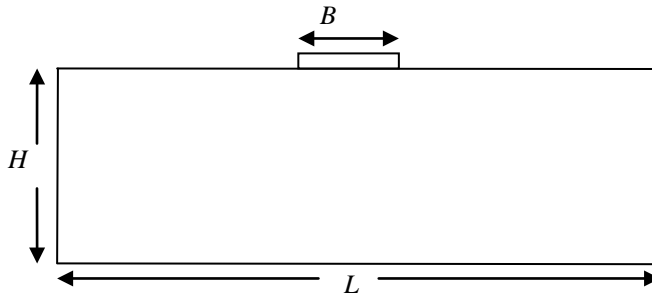


Fig. 1- Schematic shape of current model

In current study, four types of clays with different overconsolidation ratios are considered with parameters described in table I.

Table I. The parameters of the employed soils

Soil Parameters	NC	OCR=1.7	OCR=2.5	OCR=4
E_{50}^{ref}	3.2 E 3	1.6 E 4	3.75 E 4	7.5 E 4
E_{oed}^{ref}	3.2 E 3	1.6 E 4	3 E 4	6 E 4
E_{ur}^{ref}	9.6 E 3	4.8 E 4	9 E 4	2.25 E 5
ν	0.3	0.3	0.3	0.3
m	0.8	0.65	0.6	0.55
C	1	7	11	20
ϕ	24	25	25	25
ψ	0	0	0	0
γ_{unsat}	16	16	16	16
γ_{sat}	18	18	18	18
k	1.0 E - 4	1.0 E - 4	1.0 E - 4	1.0 E - 4
k_0	0.59	0.75	0.91	1.15

In table I, the E_{50}^{ref} (kN/m²) is Secant stiffness in standard drained triaxial test, E_{oed}^{ref} (kN/m²) is tangent stiffness for primary oedometer loading, E_{ur}^{ref} (kN/m²) is Unloading/reloading stiffness, ν is Poisson's ratio, m is Power for stress-level dependency of stiffness, c (kN/m²) is effective cohesion, ϕ is effective angel of internal friction, ψ is the angel of dilatancy, γ_{unsat} (kN/m³) is the unsaturated volumetric weight, γ_{sat} (kN/m³) is the saturated volumetric weight, k is the bulk modulus and k_0 coefficient of lateral earth pressure.

4. Results

The general equation for settlement analysis is introduced as:

$$S = \mu S_i + \eta S_c + S_s \quad (4)$$

Where S_i , S_c and S_s are the immediate, consolidation and secondary consolidation settlements respectively and μ and η are the correction coefficients for the immediate and consolidation settlements respectively. All the settlement components are calculated using the PLAXIS software.

The correction factors for the immediate and consolidation settlements are composed of two components: the correction factor of using foundation width less than 2m, I_i and the correction factor of employing elastic theory in the analysis, β .

$$\mu = I_i \beta_i, \quad \eta = I_c \beta_c \quad (5)$$

Where:

I_i = the correction factor for using elastic theory in the immediate settlement analysis

β_i = the correction factor for using foundation width less than 2m in the immediate settlement analysis

I_c = the correction factor for using elastic theory in the consolidation settlement analysis

β_c = the correction factor for using foundation width less than 2m in the consolidation settlement analysis

In the current analysis, foundation loading is continued up to the subsoil failure. It is evident that the pressure at which the failure occurs, in other words the bearing capacity of the foundation is related to foundation aspects. For omitting the effect of this issue, the under pressure in the foundation is divided by its bearing capacity as:

$$(6) RP = \frac{P}{BC}$$

Where RP is the relative pressure and according to its definition is the negative power of safety factor against the bearing capacity of the foundation, P is the applied load and BC the bearing capacity of the foundation. For defining the correction factor of using elastic theory in the immediate settlement analysis, I_i the result of modeling where the Hardening Soil model is used is divided by those whom the elastic theory is adopted. The results are smoothened and introduced as the I_i in Fig 2. For other overconsolidation ratios, the extrapolation should be employed.

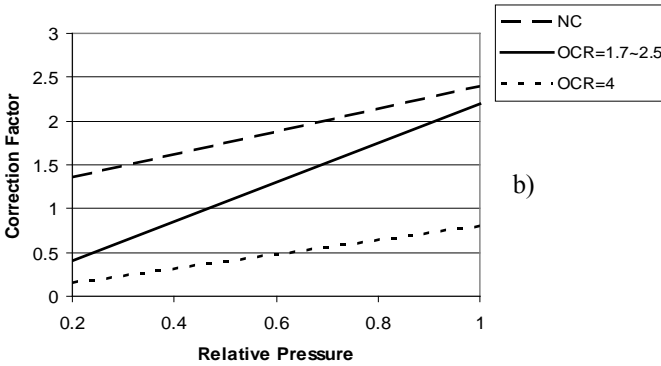
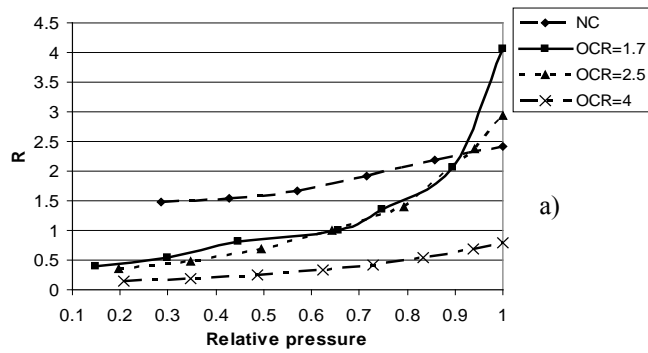


Fig. 2- a) Variation of the ratio of the settlement estimated from the Hardening Soil model over the one estimated from elastic theory, R with relative pressure for four different soils, b) Variation of I_i with relative pressure

In order to define the correction factor of using foundation width less than 2m in the immediate settlement analysis, β_i the ratio of the settlement estimated from the Hardening Soil model over the one estimated from elastic theory for foundation widths less than 2m is estimated and is divided by the results obtained for the foundation assumed to have the width equals to 2m. The results for normally and lightly overconsolidated soils are shown in figs. 3 and 4.

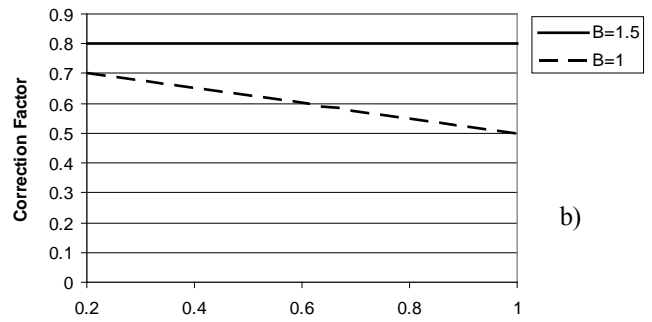
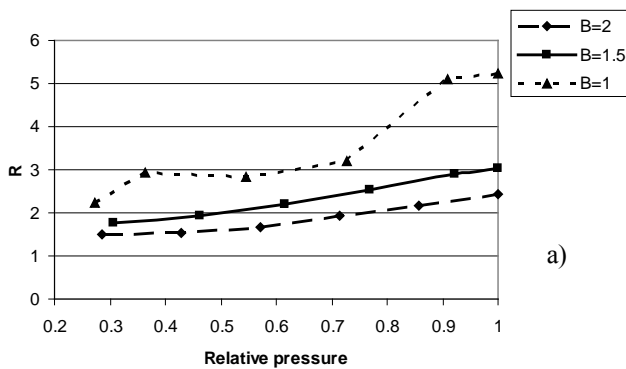


Fig. 3- a) Variation of the ratio of the settlement estimated from the Hardening Soil model over the one estimated from elastic theory, R with relative pressure for normally consolidated soil, b) Variation of β_i with relative pressure

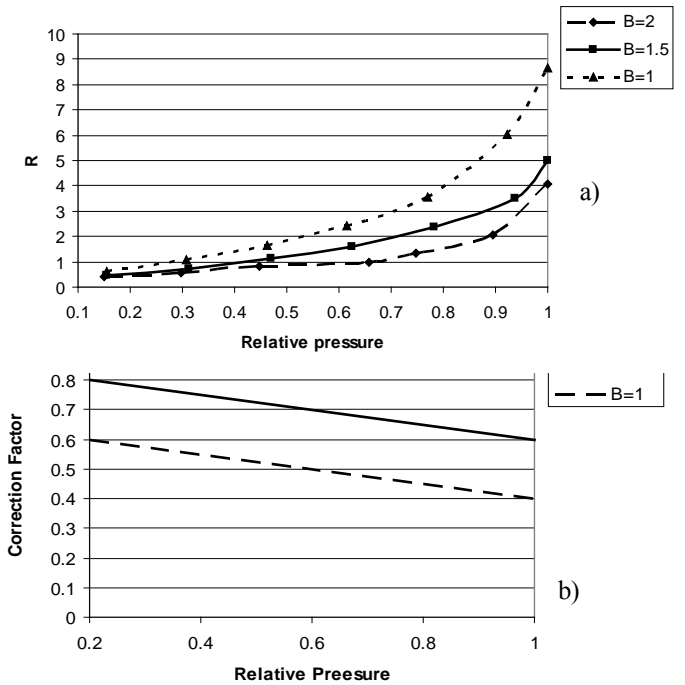


Fig. 4- a) Variation of the ratio of the settlement estimated from the Hardening Soil model over the one estimated from elastic theory, R with relative pressure for soil with OCR=1.7, b) Variation of β_i with relative pressure

The variation of β_i doesn't differ for various soil types and the graph introduced in fig. 4 can be used for soils with other overconsolidation ratios.

Definition of the correction factors for consolidation settlement is similar to those works done for immediate settlement; for obtaining the correction factor of using elastic theory in the consolidation settlement analysis, I_c and the correction factor of using foundation width less than 2m, β_c the result of modeling with assuming the soil to behave as the Hardening Soil model is divided by those whom the elastic theory is used. The results are smoothened and introduced in figs. 5, 6 and 7 for normally and lightly overconsolidated soils. Again

for other overconsolidation ratios, the extrapolation should be employed.

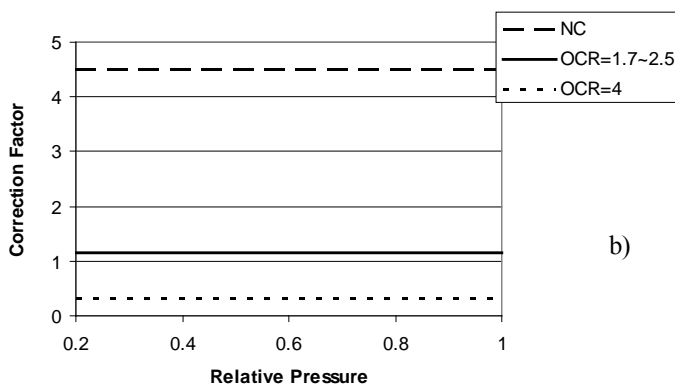
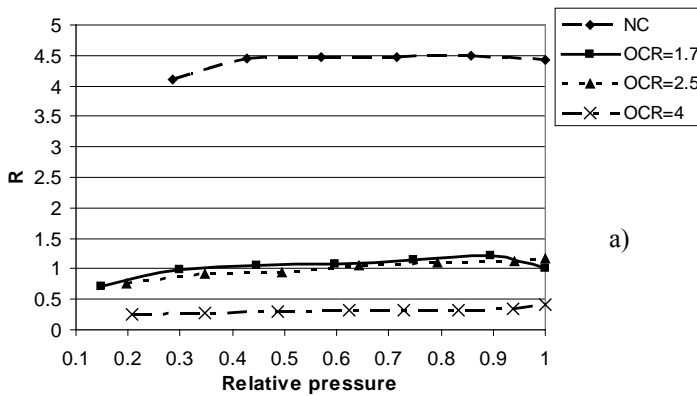


Fig. 5- a) Variation of the ratio of the settlement estimated from the Hardening Soil model over the one estimated from elastic theory, R with relative pressure for four different soils, b) Variation of I_c with relative pressure

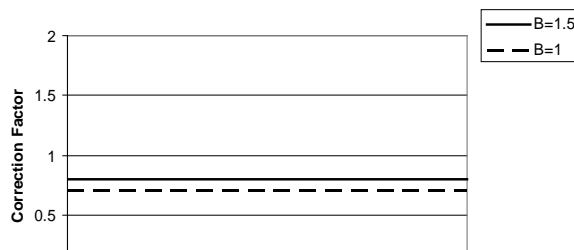
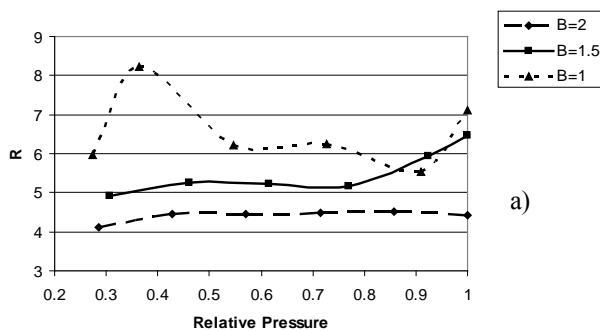


Fig. 6- a) Variation of the ratio of the settlement estimated from the Hardening Soil model over the one estimated from elastic theory, R with relative pressure for normally consolidated soil, b) Variation of β_c with relative pressure

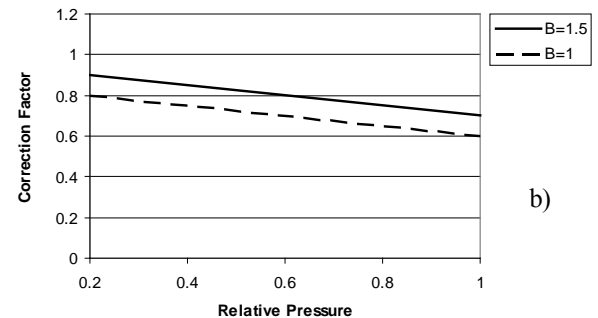
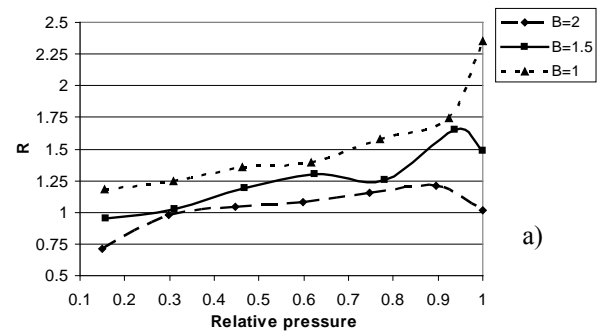


Fig. 7- a) Variation of the ratio of the settlement estimated from the Hardening Soil model over the one estimated from elastic theory, R with relative pressure for soil with OCR=1.7, b) Variation of β_1 with relative pressure

Similar to that mentioned about immediate settlement, for other soils with different overconsolidation ratios, the variation of β_c is not much different from the graph introduced in fig. 7 and this graph also works for these soils as well.

5. Conclusion

In this study, the methods introduced for estimating the settlement in shallow foundations and their limitations are considered in detail. It is concluded from prior studies that the current introduced method should consider the effects of both elastic and plastic strains

and secondary consolidation in analysis; the Hardening Soil model which is used in PLAXIS software is considered and with the aid of this software and using Hardening Soil model, a new relation is introduced for estimation of settlement in shallow foundations which is composed of three components: Initial, consolidation and secondary consolidation settlements. The relation also introduced the correction factors for Initial and secondary consolidation settlements which are estimated for four different clays with various overconsolidation ratios.

References:

- [1] Buisman K, "Results of long duration settlement tests," Proceedings 1st International Conference on Soil Mechanics and Foundation Engineering, Cambridge, 1936, Mass. Vol. 1, pp.103-107.
- [2] Burland J.B, Broms B. B. and de Mello V. F. B., "Behavior of foundations and structures", Proc. 9 ICSMFE, Tokyo, 1977, Vol. 2, pp. 495-546.
- [3] Carter J. P., Booker J. R. and Small J. C., "The analysis of finite elasto-plastic consolidation," Int. JNAMG, 1979, Vol. 3, pp. 107-129.
- [4] D'Appolonia D. J., Poulos h. G. and Ladd C. C., "Initial settlement of structures on clay," JSMFD, ASCE, 1971, 97(SM10), pp. 1359-1397.
- [5] Davis E. H. and Polous H.G, "The use of elastic theory for settlement prediction under three-dimentional conditions," Geotechnique, 1968, 18(1), pp. 67-91.

Numerical Study Of Earthquake Hazards Of Liquefaction Occurring On The Site And Stability Of Transport Pipes

Hamed Bavanpouri, Dr.Jahangir Khazaie, Dr.Hasan Sharafi
Razi University, Kermanshah- Iran

ABSTRACT

Arteries are vital components of the buried pipe for water distribution, gas, oil, etc. are used. Vulnerability of pipelines against earthquake-induced liquefaction has been observed since in many past earthquakes. There are extensive reports about. Liquefaction can be by the side, fluid fragmentation, loss of cargo, buoyancy, causing subsidence and deformation in the structure. Buried gas pipe network in some urban areas may be saturated loose sandy soil layers, are buried. The purpose of this numerical study on the liquefaction of the pipe is buried.

Keywords: liquefaction, buried pipelines, numerical analysis

1. INTRODUCTION

Better interaction between human and nature, requires detailed understanding and knowledge of natural disasters.

Among natural disasters, more attention is needed to earthquake. Due to factors such as being unpredictable, impossible to prevent the likelihood of being in crowded places, in countries like Iran every year, several large and small earthquakes occur. It requires a comprehensive protection plan in various aspects. During an earthquake, phenomena such as wave propagation and large movements of the Earth, causing damage to the pipes. Great earth movements such as fault movement, landslide and soil liquefaction of the most important factors is to count [1]. Studies on earthquake damage to buried pipes has proven above ground stations on the structures, vibrations resulting from seismic loads do not cause destruction of the buried pipe. But the great movements of Earth's major pipe failure. In other words, buried pipelines usually have the ability to withstand earthquake waves but The pipes are often unable to withstand the large motions of ground [2]. Large ground motions can be caused by phenomena such as faults, landslides and soil liquefaction. The main risk for pipelines include earthquake ground motion and transient changes lasting places of the earth. Transient ground motion caused by waves emanating from the source, releasing energy and the resonance is due to topography and local soil conditions. Earth represents a lasting shift in the earth, defeat and failure is caused by various phenomena such as : Surface faulting, the gable and landslide, lateral mass movement of soil liquefaction, the heterogeneous settlement. Research has shown that most of the earthquake seismic damage to buried steel pipelines in oil and gas by continuous change takes place as a viable land and only a few of these injuries are caused by the phenomenon of wave propagation. Psuedustatics steady shift to enter the pipeline is not necessarily a lot of intensity

but however it may cause serious damage to the pipeline. Example can be pointed to different earthquakes such as : Alaska and Nigita (1964), San Fernando (1971), Kobe (1995), Chi Chi (1999) and etc. Soil liquefaction occurring in Iran and also numerous harmful effects on arterial lines have been reported. Manjil earthquake that it can be mentioned [3].

Liquefaction effects on buried pipelines and proposed models (History Research)

Wang & Yeh [4] to the analysis of buried pipelines under liquefaction by Separating the two zones with liquefaction and no liquefaction, a beam- column model is proposed for buried pipelines. In this modeling the geometric properties, material specifications, soil stiffness, shear wave propagation velocity, and axial bending effects, the mass and diameter, the buoyancy effects of the soil mass was considered. The model assumes the soil liquefaction around the environment, all lost its shear strength and behaves like a viscous fluid. Nishio[5] dynamic strain in the buried pipeline due to liquefaction of soil analyzes. The results show that under conditions of soil liquefaction, large strains are produced in the pipe. Also with regard to slip between soil and pipe strain on the pipeline to significantly reduced. Hamada and et al did Similar studies with the large ground displacement caused by liquefaction-related chubu-Nihonkai earthquake in 1983. The shear resistance between soil liquefaction severely reduced re verberation in the sand [6].

Wang Guoxin and et al were examined seismic response of pipelines buried in soil liquefaction caused by axial and lateral waves in different directions [7]. In their model, the effective stress of soil and were floating in a spring system is used to simulate soil and pipe.

Fu-lu two methods to investigate the problem of static liquefaction and its effects on buried pipelines will provide[8].

$$\varepsilon_a = \frac{\sigma_a}{E_i} \left[1 + \frac{\alpha}{(r+1)} \left(\frac{\sigma_a}{\sigma_0} \right)^r \right] \quad (1)$$

2. Description of Numerical Model

2.1 Geometry of model

The data used in this modeling is based on information related to gas pipelines in Kermanshah of Iran .

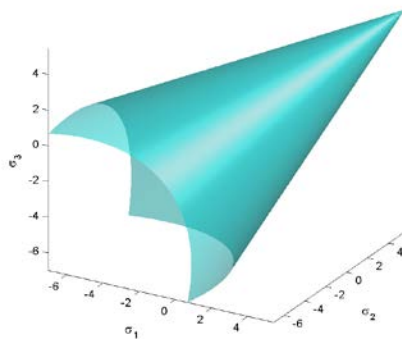
“TableI. The characteristic parameters of the pipe”

Length	Diameter	Tickness	Poisson's ratio	Young's modulus
12m	0.9m	0.1m	0.3	200e9 Pa

“Table II. The characteristic parameters of soil”

Friction angle	Dialation angle	Density	Poisson's ratio	Young's modulus
29°	2°	1700 kg/m ³	0.25	1e8 Pa

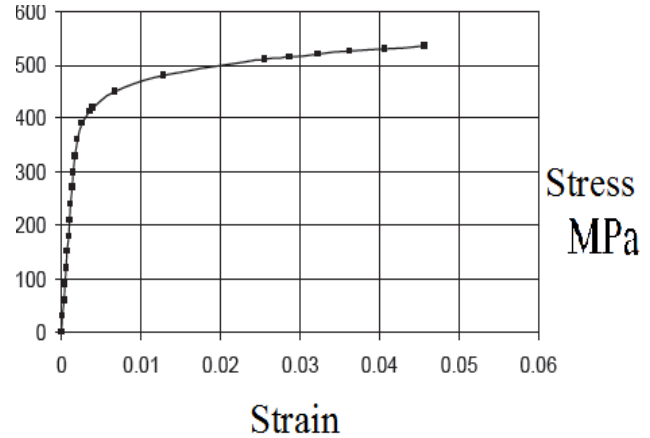
In this study , Soil environment of the elastoplastic model is intended Drucker Pragr.



“Fig. 1” Drucker Prager yield surface in 3D space

2.2 Specifications of Structural Pipe

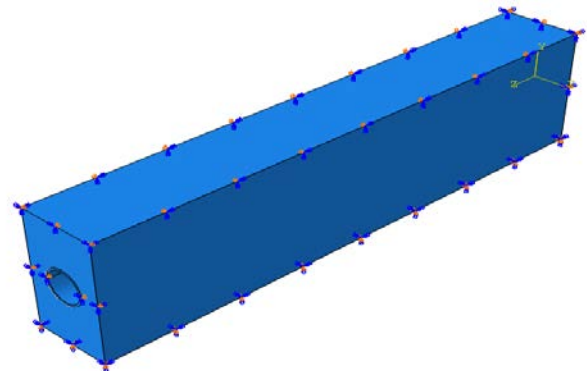
As can be seen in Fig. 3 the stress - strain curve Ramberg Osgood have used. the Ramberg Osgood relationship is :



“Fig. 2” Stress-strain curve of the pipe

2.3 Boundary conditions

In this modeling, boundary conditions of the soil medium is considered infinite. The soil environment is assumed to be symmetric and isotropic. However, given the existing conditions of the soil profile, it is fairly acceptable.



“Fig. 3” Boundary conditions of model

2.4 Pipe-soil interaction

Interaction between soil and pipe for the consideration of the contact elements are used . These elements, the contact forces are two models :

1- Vertical behavior is Hard contact. The first two levels, one of which is usually more difficult level, is defined as a reference and Another level it is defined as the function. This behavior is assigned to the two surfaces in contact causes the penetration of the surface elements of nodes in the elements

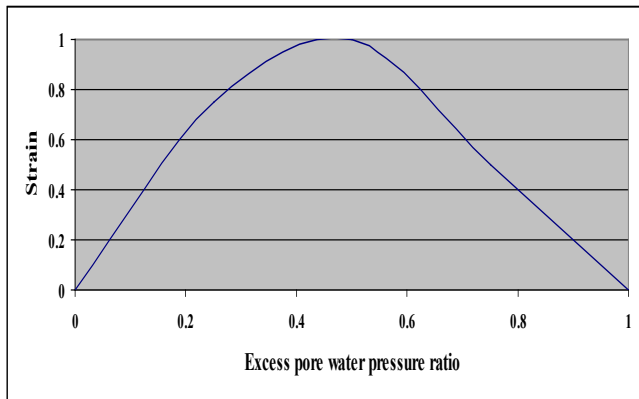
of the reference level to prevent.

2- Tangential behavior that is related to the friction between surfaces. Tangential to the friction coefficient of both fixed and variable coefficient model is available. The coefficient of constant friction, static friction to be considered , Thus reducing the coefficient of friction between the sliding surfaces are not considered But in the case of variable coefficient of friction . reducing coefficient of friction due to slippage on the dynamic load can be made exponentially decreasing model .The coefficient of static to the dynamic limit value is reduced. Represent the behavior of a weakened area around the pipe [2] .

In this study, tangential behavior considered as constant. In this case, the only parameter required is the coefficient of friction between surfaces .

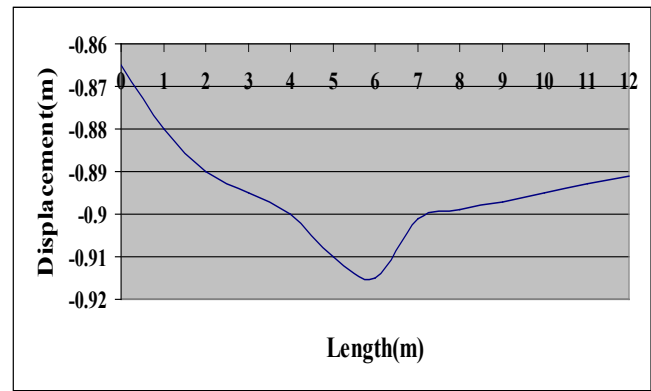
3 Numerical Results

As can be seen in Fig. 4 Relationship between excess pore water pressure ratio and strain of pipe due to liquefaction is shaped like a parabolic. With increasing excess pore water pressure ratio, the strain of pipe is increased , but the strain reaches the maximum value and then decreases the amount of strain.



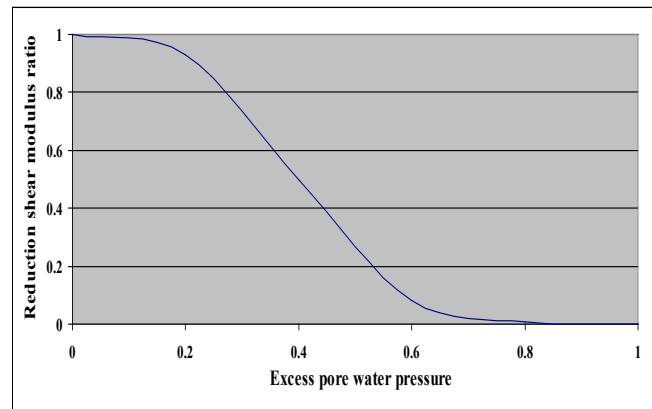
“Fig. 4” Relationship between excess pore water pressure ratio and strain

As can be seen in Fig. 5 deformation due to liquefaction is shaped like a parabolic.



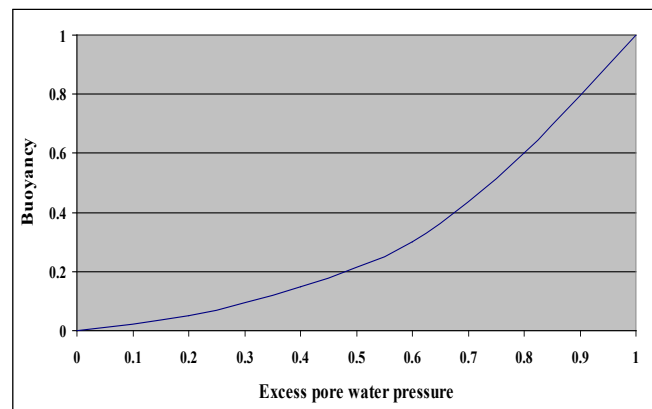
“Fig. 5” Relationship between length of pipe and displacement

As can be seen in Fig. 6 With decreasing reduction ratio of shear modulus, the excess pore water pressure reduced.



“Fig. 6” Relationship between excess pore water pressure and reduction ratio of shear modulus

As can be seen in Fig. 7 With increasing excess pore water pressure ratio, the buoyancy is also increasing



“Fig. 7” Relationship between excess pore water pressure ratio and buoyancy

4 CONCLUSION

Peak strains are caused when the excess pore water pressure rises and falls.

The vibration strain peaks when the excess pore water pressure ratio is between 0.45 to 0.55 during liquefaction process. The longer the period of incomplete liquefaction remains, the longer that of great vibration strain is.

The pipe strains should be classified according to the mechanism of generation: vibration strains which indicate pipe vibration, and accumulated residual strains which indicate the pipe bending due to uplift. Modes of pipe failure indicated by the former is different from the later.

Given the significant changes that occur in the pipe, buried pipe can be concluded that the gas network is vulnerable. And retrofit them for prevention of human and financial losses, it seems quite reasonable.

To obtain an equation to describe the pore water pressure during the liquefaction phenomenon in this region requires studies far much worse.

5 REFERENCES

- [1] Liang,j.,Sun,S.” Site Effects on Seismic Behaviour of Pipeline”,Pressure Vessel Tech.,ASME,Vol .122,pp 469-475,2000
- [2] Hoseini,M., Mehrantiv, “Seismic design guidelines for oil and gas pipelines” Tehran, International Institute of Seismology and Earthquake Engineering,1997
- [3] “International Institute of Seismology and Earthquake Engineeringuidelines for oil and gas pipelines” Manjil earthquake ,Analytical Report Number 1 , 1990
- [4] Wang L.R.L., Yeh, Y. H. “Combined Effecte of Soil Liquefaction and Ground Displacement to Buried Pipelines”. P. V. P., Vol.162,1989, PP.43-51.
- [5] Nishio N. “Dynamic Strains in Buried Pipelines due to Soil”. P. V. P., Vol.162,1989,
- [6] Hamada M., Kubo K. and Saito K. “Large Ground Displacement and Buried Pipe Failure by Soil Liquefaction during 1983 NIHONLAI-CHUBU Earthquake”. P. V. P., Vol.98-4, 1985, PP.11-18.
- [7] Guoxin Wang., Wei H. and Jianguo. “Seismic Response Liquefactional Conference on of Buried Pipelines During Seismology and Earthquake Engineering, Tehran, Iran, Vol.2, 1995, PP.1343-1351.
- [8] Fu-Lu M. “Earthquake Response of Fluid-Filled Pipeline in Soil”. P. V. P., Vol.77, 1983, PP.196-201

Analysis Of Geogrid Reinforced Soil Retaining Walls With Limit Equilibrium And Finite Difference Method

Alireza sadeghabadi¹, Jahangir khazaie² and Mostafa yousefi rad³

¹M.Sc. Student of civil Eng., Dept of civil Eng., Science & Research Branch., Islamic Azad University, Markazi(Arak), Iran; Tel: +98-9122070810; Fax: +98-2188532683; Email: alireza_sadeghabadi56@yahoo.com

²Assistant Professor of Civil Eng., Department of Civil Eng., Univ. of Razi, Kermanshah, Iran; Tel: +98-9123271926; Fax: +98-2144133580; Email: p.khazaei@razi.ac.ir

³Department of earth Science., Payame Noor university., Tehran, Iran; Tel: +98-9183638957; Email: Radyousefi@yahoo.com

ABSTRACT

Reinforced soil technologies have been widely applied during past few decades. A large variety of reinforcing materials emerged and they have been developed for construction purposes, such as geogrids. In this regards, due to increasing usage of polymeric materials such as geogrids shows the importance of investigating on behavior of these types of materials. Geogrid reinforced retaining walls, are designed by experimental and the classic methods which are often based on limit equilibrium methods. current analytical methods sometimes treat the soil and reinforcement separately, which should be evaluated with practical situations. So, in this research the experimental results compare with output results of finite difference method numerical analysis and limit equilibrium methods in these types of walls. It's shown that the "F.D.M" results performed by FLAC^{2D} software are in good agreement with those of experimental model tests and nearly manual calculations (L.E.M).

Keywords: geogrid, Geosynthetic, manual calculations, finite difference method "F.D.M", Limit equilibrium, Polymeric reinforced soil retaining walls, FLAC^{2D} software, laboratory models.

1.Introduction

Issued related to the design and factors affecting the performance of reinforced soil have been addressed by many researchers in recent times (e.g. Bathurst et al., 2005; Park and Tan, 2005; skinner and Rowe, 2005; Versuo et al., 2005; Hufenus et al., 2006; Nouri et al., 2006). Also, the behavior of reinforced earth structures has been comprehensively studied through filed observation of full scale physical model, laboratory model testing, and numerical solutions. However the cost of constructing and monitoring full scale reinforced test embankments is quiet high. An alternative method such as a numerical "experiment" or simulation by means of appropriate methods such as finite difference (F.D.M) or limit equilibrium (L.E) techniques (e.g. and Rowe, 1994) is essentially required. So, numerical modeling of reinforced systems behavior is important for the evaluation of

of extension (Mendonca 2004).

Knowledge concerning these systems, their design methodologies and also to forecast their behavior. with this goal, a real soil wall with lateral slopes reinforced with geogrids was numerically modeled. The main target of this research is to analyze the influence of reinforcement and the reinforcement geometry in the behavior of soil systems reinforced with geogrids.

2.Reinforced soil Description

A soil wall with slopes reinforced with geogrids was built between Regua and Reconcos in the main itinerary 3 (IP3) and is a part of the reestablishment 2. The reinforced slope has an extension of about 206m, is in curve and the reinforced area reaches a maximum height of about 20 m in the outside curve slope at 150 m

The maximum inclination of the reinforced slope

is about 60° in horizontal direction. On the reinforced sections higher than 10m, with variable width parallel to the road pavement was built. The maximum width of the bench was 3 m. the bench had the following objectives: to reduce minimum inclination of the slope in the zones of the larger height, to facilitate drainage and, consequently, to reduce the superficial erosion.

The simulation of the soil construction was modeled as a successive placement of 30 soil layers and equal number of geogrids levels. So, the total number of calculation phases was 30. The soil was modeled with elastic-plastic behavior with a failure criterion of Mohr- coloumb. Geosynthetic layers were modeled using linear, elastic-plastic cable elements.

The face characteristics were modeled considering in a strip of 0.5m adjacent to the face soil with a cohesion equal to 25 KN/m^2 . The reinforcements are placed horizontally and spaced 0.60 m vertically are high-density polyethylene (HDPE) uniaxial geogrids with tensile strengths selected according to the height of the soil wall.

The face units, 0.60 m high, were constructed using welded wire net with quadrangular 0.15m size openings. The face unit angle (with the horizontal) is 60° .

The characteristics of the fill material used in the slope nearby the facing were similar than that used

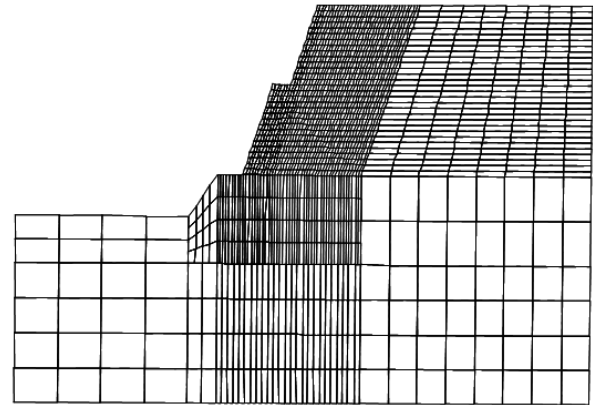
SE (sand equivalent)	(%)	33.0
Proctor	$\gamma_{d\max}(\text{g/cm}^3)$	1.95
	$W_{opt}(\%)$	10.2
CBR	95%	22.3
	Exp.	0.20
Triaxial (two tests)	$c'(\text{kPa})$	0.0
	$\phi'(^{\circ})$	36.0

Table (1). Specifications of the soil.

in the fill and are presented in Table (1). This soil is a residual granite and the layers were placed with a height of 0.30 m after compaction.

3. Numerical modeling of the reinforced soil wall.

for this work the program FLAC V4.0 was chosen. The main reason for this decision was the fact that it is commercial software and so it will be easier for geotechnical engineers' to access the code. The construction the soil wall was modeled considering the real geometry, the adopted sequence construction, the materials used and the real solicitations applied. The total number of was 1700, with 1640 square two dimensional elements representative of the soil material, 30 elements of the type representative of the face and 30 linear cable elements representative of the geogrids(figure.1)



Figure(1). Mesh elements of the embankment numerical model.

From the results of the numerical modeling presented in Figures 2 & 3 it was verified that, only in a reduced extension to the interior of the embankment face, displacements have influence on geogrids's deformations and in consequence on its tensile load distribution. Therefore, we think that it is interesting to study the effect of position and reinforcement length in the limitation of the slope deformations.

So, starting from a calculation with reinforcements with the same length (12.5 m) designated by base model, several calculations were made. In these calculations the number of reinforcements was the same as the base model.

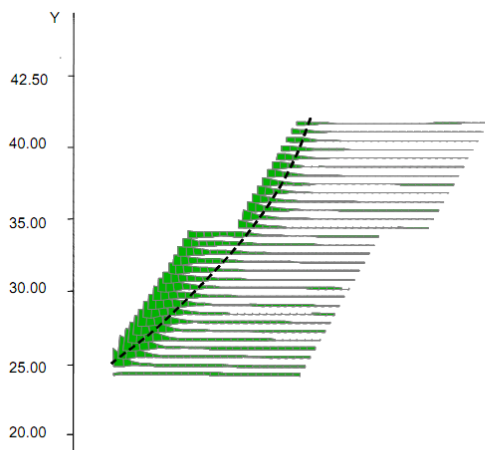
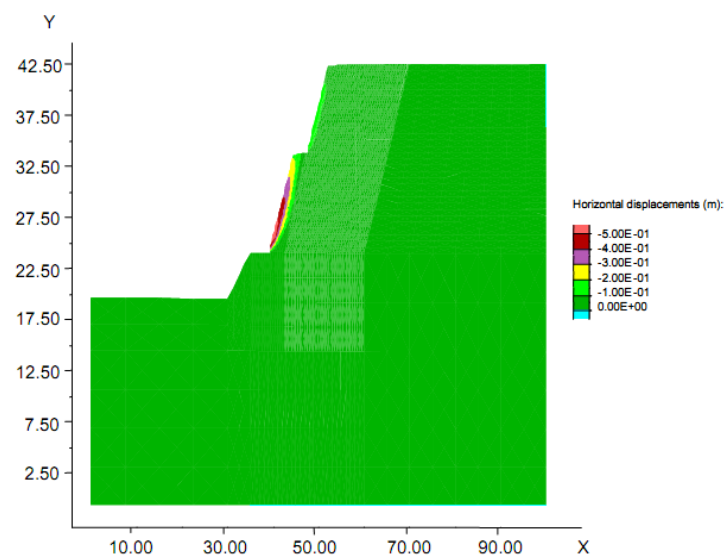


Figure (2). Geogrids displacements

Even so with two different lengths: main reinforcements spaced 1.2 m, with the length considered in the base model; and secondary reinforcements, spaced 1.2 m in the middle of the main reinforcements, with variable lengths of 8,6, 4 and 2 m. Additionally, a calculation was performed with the reinforcements spaced vertically at 1.2 m.



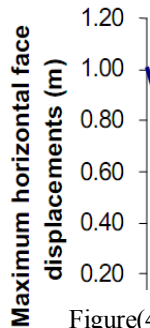
Figure(3). Contours of horizontal displacements.

The Conclusions from N.M. show that the maximum horizontal face displacements are strongly dependent on the length of the intermediate reinforcements. Figure 4 clearly shows that the face displacements decrease with the reduction of the length of the intermediate reinforcements until values of about 4m. For shorter reinforcements, the displacements in-crease significantly. Therefore, the optimum intermediate reinforcement's length, for this particular structure, is between about 4 and 6 m.

This situation results from the fact that the reinforced soil wall, with shorter intermediate reinforcements for the optimum values, are flexible in a non-uniform way and consequently the resulting rotation due to differences of stiffness along the reinforced Soil drive to a reduction of the horizontal deformation near the face. In the base model, as in models with short intermediate reinforcement length, the stiffness of the soil mass is more uniform and consequently the

horizontal face deformation, in the absence of an accentuated rotation, is controlled by the stability of the face. In limit, as it would be expected, its maximum deformation occurs when intermediate

reinforcements do not exist.



Figure(4). Effect of secondary Geoid's length on maximum horizontal face displacements.

0

Reinforcement length (m)

Applying this method to the IP3 embankment with reinforced slopes with geogrids, an alternative solution to the real structure could be the corresponding optimized calculation. That is, secondary reinforcements (with 4.0 m of length), at

middle vertical distance from primary reinforcements, spaced in the vertical of 1.2m(Fig.5)

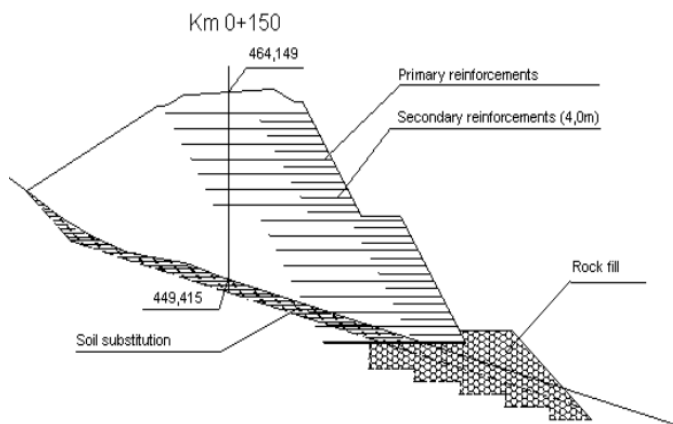


Figure 5. Normalized geogrids distribution for the geogrid reinforced soil retaining wall.

Figures (6) shows some numerical results and can be compared with those presented in Figure (3). From its analysis it is verified that the influence of the face displacements on the interior of the reinforced zone increases in the Normalized solution.

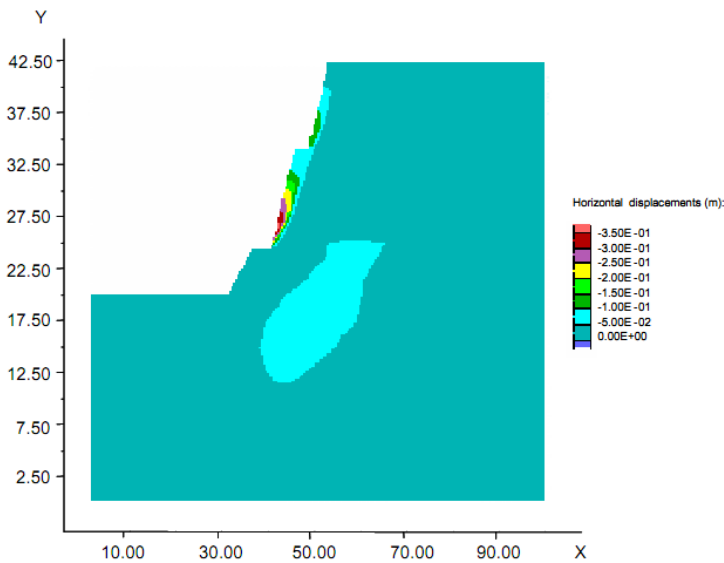


Figure (6). Horizontal displacements of the Normalized model.

4. Conclusions

Although, Internal stability analysis geogrid reinforced soil retaining walls, based on limit equilibrium, are known to be very conservative current design methods do not provide useful performance information such as wall face deformations.

Utilizing the constitutive models and properties of foundation soils published by previous researches, numerical simulations were conducted using 2D explicit Finite Difference programs, FLAC^{2D}. after

reviewing the main results of the N.M. in static conditions of the reinforced soil with geogrids built in IP3, between Regua and Reconcos, it's shown that the control of face deformations is guaranteed considering geogrids with an minimum length plus a sufficient number of long geogrids to ensure the structure's internal and external stability.

It's observed that in a normalized geogrids solution the amount of shorter geogrid's length should have between 30-50% of the long geogrid's length.

4. References

- [1]Mendonça, A.A. 2004. Study of the behaviour of geogrids re-inforced structures. Ph.D. thesis, FEUP, Porto, Portugal, (in Portuguese)
- [2] Rowe, R.K. and skinner, G.D. (2001) Numerical analysis of geosynthetic reinforced retaining wall constructed on a layered soil foundation, Geotextile and Geo-membranes, 19(7), 387-412.
- [3] ITASCA Consulting Group, Inc. 2000. FLAC – Fast Lagrangian Analysis of Continua, Ver. 4.0 User's Manual. Minneapolis: Itasca.

Recent Development In Electrokinetic Stabilization Of Soft Soil: A Review

Hossein Moayed¹, Sina Kazemian², and Bujang B. K. Huat³,

1. Department of Civil Engineering, Science and Research Branch, Islamic Azad University, Tehran, Iran.
2. Department of Civil Engineering, Bojnourd Branch, Islamic Azad University, Bojnourd, Iran.
3. Department of Civil Engineering, Universiti Putra Malaysia, Serdang, Selangor, Malaysia.

ABSTRACT

Electrokinetic (EK) stabilization is a ground improvement method which treats soils without excavation process. This is known as an important advantage over traditional grouting methods. It has been used in several soil improvement categories including consolidation, contaminant removal, dewatering, and stabilization. In addition, the EK applications cause electrochemical effects in the treated soil, leading to changes in the soil's chemical, physical, and mechanical properties. With EK injection technique, chemical stabilizing agents are electrically injected into the soils to achieve stabilization by means of ion exchange, precipitation or mineralization. The aim of this study was to review the recent development in the EK strengthening of soft soils. Enhancing the EK stabilization techniques require a deeply assessment through the colloidal surface charge and advances in the EK apparatus.

Keywords: Electrokinetic, Soil improvement, Grouting, Direct current, Soft soil.

1. INTRODUCTION

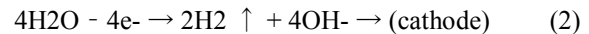
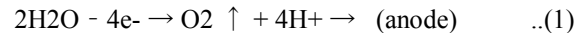
Soil improvement refers to any method or techniques that improve the engineering properties of soil, like compressibility, shear strength, stiffness, and permeability. Raju (2009) classified the soil improvement methods to following principles: (i) chemical modification (e.g. jet grouting, deep soil mixing, injection grouting), (ii) consolidation (e.g. vacuum consolidation, prefabricated vertical drains & surcharge, stone columns), (iii) reinforcement (e.g. geosynthetic reinforcement, stone columns), and (iv) densification (e.g. dynamic compaction, vibro-compaction, compaction grouting) [1, 2] (Table 1).

Majority of the companies and geo-engineers, which are working in these fields agree that the soil improvement methods are typically done based on following classifications: (i) hydraulic modifications, (ii) mechanical modifications, (iii) modifications by inclusions and confinement, and (iv) physical and chemical modifications [3]. The goals of such improvement methods include reducing soil water content, reducing compressibility, and increasing shear strength.

2. DEFINITION OF ELECTROKINETIC

EK is well known as the physicochemical transport of charge, action of charged particles, and effects of applied electric potentials on formation and fluid transport in porous media [4, 5]. As stated, the presence of the diffuse double layer (DDL) causes several EK phenomena in soil, which may result from either the movement of different phases in respect of each other including transport of charge, or the movement

of different phases relative to each other due to the applying of such electric potentials [4, 6]. Besides, application of direct current (DC) through electrodes give rises to electrolysis reactions at the electrodes [7, 8]. Oxidation of water at the anode generates an acid front and reduction at the cathode generates a base front. Electrolysis reactions are described by the Equations (1) and (2).



Within the first few days of EK processing, electrolysis reactions increase the pH at the vicinity of the cathode and decrease the pH at the vicinity of the anode. These changes are normally dependent to the total current applied [5, 9].

The EK phenomena include electroosmosis, electrophoresis, streaming potential, and sedimentation potential. Electroosmosis is defined as movement of fluid with respect to a solid wall as a result of an applied electric potential gradient [10, 11].

In other words, if the soil is placed between two electrodes in a fluid and an electromotive force is applied the fluid will move from one side to the other. Electrophoresis is the movement of suspended solid in a liquid due to application of an electric potential gradient. Streaming potential is the reverse of electroosmosis. It defines the generation of an electric potential difference due to fluid flow in soils. Sedimentation potential (or migration potential), known as Dorn effect [12], is an electric potential generated by the movement of particles suspended in a liquid [9, 13, 14].

Table 1. Various soil improvement techniques (after Hausman, 1990)

Mechanical modifications	Shallow Surface Compaction	Static Roller	Smooth Steel Rollers and Pneumatic-tired Roller
			Sheepsfoot Rollers
			Grid Roller
		Impact and Vibratory Equipment	Tamper, Rammers, and Plate Compactors
			Vibrating Rollers
		Impact Rollers	
	Deep Compaction Technique	Pre-compression	
		Explosion	
		Heavy Tamping (Dynamic compaction)	
		Vibration (Vibro-compaction and Vibro-replacement)	
	Hydro-mechanical Compaction	Hydraulic Fill	
		Dry Fill with Subsequent Spraying or Flooding	
		Compaction of Rock Fill with Water Jets	
Hydraulic modify cations	Open Sumps and Ditches		
	Gravity Flow Wells		
	Pre-loading and Use of Vertical Drains		
	Vacuum Dewatering Wells and Preloading		
	Electrokinetic Dewatering and Stabilization		
Physical and chemical modifications	Mixing Method	Shallow Mixing Method (SMM)	
		Deep Mixing Method (DMM)	
	Injection and grouting	Permeation Grouting	
		Compaction Grouting	
		Hydro fracture Grouting	
		Compensation Grouting	
Modifications by inclusions and confinement	Flexible Geosynthetic Sheet Reinforcement		
	In Situ Ground Reinforcement	Ground Anchorage	
		Rock Bolting	
		Soil Nailing	
	Soil Confinement by Formwork	Crib Walls	
		Gabions and Mattress	
		Fabric Formwork	

3. ELECTROKINETIC HARDENING OF SOIL

While conventional soil grouting can be used to stabilize soils with relatively high permeability (k typically greater than 10^{-5} m/s), other methods need to be applied for strength improvement of fine-grained soils with lower hydraulic conductivity values. These include, hydrofracture grouting, artificial ground freezing, and induced consolidation either by applying electric fields or surcharging the soil [15]. Although all of these methods result in some considerable degree of

ground movement, it still have other drawbacks [8, 15]. With the increase in urban construction and construction in mechanically substandard soils, new methods was required to stabilize soft soils with low permeability while minimizing ground movements [11]. EK stabilization is a ground improvement method which is treats soils without excavation (e.g. disturbing the soil). This is known as an important advantage over traditional methods. It has been used in several soil improvement categories including consolidation, contaminant removal, dewatering, and stabilization [7, 16-20]

3.1 Electroosmosis Consolidation

Early application of electroosmosis was intended for dewatering of wet soils and soil consolidation [21-23]. Enhanced electroosmosis with injection of cationic stabilizer into the soil has been developed significantly in recent years to improve the shear strength of soft soils [14, 15, 24-27]. The enhanced electroosmosis techniques are different than electroosmotic consolidation in that transport processes are utilized for injecting chemical grouts into the soil.

Gray and Schlocker (1969) and Gray (1970) studied electroosmosis as a transport mechanism for hardening soft soils by injecting the aluminum ions [28, 29]. In their studies, the liquid limit of montmorillonite dropped to about half of the initial value. Sutton and Alexander (1987) described using electroosmosis to draw chemicals from anode to cathode for soil stabilization, further indicating that it is possible to alter the clay properties and cause mineralization by electrochemical methods [8]. Shang et al. (2004) stated conditions that most favored for a chemical reagents used in the electrochemical cementation process are (i) the chemical compounds should increase the soil shear strength, (ii) they must be economically feasible, and (iii) they should be soluble in water so that they can be transported by the electrical current through soil pores.

While electroosmosis mobilizes the pore fluid, carrying soluble grouts toward the cathode, ionic migration effectively transports negative anions to the positive anode and positive cations to the negative cathode. The important difference is that this mode of chemical transport can potentially occur without any fluid flow, compared to the use of electroosmosis to induce chemical transport [22]. Based on this fact, Ozkan et al. (1999) presented the results of experiments for injection of phosphate and aluminum ions at the cathode and anode to improve the mechanical properties of kaolinite [30]. The premise for this work is that electroosmosis can carry phosphate ions towards the cathode while ionic migration transports phosphate ions towards the anode, resulting in more rapid, uniform soil stabilization. The results showed a 500–600% increase in kaolinite undrained shear strength after treatment. However, the strength increase was not homogeneous throughout the specimen. Previous laboratory work and case studies are summarized in Table 2.

3.2 Application of Electrokinetics in Soil Improvement

Alshawabkeh (2009) stated that application of electric gradients in soil mass will result in two important transport mechanisms; electroosmosis as well as electro ion migration (EM). Electroosmosis draws chemical stabilizers with the flowing water under electric fields. However, the EM transports ions to the electrode opposite in polarity under electric fields [9]. Electroosmosis and any other hydraulic flow will usually carry and move all types of solutes from one location to another, depending on flow direction. However,

EMs separate positively and negatively charged ions and cause their migration to opposite electrodes. As a result, hydraulic flow might improve the migration of certain ions, but retard migration of other ions (with opposite charge) [5, 9, 31]. The relative contribution of electroosmosis and migration to ion transport under electric fields varies for different soil types, type of ion, water content, boundary conditions, and pore fluid chemistry.

4. IMPORTANCE OF SURFACE CHARGE

Surface charge in turn is a function of pH and dissolved salts concentration which normally measure by the zeta (ζ) potential [38, 39]. The ζ potential is known as an intrinsic property of colloidal particles suspended in a liquid. Adsorption of ions or dipolar molecules is determined by, and also determines, this charge and potential distribution [40, 41]. The potential distribution itself determines the interaction energy between the particles, and this is in many cases responsible for the stability of particles towards coagulation and for many aspects of the flow behavior of the colloidal suspension [27, 42, 43].

5. CONCLUSION

Although EK injection technology has been seldom employed, as showed in Table 2, the majorities of applications have been successful and have proved an economic alternative to traditional ground improvement methods [14, 24, 30]. Over the last 40 years, a few hundred different compounds of chemical grout are introduced. The grouting and chemical grouting technologies have also grown over the last few decades. Besides, the EK injection is established as an effective in situ ground improvement technique in fine soils, particularly where ground movements need to be minimized. However, the origin of EK treatment performed on a few soil types as well as chemical stabilizers. For most of the soft soil, EK injection phenomena and consequences of injection of cationic (or chemical stabilizer) reagents have not been studied yet.

Table 2. Various reported case studies and researches relating to EK stabilization

Reference	Application	Soil	Stabilizer	Comments
[32]	Foundation for bridge abutment	Soft to stiff clay	Sodium silicate	Major implementation problems encountered
[33]	Laboratory investigation	Liquifiable sand	Silicate solutions, bentonite, aluminum hydroxide	Successful application
[34]	Highway subgrade, Arizona	Low-plasticity clay	Potassium chloride	Reductions in degree of swell and swell pressure
[35]	Foundation strengthening	Loess	Sodium silicate	Successful application
[5]	Large scale laboratory investigation	Fine grained sand bed and Kaolinite bed	ammonium at cathode and sulphate at the anode	Successful application
[36]	Laboratory investigation	Kaolinite	Aluminum and phosphate ions	Larger increases in shear strength for phosphoric acid than aluminum sulphate/phosphoric acid
[30]	Laboratory investigation	Kaolinite	simultaneously inject aluminum ions at the anode and phosphoric ions at the cathode	average shear strength increase of 500 – 600% was obtained in the region of the cathode
[37]	Laboratory investigation	Sand	Sodium silicate and calcium chloride	Possibility that temperature variation in ground under electric loading has an influence on strength of improved ground.
[15]	Laboratory investigation	Marine illitic soil (Boston Blue Clay)	inject phosphoric acid at the cathode	shear strength increased by 160% at the side of cathode

6. REFERENCES

- [1] Raju, VR, Ground Improvement Principles and Applications in Asia. Ground Improvement Technologies and Case Histories, 2009, pp. 43-66.
- [2] Kazemian, S, Stabilization of Peat by Cement-Sodium Silicate Grout Using Injection-Vacuum Technology. Department of Civil Engineering, Doctor of Philosophy, 2011, pp. 267.
- [3] Hausmann, MR, Engineering Principles of Ground Modifications. 1990.
- [4] Acar, YB, AN Alshawabkeh, RJ Gale, "Fundamentals of Extracting Species From Soils by Electrokinetics," Waste Management, 13(2), 1993, pp. 141-151.
- [5] Acar., YB, MF Rabbi., EE Ozsu., "Electrokinetic Injection of Ammonium and Sulfate Ions Into Sand and Kaolinite Beds," Journal of Geotechnical and Geoenvironmental Engineering, 123(3), 1997, pp. 239-249.
- [6] Acar, YB, AN Alshawabkeh, "Electrokinetic Remediation. I: Pilot-Scale Tests With Lead-Spiked Kaolinite," Journal of Geotechnical and Geoenvironmental Engineering, 122(3), 1996, pp. 173-185.
- [7] Asavadorndeja, P, U Glawe, "Electrokinetic Strengthening of Soft Clay Using the Anode Depolarization Method," Bulletin of Engineering Geology and the Environment, 64(3), 2005, pp. 237-245.
- [8] Alshawabkeh, AN, TC Sheahan, X Wu, "Coupling of Electrochemical and Mechanical Processes in Soils Under DC Fields," Mechanics of Materials, 36(5-6), 2004, pp. 453-465.
- [9] Alshawabkeh, AN, "Electrokinetic Soil Remediation: Challenges and Opportunities," Separation Science and Technology, 44(10), 2009, pp. 2171-2187.
- [10] Mitchell, JK, K Soga, Fundamentals of Soil Behavior. 2005.
- [11] Acar, YB, RJ Gale, AN Alshawabkeh, RE Marks, S Puppala, M Bricka, R Parker, "Electrokinetic Remediation: Basics and Technology Status," Journal of Hazardous Materials, 40(2), 1995, pp. 117-137.
- [12] Krut, HR, Colloid Science (I): Irreversible Systems., 1952.
- [13] Acar, YB, RJ Gale, GA Putnam, J Hamed, RL Wong, "Electrochemical Processing of Soils: Theory of pH Gradient Development by Diffusion, Migration, and

- Linear Convection," *Journal of Environmental Science and Health - Part A Environmental Science and Engineering*, 25(6), 1990, pp. 687-714.
- [14] Chien, SC, CY Ou, MK Wang, "Injection of Saline Solutions to Improve the Electro-Osmotic Pressure and Consolidation of Foundation Soil," *Applied Clay Science*, 44(3-4), 2009, pp. 218-224.
- [15] Alshawabkeh, AN, TC Sheahan, "Soft Soil Stabilization by Ionic Injection Under Electric Fields," *Ground Improvement*, 7(4), 2003, pp. 177-185.
- [16] Casagrande, L, "Electro-osmosis in Soils," *Geotechnique*, 1(3), 1949, pp. 159-177.
- [17] Azzam, R, W Oey, "The Utilization of Electrokinetics in Geotechnical and Environmental Engineering," *Transport in Porous Media*, 42(3), 2001, pp. 293-314.
- [18] Han, SJ, SS Kim, BI Kim, "Electroosmosis and Pore Pressure Development Characteristics in Lead Contaminated Soil during Electrokinetic Remediation," *Geosciences Journal*, 8(1), 2004, pp. 85-93.
- [19] Kim, SO, WS Kim, KW Kim, "Evaluation of Electrokinetic Remediation of Arsenic-Contaminated Soils," *Environmental Geochemistry and Health*, 27(5-6), 2005, pp. 443-453.
- [20] Nieto Castillo, AM, JJ Soriano, RA García-Delgado, "Changes in Chromium Distribution During the Electrodialytic Remediation of a Cr (VI)-Contaminated Soil," *Environmental Geochemistry and Health*, 30(2), 2008, pp. 153-157.
- [21] Bjerrum, L, J Moum, O Eide, "Application of Electro-osmosis to a Foundation Problem in a Norwegian Quick Clay," *Geotechnique*, 17(3), 1967, pp. 214-235.
- [22] Gray, DH, JK Mitchell, "Fundamental Aspects of Electroosmosis in Soils," *Journal of the Soil Mechanics and Foundations Division, ASCE*, 93(SM6), 1967, pp. 209-236.
- [23] Esrig, MI, "Pore Pressures, Consolidation and Electrokinetics," *J. Soil Mech. Found. Div., Am. Soc. Civ. Eng.*, 94(4 SM), 1968, pp. 899-921.
- [24] Lefebvre, G, F Burnotte, "Improvements of Electroosmotic Consolidation of Soft Clays by Minimizing Power Loss at Electrodes," *Canadian Geotechnical Journal*, 39(2), 2002, pp. 399-408.
- [25] Abdullah, WS, AM Al-Abadi, "Cationic-Electrokinetic Improvement of an Expansive Soil," *Applied Clay Science*, 47(3-4), 2010, pp. 343-350.
- [26] Ou, CY, SC Chien, HH Chang, "Soil Improvement Using Electroosmosis With the Injection of Chemical Solutions: Field Tests," *Canadian Geotechnical Journal*, 46(6), 2009, pp. 727-733.
- [27] Ou, CY, SC Chien, YG Wang, "On The Enhancement of Electroosmotic Soil Improvement by the Injection of Saline Solutions," *Applied Clay Science*, 44(1-2), 2009, pp. 130-136.
- [28] Gray, DH, "Electrochemical Hardening of Clay Soils," *Geotechnique*, 20(1), 1970, pp. 81-93.
- [29] Gray, DH, J Schlocker, "Electrochemical Alteration of Clay Soils," *Clays and Clay Minerals*, 17, 1969, pp. 309-322.
- [30] Ozkan, S, RJ Gale, RK Seals, "Electrokinetic Stabilization of Kaolinite by Injection of Al^{3+} and PO_4^{3-} Ions," *Ground Improvement*, 3(4), 1999, pp. 135-144.
- [31] Park, JY, Y Chen, J Chen, JW Yang, "Removal of Phenanthrene From Soil by Additive-Enhanced Electrokinetics," *Geoscience Journal*, 6(1), 2002, pp. 1-5.
- [32] Caron, C, "Consolidation of Clayey Soils by Using Electro-Osmosis, (Consolidation Des Terrains Argileux par Electro-Osmose)," *Ann Inst Tech Batiment Trav Pub*, (285), 1971, pp. 73-123.
- [33] Yamanouchi, T, S Matsuda, 'Proceedings of the Symposium on Recent Developments in the Analysis of Soil Behaviour,' 1975, pp. 411-421.
- [34] O'Bannon, CE, GR Morris, FP Mancini, "Electrochemical Hardening of Expansive Clays," *Transportation Research Record*, (593), 1976, pp. 46-50.
- [35] Oncescu, V, RJ Bailie, "Problems of Soil Consolidation and Waterproofing Solved by Grouting," *Studii de Cercetare in Constructii Hidraulice Si Mecanica Rocii*, 19, 1977, pp. 127-210.
- [36] Anon, "Chemical Stabilisation of Kaolinite by Electrochemical Injection," *Geotechnical Special Publication*, 81(286-297), 1998.
- [37] Fujihira, M, E Shimizu, T Konishi, S Yasuda, T Shimizu, "The Fundamental Study on Soil Prevention Method of Liquefaction Using Electrophoresis of Fixative Materials," *Zairyo/Journal of the Society of Materials Science, Japan*, 49(1), 2000, pp. 38-41.
- [38] Brunelle, MT, "Colloidal Fouling of Reverse Osmosis Membranes," *Desalination*, 32, 1980, pp. 127-135.
- [39] Niriella, D, RP Carnahan, "Comparison Study of Zeta Potential Values of Bentonite in Salt Solutions," *Journal of Dispersion Science and Technology*, 27(1), 2006, pp. 123-131.
- [40] Hlavacek, M, JF Remy, "Simple Relationships among Zeta Potential, Particle Size Distribution, and Cake Specific Resistance for Colloid Suspensions Coagulated with Ferric Chloride," *Separation Science and Technology*, 30(4), 1995, pp. 549-563.
- [41] Sabah, E, U Mart, M Çınar, MS Çelik, "Zeta Potentials of Sepiolite Suspensions in Concentrated Monovalent Electrolytes," *Separation Science and Technology*, 42(10), 2007, pp. 2275-2288.
- [42] Carlson, JJ, SK Kawatra, "Factors Affecting Zeta Potential of Iron Oxides," *Mineral Processing and Extractive Metallurgy Review*, 2011.
- [43] Gallardo, MAM, MR Calzado, MML González, GC Pérez, "Zeta Potential Aspects of Dispersed Solvents Involved in the Determination of Microbial Cell Surface Hydrophobicity," *Journal of Dispersion Science and Technology*, 27(1), 2006, pp. 23-32.

Application of Ion-Exchange Solution Soil Stabilizer in Increasing CBR Values of Clayey Soils

Reza Ziaie Moayed¹, Seyed Ali Hashemi² and Farzad Allahyari³
^{1,3}Imam Khomeini International University, Iran
²Iran Polymer and Petrochemical Institute, Iran

ABSTRACT

Soil stabilization is one of the methods for increasing soil strength. For this purpose many of materials can be used like lime, fly ash, cement and organic polymers. Using this material has some limitation and does not improve soil properties very well. One of the best materials for soil stabilization is ion-exchange solutions. There are many ion-exchange solutions soil stabilizer and one of the best and the most economical ion-exchange solution is using in this paper and its name is CBR⁺. This paper describes the application of ion-exchange solution CBR⁺ (CBR plus) for stabilization two various clayey soils. California Bearing Ratio (CBR) tests were carried out on unstabilized and stabilized soil samples. The samples were soaked in water for 96 hours. CBR values of stabilized soils in the soils with lower plasticity index are more than unstabilized. For soils with lower plasticity index CBR values increases up to the 168%.

Keywords: Soil stabilization, ion-exchange solution, CBR⁺, CBR, Atterberg limits

1. INTRODUCTION

Clay soils make up great part of soils in the ground. Clayey soils are commonly stiff in dry states but lose their stiffness when they are saturated with water. Clayey soils commonly have low bearing capacity, low stability, high settlement, and excessive swelling or shrinkage properties. For these reasons it is necessary to make such soils suitable for construction. The use of traditional geotechnical engineering techniques for infrastructure, such as the replacement of unsuitable soils for stiff and resistant embankment, is often problematic, not only for their high costs, but even more for environmental reasons. In roads, for instance, the use of granular bases becomes unsuitable when the extraction site is at a significant distance from the construction site [1]. Application of stabilization agent on soils has a long history. Many materials such as lime [2], fly ash [3] and organic polymers [4] were used as stabilizing agents. When lime is added to a clayey soil it has an immediate effect on the properties of the soil. With adding lime cation exchange begins to take place between the metallic ions associated with the surfaces of the clay particles and the calcium ions of the lime. One of the ways to make clayey soils suitable for construction is altering the properties of soil. This increases the strength, reducing compressibility, swelling or shrinkage and increasing the durability of soils. Ion exchange is one of the methods for stabilization of clayey soils. It is well-known that the swelling properties of expansive soils significantly are affected by cation exchange capacity [5]. Ion exchange occurs when some of the additive such as fly ash, lime, cement and ion exchange solution are added to these soils. Many of ranchers have investigated the improvement of the expansive soils with fly ash and they

have determined that addition of fly ash to the soil decreases the value of cation exchange capacity [6], [7].

There are many ion-exchange solutions soil stabilizer and one of the best and most economical ion-exchange solution is using in this paper and its name is CBR⁺.

The objective of this paper is to investigate the bearing ratio capacity of two clayey soils that are stabilized with CBR⁺ ion exchange solution. The tests were carried out on two clayey soils with different doses of CBR⁺ (0.0, 0.12 and 0.28 (gr/lit)) in two different curing times. The test results also were discussed in detail and compared with each other.

2. MATERIALS

2.1 Soil

In this experimental study two fine-grained clays were used. Soils are from Iran- Qazvin- Abyek. The grain size distributions of two clayey soils are presented in Fig.1.

The soils lie above the A-line in plasticity chart. Two soils are classified as low plasticity soil according to the unified soil classification system (ASTM D422-87) and their name according to USCS is CL (clayey soil with low plasticity).

The optimum moisture contents and maximum dry densities of two clayey soils were obtained according to ASTM D4318 (Fig. 2). Engineering properties of two soils are presented in Table 1.

Soil samples for CBR test were compacted with their optimum moisture contents value and the respective dry densities.

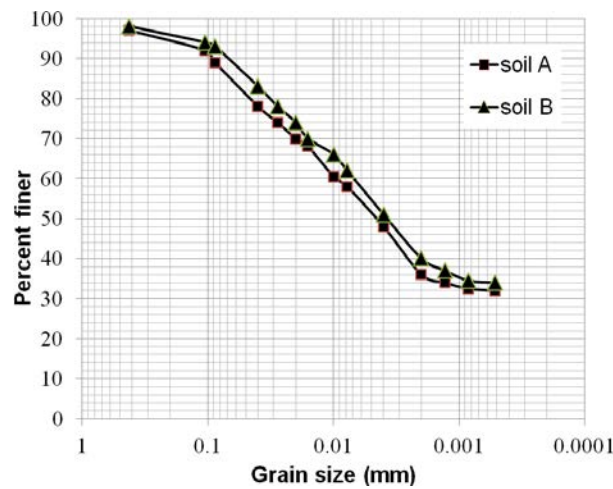


Fig.1 Grain size distribution of two clayey soils

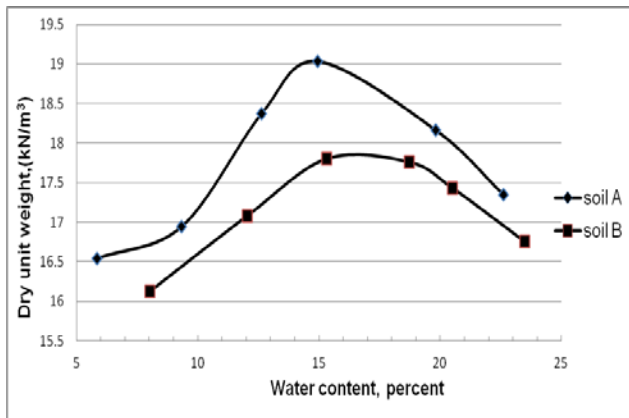


Fig.2 Compaction curves of two clayey soils

2.2 CBR⁺ Solution

CBR⁺ solution is a stabilizer for anionic soils that can improve the bearing capacity of a variety of clayey soils. Soils that normally are not suitable for road construction can now be treated with CBR⁺ for base and subbase in road construction. Clay minerals inherently have a predominantly negative electrical or anionic charge; this causes the clay minerals to have strong attraction for any cation that are presented. These negative clay minerals attract cations like iron filings to a magnet and will react with water when present. Normal temperatures and compaction pressure will not remove them. This layer of water is known as the electrostatic diffused double layer of adsorbed water [8]. Generally it can be said that CBR⁺ forms an extremely thin oily layer on the surface of soil particles and especially on clay particles. This facilitates the compaction of soil and allows water, which is normally chemically bound with the soil particles, to be driven out of the soil matrix. In this process the soil can be compacted to a higher density. Since CBR⁺ neutralizes the natural electrical charges that occur on the soil particle surface, the soil particles can be compacted to a much closer degree (especially by traffic forces). This will lead to increasing in internal friction between the soil particles, which in turn result in a higher bearing capacity for

the soil [9]. Table 2 shows physical and chemical properties of CBR⁺.

Table 1: Engineering properties of two clayey soils

property		soil A	soil B
Atterberg limits	Liquid Limits, (%)	30	42
	Plastic Limits, (%)	18	23
	Plasticity Index, (%)	12	19
Compaction parameters	Optimum Moisture Content, (%)	15	17
	Maximum dry unit weight, (kN/m ³)	19	17.8
Soil classification(USCS)		CL	CL

Table 2: Physical and chemical properties of CBR⁺ [10]

Appearance	Chocolate Brown viscous fluid
Odour	Sulphurous Odour
Physical State	Viscous Fluid
Freezing Point(°C)	<-10° C
Boiling Pint (°C)	100°C
pH	9
Specific Gravity	0.94
Coefficient Water/Oil	100% water soluble
Percent Soluble (at 20°C)	100%

3 EXPERIMENTAL PROGRAM

3.1 Test Procedure

To study the effect of various amount of ion exchange CBR⁺ and curing time on the bearing ratio of clayey soils with various plasticity index(PI), a series of bearing ratio tests were conducted on soaked samples for three different amount of CBR⁺ solution (without CBR⁺ and two different doses of it) and two different curing times. For soaked condition, the samples were immersed in water for 96 hours. The purpose of different amount of ion exchange solution and curing time is to investigate the effect of each variable on bearing ratio of different soil samples.

3.2 Preparation of Samples

The bearing ratio mold is a rigid metallic cylinder with an inner diameter of 152mm and a height of 178mm that 61mm of its height is filled with a circular metal disk.

To prepare the samples, oven-dried clayey soils were mixed with their optimum moisture content (soil A with 15% moisture and soil B with 17% moisture). The soil that was mixed with its optimum moisture was placed in five layers at the bottom of the mold. Each layer was compacted by 56 blows of a 44.5-N rammer dropped from a height of 457mm.

The samples with various clayey soils and amount of CBR⁺ solution have been cured for two various times, one day and one week. After these curing times, samples were soaked in water for 96 hours.

To prepare the soaked samples, the mold containing clayey soil was immersed in water, allowing free access of water to the top and bottom of the samples, and was allowed to soak for 96 hours (ASTM D1883-99).

3.3 California Bearing Ratio (CBR) Test

The bearing ratio is one of the fundamental parameters used to demonstrate the behaviour of soil. This test is used in many geotechnical projects including roads, railroads, pavements and airport runways. To demonstrate the influence of different variables on the bearing ratio of the clayey soil stabilized with CBR⁺ solution, a series of bearing ratio tests were carried out on stabilized and unstabilized specimens. The bearing ratio tests were conducted under soaked condition in both one day and one week curing times according to ASTM D1883-99. CBR tests are conducted with a mechanical loading machine equipped with a movable base that moved at a uniform rate of 1.27 mm/min. The diameter of the piston is 49.6 mm. The loads were recorded as a function of penetration depth up to a penetration of 10 mm.

4 RESULTS AND DISCUSSION

Bearing ratio tests were carried out for both stabilized and unstabilized clayey soils with different amount of CBR⁺ and different curing times at optimum moisture contents values of each soils. The stress-penetration curves were plotted and corrected according to ASTM D1883-99. Fig. 3a shows typical stress-penetration curves for soil A in one week curing time and Fig. 3b indicate the same curves for soil B.

4.1 Effect of Amount of CBR⁺ Solution

In this study three different ion exchange solutions doses were considered for two clayey soils to investigate the influence of the amount of this stabilizer on the strength of soaked samples. CBR values for a penetration depth of 2.5mm were calculated based on ASTM D1883-99 and the following equation:

$$\text{CBR} = [\text{stress at 2.5mm penetration} / 6.894 \text{MPa}] \times 100 \quad (1)$$

In the above equation 6.894 MPa is standard stress at 2.5 mm penetration.

Fig. 4 shows CBR values versus various doses of CBR⁺ for one week curing time. Based on these finding, it can be inferred that dose of CBR⁺ doesn't play any significant role in the behaviour of soil with higher plasticity index and this can be due to less ion exchange. It shows that soil with higher PI can't properly accept cation (positive charge) from CBR⁺ solution.

Fig. 5 shows the percentage of the increase in CBR values for two clayey soils in one week curing time. It shows that with increasing the dose of CBR⁺ up to the 0.12 gr/lit, it increases CBR values of soil A and this is because of ion exchange reaction. With increasing CBR⁺ more than this value, more solution without any reaction remain in the soil and this can

deteriorate its strength. But soil B shows reduction in CBR values with increasing the dose of CBR⁺.

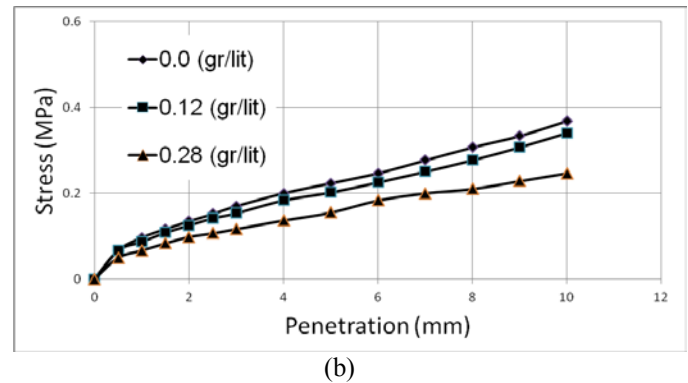
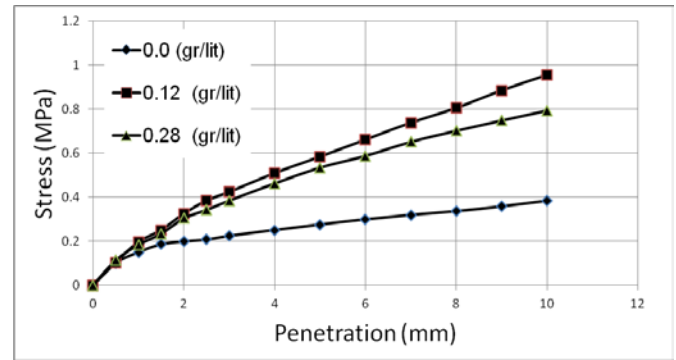


Fig.3 Typical stress-penetration curves for samples with various dose of CBR⁺ for one week curing time: (a) Soil A and (b) soil B.

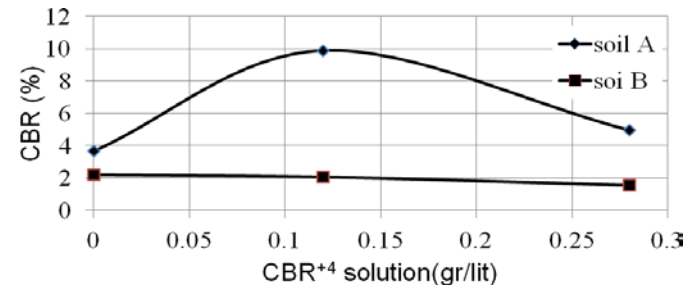


Fig.4 CBR values versus doses of CBR⁺ solution for one week curing time

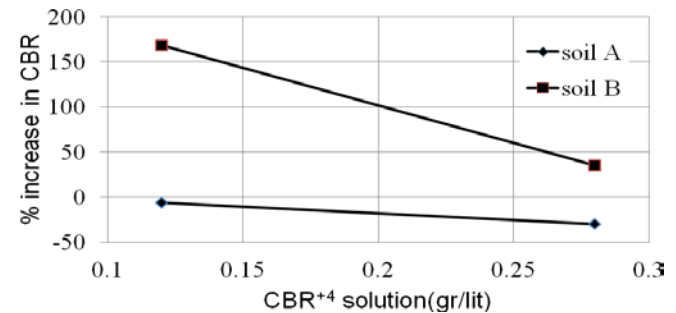


Fig.5 Percentage of increase in the CBR values for different clayey soils

4.2 Effect of the Curing Time

To investigate the effect of the curing time on the behaviour of the stabilized and unstabilized soil, two curing times were considered; one day and one week.

Fig. 6 illustrates the effect of the CBR^{+4} on the CBR values for the various curing times. It shows that the curing times don't have any significant effect on the behaviour of soil B that have higher plasticity index but curing time plays a significant role in the strength of the soil A with lower PI. It show that increasing curing time has a significant effect on the behaviour of soil A and CBR values of soil B don't show a significant change. Soil A has a complicated behaviour with adding stabilizer and curing time is an important factor. In one day curing time, increasing in dose of CBR^{+4} increase strength of soil and this is because of higher rate of reaction with further amount of this solution. With higher curing time increasing in dose up to the 0.12 gr/lit increases CBR values and this is because of ion exchange reaction, but with increasing CBR^{+4} more than 0.12 gr/lit, more solution without any reaction remain in the soil and deteriorate its strength.

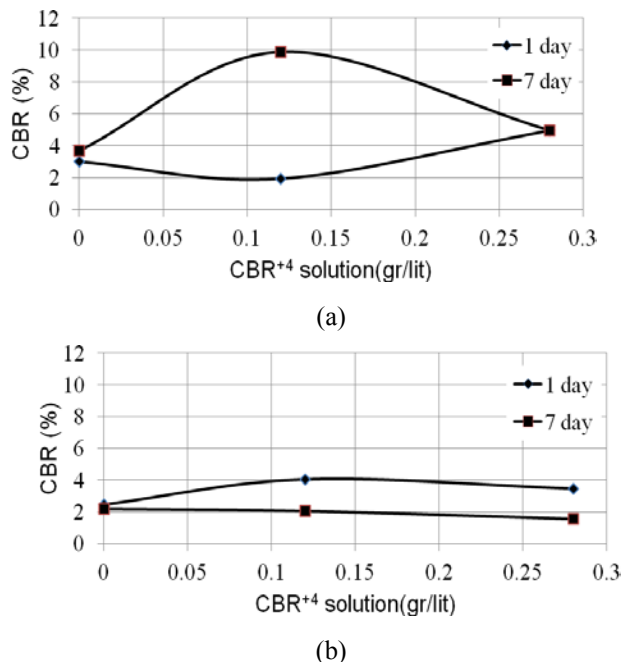


Fig.6 CBR values versus doses of CBR^{+4} solution for different clayey soils: (a) Soil A and (b) soil B.

5 CONCLUSION

To study the behavior of clayey soils that have been stabilized with CBR^{+4} ion exchange solution, several CBR tests were conducted on the stabilized and unstabilized soils. The following conclusion can be drawn from the test results:

- CBR^{+4} solution is a stabilizer that has cation ions and can be used for soils that have anion ions. Two soils that have been used in this study were clayey soils that have anion ions.
- Plasticity index (PI) plays a fundamental role and this study shows that the stabilization efficiency decreases with increasing PI.

- A greater strength for stabilized soil was achieved for samples with one week curing time and lower dose of CBR^{+4} for soil with lower PI (soil A).
- Increasing in the curing times doesn't have a constant effect on the strength of the various clayey soils and its effects are different for various soils.
- Adding excessive dose of CBR^{+4} solution have a negative effect, because some of this stabilizer remains in the soil without any reaction and reduces the strength of soil.
- Soil A that has lower PI shows the maximum strength with lower dose of CBR^{+4} and one week curing time. It shows 168% increase in CBR value.

6 REFERENCES

- [1] Da Fonseca, A.V., Caberlon Cruz, R., Cesar Consoli, N. "Strength Properties of Sandy Soil-Cement Admixture," *Geotech Geol Eng*, vol.27,2009, pp. 681-686.
- [2] Theng, B.K.G.(1982). "Clay-polymer intractions: Summary and perspectives," *Clay and Clay Minerals*, vol.30, 1982, pp.1-10.
- [3] Dermatas, D., Meng, X.G. "Utilization of fly ash for stabilization /solidification of heavy metal contaminated soils," *Engineering Geology*, vol.70, 2003, pp. 377-394.
- [4] Lahalih, S.M., Ahmed, N. "Effect of new stabilizers on the compressive strength of dune sand," *Construction and building Materials*, vol.12, 1998, pp. 321-328.
- [5] Grim, R.E. "Clay Mineralogy," Second edition, McGraw-Hill Book Company, New York, 1968, p. 596.
- [6] Nalbantoglu, Z., "Effectiveness of class C fly ash as an expansive soil stabilizer". *Construction and Building Materials*, vol.18, 2004, pp.377-381.
- [7] Nalbantoglu, Z., Gucbilmez, E." Improvement of calcareous expansive soils in semiarid environments," *Journal of Arid Environments*, vol. 47, 2001, pp. 450-463.
- [8] CBR PLUS (North America Inc.). "Effective Soil Stabilization & Dust Control for Roads," soil stabilization and dust control.
- [9] CBR PLUS (North America Inc.). "Guidelines for the CON-AID / CBR PLUS Soil Stabilizer," soil stabilization and dust control.
- [10] CBR PLUS (North America Inc.). "Material Safety Data Sheet," soil stabilization and dust control.

Assessment of Low Strain Wave Attenuation for Piles Cast in Very Dense Granular Soil

Ramli Nazir, Ph.D, P.Eng. and Osman El Hussien, M.Eng.
Faculty of Civil Engineering, Universiti Teknologi Malaysia

ABSTRACT

In low strain testing of piles, soil within which the pile is embedded causes attenuation of propagated stress wave. The pile-soil interaction effect on low strain integrity test is not properly identified; however, it may lead to inconclusive results when piles are embedded in very dense soil. In this paper a method to estimate soil effects on low strain wave attenuation is proposed. Numerical analysis is utilized to arrive to a theoretical model, which accommodates soil effects on wave propagation in pile body. The proposed model assuming pile casted in very dense granular soil is compared with PIT-S software, which simulates propagation of low strain waves for similar pile-soil conditions. Generally, wave attenuations estimated by both methods were found to be close for pile subjected to short duration light impact.

Keywords: Pile, Soil, Wave, Attenuation, Low Strain

1. INTRODUCTION

Constructed piles are usually tested in order to evaluate their integrity as part of foundation construction quality assurance. The low strain integrity test is routinely performed, because it is fast and cost effective. This test is based on wave propagation theory and the name "low strain test" is based on the fact that when a light impact is applied to a pile it produces a low strain compression wave that travels down the pile at a constant speed, and generates pile strains of around 10^{-5} micro strain (Hussein and Garlanger, 1992). Changes in cross sectional area such as a reduction in diameter or material such as a void in concrete produce wave reflections, which can be used for pile integrity assessment. This procedure is performed with a hand held hammer to generate an impact. The accelerometer or geophone is placed on top of the tested pile to measure the response to the hammer impact via data acquisition and interpretation through electronic instrument. The hammer impact induces a one dimensional stress wave into the pile that travels at speed (c), where (c) is a function of the pile density (ρ) and material elastic modulus (E). The recorded data will be processed and interpreted assuming a typical wave speed value. Pile impedance (Z) is defined as the elastic modulus "E" times the cross sectional area (A) divided by material wave speed (c) (i.e. $Z=EA/c$). Impedance changes are attributed to changes in pile cross sectional area and material quality. A sample test setup is shown in Figure 1.

The low strain pile top velocity records indicate changes in pile size or quality. However, the pile top motion is also affected by soil resistance forces. An increase in pile impedance and/or soil resistance force results in a decrease in the measured pile top velocity (Johnson and Rausche, 1996). However, the contribution of surrounding soil on the pile

integrity results is still not precisely quantified. This has led to difficulties in assessment of integrity of piles embedded in soils that produce strong resistance or damping effects on the tested piles.

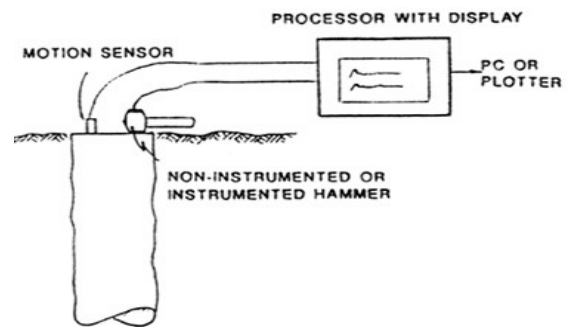


Figure 1. Components of Pile Integrity Test (PIT) (Massoudi and Teferra, 2004)

Reflections from defects are also reduced by soil damping effects. Hence, defects at deeper depths are more difficult to detect. Rausche et al. (1992) had noted that an impedance profile analysis, which yields a pile shape as function of depth must properly identify soil resistance effects before the impedance profile can be calculated.

While well developed for high strain dynamic tests, currently there is no generally accepted method available for the analysis of soil resistance effects on low strain stress wave propagation. For this reason, engineers have to make certain assumptions in order to compensate for lack of proper identification of pile/soil interaction. This may jeopardize the quality of the test output. In addition, soil resistance and damping effects may lead to inconclusive assessment of pile integrity, while it is difficult to distinguish the soil response from the pile response (ASTM, D5882). As a consequence,

GRL Engineers, the leading firm in the field of pile integrity testing, has recommended “Inconclusive” test result for piles subjected to high soil resistance and thus, lacking of clear stress wave toe reflection (Webster and Rausche, 2011).

2. METHOD OF ANALYSIS

Assuming a concrete pile shown in Figure 2 having radius (r_0), density (ρ_c), modulus of elasticity (E_c), and cross sectional area (A) is subjected to light dynamic force (F_0) causing displacement (w) in the (z) direction.

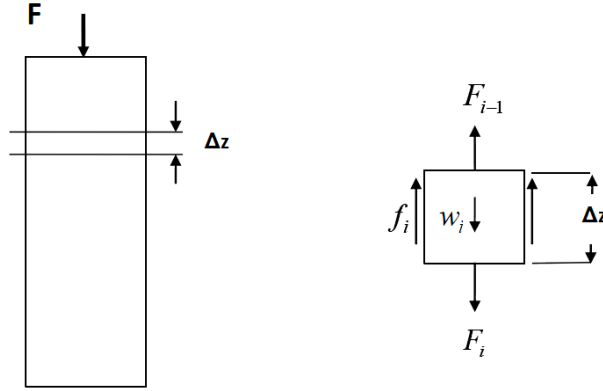


Figure 2. Schematic diagram for the proposed pile and a selected pile segment

Hence, the basic mathematical equations, assuming elastic soil resistance will be:

$$F_i - F_{i-1} - f_i A_s = \rho_c A \Delta z \frac{v_i(t + \Delta t) - v_i(t)}{\Delta t} \quad (1)$$

$$v_i = \frac{w_i(t + \Delta t) - w_i(t)}{\Delta t} \quad (2)$$

$$F_i - f_i A_s = E_c A \frac{w_{i+1} - w_i}{\Delta z} \quad (3)$$

where, (v) is particle velocity, (f) is skin friction and (A_s) is surface area.

The skin friction is assumed to be proportional to displacement as per the friction-displacement correlation of Kraft et al. (1981):

$$f_i = \frac{G}{r_0 \cdot \ln\left(\frac{r_m}{r_0}\right)} w_i \quad (4)$$

where (G) is the soil shear modulus, which can be calculated using equation (5) and (r_m) is the pile influence zone.

$$G = \frac{E_s}{2(1 + \nu)} \quad (5)$$

where (E_s) is soil Young's modulus and (ν) is soil Poisson's ratio.

Since the pile is subjected to dynamic loading, pile influence zone can be estimated using ground vibration attenuation equation (Amick and Gendreau, 2000) as follows:

$$A_1 = A_0 (r_0 / r_1)^{(\gamma)} e^{\alpha(r_0 - r_1)} \quad (6)$$

where, (A_0), (A_1) are vibration amplitudes at (r_0) and (r_1) distances, respectively, (γ) is a coefficient, which depends on wave type and (α) is material damping coefficient.

At the pile toe, the displacement caused by reflected wave (w_r) in terms of the incident wave caused displacement (w_i) is:

$$w_r = \left[\frac{1 - \frac{\rho_s v_s}{\rho_c v_c}}{1 + \frac{\rho_s v_s}{\rho_c v_c}} \right] w_i \quad (7)$$

At the pile-soil Interface, the force caused by the reflected wave (F_r) in terms of the incident wave caused force (F_i) is:

$$F_r = \left[\frac{\frac{\rho_s v_s}{\rho_c v_c} - 1}{\frac{\rho_s v_s}{\rho_c v_c} + 1} \right] F_i \quad (8)$$

where, (ρ_s) is soil density, (v_s) is wave velocity in soil and (v_c) is wave velocity in concrete.

The compressive wave velocity in the concrete pile is calculated by:

$$v_c = \sqrt{\frac{E_c}{\rho_c}} \quad (9)$$

The primary wave velocity in the soil is calculated by:

$$v_s = \sqrt{\left[\frac{2G(1 - \nu)}{\rho_s(1 - 2\nu)} \right]} \quad (10)$$

i. Sample analysis

The following pile data is used in the analysis:

Pile Length, L [m]	=	10
Concrete Density, ρ_c [t/m^3]	=	2.5
E_c [kN/m^2]	=	4.0E+07
Pile Radius, r_0 [m]	=	0.178412
Pile Cross Sectional Area, A [m^2]	=	0.1
Number of elements	=	80
Pile Element Surface Area, A_s [m^2]	=	0.140124
Wave Velocity in Concrete, v_c [m/s]	=	4000

Very dense granular soil is assumed to surround the pile. Soil parameters are as follows:

Soil Density, ρ_s [t/m^3]	=	1.8
Poisson's Ratio, ν	=	0.4
Soil Shear Modulus, G [kN/m^2]	=	36000

Wave Velocity in Soil, v_s [m/s] = 346.4102
Time Interval in Soil, Δt_s [sec] = 0.000361
 γ (equation 6) = 1
 α (equation 6) = 0.13

Applied dynamic force details are as follows:

Force Amplitude, F_0 [kN] = 1.8
Pulse duration, [sec] = 0.00025

The pile influence radial distance (r_m) is calculated using equation (6) and the abovementioned pile-soil parameters. Wave amplitude attenuation with radial distance is shown in Figure 3.

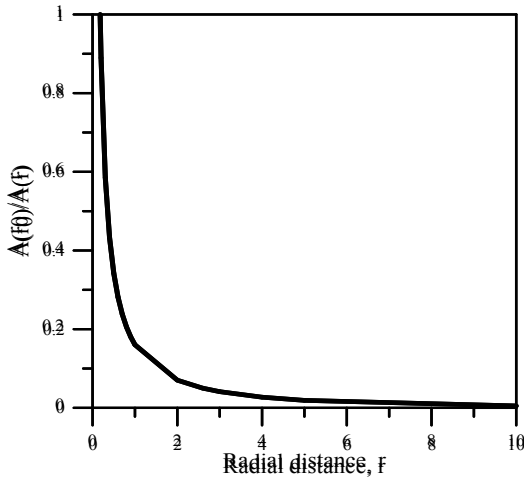


Figure 3. Wave attenuation with radial distance

As shown in the figure, the attenuation reaches 95% at 2.6m radial distance. Hence, r_m is considered to be 2.6m. The proposed model is compared with the output of PIT-S software manufactured by Pile Dynamic Inc. (PDI). PIT-S takes a user-input pile shape, soil layer properties and characteristics of the low strain hammer impact, and displays the velocity reflections versus time and versus pile length that a PIT test under such conditions would produce. PIT-S is simulation software in its most basic application, does not require any data collection. The display of force and velocity curves or of the velocity curves at two different locations along the pile (integrity testing of piles integral to a structure is accomplished by analyzing 2 velocity curves) simulate integrity tests performed with the PIT model FV.

Velocity values at 0.625m, 5.5m and 9.5m depths, calculated by PIT-S software and the proposed model are shown in the following figures:

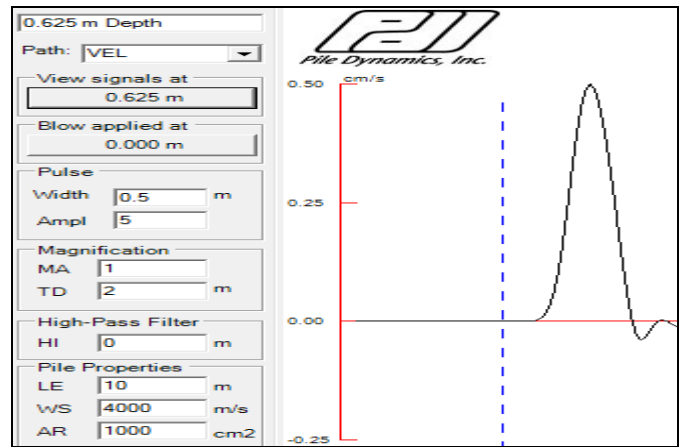


Figure 4. Velocity curve at 0.625m depth using PIT-S

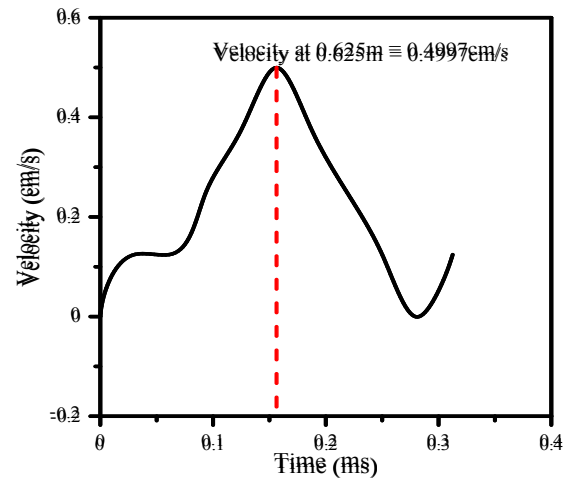


Figure 5. Velocity value at 0.625m depth using the proposed model

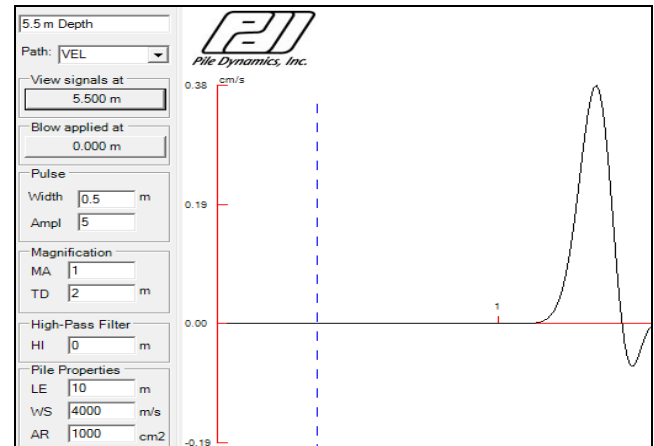


Figure 6. Velocity curve at 5.5m depth using PIT-S

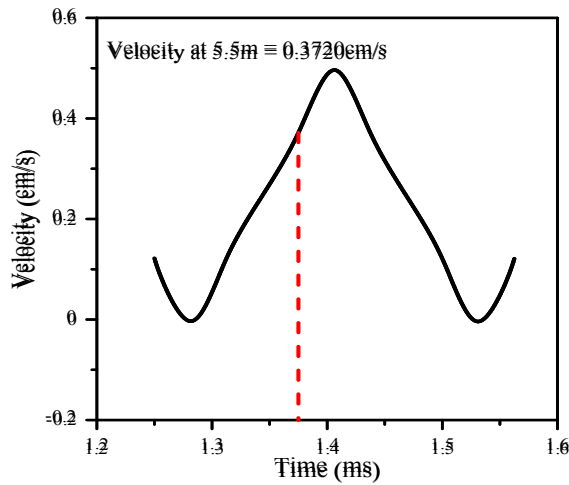


Figure 7. Velocity value at 5.5m depth using the proposed model

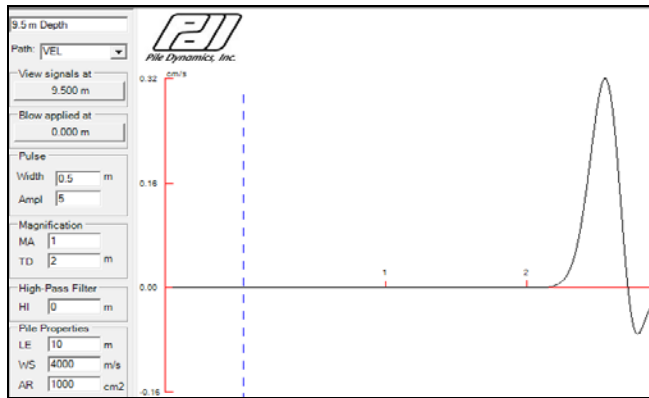


Figure 8. Velocity curve at 9.5m depth using PIT-S

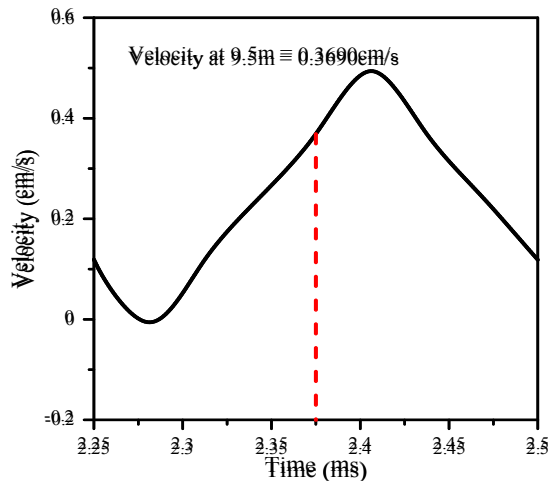


Figure 9. Velocity value at 9.5m depth using the proposed model

Summary of velocity values comparison is shown below:

Table 1. Proposed model and PIT-S produced results

Depth (m)	Time (ms)	Velocity (Proposed Model), cm/s	Velocity (PIT-S), cm/s
0.625	0.15625	0.4997	0.5000
5.500	1.37500	0.3720	0.3800
9.500	2.37500	0.3690	0.3200

The proposed analysis method had been utilized in order to estimate soil effects on two-way propagated wave after been reflected at pile toe. Hence, equations (7) and (8) were used to predict reflected wave characteristics. The pile top segment force is shown in Figure 10:

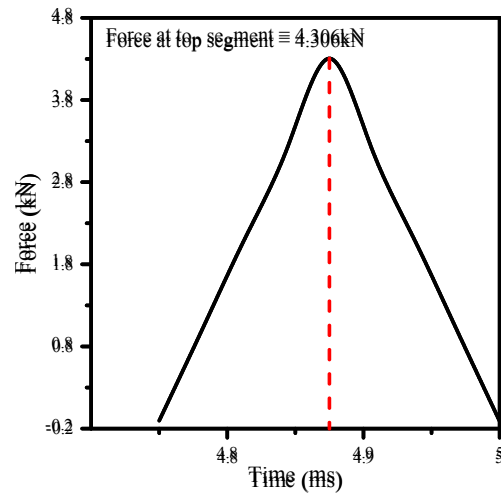


Figure 10. Force curve at pile top segment for the reflected wave

Hence, the impact force amplitude found to be attenuated from 5.000kN to 4.306kN during its travel downward and upward the pile. This attenuation is caused by soil damping at toe and skin friction on pile surface. The estimated attenuation can be summarized as follows:

Table 2: Applied force and encountered attenuations

Impact Force amplitude (kN)	5.000
Reflected force amplitude (kN)	4.356
Force amplitude at top pile segment (kN)	4.306
Attenuation at pile toe due to soil damping (%)	11.64
Attenuation due to friction (%)	2.24
Total attenuation (%)	13.88

Force amplitude values at 0.625m, 5.5m and 9.5m depths (at 0.15625ms, 1.375ms and 2.375ms time, respectively) produced from the proposed method of analysis as well as the PIT-S software is shown in Figure 11.

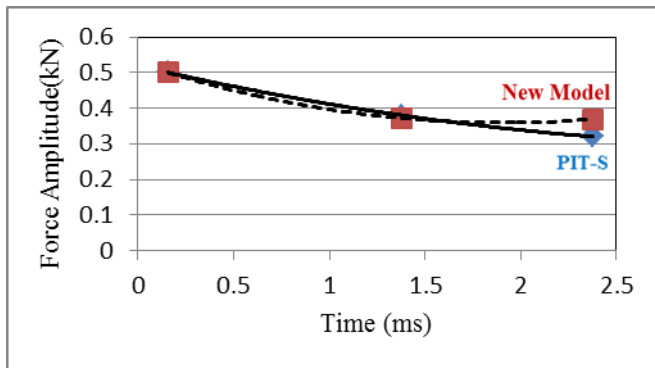


Fig. 11: Force amplitude values using PIT-S and proposed model

3. DISCUSSIONS AND CONCLUSIONS

Numerical analysis had been utilized in order to evaluate in order to evaluate low strain wave attenuation in a concrete pile subject to soil resistance in a very dense material. The numerical analysis is based on introducing the skin friction in the basic numerical equations of motion and Hooke's law. The skin friction is assumed to mobilize elastically proportional to pile displacement. In addition, wave reflection/attenuation at pile-soil interface is also considered in the analysis.

Shear stress is assumed to decrease with distance, and considered to be negligible beyond a radial distance (pile zone of influence). This radial distance was estimated assuming that soil does not deform beyond the distance where vibration amplitude will be attenuated by 95% of its original value.

Short pulse duration was assumed for the light impact comparable to the pulse chosen in the PIT-S. Despite the fact that PIT-S model includes plastic characteristics of soil, which is absent in the numerical analysis, the comparison between the two methods can still be considered as valid due to the short duration light loading type adopted, which is not expected to mobilize plastic behavior of soil.

The proposed numerical analysis showed close agreement with the PIT-S analysis for the selected pile depths (near pile top, mid of pile and near pile toe). However, the produced results diverge near pile toe, which can be attributed to the differences in evaluation of soil effect at pile-soil interface between the two methods of analysis.

Low strain F-wave amplitude was found to be attenuated by 13.88% while traveling 20.0m distance (2-way propagation) and after been reflected at pile toe, for a selected 10.0 m concrete pile cast in very dense granular soil. Soil damping at pile toe was found to be responsible of about 84% of the encountered wave attenuation based on the proposed

numerical analysis. The proposed numerical analysis need to be improved in order to accommodate plastic behavior of soil.

4. ACKNOWLEDGEMENT

The authors' wish to thank the Research Management Centre of Universiti Teknologi Malaysia and Pile Dynamic Incorporation for providing financial support and data, respectively.

5. REFERENCES

- [1] American Society of Testing and Materials (ASTM), 2006. Section 4, Vol. 04.09, Standard Test Method for Low Strain Impact Integrity Testing of Deep Foundations.
- [2] Amick, H., and Gendreau, M., 2000. Construction Vibrations and Their Impact on Vibration-Sensitive Facilities. Proc., ASCE Construction Congress 6, Orlando Florida, pp. 1-10.
- [3] Hussein, M. H., Garlanger, J., June 1992. Damage Detection for Concrete Piles Using a Simple Nondestructive Method. First International Conference on Fracture Mechanics of Concrete Structures. Breckenridge – Colorado, USA.
- [4] Johnson, M., Rausche, F., September, 1996. Low Strain Testing of Piles Utilizing Two Acceleration Signals. Proceedings of the Fifth International Conference on the Application of Stress-wave Theory to Piles 1996: Orlando, USA, FL; pp. 859-869.
- [5] Kraft, L. M., Ray, R. P., and Kagawa, T. (1981). Theoretical t-z curves, Journal Geotechnical Engineering Division, Proceedings Paper 16653, American Society of Civil Engineers, Vol 107(GT11).
- [6] Massoudi, N., Teferra, W., April, 2004. Non-Destructive Testing of Piles Using the Low Strain Integrity Method. Proceedings of the Fifth International Conference on Case Histories in Geotechnical Engineering: New York, USA, NY. (CD-ROM).
- [7] Rausche, F., Likins, G. E., Ren-Kung, S., September, 1992. Pile integrity testing and analysis. Proceedings of the Fourth International Conference on the Application of Stress-Wave Theory to Piles: The Netherlands; pp. 613-617.
- [8] Webster, K., Rausche, F., January, 2011. Pile and Shaft Integrity Test Results, Classification, Acceptance and/or Rejection. Compendium of Papers of the Transportation Research Board (TRB) 90th Annual Meeting: Washington, D.C., USA.

Dynamic Soil-Structure Interaction Considering Pore-Water Pressure Coupling

Dr. Qutayba Nazar Al-Saffar*
Civil Engineering Department
University of Mosul / Iraq

Prof. Dr. Akram Y. Al-Sa'aty
University of Mosul / Iraq

Prof. Dr. Mohamad T. Al-Layla
Civil Engineering Department
University of Mosul / Iraq

ABSTRACT

It is a fact that soils are extremely complicated engineering materials whose constitutive response depends on many factors, including soil type, density, water content, structure, particles size, drainage conditions, duration of loading, stress history, confining pressure, and stress path, (Corotis et al., 1974).

However, due to the complexity of dynamic soil-structure interaction, numerical modeling of this phenomenon still remains a challenge. There still exists many difficulties to cover all the problems listed above in one model.

From the dynamic analysis of soil-structure interaction using non-linear finite element simulation, it has been found that the developed DIANA-SWANDYNE II computer program and the solution algorithms of the u-p formulation for predicting the coupled behavior of soils are efficient for the problems solved.

The eight noded isoparametric quadrilateral elements are used in the modeling. Also, a slip-interface element is used for simulation of slippage or separation at interfaces between soil and structure.

Furthermore, it has been found that the coupling has a significant effect on the response indicated by the lower values of the displacement compared with those of uncoupled analysis.

Each of the constitutive models employed in this research proved its ability to predict the soil response for displacement and excess pore-water pressure according to the type of material under consideration. But this depends on the selection and evaluation of the parameters of each constitutive model.

Key words:

Dynamic soil-Structure Interaction, Finite element method, Coupling Phenomena.

* dr.qutaybaalsaffar@yahoo.com or dr.qutayba@gmail.com

1. Introduction

Soil mechanics is known as the science that deals with the properties and behavior of soils under stresses. However, only static stresses are most often implied. On the other hand, soil dynamics is that branch of soil mechanics which deals with engineering properties and behavior of soil under the variation of stresses imposed by dynamic loads (Das, 1983).

The behavior of soils under dynamic loading deals with additional problems due to diversity in the areas and complexity in the conditions under which dynamic loads are applied (Prakash, 1981)

Ishihara (1967) derived the equations of motion for a saturated porous elastic matrix for the two constituents of the soil separately. He related the four elastic constants of Biot's theory to the compressibility of the bulk soil, the solid material and the water. He concluded that the waves travel through the solid-water system without causing any change in the pore volume.

Bazant and Krizek (1975) extended Biot's linear elastic theory to the non-linear non-elastic case. They formulated an incremental stress-strain relationship that takes into account the non-linearity and non-elasticity of the soil.

Zienkiewicz and Bettess (1982) extended Biot's formulation to rocks and other saturated porous materials. They also presented a physical derivation of the governing equations.

The behavior of soil is nonlinear and the dynamic properties are substantially dependent on the strains caused by the dynamic loads applied to the soil. For instance, the dynamic loads due to machine foundation, the amplitude of motion and, consequently, the strains in the

soil are usually low. However, systems subjected to earthquakes or blasts exhibit large deformations and thus large strains.

The principal properties that are required for design purposes are (Das, 1983 and El-Sawwaf, 2002):

1. Shear strength and stress strain characteristics,
2. Liquefaction parameters, such as cyclic shearing stress ratio, and pore pressure response,
3. Dynamic moduli, such as Young's modulus and shear modulus,
4. Damping ratio, and
5. Poisson's ratio.

Laboratory measurements are most widely used for the determination of dynamic properties and cyclic strength of soils, for their accuracy and ability to cover various strain ranges (Ishihara, 1996).

The soil deposits, which are subjected to earthquake loadings are also capable of these two behaviors, i.e. flow liquefaction and cyclic mobility (Casagrande, 1975). These behaviors are best considered in terms of steady-state soil mechanics (Casagrande, 1975; Castro and Poulos, 1977).

The finite element techniques are now the most widely used to simulate the dynamic soil behavior because of the ease and realism with which the geometry and material properties can be modeled (Al-Saffar, 2009).

1. soil-structure interaction

A large part of geotechnical engineering is directly concerned with soil-structure interaction. In some cases, the soil may be modeled in great detail and with complicated constitutive relations while the structure is represented very simply. In dynamic problems, the addition of time as a variable increases the mass of data and the number of options.

There is no universal, ideal, or complete way to deal with problems of soil-structure interaction. The choice must be based on the relative importance of the various parts of the problems and on the time and resources available to deal with it (Salih, 2001). Dynamic interaction between soil and structure is defined as a phenomenon of transmitting kinetic energy through the interface media.

The use of multistory buildings with basement floors is very important in overcrowded cities. Considering the dynamic behavior of these types of structures under earthquake loading, many researches have neglected the dynamic interaction between soil, substructure and superstructure. They merely simulate the soil using a-series of springs and viscous damping located at the base of the structure only or use the shear beam analogy method.

There are several factors which must be considered in the design of high-rise buildings. Some of these factors are related to the superstructure such as strength, serviceability and ductility while others are soil related, such as settlement.

Either continuum approach or finite element approach can solve soil-structure interaction problem.

2. Coupling Phenomena

Coupled systems are those applicable to multiple field and dependent variables, which interact with each other, where the solution of any system being impossible without simultaneous solution of the other.

It is convenient to classify coupled systems into two categories :

Class I Problems : This class contains problems in which coupling occurs on domain interfaces via the boundary conditions imposed there.

Class II Problems : This class contains problems in which the various domains overlap either totally or partially. Here,

the coupling occurs through the governing differential equations describing different physical phenomena. The main example of this type of coupling is the soil-pore water interaction.

It is well known that the behavior of soil is strongly influenced by the pressure of the fluid (generally water) present in the pores of the material, (Zienkiewicz & Taylor, 2000).

3. Constitutive relations

The concept of the effective stress is here of paramount importance, thus if σ describes the total stress (positive in tension) acting on the total area of the soil and pores, and p is the pressure of the water (positive in compression) in the pores, the effective stress is defined as:

$$\sigma' = \sigma + mp \quad \text{---(1)}$$

where:

$$m^T = [1, 1, 1, 0, 0, 0] \quad \text{---(2)}$$

Assuming that the soil can be represented by a linear elastic model we have:

$$\sigma' = D\varepsilon \quad \text{---(3)}$$

Immediately the total discrete equilibrium equations for the solid-fluid mixture can be written in exactly the same form as is done for all problems of solid mechanics:

$$M\ddot{u} + C\dot{u} + \int_{\Omega} B^T \sigma \, d\Omega + f = 0 \quad \text{---(4)}$$

Where:

M , C and f have the usual meaning of mass, damping and force matrices, respectively.

B : is the strain-displacement matrix .

Ω : is the numerical integration domain.

We shall now consider the coupled problem discretized in the standard manner with the displacement vector approximated as:

$$u \approx \tilde{u} = N_u \tilde{u} \quad \text{---(5)}$$

and the fluid similarly approximated as:

$$p \approx \tilde{p} = N_p \tilde{p} \quad \text{---(6)}$$

where \tilde{u} and \tilde{p} are the nodal parameters of each field and N_u and N_p are appropriate shape function.

Now, the term involving the stress must be split as:

$$\int_{\Omega} B^T \sigma \, d\Omega = \int_{\Omega} B^T \sigma' \, d\Omega - \int_{\Omega} B^T m p \, d\Omega \quad \text{---(7)}$$

To allow the direct relationship between effective stresses and strain (and hence displacements) to be incorporated. For a linear elastic soil skeleton we immediately have:

$$M\ddot{\tilde{u}} + C\dot{\tilde{u}} + K\tilde{u} - Q\tilde{p} + f = 0 \quad \text{---(8)}$$

Equation (8) represents the dynamic equation of motion for the solid and fluid phase of the saturated porous media subjected to cyclic loading, where:

M : is the global mass matrix.

K : is the global stiffness matrix.

C : is the global damping matrix.

Q : is the coupling matrix.

\tilde{p} : is the global pore pressure matrix.

f : is the forces matrix for the solid phase.

\tilde{u} : is the displacement matrix in the global direction.

The standard stiffness matrix K in equation (8) can be represented as:

$$\int_{\Omega} B^T \sigma' \, d\Omega = \left(\int_{\Omega} B^T DB \, d\Omega \right) \tilde{u} = K\tilde{u} \quad \text{---(9)}$$

and the coupling matrix Q can be represented as:

$$Q = \int_{\Omega} B^T m N_p \, d\Omega \quad \text{---(10)}$$

Such damping matrices C have a physical significance and are always introduced in earthquake analyses or similar problems of structural dynamics. With the lack of any special information about the nature of damping, it is usual to assume the so called 'Rayleigh damping' in which:

$$C = \alpha M + \beta K \quad \text{---(11)}$$

, where α and β are coefficients determined by experience (see for instance Clough and Penzien, 1975 ; Seed et al., 1975).

In the above conventional discretization, the same element shapes are used for the u and p variables, though not necessarily identical interpolations. With the dynamic equations coupled to the pressure field, an additional equation is clearly needed from the transient seepage equation of the form:

$$-\nabla^T (k \nabla p) + \frac{1}{Q} \dot{p} + \dot{\epsilon}_v = 0 \quad \text{---(12)}$$

where Q is related to the compressibility of the fluid, k is the permeability and $\dot{\varepsilon}_v$ is the volumetric strain in the soil skeleton, which on discretization of displacement is given by:

$$\varepsilon_v = m^T \varepsilon = m^T B \tilde{u} \quad \text{---(13)}$$

The equation of seepage can now be discretized in the standard Galerkin manner as:

$$Q^T \ddot{\tilde{u}} + \dot{S} \tilde{p} + H \tilde{p} + q = 0 \quad \text{---(14)}$$

Equation (14) represents the dynamic equation of motion for the fluid phase of the saturated porous media subjected to cyclic loading, where:

S : is the compressibility matrix.

H : is the permeability matrix.

q : is the forces vector for the fluid phase.

The standard compressibility matrix (S) and permeability matrix (H) in equation (14) can be represented as follows:

$$S = \int_{\Omega} N_p^T \frac{1}{Q} N_p d\Omega, \text{ and}$$

$$H = \int_{\Omega} (\nabla N_p)^T k \nabla N_p d\Omega \quad \text{---(15)}$$

Finally, from the two main dynamic equations of motion (8 and 14), the format of the coupled equations using u-p formulation can be written as :

$$\begin{bmatrix} M & 0 \\ 0 & 0 \end{bmatrix} \begin{Bmatrix} \ddot{\tilde{u}} \\ \ddot{\tilde{p}} \end{Bmatrix} + \begin{bmatrix} C & 0 \\ Q^T & S \end{bmatrix} \begin{Bmatrix} \dot{\tilde{u}} \\ \dot{\tilde{p}} \end{Bmatrix} + \begin{bmatrix} K & -Q \\ 0 & H \end{bmatrix} \begin{Bmatrix} \tilde{u} \\ \tilde{p} \end{Bmatrix} = - \begin{Bmatrix} \tilde{f} \\ \tilde{q} \end{Bmatrix} \quad \text{---(15)}$$

4. DIANA-SWANDYNE II Program

DIANA-SWANDYNE II or Dynamic Interaction and Nonlinear Analysis-SWANseaDYNAMIC program version II is an improved version of the DIANA-SWANDYNE I

The program is developed by Prof. A.H.C. Chan based on his thesis (Chan 1988) under the supervision of Prof. O.C. Zienkiewicz.

The program is intended for Static, Consolidation and Dynamic analysis for problems in Geomechanics. It is a 2-Dimensional program which incorporates Plane strain and Axisymmetric analysis. The Governing equation that is being solved is the Fully Coupled, Large Deformation Biot Equation with the u-p simplification with the fluid acceleration neglected.

DIANA-SWANDYNE II is capable of performing analysis for static (drained and undrained). Consolidation and dynamic (drained and undrained). The solid and fluid are treated as separate phase in the program and different integration rule can be used for each of them.

The program is based on finite element method with triangular and quadrilateral isoperimetric elements in spatial domain. The time integration is done with the Generalized Newmark method (Newmark 1959).

5. Verifications of the program

In order to examine the approximations introduced in the (u-p) form and to verify the performance of the developed DIANA-SWANDYNE II program, problems of one-dimensional soil layer is adopted and implemented in the numerical solution procedure for this purpose.

Numerical Application

Consolidation Problems

Two problems are chosen to be solved using DIANA-SWANDYNE II, in the first problem a simulation of consolidation test is performed while, the second problem is conducted to simulate the long term field settlement.

A: Consolidation of Swansea Blue Clay in a Rowe Consolidation Cell

Lewis and Schrefler (2000) simulated the experimental results of Rowe consolidation cell using finite element program and a good agreement results are obtained. In this work the simulation of this test are performed and a comparison of the results are discussed.

Problem definition :

The problem represents an experimental consolidation test performed on a soil sample of Swansea blue Clay in (10") Rowe consolidation cell. Large sample of 10" (254 mm) in diameter and (61 mm) in height is tested (figure 1-a). One stage of consolidation loads are simulated when a load of (172 kPa) is applied and the soil properties are shown in table (1). The finite element discretization is shown in figure (1-b), where 130 elements are used to simulate the test. The solid skeleton and the pore water in the soil are each modeled with 8-nodded and 4-nodded serendipity isoparametric elements respectively. At the vertical boundaries of the solid skeleton, only vertical movement is permitted (i.e. vertical rollers). The water level is assumed to be at the ground surface (i.e. saturated state) and the pore water pressures at the free surface are taken as zero. A non-linear elasto-plastic model is used in finite element simulation of the soil behavior.

Numerical Analysis Results:

Figure (2-a) show the settlement behavior of the middle surface of the sample. The results obtained by the present study using DIANA-SWANDYNE II program found to be acceptable values with the results given by Lewis and Schrefler (2000) using non-linear consolidation finite element program. The response of the pore water pressure with time

during the test are shown in figure (2-b) and the comparison of the results indicates that the numerical results from the present study are in good agreement with the numerical results given by Lewis and Schrefler (2000). The small difference in results is due to different models used in simulation.

B: Two-Dimensional Consolidation

• Problem definition :

A two dimensional plain strain consolidation problem is solved in this section. The problem is similar to that solved by Siriwardane and Desia (1981)* using elastic and elasto-plastic models, also the same problem is solved by Lewis and Schrefler (2000) using non-linear consolidation finite element program. The adopted finite element mesh are shown in figure (3) where 30 elements have been used where the solid skeleton and the pore water in the soil are each modeled with 8-nodded and 4-nodded serendipity isoparametric plane strain elements respectively. A Cam-Clay model (critical-state model type) is used in the present study. The properties of the soil and parameters of the model used in simulation are shown in table (2).

An external load applied at the top surface of the model for a length $B=10$ varies with time as indicated in figure (3).

Numerical Analysis Results:

The predicted pore-water pressure using Cam-Clay model are compared with the results of Siriwardane and Desia (1981) and the results of Lewis and Schrefler (2000) in figure (4). The simulated pore-water pressure are non-dimensional with respect to initial applied load ($p_0=1000$), also, the non-dimensional time factor defined as ($T_v = cvt/H^2$).

A good agreement of results can be observed in the comparison and the small difference between models' results are due to the inclusion of the plasticity effects which decreases the magnitude of dissipation of pore water pressure for almost the whole time span. Therefore, the predicted pore-water pressure is higher than those from an elastic analysis.

Dynamic Analysis of Soil-Foundation Interaction

In this problem, the dynamic analysis of two-dimensional soil-foundation system is considered and the response of the system to the different type of dynamic loading are presented. In addition, the effect of pore-water pressure coupling and the interface-element are considered.

Problem definition :

Figure (5-a) shows a (2.0*0.25m) concrete strip footing supported on (H=20.0m) saturated soil stratum laying over a rigid bedrock. The soil properties are shown in table (3) while, the properties of the footing material (concrete) are shown in table (4). The footing is subjected to surface excitations (step, ramp and Sinusoidal function), which are the same as those given in (table 1). The same problem was solved and discussed by Abbas (2003) except that he used high frequency sinusoidal loading ($\omega=66.92$ rad/sec), and in the present study, an elastic and elasto-plastic model is used to solved this problem using DIANA-SWANDYNE II program.

The selected depth of the saturated layer of (20.0m) is taken to assure that the ratio ($h/b=20$) is well greater than the minimum indicated by Japon et.al (1997)*, to minimize the effect of the rigid bedrock on the dynamic response of the footing.

The finite element discretization is shown in figure (5-b), where 22 elements are used to simulate the soil-foundation system. The solid skeleton and the pore water in the soil are each modeled with 8-nodded and 4-nodded serendipity isoparametric plane strain elements respectively. At the vertical boundaries of the solid skeleton, only vertical movements are permitted (i.e. vertical rollers). The water level is assumed to be at the ground surface (i.e. saturated state) and the pore water pressures at the free surface are taken as zero. A non-linear elasto-plastic model is used in finite element simulation of the soil behavior.

• Numerical Analysis Results:

Figure (6) shows the response of the vertical displacement at point A for the strip footing when it is subjected to step and ramp surface excitations. The upper part of this figure present the result of Abbas (2003) while, the lower part shows the results of the present study. Furthermore, in the right side of the two parts the coupling effect is present. The comparison of the results indicates that the results of the present study are in good agreement with the results given by Abbas (2003).

Figures (7) shows the response of the vertical displacement at point A for the strip footing when it is subjected to surface excitations of high frequency sinusoidal loading ($\omega=66.92$ rad/sec) for both dry and saturated state , and the coupling effect is clearly shown in figure (8).

The excess pore-water pressure-time history at point B for the strip footing when it subjected to sinusoidal excitation is shown in figure (9).

In all of the results above, no relative motions allowed at the interface between soil and foundation (without interface element). A simple slip-interface model is used in the present study which is described briefly in chapter three with material properties same as the soil properties. The effects of using this model on the displacement and excess pore-water pressure response are shown in figures (10 and 11) respectively, and the interface effect is clearly shown in figures (12 and 13) respectively.

The comparison of the results indicates that the results of the present study are in good agreement with the results given by Abbas (2003). The differences in results are due to different soil models and different interface models used in simulation.

8. Conclusions

From the studying of dynamic analysis of soil-structure interaction using non-linear finite element simulation, the following are concluded:

1. The developed DIANA-SWANDYNE II computer program and the solution algorithms of the *u-p* formulation for predicting the coupled behavior of soils are found to be efficient for the problems solved.
2. The finite element method represents a powerful tool in soil dynamic in which there are no analytical solutions available yet.
3. Two-phase materials (such as saturated soil) subjected to dynamic loading could be formulated with approximate numerical solutions with an acceptable degree of accuracy.
4. The coupling has a significant effect on the response indicated by the lower values of the displacement compared with those of uncoupled analysis. This is due to the role of water in the pores which shares the solid in carrying the applied load at the earlier stages. Then, diminishes as the excess pore water pressure is dissipated with the progress of time.
5. Each of the constitutive models employed in this study proved its ability to predict the soil response in displacement and excess pore water pressure according to the type of material under consideration. But this, certainly, depends on the selection and the evaluation of the parameters of each constitutive model.

9. References

1. Al-Saffar, Q.N. (2009), "Simulation of Soil Dynamic Properties and Pore-Water Pressure Coupling Using Finite Element Method", Ph.D. Thesis, College of Engineering, University of Mosul, Iraq.
2. Bazant, Z.P. and Krizek R. J., (1975), "*Saturated Sand as an Inelastic Two-Phase Medium*". Journal of Engineering Mechanics, ASCE, Volume 101, No. EM4, pp.317-332.
3. Bowles, J.E., (1996), "*Foundation Analysis and Design*", Mc-Graw-Hill Book Co., New York.
4. Casagrande, A., (1975) "*Liquefaction And Cyclic Mobility Of Sands. A Critical Review*" Proceedings of the 5th Pan American Conference on Soil Mechanics and Foundation Engineering, Buenos Aires, Vol. 5, pp. 80-133.
5. Castro, G. and Poulos, S.J., (1977) "*Factors Affecting Liquefaction And Cyclic Mobility*" Journal of the Geotechnical Engineering Division, ASCE, Vol. 103(6), pp.501 - 516.
6. Chopra A.K., (1995), "*Dynamics of Structures-Theory and Applications to Earthquake Engineering*", Prentice-Hall, Inc., New Jersey, USA.
7. Das, B.M., (1983), "*Fundamentals of Soil Dynamics*", Elsevier Science Publishing, New York.
8. Dinesh, S.V., Sitharam, T.G. and Vinod, J.S., (2004), "*Dynamic Properties And Liquefaction Behavior of Granular Materials Using Discrete Element Method*", Current Science- Geotechnics And Earthquake Hazards-, Vol. 87, No. 10.
9. El-Sawwaf, M.A.M., (2002), "*The Effect of Dynamic Loading on The Behavior of Shallow Foundation*", Ph.D.Thesis, University of Cairo, Egypt.

10. Ishihara, K., (1967), "*Propagation of Compressional Waves in a Saturated Soil*". Proceedings of International Conference on Wave Propagation and Dynamic Properties of Earth Materials, University of New Mexico, Albuquerque, New Mexico, August 23-25, pp. 451-467.
11. Ishihara, K., (1996), "*Soil Behavior in Earthquake Geotechnics*", Oxford University Press Inc., New York, USA.
12. Khosla, V., (1985), "*Advances in The Art of Testing Soils Under Cyclic Condations*", The American Society of Civil Engineering, USA.
13. Polito, C.P., (1999), "*The Effects Of Non-Plastic and Plastic Fines On The Liquefaction Of Sandy Soils*", Ph.D. Thesis, Virginia Polytechnic Institute and State University.
14. Prakash, S., (1981), "*Soil Dynamics*", McGraw-Hill Book Company, New York.
15. Silver, M.L., Chan, C.K., Ladd, R.S., Lee, K.L., Tiedmann, D.A., Townsend, F.C., Valseara, J.E., and Wilson, J.H., (1976), "*Cyclic Triaxial Strength of Standard Test Sand*", Journal of the Geotechnical Engineering Division, ASCE, Vol. 102,GT5, pp.511 - 523.
16. Srbulov, M., (2008)", *Geotechnical Earthquake Engineering-Simplified Analyses with Case Studies and Examples*", Springer Science and Business Media B.V., United Kingdom .
17. Yang, Z., Elgamal, A. and Parra, E., (2003), "*Computational Model for Cyclic Mobility and Associated Shear Deformation*", Jornal of Geotechnical and Geoenvironmental Engineering, pp. 1119-1127.
18. Zienkiewicz, O.C., Leung, K.H., Hinton, E. and Chang, C. T., (1982), "*Liquefaction and Permanent Deformation under Dynamic Conditions-Numerical Solution and Constitutive Relations*", Chapter 5 in Soil Mechanics-Transient and Cyclic Loads, (edited by G. N. Pande and O.C. Zienkiewicz), pp. 71-103.

Table (1):

Properties of the Swansea Blue Clay

Elastic modulus	$E_i = 26000.0 \text{ kPa}$
Poisson's ratio	$\nu = 0.20$
Solid skeleton density	$\rho_s = 18.0 \text{ kN/m}^3$
Water density	$\rho_f = 10.0 \text{ kN/m}^3$
Permeability	$K = 4.83 \cdot 10^{-6} \text{ cm/min}$
Angle of internal friction	$\phi' = 8.0^\circ$
Effective cohesion	$C' = 22.8 \text{ kPa}$

Table (2):

Properties and parameters used in simulation

Elastic modulus (E_i)	13000
Poisson's ratio (ν)	0.4
Soil density (γ_s)	18.5
Water density (γ_w)	10.0
Void ratio (e_o)	0.9
Porosity (n)	0.473
Permeability ($k_x=k_y$)	$4.0 \cdot 10^{-5}$
M	1.05
λ	0.14
K	0.05
$*C_v$	0.282

*Calculated from $T_v = c_v t / H^2$

Table (3):**Prosperities for the Saturated Soil Layer**

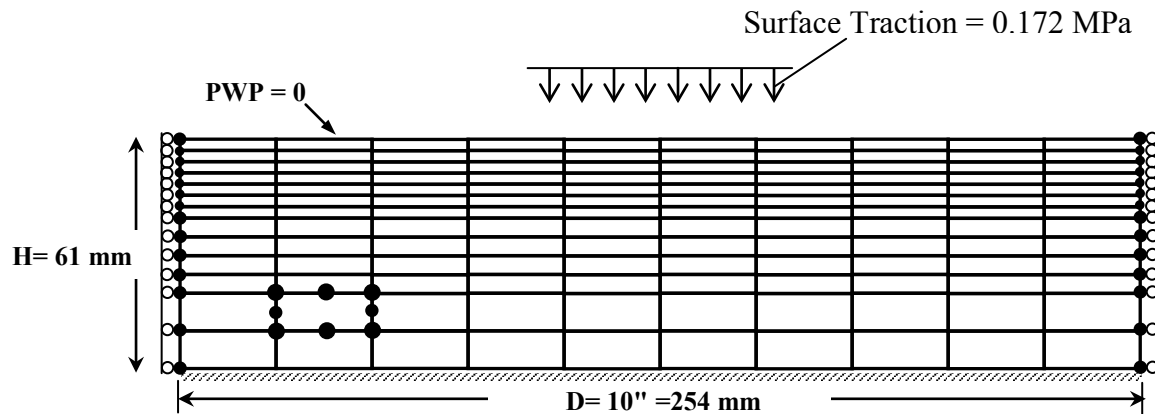
Elastic modulus	$E = 30000.0 \text{ kPa}$
Poisson's ratio	$\nu = 0.2$
Solid weight density*	$\rho_s = 30.01 \text{ kN/m}^3$
Water weight density	$\rho_f = 10.0 \text{ kN/m}^3$
Permeability	$K = 0.0015 \text{ m/sec}$
Porosity	$n = 0.333$
Solid bulk modulus	$K_s = \infty$
Pore water bulk modulus	$K_f = 400000.0 \text{ kPa}$

*Solid mass density = 3.001 gm/cm^3
 $= 30.01 \text{ kN/m}^3$ (weight density)

Table (4):**Elastic Concrete Prosperities**

Elastic modulus	$E = 42 * 10^6 \text{ kPa}$
Poisson's ratio	$\nu = 0.2$
Weight density	$\rho = 23.2 \text{ kN/m}^3$

254 x 61 mm soil sample

a- Dimension of Sample in Rowe Cell**b- Finite Element Idealization****Figure (1) Finite Element Simulation for Rowe Consolidation Cell**

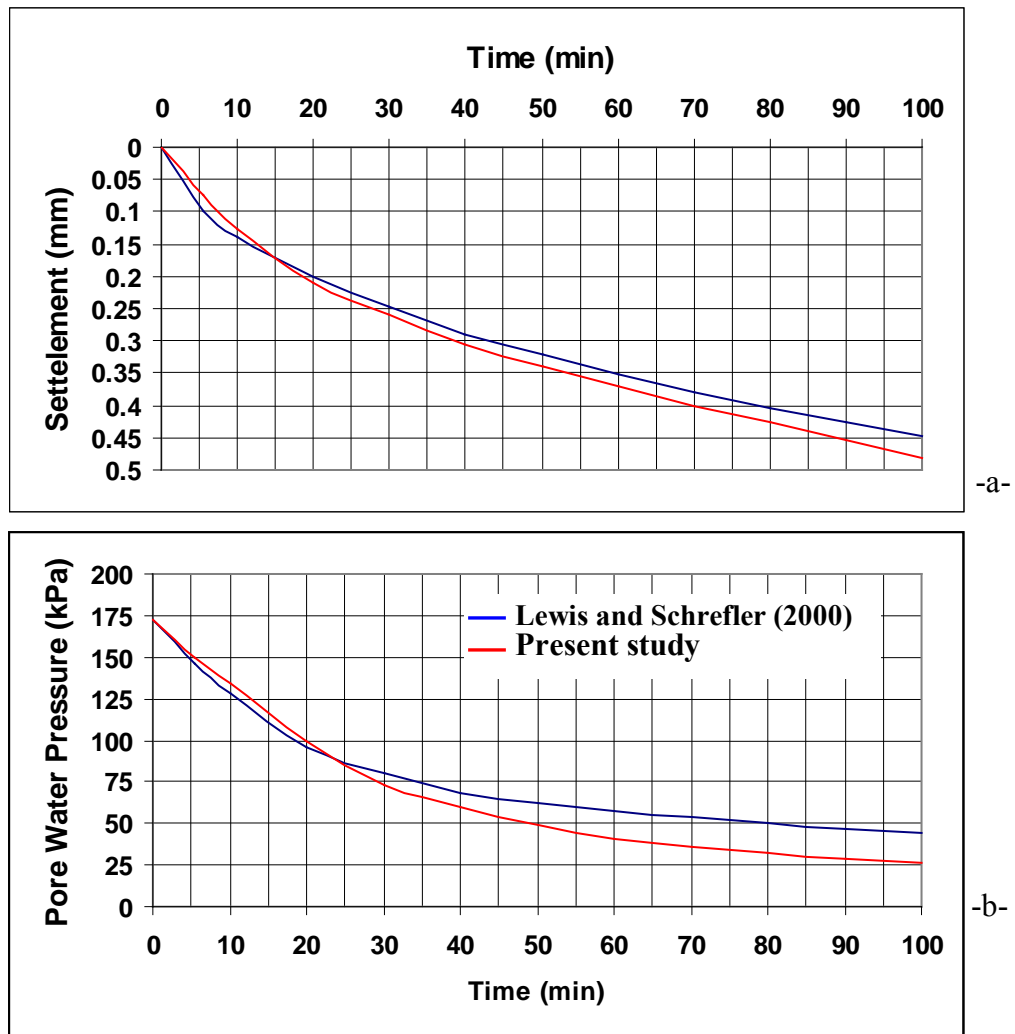


Figure (2): Results of the Simulation of Rowe Consolidation Cell

a- Settlement versus time for clayey soil.

b- Pore-water pressure versus time for clayey soil.

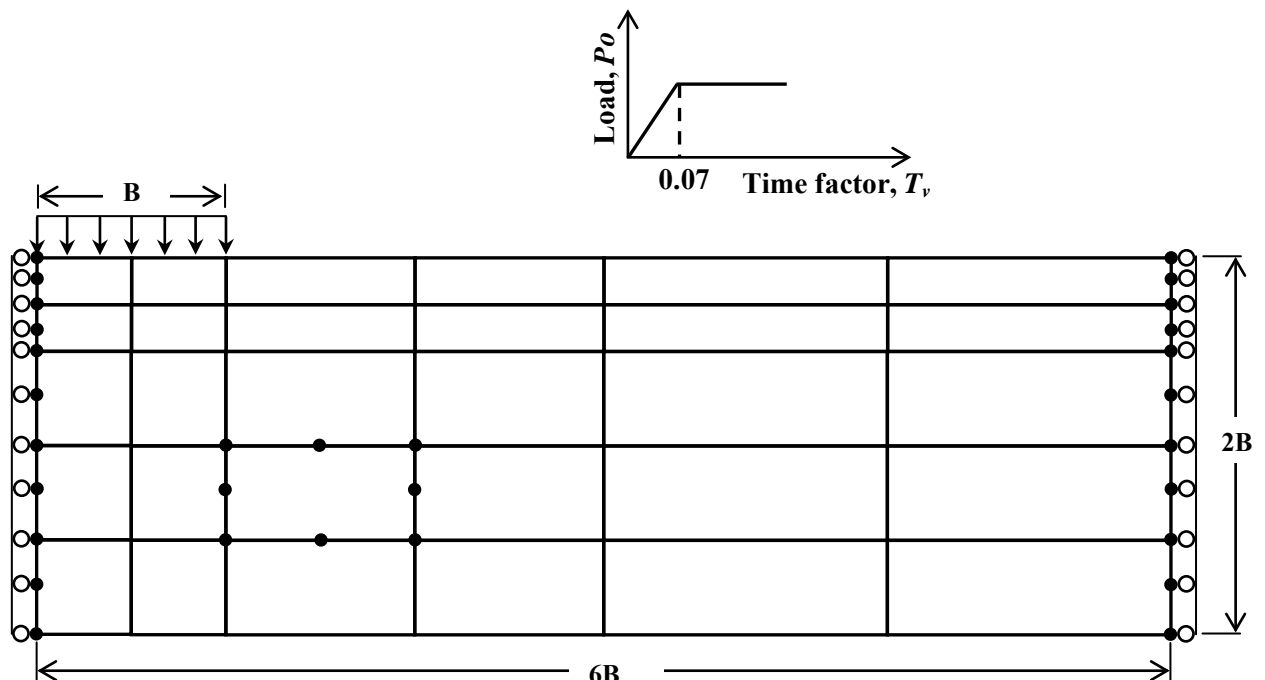
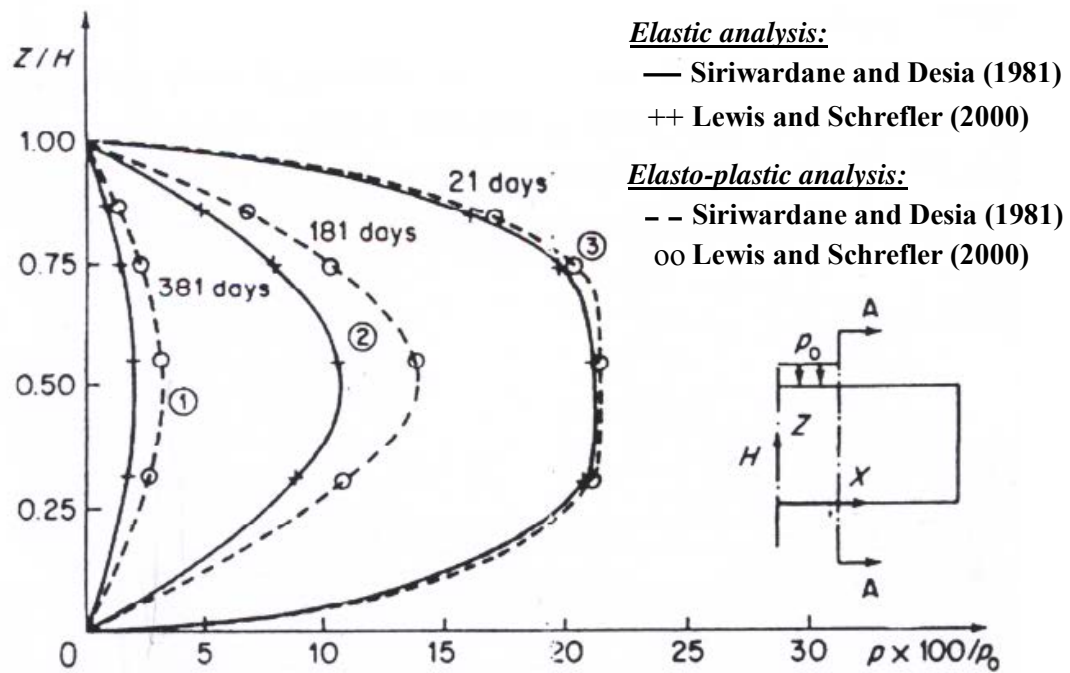
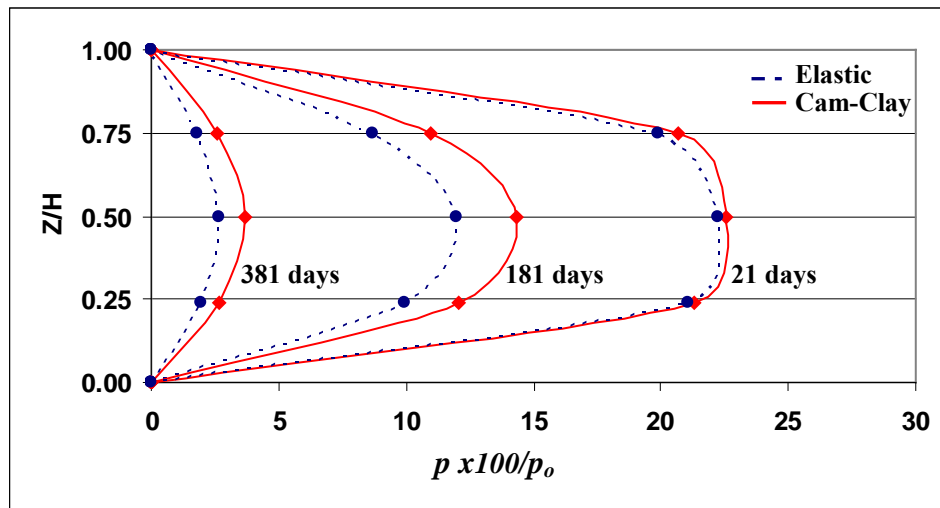


Figure (3): Finite Element Idealization and Load History



a- Results of: Siriwardane and Desia (1981); Lewis and Schrefler (2000)



b- Results of the present study

**Figure (4): Pore-water Pressure Versus Depth Along Saction A-A
at Three Different Time Values:
(1) $T_v = 0.059$, (2) $T_v = 0.504$ and (3) $T_v = 1.060$**

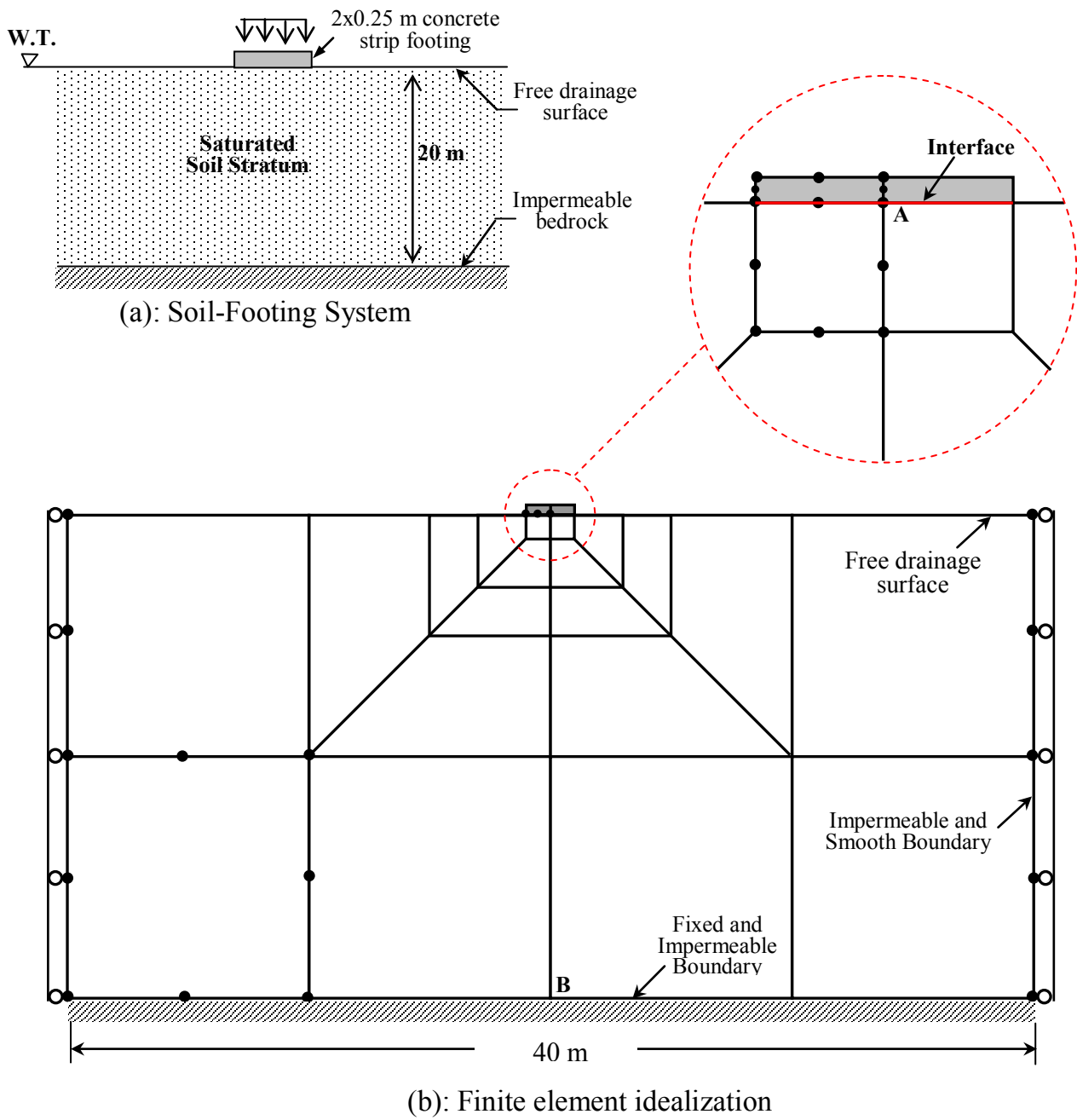
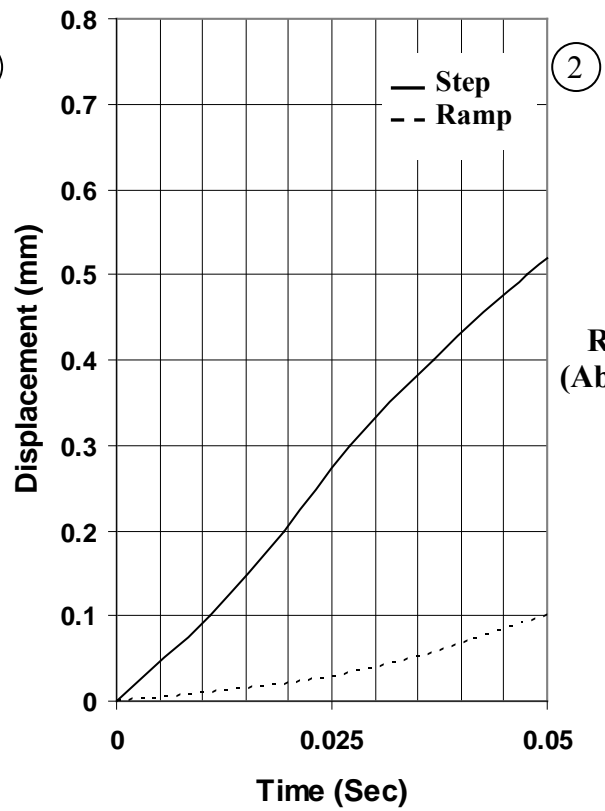
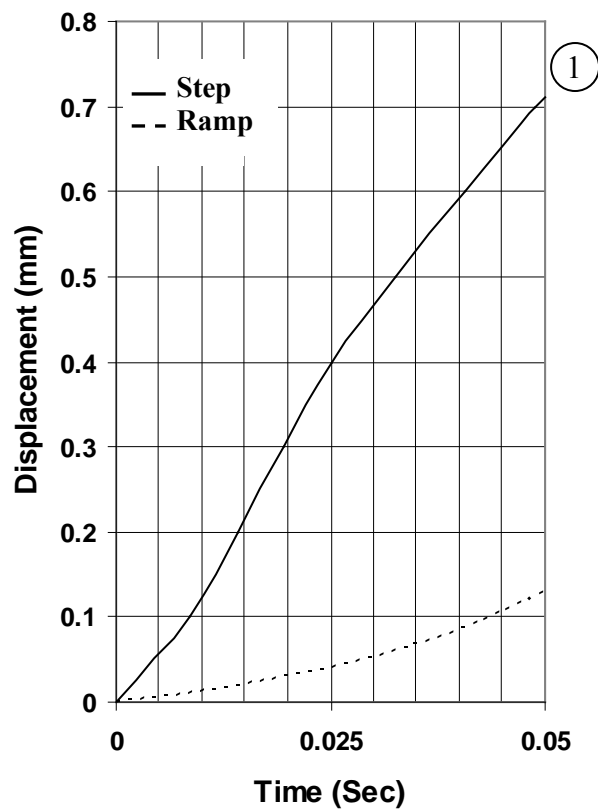
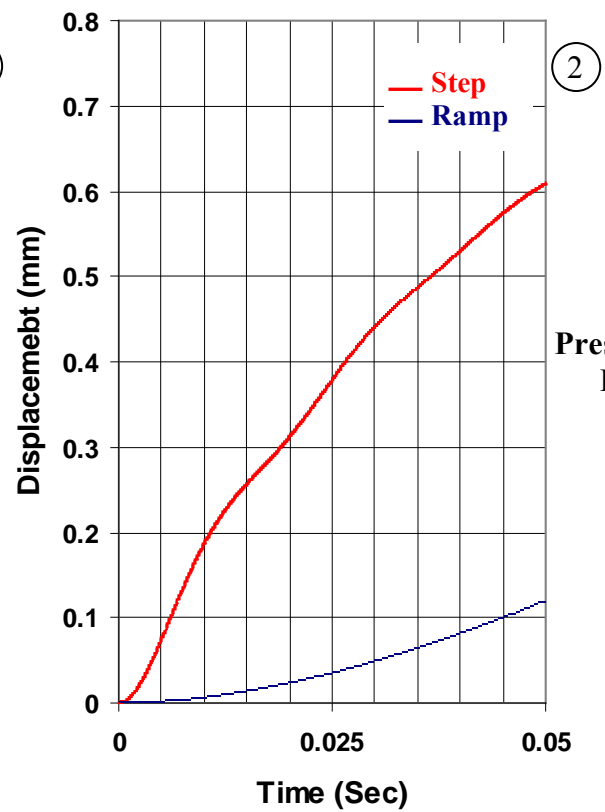
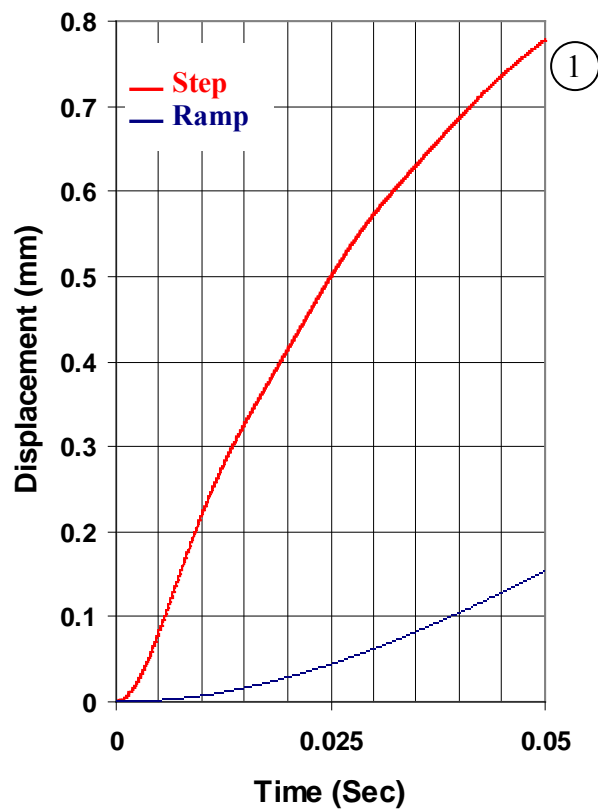


Figure (5): Strip Footing on Saturated Soil Stratum



Results of
(Abbas, 2003)



Present Study
Results

Figure (6): Vertical Displacement Time History at Point A for the Strip Footing
1: without Coupling (Dry State), 2: with Coupling Effect (Saturation State)

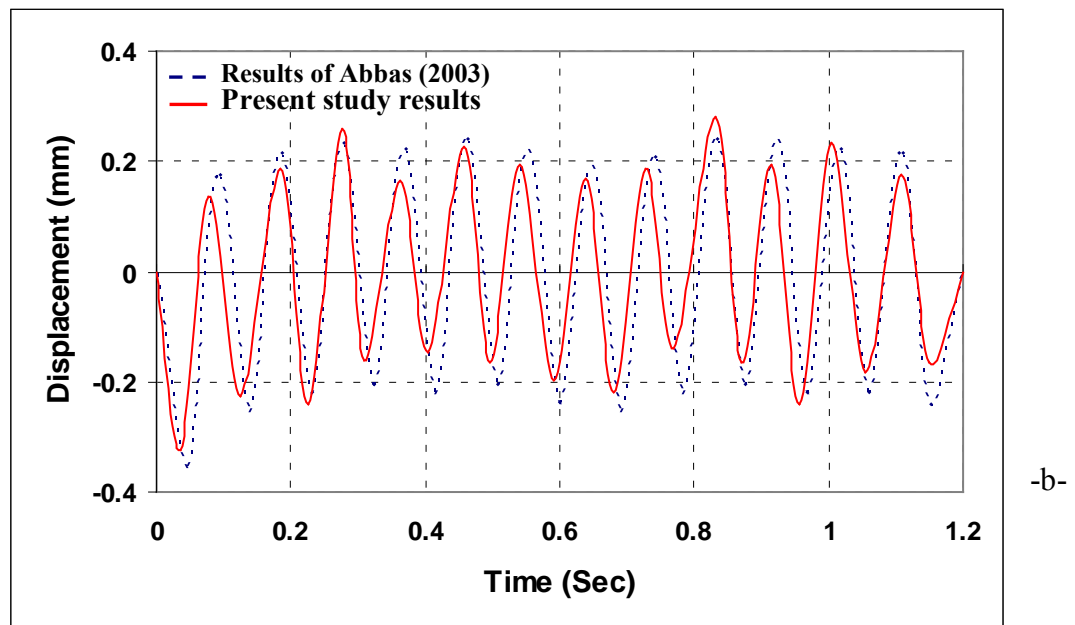
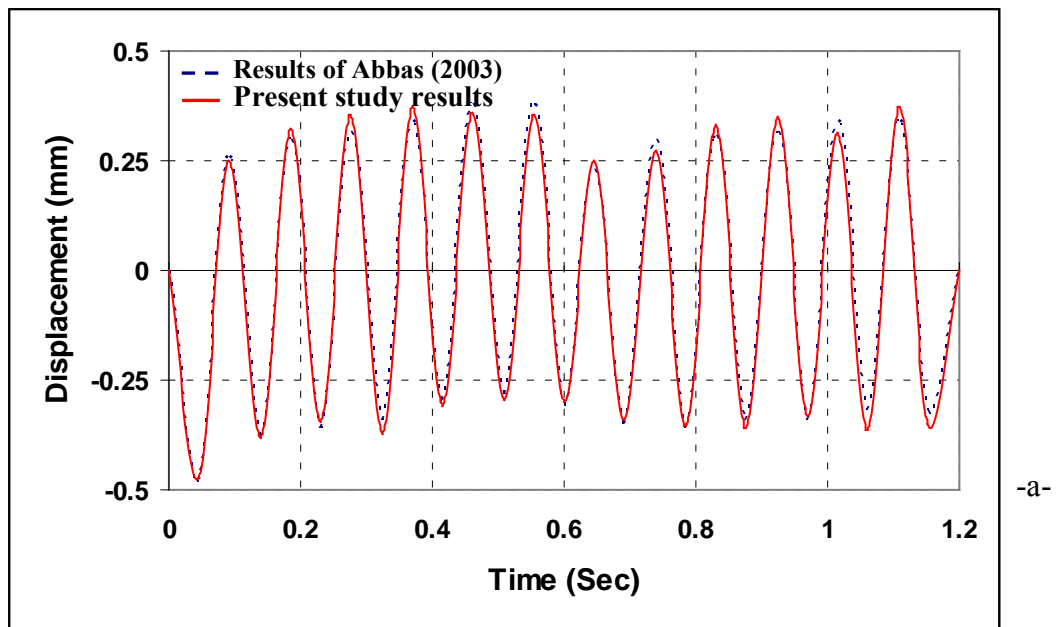


Figure (7): Vertical Displacement Time History at Point A for the Strip Footing
a- without Coupling (Dry State), b- with Coupling Effect (Saturation State)

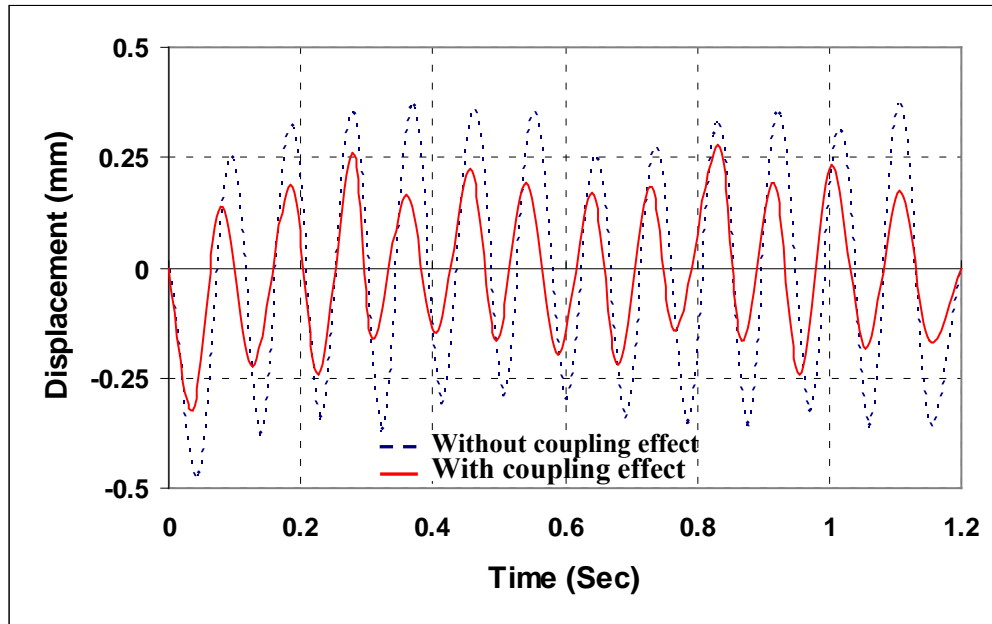


Figure (8): Coupling Effects on Vertical Displacement for the Strip Footing (present study results)

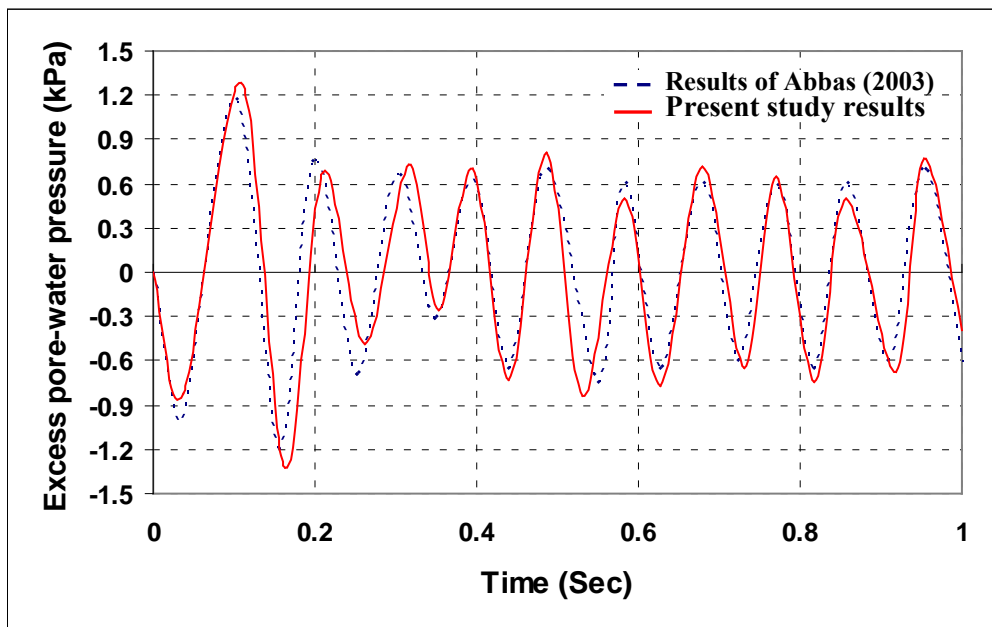


Figure (9): Excess Pore-water Pressure Time History at Point B for Strip Footing Subjected to Sinusoidal Excitation

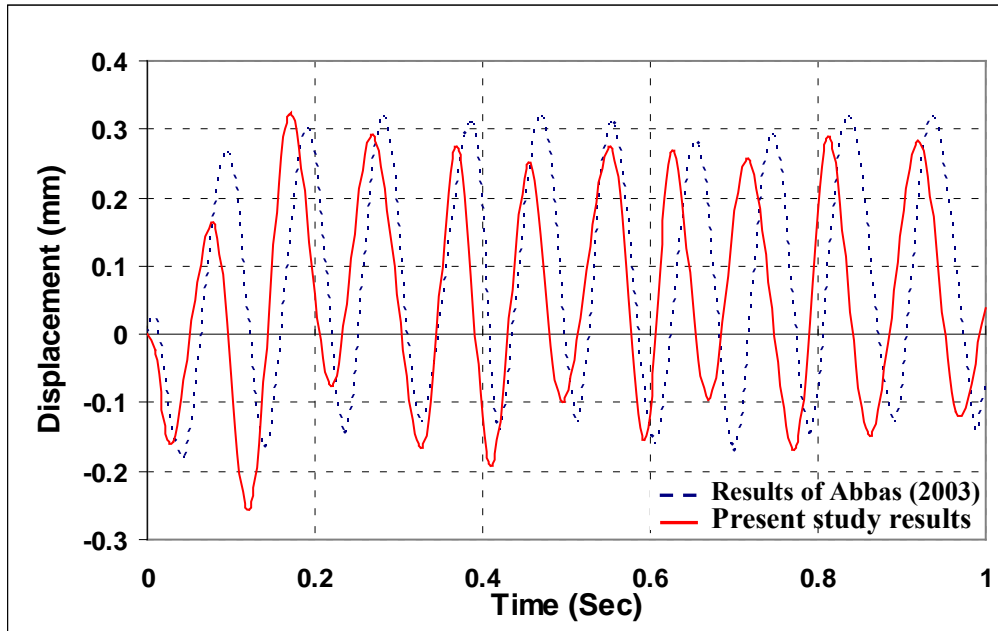


Figure (10): Interface Effects on Vertical Displacement for the Strip Footing

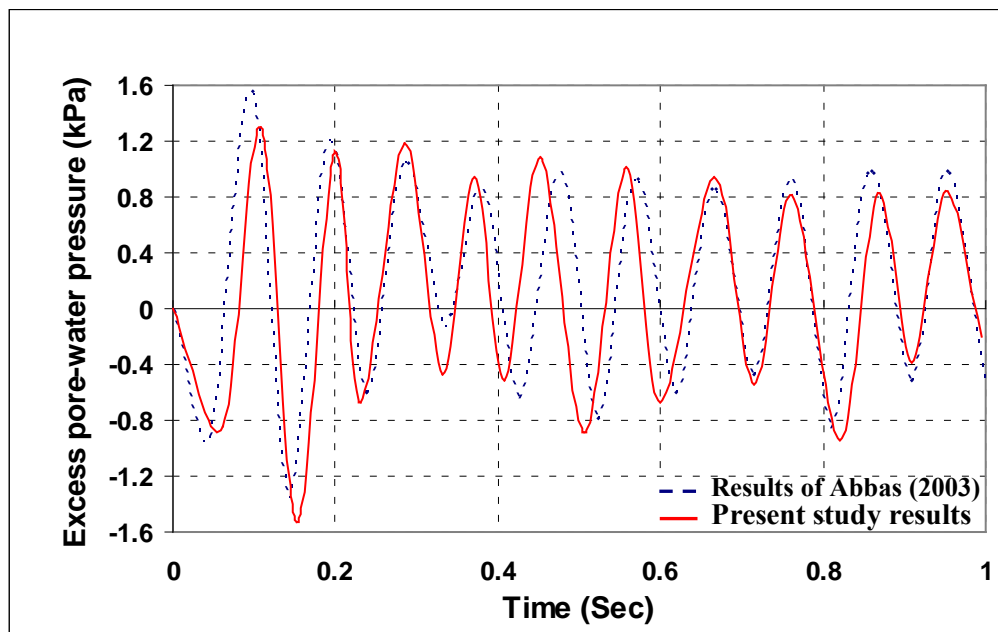


Figure (11): Interface Effects on Excess Pore-water Pressure for the Strip Footing

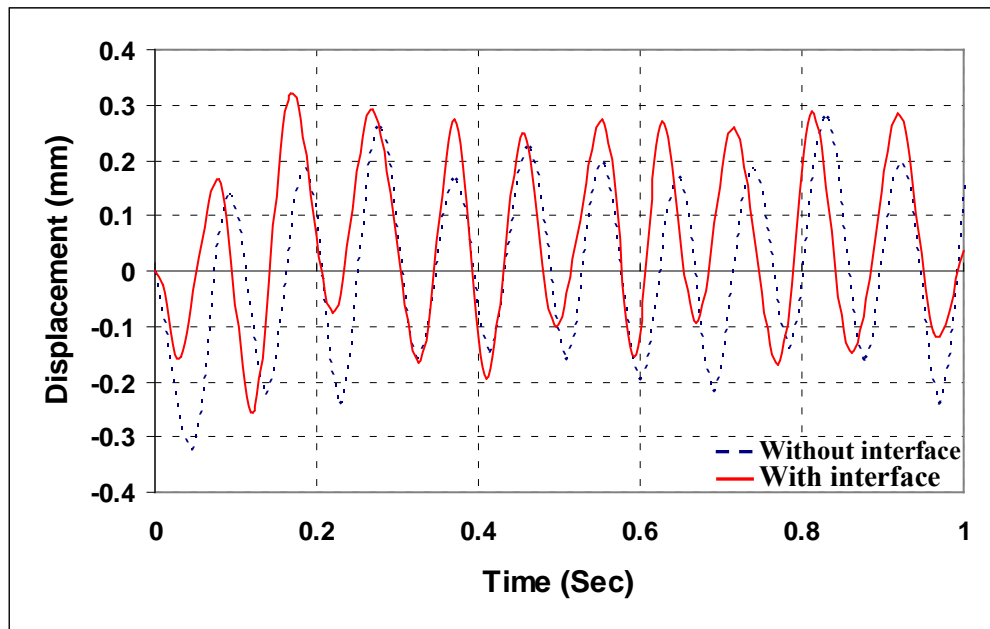


Figure (12): Interface Effects on Vertical Displacement for the Strip Footing (present study results)

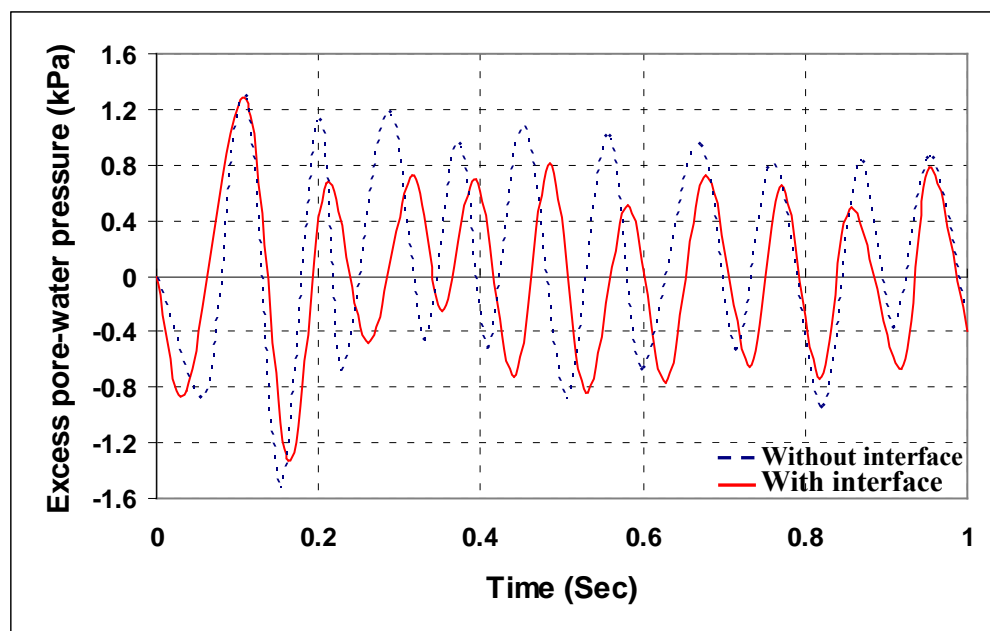


Figure (13): Interface Effects on Excess Pore-water Pressure for the Strip Footing (present study results)

Analysis And Design Of Tunnel Lining In Alluvial Soil Deposits

Prof. Dr. Nuri al-Mohamadi

Applied Science University ,Amman , Jordan ,11931 .

Formerly ; Consultant for Baghdad Metro Project ; Baghdad Rapid Transit Authority

e-mail: nalmohamadi@yahoo.com

ABSTRACT

This paper is concerned with analysis and design of a typical tunnel section of the proposed Baghdad Metro Project. A cross section of the soil profile is presented showing soil layering, which consist of a top cohesive layer underlain by a lower sand layer of fine to medium sand. A summary of soil characteristics required for tunnel analysis is given. Two loading cases are considered for the analysis of the driven bored tunnel. Load case 1 (LC 1) the water table is assumed at ground surface , while load case 2 (LC 2) the water table is assumed at bottom of tunnel. The earth pressures and water pressures acting on the tunnel for these loading cases are calculated . The tunnel lining consists of seven precast segments of 0.3 m thickness . Two tunnels of diameter $D= 6.2\text{m}$ are driven with a distance= 16.5m between center of tunnels . This distance becomes 9.0m when the tunnels approach to a station. A finite element program is used to analyze the normal forces, bending moments, shear forces and displacement of the tunnel lining . The tunnel section is idealized as a framework consisting of (a) straight beams representing the reinforced concrete segments, (b) springs which represent the soil .Spring stiffness factor is calculated from elastic theory and soil characteristics. The maximum values of normal forces, shear forces bending moments and displacements are presented.

Keywords: Alluvial soil, loading cases, precast concrete segments, tunnel lining, structural analysis.

1. INTRODUCTION

The development of transportation in large cities and the continuous increase of population require the construction of underground transportation systems.

The relative positions of tunnels and the construction procedure affect the soil deformation and internal forces shear forces and bending moments in the lining , [4]. Precast segmental linings are used in circular tunnels that are bored using shield tunnel boring machines, mainly in soft ground. shield tunnel lining in soft ground is usually designed based on empirical analytical methods with some simplifying assumptions related to soil homogeneity, stiffness and height above the tunnel, [8]. Several curved precast reinforced concrete segments are assembled inside the tunnel at the tail of the boring machine to from a complete ring. The number of segments is a function of tunnel diameter and construction method. The segments are supplied with water proofing neoprene gaskets on each edge and bolted together with high strength grip bolts to compress the gaskets and assure impermeability of the lining.

2. SOIL CONDUCTION AND GEOTECHNICAL ASSESMENTS

In Baghdad region the flood plane alluvial deposits extend to a large depth below the investigated depths of 40m and 50m. in general the top layers are cohesive layers of silty clays or clayey silts mostly of intermediate to high plasticity, overlying medium to dense or very dense silty fine sands. The upper cohesive soils contain lenses of silty fine sands, are in the order of 10 to 20m deep, occasionally may be only 3m deep and exceptionally more than 35m deep. The silty sands contain numerous randomly occurring inter-layers and lenses of cohesive soils of varying thickness and extent as well as pockets or lenses of gravelly sands. Groundwater levels are in general between 1m and 3m deep; these details are shown in figure 1.

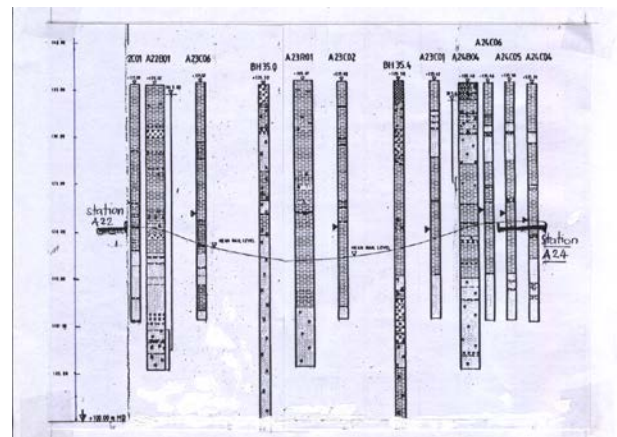


Figure 1: Soil profile and elevation of metro rail level

The moisture of the upper cohesive soils, usually in the range 20% to 30%, which is close to and often lower than the plastic limit. This conforms with the desiccated nature of the soils due to high evaporation during precipitation associated with high shrinkage stresses. The resulting soil characteristics are; over consolidation, reduced compressibility and high strength. Therefore these soils are described as stiff or even hard than would be expected from normally consolidated alluvial deposits in more temperate areas, [7], [2].the presence of sand stratum below the main cohesive layer and the highly variable soil conditions with all their random lensing, in the presence of high water table give rise to some of the more difficult problems of constructing deep underground structures, especially in the urban area where adjacent buildings may be affected and services and access have to be maintained. Tunneling will always be below water table either in the silty fine sands or more often through a silty clay – silty sand interface. All excavations must be supported with good excavation support system with minimum lateral yield to protect adjacent buildings. Control of ground

water will be essential. Recharge in nearby areas may be required to protect nearby buildings from excessive settlement and differential settlement due to water table lowering for prolonged periods.

3. GEOTECHNICAL ASSESMENT

The main geotechnical parameters required to the design of segmental tunnel lining and excavated stations are summarized in table 1,[7].

Table (1a&b): Summary of Geotechnical Parameters

(a) cohesive soils	
Parameters	Value
Bulk density (γ_b)	19.1 KN/m ³ (1.95 t/m ³)
Shear Strength Undrained (C_u)	75 KN/m ²
Drained (Φ')	25°
Elastic Modulus (E)	15 MN/m ² = 200 C_u
Poisson's Ratio (ν)	0.5
Consolidation characteristics: Compression Index (C_c)	0.2 for depth < 13m 0.3 for depth > 13m
Swelling or rebound Index (C_r)	0.05 (0-15m) depth 0.06 (15-22m) depth
Initial Void Ratio (e_0)	0.65 (0-13m) 0.72 (13-22m)
Main pre-consolidation pressure (P_c')	325 KN/m ²
Earth Pressure at Rest (K_0)	1.2 at 3m depth 0.7 at 25m depth
Sulphate Content (SO_3)	Range 0.1 to 8.7 g/l
(b) Silty Sands	
Parameter	Value
Bulk Density (γ_b)	19.1 KN/m ³ (1.95 t/m ³)
Effective Angle Of Shearing Resistance (Φ')	35°
Elastic Modulus (E_s)	30 to 50 MN/m ²
Poisson's Ratio(ν)	0.3
Earth Pressure Coefficient at Rest (K_0)	0.7 to 8m depth 0.5 at 25 depth
Permeability(K)	Order of 10 ⁻⁶ m/s

4. LOAD CASES AND GROUND WATER

Tow load cases are considered ;

4.1 load case1 (LC1)

With highest soil cover above tunnel crown (~10m) and the distance between the two tunnels is large ($d \approx 16.5m$). The ground water table is assumed at ground surface, figure2. in this loading case the tunnel lining will be subjected to the greatest normal force, so this loading case will be decisive for evaluating the normal stresses in the joints of the tunnel segments. Since the distance between the centerline of the two tunnels is wide enough ($d \approx 16.5m$), the influence of the adjacent second tunnel driving or excavation is of minor importance and it will not be necessary to be considered for the calculation. This loading case simulates the actual loading for bored tunnel. A surcharge load equivalent to a soil cover of 1.5m is

assumed to take into consideration the effect of adjacent buildings and street loads for both loading cases.

4.2 Load case 2 (LC2)

This load case simulates the loading of excavated tunnel adjacent to each station from both sides and extends to about 10 to 15 m from the station. The water is assumed at bottom of the tunnel, figure 2.

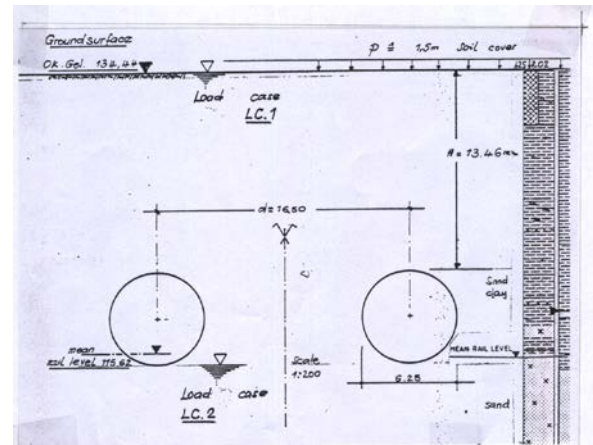


Figure 2: Loading cases LC1, LC2

The distance between the two tunnels is minimum ($d_2 = 9.0m$), so the effect of the adjacent second tunnel excavation, should be considered, i.e. the soil will be loose and the elastic modulus (compression modulus of springs) must be reduced around the horizontal center line of the tunnel facing the first tunnel, from 30 MN/m² to 20 MN/m². The calculated earth pressures and water pressures acting on the tunnel for load cases LC 1 & LC 2 are given in figures 3a & 3b.

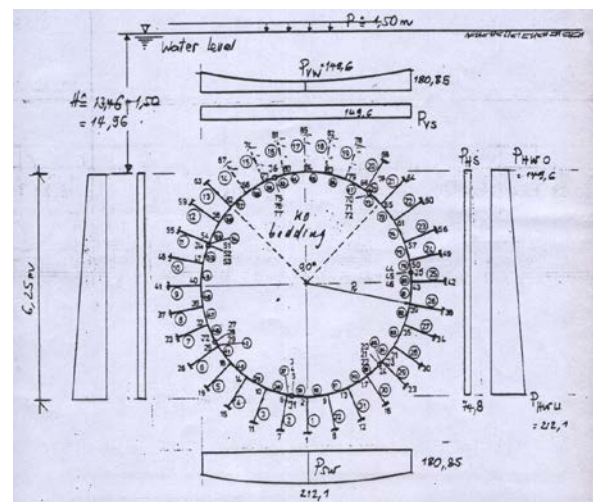


Figure 3a: Earth pressures and water pressures acting on tunnel, LC 1

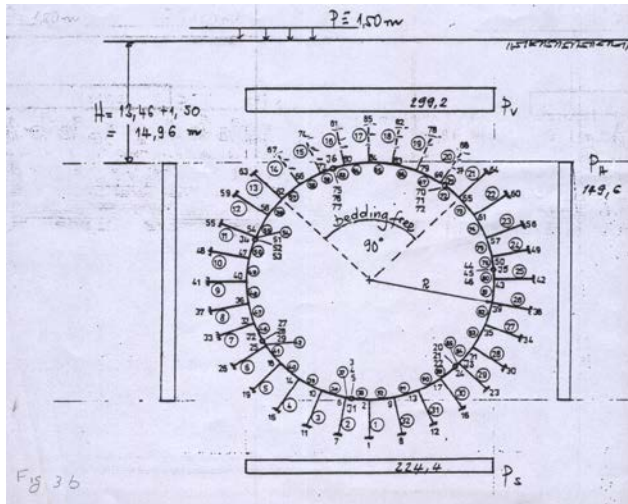


Figure 3b: Earth pressures acting on tunnel, LC 2

5.DETERMINATION OF COMPRESSION MODULUS E_s

The compression modulus E_s is required for the finite element analysis of tunnel lining. E_s can be obtained from consolidation tests results presented as void ratio e vs. log applied effective stress σ_v' .

$$E_s = \frac{\Delta \sigma_v'}{\Delta e} \quad (1)$$

$$\Delta e = e_o - (1 - e_o) * e \quad (2)$$

Where

$\Delta \sigma_v'$ = change of applied effective stress.

Δe = change of void ratio.

e_o = initial void ratio.

e = void ratio corresponding to any stress.

Since most tunneling lies in a mixed soil of clay, silt and sand, so an average value of E_s for different soil types. The consolidation test results are not presented due to space limitations.

Table (2): Calculation of compression modulus E_s

Soil type	e _o	σ _v ' KN/m ²	e	Δe	Δσ _v ' KN/m ²	E _s MN/m ²
Clay	0.52	50	0.486	0.287	1550	50
		1600	0.420	0.318		
Silt	0.6	50	0.580	0.368	750	18.75
		800	0.480	0.408		
Sand 1	0.54	50	0.524	0.299	1550	25
		1600	0.390	0.361		
Sand 2	0.68	25	0.664	0.468	750	53.57
		800	0.618	0.482		AV. E _s =36.83

Therefore a constant value of the compression modulus $E_s = 30 \text{ MN/m}^2$ is adopted for the analysis since preliminary structural analysis have shown that the possible extreme values of E_s have no significant influence on static forces, only the deformation of tunnel lining will increase slightly if E_s is varied from 30 MN/m^2 to 15 MN/m^2 .

6.CALCULATION OF SPRING CONSTANT (MODULUS OF ELASTIC SUPPORT)

The elastic deformation of the tunnel can be simulated by means of springs situated normal to the ring at constant small distances about (0.6m) so that the soil characteristics are represented as close as possible to the actual case, as shown in figures 4&5.

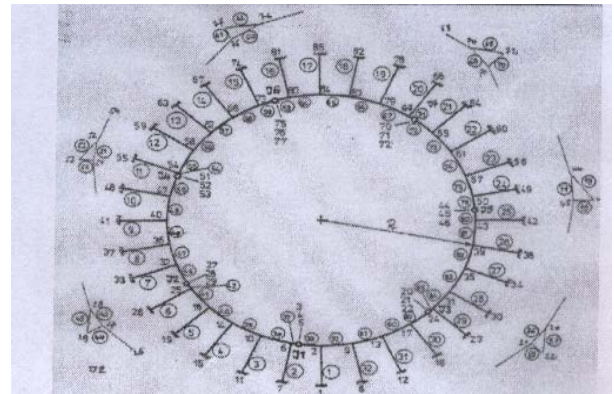


Figure 4: Simulation of segmental lining model

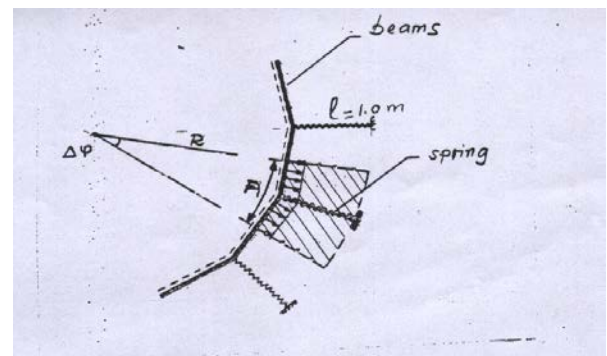


Figure 5: Tributary area for each spring

From elastic theory, the following relationships can be obtained :

$$\Delta l = \frac{\sigma}{C} \quad (3)$$

σ = Applied stress.

C = Elastic constant of the spring

$$C = \frac{E_s}{R} \quad (4)$$

Δl = Deformation of the spring

$$\sigma = \frac{P}{A} = \frac{P}{b * R * \Delta \Phi} \quad (5)$$

P = Load of the spring.

A = area of soil under consideration.

R = Radius of tunnel.

b = breadth of influence = 1.0 m in this case.

Substituting 4 and 5 in to 3 :

$$\Delta l = \frac{P * R}{R * \Delta \Phi * E_s} = \frac{P}{E_s * \Delta \Phi} \quad (6)$$

E_s = Compression modulus of soil .

According to Hook's law, the deformation of a spring Δl is obtained as follows : see figure 5.

$$\text{Strain } \varepsilon = \frac{\Delta l}{l} = \frac{\sigma}{E_s} = \frac{P/A}{E_s} \quad (7)$$

$$\Delta l = \frac{P}{E_s * A} \quad (l = 1.0m) \quad (8)$$

Equating 6 and 8

$$\frac{P}{E_s * \Delta \Phi} = \frac{P}{E * A} \quad (9)$$

$$\therefore A = \Delta \Phi \quad (10)$$

7. TUNNEL LINING SIMULATION FOR FINITE ELEMENT ANALYSIS

Physical modeling of tunnel lining and excavation in soft ground has played an important role in studies related to underground structure, [6]. These models include: analytical models using formulas in accordance with national standards with properly selected design loads, numerical models using finite element programs (2-D and 3-D) with constitutive laws in accordance with national standards to obtain; stresses, strains and bending moments,[5].

The segmental tunnel lining can be represented by beams supported by springs which represent soil and joints.

Seven joints (J1 to J7) are assumed at which the bending moment is zero , but there will be axial force and shear at these joints . Figure 4 shows the basic model for segmental tunnel lining analysis.

The system consists of:

7 joints (1 to 7) , 92 elements (1 to 92) and 85 nodes (1 to 85) , as shown on figure4.

In this paper, the thickness of segment is assumed $t_s = 0.30m$, although in the original study another thickness $t_s = 0.35m$ was also investigated internal diameter of tunnel $d_i = 5.90m$. thickness of tunnel lining $t_s = 0.30m$. mean diameter to the center of lining $d_m = 6.20m$.Mean radius to the center of lining $R_m = 3.10m$.

Member properties :

Beams : breadth $B = 1.00m$, cross sectional area $= 0.30m^2$, moment of inertia $I = \frac{Bd^3}{12} = 0.00225 m^4$.

Assumed Modulus of Elasticity for Concrete $E_{con} = 37000MN/m^2$.

Springs of foundation support :

Breadth of influence = 1.0m.

Length of spring = 1.0m .

Central angle $\Delta \Phi = \frac{360^\circ}{32} = 11.25^\circ$.

Area of influence for each spring $= \frac{11.25 * [1]}{180} = 0.1964 m^2$

Moment of inertia of spring $I_s = 0$.

Compression modulus $E_s = 30MN/m^2$.

Reinforced concrete design was carried out according to [1].

8. SUMMARY OF RESULTS OF ANALYSIS

Table 3 presents the maximum values of :

Axial forces N, shear forces V and bending moment M for a segment thickness $t_s = 0.3 m$ for both load cases LC 1 and LC 2 .

Table (3) : summary of member force , shear and bending moment (maximum values)

Load case	Axial force F_x (KN)	Shear force V_v (KN)	Moment M_z (KN.m)
LC 1	-957.4* -745.8	± 149.0 ± 149.0	-4.67* ± 59.54
LC 2	-761.6* -567.6	± 195.0 ± 195.0	9.20* -107.30

These values are decisive for design of tunnel segments .

9. STRUCTURAL DESIGN OF SIGMENTS

Details of the structural design can not be presented in this paper with very limited space available .However , detailed calculations for $t=0.3m$ thickness for LC 1 showed that the thickness is adequate and only temperature reinforcement (minimum reinforcement) is required in top and bottom faces of the segment in the both directions to limit concrete cracking .

Therefore the final decision is to use reinforced concrete segmental lining with thickness $t=0.3m$, since it is adequate , safe and economical [3].

10. NODAL DISPLACEMENTS OF THE TUNNEL.

The approximate radial displacement (Δs) at a point directly around a tunnel in an elastic soil is given by :

$$\Delta s = \frac{P_z (1 + \nu) a^2}{E * r} \quad (11)$$

Where : P_z = stress in the ground , ν = Poisson's ratio , a = radius of tunnel, r = radius of point of interest.

The finite element analysis had shown that the displacement $\Delta s = 23.6mm$ for LC 1 and lining thickness $t=0.30m$. for LC 2 the displacement is $\Delta s = 30mm$ which is the maximum value . in comparison with the diameter of the tunnel ($D = 6.20m$) , this displacement is relatively small and equal to only 0.48% . The neoprene gasket provided on all side of each segment and the high tensile strength friction grip bolts will provide construction measure that prevents endangering the impermeability of tunnel lining due to those values of displacement .

11. CONCLUSIONS

From this paper the following conclusions may be drawn :

11.1 the alluvial soil deposits in Baghdad city consist of top cohesive layers underlain by lower sand layers which extend to large depths. The top cohesive layers are over consolidated due mainly to shrinkage stresses and rise of water table , stiff to hard soils with relatively low compressibility .

11.2 precast segmental linings can be used successfully in alluvial soil deposit below water table .

11.3 this study presented the design geotechnical parameters required for analysis and design of bored tunnel .

11.4 Two load cases were considered for the design of tunnel lining; LC1, water table assumed at ground surface, LC2, water is assumed at bottom of tunnel, a surcharge of 30 KN/m^2 was assumed for both cases. The earth pressures (vertical and horizontal) and water pressures acting on the tunnel were calculated according to these assumptions, which simulate the real construction conditions.

11.5 the values of compression modulus E_s varies from 18.75 MN/m^2 for silt to 53.6 MN/m^2 for dense sand, with an average design value for the mixed soil $E_s = 30 \text{ MN/m}^2$.

11.6 the tunnel lining can be simulated as 2-D frame using finite element analysis. The analysis carried out using the obtained values of axial forces, shear forces and bending moments showed that reinforced concrete segments of 0.3m thick. will be adequate , safe and economical for this project with minimum temperature reinforcement .

11.7 the maximum displacement of the lining $\Delta s = 30 \text{ mm}$ for LC2, which is equivalent to 0.48% of the tunnel diameter. This displacement is considered relatively small and will not affect the water proofing of the lining.

REFERENCES

1. British Standard Institute, BS 8110(1997) code of practice for design of concrete structures, BSI, London.
2. British Standard Institute, BS 5930 (1999) code practice for site investigation, BSI, London.
3. British Tunneling Society, ICE(2004). Tunnel lining design guide Tomas Telford, London.
4. Chahade, F.H and Shahrour, I., (2008). Numerical analysis of the interaction between twin tunnels, Influence of the relative position and construction procedure. Tunneling and underground space technology vol.23, Iss.2.
5. Federal Highway Administration FHWA(2009), Technical manual for design and construction of road tunnels-civil elements report No.FHW-NHI-10-034, Washington D.C.20590.
6. Meguid, M.A, Saada, O, Munes, M.A & Matter, J.D (2008), Physical Models of Tunnels in Soft Ground, a Review. Tunneling and Underground Space Technology vol.23, Iss.2.
7. National Center for Construction Laboratories NCCL(1981), Site Investigation Report for Baghdad Metro Project, Baghdad Rapid Transit Authority, BRTA, Baghdad, Iraq.
8. Nunes, M.A., & Meduid, M.A (2009) A Study of the Effect of Overlying Soil Strata on the Stress Developing in Tunnel Lining . Tunneling and Underground Space Technology vol.24, Iss.6.

Effect Of Silt Content On The Anisotropic Behaviour Of Silt-Sand Mixtures

Navid Khayat¹, Abbas Ghalandarzadeh²

Ph.D. Assistance Professor, Department of Civil Engineering, Islamic Azad University Ahvaz Branch, Ahvaz,
Iran. (Khayat@iauahvaz.ac.ir)

Ph.D, Associate Professor, School of Civil Engineering, University college of engineering of Tehran, Iran,
(aghaland@ut.ac.ir)

ABSTRACT

The anisotropy of sand has not been fully studied in terms of the effects of different silt content. This study investigates the effects on anisotropy in Tehran sand with various silt contents. The tests performed in this research include some Hollow Cylinder Torsion Shear Tests conducted on 400kPa confining stresses. The samples had 0, 15, 30, and 50 percent silt contents, and the effect of the inclination angle on the major principal stress (α°) was investigated with a particular emphasis on silt content. The parameter " α " is considered as the key parameter that indicates the anisotropy characteristics, and can vary from 0° to 90° . According to the results, an increase of α° leads to more contractive behaviours in the studied sands. In all samples, increasing the silt content up to 50% causes the strength to decrease.

Keywords: Sand; strength; Silt content; anisotropy;

1 INTRODUCTION

In recent years, researchers have performed extensive and comprehensive studies on clean sand, determined different aspects of its behaviour in terms of its structure, and have made several general conclusions. However, the behaviour of clean sand containing silt is associated with several complications that make it difficult to understand. Extensive studies have focused on the effects of inherent and induced anisotropy on the behaviour of clean sand [14]-[17]-[19]-[34].

Yamamuro and Lade (1998) extensively investigated the behaviour of sands containing small amounts of silt (7%)[30]. They concluded that when a small amount of silt is added to the host sand, the obtained sand-silt mixture exhibits the opposite behaviour of that of pure sand. The sand under low confining pressure (25 kPa) is completely liquefied, and the strength of sand reaches zero. As the confining stress increases, the sand with 7% silt has more stable behaviour than that of pure sand with no liquefaction under high confining pressures. According to Yamamuro and Covrt (2001), the behaviour of silt-sand mixtures with high amounts of silt (40%) are different from those of pure sand and those of silt-sand mixtures with small amounts of fine particles [31]. In these mixtures, like the sands with 7% silt, liquefaction occurs completely under 25 and 50 kPa confining stresses; however, as the confining stress increases, the behaviour tends to be more stable. Such behaviours are similar to that of the sand with 7% silt content, but are still different from those of pure sand [31].

Parameter α° (the inclination of major principal stress with respect to the depositional (vertical) direction) is used to denote the rotation of principal stresses, and

parameter $b' = (\sigma_2 - \sigma_3) / (\sigma_1 - \sigma_3)$ indicates intermediate stresses. Different principal stress directions and b' values can cause changes in soil behaviour. Thus, α° and b' are selected as the key parameters for studying the anisotropy of sands. In this regard, Hollow Cylindrical Torsional Shear (HCTS) is the best apparatus for studying these parameters [1]. HCTS has been used in several tests conducted on sands by different researchers to study the effects of parameters α° and b' more accurately. They generally came to the conclusion that sandy samples had softer behaviour as the values of α° and b' increased in undrained tests [34]. According to Symes et al. (1985), sandy samples exhibit more contractive behaviour as the α° and b' values increased [14]-[25].

Despite extensive studies conducted on the anisotropy effects of clean sand, there are few studies that have investigated its effects on the behaviour of sand-silt mixtures. Among recent relevant studies, Bahadori and Ghalandarzade (2008) studied the inherent anisotropic effects on the undrained behaviour of sands using HCTS [4].

In this research, the anisotropic behaviour of Tehran sand with different silt contents in 400 kPa initial effective confining stress are studied. A total of 12 tests are conducted on Tehran sand with silt contents of 0%, 15%, 30% and 50%. In these tests, the effects of the inclination angle of major stress and silt content are investigated.

Material and Methods

2.1 Material properties

Tehran sand have been used in this research, which is

produced by crushing plants, This sand with greenish gray color. The physical characteristics and grading curves of this sands are shown in Fig. 1 and Table 1. The plasticity index of silt is less than 5% and can be addressed as non-plastic soil (see Table 2).

2.2 Maximum and minimum void ratios of sand-silt mixtures

An effective factor in the general behaviour of saturated sands in monotonic loading is soil relative density, a parameter that shows the sample's specifications at the end of consolidation stage. The samples prepared at low densities showed contractive behaviour in the drained tests; this behaviour causes excess pore water pressure in undrained tests which reduces the effective confined stress. The change of stress-strain from the softening to hardening state is generally related mostly to the relative density, which is observed and reported by several researchers [5]-[7]-[8]-[16].

It is clear that adding silt to the host sand changes the maximum and minimum void ratios. The parameters related to soil density are needed to compare the test results; therefore, minimum and maximum void ratios should be obtained for different percentages of silt. In this research, ASTM 4253 and ASTM 4254 are used to measure the minimum void ratio (e_{\min}) (the densest state) and maximum void ratio (e_{\max}) (the loosest state), respectively. The obtained values are plotted in Fig. 2. For host sand, the minimum void ratios decrease as the silt content of the samples increases. This trend continues up to 28 percent fine content (FC); then, the void ratio increases as the silt content increases. The minimum achieved void ratio takes place in the fine contents, which will be called the threshold fines content.

2.3 Testing apparatus and method

In order to study the inherent anisotropy, a hollow cylinder torsional shear (HCTS) device was used. For better investigation of post peak response the device can perform both stress and strain controls.

A closed loop control was applied to the machine to handle any type of desired stress history including major principal stress rotation and intermediate stress ratio. Four Electrical/Pneumatic [E/P] transducers were used to exert required pressure for the inner and outer cell pressure in addition to the torsion and axial load pneumatic actuators. An alternative DC motor for torsional strain control test was prepared in order to study the post peak behaviour. In the case of our tests, the motor was utilized since the strain control was adopted in order to study the softening response. The motor speed in all the tests remained constant and equal to 4 degrees per minute. Eleven transducers were adjusted in order to measure different parameters continuously. Three water pressure sensors, two for inner and outer cell pressures and one for pore pressure, one vertical displacement sensor to measure axial strain, and one rotation angel sensor to measure torsional strain, two differential pressure sensors, two axial and torsional stress sensors and finally two limit switch sensors

were set up. A computer program was utilized to control all test procedures by means of a PID control algorithm. Data logging device was the last part of the control system. The sample dimensions were 12 cm in height, 6 cm in inner diameter and 10 cm in outer diameter.

The maximum inclination of principal stress (α°) and intermediate stress ratio (b') are considered the critical parameters in this research. Because the torsion sensor measures the torque (T) at any moment, the $\sigma_{z\theta}$ (shear stress) value can be obtained using Eq (3), where r_i and r_o are the inner and outer radiuses of the samples, respectively. The value of σ_z (vertical normal stress) must be kept constant, and therefore, the values of σ_θ and σ_r (the circumferential and radial normal stress, respectively) obtained through Eqs (1) and (2), respectively, are also kept constant. Furthermore, P_i and P_o (inner and outer water pressures) are computed using Eq (5), F_v (vertical force) is found using Eq (4), and principle stress can be measured by equations 6 to 8 [15].

$$\sigma_\theta = \sigma_z - \frac{2\sigma_{z\theta}}{\tan 2\alpha} \quad (1)$$

$$\sigma_r = \sigma_z - \frac{\sigma_{z\theta}(\cos 2\alpha - 2b + 1)}{\sin 2\alpha} \quad (2)$$

$$\sigma_{z\theta} = \frac{1}{2} \left[\frac{3T}{2\pi(r_o^3 - r_i^3)} + \frac{T}{\pi(r_o^3 + r_i^3)(r_o - r_i)} \right] \quad (3)$$

$$\sigma_z = \frac{F_v + \pi(P_o r_o^2 - P_i r_i^2) - A_r P_o}{A_s} \quad (4)$$

$$\begin{cases} P_i = \frac{\sigma_r(r_o + r_i) + \sigma_\theta(r_o - r_i)}{2r_i} \\ P_o = \frac{\sigma_r(r_o + r_i) + \sigma_\theta(r_o - r_i)}{2r_o} \end{cases} \quad (5)$$

2.4 Experimental Program

Sample preparation method used in this study was dry deposition method, while not using water sedimentation method. That may alter the real anisotropy fabric. Dry deposition method is able to create more uniform silty sand samples according to Miura and Toki (1982) suggestion which says pluviation methods create the most significant anisotropy [12]. The sand was deposited into the frame through a funnel with a long tube. Carbon dioxide (CO_2) and deaired water were passed through the samples in their saturated states. The circulating time for the CO_2 considered in the tests conducted by Zlatovic and Ishihara (1997) were 30 minutes for clean sand and 8 hours for pure silt [35]. In the present study, the minimum and maximum times were 30 and 135 minutes for clean sand and the 50% silt mixture, respectively. After circulation of CO_2 , the deaired water entered from the bottom similar to CO_2 but in the opposite direction of gravity and was seeped into all the voids in the sample. The saturation procedure continues as the confining pressure increased, and the pore water pressure was measured in several steps. If the B-value would exceed

0.95, then the sample is assumed to be completely saturated. At this time the saturation stage was completed and the sample should be consolidated. Because all the tests conducted in this research were of the Consolidated Undrained (CU) type, all drainage valves must be opened during consolidation and connected to the system. The amount of water discharged from the sample during consolidation could be measured by reading the burette numbers at the beginning and end of this stage. After consolidation the shear stage started at which the shear speed was four degrees per minute, the lowest speed that can be applied to the system. At the end of the test the porosity of the samples was measured.

3. Results

The goal of this research was to study the influence of the amount of silt upon anisotropy features in sand-silt mixtures. For this purpose, sand were tested using 400-kPa initial confining stress and a silt content range of 0-50%. Also the Intermediate stresses parameter (b') in all tests was 0.5, Some information on these tests are given in Table 3.

All test results are presented in the form of stress-strain and effective stress path curves. According to these curves, the sample behaviours are similar to those of dense sands based on the classification of undrained sand behaviour in most conducted tests, according to Yoshimine et al. (1998) [34]. The significance of the strength of the deviator stressing phase transformation point is evident in this figure. According to Figs. 3 through 6, the sample strengths (deviator stressing phase transformation and failure points) decrease as α° increases; this indicates that the soil becomes softer. Increasing the silt content up to the threshold level will cause the strengths to decrease, and this reduction is more obvious for the 50% silt case (Figs. 6). In these samples, the test conditions were the same, and the silt percentage increased as the density increased, but unexpectedly, strength did not increase. For example, in test No.7, the value of D_r is 76, but in test No.28, which contains 50% silt, its value is 99, 6.

4. Discussing and studying the stress paths

4.1 Effect of inclination angle (α°) on the sand's behaviours

In Figs. 3 through 6, the strength of samples (deviator stressing phase transformation and failure strength) is reduced as α° increases, which indicates that the soil becomes softer. This behaviour has been described by Yoshimine and Ishihara (1998) for Toyoura sand, and by Bahadori and Ghalandarzadeh (2008) for a Firoozkuh sand-silt mixture[4]-[34].

4.2 Effect of non-plastic fines content on the sand's mixture behaviours

The effect of nonplastic fines on the behaviour of saturated sand has been studied by many researchers [6]-[13]-[23]-[29]-[32]. Adding different amounts of nonplastic silt considerably changes the sand behaviour,

and these changes are difficult to describe. Pitman et al. (1994) concluded that when silt was added to Ottawa sand, it became less collapsible in undrained triaxial compression tests. However, others found that nonplastic silt may decrease the strength (Troncoso and Verdugo, 1985; Sladen et al., 1985) [18]- [24]. Ishihara (1993) and Verdugo and Ishihara (1996) showed that the increased silt content increased the potential for sand to exist in nature in a contractive state, which includes the possibility of flow failure or liquefaction[9]- [28]. Yamamuro and Lade (1997, 1998) and Lade and Yamamuro (1997) observed that increasing the amount of nonplastic silt in Nevada sand increased the volumetric contractive character in both drained and undrained triaxial tests, even when the overall density increased[30]. Among the problems involved in these studies is the impossibility of fixing at least one of the parameters in sand-silt mixtures. In the present study, the method proposed by Bahadori and Ghalandarzadeh (2008) [4] was applied to address this problem. Based on this method, if the same conditions are considered in sampling and testing, then increasing the silt increases the density and decreases the strength. Thus, while the sample densities are equal, the sample with higher silt content has lower strength.

The sample strengths decreased in the silt-sand mixtures as the silt content increased (Fig. 7). The decreasing strength as silt is added to the host sand can be explained by Tavanayagan's classification (1999) (Fig. 8) [21]. According to Fig. 9, the void ratios of host sands are tested in the range of Tavanayagam's classification case (i); however, with 15% silt content, the intergranular void ratio (e_c) approached $e_{\max,HS}$ (Fig. 9), which is more similar to that observed in Tavanayagam's classification case (ii). In this latter case, the finer grains may support a coarser grain skeleton that is otherwise unstable. These grains act as a load transfer vehicle between some of the coarse grain particles in the soil matrix, while the remaining fine particles fill in the voids. In this case, the shear strength is derived from a combination of friction along coarse grain contacts and fine particles. In this structure, e_c increased, which decreased the strength of the samples. This behaviour is evident as the silt percentage in the mixtures increases and leads to an increase in relative density. Increasing the amount of silt content to 30% caused the intergrain void ratio, the relative density does not increase because its threshold percentage was 28%. Thus, an inter-fine-particle void ratio is used to explain its behaviour, which is similar to case (iv-2) and is shown in Fig. 9. Moreover, the inter-fine-particle void ratio in the mixture with 30% silt content is greater than that of a sample with 15% fine particle content. When the silt content is increased to 50% in all mixtures, e_f is smaller than ($e_{\max,HF}$), and ($FC_{th} < FC$); thus, their behaviours are similar to Tavanayagan's classification case (iv-2). In this case, the fine particles carry the contact and shear forces, while the coarse grains act as reinforcing elements embedded within the finer grain matrix. In this situation, the main bearing structure changes from sand to silt, and because the strength of silt is less than that of sand,

increasing the silt up to 50% decreases the strength of the mixture.

5. Conclusions

1) As α° increases, the strengths of the samples of host sand and silt-sand mixtures decrease, i.e., the soil becomes softer. Such behaviours have also been observed by Yoshimine et al. (1998) and Bahadori and Ghalandarzadeh (2008) [34]-[4].

2) As the silt content in mixtures increases, the relative density also increases, but this increase does not increase the mixture strength. An increase in relative density is one of the most marked phenomena indicating that the index of the relative density (or void) is not a suitable index for evaluating the behaviour of silt-sand mixtures.

3) In all mixtures, increasing the silt content up to 50% causes the strength to decrease. This decline in strength may be justified by parameters (e_c, e_f) , which are defined by Tavanayagam (1999) [21].

Notation

The following symbols are used in this paper:

α : the inclination of the major principal stress with respect to the vertical direction

b' : Intermediate stresses

b : Portion of fine grains that contribute to active intergrain contacts

D : Diameter of coarse grains

C_c : Coefficient of curvature

C_u : Coefficient of uniformity

D_{50} : Medium grain size

d : Diameter of fine grains

e_c : intergranular void ratio

e_f : Inter-fine-particle void ratio

e_{\max}, e_{\min} : Maximum and minimum void ratios, respectively

$e_{\max, HF}, e_{\min, HF}$: Maximum and minimum void ratios of host fine particles, respectively

FC : Fine particle content (%)

FC_{th}, FC_L : Threshold and limiting fine particle content, respectively

$(e_1 - e_3) / 2$: deviatoric axial strain

p'_c : initial effective confining stress

p_i, p_o : inner and outer water pressures, respectively

r_i, r_o : inner and outer radius, respectively

6. REFERENCES

- [1] Anhhminh, N. (2006). An investigation of the anisotropic stress-strain-strength characteristics of Eocene clay. Thesis for the degree of Doctor of Philosophy and for the Diploma of the Imperial College.
- [2] ASTM D4254. Standard Test Methods for Maximum Index Density and Unit Weight of Soils Using a Vibratory Table. ASTM Standard, (2006).
- [3] ASTM D4254. Standard Test Methods for Minimum Index Density and Unit Weight of Soils and Calculation of Relative Density. ASTM Standard (2006) e1.
- [4] Bahadori, H. Ghalandarzadeh, A. & Towhata, I. (2008). Effect of non plastic silt on the anisotropic behaviour of sand. Soils and Foundations 48, No. 4, 531-546.
- [5] Bishop, A. W., (1971). Shear strength parameters for undisturbed and remolded soil specimens. Proceeding for the Roscoe memorial symposium, Cambridge University, Cambridge, Mass, pp 3-58.
- [6] Bouckovalas, G. D, Andrianopoulos, K. I. & Papadimitriou, A. G., (2003). A critical state interpretation for the cyclic liquefaction resistance of silty sands. Soil Dynamics and Earthquake Engineering, No. 23, 115-125.
- [7] Castro, G. (1969). Liquefaction of sands. Harvard Soil Mechanics Series, No.81, Pierce Hall.
- [8] Castro, G., Poulos, S.J., France, J.W., and Enos, J.I. (1982). Liquefaction induced by cyclic loading. Geotechnical engineers Inc., Report submitted to NSF.
- [9] Ishihara, K.(1993). Liquefaction and flow failure during earthquakes. Geotechnique 43, No.3, 351-415.
- [10] Khayat, N. (2010). The investigation of the effect of inherent and induced anisotropy on the undrained behavior on Silt-Sand mixture. Thesis for the degree of Doctor of Philosophy of the Department of Civil Engineering, Science and Research Branch, Islamic Azad University, Tehran, Iran.
- [11] Lade, P.V. and Yamamuro, J.A. (1997). Effects of non plastic fines on static liquefaction of sands. Canadian Geotechnical Journal, 34.No. 6, 918-928.
- [12] Miura, S. and Toki, S. A.(1982). Sample preparation method and its effect on static and cyclic deformation-strength properties of sand, Soil and Foundation 22, No. 1, 61-77.
- [13] Naeini, S.A. & Baziar, M.H. (2004). Effect of fines content on steady-state strength of mixed and layered samples of a sand.. Soil Dynamics and Earthquake Engineering 24, 181-187.
- [14] Nakata, Y., Hyodo, M., Murata, H. and Yasufuku, N. (1998). Flow deformation of sands subjected to principal stress rotation. Soils and Foundations 38, No. 2, 115-128.

- [15] Pradhan, B. S., Tatsuoka, F. and Horii, N. (1988). Simple shear testing on sand in a torsional shear apparatus, *Soils and Foundations* 28, No. 2, 95-112.
- [16] Seed, H.B. and Idriss, I.M.(1971). Simplified procedure for evaluating soil liquefaction potential. *Geotechnical Engineering Journal* 97, No.9, 1249-1274.
- [17] Sivathayalan, S. & Vaid, Y.P. (2002). "Influence of generalized initial state and principal stress rotation on the undrained response of sands", *Canadian Geotechnical Journal*;39:63-76.
- [18] Sladenn J. A., D'Hollander, R. D. and Krahn, J. (1985a). Back analysis of the Nerlerk berm liquefaction slides. *Canadian Geotechnical Journal* 22, No.4, 564-588.
- [19] Symes, M.J., Gens, A. and Hight, D.W.(1984). Undrained Anisotropy and Principal stress Rotation in Saturated Sand. *Geotechnique* 34, No. 1, 11-27.
- [20] Symes, M.J., Gens, A. and Hight, D.W.(1985). Discussion. *Geotechnique*, 35, No. 1, 78-85.
- [21] Thevanayagam, S. (1999). Effect of fines and confining stress on undrained shear strength of silty sands. *Journal of Geotechnical and Geoenvironmental engineering* 124, No.6, 479-491.
- [22] Thevanayagam, S., Shenthann, T., Mohan, S. and Liang, J. (2002). Undrained fragility of sands, silty sands and silt. *ASCE, Journal of Geotechnical and Geoenvironmental engineering* 128, No.10, 849-859.
- [23] Thevanayagam, S. & Martin, G.R. (2002). Liquefaction in silty soils-screening and remediation issues. *Soil Dynamics and Earthquake Engineering* ,No.22, 1035-1042.
- [24] Troncoso, J.H. & Verdugo .R.(1985).Silt content and dynamic behaviour of tailing sand .*Proceeding of 11th JCSMFE, Balkema ,Rotterdam ,The Netherlands*,pp.1311-1314.
- [25] Uthayakumar, M. & Vaid, Y. P. (1998). Static liquefaction of sands under multi axial loading. *Canadian Geotechnical Journal* 32, No.2, 273-283.
- [26] Vaid ,Y.P., Sivathayalan, S.,Uthayakumar , M. And Eliadorani, A. (1995a). Liquefaction potential of reconstituted Syncrude sand. 48th Canadian Geotechnical Conference 1, pp.319-328.
- [27] Vaid ,Y.P., Uthayakumar, M.Sivathayalan, S., Robertson, P.K And Hofman,B. (1995b). Laboratory testing of Syncrude Sand . 48th Canadian Geotechnical Conference 1, pp.223-232.
- [28] Verdugo, R. & Ishihara, K. (1996). The steady state of sandy soils. *Soils and Foundations* 36, No.2, 81-92.
- [29] Xenaki, V.C. & Athanasopoulos, G.A. (2003). Liquefaction resistance of sand-silt mixtures: an experimental investigation of the effect of fines. *Soil Dynamics and Earthquake Engineering*, No.23, 183-194.
- [30] Yamamuro , J. A. & Lade, P.V. (1998). Steady-state concepts and static liquefaction of slity sands. *Journal of Geotechnical and Geoenvironmental engineering* 124, No.9, 868-877.
- [31] Yamamuro , J.A. & Covert, K.M. (2001). Monotonic and Cyclic Liquefaction of Very Lose Sands with High Silt Content. *Journal of Geotechnical and Geoenvironmental Engineering, ASCE*127, No. 4, 314-324.
- [32] Yang, S.L., Sandven, R., & Grande, L. (2006). Instability of sand-silt mixtures. *Soil Dynamics and Earthquake Engineering*, No.26, 183-190.
- [33] Youshimine, M., Ishihara, K. and Vargas, W. (1998a). Flow deformation of sands subjected to principal stress rotation. *Soils and Foundations* 38, No.3, 179-188.
- [34] Yoshimine, M. & Ishihara, K., (1998). Flow potential of sand during liquefaction. *Soils and Foundations* 38,189-198.
- [35] Zlatovic, S, & Ishihara, K., (1997).Normalized behaviour of very loose nonplastic soils: effects of fabric. *Soils and Foundations* 37, No.4, 47-56.

Table 1: Physical characteristics of sands

Sand type	C_c	C_u	$FC(\%)$	$D_{50}(mm)$
Tehran sand	0.59	2.55	0.03	0.106

Table 2: Physical properties of silt

Plastic limit (%)	Liquid limit (%)	Plasticity index (%)
22	24	2

Table 3. Characteristics of the tests

Test No.	Sand type	FC (%)	α°	e	D_r (%)	(e_f)	(e_c)
7	T	0	15	0.711	76.0	1.83	0.71
8	T	0	30	0.712	75.8	1.83	0.71
9	T	0	60	0.718	74.3	1.85	0.72
16	T	15	15	0.600	83.0	1.25	0.84
17	T	15	30	0.610	80.7	1.27	0.85
18	T	15	60	0.606	81.6	1.26	0.84
25	T	30	15	0.560	89.3	0.98	0.92
26	T	30	30	0.563	88.6	0.98	0.93
27	T	30	60	0.567	87.7	0.99	0.93
28	T	50	15	0.530	99.6	0.76	0.88
29	T	50	30	0.534	98.8	0.77	0.88
30	T	50	60	0.537	98.2	0.77	0.89

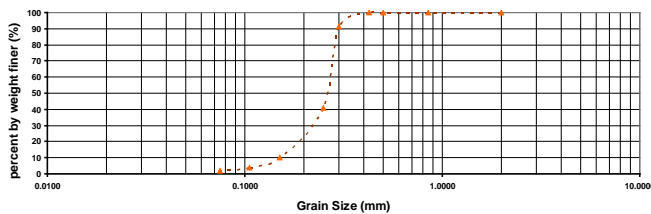


Fig. 1. Grain size distribution curves of Tehran sand

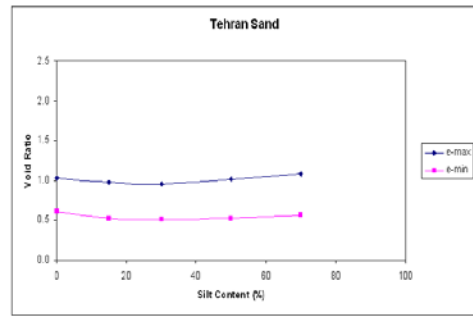


Fig. 2. Minimum and maximum void ratios for **Tehran** sand-silt mixtures

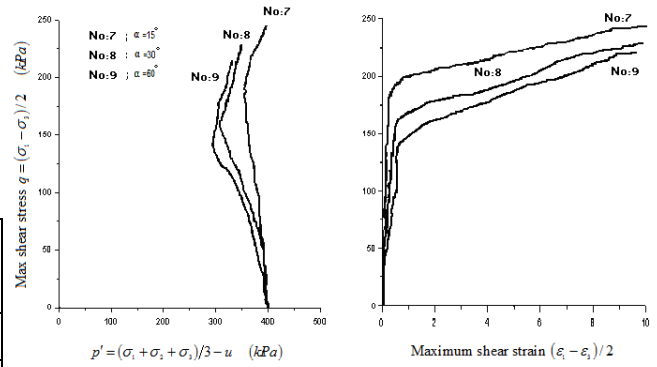


Fig. 3. Stress path and stress-strain curves in Tehran sand subjected to an initial effective stress of 400 kPa (FC=0%).

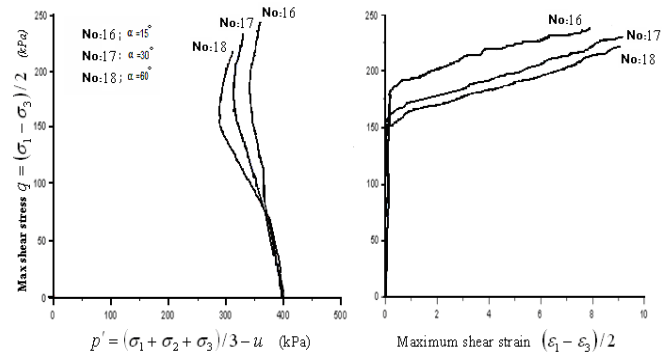


Fig. 4. Stress path and stress-strain curves in Tehran sand subjected to an initial effective stress of 400 kPa (FC=15%).

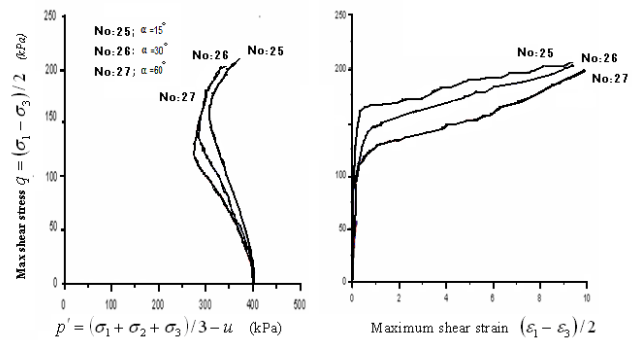


Fig. 5. Stress path and stress-strain curves in Tehran sand subjected to an initial effective stress of 400 kPa (FC=30%).

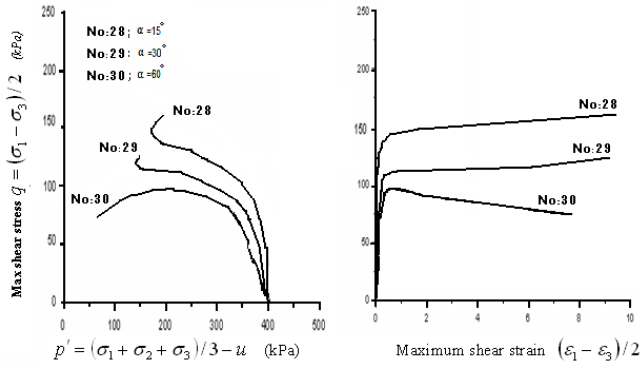


Fig. 6. Stress path and stress-strain curves in Tehran sand subjected to an initial effective stress of 400 kPa (FC=50%).

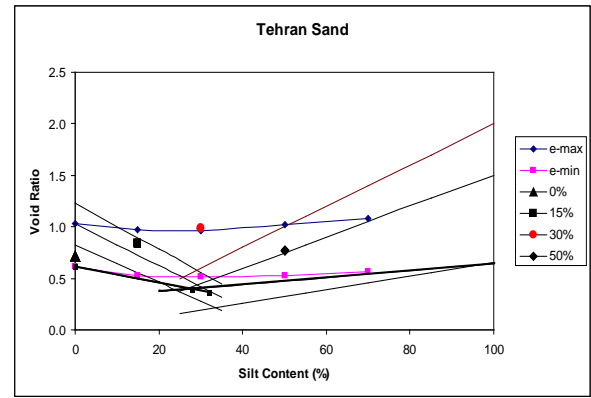


Fig. 9. Intergranular matrix phase diagram for Tehran Sand

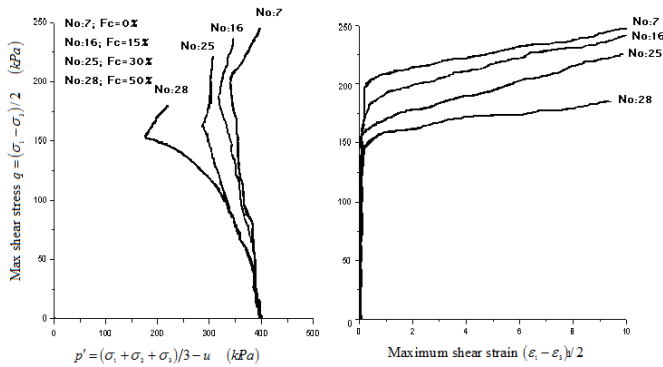


Fig. 7. Stress path and stress-strain curves in Tehran sands with different silt contents at $\alpha = 15$.

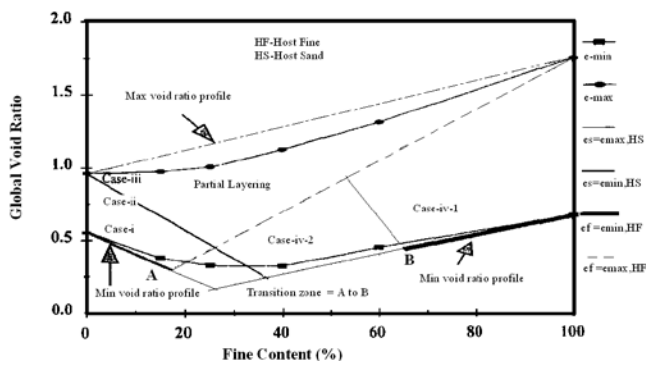


Fig. 8. Intergranular and Interfine Matrix Phase Diagram (Thevanayagam, 1999) [18]

Optimizing the twin tunnels position for reduction the surface ground movements

Mehdi Mokhberi¹, Seyed Ali Farjam²

1. Assistant Prof., Department of civil engineering, Islamic Azda University, Estahban Branch
2. M. Sc. Student, Department of civil engineering, Islamic Azda University, Estahban Branch

Abstract:

Increasing in the city's population and the necessity to access to various locations has led to use of underground structures in urban planning. In the different cities, the twin tunnels has utilized in urban transportations. This type of tunnel design effected the urban facilities specially caused the settlements of roads and structures. In the researchers studies, the tunnel deformations, ground moments and tunnel stabilities were considered. For evaluation the effect of tunnel positions on surface settlements a numerical study of twin tunnels in Shiraz City were studied. According to different type of soils and the tunnel positions, the ground deformation was analyzed and discussed. Three different configurations are taken into consideration, side-by-side tunnels, piggyback tunnels and angular-offset tunnels. Empirical correlations, derived from extensive field data, are used to calculate ground settlements caused by twin bored tunnel. Non-linear finite element analysis is used for these situations. The use of superposition was tested using the non-linear analysis to check whether or not its use with empirical methods is appropriate. The results confirm that is a clear difference in the magnitude and distribution of ground movements in tunnel positions.

Key words: twin tunnel, underground, tunneling, settlements, ground movments

1. INTRODUCTION

Underground transportation facilities in urban areas have a significant importance on the citizen lives as they provide fast and safe transportation services. Therefore, the usage of metro tunnels has improved in recent years all over the world. Constructing multiple tunnels provides increased engineering challenges e.g. excavation of twin metro tunnels side by side or piggyback requires much more attention rather than a constructing single tunnel. Ground surface settlement is an inevitable consequence of excavating and constructing tunnels [1].

In order to evaluate the multiple tunnel behavior, a number of studied were carried out. The studies focused on experimental, empirical and numerical methods. Many semi-empirical equations have been introduced by various authors for predicting the movements above single [2], [3]. The equations have been shown over many years, when compared to case history data of single tunnels, to make accurate predictions of the vertical and horizontal displacements. Furthermore numerical modeling and in situ observations were used to analyze the interaction between twin tunnels. Results show that in some configurations, the interaction could largely affect

the soil settlement and that the design of twin tunnels requires numerical analysis associated to monitoring during the design and construction [4]. The construction of the first tunnel may significantly affect the soil conditions: reduced confinement, stress release and reduction of the strength parameters of the soils. Consequently, the second tunnel will be excavated through a different material and the induced settlements related to the second tunnel will be generally greater [5]. many twin tunnel case histories do not usually have sufficient data points in critical positions and are usually given as a total profile and do not show the individual contributions made by each tunnel. Quality data that does fit this description has been reported [6], [7]. Due to the lack of data and through advancements in computing power, researchers have been aiding understanding of deformation of above twin tunnels, using the numerical methods [1], [4], [6], [8].

Unfortunately, the resulting magnitudes of settlements produced using these numerical methods do not accurately reproduce the actual magnitudes of displacement found at full scale. Hence they cannot be used directly to improve the empirical equations. In this reason, this paper presents 3D numerical analysis conducted to investigate the influence of twin tunnel spacing on the surface settlement and internal forces

resulting from the tunnel excavation. Analysis was carried out for three different tunnel situation and different twin tunnels spaces.

2. MATERIALS AND METHODS

In this study the analysis of the three types of twin tunnel configuration have considered; side-by-side, piggyback and angular-offset. Fig. 1 illustrated the tunnels status. Common practice was carried out to superimpose the independent settlements to get the final settlement

profiles. Using the finite element program analyzed the soil to evaluate the ground surface deformation. This research has performed to evaluate the tunnels behavior which constructed in the different class of soils.

2.1 Soils and lining properties

In order to use the Plaxis software the soils and lining properties are defined. 5 types of Shiraz soil properties and 35 centimeters thickness concrete fragments have been taken. The Mohr-Columb elasto-plastic criterion introduces the soil behavior. The data used in the analysis have listed in tables I and II respectively.

Table I. the data collected from different location of shiraz Metro soil

	Soil classificatio	Location	Unit weight (γ) ($\frac{KN}{m^3}$)	SPT	W%	γ_{sat} ($\frac{KN}{m^3}$)	E ($\frac{KN}{m^2}$)	ϕ (degree)	C ($\frac{KN}{m^2}$)
1	GM-GP	Moa'li Abad	21	50	5	22	60000	40	5
2	GP	Qasr Dasht	19	15	15	20	40000	30	10
3	SM-SC	Farhang Shahr	18	40	10	19	25000	25	15
4	CL-ML	Khak Shenasi	17	12	12	19	30000	20	20
5	CL	Moshir Fatemi	20	25	15	22	20000	10	30

Table II. Properties of concrete lining fragments

Parametrs	amount	unit
EA	1.4×10^7	KN/m
EI	1.43×10^5	kNm/m ²
D	0.35	m
w	8.4	KN/m/m
ν	0.15	-

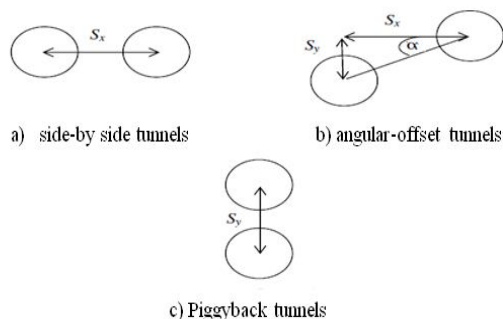


Fig. 1. the schematic position of twin tunnels

2.2 Surface effect

In order to recognize the twin tunnel settlements, surface deformation for each tunnel has founded separately. An analysis has been performed for twin tunnels and the results measured. Following discussed the obtained results:

2.2.1 Side-by-side tunnel

Figs 2 to 7 shows the effect of distance on the subsurface settlements. The 6 meters diameter tunnels are buried in depth 15 meters. The tunnels spaces are 8, 16, 20, 24, 32, 40 and 60 meters respectively. The water table position is 2 meter above the tunnel lining. The settlements are depending to the tunnels spaces. The closest tunnels have more effect and larger settlements. Keeping a way from each other, the settlement is decreasing. The maximum settlement is occurred in distance 8 from the center of each tunnel. The settlement is remains constant between 8 to 16 meters and decreases after 16 meters from center of tunnels. In the 60 meters distance the tunnels settlements have no superimpose effects.

2.2.2 Piggyback tunnels

The Piggyback tunnels analyzed in 8, 16, 20, 24, 32, 40 and 60 meters distances. . The water table position is 2 meter above the tunnel lining. Figs 8 and 9 shows the effect of vertical distance on the subsurface settlements. The results indicate that the piggyback tunnels have not interface significantly with the maximum settlements. The surface settlement is considerably depending on upper tunnel settlements.

2.2.3 Angular-offset tunnels

For the Angular-offset tunnels analyze the 25, 45 and 65 degree offset-angular have been considered. The tunnels have 8 and 14 meters offset distances and the soil class is CL. The results show a linear decay with spacing between two tunnels. Fig. 10 confirms that the settlements increases from 25 to 65 degree offset. The 25 degree twin tunnel has less settlements and the 65 degree offset have maximum superimpose settlements. The maximum amount of settlements has occurred in the center point of twin tunnels

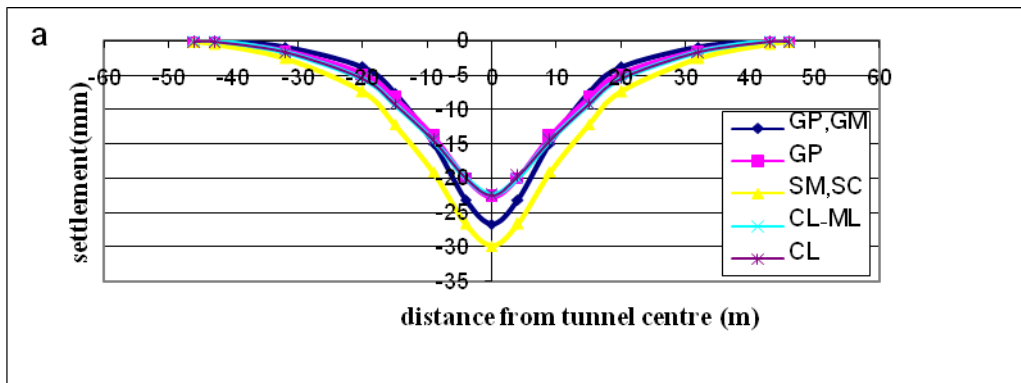


Fig. 2. the total settlements in side-by-side tunnels, tunnel diameter=6 m; tunnels spaces=8 m

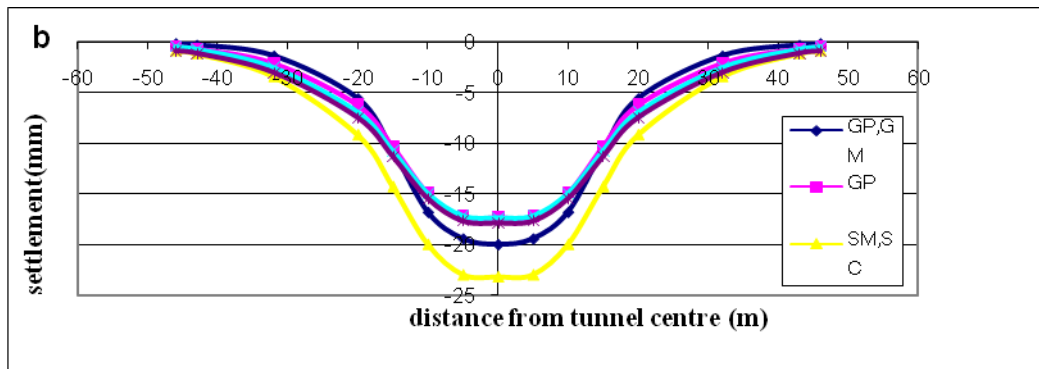


Fig. 3. the total settlements in side-by-side tunnels, tunnel diameter=6 m; tunnels spaces=16 m

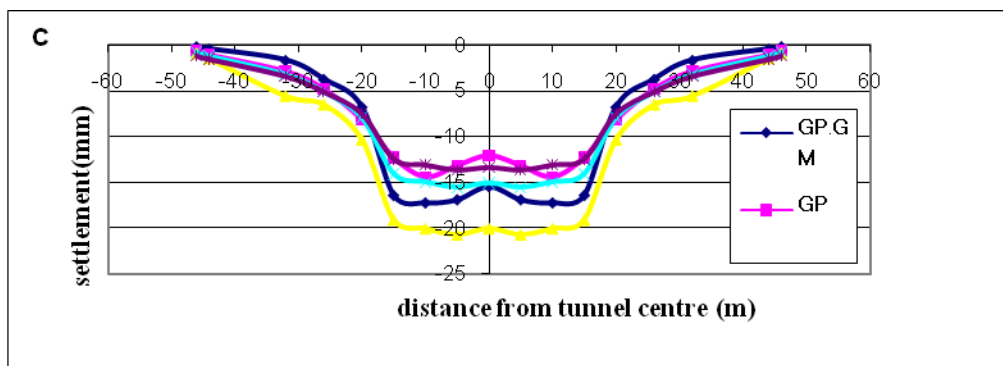


Fig. 4. The total settlements in side-by-side tunnels, tunnel diameter=6 m; tunnels spaces=20 m

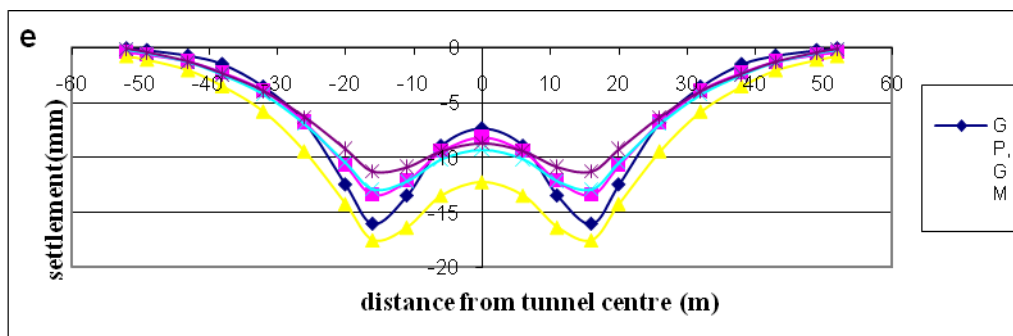


Fig. 5. the total settlements in side-by-side tunnels, tunnel diameter=6 m; tunnels spaces=32 m

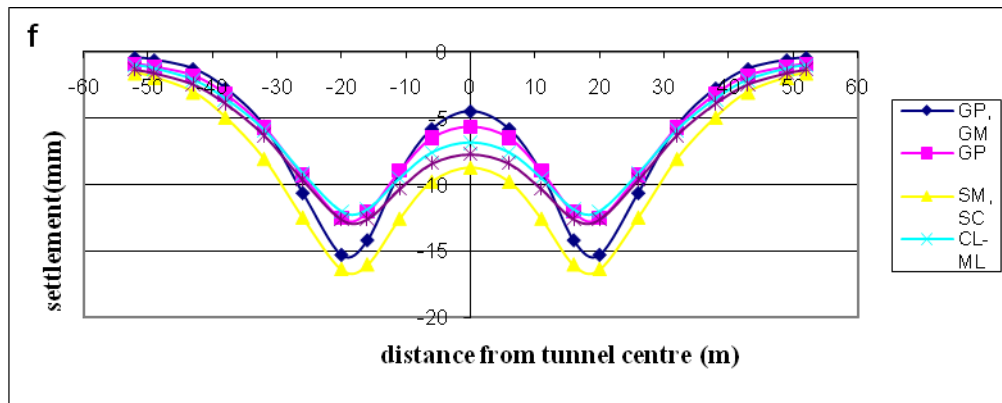


Fig. 6. The total settlements in side-by-side tunnels, tunnel diameter=6 m; tunnels spaces=40 m

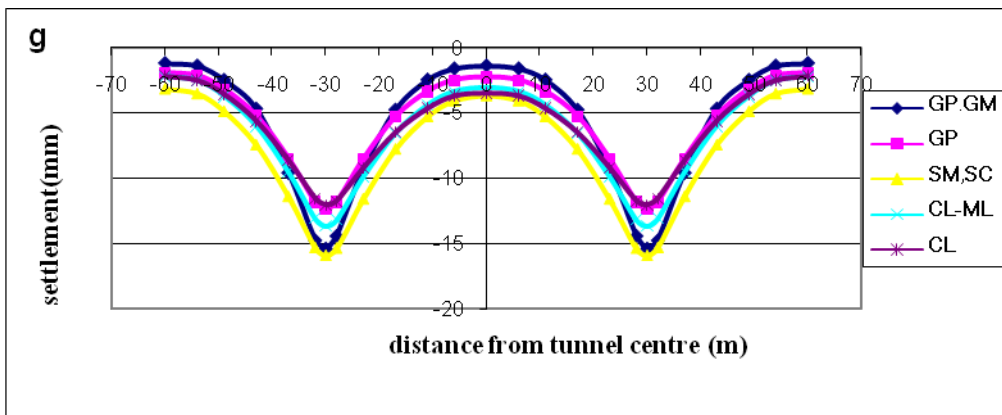


Fig. 7. the total settlements in side-by-side tunnels, tunnel diameter=6 m; tunnels spaces=60 m

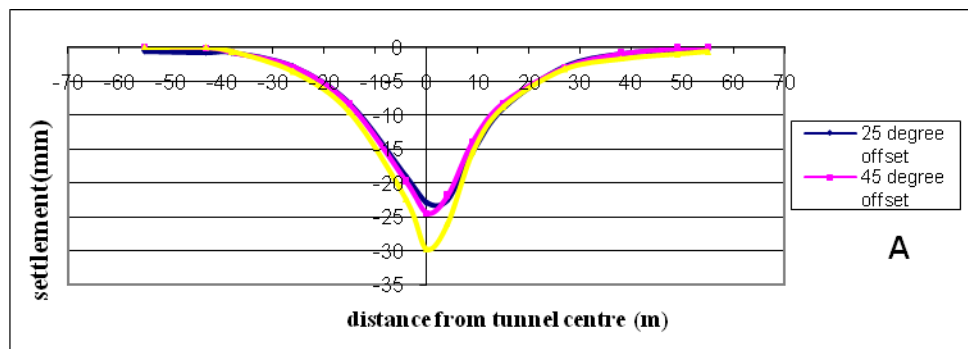


Fig. 8. the total settlements in angular-offset tunnels, tunnel diameter=6 m; spaces=8 m

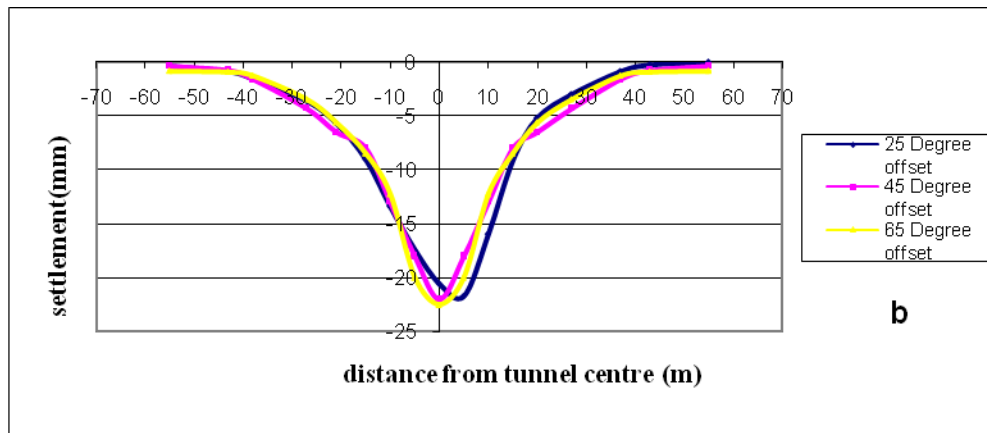


Fig. 9. The total settlements in angular-offset tunnels, tunnel diameter=6 m; spaces=14 m

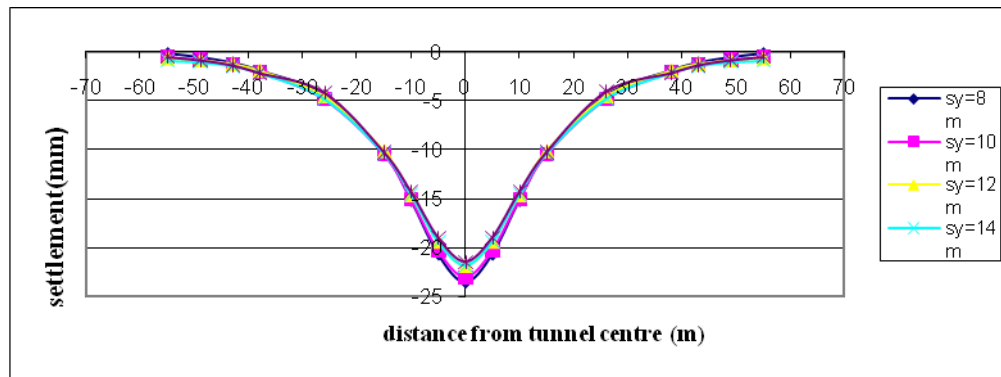


Fig. 10. The settlements in piggyback tunnel, tunnel diameter=6 m

3. CONCLUSION

The research has carried out to recognize the effect of twin tunnel situation on ground surface settlements. Using the finite element method analysis the following results could be obtained:

- In the single tunnel, Settlements decreases with increasing the distance from the tunnel center; while the settlement have maximum amount in 8 to 16 meter from the center of each tunnels in the twin tunnels, due to superimpose effect.
- In spite of soil saturation, the sand layers have considerable settlements than the other soils type.
- Settlement is increases with increasing the offset-angular degree, and it has the maximum amount in 60 degree alignments.

- The piggyback tunnels settlements is due to upper section settlements and the lower parts have least effect on superimpose settlements.

4. ACKNOWLEDGEMENTS

This paper was funded by a part of the M. Sc. Research in the Islamic Azad University, Estahban Branch. The authors are grateful to the head of University, research management and the head of the civil engineering faculty. They are thankful to Shiraz Urban Railway Organization (SURO) for cooperating in geotechnical data.

5. REFERENCES

- [1] Addenbrooke, T. I., Potis, D. M. 2001. "Twin tunnel interaction: Surface and subsurface effects". *Int. Jour. of Geomechanics*, 1 (2), 249-271.
- [2] O'Reilly, M.P. and New, B.M. 1982. "Settlements above tunnels in the United Kingdom - their magnitude and prediction". *Proceedings of Tunneling' 82 Symposium*. Institution of Mining and Metallurgy. London. pp. 173 - 181.
- [3] Peck, R., 1969. "Deep excavation and Tunneling in soft ground" In *proc 7th int conf soil Mechanics and Found engineering*, Mexico., pp. 225-231.
- [4] Chehade, F., and Shahrou, I., (2008). "Numerical analysis of the interaction between twin-tunnels: influence of the relative position and construction procedure." *Tunnelling and underground space technology*., Vol. 23, PP. 210-214.
- [5] Guglielmetti, V, Piergiorgio, G, Mahtab, A and Xu Sh, 2007. *Mechanized tunneling in urban areas*, Taylor and Francis Group, London, UK.
- [6] Cooper, M.L., Chapman, D.N., Rogers, C.D.F., 2002. "Prediction of settlement in an Existing Tunnel caused by the Second of Twin Tunnels. Design of structures" 2002, *Transportation research record* 1814, pp.103-112.
- [7] Nyren, R., 1998. "Field measurements above twin tunnels in London Clay". PhD theses, Imperial College
- [8] Chapman, D.N., Rogers, C.D.F., Hunt, D.V.L., 2003. "Investigating the settlement above closely spaced multiple tunnel constructions in soft ground". *Proc of World Tunnel Congress 2003, Amsterdam 2003*, vol 2. pp.629-635.

Evaluation of Pile Lateral Capacity in Clay Applying Evolutionary Approach

Alkroosh¹ I., Nikraz² H
Curtin University, Perth, Australia

ABSTRACT

This paper presents the development of a new model to predict the lateral capacity of piles inserted into clayey soils and subjected to lateral loads. Gene Expression Programming (GEP) has been utilized for this purpose. The data used for development of the GEP model is collected from the literature and comprise 38 data points. The data are divided into two subsets: Training set for model calibration and independent validation set for model verification. Predictions from the GEP model are compared with the results of experimental data. The model has achieved a coefficient of correlation, r , of 0.95 for training and validation sets and average prediction ratio (APR) of 0.97 and 1.04 for training and validation sets respectively. The results indicate that the GEP model performs very well and able to predict the pile lateral capacity accurately.

Keywords: Pile; Capacity; GEP; Training and validation

1. INTRODUCTION

Geotechnical engineers often recommend piles as foundations to support the proposed superstructure subjected to lateral loads. Hence, pile lateral carrying capacity is required to be evaluated.

Several researchers have attempted evaluation of pile lateral capacity based on analytical solutions [e.g. 1], semiempirical solutions [e.g. 2, 3] and finite element solutions [e.g. 4]. However, because of the nonlinearity of the soil behaviour and the variability of soil properties, the proposed methods have achieved limited success in terms of giving accurate prediction of pile lateral capacity.

In this respect, artificial intelligence techniques may be more efficient. Recently, several attempts have been made to use artificial neural networks (ANNs) for modeling the axial capacity of pile foundations [e.g. 5, 6, 7] and lateral capacity [e.g. 8]. The modelling advantage of ANNs over traditional methods is the ability of ANNs to capture the nonlinear and complex relationship between the bearing capacity and the factors affecting it without having to assume a priori formula of what could be this relationship. However, the main shortcoming of ANNs is the large complexities of the network structure, as it represent the knowledge in terms of weight matrices together with biases that are not accessible to the users [9].

In this regard, the genetic programming (GP) may represent better alternative. The main advantage of the GP over the ANNs is the ability to provide the relationship between a set of inputs and the corresponding outputs in a simple mathematical form accessible to the users. Recently, the GP has been found successful in solving several problems in the field of engineering [e.g. 10, 11].

In this paper, the lateral capacity of piles in clayey soils has been correlated with undrained shear strength and load eccentricity using a developed version of genetic programming that is gene expression programming (GEP). Recently, GEP has been applied with success in solving engineering problems [e.g. 12, 13, 14, 15, 16a, 16b]

The objectives of this paper:

1. Applying the GEP technique for modelling the lateral load capacity of pile foundations embedded in clayey soils.
2. Evaluating the performance of the GEP model by comparing its predictions with experimental data.
3. Measuring the accuracy of the GEP model via statistical analysis.

2. OVERVIEW OF GENE EXPRESSION PROGRAMMING

Gene Expression Programming is an instance of an Evolutionary Algorithm from the field of Evolutionary Computation, invented by Ferreira [17] as a global optimization algorithm. It has similarities to other Evolutionary Algorithms such as the Genetic Algorithm as well as other Evolutionary Automatic Programming techniques such as Genetic Programming. Similar to the GAs, the GEP utilizes evolution of computer programs (individuals or chromosomes) that are encoded linearly in chromosomes of fixed length and likewise the GP the evolved programs are expressed nonlinearly in a form of expression trees (ETs) of different sizes and shapes. However, the GEP implements different evolutionary computational method.

The GEP distinct itself from GAs in that the evolved solutions are expressed in forms of parse trees of different sizes and structures and unlike GP genetic variations are performed on chromosomes before they are translated into ETs. The GEP chromosomes are composed of multiple genes, each gene is encoded a smaller sub-program. Every gene has a constant length and includes a head that contains functions and

terminals, and a tail that composes of terminals only. The genetic code represents a one-to-one relationship between the symbols of the chromosome; the functions or terminals. The process of information decoding from chromosomes to expression trees is called translation which is based on sets of rules that determine the spatial organization of the functions and terminals in the ETs and the type of interaction (link) between the sub-ETs [17].

The modelling process of GEP begins with random generation of chromosomes of initial population. Each individual chromosome is expressed and its fitness is evaluated through the fitness function which measures how good the individual is at competition with the rest of the population. The best individuals are kept for modifications which are performed by the genetic operators such as mutation and recombination. New offspring of chromosomes with new traits are generated and used to replace the existing population. The individuals of the new generation are then subjected to the same developmental process which is repeated until stopping criteria are satisfied

3. DEVELOPMENT OF THE GEP MODEL

In this work, the GEP model is developed using the commercial available software package *GeneXproTools* 4.0 [18]. The data used for the model development are collected from the literature and comprise 38 data points of piles inserted in clayey soil reported by Rao and Kumar [19] and found in Das and Basudhar [8]. The piles have different sizes with diameters ranging from 6.35 mm to 25.4 mm and lengths from 130 mm to 300 mm. In order to accurately predict the pile lateral capacity, the significant factors that influence the capacity need to be identified and presented to the GEP as input variables. These include the pile geometry, load lever arm and soil properties. The pile geometry is represented by the pile diameter, D , and pile embedment length, L . The load lever arm is represented by the eccentricity, e . The soil properties are represented by the undrained shear strength, S_u . The lateral pile capacity, Q_u , is the single output.

3.1 Data Division

The next step in development of the GEP model is the data division. In this work, the data are randomly divided into two statistically consistent sets, as recommended by Masters [20] and detailed by Shahin et al. [21]. This includes a training set for model calibration and an independent validation set for model verification. In total, 29 data points (75%) of the available 38 data points were used for training and 9 data points (25%) for validation. The statistics of the data used for the training and validation sets are presented in Table 1, which includes the mean, standard deviation, maximum, minimum and range. It should be noted that, like all empirical models, GEP performs best in interpolation rather than extrapolation, thus, the extreme values of the data used were included in the training set.

Table 1 GEP model input and output statistics

Model variable and data sets	Statistical parameters				
	Mean	SD*	Max.*	Min.*	Range
Pile diameter, D (mm)					
Training	18	7	33	6	27
Validation	17	4	25	12	13
Pile embedment length, L (mm)					
Training	282	50	300	130	170
Validation	269	63	300	132	168
Load eccentricity, e (mm)					
Training	45	14	50	0	50
Validation	44	17	50	0	50
Undrained shear strength, S_u (kPa)					
Training	10	10	39	3	35
Validation	10	12	39	3	35
Pile lateral capacity, Q_u (N)					
Training	77	40	225	30	196
Validation	62	29	128	35	93

* SD: Standard deviation; Max: Maximum; Min: Minimum

3.2 Modelling Attempts

The success of the modelling process using GEP technique depends significantly on the design of the model structure. In this, the optimal model parameters are determined to ensure that the best performing model is achieved. In the search for a model using the GEP, the number of chromosomes, chromosome structure, functional set, fitness function, linking function and rates of genetic operators play important role during modelling process and choosing suitable rates of these parameters can reduce modelling time and effort and produce a robust solution.

In this work, the trial-and-error approach was used to determine the values of setting parameters. This approach involved using different settings and conducting runs in steps. During each step, runs were carried out and the values of one of the above mentioned parameters (with its optimal value being searched) were varied, whereas the values of the other parameters were set constant (i.e. number of chromosomes = 30, number of genes = 3, gene's head size = 8, functions set = +, -, ×, and /, fitness function = mean squared error (MSE), linking function = +, mutation rate = 0.04, and gene recombination rate = 0.1). The runs were stopped after fifteen thousand generations, which were found sufficient to evaluate the fitness of the output. At the end of each run, the MSE for both training and validation sets were recorded in order to identify the values that give the least MSE. The search attempts for optimal parameters values are presented in Table 2.

Table 2 Input parameters used for developing GEP model

Parameter	Used input
Number of chromosomes	15, 16, 17, ...30
Number of genes	1, 2, 3
Head size	7, 8, 9, ...12
Function set	$+, -, \times, \div, \sqrt{}, \sqrt[3]{}, \sqrt[4]{}, \text{Power}$
Fitness function	MSE (Mean Squared Error)
Linking function	$+, \times$
Mutation rate	0.045, 0.05, 0.055, ..., 0.08
Recombination rate	0.1, 0.2, 0.3, ..., 0.7

3.3 Model Formulation

As mentioned earlier, one of the advantages of the GEP is that it presents the relationship between the input and output in a form of expression trees as shown in Fig. 1. As can be seen, the figure illustrates the mathematical operations and interactions between the components of the solution. This can give insight to the nature of the relationship between the input and the output. The trees can be easily translated and arranged into mathematical expression as follows:

$$Q_p = 2D + e + \frac{L}{\sqrt[2]{e} + \sqrt[3]{\frac{S_u^2}{L}}} - \frac{e^2}{D(D+9.8)} - \frac{L}{S_u} \quad (1)$$

where;

Q_p : predicted pile lateral capacity; D : pile diameter; L : embedment depth; e : eccentricity; S_u : undrained shear strength.

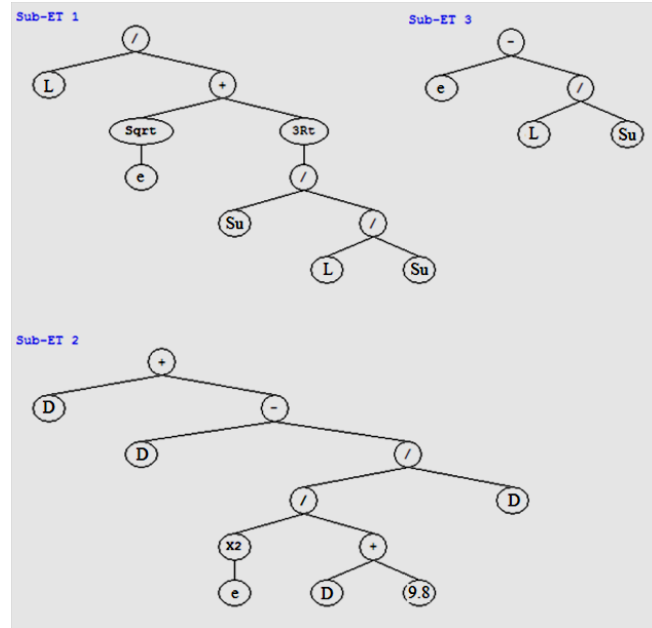


Fig. 1 Expression trees of the developed GEP model;
Sqrt = square root; 3Rt = cubic root; X^2 = to power 2

4. RESULTS AND MODEL VALIDATION

The performance of the optimum GEP model is shown numerically in Table 3 and is depicted graphically in Fig. 2. It can be seen from Table 3 that the model performs well with high coefficients of correlation, r , of 0.95 for the training and

validation sets. It can also be seen that the model has good average prediction ratios, APR , of 0.97 and 1.04 for the training and validation sets, respectively. The APR is calculated from

$$APR = \sum_{i=1}^n \left(\frac{Q_p}{Q_m} \right) / n \quad (2)$$

where;

Q_p : predicted capacity; Q_m : measured capacity and n : the number of case records. Fig. 2 also indicates that the model has minimum scatter around the line of equality between the measured and predicted pile capacities for the training and validation sets. The results demonstrate that the developed GEP model performs well and provides accurate predictions.

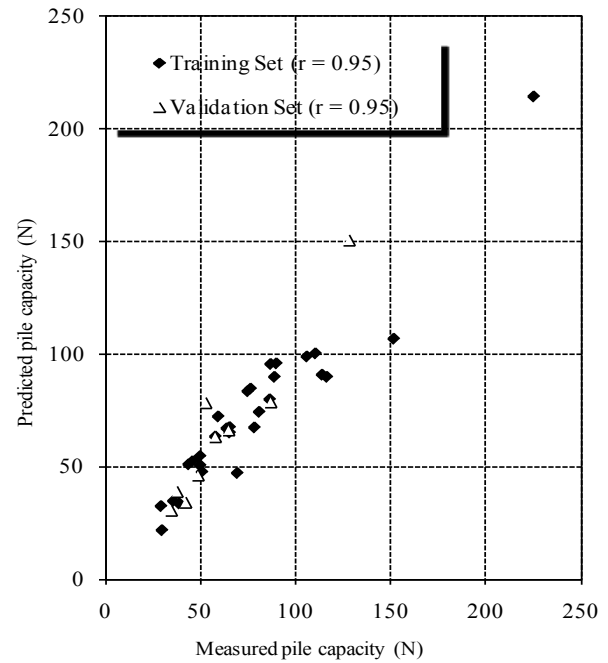


Fig. 2 GEP model performance in training and validation sets

Table 3 Numerical evaluation of the GEP model performance

Performance measure	Data set	
	Training	Validation
Correlation coefficient, r	0.95	0.95
Average prediction ratio, APR	0.97	1.04

5. CONCLUSION

The results of this study indicate that the GEP model possess a good capability in predicting the lateral capacity of piles embedded into clayey soils; the model has achieved high coefficients of correlation, r , of 0.95 for the data used in model calibration and validation. The model has also low average prediction ratio, APR , values of 0.97 and 1.04 for the data used in model calibration and validation, respectively; these values indicate that the model may tend to under-predict the pile lateral capacity. The results also demonstrate that

GEP model performs well in comparison with the experimental data. Overall, the output of this study has demonstrated that resulting model correlates pile lateral capacity and undrained shear strength of soil accurately.

2 REFERENCES

- [1] Poulos HG, and Davis EH, *Pile Foundation Analysis & Design*. New York: Wiley, 1980.
- [2] Hansen B, "The ultimate resistance of rigid piles against transversal force," Danish Geotechnical Institute, Bulletin No 12. 1961, pp. 5-9.
- [3] Brom BB, "Lateral resistance of piles in cohesive soils," *J. Soil Mech Found Eng., ASCE*, 90 (SM2), 1964, pp. 27-63.
- [4] Portugal JC, and Scao Pinto PS, "Analysis and design of pile under lateral loads", in *Proc. 11th Int. Conf. on geotechnical seminar on deep foundation on bored and auger piles*, Belgium, 1993, pp. 309-13.
- [5] Abu-Kiefa M, "General regression neural networks for driven piles in cohesionless soils," *J. of Geotechnical & Geoenvironmental Engineering*, vol. 124 (12), 1998, pp. 1177-1185.
- [6] Chan WT, Chow YK, Liu LF, "Neural network: an alternative to pile driving formulas," *J. Computer & Geotechnics*, vol. 17, 1995, pp. 135-56.
- [7] Shahin M, 2010. "Intelligent computing for modeling axial capacity of pile Foundations," *Canadian Geotechnical Journal*, vol. 47 (2), 2010, pp. 230-243.
- [8] Das SK, and Basudhar PK, "Undrained Lateral Load Capacity of Piles in Clay Using Artificial Neural Networks," *Computers and Geotechnics*, vol. 33 (8), 2006, pp. 454-459.
- [9] Rezaia M, and Javadi A, "A new genetic programming model for predicting settlement of shallow foundations," *Canadian Geotechnical J.*, vol. 44 (12), 2007, 1462-1473.
- [10] Javadi AA, Rezaia M, Nezhad MM, "Evaluation of liquefaction induced lateral displacements using genetic programming," *Computers and Geotechnics*, vol. 33 (4-5), 2006, pp. 222-233.
- [11] Bayksoglu A, Gullu H, Canakci H, Ozbakir L, "Prediction of compressive and tensile strength of limestone via genetic programming," *Expert Syst. Appl.* vol. 35 (1-2), 2008, pp. 111-123.
- [12] Cevic A, and Cabalar AF, "Modelling damping ratio and shear modulus of sandmica mixtures using genetic programming," *Expert Syst. Appl.*, vol. 36 (4), 2009, pp. 7749-7757.
- [13] Alkroosh I, Shahin M, Nikraz H, "Modelling axial capacity of bored piles using genetic programming technique," in *Proc. GEO-CHIANGMIA Int. Conf.*, Thailand, 2008.
- [14] Alkroosh I, Shahin M, Nikraz H, "Genetic programming for predicting axial capacity of driven piles," in *Proc. 1st Int. Symp. on Computational Geomechanics*. Cote d'Azur, France, 2009.
- [15] Alkroosh I, and Nikraz H, "Correlation of pile axial capacity and CPT data using gene expression programming," *Geotechnical and Geological J.*, 2011a. DOI: 10.1007/s10706-011-9413-1).
- [16] Alkroosh I, and Nikraz H, "Predicting axial capacity of driven piles in cohesive soils using intelligent computing," *Engineering Applications of Artificial Intelligence*, vol. (25), 2011b, pp. 618-627
- [17] Ferreira C. *Gene Expression Programming: Mathematical Modeling by an Artificial Intelligence*. Portugal, Angra do Heroismo, 2002.
- [18] Gepsoft, Gene Expression Programming Tool, 2002, <http://www.gepsoft.com>.
- [19] Rao KM, Suresh Kumar V, "Measured and predicted response of laterally loaded piles," in *Proc. 6th Int. Conf. and exhibition on piling and deep foundation*. India, 1996, 1.6.1-1.6.7
- [20] Master T, *Practical neural network recipes in C++*. In Academic Press. San Diego, California, 1993.
- [21] Shahin M, Maier H, Jaska M, 2004. "Data division for developing neural networks applied to geotechnical engineering," *J. Computing in Civil Eng.*, vol. 18 (2), 2004, pp. 105-114.

Effect of Reservoir Drawdown Rate on Phreatic Line Recession in Homogeneous Earth Dams

R. Ziaie Moayed¹, V. Rashidian²

1. Associate Professor, Civil Engineering Department, Imam Khomeini International University (phone: 281-837-1153; fax: 281-837-1153; e-mail: R_ziaie@ikiu.ac.ir).
2. M.Sc. Student, Civil Engineering Department, Imam Khomeini International University (e-mail: Rashidian@ikiu.ac.ir; Vahidrashidian@gmail.com).

ABSTRACT

An embankment dam, under filled up condition develops pore water pressure within the body of the dam. If the reservoir water is suddenly depleted, say due to the need of emptying the reservoir in expectation of an incoming flood, then the pore pressure cannot get released, which causes the upstream face of the dam to slump. This condition becomes critical if the materials of the upstream portion of the dam are not freely draining. Depending upon the value of the coefficient of permeability of the upstream shell material and the rate of drawdown, the phreatic line in embankment can be receded differently. In this paper a numerical analysis has been studied to evaluate the phreatic line place due to different reservoir drawdown rate. It is observed that the phreatic line level shows a delayed response with respect to the change of reservoir level. Also during drawdown process, the phreatic line takes the shape of concave.

1. INTRODUCTION

One of the important points in the study stages and during construction of earth dams is seepage through the dam body. Seepage is the continuous movement of water from the upstream face of the dam toward its downstream face. The upper surface of this stream of percolating water is known as the phreatic surface. The position of the phreatic surface influences the stability of the earth dam because of potential piping due to excessive exit gradient and sloughing due to the softening and weakening of the soil mass as if it touches the downstream slope or intersects it. Steady seepage develops after a reservoir pool has been maintained at a particular elevation (e.g., maximum storage pool) for a sufficient length of time to establish a steady line of saturation through the embankment. The seepage forces which develop in the steady state condition act in the downstream direction [1]-[3].

Another condition that may happen in earth dams is rapid drawdown of reservoir water table. When the reservoir is emptied, a phreatic surface or water table is formed in the embankment. The free water surface in the embankment does not fall as rapidly as the reservoir level. A reverse hydraulic gradient is established which results in a flow in the embankment towards the emptied reservoir. The water table in the embankment gradually recedes as water flows out towards the toe. The hydrostatic pressure in the embankment decreases as the water table falls, and the soil effective stresses increase. The period immediately after drawdown of the reservoir level is a critical one with respect to the design of the embankment. The hydrostatic pressure in the embankment causes an unstable situation as it acts towards

the free face. The effective stresses in the soil are low therefore the full strength of the soil is not established and the frictional resistance is low [4], [5].

The drawdown condition is a classical scenario in slope stability, which arises when totally or partially submerged slopes experience a reduction of the external water level. This is a common situation in riverbanks, subjected to changing river levels. Flooding conditions are critical in this case because river levels reach peak values and the velocity of decreasing water level tends to reach maximum values also.

Operation of dams requires changes in water level, which modify the safety factor against sliding of the upstream slope of earth dams. When the reservoir level is high, hydrostatic pressures help to stabilize the slope. A reduction of water level has two effects: a reduction of the stabilizing external hydrostatic pressure and a modification of the internal pore water pressures. The second effect has traditionally received considerable attention in dam design because it may lead to critical conditions of the slope. The subject has been approached from different perspectives, which have been largely dictated by current advances in soil mechanics.

Reference [6] discusses the practical implications of rapid drawdown and a number of case histories associated with total or partial failure of the upstream slope. References [7] and [8] provide further information on drawdown-induced failures.

Current approaches to analyze drawdown are classified into two different groups: Flow methods, which should be applied in relatively pervious slopes and undrained methods, which find applications in impervious soil slopes. Methods from the first group concentrate on the solution of the flow problem in a situation that involves changes in boundary conditions and a modification of the initial free surface. These methods implicitly assume that the soil skeleton is rigid and therefore they do not consider any modification of the initial water

pressure because of the change in total boundary stresses imposed by the drawdown. Methods developed to handle this problem include flow net analysis; methods based on ad hoc hypothesis (typically Dupuit-type of assumptions) finite element analysis of flow in saturated soil and finite element analysis for saturated-unsaturated flow.

The finite elements method (FEM) can be used for the stress, seepage, and stability analysis of slopes; where nonlinear material behavior and complex boundary, and loading conditions can be taken into account. It has also become possible in recent years to perform coupled analysis of stress-induced pore pressure generation and dissipation over time. This paper presents a numerical evaluation on phreatic line location within an earth dam in both steady-state and rapid drawdown condition. Different rapid drawdown rates are considered and phreatic line has been evaluated accordingly. In this study, finite element software, ABAQUS, is used to determine phreatic line. ABAQUS application is a general purpose finite element program from SIMULIA Ltd. It has a large element library and is capable of analysis of variety of problems. A large class of stress analysis problems can be solved with ABAQUS.

2. PROBLEM DEFINITION

The problem for this study is defined as in Fig. 1. The selected example is a simplified representation of typical homogeneous earth dam geometry. The dam section assumed in the present survey is a symmetric zone section with impervious foundation. The water level height in the reservoir and downstream are 32 m and 4 m respectively and the free board is 3 m; let the 1/3 be the slope of the upstream and downstream face of the earth dam; let the top width of the embankment be 5 m. The materials properties are chosen more close to reality. The dry density is 1800 kg/m^3 and the permeability of material is 0.0864 m/day . The Young's modulus of the embankment is equal to 20 MPa. The void ratio is considered to be 0.6.

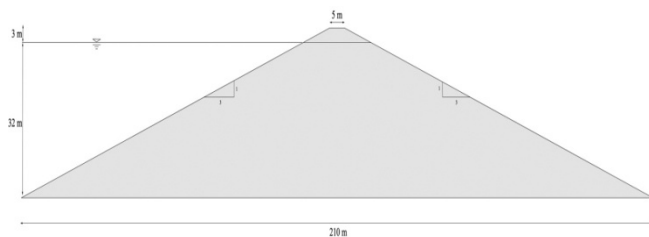


Fig. 1. The proposed model geometry

3. ABAQUS SIMULATION

The boundary conditions applied to the model are such that the whole model is restrained from moving in horizontal and

vertical direction. Pore fluid boundary condition applied to the model for Steady-state analysis comprise of water head over the upstream and downstream face. Potential seepage boundary condition is assigned to drainages outlet. The remaining boundaries are impermeable, as it is assumed that there is no flow of water through these boundaries.

In order to simulate rapid drawdown condition, it is necessary to perform Transient analyses. For this purpose, 15 Transient steps after Steady-state analysis have been defined. Each step represents 1 m drawdown of reservoir water table daily; consequently, the pore fluid boundary condition for upstream slope changes with steps.

In order to perform 2D finite element analyses, the model was discretized into basic triangle elements. Figure 2 shows the finite element mesh used in the pore fluid analyses, consisting of 1473 6-noded isoparametric modified quadratic triangle elements.

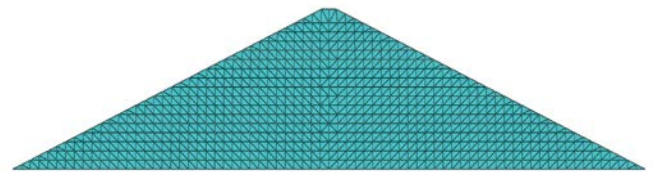


Fig. 2. Finite element mesh used in study

4. ANALYSIS AND DISCUSSION

In the simulation of rapid drawdown, initially a steady-state seepage analysis is performed to determine the phreatic line in steady-state condition. After that, a transient seepage analysis is performed to obtain seepage-induced pore pressures and free ground water surface for different drawdown rates. To model variation of water level during drawdown, linearly variable groundwater heads with time was specified as the boundary condition in the transient seepage analysis. The calculated groundwater flow parameters (hydraulic heads, pore pressures, flow rates, etc.) were later used in the deformation analysis.

Changes in pore water pressure developed immediately after the drawdown will be exclusively owing to total stress changes. Therefore, if an uncoupled analysis is run, the pore water pressures inside the slope will maintain their initial values immediately after drawdown.

Fig. 3 shows the phreatic line within the earth dam after the steady-state condition has been reached. The dam was supposed to be fully saturated at first. Above the phreatic line, Sorption would occur. It means the pore pressure above the phreatic line is negative and the degree of saturation is about 5 %. The seepage will reach the steady-state condition after 20 days. Fig. 4 shows the earth dam after the rapid draw down occurred. The water level of reservoir has been drawn down to 2 meter from 32 meter that was before reservoir rapid draw down.

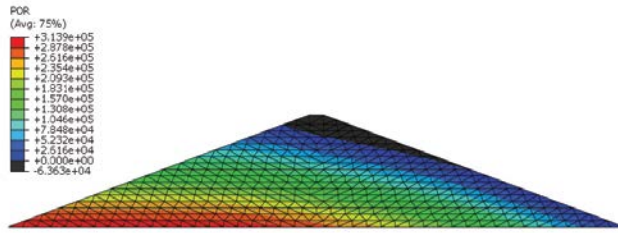


Fig. 3. Phreatic line before rapid draw down

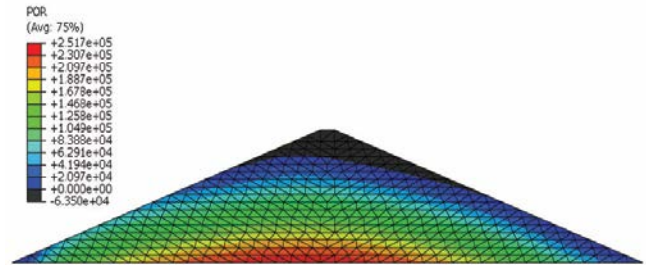


Fig 7. Receded phreatic line with rapid draw down rate of 1 meter per day

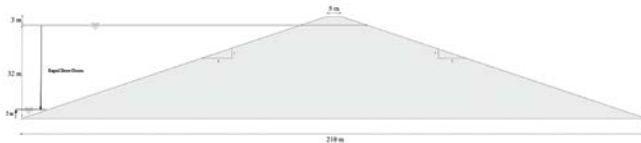


Figure 4. Water level after rapid draw down

Fig. 5 to 10 depict the phreatic line recession after 30 meter rapid draw down with rate of 0.25, 0.5, 1, 2, 4 and 8 meter per day. It can be seen from these figures that faster the rapid draw down rate, slower the phreatic line recession. Of course the receded phreatic line is very close to each other in all the rates. It means that the rapid draw down rate has a little and negligible effect on phreatic line recession and consequently on upstream slope stability.

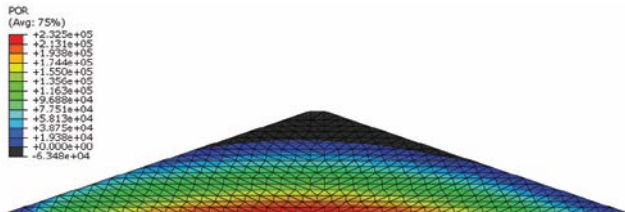


Fig 5. Receded phreatic line with rapid draw down rate of 0.25 meter per day

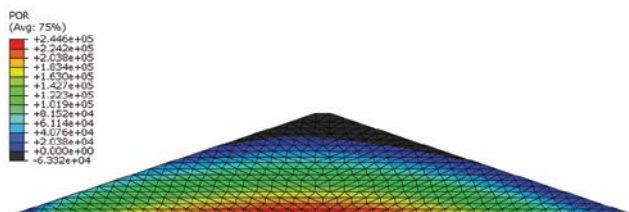


Fig 6. Receded phreatic line with rapid draw down rate of 0.5 meter per day

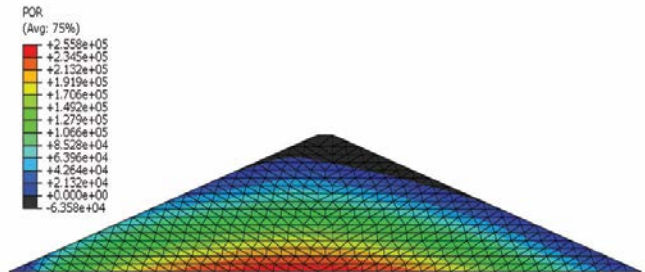


Fig 8. Receded phreatic line with rapid draw down rate of 2 meter per day

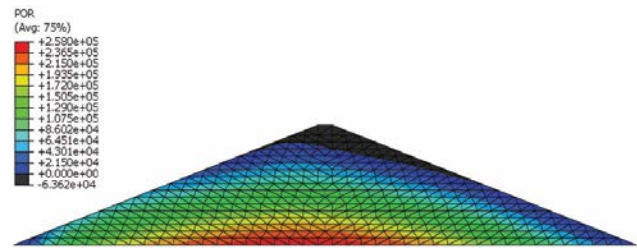


Fig 9. Receded phreatic line with rapid draw down rate of 4 meter per day

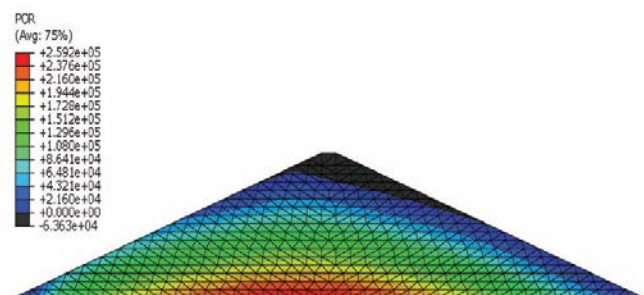


Fig 10. Receded phreatic line with rapid draw down rate of 8 meter per day

Maximum pore pressure within the dam is presented in table 1. it can be seen that the difference between the pore pressures with different rapid draw down rates is very small and almost omisable.

Table 1. Maximum pore pressure within the dam after rapid draw down

Rapid Draw Down Rate (m/day)	Maximum Pore Pressure (kPa)
0.25	+232.5
0.5	+244.6
1	+251.7
2	+255.8
4	+258
8	+259.2

5. CONCLUSION

Modern numerical methods and constitutive models enable analysis of transient seepage in order to more realistic and economical design. It is shown that the simultaneous generation of seepage and pore pressures and their dissipation with time can be computed and the distribution of excess pore pressures within the slope at any stage together the phreatic surface can be determined.

The stability of a submerged slope during drawdown is greatly influenced by the how fast its pore water drains. Even though the common design practice of assuming either freely draining (fully slow) or undrained (rapid) drawdown provides solutions for two extreme limiting conditions, it does not reflect the field behavior realistically in majority of cases where the hydraulic conductivity of soil and the rate and level of drawdown combine in a manner that results in solutions quite different than these limiting conditions.

In this paper the effect of rapid draw down rate on phreatic line recession was investigated using finite element software, Abaqus.

It was seen that the change in rapid draw down rate has a little effect on phreatic line recession and all the receded phreatic lines are almost similar to each other. Also there is a little difference between the maximum pore pressure within the dam after rapid draw down.

3. REFERENCE

[1] Casagrande, A. (1937). "Seepage through dams." J. New England Water Works Association, reprinted in Contribution to soil mechanics 1925- 1940, Boston Society of Civil Engineers, Boston, 1940.

[2] Lambe, T. W., and Whitman, R. V. (2000). *Soil mechanics*, Wiley, Singapore.

[3] Neuman, S. P., and Witherspoon, P. A. (1970). "Finite element method of analysing steady seepage with a free surface." *Water Resour. Res.*, 6(3), 889–897.

[4] Sherard, J. L., Woodward, R. J., Gizinski, S. F., and Clvenger, W. A. (1967). *Earth and earth rock dams*, Wiley, New York. Kimura S, "Journal paper title," *J. of Computer Science*, vol. 1, Aug. 1987, pp. 23-49.

[5] Taylor, R. L., and Brown, C. B. (1967). "Darcy flow solutions with a free surface." *J. Hydraul. Div., Am. Soc. Civ. Eng.*, 93(2), 25–34.

[6] Sherard, J. L., R. J. Woodward, S. F. Gizieski, and W. A. Clevenger (1963), *Earth and Earth-Rock Dams*, John Wiley, Hoboken, N. J.

[7] International Committee on Large Dams (1980), *Deterioration of Dams and Reservoirs. Examples and Their Analysis*, Balkema, Rotterdam, Netherlands.

[8] Lawrence Von Thun, J. (1985), San Luis Dam upstream slide, *Int. Conf. on Soil Mech. Found. Eng.*, 11, 2593–2598.

The Effect of lime-Microsilica Stabilization on California Bearing Ratio of Silty Soils

R. Ziaie Moayed¹, Y. Daghigh², B. Pourhadi³ and N. Sahebzamani⁴

^{1,3}Imam Khomeini International University, Iran

²Islamic Azad University, Karaj branch

⁴Islamic Republic of Iran Railways

ABSTRACT

Silty soils have some undesirable characteristics that challenge the geotechnical engineers in practical projects. These soils due to their low cohesion and friction angel cause the pavement, railways, roadways, foundation and channels to crack and break up. In this research, the effects of lime and microsilica stabilization in a silty soil are investigated. In this research, the effects of lime and microsilica stabilization in a silty soil from Ahvaz-Khorramshahr railway subgrade are investigated. Microsilica is one of the harmful byproducts that obtained from the factories's chimneys that produce silicon and ferrosilicon. Therefore to determine the best mixture of lime and microsilica to stabilize the soil, different percentage of these materials were mixed with soil. After 7day curing time, CBR tests were conducted on specimens. Results show that the California Bearing Ratios are increased as the content of mixed stabilizer increase. So it can be concluded that the microsilica waste material can be successfully used to enhance silty soil resistance.

Keywords: Soil stabilization, Silty soil, Lime, Microsilica, CBR

1. INTRODUCTION

Silt is a kind of sedimentary geomaterial consisting primarily of very fine particles, including fine sand particles, silt particles, and some clay particles which are often less than 10% by weight. Silt is a type of transitional soil between sand and clay. A soil is defined as silt if its plasticity index is no greater than 10 and the amount of particles greater than 0.075 mm is no greater than 50% of the total [1].

silty soils don't consider as suitable materials in civil engineering project due to their low cohesion and friction angel. Using the soils as a road or railway subgrade is generally not possible without stabilization as their characteristics fall below the minimum required. Consequently, stabilization is needed for this kind of soil. Application of stabilizing agents on soils has a long history. Cement was first used as stabilizing agent at the beginning of the twentieth century to mix with soils and form road materials in the United States. Since then, many other kinds of materials, such as lime [2] and special additives such as Pozzolanic materials like Fly Ash [3], Microsilica [4], and Rice Husk Ash [5], which are as waste material, may be used for soil improvement. Most of the existing stabilizers like lime and cement aren't much useful for silts, so the stabilized silts with such kind of stabilizing agents usually cannot satisfy the requirements of road construction. The encountered problems mainly are lower early strength, greater shrinkage, easy cracking, and bad water stability [6], [7].

Indeed, a successful stabilization method depends on many factors such as:

(1) Soil type and properties; (2) stabilizing agent; (3) Stabilizer content; (4) Potential use of the stabilized soil; (5) Field mixing method; and (6) Economical considerations [8]. Therefore, new methods are still being researched to increase the strength properties of silty soils. In this study we evaluate the feasibility of using stabilized silt with microsilica and lime for Karaj railway subgrade in Iran.

Microsilica (or silica fume) is one of the by-product materials which is obtained from silicon material or silicon alloy metal factories. It was discharged into the atmosphere by the factories smoke before the mid-1970s. Nowadays each year nearly 100,000 tons of microsilica is produced on purpose word wide [9]. Iran also has a large amount of microsilica production. Although the microsilica is a waste material of industrial applications, it has become the most valuable by-product among the pozzolanic materials due to its very active, high pozzolanic property and very fine particles. These particles are approximately 100 times smaller than the average cement particle [9].

In previous studies, there have been many researchers investigating the effects of microsilica on the strength and swelling characteristics of clayey soils were investigated. It was seen that microsilica improved the properties of clayey soils [10]-[13]. Likewise, recently, the effects of microsilica and lime have been investigated on CBR values of sand [9], [14]. So their effects on cohesionless soils especially silts aren't investigated enough yet. Therefore our aim in this study is to evaluate the feasibility of using stabilized silt with microsilica and lime for a railway subgrade.

2. MATERIALS

2.1 Soil

The silts involved in this research were obtained from an area in Karaj railway project in Iran. Atterberg limits tests were carried out according to ASTM D 4318. The soil Plasticity Index (PI) was 2. The soil was classified as a low plasticity soil according to the unified soil classification system ASTM D 422 - 87. The soil name is ML according to USCS (silty soil with low plasticity). The soil classification is shown in Fig 1.

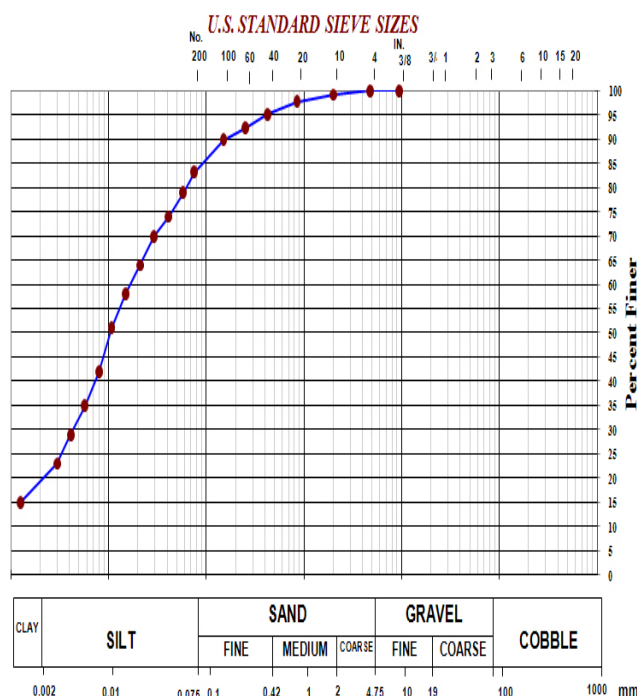


Fig. 1 Grain size distribution curve of the silty soil

2.2 Lime

Quick lime which was used in this experiment was obtained from the industrial group Qom-Iran limestone and its chemical composition is shown in Table 1.

Table 1- Chemical properties of lime

Chemical names	Percentage
K ₂ O	4
SO ₃	0.8
MgO	2.65
CaO	51.64
Fe ₂ O ₃	0.13
Al ₂ O ₃	0.24
SiO ₂	1.36

2.3 Microsilica

Microsilica has been obtained from Ferroalloy Industrial Co (I.F.I) in Azna. The composition of microsilica mineral is shown in Table 2.

Table 2. Chemical properties of microsilica

Chemical names	Percentage
MgO	0.5~2
CaO	0.5~1.5
Fe ₂ O ₃	0.3~1.3
Al ₂ O ₃	0.6~1.2
SiO ₂	90~95
C	0.2~0.4
Na ₂ O ₃	0.3~0.5
SiO ₂	0.04~0.08
MO	0.02~0.07
P ₂ O ₅	0.04
Moisture	0.01~0.4
PH	6.6~8.8

3. EXPERIMENTAL PROGRAM

3.1 Tests Procedure

To evaluate the effects of lime- microsilica on CBR values of stabilized silty soils, first we found soil optimum moisture from compaction test. Then the soil was mixed with various contents of lime and microsilica at the soil optimum moisture. Therefore the oven- dried soil was sieved from sieve #4 and lime and microsilica were added into them in 1, 3 and 5% for lime and 2, 5, 8 and 12 percent of dried soil weight for microsilica. Required amount of water was added to the mixture to obtain soil optimum moisture, beyond. The CBR tests were carried out on samples which were cured for 7 days after 96 hours immersing according to ASTM D 1883 - 99.

3.2 Compaction Tests

To determine the soil optimum water content and the soil maximum dry unit weight, the modified compaction tests were carried out according to ASTM D 1557 – 91. For this purpose, the oven- dried soil passing sieve #4 was compacted in five layers by 56 blows with 4.5 Kg hammer from 45 cm height in 6 inch mold according to procedure C from respective standard test method.

3.3 California Bearing Ratio (CBR) Tests

The California Bearing Ratio (CBR) test is one of the most widespread tests to determine strength and bearing capacity of base, sub- base and subgrades for use in road, railway and airfields pavements. To demonstrate the influence of lime-

microsilica additive on the bearing ratio of the silty soil, a series of bearing ratio tests were carried out on stabilized and unstabilized specimens. The tests were conducted according to ASTM D 1883 – 99. The soil with different mixtures of lime and microsilica were compacted in 6" modified proctor mold in five layers by 56 blows in per layer at the soil optimum moisture obtained from compaction tests. For curing the samples, they were placed in constant moisture and temperature for 7 days. To conduct the tests in soaked condition, they were immersed in water for 96 hours under the 4.5 Kg (10 pound) overload according to standard test method. The CBR tests were carried out after 20 minutes to drain the samples. Meanwhile variation of the samples maximum unit weight and water content were determined after the samples soaking and swelling potential changes were measured during the soaking time.

4. RESULTS AND DISCUSSION

4.1 Compaction Tests

Compaction tests were carried out on the silty soil and the soil optimum moisture and the soil maximum unit weight were found to be 14.2% and 17.2 KN/m³ respectively. Compaction tests results are drawn in Fig 2.

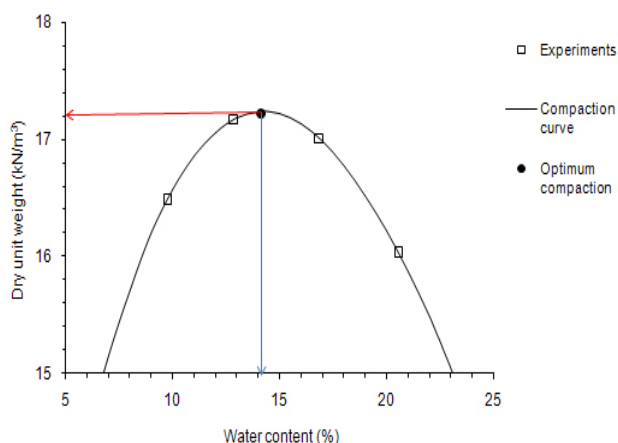


Fig. 2 Compaction test curve

4.2 Effect of Additives on the CBR

To compare the soil resistant with different amount of additive, a series of samples were prepared in modified proctor mold. The CBR tests were conducted in both stabilized and unstabilized silty soils at the soil optimum moisture with different amount of lime and microsilica. The CBR value of the unstabilized soil was 5.4%. The effect of various amount of additive on CBR values of samples are shown in Fig 3.

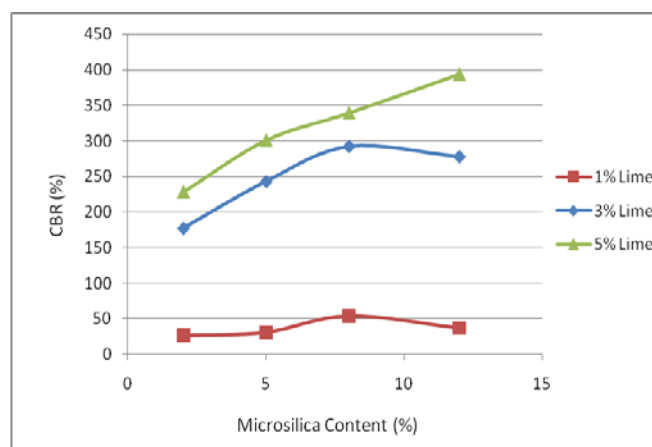


Fig. 3 The effect of various amount of lime- microsilica additive on CBR values of stabilized soil

As the Fig. 3 presents, in low amounts of lime (1 and 3 percent of dry soil) increase in microsilica amount up to 8% causes increase in CBR values and then decrease but for 5% of lime increase in microsilica amount causes increase in CBR values. The maximum CBR value of the samples which contain 5% lime and 12% microsilica increases from 5.4% to 393.2%. So it is seen that up to 388% increase in CBR value of stabilized soil in compare of unstabilized silty soil.

The samples maximum dry unit weight and moisture are determined after samples soaking. Figs 4 and 5 show their results respectively. It is observed that the maximum dry unit weight increase like CBR increase procedure and the samples moisture are increase exactly the opposite of the samples dry unit weight procedure. The reason for increase in the maximum dry unit weight of stabilized samples is assessed by void ratio decreasing due to the additive mixture with very fine particle size distribution.

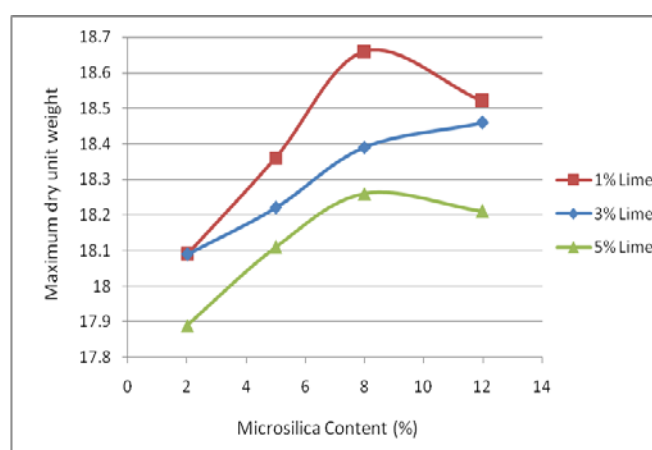


Fig. 4 The effect of lime- microsilica additive on the maximum dry unit weight

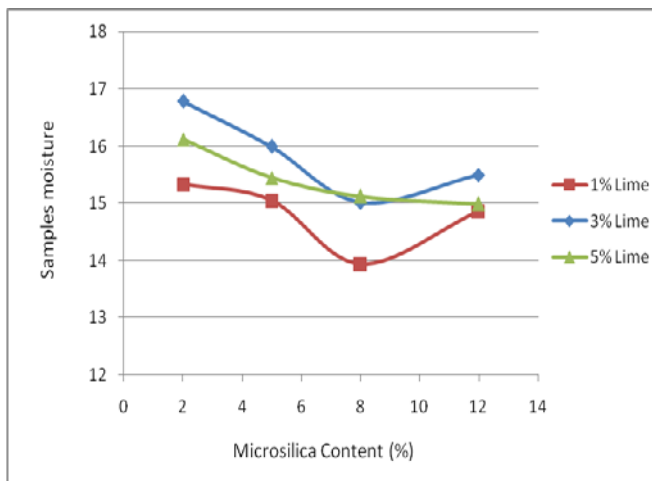


Fig. 5 The effect of lime- microsilica additive on samples moisture after soaking

4.3 Effect of Additives on Swelling

The samples swelling were measured during the 96-hour of CBR samples soaking. There were seen swelling potential rate were decreased reverse of strength. Unstabilized soil swelling was 0.55mm and stabilized swelling samples were decreased up to 0.01mm.

5 CONCLUSIONS

In this research the effects of lime- microsilica additive on silts and its utilize on railways subgrade were investigated and following conclusions were drawn:

The experimental results showed that in 1 and 3% of lime it was seen an increase on CBR values of samples with microsilica increase until 8% of microsilica and then it increased. But in 5% use of lime the CBR values were increased with microsilica increase. So it sounds the amount of sufficient amount of microsilica for 1 and 3% of lime to achieve maximum pozzolanic reaction is 8% and for 5% of lime is 12%.

The results of the samples maximum dry unit weight change is just like CBR values change procedure. The samples maximum dry unit weight increase with CBR increase.

The moisture measured after soaking stabilized and unstabilized samples decrease exactly opposite of the samples maximum dry unit weight change procedure.

There were also seen decreases on swelling rates of stabilized soil by increase the additive.

Therefore, in order to related conclusions which present considerable strength of stabilized silty soil with lime-microsilica additive in comparison of unstabilized soil, application of lime- microsilica additive is recommended for subgrad and even sub base of civil projects.

6 REFERENCES

[1] MCPRC (Ministry of Construction of the People's Republic of China), GAQSIQPRC (General Administration of Quality Supervision, Inspection and

Quarantine of the People's Republic of China). Code for design of building foundation. China Architecture and Building Press, Beijing. (in Chinese), 2002, 262pp.

[2] Bell F.G, "Lime stabilization of clay minerals and soils." Engineering Geology 42, 1996, pp. 223–237.

[3] Dermatas D, Meng X.G "Utilization of fly ash for stabilization/ solidification of heavy metal contaminated soils." Engineering Geology, 2003, pp. 377–394.

[4] Abd El Aziz, "The Effect of Silica Fume Substitution on the Characteristics of Ordinary Portland cements Pastes and Mortars." Civil Engineering Magazine, Vol. 24 No. 2, 2003, p. 715-725.

[5] Choobbasti A.J, Ghodrat H, Vahdatirad M.J, Firouzian S, Barari A, Torabi M, Bagherian A, "Influence of using rice husk ash in soil stabilization method with lime." Earth Sci. China 2010, pp. 471–480

[6] Bell F.G., "Cement stabilization and clay soils, with examples." Environmental and Engineering Geoscience, 1995, pp.139–151.

[7] Sheng A.Q, Ma M, "Experimental study on stabilization of subbase of bearing sand silt with low liquid limit (in Chinese)". East China Highway 5, 2001, pp.42–46.

[8] Mohamedzein, Y.E., Al-Rawas, A.A. and Al-Aghbari, M.Y. "Assessment of sand– clay mixtures for use in landfill liners." Proceedings of the International Conference on Geo-environmental Engineering, Singapore, December 2003, pp. 211–218.

[9] Karimi M, Ghorbani A, Daghigh Y, Kia Alhosseini S, Rabbani P, "Stabilization of silty sand soils with lime and microsilica admixture in presence of sulfates" Pan- Am CGS Geotechnical conference, 2011

[10] Kalkan E, "Influence of silica fume on the desiccation cracks of compacted clayey soils." Applied Clay Science, 2009, pp. 296–302.

[11] Kalkan E, "Impact of wetting–drying cycles on swelling behavior of clayey soils modified by silica fume." Applied Clay Science, 2011, pp. 345–352.

[12] Abd El-Aziz M.A, Abo-Hashema M.A, El-Shourbagy M, "The Effect of Lime-Silica Fume Stabilizer on Engineering Properties of Clayey Subgrade." Engineering Conference, Faculty of Engineering, Mansoura University, April 2004, Paper No. 96

[13] McKennon, J.T, Hains N.L, Hoffman, D.C, "Method for stabilizing clay bearing soils by addition of silica and lime." Patent Cooperation Treaty (PCT), International Application Published Under the Patent Cooperation Treaty (PCT), Patent Classification: C09K 17/00, Publication Number: WO 94/06884, 1994.

[14] Kalkan E, "Effects of silica fume on the geotechnical properties of fine-grained soils exposed to freeze and thaw." Cold Region Science and Technology, 2009, pp. 130–135.

Effect of Elastic Modulus Varieties in Depth on Subgrade Reaction Modulus of Granular Soils

Reza Ziaie Moayed¹, Mahdi Ali Bolandi²

Civil Engineering Department, Imam Khomeini International University, Qazvin, Iran

ABSTRACT

The subgrade reaction modulus that indicates the relation between soil pressure and deflection is one of the most efficient parameter that is used for structural analysis of foundation members. The popular practical method for estimating the modulus of subgrade reaction is the plate load test (PLT), that determines the ratio of load to displacement of circular plate with 15cm-75cm diameter. Afterward, the results modified with Terzaghi's equation (1955) and became applicable for foundation engineering problems. The subgrade reaction modulus (K_s) is dependent to some parameters like soil type, size and shape of foundation, depth and stress level. One of the principle methods for determining K_s is back numerical analysis. In this way, by using Mohr-coulomb behavior model, elastic modulus (E_s) has a significant influence on obtained results. In granular soils, due to the increase of confining stress in depth, elastic modulus is also increased. In this paper the effect of soil stress-strain modulus (E_s) varieties in depth on subgrade reaction modulus (K_s) was investigated by using finite element analysis. The results illustrate that in granular soils, by considering the elastic modulus varieties in depth, the subgrade reaction modulus would become significantly greater as compared to a constant E assumed for all depth. Therefore, it may be proposed that in subgrade reaction modulus calculation the E varieties in depth should be considered by back analysis method.

Keywords: Subgrade Reaction Modulus, Elastic Modulus, Granular Soils, Plate Load Test, Finite Element Analysis

INTRODUCTION

Soil medium has very complex and erratic mechanical behavior because of the Nonlinear, stress dependant, anisotropic and heterogeneous nature of it. Hence, instead of modeling the subsoil in its three dimensional nature, subgrade is replaced by a much simpler system called a subgrade model that dates back to the nineteenth century. The search in this context leads to two basic approaches which are Winkler approach and the elastic continuum model, which are of widespread use, both in theory and engineering practice. Winkler assumed the soil medium as a system of springs which are identical but mutually independent, closely spaced, discrete and linearly elastic and ratio of contact pressure, p , at any given point to settlement, y , produced by load application at that point, is given by the coefficient of subgrade reaction, K_s [1]:

$$K_s = p / y \quad (1)$$

A direct method to estimate both E_s and K_s is plate loading test (PLT) that requires circular or equivalent rectangular plates. PLT provides a direct measurement of the compressibility and bearing capacity of soil and essentially consists in loading a rigid plate and determining the settlements corresponding to each load increment. The results of a PLT are presented as applied contact pressure versus settlement curves (Fig. 1).

There are some current methods for subgrade reaction modulus determination like NAVFAC DM-7.1, that indicate after plotting stress- settlement curve, q_{ult} fined, and ratio of $0.5q_{ult}$ to corresponding settlement, considered as K_s [2]. According to Bowles initial tangent or initial secant line slope can be used for estimating the modulus of subgrade reaction. However, the slope of tangent line in applied stress may be used to determining the subgrade reaction modulus [3].

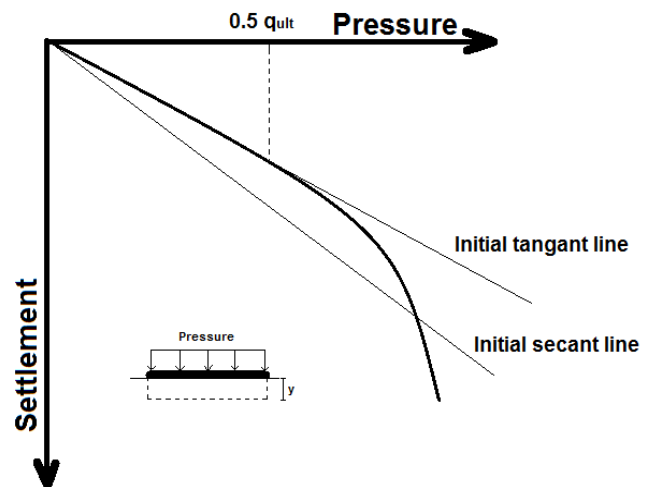


Fig 1. Typical presentation of results from a PLT

Many researches including Biot, Terzaghi, and Vesic have investigated the effective factors and determination approaches of K_s [4]-[6]. Geometry and dimensions of the foundation and soil layering are assigned to be the most important effective parameters on K_s .

Terzaghi made some recommendations where he suggested values of K_s for 1*1 ft rigid slab placed on a soil medium; however, the implementation or procedure to compute a

1.Associate Professor, Civil Engineering Department, Imam Khomeini International University, Qazvin, Iran, R_ziaie@ikiu.ac.ir

2.M.Sc. Student, Civil Engineering Department, Imam Khomeini International University, Qazvin, Iran, Eng.alibolandi@gmail.com

value of K_s for use in a larger slab was not specific. Biot solved the problem for an infinite beam with a concentrated load resting on a 3D elastic soil continuum [7]. He found a correlation of the continuum elastic theory and Winkler model where the maximum moments in the beam are equated. Vesic tried to develop a value for K_s , except, instead of matching bending moments. He matched the maximum displacement of the beam in both models. He obtained the equation for K_s for use in the Winkler model.

Several studies by Filonenko-Borodich, Hetenyi, Pasternak, and others, have attempted to make the Winkler model more realistic by assuming some form of interaction among the spring elements that represent the soil continuum [8]-[10]. One of the early contributions was that of Terzaghi, who proposed that K_s for full-sized footings could be obtained from plate-load tests using the following equations:

For clayey soil:

$$K_s = K_p (B_p / B) \quad (4)$$

For sandy soil:

$$K_s = K_p [(B+B_p) / 2B]^2 \quad (5)$$

Where

K_s = desired value of modulus of subgrade reaction for the full-size (or prototype) foundation

K_p = value obtained from a plate-load test using a 0.3m × 0.3m (1ft × 1 ft) or other size load plate

B_p = plate diameter

B = dimension of foundation.

In the present paper, the effect of elastic modulus variation on K_s determination is investigated. For this purpose, the numerical analysis are performed on four models with constant and various E in depth (two model for either PLT and mat foundation) and the subgrade reaction modulus are determined using back analysis method for each model.

2 ANALYSIS PROCEDURE

2.1 Material

2.1.1 Material Model

In current paper the value of E is expressed as a function of confining pressure σ_3 using Janbu's [11] relationship as

$$E = k_{ur} P_a (P/P_a)^n \quad (6)$$

E = tangent elastic modulus at the mean stress P

k_{ur} = modulus number

P_a = atmospheric pressure

P = mean stress = $(\sigma_1 + \sigma_2 + \sigma_3)/3$

n = exponent modulus.

Then, by replacing $P = \gamma z (1 + 2 k_0)/3$, E versus depth (z) derived (Fig 2). Afterwards, the obtained curve approximately divided to straight lines and assumed that E changes in each part, linearly. Each part considered as

different layers that E linearly change with depth. For these layers, Mohr-Coulomb model is employed.

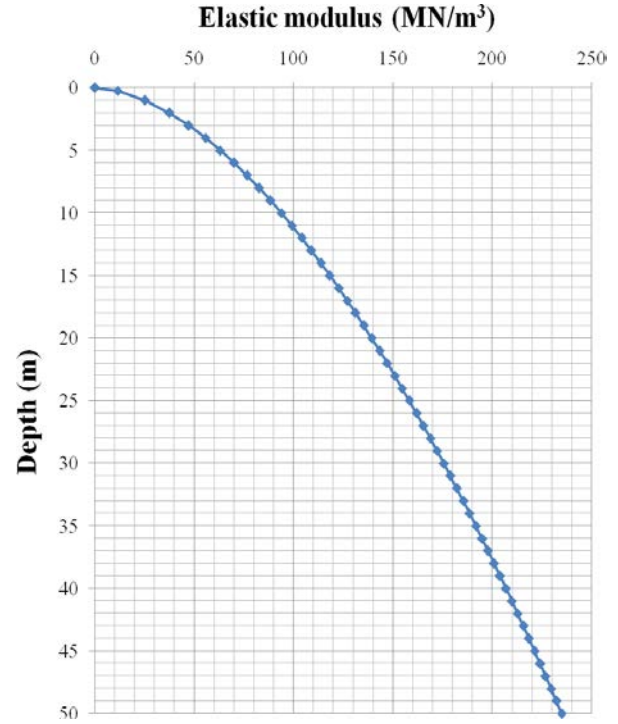


Fig 2. Elastic modulus versus depth

2.1.2 Material Properties

In present study, Sacramento River Sand properties that was given by Lade [12], dedicated to soil. Aforesaid soil parameters are presented in Table 1.

Table 1. Sacramento River sand properties.

k_{ur}	n	ν	ϕ (°)	C (kPa)	ψ (°)	ρ (kg/m³)
960	0.57	0.3	35	0	5	1417

2.2 Geometry

46 finite element analysis performed using Plaxis 8.5 software with axis-symmetric model. The 15-node triangular elements are used to model the soil layers and other volume clusters. Near the edges of a loaded area where stress concentrations are expected, mesh is refined by reducing the size of the soil surface below the position of the loading area. Analysis is performed under load control by a vertical distributed load boundary condition applied to the soil surface below the position of the loading plate. It is assumed that both horizontal and vertical displacements are zero for all nodes along the bottom boundary of the mesh. On the vertical side boundaries, the horizontal displacements have been assumed to be zero too.

The size of axis-symmetric model in X and Y direction is considered greater than 2.5D and 6D, respectively, that satisfy Bowles recommendation [3]. Four models provided to

analyze, two models for 0.75m diameter plate loading, and others assigned to circular foundation with 10 m diameter. In each of mentioned groups, one of them has layers that Elastic modulus linearly changes in depth and other has a constant E overall the model (Fig 3-4).

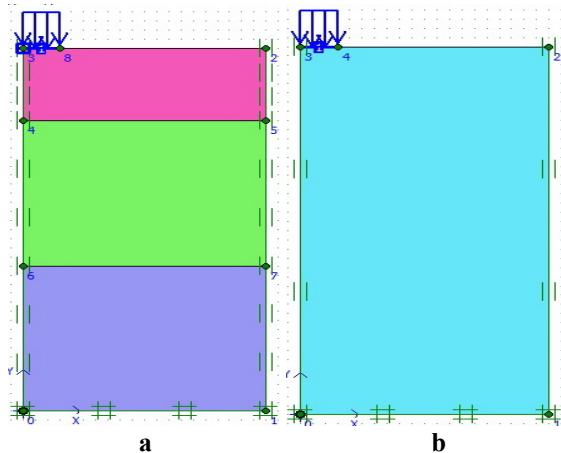


Fig 3. Geometry of model (PLT).
a: Various E, b: Constant E

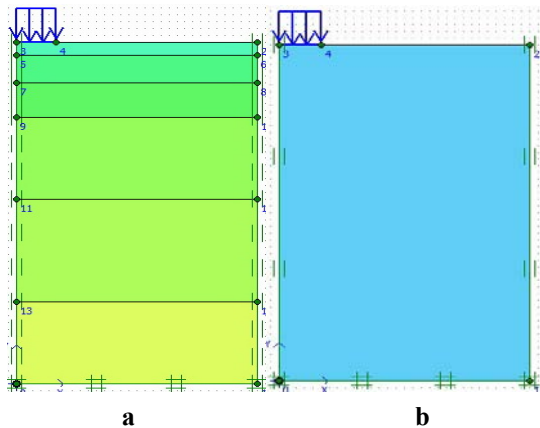


Fig 4. Geometry of model (Mat Foundation).
a: Various E, b: Constant E

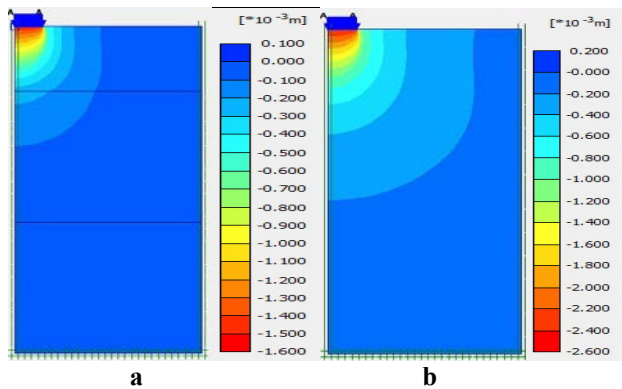


Fig 5. Vertical displacement (PLT).
a: Various E, b: Constant E

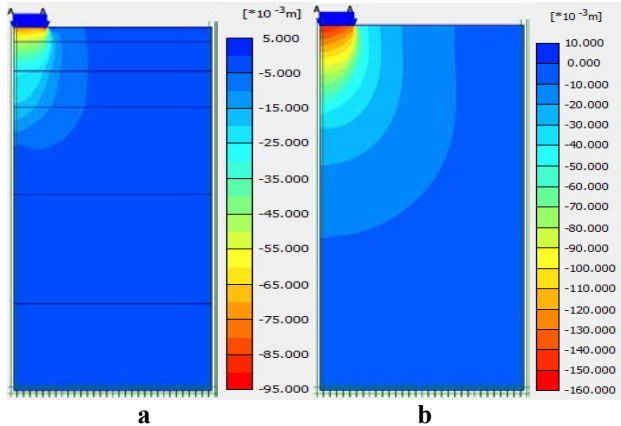


Fig 5. Vertical displacement (PLT).
a: Various E, b: Constant E

3 RESULTS

All models were analyzed (Fig 4-5) and pressure-settlement curves for each model were plotted (Fig 6-7). Therefore, the subgrade reaction modulus by estimating the slope of initial tangent line, were specified (Table 2).

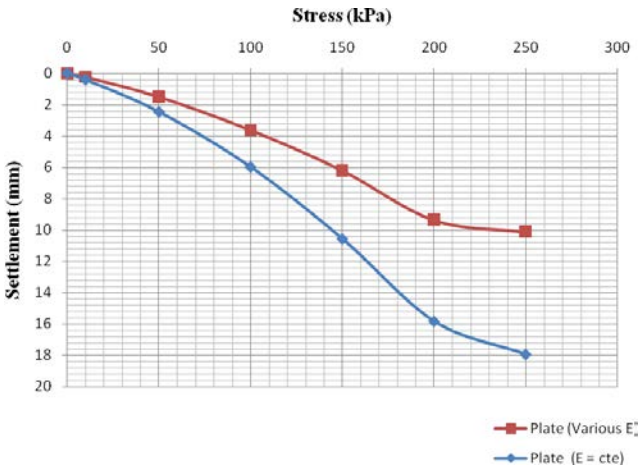


Fig 6. Stress – Settlement curves of plate loading with various and constant E.

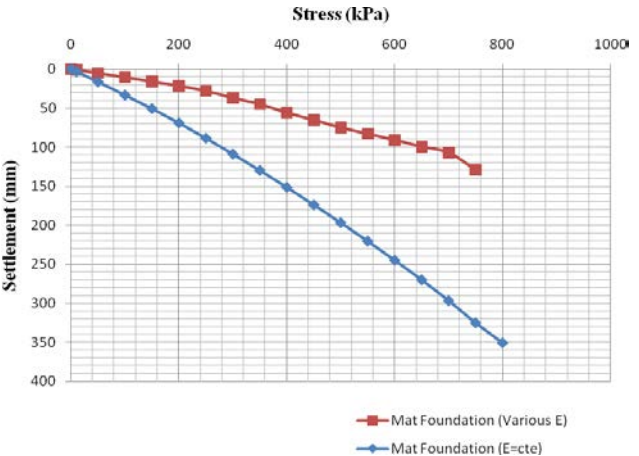


Fig 7. Stress – Settlement curves of foundation loading with various and constant E.

Table 2. Subgrade reaction modulus for models.

Type	K_s (MN/m ³)	
	Various E	Constant E
Plate	33.1	20.3
Foundation	9.4	3.0

3 CONCLUSION

1. Considering the E varieties in depth, in granular soils, confining pressure effect, caused the settlements decrease. Therefore the obtained K_s become greater as compared to constant E condition.
2. Due to significant variation of elastic modulus in low depth, the plate load test must perform exactly at the foundation level.
3. In order to calculate the subgrade reaction modulus using, a specific value of E could be misleading.
4. As foundation dimensions increase, the stress influence depth increases subsequently. Hence the effect of E variation in depth on K_s becomes considerable.
5. Based on obtained results, it may be propose that in subgrade reaction modulus calculation the E varieties in depth should be considered by back analysis method.

4 REFERENCES

- [1] Winkler E, "Die Lehre von Elastizitat and Festigkeit (on elasticity and fixity)" . Praguc. 1987
- [2] US Naval Facilities Engineering Command, 1982.
- [3] Bowels, J. E, Foundation Analysis and Design. fifth edition, The Mc Graw-Hill, 1998.
- [4] Biot, M. A, " Bending of Infinite Beams on an Elastic Foundation," Journal of Applied Science .Trans. Am. Soc. Mech. Eng., 1937, 59: A1-7.
- [5] Terzaghi, K, "Evaluation of coefficient of subgrade reaction", Geotechnique, 1955, Vol. 5, No. 4, pp 297-326.
- [6] Vesic, A. S, ' Beams on elastic subgrade and the Winkler's hypothesis", 5th ICSMFE, 1961, Vol. 1, pp. 845-850.
- [7] Biot, M. A, "Bending of Infinite Beams on an Elastic Foundation", Journal of Applied Science .Trans. Am. Soc. Mech. Eng, 1937, 59: A1-7.
- [8] Filonenko. M. & Borodich, M, "Some approximate theories of the elastic foundation", Uchenyie Zapiski Moskovskogo Gosudarstvennoho Universiteta Mekhanika, 1940, 46, pp 3-18 (in Russian).
- [9] Hetenyi, M, "Beams on elastic foundations", The university of Michigan Press, Ann Arbor, Michigan, 1946.
- [10] Pasternak, P. L, "On a new method of analysis of an elastic foundation by means of two foundation

constants", Gosudarstvennoe izdatelstro liberaturi po stroitelstvui arkhitekture. Moscow (in Russian), 1954.

- [11] Janbu, N, "Soil compressibility as determined by oedometer and triaxial tests", European Conference on Soil Mechanics and Foundations Engineering, Wiesbaden, Germany, 1963, Vol. 1
- [12] Lade P.V, "Elasto-plastic stress-strain theory for cohesionless soil with curved yield surfaces", Ind. J. Solids Structures, 1977, Vol. 13, pp. 1019-1035

Flexural Buckling Behavior of Steel Pile with Vertical Load in Liquefied Soil

Yoshihiro Kimura¹, and Koichi Onohara²
1 Tohoku University, 2 Nagasaki University, JAPAN

ABSTRACT

When slender steel piles beneath buildings experience high axial compression forces as a result of vertical loads increased by P-Δ effects with inertia forces acting on the buildings and then the soil liquefies, buckling of the piles may occur even though they are restrained laterally by the liquefied soil.

This paper describes the evaluation of the buckling length of slender piles in liquefied soil with the unified and triangular distributions of the coefficient of the subgrade reaction. The relationship between the buckling length of the slender piles and the soil-pile interaction is presented. Also, the elasto-plastic analyses are also conducted and interaction between the non-linear behavior of the steel piles and inelastic soil reaction are clarified.

Keywords: Steel Pile, Flexural Buckling Length, Coefficient of Subgrade Reaction, liquefaction, Energy Method, FEM Analysis

1. INTRODUCTION

When slender steel piles beneath buildings experience high axial compression forces as a result of vertical loads increased by P-Δ effects with inertia forces acting on the buildings and then the soil liquefies, buckling of the piles may occur even though they are restrained laterally by the liquefied soil. For example, in the case of tall structure as shown in Fig.1, the left steel pile carries out the tensile force due to P-Δ effect, and the right one carries out the compressive force due to P-Δ effect in addition to dead load of the structure. The flexural buckling will occur in the right one, and then its buckling length is corresponding to the thickness of the liquefied soil.

This paper describes the evaluation of the buckling load of slender piles in liquefied soil with the unified and triangular distributions of the coefficient of the subgrade reaction. The equations of elastic buckling load are developed with the energy methods, and the relationship between the buckling load of the slender piles and the soil-pile interaction is presented. The elastic eigen analyses are conducted to compare the solution from the equations of buckling load developed by the energy method.

The elasto-plastic analyses are also conducted and interaction between the non-linear behavior of the steel piles and inelastic soil reaction are clarified.

Finally the estimation for buckling stress is suggested with general slenderness ratio λ_c to apply to the present AIJ code design for the compressive steel members, and the analyses results are in good agreement with the design curves.

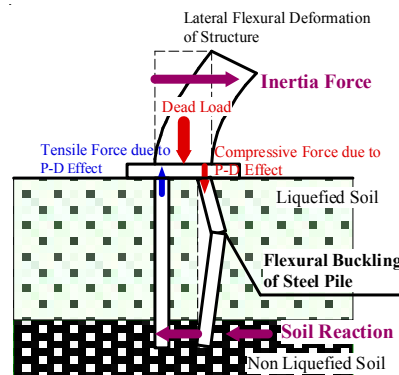


Fig.1 Concept for Flexural Buckling of Steel Pile in Liquefied Soil

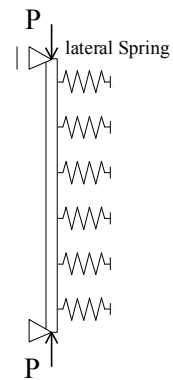


Fig.2 Analysis Model of Steel Pile in Liquefied Soil

2. ELASTIC BUCKLING LOAD FOR STEEL PILE IN LIQUEFIED SOIL

2.1 Assumption of Elastic Buckling for Steel Piles

In this paper, some assumptions are applied to develop the elastic buckling load for steel pile in liquefied soil.

- (1) The external force for a pile is only vertical load such as Fig.2.
- (2) The boundary condition is simple support, and then the displacement of the pile at the top does not occur.
- (3) The subgrade reaction is replaced to the elastic horizontal springs such as Fig.2, because there is little friction over depth between the soil and the pile. The coefficient of the subgrade reaction, K_c is expressed in the following in reference to Recommendation for Design of Building Foundations (DBF), AIJ [1].

$$K_c = k_{h1} B (\text{MN/m}^2) \quad (1)$$

$$k_{h1} = 80 E_0 B^{-\frac{3}{4}} (\text{MN/m}^3) \quad (2)$$

Where, k_{hl} is calculated with deformation modulus, E_0 and diameter of piles in reference. In Eq. (2), the unit of the diameter must be “cm”. Table 1 shows the relationship between the K_c and E_0 .

- (4) The distribution of the subgrade reaction is assumed to be the unified and triangular distributions in the followings.

$$K = K_c \quad (3)$$

$$K = \frac{2K_c}{l}(l-x) \quad (4)$$

2.2 Development of Elastic Buckling Load for Steel Piles

When a steel pile in liquefied soil is laterally buckled, the potential energy U is expressed as the following [2], [3].

$$U = \frac{1}{2} \int_0^l (EIu''^2 - Pu'^2 + Ku^2) dx \quad (5)$$

Where EI is the flexural rigidity of steel pile, K is the coefficient of the subgrade reaction such as Eq. (3) or (4), and P and u are the vertical load and the lateral displacement of the pile. The boundary conditions are simple supports such as assumption (2) in section 2.1. For the steel pile with the unified distribution of the coefficient of the subgrade reaction, the lateral deformation is expressed in the function of sine curves in the followings.

$$u = a \sin \frac{n\pi x}{l} \quad (6)$$

Substituting Eq. (6) for Eq. (5) and use a variational technique to Eq. (5), then the buckling load P_{cr} is obtained as the followings.

$$P_{cr} = \left(\frac{\pi}{l} \right)^2 EI \alpha \quad (7)$$

Where α is the ratio of the buckling load of steel pile restraint by soil to Euler buckling load in the following.

$$\alpha = n^2 + \left(\frac{l}{\pi} \right)^4 \frac{K_c}{n^2 EI} \quad (8)$$

Where n is number of the buckling mode, and the number must be selected for minimum value of α .

For the steel pile with the triangular distribution of the coefficient of the subgrade reaction, the lateral deformation is expressed in the function of sine curves in the followings.

$$u = a \sin \frac{\pi x}{l} + b \frac{2\pi x}{l} \quad (9)$$

Substituting Eq. (6) for Eq. (9) and use a variational technique to Eq. (5), then the buckling load P_{cr} is obtained as the followings.

$$P_{cr} = \frac{5}{2} \left(\frac{\pi}{l} \right)^2 EI + \frac{5}{8} \left(\frac{l}{\pi} \right)^2 K_c - \sqrt{\frac{9}{4} \left[\left(\frac{\pi}{l} \right)^2 EI - \left(\frac{l}{\pi} \right)^2 \frac{K_c}{4} \right] - \frac{256 K_c^2}{81 l^4} \left(\frac{l}{\pi} \right)^8} \quad (10)$$

Eq. (10) can be applied in less than the local minimum value of buckling load, because Eq. (9) represents only the first buckling mode.

2.3 Elastic Buckling Stress for Steel Piles

Fig. 4 shows the relationship between the elastic buckling stress, σ_{cr} for steel piles with the subgrade

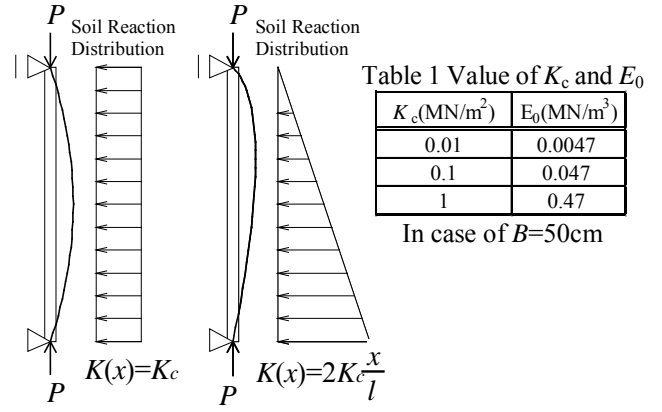


Fig. 3 distribution of Subgrade Reaction

reaction and slenderness ratio, λ . The parameters are the shapes of subgrade reaction distribution such as unified or triangle ones, the coefficient of the subgrade reaction such as 1 MN/m², 0.1 MN/m² and 0.01 MN/m². The dots are the numerical analyses results and the thin curves are drawn from Eqs. (6), (7) and (10).

The buckling stresses of piles with unified subgrade reaction distribution calculated from Eqs. (6) and (7) are almost equal to the results of numerical analyses results on this diagram. In general, the larger the slenderness ratio is, the buckling stress does not increase. So that the closed form solutions for the buckling stresses of piles are suggested in the following.

$$P_{cr} = 2\sqrt{EIK_c} \quad (l \geq \pi \sqrt{EI/K_c}) \quad (11)$$

Eq. (11) represents the stationary value of buckling stress of Eq. (7), and thick broken lines are drawn from Eq. (11).

These lines are lower limit of Eq. (7), and are similar to the square dots of numerical analyses results. Eq. (11) is transformed into Eq. (7), α can represent in the following.

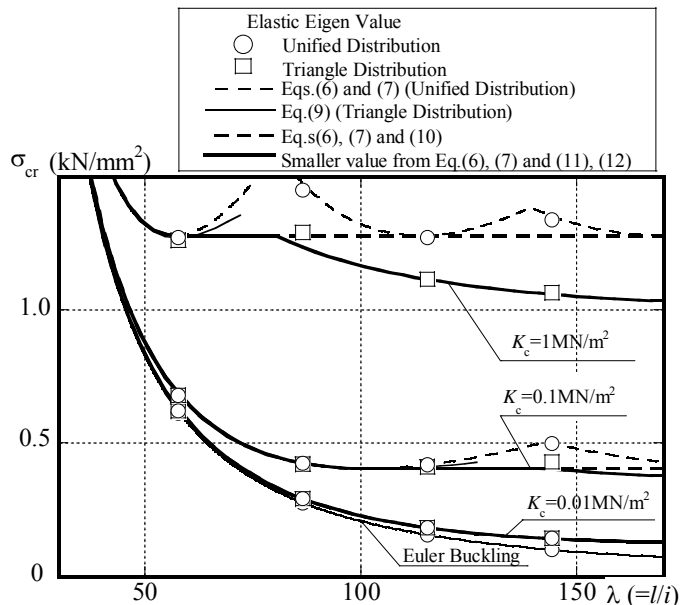


Fig.4 Elastic Buckling Stress for Steel Piles

$$\alpha = 2 \left(\frac{l}{\pi} \right)^2 \sqrt{\frac{K_c}{EI}} \quad (12)$$

On the other hand, the buckling stresses of piles with triangle subgrade reaction distribution calculated from Eq.(10) are almost equal to the numerical analyses results in the small slenderness ratio, but the numerical analyses results are lower than those from Eq.(10) in the large slenderness ratio, because Eq. (10) can be applied to less than the local minimum value of buckling load. Then it is difficult to apply Eq.(10) to the buckling stresses of the piles with large slenderness ratio.

As with the unified subgrade reaction distribution, the closed form solution for the piles with triangle subgrade reaction distribution is suggested in the following.

$$\alpha = 1 + \frac{3}{2} \left(\frac{l}{\pi} \right)^2 \sqrt{\frac{K_c}{EI}} \quad (l \geq \pi \sqrt{2EI/K_c}) \quad (13)$$

The thick solid curves from Eq. (13) are fitting well as the numerical analyses results.

3. ELASTO-PLASTIC BUCKLING BEHAVIOR FOR STEEL PILE IN LIQUEFIED SOIL

3.1 Summary of Elasto-Plastic Analyses Models

In this section, FEM analyses are performed to investigate the elasto-plastic buckling behavior for steel piles with subgrade reaction. Material properties of steel piles is shown as Fig.5, and then Yong's modulus E , yield stress σ_y and strain hardening gradient E_{st} for piles are $E=206$ (KN/mm²), $\sigma_y=400$ (N/mm²) and $E_{st}=4.2$ (KN/mm²), respectively in reference to [4]. Fig.6 shows the subgrade reaction curve as shown in reference [1].

Fig.7 shows the initial imperfection of the steel pile, and then the initial imperfections are described as the function of sine curves in the followings.

$$u = a \sin \frac{\pi x}{l} + b \sin \frac{2\pi x}{l} \quad (14)$$

$$\therefore a = \frac{l}{5000}, \quad b = \frac{l}{10000}$$

Fig.8 is the analysis model of steel pile with subgrade reaction. The analysis model and boundary conditions are same as those in the previous section. Soil is assumed to restrain the lateral deformation of steel piles, and is replaced to elasto-plastic strut with the subgrade reaction curve in Fig.6.

Fig.10 shows the elasto-plastic buckling behavior for steel piles with the subgrade reaction. Figs. 10(a)~(d) represent the compression stress, $\sigma_x(=P/A)$, the lateral displacement, u/l , lateral distribution at maximum load, u/l , and flexural moment at maximum load, M , respectively. The steel pile has 115 of slenderness ratio, and the soil has 0.1 of the coefficient of the subgrade reaction. The parameter is soil conditions such as elastic or elasto-plastic property, and

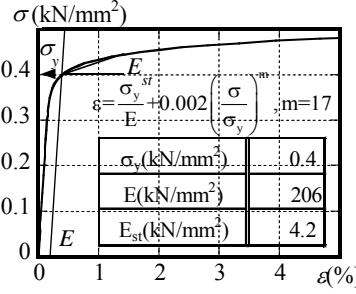


Fig.5 Stress – Strain Curve of Steel Piles

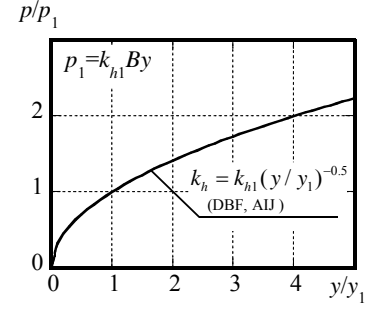


Fig.6 Subgrade Reaction Curve

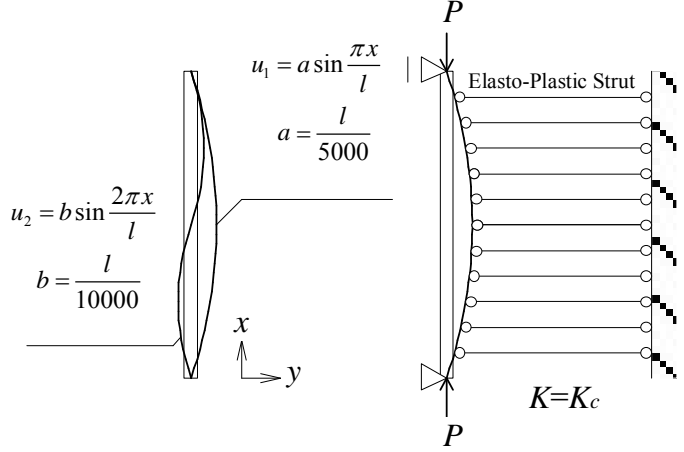
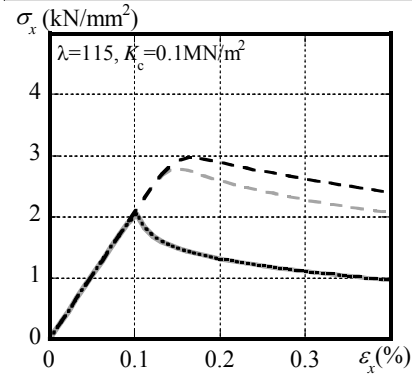
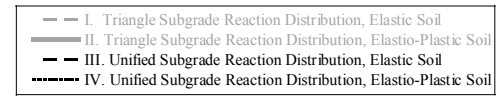
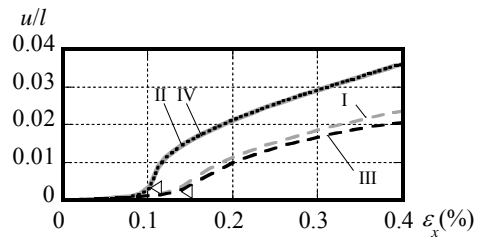


Fig.7 Initial Imperfection of Steel Piles

Fig.8 Analyses Model of Steel Pile with Subgrade Reaction



(a) Compression Load



(b) Lateral Displacement on Pile Top

unified or triangle subgrade reaction distribution. Case I is elastic soil with triangle subgrade reaction distribution, Case II is elasto-plastic soil with triangle subgrade reaction distribution, Case III is elastic soil with unified subgrade reaction distribution, and Case IV is elasto-plastic soil with the unified subgrade reaction distribution.

In Fig. 10(a), the compression load for the piles of Case II and Case IV decreases rapidly after the maximum load, because the subgrade stiffness decreases as the lateral displacement increases. On the other hand, the maximum load for Case I and III is about 1.5 times than that for Case II and Case IV, because subgrade stiffness is elastic. The maximum lateral displacement occurs at the top of pile, and for triangle subgrade reaction distribution, the value of subgrade reaction at the top of pile is 0. So that the strength for Case III is higher than that for Case I.

In Fig. 10(b), the lateral displacements at the top of pile for Case II and Case IV increase more than those for Case I and Case III.

In Fig. 10(c), the maximum deformation for Case III is larger than the others at the maximum load. It means that the pile for Case III can carry the compression load even though the large lateral deformation occurs, because the soil with elastic subgrade and unified reaction distribution can restrain the lateral deformation of the pile.

In Fig. 10(d), the maximum flexural moment for Case III becomes larger than the others, and reaches the yield moment at the maximum compression load.

4. ESTIMATION OF ELASTO-PLASTIC BUCKLING STRESS FOR STEEL PILE IN LIQUEFIED SOIL

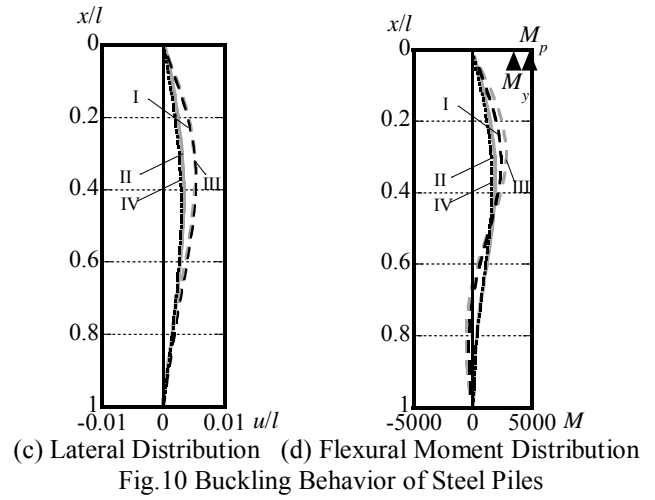
4.1 Comparison between Buckling Stress for Steel Piles with Various Soil Conditions

Fig. 11 compares the elasto-plastic buckling stress for steel piles with various soil conditions. The vertical and horizontal axes are the buckling stresses of the piles with elasto-plastic soil and elastic soil, respectively. Then they are divided by the yield stress of the piles.

White circle represents the result for distribution of unified subgrade reaction, black one represents the result for distribution of triangle subgrade reaction. In the range of less than 0.3 of $_{es}\sigma_{cr}/\sigma_y$, the piles reach the maximum load as soon as the piles deforms the laterally, so that the buckling stresses at the maximum loads are almost equal, regardless of the difference of soil condition. In the range of more than 0.75 of $_{es}\sigma_{cr}/\sigma_y$, the piles reach almost yield stress, so that the piles deform slowly after the maximum load. In these range, the buckling stresses for elastic and elasto-plastic soil are almost equal.

On the other hand, in about 0.5 of $_{es}\sigma_{cr}/\sigma_y$, the buckling stress for elasto-plastic soil is lower than that for elastic soil.

In this range, the soil restrains the lateral deformation of the piles until the pile buckles, and then the subgrade stiffness for elasto-plastic soil decreases even though that for elastic soil is constant. So that the pile with elasto-plastic soil



cannot carry the vertical load as soon as the lateral deformation increases, but that for elastic soil can carry the vertical load after lateral deformation of the pile occurs.

The lateral displacement at the buckling of the piles is assumed to be $y/y_1=0.002l$ as shown in Fig. 10 (b) and (c), and then the coefficient of the subgrade reaction at $y/y_1=0.002l\sim 0.004l$ is used as K_c' instead of K_c $y/y_1=1$. The reduction factor, χ is approximated as the ratio of K_c' to K_c in the following

$$\chi = \sqrt{I_0/l}, \quad l_0 = 500\text{cm} \quad (15)$$

Table 2 shows the relationship between the length of the piles and the reduction factor. As the length of the pile is longer, the coefficient of the subgrade reaction decreases.

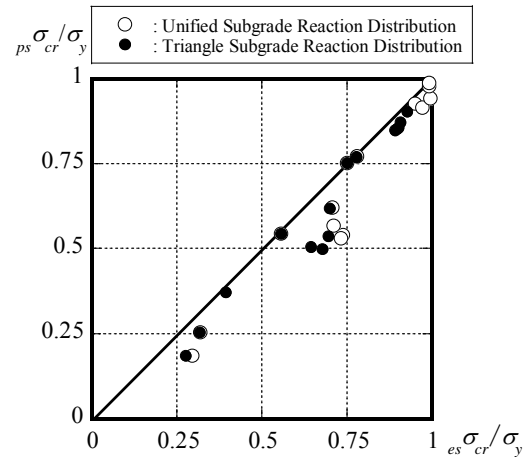


Fig.11 Comparison of Buckling Stress for Piles with Various Soil Conditions

Table 2 Relationship between length of piles and reduction factor

l (cm)	500	1000	1500	2000	2500	3000	4000
y/y_1 at $=K_c'$	1.0	2.0	3.0	4.0	5.0	6.0	8.0
$\chi (=K_c'/K_c)$	1.000	0.707	0.577	0.500	0.447	0.408	0.354

4.2 Estimation of Buckling Stress for Steel Piles in Liquefied Soil

Fig. 12 shows the elasto-plastic buckling stress for steel piles in liquefied conditions. The vertical axis represents the buckling stress for steel piles, and the horizontal axis represents the equivalent slenderness ratio. The equivalent slenderness ratio is shown as the following in Recommendation for Limit State Design of Steel Structures in AIJ (LSD) [5].

$$\lambda_c = \sqrt{P_y / P_{cr}}$$

Where P_y is the yield load and P_{cr} is Euler's buckling load in reference [5]. In this paper, when steel piles are continuously braced by the soil, Euler's buckling load in Eq. (16) is replaced on the buckling load obtained from Eqs. (7), (8), (10)~(13). Then this equivalent slenderness ratio is defined as the modified equivalent slenderness ratio. The dots are numerical analyses results, and these curves are drawn from AIJ codes such as LSD [5] and Design Standard for Steel Structures (DSS) [6].

The results of numerical analyses are exceeded for the curves drawn from LSD and distributed as the upper-bound for the curves drawn from DSS.

As the results, the elasto-plastic buckling stress for the steel piles in liquefied soil can be approximately evaluated with the equivalent slenderness ratio by LSD.

5 CONCLUSION

This paper evaluated the relationship between the buckling load for steel piles in liquefied soil. It was shown that:

- 1) In the range of small slender ness ratio, the flexural elastic buckling load for steel piles in liquefied soil is evaluated from Eqs. (7), (8), (10) developed by the energy method.
- 2) The stationary value of buckling stress for the piles with the unified subgrade reaction distribution can be calculated from Eq. (11), so that the minimum buckling stress in the range of large slenderness ratio can be estimated by Eq. (11).
- 3) In the range of large slenderness ratio, the buckling stress for the piles with the triangle subgrade reaction distribution can be approximated from Eqs. (12), (13).
- 4) From elasto-plastic large deformation analyses, in the range of less than 0.3 or more than 0.75 of the ratio of the bucking stress to the yield stress, the buckling stresses for elastic and elasto-plastic soil are almost equal, and about 0.5 of the ratio, the buckling stresses for elastic soil is higher than those for elato-plastic soil.
- 5) The elasto-plastic buckling stress for steel piles in liquefied soil can be estimated by the equations in the Japanese design codes using the modified equivalent slenderness ratio.

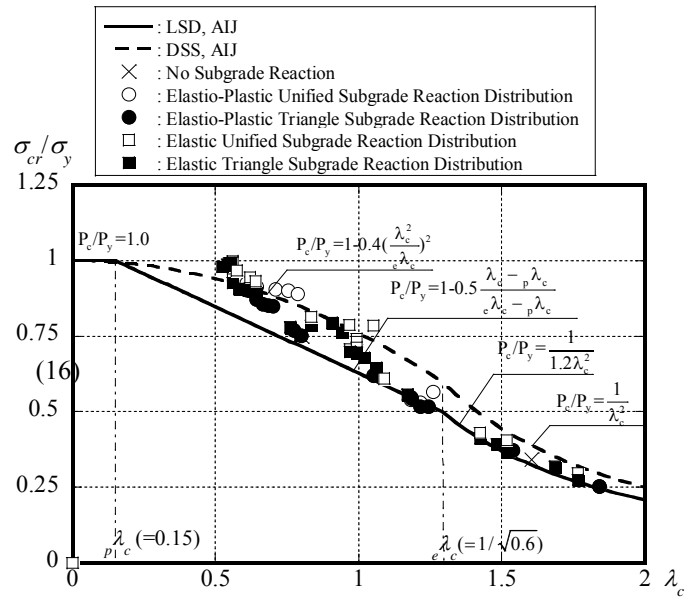


Fig.12 Buckling Stress for Piles with Subgrade Reaction

6 ACKNOWLEDGMENT

The author acknowledges support from Disaster Prevention Research Institute Kyoto University (DPRI), the Disaster Prevention Research Institute's Joint Usage/Joint Research.

7 REFERENCES

- [1] Architectural Institute of Japan, Recommendation for Design of Building Foundations, 2001, (in Japanese)
- [2] Hans H. Bleich: BUCKLING STRENGTH OF METAL STRUCTURES, McGRAW-HILL BOOK COMPANY, 1952
- [3] Kimura Y, Tokimatsu K, "Buckling Stress of Steel Pile with Vertical Load in Liquefied Soil", Jour. of Structural and Construction Engineering, No.595, Sep. 2005, pp.73-79 (in Japanese)
- [4] Kimura Y, Ogawa T and Saeki E., "The Local Buckling Behavior of Cold-Formed Circular Tubes by Different Manufacturing Process, Jour. of Steel Construction Engineering, Vol.8, No.29, March 2001, pp.27-34 (in Japanese)
- [5] Architectural Institute of Japan, Design Standard for Steel Structures, 2005 (in Japanese)
- [6] Architectural Institute of Japan, Recommendation for Limit State Design of Steel Structures, 1998, (in Japanese)

Two-dimensional finite difference pseudo-static deep-seated slope stability analysis of embankments over stone column-improved soft clay

Farshad Fayyaz Jahani¹, Mohammad Sharifipour²
Department of Civil Eng., Univ. of Razi, Kermanshah, Iran

ABSTRACT

A two-dimensional (2D) finite difference method was performed in this study to evaluate the factor of safety (FS) against deep-seated failure of embankments over stone column-improved soft clay. The parameters influencing the FS against deep-seated failure of embankments over stone column-improved soft clay were investigated including the spacing, thickness, height and friction angle of stone columns, cohesion of soft clay, friction angle, and height of embankment fill, and existence of ground water. In this study, effort to investigate the influence of these factors with different values of seismic coefficient (0.2g-0.25g-0.3g-0.35g), correspond to Iranian seismic provision (2800). The results of these analyses are summarized into a series of design charts, which can be used in engineering practice.

Keywords: factor of safety, seismic coefficient, deep-seated failure, finite difference method, stone column.

1. INTRODUCTION

Problems of slope instability present design and research challenges to geotechnical engineers. Slope stability analysis can be carried out by the limit equilibrium method (LEM), the limit analysis method (LAM), the finite element method (FEM), and the finite difference method (FDM) [1].

In recent years, finite difference method has been widely used for analyzing slope stability including the computation of its factor of safety (FS) [2]-[3]-[4]-[5].

Han et al. (2002) used the same finite software (FLAC) to obtain the identical difference corresponding FS values of unreinforced and geosynthetic-reinforced slopes as the Bishop's simplified method. Han and Leshchinsky (2004) obtained similar results for mechanically stabilized earth (MSE) walls using the finite difference method and Bishop's simplified method incorporated in the ReSSA software.

Also, several research exist only about evaluate the factor of safety of embankments in static mode, evaluate the factor of safety (FS) less attention has been in pseudo-static and dynamic analysis. Among the methods The finite difference method is perhaps one of the oldest numerical techniques used for solving sets of differential equations. In the finite difference method, every derivative in the set of governing equations is replaced directly by an algebraic expression written in terms of the field variables at discrete points in space; these variables are undefined within elements [6]. As compared with limit equilibrium methods, finite difference methods have the following advantages for calculating the factor of safety of slope stability [7]: (1) no need to define a range of trial surfaces and possible failure modes or critical slip zones determined from the numerical results (e.g., strain rate, plasticity); (2) no need to assume any functions for inter-slice force; (3) different structural elements used

(e.g., rock bolt, soil nail or geogrid) instead of equivalent forces; and (5) the solution consisting of kinematically feasible mechanisms.

The slope instability of embankments may develop locally, near the facing, within the embankment, or through the foundation soil as local, surficial, general, or deep-seated failure. Other conditions of deep-seated slope failure are creation of Rip Rap On the downstream slope. The deep-seated slope failure is also referred to as a global slope failure, mainly induced by a weak foundation existing under the embankment. Local and surficial failures develop at a shallow depth (mostly less than 1.2 m) due to low overburden stress, low density, low strength, and seepage force when the slope becomes saturated after rain. The general slope failure typically occurs through the toe of the slope [2].

A number of ground improvement techniques have been successfully adopted to prevent deep-seated slope failure, such as sand compaction piles, stone columns, and deep mixed columns. Stone columns have been commonly used as an alternative to solve deep-seated slope stability problems [8]. Stone columns can be installed using a wet or dry method. The wet method employs a vibrating probe with jetting water to form holes to be backfilled with stones from a ground surface while the dry method uses a vibrating probe with jetting air down to a depth and a feed pipe to supply stone to the bottom of the probe. The stone columns improve the ground mainly due to their higher strength and stiffness compared to the soil.

Christoulas et al. (1997) investigated the stability of embankments over stone columns using a limit equilibrium method with a slip circle, in which individual stone column and equivalent area models were analyzed. They concluded that the computed factor of safety from the individual

column method was greater than that from the equivalent area method. This paper presents a series of two-dimensional (2D) finite difference analyses to investigate the factors influencing the FS against deep-seated failure of embankments over stone column-improved soft clay in pseudo-static analysis. The finite difference method incorporated in the software – FLAC/Slope Version 5.0 is designed specifically to perform pseudo-static factor of safety calculations for slope stability analysis. The results of these analyses are summarized into a series of design charts, which can be used in engineering practice.

2. MODEL GEOMETRY

The model consists of an embankment supported by stone columns in soft clay under a two dimensional (2D) plane strain condition. The foundation soil consists of 9 m thick clay overlying 3 m thick sand. Due to the symmetry of the model, half of the cross-section was analyzed using this software. The stone columns were modeled as continuous walls parallel to the centerline of the embankment. The dimensions were selected based on a common practice in the field. These parameters of the baseline case are provided in table [1]. The groundwater table was at the ground surface. An “Exclude” function included in the FLAC/Slope software was adopted to prevent the potential failure surface from entering a 0.4 m thick surficial soil layer on the slope. In real cases the potential failure surface is prevented by Implementation Rip-Rap On the downstream slope.

Table[1] General information of model used in finite difference analysis

Thickness of stone columns	Height of stone columns	Width of fill	Height of fill
0.8 m	9 m	10 m	4 m
Slope of fill	Center to center distance of stone column	Water level	
1V:2.5 H	3 m	12 m	

3. MODEL SIZE AND BOUNDARY CONDITION

In this program the factor of safety is strongly depended on the mesh sizes, therefore the sizes of the model and mesh were determined on the basis of several trials, during which the mesh was progressively refined to 0.5 m and its horizontal boundary was extended such that zones did not influence the development of the failure surface. The size of the mesh is presented in Fig [1]. In the case of boundary condition, the bottom of model fix in two directions and nodes on the two vertical boundaries were fixed against horizontal movement but allowed to move freely in the vertical direction as shown in Fig [2].

4. MATERIAL MODEL AND PARAMETERS

The embankment fill, the foundation soils, and the stone columns were modeled as linearly elastic-perfectly plastic materials with Mohr–Coulomb failure criteria as shown in Fig [3]. The elastic properties have an insignificant effect on

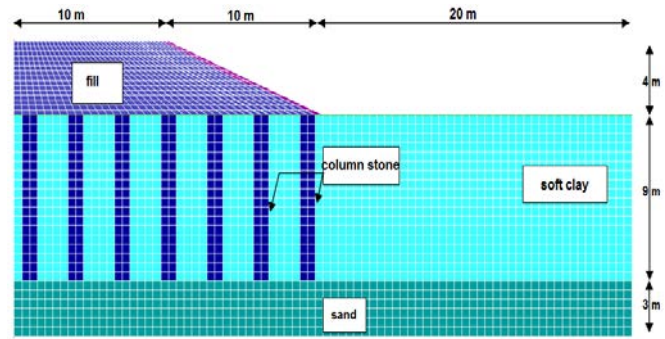


Fig [1]. Finite difference meshes of baseline model

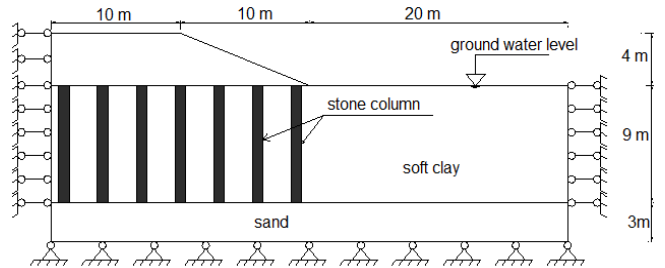


Fig [2]. Cross section of baseline model for the finite difference analysis

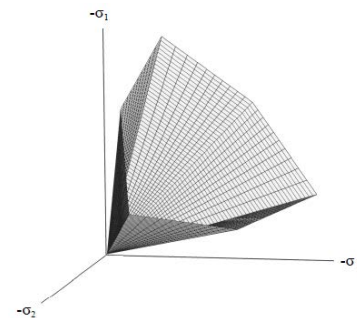


Fig [3] The Mohr–Coulomb yield surface in principal stress space ($c=0$)

the factor of safety calculation and, therefore, these properties are not required by the FLAC/Slope software (Dawson and Roth, 1999). Since soft clay is mostly normally or under-consolidated, it is more critical for an embankment over the soft clay under an undrained condition than under a drained condition [8]. Therefore, undrained cohesion was assumed for the soft clay in this study. The installation of stone columns may change the properties of the soft clay; however, field studies have shown that such property changes are minimum, especially when a wet method is used to install stone columns. Therefore, the change of the properties of soft clay is ignored in this study. Considering stone columns are formed by a cohesionless material, they have zero cohesion and their shear resistance is influenced by pore water pressure. The effect of the ground water on the stability was evaluated in this study. The FLAC software has the option to activate or de-activate the water table. When the water table option is not selected, only the unsaturated unit weight is assigned. When the water table option is selected, however, either unsaturated unit weight and porosity or saturated unit weight must be input.

The saturated unit weight of soil can be calculated as follows [6]:

$$\gamma_{\text{sat}} = \gamma_{\text{unsat}} + n \gamma_w \quad (1)$$

In which γ_{sat} , γ_{unsat} , and γ_w are saturated, unsaturated soil, water unit weights, respectively and 'n' is the porosity of soil. In the case with a ground water table, the soil above the water table was assigned an unsaturated unit weight. The material properties used in the baseline case are shown in Table [2]. Pseudo-static analysis in FLAC/Slope software is done by introducing inclined angle and resultant seismic coefficient in correspondence to different seismic coefficient (0.2g-0.25g-0.3g-0.35g) which exists in Iranian seismic provision (2800).

Table [2] Material properties of the baseline model.

parameter	unit	fill	Soft clay	Stone column	sand
Thickness	m	4	9	9	3
Cohesion	kPa	0	25	0	0
Friction angle	o	34	0	38	30
Unsaturated Unit weight	kN/m ³	17	16	17	19
Porosity	-	0.25	0.25	0.25	0.25

Table [3] Input parameter in FLAC/Slope for pseudo-static analysis.

Parameter	seismic coefficient (0.2)	seismic coefficient (0.25)	seismic coefficient (0.3)	seismic coefficient (0.35)
resultant acceleration (g)	1.02	1.0307	1.044	1.0595
Inclined angle (degree)	11.31	14.0362	16.67	19.29

5. CALCULATION OF SAFETY FACYTOR

In the finite difference program, a shear strength reduction technique was adopted to solve for the factor of safety (FS) value of slope stability. This program uses the shear strength reduction technique in the calculation of safety factor. In this technique a series of trial FS values are used to adjust the cohesion, c, and the friction angle, ϕ , of soil as follows [6]:

$$c_{\text{trial}} = c / FS_{\text{trial}} \quad (2)$$

$$\phi_{\text{trial}} = \arctan(\tan\phi / FS_{\text{trial}}) \quad (3)$$

In the Fig [5] for much understanding, the stages for calculation of safety of factor in FLAC/slope are shown in the following flowchart.

6. DISCUSION AND RESULTS

The parameters listed in abstract influencing the factor of safety against deep seated failure of embankments over stone column-improved soft clay in the pseudo-static analysis were investigated in this study. In the first stage of analysis we show that critical slip surface (maximum shear strain rates) in pseudo-static mode for baseline model in condition of without water and seismic coefficient 0.2 as shown in Fig [6].

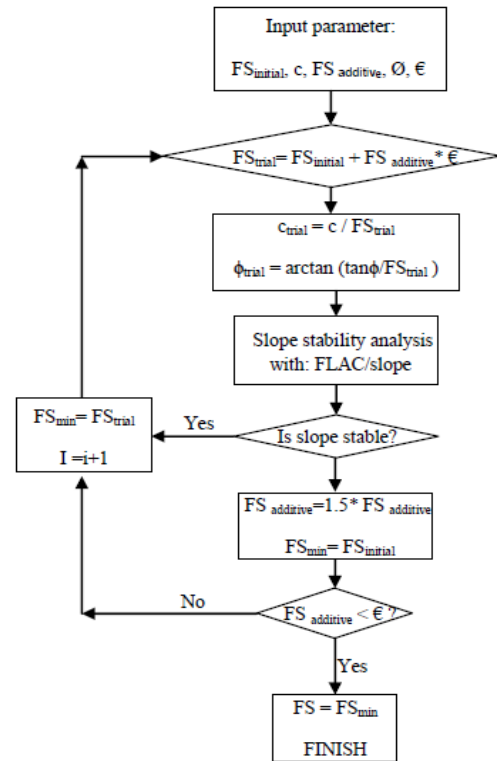


Fig [5]. Flowchart of calculating the factor of safety in FLAC/slope

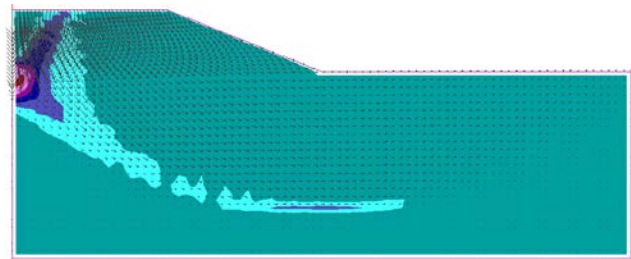


Fig [6]. Critical slip surface without considering the water table in pseudo-static mode (shaded region).

6.1 The influence of the friction angle of stone columns

The influence of the friction angle of the stone column material on the factor of safety of the embankment over stone column-improved soft clay for different seismic coefficient (0.2g-0.25g-0.3g-0.35g) and different friction angle (24-29-34-39) degree with or without water is shown in Fig [7]. The friction angles are selected based on real and applicable project. The results show that the increase of friction angle of stone column material yielded a higher factor of safety for the embankment system in all seismic coefficients. As it is apparent, with the increase in seismic

coefficient the factor of safety decreases considerably. Furthermore, since stone column was modeled as a cohesionless material, which only has a friction angle the consideration of the ground water resulted in lower FS values than that without a water table, because water pressure reduced the shear strength of the stone columns.

6.2 The influence of the spacing of stone columns

The influence of the spacing of stone columns on factor of safety of the embankment over stone column-improved soft clay for different seismic coefficient (0.2g-0.25g-0.3g-0.35g) and different Spacing of stone column (3-6-9-12) meters with or without water is shown in figure 8. The consideration of the water table resulted in lower FS values than that without a water table. As shown in fig [8] the factor of safety in distance between 3-6 meter higher than the other intervals have been changes. Indicates that a proper distance and optimal deployment of stone columns. Since stone columns as the symmetric model since the number of stone columns at intervals 6 and 9 meters is the same. The large reduction in factor of safety was not expected. The factor of safety is increased in height of 9 meters.

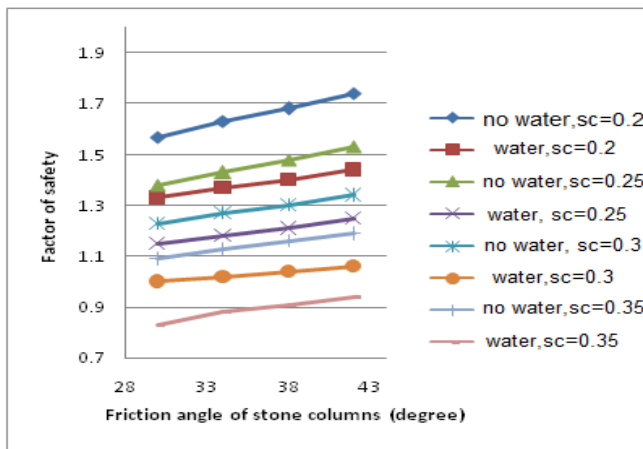


Fig [7]. Influence of friction angle of stone column with different (sc)

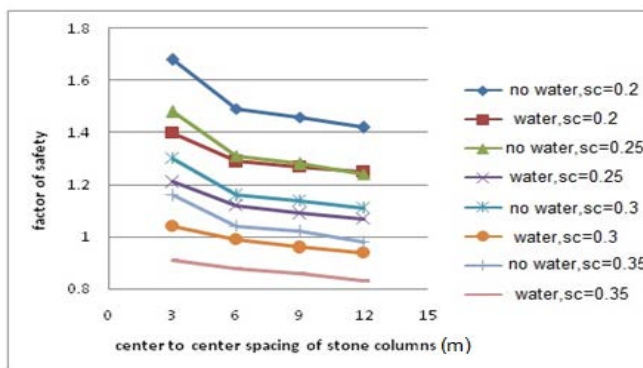


Fig [8]. Influence of spacing of stone columns with different (sc)

6.3 The influence of the height of fill

The influence of the spacing of stone columns on factor of safety of the embankment over stone column-improved soft clay for different seismic coefficient (0.2g-0.25g-0.3g-0.35g) and different the height of fill (2-4-6-8-10) meter with or without water is shown in fig [9]. Obviously, because of increasing slope and weight of fill with increasing height of fill factor of safety is reduced. It is clear that the factor of safety decreased with an increase of the seismic coefficient and height of the embankment. Height of fill will have a great impact on Safety factor.

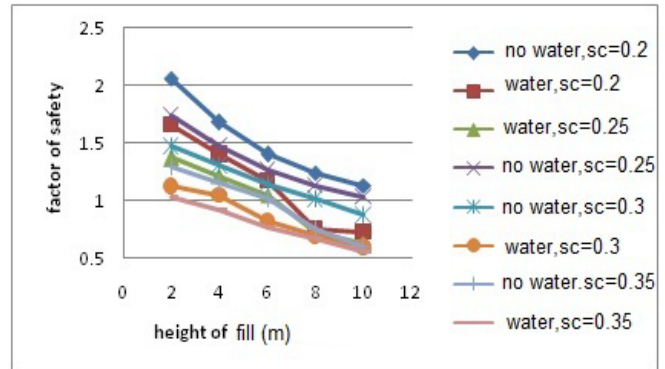


Fig [9]. Influence of height of fill with different (sc)

6.4 The influence of the cohesion of soft clay

The influence of the cohesion of soft clay on the safety factor of the embankment over stone column-improved soft clay for different seismic coefficient (0.2g-0.25g-0.3g-0.35g) and different cohesion of soft clay (15-20-25-30-35) kilopascal with or without water is shown in fig [10]. An increase of the cohesion of the soft clay increased the FS value of the fill over stone columns for all seismic coefficients. Considering Figure effect of the cohesion parameter is greater than the other parameters is discussed.

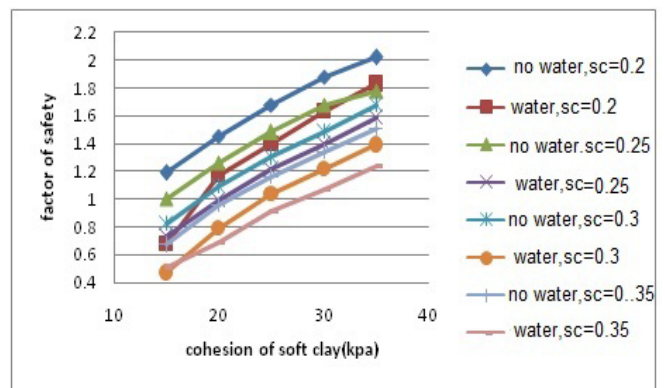


Fig [10]. Influence of cohesion of soft clay with different (sc)

6.5 The influence of the friction angle of fill

The influence of the friction angle of fill on factor of safety of the embankment over stone column-improved soft clay for different seismic coefficient (0.2g-0.25g-0.3g-0.35g) and different the friction angle of fill (24-29-34-39-44) degree

with or without water is shown in fig [11]. It is shown that the benefit of the friction angle of the embankment fill became less significant when the friction angle was higher than 29° , because the slip surface developed was deeper in the improved foundation and the contribution of the foundation became more important. Therefore, foundation-fill ratio of stiffness in applicable cases should be considered.

4.5 The influence of the height of stone columns

The influence of the friction angle of fill on factor of safety of the embankment over stone column-improved soft clay for different seismic coefficient (0.2g-0.25g-0.3g-0.35g) and different the height of stone columns (3-5-7-9) meter with or without water is shown in fig [12]. As shown in fig [11], almost at the height values from 3 to 7 meters, because no pass of failure curve through stone columns is seen little change in factor of safety occurs. In other words, failure curve pass under of stone columns and therefore participation stone columns in factor of safety will be ignored. Also it is clear that the factor of safety decreases with an increase in the seismic coefficient. Consideration of the ground water resulted in lower FS values than that without a water table, because water pressure reduced the shear strength of the stone columns as shown in fig [12]. Fig [12] indicates a proper height and optimal deployment of stone columns in increasing factor of safety can be used.

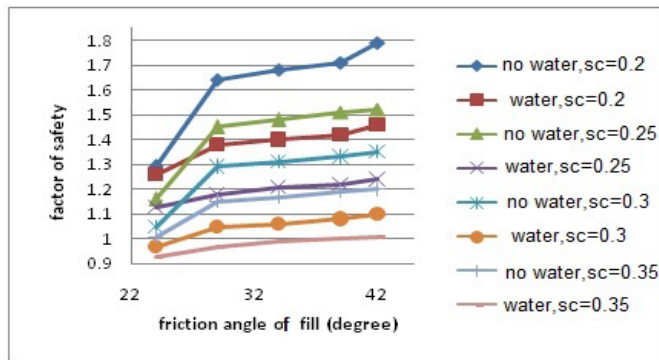


Fig [11]. Influence of height of stone columns with different (sc)

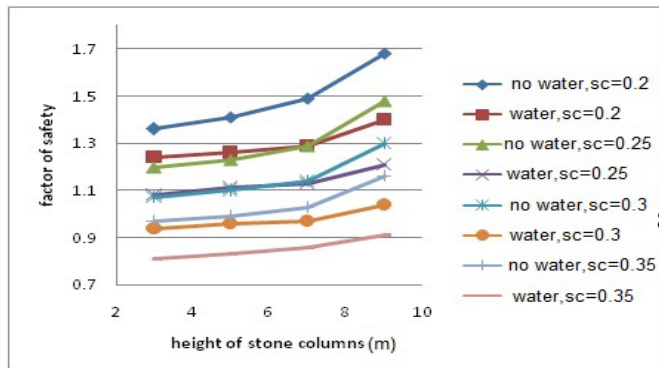


Fig [12]. Influence of friction angle of fill with different (sc)

6.8 The influence of the thickness of stone columns

The influence of the thickness of stone columns on factor of safety of the fill over stone column-improved soft clay for different seismic coefficient (0.2g-0.25g-0.3g-0.35g) and different thickness of stone columns (0.4-0.6-0.8-1.2) meter with or without water is shown in fig [13]. Such as previous items the increase of thickness of stone columns will result increase of safety of factor.

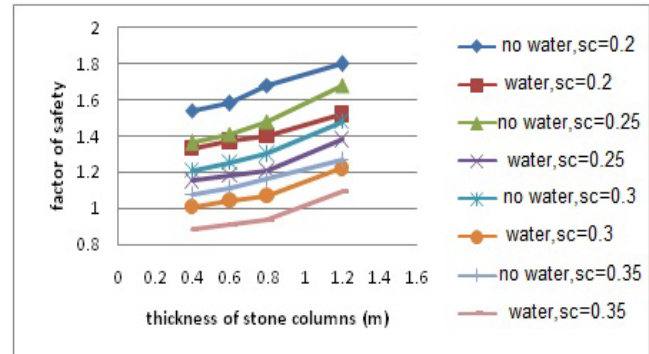


Fig [13]. Influence of thickness of stone columns with different (sc)

7 CONCLUSION

A two-dimensional (2D) finite difference method was performing in this study to evaluate the factor of safety (FS) against deep-seated failure of embankments over stone column-improved soft clay with different values of seismic coefficient (0.2g-0.25g-0.3g-0.35g) correspond to Iranian seismic provision (2800). Based on the numerical results, the following conclusions can be drawn:

1. The results of these analyses are summarized into a series of design charts, which can be used in engineering practice.
2. In all parameter discussed here the consideration of ground water resulted in lower FS values than that without ground water because pore water pressure reduced the frictional shear strength of the improved foundation.
3. In all parameter discussed here the factor of safety decreased with an increase of the seismic coefficient.
4. The increase in soil resistance parameters will not always lead to an increase in factor of safety. For example, with the increase in foundation resistance parameters the critical slip surface is formed within the fill and will not cut the stone columns. Therefore, foundation-fill ratio of stiffness in applicable cases should be considered.
5. According to the charts obtained, the effect of cohesion of soft clay on the increase of safety factor is much more than other parameters which discussed in this study.

8 REFERENCES

- [1] Han, J., Leshchinsky, D. "Stability analyses of geosynthetic-reinforced earth structures using limit equilibrium and numerical methods," in Proc. 8nd Int. Conf. on GEOSYNTHETICS, 2006, pp. 1347–1350.

- [2] Han, J., Sheth, A.R., Porbaha, A., Shen, S.L, “Numerical analysis of embankment stability over deep mixed foundations,” GEOTRANS, 2004, pp. 1385–1394.
- [3] Han, J., Parsons, R.J., Sheth, A.R., Huang, J., “Factors of safety against deep-seated failure of embankments over deep mixed columns,” Proceedings of Deep Mixing Conference, Vol. 1.2, 2005 , pp. 231–236.
- [4] Cheng, Y.M., Lansivaara, T., Wei, W.B., “Two-dimensional slope stability analysis by limit equilibrium and strength reduction methods,” J. of Computers and Geotechnics, vol 34, 2007, pp. 137–150.
- [5] Han, J., Hong, Z.S., Shen, S.L, “ Stability of levees over soft soil improved by deep mixing technology,” GEOCONGRESS ASCE ,2008, pp. 716–723.
- [6] Itasca Consulting Group, Inc., 2006. FLAC/Slope User's Guide, Version 5.0. 84.
- [7] Cala, M., Flisiak, J.,(2001), “Slope stability analysis with FLAC and limit equilibrium methods,” In: Bilaux, Rachez, Detournay, Hart (Eds.), FLAC and Numerical Modelling in Geomechanics. A.A. Balkema Publishers, pp. 111–114.
- [8] Cooper, M.R., Rose, A.N, “Stone column support for an embankment on deep alluvial soils,”. Proceedings of the Institution of Civil Engineers, Geotechnical Engineering vol 37, 1999, pp. 15–25.

Parametric Study of Geo-grid Soil Reinforced Retaining Walls under Dynamic Loading by ABAQUS Software

Prof.Atrchian Mohammad Reza¹, Prof.Daghigh Younes² Mr.Ghanbari Namin Hamed³

Islamic Azad University of Zanjan, Iran

ABSTRACT

Observation of reinforced soil retaining walls with geosynthetics system, after earthquake and laboratory studies indicate the suitable inflection behavior of these walls. For better understanding of these kind of structures under dynamic loads, in this research, at first we use finite element method (FEM) software (Abaqus) for numerical modeling of reinforced soil retaining walls under earthquake. At this phase, in order for testing and comparison of the software, results of a similar sample with small scale in shake table test, which was implemented in 2005, is compared with the results of test and analysis by the software. After correcting the model and making sure of the software's accuracy, models of several reinforced soil retaining walls with geosynthetics of 10 meter height and variable length and distance of geogrid layers are provided and dynamic analysis is performed on them. Harmonic equivalent load is used for earthquake acceleration in dynamic analysis. After implementing the analysis, by concentrating on the forces in the geosynthetics, diagrams of vertical variable displacement on soil and wall are prepared that include soil subsidence, horizontal displacement or walls bulging. Research is implemented parametrically and by studying the effects of length increase and geogrid layers spacing on displacement and results are obtained on this basis.

Keywords: Retaining walls; Reinforced soil; Earthquake; Geo-grid; Finite element method (FEM).

1. INTRODUCTION

Reinforced soil retaining walls on land areas that have nonstable and weak slopes with weak bedding makes it possible to build stable and flexible structures against shaking loads (earthquake) with increasing load bearing capacity. This results in decrease of the structures subsidence, falling, creep and swelling capability and increase of safety factor and improvement of shear strength parameters of soil [1]. Soil has a good resistance against stress and with reinforcing Geogrid that have a high tensile capacity with facing as a protective soil between Geogrid layers, it results in a stable system. Friction between soil particles and Geogrid results in a cohesion strength that has a direct relationship with Geogrid tensile resistance [2].

Points mentioned below are considered as the most important criteria to choose components of reinforced soil retaining walls:

1.1. Criteria to choose embankment: Soil that is used in this system must be conforming with the criteria and related standard in terms of optimum moisture and aggregate gradation so that the required friction between soil and reinforcement is ensured. Two kinds of criteria for these system are proposed:

a) Chemical and electrochemical criteria to prevent corrosion of the reinforcement such as limitation of chlorosulfate purity, PH limitation, and amount of organic material in soil.

1. Professor, Islamic Azad University of Zanjan, Iran, Dr.atre@yahoo.com

2. Professor, Islamic Azad University of Karaj, Keyhan khak Co. (prt)Ltd, Daghigh_y@yahoo.com

3. Geotechnical student, Islamic Azad University of Zanjan, Iran, Hghanbarinamin@yahoo.com

b) Geotechnical criteria such as prevention of vacuolate pressure and condensation of soil in horizontal layers.

1.2.criteria to choose the reinforcement: Geosynthetics alike artificial textiles are made from polymeric material such as polyethylene and polypropylene and include Geotextil, Geogrid, Geomembranes, and Geocomposits and ... and are employed as reinforcement, separation, filtration, drainage and moisture barrier.

In this research, the purpose of utilization is reinforcement. Therefore, use of Geogrids in which are only applied for the purpose of reinforcement is proposed. choosing reinforcement spaces and length of them is implemented with calculation of the inner stability of the buildings. Resistance of the reinforcement against strain and it's flexibility are the main factors of endurance.

1.3.criteria to choose facing: rigid facing are usually utilized for permanent reinforced soil structures for persistence of better appear are and ease of construction. Based on laboratory and field investigations, facing rigidity in total local state can help us in decreasing shape change while increasing structure resistance. These facing differ in term of shape, type, and profile[4] :

a) Wrapped Around Facing

b) Modular concrete blocks Facing

c) Pre-cast concrete Panels Facing

d) Gabions Facing

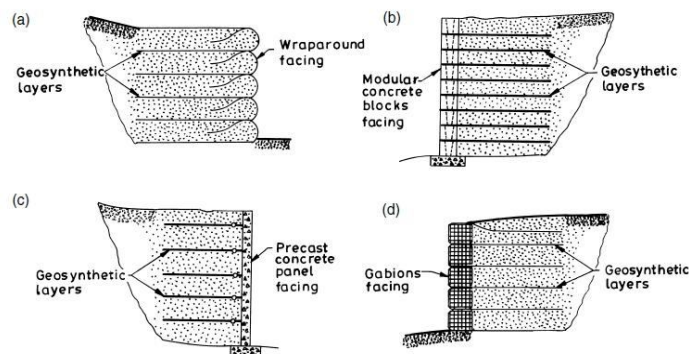


Fig.1: facing of shape, type, and profile

2. DYNAMIC STABILITY AND LITERATURE REVIEW

2.1 Dynamic stability

When earthquake occurs, seismic waves move from very deep depths of the earth to the surface and cause vibrations. The intensity and durability of this vibration is related to the intensity and magnitude of the earthquake and the environment characteristics. These waves face the decrease or increase in domain in different layers of the earth and depreciate the vibration in a specific frequency while resonate it in another frequency. This behavior is due to different characteristics of these layers and filtering behavior of them. Generally, soil slopes fracture is due to gravity effect on a mass of material that can be slid gradually and move down on an individual layer. This movement is either minor and related to failing of a few stones, or major in a vast area and cause serious damage on the infrastructure. Increasing the slope height by filling on the slope and cutting near the toe will increase instability of the slope. Owing to these changes (increasing the height and angle) thrust will increase and tangential component of thrust (shear stress in the slip surface) in the fracture surface that is one of the instability reasons will cause the mass to move down. Another reason of increasing the shear stress along the potential fracture surface is increasing

the weight of the soil zone. This pressure increment can be due to more urban construction on the slope or due to natural reasons such as falling upper slippery zones. In all cases shear stress will increase and soil zone will be instable along potential surfaces. Also, making vibration either natural or artificial will increase the shear stress along the potential fracture surfaces. During the earthquake and at the time of earth vibration, the spread waves in the soil zone change the level of forces and cause the fracture of the soil (along the weak surfaces) that is under the cyclic load and do not resist against stresses [3].

2.2 literature review

During the past years, lots of experimental research is performed to investigate the seismic performance of these soil walls by employing shaking tables and centrifuges. Richardson and Lee (1975) performed the first experimental investigation in this field. They modeled reinforced soil walls and introduced the first design criteria according to limit equilibrium method to calculate reinforced soil walls. In summary, Sakaguchi (1996), Matsu et al. (1998), Koseki et al. (1998), Siddharthan et al. (2004) and Ling et al. (2005) investigated these walls under seismic loads. Bathurst and Cai (2002) performed a quasi-static investigation on a wall that was reinforced with Geogrid and was subjected to Northridge earthquake. They found that these walls have suitable safety factors in the case of various fracture conditions. Ghalandarzadeh and Mirlatifi (2003) performed some shaking table experiments on the reinforced Geogrid walls. Then, Ghalandarzadeh and SaberMahani (2008) did a series of shaking table experiment to investigate the mode shapes and seismic response of these walls [5].

3. MATERIAL PROPERTIES AND MODEL CONSTRUCTION IN ABAQUS SOFTWARE

One of the most important parameters in the lateral soil pressure on the reinforced soil walls is the soil shear strength parameters. For the embankment material, Mohr-Coulomb (elastoplastic) model and drained behavioral are used (Table 1):

Table 1. Embankment and bed soil parameters used in the modeling

soil parameters modeling zone	Soil unit weight above g.w.l	Soil unit weight below g.w.l	(Kx)	(Ky)	Young's modulus (Eref)	Poisson's ratio (ν)	Cohesion (Cref)	Friction angle (ϕ)	Dilation angle (ψ)	Unified name
Embankment	17	18	1	1	2.5E+4	0.3	10	30	0	SW-SM
bed soil	19	20	0.413	0.413	3E+4	0.3	30	28	0	SC

In order to model, a wall with $H=10\text{m}$, $\theta=90$ (angle with horizontal), $\nu=0.2$ and continues concrete surface and a Geogrid made of Polyethylene, covered with PVC, meshed and with an axial stiffness of 3200, 2200, 1200 KN/m are considered [6].

In the case of Geotechnical modeling, usually the considered zone is big enough to be assumed infinite in calculations. Existence of any virtual boundary in these problems will cause the return of introduced waves into the calculation area after encounter to these boundaries. However, in reality, these waves can distribute in the infinite environment and be absorbed and do not return to the calculation environment. The method that is used in the program is introducing absorbing boundaries in the boundary reasons to almost completely absorb the entrance volume wave energy and prevent reflection.

After modifying the model under the name of Verification and Calibration with a similar experimental model, we build the model and perform sensitivity analysis of mesh changes and model dimensions. In the case of meshing, the average value is related to the condition that mesh size is fine. In the case of mode dimensions, all models are under the gravity load in such a way that the soil is slipped and slip cycle can be observed. According to the output of various models when the depth of the considered zone around the wall has a minimum depth equal to the height of

the wall, stress and strain calculations can be performed without any limitation. Fig.2 shows the constructed model of the reinforced Geogrid wall. In order to parametrically investigate the Geogrids' dimensions, their length is named(a) and vertical distance of Geogrids is considered as (b):

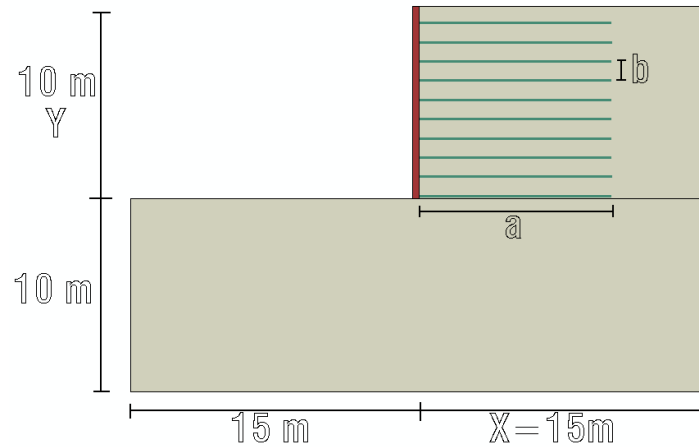


Fig.2: constructed model of the reinforced Geogrid wall

4.DYNAMIC ANALYSIS IN TERMS OF PARAMETRIC COMPARISON OF LENGTH AND VERTICAL DISTANCE OF GEOGRID IN ABAQUS

In order to investigate the effect of reinforcement on retaining walls, several different models are introduced. To determine the longitudinal parameter (e.g. a) the length of Geogrid is considered as 5.5 meters and is increased with 1.5 meters increments to 13 meters that is 2 meters less than supporting soil. Having 6 models, the minimum altitudinal parameter (e.g. b) of Geogrids are considered as 0.5 meter and is increased with 0.3 meter increments to 2 meters forming 6 more models. Totally 36 models (w1-w36) are considered in this study.

In this study dynamic analysis is performed using equivalent cyclic load of each record with a period that is defined in the seed graph for different magnitude in a distance less than 40 kilometers of the source fault. Since the most suitable method to investigate the vibration characteristics of earthquake is to change vibration movements from time domain to frequency domain using Fourier series, the frequency limit of the biggest accelerogram energy can be determined by studying the earthquake records and Fourier spectrum. Using this Information, the rate and the pattern of energy distribution in each record can be found. Also, another important application of Fourier domain spectrum of an earthquake is determining the excited vibration modes of a structure. This spectrum is employed to analyze the structure that is subjected to the earthquake, determine the effective modes of the structure and calculate structural response with an acceptable accuracy. Frequencies and damping of different modes in each step can be calculated for the whole structure by subjecting a selected degree of freedom to the earthquake and finding the response of that degree of freedom [7]. To calculate the equivalent number and amount of accelerograms SeismoSignal software is employed where earthquake accelerogram is the input and frequency is the output. Northridge earthquake happened in California State of USA in 1994 and caused severe damages. The acceleration of this earthquake in X direction is shown in fig.3 and fig.4 shows the output of SeismoSignal that is an equivalent harmonic (sinusoidal) load. In order to perform dynamic analysis and parametric investigation, the acceleration of the harmonic load is applied to the base point of the model as a horizontal component. This acceleration is applied to the system when it is in the static equilibrium. The considered acceleration for this wall is a wave with variable amplitude and the mathematical equilibrium of it is presented as:

$$\ddot{u} = \sqrt{\beta e^{\alpha t} \xi} \sin(2\pi f t) \quad (1)$$

Where $\alpha=5.5$, $\beta=55$ and $\xi=12$ are constant values. f is the frequency acceleration and t is the dynamic analysis time. The selected frequency is around the natural frequency of the system.

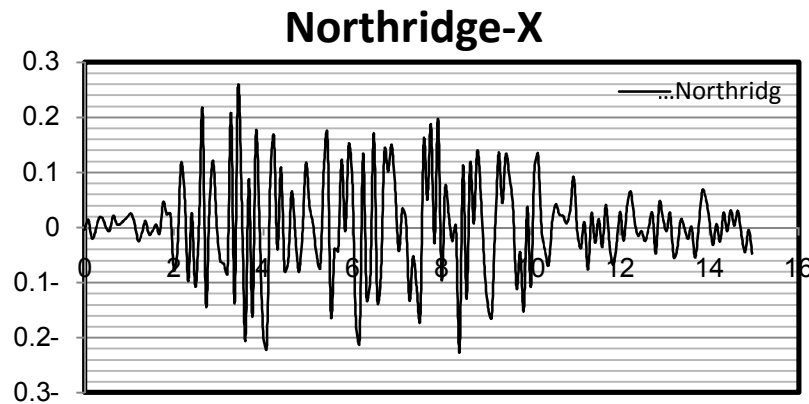


Fig.3- Northridge accelerogram in the X direction and in 14.96 seconds

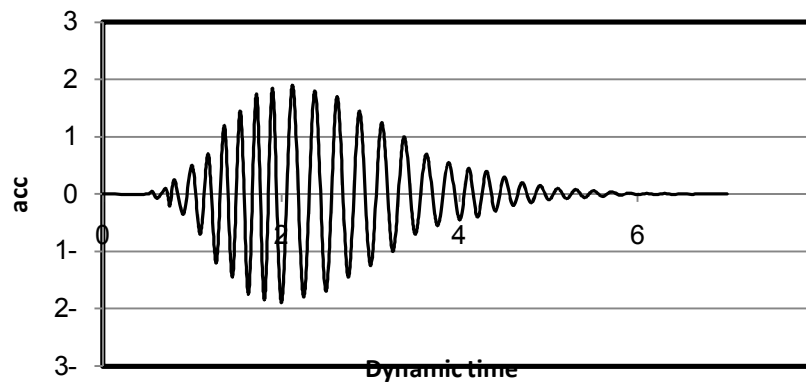


Fig.4- Subjected accelerogram to the retaining wall

The accelerogram presented in fig.4 is applied to the retaining wall and the wall displacement according to its height is the output of the models. The accelerogram is applied to the base points that are connected to the earth and the end point that is connected to the earth is restrained in the Y direction and the accelerogram is applied in the X direction.

After applying the load to W1 model (a geogrid wall with a length of 5.5 meters and a vertical distance of 0.5 meter), as it was predicted the vibration cycle is formed on the soil and the maximum settlement is 18 cm and is shown in the red part of fig.5.

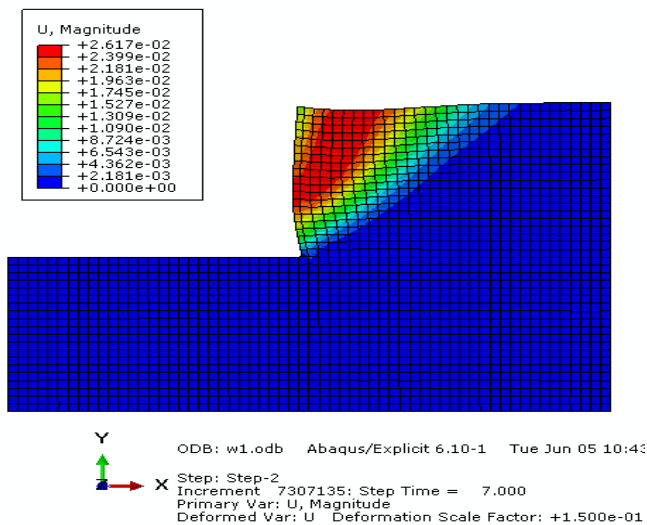
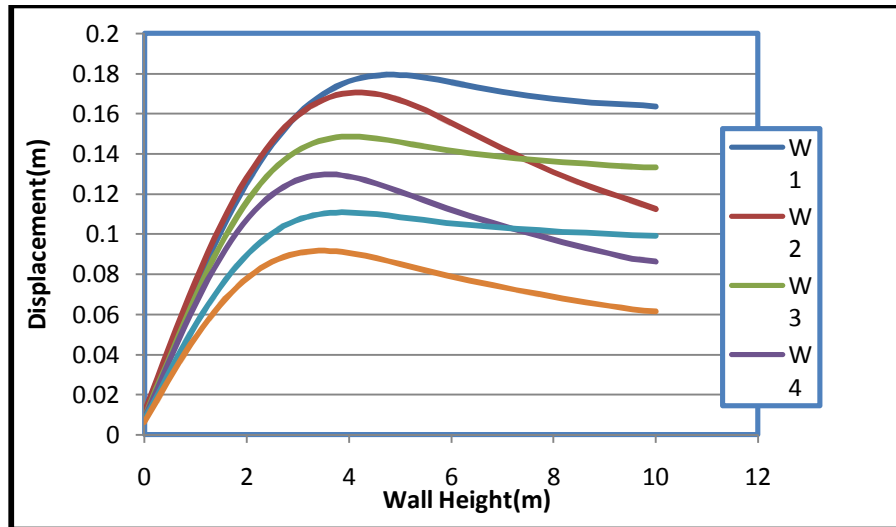
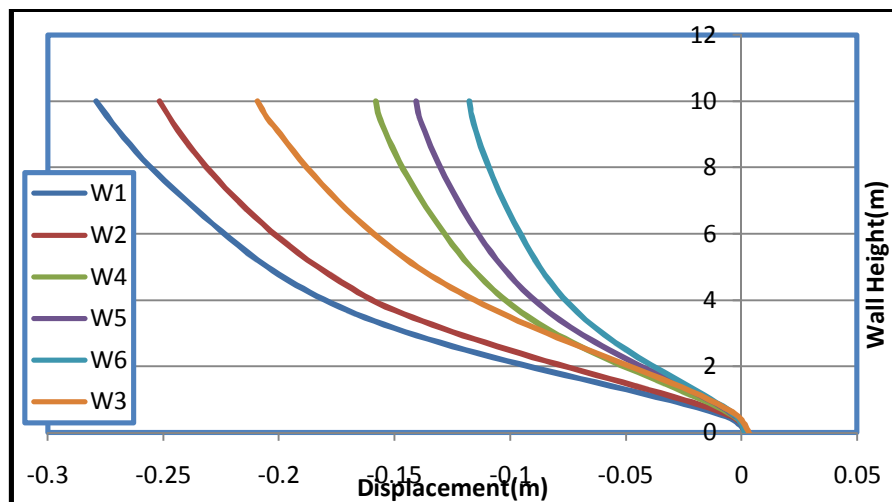


Fig.5- Total displacement contour

As it is shown in fig.5, the soil behind the wall is vibrated and the maximum horizontal displacement is approximately in the middle height of the wall. This will cause a deflection bluging at the center of the wall. In order to investigate the effect of the Geogrid's length on the wall's stability, the models with the same distance and variable length of Geogrid is compared. For this purpose models 1 to 6 are compared. The horizontal and vertical displacements of these models are compared and the results are presented in graphs 1 and 2 in terms of the vertical and horizontal displacements versus the height from the wall's base.



Graph 1-horizontal displacement versus the height from the wall's base for models w1 to w6



Graph 2- vertical displacement versus the height from the wall's base for models w1 to w6

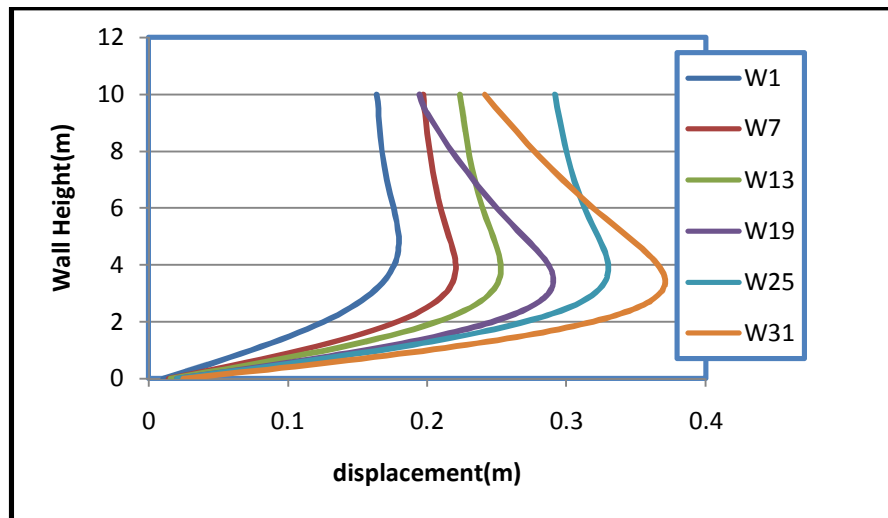
As it can be seen from graphs 1 and 2, model w1 has the biggest displacement in both vertical and horizontal direction while w6 has the lowest displacement. W1 is moved 18 cm in horizontal and 28 cm in vertical direction while these displacements are 9 and 12 cm for w6 that is showing about 50 and 57 percent reduction.

According to the above graphs it can be concluded that in the models with the same vertical distance (e.g. w1 to w6), the horizontal displacement's difference is very low; however, vertical displacements are showing a big difference. This means that the length of Geogrid has more effect on the vertical displacement. The horizontal displacement of the wall and vertical settlements are shown in Table 2.

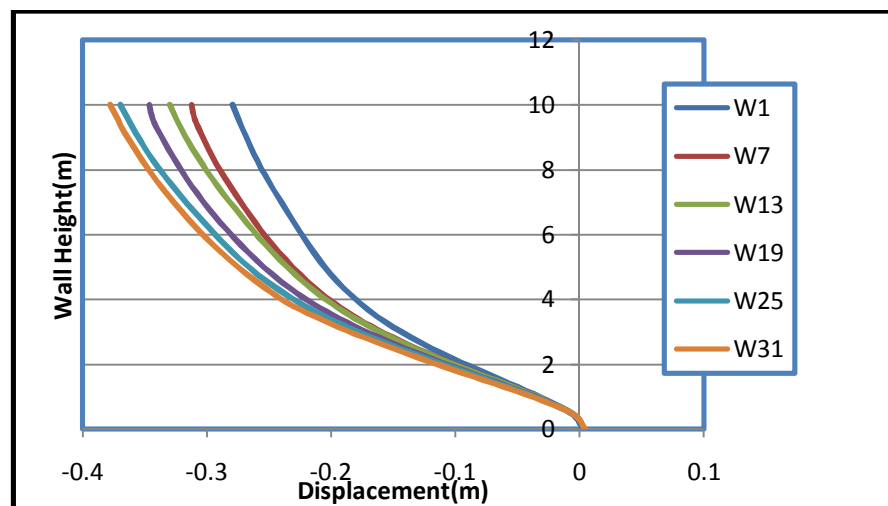
Table 2- Horizontal and vertical displacements in the investigated models

Uy(cm)	Ux(cm)	model	Uy(cm)	Ux(cm)	model	Uy(cm)	Ux(cm)	model
37	33	W25	33	25	W13	28	18	W1
31	30	W26	28	24	W14	25	17	W2
27	28	W27	24	22	W15	21	15	W3
23	25	W28	18	19	W16	16	13	W4
22	23	W29	16	17	W17	14	11	W5
21	21	W30	15	15	W18	12	9	W6
38	37	W31	35	29	W19	31	22	W7
33	33	W32	30	27	W20	27	20	W8
29	31	W33	25	25	W21	23	18	W9
26	28	W34	20	22	W22	18	15	W10
25	27	W35	19	20	W23	15	13	W11
23	25	W36	18	18	W24	14	12	W12

Graphs 3 and 4 are presenting horizontal and vertical displacements for models w1, w7, w13, w19, w25 and w31 where Geogrid length is the same but different distances between Geogrids are considered.



Graph 3-horizontal displacement versus the height from the wall's base for models w1, w7, w13, w19, w25 and w31



Graph 4- vertical displacement versus the height from the wall's base for models w1, w7, w13, w19, w25 and w31

As it can be seen from the mentioned models that have Geogrids of the same length and different distances , horizontal displacements have a significant difference compared with each other. In model w1 with Geogrid length of 5.5 m and vertical distance of 0.5 m the horizontal displacement is about 18 cm while in model w31 with the same Geogrid length and vertical distance of 2 m the horizontal displacement is 37 cm that is two times (51%) more than w1; this difference is about 10 cm (e.g. 26 %) for vertical displacement. This shows that the effect of Geogrid's length on the vertical displacements and the effect of Geogrids' distances on horizontal displacement are more.

5. CONCLUSION

After applying the dynamic load to the models, the following conclusions can be drawn:

- [1]. The soil walls reinforced with Geogrid have special characteristics; having enough strength, they are flexible and therefore more suitable for the regions with higher risk of earthquake and weaker bed.
- [2]. By introducing some changes in the length and distance of the reinforcement layers and also by duplicating the reinforcement layers in the sections with the maximum force, an optimum design can be achieved. Using this optimum design the structure will be economical, more stable, have a better performance and need less construction time.
- [3]. Frequencies and damping of different modes in each step can be calculated for the whole structure by subjecting a selected degree of freedom to the earthquake and finding the response of that degree of freedom. The frequency of the first 10 modes is calculated and is 3.71, 4.06 and 5.1 for the first, second and third modes.
- [4]. To have an accurate investigation and analysis, first of all, a sensitive analysis is needed to be done on the dimensions and the kind of mesh size. After performing the sensitive analysis, a depth of the foundation equal to the wall's height and a height of the soil behind the wall equal to 1.5 times of the wall's height are found to be suitable.
- [5]. The vibration cycle is formed on the back of the wall for all models; the total transformation nature is constant and in the form of vibration cycle and only the displacements amount change. The maximum horizontal displacement is approximately in the middle height of the wall and the maximum vertical displacement (settlement) occurs at the top of the soil behind the wall.
- [6]. The change in the vertical distance between Geogrid layers changes the relative horizontal displacements and settlements. Although increasing the vertical distance of Geogrids increases the vertical displacements, but according to the introduced graphs, it can be concluded that the effect of vertical Geogrids on the horizontal displacements is significantly more. Therefore, it is better to change the distance parameter of the Geogrids to control the horizontal displacement.
- [7]. Although increasing the length of Geogrids is efficient to increase the horizontal displacements and have a direct relation with it, but the effect of Geogrid layers length on the vertical displacements and soil settlements is more. So, in cases that the soil settlement is of crucial importance, in order to control the vertical displacement of the retaining walls, the effective parameter is the length of Geogrids.

6. ACKNOWLEDGEMENT

The authors would like to express sincere gratitude to prof.daghigh younes,Keyhan Khak Co. (prt)Ltd, for the cooperation and advice.

7. REFERENCES

- [1]. Shafabakhsh, Gh., 2005. "Reinforcing embankment and the bed of the roads using Geogrids", Education, Research and Technology Coordination, Transportation Group, Road and Urban Development Ministry.
- [2]. Vafaei, R., Aliari, H., and Hamidi, H., 2008. "Stabilizing analysis of trenches using Geogrids", Faculty of Engineering, Azad University of Tabriz.
- [3]. Mirlatif, A.R., Fakher, A., Ghalandarzadeh, A., 2009. "Reinforced soil walls' deflection investigation under earthquake", Engineering Faculties, University of Tehran.
- [4]. Vidal, H. 1966 "La Therre Armee Annles Inst ". Tech. Du. Batim. Suppl. Vol 2, No. 223-224
- [5]. Richardson, G.N. and Lee, K.L. (1975). "Seismic Design of Reinforced Earth Wall", Jol. Of Geotechnical Engineering, Vol. 101, NO. 2, PP. 167-188.
- [6]. ASTM Standard American Society For Testing and Materials, West Conshohocken, PA, USA.
- [7]. Keefer, D.K., Wilson, J.P., Youd, T.L. 1985 "Predicting Areal Limits of Earthquake-Induced Landsliding", U.S. Geological Survey, Reston, Virginia, Professional Paper PP. 317-345.

Sensitivity analysis in soil nail wall for Tehran-Tabriz railway by considering the coefficient of variation for effective parameters in stability analysis

Mohammad Moghadaripour¹, Ardalan Akbari Hamed², Ali Ghozat³

1. International Institute of Seismology and Earthquake Engineering, Tehran, I.R. Iran

2. Islamic Azad University, Central Tehran Branch, Tehran, I.R. Iran

3. Shiraz University, Shiraz, I.R. Iran

Abstract:

The construction operations of the underground section of the Tehran-Tabriz railroad executed by cut and cover tunneling method. But Due to the far distance of piles in some parts, vertical soil nail wall was used as the support of excavation system. This paper presents the sensitivity analysis of this supported wall. The effect of uncertainties has been studied through the investigation of changes by means of coefficient of variation (COV) of effective parameters such as cohesion, friction angle, and specific gravity on factor of safety. The computational results show that Some parameters are very sensitive to the changes of COV and some of them are not. Moreover, as the data scattered is more the dispersion in factor of safety is also more.

Keywords: Sensitivity analysis, Soil nailed wall, Monte Carlo simulation , Uncertainty

1.Introduction:

The construction operations of the underground section of the Tehran-Tabriz railroad to the length of 4,165 meters in district 17 and 18 of Tehran commenced on August 5th 2008 by cut and cover tunneling method. This new railroad will enable more efficient, reliable, and environmentally safe travel.

Briefly the construction stages of project consist of the following steps:

Step 1 : Installation of excavation support/tunnel structural walls (pile walls)

Step 2: Construction and waterproofing of the tunnel top slab tying it to the support of excavation walls

Step 3: Excavation of tunnel interior

Step 4: Construction of the tunnel floor slab

Due to the far distance of piles in some parts, vertical soil nail wall was used as the support of excavation system. The soil nail wall was regularly shaped and reached total heights up to 10 meters. Tight excavation requirements were defined for the project due to the location of the building, requiring fairly precise wall positions and shotcrete tolerances.

Soil nailing is a technique used to reinforce and strengthen existing slopes. Soil is a poor structural material because it is weak in tension, whilst Steel is strong. The fundamental concept of soil nailing is that soil can be effectively reinforced by

installing closely spaced grouted steel bars, called “nails” into a slope or excavation as construction proceeds from the top to down. Nails are commonly referred to as “passive” inclusions. The nail bars are forced into tension as the ground deforms laterally in response to the loss of support caused by continued excavation. The grouted nails increase the shear strength of the overall soil mass and limit displacement during and after excavation. A structural facing connected to the nails is used when the slope angle exceeds a predetermined critical value or when environmental conditions would cause deterioration of the exposed soil face over its design life [1].

For uncertainty analysis, there should be some requirements like data collection, model selection, assessing the uncertainty in the selected model and its significant characteristics, and a verification of assumptions made. The evaluation of the data sets needs recognition of the type of the uncertainties, whether the variables are dependent or independent, whether the observations are independent and whether uncertainties noted are the result of a combination of uncertainties in underlying parameters and proceeds.

The uncertainties associated with a geotechnical problem can be divided into two categories:

Aleatory and epistemic. Human errors and omissions, which are not covered herein, would fall into a third category. Within a nominally uniform

geological layer, the soil properties can be affected by both aleatory and epistemic uncertainties[2]:

- Aleatory uncertainty represents the natural randomness of a variable. Examples of aleatory uncertainty are the spatial variation of a soil parameter within a nominally uniform geological layer, the variation in the peak acceleration of a design earthquake with a given return period, the variation in the ocean wave height or wind force, and so on. The aleatory uncertainty is also called the inherent uncertainty. Aleatory uncertainty cannot be reduced or eliminated.
- Epistemic uncertainty represents the uncertainty due to lack of knowledge on a variable. Epistemic uncertainty includes measurement uncertainty, statistical uncertainty (due to limited information), and model uncertainty. Statistical uncertainty is due to limited information such as limited number of observations. Measurement uncertainty is due to for example imperfections of an instrument or of a method to register a quantity. Model uncertainty is due to idealizations made in the physical formulation of the problem. Epistemic uncertainty can be reduced, and perhaps eliminated, by collecting more data and information, improving the calculation methods.

The uncertainty sources have been introduced above. The problem of soil nailed wall also includes most of the mentioned uncertainties; hence selection of the efficacious data might be difficult and in practice the calculation will be performed by considering the critical condition. In order to provide an accurate modeling in slope stability problem, exact observation must be done. In this research for identifying the sensitive parameters, the effect of scattering in input data in analysis has been considered. In other words, the influence of scattering in input data on safety factor will be taking into account. As the result, Sensitive parameters and their effects in the design of soil nail wall will be introduced.

2. Sensitivity analysis

In problems with several uncertain parameters, it would be useful to know which parameters have tangible effect in the result of the slope stability and which do not have. A sensitivity analysis is performed to identify how each variable will change the result. In this approach, typically each variable in the problem is changed, and then the changes in the final result are observed.

The procedure of sensitivity analysis is as follows:

1- Choosing input parameters which seem to be sensitive in analysis. Soil strength parameters including cohesion (C) and friction angle (ϕ), specific gravity and seismic pseudo static coefficient (k_h) are taken into account as input parameters. The k_h is defined as fraction of the normalized horizontal acceleration (A_m), which acts at the center of gravity of the wall-soil mass (AASHTO, 1996). A_m is a function of the normalized peak ground acceleration coefficient (A), which is the actual peak ground acceleration normalized by the acceleration of gravity (g), and is defined as[3]:

$$A_m = A (1.45 - A) \quad (1)$$

2- The effect of uncertainties has been studied through the investigation of changes by means of coefficient of variation (COV) of the aforementioned parameters. The complete definition of COV will explain in part 4 (problem analysis). The COV of each parameter in the problem will change while other parameters are considered constant. For example the friction angle (ϕ) of the first layer is 5 degrees (see table I) and the coefficient of variation for this parameter has been chosen as 4, 8 and 12% (the process of selecting these COV will explain later). For any selected COV, 2000 random samplings were carried out. Every sampling concluded to a special safety factor (F.S); therefore 2000 safety factors will be elicited. Then the COV of these safety factors will be calculated and the trend of F.S changes is observable for this parameter in first layer.

3- This procedure will be carried out for all remained parameters to discern the trend of F.S changes.

3. Tehran Tabriz soil nail wall

The soil nailed wall has a depth of 10 m. The properties of the soil layers are presented in Table I. The model used in analysis was Mohr–Coulomb model. Fig. 1 illustrates a profile of the soil nailed wall.

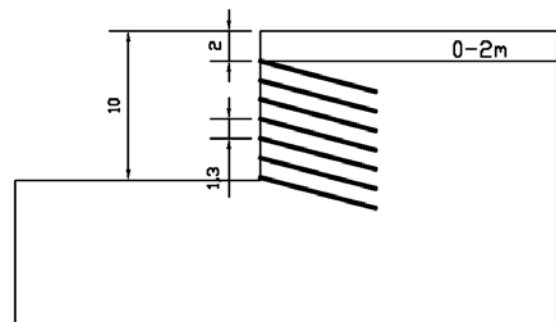


Fig. 1 Profile of soil nailed wall with depth of 10m

Table I. Geotechnical properties of excavation

Thickness of layer	Specific gravity(KN/m^3)	Friction angle	Cohesion (KN/m^2)
--------------------	-------------------------------------	----------------	------------------------------

(m)		(°)	
0-2	20	25	5
2-10	20	29	30

The stability analysis was carried out using GEOSTUDIO-W/SLOPE which is based on the Morgenstern-Price method. Recommendations for the minimum factor of safety for pull out resistance and nail bar tensile strength are set at 2 and 1.8 respectively [3]. Table II presents Characteristics of nails used in the designed excavation.

Table II. Characteristics of nails used in the designed excavation

No.	Horizontal distance (m)	vertical distance (m)	Length (m)	Diameter (mm)
1	1.5	2	8	25
2	1.5	1.3	8	25
3	1.5	1.3	8	25
4	1.5	1.3	8	25
5	1.5	1.3	8	28
6	1.5	1.3	8	28
7	1.5	1.3	8	28

4. Problem analysis through considering the coefficient of variation for effective parameters in stability analysis

In the current paper, In order to get better calculation parameters for slope stability analysis, as well as provide a better theoretical basis for slope design and reinforcement, the effect of uncertainties has been applied through the investigation of changes by means of coefficient of variation (COV) for effective parameters such as cohesion, friction angle, and specific gravity. The (COV) represents a relative and dimensionless measure of dispersion and is expressed as:

$$COV = \frac{\sigma_x}{\mu_x} \times 100\% \quad (2)$$

Where μ is average and σ is standard deviation of the selected parameter.

The COV has been commonly used to describe the variation of many geotechnical soil properties and insitu test parameters. Note that the mean, standard deviation and COV are interdependent - knowing any two will give the third. In practice, it becomes convenient to estimate moments of geotechnical soil parameters where little data are available (sparse data) by assuming that the COV is similar to previously measured values from other data sets

of the same parameter. A summary of the COV values reported in the literature is presented in Table III [4].

Table III. The range of COV reported in literature (%) [4]

Soil properties	Cohesion	Specific gravity	friction angle
COV (%)	30-45	5-15	4-12

The location of the soil nailed wall project is in Tehran. The seismic acceleration of this region is 0.35g; so the average of pseudo static acceleration coefficient is calculated as follows [3]:

$$A_M = 0.35 * (1.45 - 0.35) = 0.385 \quad (4)$$

$$k_h = 0.5 A_M = 0.385 * 0.5 = 0.19 \quad (5)$$

According to the seismic hazard research report, the coefficient of variation (COV) for the pseudo static acceleration coefficient was considered as 25% to 35%.

Based on the sensitivity analysis steps mentioned in part 2, the trend of changes in (COV) for F.S against effective parameters are achieved (see fig. 2 to 4).

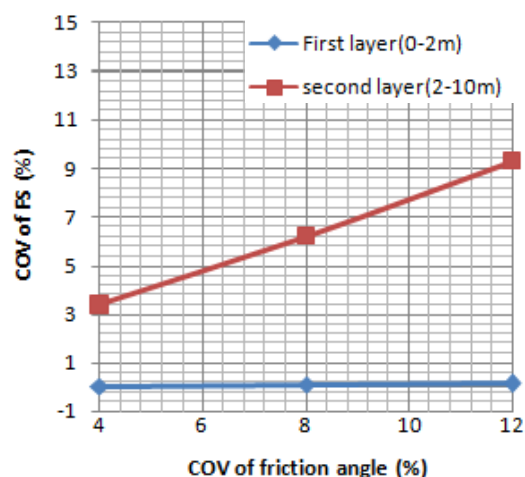


Fig. 2 Effect of friction angle variation on safety factor

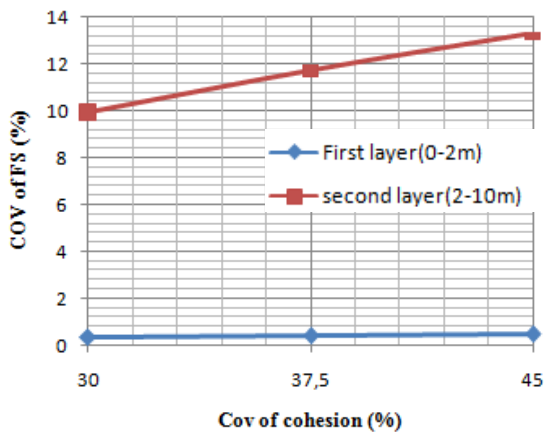


Fig. 3 Effect of cohesion variation on safety factor

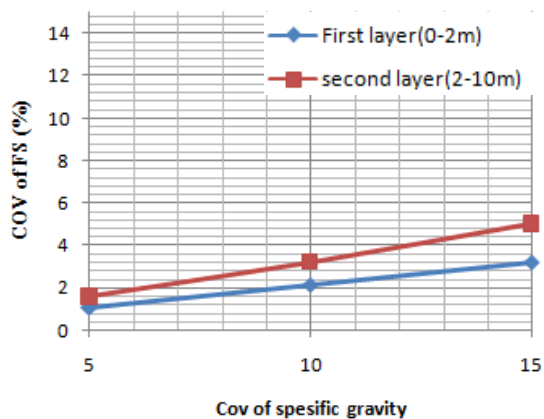


Fig. 4 Effect of specific gravity variation on safety factor

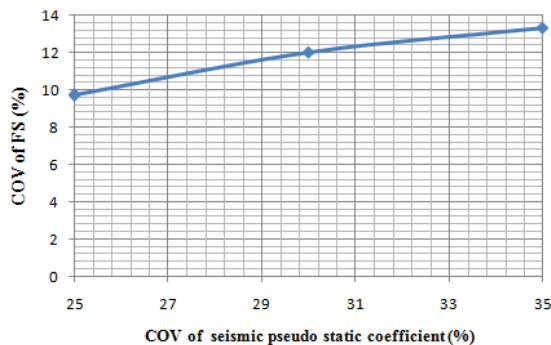


Fig. 5 Effect of K_h variation on safety factor

5. Conclusion

The results of sensitivity analysis of soil nailed wall in the project of Tehran-Tabriz rail road have been reported. Four parameters including cohesion (C) and friction angle (ϕ), specific gravity and seismic pseudo static coefficient (k_h) were considered in the analysis. Several results and features base on the analysis are summarized below:

- The COV has been put to the practical use to demonstrate the variation of soil properties and scattering of input data. As it is observed by

heeding more, dispersed data lead to ascend dispersion in the factor of safety.

- Fig.2 shows the trend of COV variation of the safety factor along the changes of friction angle (ϕ) for both layers. As it can be seen, influence of the first layer friction angle is negligible rather than the second layer. In the second layer the range of F.S variation is between 3 to 9%.

- It is clear from Fig.3 that the effect of second layer cohesion on safety factor is more significant compared to the first one. This range has been changed from 10 to 13%. The amount of F.S variation is high which shows the importance of second layer cohesion on safety factor.

- As it is observable from Fig.4, the specific gravity of both layers does not have any meaningful effect on safety factor. As an example for the second layer the F.S changes is between 2 to 4%. This amount of changes does not seem to be much effective on the results.

- From Fig.5 it can be deduced that K_h has considerable effect on safety factor. The range of changes for COV of F.S is between 10 to 13%. It shows the sensitivity of the results to K_h .

It can be concluded that the scattering in C and ϕ of the second layer and the K_h has influential effect on the safety factor; therefore, in estimating the value of effective parameters, additional consideration should be done. Moreover, in practice the result of slope stability would be more valid if the lower limit of sensitive parameter used in the analysis.

References

- [1] FHWA -SA-93-068, Federal Highway Administration .April 1994, Soil Nailing Field Inspectors Manual, prepared for us Department of Transportation, pp. 1-2.
- [2] D.V Griffiths, A.Fenton,(2007), Probabilistic Methods in Geotechnical Engineering , PP 72
- [3] FHWA 0-IF-03-017, Federal Highway Administration (2003), "Geo technical Engineering CIRCULAR NO.7 Soil Nail Walls" prepared for us Department of Transportation, pp. 4-8
- [4] Allen L. Jones, Steven L. Kramer and Pedro Arduino,2002, Pacific Earthquake Engineering Research Center, Estimation of Uncertainty in Geotechnical Properties for Performance- Based Earthquake Engineering, University of Washington, pp27-29

Evaluation of Strength Parameters of Improved Collapsible Soils with Current Additives (Case study: Atrak zone, Iran)

Mohammad Arab Ameri¹, Samaneh Kargar² and Mehdi Arab Ameri³

¹MSc, earthquake engineering, Iran

²MSc, water structures engineering, Iran

³MSc, geotechnique engineering, Iran

ABSTRACT

The collapsible soils show unusual behavior under specific situations such as uncommon loads and/or dynamic forces like earthquake. It causes the decrease of volume and large settlement with failures and cracks in the supported structures. In this paper the properties of collapsible soils and the effect of additives such as cement, lime and bentonite on physical and strength characteristics of them is investigated. For these reason, the strength tests, such as; direct shear, unconfined compressive strength and collapse potential of soil tests have been carried out. The results show that the additives cause improvement of soil properties with cement faster effects in comparison with the lime.

Keywords: Collapsible soils, Improvement, Cement, Lime, Bentonite

1. INTRODUCTION

Generally, all soils that during construction of new structures or use of existing structures encounter with problems are classified in problematic soils group. These soils exist in many forms such as soft soils, swelling soils, absorption of high water soils ... [6]. Collapsible soils are classified in problematic soils from point of view geotechnique and geology engineering [4]. Investigation of collapsible soils becomes to necessity regard of wide spread of these soils and necessity of designing of dams, channels and other structures in these zones. Geotechnical study about collapsible soils is increasing and fundamental understanding of geotechnical properties and behavior of these soils is very necessary and important job.

In 1959, Clevenger exhibited one of the first criteria for soil collapsibility potential [2]. Gibbs and Bara (1967) carried out researches about utilization of clay mortar and its injection to loess soils [3]. Bell (1993) suggested use of emulsion mixtures of cement or lime for loess stabilization [1]. Turan and etal. with investigation of compressing injection method derived that effect of earthquake and its influence such as liquefaction is minimized in these improved soils [5]. Huat and Kazemian (2009) with comparing injection method and deep soil mixing method concluded that deep soil mixing methods that extremely used for soil improvement are acceptable completely.

2. General method of investigation

In this study, examinations have been carried out in field and in laboratory. Thus soil samples of this zone were sent to laboratory for identification of geotechnical properties. Then the stabilization of soil was investigated with adding the various percentages of lime, cement and bentonite to this soil.

Therefore the tests were done on them again. In the next stage, the results of the tests were analyzed accurately and the optimum percentage of additives was specified finally.

3. Field program

One of the most important operations in soil studies is subsoil examination and soil exploration. In this study, with excavating the some boreholes, both sub layer of soil was examined and properties of soil layers were probed with sampling of soil and implementation the filed tests. In this project, three boreholes in each zone (overall 10 zones) were drilled for identification of "Atrak border line". Depth of each borehole was five meters. The in situ density of soil was obtained by implementation the sand-cone test (ASTM D1556). Undisturbed and disturbed samples were taken. Water level didn't observe up to five meters of ground surface. Results of the sand-cone tests showed that average of the in situ unit weight of soil was 15.3 KN/m³.

4. Laboratory tests

4.1 Physical tests

- Test for determination of water content of soil samples was carried out by ASTM D2216. The results of these tests showed that moisture content of samples was 8% averagely.
- Tests for determination of specific gravity of soils (ASTM D854) were done on samples and this parameter was obtained 2.64 averagely.
- Tests for particle size analysis of the soils (ASTM D422) were carried out. The soil of Atrak zone was classified to clayey silty and sandy silty loess.
- Tests for determination of liquid limit, plastic limit and plasticity Index (ASTM D4318) were done on the samples. The soil of the zone averagely had liquid limit up to 28% and plastic index up to 8%. It is important to say that the soils of some boreholes didn't have plasticity properties.

- The results that obtained from standard proctor compaction tests (ASTM D698) showed that the optimum moisture content and the maximum dry unit weight were 14.6%, 1.77 gr/cm³ respectively.

4.2 Strength tests

Purpose of these tests is determination of strength properties of soil in laboratory conditions. These tests included:

- Direct shear test (ASTM D3080) - the results have showed in table I.
- One-dimensional consolidation test (ASTM D2435) – The tests results have collected in table II.
- Test for measurement of collapse potential of soil (ASTM D5333) – results showed that the soil of zone have moderately severe to severe collapse potential that for removal of this problem, the improvement operation must be done.

Table I- The results of direct shear tests

Borehole NO.	Depth of sample(m)	Test method	c (kg/cm ²)	φ (deg)
TPF2	2	slow	0.09	25
TPF5	2.2	slow	0.01	33
TPF8	2	slow	0.06	28
TPF15	2	slow	0.03	29

Table II- The results of consolidation tests

Borehole NO.	Depth of sample(m)	c (kg/cm ²)	φ (deg)
TPF4	2	0.13	0.005
TPF5	2.2	0.12	0.004
TPF7	2	0.13	0.006
TPF8	2	0.10	0.006
TPF13	2	0.10	0.010
TPF26	2	0.16	0.005

5. Improvement operation

With respect to soil properties of researched zone, the necessity of soil improvement was quite evident. In continue of this part, admixtures and methods will introduce that have been used for modification and improvement of soil properties.

5.1 Additives

For examining the additives effect on physical and strength properties of soil, various content of lime, cement, bentonite and mixture of cement and bentonite and lime and bentonite was used. Table III shows several mixtures of additives.

5.2 Improvement tests

- **Atterberg limits test:** this test was done for all mixtures of soil and additives. Fig. 1 to 3 show additives effect on soil plasticity.

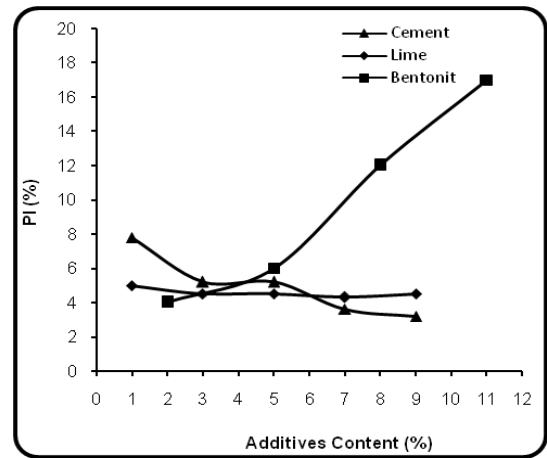


Fig. 1- Effect of additives on plasticity of investigated soil

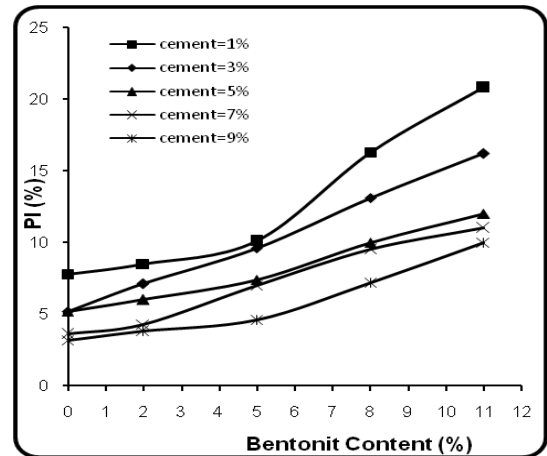


Fig. 2- Effect of cement and bentonite mixture on plasticity of investigated soil

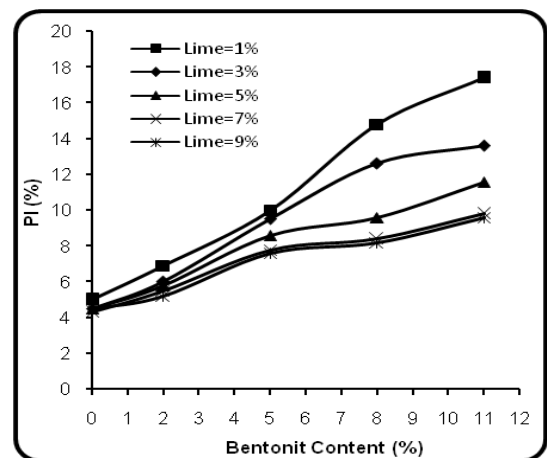


Fig. 3- Effect of lime and bentonite mixture on plasticity of investigated soil

Results show that cement or lime adding separately doesn't increase the soil plasticity but increase of bentonite exclusively, increase the soil plasticity remarkably. Fig. 2 and 3 illustrate the effect of additives mixtures on the soil plasticity. It is evident that the cement and bentonite mixture

or lime and bentonite mixture increases the plasticity of soil intensively. Also effect of cement is more than lime.

- **Direct shear test:** for investigation about the effect of additives on strength properties, direct shear test was done on the new mixture samples. The results have been showed in fig. 4-7. It is obvious clearly from them that adding the cement have very notable effect on angle of internal friction of soil. Results show that increase of cement has very large effect on angle of internal friction than cohesion but it increases the amount of both.

Adding the lime doesn't have great effect on angle of internal friction than cohesion but anyway angle of internal friction has increased but cohesion initially increased and then decreased. Manner of samples was similar to soft stones and loading on them in these tests doesn't large enough that cause to compressing the soil structure and active the friction property between ingredients. Fig. 4-7 show effect of cement and lime on strength properties of soil.

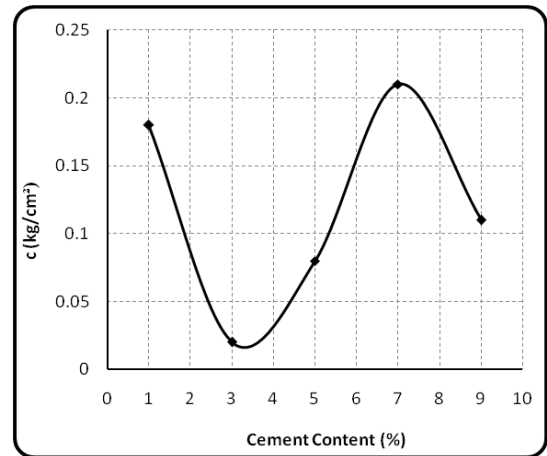


Fig. 4- effect of cement on cohesion of samples

Table III- additives mixtures

Mix. NO.	Cement content	Bentonite content	Soil content	Mix. NO.	Lime content	Bentonite content	Soil content
1	1	0	99	26	1	0	99
2	1	2	97	27	1	2	97
3	1	5	94	28	1	5	94
4	1	8	91	29	1	8	91
5	1	11	88	30	1	11	88
6	3	0	97	31	3	0	97
7	3	2	95	32	3	2	95
8	3	5	92	33	3	5	92
9	3	8	88	34	3	8	88
10	3	11	86	35	3	11	86
11	5	0	95	36	5	0	95
12	5	2	93	37	5	2	93
13	5	5	90	38	5	5	90
14	5	8	87	39	5	8	87
15	5	11	84	40	5	11	84
16	7	0	93	41	7	0	93
17	7	2	91	42	7	2	91
18	7	5	88	43	7	5	88
19	7	8	85	44	7	8	85
20	7	11	82	45	7	11	82
21	9	0	91	46	9	0	91
22	9	2	88	47	9	2	88
23	9	5	86	48	9	5	86
24	9	8	83	49	9	8	83
25	9	11	80	50	9	11	80

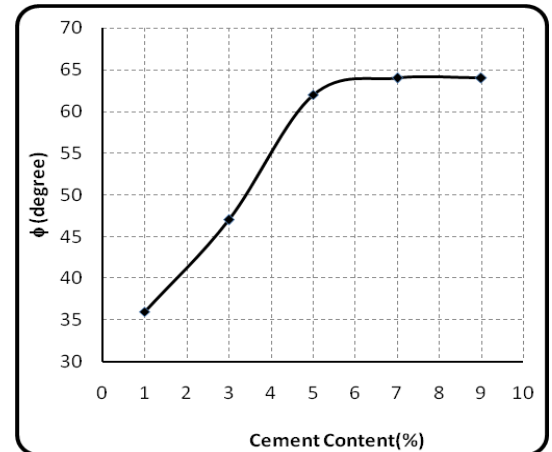


Fig. 5- effect of cement on angle of internal friction of samples

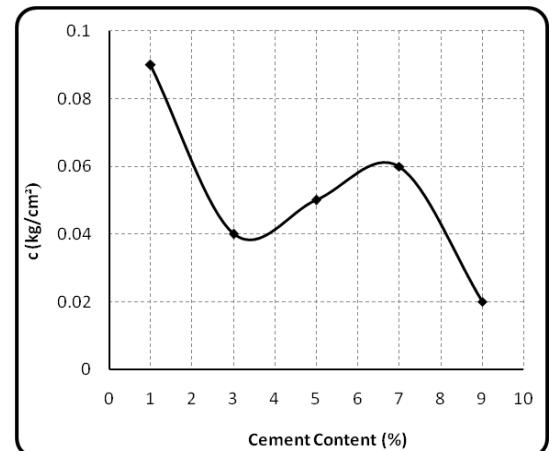


Fig. 6- effect of lime on cohesion of samples

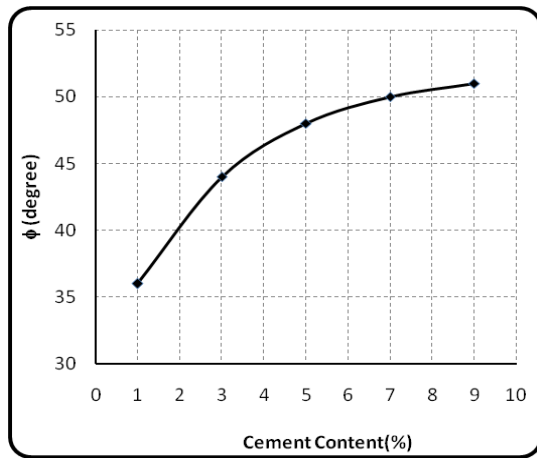


Fig. 7- effect of lime on angle of internal friction of samples

With regard of investigations can say that in the same content, cement increase has more effect than lime on shear parameters.

Cohesion of samples increases With increasing the bentonite content with constant cement or lime content. Adding the bentonite doesn't has remarkable effect on angle of internal friction of samples. Fig. 8-11 show these results. In all conditions the cohesion of improved samples has increased rather than natural soil samples.

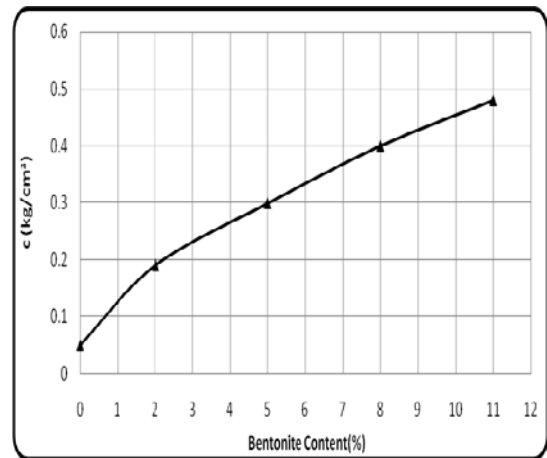


Fig. 10- effect of bentonite and 5% lime on cohesion of samples

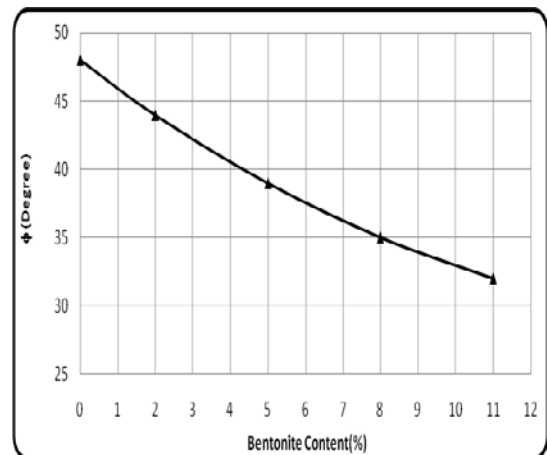


Fig. 11- effect of bentonite and 5% lime on angle of internal friction of samples



Fig. 8- effect of bentonite and 5% cement on cohesion of samples

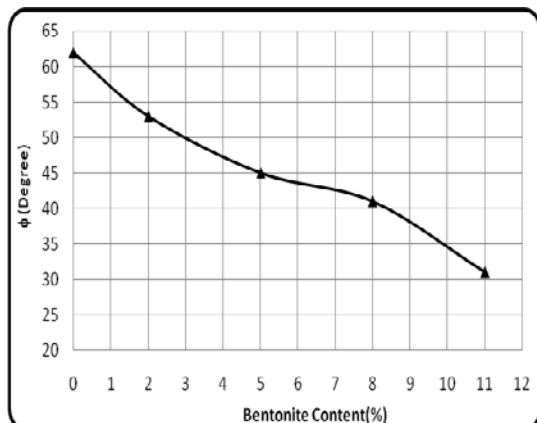


Fig. 9- effect of bentonite and 5% cement on angle of internal friction of samples

- Unconfined compressive strength test: The results of this test have pictured in Fig. 12-14. As a result of adding chemical additives to soil, several reactions is produced. one of them that has principal effect on strngth and durability of soil, is hydratasion.

The most important properties from soil stabilization with cement additives, is increase of strength with time. In general, this resistance expresses with parameters such as one dimensional strength.

It is evident from figures that effect of cement is more than lime on ultimate compressive strength.

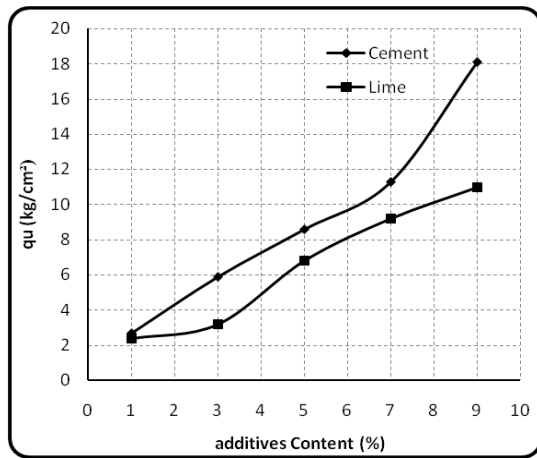


Fig. 12- effect of additives on unconfined compressive strength of samples

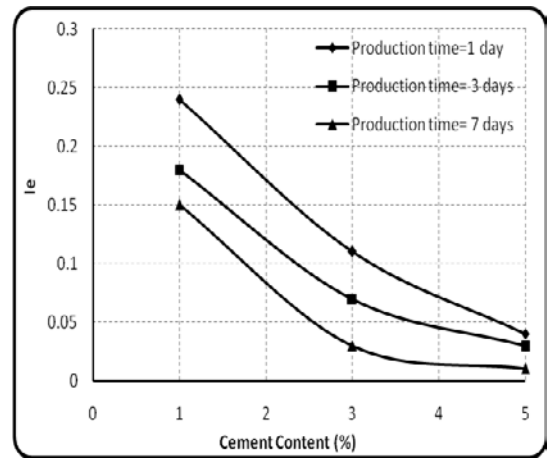


Fig. 15- effect of cement on collapse index

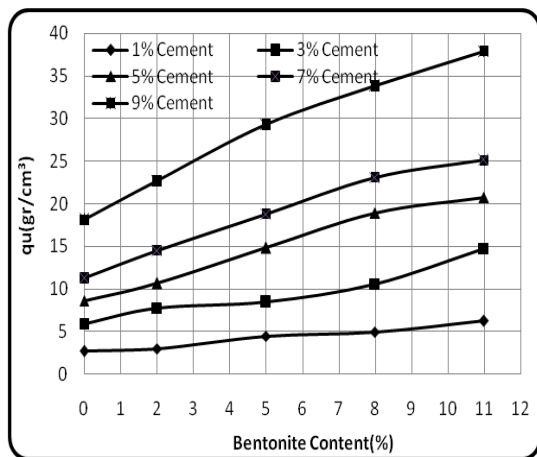


Fig. 13- effect of mixture of cement and bentonite on unconfined compressive strength of samples

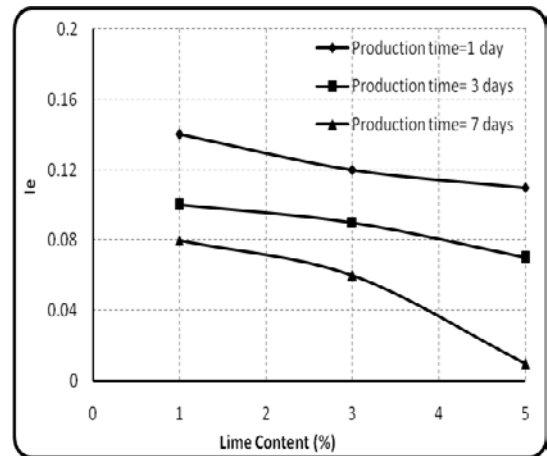


Fig. 16- effect of lime on collapse index

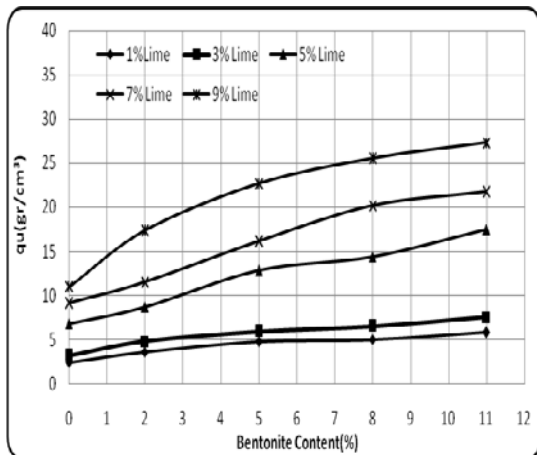


Fig. 14- effect of mixture of lime and bentonite on unconfined compressive strength of samples

- Test for measurement of collapse potential of improved soil: this test was done on samples that were mixed with additives. Fig. 15 and 16 show the effect of additives in different production time on collapse index of improved soil.

The results demonstrate that additives decrease the collapse potential of soil so that with adding 5% of each additive, soil loses its collapse potential. Indeed, if the time of production increases, the effect of additives is more.

6. Conclusion

Regard of this study and obtained results from improvement operation, these cases result:

- 1- Grain size distribution tests were done on loess soil of studied zone. It is evident from results of tests that soil of zone is in silty, clayey and sandy loesses limits. Results emphasize that the more of loess soils are silty.
- 2- Collapse potential tests were carried out on soil of zone and results show that the soil was collapsible and its degree was moderately severe to severe.
- 3- Results of atterberg tests on improved samples show that in general existence of bentonite in soil increases its plasticity extremely so that the plasticity index has increased notably. Mixtures of cement and bentonite and lime and bentonite also have caused to increase the plasticity property of soil. But plasticity index has been decreased by increasing the cement or lime content in constant content of bentonite because calcium ion replace with ions on clay mineral surface.

Plasticity index on average is 9% in improved soils of Atrak zone.

4- Existence of bentonite, cement and lime and their mixtures have been caused to changes in cohesion and internal friction angle resulted from direct shear tests. By this way that cohesion of soil has been decreased and angle of internal friction has been decreased generally with increase the cement content or lime content in constant content of bentonite. But cohesion of soil increased and angle of internal friction decreased with increase bentonite content in constant content of cement or lime. The lowest content of cohesion was 0.01 kg/cm^2 and the most content was 0.09 kg/cm^2 in soil of zone before improvement that obtained from direct shear tests. After adding the mixtures, cohesion content was increased to 0.84 kg/cm^2 . The results of improvement on loess soils of Atrak zone show that existence of bentonite together with cement or lime has remarkable effect on cohesion increase.

5- Unconfined compressive strength increases with increasing the bentonite content in constant content of cement or lime. Also, it has ascendant procedure with increase cement or lime content in constant content of bentonite.

6- Adding cement or lime to soil generally causes to removal of collapse potential of the soil. It is resulted that adding about 3% cement or 3% lime is sufficient for removal of this property. Of course the more operation time, the more decrease the collapse potential.

7- Adding lime and bentonite or cement and bentonite to loess soil causes to its stabilization that it happens as a result of chemical reactions between lime and clay or cement or clay.

7. REFERENCES

- [1] Bell FG, "Engineering Properties of Soil and Rocks," 3rd ed. Oxford, U. K. Butter worth-Heinemann, 2002, pp. 345.
- [2] Clevenger W A, "Experiences with loess as a foundation material," Transactions American Society for Civil Engineers," vol.123, 1959, pp. 51-80.
- [3] Gibbs H. J, Bara J. P, "Stability problems of collapsing soil. Proceeding American Society for Civil Engineers," Journal of Soil Mechanics Foundation Division, vol. 93, 1967, pp. 572-594.
- [4] Lutenegeger A. J, Hallberg, G. R. "Stability of loess. Engineering Geology, "vol. 25, 1988, pp.247-261.
- [5] Turan Durgunoglu H, etal. "Soil Improvement With Jet Grout Columns: A Case Study from the 1999 Kocaeli Earthquake," 5th international Conference on Histories in Geotechnical Engineering, New York, NY, April 2004.
- [6] Rafie B.M.A , et al. "Evaluation of Soil Collapsibility Potential: A Case Study of Semnan Railway Station".EJGE. vol.13, 2008.

Influences of soil material parameters in compaction simulation with soil/water/air coupled F.E. code

S. Sakamoto, K. Kawai, V. Phommachanh and A. Iizuka
Kobe University, Japan

ABSTRACT

Compacted soil is widely used for earth structures. However, the mechanism of compaction has not been explained in the framework of soil mechanics up to today. Therefore, it is difficult to grasp distributions of stress, void ratio, and soil moisture within compacted earth structure. These parameters are needed to predict the behavior of earth structures exposed to natural disasters. In this study, the influences of permeability and soil water retention characteristics on compaction quality were obtained from compaction simulations with soil/water/air coupled F. E. code. Here, we regarded compaction as compression and expansion phenomenon of unsaturated soil under drained air and undrained water conditions and formulated it in an initial-boundary-value problem. Consequently, the dependency of the compaction curve shape on permeability and soil water retention characteristics of soil could be expressed. Moreover, multi-layered compaction was examined.

Keywords: Compaction, Unsaturated soils, Soil water retention characteristics, Permeability

1. INTRODUCTION

Compaction can be defined as pushing air out of soil mass, decreasing voids and increasing dry density. The compressibility, shear strength and permeability of compacted soil strongly depend on its dry density after compaction. Therefore, compaction control by dry density is widely applied for designing and constructing compacted earth structures (Figure 1 and 2). However, soil material is not uniform and it is difficult to apply the results of lab-compaction tests to geotechnical engineering sites. Moreover, the effects of randomness of soil parameters on compaction quality cannot be estimated since compaction has not been explained in the framework of soil mechanics. Kawai et al. (2012) regarded compaction as the compression and expansion phenomenon of unsaturated soil under drained air and undrained water conditions, and formulated it as an in initial-boundary-value problem [2]. They simulated static compaction tests with a soil/water/air coupled F. E. code,

named DACSAR-MP [3] and succeeded in expressing the compaction curve and shear behavior of compacted soil.

In this study, the influences of permeability and soil water retention characteristics on compaction quality were considered and static compaction simulations with DACSAR-MP were conducted. Moreover, to grasp the distribution of state quantities, such as void ratio and soil moisture, multi-layered compaction was simulated.

2. MATHEMATICAL MODEL USED FOR ANALYSIS

The mathematical models applied to DACSAR-MP are introduced here.

2.1 CONSTITUTIVE MODEL FOR UNSATURATED SOIL APPLIED TO THE EFFECTIVE DEGREE OF SATURATION

Ohno et al. (2007) applied suction stress as a part of the effective stress for unsaturated soil and expressed changes in stiffness of unsaturated soil with an effective degree of saturation as the following equations [4]. The effective stress

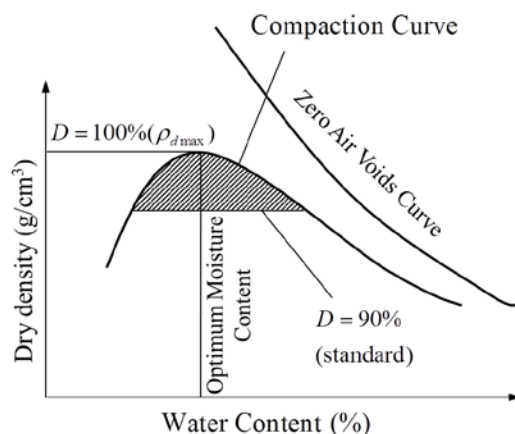


Fig.1 Concept of D-value

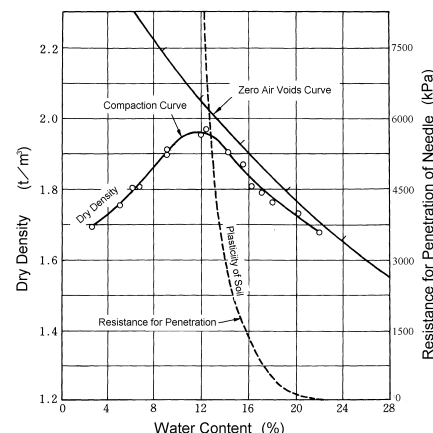


Fig.2 Procter's Concept [1]

is expressed as:

$$\boldsymbol{\sigma}' = \boldsymbol{\sigma}^{net} + p_s \mathbf{1} \quad (1)$$

$$\text{where } \boldsymbol{\sigma}^{net} = \boldsymbol{\sigma} - p_a \mathbf{1}, \quad p_s = S_e s \quad (2)$$

$$s = p_a - p_w, \quad S_e = \frac{S_r - S_{rc}}{1 - S_{rc}} \quad (3)$$

Here, $\boldsymbol{\sigma}'$ is the effective stress tensor for unsaturated soil, $\boldsymbol{\sigma}^{net}$ is the net stress tensor, $\mathbf{1}$ is the second rank unit tensor, $\boldsymbol{\sigma}$ is the total stress tensor, s is suction, p_s is suction stress, p_a is pore-air pressure, p_w is pore-water pressure, S_r is the degree of saturation, S_e is the effective degree of saturation, and S_{rc} is the degree of saturation at $s \rightarrow \infty$. The yield function is expressed as follows with an EC model which does not have a singular point on the yield surface.

$$f(\boldsymbol{\sigma}', \zeta, \varepsilon_v^p) = MD \ln \frac{p'}{\zeta p'_{sat}} + \frac{MD}{n_E} \left(\frac{q}{Mp'} \right)^{n_E} - \varepsilon_v^p = 0 \quad (4)$$

$$\zeta = \exp \left[(1 - S_e)^{n_s} \ln a \right], \quad MD = \frac{\lambda - \kappa}{1 + e_0}, \quad p' = \frac{1}{3} \boldsymbol{\sigma}' : \mathbf{1},$$

$$q = \sqrt{\frac{3}{2} \mathbf{s} : \mathbf{s}}, \quad \mathbf{s} = \boldsymbol{\sigma}' - p' \mathbf{1} = \mathbf{A} : \boldsymbol{\sigma}', \quad \mathbf{A} = \mathbf{I} - \frac{1}{3} \mathbf{1} \otimes \mathbf{1}$$

Here, n_E is the shape parameter, ε_v^p is plastic volumetric strain, M is q/p' on the critical state, D is the dilatancy coefficient, a and n_s are parameters to express expansion of the yield surface with desaturation, and λ and κ are the compression and expansion indices, respectively. Figure 3 shows the yield surface expressed as equation (4). The following elasto-plastic constitutive model for unsaturated soil is obtained from equation (4) and the associated flow rule.

$$\dot{\boldsymbol{\sigma}}' = \mathbf{D} : \dot{\boldsymbol{\varepsilon}} - \mathbf{C} : \dot{S}_e \quad (5)$$

Here, \mathbf{D} is the elasto-plastic stiffness matrix, $\boldsymbol{\varepsilon}$ is the strain tensor, and \mathbf{C} is the coefficient tensor which expresses changes in stiffness due to desaturation.

2.2 GOVERNING EQUATIONS FOR PORE-WATER AND PORE-AIR

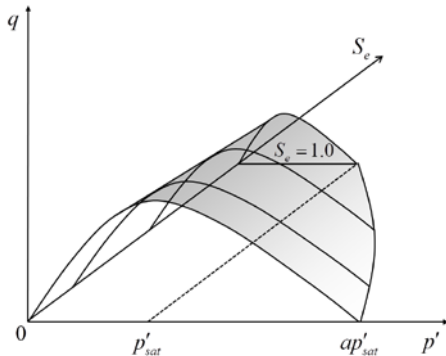
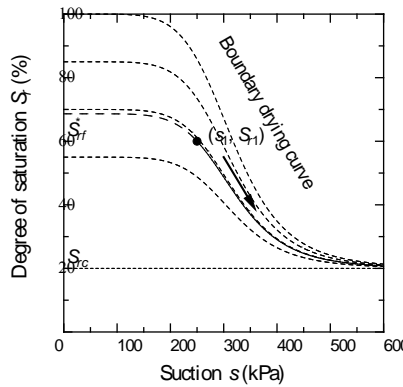
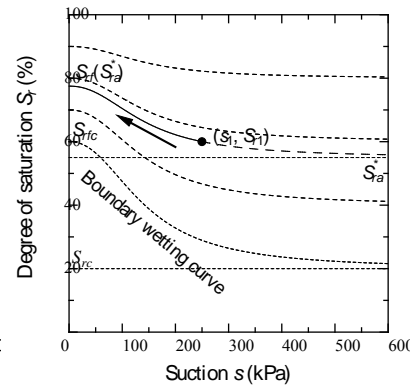


Fig.3 Yield surface for unsaturated soil



(a) Drying process



(b) Wetting process

Fig.4 SWRCC model proposed by Kawai et al.

In DACSAR-MP, the following equations are used for the governing equations after the work of Borja (2004) [5].

$$\text{Darcy's law (pore-water)} \quad \tilde{\mathbf{v}}_w = -\mathbf{k}_w \cdot \text{grad} h \quad (6)$$

$$\text{Darcy's law (pore-air)} \quad \tilde{\mathbf{v}}_a = -\mathbf{k}_a \cdot \text{grad} h_a \quad (7)$$

$$\text{Continuity equation (pore-water)} \quad n \dot{S}_r - S_r \dot{\varepsilon}_v + \text{div} \tilde{\mathbf{v}}_w = 0 \quad (8)$$

$$\text{Continuity equation (pore-air)} \quad (1 - S_r) \dot{\varepsilon}_v + n \dot{S}_r - n(1 - S_r) \frac{\dot{p}_a}{p_a + p_0} - \text{div} \tilde{\mathbf{v}}_a = 0 \quad (9)$$

Here, $\tilde{\mathbf{v}}_w$ and $\tilde{\mathbf{v}}_a$ are the flow velocities of pore-water and pore-air, respectively, \mathbf{k}_w and \mathbf{k}_a are the coefficients of pore-water and pore-air permeability, respectively, h is total water head, h_a is air pressure water head, and p_0 is gauge pressure. The soil/water/air coupled problem can be formulated with equations (5), (6), (7), (8) and (9).

2.3 SWRCC MODEL CONSIDERING HYSTERESIS

The soil-water retention characteristic curve (SWRCC) expresses the relationship between suction and saturation. It is known that SWRCC strongly depends on suction history. Shibata et al. (2010) showed that this hysteresis causes distribution of dry density and soil moisture within compacted soil [6]. In DACSAR-MP, the SWRCC model proposed by Kawai et al. (2007) [7] is used. This model can express the difference between drying and wetting processes as shown in Figure 4.

3 SIMULATIONS OF STATIC COMPACTION

The purpose of compaction is to discharge pore air and increase dry density. Here, compaction was regarded as loading and unloading under undrained air and drained water conditions on unsaturated specimens. Static compaction tests on specimens, which had various permeability and water retention characteristics, were simulated.

3.1 ANALYSIS CONDITIONS

Figure 5 shows the mesh used for this simulation. Here, 1-D compression was assumed. Deformation of the bottom was

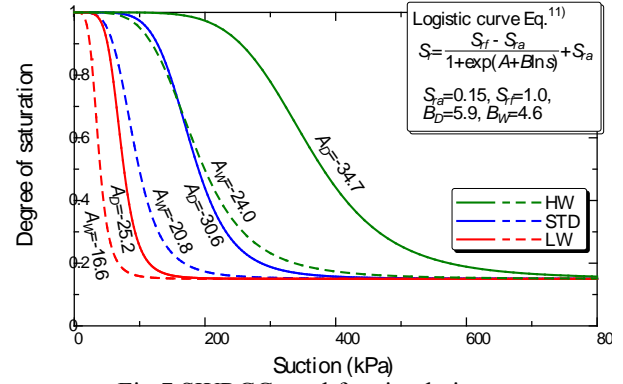
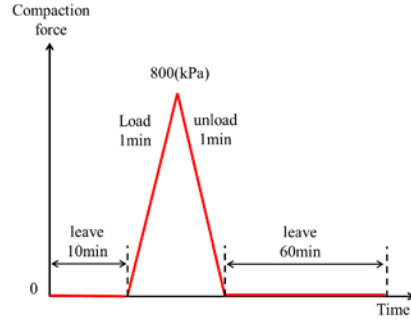
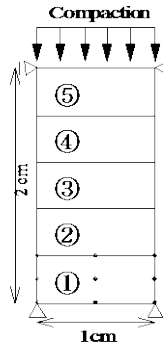


Fig.5 Simulation area Fig.6 Loading condition of compaction

Fig.7 SWRCC used for simulations

Table 1 Material parameters (STD)

λ	κ	M	ν
0.107	0.011	1.344	0.33
a	n_s	n_E	p'_{sat} (kPa)
30	1.0	1.3	73.5
k_w (m/day)	k_a (m/day)	m	e_0
0.01	1.0	0.8	0.85

Table 2 Simulation cases

CASE	SUPPLEMENT
STD(standard)	—
HP (high permeability)	$10k_w, 10k_a$
LP (low permeability)	$0.1k_w, 0.1k_a$
HW (high water retention)	$2.0A_D, 2.0A_W$
LW (low water retention)	$0.5A_D, 0.5A_W$

fixed, and that of the left and right boundaries was allowed only vertically. All boundaries were undrained water boundaries, and only air drainage from the top of the specimen was allowed. Compaction was expressed by increasing and decreasing load on top of the specimen during compaction. Figure 6 shows the loading conditions in simulations. Actual static compaction was conducted by strain control and unloading time was less than loading time. A simple form of loading and unloading was applied. Table 1 summarizes the soil material parameters used for the standard static compaction simulation (STD). Silty soil was assumed. Figure 7 shows the soil water retention characteristic curves. The simulation cases are summarized in Table 2. In order to consider the influence of permeability, high permeability (HP) and low permeability (LP) specimens are provided. High water retention (HW) and low water retention (LW) specimens were also provided. Each soil water retention characteristic curve is included in Figure 7.

To draw the compaction curve, initial water content was set between 10 to 28% while initial void ratio was 0.85. Initial suction of all nodes was assumed to take a value in relation to the initial degree of saturation on the primary wetting curve. Therefore, vertical distribution of the initial water head was uneven. Rest time prior to compaction was provided as shown in Figure 6 to allow the water head to reach equilibrium.

3.2 BEHAVIOR OF SPECIMEN UNDER STATIC COMPACTION

Fig.8 shows simulation results on STD. All results are from the middle of the specimen (element_3). It was found that the specimens compressed with loading and expanded with unloading. The yield stress of unsaturated soil increased with

desaturation. Therefore, the time taken to reach a greater compression point increased with decreased water content (Figure 8 (a)). Since simulations were conducted under undrained conditions, the degree of saturation increased with compression and decreased with expansion. Larger compressive specimens showed larger changes in degree of saturation (Figure 8 (b)). Changes of saturation in unsaturated soil brought about changes in suction. During the loading stage, the degree of saturation increased due to compression with a concomitant decrease in suction. On the other hand, during the unloading stage, the degree of saturation decreased due to expansion and suction increased. These relationships, between saturation and suction, were dominated by SWRCC (Figure 8 (c)). The influence of this relationship on SWRCC, was that specimens with higher moisture content caused more changes in suction. However, suction after compaction was higher than in specimens with lower moisture content. Also, it was found that suction after compaction became higher than before compaction (Figure 8 (d)). This behavior expresses the increase of strength and stiffness due to compaction.

The aim of compaction is to push out pore-air. Figure 8 (e) shows changes in pore-air pressure. The value of 98kPa indicates standard atmospheric pressure. Air pressure increased with loading and decreased with unloading. In specimens with low water content a relatively low degree of saturation produced high air permeability. Therefore pore-air was smoothly pushed out and returned to 98kPa after compaction. On the other hand, in high water content specimens, high air pressure appeared in the loading stage and little air pressure remained after unloading. This was due to low air permeability. Pore-water pressure showed the same behavior as air pressure (Figure 8(f)). However, change in

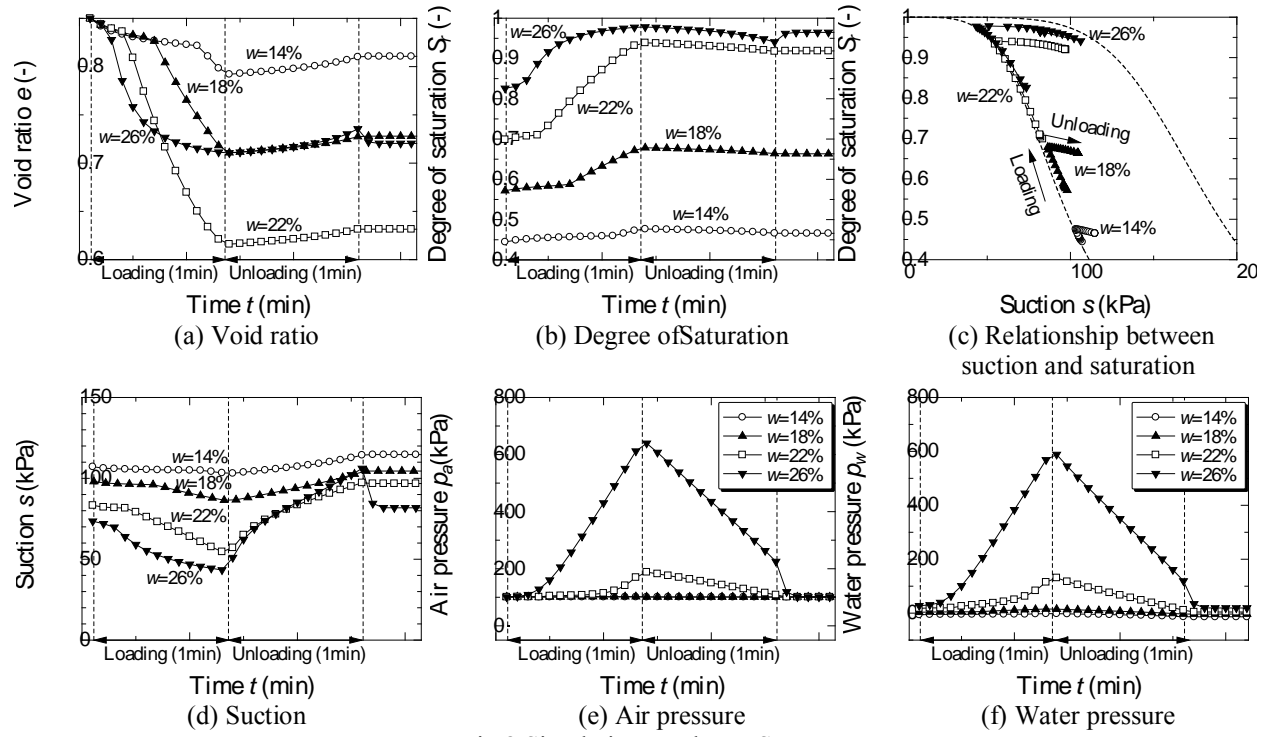


Fig.8 Simulation results on STD

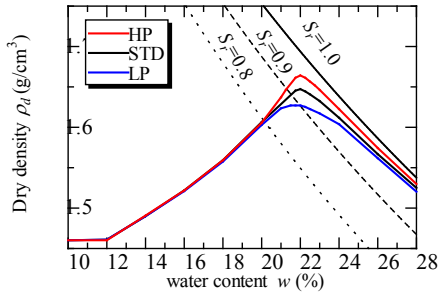


Fig.9 Influences of permeability

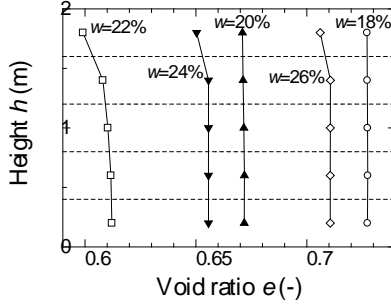


Fig.10 Distributions of void ratio (HP)

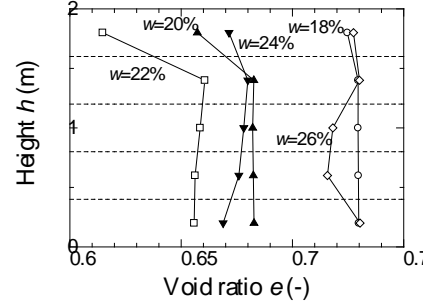


Fig.11 Distributions of void ratio (LP)

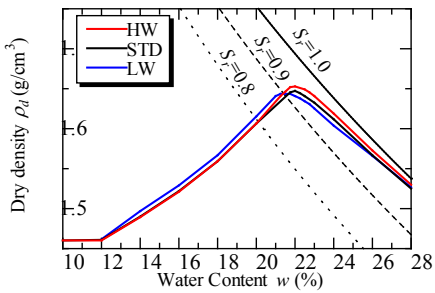


Fig.12 Influences of SWRCC

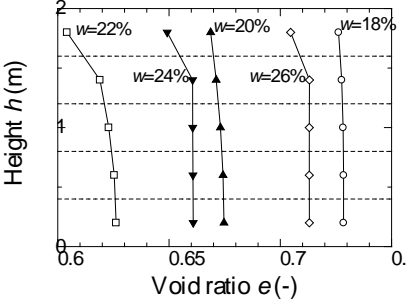


Fig.13 Distributions of void ratio (HW)

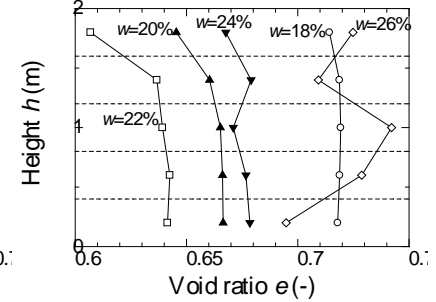


Fig.14 Distributions of void ratio (LW)

pore-water pressure was triggered by change in pore-air pressure since pore-water could not be drained while pore-air could be drained. This difference appeared as change in suction.

3.3 INFLUENCES OF PERMEABILITY

Since compaction is an initial-boundary-value-problem, it depends considerably on water and air permeability.

Figure 9 shows the relationship between dry density and

water content in three different permeability specimens, namely STD, HP and LP. The difference in permeability appears in the value of dry density. It was found that all compaction curves had the same optimum water content and corresponded to each other except in the case of 20-24% water content. In the lower water content zone of optimum water content, air permeability was high enough for air to be pushed out. On the other hand, in the higher water content

zone of the optimum water content, air was hardly drained from the specimen. Consequently, the influence of permeability appeared around the optimum water content. We can say that the compaction curve has the maximum dry density according to air permeability. The higher the air permeability is, the greater the maximum dry density.

Figures 10 and 11 show the void ratio distribution in specimens HP and LP, respectively. In the high permeability specimen, HP, void ratio gradually decreased toward the air drainage boundary. On the other hand, in the low permeability specimen, LP, void ratio was small only around the air drainage boundary.

3.4 INFLUENCES OF SWRCC

Figure 12 shows the compaction curves in various water retentivity specimens. We can say that HW is the high water-retentive specimen since it has higher air and water entry values. The difference between the compaction curves depending on water retentivity can be explained according to the shape of SWRCC during compaction. In the specimen with higher water retentivity, the gradient of the wetting curve on the loading stage was smaller and change in degree of saturation was smaller than in the lower water retentivity specimen with the under same water content. Consequently, air entrapment does not occur easily. Therefore, the optimum water content is relatively high and the compaction curve approaches the zero air void curve ($S_r = 1.0$) since entrapped air did not influence compaction even in the high water content region. This characteristic appeared as higher dry density. However, change in degree of saturation in the high water retentivity specimen was also small in the unloading stage and it is difficult to apply this explanation to the total compaction curve.

Figures 13 and 14 show the void ratio distributions in specimens HW and LW, respectively. It was found that the low water-retentive specimen, LW, was more influenced by entrapped air.

4 SIMULATIONS OF MULTI-LAYERED 1-D COMPACTION WITH VARIOUS PERMEABILITY AND WATER RETENTIVITY PARAMETERS

Shibata et al. (2010) simulated multi-layered compaction with soil/water coupled analysis and expressed the appearance of discontinuous construction gaps [8]. Here, to discuss the influences of soil material parameters on the quality of compacted earth structures, multi-layered 1-D compaction was simulated. The influences of permeability and water retentivity were also considered.

4.1 ANALYSIS CONDITION

Figure 15 shows the mesh used for this simulation. "Multi-layered" indicates that the upper layer was created after the lower layer had been compacted. In this simulation, 3 layers were used. Each layer had the same thickness and drainage, and loading conditions were the same as in the static compaction simulations.

4.2 RESULTS OF MULTI-LAYERED COMPACTION SIMULATIONS

Figure 16 shows suction distribution on STD over time. The time here indicates time after third layer compaction was completed. Suction distribution was unsteady and discontinuity appeared between the second and third layers right after compaction. For a while, vertical water balance occurred and suction distribution approached hydrostatic pressure distribution. Figure 17 shows the distribution of the void ratio. It was found that discontinuous gaps between each layer appeared. These gaps were triggered by differences in suction between the lower layer and upper layer. The lower layer had higher compression generated suction than the upper layer.

4.3 INFLUENCES OF PERMEABILITY

Figures 18 and 19 show void ratio distributions within multi-layered compactations on high permeability soil, HP, and low permeability soil, LP, respectively. Since more time was needed to reach for equilibrium in the low permeability sample, LP, changes in void ratio distribution over time can be seen in Figure 19. However, the final discontinuity gaps were more remarkable in HP than in LP since it was easier for water balance between the two layers to occur when the upper layer was lifted on the lower layer. Consequently, restively uniform distribution of void ratio appeared in multi-layered compaction of low permeability soil.

4.4 INFLUENCE OF WATER RETENTION

Figures 21 and 22 show void ratio distributions within multi-layered compactations in high water-retentive soil, HW, and low water-retentive soil, LW, respectively. In the low water-retentive soil, it was easier for the distribution of void ratio to occur, even within one layer due to the distribution of degree of saturation generated by the vertical difference of total water head. Consequently, discontinuous gaps were more remarkable in LW than in HW.

5 CONCLUSION

Static compaction and multi-layered compaction were simulated with soil/water/air coupled F.E code, DACSAR-MP, and the influences of soil material parameters on the compaction curve and compaction quality were considered. As the result, it was found that soil material parameters influences appear as a quantitative index of the compaction curve, such as optimum water content and maximum dry density.

6 REFERENCE

- [1] Procter, R. R. : Four articles on the design and construction of rolled-earth dams, *Eng. News Record*, Vol.111, pp.245-248, 286-289, 348-351, 372-376, 1933.
- [2] Kawai, K., Shibata, M., Ohtsuki, T, Phommachanh, V., Kanazawa, S. and Iizuka, A.: Simulations of static compaction with soil/water/air coupled F. E. analysis, *Proc of European Conf. on Unsaturated Soils in Napoli*, 2012 (in Printing).
- [3] Kanazawa, S.: Estimation of Compacted earth structure's

behavior with mathematical model for unsaturated soil, *Doctor Thesis, Kobe University*, 2010 (in Japanese).

[4] Ohno, S., Kawai, K. and Tachibana, S.: Elasto-plastic constitutive model for unsaturated soil applied effective degree of saturation as a parameter expressing stiffness, *Journal of JSCE*, Vol.63, No.4, p.p.1132-1141, 2007 (in Japanese).

[5] Borja, R. I.: A mathematical framework for three-phase deformation and strain localization analyses of partially saturated porous media, *Computer Methods in Applied Mechanics and Engineering*, Vol.193, pp.5301-5338, 2004.

[6] Shibata, M., Kawai, K., Kanazawa, S. and Iizuka, A.: Simulation of static compaction with unsaturated soil/water

coupled F. E. analysis, *Proc. 5th Int. Conf. on Unsaturated Soils*, pp.965-971, 2010.

[7] Kawai, K., Iizuka, A., Hayakawa, E. and Wang, W.: Non-uniform settlement of compacted earth structures caused by the deformation characteristics of unsaturated soil on wetting, *Soils and Foundations*, Vol.47, No.2, pp.195-206, 2007.

[8] Shibata, M., Kawai, K., Ozaki, S., Kanazawa, S., Tachibana, S. and Iizuka, A.: Influences of compaction procedure upon the quality of compacted earth structures, *Journal of Applied Mechanics, JSCE*, p.p.363-370, 2010 (in Japanese).

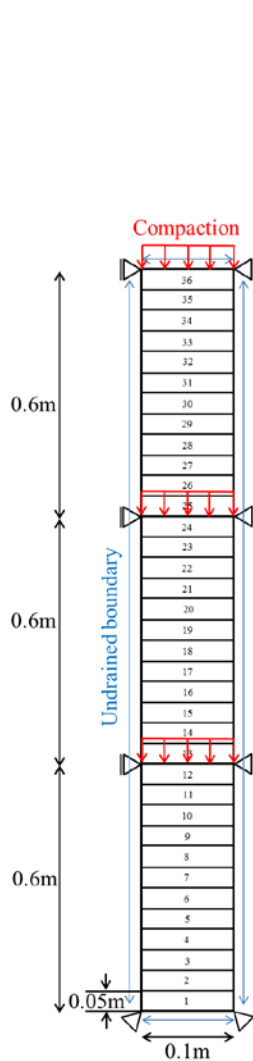


Fig.15 Mesh for Multi-layered simulation

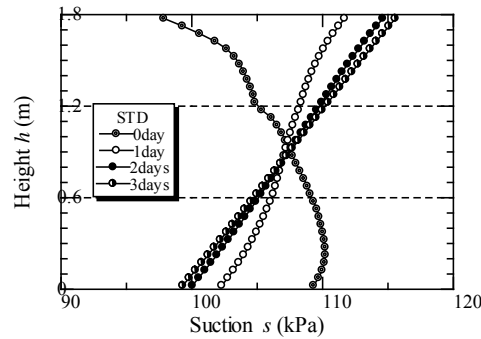


Fig.16 Changes of suction (STD)

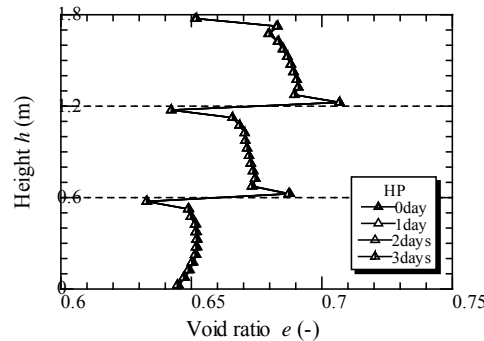


Fig.18 Changes of void ratio (HP)

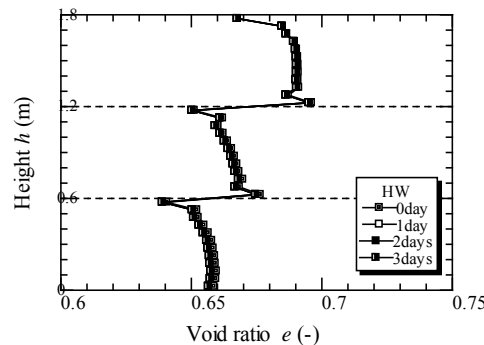


Fig.20 Changes of void ratio (HW)

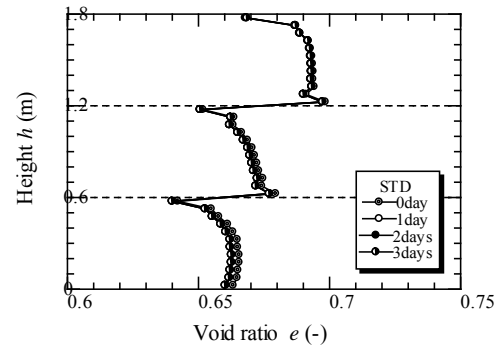


Fig.17 Changes of void ratio (STD)

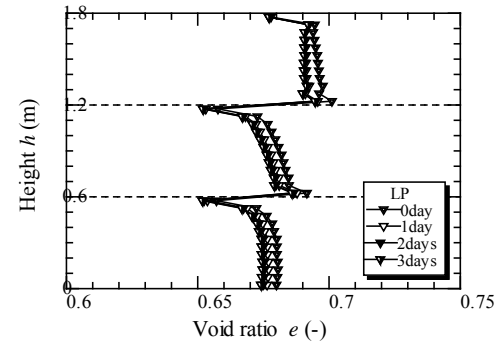


Fig.19 Changes of void ratio (LP)

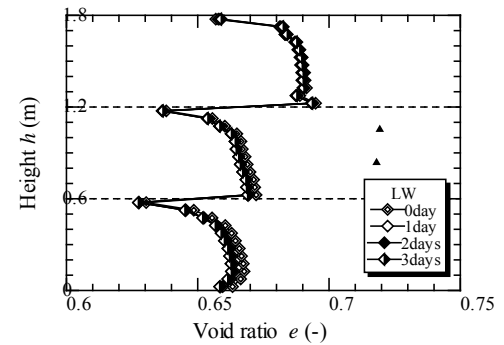


Fig.21 Changes of void ratio (LW)

Lower Bound Limit Analysis of Strip Footings Resting on Cohesive Soils

S.M. Binesh, A. Gholampour

Civil and Environmental Department, Shiraz University of Technology, Shiraz, Iran

ABSTRACT

A Novel lower bound approach is presented for the bearing capacity determination of strip footings resting on cohesive soils. The approach consists of the combination of lower bound limit theory and a mesh-free technique. In the presented method there is no need of mesh in the traditional sense and the constraints at the element discontinuities are omitted. A statically admissible stress field is constructed by the combination of mesh-free technique and the nodal integration scheme. The generated field is guaranteed to be lower bound by controlling the non-yielding condition at the entire domain. The solutions of the presented approach are compared with some well-known solutions, to demonstrate the efficiency and accuracy of the method.

Keywords: Lower bound, Mesh-free method, Strip footing

1. INTRODUCTION

Finding accurate prediction for the bearing capacity of strip footings is one of the fundamental problems in geotechnical engineering and, several researches are devoted to the subject [1]-[3]. An appealing choice to solve such problems is the application of numerical limit analysis (NLA). The use of NLA in soil mechanics problems returns back to the study of Lysmer [4] in which lower bound solutions have been found for different stability problems in the geotechnical engineering. Following Lysmer, Bottero et al [5] introduced a new finite element formulation for the limit analysis of soil structures. Sloan [6] combined the Bottero's approach and the active set algorithm [7], and developed an efficient method for the NLA of plane problems in soil mechanics. Several other attempts have been devoted to the application of NLA in stability problems in geotechnical engineering [8]-[10].

Up to now, mesh-based methods such as finite element or boundary element method are mostly used in the NLA of structures. However, these methods suffer from some deficiencies which are mainly related to mesh definition. An alternative approach to get rid of such drawbacks is the implementation of mesh-free methods as discretization tools. A great deal of research has been devoted to the application of mesh-free methods in different fields of science [11]-[12], however, a few are dedicated to the NLA of structures [13]-[15]. To the Authors knowledge, there is no study on the application of mesh-free NLA in soil mechanics problems and hence, in present paper, a new mesh-free lower bound formulation is proposed for the bearing capacity of strip foundations resting on cohesive soils. In this regard a statically admissible stress field is approximated by a mesh-free method which uses the Shepard's shape functions [16]. The stabilized nodal integration technique is adopted to

establish a collocation method for equilibrium satisfaction throughout the problem domain. The soil beneath the foundation is assumed to be a cohesive material obeying the Tresca yield criterion. Based on the derived formulations a computer code has been developed and the accuracy and efficiency of proposed method is investigated by solving an example at the end of the paper.

2. SHEPARD'S METHOD

The Shepard's method is used here for the construction of shape functions. Two distinct properties of Shepard's method make it appropriate to be used in the lower bound limit analysis (i) the shape functions constructed by Shepard's method have the Kronecker delta function property, which allows the simple imposition of boundary conditions.

(ii) Shepard's shape functions satisfy the maximum principle. According to this principle, the interpolated values always lie between the maximum and minimum nodal values used for the interpolation process. A brief description of the method is presented in this section, and for more details the reader is referred to [17].

Consider a function $F(P)$ which is defined over $P \subset R^2$. Any finite collection of distinct points in R^2 can be represented by $\{P_i\}_{i=1}^N$. The value of F at P_i is shown by F_i and, the Euclidean distance between P_i and the generic point P in R^2 is denoted by r (i.e. $r_i = [(x - x_i)^2 + (y - y_i)^2]^{1/2}$). Now the function $U(P)$ can be written as

$$U(P) = \left[\sum_{i=1}^N F_i \left(\prod_{j \neq i} r_j^\alpha \right) \right] / \left[\sum_{i=1}^N \prod_{j \neq i} r_j^\alpha \right] \quad j = 1, 2, \dots, N \quad (1)$$

where, α is a positive exponent which can affect the shape of interpolated function. Gordon and Wixom [17] suggested $\alpha > 1$ for smoothness of interpolated function. In present research α is assumed to be 3.

By the imposition of nodal values at the N nodes $\{P_i\}$, we have:

$$U(P_k) = F_k \quad k=1,2,\dots,N \quad (2)$$

The system of equations obtained from (2) leads to

$$U(P) = \sum_{i=1}^N F_i \varphi_i(P; P_1, P_2, \dots, P_N) \quad (3)$$

Where $\varphi_i(P; P_1, P_2, \dots, P_N)$ is the shape function, and can be written as

$$\varphi_i(P; P_1, P_2, \dots, P_N) = \prod_{j \neq i} r_j^\alpha / \left[\sum_{i=1}^N \prod_{j \neq i} r_j^\alpha \right] \quad (4)$$

3. LOWER BOUND LIMIT ANALYSIS

The lower bound theorem states that the collapse load obtained from any statically admissible stress field underestimates the true collapse load. A stress field is statically and plastically admissible if equilibrium and boundary conditions are fully satisfied and the yield condition is not violated anywhere.

3.1 Equilibrium satisfaction

A mesh-free collocation method is used here in conjunction with a smoothing technique to satisfy the equilibrium condition.

Assume a mesh-free scheme for a problem domain in which the interior domain and the boundaries are constructed by nodes. The general form of equilibrium equations in plane strain condition can be written as

$$\frac{\partial \sigma_{ij}}{\partial x_j} + b_i = 0 \quad (5)$$

where σ_{ij} and b_i are the stress tensor component and unit body force respectively.

Equation (5) should be satisfied at all points in the problem domain, hence a Voronoi cell is constructed around each node (figure 1) and the gradient of stress is smoothed over the cell as follows

$$\frac{\partial \tilde{\sigma}_{ij}}{\partial x_j} = \iint_{\Omega_L} \Psi \frac{\partial \sigma_{ij}}{\partial x_j} d\Omega \quad (6)$$

where $\tilde{\sigma}_{ij}$, Ψ and Ω_L are the smoothed stress, smoothing function and cell domain respectively. According to Chen's approach [18] the smoothing function can be written as

$$\Psi = \begin{cases} \frac{1}{A_L} & x \in A_L \\ 0 & x \notin A_L \end{cases} \quad (7)$$

where A_L is the area of Voronoi cell. Imposition of divergence theorem to the obtained equation from substituting (7) into (6), leads to

$$\frac{\partial \tilde{\sigma}_{ij}}{\partial x_j} = \frac{1}{A_L} \int_{\Gamma_L} \sigma_{ij} n_j d\Gamma \quad (8)$$

where Γ is the boundary of Voronoi cell and n_j is the normal unit vector in the direction of x_j . Equilibrium equation can be rewritten for the smoothed stress gradient by substituting (8) into (5) as

$$\frac{1}{A_L} \int_{\Gamma_L} \sigma_{ij} n_j d\Gamma + b_i = 0 \quad (9)$$

By satisfaction of equation (9) at all pre-defined nodes, equilibrium condition for the entire problem domain can be achieved.

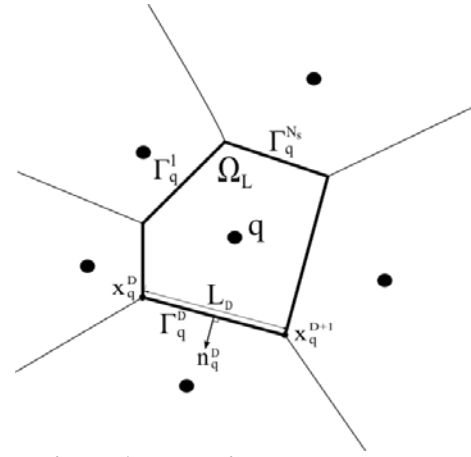


Figure 1-Voronoi cell around node q

3.2 Boundary conditions

The boundary tractions can be imposed to the problem solution by the same technique used in section 3.1 for equilibrium satisfaction. In this regard, the gradient of stress in j-direction, in each boundary node Voronoi cell, is set to be zero. According to Eq. (8) we have

$$\frac{\partial \tilde{\sigma}_n}{\partial x_j} = \frac{1}{A_{LB}} \int_{\Gamma_B} \sigma_n n_j d\Gamma = 0 \quad (10)$$

$$\frac{\partial \tilde{\tau}}{\partial x_j} = \frac{1}{A_{LB}} \int_{\Gamma_B} \tau n_j d\Gamma = 0$$

where, A_{LB} and Γ_B are related to the boundary node Voronoi cell. Knowing that the proposed shape functions have the Kronecker delta function property, the stress boundary conditions can be completely satisfied along the edge by imposing just at the boundary nodes.

3.3 Yield condition

Tresca yield criterion is adopted here for cohesive soils behavior. In plane strain condition, this criterion can be written as

$$F = (\sigma_{11} - \sigma_{22})^2 - (2\sigma_{12})^2 - (2S_u)^2 \quad (11)$$

where, S_u is the undrained shear strength of cohesive soil. For a statically admissible stress field we have

$$F \leq 0 \quad (12)$$

at every points in the problem domain. Equation (12) shows the locus of points located on and inside a circle in an X-Y plane where $X = \sigma_{11} - \sigma_{22}$ and $Y = 2\sigma_{12}$. This circle can be approximated by a polygon of P sides (Fig.2). Thus the yield condition imposes linear inequality constraints on the stresses as follows:

$$A_k \sigma_{11} + B_k \sigma_{22} + C_k \sigma_{12} \leq D \quad K = 1, 2, \dots, P \quad (13)$$

where

$$A_k = \cos\left(\frac{2\pi k}{p}\right)$$

$$B_k = -A_k$$

$$C_k = 2\sin\left(\frac{2\pi k}{p}\right) \quad (14)$$

$$D = 2S_u \cos\left(\frac{\pi}{p}\right)$$

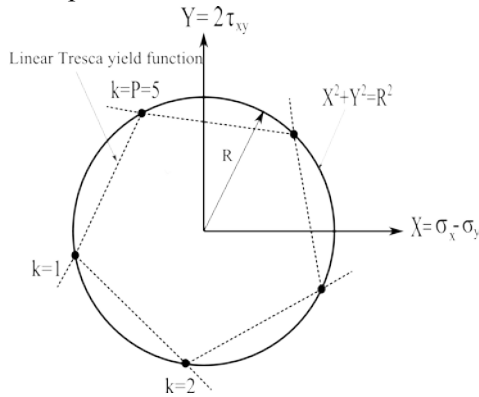


Figure 2-Linearized Tresca failure criterion

4. DISCRETE FORMULATION

According to Eq. (3), the stress values at any point \mathbf{x} can be attributed to nodal stress values as

$$\sigma_{ij}(\mathbf{x}) = \sum_{z \in K} \Phi_z(\mathbf{x}) \sigma_{ij}(\mathbf{x}_z) \quad (15)$$

where, $\sigma_{ij}(\mathbf{x})$ is the stress value at spatial coordinate \mathbf{x} , $\Phi_z(\mathbf{x})$ is the shape function defined by (4), $\sigma_{ij}(\mathbf{x}_z)$ is the nodal stress value at the spatial coordinate \mathbf{x}_z , and K is a group of nodes located in the support domain of point \mathbf{x} . The discretized stress field can be imposed into the required conditions for statically and plastically admissible stress field to derive the discrete form of constraints for lower bound analysis.

4.1 Equilibrium satisfaction

The relation between the smoothed stress gradient and the nodal stress values can be obtained by substituting Eq. (15) into Eq. (8) as follows:

$$\frac{\partial \tilde{\sigma}_{ij}(\mathbf{x})}{\partial x_j} = \sum_{z \in K} \frac{1}{A_L} \int_{\Gamma_L} \Phi_z(\mathbf{x}) n_j \sigma_{ij}(\mathbf{x}_z) d\Gamma \quad (16)$$

Substitution of Eq. (16) into Eq. (5), leads to the following matrix form

$$\mathbf{A}_{eq} \boldsymbol{\sigma} = \mathbf{B}_{eq} \quad (17)$$

where

$$\mathbf{A}_{eq} = [\mathbf{A}_1 \quad \mathbf{A}_2 \quad \dots \quad \mathbf{A}_M]^T \quad (18)$$

$$\mathbf{B}_{eq} = [\mathbf{B}_1 \quad \mathbf{B}_2 \quad \dots \quad \mathbf{B}_M]^T \quad (19)$$

$$\boldsymbol{\sigma} = [\sigma_1 \quad \sigma_2 \quad \dots \quad \sigma_M]^T \quad (20)$$

where, M is the total number of nodes and, in plane strain condition, the vector of nodal stresses ($\boldsymbol{\sigma}_i$) and body forces (\mathbf{B}_i) can be written as:

$$\boldsymbol{\sigma}_i = [\sigma_{11}(x_i) \quad \sigma_{22}(x_i) \quad \sigma_{12}(x_i)]^T \quad (21)$$

$$\mathbf{B}_i = [b_{1i} \quad b_{2i}]^T \quad (22)$$

where, b_{1i} and b_{2i} are respectively, the unit body forces in directions 1 and 2 for node i . The configuration of matrixes \mathbf{A}_1 to \mathbf{A}_M depends on the nodes located in the support domain of node 1 to M . Suppose that nodes r , s and t are located in the support domain of node i , then \mathbf{A}_i can be written as

$$\mathbf{A}_i = [0 \quad \dots \quad 0 \quad \tilde{\mathbf{A}}_r^e \quad 0 \quad \dots \quad 0 \quad \tilde{\mathbf{A}}_s^e \quad 0 \quad \dots \quad 0 \quad \tilde{\mathbf{A}}_t^e \quad 0 \quad \dots \quad 0] \quad (23)$$

where

$$\tilde{\mathbf{A}}_m^e = \begin{bmatrix} A_{m1}^e & 0 & A_{m2}^e \\ 0 & A_{m2}^e & A_{m1}^e \end{bmatrix} \quad (24)$$

$$A_{m1}^e = \frac{1}{A_L} \int_{\Gamma} \Phi_m(\mathbf{x}) n_1 d\Gamma \quad (25)$$

$$A_{m2}^e = \frac{1}{A_L} \int_{\Gamma} \Phi_m(\mathbf{x}) n_2 d\Gamma$$

4.2 Boundary conditions

The discretized form of Equation (10) can be obtained by substituting (15) into (10) as follows

$$\sum_{z \in K_B} \frac{1}{A_{LB}} \int_{\Gamma_B} \Phi_z(\mathbf{x}) n_j \sigma_n(\mathbf{x}_z) d\Gamma = 0 \quad (26)$$

$$\sum_{z \in K_B} \frac{1}{A_{LB}} \int_{\Gamma_B} \Phi_z(\mathbf{x}) n_j \tau(\mathbf{x}_z) d\Gamma = 0$$

where, K_B is a group of nodes located in the support domain of a boundary node, A_{LB} is the area of a boundary Voronoi cell and Γ_B is evaluated at the boundary Voronoi

cell. Equation (26) can be written for all boundary nodes and the obtained system of equations can be assembled in the matrix form as

$$\mathbf{A}_{b1}\boldsymbol{\sigma} = \mathbf{0} \quad (27)$$

Imposition of tractions at the boundary nodes, leads to another system of equations as follows

$$\mathbf{A}_{b2}\boldsymbol{\sigma} = \mathbf{B}_{b2} \quad (28)$$

where, \mathbf{A}_{b1} and \mathbf{A}_{b2} are the coefficient matrixes and \mathbf{B}_{b2} is the vector of specified values of tractions along the boundary.

The discretized form of constraints for boundary conditions can be written as

$$\mathbf{A}_{bo}\boldsymbol{\sigma} = \mathbf{B}_{bo} \quad (29)$$

where

$$\mathbf{A}_{bo} = \mathbf{A}_{b1} + \mathbf{A}_{b2} \quad , \quad \mathbf{B}_{bo} = \mathbf{B}_{b2} \quad (30)$$

4.3 Non-yielding condition

Since the discretization method (i.e. Shepard's method) Posses the maximum principle property, the non-yielding condition can be checked just at the pre-defined nodes. According to Eq. (13) the required constraints at all nodes, can be written in the matrix form as follows:

$$\mathbf{A}_{yi}\boldsymbol{\sigma} \leq \mathbf{B}_{yi} \quad (31)$$

where,

$$\mathbf{A}_{yi} = \begin{bmatrix} \tilde{\mathbf{A}}_I^y & 0 & 0 & 0 \\ 0 & \tilde{\mathbf{A}}_2^y & 0 & 0 \\ 0 & 0 & \ddots & 0 \\ 0 & 0 & 0 & \tilde{\mathbf{A}}_M^y \end{bmatrix} \quad , \quad (32)$$

$$\mathbf{B}_{yi} = [\tilde{\mathbf{B}}_I^y \quad \tilde{\mathbf{B}}_2^y \quad \dots \quad \tilde{\mathbf{B}}_M^y]^T$$

where

$$\tilde{\mathbf{A}}_k^y = \begin{bmatrix} A_1 & B_1 & C_1 \\ A_2 & B_2 & C_2 \\ \vdots & \vdots & \vdots \\ A_P & B_P & C_P \end{bmatrix} \quad (33)$$

$$(\tilde{\mathbf{B}}_k^y)^T = [D \quad D \quad \dots \quad D]_{1 \times P}$$

5. OBJECTIVE FUNCTION

For bearing capacity problem the objective function can be written as

$$Q = h \int_S \sigma_{nf} dS \quad (34)$$

where, Q is the limit load, h is the thickness normal to the plane, σ_{nf} is the normal stress acted over loaded area on the boundary and S is the length over which the normal stress is exerted. By application of the Gauss method, the integration in Eq. (34) can be written in a summation form as

$$Q = h \sum_{i=1}^{N_G} \omega_i \sigma_{nf} (x_G, y_G) \quad (35)$$

where, N_G is the number of Gauss points along S , ω_i is the weight of Gauss point i and (x_G, y_G) is the coordinate of Gauss point in (x, y) space. To determine the value of σ_{nf} in Eq. (35), a support domain is considered around each Gauss point (Fig.3). By the application of (15), the final discretized form of (35) can be written as

$$Q = \mathbf{C}^T \boldsymbol{\sigma} \quad (36)$$

where \mathbf{C} is the coefficient vector and $\boldsymbol{\sigma}$ is the nodal stress vector.

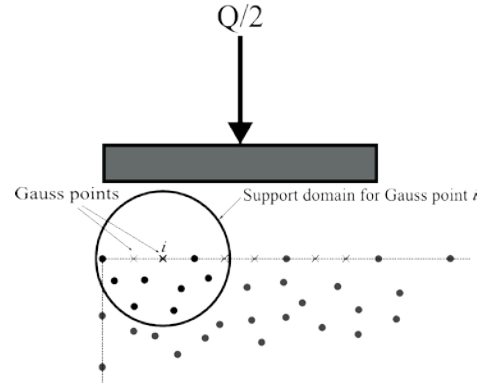


Figure 3- Support domain of a Gauss point under the loading area

6. LINEAR PROGRAMMING PROBLEM

By assembling the obtained relations for the constraints and the objective function, the problem of finding a statically and plastically admissible stress field can be written as

$$\begin{aligned} & \text{Minimize} \quad -\mathbf{C}^T \boldsymbol{\sigma} \\ & \text{Subjected to:} \quad \mathbf{A}_{tot} \boldsymbol{\sigma} = \mathbf{B}_{tot} \\ & \quad \quad \quad \mathbf{A}_{yi} \boldsymbol{\sigma} \leq \mathbf{B}_{yi} \end{aligned} \quad (37)$$

where

$$\begin{aligned} \mathbf{A}_{tot} &= \mathbf{A}_{eq} + \mathbf{A}_{bo} \\ \mathbf{B}_{tot} &= \mathbf{B}_{eq} + \mathbf{B}_{bo} \end{aligned} \quad (38)$$

An inbuilt library program, LINPROG, which is available in MATLAB, is used for solving above problem.

7. NUMERICAL STUDY

In this section, a smooth rigid footing, which is resting on a cohesive soil, is considered. The undrained shear strength of the soil is assumed to increase linearly with depth. The exact solution of this problem is presented by Davis and Booker [19] as follows:

$$q_f = F[(2 + \rho)S_{u0} + rB/4] \quad (39)$$

where q_f is the bearing capacity, S_{u0} is the undrained shear strength at the ground surface, B is the footing width and ρ is the coefficient of variation of undrained shear strength with depth. F is a non-dimensional factor which

depends on the footing roughness and $\frac{\rho B}{S_{u0}}$. By assuming

$$\frac{\rho B}{S_{u0}} = 3 \text{ and } S_{u0} = 1, \text{ for smooth foundation, } F = 1.22$$

and hence, the exact solution for bearing capacity is 7.1858. To solve the problem by the proposed method, a mesh-free model shown in Fig.4 is considered. The Voronoi diagram and the boundary conditions are also shown in the figure. The model has 811 nodes which are oriented in fan pattern. The support domain around each node is defined by an adjustable method to construct the shape functions. To guarantee that sufficient and suitable nodes are covered by the support domains, an automatically self-tuned value is devised in the code to adjust the radiuses of supports. The value of bearing capacity obtained from proposed method is 7.0324 which is about 2% lower than the exact solution result.

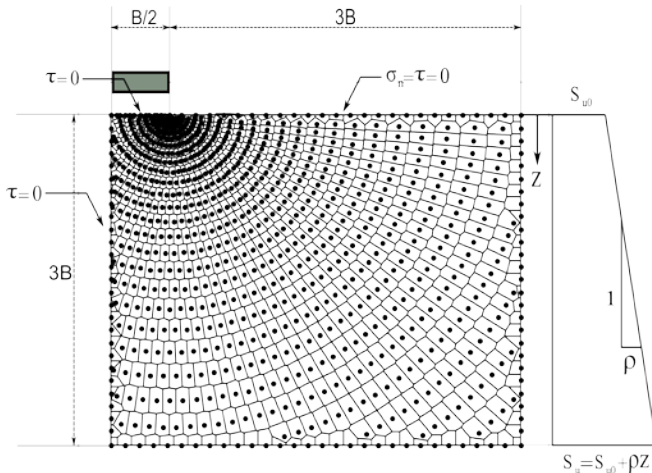


Figure 4- Problem geometry and boundary condition for 811 nodes and their Voronoi diagrams

8. CONCLUSION

A novel lower bound limit analysis formulation has been proposed for the bearing capacity determination of strip footings resting on cohesive soils. In the presented approach, there is no need of mesh in the traditional sense and, the shortcomings related to mesh definition are vanished. The results of numerical study showed very good lower bound predictions for the bearing capacity of strip footing resting on cohesive soil.

9. REFERENCE

- [1] Bolton MD, Lau CK, "Vertical bearing capacity factors for circular and strip footings on Mohr-Coulomb soil," Canadian Geotechnical Journal 1993;30(6):1024-33.
- [2] Frydman S, Burd HJ, "Numerical studies of bearing-capacity factor N_γ ," Journal of Geotechnical and Geoenvironmental Engineering (ASCE) 1997;123(1):20-29.
- [3] Kumar J, " N_γ for rough strip footing using the method of characteristics," Canadian Geotechnical Journal 2003;40(3):669-74.
- [4] Lysmer J, "Limit analysis of plane problem in soil mechanics," Soil Mechanics and Foundation Division (ASCE) 1970;96(4):1311-33.
- [5] Bottero A, Negre R, Pastor J, Turgeman S, "Finite element method and limit analysis theory for soil mechanics problems," Computer Methods in Applied Mechanics and Engineering 1980;22:131-49.
- [6] Sloan SW, "Lower bound limit analysis using finite elements and linear programming," International Journal for Numerical and Analytical Methods in Geomechanics 1988;12:61-77.
- [7] Sloan SW, "A steepest edge active set algorithm for solving sparse linear programming problems," International Journal for Numerical Methods in Engineering 1988;26:2671-2685.
- [8] Merifield RS, Sloan W, Yu HS, "Rigorous plasticity solutions for the bearing capacity of two-layered clays," Geotechnique 1999;49(4):471-90.
- [9] Kim J, Salgado R, Yu HS, "Limit analysis of soil slopes subjected to pore-water pressures," Journal of Geotechnical and Geoenvironmental Engineering, ASCE 1999;125(1):48-58.
- [10] Durand AF, Vargas EA, Vaz LE, "Applications of numerical limit analysis (NLA) to stability problems of rock and soil masses," International Journal of Rock Mechanics & Mining Sciences 2006;43:408-25.
- [11] Atluri SN, Zhu T, "A new meshless local Petrov-Galerkin (MPLG) approach in computational mechanics," Computational Mechanics 1998;22:117-27.
- [12] Liu GR, Gu YT, "A point interpolation method for two-dimensional solids," International Journal for Numerical Methods in Engineering 2001;50:937-51.
- [13] Chen S, Liu Y, Cen Zh, "Lower-bound limit analysis by using the EFG method and non-linear programming," International Journal for Numerical Methods in Engineering 2008;74:391-415.
- [14] Le CV, Gilbert M, Askes H, "Limit analysis of plates using the EFG method and second-order cone programming," International Journal for Numerical Methods in Engineering 2009;78(13):1532-55.
- [15] Le CV, Gilbert M, Askes H, "Limit analysis of plates and slabs using a meshless equilibrium formulation," International Journal for Numerical Methods in Engineering 2010;83(13):1739-58.
- [16] Shepard D, "A two-dimensional interpolation function for irregularly-spaced data," Proc. ACM Nat. conf 1968. p.517-24.
- [17] Gordon W, Wixom J, "Shepard's method of Metric Interpolation to Bivariate and Multivariate Interpolation," Mathematics of computation 1978;32(141):253-64.
- [18] Chen JS, Wu CT, Yoon S, You Y, "A stabilized conforming nodal integration for Galerkin Mesh-free methods," International Journal for Numerical Methods in Engineering 2001;50:435-66.

- [19] Davis, E. H. , and Booker, J. R., “The effect of increasing strength with depth on the bearing capacity of clays,” *Geotechnique*, Vol. 23, pp. 551–63, 1973.

Upper Bound Limit Analysis of strip footings resting on cohesive soils

S.M. Binesh, S. Raei

Civil and Environmental Department, Shiraz University of Technology, Shiraz, Iran

ABSTRACT

A novel approach is presented for the upper bound bearing capacity determination of strip footings resting on cohesive soils. The Von-Mises yield criterion is assumed for the cohesive soil behaviour. By the application of associated flow rule and the normality criterion, the relation between stress and plastic strain increment is assessed at the yield condition. The radial basis point interpolation method is used to express the strain increment field in terms of nodal velocities. An optimization problem is established and, solved by an iterative scheme. The efficiency of proposed method is investigated by solving an example at the end of the paper.

Keywords: Upper bound, Mesh-free, Strip footing

1. INTRODUCTION

The accurate prediction of the bearing capacity of strip footings is one of the fundamental problems in geotechnical engineering and, a great deal of research has been devoted to the subject [1-4]. An alternative approach for solving such problems is the numerical limit analysis (NLA) which is a robust method in solving stability problems. The use of NLA in soil mechanics problems appears to have been first proposed by Lysmer [5] who found lower bound solutions for the stability problems in geotechnical engineering. Following Lysmer, Bottero et al [6] introduced a new finite element formulation for the limit analysis of soil structures. By the implementation of Bottero's approach in conjunction with active set algorithm [7], Sloan [8] developed an efficient method for the NLA of plane problems in soil mechanics. Several other attempts have been devoted to the application of NLA in stability problems in geotechnical engineering.

Up to now, mesh-based methods such as finite element or boundary element method are mostly used as discretization tools in the NLA. However, mesh-based methods suffer from some deficiencies which are mainly related to mesh definition. An alternative approach to eliminate these drawbacks in the NLA, is the implementation of mesh-free methods as discretization tools. There has been a great deal of research into the application of mesh-free methods in different fields of science [9], however, a few are devoted to the NLA of structures [10]. To the Authors knowledge, there is no study on the application of mesh-free NLA in soil mechanics problems and hence, in present paper, a new mesh-free upper bound formulation is proposed for the bearing capacity of strip foundations resting on cohesive soils. In this regard, the Von-Mises yield criterion is

assumed for the cohesive soil behaviour and, by the application of associated flow rule and the normality criterion, the relation between stress and plastic strain increment is assessed at the yield condition. The plastic strain increment field is expressed by the nodal velocities by the application of a mesh-free technique called radial point interpolation method and, the optimization problem is established by considering an objective function and constrained obtained from upper bound limit analysis theory. An iterative scheme is proposed for the solution of optimization problem. The efficiency and accuracy of proposed method is demonstrated at the end of the paper by solving an example.

2. UPPER BOUND LIMIT ANALYSIS

The theory of upper bound limit analysis is the extension of plastic work principle [11] by Drucker et al. [12]. Based on this theory, in an admissible kinematic velocity field, the load obtained from the equality of internal dissipation power and external power, is not lower than the true collapse load. In the mathematical form we have

$$\int_{\Gamma} \mathbf{T} \cdot \mathbf{u} \, d\Gamma + \int_{\Omega} \mathbf{f} \cdot \mathbf{u} \, d\Omega \leq \int_{\Omega} \boldsymbol{\sigma} : \boldsymbol{\varepsilon} \, d\Omega \quad (1)$$

where \mathbf{T} is the traction over surface Γ , \mathbf{u} is the velocity field, \mathbf{f} is the body force in domain Ω , $\boldsymbol{\sigma}$ is the stress field and $\boldsymbol{\varepsilon}$ is the field of plastic strain rate.

3. YIELD CRITERION

The Von-Mises yield criterion is adopted here for cohesive soil behavior modeling. The general form of this criterion can be written as

$$F(\boldsymbol{\sigma}) = \boldsymbol{\sigma}^T \mathbf{P} \boldsymbol{\sigma} - 1 \quad (2)$$

where

$$\mathbf{P} = \frac{1}{S_u^2} \begin{bmatrix} 1 & -\frac{1}{2} & 0 \\ -\frac{1}{2} & 1 & 0 \\ 0 & 0 & 3 \end{bmatrix} \quad (3)$$

in which, S_u is the undrained shear strength of the soil.

4. STRESS-PLASTIC STRAIN RATE

The plastic strain used in the upper bound theory should obey the normality rule. Hence, by considering the associated flow rule, the plastic strain rate can be written as

$$\boldsymbol{\varepsilon} = \mu \frac{\partial F(\boldsymbol{\sigma})}{\partial \boldsymbol{\sigma}} \quad (4)$$

where μ is a non-negative plastic proportionality factor.

Substitution of equation (2) into (4) leads to:

$$\boldsymbol{\varepsilon} = 2\mu \mathbf{P} \boldsymbol{\sigma} \quad (5)$$

or

$$\boldsymbol{\sigma} = \frac{1}{2\mu} \mathbf{P}^{-1} \boldsymbol{\varepsilon} \quad (6)$$

Introducing (6) into (2), gives

$$F(\boldsymbol{\sigma}) = \left(\frac{1}{2\mu} \mathbf{P}^{-1} \boldsymbol{\varepsilon} \right)^T \mathbf{P} \left(\frac{1}{2\mu} \mathbf{P}^{-1} \boldsymbol{\varepsilon} \right) - 1 = \frac{1}{4\mu^2} \boldsymbol{\varepsilon} \mathbf{P}^{-1} \boldsymbol{\varepsilon} - 1 \quad (7)$$

For a point at yield surface, where $F(\boldsymbol{\sigma}) = 0$, the plastic proportionality factor can be defined as

$$\mu = \frac{1}{2} \sqrt{\boldsymbol{\varepsilon} \mathbf{P}^{-1} \boldsymbol{\varepsilon}} \quad (8)$$

Substituting (8) into (6) gives the relation between stress and plastic strain rate as follows

$$\boldsymbol{\sigma} = \frac{\mathbf{P}^{-1} \boldsymbol{\varepsilon}}{\sqrt{\boldsymbol{\varepsilon} \mathbf{P}^{-1} \boldsymbol{\varepsilon}}} \quad (9)$$

5. MESH-FREE TECHNIQUE

In this paper, there is no need of mesh in the geometry modeling and a mesh-free method is implemented as the discretization tool. In this regard a support domain, which contains the neighboring nodes, is defined around each point and the shape functions are constructed via the nodes located in the support domain. The enhanced radial basis point interpolation method is used here for the shape functions construction. Based on this method, a continue function such as $u(\mathbf{x})$ in a special coordinate \mathbf{x} can be approximated as

$$u(\mathbf{x}) = \sum_{i=1}^N R_i(\mathbf{x}) a_i + \sum_{j=1}^M P_j(\mathbf{x}) b_j \quad (10)$$

where $R_i(\mathbf{x})$ and $P_j(\mathbf{x})$ are respectively, the radial basis and polynomial terms and, a_i and b_j are their respective coefficients. The parameters N and M are the number of nodes in the support domain and the number of used polynomial terms respectively. The velocity field can be discretized into nodal velocities as follows:

$$u(\mathbf{x}) = \boldsymbol{\Phi}(\mathbf{x}) \mathbf{u}_s \quad (11)$$

where \mathbf{u}_s is the vector of nodal velocity values, and $\boldsymbol{\Phi}(\mathbf{x})$ is the vector of shape functions which can be obtained by imposing nodal values of velocity into Eq. (10) and tracing a straightforward technique described in [13].

$$\boldsymbol{\Phi}(\mathbf{x}) = [\phi_1(\mathbf{x}) \quad \phi_2(\mathbf{x}) \quad \dots \quad \phi_N(\mathbf{x})]^T \quad (12)$$

Considering the strain rate and velocity relation, we have

$$\boldsymbol{\varepsilon}(\mathbf{x}) = \mathbf{B}(\mathbf{x}) \mathbf{u}_s \quad (13)$$

where

$$\mathbf{B}(\mathbf{x}) = \begin{bmatrix} \frac{\partial \phi_1}{\partial x_1} & 0 & \frac{\partial \phi_2}{\partial x_1} & 0 & \dots & \frac{\partial \phi_N}{\partial x_1} & 0 \\ 0 & \frac{\partial \phi_1}{\partial x_2} & 0 & \frac{\partial \phi_2}{\partial x_2} & \dots & 0 & \frac{\partial \phi_N}{\partial x_2} \\ \frac{\partial \phi_1}{\partial x_2} & \frac{\partial \phi_1}{\partial x_1} & \frac{\partial \phi_2}{\partial x_2} & \frac{\partial \phi_2}{\partial x_1} & \dots & \frac{\partial \phi_N}{\partial x_2} & \frac{\partial \phi_N}{\partial x_1} \end{bmatrix} \quad (14)$$

It is note worthy that, in the presented mesh-free technique the integration process is performed by using a background mesh and the Gauss method and, there is no relation between the background mesh and the nodal arrangement.

6. CONSTRAINTS REQUIRED FOR ADMISSIBLE VELOCITY FIELD

A velocity field is admissible if it is kinematically and plastically admissible. In kinematic admissible field the compatibility condition and the kinematic boundary conditions should be satisfied. Hence, in plane strain condition with axes x_1 and x_2 , for kinematic admissibility we have

$$\boldsymbol{\varepsilon} = \mathbf{A} \mathbf{u} \quad \text{at the entire problem domain} \quad (15)$$

$$\mathbf{u} = 0 \quad \text{at the closed kinematic boundaries} \quad (16)$$

Where

$$\mathbf{A}^T = \begin{bmatrix} \frac{\partial}{\partial x_1} & 0 & \frac{\partial}{\partial x_2} \\ 0 & \frac{\partial}{\partial x_2} & \frac{\partial}{\partial x_1} \end{bmatrix} \quad (17)$$

The compatibility condition (i.e. Eq. (15)) cab be written as following relation for discretized velocity field

$$\boldsymbol{\varepsilon} = \mathbf{B}\mathbf{u}_s \quad (18)$$

A velocity field is plastically admissible if the strain rate vectors belong to the set of normals to the yield surface (normality rule) and the external power of the load is positive. The condition of normality of strain rate vectors, for Von-Mises criterion leads to

$$\varepsilon_v = 0 \quad (19)$$

where ε_v is the volumetric strain rate. The constraint for positivity of external power of load, also results in

$$\int_{\Omega} \mathbf{f} \cdot \mathbf{u} \, d\Omega + \int_{\Gamma} \mathbf{T} \cdot \mathbf{u} \, d\Gamma \geq 0 \quad (20)$$

Since in the limit analysis theory the materials are assumed rigid-plastic, and such materials are rate-insensitive, it is possible to specify the magnitude of velocity without loss of generality. Hence we assume that

$$\int_{\Omega} \mathbf{f} \cdot \mathbf{u} \, d\Omega + \int_{\Gamma} \mathbf{T} \cdot \mathbf{u} \, d\Gamma = 1 \quad (21)$$

Equations (16), (18), (19) and (21) are considered as constraints for upper bound limit analysis calculations.

7. ESTABLISHMENT OF MATHEMATICAL OPTIMIZATION PROBLEM

To establish the optimization problem, it is assumed that a ratio of external load causes the failure of material. In other words, Eq.(1) can be modified as follows:

$$\lambda \left(\int_{\Gamma} \mathbf{T} \cdot \mathbf{u} \, d\Gamma + \int_{\Omega} \mathbf{f} \cdot \mathbf{u} \, d\Omega \right) \leq \int_{\Omega} \boldsymbol{\sigma} \cdot \boldsymbol{\varepsilon} \, d\Omega \quad (22)$$

where λ is the coefficient of external loads. Considering Eq(21), we have

$$\lambda \leq \int_{\Omega} \boldsymbol{\sigma} \cdot \boldsymbol{\varepsilon} \, d\Omega \quad (23)$$

Equation (23) in conjunction with the constraints described in section 6, leads to the following optimization problem

$$\left\{ \begin{array}{l} \lambda = \min \int_{\Omega} \boldsymbol{\sigma} \cdot \boldsymbol{\varepsilon} \, d\Omega \\ \text{subjected to: } \int_{\Omega} \mathbf{f} \cdot \mathbf{u} \, d\Omega + \int_{\Gamma} \mathbf{T} \cdot \mathbf{u} \, d\Gamma = 1 \\ \varepsilon_v = 0 \quad \text{on } \Omega \\ \boldsymbol{\varepsilon} = \mathbf{B}\mathbf{u}_s \quad \text{on } \Omega \\ \mathbf{u} = 0 \quad \text{on } \Gamma \end{array} \right. \quad (24)$$

Substituting Eq. (9) into (24) and using the Gauss method for integration calculation, converted Eq. (24) into

$$\left\{ \begin{array}{l} \lambda = \min \sum_{i=1}^{N_G} \rho_i \sqrt{\boldsymbol{\varepsilon}^T \mathbf{P}^{-1} \boldsymbol{\varepsilon}} \\ \text{subjected to: } \int_{\Omega} \mathbf{f} \cdot \mathbf{u} \, d\Omega + \int_{\Gamma} \mathbf{T} \cdot \mathbf{u} \, d\Gamma = 1 \\ \varepsilon_v = 0 \quad \text{on } \Omega \\ \boldsymbol{\varepsilon} = \mathbf{B}\mathbf{u}_s \quad \text{on } \Omega \\ \mathbf{u} = 0 \quad \text{on } \Gamma \end{array} \right. \quad (25)$$

where N_G and ρ_i are the number and weight of Gauss point respectively.

For a weightless media, the optimization problem demonstrated in Eq. (25), can be written in terms of nodal velocities, using Eq. (18), as follows:

$$\left\{ \begin{array}{l} \lambda = \min \sum_{i=1}^{N_G} \rho_i \sqrt{\mathbf{u}_s^T \mathbf{B}^T \mathbf{P}^{-1} \mathbf{B} \mathbf{u}_s} \\ \text{subjected to: } \mathbf{F}^T \mathbf{u}_s = 1 \\ \mathbf{D}_v \mathbf{B} \mathbf{u}_s = 0 \end{array} \right. \quad (26)$$

Where

$$\mathbf{D}_v = [1 \quad 1 \quad 0] \quad (27)$$

$$\mathbf{F} = \int_{\Gamma} \boldsymbol{\Phi}^T \mathbf{T} \, d\Gamma \quad (28)$$

8. OPTIMIZATION ALGORITHM

In this paper the algorithm proposed by Zhang et al. [14] is used for the optimization process. In this algorithm the Lagrangian method is used in conjunction with the separation of plastic and rigid zones. In the Lagrangian method the constraints are combined with the objective function and the Lagrangian function can be written as

$$L(\mathbf{u}_s, \mathbf{q}, \boldsymbol{\mu}) = \sum_{i=1}^{N_G} \rho_i \sqrt{\mathbf{u}_s^T \mathbf{B}^T \mathbf{P}^{-1} \mathbf{B} \mathbf{u}_s} + \mathbf{q} (\mathbf{F}^T \mathbf{u}_s - 1) + \boldsymbol{\mu} (\mathbf{D}_v \mathbf{B} \mathbf{u}_s) = 0 \quad (29)$$

where \mathbf{q} and $\boldsymbol{\mu}$ are Lagrange multipliers. In order to solve the nonlinear relation shown in Eq. (29), an iterative algorithm is used. In this regard, an iterative parameter W_{icp} is defined as

$$W_{icp} = \sqrt{\mathbf{u}_s^T \mathbf{B}^T \mathbf{P}^{-1} \mathbf{B} \mathbf{u}_s} \quad (30)$$

and hence, Eq. (29) can be written as

$$L(\mathbf{u}_s, \mathbf{q}, \boldsymbol{\mu}) = \sum_{i=1}^{N_G} \rho_i \frac{\mathbf{u}_s^T \mathbf{B}^T \mathbf{P}^{-1} \mathbf{B} \mathbf{u}_s}{W_{icp}} \quad (31)$$

$$+\mathbf{q}(\mathbf{F}^T \mathbf{u}_s - 1) + \boldsymbol{\mu}(\mathbf{D}_v \mathbf{B} \mathbf{u}_s) = 0$$

The iterative algorithm is initiated by the assumption of no zero strain rates (i.e. a starting value such as 1 for W_{icp} at every Gauss points), and in the successive steps the non-differentiable regions are found and isolated by the values of W_{icp} . The algorithm can be written as follows:

Initial step :

It is assumed that $W_{icp} = 1$ for every Gauss points. Then, Eq. 31 can be written as

$$L(\mathbf{u}_s, \mathbf{q}, \boldsymbol{\mu}) = \sum_{i=1}^{N_G} \rho_i (\mathbf{u}_s^T \mathbf{B}^T \mathbf{P}^{-1} \mathbf{B} \mathbf{u}_s) \quad (32)$$

$$+\mathbf{q}(\mathbf{F}^T \mathbf{u}_s - 1) + \boldsymbol{\mu}(\mathbf{D}_v \mathbf{B} \mathbf{u}_s) = 0$$

According to the Lagrangian optimization theory, by the imposition of $\frac{\partial L}{\partial \mathbf{u}_s} = 0$, $\frac{\partial L}{\partial \mathbf{q}} = 0$ and $\frac{\partial L}{\partial \boldsymbol{\mu}} = 0$, following system of linear equations can be obtained.

$$\begin{pmatrix} 2\mathbf{B}^T \mathbf{P}^{-1} \mathbf{B} & \mathbf{F} & (\mathbf{D}_v \mathbf{B})^T \\ \mathbf{F}^T & 0 & 0 \\ \mathbf{D}_v \mathbf{B} & 0 & 0 \end{pmatrix} \begin{pmatrix} \mathbf{u}_s \\ \mathbf{q} \\ \boldsymbol{\mu} \end{pmatrix} = \begin{pmatrix} 0 \\ 1 \\ 0 \end{pmatrix} \quad (33)$$

Solution of above system of equations, leads to $(\mathbf{u}_s)_1$ and the value of λ for the first step can be defined as

$$\lambda_1 = \sum \rho_i \sqrt{(\mathbf{u}_s)_1^T \mathbf{B}^T \mathbf{P}^{-1} \mathbf{B} (\mathbf{u}_s)_1} \quad (34)$$

Step K+1 (K=1,2,...)

From step K, the values of W_{icp} are known for all Gauss points and, the rigid and plastic zones can be discerned. Using such definition, the problem domain can be divided into two parts. I_d which indicates the differentiable zones (i.e. plastic) and I_{nd} which is related to non-differentiable regions (i.e. rigid).

$$\begin{cases} I_{nd} = \left\{ i \in I, \sqrt{(\mathbf{u}_s)_k^T \mathbf{B}^T \mathbf{P}^{-1} \mathbf{B} (\mathbf{u}_s)_k} = 0 \right\} \\ I_d = \left\{ i \in I, \sqrt{(\mathbf{u}_s)_k^T \mathbf{B}^T \mathbf{P}^{-1} \mathbf{B} (\mathbf{u}_s)_k} \neq 0 \right\} \end{cases} \quad (35)$$

Now, the optimization problem at the step K+1 can be expressed as

$$\begin{cases} \lambda = \min \sum_{i=1}^{N_G} \rho_i \frac{\mathbf{u}_s^T \mathbf{B}^T \mathbf{P}^{-1} \mathbf{B} \mathbf{u}_s}{W_k} \\ \mathbf{F}^T \mathbf{u}_s = 1 \\ \mathbf{D}_v \mathbf{B} \mathbf{u}_s = 0 \quad \text{on } V \\ \mathbf{u}_s^T \mathbf{B}^T \mathbf{P}^{-1} \mathbf{B} \mathbf{u}_s = 0 \quad \text{on } I_{nd} \end{cases} \quad (36)$$

The Lagrangian of above optimization problem can be written as

$$L(\mathbf{u}_s, \mathbf{q}, \boldsymbol{\mu}) = \sum \rho_i \mathbf{u}_s^T \mathbf{B}^T \mathbf{P}^{-1} \mathbf{B} \mathbf{u}_s + \mathbf{q}(\mathbf{F}^T \mathbf{u}_s - 1) + \boldsymbol{\mu}(\mathbf{D}_v \mathbf{B} \mathbf{u}_s) + \alpha (\mathbf{u}_s^T \mathbf{B}^T \mathbf{P}^{-1} \mathbf{B} \mathbf{u}_s) = 0 \quad (37)$$

where α is the penalty factor. Again by differentiation of L with respect to its variable and, equating them to zero, the following system of linear equations is obtained

$$\begin{pmatrix} 2\mathbf{B}^T \mathbf{P}^{-1} \mathbf{B} + 2\alpha \mathbf{B}^T \mathbf{P}^{-1} \mathbf{B} & \mathbf{F} & (\mathbf{D}_v \mathbf{B})^T \\ \mathbf{F}^T & 0 & 0 \\ \mathbf{D}_v \mathbf{B} & 0 & 0 \end{pmatrix} \begin{pmatrix} \mathbf{u}_s \\ \mathbf{q} \\ \boldsymbol{\mu} \end{pmatrix} = \begin{pmatrix} 0 \\ 1 \\ 0 \end{pmatrix} \quad (38)$$

Obtaining $(\mathbf{u}_s)_{K+1}$ from above system of equations, the value of λ_{K+1} can be calculated as follows

$$\lambda_{K+1} = \sum_{i=1}^{N_G} \rho_i \sqrt{(\mathbf{u}_s)_{K+1}^T \mathbf{B}^T \mathbf{P}^{-1} \mathbf{B} (\mathbf{u}_s)_{K+1}} \quad (39)$$

The iterative calculations are continued until the following criteria are satisfied

$$\frac{|\lambda_k - \lambda_{K+1}|}{\lambda_{K+1}} \leq \eta_1 \quad (40)$$

$$\frac{\|\mathbf{u}_{K+1} - \mathbf{u}_k\|}{\|\mathbf{u}_k\|} \leq \eta_2 \quad (41)$$

where η_1 and η_2 are assumed 0.0001 here.

9. NUMERICAL STUDY

In this section the well-known problem of undrained loading of smooth strip footing, is solved by the proposed method. The exact solution of this problem is given by Prandtl [15] and can be written as

$$q_f = N_c S_u \quad (42)$$

$$N_c = 2 + \pi \quad (43)$$

where q_f and S_u are the exact collapse pressure and the undrained shear strength (i.e. cohesion), respectively. Assuming $S_u = 1$, the value of exact collapse pressure is equal to 5.14. Fig1. shows the geometry domain and the boundary conditions considered in the present problem. Due to the symmetry, only one half of the geometry is modeled. Application of mesh-free technique enables us to consider different patterns for nodes arrangement. Hence, according to Fig. 2 three patterns of nodes arrangement are considered for

the geometry modeling. The problem is solved for each pattern, and the results are shown in Table 1 As it is obvious, the fan arrangement of the nodes gives the best results, and the random arrangement deteriorate the accuracy of results. However, all obtained results are very good upper bound solutions for the problem.

To verify the convergence of proposed technique, it is necessary to show that, by increasing the density of nodes, the accuracy of results gets better. In this regards, as shown in Fig. 3, three mesh-free models with fan arrangement of nodes are considered. As shown in Table 2, all evaluated values are upper than exact solution result and, the obtained trend confirms the increase of accuracy by decrease of nodes distances.

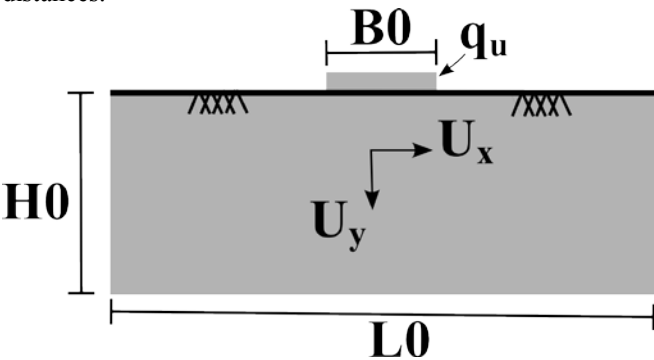


Fig1. A half-space under uniform normal pressure

Table1. Upper bound solutions for different patterns of node arrangement.

Meshless	Quantity	NLP
Fan 120 Nodes	Qu/su	8.7697
	No.of iterations	37
regular 120 Nodes	Qu/su	15.020
	No.of iterations	36
irregular 120 Nodes	Qu/su	10.700
	No.of iterations	27

Table2. Results of upper bound solution for fan arrangement

Meshless	Quantity	NLP
Fine 492 Nodes	Qu/su	5.1706
	No.of iterations	38
Medium 248 Nodes	Qu/su	7.0003
	No.of iterations	55
Coarse 116 Nodes	Qu/su	8.6329
	No.of iterations	62

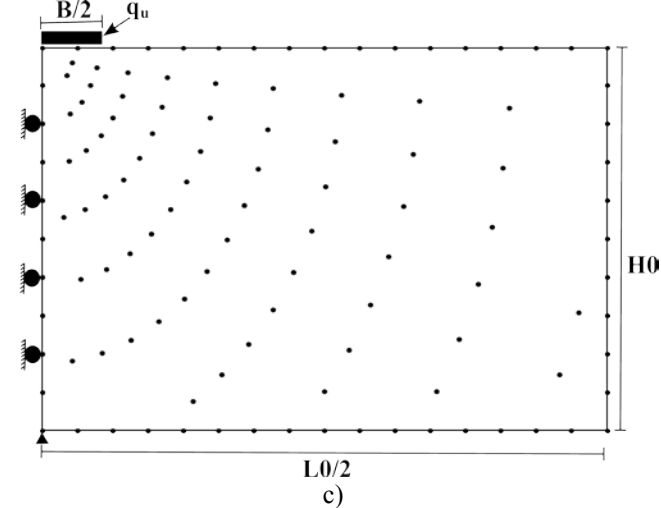
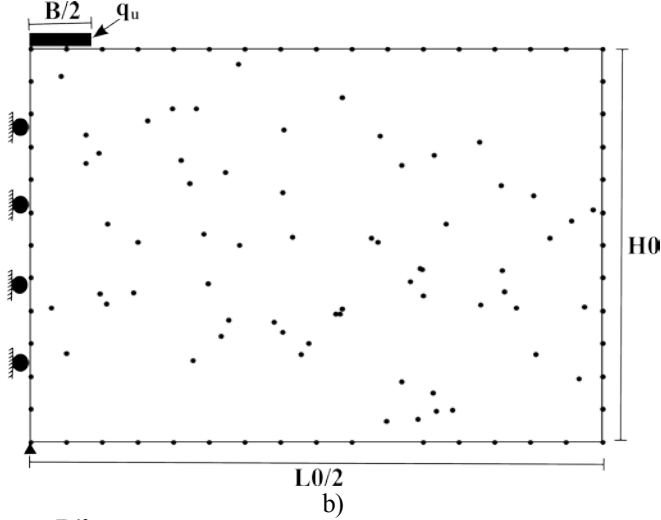
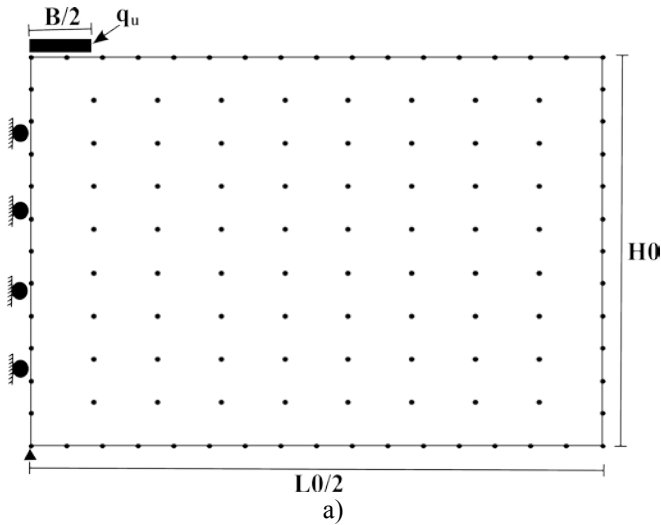


Fig2 Three patterns of nodes arrangement.

- a) uniform arrangement
- b) random arrangement
- c) Fan arrangement

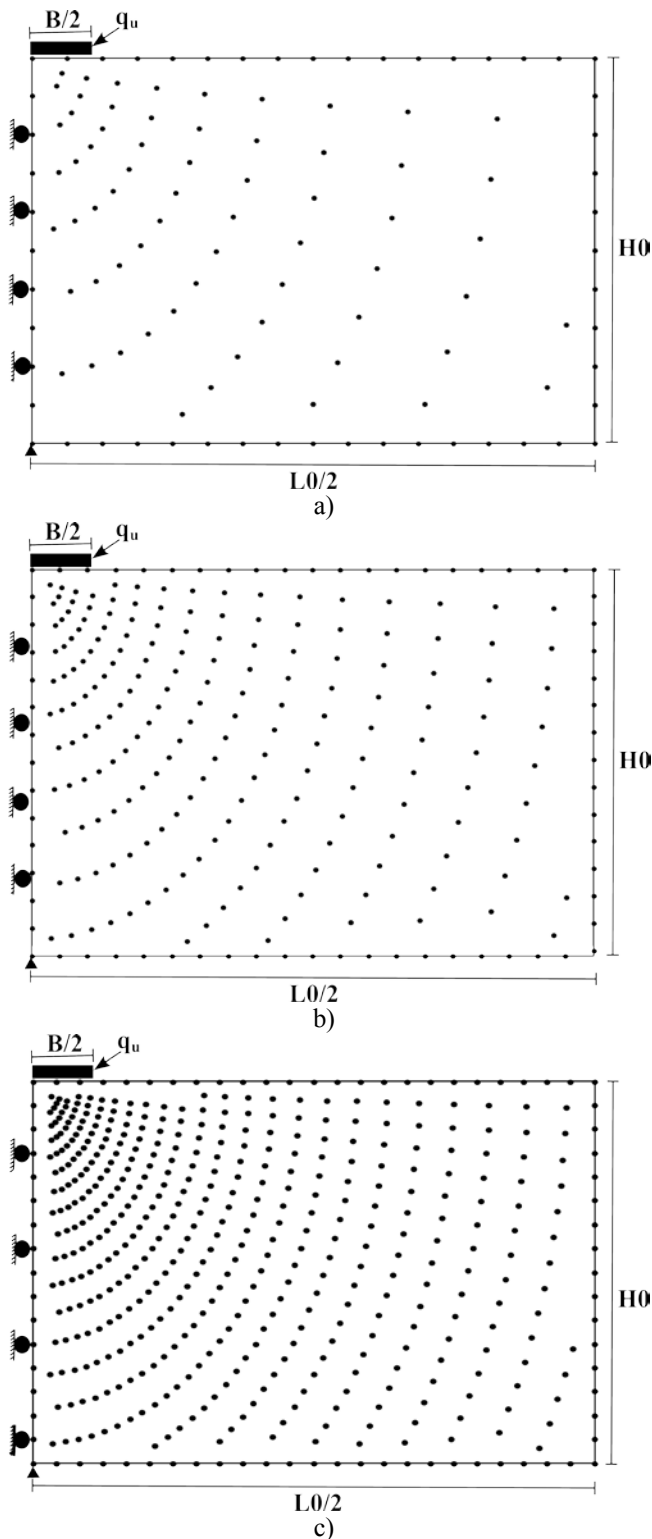


Fig3. Mesh free models with fan arrangement for a) low density b) medium density c) high density of nodes

10. CONCLUSION

A novel mesh-free upper bound solution has been proposed for the bearing capacity determination of strip footings resting on purely cohesive soils. In the proposed method there is no need of mesh in the traditional sense and hence, the

constraints related to element definition are omitted. The results of numerical study show that the proposed method provides very good upper bound solutions for the bearing capacity problem.

11. REFERENCES

- [1] Liu, Y., Zhang, X. & Cen, Z., "Numerical determination of limit loads for three-dimensional structures using boundary element method". *European Journal of Mechanics - A/Solids* 2004 ,23, 127–138.
- [2] Makrodimopoulos, A. & Martin, C. M., "Upper bound limit analysis using simplex strain elements and second-order cone programming". *International Journal for Numerical and Analytical Methods in Geomechanics* 2006b.,31, 835–865.
- [3] Capsoni, A., "A mixed finite element model for plane strain limit analysis computations". *Communications in Numerical Methods in Engineering* 1999,15, 101–112.
- [4] M. Vicente da Silva , A.N. Antão., "Upper bound limit analysis with a parallel mixed finite element formulation". *International Journal of Solids and Structures* 2008 ,45 - 5788–5804.
- [5] J. Lysmer, 'Limit analysis of plane problems in soil mechanics', *J . Soil Mech. Found. Div., A.S.C.E.,* 96 (SM4), 2008, 131 1-1334.
- [6] A. Bottero, R. Negre, J. Pastor and S. Turgeman, 'Finite element method and limit analysis theory for soil mechanics problems', *Computer Methods Appl. Mech. Eng.* 1980, 22, 131-149.
- [7] S. W. Sloan, 'A steepest edge active set algorithm for solving sparse linear programming problems'. *Int. j. numer. methods eng.* To appear. University of Newcastle, Civil Engineering Report No. 1987, 022.05.
- [8] S. W. Sloan, 'Upper bound limit analysis using finite elements and linear programming', *Int. j . numer. anal. Methods* 1989,13, 263-282 /
- [9] Monaghan JJ. , 1988. "An introduction to SPH". *Computer Physics Communications*; 48:89 -96.
- [10] Liu, G.R., Gu, Y.T., "A point interpolation method for two-dimensional solids". *Int. J. Numer. Meth. Engrg*, Vol.50, 2001,PP.937–951.
- [11] Chen, W. F."Limit analysis and soil plasticity". Elsevier Science Publishing Company, Amsterdam.
- [12] Drucker, D.C., 1953. Limit analysis of two and three-dimensional soil mechanics problems. *J. Mech. Phys. Solids* 1975, 1, 217–226.
- [13] Liu G.R.. "A point assembly method for stress analysis for two dimensional solids", *Int. J. Solids and Structures*, Vol. 2002 ,39, PP.261-276.
- [14] Zhang, P.X., Lu, M.W., Hwang, K.,. A mathematical programming algorithm for limit analysis. *Acta Mech. Sinica*1991, 7, 267–274 (in English).
- [15] Prandtl, L."U" ber die Ha"rte plastischer Ko"rper. *Nachrichten von der Gesellschaft der Wissenschaften zu Go"ttingen, Mathematisch- Physikalische Klasse* 1920 ,12, 74–85.

Evaluating and optimizing different methods of treating and cleaning contaminated soil

Dr. Mohammad Reza Atrechian¹, Seyed Salman Musavi², Khosro Ebrahimkhani³

¹Civil Engineering Faculty, Zanzan Azad University, Iran.

^{2,3} Civil Engineering Faculty, Zanzan Azad University, Iran.

ABSTRACT: One of the main environmental pollutions is soil pollution. Soils are considered as nature purifies. They also provide food and have refining characteristics. One of the main reasons of soil pollution is oil leakage and its extension which usually happens near oil refineries and transportation pipes which is sometimes unavoidable. These pollutions endanger human health and also the environment. About how to remove these items from contaminated soils, different solutions that are fully functional and relatively new are presented. In this article we have been trying to present a new optimized method from different methods around the world according to different criteria such as cost, quality, time and technology. Investigations show that biological and natural methods of cleaning contaminated soil, is to score higher than other methods.

Keywords: contaminated soil, biological, treatment, optimizing.

Introduction

Oil products is one the most dangerous pollutions which can affect the soil. Oil is usually transported by vehicles, pipelines and stored in storage tanks. These are the most common ways which can cause soil pollution. Leakage is one of the common ways in polluting the soil especially in fine grain soils such as sand. The increasing population and industrialization has made oil pollution unavoidable. This phenomena can happen in oil excavation areas, refineries and in some parts of pipelines. If the pollution penetrates into deeper depths the cost and treating operations will respectively increase and become much harder. Oil pollution can be treated by three methods: physical, chemical and biological methods. Biological methods commonly transfer the pollution into nonpoisonous materials by micro-organism procedures. This seems to be a more effective method.

Iran is between the top 5 oil producing countries so it has a high potential of being polluted by oil. Long pipelines and many oil refineries in south of Iran are a proof for this potential. Beside the

mentioned reasons, there are a lot of storage tanks inside and outside cities which are located generally underground and sometimes near the water table. The number of these storages can vary with the city population. As the population increases the number of these storage tanks increase too. In places with high water tables the pollution danger is much higher if a leakage occurs and of course the soil treatment is much harder if this pollution is happened in a residential area inside a city.

In this paper we have tried to evaluate, optimize and combine some of the soil treating methods on different types of soil. Some methods for controlling the pollution effects is as follows:

- 1- Improving the soil ventilation by plowing.
- 2- Adding nutrients to soil, like Nitrogen and phosphorous.
- 3- Combining soil with the micro-organisms which degrade oil products.

Methodology

According to the treatment methods of oil pollution and its products and due to the previous steps and treatment procedures discussed in this article, some biological methods are presented which are match with the environmental procedure of soil treatment. The output of the mentioned procedures are relatively safe for the biological cycle. From different biological methods presented by EPA, five relatively new methods were randomly selected and three of them including SVE, BV and AS were combined to make a relatively new method.

The five methods mentioned are defined as follows:

- 1- Soil Vapor Extraction.(SVE)
- 2- Air Sparging (AS)
- 3- Bio-venting
- 4- Soil Washing
- 5- Soil Flushing

METHODS

SVE: in this method special preparations are done to extract toxic and harmful chemical elements which are formed as gases from soil layers higher than the water table. These gases are produced inside the soil and treatment is done by excavating these gases.

AS: This method is used for treating soils under water table, by sparging air into soil for evacuating harmful gases. In this method, air sparging causes faster evaporation of oil products and afterwards by SVE the vapors are evacuated.SVE and AS methods are usually used together for cleaning and treating a soil.

BV: This method is similar to AS, with this difference that instead of air, Oxygen is sparged into the soil. Oxygen is combined with soil contaminations and is converted into carbon dioxide and then excavated from soil. The advantage of this method towards AS is that in this method no harmful vapors are produced and 90 % of the gases return to nature.

Soil Washing: This method is a procedure which is directly related to water and the treating is performed out of the contaminated area. This method usually treats soils which have organic and

non organic compounds. It is usually a pre treating method just to reduce the contamination so that other methods can complete the treating procedure. The contaminated soil is excavated and categorized, then the coarse grains are separated and afterwards it is washed by water and surfactants. This procedure turns the soil into two parts of clean soil and dirty soil. The advantage of this method is that it can gather the contaminations in settled soil, which this action makes the treating process faster. Soil washing reduces the total cost of treatment. Soil washing procedure is closely related to the soil type of the area. If the grains are coarse like gravel and coarse sand the process is more effective and faster than when the soil is fine grained.

Soil Flushing: This method is a developed method for treating, cleaning and gathering the contaminations of the soil in situ. Soil flushing uses water and gas compounds to make the geochemical reactions happen faster which cleans the centralized contaminations in the underground water.

Generally soil flushing has a high effect on permeable and homogenous soils such as sand and silty sand. This method can even treat the harmful products produced by chemical oxidation and even treat oil products in soil.

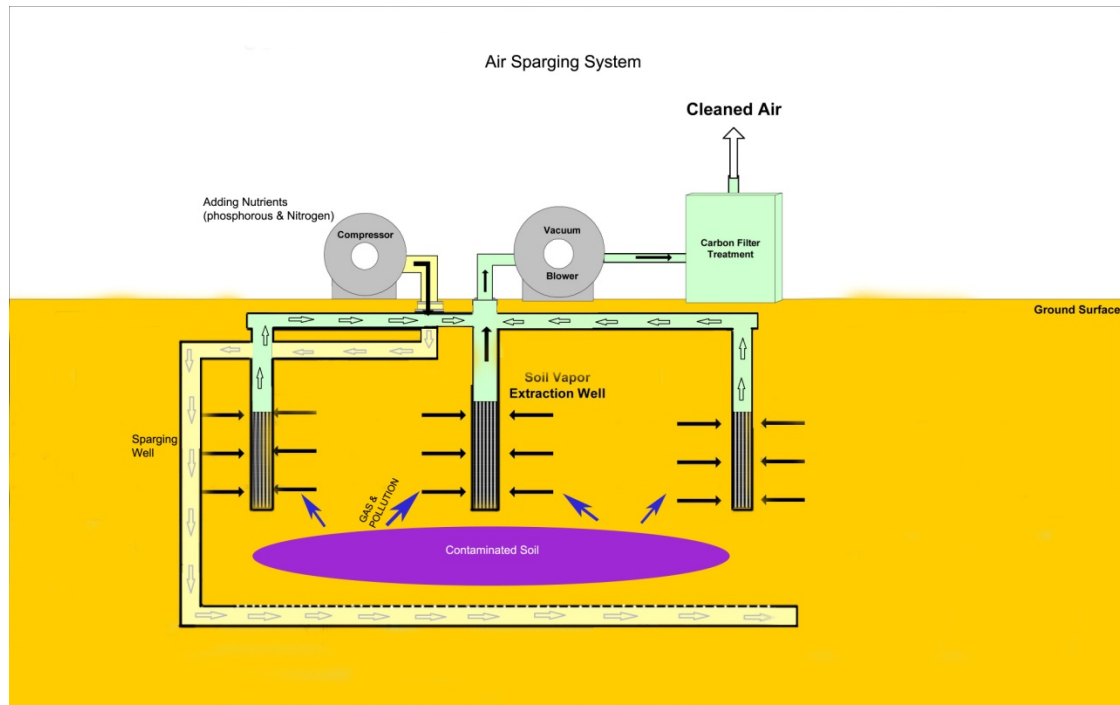
The New Presented Method

According to the mentioned methods, the offered theoretical procedure in this paper is defined as Bio Sparging (BS). As mentioned in the BV method, by injecting Oxygen (O_2) into the contaminated soil the will be treated. In the AS method by sparging the air into the contaminated region (which the air contains O_2 and possibly harmful and miserable compounds) the treatment is done. Due to environmental factors like oil pollutions in the region (liquid and gas form) , soil type according to its categorization (which has been categorized in the 2800 seismic manual of Iran) , depth, physical and mechanical properties of soil (permeability ratio, density, wetness, special mass, organic material percentage` and etc) the mentioned nutrients (Nitrogen and Phosphorous) are injected after being combined with fresh air. For injecting the air into contaminated soil, two types of wells are needed, vertical and horizontal wells. The arrangement of these wells is shown in figure 1). The horizontal wells must be installed in the

bottom of the contaminated area with defined distances from each other in parallel lines and must be screened. According to this point that the micro organisms of the natural soil can combine with the contaminations and change them into natural and biological gases which reduces the harmfulness of these gases to less than 5% can be a good

achievement. Then these gases and harmful vapors are excavated by SVE wells. Finally these vapors are taken through carbon filters and are recycled so their pollution percentage reduces to the minimum. Afterwards clean air and sometimes non toxic water are returned to the nature.

Figure 1: Air Sparging System



It should be considered that this process is completely safe and biological. In this method there are no chemical surfactants used while injecting nutrients causes the combination between them and the micro organism which results in the improvement of microbes' growth and increases the aerification of the treated and cleaned soil.

Results:

- 1- This method has a safe and biological procedure because the treating and cleaning materials used in it is O_2 and nutrients (phosphorous and nitrogen).
- 2- This method which is a combination of the biological methods in the EPA is an optimized method.
- 3- Because of the simplicity of installing the equipment, this method can prepare a proper field for the next cleaning

procedures (for probable solid oil pollutions) in the area.

References:

- [1] William C. Anderson , 1993, Innovative site remediation technology, soil washing / soil flushing. One of an Eight-Volume series. Edited by:, P.E.DEE. Executive Director, American Academy of Environmental Engineers.
- [2] U.S. Environmental Protection Agency , Off-Gas Treatment Technologies for soil Vapor Extraction systems: state of the practice, march 2006. Prepared by: Office of superfund Remediation and Technology Innovation, Office solid waste and Emergency Response,.

[3] Office of solid waste and Emergency Response (5102G), EPA 542-F-01-006. April 2001. A Citizens Guide to soil Vapor Extraction and Air Sparging. United states Environmental protection Agency.

[4] BUDIANTA Wawan, OHTA Hideki, HINODE Hirofumi, SALIM Chris, AOKI Masatoshi, IN-SITU SOIL WASHING USING INTEGRATED SYSTEM OF REMEDIATION TECHNOLOGIES. 2007

[5] ARMY, US Army Corps of Engineers Washington, DC 20314-1000, Engineering and Design SOIL VAPOR EXTRACTION AND BIOVENTING. DEPARTMENT OF THE.

Experimental Study Concerning Impact Characteristics by Collision of Weight on Sand Cushion over Steel Beam

Tam Sy HO¹, Hiroshi MASUYA² and Naoto TAKASHITA³
Kanazawa University, Japan

ABSTRACT

Sand cushion is often utilized in protection structures against rockfalls as a shock absorber. Impact by rockfall is considered one of the most important variable loads for protection structures. To clarify the evaluation method and the buffering effects of impact force, the series of weight impact experiment were conducted. A simple supported double steel beam was used to reproduce the behavior of structure. Experiments were carried out by the free fall of the weight to the sand tank installed at the center of simply supported double steel H beams. The impact force of the weight and transmitted force under the sand tank as well as displacements of beam and strains of the beam were measured. Dynamic characteristics of impact force, transmitted force to the steel beam and behavior of the beam were investigated. Dynamic interaction between sand and beam, shock absorbing effect of sand and also the transfer ratio of kinetic energy of rockfall to the structure were shown.

Keywords: Rockfall, Impact, Sand Cushion, Protection Structure

1. INTRODUCTION

Generally rockfall protection structures are classified into a net, a fence, a shelf, a wall, embankment, a rockshed etc. (Fig.1 and Fig.2) [1], [2]. Rockshed is one of the safe and important protection structures when the target rockfall has the large energy. In Japan, many prestressed concrete rocksheds and reinforced concrete rocksheds have been constructed. A certain cushion material is generally installed on the roof of the rockshed for the purpose to buffer the impact force by a rockfall. Sand is mostly used as typical cushion material in Japan. Sand and a bag in which sand is



Fig. 1 Rockshed and protection net

filled are also used for a protection shelf or protection embankment for the same purpose. Risk is rarely remained sometimes at the protection structure for the rockfall with large energy beyond initial estimation (Fig.3) [3], [4]. Research of this shock absorbing material has been done for



Fig. 2 Embankment for rockfalls



Fig. 3 Failed rockshed by large rockfall

years [5]. However, the evaluation method of impact behavior and the absorbing effects of impact force which is transmitted to the structure through the cushion are not necessarily clarified enough. It has been clear empirically that sand cushion has a large shock absorbing effect. Therefore, the use of sand cushion material for protection structures, such as a rockshed, is considered rational against the impact

force by a rockfall etc. and also in future.

When a protection structure is designed according to the idea of a performance based design, it is necessary to clarify the ultimate state of a protection structure in which sand cushion is installed. It is also required to advance suitable use of cushion material from the point of repair and reinforcement of the existing structure. In this research, the series of impact experiments to the sand cushion on H section steel beam were conducted in order to obtain the fundamental data about the impact action for designing a structure safely and rationally. This paper reports the knowledge acquired by investigating the impact force, the absorbing effect of sand cushions, dynamic interaction between structure and cushion.

2. OUTLINE OF EXPERIMENT

2.1 Method of Experiment

Fig. 4 shows the free-fall type device for impact experiment set up at Structure Engineering laboratory of the Kanazawa University. The sand tank filled up with sand cushion material was installed in the center of two H beams, which were simple supported locating in parallel. The size of a sand tank was 350 mm in width, 350 mm in depth and 500 mm in height. It was fixed to H beams with the angle steel beams and bolts.

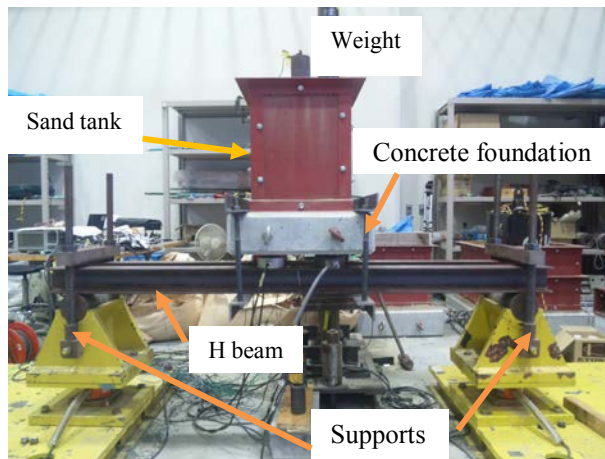


Fig. 4 Device of impact experiment

The used H beams were H-100x100x6x8 (mm). The span lengths of beams were 1.3 m, 1.8 m, 2.8 m and 3.8 m. The used weight is a steel cylinder with a diameter of 80 mm and a mass of 7.233 kg, and the tip form is spherical. Two kinds of shock absorbing materials accordingly one kind of sand and one kind of gravel were used. The characteristic values of sand and gravel are shown in Table 1. The used gravel and sand were crushed stone and loose sand with grain size ranges as shown in Fig. 5. The sand tank was covered by a thickness of 0.5 m in both cases.

Table 2 shows the list of all experiments carried out. The falling heights of the weight were seven kinds respectively 0.5 m, 0.75 m, 1.0 m, 1.25 m, 1.5 m, 1.75 m and 2.0 m. 3 times impact experiments were carried out on each condition.

2.2 Measurement Items and Measurement Method

Measurement devices involve an accelerometer (Kyowa Electronic Instruments Co., Ltd., AS-100HA), load cell (Kyowa Electronic Instruments Co., Ltd., LUK-1TBS), laser displacement meter (Keyence Corporation, LB300) and strain gauge (Tokyo Sokki Kenkyujo Co., Ltd., FLA-10-11-3-LT) as shown in Fig. 6.

Table 1 Properties of used cushions

Type	D_{10} (mm)	D_{30} (mm)	D_{60} (mm)	Effective particle size D_{50} (mm)	Uniformity coefficient C_u	Coefficient of curvature C_c
Sand	0.2	0.34	0.61	0.49	3.10	0.95
Gravel	4.0	5.5	6.5	6.1	1.63	1.16

Concretely, the accelerometer was installed at the center of the weight to measure its acceleration. The laser displacement meter was used to measure deflection of steel beams. Transmitted force of sand tank to H beams was determined through the load cells placed between the tank bottom and the beams. The strain gauges mentioned above were stuck to measure axial direction strain at the top and bottom flange of the central section of H beam.

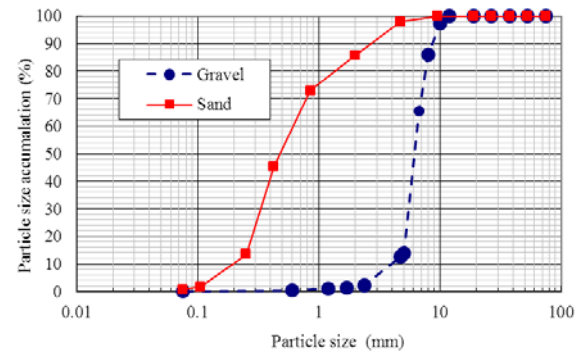


Fig. 5 Particle size accumulation curve

Table 2 List of impact experiments

Cushion	Span length of beam (m)	Falling heights of weight (m)
Sand	1.5	0.50, 0.75, 1.00, 1.25, 1.50, 1.75, 2.00
	2.0	0.50, 0.75, 1.00, 1.25, 1.50, 1.75, 2.00
	3.0	0.50, 0.75, 1.00, 1.25, 1.50, 1.75, 2.00
	4.0	0.50, 0.75, 1.00, 1.25, 1.50, 1.75, 2.00
Gravel	1.5	0.50, 0.75, 1.00, 1.25, 1.50, 1.75, 2.00
	2.0	0.50, 0.75, 1.00, 1.25, 1.50, 1.75, 2.00
	3.0	0.50, 0.75, 1.00, 1.25, 1.50, 1.75, 2.00
	4.0	0.50, 0.75, 1.00, 1.25, 1.50, 1.75, 2.00

Fig.7 shows the measurement system of this experiment. The output obtained from each measuring instrument was measured at intervals of the sampling of 100 μ s (sampling frequency: 10 kHz) and recorded by PC.

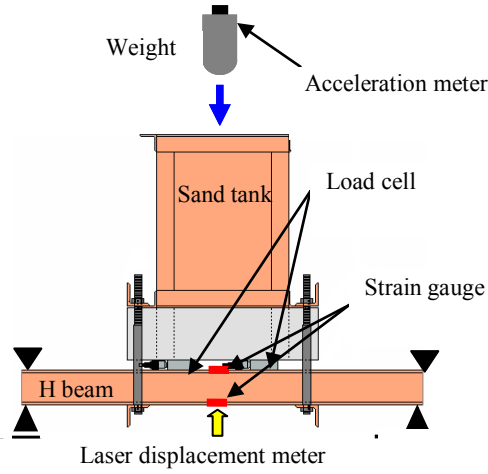


Fig. 6 Measurement devices and their locations

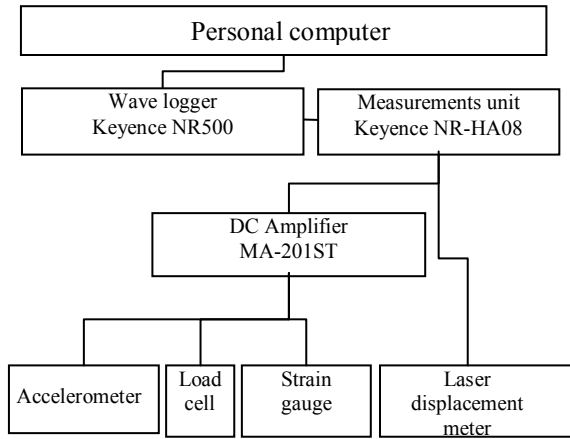


Fig. 7 Measurement system

3. RESULTS OF EXPERIMENT

3.1 Dynamic behavior of impact experiment

Fig. 8 shows the time history of measured data for the case 1.8m in span length, 2.0 m in falling height for sand cushion. The acceleration of the falling weight reached the peak at approximately 0.01 s after collision to the sand cushion and became zero at 0.02 s. Transmitted force measured under the sand tank appeared at 0.005 s, reached its peak at 0.016 s and became zero at 0.025 s. The damped oscillation of transmitted force was shown afterward. Strain and displacement appeared at 0.01 s, reached its peak also at approximately 0.016 s and became zero at 0.025 s. The similar damped oscillations were shown afterward in both time histories.

Generally the dynamic behavior of structure under hard impact load is complicated. Here, hard impact means that the

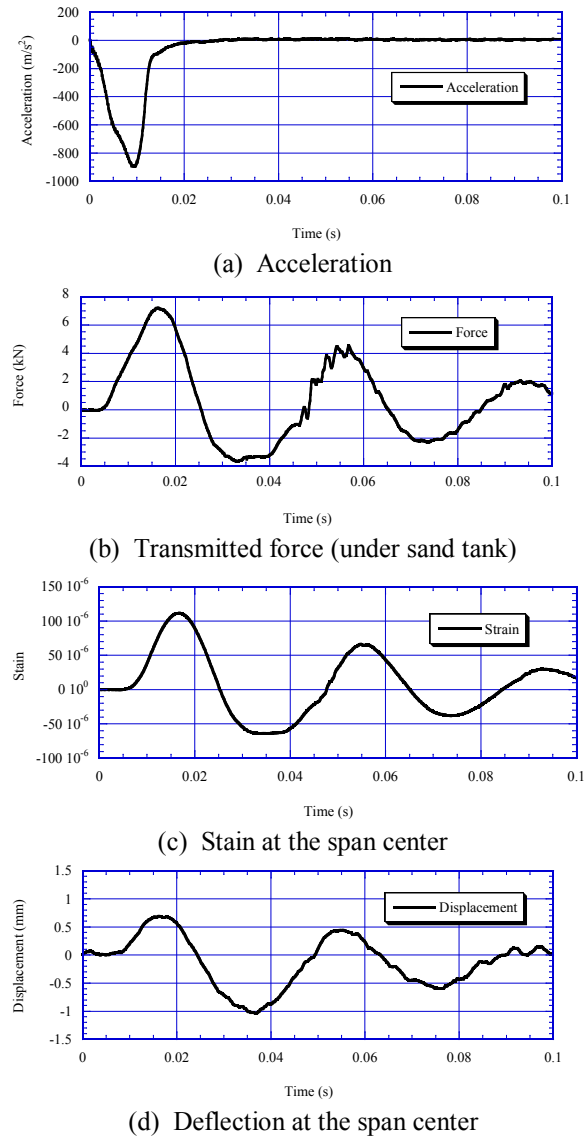


Fig. 8 Time histories of measured data (Sand, span length 1.8m, falling height 2.0m)

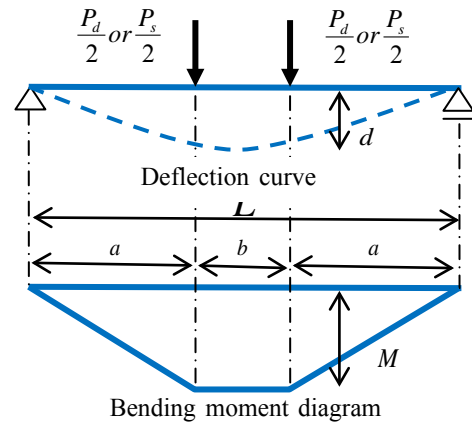
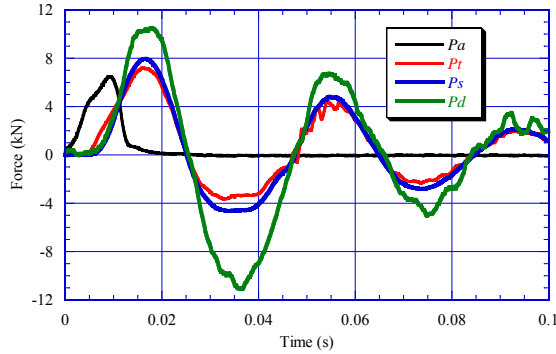


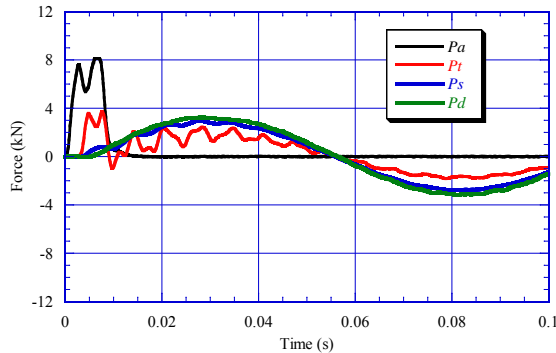
Fig. 9 Deflection and bending moment of the beam under equivalent static forces P_d and P_s

magnitude of impulse force is large and duration of impact is very short. Meanwhile, it is also known that the response of structure under relatively soft impact load is mostly quasi-static. Those beams used in this study have large mass

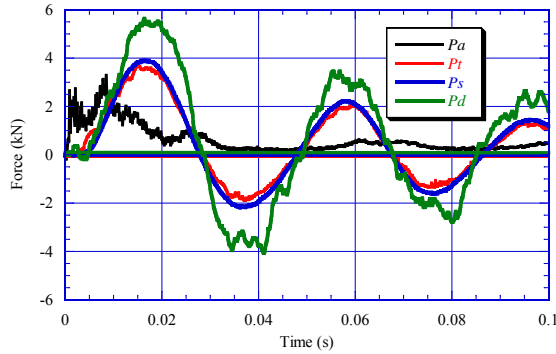
at the center of span center. Furthermore, the impact load occurred by collision of the weight to the cushion is relatively smooth because of shock absorbing effect of the cushion material. In that case, it can be assumed that the response of the beam was quasi-static. Fig. 9 shows the deflection curve and the bending moment diagram of the simple beam under two static concentrated loads. Equivalent static forces can be determined according to the deflection and the strain resulted by bending moment under this assumption. Here, P_s and P_d are equivalent forces by the strain and the deflection.



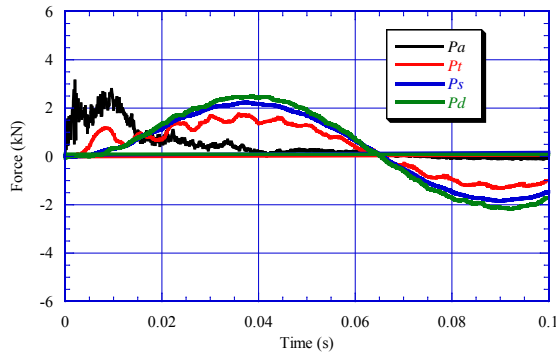
(a) Sand ($L=1.8\text{m}$, $H=2.0\text{m}$)



(b) Sand ($L=3.8\text{m}$, $H=2.0\text{m}$)

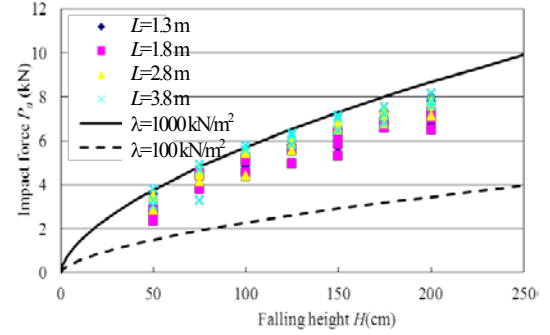


(c) Gravel ($L=1.8\text{m}$, $H=2.0\text{m}$)

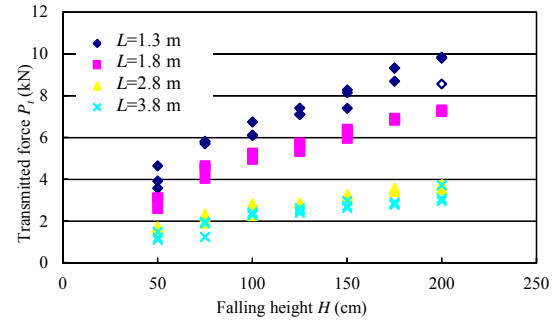


(d) Gravel ($L=3.8\text{m}$, $H=2.0\text{m}$)

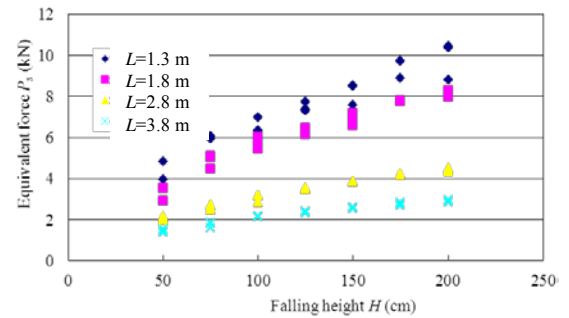
Fig. 10 Impact force, transmitted force and equivalent forces by strain and deflection



(a) Falling height and impact force P_a



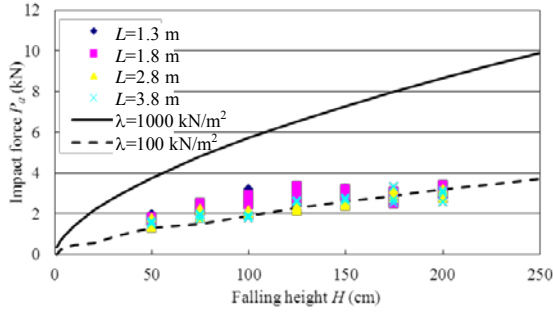
(b) Falling height and transmitted force P_t



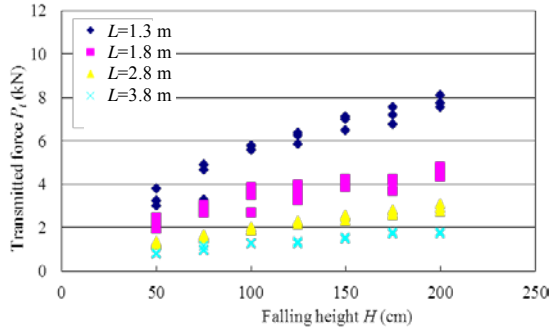
(c) Falling height and equivalent force P_s

Fig. 11 Relationship between falling height and various maximum force for sand
Fig. 10 shows time histories of impact force, transmitted force and equivalent forces by strain and deflection for four cases, namely span length $L=1.8\text{m}$ and 3.8m for sand cushion and gravel cushion. The falling height H is 2.0m in any case. The

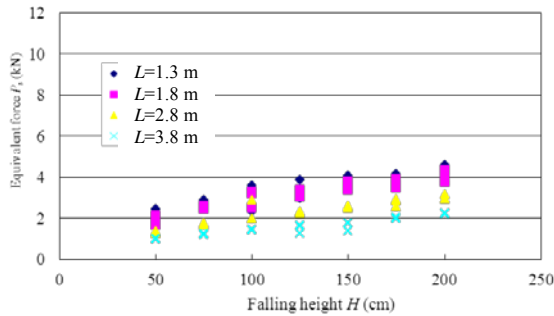
impact force P_a is smaller than other forces for sand ($L=1.8$ m, $H=2.0$ m). The maximum of force is large in the order of the transmitted force P_t , the strain equivalent force P_s and the deflection equivalent force P_d in this case. Meanwhile, the impact force P_a is larger than other forces for sand and longest span length $L=3.8$ m. The shape of first wave of transmitted force P_t is similar to the impact force P_a . However, the wave shape of P_t afterward, the equivalent forces P_s and P_d are similar with longer period than the span length $L=1.8$ m and maximum values of those are smaller than P_a . For the gravel, similar tendencies are observed.



(a) Falling height and impact force P_a



(b) Falling height and transmitted force P_t



(c) Falling height and equivalent force P_s

Fig. 12 Relationship between falling height and various maximum forces for gravel

However, maximum values of forces are smaller than those in sand. It became clear that the gravel has more excellent shock absorbing ability than sand and the large flexibility of the beam itself also contributes to the cushioning role for impact.

3.2 Maximum impact force

Fig. 11 shows the relationship between falling height and various maximum impact forces for sand. In Fig. 11(a), lines estimated by the design formula for the impact load due to rock fall are shown. The formula was drawn from the elastic contact theory and widely used in Japan. This design formula is expressed as following equation [1].

$$P = 2.108(mg)^{2/3} \lambda^{2/5} H^{3/5} \quad (1)$$

Here, m is the mass of a falling rock (ton), H is the height of a rock fall (m), λ is the Lamé coefficient of cushion material (kN/m^2) and g is the gravity acceleration (m/s^2).

There is no significant difference among span length L concerning the impact force P_a . The upper limit of the impact force is expressed by equation (1) of $\lambda=1000\text{kN/m}^2$. Concerning the transmitted force P_t , it is understood that the force becomes small, so that the span length is large. Mostly similar tendency is also observed for the strain equivalent force P_s . The strain equivalent force P_s is little larger than transmitted force P_t .

Furthermore, Fig. 12 shows the relationship between falling height and various maximum impact forces for gravel. There is also no significant difference among span length L concerning the impact force P_a as observed in the case of sand. The lower limit of the impact force is expressed by equation (1) of $\lambda=100\text{kN/m}^2$. Concerning the transmitted force P_t , it is understood that the force becomes small, so that the span length is large. Similar tendency is also observed for the strain equivalent force P_s . The strain equivalent force P_s is smaller than transmitted force P_t . It is contrary to the case of sand.

3.3 Dynamic multiplication and energy transfer

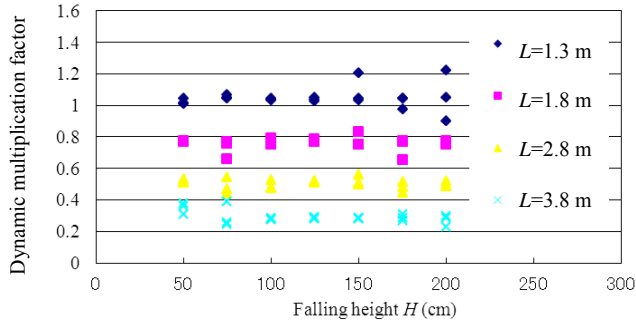
It is generally required to estimate the impact load rationally and safely for the practical design of protection structure. Some experimental results and discussions are shown here concerning dynamic multiplication and energy transfer from the falling weight to the beam.

Fig. 13 shows the results concerning dynamic multiplication for sand. Fig 13 (a) shows the relationship between the falling height H the dynamic multiplication factor. The dynamic multiplication factor is generally expressed as following equation.

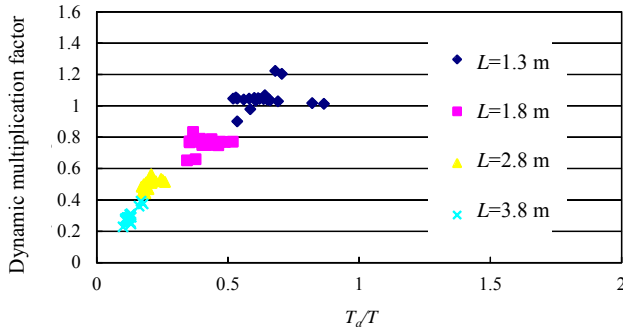
$$D_{MF} = \frac{R_{dyn}}{R_{st}} \quad (2)$$

Here, R_{st} is the response of the structure when the maximum dynamic force acts statically and R_{dyn} is the dynamic response of the structure. In this case, strain is used for the response of structure. It became clear that there is no particular relationship between the falling height H and the

dynamic multiplication factor D_{MF} and it is mostly constant. The dynamic multiplication factor D_{MF} becomes small if the span length L of the beam becomes large. Because the longer span beam has the longer first natural period T for mostly constant duration of impact force T_a . Fig 13(b) shows the Relationship between T_a/T and dynamic multiplication factor D_{MF} . It is clearly recognized that there is a proportional



(a) Falling height and dynamic multiplication factor



(b) Relationship between T_a/T and dynamic multiplication factor (T_a : duration of impact force, T : the first natural period of beam)

Fig 13 Dynamic multiplication factor by impact (sand)

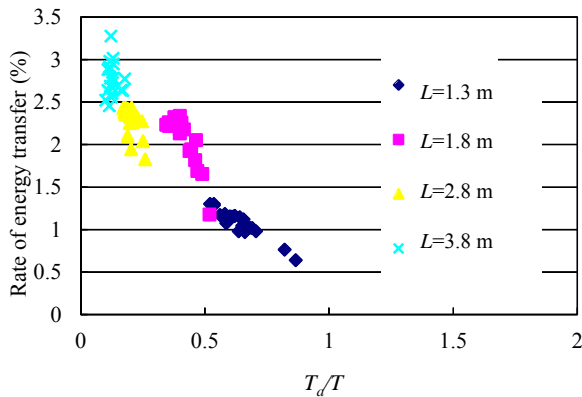


Fig 14 Relationship between T_a/T and rate of energy transfer to beam from falling weight (sand)

relationship between T_a/T and the dynamic multiplication factor D_{MF} .

Fig. 14 shows the relationship between T_a/T and rate of energy transfer to beam from falling weight for sand. The energy transfer is the transferred energy from the potential energy of the weight mgH to the beam. It has become clear that the rate of energy transfer becomes small when the ratio T_a/T becomes large. The rate of energy transfer R_E^r is important to design the member and structure under the impact. It can be considered that one of important characteristics of shock absorbing cushion is expressed by this rate of energy transfer.

We are doing further investigation concerning detailed formulation of this effect and application to design.

4 CONCLUSION

In this research, the series of impact experiments to the sand cushion on H section steel beam were conducted in order to obtain the fundamental data about the impact action. Obtained results in this research are summarized as follows.

- 1) The dynamic behaviors of H steel beam with cushion under impact were concretely shown including characteristic of impact force. The concept and actual data concerning equivalent force were introduced and shown.
- 2) The impact force P_a obtained by the acceleration of the weight is mostly equal depending only falling height H both in in sand cushion and gravel cushion.
- 3) The transmitted force at the bottom of cushion P_t becomes small when the span length L becomes large because of the effect of dynamic flexibility of the beam. The force in gravel cushion is smaller than that in sand cushion
- 4) The magnitude of equivalent force P_s or $P_{\bar{s}}$ also depends on the span length as like that of the transmitted force P_t .
- 5) The dynamic multiplication factor D_{MF} has particular relationship to the natural period of the beam T and no relation to the falling height H .
- 6) The rate of energy transfer to the beam from falling weight R_E^r was concretely shown. It has been shown that there is relationship between R_E^r and the natural period of the beam T .

5 ACKNOWLEDGMENT

Mr. A. Satoh and Mr. S. Nakamura of Nihon Samicon co. Ltd. contributed the preparation of experiments. Mr. T. Kojima and S. Eno, students of Kanazawa University, contributed effectively to pursuit of experiments. Herein, authors express sincere great gratitude to them.

REFERENCES

- [1] Japan road association "Handbook of preventatives against rockfalls", Japan road association, 2000 (in Japanese).

- [2] Vogel T., Labiouse V. and Masuya H., “Rockfall Protection as an Integral Task” *Structural Engineering International*, Vol. 9, No.3, 2000, pp.304-3124.
- [3] Schellenberg, K. ”On the Design of Rockfall Protection Galleries”, Doctoral theses, Swiss Federal Institute of Technology Zürich, No. 17924, 2009.
- [4] Delhomme F., Mommessin M., Mougin J.-P., and Perrotin P., “Behavior of a structurally dissipating rock-shed: experimental analysis and study of punching effects”, *Int. J. Solids Struct.*, Vol. 42, No.14, 2005, pp. 4203–4219.
- [5] Masuya H., Aburaya Y., Futo S., Sato A. and Nakamura S., “Experimental study of the weight collision on a sand cushion and its impact action”, *Proceedings of 8th International Conference on Shock & Impact Loads on Structures*, 2009, pp. 429-434.

Landslides in Tea Plantation Fields in Shizuoka, Japan

Jun Sugawara
Golder Associates, Australia

ABSTRACT

Shizuoka Prefecture in Japan is famous for the production of quality Japanese green tea. Approximately 45% of Japan's tea is produced in Shizuoka. In this region, tea plants are often grown in hilly terrain. Therefore, due to this topographic setting, as well as other natural characteristics including geotechnical and geological conditions, tea plantation fields are occasionally subject to landslides. This paper investigates the relationship between the tea plantation fields and landslide prone areas in Shizuoka Prefecture. In this study, tea plantation fields are described from the engineering standpoint. Typical mechanisms of landslides that have occurred in the tea plantation fields are also studied. A series of investigations reveal that there are many common points between the tea plantation fields and the landslide prone areas in this region.

Keywords: Landslides, Tea Plantation Fields

1. INTRODUCTION

Drinking green tea has been a part of everyday life for Japanese people for a long time. It is not only part of the Japanese culture, but it also provides health benefits. A number of researchers have revealed various potential positive effects of drinking green tea such as anti-cancer, anti-oxidant, fat burning, prevention of arteriosclerosis, lowering blood pressure and reducing cholesterol.

Shizuoka Prefecture in Japan is famous for the production of quality Japanese green tea. Cultivation of tea plants started this region in 1241 when a monk named Shoichi Kokushi planted green tea seeds which he brought back from China [1]. Cultivation of tea plants became economically important in the 18th century and since then this region leads the tea production in Japan. Today Shizuoka Prefecture produces 40,000 tonnes of tea, which is approximately 45% of Japan's overall tea production, refer Figure 1.

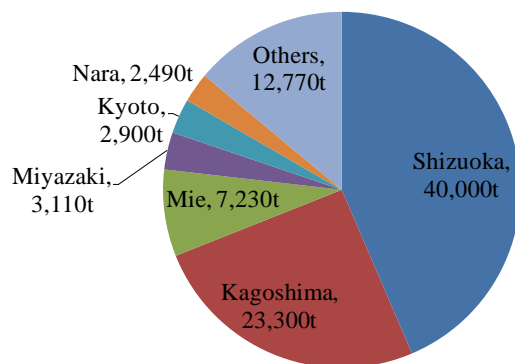


Fig. 1 Amount of Tea Production in Japan (after [2])

The author noticed that tea plants are often grown in hilly terrain and therefore tea plantation fields in Shizuoka are occasionally subject to landslides. In response to this fact, this paper investigates the relationship between the tea plantation fields and landslide prone areas in Shizuoka Prefecture from the engineering standpoint.

2. TEA PLANTATION AND LANDSLIDES

The northern part of Shizuoka Prefecture is surrounded by 3,000 meter high mountains which make up a mountain range called the Southern Alps. Many major rivers in Shizuoka Prefecture originate in this mountain range (e.g. Fuji River, Abe River and Ooi River) or the Central Alps (Tenryu River) and flow downstream to the Pacific Ocean. Due to steep river bed slopes (Fig. 2), these rivers discharge significant volumes of sediment into downstream areas following heavy rainfall events, causing a number of sediment related disasters. At the time of April 2012, there are 24,466 designated sediment related disaster areas in Shizuoka Prefecture [4]. In addition, there are number of geographical areas named after past sediment related disasters such as Hatanagi, Ooyakuzure and Ookuzure in Shizuoka Prefecture.

Major tea plantation areas in Shizuoka Prefecture, shown in Fig. 3, overlap somewhat with sediment related disaster areas. It is known that areas of frequent fog and with a significant temperature difference between day and night produce high quality tea. Hence many tea plantation fields in Shizuoka Prefecture are located on the hilly terrain at the foothills of the mountains. As a result, tea plantation fields in this region are occasionally subject to landslides.

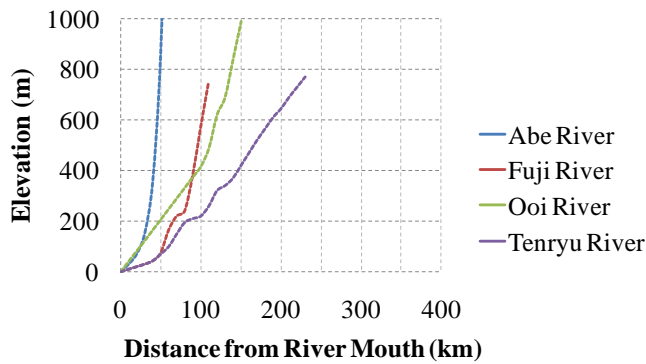


Fig. 2 Relationship between Elevation and Distance from Mouth of Class A rivers in Shizuoka Prefecture (after [3])

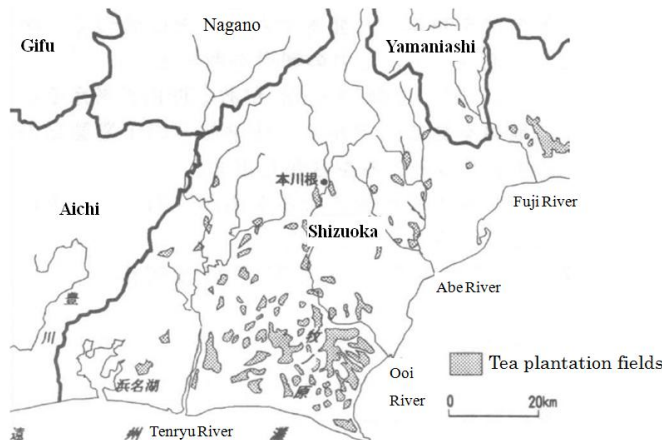


Fig. 3 Major Tea Plantation Fields in Shizuoka Prefecture (after [5])

3. MECHANISM OF LANDSLIDES IN TEA PLANTATION FIELDS

3.1 Primary Cause

In Japan, causes of landslides are generally separated into the primary cause and the triggering cause. The primary causes are factors related to topography, geology, hydrogeology etc. and the triggering causes include heavy rainfall, earthquake, earthworks, and others. In this region, it appears that there are many common points such as topography, geology, soil chemistry, hydrogeology and so on between the tea plantation fields and the landslide prone areas. The following sections will discuss typical primary cause of landslides in tea plantation areas.

3.1.1 Topography

In Shizuoka Prefecture, tea trees are often planted on sloping ground (Photo 1). This is because sloping ground can offer various advantages over flat ground, including their good natural drainage system, longer sunshine duration, larger day and night temperature difference and lower risk of cold air stagnation. All these advantages allow production of high quality teas [6] and result in hillsides being the preferred location for tea plantation fields.

Moreover, advantages of planting tea trees on slopes may not be limited to these natural conditions. For instance, choice of

productive agricultural products using hilly slopes is very limited. Among these products, tea plantations are considered as one of the most profitable business [7]. In addition, only relatively small sized machines, or no machines, are required in tea plantation fields making it easy to plant tea trees on slopes.



Photo 1 Photographs of Typical Tea Plantation Fields on Sloping Ground in Shizuoka Prefecture

According to [2], 7,377 ha (41% of overall tea plantations in Shizuoka Prefecture) of tea plantations are on ground inclined at less than 8 degrees, 4,081ha (24%) is on ground sloping between 8 and 15 degrees, 5,350 ha (32%) is on slopes steeper than 15 degrees in Shizuoka Prefecture. Since the total area of tea plantations on slopes steeper than 15 degrees is 6,074 ha in Japan, almost 70% of tea plantations on relatively steep slopes are located in Shizuoka Prefecture. This topographic characteristic is considered to be one of the primary reasons that the chance of landslides in tea plantations in Shizuoka Prefecture is significantly higher than other prefectures in Japan.

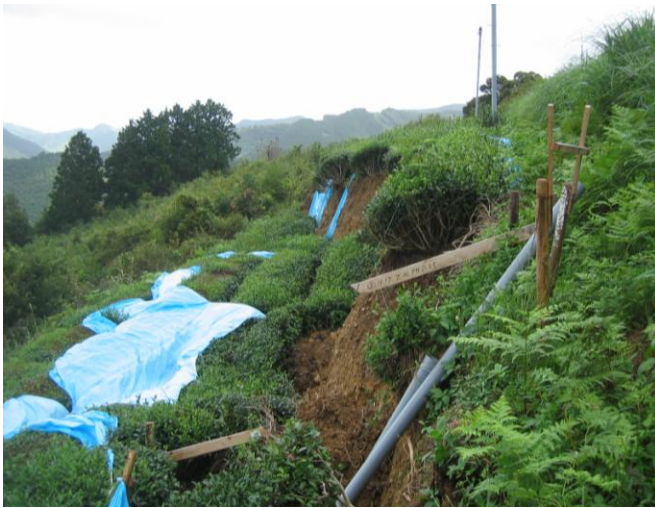


Photo 2 Crest of Landslide in Tea Plantation Fields

3.1.2 Geology and Soil Chemistry

High permeability ($> 1 \times 10^{-4}$ cm/sec), high aeration and high water retention are important soil characteristics for growing tea plants. The bedrock of tea plantation fields needs to be deep and the arable soil, free from impermeable layers, must be sufficiently thick. It is also important that the soil mass in the root system does not contain a large portion of fine particles.

The Makinohara Plateau located approximately in the centre of Shizuoka Prefecture is one of the most famous tea production areas in Japan. This area comprises approximately 20 to 30 m thick Ooi River alluvial fan sediments containing Quaternary Pleistocene uncemented gravelly layers and/or mud layers, which is overlying Miocene to Pliocene sedimentary layers. While soils in this region are suitable for growing tea plants due to their weakly acidic and high natural drainage characteristics, there are a number of slope instabilities due to their high erosion susceptibility.

In addition, colluvium slopes on hilly mountains, which are usually considered not suitable for cultivating agricultural products, are often used as tea plantation fields. This is mainly because colluvium, which tends to lose basic minerals and become acidic, is suitable for the growth of tea trees [2].

Tea plants are aluminum-philic and acid resistant. They grow well in the soil in which pH ranges between 4.0 and 5.0. Nitrogen fertilizer is often used in tea plantation fields since the quality of the tea increases with an increase of nitrogen in the soil mass. Because of this, tea plantation fields are often too acidic for other agricultural products. Therefore little beneficial effect from tree roots for reinforcing slope stability is expected in an acidic soil environment. This also contributes to the fact that tea plantation fields are susceptible to the erosion during heavy rainfall events.



Photo 3 Tea Plantation Field in Colluvium Slopes

3.1.3 Past Landslide Sites

Japan has a population of 120 million in an area of about 370,000 km² and has the one of the highest population densities in the world. Therefore the redevelopment of past landslide sites is an important engineering and social topic in Japan. To date, past landslide sites are often used as parks after rectification works in Japan (e.g., Jizukiyama memorial park and Chausuyama park in Nagano Prefecture).

In Shizuoka Prefecture, tea plantation fields are often found in the past landslide sites. The author considers that planting tea trees is a good way of utilising past landslide sites. This is because:

- Profitability of tea plantations per unit cultivable area is generally higher than other agricultural products.
- Machines required in tea plantations (e.g., green tea cut machine) are smaller in size, lighter in weight and less expensive compared with those required for other agricultural products. Therefore they are transportable to most of the tea plantation fields including difficult access areas on past landslides and hill slopes.
- Soils in the past landslide sites are often acidic due to loss of alkali ion which suite the growth of tea plants.

In the past landslides sites, tea plantations are often located in the depression zone near the landslide crown or the lobate near the landslide toe where the landslides debris are deposited and slopes become relatively gentle.

It should be noted that these past landslide areas may be used without appropriate rectification works and farmers may be using these areas without knowing about past landslide events. Landslides in these areas could be reactivated, even with relatively minor triggering events.



Photo 4 Tea Plantation Field in Past Landslide Site

3.2 Triggering Cause

Triggering causes of landslides are broadly separated into the natural causes and those related to human activity. The natural triggering causes include intense and/or long rainfall events, snowmelts, earthquakes, scouring or erosion of the toe of the slope and so on. Causes related to human activities include excavation, filling, tunneling, ponding of reservoirs, and the like.

3.2.1 Rainfall Events and Groundwater

The tea plants can grow well in areas with an average yearly temperature above 13 degree C, snowfall of not more than 1m and yearly rainfall of more than 1,400 mm [2]. More than 1,000 mm of rainfall is required during the growth period of the tea plants between April and October [9]. Many areas in Shizuoka Prefecture satisfy these requirements due to their warm and moist environment (Fig. 4) and thus tea is the one of the most representative agricultural products in this region.

While rainfall is essential to the growth of tea plants, there are a number of sediment related disasters due to the heavy rainfall events. As shown in Table 1, 86 slope failures occurred due to heavy rainfall events within a relatively short time period.

As described previously, the permeability of the soil in the tea plantation fields needs to be high. Therefore even if the groundwater level is low during the dry season, the rise of groundwater in tea plantation fields could be significant during or/and after intense rainfall events (Fig. 5).

Under such circumstances, slope failures may occur suddenly without any warnings. Once the slope starts moving, the rate of movement could be also very rapid.

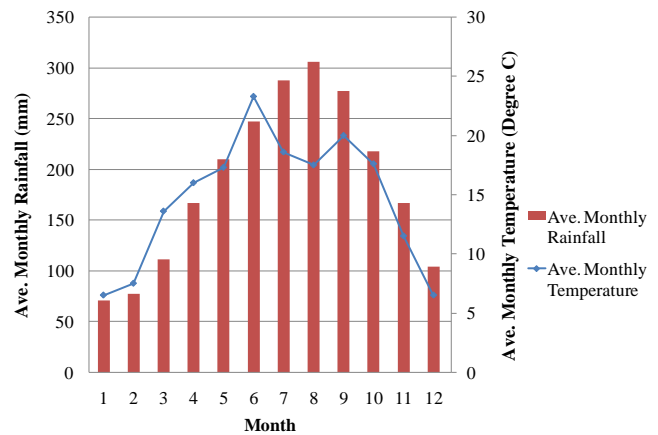


Fig. 4 Rainfall and Temperature of Makinohara City (after [9])

Table 1 Summary of Sediment Related Disasters in Shizuoka Prefecture from 1 Jan. to 3 Oct. 2011 (after [10])

Type	Triggering Cause	
	Earthquake	Heavy Rainfall (incl. Typhoon)
Debris Flow	0	13
Landslides	0	7
Rock falls	7	66
Total	7	86

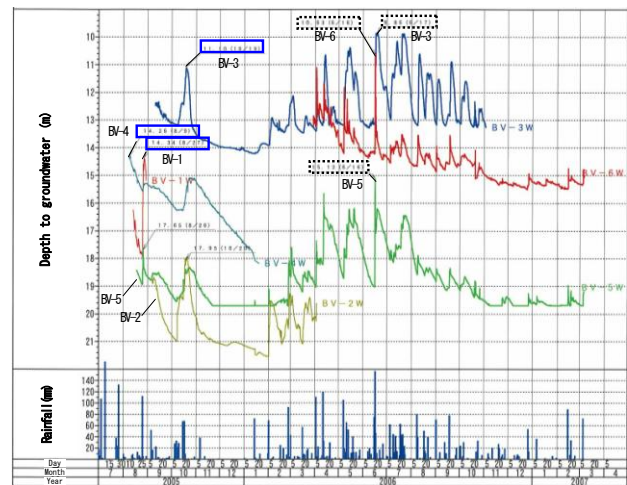


Fig. 5 Significant Rise of Groundwater Level in Tea Plantation Fields due to Rainfall Events

3.2.2 Human Activities

Shizuoka Prefecture has the largest tea plantations fields in Japan. 2.6% of lands in Shizuoka Prefecture are used as tea plantation fields. Of particular note is that about 25% of Makinohara City's land is used as tea plantation fields [9].

Therefore construction activities are often required to extend into tea plantation fields. As a result, the chance of landslides in tea plantation fields due to these human activities is inevitably high in Shizuoka Prefecture compared with other prefectures.



Photo 5 Earthworks Extended Close to Tea Plantation Field



Photo 6 Drainage Well in Tea Plantation Field

4. LANDSLIDE MITIGATION

Shizuoka Prefecture has approximately 41,200 tea farm households, which is the highest numbers in Japan. Tea farming is a very important source of income for them.

Therefore tea farmers are often reluctant to be disturbed by construction activities such as landslide rectification works, particularly during the first tea crop of the season from late April to May. Governmental administration bodies in this region are also fully aware of this issue.

One of the key aspects that needs to be taken into account during the selection of landslide rectification works is to minimise the damage to tea plantation fields. Cutting the upper portions of the slope or filling near the toe of the slope, which affects existing tea plantations fields, is therefore often considered an inappropriate technique by landholders and governmental administration bodies.

Moreover when groundwater control measures (e.g., gravity drains or drainage wells) are adopted for landslide rectification works, it is also important not to drain groundwater completely from the tea plantations fields so that sites remain suitable as tea plantation fields after rectification works.

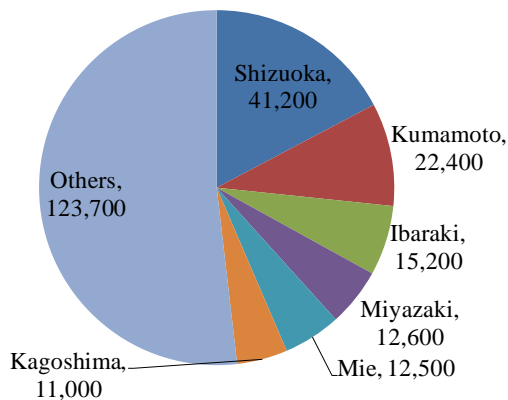


Fig. 6 Number of Tea Farm Households in Japan (after [2])

5. CONCLUSION

In this study, the relationship between the tea plantation fields and landslide prone areas in Shizuoka Prefecture was investigated. A series of investigations reveal that there are many common points between the tea plantation fields and the landslide prone areas in this region. From this study, the following conclusions can be drawn:

- Almost 70% of tea plantation fields on more than 15 degree slopes are located in Shizuoka Prefecture. This topographic characteristic is considered to be one of the primary reasons that the chance of landslides in tea plantations is high in Shizuoka Prefecture.
- Tea plants grow well in soil in which pH ranges between 4.0 and 5.0. Due to this reason as well as meteorological conditions, tea plants can grow in colluvial soils which may be susceptible to the erosion during heavy rainfall events.
- Tea trees are often planted on existing landslide sites. Hence these areas are generally susceptible to reactivation. Landslides in these areas could be reactivated even with relatively minor triggering causes.
- While rainfalls are essential to the growth of tea plants, there are numerous sediment related disasters due to heavy rainfall events.
- Construction activities are often required that extend into tea plantation fields in Shizuoka Prefecture. As a result, the chance of landslides in tea plantation fields due to these human activities is inevitably high in this region

6. ACKNOWLEDGMENT

Valuable comments were made by Aya Green Tea during writing of this paper and I am most grateful to them for their suggestions.

The author wishes to thank Amanda Barret for reviewing this paper.

7. REFERENCES

- [1] Shizuoka Prefecture, “Shizuoka Green Tea”, 2010, http://www.pref.shizuoka.jp/a_foreign/english/tea/index.html)
- [2] Rural Cultural Association, “Cha-Daihyakka”, vol. 1, Rural Cultural Association, 2008, pp. 269 – 302. (in Japanese)
- [3] Ministry of Land, Infrastructure, Transport and Tourism, “Kadou-Tokusei”, 2007, http://www.mlit.go.jp/river/basic_info/jigyo_keikaku/gaiyou/seibi/ooi_index.html (in Japanese)
- [4] Shizuoka Prefecture, “Number of designated Sediment-related Disaster Areas – Municipality Basis”, 2012, <http://www.pref.shizuoka.jp/kensetsu/ke-350/boushi/zyoukyou.html> (in Japanese)
- [5] Teikoku-Shoin, “How to Chizucho”, 2012, http://www.teikokushoin.co.jp/howto/pdf/index_16/index16/geo_36.pdf (in Japanese)
- [6] Shinseiki Koubou, 2007, <http://www.cha22.jp/daimon/001.html> (in Japanese)
- [7] Chamber of Tea Associations of Shizuoka Prefecture, “Ocha Q&A”, 2012, http://www.wbs.ne.jp/bt/chacha/main/qa_saibai.htm#Q54 (in Japanese)
- [8] Ito En, “Ocha-Hyakka”, 2006, <http://ocha.tv/production/cultivation/> (in Japanese)
- [9] Makinohara City, “Makinohara City Gaikyo”, 2012, http://www.city.makinohara.shizuoka.jp/ftp/05gt04/1_gaikyou.pdf (in Japanese)
- [10] Japan Sabo Association Shizuoka Branch, “Sabo Dayori”, vol. 175, Japan Sabo Association Shizuoka Branch, 2011, pp 2. (in Japanese)

NATURAL BASE ISOLATION SYSTEM FOR EARTHQUAKE PROTECTION

Srijit Bandyopadhyay¹, Aniruddha Sengupta² and G.R. Reddy³

¹ Graduate Student & ² Associate Professor, Indian Institute of Technology Kharagpur, India.

Email: sengupta@civil.iitkgp.ernet.in

³ Professor & Head, Structural & Seismic Engineering Section, Homi Bhabha National Institute, Mumbai, India.

ABSTRACT

The performance of a well-designed layer of sand, geo-grid, geo-textiles, and composites like layer of sand mixed with shredded tire (rubber) as low cost base isolators is studied in shake table tests in the laboratory. The building foundation is modeled by a 200 mm by 200 mm and 40 mm thick rigid plexi-glass block. The block is placed in the middle of a 1m by 1m tank filled with sand. The selected base isolator is placed between the block and the sand foundation. Accelerometers are placed on top of the footing and foundation sand layer. The displacement of the footing is also measured by LVDT. The whole setup is mounted on the shake table and subjected to sinusoidal motion with varying amplitude and frequency. The sand is found to be effective only at very high amplitude ($> 0.65g$) of motion. Among all the different materials tested, the performance of a composite consisting of 50% shredded rubber tire and sand placed under the footing is found to be most promising as a low cost effective base isolator.

Keywords: shake table; base isolation; Shredded rubber tire; model test.

1. INTRODUCTION

To find an economical and feasible way of designing new structures or strengthening existing ones for protection from the damages during an earthquake is one of the challenges in Civil engineering. The conventional approach to seismic hazard mitigation is to design structures with adequate strength and ability to deform in a ductile manner. Over the past two decades, newer concepts of structural vibration control including seismic isolation, installation of passive and active/semi-active devices ([1], [2], [3], [4]) have been growing in acceptance. Traditionally, earthquake-resistant design of low- to medium-rise buildings is particularly important, as their fundamental frequencies of vibration are within the range where earthquake-induced force (acceleration) is the highest as found during Mexico City Earthquake [5]. One possible mean to reduce the degree of amplification is to make the building more flexible [6]. In a low-to-medium-rise building, this necessary flexibility can be achieved by the use of base isolation techniques.

The primary mechanism for the reduction of shaking level in a base isolation method is energy dissipation. The concept of low-cost and effective earthquake protection techniques using natural material like sand was looked at by Qamaruddin and Ahmad [7], Qamaruddin et al. [8] and Feng et al. [9]. The use of a synthetic liner consisting of an ultra molecular weight polyethylene nonwoven geotextile, placed in the foundation of a structure, was also found to be an effective way of reducing seismic ground motion by Yegian and Kadakal [10],

and Yegian and Catan [11]. Soil reinforced with rubber demonstrates a tremendous increase in energy dissipation capability [12]. The feasibility of using shredded rubber mixed with sand as a natural base isolator was investigated theoretically by Gray et al. [13] and Tsang [14]. This paper presents results of experimental investigations into the performance of a layer of sand, geogrid, geotextile and sand mixed with shredded rubber tire as low cost base isolation systems.

2. EXPERIMENTAL SETUP

The laboratory model tests are performed on a 1m by 1m shake table. The table is shaken in a uniaxial horizontal direction by specifying a sinusoidal motion of given amplitude and frequency. The details of the shake table and its calibration can be found in Giri and Sengupta [15]. In the laboratory model tests, the building foundation or footing is assumed to be square and modeled by a 200mm by 200mm and 40mm thick, rigid plexi-glass block. The surcharge load (normal load) on the foundation due to the super structure is imparted by a number of steel plates (weights) bolted on top of the plexi-glass block. In all the cases, the surcharge load is 15kg. A coarse sand paper is glued to the bottom side of the block to model the roughness of the model footing. In the laboratory shake table tests, the model footing is placed inside a 1000mm by 1000mm and 500mm high, open plexi-glass container or tank. The plexi-glass container is made up of 12 mm thick plexi-glass sheets and reinforced with steel angles at all the corners and edges. About 30mm thick thermocol sheets are glued to all the sides of the container except one to minimize the reflection of waves at the ends. One side of the

plexi-glass container is kept clear to monitor the behavior of the model footing during a test. The whole setup is placed on top of the shake table and securely clamped to it to ensure no relative movement. The test container is then filled with sand up to 200mm height and compacted to the required density. Details of shake table arrangement are shown in Figure 1 below.

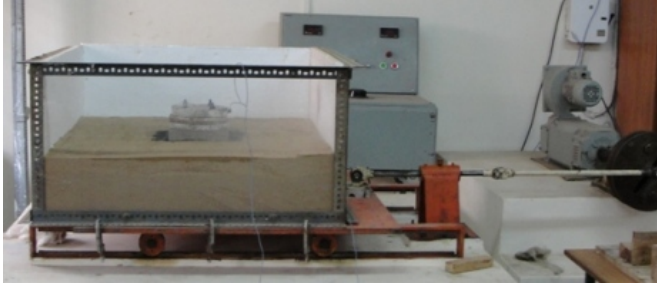


Figure 1. Shake table test setup.

The first series of tests are performed with the model footing placed on top of the sand layer at the middle of the container. The second series of tests are performed with a geogrid and a geotextile placed between the model footing and the sand foundation in the test tank. The third series of the tests are performed with the shredded rubber tire and sand mixture in different proportions as base isolator under the model footing. Before these third series of tests, a 20mm deep square excavation in the sand of the same size as that of the model footing is constructed. This excavation is then filled with the shredded rubber tire and sand mixture. The model footing is then placed over the shredded tire and sand mixture. Several proportions of shredded tire in the shredded rubber tire-sand mixture have been considered. But only the performances of sand mixed with 50% shredded rubber tire have been reported here as it yielded the best result.

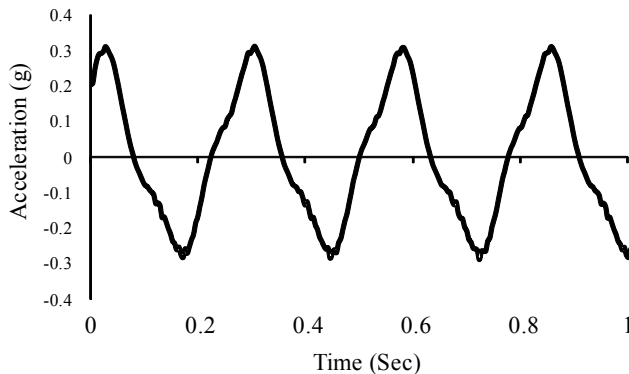


Figure 2. A typical input base motion.

3. BASE MOTIONS

The shake table along with the experimental setup is shaken in horizontal direction by a sinusoidal motions of amplitude 0.15g, 0.3g, 0.4g, 0.6g and 0.8g. The frequency of the motion is varied from test to test to study the effectiveness of the seismic isolators at different frequency of motion. The

different frequencies considered are 1.5, 3.5, and 4.5Hz. For each specified motion, vertical and horizontal acceleration of the shake table in addition to those on top of the foundation sand layer, and on top of the model footing are also recorded. Each of the motions is continued for at least 5 numbers of cycles to ensure the system had reached a steady state condition. A typical input base motion is shown in Figure 2. In all the cases, the results for the first few cycles are only shown for the clarity of the presentations. In all the cases, the results for the first few cycles are only shown for the clarity of the presentations.

4. EXPERIMENTAL RESULTS

4.1 Model footing resting on top of foundation sand

The performance of sand as a base isolator has been studied for the given base motions mentioned earlier. In this case, the model footing is resting directly on top of 200 mm deep sand layer within the test tank. The sand used in the study is a local uniform medium sand (Kansai River sand). It is classified as poorly graded sand (SP) as per Unified Soil Classification System. The specific gravity of the sand is 2.7. The maximum and minimum dry unit weights are 16.6 and 14.1 kN/m³, respectively. In all the tests, the relative density of the sand foundation within the test chamber is maintained at 65%. The shear strength (effective cohesion, c' and effective friction angle, ϕ') of the sand, as obtained from the laboratory direct tests, are given by $c'=0$ and $\phi' = 36^\circ$. Figure 3 shows the transmitted peak accelerations at the top of the footing resting on sand with respect to the peak acceleration of the base motion for different amplitude of motions (keeping the frequency constant at 3.5 Hz).

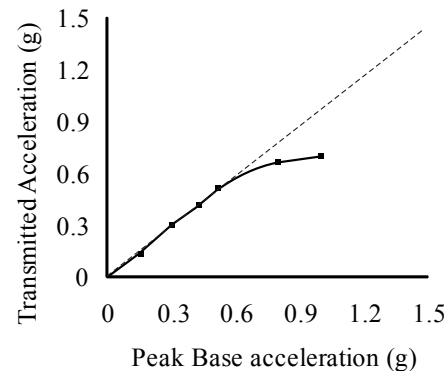


Figure 3. Footing response for different base motions with constant frequency of 3.5Hz.

The figure shows that at and around 0.6g amplitude of base motion, the sand beneath the model footing starts to dampen the base motion. This is accompanied by a sliding movement of the model footing. This back and forth sliding movement of the model footing is around 3mm in case of 1g motion of the shake table. It is clear from the above figures and tables that the sand layer in the foundation behaves as an effective base isolator only at high amplitude (above 0.6g in these

cases) of base motions.

4.2 Model footing resting on top of Geogrid & Geotextile

In this case a geo-grid/geotextile is placed underneath the model footing and on top of the sand foundation. A polyester geogrid (SF20), composed of high molecular weight, high tenacity (ultimate tensile strength= 40MPa at 4% strain), multi-filament polyester yarns, and having 19mm openings is utilized here. The geotextile utilized here is a 200gsm nonwoven geotextile. The ultimate tensile strength of the material is found to be 2.3MPa. The following figure shows the geogrid and geotextile utilized in this study. The size of the both geogrid and geotextile are 200mm by 200mm, that is, same as that for the model footing.

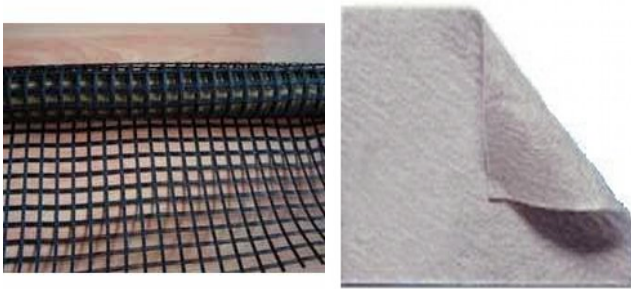


Figure 4. (a) Geogrid & (b) Geotextile utilized in the study.

Figures 5 and 6 show the responses of the footing resting on geogrid and geotextile to various base motions with constant frequency of 3.5Hz.

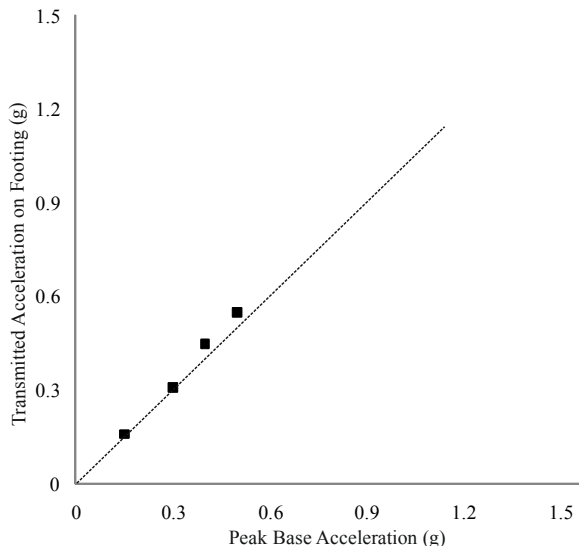


Figure 5. Response of model footing resting on geogrid for base motions with constant amplitude of 3.5Hz.

The above figure shows that the geogrid chosen is actually amplifying the base motion transmitted to the top of the

footing. The response of the model footing resting on the geotextile is marginally better than the footing resting on geogrid. As may be found from Figure 6 below, the peak acceleration transmitted to the top of the footing are 0.14g and 0.48g for the corresponding base motion of 0.15g and 0.5g, respectively.

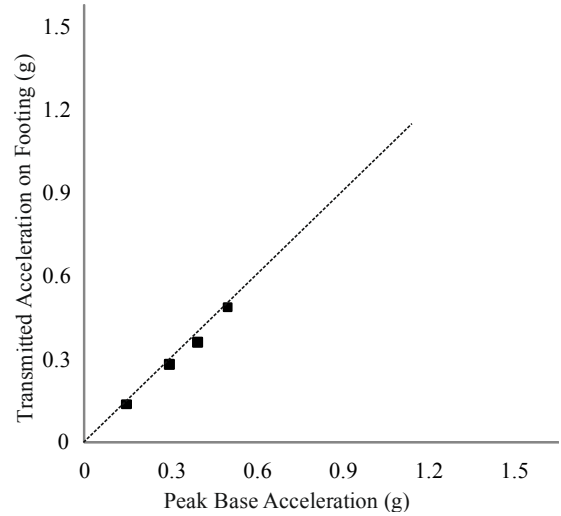


Figure 6. Response of model footing resting on geotextile for base motions with constant amplitude of 3.5Hz.

4.3 Model footing resting on top of a mixture of shredded rubber tire and sand

In this case, a 20 mm thick layer of sand and shredded rubber tire mixture is placed between the model footing and the foundation sand layer within the test tank. The shredded rubber tire is obtained from a local shop. The average length of a thread of shredded tire is 10 mm and the average diameter is 1 mm. Figure 7 shows a magnified view of shredded rubber tire and sand mixture.



Figure 7. Magnified view of 50:50 sand and shredded rubber tire mixture.

Three different proportions (by weight) of shredded rubber tire – 20%, 30% and 50% in sand have been utilized in this study as potential low cost base isolators under the model footing. However, the results of 50% shredded rubber

tire-sand mixture have been only presented here since these cases exhibit the best results under the present scenario. The direct shear strength of dry sand mixed with 50% shredded rubber tire is given by cohesion, $c'=30\text{kPa}$ and friction angle, $\phi'=30^\circ$. In these cases, a 20 mm deep square excavation in the sand of the same size as that of the model footing is constructed before the tests. This excavation is then filled with the shredded rubber tire and sand mixture in correct proportion. The model footing is then placed over the shredded tire and sand mixture (Figure 8). As done for the previous cases, in this case also the whole test setup is shaken on the shake table for the previously stated sinusoidal motions.



Figure 8. Model footing resting on 50% shredded rubber and sand mixture.

The comparison of the peak acceleration at the top of the model footing resting on sand mixed with 50 percentage of shredded rubber tire and the peak acceleration of the input (measured during the tests) base motions for a base motion of amplitude 0.3g and frequency 3.5 Hz are shown in Figure 9. The relative displacement of the model footing for this case is found to be about 1.8 mm and shown in Figure 10.

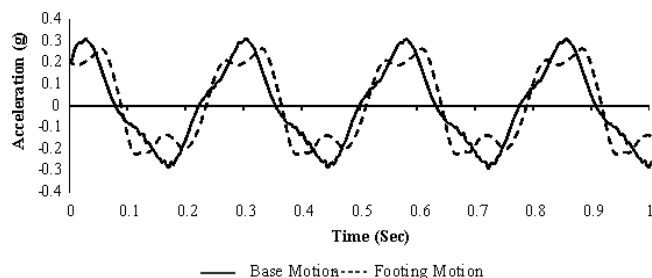


Figure 9. Footing response to a base motion of amplitude 0.3g and frequency 3.5Hz.

The comparison of the peak transmitted acceleration on top of the footing is also compared graphically with peak base acceleration in Figure 11. The test results show that, unlike in sand, even at small amplitude of base motion, the response of the model footing is remarkably less than the original base

motion. This indicates that the isolating layer consisting of sand mixed with 50% shredded rubber tire is quite effective in dampening the cyclic motions. Figure 11 attests to the effectiveness of the sand mixed with 50% shredded rubber tire as a base isolator for cyclic motions.

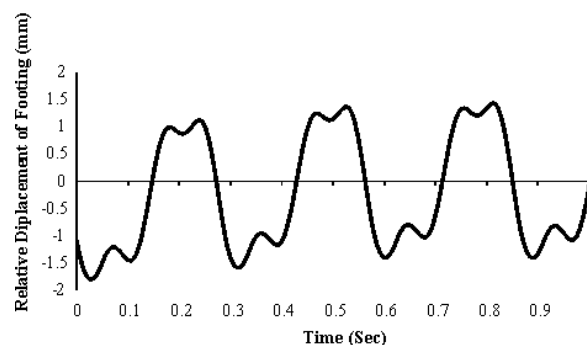


Figure 10. Relative displacement of the footing for a base motion of 0.3g and 3.5Hz frequency.

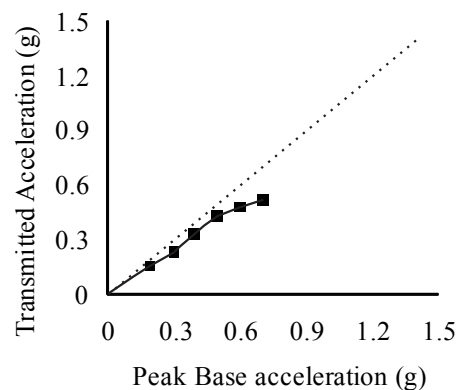


Figure 11. Comparison of the peak transmitted acceleration on top of the footing resting on 50:50 sand-shredded rubber tire mixture.

Table 1. Variation of peak acceleration at the top of footing and shake table for different frequencies of base motions with constant amplitude of 0.3g.

Frequency(Hz)	Peak Base Acceleration(g)	Peak Transmitted Acceleration(g)
1.5	0.3	0.2
2.5	0.3	0.25
3.5	0.3	0.23
4.5	0.3	0.22

Table 2. Variation of peak acceleration at the top of footing and shake table for different amplitude of base motions with constant frequency of 3.5 Hz.

Frequency(Hz)	Peak Base Acceleration(g)	Peak Transmitted Acceleration(g)
3.5	0.2	0.15
3.5	0.3	0.23
3.5	0.4	0.32
3.5	0.5	0.43
3.5	0.6	0.48
3.5	0.7	0.52

The response of the model footing resting on 50% shredded rubber tire and sand mixture to 0.3g base motions at various frequencies is shown in table 1. The effect of frequency on the response of the footing is not so clear at least for this case and other cases looked at. Table 2 shows the response of the footing to base motions of various amplitudes keeping the frequency constant at 3.5Hz. The effect of the base isolation is very clear from this table even at small amplitude of motion.

The shake table test conducted with higher than 50% shredded rubber tire in sand shows instability even at very small amplitude of base motion. The model footing with 15kg surcharge load on top starts to wobble at the very initial stage of this test and the test is discontinued.

5. CONCLUSIONS

The sand in the foundation of the model footing is found to be ineffective as a base isolator at low amplitude ($<0.6g$) of base motion. However at higher amplitude ($>0.6g$) of motion, it is quite effective in reducing the motion transmitted to the footing. At 0.8g and 1g, the accelerations at the top of the model footing show a remarkable decrease and this decrease in response is also accompanied by back and forth displacement of the footing over the sand foundation. At 1g of motion, the amplitude of this displacement is observed to be about 4mm.

The shake table tests with the model footing resting on a 20mm layer of sand and shredded rubber tire show that the proportion of shredded rubber tire should be 50% (by weight) to yield a significant favorable results. When the proportion of the shredded rubber tire is 50%, the response of the model footing is found to be significantly less than the motion of the foundation and shake table. When the percentage of rubber is further increased, the model footing is found to wobble (unstable) at 0.3g motion.

A base isolating system can be effective in two ways- 1) by reducing the input motion that the structure is subjected to, and 2) by shifting the predominant frequency of the structure from that of its base motion, so that resonance of frequency can not be achieved. This paper only addresses the base isolation by dampening of the input motion. Since all the input motions of the shake table are sinusoidal with a given frequency, the shifting of the frequency of the model footing during a test could not be studied. It is hoped to study this important aspect of the base isolation system in the next phase of the study.

6. ACKNOWLEDGMENT

The partial funding by Bhabha Atomic Research Centre (BARC), Mumbai during the course of this study in the form of scholarship for the first author during his graduate study at IIT Kharagpur is hereby acknowledged.

7. REFERENCES

- [1] Soong TT, "State-of-the-art review, active structural control in civil engineering," Engineering Structures, vol. 10, no. 2, 1988, pp. 74-84.
- [2] Jangid RS and Datta TK, "Seismic behavior of base-isolated buildings: a state-of-the-art review," Proceedings - ICE: Structures & Buildings, vol. 110, no. 2, 1995, pp.186-203.
- [3] Nagarajaiah S, "Semi-active control of structures," Proceedings of Structures Congress XV, ASCE, Portland, Oregon, 1997, pp. 1574-1578.
- [4] Ehr Gott RC and Masri SF, "Structural control applications of an electro rheological device," Proceedings of the International Workshop on Structural Control, Univ. of Southern California, Los Angeles, 1994, pp. 115-129.
- [5] Kelly J M, "Base isolation: linear theory and design," Earthquake Spectra, vol. 6, no. 2, 1990, pp. 234-244.
- [6] Paulay T and Priestley MJN, Seismic design of reinforced concrete and masonry buildings, Wiley, New York, New York, 1992.
- [7] Qamaruddin M and Ahmad S, "Seismic response of pure - friction base isolated masonry building with restricted base – sliding," J. Engg. Res., vol. 4, no. 1, 2007, pp. 82-94.
- [8] Qamaruddin M, Arya AS and Chandra B, "Seismic response of brick buildings with sliding substructure," Journal of structural Engineering, vol. 122, no. 12, 1986, pp. 558-572.
- [9] Feng M Qing, Shinozuka M and Fuji S, "Friction-controllable sliding isolation system," Journal of Engineering Mechanics, vol. 119, no. 9, 1993, pp. 1845-1864.
- [10] Yegian M K and Kadakal U, "Foundation isolation for seismic protection using a smooth synthetic liner," Journal of Geotechnical and Geo-environmental Engineering, ASCE, vol. 130, no. 11, 2004, pp. 1121-1130.

- [11] Yegian M K and Catan M, "Soil isolation for seismic protection using a smooth synthetic liner," *Journal of Geotechnical and Geo-environmental Engineering*, ASCE, vol. 130, no. 11, 2004, pp. 1131-1139.
- [12] Edil T B and Bosscher PJ, "Engineering properties of tire chips and soil mixtures," *Geotechnical Testing Journal*, ASTM, vol. 17, no. 4, 1994, pp. 453-464.
- [13] Gray D-H and Ohashi H, "Mechanics of fiber reinforcement in sand," *J. Geot. Engg.*, ASCE, vol. 112, no. 8, 1983, pp. 804-820.
- [14] Tsang HH, "Seismic isolation by rubber-soil mixtures for developing countries," *Earthquake Engineering and Structural Dynamics*, vol. 37, no. 2, 2008, pp. 283-303.
- [15] Giri D and Sengupta A, "Dynamic behavior of small scale nailed soil slopes," *Geotech. Geol. Eng.*, vol. 27, 2009, pp. 687-698.

Comparison of Effect of Percent of Compaction, Sand and Cement on The Amount and Time of Swelling of Bentonite

Mohammad S. Pakbaz and B. Rafiee
Shahid Chamran Univ. of Ahvaz

ABSTRACT

Then present paper shows the result of a research work on the effect of percent of compaction, of percent of sand, of initial water content and of percent of cement on the magnitude and time rate of swelling of a commercial bentonite. Compacted samples of soil prepared and tested free swell under surcharge pressure of 7 KPa and end of primary free swell and secondary free swell were measured in a consolidation loading frame. The result indicated that initial percent of compaction only affected the amount of secondary swelling and rate of swelling. The results also indicated that initial water content of 6 % wet of optimum affected the amount of primary swelling and time rate of primary and secondary free swell but the amount final secondary swelling after 4 days of swelling was not affected by initial water content. The result also showed that the percent sand decreased the amount of primary swell and the time to end of primary swell. The amount of primary swell and time to primary swell decreased with the percent cement.

Keywords: Four or Five Keywords Compaction, sand, swelling, bentonite, cement

1. INTRODUCTION

Problem soils are classified as expansive soils, dispersive soils, collapsible soils, liquefiable soils and organic soils (1). Expansive soils are soils that contain enough amount of montmorillonite clay mineral that makes them absorb water and expand. The most reliable method for evaluating the amount of expansion is direct measurement. The US Burue of soil conservation evaluated for the first time the problem of expansion in soils in 1938. From that time civil engineers acknowledged that the reason for many building damages occurred were due to soil expansion (2). Attention to expansive soils and damages due to theses soils increased during 1950,s. At that time many housing projects were being constructed and a lot of problems due to soil expansion were reported that caused many damages to the buildings (1).

As it was mentioned soil expansion is due to the presence of clay mineral montmorillonite. More than 2.4 million sq.km of the world land are covered by soils that contain this mineral (2). Due to importance of the subject and the presence of expansive soil in Khuzestan province of Iran and high ground water table in this area the problem of soil expansion is severe.

2. IDENTIFICATION METHODS

Direct identification of expansion potential means direct measurement of percent swelling or swelling pressure. There are mainly three direct method of evaluating the swelling potential namely (a) free swell (b) swell under surcharge and (c) constant volume swelling pressure. In this research we used method (a) for our evaluation.

3. MATERIALS AND PROCEDURES

Bentonite- the bentonite we used was available commercially, it had bright grey color with liquid limit, plastic limit, maximum dry density, and optimum water content of 170 %, 77%, 13.4 KN/m³ and 32% respectively.

Cement- the cement used was type II Portland cement manufactured in Khuzestan cement factory.

Sand-the sand used was wind blown sand available in Khuzestan and the distribution curve is shown in Fig.1.

In order to prepare soil samples for free swell tests we mixed bentonite, sand and cement according to Table 1. For each mixtures maximum dry density, optimum water content, liquid limit and plastic limit were determined. The samples were all prepared at maximum dry density and optimum water content. The samples prepared at dry densities lower than maximum had water content 2% and 6% dry and wet of optimum water content. After compaction each specimen were trimmed into consolidation ring and placed in the consolidation cell. The water was added to the specimens and the specimens were allowed to free swell under seating pressure of 7 KPa. The swelling were allowed beyond the end of primary swelling into secondary swelling.

4. TEST RESULTS

Figure 2 showed the way we determined the end of primary percent swell (e_{v100}), and time to the end of primary swell (t_{100}).

4.1 Effect of Moisture content

Figure 4 showed the effect of initial moisture content of specimens on free swell and time of swell. According to this Figure the amount of swell for specimen with moisture content 6 % wet of optimum water content was lower than specimens with moisture content 2 % wet or dry of optimum water content.

4.2 Effect of Percent of Compaction

According to Figure 3 the effect of initial percent of compaction on the free swell is negligible during the primary swelling. However the free swell during secondary free swell decreased with decrease in the percent of compaction.

4.3 Effect of percent of sand

Figure 5 shows that in general the increase in the percent of sand caused a decrease in the percent swell and time to primary swell.

4.4 Effect of percent of cement

Figure 6 shows that in general the increase in the percent of cement caused a decrease in the percent swell and time to primary swell. The time for primary swelling with the percent cement beyond 4% cement did not change very much. A major change of time to end of primary swell occurred for percent cement below 4% as compared with samples without cement

5. Conclusion

Compacted samples of soil prepared and tested free swell under surcharge pressure of 7 KPa and end of primary free swell and secondary free swell were measured in a consolidation loading frame. The result indicated that initial percent of compaction only affected the amount of secondary swelling and rate of swelling. The results also indicated that initial water content of 6 % wet of optimum affected the amount of primary swelling and time rate of primary and secondary free swell but the amount final secondary swelling after 4 days of swelling was not affected by initial water content. The result also showed that the percent sand decreased the amount of primary swell and the time to end of primary swell. The amount of primary swell and time to primary swell decreased with the percent cement.

REFERENCES

- [1] Asghari, F. and Fakher, A "Swelling and dispersion of soils from geotechnical engineer point of view" Tehran University publication, Tehran, 1993.
- [2] Chen, F. H. "Foundation, retaining and earth structures, Mac Graw Hill book Co. New York, 1988.;

Fig.2 Method used for defining primary swell and time to primary swell

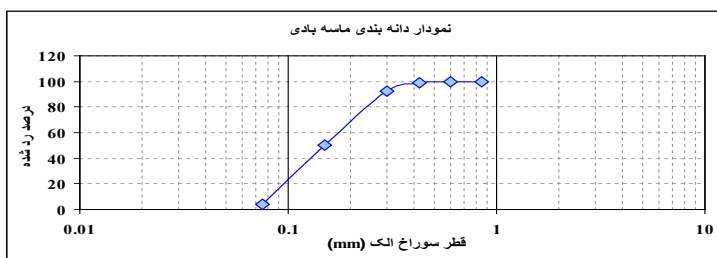
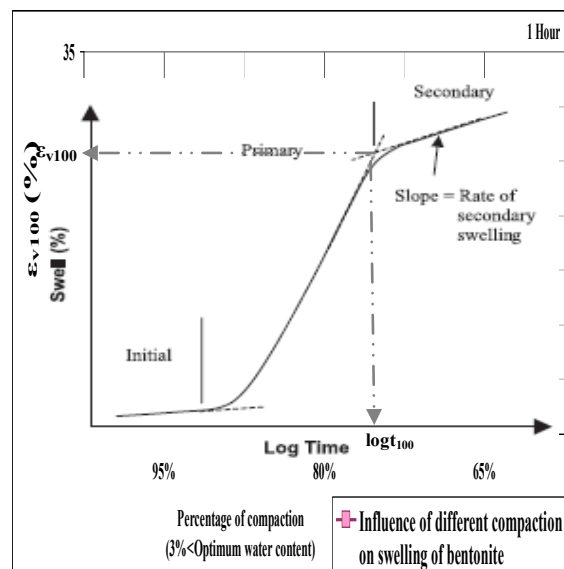


Fig.1 Grain size distribution curve for sand used

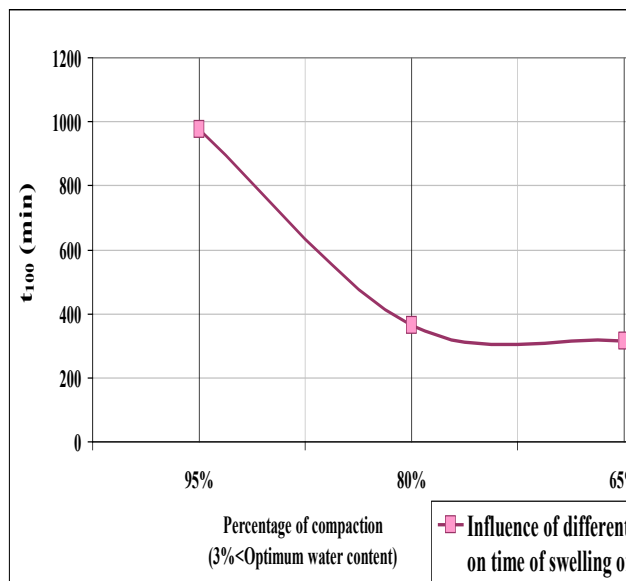


Fig.3 The effect of percent of initial compaction on the amount and time of primary swell

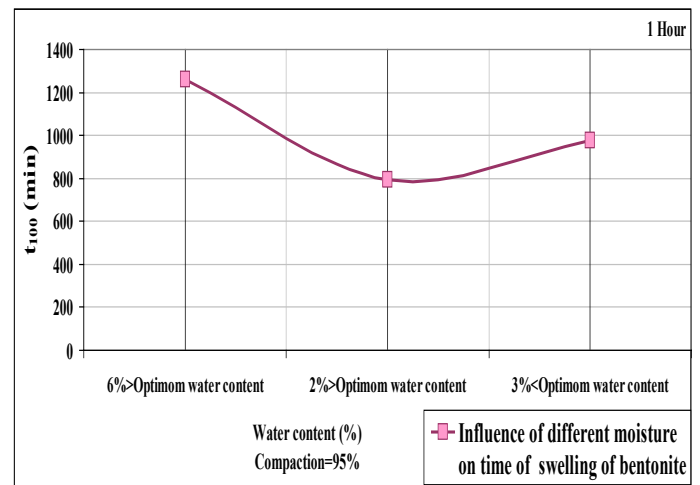


Fig.4 The effect of percent of initial water content on the time of primary swell

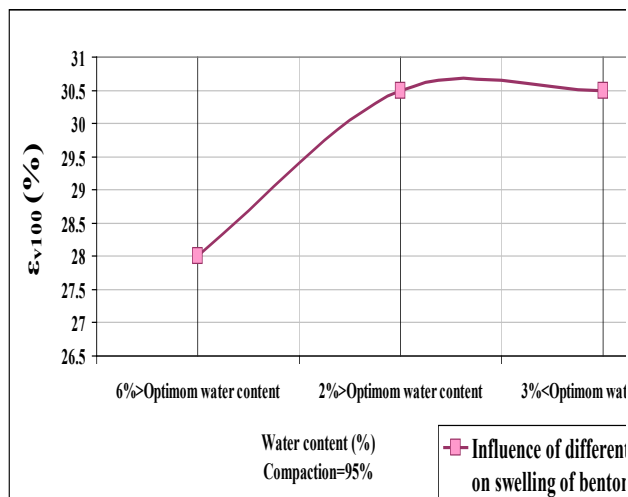


Fig.4 The effect of percent of initial water content on the amount of primary swell

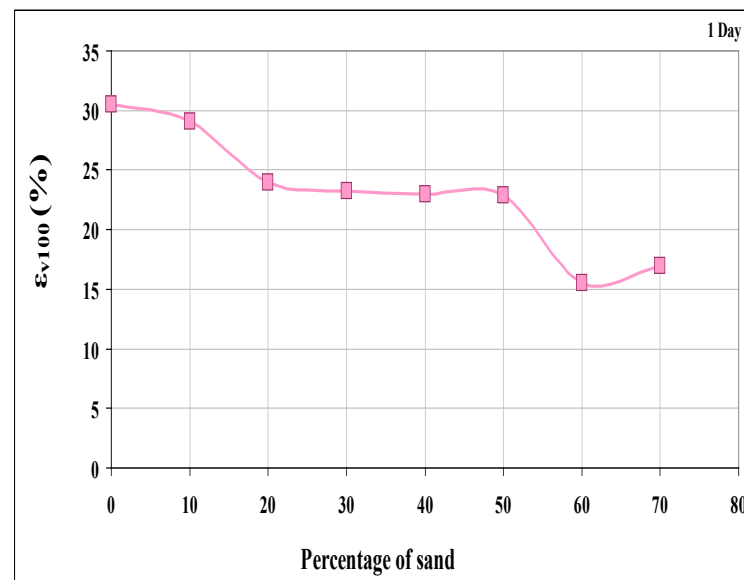


Fig.5 Effect of percent sand on the amount of primary swell

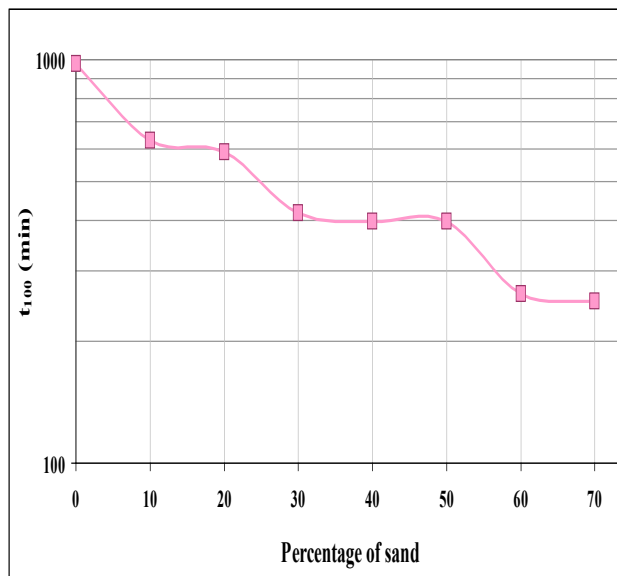


Fig.5 Effect of percent sand on the time of primary swell

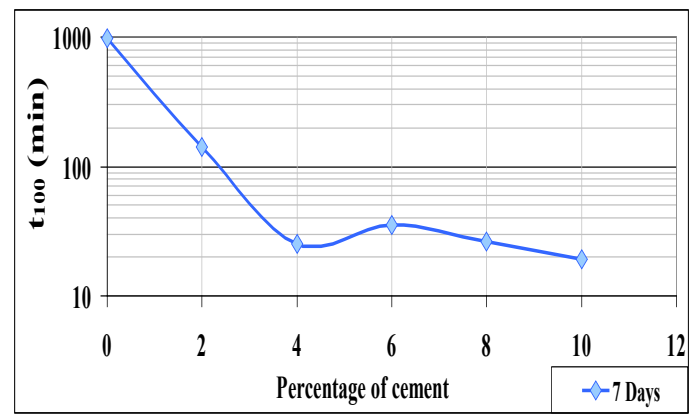


Fig.6 Effect of percent cement on the time of primary swell

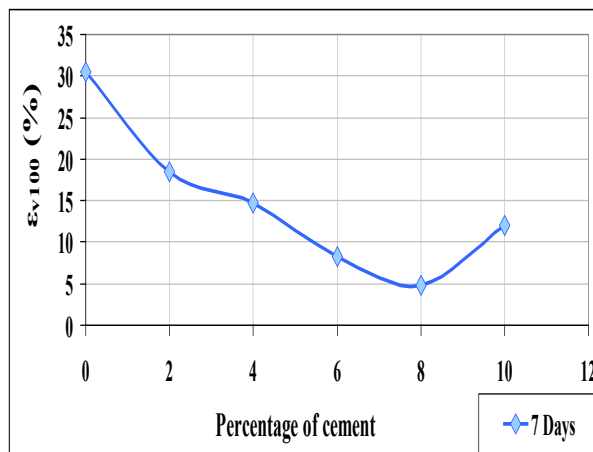


Fig.6 Effect of percent cement on the amount of primary swell

Table1 Index properties of sample tested

نمونه	LL(%)	PL(%)	PI(%)	$\gamma_d^{(opt)}$ (%)	$\gamma_d^{(max)}$ (kN/m ³)
100B	170	77	93	32	13.4
100B 2C	158	63	95	30.4	13.65
100B 4C	150	70	80	29.5	13.72
100B 6C	176	87	89	28.5	13.75
100B 8C	164	106	58	28	13.75
100B 10C	161	101	60	28.0	13.8
100B 10S	138	60	78	28	14.25
100B 20S	136	53	83	27	14.32
100B 30S	119	43	76	24	15.14
100B 40S	107	41	66	23	15.5
100B 50S	108	41	67	22	16.0
100B 60S	112	48	64	21	16.5
100B 70S	106	46	60	21	16.8

Prediction of the Axial Bearing Capacity of Piles by SPT-based and Numerical Design Methods

Issa Shooshpasha, Ali Hasanzadeh and Abbasali Taghavi
Babol University, IRAN

ABSTRACT

The prediction of the axial capacity of piles has been a challenge since the beginning of the geotechnical engineering profession. In recent years determining bearing capacity of piles from in-situ testing data as a complement of static and dynamic analysis has been used by geotechnical engineers. The Standard Penetration Test (SPT) is still the most commonly used in-situ test and pile capacity determination by SPT is one of the earliest applications of this test. On the other hand, the acceptance of numerical analyses in geotechnical problems is growing and finite element calculations are more and more used in the design of foundations. In this paper, different approaches for estimating the bearing capacity of piles from SPT data have been explained and compared with numerical method. Then, comparisons between numerical and empirical results are presented and discussed.

Keywords: Pile, Axial capacity, Standard Penetration Test, Finite Element Method

1. INTRODUCTION

The prediction of the axial capacity of piles is recognized as being the area of greatest uncertainty in foundation design. Several methods and approaches have been developed to overcome the uncertainty in the prediction. The methods include some simplifying assumptions or empirical approaches regarding soil stratigraphy, soil-pile structure interaction and distribution of soil resistance along the pile. Therefore, they do not provide truly quantitative values directly useful in foundation design [1]. Bearing capacity of piles can be determined by five approaches: static analysis, dynamic analysis, dynamic testing, pile load test and in-situ testing.

Design guidelines based on static analysis often recommend using the critical depth concept. However, the critical depth is an idealization that has neither theoretical nor reliable experimental support, and contradicts physical laws. Dynamic analysis methods are based on wave mechanics for the hammer-pile-soil system. The uncertainty in the hammer impact effect, as well as changes in soil strength from the conditions at the time of pile driving, and also at the time of loading, causes uncertainties in bearing capacity determination. Dynamic testing methods can only be used by an experienced person and the capacity estimation is not available until the pile is driven [2]. Pile load test is the best method for pile bearing capacity determination but such tests are expensive, time-consuming and the costs are often difficult to justify for ordinary or small projects. In recent years, the application of in-situ testing techniques has increased for geotechnical design. This is due to the rapid development of in-situ testing instruments, an improved understanding of the behavior of soils.

2. COMMON METHODS of PILE BEARING CAPACITY DETERMINATION by SPT

The Standard Penetration Test, SPT, is still the most commonly used in-situ test. Also SPT is the most common testing methodology adopted in the field to gain idea about the stratigraphic profile at a site. Due to its simplicity of execution (apart from the difficulty in repeatability), a field engineer finds the method to be one of the most amiable and reliable one.

The introduction in the United States in 1902 of driving a 25-mm diameter open-end pipe into the soil during the wash-boring process marked the beginning of dynamic testing and sampling of soils. Between the late 1920s and early 1930s, the test was standardized using a 51-mm O.D. split-barrel sampler, driven into the soil with a 63.5-kg weight having a free fall of 760 mm. The blows required to drive the split-barrel sampler a distance of 300 mm, after an initial penetration of 150 mm, is referred to as the SPT N-value. This procedure has been accepted internationally with only slight modifications. The number of blows for each of the three 150-mm penetrations must be recorded. Apart from its main applications in soil characterization, SPT N-value has also been extensively used for designing structural foundations and other earth structures, particularly, for the bearing capacity of piles.

Pile capacity determination by SPT is one of the earliest applications of this test that includes two main approaches, direct and indirect methods. Direct methods apply N values with some modification factors. Indirect SPT methods employ a friction angle and undrained shear strength values estimated from measured data based on different theories. Amongst the two, the direct methods are more accepted amongst the field engineers for the ease of computations. In the present study, the following common SPT-based direct

methods have been employed to predict the pile bearing capacity (Table I).

Table I: SPT direct methods for prediction of pile bearing capacity in the present study

Method	Unit Base (Q_b) and Unit Shaft (Q_s) resistance	Remarks
Meyerhof (1976)	$m N_b \leq \left(\frac{L}{D}\right) Q_b \text{ (MPa)} = k$ $Q_s \text{ (kPa)} = n_s N_s$	N_b : average of N between 10D above and 5D below pile base N_s : average value of N around pile embedment depth. bored piles: $n_s=1$, $k=0.012$, $m=0.12$ driven piles: $n_s=2$, $k=0.04$, $m=0.4$
Bazaraa & Kurkur (1986)	$Q_b \text{ (MPa)} = n_b N_b$ $Q_s \text{ (kPa)} = n_s N_s$	N_b : average of N between 1D above and 3.75D below pile base, $N_b \leq 50$ $n_b = 0.06 - 0.2$ $n_s = 2 - 4$ N_s : average value of N around pile embedment depth
Decourt (1995)	$Q_b \text{ (MPa)} = k_b N_b$ $Q_s \text{ (kPa)} = \alpha (2.8 N_s + 10)$	driven piles and bored piles in clay: $\alpha = 1$ bored piles in granular soils: $\alpha = 0.5 - 0.6$ driven piles in sand: $k_b = 0.325$ bored piles in sand: $k_b = 0.325$ driven piles in clay: $k_b = 0.1$ bored piles in clay: $k_b = 0.08$ N_b : average of N around pile base N_s : average value of N around pile embedment depth.
Shariatmadari et al.(2008)	$Q_b \text{ (MPa)} = 0.385 N_{gb}$ $Q_s \text{ (kPa)} = 3.65 N_{gs}$	N_{gb} : the geometrical average of N values between 8D above and 4D below pile base N_{gs} : geometrical average of N values along the pile

3. DETERMINATION of PILE BEARING CAPACITY by SPT (Case Study)

By performing a 15m borehole in a region in Babol (Fig 1), north of IRAN, the soil stratigraphy has been recognized(Fig 2). The groundwater table is 1.5 m below the ground surface. The average unit weight of the soil is 1.93gr/cm³ and its average modulus of elasticity is 90 kg/cm². Fig 3 depicts the variation of SPT-N values with depth of this site.

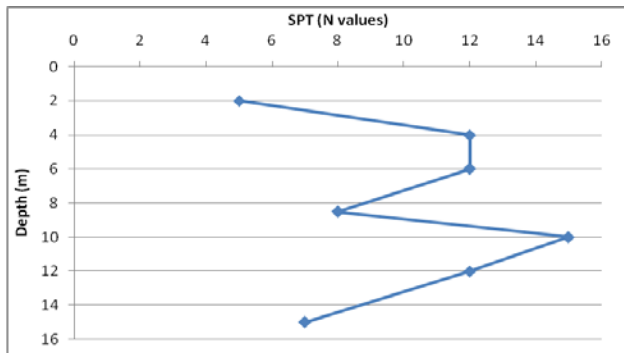
Fig 1. The region considered in this study



Fig 2. Exploratory boring log

Standard Penetration Test (No. of Blows)				PI (%)	LL (%)	Graphic Log	Soil Classification (unified)	Depth (m)
Total N	third 15 cm	second 15 cm	first 15 cm					
							Fill	0
5	3	2	2	20	37		CL	1
				NP			SP-SM	2
12	6	6	4				SP-SM	3
				NP			SP-SM	4
12	6	6	4				SP-SM	5
				NP			SW-SM	6
				6	23		CL-ML	7
8	4	4	4				SM	8
15	8	7	4	NP			SM	9
				NP			SM	10
12	6	6	4				SM	11
				NP			SM	12
7	4	3	3	16	44		ML	13
								14
								15

Fig 3. Variation of SPT-N values with depth



Based on the SPT data above, a hypothetical problem is considered wherein the bearing capacity of a bored pile ($L=7\text{m}$, $D=1\text{m}$) is determined by the methods mentioned above. (Table II).

Table II: The bearing capacity of the bored pile by common SPT-based methods ($L=7\text{m}$, $D=1\text{m}$)

Method	Meyerhof	Bazaraa & Kurkur	Decourt	Shariat madari
value(kN)	916	1102	1700	3655

4. VALIDATION

In order to validate the program, a pile load test in Germany has been analyzed. The load test investigated the load-settlement behavior of a single pile. The upper 4.5m subsoil consist of silt (loam) followed by tertiary

sediments down to great depths. These tertiary sediments were stiff plastic clay similar to the so-called Frankfurt clay, with a varying degree of overconsolidation. The groundwater table was about 3.5m below the ground surface. The considered pile had a diameter of 1.3 m and a length of 9.5m. It was located completely in the overconsolidated clay. The loading system consisted of two hydraulic jacks working against a reaction beam. This reaction beam was supported by 16 anchors. These anchors were installed vertically at a depth between 15 and 20 m below the ground surface at a distant of about 4 m from the tested pile, in order to minimize the effect of the mutual interaction between the tested pile and the reaction system. Then, loading test was carried out. The loads were applied in increments and maintained constant until the settlement rate was negligible.

The mentioned pile load test has been carried out by El-Mosallamy in Frankfurt clay, was used to verify the present numerical method. Fig 4 shows the layout of the pile load test and measurement points by El-Mossallamy. Fig 5 demonstrates a comparison between the result obtained by El-Mosallamy and that obtained in the present study. The comparison depicts a good agreement between the results.

Fig 4. Layout of the pile load test and measurement points by El-Mossallamy

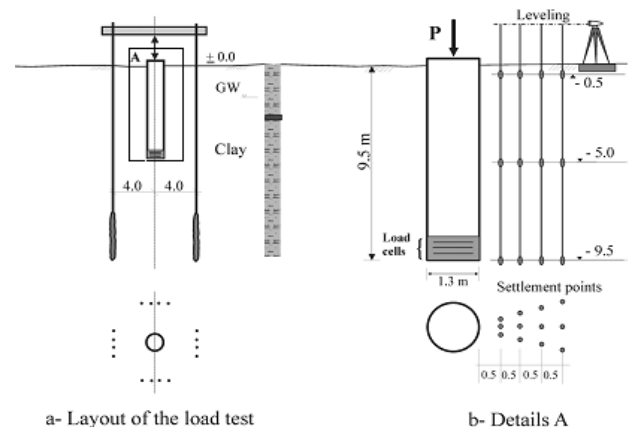
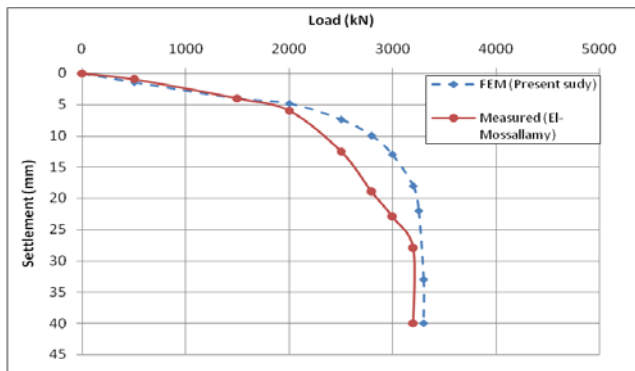
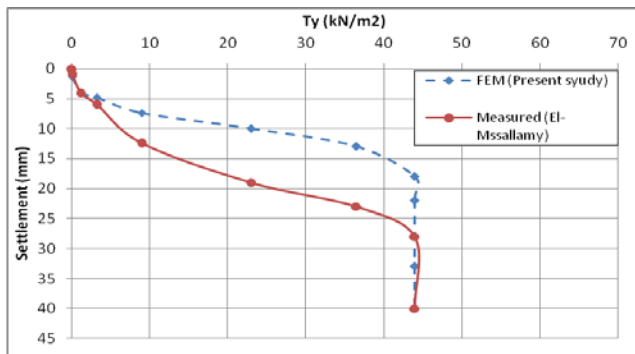


Fig 5. Comparison between the results of El-Mosallamy and the present study (a) load – settlement curve (b) stress – displacement curve



(a)

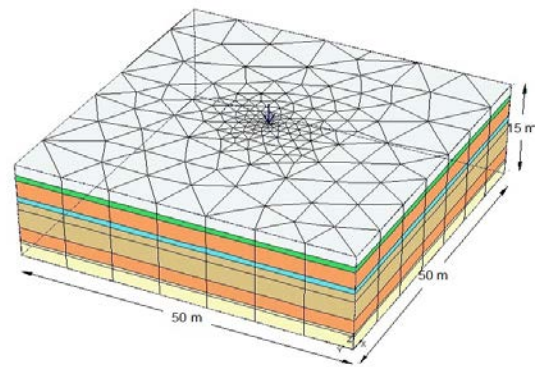


(b)

5. DETERMINATION of PILE BEARING CAPACITY by PLAXIS 3D FOUNDATION

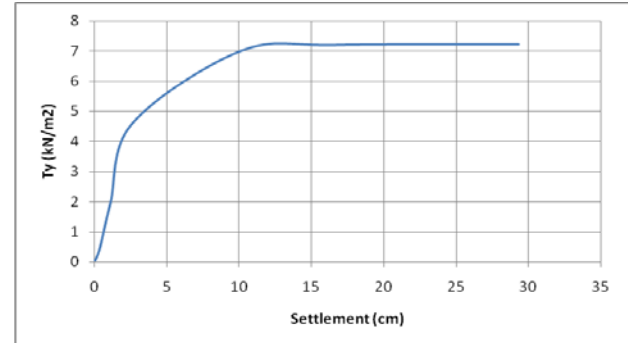
In this part, the bearing capacity of the pile mentioned above is determined by the program "plaxis 3d foundation". "Plaxis 3d foundation" is a finite element method-based three-dimensional program specially developed for the analysis of foundation structures, including off-shore foundations. This program combines simple graphical input procedures, which allow the user to automatically generate complex finite element models, with advanced output facilities and robust calculation procedures. In order to analyze the behavior of the single pile, at first a model is made. A working area 50m x 50m has been used. The pile is modelled as a solid pile using volume elements in the center of the mesh. Interfaces are modelled along the pile. The generated mesh of the system (for pile: $L=7\text{m}$, $D=1\text{m}$) by this program is as follows (Fig 6).

Fig 6. The typical mesh used in the study



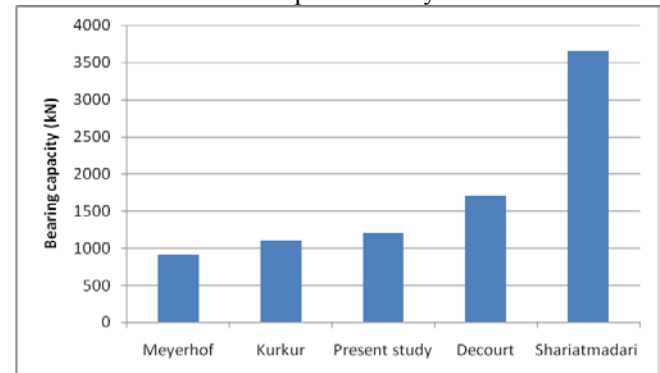
The stress-settlement behavior of the pile, analyzed by the program is presented in Fig 7.

Fig 7. Stress-settlement behavior of the considered pile



The bearing capacity of the considered pile, obtained by this program, is 1200 kN. Fig 8 shows a comparison between different methods and the present study.

Fig 8. Comparison between the results obtained by different methods and the present study FEM



6. CONCLUSION

Determining the bearing capacity of piles is an interesting subject in geotechnical engineering. The complex nature of the embedment ground of piles and lack of suitable analytical models for predicting the pile bearing capacity are the main reasons for the geotechnical engineer's tendency to pursue further research on this subject. Direct bearing capacity predicting methods for piles are developed based on in-situ testing data, specially SPT,

having applications that have shown an increase in recent years.

In this study, by analyzing the pile by FEM and comparing it with common methods, tried to find a reasonable prediction for its bearing capacity. The results indicate that, in this site, the bearing capacity predicted by Bazaraa & Kurkur method is very close to the one obtained by the finite element method (FEM). Also Meyerhof method underestimates and Shariatmadari method overestimates the bearing capacity of the single pile. Therefore, 1200 kN can be a good prediction for the bearing capacity of the bored pile considered ($L=7\text{m}$, $D=1\text{m}$) in this study.

7. REFERENCES

- [1] Eslami A & Fellenius, BH, "Pile capacity by direct CPT and CPTu methods applied to 102 case histories," Canadian Geotechnical Journal, vol. 34, 1997, pp. 886-904.
- [2] Rausche F, Goble G & Likins G, "Dynamic determination of pile capacity," J of Geotechnical Engineering, vol. 111, 1985, pp. 367-383
- [3] Meyerhof GG, "Bearing capacity and settlement of pile foundations," J of the Geotechnical Engineering Division, ASCE, vol. 102, Iss. GT3, pp.196-228.
- [4] Bazaraa AR & Kurkur MM, "N-values used to predict settlements of piles in Egypt," Proceedings of In Situ '86, New York, 1986, pp. 462-474
- [5] Decourt L, "Prediction of load-settlement relationships for foundations on the basis of the SPT-T," Ciclo de Conferencias Internationale, Leonardo Zeevaert, UNAM, Mexico, 1995, pp. 85-104.
- [6] Shariatmadari N, Eslami A & Karimpour-fard M, "Bearing capacity of driven piles in sands from SPT-applied to 60 case histories ," Iranian Journal of Science & Technology, 2008, vol .32, pp.125-140
- [7] El-Mossallamy Y "Load-settlement behavior of large diameter bored piles in over-consolidated clay," Proceeding of the 7th. International Symposium Models in Geotechnical Engineering, Graz, Austria, 1999, pp.443-450

Application of Recently Developed Mechanistic-Empirical Methods for the Design of Heavily Loaded Pavement Structures

John N. MUKABI

Engineerintel - R&D, Design & Engineering, Kensetsu Kaihatsu Limited, Nairobi, KENYA

ABSTRACT

The mechanistic-empirical approach presents a new paradigm for pavement design and analyses. Nevertheless, it is imperative that the analytical functions adopted as well as the prediction equations and models employed manifest as high a degree of precision as possible. In this Study, a unique research regime and full scale in-situ experimental testing sections were designed and constructed with varying pavement structural configurations; and subjected to different environmental conditions under both static and dynamic loading. The innovative methods of testing and analytical techniques developed and/or modified are cited. The recently developed mechanistic-empirical methods based on results from the elaborate and comprehensive testing and research regimes designed and implemented are reported and some case examples of their practical application for the design, construction and maintenance of heavily loaded pavement structures are introduced.

Keywords: Pavement, mechanistic-empirical, modulus, elastic yield (limit) strain, performance prediction

1. INTRODUCTION

1.1 Overall Background

Infrastructure development is a prerequisite for the achievement of rapid socio-economic enhancement. In particular, the development of an efficient roads network is of paramount importance as a primary mode of transportation for passengers, goods and services. Recent trends in East and Central Africa depict tendencies of increased rate of rapid development precipitated mainly by various needs due to population explosion. On the other hand, the lack of adequate resources to cope with such prevailing circumstances is a major impediment towards the achievement of any set visionary goals.

In view of this therefore, it is increasingly necessary to develop Value Engineering (VE) based cost-time effective technologies that can facilitate for the comprehensive characterization and design of pavement structures founded on research oriented unique and innovative methods of testing as well as sophisticated analytical techniques, versatile enough to expound the range of extrapolation derived on limited sets of data. Although the Mechanistic-Empirical (ME) may be a versatile application for pavement design and analysis, the main geotechnical engineering parameters that are employed in such a program are known to highly influence the results of the design, analysis and performance prediction. It is therefore imperative that the analytical functions, equations and models adopted are of the highest degree of accuracy and sophistication possible. The ME pavement design approach is based on an assumption that load-induced pavement structural responses such as stresses, strains and deflections, can be adopted in predicting the

development of pavement distress and structural deterioration, in the form of rutting and/or cracking, through the use of transfer functions. Therefore, characterization of the linear elastic properties is generally considered primarily important. In this Study, however, the importance of considering the elastic properties including the elastic moduli, elastic limit (yield) strain {initial yield surface} as well as the recently developed kinematic hardening theories [1], [2] is demonstrated, whilst new geoscientific and geotechnical engineering concepts related to this subject matter are proposed.

1.2 Brief Background on Some Challenges Regarding the ME Approach

According to the Research Results Digest 307 [3], an independent review of the MECHANISTIC-EMPIRICAL PAVEMENT DESIGN GUIDE (MEPDG) prepared by the Transportation Research Board of the National Academies within the National Cooperative Research Program of the USA, the MEPDG uses CBR for soils and granular materials as a basis to estimate resilient modulus (M_r). However, it further states that research has shown that the relationship between these parameters is not reliable for either material type due to non-linear stress-strain relations and the fact that CBR is, at best, a measure of undrained shear strength, which does not relate closely to resilient properties at relatively low stresses, but may relate to permanent deformation resistance. The report further states that some of the major challenges in regard to the use of the ME design system are: a) complexities in the calibration of the design models against actual pavement behavior in the field due to the limitations with Long Term Pavement Performance (LTPP) database and the related difficulties in dealing with design reliability; b) problems encountered in developing the software; c) the approximate nature of some of the distress prediction models;

and, d) the need for enhanced application of models that take into account the non-linear properties of geomaterials.

On the other hand, a review of the new MEPDG from a material characterization perspective by the National Research Council (NRC) Canada [4] concludes that; although the performance predictions of the laboratory measured dynamic modulus are in agreement with the patterns established in the current practice and reported in most literature, the following major challenges are still prevalent: a) the Asphalt Concrete (AC) dynamic modulus estimated using the predictive equation incorporated in the Guide proved to be substantially different from measured values, the error of which leads to gross underestimates of accumulated damage resulting in undersigning the road pavement structure; b) similarly, for unbound materials, the correlation between physical properties (including the AASHTO classification) and the resilient modulus, produced unreliable values when compared with actual measurements made in the laboratory hence applications based on moduli estimated using the Guide proposed values to run the software resulted in substantially different performance predictions compared with those produced when using measured modulus values. Recently developed concepts of circumventing some of the aforementioned challenges are proposed in this paper.

1.3 Introduction of Some Advances made in this Study

Some of the most important advances made in this Study include: a) geomathematical methods of estimating, under varying loading and environmental conditions, modulus of elasticity, resilient modulus, elastic limit (yield) strain, initial yield deviator stress and strain, elastic limiting line, the limiting elastic state, and Poisson's ratio; all parameters of which form the fundamental basis of the ME pavement design; b) correlating NDT deflection properties to NDT and DT elastic properties; c) developing correlations between elastic modulus determined from mechanical tests to that from geophysical tests; d) developing models for characterizing pavement response and performance prediction under varying conditions; e) proposing methods of determining the approximate range of dynamic and static load effects; and, f) advancing analytical methods for characterizing various Geomaterials and pavement response.

2. EXPERIMENTAL TESTING AND GI REGIMES

In Ethiopia, along the heavily trafficked Addis Ababa ~ Debre Markos international trunk road, twelve full-scale field experimental testing sections were designed and constructed with six varying pavement layers and structural configurations and subjected to varying environmental conditions over six seasonal cycles as well as different modes and cycles of static and dynamic loading. In this case, in certain sections, mechanically stabilized Graded Crushed Stone (GCS) and unbound lateritic gravel were adopted for the base and subbase layers respectively [5].

On the other hand, whilst undertaking a detailed design study for the Juba River Port access road in South Sudan, due to the heavy traffic, overloading and unconventional loading

characteristics that had been anticipated, it was imperative to initiate a comprehensive investigation in order to realize Value Engineering (VE) based cost-time effective design, that ensures enhanced structural performance as well [6]. The experimental testing and Geotechnical Investigation (GI) regimes adopted in this Study are reported in [7] and [8].

3. PROPOSED ME EQUATIONS FOR EVALUATION OF EXISTING PAVEMENTS STRUCTURES

3.1 Mechanical Testing

(1) Laboratory testing

At every project and in-situ experimental testing site, “undisturbed” and disturbed samples were extruded at designated intervals and/or at points where the soil type and/or characteristics varied; for purposes of undertaking comprehensive laboratory testing.

Conventional and modified laboratory and field methods of testing were adopted in this Study. The main mechanical methods of laboratory testing included the conventional and modified Unconfined Compressive Strength (UCS) adopting larger size specimens ($\phi \geq 20\text{cm}$), conventional Consolidated Undrained Triaxial Compression (CUTC), Consolidated Drained Triaxial Compression (CDTC), modified simple shear and modified UCS dynamic loading; carried out under varying moisture – suction and loading conditions.

In order to correct for the specimen size, some full scale plate loading tests were carried out in the field.

Basic physical and mechanical properties such as specific gravity, bulk and dry densities, Atterberg Limits, grading, moisture content and compaction were also measured and characterized. The data applied for modeling was determined from sophisticated laboratory tests and correlated to results from field seismic and other surveys.

Details of the methods of testing are reported in [8].

The following equations, developed from Consolidation and Stress Ratio (CSSR) concepts [9], were applied in correcting for the effects of destructureation due to reconstitution.

$$\left(\frac{q}{P_e}\right)^I_{\max} = \frac{\mu_e^R \cdot \eta_c \cdot (q/P_e)_f^R}{(K_{cf}^R - (\mu_e^R \cdot A\phi \cdot CSR^R))} \quad (1)$$

$$\left(\frac{p}{P_e}\right)^I = \frac{\mu_e^R \cdot \eta_c \cdot (p/P_e)_f^R}{(K_{cf}^R - (\mu_e^R \cdot A\phi \cdot CSR^R))} \quad (2)$$

where superscripts I and R denote “intact” and “reconstituted” respectively and $\mu_c^R = (q/p')_f^R$, $\eta_c = (q/p')_c$, and $K_{cf}^R = (\sigma'_r/\sigma'_a)^R_{ec}$.

(2) In-situ testing

Standard Penetration Tests (SPTs) were carried out for bridge foundation designs, while Dynamic Cone Penetration Tests (DCPTs) were undertaken for pavement structures.

The relations between the N -value and Unconfined Compressive Strength (UCS) as well as initial stiffness expressed as E_0 and UCS are presented in Eqs. (3) and (4) respectively.

$$q_u = \{[N_{SPT} + B_N] \times A_q / A_N\} - B_q \quad (3)$$

$$E_0 = [q_u + B_q] A_E / A_q \} - B_E \quad (4)$$

where, N_{SPT} is the number of blows from a Standard Penetration Test (SPT), q_u is the Unconfined Compressive Strength (UCS), E_0 is the elastic modulus, and $A_N=19.6$, $B_N=48.4$, $A_{BC}=40$, $B_{BC}=98$, $A_q=0.96$, $B_q=2.37$, $A_E=1024$ and $B_E=280$ are material and ground related constants.

3.2 Deflection Testing and Measurement

The magnitude of the Representative Rebound Deflection (RRD), δ_{RD} , for structural analysis, was computed from;

$$\delta_{RD} = [\delta_{av} + 2V^{0.5}] \times f_{\delta}^{tc} \times L_c^f \quad (5)$$

where, δ_{av} is the average value of deflection measured under a wheel load of 5tons, V is the variance of the measurements and f_{δ}^{tc} is the temperature correction factor expressed as:

$$f_{\delta}^{tc} = \frac{\delta_t^R}{\delta_t} \quad (6)$$

where, δ_t^R is the RRD determined at $t=21^\circ\text{C}$ and δ_t , which is computed from:

$$\delta_t = A_{\delta} t^3 - B_{\delta} t^3 + C_{\delta} t - P_{\delta} \quad (7)$$

where, $A_{\delta}=7.2 \times 10^{-5}$, $B_{\delta}=7.6 \times 10^{-3}$, $C_{\delta}=0.27$ and $D_{\delta}=2.7$ are deflection-temperature related constants, while t is the average temperature of the asphaltic layers; $t > 16.5^\circ\text{C}$.

Some of the equations that were developed from this investigation and applied in this Study are introduced under section 4.2 of this paper.

3.3 Geophysical Surveys

The mathematical and regression analysis carried out with consideration to various environmental factors yielded the following equations applicable for $\rho > 25\Omega\cdot\text{m}$.

$$q_u = [A_q \ln(\rho) - B_q] \text{ (MPa)} \quad (8)$$

$$E_0 = A_E \ln(\rho) - B_E \text{ (MPa)} \quad (9)$$

q_u is the Unconfined Compressive Strength (UCS), E_0 is the elastic modulus, and ρ is the geo-electromagnetic resistivity.

4 PROPOSED ME EQUATIONS FOR ENHANCED PERFORMANCE PREDICTION

4.1 Generalized Pavement Response Concept

Conventionally, traffic, materials and climate are the three main categories of input variables adopted in the MEPDG methodology. This Study proposes a modified approach that takes into account; traffic intensity and reciprocal characteristics, environmental factors and the impact thereof and unique and comprehensive geomaterial characterization. In so doing, consideration is made of both an elastic layer system which is insensitive to the rate of loading and the visco-elastic layer system whereby the pavement becomes sensitive to vehicle speed and frequency of loading. In the earlier case the behavior is simulated as linear-elastic and

recoverable, whereas in the latter case the response gradually transposes from the visco-elastic towards the plastic phase.

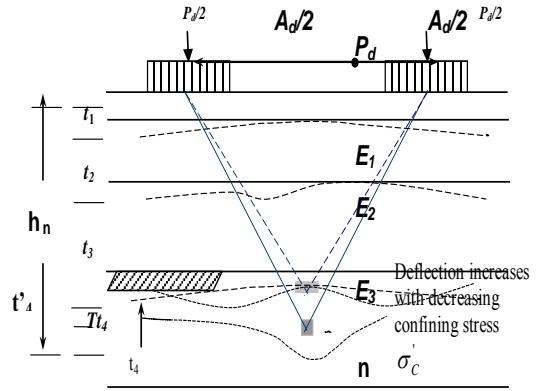


Fig. 1 Generalized characterization of pavement response

The definitive generalized equation delineating and simulating the road conditions under this conceptual framework is expressed as a function of loading conditions, pavement type (structurally), pavement layer quality, structural thickness as well as intrinsic material properties, inherent and induced characteristics as postulated in Eq. (10).

$$R_c = f[\phi_{df}, \partial t_i, P_c, P_e, \Delta t_e, \Delta \alpha_{ms}^v] \quad (10)$$

where, R_c represents road condition, ϕ_{df} is the dynamic load factor, ∂t_i defines the response mode factor of layer of the pavement structure, P_c is the pavement configuration, P_e is the pavement layer quality, Δt_e is effective structural thickness and $\Delta \alpha_{ms}^v$ = parameter delineating moisture ~ suction variation.

On the other hand, the extent of deformation can be derived by carrying out back analysis of the deformation history of an existing pavement structure. In a generalized state, this can be expressed as:

$$\varepsilon_{dh} = f[\phi', \psi', p_f^{oc}, q_f^{oc}, \phi_f^{oc}, \Sigma f_{yi}, \delta_{ij}^o] \quad (11)$$

where, ε_{dh} represents the parameter delineating deformation history, ϕ' is the consolidation stress ratio, ψ' is the modifier between Isotropic and Anisotropic stress paths, p_f^{oc} , q_f^{oc} are the invariant stresses under over consolidation conditions, ϕ_f' is the Angle of Internal Friction within the failure zone.

4.2 Characterization of Traffic Impacted Dynamic Loading Effects

The dynamic component of the traffic loading was simulated as moving constant wheel loads whose transfer mechanisms occur very slowly relative to the frequencies involved in the vertical dynamics. Computation and analysis of the stresses transmitted is presented in [5]. In carrying out these analyses, the mid-elements of each layer are analyzed in relation to the

applied stresses.

The dynamic traffic loading effects were analyzed on the basis of Eqs. (12) ~ (17), which were developed in this Study.

1) Transversal propagation of stress

The modified transformed damped oscillatory equation of motion is proposed as:

$$\delta_{rd} = c_o e^{ht} \sin \left[(h^2 - \omega_o^2)^{0.5} t + \phi_o \right] \quad (12)$$

where, δ_{rd} =rebound deflection, c_o =constant representing the initial conditions of loading, h =damping factor of the pavement structural layer stiffness, t =response time measured, ω =angular frequency and ϕ_0 =constant representing condition of deflection measurement.

The modified concept of energy was also applied in analyzing the curvature of the deflection basin in relation to the elastic moduli energy equation, which is expressed as;

$$E(t) = 0.5c_o^2 e^{-2ht} \left\{ l_a (w_0^2 + h^2) \cos^2 \left[(w_0^2 + h^2)^{0.5} t + \phi_0 \right] + f_r \sin^2 \left[(w_0^2 + h^2)^{0.5} t + \phi_0 \right] \right\} \quad (13)$$

where, f_r is the force constant and l_a =axle load. The energy is postulated to decrease exponentially with the increase in time, which is expressed in relation to the magnitude of δ_{rd} as:

$$\frac{dE(t)}{dt} = \frac{d}{dt} \left[\frac{1}{2} l_a \delta_{rd}^2 + \frac{1}{2} f_r \delta^2 \right] \quad (14)$$

2) Shear wave propagation

Assuming the deflection at any layer n is given by,

$$\delta_{rd} = \delta_{rd}(Z, t) = \Delta_{rd}(Z) e^{i\omega t} \quad (15)$$

where, Δ_{rd} is the total displacement. The proposed deflective equation of motion is then given by:

$$\rho_n \frac{\partial^2 \delta_{rd}^n}{\partial t^2} = G_n \frac{\partial^2 \delta_{rd}^n}{\partial Z^2} + \eta_n \frac{\partial^3 \delta_{rd}^n}{\partial Z^2 \partial t} \quad (16)$$

where, $\omega \eta_n = 2G_n h_n$, ρ =density of pavement layer, G =shear modulus and h is damping

3) Correlation between elastic modulus and deflection

Wave propagation techniques are usually used to determine the dynamic shear and elastic moduli of in-situ ground and geomaterials. For purposes of estimating these parameters from deflection testing, the following correlations were developed.

$$E = 2[1 + \nu] t_r^\alpha \{ \gamma_n / g \}; \quad t_r^\alpha \alpha V_s^2: G = E/2[1 + \nu] \quad (17)$$

where, E =Elastic (dynamic) modulus, ν =Poisson's ratio, t_r^α =response time between start of measurement and rebound deflection whereby α varies with type of pavement structure, layer configuration, geomaterial properties and

environmental factors; γ_n =density of layer n , g =acceleration of gravity, V_s^2 =shear wave velocity and G =shear modulus.

4.3 Equations Applied for Analyzing Impact of Environmental Factors

Most tropical soils are known to be highly sensitive and susceptible to changes in environmental factors. Development of methods that can quantify the magnitude of the impact of such variations on the performance of pavement structures is therefore of great essence.

1) Effect of swelling

$$\Delta_{sc} = \mathcal{G}_{sc} \ln \lambda_{sc} + B_{sc} \quad (\%) \quad (18)$$

where, Δ_{sc} represents swell in relation to surcharge pressure, $\mathcal{G}_{sc} = 12.9$; logarithmic gradient constant for tropical geo-materials, λ_{sc} is the surcharge pressure in Kpa, $B_{sc} = 36.5$; logarithmic intercept for most fine grained tropical problematic geomaterials.

2) Seasonal effects on resilient modulus (M_r)

The effects of seasonal changes on the resilient modulus of some tropical c geomaterials is presented in Eqs. (4) and (5).

$$\zeta_{wMr} = \alpha_{gl} \ln M_r + \alpha_{gi} \quad (19)$$

where, ζ_{wMr} represents the wet to dry Season resilient modulus (M_r) ratio, $\alpha_{gl} = 0.622$ and $\alpha_{gi} = 0.54$ are logarithmic M_r intercept constants for tropical geomaterials

3) Moisture-suction variation

The impact of the moisture-suction variation is analysed by considering the correlation between the change in moisture content as a function of the plasticity ratio. Thus the resulting resilient modulus, M_r^R is computed from:

$$M_r^R = \left[-A_{wc} \times \Delta w_c + B_{wc} \right] \times \frac{PI_R}{PI_m} \times M_r^i \quad (20)$$

where, $A_{wc} = 0.092$ and $B_{wc} = 1$ are resilient modulus related gradient and intercept constants, Δw_c is the change in moisture content expressed as a percentage, $PI_R = 16$ is the Reference Plasticity Index, while PI_m is that determined for the tested material and M_r^i is the initial resilient modulus.

The initial resilient modulus M_r^i can be determined from the modified quasi-empirical equation proposed as:

$$M_r^i = A_{Mr} \times \left[M_r^{Al} \right]^3 \times 10^{-6} - B_{Mr} \left[M_r^{Al} \right]^2 + C_{Mr} \left[M_r^{Al} \right] - D_{Mr} \quad (21)$$

where, $A_{Mr} = 2$, $B_{Mr} = 0.0012$, $C_{Mr} = 0.623$ and $D_{Mr} = 0.775$ are average constants determined for tropical geomaterials and $M_r^{Al} = 10.3 \times CBR$, is an equation proposed by the American Asphalt Institute.

4) Impact of black cotton soil ingression

- Basic equations

Basic mathematical equations that can enable the quantitative analysis of the impact of the ingression of subgrade black cotton soil (BCS) into the upper superior subbase and base course layers are proposed in this Study. The ultimate $CBR_{int.}$ is computed as:

$$CBR_{int.} = A_{BCi} \int_{BCi}^3 - B_{BCi} \int_{BCi}^2 + C_{BCi} \int_{BCi} + CBR^i \quad (22)$$

where $A_{BCi}=0.057$, $B_{BCi}=2.76$ and $C_{BCi}=15.2$ are BCS inherent characteristics related constants, while \int_{BCi} is the BCS ingression content expressed in percentage terms.

- Evaluation of impact on quality of pavement layers

The deterioration of pavement structural thickness occurs mainly as a result of cyclic action impacted by increased axle loading, moisture ~ suction variation and intrusion of subgrade fines to upper layers. In order to quantify these effects, an Intensity factor I_f , is introduced as follows:

$$I_f = \frac{T_D}{T_{EP}} x R_f (1 + \Delta S_{df} x \Delta t_s) \quad (23)$$

where, T_D = design thickness, T_{EP} = measured thickness of the existing pavement, R_f = roughness factor expressed as $Rf = [2R_i / (R_t - R_i)]^{0.25}$ given, R_i = initial roughness value, R_t = terminal roughness value, ΔS_{df} = rate of surface distress depreciation factor, Δt_s = time lapsed.

On the other hand, the effective structural layer thickness of subgrade soils can be derived from the following equation.

$$t_p^b = [A_p - B_p (\log CBR_d) + C_p (\log CBR_d)^2] \log [N / D_p] \quad (24)$$

where, $A_p=219$, $B_p=211$, $C_p=58$ and $D_p=120$.

4.4 Geomaterials characterization

For the MEP design it is a prerequisite that geomaterial properties and changes caused by loading and the environment be comprehensively analyzed. The basic mechanistic properties used to evaluate the performance of pavement geomaterials under various loading and environmental conditions are: 1) dynamic (elastic) modulus; 2) resilient modulus and, 3) Poisson's ratio. These parameters are primarily adopted in the calculation of stresses, strains and displacements within the pavement under traffic loading. Through the application of transfer functions, the computed results are then translated into pavement surface distresses based on LTPP database and performance indicators supplemented with comprehensive testing s and analyses.

The geomaterials adopted in this Study were mainly: a) black cotton subgrade (problematic) soils; b) unbound lateritic gravels; c) quasi-bound mechanically stabilized gravels employing the Optimum Batching Ratio Method (OBRM) [6], [10]; d) bound graded aggregates and gravels employing the Optimum Mechanical and Chemical Stabilization (OPMCS)

technique [6], [10]; e) geosynthetics reinforced unbound and bound materials [6]; and, f) reclaimed asphalt.

The geomaterial property input parameters that were considered include; a) elastic modulus; b) shear modulus; c) resilient modulus; d) elastic limit (yield) strain {initial yield surface} determined within the framework of the recently developed kinematic hardening theories [1], [2]; e) Poisson's ratio; f) compressive and shear strength; g) mechanical stability due to application of OBRM; h) enhanced particle agglomeration due to effects of OPMCS; i) tensile strength; j) coefficient of thermal expansion; k) creep compliance; l) thermal conductivity; m) asphalt binder stiffness; n) aggregate properties; o) heat capacity; p) hydraulic conductivity; q) moisture ~ suction variations; r) plasticity index; and, s) degree of layer contamination. Some of the input parameters influenced by the variations in environmental conditions were computed by using Eqs. (18) ~ (24), whilst the basic mechanistic properties and other input parameters were determined from Eqs. (25) ~ (42).

1) Moduli of elasticity and shear

Research on small strain elastic properties of most geomaterials within the region of linear elastic and recoverable behavior has shown that the elastic modulus is insensitive to the rate, mode and other conditions of loading as well as the consolidation shear stress-strain history provided that the geomaterials are tested under post-primary consolidation conditions and at a constant state of stress. However, it is the elastic yield strain limit $\{(\epsilon_a)_{EYLS}\}$ that varies considerably with the changes in such conditions {also ref. to [1], [2] and [13]}. Essentially therefore, $E^{dynamic} = E^{cyclic} = E^{static}$, whilst $(\epsilon_a)_{EYLS}^{dynamic} > (\epsilon_a)_{EYLS}^{monotonic}$.

This fact notwithstanding, consideration was made of the visco-elastic behavior of Hot Mix Asphalt (HMA) mainly in relation to loading and other factors such as voids contents, effective asphalt contents, binder type and effective specific gravity of aggregates, among others.

Measurement of elastic properties within the region of very small strains, however, requires sophisticated equipment, which is curtailing in terms of resources and maintenance capability. As a consequence, Eqs. (25) and (26) which correlate the initial elastic modulus, E_0 , to the maximum deviator stress (peak strength), q_{max} tested under CUTC (Consolidated Undrained Triaxial Compression) conditions using conventional apparatus, are proposed.

$$E_0 = \{(\ln 7.46 q_{max} + C_{\phi CSS}) / B_{\phi CSS}\} \times [A_{\psi E_0} \times \alpha_{\sigma_{ss}}] \quad (25)$$

$$q_{max} = A_{\psi E_0} \times \exp[B_{\phi CSS} \ln\{m^{-1} \times (\sigma_a)_{max} \times E_0\} - C_{\phi CSS}] \quad (26)$$

$A_{\psi E_0} = 0.134$, $B_{\phi CSS} = 0.418$, $C_{\phi CSS} = 0.936$, and $m^{-1} = 1.32$.

For very soft cohesive geomaterials, $\alpha_{\sigma_{ss}} = (\sigma'_{a0})_{max}$; relatively stiff to hard cohesive geomaterials, $\alpha_{\sigma_{ss}} = \{(\sigma'_{a0})_{max}\}^{-1}$; for sand stone, soft rock and mudstone, $\alpha_{\sigma_{ss}} = \{(\sigma'_{a0})_{max} \times 5 \times \sigma'_r / \sigma'_{a0}\}^{-1}$; while $\alpha_{\sigma_{ss}} = \{(\sigma'_{a0})_{max} \times 5 \times \{\sigma'_c \times OCR\}^{-1}$ for gravel.

The effects of stress states on E_o for cohesive geomaterials are accounted for by applying Eqs. (27) and (28) for drained and undrained conditions respectively.

$$E_o^D = 726e^{0.76 \times \sigma'_{a0}} \quad (27)$$

$$E_o^U = 891e^{0.76 \times \sigma'_{a0}} \quad (28)$$

For the determination of resilient modulus, M_r for unbound geomaterials in general, Eq. (29) may be adopted with the elastic yield limit stress, σ'_{EYLS} determined from Eq. (30).

$$M_r = \sigma'^2_{EYLS} / 2 E_o \quad (29)$$

$$\sigma'_{EYLS} = (\varepsilon_a)_{EYLS} \times E_o \quad (30)$$

On the other hand, E_o can be determined from Eq. (31) for stress-strain measured at $\varepsilon_a=0.001\%$ by using conventional gap sensors, which are affordable and relatively user friendly.

$$E_o = [\alpha_{E_o}(\varepsilon_a)_{=0.001\%} + \beta_{E_o}] \times 10(MPa) \quad (31)$$

where, α_{E_o} and β_{E_o} are determined simultaneously at $\varepsilon_a=0.001\%$ and 0.01% .

Prediction of shear modulus as a function of consolidation stress history and stress state can be made from Eq. (32) below.

$$[G_o]_{p'} = \left\{ \mathcal{A}_{p'_o} \left[(K_{cs})^\alpha \times \left(\frac{p'}{p'_o} \right)^\beta \right] + \mathcal{B}_{p'_o}^{K_{cs}} \right\} \times [G_o]_{p'_o} \quad (32)$$

where $[G_o]_{p'}$ is the initial shear modulus at a variable stress point p' , $K_{cs} = \sigma'_r / \sigma'_a$ is the arbitrary or designated consolidation stress ratio traced to p' , $[G_o]_{p'_o}$ is the initial shear modulus determined at in-situ overburden pressure, $\mathcal{A}_{p'_o}=0.95$ and $\mathcal{B}_{p'_o}=0.35$ are geomaterial constants, the values of which are applicable for most natural stiff to hard clayey geomaterials, while $\beta=1.16$ and $\alpha=0.4$ for stress states in the 1st quadrant and $\alpha=-1$ for stress states in the 4th quadrant accordingly.

2) Elastic Yield Limit Strain $\{(\varepsilon_a)_{EYLS}\}$ and Stress $\{\sigma_{EYLS}\}$

The importance of determining the initial yield limit strain and stress to a high degree of precision cannot be overemphasized. At a designated stress state dictated by the in-situ overburden pressures, $(\varepsilon_a)_{EYLS}$ can be determined in % from Eq. (33), which takes into account the effects of consolidation and shear stress history, \mathcal{L}_{CSSH} {Eq. (34)}, drainage conditions, φ_{DC} {Eq. (35)}, cyclic prestraining, α_{cp} {Eq. (36)}, and loading rate, $\dot{\varepsilon}_{SR}$ {Eq. (37)}.

$$(\varepsilon_a)_{YI} = \frac{\beta_{E_o} - 0.1[(E_o)_R^2 / E_o]}{\alpha_{E_o}} + f(\mathcal{L}_{CSSH}, \varphi_{DC}, \alpha_{cp}, \dot{\varepsilon}_{SR}) \quad (33)$$

Equation (33) can be conveniently computed from the ratio of $(E_o)_R^2 / E_o$, where $(E_o)_R^2$ is measured from reconstituted specimens, while E_o is determined from CU(D)TC test

performed on intact specimens, field seismic surveys or otherwise computed from Eqs. (25) ~ (28).

$$[\varepsilon_a]_{YI}^{\sigma_{ss}} = \mathcal{A}_{\mathcal{L}_{CSSH}}^{\varepsilon} \ln(\delta_{SCT} \times \phi_{OCR}) + [(\varepsilon_a)_{YI}]_{NC}^{tp} \quad (34)$$

where $\mathcal{A}_{\mathcal{L}_{CSSH}}^{\varepsilon} = 1.9 \times 10^{-3}$ is a constant, δ_{SCT} is the secondary consolidation factor, ϕ_{OCR} is the overconsolidation factor and $[(\varepsilon_a)_{YI}]_{NC}^{tp}$ is the initial yield strain determined under normally consolidated conditions at a standard time period designated after the end of primary consolidation.

$$[\varepsilon_a]_{YI}^{\varphi_{DC}} = \left[\frac{(\Delta\sigma'_a - 2\nu\Delta\sigma'_r)}{(\Delta\sigma'_a - \Delta\sigma'_r)} \right]^{\beta(d/u)} \times \left[\frac{\sigma'_r}{\sigma'_a} \right]_{KC} \times [(\varepsilon_a)_{YI}]_{\{d/u\}} \quad (35)$$

where $\Delta\sigma'_a$, $\Delta\sigma'_r$ are the effective axial and radial stresses respectively determined at the threshold of $[(\varepsilon_a)_{YI}]_{\{d/u\}}$, $[\sigma'_r / \sigma'_a]_{KC}$ is the stress ratio during consolidation, $\beta(d/u) = -1$, $\beta(u) = +1$ (d : drained and u : undrained) and ν is the Poisson's ratio computed from Eq. (38).

$$[\varepsilon_a]_{YI}^{\alpha_{cp}} = \mathcal{A}_{\alpha_{cp}}^{\varepsilon} \ln \alpha_{cp} + [(\varepsilon_a)_{YI}]_{(tp)} : BC =$$

$$\left| \frac{\partial^2 (\varepsilon_a)_{tp}}{\partial \alpha_{cp}^2} \right| = 0 \text{ and } \left[\frac{\partial^3 (\varepsilon_a)_{tp}}{\partial \alpha_{cp}^3} \right]_{\delta R} < 0 \quad (36)$$

$$[\varepsilon_a]_{YI}^{\dot{\varepsilon}_{SR}} = \left[\mathcal{A}_{\dot{\varepsilon}_{SR}} \ln \left(\frac{\dot{\varepsilon}_{ASR}}{\dot{\varepsilon}_{RSR}} \right) + \mathcal{B}_{\dot{\varepsilon}_{SR}} \right] \times (\varepsilon_a)_{YI}^{\dot{\varepsilon}_{SR}} \quad (37)$$

where, the subscripts SR denote Strain Rate, ASR : Applied Strain Rate during testing or arbitrarily designated and RSR : Reference Strain Rate.

3) Poisson's ratio $\{\nu_{pd}\}$

Under partially undrained conditions ν_{pd} can be determined from Eq. (44) as:

$$\nu_{pd} = \left\{ \frac{(E_o)_d}{(E_o)_u} (1 + \nu_u) \right\} - 1 \quad (38)$$

where $(E_o)_d$, $(E_o)_u$ are the initial drained and undrained elastic moduli respectively.

4) Mechanical stability

Quantitative analysis of the contribution of enhanced mechanical stability due to OBRM stabilization was undertaken by applying Eqs. (39) and (40).

$$M_S^f = A_{MS} \exp^{-1.16\eta} \quad (39)$$

when $\eta \geq 0.5$

$$M_S^f = M_S^{ideal} - [A_{MS} \exp^{-1.16\eta} - M_S^{ideal}] \quad (40)$$

when $0 < \eta < 0.5$

where, M_S^f is the Mechanical Stability (MS) factor, and for this case, A_{MS} is the MS constant=178.6, η is the gradation index= $\log 0.01P / \log(d/d_{max})$, $M_S^{ideal}=100\%$ for non-stabilized geomaterial.

5) Particle agglomeration

The contribution of particle agglomeration in enhancing strength and elastic modulus due to OPMC stabilization is quantitatively analyzed from Eqs. (41) and (42) respectively.

$$q_{max} = A_q \ln a_f + q_{max}^i \quad (41)$$

where, q_{max} is the maximum shear strength, $A_q = 1.06$ is a material constant and a_f is the agglomeration factor computed from the level of OPMC related factors.

$$E_0 = A_{EM} a_f^2 + B_{EM} a_f + E_0^i \quad (42)$$

where, $A_{EM} = 62.4$ and $B_{EM} = 690$ are geomaterial constants. E_0 is measured and/or expressed in MPa.

4.5 Modified Performance Prediction Equations

Studies on the modification of performance prediction equations and calibration factors aimed at enhancing their precision, versatility, reliability and confidence levels, are on-going.

4.6 Performance Prediction Models

The performance prediction models that were adopted for this Study include: a) ESDAM (Environmental, Strength and Deformation Model); b) SCDRM (Structural Capacity and Deformation Resistance Model); c) CSSRM (Consolidation and Shear Stress Model); and, d) MCSTM (Modified Critical State Theory Model).

5 ME APPROACH IN PAVEMENT STRUCTURAL DESIGN, CONSTRUCTION AND MAINTENANCE

5.1 MEP Design Approach

In this Study, the MEP (Mechanistic-Empirical Pavement) design is incorporated into the CMD (Comprehensive Method of Design) [11]. Conventionally, methods of pavement design can be grouped into five categories namely: a) empirical methods; b) limiting shear failure methods; c) limiting deflection methods; d) regression methods based on pavement performance and road test; and, e) mechanistic-empirical methods [12]. In order to undertake comprehensive design analyses for mega projects, the CMD combines all these methods through an iterative comparative analysis module. Basically, the MEP-CMD approach consists of the following steps: ① Identification of the input parameters through application of the equations and functions introduced in this paper; ② Computation of elastic/visco-elastic solutions under mechanical loading conditions; ③ Computation of elastic solutions under thermal loading conditions; ④ Computation of elastic solutions under physio-chemical loading conditions; ⑤ Conversion of the mechanical, thermal and physio-chemical elastic solutions to the counterpart visco-elastic through the application of EVCP (Elastic-Visco-elastic Correspondence Principle) and the modules introduced herein; ⑥ Introduction of the dynamic loading concept for the reciprocal loading conditions by applying the BSI (Boltzman Superposition Integral); ⑦ Analysis of integrated effects of mechanical, thermal and physio-chemical loading; ⑧ accumulation of deformations and plastic strains; ⑨ Systematic introduction of other

influencing factors based on the SAC (Systematic Approach Concept); and, ⑩ Determination of postulated failure mechanisms, mainly rutting, fatigue and thermal cracking through the application of appropriate prediction models.

5.2 Construction Quality Control

The recently developed construction quality control functions adopted for the MEP design are reported in [14].

5.3 Prediction of Maintenance Requirements

The deterioration with time of the structural capacity is predicted by adopting Eqs. (43) ~ (45). The results for the Juba River Port access road Case Study are plotted in Fig. 2.

$$f_{sc}^t = f_{sc}^i \times (\ln N_t^{0.62})^{-1} \times \left[1 + \frac{0.1 \log N_t^R}{f_{sc}^R} \right] \times e^{0.01 N_t} \quad (43)$$

where, f_{sc}^R = reference structural capacity for $N_t = 2.2$ years of post dynamic traffic loading.

Environmental factors such as moisture-suction variation due to seasonal changes, inferior material intrusion as a result of the combined effects of dynamic loading and water infiltration (pumping) and land use affecting the structural capacity and pavement structural layer thickness, are quantitatively analyzed and factored into generalized Eq. (43) by applying Eqs. (44) and (45) which incorporate the time dependant factor f_{df}^t partially defining the effects of LTPP.

$$f_{df}^t = \{e^{[0.01 f_{df}^d N_t]}\}^{-1} \quad (44)$$

The factor f_{vf}^d , which defines the variation with time in environmental factors is computed as:

$$f_{vf}^d = f_{msv}^d \times f_{int}^d \times f_{th}^d \quad (45)$$

where, f_{msv}^d = moisture~suction depreciating factor, f_{int}^d = BCS intrusion depreciating factor, f_{th}^d = pavement structural layer thickness depreciating factor.

• *Computation of Maintenance Requirement Ratio (MRR)*
The computation of the MRR is made from Eq. (46) based on the results computed and simulated by the SCDR model by adopting the T_A over a loading period N_t and Design Life, DL .

$$MRR = \frac{T_A^{(N_t=DL)}}{T_A^{(N_t=2.2)}} \times f_{SC}^{d(N_t=10)} \times \frac{T_A^{(N_t=0.5DL)}}{T_A^{(N_t=2.2)}} \times \left[\frac{N_t=0.5DL}{N_t=DL} \right] \times F_s \quad (46)$$

Figure 2 shows a comparison of the predicted and actual pavement structural performance based on the results from deflection testing and prediction made from the SCDR model for three varying pavement structural configurations [6]. It can be inferred that Type II-1 approaches the critical zone, which is an indication of the requirement of fully-fledged rehabilitation, after only 4.6 years; whereas Type II-3 is structurally sound over the whole period of the Design Life. On the other hand, based on Eq. (46) and the SCDR results, the Maintenance Requirement Ratio (MRR), was generated for the three varying pavement structural configurations over the entire period of the Design Life ($DL=20$ years). The

results indicated that; $\{Type II-1\}_{MRR} = 2.86$, $\{Type II-2\}_{MRR} = 0.88$, while $\{Type II-3\}_{MRR} = 0.43$.

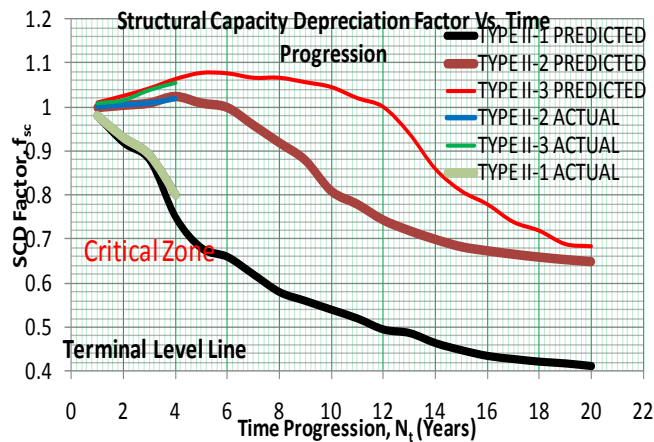


Fig. 2 Progressive time dependent structural capacity depreciation of three types of pavement structures

6 CASE EXAMPLES OF APPLICATION

The MEP-CMD has been applied for the design of heavily loaded pavement structures, foundations and other geo-structures in East and Central Africa whereby average construction cost-time savings of approximately 40% were realized, whilst the structural capacity and pavement performance were appreciably enhanced [6].

7 CONCLUSIONS

The recently developed mechanistic-empirical methods introduced in this paper form a conceptual and geoscientific basis for geotechnical engineers in general, and pavement designers in particular, to improve their design philosophies geared towards VE principles, enhance reliability and precision of prediction of overall pavement performance, effectively simulate failure modes, quantitatively determine impact of environmental changes, advance methods of characterizing inherent as well as induced material properties, improve construction quality control and technically compute maintenance requirements.

Nevertheless, the necessity of further research in this regard is significantly apparent.

8 ACKNOWLEDGMENT

The author wishes to extend special appreciation to the Japan International Cooperation Agency (JICA), and Kajima Corporation, Japan, for sponsoring most of this research as well as the Materials Testing & Research Department of the Ministry of Roads, Kenya for their support. Acknowledgement is also made of the relentless efforts of members of the Kenya Geotechnical Society Research Team.

9 REFERENCES

[1] Mukabi JN, "Characterization and modeling of various aspects of pre-failure deformation of clayey Geomaterials –

Fundamental theories and Analyses", Proc. 1st Int. Conf. on GEOMAT, Mie, 2011.

[2] Mukabi JN and Hossain Z, "Characterization and modeling of various aspects of pre-failure deformation of clayey Geomaterials – Applications in modelling", Proceedings. 1st International Conference. on Geotechnique, Environment & construction Materials, GEOMAT, Mie, 2011.

[3] Baus RL and Stires NR, "Mechanistic-Empirical Pavement Design Guide Implementation", Report submitted to the South Carolina Department of Transportation and the Federal Highway Administration, USA, 2010.

[4] Zeghal M, Adam YE, Ali O, and Elhissein HM, "Review of the new Mechanistic-Empirical Pavement Design Guide – a material characterization perspective", Report submitted to the National Research Council of Canada, 2005.

[5] Mukabi JN, Kotheki S, Ngigi A, Gono K, Njoroge BN, Murunga PA, Sidai V, "Characterization of black cotton soil under static and dynamic loading- Testing and Analyses", Proc. Int. Conf. on GE, 2010, Tunis, pp. 67-77.

[6] Mukabi JN, "Case Study Analysis of OPMC improved foundation ground, pavements and geo-structures employing the GECPRO model", to be published in Procs. Of ISSMGE Int. Symp. on Ground Improvement (IS-GI), Brussels, 2012, Vol. II, pp.II-431-II-442.

[7] Mukabi J.N, "Application of Unique Methods of Testing and Analysis for the Comprehensive Design of Geo-structures to be published in Proc. Int. Conf. on Geotechnical Engineering, Lahore, 2013.

[8] Mukabi JN, "Innovative laboratory and in-situ methods of testing in geotechnical engineering, to be published in the Proc. of the Int. Conf. of the Institute of Engineers Kenya , Nairobi, 2013.

[9] Mukabi JN, "Application of Consolidation and Shear Stress Ratio (CSSR) concepts in foundation design and construction" Proc. 14th ARC on SMGE Vol. II, Yaoundé, 2007, pp.172-193.

[10] Kogi, S.K, Mukabi, J.N, Ndeda, M, Wekesa, S, "Analysis of Enhanced Strength and Deformation Resistance of Some Tropical Geomaterials through Application of In-situ Based Stabilization Techniques", Proceedings. 1st International Conference. on Geotechnique, Environment & construction Materials, GEOMAT, Mie, 2011.

[11] Mukabi JN, "A Comprehensive Method of Analysis for Cost-effective Detailed Design of Pavement Structures" Proc. 14th ARC on SMGE Vol. I, Yaoundé, 2007, pp.82-112.

[12] Bhutta SA, "Mechanistic-Empirical Pavement Design Procedures For Geosynthetically Stabilized Flexible Pavements", PhD Thesis in Civil Engineering, Virginia Polytechnic Institute and State University, 1998.

[13] Mukabi J.N., "Recent Development in the Quantative Determination of Kinematic Hardening Sub-Yield Surface Limits", in Procs. Int. Conf. on New Developments in Soil Mechanics and Geotechnical Engineering, North Cyprus, 2012.

[14] Mukabi JN, Kimura Y, Murunga PA, Njoroge BN, Wambugu J, Sidai V, Onacha K., Kotheki S, Ngigi A, "Case example of design and construction within problematic soils", in Procs. Int. Geotechnical Conference on Geotechnical Challenges in Megacities, Geomos, Moscow, 2010, vol. 2, pp 1172-1179.

Design of Support System for Excavation in Black Cotton Soils in Guntur, India

D. Neelima Satyam¹, Akhila Manne²
Earthquake Engineering Research Centre,
International Institute of Information Technology Hyderabad,
Gachibowli, Hyderabad-32, India.

ABSTRACT

Deep excavations are one of the venturesome tasks taken up by geotechnical engineers. Adept and secure design of deep excavations in especially clayey strata is a defying task per se it involves assumptions. Controlling the mobility of clayey soil is intricate. Deformations are consequential to stress release and redistribution in deep excavations and stability controls the design of the support systems. Usually, it is the supervision of deep excavations (Burland and Hancock 1977, O'Rourke 1981; Finno et al. 1989, Hansmire et al. 1989, Ulrich 1989; Whitman et al., 1991; Ikuta *et al.*, 1994) at field that succor to attain economy and safety. It also aids in prediction of the ground settlement on adjacent structures. The objective of this paper is to discuss the design of sheet pile, supporting structures and challenges faced in the construction of a sump in clayey soil site. The case of study is located at Guntur district in the state of Andhra Pradesh, India. Standing on a bed of black cotton and plastic clays with water table as low as 0.5m, the site renders a geotechnical challenge.

Keywords: Deep excavation, Sheet pile, Finite Element Analysis, PLAXIS

[1] INTRODUCTION

Construction of deep basements, subways and service tunnels require deep excavations eventually making them contingent in the construction activities. Excavation is one of the most hazardous construction operations as the behavior is multifaceted and their failures are rapid. The effects are caused due to the decrease in vertical stress and loss in lateral support and hence requires the examination of field performance and monitoring [1]-[3]. Stability and deformation are the weightage factors in the performance of a deep foundation. If the factor of safety is small, strains are small and return the ground movements are small. The deformations damage the adjacent structures like buildings and utilities. Severity of this damage depends on the pattern and movements around the excavation.

Soil type dictates the design and performance of such excavations [4]-[6]. Including soil properties, depth of excavation and workmanship are intrinsic in controlling the earth movements [4]. To verify the performance of a deep excavation, their analysis is required. Though stability is easy to analyse using equilibrium calculations, deformations are difficult to predict and require finite element analysis.

References [7]-[11] used 3D finite element analysis to study deep excavations. Study and analysis done by [10] and [11] have shown that a significant reduction in deformation in the corners was observed when corner restraints were used when compared with that for a plane strain condition. Fig 1

illustrates the effect of support system stiffness on the wall displacements.

In this paper the design of sheet piles as temporary support system for excavation in deep clay is dealt. The excavation has a 17m x 13.26 m plan area for construction of an underground sump with 6 m excavation depth at the Reliance cash and carry construction site in Guntur located in the state of Andhra Pradesh, India.

[2] SITE DETAILS

The site is blanketed with plastic silty clays up to 7.5m below the ground surface, underlain with about 5m of sandy clays (Fig). In order to excavate to the required depth of about 6 m total is a major challenge of controlling the soil collapse as well as the lateral support of the excavation.

In detail, the ground consists of 3 layers (Fig. 1). The upper most layer is 5.0 to 7.5 m thick silty clay (layer I). Beneath the fill is sandy clay (3.5 to 4.5 m) thick layer (layer II) and it is underlain by greenish white rock fragments / reddish clayey sand gravel (11m to 13.5m, layer III). The recorded SPT 'N' value ranges from 5-36 in the topmost layer, 19-61 for the sandy clay layer and 41-99 for the rock fragments in the third layer. The groundwater level was located at about 0.5m below the ground surface during the exploration in 2011(May) but is suspected to be seepage. The results of a number of field and laboratory soil tests are summarized in Fig. 2 and Fig. 3. The natural water content varies between 37 and 7% (including the pebbles) and shows a general decreasing trend with depth.

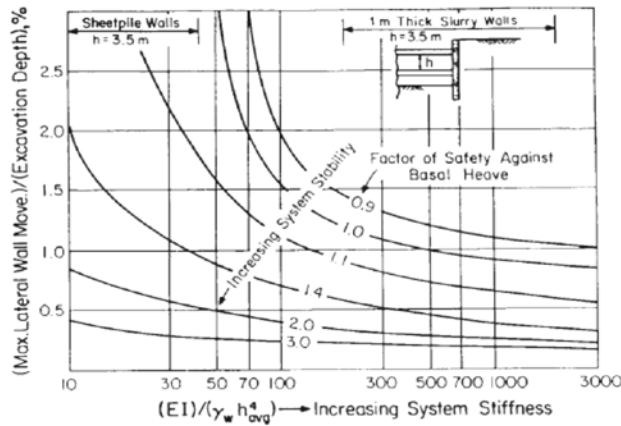


Figure 1 Chart for estimating maximum lateral wall movements and ground surface settlements for support system in clays [6].

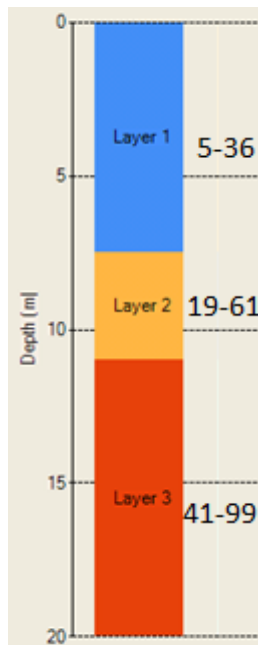


Figure 2 Predominant soil profile with SPT 'N' value

Table 1 Soil Properties

Depth (m)	Soil Type and IS Classification	SPT 'N'
0-2.5	Plastic silty clay [MH-CH]	8
2.5-4.5	Silty clay [MH-CH]	11
4.5-7.5	Plastic silty clay [MH-CH]	15-19
7.5-9.	Sandy clay +lime pebbles	30
9-12	Sandy clay +lime pebbles	32-38
12-15	Clayey sandy +pebbles [MI-CI]	46-47
15-20	Rock fragments [SC]	54-66

The liquid limit in the upper part is around 40 % which can be classified as plastic silty .Unconfined compressive strength and direct shear tests were conducted during the exploration phase.

[3] MODELING AND ANALYSIS

With the increase in the complexity of a geotechnical problem it is preferable to use a numerical model. Partial differential equations are employed with a combination of different variables and the calculations are used to mould the model. The variables maybe material parameters, stresses, and strains etc, and have a complex correlation. According to [12] the maximum horizontal wall displacement (δ_{hm}) lies between 0.5% H and 1.0 % H , on average at 0.87% H (Fig.3).

The use of the sheet piles as temporary support system for the current problem of study satisfies the limits imposed by the design specifications and also addresses the constructability of the underground water tank. Finite element analysis is used, which is vital not only in the evaluation of the behavior and design of the support system for underground sump, but also in the evaluation of its impact on adjacent structures. The analysis is primarily based on the theory of earth pressure developed by Rankine, 1857. When designing sheet pile walls, the partial coefficient method is used, both in serviceability limit state and ultimate limit state.

The finite element software PLAXIS [13] has been used to model the staged excavation of the underground sump. Fig 4,5 show the excavation pit section details and plan with structural support system.

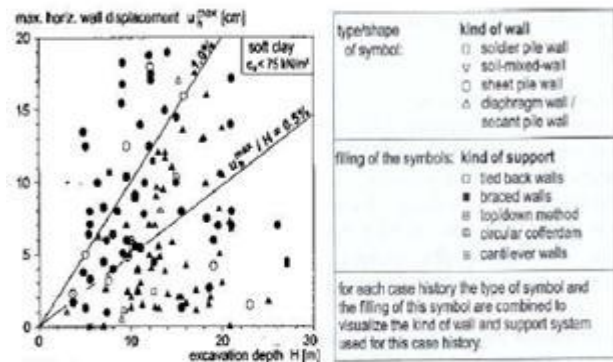
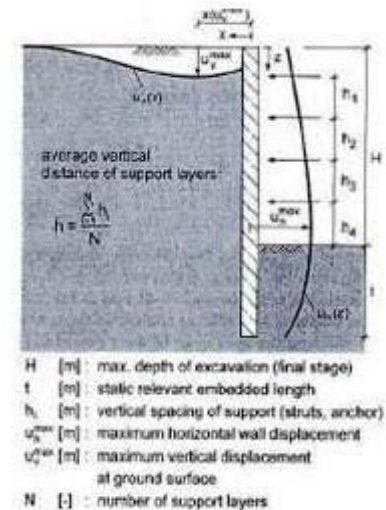


Figure 3 Variation of maximum horizontal displacements with excavation depth [12]

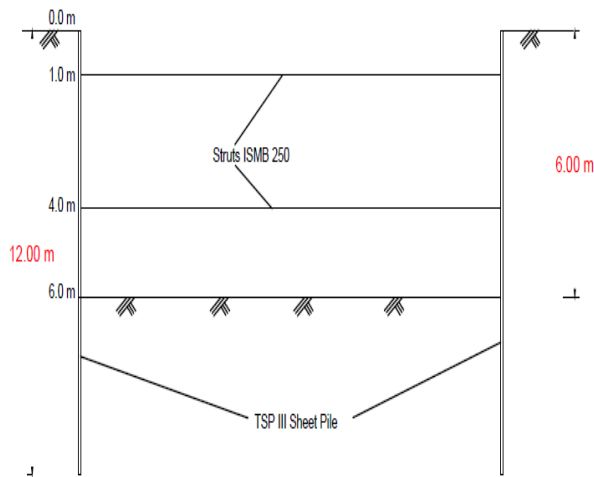


Figure 4 Excavation section with support details

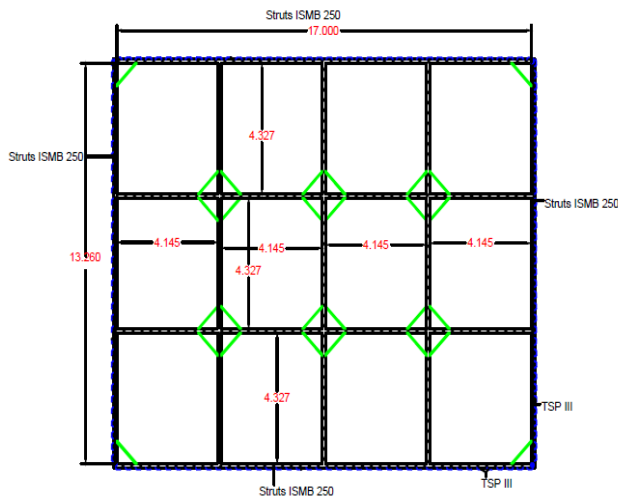


Figure 5 Excavation Plan details with support system

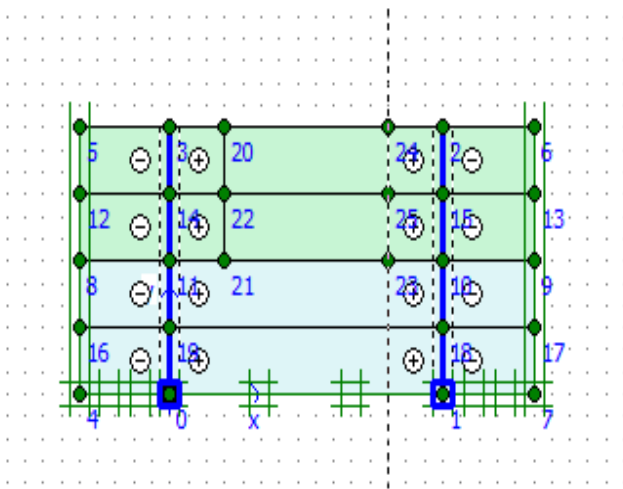


Figure 6 Geometry of the model with TSP III sheet pile for 12m

The geometry of the sheet pile used is TSP III with 400 x 125 x 13mm section piles (Fig. 6) with unit weight of 60kg/m from Hanwa Singapore is provided. In addition, soil

properties from the geotechnical investigation reports were used. Struts or braces are modeled as bar elements which have only axial forces and no resistance to bending. The connection between the wall and the strut is consequently analogous to a pin connection. Pre-loads are specified as part of the strut definition. ISMB 250 is used at two preferable levels at 1.0 and 4.0m below the EGL.

[4] RESULTS AND CONCLUSIONS

Understanding of the load transfer mechanism around the construction site, superior workmanship, soil properties information is required for deep excavations. Prediction of accurate design before the construction is necessary, especially when clay soils are being dealt. Catastrophic failures of the excavation and structural failure can be avoided by detailed deformation analysis and site inspection during construction process.

In the current case, a temporary support system using sheet piles TSP III with 400 x 125 x 13mm has been adopted for adequacy of the lateral loads. Fig.7 details the deformed mesh of the sump after the analysis. The total displacements and vertical displacements at 14.6mm and horizontal displacements at 10.58mm are shown in Figs 8-10.

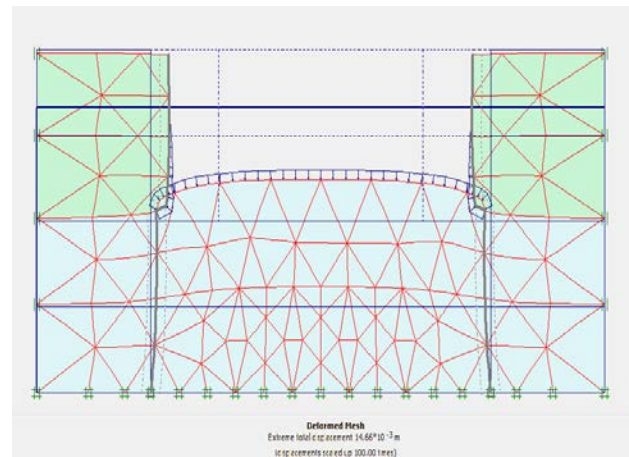


Figure 7 Deformed mesh of sump

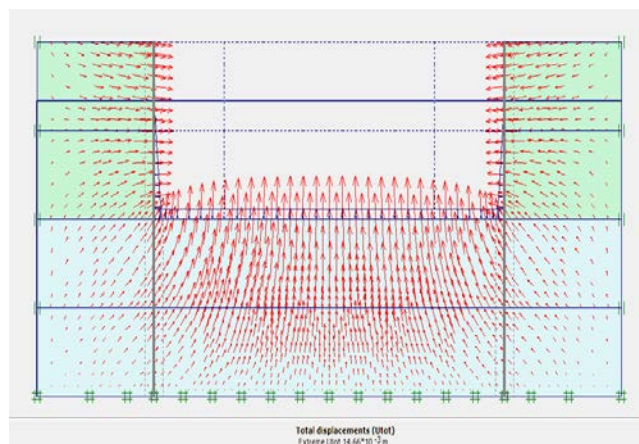


Figure 8 Total displacement (14.66 mm)

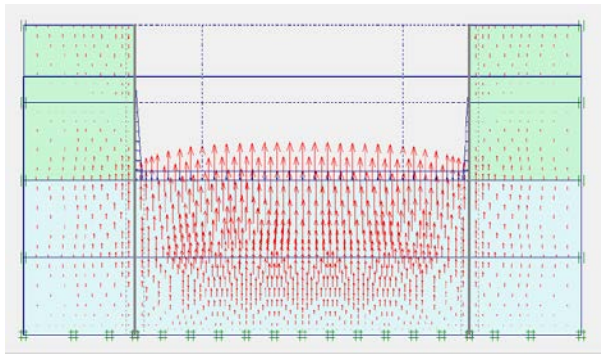


Figure 9 Vertical displacements (14.66 mm)

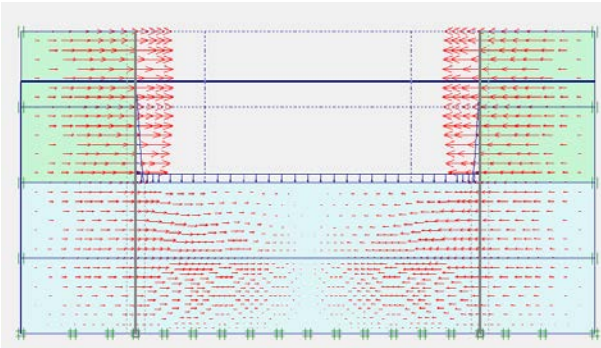


Figure 10 Horizontal displacements (10.58 mm)

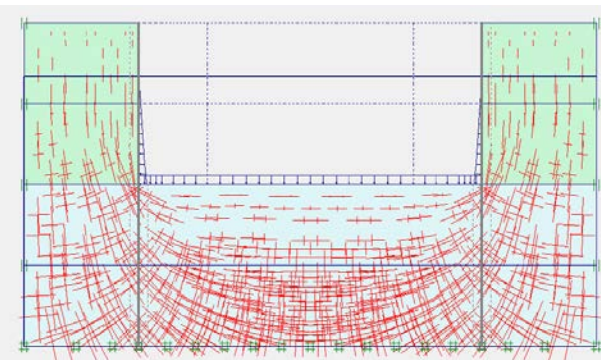


Figure 11 Effective stress (145.50 kN/m²)

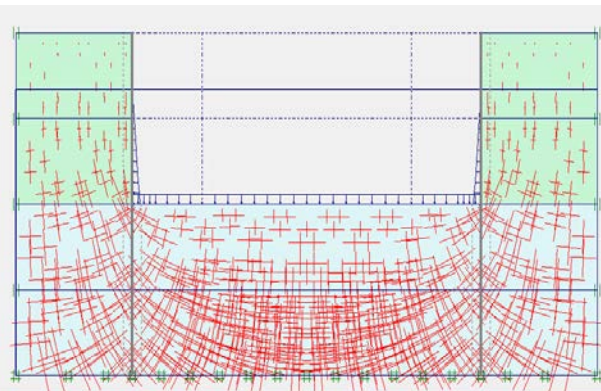


Figure 12 Total stress (208.66 kN/m²)

The values of total and effective stress are derived to be 145.5kN/m² and 208.6 kN/m² (Fig.11, 12)

Finally, sheet piling has been designed to facilitate the excavation in the site blanketed with clay as sheet piling also does not require much expertise and time. However, skill is necessary to safely install walers and toms which support the piling.

[5] REFERENCES

- [1] Burland, J.B., and Hancock, R.J.R. (1977). Underground carpark at the House of Commons, London: Geotechnical aspects. The Structural Engineer, No. 2, Volume 55, 87-100.
- [2] O'Rourke, T.D. (1981). Ground movements caused by braced excavations. J. Geotech. Engng Div. Am. Soc. Civ. Engrs 107, GT9, 1159-1178.
- [3] Finno, R.J., Atmatzidis, D.K. and Perkins, S.B. (1989). Observed performance of a deep excavation in clay. J. Geotech. Engrg., ASCE, Vol.115, No.8, pp 1045-1064
- [4] Peck, R.B. [1969]. "Deep excavations and tunneling in soft ground. State of the Art Report" Proc. Of the VII ICSMFE, Mexico, pp. 225-290.
- [5] Goldberg, D.T., Jaworski, W.E., and Gordon, M.D. (1976). "Lateral support systems and underpinning". Rep. FHWA-RD-75-128, Federal Highway Administration, Washington D.C.
- [6] Clough, G.W. and O'Rourke, T. D., (1990). "Construction induced movements of in situ Walls". In Proc. Design and performance of earth retaining structure, ASCE Special conference, Ithaca, New York, pp 439-470.
- [7] Borja, R.I. (1990). "Analysis of incremental excavation based on critical state theory", Journal of Geotechnical Engineering, ASCE, 116(6), 964-985
- [8] Schweiger, H.F. and Freiseder, M (1994) "Three dimensional finite element analysis of diaphragm wall construction" Proc. Of the Eighth Int.Conf.on Computer Methods and Advances in Geomechanics, 8(3),2493-2498.
- [9] Tabrizi, K.S., Gucunski, N., and Maher, M.H. (1995). "3-D analysis of excavation of a soil-nail wall," Second congress on computing in Civil Engineering, ASCE, 1, 812-819.
- [10] Ou, C.Y. and Chiou, D.C. and Wu, T.S. (1996). "Three dimensional finite element analysis of deep excavations". Journal of geotechnical engineering, Vol 122, No.5, May, 1996, pp337-345.
- [11] Lee, F.F., Yong, K.W., Quan, K.C.N., and Chee K.T. (1998). "Effect of corners in strutted excavations: field monitoring and case histories", Journal of Geotechnical and Geoenvironmental Engineering, ASCE, 124(4), 339-349
- [12] Moormann, C. (2004). "Analysis of wall and ground movement due to deep excavation in soft soil based on a new worldwide database", Soils and Foundations, Vol. 44, No. 1, 87-98.
- [13] Brinkgreve R.B.J. 2002. PLAXIS: Finite element code for soil and rock analyses, Balkema

Numerical Modeling Of Pullout Capacity Of A Suction Pile In Sand Under Oblique Load

Md. Iftekharuzzaman¹ and Dr. Bipul Hawlader²
Memorial University, St. John's, Newfoundland, Canada

ABSTRACT

Suction piles are widely used in mooring system for deep water oil and gas development projects. In this study three-dimensional finite element analyses are performed to estimate the pull-out capacity of a suction pile subjected to oblique loading. The numerical modeling is performed using ABAQUS finite element software. The effects of two key variables, loading angle and mooring line position, are investigated. The finite element results are compared with centrifuge test results available in the literature. The maximum pull-out capacity is obtained when the mooring line is attached at approximately 75% depth of the pile for the cases analyzed in this study.

Keywords: Suction pile, oblique load, finite element analysis, pull-out capacity.

1. INTRODUCTION

A suction pile (also known as suction caisson) is a large cylinder, usually made of steel, with an open bottom and a closed top that is installed in the ground mainly by suction applied by pumping water out of the caisson interior. Suction piles have been widely used in offshore industries ranging from anchor for floating facilities to offshore foundations. Geometrically the suction piles are larger in diameter than typical piles used for foundation [1]. Fig. 1 shows some use of suction piles for various projects in the world. Suction piles could be installed both in clay and sand sea beds, although the mechanism during installation is different. Houlsby and Byrne (2005a, b) [2], [3] present the design procedure for installation of suction piles in sand, clay and other geomaterials.

Suction piles are widely used in mooring system for deep water oil and gas development projects, where the pull-out capacity is one of main requirements. The piles are normally pulled by a chain connected to the pad eye on the side of the pile. The inclined pull-out capacity of suction pile depends on both horizontal and vertical load capacity.

Yoshimi (1964) studied the behavior of rigid vertical and batter piles in a cohesionless soil subjected to inclined loading [4]. Broms (1965) also analyzed the Yoshimi (1964) experiments and proposed an equation for the pull out resistance [5]. Poulos and Davis (1980), based on the experiments of Yoshimi (1964) and the analysis of Broms (1965), proposed a simplified theoretical method to predict the ultimate resistance of vertical pile under oblique loading [6].

Finite element analysis of a single pile under lateral and oblique pulling has also been conducted by some researchers.

Erbrich (1994) conducted a series of finite element analysis to estimate the capacity of suction caissons used as foundations for fixed offshore steel platforms [7].

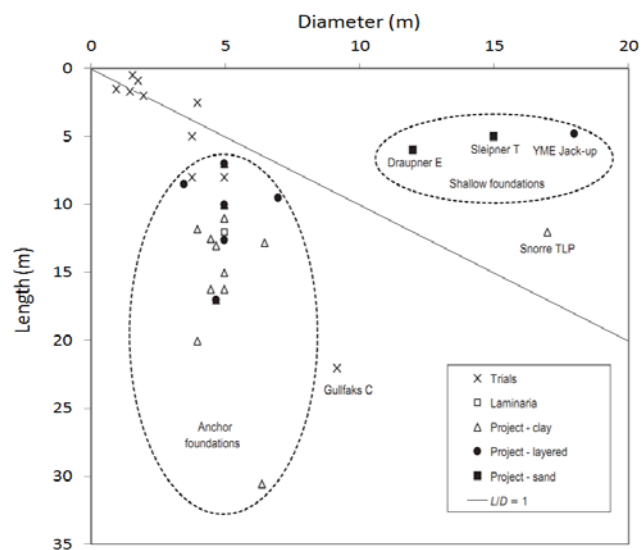


Fig. 1. Suction piles used in various projects (Byrne 2005b)

Bye et al. (1995) presented the design analyses of the Europe 16/11E and sleipner T foundation in dense sand [8]. Sukumarn et al. (1999) and Sukumaran and McCarron (1999) showed the application of the finite element method to estimate the capacity of suction pile foundations installed in soft clays and subjected to axial and lateral loads under undrained conditions [9], [10]. Handayanu et al. (1999 and 2000) used a quasi-three-dimensional finite element model to study the response of suction caissons subjected to vertical

uplift and inclined loads [11]. Deng and Carter (2000) presented finite element analyses using axisymmetric elements and proposed a simplified relationship for estimating inclined pull-out capacity under drained condition [12]. Zdravkovic et al. (2001) conducted finite element analyses to study effects of load inclination, caisson aspect ratio, soil adhesion, and soil anisotropy on behavior of suction piles [13]. Cho and Bang (2002) examined the application of the failure envelop developed by Bransby and Randolph (1999) from the observation in clay for estimating inclined load capacity of a suction pile in sand [14]. Bang et al. (2011) conducted a series of centrifuge tests to estimate the pullout capacity of a suction pile installed in sand [15].

This paper presents three-dimensional finite element analysis of a steel suction pile embedded in sand subjected to oblique loading at different load inclination and mooring positions. A total of 25 cases are analyzed to evaluate the pull-out capacity of a suction pile. The finite element results are compared with centrifuge test results. The effects of loading angle and mooring positions on ultimate pull-out capacity, lateral displacement and soil reactions on suction piles are discussed.

2. PROBLEM DEFINITION

Finite element (FE) analyses are performed to calculate the pullout capacity of suction piles. A suction pile of diameter D and length L installed in sand is loaded for different mooring positions and loading angles. The notations used in this study are shown in Fig. 2. The load is applied at five pad-eye locations as shown by solid circles on the left.

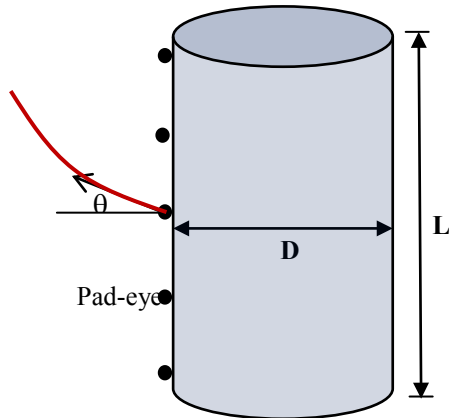


Fig. 2. Problem definition

3. NUMERICAL MODELLING

In this study, numerical analyses are carried out using finite element software ABAQUS/standard 6.10-EF-1. A cuboid soil domain of 40 m length, 20 m width and 20 m height as shown in Fig. 3 is modeled. The size of the soil domain is sufficiently large compared to the size of the pile and therefore boundary effects are not expected on calculated load, displacement and deformation mechanism. The vertical plane of symmetry is restrained from any displacement

perpendicular to it, while the other three vertical sides of the soil domain are restrained against lateral displacement using roller supports at the nodes. The bottom boundary is restrained from any vertical displacement, and the top boundary is free to displace.

The finite element mesh used in this study is shown in Fig. 3. The elements used are the solid homogeneous C3D8R element, which is an 8-noded linear brick, multi-material and reduced integration with hourglass control.

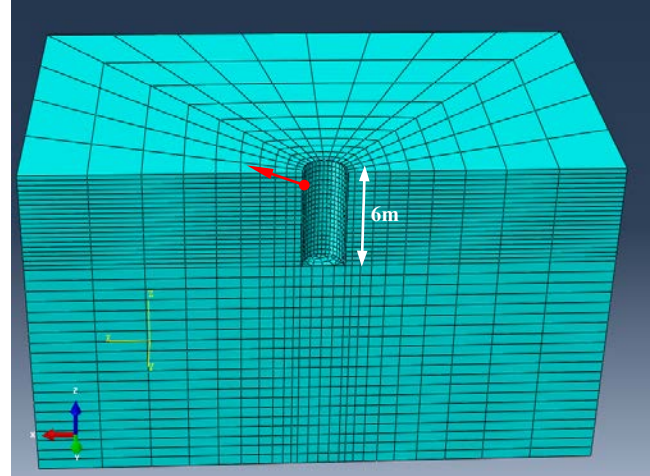


Fig. 3. Finite element model with medium dense mesh

The numerical analysis consists of two major steps: gravity and loading step. In gravity step the soil domain is loaded up to in-situ stress condition, and in the loading step preselected lateral and oblique displacements are applied on the nodes at desired depth (pad-eye location) on the left side of the outer surface of the pile as shown in Fig. 2 and Fig. 3.

3.1 Pile Modelling

A steel pipe pile of 6 m length and 3 m diameter with 100 mm wall thickness is modeled in this study. The pile is modeled as an elastic material with modulus of elasticity (E_p) of 208×10^6 kN/m² and Poisson's ratio (ν_p) of 0.3.

3.2 Soil Modelling

The sand is modeled by the Mohr-Coulomb constitutive model available in ABAQUS FE software using the following soil parameters: angle of internal friction, $\phi' = 39^\circ$; dilation angle, $\psi = 9^\circ$; modulus of elasticity, $E_s = 60,000$ kPa; and Poisson's ratio, $\nu_p = 0.3$.

The location of the groundwater table is at the ground surface. Submerged unit weight of 8.2 kN/m³ is used for soil layers. Geometry and mechanical properties used in the analysis are shown in Table 1. Note that the geometry and soil parameters mentioned above and in Table 1 are very similar to Bang et al. (2011) as the numerical results presented in this study are verified using their test results [15].

The soil/pile interaction has been modeled using Coulomb friction model, which defines the friction coefficient (μ) as $\mu = \tan(\phi_\mu)$, where ϕ_μ is the pile/soil interface friction angle.

The value of ϕ_μ is assumed to be equal to $0.7\phi'$ in this analysis.

Table 1. Geometry and mechanical properties used in the analysis

Pile:	
Length of the pile (L)	6 m
Diameter of the pile (D)	3 m
Wall thickness of the pile (t)	100 mm
Modulus of elasticity of pile (E_p)	208×10^6 kN/m ²
Poisson's ratio (ν_p)	
Soil (sand)	
Modulus of elasticity, E_s	60,000 kN/m ²
Poisson's ratio, ν_s	0.3
Submerged unit weight of soil, γ'	8.2 kN/m ³
Angle of internal friction, ϕ'_p	39°
Dilation angle, ψ	9°

3.3 Mesh Sensitivity Analysis

The size of the mesh has a significant effect on finite element modeling. Often finer mesh yields more accurate results but computational time is higher. For successful modeling of load-displacement behaviour of piles under oblique load denser mesh should be used near the pile. As shown in Fig. 4 that smaller soil elements are used near the pile and the size of the elements are increased with radial distance from the centre of the pile. Also denser mesh is used in the top 6 m of soil where the pile is located. Below 6 m depth coarser mesh is used which does not have significant effect on calculation.

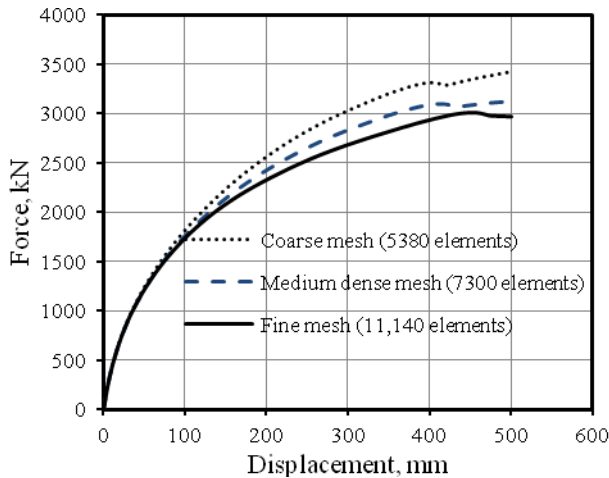


Fig. 4. Mesh sensitivity analysis

After several trial analyses with different mesh size, the optimum mesh is selected. Fig. 4 shows the lateral load versus lateral displacement of the pile for three different types of mesh. In the coarse mesh, a total of 5,380 elements, in the medium dense mesh 7,300 elements and in the fine mesh 11,140 elements are used. The distribution of mesh size is shown in Fig. 3. As shown in Fig. 4 that the number of elements has considerable effect on force-displacement behavior. As for very fine mesh the computational time is

high, the analyses presented in the following sections are conducted using medium mesh with 7,300 elements.

3.4 Centrifuge Modeling

Bang et al. (2011) conducted a series of centrifuge model test of a suction pile embedded in sand to evaluate its inclined pull-out capacity [15]. The effects of load inclination angle and the point of mooring line attachment are studied. The tests were conducted at 100g using geotechnical centrifuge. The test condition and geotechnical properties of sand are similar to those described in Section 3.1 and 3.2.

4 NUMERICAL RESULTS

Numerical modeling is carried out for a single pile applying the load at five mooring positions: 5%, 25%, 50%, 75% and 95% distance from top of the pile. At each mooring position the load is also applied at five different angles of inclination with the horizontal axes: 0°, 22.5°, 45°, 67.5° and 90°. That means, a total of 25 (5×5) numerical modeling are conducted to show the effects of inclination angle and mooring position on pull-out capacity.

4.1 Load-Displacement curves

The variation of total load with total displacement of the suction pile for loading at 5% mooring position is shown in Fig. 5. The total load is calculated from the vertical and horizontal nodal force components at the point of loading. Bang et al. (2011) reported the pull-out capacity for similar condition from of number of centrifuge tests. The range of their pull-out capacity is shown by the arrows on the right vertical axis. As shown the numerical prediction in the present analyses reasonably match with the centrifuge test results [15].

Various methods are available in the literature to estimate the pull-out capacity of a pile. In this study, the pull-out capacity is determined by the first peak load in load-displacement curve. In the absence of a clear peak, the load corresponding to the displacement of 10% pile diameter (i.e. $0.1 \times 3 = 0.3$ m) is considered as pull-out capacity of the pile [16]. The pull-out capacity is shown by the vertical arrows in Fig.5.

Fig. 6 shows the variation of the lateral load with lateral displacement for five different mooring positions. Again, the pull-out capacity obtained in centrifuge tests [15] is shown on the right vertical axis using horizontal arrows. The pull-out capacity (vertical arrows) in the present finite element analysis compares well with centrifuge test results. The pull-out capacity increases as the depth of mooring position increases. The maximum pull-out capacity is obtained for 75% mooring position. After that, for example at 95% mooring position, the pull-out capacity decreases. This is because of the displacement and rotation of the pile under mooring force, which will be further discussed in the following sections.

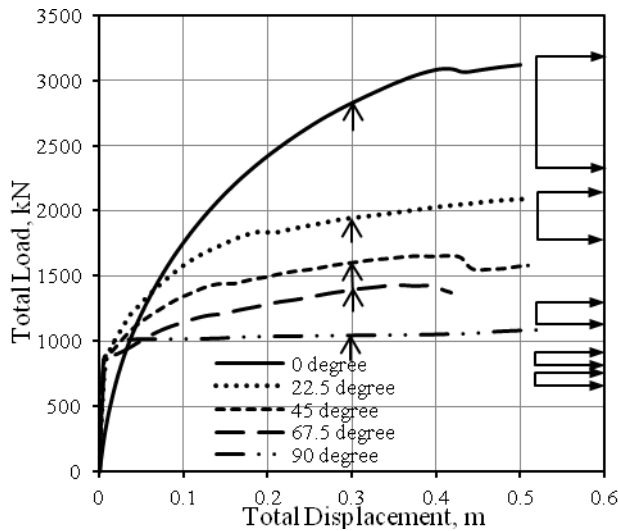


Fig. 5. Total load vs. total displacement for 5% mooring position

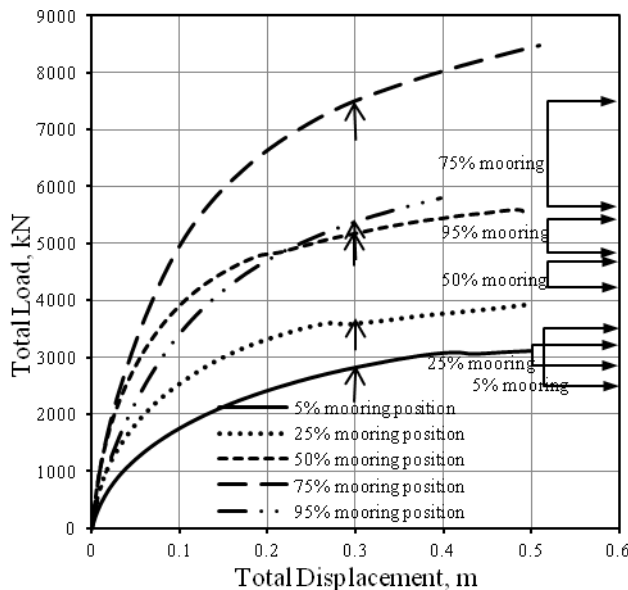


Fig. 6. Lateral load vs. lateral displacement for different mooring positions.

4.2 Pull-out Capacity

As mentioned before that a total of 25 finite element analyses are presented in this paper. The load-displacement curves obtained are very similar to curves presented in Figs. 5 and 6. The pull-out capacity obtained for various conditions is plotted against load inclination angle for different mooring positions in Fig. 7. As shown, at 75% mooring position the maximum pull-out capacity is obtained. It is to be noted here that the pull-out capacity at zero inclination angle (horizontal loading) is highly dependent on mooring position. However, for inclination angle of 90° (vertical loading) the pull-out capacity is almost independent of mooring position.

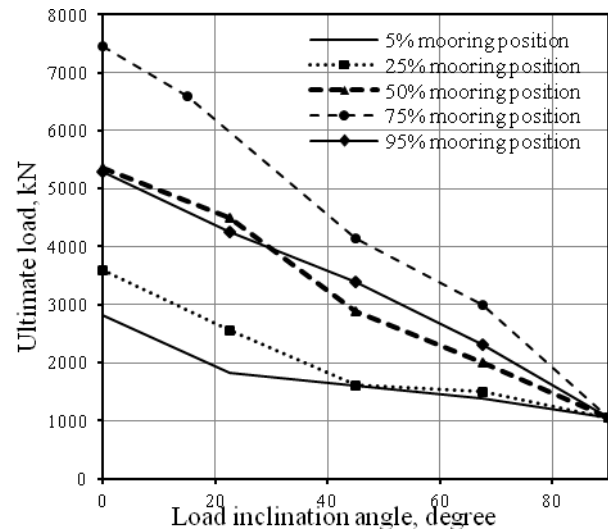


Fig. 7. Pull-out capacity for different loading angle and mooring position

4.3 Plastic Strain and Displacement Vector Diagram

Fig. 8 and Fig. 9 show the plastic strain and displacement vectors (total) for two cases. For 5% mooring position the plastic strain mainly developed on the left side of the pile. The bottom of the failed soil wedge on the left is almost linearly extent to the bottom of the pile. On the other hand the shape of the plastic zone on the left side of the pile for 75% mooring position (Fig. 9) is different from the shape shown in Fig. 8. This is again because of rotation of the pile. As the deformation pattern is different, it should be considered in estimation of pull-out capacity.

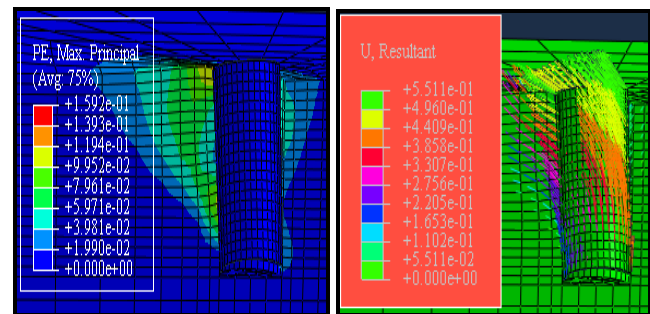


Fig. 8. Maximum principle plastic strain and displacement vector diagram for 5% mooring position and 0.5m displacement at 22.5 degree angle

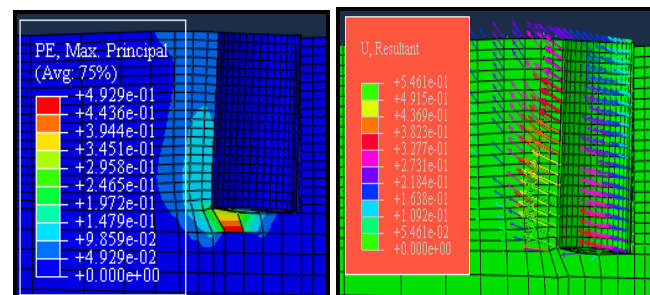


Fig. 9. Maximum principle plastic strain and displacement vector diagram for 75% mooring position and 0.5m displacement at 15 degree angle.

4.4 Lateral Displacement vs. Depth

Fig. 10 shows the variation of lateral displacement along the centerline of the caisson against depth for different loading angle at 5% mooring position at 0.3 m displacement. The lateral displacement is obtained from the displacement of the center nodes of the pile. As shown in this figure that the lateral displacement is almost linear. That means this short pile is rotated almost as a rigid body. The degree of rotation and also the center of rotation is dependent upon the angle of loading. The rotation has a significant effect on pull-out capacity.

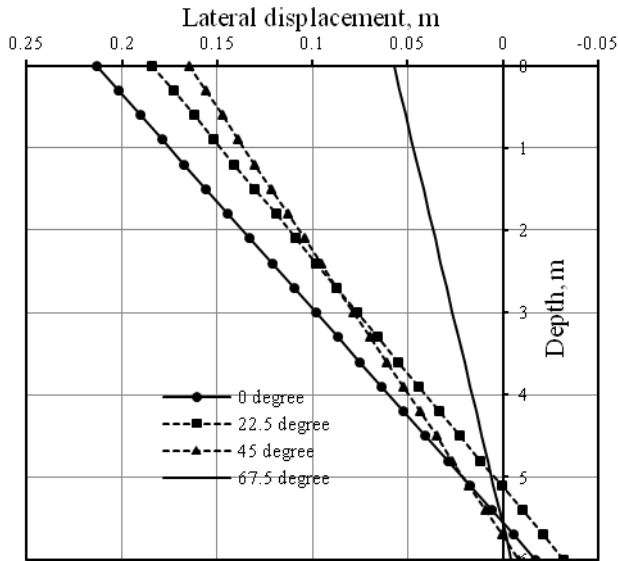


Fig. 10. Lateral displacement for different loading angle at 5% mooring position

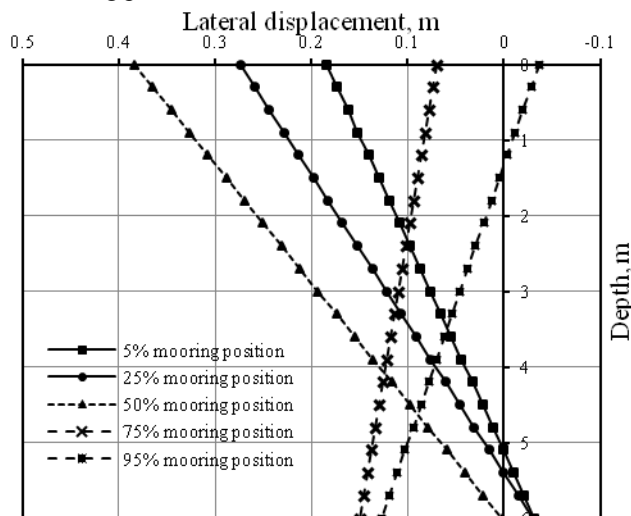


Fig. 11. Lateral displacement for different mooring positions

Fig. 11 shows the variation of lateral displacement with depth for different mooring position under lateral loading for 0.3 m lateral displacement. The suction pile is rotated toward the left when the mooring position is less than 50% while it

rotated toward the right when it is at 95%. The minimum rotation is occurred for 75% mooring position.

4.5 Mobilized Soil Reaction

Fig. 12 shows the variation of mobilized soil reaction (load per unit length of the pile) with depth at 0.3 m displacement for different loading angle at 5% mooring position. In finite element analysis, the soil reaction is obtained from the sum of the lateral component of nodal force at a particular depth dividing by the vertical distance between two node sets at the point of interest. As noted, with increase in loading angle the soil reaction decreases because of less lateral deformation and interaction between horizontal and vertical movement.

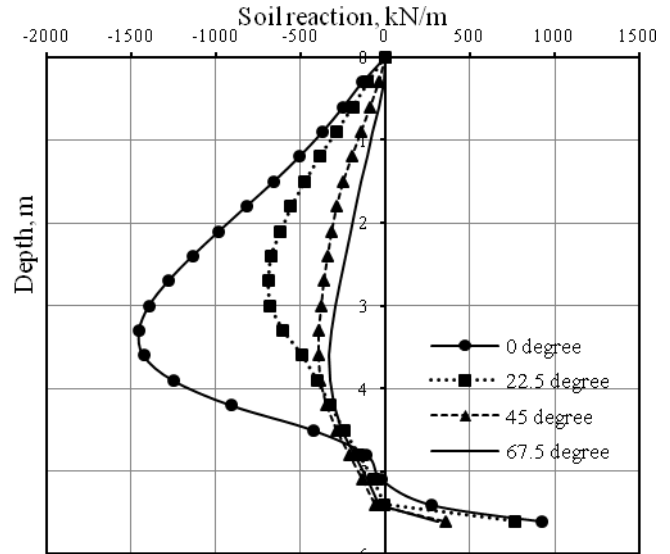


Fig. 12. Soil reaction for different loading angle at 5% mooring position

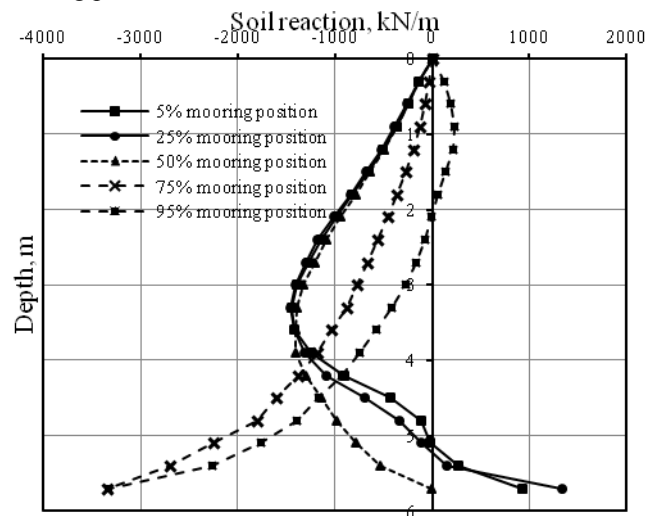


Fig. 13. Soil reaction for different mooring positions

The effect of mooring position on mobilized soil reaction is shown in Fig. 13. As shown the mobilized soil reaction is dependent on mooring position. For mooring position less than 50% the pattern of mobilized soil reaction curve is

similar while after 50% mooring position it is different, which is because of the rotation of pile.

5 CONCLUSION

A total of 25 finite element analyses are conducted to evaluate the pull-out capacity of a suction pile. The effects of two key variables examined in this study are: loading angle and mooring position. Finite element results have been compared with centrifuge test results. It is shown that the pull-out capacity of suction piles increases as the mooring position moves towards the pile tip and the 75% mooring line attachment gives the maximum pull-out capacity for the cases presented in this paper. Pull-out capacity also decreases with increase in loading angle. The shape of the soil failure wedge is dependent on mooring position and loading angle which has a significant effect on pull-out capacity.

6 ACKNOWLEDGMENT

The authors are grateful to the technical and financial supports provided by MITACS, PRAC and NSERC Discovery grant.

7 REFERENCES

- [1] Byrne, B.W., "Investigations of suction caissons in dense sand," PhD Dissertation, 2000, Magdalen College, Oxford.
- [2] Houlsby, G.T. and Byrne, B.W., "Calculation procedures for installation of suction caissons in clay and other soils," *Proc ICE - Geotechnical Engineering*, 2005b, Vol. 158, No 2, pp. 75-82.
- [3] Houlsby, G.T. and Byrne, B.W., "Calculation procedures for installation of suction caissons in sand," *Proc ICE - Geotechnical Engineering*, 2005a, Vol. 158, No 3, pp. 135-144.
- [4] Yoshimi, Y., "Piles in cohesionless soil subject to oblique pull," *Journal of the Soil Mechanics and Foundation Division, ASCE*, 1964, Vol. 90, pp. 11-24.
- [5] Broms, B. B., "Piles in cohesionless soil subject to oblique pull," *Journal of the Soil Mechanics and Foundation Division, ASCE*, 1965, Vol. 91, pp. 199-205.
- [6] Poulos and Davis, "Pile foundation analysis and design," 1980, New York: John Wiley & Sons.
- [7] Erbrich, C.T., "Modeling of a novel foundation for offshore structures," *Proceedings of the 9th UK ABAQUS User's Conference*, 1994, Oxford, England, pp. 235-251.
- [8] Bye, A., Erbrich, C., Rognlien, B., and Tjelta, T.I., "Geotechnical design of bucket foundations," *Proc. of Offshore Technology Conference*, 1995, OTC 7793.
- [9] Sukumaran, B., McCarron, W.O., Jeanjean, P., and Abouseeda, H., "Efficient finite element techniques for limit analysis of suction caissons under lateral loads," *Computers and Geotechnics*, 1999a, Vol. 24, pp. 89-107.
- [10] Sukumaran, B., and McCarron, W.O., "Total and effective stress analysis of suction caissons for Gulf of Mexico conditions," In *Analysis, Design, Construction and Testing of Deep Foundations*, Edited by J.M. Roesset, *Proceedings of the OTRC'99 Conference*, 1999b, Geotechnical special publication No. 88, pp. 247-260.
- [11] Handayanu, Swamidass, A.S.J., and Booton, M., "Behavior of tension foundation for offshore structures under extreme pull-out loads," *Proceedings of 18th International Conference on Offshore Mechanics and Arctic Engineering*, St. Johns, Newfoundland, Canada, 1999, OMAE99/OFT-4204, Pp. 635-641.
- [12] Deng, W., and Carter, J.P., "Inclined uplift capacity of suction caissons in sand," *Offshore Technology Conference*, 2000a, Houston, Texas, OTC 12196, pp. 809-820.
- [13] Zdravkovic, L., Potts, D.M., and Jardine, R.J., "A parametric study of the pull-out capacity of bucket foundations in soft clay," *Geotechnique*, 2001, Vol. 51, No. 1, pp. 55-67.
- [14] Cho, Y. and Bang, S., "Inclined Loading Capacity of Suction Piles," *Proceedings of The Twelfth International Offshore and Polar Engineering Conference*, Kitakyushu, Japan, 2002, May 26-31, pp. 827-832.
- [15] Bang, S., Jones, K. D., Kim, K. O., Kim, Y.S. and Cho, Y., "Inclined loading capacity of suction piles in sand," *Journal of Ocean Engineering*, 2011, Vol. 38, pp. 951-924.
- [16] Hesar, M., "Behaviour of pile-anchors subjected to monotonic and cyclic loading," 1989, PhD Thesis, University of Sunderland, UK.

“Slope Failure in Residual Soils of Peru”

A.Carrillo-Gil , P.E., MSc., DrEng., F.ASCE
Professor Ricardo Palma University, Lima, Peru.

A. Carrillo-Acevedo P.E., MSc., M. ASCE
Member of the Board AC Consulting Engineers, Lima, Peru.

ABSTRACT

The main objective of this paper is to present a real case occurred in residual soils from the Peruvian Amazon plane, in order to show the positive effects of the stabilization with drainage and the pore pressures dissipation that previously had originated large landslides in the season of the annual water level decrease of the Amazon River. This happens in a very short time and decreases around 12 meters in a fast way. This effect decreases the shearing strength of the saprolitic soil underlying, producing instability in its banks and important damages in the works of civil engineering over the surface. The results of the practiced instrumentation allowed a better planing and distribution of the drains in the affected area as well as an interpretation of the registered movement with biaxial inclinometers and the water pressures with pneumatic piezometers. All of them were associated with the extensive rains of the area, the movement of the riverbed and the rapid drawdown of the water, minimizing the risk and creating better possibilities for future investments.

Keywords: residual soils, slide stabilization

1. INTRODUCTION

The stability of the riverbanks in the Peruvian Amazon jungle present a great number of technical problems not existing in other places, since in very few regions of the world are present the atmospherical, environmental or hydrological conditions that prevail in this region, adding to these factors the lack of conventional construction materials. The erosion and sedimentation phenomena that alternatively occur in both margins of the Amazon river, and the continuous course changes between the subsequent years, present additional problems and large challenges to the application of the knowledge of the geotechnical engineering.

To offer some explanation to the movement of the meanders of the Amazon river, the reasons are: Soil with very low gradient and smoothly sloped toward to the East, in the order of 1: 20,000, that offers greater or smaller resistance to the water flow. The changes of water level between flood and ebb times, that reach fluctuations from 10 to 12 meters.

The tectonic movements in the Amazon zone are small, however the surface of the land bank suffers level changes, originating possible displacement in the bed of the rivers. According to what is shown previously, the Amazon river has impacted strongly on the riverbank causing considerable landslides (Fig. 1), being produced phenomena of instability. Phenomena go advancing downstream initially as erosion to end afterwards as sedimentation and therefore stabilization of the slide critical area [1].

During more than 40 years they have been producing landslides that have considerably damaged different types of

engineering works placed in the banks of the Amazon river in the region of Peru, when the river impacts directly on the critical border, and increasing gradually according to the river is going far.



Fig. 1. Landslide at the Amazon Riverbanks.

2. GEOLOGICAL AND GEOTECHNICAL SETTING

The general geology considers that a large part of the Amazon region has stayed covered during the interglacial periods of the quaternary by an interior sea of shallow water when the level of the oceans had 100 meters above of the existing now (330,000 years ago) it also to fluctuate during several glacial and interglacial periods forming terraces throughout the water courses, dropping to 100 meters below of the original level during the last Glacial Era (17,000 years ago) and remaining in these deep channels the large rivers, between them the

Amazon river, raising afterwards to the current level (6,000 years ago).

The accomplished studies establish that in the high jungle and in the limits of the low jungle are found so much igneous rocks as sedimentary, while in the low jungle prevail saprolitic soils originated by the sedimentary rocks of the tertiary and quaternary and they are formed mainly by sandstones, shales and clays. The general description of the geomorphology of the Amazon region indicates that the low jungle is substantially flat and as said remain, its height varies between 80 to 400 meters above mean sea level. Due to this small difference of elevation the rivers flow slowly, getting in the dry station the appearance of lakes. This region of the Amazon plain, can be indicated as advanced erosion type (Fig. 2). The Amazon plain is characterize by its great humidity and soil covered by a dense tropical vegetation.



Fig. 2. Erosion Consequences at the Amazon River.

3. AMAZON RIVER MEANDERS

The Amazon River is formed from the confluences of the Marañón y Ucayali Rivers nearby city of Nauta. This is located 74 miles from the city of Iquitos. It has a length of 3,762 kilometers (2,031.3 nautic miles). 570 Km (307.7 miles) correspond to Peruvian territory. Its course is predominantly to the east to the Atlantic Ocean with wide meanders and numerous islands; its stream bed varies from 1,000 and 4,000 meters in the Peruvian territory with low river banks that have floodings in high water level seasons. Human settlements are located usually in high river banks areas. River bed is formed with muddy material and fine sands. Its main affluents are the Napo River, Putumayo River by the left side, Yavari by the right side to 41, 487, and 270 miles respectively to the city of Iquitos.

The river rise happens from November to May. Its peak occurs in April and May. Drawdown happens in the second half of the month of May until September. Maximum drawdown occurs in August and September. Drawdown happens faster than the rise.

The Amazon River does not present a define bed. On contrary, it flows creating meanders over a tropical soft soil potentially variable. The meanders move downstream, originating erosion and sedimentation. Comparing information from 1948 to 2009, it is observed great erosion that allowed the meanders advance upstream but no at the velocity that the river normally used to, causing its deformation upstream and downstream and creating landslides ant the river banks slopes [2]-[4].

According to this, the Amazon River has strongly impacted its stream bed, causing deformation of its meanders at the upstream area as well, modifying its stream and creating diverse problems related to slope stability. The first registered problem as a landslide was observed in June 1992. Afterwards, large landslides happened at the critical seasons of discharge in 1993, to collapse in its entirety in 1994.

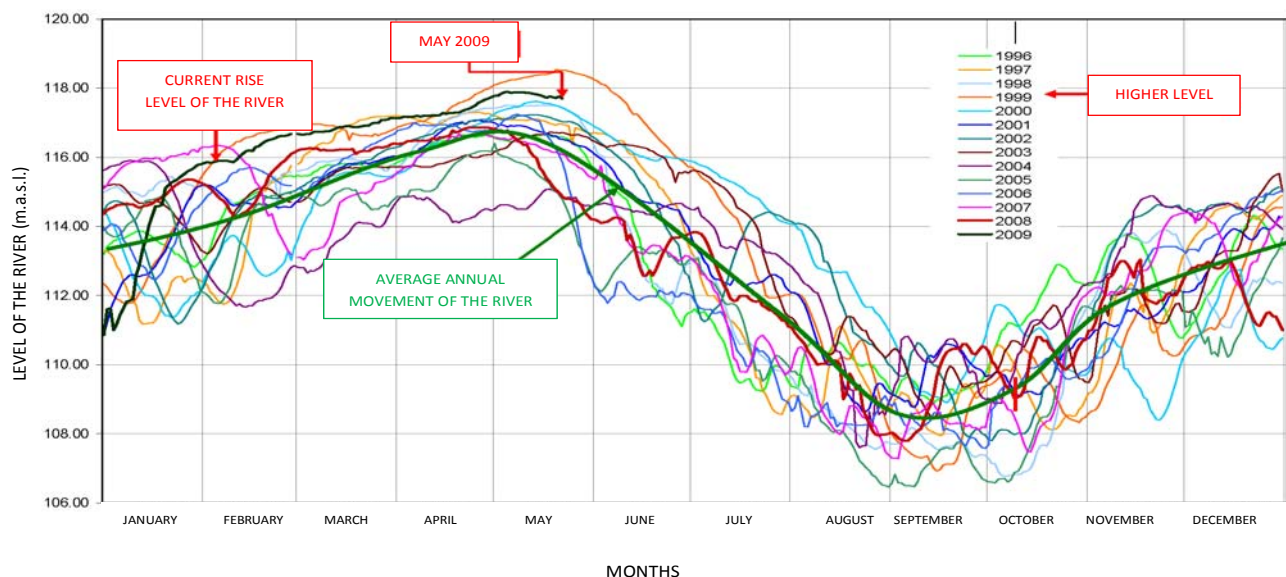


Fig.3. Behavior of the Amazon river in the area of landslides.

4. SLOPE FAILURE MECHANISM

The statistical analysis of Amazon River movements clearly established that the landslides have occurred during the stage of water level decrease in the river. This is completely different from other places around the world where rains at river high water levels season creates landslides. We consider that as a phenomenon of rapid drawdown that affects the bank, because of the water level decreases to an average of 12 meters in a very short time [3].

This rapid drawdown is interpreted as a process that increases the undrained deformation of the saturated zone in the affected banks. In other words, the reaction of the stability of the banks to the rapid movement when the water level decreases is similar to the response occurred in an open cut in which is produced a forced alleviation, due to material that previously was offered as lateral support and that was suddenly removed. In this case, as a consequence of the imbalance produced by the rapid drawdown of the river, there is water that remains within the porous structure of the soil, since its level does not decrease to the same speed that the water level (Fig. 4) This phenomenon causes an increase in the weight of the bank body, as in the pore pressure with the soil. This effect reduce the shearing strength of the soil, which, together with the effects of the river, causes the landslides (if it has not been possible to evacuate the water tricked within the soil of the bank).

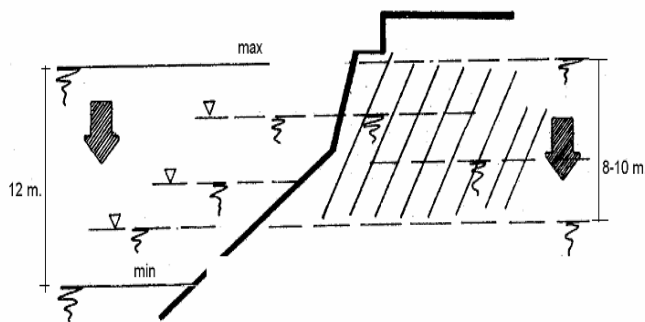


Fig. 4. Rapid drawdown when water level decrease

5. LANDSLIDES CONTROL MEASURES

The system of installed deep drainage is efficient and it has generated an adequate drainage during the critical stage of drawdown of the Amazon river in 1996, 1997 and 1998. In the better behavior area we put 31 horizontal drains of 30.meters of length, spaced each 3 meters with a slope of 3° and diameter of 4". In the adjacent section we installed wells with radial drains that arrived to lengths understood between 15 to 25 meters

The measures analyzed indicate a small displacement in direction to the Amazon river in the stage of water level decrease, and backward displacement when the water level rose. The comparison of the results obtained demonstrate that the movements registered before have reduced considerably,

probably due to the effective operation of the deep drainage system, and the additional effects produced by the sedimentation that originated due to movement of the riverbed of the Amazon river.

The results of the final piezometrics measures indicate that, as a rule, the dissipation of the pore pressures in almost all cases has been effected in correspondence with the decrease and increase of the water level. So, we found a good behavior in the drainage system installed in the critical zones. The piezometers that were installed in the zone of the last landslide from the beginning of their readings showed irregularities with respect to the dissipation of the accrued pore pressures after of the decrease of the river. It must be noted that in the location zone of these instruments was not practiced any deep drainage system or treatment for maintenance [5].

6. CONCLUSIONS

The deep drainage system, installed in the studied area (by means of wells with radial drains as well as by horizontal drains) has contributed effectively in the stabilization of these banks, and the analysis of all the measures taken during the several months of work with the instruments, prove that there is a substantial improvement in the stability conditions of the platforms included in the study, conditions that can improve in the future due to more sedimentation that presumably could be produced in the place by effect of the change of the Amazons riverbed.

The results shown in this paper provide a global vision of the stability problems of soils in the Peruvian wet tropic, generated by the changing morphology of the rivers that originate important risk situations in some cases, and increasingly growing stability in others that permits to establish the development of new behavior standards for the riverbanks of the Peruvian Amazon that in the future can be predictable with certain approximation considering their evolution in the geological time of hundreds of years, since now in certain areas it has already passed the danger, and maybe within 100 or more years, the problem return to be present and the safety factors of the banks decrease gradually until to become unstable and to produce large landslides as they occurred in sites and dates of study, considering finally that the Peruvian Amazon is located in a region of a very singular world in light of their geotechnical occurrences and of climate that create very difficult wet tropical soils to predict and handle in the construction of the earth works.

7. REFERENCES

- [1] Carrillo-Gil, A. "Stability Problems in Iquitos, Peru". Proc. VII Pan-American Conference on Soil Mechanics and Foundation Engineering, Vancouver, Canada, 1983.
- [2] Carrillo-Gil, A. , Carrillo, E. , Cardenas, J. , "Properties of the Peruvian tropical soils". X Pan-American Conference on Soil Mechanics and Foundation Engineering, Guadalajara, Mexico, 1995.

- [3] Carrillo-Gil, A. , Dominguez, E. “Failures in Amazon riverbanks, Iquitos, Peru”. Seventh International Symposium on Landslides, Trondheim, Norway, 1996.
- [4] Carrillo-Gil, A. “Peculiarities of tropical saprolitic soils of Peru”. XIV International Conference on Soil Mechanics and Foundation Engineering, Hamburg, Germany, 1997.
- [5] Carrillo-Gil, A. “Geotechnology of the Peruvian tropical soils”, (in progress) Ricardo Palma University, Lima, Peru, 2011.

Back-analysis of Frictional Jacking Forces Based on Shear Box Testing of Excavated Spoils

Choo Chung Siung¹ and Dominic Ong E. L.²

^{1,2}Swinburne University of Technology (Sarawak Campus), Malaysia

ABSTRACT

Trenchless technology has become the preferred technique for installation of buried infrastructure due to advantages such as minimised ground surface disturbances as well as reduced social disruptions. These benefits have led to an increased demand for trenchless technologies such as the pipe-jacking method, with its application well-suited for urban environments. The construction of trunk sewers in Kuching, Sarawak has been carried out using the pipe-jacking method. Critical to this micro-tunnelling technique were the associated frictional forces anticipated during the jacking process. Excessive jacking forces could damage installed pipes. The Authors have studied the use of a few well-established empirical equations to validate frictional resistance during jacking supplemented by laboratory direct shear box tests carried out on spoils obtained from pipe-jacking drives. The tested spoils were by-products of the slurry transport system for spoil removal at the tunnel face. Shear box test results have been attempted for use to predict the pipe-jacking forces based on the well-established empirical equations. The predicted jacking forces for this study show fair agreement when benchmarked against actual, measured forces. However, it is the intention of the Authors to carry out more tests to further verify the reliability of this method for a wider variety of local rock types, especially in geologically 'young' weathered rock where competent rock cores are usually difficult to obtain.

Keywords: Pipe-jacking, direct shear, back-analysis

1. INTRODUCTION

There has been a growing need for trenchless technology for the construction of various pipelines. This trend has been evidenced by its implementation in the installation of trunk sewers in Kuching, Sarawak. Sewer lines comprising of concrete pipes were installed using micro-tunnelling by pipe-jacking. This method was elected over conventional open trench methods due to the minimised socio-economic disruption and pollution. However, the technicalities of such tunnelling works required specialist expertise. During the jacking process, various components were necessary for the works to proceed. The capacity of the microtunnel boring machine (MTBM), the application of lubrication, the capacity of main jacks, the use of intermediate jacking stations, and the design of jacking pipes are constituents of the synchronous system for successful pipe-jacking. A key factor affecting the above components is the frictional jacking load.

2. BACKGROUND

Studies have been carried out to investigate the behaviour of jacking loads during the pipe-jacking process. Pioneering studies on pipe-jacking were carried out by researchers at Oxford University, U.K. Norris & Milligan [1] detailed drives entailing instrumented concrete jacked pipes were carried out. Instrumented pipes were outfitted with pore pressure probes, contact stress transducers, extensometers, and other monitoring equipment. Data on variations of normal stresses and pore pressures on the instrumented pipes provided valuable early insight into the effects of lubrication on jacking

stresses [2, 3]. Pellet-Beaucour & Kastner [4] studied the influence of various parameters on the build-up of frictional forces for drives in varying soil conditions across France. The authors proposed two frictional force models in their analyses. Staheli [5] studied the behaviour of pipe-soil interface friction by conducting laboratory shear box tests. Sand specimens were applied normally on pipe crown segments of varying roughness. A similar test was carried out by Shou et al. [6], with the addition of lubrication. Interface frictional coefficients were derived from the shear box tests and verified using three-dimensional finite element modelling. The experiences and results reported by these researchers have been carefully reviewed and understood, so as to ensure that the methodologies reported in this paper are within acceptable conditions and practice.

3. SHEAR BOX TESTING OF EXCAVATED SPOILS

2.1 Direct shear test and geology

Due to the weathered nature of the 'young' sedimentary and metamorphic rock of the Tuang Formation in the Kuching City area, intact and competent rock cores ($\geq 100\text{mm}$ in length) are usually difficult to obtain during Soil Investigation works, thus making the strength parameters (c' and ϕ') for these weathered rocks rather elusive. Rock Quality Designation (RQD) may not be the best indication of rock strength as the values are usually zero or close to zero due to its friability. However, this observation does not necessarily represent the in-situ strength of the rock mass as a whole. Hence, performing direct shear tests where excavation spoils are reconstituted with appropriate confining stress

during testing may be a worthwhile and feasible method. Direct shear test was conducted using the GeoComp ShearTrac-II direct shear system (Figure 1). The ShearTrac II system enables full automation of shear box testing. Automation of the test ensures repeatability of testing regime.



Figure 1 ShearTrac II direct shear system

Control of the ShearTrac II system is achieved through the use of the SHEAR software. Users are given control over the shear box testing regime by inputting the desired consolidation stresses and shear strain rates. Results from tests are generated regularly in terms of horizontal and vertical displacements, as well as shear stresses along the shear band. The ability of the user to obtain results at a high-resolution allows for close scrutiny of tests. The ShearTrac II system is also able to maintain the consolidation and confining pressures throughout the test, from the consolidation stage through to the shearing stage.

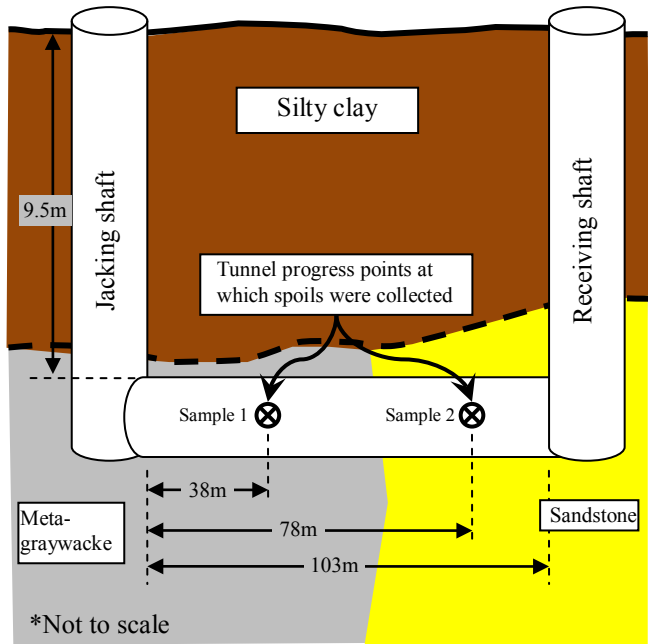


Figure 2 Estimated locations where Sample 1 (metagraywacke) and Sample 2 (sandstone) were collected as excavation spoils from slurry

2.2 Collection of excavated spoils

Excavated spoils were collected from the slurry separation plant (also known as desander). The excavated spoils were transported from the MTBM face through suspension in a pressurized slurry transport system and discharged in the desander. The desander recycles the slurry through filtration and segregates the spoils from the slurry. The slurry is then pumped back through the slurry supply line, back to the TBM face. Figure 2 shows approximate chainages at which excavated spoils were collected for testing.

2.3 Shearbox testing and results

Test samples were prepared according to AS1289.6.2.2-1998 [7]. Scalping of samples was carried out according to the allowances stated in the above-mentioned standard. The test samples consisted of grains passing the 2.36mm sieve, and retained by the 75 μ m sieve. Such scalping method has already been carried out by Bagherzadeh-Khalkhali & Mirghasemi [8]. Scalping was deemed necessary as preliminary shear box testing showed large fluctuations, particularly beyond the peak stress threshold. The consolidated drained shear box tests were conducted with samples placed in the reservoir filled with distilled water. Shearing was initially carried out at three confining pressures σ_1 , i.e. 170kPa, 180kPa, and 190kPa. These were approximate in-situ stresses acting on the pipe. Two further sets of tests were conducted at confining pressures of 100kPa and 250kPa, for better data distribution when measuring the respective strength characteristics.

Table 1 Results from shearbox testing on excavated spoils

Sample number	σ_1 (kPa)	Peak strength characteristics			Residual strength characteristics		
		τ_{peak} (kPa)	ϕ_{peak} (°)	c_{peak} (kPa)	τ_{res} (kPa)	ϕ_{res} (°)	c_{res} (kPa)
Sample 1	100	117	36	49	96	28	37
	170	179			128		
	180	171			128		
	190	186			134		
	250	227			178		
Sample 2	100	183	49	78	112	47	4
	170	282			201		
	180	282			203		
	190	282			204		
	250	360			275		

Table 1 above tabulates the results from shear box tests on the spoils. Generally, higher confining pressures, σ_1 resulted in larger shear strengths, τ_{peak} and τ_{res} . Strength characteristics were interpreted according to the Mohr-Coulomb failure criterion. Sample 2 showed higher strength characteristics than Sample 1 at both peak and residual strains. This is attributed to the particle shapes of the respective samples, with Sample 2 exhibiting generally angular particles as compared to the rounded particles of Sample 1 (Figure 3). As expected, peak strength parameters were generally higher than the residual counterparts for both samples. This is particularly evident for Sample 1. For Sample 2, the decrease in strength from peak to residual states was significantly due to a loss of cohesion. There was minimal observed decrease in friction angle of Sample 2. The residual strength of the

samples is thought to mimic the excavation process better as the in-situ rock mass is expected to be crushed till failure by the roller cutter bits found at the face of the MTBM. Besides, the continuous jacking process involved in the installation of pipes is also analogous of a shearing process in large-strain condition. The test results obtained were subsequently utilized for the prediction of frictional jacking forces.



Figure 3 (left) Sample 1 (spoils of metagraywacke); (right) Sample 2 (spoils of sandstone) used for direct shear tests

3. ANALYSIS OF FRICTIONAL JACKING FORCES

In the pipe-jacking process, jacking forces comprise of soil pressures acting on the face of the MTBM and normal stresses accumulating along the outer peripheral surface of the pipeline. The frictional component nominally forms the major portion of the jacking loads as the pipe-soil contact area increases with jacking progress.

3.1 Frictional jacking force equation

Frictional forces have been the subject of much research. The work carried out by Pellet-Beaucour & Kastner [4] employed the model shown in Eq.(1), which is expressed as a function of vertical soil stress on the pipe crown, σ_{EV} as in Eq. (2).

$$F = \mu L D_e \frac{\pi}{2} \left\{ \left(\sigma_{EV} + \frac{\gamma D_e}{2} \right) + K \left(\sigma_{EV} + \frac{\gamma D_e}{2} \right) \right\} \dots (1)$$

$$\sigma_{EV} = \frac{b(\gamma - \frac{2C}{b})}{2K \tan \delta} \left(1 - e^{-2K \frac{h}{b} \tan \delta} \right) \dots (2)$$

L is the length of the pipe string, D_e is the outer diameter of pipe, γ is the soil unit weight of ground cover, h is the height of cover at the pipe crown, K is the coefficient of lateral soil pressure, δ is the angle of wall friction in the shear plane, b is the influencing width of soil above the pipe. μ is the coefficient of soil-pipe friction, expressed as

$$\mu = \tan \delta \dots (3)$$

Pellet-Beaucour & Kastner [4] suggested upper limit values $\delta = \phi$, and lower limit values of $\delta = \phi/2$ or $\phi/3$ for soil-structure interaction calculations. They also reported values for b , δ and K by various organizations (Table 2).

Staheli [5] and Pellet-Beaucour & Kastner [4] further reported the use of some values of friction coefficient, μ . These values were obtained from Stein et al. [9].

Table 2 Summary of various parameters for use with frictional model by Pellet-Beaucour & Kastner [4]

b	δ	K
$D_e \left(1 + 2 \tan \left(\frac{\pi - \phi}{4} \right) \right)$	ϕ	1

Table 3 Friction coefficient values for various friction states from Stein (as summarized in Ref. [4])

	Static friction	Sliding friction	Fluid friction (lubrication)
Concrete on gravel or sand	0.5 – 0.6	0.3 – 0.4	0.1 – 0.3
Concrete on clay	0.3 – 0.4	0.2 – 0.3	
Asbestos or centrifuged concrete on gravel or sand	0.3 – 0.4	0.2 – 0.3	
Asbestos or centrifuged concrete on clay	0.2 – 0.3	0.1 – 0.2	

3.2 Case study for back-analysis

A case study was considered for a drive negotiating through the geology of the Kuching inner city area. The pipeline lies embedded in rock, with the crown at a level 9.5m below ground surface. The 103m alignment of 1.2m diameter concrete pipes traversed metagraywacke (metamorphic) and sandstone synonymous with the Tuang formation. As reported by Tan [10], the metagraywacke encountered in the Tuang formation is characterised as weathered, with occurrences of quartz veins. This was consistent with findings from soil investigation works. Metagraywacke in the Tuang formation is often found interbedded with moderately weathered phyllite.

The tunnel was excavated using an Iseki Unclemole Super TCS 1200. The closed-face MTBM had an outer diameter of 1.472m, creating a theoretical overcut annulus of 19mm around jacking pipes of outer diameter 1.434m. As mentioned earlier, the MBTM used the slurry transport system for maintaining a stable tunnel face, as well as for the transportation of excavated spoils. A shield embodied the machinery in the MTBM, with a succeeding sleeve attached. The cutter face was outfitted with four roller cutters arranged on the face, and three roller cutters at the peripheral for formation of the overcut.

Site data of measured jacking loads (Figure 4) from the earlier described site was used for benchmarking against predicted frictional forces. Site data could be generalised under two drive sections. The jacking forces within the initial drive portion (Section 1 – 0 to 60m) accumulated within a lower bound of 7kN/m and an upper bound of 12kN/m. The latter drive portion (Section 2 – 60m to 108m) exhibited gains in frictional loads of between 71kN/m (upper bound) and 41kN/m (lower bound). The positions where the samples were collected from are entailed in Figure 4 below, including the respective shear box test results.

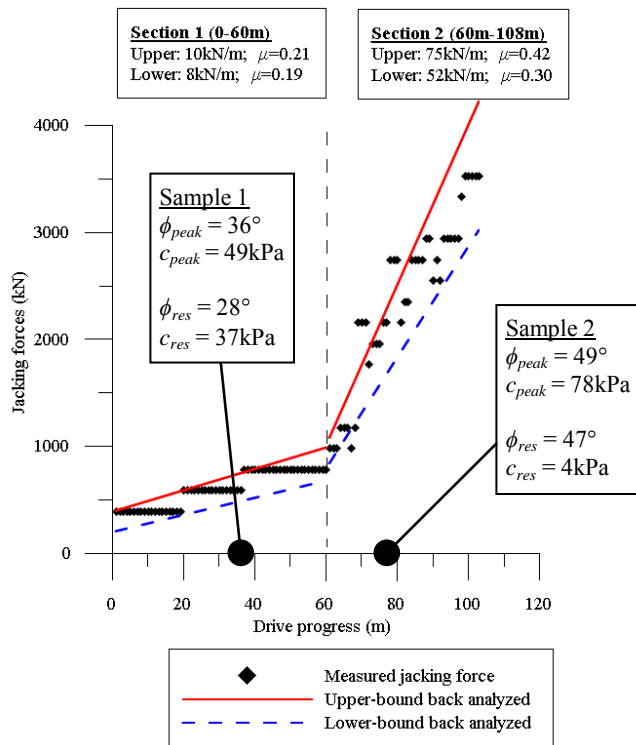


Figure 4 Back-analysed upper and lower bound jacking forces with respect to measured values including effect of stoppages in jacking in Section 2 only

Using Eqs. (1), (2) & (3) together with the residual strength properties of the excavated spoils, the required frictional coefficients for back-analysis were determined and presented in Figure 4.

The results were based on the Terzaghi set of parameters from Table 2. For the initial portion of the drive, the back-analysed frictional coefficients were 0.19 (lower-bound) and 0.21 (upper-bound), while those for the latter portion of the drive were 0.30 (lower-bound) and 0.42 (upper-bound). With reference to Table 3, the lower-bound coefficients of friction lie within the range of values reported for lubricated drives. The upper-bound frictional coefficient lies beyond the range of acceptable values for lubricated drives.

3.3 Effect of stoppage on jacking forces

In Section 2 of the drive, the disparity between upper and lower bounds for the coefficients could be explained by the stoppages in jacking works. Jacking forces in this latter section have been segregated as shown in Figure 5, thus Figure 5 shows jacking forces associated with only on-going jacking works. Frictional coefficients for the lubricated Section 2 are seen to have reduced to 0.32 (lower-bound) and 0.34 (upper-bound). These coefficient values were slightly above the upper limit of the corresponding values reported in Table 3 (under lubrication component). Figure 6 shows jacking forces, with forces attributed to stoppages presented for Section 2 of the drive. Frictional coefficients for Section 2 are 0.36 (lower-bound) and 0.42 (upper-bound), which are generally higher as re-start of jacking works after periods of stoppages are known to induce greater static frictional

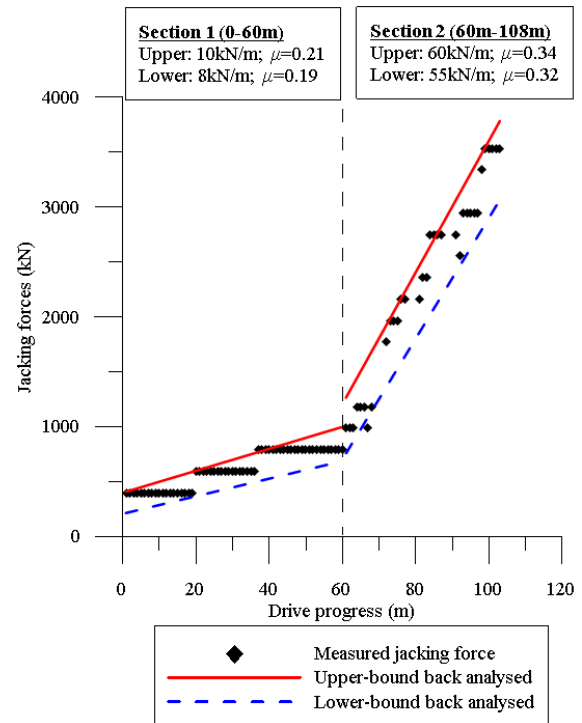


Figure 5 Back-analysed upper and lower bound jacking forces with respect to measured values, but with effect of stoppages excluded from Section 2 only

resistance and effects of lubrication are usually mitigated at this initial stage of work. This is confirmed by the back-analysed coefficients, which are comparable to those for unlubricated sliding friction for concrete on gravel or sand as per Table 3.

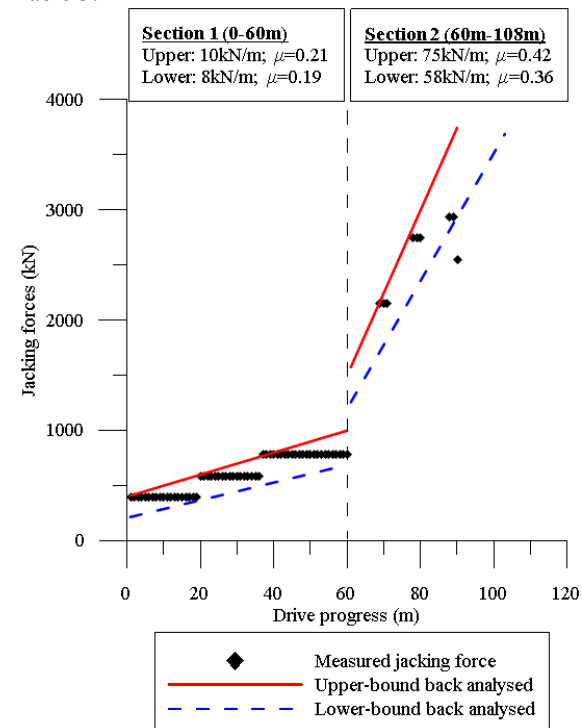


Figure 6 Back-analysed upper and lower bound jacking forces with respect to measured values, with only effect of stoppages in Section 2 only

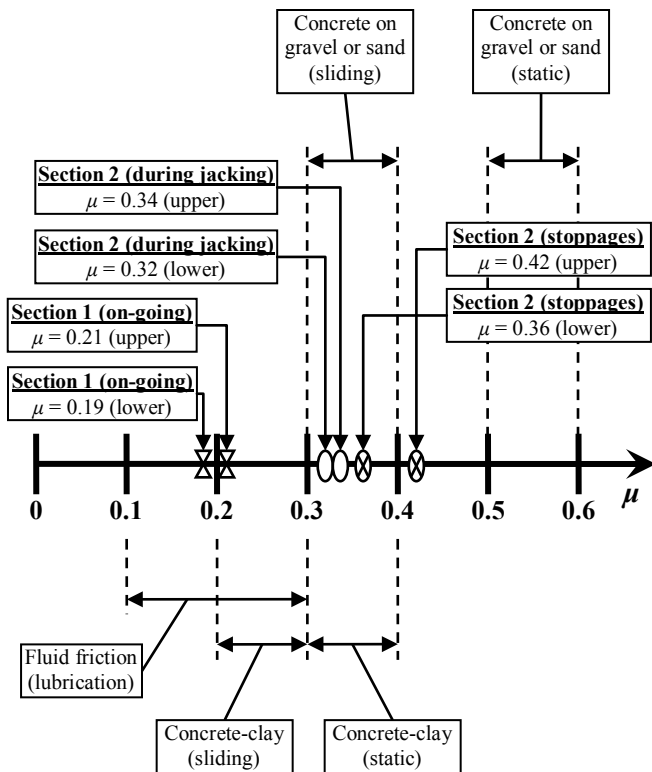


Figure 7 'Dynamic' behaviour of coefficient of friction during various stages of the pipe jacking process

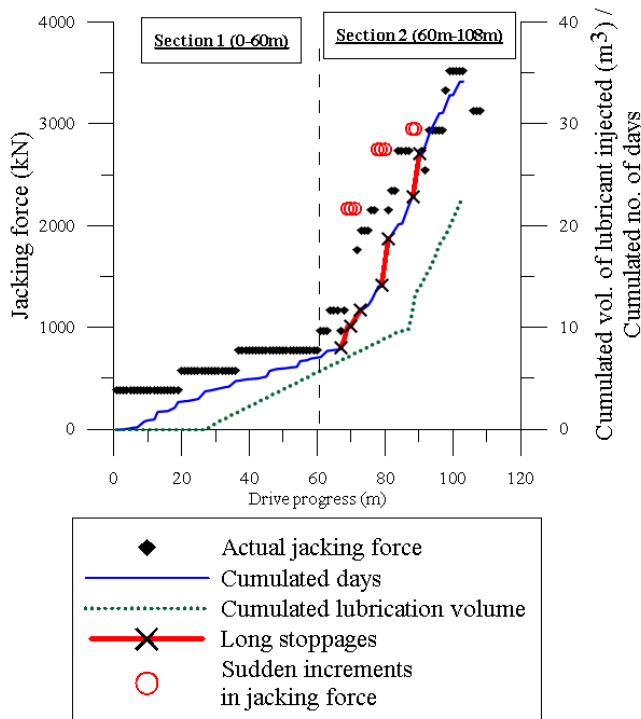


Figure 8 Development of jacking force and elapsed time in relation to stoppages and volume of lubricant injected into tunnel overcut

Figure 7 shows the 'dynamic' propagation of friction coefficients during different stages of work in the

pipe-jacking process as had been described in detail earlier and interpreted from Figures 4, 5 and 6.

Figure 8 illustrates the occurrences of extended stoppages, where sudden increments in jacking forces have been previously presented. These were not weekend stoppages as jacking was on-going through the weekends. Such stoppages in work could have been due to major maintenance works, possibly from the replacement of roller cutters. During such stoppages, lubricant injected into the overcut around the pipe peripheral could be lost through fissures in the surrounding geology as shown schematically in Figure 9.

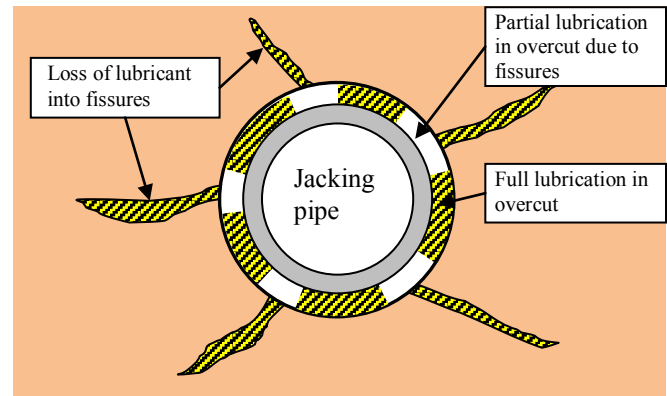


Figure 9 Schematic idealisation showing loss of lubrication through fissures in a rock mass

The pressure for lubricant injection would also be relieved, mitigating any buoyancy effect that may have reduced the frictional forces. The effect of loss of buoyancy supporting the weight of the pipe could result in higher pipe-soil contact area. There was an observed change of the lubricating regime in Section 2 of the drive, particularly upon the advent of the third major stoppage. This increase in the volume of lubricant (from 170 litres to 800 litres per metre run) was in reaction to the increased rate of frictional loads upon transition from Section 1 to Section 2 of the drive. However, this intensified effort had only been initiated after several spikes in the jacking load had been accrued.

4. CONCLUSIONS

This paper has highlighted the potential of using direct shear testing of excavation spoils to obtain residual strength values of geologically 'young' weathered rock to predict jacking forces. The main advantage of using reconstituted excavation spoils as specimens is the ability to obtain rock strength parameters which otherwise would be elusive as intact and competent rock cores ($\geq 100\text{mm}$ in length) are usually difficult to obtain in such weathered and friable conditions. One of the main factors affecting the accuracy of the back-analysis of the lower and upper bound jacking forces is the 'dynamic' or fluctuation nature of the coefficients of friction as the pipes penetrate into differing geology within a similar drive and also due to its construction activity (whether jacking is on-going or stopped for maintenance). The back-analysed coefficient of friction seems to be also affected by the fact that whether the drive is fully or partially

lubricated. Hence, soil-structure interaction is indeed an important consideration in any pipe-jacking work. Jacking forces have been observed to have increased during the re-start of jacking activities after periods of stoppages as more thrust is required to overcome static frictional resistance prior to the realisation of the positive benefits of lubrication. However, it is the intention of the Authors to carry out more tests to further verify the reliability of this method for a wider variety of local rock types, especially in geologically 'young' weathered rock.

5. ACKNOWLEDGMENTS

The authors would like to thank the generosity of Hock Seng Lee Bhd and Jurutera Jasa (Sarawak) Sdn Bhd for their support during this study. The authors are also thankful to the ground staff of Shaft & Tunnel Sdn Bhd for their assistance and patience during the study of the microtunnelling drive. The work described in this paper would not have been possible without the efforts of Leong Hsiao Yun and Lionel Foo Fang Ho.

6. REFERENCES

- [1] Norris, P. and G.W.E. Milligan, *Field instrumentation for monitoring the performance of jacked concrete pipes*, in *3rd International Symposium on Field Measurements in Geomechanics*, G. Sørum, Editor 1991, A.A. Balkema: Oslo, Norway.
- [2] Milligan, G.W.E. and M.A. Marshall. *The functions and effects of lubrication in pipe jacking*. in *World Tunnel Congress*. 1998. Sao Paulo, Brazil: Balkema.
- [3] Milligan, G.W.E. and M.A. Marshall. *The influence of lubrication on jacking loads from six monitored pipe jacks*. in *16th International ISTT No-Dig 1998*. 1998. Lausanne, Switzerland: ISTT.
- [4] Pellet-Beaucour, A.L. and R. Kastner, *Experimental and analytical study of friction forces during microtunneling operations*. *Tunnelling and Underground Space Technology*, 2002. **17**(1): p. 83-97.
- [5] Staheli, K., *Jacking force prediction an interface friction approach based on pipe surface roughness*, in *School of Civil and Environmental Engineering 2006*, Georgia Institute of Technology: Georgia. p. 385.
- [6] Shou, K., J. Yen, and M. Liu, *On the frictional property of lubricants and its impact on jacking force and soil-pipe interaction of pipe-jacking*. *Tunnelling and Underground Space Technology*, 2010. **25**(4): p. 469-477.
- [7] The Australian Standards, *AS1289.6.2.2-1998 Soil strength and consolidation tests - Determination of the shear strength of a soil - Direct shear test using a shear box*, 1998, Standards Australia: Australia.
- [8] Bagherzadeh-Khalkhali, A. and A.A. Mirghasemi, *Numerical and experimental direct shear tests for coarse-grained soils*. *Particuology*, 2009. **7**(1): p. 83-91.
- [9] Stein, D., K. Möllers, and R. Bielecki, *Microtunnelling : Installation and Renewal of Nonman-Size Supply and Sewage Lines by the Trenchless Construction Method*. 1989, Berlin, Germany: Ernst.
- [10] Tan, D.N.K., *Geology of the Kuching Area, West Sarawak, Malaysia*, 1993, Geological Survey of Malaysia: Kuching.

Lime Stabilization of Tropical Soft Soils

Dygku Salma Awg Ismail¹, Tan Jui Siang² and Siti Noor Linda Taib³
Universiti Malaysia Sarawak, Malaysia

ABSTRACT

Soft soil, naturally contains high percentage of moisture content, is having low values of compression strength and California Bearing ratio (CBR). Construction of any infrastructures over the soft soils unsurprisingly causes the soil to undergo excessive settlements and possible bearing capacity failures. Therefore, chemical stabilization has been practiced by the practitioners whereby the chemicals such as cement and lime were used in construction. In this study, lime stabilization method was opted to improve the geotechnical properties of the soft soils. The initial consumption lime tests were done at the first stage in order to determine a minimum amount of lime used for the stabilization. In addition, the unconfined compression strength (UCS) and California Bearing Ratio (CBR) tests were conducted to evaluate the effectiveness of lime stabilization with different percentage of lime content. As a result, the highest UCS and CBR value of stabilized soft soils was achieved at 9% of lime content within 28 days curing period which indicated a value of 1514.13 kPa and 92.19% respectively.

Keywords: soft soils, curing period, lime stabilization, optimum lime content

1 CONCLUSION

Soft soils are commonly tag as 'problematic' due to its typical failure characteristic of having poor resistance to deformation, highly compressible, low shear strength, low permeability and limited bearing capacity [1]. Construction of any infrastructure over soft soils unsurprisingly causes the soil to undergo excessive settlements and possible bearing capacity failure. The common construction approach in soft soil is excavation and substitutes the soft soil with stronger and better quality materials. However, this effort will lead to uneconomical design due to the requirement of purchasing and transportation for large amount of good quality soil [2]. In such conditions, alteration of the weak properties of soft soil to meet the specified engineering requirement can be achieved by adopting soil stabilization. Soil stabilization can be defined as the permanent physical and chemical alteration of soils to enhance their physical properties. Stabilization can increase the shear strength of soil and control the shrink-swell properties of a soil, thus improving the load bearing capacity of a sub-grade to support pavements and foundations [3]. The techniques of soil stabilization can be classifies into a number of categories such as vibration, surcharge load, structural reinforcement improvement by structural fill, admixtures, grouting and etc. [4].

2 RESEARCH METHODOLOGY

Hydrated lime Ca(OH)_2 was used as the chemical additive for stabilization of this study. The quality and suitability of hydrated lime used has to be ensured before the stabilization process. Table 1 shows the soil properties and Table 2

illustrates the chemical properties of the hydrated lime used in this study. A light storm given was reported to have occurred a day prior to sampling which influenced the moisture content as indicated in Table 1.

Several physical properties testing were conducted on soil and hydrated lime in order to determine the suitability of these admixtures. It was also important to conduct these tests as a control set to compare the soil properties before and after soil stabilization. After verification of soil properties and suitability of the soil and lime admixtures, estimated lime content was added to the soil for stabilization.

In this study, lime content of 7, 8, 9 and 10 percent by soil weight were used. Unconfined Compressive Strength test (UCS) and California Bearing Ratio test (CBR) were carried out on the 28 days air-cured samples to evaluate the effectiveness of lime stabilization with different concentration of lime solution. The Atterberg limit test and moisture content determination were then conducted as to investigate the effect of lime stabilization on plasticity behavior of the soil.

2.1 Initial Consumption Lime

A series of initial consumption lime tests (ICL) were carried out in which to determine the ICL value for the selected soil. The ICL value is indicating a minimum amount of lime required for soil modification in the early stage. Therefore, the lime used in the stabilization process is greater than the ICL value in order to establish soil stabilization. The ICL value was determined based on average pH of 12.4 in order to sustain the strength producing lime-soil pozzolanic

reactions. As a result, about 6% of lime was obtained from the test.

Table 1 Properties of soil

Physical properties	
Natural Moisture Content (%) before light storm	32.78
Natural Moisture Content (%) after light storm	53.12
Specific Gravity (G_s)	2.64
Liquid Limit (%)	61.50
Plastic Limit (%)	30.15
Plasticity Index (%)	31.35
Unconfined Compressive Strength (UCS) test (kPa)	167.80
California Bearing ratio (CBR) (%)	10.08
Particle size distribution	
Sand	69.50
Silt	16.70
Clay	13.80
Clay activity (A_c)	2.27
Soil Classification	
BSCS	SCH
AASHTO	A-2-7

Table 2 Chemical properties of hydrated lime

Available Lime Content	
Ca(OH)_2	85.71
CaO	64.86
pH at corrected 25 °C	12.40

2.2 Optimum Moisture Content

Optimum moisture content determination is important as a condition to prepare a fully saturated condition for lime stabilization. The result of standard proctor compaction test is given in Table 4 and the compaction curves for various lime contents are plotted in Fig. 1.

Table 4 Standard Proctor Compaction

Lime Content (% of soil mass)	Maximum Dry Density (Mg/m^3)	Optimum Moisture Content (%)
Untreated	1.44	25.5
7%	1.35	29.2
8%	1.32	33.5
9%	1.30	33.9
10%	1.28	34.2

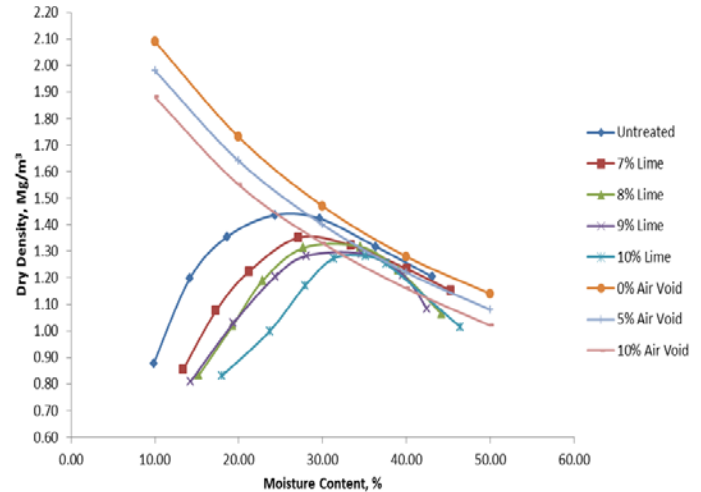


Figure 1 Standard Proctor Compaction Curve

As in Fig. 1, the compaction curves show that further addition of lime to the soil can decrease the dry density and at the same time increase the moisture content of the mixture. Moreover, the compaction curves move closer towards the zero air void line as the lime content is increased.

3 RESULTS

3.1 Unconfined Compressive Strength (UCS)

Compressive strength of a soil is a significant factor to estimate the design criteria for the use as pavement and construction material. The result of the UCS test for the soil samples at different lime content are tabulated and shown in Fig. 2. The highest strength achieved is 1514.13 kPa with 9% of lime content cured for 28 days at room temperature of $27 \pm 2^\circ\text{C}$. The reason for the strength development is due to the pozzolanic reactions between lime, water, soil silica, and alumina that form various cementing-type materials. The cementing products are calcium silicate hydrates and calcium aluminate hydrates which are the same hydrates formed during the hydration of Portland cement [6]. According to [7], the excessive lime can be detrimental in soil stabilization if the available silica in the soil is consumed. Fig. 2 shows the strength of soil-lime admixtures are considerably increased according to the increment of lime. Nevertheless, the compressive strength of the treated soil shows no further increase after optimum lime content was achieved.

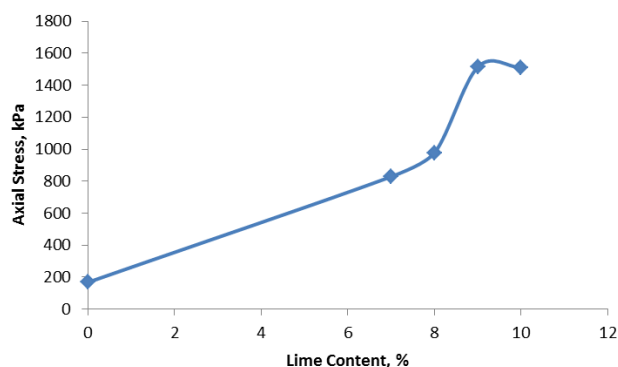


Fig. 2 Unconfined Compressive Strength Test

3.2 California Bearing Ratio (CBR)

California Bearing Ratio (CBR) value is used as an index of soil strength and bearing capacity. It is a familiar indicator test used to evaluate the strength of soils which broadly applied in the design of the base and the sub-base material for pavement [8]. CBR test without soaking are conducted to characterize the strength and bearing capacity of the soil samples with different lime percentage compacted at optimum moisture content. Fig. 3 gives the summarized result of CBR value for the untreated and lime treated soil. The results of unsoaked CBR values for lime treated soil indicated that the highest CBR of 92.19 % is observed at 9% lime stabilization. The CBR values are increasing as the lime percentage is increasing up to 9% and thereafter the CBR values started to reduce. Thus, lime stabilization is recommended at 9 % lime content.

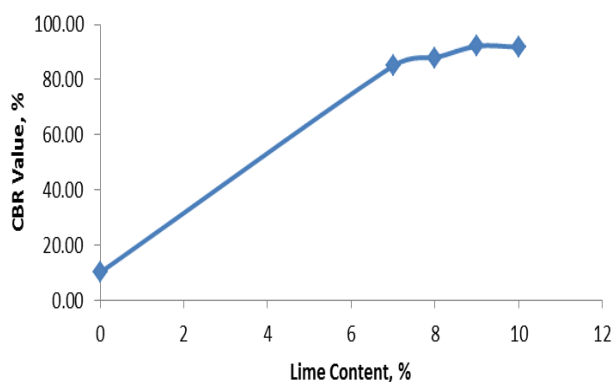


Fig. 3 California Bearing Ratio

The improvement of a cohesive material using hydrated lime changes the clay properties in plasticity index [9]. Atterberg limit test are conducted for lime treated soil as to compare the variation and differences with the untreated soil. Fig. 4 summarized the effect of the addition of lime on the plasticity of the soil sample. From the results, it is clearly shown that the addition of lime to the soil increases the plastic limit however decreases the liquid limit and linear shrinkage

of the soil sample, which results in a significant reduction in the plasticity index. This reduction in plasticity index means a marked increase in workability. The effect of lime on liquid limit is much less marked compared to the plastic limit. As indicated by Fig. 4, addition of 7 % of lime content increases 18.23 % of plastic limit while the liquid limit only decreases by 1.91%.

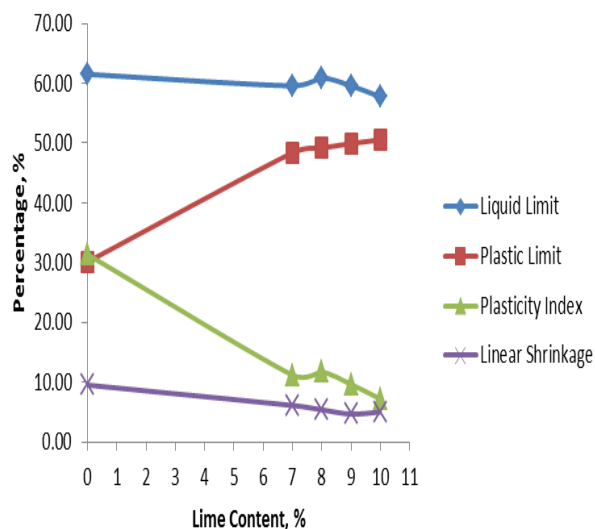


Fig.4 Influence of the Addition of Lime on Atterberg Limit

Fig. 5 presents the reduction of water moisture content of the untreated and lime treated soil after 28 days air-cured at room temperature of $27 \pm 2^\circ\text{C}$. From the result, the moisture content of the soil reduced 14 % at the lime content of 10 %. It shows that drying occurs only through the chemical changes in the soil that reduce the soil moisture holding capacity and increase its stability as for hydrated lime [10].

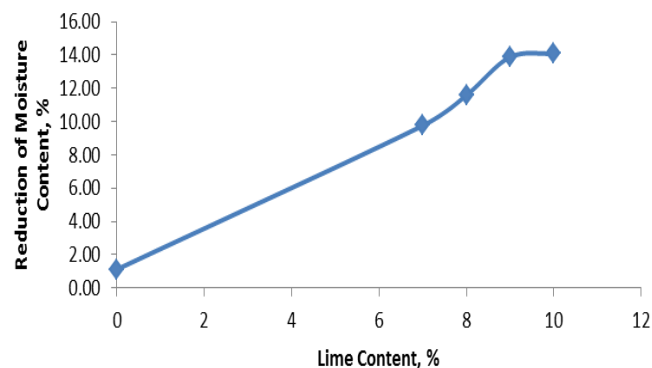


Fig. 5 Moisture Reduction of Lime Treated Soil

4 CONCLUSION

In this study, it was found that the 28 days air-cured lime-soil admixtures contributed the highest strength at 1514.13 kPa with 9% of lime content. In addition, the unsoaked CBR values for lime treated soil also indicated the highest CBR of 92.19 % at the same value of lime content. Besides, there is no further increase of strength after the stabilization reaching 9% of lime content. Therefore, the optimum concentration of lime used in this study is 9% of lime by weight of the soil.

5 ACKNOWLEDGMENT

The authors acknowledge Universiti Malaysia Sarawak for the support towards this project through UNIMAS GRANT 02 (76) /581/2006/(14).

6 REFERENCES

- [1] Gan, S., & Tan, C. (2003). Some Construction Experiences on Soft Soil Using Light Weight Materials. *2nd International Conference on Advances in Soft Soil Engineering and Technology*. Putrajaya, Malaysia.
- [2] Said J., & Taib, S. (2009). Peat Stabilization with Carbide Lime. *UNIMAS E-journal of Civil Engineering Vol. 1*.
- [3] ARRA, A. (2008). *Soil Stabilization*. Retrieved October 2011, from www.arra.org: http://www.arra.org/index.php?option=com_content&view=article&id=36:soil-stabilization&catid=20:industry-segments&Itemid=81.
- [4] Kazemian, S., & Huat, B. (2010). Assessment of Stabilization Methods for Soft Soils by Admixtures. *International Conference on Scientific & Social Science Research (CSSR 2010)*. Kuala Lumpur, Malaysia.
- [5] McNally, G. (1998). *Soil and Rock Construction Materials*. London: Routledge.
- [6] Terrel, R., Epps, J., Barenberg, E., Mitchell, J., & Thompson, M. (1979). *Soil Stabilization in Pavement Structures: A User's Manual, Volumes I and II*, FHWA.
- [7] Impe, V. (1989). *Soil Improvement Techniques and Their Evolution*. CRC Press, Taylor and Francis.
- [8] Nicholson P., K. V. (1994). *Lime and fly ash admixture improvement of tropical Hawaiian soils*. Washington DC: Transportation Research Record.
- [9] Transport, D. o. (2007). *Treatment of Fill and Capping Materials Using Either Lime or Cement or Both*.
- [10] NLA, National Lime Association. (2004). *Lime-Treated Soil Construction Manual: Lime Stabilization & Lime Modification*.

Increase Of Piles Bundle Capacity By Making A Base Joining Them

Jan Jaremski

Rzeszow University of Technology, Rzeszów , Poland, jjaremsk@prz.edu.pl

KEYWORDS: joining pile, rock eluvium, swelling soils.

ABSTRACT: The paper contains a new solution of the complex pile foundation including the base, made in the ground, and the joining piles the base with the girt. This kind of piles can be used for foundation under special geological conditions (proglacial stream valleys) for foundation reinforcement of the existing buildings and new foundations. The proposed solution may be applied in the swelling soils. . In the work possibilities of execution of joining piles in different soils like fine sands, silts, clays, clay shale, sandstones, which can be foundation for the pales, have been considered. Application of the joining pile on swelling soils.

1 INTRODUCTION

So-called joining piles represent a new idea of piling where the basic part of the pile (the base of the high-diameter pile) is located at the depth of the foundation occurrence. Depending on the ground conditions, in many pile structures the basic part of loading is carried by the pile base. The joining pile is an example of such piles. It is a combined foundation including the base made in the soil, and the post elements (a bundle of piles or micropiles) joining the base with the girt (see Fig.1).

Loading conveyance from the building object to the carrying ground zone takes place through the bundle of piles (posts) joined at the base with the solid of a big projection zone and volume. The solid is formed of the hardened soil-concrete generated from the deposited aggregate or the degraded rock with injections cement grout. Such a pile allows to distribute loading on a large surface; in a consequence load intensity becomes lower. It also allows to make a base increasing load capacity of the bundle

of piles for improvement of soil capacity of the existing foundations located on the grounds of low load capacity and on swelling ground. In many cases, direct capacity of the considered pile can be compared with high-diameter piles because of their base surfaces. The considered solution is very cheap and its realization does not require heavy equipment at the building site. It also eliminates a widely applied „forest” of prefabricated piles joined with a plate requiring much more reinforcement than beams joining the joining piles.

The joining pile is characterized by great ability to transfer horizontal loads, very important in bridge and industrial building (chimneys etc.). It can be also applied as the anchor pile in small buildings. The considered piles are used for increase of capacity of the existing foundations in the case of a superstructure and deterioration of geotechnical parameters of the base.

The discussed way of foundation was realized in the soils where a layer of gravel-sand soils occurred below the layers non-

transferring loads. In such layers the pile base can be made with cement paste injection. Such geological conditions usually exist near proglacial valleys and valleys where there are interbeddings of aggragate mud, peat, soft plastic silts clay, dust especially sensitive to changes of humidity occurring e.g. while flood states

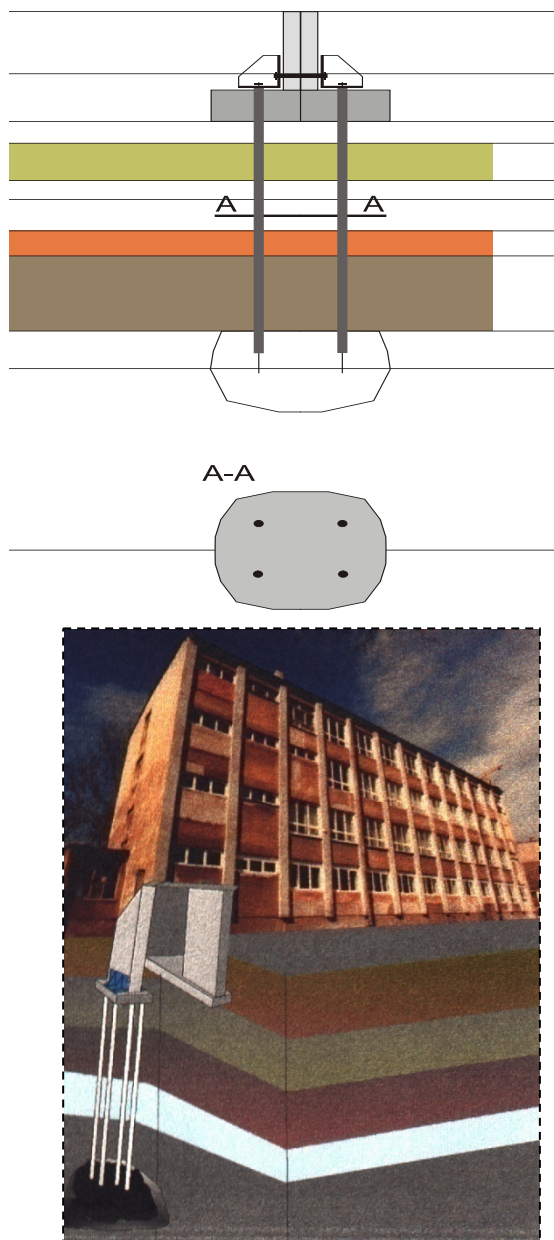


Fig. 1. A scheme of foundation reinforced with a bundle of piles joined by concrete base

In the cases realized so far, the pile bases were made in the gravel layer occurring at the depth of about 5 m below the site by means of an injection of cement paste. Such injection was performed through the holes in a bundle containing e.g. four posts (prefabricated piles with the holes inside).

There is another advantage of joining piles: they can be used at expansive soils. Such piles have relatively very small lateral surface. Moreover, it allows to transfer some forces from swelling through anchors located in the holes used for injections. Foundation on traditional piles in swelling soils transferring loadings to non-swelling layers does not protect the structures against the swelling effects because of swelling influence on lateral surfaces of the piles. The joining pile is a verified solution for foundation reinforcement in the existing buildings, it can be applied for foundation capacity increase in dangerous situations, also in the case of new solutions of intermediate foundations[7]. The calculations included possibilities of deviations in post elements with unintended eccentricity of longitudinal force applying. For calculations parameters of the stratified base were assumed, because such base usually occurs in proglacial valleys. The base joining post elements can be done only under the condition of existence of suitable layer. Thus, the proposed idea can be realized only in proglacial valleys[6].

Application of the joining piles under different conditions has been considered. Namely, it concerns the conditions where there is no layer of non-cohesive soil, and at the level of pile foundation there are shale clays, shales, sandstones, fine sands, silts, clays etc., being a base for the element joining the pile heads. It seems be possible to make an empty space necessary for generation of the pile base by explosion of an explosive material.

The formed volumes could be filled with cement grout[8].

In the considered solution, explosive materials are used while pile manufacturing. Ammonium saltpetre and potassic saltpetre are the proposed explosive materials, comparable amounts of trinitrotoluene are also considered. A possibility of such solution can be proved by an example from Shanghai, China. Ground anchors were located under the object of relatively large area. That object contains two underground storeys, and soft plastic swelling clays occur at the foundation level. The object is located on the plate mounted by means of 1100 anchors 9 meters in length with a widened base. A necessary volume for the widened base of the anchor was obtained by means of explosion of the explosive material. In such a way, an empty area of a small diameter was obtained at a proper depth in a soft rock. The area was filled with concrete. Ammonium saltpetre and potassic saltpetre were applied as explosive materials, and suitable detonators were used – application of professional procedures could eliminate accidents. Vibration and noise generating while explosion were less than permissible ones. Effects of explosion and generated shocks were analyzed. Noise measurements done in situ while explosions showed from 112 to 116 decibels.

In opinion of the scientists from China, the presented solution is a new method of foundation anchorage at expansive soils. The applied method of manufacturing is reliable and very good from the economical point of view, and it should be disseminated – the proposed design is safe, relatively cheap and its realization is easy[1].

In the case of soft rocks at the level of pile location, it is also possible to make a head of soils occurring above the eluvia of soft rocks widely assumed as non-carrying subsoil. The author analyses the possibilities of utilization of earlier investigations of application of the piles

joining in cohesive soils and the soft rocks. For many pile constructions weathering is the foundation strata and it is very complex to learn its properties and geotechnical parameters considering the difficulty of taking samples of undisturbed structure and the depth which weathering occupies. The researches, given in the early papers, can be accepted as model ones in the estimation of geotechnical parameters of weathering which is very often the foundation strata for pile constructions [3,4,]. The obtained results of the researches of the marl eluvium are ones of the standard laboratory tests of debris with disturbed structure, made successively, and also of model testing made on the samples of weathering with the smallest fractions of simulated variations of moisture-content approximated to those occurring in the deposit. The papers presented the results of non-typical investigations“ in situ ” to with the role of a verifier of numerical values of geotechnical characteristics has been attributed [5,10,]. They allow to determine the optimum bearing capacity of piles which brings about the possibility of the reduction of their number and greater safety of designed constructions. The determination of piles bearing capacity is based on test loads [2,9].

2 THE COMPLEX PILE MANUFACTURING FOR NEW OBJECTS

In case of many pile solutions (high-diameter piles) the fundamental part of loadings is transferred by the pile base. The base manufacturing requires high-diameter bore-holes made by means of heavy equipment. Such piles are rather expensive. In such cases, the joining pile can be an alternate solution. In case of such a pile, at least three prefabricated piles are introduced in a traditional way (by means of a vibrating hammer or a pile driver) at the depth of occurrence of the water bearing layer

containing coarse sands and gravel on the surface of min. 0.5m^2 . Next, injection is performed by the axial holes in piles, at least 20 in diameter; where the binding medium (for example cement grout) is introduced under pressure 3 – 150 bars. While injection into the first hole, the moment of occurrence of cement grout in the hole of the alternate pile is determined, and injection pressure treated as preliminary pressure is registered. .

The pile base formed after injection and cement grout binding, joined by piles with the girt (the plate the joining pile heads) is a complex pile foundation. For example, the joining pile manufactured by introduction of four prefabricated piles of dimensions 80×80 and the spacing about 80 cm forms after injection the base joining pile heads of a diameter comparable with the high-diameter pile 180 cm in diameter.



Fig 2. The computer simulation of the joining pale

3 APPLICATION OF THE PILE ON SWELLING SOILS

Usability of the pile joining on the expansive soils is its important advantage. Conventional piles located in swelling soils transfer loadings to non-swelling layers, but they do not protect the structure against effects of swelling because of action of forces from swelling on lateral surfaces of piles. The joining pile has a relatively small lateral surface. Moreover, it allows to transfer some forces from swelling through anchors located in the holes for injections, diameters of which can be enlarged. This solution was successfully applied in two constructions.

Swelling soils are present on many areas of the hot and temperate zones, also in many enclaves of soils and rock eluvia containing minerals belonging to the groups of montmorillonite, illite etc. Identification of swelling ability and methods of its investigations were described in [11,13]. Losses caused by soil swelling in building industry are comparable to losses caused by environment.

In the case of swelling soils, the system of piles or micropiles with the base joining their heads plays the role of the anchoring pile. After the injection, the anchors made of steel ribbed bars are introduced through the holes at the depth providing a proper anchorage. The fronts of the piles are bonded with the foundation masonry or the structural post by the steel girts.

In the case of unfavourable soil and water conditions above the base, the micropiles are made by forcing the pipe into the base. At the pipe front there is a taper with a hole for injection. When a proper depth is obtained, injections of the hardening medium are performed into the base, next the pipe with the taper is removed. Concrete mix is introduced into the existing hole, and the micropiles are formed.

4 JOINING PILES MANUFACTURING WHILE INCREASE OF LOAD-CAPACITY OF THE EXISTING FOUNDATIONS

In future it will be possible to apply the considered piles in modernized objects made of brick. It is proposed to make the joining piles with the simultaneous introduction of the beams made of steel profiles into the masonry. The beams could transfer loadings from the masonry to the posts-piles. If a frogged storey must be made, the piles could be built over. How to make such piles when load capacity of the existing foundations is increased. Here is an example. As an example cracks occurred on the walls and floor cellars at the final phase of the major overhaul of the building. Cracks occurred on the walls at the final phase of the adaptation repair of the building. Also non-uniform deformations caused by ground settlement under a part of the building, and the ground swelling were registered. It is caused by vertical cracks on the walls in the cellar in eighteen reinforced concrete cores. The supporting structure of the higher storeys included reinforced concrete frames, combined as a monolith in reinforced concrete finials of the ceilings of channel plates. After 25 years later of operating, the internal walls were damaged. During adaptation works the walls were replaced by new ones. The substrate below the building should be consolidated after so long time, and according to the geodetic measurements results a part of the object was settling, and another part was period rising. Particular layers of the substrate were tested very precisely. All the tests proved a complicated structure of the ground below the building. The soil cooperating with the foundations below all the house is and it will remain the active substrate with variable geotechnical parameters because of swelling, mineralization of organic parts of the soils occurring above the variable level of the underground water.

Under the foundation of the considered building, the heads were made – they joined the pile bases made by injection in the gravel layer occurred at the depth about 5 m.

Injection of cement grout was done by the holes occurring in the bundle of four posts (prefabricated interval piles $\phi 150$ mm and with the internal holes $\phi 42$ mm and length 140 cm). The prefabricated bundle of piles with the base was made under particular cores (hidden posts) in the foundation masonry every 3.0 m under posts of reinforced concrete frames. Such a high-diameter pile under each of 54 posts of the reinforced concrete frames allows to join a bundle of 4 posts with the cores by means of a steel girt (2 piles at each side). The girt is an angle bar reinforced in three points and joined with the post by means of 4 bolts $\phi 50$ mm.

Since swelling properties of the soils occurring along the posts (prefabricated piles) are variable, the piles play an additional role of the anchoring piles.

After injections, the bars made of ribbed steel, 20-40 mm in diameter, were introduced into the holes inside the pile to the length greater than 40 diameters. Injection was performed under pressure depending on density of the layer of coarse sands and gravel occurring in the subbase.

The joining pile should contain at least 4 prefabricated piles allowing to make a symmetric injected part of the pile. The prefabricated piles are introduced at the established depth. Assembly was realized according to requirement of the adapted building. The prefabricated piles are interval piles of $\phi 150$ mm – it is the maximum diameter of the drill applied for hole drilling. The ready holes were checked at the building site.

Introduction of the prefabricated element is preceded by making a hole $\phi 150$ mm in the soil by means

of the tapered point chisel (see Fig. 1. 3).

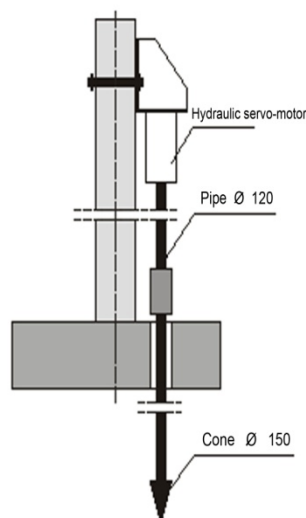


Fig 3. Diagram of the micropile introduction

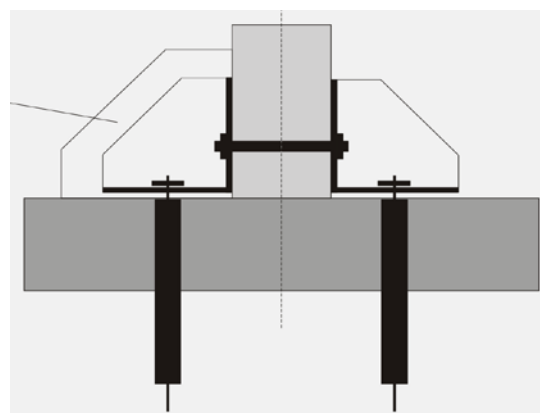
In this order, the assembly girt is mounted on the foundation masonry at the height dependent on the servo-motor and the element length. Next, the point chisel was forced into the hole.

The reinforced concrete post elements were introduced into the hole by means of the same hydraulic servo-motor. The main hole is made to the required depth by means of joined sections of thick-walled tubes $\sim \phi 100 - 140$ mm, joined with the tapered point chisel which allows to make a preliminary hole where the pile is introduced. When the taper is introduced to the required depth, the point chisel is removed by means of the hydraulic servo-motor. According to measurement of pressure, the force of the point chisel introduction was about 80kN.

Application of the considered piles does not require special equipment for earth work, especially in the case of increase of load capacity of the existing foundations on the soils of low load capacity and on the swelling soils.

The load transfer from the building object to the carrying soil zone through the bundle of micropiles joined at the base by a block of a big projection surface formed by cement grout allows to distribute the load into a large surface,

and in a consequence load intensity can be reduced. This method is much more efficient than other well-known and widely applied methods of increase of the soil load capacity. The connection butt-end micropiles it was how on Figure.



5 CONCLUSIONS

1. The planned works lead to the complex analysis of the presented problems and they should insist in tests in situ, model tests, numerical calculations. Determination of the injected zone of ground concrete is also provided. Determination of injection parameters in fluvioglacial soils is also a very important problem.
2. Application of the joining piles seems to be advantageous as compared with foundation of new objects on the high-diameter piles. Such piles are very expensive, and their manufacturing requires heavy boring rigs and much time, also application of special equipment.
3. Application of the joining piles does not require special equipment for earth works, especially in the case of increase of load capacity of the existing foundations at the soils of low capacity and swelling soils.
4. A possibility of application of the joining pile at swelling soils is its very important advantage. Traditional piles applied at swelling soils can transfer loadings to non-swelling soils, but they do not protect the structure against the swelling effects since swelling acts on the lateral surfaces of the piles.

6 REFERENS

1. Guanzhou Z. Zhiming X.(2004): The application of blown tip pile used in the saturated soft soil land single stake economic analysis. Proc. Int. Conf. on Soil Nailing, Nanjing,.
2. Gwizdała K.:(2008) Fundamenty palowe. (In polish). Wydawnictwo Naukowe PWN SA. Warszawa.
3. Jaremski J.: (1991)Characteristic of weathering as foundation strata for pile construction on the basis of the researches of the Opole marls eluvium. Proc. 4th Int. Conf. Piletalk International, Kuala Lumpur,.
4. Jaremski J.: (1997) The influence of recognition of physical and chemical processes occurring in the weathering in the estimate of the extreme values of geotechnical parameters of the Opole marls eluvium. Proc. Int. Symp. Geotechnical Engineering of Hard Soils-Soft Rocks, Athens, A.A.Balkema,.
5. Jaremski J.:(2005), The influence of physical and chemical processes occurring in the weathered Opole marls on the geotechnical parameters, Publishing House of Rzeszów University of Technology,
6. Jaremski J.:(2000) Increase of micropiles bundle capacity by making a base joining them.Zwiększenie nośności wiązki mikropali przez wykonanie łączącej je podstawy.(In polish), XLVI Konferencja Naukowa KILiW PAN i KN PZITB, Krynica,.
7. Jaremski J., Wilk K.: (2001) Zwiększenie możliwości wykorzystania pali rzeszowskich do posadowień fundamentów pośrednich (In polish), VI Międzynar. Konf. Naukowa Lwowsko- Koszycko-Rzeszowska, Lwów.
8. Jaremski J.,(2006) Possibilities of application of rzeszowski pales In cohesive soils and the soft rocks. O możliwościach zastosowania pali rzeszowskich w gruntach spoistych i skałach miękkich.(in polish),. Zeszyty Naukowe Politechniki Białostockiej, Budownictwo z. 28
9. Jaremski J.: Creep property of Opole marls weathering on the base of the model laboratory research on the research in situ. Proc. 7th Int. Cong. on Rocks Mech. Aachen, A.A.Balkema, 1991.
10. Jaremski J.:(1994) Influence of physical and chemical processes occurring in eluvium of the Opole marls and their influence on the geotechnical parameters, Proceedings of the 7th International Congress IAEG, Lisboa , A.A.Balkema,
11. Jaremski J.:(1995) Proposal for a method determining value of the maximum swelling of soil by example of the Opole marls eluvium and illite clays. Proc. of 8th Int. Cong. on Rock Mechanics, Tokyo, A.A.Balkema.
12. Jaremski J.:(2004) The influence of changes of weathering water content on the formation of landslides in the Carpathian Flysch. Proc. of 9th Australia New Zealand Conference on Geomechanics, Auckland – February 2004, New Zealand Geotechnical Society Inc.
13. Jaremski J.:(2010), Influence of moisture changes on physico - chemical processes and geotechnical parameters in soft rocks , Studia Geotechnica et Mechanica, Vol. XXXII, No. 1.

The Effects of Soil-Pile Interaction on Seismic Parameters of Superstructure

Mahdy Khari^{1 #}, Khairul Anuar Bin Kassim², Azlan Bin Adnan³

1. Department of Geotechnical Eng., Faculty of Civil Engineering, Universiti Teknologi Malaysia

2. Department of Geotechnical Eng., Faculty of Civil Engineering, Universiti Teknologi Malaysia

3. Department of Stretcher Eng., Faculty of Civil Engineering, Universiti Teknologi Malaysia

(#: Corresponding Author: Mahdy Khari)

ABSTRACT

Large superstructures such as tall buildings, important structures and bridges sometimes are founded on fluvial and alluvial soil deposits. The pile supported structures response subjected to earthquake events strongly affected by the dynamic behavior of the soil-pile interaction (SPI). The destruction of the pile-supported superstructures has raised the attention to the SSI underlying concerns. In this paper, an attempt is made to evaluate the influences of the laterally seismic excitations on the lateral response of flexible piles owing to the kinematic and the inertial interaction in the SPI. In the present approach, the nonlinear beam on Winkler foundation (BNWF) is incorporated into a finite element analyses program to calculate the piles response. The static p-y curves are implemented to simulate the soil reactions within the frame of Winkler method. The material damping was included in this method. The results obtained of the equivalent linear method of the site response analyses are utilized as the input motions. The computed responses have been shown that this approach can be used for estimating the soil-pile interaction effects on the system seismic behavior.

Keywords: Soil-Pile Interaction, BNWF, Seismic Parameters, p-y Curve, Earthquake

1. INTRODUCTION

Significant damages of superstructures supported by deep foundations from major earthquakes (e.g. Cairo Earthquake, 1992; Loma Prieta Earthquake, 1989; Alaska Earthquake, 1964) have raised concerns of approaches implemented for the design of the deep foundations. As this complex phenomenon has received considerable attention [1-2]. In the past, the seismic motions have been used as the input ground motion at the base of the superstructure without considering the site effects and the soil-pile interaction.

The soil-pile-superstructure interaction (SPSI) is included of the two sources: Inertia and Kinematic Interaction. The kinematic interaction is due to the presence of pile foundation on or in the ground surface that causes the ground motions deviate from free-field notions[3]. Inertia interaction is due to the kinematic interaction transmitted to the superstructure.

Based on these observations, the several methods have been developed to evaluate the seismic parameters of structure with considering of the soil-pile interaction such as finite element method (FEM)[4-5], boundary element method (BEM)[6-7], beam on nonlinear Winkler Foundation (BNWF) and simplified method. It is mentionable although FEM and BEM provide the powerful tools to verify the seismic behavior so that the soil is considered as the continuum medium but they are not commonly owing to the excessive computational costs used. Among these foregoing approaches, the BNWF is widely used in the design offices [8-9] because it is a versatile and economical method.

A BNWF analysis of the soil-pile-structure interaction is performed in the current paper to verify the seismic behavior of the superstructure using the general finite element analysis software.

2. SPSSI ANALYSIS WITH BNWF

BNWF approach is a simplified method that has been an old popular and widely used in professional design offices due to computationally time saving and accurate. The Winkler' foundation assumptions are implemented in the Beam on Nonlinear Winkler Foundation (BNWF) method. The main assumption of this method is that the displacement of the each layer of soil profile is without dependence on the responses adjacent layers and consequently the shear stress between soil layers is ignored. The layered soil deposit can be estimated by this approach because the soil properties are allocated to determine the soil stiffness at the each level. In addition, the energy dissipation is considered through the material and the radiation damping. The Soil-Pile behavior can be modeled nonlinearity and linearity based on solutions envisaged in the time and the frequency domain. Moreover, the nonlinearity soil behavior, the radiation damping, the hysteretic damping and gapping can be considered in BNWF models.

As Fig.1 shown, in this method, the pile is discrete to a number of elastic finite beam-column segments so that the pile mass is modeled as the lumped mass in the nodal location. Each nodal is connected to the mechanical elements to represent the soil characteristics. Based on this simulation, the soil stiffness and the damping are simulated using spring (linear or non-linear) and the damper (radiation and material damping). The springs and dashpots are connected to nodal locations. There are several methods for calculation of the spring coefficients such as the p-y curves recommended by American Petroleum Institute (API). El Naggar et al. [8] used the static p-y curves recommended by O'Neill and Murchison [10] and Matlock [11] in sand and clay(Fig.2).

The variation of the soil parameters affect on the bending moment of the pile (Khari,ISFEHAN). As regard, the kinematic bending moment at the interface is affected by the soil nonlinearity behavior and the frequency content of the seismic motion even in absence superstructure.

Modeling radiation damping (represent energy loss due to wave propagation away) is obviously an important component of the soil-pile-superstructure interaction analysis so that it is most important in the far field. Gazetas and Dobry[12] developed a plane-strain model for the radiation damping of the soil. Based on their research, The radiation-damping coefficient can be calculated using the following equations:

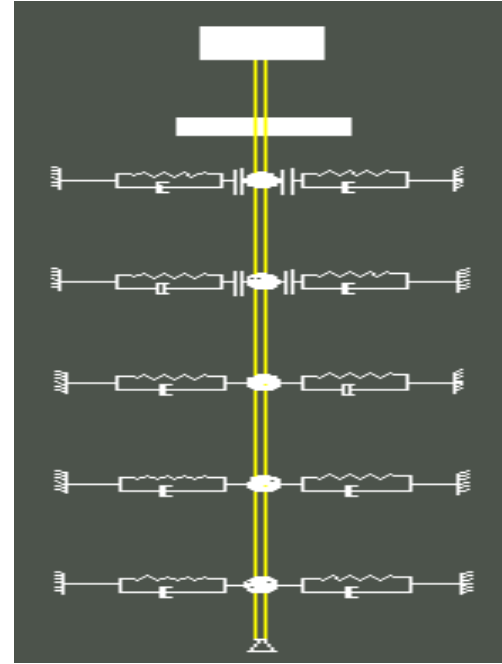


Fig.1: Schematic view of the proposed model

$$z > 2.5b \\ C_r = 4B\rho_s V_s [1 + (3.4/\pi(1-\nu)^{5/4})(\pi/4)^{0.75}a^{-0.25}] \quad (2.7)$$

$$z \leq 2.5b \\ C_r = 8B\rho_s V_s (\pi/4)^{0.75} a^{-0.25} \quad (2.8)$$

Where ρ_s and V_s are the density and the shear wave velocity of the soil, respectively; a is the dimensionless frequency factor ($a = 2\pi f B / V_s$; B =pile radius).

Material damping of the soil should be taken into account when the p-y curves are computed based on the backbone curve of a secant modulus approach. The material dashpot coefficient can be determined by the evaluation of hysteretic damping ratio (β) of the soil [13].

3. METHODOLOGY AND NUMERICAL ANALYSIS

To model of the soil-pile-structure interaction of above mentioned, ANSYS code a general-purpose finite element analysis software was performed. To evaluate the seismic behavior of the superstructure a transient analysis was implemented under the dynamic loading shown in Fig.3. A group 3x3 of steel piles (diameter=670mm; thickness=19mm) was considered in this study. Each row of this group was simulated to a equal pile with the similar

stiffness. The pile was divided into 13 elastoplastic elements

was selected owing to the dynamic parameters of the soil and the intensity of the seismic excitation.

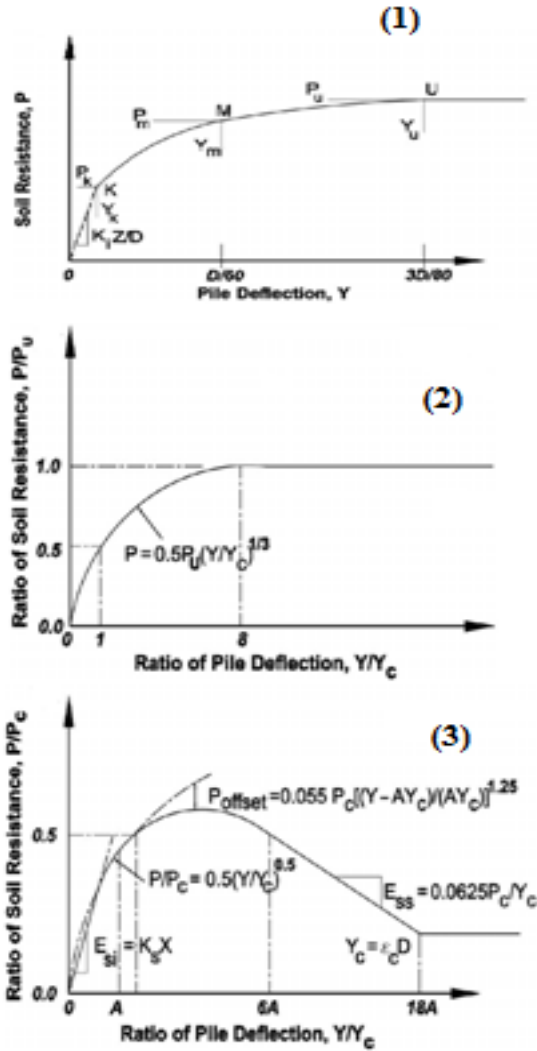


Fig.2: Characteristic shape of p-y curves;
(1) sand (2) soft clay (3) stiff clay

of “PIPE20” from elements library of above software. Mass of each part of the pile divided was lumped at the nodal location using of point element of “MASS21”. Also, each nodal was connected with a set of the nonlinear spring and the dashpots in parallel on each side of the pile. The soil stiffness was modeled using the nonlinear spring of “COMBIN39”. Newmark and full Newton-Raphson method were used to solve the non-linear equations in the software with amplitude decay factor of 0.005 and to equilibrium convergence, respectively.

The input motion was determined at the pile tip level using the site response analysis. For this reason, the nonlinear site response analysis (NERA)

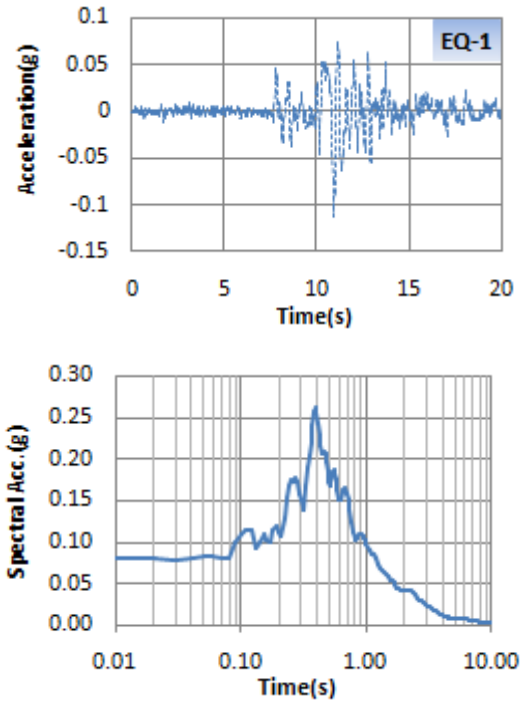


Figure 3- Acceleration time histories and response spectra at the bedrock roof

The soil profile proposed in the current paper, was included of the two horizontal layers of sand and clay. The upper layer was reconstituted clay ($\gamma=6.68 \text{ kN/m}^3$), 6.39 m thick with the plasticity index and the liquid limit equal to 48% and 80%, respectively. The lower layer was the sand with 11.1 m thick and the dry density of 1.66 Mg/m^3 , D_{50} of 15 mm and C_u of 1.5. a mass lumped (49100 kg) was attached at 3.8m above the ground surface.

4. ANALYSIS RESULTS COMPUTED

To evaluate the seismic response of the structure, the acceleration and the displacement time histories of the structure and the pile kinematic bending moment within different soil layers can be considered. Based on suggestions of some building codes, the time histories recorded are directly entered into the fixed base of the structure without considering the soil effects and the soil-pile interaction on the time histories recorded. As Fig.4 shown, this suggestion can not be used in the design and the evaluate of the dynamic response because the influences of the soil dynamic parameters and

the kinematic interaction are ignored because the value of the peak acceleration is difference with and without the site conditions.

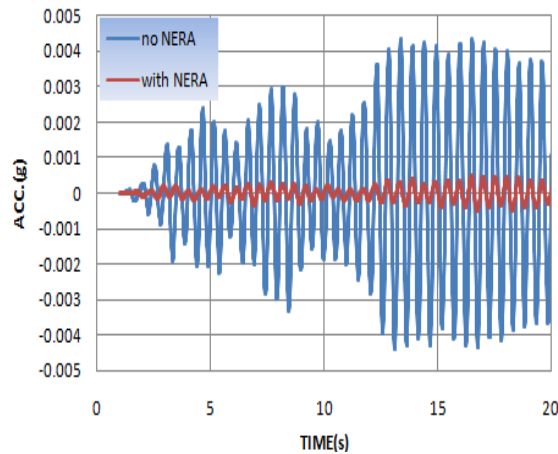


Fig.4: Acc. Time histories at the fixed based structure

the fundamental frequency of the fixed base structure and the system based on the modal analysis were equal to 1.94 Hz and 1.32 Hz in the first mode as the predominate mode, respectively. However, the natural frequency of the soil deposit was calculated based on the one-dimensional wave equation 0.78 Hz. These frequencies illustrate that the soil deposit effects play a very important rule in the interaction.

The acceleration and the displacement time histories at the three locations of the system are shown in Figs.5-6, respectively. A range of material damping ratios (0%, 5%, 10%) for the pile segments were considered in the numerical dynamic response. As regards the figures illustrated, with the increase of the material damping of the pile, the peak accelerations were decreased.

The frequency content was decreased at the different levels. So that, the time histories calculated at the below ground level shows the maximum content. Also, the maximum acceleration was decreased along the system height that it can be owing to the energy dissipation.

The maximum accelerations at the structure level were 0.0042g and 0.21g with note to the Fig.4 and Fig.5(1), respectively. It indicates the soil-pile interaction has the remarkable effects. In additional, the Fig. 5(1) shows that the existing of the damping affect the seismic responses but it is clear that its effectives is more less when the value of the material damping increase.

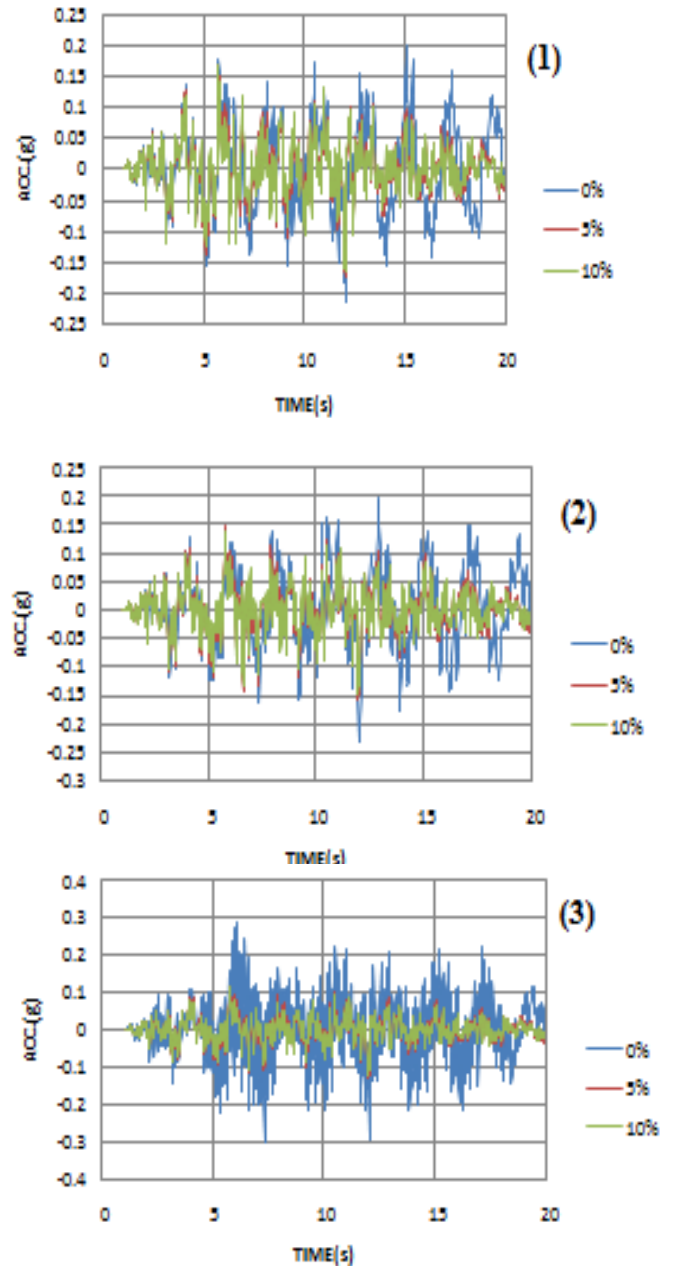


Fig.5: Acc. Time histories with damping
(1) the structure level (2) the pile cap level
(3) the below ground level

The influence of the material damping of the pile segments were more effect on the movement of the system. As Fig.6 shown, the displacement time histories are more different for the damping 5% and 10%. Point remarkable in this Fig. can be stated that the peak displacement are occurred in the higher time. The values of the maximum displacements at the pile cap and the structure level are not noteworthy.

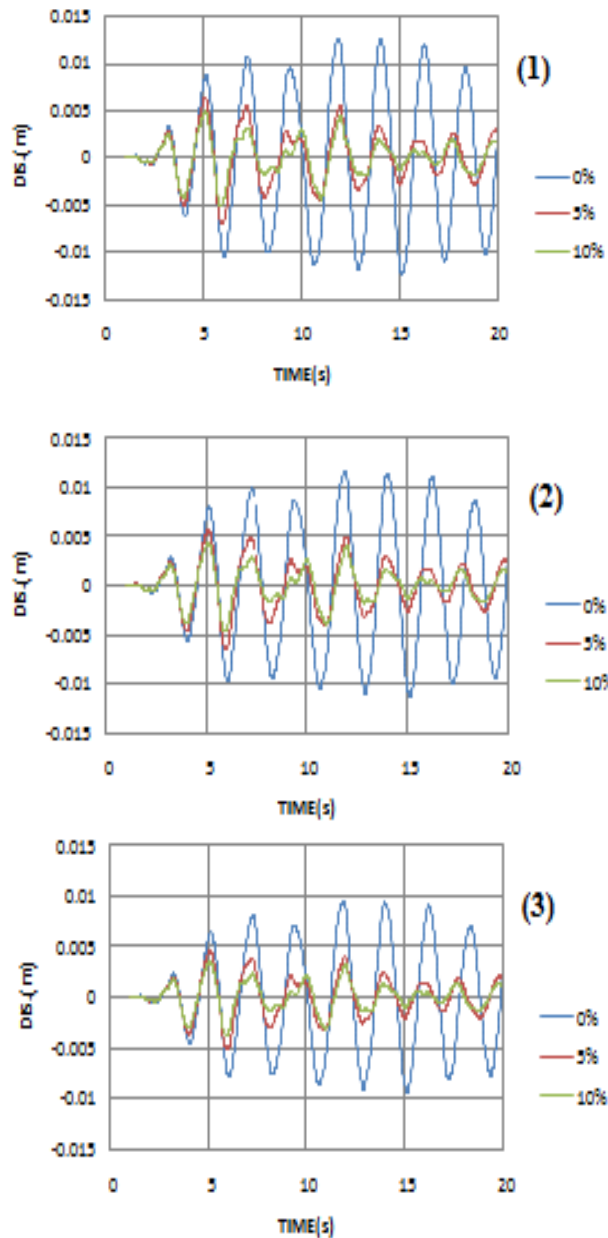


Fig.6: Dis. Time histories with damping
 (1) the structure level (2) the pile cap level
 (3) the below ground level

5. CONCLUSION

The influence of the soil-pile interaction (so-called kinematic interaction) on the seismic response of the structure was investigated in the current paper. A BNWF method was developed so that the soil stiffness and the damping (radiation and material) were considered. A range of the material damping of the pile segments were carried out. The results of this paper are applicable to linear structure and the

equivalent linear soil. Several aspects will affect the accuracy of the analysis such as the static p-y curve used to simulate the soil stiffness, not considering of the soil stiffness degradation, and decay factor in Newmark method. The results show that the peak acceleration is varied under the kinematic interaction. In additional, the material damping of the pile is more effective on the displacement time histories. However, the intensity of the seismic motion should be considered in this model.

6. ACKNOWLEDGEMENTS

The research was undertaken with support from GUP grant (No: 02H09) under the Universiti Teknologi Malaysia (U.T.M.). The first author would like to thank the Ministry of Higher Education (MOHE) and the Research Management Center (RMC) for the financial supports during this study.

7. REFERENCE

1. Khari, M., K.A. Kassim, and A. Adnan, *The Influence of Effective Confining Pressure On Site Response Analyses*. Asian Journal of Earth Sciences, 2011. 4(3): p. 148-156.
2. Khari, M., A.B.K. Khairul, and A. Adnan, *Evaluation of Kinematic Bending Moment of Piles subjected to Seismic Motions*, in *9th International Congress on Civil Engineering*. 2012: Isfahan University of Technology (IUT), Isfahan, Iran.
3. Khari, M., K.A. Kassim, and A. Adnan, *The Effects of Soil Model on Site Response Analyses*. Asian Journal of Scientific Research, 2012a. **Under Review**.
4. Maheshwari, B.K., et al., *Three-dimensional finite element nonlinear dynamic analysis of pile groups for lateral transient and seismic excitations*. Canadian Geotechnical Journal, 2004. 41(1): p. 118-133.
5. Wu, G. and W.D.L. Finn, *Dynamic nonlinear analysis of pile foundations using finite element method in the time domain*. Canadian Geotechnical Journal, 1997. 34(1): p. 44-52.
6. Cairo, R., et al., *Soil-pile kinematic interaction: from research to practice*. Italian Geotechnical Journal.
7. Kaynia, A.M. and E. Kausel, *Dynamic behaviour of pile groups*. Second International Conference on Numerical Methods in Offshore Piling, 1982.

8. *model for nonlinear seismic response analysis of offshore piles with nonlinear input ground motion analysis*. Canadian Geotechnical Journal, 2005. **42**(2): p. 365-380.
9. Nogami, T., J. Otani, and H. Chen, *Nonlinear Soil-Pile Interaction Model for Dynamic Lateral Motion*. Geotechnical and Geological Engineering, 1992. **118**(1): p. 89-106.
10. O'Neill, M. and J. Murchison, *An Evaluation of P-Y Relationships in Sands*. 1983: University of Houston.
11. Matlock, H., *Correlations for Design of Laterally Loaded Piles in Soft Clay*, in *Proc. 2nd Offshore Technology Conf.* 1970: OTC 1024, Houston. p. 577-594.
12. Gazetas, G. and R. Dobry, *Horizontal Response of Piles in Layered Soils*. Journal of geotechnical engineering, 1984. **110**(1): p. 20-40.
13. Finn L., W.D., *A Study of Piles during Earthquakes: Issues of Design and Analysis*, in *Bulletin of Earthquake Engineering*. 2005, springer. p. 141-234.

Investigation on Finite Element Modeling of Group of Stone Columns

M. Mirshekari¹, C. Behnia² and S. Fakhretaha³

¹MSc Student, School of Civil Engineering, University of Tehran, Tehran, Iran

²Associated Professor, School of Civil Engineering, University of Tehran, Tehran, Iran

³BSc Student, School of Civil Engineering, University of Tehran, Tehran, Iran

ABSTRACT

In recent years, stone columns have been widely used to increase load bearing capacity as well as settlement reduction of soft soils. 2D finite element methods are usually used for analysis of load-displacement in the soil reinforced by stone columns. Plain strain modeling of stone columns is frequently carried out by idealization of equivalent continuous stone strips. This might result in changing the failure modes of stone columns. For instance, bulging failure mode, one of the important failure modes in stone columns, is neglected in the stiff axis of equivalent stone strip. The usual method is used for defining the equivalent stone strip, does not consider the failure mode variations. In this paper a new method is purposed for 2D modeling of stone columns. Plaxis 2D is used and the analysis is carried out considering various diameters and spacing of stone columns. Floated and rigid based stone columns have been studied applying the proposed method. Comparing the results with those obtained by 3D modeling analysis shows the accuracy of the proposed method.

Keywords: Stone Columns, Finite element, Plain Strain, Equivalent Stone Strip

1. INTRODUCTION

Land scarcity near existing urban areas due to fast development and urbanization, often necessitates the use of some sites in which soil has low quality (such as soft clays). In this condition, the soil may be unsuitable for short or long-term construction activities. Hence, the soil properties must be improved.

Several methods have been presented for soil improvement such as dewatering, compaction, preloading, grouting, deep mixing, stone columns, deep densification and soil reinforcement. Many of these techniques have been used for many years. The use of stone columns as a technique of soil reinforcement is frequently implemented in soft cohesive soil. Use of stone columns leads to increase in bearing capacity accompanied by significant reduction in settlement. Using granular, freely drained material in stone columns, consolidation settlement is accelerated, and post construction settlement is minimized.

Theoretical, experimental and field study on behavior of stone columns have been investigated in last decades. Hughes and Withers (1974) performed pioneering laboratory studies of sand columns within a cylindrical chamber containing clay. They used radiography to track the deformations occurring within and outside the column. They found that confining pressure of stone columns represented the measured column behavior very well. As a result of their researchs, they proposed the ultimate vertical stress (q) as a function of lateral effective stress of stone column. Barksdale and Bachus (1983) assumed a straight rupture surface for soil improved by group of stone columns, beneath the foundation. Their assumption made a triangular failure block, as shown in Fig. 1. They proposed ultimate bearing capacity of improved soil, considering straight failure surface.

Priebe (1995) considered the effect of compressibility of the column material and the overburden. He developed design

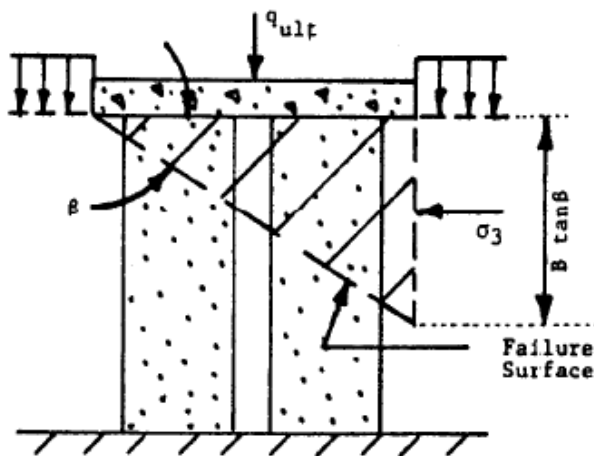


Fig. 1. Failure surface assumed by Barksdale and Bachus(1983)

charts to calculate the settlement of single and strip footing reinforced by a limit number of stone columns. Finite element method is recently used to determine the settlement of a soil improved by group of stone columns. Plaxis is a common Finite element package used for settlement determination. Results obtained by finite element modeling Plaxis have been verified with those obtained by empirical and field studies in several past studies. For example Ambily and Gandhi (2004) studied a laboratory model of single stone column in soil. In a case of static loading, they validated numerical results obtained by plaxis with the experimental results obtained by laboratory model. Barksdale and Bachus (1983) proposed idealized stone strip method to model group of stone columns as a plain strain situation. Idealized stone strip is shown in fig. 2.

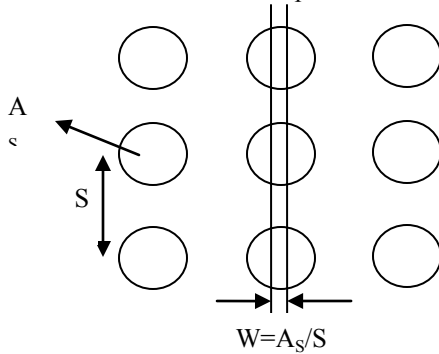


Fig. 2. Stone Column strip idealization presented by Barksdale and Bachus (1983)

In this paper a new method is purposed for 2D modeling of stone columns. Plaxis 2D is used and the analysis is carried out considering various diameters and spacing of stone columns. The results are compared with those obtained by 3D modeling analysis.

2. Modeling and analysis

In order to study on the finite element modeling of stone columns plaxis package is used in this paper. Plaxis package is one of the most prominent software's are operate with the finite element theoretical base. Plaxis package is widely used for stone columns modeling in the practical projects. Plaxis 2D, version 8.2 is used in this paper and the results are compared with palxis 3D, version 1.1 in order to define more accurate method for 2D modeling of stone columns.

3. Validation of plaxis 3D

(PLAXIS 3D) is validated by modeling of a stone column over axial loading based on load test carried out by Thompson et al. (2009). The subsurface profile at the project site consists of soft, nonuniform clay classifying as sandy lean clay (CL) to a depth of approximately 4 to 5 m. Groundwater was encountered approximately 1 m below the ground surface. The clay and gravel properties are assumed exactly as same as which presented by Thompson et al. (2009). Fig 3. Exhibit a comparison between results of modeling in plaxis 3D and the results which obtained in full scale load test is carried out by Thompson et al. (2009).

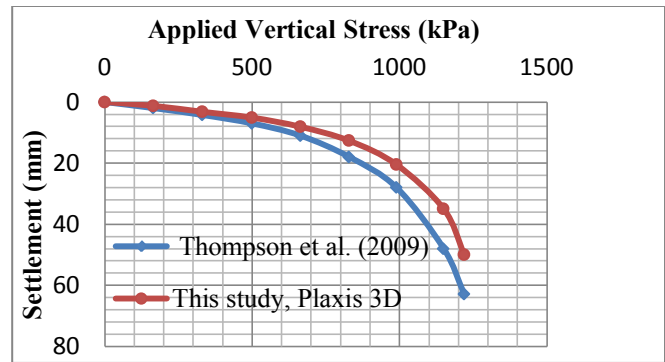


Fig. 3. Validation of Plaxis 3D

As could be seen in Fig. 3. the differences between the results of plaxis 3D modeling and full scale load test, Thompson (2009), might be neglected. Hence plaxis 3D is validated and could be used for the verification and précising of plaxis 2D models.

4. Examples

The Mohr-Coulomb criteria is used for soil and stone columns behavior. Also since in the most practical projects, gravel blanket is used above the stone columns, a gravel blanket is assumed beneath the load and above the stone columns. This gravel layer can distribute the stress between stone columns. In addition, it can dissipate excess pore water pressure. Thickness of this gravel blanket is 0.5 meter in this modeling. The columns are placed in square pattern and length of stone columns varies between 10 to 20 meter in different models. Geometry of model in plan and section are shown in Fig. 4 and Fig. 5. Stone columns diameter are between 0.8 to 1.2 meter in models. This range is most common diameters of stone columns in practical projects. The equivalent stone strip thickness is determined with barksdale and bachus method, as can be seen in Fig. 2. spacing of stone columns may vary between 2 and 3 meters. Geometrical parameters of modeling are shown in Table. I. Each column acts within a cylindrical cell with a radius of influence denoted by R_e (Fig. 6). Balaam and Booker (1981), related the radius of influence to the actual column spacing by the relation $R_e = c.S$, where S is the actual spacing (from center to center of the columns) and c is a constant having values of 0.525 and 0.564 for triangular and square patterns, respectively. Considering the radius of influence of stone columns in square pattern, the area replacement ratio(ρ), total area of stone columns over area of unreinforced soil, may be defined as :

$$\rho = \frac{d^2}{(1.13S)^2} \times 100 \quad (1)$$

By using Eq. (1) the area replacement ratio in different models varies between 6% to 28%. This range of area replacement ration may represent different stone columns geometries.

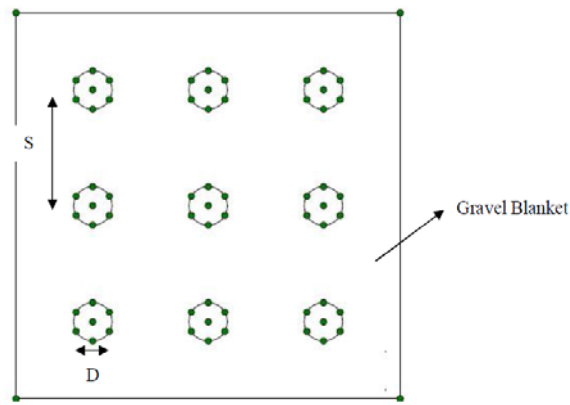


Fig. 4. Plan of Stone Columns and The Gravel Blanket

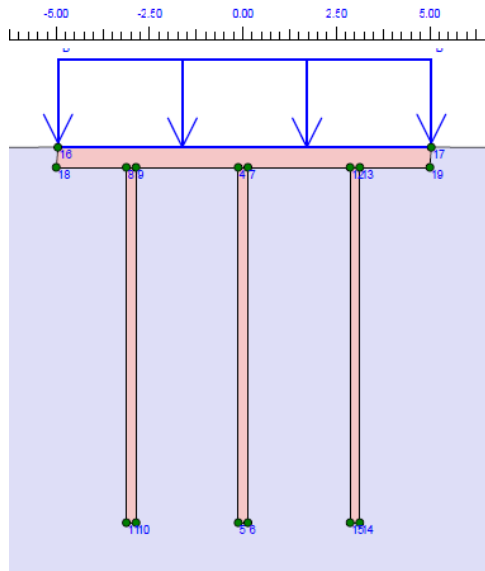


Fig. 5. Section of Stone Columns and the Gravel Blanket Modeled in Plaxis 2D

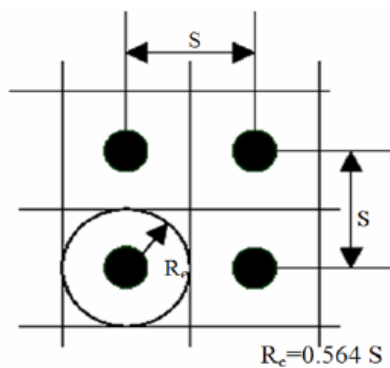


Fig. 6. Definition of radius of influence in square pattern of stone columns, Balaam and Booker (1981)

Table I. Geometrical properties of models

Spacing of Stone Columns (m)	Stone Columns Diameter (m)	Length of Stone Columns (m)	Thickness of Gravel Blanket (m)
2	0.8	10	0.5
2.5	1	15	
3	1.2	20	

In this modeling, site's soil is defined purely cohesive and stone column's material is defined purely frictional material. The soil is completely saturated and the water level is at the ground surface. Table. II indicates geotechnical parameters of soil and stone column's material.

Table. II. Site's soil and Stone Columns specifications, used in 2D and 3D Modeling

Region	Site's Soil	Stone Column Material
C (kPa)	25	0
ϕ (Degree)	0	40
E (MPa)	3	200
$\gamma_{\text{unsaturated}}$ (kN/m ³)	16	18
$\gamma_{\text{saturated}}$ (kN/m ³)	18	20

Distributed loading is assumed and the load acts in a 10*10 meter surface above the gravelly blanket. In reality it can represent a liquid storage tank or embankment load.

5. Results

The results of presented modeling are shown as a load-displacement curve. Since in the practical projects maximum displacement beneath the foundation is used as absolute settlement, in this study maximum displacement is used in load-displacement curves. All modeling results are gathered and analyzed. Fig. 7. shows the resultant of this study as a load-displacement curve.

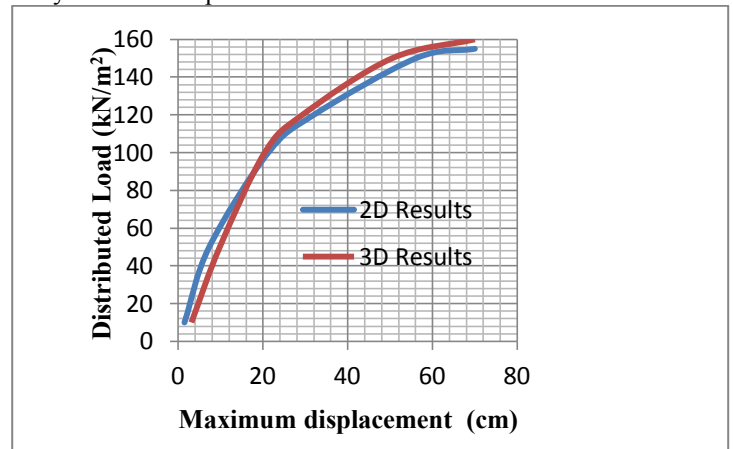


Fig. 7. Load versus maximum settlement in the 2D and 3D models of soil improved with stone columns

As might be seen the maximum displacement of soil in 3D models is higher than maximum displacement in 2D models

in light loads, and lower in heavy loads. In fact, however 3D displacements commence from a higher level, but the elasticity modulus of improved soil is higher in 3D models. So the displacement in 3D models are lower in heavy loads. It seems this difference occurs for the variation in failure mode of stone columns. For instance bulging failure mode can not occurs in the stiff axe of idealized stone strip in 2D modeling. Also the punching failure mode of stone columns happens harder in idealized stone strip. Table III shows some results too.

Table III. Results of 2D and 3D modeling of group of stone columns

Applied Load (kN/m ²)	Max Disp. 2D (cm)	Max Disp. 3D (cm)
10	1.46	3.1
50	7.31	9.8
100	21.24	20.4
120	32	29.3
150	56.1	50.5
155	70	66.1

Considering the results, it seems 2D modeling results can be improved using Eq. 2.

$$S_{3D} = S_{2D} \times 1.3 : \frac{q}{q_{ultimate}} \leq 0.5 \quad (2)$$

$$S_{3D} = S_{2D} \times 0.9 : \frac{q}{q_{ultimate}} > 0.5$$

Which

S_{2D} and S_{3D} , are the settlement in 2 and 3 dimensions

q , is the available stress level

and $q_{ultimate}$, is the bearing capacity of improved soil.

The Eq. (2) may be used to precise 2D modeling results, where plain strain model is used.

6. Conclusion

In this paper, a more accurate method is proposed to determine maximum settlement of soil which is improved with stone columns. Stone columns with different spacing's, diameters and lengths are modeled and the load-displacement curve is illustrated for the resultant of models. Differences between 2D and 3D results are seen and it seems that these differences have been occurred because of the changing in failure modes of stone columns. Finally by comparing 2D and 3D models results 2 coefficients are proposed to precise 2D finite element modeling results.

7. ACKNOWLEDGMENT

Acknowledgment is given to my dear friend Miss. Sanaz Mahmoudpour, for her kindly supports. Also,

acknowledgment is given to Prof. Ali Fakher for his astutely advices.

8. REFERENCES

- [1] Ambily, A.P. and S.R. Grandhi, 2007. "Behavior of stone columns Based on Experimental and FEM Analysis", Jour. Of Geotechnical and Geoenvironmental Engineering. ASCE, 133(4): 405-415.
- [2] Barksdale, R.D. Bachus, R. C., "Design and construction of stone column", Vol.1
- [3] Hughes, J.M.O. and Withers, N.J. (1974). "Reinforcing of Soft Cohesive Soils with Stone Columns", Ground Engineering, Vol.7, No.3, 42-49.
- [4] Hughes, J.M. O., N.J. Withers, and D.A. Greenwood, 1976. "A field trial of reinforcing effect of stone column in soil". Proc., Ground Treatment by Deep Compaction, Institution of Civil Engineers, London, 32-44.
- [5] Priebe, H.J., 1995. "The design of Vibro replacement. Ground engineering", 31-37.
- [6] Thompson, M. J., Wissmann, K. J., Pham, H. T. V., (2009), "Performance Monitoring of a Rammed Aggregate Pier Foundation Supporting a Mechanically Stabilized Earth Wall", Journal of performance of constructed facilities, July/August,2009, P 244-250.

Suction Controlled Triaxial Apparatus for Saturated-Unsaturated Soil Test

Luky Handoko, Noriyuki Yasufuku, Kiyoshi Oomine, Hazarika Hemanta
Department of Civil Engineering, Kyushu University, Japan

ABSTRACT

A suction controlled triaxial apparatus has been developed in Geotechnical Engineering Laboratory of Kyushu University. The apparatus has been designed to obtain mechanical properties of unsaturated soil such as shear strength and stiffness, as well as hydraulic properties of unsaturated soil, i.e. soil water retention curve by measuring drained water volume change during applied matric suction. Not only for unsaturated condition, this apparatus can be also used to conduct conventional test on saturated soil. This paper focuses on the performance of the apparatus, by performing a series of multistage test on unsaturated soil under drying and wetting path. The hydraulics and mechanical properties of unsaturated soil are presented and discussed.

Keywords: triaxial apparatus, unsaturated soils, suction control, hydraulics and mechanical properties

1. INTRODUCTION

Stress state variable, such as net normal stress and matric suction has been successfully governing behavior of unsaturated soils [1]. Those variables have significant influence on hydraulics and mechanics properties. Many researchers have been focusing study on determining shear strength [2]-[4], small strain stiffness [5]-[7], and soil water retention curve [8]–[9] of unsaturated soil through laboratory experimental. To obtain hydraulic and mechanical properties of unsaturated soil, an accurate control and measurement equipment is needed. Triaxial apparatus for unsaturated soil has been developed by many researchers [10]-[13].

Due to climate change, unsaturated soil prone to have hysteresis features and should no longer be ignored [14]. To investigate the hysteresis effect on unsaturated soil hydraulics and mechanics properties, an apparatus which able to control suction needs to be developed. This paper presents the development of suction controlled triaxial apparatus which can be used to conduct test on unsaturated soils as well as conventional saturated condition. The apparatus has independent control of cell pressure, pore air pressure and pore water pressure, equipped with Local Deformation Transducers (LDTs) to measure strain at small range and Pressure Differential Transducer to measure both drained water volume change and total volume change. With those equipment, it is possible to obtain both hydraulics and mechanics properties of unsaturated soil in a series of multistage test. Five centimeter diameter and ten centimeter height of silty sand specimen was used to conducted multistage triaxial test on different matric suction and stress path. Hydraulic and mechanical properties of the specimen are going to be presented and discussed.

2. SUCTION CONTROLLED TRIAXIAL APPARATUS

A suction controlled triaxial apparatus has been developed in Geotechnical Engineering Laboratory of Kyushu University collaborating with Geo-Research Institute, Kobe, shown in Fig. 1. This apparatus can be used to perform test under unsaturated condition by using axis translation technique controlling both pore water and air pressure to maintain matric suction within the specimen, as well as under saturated condition by providing a channel to apply back pressure.

Many instruments for control /measurement purposes are equipped in the apparatus, such as: external and internal load cell to measure deviator load; pressure transducer to measure cell pressure, pore water pressure at bottom of the specimen and pore air pressure at the top of specimen; Pressure Differential Transducer to measure drained water volume changes and total volume changes, LVDT to measure axial large strain range externally, LDTs and Pi-gauges to measure axial and radial small strain range internally.

Pressure control/measurement

Air pressure is supplied at a constant value about 700kPa to the pressure regulator. From pressure regulator, it is divided into four channels for controlling cell pressure, air pressure and two channel of pore water pressure independently.

Pore air pressure is applied at the top of the specimen through normal porous disk, while pore water pressure is applied at bottom through high air entry ceramic disk. The air entry value of ceramic disk is about 3 bars (300 kPa). High air entry ceramic disk was glued and completely sealed at the pedestal and connected with water channel at the bottom. At the middle of ceramic disk, metal porous disk is installed, mainly used during saturating the specimen or during saturated triaxial test. Fig. 2 shows the schematic diagram of pressure regulation in triaxial apparatus.

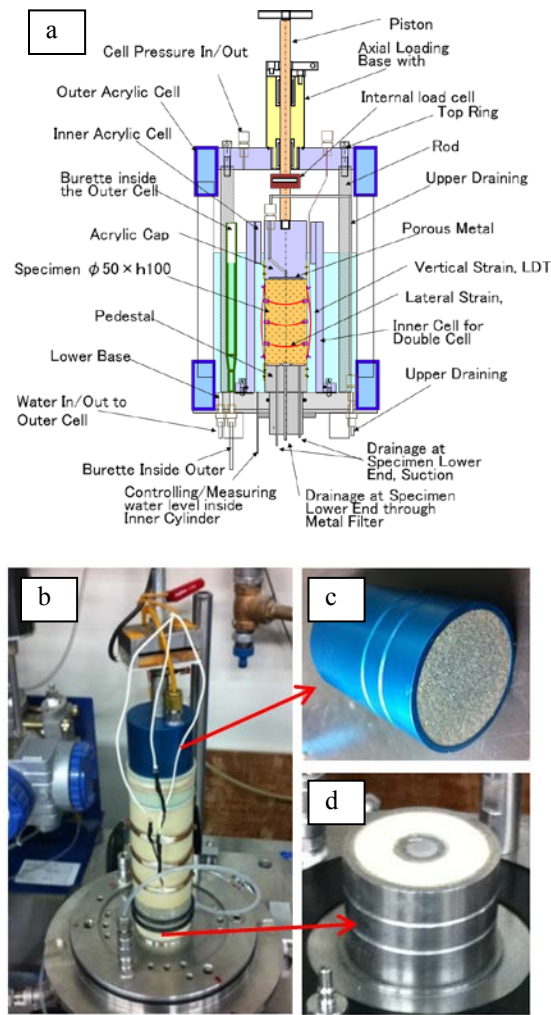


Fig. 1 Suction controlled triaxial apparatus, a) schematic diagram, b) photo, c) normal porous disk (top of specimen) and d) high air entry value disk and porous metal filter (bottom of specimen)

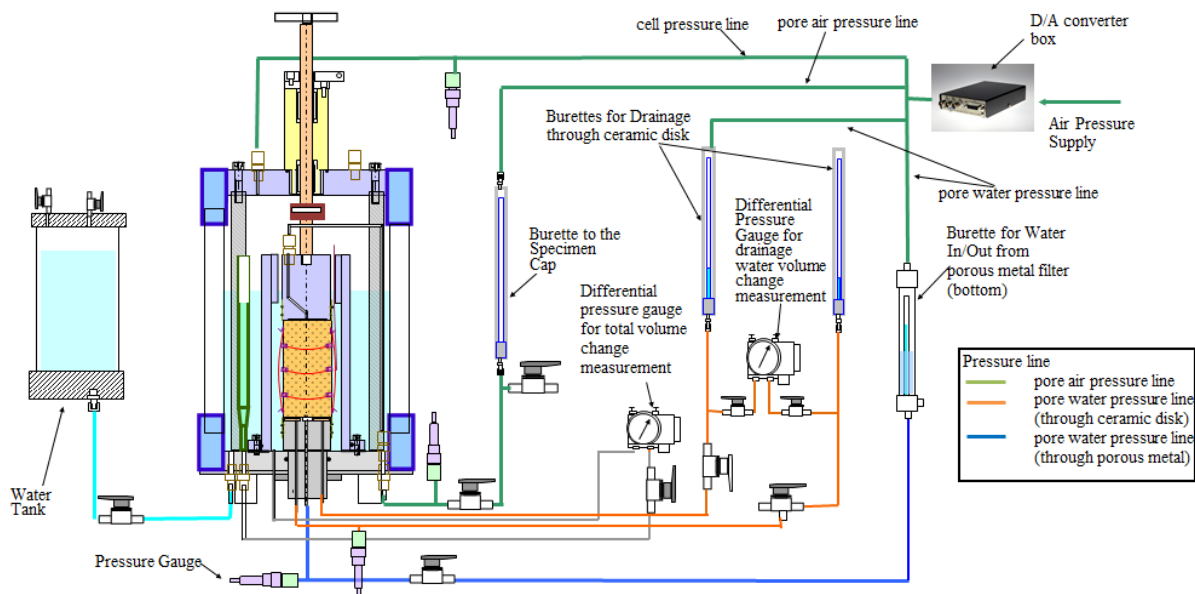


Fig. 2 Schematic diagram of pressure regulation

Volume change measurement

Total volume change and drained water volume change can be measured by using pressure differential technique [15]. Open ended inner cell is used to measure total volume change of soil. The fluctuation of water level inside the inner cell represents the change of total volume change. Drained water volume change is calculated by measuring the amount of water drained in or out of specimen. For complete description of pressure differential technique for measuring volume change please refer [15].

Strain Measurement

During shearing, strain of deformed specimen is measured externally and internally. Linear Variable Differential Transformer (LVDT) (range 0-20% strain) is placed outside the chamber to measure large strain range of specimen during shearing. Internally, LDTs [16] are attached at the specimen to measure axial strain, while other instruments so called pi-gauge are attached horizontally to measure lateral strain. The maximum displacement can be handled by LDT is about 1.5 mm (1.5% of strain). These LDTs and Pi-gauges were produced by Geo-Research Institute, Kobe.

3. TEST METHOD

3.1 Materials

Two types of soil were used in the tests; they are low plasticity silt called Red Soil from Okinawa Prefecture, Japan and sand soil called Toyoura sand. The grain size distributions are shown in Fig. 3 and the basic properties are shown in Table 1. Red soil was prepared to conduct soil water retention test, while Toyoura sand was prepared for shearing test. Specimen dimension prepared in the apparatus is 10 cm in height and 5 cm in diameter for shearing test. To reduce the time consumed in soil water retention test, specimen height was reduced to be 5 cm height, while the diameter is same.

The specimen was prepared by using moist tamping method compacted at a split mold attached to the pedestal of triaxial apparatus [17]. Required amount of dry soil was mixed with predetermined amount of de-aired water and then kept about 16 hours before used. Internal split mold was used to make the specimen, attached at the base pedestal of the apparatus. The specimen was compacted by 5 equal layers for soil water retention test and 10 equal layers for shearing test.

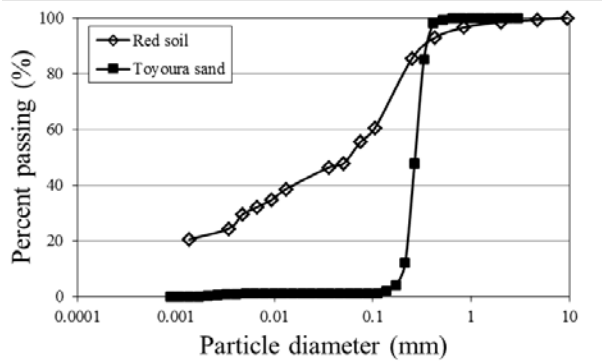


Fig. 3 Grain size distribution of Red soil and Toyoura sand

Table 1. Basic properties of Toyoura sand

Soil type	G_s	e	w (%)	γ_d (kN/m^3)	γ_b (kN/m^3)
Red soil	2.64	0.63	10.6	16.23	17.95
Toyourea	2.65	0.68	10	15.8	17.38

3.2 Test Procedures

Reference [18] explained the multistage testing procedure in triaxial apparatus by increasing soil suction of unsaturated soil. This procedure is mainly used to provide unsaturated soil properties of different applied matric suction and different path by using single soil specimen. Even though it is possible to obtain hydraulics and mechanics properties by using single soil specimen, in this test, two different tests were conducted to evaluate the performance of the apparatus. Water retention test and shearing test were conducted using the apparatus.

For water retention test, the specimen test was started from saturated condition. Pore air pressure and cell pressure was increased in the same value to maintain destined matric suction and to keep constant of net normal stress. Pore water pressure was set constant about 25kPa. Net normal stress was also set constant about 50kPa. Matric suction was varied to 3kPa, 10 kPa, 30kPa, 100kPa, 170kPa, 250kPa, 100kPa and 30kPa.

For shearing test, consolidated drained condition was chosen with shear rate about 0.01 mm per minutes. The specimen was tested initially from saturated condition. After being saturated, the specimen was sheared until reaching peak value and then unloading. After shear loading and unloading was finished, consolidation for next stage predetermined matric suction started, and then sheared again after reaching equilibrium state. This condition was repeated for next stage. A typical set of stresses for each stages are given in Table 2.

Net normal stress variable was set to constant value at 20kPa.

Table 2. Applied stress and stress state variable

Stages	u_a (kPa)	u_w (kPa)	u_c (kPa)	$u_a - u_w$ (kPa)
I	25	25	45	0
II	30	25	50	5
III	40	25	60	15
IV	30	25	50	5

2 RESULT AND DISCUSSION

Among of equipment mentioned above, LDTs performance may change with their use, so calibration is needed after used few times. For use in multistage test, LDTs will experience loading and unloading of deviatoric stress for many times in one series of test. This equipment needs to be calibrated properly before used by using digital micrometer as shown in Fig. 4.

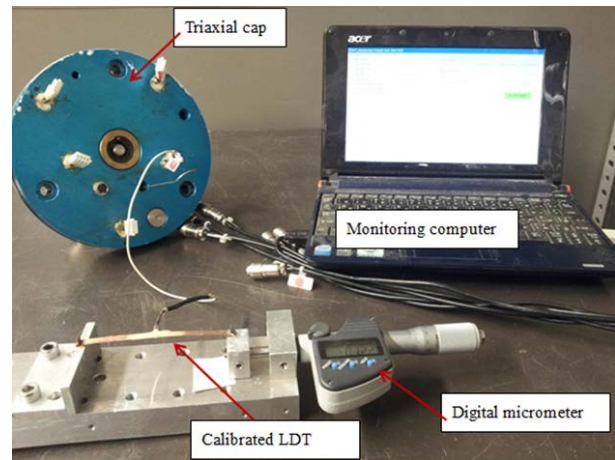


Fig. 4 LDT calibration techniques

Calibration for LDT is polynomial order two, while pi gauges follows linear curve. Fig. 5 shows the repeated calibration by loading and unloading for 2 times. It shows that LDT and pi gauges are still in good calibration due to repeated loading. The calibration curve does not change so much, and expected to work properly during multistage test.

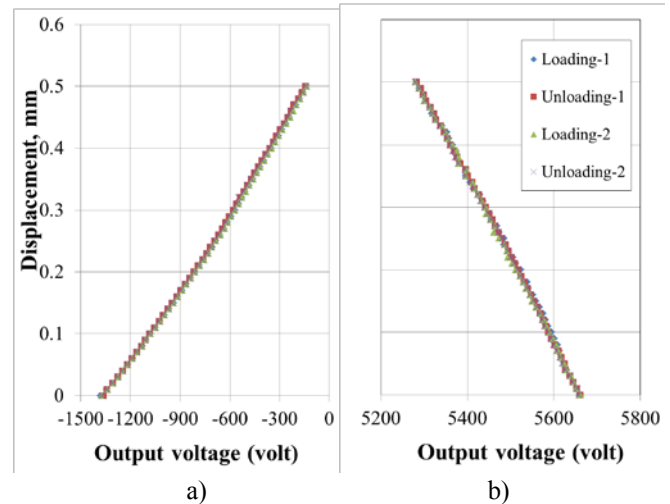


Fig. 5 Repeated calibration for a) LDT and b) pi-gauges
Soil Water Retention Test

Fig. 6 shows the drained water evolution versus time. It shows that drained water volume change can be monitored well. The result shows that red soil reaches equilibrium time about 8-10 days. After finish all consolidation step, water content of specimen was measured, and then recalculating water content for each applied matric suction by back calculation. As the result, SWRC of red soil can be drawn in Fig. 7. This figure shows the hydraulic hysteresis of red soil. At the same matric suction, wetting process will give lower water content than drying process. Environmental condition of specimen during soil water retention test is more similar with field condition by applying radial pressure (cell pressure) at the specimen. This is one of the advantages of using triaxial apparatus to measure soil water retention curve.

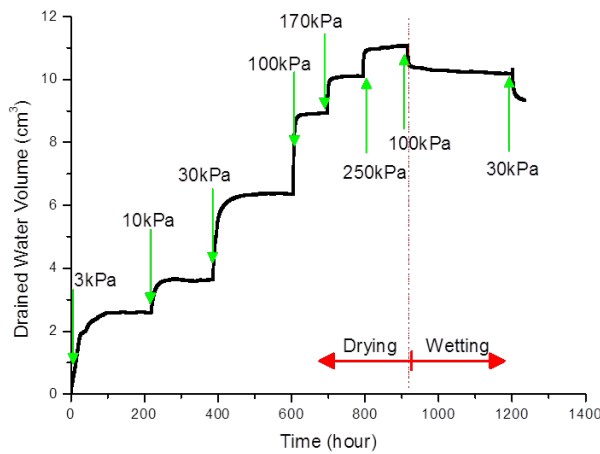


Fig. 6 Monitored drained water volume change

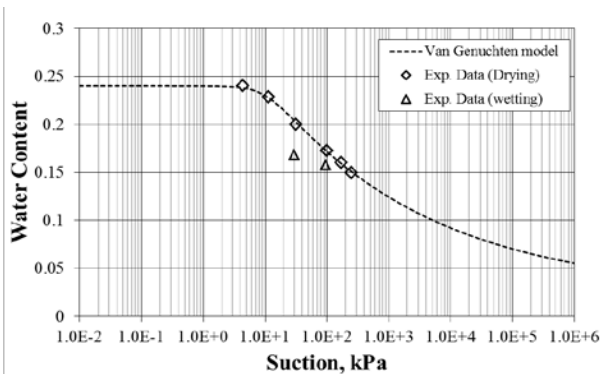


Fig. 7 SWRC experiment data fitted with Van Genuchten fitting curve

Shearing test

The stress-strain relationships for 4-stages (different matric suction) shearing test is shown in Fig. 8. It shows that the strength of soil increases as the increasing matric suction. And also, the curve is steeper as the increasing matric suction, means that stiffness is also increasing. At the early shearing test (matric suction = 0kPa), the graph seems to be incorrect. This problem may occur when the LDT was not attached properly. In this test, the LDT were attached manually by

using hand, and may unstable. Reference [16] suggests a fixing device to attach the LDT, so it can be aligned properly. Expected correct line is drawn in red line. Smaller strain range (below 0.01%) of stress-strain diagram and related elastic moduli at small strain are presented in Fig. 9 and Fig. 10. These figure more clearly show the stiffness of soil at small strain range. It shows that in small strain range, the stress-strain relationship can be represented by linear line. Elastic moduli of soil changes depend on the matric suction applied.

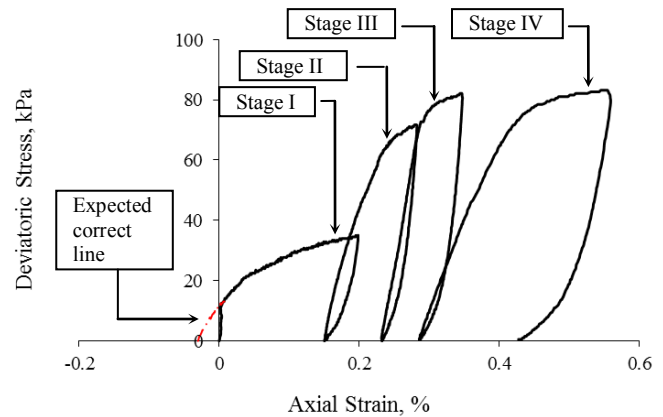


Fig. 8 Stress strain relationship of 4-stages multistage triaxial test

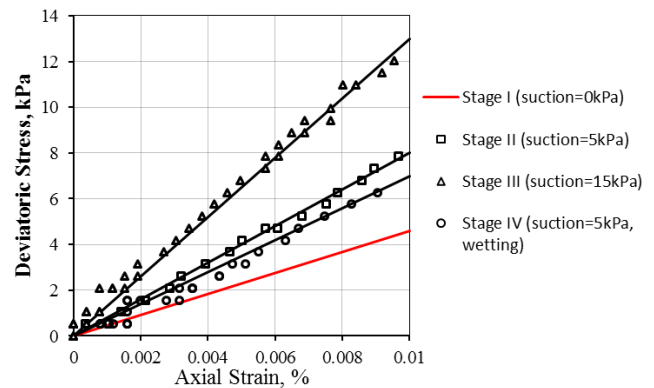


Fig. 9 Stress-strain diagram in small strain range of each stage

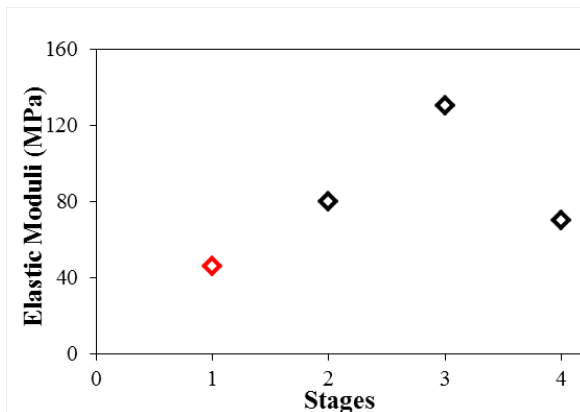


Fig. 10 Elastic moduli of each stage

3 CONCLUSION

A suction controlled triaxial apparatus has been developed in Geotechnical Engineering Laboratory of Kyushu University collaborating with Geo-Research Institute, Kobe. The apparatus has an automatic system to collect and store the data. It can be used to conduct multistage test to obtain hydraulic (SWRC) and mechanics (shear strength and stiffness) properties of soil. Two different series of multistage test has been conducted to evaluate the performance of the apparatus. From the experimental test result, it can be conclude that:

- the developed suction control apparatus is able to provide good monitoring and storing data automatically,
- the apparatus equipped with LDTs is to measure small strain range and works well based on the test result,
- unsaturated soil is having hysteresis features due to different process (drying and wetting). This apparatus is able to observe this phenomenon. It can be shown clearly in the hydraulic properties (SWRC) test result.

4 ACKNOWLEDGES

This research was financially supported by Grant-in Aid for scientific research (A) No. 22246064 from JSPS lead by N. Yasufuku. Authors also gratefully acknowledge support from Geo-Reserch Institute for the good collaboration to develop the apparatus.

5 REFERENCES

- [1] Fredlund, D.G., and Morgenstern, N.R. Constitutive relations for volume change in unsaturated soils, *Canadian Geotechnical Journal*, 1976, 13(3): 261–276
- [2] Escario, V. and J. Saez . "The Shear Strength of Partly Saturated Soils." *Geotechnique*, 1986, 36(3): 453-456.
- [3] Rassam, D. W. and F. Cook. "Predicting the Shear Strength Envelope of Unsaturated Soils." *Geotechnical Testing Journal*, 2002, 25(2): 215-220.
- [4] Guan, G. S., H. Rahardjo, et al. "Shear Strength Equations for Unsaturated Soil under Drying and Wetting." *Journal of Geotechnical and Geoenvironmental Engineering*, 2010, 136(4): 594-606.
- [5] Mendoza, C. E., J. E. Colmenares, et al. Stiffness of an Unsaturated Soil Mechanics. *Advanced Experimental Unsaturated Soil Mechanics*. A. Tarantino, E. Romero and Y. J. Cui. Trento, A. A. Balkema Publishers, 2005, 199-204.
- [6] Mendoza, C. E. and J. E. Colmenares. Influence of the Suction on the Stiffness at Very Small Strains. *Proceedings of the Fourth International Conference on Unsaturated Soils*. G. A. Miller, C. E. Zapata, S. L. Houston and D. G. Fredlund. Arizona, ASCE, 2006.
- [7] Nyunt, T. T., E. C. Leong, et al. "Strength and Small-Strain Stiffness Characteristic of Unsaturated Sand." *Geotechnical Testing Journal*, 2011, 34(5).
- [8] Tami, D., H. Rahardjo, et al. "Characteristics of Scanning Curves of Two Soils." *Soils and Foundations*, 2007, 47(1): 97-108.
- [9] Liu, Q., et al. Automatic soil water retention test system with volume change measurement for sandy and silty soils. *Soils and Foundation*, 2012, 52(1): 368-380.
- [10] Aversa, S. and M. V. Nicotera. "A Triaxial and Oedometer Apparatus for Testing Unsaturated Soils." *Geotechnical Testing Journal*, 2002, 25(1): 3-15.
- [11] Lauer, C. and J. Engel. A triaxial device for unsaturated sand — New Developments Unsaturated Soils: *Experimental Studies*. T. Schanz, Springer Berlin Heidelberg, 2005, 93: 301-314.
- [12] Cabarkapa, Z. and T. Cuccovillo. "Automated Triaxial Apparatus for Testing Unsaturated Soils." *Geotechnical Testing Journal*, 2006, 29(1): 21-29.
- [13] Padilla, J. M., W. N. Houston, et al. An Automated Triaxial Device for Unsaturated Soils. *Proceedings of the 4th International Conference on Unsaturated Soils*. Arizona, ASCE, 2006, 1775-1786.
- [14] Li, X. S. Modelling of Hysteresis Response for Arbitrary wetting/drying Paths. *Comput. Geotech*, 2005, 32, No. 2, 133–137.
- [15] Ng, C. W. W., L. T. Zhan, et al. "A New Simple System for Measuring Volume Changes in Unsaturated Soils." *Canadian Geotechnical Journal*, 2002, 39: 757-764.
- [16] Goto, S., F. Tatsuoka, et al. "A Simple Gauge for Local Small Strain Measurements in the Laboratory." *Soils and Foundations*, 1991, 32(1): 169-180.
- [17] Ladd, R. S. "Preparing Test Specimens Using Undercompaction." *Geotechnical Testing Journal*, 1978, 1(1): 16-23.
- [18] Ho, D. Y. F. and D. G. Fredlund. "A Multistage Triaxial Test for Unsaturated Soils." *Geotechnical Testing Journal*, 1982, 5: 18-25.

Monitoring Program and Dilapidation Survey for Grouting of Karst Cavities

Hasan A. Kamal and Hassan J. Karam
Kuwait Institute for Scientific Research, Kuwait

ABSTRACT

A total of eight ground-surface subsidence were detected in a residential suburb. The subsurface failure cases in the suburb were investigated in detail after their development. Results of the investigations indicated that the geological profile in this suburb consists of overburden soil which is underlain by limestone bedrock. It was concluded that raveling of the overburden soil into the underlying Karst cavities was the main cause of ground-surface subsidence development. Filling the Karst cavities with cementitious grout was chosen as a treatment measure for the cavity problems. Before and during the grout works for filling the Karst cavities, continuous monitoring of elevations in some selected points at critical locations were considered an essential tool to detect any slight movement or change that may be evaluated and considered a warning for larger movements or cavity and ground-surface subsidence formations. The continuous monitoring program was based on two major elements; dilapidation survey of selected high risk locations and the measurement of water levels for determining water fluctuations. Dilapidation was achieved through topographical site surveys including houses, utilities and general surveys along with a set of pictures illustrating important features. Station points were set all over the site and their elevations were checked regularly. Regular periodic evaluation of elevations, water-table levels and crack-meter readings were used as tools to evaluate the impact of the grouting works. Status of existing structures was checked regularly using crack-meters along with water-table levels through available piezometers. This paper contains description of the conducted dilapidation and topographical survey. Results of the monitoring program of the grouting works and their impact on the ground-surface subsidence is also presented in this paper.

Keywords: subsidence; grout; Karst; soil; topographical

1. INTRODUCTION

A number of ground surface subsidence in the form of sinkholes of various sizes had been occurring in a residential suburb in State of Kuwait [1]. The first sinkhole of April 1989 (SH-1) was immediately backfilled with gravel, sand, and concrete. The occurrence of the second and third sinkholes during the same months led to the decision to evacuate more than 130 surrounding houses [2]. Extensive investigation studies had been conducted in this affected residential suburb in order to understand the causes of those sinkholes and recommend appropriate treatment methods [2]-[4]. The studies that included topographic and geophysical surveys, geological, and geotechnical investigations revealed the existence of underground Karst cavities within the Limestone bedrock underlying the overburden soil caused the sinkholes.

The studies also reported that the geological profile of this residential suburb consists of 35 to 40 m thick overburden soil comprising dense to very dense predominantly quartz sand, overlying the Karst limestone bedrock. The cause of the sinkholes had been attributed to the dissolution of the limestone bedrock and subsequent raveling of the overburden soil cover into the underlying Karst cavities.

Accordingly, treatment methods were recommended to minimize the recurrence of the sinkholes composing of filling the underground cavities by injecting cement grout at depths varying between 32 to 60 m in a pilot area and by

eliminating the possibilities of collapse of the upper level Karst cavities within the limestone bedrock [5].

The pilot area located in Sector A1 of the residential area classified as the evacuated area (Fig. 1), was divided into six treatment zones, TA1 to TA6, for sequential injection of grout according to these zones. In general terms, the grouting program work required performing dilapidation survey, drilling exploratory holes with in situ testing and sampling; designing a grout mix, and developing quality assessment program; filling in of deep limestone cavities using cement-based mortar; permeation grouting of remaining deep voids and fractured rocks using cement-based grout; drilling control holes at the end of grouting and overburden treatment.

In this paper, the monitoring program used during the treatment implementation methods is described. The continuous monitoring program focused on the impact of the treatment drilling and grouting works on the existing structures on the site, ground surface movement and fluctuation of water-table levels. The results are presented and discussed and conclusions are illustrated.

2. METHODOLOGY OF MONITORING PROGRAM

The purpose of the monitoring program is to monitor the potential impacts of drilling and grouting works for the implemented treatment methods on the existing structures and ground surface condition.

The monitoring program focused on the sinkholes and their behavior during and after the period of treatment

implementation works to detect impacts resulted from the treatment campaign. The following subsections describe the methods used for monitoring the treatment effects in the area under study.



Fig. 1 The six treatment zones, TA1-TA6, in the pilot area.

2.1 Dilapidation Survey

Dilapidation survey is a detailed record of land and buildings at a specific point in time. The survey started before implementing the treatment methods by describing the condition of the existing structures, indentifying any defects, and a schedule of pictures for existed defects.

Large numbers of pictures were taken including general views of the area, description and close up photos of some parts of the structures and utilities (Fig. 2). Detailed identification of location, date of picture taken, image number, and location on key map were also recorded for each photo.



Fig. 2. Dilapidation picture in area TA1.

2.2 Topographical Site Survey

At the beginning of the monitoring program, a site survey of the area under study was carried out. The output results of this part were drawings for locations of all existing buildings and facilities such as structures, fences, walls, roads, sidewalks, over and under-passes, gardens, open yards, trees, ditches, cannels, culverts and wells, services and related structures (both above and below ground) such as water mains, sewers and electricity and telephone poles. They were considered as the “As-Built” drawings.

The topographical survey concentrated mostly on regular recording of elevations inside and around the treated areas. Elevation points were distributed on the ground surface forming a grid of less than 50 m spacing, in addition to points selected in each housing unit. The readings were evaluated and recorded using a total-station surveying instrument. Any signs of undesired ground movement were detected and projected into maps and tables.

2.3 Crack Propagation

Crack-meters of an accuracy of 0.001 mm were used to record movements of selected elements (Fig. 3). Crack meters were located on site mostly on structures, around sinkholes and other sensitive areas suspected with occurring movement. A number of crack-meters were set on columns, slabs, and on structural joints on ground and upper floors. One crack meter was set on the asphalt close to the progressing sinkhole SH-1. Each crack-meter was identified by a label with all necessary information on the location and the structure on which it is set.

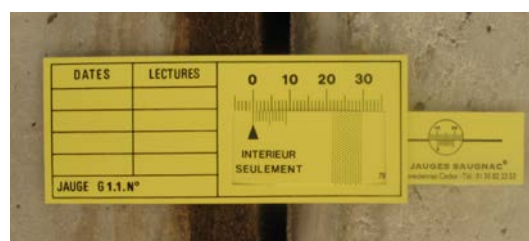


Fig. 3. A crack-meter sample used to monitor movements.

2.4 Water-Table Fluctuation

Evaluation and monitoring of groundwater and water-table levels is essential for detecting changes or risks, as the water content affects the soil behavior and stability. Three piezometers were drilled and were used to evaluate water-table levels since 2002. These holes were unfortunately blocked during the heavy work on site.

Three new holes were drilled and are currently being used to evaluate water-table levels and detect groundwater fluctuations. The locations of those new piezometers are shown in Fig. 4.

Fig. 4. Location of the piezometers.

2.5 Visual Inspection

A visual inspection was performed to document the common defects, whether they are due to demolishing, aging, construction etc. A sample picture of those defects is shown in Fig. 5. Those cases pictures reflect the general status and condition of the site and structures.



Fig. 5. Exposed corroded reinforcement and expelled concrete at the bottom of a ground floor column.

3 RESULTS AND DISCUSSION

In the monitoring program, effects of drilling and grouting on ground surface and existing structures were considered. The drilling is carried out with a drilling fluid, either water with polymer or air alone. The fluid has an ability to permeate more easily in the underground channel because it is light and not loaded with too much particles. Two types of grouting treatment were used which included mortar filling and permeation grouting.

Cavity filling with mortar was carried out as specified by the gravity process and, consequently, the pressure exerted during the process was not very high (~ 5 bars). Therefore, there was no change was recorded in any elevation consecutive to the cavity filling.

A higher pressure of 30 bars was applied during the permeation grouting stage. No perceivable changes in the elevation of the surveyed points were recorded as a result of the permeation grouting. This indicates that there was sufficient room for the voids to redistribute in the ground without impacting the surface.

Dilapidation pictures show general views of the area, description and close up photos of some parts of the villas, utilities, etc. Detailed identification of location, date of picture taken, image number, and location on key map are presented as well on each photo.

For the topographical survey, appraisal of the readings recorded for elevation points by a total station was monitored through any sign of ground undesired movement. Safety of the housing units is the most important issue before and after treatment implementation,

therefore; points are concentrated on the houses and around the old sinkhole locations. Fig. 6 shows the selected monitoring points and their elevations, and Fig. 7 shows sample records for selected points in zone TA3 which indicates no significant changes in the elevation of those points during the treatment implementation period.



Fig. 6. Coordinates and elevations of selected points.

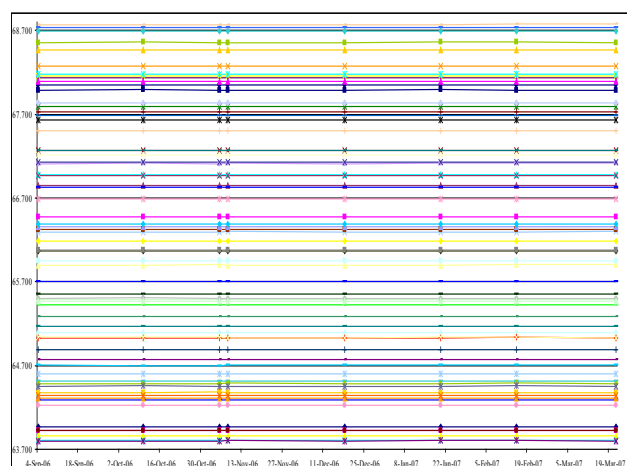


Fig. 7. Display of elevations for area TA3.

For crack propagation monitoring, a number of crack-meters were mounted at different locations and readings were taken periodically. Fig. 8 is a plan view of the treated area where the rectangular red marks and numbers show the locations of the mounted crack meters. Table 1 is a summary of the accumulated readings of a sample of crack-meters.

The amplitude recorded varies from 0 to 0.5 mm for the typical cracks and 0-3 mm for the dilatation joints. It may be said that these recorded data are expected and could be attributed exclusively to the thermal effect. The readings showing the more significant displacements are recorded along the dilatation joints at upper floor during the wintertime when thermal effect is measured. The crack meters have confirmed the fact that there was no impact recorded from the general survey.

For the water-table level monitoring, the ground water and its effect on the soil is of real importance in evaluating the treatment method. The water-table level was targeted since

few years before the treatment implementation. Table 2 lists sample reading for the water-table level for the new piezometers. In general, slight rise in the water-table level was observed during the treatment implementation campaign.



Fig. 8. Locations of crack meters.

Table 1. Summary of Crack-Meter Readings

No.	Min. (mm)	Max. (mm)	Difference (mm)	Location			
				Zone (TA)	Unit	Floor	Unit Adjacent
1	0.50	2.70	2.20	3	9	1st	11
2	-3.00	1.00	4.00	3	9	1st	11
3	1.50	1.50	0.00	1	19	GF	-
4	0.00	1.50	1.50	1	19	1st	17
5	2.00	2.00	0.00	1	23	1st	25
6	0.50	1.00	0.50	1	23	1st	-
7	0.00	0.00	0.00	3	Asphalt	-	-
8	0.00	0.00	0.00	3	A2	1st	-
9	0.50	0.50	0.00	3	8	1st	-
10	0.00	0.00	0.00	3	11B	1st	13
11	0.00	0.00	0.00	2	35	1st	36
12	0.00	0.00	0.00	4	63	GF	65
13	-0.50	-0.50	0.00	4	3B	1st	-
14	0.00	0.00	0.00	4	5	1st	7
15	-0.50	-0.50	0.00	1	40	1st	42

Table 2: Sample records for the water-table level

Date	Hole 7	Hole 11	Hole 18
	Net Depth of Water (m)	Net Depth of Water (m)	Net Depth of Water (m)
20/11/2006	27.89	29.91	30.48
17/12/2006	27.91	29.92	30.52
02/01/2007		29.89	30.51
03/02/2007		29.86	30.50
20/02/2007	27.77	29.79	30.51
21/02/2007	27.70	29.9	30.61
25/03/2007		29.84	30.60
14/4/2007	27.82	29.88	30.64
15/11/2007	27.86	29.91	30.64
31/1/2008	27.83	29.86	30.62

4 CONCLUSION

The outputs of the pilot area under study mainly depends on the geological profile encountered and the type of the works, the porosity of the sand. The thickness of the overburden is of 30 meters which here is sufficient to allow redistribution of the porosity during the grouting and the rock grouting took place with a rather limited pressure.

The monitoring and surveying campaign represented an important essential component of the treatment implementation process of underground cavities in the area under study. The area was intensively treated using two different types of rock treatments; cavity filling and permeation grouting.

Regular periodic evaluation of elevations, water-table levels and crack-meter readings were used as tools to evaluate the impact of the drilling and grouting works of the treatment implementation program. During the treatment implementation using low and high pressure grouting, no alarming signs or significant move or settlement was observed due to the grouting works. It signify that sufficient space for the voids were available to redistribute in underground level without impacting the surface.

Continuous monitoring was recommended to be achieved by regular evaluation of elevations in selected higher risk locations reporting any alarming changes, along with monitoring water-table levels through available piezometers in order to assure the safety of the area and its occupants.

5 ACKNOWLEDGMENT

The authors would like to express their appreciation to the Public Authority for Housing Welfare (PAHW) and Kuwait Institute for Scientific Research (KISR) for their facilitative and support of this project.

6 REFERENCES

- [1] Abdullah W., and Kamal H., "Characterization of Desert Karst Terrain in Kuwait and the Eastern Coastline of the Arabian Peninsula," in Proc. Sinkholes and the Engineering and Environmental Impacts of Karst, San Antonio, Texas, 2005, pp. 35-45.
- [2] Al-Rifa'iy A., "Land subsidence in the Al-Dhahar residential area in Kuwait: a case history study," Q. J. of Eng. Geol. London, vol. 23, 1990, pp. 337-346.
- [3] Abdullah W., Mollah M., Al-Mutairi N., Al-Fahad F., and Mussallam H., "Evaluation and Treatment of Underground Cavities at Al-Dhahar Area", Vol. II, Subsurface Exploration Study in the Al-Dhahar Area, 1998, Final Report, Kuwait Institute for Scientific Research.
- [4] Al-Mutairi N., Eid W., Abdullah W., Misak R., Mollah M., Awany R, Al-Fahad F., "Evaluation and Treatment of Underground Cavities at Al-Dhahar Area", Vol. I, Evaluation and Treatment of Subsurface Conditions at Al-Dhahar Area, 1998, Final Report, Kuwait Institute for Scientific Research.
- [5] Kamal H., and Abdullah W. "Sinkholes' Detection in a Residential Area in the State of Kuwait", Arabian Journal for Science and Engineering, accepted, 2011.

Numerical analysis of soil nail walls under seismic condition for different geometry of the nails

Siavash Zamiran¹, Hamidreza Saba²

¹Department of Civil Engineering, Science and Research Branch, Islamic Azad University, Iran,
zamirans@gmail.com

²Amirkabir University of Technology, Tehran, Iran

ABSTRACT

In this paper, numerical simulations of soil nail walls under simulated vibrational input have been carried out and the results are compared with the function of soil nail walls under ordinary statistical loading. The behaviour of geometry of nails is mentioned under static and seismic analysis. The analysis is carried out with finite difference software called FLAC. The results are prepared as lateral displacement of the walls and normalized maximum tensile forces for nails. These results can demonstrate the behaviour of external and internal resistance of soil nail walls under dynamic and static analysis. The deformation of wall under static and dynamic manner varies in a wide range. On the other hand tensile loads that are produced in nails under static manner are namely 50% less than the dynamic manner.

Keywords: Soil Nail Walls, Dynamic Analysis, Finite Deference Analysis, FLAC

1. Introduction

The behaviour of soil nail walls is the function of soil and nail strength parameters, geometry of wall, etc. Numerous investigations are carried out to demonstrate the static and seismic behaviour of soil nail walls. However, with respect to different parameters that influence on the behaviour of these systems, more investigations about soil nail walls are necessary. In this research, deferent geometry parameters of soil nail walls are mentioned in static and dynamic behaviour of soil nail systems. The strength function of the wall under Manjil earthquake acceleration (Iran 1990) loading condition is mentioned by wall deformation and vibration of soil nail forces.

Mohr-Coulomb constitutive model is selected for numerical study in this research. The strength function of nail and shotcrete is considered as elastic. The finite deference software called FLAC is used for numerical study. FLAC can model the interaction between nail and soil properly as static and dynamic analysis in the soil medium.

2. Verification of the finite deference model

Thompson and Miller (1990) investigated the Seattle's first nailed walls. For this vertical soil nail wall, nails were mostly installed at 1.8m spacing horizontally and vertically. The nail length is 10.7m, except for the length of the top row which is 9.8m. The diameter of the drilled holes is 203mm. Nail bars are installed at an inclination of 15 degrees, though the first row on the high wall was installed at 20 degrees to avoid utilities. A typical section of the high wall is shown in Fig. 1, [1]. In this research, the stability of this soil nailed vertical cut is analysed by FLAC.

Thompson and Miller measured the highest nail forces by inclinometer and calculated the values by the finite-element method. A comparison of maximum nail forces in measured values and finite-element calculations in each row is shown in Fig. 2 with the values that gain from finite deference method, FLAC. The results show reliable convergence among calculated values, FEM and FDM. Fig. 3 shows the reliable convergence of the places that maximum tensile loads occur through the nail lengths.

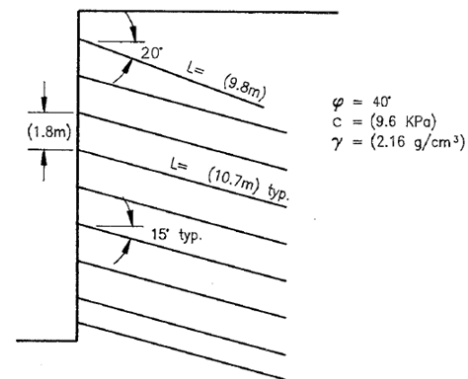


Fig. 1) Typical section of Seattle's wall

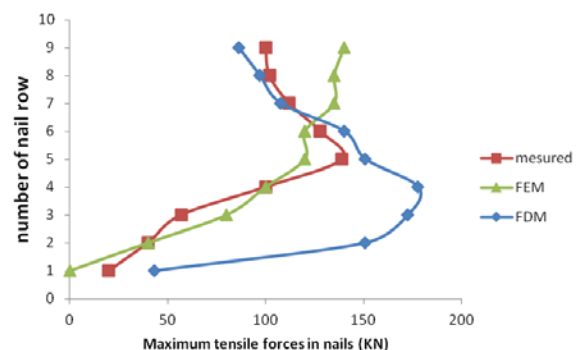


Fig. 2) Comparison of maximum nail forces

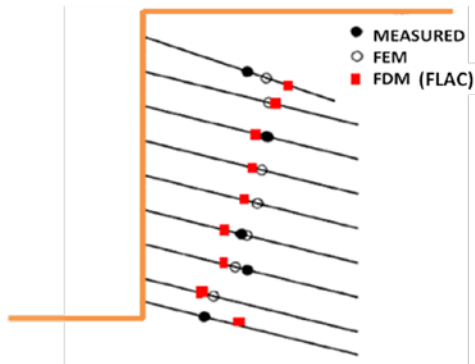


Fig. 3) The places that maximum tensile loads occur through the nail lengths.

3. Numerical modeling considerations

In this study, a 9 meters soil nail wall is considered. 9 rows of nails with the length of 9 meters are selected for stabilizing the wall. The selection of the first geometry is based on the FHWA design booklet. Nail inclination in the first model is 10 degrees, and the horizontal and vertical space between nails is 1 meter.

Static equilibrium of the wall is obtained with step by step excavations. Soil mass is modelled in the software by popular constitutive model, Mohr-Coulomb. Elastic modulus of soil is 20 Mpa; Poisson's ratio is 0.3; unit weight is 17.6 kN/m³; internal friction angle is 31 degree and cohesion strength is 20 Mpa.

Cable structural element is used to modeling the nail. Also beam structural element is used to simulate shotcrete in numerical models.

According to some researchers like Wei and Cheng, a thin layer of material with a thickness of 4.0 mm surrounding the nail is used to model the shearing zone between the nail and the soil that is shown in Fig. 4. [2]

The shear stiffness of the shear zone (grout), Kg, can be estimated in Eq. (1).

$$Kg = \frac{2\pi G}{10 \ln(1 + 2tD)} \quad (1)$$

Where G is shear modulus of the shear zone and identical to shear modulus of soil. D is drilled hole diameter and t is annulus thickness of the shear zone and is considered equal to 0.004 m. The shear zone cohesive strength (slider) per unit length can be estimated as Eq. (2).

$$cg = \pi c(D + 2t) \quad (2)$$

Where c is cohesion of soil. Shear zone friction angle is nearly equal to friction angle of surrounding soil.

The properties of cable and beam elements for nail and shotcrete is shown in Table 1.

Earthquake loading is based on shear stress history that is applied to the base of the model. Quiet boundary should adjust for bottom boundary of the model. To avoid rejection of the earthquake wave to the model, free field boundary is used for left and right side of the model.

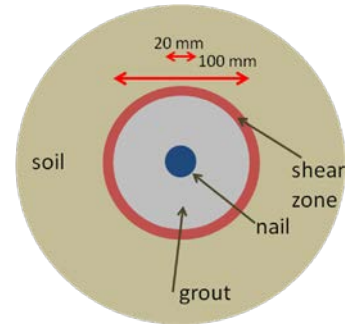


Fig. 4) Idealization of the soil nail system.

Table 1) Cable parameters for simulation of nail

parameter	value	unit
Nail diameter		mm
Drill hole diameter	100	mm
Young's modulus of nail	200	GPa
Young's modulus of grout	22	GPa
Young's modulus of grouted nail	29.12	GPa
Annulus thickness	0.004	m
Nail shear zone cohesive strength	6.28	kPa
Nail shear zone friction angle	31	degree
Nail shear stiffness of the shear zone	219.6	MPa
Compressive yield strength of the grouted nail	30	MPa
Tensile yield strength of the grouted nail	30	MPa
density of grouted nail	2200	kg/m ³
Young's modulus of shotcrete	24.5	Gpa
Poisson's ration of shotcrete	0.3	
Density of shotcrete	2200	kg/m ³

Rayleigh damping is used in the seismic analysis of soil nail walls. Rayleigh damping is specified in FLAC with the parameters f_{min} in Hertz (cycles per second) and ξ_{min} . For geological materials, damping (ξ_{min}) commonly falls in the range of 2 to 5% of critical; for structural systems, 2 to 10% is representative. [3]

The idea in the dynamic analysis is to adjust f_{min} of the Rayleigh damping so that it is 3:1 range coincides with the range of predominant frequencies in the problem. The "predominant frequencies" are neither the input frequencies nor the natural modes of the system, but a combination of both. The idea is to try to get the right damping for the important frequencies in the problem. [4]

Numerical distortion of the propagating wave can occur in a dynamic analysis as a function of the modeling conditions. Both the frequency content of the input wave and the wave-speed characteristics of the system will affect the numerical accuracy of wave transmission. Kuhlemeyer and Lysmer (1973) show that for accurate representation of wave transmission through a model, the spatial element size, l, must be smaller than approximately one-tenth to one-eighth of the wavelength associated with the highest frequency component of the input wave [5]. In this research, finite element mesh size is considered for accuracy of wave transmission.

4. Influence of nail length in static and dynamic analysis

The numerical model that is described in part 3 is used to investigate the influence of nail length during static and dynamic analysis. The only exception is the variation in nail length that is varied in 5, 7, 9 and 11 meters. The dynamic analysis is carried out by Manjil velocity history. Fig. 5 shows lateral displacement of the wall during static and dynamic analysis. As shown in Fig. 5 displacement behaviour defers in the static and dynamic analysis. The maximum displacement of the wall in the dynamic analysis happens on the top of the wall. Other than the displacement of the wall in the static analysis happens on the one-third height of the wall. The variation of nail length effects on the stability of the wall in the dynamic analysis more than static stability of the wall. Fig. 6 shows maximum normalized axial force of the nails during static and dynamic analysis. As shown in Fig. 6 mobilized axial force behaviour nearly is same in the static and dynamic analysis.

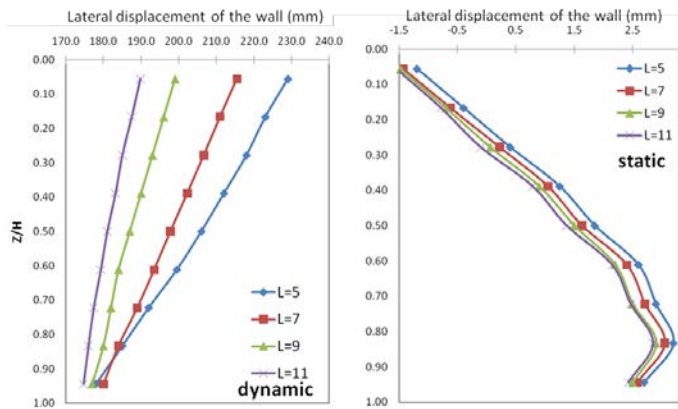


Fig. 5) Lateral displacement of the wall in static and dynamic analysis

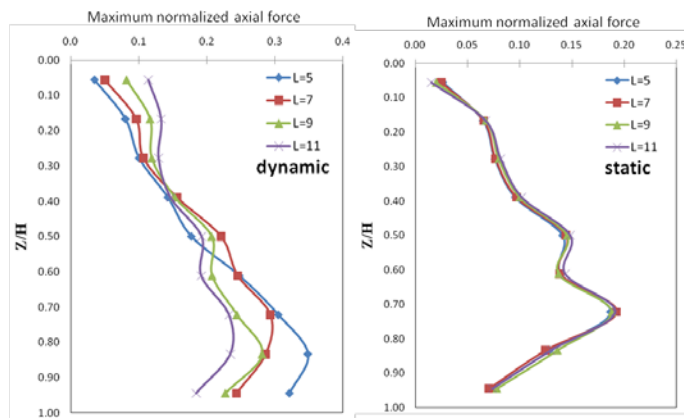


Fig. 6) Maximum normalized axial force of the wall in static and dynamic analysis

6. Influence of nail inclination angle in static and dynamic analysis

The same numerical model is used to investigate the influence of nail inclination angle during static and dynamic analysis. The only exception is the variation in nail inclination angle that is varied in 0, 10, 20 and 30 degrees. The dynamic analysis is carried out by Manjil velocity history. Fig. 7 shows lateral displacement of the wall during static and dynamic

analysis. As shown in Fig. 7 displacement behaviour defers in the static and dynamic analysis. The maximum displacement of the wall in the dynamic analysis happens on the top of the wall. Other than the displacement of the wall in the static analysis happens on the one-third height of the wall. As shown in Fig. 7 minimum displacement of the wall occurs in the models with 10 and 20 degrees of inclination angle. Otherwise walls with 0 and 30 degrees of inclination angle have larger displacement. This situation shows that there is an optimum inclination angle in both static and dynamic manners between 10 and 20 degrees.

Fig. 8 shows maximum normalized axial force of the nails during static and dynamic analysis. As shown in Fig. 8 there is similar function of nail axial force in both dynamic and static analysis. In the upper nails, lower inclination of nails causes lower axial force. Otherwise in the downer nails, lower inclination of nails causes higher axial force.

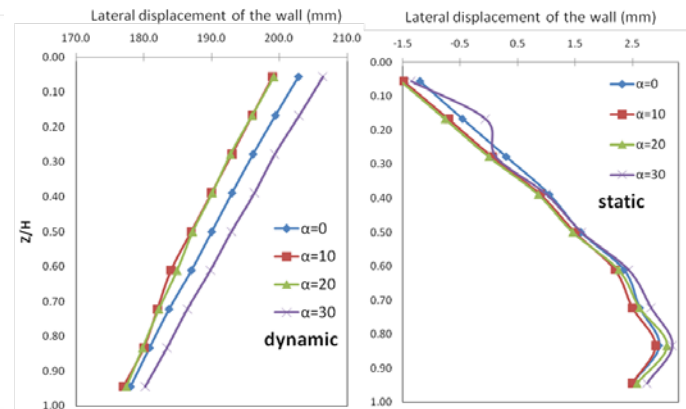


Fig. 7) lateral displacement of the wall during static and dynamic analysis

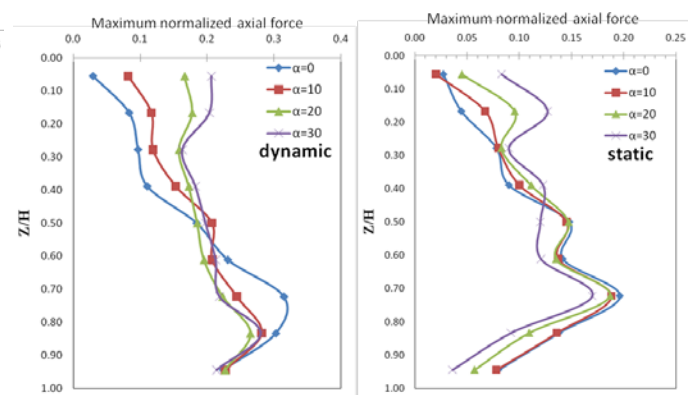


Fig. 8) Maximum normalized axial force of the nails during static and dynamic analysis.

7. Conclusion

In this paper static and dynamic analysis is carried out on a soil nail model. Manjil earthquake acceleration is selected for the dynamic analysis. Two main geometry parameters of soil nail walls are considered for comparison between dynamic and static behaviour of soil nail walls: nail length and nail inclination angle. The results are gained by lateral displacement of the wall and maximum axial nail force.

These two parameters can explain the external and internal response of the system respectively.

The results show that the maximum displacement of the wall in the dynamic analysis happens on the top of the wall. Other than the displacement of the wall in the static analysis happens on the one-third height of the wall. The variation of nail length effects on the stability of the wall in the dynamic analysis more than static stability of the wall. In the upper nails, lower inclination of nails causes lower axial force. Otherwise in the downer nails, lower inclination of nails causes higher axial force.

Reference

- [1] Thompson, S. R., and Miller, I. R., "Design, Construction and Performance of a Soil Nailed wall in Seattle, Washington", Design and Performance of Earth Retaining Structures, Geotechnical Special publication, No. 25, ASCE, 1990, pp. 629-643.
- [2] W.B. Wei, Y.M. Cheng, "Soil nailed slope by strength reduction and limit equilibrium methods", Computers and Geotechnics journal, 2010.
- [3] Biggs, J. M. Introduction to Structural Dynamics. New York: McGraw-Hill, 1964.
- [4] Itasca Consulting Group, Inc. , "Fast Lagrangian Analysis of Continua in 2 Dimensions, FLAC2D" Dynamic Analysis, 2005, pp 13
- [5] Kuhlemeyer, R. L., and J. Lysmer. "Finite Element Method Accuracy for Wave Propagation Problems," J. Soil Mech. & Foundations, Div. ASCE, 1973, 99(SM5), 421-427.

SHEAR STRENGTH IMPROVEMENT OF FIBROUS PEAT DUE TO CONSOLIDATION PRESSURE

Vivi Anggraini¹, Nurly Gofar² and Bujang bin Kim Huat¹

¹Universiti Putra Malaysia, ²Universiti Teknologi Malaysia, Department of Civil Engineering, Malaysia

ABSTRACT

A major problem related to construction on peat deposit is the low shear strength of the soil. However previous researches indicated that the shear strength could increase upon consolidation and hence some improvement methods have been developed to increase the bearing capacity of the peat deposit by utilizing consolidation pressure. The aim of this paper is to evaluate the shear strength improvement of fibrous peat due to consolidation. The initial undrained shear strength was obtained from vane shear test in-situ. Subsequently, samples were prepared under several consolidation pressures: 50 kPa, 100 kPa, 150 kPa, and 200 kPa. The shear strength of the samples was obtained by triaxial compression test under unconsolidated undrained condition. The results showed that there is an increase in shear strength due to application of consolidation pressure as compared to the initial shear strength obtained by field vane shear test. However, the ratio of strength increase for peat in this study is only 0.06 which is much lower than previously published data may be due to high fiber content.

Keywords: Peat Soil, Shear Strength, Unconsolidated Undrained, Consolidation Pressure

1. INTRODUCTION

Initial stability of construction on peat is the most critical problem due to low undrained shear strength of peat in normally consolidated state and hence low bearing capacity of foundation soil. Conventional solution is to replace the poor soil by suitable imported fill materials. This practice is naturally very expensive. In addition, there must be an environmentally acceptable location to waste excavated soil within an economically acceptable haul distance [1]. This method also need maintenance work related to long term settlement and horizontal movement [2]. The fill induces a consolidation pressure, thus increases the shear strength of the peat. Laboratory compression tests have to be performed in order to estimate and take into account the rate of increase of undrained shear strength as a function of consolidation and subsequent densification of peat. The undrained shear strength of peat is typically determined by vane shear in the field and undrained triaxial compression test in the laboratory. The ratio of increase can be applied to the in-situ shear strength obtained from vane shear test. Therefore the thickness of fill for each stage can be increased as a consequence of the increase in shear strength.

Based on his study, Magnan [2] suggested a ratio of shear strength increase due to increase in overburden pressure of 0.5 for peat soil. Furthermore, Edil and Wang [3] collected normalized undrained strength (c_u/σ'_{3c} or c_u/σ'_{1c}) as a function of organic content for all peat and organic soil. The study showed that fibrous and amorphous peat presents no perceptible differences and gives an average

normalized undrained strength to consolidation pressure of 0.59 with most of the data falling between 0.5 and 0.7. These c_u/σ'_v values appear unusually high compared to the typical values for inorganic clays that lay between 0.2 and 0.25. Chen and Tan [4] found that the ratio of shear strength increase due to consolidation for clay obtained from Klang, Malaysia is 0.25. However, there is no published data for the ratio of shear strength increase for peat found in Malaysia.

2. EXPERIMENTAL PROGRAM

2.1 Physical and Chemical Properties

The peat sample for this study was obtained from Pontian, Johor. Observation made in the location showed that the peat is categorized as deep peat with thickness of more than 5 m. Ground water table exists at depth less than 1 m at the time of sampling, thus samples were taken from depth of 1 to 2 m from ground surface. The samples were taken below water table; thus it is expected to be in fully saturated condition. Visual identification showed that the peat is dark brown, very soft, and contains a large amount of fiber. Plant structures such as roots are easily recognizable from the soil. Long, slender roots, and rootlets are identified as the remaining of forest vegetation. The texture is coarse and may results in large permeability.

In-situ measurement of water content was not possible. Thus, sufficient care was taken during the sampling of the peat in order to maintain the natural water content. The preliminary identification of the soil was made based on the index properties and classification tests. Index properties include the determination of water content, specific gravity, bulk unit

weight, and the initial void ratio. The summary of index properties is presented in Table 1.

Table 1. The summary of index properties of peat soil in West Malaysia peat [5]

Parameters	Results	Published data (ranges)	
Natural moisture content (%)	608	200-700	[6]
Specific Gravity (Gs)	1.47	1.30-1.90	[6]
Bulk unit weight (kN/m ³)	10.02	8.30-11.50	[6]
Dry unit weight(kN/m ³)	1.4	1.00-1.65	[7]
Initial void ratio (e ₀)	8.92	3.00-15	[6]
Acidity (pH)	3.24	3.00-4.5	[8]

The average natural water content obtained from laboratory tests is 608 %which indicates that the peat has a high water-holding capacity. This value is within the range obtained by previous researches for peat soil in West Malaysia. The average specific gravity obtained using kerosene on pycnometer test is 1.47 and it is within the range for fibrous peat. The initial void ratio is 8.92 which is within the range given by Huat [6]. The average unit weight of the peat is 10.02 kN/m³ which give a bulk density of 1.002 Mg/m³ which is also within the range given in Table 1. The dry unit weight of the peat is 1.40 kN/m³ and it is slightly less than predicted by Al-Raziqi et al. [7]. From the information indicated above, the unit weight of the peat in this study is close to the unit weight of water; hence in-situ effective stress is very low and the void ratio of the peat is very large.

The void ratio also includes the volume of gas generated during decomposition process. The average void ratio for the 51 fibrous peat obtained in Pontian is 8.92 and this is within the range given for West Malaysian peat (3 -15) presented by Huat [6]. Peat in Malaysian Peninsular is known to have low pH value and the acidity tends to decrease with depths. The test results showed that the average pH value of the fibrous peat used in this study is 3.24 which is in the lower side of the range published for Malaysia peat (3.0 - 4.5) presented by Muttalib et al. [8].

2.2. Classification

The peat in this study was classified based on the degree of humification [9] and the organic and the fiber content. The von Post scale is based on the appearance of soil water that is extruded when a sample of the soil is squeezed in the hand and the soil is classified based on Table 2. When the test was performed on the samples used in this study, brown water comes out from the soil and the soil left in hand has a large amount of fiber; thus the peat can be classified as fibrous peat with H4 degree of decomposition according to von Post scale. The organic content the peat is 97 % which is quite high but within the range of published data on peat soil found in Malaysia.

The ash content is 3 %. The fiber within the range of published data on peat soil content of 90 % is considered very high as compared to published data around the world (Table 2) but this is a typical fibrous peat obtained in West coast of Peninsular Malaysia [6],[8]. The average percentage of particle passing from 0.063 mm sieve is 2.37 % which show that the soil contain a large amount of fiber. The summary of the classification tests results is presented in Table 2.

Table 2. The summary classification test results in West Malaysia peat [5]

Parameters	Results	Published data (ranges)	
Von Post humification of peat	H4	H1-H4	[9]
Organic content (%)	97	> 90	[6]
Ash content (%)	3	< 10	[6]
Fiber content (%)	90	> 20	[10]

2.3 In-situ Shear Strength

The in-situ shear strength was obtained by field vane test conducted at depth of 1 and 2 m in the site. The average initial undrained shear strength of peat obtained by the field vane shear test is 10.10 kPa which is comparable to the range of the undrained shear strength of peat in West Malaysia (3-15 kPa) and Sarawak (10 kPa) as indicated by Huat [6]. The peat is identified as very sensitive to disturbance with sensitivity of 5.64, which is also within the range of published data 4-12 [7].

2.4 Remoulded Sample Preparation

Remolded sampler preparation equipment was used for soil sample preparation. The remolded sampler was designed as shown in Fig 1. Soil sample was put into the remolded sampler equipment. The plate with some holes was placed at the bottom of the sampler to drain water from the sample. The soil sample was then loaded using steel load platen. Pressure was applied on the steel load platen by compressed air. The air pressure supply was from the centralized air compressor and pressure panel system in the geotechnical engineering laboratory, Universiti Teknologi Malaysia (UTM). Air pressure applied to the soil sample was based on the maximum applied pressure needed for remolded sample preparation. The pressure for the remolded sample was adjusted from the dial gauge attached on the top of the load platen. Samples were placed into 152 mm diameter remolded sampler equipment under various consolidation pressure; consist of 50 kPa, 100 kPa, 150 kPa and 200kPa. The consolidation was assumed completed when there is no more water draining out from the bottom of the remolded sample equipment.



Fig. 1: Remoulded sampler preparation equipment

3. RESULT AND DISCUSSION

3.1 Shear Strength Obtained from Triaxial Test

Twelve sets of test containing three soil samples were conducted on Triaxial test apparatus under Unconsolidated Undrained (UU) condition [11]. In this project the tests were carried out in the triaxial apparatus on the specimens of diameter 38 mm and height 76 mm and were subjected to cell pressures of 50 kPa, 100 kPa, 150 kPa, and 200 kPa. The results obtained from the triaxial test were used to analyze the shear strength parameters of fibrous peat soil from Pontian by determining the undrained cohesion (c_u) and the angle of internal friction (ϕ_u). The test results were used to evaluate the increase of shear strength due to consolidation pressure.

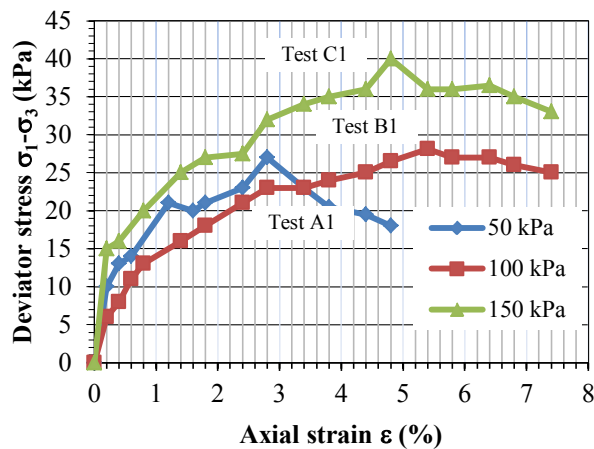


Fig. 2: Typical curve for deviator stress versus axial strain for set 1

Fig.2 shows the relationship between principal stress difference ($\sigma_1 - \sigma_3$) and the axial strain from triaxial test under UU condition and cell pressures 50 kPa, 100 kPa and 150 kPa. The results show the increase in shear strength up to a peak value and then the reduction in shear strength. The maximum deviator stress for sample A1 with cell pressure of 50 kPa is 26.7 kPa, for sample B1 with cell pressure 100 kPa is 28.10 kPa and for sample C1 with cell pressure 150 kPa is 40.6 kPa. Axial strain at maximum deviator stress is less than 5 % which shows that the sample is of high quality.

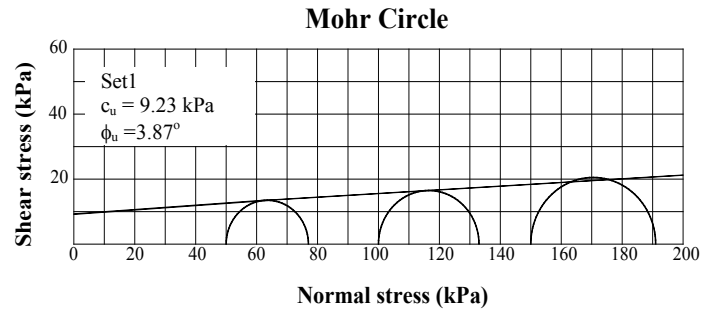


Fig.3: Shear stress at failure (τ_f) versus normal stress (σ_n)

Fig.3 shows the typical Mohr circle obtained from set 1 sample for each specimen. The shear stress at failure (τ_f) is plotted against the corresponding normal stress (σ_n). A line that the best fit through the corresponding points of the graph is drawn and results in the cohesion of 9.23 kPa and the angle of internal friction (ϕ_u) of the failure envelope is 3.87°. The angle of internal friction obtained from the test is very close to 0.

The angle of internal friction (ϕ_u) for undrained cohesion is theoretically equal to zero but the range of 0°-5° is acceptable due to the presence of air in the specimen resulted in perfect undrained condition is maintained during the test [12]. Shearing induced by unconfined compression, unconsolidated undrained compression and consolidated undrained compression did not result in the formation of a plane of failure. The shear strength obtained from unconfined compression tests increased from a negligible value to about 25 kPa, while the envelope of Mohr circles of total stress for consolidated undrained tests was inclined at an angle of 5° [13]. Air being highly compressible and reduces air voids proportionally with higher lateral pressures, thereby reduce the total volume of the specimen under testing.

Table.3 shows the summary of triaxial compression test results for each test set under unconsolidated undrained condition in terms of undrained cohesion and undrained angle of internal friction. The average cohesion is 10.44 kPa and the average angle of internal friction is 3.60°.

Table 3. Result of Triaxial Compression Test

Test	Parameter of Shear Strength	
	Cohesion c_u (kPa)	Angle of friction ϕ_u °
Set 1	9.23	3.87
Set 2	6.36	4.11
Set 3	10.84	3.91
Set 4	12.5	3.21
Set 5	15.74	2.2
Set 6	8.98	4.34
Average	10.44	3.6

3.2 Effect Consolidation on Strength

The effect of consolidation pressure on the shear strength of peat is studied by performing triaxial compression test under UU condition on samples prepared under different consolidation pressure. In this study, consolidation pressure of 50 kPa, 100kPa, 150 kPa and 200 kPa were used. The results are shown in Table 4. The average undrained shear strength from test results from four different consolidation pressures are 13 kPa, 15.66 kPa, 21 kPa and 21.66 kPa.

Table 4.Result summary of shear strength under consolidation pressure

Consolidation Pressure (kPa)	Sample	Initial cell pressure	c_u	c_u Average (kPa)
50	A1	50	11	13
	A2		13	
	A3		15	
100	B1	100	11	15.66
	B2		16	
	B3		20	
150	C1	150	19	21
	C2		21	
	C3		23	
200	D1	200	19	21.66
	D2		21	
	D3		25	

It can be seen from Table 4 that the undrained cohesion (c_u) increases as the consolidation pressure increases. These data, together with the in-situ shear strength obtained by vane shear test were used to develop the correlation between the shear strength and the consolidation pressure. The relationship between the strength of peat under consolidation pressure and initial shear strength and the effective consolidation pressure can be expressed in the following form:

$$c_{u(mod)} = c_{u(initial)} + \lambda \sigma_{vc} \quad (1)$$

where:

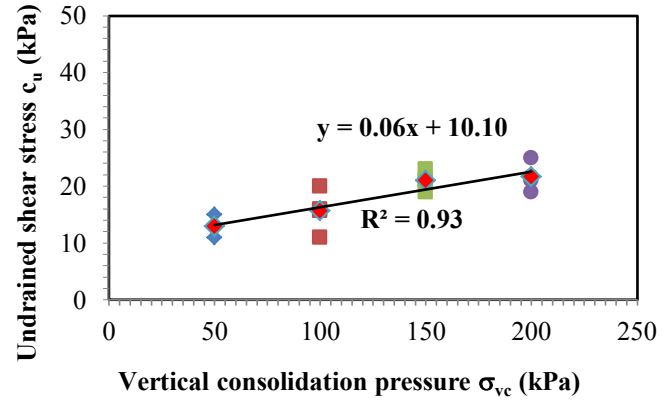
$c_{u(mod)}$ = Shear strength under consolidation pressure,

$c_{u(initial)}$ = Initial shear strength obtained from vane shear test,

λ = Ratio of strength increase, and

σ_{vc} = Consolidation pressure.

This relationship is illustrated in Fig 4. It can be observed that there is not much scattered of data obtained from the test indicated by R squared value of 0.93 which gives a strong relationship between undrained shear strength and consolidation pressure.

Fig 4. Undrained shear stress c_u versus vertical consolidation pressure σ_{vc}

The equation relating the shear strength and the effective consolidation pressure for fibrous peat used in this study is:

$$C_{u(mod)} = 10.10 + 0.06 \sigma_{vc} \quad (2)$$

It can be seen from Eq.(1) that the initial undrained shear strength of the peat soil predicted by the equation agrees with average undrained shear strength obtained by field vane shear test. The initial value of undrained shear strength from vane shear in the field ($c_{u(mod)}$) is 10.10 kPa. The increase in undrained shear strength is small, however, very small as compared to the published data may be due to the anisotropy of the fiber in the soil. The relationship shown in Eq.(2) allows the estimation of strength allows a means of estimation strength gain due to consolidation pressure and to get the modified shear strength $c_{u(mod)}$ of the peat. The result proves that the shear strength value can be improved when subjected to consolidation pressure; even though the increase is small.

4. SUMMARY AND CONCLUSION

The study on the shear strength improvement of peat due to application of consolidation pressure was conducted on this project for fibrous peat sampled from Pontian, Johor. The objective was to find the ratio of strength increase with the increase in consolidation pressure. Consolidation pressure applied to the soil prior to Triaxial Compression Test under Undrained Unconsolidated condition have the effect of increasing the shear strength obtained from the test. The

average value of undrained shear strength from test results are 13 kPa, 15.66 kPa, 21 kPa and 21.66 kPa under consolidation pressure of 50 kPa, 100kPa, 150 kPa, and 200 kPa respectively. The relationship derived from the Triaxial test results shows an initial undrained shear strength equal to that obtained from field vane shear test ($c_u = 10.10$ kPa). However, the ratio of strength increase is only 0.06 which is much lower compared to previously published data may be due to high fiber content.

NOTATION

The following symbols are used in this paper:

c	Cohesion value of soil
c'	Apparent cohesion in terms of effective stress
c_u	Undrained shear stress
$c_{u(mod)}$	Undrained shear stress modify
$c_{u(initial)}$	Undrained shear stress initial
ϕ	Angle of internal friction soil
ϕ_u	Undrained angle of internal friction soil
τ_f	Shear stress at failure of soil
τ	Shear stress of soil
ε	Strain
σ_n	Normal stress due to applied vertical load
σ'_v	Effective vertical consolidation pressure
σ_{vc}	Vertical consolidation pressure
σ_1	Major principal stresses
σ_2	Intermediate principal stresses
σ_3	Minor principal stresses
σ'_{1c}	Effective major principal stresses
σ'_{3c}	Effective minor principal stresses
$\sigma_1 - \sigma_3$	Principal total stress difference
$\sigma'_1 - \sigma'_3$	Principal effective stress difference
σ_1 / σ_3	Principal effective stress ratio
σ'_1 / σ'_3	Principal total stress ratio
λ_{cu}	Coefficient ratio of undrained shear strength
λ	Coefficient ratio of shear strength

REFERENCES

- [1] Jarrett, P.M. Geoguide 6. Site Investigation for organic soils and peat. JKR: Document 20709-0341-95. Institut Kerja Raya Malaysia.1995.
- [2] Magnan, J (1994). Construction on peat. State of the art in France. *Advances Understanding and Modelling the mechanical behaviour of peat*, ed. Den Haan et al.,1994.pp.369-380.
- [3] Edil, T. B. and Dhowian, A. W. At-rest Lateral Pressure of Peat Soils. *Conf. on Sedimentation and Consolidation Model*, ASCE, San Fransisco.1981.pp 411-424.
- [4] Chen, C.S & S.M Tan. Some engineering properties of soft clay from Klang Area.2nd Int.Conference on Advances in Soft Soil Engineering and Technology.2003. pp.79-87, 2-4 July 2004, Putra Jaya.
- [5] Nurly Gofar and Yulindasari Sutejo. Properties of Fibrous Peat. Senai (Malaysia): *Seminar Penyelidikan Kejuruteraan Awam (SEPKA)*, Universiti Teknologi Malaysia (UTM).2005.
- [6] Huat, B. B. K.. *Organic and Peat soil engineering*. Univ Putra Malaysia Press.2004.ch.3 and ch.4.
- [7] Al-Raziqi, A. A., Huat, B. B. K. and Munzir, H. A. Potential Usage of Hyperbolic Method for Prediction of Organics Soil Settlement. In *Proceeding of 2nd International Conferences on Advances in Soft Soil Engineering and Technology*, ed. Huat et al., Putrajaya Malaysia.2003. pp 439-445.
- [8] Mutallib, A.A.,J.S. Lim, M.H. Wong & L.Koonvai.Characterisation, distribution and utilization of peat in Malaysia. In *Proceedings International Symposium on Tropical Peat Land*, 2001. pp.7-16, Kuching, Sarawak.
- [9] von Post, L. Sveriges Geologiska Undersoknings Torvinventering Och nagre av Dess Hittills Vunna Resultat, Sr.Mosskulturfor. Tidskr 1.1992. pp.1-27.
- [10] Molenkamp,F. Investigation of requirements for plave strain elements tests on peat. In *Advances in Understanding and Modeling the Mechanical behaviour of Peat*, ed. Den haan et al. Balkema.1994.
- [11] Head, K.H. *Manual of Soil laboratory Testing*, Volume 3. Pentech Press, London.1981.
- [12] Mandal J. N. *Soil Testing in Civil Engineering*.A.A Balkema. Rotterdam.1995.
- [13] Hanrahan, E. T. An Investigation of Some Physical Properties of Peat. *Geotechnique*, London, England, 4(2).1954.pp.108-123.

Factors affecting the stability analysis of earth dam slopes subjected to reservoir drawdown

T. Souliyavong¹, C. Gallage¹, P. Egodawatta¹ and B. Maher²

¹Queensland University of Technology, Australia. ²South East Queensland Water, Australia

ABSTRACT

The drawdown of reservoirs can significantly affect the stability of upstream slopes of earth dams. This is due to the removal of the balancing hydraulic forces acting on the dams and the undrained condition within the upstream slope soils. In such scenarios, the stability of the slopes can be influenced by a range of factors including drawdown rates, slope inclination and soil properties. This paper investigates the effects of drawdown rate, saturated hydraulic conductivity and unsaturated shear strength of dam materials on the stability of the upstream slope of an earth dam. In this study, the analysis of pore-water pressure changes within the upstream slope during reservoir drawdown was coupled with the slope stability analysis using the general limit equilibrium method. The results of the analysis suggested that a decrease in the reservoir water level caused the stability of the upstream slope to decrease. The dam embankment constructed with highly permeable soil was found to be more stable during drawdown scenarios, compared to others. Further, lower drawdown rates resulted in a higher safety factor for the upstream slope. Also, the safety factor of the slope calculated using saturated shear strength properties of the dam materials was slightly higher than that calculated using unsaturated shear strength properties. In general, for all the scenarios analysed, the lowest safety factor was found to be at the reservoir water level of about 2/3 of drawdown regime.

Keywords: reservoir drawdown, earth dam, slope stability, hydraulic conductivity, unsaturated shear strength.

1. INTRODUCTION

Rapid drawdown of storage water level is a critical design mechanism for most reservoirs particularly in situations such as post earthquake damage or piping events. Rapid drawdown of water levels in reservoirs with earth dams can lead to failure of the upstream slope. A number of such failures are listed by Morgenstern [8].

Prior to reservoir drawdown, steady-state seepage conditions can be assumed within the dam materials and the hydrostatic pressure resulting from the reservoir water helps to partially stabilize the upstream dam slope. The reservoir drawdown could establish undrained conditions and development of excess pore-water pressures that could dissipate with time (transient seepage). These scenarios could cause instability and consequently lead to failure of the slope. The instability of the slope during a reservoir drawdown can be affected by a range of factors including drawdown rates, slope inclinations and soil properties of earth dam materials [1], [2], [7], [8], [11]. Transient seepage and the instability of the earth dam slope induced by rapid drawdown can be affected by the unsaturated properties of dam materials such as hydraulic conductivity functions and unsaturated shear strength.

This paper presents the analytical outcomes of an earth dam during a drawdown regime. The analysis undertaken

considered the effects of the saturated and unsaturated properties of dam materials, the saturated hydraulic conductivity of the dam embankment soil, and the drawdown rate of the reservoir on the upstream slope stability of the dam. The influences of pore-water pressures or transient seepage on the slope stability were analysed by coupling SEEP/W [5] with a stability analysis tool, SLOPE/W [6]. The outcomes generated from this analysis could form the basis for determining a safe drawdown rate and a safe drawdown level for some Queensland earth dams.

2. MODEL DAM AND MATERIAL PROPERTIES

The dam configuration shown in Fig. 1 and material properties listed in Table 1 were used in this study. The dimensions, material zones and soil properties of the dam cross section were chosen to be generic representatives of existing earth dams in Queensland, Australia. For this, geometries and material properties of a range of earth dams were studied based on the data provided by the Queensland Bulk Water Supply Authority (Seqwater); the dam owner in South East Queensland.

Apart from basic geometry and material properties, the soil water characteristic curves (SWCCs) form a critical part in the analysis of the earth dam with unsaturated material conditions. Since the measured SWCCs for the dam materials were not available, SWCCs (see in Fig. 2) assigned for the clay core, embankment soil and sand filter were estimated from their grain-size data [4].

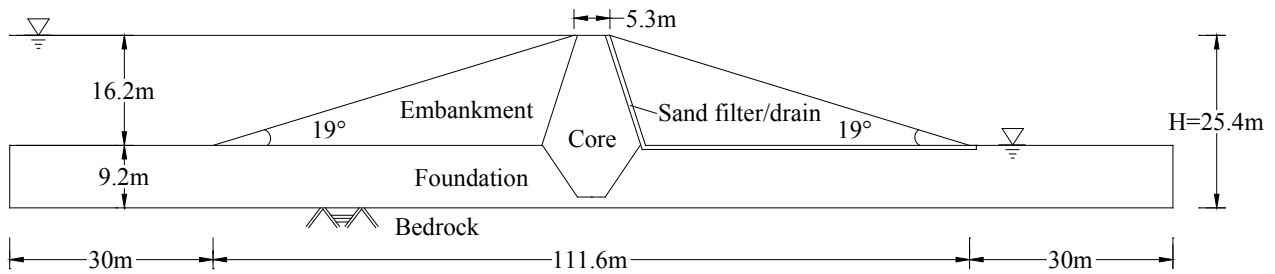


Fig. 1. Geometry and material zones of the earth dam

Table 1. Properties of the earth dam materials

Material properties	Symbol	Unit	Value			
			Clay core	Embankment	Sand filter	Foundation
Saturated hydraulic conductivity	k_{sat}	m/sec	1.2×10^{-10}	3×10^{-7}	4.9×10^{-3}	3.9×10^{-6}
Saturated unit weight	γ_{sat}	kN/m ³	20	20.5	20.5	19.2
Effective cohesion	c	kPa	7	18	0	21
Effective friction angle	ϕ	degree	29	30.8	34	32.3
Volume compressibility coefficient	M_v	m ² /kN	18×10^{-5}	12×10^{-6}	0	12×10^{-6}
Volumetric water content	θ_w	m ³ /m ³	0.4	0.35	0.31	0.33
Diameter at 10% passing on a grain-size curve	D_{10}	mm	0	0.06	0.3	0.05
Diameter at 30% passing on a grain-size curve	D_{30}	mm	0.004	0.6	1	0.5
Diameter at 60% passing on a grain-size curve	D_{60}	mm	0.07	0.8	1.6	1.2
Liquid limit	LL	percent	51	30	0	31
Plastic limit	PL	percent	20	16	0	13

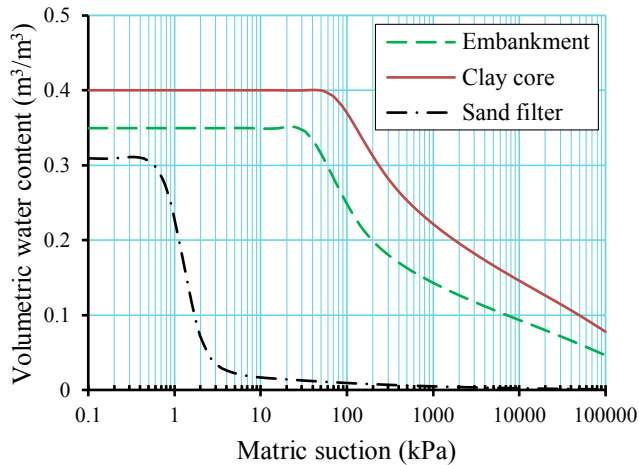


Fig. 2. SWCCs for dam materials

3. MODELLING AND ANALYSIS

The analysis undertaken includes transient seepage analysis to determine pore-water pressures during drawdown and stability analysis of the upstream dam slope. Both analyses were conducted in automatic coupled mode. For the analysis, each material zone was assumed to be homogeneous and isotropic.

3.1 Seepage Analysis

The finite element (FE) method available in SEEP/W was employed to simulate 2-D steady-state and transient seepage in the earth dam before and during the rapid drawdown, respectively. This program solves the general governing differential equation for two-dimensional seepage shown in Eq. (1) using FE method.

$$\frac{\partial}{\partial x} \left(k_x \frac{\partial H}{\partial x} \right) + \frac{\partial}{\partial y} \left(k_y \frac{\partial H}{\partial y} \right) + Q = \frac{\partial \theta}{\partial t} \quad (1)$$

where H = total head, k_x = hydraulic conductivity in the x -direction; k_y = hydraulic conductivity in y -direction; Q = applied boundary flux; θ = volumetric water content; and t = time.

The FE mesh shown in Fig. 3 was used to replicate the dam structure. The mesh was defined as an unstructured pattern of quadrilateral and triangular elements with 3 and 4 nodes respectively. Prior to drawdown simulation, the dam was analysed for steady-state seepage conditions, assuming the reservoir water level at the dam crest (elevation of 25.4 m) is a critical situation. For this, the boundaries ABC and DE in Fig. 3 were defined as constant total head boundaries with the values of 25.4 m and 9.2 m respectively. The corresponding saturated hydraulic conductivity values

tabulated in Table 1 were assigned for the defined material zones in the dam.

Outcomes of the steady-state seepage analysis were then used to define the initial pore-water pressure distribution for the transient seepage analysis. To simulate the reservoir drawdown numerically, the upstream boundary (ABC) condition was defined by a total head function. This type of boundary will allow the user to define the change in total head as a function of time. For transient seepage analysis, the total head of the upstream boundary was decreased linearly from 25.4 m to 9.2 m at different rates of the reservoir drawdown. During the drawdown, the conditions of the dam materials could change from saturated to unsaturated and thereafter the saturated hydraulic conductivity of each dam material should be defined as a function of suction. Since the laboratory measured hydraulic conductivity functions of the dam materials were not available, Fredlund and Xing's method [3] was used to estimate the hydraulic conductivity function of each material using its SWCC and saturated hydraulic conductivity. The transient seepage analysis of the dam during reservoir drawdown will give the variation of pore-water pressures with drawdown time throughout the FE mesh.

3.2 Stability Analysis

To analyse the stability of upstream slope of the dam during drawdown, the GLE method available in SLOPE/W was employed. In this study, the entry (DEFG) and exit (ABC) method was used to define trial failure surfaces (as shown in Fig. 4) for each simulation scenario. The software analyses all the trial surfaces to obtain a critical surface with a minimum safety factor for each drawdown scenario.

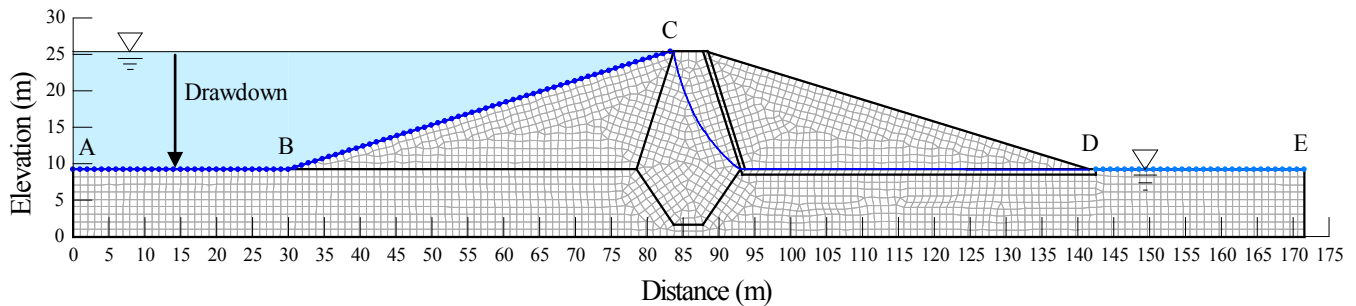


Fig. 3. Finite element mesh of the earth dam used in SEEP/W

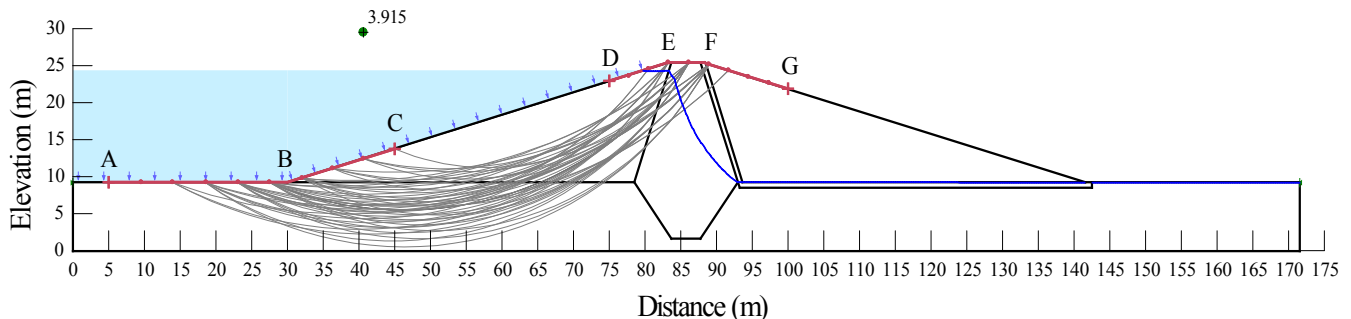


Fig. 4. Model dam and some of trial failure surfaces used in stability analysis in SLOPE/W

Since the drawdown of reservoir produces unsaturated conditions in the dam materials such as clay core, embankment and sand filter, the unsaturated shear strengths of the materials were taken into account. In this analysis, Eq. (2) proposed by Vanapalli et al. [10] was used to estimate the unsaturated shear strength of the materials. Therein, effective shear strength parameters and SWCCs were needed to estimate the unsaturated shear strength of the materials.

$$\tau = c' + (\sigma_n - u_a) \tan \phi' + (u_a - u_w) \left[\left(\frac{\theta_w - \theta_r}{\theta_s - \theta_r} \right) \tan \phi' \right] \quad (2)$$

where τ = shear strength of saturated/unsaturated soil; c' = effective cohesion of unsaturated soil; σ_n = total normal stress on the failure plane of the soil; ϕ = effective friction angle; $(u_a - u_w)$ = matric suction in the failure plane of the soil; u_a = pore-air pressure in unsaturated soil; u_w = pore-water pressure; θ_w = volumetric water content; θ_s = saturated volumetric water content; and θ_r = residual volumetric water content which can be assumed to be equal to 10% of θ_s .

In this study, pore-water pressure changes obtained from the transient seepage analysis were used for the stability analysis of the upstream dam slope at different stages of drawdown.

4. RESULTS AND DISCUSSIONS

4.1 Effects of Saturated Hydraulic Conductivity of Embankment Soil on the Slope Stability

To investigate the effects of saturated hydraulic conductivity (k_{sat}) of embankment soil on the stability of the upstream dam slope in terms of safety factor (FOS), the analysis

described in section 3 was repeated for different k_{sat} values of embankment soil (e.g., 3×10^{-3} , 3×10^{-5} , 3×10^{-7} , 3×10^{-9} m/s). For this, the reservoir drawdown rate of 1 m/day was used. It is reported that the common range of drawdown rate is from 0.5 to 1 m/day in dam engineering applications [9]. The SWCCs of the dam materials were used for the entire analyses. The results of the analyses are shown in Fig. 5.

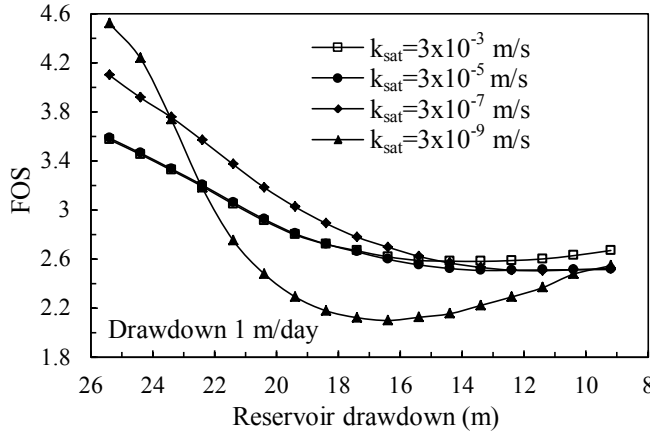


Fig. 5. Variation of FOS of upstream dam slope with reservoir drawdown and unsaturated soils.

As shown in Fig. 5, for a given k_{sat} of embankment soil, the FOS of the upstream slope of the earth dam decreases with the reservoir drawdown and reaches the lowest value when the reservoir is lowered about 1/2 to 2/3 of the adopted drawdown regime (16.2 m). The removal of the balancing hydraulic forces acting on the upstream slope due to the reservoir drawdown is the main reason for a decrease in the FOS of the slope. The temporary undrained condition within the dam created by the drawdown leads to a decrease in the shear strengths of the dam materials which, in turn, cause the FOS of the slope to decrease. As shown in Eq. (2), an increase in pore-water pressures causes a decrease in the shear strengths of the dam materials. The FOS of the slope increases slowly from its minimum value as the reservoir water is further drawn. When the reservoir level is reduced from 1/2 to 2/3 to the end of the drawdown regime, the shear strengths of the dam materials increase due to the pore-water dissipation. This has positive effects on the stability of the slope.

Saturated hydraulic conductivity (k_{sat}) of the embankment soil exerts a significant influence on the upstream slope stability during reservoir drawdown. It can be seen from Fig. 5 that during the early stages of drawdown (0 to 1/4 of drawdown regime) the upstream slope of the dam embankment constructed with low k_{sat} soil is more stable than that constructed with high k_{sat} soil. However, as the reservoir level decreases further, this behaviour changes by making the high k_{sat} embankment soil more stable than the low k_{sat} embankment soil. It was noted that the saturated zone (area below the phreatic surface) under the steady-state

seepage conditions is larger for the high k_{sat} embankment soil than the low k_{sat} soil. Since a high k_{sat} embankment soil allows water to penetrate deeper into the dam, the production of a larger saturated zone would be the primary reason for having the low FOS during the early stages of drawdown for the high k_{sat} embankment soil. The pore-water pressures in a smaller saturated area within the low k_{sat} soil may dissipate faster than that of a larger saturated area within the high k_{sat} soil and so an embankment slope with less excess pore-water pressures is more stable than that with more excess pore-water pressure or a larger saturated area. When the reservoir water level is decreased further (about 1/4 to the end of the drawdown regime), the difference between the areas of the saturated zone within the dam constructed with the low k_{sat} embankment soil and that within the high k_{sat} soil is of no consequence. Also, the pore-water pressure within the high k_{sat} embankment soil can dissipate faster than that within the low k_{sat} soil. As a result, at the given drawdown level, the shear strength of the high k_{sat} soil is larger than that of the low k_{sat} soil.

In this study, the effects of using saturated and unsaturated shear strength properties for the stability of the upstream slope during rapid drawdown of the reservoir were investigated. The pore-water pressures obtained from the transient seepage analyses conducted at the reservoir drawdown rate of 1m/day for different saturated hydraulic conductivity values of the embankment soil (e.g., 3×10^{-3} and 3×10^{-7} m/s) were used for stability analysis with saturated shear strength (τ_{sat}) and unsaturated shear strength (τ_{unsat}) properties of dam materials. Hydraulic conductivity functions and SWCCs were not considered for the calculations of saturated shear strengths of the dam materials.

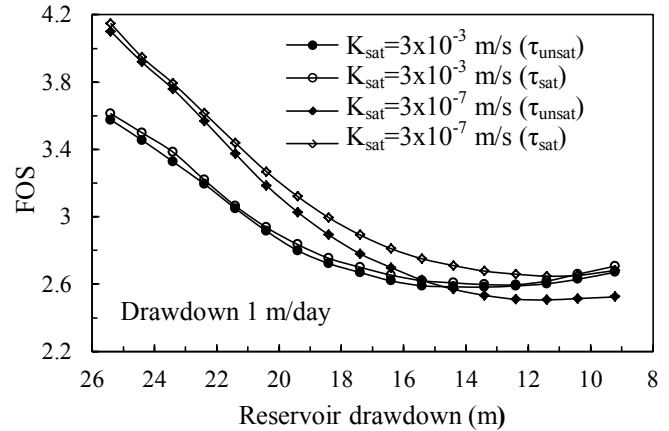


Fig. 6. Variation of FOS of upstream dam slope with unsaturated and saturated soils.

The results shown in Fig. 6 depict that the trend of the FOS variation of the upstream dam slope with saturated shear strength is similar to that observed for the dam materials with unsaturated shear strength. During the drawdown, the

slope stability calculated using saturated shear strength is slightly higher than that calculated using unsaturated shear strength. It is noted that the saturated (wetting) zone under the steady-state seepage is larger in the dam with unsaturated materials than that with saturated soils. Since the unsaturated materials allow water to penetrate deeper into the dam due to soil suction, the production of a larger wetting zone would be a primary reason for having the low FOS for the dam with unsaturated materials. The pore-water pressures in a smaller wetting zone within the dam with saturated materials may dissipate faster than that in a larger wetting zone within the unsaturated dam materials and so a dam with low pore-water pressures or smaller wetting zone is more stable than that with high pore-water pressures and larger wetting area. As a result, the upstream slope of saturated dam materials is more stable than that of unsaturated dam. However, it is noted that defining saturated conditions for the dam materials may lead to inaccurate results. In the real situation earth dam materials such as clay core, embankment and sand filter are not fully saturated even though the reservoir level is level to the dam crest.

4.2 Effects of Drawdown Rate on the Slope Stability

To investigate the effects of drawdown rate (R) on the stability of the upstream slope during the reservoir drawdown, the method of analysis described in section 3 was repeated for various drawdown rates (e.g., 8 m/day, 6 m/day, 2 m/day and 0.5 m/day). The results of the analysis are shown in Fig. 7.

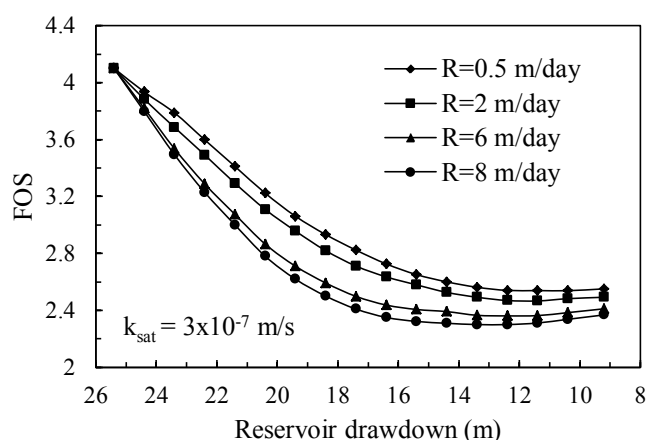


Fig. 7. Variation of FOS of upstream dam slope with different drawdown rates

As shown in Fig. 7, the FOS of the upstream slope of the dam increases as the drawdown rate decreases. The low drawdown rate allows more time for the pore-water pressure dissipation from the saturated zone within the dam. According to Eq. (2), the dissipation of pore-water pressure increases the shear strength of the dam materials. The pore-water pressure within the materials can reduce to a negative value (suction) during the dissipation process, and

consequently the slope stability increases. By contrast, the higher drawdown rate or rapid drawdown (e.g., 8 m/day) will not allow enough time for pore-water pressure dissipation. Therefore, the shear strength increase of the dam materials subjected to a higher drawdown rate is less than that of the materials at a lower drawdown rate.

5. CONCLUSION

The effects of saturated hydraulic conductivity of embankment soil and the drawdown rate of the reservoir on the stability of the upstream slope of an earth dam subjected to reservoir drawdown were investigated incorporating unsaturated soil properties. The following conclusions were drawn from this analysis:

- Stability (FOS) of the upstream slope of an earth dam decreases with the drawdown of the reservoir and reaches the minimum FOS at a reservoir water level of about 2/3 of the total drawdown height. Further decrease in the reservoir water level induces a gradual increase in the FOS of the upstream slope.
- During the drawdown of reservoir, the upstream slope of the earth dam constructed with highly permeable embankment soil is more stable than that of the dam with low permeable embankment soil.
- A low rate of reservoir drawdown increases the stability of the upstream slope of the earth dam.
- Throughout the drawdown regime, the stability of the upstream slope calculated using the saturated shear strength of the dam materials is slightly higher than that calculated using unsaturated shear strength.

6. ACKNOWLEDGMENT

The authors wish to acknowledge the Australian Agency for International Development (AusAID) for providing a scholarship for the first author's studies at Queensland University of Technology (QUT).

7. REFERENCES

- [1] Berilgen MM, "Investigation of stability of slopes under drawdown conditions," J. of Computers and Geotechnics, vol. 34, 2007, pp. 81-91.
- [2] Desai CS, "Drawdown analysis of slopes by numerical methods," J. of the Geotechnical Engineering Division, ASCE, 103 (GT7), 1977, pp. 667-676.
- [3] Fredlund DG and Xing A, "Equations for the soil-water characteristic curve," J. of Canadian Geotechnical Journal, vol. 31, 1994, pp. 521-532.
- [4] Fredlund MD, Wilson GW and Fredlund DG, "Use of the grain-size distribution for estimation of the soil-water characteristic curve," J. of Canadian Geotechnical Journal, vol. 39, 2002, pp. 1103-1117.

- [5] GEO-SLOPE International Ltd., Seepage Modeling with SEEP/W 2007: An Engineering Methodology (4th ed.). Alberta: GEO-SLOPE International Ltd., 2010.
- [6] GEO-SLOPE International Ltd., Stability Modeling with SLOPE/W 2007 Version: An engineering methodology (4th ed.). Alberta: GEO-SLOPE International Ltd., 2010.
- [7] Lane PA and Griffiths DV, "Assessment of Stability of Slopes under Drawdown Conditions," J. of Geotechnical and Geoenvironmental Engineering, vol. 126, 2000, pp. 443-450.
- [8] Morgenstern NR, "Stability charts for earth slopes during rapid drawdown," Geotechnique, vol. 13, 1963, pp. 121-131.
- [9] Pinyol NM, Alonso EE and Olivella S, "Rapid drawdown in slopes and embankments," Water Resources Research, vol. 44, Sept. 2008, pp. 1-22.
- [10] Vanapalli SK, Fredlund DG, Pufahl DE and Clifton AW, "Model for the prediction of shear strength with respect to soil suction," Canadian Geotechnical Journal, vol. 3, 1996, pp. 379-392.
- [11] Viratjandr C and Michalowski RL, "Limit analysis of submerged slopes subjected to water drawdown," Canadian Geotechnical Journal, vol. 43, 2006, pp. 802-814.

Lateral stress induced due root-water-uptake in unsaturated soils

Mu'azu Mohammed Abdullahi¹ and Nazri Bin Ali²

¹Department of Civil Engineering and Built Environment

RAZAK School of Engineering and Advanced Technology,

Universiti Teknologi Malaysia, 54100 Kuala Lumpur Campus, Malaysia.

²Department of Geotechnics and Transportation, Faculty of Civil Engineering, Universiti Teknologi Malaysia

81310 UTM Skudai, Johor Bahru, Johor, Malaysia.

Email: ¹muazu@ic.utm.my, ²nazriali@utm.my

ABSTRACT

A two-dimensional (2-D) lateral stress was modeled as a result of matric suction change caused by vegetative induced moisture transfer. The negative pore-water pressures are estimated through governing partial differential equations for unsaturated soils. The results of the of simulated root water uptake are used as an input for the prediction of 2-D lateral stress in a stress-deformation analysis in an uncoupled manner. The soil is allow to expand and contract free laterally, as the as water is being abstracted from the soil. A mature Lime tree located on a Boulder clay sub-soil for period covering a full spring/summer drying period was used as a case study. The result shows interdependence of lateral and vertical stress generated resulting from root water-uptake.

Key words: *Unsaturated soils, numerical, water-uptake, simulation, stress-deformation, experimental.*

1. INTRODUCTION

When a material is compressed in one direction, it usually tends to expand in the other two directions perpendicular to the direction of compression, this phenomenon is known as the Poisson effect. The coefficient of lateral stress is a measure of the magnitude of the Poisson effect. In general soil mechanics, the deformation of soil matrix is analyzed as a result of increase in applied load, whereas in groundwater field, the soil deformation is studied due to extraction of groundwater. In both cases, a soil displacement takes place, because pore volume decreased [1]. Withdrawal of water by plant roots results in change in water pressures and moisture content in the soil. Soil settlement occurs whenever there is an increase in effective confining stress. In prediction of soil movement two fundamental stages are generally involved; an assessment of the changes in moisture conditions and the knowledge of the volumetric strains induced by these change. A horizontal and vertical distribution of roots determines the dispersal of root water-uptake [1]-[2]

This paper employed two-dimensional axi-symmetrical finite element approach to solve the transient partial coupled flow and stress-deformation equations. The study was based on case study of mature single lime tree on a Boulder Clay as reported by [3], with the following objectives; to employ two-dimensional axi-symmetrical finite element approach to solve the transient partial coupled flow and deformation equations and to simulate the water-uptake and deformation. The capillary potential was estimate as a result of the root water-uptake was partial coupled to estimate the lateral and vertical

displacements as a result of vegetative induced matric suction changes.

2. THEORETICAL FORMULATIONS SOIL MOISTURE MOVEMENT

The first step is dealt with through the use of modified Richard equation [4]; two-dimensional axi-symmetric governing equation for unsaturated soils with sinks term:

$$\frac{\partial \theta}{\partial \psi} \cdot \frac{\partial \psi}{\partial t} = \frac{\partial}{\partial z} \left[K(\psi) \frac{\partial \psi}{\partial z} \right] + \frac{1}{r} K \frac{\partial \psi}{\partial r} + \frac{\partial}{\partial r} \left[K(\psi) \frac{\partial \psi}{\partial r} \right] + \frac{\partial K(\psi)}{\partial z} - S(\psi, r, z) \quad (1)$$

Where $K(\psi)$ is the unsaturated hydraulic conductivity, t is the time, r and z are the coordinate, θ is the volumetric moisture content and ψ is the capillary potential, $S(r, z)$ is the root water extraction function and r is the radial coordinate.

The root water-uptake extraction function is the sink term $S(\psi, z, r)$ in the Equation 1; for water-uptake in two-dimensional axi-symmetric form [5]. Comprising of vertical and radial components incorporating water stress function when soil moisture is limiting:

$$S(\psi, z, r) = \frac{4T}{z_r r_r} \alpha(\psi) \left[1 - \frac{z}{z_r} \right] \left[1 - \frac{r}{r_r} \right] \quad (2)$$

Where $\alpha(\psi)$ (dimensionless) is a prescribed function of the capillary potential referred to as water-stress function.

The numerical solution of Equation 1 was achieved via the finite element spatial discretization procedure and a finite-difference time-stepping scheme adopting particular Galerkin weighted residual approach. The parabolic shape functions and eight-node isoperimetric elements are employed [6].

3 GROUND DISPLACEMENT THEORETICAL FORMULATION

The second step is tackled through stress-deformation formulation considering unsaturated soil mechanics concept using ground water field concept. Constitutive relationships are to compliment governing flow equation, thus, providing additional relationship between deformation and stress state variables. A change in the negative pore-water pressure occurs as a result of root water-uptake and can be related to changes in soil volume through the use of constitutive relations. Swelling in the field occurs along the rebound curve at an overburden pressure. Shrinkage occurs along either a recompression curve or the virgin compression curve. While the soil is a normally consolidated clay with a consolidation behavior that can be described by;

$$de = C_r \ln \left(\frac{\sigma_v + \Delta\sigma_v - u_{wf}}{(\sigma_v - u_a) + (u_a - u_w)_e} \right) \quad (3)$$

Where de is the change of void ratio in the element, C_r is the re-compression index, σ_v is the vertical total stress, $\Delta\sigma_v$ is the change in the total vertical stresses, u_{wf} is the final pore water pressure, and $(u_a - u_w)_e$ is the matric suction equivalent [7].

4 DISCRETIZATION, BOUNDARY AND INITIAL CONDITIONS

The mesh consists of 8-noded isoperimetric linear strain quadrilateral elements. The entire finite element mesh consists of 1281 nodes and 400 elements; the axi-symmetric domain is shown in Figure 1. The mesh was configured to offer some refinement within the root zone area, since this is the region where the most significant moisture content variations were expected to occur. Spatial discretisation has been achieved via the finite element mesh shown in Figure 1.

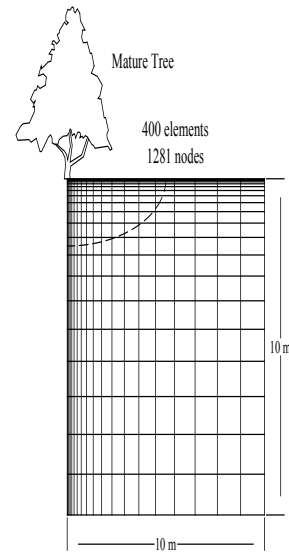


Figure 1 Finite element mesh (10 m x 10 m)

The simulation employs a time-step size of 21600 seconds, which was held constant for the entire period considered. The lower boundary of the domain and the far-field vertical and horizontal boundaries remained unconstrained (natural) throughout the simulation. The soil parameters are shown in Table 1 for Boulder clay. Based on the field observations provided by [3], the root zone of matured Lime tree is assumed to extend to a depth of 2.0 m and a radial distance of 5.0

Table 1 Parameters used in the analysis for Case I

Parameters	Values	References
k_s	10^{-6} m/s	[3]
T_a	5 mm/day	[3]
ψ_d	1500 kPa	[8]
γ	19.65 kN/m ³	[9]
e_0	1.25	[10]
C_r	0.023	[11]
μ	0.30	[12]
θ_r	0.1	[5]
θ_s	0.55	[5]
α	0.028	[5]
m	0.29	[5]
n	1.4	[5]
l	0.5	[5]

Where K_s is saturated hydraulic conductivity, T_a is actual transpiration rate, ψ_w is suction at wilting point, γ is unit weight of soil, e_0 is initial void ratio, C_r is re-compression index, μ is Poisson's ratio, θ_r is residual water content, θ_s is saturated water content, α is water stress, m is empirical shape fitting parameters, n is empirical shape fitting parameters and l is soil specific parameter generally assumed to be 0.5. The required soil moisture retention characteristics and unsaturated

hydraulic conductivity was simulated from the closed form equation developed by [13].

5 CASE STUDY ON MATURE LIME TREE ON BOULDER CLAY

The particular experimental data is based on the field measurements undertaken at a site located at Stacey Hall, Wolverton, England [14]. The case considered here relates to a single mature Lime tree, 15 m in height, located on a Boulder clay sub-soil. A uniform initial value of capillary potential of -17 cm was applied throughout the domain; representing an initial volumetric water content of 37.5 % which corresponds to a degree of saturation of approximately 93.75 % was used as an initial value of capillary potential. The initial value of capillary potential would be in steady state and the subsequent steady state value is applied to the simulation. The drying phase was represented via the application of the transpiration rate.

6 Results and Discussions

The graphs of variation of lateral and vertical ground displacement with depth at various lateral distances from Lime tree after 30 days are shown in Figs. 2 and 3. Lateral ground displacements are denoted with positive signs while the vertical ground displacements are denoted with negatives signs.

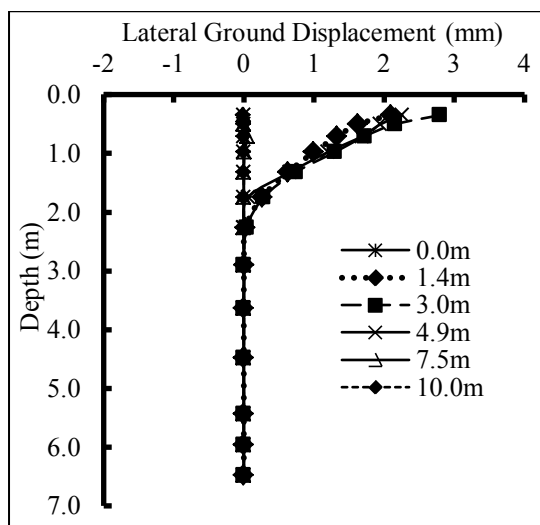


Fig. 2 Variation of lateral ground displacement with depth at various lateral distances from Lime tree after 30 days.

The vertical displacements seem to be larger in magnitude than the lateral displacements. For 30 days simulation 7.13 mm vertical ground displacement at zero lateral distance from the Lime tree was achieved compared to zero lateral ground displacement at the same lateral away from the lime tree. The result shows that there is no lateral ground displacement beneath the Lime tree.

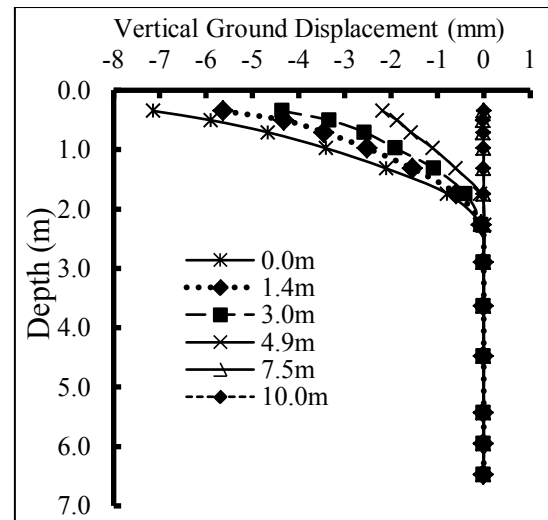


Fig. 3 Variation of vertical ground displacement with depth at various lateral distances from Lime tree after 30 days.

The variations of lateral and vertical ground displacement with depth at various lateral distances from Lime tree after 190 days are shown in Figs. 4 and 5. Fig. 4 show lateral ground displacement for 190 days simulation, a zero lateral displacement was recorded at zero lateral distance from the Lime tree. 18.67 mm, 19.34 mm and 6.76 mm lateral ground displacements at 1.4 m, 3.0 m and 4.9 m away from the lime tree respectively are simulated. At distance of 7.5 m and 10.0m away from Lime tree, -12.23 mm and -15.11 mm lateral ground displacements are simulated. This means at the distance of 7.5 m and 10.0 m away from the lime tree the effect of root water uptake is negligible. This shows that there is likely expansion instead of lateral shrinkage of the Boulder Clay.

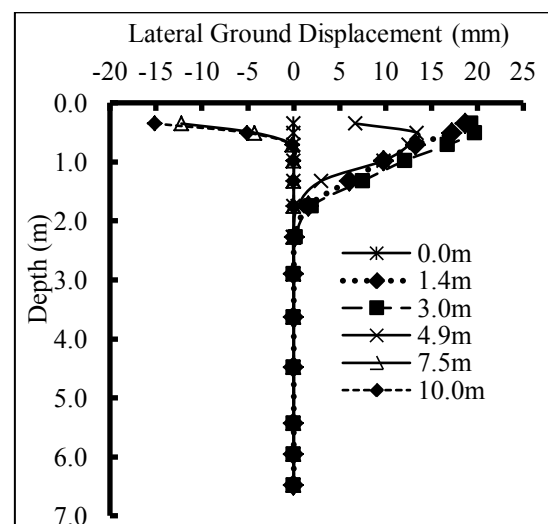


Fig. 4 Variation of lateral ground displacement with depth at various lateral distances from Lime tree after 190 days.

The vertical ground displacements are shown in Fig. 5. Vertical ground displacements -79.16 mm, -48.70 mm, -29.64 mm and -6.58 mm at 0.0 m 1.4 m, 3.0 m and 4.9 m away from the lime tree respectively are shown in Fig. 5. At distance of 7.5 m and 10.0m away from Lime tree, 6.70 mm and 6.11 mm vertical ground displacements are simulated. Similarly, its means at the distance of 7.5 m and 10.0 m away from the lime tree the effect of root water uptake is negligible. This shows that there is likely heave instead of vertical ground displacement of the Boulder Clay.

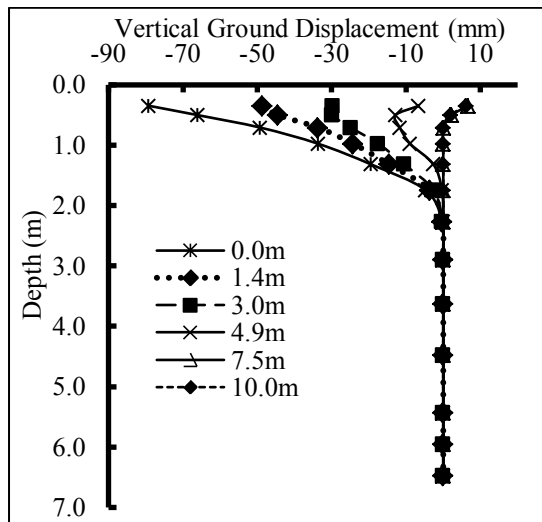


Fig. 5 Variation of vertical ground displacement with depth at various lateral distances from Lime tree after 190days.

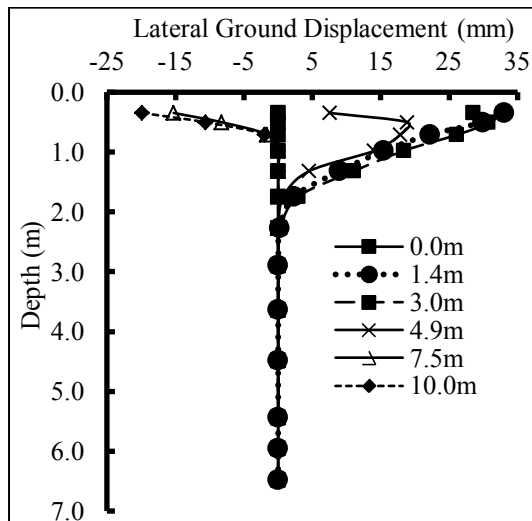


Fig. 6 Variation of lateral ground displacement with depth at various lateral distances from Lime tree after 270 days

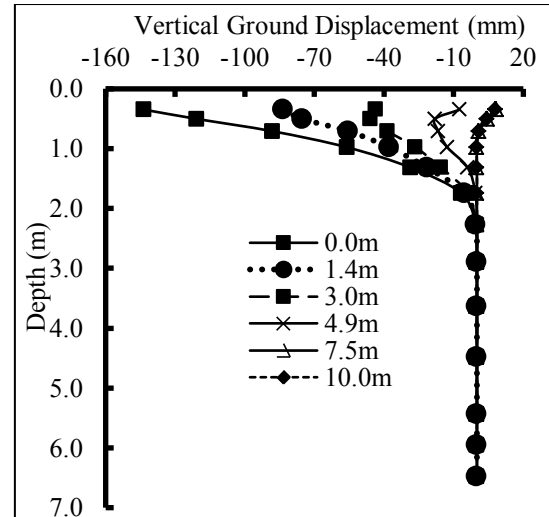


Fig. 7 Variation of vertical ground displacement with depth at various lateral distances from Lime tree after 270 days

Lateral and vertical ground displacements with depth at various lateral distances from Lime tree after 270 days are shown in Figs. 6 and 7. The sequence is the same with Figs. 2, 3, 4 and 5, both vertical and lateral displacement increase with an increase in elapse time and decreases with depth.

7. CONCLUSIONS

The approach proposed utilizes radial symmetry and a linear distribution of water extraction rate with both depth and radius. The results of the root water-uptake analysis are then used as an input for the prediction of displacements in a stress-deformation analysis in an uncoupled manner. A mature Lime tree located on Boulder clay sub-soil covering a full spring/summer drying period was considered for the case study. The majority of the moisture extraction occurred near the surface; likewise, the ground displacement occurred mostly near the ground surface. Ground displacement reduced significantly when the distance from the tree increased. Both lateral and vertical displacements are time and space dependent. The accuracy of the lateral ground displacement simulation depends on accurate determination of the magnitude of the Poisson effect.

8. REFERENCES

- [1] Ali N, Mu'azu MA, Kamarudin A (2010). 2-D Axi-Symmetric of Root Water-Uptake. The 8th International Conference on Geotechnical and Transportation Engineering, Sustainability in Geotechnical and Transportation Engineering, (GEOTROPIKA 2010) 1-3 December 2010. Kota kinabalu, Malaysia, pp. 1-5.
- [2] Mu'azu MA, Ali N, Ahmed K (2010). Rainfall evaluation of root water-uptake

- induced deformation, *ARPN Journal of Eng. and Applied Science*, 5(8): 32-41.
- [3] Biddle PG (1998). Tree Root Damage to Buildings, Pattern of soil Drying in Proximity to Trees on Clay Soils. 1st Edn., Vol. 2, Willow mead Publishing Ltd, Wantage, pp: 88-93.
 - [4] Richards LA (1931). Capillary conductance of liquids through porous mediums, *Physics* 1, pp. 318-333.
 - [5] Rees SW, Ali N (2006). Seasonal water uptake near trees: A numerical and experimental study. *Geomechanics and Geo-Engineering*, 1(2): 129-138.
 - [6] Zienkiewicz OC, Taylor RL (1989). The Finite Element Method. 4th Edn., Vol. 1, McGraw-Hill, USA., pp: 648.
 - [7] Fredlund DG, Rihardjo H (1993). Soil Mechanics for Unsaturated Soil. 1st Edn., John Wiley and Sons Inc., New York, pp: 346-373.
 - [8] Feddes RA, Kowalik PJ, Malink KK, Zaradny H (1976). Simulation of field water uptake by plants using a soil water dependent root extraction function. *J. Hydro*, 31: 13-26.
 - [9] Indraratna B, Fatahi B, Khabbaz H (2006). Numerical analysis of matric suction effects of tree roots." *Geotechnical Engineering*, 159(2):77 – 90.
 - [10] Samuels SG (1975). Some properties of the Gault Clay from Ely-Ouse Essex water tunnel, *Geotechnique*, 25(2): 239-264.
 - [11] Ng CWW (1998). Observed performance of multi-propped excavation in stiff clay, *J. Geoenv.*, 124(9): 889-906.
 - [12] Almeida MSS, Britto AM, Perry RHG (1986). Numerical modeling of a centrifuged embankment on soft clay, *Canadian Geotechnical Journal*, 23(20): 103-114.
 - [13] vanGenuchten MT (1980). A closed-form equation for predicting the hydraulic conductivity of unsaturated soils. *Soil Sci. Soc. Am. J.*, 44(5): 892-898.
 - [14] Bureau of Meteorology (2006) United Kingdom Bureau of Meteorology Meteorological Rainfall Data (1979-1980), Meteorological Office, Exeter, United Kingdom, 2006

The effect of pre-tensioned rock bolts on seismic behavior of urban tunnels

Farshad Fayyaz Jahani¹, Mohammad Sharifipour²
Department of Civil Eng., Univ. of Razi, Kermanshah, Iran

ABSTRACT

The distribution of seismic waves from the bedrock through the soil layers can cause severe damages not only to the structures on the soil surface but also to the subsurface structures. Previous studies have indicated the significant role of the site condition in modifying and changing the characteristics of the strong ground motion data. The importance of the pre-tensioned force of rock bolts has been recognized by many researchers. But the studies of seismic behavior of pre-tensioned rock bolts have been considered by fewer researchers. To investigate the impact of seismic behavior of pre-tensioned rock bolts on force redistribution and displacement around urban tunnels, a numerical analysis was carried out using finite element method. The analysis performed by considering three actual ground motion records representing seismic motions with low, intermediate and high frequency content. The results show that the pre-tensioned rock bolts have a minor effect on decreasing the total displacement on the urban tunnels in all seismic content and intermediate influence on the lateral force decrease.

Keywords: pre-tensioned rock bolts, seismic behavior, urban tunnels, finite element method

1. INTRODUCTION

When a roadway is introduced in a rock mass, its natural state of stress is disturbed locally as the rock mass attains a new state of equilibrium. These redistributed or induced stresses have a definite zone of effect within which rock failure may occur, creating a zone of disturbed or failed rock which should be supported [1]. In urban subway, rock bolts have been introduced in recent years and the mechanism of rock bolting has been studied by a great many scientists [2]. Consideration of earthquake ground motions, the way they propagate through the earth, their characteristics description at a certain location and methods for incorporating this information into engineering designs have been the subject of considerable research and interest so far. The energy released from a source mechanism will travel in the form of seismic waves through the rock formation where some energy absorption takes place. The seismic waves will be reflected and refracted as they approach the zone of special interest. Numerous studies on different earthquakes where site amplification caused substantial damage and collapse of many buildings are available (Romo and Seed 1986). Observations made after the destructive earthquakes have shown a correlation between damage and local geology, with the destruction being larger on soft soil than hard soil or rock (Duck 1958; Medvedev 1965; Seed, 1986) [3]. Dynamic effects on underground structures have often been neglected based on the assumption that their response to earthquake loading is relatively safe as compared to that of surface structures. Nevertheless, several examples of recorded

damage to underground structures for which seismic forces were not considered in the original design can be quoted. For example, Hashash et al. [1] describe the collapse of the Daikai subway station in Kobe during the 1995 Hyogoken-Nambu earthquake, the damages to highway tunnels in Central Taiwan during the 1999 Chi-Chi earthquake and the collapse of the Bolu tunnel in Turkey during the 1999 Kocaeli earthquake. Another example is the south-Hyogo earthquake of 17th Jan 1995 did serious damage to subway stations in Kobe. So investigating the effects of earthquakes on underground structures and their behavior during earthquakes has been the subject of many studies so far (Konagai 1998, Hashash et al 2001). In this study the analysis performed by considering three actual ground motion records representing seismic motions with low, intermediate and high frequency content of a/v (pick ground acceleration in g to pick ground velocity in m/s) so as to discuss the effect of frequency content on seismic response of pre-stress rock bolt on displacement and force on the urban subway tunnel. The principal object of rock bolting is to help the rock mass to support itself. Bolts often act to increase the stress and the frictional strength across joints, encouraging loose blocks or thinly stratified beds to bang together and act as a composite beam [4]. Rock bolts are always installed with tension and the pre-tensioned effect has been studied by a number of researchers and most results are reported to be positive. Firth and Thomas argued that active preloads modify roof behavior by dramatically reducing bed separation and delimitations in the immediate 0.5–0.8 m of the roof [5]. Peng stated that resin-assisted point-anchor tensioned bolts can be used to clamp thinly laminated roof beds into a thick beam that is more resistant to bending [6]. Stankus and Peng added that by “increasing

frictional resistance along bedding planes, roof sag and deflection is minimized and the lateral movement due to horizontal stress is unlikely to occur” [7]. Kang and Zhang also stated positive attributes on the pre-tensioned rock bolts [4]. Generally, pre-tensioned rock bolts are said to be more efficient than bolts without pre-tension, because a stronger beam can be built with the same bolt by utilizing a larger installed load. But in these all investigations researcher consider only the static behavior of rock bolt and therefore seismic behavior of pre stressed rock bolt is less or not taken into consideration. Therefore in this study we tend to describe the effect of pre-tensioned rock bolt in three different of frequency content and three pre-tensioned force on the seismic behavior of urban tunnels.

2 GENERAL PROPERTIES OF THE SIMULATED MODEL AND OTHERS

A circular tunnel is considered with 6 (m) interior diameter and the 30 (cm) thickness the center of model is located 16 (m) below the ground surface, is selected as the reference underground structure for the present case study. The lining is assumed to be composed by 0.35m thick precast concrete segments characterized by the following linear visco-elastic parameters as shown in table [2].

In the analyses, first, the primary state (static analyses) is defined then the dynamic analysis is performed. soil and the concrete body of the tunnel are both modelled using visco-elastic constitutive model with consideration of Rayleigh damping coefficients of the materials in general, when linear-elastic or linear-visco-elastic models are employed to describe the soil behavior, particular effort should be put in the selection of the stiffness and damping parameters compatible with the effective deformation level expected during the earthquake. The physical properties and mechanical parameters of both materials are reported in Table [1]. The assumed profile of the small-strain shear stiffness G_0 with depth (Fig [1]) was calculated adopting the relationship proposed by Viggiani and Atkinson used in this study [8].

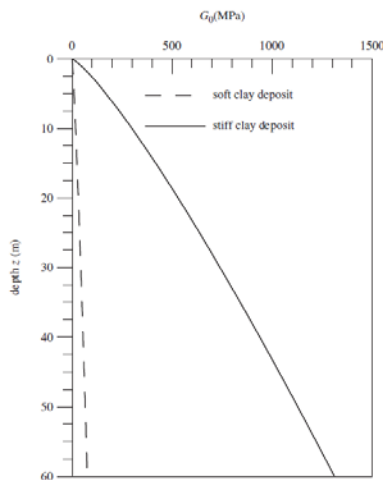


Fig [1]. Profile of small-strain shear stiffness G_0

In the present study, all of the models are subjected to three different natural ground motion records with different frequency contents representing seismic motions with high intermediate and low magnitude of a/v (pick ground acceleration in g to pick ground velocity in m/s) classified as Hav, Iav and Lav, respectively, as shown in figures [2],[3] and [4]. The earthquakes' properties are presented in Table [1] including their magnitude, maximum acceleration, velocity, time duration, their classification, and location of their occurrence. In order to investigate the effect of pre-tensioned rock bolts on the seismic behavior around the roadway tunnel, five similar models were constructed in our present study. All model parameters, except the tunnel support patterns, were similar in the five models. The first model was unsupported and the second model was supported with no pre-tensioned force, other three models were supported by pre-tensioned rock bolts with pre-tensioned forces (20-60-100) kN/m, respectively. On the other hand, the number of bolts used in this study is 4 and 8 that have been used as a symmetric and spacing from each other in Z direction is selected 1 m.

Table [1].Earthquakes properties

Category	Hav	Iav	Lav
Specified criteria	$a/v > 1.2$	$0.8 < a/v < 1.2$	$a/v < 0.8$
Location	Pinnacles	Loma Prieta	Indonesia
Magnitude	3.7	7.1	7
Time duration (sec)	28	82	30
Max. Acceleration(g)	0.105	0.1044	0.146
Max. velocity(m/s2)	0.0338	0.105	0.192
a/v	3.1	0.99	0.76

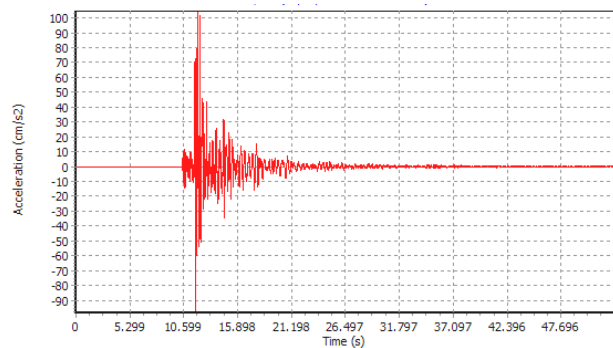


Fig [2]. Selected accelerogram for hav earthquake

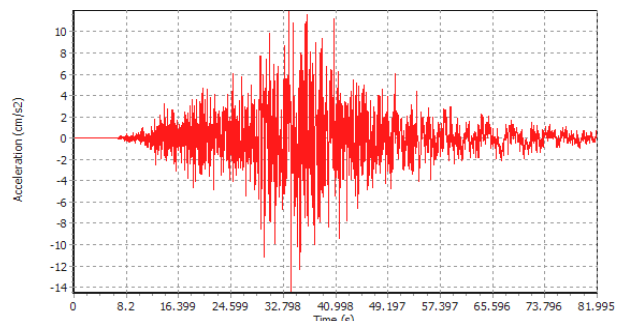


Fig [3]. Selected accelerogram for Iav earthquake

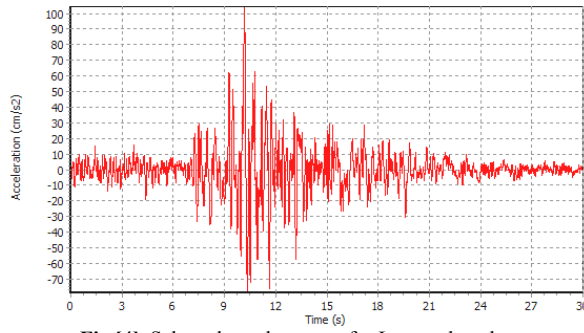


Fig [4]. Selected accelerogram for Lav earthquake.

Table [2]. Material properties used in this analysis.

Parameter	Soil	Rock bolt	Tunnel	Geogrid
Density (KN/m³)	17	-	-	-
Elastic Modulus(Pa)	2.5e4	-	-	-
Friction Angle (degree)	28	-	-	-
Cohesion (kpa)	10	-	-	-
Poisson's ratio	0.3	-	0.15	-
axial stiffness (KN/m)	-	2e5	1.4e8	1e5
bending stiffness (KNm²/m)	-	-	1.43e6	-
Equivalent Thickness(m)	-	-	0.35	-
Damping ratio α	Calculate with PLAXIS	-	2.83	-
Damping ratio β	-	-	8.74E-4	-
Interface	0.7	0.7	0.7	0.7

3 FINITE ELEMENT MODELING

The length, width and height of the model were 150 m, 1 m and 60 m respectively. A circular roadway (internal diameter 6 meter) was placed in the center of model is located 16 (m) below the ground. The coupled numerical analyses were performed with the finite element code PLAXIS2D [9], a two-dimensional (plane strain and axi-symmetric) FE code that implements the coupled Biot dynamic equations [10], adopting the so-called u-p simplification (where u is the skeleton displacement and p the pore pressure), assuming as negligible the fluid acceleration relative to the solid skeleton. The code adopts the Generalised Newmark method [11] for the time integration under dynamic conditions. In this study, the following standard values of the Newmark's constants were selected in all the analyses illustrated in this paper: $\alpha_N=0.3025$ and $\beta_N=0.6$. Those values ensure that the algorithm is unconditionally stable, while being dissipative only for the high- frequency modes. In the dynamic solution, the code allows to introduce frequency-dependent viscous damping by means of the Rayleigh formulation, the damping matrix being defined as follows:

$$[C] = \alpha_R [M] + \beta_R [K] \quad (1)$$

Where M and K are the mass and the stiffness matrix of the system, respectively. The coefficients α_R and β_R are obtained considering the following relationship with the damping ratio D [12]:

$$\begin{Bmatrix} \alpha_R \\ \beta_R \end{Bmatrix} = \frac{2D}{\omega_n + \omega_m} \begin{Bmatrix} \omega_n \omega_m \\ 1 \end{Bmatrix}$$

Where ω_n and ω_m are the angular frequencies related to the frequency interval f_n/f_m in which the viscous damping is equal to or lower than D.

The boundary conditions adopted for the static stages of the analyses were the standard ones: nodes at the bottom of the mesh were fixed in both vertical and horizontal directions, while those along the lateral sides were only fixed in the horizontal direction. In the dynamic analyses, the bottom of the model was assumed to be rigid and the lateral sides were characterised by the viscous boundaries proposed by Lysmer and Kuhlmeyer with parameters $a=1$ and $b=0.25$

Suitable constitutive elasto-plastic relations were chosen to represent the mechanical behavior of the soil and concrete body of the tunnel using the Mohr-Coulomb failure criterion which has been adopted throughout the PLAXIS2D analysis. In addition to its robust constitutive models, PLAXIS2D also includes various structural support elements. The structural element called 'node to node anchor' represents rock and soil support as an axial force along a line and this approach suffices for most soil and cable bolts under practical conditions. In this study the length bolts are selected 3 meter. The grout around the node to node anchor is modeled with geogrid that can be tolerated only tension. Impervious interface elements were also introduced to model the interaction between the lining and the soil, soil and node to node anchor according to the formulation summarised in the manual of the code. In particular, the interface was characterised by values of the shear strength parameters equal to 0.7 those of the surrounding soil. The mesh employed in the present study is reported in Fig [5]: it is characterised by a width equal to eight times its height, in order to minimise the influence of boundary conditions on the computed results. The domain was discretised in a total number of 1580, 15-node plane strain triangular elements. In the central part of the mesh, where the tunnel is located, the characteristic dimension of the elements h always satisfies the condition:

$$h \leq h_{\max} = V_s / 0.857 f_{\max}$$

Where V_s is the shear wave velocity and f_{\max} is the maximum frequency of the seismic signal.

In this study in order to demonstrate displacements and lateral forces, two nodes A and B are selected located on the lateral and top of tunnel, respectively.

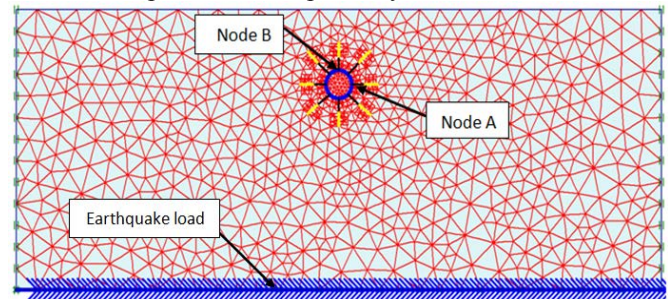


Fig [5] Mesh geometry in the FE analyses and location of nodes A and B

4 RESULTS AND DISCUSION

First, for example, we show the deformed mesh and changing in the position of the tunnel for (lav) earthquake.

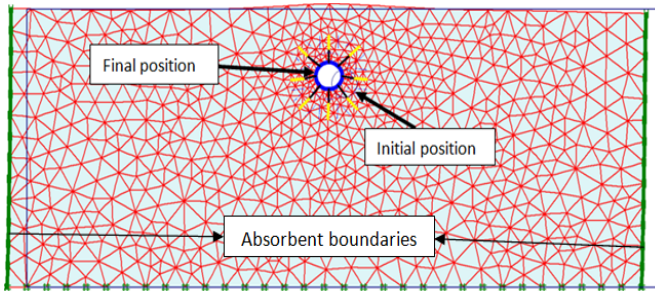


Fig [6]. Final deformed mesh and change the position of the tunnel for lav earthquake

As shown in Fig [6], in the seismic analysis and occurrences of earthquake due to more stiffness of tunnel to soil, the deformation shape of the tunnel ground top surface is shown as lump. In addition, by comparing figures 2 and 3 it can be said that the position of tunnel has changed and the shape of the tunnel, due to earthquake load, is an ellipse as shown in Fig [6]. In order to consider the effect of pre-stress force, three different rock bolt forces (20, 60 and 100 KN/m) have been modeled representing pre-tensioned. On the other hand, influence of earthquake's frequency content has been investigated on seismic behavior (displacement and lateral force on specified points that located on right and top of the tunnel as shown in Fig [5]) of urban tunnels by consideration of forenamed ground motion records. Analyses are performed in two separate parts: the free field analysis which considers only the soil medium without the tunnel for generating insitu stresses and soil-tunnel-rock bolt analysis which includes the tunnel structure and rock bolt in the soil medium. The results of these analyses are summarized into a series of charts shown in Figures [7] – [24]. It should be noted that in all figures shown in this study, we consider only effect of pre-tensioned rock bolts on seismic behavior of urban tunnels. This means that, after generating the initial stress, the total displacement sets to zero. All displacement and lateral forces shown in all figures related to seismic analysis.

The total displacement of node A and B in low frequency content earthquake in no bolt mode is minimum and in with bolt mode (number of bolt 4), the total displacement of node A is increased. On the other hand with increasing in pre-stress force the total displacement of node A and B decreased. But the total displacement into with bolt mode is more yet. With increasing in pre-stress force particularly in 100 KN/m, the applied lateral force on the node A decreases. A little difference exists between two pre-stress forces 20, 60 KN/m.

In with bolt mode and number of bolt 8, in low frequency content earthquake, the result is the same with the number of bolt 4 but there is difference among different pre-stress forces on the total displacement in prescribe nodes. Note that in this mode (number of bolt 8) increases in pre-stress force have a minor effect on the reduction of occurred lateral force

on the tunnel. In intermediate frequency content earthquake and with number of bolt 4, the pre-stress force don't effect on the displacement on prescribe nodes and have a minor effect on the applied lateral force but with increasing in pre-stress force, it is reduced. But in high frequency content earthquake the obtained results is differ from other two type of earthquake. In other words the effective of pre-stress rock bolt is appearing in high frequency content earthquake. With comparison between Fig [15] and Fig [21] can be said that in high frequency content earthquake, the applied lateral force extremely decreased than intermediate frequency content earthquake. Also in high frequency content earthquake due to low period the behavior of model will be somewhat close to static mode.

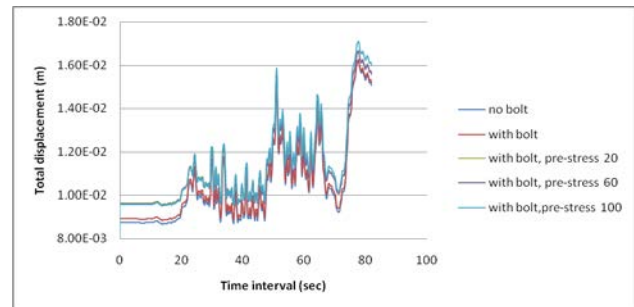


Fig [7]. Total displacement of node A in (lav) with number of bolt 4

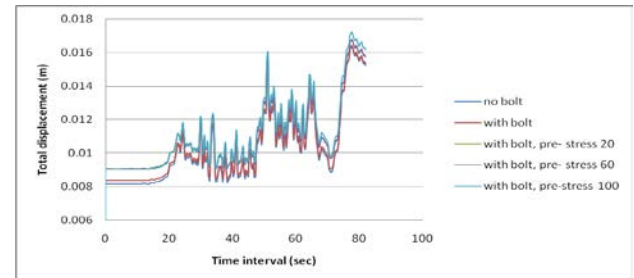


Fig [8]. Total displacement of node B in (lav) with number of bolt 4

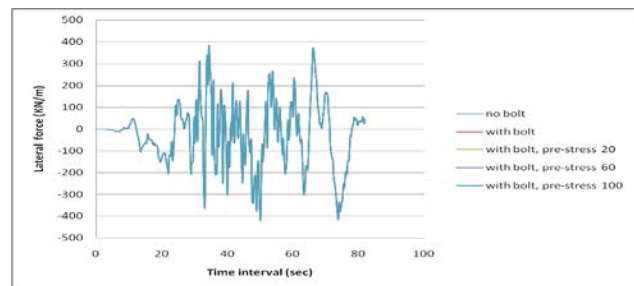


Fig [9]. Lateral force of node A in (lav) with number of bolt 4.

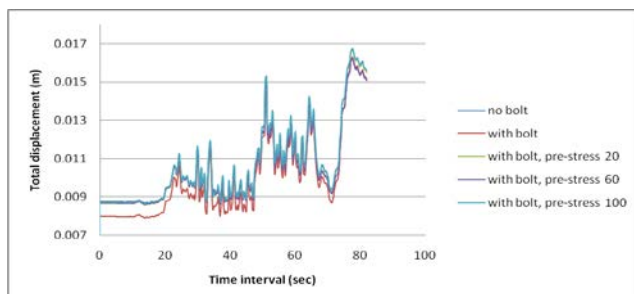


Fig [10]. Total displacement of node A in (lav) with number of bolt 8

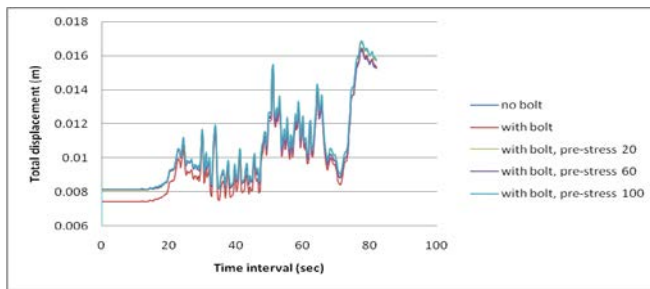


Fig [11]. Total displacement of node B in (lav) with number of bolt 8

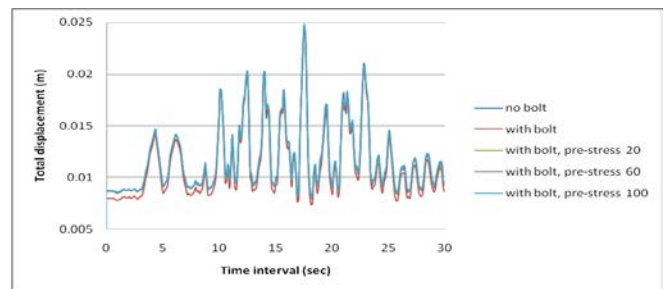


Fig [16]. Total displacement of node A in (lav) with number of bolt 8

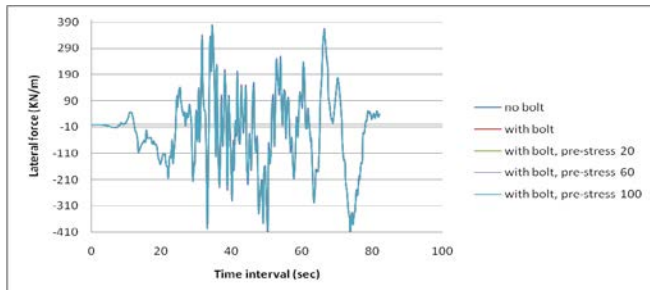


Fig [12].lateral force of node A in (lav) with number of bolt 8

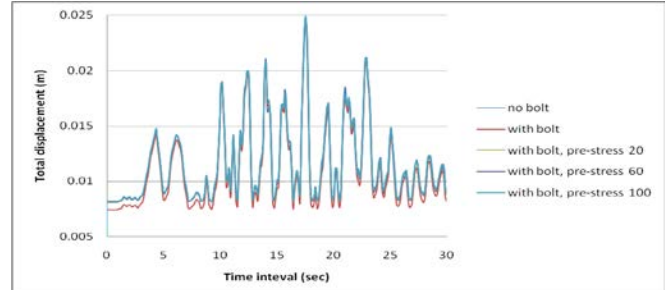


Fig [17]. Total displacement of node B in (lav) with number of bolt 8

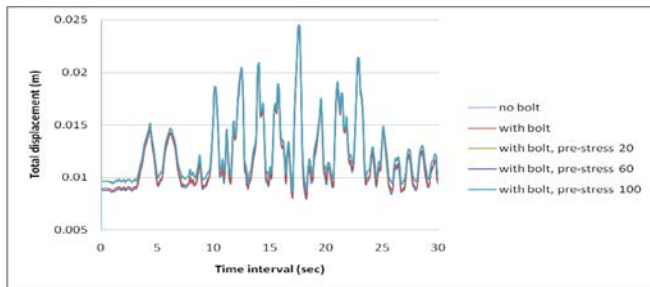


Fig [13]. Total displacement of node A in (lav) with number of bolt 4

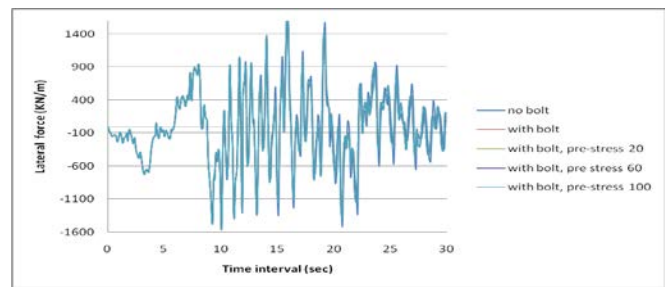


Fig [18].Lateral force of node A in (lav) with number of bolt 8

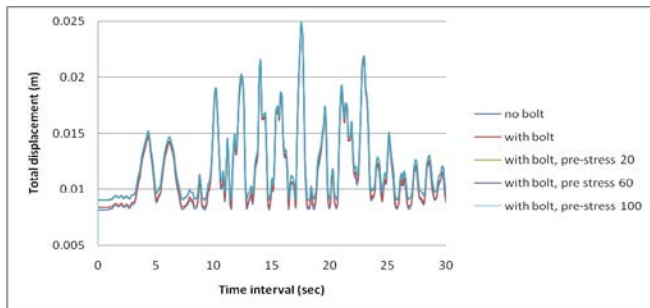


Fig [14]. Total displacement of node B in (lav) with number of bolt 4

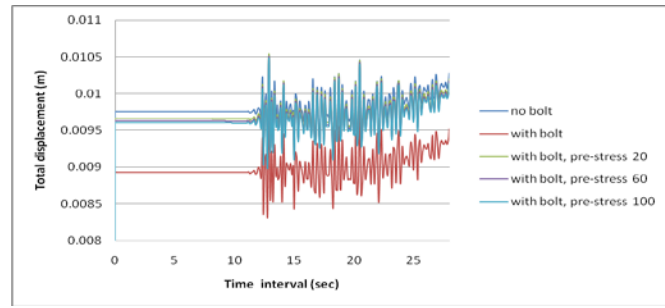


Fig [19]. Total displacement of node A in (Hav) with number of bolt 4

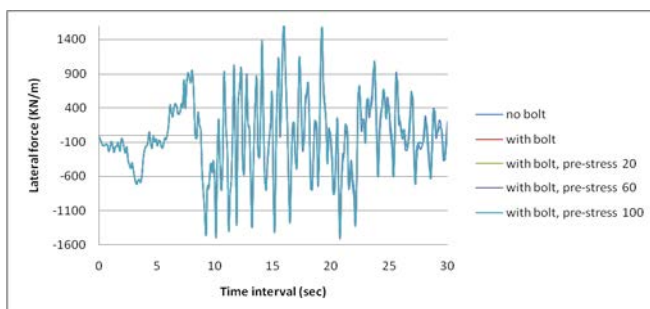


Fig [15]. Lateral force of node A in (lav) with number of bolt 4

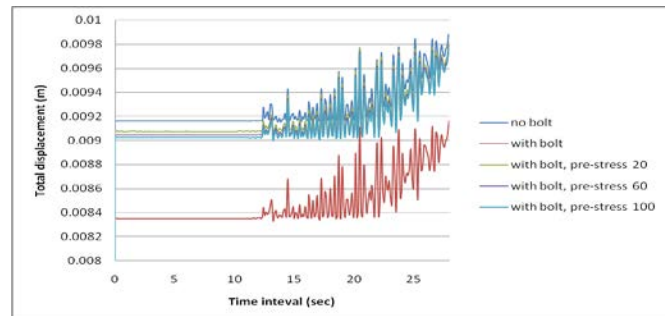


Fig [20]. Total displacement of node B in (Hav) with number of bolt 4

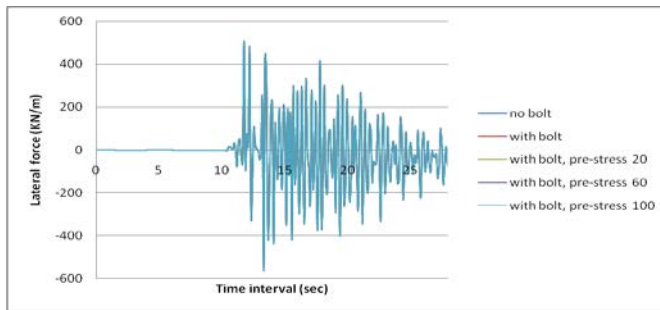


Fig [21].lateral force of node A in (Hav) with number of bolt 4

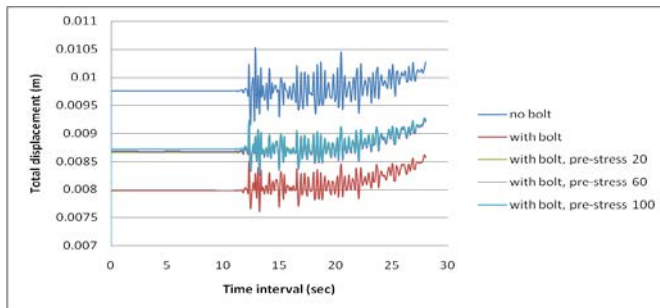


Fig [22]. Total displacement of node A in (Hav) with number of bolt 8

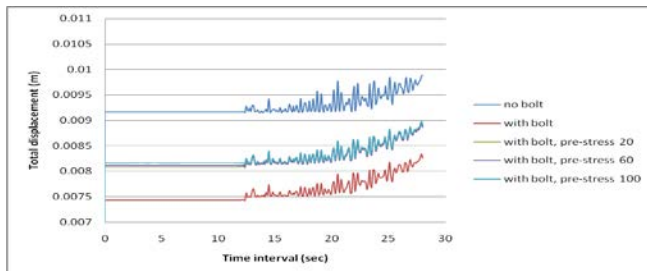


Fig [23]. Total displacement of node B in (Hav) with number of bolt 8

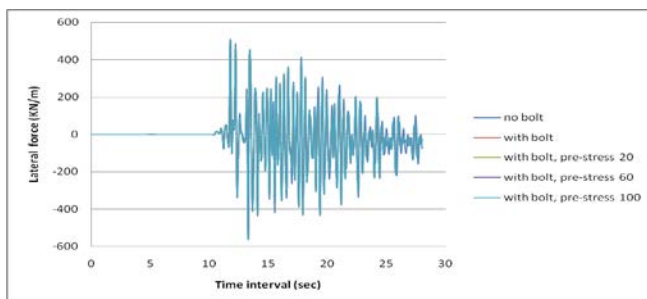


Fig [24].Lateral force of node A in (Hav) with number of bolt 8

5 CONCLUSION

In this paper, effect of pre-tensioned rock bolts on seismic behavior of urban tunnels on total displacement and lateral forces of the tunnel lining have been evaluated by using finite element method with PLAXIS software. For this purpose, the tunnel is considered with 6 (m) diameter and the center of which is located 16 (m) below the ground surface. Then the effect of dynamic loading with various frequencies content earthquakes (high, intermediate, low) on the variations of displacement and forces in described nodes in the tunnel lining have been assessed. In the modeling, the visco-elastic

constitutive model is used to consider the behavior of soil and the concrete body of the tunnel with consideration of Rayleigh damping coefficients of these materials. According to this assessment, the results show that the pre-tensioned rock bolts have a minor effect on decreasing the total displacement on the urban tunnels in all low and intermediate (lav and iav) seismic content. But in high frequency content (hav), the result of total displacement between the different forces pre-tensioned rock bolts model and with bolt model differ from each other considerably. In other words in (hav) earthquake use of pre-tensioned rock bolt increases the total displacement. But does not mean that the use of pre-tensioned have a negative effect on tunnel displacement. The applied lateral force in low and high frequency content earthquake is less than the intermediate earthquake. Therefore, the use of pre-tensioned rock bolts is efficient in (lav) and (hav) earthquake for decreasing lateral force that applied on the urban tunnel. Also the use of model with the number of bolt 8 than the model with number of bolt 4 is more efficient.

2 REFERENCES

- [1] Karakus M, Fowell R J, "Back analysis for tunnelling induced ground movements and stress redistribution," J. of Tunnelling and Underground Space Technology, vol. 6, 2005, pp. 514–524.
- [2] Kang H P, Jiang T M, Gao F Q, "Effect of pre-tensioned stress to rock bolting," J. of China Coal Society, vol. 7, 2007, pp. 680–685.
- [3] Saleh Asheghabadi M, Matinmanesh, H, "Finite Element Seismic Analysis of Cylindrical Tunnel in Sandy Soils with Consideration of Soil-Tunnel Interaction," in Proc. 12nd Int Conf. on Structural Engineering and Construction, 2011, pp. 3162-3169.
- [4] Mark C, "Design of roof bolt system," New Technology for Coal Mine Roof Support, Pittsburgh: U.S. Department of Health and Human Services, 2000.
- [5] Frith R, Thomas R, "The pre-tensioning pedigree," J. of Australia's Mining Monthly Supplement-Underground Equipment and Technology, vol.7, 1998, pp.68–72.
- [6] Peng S S, "Roof bolting adds stability to weak strata," Coal Age Magazine, vol. 11, 1998, pp. 32–38.
- [7] Stankus J C, Peng S S, "A new concept for roof support," Coal Age Magazine, vol. 9, 1996, pp. 2–6.
- [8] Viggiani GMB, Atkinson HJ, "Stiffness of fine-grained soils at very small strains. J. of Geotechnique ,vol.2, 1995, pp. 249–65.
- [9] Plaxis 2D. Reference Manual, version 8, 2003.
- [10] Biot MA, "General theory of three-dimensional consolidation," J. of Applied Physics , vol.12, 1941, pp. 155–64.
- [11] Katona MC, Zienkiewicz OC, "A unified set of single step algorithms. III. The beta-m method, a generalization of the Newmark scheme," J. of Numerical Methods in Engineering, vol. 7, 1985, pp.1345–59.
- [12] Clough R, Penzien J, "Dynamics of structures". New York: McGraw H

Effect Of Silt Content On The Anisotropic Behaviour Of Silt-Sand Mixtures

Navid Khayat¹, Abbas Ghalandarzadeh²

Ph.D. Assistance Professor, Department of Civil Engineering, Islamic Azad University Ahvaz Branch, Ahvaz,
Iran. (Khayat@iauhvaz.ac.ir)

Ph.D, Associate Professor, School of Civil Engineering, University college of engineering of Tehran, Iran,
(aghaland@ut.ac.ir)

ABSTRACT

The anisotropy of sand has not been fully studied in terms of the effects of different silt content. This study investigates the effects on anisotropy in Tehran sand with various silt contents. The tests performed in this research include some Hollow Cylinder Torsion Shear Tests conducted on 400kPa confining stresses. The samples had 0, 15, 30, and 50 percent silt contents, and the effect of the inclination angle on the major principal stress (α°) was investigated with a particular emphasis on silt content. The parameter " α " is considered as the key parameter that indicates the anisotropy characteristics, and can vary from 0° to 90° . According to the results, an increase of α° leads to more contractive behaviours in the studied sands. In all samples, increasing the silt content up to 50% causes the strength to decrease.

Keywords: Sand; strength; Silt content; anisotropy;

1 INTRODUCTION

In recent years, researchers have performed extensive and comprehensive studies on clean sand, determined different aspects of its behaviour in terms of its structure, and have made several general conclusions. However, the behaviour of clean sand containing silt is associated with several complications that make it difficult to understand.

Extensive studies have focused on the effects of inherent and induced anisotropy on the behaviour of clean sand [14]-[17]-[19]-[34].

Yamamuro and Lade (1998) extensively investigated the behaviours of sands containing small amounts of silt (7%)[30]. They concluded that when a small amount of silt is added to the host sand, the obtained sand-silt mixture exhibits the opposite behavior of that of pure sand. The sand under low confining pressure (25 kPa) is completely liquefied, and the strength of sand reaches zero. As the confining stress increases, the sand with 7% silt has more stable behaviour than that of pure sand with no liquefaction under high confining pressures. According to Yamamuro and Covrt (2001), the behaviours of silt-sand mixtures with high amounts of silt (40%) are different from those of pure sand and those of silt-sand mixtures with small amounts of fine particles [31]. In these mixtures, like the sands with 7% silt, liquefaction occurs completely under 25 and 50 kPa confining stresses; however, as the confining stress increases, the behavior tends to be more stable. Such behaviours are similar to that of sand with 7% silt content but are still different from those of pure sand [31].

Parameter α° (the inclination of major principal stress with respect to the depositional (vertical) direction) is used to denote the rotation of principal stresses and parameter $b' = (\sigma_2 - \sigma_3) / (\sigma_1 - \sigma_3)$ indicates intermediate stresses. Different principal stress directions and b' values can cause changes in soil behaviour. Thus, α° and b' are selected as the key parameters for studying the anisotropy of sands. In this regard, Hollow Cylindrical Torsional Shear (HCTS) is the best apparatus for studying these parameters [1]. HCTS has been used in several tests conducted on sands by different researchers to study the effects of parameters α° and b' more accurately. They generally came to the conclusion that sandy samples had softer behaviour as the values of α° and b' increased in undrained tests [34]. According to Symes et al. (1985), sandy samples exhibit more contractive behaviour as the α° and b' values increased [14]-[25].

Despite extensive studies conducted on the anisotropy effects of clean sand, there are few studies that have investigated its effects on the behaviour of sand-silt mixtures. Among recent relevant studies, Bahadori and Ghalandarzade (2008) studied the inherent anisotropic effects on the undrained behaviour of sands using HCTS [4].

In this research, the anisotropic behaviour of Tehran sand with different silt contents in 400 kPa initial effective confining stress are studied. A total of 12 tests are conducted on Tehran sand with silt contents of 0%, 15%, 30% and 50%. In these tests, the effects of the inclination angle of major stress and silt content are investigated.

2 Material and Methods

2.1 Material properties

Tehran sand, which is produced by crushing plants, This sand with greenish gray color. The physical characteristics and grading curves of this sands are shown in Fig. 1 and Table 1. The plasticity index of silt is less than 5% and can be addressed as non-plastic soil (see Table 2).

2.2 Maximum and minimum void ratios of sand-silt mixtures

An effective factor in the general behaviour of saturated sands in monotonic loading is soil relative density, which is a parameter that shows the sample's specifications at the end of consolidation stage. The samples prepared at low densities showed contractive behaviours in the drained tests; this behaviour causes excess pore water pressure in undrained tests, which reduces the effective confined stress. The change of stress-strain from the softening to hardening states is generally related mostly to the relative density, which is observed and reported by several researchers [5]-[7]-[8]-[16].

It is clear that adding silt to the host sand changes the maximum and minimum void ratios. The parameters related to soil density are needed to compare the test results; therefore, minimum and maximum void ratios should be obtained for different percentages of silt. In this research, ASTM 4253 and ASTM 4254 are used to measure the minimum void ratio (e_{\min}) (densest state) and maximum void ratio (e_{\max}) (loosest state), respectively. The obtained values are plotted in Fig. 2. For host sand, the minimum void ratios decrease as the silt content of the samples increases. This trend continues up 28 percentage fine content (FC); then, the void ratio increases as the silt content increases. The minimum achieved void ratio takes place in the fine contents, which will be called the threshold fines content.

2.3 Testing apparatus and method

In order to study the inherent anisotropy, a hollow cylinder torsional shear (HCTS) device was used. For better investigation of post peak response the device can perform both stress and strain controls.

A closed loop control was applied to the machine to handle any type of desired stress history including major principal stress rotation and intermediate stress ratio. Four Electrical/Pneumatic [E/P] transducers were used to exert required pressure for the inner and outer cell pressure in addition to the torsion and axial load pneumatic actuators. An alternative DC motor for torsional strain control test was prepared in order to study the post peak behaviour. In the case of our tests, the motor was utilized since the strain control was adopted in order to study the softening response. The motor speed in all the tests remained constant and equal

to 4 degree per minute. Eleven transducers were adjusted in order to measure different parameters continuously .Three water pressure sensors, two for inner and outer cell pressures and one for pore pressure, one vertical displacement sensor to measure axial strain, and one rotation angel sensor to measure torsional strain, two differential pressure sensors, two axial and torsional stress sensors and finally two limit switch sensors were set up. A computer program was utilized to control all test procedures by means of a PID control algorithm. Data logging device was the last part of the control system. The sample dimensions were 12 cm in height, 6 cm in inner diameter and 10 cm in outer diameter.

The maximum inclination of principal stress (α°) and intermediate stress ratio (b') are considered the critical parameters in this research. Because the torsion sensor measures the torque (T) at any moment, the $\sigma_{z\theta}$ (shear stress) value can be obtained using Eq (3), where r_i and r_o are the inner and outer radiuses of the samples, respectively. The value of σ_z (vertical normal stress) must be kept constant, and therefore, the values of σ_θ and σ_r (circumferential and radial normal stress respectively) obtained through Eqs (1) and (2), respectively, are also kept constant. Furthermore, P_i and P_o (inner and outer water pressures) are computed using Eq (5), F_v (vertical force) is found using Eq (4) and principle stress can be measured by equation 6 to 8 [15].

$$\sigma_\theta = \sigma_z - \frac{2\sigma_{z\theta}}{\tan 2\alpha} \quad (1)$$

$$\sigma_r = \sigma_z - \frac{\sigma_{z\theta}(\cos 2\alpha - 2b + 1)}{\sin 2\alpha} \quad (2)$$

$$\sigma_{z\theta} = \frac{1}{2} \left[\frac{3T}{2\pi(r_o^3 - r_i^3)} + \frac{T}{\pi(r_o^3 + r_i^3)(r_o - r_i)} \right] \quad (3)$$

$$\sigma_z = \frac{F_v + \pi(P_o r_o^2 - P_i r_i^2) - A_r P_o}{A_s} \quad (4)$$

$$\begin{cases} P_i = \frac{\sigma_r(r_o + r_i) + \sigma_\theta(r_o - r_i)}{2r_i} \\ P_o = \frac{\sigma_r(r_o + r_i) + \sigma_\theta(r_o - r_i)}{2r_o} \end{cases} \quad (5)$$

2.4 Experimental Program

Sample preparation method used in this study was dry deposition method. That may alter the real anisotropy fabric; water sedimentation method was not used. Dry deposition method is able to create more uniform silty sand samples according to Miura and Toki (1982) suggestion which says pluviation methods create the most significant anisotropy [12]. The sand was deposited into the frame through a funnel with a long tube. Carbon dioxide (CO_2) and deaired water

are passed through the samples in their saturated states. The circulating time for the CO_2 considered in the tests conducted by Zlatovic and Ishihara (1997) were 30 minutes for clean sand and 8 hours for pure silt [35]. In the present study, the minimum and maximum times were 30 and 135 minutes for clean sand and the 50% silt mixture, respectively. After circulation of CO_2 , the deaired water entered from the bottom similar to CO_2 but in the opposite direction of gravity and was seeped into all the voids in the sample. The saturation procedure continues as the confining pressure increased, and the pore water pressure was measured in several steps. If the B-value would exceed 0.95, then the sample is assumed to be completely saturated. At this time the saturation stage was completed and the sample should be consolidated. Because all the tests conducted in this research were of the Consolidated Undrained (CU) type, all drainage valves must be opened during consolidation and connected to the system. The amount of water discharged from the sample during consolidation could be measured by reading the burette numbers at the beginning and end of this stage. After consolidation the shear stage started at which the shear speed was four degrees per minute, the lowest speed that can be applied to the system. At the end of the test the porosity of the samples was measured.

3. Results

The goal of this research was to study the influence of the amount of silt upon anisotropy features in sand-silt mixtures. For this purpose, sand were tested using 400-kPa initial confining stress and a silt content range of 0-50%. Also the Intermediate stresses parameter (b') in all tests was 0.5. Some information on these tests are given in Table 3. All test results are presented in the form of stress-strain and effective stress path curves. According to these curves, the sample behaviours are similar to those of dense sands based on the classification of undrained sand behaviour in most conducted tests, according to Yoshimine et al. (1998) [34]. The significance of the strength of the deviator stressing phase transformation point is evident in this figure. According to Figs. 3 through 6, the sample strengths (deviator stressing phase transformation and failure points) decrease as α° increase, which indicate that the soil becomes softer. Increasing the silt content up to the threshold level will cause the strengths to decrease, and this reduction is more obvious for the 50% silt case (Figs. 6). In these samples, the test conditions were the same, and the silt percentage increased as the density increased, but unexpectedly, strength did not increase. For example, in test No.7, the value of D_r is 76, but in test No.28, which contains 50% silt, its value is 99, 6.

4. Discussing and studying the stress paths

4.1 Effect of inclination angle (α°) on the sand's behaviours

In Figs. 3 through 6, the strength of samples (deviator stressing phase transformation and failure strength) is reduced as α° increase, which indicates that the soil becomes softer. This behaviour has been described by Yoshimine and Ishihara (1998) for Toyoura sand and by Bahadori and Ghalandarzadeh (2008) for a Firoozkuh sand-silt mixture [4]-[34]. It seems regardless of type of sand, similar behaviour can be observed in all studied cases here.

4.2 Effect of non-plastic fines content on the sand's mixture behaviours

The effect of nonplastic fines on the behaviour of saturated sand has been studied by many researchers [6]-[13]-[23]-[29]-[32]. Adding different amounts of nonplastic silt considerably changes the sand behaviour, and these changes are difficult to describe. Pitman et al. (1994) concluded that when silt was added to Ottawa sand, it became less collapsible in undrained triaxial compression tests. However, others found that nonplastic silt may decrease the strength (Troncoso and Verdugo, 1985; Sladen et al., 1985) [18]- [24]. Ishihara (1993) and Verdugo and Ishihara (1996) showed that the increased silt content increased the potential for sand to exist in nature in a contractive state, which includes the possibility of flow failure or liquefaction [9]-[28]. Yamamuro and Lade (1997, 1998) and Lade and Yamamuro (1997) observed that increasing the amount of nonplastic silt in Nevada sand increased the volumetric contractive character in both drained and undrained triaxial tests, even when the overall density increased [30]. Among the problems involved in these studies is the impossibility of fixing at least one of the parameters in sand-silt mixtures. In the present study, the method proposed by Bahadori and Ghalandarzadeh (2008) [4] was applied to address this problem. Based on this method, if the same conditions are considered in sampling and testing, then increasing the silt increases the density and decreases the strength. Thus, while the sample densities are equal, the sample with higher silt content has lower strength.

The sample strengths decreased in the silt-sand mixtures as the silt content increased (Fig. 7). The decreasing strength as silt is added to the host sand can be explained by Tavanayagan's classification (1999) (Fig. 8) [21]. According to Fig. 9, the void ratios of host sands are tested in the range of Tavanayagan's classification case (i); however, with 15% silt content, the intergranular void ratio (e_c) approached $e_{max,HS}$ (Fig. 9), which is more similar to that observed in Tavanayagan's classification case (ii). In this latter case, the finer grains may support a coarser grain skeleton that is otherwise unstable. These grains act as a load transfer vehicle between some of the coarse grain particles in the soil matrix, while the remaining fine particles fill in the voids. In this

case, the shear strength is derived from friction along coarse grain contacts and fine particles. In this

structure, e_c increased, which decreased the strength of the samples. This behaviour is evident as the silt percentage in the mixtures increases and leads to an increase in relative density. Increasing the amount of silt content to 30% caused the intergrain void ratio increased, the relative density does not increase because its threshold percentage was 28%. Thus, an inter-fine-particle void ratio is used to explain its behaviour, which is similar to case (iv-2) and shown in Fig. 9. Moreover, the inter-fine-particle void ratio in the mixture with 30% silt content is greater than that of a sample with 15% fine particle content. When the silt content is increased to 50% in all mixtures, e_f is smaller than ($e_{\max, HF}$), and ($FC_{th} < FC$); thus, their behaviours are similar to Tavanayagan's classification case (iv-2). In this case, the fine particles carry the contact and shear forces, while the coarse grains act as reinforcing elements embedded within the finer grain matrix. In this situation, the main bearing structure changes from sand to silt, and because the strength of silt is less than that of sand, increasing the silt up to 50% decreases the strength of the mixture.

5. Conclusions

- 1) As α° increases, the strengths of the samples of host sand and silt-sand mixtures decrease, i.e., the soil becomes softer. Such behaviours have also been observed by Yoshimine et al. (1998) and Bahadori and Ghalandarzadeh (2008) [34]-[4].
- 2) As the silt content in mixtures increases, the relative density also increases, but this increase does not increase the mixture strength. An increase in relative density is one of the most marked phenomena that indicate that the index of the relative density (or void) is not a suitable index for evaluating the behaviour of silt-sand mixtures.
- 3) In all mixtures, increasing the silt content up to 50% causes the strength to decrease. This decline in strength may be justified by parameters (e_c, e_f), which are defined by Tavanayagam (1999) [21].

Notation

The following symbols are used in this paper:

α : the inclination of the major principal stress with respect to the vertical direction

b' : Intermediate stresses

b : Portion of fine grains that contribute to active intergrain contacts

D : Diameter of coarse grains

C_c : Coefficient of curvature

C_u : Coefficient of uniformity

d : Diameter of fine grains

e_c : intergranular void ratio

e_f : Inter-fine-particle void ratio

e_{\max}, e_{\min} : Maximum and minimum void ratios, respectively

$e_{\max, HF}, e_{\min, HF}$: Maximum and minimum void ratios of host fine particles, respectively

FC : Fine particle content (%)

FC_{th}, FC_L : Threshold and limiting fine particle content, respectively

$(e_1 - e_3)/2$: deviatoric axial strain

p'_c : initial effective confining stress

p_i, p_o : inner and outer water pressures, respectively

r_i, r_o : inner and outer radius, respectively

6. REFERENCES

- [1] Anhminh, N. (2006). An investigation of the anisotropic stress-strain-strength characteristics of Eocene clay. Thesis for the degree of Doctor of Philosophy and for the Diploma of the Imperial College.
- [2] ASTM D4254. Standard Test Methods for Maximum Index Density and Unit Weight of Soils Using a Vibratory Table. ASTM Standard, (2006).
- [3] ASTM D4254. Standard Test Methods for Minimum Index Density and Unit Weight of Soils and Calculation of Relative Density. ASTM Standard (2006) e1.
- [4] Bahadori, H. Ghalandarzadeh, A. & Towhata, I. (2008). Effect of non plastic silt on the anisotropic behaviour of sand. Soils and Foundations 48, No. 4, 531-546.
- [5] Bishop, A. W., (1971). Shear strength parameters for undisturbed and remolded soil specimens. Proceeding for the Roscoe memorial symposium, Cambridge University, Cambridge, Mass, pp 3-58.
- [6] Bouckovalas, G. D., Andrianopoulos, K. I. & Papadimitriou, A. G., (2003). A critical state interpretation for the cyclic liquefaction resistance of silty sands. Soil Dynamics and Earthquake Engineering, No. 23, 115-125.
- [7] Castro, G. (1969). Liquefaction of sands. Harvard Soil Mechanics Series, No.81, Pierce Hall.
- [8] Castro, G., Poulos, S.J., France, J.W., and Enos, J.I. (1982). Liquefaction induced by cyclic loading. Geotechnical engineers Inc., Report submitted to NSF.
- [9] Ishihara, K. (1993). Liquefaction and flow failure during earthquakes. Geotechnique 43, No.3, 351-415.
- [10] Khayat, N. (2010). The investigation of the effect of inherent and induced anisotropy on the undrained

- behavior on Silt-Sand mixture. Thesis for the degree of Doctor of Philosophy of the Department of Civil Engineering, Science and Research Branch, Islamic Azad University, Tehran, Iran.
- [11] Lade, P.V. and Yamamuro, J.A. (1997). Effects of non plastic fines on static liquefaction of sands. *Canadian Geotechnical Journal*, 34, No. 6, 918-928.
- [12] Miura, S. and Toki, S. A. (1982). Sample preparation method and its effect on static and cyclic deformation-strength properties of sand, *Soil and Foundation* 22, No. 1, 61-77.
- [13] Naeini, S.A. & Baziar, M.H. (2004). Effect of fines content on steady-state strength of mixed and layered samples of a sand. *Soil Dynamics and Earthquake Engineering* 24, 181-187.
- [14] Nakata, Y., Hyodo, M., Murata, H. and Yasufuku, N. (1998). Flow deformation of sands subjected to principal stress rotation. *Soils and Foundations* 38, No. 2, 115-128.
- [15] Pradhan, B. S., Tatsuoka, F. and Horii, N. (1988). Simple shear testing on sand in a torsional shear apparatus, *Soils and Foundations* 28, No. 2, 95-112.
- [16] Seed, H.B. and Idriss, I.M. (1971). Simplified procedure for evaluating soil liquefaction potential. *Geotechnical Engineering Journal* 97, No.9, 1249-1274.
- [17] Sivathayalan, S. & Vaid, Y.P. (2002). "Influence of generalized initial state and principal stress rotation on the undrained response of sands", *Canadian Geotechnical Journal*, 39:63-76.
- [18] Sladenn J. A., D'Hollander, R. D. and Krahn, J. (1985a). Back analysis of the Nerlerk berm liquefaction slides. *Canadian Geotechnical Journal* 22, No.4, 564-588.
- [19] Symes, M.J., Gens, A. and Hight, D.W. (1984). Undrained Anisotropy and Principal stress Rotation in Saturated Sand. *Geotechnique* 34, No. 1, 11-27.
- [20] Symes, M.J., Gens, A. and Hight, D.W. (1985). Discussion. *Geotechnique*, 35, No. 1, 78-85.
- [21] Thevanayagam, S. (1999). Effect of fines and confining stress on undrained shear strength of silty sands. *Journal of Geotechnical and Geoenvironmental engineering* 124, No.6, 479-491.
- [22] Thevanayagam, S., Shenthan, T., Mohan, S. and Liang, J. (2002). Undrained fragility of sands, silty sands and silt. *ASCE, Journal of Geotechnical and Geoenvironmental engineering* 128, No.10, 849-859.
- [23] Thevanayagam, S. & Martin, G.R. (2002). Liquefaction in silty soils-screening and remediation issues. *Soil Dynamics and Earthquake Engineering* ,No.22, 1035-1042.
- [24] Troncoso, J.H. & Verdugo .R. (1985). Silt content and dynamic behaviour of tailing sand .Proceeding of 11th JCSMFE, Balkema ,Rotterdam ,The Netherlands, pp.1311-1314.
- [25] Uthayakumar, M. & Vaid, Y. P. (1998). Static liquefaction of sands under multi axial loading. *Canadian Geotechnical Journal* 32, No.2, 273-283.
- [26] Vaid ,Y.P., Sivathayalan, S., Uthayakumar , M. And Eliadorani, A. (1995a). Liquefaction potential of reconstituted Syncrude sand. 48th Canadian Geotechnical Conference 1, pp.319-328.
- [27] Vaid ,Y.P., Uthayakumar, M. Sivathayalan, S., Robertson, P.K And Hofman, B. (1995b). Laboratory testing of Syncrude Sand . 48th Canadian Geotechnical Conference 1, pp.223-232.
- [28] Verdugo, R. & Ishihara, K. (1996). The steady state of sandy soils. *Soils and Foundations* 36, No.2, 81-92.
- [29] Xenaki, V.C. & Athanasopoulos, G.A. (2003). Liquefaction resistance of sand-silt mixtures: an experimental investigation of the effect of fines. *Soil Dynamics and Earthquake Engineering*, No.23, 183-194.
- [30] Yamamuro , J. A. & Lade, P.V. (1998). Steady-state concepts and static liquefaction of silty sands. *Journal of Geotechnical and Geoenvironmental engineering* 124, No.9, 868-877.
- [31] Yamamuro , J.A. & Covert, K.M. (2001). Monotonic and Cyclic Liquefaction of Very Loose Sands with High Silt Content. *Journal of Geotechnical and Geoenvironmental Engineering*, ASCE 127, No. 4, 314-324.
- [32] Yang, S.L., Sandven, R., & Grande, L. (2006). Instability of sand-silt mixtures. *Soil Dynamics and Earthquake Engineering*, No.26, 183-190.
- [33] Youshimine, M., Ishihara, K. and Vargas, W. (1998a). Flow deformation of sands subjected to principal stress rotation. *Soils and Foundations* 38, No.3, 179-188.
- [34] Yoshimine, M. & Ishihara, K., (1998). Flow potential of sand during liquefaction. *Soils and Foundations* 38, 189-198.
- [35] Zlatovic, S, & Ishihara, K., (1997). Normalized behaviour of very loose nonplastic soils: effects of fabric. *Soils and Foundations* 37, No.4, 47-56.

Table 1: Physical characteristics of sands

Sand type	C_c	C_u	$FC(\%)$	$D_{50}(mm)$
Tehran sand	0.59	2.55	0.03	0.106

Table 2: Physical properties of silt

Plastic limit (%)	Liquid limit (%)	Plasticity index (%)
22	24	2

Table 3. Characteristics of the tests

Test No.	Sand type	FC (%)	α°	e	D_r (%)	(e_f)	(e_c)
7	T	0	15	0.711	76.0	1.83	0.71
8	T	0	30	0.712	75.8	1.83	0.71
9	T	0	60	0.718	74.3	1.85	0.72
16	T	15	15	0.600	83.0	1.25	0.84
17	T	15	30	0.610	80.7	1.27	0.85
18	T	15	60	0.606	81.6	1.26	0.84
25	T	30	15	0.560	89.3	0.98	0.92
26	T	30	30	0.563	88.6	0.98	0.93
27	T	30	60	0.567	87.7	0.99	0.93
28	T	50	15	0.530	99.6	0.76	0.88
29	T	50	30	0.534	98.8	0.77	0.88
30	T	50	60	0.537	98.2	0.77	0.89

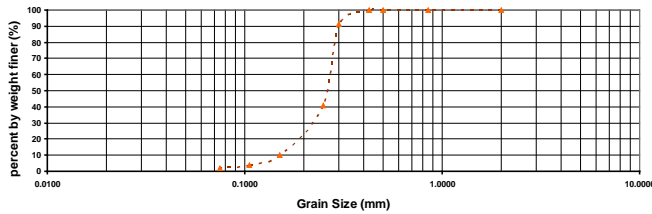


Fig. 1. Grain size distribution curves of Tehran sand

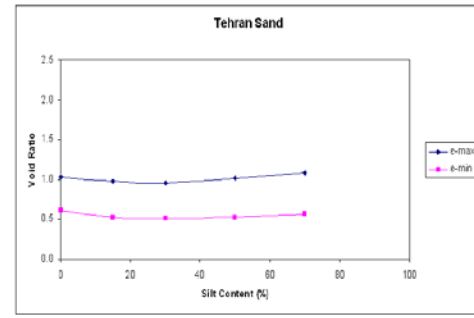


Fig. 2. Minimum and maximum void ratios for the Tehran sand-silt mixtures

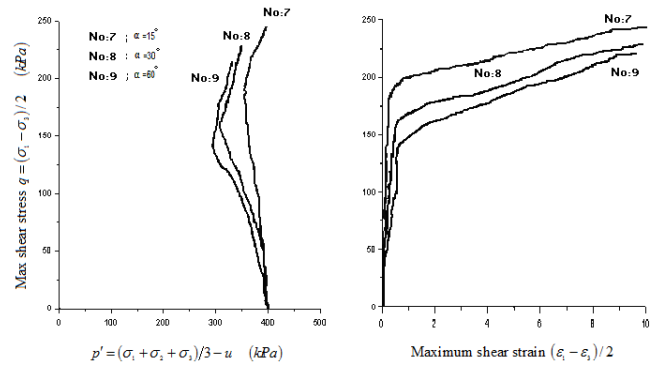


Fig. 3. Stress path and stress-strain curves in Tehran sand subjected to an initial effective stress of 400 kPa (FC=0%).

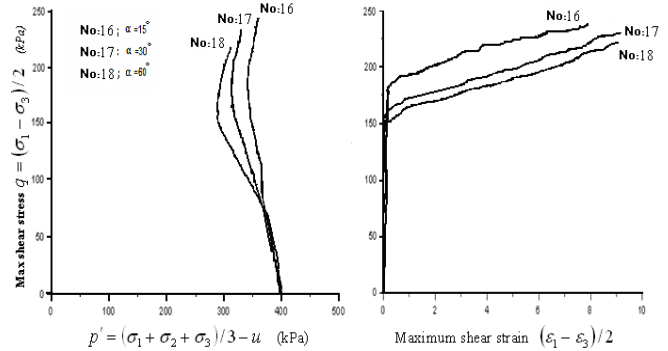


Fig. 4. Stress path and stress-strain curves in Tehran sand subjected to an initial effective stress of 400 kPa (FC=15%).

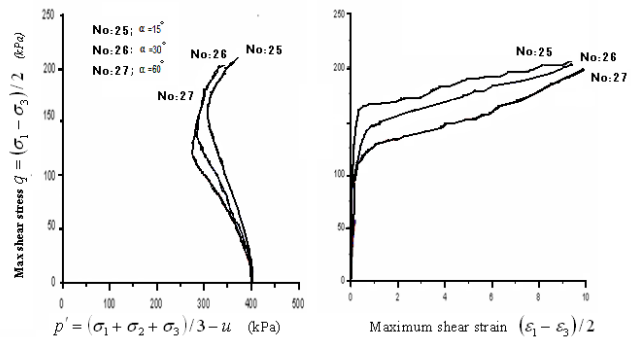


Fig. 5. Stress path and stress-strain curves in Tehran sand subjected to an initial effective stress of 400 kPa (FC=30%).

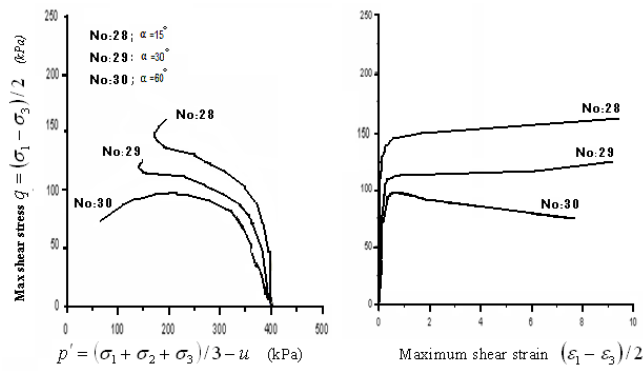


Fig. 6. Stress path and stress-strain curves in Tehran sand subjected to an initial effective stress of 400 kPa (FC=50%).

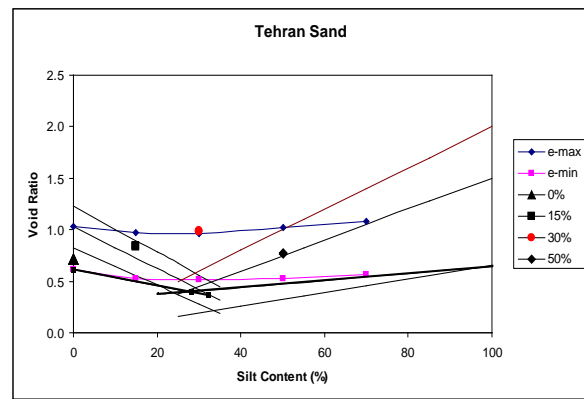


Fig. 9. Intergranular matrix phase diagram for Tehran Sand

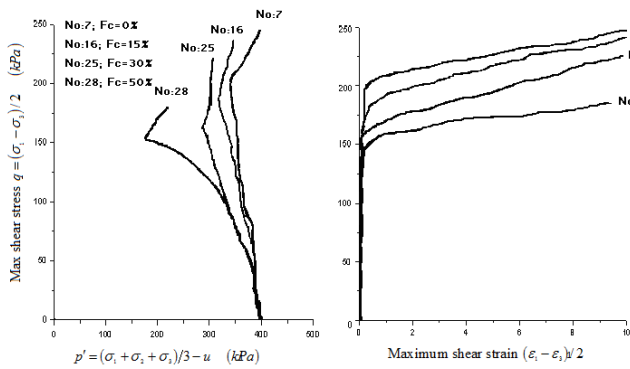


Fig. 7. Stress path and stress-strain curves in Tehran sands with different silt contents at $\alpha = 15$.

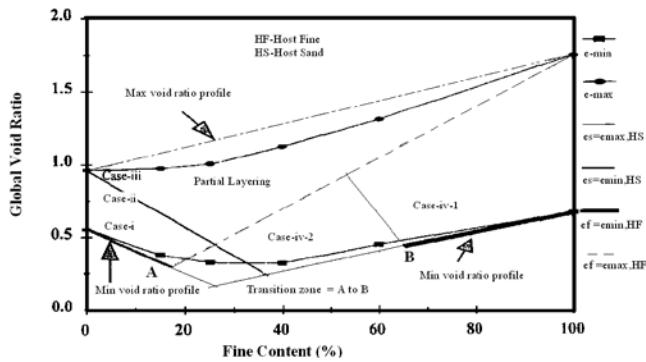


Fig. 8. Intergranular and Interfine Matrix Phase Diagram (Thevanayagam, 1999) [18]

Production and Properties of High Strength Concrete for Heightening Concrete Dam in Sudan

Osama M. A. Daoud¹ and, H. S. Sagady²

¹Building and Road Research Institute, University of Khartoum, Sudan

² Senior Material Engineer, SMEC International Co. Ltd., Sudan

ABSTRACT

This paper presents a part of an ongoing experimental laboratory investigation being carried out for production and characterization of high strength concrete (HSC) for heightening of an existing concrete dam in the middle of Sudan. Brief description of the main features of the dam and concrete works is presented. Hundreds of trial mixes were performed and tested using local Sudanese aggregates with addition of mineral admixtures (Silica Fume and Fly Ash) and Super plasticizers. Six grades of HSC (50, 60, 70, 80, 90, 100 MPa) had been success fully produced and their mechanical properties were measured and documented. Statistical analysis of tests results was performed and simple correlations were developed relating compressive strength to flexural and Splitting Strengths.

The results have offered an important insight for optimizing the rheological characteristics of HSC and permitted to develop guidelines for optimum mix design methods for HSC from locally available aggregates in Sudan. The effect of w/c ratio on strength of HSC was also highlighted. It is concluded that local concrete materials, in combination with mineral admixtures can be utilized in producing High Strength Concrete in Sudan.

Keywords: High Strength Concrete, Silica Fume, Fly Ash, Dams, Sudan.

1. INTRODUCTION

Concrete, a composite material consisting of aggregates enclosed in a matrix of cement paste including possible pozzolans, has two major components, cement paste and aggregates. The strength of concrete depends upon the strength of these components, their deformation properties, and the adhesion between the paste and aggregate surface [1].

In recent years, the construction industry has shown significant interest in the use of high strength concrete (HSC), in applications such as dams, bridges and high rise buildings. This is due to significant structural, economic and architectural advantages that HSC can provide compared to conventional, normal strength concrete (NSC).

Although high strength concrete is often considered a relatively new material, its developed has been gradual over many years. Definition of the minimum strength value for high – strength concrete varies with time and geographical location depending on the availability of raw material and the technical Know-how, and the demand form the industry [2]. Starting form a value of 34 MPa in the 1950s in the United States moving to upper values, the ACI 363, 1999 [4] on high strength concrete defines a value of 51 MPa (cube strength) as a minimum value for high for high strength concrete.

Production of HSC may or may not require special materials, but it definitely requires materials of highest quality and their optimum properties [3]. The production of HSC that consistently meets the requirements for workability and strength development places more stringent requirements on material selection than that for lower strength concrete (ACI

363R, 1999) [4]. However, many trial batches are often required to generate the data that enables the researchers and professionals to identify the optimum mix proportions for HSC [3].

2. GENERAL DESCRIPTION OF ROSEIRES DAM

Roseires Dam is located in Damazin city in the Blue Nile State, about 520Km south-east of Khartoum. The Dam was originally designed to be constructed in two phases, the first phase was completed in 1966 to maximum water level of Alexandria Datum (AD) 483 m with allowance for it to be raised to AD 493 m at a future date.

The Dam is a composite dam with a central 1000 m long concrete buttress dam section that contains the deep level sluices, gated spillways, power intakes for a service power station and head works for future irrigation canals on either side of the river. The maximum height of the existing concrete section is 68 m. It embodies specialized section for deep sluices, spillway, west and east bank irrigation canal head works, main power station (280 MW) and service power station (2 MW). The Embankment Dam is 8500 m long on the left (west) bank and 4000 m long on the right (east) bank. The maximum height of Embankment Dam is 30 m and the maximum width 230 m. Once raised, Roseires Dam will have a combined length of 25 Km (Fig. 1). Table 1 shows the main features and important numbers of the different components of the dam before and after the heightening. As one of the major development projects in Sudan, this project was given a top priority in the strategic planning of the Sudanese government in the last ten years.

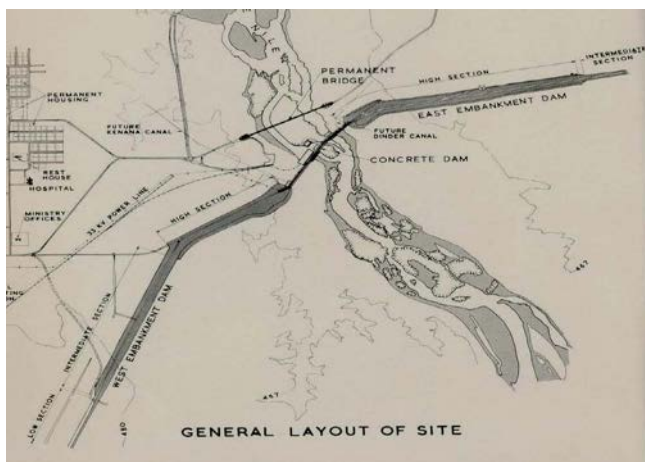


Fig. (1): General Layout of Dam site

Table 1: Main Features of the Dam

Description	Existing Dam	After Heightening
Reservoir		
Volume (without siltation)	3,000 million m ³	7,400 million m ³
Area	290 Km ²	627 Km ²
Maximum Water Level (FSL)	AD 483.02m	AD 493.02m
Overtopping Level (Concrete Dam)	AD 485.22m	AD 495.22m
Overtopping Level (Embankment)	AD 485.52m	AD 495.52m
Minimum Draw down level	AD 438.52m	AD 438.52m
Tailwater		
Maximum Water Level	AD 459.02m (PMF)	AD 459.02m (PMF)
Nominal Wet Season Tailwater level	AD 451.02m	AD 451.02m
Minimum Tailwater level	AD 443.02m	AD 443.02m
Contract Dam		
Roadway level	AD 484.22m	AD 494.22m
Maximum level above Foundation	68.0m	78.0m
Crest Length	1,000m	1,000m
Concrete Volume	850,000 m ³	155,000 m ³
Embankment Dam		
Crest Length (east)	4,000 m	8,500 m
Crest Length (west)	8,500m	15,500m
Fill Volume	5 million m ³	17 million m ³

SMEC International in association with Coyne et Bellier of France undertook a review of the tender design and tender documents which were prepared during the early 1990,s and has updated the design as necessary, including preparation of new tender documents.

In January 2009, Lahmeyer International (LI) of Germany substituted Coyne et Bellier as sub-consultant to SMEC. The main contractor of the project was CCMD Joint Venture of SINOHYDRO and CWE (two Chinese companies).

The Accepted Contract Amount for Roseires Dam Heightening was around three hundred and ninety-six million United States Dollars (USD 396,000).

Time required for Completion of the Works is 1308 days, making October 2012 as the completion date for the whole of the works. All concrete works are expected to finish by the end of May 2012, while the rest of other electromechanical and earth embankments works are expected to finish by October 2012.

1.2 Main Concrete Works

The major concrete works in the project included the heightening of the existing concrete dam by ten meters above the existing concrete level (483.02 m AD) which will accordingly increases the crest levels of both eastern and western embankments from 4000 m to 8,500 m and from 8,500 to 15,500 m respectively. The heightening of the concrete dam will increase the volume of the reservoir from 3,000 million m³ to 7,400 million m³ of water per year. A total of 155,000 cubic meters of high strength concrete were properly prepared, mixed, casted and cured using locally Sudanese aggregates, flay ash and locally produced ordinary Portland cement.

Heightening of the existing concrete dam required extension, web thickening and strengthening of buttress and enlargement of the deep sluices (Fig. 2). In order to pour the new high strength concrete on the existing old concrete, anchor bars and high tensile strength epoxy resin was used as a grout after demolishing and roughening the surfaces of existing concrete. Table 2 below shows the details of anchor bars. Fig. 3 shows a general view of the dam when most of concrete works were finished.



Fig. 2: Thickening and Strengthening of buttresses

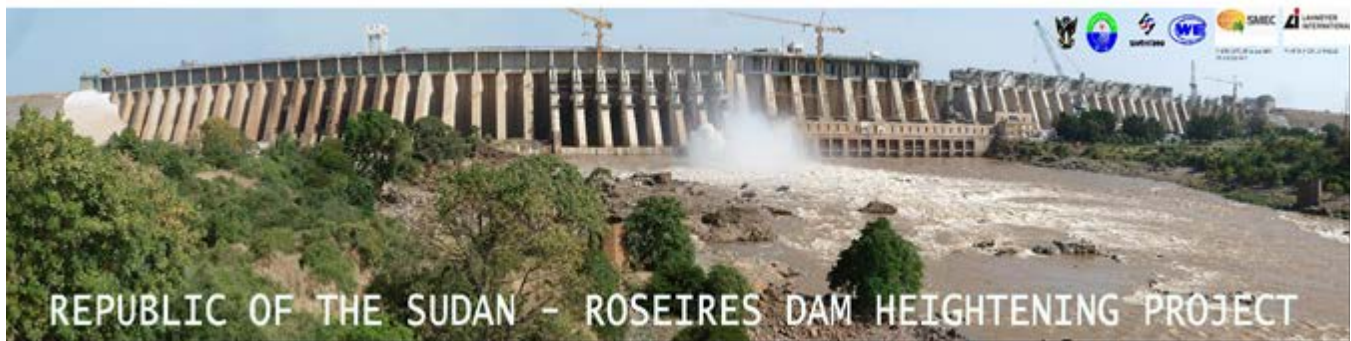


Fig. 3: General View of Concrete Dam Almost Finished

Table 2: Details of anchor bars

Anchor Bars Diameter (mm)	Anchor Bars Length (mm)	Diameter of Drilled hole (mm)	Length of Drilled hole (mm)	Spacing at site staggered (mm)
16	1400	25	700	1000
32	2800	45	1400	1500

3. EXPERIMENTAL PROGRAM

The following subsections present the details of the materials used in the production of HSC and the related testing and specifications.

3.1 Concrete Ingredients

Cement

In this research, a locally produced ordinary Portland cement type I, conforming to ASTM C150 (OPC 42.5N) [5] which is extensively used in Sudan, was used in the trial batches production. The specific gravity of cement used was 3.15, initial and final setting time were 3:17 and 4:38, other physical and mechanical properties test for cement are shown in Table 3.

Table 3: Physical and Mechanical Properties of Cement

Test		Result
Normal Consistency		29%
Setting Time		
	Initial Setting Time	3:17 hrs
	Final Setting Time	4:38 hrs
Loss on ignition		2.29%
Compressive Strength		
	2 Days	20.8 Mpa
	28 Days	56.4 Mpa

Aggregates:

The coarse and fine aggregates used in this study were crushed marble processed from the local quarries around Damazin City, the quarry for Roseires Dam Heightening Project. The maximum aggregate size was 20 mm, the grading of the coarse and fine aggregates is shown in Figure 4. The specific gravity and absorption of the coarse aggregates, determined in according with ASTM C127 [8] were 2.84 and 0.25 respectively, whereas those of fine aggregates, determined in accordance with ASTM C128 [9] were 2.839 and 0.45 respectively. All the sand samples were tested for their absorption percentage in saturated surface dry (SSD) condition. Organic impurities in sand were tested in accordance with ASTM C-40 [10]. The water-cement ration of all trial mixes were based on saturated surface dry condition (SSD) of the aggregates. For the mix HSC6, different type of aggregates from another quarry was used. To compare with marble, granite aggregates from Merwei Dam (recently constructed another concrete dam in the north of Sudan) location were used.

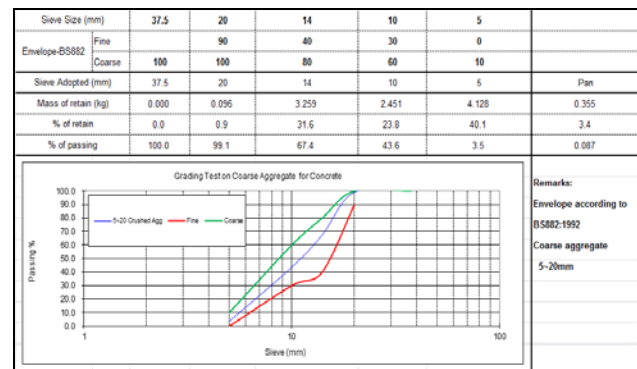


Fig. 4: Gradation of Fine & Coarse Aggregates

Chemical Admixtures (Superplasticizer)

The superplasticizer used in this study has the trade name of "PCA-(I)" from Jiangsu Bote New Materials Company-China. PCA-(I) is a polycarboxylate polymer-based composite admixture. It is a liquid which has the performance of high range water reduction, excellent slump retention and strengthening. The specific gravity of the

superplasticizer was 1.085 and the PH was 8.11 with nil chloride content percentage by weight. It is specially adapted for the production of high durability concrete, self-compacting concrete, high compressive strength concrete, and high workability concrete. PCA-(I) superplasticizer is formulated to comply with the ASTM specifications for concrete admixture: ASTM494, Type G [11].

Mineral Admixtures (Silica Fume and Fly ash)

Silica Fume

Silica fume (SF) is a by-product of the manufacture of silicon metal and ferro-silicon alloys. The process involves the reduction of high purity quartz (SiO₂) in electric arc furnaces at temperatures in excess of 2000°C. SF is a very fine powder consisting mainly of spherical particles or microspheres of mean diameter about 0.15 microns, with a very high specific surface area (15,000-25,000 m²/Kg). Each microsphere is on average 100 times smaller than an average cement grain. At a typical dosage of 10% by mass of cement, there will be 50,000-100,000 SF particles per cement grain. In bulk, SF is generally dark grey to black or off-white in colour and can be supplied as a densified powder or slurry depending on the application and the available handling facilities. SF is available globally. There is no health hazard associated with the use of SF as non-crystalline silica is non-hazardous. The dense microstructure of concrete containing SF leads to major improvements in mechanical performance and resistance to chemicals (such as acids, fuel oil, chlorides and sulfates). SF is ideally suited to the most demanding applications, such as concrete slipways, dam spillways and hard standings, where chloride, chemical or abrasion resistance are required. SF concretes have performed well under these circumstances, as they are chemically stable and have very low permeability. The SF used in this study was in accordance with the most international standards such the European BS EN 13263 Silica fume for concrete, Part 1:2005 Definitions, requirements and conformity criteria Part 2:2005 Conformity evaluation, and the American ASTM C1240-97b Standard specification for silica fume for use as a mineral admixture in hydraulic- cement concrete, mortar and grout. The specific gravity of the silica fume silica fume used in this study was 2.373. SF the pozzolanic high activity, which can be filled the gap between cement, increase the density of the system, so as enhance strength, impermeability, wear proof, anti-corrosion, anti-scour, antifreeze, and strong early performance.

Table 4: Physical Properties of Silica Fume

Moisture Content %	Loss on ignition %	Fineness Retain 0.045 mm	Expansion (mm)	Water Requirement %
0.22	0.48	6.67	1	88.9

Fly ash:

Fly ash used in this study was manufacture by Shandong Zouxian-China.the specific gravity of the fly ash is 2.4, loss on ignition 0.48, the other properties of fly ash are presented in Table 5. ASTM C618; the requirement for Class F and Class C fly ashes, and the raw or calcined natural pozzolans, Class N, for use in concrete. Fly ash properties may vary considerably in different areas and from different sources within the same area. The preferred fly ashes for use in high strength concrete have a loss on ignition not greater than 3 percent, have a high fineness, and come from a source with a uniformity meeting ASTM C 618 requirements [12].

Table 5: Physical Properties of Fly Ash

Moisture Content %	Loss on ignition %	Fineness Retain 0.045 mm %	Density Kg/m ³
0.67	2.7	0.23	2373

3.2 Proportioning, Mixing and Casting of Specimens

There is no empirical method available for proportioning high strength concrete. The procedure to get the proportions in this study is the approach that recommended the in ACI 211.4R-08[13], by starting with mixture proportion that has been used successfully on other projects with similar requirements. Given this starting point, trial mixtures were made in the laboratory and under field conditions to verify performance with actual project materials. Hundreds of trial batches were performed in the laboratory and several adjustments were carried out in order to identify the optimum proportions. The final optimum and best trials used in the construction of the concrete dam are shown presented in Table 6. A concrete fixed mixer with capacity of 0.125 m³ was used, the mixes from Table 6 were scaled down depending on number of molds for different tests, and the mixer was buttered by mixing amount of cement, sand with water because it is difficult to recover all the mortar from the mixer. The mortar adhering to the mixer after discharging is intended to compensate for loss of mortar from the test batch. The following steps were to mix each batch; all the mixing ingredients, including the mixtures, were scaled down and weight out. The coarse and fine aggregates, cement and other cementitious materials were added to the mixer. The mixer rotated for 2 minutes (dry mixing). Superplasticizer was dispersed in about 2/3 of water before added to the mixer and started rotated the mixer again for 2 minutes. The mixer was shut off about 1 minute to let the aggregate absorb some of the paste, the aggregates were approximately in saturated surface dry condition (SSD) at the time the batch was prepared. The aggregates were sprayed with water and covered by burlaps for at least 24 hours.

3.3 Curing and Testing of Specimens

Two different curing methods were used in this study; lime saturated-water curing and the curing compound methods.

The effect of different curing method was studied and commented on. After mixing, a portion of the fresh concrete was placed aside for plastic properties determination. Slump of fresh concrete was measured according to ASTM C143. Precautions were taken to keep the slump between 150-200 mm to obtain pumpable concrete for dam construction. Concrete casting was performed according to ASTM C192. Molds were covered to prevent loss of water from evaporation. Specimens were kept for 24 hours in molds at a temperature of about 23 C in casting room, and then cured for the specified time at approximately 23 C \pm 2 C. The specimens were tested in dry state for compressive, flexural, and splitting strengths tests in accordance with BS EN 12390-2:2000[12], ASTM C78 or ASTM C29, and ASTM C496 respectively.

4. RESULTS AND DESCUSSION

4.1 Optimum Proportions

Table 6 presents the optimum mix proportions for the different grades used in the dam construction project. From the table it is clear that five different grades of high strength concrete (60, 70, 80, 90, 100MPa) were successfully produced using local Sudanese aggregates and fly ash. Three w/c ratios 0.22, 0.32, and 0.35 were found to produce the maximum values of strength in the different grades of concrete. SF and FA replacements in the range of 10 to 15% for each one were found in the optimum combinations of ingredients to produce high strength concrete. Cement content between 390 and 560 Kg/m³ for the five grades.

Table 6: Optimum Mix Proportion for Different Grades of HSC

Mix Design	Concrete Class	W/C	Sand %	Cement (Kg/m ³)	Water (Kg/m ³)	Fly ash (Kg/m ³)	Silica Fume (Kg/m ³)	Admixture (Kg/m ³)	Crushed Sand (Kg/m ³)	Aggregate (5-20) (Kg/m ³)	Unit Weight (Kg/m ³)
HSC1	50 MPa	0.46	42	390	179	0	0	3.21	798	1102	2473
HSC2	60 MPa	0.35	40	419	163	47	0	3.72	746	1119	2496
HSC3	70 MPa	0.32	38	486	173	0	54	6.48	667	1089	2475
HSC4	80 MPa	0.3	38	500	167	0	56	8.896	665	1086	2483
HSC5	90 MPa	0.22	36	585	143	0	65	10.4	621	1104	2528
HSC6	100 MPa	0.22	34	560	154	70	70	12.6	522	1014	2403

4.2 Compressive Strength

Fig. 6 shows the variation of strength concrete for the different grades with time. Starting form three days up to 28 days, it is clear that it was possible to produce high strength concrete (up to 110 MPa) with stable and acceptable rate of strength gain. Considering the type of cement used in this study (ordinary Portland cement) and the relatively small ration of SF, it is also clear that it was possible to produce high strength concrete with very high rates of early strength gain using the same local materials. Different relations were obtained from data accumulated from the tests results. High strength concrete shows a higher rate of strength gain with age than normal strength. Parrott reported typical ration of 7

days to 28 days strength of 0.8 ~ 0.9 for high strength and 0.7 ~ 0.75for normal strength (ACI). The high strength gain with age in this study of 3 to 28 and 7 to 28 days are 0.5~ 0.64 and 0.75 ~ 0.86 respectively.

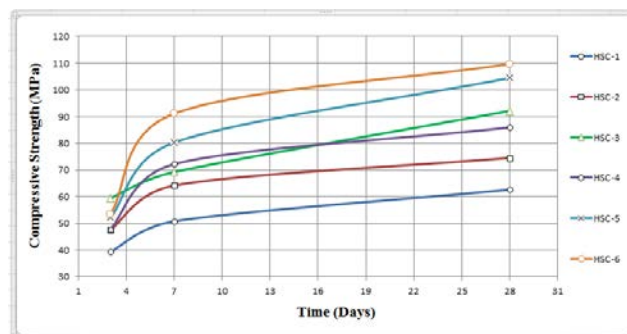


Fig. 6: Variation of Compressive Strength with Time for Different Grades

Fig. 7 shows the variation of the compressive with the water-cementitious materials ratio. Non-linear regression analysis performed for the tow parameters concluded that an exponential formula strongly related the compressive strength and the water-cementitious materials ratio. The exponential formula is shown in the figure. Fig. 8 shows the effect of san content on the compressive strength of HSC. Non-linear regression analyses performed have shown that a quadratic formula strongly relates these two parameters.

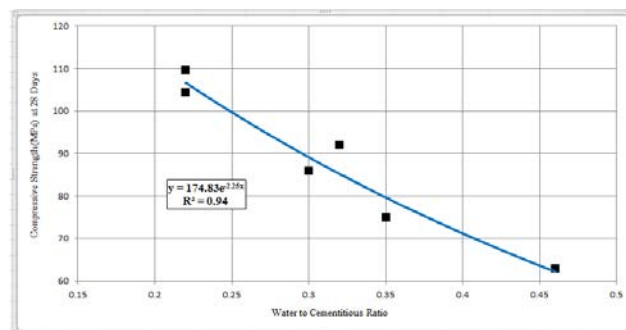


Fig. 7: Effect of Water-Cementitious Ratio on Compressive Strength

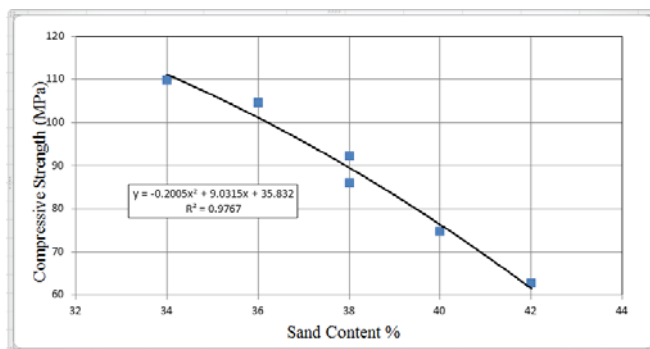


Fig. 8: Effect of Sand Content on Compressive Strength

4.3 Flexural Strength

Fig. 9 shows an exponential correlation between flexural strength and compressive strength of HSC. This correlation obtained from the non-linear regression analysis performed for data collected during the experimental program. A simple linear relationship was found between the flexural strength and the water-cementitious materials ratio and shown presented in Fig. 10.

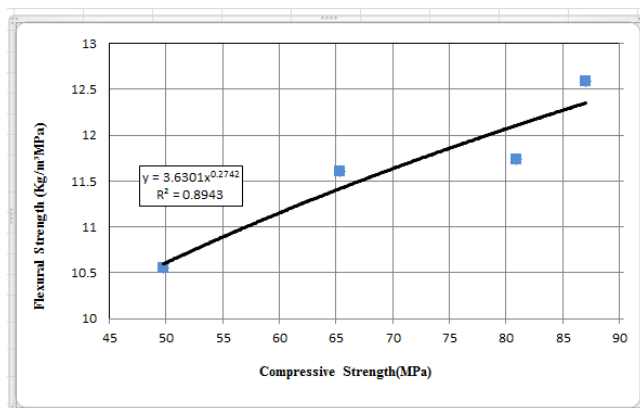


Fig. 9: Variation of Flexural strength with Compressive Strength

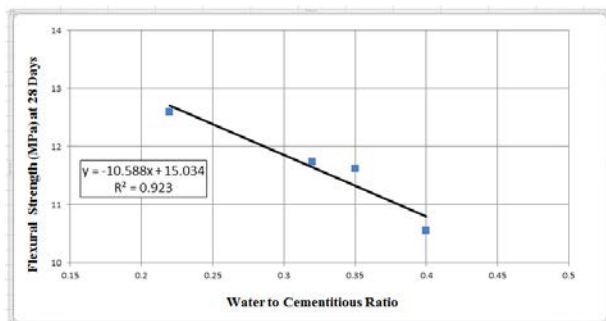


Fig. 10: Variation of Flexural strength with Water-Cementitious Ratio

4.4 Tensile Splitting Strength

Fig. 11 shows the non-linear exponential relation between the splitting tensile strength and the compressive strength of HSC. A non-linear quadratic relation was found to describe the effect of water-cementitious materials ratio on the splitting tensile strength. This relation is shown presented in Fig. 12.

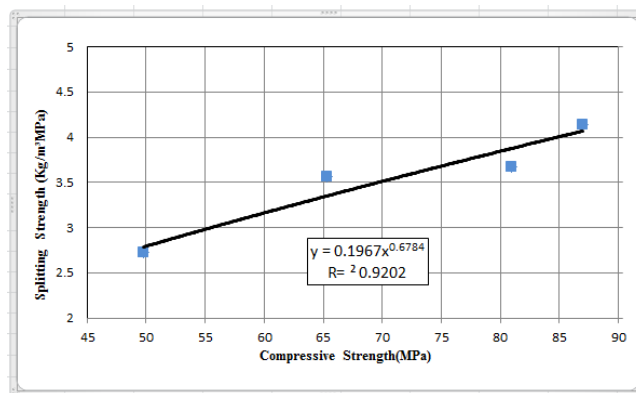


Fig. 11: Variation of Splitting strength with Compressive Strength

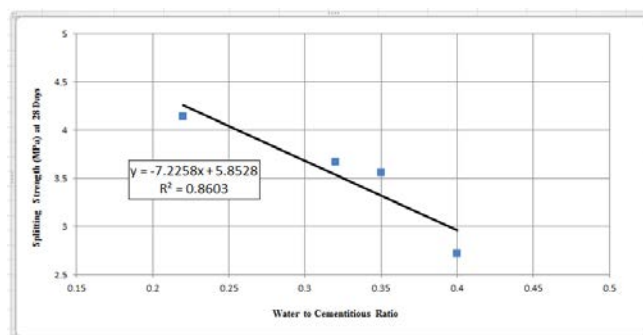


Fig. 12: Variation of Splitting strength with Water-Cementitious Ratio

5. CONCLUSIONS

Based on the findings of this study the following conclusions were made:

- When carefully mixed and cured, locally produced concrete materials (aggregates, fly ash and ordinary Portland cement) of good quality and with their optimum proportioning can be successfully used with other chemical and mineral admixtures to produce high strength concrete of excellent properties.
- It is essential to optimize the doses of mineral and chemical at admixtures (silica fume, fly ash, and super plasticizer) when producing mass high strength concrete in order to control the cost of materials.
- With other mix proportioning parameters held constant, the results of the present investigation indicated that the maximum compressive and flexural strength occurred at

about 10 to 15% Silica fume content and 20% fly ash content.

- iv. The present study shows that the maximum values of compressive strength for different grades were obtained at water-cementitious materials ratios between 0.22 and 0.35.
- v. Both compressive and flexural strengths of concrete continue to increase as the percentage of silica fume increases.
- vi. Non-linear regression analysis was used to correlate different parameters involved in the characterization of high strength concrete produced from local Sudanese aggregates, such as compressive, tensile, and flexural strengths, water-cementitious ratio, sand content, and cementitious content.

ACKNOWLEDGEMENTS

The authors thank SMEC International Company for their cooperation during the part of the experimental testing program of this research. The authors also thank the Dams Implementation Unit (DIU) of Sudan for allowing the authors to use the information and photographs needed in this research paper.

REFERECES

- [1] Berntsson, L.; Chandra, S. and Kutti, T. (1990), "Principles and Factors Influencing High-Strength Concrete Production," *Concrete International*, December, pp.59-62.
- [2] Cetin, A. and Carrasquillo, R. L. 1998. High-Performance Concrete: Influence of Coarse Aggregates on Mechanical Properties, *Journal of ACI Materials*, 95:252-261.
- [3] Muhammad A. Rashid & Mohammad Abul Mansur (2009), "Considerations in the Producing High Strength Concrete", *Journal of Civil Engineering (IEB)*, 37(1) (2009) 53-63.
- [4] ACI 363R-92: "State-of-the- Art Report on High Strength Concrete", American Concrete Institute, Farmington Hills, Mich., 394 pp.
- [5] ASTM C-150 Standard Specifications for Ordinary Portland Cement, Type I. American Society for Testing and Materials, Tests Specimens and Laboratory, Philadelphia, PA, 2003.
- [6] ASTM C-136, Standard Test Method for Sieve Analysis of Fine and Coarse Aggregates, Philadelphia, PA: American Society for Testing and Materials, 2001.
- [7] ASTM C-33, Standard Specification for Concrete Aggregates, Philadelphia, PA: American Society for Testing and Materials, 2003.
- [8] ASTM C-127 Standard test method for Determination of The Specific Gravity and Absorption of the Coarse Aggregates, Philadelphia, PA: American Society for Testing and Materials, 2000.
- [9] ASTM C-128 Standard test method for Determination of The Specific Gravity and Absorption of the Fine Aggregates, Philadelphia, PA: American Society for Testing and Materials, 2000.
- [10] ASTM C-40, Standard test method for organic impurities in sand for concrete, Philadelphia, PA: American Society for Testing and Materials, 2003.
- [11] ASTM C-494: Standard Specifications for Concrete Super plasticizing Admixtures, Philadelphia, PA: American Society for Testing and Materials, 2003.
- [12] ASTM C-618:" Standard Test Method for Physical Properties of Fly Ash", PA: American Society for Testing and Materials, 2001.
- [13] ACI 211.4R-93:"Guide for Selecting Proportions for High-Strength Concrete", American Concrete Institute, Report 211.4R-93, Detroit, 1993.
- [14] British Standards Institution, "Methods for making concrete cubes in laboratory," BS-1881-116: Part 110, 1990.
- [15] British Standards Institution, "Methods for Determination of compressive strength of concrete cubes" BS 1881-108: Part 110, 1990.

BEHAVIOR OF FOLDED PLATE ROOFING SYSTEMS WITH OPENINGS LOCATIONS

***HALA ELKADY -**AHMED HASSAN**

***Professor, National Research Center** Beni Suef University, Egypt and Umm Al-Qura Univeristy, Saudi Arabian**

ABSTRACT

This paper investigates the effect of openings locations on the structural behavior of quadratic folded plate (Q.F.P) roofs by using different geometric configurations for the main elements of the system. Furthermore, the impact of such variance on the behavior of the structure system under both static and dynamic conditions is investigated in this study. The selected and investigated parameters in this study are openings locations and folded plates rise (height). Different spans of 14, 20 and 26 meters were selected for all the investigated parameters. 3-D Finite Element Model (FEM) was adopted to examine the suggested variables to meet the target of this study. Linear static analysis was performed to analyze the effect of the investigated parameters on system deflections, moments, tension and compression stress. Quadratic folded plate Q.F.P slabs with rise varying from 90 to 180 cm were studied. Results indicated that the difference in the rise reduced the roof deflection by 72%. Moreover, the behavior of the folded plate with openings at different locations was improved.

Also, results indicated that the maximum bending moment for intermediate beams increased by 69% in case of center openings locations at beam center. The maximum bending moment at 0.57 L (intermediate beam length) for quarter openings locations was increased by 64%. The edge openings locations had a slight effect on the diaphragm bending moment and the intermediate beam fixed end moment.

Three Dimensional dynamic modal analyses were performed and the effect of different openings locations on the fundamental modes was investigated. Results of modal analysis showed that openings locations had no significant effect on the fundamental frequencies and Fundamental mode shapes. The obtained results from this study emphasized on the importance of elaborate numerical analysis to deal with such sensitive models, as the geometric properties and openings locations for each contributing element which had a clear effect on the overall performance of the system.

Finally, model results proved that folded plate openings locations at center is the most effective parameter compared to the others investigated parameters, while edge openings locations in the folded plate had the lowest effect on both static and dynamic behavior of the investigated system.

Keywords: Folded plates; Height; Openings location; Free vibrations

1. INTRODUCTION

Folded plate is one of the most practical structures used in civil engineering applications since it has many merits such as lightweight, easy to form, low cost and high resistance for loads. It is used in many applications such as roofs, sandwich plate cores and cooling towers. As the use of folded plates has many merits compared to flat plates, it is essential to investigate their behavior with openings and without openings under different load conditions. Subsequently, there are several methods available to analysis this type of structure (1 to 8). Conventional analysis methods are simple and easy while they have some limitations of generality of application and precision.

Early researchers solved folded plate problems approximately with the use of beam method or the theory that neglected the relative joint displacement (2). However, these two methods met difficulties in dealing with the generalized folded plate problems. Both computational approaches and numerical methods for the analysis of the folded plates offer more precise solutions compared to

Conventional analysis methods. The methods of interest are including finite strip methods, one of the earliest work presented based on this method was introduced by Cheung (1969) through the work presented by Golley and Grice (1989) along with the work presented in the same year by Eterovic and Godoy (1989). The combined boundary element-transfer matrix method [Ohga et al., 1991] and finite element method (FEM) which was a topic of research for many previous researchers [Liu and Huang, 1992; Perry et al., 1992; Duan, 2002]. From these methods, the FEM is the most convenient method because it can be applied to analyze large complex structures as well as all kinds of boundary conditions and loadings can be easily implemented. Subsequently, most of commercial software used for structural analysis used FEM method.

Quadratic folded plate Q.F.P roofs are one of the most common types used for roofing systems and that is why it was selected in this study. The presented parametric study on the effect of openings locations on folded plate behavior were examined by using Finite Elements analysis and Linear Static Three Dimensional F.E. analysis. The effects of openings locations and folded plate rise on slab deflection, intermediate beam moments, and stress distribution on slab,

maximum stress were executed.

In some cases, Quadratic folded plate Q.F.P slabs system should include openings. They may have small dimensions, like those needed to accommodate heating, plumbing, and ventilating risers, floor and roof drains, and access hatches but in some cases openings may be larger than the code limitation in size and position. The large openings presence in slab system reduces the stiffness and increases the deflection and then there are previous studies investigated the openings on the behavior of flat plate structure.

Based on the output of models, design charts for this particular system will be presented to select the best openings locations and also the parameters effect on the behavior of the structural system will be evaluated. Recommendations will be given in accordance with the impact of openings locations on the behavior of structural system.

2. FINITE ELEMENTS ANALYSIS

2.1 Geometry and Dimensions of the Investigated Systems

Q.F.P. panels of 7.8 ms width were studied as presented in Figure 1. This width was kept constant throughout the analysis, while the three different spans of 14, 20, and 26 m were changed to investigate their effect on the behavior of structural system. A constant openings size of (3m×2m) which is located in the top surface of the folded plate slab at different positions (center- quarter – edge) were considered for each panels. Models heights are varying from 90 to 180 cm. A 3-D F.E. analysis was performed and the roof was modeled using 3-D quadratic shell elements which are presented in Figure 2. While intermediate beams, end diaphragms, and columns were modeled as 3-D frame elements as shown in Figure 2.

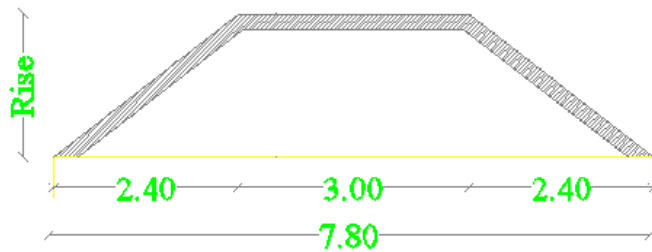


Figure 1: Cross section dimensions of investigated models

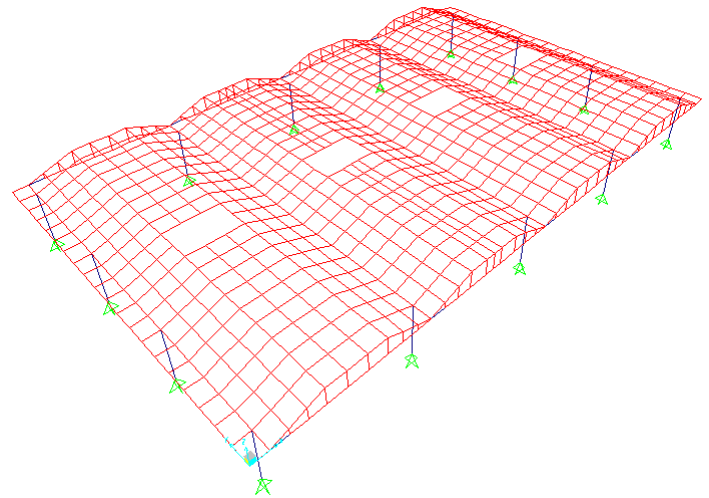


Figure 2: 3-D model of investigated folded plates panels and center openings locations.

2.2 Static Analysis of Q.F.P System

3-D Static linear F.E. analysis was performed by applying each of the parameters under study separately as openings locations and folded plate rise. An imposed static load of 150 kg/cm² was applied on all the models, as a make up for flooring and service load. Throughout the analysis, the following straining actions and deformations are monitored and compared. Deflections and stresses of the folded plate are checked and the maximum bending moments at the intermediate beams and diaphragm are reported. The effect of the tested parameters will be presented in details later.

2.2.1 Effect of Openings Locations on the Q.F.P. System

Maximum Deflection for the Constant Rise

The first investigated parameter was the effect of the folded plate openings locations on the maximum deflection at the center of the folded plate. There are three different spans of 14, 20, and 26 meters were studied. Figure 3 shows the maximum deflection for the folded plate slabs at the center point in the case of different lengths used versus openings locations for folded plate. In case of center openings locations, it is obvious that the maximum deflections for the span length of 26 m and 0.9 m rise is increased from 47.6 mm to 58.2 mm, with a percentage increase of 22%. The increase of the central deflection in the case of quarter openings locations was found 51.8 mm, with a percentage increase of 9 %. The central deflection was found 47.6 mm in case of edge openings locations, which has minor, effect on the center deflection point. The measured deflection value in these cases is approximately the same as in the case of control model.

For the 20 m Q.F.P span when the rise of folded plate equals 0.9 m, the central deflection was found 15.7 mm as presented in Figure 3. The openings locations have a significant effect on the increase of the central deflection in the most investigated cases. For example, the deflection increased to 19.3 mm and 17 mm, which equals 23% and 8% in case of

center and quarter openings locations respectively, in some investigated points compared to the control case.

The central deflection for the folded plate with 14 m span was found 3.73 mm and this case is considered as a control model. The effect of the openings locations on the central deflection were 4.45 mm (increasing by 19 %), 3.89 mm (increasing by 4 %), and 3.77 mm which corresponding to center, quarter, and edge openings locations, respectively.

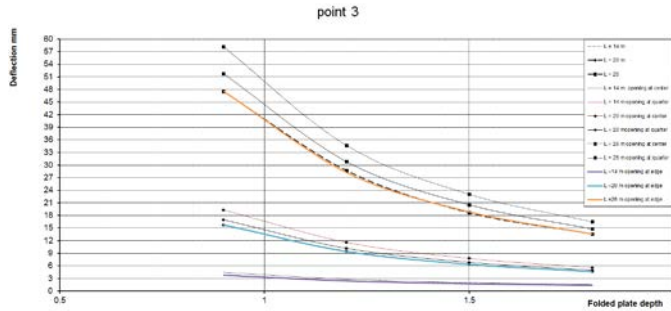


Figure 3: Q.F.P. slabs maximum deflection versus different opening locations for different rise.

2.2.2 Effect of Folded Plate Rise to the Maximum Deflection

The investigated folded plate rise in this study was varying from 90 cm to 180 cm. The folded plate rise has a significant effect on decreasing the central deflection as shown in Figure 3. For the longest investigated span of 26m, the increase of the folded plate depth (rise) from 0.9 m to 1.8 m with center openings locations results in the reduction of deflection from 58.2 mm to 16.5 mm. While, the deflection induced at the quarter openings locations reduced from 51.8 mm to 14.8 mm in the case of the folded plate rise 0.9 m to 1.8 m.

The case of 20 m model doubling, the folded plate rise from 0.9 m to 1.8m reduced the central deflection from 19.3 mm to 5.62 mm at the center openings locations while at the quarter openings locations reduced the center point deflection from 17 mm to 5 mm.

In the case of 14 m folded plate span, the reduction percent on the central deflection was found 65 % at both center and quarter opening locations as presented in Figure 3. The Q.F.P slab rise is reduced the effect of openings locations on the maximum deflection.

2.2.3 Effect of Folded Plate Openings Locations on the Intermediate Beam Moments.

Three trials for the openings locations of Q.F.P. slabs were considered in this study; center, quarter and edge. These openings have a significant effect on the increase of the maximum bending moment of the intermediate beam and the value of moment is depending on the opening positions. In the case of 26 m length without openings, the maximum bending moment at the center of the intermediate beam was found 16.8 m.t, while at the center openings locations the bending

moment was found 28.37 meter ton (increasing by 67 %). For the 20 m and 14 m folded plate lengths, the maximum bending moments increased by 60% and 42 % respectively. The effect of opening locations at quarter or edge has no effect on the maximum moment at the center and this result close to the control model result as shown in (Fig.6). The maximum moment was found at the quarter of the intermediate beam at the openings locations and it increased by 64 %, 46% and 30% which corresponding to different model lengths of 26 m, 20 m and 14m respectively as shown in Figure 5. The edge openings locations have a limited significant effect on the intermediate beam bending moment as shown in Figure 4.

Figure 4-6 gathers the effect of both opening locations and Q.F.P. rise on the bending moment of the intermediate beam. It is obvious from these Figures that for all investigated models, the increase of the folded plate rise from 0.9 to 1.8 m results in a reduction for moment of the intermediate beam at different locations.

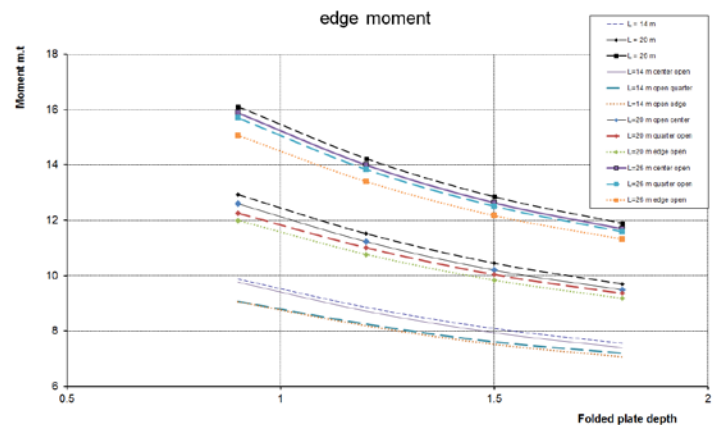


Figure 4: intermediate beam fixed end moment versus different opening locations.

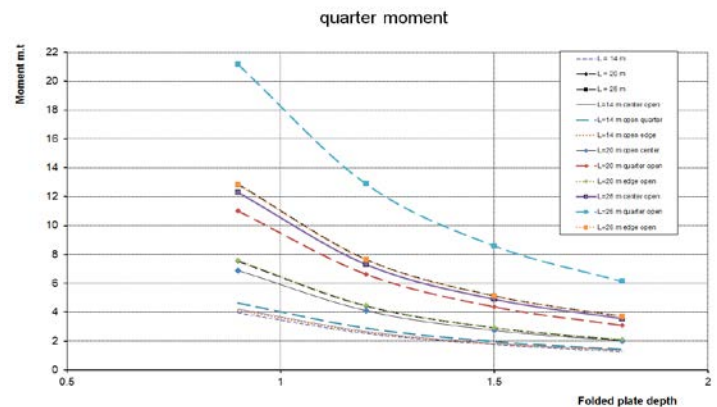


Figure 5: intermediate beam moment at quarter versus different openings locations.

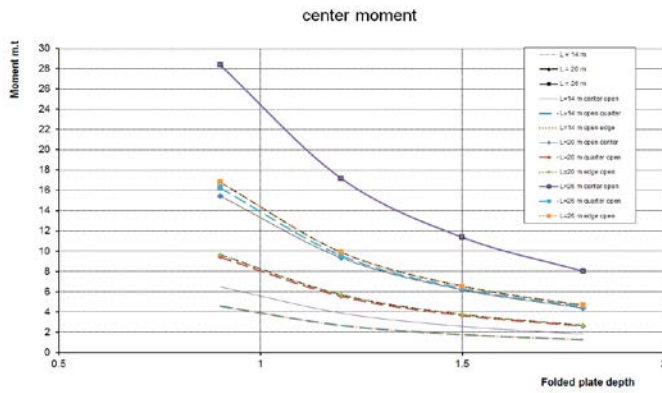


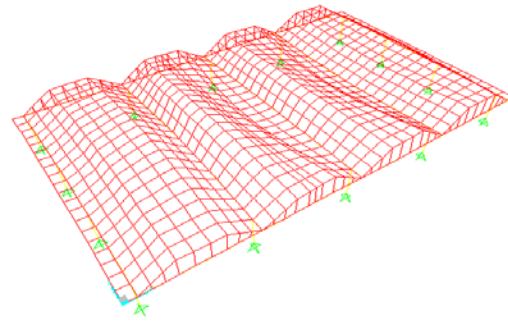
Figure 6: maximum moment of intermediate beam versus different openings locations.

2.3 FREE VIBRATIONS ANALYSIS

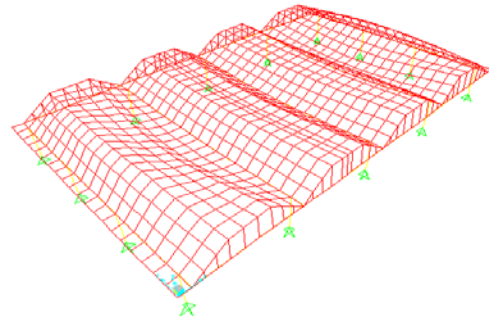
The investigated systems were subjected to free vibrations analysis. Eigen values analysis was adopted in the linear dynamic analysis. For the investigated spans, with different parameters arrangement of mode shapes was consistent. Columns sway dominates the first three modes and then the roof deformations is controlled the next ones. Figure 7 displays the roof modes and it can be seen from this Figure that the dominating mode for the Q.F.P. slab is intermediate symmetric bending mode. The second mode was anti-symmetric bending, followed by symmetric bending of the external spans and then followed by alternative modes of anti-symmetric and symmetric plate bending.

In Figure 8, the fundamental frequencies of the system were given for Q.F.P. slabs with spans of 14, 20 and 26 meters. It is noticed from this Figure that the first three modes were columns lateral displacements. Fundamental modes for the folded plate roof started from the fourth mode. The frequency of three fundamental modes for the roof of 14 and 20 meters spans were found very close, while the 26 meters frequencies was found 27% lower than the 14, and 20 meters spans.

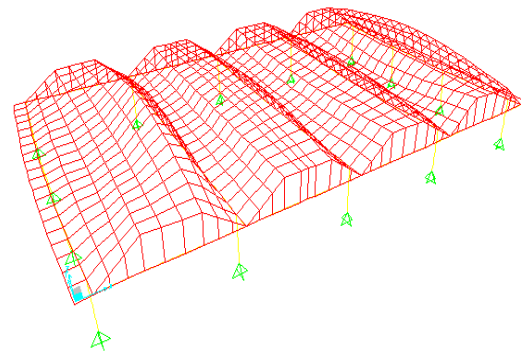
Figure 9 presents the effect of the roof rise on the fundamental frequencies of the system with includes span of 20 meters. Two rises were investigated which were 90, and 180 cm. It is observed that the system with higher rise of (180 cm) has higher fundamental frequencies by 20%. This result is probably attributed to the higher stiffness of the used roof. The change in the openings locations has no effect on the roof modes as well as the fundamental frequencies when free vibration analysis is subjected.



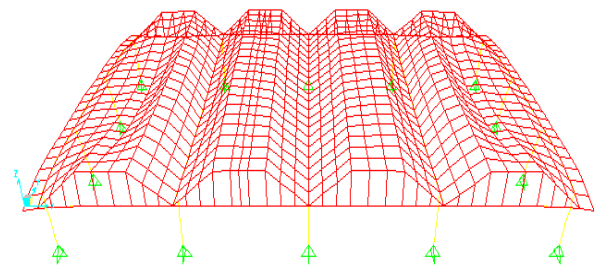
Q.F.P.slab second mode shape



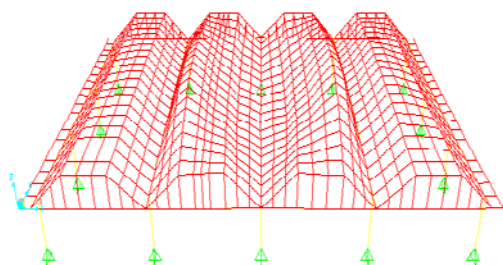
Q.F.P.slab third mode shape



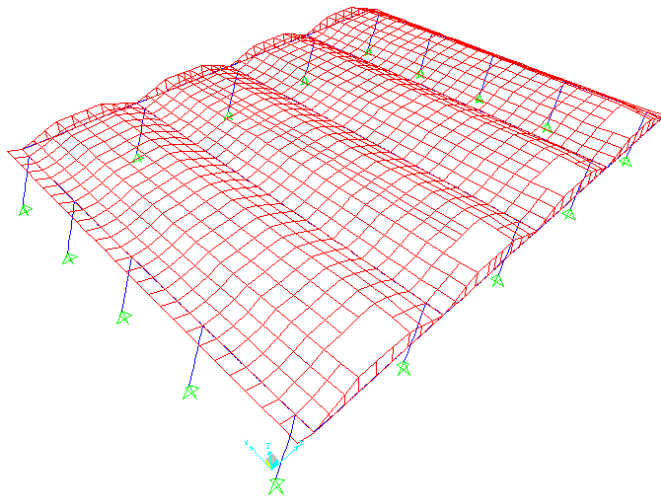
Q.F.P.slab fourth mode shape



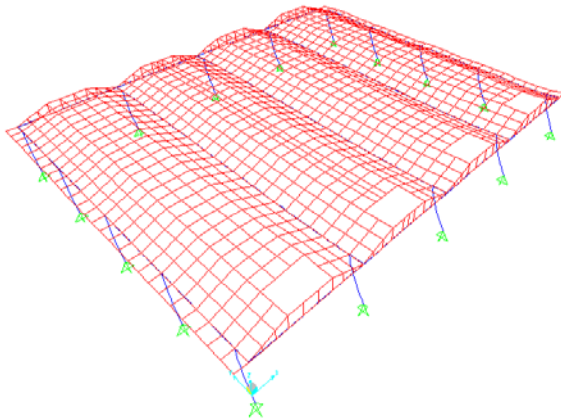
Q.F.P.slab fifth mode shape



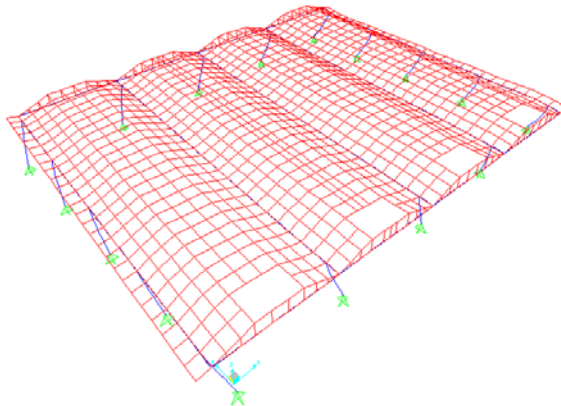
Q.F.P.slab First mode shape



Q.F.P. slab with edge opening third mode shape



Q.F.P. slab with edge opening fourth mode shape



Q.F.P. slab with edge opening fifth mode shape

Figure 7: Fundamental mode shapes of Q.F.P. slab

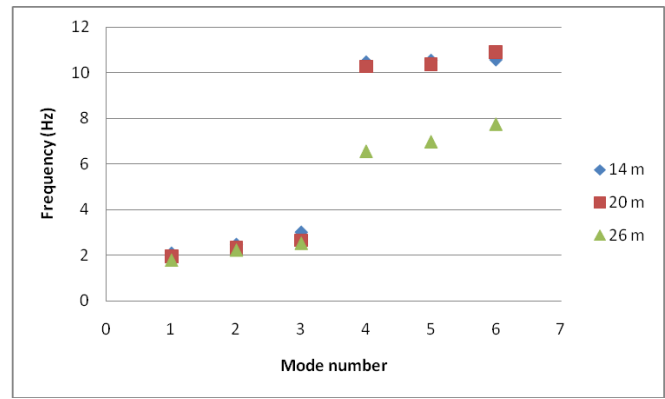


Figure 8: Fundamental modes frequencies for folded plate roofs with different spans.

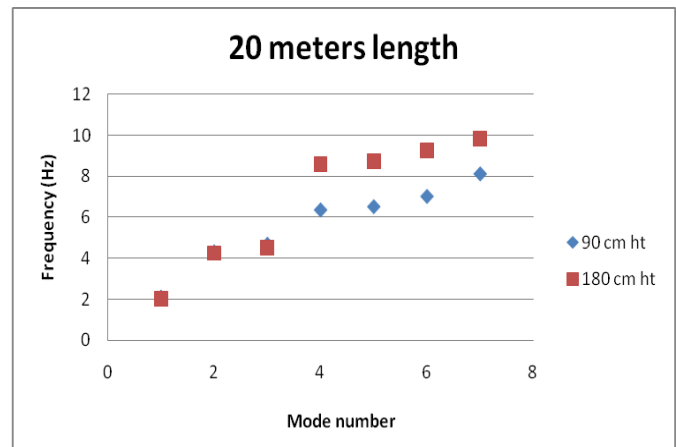


Figure 9: Effect of folded plate rise on fundamental frequencies under free vibrations.

3. DISCUSSION OF RESULTS

For the tested models edge openings locations has a limited effect on the Q.F.P roofs central deflection, maximum bending moment, edge moment of intermediate beam and the diaphragm bending moment. This effect did not exceed more than 3% as shown in Figure 10. The center openings locations have a clear effect on the central deflection compared to the deflections induced in both quarter and edge openings locations. The center openings locations increased deflection by 14 % more than quarter opening effect for 14 m and 20 m but in Case of 26 m this percentage was 12%.

Doubling the height of the investigated folded plate from 0.9 meters to 1.8 meters is associated with a reduction in deflection by an average value of 72% as shown in Figure 12. From the same figure it is shown that there is no variation in the increase of the percentage of central deflection for the different spans used from 26 m to 20 m, while the effect of the opening locations at 14 m folded plate length was found lower than the induced in the cases of 20 m and 26 m folded plate spans.

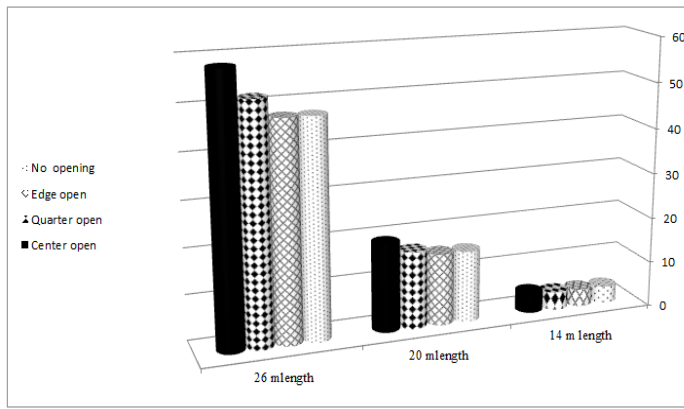


Figure 10: Q.F.P. slabs maximum deflection versus different opening locations for different length.

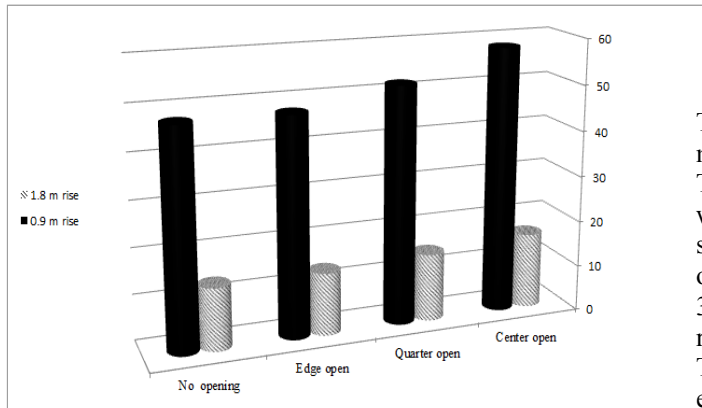


Figure 11: Q.F.P. slabs maximum deflection versus different opening locations for different length.

The maximum moment location was found at the intermediate beam center in the case of the control model and center openings locations model. In the case of quarter openings locations, the maximum moment's position was found at a length of 0.75 (at openings locations) for the intermediate beam length. The maximum moment in case of edge openings locations was found close to the maximum moment of control model as presented in Figure 12.

Varying the openings locations has a significant effect on the maximum moment of intermediate beam. The center openings locations increased the maximum moment by 67%, 60% and 42% which corresponding spans of 26 m, 20 m, and 14 m, respectively. The maximum moment is located at the quarter of the intermediate beam at openings locations and it increased by 64 %, 46% and 30% which corresponding to different model lengths of 26 m, 20 m and 14m, respectively as reported in Figure 12. The openings locations have a limited effect on the edge moment and diaphragm bending moment, which did not exceed more than 3%. At the quarter openings locations there is no effect on the maximum

moment at intermediate beam center and edge moment observed.

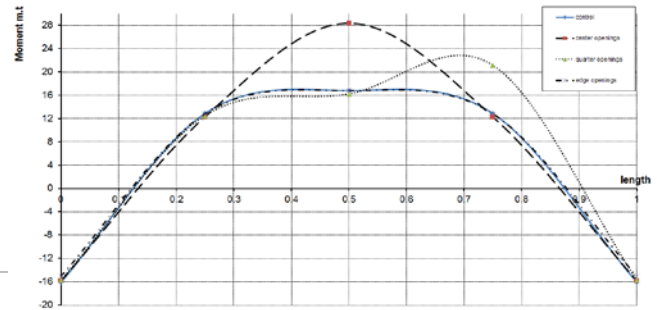


Figure 12: Intermediate beam moment versus different openings locations.

The variations of openings locations have minor effect on the maximum tensile stress. This effect do not exceed than 4%. These openings have a great effect on the compression stress, which increased by 174%, 170%, 120% for the different spans of 26 m, 20m and 14m respectively. The quarter openings locations increased the compression stress by 56%, 30%, and 5% for different spans 26 m, 20m, and 14m respectively.

The openings locations from center to edge have a limited effect on the fundamental frequency of the Q.F.P slab. Mode shapes patterns arrangement was not affected by the variation in the openings locations from center to the edge. In other words, it can say that the mode shapes came in the same order for all the investigated spans.

4. CONCLUSION

- The propose approximate static solutions for the fixed boundary conditions at the end diaphragms for the Q.F.P slab ends (9, 10, and 11) are not reliable for the longer spans, especially for spans higher than 20 meters. Subsequently, the stiffness should be recommended in the numerical modeling.
- Increasing folded plate rise was the most significant factor in improvement the static analysis for deflection control, on the other hand increasing the roof rise lead to an increase in the fundamental frequencies of the system.
- Rise effect was most effective in shorter spans.
- Increasing folded plate rise enhanced the structural behavior of the overall Q.F.P. system.
- Edge openings locations have a limited effect on the Q.F.P roofs static and dynamic behavior.
- Center and quarter openings locations have an effect on the change in static deflections, or straining actions of the system.

- Spans from 14 to 20 meters for the investigated Q.F.P. slabs had very close fundamental frequencies, this effect widens noticeably on analyzing longer spans.
- Center openings locations has a great effect on the Q.F.P. slabs deflection greater than quarter openings locations by 14%.
- The variation of the openings locations has a significant effect on the maximum moment of intermediate beam, while the center openings locations increased the maximum moment by 67%, 60% and 42% which corresponding spans of 26 m, 20 m, 14 m, respectively.
- The openings locations has a limited effect on the edge moment and diaphragm bending moment, which did not exceed more than 5%
- At the quarter openings locations there is no effect on the maximum moment at intermediate beam center and edge moment observed. The maximum moment is located at the quarter of the intermediate beam at openings locations and it increased by 64 %, 46% and 30% which corresponding to different model lengths of 26 m , 20 m and 14m, respectively.
- The openings locations from center to edge have a limited effect on the fundamental frequency of the Q.F.P slab.
- Mode shapes patterns arrangement was not affected by the variation in the openings locations from center to the edge. In other words, it can say that the mode shapes came in the same order for all the investigated spans.

5. REFERENCES

- [1] Cheung YK., "Folded plate structures by finite strip method.", *Jr of Struct Div ASCE* 1969;95:2963–79.
- [2] Golley BW, Grice WA., "Prismatic folded plate analysis using finite strip-element.", *Comput Methods Appl Mech Eng* 1989;76:101–18.
- [3] Eterovic AL, Godoy LA., "An exact-strip method for folded plate structures.", *Comput Struct* 1989;32(2):263–76.
- [4] Ohga M, Shigematsu T, Kohigashi S., "Analysis of folded plate structures by a combined boundary element-transfer matrix method", *Jr. of Comput Struct* 1991;41(4):739–44.
- [5] Liu WH, Huang CC., "Vibration analysis of folded plates.", *Jr. of Sound Vibr* 1992;157(1):123–37.
- [6] Perry B, Bar-Yoseph P, Rosenhouse G., "Rectangular hybrid shell element for analyzing folded plate structures.", *Comput Struct* 1992;44(1–2):177–85.
- [7] Duan M, Miyamoto Y. , "Effective hybrid/mixed finite elements for folded-plate structures.", *J Eng Mech* 2002;128(2):202–8.
- [8] Guha Niyogi A, Laha MK, Sinha PK., "Finite element vibration analysis of laminated composite folded plate structures", *. Jr. of Shock Vibr* 1999;6:273–83.
- [9] Bar-Yoseph P, Hersckovitz I., "Analysis of folded plate structures.", *Jr. of Thin-Walled Struct* 1989;7:139–58.
- [10] Bandyopadhyay JN, Laad PK., "Comparative analysis of folded plate structures.", *Jr. of Comput Struct* 1990;36(2):291–6.
- [11] Peng L.X, Kitipornchai S., Liew K.M. , "Bending analysis of folded plates by the FSDT meshless method", *Journal of thin walled str.* 44, 2006, p 1138-1160.
- [12] Belytschko T, Lu YY, Gu L. , "Element-free Galerkin methods", *. Int J Numer Methods Eng* 1994;37:229–56.
- [13] Liew KM, Ng TY, Wu YC., "Meshfree method for large deformation analysis—a reproducing kernel particle approach.", *Eng Struct* 2002;24(5):543–51.
- [14] Bernadou .M, "Finite Element Methods for Thin Shell Problems", *J. Wiley & Sons*, 1996.
- [15] Chapelle B, K.J. Bathe, "Fundamental considerations for the finite element analysis of shell structures", *Comput. Struc.* 66 (1998) 19–36.
- [16] Liew KM, Wu YC, Zou GP, Ng TY., "Elasto-plasticity revisited: Numerical analysis via reproducing kernel particle method and parametric quadratic programming", *Int J Numer Methods Eng* 2002;55(6):669–83.
- [17] Liew KM, Huang YQ, Reddy JN. "Moving least square differential quadrature method and its application to the analysis of shear deformable plates.", *Int J Numer Methods Eng* 2003;56(15):2331–51.
- [18] Liew KM, Zou GP, Rajendran S., "A spline strip kernel particle method and its application to two-dimensional elasticity problems.", *Int J Numer Methods Eng* 2003;57(5):599–616.
- [19] Liew KM, Chen XL., "Buckling of rectangular Mindlin plates subjected to partial in-plane edge loads using the radial point interpolation method", *. Int J Solids Struct* 2004;41(5–6):1677–95.
- [20] Liew KM, Cheng Y, Kitipornchai S., "Boundary element-free method (BEFM) for two-dimensional elastodynamic analysis using Laplace transform.", *Int J Numer Methods Eng* 2005;64(12):1610–27.
- [21] Liew KM, Ren J, Reddy JN., "Numerical simulation of the thermomechanical behaviour of shape memory alloys.", *Int J Numer Methods Eng* 2005;63(7):1014–40.
- [22] Liew KM, Cheng Y, Kitipornchai S., "Boundary element-free method (BEFM) and its application to two-dimensional elasticity problems.", *Int J Numer Methods Eng* 2006;65(8):1310–32.
- [23] Chen JS, Pan C, Wu CT, Liu WK., "Reproducing kernel particle methods for large deformation analysis of nonlinear structures.", *Comput Methods Appl Mech Eng* 1996;139:195–227.
- [24] Liew KM, Wang J, Tan MJ, Rajendran S. , "Postbuckling analysis of laminated composite plates using the mesh-free KP–Ritz method ", *. Comput Methods Appl Mech Eng*

Improving concrete compressive strength using natural additive

Abdoullah Namdar, Ideris Bin Zakaria and Nurmunira Binti Muhammad @ Atan
Faculty of Civil Engineering & Earth Resources
Universiti Malaysia Pahang, Malaysia
anamdar@ump.edu.my

ABSTRACT

Construction material quality is one of the important issues for eliminating any types of problems may face civil engineering structures. For improving concrete quality and reducing construction cost a simple procedure has been evaluated. Thermally treated bentonite of 6% quantity of cement content in concrete mixture design is used as a concrete additive to assess concrete compressive strength. The XRD experimental for studying crystal structure of modified bentonite has been conducted. The result indicated acceptable improving concrete compressive strength. And in compare to the natural additive cost the method has economic effective, and can be produced at any situation, and helps to reduce construction cost especially for low cost construction.

Keyword: Bentonite; crystal structure; compressive strength; natural additive; low cost construction

1. Introduction

The mineral additives could have different effects on the properties of concrete due to different mineralogical and chemical process [1]. The mineral admixture has different effect on high strength concrete. And full loads apply to concrete structure on early age is important to a construction programme [2]. There is an investigation on natural mixed minerals to analyze compressive concrete strength through effect of natural mixed minerals on composition of the gel phase and its structure [3]. It has been instructed that the mineral admixture in concrete mixed design decreased both unit weight and compressive strength [4]. From this point of view European Standards (EN 206-1) restrict the use of mineral additions to low proportions during the manufacture of concrete [5]. It is due to some mineral addition in high percentages as a replacement for cement can result in a concrete with lower compressive strength. From other hand using proper combination of minerals results in produce economical concrete and CO₂ emissions reductions for sustainable development [6]. To enhancement of concrete strength using mineral mixture technique some empirical relations has been investigated [7]. The rational methods have also been proposed to analysis mineral additives effect on concrete strength in specific age [8]. There is reported an artificial neural networks study for predicting the core compressive strength of self-compacting concrete (SCC) mixtures with mineral additives [9]. In view of sustainable development, mineral admixture commonly is used to replace part of cement in concrete as supplementary cementitious materials [10], [11]. One of method is performance of steam cured concrete by adding mineral admixtures to determined concrete compressive strength in short and long term tests [12].

The mineral admixtures to partially replace cement preserve the non-renewable resources required for the production of cement [13-15]. In attention to the mineral admixture is utilized for many years either as supplementary cementitious materials in Portland cement concretes or as a component in blended cement [16]-[20], the objective of this study is to asses best heat level in modify bentonite to develop appropriate mineral under laboratory condition for enhancement concrete compressive strength in early age, produce low cost concrete, reducing chemical additive and cement consumption in concrete mixture design which decreases environment pollution.

2. Methodology and Experiments

In this research work the bentonite has been selected for improve concrete compressive strength. The bentonite was subjected to the heat for 1 hour for 200 °C, 400 °C, 600 °C and 800 °C. The concrete mixed design is made to reach acceptable compressive strength. The unheated and heated bentonite hais mixed in concrete mixture design in 6% quantity of consumed cement. The concrete compressive strength for 7 days, 14 days and 28 days have been tested. To study macro properties of bentonite-cement mixture X-ray is used.

3. Result and discussion

In an experimental investigation on Pakistani bentonite (from Jehangira, Swabi District) is treated by heat at 500 °C and 900 °C and the cement in mortar and concrete was replaced with the bentonite at 0%, 20%, 30%, 40% and 50% by cement mass. And used as a cement replacement material in mortar and concrete, it was reported that Pakistani bentonite can be used to replace up to 30% of cement to produce concrete with sufficient

compressive strength for low-cost construction resistant to sulphate attack [21]. The proportion of bentonite, (3%, 6%, 9%, 12%, 15%, 18% and 21% by weight of cement) is used as replacement. And has been found that the workability, fresh concrete density and water absorption decreased as bentonite usage is increased. The comparative compressive strength analysis indicated that at 3 days of testing, the mixes containing bentonite showed lower strength than control mix while at 56 days of testing, the bentonite mixes showed higher strength than the control mix [22]. When bentonite is thermally treated by heat for one hour under 200 °C the Montmorillonite-15A has been developed, this mineral has strong negative effect on concrete compressive strength (table 1 and figure 1). In second part of experiment in thermally treated of bentonite, 400 °C, heat for one hour has been used to observe new

modification in bentonite. In this stage Rectorite is created. The Rectorite mineral has reduced concrete compressive strength significantly. Up to this level of research thermally treating bentonite is presented disappointing results. The 600 °C heat is submitted to the bentonite for one hour, several minerals have been developed (figure 2 and table 2), these minerals improve concrete compressive strength due to number of minerals it is difficult to conclude effect of them on improving concrete compressive strength. In continuing investigation 800 °C heat has been applied to the bentonite for one hour and quantity of 6 % new developed minerals is added to concrete mixed design. The concrete compressive strength test had shown that in improving around 8% concrete compressive strength in early age of 7 days and also 13% in 28 days.

Table. 1. Concrete compressive strength

Concrete type	% of Bentonite	7days	14 days	28 days
		Stress (N/mm ²)	Stress (N/mm ²)	Stress (N/mm ²)
Unmixed bentonite	-	25.77	30.86	34.42
Unheated bentonite	6	23.13	27.76	31.24
bentonite 200 °C	6	15.5	18.46	27.77
bentonite 400 °C	6	11.8	14.71	23.33
bentonite 600 °C	6	27	30.36	31.5
bentonite 800 °C	6	27.95	35.65	38.95

Table. 2. Minerals is developed in bentonite thermally treated

Bentonite type	Name of minerals
Unheated	alpha-Si O ₂ , quartz low high HP, syn
200 °C	Montmorillonite-15A, alpha-Si O ₂ , quartz low,
400 °C	Rectorite, alpha-Si O ₂ , quartz low,
600 °C	Zinc aluminum succinate dihydrate, 3-Amino-4-nitro-6-methyl-8-oxopyrazolo(1,5-a)pyrimidine, Sodium Aluminum Silicon Oxide, Zircon, Quartz alpha, alpha-Si O ₂ , Cobalt Sulfide,
800 °C	cyclo undecasulfur, Quartz, syn,

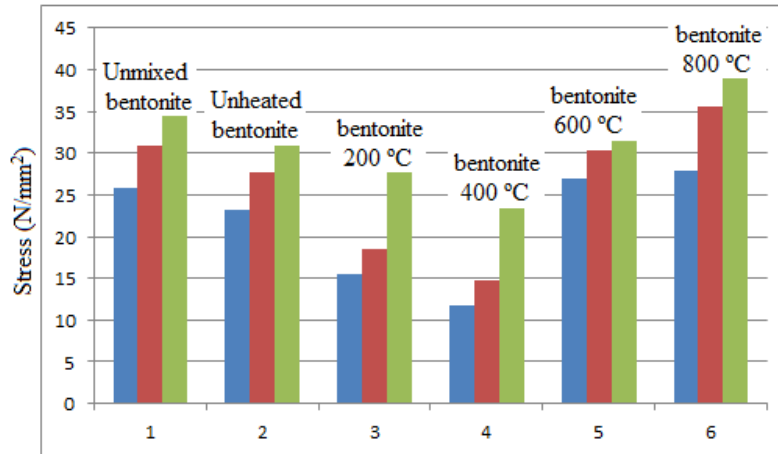


Fig. 1. Concrete compressive strength in 7, 14 and 28 days

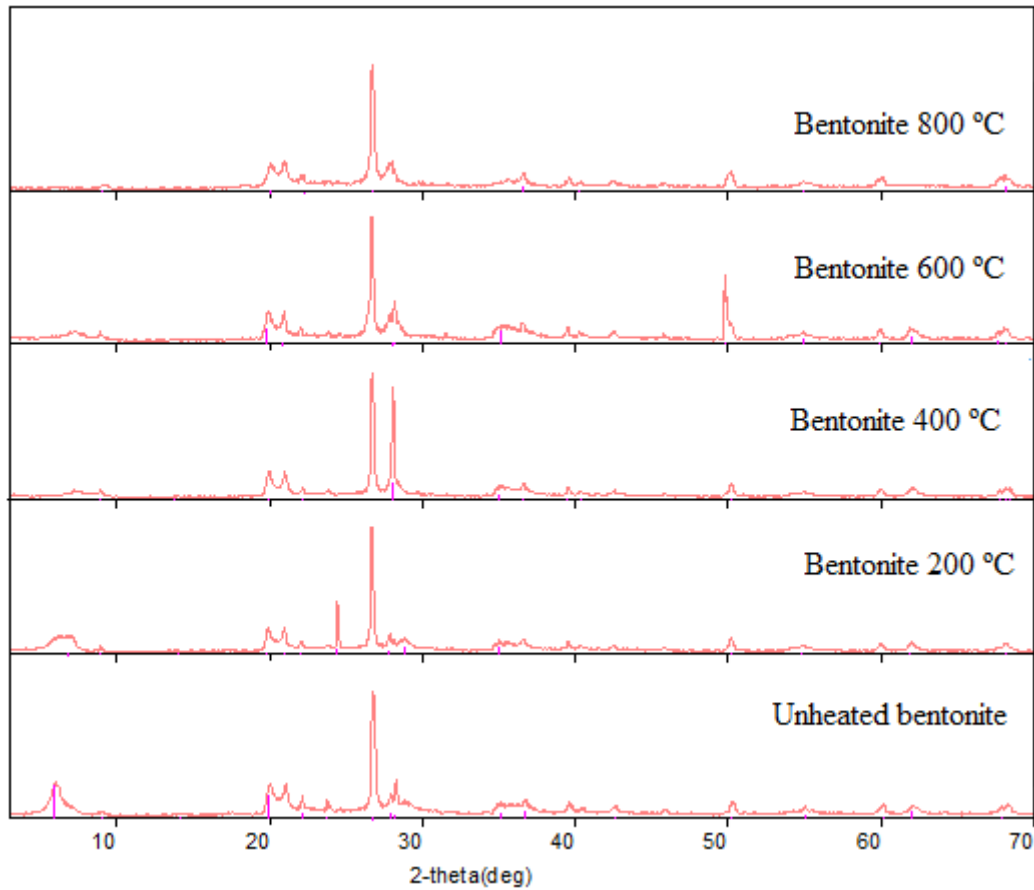


Fig. 2. XRD pattern of thermally modifying bentonite

5. Conclusion

The mineral mixture in concrete mixed design has significant effect on setting time and final strength in concrete. The quantity of used thermally treated bentonite is very less and it made this product economic and also helps in reducing CO₂ producing in the environment.

Rectorite and Montmorillonite-15A have strong negative effect on concrete compressive strength. The low cost concrete with better compressive strength is main product of this research work.

References

- 1) Gesoglu M, Ozbay E, "Effects of mineral admixtures on fresh and hardened properties of self-compacting concretes: binary, ternary and quaternary systems," *Mater Struct*, vol 40, 2007, pp. 923-37.
- 2) M.A. Megat Johari, J.J. Brooks, Shahid Kabir, Patrice Rivard, "Influence of supplementary cementitious materials on engineering properties of high strength concrete," *Construction and Building Materials*, vol 25, 2001, pp. 2639-2648.
- 3) Dali Bondar, C.J. Lynsdale, N. B. Milestone, N. Hassani, A.A. Ramezaniapour, "Effect of adding mineral additives to alkali-activated natural pozzolan paste," *Construction and Building Materials*, vol 25, 2011, pp. 2906-2910.
- 4) Demirel B, Keleştemur O, "Effect of elevated temperature on the mechanical properties of concrete produced with finely ground pumice and silica fume," *Fire Safety Journal*, vol 45(6-8), 2010, pp. 385-391.
- 5) NF EN 206-1. Béton, Partie 1: Spécification, performances, production et conformité, AFNOR, 2004 from EN 206-1. Concrete - part 1: specification, performance, production and conformity.
- 6) Malhotra VM, "Reducing CO2 emissions - the role of fly ash and other supplementary cementitious materials," *Concr Int*, 2000, pp. 42-5.
- 7) Bilodeau A, Malhotra VM, "High-volume fly ash system: concrete solution for sustainable development," *ACI Mater J*, vol 97(1), 2000, pp. 41-50.
- 8) Smith LA, "Proceedings institution of civil engineers," vol. 36. London, April; 1967, pp. 769-90.
- 9) Mucteba Uysal, Harun Tanyildizi, "Predicting the core compressive strength of self-compacting concrete (SCC) mixtures with mineral additives using artificial neural network," *Construction and Building Materials*, vol 25, 2011, pp. 4105-4111.
- 10) Tiong HW, Yoshihisa M, Yoshiharu W, "Microstructure and strength properties of high strength concretes containing various mineral admixtures," *J Cem Concr Res*, vol 25, 1995, pp. 715-20.
- 11) Halit Yazici, "The effects of curing conditions on compressive strength of ultra high strength concrete with high volume mineral admixtures," *J Build Environ*, vol 42, 2007, pp. 2083-9.
- 12) He Zhimin, Liu Junzhe, Zhu Kangwu, "Influence of Mineral Admixtures on the Short and Long-term Performance of Steam-cured Concrete," *Energy Procedia* 16, 2012, pp. 836 - 841.
- 13) Aitcin, PC. High-performance concrete. E & FN Spon, 1998, p. 591.
- 14) Malhotra VM, Mehta PK, "Pozzolan and cementitious materials," *Advances in concrete technology*, Gordon and Breach Publishers, vol 1, 1996, p. 191.
- 15) Mehta PK, Monteiro PJM, "Concrete - microstructure properties and materials," 3rd ed. McGraw-Hill, 2006, p. 659.
- 16) Ho DWS, Lewis RK, "Carbonation of concrete incorporating fly ash or a chemical admixture," In: *Proceedings of the first international conference on the use of fly ash, silica fume, slag and other mineral by-products in concrete*, Canada, SP-79, 1983, pp. 333-46.
- 17) Byfors K, "Carbonation of concrete with silica fume and fly ash," Oslo: *Nordic Concrete Research*, vol 4, 1985, pp. 26-35.
- 18) Ogha H, Nagataki S, "Prediction of carbonation depth of concrete with fly ash," In: *Proceedings of the third international conference on fly ash, silica fume, slag and natural pozzolans in concrete*. Trondheim, Norway, SP -114, 1989, pp. 275-94.
- 19) Cabrera JG, Woolley GR, "A study of 25 year old pulverized fuel ash concrete used in foundation structures," In: *Proceedings of instrumentation civil engineering Part*, vol 2, 1985, pp. 149-65.
- 20) Atis, CD, "Accelerated carbonation and testing of concrete made with fly ash," *Constr Build Mater*, vol 17, 2002, pp. 147-52.
- 21) Ahmad S, Barbhuiya SA, Elahi A, Iqbal J, "Effect of Pakistani bentonite on properties of mortar and concrete," *Clay Miner*, vol 46, 2011, pp. 85-92.
- 22) Shazim Ali Memon, Rao Arsalan, Sardar Khan, Tommy Yiu Lo, "Utilization of Pakistani bentonite as partial replacement of cement in concrete," *Construction and Building Materials*, vol 30, 2012, pp. 237-242.

DEM Simulations and Laboratory Experiments on Physical and Mechanical Properties of Sand-Gravel Mixtures

Janaka J. Kumara¹, Kimitoshi Hayano², Yuuki Shigekuni² and Kota Sasaki²

1 Dept. of Civil Engineering, 2 Dept. of Urban Innovation, Yokohama National University, Japan

ABSTRACT

In railway tracks, ballast fouling due to fine materials mixing with ballast has been identified as a challenging issue nowadays. In this research, deformation characteristics of sand-gravel mixtures, repressing fine-ballast mixtures, were studied using laboratory and DEM simulated triaxial compression tests. DEM simulations were done in Yade, an open source developed based on DEM. Initially, void ratio characteristics of sand-gravel mixtures were studied. After void ratio results were obtained, triaxial compression tests were conducted on specimens with 50% and 80% of relative densities. Void ratio results indicated that the specimen with 30% sand showed the smallest void ratios (i.e., the densest packing) in DEM simulations. Triaxial test results indicated that the specimens with 30% sand experienced the highest deviator stress in both 50% and 80% of relative density cases, showing clear relation of void ratio and deviator stress.

Keywords: DEM Simulations, Laboratory Tests, Mechanical Properties, Physical Properties, Sand-Gravel Mixtures

1. INTRODUCTION

In railway tracks, due to repeated heavy train loads, fine materials mix with ballasts. The fine materials come mainly from the underneath layers and to a lesser extent due to particle crushing as well [1]. Changes in deformation properties of ballasts due to sand intrusions have been identified as a major problem in railway engineering. In many cases, ballasts containing sands shows large settlements, which is induced mainly by railway traffic loading. However, degree of settlement depends not only on traffic volume but also on physical and mechanical properties of the ballasts. Though there had been various researches conducted on pure materials of ballasts and fines [2]-[3], there had not been sufficient researches conducted on deformation characteristics of fine-ballast mixtures simulating actual field rail-track conditions. Perhaps, difficulties in simulating multi-size particles in numerical simulations would have been the main issue behind less number of researches on fine-ballast mixtures. However, it is very important to understand effects of fine materials mixing on deformation characteristics of ballast to understand degradation of ballast layers and to propose maintenance works for degraded ballast layers.

After development of DEM [4], DEM simulations became the most widely used numerical method to study deformation characteristics of granular materials. As laboratory experiments are complicated and expensive for various types of field conditions, nowadays, numerical simulations are preferred in many research works. However, laboratory experiments are still required to verify the accuracy of the numerical simulations. In this research, deformation characteristics of granular materials including sand-gravel mixtures were studied using triaxial compression tests in Yade [5] as the numerical method in addition to laboratory triaxial compression tests.

1.1 Yade

Yade is an extensible open-source framework for discrete numerical models, focused on Discrete Element Method. Yade is a 3-D numerical method. The original code was modified to obtain particle size distribution of sand-gravel mixture since the original code does not allow gap graded particle size distribution curves like in sand-gravel mixtures. Widulinski et al. (2009) [6] and Sayeed et al. (2011) [7] have also conducted triaxial compression tests using sphere particles in Yade recently. They found good agreement with experimental results.

2. METHODOLOGY

In this research, since size of ballast (i.e., 10-60mm) is too large to use in triaxial compression test (specimen size is 100x200mm), gravel with the size of 1/5 of actual ballast, was selected. Medium size sand was used as the fine material. At the initial stage, void ratio characteristics of sand-gravel mixtures were evaluated using laboratory density tests and DEM triaxial simulations. Density tests were conducted according to JIS A 1204-2009 [8]. In the next stage, deformation characteristics of sand-gravel mixtures were evaluated on the specimens prepared with 50% and 80% of relative densities. Deformation characteristics were evaluated using both laboratory and DEM simulated triaxial compression tests.

2.1 Laboratory Triaxial Compression Tests

Laboratory triaxial compression tests were conducted according to JGS 0527 [9]. Triaxial compression tests were conducted using the apparatus shown in Fig. 1. Axial deformations were measured by an external displacement transducer and a pair of LDTs [10]. However, the measurements of LDTs used to determine small strain deformation properties, are not included in this paper. Triaxial compression tests were conducted under 80kPa of confining pressure.

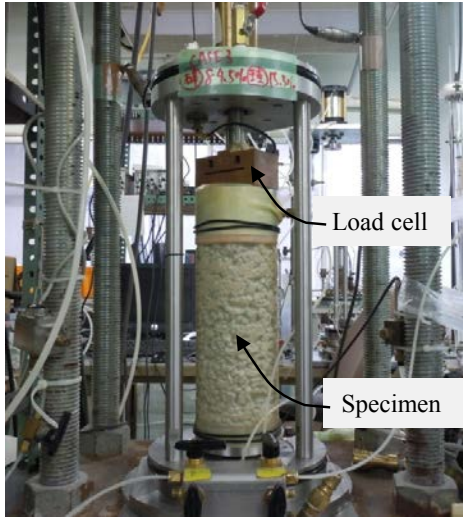


Fig. 1: Triaxial apparatus

2.2 DEM Simulations

In triaxial test simulations, void ratio is determined by friction angle, ϕ_c , during isotropic compression. After maximum and minimum void ratios, e_{\max} and e_{\min} , of the specimens were determined, void ratios related to 50% and 80% of relative densities, e_{50} and e_{80} , were obtained using Eq. (1). Then, the values of ϕ_c related to e_{50} and e_{80} were determined. In DEM simulations, particle size was simulated as 100 times larger than the size of laboratory specimens to reduce simulation time. DEM simulations were done using sphere particles. The input parameters used in DEM simulations are given in Table 1. Though 5m/s of V_w was used for gravel specimens, smaller values of V_w (1m/s used here) were required for the specimens of small size particles to stabilize the simulations.

Table 1: Input parameters of DEM triaxial simulations

Parameter	Value	Remarks
Stability criterion	0.01	Help to stabilize system
Friction angle of spheres during isotropic compression, ϕ_c	See Table 2	ϕ_c determines void ratio
Coefficient of Cundal non-viscous damping	0.2	Default value
Max. time step, Δt (s)	0.000658	Default value
Density of spheres, ρ_s (kg/m ³)	2600	
Max. velocity of walls, V_w (m/s)	1.0/5.0*	Help to stabilize the system
Number of particles, N	10000	
Confining pressure, σ_c (kPa)	80	
Friction angle of spheres just before shearing, ϕ_s (degree)	30	
Ratio of shear and normal contact stiffness for spheres, K_s/K_n	0.5	
Stiffness of spheres, E_s (MPa)	15	
Strain rate (s ⁻¹)	0.1	

Note: * Used for gravel specimen

$$D_r = \frac{e_{\max} - e}{e_{\max} - e_{\min}} \times 100(\%) \quad (1)$$

2.3 Sample Preparation

Six specimens each were prepared with different amount of fines as given in Table 2 for both laboratory experiments and DEM simulations. Two specimens were prepared with sand and gravel separately to compare the results with those of sand-gravel specimens.

Table 2: Details of friction angle and void ratio

Fines (%)	Friction angle, ϕ_c (degree)		Void ratio, e	
	$D_r = 50\%$	$D_r = 80\%$	$D_r = 50\%$	$D_r = 80\%$
0	16.5	4.5	0.632	0.566
15	11.8	3.8	0.485	0.429
30	16.3	4.2	0.403	0.342
50	20.0	5.0	0.450	0.396
70	17.15	4.4	0.519	0.460
100	16.4	3.5	0.646	0.574

3. RESULTS AND DISCUSSIONS

Fig. 2 shows particle size distribution of laboratory specimens. Particle size distribution of soil samples was evaluated using sieve analysis test according to JIS A 1204 [11]. Fig. 3 shows particle size distribution of DEM simulations. As shown in Fig. 3, particle size of DEM simulated specimens is 100 times larger than that of laboratory specimens.

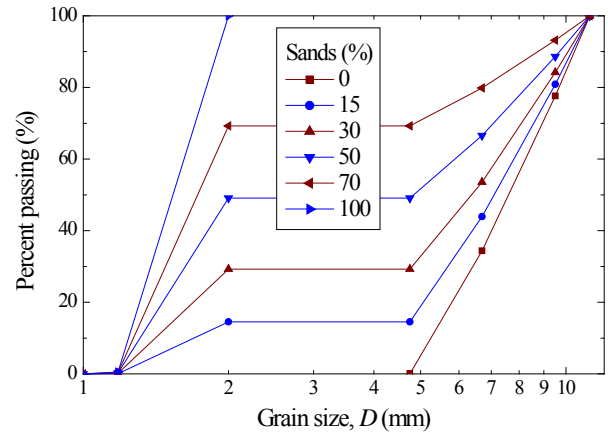


Fig. 2: Particle size distribution of laboratory specimens

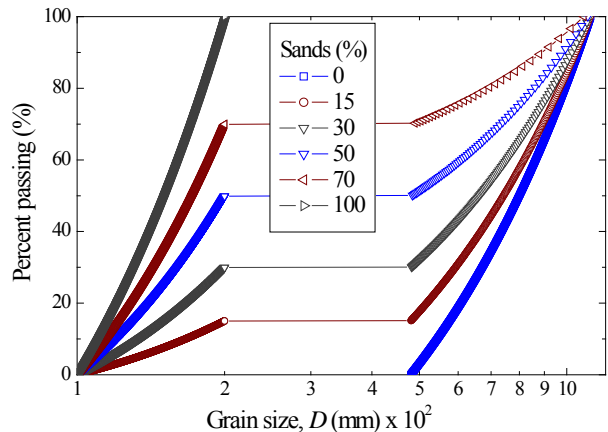


Fig. 3: Particle size distribution of DEM simulated specimens

3.1 Void Ratio Characteristics

Fig. 4 shows relation of void ratio of the specimens with % sands. In Fig. 4, $e_{\max, \text{exp}}$ and $e_{\max, \text{DEM}}$ represent maximum void ratios of experimental and DEM simulated specimens respectively. In Fig. 4, e_{50} and e_{80} represent void ratios of the specimens with 50% and 80% of relative densities respectively. As shown in Fig. 4, void ratios (both e_{\max} and e_{\min}) reduce with sands at initial level, then, after certain amount of sands, increase with sands. Minimum value of void ratios (both e_{\max} and e_{\min}) reached at 50% and 30% of sands for laboratory and DEM simulated specimens respectively. The difference in amount of sands to reach minimum value of void ratios would be attribute to particle shape as DEM simulations were done using sphere particles whereas laboratory specimens consist of irregular shape particles. Lade et al. (1998) [12] also showed similar results for binary mixtures of sphere particles where minimum values of void ratios were observed mainly at 20% - 40% fines depending on diameter ratio of two mixtures.

The results also showed that void ratios of DEM simulated specimens are smaller than laboratory specimens for the specimens with larger particles (e.g., gravel specimen). It should be, however, noted that void ratio of DEM simulated specimens were measured at the end of isotropic compression (under 80kPa) whereas in laboratory specimens, void ratios were measured before the isotropic compression. As shown in Fig. 4, the difference in void ratios of laboratory and DEM simulated specimens become small for the specimens with more sands than those with more gravel particles. The large difference in void ratios for the specimens with larger particles should be attribute to different particle shapes in laboratory specimens and DEM simulations. Fig. 4 also shows that DEM simulations can give same void ratios as laboratory results for sands (i.e., for specimens with small particles). Fig. 5 shows relation of e_{\max} and e_{\min} for both laboratory and DEM simulated specimens. Fig. 5 clearly shows that both relations are linear with a same gradient (i.e., increasing rate) though experimental data shows higher void ratios. As explained, smaller void ratios in DEM simulations should be attribute to change in particle shapes in the two methods.

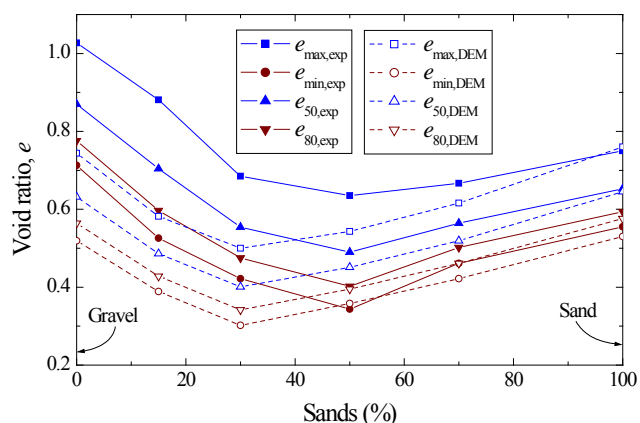


Fig. 4: Void ratio of laboratory and DEM simulated specimens

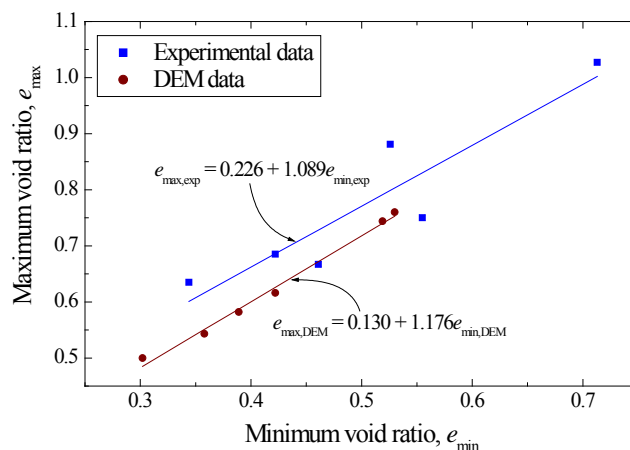


Fig. 5: Comparison of relations of maximum and minimum void ratios

3.2 Triaxial Test Results

Fig. 6 shows a DEM triaxial test simulation at different steps. Specimens were prepared in a box as shown in Fig. 6. As shown in Fig. 6 (a), at the beginning of particle generation, packing is very loose. At the end of isotropic compression (i.e., Fig. 6 (b)), void ratios were obtained to compare with those of laboratory specimens. Fig 7 shows deviator stress vs. axial strain for laboratory specimens of 50% of relative density. Fig. 8 shows deviator stress vs. axial strain for DEM simulated specimens of 50% of relative density. As shown in Fig. 7, the specimen with 30% sands experienced the highest deviator stress, followed by the specimen with 15% sands. The results also showed that gravel specimen experienced higher deviator stress than that of sand specimen. In DEM simulations too, as shown in Fig. 8, the specimen with 30% sands experienced the highest deviator stress, followed by the specimen with 15% sands. In DEM simulations too, gravel specimen experienced higher deviator stress than that of sand specimen. However, it should be noted that laboratory specimens experienced higher deviator stress compared to DEM simulated specimens. The difference in deviator stresses between the two methods should be attribute to different particle shapes as DEM specimens consist of sphere particles while laboratory specimens consist of irregular shape particles. Lin and Ng (1997) [13] also showed that irregular shape particles give higher deviator stress than that of sphere particles. He compared deviator stress for the samples made of ellipsoid and sphere particles. Yan et al. (2009) [14] also studied effects of particle shapes on strength characteristics and found that sphere particles give smaller stress ratio compared to clump particles. He also observed that DEM simulations (using PFC3D) give smaller stress ratio than that of experimental specimens.

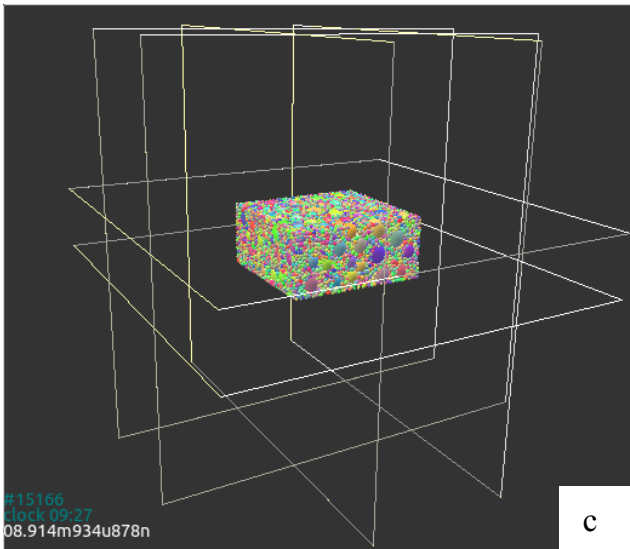
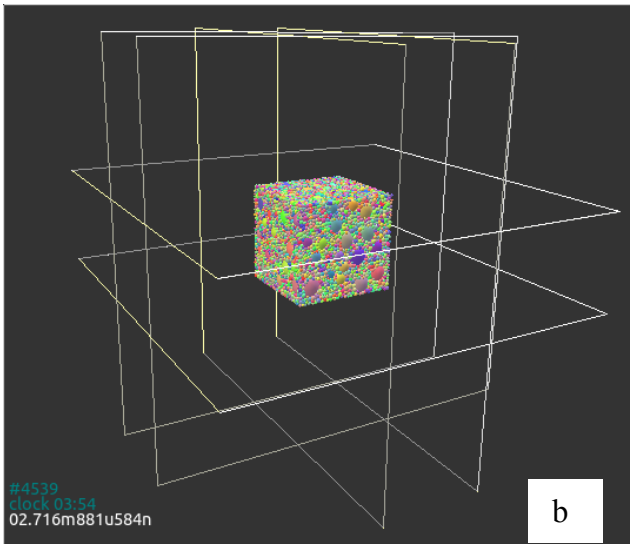
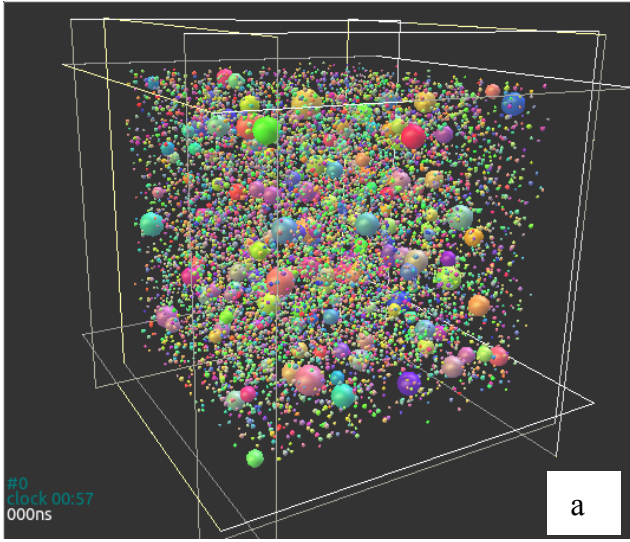


Fig. 6: A DEM triaxial test simulation (a) at the particle generation, (b) after isotropic compression and (c) at the end of simulation (a sample with 30% sands)

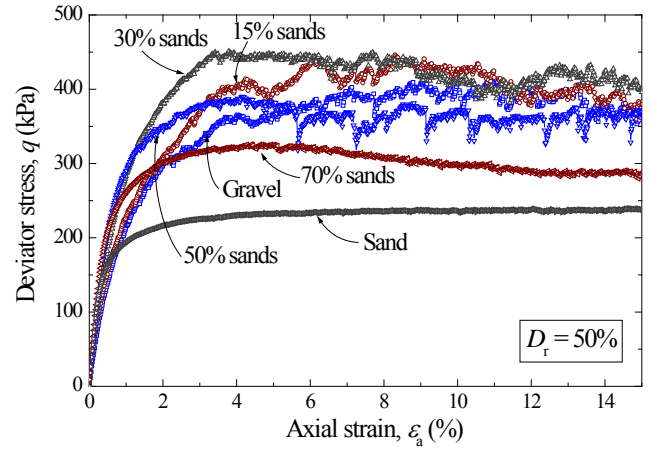


Fig. 7: Deviator stress vs. axial strain from laboratory specimens with 50% of D_r

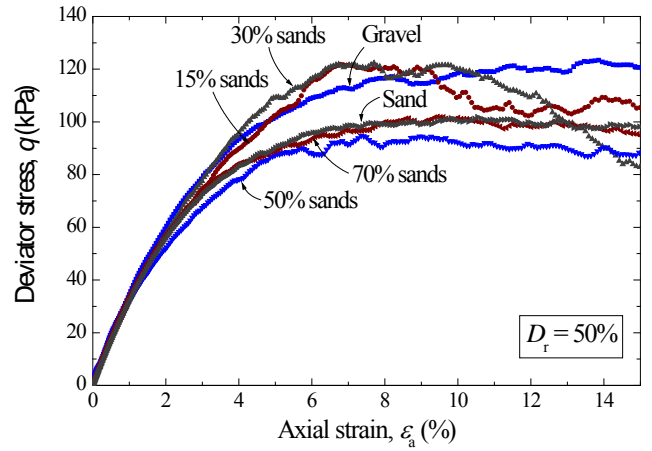


Fig. 8: Deviator stress vs. axial strain from DEM simulations with 50% of D_r

Fig. 9 shows deviator stress vs. axial strain for laboratory specimens of 80% of relative density. Fig. 10 shows deviator stress vs. axial strain for DEM simulated specimens of 80% of relative density. As shown in Fig. 9, some specimens (i.e., the specimens with 30%, 50% and 70% sands) reached a peak value in deviator stress and then reduced deviator stress same as a dense specimen. Out of these three specimens, the specimen with 30% sands experienced the highest deviator stress. However, gravel specimen experienced the highest deviator stress showing stress-strain behaviour of a loose specimen where there is no any clear peak value in deviator stress. As shown in Fig. 10 for DEM simulations, the specimen with 30% sands experienced the highest deviator stress, followed by the specimens with 50% and 70% sands until 4% axial strain. However, after 4% axial strain, gravel specimen experienced higher deviator stress than the specimens of 50% and 70% sands. In 80% of relative density case too, gravel specimens experienced higher deviator stress than those of sand specimens. The triaxial test results show that sand-gravel specimens with 30% sands experienced the highest deviator stress showing the densest packing.

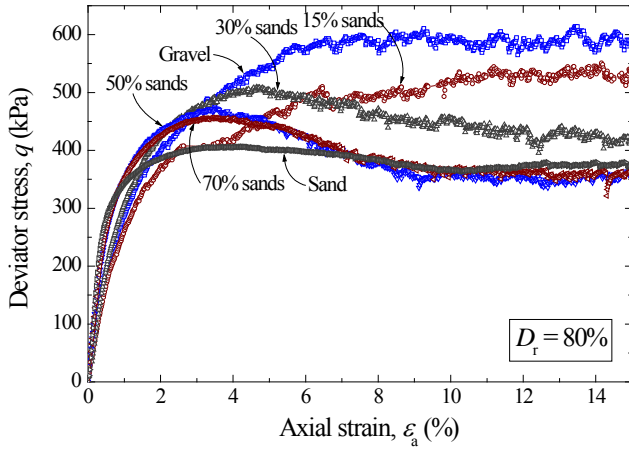


Fig. 9: Deviator stress vs. axial strain from laboratory specimens with 80% of D_r

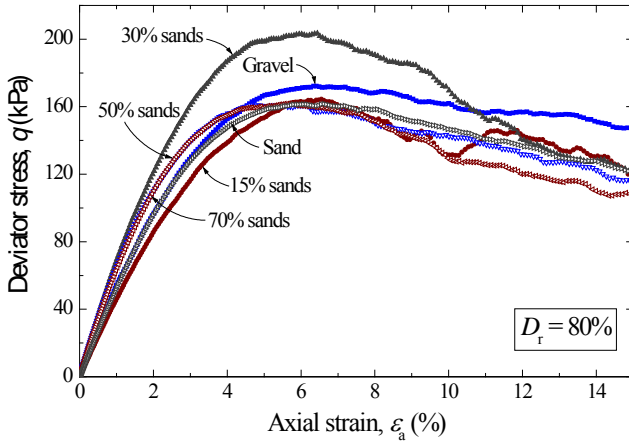


Fig. 10: Deviator stress vs. axial strain from DEM simulations with 80% of D_r

Figs. 11 and 12 show comparisons of deviator stress vs. axial strain between laboratory tests and DEM triaxial test simulations for 50% and 70% of relative densities respectively. Though Figs. 11 and 12 do not show a very clear relation of different deviator stresses for the two specimens (i.e., gravel and 30% sands specimens) for both cases, Fig. 11 showed that the specimen with 30% sands experienced higher deviator stress than the gravel specimen in laboratory tests while Fig. 12 showed that the specimen with 30% sands experienced higher deviator stress than the gravel specimen in DEM simulations.

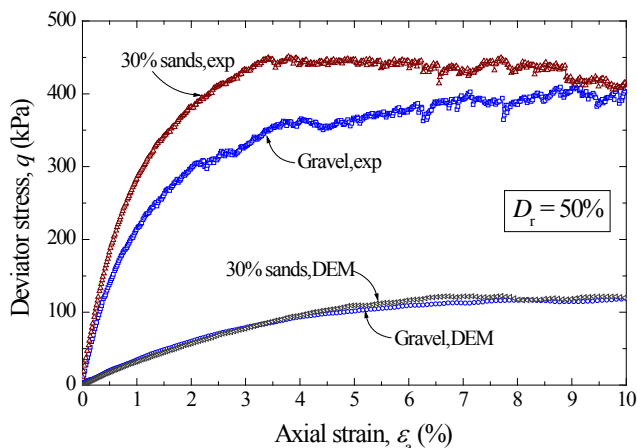


Fig. 11: Comparison of deviator stress vs. axial strain for the specimens with 50% of D_r

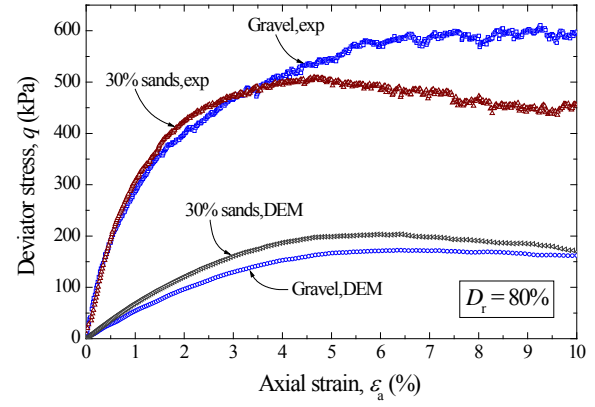


Fig. 12: Comparison of deviator stress vs. axial strain for the specimens with 80% of D_r

Fig. 13 shows failure friction angle, ϕ_f , vs. dry density, ρ_d , of sand-gravel specimens from laboratory triaxial compression tests. As shown in Fig. 13, the highest ρ_d was observed for the specimen with 50% sands in both 50% and 80% of relative densities. In case of 80% of relative density, the gravel specimen has the largest ϕ_f , which gradually reduced until the sand specimen. In case of 50% of relative density, ϕ_f increases until the specimen with 30% sands, then reduced until the sand specimen. Fig. 14 shows failure friction angle, ϕ_f , vs. dry density for DEM simulated specimens. As shown in Fig. 14, both dry density and failure friction angle increased with sands (up to 30% sands) and reached peak values for the specimens with 30% sands in 80% of relative density. In case of 50% of relative density, ϕ_f remains same for the specimens with 0% - 30% sands, then, reduced for the specimen with 50% sands and then remains same until the sand specimen same as 80% of relative case. As an overall finding, it is clear the specimen with 30% sands showed densest behaviour, particularly, in case of 50% of D_r in laboratory experiments and 80% of D_r in DEM simulations. The results showed that mixing of sands in gravel (i.e., mixing of fines in ballast) change failure frictional angle of the mixtures.

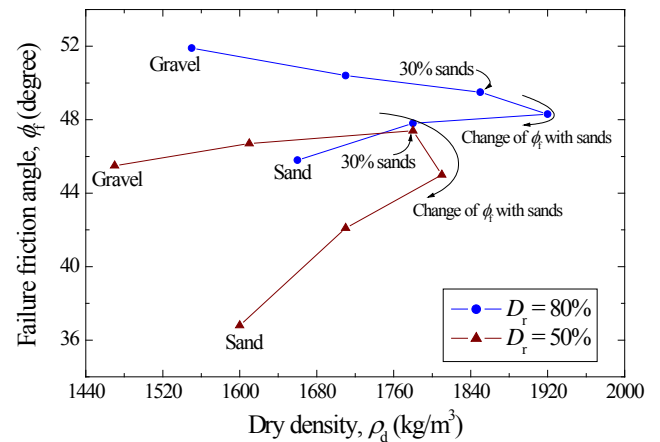


Fig. 13: Change of failure friction angle of sand-gravel specimens with sands from laboratory experiments

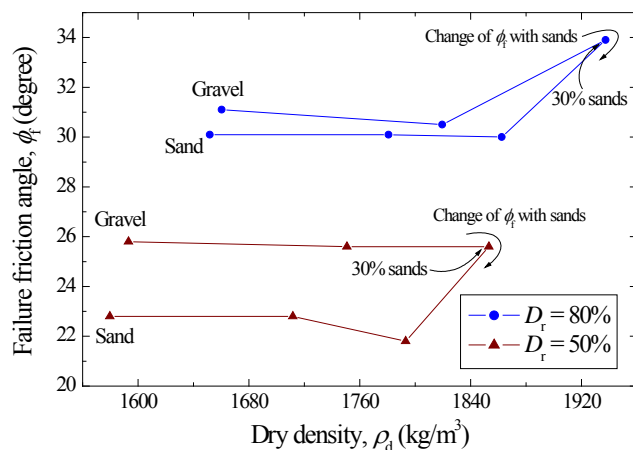


Fig. 14: Change of failure friction angle of sand-gravel specimens with sands from DEM simulations

4. CONCLUSION

Triaxial compression tests were conducted on sand-gravel mixtures to study effects of fine material mixings in ballast in railway tracks. Triaxial tests were conducted in the laboratory and using Yade, a DEM application as the numerical simulations. Triaxial compression tests were conducted on specimens having 50% and 80% of relative densities. The following conclusions were made,

- ❖ Void ratios (both e_{\max} and e_{\min}) reduced with initial addition of sands. After reaching a minimum value, void ratios increase with sands. Minimum value of void ratios in DEM simulations were observed on the specimens with 30% sands while it was 50% sands for laboratory specimens.
- ❖ Void ratios observed in DEM simulations were smaller than those of laboratory specimens. The difference in void ratios can be attribute to difference in particle shapes in DEM simulations and laboratory experiments. However, relations of void ratio change with sands were approximately same in DEM simulations and laboratory specimens.
- ❖ The results also showed that void ratios can be simulated in DEM simulations same as in laboratory experiments for specimens with small particles (e.g., sands).
- ❖ As an overall finding, in both laboratory experiments and DEM simulations, the highest deviator stress was observed on the specimens with 30% sands. The results indicated that specimens with smaller void ratios experienced higher deviator stress.
- ❖ However, there is difference in deviator stresses between the two methods, experimental specimens showing higher deviator stresses. The difference in deviator stress should be due to difference in particle shapes in the two methods. However, the results showed similar patterns in a qualitative manner.
- ❖ The specimens with 30% sands achieved the highest dry density and maximum friction angle in DEM simulations. In experimental specimens, it was quite same for 50% of relative density.

5. ACKNOWLEDGMENT

Japanese Government is highly acknowledged for providing financial assistance to the first author to study in Yokohama National University, Japan through a Monbukagakusho scholarship.

6. REFERENCES

- [1] Thakur PK, Vinod JS and Indraratna B., Effect of particle breakage on cyclic densification of ballast: a DEM approach, In Proc., IOP Conf. Series: Materials Science and Engineering, 2010, pp. 122-129.
- [2] Raymond GP, Reinforced ballast behaviour subjected to repeated load, Geotextiles and Geomembranes, vol. 20, 2002, pp. 39-61.
- [3] Indraratna B, Khabbaz H, Salim W and Christie D, Geotechnical properties of ballast and the role of geosynthetics in rail track stabilization, Journal of Ground Improvement, vol. 10, No. 3, 2006, pp. 91-102.
- [4] Cundal PA and Strack ODL, A discrete numerical model for granular assemblies, Geotechnique, vol. 29, No. 1, 1979, pp. 47-65.
- [5] Smilauer V, Catalano E, Chareyre B, Dorofeenko S, Duriez J, Gladky A, Kozicki J, Modenese C, Scholtes L, Sibille L, Stransky J, Thoeni K (2010), Yade Reference Documentation, In Yade Documentation (V. Smilauer, ed.), The Yade Project, 1st ed. (<http://yade-dem.org/doc/>).
- [6] Widulinski L, Kozicki J and Tejchman J, Numerical simulations of triaxial test with sand using DEM, Archives of Hydro-Engineering and Environmental Mechanics, vol. 56, No. 3-4, 2009, pp. 149-171.
- [7] Sayeed MA, Suzuki K and Rahman MM, Strength and deformation characteristics of granular materials under extremely low to high confining pressures in triaxial compression, International Journal of Civil & Environmental Engineering, vol. 11, No. 4, 2011, pp. 1-6.
- [8] JIS A 1224, Test method for minimum and maximum densities of sands, 2009.
- [9] JGS 0527, Method for triaxial compression test on unsaturated soils, 1998.
- [10] Goto SF, Tatsuoka F, Shibuya S, Kim YS and Sato T, A simple gauge for local small strain measurements in the laboratory, Soils and Foundations, vol. 31, No. 1, 1991, pp. 169-180.
- [11] JIS A 1204, Test method for particle size distribution of soils, 2009.
- [12] Lade PV, Liggio CD and Yamamuro JA, Effect of non-plastic fines on minimum and maximum void ratios of sand, Geotechnical Testing Journal, ASTM, vol. 21, No. 4, 1998, pp. 336-347.
- [13] Lin X and Ng TT, A three-dimensional discrete element model using arrays of ellipsoids, Geotechnique, vol. 47, No. 2, 1997, pp. 319-329.
- [14] Yan G, Sui YH and Glenn M, Simulation of granular material behaviour using DEM, In Proc., 6th International Conference on Mining Science & Technology, 2009, pp. 598-605.

Rock slope stability problems in Gold Coast area, Australia

Shokouhi Ali, Gratchev Ivan, Charrismanagara Arry
Griffith University – Gold Coast campus - Australia

ABSTRACT

The Tamborine Mountain area of the Gold Coast, Australia often faces rock slope failures during rainy seasons. To have a better understanding of the factors that may affect the slope stability, several rock slope sites have been examined in detail to assess the effect of discontinuities formed in the rock masses, and degree of weathering of the rocks on the overall stability of slopes. Different methods of slope stability analysis such as kinematic approach and slope mass rating, were applied to investigate the potential failure mode and predict the behavior of rock slopes in the future. This paper will present results of this work and make comparisons between different methods of rock slope stability analysis. Keywords: slope stability, discontinuity, kinematic approach, SMR

1. INTRODUCTION

Tamborine Mountain, located in south of Brisbane and inland from the Gold Coast, is a plateau formed on sub-horizontal basalt lavas of Tertiary age[1]. It is covered by forest. The basalt plateaux of southeast Queensland potentially has hazard of landsliding[1], and often faces rock slope failures during rainy seasons.

Many of residences in Tamborine Mountain are located near the rock slopes which have potential hazard of movement and instability. Failure of these rock slopes can lead to damaging results and will have a deep economic and social impact on the society of this area. Also the slope failure can be very harmful for infrastructures located in Tamborine Mountain such as roads. Every year during the rainy seasons, many of access roads are closed by failed slopes.

The objective of this study is to investigate some cut slopes through the main roads and analyze them with using kinematic approach Slope Mass Rating (SMR) to identify the potential failure modes of them and to determine the condition of slopes located along roads.

The investigation field was located along Beaudesert – Nerang Road, immediately south-east of the Beaudesert – Nerang Road / Arunta Drive intersection, on the Gold Coast (Fig.1). The approximate length of the existing cut slope is 200m and with the height of approximately 7m. (Fig.2)

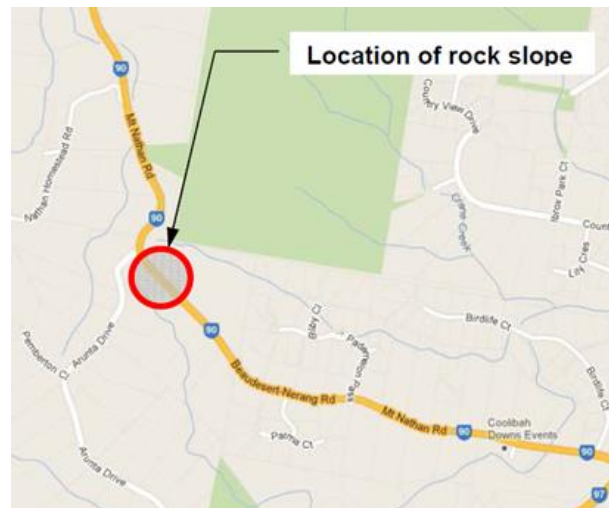


Figure 1 - Location on investigated slopes



Figure 2 - One of investigated slopes

2. Geology and landslides types

The regional geological structure of the Tamborine Mountain and detailed geology of the basalt lavas forming the plateau surface area have been described by Willmott[1], Cranfield et al [2], and Green [3].

The investigation field was located on the eastern part of Tamborine Mountain and made of metasediments of Neranleigh-Fernvale Beds. Based on investigation performed by [1], this sequence of mainly sedimentary rocks was deposited in Devonian to Carboniferous times. These rocks have been deformed, indurated and slightly metamorphosed, probably in the Carboniferous; they now can be termed metasediments. The main rock types present are argillite (derived from siltstone and shale), greywacke dark sandstone with abundant rock fragments), quartzite (derived from chert) and greenstone (metamorphosed submarine basalt lavas). Conglomerate horizons are known in a few areas. In some places, the argillite is sheared and has the appearance of phyllite.

In 1981 a slope stability investigation performed by [1], on Tamborine Mountain, his investigation showed that few landslides are known on the plateau surface of the mountain, but numerous slides, some very large, have occurred on the cliff lines and benches below, and on the fans of colluvial debris along the lower western flanks of the mountain. Based on his investigation, amongst different types of slope instability, four main types of landslides can occur in Tamborine mountain including: Rock falls, Debris flows, small rotational slides and complex multiple rotational slides.

3. Field survey

To assess the impacts of formed discontinuity and weathering on the rock slopes located in Tamborine Mountain, site investigations were performed in 2012 to collect the relevant and required data such as: Geometric properties of discontinuities such as: dip, dip direction, spacing, etc., compressive strength by using Schmitt hammer and types of rocks.

Three locations were selected along the rock slope located in the side of main road for these investigations.

The following data were collected:

Table I- Collected data

Location 1				
Set #	Dip	Dip direction	Aperture (mm)	Compressive Strength of rocks (Mpa)
1	55	220	0.5	27
2	50	135	0.5	27
3	55	50	2	27
Location 2				
Set #	Dip	Dip direction	Aperture (mm)	Compressive Strength of rocks (Mpa)
1	61	70	1-2	40
2	73	170	1-2	27

Location 3				
Set #	Dip	Dip direction	Aperture (mm)	Compressive Strength of rocks (Mpa)
1	40	40	0.5	45
2	73	170	1-2	27
3	25	240	3-5	27

4. Data analyses

The collected data were analyzed by Dips computer software to identify the potential failure modes of the investigated slopes. The results from kinematic analysis indicate that at location 1, there is only one potential failure mode. Planar sliding is the most likely failure mode that may occur at this location (Fig.3). As can be seen in Fig3 some of the discontinuities are located in gray shade that shows the potential planar sliding area. Toppling and wedge failure analyses show, there are no toppling and wedge potential failure at location 1.

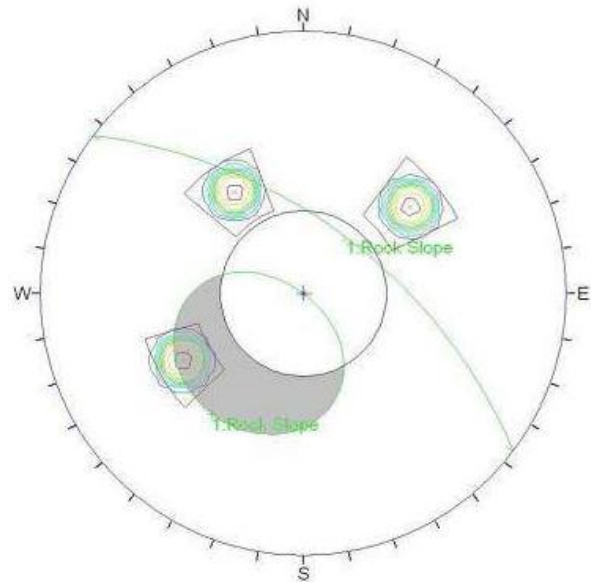


Figure 3 - Planar sliding of location 1

In location 2, the results produced by kinematic analysis suggest that there may be a potential toppling failure (Fig.4). In Fig.4, a part of the contour lines fall within the toppling failure zone that indicates the potential toppling failure.

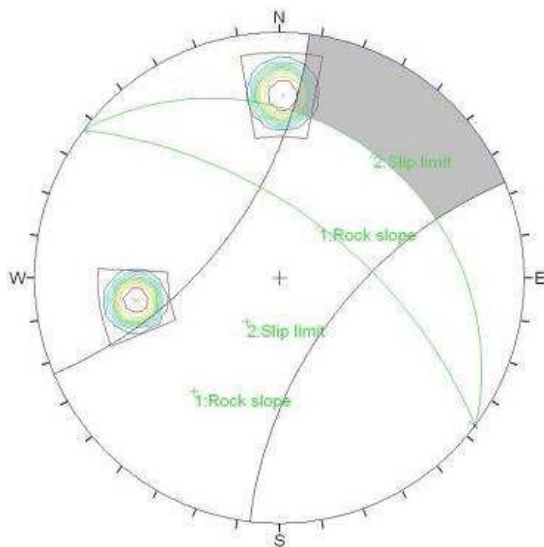


Figure 4 – Toppling failure of location 2

The results of kinematic analysis show that the rock slope at location 3 has two potential failure modes, planar sliding and wedge sliding. In Fig. 5, the discontinuity set #3 falls within the failure zone (grey shaded area) for planar sliding analysis. This means that planar sliding may occur along this failure plane.

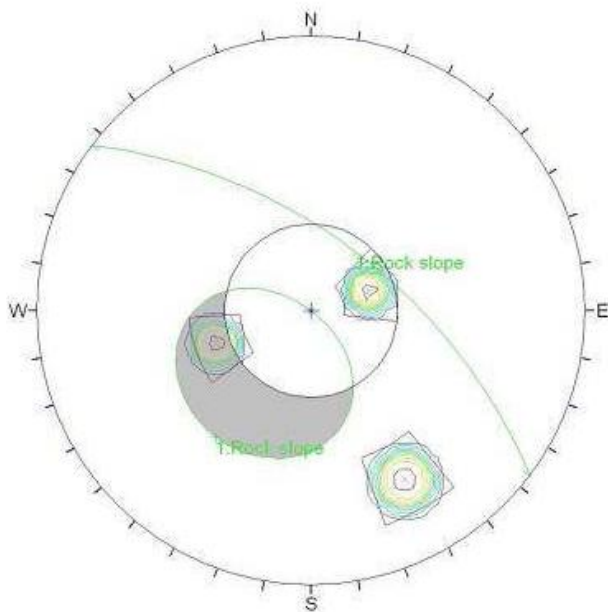


Figure 5 – Toppling failure for location 3

Fig.6 shows that there is a mean joint set orientation (shown by black dots) that falls within the wedge failure zone (grey shaded area). This indicates that a wedge failure may potentially occur at location 3.

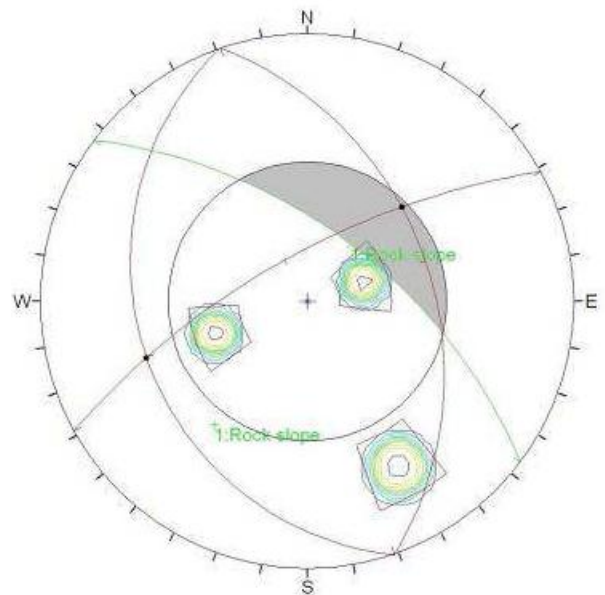


Figure 6 - Wedge failure of location 3

Besides the kinematic analysis a SMR (Slope Mass Rating) analysis was also conducted to assess the slopes. Following table indicates the results of SMR analyses.

Table II- SMR results

Location	SMR	Slope Mass Class
1	40	IV, Poor
2	83	I, Very good
3	14	V, Very poor

The results from SMR analyses consistently show that location 2 has the best rock mass condition out of the three locations, followed by location 1, and location 3 has the worst. These results reflect the evidence that there was a significant recent rock fall at location 3. At location 1, the rock fall was deemed to be minor, however, small fragments of rock blocks were found along the toe of the rock slope.

5. Concluding remarks

The results of kinematic analyses show that at location 1, the rock is unstable under current conditions. However, in an event of a rock slope failure, it will only be a minor one. At location 2 of the rock slope, the geometry condition and high strength of rock due to less weathering lead to a better condition than the other two locations. The SMR analysis result of this location indicates that the rock slope is class 'I', which means that the slope is completely stable. However, the results from kinematic analysis suggest that there may be a possibility that the rock slope at this location will fail in toppling.

All the analysis done on the rock slope at location 3, point out that this section of the slope is the least stable out of the three.

The following table illustrates the comparison of results

between these two different approaches (Kinematic and SMR).

Table III- Comparison of results

Set #	SMR		Kinematic approach		
	SMR	Grade	Toppling	Planar	Wedge
1	40	IV, Poor	-	+	-
2	83	I, Very good	+	-	-
3	14	V, Very poor	+	-	+

It can be deduced from the above table that, the results of both analyses have a good concordance with each other and in term of stability both show same outcomes.

6. REFERENCES

- [1] Willmott, W.F., *Slope Stability and Its Constraints On Closer Settlement On Tamborine Mountain, Southeast Queenslan*, 1981, Department Of Mines Geological Survey Of Queensland.
- [2] CRANFIE, L.C., SCHWARZBOCK, H., & DAY, R.W., *Geology of the Ipswich and Brisbane 1:250 000 Sheet areas*, in *Geological Survey of Queensland, Report 95*, 1976.
- [3] GREEN, D.C., *The volcanic rocks of Mt Tamborine, South-East Queensland.*, in *Department of Geology* 1964, University of Queensland.

Techno-commercial development of pre-fabricated structures using geopolymer concrete

J. Santhosh¹, R.Sanjeev², P.Sethu Raja³, A. Rajendra Prasad^{a1}

A. Abdul Rahman^{a2},

Sri Sai Ram Engineering College, Chennai, India.

1. ABSTRACT:

It is known that cement production releases high amount of CO₂ to the atmosphere. The cement is used for civil construction purposes including the structures like railway sleepers, electric power poles, fencing and waste containments, etc. In the present project geopolymer concrete is developed by using fly ash, mixing with the alkaline material and hardening the structure by polymerization using alkaline solutions like NaOH/KOH. A waste material such as rice husk ash which contains silica is utilized.

In the case of bamboo, a separate treatment technology is developed to increase the rigidity and flexibility in order to increase the life span and eliminate its bio-degradability. This is done by using certain metal ions in the freshly harvested bamboo. For making pre-fabricated structure, the bamboo is split into two halves equally and geopolymer concrete is embedded and the bamboo halves are united. The entire pre-fabricated structure is cured over a period of time.

2. INTRODUCTION:

Many concrete structures have life span of two to three decades. These structures deteriorate after specific period. Many buildings are also demolished after a period of 40 years. This indicates that the raw materials used for construction last only for a specific period. Under these circumstances, the cement production increases.

One ton of cement production releases equally one ton of CO₂ thus contributing 7% of world CO₂ emission that leads to global warming. Cement is also known as most energy intensive material.

In most countries, concrete is widely used as the foundation for the infrastructure. Concrete is used largely because its ability to support large compressive loads. However, the use of concrete is limited because it has low tensile strength. For this reason, it is reinforced, and one of the more popular reinforcing bars (rebar) is steel.

Steel is available and is affordable in most developed countries but unfortunately not all parts of the world. In many countries, none or very little steel reinforcement is used in construction. In some parts of the world many buildings are constructed only with concrete or mud-bricks. This is dangerous in case of seismic activity. These buildings have little hope of standing in the case of an earthquake. Steel reinforcement would be an ideal solution, but cost is a considerable problem.

3. MATERIALS AND METHODS:

The cement is a mixture of magnesium oxide (burnt magnesite) with magnesium chloride with chemical formula $Mg_4Cl_2(OH)_6(H_2O)_8$, corresponding to a weight ratio of 2.5–3.5 parts MgO to one part MgCl₂. It has the capacity to withstand about 10,000 to 12,000psi whereas the Ordinary Portland Cement has a capacity to withstand only around 2,000psi. MgCl₂ is the most effective chemical which acts as dust suppressant. The requirement of MgO and MgCl₂ are made available from the bittern, an inexhaustible resource from the salt field and it is cost effective.

Nearly 250 million tonnes of fly ash is being dumped in developing and developed countries each and every year. Developed countries allocate high financial resource for dumping these wastes. Since developing countries find it difficult to allocate this high financial resource this poses problems in the form of land use, health hazards, and environmental dangers both in disposal and in utilization. The other problems are as contamination of ground water as it can

leach into the subsoil, lowering of soil fertility, siltation and clogging the system, reduction in the pH balance, interference in the process of photosynthesis of aquatic plants and thus disturbs the food chain, corroding exposed metallic structures in its vicinity [1]. Fly ash which has self-cementing properties is produced in bulk quantity from thermal power plants. It is known to be useful for road construction and at the same time, it is a good material that blends with concrete [1].

It contains about 50% of silica and around 14% of ferric oxide which are some of the source materials that imparts strength to concrete. Ordinary Portland Cement contains only about 21% of Silica and 4% of Ferric Oxide. Fly ash not only increases the strength but also increases the volume since it acts as a dead weight material [2]. Class C fly ash which consists of about 20% of CaO is used here. It has the property of gaining strength over time.

The other source material used in the present study is the ash of rice husk which contains high silica content. It provides excellent thermal insulation property which helps maintaining a pleasant and cool environment.

The process of using fly ash is to be evolved by mixing with alkaline material which is also considered as waste material which will form a good product as cementitious paste. This material is hardened by adding chemical agents for polymerization. The temperature for polymerization is around 60°C to 90°C. A combination of NaOH or KOH with other chemical components in the raw material gets hardened like concrete. In addition, another biological waste material such as rice husk is used.

In the process of polymerization, the alkaline solution induces the Silica atoms especially in the source materials like fly ash and/or husk ash. In this process a gel is formed when it is applied with heat. This gel binds the aggregates of the unreacted source material and this source material due to polymerization at high temperature forms a product known as geopolymer concrete. This is used for mould preparation.

4. BAMBOO AS A RE-INFORCING MATERIAL:

Bamboo reaches its full growth in just a few months and reaches its maximum mechanical strength in just few years [3]. Its abundance in tropical and subtropical regions makes it an economically advantageous material. Some of the positive aspects such as a lightweight design, better flexibility, and toughness due to its thin walls with discretely distributed nodes and its great strength make it a good reinforcing material. Bamboo is used as structural material for scaffolding at construction sites in India, China and other countries as it is a tough, flexible, light weight and low cost material. In nature when bamboo is covered with heavy snow, it will bend until it touches the ground without breaking. This implies that bamboo has greater flexibility than wood. The tensile strength of bamboo is very high and can reach 380 N/mm² [2]

It is estimated that one billion people live in bamboo houses. In India and China bamboo is used in construction of temporary suspension bridges.

4.1 BAMBOO CHARACTERISTICS:

Bamboo culms are a cylindrical shell divided by solid transversal diaphragms at nodes and have some intriguing properties such as high strength in the direction parallel to the fibers, which run longitudinally along the length of the culm, and low strength in a direction perpendicular to the fibers. The density of fibers in cross-section of a bamboo shell varies with thickness as well as height. Fiber distribution is more uniform at the base than at the top or the middle. This is because bamboo is subjected to maximum bending stress due to wind at the top portion of the culm. The strength of bamboo is greater than most of the timber products.

The mechanical properties vary with height and age of the bamboo culm. Research findings indicate that the strength of bamboo increases with age. The optimum strength value occurs between 2.5 and 4 years. The strength decreases at a later age. The function of the nodes is to prevent buckling and they play a role of axial crack arresters.

One of the amazing aspects of bamboo is the way it interacts with the environment. It has been discovered that bamboo can prevent pollution by absorbing large amounts of nitrogen from waste water and reducing the amount of carbon dioxide in the air.

4.2 COMPARISON OF BAMBOO AND STEEL:

One of the properties that would make bamboo a good substitute to steel in reinforced concrete is its strength. The strength of bamboo is greater than most timber products which are advantageous. Bamboo is easily accessible as it grows in almost every tropical and subtropical region; this lowers the cost of construction and increases the strength of the buildings that would otherwise be unreinforced.

One major problem with bamboo is that it attracts living organism such as fungi and insects. Bamboo is more prone to insects than other trees and grasses because it has a high content of nutrients. In order to combat this problem, it becomes necessary to treat bamboo to protect it from bio-degradation. Steel does not have this problem but it also needs to be coated in order to protect it from rusting.

4.3 BAMBOO TREATMENT:

The physical structure of bamboo makes it very strong. Like reinforced cement concrete bamboo represents a composite material. As a result of structural peculiarities bamboo is very strong in spite of being light. Bamboo poles are treated to reduce their bio-degradability using 400gms of

Sodium dichromate, 300gms of Copper Sulphate and 150gms of Boric Acid in 10 litres of water. The outer surface of the bamboo culms is hard and impermeous. Therefore the solution is not absorbed. It is the inner surface of the culms through which the solution is absorbed.

Bamboo culms can also be treated with Potassium Dichromate which makes it more rigid like steel rod. It can be used as a steel rod and such structures are reinforced in geopolymer concrete.

The bamboo strips are also to be placed in a tank filled with above solution. Soaking is done for about 48 hours to make the treatment effective. However, it is proposed to use electrically driven compressor to impregnate the solution into the bamboo for future studies. The complete process has been explained in Fig.1.

4.3.1 PROCESS PLANNING:

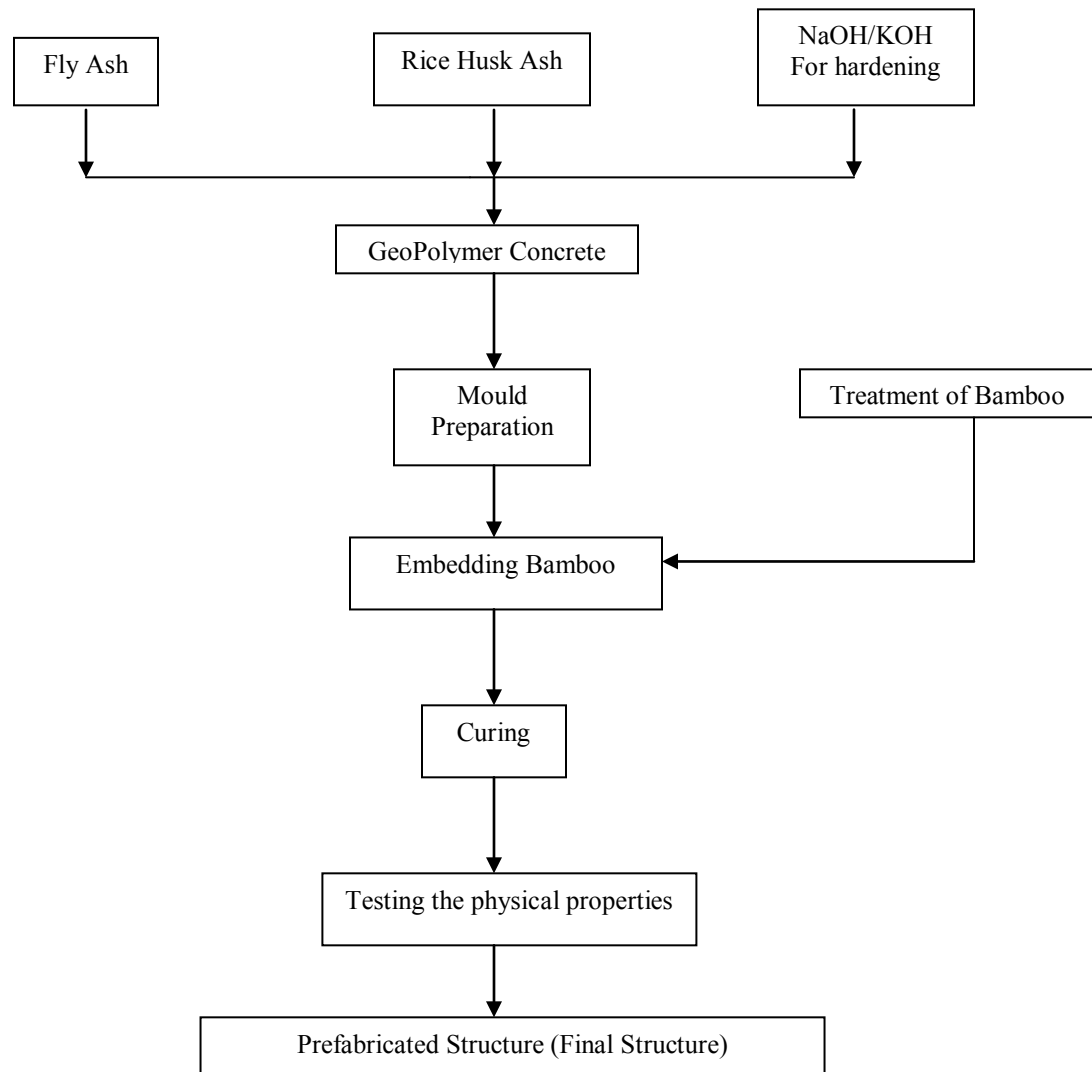


Fig.1

5.1 PRODUCTION ADVANTAGES:

The Polymerization temperature is only about 90°C, hence furnaces with high refractoriness are not required, thereby reduces the production cost further. Geopolymer concrete is more resistant to corrosion and fire, has high compressive and tensile strengths, and it gains its full strength quickly (cures fully faster). It also shrinks less than standard concrete.

5.2 SOCIAL IMPACT:

CO₂ emission reduces significantly thereby reducing global warming. The local NGO and Self Help Groups can be trained to fabricate their own fencing poles.

6. DISCUSSION:

Sorel Cement of Magnesium Oxide and Magnesium Chloride can withstand a compressive force of about 10,000 to 12,000psi whereas the Ordinary Portland Cement can withstand a pressure of only about 2,000psi. Fly ash consists of about 50% of Silica and 14% of Ferric Oxide which adds strength to the concrete whereas it is only about 21% of Silica and 4% of Ferric Oxide.

The load required to cause the failure of concrete beams reinforced with bamboo was from 4 to 5 times greater than that required for concrete members having equal dimensions and with no reinforcement. Fabricated product is fire-proof with low permeability, eco-friendly with

excellent properties in both acid and base environment. When curing period in oven is prolonged and polymerization temperature is increased, good structural property can be achieved. Life of structures made of geopolymer concrete lasts for more than 6 decades.

Concrete beams reinforced with unseasoned bamboo showed slightly greater load capacities than that with seasoned untreated bamboo. High early strength, low shrinkage, sulphate resistance and corrosion resistance are some of the characteristics. Bamboo reduces the intensity of damage to buildings due to earthquake. Such treated bamboo is free from termite attack and acts as a biological steel rod.

7. REFERENCES:

- [1] Malhotra, V.M., "Introduction: Sustainable Development and Concrete Technology", Concrete International, V.24, No.7, July 2002, p.22
- [2] Mehta, P.K., "Reducing the Environment Impact of Concrete", Concrete International, V.23, No. 10, Oct, 2001, pp.61-66.
- [3] Davidovitis, J. "Chemistry of Geopolymeric Systems, Terminology", Geopolymer'99 International Conference, France, 1999, pp. 9-40.
- [4] Malhotra, V.M., "Making Concrete 'Greener' with Fly ash", Concrete International, V.21, No.5, May 1999, pp. 61-66.

Mechanical Properties of Recycled Steel Fibre Reinforced Concrete

A.S.M. Abdul Awal¹, Lim Lion Yee¹, M. Dianah¹ and M. Zakaria Hossain²

¹Faculty of Civil Engineering, Universiti Teknologi Malaysia, Johor Bahru, Malaysia

²Graduate School of Bioresources, Mie University, Tsu-city, Mie, Japan

ABSTRACT

This paper presents some results, and discusses the feasibility of adding recycled steel fibre from scrap tires as reinforcement in concrete. A number of tests were conducted to investigate fresh and hardened state properties like slump, Ve-be time, ultrasonic pulse velocity, compressive, tensile and flexural strength of recycled steel fibre reinforced concrete (RSFRC). The effect of incorporation of recycled steel fibre on various aspect ratios (l/d) of 45, 67 and 89, and volume fraction (V_f) of 1, 1.5 and 2% were experimentally investigated. Test specimens comprising of cube, cylinder and prism were prepared and tested after 1, 7 and 28 days of water curing. It has been found that the workability of RSFRC, in general, was reduced as the volume fraction of the fibre increased. The compressive strength and splitting tensile strength of RSFRC reached a maximum at l/d ratio of 67. In terms of volume, the compressive strength of RSFRC was not significantly increased by incorporation of recycled steel fibre. However, the tensile and flexural strength of RSFRC was remarkably improved with the increase of fibre content. The results obtained and the observation made in this study suggests that recycled steel from waste tires can successfully be used as fibre reinforcing material in concrete.

Keywords: Fibre reinforced concrete, scrap tire, steel fibre, workability and strength.

1. INTRODUCTION

The technology of concrete reinforcement is not new, and fibres have been used for reinforcement since ancient times. Fibre reinforced concrete is a type of concrete that includes fibrous substances homogeneously dispersed and oriented in the concrete matrix. Fibres commonly used in concrete are steel fibers, synthetic fibres, glass fibres, and natural fibres. Since the advent of fibre reinforcing of concrete, a great deal of testing has been conducted on various fibrous materials to determine the actual characteristics and advantages for each product. Over the decades different types of steel fibres have been successfully used to reinforce concrete.

Steel fibres may be produced either cutting wire, by shearing sheets or from a hot-melt extract. The first generation of steel fibres was smooth so they did not develop sufficient bond with the cementitious matrix. Major efforts have been made in recent years to optimize the shape and size of the steel fibres to achieve improved fibre-matrix bond characteristics [1],[2]. It was found that steel fibre reinforced concrete (SFRC) containing hook-ended stainless steel wires has better physical properties than those containing straight fibres. This is attributed to the better anchorage provide and higher effective aspect ratio than that for the equivalent length of straight fibre [3]. The addition of steel fibres to concrete necessitate an alteration to the mix design to compensate for the loss of workability due to the extra paste required for coating the surface of the added steel fibres.

The utilization of SFRC over the past years has been so varied and widespread. The most common applications are pavements, tunnel linings, bridge deck slab repairs, and so on. Unfortunately the fibres themselves are relatively expensive. A 1% steel fibre addition, for instance, will

approximately double the material cost of the concrete, and this has tended to limit the use of SFRC to special applications. In recent years, there has been an increased interest in using the recycled steel waste especially from tire products. In all parts of the world large quantities of scrap tires are generated each year resulting in environmental hazards. It has been estimated that over 8 million units of scrap tire have been generated in Malaysia, and 60% of the scrap tires are disposed via unknown route [4]. These scrap tires are dangerous not only due to potential environmental threat, but also from fire hazards and provide breeding grounds for rats, mice, and mosquitoes. Today, scrap tire disposal has become a serious issue and research works have been devoted to the use of steel fibres recovered from waste tires in concrete. Concrete obtained by adding recycled steel fibres has evidenced a satisfactory improvement of the fragile matrix, mostly in terms of toughness and post-cracking behavior [5],[6]. This paper highlights the use of recycled steel fibre from scrap tires as reinforcement of normal concrete and discusses various fresh and hardened state properties of concrete containing the fibre.

2. MATERIALS AND TEST METHODS

The aim of this study as mentioned above, is to investigate the properties of concrete reinforced with recycled steel fibre recovered from waste tires. The fresh properties of recycled steel fibre reinforced concrete (RSFRC) were slump and Vebe times while the hardened properties of were compressive strength, splitting tensile strength, flexural strength and ultrasonic pulse velocity. The materials used and the methods followed for conducting the tests are given in the following sections.

2.1 Materials

Cement corresponding to ASTM Type I from a single source was used throughout the experimental work. The coarse aggregate was crushed granite with a maximum size of 20mm. Natural river sand with fineness modules of 2.5 was used as a fine aggregate. Both coarse and fine aggregates were batched in a saturated surface dry condition. Supplied tap water was used throughout the study in mixing, curing and other purposes.

A commercial polynaphthalene sulfonate type superplasticizer conforming to ASTM C494-92 was utilized as high range water reducing agent in the concrete. The dosage of superplasticizer was kept constant for all concrete mixes in order to eliminate any probable effect of this parameter on the properties of hardened concrete.

2.2 Preparation of Recycled Steel Fibre

Steel fibres used in this research were recovered by a shredding process of waste tires. The steel was successively separated from rubber by a pyrolysis process. The steel fibres shown in Fig.1 are characterized by different diameters and length. The average fibre length was 30mm with an average tensile strength of 1033 MPa.

A preliminary characterization was carried out by a statistical analysis in order to evaluate the variability of the geometric properties after the shredding process without any further treatment. The characterization is fundamental to eventually defining the opportune treatments for improving the final properties of the concrete. A sample of about 200 steel fibres, extracted randomly after the shredding process, was analysed. The diameter of each fibre was recorded by a micrometer and determined averaging three measures, namely at the two extremities of the fibre and at the midpoint.

2.3 Concrete Mix and Sample Preparation

The recycled steel fibres were added at different aspect ratio (l/d) and volume fraction (V_f) to determine the applicability of the fibre as reinforcement in concrete. The steel fibre recovered from waste tyre was employed to concrete mixtures with aspect ratios (l/d) of 45, 67 and 89 followed by volume fractions of 0.5%, 1.0%, 1.5% and 2.0%. A total



Fig. 1: Recycled steel fibre before and after shredding.

of 63 cubic specimens, 21 cylindrical specimens and 21 prismatic specimens was fabricated and cured in water until testing. Water to cement ratio was settled to 0.4 according to ACI Committee such as to provide good mechanical strength and adequate workability of the mixtures. The mix proportion of recycled steel fibre reinforced concrete is shown in Table 1.

The mixing procedure was divided into three stages. In the first stage cement, fine and coarse aggregates were weighed and mixed by hand until all the constituents are mixed uniformly. In the second stage, the recycled steel fibres were added slowly and uniformly to eliminate the recycled steel fibres clumped together. In the final stage, measured water and superplasticizer were added and mixed thoroughly until a homogeneous mix is obtained.

2.4 Tests on Fresh and Hardened Concrete

Slump test, following ASTM C143 standard was carried out to measure the consistency of a concrete which has a close indication to workability. Along with slump test, the Vebe test was conducted conforming to ASTM C 1170. In order to investigate the compressive strength of concrete, uniaxial compression test was carried out on 100 mm cube specimen following BS 1881-127:1990. The splitting tensile test was, however, performed on the standard test cylinders measuring 100x200mm conforming ASTM C496/C496M-04. The flexural strength test was conducted using 100x100x500mm beams under third point loading following

Table 1: Mix design of recycled steel fiber reinforced concrete.

Mixture code	l/d ratio	V_f (%)	Cement (kg/m ³)	Water (L/m ³)	Coarse aggregate (kg/m ³)	Fine aggregate (kg/m ³)	Fibre (kg/m ³)	SP (kg/m ³)
PC	-	-	562	225	925	670	-	5.63
RSFRC -1	45	0.5	562	225	925	670	12.5	5.63
RSFRC -2	67	0.5	562	225	925	670	12.5	5.63
RSFRC -3	89	0.5	562	225	925	670	12.5	5.63
RSFRC -4	67	1.0	562	225	925	670	25.0	5.63
RSFRC -5	67	1.5	562	225	925	670	50.0	5.63
RSFRC -6	67	2.0	562	225	925	670	70.0	5.63

the ATSM C1609/C1609M -10.

In addition to compressive, tensile and flexural strength tests, an ultrasonic pulse velocity test (conforming ASTM C597) was also conducted to measure the uniformity of concrete, and to investigate the relationship between compressive strength and ultrasonic pulse velocity of concrete cubes with different fibre volume fractions.

3. RESULT AND DISCUSSION

3.1 Properties of Fresh Concrete

Both the slump and Vebe time tests were conducted to investigate workability of concrete. The slump value and the Vebe time of all the concrete mixes for different aspect ratio (l/d) and fibre volume fraction (V_f) are tabulated in Table 2. As shown in the Table 2, slump values of concrete decreased as the l/d ratio and V_f increased. Meanwhile, Vebe time of concrete increased as the l/d ratio and V_f increased. For fibre volume of 1% and above the workability of concrete is dramatically decreased. The interlocking of fibres resists the flow of fresh concrete affecting the workability of concrete. The result on unit weight of concrete, presented in the same table reveals that the unit weight of concrete increased uniformly with the increase in fibre volume fraction. This is obvious as the specific gravity of recycled steel fibres are higher than those of other components of concrete. Regardless of fibre volume, it was further observed that the unit weight of RSFRC decreased by the increase of fibre aspect ratio because of air content in the concrete by orientation and distribution of long fibres.

Aspect ratio (l/d) of recycled steel fiber has a predominant effect on the workability concrete mixtures. The slump value has been found to decrease in concrete mixture realized with fiber aspect ratio of 45 and 67. A significant drop from 50mm to 30mm for concrete mixture was realized with fiber aspect ratio of 89. Table 2 reveals that higher the aspect ratio higher was the Vebe time for the same fibre content. This is due to the fact that long fibres tend to mat together while short fibres does not interlock and can be dispersed easily by vibration.

The experimental results obtained in this study are in close agreement with the research findings from Yazici et al. [8]. It has been shown that slump of concrete decreased as the l/d ratio of steel fibre increased. Like that of slump value, the Vebe time also found to be influenced by the aspect ratio of recycled steel fibers.

Like aspect ratio, the amount of fibre i.e. the volume fraction (V_f) significantly influenced the workability of fibre reinforced concrete. Higher the amount of fibre lower was the slump value. With an increase in the amount of fibre for 1 to 2 percent, the Vebe time of the SFRC has been found to be almost double. This is to be expected because lower amount of fibre can easily disperse in the concrete matrix.

With further addition the fibres start to clump together showing a balling effect (Fig. 2) Furthermore, the interlocking and entangled around aggregate particles and considerably reduce the workability. A similar observation has been made by Uygunoglu [7] who found that the unit weight of SFRC increased with the increase in fibre content for both 30mm and 60mm steel fibre.

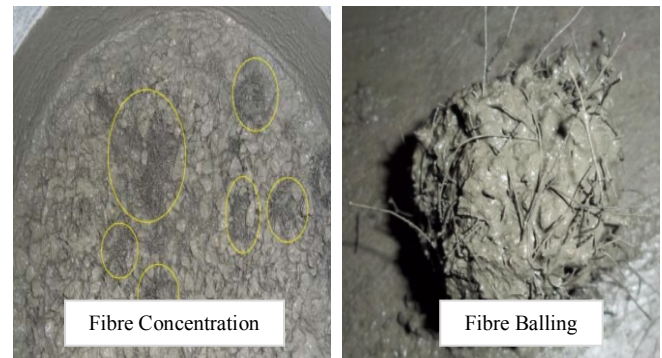


Fig. 2: Fresh concrete showing fibre concentration and balling effect.

3.2 Hardened Properties of Concrete

The mechanical properties of recycled steel fibre reinforced concrete investigated in this study are compressive strength, splitting tensile strength and flexural strength. The results

Table 2: Slump, Vebe time and unit weight of concrete mixtures.

Mixture code	l/d ratio	V_f (%)	Slump (mm)	Vebe time (s)	Unit weight (kg/m^3)
PC	-	-	50	3.05	2
RSFRC-1	45	0.5	45	3.88	2
RSFRC-2	67	0.5	40	4.06	2
RSFRC-3	89	0.5	30	5.62	2
RSFRC-4	67	1	25	6.35	2
RSFRC-5	67	1.5	20	7.85	2
RSFRC-6	67	2	10	12.32	2

obtained for all categories of strength investigation are presented in Table 3. Along with strength, ultrasonic pulse velocity of the concrete specimen was also studied to examine the relationship.

3.2.1 Compressive Strength

The 28-days compressive strength values are 57.15, 58.50 and 57.85MPa respectively. Among the three aspect ratios, the l/d ratio of 67 (RSFRC-2) exhibited the maximum compressive strength value. It can be seen that on average, compressive strength of RSFRC are about 2-6% higher than that of control mixture. RSFRC with fibre volume of 1.5% showed the highest compressive strength for aspect ratio of 67. A close observation has been made by Modtrifi et al. [9] who reported that an addition of 0.7% recycled steel fibres in concrete resulted in an increase of approximately 12% in compressive strength.

Although the compressive strength of SFRC was much affected by the presence of fibre, the failure mode, however, exhibited a considerable change from fragile to ductile state. Due to bridging effect of the fibre, the cubic specimens did not crush but held their integrity up to the end of the test. Fig. 3 illustrates the typical failure mode of plain concrete and recycled steel fibre reinforced concrete.

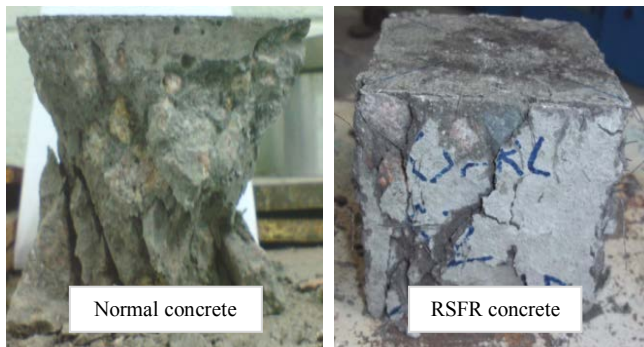


Fig. 3: Typical failure mode of normal and recycled steel fibre reinforced (RSFR) concrete cube.

There appears to be a good correlation between compressive strength and ultrasonic pulse velocity containing recycled steel fibre. The relationship shown in Fig. 4 suggests that higher the compressive strength higher was the ultrasonic pulse velocity. This is in agreement with the research findings in concrete containing recycled aluminium can fibre [10] and the relationship demonstrated by Neville and Brooks [11].

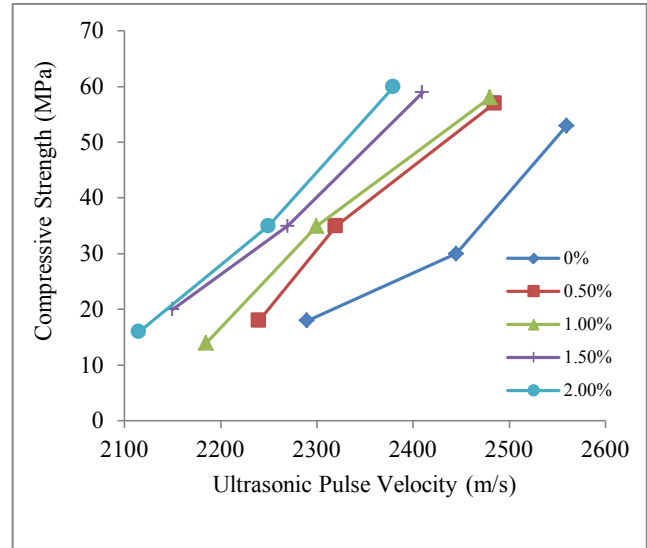


Fig. 4: Relationship between compressive strength and ultrasonic pulse velocity of concrete with different amount of fibre.

3.2.2 Splitting Tensile Strength

In general, the tensile strength of RSFRS was found to increase with increasing amount of fibre. But in all mixes, concrete with fibres volume fraction of 0.5%, l/d ratio of 67 (RSFRC-2) showed the maximum strength gain. The relative splitting tensile strength values of RSFRC according to V_f and l/d ratio are also given in Table 3. The test results indicated that splitting tensile strength of RSFRs is about

Table 3: Mechanical properties of concrete mixtures.

Mixture code	l/d ratio	V_f (%)	Compressive strength, f_c (MPa)	Relative, f_c (%)	Splitting tensile strength, f_{st} (MPa)	Relative, f_{st} (%)	Flexural Strength, f_f (MPa)	Relative, f_f (%)
PC	-	-	55.85	100	3.80	100	4.60	100
RSFRC-1	45	0.5	57.15	102	6.50	172	5.20	113
RSFRC-2	67	0.5	58.50	105	6.90	181	5.45	118
RSFRC-3	89	0.5	57.85	104	6.65	175	5.65	123
RSFRC-4	67	1	58.20	104	7.10	187	5.75	125
RSFRC-5	67	1.5	59.00	106	8.15	215	6.15	134
RSFRC-6	67	2	58.70	105	9.45	249	6.95	151

70-149% higher than the control mixture. Indeed, recycled steel fibres significantly improved the splitting tensile strength of concrete as compared to compressive strength. The results obtained in this study are consistent with previous studies [9], [10], [12].

During the splitting tensile test, the effect of the recycled steel fibres was apparent. The recycled steel fibres appear to control the cracking of RSFRC and alter the post cracking behaviour. The recycled steel fibres seem to provide a load redistribution mechanism after initial cracking. Unlike in normal concrete, it was difficult to separate the fractured specimens because the recycled steel fibres were bridging the gap that kept the two concrete parts together, as shown in Fig. 5.



Fig. 5: Concrete cylinder after splitting tensile test.

3.2.3 Flexural Strength

Data shown in Table 3 reveals that flexural strength of RSFRC are about 14-52% higher than the control sample. The flexural strength of control specimen, for example, is 4.60MPa. For l/d ratio of 45 (RSFRC-1), 67 (RSFRC-2) and 89 (RSFRC-3) the flexural strength values are 5.20, 5.65 and 5.45MPa respectively. The relative flexural strength values of RSFRC according to V_f and l/d ratio also given in Table 3. Evidently the flexural strength of concrete has significantly been improved by incorporating recycled steel fibres. Higher the aspect ratio and volume fraction higher was the strength gain.

An important aspect that can be outlined from experimental results is the ductility and tenacity of RSFRC increase when fibre content volume is increased, and for the same fibre content, when fibre length is increased. This phenomenon could be due to the higher deformability and energy absorption of RSFRC during the cracking phase.

Interestingly the RSFRC shows a higher bending stiffness and a different cracking pattern than the normal concrete. Most cracks showed a reduced width and they appeared from casting surface due to the presence of recycled steel fibres, which tend to move to the lower portion of the specimen. The differences in the failure mode of plain and RSFRC are illustrated in Fig. 6 and Fig. 7.



Fig. 6: Failure mode of plain concrete beam in flexure.



Fig. 7: Failure mode of RSFRC beam in flexure.

4 CONCLUSION

The experimental works carried out in this research draw some conclusions. These are:

- 1) The inclusion of recycled steel fibre significantly affected the workability of concrete. It has been found that the workability of concrete mixes decreased with the increase in the aspect ratio (l/d) and the volume fraction (V_f) of fibre.
- 2) Recycled steel fibre has been found to improve the overall strength of concrete. This improvement has been shown to be prominent in case of splitting tensile and flexural strength as compared to that of compressive strength. Generally, higher the l/d and V_f , higher was the strength development.
- 3) There has been a good co-relation between compressive strength and ultrasonic pulse velocity of concrete. The ultrasonic pulse velocity of concrete was found to increase with the increase of compressive strength.
- 4) The result obtained and the observations made in this study suggest that the recycled steel fibre from waste tire has a good potential as reinforcing material. Long-term research work including deformation behavior and durability aspects of concrete, however, has been put forward for future study to obtain better understanding of this material in concrete.

REFERENCE

- [1] Mindess, S, Young, FJ, Darwin, D. Concrete. New Jersey. Pearson Education, 1996.
- [2] Colin, DJ. "Steel fibre-reinforced concrete – present and future in engineering construction". Composites, 1982, pp. 113-121.
- [3] Swamy, RN, Mangat, PS, "The interfacial bond stress in steel fiber cement composites". Cement and Concrete Research, vol. 6, 1976 pp. 641-650.
- [4] Jalil, MA, "Sustainable development in Malaysia: A case study on household waste management," J. of Sustainable Development, vol. 3, No. 3, 2010, pp. 91-102.
- [5] Tlemat, H, Pilakoutas, K, Neocleous, K, "Design issues for concrete reinforced with steel fibre recovered from waste tires," J. of Materials in Civil Engineering, ASCE 18 (September/October), 2006, pp. 677–685.
- [6] Naik, TR, Singh, SS. Utilization of discarded tires as construction materials for transportation facilities. Report No. CBU-1991-02, UMW Center for by-products utilization, University of Wisconsin-Milwaukee. 1991, pp.16.
- [7] Uygunoglu T, "Effect of fibre type content on bleeding of steel fibre reinforced concrete," Construction and Building Materials, 2010, pp. 766-772
- [8] Yazici S, Inan G, Tabak V, "Effect of aspect ratio and volume fraction of steel fibre on the mechanical properties of SFRC," Construction and Building Materials, vol. 21, 2007, pp. 1250-1253.
- [9] Modtrifi N, Ibrahim IS, Rahman AB, "Mechanical properties of concrete containing recycled steel fibres," in Proc. 3rd Int. Conf. of EACEF (European Asian Civil Engineering Forum) Universitas Atma Jaya Yogyakarta, Indonesia, September 20-22, 2011, pp. B-135 - B140.
- [10] Awal, ASMA, Mazlan, D, Mansur, ML, "Ultisation of soft drink can as reinforcement in concrete" in Proc. 3rd Int. Conf. of EACEF (European Asian Civil Engineering Forum) Universitas Atma Jaya Yogyakarta, Indonesia, September 20-22, 2011, pp. B15-B20.
- [11] Neville, AM, and Brooks, JJ, Concrete Technology, ELBS Edition, Longman Group UK Ltd., 1994.
- [12] Papakonstantinou, CG, and Tobolski, MJ, "Use of waste tire steel beads in Portland cement concrete," Cement and Concrete Research, vol. 36, 2006, pp.1686-1691.

Effects of Gradation of Various Sand Deposits of Pakistan on Strength of Hardened Concrete

Gauhar Sabih¹, S. Muhammad Jamil¹ and Kamran Akhtar¹

¹School of Civil and Environmental Engineering, National University of Science and Technology, Islamabad, Pakistan

ABSTRACT

Various sand deposits of varying gradation are available in different regions of Pakistan. The gradation of different sands was compared with the ASTM specifications. It was revealed that only two sands satisfy the ASTM gradation limits. The same was also confirmed by the results of workability and compressive strength. For betterment of the construction industry, optimization of sand was carried out. The grading curves of optimized sands became compatible with the ASTM specifications and the concrete made with improved sands showed up to 39% increase in compressive strength. The optimized sands were cost effective also.

Keywords: sand, concrete, Pakistan, Lawrencepur, stone dust, compressive strength

1. INTRODUCTION

Since up to 30 percent of the total volume of concrete consists of sand/fine aggregate consequently fine aggregate characteristics significantly affect the performance of fresh and hardened concrete and have an impact on the cost effectiveness of concrete [1]. Gradation or particle size distribution of sand affects the properties of concrete like packing density, voids content, workability and strength [2]. Uniformly distributed mixtures generally lead to higher packing resulting in concrete with higher density and less permeability, and improved abrasion resistance. Consequently, uniformly distributed mixtures require less paste, thus decreasing bleeding, creep, and shrinkage [3]-[4]. The fine aggregate should be uniformly graded. If fine aggregate is too coarse it will produce bleeding, segregation and harshness, but if it is too fine, the demand for water will be increased [5].

Various sand deposits of varying gradation are available in different regions of Pakistan. The existence of large water reservoirs usually transports finer sands towards downstream; consequently the sand in the Northern region is coarser as compared to the sand from Central and Southern regions. There is a general trend in the country to use coarser sand from Lawrencepur, a site located in the Northern region. Transportation cost of sand from this place to far flung areas in Centre and South makes any project cost intensive. This study was aimed at evaluating the grain size distribution and absorption of various types of sands in the light of ASTM standards and to contrast the effects of gradation on the strength and workability of concrete. Finally devising a technique for optimizing the gradation of fine sands by sieving the stone dust and mixing different fractions of stone dust

with the natural sand to get optimized sand gradation and evaluating its effects on strength of hardened concrete.

2. IDENTIFICATION OF SAND DEPOSITS

Various well known material suppliers and construction firms were approached for identification of major sand deposits of the country. The locations of identified sand deposits are shown in Fig 1.

3. EXPERIMENTAL PROGRAM

3.1 Sieve Analysis and Classification

All the sand samples were classified by sieve analysis, carried out according to ASTM C-136-96 [6] and the classification of sand was done according to ASTM D-2487-93 [7]. ASTM C-33-03 specifies the gradation limits for sands to be used as fine aggregate in concreting [8]. The gradation curves of all the sands were compared with the ASTM gradation limits to contrast the variations.

3.2 Absorption Percentage

All the sand samples were tested for their absorption percentage in saturated surface dry (SSD) condition according to ASTM C-128.

3.3 Organic Impurities in Sands

This test was conducted for all the sands according to ASTM C-40 [9]. The test procedure consisted of making a reference standard colour solution by dissolving reagent grade potassium dichromate in concentrated sulfuric acid at the rate of 0.25 gram per 100 ml of acid. The sand sample was filled in a glass bottle up to 130 ml mark and sodium hydroxide solution (3% by mass in 97% water)



Fig 1. Locations of Identified Sand Deposits

was added up to 200 ml mark. The bottle was shaken vigorously and allowed to stand for 24 hours. After 24 hours the colour of the sand solution was compared with freshly made reference colour solution. The darker colour than reference colour indicates the possibility of sand containing injurious organic impurities and requires further testing for sand before use in concreting. The lighter or equal colour means that the sand does not contain injurious organic impurities and no further testing is required.

3.4 Evaluation of Sands in Concreting

3.4.1 Concrete Mix

The concrete mixes were prepared using sand / fine aggregate from eight different sources and remaining variables as constant with the cement: sand: coarse aggregate ratio of 1: 2: 4 (by weight) respectively, cement content (201.7 kg/cum) and water cement ratio of 0.5 with constant slump value. The course and fine aggregates were used in SSD condition. The course aggregate used was taken from Margallah quarry located in the Northern region. The cement used was Fauji cement (type 1, portland cement). The water used was normal tap water without any undesired colour.

3.4.2 Workability of Fresh Concrete

The workability was evaluated by measuring the slump of fresh concrete according to ASTM C-143. The concrete was filled in the slump cone in 3 equal layers with 25 blows of tamping rod each. After leveling the

top layer, the cone was lifted and slump was measured as reduction in original height.

3.4.3 Compressive Strength of Hardened Concrete

The test was conducted on 4x4 inches cubes (as per BS-1881) and 4x8 inches cylinders (as per ASTM C-39). The compressive strength was determined at the age of 3, 7, 14 and 28 days [10]-[11].

4. TEST RESULTS AND DISCUSSIONS

4.1 Sieve Analysis and Classification

All the sand types are poorly graded sands classified as SP, except the Wadd sand which contains silt as well and classified as SP-SM. The Percentage of micro fines (material passing No. 200 sieve) is below 5% in all sands except Wadd sand which contains 9% micro fines. According to ASTM C-33, the allowable limit of micro fines in sand for concreting is up to 5% so all the sands satisfy the ASTM criteria except the Wadd sand.

4.2 Comparison of Gradation with ASTM Gradation Limits

The comparative results of all the sands with the ASTM gradation limits are shown graphically in Fig 2. All the sands are finer than ASTM gradation limits except the Qiblabandi and Bollari sand. The Qiblabandi sand is the best match to ASTM gradation limits while Bollari sand is little finer than Qiblabandi sand.

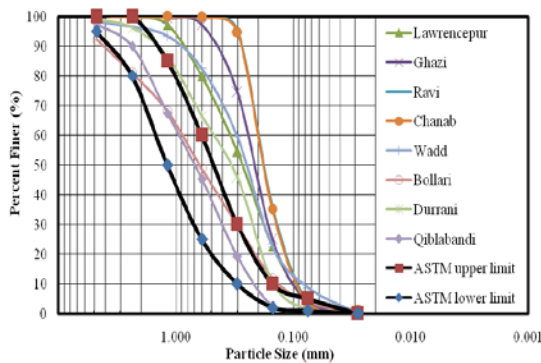


Fig 2. Sand Gradation versus ASTM Gradation Limits

4.3 Absorption Percentage

All the sands have absorption less than 3 % so they are within range of the limiting range as per BS-8007. The Qiblabandi sand has the lowest absorption percentage i.e. 1.75% being the coarsest sand of all types while the Bollari sand has the highest absorption percentage of 2.11% but it is also within range of the acceptable limit.

4.4 Organic Impurities in Sands

All the sand sample solutions have the colour lighter than the reference standard colour solution so all the sands do not contain injurious organic impurities and no further testing is required for the organic impurities (according to ASTM C-40). Consequently all the sands are suitable for concreting as per the results of this test.

4.5 Workability of Fresh Concrete

The slump values of the concrete made with different types of sands are ranging between 1.1 to 1.2 inches with same water cement ratio. This slump value was taken as constant for further compressive strength testing of hardened concrete. According to specifications, hand tamping was resorted in the preparation of cubes while vibrator insertions were used in preparation of cylinders [12]-[13].

4.6 Compressive Strength of Concrete Cylinders and Cubes

The compressive strengths of both of concrete cubes and cylinders follow the same trend line thus confirming the results. The comparative results of compressive strength of concrete cylinders are graphically shown in Fig 3. The Qiblabandi sand proved to be the best fine aggregate giving highest compressive strength of 3463 psi. Gradation meeting the ASTM specifications, lowest percentage of micro fines and within range fineness modulus of Qiblabandi sand are the supporting factors for the highest compressive strength. The trend of gradation of different sands as compared with the ASTM gradation limits is also confirmed by the results of the compressive strength. The Ghazi, Ravi and Chanab sands are below 3000 psi which is not desirable for concreting works.

5. OPTIMIZATION OF SAND GRADATION

Having observed the gradation of various sands, an endeavor was made to bring them within the specified limits of ASTM by adding a fraction of coarse material. The stone dust from Margallah, crusher site was taken and various fractions of stone dust were produced by sieving the stone dust on Number 4, 8, 16, 30 and 50 sieves (stone dust can be taken from any crusher site as the lab tests showed compatible results on use of stone dust from various crusher sites). Different percentages of various fractions of stone dust were added to the sand samples and optimized samples were produced. The optimized samples were then tested for their gradation to check the compatibility with ASTM limits. The optimized samples were then used for making concrete cubes and cylinders thus determining the improvement in the compressive strength of concrete specimens.

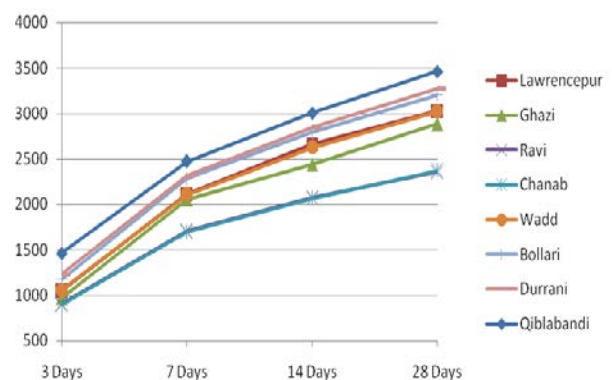


Fig 3. Comparison of Compressive Strength of Concrete Cylinders (psi)

This resulted in significant improvement of sand gradation as well as the compressive strength of concrete. Six sands which were out of range of ASTM standards were optimized. Various different combinations were tried for making the improved sand samples to attain the best mix.

5.1 Gradation of Optimized Sands

The gradation curves of optimized sands were compared with the gradation curves of original sands in the light of ASTM gradation limits to determine the effects on the gradation curves. The comparison clearly shows that the gradation curves of optimized sands are satisfying the ASTM gradation limits where as the original ones were out of the limits. The comparison of original and optimized gradation curves is shown in Fig 4.

5.2 Compressive Strength of Concrete

The optimized sand samples were tested by making concrete cubes and cylinders with the cement: sand: coarse aggregate mix of 1: 2: 4 (by weight) and the variables like cement (201 kg/cum), water-cement ratio (0.5), curing conditions and coarse aggregate (Margallah) as constant. The concrete specimens were then tested for compressive strength at the age of 3, 7, 14 and 28 days to get the improved compressive

strengths. These improved strengths were than compared with the original compressive strength values to get the percentage improvement.

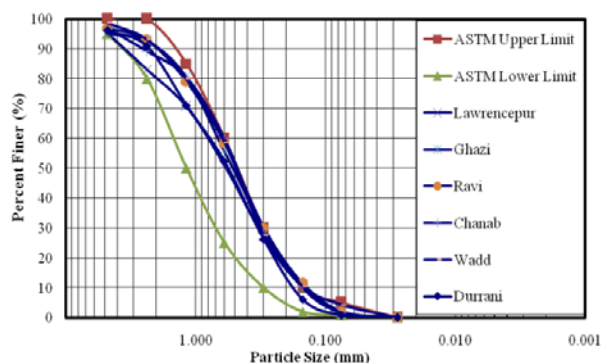


Fig 4. Comparison of Optimized Gradation Curves with ASTM Limits

5.3 Results of Compressive Strength of Optimized Sands

The compressive strengths of both cubes and cylinders follow the same trend line thus confirming the results. The comparative results of compressive strength of concrete cylinders are graphically shown in Fig 5. The results show that there is significant improvement in the compressive strengths and all the improved sands are above 3000 psi which is the foremost requirement for a sand to be used in concreting works. The improved Lawrencepur sand and Durrani sand (with fineness modulus of 2.62 and 2.58) respectively are giving the highest strength of 3441 psi and 3547 psi respectively.

6. COMPARISON OF ORIGINAL AND OPTIMIZED SAND PROPERTIES BASED ON COMPRESSIVE STRENGTH OF CONCRETE

The cylindrical compressive strengths of optimized sands at the age of 28 days were than compared with the cylindrical compressive strength values of original sands to get the percentage improvement.

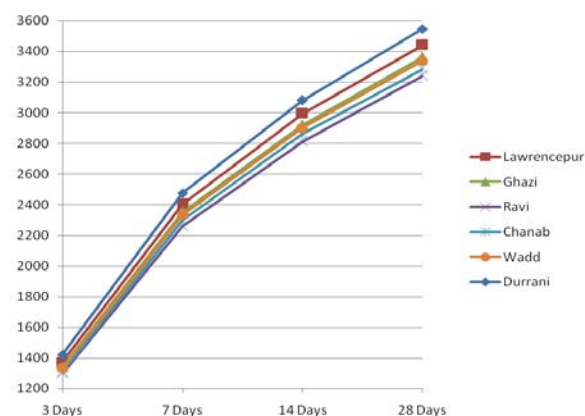


Fig 5. Comparison of Improved Compressive strength of Cylinders (psi)

6.1 Comparative Results of Cylinder Strength

The comparative summary is shown graphically in Fig 6. The comparison of percentage improvement of optimized sands in comparison to original sands is shown in Fig 7. The results show that all the optimized sands gave increased compressive strength. The optimized Ravi and Chanab sands show the most significant increase of 37% to 39% in the compressive strength when compared with original sands.

7. CONCLUDING REMARKS

Based on laboratory investigations and data analyses, following conclusions are drawn:

- Local sands can be utilized in the construction projects by optimizing the gradation using stone dust to avoid high costs of transportation.
- Even the best considered sand deposit requires fractions of stone dust to maximize its potential in concreting.
- The optimized Ravi and Chanab sands show the most significant improvement of 37% to 39% in the compressive strength while the optimized Lawrencepur, Ghazi, Wadd and Durrani sands also show greater strength than original sands with percentage improvement of 8% to 16%.
- The optimized Ghazi, Ravi and Chanab sands can be utilized in concreting works where as they were not suitable for concreting in their original form.
- All the optimized sands show higher compressive strength than the original sands in concrete cubes and cylinders both and are above 3000 psi which is the minimum criteria for any sand to be used as fine aggregate in concreting works.
- The improved performance of optimized sands can be directly related to various factors out of which, improved sand gradation is a major factor as per the analysis of this study.

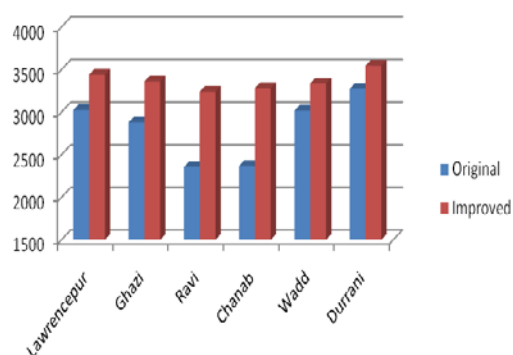


Fig 6. Comparison of Original versus Improved Cylinder Strength

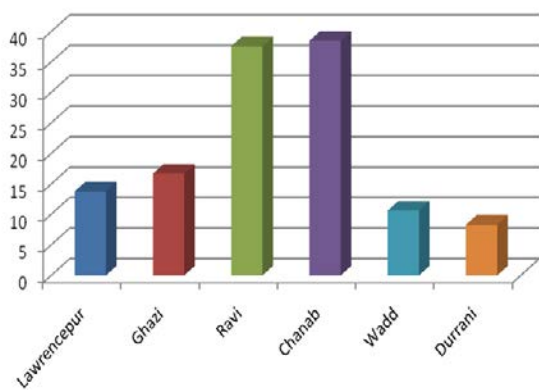


Fig 7. Comparison of Percentage Improvement of Optimized Sands

ACKNOWLEDGEMENTS

The authors thank Dr. S. Ali Rizwan for his critical review which greatly helped in improving the manuscript. The study was funded by the National University of Sciences and Technology.

REFERENCES

- [1] Hudson, B.P, "Concrete Workability with High Fines Content Sands", 1999.
- [2] Golterman, P., Johansen, V., Palbfl, L., "Packing of Aggregates: An Alternative Tool to Determine the Optimal Aggregate Mix," ACI Materials Journal, Vol. 94, No. 5, 1997.
- [3] Shilstone, J. M., "The Aggregate: The Most Important Value-Adding Component in Concrete," Proceedings, Seventh Annual International Center for Aggregates Research Symposium, Austin, Texas, 1999.
- [4] Washa, G.W., Workability, Chapter 5, Concrete Construction Handbook, 1998, 4th edition, New York.
- [5] Galloway, J. E. Jr., "Grading, Shape, and Surface Properties," ASTM Special Technical Publication No. 169C, Philadelphia, 1994.
- [6] ASTM C-136, Standard Test Method for Sieve Analysis of Fine and Coarse Aggregates, Philadelphia, PA: American Society for Testing and Materials, 2001.
- [7] ASTM D-2487, Standard classification of soils for engineering purposes (Unified soil classification system), Philadelphia, PA: American Society for Testing and Materials, 1993.
- [8] ASTM C-33, Standard Specification for Concrete Aggregates, Philadelphia, PA: American Society for Testing and Materials, 2003.
- [9] ASTM C-40, Standard test method for organic impurities in sand for concrete, Philadelphia, PA: American Society for Testing and Materials, 1992.
- [10] ASTM C-192, Standard Practice for Making and Curing Concrete Tests Specimens in the Laboratory, Philadelphia, PA: American Society

for Testing and Materials, 2000.

- [11] British Standards Institution, "Methods for making of concrete cubes in laboratory," BS-1881-116: Part 110, 1990.
- [12] British Standards Institution, "Methods for Determination of compressive strength of concrete cubes," BS 1881-108: Part 110, 1990.
- [13] ASTM C-39, Standard Specification for Compressive Strength of Cylindrical Concrete Specimens, Philadelphia, PA: American Society for Testing and Materials, 2003.

Assessment of recycled concrete aggregates for road base and sub-base

S. Jayakody, C. Gallage, A.Kumar

*School of Urban Development, Faculty of Built Environment & Engineering, Queensland University of
Technology, Brisbane, Australia*

ABSTRACT

Population increase and economic developments can lead to construction as well as demolition of infrastructures such as buildings, bridges, roads, etc and used concrete is the main waste product of them. Recycling of waste concrete to obtain the recycled concrete aggregates (RCA) for base and/or sub-base materials in road construction is a foremost application to be promoted to gain economical and sustainable benefits. As the mortar, bricks, glass and asphalt present in different constituents in RCA, it exhibits inconsistent properties and performance. In this study, six different types of RCA samples were subjected classification tests such as particle size distribution, plasticity, compaction test and California Bearing Ratio (CBR). Results were compared with those of the standard road materials used in Queensland, Australia and found that 'RM1-100/RM3-0' and 'RM1-80/RM3-20' samples are sitting in the margin of the minimum required specifications of base materials while others are lower than that.

Keywords: Recycling, Waste concrete, Road materials

1. INTRODUCTION

Demolished materials are becoming more popular to recycle and reuse due to shortage of natural mineral resources, increasing waste disposal cost, and increasing the demand of materials. Conversely supplying the conventional aggregates for construction purposes make impact on resource depletion, environmental degradation, and energy consumption. Therefore reusing the recycled materials creates many economical and environmental benefits.

Crushed concrete can be considered and promoted as an alternative and a sustainable source of aggregate for construction industry. Successful studies have been revealed that recycled concrete aggregates can be applied as a partial or complete substitution of natural aggregates in the production of ordinary concrete [1], [2], [3]. However Hansen in 1992 [4] has proven that fine portion of RCA makes detrimental effects on the harden properties of concrete and the coarse RCA are the best use.

The studies on RCA as pavement materials are widely reported in last decades. Reference [5] shows the evaluation of the performance of RCA using as a base material under hot mix asphalts and as an aggregate in Portland cement concrete pavement while [6] reported that the performance of the subbase materials prepared with both coarse and fine RCA was comparable to that of conventional subbase materials. Reference [7] introduced RCA as base and subbase material for supporting a concrete pavement while [8] concluded the feasibility of using RCA and crushed clay bricks as blended materials for un-bound granular subbases. Although these research findings have demonstrated the feasibility of using RCA as

subbase material as well as for base course of the concrete pavements, a detailed investigation of RCA as base and subbase material for unbound pavements is required including classifications considering the variability of RCA compositions, performance characteristics under repeated loading, and evaluation of the performance of a granular pavement constructed using RCA and subjected to real traffic loading. As the first step of such a detailed investigation of RCA, this paper presents the results of classification tests of six different RCA samples to analyze the feasibility of using them in unbound granular pavement constructions comparing their classification properties with those of the conventional unbound granular materials used in Queensland.

2. MATERIALS USED

For this investigation, two main commercially available RCA products, namely RM001 and RM003, obtained from a leading concrete recycling plant in Queensland were utilized. Material sources are demolished building (slabs, floors, columns and foundations), bridge supports, airport runways and concrete road beds. The collected materials are undergone specified crushing process to produce RM 001 and RM 003. Table 1 shows the maximum percentages of the constituents that can be consisted in RM001 and RM003 at the plant output. These two materials were blended in different percentages by weight to form another four samples to represent various combinations of constituents. New sample types with their blending percentages are showing in Table 2.

Table 1: Percentage limits of constituents of two main RCA materials.

Recycled Material Type	Maximum Limit of each Constituent (Percentage by mass)		
	Reclaimed Concrete	*RAP	Brick
RM 001	100	-	-
RM 003	100	20	15

*RAP – Reclaimed Asphalt Pavement

Table 2. New RCA samples with blending percentages

Material name	Mixing percentages by mass (%)	
	RM001	RM003
RM1-100/RM3-0	100	0
RM1-80/RM3-20	80	20
RM1-60/RM3-40	60	40
RM1-40/RM3-60	40	60
RM1-20/RM3-80	20	80
RM1-0/RM3-100	0	100

3. LABORATORY TESTING, RESULTS AND DISCUSSION

Usually RCAs are highly heterogeneous and consist in different amounts of impurities and their quantities are not steady. This makes RCA to have inconsistent classification properties. Therefore it is essential to characterize the properties of RCAs through classification tests such as sieve analysis test, atterburg limits test, proctor compaction test and California bearing ratio (CBR) to investigate the possible range of variation of classification parameters. The results were compared with the specifications of base and subbase materials of Department of Main Roads in Queensland.

3.1 Grain Size Distribution

Particle size distribution of a particular pavement aggregate type affects its compressibility, permeability, density...etc [9]. Grain size distribution curves of all six testing RCA samples obtained from sieve analyses are shown in Fig 1. Further the maximum and minimum grading curves of material subtype 2.1 have been drawn in same figure. Material subtype 2.1 is applied for base layers by Department of Main Roads, Queensland and its gradation curves are drawn as their specifications. These demarcating lines are showing that fine content of the six samples are within required range but close to the minimum curve, while the coarse particles have exceeded the maximum gradation curve at the top. But all the curves show that a greater fraction of their curves are laid within the specified range.

According to the unified soil classification system (USCS), except 'RM1-0/RM3-100', other five samples are categorized as 'well graded gravel'. The 'RM1-0/RM3-100' present

approximately half of sand and half of gravel with slightly susceptible to gravel.

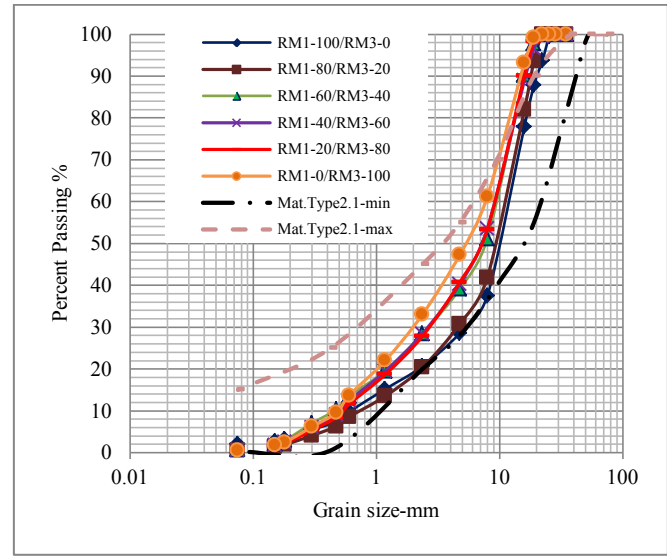


Fig 1. Gradation curves for six samples and maximum & minimum curves of subtype 2.1 materials

Table 3. Plasticity Index of two main materials

Fine Sample	RM1-100/RM3-0	RM1-0/RM3-100
LL	21	27
PL	15.6	20
PI	5.4	7

3.2 Plasticity

Cone-penetrometer method was followed to determine the liquid limit (LL) as well as plastic limit test was done for plastic limit (PL) for the sample of fines passing 0.475 mm sieve. Fines of only 'RM1-100/RM3-0' and 'RM1-0/RM3-100' were tested since other four samples are blended of these two. The LL values and mean values of plastic limit (PL) test (Atterberg limit test) were summarized in Table 3. According to the Department of Main Roads specifications the maximum plasticity index (PI) is 6 for material subtype 2.1 (See section 3.1). 'RM1-100/RM3-0' is within that range but 'RM1-0/RM3-100' having PI of material subtype 2.3 which is given maximum PI as 8. The subtype 2.3 is applied for upper subbase layers by Main Roads.

3.3 Compaction

The moisture density curve (compaction curve) of a soil is an indicator of the sensitivity of the density with respect to the variation of moisture content in the materials [10]. Materials with flat curves can tolerate a greater amount of variations in the moisture content without compromising much of the achieved density from compaction. In contrast, materials with sharp curves are extremely sensitive to the optimum value during compaction.

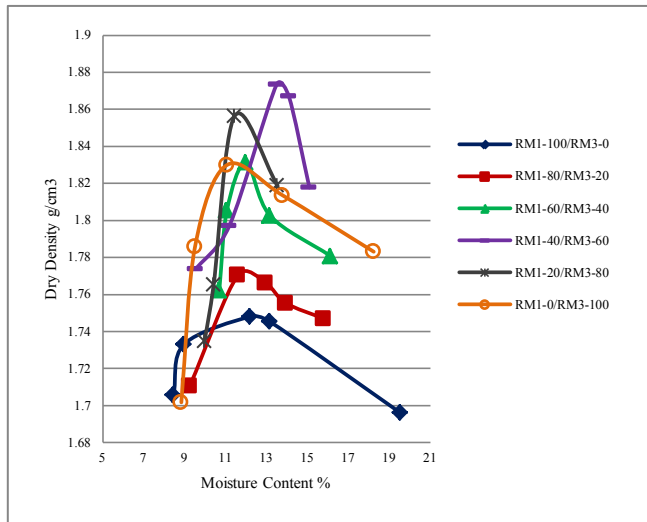


Fig 2. Compaction curves for Six Samples

Table 4. Optimum Moisture Content and Maximum Dry Density for Six Samples

Sample Type	Optimum Moisture Content %	Maximum Dry density (g/cm ³)
RM1-100/RM3-0	13.2	1.748
RM1-80/RM3-20	13.2	1.768
RM1-60/RM3-40	13.3	1.822
RM1-40/RM3-60	13.5	1.856
RM1-20/RM3-80	14.0	1.836
RM1-0/RM3-100	14.2	1.846

Standard proctor compaction test in accordance with Australian Standards [11] was performed on each testing sample and the results are shown in Fig 2. Optimum Moisture Content (OMC) and Maximum Dry Density (MDD) values of each material obtained from Fig. 2 are tabulated in Table 4. The range of the variation of MDD and OMC are relatively small as 1.748-1.846 g/cm³ and 13.2-14.2%, respectively. It can be seen that with the increase in fines contents of a material, both OMC and MDD increase as fines can absorb more water and can reduce the void volume by filling the voids between larger particles.

Furthermore, with the increase in fine in the samples the curves are more pointed showing the sensitivity of mixture of water. And it is also interesting to note that all the samples are more sensitive to the moisture variation on the dry side of the OMC curves than the wet side of the OMC.

Table 5. Variation of CBR values with different moisture homogenization periods

Sample Type	CBR %		
	No moisture homogenization period	3 hrs moisture homogenization period	*8 hrs moisture homogenization period
RM1-100/RM3-0	61	74	55
RM1-80/RM3-20	56	63	-
RM1-60/RM3-40	55	66	-
RM1-40/RM3-60	50	61	-
RM1-20/RM3-80	48	60	-
RM1-0/RM3-100	46	50	53

*CBR was conducted only for two samples to observe the strength gaining pattern

3.4 CBR tests

CBR characterization is widely used in pavement industry to provide a relative measure of strength, elastic modulus and moisture durability across various road materials for structural design purposes [9]. CBR tests were performed as specified in AS 1289.6.1.1 – 1998 [12] on the six samples compacted at their corresponding OMCs.

In order to find out the optimum moisture homogenization period (time between material mixing with water and compaction), a series of CBR tests were performed on RCA samples prepared allowing different moisture homogenization periods (e.g. 0, 3, 8 hours) since the main components of crushed concrete; aggregates, cement mortar, sand need specific time period for uniformly moisture distribution. The results of these CBR tests are tabulated in Table 5.

The samples under ‘No moisture homogenization period’ have given the lowest CBR values since they did not have enough time for homogenization of moisture and therefore lower the compaction and CBR values. 3 hours curing period showed higher CBR values since the materials have taken sufficient time for uniformly moisture distribution which helps for properly compaction of the samples. But RM1-100/RM3-0 showed lower CBR values for 8 hours curing period while RM1-0/RM3-100 had its highest CBR value than previous conditions. RM1-0/RM3-100 consists on more fines, clay bricks, and RAP particles which need more time and 3 hours insufficient for uniformly moisture distribution. In the RM1-100/RM3-0 neither clay bricks nor

RAP, but when higher the curing time (8 hours) the cement motar separately harden themselves and the inter particle connection between those the harden cement motar and recycled aggregates caused poor compaction as well as poor load transfer through materials under loading. Therefore 3 hours moisture homogenization was followed for the next CBR test series.

3.4.1 CBR test for unsoaked samples

Next CBR test series were conducted to investigate the effects of unsoaked curing periods of the compacted samples on CBR values. Each sample was prepared following the 3 hours curing period and followed standard compaction procedure. The sample compacted into the mould was cured (unsoaked) in a sealed container for different periods (e.g. 4 and 8 days) with 4.5kg surcharged load before testing. The variations of CBR values with curing periods for each RCA are shown in Table 6. 4 days curing for compacted samples were followed since it is followed for standard aggregates by the Department of Main Roads. 8 days curing period for compacted samples were applied to observe the strength gaining with time. RM1-100/RM3-0 and RM1-80/RM3-20 had slightly lower values of their CBR after 8 days curing of the compacted samples. The fine particles of these compacted samples were settled themselves under 4.5 kg surcharge load for 8 days. This caused to form little voids between irregular shapes recycled aggregates since these two sample types have very low amount of fines comparatively other samples. This makes weak inter connection in the upper part of the compacted sample while load transferring and caused for low CBR values.

Table 6. CBR Values for Different Curing Period of Compacted Samples

Sample Type	CBR %	
	Mixture-3 hrs curing & compacted sample cured 4days	Mixture-3 hrs curing & compacted sample cured 8days
RM1-100/RM3-0	81	78
RM1-80/RM3-20	77	75
RM1-60/RM3-40	74	75
RM1-40/RM3-60	63	64
RM1-20/RM3-80	60	60
RM1-0/RM3-100	58	41

RM1-60/RM3-40, RM1-40/RM3-60, RM1-20/RM3-80 had almost same but slightly higher CBR values respectively. Higher compactability due to the high fine fraction and high water absorption for cement motar strength gaining affect their greater load bearing strength.

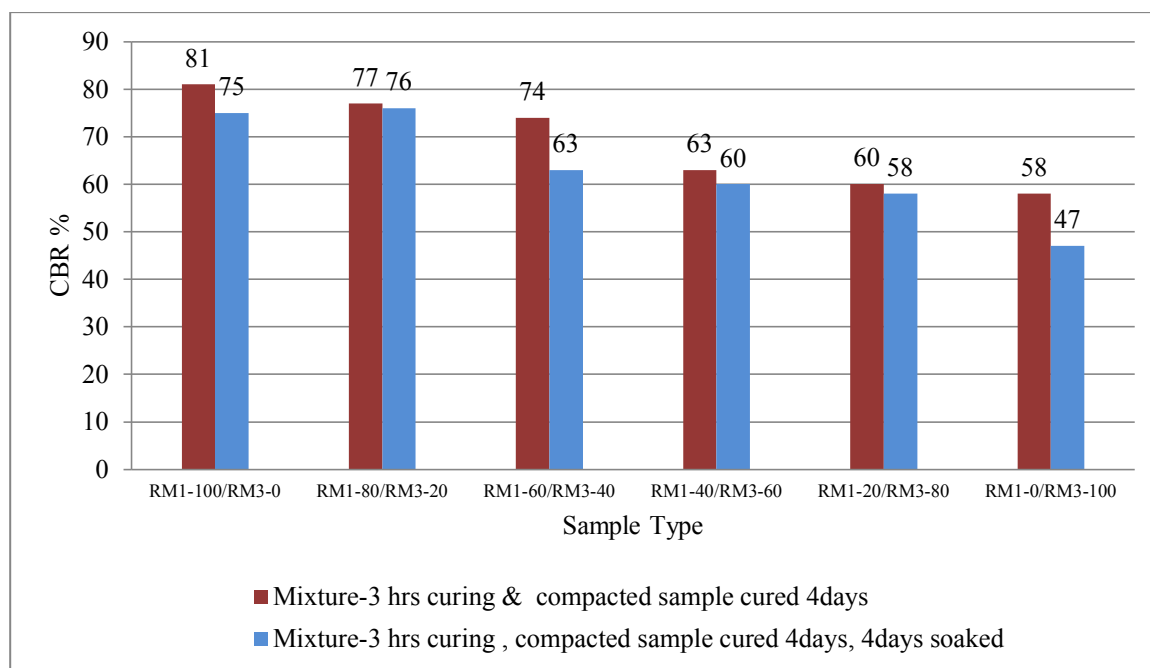


Fig 3. Summary of CBR values for best unsoaked and soaked results

RM1-0/RM3-100 had its lowest CBR values and this is due to the lower intrinsic particle strength of crushed bricks and reclaimed asphalts (RAP) which led to lower overall bearing strength of RCA [13]. Also the poor interlocking system due to the crushed clay brick and sand decrease the load transfer capacity of the compacted samples.

3.4.2 CBR test for soaked samples

Testing the CBR values of pavement materials after soaking is more significant to observe the strength of materials under fully saturated condition. This is highly applicable for flood risk areas in material selecting and pavement designing. The Department of Main Roads in Queensland has introduced minimum required soaked CBR value as 80 for base layers. The soaked CBR results and the best CBR values which were shown by the mixture cured 3 hours and compacted samples cured 4 days are shown in Fig 3. For the soaked test, materials were cured 3 hours prior to compaction and the compacted samples also cured for 4 days with 4.5kg surcharged load prior to testing. It shows that soaked CBR values are slightly less than the unsoaked values which has the same curing times but not reached the minimum requirement of the Main Road's specifications.

4 CONCLUSION

- RCAs have fewer fines but higher percentage of coarse fraction. The six curves are shown minimum required particles size distribution of material subtype 2.1.
- The proctor compaction test gave relatively higher water absorption for maximum dry density. Cement, rock dust and clay bricks cause for higher compaction with increase the RM 003 portion but lower the density. However the density varied in a small range giving the lowest value for 'RM1-100/RM3-0' which represents only crushed concrete aggregate.
- 'RM1-100/RM3-0' sample has certainly very appreciable results at CBR test at the both soaked and unsoaked. 'RM1-80/RM3-20' sample also has come close to 'RM1-100/RM3-0' with CBR results but lesser values. However, this improvement is laid in the margin of the minimum requirement of the pavement aggregates' CBR values which employ for base layer (CBR 80 for soaked condition, [14]) as introduced by Main Roads in Queensland. But it is possible to conclude that six sample types are showing appropriate strength for employing as a subbase aggregate as well as being able to be reusing in base for low or average traffic pavements.

ACKNOWLEDGMENT

The authors thank Alex Fraser Group, Queensland for providing recycled concrete aggregates for this experimental investigation.

5 REFERENCES

- [1] Amnon K. Properties of concrete made with recycled aggregate from partially hydrated old concrete. *Cement and Concrete Research* 2003; 33:703-711.
- [2] Kou S-c, Poon C-s, Agrela F. Comparisons of natural and recycled aggregate concretes prepared with the addition of different mineral admixtures. *Cement and Concrete Composites* 2011; 33:788-795.
- [3] Poon C S, Shui Z H, Lam L. Effect of microstructure of ITZ on compressive strength of concrete prepared with recycled aggregates. *Construction and Building Materials* 2004; 18:461-468.
- [4] Hansen T C. Recycling and demolished concrete and masonry. In: Taylor & Francis e-library; 1992.
- [5] Chini S A, Serghian T J, Marmaghani J. Use of recycled aggregates for pavement. In: *Materials for the new millennium* Washington: 2001.
- [6] Nataatmadja A, Tan Y L. Resilient Response of recycled concrete road aggregates. *Transportation engineering* 2001.
- [7] Park T. Application of construction and building debris as base and subbase materials in rigid pavement. *Journal of Transportation Engineering* 2003; 129:558-563.
- [8] Poon C S, Chan D. Feasible use of recycled concrete aggregates and crushed clay brick as unbound road sub-base. *Construction and Building Materials* 2006; 20:578-585.
- [9] Papagiannakis A T, Masad E A. *Pavement design and materials*. John Wiley & Sons Inc. Hoboken New jersey; 2008.
- [10] Poon C-S, Qiao X C, Chan D. The cause and influence of self-cementing properties of fine recycled concrete aggregates on the properties of unbound sub-base. *Waste management* 2005:1166-1172.
- [11] Australia C o S. Methods of testing soils for engineering purposes. In: Method 5.1.1: Soil compaction and density tests-determination of the dry density/moisture content relation of a soil using standard compactive effort. 2003.
- [12] Australia C o S. Methods of testing soils for engineering purposes. In: Method 6.1.1: Soil strength and consolidation tests-determination of the California Bearing Ratio of a soil-standard laboratory method for a remoulded specimen. 1998.
- [13] Boudlal O, Melbouci B. Study of the behavior of aggregates demolition by proctor and CBR tests. In: *Material, design, construction, maintenance, and testing of pavement*. Changsha, Hunan, China: 2009.
- [14] MainRoads Q D o T a. Main roads technical standard: MRTS35 - Recycled materials for pavements. In: 2010.

Estimation of consolidation properties of Holocene clays with artificial neural network

Kazuhiro ODA¹, Minsun Lee² and Shotaro Kitamura³
Osaka University, Japan

ABSTRACT

It is required to estimate appropriately the spatial distribution of consolidation properties, in order to predict accurately the consolidation settlement of sea bed ground due to large scale reclamation. It is necessary to estimate the soil properties at arbitrary position in the ground from the data of soil investigation. In this study, an artificial neural network was applied to interpolate spatially the consolidation properties, such as natural water content, void ratio, plastic index, compression index and pre-consolidation pressure. The estimation accuracy of consolidation properties was judged based on the four indexes, such as R^2 , G , $MARE$ and SR . The artificial neural network estimates the appropriate consolidation properties with high accuracy, so that the availability of spatial interpolation of consolidation properties through artificial neural network was confirmed.

Keywords: Neural Network, Geo-informatics, Spatial interpolation, Osaka Bay, Consolidation properties

1. INTRODUCTION

Many man-made islands such as Kansai International Airport, Port Island, Yumeshima Island et al have been constructed in the Osaka Bay. In addition, the construction of some man-made islands is planned presently. Man-made islands are usually constructed for a long term, because man-made islands are very large. On construction of man-made islands, they are usually divided into some construction of sections. The construction histories are different in each construction of section, differential settlement of man-made islands occurs necessarily. Therefore, the prediction of differential settlement must be required to control the construction work of man-made islands.

Holocene clays more than 20m, which is under almost normally consolidated condition, accumulate in Osaka Bay. The differential settlement of man-made islands in Osaka Bay is dependent on mainly the consolidation behavior of Holocene clay layer. The spatial distribution of consolidation properties, such as compression index, coefficient of permeability et al, in Holocene clay layer must be elucidated to predict the differential settlement of man-made islands accurately. However, it is difficult to estimate the spatial distribution of consolidation properties from limited number of soil investigations.

By the way, an artificial neural network is one of the information processing systems which have been advanced recently. This technique has been applied to data mining. Data mining is the process of discovering new patterns from large number of data sets. That is, locations at which soil investigations were carried out and geotechnical information obtained from soil investigations can be chosen as data sets. The connection between the locations at soil investigations

and geotechnical information could be given through applying an artificial neural network. The authors have studied about the spatial interpolation of soil properties by artificial neural network [1]-[3]. Consequently, the artificial neural network was applied to estimate the soil properties at an arbitrary position in the ground. That is, the spatial interpolation of soil properties was carried out through an artificial neural network.

In this study, the spatial distribution of soil properties, which are used to predict the differential settlement of man-made islands, is carried out through an artificial neural network. That is, an artificial neural network is applied to estimate the soil properties at an arbitrary position in Holocene clay layer. The accuracy of estimation to the soil properties is judged through various statistical indices. Also, the spatial distribution of soil properties in Holocene clay layer is visualized. The availability of artificial neural network to spatial interpolation of soil properties is discussed based on the accuracies.

2. ARTIFICAIL NEURAL NETWORK

An artificial neural network is an information processing systems, in which the nerve cells (neurons) in human brain are mimicked mathematically. Fig. 1 illustrates the architecture of artificial neural network used in this study. This type of artificial neural network is called back propagation neural network, which has been most popularly used. The back propagation neural network is consists of the input-layer, one or more hidden-layer, and the output-layer. Each layer is connected by neurons. In this study, the soil properties at an arbitrary position in the ground should be estimated. Then, the latitude, longitude, and altitude at target position at which the soil properties should be estimated were corresponded to items of the input-layer. Further, the consolidation pressures in the oedometer tests were added to

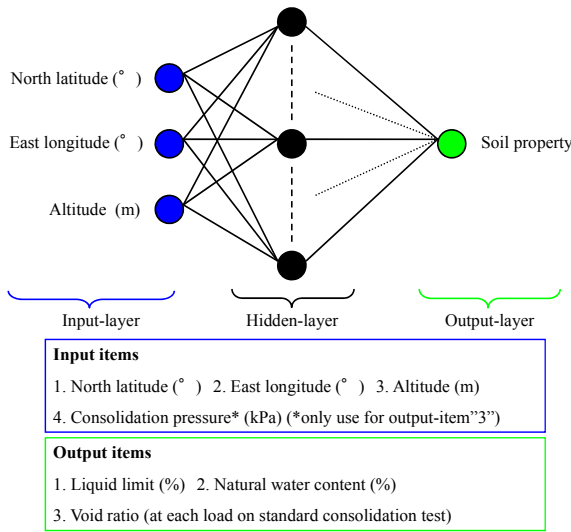


Fig. 1. Architecture of artificial neural network

items of the input layer provided that one dimensional compression curves were estimated. On the other hand, estimated soil properties were corresponded to items of the output-layer.

3. ANALYSIS

3.1 Subject Area for Spatial Interpolation

There are large amounts of geotechnical information obtained from soil investigations in many construction projects in Kansai area and they have been accumulated into geo-informatics database, called Gibase [4]. Figure 2(a) shows locations at soil investigations included in Gibase. The red dots in Fig. 2 denote the locations at which soil investigations were carried out. Over 25,000 boring investigations in Kansai Area is accumulated into Gibase. In this study, the spatial interpolation of soil properties in Holocene clay (Ma13) in Kobe Airport in Osaka bay was carried out. Figure 2(b) shows the locations at soil investigation in the subject area of this study. 99 boring

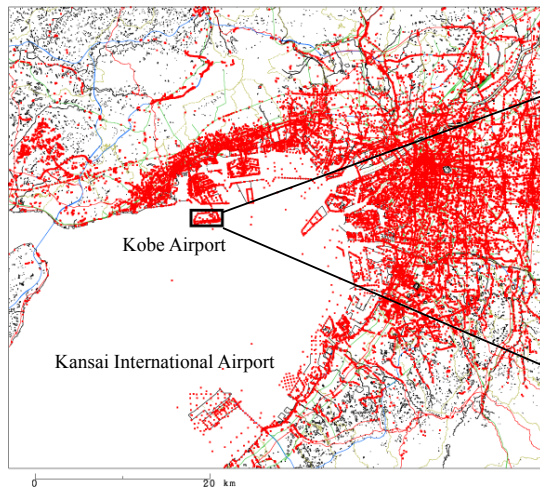


Fig. 2(a). Locations at soil investigation in Gibase.

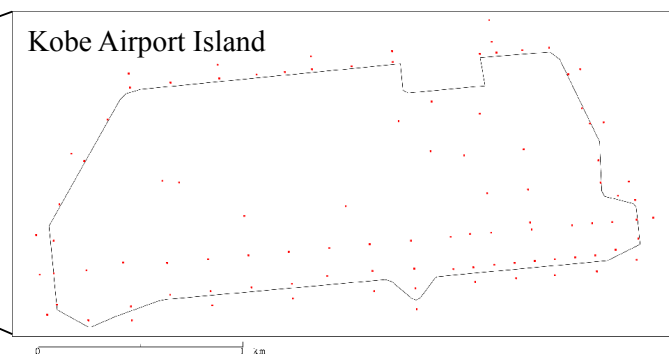


Fig. 2(b) Locations of boring investigation for subject area

investigations were applied to determine the optimum architecture of artificial neural network.

3.2 Analysis Procedure

The architecture of artificial neural network must be determined to estimate optimally the soil properties at an arbitrary position in the ground. The determination process of the architecture is called as "Training". A large number of pairs of the input and output items is required in "Training" process. The method of "Training" to the artificial neural network is the following. Firstly, the initial network has randomly assigned weights. When input data are given to input-layer of this network, they are propagated through the hidden-layer to output-layer, and then output data can be obtained. However, there are differences between the estimated output values and real values. Then, the network and weights are updated automatically to minimize the errors. "Training" is repeated until the repetition reaches preliminarily given number. The optimal network structure is determined in this way.

3.3 Indexes for judging Optimum

The following four indexes, R^2 , G , $MARE$ and SR , were used to choose the optimum architecture of artificial neural network.

R^2 (coefficient of correlation) is popularly used in statistics for in a liner regression between estimated value and target one. It is defined as follows:

$$R^2 = \frac{\frac{1}{N} \sum_{i=1}^N (x_i^o - \bar{x}^o)(x_i^p - \bar{x}^p)}{\sqrt{\frac{1}{N} \sum_{i=1}^N (x_i^o - \bar{x}^o)^2} \sqrt{\frac{1}{N} \sum_{i=1}^N (x_i^p - \bar{x}^p)^2}} \quad (1)$$

where N number of pair of samples, x_i value of each sample, \bar{x} mean value of samples. Also, superscripts o and p denote estimated value and target value, respectively.

G (prediction accuracy) is defined as follows [5].

$$G = \left(1 - \frac{RMSE}{RMS}\right) \times 100 \quad (2)$$

where $RMSE$ (root mean squared error) and RMS (root mean squared) are defined respectively, as follows:

$$RMSE = \sqrt{\frac{1}{N} \sum_{i=1}^N (x_i^p - x_i^o)^2} \quad (3)$$

$$RMS = \sqrt{\frac{1}{N} \sum_{i=1}^N x_i^{o2}} \quad (4)$$

The higher the estimation accuracy is, the higher both R^2 and G is. $MARE$ (mean absolute relative error) is defined as follows:

$$MARE = \frac{1}{N} \sum_{i=1}^N |x_i^p - x_i^o| \quad (5)$$

The higher the estimation accuracy is, the lower $MARE$ is. Also, both G and $MARE$ are indexes to judge the estimation accuracy to a set of estimated values. On the other hand, SR (success rates) is used to judge the accuracy of each estimated value. It is based on an absolute error r at each estimated value. r_i is defined as follows:

$$r_i = \frac{|x_i^p - x_i^o|}{x_i^o} \quad (6)$$

In this study, in the judgment of the estimation accuracy, three different ranges of SR (%) were used with $r_i < 10\%$, with r_i between 10% and 15% and with $r_i > 15\%$ [6].

4. ESTIMATION ACCURACY

4.1 Natural Water Content

Table 1 shows the estimation accuracy in natural water content. In each case, the value of R^2 is over 0.9, the value of G is almost 80% and the value of $MARE$ is less than 12%, so that natural water content could be estimated through artificial neural network. Especially, in WN-1, G is highest and $MARE$ is lowest. Also, SR with $r < 10\%$ is highest. It was considered that the estimation accuracy in WN-1 is highest in the four cases. The artificial neural network could reproduce the distribution of natural water content.

Fig. 3 shows the 3-dimensional distribution of natural water content. The natural water content in Fig. 3 was estimated by WN-1. Firstly, the subject area was divided into about 67,000 regions. Secondly, the latitude, longitude and altitude in each region were calculated. Finally, the natural water content in each region was estimated by applying the latitude, longitude and altitude to the artificial neural network in WN-1. It is very easy to recognize visually the distribution of natural water contents in Fig. 3. The natural water content decreases in east to west direction. The natural water content at southeast corner of sea bed surface in the subject area is highest. It is over 100%. The natural water content is about 90% at northwest corner of sea bed surface in the subject area. Also, the natural water content decrease in the direction to depth. The natural water content in bottom layer in Holocene clay is about 50%. The natural water content hardly varies in north to south direction.

4.2 Void ratio

Table 2 shows the estimation accuracy of void ratio. In each case, the value of R^2 is over 0.9, the value of G is more than 93% and the value of $MARE$ is only slightly over 5%, so that void ratio could be estimated through artificial neural network. The artificial neural network in VR-3 can be

Table 1. Estimation accuracy in natural water content

Case	Repetition Number	R^2	G (%)	$MARE$ (%)	SR (%)		
					$r < 10$	$10 < r < 15$	$r > 15$
WN-1	5000	0.934	87.10	11.56	80.9	6.6	12.6
WN-2	10000	0.935	87.13	11.63	79.9	6.8	13.3
WN-3	15000	0.936	87.15	11.60	80.7	7.2	12.2
WN-4	20000	0.936	87.16	11.58	79.3	8.9	11.8

Table 2. Estimation accuracy in void ratio

Case	Repetition Number	R^2	G (%)	$MARE$ (%)	SR (%)		
					$r < 10$	$10 < r < 15$	$r > 15$
VR-1	5000	0.912	93.46	5.29	89.2	6.7	4.1
VR-2	10000	0.911	93.36	5.21	90.2	5.7	4.1
VR-3	15000	0.908	93.16	5.45	88.1	6.2	5.7
VR-4	20000	0.911	93.49	5.20	88.7	7.2	4.1

estimated most accurately in the four cases, judging from *SR*. Fig. 4 shows the 3-dimensional distribution of void ratio. The void ratio in Fig. 4 was estimated by the artificial neural network in VR-3. The same way for estimating the natural water contents was applied to make Fig. 4. The void ratio decreases in east to west direction. The void ratio at southeast corner of sea bed surface in the subject area is highest. It is about 3.0. It is about 2.5 at northwest corner of sea bed surface in the subject area. Also, the void ratio decreases in the direction to depth. The void ratio in bottom layer in Holocene clay is about 1.5. The void ratio hardly varies in north to south direction.

The distribution of void ratio corresponds to that of natural water content as shown in Fig. 3. The Holocene clay layer in east side of Kobe airport is thicker than that of the west side.

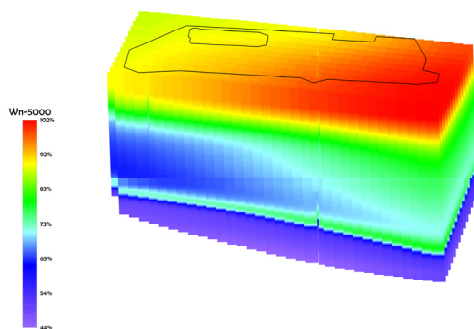


Fig. 3. 3-dimensional distribution of natural water content (WN-1)

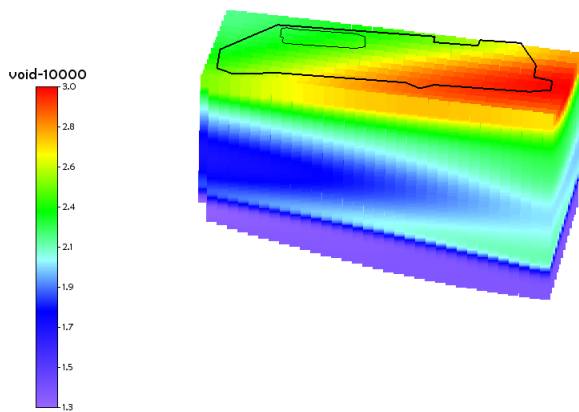


Fig. 4. 3-dimensional distribution of void ratio (VR-3)

Also, both natural water content and void ratio in east side of the airport are higher than that of the west. It was predicted that the settlement in east side of the Kobe airport is larger than that in the west side in the construction. The construction work of the Kobe airport was controlled in consideration of occurrence of differential settlement.

4.3 Plastic index

Table 3 shows the estimation accuracy of plastic index. In each case, the value of R^2 is almost 0.94, the value of G is almost 90% and the value of $MARE$ is about 8%, so that plastic index could be estimated through artificial neural network.

Fig. 5 shows the 3-dimensional distribution of plastic index. The plastic index in Fig. 5 was estimated by the artificial neural network in IP-1. The same way for estimating the natural water contents and void ratio was applied to make Fig. 5. The plastic index decreases in east to west direction in the same way as the natural water content and void ratio. The plastic index at southeast corner of sea bed surface in the subject area is highest. The plastic index is lowest at the northwest corner of sea bed surface in the subject area. Also, the plastic index decrease in the direction to depth. Especially, the variation of plastic index around both surface and bottom is significant. The void ratio hardly varies in north to south direction.

4.4 Compression index

Table 4 shows the estimation accuracy of compression index. In each case, the value of R^2 is over 0.8. This value is lower

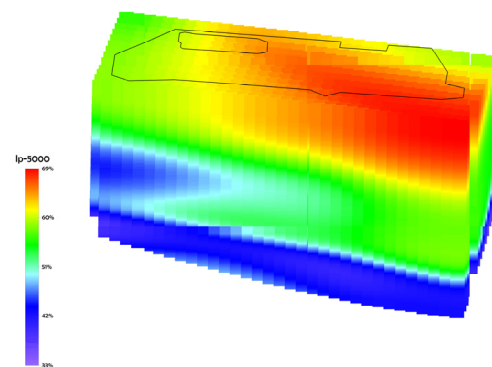


Fig. 5. 3-dimensional distribution of plastic index (IP-1)

Table 3. Estimation accuracy in plastic index

Case	Repetition Number	R^2	G (%)	$MARE$ (%)	SR (%)		
					$r < 10$	$10 < r < 15$	$r > 15$
IP-1	5000	0.934	90.31	7.67	72.3	12.3	15.4
IP-2	10000	0.935	89.84	7.78	68.7	14.4	16.9
IP-3	15000	0.936	89.61	8.09	71.3	12.3	16.4
IP-4	20000	0.936	90.12	7.79	72.8	11.3	15.9

than that in natural water content, void ratio and plastic index. The value of G is almost 87% and the value of $MARE$ is almost 10%. The estimation accuracy in compression index is slightly lower than that in natural water content, void ratio and plastic index. The artificial neural network in CC-3 can be estimated most accurately in the four cases, judging from all four indices for judging optimum.

Fig. 6 shows the 3-dimensional distribution of compression index. The compression index in Fig. 6 was estimated by the artificial neural network in CC-2. The same way for estimating the other soil properties was applied to make Fig. 6. The compression index in upper and middle part of Holocene clay layer is almost 0.9. It slightly decreases in east to west direction. However, its variation is extremely little. The compression index in lower part increases in the direction to depth. It decreases significantly in bottom part of Holocene clay layer. The maximum of compression index in lower part in the east side of the subject area is greater. That decrease in

east to west direction.

4.5 Pre-consolidation pressure

Table 5 shows the estimation accuracy of pre-consolidation pressure. In each case, the value of R^2 is over 0.95, the value of G is more than 87% and the value of $MARE$ is almost 12%. However, SR with $r < 10\%$ is about 53% to 61%. Also, SR with $r > 15\%$ is about 24% to 27%. It is implied that estimation value with errors less than 10% is made up about 53% to 61% of the total and that with errors greater than 15% is made up about 24% to 27%. The artificial neural network in PC-4 can be estimated most accurately in the four cases, judging from SR .

Fig. 7 shows the 3-dimensional distribution of pre-consolidation pressure. The pre-consolidation pressure in Fig. 7 was estimated by the artificial neural network in PC-4. The same way for estimating the other soil properties was applied to make Fig. 7. The pre-consolidation pressure

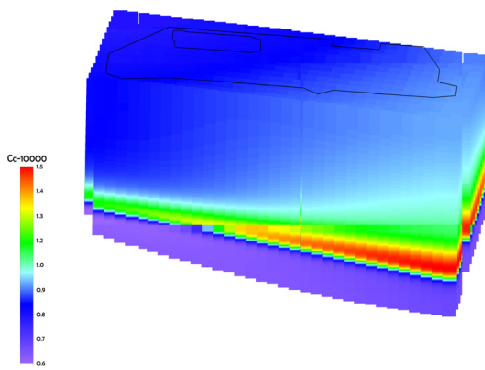


Fig. 6. 3-dimensional distribution of compression index (CC -2)

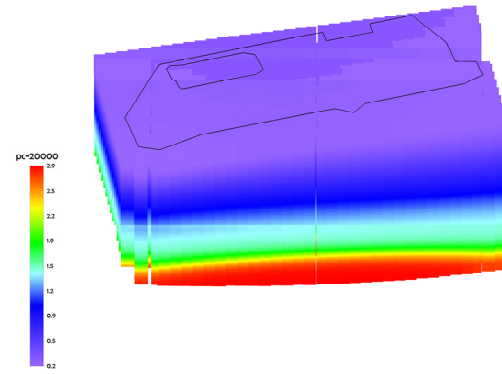


Fig. 7. 3-dimensional distribution of pre-consolidation pressure (PC-1)

Table 4. Estimation accuracy (compression index)

Case	Repetition Number	R^2	G (%)	$MARE$ (%)	SR (%)		
					$r < 10$	$10 < r < 15$	$r > 15$
CI-1	5000	0.832	87.10	10.48	60.3	20.6	19.1
CI-2	10000	0.852	87.80	10.23	67.0	16.0	17.0
CI-3	15000	0.848	87.55	10.44	62.9	17.5	19.6
CI-4	20000	0.813	86.49	11.09	63.9	19.1	17.0

Table 5. Estimation accuracy (pre-consolidation pressure)

Case	Repetition Number	R^2	G (%)	$MARE$ (%)	SR (%)		
					$r < 10$	$10 < r < 15$	$r > 15$
PC-1	5000	0.963	87.33	12.74	52.6	20.1	27.3
PC-2	10000	0.964	87.67	12.35	53.6	20.1	26.3
PC-3	15000	0.962	87.38	12.21	56.2	19.1	24.7
PC-4	20000	0.964	87.66	12.06	60.8	14.9	24.2

increases in the direction to depth. There are hardly distinguishing spatial variation in the subject area.

5 CONCLUSION

In this study, the spatial interpolation of consolidation properties in Holocene clay in Kobe Airport was carried out through artificial neural network. Main conclusions are summarized as follows:

1. An artificial neural network could be applied to estimate the consolidation properties at an arbitrary position in Holocene clay layer in Osaka Bay.
2. The estimation accuracy in consolidation properties by an artificial neural network was high. Especially, the estimation accuracy in natural water content, void ratio and plastic index was excellent.
3. The spatial interpolation of consolidation properties could be carried out through an artificial neural network.
4. The consolidation properties interpolated spatially could be visualized three dimensionally, so that it is very easy to recognize the distribution of consolidation properties.

6 REFERENCES

- [1] Oda, K, Ikeda, S and Tokida, K, "Spatial interpolation of soil properties in Osaka Bay area through artificial neural network," Proc Symposium on Geoinformatics and Zoning for Hazard Mapping, 2009, pp. 178-181.
- [2] Oda, K, "Spatial Interpolation of soil properties in north area of Osaka bay through artificial Neural Network," Advances in Ground Technology & Geo-Information, 2011, pp. 143-150.
- [3] Oda, K, Kitamura, S, Lee, MS, "Applicability of Artificial Neural Network to Spatial Interpolation of Soil Properties in Kansai International Airport," Proceedings of the Twenty-second (2012) International Offshore and Polar Engineering Conference, 2012, pp. 583-586.
- [4] Tanaka, Y, and Tsukada, Y, "Geotechnical Database of Kansai – History and Developments," Proc Symposium on Geoinformatics and Zoning for Hazard Mapping, 2009, pp. 85-92.
- [5] Juang, CH, Jiang, T and Christopher, RA, "Three-dimensional site characterization: neural network approach," Geotechnique, Vol. 51, No. 9, 2001, pp. 799-809.
- [6] Erdal, U, Mustafa, L, Ahmet, S and Bekir, KH, "Prediction of lateral effective stresses in sand using artificial neural network," Soils & Foundations, Vol 48, No. 2, 2008, pp. 141-153.

Measurement of The Crack Displacement Using Digital Photogrammetry for Evaluation of The Soundness of Tunnels

A.Kanazawa¹, S.Nishiyama², T.Yano³

Department of Urban Management, Graduate school of Engineering, Kyoto University, Japan

T.Kikuchi⁴

J-POWER Design Co.,Ltd., Japan

ABSTRACT

The purpose of this study is to develop a measurement technique for crack deformation monitoring by using the digital image-processing. In the measurement technique proposed here, reflective targets are established at the measurement points on both sides of the crack as a gauge and the two dimensional displacement of the crack is calculated based on the coordinates of targets. In this paper, experiments were performed to verify the accuracy and precision of the measurement and the results showed that the changes of the tensile and shear displacement of the crack we could measure were found to be about 20 μ m by using the image taken 1m away from the crack. This paper also presents the actual tunnel measurement results to demonstrate that the cracks on the tunnel wall can be identified through simple measurements. After the regular measurements through a year, we found that the tendency of crack deformation and that of slide movement were in close agreement.

Keywords: photogrammetry, image processing, crack displacement, tunnel

1. INTRODUCTION

In Japan, many infrastructures have been constructed during the rapid economic growth period in 1960s, and moreover, Japan often suffers natural disasters such as earthquakes and typhoons. One of the most challenging issues in Japan is to know whether these old infrastructures are safe or not, and the inspection to evaluate their soundness will play an important role for countermeasure such as reinforcement, repair and reconstruction. In infrastructures consisted of concrete such as bridges and tunnels, width and patterns of cracks which occur on surfaces of the infrastructures are one of the most important signs to estimate their soundness [1]. The prediction of the change of the crack width and length and the prevention of resultant damages require the establishment of crack behavior monitoring technology. Generally, vernier caliper and crack gage are usually used as measurement tools, but these methods heavily depend on human efforts, which cause nonobjective evaluation [2]. Considering this situation, this paper presents a study on the application of a measurement technique using digital image processing and photogrammetry to the development of a new measurement system for crack monitoring. In the measurement technique proposed here, the deformation of the crack is calculated based on the image taken from an arbitrary camera position. This system has the following advantages.

- Measurement can be carried out only by taking an image and does not need human skill, knowledge and experience [3].

- The necessary measurement hardware consists of a digital camera and a PC, which holds measurement cost in very low level. [4]

- Digital photogrammetric measurement is superior to conventional measurement in objectivity and reproducibility [5].

- It is possible to make a database including also the number of cracks and the crack length by using a digital image [6].

The study aims to develop the measurement method of the crack displacement on the digital image. In our developed method, reflective targets are established at the measurement points around the crack as gauges and the two dimensional displacement of the crack, which are tensile and shear displacement, is calculated based on the coordinates of the targets on an image taken from arbitrary position. In this paper, experiments were performed to verify the accuracy and precision of the measurement. In the experiments, we measure the relation between the distance and angle of photographic positions from targets and the accuracy and precision of the measurement results. This paper also presents the measurement results of the crack displacements in the actual tunnel damaged by landslide in order to demonstrate that the soundness of the infrastructure can be identified through simple measurements.

2. PRINCIPLE OF CRACK MEASUREMENT

This section explains techniques and principle for measuring cracks on digital images taken.

2.1 The process of the measurement

We measure the width and length of the crack as follows.

- 1) Reflective targets shown in Fig.1 were attached

around the crack as gauges. These targets were designed with glass beads arranged in circles to induce a strong diffuse reflection of incident light. There are four circles on each target. The distance of one pair of circles on both sides of the crack is measured and the change of the distance means the displacement. The circles on the target also act as marks for the perspective projection.

- 2) A digital image of the targets is taken from an arbitrary camera position and camera angle. The picture of the condition of measuring is shown in Fig.2. The digital image taken at an arbitrary camera angle is converted to the image facing the target by the perspective projection.
- 3) The 2-dimensional coordinate values of the centroids of the circles on the image are measured by using the image processing.
- 4) The distances between the circles of the targets on the both sides of the crack indicate the tensile and shear displacements.

The measurement procedure we developed has the following characteristics [7]:

-Measurement involves photographing can eliminate the need for human skill to improve accuracy as in conventional measurement.

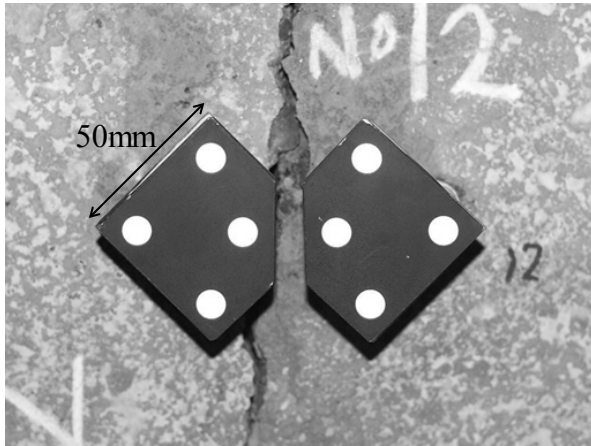


Fig.1 Reflective targets are established on both sides of crack.

-The necessary measurement hardware consists of a digital camera and a PC. That's why this measurement system brings down measurement cost.

2.2 Basic principles of coordinate measurement of target

Image processing is used to make it easier to identify centroids of circles taken on the images. The measurement precision/accuracy in our measurement system is strongly dependent on the measurement precision/accuracy of 2-dimensional coordinates of centroids of the circles on the targets as measurement points. Thus, to improve this 2-dimensional measurement precision/accuracy in the present study, reflective targets that consist of garranged in circles were established at the measurement points. The glass beads can induce a strong diffuse reflection of light. The digital imageries are categorized into gauge imageries in white and other areas in black through binarization by a threshold of intensity value. The 2-dimensional coordinates of the centroids are obtained by calculating the center of mass of white areas for each circle [8]. Assuming the x - and y -coordinates are $x=1\sim n$ and $y=1\sim m$ in the image coordinate system, the coordinate values (x,y) of the gauge imageries are calculated by using the following equation. In other words, the coordinates of centroids of the circles on the images are obtained by calculating the center of mass of a particular imagery's gauge.

$$x = x_0 + a_x \frac{\sum_{i=1}^n \sum_{j=1}^m (q(i, j) \times x_{ij})}{\sum_{i=1}^n \sum_{j=1}^m q(i, j)} \quad (1)$$

$$y = y_0 + a_y \frac{\sum_{i=1}^n \sum_{j=1}^m (q(i, j) \times y_{ij})}{\sum_{i=1}^n \sum_{j=1}^m q(i, j)} \quad (2)$$

where, x_0 and y_0 are the origin of the image coordinate system, a_x and a_y are the pixel size, $q(i, j)$ is the intensity value of the pixel (i, j) .

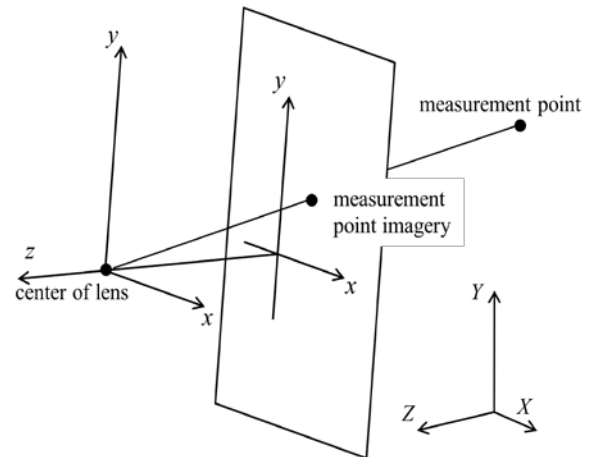


Fig.3 Measurement point means a circle of the reflective targets.

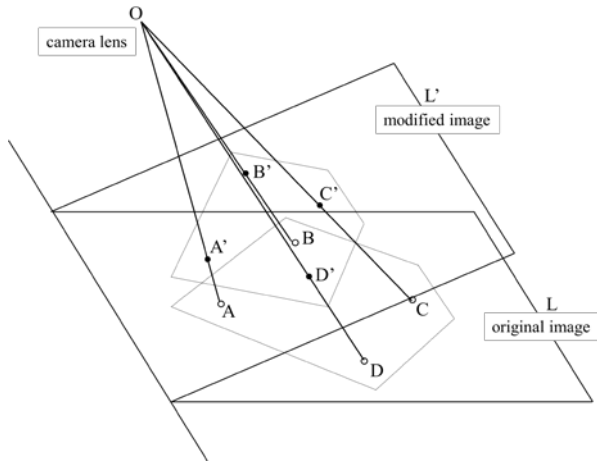


Fig.4 The image L' seen from the front view of target is calculated by this perspective projection.

Next, the image seen from the front view of the targets are calculated using the perspective projection [9]. The perspective projection is based on the collinearity condition, which means that a measurement point, the camera and the measurement point's imagery appearing on the image taken can be connected by a straight line [10]. The concept of collinearity condition is shown in Fig.3. The Eq.(3)&(4) show the relation between the coordinates (x, y) in the original image coordinate system and the coordinates (x', y') in the image coordinate system seen from the front view of the targets (see Fig.4). There are 8 unknowns in total, namely b_i ($i = 1 \sim 8$). Because Eq.(3)&(4) are established for one known point, 4 or more known points are required to solve the equation. The xy coordinates of the reflective target is illustrated in Fig.5.

$$x' = \frac{b_1x + b_2y + b_3}{b_7x + b_8y + 1} \quad (3)$$

$$y' = \frac{b_4x + b_5y + b_6}{b_7x + b_8y + 1} \quad (4)$$

These xy coordinates of centers of four circles are



Fig.2 A digital image is taken from an arbitrary position.

substituted for (x', y') in Eq.(3)&(4) and unknown b_i is calculated. In practice, unknown b_i is obtained by the least-squares method [11].

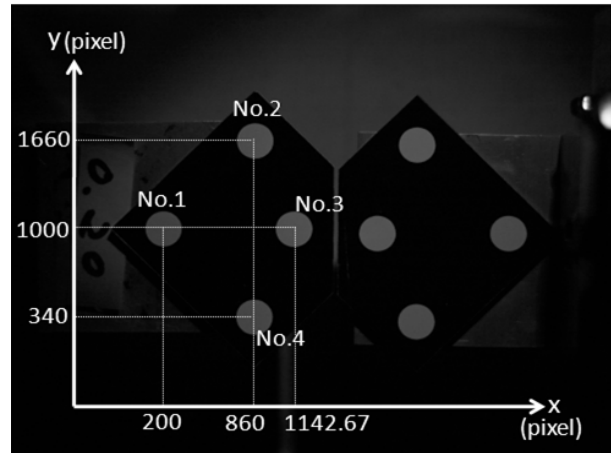


Fig.5 The origin of the coordinate axes is at an arbitrary point. It is just important to substitute the precise distance of four centers for (x', y') in Eq.(3)&(4).

Finally, the distance between the pair of circles on both sides of the crack is calculated and the change of the distance is evaluated as that of crack width and crack length.

3. EXPERIMENTS AND DISCUSSION

Experiments were performed to evaluate the accuracy and precision of the measurement system we developed. The measurement errors of the coordinates of the centroids affect the accuracy and precision of the measurement system. The imagery of target appearing on the image

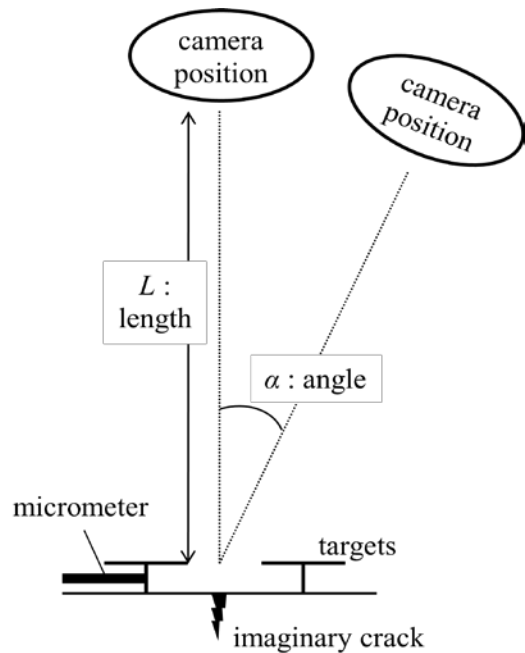


Fig.6 One target is fixed and another target is displaced by a micrometer.

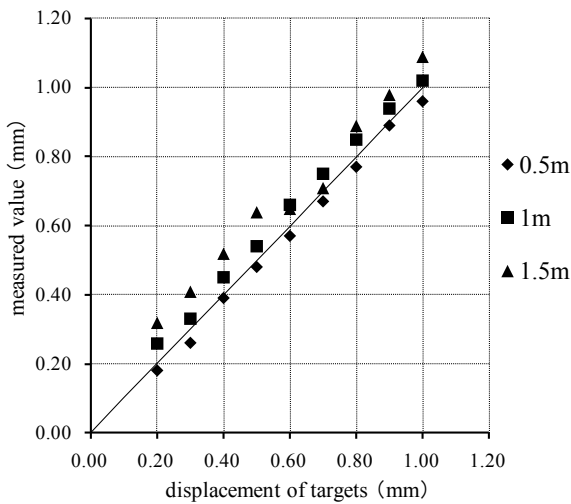


Fig.7 Points are the relation between the displacement of targets and the measured value. The values of distance in the figure mean camera length L .

taken becomes small with an increase of the distance between photographic position and the target. The measurement errors of the coordinates of the centroids depend on the size of the imagery of the target, and increasing of camera angle also causes an increase of the measurement errors of the coordinates of the centroids. That's why we measured the relation between the accuracy and precision of the displacement measurement and camera positions and camera angle. All of images were taken with the digital camera of 13 million pixels.

To verify the measurement accuracy and precision, a reflective target is placed at a fix position and another reflective target was attached to a micrometer, and the digital images were taken at different camera positions and camera angles. The distance of the micrometer's artificial movement D_0 and measured displacement D using the images taken were obtained to calculate the differences between the two. Accuracy is defined as the average of difference between D_0 and measured displacement D , and precision is defined as measurement value's dispersion. Fig.6 shows the camera positions L and camera angles α in the experiments.

Fig.7 and Table 1 show the relation between the distance of the micrometer's artificial movement D_0 and measured displacement D . All images were taken at the camera angle

Table 1 Relation between the accuracy/precision and L (unit: mm) Target size is 50mm by 50mm and focal length is 50mm.

L	0.5m	1m	1.5m
Accuracy	0.02	0.04	0.08
Precision	0.01	0.02	0.04

of 0° . The focal length was 50mm. Increasing L caused the deterioration of accuracy and precision of the measurement value, but we can measure the displacement with accuracy/precision of less than 0.02mm when we taken images up to 1m away from targets. Table 2 shows the relation between the camera angle α and the accuracy and precision. The images were taken at camera position of 0.36m. At

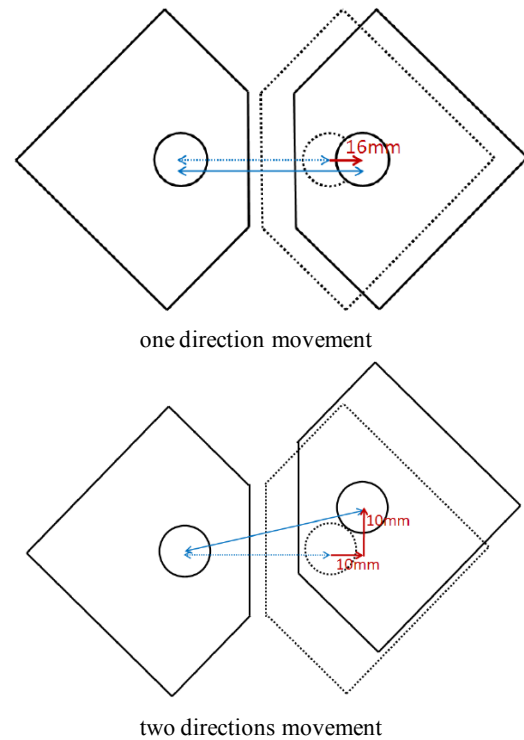


Fig.8 Upper figure shows that only tensile displacement occurs, whereas lower figure shows that shear displacement occurs simultaneously. The measurements of displacement need to be recognized whether only tensile displacement occurs or not.

Table 3 Accuracy/precision of measured displacement x means tensile displacement and y means shear displacement. (unit: mm)

	x	y
Accuracy	0.03	0.02
Precision	0.04	0.02

different camera angles α , when we take images at less than 20° , we can measure the displacements with good accuracy/precision of 0.01mm. Increasing camera angle α caused the deterioration of accuracy and precision of the measurement value. When camera angle α was 60° , accuracy deteriorated by 0.05mm, and precision deteriorated by 0.01mm

In general, visual inspection using a vernier caliper can measure only tensile displacement as the change of crack width. When displacement of 16mm occurs, we cannot know whether only tensile displacement or not in case of using conventional method. The feature of our measurement system used is to measure tensile and shear displacement respectively shown in Fig.8. Another experiment were performed to verify the accuracy and precision of measured tensile and shear displacement. Table 3 shows the accuracy and precision of measured shear displacement comparing with those of measured tensile displacement. All images were taken at the camera angle α was 0° and at the photogrammetric position L was 0.5m. This figure demonstrated that we can measure the shear displacement and the tensile displacement

Table 2 Relation between the accuracy/precision and α (unit: mm)

α	0	10	20	30	45	60
Accuracy	0.01	0.01	0.01	0.03	0.02	0.06
Precision	0.01	0.01	0.01	0.01	0.02	0.02

simultaneously with high degree of accuracy and precision.

In the experiments mentioned above, all images were taken

Table 5 Relation between the accuracy/precision and L (unit: mm). Target size is 400mm by 400mm and focal length is 300mm.

	25m	50m	100m
Accuracy	0.11	0.33	0.57
Precision	0.07	0.25	0.46

within 1.5m from targets. In actual measurements, it can be considered that we have to take images more than 1.5m away from targets. It can be estimated from Table 1 that the accuracy/precision is in proportion to the camera length L . We are able to assume easily that the accuracy/precision of measurement become worth more when camera length L is more than 1.5m. Therefore, two types of the bigger targets were used in the further experiments. One was the twice size and another was the eight times size of the conventional target. Furthermore, the lens which focal length was 300mm was used. Table 4 shows the relation between the accuracy/precision and L

(5m, 7m, 10m, 15m, 20m). Twice size of targets (100mm by 100mm) and the lens which focal length was 300mm were used. Table 5 shows the results when L was more than 25m and eight times size of targets (400mm by 400mm) were used. From these results, increasing L caused the deterioration of the accuracy/precision, in the same way the experiment described above revealed. Table1, 4, and 5 are summarized in Fig.8. In three experiments, not only camera length L but also the target size and focal length were varied. This is why the x -axis of Fig.8 is not camera length L but the diameter of circles in images. Fig.8 shows that the accuracy/precision of measurement is agree with the diameter of circles in images.

4. EXA MPLE OF MEAS URE MENT IN AN ACTU AL TUNN EL

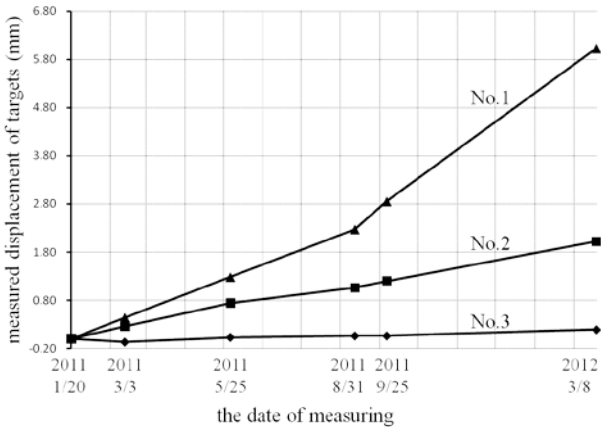


Fig11 The values of the change of cracks' width are plotted. +5.80mm means that the crack displaced in 5.80mm in the tensile direction. (Tensile is plus.)

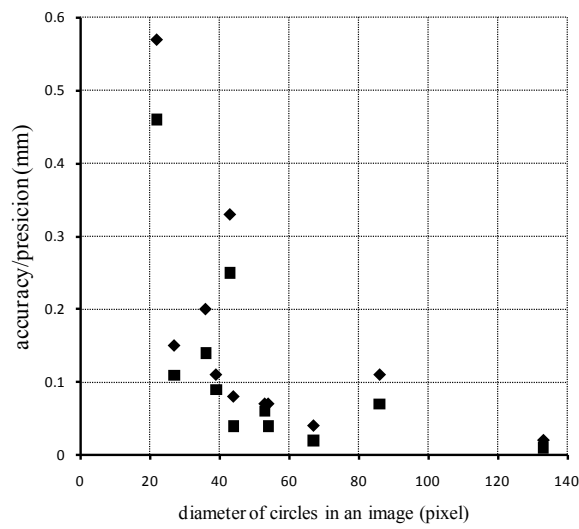


Fig.8 Points are the relation between the diameter of circles in an image and the accuracy/precision. Diamond points mean the accuracy and square points mean the precision.

We applied the proposed method to the crack measurement in the actual tunnel. This tunnel was constructed 20 years ago to prevent the occurrence of the landslide by draining groundwater in the slope. The measurements of extensometers indicate the movement of 2-3mm per year in the slope. Fig.9 shows the diagram of the slope and the tunnel. The existence of two slide planes were revealed by the records of boring. The track curves to the left at a point about 50m from the entrance and goes straight on parallel to the slide A and B. At a point about 280m from the entrance, two tracks diverge; one track keeps straight on and another track turns at right angles. In other words, this track crosses the both slide plane A and B. The picture of this tunnel is shown in Fig.10. Diameter of the tunnel is 2m, and there are more than 300 cracks caused by landslide in the tunnel. In order to investigate the soundness of the tunnel quantitatively, we tried to apply our crack measurement system to this tunnel and investigated the relation between the effect of slide and the displacement crack. Targets were placed on 30 locations, and measurement of crack behaviors were performed per every two month. In this paper, we report three examples of the results of the measurements of cracks. Target No.1 is located on the vertical crack at a point 15m from the entrance. This area is in the slide plane A, therefore about 100 vertical cracks occur from a point 0-50m. Target No.2 is also established on the vertical crack in the branch tunnel at a point 300m. This target is directly under the slide B, so that there are more than 100 cracks around target No.2. Last, Target No.3 was placed on the horizontal crack at a point 100m. The track around target No.2 is parallel to slide A and B, so this area is difficult to be affected by the landslide and there are hardly any cracks around here. Fig.11 shows the three examples of the results of the change of crack width measured by our system. It can be seen from Fig.11 that the targets No.1 and No.2 have displaced at a constant pace for a year. On the other hand, target No.3 has hardly displaced for a year. From this result, it can be concluded that cracks in or under the slide plane have displaced and cracks which are not under the slide plane have hardly moved. This conclusion suggest that it is not necessary to monitor all more than 300 cracks

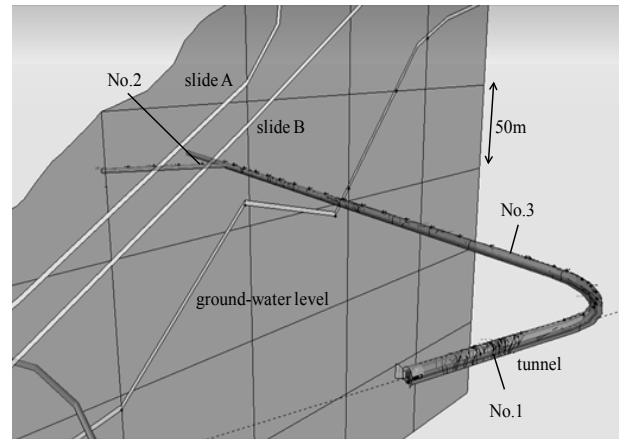


Fig.9 The sectional diagram of the mountain is illustrated along the branch tunnel which was drilled from the diverging point. Slide A and B are parallel to the tunnel and cross the tunnel around the target No.1.

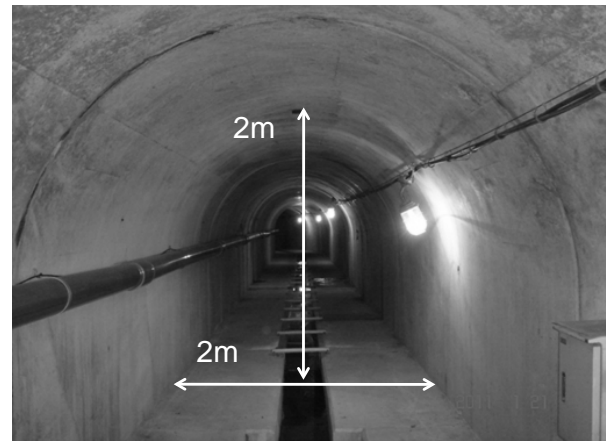


Fig.10 Due to the thin diameter of the tunnel, we were able to take the digital images of targets less than 0.5m away from targets.

but to focus on only 10-20 cracks under the slide plane. With regard to the values of the displacement of targets, the tensile displacement of target No.1 is 5.3mm/year and that of the target No.2 is 1.8mm/year. These results of the change of crack width and the result of the measurements of extensometers described above are in close agreement.

5. CONCLUSIONS

In this study, we developed a measurement technique for crack deformation monitoring by using a digital camera image. In this measurement, reflective targets are established at the measurement points around the crack as gauges and the digital camera image of the targets is subjected to a process that consists of photogrammetry and image processing. Experiments were performed to verify the accuracy and precision of the measurement and the results showed that the changes of the tensile and shear displacement of the crack we could measure were found to be about 20μm by using the image taken 1m away from

the crack. We also present the actual tunnel measurement results to demonstrate that the cracks on the tunnel wall can be identified through simple measurements. Measurements through a year revealed that the tendency of the displacement of cracks is consistent with the results of the measurements of extensometers. This conclusion shows that it is enable to measure only cracks in the slide plane. This may make us decrease much labor and time of measurements. We plan to do further research response to the requirement of actual site with the aim to complete our measurement.

REFERENCES

- [1] Yamada, T., Sano, N., Baba, K., Yoshitake, I., Nakagawa, K., and Nishimura, K.. "A quantitative criterion for evaluation of tunnel lining concrete," *Journal of Structural Mechanics and Earthquake Engineering*, Vol.63, No.1, 2007, pp. 86-96.
- [2] Kimoto, R., Fujita, Y., Kawamura, K., Hamamoto, Y. "A fundamental study on automated crack measurement for concrete structures using image processing," 26th Fuzzy System Symposium, 2010.
- [3] Fraser, C.S. "High accuracy ground surface displacement monitoring," *Photogrammetric Record*, Vol.14, No.81, 1993, pp. 505-521.
- [4] Zhang, C., Ohnishi, Y., Hayashi, K. "Rock displacement measurement by precise close range photogrammetry system," *Proceedings of the fifth international symposiumon field measurement in geomechanics*, Singapore, 1999, pp. 71-76.
- [5] Ryu, M., Ohnishi, Y., Nishiyama, S., Nakai, T. "Study on application of digital vision metrology to slope monitoring system," *Japanese Geotechnical Journal*, Vol.3, No.2, 2008, pp. 109-119.
- [6] Nishiyama, S., Ohnishi, Y., Yano, T., Ryu, M. "A measurement method of tunnel deformation using digital photogrammetry," *Journal of Geotechnical Engineering*, Vol.64, No.3, 2008, pp. 598-606.
- [7] Hattori, S., Akimoto, Y., Ohnishi, Y., Miura, S. "Semi-automated tunnel measurement by vision metrology using coded-targets," *Modern Tunneling Science and Technology*, Vol.1, 2001, pp. 285-288.
- [8] Trinder, J.C. "Precision of digital target location," *Photogrammetric Engineering and Remote Sensing*, Vol.55, 1989, pp. 883-886.
- [9] Penna, M.A. "Determining camera parameters from the perspective projection of a quadrilateral," *Pattern Recognition*, Vol.24, No.6, 1991, pp. 533-541.
- [10] Ohnishi, Y., Nishiyama, S., Yano, T., Matsuyama, H., Amano, K. "A study of the application of digital photogrammetry to slope monitoring systems," *International Journal of Rock Mechanics and Mining Science*, Vol.43, 2006, pp. 756-766.
- [11] Murakami, O., Amano, K., Nishiyama, S. "Automatic target detection for vision metrology with using colored target," *Journal of the Japan society of photogrammetry and remote sensing*, Vol.46, No.1, 2007, pp. 39-46.

Numerical modeling of a small scale shallow foundation reinforced by Soil-Mixing

Anna GRZYB, Mahmoud DHAYBI and Frederic PELLET

Laboratory of Civil and Environmental Engineering, Institut National des Sciences Appliquées, Lyon, France

ABSTRACT

Soil improvement for the reinforcement of existing foundations has become an important challenge for civil engineers. One of the major difficulty is to balance efficiency and cost of a method. The study, presented in this paper, is based on the concept of using the Soil-Mixing (SM) column as a reinforcement for shallow foundations. The numerical finite element simulation in ABAQUS allows one to identify the influence and the consequences of the SM method on the behavior of soil and foundation. Parametric study is carried out to investigate the impact of soil constitutive law (the Drucker-Prager criterion and the Modified Drucker-Prager with cap) on the foundation bearing capacity for two cases: a shallow foundation without reinforcement and a shallow foundation reinforced by a central SM column. Calibration of the numerical models' parameters was achieved according to the reduced scale laboratory model.

Keywords: Soil-Mixing, ABAQUS, shallow foundation, Drucker-Prager, small scale model

1. INTRODUCTION

The increasing densification of constructions in urban area and development of transport network creates new challenges for civil engineers. Soils, which used to be classified as inappropriate for construction purposes, need to be redefined because of the economical reasons. Renovations of existing buildings, which usually lead to an additional loading transferred to the foundations, require foundations' support. One of the major difficulties is to balance efficiency and cost of a method. Up to now many reinforcement methods have been developed. Some of the most common techniques are: pre-fabricated vertical drains, preloading, jet-grouting columns, geosynthetics, light-weight fill, vertical rigid inclusions (concrete piles, stone columns), Soil-Mixing method (known also as Deep Mixing), etc.

The objective of this paper is to present results of Finite Element Method (FEM) numerical simulation, of a small scale shallow foundation reinforced by the Soil-Mixing (SM) technique. The parametric study leads to investigate the influence of soil constitutive law on the foundation bearing capacity. The axisymmetric analysis of the homogeneous soil layer is conducted with elastic perfectly plastic constitutive model with two failure criterions: the Drucker-Prager and the Modified Drucker-Prager with cap. The study takes into account the effect of cap parameters such as eccentricity, its location and evolution and transition surface radius. Results are compared with the experimental measurements.

1.1 The Soil-Mixing method

The SM method is frequently applied as a soil improvement, since 1960s, when it was created in Japan, USA and Scandinavian countries [14]. Originally the technique was dedicated to soils reinforcement but presently it is also used in other geotechnical applications. The major areas of

application are: foundation engineering, excavation control, ground improvement, hydraulic cut-off walls, liquefaction mitigation, environmental remediation and as a reinforcement of the existing foundations. The technique is able to fulfill cost-efficiency criteria while being environmental friendly. The SM method consists in the creation of elements of mixed-in-place soil with a cementitious material in order to create composite stiff elements (Fig. 1).

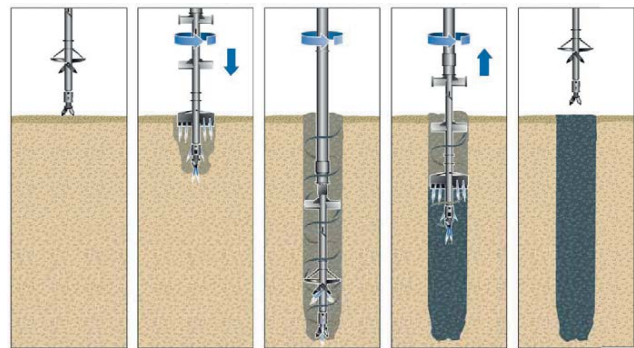


Fig. 1 The Soil-Mixing column production process [12].

The shape of the SM element and its appliance depend on its production method. The SM technique classification, proposed in the Federal Highway Administration Report [4], is presented in Fig. 2. The improvement patterns of the SM columns can be classified into four categories: single, wall type, block type and grid type. All the plane layout patterns of these improvement modes are shown in Fig. 3. In this study behavior of the single SM column has been analyzed. Until now, no specific algorithm for designers has been created. Therefore, the investigation by field loading tests is necessary. However, this type of measurements increases the project costs. In this context, it seems that numerical approach can be complementary or even an alternative solution. Many experimental ([3], [7], [8]) and numerical ([2], [4], [7], [11])

studies have been performed to investigate the behavior of soil reinforced by the SM method.

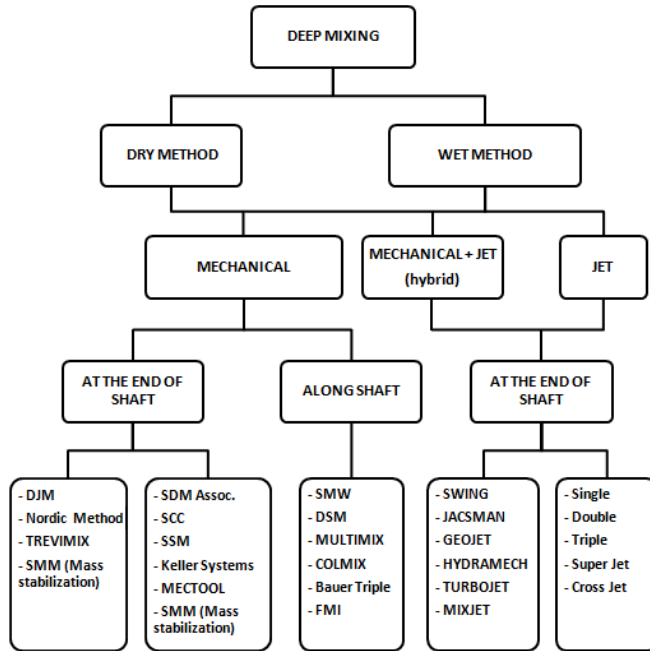


Fig. 2 The Soil-Mixing technique classification proposed in the Federal Highway Administration Report [4].

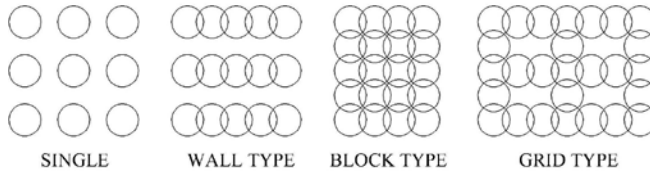


Fig. 3 The improvement patterns of SM method [7].

2. CONSTITUTIVE MODELS

Soils are heterogeneous materials, whose behavior is strongly dependent on factors like: grain size, mineralogy, structure, initial stress state etc. Various models and criteria have been proposed [15] (Mohr-Coulomb, Drucker-Prager, Duncan Chang, Cam Clay) to describe accurately different aspects of soil behavior. Some of them have been also apply in the finite element modeling for geotechnical engineering applications. Decision, which constitutive law is the most suitable to describe behavior of analyzed material, has a significant influence on the final result. The choice of using one or another constitutive law depends on: soil type, geotechnical problem and, most of the time, the possibilities of estimating constitutive parameters.

The elastic perfectly plastic model with the Mohr-Coulomb failure criterion is one of the most commonly used strength theories in geotechnical analysis. Apart of its advantages, user needs to deal with some limitations. Firstly, the intermediate principal stress σ_2 has no influence on the yield. Only the major and the minor principal stresses, σ_1 and σ_3 respectively, are taken into consideration. It leads to underestimation the yield strength of soil and discrepancy with experimental evidence. Secondly, an irregular hexagonal section of the yield cone in deviator plane induces the

convergence problems in flow theory, due to six sharp corners [10].

2.1 The Drucker-Prager criterion

The criterion proposed by Drucker and Prager in 1952 [6], also known as the Extended von Mises criterion, is widely used in engineering. The yield function of the linear Drucker-Prager criterion can be expressed by Eq. (1). Where J_2 is the second stress invariant, I_1 is the first stress invariant, α and k are material constants.

$$F = \sqrt{J_2} - \alpha I_1 - k \quad (1)$$

In ABAQUS [1], the linear Drucker-Prager criterion is written as Eq. (2) and can be illustrated in p-t plane (Fig. 4) and in deviator plane (Fig. 5). The p parameter is the equivalent pressure stress, β and d are the friction angle and cohesion respectively and t is defined by Eq. (3).

$$F_s = t - p \tan \beta - d \quad (2)$$

$$t = \frac{q}{2} \left[1 + \frac{1}{K} - \left(1 - \frac{1}{K} \right) \left(\frac{r}{q} \right)^3 \right] \quad (3)$$

Where q is the von Mises equivalent stress, r is the third invariant of the deviator stress and K is a ratio between the yield stress in triaxial compression and tension. The K parameter controls the dependency of the yield surface on the value of the intermediate principal stress. When the triaxial tension is equal to the triaxial compression $K = 1$ and $t = q$ (Fig. 5). It is required that $0.778 \leq K \leq 1$ to ensure that surface is convex. The Mohr-Coulomb parameters, cohesion c and friction angle ϕ , can be converted to the Drucker-Prager parameters as follows:

$$\tan \beta = \frac{6 \sin \phi}{3 - \sin \phi} \quad (4)$$

$$d = \frac{18c \cos \phi}{3 - \sin \phi} \quad (5)$$

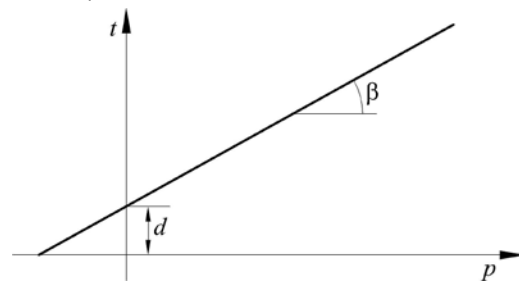


Fig. 4 The Drucker-Prager yield surface in p-t plane [1].

2.2 The Modified Drucker-Prager with cap

The modification added to the model with the Drucker-Prager criterion allows taking into account effect of the soil hardening. Moreover, the cap model is able to consider the effect of stress history, stress path and compaction [1]. The yield surface of this constitutive law consists of three parts (Fig. 6): a Drucker-Prager shear failure surface, defined previously, an elliptical cap, which intersects p axis at a right angle, Eq. (7), and a smooth transition region between the shear failure surface and the cap, Eq. (8).

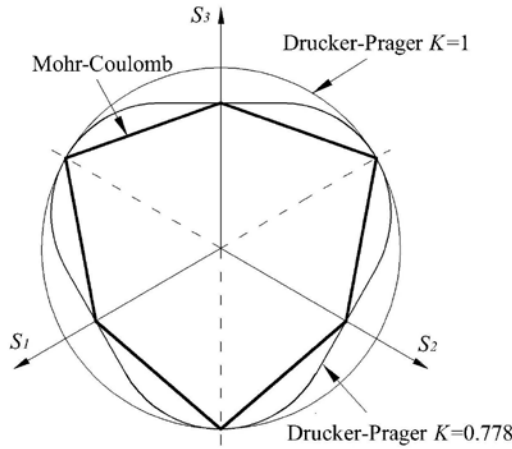


Fig. 5 The Drucker-Prager yield surface in deviator plane [1].

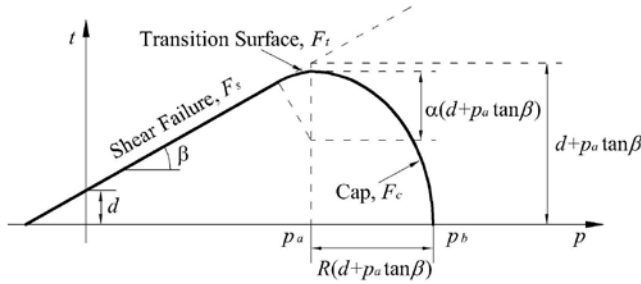


Fig. 6 The Modified Drucker-Prager with cap model yield surfaces [1].

Where R is cap eccentricity (controls the shape of the cap), α is a parameter use to define a smooth transition region (small number, typically 0.01-0.05) and p_a is an evolution parameter that represents the volumetric plastic strain driven hardening or softening, which is defined by Eq. (9). The cap model uses associated flow ($\psi = \beta$) in the cap surface and non-associated flow ($\psi \neq \beta$) in the shear failure and transition region. The hardening/softening phenomenon is described as a function that associates the hydrostatic compression yields stress p_b and the volumetric plastic strain ϵ_{vol}^{pl} , as it is illustrated in Eq. (10). $\epsilon_{vol}^{pl}/0$ is the initial cap yield surface position. The hardening curve is obtained from isotropic consolidation test.

$$A = d + p_a \tan \beta \quad (6)$$

$$F_c = \sqrt{(p - p_a)^2 + \left(\frac{Rt}{1 + \alpha - \frac{\alpha}{\cos \beta}} \right)^2} - RA \quad (7)$$

$$F_t = \sqrt{(p - p_a)^2 + \left[t - A \left(1 - \frac{\alpha}{\cos \beta} \right) \right]^2} - \alpha A \quad (8)$$

$$p_a = \frac{p_b - Rd}{1 + R \tan \beta} \quad (9)$$

$$p_b = p_b \left(\epsilon_{vol}^{pl} \right) + \epsilon_{vol}^{pl} \quad (10)$$

3 NUMERICAL MODEL

The numerical analysis of the small scale shallow foundation without and reinforced by a centrally situated SM column have been carried out to reproduce physical test. The model parameters are obtained according to the reduced scale (1:10) laboratory model which consists of a vertically loaded rectangular foundation, laying centrally on the surface of 1m^3 of fine Hostun sand [5]. Two SM columns, the 7 days old and the 14 days old, have been analyzed. In this research, the solutions are obtained using the finite element method code ABAQUS.

3.1 Model geometry and material properties

The shallow foundation bearing capacity has been analyzed by axisymmetric model. Hence, rectangular rigid foundation requires to be modeled as a circular one. The equivalent radius, $r_{eq} = 130\text{ mm}$, is calculated according to Eq. (11), where S_m is the foundation cross section.

$$r_{eq} = 0.5 \sqrt{\frac{4S_m}{\pi}} \quad (11)$$

The behavior of sand is simulated using the elastic perfectly plastic model with the Drucker-Prager criterion (DP) and the Modified Drucker-Prager with cap (DPC) with parameters computed from the classical Mohr-Coulomb (MC). The SM column is characterized by model with the Mohr-Coulomb criterion. Properties of the sand for different constitutive laws are presented in Table I. The cap parameters used in calculations are $R = 1.2$, $\alpha = 0.05$ and $\epsilon_{vol}^{pl}/0 = 0$. The properties of the 7 days old and the 14 days old columns are given in Table II. Figure 8 shows dimensions and mesh used in the analysis. The mesh consists of 6-node modified quadratic axisymmetric triangle elements (CAX6M). In order to simulate contact between the SM column and soil, interface elements with zero initial thickness with the Coulomb failure criterion are used. The friction coefficient is taken as tangent of $2/3$ of the soil friction angle, $\mu_f = 0.4$.

Parameter	Unit	DP / DPC	MC
Density	ρ [kg/m ³]	1450	1450
Young's modulus	E [MPa]	50	50
Poisson's ratio	ν [-]	0.3	0.3
Friction angle	β, ϕ [°]	52	32
Cohesion	d, c [kPa]	1.24	0.2
Yield stress ratio	K [-]	1	-

Table I Sand properties.

3.2 Loading and boundary conditions

The numerical model boundary conditions are no horizontal displacement at the two lateral vertical sides. In the bottom boundary, displacements are restricted in direction (Fig. 8). The rigid shallow foundation is modeled by imposed displacement to the surface, with previously presented equivalent radius.

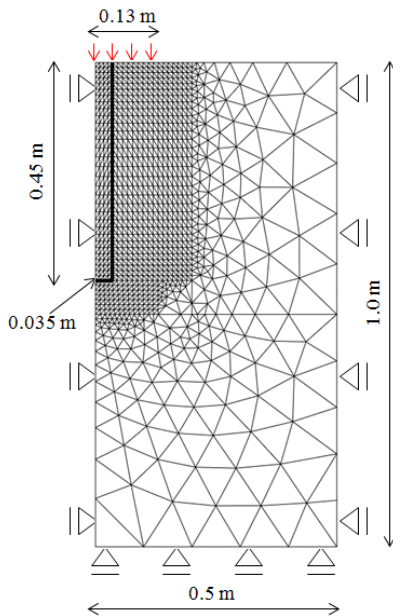


Fig. 8 Finite element mesh and boundary conditions used in numerical modeling.

4 RESULTS

4.1 Preliminary calculation

Preliminary calculation has been carried out for the case of unreinforced foundation with soil characterized by a model with the Drucker-Prager criterion (Table I). In Fig. 9, both curves represent the bearing capacity of the vertically loaded shallow foundation. Curves show good agreement for lower values of displacement but the final bearing capacity and the final displacement are different. As it can be seen, in the first stage of loading, until 6.5 mm, the increase of displacement in the numerical case is slower than the measured one. Afterwards, the situation inverts.

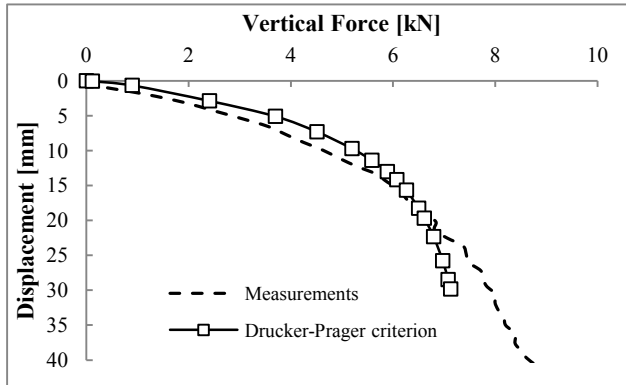


Fig. 9 Comparison between preliminary calculation result and measurements.

The final value of the force borne by the foundation is higher and the displacement domain is larger in the measurements than in the numerical prediction. It can be explained by inappropriate constitutive model due to the fact that the failure surface is limited only by shear failure. Since there is no limit imposed on the compaction, numerical prediction is unable to properly reproduce soil behavior.

4.2 Parametric study of unreinforced foundation

To acquire a better accordance between measurements and numerical prediction, a more advanced constitutive law has been used. The Modified Drucker-Prager with cap, presented above, allows taking into consideration sand's compaction hardening. The basic material properties are chosen as for the preliminary calculation (Table I). The cap parameters calibration has been achieved according to parametric study and comparison with measurements. The effects of the parametric study and influence of each parameter on bearing capacity of unreinforced foundation is presented below.

4.2.1 Cap eccentricity, R

The influence of different cap eccentricity, R , is presented in Fig. 10. Another three cap parameters are assumed as: $\alpha = 0.05$, $\varepsilon_{vol}^{pl}/\sigma_0 = 0$ and hardening, for analyzed Hostun sand, is obtained from isotropic consolidation test (Fig. 11).

Figure 10 depicts five curves. The best fit curve is obtained from $R = 1.20$. As can be seen, in case of $R = 0.75$ the increase of displacement is the slowest. Also the lowest value of final displacement is obtained for this case. The quickest displacement occurs for $R = 2.00$. In cases of $R = 0.75$, $R = 1.00$, $R = 1.20$, values of borne force are overestimated, in contrast $R = 2.00$ case. The more the displacement increases, the greater the difference between measurements and prediction for $R = 2.00$ appears.

According to results of the cap eccentricity parametric study, $R = 1.20$ has been selected for the following calculations.

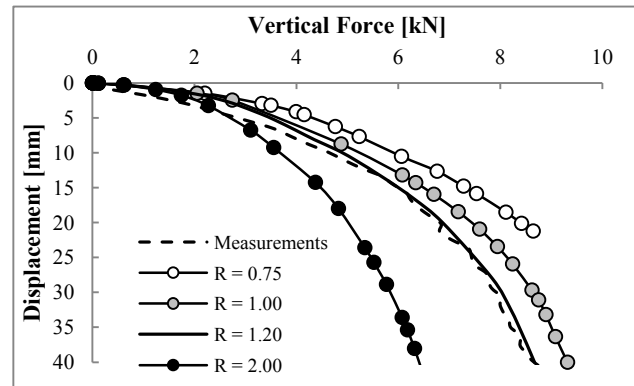


Fig. 10 The influence of different cap eccentricity, R , on bearing capacity of unreinforced foundation.

4.2.2 Transition region parameter, α

The influence of different transition region parameter, α , is presented in Fig. 12. Cap parameters are assumed as previously. In Fig. 12, solid line illustrates the best fit curve obtained from numerical model, $\alpha = 0.050$. Other numerical results correspond to $\alpha = 0.000$, $\alpha = 0.010$, $\alpha = 0.100$, respectively. The spectrum of numerical results is quite narrow. The beginnings of all four curves are almost the same until about 5 mm. Afterwards, the increase of displacement, for curve corresponds to $\alpha = 0.100$, starts to be faster than for the others. The difference between results obtained for $\alpha = 0.000$ and $\alpha = 0.010$ is negligible. The decrease of α causes an increase of the final bearing capacity of the foundation. Based on these results, $\alpha = 0.050$ has been chosen as the most appropriate one.

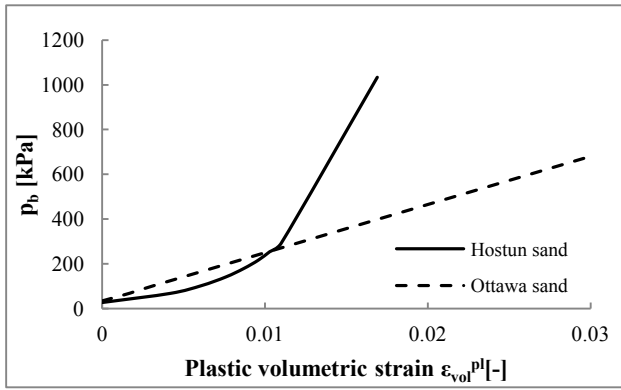


Fig. 11 Hardening law of sands used in calculations.

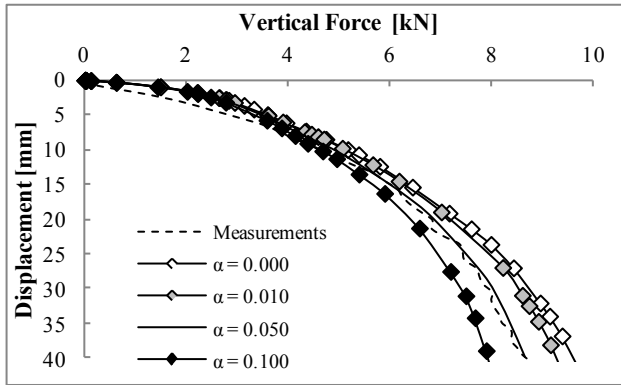


Fig. 12 The influence of different transition region parameter, α , on bearing capacity of unreinforced foundation.

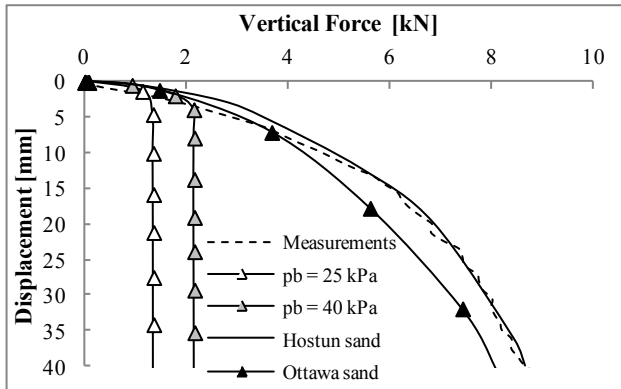


Fig. 13 The influence of different hydrostatic compression yield stress, p_b , and hardening on bearing capacity of unreinforced foundation.

4.2.3 Hydrostatic compression yield stress, p_b , and hardening

The last but not least analyzed parameter is hydrostatic compression yield stress, p_b , in relation to material hardening. As it can be seen in Fig. 13, calculations for four possibilities, have been carried out. Obtained results can be divided into two categories: p_b is defined as constant or p_b is a function according to Eq. (10). Cases, which belong to first category, $p_b = 25$ kPa and $p_b = 40$ kPa, are characterized by early plastic failure, represented by a sudden drop in bearing capacity. The higher value of p_b , the higher final bearing capacity of foundation. For the second category, sand is

described by two hardening functions (Fig. 11). The line with black markers corresponds to results acquired with Ottawa sand hardening [9]. Even the first assumed Ottawa sand characteristics, reproduces quite well measurements' curve. However it is recommended to perform isotropic consolidation test for better material characterization. The best fit result has been accomplished by using Hostun sand hardening.

4.3 Reinforced foundation

Reinforced foundation, has been analyzed with the soil properties obtained by parametric study. As it has been mentioned before, the SM column is described by model with the Mohr-Coulomb criterion. The 7 and the 14 days old columns' properties are reported in Table II. Figure 14 provides measurements and numerical in terms of vertical forces and vertical displacements.

Parameter	Unit	7 days	14 days
Density	ρ [kg/m ³]	2000	2000
Young's modulus	E [GPa]	1.8	3.0
Poisson's ratio	ν [-]	0.2	0.2
Friction angle	ϕ [°]	40	40
Dilation angle	ψ [°]	15	15
Cohesion	c [kPa]	700	1100

Table II Soil-Mixing columns properties.

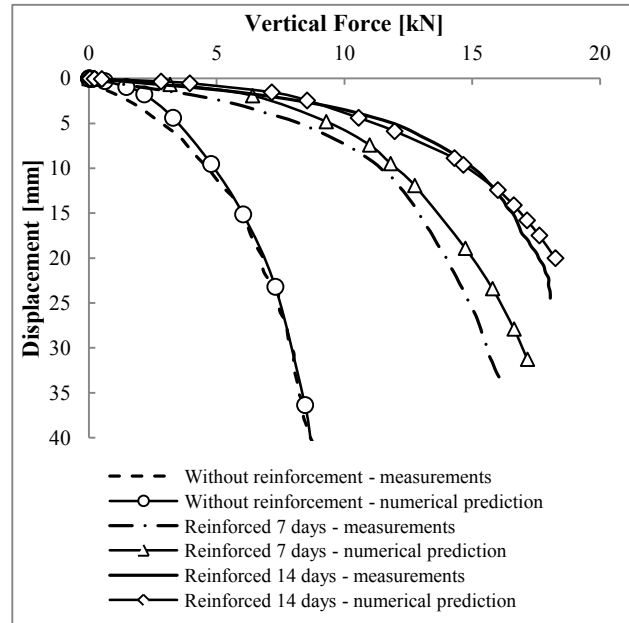


Fig. 14 Comparison between numerical predictions and measurements SM reinforced foundation.

Numerical prediction of the behavior of the 7 days old SM column presents a good agreement with measurements., despite the fact that predictions overestimate a little bit the force. Displacement results between 0 and 2 mm have almost the same values for both columns. Numerical predictions for both reinforced cases are similar to each other and the final bearing capacity of the reinforced shallow foundation is higher. In case of the 14 days old column, predictions overestimate force for displacements 0 – 3 mm and 12 mm – 20 mm, and slightly underestimate between 3 mm and 12.

Despite the small differences, obtained results represent well the behavior of reinforced and unreinforced foundation. The mentioned differences might be due to the definition of the interface between SM column and sand or idealized contact between the foundation and soil layer.

5 CONCLUSIONS

This study was based on the concept of using the SM method as reinforcement for a shallow foundation. The numerical simulation was an attempt to identify the influence and the consequences of the SM method on the behavior of the soil and the foundation. The finite element axisymmetric analysis provided good values in terms of the bearing capacity. The positive effect of the reinforcement on the foundation was clearly highlighted. The value of the load to be borne by the foundation is increased significantly, and the displacements are substantially reduced.

The results lead us to conclude that the more advanced constitutive law needs to be used. The models we recommend are models which take into account, not only shear failure of the soil, but also compaction which is properly described by a cap. Performed parametric study, with the Modified Drucker-Prager with cap, leads us to the conclusion that the most influential parameter is hydrostatic compression yield stress, p_b , which is directly related to hardening phenomena. The slightly smaller impact on the result is due to cap eccentricity, R . The transition region parameter, α , seems to be less significant.

Preliminary prediction evidenced that calculation which only includes the Drucker-Prager criterion, may be helpful but insufficient in the design process. Therefore, when it is possible to analyze soil in laboratory, more advanced constitutive laws should be used. Taking these paper findings into account, we can see that results obtained from the advanced calculations, might be considered on a par with the field test. However, the necessity of calibration model parameters according to physical test generates some difficulties. Therefore, a back-calculation method should be used to complete this study.

6 ACKNOWLEDGMENT

The authors would like to thank the French Ministry of Economy, Finances and Industry, the local authorities (Départements 77 and 93) which supported this research program named RUFEX (Renforcement et Reutilisation des plateformes Ferroviaires et des Fondations Existantes)

7 REFERENCES

- [1] ABAQUS Theory Manual. Version 6.10, 2010
- [2] Archeewa E., Puppala A.J., Saride S., Kalla S., "Numerical Model Studies of Deep Soil Mixing (DSM) Column to Mitigate Bridge Approach Settlements" in Proc. Geo-Frontiers: Advances in Geotechnical Engineering, 2011, pp. 3286 – 3295.
- [3] Bergado, D.T., Ruenkairergsa, T., Taesiri, Y. and Balasubramaniam, A.S., "Deep soil mixing used to reduce embankment settlement" in Proc. ICE - Ground Improvement, 1999, pp. 145-162.
- [4] Bruce D., Federal Highway Administration Report, USA 2000.
- [5] Dhaybi M., Grzyb A., Trunfio R., Pellet F., "Foundations reinforced by soil-mixing: Physical and numerical approach" in Proc. TC 211 IS-GI Brussels, vol. III, 2012, pp. 137-146.
- [6] Drucker D.C., Prager W., "Soil mechanics and plastic analysis or limit design", Quarterly of Applied Mathematics, vol. 10(2), 1952, pp. 157-165.
- [7] Fang Z., "Physical and numerical modelling of the soft soil ground improved by deep cement mixing method" PhD Thesis, Dept. of Civil & Structural Engineering, The Hong Kong Polytechnic University, May 2006.
- [8] Han, J., Sheth, A.R., Porbaha, A. and Shen, S.L., "Numerical analysis of embankment stability over deep mixed foundation" Geotechnical Special Publication ASCE, vol. 126(2), 2004, pp. 1385-1394.
- [9] Helwany S., "Applied Soil Mechanics with ABAQUS Applications", J. WILEY & SONS, INC., 2007, pp. 61-67.
- [10] Jiang H., Xie J., "A note on the Mohr-Coulomb and Drucker-Prager strength criteria", Mechanics Research Communications, vol. 38, 2011, pp. 309-314.
- [11] Kitazume, M., Okano, K. and Miyajima, S., "Centrifugal model tests on failure envelope of column type deep mixing method improved ground", Soils and Foundations, vol. 40(4), 2000, pp. 43-55.
- [12] LIEBHERR, LB series – Soil mixing. Technical report, Austria, 2012.
- [13] Navin M.P., "Stability of Embankments Founded on Soft Soil Improved with Deep-Mixing-Method Columns" PhD Thesis, Faculty of the Virginia Polytechnic Institute and State University, Aug. 2005.
- [14] Porbaha A., "State of the art in deep mixing technology: part I. Basic concepts and overview" in Proc. ICE - Ground Improvement, 1998, pp. 81 –92.
- [15] Ti K.S., Huat B.B.K., Noorzaei J., Jaafar M.S., Sew G.S., "A Review of Basic Soil Constitutive Models for Geotechnical Application", Electronic Journal of Geotechnical Engineering, vol. 14, 2009, pp. 1-18.

Physical modelling of a small scale shallow foundation reinforced by Soil-Mixing

Mahmoud DHAYBI and Frederic PELLET

Institut National des Sciences Appliquées, Department of Civil and Environmental Engineering, Lyon, France

ABSTRACT

Soil mixing is a stabilization technique which consists in mixing soil with a stabilizing agent to improve its behavior. The aim of this research project is to identify the influence of Soil Mixing (SM) and analyze the consequences on the foundation's behavior. First, laboratory tests are performed to characterize the SM material. The study of unconfined compressive strength and Young modulus of different mixtures shows the effect of curing age and cement content. Second, a reduced scale model is developed in order to show the influence of SM reinforcement on shallow foundations. It consists in a rectangular foundation, vertically loaded, and laying on the top of a 1m³ tank filled with Hostun sand. The effects of age of SM columns and soil density were carefully studied. The difference between the behavior of unreinforced and reinforced cases is clearly demonstrated by physical modeling.

Keywords: soil mixing, shallow foundation reinforcement, Hostun sand, small scale model, bearing capacity

1 INTRODUCTION

The growth of infrastructure in urban areas in most countries of the world has led to a dramatic rise in land prices. Consequently, areas with poor soil conditions become more and more attractive for development and construction. The solution to overcome the difficulties of construction on poor quality ground is either improving the compressible soil or installing deep foundations. The foundation techniques such as various methods of soil improvement are usually more cost effective compared to deep foundations such as driven piles, bored piles or drilled piers [1]. The basic concepts of soil improvement, which are, densification, solidification, dehydration, strengthening, were developed. However, over the last three decades, many techniques have been developed and applied to complicated soil, and it is expected that new techniques for soil improvement continue to be developed. While conventional methods of soil strengthening pass through the construction of rigid foundation elements for transferring the entire loading to a supporting layer, the SM method opens the door to a new conception of reinforcing foundations. It is based on the effort distribution between the column of improved soil and the surrounding soil. The process of SM sets up a new material whose characteristics are intermediate between those of concrete and soil. This ground modification improves soil bearing capacity, contributes in the reduction of foundation settlements and prevents shear deformation [2]. Several soil improvements by SM are available. Soil reinforcement with SM columns is one of the most well known shapes used as an alternative solution to conventional deep foundations for buildings [2]. The addition of binder to soil leads to significantly changes in

its properties which have been investigated in different studies. The addition of few cement percentages was able to

increase the drying rate of soil, change optimum water content and increase compressive strength [3]

The main objective of this research project is to highlight the effect of SM columns and their contribution in increasing foundation bearing capacity subjected to vertical load. Age of columns and soil density were the studied parameters to investigate the load transfer between column and soil.

2 SOIL MIXING CHARACTERIZATION

With the aim to characterize the behavior of SM material, some laboratory tests are performed to determine the characteristics of three different mixtures with different cement content (Table 1).

Mix	Cement content	Ratio C/S	Ratio C/W
Mix 1	280 Kg/m ³	0.2	0.7
Mix 2	210 Kg/m ³	0.15	0.55
Mix 3	140Kg/m ³	0.1	0.4

Table 1: Mix composition (S: Sand, C: Cement, W: Water)

The soil under study is Hostun dry sand HN 31[4] (fig 1) and cement CEM III/C 32.5N is used as a binder. Sand, cement and water are mixed together during 10 minutes under a rotation velocity of 62.5 RPM. Some characterization tests were performed to assess the mixture consistency. Slump tests (2 to 4 cm slump) and flow test (27 to 32 cm spread) show that our mix is of considerable consistency [5]. Small cylindrical specimens of 45 mm diameter and 90 mm height were prepared according to a specific procedure [6]. The preparation of specimens should be performed immediately after the mixing operation. The

mixture is placed in cylindrical molds in three layers and the material is vibrated manually to allow the evacuation of trapped air. The blending and the casting must be completed in less than 40 minutes. Produced specimens were sealed with PVC lids and stored vertically in dry bags with paper towel soaked in water. The temperature must be maintained at about 20 °C.

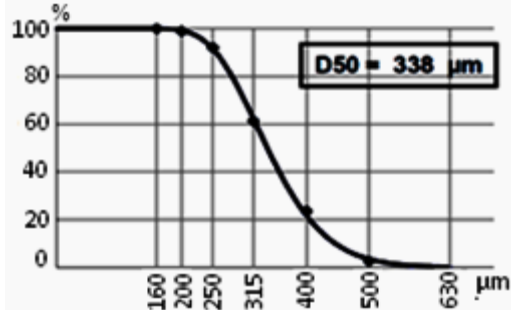


Fig1: Particle size distribution curve for Hostun sand

Unconfined compression tests were carried out on these SM specimens at 7, 14, 21 and 28 days in order to evidence the effect of curing time on specimen's behavior. In every test, three specimens of the same mix are tested at the same day. Results show that specimens with the highest cement content have higher UCS (Unconfined Compressive Strength) which can reach 7 MPa. However, specimens of mix 3 have the lowest UCS. It's even hard to unmold them at day 7 and they can barely achieve 1.2 MPa at day 28.

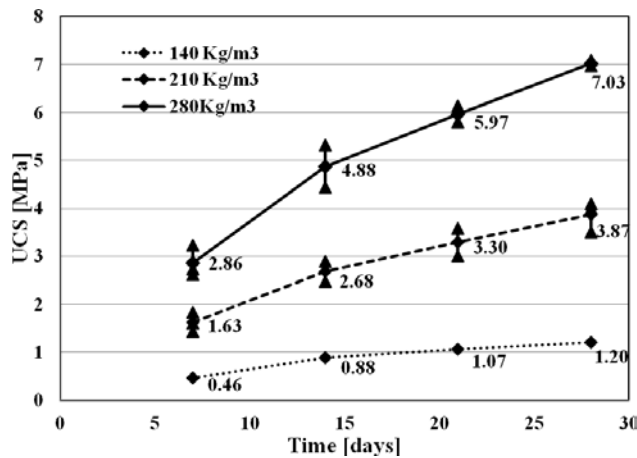


Fig 2: Evolution of Unconfined Compressive Strength (UCS) of SM specimens versus curing time

For 3 mixtures, the slope of the curve of the UCS as a function of cure time is significant between 7 and 14 days and then it is reduced. At 14 days the UCS is substantially increased. Our study was carried on with mix 2 because it proves a good compromise between resistance and economy. On each specimen, three strain gages are installed to measure axial strain and determine Young's modulus. Additionally, dynamic elastic modulus of the specimens is determined by measuring the resonance frequency on specimens of prismatic shape of 4 cm x 4 cm x

16 cm (fig 3).

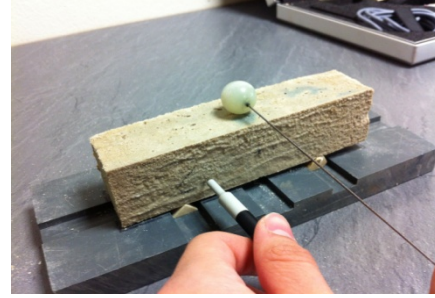


Fig 3: SM prismatic specimen for dynamic Young modulus measurement

Table 2 below shows the variation of resistance and Young modulus with age. Results show a good agreement with other research [7], [8]. The range of the UCS lies between 1.5 MPa for fine sand and 5 MPa for medium sand with binder factor between 120 and 300 Kg/m³. Dividing UCS at 28 days by UCS at 7 days, we get a factor of 2.3 which is in agreement with other studies carried on Fontainebleau sand [9]. Our results show also that dynamic Young modulus is higher than secant Young modulus by 25-40%. This results match with other studies carried on concrete, where difference was by 37% [10].

Age (days)	Resistance [MPa]	E ₅₀ tangent [GPa]	E ₅₀ secant [GPa]	Dynamic Young modulus [GPa]
7	1,6	2,2	2,8	3.6
14	2,6	3,3	4	5.7
21	3,3	3,8	4,5	7.1
28	3,8	4,3	4,9	8.3

Table 2: Evolution of static and dynamic young modulus with age of mix 2 specimens

3 EXPERIMENTAL SMALL SCALE MODEL

In order to analyze the behavior of shallow foundations reinforced by SM columns and composite interface mechanisms, an experimental setup inspired from WANG [11] has been built. It consists of a tank 2m long, 1m wide and 1m high divided into two parts, 1 m³ each, in which a 1/10 scaled model is placed. The tank is filled by layers of Hostun dry sand 10 cm thick to ensure appropriate homogeneity and good compaction of the soil mass.

Since the aim of the experiment is to study the behavior of soil and not to dimension the structure, a rectangular steel plate 25 cm x 20 cm is installed on the top surface of the fill and models the shallow foundation 2.5 m x 2 m. The plate is vertically loaded using a servo- hydraulic jack. A special metal frame based on a guidance system on rails allows the jack to be moved easily in the horizontal plane, covering the entire upper surface of the tank.

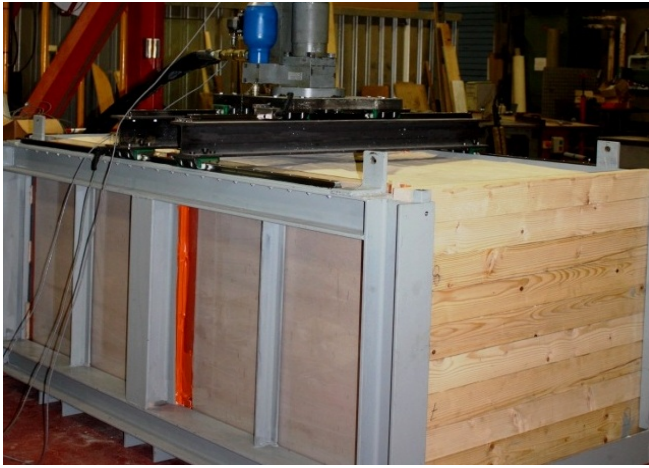


Fig 4: Photo of the constructed tank

Setting up SM column is done by sinking a steel tube in soil (fig 5). Sand in the tube is extracted using vacuum. Then the mixture prepared in the laboratory is poured into the tube. The SM column, which is 450 mm in length and 70 mm in diameter, remains in sand for the curing period (7 days, 14 days).

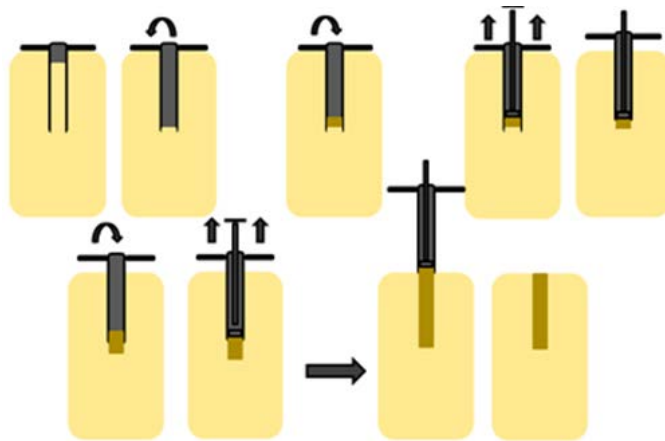


Fig 5: Procedure of setting up-mixing of soil columns

The instrumentation of the tank consists in different sensors. A 100 kN load cell is placed between the plate and the jack to measure the vertical force. Two stress sensors are installed between the plate and the soil to measure the pressure borne by the soil. A small force sensor is placed between the head of the SM column and the steel plate to measure the pressure applied on the reinforcement column. Three displacement sensors are installed on the plate to check that it remains horizontal.

In order to determine the effect of column age and soil density 12 loading tests were performed (table 3). In these tests, soil density varies from 15 kN/m^3 to 13.6 kN/m^3 . In the first case, each layer is compacted using a rectangular heavy steel plate to make the soil denser and more homogeneous. In the second case, the filling process is carried without any compaction. In both cases, loading tests were performed for column age 7 and 14 days.

Test	Type of soil	Age of column (days)	Number of tests	Soil density (KN/m^3)
Test 1	Dense	7 days	3	15
Test 2	Dense	14 days	3	15
Test 3	Loose	7 days	2	13.6
Test 4	Loose	14 days	2	13.6
Test 5	Dense	-	2	15

Table 3: Performed loading tests

3.1 Loading tests on dense soil

Figure 6 shows the evolution of the bearing capacity of the foundation subjected to increasing vertical displacement in test 1. After 7 days, foundation and columns exhibit almost the same behavior. For reinforced cases, vertical stress increases very sharply, causing the pressure to rise considerably after 4-5 mm vertical displacement.

Curve for this reinforced case can be divided into three parts. They start with a sharp increase of axial force (0-5 mm), the slope decreases later on (5-12.5 mm). The third part of the curves corresponds to the lower slope.

To verify the total force measured by the load cell, force resulting from the pressure on the soil and force measured on the column head were added. A little difference exists possibly due to presence of pressure cells at the bottom of the steel plate which could lead to the creation of rigid corners. Thus, pressure measured by soil pressure cells is a little bit overestimating the real pressure under the steel plate.

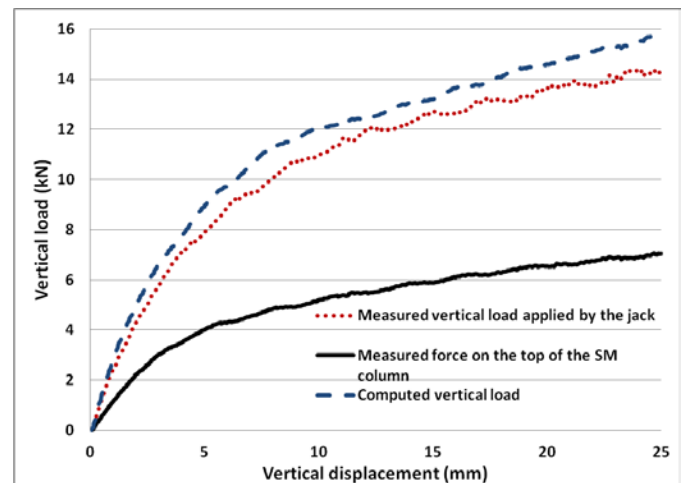


Fig 6: Loading test 1 – dense soil mass

Figure 7 shows the evolution of pressure under the foundation with vertical displacement. Stress supported by soil corresponds to almost 60% of the total stress. For a 25 mm displacement, stress applied on soil under the foundation is around 0.2 MPa while 0.32 MPa is the original stress applied on the steel plate.

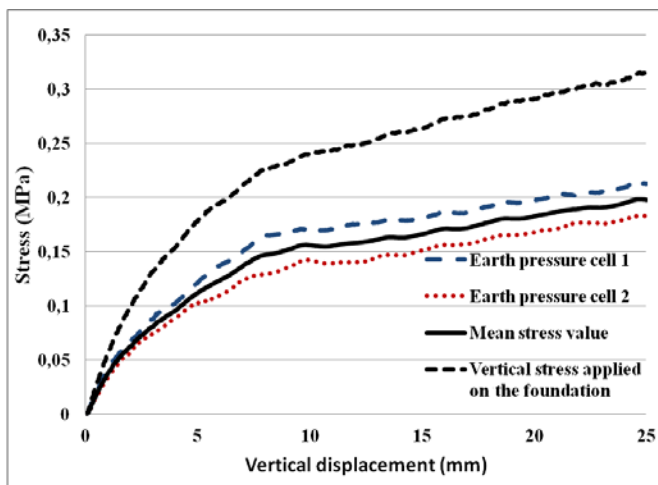


Fig 7: Total stress applied on the foundation- stress registered by soil pressure cells.

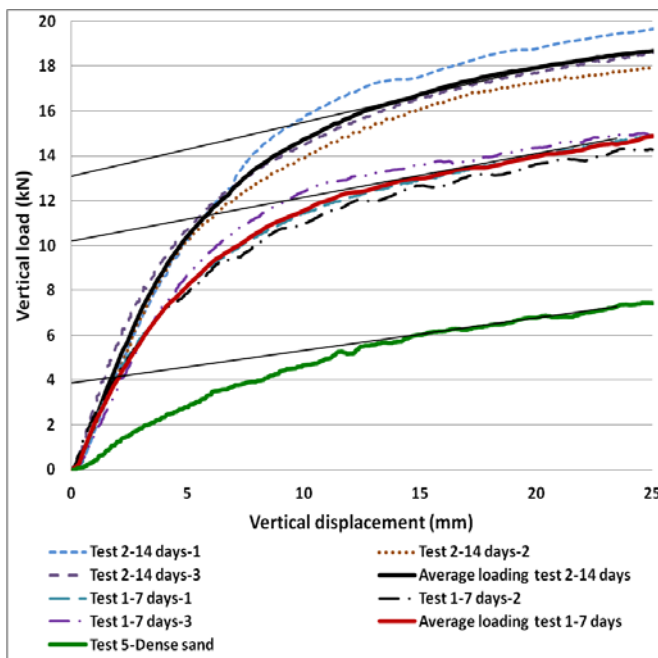


Fig 8: Loading test results carried on dense sand- reinforced and unreinforced cases

Figure 8 shows results of loading tests carried on dense sand. Test 1, 2 and 5 were repeated to verify the good reproducibility of the tests. Regarding the results shown above where soil mass density is 15kN/m^3 ; there is strong evidence that SM columns have a positive effect on foundation behavior. After reinforcement, the bearing capacity of the foundation increased more than twofold after 7 days and almost threefold after 14 days. Reinforced foundations with different column age have a similar behavior, but with age, foundation becomes stiffer. Settlement of the foundations is another aspect which has to be taken into account. It was reduced after reinforcement even for low loading values. As shown for a loading of 4 kN, the unreinforced foundation resulted in a settlement of 8 mm. On the contrary, reinforced foundations undergo settlements

less than 3 mm even after 7 days. In terms of higher loading, the difference increases more significantly and the contribution of reinforcement also increases.

For 7 kN, the unreinforced foundation resulted in a displacement of 22 mm, whereas reinforced ones do not exceed 4 mm.

Taking recent findings into account, we can see that reinforcing foundations with soil mixing columns leads to increasing the bearing capacity of foundations and greatly reduces the extent of settlements.

Contribution of SM columns to support the applied loading was also investigated (Fig 9). Contribution of SM column and soil are the ratio between the vertical loading supported by the element (soil or SM columns) and the total vertical applied load. Figure 9 shows that SM column takes around 45% of total charge applied on the foundation. The presence of a stiff element in contact with the foundation gives to the foundation a higher bearing capacity because it takes an important part of the charge.

On the other hand, the same analysis was carried on reinforced foundation at day 14. It shows that SM columns take 55% of total applied charge. With aging, SM columns become stiffer due to cement curing, which makes their Young modulus higher and makes the stiffness difference between soil and column larger.

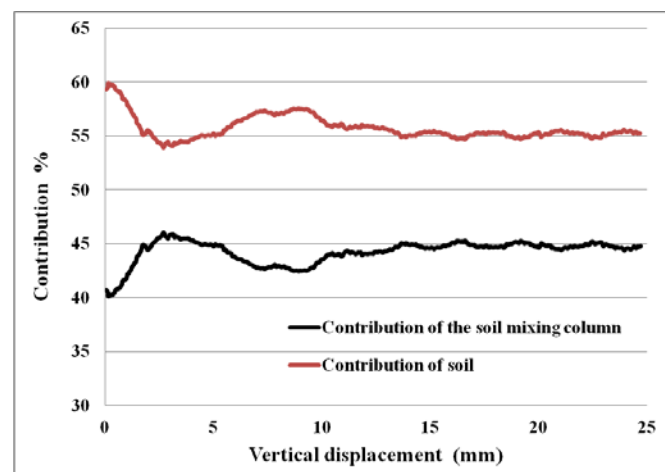


Fig 9: Contribution of soil and SM column to take charge of the applied load

3.2 Loading tests on loose soil

In this part, loading tests are performed on loose soil mass reinforced by SM columns. Composition of columns and their installation process are the same as before. Filling the tank is achieved by layers of 10 cm thick of Hostun dry sand without any compaction. Sand is properly spread to ensure a good homogeneity.

In terms of vertical applied load (fig 10), a sharp increase in vertical stress takes place at the beginning for a small amount of vertical displacement (0-2mm). This is due to the presence of a stiff element under the foundation which takes the most part of the applied load.

After this phase, curve slopes become lower and the verification force is calculated, as explained before. In terms of vertical displacement, reinforced foundations in loose sand present much higher vertical displacements in comparison with dense sand presented before. At the beginning the presence of SM column gives a sharp increase in bearing capacity. On the other hand, the tip of SM column is also in loose sand, which makes tip resistance lower.

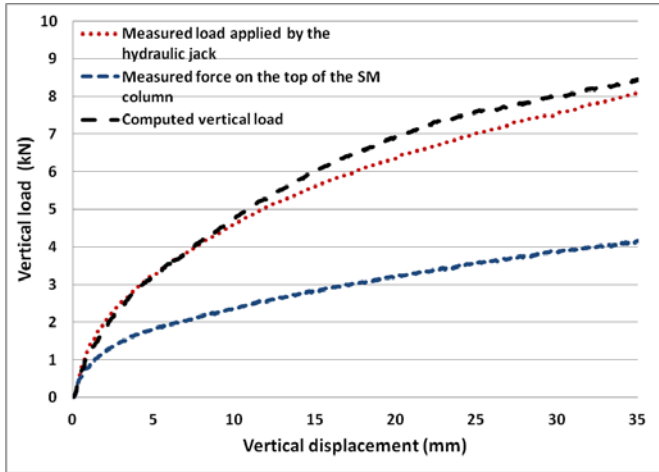


Fig 10: Loading test 3 –loose soil mass

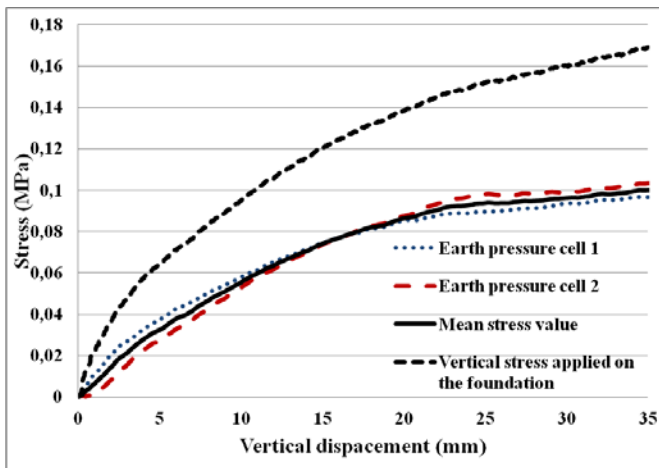


Fig 11: Total stress applied on the foundation- stress registered by soil pressure cells.

In terms of stresses, pressure cells were also installed between foundation and soil (Fig 11). It can be seen, these cells record almost the same pressure. At the beginning and for small vertical displacements, stress on soil is between 30 and 45% of the total vertical stress. Higher displacements results higher stress on soil that becomes between 55 and 60% of the total applied stress.

Figure 12 shows the contribution of soil and SM columns. For small displacements (0-6mm), column takes the higher part of the vertical applied load. Later on, soil and SM column have the same contribution, and total load is shared between these two elements.

At the beginning of the loading test, soil is loose and SM column is the stiff element underneath the foundation which explains his high contribution. Increasing displacements leads soil compaction . As a result, soil under the foundation becomes denser which explains the increase in soil contribution. The system soil-column is plastified when displacements are higher than 4 mm.

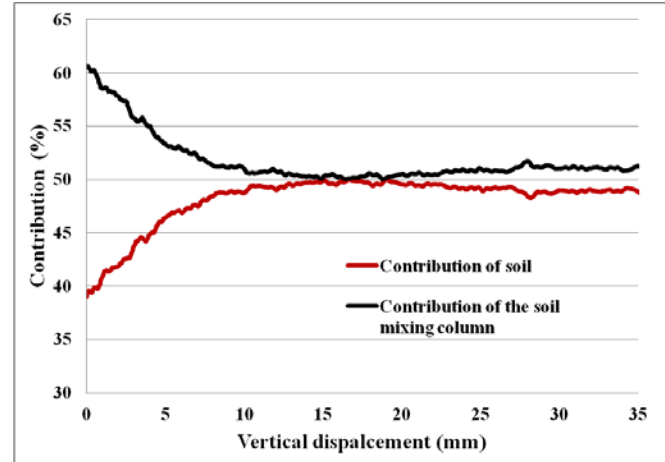


Fig 12: Contribution of soil and SM column to take charge of the applied load

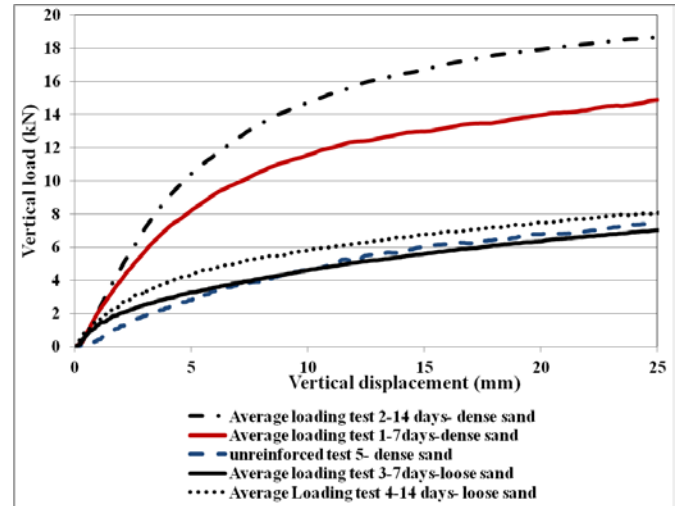


Fig 13: Loading test results carried on dense sand, loose sand and unreinforced dense sand

Figure 13 shows average results of performed tests (table 3). Curve from unreinforced foundation in dense sand is similar to the reinforced foundation in loose sand loaded at day 7. This similarity shows the importance of the reinforcement since we could have the same behavior of a dense soil with a stiffer behavior at the beginning of vertical displacement. Difference between bearing capacity at 7 and 14 days in both cases (loose and dense sand) is around 23 %. This difference is due to cement hydration which makes column stiffer and able to take higher load.

4 CONCLUSION

The laboratory investigation on the influence of age and cement content of soil mixing specimens provided valuable results in terms of resistance, Young modulus and consistency.

The physical model tests highlight some major differences in the behavior of reinforced and unreinforced foundations. With reinforcement, bearing capacity becomes higher and foundations undergo lower settlements.

Age of SM columns has also an important effect on foundation's bearing capacity which is 23% higher at day 14 than at day 7.

In dense soil mass, SM columns contribute to take 45% of the total vertical loading at day 7 and 55% at day 14. In loose soil mass, SM columns contribute to take almost half of the total vertical loading at day 7 and 55% at day 14.

As a result, SM columns take an important part of the loading applied on the foundation, which increase its bearing capacity and reduce stress applied on soil.

Reinforcing loose soil mass with SM columns, makes the foundation behaves as if it lays on a dense soil mass and even better at small vertical displacements.

This study will be extended by additional tests. Other reinforcement models have to be tested, especially to emphasise the role of an intermediate granular layer between the footing and the column. Heterogeneous soil, where deeper soil layers are denser than the upper ones will also be studied.

5 ACKNOWLEDGMENT

The authors would like to thank the French Ministry of Economy, Finance and Industry, the local authorities (Departements 77 and 93) which supported this research programme named RUFEX (Renforcement et reUtilisation des plateformes Ferroviaires et des fondations EXistantes).

6 REFERENCES

- [1] Porbaha A., "State of the art in deep mixing technology: part I. Basic concepts and overview" in Proc. ICE - Ground Improvement, 1998, pp. 81 –92.
- [2] Porbaha A., "State of the art in deep mixing technology: part I. Basic concepts and overview" in Proc. ICE - Ground Improvement, 1998, pp. 81 –92.
- [3] Sarisseries F., Muhunthan B., "Effect of cement treatment on geotechnical properties of some Washington state soils", J. Engineering geology, 2009, pp.119-125.
- [4] Technical data sheet of Hostun sand http://www.sibelco.fr/item_img/medias/images/ft1_2_hn31.pdf, Last visit June 19th 2012.
- [5] AFNOR, "NF EN 206-1: concrete - Part1: specification, performance, production and conformity", Fresh concrete, consistence classes.
- [6] Guimond-Barrett A., " Protocole de référence pour la réalisation des mélanges sol-ciment en laboratoire", IFSTTAR laboratory, 2011.

- [7] Porbaha A., "State of the art in deep mixing technology: part III. Geometrial characterization" in Proc. ICE - Ground Improvement, 2000, pp. 91 –110.
- [8] Topolnicki M., "General overview-Deep mixing short course", International symposium of ground improvement , IS-GI Brussels 2012
- [9] Guimond-Barrett A., "On the strength and durability of cement-stabilised sands", in Proc. International symposium of ground improvement , IS-GI Brussels 2012
- [10] Zheng L., Sharon Huo X., Yuan Y., "Experimental investigation on dynamic properties of rubberized concrete", J. Construction and building materials, 2008, pp.937-947.
- [11] Wang X., Zheng J., YIN J., "On composite foundation with different vertical reinforcing elements under vertical loading: a physical model testing study" J. of Zhejiang university, November 2010, pp. 80-87.
- [12] Fioravante V., "Load transfer from a raft to a pile with an interposed layer", Géotechnique, pp.121-132.

Prediction compressive strength of concretes containing silica fume and styrene-butadiene rubber (SBR) with a mathematical model

A.Hagholahi, M.Shafieyzadeh

Shaid Rajaee Teacher Training University, Iran

ABSTRACT

This paper deals with the interfacial effects of silica fume (sf) and styrene-butadiene rubber (SBR) on workability and compressive strength of concrete. Analyzing the compressive strength results of 32 concrete mixes performed over two water-binder ratios (0.35, 0.45), four percentages replacement of silica fume (0%, 5%, 7.5%, 10%) and four percentages of SBR (0%, 5%, 10%, 15%) were investigated. The results of experiments were shown that in 5% SBR, compressive strength rises slightly, but when the polymer/binder materials ratio increases, compressive strength of concrete decreases. A mathematical model base on Abrams' law has been proposed for evaluation strength of silica fume-SBR concretes. This simplified model might serve as useful guides for commixture concrete admixtures containing of silica fume and SBR. The accuracy of the proposed model is investigated.

Keywords: Concrete, Silica fume, SBR, Compressive strength, Mathematical modeling

1. Introduction

The strength of concrete is affected by many factors, such as cement composition and fineness, water-to-cement ratio, aggregate, age and temperature of curing. There is as yet no such formula (mathematical model) that could reproduce the effects of all these factors adequately in a quantitative manner, primarily due to a high number of variables [1].

Abrams' water-cement ratio law in 1918 is still considered as a milestone in the history of concrete technology, it is accepted that the largest single factor that governs the strength of concrete is the water to cement ratio. Originally, concrete was made by mixing cement, aggregates and water, and uses of admixtures were unknown. The only cementations material was cement. The present-day, new-generation concretes contain mineral admixtures and latexes for a variety of reasons. These materials increase abrasion strength or durability and decrease permeability [2-5], and Abrams' formulation needs to be modified.

Two different ways of adding polymers to cement composites have been described [6]:

1. Keeping constant the water-to-cement ratio (W/C) to obtain a similar hydration of the cement paste.
2. Fitting the consistency of the composite, by adjusting the W/C.

In this research, the water to binder ratio is constant (0.35, 0.45) considered and the effects of SBR emulsion and silica fume on fluidity and compressive strength of concrete are investigated and a relationship between compressive strength of concrete with the ratio of polymer, silica fume, water to binder materials and time of curing in water is proposed.

2. Test program and procedure

In this research, two series of samples with water-binder materials ratios of 0.45 and 0.35 were prepared. Intend to investigation interfacial effects of silica fume and SBR on compressive strength, experiments base on four levels of replacement silica fume (0%, 5%, 7.5%, 10%) and four levels of SBR (0%, 5%, 10%, 15%) were performed.

Cubes 150×150×150 mm were cast for compressive strength test. Before casting, coarse aggregate, sand and mixture of water and silica fume were mixed first. Then, cement, SBR latex and rest water together with supper plasticizer were put in the mixer and completely mixed. The mixed concrete were cast in molds to make specimens, and compacted by mechanical vibration. The specimens were subjected to the following three different curing systems:

- 1) 7-day water curing at 20⁰ c and 53-day dry curing at 20⁰ c (7W53D).
- 2) 14-day water curing at 20⁰ c and 46-day dry curing at 20⁰ c (14W46D).
- 3) 28-day water curing at 20⁰ c and 32-day dry curing at 20⁰ c (28W32D).

SBR latex as an aqueous polymer dispersion prefers dehydration and solidification under the dry conditions [7]. The cement hydration and polymer film in the modified concretes develop with prolongation cured age, which results in enhanced strength. In other words, the combination of the wet and dry curing is effective for the strength development of the polymer-modified concretes. A co-matrix is formed by both processes [4,8-10]. The specimens were tested for compressive strength according to BS standard.

3. Materials

The materials used in this research, were:

Ordinary Portland cement (Type 1) produced by Tehran factory, and silica fume, a by-product of the ferrosilicon Deligan factory. Chemical Properties of cement and silica fume are given in table 1.

Coarse aggregate with a maximum particle size of 17 mm and fine aggregate with a 3.01 fines modulus were used in the experiment. The specific gravity and water absorption of coarse and fine aggregates were 2.55 and 1.6%, 2.25 and 2.4%, respectively. A water reducer agent with the commercial name of Gelenium 110p from BASF was used to adjust the workability of the concrete mixtures. The base of this super- plasticizer is a unique carboxylic ether polymer with long lateral chains.

The polymer latex used was styrene-butadiene rubber (SBR) latex with commercial name of Rheomix 141p from BASF. The properties of SBR latex is presented in table 2.

Table 1- chemical Properties of cement and silica fume

Composition (%)	Cement	Silica fume
Sio2	21.46	91.7
Al2o3	5.55	1.0
Fe2o3	3.46	1.0
Mgo	1.86	1.8
Cao	63.95	0.9
So3	1.42	0.87
K2o3	0.54	—
Na2o	0.26	—
C3S	50.96	—
C2S	23.1	—
C3A	8.85	—
C4AF	10.53	—

Table 2 - Properties of SBR

Density (gr/cm ³)	Mean particle Size (micron)	Butadiene content	PH
1.01	0.17	40%	10.5

4. Test results and discussion

4.1. Effects of silica fume and SBR on fluidity of concrete

Silica fume decreases fluidity of concrete but SBR increases fluidity of concrete. Adding of 15 percent of SBR to samples with water to binder materials ratio 0.45 induces self-compacting concrete. The effect of SBR in increasing fluidity of concrete is more than the decreasing effect of silica fume in fluidity.

4.2. Effects of SBR on compressive strength

In polymer-cement ratio (5%), the compressive strength of modified samples was equal and even slightly higher than that of no polymer samples (Fig. 1). The filling effect of polymer cause increasing a little of Compressive strength. The compressive strength is mostly influenced by the bonding forces generated by hydration reaction of cement [11-13], and a little of increasing is observed. It seems at a p/c ratio 5%, the continuity of polymer film is only present through small tiny bridges on a limited number of spots. Although, the structure between the polymer film and cement hydrates develops at a p/c of 10%, the compressive strength of concrete decreases in comparison of no polymer concrete. In other words, the inclusion of SBR latex in concrete produces a decrease of compressive strength, due to a lower mechanical capacity of latex with regard to cement paste.

4.3. Effects of silica fume on compressive strength

It is observed a significant improvement in compressive strength of concrete because of the high pozzolanic nature and void filling ability of silica-fume [14-16]. The compressive strength of silica-fume-concrete continuously is increased with respect to reference concrete and reached a maximum value of 7.5% replacement level (Fig. 2). The effect of silica fume in water –binder 0.35 is less than water –binder 0.45.

4.4. Interfacial effects of silica fume and SBR on compressive strength of concrete

The compressive strength of concrete is affected by the ratio of SBR and silica fume to binder materials. When the ratio of polymer/binder is certain, the amount of silica fume affects strength of concrete. The percentage of silica fume that optimizes compressive strength remains 7.5% (Fig. 3).

In samples with 5% polymer and 7.5% silica- fume (water to binder ratio 0.45) a decrease in compressive strength is observed (Fig. 4). The cavitation of super plasticizer induces a decrease in compressive strength of these samples. (In making of these samples, the ratio of super plasticizer was kept constant.)

In 15% polymer, with decreasing water to binder materials ratio from 0.45 to 0.35, decreasing of compressive strength is compensated by the reduction of w/b due to the plasticizer effect of SBR. Both phenomena together remain compressive strength constant.

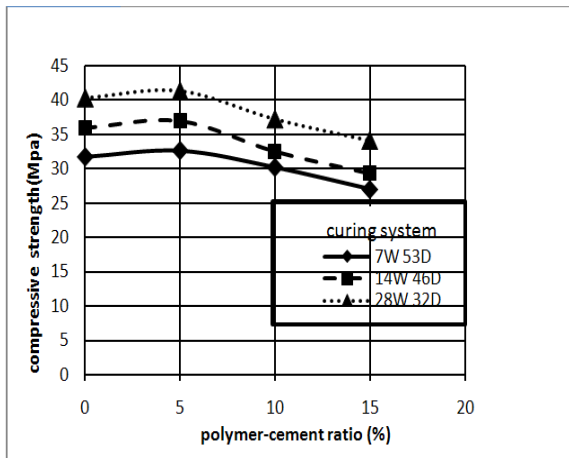


Fig. 1. Effect of polymer-cement ratio on the compressive strength of concrete (w/c=0.35 and 0% silica fume)

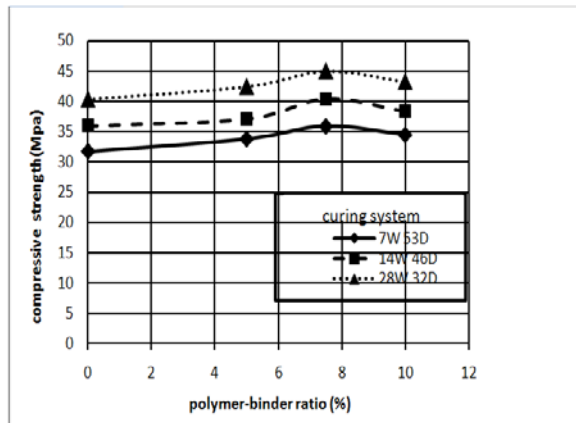


Fig. 2. Effect of silica fume- binder ratio on the compressive strength of concrete (w/b=0.35 and 0% SBR)

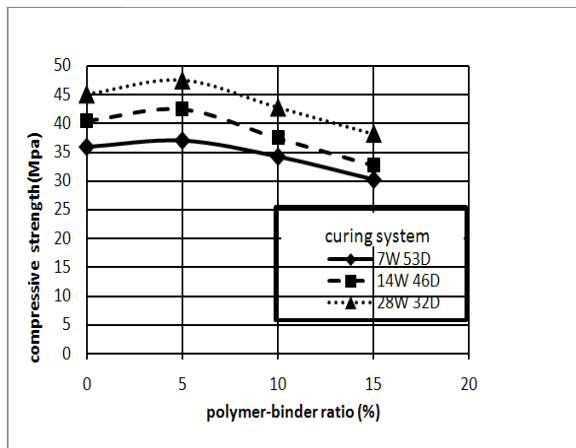


Fig. 3. Effect of polymer-binder materials ratio on the compressive strength of polymer modified concrete (w/b=0.35 and 7.5% silica fume)

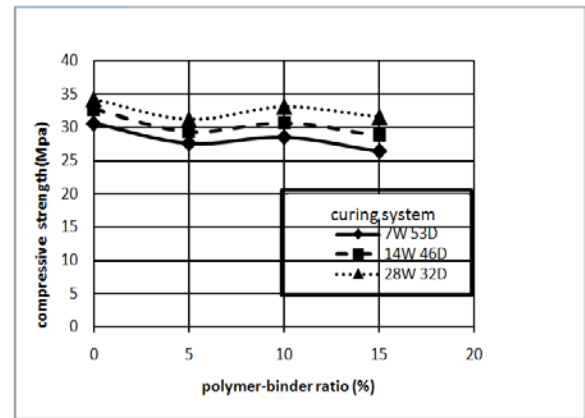


Fig 4. Effect of polymer-binder ratio on the compressive strength of polymer modified concrete.

(W/b=0.45 and 7.5% silica fume)

4.5. Investigation of main effects and interaction effects of factors in compressive strength

The main effect of each factor is shown in Fig 5. This diagram shows means of the compressive strength at various levels of each factor. It is observed that decreasing of water to binder material from 0.45 to 0.35 increases compressive strength about 26% ($\frac{36.7-29.06}{29.06} \times 100$). Averagely, 7.5% of replacement silica fume increases compressive strength about 13%. Also adding 15% of SBR decreases compressive strength about 14%.

A single diagram of interaction effects of factors in compressive strength is shown in Fig 6. Parallel lines in an interaction diagram indicate there is no interaction effect between variables. The greater the departure of lines from the parallel state indicates the higher the degree of interaction, in this situation, the response at a factor level depends upon the levels of other factors. For example, between SBR and silica fume in level of 5% SBR with other levels is observed an interaction effect. (A decrease in compressive strength of samples with 5% SBR and 7.5% silica fume in water to binder ratio 0.45 is happen.)

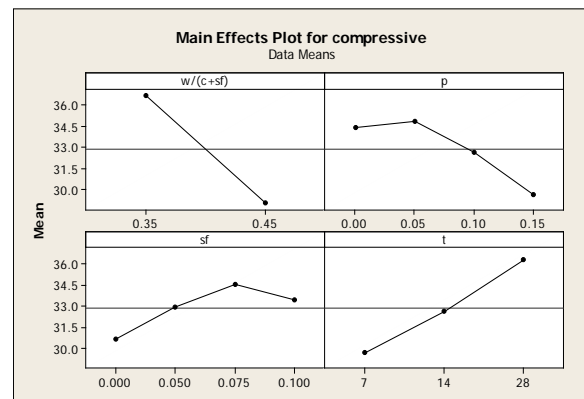


Fig 5. Main effects of diagram for compressive strength

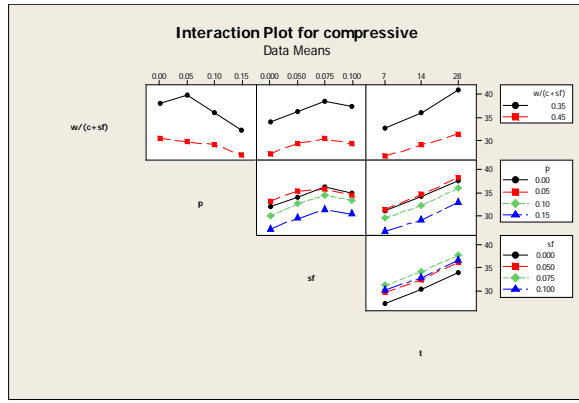


Fig 6. Interaction effects of factors in compressive strength

5. Mathematical model

The primary factors that affected the compressive strength of concrete are the ratios of water, SBR, silica fume to binder materials and time of curing in water. As per the classical formulation of Abrams' law, there exists an inverse relationship between the compressive strength and water-to-cement ratio of concrete [17,18]. A lot of researchers introduce relationship between compressive strength and time of curing in water with a logarithmic equation. Some of researchers propose power equations for the effect of silica fume on compressive strength of concrete [19,20]. But relationship between compressive strength with all variables is yet to be well known. In this situation where there is no prior known relationship between the compressive strength of concrete with all variables, scatter diagrams are prepared and means of values are portrayed in diagrams.

The scatter diagrams for all of the specimens exhibited a nonlinear relationship between the compressive strength with the ratios of silica fume and SBR to binder materials. From the scatter diagrams, it was observed that a two degree parabolic might be appropriate for showing the effect of silica- fume or SBR in compressive strength of concrete. The relationship of compressive strength with every variable is shown in Figs (7-9). The relationship between compressive strength with every factor is determined base on regression.

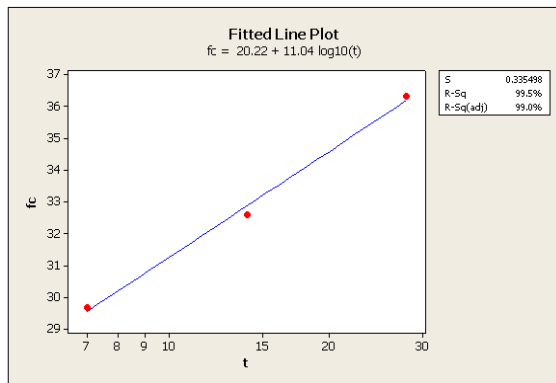


Fig 7. Relationship between compressive strength and time of curing in water

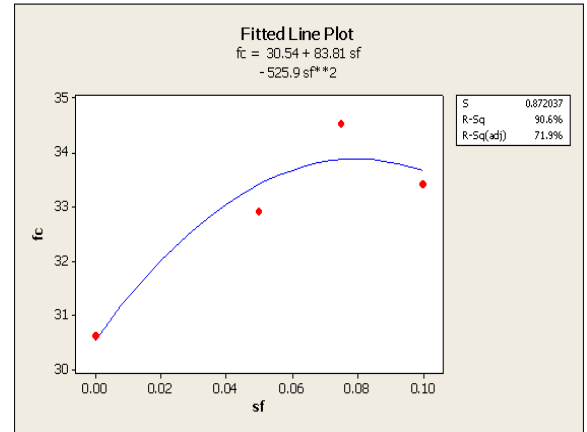


Fig 8. Relationship between compressive strength with Silica fume to binder materials ratio

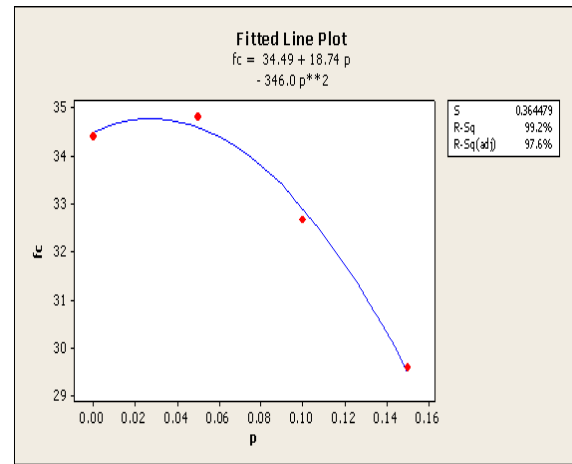


Fig 9. Relationship between compressive strength with SBR to binder materials ratio

The relationship between compressive strength with considered variables may be represented by:

$$F_c = \frac{a_1}{a_2 \left(\frac{w}{b}\right)} \times (11.04 \times \log(t) + 20.22)^{a_3} \times (-525.9s^2 + 83.81s + 30.54)^{a_4} \times (-346p^2 + 18.72p + 34.49)^{a_5} \quad (1)$$

Where F_c is the compressive strength (Mpa), $\frac{w}{b}$ is the ratio of water to binder materials, t is time of curing in water (day), s is the ratio of silica fume to binder materials, p is the ratio of sbr polymer to binder materials. a_1, a_2, a_3, a_4, a_5 are constant coefficients. The above equation can be written the following form:

$$\log(F_c) = \log(a_1) - \log(a_2) \times \frac{w}{b} + a_3 \times \log((11.04 \times \log(t) + 20.22)) + a_4 \times \log(-525.9s^2 + 83.81s + 30.54) + a_5 \times \log(-346p^2 + 18.72p + 34.49) \quad (2)$$

Where a_1, a_2, a_3, a_4, a_5 can be determined with multiple linear regression. The values of these coefficients are shown in below table. The value of the multiple correlation coefficients (r) has been obtained as 0.95.

a_1	a_2	a_3	a_4	a_5
2.637	0.999	0.98	1.005	0.977

With replace of one to coefficients that are near one, below equation is obtained.

$$F_c = \frac{49.2}{10^{\left(\frac{w}{b}\right)}} \times (0.546 \times \log(t) + 1)(-17.22S^2 + 2.74S + 1)(-10P^2 + 0.54P + 1) \quad (3)$$

From above equation can be determined the compressive strength of concrete containing of silica fume and SBR. To investigate of the accuracy of above equation, diagrams of residuals (the difference of observed and fitted values) for compressive strength has been drawn (Fig 10). The diagram of residuals for compressive strength shows that the maximum percent of error for compressive strength is about 10%.

The histogram of residuals has been shown in figure 11. Although, the distribution residuals doesn't completely obey from normal distribution but mean and maximum values of histogram of residuals is located near zero.

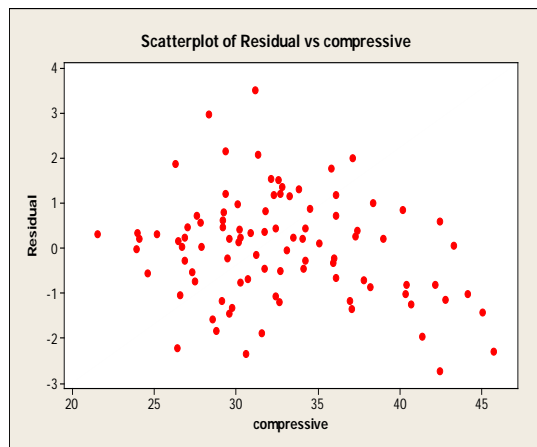


Fig 10. Diagram of residuals for compressive strength

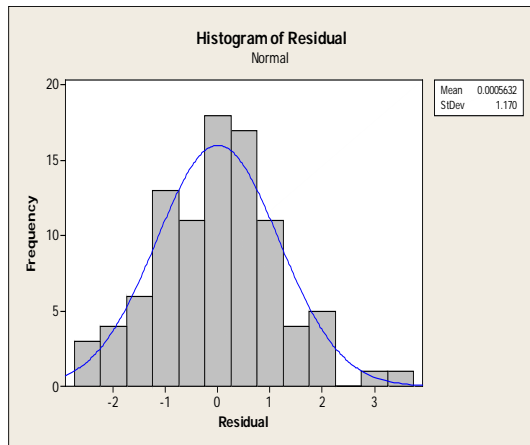


Fig 11. Histogram of residuals for compressive strength

6. Conclusion

1) The effect of SBR in increasing of fluidity of concrete is greater than the effect of silica fume in decreasing of fluidity of concrete.

2) In constant of water to binder ratio and combined curing system, the compressive strength of concrete in 5% SBR rises slightly, but when polymer/binder ratio increases, the compressive strength of concrete decreases.

3) Cement replacement up to 7.5% with silica fume leads to increase in compressive strength.

4) The decrease of compressive strength is compensated by the reduction of w/b due to the plasticizer effect of SBR. Both phenomena together remain compressive strength approximately constant.

5) The percentage of silica fume that optimize the compressive strength with adding SBR doesn't change.

6) The Abram's law with some modification is applicable to the compressive strength of concretes contain of silica fume and SBR and according to main effects of diagram is proposed the bellow equation:

$$F_c = \frac{49.2}{10^{\left(\frac{w}{b}\right)}} \times (0.546 \times \log(t) + 1)(-17.22S^2 + 2.74S + 1)(-10P^2 + 0.54P + 1)$$

The proposed model provides the opportunity to predict the compressive strength based on the time of curing in water(t), and water, silica fume and SBR to binder materials ratios that we show them with $\left(\frac{w}{b}\right)$, (s) and (p), briefly.

7. References

- [1] J. Zelic, D. Rusic, R. Krstulovic. A mathematical model for prediction of compressive strength in cement-silica fume blends, Cement and Concrete Research 34 (2004) 2319-2328.
- [2] V. Bhikshma, K. Nitturkar and Y. Venkatesham. Investigations on mechanical properties of high strength silica fume concrete, Asian journal of civil engineering building and housing vol.10.no.3(2009) 335-346.
- [3] O.Rozenbaum, R.J.-M.Pellenq and H.Van Damme. An experimental and mesoscopic lattice simulation study of styrene-butadiene latex-cement composites properties, Materials and structures (2005) 467-478.
- [4] Ru Wang, Pei-Ming Wang, Xin-Gui Li. physical and mechanical properties of styrene-butadiene rubber emulsion modified cement mortars, cement and concrete Research 35 (2005) 900-906.
- [5] S. Bhanjaa, B. Sengupta, Modified water-cement ratio law for silica fume concretes, Cement and Concrete Research 33 (2003) 447- 450.
- [6] G. Barluenga, F. Herna'ndez-Olivares. SBR latex modified mortar rheology and mechanical behavior. Cement and Concrete Research 34 (2004) 527-535.
- [7] Bing Chen , Juanyu Liu. Mechanical properties of polymer-modified concretes containing expanded polystyrene beads. Construction and Building Materials 21 (2007) 7-11.
- [8] A. Beeldens, D.Van Gemert, H.Schorn, Y.Ohama and L.Czarnecki. From microstructure to macrostructure : an integrated model of structure formation in polymer-modified concrete. Materials and Structures 38 (2005) 601-607.
- [9] LIU jun, XU Chang-wei, ZHU Xiao-yan, WANG Ling-ling, Modification of high performances of polymer cement concrete. Journal of wuban university of Technology-Mater vol.18 No.1 (2003).
- [10] João Adriano Rossignol, Interfacial interactions in concretes with silica fume and SBR latex (2009), Construction and Building Materials 23 (2009) 817-821.

- [11] Eui-Hwan Hwang, Young Soo Ko, Comparison of mechanical and physical properties of SBR-polymer modified mortars using recycled waste materials.
- [12] Ke-Ru Wu, Dong Zhang, Jun-Mei Song, Properties of polymer-modified cement mortar using pre-enveloping method, *Cement and Concrete Research* 32 (2002) 425-429.
- [13] Eui-Hwan Hwang, Young Soo Ko, Jong-Ki Jeon, Effect of polymer cement modifiers on mechanical and physical properties of polymer-modified mortar using recycled artificial marble waste fine aggregate, *Journal of Industrial and Engineering Chemistry* 14 (2008) 265-271.
- [14] S. Bhanja, B. Sengupta. (2005). Influence of silica fume on the tensile strength of concrete, *Cement and Concrete Research* 35 (2005) 743–747.
- [15] H. Katkhuda, B. Hanayneh and N. Shatarat. (2009). Influence of silica fume on high strength of light weight concrete, *World Academy of Science, Engineering and Technology* 58.
- [16] K.C. Biswal and Suresh Chandra Sadangi. (2010) . Effect of superplasticizer and Silica Fume on Properties of Concrete. *Proc. of Int. Conf. on Advances in Civil Engineering*.
- [17] Sandor Popovics, Strength and related properties of concrete a quantitative approach. (1998) John Wiley and sons.
- [18] mehta,p.kumar, concrete : Micro structure,properties and materials . (2006).
- [19] S. Bhanjaa, B. Sengupta, Investigations on the compressive strength of silica fume concrete using statistical methods, *Cement and Concrete Research* 32 (2002) 1391–1394.
- [20] Mohammad Iqbal khan, Analytical model for strength prediction of HPC consisting of cementitious, *Architecture civil engineering environmental* (2009).

Sliding Stability of Dry Masonry Block Retaining Wall Structure with a Resistance Plate

Akihiro HASHIMOTO¹, Yoshio SUEMATSU¹, Kazuo FUJITA¹, Toshimitsu KOMATSU¹ and
Noriyuki YASUFUKU¹

¹⁾ Department of Civil Engineering, Kyushu University, Fukuoka, Japan

ABSTRACT

There are two types of block masonry in the structural retaining wall, one is "dry masonry" and the other one is "wet masonry". However, the sliding stability of the dry masonry type retaining wall may be inferior to that in wet masonry block. Therefore, when focusing on the dry masonry type retaining wall, some arrangements are necessary to increase the sliding resistance. In this study, a new dry masonry type retaining wall is discussed, which is not only environmental friendly but also structurally stable. A resistance plate is newly attached to the boundary between upper and lower blocks to enhance the sliding resistance, which is due to the passive earth pressure mobilized in the plate. In this study, a series of model tests was carried out, paying attention to the position of the resistance plate, mobilized earth pressure in the plate and the horizontal movement of the blocks. It was indicated from the model tests results that the position of the resistance plate becomes very important to effectively increase the block stability.

Keywords: Sliding resistance, Retaining wall, Dry masonry, Resistance plate, Passive earth pressure

1. INTRODUCTION

There are two types of retaining block masonries namely "dry masonry" and "wet masonry" to construct the retaining wall. There is a "dry masonry" and "wet masonry" in the construction of retaining wall block masonry. Since, wet masonry cannot offer certain safety factor against the sliding, a projection at the bottom of basis [1] is given to enhance the sliding resistance on dry masonry retaining wall. In the case that a certain safety factor against sliding cannot be secured in wet masonry retaining wall, there is a method to enhance the sliding resistance by providing a projection at the bottom of basis [1]. However, this method has not been used much in clayey ground because the contact between the projection and the surrounding ground becomes loose. At the same time the construction cost is also relatively higher.

When the effect of projection in the clayey ground is properly mobilized, the construction of retaining wall can achieve the excellent safety with minimizing the construction cost. When the effect of projection in the clayey ground can be properly mobilized, which can be easily constructed at low cost, the construction of retaining wall with excellent safety and economy becomes possible.

On the other hand, the dry masonry type of retaining wall has an advantage in the environmental and economic efficiency. However, it generally resists against the sliding of the block due to the friction of filling geo-materials, it is considered to be unstable comparing with the wet masonry retaining wall. On the other hand, as the retaining wall in dry masonry type, which has an advantage in environmental and economic efficiency, generally resists against the sliding of the block due to the friction of filling geo-materials, it is considered to

be unstable comparing with the retaining wall in wet masonry type. Thus, it is instructed by adding a projection into each block or by using the block with an engagement structure [2] through the method of unifying each block. Thus, it is instructed to use the method unifying each block by adding a projection into each block or by using the block with an engagement structure [2]. In addition, an alternative method to enhance the sliding resistance by connecting each block with furniture has also been studied [3]. However, more effort is still required to eliminate the anxiety of the stability of blocks. When enough sliding resistance is achieved in dry masonry retaining wall compared to wet masonry retaining wall, the significant advantages can be expected in relation to constructive, economic and environmental aspects. When achieving an enough sliding resistance in retaining wall with dry masonry which exceeds that in retaining wall with wet masonry, the significant advantages can be expected in relation to constructive, economic and environmental aspects. Corresponding to these concerns, the authors have developed a reinforced dry masonry block retaining wall in which a new plate is set up at the boundary of upper and lower block. Corresponding to these concerns, the authors have developed a dry masonry block retaining wall reinforced the sliding resistance of each block to set up a new plate at the boundary of upper and lower block. In this study, a series of vertical stress loading tests were first carried out for investigating the effect of resistance plate on the sliding stability, and then for evaluating its effectiveness.

2. OVERVIEW OF PROPOSED DRY MASONRY BLOCK STRUCTURE WITH A RESISTANCE PLATE

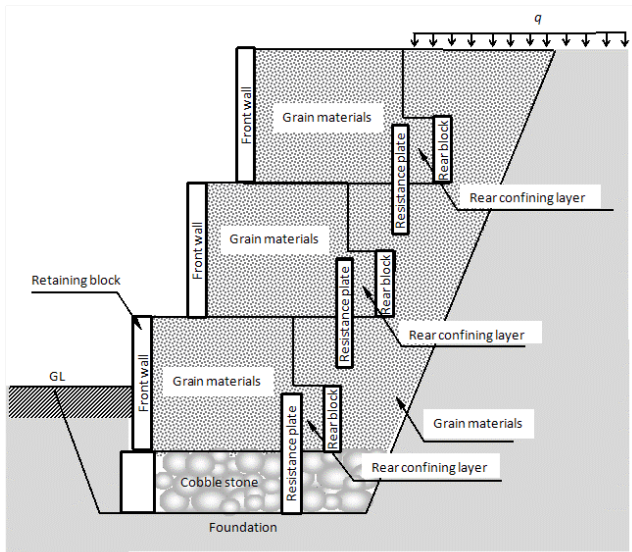


Fig. 1 A conceptual diagram of a dry masonry block structure with a resistance plate

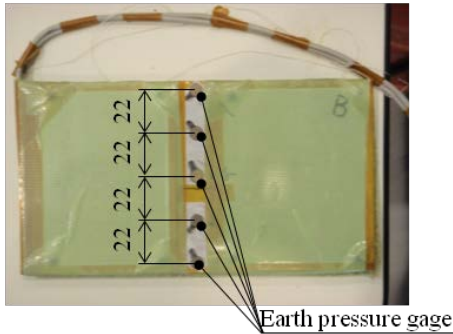


Photo. 1 Earth pressure gage

Figure 1 shows a conceptual diagram of a dry masonry block structure with a resistance plate. Each block used in the present structure has a side wall connecting the right and left of the front wall and rear wall, which is characterized by bottomless plate shown in Fig. 1. Each block used in the present structure has a side wall connecting the right and left of the front wall and rear wall, which is characterized by that there is no bottom plate shown in Fig. 1. Newly added resistance plate is perpendicular to the horizontal boundary surface between the upper and lower block, which is set up by keeping a spacing from the inner surface of the rear wall. Then, each inner space of the block and the space behind the block are densely filled in grain materials. As a result, a confining layer is produced in the space between the resistance plate and the rear wall, which is named as “rear confining layer”.

3 OUTLINE OF CONDUCTING MODEL TESTS

Figure 2 shows schematics of the experimental apparatus and model test specimen used in this experiment. All of model tests were conducted by applying the vertical load to the back filling and then resultantly by giving the horizontal load to the

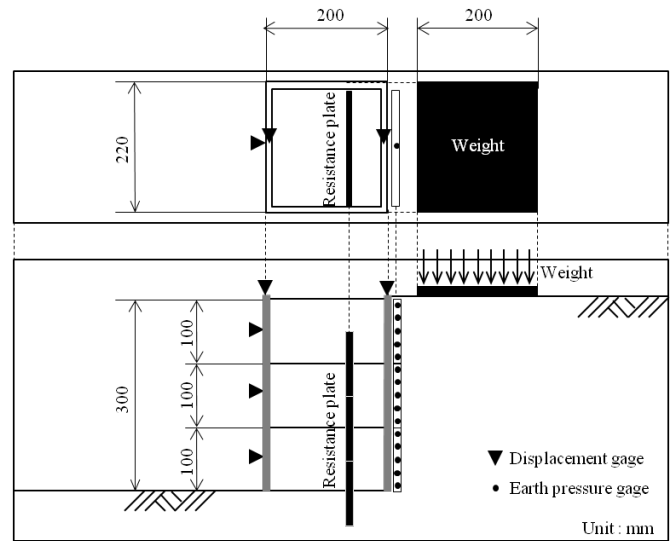


Fig. 2 A schematics of the experimental apparatus and model test specimen



Photo. 2 Experimental setup

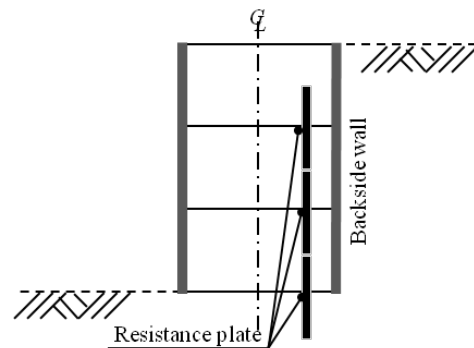


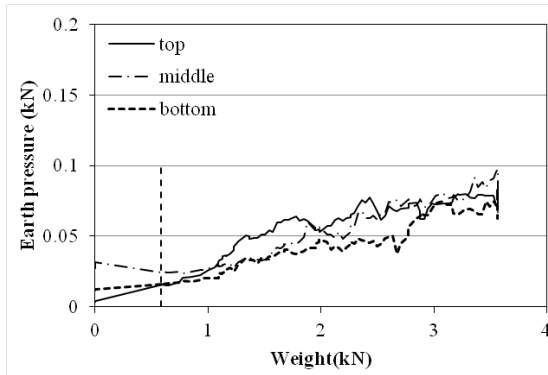
Fig. 3 Position of the resistance plate (ex. Case2)

Table 1 Fundamental properties of sand

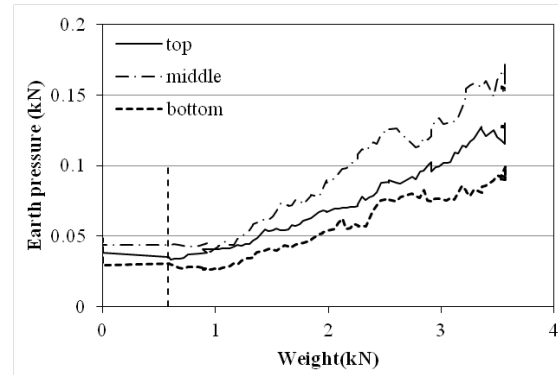
D_{50}	0.412mm
U_c	1.90

Table 2 Experimental conditions

Case	Position of a resistance plate
Case1	No plate
Case2	Back
Case3	Center
Case4	Attached on the back side wall

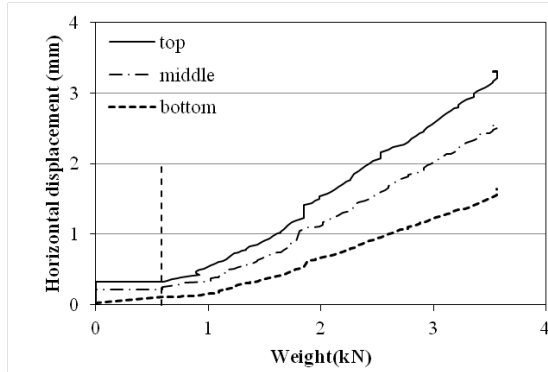


(a) Case 1 (No plate)

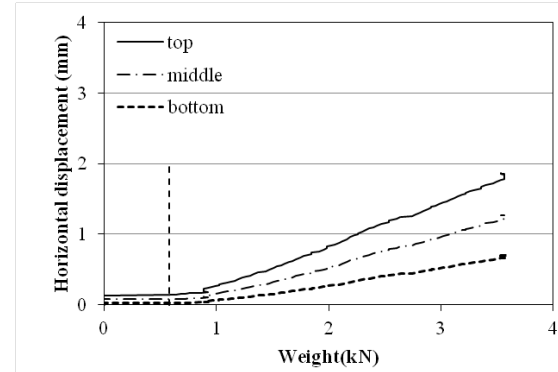


(b) Case 2 (Back)

Fig. 4 Relationship between earth pressure and vertical load



(a) Case 1 (No plate)



(b) Case 2 (Back)

Fig. 5 Relationship between horizontal displacement and vertical load

back side wall of the block. Scale of a model block made of acrylic with 15mm in thickness has 220mm front wall width, 200mm depth and 100mm height. Specimen with 300mm high wall has been created by overlaying a 3-stage block. Scale of a model block made of acrylic with 15mm in thickness is around 220mm in front wall width, 200mm in depth and 100mm in height. Specimen with 300mm high wall has been created by overlaying a 3-stage block. In this experiment, the steel plate with 2.3mm in thickness, 100mm in vertical height and 180mm in horizontal width were used as a model resistance plate.

Horizontal geostatic stress acting on the rear of the specimen was measured by ultra-compact earth pressure gauge (PDA-200KPA) as shown by Photo 1. Five earth pressure gages are installed to a plate with 100mm in length, 180mm in width and 7mm in thickness, which was bonded to two acrylic sheets and an aluminum sheet with 1mm thickness. As shown in Photo 1, the pressure gages are vertically attached to the central part of the plate at intervals of 22mm. Then, the lateral earth pressure was measured in a total of 15 points by attaching the plate with the pressure gages to the back of each block. A typical sea sand is used as filling and backfilling materials of the model ground, whose fundamental properties are summarized in Table 1. In order to prepare the model ground, all the specimens were prepared by compacting the sea sand under air-dried condition.

Vertical load was applied to the rubber plate put on the surface of backfill model ground through the water tank in

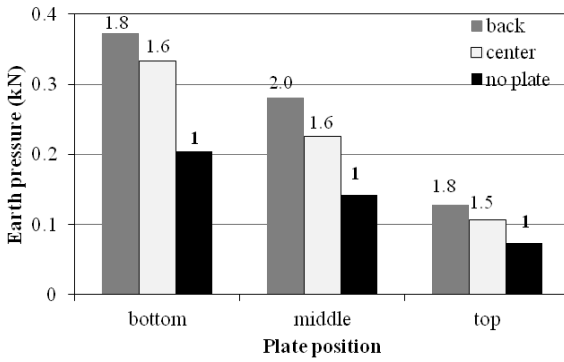
which the increasing rate of amount of water is constantly controlled. In this study, the rubber plate with 220mm width, 200mm in length and 50mm in thickness is set up to 50mm behind the back side of the block as shown in Photo 2 and the applicable applied load was limited to be around 4kN.

Also, in order to measure the lateral displacement of each block and the vertical displacement on the surface of the top block, the displacement sensor was set in the center front of each block wall. At the same time, two sensors were also put on the surface of the front and rear sides of the top block. Figure 3 shows the position of the resistance plate. A series of experiments were conducted paying attention to the effect of the position on the sliding stability. The position of a resistance plate selected is summarized in Table 2.

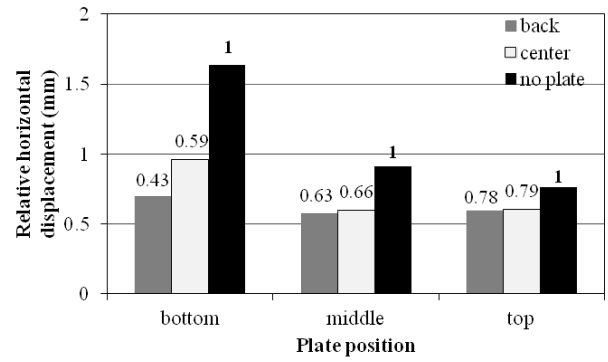
4 RESULTS AND DISCUSSIONS

4.1 Characteristics of mobilized rear earth pressure and horizontal displacement

Figures 4(a) and (b) show the results of rear earth pressure acting on the block body without and with resistance plate against applied vertical loads respectively. Figures 5 (a) and (b) also show the results of the horizontal displacements of the block body without and with resistance plate against applied vertical loads, respectively. Dotted lines in each figure indicate the start point of the loading which is around 0.59kN. Here, the total force acting on each rear of the block body (kN) was calculated by multiplying the average value of



(a) Total rear earth pressure



(b) Relative horizontal displacement

Fig. 6 The characteristics of (a) total rear earth pressure and (b) relative horizontal displacement at final loading stage

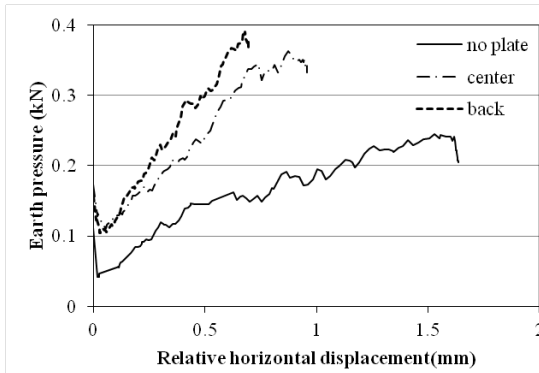


Fig. 7 Relationship between total rear earth pressure and relative horizontal displacement at the bottom block

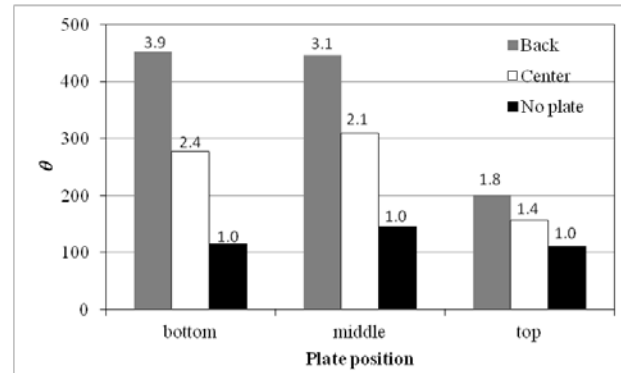


Fig. 8 Relative effect of resistance linked with plate position, θ defined as a gradient in the relationship between P_H values normalized by $\gamma H^2 B/2$ and the relative horizontal displacement δh normalized by the depth of the block D

the five measured earth pressures by the area of the plate resistance. It can be confirmed from these figures that the horizontal displacement and earth pressure at each block have increased with the increase of the loading in both cases. However, paying attention to the increment rate, the rate of earth pressure in case with resistance plate becomes greater comparing with that in case without resistance plate. On the other hand, the incremental rate of horizontal displacement in case with resistance plate is kept smaller comparing with that in case without resistance plate.

4.2 Evaluation of effect of resistance plate against sliding

It means that the sliding of the block is suppressed more effectively when a horizontal displacement of the block body becomes smaller against a same earth pressure action on the wall. Here, the effect of resistance plate on the sliding of the block is discussed from the relationship between horizontal displacement and mobilized earth pressure. In this study, the sum of the earth pressure acting on each block is defined as a force to slide the bottom surface of the block. For instance, sum of the rear earth pressure action on middle and top block bodies is used, when focusing on total earth pressure at the bottom of the surface in the middle block body. This is defined as total rear earth pressure P_H . In addition, the relative horizontal displacement between each block is used for

considering the results obtained. Figures 6 (a) and (b) are summarized in the bar diagram to indicate the characteristics of total rear earth pressure P_H and relative horizontal displacement at final loading stage. The numerical values shown above the bar diagram is obtained by normalizing the magnitudes of P_H in case 2 and 3 by the magnitude in case 3, which corresponds to the case without any resistance plates. It is clear that although the magnitudes of P_H in the cases with resistance plates become much greater comparing with that in case without any resistance plates, the relative horizontal displacement becomes smaller. For instance, the relative horizontal displacement of bottom block in case 3 has been reduced to less than half. In addition, the effect of resistance plate on sliding is clearly dependent on the position. Namely, when the resistance plate is set up on the back side of the block, the effect becomes much greater comparing with the case whose resistance plate is set up on the middle of the block.

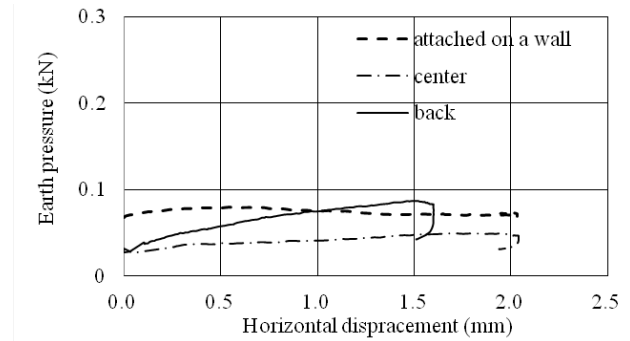
Figure 7 shows the relationship between relative horizontal displacement and total rear earth pressure P_H at the bottom block body in three cases. It is confirmed from this figure that P_H values for the case with resistance plate quickly increases comparing with the case without any resistance plates. A similar tendency was also confirmed in middle and top block bodies. Therefore, the incremental rate of P_H values against

relative horizontal displacement is introduced to evaluate the effect of the resistance plate. Figure 8 shows an index θ which may indicate the relative effect of resistance linked with plate position, where θ is defined as a gradient in the relationship between P_H values normalized by $\gamma H^2 B/2$ and the relative horizontal displacement δh normalized by the depth of the block D , where γ is unit weight of soil ($=17.5\text{kN/m}^3$), H is height of the block specimen and B is width of the block. Numbers indicated in Figure 8 mean the value which was calculated by dividing the value of θ for the two other cases by the value in corresponding each block without any resistance plate. It is indicated that the resistance potential against sliding at the bottom block in case 3 whose resistance plate sets up on the back side of the block body becomes relatively 3.9 times greater. Similarly, the resistance potential in case 2 whose resistance plate sets up on the middle of the block body becomes relatively 2.4 times greater. In addition, the resistance potential against sliding is clearly dependent on the position of the block body, even if the resistance plate set up on the same position of the block body. It means that the sliding resistance of the plate is influenced by the induced overburden pressure.

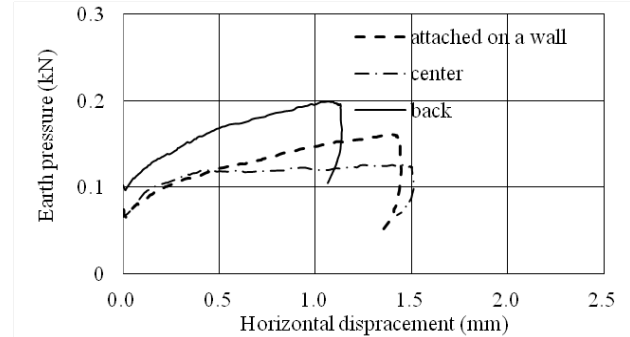
5 EARTH PRESSURE ACTING ON THE RESISTANCE PLATE

The resistance plate has been confirmed in Chapter 4 to be effective to suppress the sliding of the block body. This is probably due to earth pressure acting on the resistance plate, which is named as a passive mobilized earth pressure in this study. So, in order to make clear the effect of the position of resistance plate on the block sliding, the horizontal earth pressures action on the resistance plates were measured in case 2 and case 3, together with case 4 that the resistance plate is attached on the back side of the block.

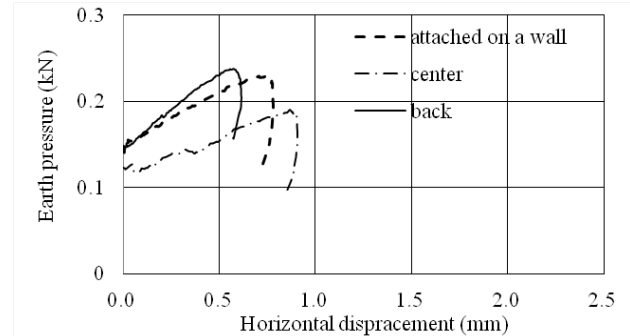
Figure 9 shows the relationship between the total horizontal earth pressure acting on the plate and the mobilized horizontal displacement of the block body, where the total horizontal pressure is estimated by multiplying an average horizontal earth pressure by an area in the resistance plate. Figures 9(a), (b) and (c) show the results in top, middle and bottom block body respectively. In Figure 9(c), the mobilized passive total earth pressure in case 2, 3 and 4 becomes 0.24kN, 0.19kN, and 0.23kN respectively. On the other hand, the amount of horizontal displacement becomes 0.62mm, 0.9mm, and 0.78mm in case 2, 3 and 4 respectively. Based on these results, it shows that greater the mobilized passive total earth pressure, relatively smaller the corresponding horizontal displacement. Conversely, it reflects that smaller the mobilized passive total earth pressure, relatively greater the corresponding horizontal displacement. Similar tendency is also indicated in Figures 9 (a) and (b). It is mentioned that the effect of a resistance plate against sliding is due to the mobilized earth pressure action on the resistance plate. The magnitude of the earth pressure is also dependent on the overburden pressure by the filling materials in the block. Further considering the results, the mobilized earth pressure in case 2 becomes greater than that



(a) Top



(b) Middle



(c) Bottom

Fig. 9 Relationship between the total rear earth pressure and acting on the plate and mobilized horizontal displacement of the block body

of case 4. It is concluded that the resistance plate set up on the back side of the block works well for increasing sliding resistance of dry masonry retaining structure, comparing with the case in which the resistance plate was set on the position attached on a wall at block body. It is considered that this is due to a constraining effect induced by a granular layer between the position of the resistance plate and back side of block body.

6 CONCLUSIONS

In this study, a series of vertical stress loading tests were carried out for investigating the effect of resistance plate on the sliding stability. The main conclusions obtained are summarized below:

1) Based on the small model test results, it is clearly confirmed that the resistance plate contributes well to induce a greater horizontal earth pressure acting on the block body

and to reduce the horizontal displacement of block body. In addition, the effect becomes greater when the resistance plate set up on the back side of the block body, rather than set up on the middle position of the block.

2) Based on the small model test results, the resistance potential against sliding at the bottom block in case whose resistance plate sets up on the back side of the block body became 3.9 times greater than that of the case without any resistance plate. Similarly, the resistance potential in case whose resistance plate sets up on the middle of the block body became relatively 2.4 times greater.

3) It is confirmed from the characteristics of mobilized earth pressure acting on the resistance plate that the effect of the plate against sliding is due to the mobilized earth pressure action on it. Furthermore, it is concluded that the resistance plate set up on the back side of the block works well for increasing sliding resistance of dry masonry retaining structure, comparing with the case in which the resistance plate was set on the position attached on the wall at block body. One of the reasons is considered that this is due to a constraining effect induced by a granular layer between the position of resistance plate and back side of block body.

7 REFERENCES

- [1] Doro dokou kasetsukozobutsu-ko shishin, Japan road association, 1999, pp.74-75.
- [2] Doro dokou kasetsukozobutsu-ko shishin, Japan road association, 1999, p.82.
- [3] “Effect of connecting method on dynamic behavior of concrete block retaining wall”, 29(3), pp. 523-528, 2007

Evaluation and Prediction Method on Neutralization of Supplied Long-term Hydraulic Concrete Structure

Man-Kwon Choi¹, Yuki Hasegawa², Shinsuke Matsumoto³, Shushi Sato³ and Tsuguhiro Nonaka⁴

¹The United Graduate School of Agricultural Science, Ehime University, Japan

²Graduate School of Integrated Arts and Science, Kochi University, Japan

³Faculty of Agriculture, Kochi University, Japan

⁴Faculty of Life and Environmental Science, Shimane University, Japan

ABSTRACT

Velocity of neutralization is occupied by three factors; W/C ratio in mixture proportion, type of cement and supplied environmental condition. Hydraulic concrete structures are objective in this study. Influences of supplement condition to neutralization characteristics were evaluated. As a result, coefficient of neutralization velocity of concrete exposed to air is larger than that of concrete exposed to water. However, as for hydraulic concrete structure, mortar is disappeared and coarse aggregate is exposed from concrete surface in water during long-term supplement. It means that coefficient of neutralization velocity of concrete in water could be an apparent coefficient and actual coefficient was almost same with that of concrete in air. On the other hand, coefficient of neutralization velocity of concrete canal was smaller than that of general engineering structures. Furthermore, neutralization depth and velocity of concrete canal was different even in same member. Therefore, it seems reasonable to conclude that evaluation of neutralization should be careful when concrete in water is measured.

Keywords: Neutralization, Phenolphthalein method, Neutralization depth, Prediction method, Coefficient of neutralization velocity

1. INTRODUCTION

Neutralization of concrete generates at anywhere where carbon dioxide gas is supplied. This deterioration, commonly progresses from surface to inner part of concrete, gives serious damage to reinforced concrete. Investigation and diagnosis are necessary to carry out from the viewpoint on restriction of reinforcement corrosion in concrete.

Neutralization depth is the general expression for the evaluation of this deterioration. This depth is indicated with following Eq. (1);

$$y = at^b \quad (1)$$

where y is neutralization depth (mm), t is time (year), a and b are the constants; especially a is called as coefficient of neutralization velocity. In general, a constant b is stipulated as 0.5, which was confirmed from many previous studies.

Thus, the progress estimation of neutralization will also be achieved if there were plural measured data concerned to neutralization depth and supplied year [1].

On the other hand, following Eq. (2) is described for the estimation of neutralization depth when there were no measured data;

$$y = (-3.57 + 9.0W/B)\sqrt{t} \quad (2)$$

where W/B is the effective ratio of water per binder, W is the unit weight of water and B is the unit weight of effective binder [1]. However, it is difficult to identify W/B because the drawings and specifications of most existing old structures have disappeared during their long-term supplement. Moreover, progress velocity of neutralization is commonly occupied by two main factors; W/C ratio in mixture proportion of concrete (penetration velocity of carbon dioxide gas) and supplied environmental condition of concrete structures. It means that Eq. (2) is not always available for the prediction of neutralization if neither inspection data nor drawing and specifications were remained. Furthermore, Kawanishi et al. have reported that constant a was changed under some distinctive environmental conditions [2]. As the mix, proportion of hardened concrete is impossible to estimate accurately, it is necessary to clarify the influence of supplemental environment to neutralization of concrete in order to improve the precision on evaluation and prediction of neutralization.

Concrete canals for the agricultural use, one of the hydraulic concrete structures, are supplied long period under sever environmental condition. At the same time, concrete canals have one characteristic supplied environmental condition. The supplied condition of concrete canal is divided into two parts; the part that sunk into the water (call "water part") and the part exposed to the open air (call "air part") for comparatively long period. On the whole, it is considered that transfer velocity of carbon dioxide gas of concrete exposed to liquid phase is quite slower than that of concrete exposed to gaseous phase, and the progress of neutralization is possible

to disregard. However, in case of concrete canal, water contacted to concrete surface is continually moving, there is a possibility that various ionic compounds become easy to dissolve and transfer due to water flow. Furthermore, exposure of coarse aggregate, one of the distinguishing trait deterioration of concrete canal, also can affect to the neutralization of concrete.

This research aimed to clarify the influence of different environmental conditions to the neutralization depth of concrete experimentally. Objective structures were actual concrete canals for the agricultural use that were supplied for long terms. To be specific, the surfaces in water and in air of concrete canal were shaved by the rock drill. Phenolphthalein method was applied and measured the neutralization depth. Relationship between supplied year and neutralization depth, as well as the influence of different supplied conditions, in air and in water, to the progress of neutralization, were investigated in this study. Finally, applicable prediction method for the evaluation of neutralization against concrete canal was examined.

2. RESEARCH SIGNIFICANCE

Neutralization of normal civil engineering structure has been studied and their tendency about this deterioration has clarified sufficiently. In spite, huge number of hydraulic concrete structures has been constructing in this world, their specific supplied condition and effect against neutralization has not focused enough yet. Hydraulic concrete structures are considered to face the multiple deterioration; not only the neutralization but also the abrasion. It will be necessary to evaluate both deterioration for accurate evaluation and prediction of them. The authors believe that this study will work for the review on the effect of supplied environment to the neutralization of concrete.

3. EXPERIMENTAL PROCEDURE

The subject of this study is accumulating the neutralization

data of hydraulic concrete structures in order to grasp the tendency and clarify the influence on supplied environment to the neutralization. An object of this study was the large concrete open channel supplied for long periods. Especially a side wall of concrete canal was focused member for the investigation because the side wall has both water part and air part in same member.

3.1 Objective Concrete Canals

Open canal network focused in this study was located in the center of Kochi prefecture, Japan. This canal network was developed from 1968 to 1985 consecutively under prefectural management for improving the water utilization of paddy field. In Japan, even though these projects had public infrastructural aspect, but the part of construction cost should be paid by the beneficiaries (the beneficiary pays principle). The size of beneficial area was 1,860 hectares paddy fields, and the length of this main canal network was 36kilometers. Designed service life of mainstay concrete open channel for the agricultural use is established for 40 years, and design criteria strength of concrete was estimated to 21MPa (approximately 200kgf/cm²). Supplied periods of investigated concrete canal were between 23 to 39 years. Moreover, additional two concrete canals supplied longer periods, 42 and 47 years, were examined in order to analysis the relationship between service periods and neutralization depth in detail.

3.2 Field Investigation Method

Concrete surface was shaved as one of the partial destructive method for the diagnosis of concrete. Phenolphthalein method was applied against these shaved phases of concrete. 1.0% concentration of phenolphthalein ethanol solution was used in this study. Measurement procedure was described as follows; this solution was sprayed after opening at least 50mm depth of hole at the side wall of concrete canal and blowing off the fine powders of concrete completely. Waiting for a couple minutes, then, measured the depth of discoloration boundary from the surface. Phenolphthalein

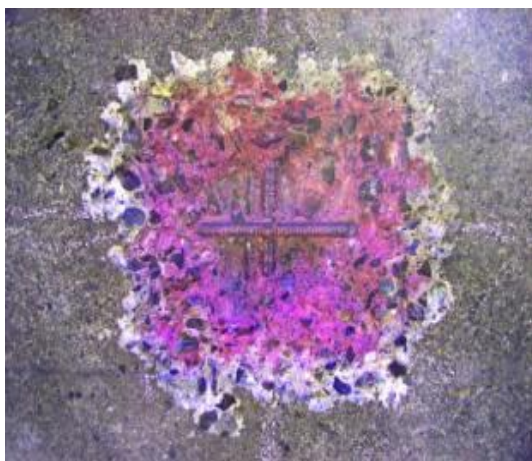


Fig.1 State of Discolored Condition by Phenolphthalein Solution

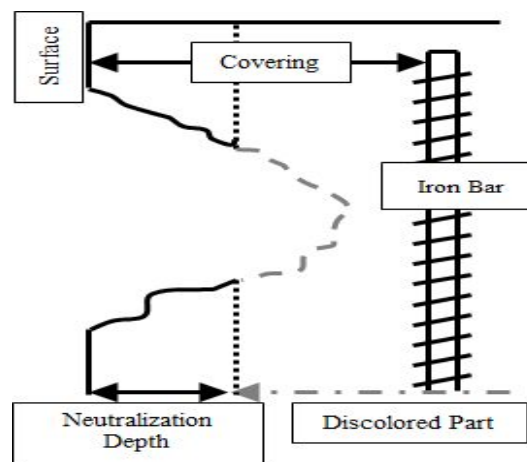


Fig.2 An Overview on Evaluation of Neutralization Depth

ethanol solution is one of a coloring reagent and applies for the evaluation of neutralization depth of concrete as this solution change the color from clear into deep red-violet when the concrete has enough alkalinity. In general, discoloration generates when the potential of hydrogen (pH) of concrete is higher 8.2 to 10. Authors have also confirmed the discoloration boundary of this solution and clarified the threshold value on potential of hydrogen was 10 experimentally [3]. The state of discolored condition by the phenolphthalein solution is shown in Fig.1, and an overview on evaluation of neutralization depth is shown in Fig.2. The neutralization depth, distance from surface of concrete to discoloration boundary is measured using depth gage. Three holes were drilled at air part and water part in each one member, and calculated the average depth.

4. RESULTS AND DISCUSSION

4.1 Neutralization Depth and Supplied Periods

Relationship between neutralization depth and supplied periods are shown in Fig.3. As a whole, neutralization depths are less than 30mm in spite of their different service periods. In addition, we cannot see the correlation between them. Basically the neutralization depth would be larger as the supplied periods were longer. It is considered that the progress velocity of neutralization had a great influence to the neutralization depth. Say in other words, it is necessary to pay attention not only to the service periods but also to the coefficient of neutralization velocity (call CNV here after) for the evaluation of neutralization.

Comparing the neutralization depth of air part and water part, we can confirm big difference between them. There is a tendency that the neutralization depth of water part is smaller than that of air part. Phenomenologically, it would be resulted that external factors such as the difference on concentration of carbon dioxide gas and humidity affect to the neutralization velocity. However, coarse aggregates were exposed at most of all water part on the side-wall of concrete canal shown in Fig.4, and this phenomenon is omnipresent as the deterioration of hydraulic concrete structures. Neutralization depth of water part should be evaluated if the equivalence of evaluation with that of air part was necessary to secure. Therefore, it is revealed that measured neutralization depth could not be the enough data for the accurate evaluation of hydraulic concrete structures if the coarse aggregates were exposed on their surface.

4.2 Substantial Neutralization Depth of Hydraulic Concrete Structures

Described as foregoing paragraph, neutralization depth of water part has possibility that its evaluation result was the apparent neutralization depth. According to author's previous study concerning to the explosion of coarse aggregate, this phenomenon would be actualized when 6mm thickness of mortar was disappeared from the surface of concrete despite of water cement ratio [4]. It was considered that at least 6mm thickness of mortar has already abraded if the coarse

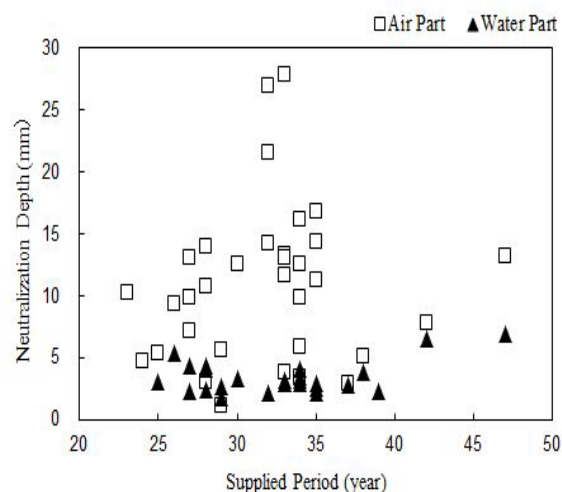


Fig.3 Relationship between Neutralization Depth and Supplied Periods

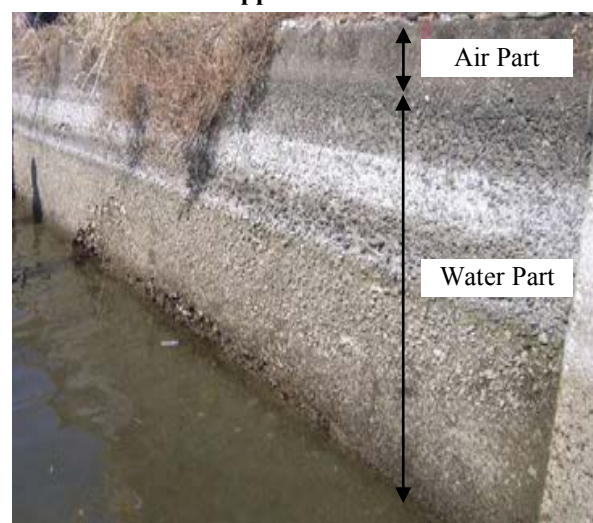


Fig.4 An Overview of Abraded Surface of Concrete Canal

aggregate were exposed at the side wall of concrete canal. Relationship between estimated neutralization depth taking into account the 6mm thickness of disappeared mortar and supplied periods are shown in Fig.5. Without this consideration, 96% of neutralization depth of air part was higher than that of water part. However, thus, in addition to this consideration, only 48% of neutralization depth of water part could show the same result. As a result, the assumption concern to the general theory that the neutralization velocity of water part is smaller than that of air part cannot be comprised all the time against hydraulic concrete structures. Significant abrasion of concrete canal is observed frequently at the draft level; the highest frequency water level. Therefore, evaluation of neutralization at this water level will be also more important for securing the accuracy on this deterioration.

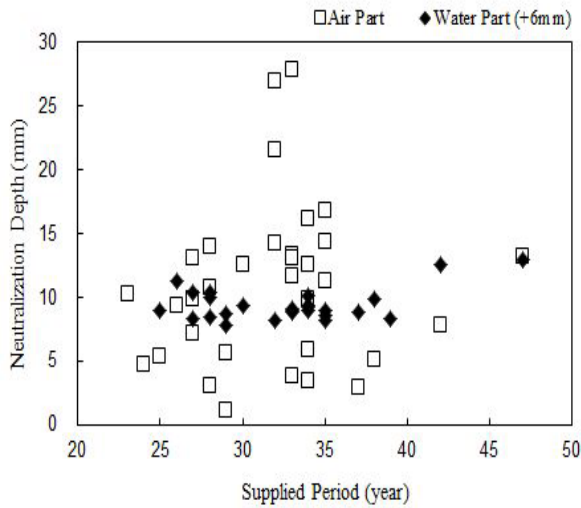


Fig.5 Relationship between Neutralization Depth Considering 6mm Thickness of Disappeared Mortar and Supplied Periods

4.3 Comparison on Coefficient of Neutralization Velocity (CNV)

A fundamental equation on the neutralization depth was shown as Eq. (1). Now CNV was calculated on assumption that the neutralization advances in proportion to a square root of time. In short, CNV was calculated from the measured data and supplied years. A histogram of CNV was shown in Fig.6, and their average and standard deviation were shown in Table I. Around 55% of CNV of air part was less than 2.0 in the whole. However, around 90% of CNV of water part was less than 1.0. In addition, if considering the disappeared mortar thickness in water part was 6mm as an assumption, around 95% of CNV in water part was less than 2.0. Previous study has reported that the highest frequency range on CNV of general civil structures (nominal strength: 16 to 21MPa) were 0.0 to less than 2.0. All the results from air part, water part, and water part of additional condition, showed the same tendency with the past study [5]. In the same literature, percentages of CNV under the range distribution of $0 < \text{CNV} < 2$, $2 < \text{CNV} < 4$, $4 < \text{CNV} < 6$ were around 50%, 35% and 15%, respectively. Comparing the same range distribution between it and our results, CNV of air part of concrete canal was approximately same or smaller than the result of civil engineering structures; $0 < \text{CNV} < 2$, $2 < \text{CNV} < 4$, $4 < \text{CNV} < 6$ were around 55%, 40% and 5%, respectively.

As for the average and standard deviation results of CNV shown in Table I, average on CNV of air part was three times larger than that of water part. As well, the standard deviation on CNV of air part was five times larger than that of water part. In particular, the difference of standard deviation between air part and water part was generated from the supplied environmental conditions. It was considered to be the difference of humidity; the air part was faced to various conditions of dryness and moisture due to the rainfall and

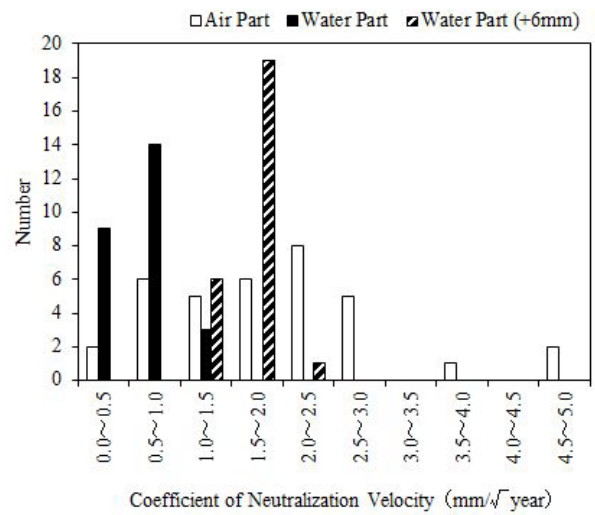


Fig.6 Histogram on Coefficient of Neutralization Velocity of Hydraulic Concrete Structures

Table I Average and Standard Deviation of Coefficient of Neutralization Velocity

	Average (mm)	Standard deviation (mm)
Air part	1.92	1.08
Water part	0.60	0.20
Water part (+6mm)	1.65	0.21

solar radiation, on the contrary, water part was more stable condition rather than air part. These environmental conditions affected to the difference of standard deviation of them.

4.4 Prediction of Neutralization Considering the Disappeared Mortar

It was considered that the mechanism on progress of neutralization was different between air part and water part of concrete canal. To be more precise, neutralization at the air part of hydraulic concrete structures advanced with the same way with general civil engineering structures, however, at the water part, the exposure of coarse aggregate due to abrasion is going on at the same time with the progress of neutralization. Therefore, it would be impossible to express the equation for prediction of neutralization such as Eq. (1) when the partial loss of surface is going on such as water part of hydraulic concrete structures.

For example, as for the predictive equation against sulfate acid attack, one kind of serious deterioration of concrete, different equations are applied due to their deteriorative conditions; while the original shape of structure is keeping or not. In specific terms, deterioration velocity increased in proportion to the square root of time if the shape of original structure was remaining as it was. On the contrary, deterioration velocity increased in proportion to the time if

the shape was partially loss [6]. Then predictive equation was assumed to follow to the latter theory, and expressed the equation for the water part could be as follows:

$$y = at \quad (3)$$

Average and standard deviation of CNV were calculated with this Eq. (3) and gained 0.29 and 0.05, respectively. Comparing this result with the result from Eq. (1), CNV was extremely small. In other words, progress velocity of neutralization in water part should be smaller than the air part because the mortar area is becoming smaller due to the exposure of coarse aggregate, and as a result, penetration amount of carbonate ion into mortar was decreased relatively. On the other hand, neutralization depth drawn in Fig.3, the approximation line should be sloped from right to left. However, the neutralization depths were constant nevertheless the progressing of time. It was considered that the reason was the assumed thickness of disappeared mortar; constant 6mm thickness of mortar. It meant that the exposure of coarse aggregate was actualized when the 6mm thickness of mortar was disappeared, but it would be difficult to evaluate the actual disappearance accurately at the presence in case if more than 6mm thickness of mortar had lost. Thus, it will be possible to evaluate the actual neutralization depth if the actual disappearance thickness of mortar could be obtained in detail in the future.

5 CONCLUSIONS

Based on the results of this experimental investigation concerns to neutralization of actual hydraulic concrete structures, the following conclusions are drawn:

- 1) Comparing the air part and water part of neutralization depth and coefficient of neutralization velocity, both values of water part were smaller than those of air part. Moreover, standard deviation also showed the same tendency with above result.
- 2) Those differences between air part and water part were not confirmed when considering the estimated thickness 6mm of disappeared mortar.
- 3) Coefficient of neutralization velocity of hydraulic concrete structures was smaller than that of general civil engineering structures even though the nominal strength was equivalent each other.

6 FURTHER RESEARCH

It has not clarified the exact progressive process of neutralization in water part. For establishing the progressive prediction method, further studies concerns to the deterioration mechanism on water part of concrete should be examined, including the relationship between neutralization and abrasion of hydraulic concrete structures.

7 ACKNOWLEDGMENTS

The authors wish to express their gratitude and sincere

appreciation to Mr. Kenichirou Uchida and Shutaro Yamasaki, now the staffs of Kochi Prefectural Office, to their kindly support while they were belonging to master course student in Kochi University, Japan. A part of this work was supported by JSPS KAKENHI (22780219) (Grant-in Aid for Young Scientists (B), A representative: Shushi SATO) and the authors are also grateful for their financial support to this research work.

8 REFERENCES

- [1] Japan Society of Civil Engineering, Standard specifications for concrete structures-2007, maintenance: JSCE, 2007, pp. 92-73.
- [2] Kawanishi T, Hamasaki H and Masuda Y, "Analysis on the carbonation of concrete based on investigation of existing buildings," J. of Structure and Construction Engineering, No.608, Oct. 2006, pp. 9-14.
- [3] Sato S, Masuma Y, Hasegawa Y, Natsuka I, Aoyama A and Yokoi K, "Development on specific evaluation technique for the prediction of neutralization of concrete," in Proc. 36th Int. Conf. on OWCS, 2011, pp. 373-380
- [4] Sato S, Ogata H, Nonaka T and Hattori K, "Fundamental study on the evaluation of exposed coarse aggregate in concrete channel," J. of Japan Concrete Institute, 2008, pp. 699-704.
- [5] Public Works Research Institute, and Nippon Structural Inspection and Technology Association, Manual for inspecting soundness level of concrete structures using nondestructive testing: Gihodo Shuppan Co. LTD., 2003, pp. 50-55.
- [6] Japan Society of Civil Engineering, Standard specifications for concrete structures-2007, maintenance: JSCE, 2007, pp. 147-149.

MEASUREMENT OF TENSILE PROPERTIES OF GEOGRIDS

Raid R. Al-Omari¹ and Mohammed K. Fekheraldin²

¹Professor, Civil Engineering Department, Nahrain University, Baghdad, Iraq, Email: tosharaid@yahoo.com, Mobile: 00964-7901699487

²Assistant Lecturer, Civil Engineering Department, Kufa University, Najaf, Iraq, Email: Kadum_fekheraldin@yahoo.com, Mobile: 00964-7811497218

ABSTRACT

Geogrid reinforcement of soil has been successfully used for many years in a wide variety of applications. A huge development plan is expected in Iraq. The use of modern techniques like geogrid reinforced earth is expected. It is essential to gain experience in testing methods of geogrids using the available materials produced nationally, in neighboring countries and in developed countries. Some manufacturers do not provide sufficient data on the tensile properties of their products.

This paper presents data obtained from a series of laboratory tests performed on various configurations of geogrids. The tests are conducted to determine the physical properties of various seven types of geogrids, these types of geogrids were manufactured in Iraq, Iran, China and Britain. The mechanical properties included peak tensile strength, modulus of elasticity, upper yield strength, lower yield strength, tensile strength, non-proportional extension strength, total extension strength, fracture elongation, elongation at maximum load and total elongation as well as other physical properties such as aperture size, mass per unit area, rib thickness, rib width, junction thickness, roll width, mesh type, standard color and polymer type. The single rib strength test according to ASTM 6637-01 was performed using a computer controlled electronic universal testing machine. The results were compared with some information available from the manufacturers. Good agreement was found between the results obtained from the present tests and those given by manufacturers.

Keywords: geogrid, tensile strength, modulus of elasticity, elongation, polymer type.

1. INTRODUCTION

Geosynthetics include exclusively man made polymeric products such as geotextiles, geogrids, geonets, geomembranes, geosynthetic clay liners, and geocomposites. Polypropylene, polyester, polyethylene, polyamide, polyvinyl chloride, and polystyrene are the major polymers used to manufacture geosynthetics. It is not the properties of the polymers, but the properties of the final polymeric products that are of interest to civil and environmental engineering applications. Geosynthetics are used as part of the geotechnical, transportation, and environmental facilities. Geosynthetic products perform five main functions: separation, reinforcement, filtration, drainage, and containment (hydraulic barrier). However, in most applications, geosynthetics typically perform more than one major function [1].

Geogrids are matrix like materials with large open spaces called apertures, which are typically 10 to 100mm between ribs that are called longitudinal and transvers respectively. The ribs themselves can be manufactured from a number of different materials, and the rib cross-over joining or junction-bonding methods can vary. The primary function of geogrids is clearly reinforcement [2].

Geogrid, is also defined as a geosynthetic formed by a regular network of integrally connected elements and possess apertures greater than 6.35 mm (1/4 inch) to allow interlocking with surrounding soil, rock, earth, and other surrounding materials to primarily function as reinforcement [3].

Ribs for geogrids are the continuous elements of a geogrid which are either in the machine (MD) or cross-machine direction (XMD) as manufactured; Junction is the point where geogrid ribs are interconnected to provide structural and dimensional stability.

Geogrid is stiff or flexible polymer grid-like sheets with large apertures used primarily for stabilization and reinforcement of unstable or weak soil. The general types of geogrid are:

- 1- Unidirectional geogrid.
- 2- Bidirectional geogrid.
- 3- Extruded geogrid.
- 4- Bonded geogrid.
- 5- Woven geogrid, [2]-[3].

A significant development plan is expected in Iraq. The use of geosynthetics in the construction is anticipated. There is no local experience in measuring the mechanical properties of geogrids, in this work an experience has been built up. Also it is necessary to establish an idea of the available types of geogrids first in Iraq, second in neighboring countries and third in developed countries in order to be readily aware of the available options in the markets.

2. EFFECT OF GEOGRID PROPERTIES

The principal requirements of reinforcing materials are strength and stability (low tendency to creep), durability, ease of handling, a high coefficient of friction and or adherence with the soil, together with low cost and ready availability [4]. The selection of fabric for a particular construction application must necessarily depend upon adequate and suitable fabric properties and characteristics [5].

Geogrid tests are unique in a number of aspects when compared with geotextiles. Properties relating to separation, filtration, drainage, and barrier applications are not included since geogrids always serve the primary function of reinforcement [2].

The effective important properties of geogrids may be concerned in three main properties:

- 1- Physical properties.
- 2- Mechanical properties.
- 3- Endurance properties.

Many of the physical properties of geogrids including the weight (mass), type of structure, rib dimensions, junction type, aperture size, and thickness can be measured directly and are relatively straightforward. Other properties that are of interest are mass per unit area, which varies over a tremendous range from 200 to 1000 g/m², and percent open area, which varies from 40 to 95%. The latter suggests that almost all soils will communicate, or strike-through the plane of geogrids, [2].

The effect of geogrid aperture size on the obtained enhancement in strength was previously studied. Al-Omari, et al., (1987) investigated the effect of interlocking mechanism between soil particles and the aperture of the mesh using triaxial compression tests. It was concluded that the strength enhancement in mesh reinforced sand depends on the mechanism of interlocking which in turn affected by the ratio of aperture size to particle diameter [6].

The mechanical properties of geogrids include the geogrid stiffness, the peak tensile strength, modulus of elasticity, upper yield strength, lower yield strength, tensile strength, non-proportional extension strength, total extension strength, fracture elongation, elongation at maximum load and total elongation.

Al-Omari and Hamodi (1991) studied the effect of geogrids of varying stiffness values embedded in clays of different plasticity indices and they concluded that the reduction in swell increased with increasing the geogrid stiffness [7]. Also Al-Omari, et al., (1995) investigated the effect of stiffness of geogrids using triaxial test on plastic mesh reinforced sand. The sand density, mesh stiffness and the number of reinforcing layers were varied and they concluded that there may be limiting reinforcement stiffness, influenced by the number of reinforcing layers after which there will be no further gain in strength [8].

As geogrid are used in critical reinforcement applications, some of which require long service lifetimes, it is generally necessary to evaluate selected endurance properties [2].

3. Tensile Properties of Geogrids using the Single or Multi-Rib Tensile Method

The single or multi-rib tensile test methods cover the determination of the tensile strength properties of geogrids by subjecting strips of varying width to tensile loading. Three alternative procedures are provided to determine the tensile strength, as follows:

3.1 Method A—Testing a Single Geogrid Rib in Tension (N or lbf).

In this method, a single, representative rib specimen of a geogrid is clamped and placed under a tensile force using a constant rate of extension testing machine. The tensile force required to fail (rupture) the specimen is recorded. The ultimate single rib tensile strength (N or lbf) is then determined based on the average of six single rib tensile tests [3].

The initial tendency when assessing a geogrid tensile strength is to pull a single rib in tension until failure and then to note its behavior. A secondary tendency is to evaluate the in-isolation junction strength by pulling a longitudinal rib away from its transverse rib junction. It is important to state “in-isolation” since there is no normal stress on the junction; strength test must be done with the entire geogrid structure contained within soil embedment, [2].

A single rib tension strength test merely uses a constant rate-of-extension testing machine to pull a single rib to failure. For unidirectional geogrids, this would most likely be a longitudinal rib. For bidirectional geogrids, both longitudinal and transverse ribs require evaluation. By knowing the repeat pattern of the ribs, equivalent wide-width strength can be calculated. Alternatively, a number of ribs can be tested simultaneously to obtain a more statistically accurate value for the wide-width strength [3].

An in-isolation junction or node strength test can also be performed. The test method uses a clamping fixture that grips the transverse ribs of the geogrid immediately adjacent to and on each side of the longitudinal rib as shown in Fig. 1. The lower portion of the longitudinal rib is gripped in a standard clamp, and both clamps are mounted in a tensile testing machine, where the test specimen is pulled apart. The strength of the junction, in force units, is obtained [2].

The sample may be taken from the end portion of a roll provided there is no evidence it is distorted or different from other portions of the roll. The specimens shall consist of three (3) junctions or 300 mm in length (12 in.), in order to establish a minimum specimen length in the direction of the test (either the machine or cross-machine direction). All specimens should be free of surface defects, etc., not typical of the laboratory sample. Take no specimens nearer the selvage edge along the geogrid than 1/10 the width of the sample. Prepare each finished specimen, as shown in Fig. 1, to contain one rib in the cross-test wide by at least three junctions (two apertures) long in the direction of the testing, with the length dimension being designated and accurately cut parallel to the direction for which the tensile strength is being measured. The outermost ribs are cut prior to testing to prevent slippage from occurring within the clamps. For those

cases where the outermost ribs are severed, the test results shall be based on the unit of width associated with the number of intact ribs [3].

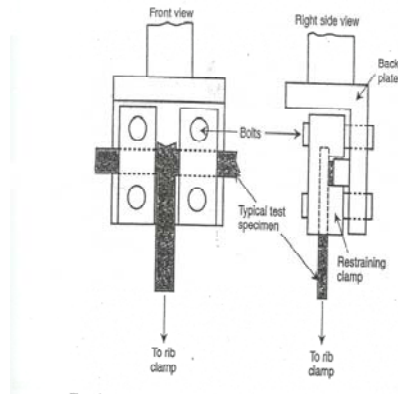


Figure 1: Test fixture measuring in-isolation junction strength

3.2 Method B—Testing Multiple Geogrid Ribs in Tension (kN/m or lbf/ft).

A relatively wide specimen is gripped across its entire width in the clamps of a constant rate of extension type tensile testing machine operated at a prescribed rate of extension, applying a uniaxial load to the specimen until the specimen ruptures. Tensile strength (kN/m or lbf/ft), elongation, and secant modulus of the test specimen can be calculated from machine scales, dials, recording charts, or an interfaced computer [3].

3.3 Method C—Testing Multiple Layers of Multiple Geogrid Ribs in Tension (kN/m or lbf/ft)

A relatively wide, multiple layered specimen is gripped across its entire width in the clamps of a constant rate of extension type tensile testing machine operated at a prescribed rate of extension, applying a uniaxial load to the specimen until the specimen ruptures. Tensile strength (kN/m or lbf/ft), elongation and secant modulus of the test specimen can be calculated from machine scales, dials recording charts, or an interfaced computer [3].

4. The used geogrids

With BS 8006, FHWA-SA-96-071, and independent certification of product characteristics by the British Board of Agreement, a sound base for the use of reinforcing products, whether flexible or stiff, is now available. A range of geogrid products with varying strength and made in different ways is now available from which users can select the product best suited to their purpose. The strength of the geogrids varies between 20 and 250 kN/m, and they are used in both road

constructions and reinforced slopes. Geogrids can be divided into two groups [9]:

Stiff geogrids, mostly high density polyethylene (HDPE) with a monolithic mesh structure.

Flexible geogrids, mostly polyethylene terephthalate (PET) with poly vinyl chloride (PVC) or acrylic coating with mechanically connected longitudinal and transverse elements.

The main design requirements for the use of geogrids in soil structures result from the geotechnical design. This includes the calculation of different failure modes resulting in requirements for: axial tensile design strength of the geogrid and maximum strain requirements in the geogrid [9].

In this work the stress-strain properties of various types of geogrids (seven types) manufactured in four different countries are investigated. The following types of geogrids have been employed in this work: Netlon CE121 and Tensar SS2, manufactured in Britain, a type of geogrid manufactured in Iraq and a type manufactured in China, SQ12, SQ15 and CE131 manufactured by Pars Mesh Polymer in Iran, Fig. 2 shows the types of geogrids.

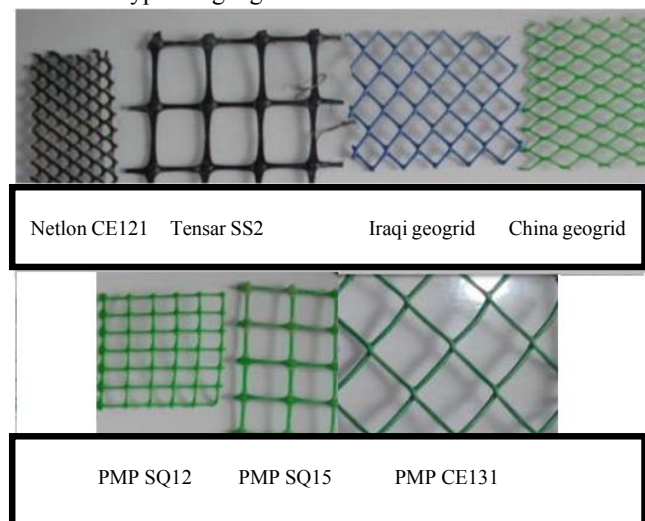


Figure 2: The various types of geogrids used in the work

5. Experimental Results

In the present work a large number of samples (90 samples) were tested by computer controlled electronic universal testing machine and this machine give the information as follow; peak tensile strength, modulus of elasticity, upper yield strength, lower yield strength, tensile strength, non-proportional extension strength, total extension strength, fracture elongation, elongation at maximum load and total elongation after completing test for each geogrid type. Figure 3 shows sample test using the computer controlled electronic universal testing machine and Fig. 4 demonstrates the information given from this testing machine.



Figure 3: Computer controlled electronic universal testing machine

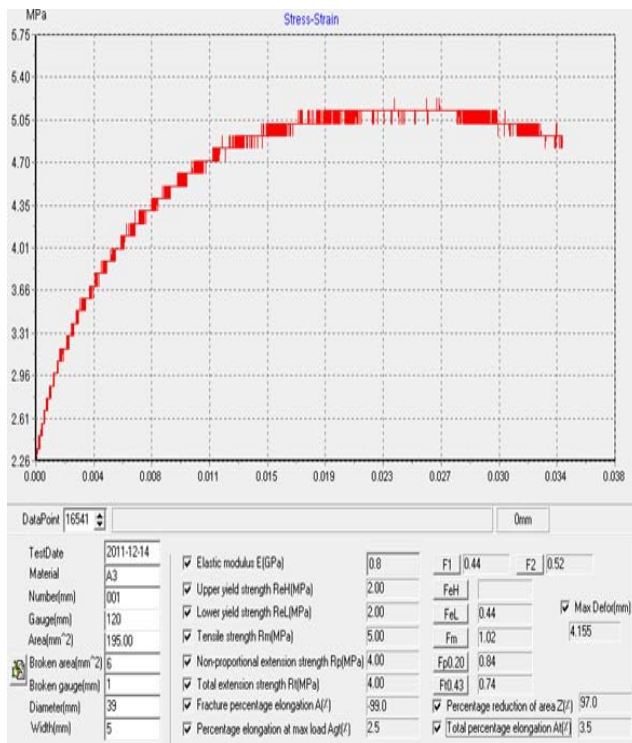


Figure 4: Information given after test from computer controlled electronic universal testing machine

The properties of the geogrids employed in this work are as follow;

Netlon CE 121

This geogrid was manufactured by the British Company Netlon ltd. The physical and the presently determined mechanical properties of this type of geogrid are summarized in Table 1. The results of single rib test, as determined in the present work, are shown in Figs. 5a and b.

Table 1: The physical and mechanical properties of Netlon CE121 geogrid

The physical properties		
Property	Data	
Mesh type	Diamond	
Standard color	Black	
Polymer type	HDPE	
Packaging	Rolls	
Dimensional Properties		
Property	Unit	Data
Aperture size(MD/XMD)	mm	6*8
Mass per unit area	g/m ²	740
Rib thickness	mm	1.6/1.45
Rib width	mm	2/2.75
Junction thickness	mm	2.75
Roll width	m	4
Roll length	m	50
The Mechanical Properties		
Peak Tensile Strength	kN/m	6.4
Elastic modules	GPa	0.39
Upper yield strength	MPa	5
Lower yield strength	MPa	5
Tensile strength	MPa	9
Non-proportional extension strength	MPa	6
Total extension strength	MPa	5
Fracture elongation	%	-99
Elongation at maximum load	%	6
Tota elongation	%	11

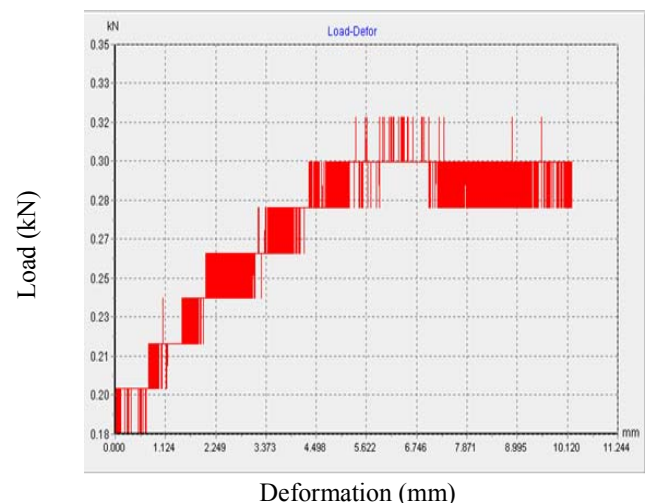
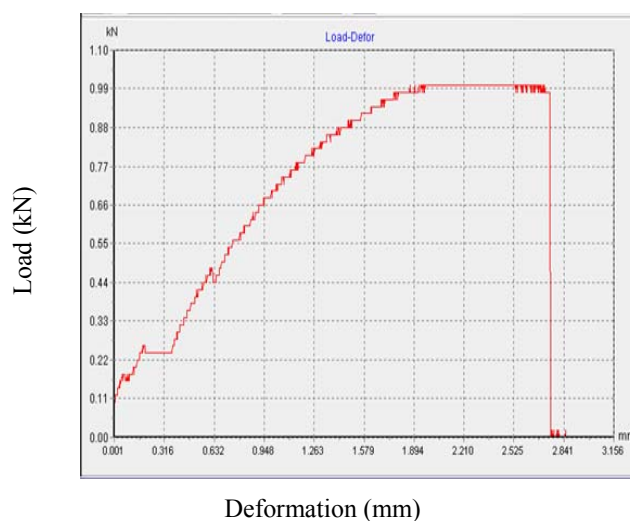
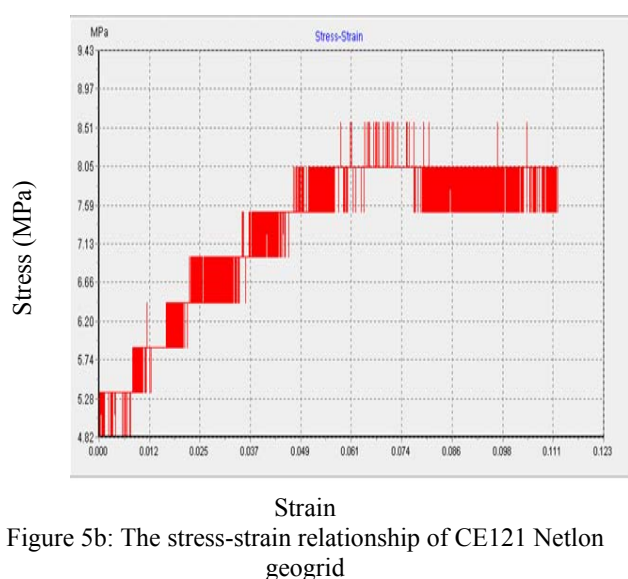


Figure 5a: The load-deformation relationship of CE121 Netlon geogrid

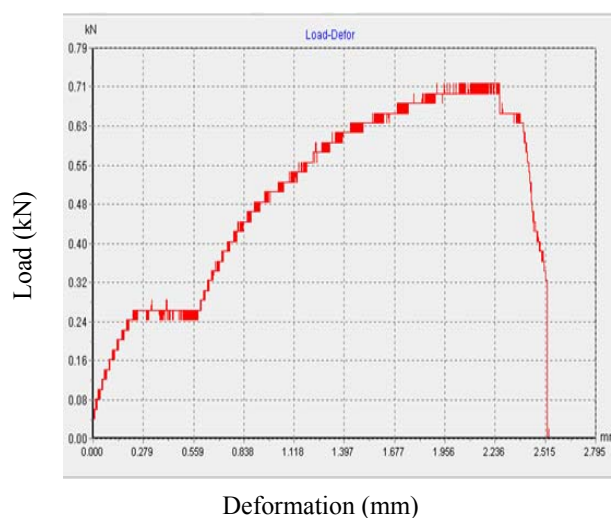
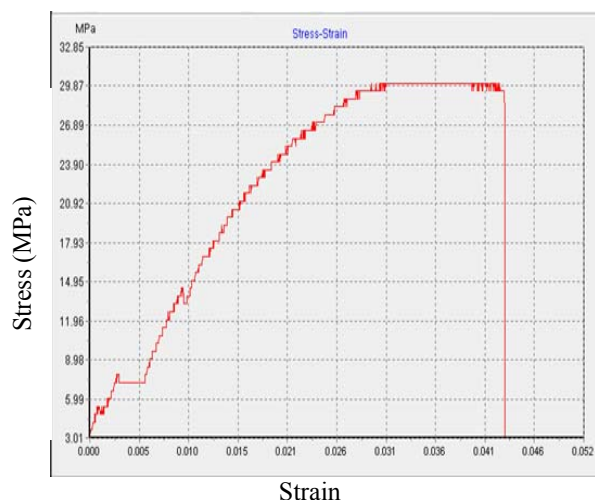


Tensar SS2

This geogrid was manufactured by the British Company Netlon ltd. The physical and the presently determined mechanical properties of this type of geogrid are summarized in Table 2. The results of single rib test, as determined in the present work, are shown in Figs. 6a, b, c and d.

Table 2: The physical and mechanical properties of Tensar SS2 geogrids

The physical properties		
Property	Data	
Mesh type	square	
Standard color	Black	
Polymer type	HDPE	
Packaging	Rolls	
Dimensional Properties		
Property	Unit	Data
Aperture size(MD/XMD)	mm	28/40
Mass per unit area	kg/m ²	0.3
Rib thickness MD/XMD	mm	1.2/1.1
Junction thickness	mm	3.9
Longitudinal rib width <i>lw</i>	mm	3
Transverse rib width <i>tw</i>	mm	3
Roll width	m	4
Roll length	m	50
The Mechanical Properties		
Peak Tensile Strength MD/XMD	kN/m	14.4/28.2
Elastic modules MD/XMD	GPa	0.57/0.99
Upper yield strength MD/XMD	MPa	1 /3
Lower yield strength MD/XMD	MPa	1/3
Tensile strength MD/XMD	MPa	24/30.7
Fracture percentage elongation MD/XMD	%	-98/-98
Percentage elongation at maximum load MD/XMD	%	3.5/2.9
Total percentage elongation MD/XMD	%	5/4.25



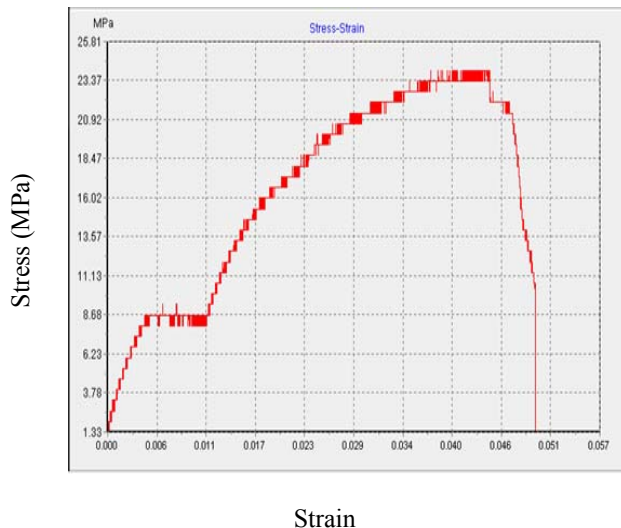


Figure 6d: The stress-strain relationship of Tensar SS2 geogrid in MD direction

The results of the present tests reasonably agree with results provided by the manufacturer, Tensar specification of geogrid SS2 in mechanical properties of single rib test. The results provided by the manufacturer are 17.5 kN/m and 31.5 kN/m for MD and XMD respectively, while the values from the single rib test of Tensar SS2 by computer controlled electronic universal testing machine are 14.4 and 28.2 kN/M for MD and XMD respectively. The percentages of agreement are 82.3% and 89.5 for MD and XMD respectively.

The Iraqi Geogrid

A geogrid product manufactured in Iraq is employed. The physical and presently determined mechanical properties are illustrated in Table 3. Figure 7a and b demonstrates the obtained stress-strain and load-deformation relationships.

Table 3: The physical and mechanical properties of Iraqi geogrid

The physical properties		
Property	Data	
Mesh type	Diamond	
Standard color	Blue	
Polymer type	HDPE	
Packaging	Rolls	
Dimensional Properties		
Property	Unit	Data
Aperture size	mm	21*18
Mass per unit area	g/m ²	255
Rib thickness	mm	1.4/2.25
Junction thickness	mm	3.3
Rib width	mm	1.6/2
Roll width	m	1.2
Roll length	m	30
The Mechanical Properties		
Peak Tensile Strength	kN/m	1.6

Elastic modules	GPa	0.083
Upper yield strength	MPa	0
Lower yield strength	MPa	0
Tensile strength	MPa	7.5
Fracture percentage elongation	%	-99
Percentage elongation at maximum load	%	9
Total percentage elongation	%	21.1

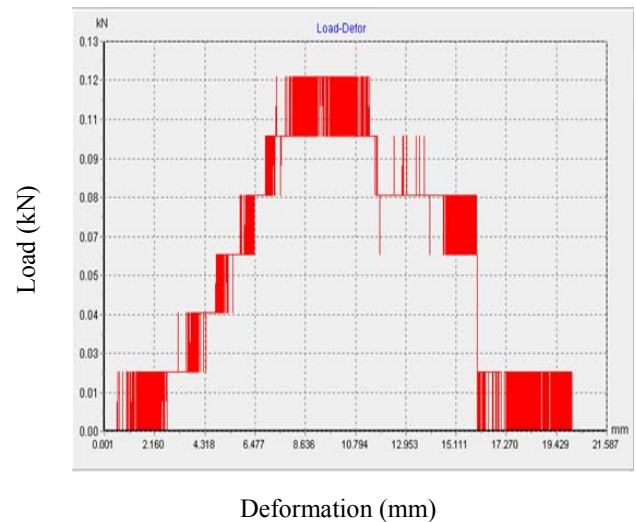


Figure 7a: The load-deformation relationship of Iraqi geogrid

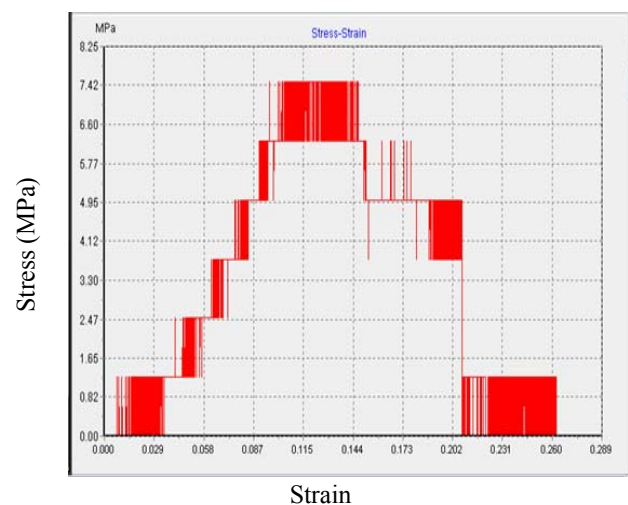


Figure 7b: The stress-strain relationship of Iraqi geogrid

The China Geogrid

A geogrid produced in China is employed. The physical and the presently determined mechanical properties are illustrated in Table 4. Figure 8a and b demonstrates the obtained stress-strain and load-deformation relationships.

Table 4: The physical and mechanical properties of China geogrid

The physical properties		
Property	Data	
Mesh type	Diamond	
Standard color	Green	
Polymer type	HDPE	
Packaging	Rolls	
Dimensional Properties		
Property	Unit	Data
Aperture size	mm	12*15
Mass per unit area	g/m ²	283
Rib thickness	mm	1.2/1.1
Junction thickness	mm	1.9
Rib width	mm	1.4/1.25
Roll width	m	1.2
Roll length	m	30
The Mechanical Properties		
Peak Tensile Strength	kN/m	1.1
Elastic modules	GPa	0.03
Upper yield strength	MPa	-----
Lower yield strength	MPa	-----
Tensile strength	MPa	6.5
Fracture percentage elongation	%	-99.5
Percentage elongation at maximum load	%	22.7
Total percentage elongation	%	31.9

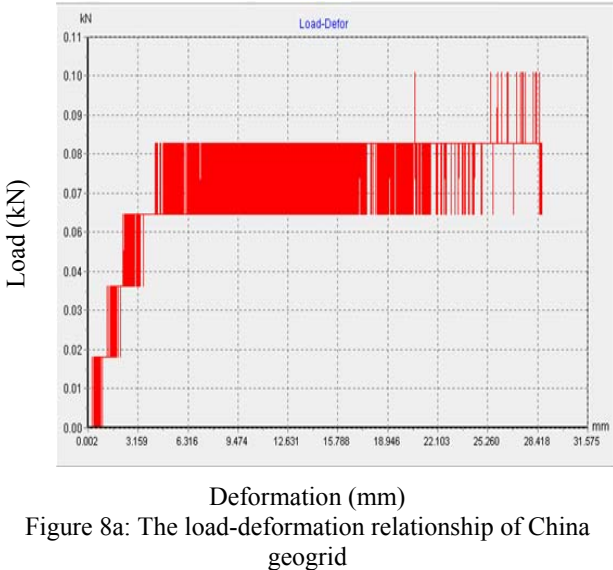


Figure 8a: The load-deformation relationship of China geogrid

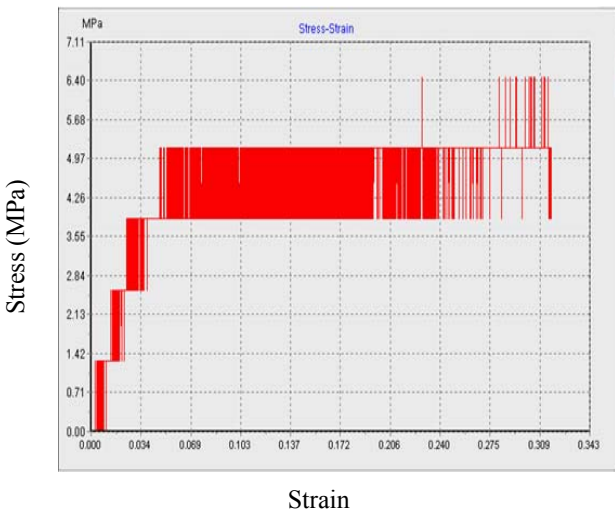


Figure 8b: The stress-strain relationship of China geogrid

PMP SQ12

This geogrid is manufactured by the Iranian company Pars Mesh Polymer. The physical and the presently determined mechanical properties of this geogrid are summarized in the Table 5. The results of single rib test, as determined in the present research are shown in Figs. 9a and b.

Table 5: The physical and mechanical properties of SQ12 geogrids

The physical properties		
Property	Data	
Mesh type	Square	
Standard color	Green	
Polymer type	HDPE	
Packaging	Rolls	
Dimensional Properties		
Property	Unit	Data
Aperture size	mm	12*12
Mass per unit area	g/m ²	318
Rib thickness	mm	1.7
Junction thickness	mm	1.6
Longitudinal rib width <i>lw</i>	mm	1.3
Transverse rib width <i>tw</i>	mm	1.6
Roll width	m	1.2
Roll length	m	30
The Mechanical Properties		
Peak Tensile Strength	kN/m	0.25
Elastic modules	GPa	0.28
Upper yield strength	MPa	-----
Lower yield strength	MPa	-----
Tensile strength	MPa	2
Fracture percentage elongation	%	-99.5
Percentage elongation at maximum load	%	1
Total percentage elongation	%	5.5

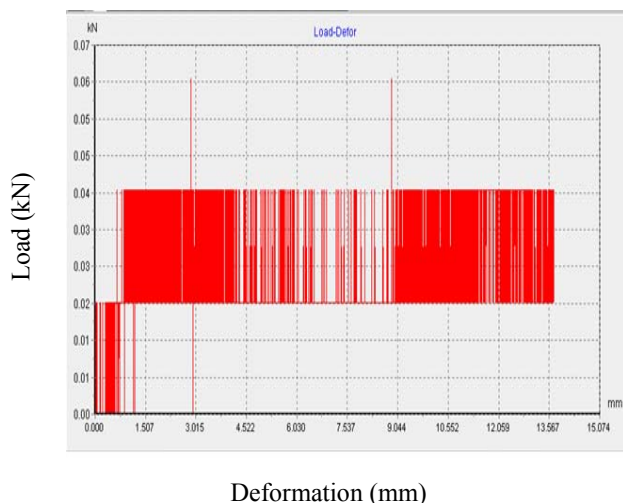


Figure 9a: The load-deformation relationship of SQ12 geogrid

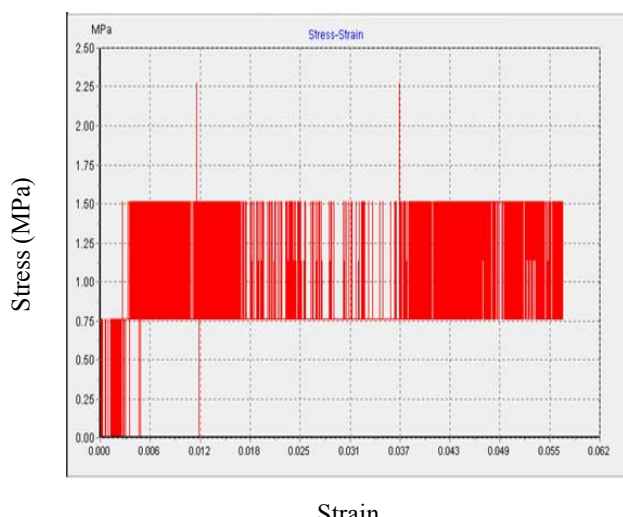


Figure 9b: The stress-strain relationship of SQ12 geogrid

PMP SQ15

This geogrid is manufactured by the Iranian company Pars Mesh Polymer. The physical and the presently determined mechanical properties of this geogrid are summarized in Table 6. The results of single rib, as determined in the present tests are shown in Figs. 10a and b.

Table 6: The physical and mechanical properties of SQ15 geogrids

The physical properties	
Property	Data
Mesh type	Square
Standard color	Green
Polymer type	HDPE
Packaging	Rolls
Dimensional Properties	

Property	Unit	Data
Aperture size	mm	24*24
Mass per unit area	g/m ²	385
Rib thickness	mm	2
Junction thickness	mm	3.3
Longitudinal rib width l_w	mm	2.5
Transverse rib width t_w	mm	2.2
Roll width	m	1.2
Roll length	m	20
The Mechanical Properties		
Peak Tensile Strength	kN/m	2.41
Elastic modulus	GPa	0.12/0.54
Upper yield strength	MPa	----/----
Lower yield strength	MPa	----/----
Tensile strength	MPa	2
Fracture percentage elongation	%	-9%
Percentage elongation at maximum load	%	0.0
Total percentage elongation	%	2

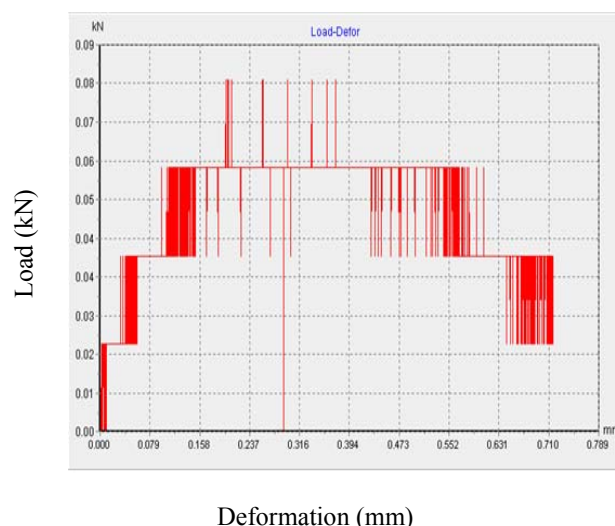


Figure 10a: The load-deformation relationship of SQ15 geogrid

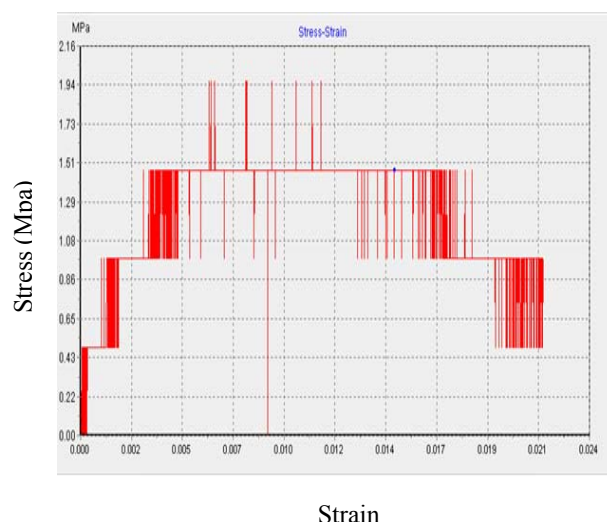


Figure 10b: The stress-strain relationship of SQ15 geogrid

PMP CE131

This geogrid is manufactured by the Iranian company Pars Mesh Polymer. The physical and the presently determined mechanical properties of this geogrid are summarized in Table 7. The results of single rib test, as determined in the present research are shown in Figs. 11a and b.

Table 7: The physical and mechanical properties of CE131 geogrids

The physical properties		
Property	Data	
Mesh type	Square	
Standard color	Green	
Polymer type	HDPE	
Packaging	Rolls	
Dimensional Properties		
Property	Unit	Data
Aperture size	mm	34*34
Mass per unit area	g/m ²	429
Rib thickness	mm	2.8
Junction thickness	mm	5
Longitudinal rib width <i>lw</i>	mm	3.1
Transverse rib width <i>tw</i>	mm	3.1
Roll width	m	1.2
Roll length	m	30
The Mechanical Properties		
Peak Tensile Strength	kN/m	1.92
Elastic modules	GPa	0.3 [†]
Upper yield strength	MPa	-----
Lower yield strength	MPa	-----
Tensile strength	MPa	1
Fracture percentage elongation	%	-9^,0
Percentage elongation at maximum load	%	1.5
Total percentage elongation	%	8.5

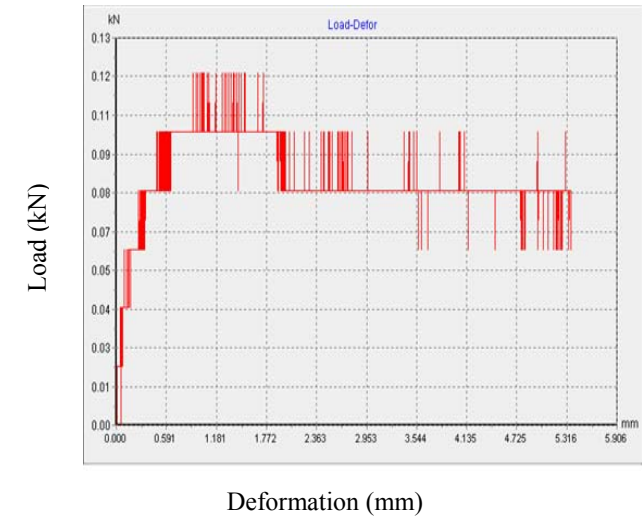


Figure 11a: The load-deformation relationship of CE131 geogrid

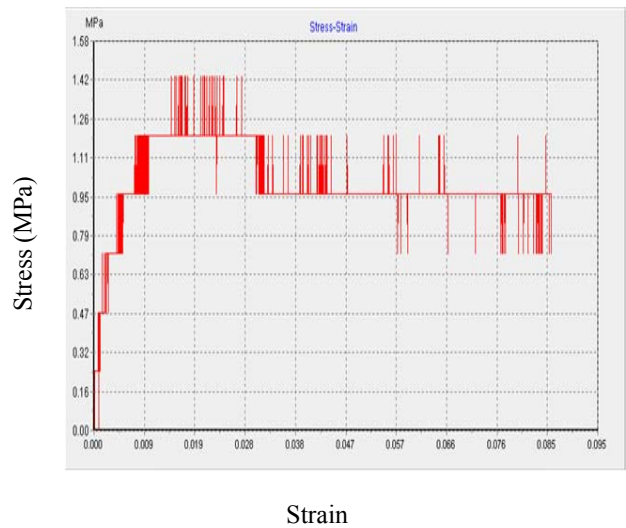


Figure 11b: The stress-strain relationship of CE131 geogrid

6. Discussion of test results

This study was carried out to investigate the parameters that govern the behavior of geogrids. The most significant results obtained from the present work are summarized in Table 8. It is obvious that Tensar SS2 and Netlon CE121 possess the higher tensile strength and modulus of elasticity. All other geogrids may be used for temporary structures or where modest strength is accepted.

Table 8: Results of various geogrids

Geogrid type	Peak tensile strength MD/XMD (kN/m)	Modulus of elasticity MD/XMD (GPa)	Rib Thickness MD/XMD (mm)	Mass per unit area (g/m ²)	Rib width <i>Lw/tw</i> (mm)
Netlon CE121	6.4	0.39	1.6/1.45	740	2/2.75
Tensar SS2	14.4/28.2	0.57/0.99	1.2/1.1	300	3/3
Iraqi geogrid	1.6	0.083	1.4/2.25	255	1.6/2
China geogrid	1.1	0.03	1.2/1.1	283	1.4/1.25
PMP SQ12	0.25	0.28	1.7	318	1.3/1.6
PMP SQ15	2.41	0.12/0.54	2	385	2.5/2.2
CE131	1.92	0.32	2.8	429	3.1/3.1

7. CONCLUSION

Based on this experimental study the following conclusions may be drawn:

- 1- The geogrids Netlon CE121 and Tensar SS2 have tensile strength and elastic modulus higher than other geogrids made by different manufactures.
- 2- The tensile strength and elastic modulus are not dependent on the density of materials but dependent on type of polymer used and method of manufacture.
- 3- The dimensional properties such as rib thickness, junction thickness, longitudinal and transverse rib width of geogrid play important role in the mechanical properties such as tensile and elastic modulus.
- 4- The effect of tensile strength and stiffness is more significant than elastic modulus when geogrids are used as reinforcement in the soil.

8. ACKNOWLEDGMENTS

The experimental part of the work was conducted in the laboratory of Materials Engineering Department in College of Engineering of Kufa University. Special thanks are presented to Dr. Ali Sabaa Hummoud, the chairman of Materials Engineering Department and deepest wishes to Miss. Batool Hatim, responsible on laboratory of materials engineering.

9. REFERENCES

- [1] Hoe I. Ling, "Civil and Environmental Applications of Geosynthetics," Reinforced Soil Engineering. Advances in Research and Practice, 4th ed. vol. 1, Hoe I. Ling, Dov Leshchinsky and Fumio Tatsuoka, Ed. Library of Congress Cataloging: Publisher's, 2003, pp. 14-31.
- [2] Robert M. Koerner, Designing with Geosynthetics, Library of Congress Cataloging: Publisher's, 2005, Ch. 3.
- [3] ASTM D6637-01-2009, "Standard Test Method for Determining Tensile Properties of Geogrids by the Single or Multi-Rib Tensile Method".
- [4] Colin JFP Jones, Earth Reinforcement and Soil Structure, British Library Cataloging: Publisher's, 1985, Ch. 5.
- [5] Robert M. Koerner and Joseph P. Welsh, Construction and Geotechnical Engineering Using Synthetic Fabrics, Library of Congress Cataloging: Publisher's, 1980, Ch. 4.
- [6] Al-Omari, R.R., AL-Dobaissi, H.H. and Al-Wadood, B.A. "Inextensible geomesh included in sand and clay". Proceedings, International Symposium on Prediction and Performance in Geotechnical Engineering, Calgary, 1987, pp. 155-160.
- [7] Al-Omari, R.R. & Hamodi F. J. "Swelling Resistant Geogrid- A new Approach for the Treatment of Expansive Soils" J. of Geotextiles and Geomembranes, 1991, , pp. 295-317.
- [8] Al-Omari, R.R., Nazhat, Y.N. & AL-Dobaissi, H.H. "Effect of Stiffness and Amount of Reinforcement on Strength of Sand" J. of Engineering Geology, 1995, pp. 363-367.
- [9] Voskamp W." Performance Properties of Geogrids" Reinforced Soil Engineering. Advances in Research and Practice, 4th ed. vol. 1, Hoe I. Ling, Dov Leshchinsky and Fumio Tatsuoka, Ed. Library of Congress Cataloging: Publisher's, 2003, pp. 32-48.

Modeling the Swelling strain and pressure of Weak Rock using Adaptive Network-Based Fuzzy Inference System

Ramin Doostmohammadi
Mining Engineering Department, University of Zanjan, Iran

ABSTRACT

Some of civil engineering projects (such as dam construction, excavation of road way tunnels) or mining projects (such as underground excavation of coal and gypsum ores) are performed in vicinity of weak rocks with swelling potential. Therefore, the swelling strain and swelling pressure of such rocks can develop under different boundary conditions, simultaneously. This paper uses the information of swollen clay content and different boundary stiffness in combination with Adaptive Network-Based Fuzzy Inference System (ANFIS) to predict the swelling pressure and strain of weak rock. The result of this method is compared with the previously presented method, Artificial Neural Network (ANN). Differing from ANN, ANFIS is transparent rather than a black box.

Keywords: Swelling strain, swelling pressure, Adaptive Network-Based Fuzzy Inference System

1. INTRODUCTION

In an excavation without any support system, swelling rock moves inside and causes problems associated with reduced cross sectional area. When excavation is reinforced by support systems, swelling will usually cause considerable damages to the support system. The pressure from swelling rocks to the support system and lining of underground openings has been the focus in recent years.

Basma et al. (2000) implemented ANNs for modeling the time dependent swelling of expansive soils [1]. They attempted to implement sequential ANN for modeling the time dependent swelling strain of expansive soils. Soil samples with varying properties were selected and tested for expansion under three different initial applied pressures (25, 100, and 200 kPa) to develop the database used for training and testing the neural network. The input parameters used in the network included the soil initial dry unit weight, water content, initial applied pressure, percent clay content, plasticity index and the percent swell at time i . Different models based on the ANN approach were developed for determination of the swelling parameters of some clayey soils present in the Oltrepo Pavese area by Meisina and Najjar (2004). Some models were developed to estimate the swelling pressure and others were employed to estimate the swelling strain. A different number of variables (atterberg limit, clay content, methylene blue absorption, water content, dry density and soil suction) were selected to represent the inputs for the models [2]. Moosavi et al. (2006) modeled the cyclic swelling behavior of mudstone using ANNs. Each sample has its own swell model and a general model for all studied samples is lacking. The duration of a swelling cycle is divided to twelve equal points. The swell pressure of a desired point is

predicted according to its four previous points [3]. In a recent research, Doostmohammadi et al. (2008) have used ANN for predicting the swelling strain and pressure of mudstone under different boundary conditions [4]. The input data for their model are the result of some standard laboratory tests that have been proposed by ISRM and Madsen [5]-[6]-[7].

2. SWELLING TESTS AND SAMPLE CHARACTERIZATION

Mudstone cores for experimental study were obtained from drilled holes at Masjed-Soleiman Underground hydroelectric power plant (UHEPP). Table 1 shows the mineral composition of six samples taken from mudstone at different locations of Power House Cavern (PHC).

2.1 Free swelling strain test

This test is intended to measure the swelling strain developed when an unconfined, undisturbed rock specimen is immersed in water [7]. Such conditions happen in ground surface and shallow trenches. Some results of this test on mudstone samples are shown in Fig.1.

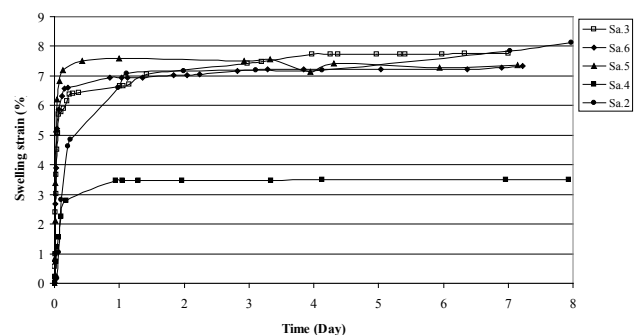


Fig.1. The result of the free swelling tests for mudstone samples

Table 1. The mineralogy of mudstone samples.

Sample number	Sa.1	Sa.2	Sa.3	Sa.4	Sa.5	Sa.6
Montmorillonite (%)	5.9	3.6	3	2.8	3.8	2.5
Illite (%)	4.2	8.2	8.5	5.5	10.3	7.6
Kaolinite (%)	7.9	3.6	0	2.8	3.4	4.1
Chlorite (%)	8.8	6.4	4.5	5.6	7	2.7
Quartz (%)	11.3	10.3	14.2	15.25	12.1	18
Feldspar (%)	10.2	12.5	6	3.4	3.4	3.1
Calcite (%)	36.9	39.8	48.7	49.6	49.6	49.7
Dolomite (%)	14.8	15.6	15.1	15.05	10.4	12.3

2.2 Semi confined swelling strain test

This test is intended to measure the axial swelling strain under a constant axial load of a radially confined, undisturbed rock specimen when immersed in water [7]. Examples of such conditions are tunnel invert or swelling ground under foundations. Some results of this test on mudstone samples are shown in Fig. 2.

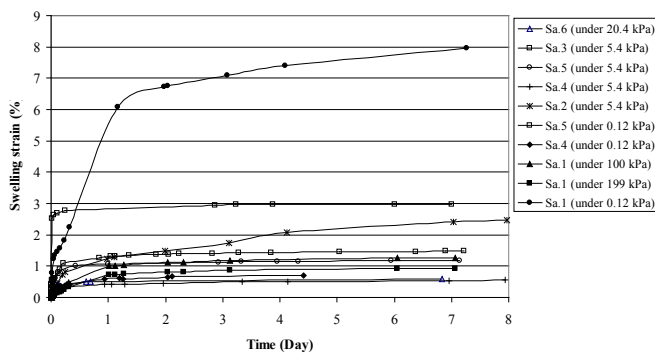


Fig.2. The result of the semi confined swelling strain test for mudstone samples

2.3 Swelling pressure test

This test is intended to measure the pressure necessary to constrain an undisturbed rock specimen at constant volume when it is immersed in water [7]. Such conditions happen in lined tunnels containing swelling rock beds. Some results of this test on mudstone samples are shown in Fig. 3. The high swelling pressure is referred to osmotic or double layer swelling as reported by seedsman [8].

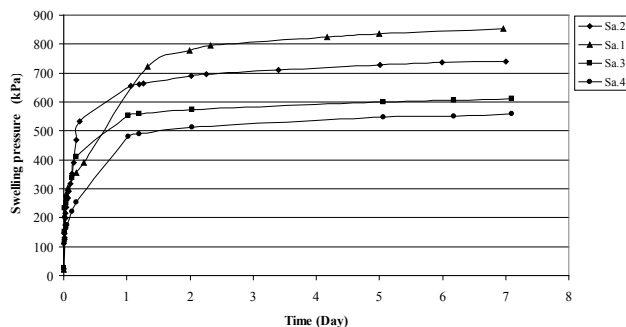


Fig.3. The result of the swelling pressure test

2.4 Semi confined swelling strain and pressure test

This test is intended to measure the axial swelling strain and pressure of specimen in contact of deformable axial boundary condition. An example of such conditions is the roof of tunnels supported by deformable reinforcements. Some results of this test on mudstone samples are shown in Fig.4 and Fig.5.

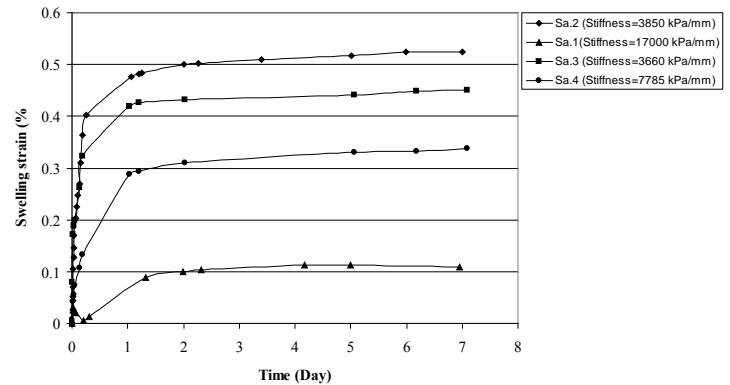


Fig.4. The result of the variation of the swelling strain under constant axial stiffness

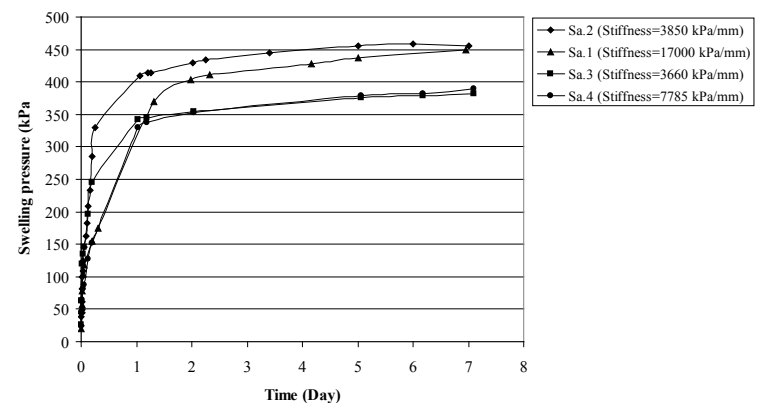


Fig.5. The result of the variation of the swelling pressure under constant axial stiffness

3. DEVELOPMENT OF ANFIS FOR MODELING THE SWELLING POTENTIAL

3.1 Concept of ANFIS

The fuzzy logic approach is based on the linguistic uncertain expression rather than numerical uncertainty. The main problem with this approach is that there is no systematic procedure for a design of fuzzy controller. Basically a fuzzy inference system (FIS) is composed of five functional blocks (Fig. 6).

- A rule base containing a number of fuzzy if-then rules;
- A database which defines the membership functions of the fuzzy sets used in the fuzzy rules;
- A decision-making unit which performs the inference operation on the rules;

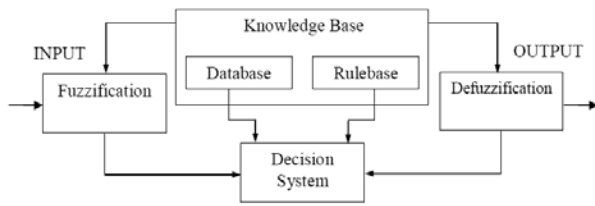


Fig.6. The general structure of the fuzzy Inference System

- A defuzzification interface which transform the fuzzy results of the inference into a crisp output.

Jang (1993) introduced a novel architecture and learning procedure for the FIS that uses a neural network learning algorithm for constructing a set of fuzzy if-then rules with appropriate membership functions from the stipulated input-output pairs. This procedure of developing a FIS using the framework of adaptive neural networks is called an adaptive network-based fuzzy inference system [9].

ANFIS is a Sugeno-type FIS. The general structure of the ANFIS is presented in Fig.7. It is assumed that the FIS has two inputs x and y and one output z . suppose that the rule base contains two fuzzy if-then rules of Takagi and sugeno's type:

If x is A_1 and y is B_1 Then $f_1 = p_1 \cdot x + q_1 \cdot y + r_1$ (1)

If x is A_2 and y is B_2 Then $f_2 = p_2 \cdot x + q_2 \cdot y + r_2$ (2)

Where A_1, A_2 and B_1, B_2 are the membership functions for inputs x and y , respectively; p_1, q_1, r_1 and p_2, q_2, r_2 are the parameters of the output function. Fig.7(a) illustrates the fuzzy reasoning mechanism for this Sugeno model to derive an output function (f) from a given input vector $[x, y]$. The corresponding equivalent ANFIS architecture is presented in Fig.7(b), where nodes of the same layer have similar functions. The functioning of the ANFIS is as follows:

Layer 1: Each node in this layer generates membership grades of an input variable. The node output OP_i^1 is defined by:

$$OP_i^1 = \mu_{A_i}(x) \text{ for } i=1, 2 \quad (3)$$

$$OP_i^1 = \mu_{B_{(i-2)}}(y) \text{ for } i=3, 4 \quad (4)$$

Where x (or y) is the input to the node; A_i (or B_{i-2}) is a fuzzy set associated with this node, characterized by the shape of the MFs in this node and can be any appropriate functions that are continuous and piecewise differentiable such as Gaussian, generalized bell, trapezoidal and triangular shaped functions.

Layer 2: Every node in this layer multiplies the incoming signals.

Layer 3: The i th node of this layer, labeled as N_i , computes the normalized firing strengths.

Layer 4: Node i in this layer computes the contribution of the i th rule towards the model output, with the following node function:

$$OP_i^4 = \bar{w}_i f_i = \bar{w}_i (p_i x + q_i y + r_i) \quad (5)$$

where \bar{w}_i is the output of layer 3 and $\{p_i, q_i, r_i\}$ is the parameter set.

Layer 5: The single node in this layer computes the overall output of the ANFIS as:

$$OP_i^5 = \text{Overall_output} = \sum_i \bar{w}_i f_i = \frac{\sum_i w_i f_i}{\sum_i w_i} \quad (6)$$

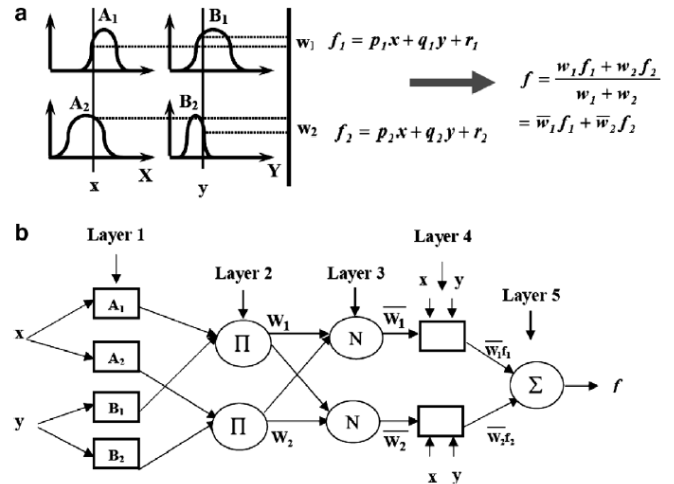


Fig.7. Schematic of fuzzy and neurofuzzy paradigm: (a) fuzzy inference system and (b) equivalent ANFIS architecture

The parameters for optimization in an ANFIS are the premise parameters $\{a_i, b_i, c_i\}$, which describe the shape of the MFs, and the consequent parameters $\{p_i, q_i, r_i\}$, which describe the overall output of the system. The basic learning rule of an adaptive network, the back propagation algorithm which is based on the gradient descent rule, can be successfully applied to estimate these parameters[10].

3.2 ANFIS model development

The swell potential tests according to part 3 were performed to develop and assess the ANFIS model. Swelling potential tests including 354 data points are used for training (283 data

Table 2. Maximum swelling strain and pressure using ANFIS and ANN models

	Maximum swelling strain(%)			Maximum swelling pressure(kPa)		
	Real Data	ANN	ANFIS	Real Data	ANN	ANFIS
Test 1	0.45	0.49	2.06	382	448	546
Test2	0.001	0.001	0.00	737	730	607

Table 3. Correlation coefficient and error in predication of swelling strain and pressure

	Time dependent swelling strain(%)				Time dependent swelling pressure(kPa)			
	Error		Correlation coefficient		Error		Correlation coefficient	
	ANN	ANFIS	ANN	ANFIS	ANN	ANFIS	ANN	ANFIS
Test 1	0.102	3.57	0.963	0.845	0.174	0.43	0.984	0.960
Test 2	0.00	1.00	0.998	0.998	0.0095	0.176	0.978	0.954

points) and testing (71 data points) the model. The training and testing data points include 80% and 20% of the total data points are selected randomly from the total data points.

The input parameters are selected according to the important affecting factors in swelling potential and boundary conditions. Five parameters are considered for modeling the swelling potential: time at which swell potential is measured, stiffness in radial direction, percentage of swollen clays (montmorillonite) content, initial dead pressure in axial direction and stiffness in axial direction. The output parameters are swelling strain and swelling pressure.

In the present study, two triangular membership functions have been assigned to each input variable. Each input variable is classified into two fuzzy categories with linguistic attributes. The initial values of the premise parameters are set in such a way that the centers of the MF are equally spaced along the range of each input variable.

The model structure is implemented using the fuzzy logic toolbox of MATLAB software package.

The hybrid algorithm used in the present study for optimizing the parameters allows a fast identification of parameters and substantially reduces the time needed to reach convergence. Fig.8 shows the final MFs for ANFIS pressure model after training.

The ANFIS model is tested using a matrix of 71 samples obtained from different laboratory testing groups. These data points were not used in training the model. The ANFIS model is used to predict the swelling strain and pressure. The real and predicted maximum strain and pressure for two test dataset are presented in Table 2.

The performance of the ANFIS model is evaluated by statistical indexes and is compared to that of ANN method. The error and correlation coefficient are determined as follows:

$$Error = \left(\frac{1}{N} \sum_{i=1}^N (x_i - y_i)^2 \right)^{\frac{1}{2}} \quad (7)$$

$$Corr = \frac{\sum_{i=1}^N (x_i - \bar{x}) \cdot (y_i - \bar{y})}{\left(\sum_{i=1}^N (x_i - \bar{x})^2 \cdot \sum_{i=1}^N (y_i - \bar{y})^2 \right)^{\frac{1}{2}}} \quad (8)$$

Where \bar{x} =forecasted values, \bar{y} =measured values, \bar{x} =mean of forecasted values, \bar{y} =mean of measured values and N= number of data points.

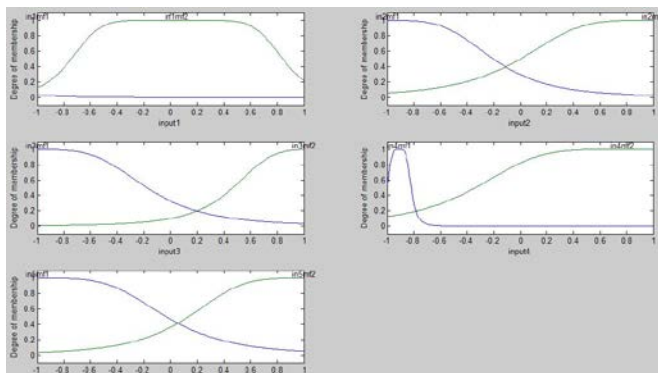


Fig.8. Final MFs for swelling pressure after training

The correlation coefficient and error for predicted strain and pressure using ANFIS and ANN model are presented in Table 3, also.

It is observed that ANFIS predicts the swelling potential with higher error and lower correlation coefficient in comparison with ANN.

4 CONCLUSIONS

a) The results of standard swelling potential tests are correlated using ANFIS method. The ANFIS uses the time at which swell potential is measured, stiffness in radial direction, percent of swollen clay content, initial dead pressure in axial direction, stiffness in axial direction as input parameters to develop the model. It was shown that ANFIS model can be employed to simulate the swelling potential of mudstone.

b) The proposed model can be used to determine the swelling response of rocks under different boundary conditions (free radial boundary, rigid radial boundary, free axial boundary, rigid axial boundary and deformable axial boundary). The result of this model can be applied to predict the interaction of swelling rocks and support systems in underground excavations which usually have argillaceous boundaries.

c) The difference in the maximum swelling strain obtained from the two methods is large as given in table 2. It has been observed that ANN (which has been found in literature) outperforms ANFIS. Differing from ANN, ANFIS is transparent rather than a black box.

4. REFERENCES

- [1] Basma AA, Barakat SA, Omar M, "Modeling time dependent swell of clays using sequential artificial neural networks," *Environmental & Engineering Geoscience*, Vol.9, 2003, pp.279-288.
- [2] Meisina C, Najjar Y, "Assessing the swelling /shrinkage potential of Italian soils via neural network approach, " *Proceeding of 9th Symposium on Numerical Models in Geomechanics*, 2004, pp.187-193.
- [3] Moosavi M, Yazdanpanah MJ, Doostmohammadi R, "Modeling the cyclic swelling pressure of mudrock using artificial neural network," *Engineering Geology*, Vol.87, 2006, pp.178-194.
- [4] Doostmohammadi R, Moosavi M, Araabi BN, "Modelling time dependent swelling potential of mudrock using laboratory tests and artificial neural network," *Mining Technology*, Vol.117, 2008, pp.32-41.
- [5] ISRM, "Characterisation of Swelling Rock," Pergamon Press, 1983, pp. 49-75.
- [6] ISRM, "Suggested methods for laboratory testing of argillaceous swelling rocks," *International Journal of Rock Mechanics and Mining Sciences and Geomechanics Abstracts*, Vol. 26, 1989, pp.415-426.
- [7] Madsen FT, "Suggested methods for laboratory testing of swelling rocks", *International Journal of Rock Mechanics and Mining Sciences and Geomechanics Abstracts*, Vol.36, 1999, pp.211-225.
- [8] Seedsman RW, "Comprehensive rock engineering. characterizing clay shales," Vol. 3, John A. Hudson: Pergamon Press, 1993, chap.7, pp. 151-164.
- [9] Jang JSR, "ANFIS: Adaptive network based fuzzy inference system," *IEEE Trans Syst Man Cybernet*, Vol.23, 1993, pp.665-83.
- [10] Jang, JSR, Sun, CT, "Neurofuzzy modeling and control," *Proceeding of IEEE*, 1995, pp. 378-406.

Centrifuge Modeling Of Reinforced Embankments On Soft Foundation

Ali Sobhanmanesh¹, Nurly Gofar²
University Teknologi Malaysia, Malaysia

ABSTRACT

A series of centrifuge tests were fulfilled at small centrifuge equipment of national university of Malaysia (UKM) on reinforced and unreinforced embankments built over soft and stiff foundations to observe the effect of reinforcement, investigate the reinforcement mechanism and deformation behavior of models. Five different cases were analyzed based on different strength of foundation and embankment soil. A proper textile used as a reinforcement material and clayey-sand used as fill material. Kaolin and dry sand used as soft and stiff foundations respectively. The results show that surface settlement and deformation behavior of reinforced models are changed and reduced significantly compare to unreinforced models.

Keywords: Reinforced Embankment, Centrifuge test, Soft foundation

1. INTRODUCTION

Many embankments constructed on soft grounds are susceptible to failure and large settlements [1]. These stability problems of embankments on soft soils occur due to high compressibility and low shear strength of soil. Many of the ground improvement techniques, which have been used in the past to increase the shear strength of the soil, are time-consuming and uneconomical. Hence an alternative method such as soil reinforcing by geosynthetics is needed to solve this problem. The emergence of geosynthetic reinforcement in recent times has revolutionized the concept of ground improvement. The idea behind this technique is to make use of the tensile strength of the reinforcement to limit the spreading of the embankment and lateral displacement of the soft foundation [2]. Although geosynthetics have been widely used in practice to improve the stability of various geotechnical projects, the reinforcement mechanisms are still far from clear [3], so designing an embankment on a soft soil still raises several concerns related to the weak geotechnical properties of the soft soil. In recent years, there have been a series of centrifuge tests conducted on scaled-down geosynthetics-reinforce structures to investigate the reinforcement mechanisms.

This paper deals with the study of settlement and deformation behavior of reinforced and unreinforced embankments subjected to accelerate gravity conditions in small beam centrifuge at the department of geology of Universiti Kebangsaan Malaysia (UKM). Series of centrifuge tests have been conducted by varying the characteristics of foundation soil material.

2. Centrifuge Modeling

Reduced scale models are economical and timesaving alternatives to full scale testing. Centrifuge model testing is an example of small-scale models and is a useful tool in the investigation of geotechnical problems because of its ability to reproduce the same stress levels in a small-scale model as those present in a full-scale prototype [2].

The focus of this paper is on geotextile reinforced embankment and its deformation behavior is highly influenced by the presence of prototype stress conditions and it is possible to achieve those levels of stresses in the laboratory with the help of centrifuge modeling technique [4].

2.1 Description of small geotechnical centrifuge

Centrifuge tests were carry out with small geotechnical centrifuge apparatus at department of geology, faculty of Science and technology FST, national university of Malaysia (UKM), under the supervision of associated professor Dr. Wan Zuhairi Wan Yaacob.

The apparatus is a small-size beam-type centrifuge, designed to allow centrifuge testing of soil package up to 6Kg with a maximum rotational speed of 500rpm and can accelerate up to 140 in units of times gravity at an effective radius of 0.5 m. The capacity of the small geotechnical centrifuge is 0.84 *g-ton* machine (140 *g* x 0.6 kg). For observing the performance of model during the test, the centrifuge apparatus is equipped with colored digital video camera and high-speed stroboscope. The recorded of moving images can be stored directly into the computer. Real time video images can also be observed on the LCD monitor installed in the operation room.

An overall view of centrifuge apparatus and its equipment is shown in Fig. 1.

¹PhD Candidate, department of civil engineering, University Teknologi Malaysia

²Associate professor, department of civil engineering, University Teknologi Malaysia



Fig. 1. Overall view of small geotechnical centrifuge apparatus.

2.2 Test Box

The soil sample box with dimensions of 28cm (length) x 10cm (width) x 19.5cm (height) was placed in a strongbox that was fixed to the centrifuge arm. The strongbox constructed with aluminum walls and Perspex at the front to allow the sample to be seen during the test. To adjust the balance during the flight a counterweight was placed at the opposite centrifuge arm (Fig. 2). The front wall Perspex allows viewing and measuring the settlements and deformations of models after each test. To monitor the soil settlement during testing, a sketch of embankment and foundation layers were drawn on the front surface of the model specimens [5].

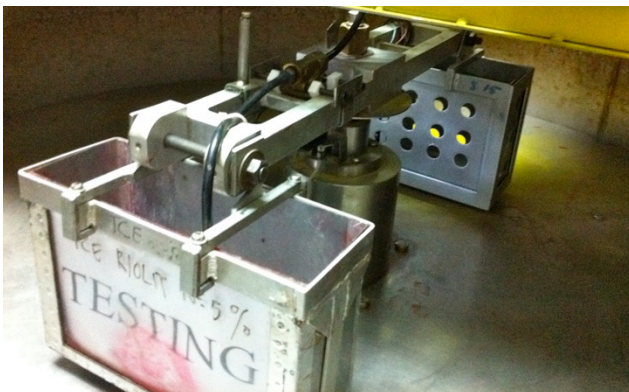


Fig 2. Small-sized beam- type centrifuge

Details of the small geotechnical centrifuge are shown in Table 1.

Table I. Specification of small geotechnical centrifuge

Parameter	Value
Package volume	290mm x 100mm x 195mm
Package mass	6 kg
Drive Power	600 W
Rotational speed	80 to 500 rpm
Radius at base package	0.5 m
Acceleration	3 to 140 g
Centrifuge capacity	0.84 g-ton

2.3 Centrifuge models

In this research study, five distinct models base on different conditions of embankment/foundation and different conditions of reinforcement are tested in centrifuge apparatus.

□ Case I: Stiff embankment on soft soil foundation (Clay/Kaolin).

□ Case II: Unreinforced soft soil embankment (Clayey sand) on stiff soil foundation (Compacted sand).

Case III: Unreinforced soft soil embankment (Clayey sand) on soft soil foundation (clay/kaolin).

Case IV: Reinforced soft soil (clay/kaolin) embankment on stiff soil (Compacted sand).

Case V: Reinforced soft soil (clayey sand) embankment on soft soil foundation (clay/kaolin).

The general condition of each case is listed in Table II. In four models clayey-sand is used as fill material and in one model a wooden embankment is used to simulate a stiff rigid embankment. Compacted sand was modeled as hard soil foundation while the consolidated kaolin was modeled as soft soil foundation. Three models are unreinforced and two models are reinforced with textile.

The scaled-down centrifugal embankment has a height of 5cm, a crest width of 14cm and slope of 1V to 1H, underlain by a soft kaolin foundation of 7cm thickness. Due to inherent symmetry about the centerline, only one half of the structure was modeled. Sectional view of model is shown schematically in fig. 3.

Table II. Condition of embankments and foundations in centrifuge tests

NO.	Foundation	Fill Material	Reinforcement
1	Kaolin	Wooden block	-
2	Sand	Clayey-Sand	-
3	Kaolin	Clayey-Sand	-
4	Sand	Clayey-Sand	Textile
5	Kaolin	Clayey-Sand	Textile

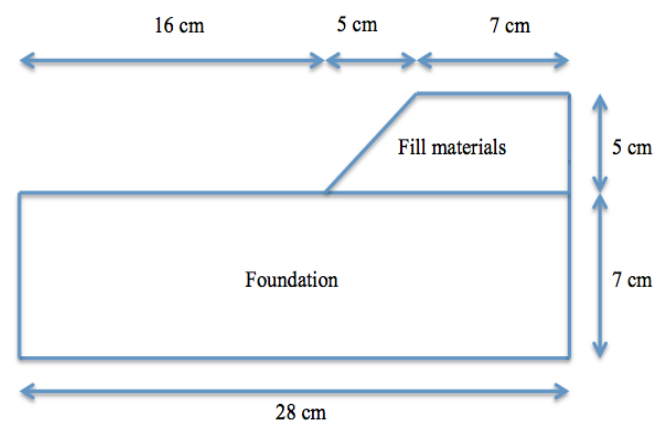


Fig. 3. Sectional view of embankment model

3. Model Preparation

3.1 Foundation Material

For soft foundation models, kaolin was mixed with an amount of water to obtain the moisture content of 31% (between optimum moisture content and liquid limit) and then placed in the test box to a thickness of a little bit higher than 7 cm. The kaolin layer in the test box was rotated using the centrifuge rotation speed of 50g for about 1 hour to consolidate and produce homogenous soft soil. At this condition, the undrained shear strength of kaolin was found to be 14 kPa, tested by mini vane shear equipment.

For models with stiff foundation soil, dry sand was poured into sample box using raining technique and then rotated about 30 minutes with the speed of 50g. Table III and IV show the properties of kaolin and sand. The properties of the geotextile were obtained from tensile strength test at department of civil engineering, University Teknologi Malaysia (UTM) and are given in table V.

Table III. Properties of kaolin

Parameter	Value
Unsaturated unit weight (kN/m^3)	14
Saturated unit weight (kN/m^3)	17
Young's modulus (kN/m^2)	1000
Poisson's ratio	0.33
Cohesion (kN/m^2)	5
Friction angle	15
Optimum moisture content (%)	16.5
Liquid limit, LL (%)	38
Plastic limit, PL (%)	29.7
Plasticity index, I_p (%)	8.3

Table IV. Properties of sand

Parameter	Value
Unsaturated unit weight (kN/m^3)	16
Saturated unit weight (kN/m^3)	20
Young's modulus (kN/m^2)	10000
Poisson's ratio	0.3
Cohesion (kN/m^2)	1
Friction angle	33

Table V. Properties of textile

Parameter	Value
Thickness (mm)	0.17
Tensile stress (kN/m)	6.1
Elasticity modulus (Mpa)	65.3
Tensile strain (%)	53.4

Fig. 4 and 5 show the kaolin placement before and after centrifuge test, respectively.

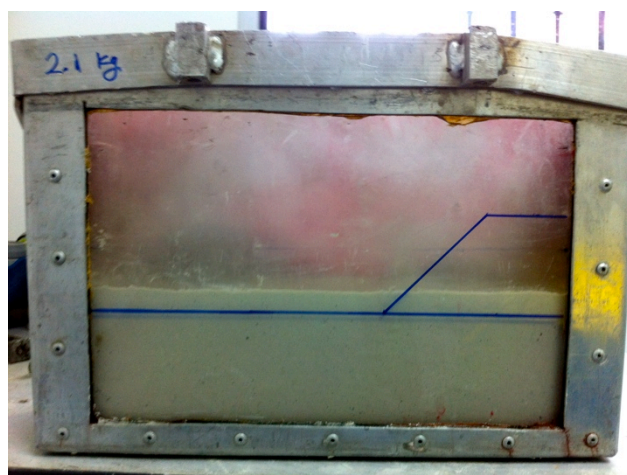


Fig. 4. The state of placed kaolin, before performing the centrifuge test

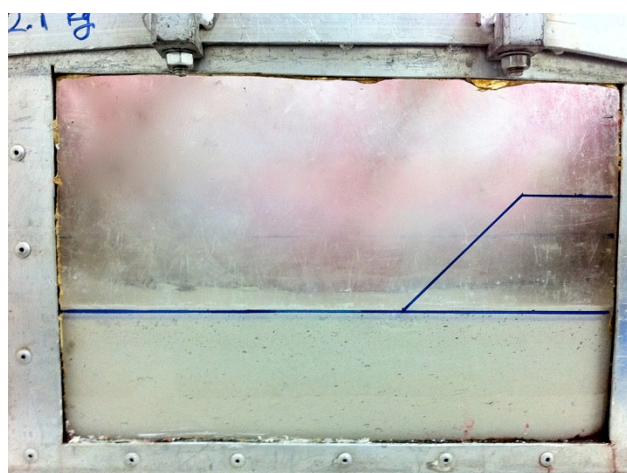


Fig. 5. The state of placed kaolin, after performing the centrifuge test

3.2 Fill Materials

In the first model, a wooden block with the dimension of embankment was used to simulate a rigid, stiff embankment. For other models oven-dried kaolin mixed with oven-dried sand to provide clayey sand with 20% kaolin and 80% sand. Properties of clayey-sand are shown in table VI. To prepare the embankment in the centrifuge box, a specific mold is used on the foundation soil and embankment was constructed by spreading the clayey sand into the mold and compacted in three layers by wood rod to simulate a similar compactive effort for all models.

Table VI. Properties of Clayey-Sand

Parameter	Value
Unsaturated unit weight (kN/m^3)	16
Saturated unit weight (kN/m^3)	19
Young's modulus (kN/m^2)	6000
Poisson's ratio	0.3

Fig.6 and Fig.7 show the clayey-sand soil embankments on sand and kaolin foundation before the centrifuge test, respectively.

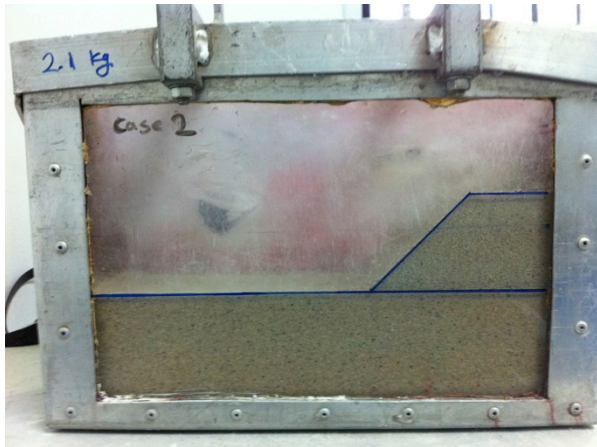


Fig. 6. Embankment on compacted sand foundation



Fig. 7. Embankment on soft kaolin foundation

4. Centrifuge Test Methodology

After preparing the model in sample box, the model was weighted and then the sample box was fixed to the centrifuge arm. To balance the system, a counterweight equal to weight of sample added to opposite side of the centrifuge arm. To reduce the side friction, the sides of the strongbox were lubricated by applying silicon gel, which was especially necessary as only half of the embankment was modeled.

The model was initially run at low acceleration. The models were subjected to a progressively increasing centrifugal acceleration limited to 50 g in about 60 minutes. At certain accelerations the test was maintained constant for certain times and then again the acceleration continued to increase. These certain accelerations and time maintained is shown in Table VII.

Table VII. Gravity acceleration and time maintained of centrifuge test

Time Maintained (minute)	ω (rpm)	Gravity (g) $G=(1.18 \times 10^{-3}) \times r^* \omega^2$
5	120	8.5
5	185	20
5	225	30
15	250	37
10	285	48
20	300	50

5. Results

Case II: Fig. 8 and 9 show the deformation behavior of model II (unreinforced embankment on stiff foundation) after 60 minutes centrifugal rotation.



Fig. 8. Deformation behavior of model II (unreinforced embankment on stiff foundation)

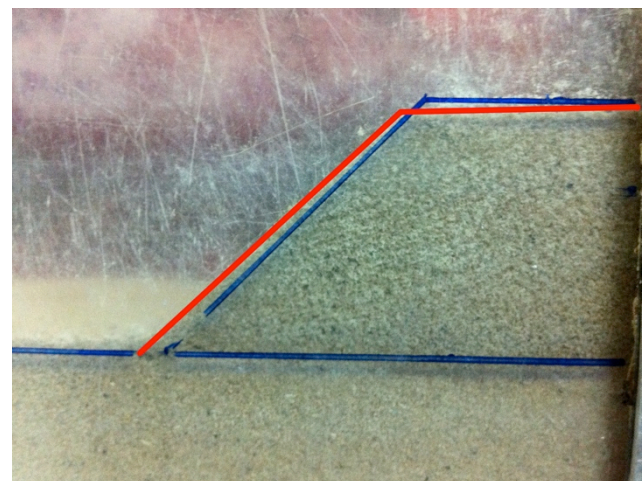


Fig. 9. Deformation behavior of model II (unreinforced embankment on stiff foundation)

The measured settlement on the top of embankment after the centrifuge test is about 3 mm.

Case III: the side view deformation behavior of model III

(unreinforced embankment on soft foundation) are displayed in Fig 10, 11 and 12 after 60 minutes centrifugal rotation.

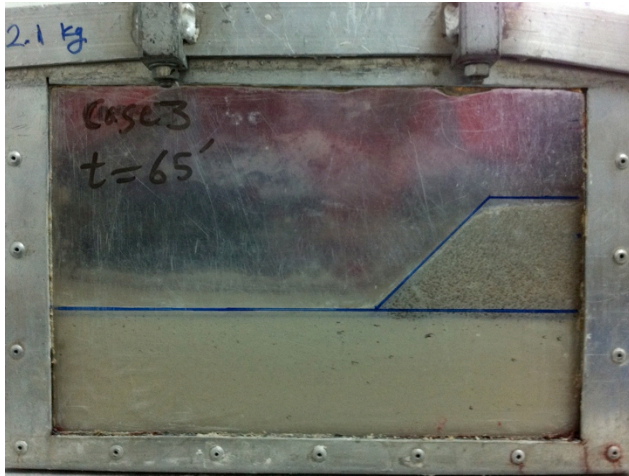


Fig 10. Deformation behavior of model III (unreinforced embankment on soft foundation)



Fig. 11. Deformation behavior of model III (unreinforced embankment on soft foundation)



Fig. 12. Deformation behavior of model III (unreinforced embankment on soft foundation)

The measured settlement on the top of embankment is

about 7 mm.

Case IV: Fig 13 and 14 show the deformation behavior of model IV (reinforced embankment on stiff foundation) after 60 min centrifugal rotation.

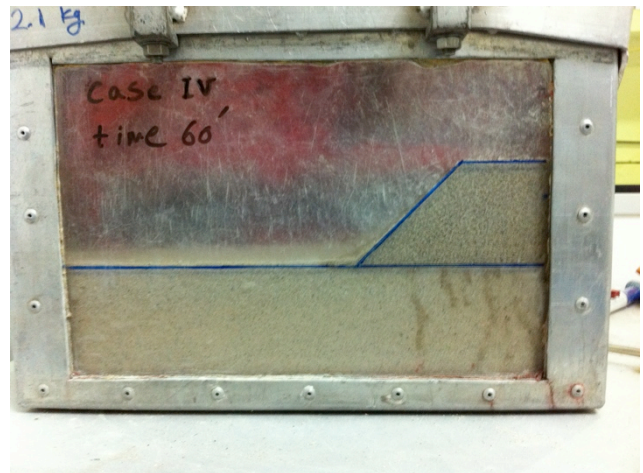


Fig. 13. Deformation behavior of model IV (reinforced embankment on stiff foundation)

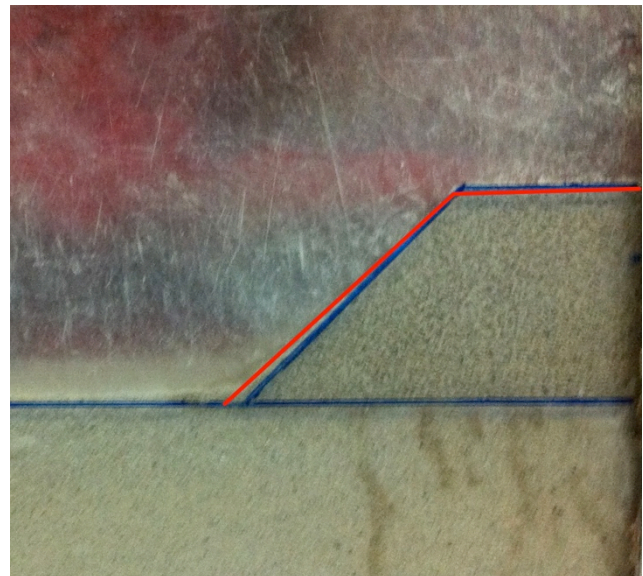


Fig. 14. Deformation behavior of model IV (reinforced embankment on stiff foundation)

The measured settlement on the top of embankment after the centrifuge test is about 0.5 mm.

Case V: the side view deformation behavior of model V (reinforced embankment on soft foundation) are displayed in Fig 15, 16 and 17 after 60 minutes centrifugal rotation.

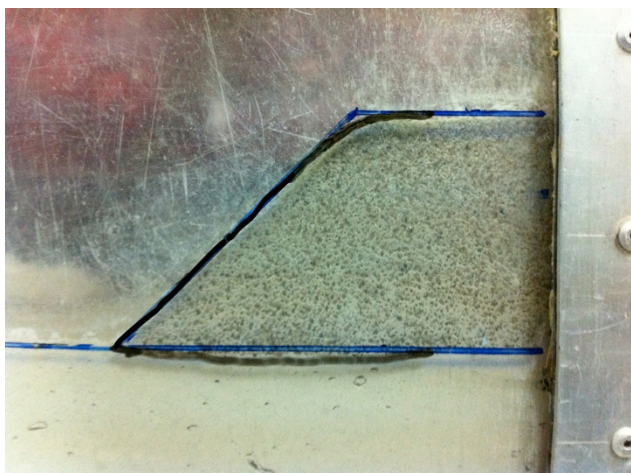


Fig. 15. Deformation behavior of model V (reinforced embankment on soft foundation)



Fig. 16. Deformation behavior of model V (reinforced embankment on soft foundation)



Fig. 17. Deformation behavior of model V (reinforced embankment on soft foundation)

The measured settlement on the top of embankment after the centrifuge test is about 2 mm.

1. CONCLUSION

Five centrifuge tests were performed based on different conditions of foundation strength and embankment reinforcement at the small centrifuge equipment of UKM. The mini-centrifuge equipment of UKM, does not enable a comprehensive study of reinforced embankments. This refers obviously to the capacity of the centrifuge. The payload limitation compels one to choose problems with lesser complexities. The size of the strongbox is designed to take into account this limitation and hence make it possible to study a slope of 1:1 only. However, this apparatus has enabled the qualitative behavior of the phenomenon to be studied.

As expected deformations of model 3 (soft embankment fill materials on soft foundation materials) was more than other models. To reduce deformations, the embankment was reinforced with textile. The results show that surface settlement and deformations of reinforced models are reduced about 71% for embankment on soft foundation and 83% for embankment on stiff foundation.

As shown in figures the type of deformation for unreinforced embankment on soft soils (model 3) is deep-rotational slide type but for other models is shallow-rotational slide type. This change is due to increasing the soil strength because of reinforcing the soil with textile (model 5) or using stiff foundation at models 2 and 4.

The effect of side friction between soil and sidewall on deformation behavior is significant and should be considered. Efforts should be made in the centrifuge work to minimize the effects of side friction by using some materials like silicon grease to reduce the friction

Acknowledgment

The author would like to thank to associate professor Dr. Wan Zuhairi Wan Yaacob for his kind guides on centrifuge test process.

References

- [1] Koerner, R.M., "Designing with geosynthetics" 5th edition. Ed. Pearson Education, 2005.
- [2] Sharma, J.S., Bolton, M.D. "Centrifuge modeling of an embankment on soft clay reinforced with geogrid." *Geotextile and geomembrane*. 14 (1): 1-17, 1996.
- [3] Chen, J. F., Yu, S.B. and Han, J., "Numerical modeling of a reinforced embankment based on centrifuge test dimensions." *ASCE GeoHunan International Conference*, 2009.
- [4] Viswanadham, B.V.S., Mahajan, R., "Modelling of geotextile reinforced highway slopes in a geotechnical centrifuge" *Geotechnical Engineering for Transportation Projects: Proceedings of Geo-Trans, ASCE*, 637-646, 2004.
- [5] Muhandi, "Pulverized fuel ash as structural fill for embankment construction." 2011.

Centrifuge Model Tests and Finite Element Analyses on Seismic Behavior of Quay Walls Backfilled with Cement-Treated Granular Soils

Hayano, K.¹, Morikawa, Y.², Fukawa, H.³, Takehana, K.⁴ and Tanaka, S.¹

¹Yokohama National Univ., ²Port and Airport Research Institute, ³Toa Corporation, ⁴Geodesign, Japan

ABSTRACT

Dynamic centrifuge model tests and finite element analyses (FEA) were conducted to investigate the seismic behavior of quay walls backfilled with cement-treated granular soils (CTGS). In particular, the effects of the CTGS fill depth and fill range on seismic behavior were investigated. The centrifuge model tests showed that no liquefaction was generated in the CTGS backfills. The quay wall's horizontal displacement induced by the seismic loading decreased with increases in the CTGS fill depth because the earth pressure acting on the quay wall was reduced. In addition, a wedge-shaped CTGS fill was found to be effective at reducing the horizontal displacement of the quay wall. However, the results of the dynamic FEA indicate that the wedge angle of the CTGS fill should be carefully designed.

Keywords: Ground improvement, Cement-treated granular soil, Centrifuge model test, Finite element analyses

1. INTRODUCTION

Attempts have been made recently to reuse soft soils obtained from dredging conducted near ports and harbors. The methods developed so far include dehydration, segregation, and cement-treated techniques. Disadvantages as well as advantages have been found for each method. For example, dehydration and segregation methods usually take a long time to stabilize a large amount of dredged soils. Cement-treated methods take a shorter time compared to dehydration and segregation methods. However, cement-treated materials show brittle behavior; cracks are generated when the foundation layers show differential settlement owing to consolidation.

The focus of this study is on a granulating technique, which is used for overcoming these difficulties. The method converts the dredged soils with their high water content to granular materials by adding cement and polymer. To date, the authors' research group has conducted fundamental studies on the geotechnical characteristics of cement-treated granular soils (CTGS) [1], [2]. These studies established the mixture design and the production method to obtain CTGS at low cost. Based on these findings, Dong et al. (2011) performed a series of laboratory tests to investigate the physical and mechanical properties of CTGS [3]. It was concluded that CTGS is a lightweight material because the particles include many voids. Therefore, it can be expected that CTGS would reduce the earth pressure acting on retaining walls if used as backfill soils. However, the applicability is not fully understood at present. In particular, it is important to clarify the effects of the CTGS fill depth and

fill range on the seismic behavior of a quay wall.

Therefore, in this study, a series of dynamic centrifuge model tests and finite element analyses (FEA) were conducted to investigate the seismic behavior of quay walls backfilled with CTGS.



Figure 1 Cement-treated granular soils (CTGS) prepared for centrifuge model tests

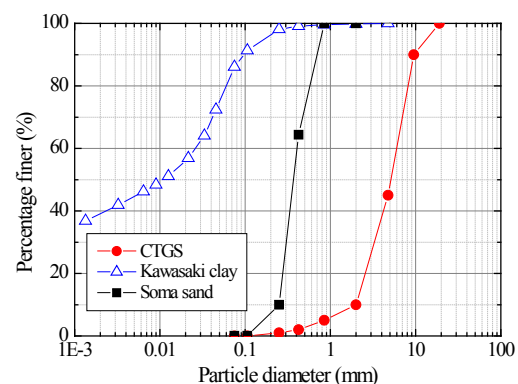


Figure 2 Particle size distributions of CTGS, Kawasaki clay, and Soma sand

2. CENTRIFUGE MODEL TESTING METHOD

2.1 Materials

CTGS were produced in the following manner for centrifuge model tests: First, the water content of a dredged soil called Kawasaki clay was adjusted to 60%. Then, the soil was mixed with a small amount of polymer with a weight of 0.1% of the clay. Owing to the effect of the polymer, the plasticity of the mixture became lower. After the plasticity change was observed, Ordinary Portland Cement was added and the mixture was stirred for about 10 min. Granular particles (shown in Fig. 1) gradually appeared because of the effect of cementation. The weight of the cement added to the mixture was 5% of the clay. Finally, the granular particles thus obtained were cured for more than 28 days.

Figure 2 shows the particle size distributions of the CTGS and Kawasaki clay, as well as that of Soma sand, which was also prepared for the centrifuge model tests. It is clear that Kawasaki clay was converted to a gravel-type soil (CTGS) by the granulation process.

2.2 Model preparation

Four models (denoted by Cases 1 through 4) were prepared to physically simulate a quay wall, as shown in Fig. 3. The quay wall consisted of a foundation layer, a caisson, and backfill soils. As seen in the figures, CTGS and Soma sand were used as the backfill soils. The foundation layer of each model was made with Soma sand of 90% relative density and had a 2.5-m thickness at prototype scale.

The sandbox used for Cases 1 and 2 had dimensions of 410 mm (height) by 556 mm (width) by 200 mm (length), whereas that used for Cases 3 and 4 had dimensions of 512 mm (height) by 710 mm (width) by 200 mm (length) at model scale.

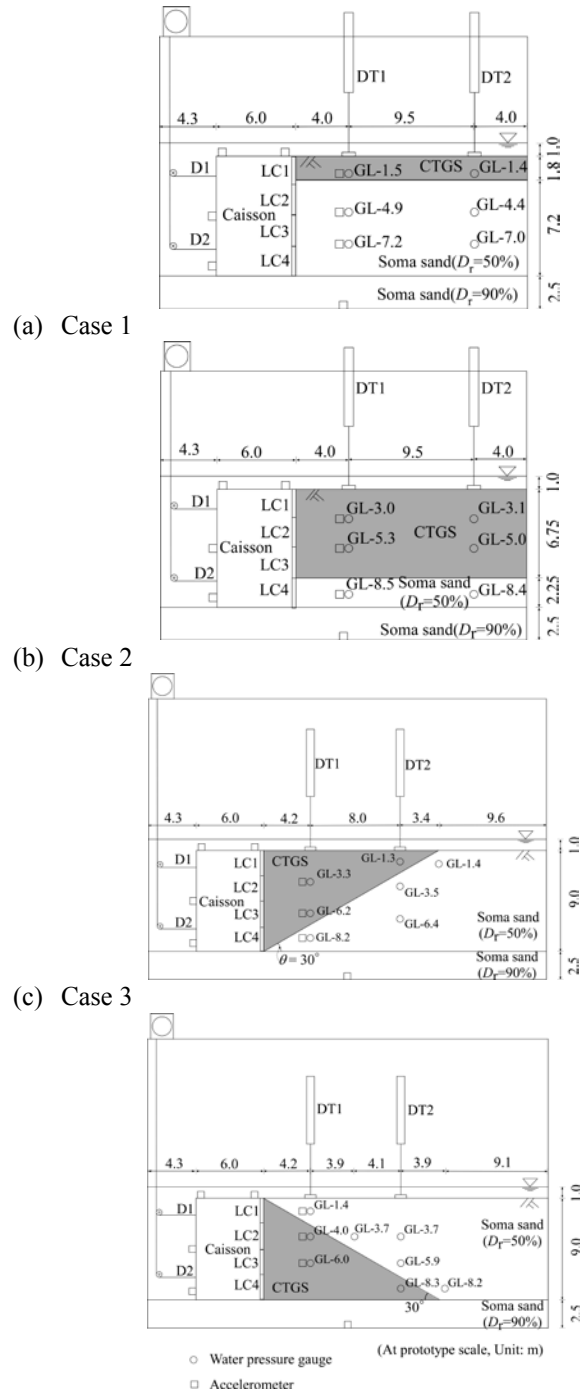
As seen in Figs. 3(a) and (b), the caisson in Cases 1 and 2 was backfilled with two horizontally layered soils. In Case 1, the overlying layer was filled with CTGS that was 1.8 m thick (20% of the total thickness of the backfilled ground) at prototype scale. The underlying layer was Soma sand that was 7.2 m thick. Case 2 was similar, but the overlying layer was 6.75 m thick (75% of the total thickness of the backfilled ground) and the underlying layer was 2.25 m thick.

In Cases 3 and 4, the CTGS was placed in a wedge shape with one edge of the wedge adjacent to the caisson. In Case 3, the right angle of the wedge was at the upper left corner of the backfill, as shown in Fig. 3(c). The remaining part outside the wedge was filled with Soma sand. In contrast, the right angle of the wedge in Case 4 was in the lower left corner of the backfill, as shown in Fig. 3(d). The remainder was filled with Soma sand.

In all cases, first, Soma sand was poured using the air pluviation method, resulting in a foundation layer of relative density of 90%. Next, in Cases 1, 2 and 3, Soma sand was filled using the air pluviation method to become about 50 % relative density. Then, a small shovel was used to place CTGS in the sandboxes at zero height, such that a loose state was achieved. In Case 4, CTGS was filled, followed by the

fill of Soma sand of 50% relative density.

In each case, two displacement transducers (denoted by D1 and D2 in the figures) were set at the seaward side of the caisson to measure its horizontal displacement. The other two displacement transducers (denoted by DT1 and DT2) were set above the backfill soils to measure the ground surface settlement. Pore water pressure gauges and accelerometers were installed inside the backfill soils at prefixed positions, as shown in the figures.



(d) Case 4
Figure 3 Schematic images of models prepared for centrifuge model tests

To evaluate the earth pressure distribution acting on the caisson, four load cells (denoted by LC1 through LC4) were built in the caisson. A rigid rectangular plate that directly contacted the backfill soils was connected to each load cell. The plate surface was set to be smooth in this study. A small space was allowed between the plates, so that they would not interfere with each other.

In preparing the models, efforts were made to minimize the friction between the inside of the box and the model soils by inserting thin, smooth films.

2.3 Centrifugal acceleration and dynamic shaking

A geotechnical centrifuge facility known as Mark II at the Port and Airport Research Institute was used in this study. The beam radius of the centrifuge is about 3.8 m and the maximum loading mass is 2.76 ton. Detailed information can be found in Kitazume and Miyajima (1995) [4].

Centrifugal acceleration and dynamic shaking were conducted in the following manner: First, after each model was prepared, it was set on the shaking table installed on the centrifuge platform. The model was then accelerated up to 20 G by the centrifuge. At the 20-G acceleration field, viscous fluid was infiltrated into the ground from the bottom to saturate the soils. The high saturation degree of the soils was obtained as proposed by Okamura and Kitayama (2008) [5]. The fluid's viscosity was set to be 50 times that of water to satisfy the similitude of the pore water dissipation of the ground. Then, the centrifugal acceleration was increased up to 50 G, and dynamic shaking was applied six or seven times. In each shaking period, 20 cycles of the sinusoidal waves of 2-Hz frequency at prototype scale were applied. The maximum amplitude of acceleration applied to the ground was increased stepwise up to about 400 Gals.

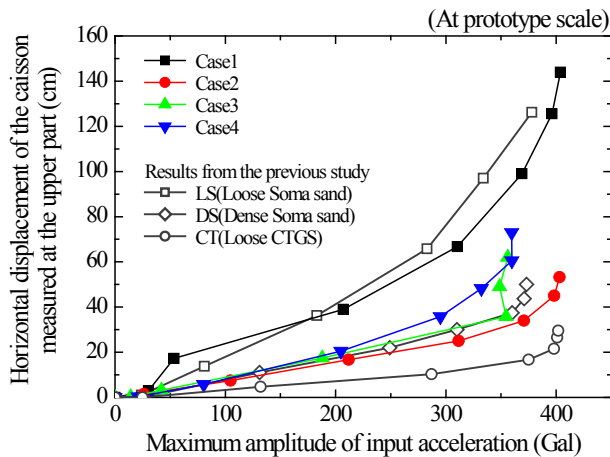


Figure 4 Relationship of input acceleration and caisson horizontal displacement

3. CENTRIFUGE TEST RESULTS

3.1 Horizontal displacement of the caisson and the ground surface settlement

Figure 4 shows the relationship between the maximum amplitude of the input acceleration and the cumulative horizontal displacement of the caisson for each case. The horizontal displacement was measured at the upper part of the seaward side of the caisson (see Fig. 3). The relationships obtained from the previous study [6],[7] were also shown in Fig. 4.

The previous study included three centrifuge model tests, denoted here by loose sand (LS), dense sand (DS) and CTGS (CT). The LS model was backfilled solely by Soma sand of 50% relative density, while the DS model was backfilled only by Soma sand of 95% relative density. The CT model was backfilled solely by loose CTGS. The caisson used in the LS, DS, and CT tests was the same as that used in this study.

Figure 4 shows that LS had the largest horizontal displacement at the higher accelerations. This was because the Soma sand was liquefied, and the earth pressure acting on the caisson increased as compared to other models. This will be discussed in detail in sections 3.3 and 3.4.

The caisson's horizontal displacement in Case 1 was close to that of LS, despite the fact that the upper part (20% of the total thickness) of the backfill ground consisted of CTGS. On the other hand, the caisson did not show a large horizontal displacement in Case 2. The horizontal displacement was close to that of DS. The caisson showed the smallest displacement in the CT case. These facts indicate that the caisson's horizontal displacement was reduced as the fill depth of the CTGS increased.

Looking at the results of Cases 3 and 4 in Fig. 4, the caissons show a horizontal displacement close to that of Case 2. This fact suggests that CTGS filled in the shape of a wedge or a reversed wedge can be effective at reducing the caisson's horizontal movement. The total CTGS volume required for Case 3 or 4 was lower than that required for Case 2.

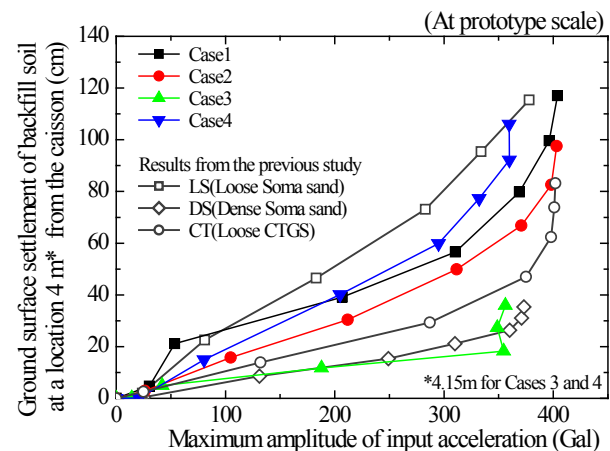


Figure 5 Relationship of input acceleration and backfill surface settlement

Figure 5 shows the relationships between the maximum amplitude of the input acceleration and the cumulative settlement of the ground surface. The surface settlement was measured at locations 4.0 or 4.2 m from the caisson edge (see Fig. 3). As shown in the figure, LS has the largest ground surface settlement, owing to the liquefaction of the Soma sand.

Wedge-shaped CTGS fills were a common characteristic between Cases 3 and 4; however, Case 3 shows a notably smaller ground surface settlement than Case 4. The ground surface settlement of Case 3 was close to that of DS. The reason why a small ground surface settlement was observed in Case 3 will be discussed in section 4.3.

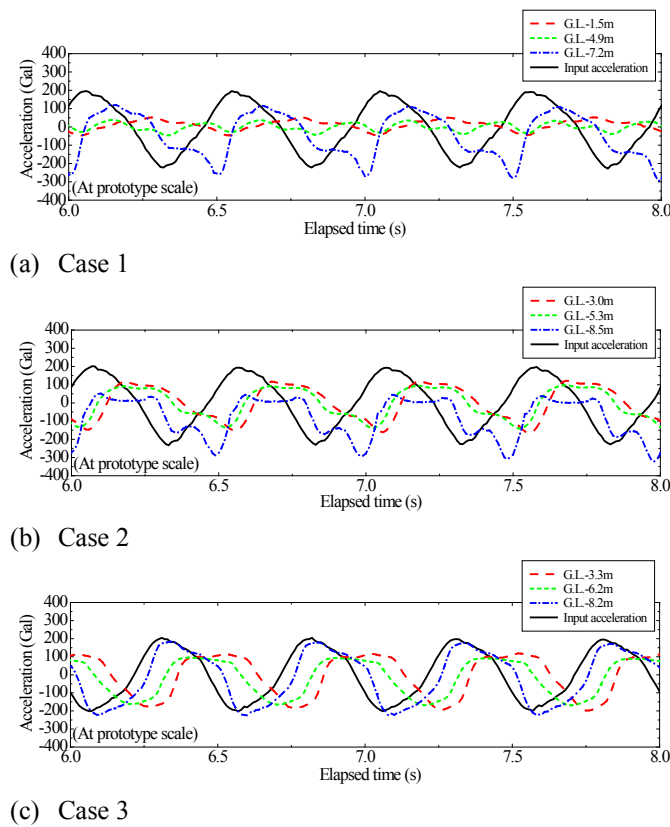


Figure 6 Time histories of ground response and input accelerations

3.2 Ground response acceleration

Figure 6 shows the time histories of the accelerations recorded in the backfill soil in Cases 1, 2, and 3. The data presented here were obtained in each case during the 6–8 s that elapsed after the start of the third shaking period. The ground acceleration was measured at locations 4.0 or 4.2 m from the caisson. Acceleration time histories were not obtained in Case 4 owing to connection errors with the accelerometers.

The ground accelerations were attenuated in each model as seen in the figures. In particular, the maximum amplitude of accelerations obtained at ground depths of 1.5 and 4.9 m in

Case 1 were smaller than those obtained in Cases 2 and 3. It is believed that the stiffness of Soma sand was considerably reduced by liquefaction and that the shear stress transmitted in the ground was attenuated in Case 1.

Phase delays were also observed in the ground acceleration waves. The wave phase differences between the acceleration obtained at a depth of 1.5 or 4.9 m and the input acceleration were about 0.2–0.3 s in both Cases 2 and 3.

3.3 Excessive pore water pressure

The ratio of the maximum excessive pore water pressure to the effective overburden pressure $\Delta u/\sigma_v'$ was evaluated based on measurements made with the pore water pressure gauges. Figure 7 shows the relationships between $\Delta u/\sigma_v'$ and the ground depths for Cases 1–4. The excessive pore water pressure was measured at locations 12.2 or 13.5 m from the caisson. The data presented here were obtained at the third, fourth, and fifth shaking periods (periods 3–5) in each case. The calculated effective overburden pressure was also shown in the figures.

As shown in Fig. 7(a), the values of $\Delta u/\sigma_v'$ obtained at ground depths of 4.4 and 7.0 m were close to 1.0, which indicated the liquefaction of loose Soma sand in Case 1. In addition, the values of $\Delta u/\sigma_v'$ obtained at the Soma sand layers in Cases 3 and 4 were close to 1.0, as seen in Figs. 7(c) and (d). This was also because of liquefaction.

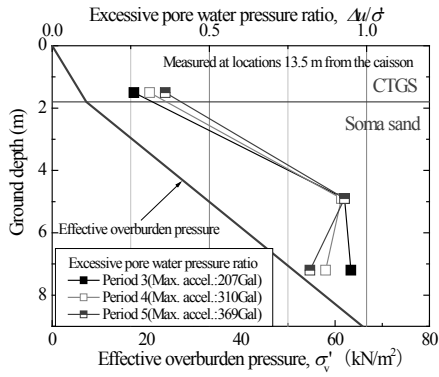
On the other hand, $\Delta u/\sigma_v'$ obtained at a ground depth of 1.4 m in Case 1 was about 0.3. Small $\Delta u/\sigma_v'$ values were also observed at ground depths of 3.1 and 5.0 m in Case 2, 1.3 m in Case 3, and 8.3 m in Case 4. These values were all obtained with the pore water pressure gauges installed in the CTGS. These findings verified that liquefaction was not observed in CTGS, even though the CTGS fill was loose and at shallow ground depths. The low liquefaction potential of CTGS can be explained by the high permeability characteristic of CTGS, which is suggested by the grain-size distribution shown in Fig. 2.

3.4 Dynamic earth pressure distribution

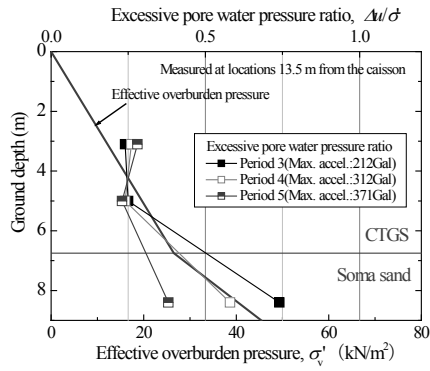
Figure 8 shows the dynamic earth pressure distribution acting on the caisson in each case. The dynamic earth pressure presented here was the minimum–maximum range obtained during period 3. The dynamic earth pressure was calculated by subtracting hydrostatic pressures from the total earth pressures measured with the load cells.

The figures show that the dynamic earth pressure at ground depths of 3.2, 5.3, and 7.4 m in Case 1 was higher than those obtained in the other cases. Similarly, a higher dynamic earth pressure was observed at a ground depth of 7.4 m in Case 2. These higher pressures were induced by the effect of the liquefaction of the Soma sand.

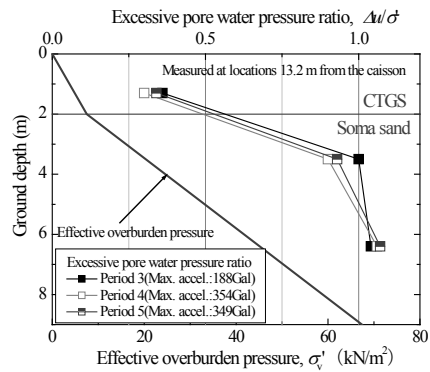
On the other hand, the dynamic earth pressure obtained at a ground depth of 1.1 m in Case 1 and at ground depths of 1.1, 3.2, and 5.3 m in Case 2 were not so high. In addition to the fact that no liquefaction was generated in CTGS, it is believed that the CTGS layers in Cases 1 and 2 induced a small



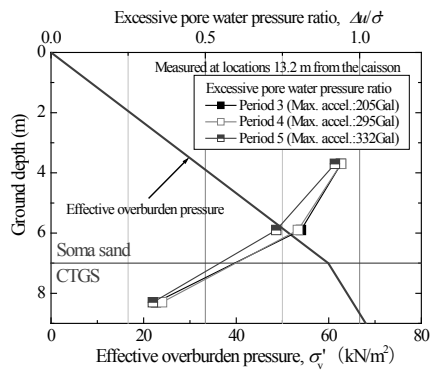
(a) Case 1



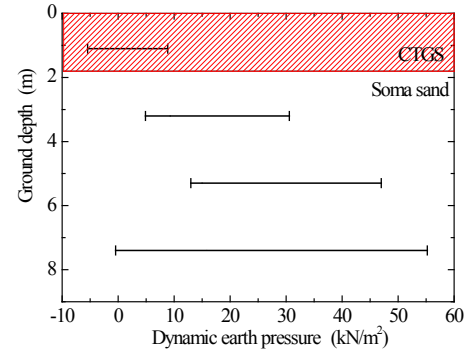
(b) Case 2



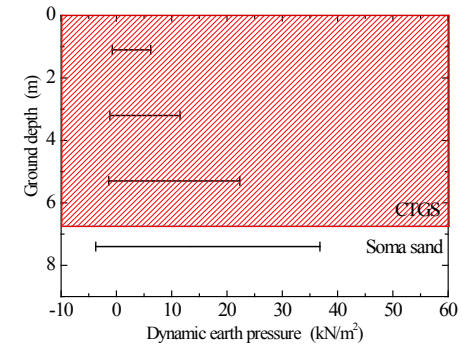
(c) Case 3



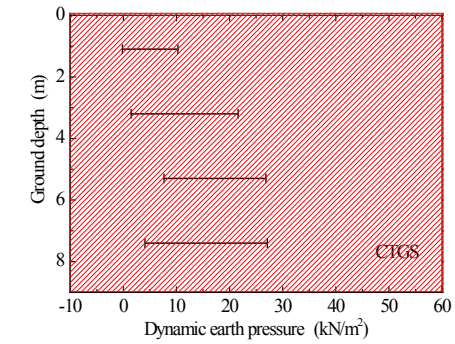
(d) Case 4



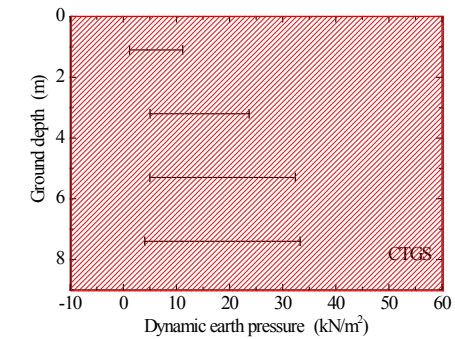
(a) Case 1



(b) Case 2



(c) Case 3



(d) Case 4

Figure 8 Depth distributions of dynamic earth pressure distributions at caisson wall

Figure 7 Depth distributions of excess pore water pressure ratio and effective overburden pressure

dynamic earth pressure because of their light weight. This light weight characteristic is attributable to the fact that many small voids were included in the particles. Please see Dong et al. (2011) [3] for further information related to this issue.

The dynamic earth pressures obtained at ground depths of 3.2 and 5.3 m in Cases 3 and 4 were slightly higher than those in Case 2. This was probably induced by the liquefaction of the Soma sands filled behind the CTGS. This suggested that the effect of liquefaction of Soma sand filled behind the CTGS might be higher if the fill zone range of a wedge of CTGS became smaller. This matter will be investigated in detail in the following sections.

4 FINITE ELEMENT ANALYSES

4.1 Software and numerical analysis conditions

The centrifuge model test results indicated that the wedge-shaped fill of CTGS in Case 3 was effective at reducing the caisson's horizontal displacement and the backfill ground surface settlement when the quay wall was subjected to the dynamic loading. However, owing to the limited conditions of the centrifuge model tests, the appropriate range of the wedge-shaped zone was not well understood. Therefore, dynamic FEA were conducted to obtain the effect of the wedge-shaped zone range (in particular, the effect of the wedge angle) on the caisson's horizontal displacement.

Dynamic FEA software named FLIP was used in this study. The software is widely used for seismic designs of port and harbor structures in Japan (e.g., Iai and Kameoka, 1993[8], Iai et al., 1998[9]). First, the analyses using FLIP were focused on simulating the effect of the fill depth of CTGS on the caisson's horizontal displacement. The centrifuge models (Cases 1 and 2 in this study and LS and CT in the previous study) were simulated. An analysis was also conducted to simulate the model in which the upper half of the backfill was CTGS.

As an example, the finite element meshes used to simulate Case 1 are shown in Fig. 9. The scales of the foundation layer, the caisson, and the backfill layers in the figure were set to be the same as those of Case 1 at the prototype scale (see Fig. 3). For the dynamic acceleration, sinusoidal waves that were the same as those of the centrifuge model tests were introduced into the FEA. The maximum amplitude of the acceleration was adjusted to 200 Gal.

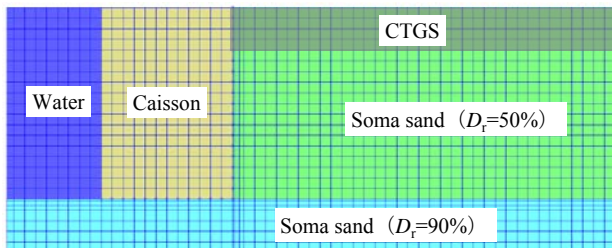


Figure 9 Finite element meshes adopted to simulate Case 1 in dynamic FEA

Table 1 Strength parameters used in dynamic FEA based on CD triaxial tests

Material	Submerged unit weight, γ' (kN/m ³)	c_d (kN/m ²)	ϕ_d (kN/m ²)
Soma sand ($D_r = 50\%$)	8.5	0.6	36.1
Soma sand ($D_r = 90\%$)	9.5	8.6	40.4
CTGS	4.3	0.0	26.6

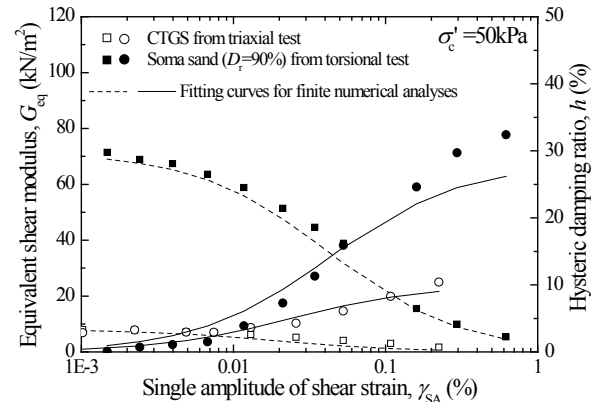


Figure 10 Comparison of laboratory and FEA results for equivalent shear modulus and hysteric damping ratio as a function of shear strain

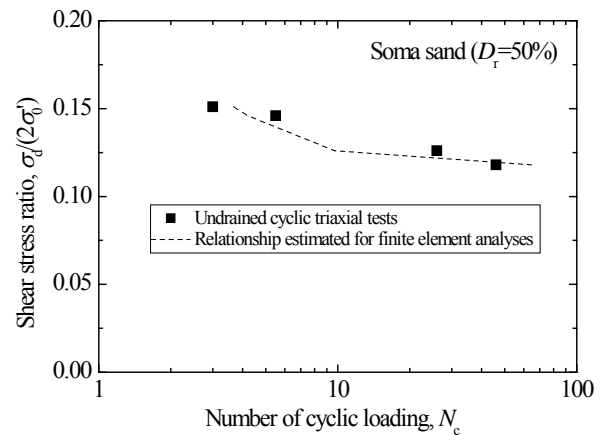


Figure 11 Comparison of liquefaction resistance curves obtained from laboratory tests with those estimated based on FEA

The material parameters related to the strength properties of CTGS and Soma sands were determined based on the consolidated drained triaxial tests are listed in Table 1, and those related to the deformation properties were determined based on cyclic triaxial tests or cyclic torsional tests, as shown in Fig. 10. Laboratory experiments were conducted according to JGS 0524-2009, JGS 0542-2009 and JGS 0543-2009.

The liquefaction parameters necessary for simulating the liquefaction behavior of Soma sand were evaluated based on the cyclic undrained triaxial tests (JGS 0541-2009), as shown in Fig. 11. The CTGS were treated as nonliquefiable soils

based on the centrifuge model test results. Detailed information on the input parameters required for FLIP and the constitutive material models can be found in Morita et al. (1997)^[10].

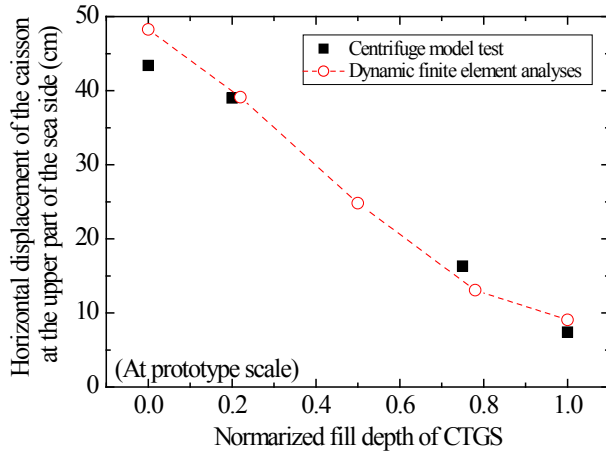


Figure 12 Comparison of centrifuge model tests and FEA results for caisson horizontal displacement as a function of fill depth

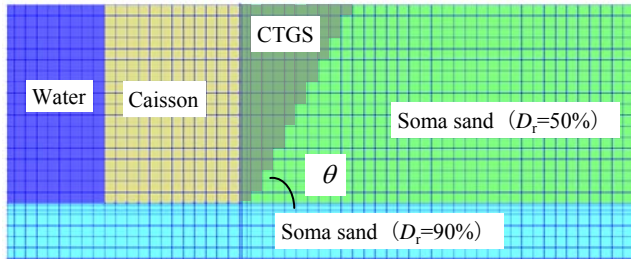


Figure 13 Example of finite element meshes adopted to represent wedge-shaped CTGS fill ($\theta = 60^\circ$)

4.2 Numerical analysis results on the effect of the filling depth of CTGS

Figure 12 shows the relationship between the fill depth of CTGS and the horizontal displacement of the caisson. The fill depths of CTGS were normalized by the total thickness of the backfill soil. The horizontal displacements of the caisson were evaluated at the upper part of the seaward side of the caisson, the same as for the centrifuge model tests (see Fig. 3). For comparison, the centrifuge model test results are also shown in the figure. The figure shows that the FEA results in horizontal displacements that are close to the centrifuge model test results. These results suggest that the horizontal displacement of the caisson was reduced proportionally to the normalized fill depth.

4.3 Numerical analysis results on the effect of the range of the wedge-shaped fill zone

As described in the previous section, the horizontal displacement of the caisson could be reasonably predicted by the finite element analyses by introducing the appropriate parameters into the numerical models. Then, using the same

parameters and the constitutive models, analyses were conducted to investigate the effect of range of the wedge-shaped CTGS fill zone (in particular, the effect of the wedge angle) on the caisson's horizontal displacement. The wedge angle θ was defined as the inclination angle of the wedge plane from the horizontal plane. Typically, as shown in Fig. 13, the wedge angle θ was set to 0° , 30° , 45° , 60° , and 90° in each analysis. The scales except for the wedge angle were designed to be as same as those of the centrifuge model tests.

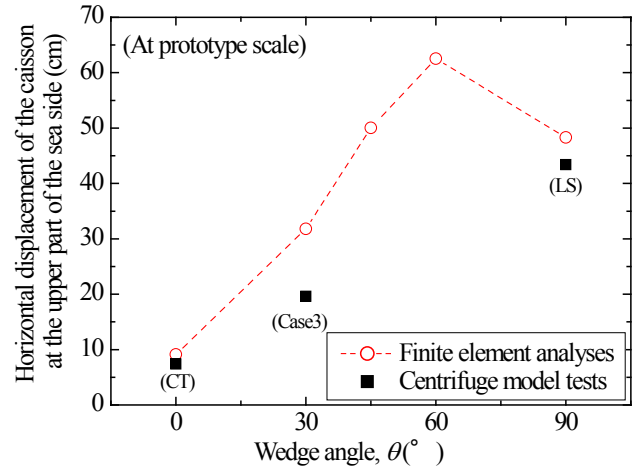


Figure 14 Comparison of centrifuge model tests and FEA results for wedge-angled CTGS fill and caisson horizontal displacement

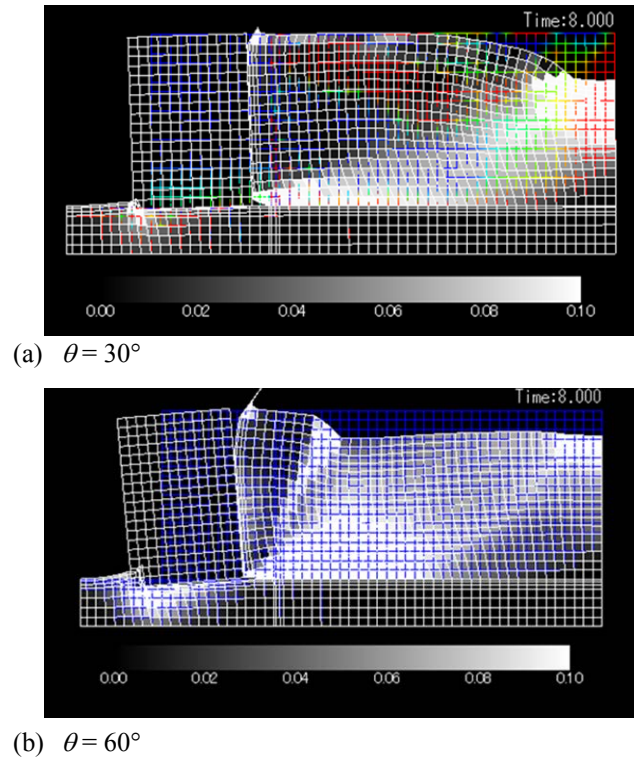


Figure 15 Maximum shear strain distribution obtained from dynamic FEA

Figure 14 shows the relationship between the wedge angle θ and the horizontal displacement of the caisson. The centrifuge model test results were also shown in the figure. Here, the wedge with the 0° angle represented the backfill ground solely filled by CTGS (CT) and that of the 90° angle represented the backfill ground solely filled by Soma sand (LS). It can be seen in the figure that the wedge with a 60° angle showed the largest horizontal displacement.

Figure 15 shows the maximum shear strain distributions of the grounds for the wedges with 30° and 60° angles. The results indicate that higher shear strain was concentrated near the boundary between CTGS and Soma sand in the 60° wedge case compared to that in the 30° wedge case. This may suggest that the range of the wedge-shaped CTGS fill would be better designed to cover the active failure zone of backfill ground.

In addition, Figure 15 shows that Soma sand moved in the horizontal direction toward the caisson after it was liquefied. This sand appeared to push the CTGS up toward the ground surface during the movement because the density of the liquefied soil was much higher than that of CTGS. This mechanism can explain the reason why a small amount of ground surface settlement was observed in Case 3 but not in Case 4 in the centrifuge model tests.

5 CONCLUSIONS

Dynamic centrifuge model tests and finite element analyses (FEA) were conducted to investigate the seismic behavior of quay walls backfilled with cement-treated granular soils (CTGS). Effects of the fill depth and fill range of CTGS on the seismic behavior were investigated. The following results were obtained:

- 1) The centrifuge model tests showed that no liquefaction was generated in the CTGS backfills. The low liquefaction potential of CTGS was due to the highly permeable characteristic of CTGS resulting from the coarse grain-size distribution.
- 2) The quay wall horizontal displacement induced by the seismic loading was decreased as the CTGS fill depth increased because the earth pressure acting on the quay wall was reduced. The small earth pressure was attributed to the light weight characteristic of the CTGS.
- 3) The centrifuge model tests also showed that the wedge-shaped CTGS fill was effective at reducing the quay wall's horizontal displacement and the ground surface settlement.
- 4) The dynamic FEA using FLIP could reasonably give the caisson's horizontal displacements, which were close to those of the centrifuge model tests. The FEA also indicated that the wedge angle of the CTGS fill zone should be carefully designed to cover the active failure zone of the backfill ground.
- 5) The dynamic FEA for the wedge-shaped fill also showed that liquefied Soma sand filled behind the CTGS and pushed the CTGS up toward the ground surface. This contributes to the fact that a small ground surface settlement was observed for the wedge-shaped CTGS fill in the centrifuge model tests.

REFERENCES

- [1] Dong, P. H., Hayano, K., Okusa, Y., Takahashi, H. and Morikawa, Y., "Mechanical Properties of Lean-Mixed Granular Cement Treated Soil from Consolidated Drained Triaxial Tests", Proc. of International Symposium on Geotechnical Engineering, Ground Improvement, and Geosynthetics for Sustainable Mitigation and Adaptation to Climate Change Including Global Warming, pp. 319–330, 2009.
- [2] Dong, P. H., Hayano, K., Takahashi, H. and Morikawa, Y., "Effects of Mixture Design on the Mechanical Properties of Cement Treat Granulate Soil," Proc. of Sixth International Congress on Environmental Geotechnics, Vol. 1, pp. 594–599, 2010.
- [3] Dong, P. H., Hayano, K., Kikuchi, Y., Takahashi, H., and Morikawa, Y., "Deformation and crushing of particles of cement treat granulate soil", Soils and Foundations, Vol. 51, No. 4, pp. 611–624, 2011.
- [4] Kitazume, M. and Miyazima, S., "Development of PHRI Mark II geotechnical centrifuge", Technical Note of the Port and Harbor Research Institute, No. 817, pp. 1–33, 1995.
- [5] Okamura, M. and Kitayama, H., "Preparation of Fully Saturated Model Ground in Centrifuge and High Accuracy Measurement of Degree of Saturation, Journal of JSCE, Division C: Geotechnics, Vol. 64, No. 3, pp. 662–671, 2008 (in Japanese).
- [6] Morikawa, Y., Takahashi, H., Hayano, K. and Okusa, Y., "Centrifuge Model Tests on Dynamic Behavior of Quay Wall Backfilled with Granular Treated Soil," Proc. of the 8th International Conference on Urban Earthquake Engineering, pp. 279–284, 2011.
- [7] Takahashi, H., Morikawa, Y., Hayano, K. and Okusa, Y., "Seismic behavior of gravity-type quay wall backfilled with granular soil", Japanese Geotechnical Journal, Vol. 6, No. 2, pp. 169–179, 2011 (in Japanese).
- [8] Iai, S. and Kameoka, T., "Finite element analysis of earthquake induced damage to anchored sheet pile quay walls," Soils and Foundations, Vol. 33, No. 1, pp. 71–91, 1993.
- [9] Iai, S., Ichii, K., Li, H., and Morita, T., "Effective stress analyses of port structures," Soils and Foundations, Special Issue on Geotechnical Aspects of the January 17 1995 Hyogoken-Nambu Earthquake No.2, pp. 97–114, 1998.
- [10] Morita, T., Iai, S., Liu, H., Ichii, K. and Sato, Y., "Simplified Method to Determine Parameter of FLIP", Technical Note of the Port and Harbor Research Institute, Ministry of Transport, Japan, No. 869, pp. 1–36, 1997 (in Japanese).

Response of Piered Retaining Walls to Lateral Soil Movement Based on Numerical Modeling using Matlab

Siamak Pahlevanzadeh¹

¹ Griffith School of Engineering, Griffith University, Gold Coast Campus, QLD 4222, Australia; PH (0061) 7-5552 7608; FAX (0061) 7-5552 8803; email: s.pahlevanzadeh@griffith.edu.au

ABSTRACT

The response of individual retaining walls employed as a preferred slope stabilization technique, to lateral loading has been widely explored in the literature. The present study focuses on the response of piered retaining walls, i.e. retaining walls supported by a pile foundation system, to lateral soil movement. Numerical analysis results by MATLAB have revealed wall-soil-pile interaction mechanism with different effective height of wall, spacing, diameter and number of piles, using different soil properties, which quantifies the behavior of piered retaining walls owing to lateral soil movement. Based on a numerical configuration sensitivity study, the relationship between lateral loading and pile/wall deflection, shear and bending moment under different influencing parameters has been established. Optimum effective parameters are accordingly defined and relevant guidance on choosing appropriate piling configuration is provided, which can be of practical use in engineering design.

Keywords: Piered Retaining Wall, Lateral Soil Movement, Numerical Modeling, Matlab

1. INTRODUCTION

The problem associated with lateral earth pressure and retaining wall stability is one of the most common in the civil engineering field and a segment of soil mechanics that has been receiving widespread attention from engineers for a long time.

The typical structures whose primary or secondary purpose is to resist earth pressures may include various types of retaining walls, sheet piling, braced sheeting of pits and trenches, bulkheads or abutments, and basement or pit walls. These may be self-supporting (e.g., gravity or cantilever concrete walls) or they may be laterally supported by means of bracing or anchored ties. The lateral earth pressure depends on several factors [1]:

- The physical properties of the soil
- The time-dependent nature of soil strength
- The interaction between soil and retaining structure at the interface
- The general characteristics of the deformation in the soil-structure composite
- The imposed loading (e.g., height of backfill, surcharge loads).

Due to virtually no analytical, theoretical or field testing data on piered retaining walls, this review will focus on the literature on wall-soil interaction and the behavior of piles subjected to a lateral loading. Although the integrated structure will behave differently, numerical modeling can still be employed on the basis of how each section would behave

in a traditional situation, i.e. the retaining wall behaves as a piling cap with an additional moment force due to earth pressure.

Although much research has been performed and appreciable advancement made during the past two centuries regarding the distribution of earth pressures and on the analysis of a wide range of earth-retaining structures, some of the theories formulated by Coulomb (1776), Rankine (1857) and Mononobe-Okabe (1929) still remain as the fundamental approaches to the analysis of most earth-supporting structures, particularly for sandy soils. Furthermore, although some research data and experience indicate that assumptions related to pressure distributions on retaining walls, or on the failure surface of the backfills, are not quite those depicted by these early investigators, substantial evidence exists that the analysis and design efforts based on their theories give acceptable results for most cases of cohesion-less backfills. The results are significantly less dependable for the more cohesive soils.

Recent analyses have tended to concentrate on numerical methods, in particular, the three-dimensional finite element methods. The importance of incorporating interface elements to simulate possible slippage and separation between the wall and soil, and capturing the soil nonlinearity using advanced constitutive models, has been widely recognized.

Advanced numerical analysis may be appropriate and necessary for detailed design; generally, the wall-soil interaction may be addressed with numerical simulations based on either the finite-element method (FEM), or the finite-difference method (FDM).

Goh (1993) performed finite element analyses to investigate the effects of subsoil stiffness, wall stiffness, and wall

roughness on the lateral earth pressure for concrete cantilever retaining walls, and proposed a modified earth pressure distribution.

In spite of recent published methods, the tendency today in practice is to use the values given by Caquot and Kerisel (1948) [2] and Kerisel and Absi (1990) [3].

Benmebarek et al. (2007) [4] concerned with the numerical evaluation of passive earth pressure coefficients for a rigid rough vertical retaining wall with horizontal ground surface and limited breadth subjected to translation. They conducted a numerical study of 3D passive earth pressures induced by the translation of a rigid rough retaining wall for associative soils. Using the explicit finite difference code FLAC^{3D}, the increase of the passive earth pressures due to the decrease of the wall breadth was investigated. FLAC uses an explicit finite difference program to study numerically the mechanical behavior of a continuous 3D medium as it reaches equilibrium or steady plastic flow. The explicit Lagrangian calculation scheme and the mixed-discretization zoning technique as presented by Cundall (1987) [5], is used in FLAC to ensure that plastic failure and flow are modeled accurately.

Numerical methods including both finite element and finite difference methods have been widely employed to study the wall-soil interaction under active and passive lateral loading due to soil movements. These methods mainly satisfy the compatible relationship between the lateral pressure and the movement. However, relatively little effort is made to assess the response of the piered retaining walls under the action of the lateral soil movements.

2. NUMERICAL MODELING

2.1 Method

The numerical model was created by combining two methods (Fig. 1) using C⁺⁺ script in Matlab:

- Finite Difference Method, FDM, (Matlock and Reese, 1960) [6] revised by Guo (2003) [7],
- Finite Element Method, FEM, reviewed and verified by Chen (1998) [8] as the method of superposition, namely flag pole analysis

Basic mechanics of materials formulae is used to determine elastic deflection in the retaining wall, boundary conditions to have a statically determinant cantilever wall which can be used to determine the degree of deflection the wall itself undergoes.

Numerical modeling using Matlab is designed to calculate deflection when subject to a variety of parameters, maximum shear in each pile correlating to the applied load and bending moment at different depths, to find where the maximum moment occurs. Numerical modeling is also designed to highlight the impact of input parameters on the performance of a piered retaining wall to facilitate the development of design guidelines.

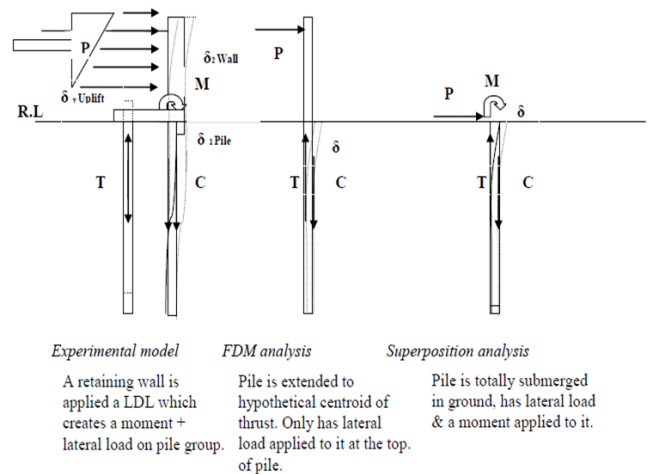


Figure 1 - The numerical model was created by combining two methods, FDM and FEM

By implementing the popular p-y method, Rankine's Coulomb's and Mononobe-Okabe's general formulas for a case of static equilibrium using Matlab, results can be obtained to verify the accuracy of existing methods applied to an unfamiliar situation. This method can only be reliable for a pile group with S/D of 6 or greater where S, is the spacing between piles and D, is the diameter of each pile.

2.2 Analysis

The numerical model uses the FDM to determine the maximum bending moment and the angle of rotation in the piles, and the FEM analysis to determine pile deflection. Mechanics of materials formulae is also used to determine elastic deflection in the retaining wall. The method of critical pile depth was utilized to establish pile flexibility and boundary conditions required for a statically determinant cantilever wall to be used to determine the deflection of the wall.

The type of piered retaining wall modeled, can be either a cantilever or gravity wall retaining wall interface, with one or two rows of piles beneath it. Finite element analysis is used to determine this behaviour. The retaining wall's deflection is determined with an extension of the P-y method using the general limit static equilibrium case. The force profile and behaviour of piles are modelled with p-y curves to determine the elastic-plastic sliding depth and bending moment for a non-linear loading distribution profile.

The model is developed for a piered retaining wall subjected to active earth pressure, which behaves as a pile with fixed head. Piles are subject to passive earth pressure loading case, where soil movement occurs exclusively at and above the bottom of the retaining wall. The Matlab script is split up into three parts, input parameters, deflection calculation and pile analysis. It basically calculates the percentage of the loading transferred from the wall to the piles due to the lateral soil movement and then quantifies the behavior of piles due to the load transferred.

2.3 Model Modifications

A variety of modifications have been made to the numerical

model to account for the wall – pile interaction. It was found that the numerical model best suited for a piered retaining wall which is developed for substantially long piles. In order to counteract this problem, modifications were made by imposing a relationship between the critical pile depth and the total pile length, such that the deflection was not underestimated.

Basically if a pile decreases in length the deflection will decrease, past a certain point namely critical pile depth and if a pile decreases in length below the critical pile depth, deflection will increase. After satisfactory equations were derived and verified, numerical results have been produced. Comparisons and conclusions have been obtained to deduce the suitability and feasibility of implementing piered retaining walls. The purpose of these comparisons is to determine the sensitivity of the numerical model to the influencing parameters which establishes the performance of the piered retaining wall.

2.4 Results and Discussion

Fig. 2 shows the comparison between three different piling configurations for a concrete retaining wall. It includes:

- two piles, diameter of each pile 177mm, S/D>6
- Six piles, diameter of each pile 100mm, S/D>6
- Ten piles, diameter of each pile 78mm, S/D<6

The maximum shear force per pile due to a certain lateral load decreases considerably by increasing the number of piles from 2 to 6; however increasing the number of piles from 6 to 10 slightly decreases the maximum shear force per pile. The bending moment per pile at a certain depth also decreases considerably by increasing the number of piles from 2 to 6; however increasing the number of piles from 6 to 10 slightly decreases the bending moment force per pile.

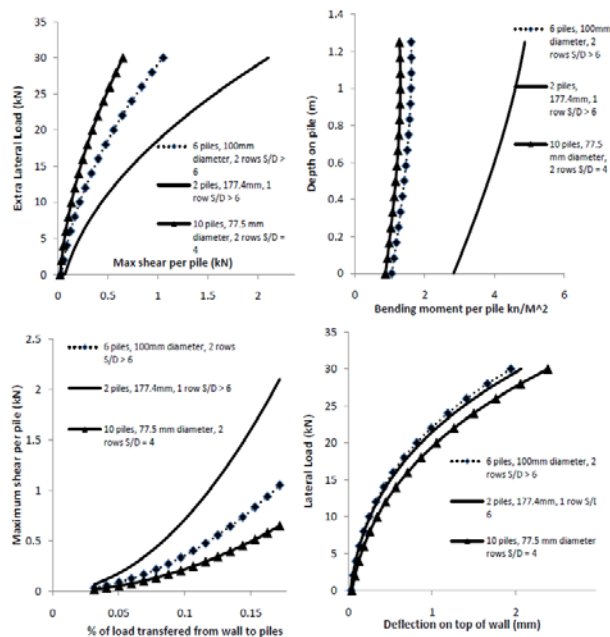


Figure 2 - Numerical comparison between three different piling configurations for a concrete retaining wall

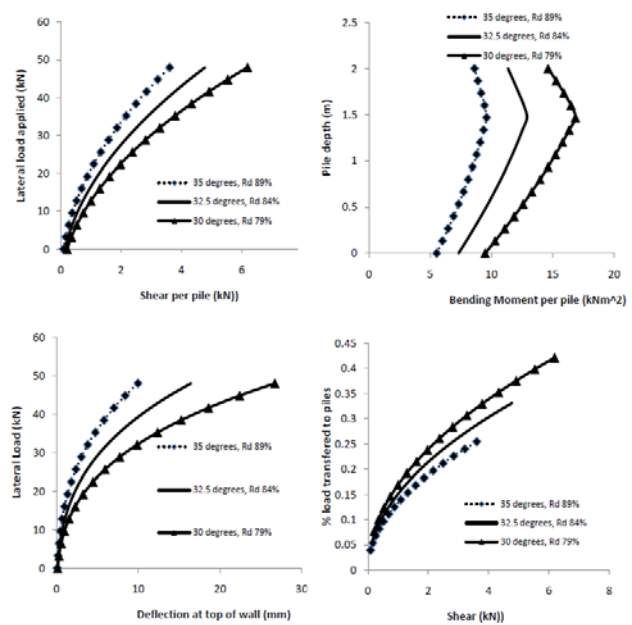


Figure 3 - Numerical comparison between three different cases of soil properties for a large reinforced concrete piered retaining wall

Fig. 3 shows the comparison between three different cases of soil properties for a large reinforced concrete piered retaining wall. These cases are including sand with:

- $\phi = 30^\circ$ friction angle and 79% relative density
- $\phi = 32.5^\circ$ friction angle and 84% relative density
- $\phi = 35^\circ$ friction angle and 89% relative density

The maximum shear force per pile due to a certain lateral load increases by decreasing the friction angle and relative density of soil. The bending moment per pile at a certain depth also increases by decreasing the angle of friction and relative density of soil.

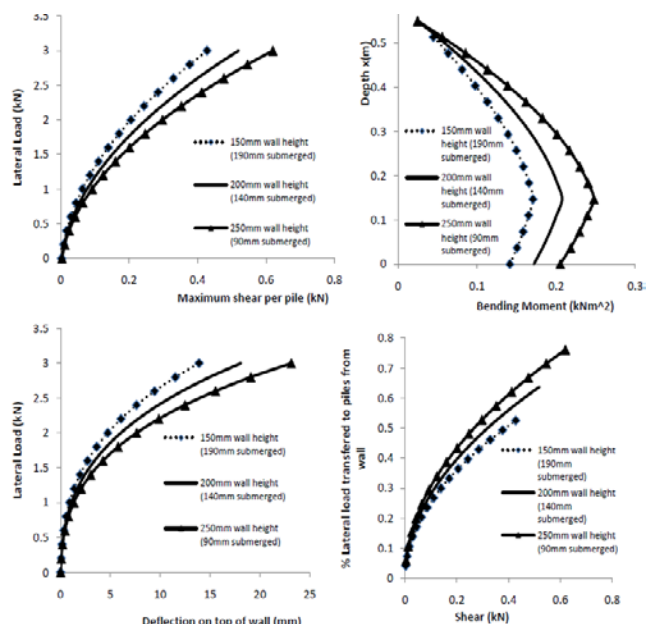


Figure 4 - Numerical comparison between effective wall heights 150mm, 200mm, and 250mm

The deflection at top of wall due to a constant lateral loading increases accordingly by decreasing the angle of friction and relative density of soil.

Fig. 4 shows the comparison between three different cases of effective wall heights for a large reinforced concrete piered retaining wall. These cases are including piered retaining wall with:

- $h = 150\text{mm}$, 190mm submerged into the soil
- $h = 200\text{mm}$, 140mm submerged into the soil
- $h = 250\text{mm}$, 90mm submerged into the soil

Where h is the effective wall height. The maximum shear force per pile due to a certain lateral load increases by increasing the effective wall height. The bending moment per pile at a certain depth also increases by increasing the effective wall height. The deflection at top of wall due to a constant lateral loading increases accordingly by increasing the effective wall height.

3 CONCLUSION

To gain a relatively better understanding of the effect of piling beneath a simple typical retaining wall, a numerical modeling and analysis has been conducted using Matlab. The model utilizes a combination of both FDM and FEM methods in order to calculate the earth pressure on the wall due to applied lateral loading, determine the percentage of load transferred from wall to piles and quantify the pile behavior accordingly.

Discussing the improvement of the engineering behavior of a simple typical retaining wall by piling beneath the retaining wall also reveals that:

- There is optimum number of piles to use beneath any particular retaining wall, since the numerical modeling indicates that the maximum shear force per pile due to a certain lateral load and the maximum bending moment at a certain depth decrease by increasing the number of piles to a certain number and additional piling will not considerably improve the lateral capacity. This optimum number of pile can be determined running the developed numerical model in the present study.
- Decreasing the friction angle and relative density of soil, increases the maximum shear force per pile due to a certain lateral load and also the bending moment per pile at a certain depth. This conclusion illustrates the effect of soil properties on the model. The deflection at top of wall due to a constant lateral loading increases accordingly by decreasing the angle of friction and relative density of soil. The numerical model developed in the present study is able to consider different soil properties in order to produce appropriate outcome.
- There is optimum effective wall height, since increasing the effective wall height will result to increase in the maximum shear force per pile due to a

certain lateral load and also the bending moment per pile at a certain depth. The deflection at top of wall due to a constant lateral loading increases accordingly by increasing the effective wall height. This shows the effect of piered retaining wall dimensions on the total improve in the lateral capacity. The optimum effective wall height can be determined using the numerical model developed in the present study.

A generalized improvement over a retaining wall can be shown by running this numerical model in Matlab. If the percentage of load transferred to piles from the wall is low, the piling impact is not substantial and using piered retaining wall is arguable, since the use of piles beneath the retaining wall will not considerably improve the total lateral capacity. As the percentage of load transfer from wall to piles increases, the impact of piles becomes more prevalent and the necessity to utilize a piered retaining wall to achieve a desired lateral capacity instead of a simple typical wall becomes more obvious.

4 ACKNOWLEDGMENT

The author would like to acknowledge Dr. Wei Dong Guo for his guidance, mentoring and support and Mr. Nick Thill for his contribution during the numerical modeling process.

5 REFERENCES

- [1] Andraws, K. Z., and El-sohby, M. (1973). Factors affecting coefficient of earth pressures K_0 . ASCE Journal of Geotechnical Engineering, vol. 99.
- [2] Caquot, A., and Kerisel, J. (1948). Tables for the calculation of passive pressure, active pressure and bearing capacity of foundations. Paris: Gauthier- Villard.
- [3] Kerisel, J., and Absi, E. (1990). Tables de pousse'e et de but'e des terres. 3rd ed. Presses de l'E' cole Nationale des Ponts et Chausse'es, Paris.
- [4] Benmebarek, S., Khelifa, T., Benmebarek, N. and Kastner, R. (2007). Numerical evaluation of 3D passive earth pressure coefficients for retaining wall subjected to translation. Computers and Geotechnics, 35, 47-60.
- [5] Cundall, P. A. (1987). Distinct element models of rock and soil structure. Analytical and computational methods in engineering rock mechanics. London: Allen & Unwin, chap 4-pp187-190.
- [6] Matlock, H., and Reese, L. C. (1960). Generalized solutions of laterally loaded piles. Journal of Geotechnical Engineering, ASCE, 86(5):63-91.
- [7] Guo, W. D. (2003). A simplified approach for piles due to soil movement. Proc. of the 12th Pan-American Conference on Soil Mechanics and Geotechnical Engineering, Cambridge, MIT, U.S.A. Vol. 2, 2215-2220.
- [8] Chen, Z. Y., and Li, S. M. (1998). Evaluation of active earth pressure by the generalized method of slices. Canadian Geotechnical Journal, 35(4):591-599.

Evaluation of Thermal Response Tests in Energy Piles

Seung-Rae Lee¹, Seok Yoon², Hyun-Ku Park³, Gi-Dae Oh⁴

¹ PhD. Professor, Dept. of Civil and Environmental Engineering, KAIST, Daejeon, Korea

² PhD Student, Dept. of Civil and Environmental Engineering, KAIST, Daejeon, Korea

³ PhD. Post Doctor, Dept. of Civil and Environmental Engineering, KAIST, Daejeon, Korea

⁴ MSc. Senior Researcher, Power System Lab, KEPRI, Daejeon, Korea

ABSTRACT

This paper describes an experimental and analytical study on thermal response test in precast-high strength concrete (PHC) energy piles. The thermal response tests (TRTs) of PHC energy pile were carried out using two type of ground heat exchangers (GHEs) : W and 3U-shaped heat exchangers. Ground thermal conductivity was measured by laboratory test using transient hot wire method and inversely estimated from TRT results. Total thermal resistance was also measured by TRT and compared with an analytical solution. Ground thermal conductivity of W-shaped heat exchanger was higher, and total thermal resistance was smaller than 3U-shpaed heat exchanger because of different conditions such as pile size and volume of grout.

Keywords: Ground thermal conductivity, Thermal Response Tests, Thermal Resistance, Ground Heat Exchangers

1. INTRODUCTION

Subsurface geothermal resources represent a great potential of directly usable energy, especially in connection with foundations and heat pumps. Geothermal energy used to be called ubiquitous energy because it can be used at any time at any place. Geothermal energy can be obtained by means of borehole heat exchangers. With geothermal cooling/heating systems, heat energy is fed into and withdrawn from the ground via GHEs. Conventional GHEs consist of U-shaped GHEs inserted into a borehole. Moreover, recently, energy foundations substitute boreholes in the heat exchanger system. That is, GHEs can be embedded in piles, and thus it decreases initial construction cost. Energy pile generally has shorter length in the rage of several tens of meters. In Korean practices, PHC piles are broadly used [1].

This research investigates an experimental and analytical study of energy piles which are composed of 3U and W shaped heat exchangers. PHC energy piles were installed at an electric substation in Suwon, Korea. TRT results were calculated using simple line source theory to derive effective ground thermal conductivity. Thermal resistance was also calculated and compared by both experimental and analytical solutions.

2. THEORETICAL BACKGROUND

2.1 Heat transfer mechanism of GHE

In the GHEs system, heat is extracted from or released to surrounding ground through fluid circulating, for example, in a U-type pipe embedded in a borehole. The heat transfer

mechanism of a ground heat exchanger is quite complex and conjugated because of various heat transfer mechanisms involved inside and outside GHEs. Soil is a multiple phase system involving complex heat transfer mechanisms, but heat transfer in soils occurs mainly through conduction [2], whereby energy is passed from one region of a medium to another by molecular transfer. According to Fourier's law, the heat flux through an arbitrary area (A) during time t can be written as

$$q = \frac{Q}{At} = \frac{\dot{Q}}{A} = -\lambda \frac{\partial T}{\partial x} \quad (1)$$

where λ is the thermal conductivity and $\partial T/\partial x$ is the temperature gradient. Heat exchange rate of circulating water in the GHE by conduction can be represented by temperature difference between initial temperature of soils and fluid divided by total thermal resistance. The heat transfer process can be divided into steady state inside the borehole, and transient state outside it. Thermal resistance inside the borehole is composed of fluid convection, pipe conduction, grout conduction and pile conduction. Thermal resistance outside the borehole is that of conduction in the soil [3], [4].

$$\frac{Q}{L} = \frac{[(t_i + t_o) / 2] - t_\infty}{\sum R} \quad (2)$$

Here, L : length (m)

t_∞ : initial temperature of soils

t_i, t_o : inlet and outlet temperature of GHEs, respectively

$\sum R$: total thermal resistance

$$(\sum R = R_{soil} + R_{pile} + R_{grout} + R_{pipe} + R_{convection})$$

Based on equation (1) and (2), two kinds of models such as analytical models and numerical models can be applied to obtain the thermal conductivity. The applicability depends on the assumption and the methodology adopted in the models. Among many models, a line source model is widely used for simplicity and convenience. The governing equation of the model represents a linear characteristic for long time measurement. The GHEs pipe can be assumed as a line source because the radius (r_b) is much smaller than the length of borehole. An effective thermal conductivity (λ) can be solved by equation (3). In the equation, T_f represents an average temperature of fluid that flows inside the borehole. T_o is an initial temperature, Q is an input power (W), L is a length of borehole (m), a is a thermal diffusivity (m^2/s), R_b is a thermal resistance of borehole, and γ is an Euler constant (0.5772).

$$T_f - T_o = \frac{Q/L}{4\pi\lambda} \ln t + \frac{Q/L}{4\pi\lambda} \left(\frac{4at}{r_b^2} - \gamma \right) + \frac{Q}{L} R_b + T_o + \frac{Q/L}{4\pi\lambda} \left(\frac{4at}{r_b^2} \right) \left(1 - \frac{r_b^2}{16at} \right) \quad (3)$$

An average temperature of fluid (T_f) can be expressed by a 1st linear equation with respect to $\ln t$, and it can be described by

$$T_f = bx + c \quad (4)$$

$$b = \frac{Q/L}{4\pi\lambda}, \quad x = \ln t, \quad \text{and} \quad c = b \left(\frac{4at}{r_b^2} - \gamma \right) + \frac{Q}{L} R_b + T_o.$$

Once b can be solved, an effective thermal conductivity (λ) can be obtained by

$$\lambda = \frac{Q/L}{4\pi b} \quad (5)$$

Therefore, fluid temperatures at inlet and outlet of GHEs can be measured with respect to time by the thermal response test, and an effective thermal conductivity can be obtained with the value of the slope (b) from the $T_f - \ln t$ relationship.

3. EXPERIMENTAL SETUP

3.1 Thermal Response Test

PHC piles were installed for an energy pile system (Fig.1). Table 1 shows dimensions of energy piles and GHEs. 3U and W shaped polybutylene pipes (inner/outer diameter of pipe=0.016/0.2m) were used. The depth and inner diameter of PHC pile between 3U and W-shaped GHEs were not equal because of construction condition. Cement grout with cement to water ratio of 0.5 was poured and cured for more than 28 days. The ground was composed of weathered granite soil and stiff weathered rock.

Ground water level was 4.5m below from the top of embedded energy pile. Average void ratio e and water content w of soil below and above the ground water table were measured as follows: $e=0.66$, $w=12.4\%$ above G.W.T. and $e=0.45$, $w=16.7\%$ below G.W.T.

Thermal conductivity of the weathered granite soil was measured using TP-02 device (Hukseflux Thermal Sensors Inc.), based on a transient hot-wire method. Soil was remolded to have the same void ratio and water content of the construction site. Thermal conductivities of soils above and below ground water table were measured as 1.1 and 2.4 W/m-K, respectively.

Fig. 2 shows an experimental system for the thermal response test. Constant heat flux was applied to water tank using an electric heater, and TRTs were performed until steady state condition was attained. Temperatures of water at inlet and outlet were monitored during the tests, and flow rate was also measured at outlet. Different heat flux and flow rate were applied for the energy pile with 3U and W-shaped GHEs as follows: 1,000W and 17 *lpm* (liter per minute) for 3U case, 800W and 16 *lpm* for W case.

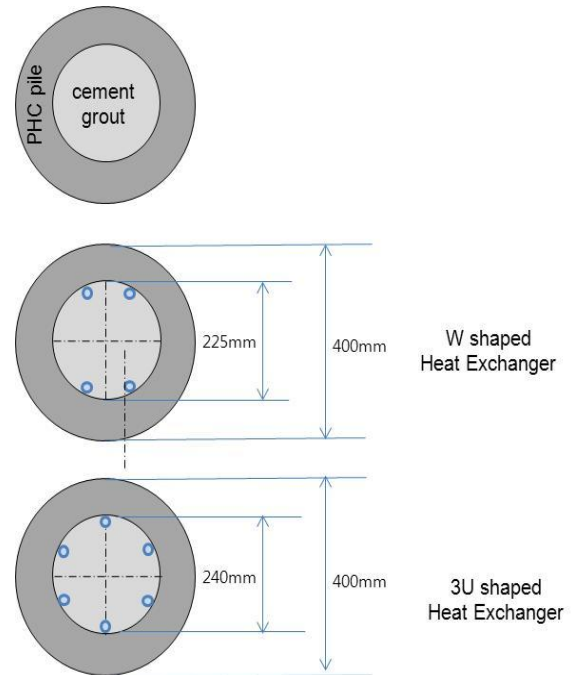


Fig. 1 Plane view of energy pile with 3U and W GHEs

Table 1 Dimensions of energy pile with 3U and W GHEs

Dimension of pile	3U	W
Pile Depth (m)	13.75	13.27
Pile Inner Diameter (mm)	240	225
Pile Outer Diameter (mm)	400	400

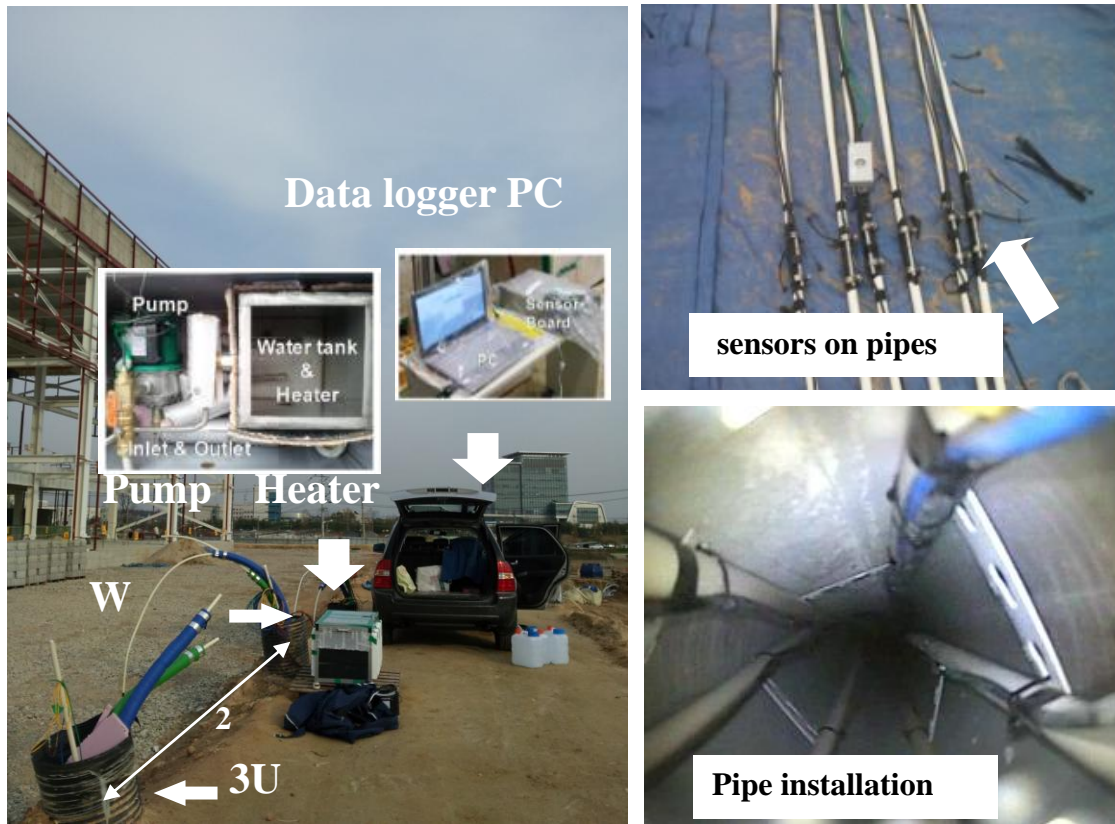


Fig. 2 Experimental system for thermal response tes

3.2 Test Results

The thermal response test was conducted for more than 30 hours. Mean circulating fluid temperature-time curves measured during TRTs are plotted in Fig. 3. Initial temperature of soil was between 16~17 °C. Temperature of fluid in 3U-shaped GHE reached to 30.19 °C, and 27.52 °C in W-shaped GHE. As a mean circulating fluid temperature reaches to lower value, heat can be well transferred to the ground. An effective ground thermal conductivity can be calculated using Eq (5), and total thermal resistance can be calculated using Eq (2). The ground thermal conductivity of 3U and W-shaped GHEs was 2.14 and 2.32 W/m·K, respectively. Total thermal resistances of 3U and W-shaped

GHEs were 0.1772 and 0.1702 m·K/W. W-shaped GHE has a higher ground thermal conductivity and lower thermal resistance than 3U-shaped GHE from experimental data. Total resistances of 3U and W-shaped GHEs from the analytical solution were 0.1998 and 0.1991 m·K/W. The relative error between experimental and analytical results was between 12~17%. W-shaped GHE has lower total thermal resistance than 3U-shaped GHE. It is thought that there is a difference of inner diameter in PHC pile, and it came up with different grout thermal resistance. Total thermal resistance from the analytical solution under the same condition with equal size of PHC pile and pile depth was also calculated. Total thermal resistances of 3U and W-shaped GHEs above the condition were 0.1953 and 0.1991 m·K/W, respectively.

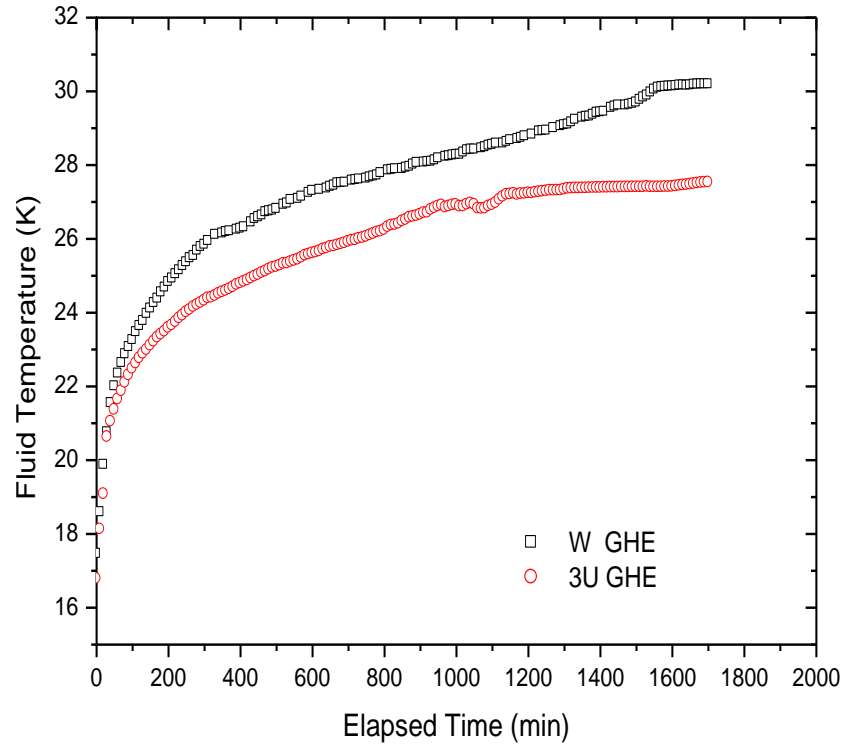


Fig. 3 Temperature variation of fluid

Table 2 Summary of TRTs

GHE type	Input Heater (W)	Released Heater (W)	λ_{ground} (W/m·K)	ΣR , Experiment (m·K/W)	ΣR , Analytical (m·K/W)	ΣR , Analytical (same condition)
3U	1000	997	2.14	0.1772	0.1998	0.1953
W	800	838	2.32	0.1702	0.1991	0.1991

It can be seen that 3U-shaped GHE has a little lower thermal resistance than W-shaped GHE under the same condition. However, it is necessary to consider a proper pile inner size to consider heat transfer mechanism between 3U and W-shaped GHEs.

4. CONCLUSION

An experiment system for thermal response test for energy piles was established in the field. TRTs were performed for two prototype PHC piles with 3U and W-shaped GHEs in a partially saturated weathered granite soil and rock condition. The ground thermal conductivity of 3U and W-shaped GHEs was 2.14 and 2.32 W/m·K, and total thermal resistance of 3U and W-shaped GHEs was 0.1772 and 0.1702 m·K/W from

TRTs, respectively. W-shaped GHE has a higher ground thermal conductivity and lower thermal resistance than 3U-shaped GHE based on experimental data. Total resistance of 3U and W-shaped GHEs from analytical solution was 0.1998 and 0.1991 m·K/W, respectively. However, if the condition is same, total thermal resistance of 3U and W-shaped GHEs will be 0.1953 and 0.1991 m·K/W, respectively. It can be concluded that 3U and W-shaped GHEs show a very similar heat transfer mechanism for small diameter energy piles. However, it is indispensable to consider the effect like of inner size and pile depth in order to analyze heat transfer in detail.

5. ACKNOWLEDGEMENT

This study was financially supported by National Research Foundation of Korea funded by the Ministry of Education, Science, Technology (under grant No. 2010-00014639) and 2011 Construction Technology Innovation Project, (11 Technology Innovation E04).

6. REFERENCES

- [1] Baek, S.K. An, H.J, Lim, S.K. Development of ground heat exchangers installed in building foundation. Proceedings of SAREK Summer Annual Conference 2007. p. 277-282,
- [2] Brandl, H. Energy foundation and other thermo-active ground structures. *Geotechniques* 2006, 56(2), p. 81-122.
- [3] Liu Jun, Zhang Xu, Gao Jun, Yang Jie. Evaluation of heat exchange rate of GHE in geothermal heat pump system. *Renewable Eenergy* 2009, 34, pp. 2898-2904
- [4] Min, H.S. Yun, T.S. Jeong, S.S. Effect of Group Spacing of Energy Piles on Thermal Analysis, *Journal of Korean Geotechnical Society* 2011, 27(8), pp. 39-50.

Experimental Study on Mechanical Characteristics of Soil-Geosynthetic Interface

Md. Bellal Hossain, Md. Zakaria Hossain and Toshinori Sakai
Department of Environmental Science & Technology, Mie University, Japan

ABSTRACT

The shear deformation behaviour along soil–geosynthetic interfaces has been investigated and the results are compared based on the backfill material, types of inclusion, and interface mechanical properties. Three soils (sandy, clayey, and pure sand) in combination with four different geosynthetics (one geotextile and three geogrids) were tested at various loading conditions in direct shear. Test results reveal that the stress-deformation behaviour of the geotextile and geogrid interfaces with sandy and clayey backfills can be defined as hyperbolic. For the pure sand-geogrid interfaces, the relationship is followed by displacement hardening and softening behaviour. The dilatancy behaviour of a particular soil-geosynthetic interface is found similar at all normal stresses. Both contractive and dilative nature is observed for the interfaces with pure sand. On the contrary, only negative dilatancy or contractive behaviour is observed for sandy and clayey backfills with all geosynthetics. Based on the test results, a simplified equation has been proposed for the nonlinear soil-geosynthetic interface shear strength envelopes which was in good agreement with the experimental data.

Keywords: Geosynthetics, Interface behaviour, direct shear test, shear strength envelop

1. INTRODUCTION

The practice of reinforcing the soil with various tensile inclusions has been widely implemented in geotechnical engineering for the last few decades. The interaction between soil and reinforcement is of utmost importance for the design and performance of reinforced soil structures, and this interaction can be very complex depending on the nature and properties of the reinforcement. Various types of geosynthetic materials have been used for soil reinforcement including geotextiles (woven and nonwoven), geogrids and geocells. Whatever the reinforcement and backfill materials are used for the design of a reinforced soil structure, the interaction properties of soil-reinforcement interface play an important role. The interaction mechanism between the reinforcement and the soil can be classified into two types; sliding of soil over the reinforcement and pullout of reinforcement from the soil [1]. The direct shear and pullout tests are widely used methods to study quantitatively these interaction mechanisms.

Practically, the direct shear test is a suitable mean to study the interaction between soil and reinforcement because it can simulate the shear mechanism along a potential failure plane in reinforced earth structure. Proper representation of the soil-geosynthetic interfaces under direct shear mode is also important for numerical simulation of the deformation response for retaining structures.

The shear strength of soil-geosynthetic interfaces has been investigated using direct shear tests by a number of researchers [1-9]. They used various types of geosynthetic materials like High density polyethylene (HDPE), poly propylene (PP), Polyester (PET) yarns coated with PVC, basalt fiber geotextile and geogrids etc. The present study is

the continuation of the previous study conducted by the Authors [9]. Here, in addition to Toyoura sand, two different soils (sandy and clayey) have been used as backfill materials to describe the interface behaviour for the same geosynthetic materials. From test results, the shear strength parameters and stress-deformation behaviour have been compared and discussed briefly.

2. MATERIALS AND METHODS

2.1 Backfill materials

Three types of soils were used as backfill material in this study. Air-dry pure silica sand named as Toyoura sand, one sandy and one clayey soil have been used to evaluate the interface behaviour with the same geosynthetic materials. Before conducting the interface direct shear tests, the physical

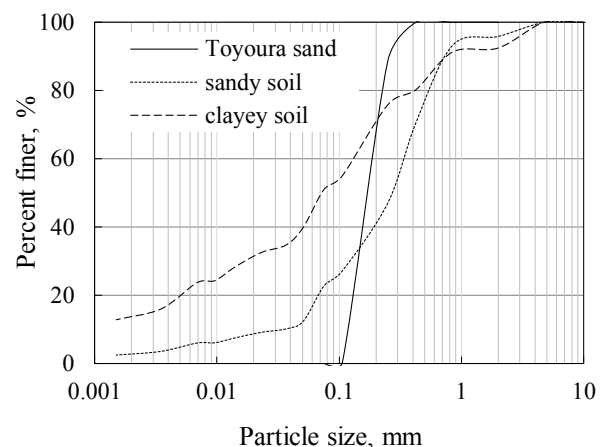


Fig. 1 Gradation curve of experimental soils

properties of the soils were tested in the laboratory. The tests of physical properties reveal that Toyoura sand has no fine content less than 0.075mm with effective diameter D_{10} of 0.01 mm, D_{30} of 0.15 mm, D_{60} of 0.19 mm, the uniformity coefficient (Cu) of 15.45, and the coefficient of curvature of the gradation curve (Cc) of 9.89. The specific gravity, maximum and minimum void ratio are $G_s=2.64$, $e_{max}=0.98$ and $e_{min}=0.61$, respectively. The water content of sand was less than 1%, which corresponds to air-dried condition. The optimum water content of sandy and clayey soils was 12% and 15%, respectively. Fig.1 represents the gradation curves of the experimental soils. According to JGS engineering classification system, the sandy and clayey soils are classified as SF and CL, respectively. The major physical properties of the soils are listed in Table 1.

Table 1 Physical properties of the backfill soils

Properties	Clayey	Sandy
Particle density, ρ_s	2.7g/cm ³	2.64g/ cm ³
Water content, W_{opt}	15%	12%
Liquid limit, LL	42.7%	---
Plastic limit, PL	25.0%	---
Plasticity index, PI	17.7	---
Sand (75 μ m-2mm)	41%	73%
Silt (5 μ m-75 μ m)	32%	19%
Clay <5 μ m	20%	4%

2.2 Geosynthetics

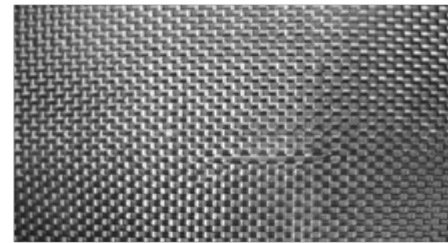
One woven geotextile and three geogrids, made of Basalt fiber, are used in this study. These materials possess good property of elasticity and stretch tension with good resistance to acid, alkali, heat and vibration. It has also non-conductive and non-magnetic resistance. The physical characteristics of these geosynthetics are listed in Table 2. For the purpose of discussion, the geotextile is noted as GT and the geogrids are noted as GG1, GG2 and GG3 as shown in Fig. 2.

Table 2 Physical properties of geosynthetic

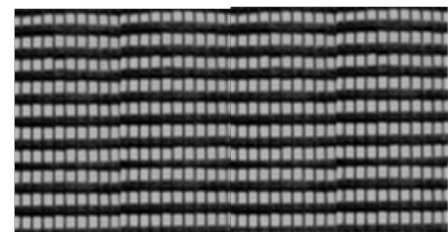
Properties	Type of geosynthetics			
	GG1	GG2	GG3	GT
Specific weight, gm/m ²	165	165	350	450
Percent open area, %	45	65	70	---
Ultimate tensile strength (kN/m)				
Machine direction	50	50	50	1870
Cross direction	40	40	50	1600

3. TESTING METHODS

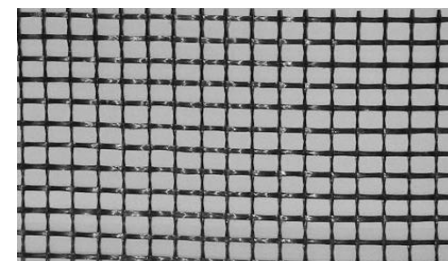
A small scale direct shear testing device which consists of a fixed lower box and a moving upper shear box has been used in this study. Both the shear boxes have same inside dimension of 150mm in length and 100mm in width. Detail of this device is also available at [9]. The applied shear force, horizontal and vertical displacements were recorded using one load cell, and two displacement transducers (one for horizontal and other for vertical displacement measurement) connected to a computer through a data-acquisition system. The geosynthetic specimens were positioned on a substrate



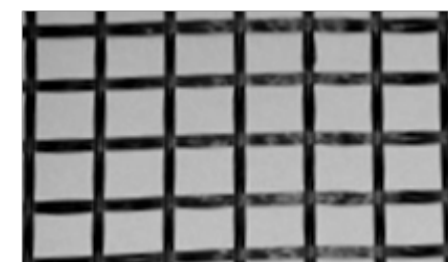
GT



GG1



GG2



GG3

Fig. 2 Geosynthetic samples used in this study

placed on the top of the lower box. Subsequently, the specimen was clamped on the front edge of the substrate steel plate using four aligned bolts and two steel clamping blocks. In case of pure sand, the upper shear box was filled by raining the sand from a height passing through two consecutive sieves. The dry unit weight of the sand mass in upper box was 1.63 g/cm^3 (15.9 kN/m^3) which corresponds to relative density (D_r) of 95%. The height of the sand layer in upper shear box was 70mm. For sandy and clayey soils, water was added to the soil samples to its optimum level before filling up the shear box. The upper box was filled by the soil in three steps with same compaction energy for every step. Thus, the density of backfill soil was kept almost constant. The direct shear tests were conducted using four different normal stresses of 40, 80, 120 and 160 kPa. All the tests involved applying the normal stress and monitoring the vertical displacement. The shear load was only applied after the vertical displacement had reached equilibrium. The normal load was maintained constant during shearing process. The rate of shearing was maintained at 0.5mm/min for all the tests. The maximum shear strength obtained during the shear process was recorded as the peak shear strength. The same procedure was repeated for all types of geosynthetics. For three soils and four types of geosynthetics, a total of 48 Nos. of tests were conducted in this study.

4. RESULTS AND DISCUSSION

4.1 Shear stress-displacement relationship

A series of direct shear tests were performed to obtain the stress-deformation characteristics of the geosynthetic interfaces for different backfill soils. The test results reveal that the relationship between shear stress and relative displacement largely depends on the type of backfill rather than the type of geosynthetics. Fig.3 represents the stress-displacement relationship between different backfill soil and geosynthetic interfaces for the constant normal stresses of 40 and 160kPa. Since, similar relationship is observed for the normal stresses of 80 and 120kPa, related data are not presented here. It is seen that the stress-displacement relationship of geotextile (GT) interfaces is same for all the backfill soils (Toyoura sand, sandy soil and clayey soil). The relationship for GT interfaces can be defined as hyperbolic in nature where no displacement softening behaviour is observed. In case of pure sand, however, some insignificant softening behaviour is observed at normal stress of 40kPa. In case of geogrid interfaces (GG1, GG2 and GG3), with sandy and clayey soils, the stress-displacement relationship is found similar to its GT interfaces. But, with Toyoura sand, the geogrid interfaces produce a well defined peak and residual shear stresses for all applied normal stresses. Before and after the peak shear stress, displacement hardening and softening behaviour is clearly observed. Maximum shear resistance mobilizes within 3-6mm of shear displacement for geogrid interfaces with pure sand backfill. The shear strength is found increasing with the increase of normal stress which is a common phenomenon for all soil-geosynthetic interfaces tested in this study.

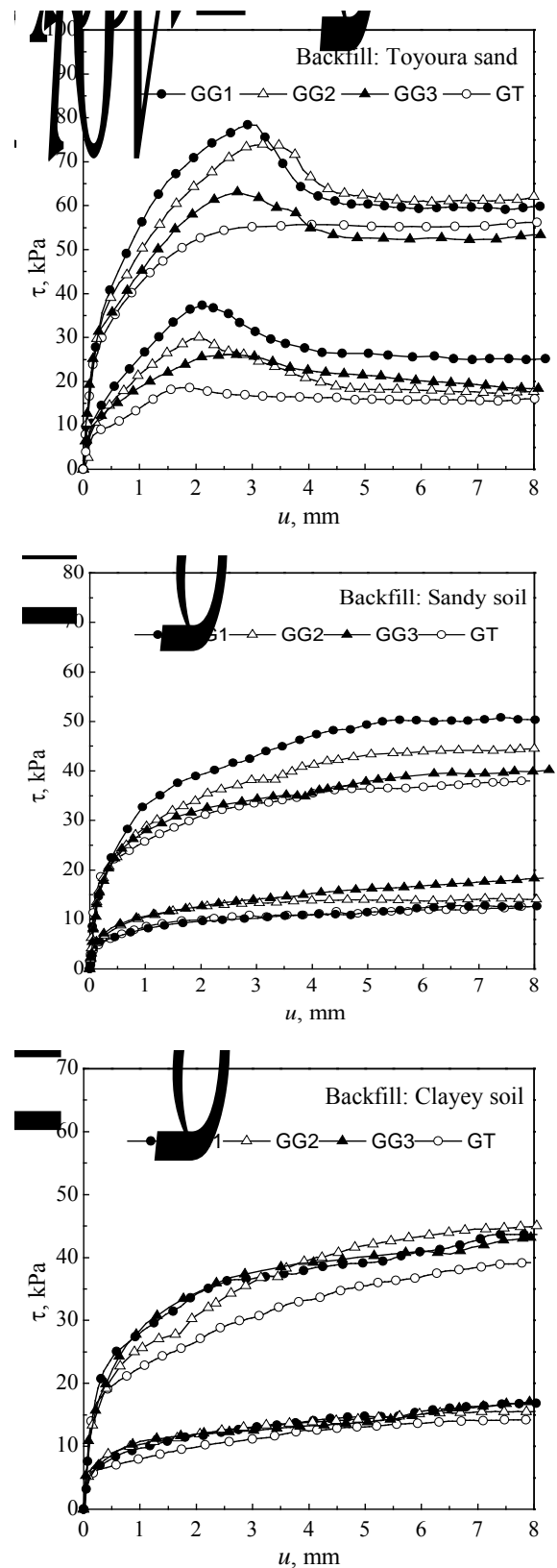


Fig. 3 Shear stress-displacement relationship of the interfaces for constant normal stresses of 40kPa and 160kPa. τ , shear stress; u , relative displacement.

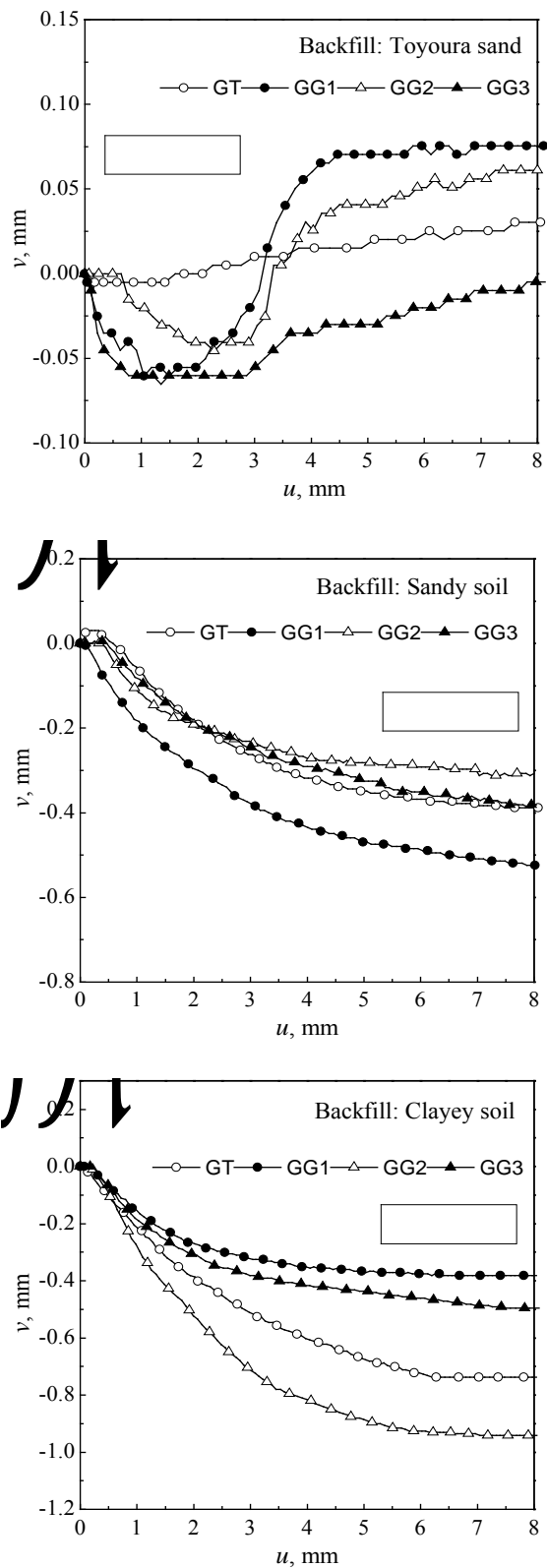


Fig. 4 Vertical vs. shear displacement relationships of the geosynthetic interfaces with different backfill materials. v , vertical displacement; u , shear displacement.

4.2 Dilatancy behaviour

From test results, it is observed that the dilatancy behaviour of a particular interface is similar for any normal stress. Thus, for comparison, the vertical versus shear displacement curves obtained from the direct shear tests on the soil-geosynthetic interfaces at 160kPa applied normal stress are shown in Fig. 4. Both contractive and dilative nature is observed for the interfaces with the backfill material of pure sand. On the contrary, for the sandy and clayey backfills, only contractive nature is observed for all the interfaces (Fig. 4). For pure sand-geosynthetic interfaces, the dilation with shearing indicates the presence of some degree of particle rolling and interlocking as dilation is required for the shearing and rearrangement of angular particles. For geogrid interfaces with pure sand, it is interesting to note that the value of maximum vertical displacement reduces with the increase of the percent open area of geogrid for a particular normal stress. And, the amount of dilation is seen higher at lower normal stresses and comparatively less at higher normal stresses. However, no such relationship is observed in case of sandy and clayey backfills which were mostly fluctuating in nature.

4.3 Interface Shear strength

The shear strength of a soil-geosynthetic interface is an essential parameter of slope stability analysis where slip surface runs along the geosynthetic. The test results show that the interface shear strength values are not linearly dependent on the normal stress. The relationship between interface shear strength and normal stress at the interface is generally considered to be linear and defined by (1).

$$\tau = a + \sigma_n \tan \delta \quad (1)$$

Where, τ is the soil-Geosynthetic interface shear strength; a is the interface adhesion; σ_n is the stress normal to the interface; and δ is the interface friction angle. In many cases, results from shear box tests showed that the relationship between τ and σ_n is not linear [10]. Usually, in those cases, approximate linear relationships (1) are often considered. This linear relationship may lead to significant errors where factor of safety of a slope is concerned.

For utilizing interface shear strength data and to prevent the errors, Giroud et al. [10] proposed a hyperbolic equation to represent a nonlinear relationship consistent with interface shear strength values obtained in laboratory shear box tests. The equation contains five parameters to be determined, and the determination of the order of hyperbola is a bit complex. However, it is observed that the interface shear strength data may be linear or nonlinear against the normal stress depending on the characteristics of geosynthetic and backfill materials. Therefore, it has been found that a similar type of generalised nonlinear equation is appropriate to represent both the linear and nonlinear peak shear strength data for the soil-geosynthetic interfaces studied in this research. The equation for interface shear strength, τ , can be expressed as

$$\tau = a_0 + \frac{\tau_0}{1 + \tau_0^m/a_i} \quad (2)$$

- Where, $\tau_0 = \sigma_n \tan \delta_0$
 σ_n = Normal stress
 δ_0 = Interface friction angle at very low normal stresses.
 a_0 = Pseudo adhesion at $\sigma_n = 0$ (i.e. intercept of the nonlinear curve with τ axis).
 a_i = Pseudo adhesion for higher values of σ_n .
 m = Curve fitting parameter; the value ranges from 0 to 1.

If the experimental data is available for very low normal stresses, a_0 can be obtained by extrapolating the curve of τ and σ_n . Otherwise, for practical purposes, a_0 can be taken as zero for the interface between geosynthetic and cohesionless soil. a_0 may not be zero for the interface with cohesive soil of high moisture content. In that case, the value of a_0 can be obtained by best fitting the nonlinear curve with the experimental data using a computer program. The interface friction angle, δ_0 , is initially calculated using the data of very low normal stresses. By the way of curve fitting, the value of δ_0 can be optimized if the data of low normal stress is not available. The value of a_i and m is completely depends on the available data of higher normal stresses. a_i can be obtained initially by fitting and extrapolating the straight line with the shear strength data points at higher normal stresses towards τ axis. The curve fitting parameter, m , is determined by the method of least square which is easy by using a computer program. Once m is obtained, the values of a_0 , δ_0 , and a_i can be optimized, if necessary, to get higher coefficient of regression (R^2) value. In case of truly linear data, the value of a_0 and a_i should be same and the value of m would be near zero or may be negative. In that case, equation (1) is recommended which is simple and convenient for linear data. The proposed equation is not an empirical equation and the parameter values are adjustable based on the extent of the available experimental data. Thus, it may not be realistic to use the equation for the purpose of prediction. Because it is found that the value of a_i and m is controlled by the experimental data of higher normal stresses.

The equation is found suitable for better representation of nonlinear experimental data and minimizing the errors where appropriate shear strength value is very important such as in slope stability analysis of reinforced earth structure.

The shear strength envelopes as shown in Fig. 5 were generated using (2) for the geotextile (Fig. 5a) and one geogrid (Fig. 5b) interfaces with Toyoura sand (T), sandy soil (S) and clayey soil (C). Here, for pure sand, the value of interface adhesion, a_0 , is taken as zero. The parameters value of the shear strength envelopes used in Fig. 5 are listed in Table 3. It is seen that the nonlinear shear strength envelopes are in good representation with the experimental data points.

4. CONCLUSIONS

The interface direct shear tests were carried out to evaluate the mechanical properties of a new type of geosynthetic material with three different backfill soils.

The constitutive behaviour of the geotextile and geogrid interfaces with sandy and clayey soil is found similar in nature which can be defined as hyperbolic relationship. In case of pure sand-geotextile interface, the behaviour is also hyperbolic. However, for sand-geogrid interfaces, the constitutive behaviour is followed by displacement hardening and softening behaviour. The dilatancy behaviour of a particular soil-geosynthetic interface is found similar for all normal stresses. Both contractive and dilative nature is observed for the interfaces with pure sand. On the contrary, only negative dilatancy or contractive behaviour is observed for sandy and clayey backfills with all geosynthetics.

Based on the test results, a simplified nonlinear equation has been proposed for the soil-geosynthetic interface shear strength envelopes which was in good agreement with the experimental data.

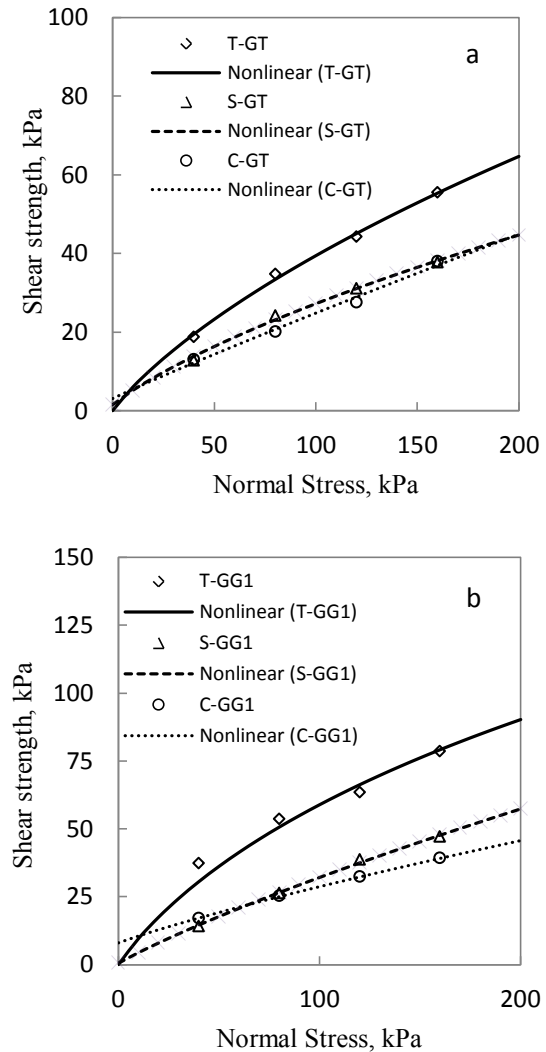


Fig. 5 Nonlinear shear strength envelopes for the geotextile (a), and geogrid (b) interfaces with different backfill soils.

Table 3 The parameter values of the interface shear strength envelops plotted in Fig. 5

Interfaces	a_0	m	a_i	δ_0	R^2
T-GT	0	0.53	10.5	37.7	0.993
T-GG1	0	0.71	31.2	48.5	0.965
S-GT	1.5	0.53	10.0	24.2	0.990
S-GG1	0.5	0.47	15.0	23.9	0.996
C-GT	3.1	0.24	7.9	15.5	0.982
C-GG1	8	0.42	10.0	16.3	0.999

5. REFERENCES

- [1] Jewell, R.A. and Milligan G.W.E., Sarsby, R.W., and Dubois, D., "Interaction between soil and geogrids", Polymer Grid Reinforcement, Thomas Telford Limited, London, March 1984, pp. 18-30.
- [2] Ingold, TS., "Laboratory pull-out testing of grid reinforcements in sand", Geotech. Testing J., Vol. 6, No. 3, 1983, pp. 101-111.
- [3] Palmeria E M and Milligan GWE, "Scale and other factors affecting the results of pull-out tests of grids buried in sand", Géotechnique, vol.39, No. 3, 1989, pp. 511-524.
- [4] Bergado, D. T., Chai, J.C., Abiera, H. O., Alfaro, M.C., Balasubramaniam, "Interaction between Cohesive-Frictional Soil and Various Grid Reinforcements", Geotextiles and Geomembranes, Vol. 12, No. 4, 1993, pp. 327 – 349.
- [5] Bergado D. T., Shivashankar R., Alfaro M. C., Chai JC, Balasubramaniam A. S., "Interaction behaviour of steel grid reinforcements in a clayey sand", Géotechnique, 1993, vol.43, No.4, pp. 589-603.
- [6] Cancelli, A., Rimoldi, P., and Togni, S., "Frictional characteristics of geogrids by means of direct shear and pullout tests", Proc., Int. Symp. on Earth Reinforcement , Kyushu Univ., Fukuoka, Japan, 1992, pp. 51–56.
- [7] Cazzuffi, D., Picarelli, L., Ricciuti, A., and Rimold, P., "Laboratory investigations on the shear strength of geogrid reinforced soils", ASTM Spec. Tech. Publ., 1993, 1190, pp. 119–137.
- [8] Bakeer, R. M., Sayed, M., Cates, P., and Subramanian, R., "Pullout and shear test on geogrid reinforced lightweight aggregate", Geotextiles and Geomembranes, vol. 16, No. 2, 1998, pp. 119–133.
- [9] Hossain, M. B., Hossain, M. Z. and Sakai, T., "Interface Behaviour of Basalt Geosynthetic with Sand Using Direct Shear Device", in Proc. 1st International Conference on Geotechnique, Construction Materials and Environment, Mie, Japan, Nov.21-23, 191-196, 2011.
- [10] Giroud, J. P., Darrasse J., and Bachus, R. C., "Hyperbolic expression for soil-geosynthetic or geosynthetic-geosynthetic interface shear strength", Geotextiles and Geomembranes, Vol. 12, No. 3, 1993, pp. 275 -286.

An Interpretation of Mechanical Properties of Bentonite as a Non-linear Elastic Material

Y. TAKAYAMA, S. TSURUMI, A. IIZUKA, K. KAWAI
KOBE UNIVERSITY, JAPAN
S. OHNO
KAJIMA CORPORATION, JAPAN

ABSTRACT

Due to its low permeability and remarkable expansion characteristics, bentonite has an excellent potential to be used as a buffer in the disposal of nuclear waste. In order to examine the long-term safety of bentonite buffer in the disposal of nuclear waste, constitutive modeling of bentonite materials and numerical simulations based on the constitutive models have been actively pursued in recent years. Bentonite materials are usually modeled as a geo-material with elasto-plastic isotropic compression/expansion and plastic dilatancy characteristics. However, based on recent experimental data, the authors feel that mere constitutive modeling for geo-materials may not be applicable to bentonite materials. In this paper, fundamental considerations of elasto-plastic constitutive modeling for fully saturated bentonite materials are investigated. According to uniaxial compression test data by Sasakura et al. (2003), where lateral earth pressure was measured, it was found that the hysteresis response between loading and unloading processes does not appear. It suggested that bentonite is an elastic material in which the swelling line corresponds to the normally consolidated line in the 'e-logp' relationship. Also, according to triaxial CU test results of bentonite materials, it was seen that the effective mean stress remains almost unchanged during shearing. This implies that bentonite does not have dilatancy characteristics as defined by the critical state theory. Similar interpretation can be derived from the experimental results obtained from a series of triaxial CD tests by Cui et al. (2006).

1. INTRODUCTION

Bentonite is known to be a material that has remarkable expansion characteristics and very low permeability. Therefore, bentonite as a material, is expected to be useful as a buffer in the geological disposal of nuclear waste facility. As a result, its mechanical and mineralogical properties have been widely investigated. At nuclear disposal sites, bentonite is expected to play a role as a buffer, preventing leakage of radioactively polluted water by its abilities to self-seal and to mitigate stresses generated due to creep of base rock. Also, the geological disposal of nuclear material at such a facility needs to be stable and safe for an extremely long period of time. In order to address such problems, it is necessary to predict the long-term behavior of geological disposal at a nuclear waste facility and reliable numerical simulation techniques are required that can reliably address these issues. Constitutive modeling that describes the mechanical properties of a material is a key technique in such numerical simulations. Constitutive models for bentonite materials have been formulated phenomenologically based on the elasto-plastic response under loading and unloading processes and dilatancy characteristics during shearing, like other clayey materials. However, in the case of bentonite materials, we feel that the available experimental data to support constitutive modeling is not sufficient. Remarkable expansion characteristics on water absorption and very low permeability of bentonite make it difficult to interpret its fundamental mechanical behavior. The aim of this paper is to reconsider the fundamental mechanical behavior of bentonite

materials based on recent experimental data and to discuss the theoretical formulation of constitutive modeling for bentonite materials.

2. Isotropic compression and swelling characteristics of saturated bentonite materials

Usually, isotropic compression and swelling characteristics are discussed based on the experimental data obtained from triaxial tests under a drained condition. However, in the case of bentonite materials, available experimental data on the compression and swelling characteristics obtained from triaxial tests under the drained condition are neither sufficient nor reliable. The primary data used to justify constitutive models have come from oedometer tests. Compression and swelling behavior of bentonite materials obtained from the oedometer tests are not directly applicable for discussing compression and swelling characteristics under isotropic confining pressure, because the lateral stress cannot be measured in the oedometer tests. If the lateral stress could reliably be estimated, more intensive discussion and more strict interpretation on the compression and swelling characteristics of bentonite materials would have been possible. In this paper, we cite experimental data on bentonite materials where lateral stress was measured with a special oedometer test apparatus by Sasakura et al. (2003). We also discuss the compression and swelling characteristics of bentonite materials under isotropic confining pressure, which are the fundamental mechanical properties for constitutive modeling.

(1) K_0 compression and swelling test

Sasakura et al. (2003) carried out one-dimensional compression and swelling tests for Kunigel V-1, which is typically made of sodium bentonite and is planned to be used in nuclear waste disposal sites in Japan. The authors tried to measure lateral stress under one-dimensional loading and unloading processes with a special oedometer test apparatus. Their experimental results are shown in Fig. 1. It was found that the coefficient of earth pressure at rest, K_0 , remains almost at 1.0 under the normal compression process and then increases with OCR under the unloaded swelling process. The relationship between K_0 value and OCR is indicated in Fig. 2. In this figure, experimental data by Sasakura et al. (2003) is indicated by white circles and is compared to the empirical relation, Eq. (1) which relates K_0 -value and OCR through the evaluation parameter m as:

$$K_{0-NC} = K_{0-OC} OCR^m \quad (1)$$

where K_{0-NC} is the coefficient of earth pressure at rest under the normal compression process, K_{0-OC} is the coefficient of earth pressure at rest under the unloaded swelling process, OCR is the over-consolidation ratio defined by σ'_{v0}/σ'_v , σ'_{v0} is the pre-consolidation vertical stress, σ'_v is the current vertical stress and m is the evaluation constant. According to Fig. 2, Eq. (1) with $m=0.6$, it seems to satisfactorily explain

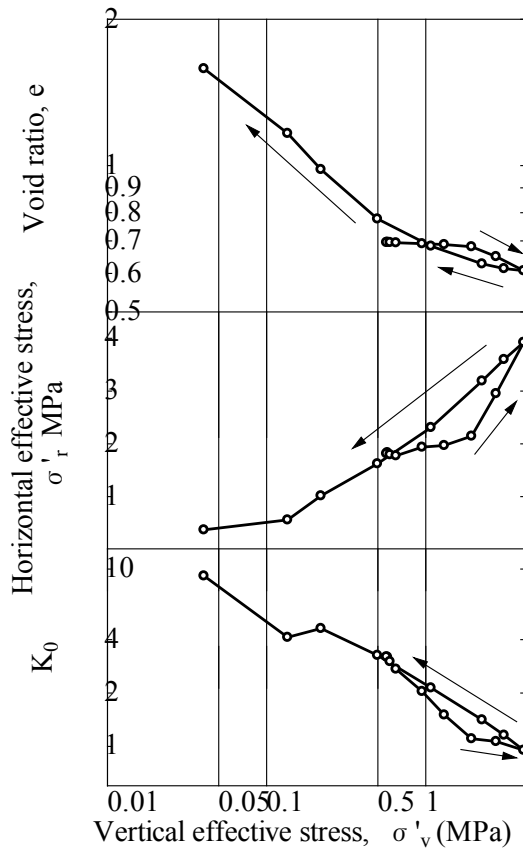


Fig. 1 K_0 compression and swelling test result

the experimental results of bentonite, Kunigel V-1. If one employs Eq. (1) with 0.6 as the value of m , in converting the vertical stress into the isotropic confining pressure, fundamental mechanical properties on compression and swelling characteristics under isotropic confining pressure can be discussed using experimental data obtained from the oedometer test.

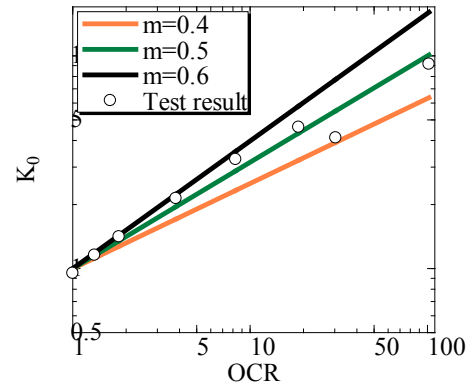


Fig. 2 Relationship between K_0 value and OCR

(2) Isotropic deformation characteristics

Fig. 3 shows one dimensional compression (consolidation) characteristics of Kunigel V1, obtained from oedometer tests by Sasakura et al. (2002) and Ishikawa et al. (1997). Normally, the consolidation lines by Sasakura et al. (2002) and Ishikawa et al. (1997) do not correspond to each other. This is because the nature of the bentonite slightly differs depending on the year it was produced and the content of the montmorillonite could be slightly different even in the same bentonite sample.

According to Kobayashi et al. (2007), one-dimensional normal consolidation characteristics of bentonite under fully

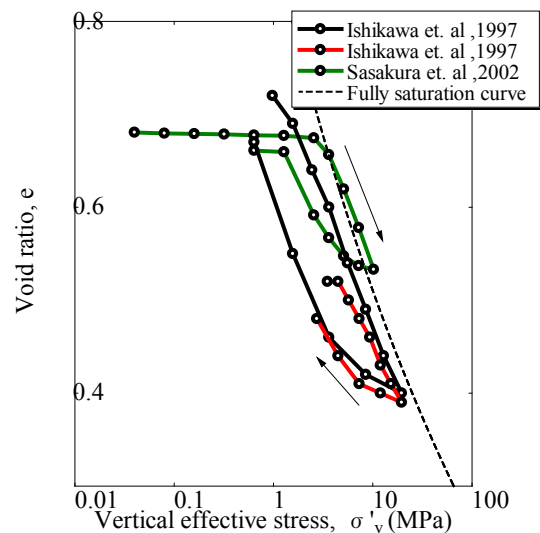
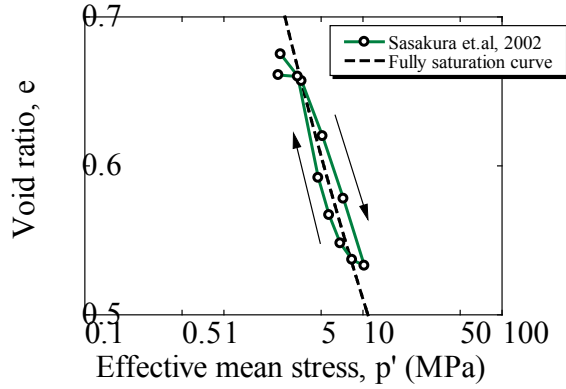


Fig. 3 One-dimensional compression (consolidation) characteristics of Kunigel V1

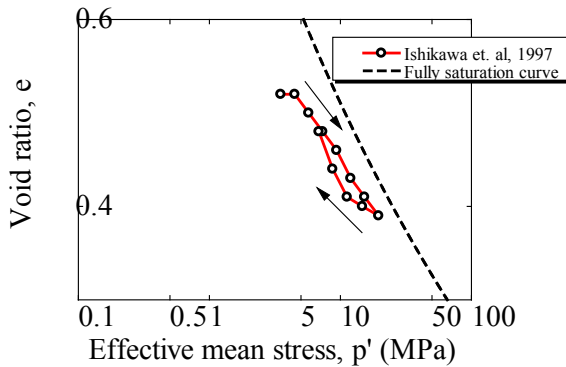
saturated state is uniquely expressed as:

$$e = \lambda_p \ln \frac{\sigma'_{v\max}}{\sigma'_v} \left/ \left(G_s - \lambda_p \ln \frac{\sigma'_{v\max}}{\sigma'_v} \right) \right. \quad (2)$$

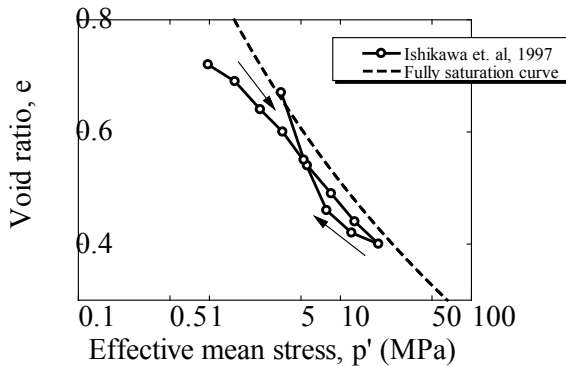
where λ_p is the material constant, G_s is the specific gravity of soil particle and $\sigma'_{v\max}$ is the reference and maximum vertical stress corresponding to the void ratio vanishing. This curve is called the full saturation curve. In the case of data by Sasakura et al. (2002), $\lambda_p = 0.156$, $G_s = 2.733$,



(A)



(B)



(C)

Fig. 4 Isotropic compression and swelling characteristics of saturated bentonite materials

$$\sigma'_{v\max} = 3.73 \text{ GPa}.$$

The effective vertical stress can be converted into an effective mean stress using Eq. (1) as:

$$p' = \frac{\sigma'_v + 2K_0\sigma'_v}{3} \quad (3)$$

where p' is the effective mean stress, σ'_v is the effective vertical stress and K_0 is the coefficient of earth pressure at rest. All data in Fig. 3 has been converted in terms of the effective mean stress using Eq. (3) and is depicted in Fig. 4 as a relation between the void ratio and the effective mean stress, in which $K_{0-NC} = 1$ and $m = 0.6$. It is found that the hysteresis-loop, between loading and unloading processes, disappears and the swelling line corresponds to the compression line in Fig. 4. If the compression and the swelling responses in Fig. 4 can be interpreted as isotropic compression and swelling characteristics of bentonite, the bentonite can be regarded as a material with no plastic deformation. In other words, it can be said that the bentonite is a non-linear elastic material.

3. Dilatancy characteristics of saturated bentonite materials

In this section, we examine the dilatancy characteristics of bentonite. Usually, dilatancy characteristics are examined by conducting triaxial CD tests in which the principal mean effective stress is maintained as a constant. However, in the case of bentonite materials, there is not sufficient reliable data being obtained from such tests. Therefore, we examine the dilatancy characteristic using the results of the triaxial CU test on bentonite.

(1) Triaxial CU test

Results of triaxial CU test on a few kinds of bentonite are shown in Fig. 5-8. These figures show the relationship between effective mean stress and

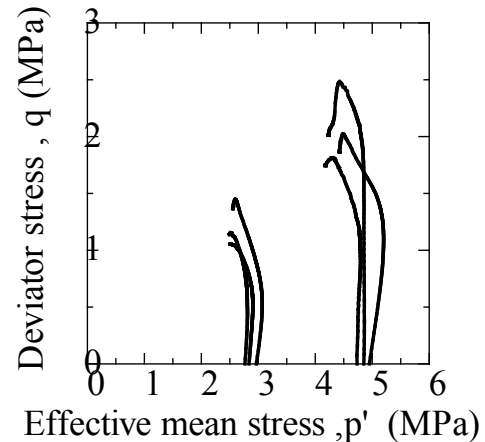


Fig. 5 Triaxial CU test result on sodium type of bentonite conducted by Sasakura et al. (2002)

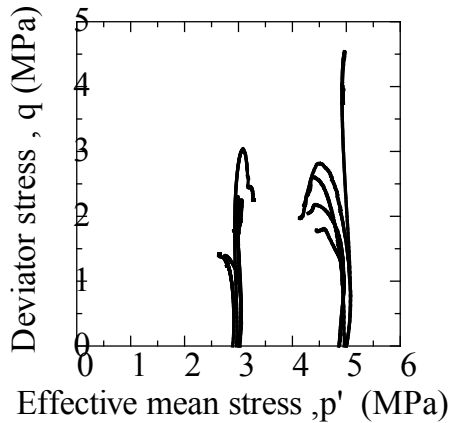


Fig. 6 Triaxial CU test result on calcium type of bentonite conducted by Sasakura et al. (2002, 2003)

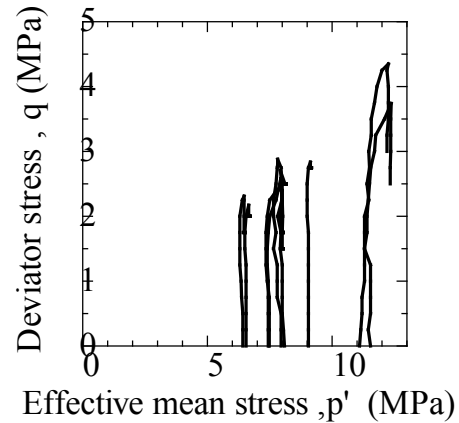


Fig. 8 Triaxial CU test result on MX-80 conducted by Ann et al. (2010)

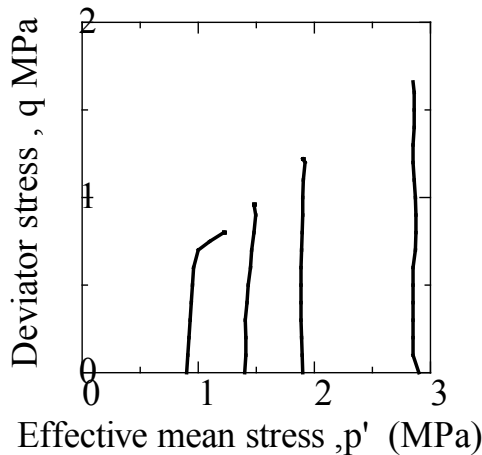


Fig. 7 Triaxial CU test result on OT-9607 conducted by Takaji et al. (1999)

deviator stress. According to these test results, it can be seen that the effective mean stress is almost unchanged during shearing. Usually, the effective mean stress decreases with increasing shear stress because of negative dilatancy, when triaxial CU test on normally consolidated clay is conducted. It is therefore implied that the bentonite does not have dilatancy characteristics based on the critical state theory.

4. Swelling characteristic of saturated Bentonite

An important mechanical property of bentonite is the swelling characteristic associated with the process of saturation from an unsaturated state. There are two kinds of tests for measuring swelling characteristics: the swelling deformation test and the swelling pressure test. Swelling deformation test reports deformations when the bentonite materials suck water to control the stress, and the swelling pressure test measures the swelling pressure when bentonite

materials suck water to keep uniformity in the volume. Typically, these results are interpreted as a connection between pressure at saturation to dry density. However, the relationship between the results of this test and full saturation line are not perfectly correlated. Saturated bentonite is an elastic body, so it always lies on the full saturation line. Because of this, we estimate that the final value of these swelling tests reach the full saturation line. Below, we examine the relationship between swelling characteristic and full saturation line, based on the results of this swelling test.

(1) Bentonite's swelling deformation test

Cui (2006) conducted swelling deformation tests and isotropic unloading tests by controlling principal stress. These tests were performed on samples of compacted Kunigel V-1/Toyourasa mixture with Kunigel V-1 content of 50% in dry mass. In the tests, they set the initial dry density at three patterns: 1.69, 1.54 and 1.2g/m³; and then performed water absorption tests under hydrostatic stress, based on the condition that the tests maintain mean principal stress settled. The sample's initial values, initial dry density and initial water content ratio, and the value of mean effective principal stress under which the samples suck water in are shown in Table-1.

Additional isotropic unloading tests were also performed, these reduce the load under 49kPa after the sample sucked water with mean principal stress set at 392 kPa. Fig. 9 shows these results: the relationship between mean effective principal stress and void ratio at the finish of retting and swelling of these three cases of initial dry density as well as the relationship between mean principal stress and void ratio when the test goes on isotropic unloading. In the case that it gave the sample some water in same mean stress, Fig. 9 shows that the void ratio takes the same value regardless of initial dry density. Furthermore, the value of unloading pass at isotropic unloading shows almost the same result as the swelling deformation test. This leads us to interpret that three words have the same meaning: full saturated line, normal consolidation line, and isotropic unloading line. Based on these results, one can conclude that the value, in the case of

the swelling test, lies on the full-saturated line under saturated conditions. Next, swelling tests were conducted with different stress ratios $R(= \sigma_a / \sigma_r)$ where the principal mean stress and the principal stress ratios were held constant. The initial values of the sample are: 1.69g/m^3 for dry density and 18.7% as the initial water content ratio. We show the relationship between the void ratio and the mean principal stress at the end of soaking in Fig. 10. This figure shows that the void ratio and the mean stress exhibit a one-to-one correspondence regardless of the principal stress ratio. So, our examination

ρ_{d0} (g/cm^3)	w_0 (%)	p (kPa)
1.69	18.7	49,98,147,196
1.54	18.7	19.6,49,88,196,294,392
1.2	19	49,98,196,392

Table 1 Initial value

that suggests saturated bentonite is a nonlinear elastic material without the characteristic of dilatancy coincides with the result of Cui's test.

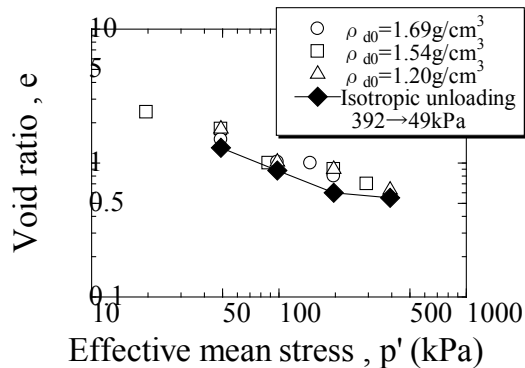


Fig. 9 Result of amount of swelling test

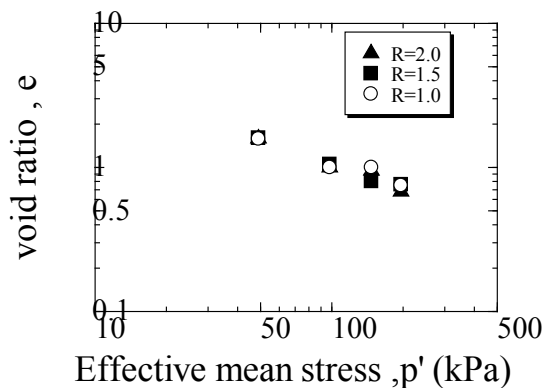


Fig. 10 Results of swelling test

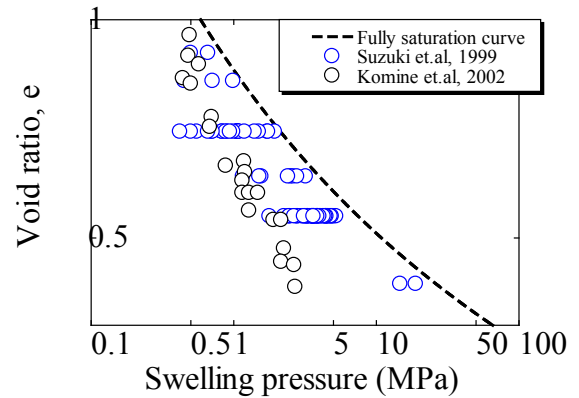


Fig. 11 the result of swelling pressure test

(2) Swelling pressure test for bentonite

A swelling pressure test, using equipment similar to that of the one-dimensional consolidation equipment, is a test that measures the counter force along the vertical direction caused by vertical soaking under settled volume. Fig. 11 shows the result of the swelling pressure test of Kunigel V-1, and the relationship between the void ratio and the vertical swelling pressure at saturation. This figure conveys that when the void ratio is smaller, the swelling pressure becomes larger and the swelling pressure value varies in the same void ratio, but the value never crosses the full-saturated line. However, considering the results obtained so far, these separate variability values result from measuring only vertical swelling pressure. So, if we take account of lateral stress and reconsider it using mean stress, we consider that all values are on the fully saturated line.

5. Conclusion

This study examines the mechanical characteristics of bentonite based on recent experimental data. The conclusions are summarized as follows:

- (1) The swelling line at $S_r = 1.0$ corresponds to the Normal Consolidation line. We also show that saturated bentonite does not have dilatancy characteristics. Therefore, saturated bentonite is a non-linear elastic material.
- (2) When water is supplied and the unsaturated state is transformed to a saturated state, the final, or saturation, points achieve the full saturation curve.

In Fig. 12, the schematics of relationship between void ratio and the principal mean stress during loading, unloading and swelling are summarized.

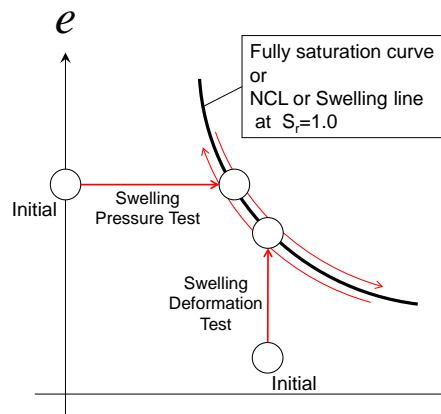


Fig. 12 Schematics of relationship between void ratio and the principal mean stress

REFERENCES

- [1] SASAKURA, T., KUROYANAGI, M., KOBAYSHI, I., OKAMOTO, M. "Studies on mechanical behavior of bentonite for development of the constitutive model II", 2003, JNC TJ8400 2003-048. (in Japanese)
- [2] SASAKURA, T., KUROYANAGI, M., OKAMOTO, M. "Studies on mechanical behavior of bentonite for development of the constitutive model", 2002, JNC TJ8400-2002-025. (in Japanese)
- [3] ISHIKAWA, H., ISHIGURO, K., NAMIKAWA, T., SUGANO, T. "Consolidation Properties of Buffer Material" 1997, PNC TN8410 97-051. (in Japanese)
- [4] KOBAYSHI, I., TOIDA, M., SASAKURA, T. and OHTA, H. "Interpretation of compression/swelling behavior of compacted bentonite using constant water-content line and constant degree-of-saturation line", 2007, JSCE Journal of Geotechnical Engineering, 63(4): 1065-1078. (in Japanese)
- [5] TAKAJI, K., SUZUKI, H. "Static Mechanical Properties of Buffer Material" 1999, JNC TN8400 99-041. (in Japanese)
- [6] Ann Dueck, Lennart Börgesson, Lars-Erik Johannesson. "Stress-strain relation of bentonite at undrained shear" 2010, SKB Technical Report TR-10-32.
- [7] Hongbin CUI, De'an SUN, MATSUOKA, H. "Swelling characteristics of Sand-Bentonite mixtures under isotropic and anisotropic stress States" 2006, JSCE Journal of Geotechnical Engineering, 62(3): 657-666. (in Japanese)
- [8] SUZUKI, H. and FUJITA, T. "Swelling Characteristics of Buffer Material" 1999, JNC TN8400 99-038. (in Japanese)
- [9] KOMINE, H. and OGATA, N. "Swelling characteristics of sand-bentonite mixture and various kinds of bentonite", 2002, JSCE Journal of Geotechnical Engineering, 701(III-58): 373-385. (in Japanese)

Effect of carbonation on strength of cement treated sand

Kenichiro NAKARAI¹ and Tomomi YOSHIDA²

¹ Hiroshima University, Graduate School of Engineering, Japan

² Gunma University, Graduate School of Engineering, Japan²

ABSTRACT

It is well known that the strength of cement treated soil increases for several years. The long-term increase in the strength is thought to be caused by pozzolanic reaction between cement paste and soil. On the other hand, carbonation of cementitious material can increase its strength. In this study, the effect of carbonation of cement treated sand on its strength was investigated. In the experiment, the specimens of the cement treated Toyoura sand were cured in three conditions; sealed condition, natural condition, accelerated carbonation condition. The concentrations of CO₂ in the curing conditions are 0%, 0.03%, and 5%. The measured strength of the specimens cured in the sealed condition didn't increase after 28 days while the strength of the specimens cured in the air or accelerated carbonation condition increased after 28 days due to carbonation. These results indicated that the carbonation can be one of the main reasons of the long-term increase in the strength of the cement treated sand.

Keywords: Cement, carbonation, strength, sand

1. INTRODUCTION

Cement treated soils, which are the soils mixed with cements, are widely used to improve the properties of foundations. It is well known that the strength of cement treated soil increases for several years. The long-term strength after a few years becomes several times of the strength at 28 days [1], [2]. It is unique property of the cement treated soil because the increase in the strength of concrete after 28 days is usually less than twice. The mechanism of the increase in the strength of the cement treated soils usually explained by the combination of the original strength of the soil without cement, improvement of the basic soil properties due to the decrease in water contents, cement hydration and pozzolanic reaction (Fig. 1 [3]). Continuous long-term increase in the strength of the cement treated soils is explained by the pozzolanic reaction between soils and cement paste due to high alkaline condition. However, there is no quantified

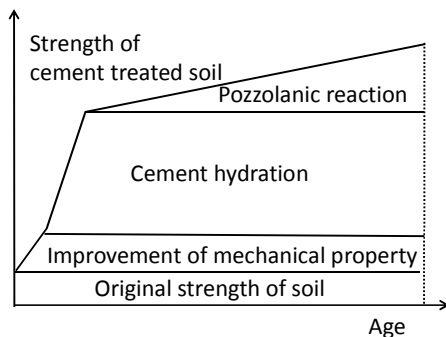


Fig.1 Proposed mechanism of increase in strength of cement treated soils [3]

investigation on the contribution of the pozzolanic reaction.

On the other hand, the cementitious material such as cement treated soil and concrete are affected by carbonation. Carbonation is a process by which carbon dioxide in the ambient air penetrates the cementitious materials and reacts with the calcium hydroxides and other cement hydrated products in the cement paste to form carbonates. A lot of studies on carbonation of concrete have been published because the carbonation is one of the main reasons of the corrosion of steels embedded in reinforced concrete structures. According to the past studies in the concrete engineering, the carbonation significantly lowers the alkalinity by the consumption of calcium hydroxides while it makes pore structure dense by the precipitation of carbonate. The decrease in the alkalinity causes the steel corrosion while the densification increases in the strength [4]. Because the speed of the carbonation of the porous cementitious materials such as cemented treated soil is faster than that of normal concretes, the influence of the carbonation on the cement treated soils may be larger.

In this study, the effect of carbonation of the cement treated sand on its strength was investigated. In the experiment, the specimens of the cement treated Toyoura sand were cured in three conditions; sealed condition, air condition, accelerated carbonation condition. Then, the strength development and the amount of carbonates were analyzed.

2. OUTLINE OF EXPERIMENT

2.1 Specimens

The cement treated specimens were prepared by mixing Toyoura sand, ordinary Portland cement and water. The designed values of the cement to sand ratio, the water content, the water to cement ratio, the void ratio, the density of the specimen were 8 %, 6 %, 70 %, 30 % and 2.8 Mg/m³,

respectively. After mixing, the cylindrical specimen having a diameter in 100 mm and a height in 200 mm were compacted by a weight of 2.5 kg. The number of the compaction times was 25 for one of three layers of the specimen.

Table 1 shows the curing conditions of the specimens. The specimens for investigating the effect of the carbonation were cured in the sealed condition for 5 days and then cured in the water for 1 day. After that, the specimens were cured in the environmental test room (natural condition) and chamber (accelerated condition). The average concentration of CO_2 , the temperature, and the relative humidity in the natural condition were around 0.03 %, 20 °C and 60 %, respectively while the concentration of CO_2 , the temperature, and the relative humidity in the accelerated condition was controlled to be 5 %, 20 °C and 60 %, respectively, to promote carbonation of the specimens. In addition, the specimens cured in the sealed condition were prepared to investigate the strength development excluding carbonation effect.

Table 1 Curing conditions of the specimens

Curing condition	Method of curing [days]			
	0-1	1-6	6-7	7-
Natural (CO ₂ ≅0.03%)	Sealed (T=20°C)	Room (T=20°C, RH=60%, CO ₂ =0.03%)	Water (T=20°C)	Room (T=20°C, RH=60%, CO ₂ ≅0.03%)
Accelerate d (CO ₂ =5%)				Chamber (T=20°C, RH=60%, CO ₂ =5%)
Sealed (CO ₂ =0%)		Sealed (T=20°C)		

2.2 Unconfined uniaxial compressive test

After prescribed curing periods, the unconfined compressive strength of specimens were investigated by the uniaxial compressive tests based on JIS A1216. For filling the gap between the specimen and the loading plate of the test machine, the gypsum was used. The displacement of the specimen cured in the natural or accelerated condition was measured by using LDT.

2.3 Thermo-gravimetric analysis

The amounts of calcium hydroxide ($\text{Ca}(\text{OH})_2$) and calcium carbonate (CaCO_3) were measured by using the thermo-gravimetric analysis (TGA). The sample was taken from the part of around 50 mm from the bottom of the cylindrical specimen after the compressive test and it was grinded. Then, the changes in the mass of the powder sample were measured from room temperature to 1000 °C. The temperature rise rate was set to 10 °C/min. The amount of $\text{Ca}(\text{OH})_2$ was determined by the mass decrease between 390 and 450 °C while the amount of CaCO_3 was determined by the mass decrease between 450 and 750 °C. In the discussion, they were modified based on the measured chemically bound water between 105 and 1000 °C to consider the variety of the composition of cement paste and sand in the sample.

2.4 X-ray diffraction analysis

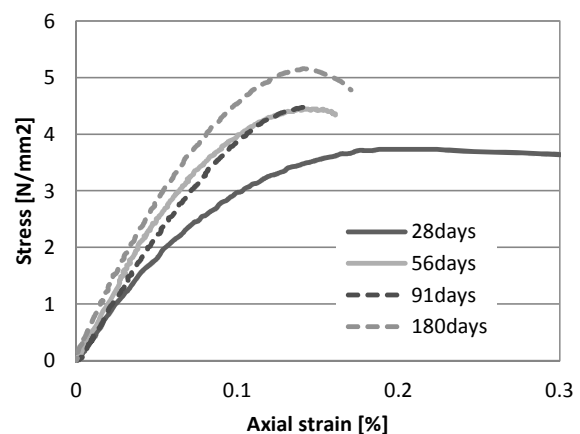
Crystalline phases, especially phase of CaCO_3 (calcite, vaterite, and aragonite), were identified by X-ray diffraction (XRD) analysis for the power sample after the compressive test.

3. RESULTS AND DISCUSSIONS

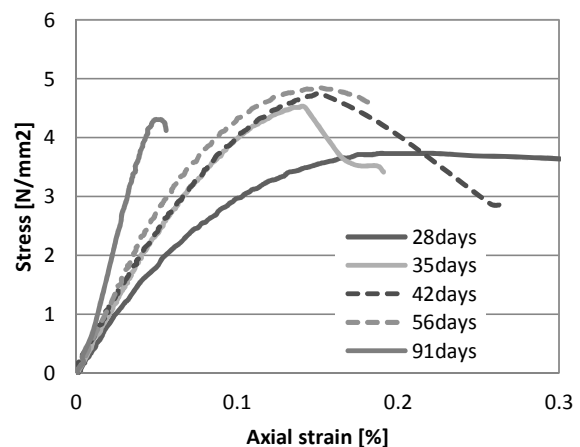
3.1 Results of unconfined compressive strength

Figs. 2 show the measured stress-strain relation of the representative specimens cured in the natural and accelerated conditions. Table 2 shows the compressive strengths and the elastic coefficient of the specimens. Each data is the average value of three results under the same condition. Figs. 3 and Fig 4 show the changes in the compressive strengths and the elastic coefficient with time, respectively.

In the sealed condition, the strength of the specimen was almost constant after 28 days until half a year. In the natural conditions, the strength of specimen constantly increased. The strength at the age of 180 days was 1.4 times of the strength at the age of 28 days. In the accelerated carbonating condition, the strength initially increased and then decreased. The maximum strength at the age of 56 days was 1.3 times of



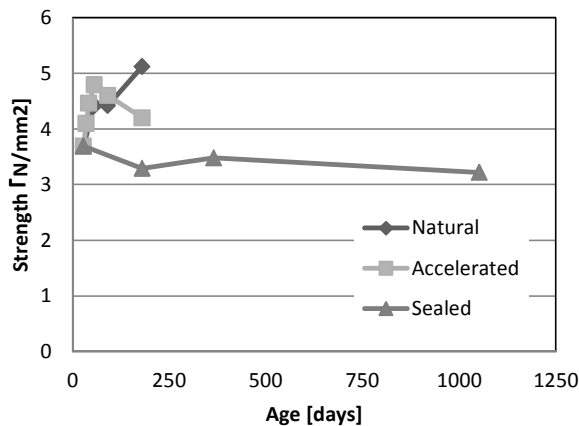
(a) Specimens cured in the natural condition ($\text{CO}_2 \cong 0.03\%$)



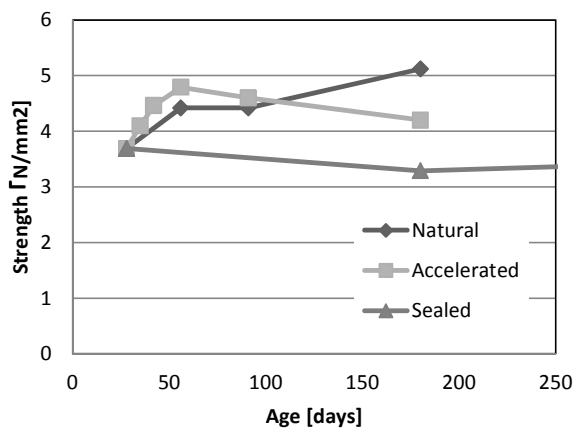
(b) Specimens cured in the accelerated condition ($\text{CO}_2=5\%$)
Figs. 2 Strain-stress relation

Table 2 Measured unconfined compressive strength

Curing condition	Age [days]	Strength [N/mm ²]	E ₅₀ [kN/mm ²]
Initial curing (1day sealed, 5days dried, 1day water, and then 21 days dried)	28	3.69	3.71
Natural (CO ₂ =0.05%)	56	4.42	5.21
	91	4.42	5.13
	180	5.12	5.85
Accelerated (CO ₂ =5%)	35	4.10	6.16
	42	4.46	5.38
	56	4.79	5.17
	91	4.60	9.80
	180	4.20	4.08
Sealed (CO ₂ =0%)	180	3.29	-
	365	3.48	-
	1052	3.22	-



(a) Data in whole periods



(b) Data until half a year

Figs.3 Changes in strength under different curing conditions

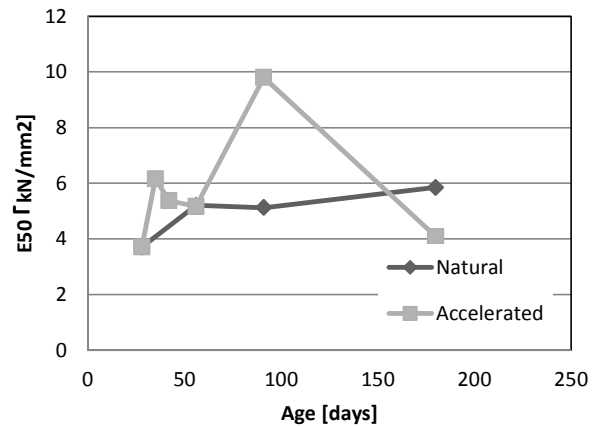


Fig.4 Changes in elastic coefficient due to carbonation

the strength at the age of 28 days.

The elastic coefficient, E_{50} , of the specimens showed almost similar behaviors as the strength. In the natural conditions, the elastic coefficient constantly increased. On the other hand, in the accelerated carbonating condition, the elastic coefficient initially increased and then decreased. The maximum elastic coefficient in the accelerated condition was observed at the age of 91 days, which is later than the age for the maximum strength.

3.2 Results of thermo-gravimetric analysis

Figs 5 and 6 show the results of the thermo-gravimetric analysis on $\text{Ca}(\text{OH})_2$ and CaCO_3 , respectively. Here, we calculated the ratios of $\text{Ca}(\text{OH})_2$ and CaCO_3 to cement. In the calculation, the amount of chemically bound water was assumed to be 23% of the cement considering the past study [5].

Regardless to the CO_2 concentration in the atmosphere, the amount of $\text{Ca}(\text{OH})_2$ decreased and the amount of CaCO_3 increased due to carbonation with time. The changes in the accelerated condition were larger than that in the natural condition because the high CO_2 concentration accelerates the progress of the carbonation.

Fig. 7 shows the relationship between the increase ratios of the unconfined compressive strength and the amount of CaCO_3 . Here, the increase ratios of the strength and CaCO_3 after 28 days were calculated. In the natural condition, the strength was almost constantly increased with the increase in CaCO_3 . In the accelerated condition, the strength was firstly increased until 56 days and then decreased with the increase in CaCO_3 . The increase ratio of the strength to CaCO_3 (the slope of plots in Fig. 7) in the natural condition was larger than that in the accelerated condition. These results suggested that the effect of the carbonation on the strength depends on the concentration of CO_2 and the carbonation progressed in the low CO_2 concentration effectively increases the strength.

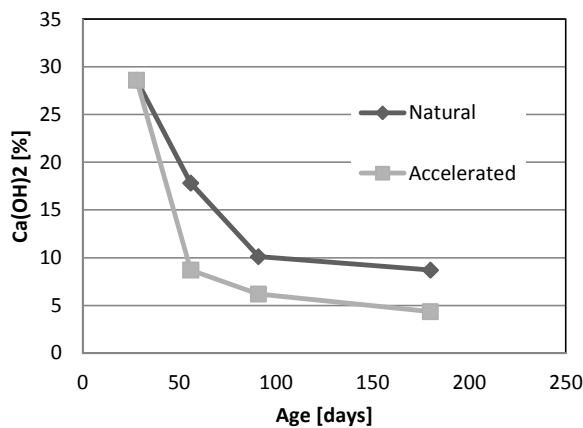


Fig.5 Changes in amount of Ca(OH)_2 under different curing conditions

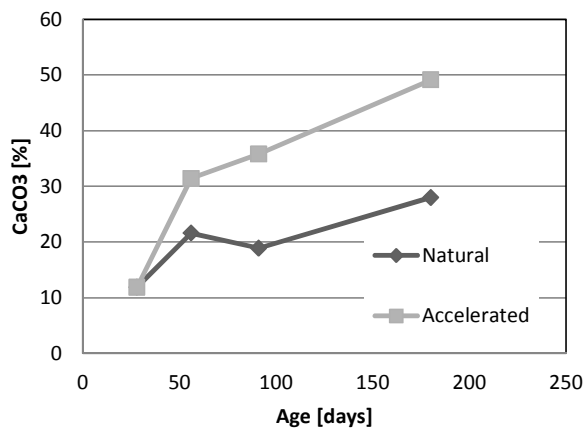


Fig.6 Changes in amount of CaCO_3 under different curing conditions

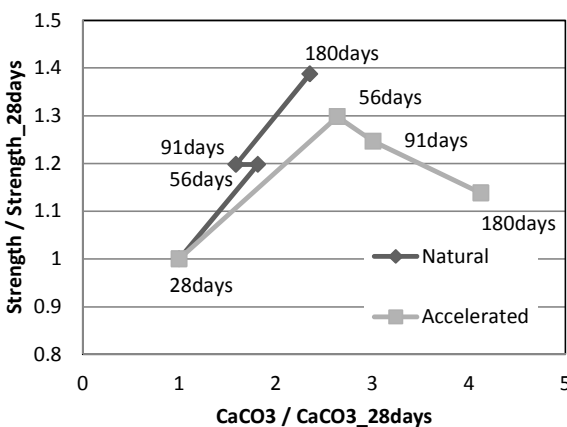


Fig.7 Relationship between unconfined compressive strength and CaCO_3 (increase ratios after 28 days)

3.2 Results of X-ray diffraction analysis

Table 3 shows the results of the X-ray diffraction analysis. Here, the peak strengths of the phases of CaCO_3 (calcite, vaterite, and aragonite) measured by X-ray diffraction

analysis were indicated.

At the age of 56 days, the main phase of the generated CaCO_3 was analyzed as calcite. On the other hand, the main phase of the generated CaCO_3 at the age of 91 days in the accelerated carbonating condition was analyzed as vaterite. It suggested the carbonation of C-S-H gel and the transformation of calcite to vaterite in the accelerated condition after 56 days. By comparing with the results of the strength in Fig. 1, it was suggested that the generation of vaterite caused the decrease in the strength in the accelerated condition.

Table 3 Peak strength measured by X-ray diffraction analysis

Curing condition	Age [days]	calcite	vaterite	aragonite
Natural ($\text{CO}_2=0.05\%$)	56	+++	+	+
Accelerated ($\text{CO}_2=5\%$)	56	+++	+	+
	91	++	+++	+

+++ : strong peak, ++ : weak peak, + very weak peak, blank : no peak

4 CONCLUSION

This study investigated the effect of carbonation on the strength development of the cement treated Toyoura sand by using the specimens cured in three conditions; sealed condition ($\text{CO}_2=0\%$), natural condition ($\text{CO}_2\approx 0.03\%$), accelerated carbonating condition ($\text{CO}_2=5\%$). Then, the experimental results showed the followings.

In the sealed condition, the strength was almost constant after 28 days. The carbonation in the natural condition constantly increased the strength and elastic coefficient. The carbonation in the accelerated condition firstly increased the strength and elastic coefficient and then decreased them. The results of XRD analysis suggested that the generation of vaterite caused the decrease in the strength in the accelerated condition.

5 REFERENCES

- [1] Horpibulsuk S., Miura N., & Nagaraj T.S., "Assessment of strength development in cement-admixed high water content clays with Abrams' law as a basis," *Geotechnique*, 53 (4), 2003, pp. 439-444
- [2] Kongsukprasert L., Tatsuoka F., & Takahashi H., "Effects of curing period and stress conditions on the strength and deformation characteristics of cement-mixed soil," *Soil and foundation*, 47(3), 2007, pp.577-596.
- [3] Express highway research foundation of japan, "Research report on planning, design, and construction of cement/lime stabilized roadbed," 1978, p.6. (in Japanese)
- [4] Leber I. and Blakey F.A., "Some effects of carbon dioxide on mortars and concrete," *Journal of the American Concrete Institute*, 28(3), 1956, pp. 295-308.
- [5] Powers T.C., "The Physical structure of Portland cement paste," *The Chemistry of Cement*, edited by H. F. Taylor, Academic Press, 1964, pp.391-416.

Application of PML to Analysis of Nonlinear Soil-Structure-Fluid Problem Using Mixed Element

Pahaiti Rehemani¹, Hiroo Shiojiri²,

¹Graduated School of College of Science and Technology, Nihon University, Japan

²College of Science and Technology, Nihon University, Japan

SUMMARY:

Mixed element may be conveniently used to express non-linear constitutive equation of fluid and to avoid volumetric locking. X-FEM may be well suited to model discontinuity of displacements between solid and fluid. Appropriate boundary conditions should be set at the boundaries of numerical models not to reflect outgoing waves. In this paper, complex frequency shifted convolution-PML without splitting of variables is developed for mixed element, and the performances of PML are confirmed. The formulation of PML is completely consistent with corresponding FEM or X-FEM. It can be easily extended to any type of element and any nonlinear constitutive equations of the corresponding FEM or X-FEM. The resulting mass and stiffness matrices for PML are symmetric for linear models.

Keywords: Soil-structure-fluid interaction, X-FEM, Mixed formulation, Complex Frequency shifted PML

1. INTRODUCTION

Soil-structure-fluid interaction may have significant effects on seismic responses of structures. Mixed element may be conveniently used to express non-linear constitutive equation of fluid and to avoid volumetric locking. X-FEM may be well suited to model discontinuity of displacements between solid and fluid. In the X-FEM analysis, as well as FEM and FDM analyses, appropriate boundary conditions should be set at the boundaries of numerical models not to reflect outgoing waves.

Several methods are proposed (Wolf 1988). The first is the extensive mesh models using a finite element method or a finite difference method with approximate energy transmitting boundaries. The second is the substructure method using, for example, finite element and time domain boundary element method. In the former, the degrees of freedom of the models are often very large. The latter method may be more efficient, but the nonlinearity must be restricted within the nearby portion of structures modeled by finite element method, i.e., constitutive equations are assumed to be linear at and outer domain of the boundary. The third is FEM with PML or convolution PML (Berenger 1994, Collino 2001, Basu 2003 2004, Drossaert 2007). PML and convolution PML are proved to have efficient wave absorbing capability for linear elasto-dynamic problem, and, the nonlinearity must be restricted within finite element domain. In the severe earthquakes, however, soil may become nonlinear to a large extent so that the second and the third methods may be inadequate. Convolutional PML is extended to cope with non-linear problem, so that nonlinear soil can be analyzed

with a limited number of meshes without loss of accuracy (Shiojiri 2010, Rehemani 2011). But, it is restricted to displacement based FEM.

Here, complex frequency shifted convolution-PML without splitting of variables is developed for mixed finite element and for X-FEM, and the performances of PML are confirmed. The formulation of PML is completely consistent with corresponding FEM or X-FEM. It can be easily extended to any type of element and any nonlinear constitutive equations of the corresponding FEM or X-FEM. The resulting mass and stiffness matrices for PML are symmetric for linear models.

2. METHOD

2.1 PML Formulation of Mixed Element for Fluid

Assuming that the effect of viscosity is negligible and that change of density is small, the equations of motion of fluid is given as:

$$\rho_0 \ddot{u}_i + \frac{\partial}{\partial x_i} p = 0 \quad (2.1)$$

,where ρ_0 is time averaged density of fluid, p is dynamic pressure, u_i is with component of displacement, and x_i denotes i th coordinate. Relationship between density and displacements is given as:

$$\rho + \rho_0 \sum_i \frac{\partial u_i}{\partial x_i} = 0 \quad (2.2)$$

,where ρ is difference between current density and time averaged density. Relationship between dynamic pressure and ρ is expressed as follows.

$$p = f(\rho) \quad (2.3)$$

,where $f(\rho)$ is given as:

$$f(\rho) = c^2 \rho \quad \text{for } p > p_v - p_0 \quad (2.3a)$$

$$f(\rho) = (\beta_0 c)^2 \rho + (1 - \beta_0^2)(p_v - p_0) \quad \text{for } p < p_v - p_0 \quad (2.3b)$$

,in which c is velocity of sound, p_v is vapor pressure, p_0 is static pressure ,and β_0 is reduction ratio of sound velocity after cavitation.

Following the PML procedure, we introduce complex coordinate stretching function in frequency domain as:

$$\tilde{x}_i = \int_0^{x_i} \lambda_i(s) ds \quad (2.4)$$

, where x_i denotes i th coordinate, and \tilde{x}_i the corresponding transformed coordinate, and λ_i is given as:

$$\lambda_i = k_i + \frac{\sigma_i}{\alpha_i + i\omega} \quad (2.5)$$

, where i is pure imaginary number, ω circular frequency, and k_i , α_i and σ_i non-negative continuous functions, such that $k_i=1$, and $\sigma_i=0$ at FEM-PML interface. At first, all equations are formulated in \tilde{x}_i coordinate in frequency domain, and then transformed to x_i coordinate.

Equations of motion are given as:

$$-\omega^2 \rho_0 \bar{u}_i + \frac{\partial}{\partial \tilde{x}_i} \bar{p} = 0 \quad (2.6)$$

,where ω is circular frequency, and \bar{u} and \bar{p} are displacement and pressure amplitudes in frequency domain respectively. The relationship between density and displacement are given as:

$$\bar{p} + \rho_0 \sum_i \frac{\partial \bar{u}_i}{\partial \tilde{x}_i} = 0 \quad (2.7)$$

,where \bar{p} is relative density amplitudes in frequency domain.

Considering $\partial / \partial \tilde{x}_i = (1 / \lambda_i) \partial / \partial x_i$, and multiplying both sides of Eqn.2.6 and Eqn.2.7 by $\lambda_1 \lambda_2$, we get;

$$-\lambda_1 \lambda_2 \omega^2 \rho_0 \bar{u}_i + \lambda_+ \frac{\partial \bar{p}}{\partial x_i} = 0 \quad (2.8)$$

$$\lambda_1 \lambda_2 \bar{p} + \rho_0 \sum_i \left(\lambda_+ \frac{\partial \bar{u}_i}{\partial x_i} \right) = 0 \quad (2.9)$$

,where $+$ denotes an integer other than i . Introducing weight functions w_i for displacements, and q for pressure, weak form equations for Eqn.2.8 and Eqn.2.9 are given as follows.

$$\begin{aligned} & - \int_V w_i \lambda_1 \lambda_2 \omega^2 \rho_0 \bar{u}_i dv - \int_V \frac{\partial w_i}{\partial x_i} \lambda_+ \bar{p} dv \\ & = - \int_S w_i n_i \lambda_+ \bar{p} ds \end{aligned} \quad (2.10)$$

$$\int_V q (p - f(\rho)) dv = 0 \quad (2.11)$$

Considering the fact that $-\omega^2, i\omega$, and $k_1 + \sigma_1 / (\alpha_1 + i\omega)$ in frequency domain corresponds to d^2 / dt^2 , d / dt , and $k + \sigma e^{-i\alpha t} *$ in time domain, equations in time domain are written as:

$$\begin{aligned} & \int_V \rho_0 w_i \left\{ k_1 k_2 \ddot{u}_i + \sum_j \frac{k_+ \sigma_j (\alpha_+ - \alpha_j) + \sigma_1 \sigma_2}{\alpha_+ - \alpha_j} e^{-\alpha_j t} * \ddot{u}_i \right\} dv \\ & - \int_V \frac{\partial w_i}{\partial x_i} (k_+ p + \sigma_+ e^{-\alpha_+ t} * p) dv \\ & = - \int_S w_i n_i (k_+ p + \sigma_+ e^{-\alpha_+ t} * p) ds \end{aligned} \quad (2.12)$$

$$\begin{aligned} & \kappa_1 \kappa_2 \rho + \sum_j \frac{k_+ \sigma_j (\alpha_+ - \alpha_j) + \sigma_1 \sigma_2}{\alpha_+ - \alpha_j} e^{-\alpha_j t} * \rho \\ & = - \rho_0 \sum_i \left(k_+ \frac{\partial u_i}{\partial x_i} + \sigma_+ e^{-\alpha_+ t} * \frac{\partial u_i}{\partial x_i} \right) \end{aligned} \quad (2.13)$$

,where $*$ denotes convolution integral. Denoting $e^{-\alpha t} * f(t) = \int_0^t e^{-\alpha(t-t')} f(t') dt' = F(t)$,

and introducing approximation

$$F(t + \Delta t) = \Delta t \left\{ (1 - \theta) e^{-\alpha \Delta t} f(t) + \theta f(t + \Delta t) \right\} + e^{-\alpha \Delta t} F(t),$$

we get

$$\begin{aligned} & \int_V \rho_0 w_i r_{12} \ddot{u}_i(t + \Delta t) dv \\ & + \int_V \rho_0 w_i \sum_{j=1}^2 U_{ij}^*(t) dv \\ & - \int_V \frac{\partial w_i}{\partial x_i} \{ r_+ p(t + \Delta t) + P_+^*(t) \} dv \\ & = - \int_S w_i n_i \{ r_+ p(t + \Delta t) + P_+^*(t) \} ds \end{aligned} \quad (2.14)$$

,where

$r_{12} = k_1 k_2 + \theta \Delta t (k_2 \sigma_1 + k_1 \sigma_2)$, $r_+ = k_+ + \theta \Delta t \sigma_+$, and we define as followings:

$$\begin{aligned} P_+^*(t) &= \sigma_+ \left\{ e^{-\alpha_+ \Delta t} \int_0^t e^{-\alpha_+(t-t')} p(t') dt' \right. \\ & \quad \left. + e^{-\alpha_+ \Delta t} \Delta t (1 - \theta) p(t) \right\} \\ &= e^{-\alpha_+ \Delta t} \{ P_+^*(t - \Delta t) + \Delta t \sigma_+ p(t) \} \end{aligned} \quad (2.15)$$

$$\begin{aligned}
U_{ij}^*(t) &= \frac{k_{\pm}\sigma_j(\alpha_{\pm}-\alpha_j)+\sigma_1\sigma_2}{\alpha_{\pm}-\alpha_j} \\
&\left\{ e^{-\alpha_j\Delta t} \int_0^t e^{-\alpha_j(t-t')} \ddot{u}_i(t') dt' + e^{-\alpha_j\Delta t} \Delta t (1-\theta) \ddot{u}_i(t) \right\} \\
&= e^{-\alpha_j\Delta t} \left\{ U_{ij}^*(t-\Delta t) \right. \\
&\quad \left. + \Delta t \frac{k_{\pm}\sigma_j(\alpha_{\pm}-\alpha_j)+\sigma_1\sigma_2}{\alpha_{\pm}-\alpha_j} \ddot{u}_i(t) \right\}
\end{aligned} \quad (2.16)$$

Likewise, from Eqn.2.13, we get:

$$\begin{aligned}
&r_{12}\rho(t+\Delta t) + R_{12}(t) \\
&= -\rho_0 \sum_i r_{\pm} \frac{\partial u_i}{\partial x_i}(t+\Delta t) - V_{12}(t)
\end{aligned} \quad (2.17)$$

,where $R_{12}(t) = \sum R_i^*(t)$, $V_{12}(t) = \sum V_i^*(t)$, and $R_i^*(t) =$,

$$\begin{aligned}
&e^{-\alpha_i\Delta t} [R_i^*(t-\Delta t) + \Delta t \rho(t) [k_{\pm}\sigma_i(\alpha_{\pm}-\alpha_i) \\
&\quad + \sigma_1\sigma_2] / (\alpha_{\pm}-\alpha_i)] \\
V_i^*(t) &= e^{-\alpha_i\Delta t} \left(V_i^*(t-\Delta t) + \Delta t \rho_0 \sigma_{\pm} \partial u_i / \partial x_i \right)
\end{aligned}$$

From Eqn.2.17, Eqn.2.3a, and Eqn.2.11, we get,

$$\begin{aligned}
&\int_V q \left\{ r_{12}p(t+\Delta t) + \rho_0 c^2 \sum_j r_{\pm} \frac{\partial u_j}{\partial x_j}(t+\Delta t) \right\} dv = \\
&- \int_V q c^2 \{ R_{12}(t) + V_{12}(t) \} dv
\end{aligned} \quad (2.18)$$

Discretizing domain of analysis by finite element, adopting Galerkin's formulation, and let \mathbf{u}^e , \mathbf{P}^e , \mathbf{N}_s and \mathbf{N}_p denote displacement and pressure vector at nodal points of a element, and interpolation matrices for displacement and pressure, respectively, matrix form equations are obtained. From Eqn.2.14, we get,

$$\begin{aligned}
&\rho_0 \int_V r_{12} \mathbf{N}_s^T \mathbf{N}_s dv \ddot{\mathbf{u}}^e(t+\Delta t) + \rho_0 \int_V \mathbf{N}_s^T \mathbf{U}(t) dv \\
&\quad - \int_V \mathbf{B}^T \mathbf{R}_m \mathbf{N}_p dv \mathbf{P}^e(t+\Delta t) \\
&\quad - \int_V \mathbf{B}^T \mathbf{S} dv \mathbf{P}(t) \\
&= - \int_S \mathbf{N}_s^T \mathbf{N} \mathbf{R}_m \mathbf{N}_p ds \mathbf{P}^e(t+\Delta t) \\
&\quad - \int_S \mathbf{N}_s^T \mathbf{N} \mathbf{S} ds \mathbf{P}(t)
\end{aligned} \quad (2.19)$$

,where

$$\mathbf{U}(t) = \left\{ \begin{matrix} \sum_{j=1}^2 U_{1j}^*(t) \\ \sum_{j=1}^2 U_{2j}^*(t) \end{matrix} \right\}, \mathbf{B} = \begin{bmatrix} \frac{\partial}{\partial x_1} & 0 \\ 0 & \frac{\partial}{\partial x_2} \end{bmatrix} \mathbf{N}_s, \mathbf{N} = \begin{bmatrix} n_1 & 0 \\ 0 & n_2 \end{bmatrix},$$

$$\mathbf{R}_m^T = [r_2 \quad r_1], \mathbf{S} = \begin{bmatrix} \mathbf{N}_p & \mathbf{0} \\ \mathbf{0} & \mathbf{N}_p \end{bmatrix}, \mathbf{P}(t) = \left\{ \begin{matrix} \mathbf{P}_2^*(t) \\ \mathbf{P}_1^*(t) \end{matrix} \right\},$$

$$\mathbf{P}_i^*(t) = e^{-\alpha_i\Delta t} \left\{ \mathbf{P}_i^*(t-\Delta t) + \Delta t \sigma_i \mathbf{P}^e(t) \right\}$$

From Eqn.2.18, we get,

$$\begin{aligned}
&\int_V r_{12} \mathbf{N}_p^T \mathbf{N}_p dv \mathbf{P}^e(t+\Delta t) \\
&\quad + \rho_0 c^2 \int_V \mathbf{N}_p^T \mathbf{R}_m^T \mathbf{B} dv \mathbf{u}^e(t+\Delta t) = \mathbf{R}(t)
\end{aligned} \quad (2.20)$$

,where

$$\mathbf{R}(t) = -c^2 \left\{ \int_V \mathbf{N}_p^T \mathbf{N}_p dv \mathbf{R}_{12}(t) + \int_V \mathbf{N}_p^T V_{12}(t) dv \right\}$$

$$\begin{aligned}
&\mathbf{R}_{12}(t) = \mathbf{R}_1^*(t) + \mathbf{R}_2^*(t), \text{ and } \mathbf{R}_i^*(t) = \\
&e^{-\alpha_i\Delta t} [\mathbf{R}_i^*(t-\Delta t) + \Delta t \{ k_{\pm}\sigma_i(\alpha_{\pm}-\alpha_i) + \sigma_1\sigma_2 \} \\
&\quad / \{ (\alpha_{\pm}-\alpha_i) c^2 \} \mathbf{P}^e(t)]
\end{aligned}$$

Let \mathbf{H} and \mathbf{G} be defined as

$$\mathbf{H} = \int_V r_{12} \mathbf{N}_p^T \mathbf{N}_p dv, \mathbf{G} = \int_V \mathbf{N}_p^T \mathbf{R}_m^T \mathbf{B} dv. \text{ Then, we get:}$$

$$\begin{aligned}
&\rho_0 \int_V r_{12} \mathbf{N}_s^T \mathbf{N}_s dv \ddot{\mathbf{u}}^e(t+\Delta t) \\
&\quad + \rho_0 c^2 \mathbf{G}^T \mathbf{H}^{-1} \mathbf{G} \mathbf{u}^e(t+\Delta t) \\
&= - \int_S \mathbf{N}_s^T \mathbf{N} \mathbf{R}_m \mathbf{N}_p ds \mathbf{P}^e(t+\Delta t) \\
&\quad - \int_S \mathbf{N}_s^T \mathbf{N} \mathbf{S} ds \mathbf{P}(t) \\
&\quad - \rho_0 \int_V \mathbf{N}_s^T \mathbf{U}(t) dv + \mathbf{G}^T \mathbf{H}^{-1} \mathbf{R}(t) \\
&\quad + \int_V \mathbf{B}^T \mathbf{S} dv \mathbf{P}(t)
\end{aligned} \quad (2.21)$$

Element stiffness matrix $\rho_0 c^2 \mathbf{G}^T \mathbf{H}^{-1} \mathbf{G}$ has many hourglass mode and may lead to unstable solution. Since vorticity is preserved in non-viscous flow, and since fluid is assumed to be static in the beginning, the following equation is valid:

$$\varepsilon_c = \frac{\partial u_2}{\partial x_1} - \frac{\partial u_1}{\partial x_2} = 0 \quad (2.22)$$

So, in PML domain, the following equation is assumed.

$$\lambda_1 \lambda_2 \bar{\varepsilon}_c = \lambda_2 \frac{\partial \bar{u}_2}{\partial x_1} - \lambda_1 \frac{\partial \bar{u}_1}{\partial x_2} \quad (2.23)$$

$$\lambda_2 \frac{\partial \bar{\varepsilon}_c}{\partial x_1} = \lambda_1 \frac{\partial \bar{\varepsilon}_c}{\partial x_2} = 0 \quad (2.24)$$

,where $\bar{\varepsilon}_c$ is amplitude of vorticity in frequency domain.

Converting Eqn.2.23 into time domain, and introducing approximation for convolution integral, we get,

$$\begin{aligned}
&r_{12} \varepsilon_c(t+\Delta t) + \sum_{j=1}^2 \frac{k_{\pm}\sigma_j(\alpha_{\pm}-\alpha_j)+\sigma_1\sigma_2}{\alpha_{\pm}-\alpha_j} E_j^*(t) \\
&= \sum_j \left\{ (-1)^{j-1} r_{\pm} \frac{\partial u_{\pm}}{\partial x_j}(t+\Delta t) + U_{\pm}^*(t) \right\}
\end{aligned} \quad (2.25)$$

,where

$$E_j^*(t) = e^{-\alpha_j\Delta t} \left\{ E_j^*(t-\Delta t) + \Delta t \varepsilon_c(t) \right\}$$

$$U_{12}^*(t) = e^{-\alpha_1\Delta t} \left\{ U_{12}^*(t-\Delta t) + \Delta t \sigma_1 \partial u_1(t) / \partial x_2 \right\}, \text{ and}$$

$$U_{21}^*(t) = e^{-\alpha_2\Delta t} \left\{ U_{21}^*(t-\Delta t) + \Delta t \sigma_2 \partial u_2(t) / \partial x_1 \right\}.$$

Introducing weight function w_1, w_2 and deriving weak form equation from Eqn.2.24, we get,

$$\begin{aligned}
& - \int_V \alpha \left(w_2 \lambda_2 \frac{\partial \bar{\varepsilon}_c}{\partial x_1} - w_1 \lambda_1 \frac{\partial \bar{\varepsilon}_c}{\partial x_2} \right) dv \\
& = - \int_S \alpha (w_2 n_1 \lambda_2 - w_1 n_2 \lambda_1) \bar{\varepsilon}_c ds \\
& \quad + \int_V \alpha \left(\lambda_2 \frac{\partial w_2}{\partial x_1} - \lambda_1 \frac{\partial w_1}{\partial x_2} \right) \bar{\varepsilon}_c dv = 0
\end{aligned} \tag{2.26}$$

Transforming Eqn.2.26 into time domain equation, and introducing approximation for convolution integral, and substituting Eqn.2.25, we get,

$$\begin{aligned}
& \int_V \frac{\alpha}{r_{12}} \left(r_2 \frac{\partial w_2}{\partial x_1} - r_1 \frac{\partial w_1}{\partial x_2} \right) \left(r_2 \frac{\partial u_2}{\partial x_1}(t + \Delta t) - r_1 \frac{\partial u_1}{\partial x_2}(t + \Delta t) \right) dv \\
& \quad + \int_V \alpha \left(\frac{\partial w_2}{\partial x_1} \sigma_2 E_2^* - \frac{\partial w_1}{\partial x_2} \sigma_1 E_1^* \right) dv \\
& \quad + \int_V \frac{\alpha}{r_{12}} \left(r_2 \frac{\partial w_2}{\partial x_1} - r_1 \frac{\partial w_1}{\partial x_2} \right) E(t) dv \\
& = \int_S \alpha \left\{ (w_2 n_1 r_2 - w_1 n_2 r_1) \varepsilon_c + (w_2 n_1 \sigma_2 E_2^* - w_1 n_2 \sigma_1 E_1^*) \right\} ds
\end{aligned} \tag{2.27}$$

,where $E(t) =$

$$- \sum_{j=1}^2 \{ k_j \sigma_j (\alpha_j - \alpha_j) + \sigma_1 \sigma_2 \} E_j^*(t) / (\alpha_j - \alpha_j) + U_{21}^*(t) - U_{12}^*(t),$$

$$E_j^*(t) = e^{-\alpha_j \Delta t} \times$$

$$\left\{ E_j^*(t - \Delta t) + \Delta t \varepsilon_c(t) \right\}, U_{12}^*(t) = e^{-\alpha_1 \Delta t} \left\{ U_{12}^*(t - \Delta t) + \Delta t \sigma_1 \partial u_1(t) / \partial x_2 \right\},$$

$$\text{and } U_{21}^*(t) = e^{-\alpha_2 \Delta t} \times \left\{ U_{21}^*(t - \Delta t) + \Delta t \sigma_2 \partial u_2(t) / \partial x_1 \right\}.$$

Introducing interpolation matrices, the following equations are obtained.

$$\begin{aligned}
& \int_V \frac{\alpha}{r_{12}} \mathbf{B}_c^T \mathbf{B}_c dv \mathbf{u}^e(t + \Delta t) \\
& = - \int_V \alpha \mathbf{B}_c^T \left\{ \begin{matrix} E_1^* \\ E_2^* \end{matrix} \right\} dv - \int_V \frac{\alpha}{r_{12}} \mathbf{B}_c^T E(t) dv
\end{aligned} \tag{2.28}$$

,where

$$\mathbf{B}_c = \begin{bmatrix} -r_1 \frac{\partial}{\partial x_2} & r_2 \frac{\partial}{\partial x_1} \end{bmatrix} \mathbf{N}_s, \mathbf{B}_c = \begin{bmatrix} -\sigma_1 \frac{\partial}{\partial x_2} & 0 \\ 0 & \sigma_2 \frac{\partial}{\partial x_1} \end{bmatrix} \mathbf{N}_s$$

By adding Eqn.2.21 and Eqn.2.28, we get final matrix form equations. Substituting interpolation function for X-FEM, we get PML for XFEM.

3 NUMERICAL EXAMPLE

3.1 Reservoir Model

Reservoir with 100m depth subjected to horizontal rigid wall motion is analyzed using proposed mixed formulation FE-PLM. Length of reservoir model varies from 100m to 600m. Boundary conditions assigned on upstream boundary are fixed boundary, viscous boundary with viscosity ρc , and PML. Meshes of models are shown in Fig.3.1~3.3. Meshes with sign x indicate PML. Forced horizontal vibration of rigid

wall on the left end of reservoir is assumed. The results are shown in Fig.3.4~3.9. Fixed boundary results show strong dependency on the location of upstream boundary. The results with viscous boundary show less dependency on the location of boundary for 1Hz excitation, but large dependency for 5Hz excitation. Proposed PML boundary shows very little discrepancy between different boundary locations for both 1Hz and 5Hz excitation.

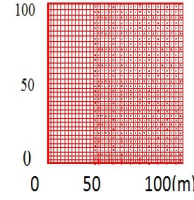


Fig.3.1. Reservoir Mesh (length 100m)

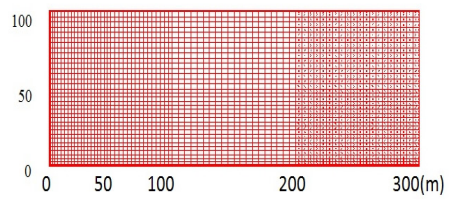


Fig.3.2. Reservoir Mesh (length 300m)

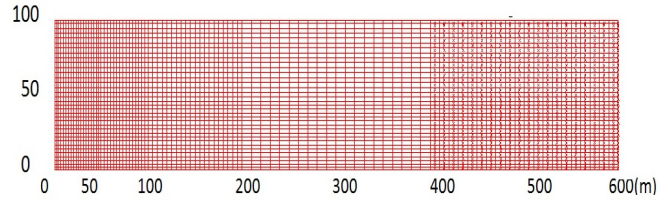


Fig.3.3. Reservoir Mesh (length 600m)

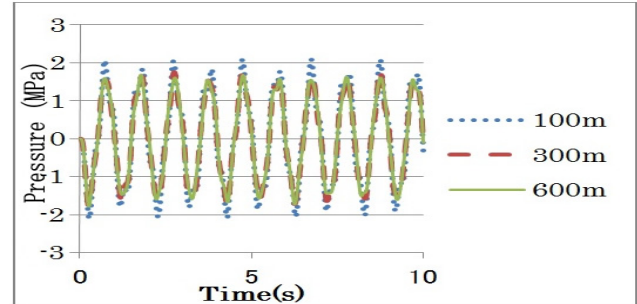


Fig.3.4. Fixed Boundary (1Hz)

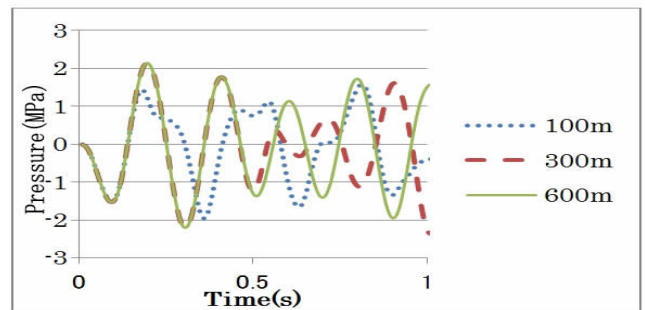


Fig.3.5. Fixed Boundary (5Hz)

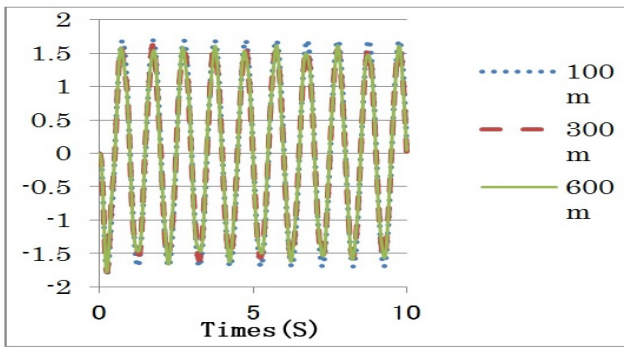


Fig3.6. Viscous boundary(5Hz)

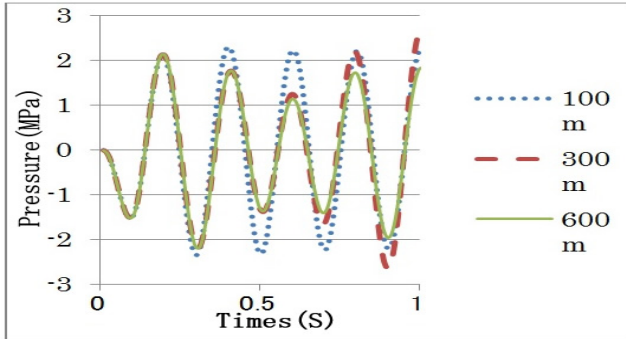


Fig3.7. Viscous boundary(5Hz)

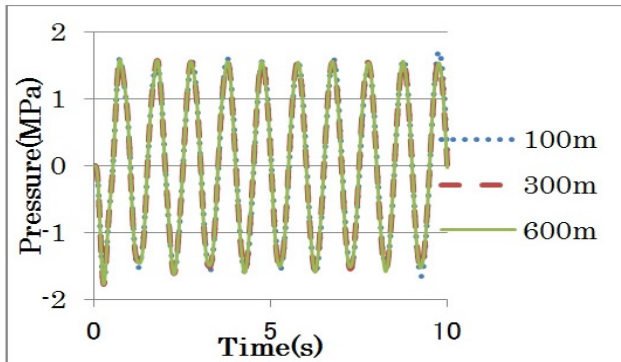


Fig 3.8. PML(1Hz)

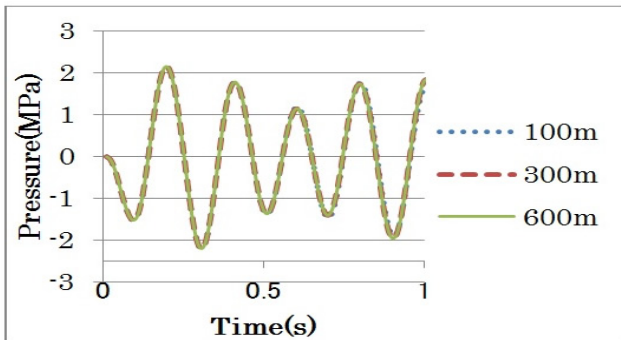


Fig3.9. PML(5Hz)

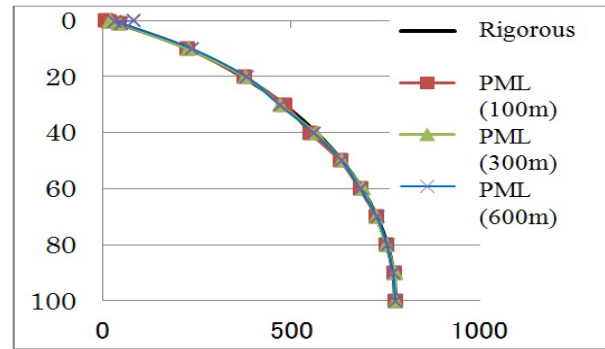


Fig 3.10. Pressure Distribution(1Hz)

3.2 Dam- Reservoir-Foundation Model

Dam-reservoir-foundation model was constructed using X-FEM for tangential discontinuity of displacement at solid-fluid interface ,and combining proposed mixed formulation FE-PML for fluid with FE-PML for solid (Fig3.11) . Two kinds of meshes are used (Fig.3.12, Fig.3.13). Discontinuous displacement in tangential direction near the top of dam is shown in Fig.14, indicating the effect of discontinuous interpolation function of X-FEM. In Fig.15-17, responses of dam top using two mesh models subjected to sinusoidal horizontal ground motion are compared. The results of two mesh model coincide each other, indicating that model size has little effect when proposed PML is used.

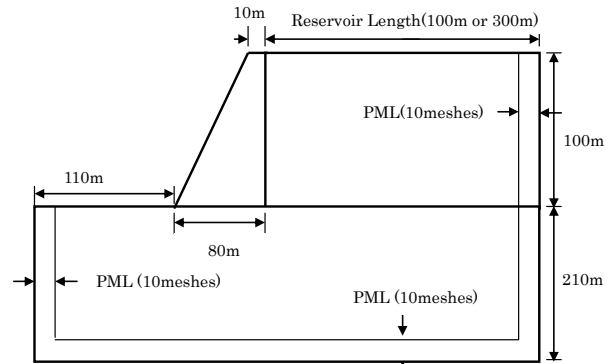


Fig 3.11. Dam-reservoir-foundation model

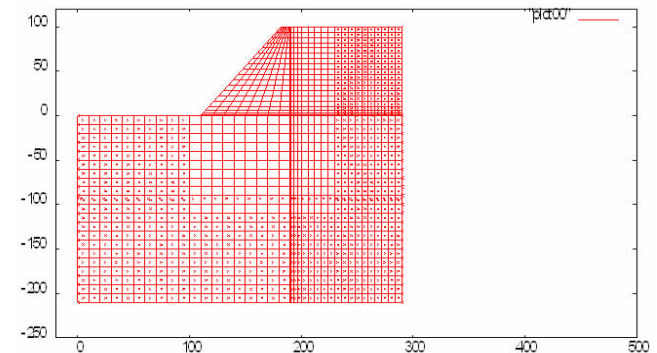


Fig 3.12. Meshes (reservoir length=100m)

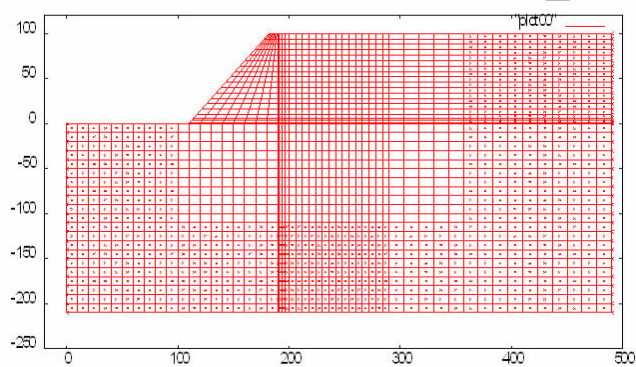


Fig 3.13. Meshes(reservoir length=300m)

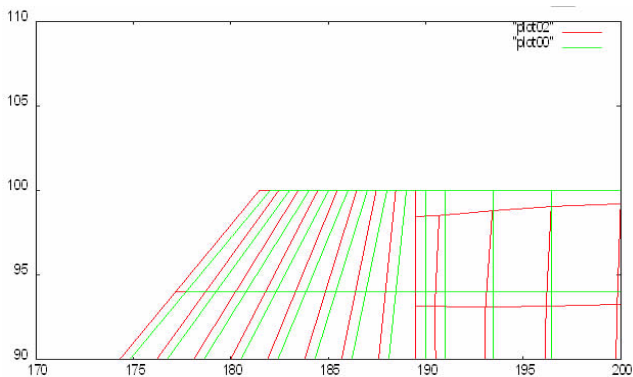


Fig 3.14. Displacements near top of dam

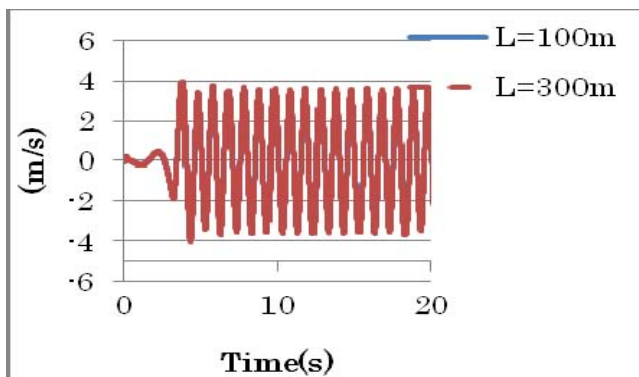


Fig 3.15. Response of dam top (1Hz)

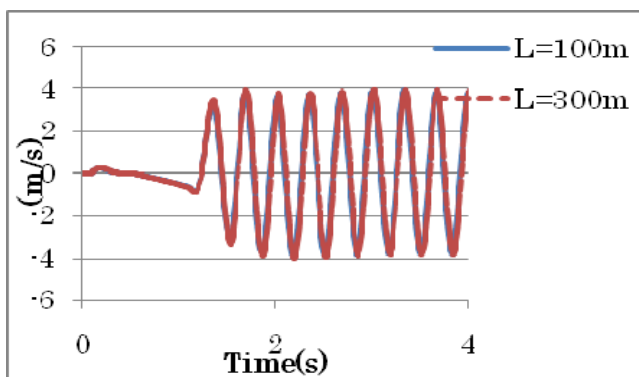


Fig 3.16. Response of dam top (3Hz)

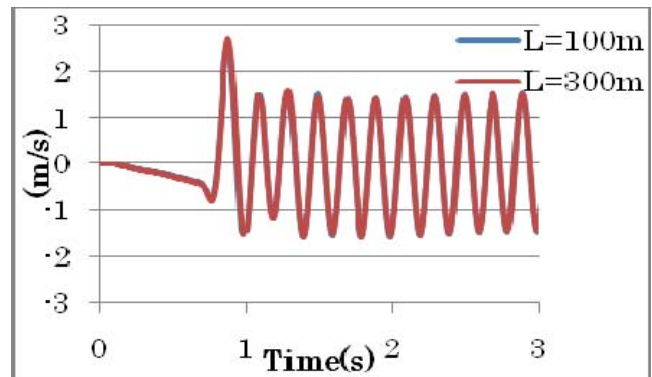


Fig 3.17. Response of dam top (5Hz)

4 CONCLUSION

Convolution PML based on mixed formulation is formulated and computer code is developed for FEM and X-FEM. It was applied to reservoir model and the performance of absorbing outgoing wave was much better than conventional boundary. By applying to dam-reservoir-foundation model including FEM and X-FEM, it was demonstrated that the formulation was quite general, and that it has wide class of application.

5 REFERENCES

- [1] Wolf, J.P.(1988). Soil-Structure-Interaction Analysis in time Domain, Prentice-Hall, Engelwood Cliffs.
- [2] Berenger P.(1994).A Perfectly Matched Layer for the Absorption of Electromagnetic Waves, Journal of Computational Physics, 114, 185-200..
- [3] Collino,F. ,and Tsogka,C.(2001).Application of the perfectly matched absorbing layer to the linear elastodynamic problem in anisotropic heterogeneous media, Geophysics, 66 :1,294-307.
- [4] Drossaert,F.H.,abd Giannopoulos,A.(2007) Complex frequency shifted convolution PMI for FDTD modeling of elastic waves, Wave Motion ,1.44:8593-604.
- [5] Basu,U ,and Chopra, A.K.(2004).,Perfectly Matched layers transient elastodynamics of unbounded domains, Int.J.Numerical Methods Eng..59, 1039-1074.
- [6] Basu,U. ,and Chopra, A.K.(2003), Perfectly matched layers for time-harmonic elesto dynamics of unbounded domains: theory and finite-element implementation, Comput. Methods Appl. Mech. Eng.192, 1337-1375.
- [7] H.Shiojiri,,P.Reheman. & Li J.F.(2010) Application of PML for Non-Linear Soil-Structure Problem,, 14ECEE,Ohrid, 1-8CD.
- [8] P. Reheman,H.SHIOJIRI, Jeng-Feng LI(2011) Analytical Method for Nonlinear Soil-Structure Interaction using PML,Eurodyne, Leuven, Belgium, 1-6CD.

Recycled Bassanite as a Stabilizing Agent for Cohesion-less Soil

Aly Ahmed¹ and Keizo Ugai²

¹Department of Civil Engineering, Beni-Suef University, Beni-Suef, Egypt

^{1,2} Department of Civil and Environmental Engineering, Gunma University, Gunma, Japan

ABSTRACT

This study evaluates the use of recycled bassanite, which is derived from gypsum waste plasterboard, to enhance the performance of two types of cohesion-less soil. Recycled bassanite was utilized as a stabilizing agent to improve both compressive and splitting strengths of tested soil. The effect of bassanite content, soil type, water content, and curing time were investigated to explore the behavior of treated soil with recycled bassanite. Test results showed that increase of bassanite content is associated with increase in optimal moisture content, while no significant increase in the dry unit weight was observed. Both compressive and splitting tensile strengths enhanced with the additives of recycled bassanite. The increase of bassanite content had a more significant effect on the compressive strength compared with the effect on tensile strength. The use of recycled bassanite to enhance the strength of sandy soil had a more significant effect compared with silty soil. The effect of curing time on the strength of treated samples was more significant in early curing ages compared with late curing ages. The strength decreased significantly in case of stabilized samples prepared with water content at the wet-side of the compaction curve. However, insignificant decrease in the strength of the stabilized sample was detected with moisture content at the dry-side of compaction curve.

Keywords: Soil Stabilization, Waste Materials, Soil Strength, Recycled Bassanite

1. INTRODUCTION

Nowadays, researchers are focused on obtaining a desirable way to eliminate waste materials by using them as alternatives in the applications of civil and industrial engineering. Gypsum waste plasterboard is considered one example of these waste materials. Large quantities of gypsum plasterboard, approximately 80 million tons in the world, are produced annually. Around 85% of this production accounts for Europe, USA, and Japan. Out of the latter figure, about 15 million tons is sent to landfill sites [1]. Plasterboard is made from gypsum sheets covered on both sides with paper sheets. Subsequently, increasing the amount of gypsum waste plasterboard results in more quantities, which are disposed in landfills. Hence, it is deemed necessary to find alternative solutions to such problems due to the following reasons. First, gypsum waste plasterboard in landfills is known under certain circumstances to cause hydrogen sulfide gasses, which are potentially harmful and/or lethal. Second, there is currently an increase in the cost of disposal in landfill and decrease in available ground spaces specified for landfills sites. Third, landfill regulations in Japan require that quantities based on gypsum materials are disposed to landfills, and that the waste must be sent to control waste disposal site, which in turn leads to increase in disposal cost.

Several researchers have conducted investigations to improve the physical and mechanical properties of soil by using different types of waste materials, such as cement kiln dust, fly ash, bottom ash, blast furnace slag, stone dust, and factory-waste roof shingles [2-6]. Most of the previous

studies investigated the use of recycled gypsum waste plasterboard in agriculture applications, while a few studies focused on the use of recycled gypsum/bassanite in civil and construction engineering applications. The new unfired gypsum-clay blocks were manufactured by using processed plasterboard from recycled sources. The blend of production blocks comprises 50% of recycled plasterboard. Results indicated that the product has a good physical properties compared with natural clay [7]. Laboratory and field investigations were conducted to develop effective novel cementation mixes using recycled gypsum and a range of mineral wastes for road foundation construction. For this purpose, a series of laboratory trials were carried out to determine the optimum proportions of recycled gypsum and mineral wastes of a binder paste to achieve the highest compressive strength. The optimum combination for the novel binder was a mix of 15% recycled gypsum from waste plasterboard, 5% bypass dust, and 80% basic oxygen slag, which gave a high compressive strength. Results indicated that plasterboard waste can be used in low-strength concrete mixes for the foundations of minor roads and car parks [8]. Generally, recycled bassanite derived from gypsum waste plasterboard has a potential to be used as a cementation material because gypsum is the main key of cementation products. Therefore, the main objective of this research is to investigate the use of recycled bassanite derived from gypsum waste plasterboard as a stabilized agent to possibly improve the strength of cohesion-less soil.

2. MATERIALS AND METHODS

Three types of materials, which include two different types of soil, recycled bassanite, and Portland cement, were used in the current study. The two soil types used were brought from Gunma prefecture, Japan. The two types of soil were named as soil-A and soil-B. All physical and mechanical properties of tested soils are shown in Table I. The grain size distribution curves for all tested soil are shown in Figure 1.

Recycled bassanite used in this work was derived from gypsum waste plasterboard. The crushed plaster gypsum waste ($\text{CaSO}_4 \cdot 2\text{H}_2\text{O}$) was heated at a temperature ranging from 130 to 160°C for a certain time results in a hemi-hydrate calcium sulphate ($\text{CaSO}_4 \cdot 0.5\text{H}_2\text{O}$) with three quarters of the water removed. Firstly, gypsum waste plasterboard was pulverized and then screened to remove any impurities such as papers, paints, and any solid material. Afterward, the powder of gypsum waste plasterboard was placed on specified plate and then the process of heating was started. The preparation of recycled bassanite was done in some construction companies in Gunma prefecture, Japan and Figure 2 is a schematic diagram for preparing the recycled bassanite. Four different contents of recycled bassanite 5%, 10%, 15%, and 20% per soil weight were investigated.

The ordinary Portland cement was used in this research with content of 3% by dry soil mass, which was added to the tested soil sample. The main reason for adding the cement was to prevent the solubility of gypsum when water was introduced since hydrate calcium sulphate ($\text{CaSO}_4 \cdot 2\text{H}_2\text{O}$) is a known water-soluble material.

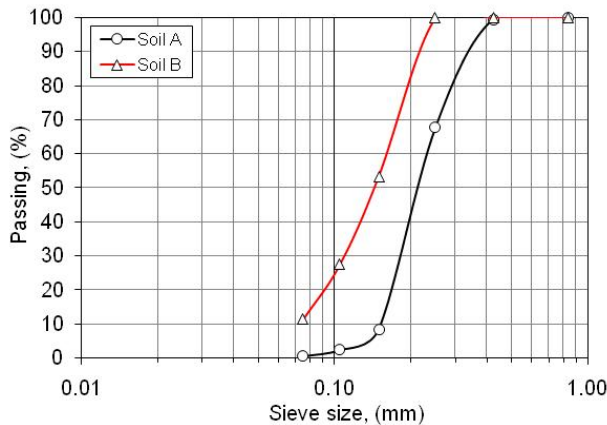


Figure1. Grain size distribution curve for used soils

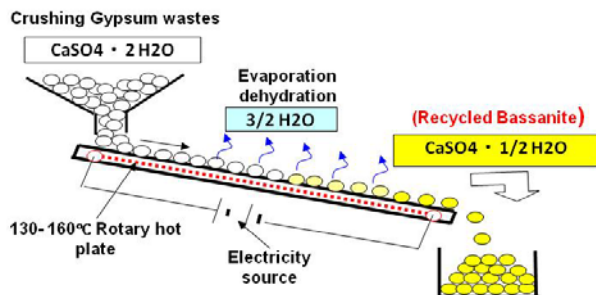


Figure 2. Schematic diagram for producing recycled bassanite from gypsum waste plasterboard

Table 1: Physical and mechanical properties for used soils

Property	Soil A	Soil B
Effective diameter, (D_{10}), (mm)	0.15	0.06
Nominal mean size, (D_{50}), (mm)	0.21	0.15
Uniformity coefficient, (C_u)	1.53	2.72
Curvature coefficient, (C_c)	0.94	1.02
Passing from sieve No. 200	0.40	11.30
Max. dry unit weight, (N/mm^3)	1.57e-5	1.43 e-5
Optimum moisture content, (%)	13.20	20.40
Specific gravity, G_s	2.60	2.67
Max. void ratio	0.85	1.28
Min. void ratio	0.60	0.79
Soil classification (USCS)	SP	SP
	A-3	A-2-4
Soil classification (AASHTO)	Fine sand	Silty sand

3. SAMPLE PREPERATION

The effect of using recycled bassanite on the strength of tested soil was evaluated by conducting a series of unconfined compression and splitting tensile strength tests. Cylindrical samples having a 50-mm diameter and 100-mm height were used. The cylindrical mold, which was used to form the soil samples, was made from high grade plastic with 5-mm thickness to resist any external pressure during the process of compaction. The reason of using plastic molds was to prevent the friction between soil samples and the inner sides of the mold during sample extraction. In addition, the use of oil to lubricate the inner sides of the mold was to make sure that no friction will be occurred during sample extraction. The samples were placed into the molds and compacted statically using a static method by hydraulic Jack to reach the required density. By knowing mold volume, which is constant for all tests and the desired density, the weight of soil was determined to validate the required density. Homogeneity of the samples was of main concern during preparation and extraction. The soil samples were extracted from the molds after 24 hours. More details for preparing stabilized soil samples were described previously [6]. All samples tests were conducted after seven days of curing at temperature ($21 \pm 1^\circ\text{C}$) and relative humidity $> 90\%$. Some samples were tested after 3, 14, 28, and 56 days of curing under the same conditions to investigate the effect of curing time on the strength of samples treated with recycled bassanite.

All tests were conducted at the optimal moisture content and maximum dry unit weight to simulate field conditions. A standard compaction test was carried out to determine the dry density/moisture-content relationship of untreated and treated soil with different contents of recycled bassanite, according to ASTM D 698-70 specifications. The oven-dried soil and recycled bassanite mixtures was firstly dry mixed then the amount of water tap was added to obtain the moisture content for all tested soils.

4. RESULTS AND ANALYSIS

The dry density/moisture-content relations for soils A and B treated with different contents of recycled bassanite are shown in Figures 3 to 4, respectively. It is clear that the increase of recycled bassanite content is associated with a significant increase in optimum moisture content in both two soil types used. It was attributed to two reasons: firstly, due to the tendency of hemi-hydrate calcium sulphate ($\text{CaSO}_4 \cdot 0.5\text{H}_2\text{O}$) to obtain the three quarters of the water that was missed before during heating process, in order to change to hydrate calcium sulphate ($\text{CaSO}_4 \cdot 2\text{H}_2\text{O}$). The second reason is related to when fine content such as recycled bassanite was mixed with soil, more water was required in compaction in order to achieve the maximum dry unit weight [9]. In the case of soil type B (silty soil), the increase of bassanite content up to 15% was associated with a slightly increase in dry unit weight. This was attributed to the calcium component in bassanite, which promotes soil particles to flocculate. Thus, attraction between soil particles was developed due to this property of flocculation. It may be assumed that the flocculation occurred due to the fine components of the soil which normally carry negative charges and attract calcium, which carries two positive charges. This behavior could be related to the tested soil-B comprising more than 10% content of silty clay, which can subsequently behave as fine minerals. The reason of the slightly increase of dry unit weight is related to the increase of optimal moisture content in the soil-bassanite mixture as compared to pure soil. Consequently, the maximum dry unit weight increased slightly. While in the case of soil type A (fine sand), slight increase in dry unit weight was related to the particles of bassanite which are very fine compared to soil particles. That makes it easy for some bassanite particles to fill the small pores within the particles of sandy soil. It is difficult, from a practical view, to fill the pores completely during compaction process in the case of pure sand. For the same volume of compacted sample, the weight of the bassanite-sand mixture was slightly higher than the weight of pure sand that was associated with the slight increase in dry unit weight. On the contrary, if the difference between soil particles was high such as in coarse sand, the dry unit weight would be decreased.

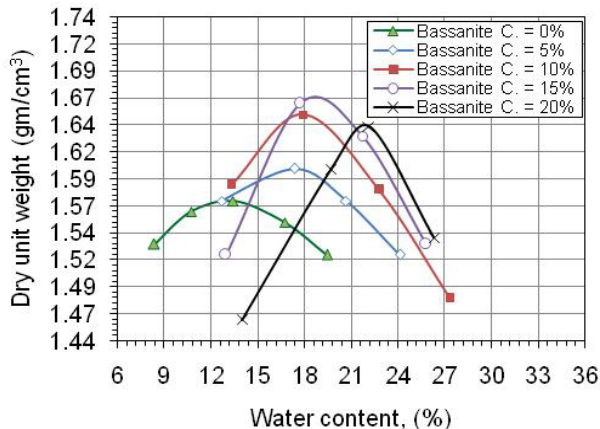


Figure 3. Dry density/moisture-content curves for tested soil-A at different contents of recycled bassanite used.

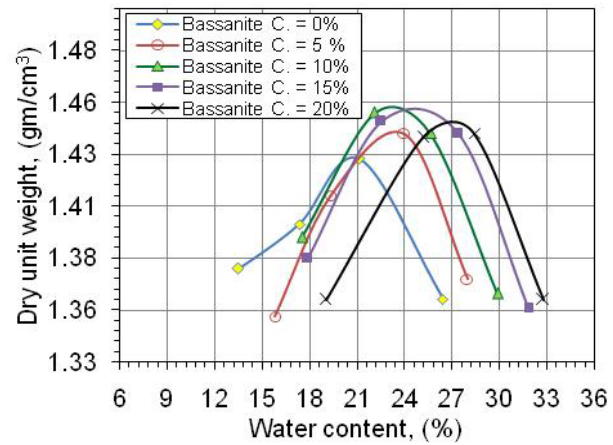


Figure 4. Dry density/moisture-content curves for tested soil-B at different contents of recycled bassanite used.

The results presented herein are only for soil-B because the same results were obtained with another type of soil-A. The results of unconfined compression tests, stress-strain relationship, for soil-B type treated with different contents of recycled bassanite are shown in Figure 5. Obviously, the compressive strength increased with the increase of bassanite content. These results suggested that recycled bassanite can be used as stabilizer material in ground improvement. These results are in agreement with the previous results [10, 11]. Improvement indexes for both compressive and splitting tensile strengths against the content of bassanite are shown in Figure 5. Improvement stress index was obtained by dividing the ultimate stress for treated sample to the ultimate stress of identical un-treated sample. Figure 6 indicates that both compressive and splitting strengths were enhanced with the increase of recycled bassanite content. The improvement in compressive strength was more significant than that in tensile strength. This is attributed to stabilized soil cement, which is weak in tension compared with compression state. An increase of bassanite content up to 15% enhanced the improvement of splitting strength compared to the other lower contents used, as shown in Figure 5. To sum up, the use of bassanite as a stabilizing agent to improve the strength of cohesion-less soil can be acceptable in both compressive and splitting strengths.

Figure 7 shows the stress-strain relationship for different two soil types treated with 10% content of recycled bassanite. It can be observed that the higher performance was obtained in the case of soil-A compared with the case of soil-B. The use of bassanite had a significant effect on the strength enhancement of sandy soil compared to silty soil. This effect could be due to the friction between soil particles of sandy soil was higher than that in silty soil. Besides, the developed cohesion between particles of sandy soil was greater than that in silty soil due to the contact surface area between sand soil particles and bassanite is strong. Thus, the effect of using bassanite to enhance the strength of sandy soil was much pronounced compared to silty sand soil. The same behavior was obtained in the case of splitting tensile strength.

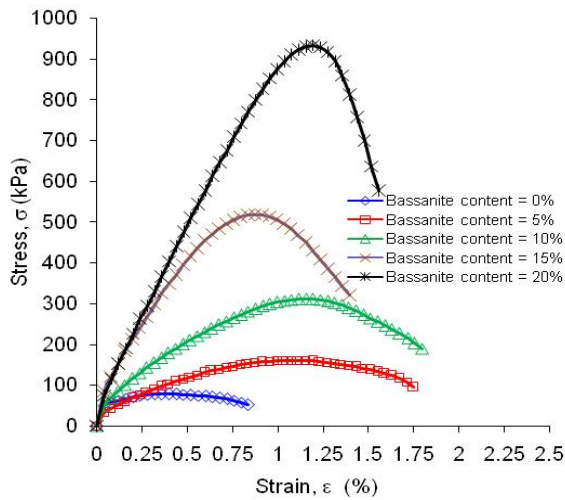


Figure 5. Stress-strain relationships for soil-B with different bassanite contents

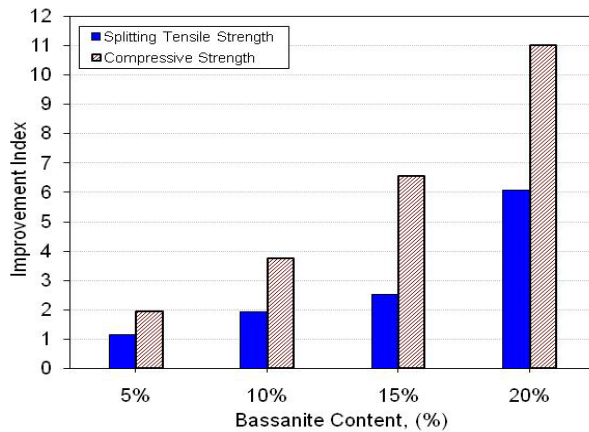


Figure 6. Improvement index for both compressive and splitting tensile strengths in case of soil-B treated with different bassanite contents

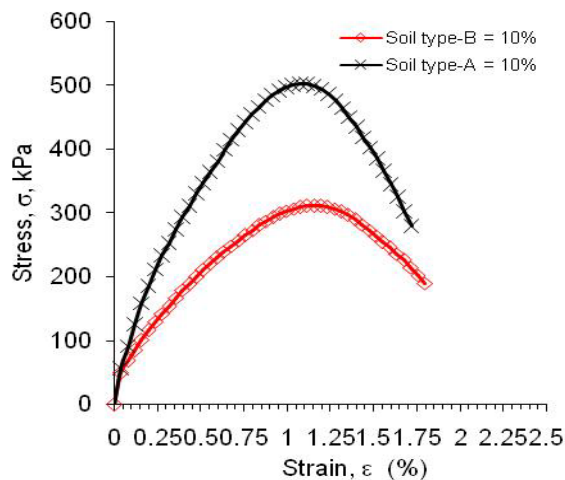


Figure 7. Stress-strain relationships for different soil types used treated with 10% content of recycled Bassanite.

To investigate the effect of water content condition on the strength of soil treated with recycled bassanite, three different moisture contents including optimal moisture content (OMC)

and moisture contents in dry and wet sides that corresponding to 95% of maximum dry unit weight, were used, respectively. The main reason for the use of 95% maximum dry unit weight was to simulate field conditions. Unconfined compression test was conducted on treated samples of soil-B with recycled bassanite contents of 5% and 15%, respectively for different investigated cases of water contents. The suggested contents of 5% and 15% of recycled bassanite were representing the smallest and highest content in this study. The tests were conducted after 7 and 14 days of curing age to investigate the effect of water content on the age of treated samples. The effects of water content on the strength of treated samples are shown in Figures 8 and 9. It is clear that for both age of samples, the high strength was obtained with samples prepared at optimal moisture content compared to other two used water contents. These results are consistent with the expected routine results of compaction test. The effect of water content on the strength of 7-day old samples was much pronounced than the 14-day old samples. The latter difference may be due to the increase of curing age of the samples. This was associated with the increase of strength and consuming most of the excess water as a result of the reaction between soil particles and bassanite. Also, it can be noted that the effect of water content on the samples having highest bassanite content was more prominent than the samples having smallest bassanite content. This behavior could be related to both increase in bassanite content and water content, as illustrated before. Subsequently, the effect of water content in the case of the samples having the highest bassanite content was significant especially at moisture content in the wet side. Furthermore, these figures in the case of samples having smallest bassanite content of 5% showed not much difference between the strength of samples prepared at moisture content in dry side and samples prepared at optimal moisture content. This result also did not match with the theory of compaction test because these samples were impure soil. However, they were treated with some cementation materials thus their behaviors were different. In other words, the amount of moisture content in this case meets the required amount of water to complete a good reaction between cementation material and soil particles. Additionally, the decrease of water content was associated with the increase of strength. Generally, it was found that the unconfined compressive strength decreased significantly in the case of water content at wet side that corresponding to 95% of maximum dry unit weight, while the strength of water content at dry side was slightly decreased.

The effect of curing time on the compressive strength of untreated and treated samples with the smallest content of 5% and largest content of 15% was investigated. Consequently, five different curing times included 3, 7, 14, 28 and 56 days were studied. As aforementioned, all samples were subjected to curing under temperature ($21 \pm 1^\circ\text{C}$) and relative humidity more than 90%. Figure 10 shows the effect of curing time on the compressive strength for tested soil-B at different curing times. The compressive strength for all cases, treated and

untreated samples, increased as curing time increased. This finding is consistent with the theory of curing time for cementation materials. The proportion of improvement in the strength of treated samples in the early curing days was significantly higher than later curing time days. In other words, the improvement in strength for treated samples after seven days curing time was increased slowly in relation with the increase of curing time. This behavior could be explained by the short time required to complete the setting of soil-bassanite mixture, subsequently the treated samples regained most of their strength. Hence, the improvement in strength for treated samples was evident especially in the first days of curing after which the rate of improvement was sluggish mainly with the largest gypsum content. It is worth mentioning that after 14 days of curing time for both bassanite contents, the effect of curing time was insignificant in the context of the strength improvement. The early strength for soil-bassanite mixture is actually a vital property in some projects, such as embankments. This property helps to open embankments for trafficability after compaction process directly. Subsequently, the time of construction decreases and that leads to a reduction in construction cost.

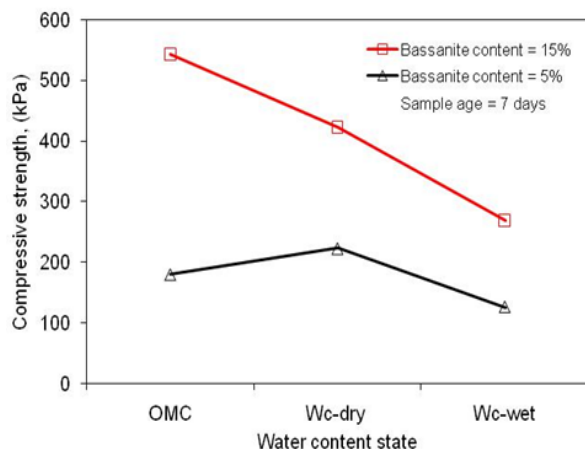


Figure 8. Ultimate strength against water content for soil type-B treated with bassanite and tested after 7 days curing.

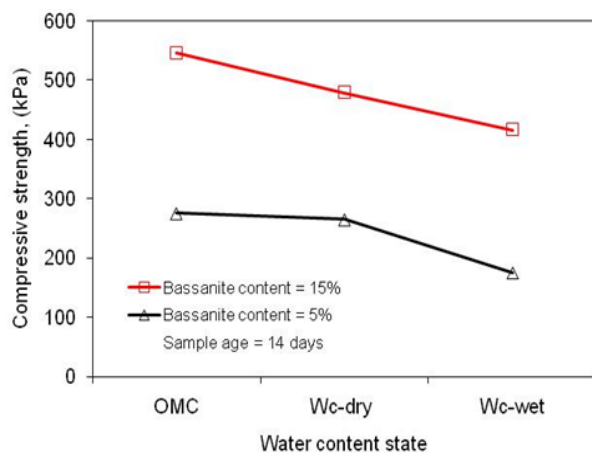


Figure 9. Ultimate strength against water content for soil type-B treated with bassanite and tested after 14 days curing.

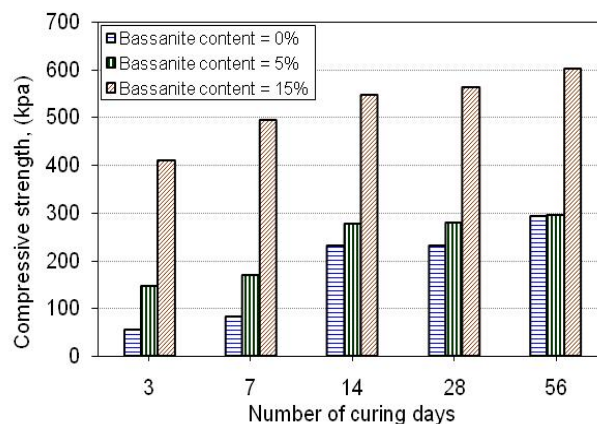


Figure 10. Ultimate strengths for soil type-B tested at different curing times.

5. CONCLUSIONS

This research meets the demand to reduce the quantities of gypsum waste plasterboard, producing useful material from waste materials. The use of recycled bassanite enhanced the performance of all tested soils. Based on test results, the following conclusions can be drawn:

- [1] The compressive and splitting strengths increased as recycled bassanite content increased. The content of recycled bassanite had a more significant effect on the compressive strength compared to the splitting tensile strength.
- [2] The use of recycled bassanite enhanced the performance of all tested types of soil. However, high performance was obtained with only sandy soil.
- [3] Unconfined compressive strength decreased significantly in the case of water content at the wet side compared to other cases of optimal moisture and water content at the dry side of the compaction curve.
- [4] The effect of curing time for samples treated with recycled bassanite was significant regarding the improvement of strength, especially in the early curing days compared with other curing says. The effect of curing time was not significant after 14 days of curing.

6. ACKNOWLEDGEMENTS

Funding of this research was provided through a grant from Japan Society for the Promotion of Science (JSPS) under project number P-10377.

7. REFERENCES

- [5] Gypsum recycling International, (GRI). Available: <http://www.gypsumrecycling.biz/> (accessed on June, 2010)
- [6] Baghdadi Z.A., Fatani M.N., Sabban N.A. Soil modification by cement kiln dust. Material Civil Eng. J. 1995, 7(4): 218-222.

- [7] Miller G.A. and Azad S. Influence of soil type on stabilization with cement kiln dust. *Construction and Building Materials J.* 2000, 14(2): 89-97.
- [8] Sreekrishnavilasam A., Rahardja S., and Santagta M. 2007. Soil treatment using fresh and landfilled cement kiln dust. *Const. and Building Materials J.* 2007, 21(2): 318-327.
- [9] Ahmed A., Shehata M. and Easa S. Enhancing the Strength of Roadway Subgrades Using Factory-waste Roof Shingles. In the Proceedings of 37th CSCE 2008 Annual Conference, 10-13 June, 2008, Québec, Canada, vol. 4, pp. 2546-2555.
- [10] Ahmed A., Shehata M. and Easa S. Use of factory-waste shingles and cement kiln dust to enhance the performance of soil used in road works. *Advances in Civil Engineering Journal*, Article ID 143750, 9 pages, doi:10.1155/2009/143750, December 2009.
- [11] Waste & Resources Action Programme, (WRAP-1). Plasterboard technical report: Use of recycled plasterboard in unfired clay-gypsum blocks. Project code: PBD6-403, Banbury, Oxon, UK, 2007. Available: www.wrap.org.uk (accessed on June, 2010)
- [12] Waste & Resources Action Programme, (WRAP-2). Plasterboard case study: Recycled gypsum in a novel cementations material. The Old Academy, 21 Horse Fair, Banbury, Oxon, UK, 2007. Available: www.wrap.org.uk (accessed on June, 2010)
- [13] Holtz R.D. and Kovac W.D. *An Introduction to Geotechnical Engineering*. Prentice Hall, New Jersey, 1981.
- [14] Kamei T., Kato T. and Shuku T. Effective use for bassanite as soil improvement materials - recycling of waste plasterboard. *Electronic Japanese Geotechnical Journal*, 2007, 2(3): 245-252. (In Japanese).
- [15] Ahmed A., Ugai K. and Kamei T. Investigation of recycled gypsum in conjunction with waste plastic trays for ground improvement. *J. Construction and Building Materials*, 2011, 25(1): 208-217.

THE EFFECTS OF ENVIRONMENTAL ON TODAY CONSTRUCTION INDUSTRY

Hooman Abadi, Rouzbeh Abadi, Poona Abadi

Universiti Kuala Lumpur (Unikl) /Business school, Kuala Lumpur, Malaysia,

Universiti Teknologi Malaysia (UTM), Faculty of Civil Engineering, Kuala Lumpur, Malaysia,

Universiti Teknologi Malaysia (UTM), Faculty of Management, Kuala Lumpur, Malaysia

hooman_abadi@yahoo.com

rouzbeh.abadi@me.com

abadi.poona@gmail.com

ABSTRACT:

We know three degrees for architecture usefulness, stability and resistance..

Of collection what address to define a correct architecture design from the past to now and can be concluded that basically a good design has three characters of simplicity, unity and necessity based on what considered as final aims in construction design. On the other hand, the basic needs that a construction system must answer it includes sat and economy function. The construction success rate to meet these needs have been investigated respecting defined characters. So a plan that supplies the application needs practically and economically, just has answered at least ``to expectations that there is of a plan.

This article indicates that although the aim to design structure is to generate structure forms that as providing application needs, tolerate the loads and the structure with economic methods and the most high structure outcomes, but the aim to design the structure in addition to achieve to finally it is addressed the role of structure engineering art in forming the new form in the architecture of today's world and the necessity at evolving at the architecture instruction in the construction industry in order to achieve this goal, as is explained analytically.

Keywords: Construction Industry, Architecture, Challenges, Requirement Effects, Process Design

INTROUDUCTION

Generally, in people's mind, structural engineering is limited to understanding mathematical concepts, structure analysis, descriptive visualization of structural systems and designing them. Most of the people think that task of a structural engineer is to answer needs of an architectural design for creating a structural system that while can withstand entering forces have predictable behaviors in different conditions of loading and also have necessary safety, a process of design that needs vast amount of calculations for determining tensions and deformations. Although structural engineers really doing these calculations, but they should have a very much more portion than only calculation of structures in forming a modern architectural plan and this should be noticed as a part of their training while study civil engineering. The aim of structural design is to create strong buildings that fulfill considered functional requirements as well as aesthetics needs. Designer should not only consider a vast domain of various choices but also should as well accurately study behavior of these systems in various

loading conditions and should be sure of securing other requirements of the plan.

In this article, role and fundamental effect of structural engineers in forming a correct, good, and acceptable architecture will be analyzed and possible solutions for realizing the suitable real role of a structural engineer in designing form and forming various elements of a building will present. Furthermore, the effect of innovativeness of structural engineers and utilizing structural engineering knowledge in presenting structural forms that provide architectural requirements and aesthetic factor needs of a building will be discussed in details and needs of noticing this matter in architectural training of civil engineering in accordance to realizing this goal will be stated.

Objectives of structural Design:

Various definitions have presented for a proper, correct and excellent design. Usefulness, stability and beauty, from whatever has been stated in defining a excellent design from past, until now, and based on what is considered in structure design as a final goal, it can be concluded that basically a good design has below characteristics:

- a- Simplicity
- b- Unity
- c- Necessity

Each of these characteristics should be considered in all stages of design and even in stages of determining details and designing building elements should be observed accurately.

Simplicity:

This principle is vastly considered in all variety of arts and is a common principle in various field of designing from architectural design to industrial design, and its result is relation and comfort feel that resulted from the intensive effort of designer to realize this very important principle. Structures that in them securing needs and requirements and comfort of users realize to very hardly don't have simplicity. Being simple does not mean being primitive; structures that match requirements of the plan and are simply practicable and also does not have calculation and analysis complexity can be defined as a structure having a simplicity characteristics.

Unity:

Unity of a plan means coordination, integrity, and being coherent, not being a unite object. Definition of unity in a flyover bridge is very unusual than the definition of it in a power plant. These buildings consist of unusual elements, which have to place together to realize a resolved goal. If elements of a plan have designed for achieving a decided goal, unity will be visible in all elements of the plan. A type of artificial unity is there that should be avoided. A set of improper, incoherent, and imbalanced elements can possibly put together but when this set cannot achieve a unique goal, the result cannot be something other than unacceptability of the plan.

Necessity:

This principle is somehow the key solution of designing, but result can be achieved when all the predicted requirements of a project realized. This principle derived from noticing innate needs of human. Human mind feel comfort while accepting something, which is needed, and in presence of extra unnecessary dummies feels unrest.

These principles (simplicity, unity and necessity) should not be considered only in design stage of a plan; these characteristics are as factors that a good plan can be evaluated according to them. Teaching these three characteristics of simplicity, unity and necessity in civil engineering subjects is one of the most important requirements to realize such these goals in plans and projects and this matter needs a new view in educational planning of this field and creates a change in noticing architect with modern definition in a civil engineering field.

Performance, Safety, economy:

Generally, basic needs that a structural system has to answer them are performance, safety, and economy. The success rate of building in realizing these needs can be evaluated based on the stated characteristics. Therefore, a plan that secures functional needs practically and economically has just answered minimum expectations from a plan. Heavy duty of designing for achieving simplicity, unity, and necessity make it mandatory to put maximum efforts for achieving best solutions and realizing these characteristics.

Structural Engineering, conception and expectations:

Structural engineering is a modern and rather a new phenomenon. For a long time, there was no difference between designers, architectures, and engineers, and even between engineers and builders. Differentiation of various specialties and separating duties of structural design from architectural design and defining structural engineering and determining limited and special duties for structural engineers in terms of structural calculations created a non-innovative image of structural engineers to the extent that structural engineers considered as people who just like mathematical science and complicated calculations related to forces and deformations; and because of this today structural engineer have lots of problems to prove their imagination and innovation ability.

For most of the people and even specialists in general is very difficult to recognize a real role of these engineers. Main part of engineering work will be hidden and because of that understanding, it is not simple.

In this situation, it is not strange if architectures see structural engineers of the plan as a technician. Exchanging ideas is a necessity for a successful cooperation between an architect and a building engineer. Engineers have to analyze behavior and reaction of a building in various conditions of loading. This responsibility make building engineers more conservative compared to those who don't have required technical knowledge and do not understand the sensitivity role of engineers and difficulties. Above studies shows that the necessity of change in the academic plan of civil engineering field and also noticing this matter that building engineers should be familiar with successful classic and modern patterns of art in the design field just like architectures, artists, and musicians. Building engineers can achieve very high imagination and understanding power if they can gain this ability to describe why a special structure designed perfectly and why other structures does not have a good design.

Structural Engineering Skills:

Generally, for someone who is not a structure engineer is difficult to understand necessary skills in the structural design process. This matter is because

the only remaining footprint of a designing activity that people will see is completed building that normally a structure of building is hidden inside it. Recognizing structural engineering skills includes what structural engineers know and activities that they do during the structure design process. These skills can be effective in achieving path of aesthetic principles of structure. Below points include a list of these skills that some parts of it is already predicted in the academic plan of civil engineering, and some parts have to be noticed in a revised syllabus of this filed:

- Predicting possible loading of a building and role of reactions of them
- Studying possible ruptures of a structure under effect of forces from both behavior of consisted elements and general stability of the whole structure against forces as a unit set
- Ability of evaluating forces to a structure from qualitative and quantitative point of views
- Having comprehensive knowledge about characteristics and behaviors of materials and structures
- Ability of matching thinking and view point method to materials, structure, and its behavior according to different situations
- Ability of creating a mathematical model of structure using geometry, algebra, trigonometry and probability, etc.
- Ability of creating a process for designing and building structures that are not implemented yet.
- Building sample models in smaller dimensions for evaluation and testing structural theories
- Interpretation ability of achieved results of built samples for utilizing in real dimensions
- Choosing practical factors based on evaluations of a structure and determining limits that value and quantities should not cross them.
- Understanding mutual effect of requirements and criterions of the plan (such as cost of building, infrastructures of building, services, useful life span, durability, resistance against fire, and, etc.) on building structure and vice versa
- Evaluating ability and possibility of building proposed plans
- Proposing plans that can be implemented simply and with lower cost.
- Understanding this matter that in which time and with which situation structure design has completed properly.

Architects and Engineers:

Although structure of building and its function seems separated from each other but constantly a structure has a determining role in architecture of building. Structure, firstly, is compulsory part of a building that cannot be

deleted and secondly, structure should constantly follow nature and physics rules and therefore, cannot secure every single demand in architectural design and thirdly, although structure is a essential part of each building but generally is hidden and in most of the cases, it seems so it does not have effect on architecture of building and finally, building structure have some cost. Howsoever, cost of structure building compared to other costs of building is not major cost, but even so, it cost money and generally in building's cost of creating a structure is one-third to be one-fourth of whole cost of the building. In some buildings such as bridges or halls with higher numbers of gates, structure cost is the most part of cost of building. Structure is a factor that can create disagreement between architect and building engineer. Today a good architect should have general knowledge about behaviors of structures. Moreover, he/she should be an artist, bound and committed to observing principles of architectural design and aesthetical factors. A plan is successful if its architecture understands its structure behavior properly, and its structural engineer has proper knowledge and be committed to architectural design and aesthetical factors. Finally, architect is the leader of a team that is responsible for design and implementing of a building and all responsibilities and also credit of success of the project in this section will be granted to him/her.

A result derived from being knowledgeable and commitment of a structural engineers on building design, and aesthetical factors is clearly evident the need of change in the academic plan of architecture training in a civil engineering field to achieve above-mentioned goals as studying notable architectural and engineering works of the world obvious necessity of such this change.

CONCLUSION

As it has shown in "Objectives of structural design" section, before anything, building design should be recognized as a joint activity and a group work with participation of architect, and structural engineer and therefore, relating engineering plans to specific persons is difficult. A modern and innovative design for a building is possible when a process of design and formation of different stages of the plan is resulted of consultation, cooperation, and effort of an architect, building engineer, infrastructure engineer and even their builders in this path. This matter manifest necessity of teaching required fundamentals for being sure of realizing such these goals in projects and plan to include three characteristics of simplicity, unity, and necessity and also dominant principles on combined realization of three principles of performance, safety, and economy in a civil engineering field.

Mentioned subjects in “Structural Engineering, conception and expectations” section shows that structural engineer is a member of design and building team that has extensive knowledge about behaviors of structures under effect of different loads. And also understand production and build process properly. Structure engineer in the process of formation of an architectural plan should take monumental responsibility of structure design, and implementing it in form of building calculations, designing structure form, designing elements of structure and joints of it with realizing designing criterions, necessities and limitations of the plan in various dimensions. From studying subjects of this section it can be concluded that principal goal of architectural design should be creating such forms that secure operational requirements of the building and also be successful in terms of aesthetic. The main goal of designing structure should be creating structural forms that while securing functional requirements can withstand applied loads in best way and economically. In close cooperation that should be present between architects and structural engineers, the duty of structure engineers is to create plans than from functional view point answer requirements of the plan and from technical view, point should be implementable, economic and having necessary conditions and moreover, from the desirable exterior of building view point complete aesthetical feeling of an architect. Difference between different and yet very important roles of architect and engineer should understand well to recognize the real value of work of each one of them. Finally, relation between design and construction can only change to a positive and constructive competition that this recognition secured properly. Study in this section has shown a necessity of the academic plan of civil engineering and noticing this matter that civil engineer should be familiar with the successful patterns in the field of classic and modern design art like architectures and artists. Structural engineers should gain high level of imagination and understanding exact behavior of structures and not only their precise calculations, and then they will have this ability to understand suitably how a specific building can answer requirement and criterions of architectural design with proper and correct design while observing principles of stability of structure. “Structural engineering skills” and “role of architects and engineers” sections show that the art of structural engineering is using calculation and design theories of structures for transforming ideas and concepts into buildings that can function correctly, utilize materials economically and answer positively to aesthetical needs of a building. In this situation, structural engineer will perform its job to reinforce architectural design of the building. Studies in this section have shown that

“Structural engineering is an art” which its goal is to create buildings that can answer functional requirements, aesthetical factors, requirements of function period, and limitation of conditions related to construction of building. Structural engineer in this path not only should consider principles of structural design in choosing the most proper structural system but should accurately study and evaluate the functionality of these systems in various situations for achieving requirements and mentioned criterions so the process of architectural design and structural calculations reach a unique and common result that can secure all the requirements of the plan. Study a list of skills of the structural engineers shows that some parts of it is already present in the academic syllabus of civil engineering subjects and some parts too should be noticed in a revision of the contents of this field. This matter needs a modern view point to academic plan of civil engineering filed and create a change in noticing architecture with a fresh definition in this filed.

REFERENCES:

- [1] Salvadori M. and Levy M., 1981, “Structural Design in Architecture”, Cliffs, N. J., USA, Prentice-Hall Inc.
- [2] Frampton K., 1985, “Modern Architecture (A Critical Histoty)”, Thames and Hudson Limited.
- [3] Mainstone R.J., 2002, “Developments in Structural Form”, Cambridge, the MIT Press.
- [4] Margolius I., 2002, “Architects + Engineers = Structures”, Willey - academy, London.
- [5] Davies C., 1991, “High Tech Architecture”, London, Thames and Hudson Ltd.
- [6] Zunz J., 1992, “Mirror on the Wall, How Fair Is the Engineering Image?” London, Arup Journal.
- [7] Snelson K., 1989, “The Nature of Structure”, New York, The New York Academy of Science.
- [8] Siegel C., 1975, “Structure and Formin Modern Architecture”, Huntington, New York, Robert E. Kreiger.
- [9] Salvadori M., 1990, “Why Buildings Stand Up, The Strength of Architecture”, New York, W.W.Norton & Company Inc.
- [10] Rice P., 1992, “Royal Institute of British Architects (RIBA) Gold Medal Speech”, London.
- [11] John Chilton, 2000, “Space Grid Structures”, Oxford, Architectural Press.
- [12] Roth L.M., “Understanding Architecture”, Herbert Press, 1993.

- [13] Golabchi M., 1994, "Selection of Appropriate Structural Systems for Large Spans", Department of Civil Engineering, University of Leeds, England.
- [14] Golabchi M., 1995, "The Art and Practice of Structural Engineering", 4th Civil Engineering Seminar, University of Manchester, England.
- [15] Berger H., 1996, "Light Structures – Structures of Light", Basel, Switzerland, Berkhauser.
- [16] Cowan H., 1971, "Architectural Structures", New York, Elsevier.
- [17] Huxtable A. L., 1960, "Pier Luigi Nervi", New York, Braziller.

A Case History of Quay Wall Failure and Remedial Design

C. S. Chen
SSP Geotechnics Sdn Bhd, Malaysia

ABSTRACT

A case history of investigation into the failure of a precast reinforced concrete quay wall and the remedial design is presented in this paper. The quay wall was about 6.5m high. The soil investigation carried out during design stage indicated that the subsoil below seabed mainly composed of soft clay layer. To enhance the stability, all soft clay was designed to be removed and replaced by granular material. The quay wall was designed to be founded on top of this granular material slope which to be protected by armour rock revetment. However, a stretch of the quay wall moved excessively during the backfilling works. Investigation was carried out after the incident. Boreholes were sunk to investigate the subsoil condition and the results showed that there was a localized very soft clay layer between the backfilled granular soil layer and the hard soil layer. Few remedial options were considered and stone columns option was adopted. The quay wall was successfully re-built after the stone columns were installed.

Keywords: Quay wall, stone column, soft clay, slope.

1. INTRODUCTION

A harbour basin had been planned for a marina project in a mixed development on a piece of coastal land. The existing ground was generally on low lying area with most of the time submersed under water. In order to allow boats and yachts to sail from the open sea into the marina project site and berth inside, about 8 to 9m deep dredging from the existing ground surface was required to form a basin. For the surrounding area of the basin, reclamation was required to form a platform higher than the tide level. Quay wall of about 6.5m high was designed to be constructed at the perimeter of the basin to retain the backfilled soil. Fig. 1 shows the proposed layout plan and Fig. 2 is the model of the proposed marina project.

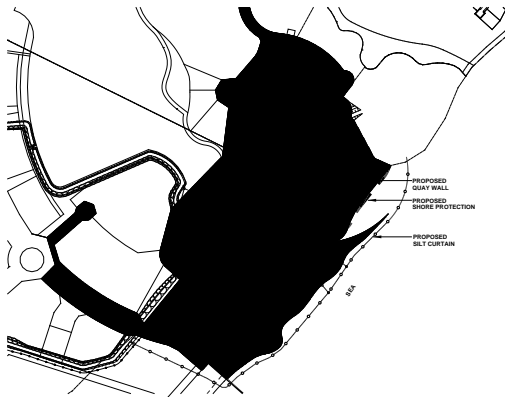


Fig.1 Layout plan of the marina project.

During the planning and design stage, soil investigation

mainly composed of boreholes was carried out. The subsoil information gathered showed that there is a thick layer of soft cohesive soil below the existing ground surface. It was decided to remove the soft soil and replaced by granular material which mainly consisted of sand in order to ensure the long term stability of the basin slope and sufficient bearing capacity for the proposed quay wall.



Fig. 2 Model of the proposed marina project.

However, a stretch of the quay wall moved excessively during the backfilling of soil behind the quay wall. Investigation was carried out to identify the possible causes of failure and to gather additional information for remedial design. This paper presents the subsoil information at site gathered from the soil investigation, findings and possible causes of failure from the failure investigation and the remedial design.

2. SUBSOIL CONDITION

Soil investigation mainly consisted of boreholes was carried out during the planning and design stage to gather the subsoil profile and engineering properties. Typical subsoil profile at the proposed basin area is shown in Fig. 3. In general, soft clay was found below the existing seabed with thickness varied from few meters to about 10m. Liquid Limit and Plasticity Index for this soft clay layer are in the range of 40% to 101% and 16% to 77% respectively. A layer of loose sand of silt could be found below the soft clay layer. The very dense sandy soil layer or hard bearing stratum is generally at about 13 to 15m below the existing seabed.

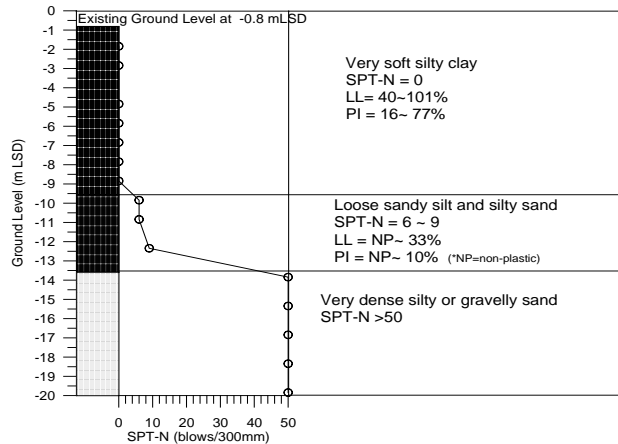


Fig. 3 Typical subsoil profile.

3. DESIGN OF THE QUAY WALL

The existing ground was a low lying mangrove swamp land with the ground levels were mostly in the range of +1m LSD (Land Survey Datum) to -1m LSD. At normal and high tide period, the ground was submersed underwater. The design of the basin required to excavate the existing ground to the designed level of -8.5m LSD. The land surrounding the basin was required to be backfilled to a higher platform level of about +3.1m LSD. Quay wall of about 6.5m height was designed to retain the backfill soil.

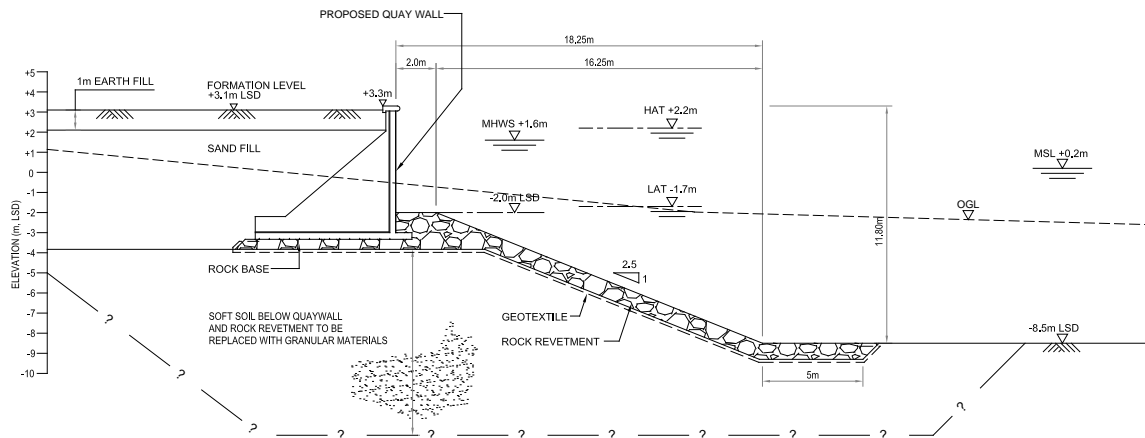


Fig. 4 Typical design of quay wall

For ease of construction, quay wall will be precast at factory and delivered to site during construction. Fig. 4 shows the typical design cross section of the proposed quay wall. As it was expected that the quay wall could be founded on the soft clay layer, stability of the quay wall was a concern in the design. Stability analysis carried out indicated that with the removal of the soft material and replaced with granular soil, the wall will be stable. It was decided to remove all soft material beneath the quay wall foundation. To prevent scouring or erosion takes place, the granular slope was protected by a layer of rock revetment.

4. FAILURE OF THE QUAY WALL

Dredging work was carried out immediately after the design was completed. The basin was dredged to the designed level. For areas below the quay wall and the slope, over-dredged was required in order to remove all soft material which may affect the stability of the quay wall. Once the removal of soft soil was completed and granular material was filled to the designed founding level, quay wall was installed and backfilling started subsequently.

However, a stretch of the quay wall moved excessively into the basin before the backfill reached to the designed platform level. The backfill material behind the quay wall was immediately removed to mitigate the wall movement. Investigation of the failure was carried out after the incident. Fig. 5 shows the failure condition of the quay wall.

5. CAUSE OF FAILURE

The design of the quay wall was reviewed. It was found that the design should be adequate. The construction method and sequence of work were also being reviewed and it was concluded that these should not be the cause of failure. Initially it was suspected that the rock revetment could have been washed away by the current which undermined the material below the quay wall and caused the wall to move excessively. However, probing results indicated that rock revetment and the slope profile still maintained. The abnormal observation was that there were signs of heaving at

the toe of the slope. To gather more subsoil information and engineering properties at the failure zone, boreholes were planned and carried out. Fig. 6 presents the gathered subsoil information. Generally the subsoil profile was consistent with the design assumption. Backfilled sandy soil was found behind and below the founding level of the quay wall. However, a layer of soft clay was detected in within the backfilled sandy soil and the medium stiff to hard soil layer. Stability analysis was carried out based on the obtained soil profile and the result showed that the slope was unstable. It was concluded that the failure of the quay wall was mainly caused by the existence of this soft clay layer. In the design, this soft clay layer was required to be removed. However, this requirement was not fully implemented during the dredging stage. Although some exploratory holes had been sunk prior to the dredging work to establish the expected depth for soft clay removal, Part of the reason was that the workers followed the estimated depth of removal which was established from the results of exploratory holes carried out prior to the commencement of dredging work.



Fig. 5 Conditions of failed quay wall.

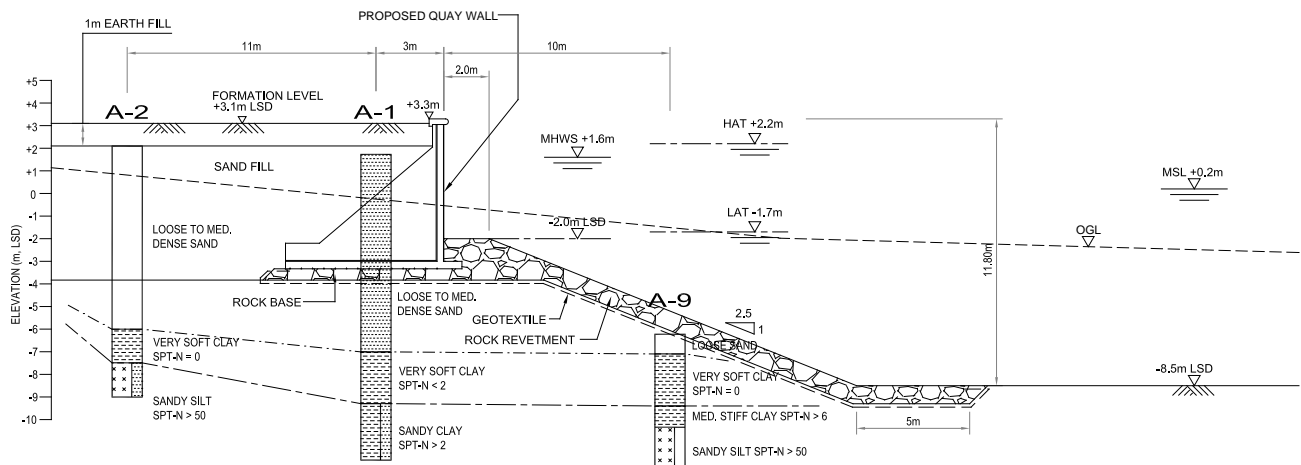


Fig. 6 Subsoil profile from the investigation results

Also, it was difficult for a non-experienced engineer to determine whether the subsoil is soft or medium stiff at site to decide the actual depth of removal. This incident could have been avoided if (a) there was an experienced site staff to inspect the dredged subsoil and determined the actual required depth for removal of soft soil and (b) carry out some verification measures to ensure that all soft soil had been removed prior to the backfilling work.

6. THE REMEDIAL DESIGN

The failure occurred at localized stretch only. For quay wall at other area, the backfilling work had reached to the designed platform level and the wall was found in stable condition. In selection of suitable remedial measure, one of factors needed to be considered was not to disturbed the already constructed quay wall.

Few options had been considered. The advantages and disadvantages of each option are discussed as follow:

6.1 Replacement Option

This option was similar to the original design, i.e. to re-dredge the soft clay which was found from the investigation and replaced with granular material. The advantage of this option is that the staff at site was fully aware of the failure cause and they will ensure all soft soil underneath to be removed. Also, they were familiar with the sequence of work. The disadvantage was this will affect the stable quay walls at both sides of the failure stretch.

6.2 Ground Improvement Option

This option is to improve the strength of the soft clay layer in order to enhance the global stability of the quay wall. A wide range of soil improvement methods [1] is available. For this site, vibro stone columns, cement mixed columns and grouting are more suitable. Surcharging method with or without Prefabricated Vertical Drains was not considered as this option required longer time. The main advantage of this

option is minimum disturbance to the adjacent quay wall. The disadvantage is that the cost is usually higher as compared with the first option. Vibro stone column was the better option as compared with cement mixed column and grouting after consideration of the availability of materials, experiences and machinery.

6.3 Structural Option

This option was to use structure such as steel sheet piles or contiguous bored piles to stabilize the slope. The advantage is the construction is fast and straightforward. However, this option is the most expensive option.

6.4 The Vibro Stone Column Remedial Works

In order to minimize the disturbance to the adjacent quay wall and to maintain the cost within acceptable level, vibro stone column option was selected. The design of stone column can refer to [2]. It was decided to adopt 800mm diameter stone columns with center to center spacing of 1.8m in triangular grid after analysis was performed to improve the soft clay soil underneath. Fig. 7 presents the typical section of the stone column option.

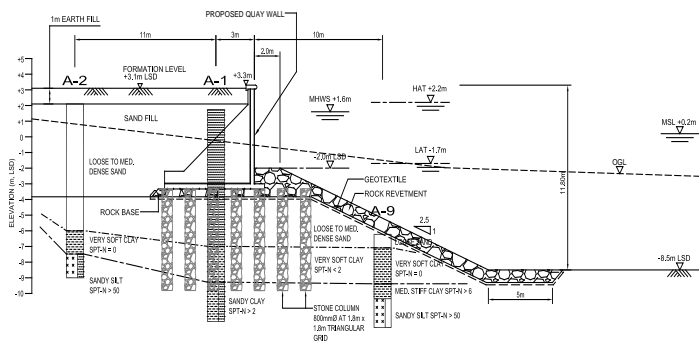


Fig. 7 Typical design of stone column option

The remedial work started by removing the affected quay wall. A working platform was then prepared to allow the movement of the machinery and installation of stone columns. Fig. 8 shows the stone column installation work carried out at site. The vibroflot with water jetting created an open hole to the designed depth. A long arm excavator was used to feed in the required stones and the vibroflot started to compact the stones until the stone column was formed. The quay wall was successfully built after the completion of the installation of stone columns. Fig. 9 shows the quay wall condition a year after the completion of the construction work.

7 CONCLUSION

A stretch of quay wall moved excessively before the backfill behind the wall reached to the design level. Investigation results show that there was a layer of soft clay below the quay wall which was required to be removed in the design. Due to the low strength of this soft clay layer, the quay wall was unstable. Stone column option was adopted to improve the subsoil strength. The quay wall was successfully built after the stone columns were installed.



Fig. 8 Stone column installation work at site



Fig. 9 Condition of the successfully built quay wall

8 REFERENCES

- [1] Mitchell J.M. and Jardine F.M, A guide to ground treatment. CIRIA publication C573, 2002.
- [2] Priebe, H.J, "The design of vibro-replacement". Ground Engineering, Vol. 28, No. 10. 1995, pp.31-37.

Environmental Economical Efficiency in Treatment/Reutilization of Construction Sludges considering Delay in Process Flow

Shinya Inazumi¹, Hiroyasu Ohtsu¹ and Takayuki Isoda¹
¹Kyoto University, Japan

ABSTRACT

In Japan, although the recycling of waste has been promoted, there may be various obstacles. In this study, we focus on construction waste, more specifically, construction sludge, which is less advanced in terms of recycling. Processing cost for materials recycled from construction sludge is higher compared to the cost of mining virgin materials. There are some additional difficulties including delays in schedules due to the time required for processing and the balance between supply and demand. Therefore, we quantitatively assess the benefit of recycling by adding the time factor to the evaluation model with consideration for cost and environmental load. As a result, it is shown that the bottlenecks of construction sludge recycling are higher cost than the cost of mining of virgin materials, high heavy metal contents in the construction sludge, and delays in the recycling process.

Keywords: Environmental Economics, Environmental Impact Assessment, Construction Sludge, Construction waste, Processing, Recycling

1. INTRODUCTION

Although recycling of construction waste is advancing, there are still many problems to be solved. One of the main factors limiting recycling of construction waste is the higher unit price of recycled materials compared to that of virgin materials because of the necessity of processing for recycling. In addition, it takes time for such processing for recycling, and if recycled materials are used, the construction schedules could be extended, resulting in a possible increase in the construction cost. However, we can look upon these problems as being the result of considering recycling only in terms of cost. The purpose of recycling consists of enabling society to undertake sustainable development through environmental preservation. Thus, in evaluating the business potential of waste recycling, not only the required actual cost but also the effects on the environment should be considered. In other words, it is important that business activities related to waste recycling should be evaluated according to environmental economics, which employs a well-balanced consideration between actual cost and environmental effects by accounting internally for environmental impact over the life cycle based on the concept of environmental economics.

In the previous studies regarding construction waste, we examined the environmental impact assessment and environmental accounting approach to evaluate recycling of construction waste by environmental economics in which environmental load converted to environment cost in addition to direct cost is considered [1]-[2]. In this study, we focus on the extension of construction schedules caused by process delay brought about from processing for recycling that is one of the obstacles for recycling of construction waste.

Specifically, regarding recycling of construction waste, we use environmental impact assessment and the environmental accounting approach to perform environmental economic evaluation with consideration of process delays in processing for recycling. In this study, among construction waste that is supposed to be a recycling resource, we look at construction sludge, which is less advanced in terms of recycling.

2. DEFINITION OF CONSTRUCTION SLUDGE

2.1 Present Situation of Construction Sludge

According to the Ministry of the Environment, the data for industrial waste by industry (2008) shows that the construction industry discharged 700 x 104 tons, 18.9% of the total, which was the third largest amount [3]. Similarly, according to the field survey about byproducts of construction by the Ministry of Land, Infrastructure, Transport and Tourism, the data for construction waste by item (2008) shows construction sludge was 450 x 104 tons [4]. Construction sludge did not constitute such a large proportion of the total construction waste, but the data for the final disposal by item of construction waste (2008) shows that construction sludge was 67 x 104 tons, approximately 15% of the total construction waste, 402 x 104 tons [4]. When it is compared with the previous field survey of construction byproducts (2005), it can be considered that the situation regarding the final disposal of construction sludge improved, because the final disposal of construction sludge was 192 x 104 tons and it constituted approximately 30% of the total, but it was still a large proportion [5]. On the other hand, as for the recycling of construction waste in 2008, the total recycling rate was 93.7%, and the recycling rate of construction sludge was 85.1% [4]. This was also an improvement from the previous survey. However, the recycling rate for construction sludge was still smaller than

the rate for the other construction waste. The recycling rate is defined as a percentage of the recycled amount or the reduced amount against the total amount. And the effective availability rate of displaced soil at construction is defined as a percentage of the displaced soil at construction against the total soil used for construction.

2.2 Obstacle for Recycling of Construction Sludge

It is preferable to use the discharged construction sludge during the construction period. However, according to the field survey of construction byproducts in 2008, the percentage of the use during the construction period was only 2% [4]. This was because there are few facilities available for recycling and it required long distance transportation between a construction site and a processing facility in many cases. In other words, transportation cost increases and furthermore, lots of air pollution is produced. In addition, for recycling of construction sludge there should be construction sludge in the first place. Even if construction needs recycled materials, recycled materials cannot be supplied without construction sludge at the processing facility. In addition to these disadvantages, recycling takes time and it may cause a delay in construction. If the construction schedule is delayed, it will lead to an increase in costs, such as labor cost or lease payments for the equipment. Thus, constructors are forced to use virgin materials instead of recycled materials. The possible delay in the construction schedule is one of the obstacles for the recycling of construction sludge.

3. ENVIRONMENT IMPACT ASSESSMENT AND ENVIRONMENTAL ACCOUNTING APPROACH

3.1 Quantification of Direct Cost

For recycling of construction waste, an inevitable cost including transportation cost and processing cost for recycling is required. In this study, we refer to these types of cost as direct cost. When we roughly classify them, we have an initial cost and running cost (including processing cost, transportation cost and storing cost) [6]. The direct cost can be calculated by the Eq. (1). We apply the Eq. (1) to the manufacturing of virgin materials, manufacturing of recycled materials and disposal. The elements in Eq. (1) indicate unit price of unit construction work.

$$C = C_I + C_S + C_T + C_K \quad (1)$$

$$C_S = WS \quad C_T = WLT \quad C_K = WDK$$

Where, C : direct cost (yen), C_I : initial cost (yen), C_S : processing cost (yen), C_T : transportation (yen), C_K : storing cost (yen), W : mass (t), S : unit price required for processing of each material (yen/m³), L : transportation distance (km), T : unit price required for transportation (yen/t-km), D : storing days (day), K : unit price required for storing each material (yen/t-day)

3.2 Quantification of Environmental Cost

In this context, it is necessary for people to understand environmental value through its conversion into monetary

value. In this study, we refer to detected environmental load converted into a cost-based figure just like direct cost as environmental cost.

In the evaluation and comparison based on environmental economic efficiency performed in this study, Eq. (2) shows the environmental cost element to which we pay special attention. We apply Eq. (2) to the manufacturing of virgin materials, manufacturing of recycled materials and disposal. Each element in Eq. (2) indicates the unit price of unit construction work. Here, we refer to the results of the study of [7]-[8] and other previous studies [2] for extraction of environmental cost elements.

$$E = E_O + E_T + E_{C1} + E_{C2} + E_{C3} + E_{C4} \quad (2)$$

Where, E : environmental cost (yen), E_O : environmental cost accompanied with operation of facilities (yen), E_T : environmental cost accompanied with transportation (yen), E_{C1} : environmental cost related to public functions such as forests (yen), E_{C2} : environmental cost related to impact on ecological system (yen), E_{C3} : environmental cost related to exploitation of natural resources (yen), E_{C4} : environmental cost related to worsening of residential environment (yen).

3.3 Business Effect of Recycling of Construction Waste

It is thought that recycling of construction waste contributes to the slowdown in the decrease of the remaining capacity of the final disposal sites through reduction of waste, and to cost reduction of waste disposal [9]. In this study, we regard these benefits of recycling as business effects caused by reduction of cost required for waste disposal. The evaluation of the business effect is calculated by multiplying the amount of construction waste by the unit price of final disposal as shown in Eq. (3). However, since the business effect means cost reduction, the calculated result should be a negative value.

$$B = -W \times S \quad (3)$$

Where, B : business effect of recycling of construction waste (yen), W : amount of construction waste (m³), S : unit price of final disposal (yen/m³).

3.4 Total Cost

The environmental assessment and environmental accounting approach defines the total cost shown by Eq. (4) as one of the indexes of environmental economic efficiency. The total cost is considered as a social cost with consideration of the environmental impact.

$$T = C + E + B \quad (4)$$

Where, T : total cost (yen), C : direct cost (yen), E : environmental cost (yen), B : business effect by recycling (yen).

3.5 Consideration of Delay in Processing Process

One of the obstacles for recycling is that the supply of recycled materials does not fit well with the construction schedule [5]. This is because the recycling of construction waste has some uncertainties including that construction waste is not constantly supplied to the disposal site, that it takes time for recycling to be certified because the method of recycling is complicated or imprecise, and that the time required for processing fluctuates because the quality of construction waste varies depending on the site. As a countermeasure to any delay that may occur in the process of disposal, storage of waste at the stock yard has been proposed. In this study, we assume soil material used for soil structures can be stored until the specified storage capacity of the site is reached. The number of days for storage is determined by the amount that can be dug in a day in case of virgin material or by the amount that can be manufactured in a day in case of recycled material. If the material stays at the stock yard long, the cost for storage increases. The number of days for storage is defined by Eq. (5).

$$D = W / W_i \quad (5)$$

Where, D : the number of days for storage (day), W : required amount of soil for a soil structure (m^3), W_i : amount of soil (virgin or recycled) that can be produced in a day (m^3/day).

3.6 Evaluation by Monte-Carlo Simulation

There are various approaches to analyze the recycling of construction waste while considering every uncertainty. In this study, we adopted the Monte Carlo simulation. The Monte Carlo simulation is a technique to comprehend all the possible combinations by changing every uncertain element at the same time. By using the Monte Carlo simulation, we can obtain frequency distributions of the output and apply the results to evaluate business risk.

4. EVALUATION OF ENVIRONMENTAL ECONOMIC EFFICIENCY OF CONSTRUCTION SLUDGE RECYCLING

In this chapter, we apply the environmental impact assessment and environmental accounting approach to recycling of construction waste and perform evaluation and comparison of virgin materials (not regenerated soil materials) and recycled materials (regenerated construction sludge) based on environmental economic efficiency.

4.1 Assumptions

The following are assumptions for evaluation and comparison for recycling of construction sludge based on environmental economic efficiency.

- (1) The amount of soil for the target soil structure is $3,000\text{m}^3$.
- (2) For each element of uncertainty, the minimum, median (base case) and maximum are specified as shown in

Table 1. We decided the medians either from the averages of the values in literature search or based on what we obtained from interviews [7], [10]-[11].

- (3) The processing for recycling of construction sludge is a stable treatment.
- (4) As shown in Fig. 1, when the processing cost increases, the amount of materials and energy required for processing as well as the environmental cost accompanied with operation of the facility (processing) increase.
- (5) For digging, the rate of change is assumed. When soil is dug up, gaps appear in the soil. As a result, the mass of the soil on the ground or after digging becomes larger than the mass after compaction. This rate of change in soil mass is defined as the soil conversion factor.
- (6) The quality of virgin material and recycled material is assumed to be same and it is assumed that there is no difference in construction technique.
- (7) The material (virgin and recycled) for a soil structure is used 100% without being discarded.
- (8) The possible heavy metal contained in construction sludge is lead (Pb).
- (9) When the cost of processing for recycling increases, the heavy metal content in the recycled soil will be reduced as shown in the Fig. 2. In this study, we assume the removal of heavy metals is included in processing for recycling.
- (10) Virgin material and recycled material are stored in the stock yard and the construction work starts when the amount in storage reaches the amount required for the construction work.
- (11) Recycled material receives curing at the stock yard for three days.

Heavy metals contained in construction sludge can be an obstacle to recycling, but in fact there are few examples of heavy metals contained in recycled materials [4]. At the same time, the Guideline for construction sludge recycling [10] under the editorship of the Ministry of Construction does not specifically mention the measures related to heavy metals contained in recycled materials. Thus, we use two assumptions for calculating environmental cost. One is recycled material contains heavy metals and the other is recycled material does not contain heavy metals. In the latter assumption, we do not consider environmental cost regarding the ecosystem.

4.2 In Case of No Delay of Processing for Recycling

Figs. 3 and 4 show the results of the Monte Carlo simulation focusing on total cost (histograms show frequency distributions). They show two cases: recycled material contains heavy metals and recycled material does not contain heavy metals. In the case of recycled material does not contain heavy metals, for 96.8% of all the results, the appraisal value became 0 or larger, which means recycled material is superior to virgin material in terms of total cost. In summary, the environmental economic efficiency of recycled material is better than that of virgin material in most of the

Table 1 Minimum, medium, maximum value in each uncertainty factor

	Min. value	Med. value	Max. value
Volume of compacted soils (m ³)	-	3,000	-
Volume of mining (m ³ /day)	-	600	-
Volume of recycling (m ³ /day)	-	600	-
Mining cost (yen/m ³)	1,000	3,000	5,000
Recycling processing cost (yen/m ³)	2,000	5,000	8,000
Storing cost (yen/m ³ /day)	-	1,500	-
Unit cost of final disposal (yen/m ³)	4,000	7,000	10,000
Unit cost of transportation (yen/t/km)	58	68	83
Rate of change volume of soils	1.26	1.47	1.70
ΔNPP	0	2	9
Heavy metals contents (mg/kg)	0	23.1	150
Mining area (ha)	-	0.1	-

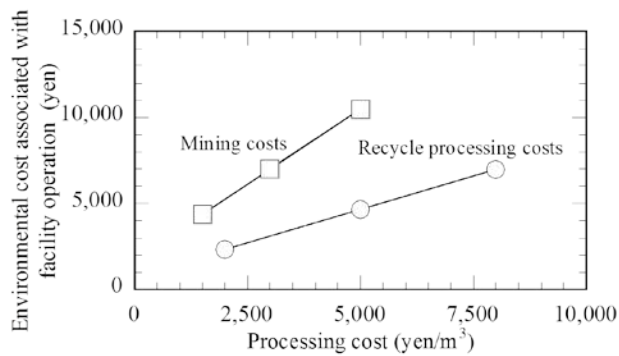


Fig.1 The relation between processing cost and environmental cost

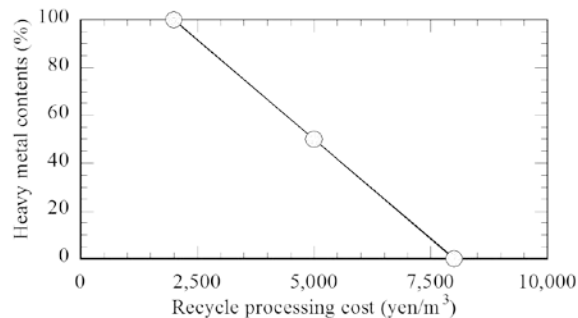


Fig.2 The relation between processing cost and heavy metal contents

cases. On the contrary, in case of recycled material contains heavy metals, for 78.3% of all the results, the appraisal value became 0 or larger, which means the probability that recycled material is superior in economic efficiency to virgin material is rather high. However, it has been clarified that the significance of the evaluation regarding recycling of

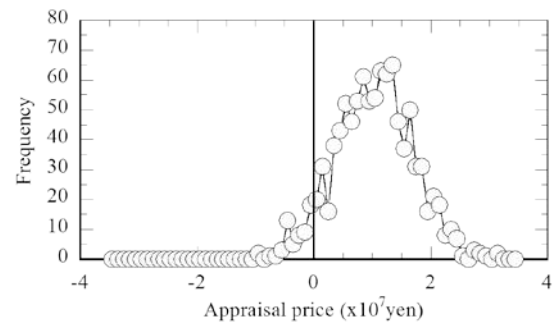


Fig. 3 The result of MonteCarlo simulation when heavy metals are not considered in case of No delay

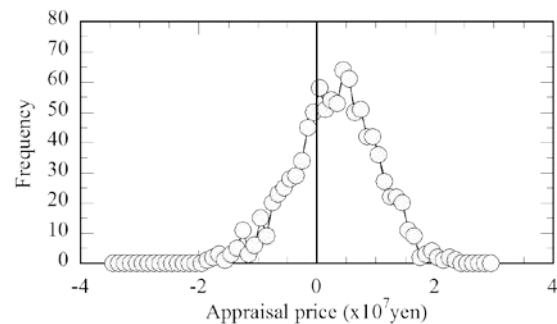


Fig. 4 The result of MonteCarlo simulation when heavy metals are considered in case of No delay

Table 2 Acquired correlations in case of No delay

	Heavy metals are not considered	Heavy metals are considered
Mining cost	0.421	0.371
Recycling processing cost	-0.602	-0.121
Final disposal cost	0.577	0.545
Unit cost of transportation	-0.072	-0.069
Transported distance in virgin materials	0.12	0.101
Transported distance in recycling materials	-0.163	-0.119
ΔNPP	0.054	0.017
Heavy metal contents	-	-0.599

Table 3 The degree of correlations

±0.7~±1	High correlation
±0.4~±0.7	Medium correlation
±0.2~±0.4	Low correlation
±0~±0.2	Little correlation

construction sludge becomes far larger when evaluated by total cost considering the load on the environment than when evaluated only by direct cost.

Yet there is a case in which recycling is not necessary even when evaluated by total cost, and analysis of such cases should be undertaken. Nevertheless, it takes many labor hours

to analyze a great number of uncertainties, which may bring about an obstacle to recycling because of the cost increase or a delay in the construction schedule. Therefore, we considered that we should focus on uncertain elements that have large influences and seek the correlation between uncertain elements and appraisal value. Tables 2 and 3 show the acquired correlations and the degree of the correlations. Here, positive correlation implies that the appraisal value increases as the value of uncertain element increases, while negative correlation implies that the appraisal value decreases as the value of uncertain elements decreases. Table 2 shows that for recycled material that does not contain heavy metals the digging cost has the positive correlation of the medium degree and the processing cost for recycling has the negative correlation of the high degree, and that for recycled material that contains heavy metals, similarly, the digging cost has the positive correlation of the medium degree and the inclusion of heavy metals has the negative correlation of the high degree. In addition, for both cases, the disposal cost, meaning the business effect of recycling of construction sludge, has the correlation of the high degree. According to these results, especially digging cost, processing cost for recycling, content of heavy metals and final disposal cost are important when we analyze the environmental economic efficiency of recycled materials. These four become important indexes in order to promote recycling of construction sludge.

4.3 In Case of Delay of Processing for Recycling

Similarly in the previous section, we conducted an assessment by using the appraisal value which is the differential of the total cost between virgin material and recycled material as the index. When we compared recycled material that does not contain heavy metals with virgin material, the probability of the appraisal value being 0 or larger, meaning recycled material that does not contain heavy metals is superior, was 76.2%. In contrast, when we compared recycled material that contains heavy metals with virgin material, the probability of recycled material that contains heavy metals being superior became 40.5% (see Figs. 5 and 6) Here, we conducted an assessment of the case without considering a process delay of processing for recycling, and the resultant probabilities are as follows: the probabilities of the appraisal value being 0 or larger became 96.8% for the case of recycled material does not contain heavy metals and 78.3% for the case of recycled material contains heavy metals. In summary, the result showed process delay of processing for recycling caused the usefulness of recycling to be reduced.

In case of considering a process delay of processing for recycling, the usefulness of recycling decreases and more detailed pre-examination is required. Table 4 shows the correlation between uncertain elements and appraisal values. For recycled material does not contain heavy metals, the manufacturing amount of recycled material as well as the disposal cost have positive correlations to the medium degree, and the processing cost for recycling has a negative correlation to the medium degree. Also for recycled material

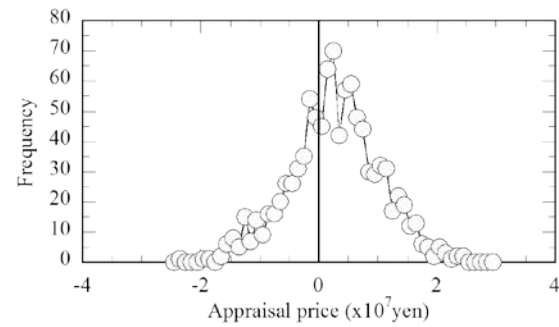


Fig. 5 The result of MonteCarlo simulation when heavy metals are not considered in case of Delay

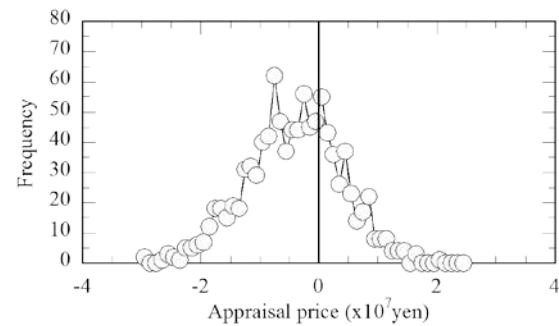


Fig. 6 The result of MonteCarlo simulation when heavy metals are considered in case of Delay

Table 4 Acquired correlations in case of Delay

	Heavy metals are not considered	Heavy metals are considered
Volume of recycling	0.556	0.518
Mining cost	0.338	0.298
Recycling processing cost	-0.455	-0.094
Final disposal cost	0.468	0.471
Unit cost of transportation	-0.049	-0.055
Transported distance in virgin materials	0.029	0.037
Transported distance in recycling materials	-0.168	-0.159
Δ NPP	-0.046	-0.011
Heavy metal contents	-	-0.484

contains heavy metals, the manufacturing amount of recycled material as well as the disposal cost has positive correlations to the medium degree. In addition, it was found that the content of heavy metals has a negative correlation to the medium degree. According to these findings, the stable manufacture and supply of recycled material has a very large influence. In order to promote recycling, it is essential to establish a system in which the stable supply of recycled material can be performed. In particular, information about the quality and the amount of soil material required for construction of a soil structure as well as about the

manufacturing amount at a facility of processing of recycling should be closely shared among the related parties. This way, the supply and demand of soil material can be comprehended precisely, and more flexible use of virgin and recycled materials can be performed, so that the bad effects of a process delay of processing for recycling of construction sludge can be controlled.

5. CONCLUSIONS

The results we obtained are as follows:

- (1) Regarding evaluation and comparison of environmental economic efficiency of recycling of construction waste, we could include the environmental load that was not convertible into CO₂ in the cost base in addition to the conventional cost depending only on CO₂ emissions. This way, we were able to combine environmental load and direct cost, which have different dimensions, and create a new index: total cost.
- (2) By performing evaluation and comparison of environmental economic efficiency through the Monte Carlo simulation, we considered the uncertainty of assumed elements. And we showed that the relative significance of evaluation regarding recycling of construction sludge increased when evaluated by total cost than when evaluated only by direct cost.
- (3) We showed the usefulness of recycling decreased quantitatively by considering a process delay in processing for recycling owing to unstable supply of construction sludge as well as a variance in the period required for processing for recycling.
- (4) We clarified that limiting factors for recycling of construction sludge include the processing cost for recycling is higher than the digging cost of virgin material, construction sludge contains heavy metals and a process delay in processing for recycling.

6. REFERENCES

- [1] Kunibe K, Itsubo T and Mizuguchi T, "Environmental Accounting", Yuhikaku Publishing, 2007.
- [2] Inazumi S, Ohtsu H, Isoda T and Shigematsu Y, "Evaluation of social environmental efficiency on recycling of construction sludges as ground materials", JSCE Journal of Geotechnical Engineering, JSCE, Vol.68, No.1, 2012, pp.163-174.
- [3] Ministry of the Environment, "The Report of the Emission and Disposition of Industrial Waste in 2008", Announce Document, Ministry of the Environment, 2008.
- [4] Ministry of Land, Infrastructure, Transport and Tourism, "The Report of the Investigation of Construction Waste in 2008", Announce Document, Ministry of Land, Infrastructure, Transport and Tourism, 2008.
- [5] Ministry of Land, Infrastructure, Transport and Tourism, "The Report of the Investigation of Construction Waste in 2006", Announce Document, Ministry of Land, Infrastructure, Transport and Tourism, 2006.
- [6] Matsuo M and Honjo Y, "New View of Geotechnical and Environmental Engineering -The Efficient Use of Displaced Soils at Construction-", Gihodo Shuppan, 1999.
- [7] Omine K and Matsuyuki K, "Environmental economic model for recycling of construction surplus soil and waste material", The Magazine of the Japanese Geotechnical Society, JGS, Vol.51, No.5, 2003, pp.10-12.
- [8] Omine K, "Life Cycle Assessment", The Magazine of the Japanese Geotechnical Society, JGS, Vol.55, No.10, 2007, pp.40-41.
- [9] Agriculture, Forestry and Fishers Bio Recycling Laboratory System Team, "Design and Analysis of Biomass Utilization System", National Institute for Rural Engineering, 2006.
- [10] Advanced Construction Technology Center, "The Guideline in Construction Sludge", Taisei Publishing, 1999.
- [11] Itsubo T and Inaba A, "Life-cycle Impact Assessment Method based on Endpoint Modeling", Maruzen Publishing, 2005.

Evaluation and validation of elastic-fragile damage modeling for unsaturated porous media in θ -Stock

B. Gatmiri^{1,2}, M. Fathalikhani³

¹Center of Excellence for Engineering and Management of Infrastructures (CE-EMI). Department of civil engineering, University of Tehran, Tehran, Iran

² ANDRA, Direction Scientifique - Mécanique des Fluides et des Solides, Paris, France

³Department of Civil Engineering, university of Tehran, Tehran, Iran

ABSTRACT

This paper presents a framework for the modeling of damage in continuous unsaturated porous geomaterials. The THHMD model developed by Gatmiri & Arson (2008) has been formulated in net stress, thermal stress and suction independent state variables. The behaviour law stems from both micromechanical and phenomenological concepts. Correspondingly, the strain tensor has been split into two independent thermodynamic strain components. A crack related intrinsic water permeability has been introduced.

A numerical modeling is simulated with θ -Stock finite element program [1] to study damage in heated samples of unsaturated bentonite. In this paper the results of this simulation will be discussed.

Keywords: Unsaturated soil, Thermohydrromechanical behavior, Finite element method, Damage modeling, Multiphase porous media

1. INTRODUCTION

The purpose of this study is to predict the behavior of the Excavation Damage Zone surrounding nuclear waste disposals. The geological barriers, often made of quasi-brittle material like granite or clay-rock, undergo damage during the excavation phase. Hydro-mechanical interaction may occur in the neighborhood of the engineered barrier, which is generally constitute of unsaturated compacted clay.

In Continuum Damage Mechanics, almost all models developed for unsaturated media are based on the concept of Biot's effective stress, stemming from Bishop's definition of stress. Some important aspects of the behavior of unsaturated soils, like wetting collapse, cannot be represented by this theoretical frame [2]. Alternatively, the THHMD model involves independent state variables (net stress, suction and thermal stress), in order to emphasize the role of suction rigidity [3]. Waste is a heat source which can generate traction, and thus cracks; therefore, the design of deep nuclear waste repositories requires the modelling of the effects of thermal loadings in the Excavation Damaged Zone (EDZ). The theoretical frame is briefly recalled in the first part of this paper, also the numerical parametric study is performed in order to determine the main parameters controlling the generation of damage in THHMD model.

2. BASIC CONCEPTS OF THHMD DAMAGE MODEL

2.1 A Formulation in Independent State Variables

In this section we just present the main concepts of damage model in order to help us to deduce and adapt the deductions to the damage concepts and basic theories.

Use Supposing for example that the material is fractured in

three principal directions $\frac{n_i}{n_i}$, the damage variable Ω can be written as a diagonal tensor whose eigenvalues d_i represent crack densities:

$$\underline{\underline{\Omega}} = \sum_{i=1}^3 d_i \underline{n_i} \otimes \underline{n_i} \quad (1)$$

Adopting the definition 1 implies that damage can be quantified by three fictive homogenized fractures

characterized by a normal vector $\frac{n_i}{n_i}$ and a relative volume d_i . The stress state variables chosen to formulate the model are net stress, $\sigma_{ij}'' = \sigma_{ij} - p_a \delta_{ij}$, suction $s = p_a - p_w$ and thermal stress pT [4].

Here, net stress and suction are thermodynamically conjugated with mechanical (ϵM) and suction-related strains (ϵSv) respectively. Both of these components are split in a reversible and an irreversible part:

$$\begin{aligned} d\epsilon_{ij} &= d\epsilon_{M\ ij}^{rev} + \frac{d\epsilon_{Sv}^{rev}}{3} \delta_{ij} + d\epsilon_{M\ ij}^{irr} + \frac{d\epsilon_{Sv}^{irr}}{3} \delta_{ij}, \quad d\sigma_{ij}'' \\ &= D_e(\Omega)_{ijkl} d\epsilon_{M\ lk}^{rev}, \quad ds = \beta_s(\Omega) d\epsilon_{Sv}^{rev} \end{aligned} \quad (2)$$

Ω is the damage tensor, and $D_e(\Omega)$ and $\beta_s(\Omega)$ are the damaged mechanical and capillary rigidities respectively.

2.2 Behavior laws

The following expression of the free energy has been postulated, on the basis of the approach introduced by Halm and Dragon [5]:

$$\begin{aligned} \psi_S(\varepsilon_{Mij}, \varepsilon_{Sv}, \varepsilon_{Tv}, \Omega_{ij}) = & \frac{1}{2} \varepsilon_{Mji} De_{ijkl}(\Omega_{ij}) \varepsilon_{Mlk} \\ & + \frac{1}{2} \varepsilon_{Sv} \beta_s(\Omega_{ij}) \varepsilon_{Sv} + \frac{1}{2} \varepsilon_{Tv} \beta_T(\Omega_{ij}) \varepsilon_{Tv} \\ & - g_M \Omega_{ji} \varepsilon_{Mji} - \frac{g_S}{3} \delta_{ij} \Omega_{ji} \varepsilon_{Sv} - \frac{g_T}{3} \delta_{ij} \Omega_{ji} \varepsilon_{Tv} \end{aligned} \quad (3)$$

The Helmholtz free energy $\psi_S(\varepsilon_{Mij}, \varepsilon_{Sv}, \varepsilon_{Tv}, \Omega_{ij})$ is written as the sum of damaged elastic energies and residual strain potentials [6]. $g_M \Omega_{ji} \varepsilon_{Mji}$, $\frac{g_S}{3} \delta_{ij} \Omega_{ji} \varepsilon_{Sv}$ and $\frac{g_T}{3} \delta_{ij} \Omega_{ji} \varepsilon_{Tv}$ are residual strain potentials, which quantify the remaining openings due to cracks after unloading. g_M , g_S and g_T are rigidity-like scalar material parameters. The derivation of the free energy $\psi_S(\varepsilon_{Mij}, \varepsilon_{Sv}, \varepsilon_{Tv}, \Omega_{ij})$, provides the whole stress/strain relations. The damage stress Y_d , conjugated to damage, writes:

$$\begin{aligned} Y_{dij} = & -\frac{1}{2} \varepsilon_{Mmn} \frac{\partial D_{emij}(\Omega_{kl})}{\partial \Omega_{qp}} \varepsilon_{Mpq} \\ & - \frac{1}{2} \varepsilon_{Sv} \frac{\partial \beta_s(\Omega_{kl})}{\partial \Omega_{ij}} \varepsilon_{Sv} - \frac{1}{2} \varepsilon_{Tv} \frac{\partial \beta_T(\Omega_{kl})}{\partial \Omega_{ij}} \varepsilon_{Tv} \\ & + g_M \varepsilon_{Mij} + \frac{g_S}{3} \varepsilon_{Sv} \delta_{ij} + \frac{g_T}{3} \varepsilon_{Tv} \delta_{ij} \end{aligned} \quad (4)$$

The damage yield function is assumed to depend on the tensile strains involved in $g_M \varepsilon_{Mij} + \frac{g_S}{3} \varepsilon_{Sv} \delta_{ij} + \frac{g_T}{3} \varepsilon_{Tv} \delta_{ij}$ only. The corresponding thermodynamic variable is noted Y_{d1}^+ . The yield function ensures the convexity of the elastic domain:

$$f_d(Y_{dij}, \Omega_{ij}) = \sqrt{\frac{1}{2} Y_{d1ij}^+ Y_{d1ij}^+} - C_0 - C_1 \delta_{ij} \Omega_{ji} \quad (5)$$

C_0 is initial damage-stress rate that is necessary to trigger damage. C_1 controls the damage increase rate. The damage evaluation law is computed by an associative flow rule.

2.3 Transfer laws

The details of thermo-hydraulic transfers in intact unsaturated porous may be found in [3].

Moisture flows have been assumed to be diffusive [3]:

$$V_w = -\frac{\psi_R(\theta_w)}{\sigma(T_{ref})} \frac{d\sigma(T)}{dT} K_w \nabla(T) + \frac{1}{\gamma_w} \frac{\sigma(T)}{\sigma(T_{ref})} K_w \nabla(s) - K_w \nabla(z) \quad (6)$$

$$V_{vap} = \frac{\rho_{vap}}{\rho_w} V_{vap} = -D_{Tvap} \nabla(T) + D_{Pvap} \nabla(s) \quad (7)$$

V_w and V_{vap} refer to liquid water and vapour relative velocities, respectively. ψ_R is the relative hydraulic potential:

$$\psi_R(\theta_w) = (P_w - P_a) / \gamma_w \quad (8)$$

$\sigma(T)$ is the superficial energy of pore water (in J.m⁻²). D_{Tvap} and D_{Pvap} are the thermal and capillary vapour conductivities, respectively. The water permeability tensor is split in an intrinsic part and in relative components:

$$K_w = k_T(T) k_r(S_w) K_{int}(n, \Omega_{ij}) \quad (9)$$

The thermal and capillary relative permeabilities $k_T(T)$ and $k_r(S_w)$ are related to heat and to the behaviour of pore fluids as follows:

$$k_T(T) = \frac{\mu_w(T)}{\mu_w(T_{ref})}, \quad k_r(S_w) = \left(\frac{S_w - S_{w,r}}{1 - S_{w,r}} \right)^3 \quad (10)$$

In which $\mu_w(T)$ is the dynamic viscosity of liquid water, and $S_{w,r}$ is the residual water saturation degree. The water saturation degree S_w evolves on a thermo-hydraulic state surface. This latter is defined by Van Genuchten [7] and assumption of exponential thermal effects done by Gatmiri [3]:

$$\begin{cases} S_w = [(1 - S_{w,r})(1 + (\alpha s)^n)^{-1 + \frac{1}{n}} + S_{w,r}] \\ \quad \times \exp(d_s(T - T_0)) & \text{if } s \geq 0 \\ S_w = 1 & \text{if } s < 0 \end{cases} \quad (11)$$

Only the intrinsic water permeability, which depends on the behaviour of the solid skeleton, is influenced by damage [6]:

$$K_{intij}(n, \Omega_{rs}) = k_{w0} 10^{\alpha_w e^{rev}} \delta_{ij} + k_{2ij}(n^{frac}, \Omega_{ij}) \quad (12)$$

The crack related component $k_{2ij}(n^{frac}, \Omega_{ij})$ has been computed by introducing an internal length parameter. The

same approach has been used to model the influence of cracking on vapour flow [4]
Air and heat flows have been modeled by using the same flow rules as an intact porous medium [1]. Damage affects flows indirectly and isotropically, through the damaged porosity [4].

3. PARAMETRIC STUDY

Here we are interested in the effects of different Van Genuchten water retention curves introducing by A to E in Fig. 2 , on the variation of different parameters of damage model.

The numerical simulation has been inspired from the laboratory test of Pintado (2002) [8], and the simulation has been performed with θ -Stock Finite Element code [1]. The objective of the Pintado test is to apply a controlled flux of heat at the top of a cylindrical bentonite sample, the bottom being maintained at a constant temperature (Fig. 3 and 4). The initial pore water pressure (p_w0) is calculated by inversion of the function of the degree of saturation state surface. The initial saturation degree S_{w0} is equal to 0.63 like in the experiment conditions. After a heating period of one week, a relaxation period of seven weeks is observed. All of the imposed boundary conditions are given on Fig. 4.

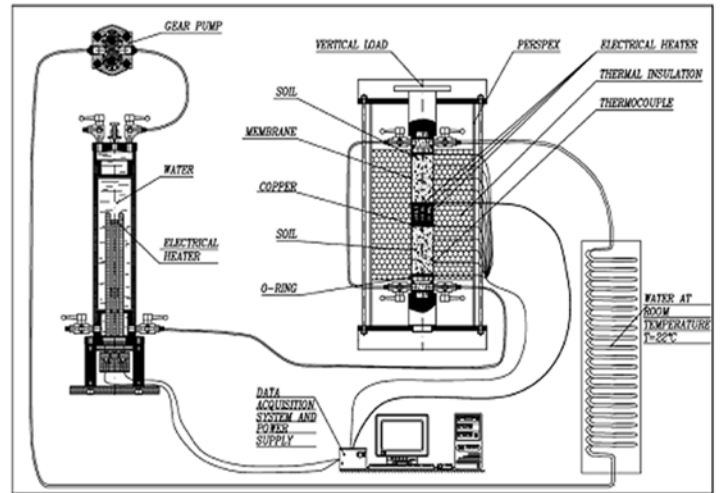


Figure 1. Bentonite heating test [8]. Scheme of experimental devices.

Table 1. Parameters of the five Van Genuchten water retention curves

Graph	$\alpha(\text{VG})$	$n(\text{VG})$
A	$1.857 \cdot 10^{-8}$	1.2
B	$1.857 \cdot 10^{-8}$	1.429
C	$2.857 \cdot 10^{-8}$	1.429
D	$3.875 \cdot 10^{-8}$	1.429
E	$3.875 \cdot 10^{-8}$	1.5

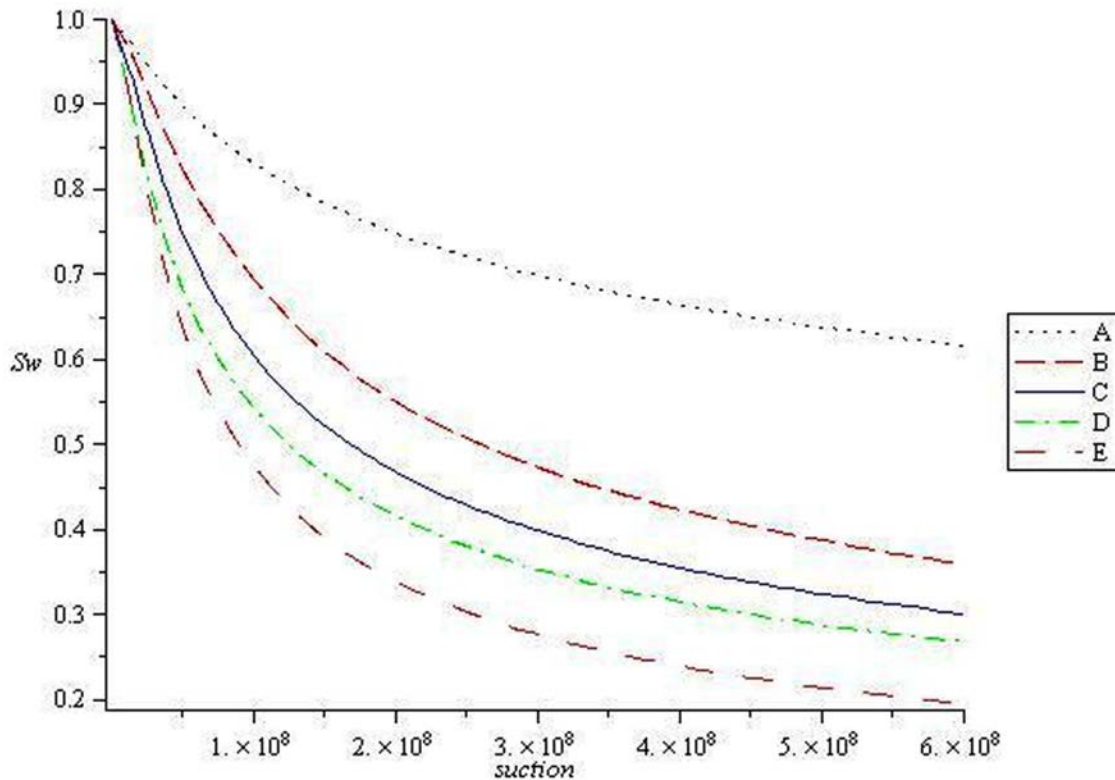


Figure 2. Five used Van Genuchten water retention curve

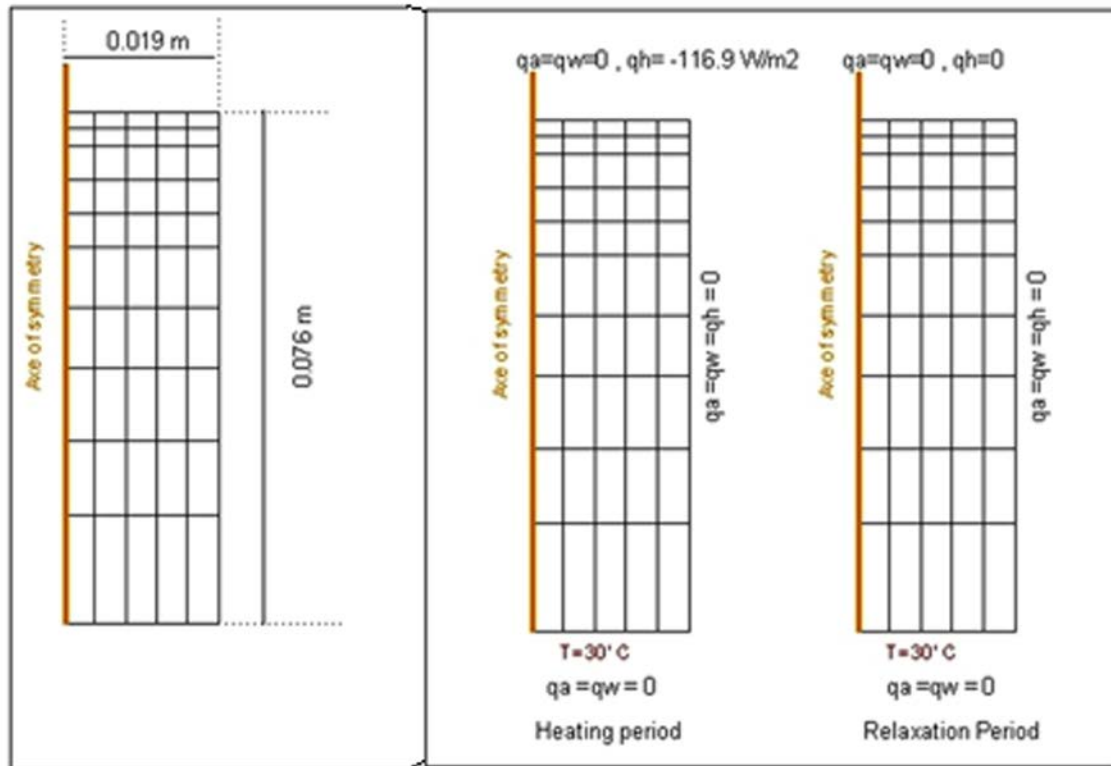


Figure 3. Bentonite heating test [8]. Mesh.

Figure 4. Bentonite heating test ([8]. Boundary conditions.

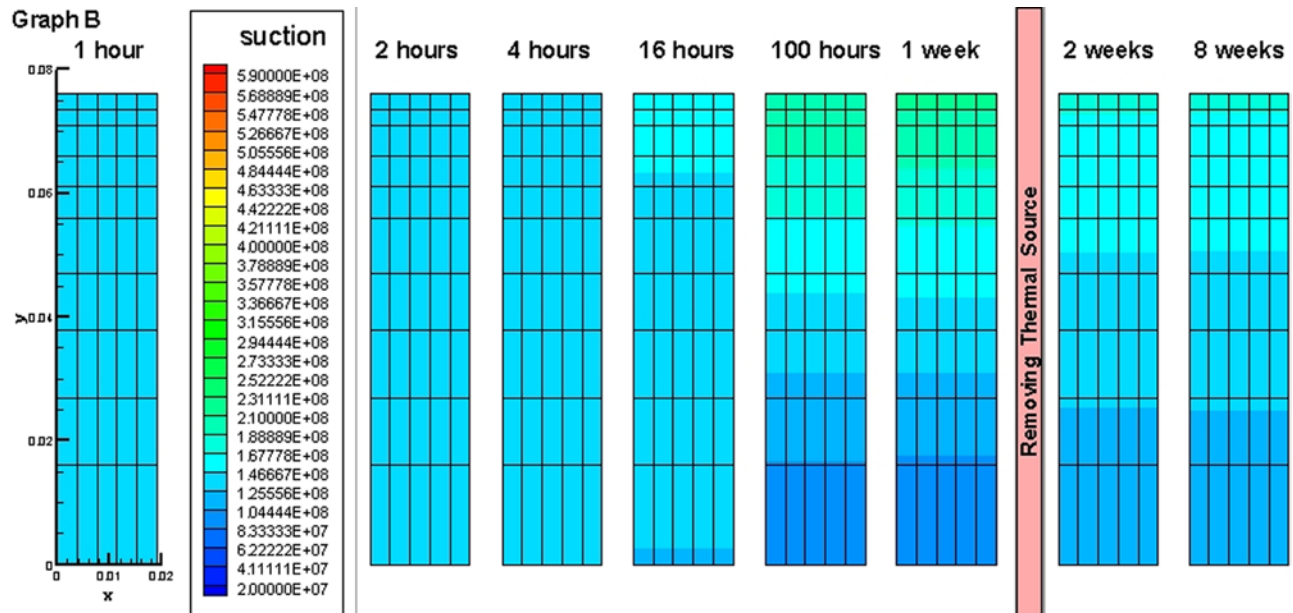


Figure 5. Space evaluation of suction of specimen B.

As shown in Fig. 5 and 5 in the higher levels of specimens which are drier since they are near the heat source, the magnitude of suction increases. It reaches to its minimum value at the bottom of specimens. During the heating period,

in the top part of specimen suction goes up while it decreases in the relaxation period, besides in the lower part of specimen, suction falls whereas it increases in the remaining seven weeks. It can be clearly seen that the direction of liquid flow

is from the top of specimen to its bottom; while it inverses during the relaxation period.

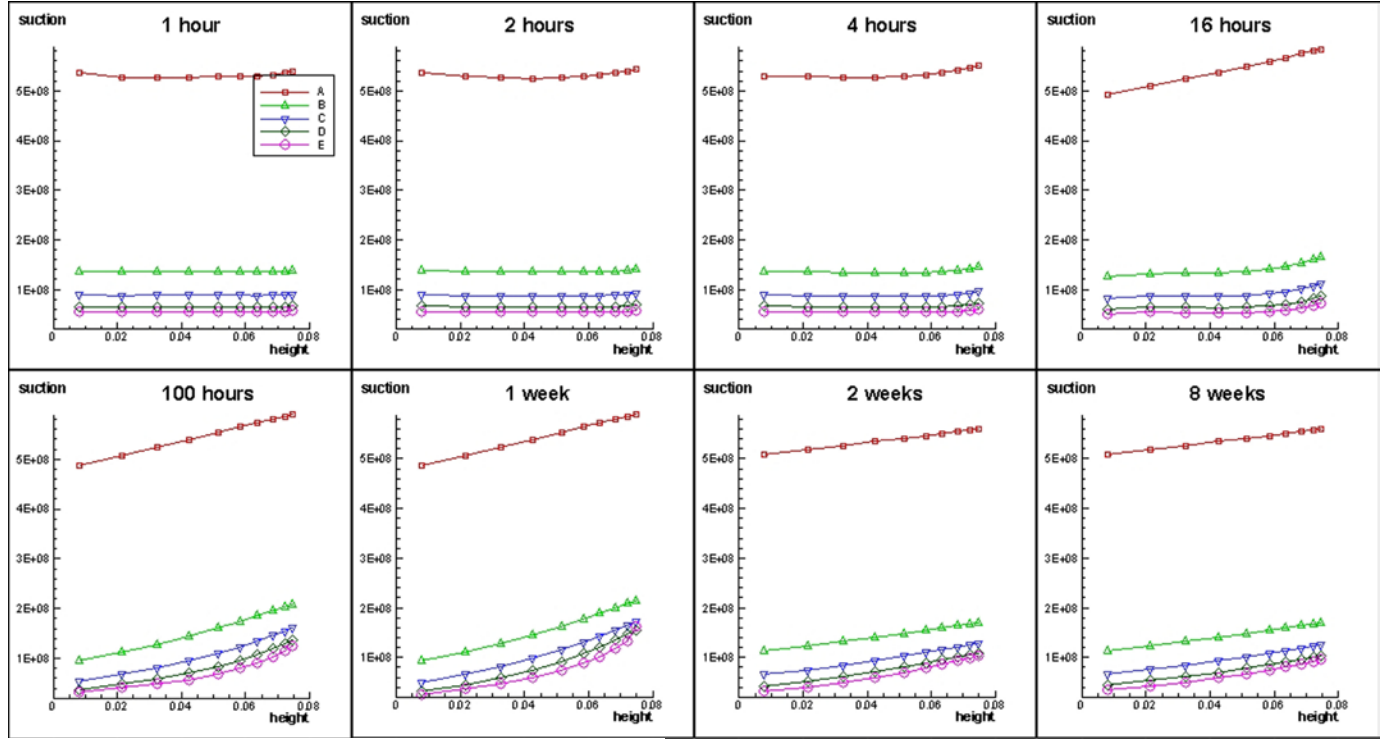


Figure 6. Evaluation of suction of all specimens at the whole testing time

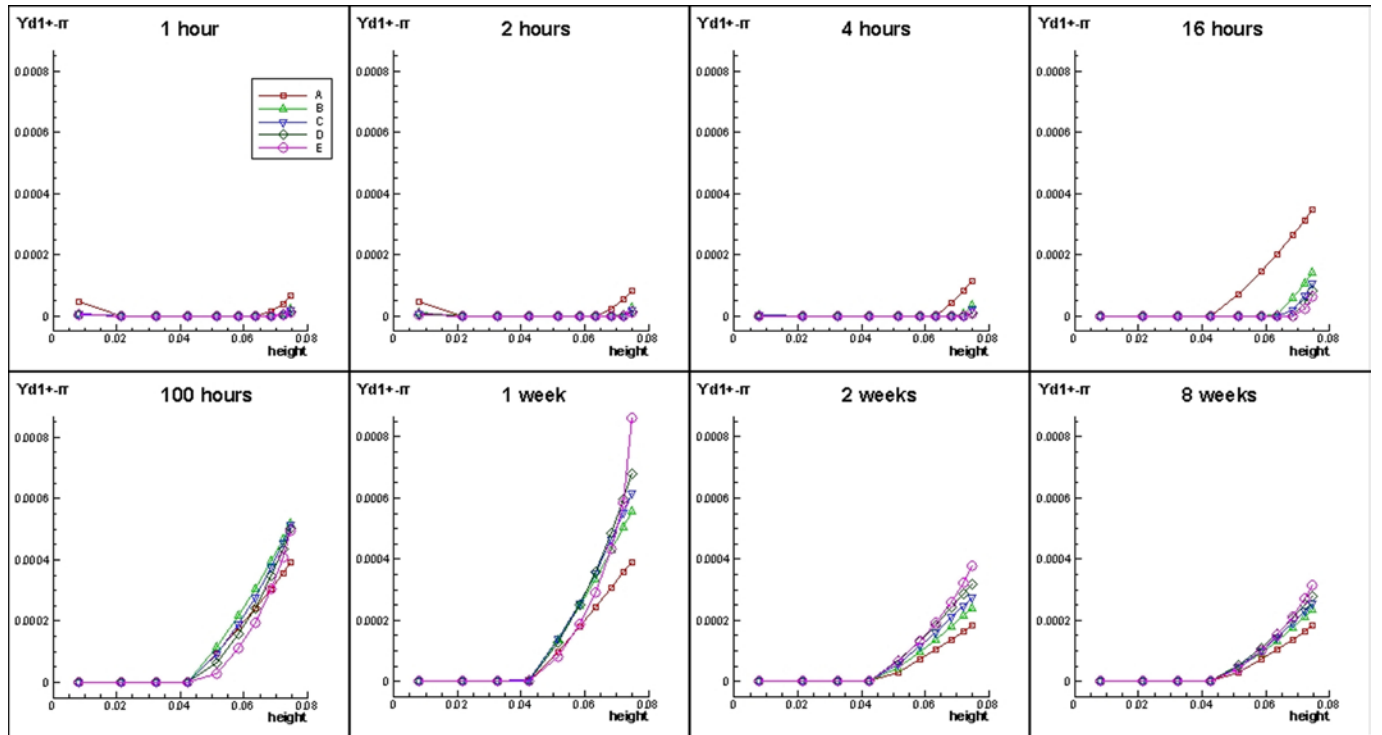


Figure 7. Evaluation of damage force in all specimens at the whole testing time.

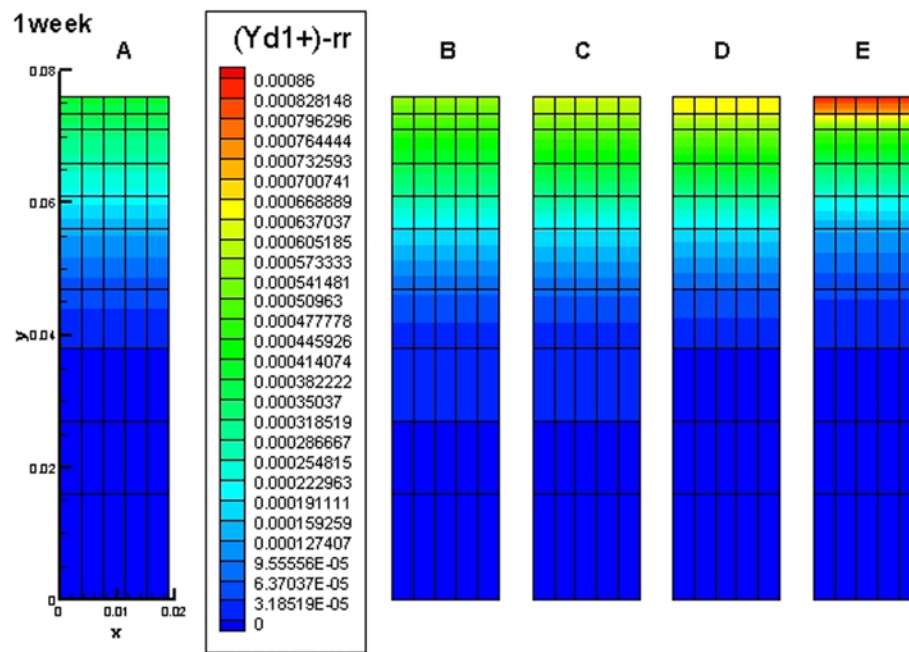


Figure 8. Space evaluation of damage force in all specimens at time= one week.

Fig. 7 and 8 also show that the part of the sample which is the close to the heater has higher amount of damage force, therefore it is the most damaged part. The Fig. 7 shows by increasing the heating time, $Y_{d1}^+ - rr$ grows, whereas $Y_{d1}^+ - rr$ falls in the relaxation period. Each graph of Fig. 7 compares the amount of damage force in the different Van Genchtun water retention curves, it can be implied that the damage force is produced earlier in the drier specimen. It should be mentioned that at the top part of specimens the graphs get wetter from A to E. There is damage force in the lowest element of specimen at beginning times of test while there is no initial damage force, but it vanishes in the resuming times. This anomaly occurs in numerical simulations and it is because of the effects of boundary conditions.

4 CONCLUSION

Fractured unsaturated porous media is studied with the "THHMD" damage model [3], formulated in independent state variables. A representation of damage is required to predict the evolution of fracturing in the neighbouring of excavated galleries. Saturation variations around galleries hugely influence the Excavation Damaged Zone. That is why damage has to be included in hydraulic transfer models and mechanical damage theories have to be extended to unsaturated porous media. A parametric study has been performed on a cylindrical sample according to laboratory test of Pintado. Distribution of suction and damage force in bentonite sample has been presented and discussed.

5 REFERENCES

- [1] Gatmiri, B., and C. Arson, "0-STOCK, a powerful tool of thermohydronechanical behaviour and damage modeling of unsaturated porous media," *Computers and Geotechnics*, 2008, 35(6): 890-915
- [2] D.G. Fredlund, N.R. Morgenstern, "Stress state variables for unsaturated soils," *J. Geotech. Engng Am. Soc.* 1997, Civ. Engrs;103, 5, 447-466
- [3] Arson C., & Gatmiri B., "On damage modelling in unsaturated clay rocks," *Physics and Chemistry of the Earth*, 2008, 33:S407-S415.
- [4] Arson, C., & B. Gatmiri., "Parametric study on the performance of a THM damage model for unsaturated porous media," 1st International Symposium on Computational Geomechanics, 29 April - 1st May 2009, pp. 553-562, Juan-les-Pins, France
- [5] Halm & A. Dragon, (1998), "An anisotropic model of damage and frictional sliding for brittle materials," *Eur. J. Mech. A/ Solids*, 17(3):439-460
- [6] Arson C. & Gatmiri B., "A mixed damage model for unsaturated porous media," *Comptes-Rendus de l'Académie des Sciences de Paris, section Mécanique*, 2009. vol. 337, pp.68-74
- [7] VanGenuchten, M., "A closed-form equation for predicting the hydraulic conductivity of unsaturated soils," *Soil Science Society of America Journal* 44, 1980, 892-898.
- [8] Pintado X., Ledesma A., Lloret A., "Backanalysis of thermohydraulic bentonite properties from laboratory tests," *Engineering Geology*, 2002, 64,91-115

Estimation of the Landslide Dam Sustainability in the Gigantic Seimareh Landslide Using the Rate of Sedimentation

Zieaoddin Shoaee

Soil Conservation and Watershed Management Research Institute, Tehran-Iran I.R.

ABSTRACT

On the border of Ilam and Lorestan Provinces in southwest of Iran, and in the heart of Zagros Range of mountains, lies the gigantic Seimareh Landslide that has been globally recognized as one of the largest mass movements of rocks in the world. Beside the geomorphic alterations in the landslide site and the depositional area, a major change is the disturbance of drainage pattern and closure of the rivers. Also, common post-failure feature is landslide lakes which formed behind the displaced material blocking the rivers. Seimareh and Jidar Landslide dams over Seimareh and Kashkan Rivers formed Seimareh and Jidar Lakes. The present study aimed to explain the formation and the time of washing off of the landslide dams, using the annual sedimentation rate data and measuring the sediment deposit in these lakes. It was concluded that the Seimareh Landslide dam has been in place for about 935 years after the landslide event.

Keywords Landslide Dam, Lake sediment, Dam Sustainability

1. INTRODUCTION

Aproximately, 50 percent of Iranian land is mountainous. Due to steep slopes, relatively high precipitation, and variations in geological settings along with frequent earthquakes, these vast mountains are prone to slope instabilities and landslides. Seimareh Landslide in southwest of Iran (Fig.1), is one of the largest known landslides in the world. The first document reporting Seimareh Landslide was published in 1935 during oil exploration projects [1] that called this landslide as a landslip in 1:100,000 prepared geological map. The most recent study was published by the author [2] with a complete review on previous studies and some detailed field works. Beside the geomorphic alterations in the landslide site and the depositional area, a major change is the disturbance of drainage pattern and closure of the rivers. Also, common post-failure feature is landslide lakes which formed behind the displaced material blocking the rivers. Seimareh and Jidar Landslide dams over Seimareh and Kashkan Rivers formed Seimareh and Jidar Lakes. The present study aimed to explain the formation and the time of washing off of the landslide dams, using sediment deposit thickness in these two lakes and the annual sedimentation rate.

Methodology

In the first step, a detailed plan map was produced on which the boundaries of the landslide area, displaced debris and landslide dam lakes sediment were defined (Fig. 1). Then, by using the topographic map and field data from selected benchmark, the longitudinal section along the axis of the Seimareh River was prepared.

The hydrology of the rivers in the landslide area and some in the adjacent basins were studied. Assuming that climatic conditions of the landslide area at the time of failure remained unchanged, the thickness of Jidar and Seimareh

Lakes and the rate of sedimentation in these two lakes were compared with the suspension sediment load in these rivers at present. The result was used to measure the standing period and the time of wash off of these dams.

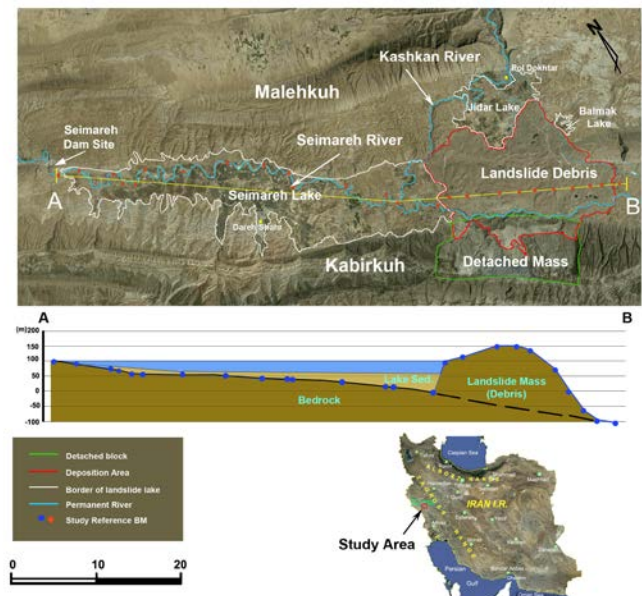


Fig. 1 Plan view of detached block, deposited debris, generated lakes (top) and cross section of Seimareh Dam and Seimareh Lake along Seimareh River (bottom).

2. Study Area

The study area was selected to cover the entire landslide anatomy, the affected post-failure area, and also the geological features of the surrounding region. This zone was located between 32°: 50'E and 33°: 15'E, and 47°: 30'N to 47°: 30'N. These coordinates cover the mid-Zagros Range with

NW-SE trend that forms the mountainous regions of the southwestern provinces of Iran.

The study area is part of the Zagros range including a series of smooth and mild folding with NW to SE trend along the fault system of the area. The presence of gypsum and gypsum lime with severe erodibility resulted to deep valleys formation in the area. Thus, a relatively wide valley is formed between northern and southern walls. The Siemareh valley was formed between Kabirkuh and Mallehkuh (Fig. 1). Mt. Kabirkuh is emerged as limestone ridge anticline of Mid-Cretaceous in the southern part of the area.

3.1 Seimareh Landslide

Among dozens of landslides observed on aerial photos and satellite images in Zagros range, Seimareh Landslide is identified as the largest one in the entire region. The complex and mega landslide of Seimareh is one of the largest instability events not only in this region, but also among all continental landslides all over the globe. The massive Seimareh Landslide in west of Iran is located at the boundary of Ilam and Lorestan provinces (33°: 03' N and 47°: 41' E). Seimareh Landslide is in a basin south of Pole-Dokhtar City (Fig. 1). This plain is surrounded by Mt. Malehkuh in the north and Mt. Kabirkuh in the south. Kashkan and Seimareh Rivers are currently flowing in this plain and are called Karkheh River after merging and continuing towards Khuzestan Province in south-west of Iran. The mega landslide of Seimareh has occurred in southern part of this plain and northern hill slope of Mt. Kabirkuh. Seimareh Landslide is initiated by a block sliding of Cretaceous limestone and its underlying sediment with 16km length, 6km width, and average thickness of 400m, detached from the edge of Mt. Kabirkuh (3200m). Subsequently, a 38km³ of debris flowed over two valleys in south of Kabirkuh to a distance of approximately 20km on an average slope angle of about 5°. Along the way, the slope angle of the route becomes -5° (upward) at some areas.

Assuming that the average density of the hard limestone, shale, and sandstone is 2.1 t/m³, the displaced material might be estimated at over 79 billion metric tons, qualifying the Seimareh Landslide as one of the few mega landslides on the earth [2], [3]. The detached and displaced material has covered an area of approximately 200km² with a mixture of mainly limestone and its underlying formation such as marl and limestone with low sorting ranges from fine grains to large blocks. Due to the extremely uneven topography and undeveloped drainage network in the area, many ponds with various areas still exist in the debris of the landslide (Fig.1)

Remnants of the thick lake sediments in the area indicate the existence of a huge lake subsequently formed behind the landslide dam. The remains of buried vegetation at the bottom of the lake sediments can be used to date the landslide occurrence. Oberlande [4], Watson and Wright [5], and van Zeist and Bottema [6] conducted some research on dating the landslide by means of C₁₄ isotope from the Seimareh lake sediments. Reviewing the available literature and resources and comparing their results showed that the approximate date of Seimareh Landslide is around 10000 (±120) years BP.

3.2 Landslide Dam Lakes

Beside the geomorphic alterations in the landslide site and the depositional area, a major change is the disturbance of drainage pattern and closure of the rivers. Because of the lack of developed drainage network, many ponds formed on the deposited material. Currently, some of these ponds are utilized as water supply sources for locals. Another common post-failure feature is landslide lakes which formed behind the displaced material blocking the rivers. In Seimareh region, due to the enormous volume of displaced material, these features were extremely vast. Seimareh Landslide dam over Seimareh River formed Seimareh Lake (Fig. 1). Western portion of the debris clogged Kashkan River to form Jidar Lake on the southern part of Pole-Dokhtar city. At the eastern part of the debris, Balmak Lake was formed likely by blocking some temporary streams in the north of Chenareh anticline. Amongst these three lakes, Seimareh and Jidar Lakes were drained naturally and dried out later.

3. Sustainability of Seimareh Dam

The Jidar Lake, as the second largest one, has an area of about 46km². It has been formed by the debris blocking Kashkan River (Fig. 1). The maximum possible height of the Jidar Dam (which is washed away) is 50m at the southern part and could hold approximately 1.15 billion m³ of water. Thus, considering Kashkan River water discharge (1.344 billion m³/yr), (Table 1) it is expected that the dam was overflowed by the second year after the occurrence of landslide. Another largest post-failure feature in the region is Seimareh Lake that is completely drained and dried.

Table 1. Kashkan and Seimareh Rivers discharge and the corresponding sediment yield

River	Area of the Basin	Water		Sediment		
		Discharge	Total Volume of Water	Discharge	Annual Sediment yield	
	km ²	m ³ /sec	×10 ⁹ m ³ /yr	g/lit	t/m ²	×10 ⁶ t/yr
Kashkan	9400	43.2	1.344	6.00	0.006	8.064
Seimareh	28400	125.4	3.900	1.60	0.0016	6.245
Total	38800	168.6	5.244	7.60	0.0076	14.309

Figure 1 shows that Seimareh Dam must have had 100 m height over Karkheh River resulting in a dam with a reservoir of 46.3km in length and a total area of 259km² after being filled up. By using the measured altitude of the selected bench marks and other field surveys data, it seems that the dam reservoir should have contained 11.84 billion m³ of water.

Considering the discharge of Seimareh River (Table 1), Seimareh Lake must have overflowed 4 years after the landslide occurrence. However, thick lake bed sediments in

these two lakes indicate that the dams have not been abruptly washed away and there has been plenty of time for sediment accumulation in the lakes. Thus, measuring water yield and the volume of the lakes is not a consistent dating method for dam standing period.

The entire sediments of these two lakes (Seimareh and Jidar) are persevered at some spots and can be used as a better evidence to estimate the sustainability of the landslide dams. Lake sediment structures such as cross beddings, laminations, graded-beddings, convoluted structures, and nodules, and also biological structures including root-casts, plant remains, and freshwater gastropod shells appear in these sediments beds that make its boundary distinct from the surrounding sediments. Because of high discharge of Kashkan River and smaller reservoir of Jidar Lake, it is possible that, after some certain time, Jidar Lake has drained into Seimareh Lake. To find out the average thickness of the lakes sediments a thorough field survey was conducted. Although because of the ragged bedrock it was not easy to estimate the sediments, thus, by dividing the area into several blocks and using sections of each block, the average sediment thickness of 60m in Seimareh Lake and 30m for Jidar Lake were estimated. Sediment beds become shallow towards the upstream.

The basic concept using the sediment thickness for dating is illustrated in Fig. 2. This model was employed to estimate the stability period for Jidar and Seimareh Lakes. At the time of landslide occurrence (T_0), sedimentation began in Jidar and Seimareh Lakes at the rate for Kashkan River and Seimareh River sediment yield separately. This continued until T_1 , when Jidar dam broke and the total sedimentation in Seimareh Lake presumably became the sums of Kashkan and Seimareh Rivers. Finally, at T_2 , Seimareh Dam broke to bring the sedimentation process to its end. In this study, to estimate the stability of the landslide dams (the time period between landslide event and the break of the Seimareh Dam) a rate of annual sediment yield over the total sediment was applied.

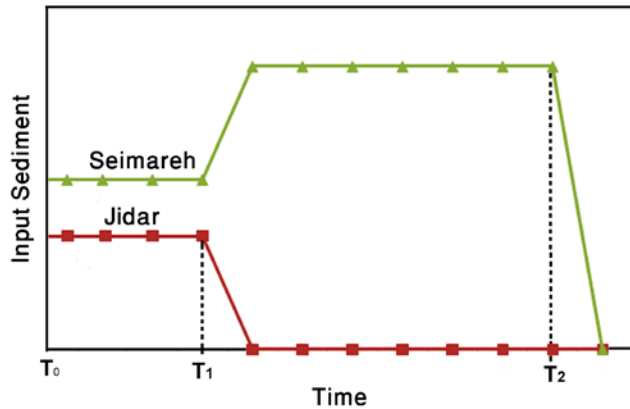


Fig. 2 A conceptual model for sedimentation process and dam stability

Based on the hydrographs of 30 years sediment yield records at Pole-Dokhtar and Karkheh River stations, the weight of the annual sediment carried by these rivers was estimated. Then,

by applying the field density of the sediments, the weight was converted to volume and then to the thickness of sediment beds. The estimated thickness was compared with the measured sediment beds thickness in the field to evaluate the period when Seimareh Dam has been standing. Because Jidar Dam was washed away earlier with a major impact on Seimareh Dam sedimentation process, the time of standing should be measured separately. Applying the data presented in Table 1, the following measurements were carried out:

$$d_{Jy} = \frac{(Q_k) \times (86400 \times 360) \times (S_k)}{(\gamma_d) \times (A_j)}$$

$$d_{Jy} = \frac{(43.2) \times (86400 \times 360) \times (0.006)}{(1.7) \times (46 \times 10^6)} \cong 0.093m$$

Where, d_{Jy} is the thickness of sediment for each year, Q_k is discharge of Kashkan River per second, S_k is sediment yield of Kashkan River (sediment per unit volume of water), γ_d is density of sediments at Jidar Lake, and A_j is the area covered by Jidar Lake sediment.

Then, by dividing the total thickness of the sediments measured in Jidar Lake by the annual sediment thickness increment, the time required for sedimentation, or the period when Jidar Dam was standing, could be calculated as follows:

$$T_J = \frac{d_J}{d_{Jy}} = \frac{30}{0.093} \cong 325yr$$

Where, T_J is the period of Jidar Dam standing, d_J is the sediment thickness measured in Jidar Lake, and d_{Jy} is the annual sediment thickness increment.

During this period, the sedimentation continued in Jidar Lake and Seimareh Lake received the sediment carried by Seimareh River:

$$d_{s1} = \frac{T_J \times S_s}{\gamma_d \times A_s}$$

$$d_{s1} = \frac{325 \times 6,245,000}{1.7 \times (259 \times 10^6)} \cong 5m$$

Where d_{s1} is the sediment deposited in Seimareh Lake before the break down of Jidar Lake, S_s is weight of annual sediment yield of Seimareh River, γ_d is the density of sediments, and A_s is the area covered by Seimareh Lake sediment.

As the 5m of sediments in Seimareh Lake was formed when Jidar Dam was standing, then:

$$d_{s2} = d_s - d_{s1}$$

$$d_{s2} = 60 - 5 = 55m$$

Where, d_s is the total thickness of sediment beds in Seimareh Lake at present, d_{s1} is previously defined, and d_{s2} is the thickness of sediment deposited in Seimareh Lake after the break of Jidar Dam.

To estimate the time required for 55 m of sedimentation in the Seimareh Lake, the same approach as used for Jidar was applied:

$$d_{K+S} = \frac{(Q_{K+S}) \times (86400 \times 360) \times (S_{K+S})}{(\gamma_d) \times (A_s)}$$

$$d_{K+S} = \frac{(168.6) \times (86400 \times 360) \times (0.0076)}{(1.7) \times (259 \times 10^6)} = 0.0905m$$

Where d_{K+S} is the annual sedimentation in Seimareh Lake from Kashkan and Seimareh Rivers, Q_{K+S} is total discharge of the two rivers, S_{K+S} is the two rivers sediment yield per unit volume of water, γ_d is the density of lake sediments, and A_s is the area covered by Seimareh Lake sediments. Finally, considering the sedimentation rate and the thickness of deposited sediment after the break down of Jidar Dam, the time requires for 55 m of sedimentation can be calculated:

$$T_s = \frac{d_{s2}}{d_{K+S}}$$

$$T_s = \frac{55}{0.0905} \cong 610yr$$

Where T_s is the time requires for 55 m of sedimentation, d_{s2} is the thickness of sediment deposited in Seimareh Lake before the break of Jidar Dam, and d_{K+S} is the annual sedimentation in Seimareh Lake from Kashkan and Seimareh Rivers' sediment.

The total time for Seimareh Dam standing is the sum of times taken for 30m sedimentation in Jidar Lake and 55m in Seimareh Lake:

$$T = T_j + T_s$$

$$T = 325 + 610 = 935yr$$

Sustainability of Seimareh Dam for 935 years after the landslide event might be due to its composition of debris that formed a resistant structure.

Conclusions

- The study of post-failure events can be a good indicator to study and clarifying the history of the landslide dam and post events.
- Assuming that climatic conditions of the landslide area at the time of failure remained unchanged, the recent 30-year hydrometric data indicate that the Kashkan and Seimareh Rivers could fill the largest lake of Seimareh in two or three years. However, because of the permeability of the dam body or some overflow from the banks of the dam, the filling time estimation may not be very accurate.

- Thus, for accurate estimation of the period of Seimareh dam stability, investigation of the lake bed sediments seemed to be a better approach. Comparing the sediments entering Seimareh Lake (based on the recent 30-year data) with the volume and thickness of the deposited sediments, the period of Seimareh Landslide dam standing was calculated to be 935 years, which seems to be a reasonable estimation.
- For more accurate dating of landslide occurrence and breaking of the Seimareh Dam, more reliable dating methods such as cosmic ray dating and more precise carbon dating is recommended.

Acknowledgment

This study is a part of an International Program on Landslide IPL (IPL M-134) and was supported and financed by Soil Conservation and Watershed Management Research Institute (SCWMRI), Ministry of Jihad-e-Agriculture, Iran.

References:

- [1] Harrison, J. V., N. L. Falcon and P. B. Mailing 1935, The Geology of Lorestan from reconnaissance, NIOC report No. 490.
- [2] Shoaiei, Z. and J. Ghayoumian, Seimareh, the largest complex slides in the world In Proc. 8th Int. Cong. on Engineering and the Environment, 1998, pp. 1337-1342.
- [3] Shoaiei, Z., Seimareh Landslide, western Iran; one of the world's largest complex landslides, In Landslide News Letter, 2000, Vol. 13, pp.23-27
- [4] Oberlander, T., The Zagross Stream: a New Interpretation of Transverse Drainage in an Organic Zone, 1965, Syracuse Univ. Press, Syracuse Geography Ser. 168 pages.
- [5] Watson, R. A. and Jr. H. E. Wright 1969. The Saidmarreh Landslide, Iran. Geol. Soc. Am. Inc., Sp. pp. 123, 115-1387.
- [6] van Zeist, W. & S. Bottema, Palynological Investigation in Western Iran, 1977, Palaeohistoria, XIX. 20-85.

Influence of soil and rock mineralogy and geomorphology on landslides Occurrence and soil erosion in the Merek Catchment, Iran

Mosayeb Heshmati^{*a}, Nik Muhamad Majid^{**b}, J. Shamsuddin^{***c}, Arifin Abdu^{**d} and Muhamad Ghaituri^{*}

^{*} Department of Watershed Management, Agriculture and Natural Research Center, Kermanshah, Iran.

^{**} Department of Forest Management, Faculty of Forestry, Universiti Putra Malaysia, 43400 UPM, Serdang, Selangor, Malaysia

^{***} Department of Land Management, Faculty of Agriculture, Universiti Putra Malaysia, 43400 UPM, Serdang, Selangor, Malaysia

a. heshmati46@gmail.com

b. nik@putra.upm.edu.my; fax: +603-89432514

c. samsudin@agri.upm.edu.my; fax: +603-89434419

d. arifinabdu@putra.upm.edu.my; fax: +603-89432514

Abstract

Part of the mountainous semi-arid areas of Iran is geologically and topographically susceptible to landslides and gully erosion. A study was conducted at the Merek catchment, Iran which is geologically characterized by limestone, sandstone, shale and marls so as to determine the soil and mineralogical factors responsible for the occurrence of landslides and erosion. In this study, geomorphological units within the catchment were mapped by overlapping geological, topographical, land use and erosion data, using satellite image and GIS. Rocks and soils were sampled within each unit to determine their physico-chemical and mineralogical properties. The respective affected areas of landslides, gully, rill and inter-rill was found 16, 41, 18 and 24%, being eroded at the rate of 10–18.5 t ha⁻¹yr⁻¹. These landslides and gullies were initiated by crack formation in areas having smectite and smectite/mica, respectively. Smectite can swell and contract, depending on the availability of water and was found the dominant mineral in about 80% of the area affected by landslides. Field verification showed that landslides occur mainly in the forest where the canopy cover is less than 15% with slope of 10-45% and triggered through crack and piping phenomena due to deforestation and overgrazing, whereas gullies mainly are dominated in agricultural area where slope is gentle (less than 10%) and developed by agricultural activities, especially improper tillage practices in this catchment.

Key words: Geology; Gully; Landslide; Marl; Piping; Rill; Smectite

1. Introduction

Landslide and gully erosion occur frequently in the semi-arid regions of Iran. They are contribute to damage to the environment worldwide through soil disturbance and sedimentation. These phenomena are reported as the dominant soil degradation process in the steep slope and agricultural areas, respectively and affected by improper human activities such as road construction, land use change, tillage practice and natural plant clearance [18], [25], [26], [22], [23]. However, gully and landslide are considerable in the forest and arable lands in the Zagros Mountain of Iran comprising fine grained sedimentary rocks (marl and shale layers) that produce soils with high erodibility [7]. The economic loss due to landslides in Iran is significant, with the estimated annual fiscal loss of about USD 600 million

[17] and their off-site impacts such as siltation, soil nutrient decline and CO₂ emission are also significant. In the study area, suspended sediments through landslide and gully contribute to reduction in incapacity of Karkheh hydro-electrical dam which has been built in down stream. These soil erosion features are accelerated through human activities such as forest clearing, overgrazing and improper tillage practices resulting in carbon emission. In the deforested areas, landslide incidence contributes to transferring $0.94 \pm 0.23 \text{ Mg C ha}^{-1}\text{yr}^{-1}$ to aquatic ecosystem [9], [4], [23].

Marls in the Zagros are susceptible to landslides where are devoid of vegetative and slope is 20-40%, while there were prone to gully erosion with gentle slope and agricultural activities [2]. Weathering of marls (containing mica) usually results in the formation of smectite. In some areas where marl layers are overlain by limestone, swelling of smectite causes sliding of soil layers. This soil mineral shrinks upon dehydration that leads to cracking phenomenon because of its low shear strength and can expand up to 30% of its volume [14], [8], [5]. Smectite increase weight of soil layer during the rainy season due to high water absorption capacity and consequently sliding incidence. Without doubt landslide and gully has increased over the years partly due to uncontrolled forest clearing, mining, road construction and unsuitable agricultural activities. The objectives of this study were (i) to determine the important factors affecting landslides and gully occurrence in semi-arid regions in the Merek catchment, Iran; and (ii) to compare these factors among different agro-ecological zones.

2. Materials and methods

2.1. The study area

This study was conducted at the Merek catchment, located in Kermanshah, Iran. It is the upper catchment of the Karkheh River Basin (KRB) within the Zagros Mountain Chains (western Iran) (Fig. 1). This catchment has an area of about 23,000 ha that lies between 34° 00' 38" and 34° 09' 3" N and 47° 04' 25" and 47° 22' 18" E, comprising plains, hilly and mountainous areas with forest, rangeland and agricultural lands. The mean annual precipitation and temperature are 481 mm and 17.7 °C, respectively.

2.2. The geomorphological units

A major part of the Merek catchment is occupied by the sedimentary rocks which have been folded into a series of huge anticline and syncline [13]. Marl, limestone, sandstone

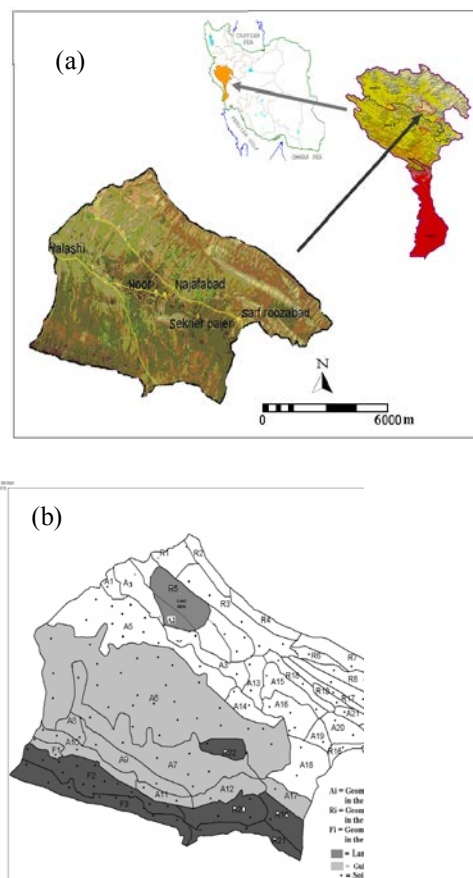


Figure 1: a- A map showing the location of the Merek catchment, b- Geomorphological units with incidence of landslide and gully erosion

and shale are the important materials/sediments forming the geological formations. Geomorphological unit (facies) is a homogenous area in the catchment with specific characteristics of geology, topography, land use and erosion for management practices and soil conservation measures [1]. This map was prepared by overlapping the digitized maps of geology, topography (slope steepness, elevation), erosion features and land use type using satellite image (Landsat ETM⁺ 2002) and GIS software (ILWIS 3.5).

2.4. Rock/soil sampling and analyses

Rock/soil samplings and field verifications were carried out within each geomorphological facies. About 270 soil samples at the depth of 0-20 and 20-40 cm were taken followed by stratified random soil sampling and their coordinates were determined by GPS. Soil physico-chemical characteristics were determined in the laboratory using standard methods for particle-size distribution, aggregate stability, pH, organic carbon, EC, Exchangeable sodium and carbonate content and their results statistically were analyzed using SAS software. The mineralogy of the soil and rock (XRD) was determined according to the standard procedure [26].

3. Results

3.1. The geology

Field verifications and geology map showed that geological formations are mainly prone to landslides and gully hazard. The north part of study area hilly topography consists limestone with intermittent layers of shale and conglomerate resulted in limited occurrence of surface landslides and gully erosion (Gurpi and Ilam Formations), while in the southern part outcrop of Kashkan Formation shows the presence of claystone, siltstone and sandstone, which are more subjected to landslide in the steep slope and its deposits (Quaternary) in the gentle slope comprise materials containing marl, argillaceous materials, sand and silt resulting in gully erosion.

3.2. Topography and land use

As shown in Fig. 2, the respective areas of landslides occur are forest, rangeland and agriculture. In contrast, gully erosion is occurs mainly in the agriculture area where soil at the Quaternary has been inherited mainly as same as landslide areas (Kaskan Formation). Although soil, geology and mineralogical factor affecting to landslide incidence roughly is similar to gully erosion, topographic and land use characteristics are different between them. Field verification showed that landslides occur at 10-60% slope and is more frequent where slope is 20-45% with 1500-1700 m above the sea level, while gully is dominant erosion feature in gentle slope (<10%) with 1400-1500 m above the sea level. Landslide in Iran occurred frequently where the slope was 20-40% [1]. In the present study, it was observed that most of the landslides occur in the northern aspect of the mountain chain. Soils in the northern slope aspect can maintain more moisture than others due to the low evaporation [20]. This condition can provide water for the expanding smectite. In addition, main land use of landslide is forest, but for gully is agriculture. The depth of the landslides in arable land was found to be shallower than that of the forest and rangeland zones because of its lower slope. In reality, about 3400 ha (15%) of the study area is affected by landslides (mainly forest zone), but gully affects 9367 ha (about 41%) which are roughly arable lands.

3.3. The physico-chemical properties of the soils

Table 1 shows the soil physicochemical properties. The soils in the landslide and gully areas are mainly clayey in nature. The respective average sand, silt and clay were 17, 42 and 41 percent. T-test of particle-size distribution showed that there was no significant difference within soil layers in all zones, but the ANOVA analysis revealed that sand value in the agriculture zone is significantly lower than that of the other zones. Inter correlation analysis also explored that clay particle was correlated with sand, SOC and pH. Clay particles control soil strength and shearing mechanism when their proportion is more than 30% and water holding capacity is strongly controlled by the clay content that can be increased up to 210 mm water/m soil depth [8] and [10]. On the other hand, increase in saturation percentage enhances water absorption capacity that increases the weight of the slipping layer in the slope area or contributes to gully process through washing away fine fractions.

Although the mean aggregate stability (AS) of the surface soil layers was about 59% in the study areas, there was significantly lower in the agriculture areas promoting piping and gully erosion. There was a good inverse relationship between soil aggregate stability and piping density on clayey soils [6]. By and large, the contribution of the physical characteristics on the incidence of landslides in Merek catchment was found to be more than those of the soil chemical properties due to low values of ESP, Na and EC as well as moderate alkaline pH (Table 1). The respective pH, exchangeable sodium and electrical conductivity values were 7.75, 0.50 cmol_c kg⁻¹ and 0.70 dS/m indicating the moderate alkaline soil and not expected to have any significant relationship with the landslides and gully erosion. The mean organic carbon level in the topsoil and subsoil of the agriculture, rangeland and forest was 1.35, 1.56 and 2.14%, respectively and t-test and ANOVA analyses showed that their means are significantly different from each other among agro-ecological zones. The burning of crop residues and improper tillage practices, especially in the hilly areas of the agriculture zone has reduced its OC significantly. Improper tillage practices strongly accelerate soil erosion processes by destroying soil organic matter and soil structures [19]. Overgrazing contributes to the reduction of OC through defoliation phenomenon and improper tillage practice can decrease about 12% of soil organic carbon [11], [24]. Heavy sheep grazing decreased about 16.5 kg of OC per ha [15]. Carbonate content in the soils of the study area is high (about 35%) and carbonate indirectly affects incidence of landslides

Table 1: ANOVA analysis of soil variables in the agro-ecological zones of Merek catchment, Iran

Soil Variable	Soil Depth (cm)	Agro-ecological Zone			Pr> F
		Agriculture	Rangeland	Forest	
Sand (%)	0 - 20	16.46 ^{b*}	19.33 ^a	19.50 ^a	0.007
	20 - 40	16.50 ^b	19.55 ^a	19.33 ^a	0.021
Silt (%)	0 - 20	42.80 ^a	39.62 ^{ab}	37.63 ^b	0.003
	20 - 40	42.88 ^a	41.64 ^{ab}	37.68 ^b	0.048
Clay (%)	0 - 20	39.84 ^a	40.55 ^a	42.70 ^a	0.284
	20 - 40	41.13 ^a	42.20 ^a	41.30 ^a	0.866
Saturation percentage	0 - 20	51.31 ^a	50.86 ^a	51.07 ^a	0.044
	20 - 40	49.59 ^a	50.5 ^a	51.14 ^a	0.631
Aggregate Stability (%)	0 - 20	53.41 ^b	60.95 ^{ab}	63.89 ^a	0.0151
	20 - 40	57.42 ^a	62.25 ^a	63.94 ^a	0.248
pH	0 - 20	7.72 ^a	7.76 ^a	7.80 ^a	0.195
	20 - 40	7.81 ^a	7.85 ^a	7.84 ^a	0.479
Exchangeable sodium cmol _c kg ⁻¹	0 - 20	0.444 ^{ab}	0.412 ^b	0.512 ^a	0.102
	20 - 40	0.490 ^a	0.408 ^b	0.517 ^a	0.021
Electrical conductivity (dS/m)	0 - 20	0.768 ^a	0.632 ^a	0.742 ^a	0.0221
	20 - 40	0.711 ^a	0.58 ^b	0.778 ^a	0.004
Organic carbon (%)	0 - 20	1.36 ^a	1.56 ^b	2.15 ^c	0.0001
	20 - 40	1.03 ^b	1.35 ^a	1.45 ^a	0.0001
Carbonate (%)	0 - 20	32.18 ^a	30.01 ^a	32.18 ^a	0.388
	20 - 40	36.94 ^{ab}	33.51 ^a	40.31 ^b	0.018

*Means with the same letters are not significantly different at P ≤ 0.05% using SNK test for variables

through the formation of hardpan, especially in some areas of the rangeland. This in the end would increase the incidence of shallow landslides.

3.4. The mineralogy of rock and soil

Fig. 1 (a) gives the XRD diffractogram of the clay minerals present in the gully areas showing the presence of peaks at 14.04 Å, 7.213 Å, 3.301 Å, 3.030 Å, and 2.104 Å indicating

the presence of vermiculite, kaolinite, quartz, calcite and dolomite, respectively. Soils in this area contain about 40% clay which potentially contributes to gully erosion, but there was 12.060 Å (K), 9.960 Å (Mg) and 10.140 Å (Mg-glycol) indicating the presence of mica-smectite. Fig.1 (b) is the Mg-treated sample in the landslide areas showing a peak at 14.81 Å, indicating the presence of smectite, vermiculite, chlorite or all of them. Glycolating the Mg-saturated sample produced a peak at 16.184 Å (Fig. not shown). This shows clearly the presence of smectite in the sample. Treatment with K gave a peak at 12.755 Å, while peak at 14 Å peak was absent (Fig. not shown). This shows that chlorite is absent in the sample. Field observations revealed that crack formation was the first step in the development of both landslide and gully. The cracks are formed in the fine grained layers containing smectite, mica-smectite

and vermiculite, running parallel and across the direction of the slope. The soils having these minerals can expand when absorb water, while during dry season, they loss their and consequently the crack formation with different sizes (1-10 cm). Smectite can absorb water (up to 30% of its original volume) resulting in swelling of the crystals and increase in weight during rainy season resulting in instability and sliding [14], [12], [16], [3].

5. Conclusions

Landslide and gully are an important feature of land degradation in the Merek catchment, Iran that has affected about 56% of the area. Their occurrence is somewhat related to the high soil erosion intensity, which was estimated about 18 t ha⁻¹yr⁻¹. Incidence of landslides and gully are mainly influenced by the geological, topographical and soil physical properties. Landslides occur frequently on the geological formations, which are composed of fine grained materials, developed from marl and shale strata. These layers weathered to form smectite and vermiculite, which are subjected to the process of swelling and shrinking, depending on the availability of water. These phenomena decrease soil stability and eventually result in the occurrence of soil erosion and landslides. The situation is made worse by the uncontrolled deforestation, improper tillage practices and overgrazing. Most of these landslides and gullies are initiated by cracking and piping processes. Cracks appear in the soils when smectite and vermiculite loss

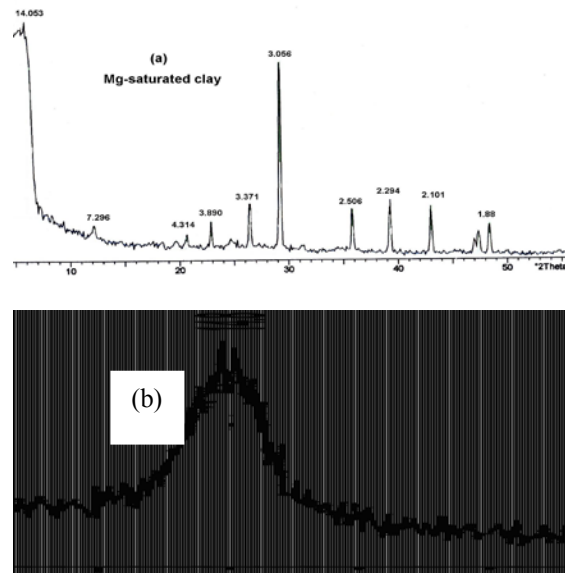


Figure 1: X-ray diffraction patterns of the clay fractions treated with Mg: a)-from gully erosion areas (agriculture) which is dominated by vermiculite, and b)- dominated by smectite in the sliding areas (forest),

their water during dry season; however, during wet season the mineral absorbs water and expands. This phenomenon accelerates soil erosion in the Merek catchment, which in turn, increases cracking, piping and landslides/gully. Field verification showed that both landslides and gully erosion are mainly accelerated by forest clearance and up-down to the slope tillage practice and landslide was more frequent where plant canopy of forest was less than 20 percent.

Acknowledgements

The authors would like to acknowledge Universiti Putra Malaysia (UPM) and Agricultural Research and Education Organization of Iran (AREO) for financial and technical support.

References

- [1] Ahmadi, H., 2003. Applied Geomorphology; water erosion (2nd edition) 2. Tehran University Press, Tehran, Iran.
- [2] Ahmadi, H. and Esfandarani, A.T. 2002. Study of effective factors on mass movements (landslide); case study: Ardal Region of Chaharmahale Bakhtiari province, Iran. *Natural Resources (Iran)*, 54: 323-329.
- [3] Azañón, J.M., Azor, A., Yesares, J., Tsige, M., Mateos, R.M., Nieto, F., Delgado, J., López-Chicano, M., Martín, W., Rodríguez-Fernández, J., 2010. Regional-scale high-plasticity clay-bearing formation as controlling factor on landslides in Southeast Spain. *Journal of Geomorphology*, 120(1-2): 26-37.
- [4] Blanco, H., Lal, R., 2008. Principles of Soil Conservation and Management. Springer publisher, USA.
- [5] Borchardt, G., 1989. Smectites. In: J.M. Bigham, Dixon, J.B., Milford, M.H., Roth, C.B., Weed, S.B., (Eds.), Minerals in Soil Environments (2nd edition) Soil Science Society of America, Madison Wisconsin, USA, pp. 967-728.
- [6] Diaz, R.P., Sanleandro M.A., Sanchez F.B., Faulkner H., 2006. The causes of piping in a set of abandoned agricultural terraces in southeast Spain. *CATENA*, 17: 233-245.
- [7] Eberhardt, E.K., Luginbuehl, M., 2005. Slope instability mechanisms in dipping inter-bedded conglomerates and weathered marls in the 1999 Ruffi landslide, Switzerland. *Engineering Geology*, 77: 35-56.
- [8] Frydman, S.T., Alesnick, M., Geffen, S., Shvarzman, A., 2007. Landslides and residual strength in marls profiles in Israel. *Engineering Geology*, 89: 36-46.
- [9] Glade, T., 2003. Landslide occurrence as a response to land use change: a review of evidence from New Zealand. *CATENA*, 51(3-4): 297-314.
- [10] Hazelton, P., Morphy, B., 2007. Interpreting Soil Test Results. CSIRO Press, Sydney, Australia.
- [11] Hodgkinson, K.C., 1993. Tactical grazing can help maintain stability of semi-arid woodlands 17th International Grassland Congress, Palmerston North, New Zealand, pp. 75-76.
- [12] Istanbuloglu, E., Bras R.L., Cervantes, H.F., 2005. Implication of bank failures and fluvial erosion for gully development: field observations and modeline. *Geophysical Research Earth Surface*, 145: 50-70.
- [13] Karimibavandpoor, A., Hajihosaini, A., Shahandi, M., 1999. Geological Map of Kermanshah, Iran (1:100,000, Series: 5458). Geological Survey Service Press, Tehran, Iran.
- [14] Krenz, J., Lee, B., Owens, P., 2000. Swelling Clays and Septic Systems: High Water Tables and Septic System Perimeter Drains. Department of Agriculture (USDA), USA. www.ces.purdue.edu/extmedia/RW/RW-1-W.pdf.
- [15] Li, C., Hao, X., Zhao, M., Han, G.W., 2008. Influence of historic sheep grazing on vegetation and soil properties of a desert steppe in Inner Mongolia. *Agriculture, Ecosystems and Environment*, 128 109-116.
- [16] Lutengger, A.J., Cerato, A.J., 2008. Surface Area and Engineering Properties of Fine-grained Soil. University of Massachusetts Press, Amherst, USA.
- [17] Jaada, M. 2009. Landslides Hazard Analysis Using Frequency Ratio Model, Universiti Putra Malaysia, Serdang, pp.181.
- [18] Morgan, R.P.C., 2005. Soil Erosion and Conservation. *Blackwell Publisher, Oxford, London*
- [19] Rosa, D.L., Romero, M.A., Pereira, E.D., Heredia, N., Shahbazi, F., 2009. Soil specific agro-ecological strategies for sustainable land use - A case study by using MicroLEIS DSS in Sevilla Province (Spain). *Land Use Policy*, 26: 1055-1065.

- [20] Ohlmacher, G.C., 2000. The relationship between geology and landslide hazards of Atchison, Kansas and Vicinity. Kansas Geological Survey, Current Research in Earth Science, Bulletin 244, part 3. <http://www.kgs.ukans.edu>.
- [21] Page, M., Trustrum, N., Brackley, H., Baisden, T., 2004. Erosion-related soil carbon fluxes in a pastoral steep-land catchment. *Ecosystems and Environment (New Zealand)*, 103: 561-579.
- [22] Parkner, T., M., M. Page, N. Marden. and Marutani, T. 2007. Gully systems under undisturbed indigenous forest, East Coast Region. *J. Geomorphology (New Zealand)*, 84: 241-253.
- [23] Preuth, T., Glade, T., Demoulin, A., 2010. Stability analysis of a human-influenced landslide in eastern Belgium. *Geomorphology*, 120(1-2): 38-47.
- [24] Senthilkuma, S., Basso, B., Kravachenko, A.N., Robertson, G.P., 2009. Cotemporary evidence of soil carbon loss in the U.S corn belt. *Soil Society of American*, 73(6): 278-2085.
- [25] Valentin, C., Poesen J. and Li, Y. 2005. Gully erosion: Impacts, factors and control. *CATENA*, 63:132-153.
- [26] Whitton, S., Churchman, G.J., 1987. Standard Methods for Mineral Analyses of Soil Survey Samples for Characterization and Classification in New Zealand Soil Bureau, NZ Soil Bureau Scientific Report 79, 27.

The effect of historical land use on landslide initiation

Gholamreza Shoaee

Assistant Professor, Engineering Geology Group, Geology Section, Basic Sciences Faculty, Tarbiat Modares University, P.O. Box: 14115-175, Tehran, Iran; shoaei@modares.ac.ir

ABSTRACT

An unlikely combination of relatively low rainfall intensity and gentle slopes produced numerous landslides and debris flows during a storm in July, 2006, around Okaya City, Japan. A detailed investigation was conducted on a landslide/debris flow near Okaya City, where the highly variable soil characteristics led to examine the variability of physical and hydrological properties throughout the soil profile. A zone of black organic soil found at depths ranging from 20 to 280 cm upslope of the landslide scar is indicative of sequential forest burning practiced during Jomon age hunting and gathering. Previous C-14 dates indicate that anthropogenic practices took place between 10,200 and 4510 years BP at this site. The results of field surveys, laboratory tests, and computer simulations show that the existence of an ancient anthropic organic soil at the middle of the soil profile altered the hydraulic response of the soil, and could be the cause of the landslide. Removing the organic ancient soil made the slope stable and thus, the landslide might not be initiated.

Keywords: Anthropic Soil, Historical land use, Soil profile variability, Rainfall induced landslides, Hydrological Modeling

1. INTRODUCTION

Landslides are important natural geomorphic agents that shape mountainous areas and redistribute sediment in gentler terrain. Much of the present Earth's landscape has been extensively sculpted by episodic landslides [1]. Landslides depend on a combination of variables such as slope, rainfall amount, rainfall intensity, soil mantle thickness, soil state parameters, subsurface hydrology and vegetation [2], [3]. Reference [4] showed that probabilistic analysis which ignores the spatial variability of undrained shear strength or effective cohesion of the soil underestimates the probability of slope failure. One of the major factors affecting slope stability is land use pattern. Most of the tremendous number of researches dedicated to unveil such effect have focused on the relatively recent impact of land use change (*e.g.* population growth, timber harvesting, forests clear cut, road construction) within the last few decades [5], [6], and [7]. Their approaches and consideration of land use change, only through past century, might be reasonable and acceptable; however, in this research, a new consideration on the possible effect of ancient land use is raised and could be a new approach for understanding the cause of some slope failures.

An unlikely combination of relatively low rainfall intensity and gently sloping topography produced numerous landslides and debris flows during a prolonged storm in July 2006 around Okaya City, Nagano Prefecture, Japan, and indicated the existence of other factors contributing to the landslide initiation. This research focused on detailed investigation on a relatively large landslide/debris flow near Okaya City (Fig. 1) where the highly variable soil characteristics in the landslide

scarp led to examine the variability of physical and hydrological properties throughout the soil profile and within the area above the landslide.

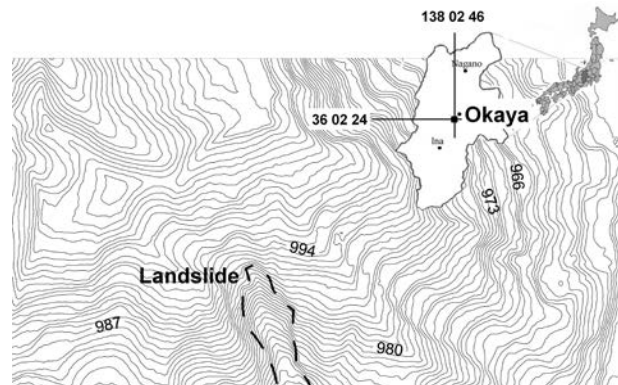


Fig. 1 The location of study area

Based on 62 yr of rainfall data from the nearest AMeDAS meteorological station in Suwa City (6 km east of the landslide site), July (during the Baiu season) has the highest total monthly rainfall. Among all 62 yr, July 2006 had the highest rainfall for this month (506 mm). Average July precipitation near the study area is 200.5 mm. Total precipitation during the July 17-19, 2006 period exceeded 358 mm. Landslides were triggered when cumulative 3-day rainfall reached about 330 mm, most of the total July rainfall. However, the storm had a relatively low intensity; maximum intensity was 22.5 mm h⁻¹ near the beginning of the storm and it never exceeded 16 mm h⁻¹ throughout the next 3 days.

The region is located approximately 53 km to the east of Japan's second largest volcano, Ontake. The geology of the area is relatively simple because of its volcanic nature and also due to its location in the middle of the main island of

Japan (Honshu). Several local faults exist in this region; however, it seems that the geological setting has not been significantly affected. Dominant lithology in the area is tuff, andesite, and pyroclastics. Andesite breccias containing large amounts of tuff breccia composed the lower layer of Pleistocene bedrock.

Soils around the landslide scarp are about 3.5 m deep and overly andesitic bedrock. Soils at this landslide site are formed primarily by erosion processes, where transported soils are deposited over approximately 0.5 m of residual soil. Soil profiles at the site indicate considerable small-scale heterogeneity and anisotropic characteristics. For example, a sequence of black soil layers appears near the middle of the profile, whereas the soil overlying the bedrock below the black layers is brownish. The anthropic black soil in the study area is an ancient buried surface soil remnant from earlier land use (*e.g.*, episodic burning of vegetation), which was later covered by eroded soil. The spatial propagation of this black soil layer appears discontinuous. The soil around the landslide is dominated by the black layer, whereas a nearby landslide behind the same hill contains brownish soil over bedrock overlain by a thin layer of organic-rich soil on the surface (*i.e.*, no black layer). Repetitive agricultural activities at the study site formed more than a meter of such organic-rich surface soil [8].

2. METHODOLOGY

To investigate the role of soil profile heterogeneity, a detailed investigation on soil variability and its effect on pore pressure distribution through and after the storm was planned including:

I) An integrated and precise study of the soil including vertical and spatial characteristics and distribution, physical, and hydrological properties; variation in texture and structure; and composition and genesis of the soil. Soil characteristic curves and K_s of the soil profile were measured in the laboratory for different soil layers. In addition, an extensive study was conducted on the history of the region to discover the stages of land use around the study area. This was to figure out a comprehensible scenario for soil heterogeneous profile forming process.

II) Field measurements from multi-depth tensiometers to monitor soil water potential (both tension and positive pore water pressure) fluctuations during recorded rainfall to capture the real-time response of the soil to the storms. To model the water movement and development of suction/pressure fluctuations in the soil due to rain, eight tensiometers were installed in field above the investigated landslide. The tensiometers were arranged in two sets, each at four different depths: 20 cm, 50 cm, 100 cm, and 167 cm. This depth arrangement allowed the tensiometers to monitor the middle of the surface soil, middle of subsurface soil, bottom of the subsurface soil, and a deeper soil at the middle of the profile, respectively. To reach the soil below the black layer and monitor the effect of this low permeable soil layer, the deepest tensiometers were installed at 167 cm below the shallow black layer. A group of four tensiometers was set up a few meters above the landslide. The second set was installed

10 m further upslope from the first set. An eight-channel logger connected to the transducer and powered by a car battery (for longer life) recorded soil suction data at 10 min intervals.

III) Modeling the process of rain water infiltration into the soil by applying field data from different soil horizons, including inherent variations. The model will be calibrated based on the recorded tensiometer data and simulations are then being conducted for the landslide-inducing storm of July 2006 to capture the process of transient unsaturated-saturated flow in the soil. The goal of this study was to simulate the infiltration and propagation of rain water within the soil, both vertically and laterally in an at least 2-D model, which caused the landslide of July 19, 2006. Thus, a suitable model needs to be selected to fulfill some of the vital criteria for simulation. These model criteria can be summarized as: 1) ability to incorporate transient rainfall; 2) handle large pressure or water content gradients between the elements of the slope allowing accretion of sharp pressure head fronts progressing through the soil during short-term, high intensity rains; 3) model soil layering effects in the profile with variable hydrological properties; 4) work with an acceptable number of soil properties; and 5) numerically solve the governing equation so it can be easily compared and fitted to field observations. Considering all the parameters mentioned above, HYDRUS 2D/3D (Pc-Progress Co.) seems to fulfill most of the requirements for the modeling in this study by: offering a user friendly interface in modeling preparations steps, being capable of a large iteration process and time step control to optimize the required running time for the simulation, receiving the topographic and soil layer data from a prepared file, and thus accepting incredible slope details, and giving a good control on 'mesh elements' generating process. Thus, HYDRUS 2D/3D was chosen to conduct the modeling.

3. RESULTS AND DISCUSSION

The study area, located west of a large fresh water lake and drained by several streams, was an appropriate location for such habitation and agriculture starting from the early Jomon period 14,000 to 4000 BC (*e.g.* [9]). The black soil layer is an indicative soil horizon around this study area near Okaya City which supports the existence and propagation of Jomon culture throughout the region. ^{14}C dating analysis of charcoal in the black layer indicates a wide age range from 10,200 to 4510 yr BP [10]. The beginning of Jomon era coincided with a warmer climate in Japan [9]. This warmer climate supported flourishing primitive practices, such as hunting and associated burning of forests around Okaya City for an extended period. The Jomon people lived by food gathering and hunting, and therefore this destructive interaction with nature began. There is no firm evidence indicating the process of hunting, whether it was a group activity or an individual practice, however, it involved hunting and clearing the forests and regenerating vegetation by fire, possibly on an annual basis (*e.g.*, [9]). The anthropogenic origin of the black soil has been mentioned in some previous publications (*e.g.* [11]), although it has never been connected chronologically to any particular era or ancient civilization. Based on ^{14}C dating

results, burnt wood and brush accumulated over the soil for about 5700 yr until about 2500 BC. More results and discussion about the genesis of the soil and its possible historical origin are presented in reference [8].

Data collected on soil thickness and distribution by field surveys show that the soil mantle at the area above the landslide can be divided into two portions: I) shallow soil with maximum depth of 1 m (Fig.2), and II) deep soil from 1 to ≈ 4 m deep.

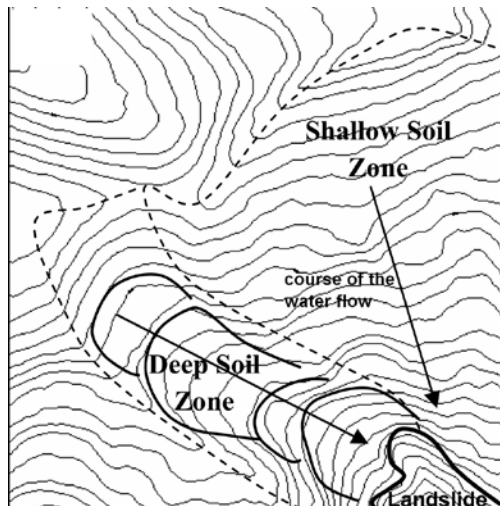


Fig.2. Location of shallow and deep soil mantle

The delayed initiation of the landslide in the July 2006 indicates that cumulative rain exerts a greater influence on critical pore pressure accretion than rainfall intensity. This phenomenon is important related to simulating the pore pressure response in the deeper soil zone, since it captures the effect of delayed hydrological response of the soil, due to water percolation process within the thick soil layer. To control the simulation of soil response to the storm, six observation points (in the model, Fig. 3) was set to read the pore pressure at the landslide spot and on particular depths.

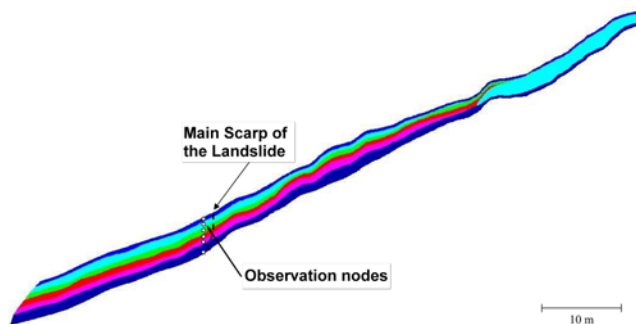


Fig 3. The modeled soil and slope and observation nodes.

Fig 4 shows the model simulations for after the long process of calibration at the depths of tensiometers installation. As shown, the simulated pore pressures fit the tensiometers response. After this stage, the model was set to run for the storm of July, 2006, to simulate the pore pressure at the site of the landslide.

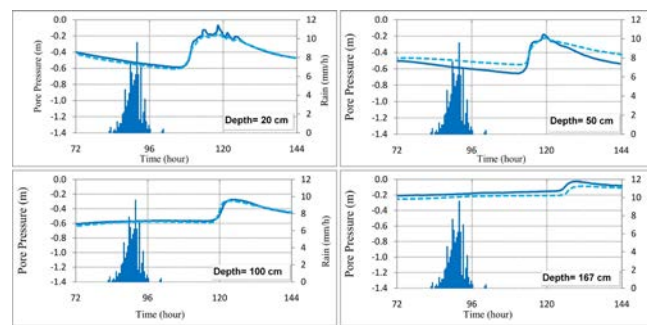


Fig.4. Calibrated model based on tensiometers data recorded on July 2007.

run for the storm in July, 17-19, 2006, as 88-h of rain (Fig 5).

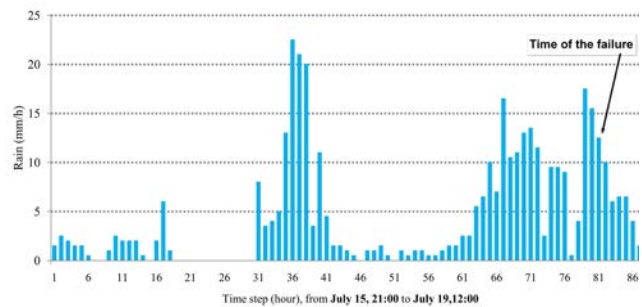


Fig.5. The storm of July, 17-19, 2006.

The result for the first set of simulations is presented in Fig 6. The curves represent the pore water pressure at the observation nodes 0.20 m to 3.50 m at the bottom the soil on the bedrock contact. The fig shows that at the time of landslide initiation and around the soil-bedrock contact, pore water pressure exceeds 3.00 mH₂O.

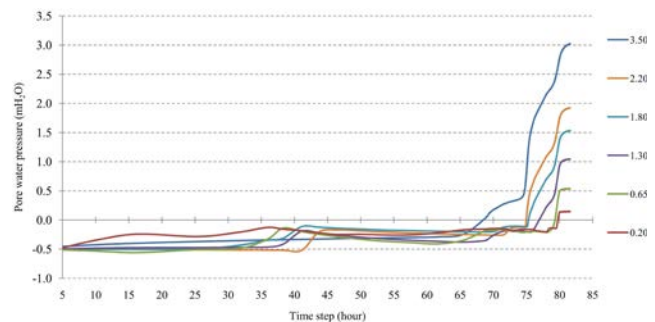


Fig.6. The model simulation for actual soil profile.

On the other set of runs, black anthropogenic soil layers were removed to simulate the propagation of pore water pressure in the absence of human effects. Fig 7 presents the result of pore pressure in the lack of black soil layer. The pore water pressure does not rise above 2.50 mH₂O when there is no anthropogenic black layer. It seems that the black soil intercept the lateral flow of the water from upslope to build a higher pore pressure around the time of failure, whereas, in the absence of the black soil layer, the water passes through the slope to build a delayed pore pressure at the location of landslide. Such difference in the built up pore water pressure may change the timing of the failure. Considering that the failure occurred toward the end of storm, the increase the in

pore water pressure might not continue to make the slope unstable and cause the landslide.

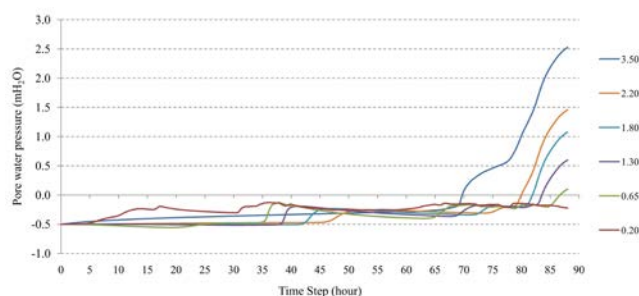


Fig. 7. The model simulation for No-Black soil scenario

4. CONCLUSION

In this study, a 2D model was applied to the entire contributing area above the actual landslide. This model included all the details of the slope characteristics and soil properties in order to examine the effect of the anthropogenic soil historically embedded into the soil profile. The simulations showed the effects of soil layering as a result of historical land use and anthropogenic activities, and thus, provide a unique look into the extended influence of human activities. Large differences were found between the hydrological and stability simulation results with original slope conditions and the assumed scenarios of no human effects. The more accurate simulations that were observed with anthropogenic effects included in the model suggest that the historical human life styles and land use activities affected contemporary mass movement phenomenon by: 1) being the probable cause of the 2006 failure, and 2) altering the timing of the landslide by changing the response of pressure head distribution in the soil during the storm, which likely could change the magnitude of economic and human life loss in such events (July, 2006, occurred early morning). Thus, the result of this study may introduce a new concept to assess the historical aspects of anthropogenic soil on contemporary landslide behavior. In contrast to earlier studies, this research extends the concept of land use and its effect of landsliding from conventionally a few decades to historical land use. Because such a long history affects the genesis, and thus the layering and properties of the soil, and imposes heterogeneity and anisotropy, the effects of historical anthropogenic activities have a direct link to the contemporary physical, hydrological, and mechanical characteristics of the soil. The results suggest that although recent human activities may affect the frequency and the number of landslides, the ancient anthropogenic activities play a more chronic role by gradually contributing to catastrophic mass movement events over time.

5. ACKNOWLEDMENT

This paper is a part of an extensive study on July 2006 landslide. I am grateful to Dr. Roy C. Sidle and Dr. Ken'ichiro Kosugi for their helps and inputs through this study at Kyoto University. Also special thank to Monbokagakusho for funding this study.

6. REFERENCES

- [1] Sidle, R.C., Ochiai, H., Landslides Processes, Prediction, and Land Use, American Geophysical Union, Water Resource Monograph No. 18, AGU, 2006, Washington DC, USA.
- [2] Dietrich, W.E., Bellugi, D., Real de Asua, R., Validation of the shallow landslide model SHALSTAB, for forest management. In: Wignosta, M.S., Burges, S.J. (Eds.), Land Use and Watersheds: Human Influence on Hydrology and Geomorphology in Urban and Forest Areas, Water Science and Application. American Geophysical Union, 2006, Washington, p. 195–227.
- [3] Rybar, J., Stemberk, J., Wagner, P., Landslides: Proceedings of the First European Conference on Landslides, Prague, 2002, Czech Republic, Taylor and Francis, London.
- [4] Griffiths DV, Fenton GA. Probabilistic slope stability analysis by finite elements. *J Geotech Geoenviron Eng ASCE*, 2004;130(5):507–18.
- [5] Sidle, R.C., Ziegler, A.D., Negishi, J.N., Abdul Rahim, N., Siew, R, Turkelboom, F., Erosion processes in steep terrain – Truths, myths, and uncertainties related to forest management in Southeast Asia. *Forest Ecology and Management*, 2006, 224(1-2):199-225.
- [6] Anderson, M.G., Holcombe, Liz, Renaud, Jean-Philippe. Assessing slope stability in unplanned settlements in developing countries. *Journal of Environmental Management*, 2007, 85:101–111
- [7] Imaizumi, F., Sidle, R.C., Kamei, R., Effects of forest harvesting on occurrence of landslides and debris flows in steep terrain of central Japan. *Earth Surface Processes and Landforms*, 2008, 33:827-840.
- [8] Shoaiei, G., Sidle, R.C., Variation in soil characteristics and hydrologic properties associated with historic land use near a recent landslide, Nagano Prefecture, Japan. *Geoderma*, 2009, 153:37–51.
- [9] Yoneda, M., Suzuki, R., Shibata, Y., Morita, M., Sukegawa, T., Shigehara, N., Akazawa, T., Isotopic evidence of inland-water fishing by a Jomon population excavated from the Boji site, Nagano, Japan. *Journal of Archaeological Science*, 2004, 31:97–107.
- [10] Okamoto, T., Katakura, M., Togashi, H., Shimizu, Y., Kitahar, H., Ochiai, H., Kawasaki, N., Kume, Y., Ages of buried humus horizons in landslide disaster sites caused by July 2006 heavy rainfall around the Suwa Region, Nagano Prefecture, *Proceedings of the General Meeting of the Association of Japanese Geographers*, 2007, 72:133 (in Japanese).
- [11] Yamanoi, T., Geological investigation on the origin of the black soil, distributed in Japan, *Journal of Geological Society of Japan*, 1996, 102(6):526-544; (Abstract in English)

Integrated Environmental Management for Sustained Development

J.RAJARAMAN¹ and K.THIRUVENKATASAMY²
AMET UNIVERSITY CHENNAI INDIA

ABSTRACT

Lowland problems are many. Many urban settlements are on the coastal belt, worldwide. In the past, many urban areas grew in an uncontrolled manner. The urban populations experienced increased risks, a poorer quality of life, and health problems. However, in general, there has been increasing management of many urban environments through Land use planning, building, environmental, health and safety regulations and management of emergencies, collectively balancing social, economic and environmental requirements. In this paper the complexities of urban cities are illustrated through many examples without naming any particular city. Since in modern times, globalization has created an environment where economic borders only exist. The systems are usually administered by separate authorities, which need to act together to secure sustainable urban management. Therefore actions and responses are frequently disconnected and are sometimes conflicting. To attain sustainable growth common sources of information are necessary. To emphasis the following eleven illustrative examples of some urban cities and their issues are discussed.

Keywords: Environmental Geology, Aquifer, Sustained development, Geomorphology.

1. INTRODUCTION

Urban areas are extreme cases where human activities have the greatest impacts on the local environment, and environmental processes can affect the greatest numbers of people. They need separate attention. Decisions made by developers and urban authorities have major implications for health, safety, the economy and the environment. Since ground processes and the nature of the underlying materials influence the occurrences of geological resources and hazards, it is important that these should be properly understood so that appropriate actions are taken to safeguard natural resources, reduce risk to people.

In this paper the need for good communication between urban authorities, developers and geoscientists.

2. GROWTH AND RENEWAL IN URBAN AREAS

The geographical origins of towns and cities are diverse. Most develop in response to natural and local conditions. The following factors influence settlements:

1. Convenient stopping places on routes such as passes between hills, convenient points on rivers, or at water sources in arid areas.
2. Ports on sea coasts, rivers or lakes.
3. Location in farming areas where routes meet allowing the development of markets.
4. Defensive sites, often on rocky prominences with areas below that could be used for building dwellings.
5. Administrative centres normally at prosperous settlements developed for other reasons but sometimes separately, for instance to refocus activity by removing administration from a coastal town to a site in the interior to promote development.

All but the last of the above mentioned factors are associated with specific Geomorphological settings that reflect underlying geology

3. MANAGEMENT OF THE URBAN ENVIRONMENT

In the past, in many countries, especially in developing countries urban areas grew in an uncontrolled manner. The urban population experienced increased risks, a poorer quality of life, and increased health problems. This trend continues where migration from rural to urban areas is very rapid. However, there has been increasing management of many urban environments through a variety of regulatory regimes.

1. Land use planning – which is concerned essentially with locating development in the most appropriate places, while protecting areas worthy of conservation, so that development is undertaken at the best balance of social, economic and environmental cost.
2. Building regulations- which aim to ensure that built structures are properly constructed and are fit for use.
3. Environmental regulations- regulating the operation and occupancy of sites, ensuring that waste and emissions are properly controlled and dealt with and that air and water are protected, so as to minimize social and environmental damage, including risks to health, conserving natural habitats and maintaining biodiversity.
4. Health and safety regulations – to ensure that employees, and other people entering places of employment, are safeguarded from unnecessary risks.
5. Environmental health regulation – to ensure that people are not exposed to potential hazards to health.

6. Management of emergencies – setting out and disseminating procedures for protection, evacuation and relief, making provision for emergencies services in relatively low hazards locations, and minimizing the likelihood of major accidents.

4. EXAMPLES OF URBAN ISSUES

4.1 THE CITY SCENARIO 1

In a city an industrial centre grew on the basis of local coal and ironstone mining that supported heavy industry. The uncontrolled outcome is shown in figure 1.

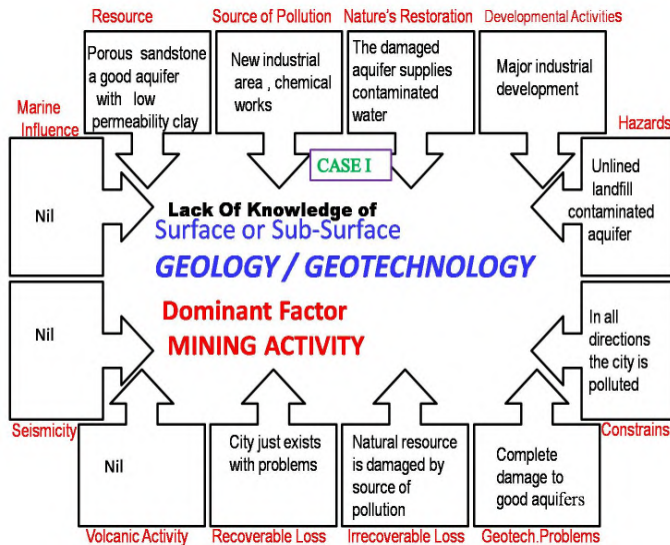


Fig.1

4.2 THE CITY SCENARIO 2

In the initial stage small quarries were opened for the extraction of limestone many years ago. The stones were used in the construction of major local buildings. The quarries were then abandoned. The buildings became part of the cultural heritage. The city expanded over the stone resource area. The uncontrolled outcome is shown in fig.2.

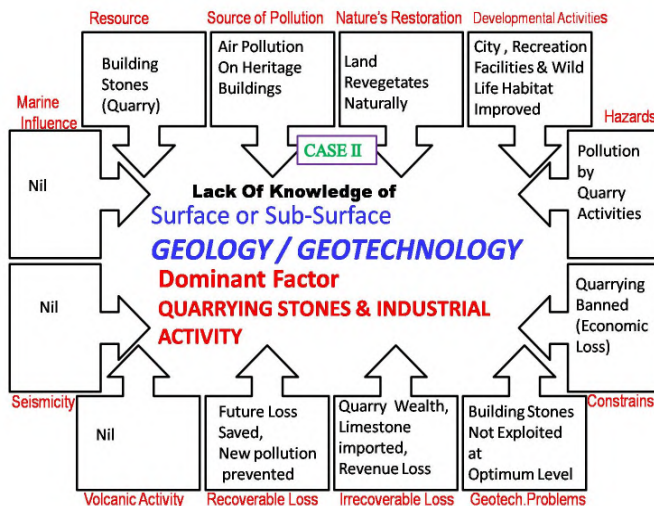


Fig.2

4.3 THE CITY SCENARIO 3

A major manufacturing city was linked to a sea port by an aging railway that had been constructed through a range of hills, along a river valley. Because of poor maintenance and increase in traffic the uncontrolled outcome is shown in fig.3.

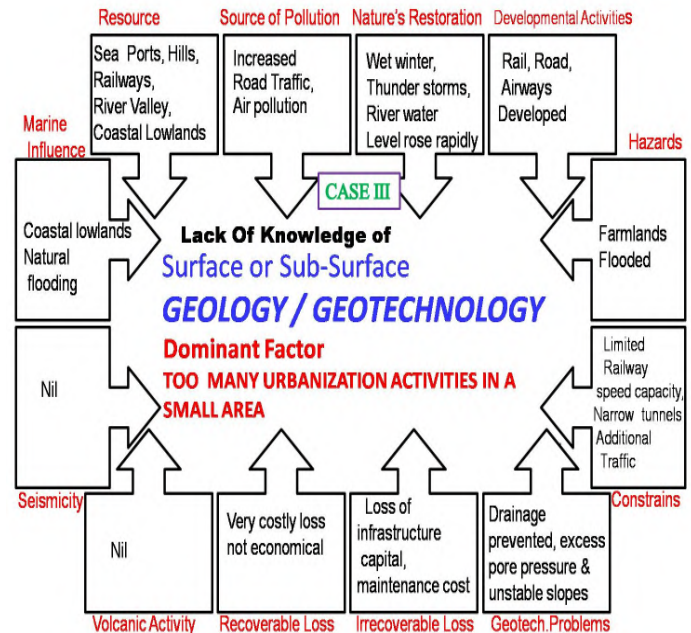


Fig.3

4.4 THE CITY SCENARIO 4

A city is located beside a bay with a narrow coastal plain backed by mountains. It was a port but expanded along the coast as housing, industry and tourism developed. Because of dredging the uncontrolled outcome is shown in fig.4

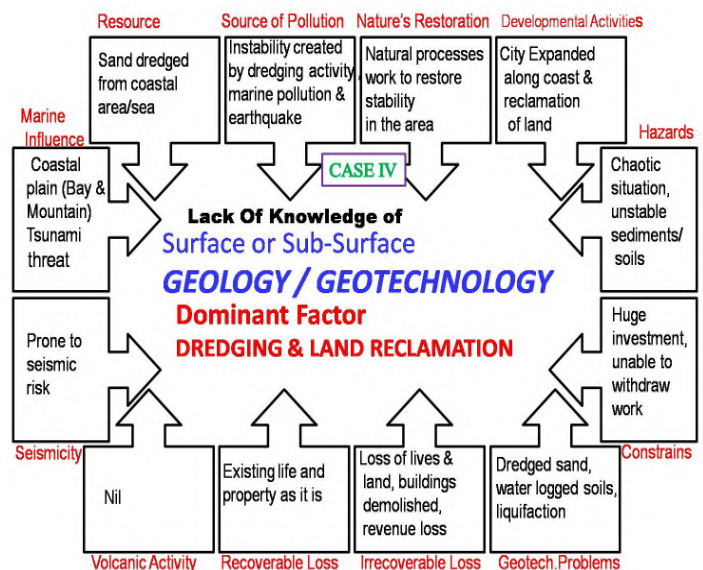


Fig.4

4.5 THE CITY SCENARIO 5

A city had been a major manufacturing centre. More recently, traditional industries had declined and a thriving service sector was now the main employer. The excess ground water created uncontrolled outcome as shown in fig.5

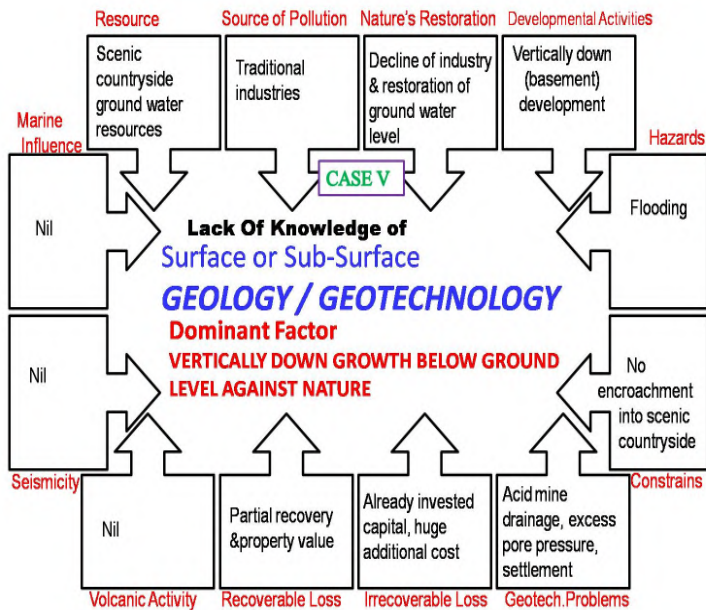


Fig.5

4.6 THE CITY SCENARIO 6

A major industrial area developed in and around a city. The complex was powered by coal and by manufacturing of gas and coke. Ash was tipped on areas between the factories and gave rise to localized contamination. This contamination caused uncontrolled outcome as shown in fig.6

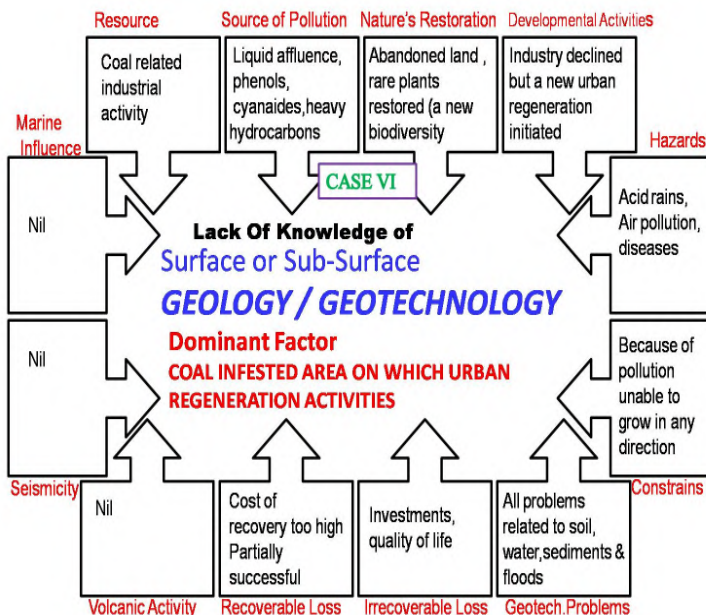


Fig.6

4.7 THE CITY SCENARIO 7

Porous sandstone beneath part of a city is the major source of local water suppl. The aquifer is overlying in places by sand and gravel and elsewhere by low permeability clay. A major chemical works contributed uncontrolled outcome as shown in fig.7.

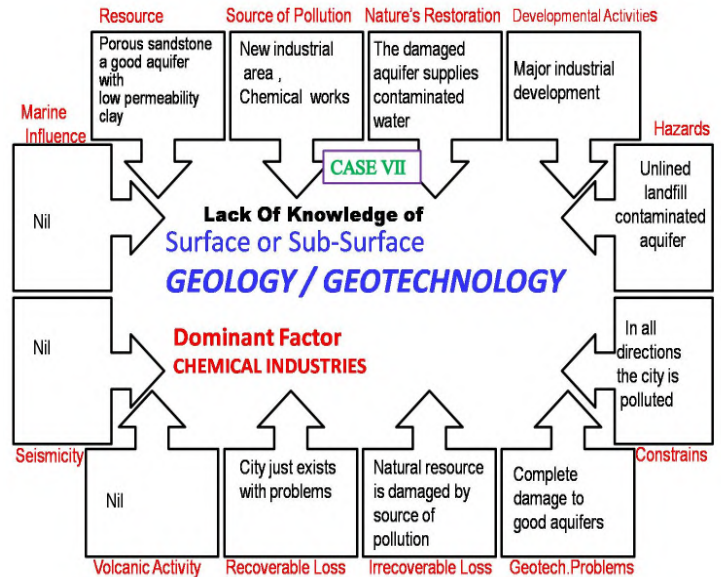


Fig.7

4.8 THE CITY SCENARIO 8

An area of uplands was rich in timber of high commercial value. Because of the need to earn foreign currency the government licensed major logging concessions. The logging company wished to maximize its profits and undertook rapid tree felling over a few years. Cutting of trees created uncontrolled outcome as shown in fig.8

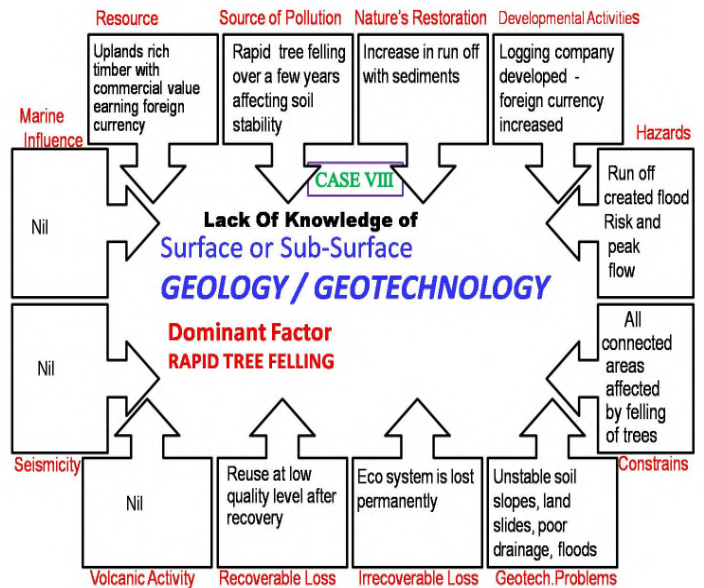


Fig.8

4.9 THE CITY SCENARIO 9

The low lying coastal area, lined by dunes, marshes and areas of mangroves was located to the west of a major port that had been designated for expansion. This involved the building of a breakwater to the east of the undeveloped coast and the dredging of a deeper access channel. The breakwater and the dredging operations created uncontrolled outcome as shown in the fig.9.

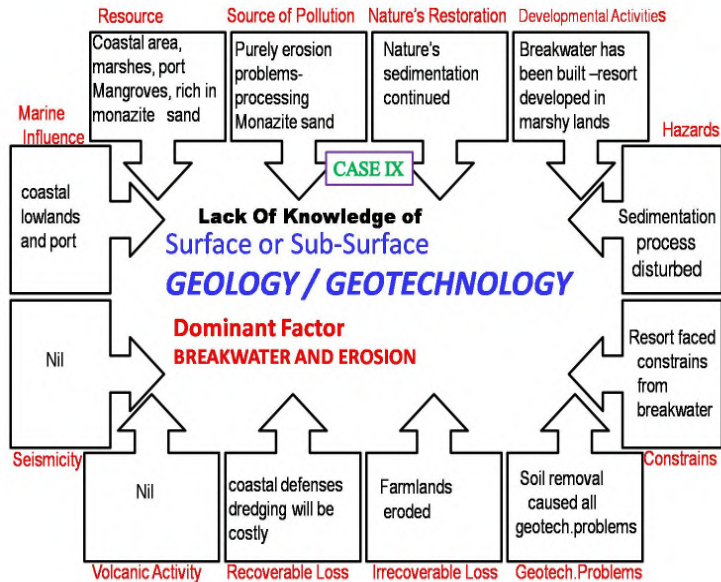


Fig.9

4.10 THE CITY SCENARIO 10

Major population growth took place in a city before mains drainage was constructed severe pollution of surface water and wells by sewage occurred. The unplanned expansion and population explosion created uncontrolled outcome as shown in fig.10.

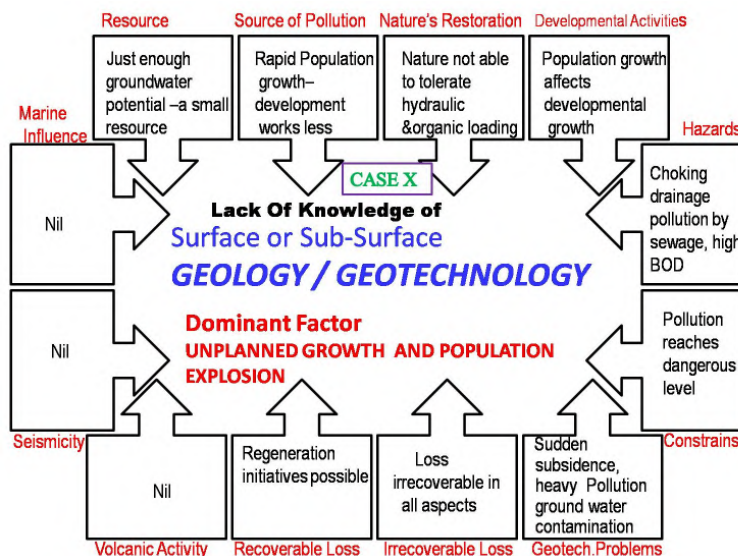


Fig.10

4.11 THE CITY SCENARIO 11

An important town grew several hundred years ago on the slopes of the mountain. It was initially a market center for farming based on rich local soils and plentiful rainfall on the slope. From time to time, there were volcanic eruptions but most of these were limited to small scale ash falls. But the volcanic eruptions were very active over the past few hundred years. The scientists found that many of these cities key emergency services and a key evacuation route for the population were located in the area that was at greatest risk. The volcanic eruptions, seismicity and ground movements contributed to uncontrolled outcome as shown in fig.11.

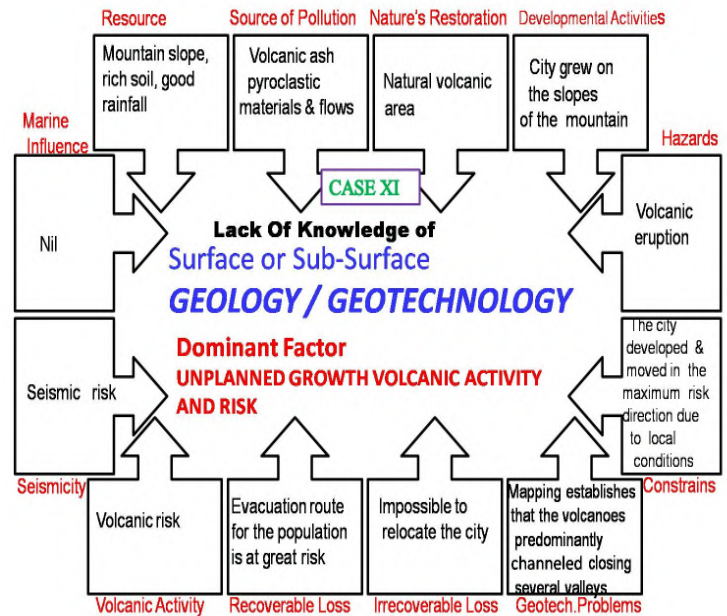


Fig.11

Many more examples could be cited throughout the world. These examples make clear the diversity of issues that may affect urban areas and the nature of the information that is needed to address them. The information comes from many sub-disciplines, some of which are rooted in Geoscience but others extend, to Ecology, Economics, Sociology, Architecture, and Archaeology. Multi-disciplinary studies are needed. In some cases communication may be straight forward but often there are barriers of unfamiliarity and technical complexity that can stand in the way of prompt and effective action. To achieve satisfactory results it is necessary to understand the implications of the Geology and Earth surface processes of the area and to explain them clearly in terms that can be understood widely. This needs adequate, easily accessible, and readily understood information, advice, guidance and training on how to deal with these issues.

5. LOWLAND CITIES AND THEIR ISSUES IN A COMPREHENSIVE TABLE

Table I Lowland cities and their issues

Example	Activity (MANMADE)	Basis of growth	Growth	Consequences
1.	Coal iron stone mining	Labour	Temporary growth	Damage to ground water aquifer, low river capacity, disappearance of natural springs
2.	Building castle, major local buildings	Heritage	The city expanded.	The remaining potential of building stones cannot be utilized because the city is above the stone reserves.
3.	Rail and Road Transport systems	Transportation	Rapid transport system	Flooding, run off water stagnant, no drainage system
4.	Land reclamation	Real estate, land value	Urban	Unstable geology, soil losses natural compaction
5.	Vertically down expansion (basement) near health resort	Tourism	Land use improved	Aquifers damaged, deterioration of public health
6.	Coal,gas and coke industries	Industrial	Urban	Water resources lost
7.	Chemical industries	Horizontal expansion	Expected growth but not sustainable	Ground water contamination, air pollution, land fill leakage
8.	Standing timber felling and timber products	Export	Economic	Loss due to floods, destruction of farm lands, damage to aquifers
9.	Construction of break water	Employment	Urban employment surge	Severe erosional problems, increasing dredging cost
10.	Civil works not keeping pace with need based growth	Urbanization	Growth with risk	River capacity reduced, subsidence of buildings, ground water loss
11.	Normal slope urban activity	Need based	Growth with risk	The city right on severe seismic zone with high risk.

The solution is “be wise at least after the event.” [1],[2],[3].

6. INFORMATION, GUIDANCE AND COMMUNICATION

The eleven city examples discussed bring together the need for coordination by authorities responsible for land use planning, environmental protection including catchment management, health and safety at work, and environmental health. In some cases land use and emergency planning are required to solve the problem. In some special cases shoreline management is also needed to regulate the activities.

In many cases the information necessary comes from many disciplines but main focus is on the Geosciences. Therefore the following are particularly relevant:

- 1). Resources – minerals, water, soils, landscape, good building land- types, extent, quality and significance (safeguarding and potential)
 - 2) Hazards and constrains – subsidence, slope instability, flooding, storms, natural and manmade contamination, erosion, volcanic activity, seismicity- types, extent and relative significance. Information is needed on all environmental issues that are relevant to a particular area at both the regional and more detailed levels.
- It is important that adequate basic Geological, Hydrogeological, Geomorphological, Geotechnical is undertaken at the strategic and more local level in order that applied outputs and modeling procedures can be securely based.

7. CONCLUSIONS

1. Traditionally Geosciences information has been presented on paper maps. These maps are essentially in two dimensional representations that can be interpreted in three dimensions by specialist users but not readily by non-specialists. Environmental and engineering Geology Mapping will help to overcome the barriers with some success.
2. The urban area has often been regarded as if it intrudes within and is therefore separate from the Eco-System. But in practice urban areas have major effects on their surroundings and processes in nearby areas have impacts on towns and cities. Therefore the urban area should be regarded as an integral part of the overall functioning of the Eco-System if environmental issues are to be properly analyzed and resolved.
3. There is a considerable diversity of environmental issues that have a Geosciences element and many problems involve multi-disciplinary consideration within a variety of management systems, often administered by different authorities.
4. These authorities often need to draw on the same body of knowledge with varying degrees of emphasis but they can only do so if they are aware of the relevant issues and significance and availability of the necessary information.
5. In practice, there is commonly a communication gap between various groups of administrators and specialists, as well as with the general public and politicians.
6. This arises partly from limitations on education in the Geosciences and a lack of dialogue and mutual learning.
7. A key aspect is for stakeholders to know who to ask, when to ask, and what to ask when problems arise.
8. A key to sound urban management is the compilation and maintenance of data bases not only for the urban area but also for its regional surroundings. These are particularly valuable if linked to GIS, Environmental information systems and software for modeling potential outcomes of possible decisions.
9. Experience shows that authorities are often unwilling to invest in research even though the outlay can lead to considerable savings in the future.
10. In addition it is often difficult to secure funds for maintenance of the data system. Few public authorities are equipped to do this even though the cost are very small compared with the development cost and the bill for putting problems right after the event.

8. REFERENCES

- [1]. Marker, B.R. (1996). Urban development – Identifying Opportunities and dealing with problems. In: McCall et al (Eds) pp 181-214.
- [2]. Brook D. and Marker B.R. (1998). Geomorphological Information needed for Environmental policy formulation In: Hook, J.M. (Ed) Geomorphology in Environmental policy J. Wiley (Chichester) pp 247-262.
- [3]. Igor S. Zektser Geology and Eco-systems, Springer (2006) pp 123 - 147

Lowland Environmental Geotechnology of Seismosediments of Kandla Port in India



J.RAJARAMAN¹ and K.THIRUVEKATASAMY²

ABSTRACT

The Gujarat coast in India is vulnerable to various natural disasters such as earthquakes, cyclones, tsunamis and agricultural droughts. The nearby main town on main land is Gandhidham. Kandla is located at a distance of about 4 km from Gandhidham. A 20 m wide road connects Gandhidham and Kandla. Geographically, Kandla could not be considered as a port because, there is water on almost 340° of this port. Kandla is almost an island. There is only one escape route via the bridge. In case the bridge gets damaged due to natural disasters, then there is no alternate route for rescue, evacuation and escape. At present huge amount of dredging is regularly being undertaken at the Kandla port. On an average about half million cubic meters of dredged materials is excavated, carried and is dumped in deep sea. In this paper an integrated approach to the clay behavior (including seismosediments) is considered mainly to relate cohesion and friction under different environmental conditions in lowlands, to shear strength by different types of clay.

Keywords: Lowlands, seismosediments, lateral earth pressure, clay minerals

1. INTRODUCTION

In flood affected lowland areas the loss of stability due to drastic variation in clay behavior and lateral pressure is a problem that needs separate treatment. The accumulated sediments due to huge amount of dredging adds more complications to the already existing problems. On an average about half million cubic meters of dredged materials is excavated, carried and is dumped in deep sea. The heterogeneity of the sediments is due to many factors in which seismosediments are one of the important factors.

1.1 Seismosedimentation And Seismosediments

Geological materials which are crushed, fractured, loosened or displaced directly or indirectly as a result of an earthquake induced processes such as landslides, landslips, slumps, mudflows, avalanches, liquefaction, rockfalls, rockslides, tsunamis and soils moved under gravity in the coastal areas or in the vicinity of the river are defined as seismosediments and the process is defined as seismosedimentation.

1.2 Textural Inversions

Textural inversions also cause mixing of different clay sediments to create more heterogeneity in soils. For example quartz Arenites are more poorly sorted and many contain high percentage of sub angular and angular grains. Some quartz Arenites exhibit textural inversions such as a combination of poor sorting and high rounding, a lack of correlation between roundness and size, such as small round grains and larger angular grains, or mixtures of rounded and angular grains within the same size fraction. These textural inversions probably result from mixing of grains from different sources, erosion of older sandstones, or environmental variables such

as floods, tsunamis and wind transport of rounded grains into a quiet water environment. Angular grains may result also from diagenetic development of secondary overgrowth.

1.3 Clay Minerals and Sediments

The dredged material in Kandla port consists of fine sandy clay or clayey sand. In these sediments mainly three types of clays are involved. They are Kaolinite, Illite and Montmorillonite. Due to the mixing factors discussed above the soil becomes highly heterogeneous. The Geotechnical properties vary from pocket to pocket in an erratic manner. A separate treatment of Geotechnical methods for coastal lowlands is necessary.

2. PROPERTIES OF CLAYS

Plastic property of clay is due to adsorbed water that surrounds the clay particles. This property is affected by type of clay minerals and their proportional amounts in a soil. The ultimate effect is that different clay soils possess different liquid and plastic limits.

2.1 Activity of Clay

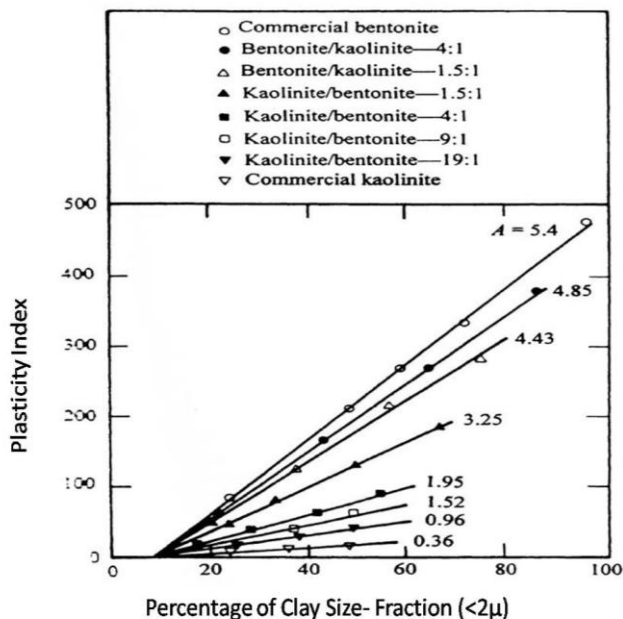
Skempton defined a quantity called Activity i.e. the slope of the line correlating PI (Plasticity Index) and percent finer than 2 μ therefore Activity A

$$A = \frac{PI}{(\text{percentage of clay size fraction, by weight})}$$

Seed and others studied the plastic property of several artificially prepared mixtures of Bentonite and Kaolinite. The results are shown in figure 1

TABLE I Activities Of Clay Minerals

MINERAL	ACTIVITY(A)
Smectites (Montmorillinite)	1 - 7
Illite	0.5 - 1
Kaolinite	0.5



Relationship between Plasticity Index and Clay size Fraction by Weight for Kaolinite / Bentonite clay mixtures.

Fig.1 [1]

2.2 Clay Minerals and Angle of Internal Friction ϕ

For normally consolidated clays cohesion $C = 0$. The equation of the Mohr – Coulomb failure envelope is given by $S = \sigma' \tan \phi$. Where ϕ is angle of internal friction and S is shear

strength . Then $\sin \phi = \frac{\sigma'_1 - \sigma'_3}{\sigma'_1 + \sigma'_3}$. (1)

The modified forms of Mohr's failure envelope for pure clay minerals are shown in the figure 2. In a consolidated drained test the total stress is equal to the effective stress, since the excess pore water pressure is zero. At failure, the maximum effective principal stress is $\sigma'_1 = \sigma_1 = \sigma_3 + \Delta\sigma_f$, where $\Delta\sigma_f$ is the deviator stress at failure. The minimum effective principal stress is $\sigma'_3 = \sigma_3$

The modified form of Mohr's failure envelope of pure clay minerals and quartz with typical values of ϕ is grouped as in Table II

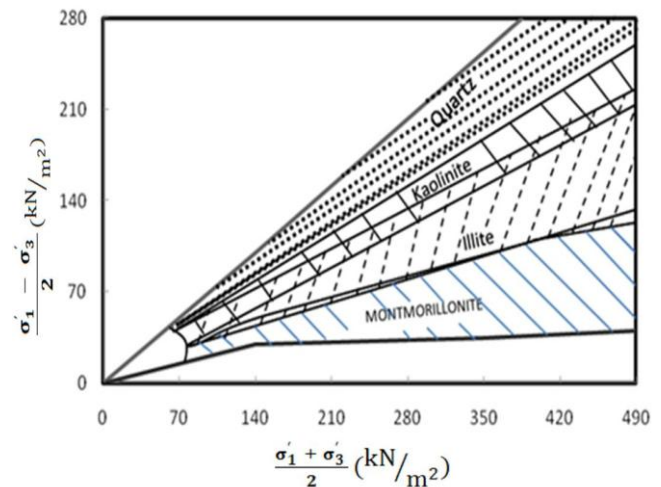


Fig.2 [2]

TABLE II

Variation of ϕ with Types of Clay Minerals

Sl.No:	MINERALS	TYPES	VALUES ϕ
1.	Clay Minerals : Montmorillonite Illite Kaolinite	Type 1	25 – 30
		Type 2	30 - 35
		Type 3	35 - 40
2.	Quartz	Type 4	40 - 45

2.3 The Random Nature of Clay

Kaolinite and Illite have nonexpansive lattices whilst that of Montmorillonite is expansive. There is no particular value of plastic limit that is characteristic of an individual clay mineral type. Similarly there is no single liquid limit which is characteristic of a particular clay mineral. The liquid limits for Illites fall in the range of 60 – 90 % whilst those for Kaolites vary from 30 -75%. The presence of 10% Montmorillonite in an Illitic or Kaolinitic clay can cause a substantial increase in their liquid limits. The plasticity indices of Na and Li Montmorillonite clays have exceedingly high values, ranging between 300 to 600 %. The Mohr-Coulomb envelope only indicates an ultimate shear strength value. It is the final compromised state of equilibrium of many random variables.

3. STRESS PATH AND LATERAL EARTH PRESSURE

Consider a normally consolidated clay specimen subjected to a consolidated drained triaxial test fig.3 (a). At any time during the test, the stress condition in the specimen can be represented by Mohr's circle as shown in fig.3(b). In a drained test, total stress is equal to effective stress so $\sigma_3 = \sigma'$ (minor principle stress).

$\sigma_1 = \sigma_3 + \Delta\sigma = \sigma'_1$ (major principal stress).

At failure, Mohr's circle will touch a line (Mohr-Coulomb failure envelope). This makes an angle ϕ with the normal stress axis.

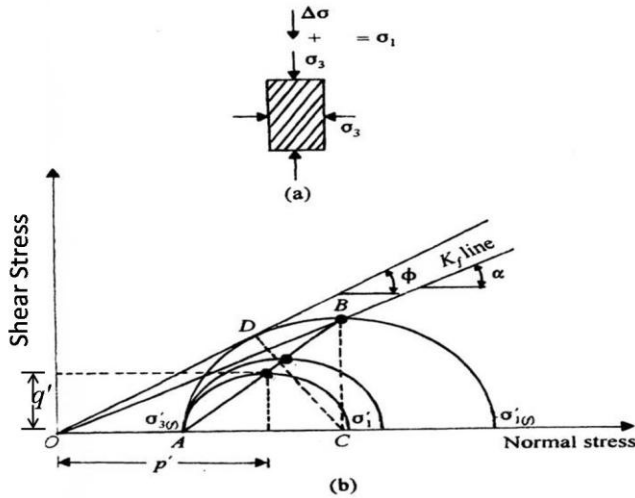


Fig.3 [3]

Now considering the effective normal and shear stresses on a plane making an angle of 45° with the major principal plane,

Effective normal stress,

$$p' = \frac{\sigma'_1 + \sigma'_3}{2} \quad (2)$$

Shear stress,

$$q' = \frac{\sigma'_1 - \sigma'_3}{2} \quad (3)$$

The points on Mohr's circle having coordinates p' and q' are shown in fig.3b. If the points with p' and q' coordinates of all the Mohr's circles are joined, will result in the line AB. The line is called a stress path. The straight line joining the origin and point B is defined here as the K_f line. The K_f line makes an angle α with the normal stress axis. Now

$$\tan \alpha = \frac{BC}{OC} = \frac{(\sigma'_{1(f)} - \sigma'_{3(f)})/2}{(\sigma'_{1(f)} + \sigma'_{3(f)})/2} \quad (4)$$

Where $\sigma'_{1(f)}$ and $\sigma'_{3(f)}$ are the effective major and minor principal stresses at failure.

Similarly,

$$\sin \phi = \frac{DC}{OC} = \frac{(\sigma'_{1(f)} - \sigma'_{3(f)})/2}{(\sigma'_{1(f)} + \sigma'_{3(f)})/2} \quad (5)$$

From equations (4) and (5), $\tan \alpha = \sin \phi$. (6)

4. SETTLEMENT CALCULATION USING STRESS PATH

From Lambe's stress path the following conclusions are made:

1. The stress paths for a given normally consolidated clay are geometrically similar, and

2. When the points representing equal axial strain say (ϵ_1) are joined, will be approximate straight lines passing through the origin. Now considering a soil specimen subjected to one dimensional consolidation type of loading we can write

$$\sigma'_3 = K_0 \sigma'_1 \quad (7)$$

This equation (7) is very important because it gives a relationship between σ'_1 , σ'_3 and the coefficient of earth pressure at rest (K_0). According to Jaky, $K_0 = 1 - \sin \phi$. This equation connects various types of clay and their respective angle of internal friction ϕ . From the following fig. 4 in the Mohr's circle the coordinates of point E is given by

$$q' = \frac{\sigma'_1 - \sigma'_3}{2} = \frac{\sigma'_1 (1 - K_0)}{2} \quad (8)$$

$$p' = \frac{\sigma'_1 + \sigma'_3}{2} = \frac{\sigma'_1 (1 + K_0)}{2} \quad (9)$$

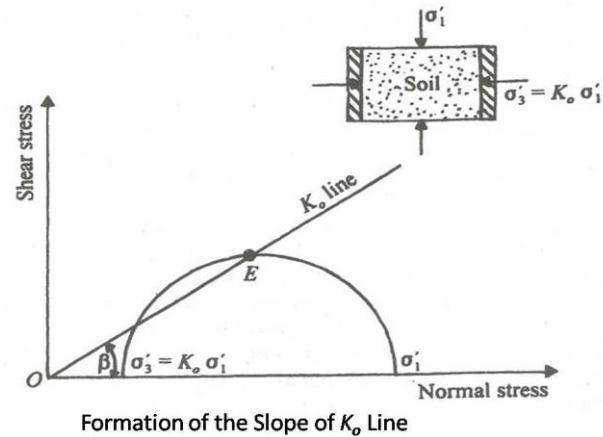


Fig.4 [3]

From the plot of p' versus q' with K_0 and K_f lines as shown in fig.5

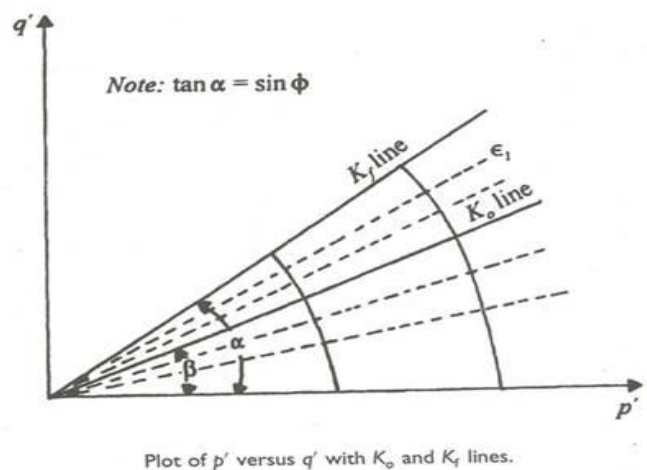


Fig 5 [3]

The angle

$$\beta = \tan^{-1} \left(\frac{q'}{p'} \right) = \tan^{-1} \left(\frac{1 - k_0}{1 + k_0} \right) \quad (10)$$

Where β is the angle that the line OE (K_0 line) makes with the normal stress axis.

5. KANDLA PORT ENVIRONMENT

The Kandla Port is surrounded on all sides by water. There are two creeks viz Nakti creek and the Kandla creek surround the port and there is water on about 340 degrees. At the Kandla end of the bridge, the two creeks almost meet one another. The above-mentioned route is the only connecting link between Kandla and Gandhidham.

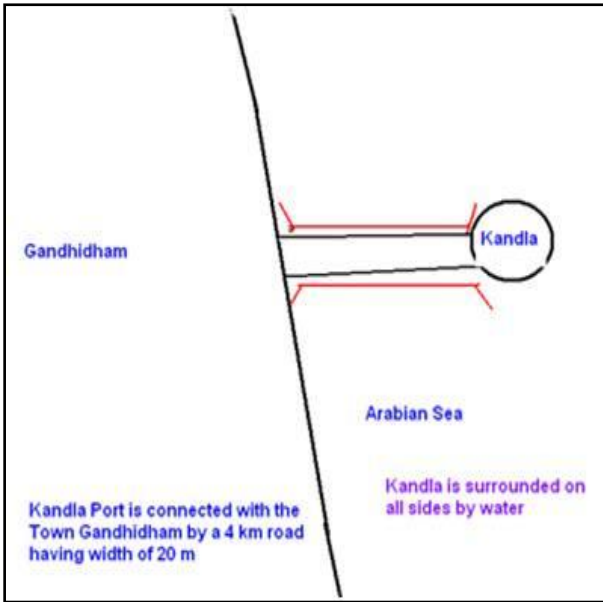


Fig 6 [4]

Arun Bapat suggested for a construction of vertical evacuation facility (VEF). Instead of dumping into the deep sea the dredged material could be used to build a vertical evacuation facility. A vacant and large area of about 100 sq.km is available at Kandla. This land is in S.W. direction and south of Khari creek. This is very near the port. This land can be used for VEF.

The facility will be a construction of small hill like structure with a shape of tapering conical or a flat top cone with one or two tops. For this purpose, retaining wall along the periphery of VEF will be required. A hillock of about 15 to 20 m high with a base of about 200 to 250 m diameter could accommodate about fifteen to twenty thousand people or more. The dredged material consists of fine sandy clay or clayey sand. This could be suitably compacted so that the structure will be in maximum stability conditions. It could have a wide ramp with gentle slope for rapid movement of large population. This ramp would be winding the small hillocks in serpentine way. Suitable shady trees could be planted at various terraces of the VEF so that it becomes stable. Construction of such VEF would help in saving several thousand lives in the case of tsunami attack at Kandla. According to the view of Arun Bapat the sketch of the VEF at Kandla will appear as shown in the fig.7

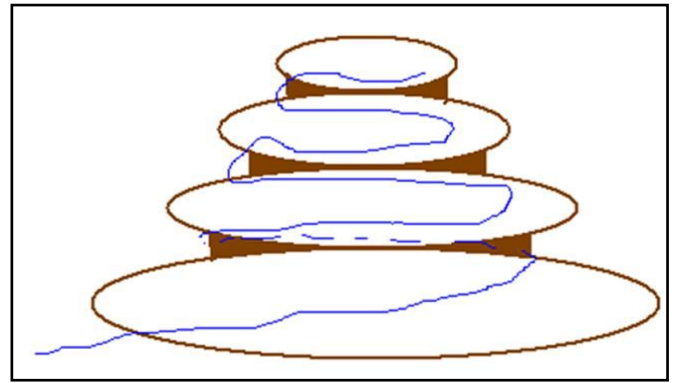


Fig.7 Sketch of VEF at Kandla [4]

6. THE ENVIRONMENTAL GEOTECHNICAL PROBLEMS

The environmental Geotechnical problems are highly complex. These problems are associated with seismosediments, dredged materials, clay minerals. Basically the dredged soils will show different soil characteristics than the natural soils with natural compaction. Therefore a detailed micro-studies related to soil mechanics alone will yield good solutions. The settlement calculation will clearly indicate the complex nature of the problems.

6. 1 Settlement Calculation

An illustrative example is shown in fig.8

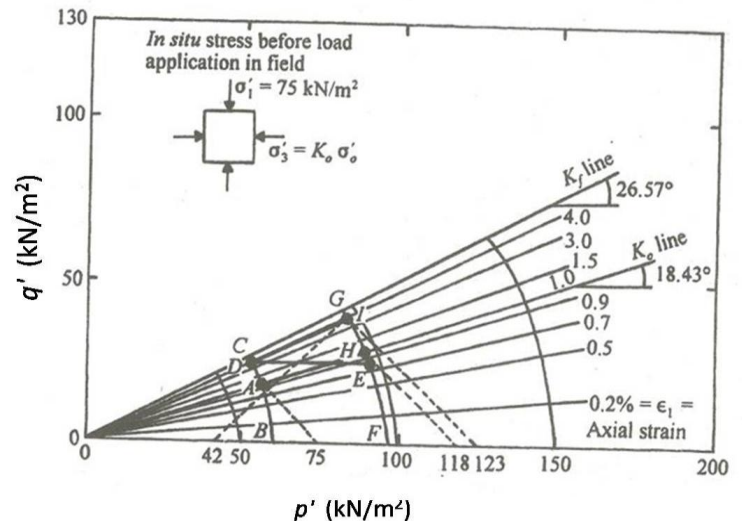


Fig.8 [5]

Fig.8 represents the stress – strain contours for a given normally consolidated clay specimen obtained from an average depth of a clay layer. Taking compression index $C_c = 0.25$ and e_0 and the drained friction angle ϕ as 30° and from equation (10),

$$\beta = \tan^{-1} \left(\frac{q'}{p'} \right) = \tan^{-1} \left(\frac{1 - k_0}{1 + k_0} \right)$$

And $k_0 = 1 - \sin \phi = 1 - \sin 30^\circ = 0.5$

$$\beta = \tan^{-1} \left(\frac{1 - 0.5}{1 + 0.5} \right) = 18.43^\circ$$

Knowing the value of β the k_0 line is formed as shown in fig. 8. Since $\tan \alpha = \sin \phi$, angle $\phi = 30^\circ$, $\tan \alpha = 0.5$. So $\alpha = 26.57^\circ$. The settlement is calculated for the clay layer from the following conditions :

1. Insitu average effective over burden pressure $\sigma'_1 = 75 \text{ kN/m}^2$.

2. Total thickness of clay layer $= H_t = 3 \text{ m}$

Owing to the construction of a structure, the increase of the total major and minor principal stresses at an average depth of $\Delta \sigma_1 = 40 \text{ kN/m}^2$
 $\Delta \sigma_3 = 25 \text{ kN/m}^2$

Assuming that the load is applied instantaneously. Insitu

minor principal stress at rest pressure is $\sigma_3 = \sigma'_3 = k_0 \sigma'_1 = 0.5(75) = 37.5 \text{ kN/m}^2$.

So before loading,

$$p' = \frac{\sigma'_1 + \sigma'_3}{2} = \frac{75 + 37.5}{2} = 56.25 \text{ kN/m}^2$$

$$q' = \frac{\sigma'_1 - \sigma'_3}{2} = \frac{75 - 37.5}{2} = 18.75 \text{ kN/m}^2$$

The stress conditions before loading can now be plotted in fig.8 from the above values of p' and q' . This point is A. Since loading is instantaneous(i.e., undrained), the stress conditions in clay represented by the p' versus q' plot immediately after loading, will fall on the stress path BCA.

Immediately after loading,

$\sigma_1 = 75 + 40 = 115 \text{ kN/m}^2$ and $\sigma_3 = 37.5 + 25 = 62.5 \text{ kN/m}^2$. So,

$$q' = \frac{\sigma'_1 - \sigma'_3}{2} = \frac{\sigma_1 - \sigma_3}{2} = \frac{115 - 62.5}{2} = 26.25 \text{ kN/m}^2$$

With this value of q' , we can locate point D. At the end of consolidation, $\sigma'_1 = \sigma_1 = 115 \text{ kN/m}^2$ $\sigma'_3 = \sigma_3 = 62.5 \text{ kN/m}^2$
 So,

$$p' = \frac{\sigma'_1 + \sigma'_3}{2} = \frac{115 + 62.5}{2} = 88.75 \text{ kN/m}^2$$

and $q' = 26.25 \text{ kN/m}^2$.

The preceding values of p' and q' are plotted as point E.

FEG is a geometrically similar stress path drawn through E.

ADE is the effective stress path that a soil element, at average depth of the clay layer, will follow. AD represents the elastic settlement, and DE represents the consolidation settlement.

For elastic settlement (stress path A to D),

$$s_g = [(\epsilon_1 \text{ at D}) - (\epsilon_1 \text{ at A})]H_t = (0.04 - 0.01) 3 = 0.09 \text{ m}$$

For consolidation settlement (stress path D to E), based on previous valid assumption the volume metric strain between D and E is the same as the volumetric strain between A and H. Note that H is on the k_0 line. For point A, $\sigma'_1 = 75 \text{ kN/m}^2$, and for point H, $\sigma'_1 = 118 \text{ kN/m}^2$. So the volumetric strain, ϵ_v

$$\epsilon_v = \frac{\Delta e}{1 + e_0} = \frac{C_c \log(118/75)}{1 + 0.9} = \frac{0.25 \log(118/75)}{1.9} = 0.026$$

The axial strain ϵ_1 along a horizontal stress path is about one-third the volumetric strain along the k_0 line, or

$$\epsilon_1 = \frac{1}{3} \epsilon_v = \frac{1}{3} (0.026) = 0.0087$$

So, the consolidation settlement is

$S_c = 0.0087 H_t = 0.0087(3) = 0.0261 \text{ m}$ and hence the total settlement is

$$S_e + S_c = 0.09 + 0.0261 = 0.116 \text{ m.}$$

7. CLAY AND LATERAL PRESSURE

In the following Table III the variation of k_0 , the lateral pressure and clay type is shown.

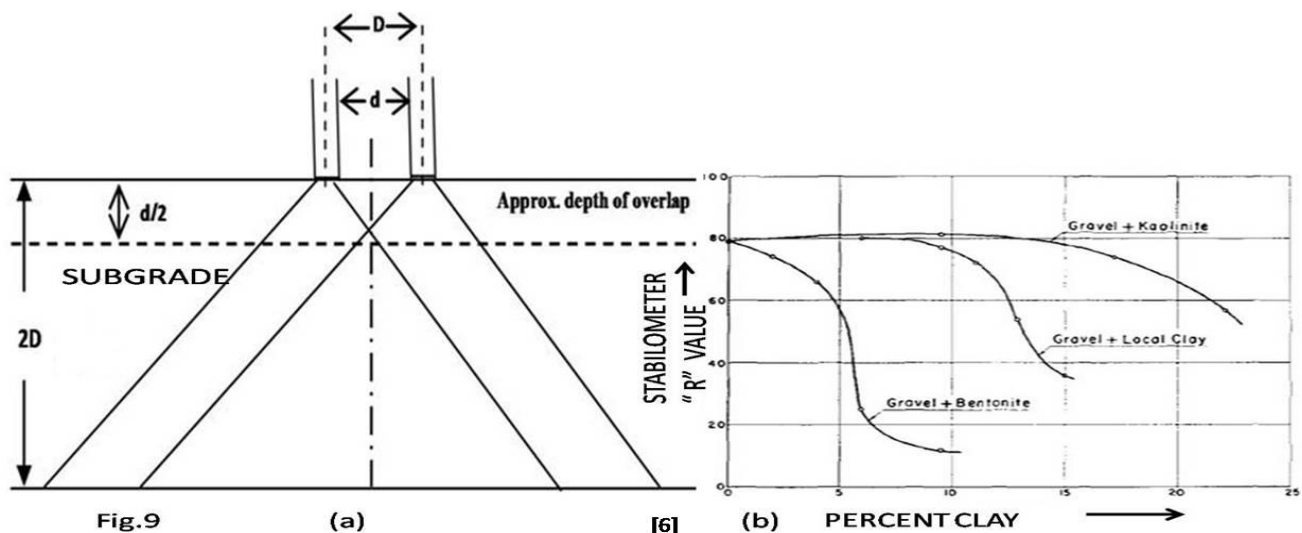
TABLE III

Sl. No	ϕ°	$\sin \phi$	$K_0 = 1 - \sin \phi$	Clay Type
1.	25	0.42	0.58	Montmorillonite
2.	30	0.50	0.50	Montmorillonite Illite
3.	35	0.57	0.43	Illite Kaolinite
4.	40	0.64	0.36	Kaolinite
5.	45	0.70	0.30	QUARTZ

K_0 values are different and therefore the settlement and differential settlement will be also different. The activity of each type of clay (Table I) will further complicate the problem in the presence of flood water. The clay Montmorillonite and its swelling potential will be a major problem.

8. IMPORTANCE OF CLAY IN APPLIED ENVIRONMENTAL GEOTECHNOLOGY

Interparticle friction is the principal property which permits soils and granular materials to resist load without formation. Dry soils of virtually all types are highly stable. The suitability of soils for engineering purposes depends largely upon their ability to remain in place and support whatever loads may be placed upon them, either by a permanent engineering structure or by transient vehicle loads. A study of the properties which distinguish the more satisfactory from the less satisfactory soils indicates that in the majority of cases clays are detrimental to stability. It is apparent that wet clay has the effect of a lubricant in diminishing the natural resistance due to friction that would otherwise exist. It is necessary that the civil engineer responsible for construction of any form of earth work should be informed not only concerning the Quantity of clay minerals that are present but also about their nature and their potential influence on the engineering properties of the soil.



Wheel load and subgrade

As the ability of soils to resist deformation depends very largely on the internal friction, wet clay has the effect of reducing or canceling out the frictional resistance. It may also be pointed out that the so-called cohesive resistance is induced almost entirely by the clay fractions, and therefore that clean sands are noncohesive. Again we must note the important part played by water, as finely ground dry clay particles exhibit no cohesive properties. If water is added to a dry soil, the cohesive resistance will normally increase with the addition of moisture and in most cases the frictional resistance will not be greatly impaired until a certain amount of moisture is added. Beyond this point, the friction will diminish but the cohesive resistance may continue to increase up to some point of higher moisture content, after which both values will diminish as the soil approaches a completely fluid state.

Metals are typical substances having little or no internal friction; in them, resistance values are almost entirely a result of the cohesive or tensile strength.

Fig. 9(a) shows wheel load and subgrade in road construction in lowland coastal area. Fig. 9(b) is a chart showing characteristic curves illustrating loss in stability or internal resistance of a crushed sandy gravel due to the addition of increments of plastic clay. The combined figures 9(a) and 9(b) clearly indicates the instability created by Montmorillonite (Bentonite), Illite (local clay), and Kaolinite in the presence of water. Bentonite fails first followed by Illite. Kaolinite is more stable.

9. CONCLUSIONS

1. Every port has its own Geological setup and environmental Geotechnology.
2. Seismosediments create heterogeneous nature to the soil. They represent accumulated disturbed samples.
3. The ϕ value for clay varies with type of clay.
4. Calculation of settlements by using strain methods reveals more intrinsic nature of clay behavior than stress oriented methods.

Stability and percent of clay

5. Increase in stability of a soil is not a function of cohesion and angle of internal friction alone because water introduces "turn around stages" and create instability especially in coastal area lowlands.
6. In a mixed sediments (seismosediments, flood sediments) a depth of 3m of clay (say Kaolinite 1m, Illite 1m and Montmorillonite 1m) KIM – will create 24 different Geotechnical sequences which in turn will increase the complexity of the Geotechnical problem. They are : KIM,MIK,IMK,KKK,III,MMM,KII,IKI,IKK,IKK,KIK,KKI,MII,IMI,IIM,KMM,MKM,MMK,KMI, IMM, MIM, MMI, MKI, IKM.
7. The final conclusion is that the construction techniques or site preparation should match with Geotechnical properties of different mixed types of clays.

10. REFERENCES

- [1] Seed, H.B., R.J. Woodward, & R. Lundgren, Clay Mineralogical Aspects Of The Atterberg Limits, J. Soil Mech. Found. Eng. Div., Am. Soc. Civ. Eng. Vol. 90, no. SM4, pp. 107- 131, 1964a.
- [2] Olson, R.E., Shearing Strength Of Kaolinite, Illite, And Montmorillonite, Geotech. Eng. Div., Am. Soc. Civ. Eng. Vol. 100, no. GT11, pp. 1215-1230, 1974.
- [3] Lambe, T.W., Methods Of Estimating Settlement, J. Soil Mech. Found. Div., Am. Soc. Civ. Eng., Vol. 90, no. 5, pp 43- 54, 1964
- [4] Arun Bapat Tsunamigenic Vulnerability of Kandla Port and use of Emergency Vertical Evacuation Facility, Pro. Nat. Conf. on Coastal Processes, Kerala, pp. 378-381
- [5] Braja M. Das Advanced Soil Mechanics, Taylor and Francis group Indian reprint 2010
- [6] Francis N. Hveem, Importance of Clay in Applied soil Mechanics, Clays and Clay Minerals; 1952 v. 1; no. 1; pp. 191-195;

Single-Step Extraction to Determine Soluble Lead Levels in Soil

Masahiko KATOH¹⁾, Satoshi MASAKI¹⁾, Takeshi SATO¹⁾

1) Department of Civil Engineering, Gifu University, Japan

ABSTRACT

This study investigated single-step extraction using EDTA to extract the amount of potentially soluble Pb in soil, which would be almost as much as that in the first four Pb fractions of Tessier's sequential extraction procedure (SEP), with or without the immobilization amendment hydroxyapatite under different extraction conditions such as concentration and extractant pH. The results clearly showed that 0.1M EDTA (pH 7.5) with a soil/extractant ratio of 1:100 can extract almost 90% of the first four Pb fractions of SEP, and EDTA-extracted Pb was positively correlated with the first four Pb fractions even in Pb-immobilized soil. In conclusion, single-step extraction using EDTA was found to be a useful method to evaluate potentially soluble Pb even in Pb-immobilized soils.

Keywords: EDTA, Immobilization, Pb-Contaminated Soil, Potentially Soluble Pb, Single-Step Extraction

1. INTRODUCTION

Heavy metal contamination, which is common in soil throughout the world, poses a potential risk to human and animal health owing to migration through soil profiles into groundwater. Therefore, various remediation techniques have been applied to reduce the mobility and bioavailability of heavy metals in soil.

To effectively remediate heavy-metal-contaminated soil, it is necessary to know the amount of toxic elements in the soil. However, only determining the total concentration of heavy metals in soil is not sufficient because mobility and bioavailability are strongly dependent on the chemical phases of heavy metals in soil [1], [2]. Therefore, determining the chemical forms of such heavy metals is especially important for chemical remediation such as in-situ immobilization and ex-situ soil-washing techniques.

Heavy metals in soil exist in various chemical forms including exchangeable, inorganic such as carbonates, bound to Fe/Mn oxide and organic matter, and retained in a clay mineral. Heavy metals bound to Fe/Mn oxide and organic matter, which are less mobilizable than exchangeable heavy metals, have the potential to solubilize with changes in soil conditions such as pH and oxidation-reduction. Therefore, to remediate contaminated soil, especially by using chemical remediation techniques, it is necessary to evaluate the amount of potentially soluble heavy metals including heavy metals bound to Fe/Mn oxide and organic matter as well.

A sequential extraction procedure (SEP) has been widely used to analyze the chemical phases of heavy metals in soil. Tessier's SEP divides the chemical phases into five fractions: exchangeable, carbonates, Fe/Mn oxide, organic matter, and residual [3]. The residual fraction should only be insoluble under natural environmental conditions, which suggests that the first four SEP fractions are possibly being solubilized by

ion-exchange and sorption/dissolution onto soil particles. However, SEP is not suitable for analyzing a large number of different contaminated soils because it is time consuming and the analytical technique requires special facilities.

Ethylenediaminetetraacetic acid (EDTA) is the most widely used chelating agent owing to its ability to form strong chelate complexes with many heavy metals. The extraction efficiency of EDTA, which is closely dependent on many factors of extractant such as its concentration and pH, and the types of contaminated soil [4]-[6], has been extensively studied to predict the mobility and bioavailability of heavy metals in contaminated soil [7], sediments [8]-[10], and wastes [7], [8] as well as to improve the efficiency of soil-washing techniques [6], [11]-[13]. However, only a few studies have compared the amount of heavy metal extracted with EDTA and the amount of each fraction of SEP [8]. It has not been determined whether EDTA can extract the first four fractions of Tessier's SEP. Moreover, EDTA extraction has never been applied to contaminated soil after the addition of an immobilization amendment that would alter the chemical phases of heavy metals in soil. To assess the effectiveness of the chemical remediation technique applied, it is important to be able to determine the amount of potentially soluble heavy metals in soil after chemical remediation.

The present study focused on Pb, which is one of the most toxic and prevalent heavy metal contaminants in Japan and throughout the world, and investigated single-step procedure using EDTA to extract potentially soluble Pb from soil. We speculated that the amount of potentially soluble Pb would be almost the same as the amount of Pb extracted in the first four fractions of Tessier's SEP. In conjunction with potentially soluble Pb, we also investigated whether the same result could be obtained after an immobilization amendment was added.

2. MATERIALS AND METHODS

2.1 Study area

This study was conducted at two shooting ranges: Tajimi and Nakatsugawa located in Gifu, Japan. The mean annual precipitation and temperature of both shooting ranges are 2200mm, 14°C, respectively and this area lies between 35° 20' 8" and 35° 28' 6" N and 137° 06' 5" and 137° 29' 2" E.

2.2 Soil Preparation and Characterization

The Pb-contaminated soils were collected from depths of 5–15 cm at both shooting ranges. At Tajimi, seven soil samples were collected at 3-m intervals from the shooting point where shooter fires a bullet toward the shooting direction. Table I shows the chemical properties of the Pb-contaminated soils collected at Tajimi (t) and Nakatsugawa (n). Sample t-1 was collected closest to the shooting point; sample t-7 was collected at a point farthest from the shooting point. The Tajimi samples used for chemical analysis were air-dried and passed through a 2-mm sieve without adding any immobilization amendments. One soil sample (n-1) was collected at Nakatsugawa. Hydroxyapatite (hereafter, HAp) was added to sample n-1 at a ratio of 1, 2.5, and 10% (w/w), hereafter, n-2, n-3, and n-4, respectively. After adding HAp, water was added to maintain a water holding capacity of 60%, and then the samples were incubated for 1 week. After incubation, the Nakatsugawa samples were also air-dried and passed through a 2-mm sieve prior to chemical analysis.

The water-extracted Pb and total Pb, Fe, Mn, and C contents of the Tajimi and Nakatsugawa soil samples were determined. The water-extracted Pb was determined by extraction with water at soil/water ratio 1:10. To obtain the total Pb, Fe, and Mn contents in soil, the soil samples were digested with HNO₃ and HCl using a microwave oven. All solutions were filtered with a 0.45-μm filter and analyzed for element concentrations by ICP-OES (ULTIMA 2, Horiba). The total C content in the soil was determined by CHO analyzer (JM10, J-SCIENCE LAB). These analyses were not performed on samples n-2, n-3, and n-4.

2.3 Determination of Lead Phases in Soil by Tessier's SEP

SEP was performed on the soil sample following the procedure described in [3]. 1.0 g of soil that has been passed through a 0.425-mm sieve was extracted with 25 mL of a 1 M MgCl₂ solution (exchangeable Pb). The soil remaining after the first extraction procedure was extracted with 25 mL of a 1 M sodium acetate solution with pH 5 (Pb carbonate). The soil remaining after the second extraction was further extracted with 20 mL of 0.04 M NH₂OH-HCl in 25% (v/v) HOAc in a 95 °C water bath with occasional agitation (Pb bound to Fe/Mn oxide). The soil remaining after the third extraction was extracted with 3 mL 0.02 M HNO₃ and 5 mL 30% H₂O₂ solution in an 85 °C water bath with occasional agitation. After 3 h of extraction, 5 mL 3.2 M NH₄OAc in 20% (v/v) HNO₃ was added and the soil was shaken for 20 min (Pb bound to organic matter). The remaining soil was digested with 5 mL HNO₃ and 2 mL HCl using a microwave oven (residual Pb) and diluted in a 50 mL measuring cylinder. After digestion was complete, the solution was passed through a 0.45-μm filter and analyzed for Pb concentration by ICP-OES.

2.4 Single-Step Extraction using EDTA

The effects of EDTA concentration, extractant pH, and soil/extractant ratio on the amounts of Pb extracted from soil were investigated using t-1, t-2, t-3, t-5, and t-7 to evaluate the amount of potentially soluble Pb by single-step extraction (SSE) with EDTA.

2.4.1 Concentration

10 mL of 0.5, 0.1, and 0.05 M EDTA (pH 7.5) was added to a 15 mL polypropylene tube containing 1.0 g soil samples t-1, t-2, t-3, t-5, and t-7 (1:10 soil/extractant ratio), and then, the tube was shaken for 1 h.

2.4.2 pH

10 mL of 0.1 and 0.05M EDTA adjusted to pH 3.5 using 1M HCl was added to a tube containing 1.0 g soil (1:10 soil/extractant ratio), and then, the tube was shaken for 1 h.

Table I Chemical properties of Pb-contaminated soils

No.	Sampling location	Amendment (Type/ratio(w/w))	Water-extracted Pb (mg/kg)	Total			
				Pb (mg/kg)	C ----- (g/kg)	Fe (g/kg)	Mn -----
t-1	Tajimi	-	0.4	91	8.8	35.8	1.7
t-2	Tajimi	-	0.5	229	19	32.6	1.6
t-3	Tajimi	-	0.7	1551	79	25.8	1.2
t-4	Tajimi	-	0.7	986	37	28.3	1.0
t-5	Tajimi	-	1.0	1341	58	21.0	1.0
t-6	Tajimi	-	1.3	2060	174	13.8	1.0
t-7	Tajimi	-	3.8	9289	135	24.8	6.4
n-1	Nakatsugawa	-	20.8	3966	6.0	30.4	6.0
n-2	Nakatsugawa	HAP/1%	N.A.*1	N.A.	N.A.	N.A.	N.A.
n-3	Nakatsugawa	HAP/2.5%	N.A.	N.A.	N.A.	N.A.	N.A.
n-4	Nakatsugawa	HAP/10%	N.A.	N.A.	N.A.	N.A.	N.A.

*1 Not Analyzed

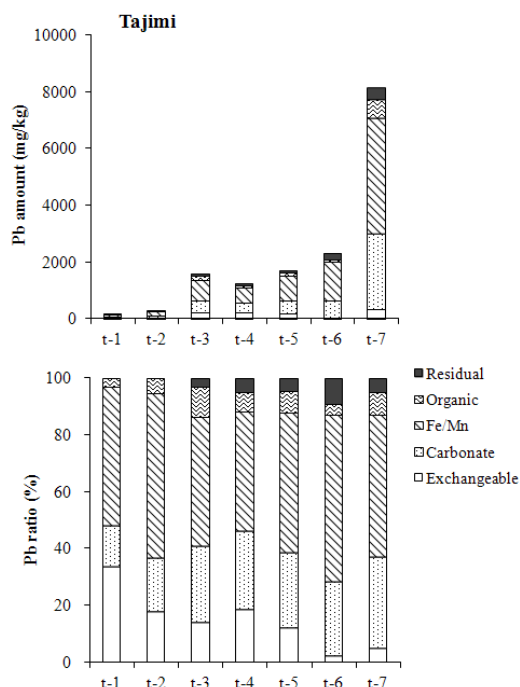


Fig. 1. Sequential extraction of Pb from Tajimi soil

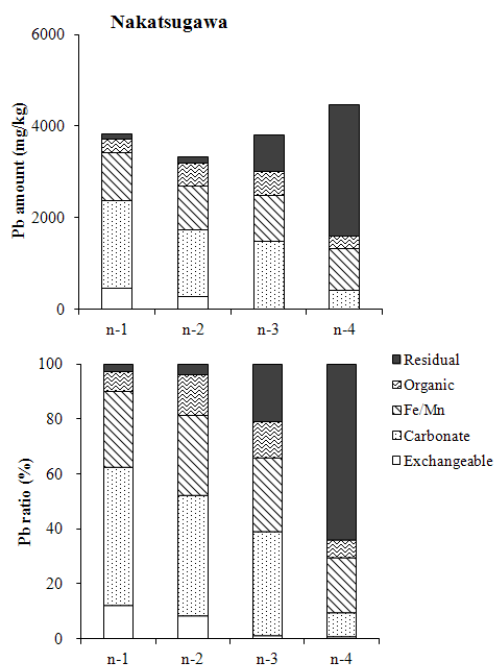


Fig. 2. Sequential extraction of Pb from Nakatsugawa soil.

2.4.3 Soil/Extractant Ratio

100 mL of 0.1 and 0.05M EDTA (pH 7.5) was added to a 100mL tube containing 1.0 g soil (1:100 soil/extractant ratio), and then, the tube was shaken for 1 h. After shaking, all solutions were passed through a 0.45-μm

filter and analyzed for Pb concentration by ICP-OES. All experiments were performed in triplicate, and the average values were calculated.

The extraction ratio in this study, defined as the ratio of EDTA-extracted Pb to the first four fractions of Tessier's SEP, was calculated according to the following equation:

$$R\% = \frac{Pb_{SSE}}{Pb_{SEP}} \times 100 \quad (1)$$

where Pb_{SSE} (mg/kg) is the amount of EDTA-extracted Pb and Pb_{SEP} (mg/kg) is the amount of the first four fractions of Tessier's SEP.

EDTA-extracted Pb of the t-4, t-6 samples was determined by extraction with 0.1M EDTA (pH 7.5) at a soil/extractant ratio of 1:100 following the procedure described above.

2.5 Single-Step Extraction using EDTA on Immobilized Soil

Based on the results obtained in the procedures described in Section 2.4, the extraction with 0.1M EDTA (pH 7.5) at a soil/extractant ratio of 1:100 would be suitable to predict potentially soluble Pb in soil. Moreover, the suitability of SSE for Pb-immobilized soils amended with HAp, which would gradually alter the amount of the residual Pb fraction in SEP, was investigated following the procedure described above.

3 RESULT AND DISCUSSION

3.1 Soil Chemical Properties

The water-extracted Pb and total Pb, C, Fe, and Mn contents in the soil used in this study are shown in Table I. The amount of the water-extracted Pb in Tajimi soil tended to increase with the distance from the shooting point. The amount of the water-extracted Pb in both Tajimi and Nakatsugawa soils exceeded environmental standards for soil contamination in Japan. The total Pb content in Tajimi soil was the lowest for t-1 and then increased gradually with the distance from the shooting point. This increase in the total Pb content might be attributed to the different number of Pb bullets that landed on the soil. From the evidence that the total Pb content in t-7 exceeded 9000 mg/kg, it was considered that heavy Pb contamination has occurred in Tajimi soil. The total C contents in t-6 and t-7 (135–174 mg/kg) were higher than those in t-1 to t-5 (8.8–79 mg/kg). The total Fe content ranged from 13.8 to 35.8 mg/kg. The total Mn content in t-7 was 6.4 mg/kg and was higher than that in the other samples. The water-extracted Pb and total Pb content in Nakatsugawa soil were 20.8 and 3966 mg/kg, respectively. The total Pb content was lower than that in t-7, whereas the water-extracted Pb was higher. This probably resulted from the difference between the Pb phases in Tajimi and Nakatsugawa soils. This result will be discussed in greater detail in the following section.

From these results, it was confirmed that the soils used in this study had different chemical properties such as

Table II EDTA-extracted Pb and extraction ratio under different conditions.

Table 1: EDTA-Extracted Pb and extraction ratio under different conditions.											
	Concentration	pH	S/E ratio	EDTA-extracted Pb					Ave.	S.D.	C.V.
				t-1	t-2	t-3	t-5	t-7			
				----- (mg/kg) -----							
EDTA-extracted Pb (a)	0.5 M	7.5	1:10	43	175	1029	1096	6552			
	0.1 M	7.5	1:10	59	203	1214	1554	8747			
	0.05 M	7.5	1:10	68	198	1271	1375	7713			
	0.1 M	3.5	1:10	68	210	1342	1650	8253			
	0.05 M	3.5	1:10	83	245	1466	1797	8493			
	0.1 M	7.5	1:100	138	365	1130	1100	6796			
	0.05 M	7.5	1:100	141	180	755	1040	7501			
First four fractions of SEP. ^{*1} (b)				156	268	1529	1631	7705			
Extraction ratio ^{*2}	0.5 M	7.5	1:10	27	65	67	67	85	62.4	21.3	34.1
	0.1 M	7.5	1:10	38	76	79	95	114	80.4	28.0	34.8
	0.05 M	7.5	1:10	43	74	83	84	100	77.0	21.0	27.3
	0.1 M	3.5	1:10	44	79	88	101	107	83.6	25.0	29.9
	0.05 M	3.5	1:10	53	92	96	110	110	92.2	23.3	25.3
	0.1 M	7.5	1:100	88	137	74	67	88	90.9	27.1	29.8
	0.05 M	7.5	1:100	90	67	49	64	97	73.6	19.8	26.9

*1: Pb amount of first four fractions of SEP

*2: (b)/(a)*100

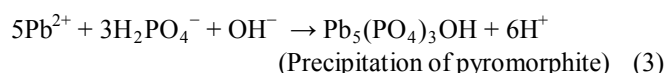
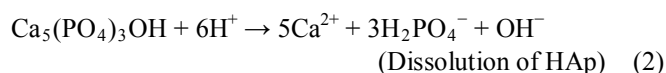
water-extracted Pb and total Pb, C, Fe, and Mn contents.

3.2 Lead Phases in Soil by Tessier's SEP

Figs. 1 and 2 show the results of Pb fractions in Tessier's SEP for Tajimi and Nakatsugawa soils, respectively. In both figures, the upper and lower graphs show the amount and ratio of the Pb fraction, respectively. The average recovery ratio, defined in this study as the ratio of the total amount from SEP to the total amount of Pb amounts in the soil shown in Table I, was 110±22%.

The ratio of the Pb fraction in Tajimi soil was the highest in the fraction bound to Fe/Mn oxide and ranged from 42 to 59%; the second highest was in carbonate ranged from 15 to 32%. In contrast, the highest ratio of Pb fraction in Nakatsugawa soil was carbonates; it was around 50% in n-1 with no added immobilization amendments. The amount and ratio of exchangeable Pb in n-1 were 460 mg/kg and 12%, respectively, although those in t-1 were 355mg/kg and 4%, respectively. In spite of a lower total Pb content in n-1 than in t-7, the water-extracted Pb in n-1 was higher than that in t-7, which probably resulted from the greater amount of exchangeable Pb in n-1 than in t-7.

The residual fractions in n-3 and n-4, where HAp was applied at 2.5% and 25% (w/w), respectively, were significantly increased, although the composition of the Pb fraction in n-2, where HAp was applied at 1% (w/w), was not significantly different from that in n-1. It is widely known that adding HAp to Pb-contaminated soil probably results in the precipitation of Pb phosphate minerals such as pyromorphite ($\text{Pb}_5(\text{PO}_4)_3\text{X}$: X = OH, Cl, F) by immobilizing Pb in the contaminated soil according to the following reactions [14], [15]:



Pyromorphite has a lower solubility product constant at $\log K_{sp} = -25.05$ [16] and is probably included in the residual fraction of SEP. From this consideration, pyromorphite might be precipitated by HAp to increase the residual fraction in n-3 and n-4. On the other hand, the low percentage of HAp added in n-2 probably caused no difference in the Pb composition between n-1 and n-2.

From these results, it was confirmed that the soils used in this study had significant differences in the amount and composition of Pb phases.

3.3 Single-Step Extraction by EDTA

3.3.1 Concentration

The EDTA-extracted Pb and extraction ratio are shown in Table II. The extraction ratios for all concentrations tended to be lower at distances closer to the shooting point. It is widely accepted that EDTA forms stable complexes with many heavy metals. Therefore, EDTA can extract Pb sorbed to Fe/Mn oxide and organic matter in soil as well as inorganic Pb compounds such as Pb carbonate. However, Palma and Mecozzi [10] reported that it was more difficult to extract the exchangeable form compared with other phases. Hence, the extraction ratio in Tajimi soil might be decreased at distances closer to the shooting point owing to a higher ratio of exchangeable Pb. In addition, the extraction ratio for 0.5M

EDTA was not higher than that for 0.1 and 0.05M EDTA. samples were 90.9 ± 27.1 and $73.6 \pm 19.8\%$ for 0.1 and 0.05M

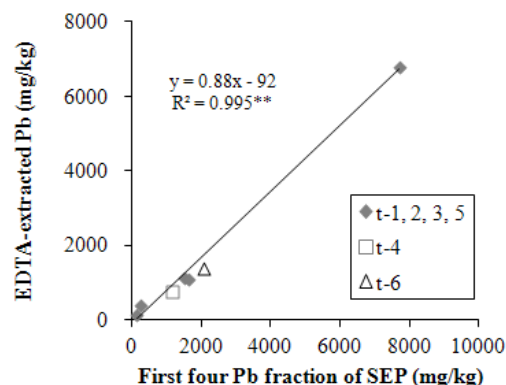


Fig. 3. Relationship between first four Pb fractions of SEP and EDTA-extracted Pb in Tajimi soil.

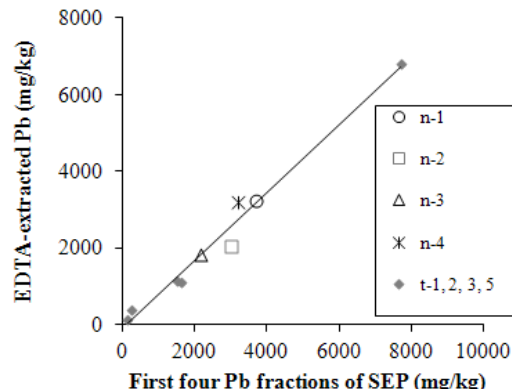


Fig. 4. Relationship between first four Pb fractions of SEP and EDTA-extracted Pb in Nakatsugawa soil.

Table III EDTA-extracted Pb and extraction ratio in Nakatsugawa soil

No.	EDTA-extracted Pb (a)	First four fractions of SEP ^{*1} (b)	Extraction ratio ^{*2}
	-----	(mg/kg) -----	(%)
n-1	3246	3701	88
n-2	2039	2996	68
n-3	1835	2151	85
n-4	3190	3183	100
Ave.			85.3
S.D.			13.2
C.V.			15.5

*1: Pb amount of first four fractions of SEP

*2: (b)/(a)*100

According to Elliott and Brown [5], the extraction ratio would not become greater above a certain concentration. Moreover, Finzgar and Lestan [6] revealed that EDTA extraction efficiencies decreased as the molar ratio of EDTA to total Pb in soil increased. From these results, it was considered that 0.1 and 0.05M EDTA should be suitable for the extraction of potentially soluble Pb in soil. Therefore, 0.5M EDTA was not used in the following investigation.

3.3.2 pH

SSE using EDTA was performed again with pH changed to 3.5 (Table II). Although compared with that at pH 7.5, the extraction ratio at pH 3.5 was improved for all samples, the ratio especially in t-1 was still low at 44% and 53% for 0.1 and 0.05M EDTA (pH 3.5), respectively. To perform a simplified analysis rapidly in the field, it is certainly recognized that a neutral pH range is suitable for extractant pH. From these results, it was proposed that an extractant pH of 7.5 would be suitable.

3.3.3 Soil/Extractant Ratio

SSE using EDTA was performed again with the soil/extractant ratio changed to 1:100 (Table II). Compared with the results obtained above, the extraction ratio for 0.1 and 0.05M EDTA (pH 7.5) was improved even in t-1 at 88% and 90%, respectively. The average extraction ratios of five

EDTA (pH 7.5), respectively, and it appears that 0.1M EDTA (pH 7.5) with soil/extractant ratio 1:100 may extract potentially soluble Pb in soil. This extraction condition is consistent with that for the soil-washing technique proposed by Garrabrants and Kosson [7].

Fig. 3 shows the relationship between the amounts of 0.1M EDTA-extracted Pb with pH 7.5 and soil/extractant ratio 1:100 and the amount of the first four Pb fractions of SEP. The relationship calculated using the software JMP 8 could be expressed as follow: $y = 0.88x - 92$ $R^2 = 0.995^{**}$, where y (mg/kg) is the total Pb in the first four fractions of SEP and x (mg/kg) is the EDTA-extracted Pb. The slope of the line was 0.88, suggesting that 0.1M EDTA can extract almost 90% of the first four Pb fractions of SEP.

The EDTA extraction was performed for the t-4 and t-6 samples under the same conditions, and the results could be represented by the equation presented above (Fig. 3). These results indicated that 0.1M EDTA (pH7.5) with soil/extractant ratio 1:100 can extract almost 90% of the first four Pb fractions of SEP.

3.4 Single-Step Extraction of Pb from Immobilized Soil with EDTA

Immobilized Nakatsugawa soil samples were extracted with 0.1M EDTA (pH 7.5) with soil/extractant ratio 1:100 (Table III). The average extraction ratio was $85.3 \pm 13.2\%$ regardless

of the amount of HAP amended and was approximately the same as that for Tajimi soil. If the results of the Nakatsugawa soil samples are plotted in the same manner as shown in Fig. 3, the amounts of EDTA-extracted Pb can also be represented by the same equation for the Tajimi soil samples (Fig. 4). These results suggested that it would be possible to extract potentially soluble Pb in spite of different kinds of soils and the addition or non addition of immobilization amendment. In addition, pyromorphite, which would be precipitated with the addition of HAP, would remain in soil without dissolution and/or complexation with EDTA owing to its very low solubility.

In this study, we have used only two kinds of soils and one type of amendment. Further investigation should consider more types of soil and amendment. Moreover, it is desirable to improve the extraction ratio up to approximately 100%. However, this study did suggest that it would be possible to extract potentially soluble Pb even in immobilized soil with EDTA.

4 CONCLUSION

This study investigated single-step extraction using EDTA of potentially soluble Pb that could be almost as much as the amount of Pb in the first four fractions of Tessier's SEP. In conjunction with potentially soluble Pb, we also investigated whether the same result could be obtained after the addition of an immobilization amendment. The results obtained in this study were mainly as follows:

- 1) EDTA extraction under different extraction conditions from soils having different total Pb amounts and different Pb phase compositions was investigated. The results clearly showed that 0.1M EDTA (pH 7.5) with soil/extractant ratio 1:100 can extract almost 90% of the first four Pb fractions of SEP, and EDTA-extracted Pb was positively correlated with the first four Pb fractions of SEP.
- 2) The soils with immobilized Pb using HAP were extracted using 0.1M EDTA (pH 7.5) with soil/extractant ratio 1:100. The results showed that the amount of EDTA-extracted Pb was also almost 90% of the amount of the first four Pb fractions and could be represented by the same equation as that of the non amended soils.
- 3) In conclusion, single-step extraction using EDTA was found to be a useful method to evaluate potentially soluble Pb even in Pb-immobilized soils.

5 ACKNOWLEDGMENT

The ICP-OES and CHO analyzer instruments used for chemical analysis in this study were made available by the Division of Instrumental Analysis at Gifu University.

6 REFERENCES

- [1] Brown S, Chaney R, Hallfrisch J, Ryan J A, Berti W R, "In situ soil treatments to reduce the phyto- and bioavailability of lead, zinc, and cadmium," *J. of Environ. Qual.*, vol. 33, 2004, pp. 522-531.
- [2] Arnich N, Lanhers M C, Laurensot F, Podor R, Montiel A, Burnel D, "In vitro and in vivo studies of lead immobilization by synthetic hydroxyapatite," *Environ. Pollut.*, vol. 124, 2003, pp. 139-149.
- [3] Tessier A, Campbell P G C, Bisson M, "Sequential extraction procedure for the speciation of particulate trace metals," *Anal. Chem.*, vol. 51, 1979, pp. 844-851.
- [4] Karamanos R E, Bettany J R, Rennie D A, "Extractability of added lead in soils using lead-210," *Can. J. Soil Sci.*, vol. 56, 1976, pp. 37-42.
- [5] Elliott H A, Brown G A, "Comparative evaluation of NTA and EDTA for extractive decontamination on Pb-polluted soils," *Wat. Air Soil Pollut.*, vol. 45, 1989, pp. 361-369.
- [6] Finzgar N, Lestan D, "Multi-step leaching of Pb and Zn contaminated soils with EDTA," *Chemosphere*, vol. 66, 2007, pp. 824-832.
- [7] Garrabrants A C, Kosson D S, "Use of a chelating agent to determine the metal availability for leaching from soils and wastes," *Waste Manag.*, vol. 20, 2000, pp. 155-165.
- [8] Cid B P, Gonzalez M J, Gomez E F, "Comparison of single extraction procedures, using either conventional shaking or microwave heating, and the Tessier sequential extraction method for the fractionation of heavy metals from environmental samples," *Analyst*, vol. 127, 2002, pp. 681-688.
- [9] Barreto S R G, Nozaki J, Oliveira E D, Filho V F D N, Aragao P H A, Scarminio I S, Barreto W J, "Comparison of metal analysis in sediments using EDXRF and ICP-OES with the HCl and Tessie extraction methods," *Talanta*, vol. 64, 2004, pp. 345-354.
- [10] Palma L D, Mecozzi R, "Heavy metals mobilization from harbour sediments using EDTA and citric acid as chelating agents," *J. Hazard. Mater.*, vol. 147, 2007, pp. 768-775.
- [11] Sun B, Zhao F J, Lombi E, McGrath S P, "Leaching of heavy metals from contaminated soils using EDTA," *Environ. Pollut.*, vol. 113, 2001, pp. 111-120.
- [12] Steele M C, Pichtel J, "Ex-situ remediation of a metal-contaminated superfund soil using selective extractants," *J. Environ. Eng.*, vol. 124, 1998, pp. 639-645.
- [13] Peter R W, "Chelant extraction of heavy metals from contaminated soils," *J. Hazard. Mater.*, vol. 66, 1999, pp. 151-210.
- [14] Mn Q Y, Traina S J, Logan T J, "In situ lead immobilization by apatite," *Environ. Sci Technol.*, vol. 27, 1993, pp. 1803-1810.
- [15] Ma Q Y, Longan T J, Traina S J, "Lead immobilization from aqueous solutions and contaminated soils using phosphate rocks," *Environ. Sci. Technol.*, vol. 29, 1995, pp. 1118-1126.
- [16] Miretzky P, Fernandez-Cirelli A, "Phosphate for Pb immobilization in soils: a review," *Environ. Chem. Lett.*, vol. 6, 2008, pp. 121-133.

Biogas Production from Tannery Sludge

A.Rajendra Prasad, A.Dhanalakshmi, S.Usha and A.Abdul Rahman
Sri Sai Ram Engineering College, Chennai, India.

1.ABSTRACT

The present study was conducted using Pilot plant scale Bio gas generator in CETP at Chennai during 2012. Bio-gas was generated using two sintex tanks-anaerobic digestion chamber and floating gas holder respectively. Cow-dung was used initially to generate biogas, supplemented by tannery sludge. The sludge generated from the Tannery effluent treatment plant is pre-digested using extremophiles and the slurry is used as a feed to generate biogas.

Qualitative and quantitative analysis of biogas were performed. The processed sludge was fed into the biogas chamber to optimise the emission of biogas. Daily production/emission of biogas is being monitored. The Pilot plant now produces 700 litres of bio-gas and the continuous burning time is 2 hours. The biogas is useful as a fuel substitute being non-polluting, renewable and CO₂ neutral.

There is no simple treatment to purify contaminated or polluted air. It is therefore necessary to reduce the pollutant load in the air at the source itself. Methane which contains the other gases such as CO₂, NH₃ and H₂S are now treated and the efficiency of methane is also increased.

2. INTRODUCTION:

In tanneries, various types of solid wastes are generated from the effluent treatment plant such as soak liquor, lime liquor and chrome liquor. Among these effluents, soak liquor forms the organic wastes predominantly constituting the flesh, albumen, dung and particularly the salts.

However, it is the lime liquor which contributes as primary and secondary sludges are being the major portion of the solid waste need proper treatment and disposal.

However, in the case of chrome liquor, there is recovery of chromium and being recycled and hence it is not taken into consideration.

In the case of primary and secondary sludges the disposal becomes major concern. In addition to the sludge, there is considerable amount of lime flesh which is generated as solid waste. The lime flesh after proper washing of the lime in the flesh is used for the biomethanisation.

Solid waste, emanating from the tannery effluent treatment plant, is the primary sludge. About 40% of this is organic matter. It is an appropriate source for conversion into biogas. A substantial quantity of sludge from tannery effluent treatment plant is currently disposed in either safe landfills or dumped in the vacant lands, again causing an environmental hazard.

3. OBJECTIVES:

The objectives of this initiative are,

To evaluate the technology for generation of biogas from primary sludge from a Tannery Effluent treatment plant under conditions prevailing in the CETP at Pallavaram, Chennai.

To evaluate the quality and volume of gas produced with reference to raw material fed.

To obtain relevant data for assessing the consumption of gas produced and to initiate the treatment of biogas in order to increase the methane.

The overall solid waste generation from Tanneries is 59.3%. Out of this the fleshing constitutes 13.9%.

3. MATERIALS AND METHODS:

Fabrication of Bio-gas pilot Plant requires two Sintex tanks having 1000 litre capacity with diameter of 110cm as fermenter and 750 litre capacity with diameter of 103cm as gas holder. The top portion of the tanks have been removed to accommodate the small tank of 750 litre capacity into big tank of 1000 litre capacity.

Two holes in the bottom and one in the top of the fermenter tank have been made and appropriate PVC pipe lines have also been provided. The bottom pipe serves to remove the sludge in case of heavy accumulation of sludge. Another hole is made with 90mm capacity through which inlet pipe has been provided. In top portion of the fermenter another hole is provided with outlet to remove excess amount of waste water.

The 750 litre capacity tank is provided with the gas holder with a PVC pipe with holes inside pipe for emission of gas through the pipe line from the gas holder and to the burner.

3.1 METHODOLOGY

During the initial stage of installation, the biogas started accumulating in the gas holder. Daily record of increase in the volume of biogas was also noted on the outer surface of the gas holder. When 75% of the gas holder is raised, the gas was also tested. It is determined that 1000 litre fermentation tank, with 750 litre gas holder will have 700 litre of biogas which can be used as a fuel for 2hrs. The process is now monitored. The outlet gas showed blue flame when external oxygen is mixed with it.

3.2 PREDIGESTION OF TANNERY SLUDGE

Tannery sludge was collected from the primary settling tank and was used as the primary source of energy for the biogas production. However, during the study, sludge was also collected from the secondary and tertiary settling tanks and the Carbon-Nitrogen ratio was evaluated for selecting the primary sludge for the purpose.

The same primary sludge was also converted as compost in view of its nitrogen source. Taking this into consideration the primary sludge was fermented using Bacterial consortium. The bacterial consortium was produced from the culture of the cow dung as the raw material and the molasses was used as a medium to culture the bacteria.

The bacterial consortium consists of various types of anaerobes are used for the present study to make the sludge into semi solid and slurry like organic biomass. This was fed into the biogas chamber. Initially, 4 litres of slurry was introduced into the chamber followed by 10 litres of chlorine-free water. However, after ten days of trial, the feed material was increased to 10 litres and consistent production of biogas was obtained. Therefore, adding slurry to the bio-gas plant was standardized.

The tannery sludge is used effectively to produce biogas in pilot plant scale. This reduces the dumping of solid waste, minimize solid waste generation, recycling of tannery sludge. The biogas generation encourages to produce biogas fuel utilizing huge quantity of tannery sludge waste effectively. The biogas was collected, separated and purified.

3.3 PRINCIPLE OF BIOMETHANATION:

Anaerobic or methane formation is brought about by extremophile -complex bacteria.

The various forms of degradation of complex organic matter in the various anaerobic process go through three distinct phases namely,

Hydrolysis and acidogenesis phase.

Acetogenesis phase.

Methanogenesis phase.

The first phase is performed by hydrolysis and results in a mixture of volatile fatty acids, neutral compounds such as ethanol and gaseous products such as CO_2 and hydrogen.

The acetogenesis phase refers to acetate production and is brought about by bacteria, which produce hydrogen. Thus this phase is sensitive to the presence of hydrogen.

Methane – producing micro-organisms bring about the methanogenesis are denitrifiable. In the first, hydrogen and CO_2 form water and methane. In the second, acetate is broken down into CO_2 and CH_4 .

It is the second method, which produces about 70% CH_4 .

The composition of gas generated depends on the composition of the substrate and conditions of operation. Gas production is the simplest criterion to measure the quality of digestion and it depends on two main factors namely temperature and retention time.

4. PROCESS FLOW:

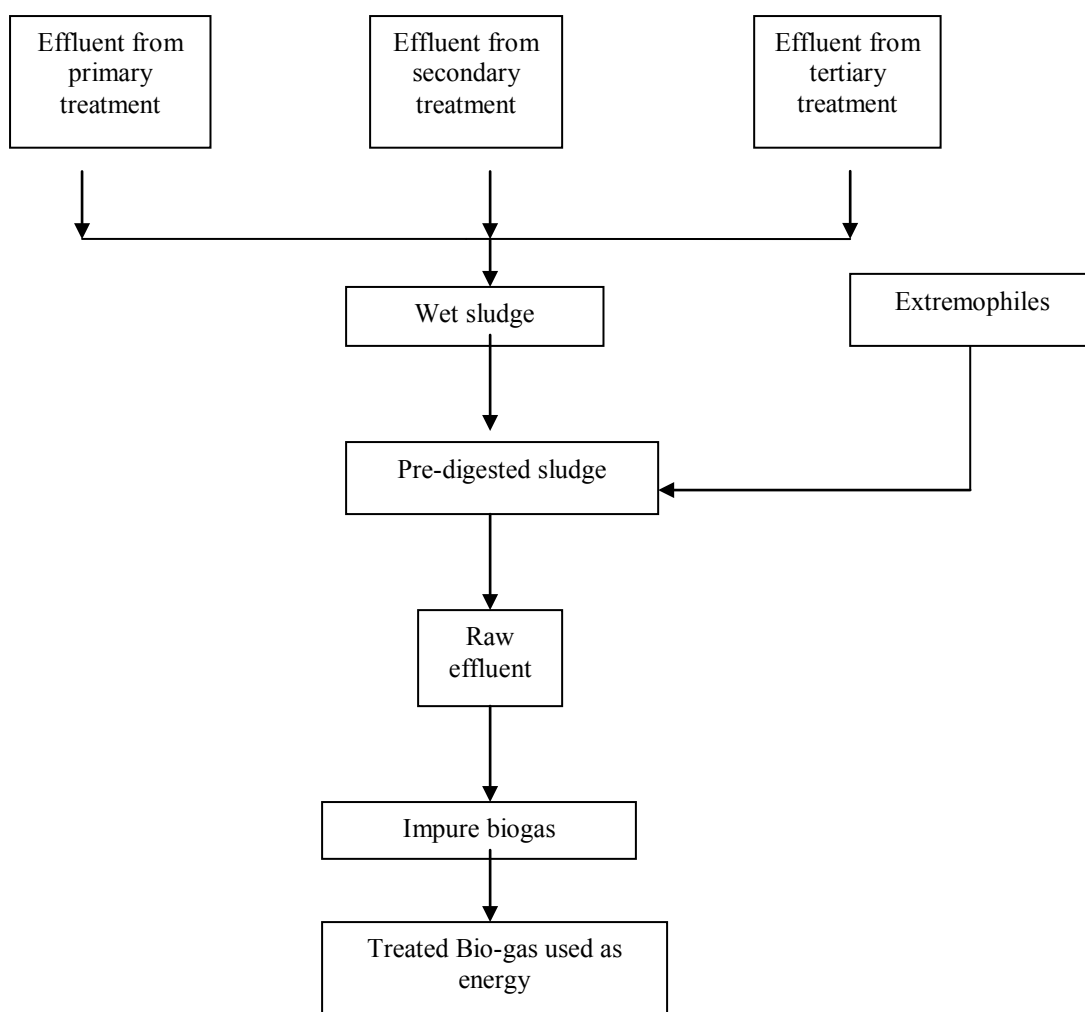


Fig.1

5. RESULTS AND DISCUSSION

Characteristics of sludge from CETP in Pallavaram, Chennai, Tamilnadu, India.

Sno.	Parameter*	CETP Pallavaram
1.	pH	7.7 -8.8
2.	Total Solids	45052.00
3.	Total Ash	27533.00
4.	Total volatile solids	17519.00
5.	COD total	22259.33
6.	COD soluble	2180.67
7.	Calcium as Ca	2000.00
8.	Sulphate as SO_4^{2-}	606.67
9.	Total Sulphide as S	370.67
10.	Total Phosphorus as P	43.29
11.	Ammonia Nitrogen	430.00
12.	TKN	1314.67
13.	Sodium as Na	3953.33
14.	Total chromium as Cr	317.00
15.	Chloride as Cl	9933.33

*unit as mg/L other than pH

According to Thabaraj et al tannery waste water could be treated to a level of BOD30mg/litre through activated sludge process at HRT 24 hrs. The MLSS concentration of activated sludge process was required to be at 4000 mg/litre for a removal of 83% COD and 92% Sulphide [(Cooper et al) 1976]. The primary clarification of tannery effluent with alum, ferrous sulphate or ferric chloride and settling before aerobic biologic treatment

5.1 TREATMENT OF BIOGAS

The impure biogas constituted 60% methane rest being other gases. However the moisture content increased in the treated biogas after removal of other gases. Hence to remove excess moisture activated carbon and glycol was used. This has increased the calorific value of methane.

The methodology for removal of CO_2 is using common solvent water. The solubility of CO_2 depends on pressure, temperature and pH. In addition to it, $\text{Ca}(\text{OH})_2$ was also used to form CaCO_3 and CaS

However, it is proposed to use organic solvents such as polyethylene glycol to make it

assisted in reducing COD by 93.6% (Cheda et al 1984).

Thus the treatment of effluent generated sludge and this sludge was used as feed for biogas plant after making pre-digested sludge.

cost effective, without sacrificing the efficiency of calorific value of methane gas. However, using activated carbon has produced useful result but the efficiency is not encouraging.

Hence, it is also proposed to use different molecular sieve and mesh size of activated carbon and to evaluate the suitability of particular molecular sieves and mesh size which absorbs CO_2 under NTP having uniform calorific value.

The traces of H_2S needs removal. The treated biogas dried using silica gel. Alternatively Al_2O_3 in case of low dew point need to be achieved.

An alternative method of drying using glycol or hygroscopic salt is also tried for absorption of moisture in the treated biogas. The result will be evaluated for upscaling the technology in future.

5.2 BIOGAS ANALYTICAL DATA

S.NO	CONTENT	IMPURE % W/W	TREATED % W/W
1	CH ₄	60	80
2	CO ₂	22.5	NIL
3	NH ₃	1.0	NIL
4	H ₂ S	0.5	NIL
5	MOISTURE	6.0	10
6	OTHER IMPURITIES	10	10

REFERENCES

1. Cheda, P.V., U.V. Mandelkar, B.K. Handa and P. Khanna 1984. Joint wastewater management for a cluster of tanneries at Kanpur. 39th Industrial waste conference, Purdue University proceeding pp 151-162
2. Cooper J.E., W.T. Happich, E.F. Melton and J. Naghaki, 1976. Activated Sludge treatment of tannery wastes. JALCA. 71(1) 6-24.
3. Thabaraj, G.J., S.M. Bose and Y. Nayudumma, 1964. Utilisation of tannery effluents for agricultural purposes. Indian Journal of Environment Health 1:28-36.

Water Harvesting and Salinization Prevention by Capillary Barrier of Soil

Toshihiro Morii¹, Mitsuhiro Inoue², Kaoru Kobayashi³, Tetsuya Suzuki¹ and Takayuki Kawai¹

¹Research Institute for Natural Hazards and Disaster Recovery, Niigata University, Niigata, Japan

²Arid Land Research Center, Tottori University, Tottori, Japan

³Research Institute of Technology, Tobishima Corporation, Chiba, Japan

ABSTRACT

A simple soil layer system which is composed of a finer soil layer underlain by a coarser soil layer provides a characteristic property of capillary barrier. Water infiltrated into soil is suspended just above an interface between soil layers due to a physical difference in unsaturated hydraulic properties of soil. As their roots can easily utilize the water retained in the upper soil layer, agricultural plants grow even under water saving irrigation. Because the gravel layer embedded in the soil cuts upward movement of water from groundwater, the capillary barrier of soil is expected to provide an effective prevention of salinization which is caused by salt included in the groundwater. Two series of field experiment are conducted on the sand soil where the gravel layer is embedded to investigate a practical effectiveness of the capillary barrier of soil in the water saving irrigation/ water harvesting and the salinization prevention.

Keywords: Capillary Barrier of Soil, Water Harvesting, Salinization Prevention, Field Experiment

1. INTRODUCTION

A simple soil layer system which is composed of a finer soil (usually sand) layer underlain by a coarser soil (gravel) layer provides a characteristic property of capillary barrier [1]-[4]. Water infiltrated into soil is suspended just above an interface between soil layers due to a physical difference in unsaturated hydraulic properties of soils as shown schematically in Fig. 1. In the case of tilted interface, the suspended water flows downward along the interface and a vertical movement of water into deeper soils below the interface will be prevented within some length along the interface. This leads to a practical application of the capillary barrier system (CBS) to a top cover of waste disposal landfill [5] and a slope repair [6]. In the case of a horizontal interface, plant can easily consume the water retained in the upper soil layer for its growth [7]. Because of this, the CBS may be well employed for an

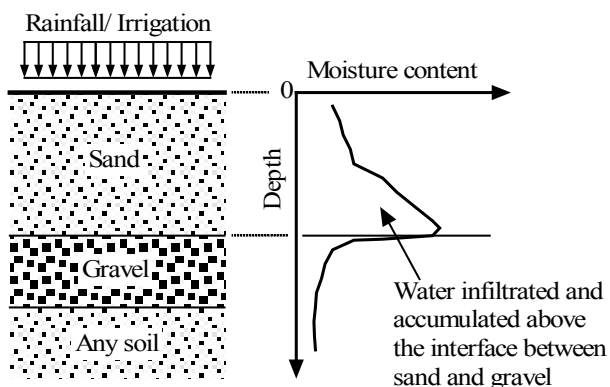


Fig. 1 Schematic diagram to show water accumulation above an interface between finer soil (sand) and coarser soil (gravel) caused by capillary barrier of soil.

effective water harvesting and saving irrigation in an area where water resource is scarce. As the gravel layer of the CBS embedded in the soil cuts upward movement of water from groundwater, it may be expected that the CBS will provide an effective prevention of salinization which is caused by salt included in the groundwater.

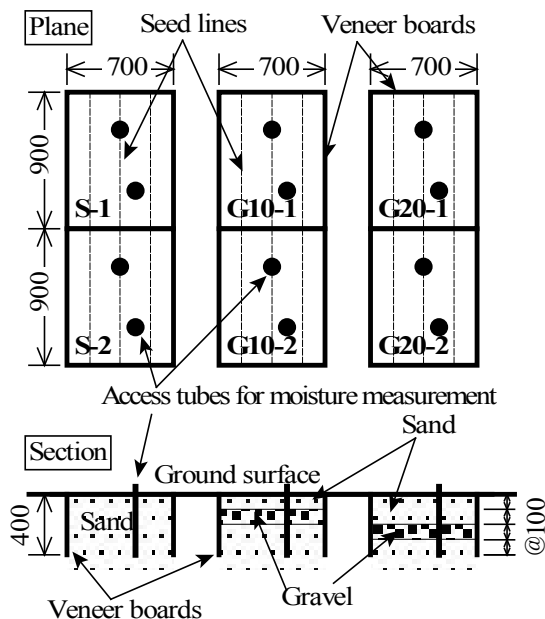
In the study, two series of field experiment were conducted on the CBS soil where the gravel layer was embedded in the sand soil in order to investigate a practical effectiveness of the CBS in water harvesting and salinization prevention. In the field experiment for water harvesting [7], experiment plots of the CBS soil were constructed, green vegetables were planted on them, and soil moisture contents were measured after seeding to harvesting of the plant. The water retained in the upper sand layer was observed, and its effect on the plant growth was quantified by a statistical analysis of the plant harvest. In the series of field experiment for salinization prevention, a number of the CBS soil were constructed in polyester containers, and connected to a water tank which could supply an artificial groundwater, 10,000ppm of NaCl, to the CBS soils with a constant head of water. Soil moisture content and electric conductivity in the upper sand layer, the gravel layer and the lowest sand layer overlain by the gravel layer were measured after plant to harvest of the green vegetable. It was observed that the gravel layer embedded in the CBS soil at some depth above the groundwater surface can well prevent the water from moving upward from the groundwater surface. This excellent interception of upward water movement was also observed by the plant death due to the salinization in the soil without the gravel layer.

Both series of field experiment reveals that the CBS is well applicable to the water harvesting and the salinization prevention, which may suggest some new progress of geotechnical engineering to green technology.

2. FIELD EXPERIMENT FOR WATER HARVESTING

2.1 Experiment Plots

Six experiment plots, each 70 cm wide and 90 cm long, were constructed to compare plant growth in the greenhouse as shown in Fig. 2. The sand soil was excavated into a depth of about 40cm, and veneer boards were placed to retain soil wall and to prevent lateral flow of soil water during the experiment. Then the sand soil was filled back into the first two of six experiment plots, S-1 and S-2 in Fig. 2, and compacted uniformly along all the depth. In other two experiment plots, G10-1 and G10-2, after the sand soil was filled back and compacted along the depth 40 to 20cm, a gravel layer 10 cm in thickness was placed and compacted, and then the sand soil was filled back and compacted uniformly from the depth of 10cm to the soil surface. In the remaining two experiment plots, G20-1 and G20-2, a gravel layer 10cm in thickness was placed and compacted between the depth of 30cm and 20cm. A polyester nonwoven sheet was placed over the compacted gravel layer so that the sand soil particles did not fall into voids formed in the gravel layer. This sheet was tested to be completely permeable. Numerals 1 and 2 given after a hyphen in the experiment plot number mean a repetition for experimental design.



Note: Length and depth are in mm.

Fig. 2 Plane and sectional configuration of experiment plots constructed on the sand soil.

2.2 Materials

Fig. 3 shows grain size distribution curves of sand and gravel employed in the experiment plots. The sand has less-5% fine and coarse fractions; the gravel, commercially available, is siliceous with a mean particle size of 5 to 6mm. Soil particle density, dry density of compacted soils and

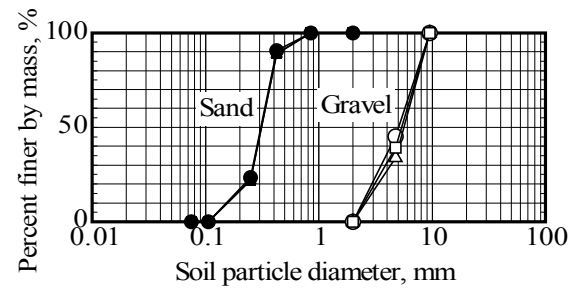


Fig. 3 Grain size distributions of sand and gravel used to construct the experiment plots.

Table I Soil particle density, dry density of compacted soils and hydraulic conductivity.

Properties	Sand	Gravel
Soil particle density, Mg/m ³	2.626	2.653
Dry density of soil, Mg/m ³	1.46-1.56	1.69-1.80
Hydraulic conductivity*, m/s	0.99×10^{-4}	1.04×10^{-2}

*Corrected to water temperature at 15 degrees Celsius.

hydraulic conductivity of sand are summarized in Table I. Dry density of soil was calculated by dividing a mass of soil compacted into the layer by a volume of the layer. Saturated hydraulic conductivity of sand was determined by interpolating the results of laboratory seepage test to the mean value of dry density of sand layer, that is, 1.51Mg/m³. Saturated hydraulic conductivity of gravel was measured by the laboratory seepage test under unit hydraulic gradient. Relationships of negative pore pressure with volumetric moisture content of sand and gravel were measured by a laboratory soil column test, and are plotted in Fig. 4(a). Soil-water characteristic curves are determined by using van Genuchten equation [8]. Fig. 4(b) shows unsaturated hydraulic conductivity of sand and gravel estimated from Fig. 4(a) using the van Genuchten equation. It is found that, when the negative pressure head just above the interface between sand and gravel decreases to 3 to 4cm due to accumulation of water, the hydraulic conductivity of gravel becomes larger than that of sand and the accumulated water will begin to infiltrate into the gravel layer. But, because nearly 100% saturation within the sand layer as estimated from Fig. 4(a) rarely occurs under evaporation condition with a restricted supply of water, the breakthrough of accumulated water into the lower gravel layer may not either.

2.3 Planting

Potherb Mustard was seeded at 5cm intervals along seed lines shown in Fig. 2(a) on 11 July, thinned on 28 July in all the experiment plots, and harvested on 14 August to measure height, fresh mass and dry mass of plant. Water corresponding to 100 % of pan evaporation measured the day before was supplied by a watering can every morning during a period from seeding to thinning, and 50 % during thinning to harvesting. Volumetric moisture content of soil in the experiment plots were measured by using Profile Probe

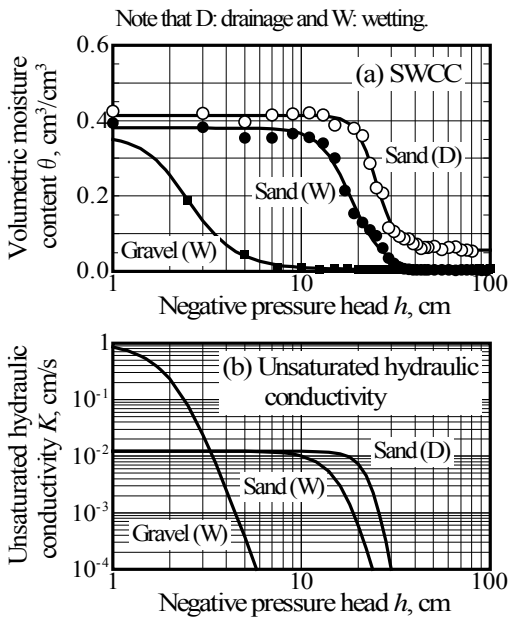


Fig. 4 Soil-water characteristic curves (SWCC) of sand and gravel measured by laboratory soil column test and estimated by using van Genuchten equation in (a). Unsaturated hydraulic conductivities of sand and gravel are estimated in (b).

PR2/4 with a moisture meter HH2 (Delta-T Devices Ltd.), at positions given by painted circles in Fig. 2 along the depth of soil surface to 40 cm at 10 cm intervals. Relationships between output of PR2/4 and volumetric moisture content of soil were calibrated along the probe in the laboratory.

2.4 Results

Evaporation was measured to be about 1 mm to 6 mm during the field experiment as shown in Fig. 5. The volumetric moisture contents were measured along the depth of soil at weekly intervals after seeding, and given in Fig. 6 together

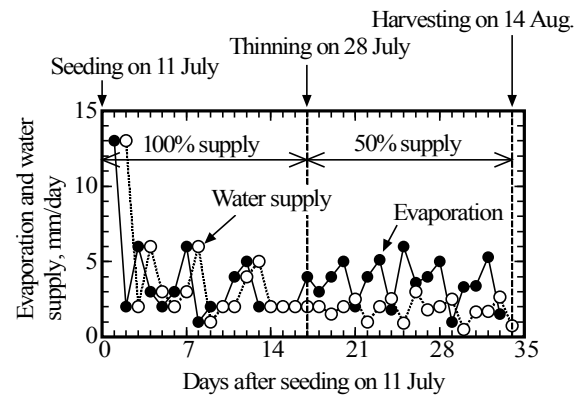


Fig. 5 Evaporation measured during the experiment, and water supply.

with the position of the gravel layer. In Fig. 6(a) which shows soil water profiles in the experiment plot S-1 composed of sand alone, it is seen that the water supplied on the soil surface infiltrates into the deeper position. On the contrary, in Fig. 6(b) and Fig. 6(c) in the experiment plots with the gravel layer at depth 10cm and 20cm respectively, it is found that water supplied on the soil surface infiltrates into the sand layer and then accumulates just above the interface between sand and gravel layers with less infiltration into the gravel layer. It may make sense to think that the plants can easily absorb the accumulated water to consume for their growth.

2.5 Effect of Accumulated Water on Plant Growth

An effect of water accumulated due to the CBS on the plant growth was investigated by using a statistical analysis. In Fig. 7, mean values of plant height excluding root length, fresh mass and dry mass of plant are plotted in thick bar together with standard deviation given by thin line. The number of plant harvested and analyzed is 44, 43 and 51 in the experiment plot S (that is S-1 plus S-2), G10 (G10-1 plus G10-2) and G20 (G20-1 plus G20-2), respectively. Alphabets

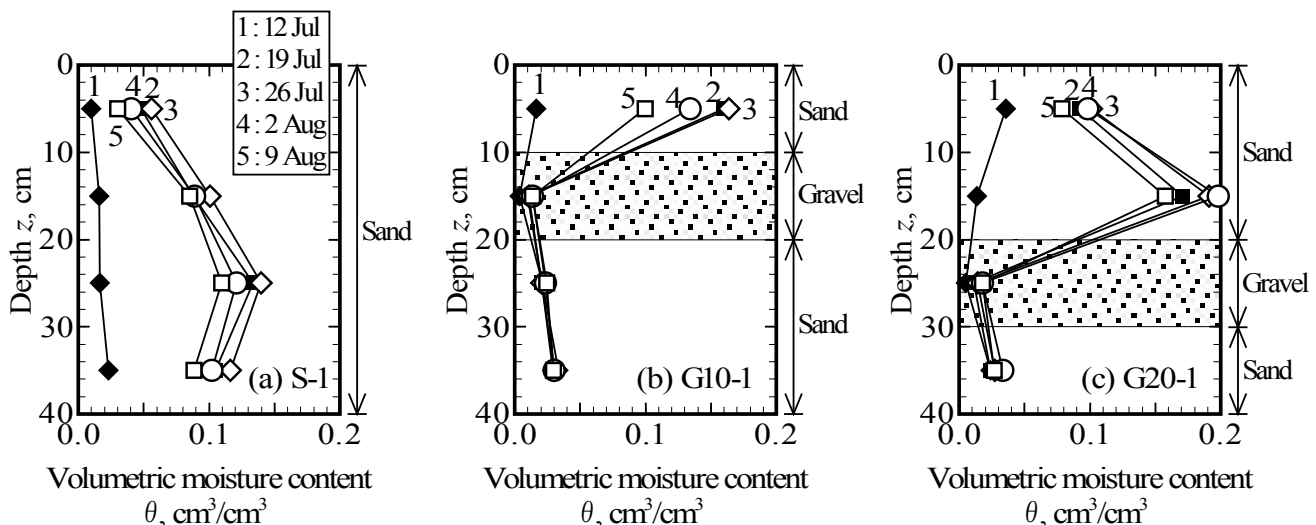


Fig. 6 Volumetric moisture content along depth of the experiment plots measured during a period from seeding to harvesting. Data are plotted at weekly intervals.

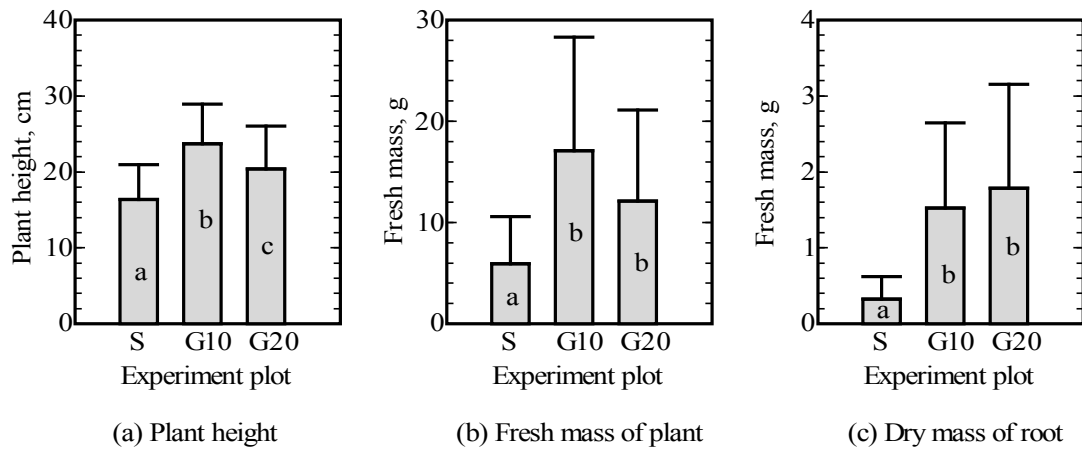


Fig. 7 Multiple comparisons to show the effect of the CBS on the plant growth. The experiment plots de-noted by different alphabets such as “a” and “c” are statistically different each other with a significant level of 5%.

‘a’, ‘b’ and ‘c’ given in Fig. 8 show the result determined by the multiple comparison analysis based on Scheffe's method. The experiment plots denoted by different alphabets such as ‘a’ and ‘c’ are statistically different each other with a significant level of 5%. According to this analysis, it is found in Fig. 7 that the plant height, the fresh mass and the dry mass of plant grown in the experiment plots G10 and G20 are significantly larger than those in the experiment plot S. This suggests water accumulated in the sand layer due to the capillary barrier of soil was consumed effectively by the plant for its growth. It is also found that the plant height in the experiment plot G10 is significantly higher than that in G20 in Fig. 7(a), and the fresh mass of plant in G10 are larger than those in G20 in Fig. 7(b). This is because, as the plant roots were observed to grow thick within the soil about 10cm deep, they could not effectively absorb water accumulated within the sand layer in the experiment plot G20.

3 FIELD EXPERIMENT FOR SALINIZATION PREVENTION

3.1 Experiment Plots

In the field experiment to investigate the salinization prevention effect of the CBS, a polypropylene container box 61 cm long, 41 cm wide and 31.5 cm deep was used to construct the experiment plot as shown in Fig. 8. In the plot G25 and G50, gravel layer 2.5 cm and 5 cm in thickness were embedded in the container boxes, respectively. No gravel layer was placed in the container boxes in the plot S. A line linking three container boxes is connected to a water supply tank which can supply groundwater into the container boxes with constant head of water.

The sand soil was excavated into the depth of about 30 cm, and the container boxes were placed. Then the sand soil was filled back to the container box and compacted uniformly into the thickness of 16.5 cm, that is, along the depth 31.5 cm (the bottom of the container box) to 15 cm. In three container boxes along the plot G25, gravel layer 2.5 cm in thickness

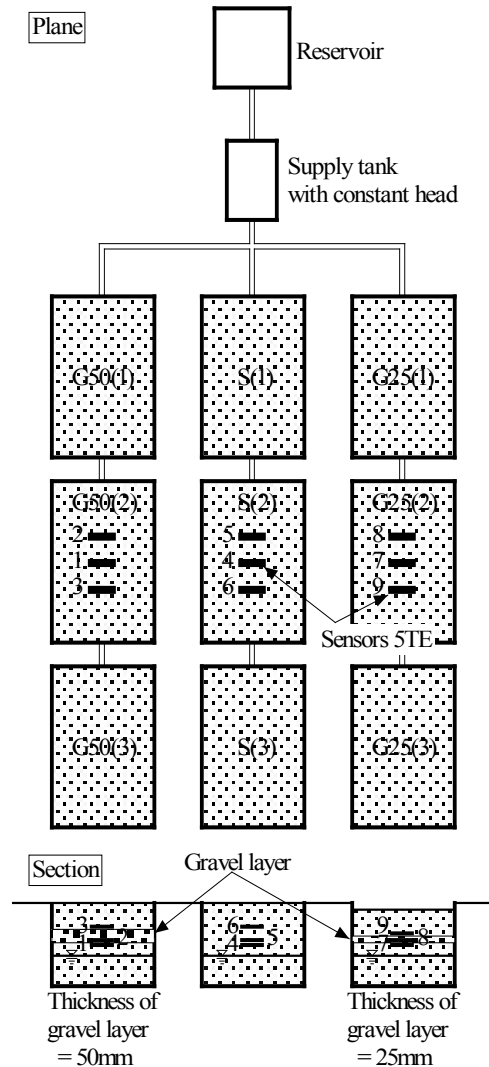


Fig. 8 Experiment plots to investigate the salinization prevention by the CBS. See also Fig. 10.

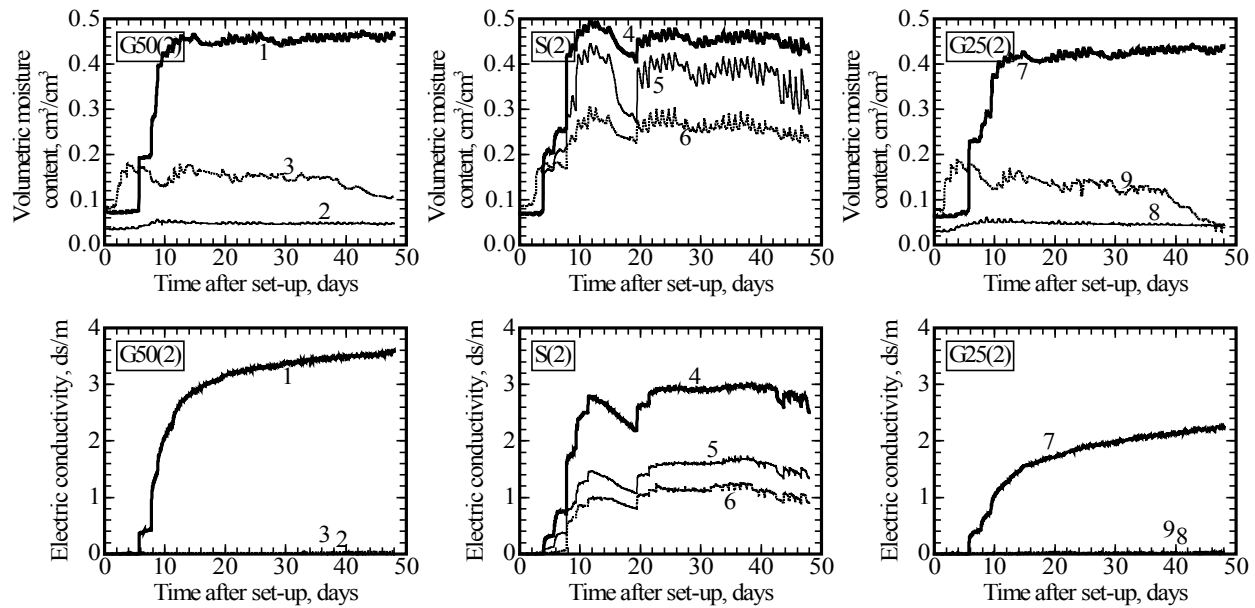


Fig. 9 Volumetric moisture content (upper three graphs) and electrical conductivity (lower three graphs) measured by the 5TE sensors in the capillary barrier soil G25 and G50 and in the sand soil S. Numerals 1 to 9 indicate the number of the 5TE sensor embedded in the soil as shown in Fig. 8.

was placed and lightly compacted, the same polyester nonwoven sheet as one used in the preceding experiment was spread on the gravel layer, and the sand soil was again filled back and compacted uniformly into the thickness of 10 cm. In three container boxes along the plot G50, the gravel layer 5 cm thick, the polyester nonwoven sheet and the sand 10 cm thick were placed in sequence. In the plot S, the sand soil was continuously filled back and compacted uniformly from the remaining depth 15 cm to the soil surface. The sand and gravel are the same as ones used in the field experiment described in Section 2, and their grain size distribution and the material properties are given in Fig. 3 and Table I. The groundwater level was kept 11.5 cm above the bottom of the container boxes, with the result that vertical distance between the groundwater level and the lower interface of the gravel layer was 5 cm. As a water-entry pressure head of the sand soil is estimated to be about 10 cm along the wetting curve, this value of 5 cm is sufficiently small to investigate the effect of the gravel layer on the upward movement of water from the groundwater. Sodium chloride was used to supply saline groundwater, 10,000 ppm in mass.

3.2 Planting and Measurements

The groundwater was supplied to all the container boxes on 3 September. The young vegetables of *Potherb Mustard* were planted into the container box, and harvested on 21 October. 750 to 1,000 cm³ of water per a container box was supplied every morning by using the watering can. During the experiment, the volumetric moisture content and the electrical conductivity were monitored by using the water content, EC and temperature sensor 5TE manufactured by Decagon Devices, Inc. As shown in the section of Fig. 8, the 5TE sensors No.1, 4 and 7 were embedded just below the lower

interface of the gravel layer or at the position of 16 cm above the bottom of the container box; No. 2, 5 and 8 just above the lower interface of the gravel layer or at the position of 17 cm above the bottom of the box; No. 3 and 6 just above the upper interface of the gravel layer or at the position of 22 cm above the bottom of the box and No.9 at the position of 19.5 cm above the bottom of the box.

3.3 Results

The volumetric moisture content and the electrical conductivity measured by the 5TE sensors in the capillary barrier soil, the plots G25 and G50, and in the sand soil, the plot S, are given in Fig. 9.

At around 1 week after the saline water was supplied into the experiment plots with the constant level of groundwater, both the volumetric moisture content and the electrical conductivity measured in the sand soil below the gravel layer increase rapidly in the experiment plots G25 and G50, and at around 2 weeks the volumetric moisture content reached its saturated value (No. 7 in the G25 and No. 1 in the G50). However, during this 2 weeks and from then, no or negligible change in the volumetric moisture content and the electrical conductivity is found in the gravel layer as given by No. 8 in the G25 and by No. 2 in the G50, which means no upward movement from the groundwater into the gravel layer. Small increases in volumetric moisture content measured by No. 9 in G25 and by No. 3 in the G50 are caused by continuous accumulation of infiltrated water just above the interface between the upper sand layer and the gravel layer as shown in Fig. 6. The electrical conductivity which has a strong relationship with pore water salinity indicates almost zero just above the interface of the CBS in the G25 (No. 9) and G50 (No. 3) during the experiment period. It may be concluded



Fig. 10 Vegetables at the end of the experiment. Although the plants grew successfully in the G25 (the right row of the container boxes) and in the G50 (the left row), they withered completely in the S (the central row) due to the soil salinization.

from these measurements shown in Fig. 9 that the saline water was completely prevented from moving upward from the groundwater into the gravel layer and into the upper sand layer where the vegetables were planted. In the experiment plot S without the gravel layer, both the volumetric moisture content and the electrical conductivity increase according to the upward movement of saline water from the groundwater because there was no prevention of water movement by the capillary barrier.

Fig. 10 shows a picture of the plots taken at the end of experiment. All the vegetables planted in the experiment plot S without the gravel layer completely withered due to the soil salinization. Be sure that, because the soil was not fertilized to avoid an effect on measurement of the electrical conductivity by the 5TE sensors, plant growth was not sufficient in the G25 and the G50 in Fig. 10.

4 CONCLUSIONS

Two series of the field experiment were conducted on the capillary barrier soil in order to investigate a practical effectiveness of the CBS in water harvesting and salinization prevention. In the field experiment for water harvesting, experiment plots of the capillary barrier soil were constructed, green vegetables were planted on them, and soil moisture contents were measured after seeding to harvesting of the plant. The water retained in the upper sand layer was observed, and its effect on the plant growth was quantified by a statistical analysis of the plant harvested. In the series of field experiment for salinization prevention, a number of the capillary barrier soil were constructed in polyester container boxes, and connected to the water tank which could supply an artificial groundwater, 10,000ppm of NaCl, to the experiment plots with a constant head of water. Soil moisture content and electric conductivity in the upper sand layer, the gravel layer and the lowest sand soil overlain by the gravel layer were measured after plant to harvest of the green vegetable. It was observed that the gravel layer embedded in the capillary barrier soil at some depth above the groundwater surface can

well prevent the water from moving upward from the groundwater surface. This excellent interception of upward water movement was also observed by the plant death due to the salinization in the soil without the gravel layer.

Both series of field experiment reveals that the CBS is well applicable to the water harvesting and the salinization prevention, which may suggest some new progress of geotechnical engineering to green technology [9].

5 ACKNOWLEDGMENTS

The present study is supported by the Grant-in-Aid for Scientific Research (B), No. 22380127, made by the Ministry of Education, Science, Sports and Culture of Japan, and by the Joint Research Grant made by the Arid Land Research Center, Tottori University, Japan. Misses M. Sugisaki and K. Takahashi and Mr. S. Furukawa are gratefully acknowledged for their help in conducting the field experiment.

6 REFERENCES

- [1] Ross B, "The diversion capacity of capillary barriers," *Water Resources Research*, vol. 26, No. 10, 1990, pp. 2625-2629.
- [2] Walter M, Kim J, Steenhuis T, Parlange J, Heilig A, Braddock R, Selker J and Boll J, "Funneled flow mechanisms in a sloping layered soil: Laboratory investigation," *Water Resources Research*, vol. 36, No. 4, 2000, pp. 841-849.
- [3] Rahardjo H, Krisdani H and Leong E, "Application of unsaturated soil mechanics in capillary barrier system," *Proceedings of the Third Asian Conference on Unsaturated Soils*, 2007, pp. 127-137.
- [4] Morii T, Takeshita Y, Inoue M and Matsumoto S, "Alternative measures for soil slope stability using capillary barrier of soil," *Proceedings of the Fourth Asia-Pacific Conference on Unsaturated Soils*, 2009, pp. 319-324.
- [5] Morii T, Kobayashi K, Matsumoto K, Suzuki T and Kawai T, "Practical application of capillary barrier of soil into a shallow land waste repository," *Proceedings of the Fifth China-Japan Geotechnical Symposium*, 2012. (to be published)
- [6] Rahardjo H, Satyanaga A and Leong E, "Unsaturated soil mechanics for slope stabilization," *Proceedings of the Fifth Asia-Pacific Conference on Unsaturated Soils*, vol. 1, 2011, pp. 103-117.
- [7] Morii T, Inoue M, Komatsu G, Kadoguchi R and Takeshita Y, "Effective water harvesting using capillary barrier of unsaturated soils," *Proceedings of the Fifth Asia-Pacific Conference on Unsaturated Soils*, vol. 2, 2011, pp. 857-860.
- [8] Stephens D, *Vadose Zone Hydrology*. Florida: CRC Press, Inc., 1996, ch. 4.
- [9] Morii T, Inoue M and Takeshita Y, "Green technological effect of capillary barrier of soil on agricultural plant growth," *Proceedings of the Second Japan-Korea Joint Workshop on Unsaturated Soils and Ground*, 2011, pp. 249-256.

Study of the Performance of anaerobic digestion of greasy skim as a renewable energy source

Salam J. Bash Al-Maliky
AlMustansiriya University, Iraq

ABSTRACT

Five laboratory scale batch reactors (each of 10 L working volume) were used to test the effect of different Induced Air Flotation IAF skim to working volume ratios; namely 0.5, 1.5, 2.5, 4.0, 5.0:10 (R1-R5), with the rest of working volume was filled with livestock manure (as inoculums). These reactors were operated at two different temperatures (25C and 45C), to determine the temperature effects on digestion performance. Chemical Oxygen Demand (COD) removal efficiencies of 72.6%, 68.6%, 60.1%, 52.1%, and 43.25% were achieved for R1-R5 respectively, at temperature of 25C. These removal efficiencies were significantly improved at temperature of 45C, where efficiencies of 91.2%, 81.5%, 72.1%, 60.7% and about 50% were achieved for these reactors. Very promising biogas production rates of 4.5- 5.8 l/day were determined at operation temperatures of 45C (compared with 3- 4 l/day at 25C) for the majority reactor life times.

Key words: Anaerobic digestion, biogas, digestion temperature, Induced Air Flotation, substrate composition.

1. Introduction

Many recent researches and studies had demonstrated the great feasibility of applying the IAF approach for the removal of Oil and Grease (OG) from the effluents of municipal and industrial activities (Al-Maliky, 2010; Arnold and Stewart, 2008; Pan Li and Hideki Tsuge, 2006). IAF may simply be explained as a treatment process often used to remove this insoluble particulate matter from the wastewater, essentially to reduce the OG constituent, Biological Oxygen Demand (BOD), COD and Suspended Solids SS loads of the wastewater to avoid surcharges when discharging to surface water or municipal wastewater treatment plants. The process is achieved by injecting air bubbles into the water or wastewater in a flotation tank or basin. The small bubbles adhere to the suspended matter causing the suspended matter to float to the surface of the water where it may then be removed by a skimming device. The feed water to the IAF float tank is often dosed with a coagulant to flocculate the suspended matter (Hayatdavoudi, 2006). Many studies had suggested various design and operation parameters for the IAF unit to achieve high performances in oil/water separation, reduction of BOD, TSS and COD (Al-Maliky, 2010; Van Ham, Behie and Svrcek, 2009), and in turn the production of skim sludge at the upper layer of a typical IAF unit that is characterized by high concentrations of OG, COD and TSS. Although that skim is typically rendered or land applied, but its poor natural degradability and high energy potential contents make it a potential candidate for anaerobic digestion. This approach needs careful handling to overcome the tendency of high OG concentrations to form a scum layer on the digester's liquid surface due to the poor solubility of OG at typical digester temperatures and the tendency

to form a separate phase above the aqueous digester contents (Halalsheh et al., 2005). Suggestions to handle the later obstacle were either to reduce the IAF skim amounts to be digested or the use of some inoculums such as the agricultural wastes that improve microbial nutrition and provide pH buffering capacity (Bouallagui et al., 2009).

Anaerobic treatment consists of the decomposition of organic material in the absence of free oxygen and this process produces biogas enriched in methane, carbon dioxide, ammonia and traces of other gases and Volatile Fatty Acids (VFA) within the reactor. The anaerobic treatment process has been employed in several developed countries with the aim of bio-stabilizing fermentable organic waste produced by rural and urban activities (Fernández, Pérez and Romero, 2010).

The main coal of this paper was to study the feasibility of an anaerobic digestion process as a final treatment of the skim of IAF unit that handles dairy industry's waste water, and the potential of such process as renewable energy source, under different set ups of digest mixtures (IAF skim and livestock manure) and operation temperatures. Livestock manure was collected from Green Grass Farms, Athens, Ohio, USA.

1.1 Characteristics of IAF skim

The characteristic of having high COD concentration (425 g/L) as shown in Table 1 gave the IAF skim a high potential of biogas production and encouraged increasing the ratio of IAF skim to manure in the reactor feed to supply a promising source of economic renewable energy, subject to the constraints due to microbial nutrition and pH buffering.

1.2 Experimental Setup

Five batch reactors (10 L working volume) were adopted for the test of anaerobic digestion parameters, as

illustrated in Fig.1. Each reactor has an independent rotary blade mixer LIGHTNIN SPX so as to maintain uniform moisture content and to homogenize the soluble substrate and bacterial distribution. Also, an internal DUREX coil heater was inserted in each reactor, with thermostat so as to supply the required heat to meet the test's operational temperature.

Under Each set of operational parameters, reactors were fed initially with 10 L of diluted sludge (animal manure diluted with fresh water) until the appearance of some low biogas production rates for successive operation days and in turn the obtained digested sludge would serve as inoculums for reactors.

Sludge masses were made of dewatered IAF unit skim and kept at -20 C prior to use as the feed for reactors. Initially, the pH of digested sludge was adjusted to the range 6- 8 via 2N solution of Sodium Hydroxide. This pH was monitored continuously to make sure it is in that range.

Analysis of COD, TSS and pH were determined according to the standard methods (APHA, 2010). The biogas production was determined by the displacement of water in a graduated column.

Digest substrates were made of 0.5, 1.5, 2.5, 4.0 and 5.0:10, IAF skim to the total working volume (each in one reactor; R1, R2, R3, R4 and R5 respectively) at each of the test temperatures (25C and 45C). These combinations were initially mixed via a commercial laboratory blender LBC15.

The five reactors were operated for a period of 30 days under each certain set of operational parameters.

2. Results and Discussions

Although disturbances in reactors performance were expected for the early periods of operation, pH values were mainly within the acceptable rang of 6-8 as shown in Fig.2 for the majority of reactors life times, which indicates well buffering balance of substrate mixtures.

2.1 Digestion Performance

In general, it takes a period of time for the reactor to acclimate and start being effective in the sense of COD removal due to long-chain fatty acids released from the hydrolysis of triglycerides constituents of OG, and the length of this lag period depends upon the IAF skim: working volume ratio; the higher it was, the longer the lag period. From another side, Fig. 3 (a) indicates that higher IAF skim portions had led to lower COD removal efficiency; that is, while the maximum achieved efficiency with reactor R1 was about 72.6%, it did not exceed 43.25% with reactor R5, when operated at temperature of 25C (68.6%, 60.1% and 52.1% for R2-R4 respectively). Remarkable enhancements were achieved for the COD removal efficiencies that reached the values of 91.2%, 81.5%, 72.1%, 60.7% and about 50% for R1- R5 respectively, by operating the reactors at higher temperature of 45 C, as shown by Fig.3 (b). This may be attributed to the thermophilic characteristic of

OG content of the IAF skim; e.g., at higher temperatures, OG tends to be more soluble that in turn enhances its biodegradability.

Regarding the TSS constituent, the performance trend of reduction was almost similar to that of COD, which is a reference to the degradable organic composition of the majority of these solids. At operation temperature of 25C, the reduction percentages were 83- 49% for the reactors R1-R5, respectively. The same scenario of high COD removal enhancement at operation temperature of 45C, was repeated with the TSS, where these percentages had the values of 95- 77% for the same mixing ratios.

2.2 Biogas Production

Biogas production in Fig.4 (a) and (b) has shown significant increase via operating the different reactors with the mixed substrates compared to that during the anaerobic digestion of the diluted livestock manure only, as shown in Fig.5. Also, these results had clearly demonstrated, that higher IAF skim (higher COD) has the tendency of higher biogas production at both operation temperatures (25C and 45C). The greater biodegradability and energy potential of carbohydrates that constitute IAF skims might be the main causal for that, in agreement with Thomas et al. (2007).

Highest biogas production rate was measured for R2 (about 4.2 l/day), in comparison with that for R1 (about 3.7 l/day), that hosted the highest IAF skim: working volume ratio at an operation temperature of 25C (Fig.4 (a)). This may be attributed to the higher OG content and salt concentration in the later mixture that inhibits biological transformation at that temperature, and hence, adversely affects the biological activity. That decrease of biogas production rate at higher concentration of IAF skim was overcome by operating the digestion reactors at 45C, (rates of 5.8 l/day and about 5.0 l/day were achieved with R1 and R2 respectively), due to the enhanced solubility at high operation temperatures as shown in Fig.4 (b).

3. Conclusions

The anaerobic digestion of wastes that are characterized by high constituency of COD and OG (IAF skim for this study) was tested via co-digestion with livestock manure at different mixing ratios and two operation temperatures in laboratory scaled batch reactors. Good COD removal efficiencies (about 72.6%- 68.6%) were achieved while using low portion of these wastes (5% - 15% of the total working volume, respectively) at operation temperature of 25C. This removal efficiency was significantly improved to the values of 91.2%- 81.5% for the same mixing ratios, at operation temperature of 45C, which leads to the recommendation of operating such digesters at high temperatures to make benefit of the thermophilic characteristic of such wastes. That later conclusion was so demonstrated by the great enhancement of the biogas production rate of such reactors when operated at high temperatures; while the highest biogas production rate

was in the range of 3-4 l/day at temperature 25C, it was raised to the range of 4.5- 6 l/day at the temperature 45C.

4. References

- Al-Maliky Salam B., (2010). Effect of geometrical dimensions and waste water temperature on the performance of an induced air flotation unit for the treatment of industrial waste water. *Journal of Modern Applied Science Vol.4 No.6, pp. 14-19*.
- APHA (2010), Standard Methods for the Examination of Water and Wastewater, Edited by Lenore S. Clesceri, Arnold E. Greenberg and Andrew D. Eaton. (20th Edition).
- Arnold, K.E., Stewart,M., (2008). Surface production operations-design of oil handling systems and facilities. (Vol. 1, 3rd ed.), *Gulf Publishing Co, Houston, Texas*.
- Bouallagui, H., Lahdheb, H., Ben Romdan, E., Rachdi, B., Hamdi, M., (2009). Improvement of fruit and vegetable waste anaerobic digestion performance and stability with co-substrates addition. *Journal of Environmental Management* 90, 1844–1884.
- Fernández J., M. Pérez b, Romero L.I., (2010), Kinetics of mesophilic anaerobic digestion of the organic fraction of municipal solid waste: Influence of initial total solid concentration. *Journal of Bioresource Technology*, 101, 6322–6328.
- Halalsheh, M., Koppes, J., den Elzen, J., Zeeman, G., Fayyad, M., Lettinga, G., (2005). Effect of SRT and temperature on biological conversions and the related scum forming potential. *Journal of Water Resources*. 39, 2475–2482.
- Hayatdavoudi A., (2006). Removing Oil and Grease from Produced Water Using Micro-Bubble Flotation Technique. *Offshore Technology Conference, Texas, USA*.
- Pan Li and Hideki Tsuge (2006). Water Treatment by Induced Air Flotation Using Microbubbles. *Journal of chemical engineering of Japan*, Vol.39, No.8, pp. 896-903.
- Thomas, A., Barbara, A., Vitaliy, K., Werner, Z., Karl, M., Leonhard, G., (2007). Biogas production from maize and dairy cattle manure: Influence of biomass composition on the methane yield. *Agriculture Ecosystems and Environment* 118, 173–182.
- Van Ham Niel, Behie Leo A., Svrcek William Y. (2009). Effect of air distribution on the induced air flotation of fine oil in water emulsions. *The Canadian Journal of Chemical Engineering*, Vol. 61 Issue 4, pp. 541 – 547.

Table 1 Characteristics of IAF skim under study

Characteristic	Amount
pH	4.5- 5
COD (g/l)	425
TSS (g/l)	120
OG (mg/l)	870

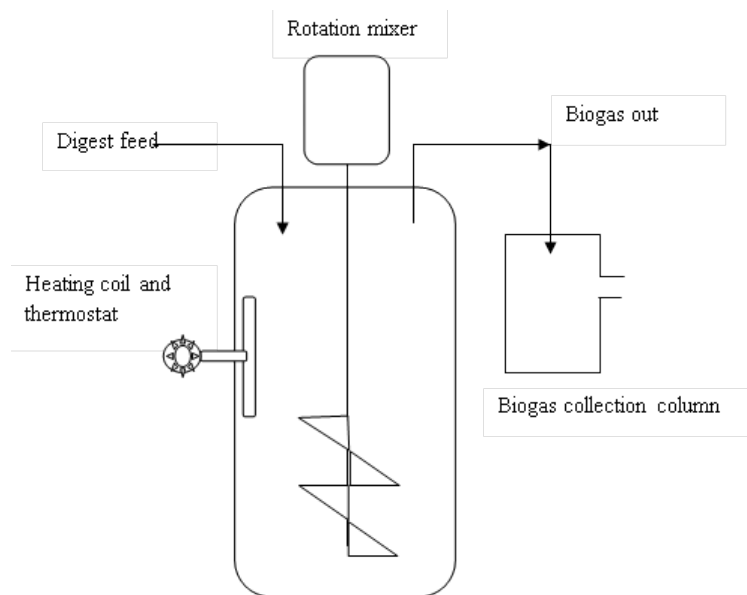


Figure 1 schematic of anaerobic digestion reactor

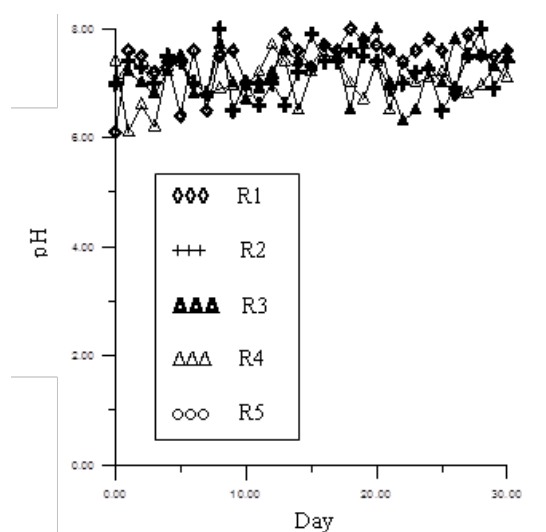
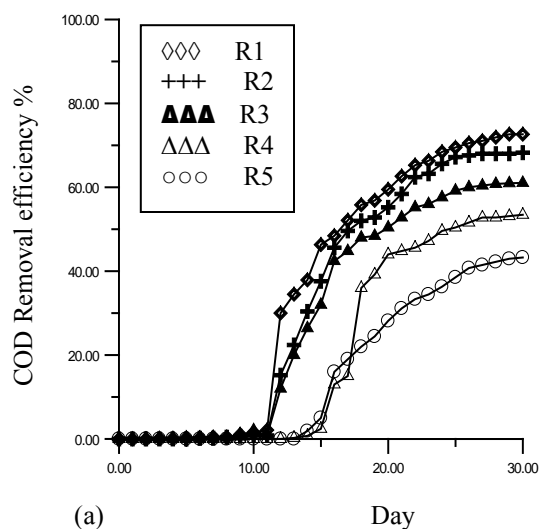
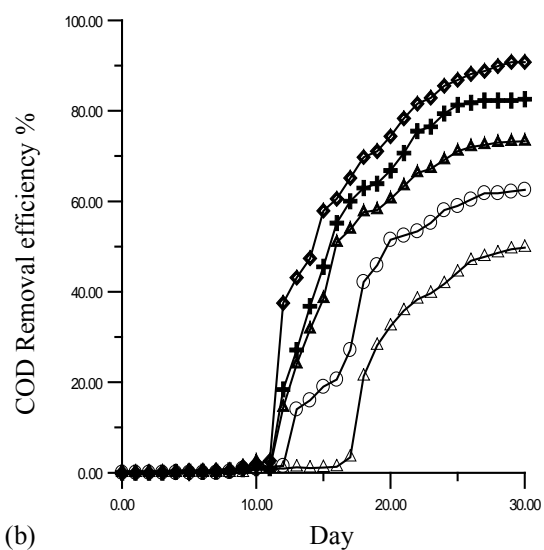


Figure 2 average daily pH values for test reactors

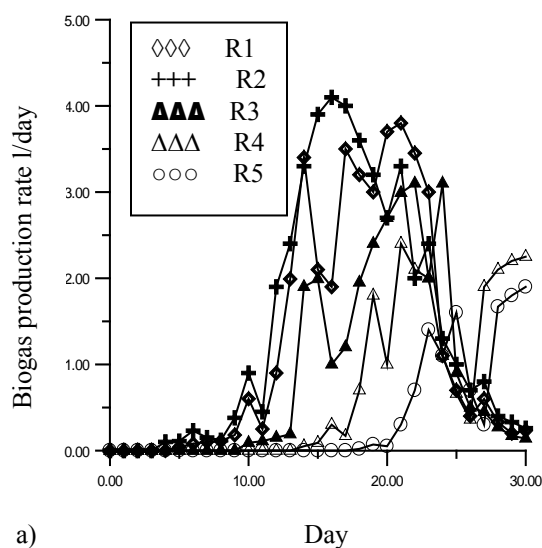


(a)

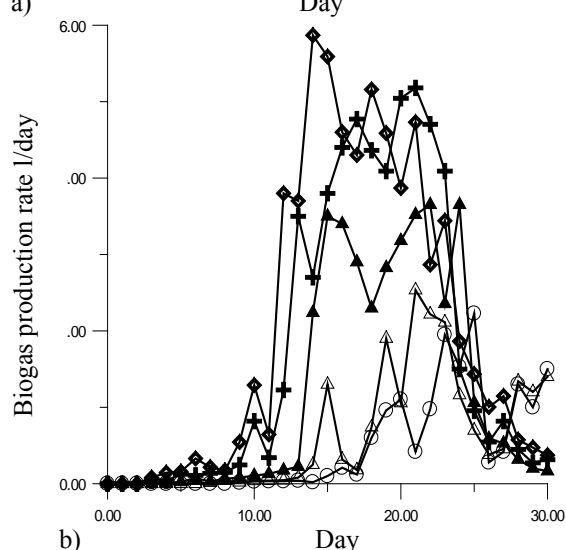


(b)

Figure 3. Daily COD removal efficiencies for the reactors R1-R5at; (a) Temperature of 25C. (b) Temperature of 45C.



a)



b)

Figure 4. Daily biogas production rate for the reactors R1-R5at; (a) Temperature of 25C. (b) Temperature of 45C.

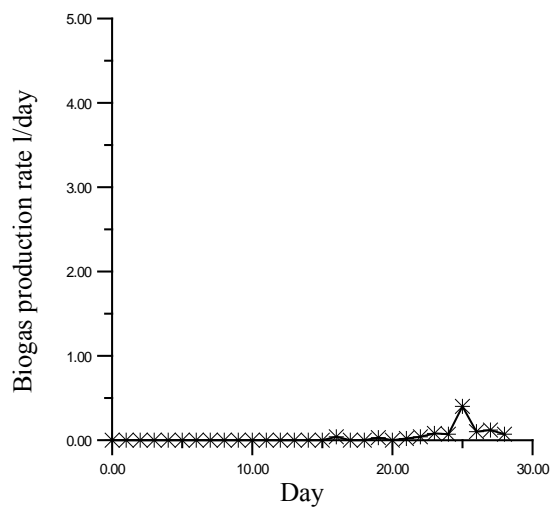


Figure 5. Biogas production rate for anaerobic digestion of livestock manure only.

Seismic evaluation of NARGES soil nailed wall under Cyclic loading and Pseudo Static forces

Ardalan Akbari Hamed¹, Mohammad Moghadaripour², Ali Ghozat³

1. Islamic Azad University, Central Tehran Branch, Tehran, I.R. Iran
2. International Institute of Seismology and Earthquake Engineering, Tehran, I.R. Iran
3. Shiraz University, Shiraz, I.R. Iran

Abstract

The more widespread use of soil nailed walls contemporary is due in large part to the demand for the construction of high-rise structures and shopping malls. Design of retaining wall needs the complete knowledge of earth pressures for both active and passive conditions. Moreover under earthquake condition, the design requires special attention. In this paper NARGES soil nailed model has been employed to study the seismic behavior. It is attempted to achieve a relation between ground seismic coefficient and ground motion amplitude to conclude the value of seismic coefficient and seismic study of this wall. Two numerical analysis methods (i.e. cyclic time history and pseudo-static) are applied to simulate the seismic behavior. The computational results show that seismic coefficient is in form of a limited range of ground seismic normalized horizontal acceleration.

Keywords: soil nailed walls, natural frequency, resonance, seismic coefficient

1. Introduction

Soil nailing consists of the passive reinforcement (i.e., no post-tensioning) of existing ground by installing closely spaced steel bars (i.e., nails), which are subsequently encased in grout. As construction proceeds from the top to bottom, shotcrete or concrete is also applied on the excavation face to provide continuity [1]. Deep excavations and retaining structures are constructed in the city of Tehran at different locations of the city due to the recent demand for the construction of high-rise structures having various basements. Tehran is located at a very seismically active region and a major earthquake magnitude of $M_w > 7.0$ is expected to occur. It is well known that flexible earth retaining structures in cuts, such as soil nailed walls, offer a great advantage for seismic conditions. As a result many soil nailed walls having of different heights have been constructed recently in the city.

The pseudo-static method is routinely used for the seismic stability analysis of soil nail walls. In this method, an equivalent seismic coefficient (k) is used within a numerical slope stability calculation. Since the seismic coefficient (k) designates the horizontal force to be used in the stability analysis, its selection is crucial. The coefficient is related to the site peak ground acceleration components.

The objectives of current paper are to observe the stability of a specific wall under seismic loads, determine the value of seismic coefficient and seismic study by pseudo static method, it is attempted to use the gained relation between ground seismic coefficient and ground motion amplitude.

2. NARGES soil nailed wall

In this research, a soil nailed wall which is located in Tehran is selected as a case study. The soil nailed wall has a depth of 23 m. The properties of the soil layers are presented in Table I. The model used in analysis was Hardening model. Fig. 1 illustrates a profile of the soil nailed wall.

Table I. Geotechnical properties of excavation

Thickness of layer	0-15	15-20	20-24	24-28	28-30	30-39	39-50
Friction angel (°)	25	28	32	25	31	33	28
cohesion (KN/m ²)	37	31	8	13	14	11	16
specific gravity (KN/m ³)	17.5	18	19	18.5	18.6	19	19

The stability analysis was carried out by using PLAXIS software which is based on the finite element method. Recommendations for the

minimum factor of safety for pull out resistance and nail bar tensile strength are set at 2 and 1.8 respectively [1]. Table II presents Characteristics of nails used in the designed excavation.

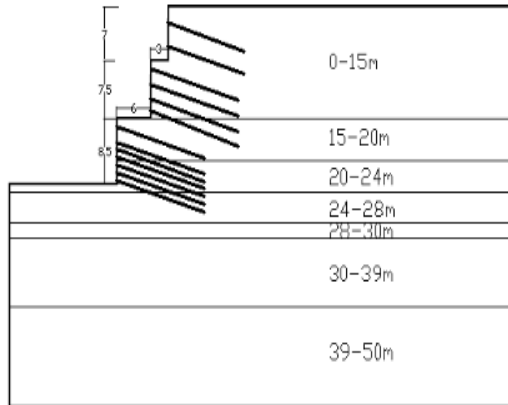


Fig. 1 Soil nailed wall with depth 23m

Geogrid and Beam elements were used to model nails and facing elements, respectively. Input parameter definitions in PLAXIS require averaging the effect of a three-dimensional problem to a two-dimensional problem. The simulation of the entire soil-nail wall construction process was carried out in a sequence of stages. In each construction stage a sufficient number of calculation steps was used to obtain an equilibrium-state.

Table II. Characteristics of nails used in the designed excavation

No.	Horizontal distance(m)	Length(m)	Diameter (mm)
1	2	12	28
2	2	12	28
3	1.5	14	32
4	1.5	14	32
5	1.5	14	32
6	1.5	14	32
7	1.5	14	32
8	1.5	14	32
9	1.5	14	32
10	1.5	14	32

11	1.5	14	32
12	1.5	14	32
13	1.5	14	32

2.1 Hardening Model

The hardening soil model is an advanced model for the simulation of soil behavior. In contrast to an elastic perfectly – plastic model, the yield surface of a hardening plasticity model is not fixed in principal stress space, but it can expand due to plastic straining. Distinction can be made between two main types of hardening, namely shear hardening and compression hardening. Shear hardening is used to model irreversible strains due to primary deviatoric loading. Compression hardening is used to model irreversible plastic strains due to primary compression in oedometer loading and isotropic loading. Both types of hardening are contained in the present model [2].

2.2 Damping

Natural dynamic systems contain some degree of damping of the vibration energy within the system; otherwise, the system would oscillate indefinitely when subjected to driving forces. In soil and rock, natural damping is mainly hysteretic — i.e., independent of frequency (Gemant and Jackson(1937) and Wegel and Walther (1935)). Rayleigh damping was originally used in the analysis of structures and elastic continua, to damp the natural oscillation modes of the system. A damping matrix, C , is used, with components proportional to the mass (M) and stiffness (K) matrices:

$$C = \alpha M + \beta K \quad (1)$$

where α = the mass-proportional damping constant; and β = the stiffness-proportional damping constant [2]. The damping ratio of soils generally varies between 2 – 5%, and this value for the structures varies between 2 – 10% (Biggs 1969) [3]. Within the scope of this study, the damping ratio used is 5%.

3. Problem Analysis

It is attempted to achieve a relation between ground seismic coefficient and ground motion amplitude to conclude the value of seismic coefficient and seismic study of this wall. The procedure of analysis is as follows:

- Dominant frequency was obtained by the following procedure. First of all different loading

frequency with a specific duration was applied to the model. Amplitude of the vibration is a factor of system response; so the vibration amplitude of each selected loading frequency was extracted and finally the Frequency corresponding to maximum response of the system is the dominant frequency of the structure. Usage of this method, was concluded to the natural frequency of 2hz for this wall (see fig. 2).

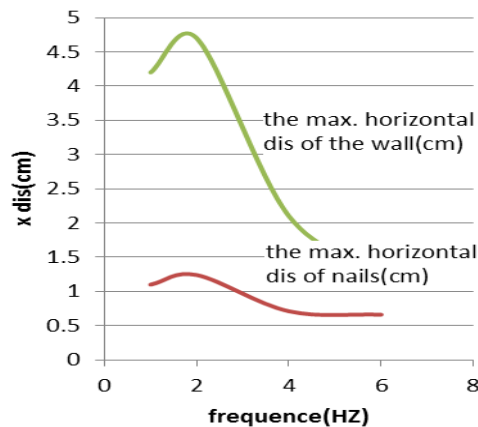


Fig 2: Reactions by different parts of wall to different frequencies

- The wall was induced by different pseudo static analysis to obtain critical seismic coefficient (a factor of safety equal to one). The k_h is defined as fraction of the normalized horizontal acceleration (A_m), which acts at the center of gravity of the wall-soil mass (AASHTO, 1996). A_m is a function of the normalized peak ground acceleration coefficient (A), which is the actual peak ground acceleration normalized by the acceleration of gravity (g), and is defined as[1]:

$$A_m = A (1.45 - A) \quad (2)$$

Assuming linearity of variable changes, the critical pullout displacement was achieved.

- At last through cyclic loading the wall was induced by different seismic amplitudes.

- By using plot of peak seismic amplitude versus critical pullout displacement which has been achieved through second step, the critical seismic amplitude can be obtained.

4. Analysis Results

The maximum axial forces mobilize in the bottom-row nails with increasing the dynamic forces.

Therefore these bottom-row nails avoid from slope failure by having anchoring effect and whenever plastic surfaces propagate behind the whole nails, It means that the bottom-row nails lost their anchoring effect and the structure will fail. Failure may occur at a specified pullout displacement of bottom-row nails. Hereafter the mentioned pulling out displacement will be known as critical pulling out displacement[4].

This method is based on supposition that failure occurs at the constant pullout displacement of bottom-row nails for both cyclic and pseudo-static analysis methods. Using this concept, relation between the critical seismic coefficient and the critical peak acceleration can be achieved. The wall was induced by different pseudo static analysis to obtain critical seismic coefficient (a factor of safety equal to one). Clearly, critical seismic coefficient is obtainable by a linear regression between seismic coefficient with the factor of safety values. The below diagram (Fig.3) presents safety factors obtained for different seismic coefficient by pseudo static analysis.

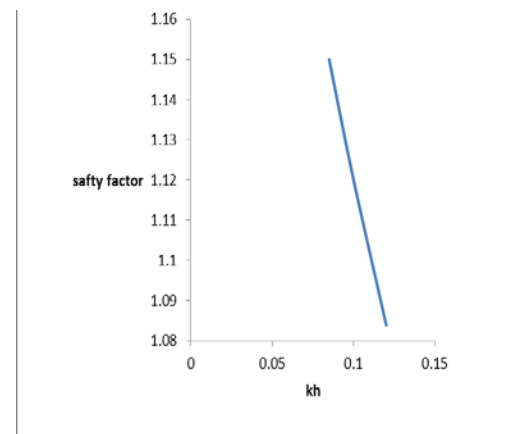


Fig. 3 Safety factors obtained for pseudo static analysis against horizontal seismic coefficient

From the above data (Fig.3), critical seismic coefficient (a factor of safety equal to one) by assuming linear change of variables and through linear regression would be achieved 0.165g. Plot of pullout displacement for bottom-row nails versus different seismic coefficients is presented in Fig. 4.

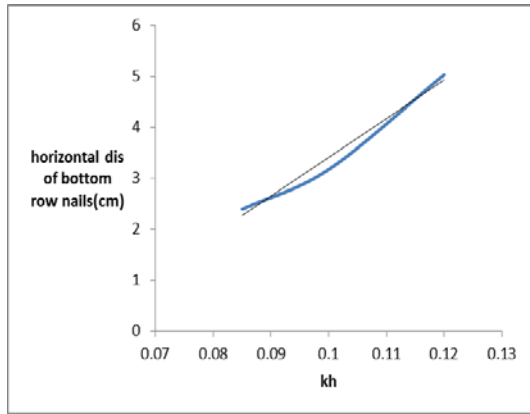


Fig 4: displacements caused by pseudo static analysis versus corresponding seismic coefficients

Assuming linearity of variable changes, based on the above diagram (Fig.4), critical displacement for critical seismic coefficient of 0.165g was obtained 8.3cm. From the above results, the critical pullout displacement achieved. Through cyclic loading the wall was induced by different seismic amplitudes and different number of cycles.

- Results of loading with frequency of 2hz and 5 cycles on the soil nailed wall is illustrated as below (see Fig.5) :

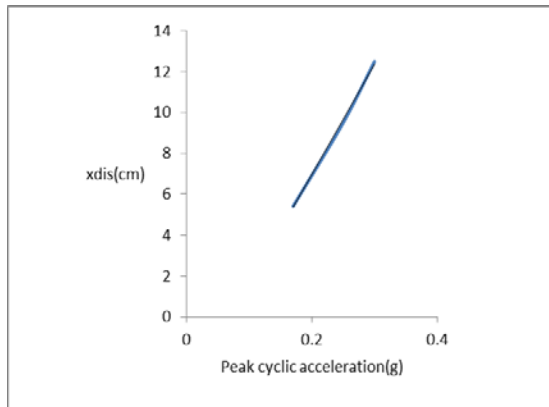


Fig. 5 displacements were conducted by seismic loading on wall for 5 cycles, frequency of 2hz and different peak amplitudes

By using the plot of peak seismic amplitude versus critical pullout displacement and the estimate of seismic amplitude at the critical pullout displacement, the critical seismic amplitude can be obtained (see Fig 5). Based on the Fig.5, maximum seismic acceleration (A) was obtained 0.22g. This value equals to 0.27g for normalized seismic acceleration (Am).

$$A_m = A * (1.45 - A) \quad (2)$$

$$k_h / A_m = 0.16 / 0.27 = 0.59$$

- Results of loading with frequency of 2hz and 8 cycles is expressed as follows (see Fig 6):

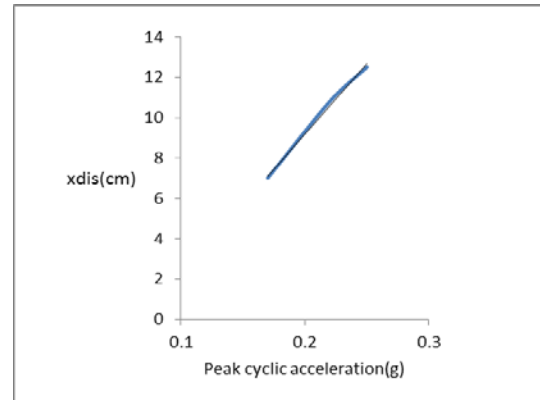


Fig. 6 displacement caused by seismic loading on the wall for 8 cycles, frequency of 2hz and different amplitude

As illustrated in the Fig.6 maximum seismic acceleration was obtained 0.18g. This amount is comparable with 0.23g for normalized seismic acceleration (Am).

$$A_m = A * (1.45 - A)$$

$$k_h / A_m = 0.16 / 0.23 = 0.69$$

- Results of loading with frequency of 2hz for 10 cycles is as follows:

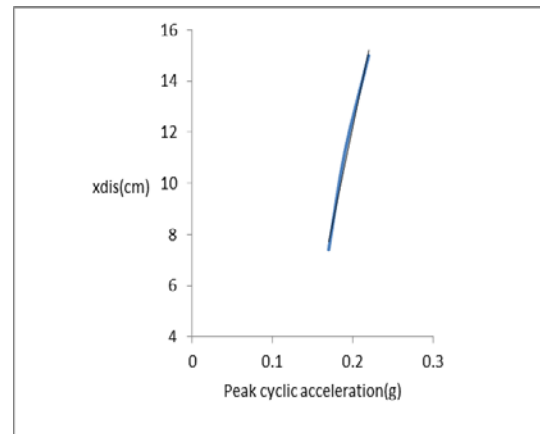


Fig. 7 displacement caused by seismic loading on the wall for 10 cycles, frequency of 2hz and different amplitudes

As illustrated in the Fig.7, maximum seismic acceleration was obtained 0.172g. This amount is comparable with 0.22g for normalized seismic acceleration (Am).

$$A_m = A * (1.45 - A)$$

$$k_h/A_m=0.16/0.22=0.72$$

The rate of critical seismic coefficient to normalized critical seismic coefficient, as shown by the results (see Fig 5 to 7), is a limited range between 0.59 to 0.72.

5. Conclusion

The results of seismic analysis of soil nailed wall in the project of NARGES have been reported. Two numerical analysis methods are applied to simulate the seismic behavior. The computational results are as below:

The values of A_m depend on the regional tectonic setting and are obtained from seismic maps, for the project region this amount is 0.35g. Obtained results from this method indicates that seismic coefficient is in form of a limited range of ground seismic normalized horizontal acceleration (i.e., 0.59 - 0.72). It means that the seismic coefficient is in form of a range (0.2g to 0.25g) which it is higher than critical seismic coefficient (0.165g).

The comparison of these values with the critical seismic coefficient indicates that this wall is probably vulnerable under earthquake effects, so its seismic resistance should be increased.

6. References

1. Federal Highway Administration Geotechnical Engineering CIRCULAR NO.7 Soil Nail Walls" prepared for us Department of Transportation , FHWA 0-IF-03-017, 2003
2. Plaxis Manual , Version 8.2 , A.A.Balkema , Netherland , 1998
3. Itasca. 2000. "FLAC (Fast Lagrangian Analysis of Continua) User's Manuals". Minneapolis: Itasca Consulting Group, Inc.
4. Komak panah, A. and Majidian, S. "Assessment of soil nailed excavations seismic failure Under cyclic loading and pseudo-static forces. International conference on Recent advances in geotechnical earthquake engineering and soil dynamics, 2010

Purification System of Ocean Sludge by Using Coagulants and Activating Microorganisms

Kyoichi OKAMOTO¹ and Kenji HOTTA¹
CST, Nihon University, Japan

ABSTRACT

Ocean sludge exerts a very big environmental load to local sea area. Here, attention was paid to micro-bubble technology for application to the purification of the sludge. The important point in this technique is to activate the bacteria existing in the area by micro-bubbles. We had developed a method for decomposing the sludge by using of microorganisms in an aerobic state by micro-bubble. We had very good results by the method, and also understood that hydrogen sulfide is reduced at first and then the nutrients will be reduced. Here, we have also a technique for purification by using “coagulants”. Therefore, we proposed the experimental way which hydrogen sulfide is reduced at first by using “coagulants” and then the nutrients will be reduced by micro-bubble and activating microorganisms. Here, we used the detergents including enzyme as the microorganism activator. Our research object in this paper is to check the purification performance for sludge by our proposed experimental system. From the results of our experiments, we succeeded in reducing the time needed to purify the sludge, and we obtained the very good performance.

Kyoichi Okamoto, Kenji Hotta, Purification System of Ocean Sludge by Using Coagulants and Activating Microorganisms

1. INTRODUCTION

It is very important to reduce sedimentary sludge in the ocean. Plans to reduce the sludge are usually dredging or sand covering. Dredging is a simple way and aims to cut off the sludge. But after cutting off, treating the dredged sludge takes much more time and, of course, cost. Sand covering, in general, gives a big load to living organisms and the ecological system. Here, a more efficient way is needed to reduce the sludge while not imparting environmental load in the local sea area.

Now, we have micro-bubble technology. Micro-bubbles (that is MB) can change conditions into an aerobic state. So, we had developed a method for decomposing the sludge by using of microorganisms in an aerobic state by micro-bubble. We had very good results by the method in [1], [2]; for example, it could be reduced the treatment days to 5 days. We had also understood that hydrogen sulfide is reduced at first in an aerobic state by micro-bubble and then the nutrients will be reduced, shown in Fig. 1.

Here, we have also a technique for purification by using “coagulants”. We had also very good results by using coagulants in [3].

Therefore, we propose the way which hydrogen sulfide is reduced at first by using coagulants and then the nutrients will be reduced in an aerobic state by micro-bubble and activating microorganisms, since we are going to reduce the treatment days more.

We used the detergents including enzyme as the microorganism activator, since we can obtain it easily and also put on the market, in [4].

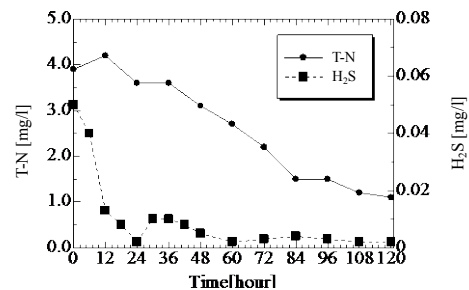


Fig.1 General results of H₂S and T-N by our experiments

Our research object in this paper is to check the purification performance for sludge by our proposed experimental system.

2. EXPERIMENTAL SYESTEM

Our proposed method for purification experiment has 2 steps. First step is that a hydrogen sulfide is reduced at first by using coagulants. Second step is that the nutrients will be reduced in an aerobic state by micro-bubble and activating microorganisms.

2.1 Experimental Apparatus and Procedure in Step 1

Sludge and seawater were put in the tank (Long70 xWidth47 xHeight 28cm) and then were mixed by a water pump (300litter/hour) for 10 minutes after coagulants were put in, shown in Fig.2.

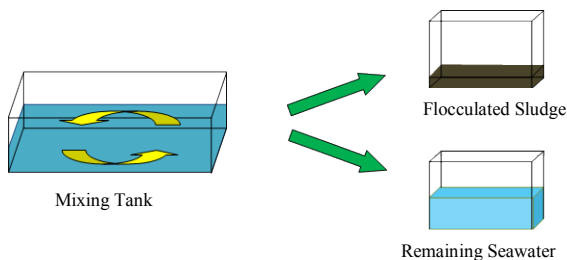


Fig.2 Schematic Representation of Experimental Apparatus in Step 1

Here, seawater is 90 (litter) and ocean sludge is 3 (kg) which were picked up from Funabashi Port in Tokyo in Japan, as shown in Fig.3 and 4. Concentration of coagulants was 400 (ppm). After sludge was changed into flocculated situation, flocculated sludge will be used for reuse and the remaining seawater is used for next experiment in step 2.



Fig.3 Gathering Instrument for Sludge

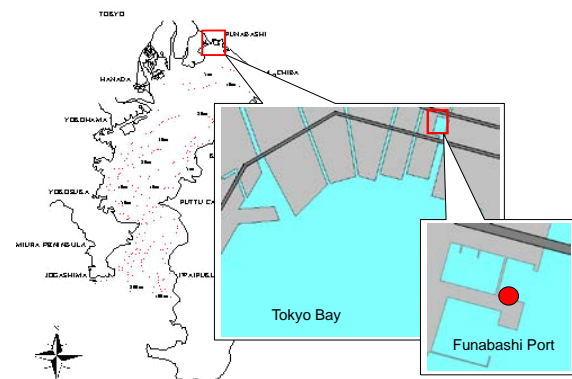


Fig.4 Catching Point of Sludge at Funabashi Port in Tokyo Bay



Fig. 5 Coagulants in this Research

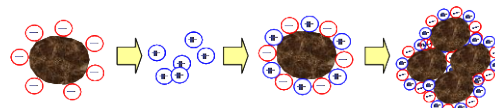


Fig. 6 Mechanism of Coagulants

2.2 Coagulants in this Paper

Our used coagulants are neutral and inorganic substance, shown in Fig.5. This is neutral and inorganic and the main ingredients of this are compound alumina and silicate. When we use this, we have to mix strongly with water after putting in. This has a characteristic of adsorption and fix-separation to cohere not only nasty substance of floating but also dissolving. This has also a characteristic of good desiccate and fixing heavy metal stable. Reaction mechanism of the coagulants is shown in Fig.6, in [5].

2.3 Experimental Apparatus in Step 2

The experimental devices in step 2 consist of two parts, shown in Fig. 7 and 8. The water circulates through two tanks. In one tank (Width40xLength28xHight28cm), micro-bubbles are generated. The micro-bubbles have micro-size diameter and high solubility. This means the water with high concentration of dissolved oxygen circulates through these tanks. The other part is the experimental tank (W60xL29 xH35cm). The remaining seawater in step 1of our experiment is put in this tank. Here, a micro-bubble generator is based on [6] and the flow rate is 1200 (litter/hour). The flow rate of water pumps connected each tanks are 300 (litter/hour).

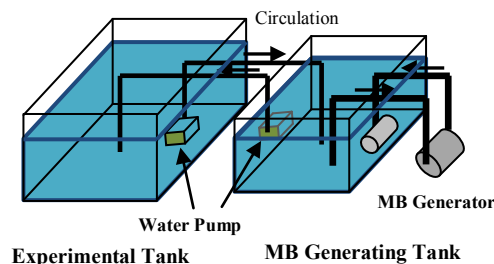


Fig. 7 Schematic Representation of Experimental Apparatus in Step 2

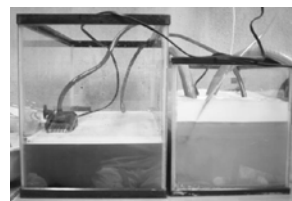


Fig. 8 Picture of Experimental Apparatus in Step 2

2.4 Experimental Procedure in Step 2

After creation of flocculated sludge by experiment as Step 1, the remaining seawater was put in the tank, and then the micro-bubble device and the water pumps were powered on. Here, room temperature was set 25 degrees Celsius by an air conditioner. After 6 hour, the microorganism activator was put in the experimental tank.

In this experiment, one kind of detergent including enzyme as the microorganism activator is used by the reasons denoted the best results in [4]. Including enzyme in the detergent are mainly lipase, protease and amylase. Amount of the detergent as experimental conditions are shown in Table. 1. The appropriate weight of this detergent is 10 (gram). For comparison, there is one more case by using the microorganism activator which had been getting effective results in purification for grease trap at gas station, written by [2], so this case is named “Case 4, 2008”.

The amount of sludge and seawater is 1(kg) and 30(litter), per an experimental case.

Dissolved oxygen (DO), water temperature and pH are measured by using of multi-parameter water quality meter. Ammonium nitrogen ($\text{NH}_4\text{-N}$), total nitrogen (T-N) and total phosphorus (T-P) are measured by using of digital-water-analyzer by digital “Packtest”, by water filtered after sampling in experimental tank.

Table. 1 Amount of Detergents as Experimental Conditions

Case	Amount(Times) (Additional / Appropriate)
①	5
②	6
③	7
④	Reference by Okamoto et al. in 2008

3 RESULTS AND CONSIDERATION

3.1 Effects on Experiment of Step 1

Results of the experiment of step 1 by using coagulants are shown in Table. 2. The results on water temperature and pH are a little change, compared with each other. We can see the situation changed into an aerobic state from the results on DO by mixing sludge with coagulant. We can also see the results of H_2S were decreased zero by the experiment of Step 1. On the other hand, the results on the nutrients; $\text{NH}_4\text{-N}$ and T-N also decrease to 70 and 53%.

Table. 2 Results on Experiment of Step 1

	Before	After
Temp. [deg. Celsius]	22.32	23.80
pH	7.37	7.95
DO [mg/l]	0.70	6.82
H_2S [mg/l]	0.02	0.00
$\text{NH}_4\text{-N}$ [mg/l]	3.42	2.38
T-N [mg/l]	2.6	1.4

3.2 Effects on Experiment of Step 2

(1) Effects on the density of sulfate and the contents of sulfur.

Checking the mechanism in this experimental system, the density of sulfate was analyzed in Case 2. The density of sulfate is shown in Fig. 8, adding the results by [2] in 2008 which is Case 4. The results were obtained by the iron chromatography. It seems that sulfate increases due to the activity of sulfur bacteria in Case 4. But the density of sulfate in Case 2 doesn't increase. It seems the reduction of H_2S became by lower density of sulfate, and microorganisms also were reduced a little by experiment of step 1.

The content of sulfur is shown in Fig.9, adding the results by [2] in 2008 which is Case 4. The results were obtained by the elementary analysis. Especially in Case 4, the content of sulfur up to 6 hours did not change but after 6 hours it decreased rapidly since the activator of microorganisms was put in the experimental tank after 6 hours. But the content of sulfur in Case 2 is almost zero. It seems that microorganisms changed the sludge into the sulfur by the ordinary method, but the present method could not change the sludge into the sulfur.

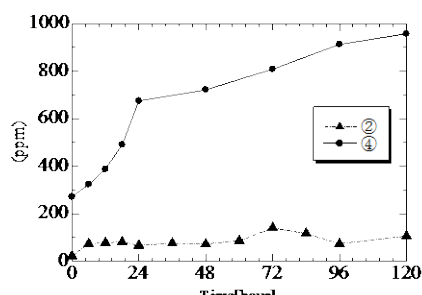


Fig. 8 Results of the Density of Sulfate in Step 2

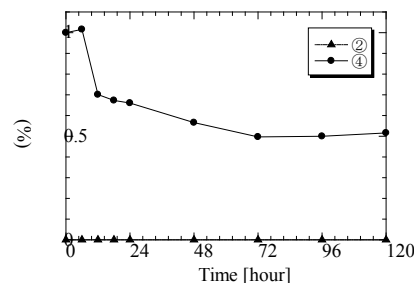


Fig.9 Results of the Content of Sulfur in Step 2

(2) Effects on H_2S .

Measured results of H_2S in all cases are shown in Fig.10. The result in Case 4 is a usual tendency. On the other hand, the results in Case 1, 2 and 3 are almost zero. It seemed coagulants in the experiment of Step 1 reduced H_2S . From the results, our method is very good.

(3) Water Temperature, pH and DO as Environmental Conditions for Experiment of Step 2.

Measured results of water temperature, pH and DO in all experimental cases are shown in Fig.11 to Fig.13, respectively. Water temperature up to 24 hours increased rapidly and then became constant about 25 to 30 degree Celsius. It seems this was caused by the heat from friction of the micro-bubble device. The tendency of pH has up and down in Case 1, 2 and 3, but became constant about 7.6 to 8.5. It seemed it is better to use for experiment. Dissolved oxygen (DO) in Case 4 up to 12 hours increased and then became constant. It seems oxygen dissolved and reached the saturation point. Case 1, 2 and 3 have a tendency of up and down but these have enough oxygen by experiment of Step 1. From these results, we can recognize anaerobic state changing into aerobic state. It seems that these results are very good conditions for growth of microorganisms.

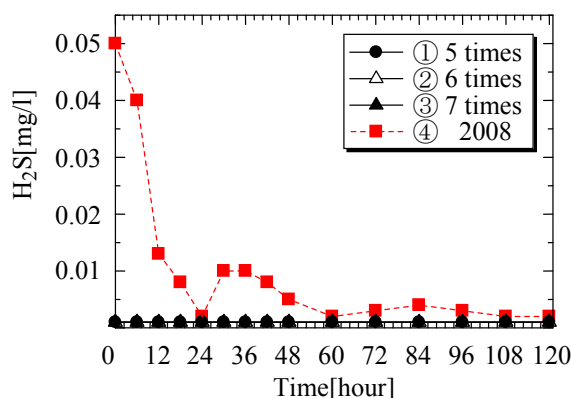


Fig.10 Changes in H_2S by Experiment of Step 2

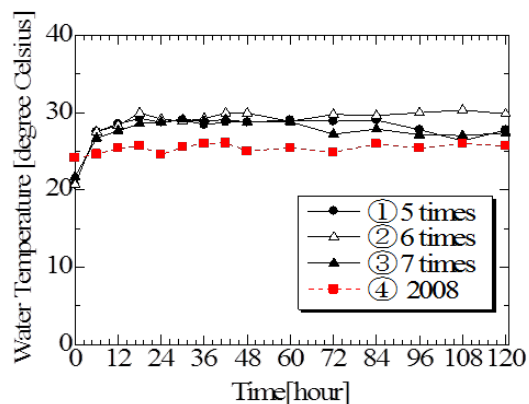


Fig.11 Changes in Water Temperature as Environmental Conditions by Experiment of Step 2

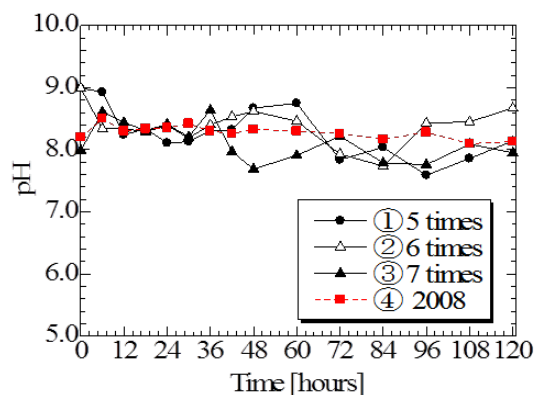


Fig.12 Changes in pH as Environmental Conditions by Experiment of Step 2

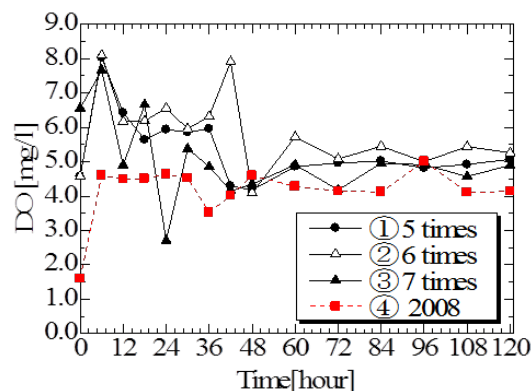


Fig.13 Changes in DO as Environmental Conditions by Experiment of Step 2

(4) Effects on NH_4-N , T-N and T-P.

Measured results of NH_4-N in Cases 1, 2 and 3 are shown in Fig.14. The results of NH_4-N in Case 1 and 2 decrease and become zero until 24 hours. But the result after 84 hours in Case 1 and 3 increase a little. It seemed the Case 2 has very good result, compared with Case 1 but Case 1 and 3 become no effect after 84 hours. Measured results of T-N and T-P in all cases are shown in Fig.15 and Fig.16. The results of T-N have a tendency of decrease until 84 hours. Case 2 has very good results that T-N is purified until 24 hours. On the other hand, the results in Case 1, 2 and 3 after 96 hours increase unexpectedly. It seemed Case 2 has very good performance for T-N, but the results are not effective after 96 hours. The results of T-P in Case 1 and 2 have good performance, compared with Case 4 by results in 2008. The results of T-P in Case 2 become no effect after 96 hours. From this experiment, we pointed out the decrease on T-N

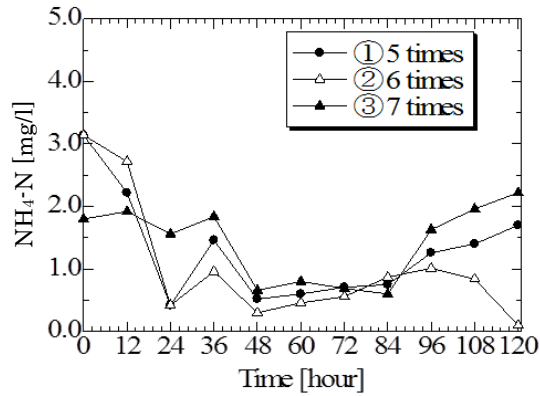


Fig. 14 Changes in $\text{NH}_4\text{-N}$ for Experiment of Step 2

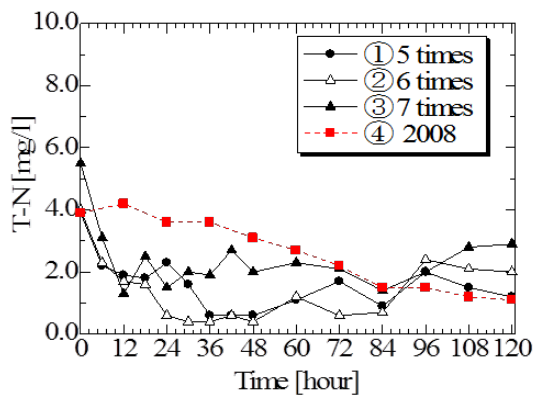


Fig. 15 Changes in T-N for Experiment of Step 2

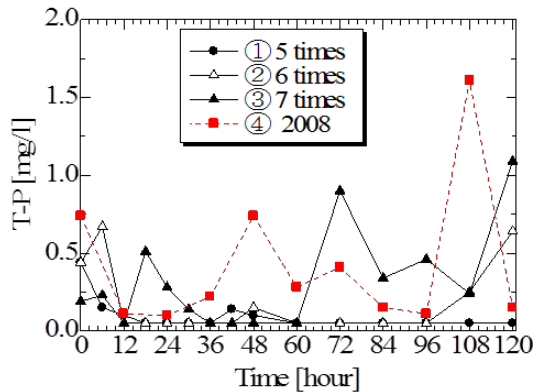


Fig. 16 Changes in T-P for Experiment of Step 2

4 RESULTS OF RE-EXPERIMENT AND CONSIDERATION

It seems our proposed method is very good until 84 hours from the results of experiment of Step 2. For getting the best purification, we had carried out re-experiments to put the activator twice in experiment of step 2, because the results are not effective after 96 hours.

4.1 Re-Experiments

Experimental conditions for the method of adding the activator twice are shown in Table. 3. Second adding amount of Case 5, 6, 7 is 2, 4, 6 times of activator at time=60hours, respectively. For comparing the effects, the results of Case 2 in experiment of step 2 are used. The other conditions are almost same of experimental of step 2. Measured results on environmental condition of this re-experiment were also almost same of experiment of step 2.

4.2 Effects on $\text{NH}_4\text{-N}$ and T-N

Measured results of $\text{NH}_4\text{-N}$ in Cases 5, 6 and 7 are shown in Fig.17, with Case 2 in experiment of step 2. The results of T-N are also shown in Fig.18.

The re-experimental system has very good performance from these results. $\text{NH}_4\text{-N}$ of Case 5 can be purified until 72 hours. T-N of Case 5 and 6 can be also purified until 84 hours. It seems that we could get very good performance for purification by adding the activator of microorganisms and reduce the time for purification, since purification performance was shortage from the results in experiment of step 2.

Table. 3 Method of Adding Activator as Re-Experimental Conditions

Case	Method of Adding Activator (Amount(Times)=Additional/Appropriate)	
	First adding at time=0	Second adding at time=60hour
⑤	6 times	2 times
⑥		4 times
⑦		6 times
②		0

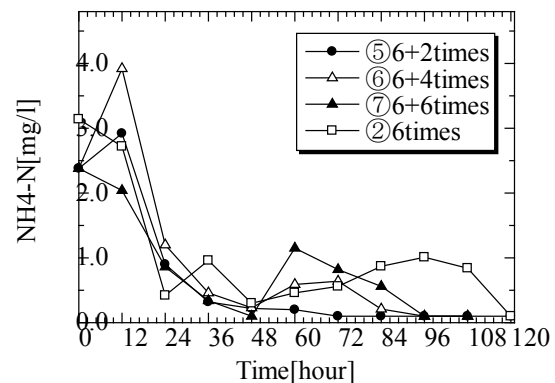


Fig.17 Results on $\text{NH}_4\text{-N}$ by Re-Experiment

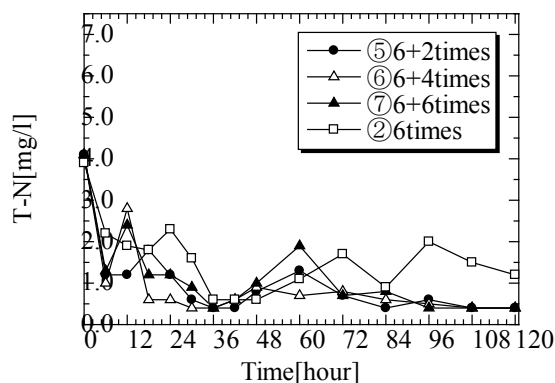


Fig.18 Results on T-N by Re-Experiment

5 CONCLUSIONS

We proposed the system which hydrogen sulfide is reduced at first by using coagulants and then the nutrients is reduced in an aerobic state by micro-bubble and activating microorganisms. Here, we used the detergents including enzyme as the microorganism activator.

We also carried out purification experiments and then checked the purification performance for sludge by our proposed experimental system. From the results by the experiment of Step 1 and 2,

- 1) It seemed coagulants in the experiment of Step 1 reduced H_2S .
- 2) It seemed microorganisms also are reduced a little by coagulants in the experiment of step 1.
- 3) The performance of purification in Case 2 is very good for the results on T-N and also NH_4-N , until 84 hours.
- 4) The results of T-P in Case 1 and 2 have good performance, compared with the results in 2008.

Here, we carried out re-experiment which was put twice of activator at 0 and 60 hours, since the purification performance was shortage from the results in experiment of step 2.

From the results by re-experiment, we could get very good performance for purification and reduced the time for purification.

Finally, it is seemed our proposed experimental system is very good.

6 ACKNOWLEDGMENT

The authors would like to express sincere thanks to Dr. T. Toyama, Nihon University, in Japan

7 REFERENCES

- [1] Okamoto K, Hotta K, Toyama T, and Kohno H, "Experiments on purification of ocean sludge by activating microorganisms," Proc. of ISOPE-2011-TPC-574.
- [2] Okamoto K, and Hotta K, "Purification experiments on sedimentary sludge by microorganism activator," Proc. of Pacific Congress on Marine Science and Technology (PACON2008).
- [3] Okamoto K, and Hotta K, "Experiment on purification for water quality by using of cohesion powder," Proc. of ISOPE-2006-JSC-306.
- [4] Okamoto K, Hotta K, Toyama T, and Kohno H, "Purification experiments of ocean sludge by activating microorganisms -by using detergent including enzyme as the activator-, " Proc. of ISOPE-2012-TPC-379.
- [5] Matsui R, Okamoto K and Hotta K, "Water Purification Experiments by Micro Bubble," Book of Recent Advances in Marine Science and Technology, 2006, pp.119-126.
- [6] Imai T, Shiohige K, Ukita M, Sekine M, Higuchi T, Fukagawa K and Fujisato T, "Development of Device for Dissolving High Concentration Gas for Purification at bottom layer around enclosed water area like Dam Lake," Proc. 39th Forum on Environmental Engineering of Civil Engineering Society, 2002, 10-12.
- [7] Matsuo K, Maeda, K, Ohnari, H, Tsunami, Y, and Ohnari, H, "Water Purification of a Dam Lake Using Micro Bubble Technology," Progress in Multiphase Flow Research I, 2006, pp.279-286
- [8] Mizoguchi M, "Observation of Water Purification Process in a Moat by Microbiological Treatment Technique," Proc. of Biological Resource in Mie University, No.16, 1996, pp.25-37.
- [9] Hibino T and Matsumoto H, "Distribution of Fluid Mud Layer in Hiroshima Bay and its Seasonal Variation", Proc. Civil Engineering, Vol. 62, No 4, 2006, pp.348-359.

Mechanical properties of volcanic products mixed with industrial wastes

K. Yamamoto¹, T. Negami², M. Hira¹, N. Aramaki³ and Y. Hayashi⁴

¹Kagoshima University, ²Saga University, ³Sojo University and ⁴Kyushu Sangyo University, Japan

ABSTRACT

Mt. Shinmoedake, located on the boundary between Kagoshima and Miyazaki has erupted on January 26, 2011 after an interval of 189 years. The Volcanic products are estimated to be a maximum of 40-80 million tons. On the other hand, the frequency of eruptions at Mt. Sakurajima in Kagoshima peaked in 2011, the highest since observations began in 1955. Large amounts of volcanic ashes from Mt. Sakurajima were falling in the surrounding areas. Most of volcanic products have been disposed as industrial wastes, but the supply of these volcanic products is anticipated to be unending for the foreseeable future. The purpose of this study is to contribute to the formation of a recycling-oriented society in the Southern Kyushu area by utilizing the volcanic products as local natural resources. This study investigates the mechanical properties of these volcanic products mixed with industrial wastes for environmental protection.

Keywords: volcanic products, compaction, California bearing ratio, recycling-oriented society

1. INTRODUCTION

Mt. Shinmoedake and Mt. Sakurajima are located in Southern Kyushu and are both active volcanoes in Japan. Due to the recent serious seismic activities in Japan, these eruptions have been recently activated. A large amount of volcanic products are already supplied in the Southern Kyushu area and the constant supply of these products is anticipated from now on. The purpose of this study is to contribute to the formation of recycling-oriented society by utilizing the volcanic products as local natural resources. This study investigates the mechanical properties of the volcanic products mixed with industrial wastes for environmental protection. The mixture of industrial wastes is scrapped ceramics, reclaimed (recycled) gypsum and slaked lime, etc. The mixture ratio is the weight ratio for the natural water content of the volcanic products. In this paper, the possibility of the effective use as a frictional geomaterial (ϕ materials) is considered.

2. PHYSICO-CHEMICAL PROPERTIES OF VOLCANIC PRODUCTS

The volcanic products of Mt. Shinmoedake and Mt. Sakurajima sampled in Miyakonojyo and Kagoshima, as shown in Figure 1. Figure 2 shows the microscopic observation of each volcanic product. It can be observed that the particle size of Shinmoedake is obviously larger than that of Sakurajima. Table 1 shows the physico-chemical properties of each volcanic product. The volcanic products of Sakurajima showed heavier density and lower permeability than those of Shinmoedake. In addition, those of Shinmoedake and Sakurajima were found to have weak acidity and alkaline, respectively.

Figure 3 shows the grain size distribution curve. The volcanic products of Shinmoedake were mainly sand, but the content (by percentage) of fines was higher for material from Sakurajima. Thus, the mixture of each volcanic product was taken into account, because the properties of pH and grain size distribution were different. The mixture ratio was set as the weight ratio 70:30, 50:50, 30:70 (%) for the natural water content of each volcanic product. When the mixture ratio of Shinmoedake increases, the percentage content of fines is reduced. Next, Figure 4 shows the compaction curve for each volcanic product. The compaction test [1] was conducted by A-a method, where the compaction energy is low and the sample is repeatedly used. It is found that the volcanic products of Shinmoedake show a higher optimum water content and lower maximum dry density than those of Sakurajima.

3. RESULTS AND DISCUSSION

The California bearing ratio (CBR) test [2], which is available for the evaluation of the strength of subgrade or subbase was carried out in the laboratory to obtain the design CBR value. Slaked lime, reclaimed gypsum and scrapped ceramics are used as the mixture of industrial wastes, and the mixture ratio is the weight ratio for the natural water content of each volcanic product. Figure 5 shows the loading pressure-penetration curve for each artificial geomaterial. Figures 5(a) and (b) are the cases of Shinmoedake and Sakurajima mixed with slaked lime. The loading pressure of mixtures of Shinmoedake is higher than that of only Shinmoedake, when the mixture ratio of slaked lime increases. On the other hand, Sakurajima mixed with slaked lime at ratios of 10% and 20% can not exceed the loading pressure of only Sakurajima. This is because the volcanic products of

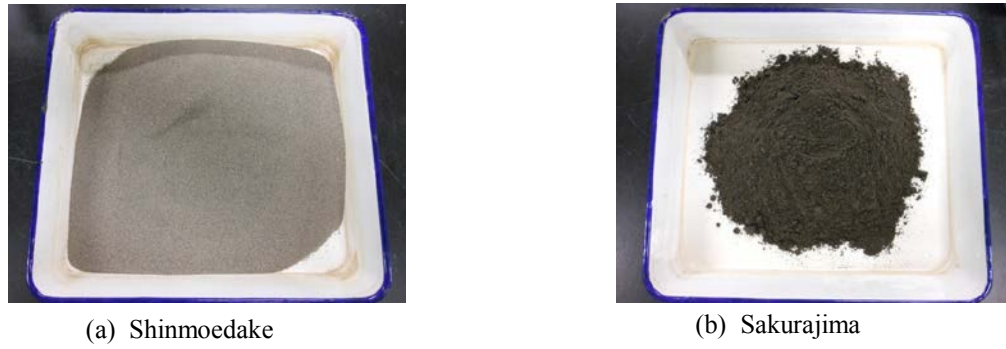


Figure 1 Volcanic products sampled in southern Kyushu area.

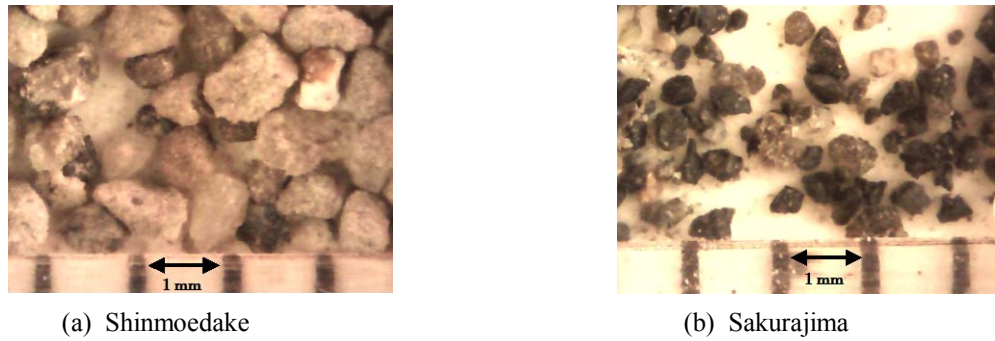


Figure 2 Microscopic observation of volcanic products.

Table 1. Physico-chemical properties of volcanic products

	Shinmoedake	Sakurajima
Natural water content (%)	10.5	10.5
Soil particle density (g/cm^3)	2.685	2.708
Minimum density (g/cm^3)	1.126	1.385
Maximum density (g/cm^3)	1.460	1.654
Permeability coefficient (cm/s)	1.6×10^{-2}	2.0×10^{-4}
pH	6.40	7.91

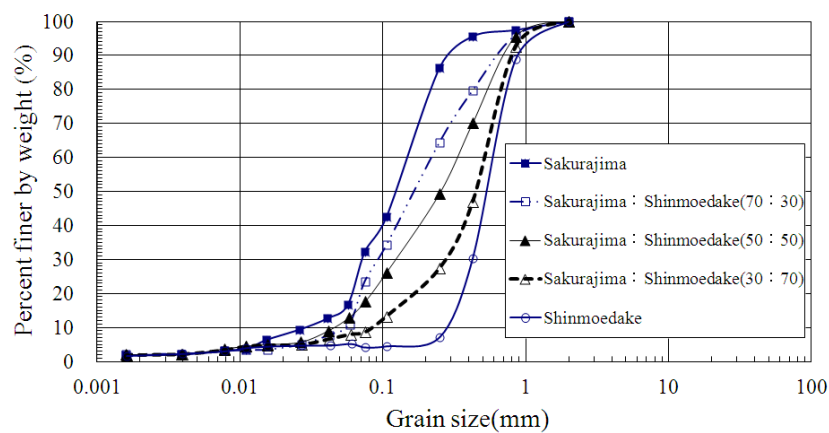
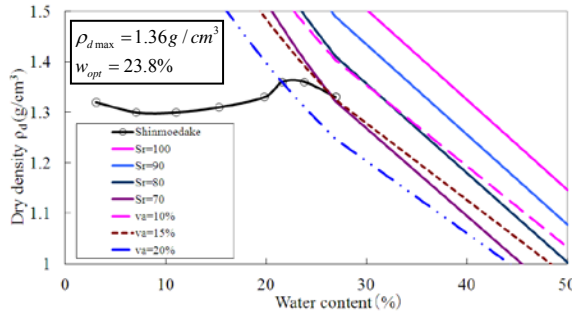
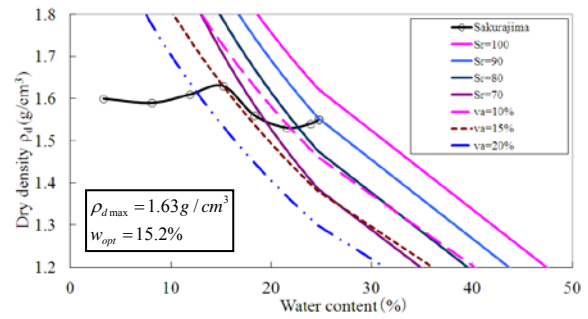


Figure 3. Grain size distribution curve.

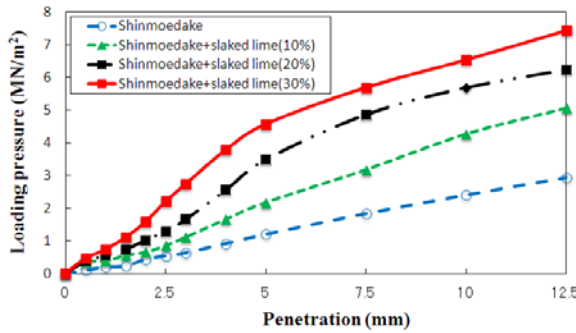


(a) Shinmoedake

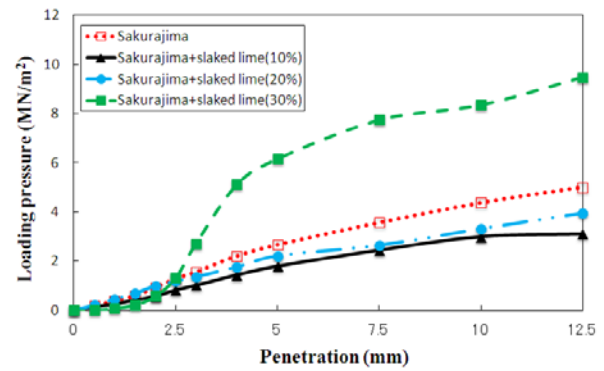


(b) Sakurajima

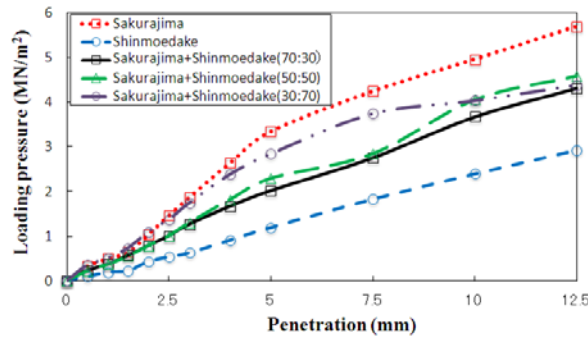
Figure 4 Compaction curve.



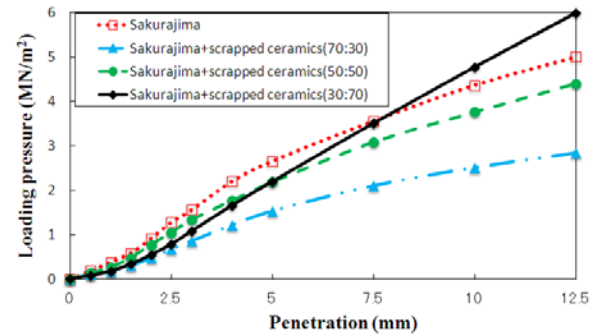
(a) Shinmoedake plus slaked lime



(b) Sakurajima plus slaked lime



(c) Shinmoedake plus Sakurajima



(d) Sakurajima plus scrapped ceramics

Figure 5 Loading pressure-penetration curve.

Shinmoedake are mainly sand with weak acidity and those of Sakurajima are a finer sand and alkalinity.

Figure 5(c) shows the case of the mixture of each volcanic product (Shinmoedake and Sakurajima). The obvious difference in the loading pressure between only Shinmoedake and Sakurajima is seen and the loading pressure-penetration curves of the mixture of each volcanic product are caught between the curves of only Shinmoedake and Sakurajima. The loading pressure of Sakurajima is clearly higher than that of Shinmoedake. Additionally, we have confirmed that the

loading pressure is somewhat dependent on the mixture of samples by the inside observation of samples after the penetration.

Figure 5(d) is the case of Sakurajima mixed with scrapped ceramics. When the mixture ratio of scrapped ceramics increases, the loading pressure tends to become higher. But the mixture of scrapped ceramics to Sakurajima has no effect before the penetration reaches 5 mm. The trend was the same for Shinmoedake. It is thought that the interlocking between these volcanic products and scrapped ceramics would not be

Table 2. CBR (%) obtained from volcanic products and those mixture

	Shinmoedake	Sakurajima	Mixture
only volcanic products	11.59	25.86	
volcanic products plus slaked lime 10%	21.04	17.30	
volcanic products plus slaked lime 20%	33.88	21.40	
volcanic products plus slaked lime 30%	44.40	59.74	
volcanic products plus reclaimed gypsum 10%	28.09	51.07	
volcanic products plus reclaimed gypsum 20%	42.65	113.43	
volcanic products (70%) plus scrapped ceramics (30%)	5.44	14.89	
volcanic products (50%) plus scrapped ceramics (50%)	4.28	21.22	
volcanic products (30%) plus scrapped ceramics (70%)	-	21.31	
Sakurajima (30%) plus Shinmoedake (70%)			27.64
Sakurajima (50%) plus Shinmoedake (50%)			22.29
Sakurajima (70%) plus Shinmoedake (30%)			19.62

effective. Note that there was no expansion in all cases shown in Figure 5. Furthermore, the mixture of reclaimed gypsum to each volcanic product is more effective than that of slaked lime for the loading pressure-penetration curve. Finally, the design CBR(%) values from volcanic products and these mixtures are summarized in Table 2. The volcanic products of Shinmoedake mixed with slaked lime 10% and 20% show higher CBR values than those of Sakurajima. In other all cases, the tendency was the reverse (the mixtures of Sakurajima are almost always a higher loading pressure than those of Shinmoedake).

4. CONCLUSIONS

In general, it would be valid to utilize these volcanic products as frictional geomaterials under sufficient compaction control. Also, there are no problems in using each volcanic product as a subgrade soil because the design CBR values of volcanic products only are greater than 10% with no expansion. The mixture of slaked lime and reclaimed gypsum were effective for the volcanic products of Shinmoedake, but the mixture of reclaimed gypsum was more effective than that of slaked lime for those of Sakurajima. Furthermore, since the volcanic products of Sakurajima are mainly finer sand and very little spread, the strength of the mixtures of Sakurajima tends to vary a little than those of Shinmoedake.

For future work, it will be possible to consider the development of base materials for fishing banks and seaweed beds as a practical use of these volcanic products and industrial wastes.

5. REFERENCES

- [1] Japanese Geotechnical Society, Soil test –basis and guideline- (first revised edition): Maruzen Print Co. Ltd., 2011, pp. 71-78 (in Japanese).
- [2] Japanese Geotechnical Society, Soil test –basis and guideline- (first revised edition): Maruzen Print Co. Ltd., 2011, pp. 79-90 (in Japanese).

Measurement of Hydraulic Conductivity for Peat Ground Using CPTU

Hirochika Hayashi and Satoshi Nishimoto
Civil Engineering Research Institute for Cold Region, Japan

ABSTRACT

In-situ permeability tests were conducted on peaty ground in Hokkaido, Japan to clarify the permeability of such ground and a method for determining permeability parameters for related finite element (FE) analysis. As a result, it was confirmed that the hydraulic conductivity (coefficient of permeability k_i) obtained from in-situ permeability testing which presents the mean permeability of the peat layer ranged from 1.7×10^{-7} to 1.1×10^{-5} (m/s). In addition, a dissipation test using the CPTU was conducted and time values for 50% dissipation of excess pore water pressure (t_{50}) were measured. It was found that the coefficient of permeability k_i of peat decreased with an increase in the t_{50} .

Keywords: peat, coefficient of permeability, in-situ permeability test, CPTU, oedometer test

1. INTRODUCTION

Peat ground, which consists of very soft and problematic soil, is widely distributed in Hokkaido, Japan. When constructing embankments on soft ground types such as peat, considerable ground deformation occurs caused by both the consolidation and shear (Fig. 1). A highly effective method of analyzing such ground deformation is soil/water coupled finite element analysis (FE analysis) using a constitutive model that can take both consolidation and shear into account. Hayashi et al. [1] clarified that FE analysis using Cam clay model (Schofield and Wroth [2]) was effective in analyzing peat ground. It can therefore be understood that FE analysis using an elasto-plastic or visco-plastic model for clay is a suitable method for clarifying the deformation of peat ground.

Peat ground has many engineering properties that have not yet been clarified, which poses the practical problem of how to determine the soil parameters for analysis. Hayashi et al. [3] proposed a method of determining parameters for elasto-plastic FE analysis of peat, but merely reached a tentative conclusion in terms of hydraulic conductivity (coefficient of permeability) determination. Therefore, the

coefficient of permeability and changes in this value resulting from consolidation for peat ground were investigated based on the results of an in-situ permeability test and oedometer test, and influences related to differences in the coefficient in peat ground on the results of FE analysis were studied.

2. INVESTIGATION SITES

The permeability characteristics of peat ground were investigated at nine sites (Mihara and Shinotsu in Ebetsu City, Tsuruno in Kushiro City, Warabidai in Toubetsu Town, Riyamunai and Kami-Riyamunai in Kyowa Town, Taura in Mukawa Town, Onobunai in Teshio Town and Asajino in Sarufutsu Village) in Japan's Hokkaido area.

The natural water content (W_n) of the peat studied ranged from 240 to 1,023%, and ignition loss (L_i) was 23 to 95%. The study was conducted for peat with a wide variety of engineering properties, from the mostly decomposed low-water-content type to the high-water-content fibrous type. For comparison with peat, organic clay and clay underlying the peat ground were also tested.

3. TEST PROCEDURES

An in-situ permeability examination involving a borehole and dissipation of pore water pressure using the electric cone penetration test (CPTU) method was conducted. In the laboratory, an oedometer test was conducted with undisturbed samples, and the results were used to determine coefficients of permeability. The test methods are detailed below.

3.1 In-situ permeability test

The in-situ permeability test was conducted in accordance with the Method for Determination of Hydraulic Properties of Aquifer in Single Borehole (JGS 1314-2003) in the Japanese Geotechnical Society standards (Fig. 2). The in-situ coefficients of permeability were found using Eq. (1), in

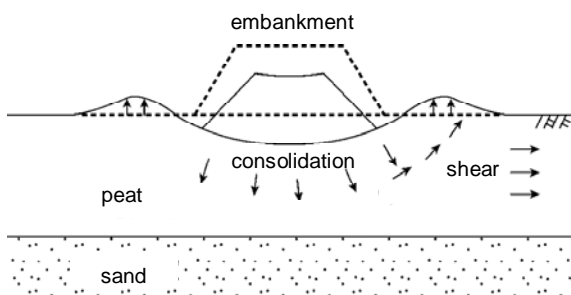


Fig. 1 Typical deformation of peat ground caused by embankment loading

which k_i is the on-site coefficient of permeability (m/s), d is the diameter of the water level measurement section (m), L is the length of the test section (m), D is the diameter of the test section (m), m is the slope of the straight section of the log s - t curve found from water level measurement, s is the difference between the steady and measured water levels (m), and t is the elapsed time (s).

$$k_i = 0.66 d^2 / L \log (2L / D)^m \quad (1)$$

3.2 Dissipation test using the CPTU method

In the CPTU method, pore water pressure is generated when a cone penetrates the ground. If the ground is left untouched after penetration stops, the pore water pressure generated dissipates over time, and the time it takes to do so is closely related to ground permeability. Dissipation testing of pore water pressure using the CPTU method involves estimation for the coefficients of ground permeability and consolidation based on this phenomenon. High applicability of the test for clay ground has been reported previously (e.g., Robertson et al. [4]; Tanaka et al. [5]).

Figure 3 shows the shape of the cone used in this study. It had a base area of 1,000 mm² and a point angle of 60°. The filter for pore water pressure measurement was placed 19.0 mm behind the base of the cone, as shown in Fig. 3. The filter was ceramic and saturated with deaired water. The cone was used to penetrate the ground with these specifications at a rate of 20 mm/s, and penetration was stopped at the depth where the in-situ permeability test was conducted. Changes in pore water pressure were subsequently measured with the cone in place. To avoid interference between the in-situ permeability test and CPTU application, the test sections were positioned at least 2 m apart.

3.3 Oedometer test

The oedometer test was conducted in accordance with the Japanese Geotechnical Society standard on undisturbed samples (dimensions: 60 mm in diameter and 20 mm in thickness) collected using a thin-walled tube sampler with a fixed piston. As the effective overburden pressure of peat is very small, consolidation pressure at the first stage was set to 4.9 kN/m², which was half the standard value. The laboratory coefficient of permeability was found using Eq. (2), where k_l is the laboratory coefficient of permeability (m/s), c_v is the coefficient of consolidation (cm²/d), m_v is the coefficient of volume compressibility (m²/kN) and γ_w is the unit weight of water (= 9.81 kN/m³).

$$k_l = c_v m_v \gamma_w / (8.64 \times 10^8) \quad (2)$$

4. COEFFICIENT OF PERMEABILITY OBTAINED FROM IN-SITU PERMEABILITY TESTS AND OEDOMETER TESTS

Figure 4 shows the relationship between the natural void ratio

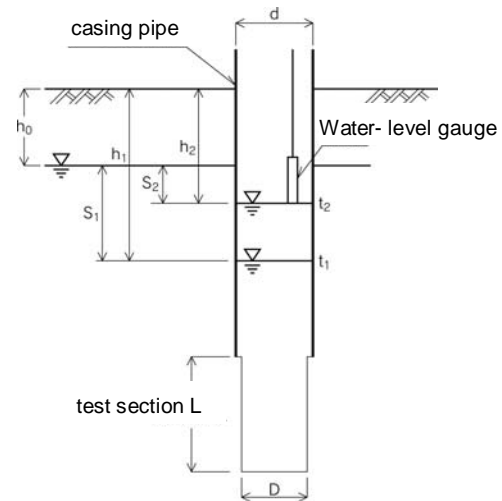


Fig. 2 In-situ permeability testing method

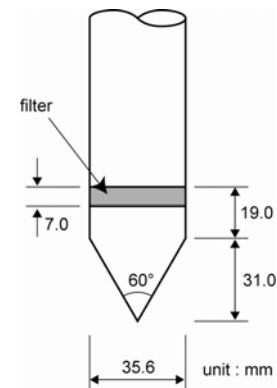


Fig. 3 Shape of CPTU

and the field coefficient of permeability. Permeability coefficient of peat, which ranged from 1.7×10^{-7} to 1.1×10^{-5} (m/s), was greater by one or two orders of magnitude than those of clay and organic clay. The field permeability coefficient of peat increased almost linearly on the logarithmic axis with higher values of the natural void ratio. The natural void ratio of peat approximately ranged from 8 to 15. These values were much larger than those for ordinary soils, indicating that peat is predominantly composed of voids. It should be noted, however, that the coefficient of permeability for peat is smaller than that for sand, which has a lower natural void ratio. Ohira [6] pointed out that most voids in peat were enclosed in plant remains and only approximately 20% of all voids were effective as macroscopic pore water flow paths. Kogure [7] reported that water in peat contained humus formed as organic matter decomposition, and was therefore higher in viscosity than that found in ordinary soil. These factors can support that the coefficient of permeability in peat shows middle value between that of clay and sand despite of its very high natural void ratio.

The relationship between the field and laboratory coefficients of permeability is shown in Fig. 5. The

laboratory coefficient values correspond to the effective overburden pressure from the relationship between the consolidation pressure P and the coefficient of permeability k (the log P -log k relationship) obtained in the oedometer test. The ratio of the field coefficient to the laboratory coefficient of permeability (k_i/k_l) ranged approximately from 3 to 7 for clay but was larger for peat, mostly ranging approximately from 10 to 100. Kogure [7] pointed out that areas surrounding large dead plant and shrub remains in peat ground likely became to water flow paths. In oedometer tests for peat, samples are limited in size and need to be prepared while avoiding large dead plant remains. For this reason, the coefficient of permeability obtained from oedometer tests fails to evaluate macroscopic water flow paths in peat, and may underestimate the permeability of the entire soil layer.

The relationship between in-situ void ratio and k_i/k_l is shown in Fig. 6. k_i/k_l roughly increases with an increase in in-situ void ratio. Peat with higher values of in-situ void ratio contains larger amounts of undecomposed large dead plant re-mains. It can be inferred that this tendency is a result of accumulation containing a large number of macroscopic pore water flow paths.

5. IN-SITU PERMEABILITY ESTIMATION FROM DISSIPATION TESTING USING THE CPTU

This section describes estimation of the in-situ coefficient of permeability in peat ground based on dissipation testing of pore water pressure using the CPTU method. Figure 7 shows the time history of pore water pressure generated by cone penetration (for the Riyamunai site at a depth of 3.0 m) as a typical measurement result. The pressure reached an almost steady state approximately 1,000 seconds after penetration stopped, and showed a value of 28.1 kPa thereafter. The result of pore water pressure estimation after the measurement period (until 10,000 seconds) using the hyperbola method also confirmed that the steady water pressure (U_f) value was 28 kPa. As the groundwater level of this site was 0.26 m below the surface, the static water pressure at the depth where the dissipation test was conducted (G.L. -3.0 m) was 27.4 kPa, which was almost the same as the U_f value. Similar results were obtained at other sites.

Past studies (e.g., Robertson et al. [4]; Tanaka et al. [7]) used the time taken for 50% of pore water pressure to dissipate (t_{50}) in the dissipation curve (Fig. 7) as an index to represent the dissipation status. Figure 8 shows the relationship between t_{50} and the in-situ coefficient of permeability described in Section 5 based on a double logarithm. There is a proportional relationship between the two, and the in-situ coefficient of permeability decreases linearly with higher values of t_{50} . Robertson et al. [7] also reported that the coefficient of permeability fell with increases in t_{50} based on examination of the relationship between these values for clay.

The relationship shown in Fig. 8 is approximated using Eq. (3), where k_i is the in-situ coefficient of permeability (m/s) and t_{50} is the time taken for 50% of the pore water

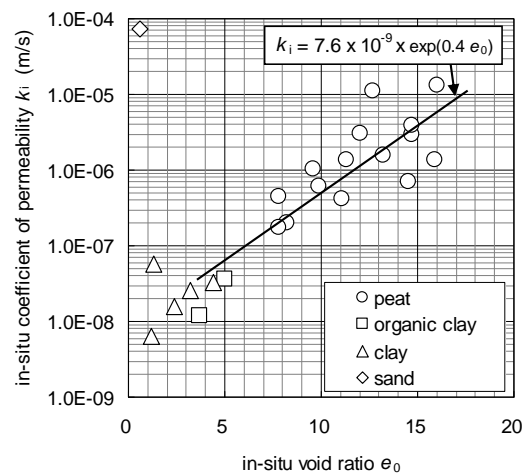


Fig. 4 The relationship between in-situ void ratio and in-situ coefficient of permeability

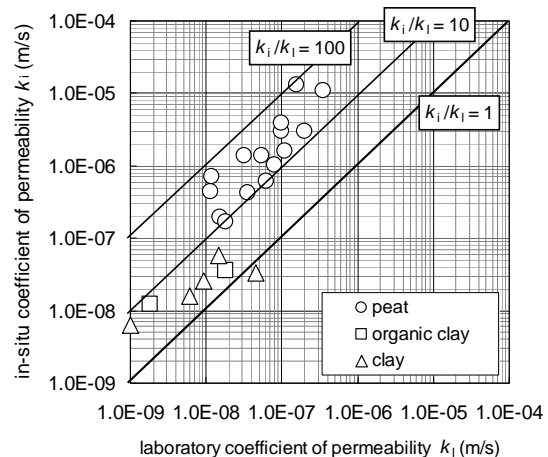


Fig. 5 The relationship between laboratory and in-situ coefficient of permeability

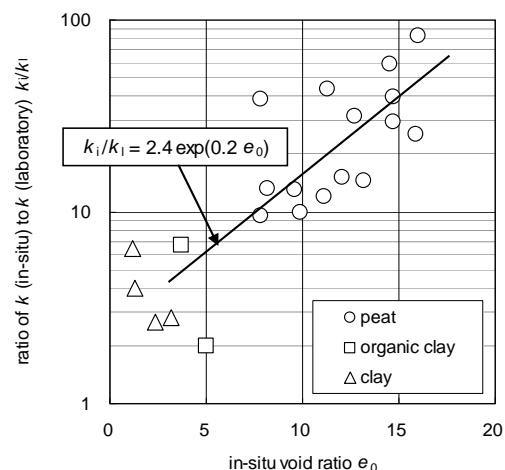


Fig. 6 The relationship between in-situ void ratio and ratio of in-situ to laboratory coefficient of permeability

pressure to dissipate (min.). It is considered possible to estimate the in-situ coefficient of permeability in peat ground based on this relationship from dissipation testing of pore water pressure and Eq. (3). Tanaka et al. [8] reported that the accuracy of pore water pressure estimation is low when U_f is calculated using the hyperbola method under conditions without pore water pressure measurement over a sufficient period of time. Attention must be paid to the problem when this estimation method is used.

$$k_i = 5.3 \times 10^{-6} t_{50}^{-0.75} \quad (3)$$

6. CONCLUSION

In this study, tests relating to in-situ permeability were conducted to determine the permeability characteristics of peat ground. The results can be summarized as follows:

- (1) The in-situ coefficient of permeability in peat ground was one or two orders of magnitude greater than that of clay or organic clay, ranging from 1.7×10^{-7} to 1.1×10^{-5} (m/s).
- (2) The laboratory coefficient of permeability in peat ground ranged from around 1/10 to 1/100 of the in-situ coefficient. Matter from large plants and other objects must be avoided when consolidation testing of peat ground is conducted. Accordingly, the laboratory values obtained in this test are considered to represent underestimations of the ground's macroscopic permeability.
- (3) The ratio of the in-situ coefficient of permeability k_i to the coefficient of permeability k_l (k_i/k_l) rose with higher in-situ void ratio, indicating that the influence of the volume of water passages in peat ground becomes significant with greater in-situ void ratio.
- (4) The in-situ coefficient of permeability decreased linearly with higher values of t_{50} , which is the result of the pore water pressure dissipation test using the CPTU method. This relationship can be used to estimate the in-situ coefficient of permeability in peat ground.

REFERENCES

- [1] Hayashi, H., Nishikawa, J., Odajima, H., Mitachi, T. and Fukuda, F., Deformation Analysis of Peaty Ground with Cam Clay Model, Proceedings of IS-Hokkaido '94, Vol.1, pp.575-581, 1994.
- [2] Schofield, A and Wroth, P., Critical State Soil Mechanics, McGraw-Hill, London, 1968.
- [3] Hayashi, H., Mitachi, T., Tanaka, H. and Nishimoto, S., Determination Procedure of Soil Parameters for Elasto-plastic FE Analysis of Peat, Proceedings of 13th of the Asian Regional Conf. on SMGE, Vol.1, pp.145-148, 2007.
- [4] Robertson, P., Sully, J., Woeller, D., Lunne, T., Powell, J. and Gillespie, D., Estimating coefficient of consolidation from piezocone tests, Canadian Geotechnical Journal, 29, pp.539-550, 1992.
- [5] Tanaka, H., Sakakibara, M., Goto, K., Suzuki, K. And Fukazawa, T., Properties of Japanese normally consolidated marine clays obtained from static piezocone

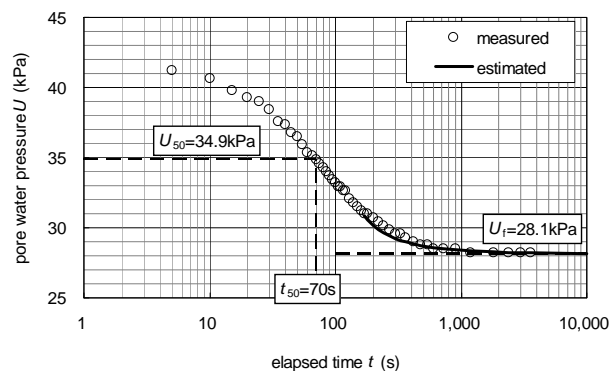


Fig. 7 The typical time history of measured pore water pressure from CPTU dissipation test (Riyamunai site at depths of 3.0 m)

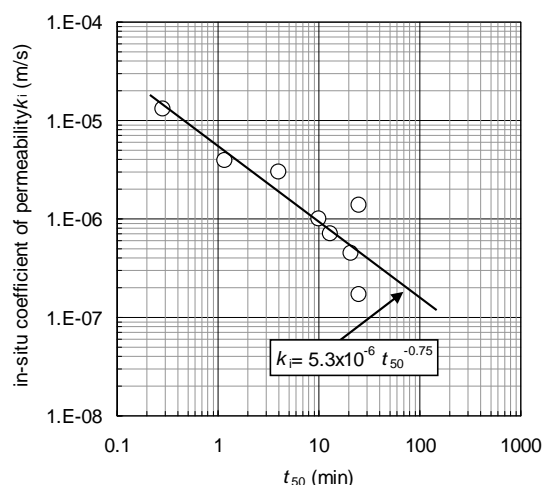


Fig. 8 The relationship between t_{50} and in-situ coefficient of permeability

penetration test, Report of The Port and Harbour Research Institute, 31(4), pp.62-92, 1992. (in Japanese).

- [6] Ohira, Y., Peat - engineering properties, investigation and design -, Sekohgizyutsu, 4(6), pp.146-148, 1971. (in Japanese)
- [7] Kogure, K., Geoenvironment of highly organic soils, Toyo-shoten co. ltd., Tokyo, pp.56-68, 1995. (in Japanese)

Extraction of temporal and spatial properties on habitat of snail by means of statistical approach

Masaaki KONDO and Takamitsu KAJISA
Graduate School of Bioresources, Mie University, Japan

ABSTRACT

A lot of fireflies, which are seen in early summer night, feed on snails. In recent years, public works are increasingly carried out with sufficient attention given to biology in the way to low-impact. There are water channel suitable for firefly as ecological zone, which are developed as a way of attention to biological environment. The notion of attention to biological environment is important in not only city life but rural human life space. National Monitoring of Biological Indices in Rivers has been conducted for many years in Japan. The data of biology and other indices have been accumulated, and it is necessary to analyze the observations. Snails living on the bottom of rivers cannot help but suffer from variation of discharge such as flood, and decline of water quality at times. These are many biological studies on snail, but it seems to be less study in terms of hydrological study and water quality. In this study area properties and temporal properties on snails were obtained by analyzing data set on stream in Mie Prefecture using quantification theory. Properties of habitat were investigated on Oomatagawa River in the south of Mie Prefecture.

Analysis of data showed useful results on temporal properties and areal properties of snail habitat. It is noted that quantification theory resulted that snail adjust to the environment of the area such as river width and bed material in river, which are important parameters. It is expected that potentiality of habitat on snail are evaluated by SOMs.

Keywords: snail, hydraulic, water quality, soil, quantification theory, self-organizing map

1. INTRODUCTION

It is fairly obvious that precipitation affects benthos in river such as rivers snails, as well as civil parameters such as flow discharge and bed materials. These are closely related to each other.

Biological monitoring methods in Japan have been improved, and their data has been accumulated for many years [1]. Part of the data is made public on the Internet. It is expected that monitoring data will be investigated and applied. While public work is carried out considering the care of rare species and their habitat, sometimes the care is not sensitive enough to the environment. Water channels suitable for fireflies similar to habitats in natural environments are often developed to enrich human life quality [2]. It is expected that monitoring data will be used to develop management procedures and protection procedures for habitats.

Mie Prefecture is suitable to investigate the impact of rivers on benthos as shown in Fig. 1. Because Mie Pref. stretches far to the north and south, and a local region in Mie Pref. has one of the heaviest rainfalls. Rainfall can affect the habitat of benthos in rivers such as snails. In this study, the relation between civil parameters, habitat, and their properties is grasped. First, the time series properties and local area properties are grasped by quantification theory. Next, the properties of potential habitats are extracted by self-organizing map (SOM).

2. DATA AND METHOD

2.1 Data and Quantification Theory

2.1.1 Data of Hydraulics, Water Quality, Soil, and Biology

Data of National Monitoring of Biological Indices in Rivers are offered by Ministry of the Environment [3] in Japan. It is characterized that monitoring is carried out on the basis of

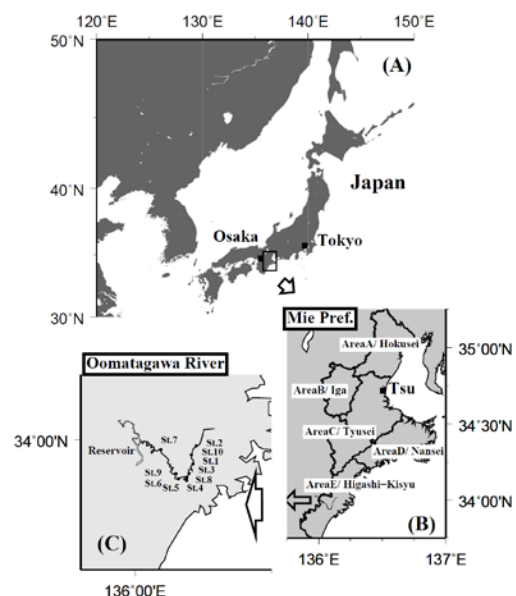


Fig.1 Location of (A) Mie Pref., (B) local areas, (C) Oomatagawa River, and observation stations in the river (JDG2000)

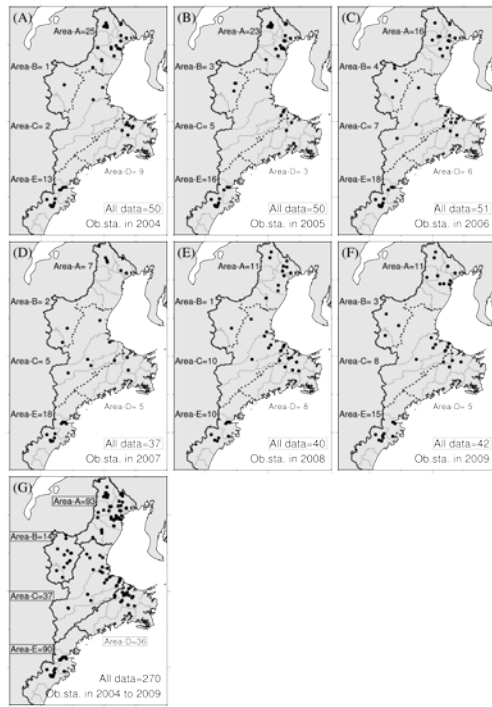


Fig.2 Location of observation stations between 2004 and 2009 for analysis, (A) to (F), for time series analysis; (G), for local area analysis (Numbers showed at each local area are one of station)

Table 1 Number of observation station

Analysis of time series		Analysis of local area	
Year	Number of observation station in all Mie Pref.	Local area	Number of observation station for six year
2004	50	Area A / Hokusei	93
2005	50	Area B / Iga	14
2006	51	Area C / Tyusei	37
2007	37	Area D / Nansei	36
2008	40	Area E / Higashi-kisyu	90
2009	42		
Total	270	Total	270

reliable procedures and not only organism species in rivers but also civil parameters are measured. Almost all of the monitoring was carried out in the summer vacation because many elementary and junior high school students participated in the monitoring. They identified organism species with the assistance from experts in biology.

The data on rivers selected in all of Mie Pref. were analyzed between June and September between 2004 and 2009. Fig. 2 shows the location of observation stations for analysis. Table 1 shows the number of observation stations. A total of 270 stations for 58 rivers were investigated for six years.

The number of stations where one-year analysis was used was between 37 and 51 stations. The number of station of the local area analysis totaled between 14 and 93 stations during 2004 - 2009.

Hydraulics parameters such as river width, depth, and flow velocity, and water quality parameters such as temperature, turbidity, and soil parameters of bed material are selected for analysis from the many items measured in civil parameters. We analyzed the river snail as benthos.

Table 2 Measured item and quantify

Quantity	Hydraulics			Water quality		Soil	Quantity	Biology
	Width	Depth	Flow velocity	Water temperature	Turbidity	Bed material	Quantity	Snail
1	0 - 5 m	0 - 10 cm	Slow / 0 - 30 cm/s	<10°C	Clear	Head-sized gravel	0	None
2	5 - 10 m	10 - 20 cm	Normal / 30-60 cm/s	10 - 20°C	Low	Fist-sized gravel	1	Few
3	10 - 20 m	20 - 30 cm	Fast / >60 cm/s	20 - 30°C	High	Small gravel and sand	2	Many
4	>20 m	>30 cm		>30°C		Sand and mud		
5						Wide particle size distribution		
6						Others		

2.1.2 Rejection and Translation of Datasets

After rejecting incorrect datasets, the qualitative datasets are quantified for analysis. Datasets lacking in analysis items and a few datasets measured on rainy days were rejected from analysis. Furthermore, the research manual advised avoiding swollen streams and rivers [4]. Thus, datasets used in analysis seem to be the ones for normal river conditions. It appears that turbidity is composed of less soil particle components and more organic algae component. Next, datasets suitable for analysis of hydraulics, water quality, soil, and river snails were translated into integers on the basis of Table 2.

2.1.3 Precipitation, BOD, and COD

Using data on precipitation between 2004 and 2009 provided by the Japan Meteorological Agency [5], the annual amount of precipitation was calculated for five regions in Mie. Mie Pref. publishes monthly data on biochemical oxygen demand (BOD) and chemical oxygen demand (COD), which are reported on the Yearly Data Book of Water Quality in Public Waters [6]. Annual average BOD and COD are calculated for five regions in Mie during 2004 and 2008.

2.1.4 Analysis by Quantification Theory

Mathematical quantification theory class II shows the explanation of external criterion as qualitative through explanatory variables shown as qualitative [7], [8]. Civil parameters such as hydraulics, water quality, and soil correspond to explanatory variables, and the snail parameter is equal to the external criterion.

The method of mathematical quantification theory class II was used for time series analysis and local area analysis. Concerning time series analysis, datasets in all of Mie Pref. were subjected to analysis one by one year as shown in Fig. 2 (A) - (F). the area and data of Mie Pref. is divided into five regions: Hokusei, Iga, Tyusei, Nansei, and Higashi-Kisyu as shown in Fig. 1 (B). Data composited for six years for each area were analyzed (Fig. 2 (G)).

2.2 Data on Oomatagawa River and Analysis by Self-Organizing Map

The studying of potential of habitat focused on only Oomatagawa River as shown in Fig. 1 (B) and (C). The fact that there were few snails in the rivers of Higashi-Kisyu indicates that the environment will be sensitive to the effects

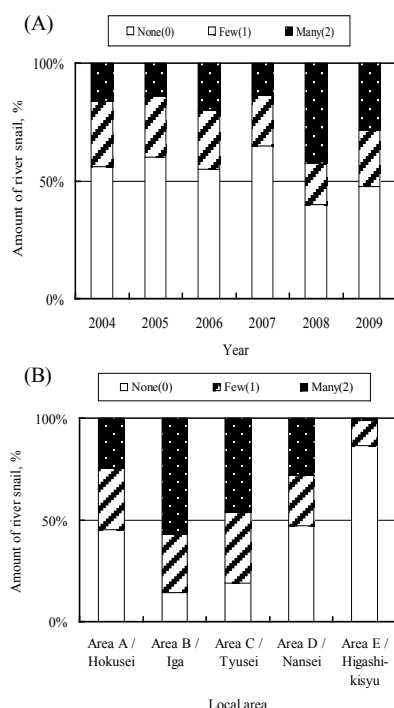


Fig.3 (A) Change of amount of river snail with time in all Mie Pref., (B) amount of river snail in local area for six year.

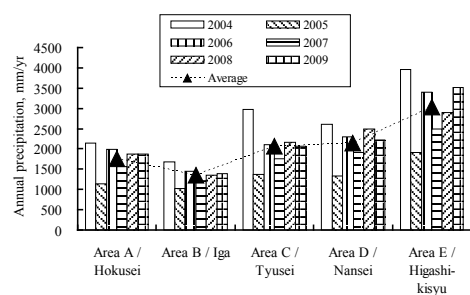


Fig.4 Annual precipitation in local area

on snails. A lot of monitoring points were set up and have continued to investigate the situation in Oomatagawa River. Oomatagawa River is suitable for investigating the existence of habitat.

It is noted that only Oomatagawa River was focused on than comparing various rivers because of avoiding the particular effect of pesticide, releasing snail in river, and heavy metals [9]. Furthermore, it is difficult to analyze rivers of many snails because of keeping the same condition.

2.2.1 Data on Oomatagawa River

Table 3 lists the monitoring data of observation stations for Oomatagawa River shown in Fig. 1 (C). The data are selected between June and September between 2004 and 2009 to grasp the recent trend. Parameters, such as river width, depth, and water temperature in Table 3 are continuous values, the others are flag values. The parameter of river snails is excluded from analysis. The analysis data has 15 dimensions. The values of BOD and COD are not measured in individual observation stations.

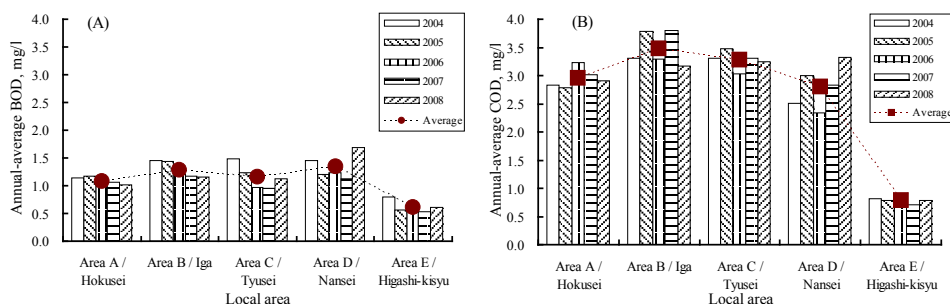


Fig.5 (A) Annual-average BOD concentration, (B) annual-average COD concentration in local area

Table 3 Data list of Oomatagawa River for SOM analysis

Year	Observation station	Station number at Fig.1	Mark at Fig.6	15 dimensions													Snail		
				WT	Width	Depth	Flow velocity	Flow velocity	Flow velocity	Flow velocity	Flow velocity	Flow velocity	Flow velocity	Flow velocity	Flow velocity	Flow velocity	None	Few	Many
2004	Asuka elementary school	SL1	★04	22	10	30	0	1	0	0	0	0	0	0	0	0	0	1	0
	Tyobokiyu lumberyard	SL2	★04	20	10	25	0	1	0	0	0	0	0	0	0	0	0	1	0
	Shikimato	SL3	★04	23.5	8	30	0	1	0	0	0	0	0	0	0	0	0	1	0
	Genbokuchiba market	SL4	★04	24	10	30	1	0	0	0	0	0	0	0	0	0	0	1	0
	Sawataribashi bridge	SL5	★04	23.9	20	20	1	0	0	0	0	0	0	0	0	0	0	1	0
	Nishin elementary school	SL6	★04	22	13	20	0	1	0	0	0	0	0	0	0	0	0	1	0
	Issuato elementary school	SL7	★04	24.7	30	40	0	1	0	0	0	0	0	0	0	0	0	1	0
	Issuato elementary school	SL7	★04	26.7	30	30	1	0	0	0	0	0	0	0	0	0	0	1	0
	Tyobokiyu	SL2	★05	18	8	15	0	1	0	0	0	0	0	0	0	0	0	1	0
	Asuka elementary school	SL1	★05	19	10	15	0	1	0	0	0	0	0	0	0	0	0	1	0
2005	Shikimato	SL3	★05	21	10	20	0	1	0	0	0	0	0	0	0	0	0	1	0
	Genbokuchiba	SL4	★05	24	15	15	1	0	0	0	0	0	0	0	0	0	0	1	0
	Sawataribashi Bridge	SL5	★05	21	10	10	0	1	0	0	0	0	0	0	0	0	0	1	0
	Nishin elementary school	SL6	★05	19	10	15	0	1	0	0	0	0	0	0	0	0	0	1	0
	Issuato elementary school	SL7	★05	23.5	15	20	0	1	0	0	0	0	0	0	0	0	0	1	0
	Issuato elementary school	SL7	★05	23.5	15	20	1	0	0	0	0	0	0	0	0	0	0	1	0
	Asuka elementary school	SL1	★06	20.5	10	20	0	1	0	0	0	0	0	0	0	0	0	1	0
	Tyobokiyu	SL2	★06	19	10	20	0	1	0	0	0	0	0	0	0	0	0	1	0
	Shikimato	SL3	★06	21.5	10	20	0	1	0	0	0	0	0	0	0	0	0	1	0
	Genbokuchiba	SL4	★06	23	10	20	0	1	0	0	0	0	0	0	0	0	0	1	0
2006	Nishin elementary school	SL6	★06	20.5	18	25	0	1	0	0	0	0	0	0	0	0	0	1	0
	Sawataribashi Bridge	SL5	★06	22	10	10	0	1	0	0	0	0	0	0	0	0	0	1	0
	Issuato elementary school	SL7	★06	22.5	15	40	1	0	0	0	0	0	0	0	0	0	0	1	0
	Issuato elementary school	SL7	★06	25	15	20	1	0	0	0	0	0	0	0	0	0	0	1	0
	Issuato elementary school	SL7	★06	23.5	10	15	1	0	0	0	0	0	0	0	0	0	0	1	0
	Issuato elementary school	SL7	★06	25.5	8	15	1	0	0	0	0	0	0	0	0	0	0	1	0
	Nishin elementary school	SL6	★07	19	20	20	0	1	0	0	0	0	0	0	0	0	0	1	0
	Sawataribashi Bridge	SL5	★07	18.8	15	20	0	1	0	0	0	0	0	0	0	0	0	1	0
	Asuka elementary school	SL1	★07	20.5	10	25	0	1	0	0	0	0	0	0	0	0	0	1	0
	Tyobokiyu	SL2	★07	19	10	25	0	1	0	0	0	0	0	0	0	0	0	1	0
2007	Marubuchi	SL8	★07	22.5	15	30	0	1	0	0	0	0	0	0	0	0	0	1	0
	Issuato elementary school	SL7	★07	24.8	15	40	1	0	0	0	0	0	0	0	0	0	0	1	0
	Issuato elementary school	SL7	★07	24.5	15	20	1	0	0	0	0	0	0	0	0	0	0	1	0
	Asuka elementary school	SL1	★08	18.2	10	20	0	1	0	0	0	0	0	0	0	0	0	1	0
	Marubuchi	SL8	★08	21.8	10	25	1	0	0	0	0	0	0	0	0	0	0	1	0
	Noguchi	SL9	★08	19	20	25	0	1	0	0	0	0	0	0	0	0	0	1	0
	Issuato elementary school	SL7	★08	27	10	35	1	0	0	0	0	0	0	0	0	0	0	1	0
	Issuato elementary school	SL7	★09	19.2	10	40	1	0	0	0	0	0	0	0	0	0	0	1	0
	Marubuchi	SL8	★09	18	10	25	1	0	0	0	0	0	0	0	0	0	0	1	0
	Noguchi	SL9	★09	19	20	25	0	1	0	0	0	0	0	0	0	0	0	1	0
2008	Tyobokiyu	SL2	★09	16.8	10	25	0	1	0	0	0	0	0	0	0	0	0	1	0
	Asuka elementary school	SL1	★09	18.7	10	20	0	1	0	0	0	0	0	0	0	0	0	1	0
2009	Issuato elementary school	SL7	★09	21	20	30	0	1	0	0	0	0	0	0	0	0	0	1	0
	Issuato elementary school	SL7	★09	21	20	30	0	1	0	0	0	0	0	0	0	0	0	1	0

Note: WT=Water temperature

Analysis data are normalized in most of the SOM study. In this study, data are normalized so that the mean is equal to zero and dispersion is equal to one.

2.2.2 Analysis by Self-Organizing Map

A self-organizing map (SOM, also called Kohonen's map) was used as an analysis method [10], [11]. The SOM produced a two-dimension map from multidimensional elements on monitoring data, and it visualized classification. Kohonen et al. (1995) of Helsinki University of Technology developed the software of SOM_PAK called Basic SOM and publish it on their website [12]. The 15-dimension data of Oomatagawa River on factors such as hydraulics, water quality, and soil property were applied to the analysis. The class of observation station is visualized to consider the results.

Values of learning parameters for SOM were set as follows: map size is 15 in the x-direction and 10 in the y-direction, limit on time iteration is 10,000, learning restraint is 0.05, and neighborhood function is 21.

Table 4 Result of time series analysis ((A), Item; (B), detail; (C), total evaluation)

(A)	Ranking and score (SA) of items					
	No.1 6 pt	No.2 5 pt	No.3 4 pt	No.4 3 pt	No.5 2 pt	No.6 1 pt
2004	Bed	Turbidity	Depth	Flow	Width	WT
2005	Bed	Depth	Turbidity	Flow	Width	WT
2006	Bed	Turbidity	Width	Flow	Depth	WT
2007	Bed	Turbidity	Width	Depth	Flow	WT
2008	Width	Bed	Flow	Turbidity	Depth	WT
2009	Width	Bed	Turbidity	Depth	Flow	WT

Note; Bed=bed material; WT=water temperature; Flow=flow velocity

(B)	Ranking of details (DB)					
	No.1	No.2	No.3	No.4	No.5	No.6
2004	Wide particle size distribution	Cloudy	20-30cm	Normal	0-5m	20-30°C
2005	Sand and mud	>30cm	Dirty	Normal	0-5m	20-30°C
2006	Others	Dirty	0-5m	Fast	20-30cm	10-20°C
2007	Sand and mud	Clear	0-5m	10-20cm	Normal	20-30°C
2008	0-5m	Sand and mud	Fast	Cloudy	>30cm	10-20°C
2009	0-5m	Wide particle size distribution	Clear	0-10cm	Slow	20-30°C

(C)	Details (Xi) and each score (SC)					
Item						
Width	0-5m	5-10m	10-20m	>20m		
	24pt	0pt	0pt	0pt		
Depth	0-10cm	10-20cm	20-30cm	>30cm		
	3pt	3pt	6pt	7pt		
Flow	Slow	Normal	Fast			
	2pt	8pt	7pt			
WT	<10°C	10-20°C	20-30°C	>30°C		
	0pt	2pt	4pt	0pt		
Turbidity	Clear	Low	High			
	9pt	8pt	9pt			
Bed	Head-sized gravel	Fist-sized gravel	Small gravel and sand	Sand and mud	Wide particle size distribution	Others
	0pt	0pt	0pt	17pt	11pt	6pt

Note; Bed=bed material; WT=water temperature; Flow=flow velocity

3. RESULT AND DISCUSSION

3.1 Characteristics for Analysis Data Based on Statistics

The modal class on civil parameters is: 5-10 m of river width, 20-30 m of depth, normal flow velocity, fist-sized gravel bed material. Data selected during the summer observation caused the water temperature to be 20-30°C at most, and there was no data for below 10°C. Clear turbidity was most common, low turbidity was present in 52 out of 270, and high turbidity, which was rare, was present in three out of 270.

Fig. 3 indicates the amount of river snails for the time series and each local area. River snails were observed in many sites in 2008 as shown in Fig. 3 (A). Iga and Tyusei, Hokusei and Nansei, and Higashi-Kisyu were ranked in descending order of snails in each area. There were fewer snails in Higashi-Kisyu/Area E than in other areas.

Fig. 4 shows the amount of rainfall in each local area. In accordance with the local area, rainfall in Higashi-Kisyu/Area E, where it naturally rains a lot, is markedly high.

Fig. 5 shows annual average BOD and COD in rivers. BOD and COD are low in all of Mie pref. In accordance with the environmental quality standard in Japan [13], river water

meets the level of drinking water needing normal purification. Water in all of Mie Pref. is recognized as clear; in particular, water from Higashi-Kisyu, showed in Fig. 1 (B) as Area E, is clear. Therefore, the organic matter on which snails feed is less in Higashi-Kisyu.

3.2 Properties of Time Series Using Quantification Theory

Table 4 indicates the results of the analysis. Bed material, river width, and turbidity seem to contribute highly to snail habitat as shown in Table 4(A). It is difficult to understand the properties without including the data shown in Table 4(B). To provide the scores depending on the order, Table 4(C) was rearranged using the following equation (1):

$$SC(X_i) = \sum_{yr} \{SA_{yr} \times Y(X_i - DB)\} \quad (1)$$

where SC is a score of X_i , X_i is a detail in Table 4(C), DB is a detail in Table 4(B), yr is year, SA is the score in Table 4(A), and Y is the step function; if $X_i = DB$, $Y = 1$, and if X_i is not equal to DB , $Y = 0$.

Table 4(C) shows that the properties of the time series resulting from aggregating the contents shown in both Table 4 (A) and (B) have greater accuracy. 0-5 m of river width (24 points), sand and mud bed material (17 points), clear or high turbidity (both 9 points), and other items such as flow velocity, depth, and water temperature are presented in descending order of points.

First, the top three of all items: river width, bed material, and turbidity are explained as follows. The relatively narrow 0-5 m river width corresponds to a flume or small stream in Japan. Snails prefer narrow rivers into wide rivers (Murakami (2007) [14]). The analysis results agree with his description.

Sand and mud bed material showed high point. Furujo and Tomiyama (2000) [15] indicated that snails prefer gravel, sand, and mud. Murakami (2007) [16] also indicated that that snails in upstream sites feed on periphyton on gravel and withered leaves. It is considered that since the light material such as sand, mud, and withered leaves are easy to sediment in the condition of low velocity, snails prefer the sedimentary surrounding.

Table 5 Result of local area analysis ((A), Item; (B), detail)

(A)	Ranking and score of items					
Local area	No.1	No.2	No.3	No.4	No.5	No.6
Area A / Hokusei	Bed	Turbidity	Width	Flow	Depth	WT
Area B / Iga	Bed	Flow	Width	Depth	WT	Turbidity
Area C / Tyusei	Bed	Width	Depth	Flow	Turbidity	WT
Area D / Nansei	Depth	Bed	Width	Flow	Turbidity	WT
Area E / Higashi-kisyu	Turbidity	Depth	Bed	WT	Width	Flow

Note; Bed=bed material; WT=water temperature; Flow=flow velocity

The effect of turbidity as feed will be an important factor for snails because non-clear turbidity, summing up eight points of low and nine points of high turbidity, is more than the nine points of clear turbidity. Non-clear turbidity affects the habitat of snails.

Next, Flow velocity, depth, and water temperature in the low ranks are explained. Snail on river beds can be flushed away at flow velocities of more than one m/s [17]. Snails are observed in riffles with high velocities [15]. It does not mean that high velocity is a bad condition. Thus, the fact that the flow condition is uncertain leads to a low position in Table 4. Snails are fed on by enemies such as fireflies, river crabs, rats [18]. Deep water may protect snails from these enemies. However, snails are observed regardless of the depth of the river [15]. It is considered that the habitat condition on depth is ambiguous.

The reason why data of water temperature was restricted in summer caused to be low points in Table 4.

3.3 Properties of Local Area Using Quantification Theory

Table 5 indicates the results of local area analysis. As shown in Table 5(A) and (B), the analyzed order of local area resulted in difference from each other. Area A / Hokusei has sand and mud bed material, low turbidity, and 0-5 m river width in sequence. Area B / Iga has head-sized gravel bed material, fast flow velocity, and 0-5 m river width. Area C / Tyusei has wide particle size distribution bed material, 5-10 m river width, and 10-20 cm depth. Area D / Nansei has over 30 cm depth, other bed material, and 5-10 m river width. Area E / Higashi-Kisyu has low turbidity, 0-10 cm depth, and fist-sized gravel bed material.

Thus, the property of a local area is similar to the property of time series regarding of an importance of river width, bed material, and turbidity. The property of Higashi-Kisyu is different from the others; turbidity resulted in high contribution toward the habitat of snails.

There are few snails in Higashi-Kisyu as described in section 3.1. Snails in clear or pure rivers like the upper portion of a river feed on periphyton on gravel or spoiled leaves [16]. A lot of rainfall causes damage to the surface of gravel by their rolling, and it is hard for periphyton to grow on gravel. This may result in few snails and in less BOD and COD

(B)	Ranking of details					
Local area	No.1	No.2	No.3	No.4	No.5	No.6
Area A / Hokusei	Sand and mud	Low	0-5m	Slow	20-30cm	20-30°C
Area B / Iga	Head-sized gravel	Fast	0-5m	0-10cm	10-20°C	Low
Area C / Tyusei	Wide particle size distribution	5-10m	10-20cm	Normal	High	20-30°C
Area D / Nansei	>30cm	Others	5-10m	Slow	Low	20-30°C
Area E / Higashi-kisyu	Low	0-10cm	Fist-sized gravel	10-20°C	>20m	Normal

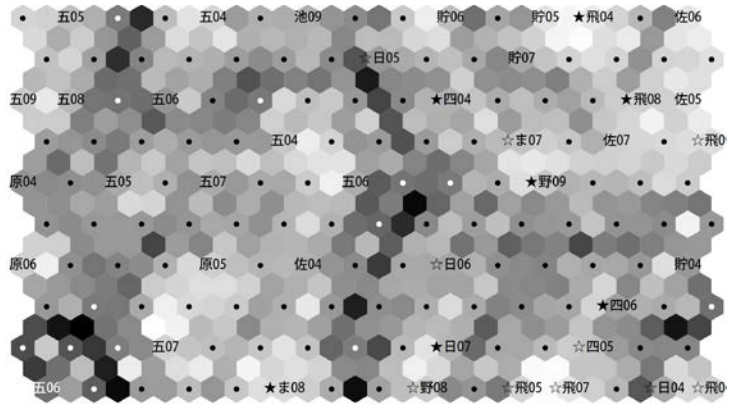


Fig.6 Self-organizing map on observation stations in Oomatagawa River (Marks in the figure are showed in Fig.1 and Table 3)

considered as a feed index.

3.4 Results using SOM

Fig. 6 indicates the SOM on Oomatagawa River. A black star means that the snail was captured, a white star means the snail was not captured but was captured in another year, no mark means the snail was not captured. Not-captured sites like Itsusato are located on the left side of the map. Most of the black stars, all of the white stars, and a few of the locations with no marks such as Sawataribashi Bridge and Tyobokujyou lumberyard are located on the right side. The right side is under the mixed conditions.

The results of analysis are interpreted as follows; it is almost impossible to observe snails on the site of left side because almost all were not captured. However, it is highly possible to observe snails on site of the right side because of the mixing conditions.

Snails have not been observed at the Itsusato site. It will be hard to observe snails there. The Itsusato site is located on nearby reservoir and downstream with wide river width (Fig. 1(C)). Thus, it is considered that sand accumulated around the Itsusato site damages periphyton on the gravel surface and no snails are observed.

4. CONCLUSION

In this study, it was investigated that the civil parameters

exerted on habitat of river snail and the possibility of habitat. Data of civil parameter on rivers and snail concerning Mie Pref. in Japan were subject to the analysis by the method of both quantification theory and self-organizing map.

1) Relationship between habitat of snail and quantification theory was investigated. Compared with references published by the experts and their experience, river width, bed material, and turbidity made a large contribution to habitat.

2) Possibility of habitat for river snail is showed on a SOM. It is possible to distinguish between easy habitat and difficult one to live. It suggested that the rolling of gravel and sedimentation cause bed variable to make hard habitat for continuously-growing snail.

2004, p.35.

REFERENCE

- [1] Tanida K, "Index biology on river environment", Tokyo, Hokuryukan Publishing, 2010, pp.142-151.
- [2] Sekine M, Goto M, Ito N, Tanaka K, Kanao M, and Inoue T, Construction of a firefly stream by using a physical habitat evaluation method, *Ecol. Civil Eng.* 10(2), pp.103-116, 2007.
- [3] Ministry of the Environment (2004-2009), "Data of National Monitoring of Biological Indices in Rivers", <<https://www2.env.go.jp/water-pub/mizu-site/mizu/suisei/>>, browsed on April 1st, 2012.
- [4] Ministry of the Environment and Ministry of Land, Infrastructure, Transport and Tourism, "Kawa no ikimono wo sirabeyou (research manual)", Japan Society on Water Environment, 2000.
- [5] Japan Meteorological Agency (2004-2009), "Table of Hourly Weather Observations", < http://www.jma.go.jp/en/amedas_h/map38.html>, browsed on April 1st, 2012.
- [6] Mie Pref., "Yearly Data book of Water Quality in Public Waters", Mie Pref., 2004-2009.
- [7] Hayashi C., "On the quantification of qualitative data from the mathematico-statistical point of view -An approach for applying this method to the parole prediction-", *Ann. Inst. Statistical Math.*, 2, pp.35-47, 1950.
- [8] Hayashi C., "On the prediction of phenomena from qualitative data and the quantification of qualitative data from the mathematico-statistical point of view", *Ann. Inst. Statistical Math.*, 3, pp.69-98, 1951.
- [9] Iskizaki S and Hamada H, "Effects of Heavy Metals on the Freshwater Snail, *Semisulcospira bensoni*, in a Closed Mining Area", *Jpn. J. Limnol.*, 48(2), pp.91-98, 1987.
- [10] Kohonen T, "Self-Organizing Maps", Tokyo, Springer, 2010.
- [11] Ookita M, Tokutaka H, Fujimura K, and Gonda E, "Self-Organizing Maps and its Software", Tokyo, Springer, 2008.
- [12] Kohonen T, Hynninen J, Kangas J, and Laaksonen J, "SOM_PAK -Self-Organizing Map Program Package", Helsinki University of Technology, 1995.
- [13] Announcement by Ministry of the Environment (1971), "Environmental standards concerning water pollution -appended table 2-", <<http://www.env.go.jp/kijun/mizu.html>>, browsed on April 1st, 2012.
- [14] Murakami M, "How to breed and to photograph firefly in freshwater", Powersha, 2007, p.87.
- [15] Furujo Y and Tomiyama K, "Distribution and Microhabitat of Coexisting Two Freshwater Snail Species, *Semisulcospira libertina* (Gould) (Prosobranchia; Pleuroceridae) and *Clithon retropictus* (Martens)(Prosobranchia : Neritidae)", *Venus : the Japanese j. of malacology* 59(3), pp.245-260, 2000.
- [16] Murakami M, "How to breed and to photograph firefly in freshwater", Powersha, 2007, p.4.
- [17] Mori S, "Some ecological notes on the fresh water snails - second -", *Venus*, 6(1), pp.15-21, 1936.
- [18] Tokyo Fireflies Ecology Institute, "Hotaru hyakka", Tokyo, Maruzen,

The use of Nano Zero Valent Iron to remediation of contaminated soil and groundwater

Taghizadeh Maryam¹, Yousefi Kebria Daryoush² and Gholamreza Darvishi³
Babol University of Technology, Iran

ABSTRACT

Environmental contaminants have been known to be present in many hazardous waste sites, which made an enormous impact on the quality of groundwater, soil and associated ecosystems. Remediation of these contaminated sites is an important challenge facing the scientific and technical community. Nanotechnology is the use of manipulating matter on an atomic at least one dimension sized from 1 to 100 nanometers and molecular scale. Nano Zero Valent Iron (nZVI) is emerging as new option for the treatment of contaminated soil and groundwater. Due to their small size, the particles are more reactive than granular iron which is conventionally applied in reactive barriers and can be used for in situ treatment. nZVI effectively reduces chlorinated organic contaminants (e.g. PCB, TCE, PCE, TCA, pesticides, solvents) and also inorganic anions (perchlorate). This present research gives an overview over the characteristics and application of nano zero valent iron (nZVI) in general and summarizes of the experiences on groundwater remediation with other scientists.

Keywords: Remediation – Nanotechnology - groundwater - Nano Zero Valent Iron (nZVI)

1. INTRODUCTION

Maintaining and restoring the quality of air, water and soil is one of the great challenges of our time. Most countries face serious environmental problems, such as the availability of drinking water, the treatment of waste and wastewater, air pollution and the contamination of soil and groundwater.

Enormous effort has been made to find efficient and effective ways to remediate petroleum contamination in soil and groundwater [1].

Petroleum compounds and its derivatives are cause contamination groundwater and soil, however petroleum materials penetrated to more depth of soil, decontamination will be more difficult. Techniques that are used for cleanup of soil and ground water include the use of water for to remove pollutants, chemical solvent, incineration and help to organism to break down the pollutant molecules.

Thousands of sites exist in the United States and worldwide where subsurface soils and groundwater have been contaminated with a wide range of toxic organic compounds and heavy metals.

In particular, halogenated organic contaminants, such as Pentachlorophenol, Trichloroethylene, Trichloroethane, Dinitrotoulene, and Trinitrotoluene, are present at several sites, and these contaminants are listed as priority pollutants by the United States Environmental Protection Agency (USEPA) due to their toxicity and carcinogenicity.

These contaminants are persistent in the environment slowly by natural processes [2].

The conventional methods of treating these contaminants include soil washing/ flushing, thermal desorption, vitrification, and bioremediation; however, these methods are relatively expensive, slow, or limited by the production of secondary waste streams that require subsequent disposal or treatment[3].

Nanoscale iron particles represent a new generation of environmental remediation technologies that could provide cost-effective solutions to some of the most challenging environmental cleanup problems. Nanoparticles show a higher catalytic activity because of their small size (10-100 nm) and their large specific area.

Nanotechnology is a branch of applied sciences that can be defined as particles of size ranging from one to hundred nanometers (nm) in any dimension. The size of nano particles is of several times smaller than even the red blood cells.

Nanotechnology is very diverse, ranging from extensions of conventional device physics to completely new approaches based upon molecular self-assembly, from developing new materials with dimensions on the nanoscale to direct control of matter on the atomic scale [4].

Andreta is showed that nanotechnology is the actions and reactions that occur at the atomic level, a more accurate interpretation nanotechnology is new revolution for all science in the future. This technology can improve methods assessment , management and reduce risks for the environment and will provide opportunities for new products [5].

2. NANOTECHNOLOGY APPLICATION IN ENVIRONMENTAL

Nanotechnology has provided the possibility of producing product with high quality, low cost and high speed. One of the important areas of application of nanotechnology in the

environmental is removal or cleanup of chemical contaminants such as chemical pesticides or convert them to substances that have less risk of toxicity. For example, can be used of nano zero valent iron for the cleanup of soil and groundwater for a variety of chemical contaminants. These nanoparticles as a catalyst was caused accelerate the oxidation process and cause the Organic pollutants such as chemical pesticides are broken down into smaller carbon compounds that have less toxicity. The same projects about removal of microbial and chemical contaminants of water, soil and air is in progress in anotechnologies centers at various countries around the world, that represent the capabilities of nanotechnology in this field.

2.1 ENVIRONMENTAL CLEANUP OF HYDROCARBON CONTAMINANTS

There are different methods for improvement and cleanup of soil and groundwater, for example in pump and treat method, which is one of the conventional methods, groundwater pumped and after filtration and removal of contaminants, groundwater aquifers are returned again, this method is very costly and take a long time.

Iron was first recognized and patented in 1972 as a chlorinated pesticide degrader. In 1981, Sweeny utilized iron powders to degrade various hydrocarbons, such as trichloroethylene [6]. Additional suggestions for using zero valent iron to degrade trichloroethylene and trichloroethane were made in the late 1980's by Senzaki (1988) [7]. In 1993 a patent was lodged by the University of Waterloo for using zero valent iron for treating contaminated groundwater in-situ, demonstrating the identification of zero valent iron as a remediation constituent.

Nanoscale zero valent iron (NZVI) is more effective at reaching deep zones of contamination, and is more effective at contaminant degradation than iron of larger size. (NZVI) can induce greater rates of reaction because of its greater specific surface area, which allows a greater exposure of the iron particle to the contaminant per unit weight of iron than other larger particles. Additionally, as particle size decreases and tend towards 10 nm, thermodynamic properties, such as work-function and free energy being to alter and can increase reactivity. Gavaskar et al has found that NZVI is significantly more reactive than granular iron, and states that it can remediate a plume in a much shorter time scale [8]. Henry et al states that nanoscale zero iron has a superior pore penetration ability when compared to larger particulate zero valent iron [9].

Zero valent iron has been shown to react and degrade many types of chemicals[8], including halogenated aliphatics, polyhalogenated aromatics and nitrates and trichloroethene [10],[9].

The standard half reaction for zero valent iron reacting to yield a ferrous cation and 2 electrons is:



This reaction has a standard reduction potential of +0.44 V [11].

Alkyl halides have a typical half reaction as such, where RX indicates a halogenated hydrocarbon, and X⁻ represents a halogen anion:



These types of half reactions have reduction potentials ranging from +0.5 V to +1.5V at pH 7 (Matheson 1994), the variation is attributed to the wide range of alkyl halides that this reaction applies to.

When combined, these two half reactions yield a thermodynamically spontaneous reaction:

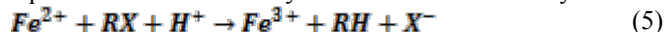


This constitutes the most basic mechanism for halogenated hydrocarbon degradation by zero valent iron, yielding a ferrous cation, an aliphatic hydrocarbon and a halogen anion (Matheson 1994).

A second mechanism for degradation of halogenated hydrocarbon by zero valent iron is the oxidation of zero valent iron to a ferrous cation by water (Matheson 1994). The ferrous ion then further oxidizes to a ferric cation by the following half equation:

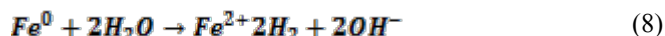


This oxidation reaction can be coupled with the reduction half equation to reduce the alkyl halide shown above to yield:



This is a second mechanism for the degradation of an alkyl halide (Matheson 1994) by zero valent iron.

Matheson (1994) describes a third mechanism, which involves the zero valent iron reacting with water to yield the ferrous cation, the hydroxyl anion and hydrogen gas (H₂). It is combination of the two following half reaction:



The H₂ gas generated can then continue on to react with an alkyl halide in a reaction known as addition reaction to yield a dehalogenated aliphatic, a halogen anion and a proton in the following manner:



It is important to note that the H₂ can only react with the alkyl halide if a suitable catalyst is present.

3. ADVANTAGES OF ZERO VALENT IRON NANOPARTICLES

Using zero valent iron has the following advantages as a remediation technology [10]:

- I. It is relatively inexpensive.
- II. It is non-toxic.
- III. It degrades certain chemical faster than other techniques of remediation, such as biotic remediation
- IV. It has high energy effectiveness.

A widely used technique to treat contaminated groundwater in-situ is by utilizing Passive Reactive Barriers (PRB). The location of the PRB must first be ascertained, then the existing soil must be excavated and the void space filled with the reactive medium with relatively high hydraulic conductivity.

Some of the initial field testing of PRBs was done using zero valent elemental iron filings [12],[13]. Incorrect understanding of the frequently complex hydrogeology of various contamination sites can lead to incorrect barrier wall placement, which can leave contaminated zones outside of the barriers untreated.

Passive Reactive Barrier have proven to be effective at treating a great number of contaminated groundwater plumes; they have certain limitations [14]:

- I. They only target contaminant plume, and not the source of contamination. They therefore have to wait for the contaminant to be leached into or advected with the groundwater before treatment can be initiated.
- II. They are unfeasible solutions in certain situations of complex hydrogeological conditions, such as fractured rock.
- III. Most Passive Reactive Barriers have been installed to a depth of approximately 15 meters, although there have been instances of depths up to 35 meters[9]. They cannot penetrate deep into the soil, rendering them wholly ineffective with deep plumes, as they cannot reach the target zone.

A comprehensive understanding of the hydrogeological conditions at the contamination site is required for this technology to work, as the positioning of PRB is of utmost importance.

4. SOIL AND GROUNDWATER REMEDIATION WITH NANOPARTICLES

Environmental remediation methods can be classified as adsorptive and reactive and as in situ or ex situ [15],[16]. The use of nanomaterial in all these scenarios has been investigation. In soil and groundwater remediation, for in situ treatment, it is necessary to create either an in situ reactive zone with relatively immobile nanoparticles or a reactive nanoparticles plume that migrates to contaminated zones.

There are two ways to use nZVI in groundwater and soil remediation[15],[17]:

- nZVI is injected to form a reactive barrier of iron particles.
- nZVI is injected in surface- modified form to establish a plume of reactive iron, which destroys any organic contaminants within the aqueous phase

Several studies have shown that nZVI as a reactive barrier is very effective in the reductive degradation of halogenated solvents, such as chlorinated methane, brominated methane, trihalomethane, chlorinated ethene, chlorinated benzenes and other polychlorinated hydrocarbons, in groundwater [18], [19]. nZVI has also been shown to be effective against pesticides and dyes [18]. Efficient removal by nZVI of

polycyclic aromatic hydrocarbons (PAHs) adsorbed to soils has been reported at room temperature [20],[21], while under the same conditions only 38% of the polychlorinated biphenyls (PCBs) were destroyed because of the very strong sorption of PCBs to the soil matrix [22].

Krishna investigated electrokinetic delivery of nanoscale iron particles for remediation of pentachlorophenol in clayey soil. The results showed that 80 to 98% PCP was removed from the soil within an hour, but PCP reduction was increased from 50 to 78% at 1h to 40 to 90% at 24h reaction time for different NIP concentrations. There was no significant effect of NIPs concentration on the PCP removal, but the amount of PCP reduction increased with increase concentration of NIP.

According to Tratnyek and Johnson (2006), nZVI used in real- world groundwater remediation has a particle size larger than 100 nm and is thus strictly speaking outside the standard definition of NP size. These authors also state that the mobility of nZVI will be less than a few meters under almost all relevant conditions as nZVI tends to aggregate, producing clusters that may approach several micrometers in size and thus be easily removed from the pore water[15]. Companies are therefore functionalizing nZVI particles to stop them from aggregating, for example, with surfactants or polymers. Other approaches combine the nZVI with carbon platelets or embed the nZVI in oil droplets to facilitate particle delivery into the contaminated area [19]. In the United States, it is common to combine the nZVI with other metals, such as palladium, to increase the reactivity. In Europe such bimetallic particles are not used due to their possible toxicity and the limited additional benefit [19].

Tratnyek and Johnson (2006) state that high reactivity tends to correlate with low selectivity. For this reason, remediation with nZVI may be inefficient because nZVI particles may react with non-target substances, including dissolved oxygen, sulphate, nitrate and water. This also implies that nZVI will have a limited lifetime in porous media and reinjection of nZVI may be necessary, which makes the treatment more costly[15].

5. CONCLUSION

Emergence of nanotechnology, particularly synthesis of nanoscale iron particles (NIP), has provided opportunities to develop innovative site remediation technologies. The small particles have great sorption capacity. However, technical challenges, such as the delivery of the particles to the target area, have to be solved.

The reaction pathways of NIP with target halogenated organic contaminants are similar to that of zero-valent iron (iron filings) commonly used in a permeable reactive barrier technology. However, due to their infinitesimally small size, NIP can be highly reactive due to their high surface to volume ratio and greater number of reactive sites and higher intrinsic reactivity on reactive sites. In addition, NIP can be injected directly into the contaminated zones, making the in-situ remediation faster and effective. Due to their small size, the particles are very reactive (more reactive than granular iron

which is conventionally applied in reactive barriers) and can be used for in situ treatment. NZVI effectively reduces chlorinated organic contaminants (e.g. PCB, TCE, PCE, TCA, pesticides, solvents) and also inorganic anions (perchlorate). It can even be used to recover/remove dissolved metals from solution (e.g. Cr (VI), U (VI)). Also nanoscale zero valent iron is more effective at reaching deep zones of contamination, and is more effective at contaminant degradation than iron of larger size.

6. REFERENCES

- [1] Rickerby, D. and M. Morrison, *Report from the Workshop on Nanotechnologies for Environmental Remediation*, JRC Ispra, 2007.
- [2] Vogel, T.M., Criddle, C.S. and McCarty P.L., *Transformation of Halogenated Aliphatic Compounds* Environmental science & technology, 1987. **21**(8): p. 722-736.
- [3] Sharma H.D., R., K.R., *Geoenvironmental Engineering: Site Remediation, Waste Containment, and Emerging Waste Management Technologies*. John Wiley, Hoboken, NJ, 2004.
- [4] Breytenbach, J.H., *The Metris of vaccination international poultry production*. Savian Influenza Control, 2005. **13**(4): p. 15-17.
- [5] Andreta, E., *Nanosciences and Nanotechnologies: What Future for Research*. rfuture Conference and Expo, Chiba- shi, Chiba, Tokyo, Japan, 2003.
- [6] Sweeny, K. and J. Fischer, *Reductive degradation of halogenated pesticides*. 1972.
- [7] Senzaki, T., " *Removal of Chlorinated Organic Compounds by Iron and Manganese Powders in Buffered Water and Landfill Leachate*" Chemosphere, 1988. **29**: p. 1743-1753.
- [8] Gavaskar, A., L. Tatar, and W. Condit, *Cost and performance report nanoscale zero-valent iron technologies for source remediation*. 2005, DTIC Document.
- [9] Henry, S.M. and S.D. Warner, *Chlorinated solvent and dnapl remediation innovative strategies for subsurface cleanup*. Recherche, 2003. **67**: p. 02.
- [10] Zawaideh, L., C. Chew, and T. Zhang. *Remediation of nitrate-contaminated water and soil by Fe0-promoted processes*. 1997.
- [11] Atkins, P., *Physical Chemistry*. 6th. 1998, Oxford University Press, Oxford, Melbourne, Tokyo.
- [12] Gillham, R.W., S. O'Hannesin, and W. Orth. *Metal enhanced abiotic degradation of halogenated aliphatics: Laboratory tests and field trials*. 1993.
- [13] Gillham, R.W. and S.F. O'Hannesin, *Enhanced degradation of halogenated aliphatics by zero - valent iron*. Ground water, 1994. **32**(6): p. 958-967.
- [14] Pankow, J.F. and J.A. Cherry, *Dense chlorinated solvents and other DNAPLs in groundwater: History, behavior, and remediation*. 1996.
- [15] Tratnyek, P.G. and R.L. Johnson, *Nanotechnologies for environmental cleanup*. Nano today, 2006. **1**(2): p. 44-48.
- [16] Hodson, M.E., *The need for sustainable soil remediation*. Elements, 2010. **6**(6): p. 363-368.
- [17] Nowack, B. and T.D. Bucheli, *Occurrence, behavior and effects of nanoparticles in the environment*. Environmental Pollution, 2007. **150**(1): p. 5-22.
- [18] Zhang, W., *Nanoscale iron particles for environmental remediation: An overview*. Journal of nanoparticle Research, 2003. **5**(3): p. 323-332.
- [19] Mueller, N.C. and B. Nowack, *Nanoparticles for remediation: Solving big problems with little particles*. Elements, 2010. **6**(6): p. 395-400.
- [20] Chang, M.C., et al., *Using nanoscale zero-valent iron for the remediation of polycyclic aromatic hydrocarbons contaminated soil*. Journal of the Air & Waste Management Association, 2005. **55**(8): p. 1200-1207.
- [21] CHANG, M.C., et al., *Remediation of soil contaminated with pyrene using ground nanoscale zero-valent iron*. Journal of the Air & Waste Management Association, 2007. **57**(2): p. 221-227.
- [22] Varanasi, P., A. Fullana, and S. Sidhu, *Remediation of PCB contaminated soils using iron nano-particles*. Chemosphere, 2007. **66**(6): p. 1031-1038.

A Multi-parameter Water Quality Analysis by Onsite Filtered 2mL Sample to Monitor Urban River Eutrophication

Akira Kikuchi^{1,2}, Nor Eman Ismail², Narges Janalizadeh^{1,2}, Musa Mutah^{1,2}, and Muhamad Faiz^{2,3}

¹Institute of Environmental and Water Resource Management, ²Faculty of Civil Engineering, Universiti Teknologi Malaysia, ³SAJ Holdings SDN. BHD. Johor Malaysia

ABSTRACT

A new approach for ecosystem level water quality prospecting was examined. Full-automated Ion Chromatography system (TOSOH IC2010) was modified for integration with Flow Injection Analysis. 13 of 2mL samples were collected after onsite filtration by 0.45 μ m syringe filter from river in UTM Johor campus, representing common human impacted river environment, on 24 February 2012. Then four analytical modes were applied for standard solutions and the environmental samples. The detection limit that was signal-noise ratio three in μ M/L were as follows, SO₄²⁻ (0.31), Cl⁻ (0.50), NO₃⁻ (0.89), Na⁺ (0.52), NH₄⁺ (0.94), K⁺ (1.24), Mg²⁺ (0.76), Ca²⁺ (1.75), NO₂⁻ (0.02), and PO₄³⁻ (0.12), and its EC was 0.03 μ S/cm. Comparing these values with water qualities of environmental samples, our analytical approach was satisfactory. The onsite filtration drastically improved the sampling process as simple, and μ M/L level analyses were obtained by only one equipment with 2mL sample. This analysis can be extend to COD, total nitrogen/phosphorous, and etc, which will contribute strategic environmental assessment due to rapid delivered, low-cost, and integrated data.

1. INTRODUCTION

Environmental assessment has multiple scheme [1][2]. The assessments for environmental acts implementation in the higher planning processes than project level is particularly categorized as strategic environmental assessment (SEA) [1]. Then, the conventional environmental impact assessment (EIA) functions under the SEA at project level [2]. It is clear from the viewpoint of environmental decision-making processes, in the sense that as one move down the hierarchy from policies, plans, program (PPPs), and then to project, the nature of decision-making has prescribed specifications [2]. There in the water matters, standard methods for water quality analysis [3] have been main technical procedure for EIA under such object specified conditions. On the other hand, even though SEA at higher PPPs process has unique function to enhance more useful problem prospecting and effective environmental programs-projects development [1][2], however the methodologies for suitable water quality monitoring for SEA are still on a development process [4][5]. Hence, technical development for strategic water quality assessment for SEA has been focused on in this study.

Elevated levels of phosphorous in conjunction with nitrogen can negatively affect aquatic ecosystems in many ways in terrestrial fresh water bodies [6][7]. The increased growth of algae and aquatic macrophytes and distinct shifts in species composition are a prominent symptom of eutrophication [8]. These blooms generally contribute to a wide range of water quality problems including summer fish kills, foul odours, and tainted drinking water. Furthermore, certain cyanobacteria produce and release toxins that can kill livestock and may pose serious health threat to humans. To monitor phosphorous and nitrogen concentration of

environmental water is important [6][7]. From another view point in general environmental water quality monitoring, the measurement of common anions (SO₄²⁻, Cl⁻, and NO₃⁻) and cations (Na⁺, K⁺, NH₄⁺, Mg²⁺, and Ca²⁺) found in environmental water is essential for some environmental waters including rain, lake, underground, and river water [9].

Ion Chromatography (IC) have been recognized to be very useful approach for the determination of anions and cations, and Flow Injection Analysis (FIA) is also very fundamental for environmental chemistry. Herein an integration of IC and FIA was examined on analysis for phosphorus, inorganic nitrogen ions, other common anions and cations analysis by only one vial of 2mL onsite filtered sample as a convenient multi-parameter water quality analysis.

2. Experimental

2.1 IC-FIA integration

IC-FIA integration was performed on a TOSOH model IC2010 equipped with the following devices: vacuum degasser, double plunger pump that capacity is 6 μ L x 2, column oven, auto sampler of capacity 150-300 samples, and conductivity detector (TOSOH, Tokyo, Japan). The integration with FIA was proceeded by modification of merging process of double plunger pump by installing a 1-2, 3 switching valve (Fig. 1). Applying 1-2 position of the switching valve, eluent from double plunger pumps were merged before sample injector as conventional IC system. Then, applying 1-3 position of the switching valve, a plunger pump sent carrier and a sample segment was injected in the carrier flowing, and reagent sent by the other plunger pump was merged after the sample injector. Whereas, injected sample and reagent were merged for every 6 μ L alternately.

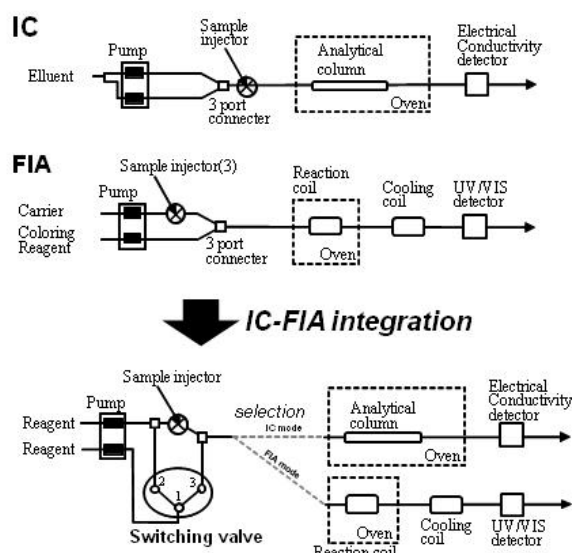


Fig. 1. Schematic depiction of IC and FIA system, and its integration by a switching valve.

2.2 Manifold for IC and FIA analysis

Using, IC mode that was by 1-3 position of switching valve, simultaneous anions and cations separation was carried out using TSK gel Super-IC-A/C (3 μm particle size, 0.2 mequiv./ml cationic exchange capacity, 150 x 6.0mm I.D.) with conductivity detector. Using FIA mode that was by 1-2 position of switching valve, two channels FIA manifolds were carried out, in which, 2m SAS tube was applied for reaction at 40 °C for EC analysis, and 5.5m and 4.0m PTFE tube were applied for reaction at 40 °C for NO_3^- and PO_4^{3-} analysis, with 540nm and 660nm spectrophotometric detector, respectively.

2.3 Chemicals and analytical conditions

All reagents used in this study were analytical-reagent grade purchased from Sigma Aldrich and Merck, and ultra pure water system (Millipore Direct Q3) was used to prepare standard solutions, washing solvents and eluents. Analytical balance, ATY 224 (Shimadzu, Tokyo, Japan) was used to balance reagents.

Common Anion and Cation analysis: A stock solution of Na_2SO_4 , KNO_3 , NH_4NO_3 , and MgSO_4 , and a different CaCl_2 solution were solved to 0.1M/L, respectively. These two stock solutions were mixed with the ultra pure water for calibration purpose for common anions and cations simultaneous analysis. 10m M/L tartaric acid with 3m M/L 18-C-6 was prepared for eluents [10]. Flow rate was 1.0 mL/min, injection volume was 50 μL , and duration of an analysis was 7.5min.

NO_2^- analysis: Stock solution of NaNO_2 (0.069g) was solved to 50mL ultra pure water as 20mM/L stock solution, and mixed with the ultra pure water for calibration purpose for NO_2^- analysis. Concentrated hydrochloric acid (12M/L, 417 μL) was dissolved to 50mL ultra pure water as 0.1M/L HCl solution. Sulfanil amide (0.5g) was dissolved to 50mL

0.1Mol/L HCl as reagent solution A, and N-(1-Naphthyl)ethylene diamine dihydrochloride (0.05g) was dissolved to 50mL ultra pure water as reagent solution B. The reagent solution A and B are mixed just before analysis as coloring reagent for FIA to analyze NO_2^- [11]. Flow rate was 0.25 mL/min x 2, injection volume was 50 μL , and duration of an analysis was 3min.

PO_4^{3-} analysis: Stock solution of KH_2PO_4 (0.06804g) was solved to 50ml ultra pure water as 0.01 M/L stock solution, and mixed with the ultra pure water for calibration purpose for PO_4^{3-} analysis. Ammonium molybdate (0.274g), antimony potassium tartrate (0.0125g), concentrated sulfuric acid (3.35mL), L-ascorbic acid (1.5g), and sodium dodecylsulfate (0.05g) were dissolved to 50mL ultra pure water as coloring reagent [12]. Flow rate was 0.5 mL/min x 2, injection volume was 50 μL , and duration of an analysis was 3min.

EC analysis: 0.1 mM/L KCl was used for 147 $\mu\text{S/cm}$ standard solution for EC at 40°C. Flow rate was 1.0 mL/min, injection volume was 50 μL , and duration of an analysis was 3min.

2.4 Field sampling (add onsite filtration)

13 environmental water samples were collected into each of 2mL plastic vials by onsite filtration (0.45 μm nylon filter). Sampling locations were where groundwater discharging from a cut slope beside a road (S1), forested upstream (S2-S3) and its downstream of developed campus area (S4-S6), and discharge from the campus (S7), and oxidation pond (S8-S13) that discharge to river between S5 and S6 in UTM Johor campus. These are representing human impacted water environment. The sampling was performed of 12:00 to 13:00 on 24 Feb. 2012.

3 RESULTS

Calibration graphs were obtained by plotting peak area against the concentration of standard solutions. Linear calibration graphs ($r^2 > 0.999$) were obtained for anions and cations simultaneous analysis in the concentration range 0-0.8mM for common anions (SO_4^{2-} , Cl^- , and NO_3^-), 0-0.4mM for cations (Na^+ , NH_4^+ , K^+ , Mg^{2+} , and Ca^{2+}), 0.0002-0.025mM for NO_2^- , 0.00005-0.05mM for PO_4^{3-} , and 0.005-2.0mM (7.35-2940 $\mu\text{S/cm}$) for KCl.

The detection limits determined at a signal-to-noise ratio of three were 0.31 $\mu\text{M/L}$ for SO_4^{2-} (29.5 ppb), 0.50 $\mu\text{M/L}$ for Cl^- (17.7 ppb), 0.89 $\mu\text{M/L}$ for NO_3^- (12.5 ppb), 0.52 $\mu\text{M/L}$ for Na^+ (11.9 ppb), 0.94 $\mu\text{M/L}$ for NH_4^+ (13.2 ppb), 1.24 $\mu\text{M/L}$ for K^+ (48.5 ppb), 0.76 $\mu\text{M/L}$ for Mg^{2+} (18.4 ppb), 1.75 $\mu\text{M/L}$ for Ca^{2+} (70.0 ppb), 0.02 $\mu\text{M/L}$ for NO_2^- (0.7 ppb), 0.12 $\mu\text{M/L}$ for PO_4^{3-} (11.4 ppb), and 0.03 $\mu\text{S/cm}$ for EC (Table 1).

As shown in Table 1, the water quality of stream water were ranging 4.6-213.4 $\mu\text{M/L}$ for SO_4^{2-} , 68.6-689 $\mu\text{M/L}$ for Cl^- , 3.0-19.0 $\mu\text{M/L}$ for NO_3^- , 79.1-592.8 $\mu\text{M/L}$ for Na^+ , 1.2-416.5 $\mu\text{M/L}$ for NH_4^+ , 3.8-91.9 $\mu\text{M/L}$ for K^+ , 32.9-96.2 $\mu\text{M/L}$ for Mg^{2+} , 61.6-360.4 $\mu\text{M/L}$ for Ca^{2+} , 0.2-2.4 $\mu\text{M/L}$ for NO_2^- , 0.2-22.4 $\mu\text{M/L}$ for PO_4^{3-} , and 292.4-2490.9 $\mu\text{S/cm}$ for

Table 1. Water quality of stream water in Univeristy Teknologi Malaysia on 24 Feb. 2012.

		SO ₄ ²⁻	Cl ⁻	NO ₃ ⁻	Na ⁺	NH ₄ ⁺	K ⁺	Mg ²⁺	Ca ²⁺	NO ₂ ⁻	PO ₄ ³⁻	EC
		[uM/L]	[uM/L]	[uM/L]	[uM/L]	[uM/L]	[uM/L]	[uM/L]	[uM/L]	[uM/L]	[uM/L]	[uS/cm]
S1	Groundwater discharging from cut slope	14.7	124.1	18.8	111.9	3.6	3.8	45.3	61.6	2.4	0.190	344.9
S2	Natural stream in forested area	4.6	68.6	6.3	79.1	2.6	5.7	52.5	72.5	0.2	0.174	292.4
S3	Nagural stream after small human effect	15.3	93.5	15.4	105.8	2.7	8.5	45.4	79.4	0.8	0.183	358.2
S4	Up stream, open water	14.1	77.4	8.8	93.7	2.6	7.5	96.2	165.6	0.2	0.207	554.1
S5	River, upstram of oxidation pond	36.9	109.5	3.0	130.2	1.2	17.8	33.6	200.7	0.2	0.168	594.6
S6	Downstream of oxidation pond	108.5	287.9	9.9	259.0	119.3	43.5	36.3	292.1	0.9	0.280	1166.6
S7	River, infront of security gate	110.2	311.0	19.0	263.3	111.8	50.4	37.3	294.4	1.6	0.620	1206.0
S8	Oxidation pond (NE)	160.4	404.3	9.2	318.0	143.4	58.5	40.0	315.9	2.0	0.348	1451.8
S9	Discharge from oxidation pond	157.2	428.8	11.5	352.5	235.9	61.4	37.6	327.9	0.9	0.504	1641.2
S10	Oxidation pond (NW)	155.3	454.1	6.4	371.3	227.0	65.7	34.9	314.1	0.5	0.541	1610.5
S11	Oxidation pond (SE)	167.0	481.9	6.8	379.7	255.6	70.1	32.9	315.5	0.2	0.696	1720.7
S12	Oxidation pond (SW)	174.6	517.1	7.9	404.6	360.5	78.4	37.8	352.9	0.2	7.340	2022.1
S13	Inflow water to oxidation pond	213.4	689.0	12.9	592.8	416.5	91.9	40.6	360.4	1.7	22.364	2490.9
	Environmental sample data (max)	213.4	689.0	19.0	592.8	416.5	91.9	96.2	360.4	2.4	22.4	2490.9
	Environmental sample data (min)	4.6	68.6	3.0	79.1	1.2	3.8	32.9	61.6	0.2	0.2	292.4
	Caribration graph range (max)	400	400	400	400	400	400	400	400	25	50	2940
	Caribration graph range (min)	0	0	0	0	0	0	0	0	0.2	0.05	7.4
	Detection Limit*	0.31	0.5	0.89	0.52	0.94	1.24	0.76	1.75	0.02	0.12	0.03

*: The detection limits determined at a signal-to-noise ratio of three.

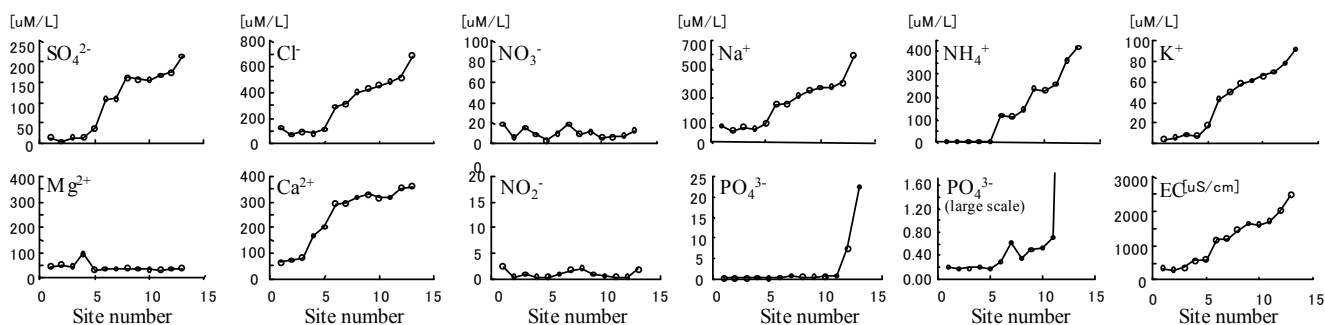


Fig. 2 Water quality of stream water in Universiti Teknologi Malaysia on 24 Feb. 2012. Comparing to detection limit shown in table 1, the resolution among analyte anions, cations, and EC were quite satisfactory, and the methods were useful for the accurate determination of these parameters in common river water.

EC (Table 1). Comparing to detection limit shown in Table 1, the resolution among analyte anions, cations, and EC were satisfactory in order to assess the trend of environmental water quality difference in UTM campus (Fig. 2).

4 DISCUSSION

In this study, common anions and cations simultaneous analysis for SO₄²⁻, Cl⁻, NO₃⁻, Na⁺, NH₄⁺, K⁺, Mg²⁺, and Ca²⁺ were performed by IC mode. Then the analytical resolution was satisfactory and can be considered useful for the accurate determination of these common anions and cations. Moreover, the analysis is a part of an advanced non-suppressor type IC by “polyacrylate– based weakly acidic cation-exchange resin column” with weak-acid eluent [13][14]. By the analytical column, a series of very functional water quality analysis are obtained, such as, these 8 ions plus PO₄³⁻ and SiO₄²⁻ simultaneous analysis[15], HCO₃⁻ analysis[16], simultaneous heavy metal analysis for Ni²⁺, Zn²⁺, Co²⁺, Mn²⁺, and Cd²⁺ [17]. Applying this advanced IC, there is a potential to develop integrated IC for common cation and anion, nutrients, and heavy metals by only one analytical column and equipment.

However, some important parameters, for example COD, total nitrogen (TN), total phosphorous (TP) are impossible to analyze by conventional IC, and generally seawater samples are not applicable for IC. In addition, some parameters, for example IC for phosphorous has low sensitivity for environmental monitoring [15]. On the contrary, FIA has

advantage for these analyses [11][12][18][19]. Accordingly, because of similarity for system design between IC and FIA, these analytical systems were integrated in this study (Fig. 1). Consequently, SO₄²⁻, Cl⁻, NO₃⁻, Na⁺, NH₄⁺, K⁺, Mg²⁺, Ca²⁺, NO₂⁻, PO₄³⁻, and EC were able to be analyzed from only 2mL onsite filtered sample in a plastic vial. This multi-parameter analysis can be extended to TP [12], TN [18], COD [19], HCO₃⁻ [16] within another one 2mL vial sample, easily, and the analytical capacity is several hundred samples regarding the capacity of auto sampler of IC2010.

In order to embark on effective environmental restoration programs and projects, SEA is quite important [1], where new methodologies for SEA need to be developed [8][9]. According to literature [8][9], expected properties of such new approach is “rapid delivery of results, on-site, low-cost, and capacity to acquire large number of observations within a short time frame”. Regarding the requirement, the concept of on-site analysis was eliminated, and time frame for rapid delivery of result is assumed as one day, and then, convenient experiment procedure, satisfactory accuracy, capacity of automated large number sample analysis, and integrated multi-parameter analysis were of more concern in this study. According to our analytical approach, because of reduction of sample volume, even concept of onsite analysis was eliminated, field sampling process and sample transportation process were drastically improved, and then, convenient and enough accuracy of multi-parameter large number sample was available, which will contribute to SEA as a new

technical approach that improves problem recognition processes in environmental prospective and profiling.

In water environmental management, the communication gap (CG) between water authorities and public causes difficult chronic management problem in water-environment monitoring and assessment [5]. The potential solution is to prepare useful information, where our multi-parameter convenient approach will contribute to give new approach to solve the CG by rapid delivery of data, low-cost, and high capacity to acquire large number of observations of integrated data.

5. CONCLUSION

Ion Chromatography and Flow Injection Analysis integration was performed, which was satisfactory to analyze SO_4^{2-} , Cl^- , NO_3^- , Na^+ , NH_4^+ , K^+ , Mg^{2+} , Ca^{2+} , NO_2^- , and PO_4^{3-} in $\mu\text{M/L}$ level, and EC in $\leq 0.03 \mu\text{S/cm}$ by only one equipment within 2mL onsite filtered sample. The analysis can be extended to COD, TP, and TN. A convenient water quality prospecting was available for strategic environmental monitoring due to rapid delivered, low-cost, and integrated data.

6. ACKNOWLEDGMENT

This study was supported by FRGS (4F089) and ERGS (4L015) fund by Ministry of Higher Education, Malaysia. We express our gratitude to TOSOH for all the support for this study.

7. REFERENCES

- [1] Gauthier M, Simard L, Waaub JP, "Public participation in strategic environmental assessment (SEA): Critical review and the Quebec (Canada) approach," *Env. Impact Assessment Review*, 2011, vol.31, pp48-60.
- [2] Fischer BT, Wood CJC, "Policy, plan, and program environmental assessment in England, the Netherlands, and Germany: practice and prospects," *Env. and planning*, 2002, vol.29, pp.159-172.
- [3] Clesceri LS, Greenberg AE, Eaton AD, "Standard methods for the examination of water and wastewater" 20th ed. American Public Health Association, Washington, 1998, 1325 p.
- [4] Graveline N, Maton L, Luckge H, Rouillard J, Strosser P, Palkaniete K, Rinaudo JD, Taverne D Interviews E, "Potential uses and constraints of emerging water quality Monitoring tools: an operational perspective," *Trends in Analytical Chemistry*, 2010, vol.29, pp.378-384.
- [5] Kikuchi A, Hakim L, Heryansyah A, Romaidi R "Significance of the Easy-to-use Water Quality Checker for Participative Environmental Monitoring and Experience Based Learning," *Journal of Tropical Life Science*, 2010, vol.1, pp17-21.
- [6] Smith VH, Tilman GD, Nekola JC, "Eutrophication: impacts of excess nutrient inputs on freshwater, marine, and terrestrial ecosystems," *Env. Pollution*, vol. 100, 1999, pp.179-196.
- [7] Elser JJ, Bracken MES, Cleland EE, Gruner DS, Harpole WS, Hillebrand H, Ngai JT, Seabloom RW, Shurin JB, and Smith JE, "Global analysis of nitrogen and phosphorus limitation of primary producers in freshwater, marine and terrestrial ecosystems," *Ecology Letters*, 2007, vol. 10, pp.1135-1142.
- [8] Carpenter SR, Caraco NF, Correll DL, Howarth RW, Sharpley AN and Smith VH, "Nonpoint pollution of surface waters with phosphorus and nitrogen," *Ecological Applications*, 1998, vol. 8, pp.559-568.
- [9] Stumm W, Mrgan JJ, "Aquatic Chemistry; an Introduction Emphasizing Chemical Equilibria in Natural Water," 2nd ed., Wiley, New York, 1981, pp.780.
- [10] Masuda W, Tanaka K, Goto R, Hasebe K, Kikuchi A and Nakagoshi N, "Ion-exclusion/cation-exchange chromatography for water quality monitoring of river waters," *J. Japan Industrial Water Association*, 2007, vol. 585, pp.80-86.
- [11] Higuchi K, Motomizu S, "Flow-Injection Spectrophotometric Determination of Nitrite and Nitrate in Biological Samples," *Analytical Science*, 1999, vol. 15, pp129-134.
- [12] Higuchi K, Tamanouchi H, Motomizu S, "On-line Photo-Oxidative Decomposition of Phosphorous Compounds to Orthophosphate and Its Application to Flow Injection Spectrophotometric Determinations of Total Phosphorus in River and Waste Waters," *Analytical Sciences*, vol. 14, 1998, pp941-946.
- [13] Tanaka K, Ohta K, Fritz JS, Matsushita S Miyanaga A, "Simultaneous ion-exchange chromatography with conductimetric detection of anions and cations in acid rain waters," *J. Chromatography A*, 1994, vol. 671, pp.239-248.
- [14] Mori M, Tanaka K, Helaleh MIH, Xu Q, Ikedo M, Ogura Y, Sato S, Hu W, Haebe K Haddad PR, "High-speed simultaneous ion-exchange chromatography of anions and cations on a weakly acidic cation-exchange resin column," *J. Chromatography A*, 2003, vol. 997, pp219-224.
- [15] Nakatani N, Kozaki D, Masuda W, Nakagoshi N, Hasebe K, Mori M, Tanaka K "Simultaneous spectrophotometric determination of phosphate and silicate ions in river water by using ion-exchange chromatography separation and post-column derivatization," *Analytical Chimica Acta*, 2008, vol. 619, pp110-114.
- [16] Mori K, Ikedo M, Hu W, Helaleh MIH, Xu Q, Itabashi H Tanaka K, "High-speed ion-exchange chromatography of dissolved carbon dioxide on a small weakly acidic cation-exchange resin column with ion-exchange enhancement columns of conductivity detection," *J. of Chromatography A*, 2005, vol. 1092, pp250-253.
- [17] Mori K Tanaka K, "Separation of Heavy Metal Ion(Ch.2.5)," *The practice of ion chromatography*, Tanaka K, Ed. Mimizukusya, Tokyo, Japan. 2009, p228.
- [18] Kitami H, Ishihara Y, "Simultaneous Determination of Total Nitrogen and Total Phosphorous in Sewage Water by Flow Injection Analysis after Continuous Flow Sample Degradation Using Heating Aluminum Block," *BUNSEKI KAGAKU*, 2009, vol. 58, pp.839-844.

- [19] Vallejo-Pecharroman B, Izquierdo-Reina A, de Castro MDL, "Flow injection determination of chemical oxygen demand in leaching liquid," *Analyst*, vol. 124, 1999, pp.1261-1264.

THE INTELLIGENT PERFORMANCE INSTALLATIONS IN ENERGY EFFICIENCY IN GREEN BUILDINGS

Hooman Abadi, Rouzbeh Abadi, Poona Abadi

Universiti Kuala Lumpur (Unikl) /Business school, Kuala Lumpur, Malaysia,

Universiti Teknologi Malaysia (UTM), Faculty of Civil Engineering, Kuala Lumpur, Malaysia,

Universiti Teknologi Malaysia (UTM), Faculty of Management, Kuala Lumpur, Malaysia

hooman_abadi@yahoo.com

rouzbeh.abadi@me.com

abadi.poona@gmail.com

ABSTRACT:

Increasing population, growth and diversity of the people demands in the work and communal activity and living issues like achieving to the participated aims, move welfare, change the life culture and public in structure and or expansion of the building's foundation level and or possibility to enjoy of the day and fresh technology in the life brought out the unused issues in the different fields such as safe, protection, repair and maintain of the instruments and installations, presenting the favorable service, suitable consumption and consumption optimization in the various energies

in collection. Remedies about the protection issues in scattered and some had acceptable solutions, Supervision on good performance and leading of installations and instruments in order to the suitable exploitation and the move suitable service presentation has been applied the traditional methods and the limited solutions with significant cost. But it needed do the abundant effective practical measures to apply the modern management in order to the suitable exploitation of a building in generally such as useful age of installations and instruments, in time service and maintenance, optimum consumption of kinds of energy and determining at least cost in any country.

It can be said in courage that is needed a basic turn to the views. Perhaps, there are fewer green buildings in the world that presents a statistic of the energy consumptions, their wastes, to determine the costs based on statistics of them.

In the present paper management techniques and integrated quick control equipment while define the mechanical and electrical installations and instruments coordinated clever management system and this system. How has efficiency a powerful instrument to manage a building (construction)

Keywords: Intelligent, Performance Installations, Energy Efficiency, Green Buildings

INTRODUCTION

Increasing energy consumption and as a result increasing prices during the current decade caused many energy consumers, and even retail consumers try to reduce consumption, and it results from various kinds of savings. Meanwhile, some scholars believe that increasing price of energy as a driving factor for savings, although bio environmental damages resulted from excessive consumption of energy caused to consume wisely too. For answering new requirements such as lower consumption and more efficiency, notice and resorting to innovation and inventions and utilizing new technologies in all sections of production, as well as transportation and distribution of energy, and also in consumption section is unavoidable. Therefore, for managing and steering a building and dealing with events with the lowest unsuitable effect for presenting

proper services need of changing view and exploiting management methods from traditional and manual methods to contemporary ones can be felt clearly. Because humane based on their physiological structure and limited capacities in time of unacceptable events are vulnerable and will lose their sagacity and mental control for resisting or if controlling or supervision domain is vast, negative effects of tediousness or lack of concentration will occur. accordingly, new modern machineries as a type of movement with the goal of subsiding humane force with mechanical and electronic ones should be utilized. Geographical situation of Iran from one hand and necessity of saving in costs and avoiding wasteful and maintaining national capital such as water resources, energy, electricity, repairs, precautionary service of equipment and important huge building infrastructures such as health

centers from the other hand demands this change of method in country level, which has stated below:

- 1- Relying on sectional scientific specialists and topical technical knowledge
- 2- Designing and building required mechanical equipment inside the country (as much as possible)
- 3- Having services and customer services after implementation

This movement for building exploitation management from the manual system to an effective electronic system with an ability of integration in further stages is from inside the country and with relying on all of local specialist forces and immediate facilities than with a proper investment and along with a codified and assured plan, this movement for buildings of the country will be achieved its goals. It is believed that considering current capabilities and facilities and with utilizing them and infrastructures with utilizing the intelligent management system, this national capital will be maintained and save in cost and also functionality of equipment will be coordinated and competent.

A requirement of Management of a building:

Each building and especially huge buildings such as tall or wide in ground level regarding their functional requirements and number of infrastructures and equipment presented in them have some requirements in managing and proper and efficient exploitation of them which some of them are as follows:

- Reducing power consumption without creating a lack of services
- Lack of presence of identity and repair record of infrastructures and equipment and number of services
- Lack of precautionary and on time services for present equipment
- Any kind of setting or control is done manually by operators, and no automatic setting equipment is using. Therefore, settings are fully depended on technical knowledge and personal preferences of the operator not to a systematic knowledge and what should be done technically.
- High cost of human-resource wage for operating and maintaining equipment
- High rate of depreciation because lack of the intelligent system as a tool for maintainer's forces and operators for controlling functional quality
- Lack of presence of a precautionary maintenance program (P.M) for equipment and building infrastructures
- Planning with saving goals in cost of electricity power, fossil fuel, etc. is not functional

because of lack of required information and needed equipment that its result is various high costs and undesirable and inefficient results.

- Really accurate value of activity of backup services manager is not clear because of lack of information about the way they work and not being familiar with their facilities and method of their reactions to needs.
- Lack of using expert specialists for presenting proper technical services to buildings, especially in deprived regions

To the above issues, controlling another equipment including always on and non-always on such as starting and stopping elevators according to requirements, opening and closing special doors such as emergency doors in time of disasters and such these will be added. Necessity of answering these needs for desirable managing a building caused to invent electronic systematic solutions that are defined for a specific job which efficient management of buildings will be possible with relying on these tools.

What is the meaning of intelligent management of a building?

One of the tasks of management is evaluating deviance from the goal and guiding the set in each time period intervals so the set under management is moving toward goals and achieve its goal. Building management with the aim of presenting on time and desirable services and with optimum cost is not separated from this subject too. For this reason, some tools are needed including gathering information from equipment and installations of building in form of signals such as temperature of warm water, the amount of consumed cold water, being in ON or OFF state of equipment, pumps and such as these installations. Being in move or stopped state of facilities such as elevators or some information of the security system, lighting system, Coccus and, etc. and then this gathered information is placed for analysis process that can be handled by one or more persons manually or through electronic systems and by computer automatically. It seems that regarding the number of signals and number of different requirements of exploitation and capabilities of electronic machines and present today microprocessor equipped machines such as computers, analyzing these signals automatically is unavoidable. In this situation, all the varying possibility is predicted by functional software or a desirable algorithm, logical continuity of cases observed and in case of mistakes, a warning will be issued or another decision will be made an issue order to implement that.

Results of analysis prepared in form of made decisions ready for implementation, and managerial order will issue. These orders and commands can be in various digital forms such as make consumer keys on or off such as lighting keys, starting pumps and electrometer or includes combined and group functions such as stopping all of elevators or opening all emergency doors. Implementing decisions too can be granted to a person or a group, or it can be granted to some machines because most of the information is gathered during 24-hour day and night, therefore, management of a building is like management of a factory that is running 24/7. In addition to managing daily routines, another management requirement is observing functional in building in time, day, month, season and year, which are relying on the same gathered information that preparing statistics, generating periodical reports, and codifying proper algorithm for operation of equipment is a part of this task. Such this system, including, transmitting and receiving signals, commands, reports to remote location and having records of operations in an active archive called intelligent management of building, which is consisted of hardware, software, and controlling systems.

Capabilities and technical advantages of Intelligent Management of building:

Once such these powerful and efficient tools are provided for managing a building, in addition to habitual and communal jobs in building management modern capabilities can be achieved, which were impossible, until now, while even for doing customary and shared tasks too, unused definitions and capabilities will be stated that below points can be mentioned:

Collect, register and record all input data:

Input data are analog and digital signals that transmit all required information about situation and state of equipment and installations such as determining energy's consumption rate, determining the excessive or shortcoming amount of consumption compared to factors, temperature of water, flow of water, leakage in pipes, voltage and amperage and power consumption of a machine or a set of consumer machines, being in on or off state of an electrometer, state of an elevator in each moment of time, or a door or window being open or close, and such these data sent to the system. With collecting data, record and analyzing and processing them, diagrams and process of their changes in a desired period of time can be prepared, viewed or study or transmitted for a specific reason to a remote location.

Controlling decision making based on collected data:

Recorded data of quantities compared to a source quantity, for example, temperature of received warm water compared to desired temperature, and decision will be made based on it and if water is warm enough heater will be turned off. Generally such these

controlling and commands are done on installations but functional history of parameters and mechanism of control will not be recorded. Moreover, any decision about controlling circuit should be done in the location which equipment is installed while in the intelligent management system of building change order in reference quantity's values (set points) or mechanism of control (such as PID or PI) or operation command can be issued from command room and utilize software flexibility in the system too.

It coordinated and on time operation in the building:

In buildings function of equipment and installations traditionally grouped into various groups, for example, control and operating powerhouse is granted to a group and repairing and supervising power systems is granted to other groups and maintain and securing is granted to securities, but integrity and coordination between functions such as coordination of job of a fire alarm system with air-conditioning system and elevators for building management is very desirable and have importance. This coordination will lead to a major saving in costs, energy consumption, and depreciation.

Expanding managerial services in form of the management information system:

Increasing buildings in country and need of technical specialist for control, operate, service, and maintaining equipment and installations from one hand and lack of the possibility of utilizing required specialists, especially in remote areas from other hand state necessities

of intelligent management of building so with this method it will be possible to transmit registered and recorded information through telecommunication networks to users and experts in remote location far from building hence management of building both technical and non-technical relying on transmitted data in form of management information system (MIS) and based on real statistics can make important decisions that lead to major savings in consumption of water, electricity, fuel, depreciation, and avoid lack of coordination.

Scheduling and planning for service and repair:

One of the weaknesses that there is in maintaining, servicing and operating of technical systems of building in the country, including industrial and non-industrial is that preparing repair history and scheduling for repair and precautionary maintenance (PM), if not considered as impossible but is very difficult and cost lots of money and is inactive. With the intelligent management system, it is possible to record functional history of equipment and utilize it in the future. This matter, especially when it comes to ordering for spare parts, warehouse handling, and reducing costs is very important. With the help of the intelligent management system, it is possible to schedule for periodical repairs and determine current or yearly repairs, and with the

possibility of necessary predictions reduce most of the costs and also for precautionary service and maintenance by the system it will be possible to fight against majority of dangers and prevent loss.

Increasing useful life span of equipment:

Implementing ordered plan and precautionary service and maintenance will cause to determine working hours of each machine in advance, identity card of each machine, including record of all past problems, and spare parts replaced should be prepared and through a software program service and maintain. Implementing these steps will lead to decreasing depreciation and energy consumption and will increase the useful life span of equipment and make them always stand by and ready to work.

Savings:

Getting statistics of consumption of water, electricity, gas or diesel is the first step for finding a solution for saving that with the help of intelligent management such as these statistics is provided easily. And based on it is possible to calculate what type of saving in which part can be done. These calculations are simply done by computers and cost of any type of control for each part is determined. Managing power distribution system, making lighting system intelligent, controlling air-conditioning system with observance of saving energy, and efficient managing of warm water installations and radiators or chillers after implementing parameters of savings are all possible with the help of the intelligent management system.

For example, it is reported that in a tall building in United States between 20 to 41% in energy cost for each unit of infrastructure saved. Moreover, according to various reports, including presented information in table no.1, recorded statistics showed definitive savings after utilization of the intelligent management system in all various economic sections, including urban installations.

Economic effects of the intelligent management system: Because of various utilizations of buildings, servicing, maintaining, and keep all equipment and installations including power, mechanical, and low pressure in buildings ready to work has special importance and necessity of on time and proper service to residents and guests is clear. With a glance to maintaining cost of building and installations and also fuel, electricity, lighting of some buildings including health centers, it will be determined that while presenting proper services for stopping increasing mentioned case's costs or even decreasing them a solution should be thought. Equipping buildings with the intelligent management system along with technical and efficient effects of that which has mentioned because of creating the proper basis for creating job opportunity in technical level and current technology for university graduates and

therefore, increasing technical level of services and maintaining of buildings from one hand and service, maintain, and consumption of fuel, electricity and energy from the other hand bring suitable economic effects. Moreover, implementation level of this system in building with a scheduled plan in a few years can be upgraded and utilization of system and level of savings will be increased.

CONCLUSION:

Presenting suitable and on time service along with economic savings in energy consumption and electricity energy is one of the first and most important actions in proper management of building. Utilization of buildings in all over the country raises another case that for presenting suitable services should find new solutions. Building management now needs new tools that intelligent management system is designed and created for answering these needs. With the help of this system in addition to common savings, it is possible to manage different parts of a building under an integrated and coordinated control and from a remote location supervise and control buildings and till some extent diagnose technical difficulties in them. From other hand this system with presenting managerial services such as possibility of preparing periodical reports and service and maintenance reports and such these present special facilities to the managers of buildings. Valuable experiences in design, build and implementing this system shows that with spending a little cost can achieve noticeable savings.

REFERENCES:

- [1] J.B. Brodrick et al, "A New Approach to Buildings and Energy Analysis", ASHRAE J, Aug, 1990 pp 15-20.
- [2] Weidmuller interface, Profit by peak load Limitation, Weidmuller Co., Cat. No 51296-0493.
- [3] H. Ghaeini, Feasibility Study on BMS implementation in MP, S Offices, Sheraguima Co. (in Farsi) 1992
- [4] Eastwell A. (1988). "Building Energy Management" from McClelland, S. (ed) Intelligent Buildings: An IFS Executive Briefing, IFS Publications, UK.
- [5] Hartman, T. (2001). "Occupant connectivity for building controls", an article in AutomatedBuildings.com, March issue, retrieved 10/8/2001 from the web: <http://www.automatedbuildings.com/>

- [6] Mustafa, H. and Bansal, P. (2002). "Building Intelligence via building management systems" thesis, University of Auckland, New Zealand
- [7] Newman, H. (1996). "Integrating Building Automation & Control Products Using the BACnet Protocol", ASHRAE Journal, Vol.38, Nov. issue, USA.
- [8] Sinclair, K. (2001c). "The greening of buildings with automation", engineered systems online, Feb. issue, retrieved 10/10/2001 from the web: <http://www.esmagazine.com/es/cda/articleinformation/>
- [9] A. Mahdavi, "Simulation-based control of building systems operation," Building Environ., vol. 36, no. 6, pp. 789–796, 2001.
- [10] T. Pfeifer, A. Micklei, and H. Hartenthaler, "Internet-integrated building control: leaving the lab-robust, scalable and secure," in Proc. 26th Annu. IEEE Conf. Local Computer Networks (LCN2001), 2001, pp. 306–315.
- [11] H. M. Newman, Direct Digital Control of Building Systems: Theory and Practice. New York: Wiley, 1994.
- [12] Building Automation and Control Systems (BACS)—Part 2: Hardware, ISO Std. 16 484-2, 2004.
- [13] Thermal Environmental Conditions for Human Occupancy, ANSI/ASHRAE Std. 55, 2004.
- [14] D. Snoonian, "Smart buildings," IEEE Spectr., vol. 40, no. 8, pp.18–23, Aug. 2003.
- [15] J. Plönnings, M. Neugebauer, and K. Kabitzsch, "A traffic model for networked devices in the building automation," in Proc. 2004 IEEE Int. Workshop Factory Communication Systems (WFCS 2004), pp. 137–146. [14] E. Finch, "Is
- [16] Home and Building Electronic Systems (HBES), Eur. Family of Std. 50 090.
- [17] (2005). Open Building Information Exchange. [Online]. Available: <http://www.obix.org>
- [18] K. Eaton, A. Amato, A Comparative Environmental Life Cycle Assessment of Modern Office Buildings, Steel Construction Institute, Ascot, UK, 1998.
- [19] B. Berge, the Ecology of Building Materials, Architectural Press, Oxford, UK, 2000.
- [20] D.J. Clements-Croome, K.G. Jones, G. John, Through life environmental business modeling for sustainable architecture, CIBSE Proceedings of Conference on Building Sustainability, Value and Profit, Edinburgh, UK, 2003.

Study the Effect of Polyvinyl Chloride (PVC) Addition on the Permeability of Anbar Soils

Dr. Ahmed H. Abdul Kareem & Omar Mustafa
Engineering College-Anbar University, Iraq

ABSTRACT

The soil is considered the most abundant building material in the world and after the only local resource available to the engineer for his work. On the other hand, the inclusion of materials such as soil stabilizing agents allowed to improve some of its properties (mainly strength, permeability), reduce costs and environmental effects, especially if such materials from industrial by products. The aim of this research is to study the effect of PVC addition on the permeability of Anbar soils. Permeability testing for these soils by laboratory tests working (i.e. the addition of different percentages of PVC, 5%, 10%, 15%, and 20%) to four types of fill soils from different areas in Anbar government. Classification tests were done on these soils. The addition of PVC to the soils lead to significant decrease in soil permeability and this serves in improving the soil layers that are placed under buildings and roads as sub-base or sub-grade layers. Also, the study found that the addition of PVC at least 15% to the soils will reduce the coefficient of permeability, k , by up to 99% and that help to use it instead of concrete in the lining of the water treatment plants. The study also found the coefficient of permeability, k decrease significantly in soils containing a high proportion of gypsum.

Keywords: Permeability, Soil Stabilize, PVC addition, Anbar soil

1. INTRODUCTION

According to Lamb (1999), the soil is considered the most abundant building material in the world and after the only local resource available to the engineer for has work in the case, it is intended that its characteristics meet the requirements demanded by these jobs [1].

The inclusion of materials such as soil stabilizing agents allowed to improve some of its properties (mainly strength, permeability), reduce costs and environmental effects, especially if such materials from industrial-by products or recycling, and updated the stabilization techniques, modification or improvement of soils through the inclusion of alternative materials.

The concern to stabilize or modify the soil has generated inventive approaches, although based on conventional systems make use of additive and processes following this trend, we present this research which studies the behavior in terms of coefficient permeability in its natural state, and the same material added product that until now had not been used as modifying agent in this such materials PVC.

The work focuses on the analysis of behavior in terms of permeability, for being the most commonly used test in the different soils in earth dam, and reservoir dams.

The purpose of using PVC is improved the coefficient permeability, k . These additives can be used with a variety of soils help improve their natural soil these additives depends on the soil treated and the amount of additive used.

2. SOIL STABILIZATION

The soils are stabilized to modify existing properties making them able to best comply with their requirements,

especially looking for a good stress-strain behavior and permeability.

The properties that are attempting to change into soils through a process of stabilization are: volume stability, strength, permeability, compressibility and durability.

With respect to soil stabilization methods, the following have been referenced in literature (April & Castrillon, 1993, Aguirre & Velez, 2005, Amaya et al., 1978, Caicedo & Herrera, 2004, and Gomez et al., 1983) to stabilize granular sub-bases: mechanical stabilization through mixtures, mechanical stabilization by compaction, stabilization and drainage, lime stabilization, stabilization with lime and fly ash, stabilization with asphalt and cement stabilization [2,3,4,5,6].

The most commonly used to stabilize granular sub base under the concrete, asphalt, compaction and lime; however are currently investigating methods and unconventional materials which stabilize optimal from the standpoint of technical, economic, and environmental [7].

3. POLYVINYL CHLORIDE (PVC)

Polyvinyl chloride, $-(CH_2-CHCl-)_n$ – is a synthetic polymer which is obtained by addition polymerization of vinyl chloride, and is the raw material for preparation of PVC.

Raw materials which results in the PVC are common salt and oil or natural gas. Oil or gas ethylene is obtained through a cracking process, the salt dissolves in water and subjected to electrolysis to separate the chlorine in it. Ethylene, 43%, and chlorine by 57%, are then combined under heat to obtain a gas monomer, vinyl chloride. Monomer molecules are linked as results of a reaction know as polymerization. The product of this process is the

PVC resin in its virgin, whose appearance is a fine white powder [8].

Most times the polyvinyl chloride used with additives that improve their finish, these are: plasticizers (give flexibility to the polymeric materials), heat stabilizers (to prevent thermal degradation during processing and increase shelf life), lubricants (help fluidity during processing and prevent adhesion to metal surfaces), fillers (lower costs) and pigment (give color, opacity and weathering).

Because faculty have mixed resins with various additives, PVC has been used for various products, ranging from the rigid and durable used for drinking water supply and energy to the flexible and extensible films for food packaging.

The construction and infrastructure accounts for 60% of products made with PVC benefiting the areas of modern life or to meet human needs

Plastics are also called synthetic resins and are broadly classified into two categories; thermosetting resins and thermoplastic resins. The thermosetting resins include phenol resin and melamine resin, which are thermally hardened and never become soft again. Thermoplastic resins include PVC, polyethylene (PE), polystyrene (PS) and polypropylene (PP), which can be re-softened by heating.

4. PVC's PHYSICAL PROPERTIES

PVC, PE, PP and PS are general purpose plastics. The features of the particular plastic are determined by its chemical composition and type of molecular structure (molecular formation: crystalline/amorphous structure) PVC has an amorphous structure with polar chlorine atoms in the molecular structure. Having chlorine atoms and the amorphous molecular structure are inseparably related. Although plastics seem very similar in the context of daily use, PVC has completely different features in terms of performance and functions compared with olefin plastics which have only carbon and hydrogen atoms in their molecular structures. Chemical stability is a common feature among substances containing halogens such as chlorine and fluorine. This applies to PVC resins, which furthermore possess fire retarding properties, durability, and oil/chemical resistance.

5. MECHANICAL STABILITY

PVC is a chemically stable material, which shows little change in molecular structure, and also exhibits little change in its mechanical strength. However, long chain polymers are viscous as in 1 materials and can be deformed by continuous application of exterior force, even if the applied force is well below their yield point.

6. PERMEABILITY

Flow of soil water for non-turbulent conditions has been expressed by Darcy as

$$v = k i \quad (1)$$

Where

i = Hydraulic gradient h/L

k = Coefficient of permeability (or hydraulic conductivity) as proposed by Darcy, Length/time.

v = Discharge velocity, which is due quantity of water flowing in unit time through a unit gross section area of soil at right angle to the direction of flow.

Table (1) lists typical order of magnitude (exponent of 10) values for various soils.

Table (1) Order-of-magnitude values for permeability k , based on description of soil and by the Unified Soil Classification System, m/s [9].

10^0	10^{-2}	10^{-5}	10^{-9}	10^{-11}
Clean gravel GW, GP	Clean gravel and sand mixtures GW, GP SW, SP GM	Sand-silt mixtures SM, SL, SC	Clays	

The quantity of flow q through a cross section of area A is

$$Q = k i A \quad \text{Volume/time} \quad (2)$$

Permeability is a measure of the ease in which water can flow through a soil volume. It is one of the most important geotechnical parameters. However, it is probably the most difficult parameter to determine. In large part, it controls the strength and deformation behavior of soils. It directly affects the following:

- Quantity of water that will flow toward an excavation
- Design of cutoffs beneath dams on permeable foundations
- Design of the clay layer for a landfill liner.

Two tests commonly used in the laboratory to determine k are the *constant-head* and *falling-head* methods. Figure 1 gives the schematic diagrams and the equations used for computing k . The falling-head test is usually used for $k < 10^{-5}$ m/s (cohesive soils), and the constant-head test is usually used for cohesionless soils [9].

7. ORDINARY METHOD

When the soil $k < 10^{-5}$ m/s Falling-head permeability test using the standard compaction-mold permeameter as shown in Figure 3 where both a disassembled device and a test setup using a 100-ml burette. Great care is required in assembly to avoid leaks. Use a meter stick to measure the hydraulic heads, h_1 and h_2 , and the coefficient of permeability could be found by Applying Eq. (3) with small hydraulic gradients exercise care that sample does not drain [10].

$$k = 2.303 * \frac{aL}{At} \log \frac{h_1}{h_2} \quad (3)$$

Where :

k =Coefficient of permeability (or hydraulic conductivity) as proposed by Darcy, Length/time.
 a = Inside area of standpipe, cm^2
 A = Cross - sectional area of specimen, cm^2
 L = Length of specimen, cm
 t = Elapsed time of test, sec
 h_1 =Hydraulic head across sample at beginning of test($t=0$)
 h_2 = Hydraulic head across sample at end of test ($t=t_{\text{test}}$)

8. CHARACTERISTIC OF SOILS

Four soils from different areas in Anbar government were selected for use in the admixture evaluation. The soil properties were determined in general accordance with ASTM and BS. Tests included Grain Size Distribution (ASTM D 422-02), Atterberg Limit testing (ASTM D 4318), compaction test (ASTM D 698), specific gravity (D 854) and gypsum Content, (BS 1377). Material classifications were made in accordance to the Unified Soils Classification System (USCS). A summery of the soil properties determined in the laboratory and the corresponding standard testing identification is presented in Fig.(1) and Table (2).

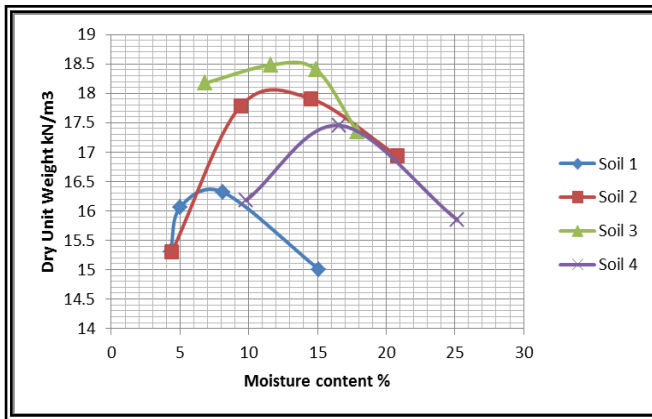


Fig. (1) Results of compaction tests for four Soils

Table (2) Material Index Properties

Parameters	Soil 1	Soil 2	Soil 3	Soil 4
Location	Ramadi	West Ramadi	East Ramadi	North Ramadi
Liquid Limit, LL (%)	NL	NL	NL	18
Plasticity Index, PI (%)	NP	NP	NP	7
Particle Size Distribution				
Finer %	27	14.8	16.6	84.6
Sand %	73	85.2	83.4	15.4
Gravel %	0	0	0	0
Compaction Test				
Dry Unit Weight (kN/m^3)	16.38	17.96	18.53	17.46
Optimum Moisture Content %	7.2	13.4	13.4	16.6
USCS System	SM 799	SM	SM	CL-ML
Description of Soil	Silty Sand (Gypseous Soil)	Silty Sand	Silty Sand	Silty Clay with Sand
Specific Gravity (Gs)	2.43	2.64	2.58	2.6
Gypsum Content %	47	8.02	13.75	7.74

9. TEST PROCEDURE OF PERMEABILITY

Three SM soils, and one soils of type CL-ML were used. PVC addition was mixed with each of the soils. PVC was added to the soils at rate of (5, 10, 15, 20) percent by weight of the dry soil. Each PVC/ soil combination was compacted to maximum dry unit weight and optimum moisture content (O.M.C) for each soil. After the prepared the compacted test samples which used in falling permeability testing [11].

10. RESULTS AND DISCUSSION

After examination and obtaining the basic results, PVC has been added to each soil and at different rates and in a manner to bring the weight of the PVC replaced by equivalent weight of the soil then see the changes on soil properties by comparing the results of permeability before and after Addition.

10.1 Soil No.1

The addition of PVC into the soil 1 (SM, silty sand gypseous soil) calculated value of k as shown in Fig (2). From this figure, it can be seen that the addition of PVC to the soil at different rates lead to a decrease in k values. The ppercentage decrease in the k value reaches 97% when the addition of PVC by 20%.

10.2 Soil No.2 and 3

The effect of PVC addition on coefficient of permeability, k , for soil 2 and 3 (silty sand) shown in Fig. (3) and (4). These figures show that increasing the proportion of addition of PVC to the soil leads to a decrease of k values and this tells us in improving the soil layers that are under the foundations of buildings or roads and prevent the rise of groundwater, which causes them to reduce the shear strength of soil. The ppercentage decrease in the k value reach to 99.2% and 99.7% when the PVC addition of 20%

and 15% for soil2 and 3. Fig. (5) show effect of PVC addition on coefficient of permeability, k, for soil 1 to 3 respectively.

10.3 Soil No.4

The soil is silty clay with sand (CL-ML). The addition of PVC will decrease the coefficient of permeability, k, for all addition as shown in Fig. (6). The decrease of the coefficient of permeability, k, percentage to 99.8% when the PVC addition of 20%. In Table (3), we can see the final results are calculated to effect PVC addition on coefficient of permeability, k, for different soil.

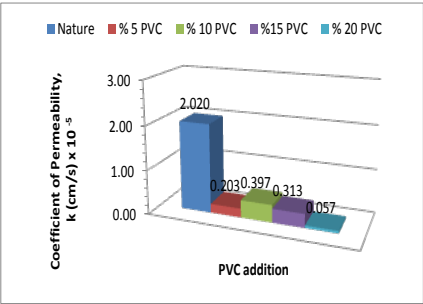


Fig. (2) Effect of PVC addition on coefficient of permeability, k, for soil 1.

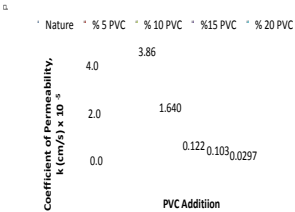


Fig. (3): Effect of PVC addition on coefficient of permeability, k, for soil2.

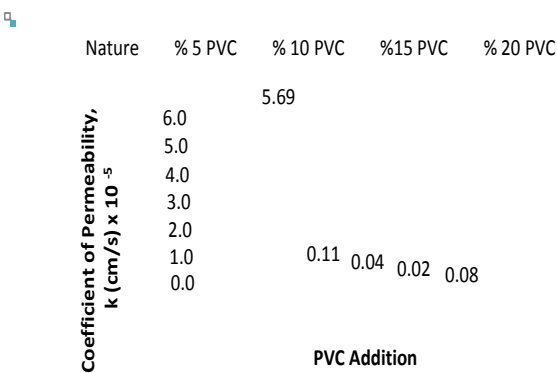


Fig. (4) Effect of PVC addition on coefficient of permeability, k, for soil 3.

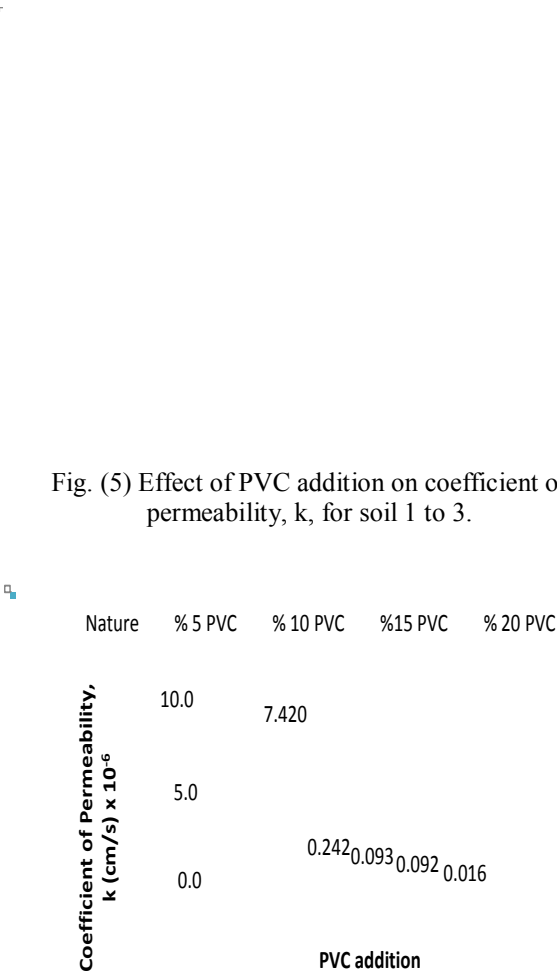


Fig. (6): Effect of PVC addition on coefficient of permeability, k, for soil 4.

Table (3) Values of permeability coefficient, k, for different soils with different PVC addition and the percentage decreasing.

Type of Soil	PVC addition %	Coefficient of Permeability, k, cm/s	The Percentage Decreasing, %
Soil 1	0	2.02×10^{-5}	0.00
	5	2.03×10^{-6}	90.0
	10	3.97×10^{-6}	80.0
	15	3.13×10^{-6}	84.5
	20	5.70×10^{-7}	97.0
Soil 2	0	3.86×10^{-5}	0.00
	5	1.64×10^{-5}	57.5
	10	1.22×10^{-6}	96.8
	15	1.03×10^{-6}	97.3
	20	2.97×10^{-7}	99.2
Soil 3	0	5.69×10^{-5}	0.00
	5	1.07×10^{-6}	98.0
	10	4.17×10^{-7}	99.0
	15	2.48×10^{-7}	99.7
	20	7.6×10^{-7}	98.7
Soil 4	0	7.42×10^{-6}	0.00
	5	2.41×10^{-7}	96.7
	10	9.28×10^{-8}	98.7
	15	9.20×10^{-8}	98.7
	20	1.66×10^{-8}	99.8

11. CONCLUSIONS

The following conclusion can be drawn from the results of this research:

- 1-The PVC is classified as a durable product that is not affected by humus, corrosive, acidic solution, basic solutions, saline solution, solvents and chemicals, also is resistant to the aggression produced by the environmental.
- 2-Addition of PVC to the granular soils at different rates leads to a decrease in soil permeability significantly and this serves us in improving the soil layers that are placed under buildings and roads as sub-base or sub-grade layers.
- 3-Addition of PVC to the clay soils at different rates lead to a substantial decrease in the permeability of the soil and this tells us to use this type of soils in the lining of the docks used in water treatment plants as a cheap alternative to heavy concrete material.
- 4-When used percentages of PVC equal to or greater than 15%, decrease the permeability coefficient, k until to 99%.
- 5- Addition of PVC to gypseous soils by not less than 15% lead to a decrease in permeability and significantly and this will reduce the melting of crystals of gypsum surrounding soil and prevents the occurrence of the phenomenon of piping that causes the collapse of the soil suddenly.

12. REFERENCES

- [1] Lamb, W. & Whitman, R. 1999. Soil Mechanics Mexico DF Limusa. 250 pp.
- [2] April, N. & Castrillon, L. 1993. Acorn stabilization with asphalt emulsions: an expeditious alternative to produce competent bases. Universidad Nacional de Colombia. Faculty of Civil Engineering. Bogota' DC Labor Grands 105 pp.
- [3] Aguirre, C. & Velez, M. 2005. Granular sub base stabilization using PVC waste. . Catholic University of Colombia. Faculty of Civil Engineering. Bogota' DC Labor Grands 94 pp.
- [4] Amaya, C. Rodriguez, G & Valdez, J. 1978. Soil stabilization with lime and ash Universidad Nacional de Colombia. Faculty of Civil Engineering. Bogota' DC Labor Grands 140 pp.
- [5] Caicedo, L. & Herrera, O. 2004. Studying the behavior of hot dense mixtures made with modified bitumen, polyvinyl chloride waste. Catholic University of Colombia. Faculty of Civil Engineering. Bogota' DC Labor Grands 77 pp.
- [6] Gomez, R., Moreno, C. & Reyes, H. 1983. Stabilization materials with additives of conventional and unconventional. Universidad Nacional de Colombia. Bogota' DC Labor Grands 140 pp.

- [7] Areizaga, J., Cortazar, M. & Elorsa, J. 1992. Polymers. Madrid: Editorial Sintesis 356pp.
- [8] Edgar, R., Hugo,Q., Diana, F., & Leidy, A. 2006. Influence of the inclusion of PVC waste on the CBR of subbase granular material type. Revista Universidad de Medellin Engineering Magazine. Vol.5 no.9 , 1-11pp.
- [9] Bowles, J. E. 1997, Foundation analysis and design. 5th ed., McGraw-Hill, New York, 46, 52-53pp.
- [10] Tavenas, F., et al. 1983. The permeability of natural soft clay. Part I: Methods of Laboratory Measurement. " Canadian Geotechnical Journal, Vol. 20, No.4, Nov., 629-644pp.

Monitoring deforestation and rangeland destruction through land use alteration during 1955- 2002, using GIS and RS in the Merek river basin, Iran

Mohammad Gheitury^{*a}, Mosayeb Heshmati^{*b}, Mohammad Ahmadi^{*} and Nik Muhamad Majid^{**c}

^{*} Department of Watershed Management, Agriculture and Natural Research Center, Kermanshah, Iran.

^{**} Department of Forest Management, Faculty of Forestry, Universiti Putra Malaysia, 43400 UPM, Serdang, Selangor, Malaysia

a. m_ghatori50@yahoo.com

b. heshmati46@gmail.com

c. nik@putra.upm.edu.my; fax: +603-89432514

ABSTRACT

Land use changing is considered by decision makers and can be precise evaluated by GIS and RS techniques. However, land use alteration should be evaluated for monitoring and curtailing the land degradation, especially deforestation and destruction of rangeland. This research carried out in the Merek river basin, west Iran for evaluation of land use change during 1955- 2002 using aerial photos (1955) and satellite images (TM 1989, ETM 2002). The border and area of agriculture, forest and rangeland were distinguished and interpreted for each period (1955, 1989 and 2002). Result showed that forest and rangeland suffered from accelerated destruction during 1955– 2002 period. The area reduction rate in the forest and rangeland were 64 and 172 ha/yr, respectively. In contrast, the area of rain-fed agriculture and mixed land use (forest- rangeland and rain-fed) were increased annually 500 ha. Rill and gully erosion features usually were obviously found in converted area, especially in the rain-fed lands, indicating soil erosion, siltation and other environmental problems such as deforestation and carbon dioxide emission. In addition irrigated lands were increased 40 ha annually due to enhancing ground water extraction through water well drilling. Currently, excessive water extraction cause negative balance of ground water table and consequently water scarcity in this basin. The mix land-use was found more vulnerable to soil erosion and deforestation problems.

Keywords:

Land use Change, Merk river basin, Rangeland Destruction, SatelliteImage

1. Introduction

Land use change is become more concern for relevant expert and decision makers as the main environmental problem around the world and has been evaluated in many countries. It is carried out using better and more accurate techniques such as Remote Sensing (RS) and Geographic Information System (GIS). Remote sensing through aerial photos and satellite images can be used for land use monitoring over time. These techniques are used extensively and despite their short history they are increasing at work in modern research on land resources which without them, some environmental issues such as land degradation, deforestation and agricultural activities is more difficult and

maybe impossible. Aerial photo was prepared for Iran in 1955 at the 1:55,000 scale and was used for evaluation of forest, rangeland and soil erosion for first time by Faculty of Natural Resources, Tehran University, Iran [2]. The satellite images is common tool for evaluation of forest and rangeland vegetation in Iran and reduction in natural vegetation within watershed in the Kabir Kouh of Ilam province (Zagros area) was evaluated using satellite images (1989- 2002). The results indicated that forest area was reduced from 108,000 ha (1989) to 98,000 ha (2002) [1].

Nowadays, experts and managers are used GIS and RS with developed software as the common and necessary tools for better and more accurate planning in how to use land. Because these techniques can enable us to determine with much ease specify the environmental planning. These techniques are also valuable tool for soil erosion study in Iran [3].

An investigation by Srivastava and Gupta [5] showed that during 1994-2000 about 8 km² of natural resources and 2 km² of arable lands were converted to urban area [5]. and use change in Catmando valley (Nepal), was estimated during 1989- 2005 using satellite images. The result showed 14 % reduction in agricultural lands and adversely 17% increase in urban and rural area [4]. The same investigation in North Iran (Roud Sary) showed 7 % reduction in forest area during 1967-1994 that main forest clearance was found where slope was less than 20% [3]. This research carried out in the Merek sub-basin, west Iran for evaluation of land use change during 1955, 1989 and 2002, using aerial photos (1955) and satellite images (TM 1989, ETM 2002) and the border and area of agriculture, forest and rangeland were distinguished and interpreted for each period.

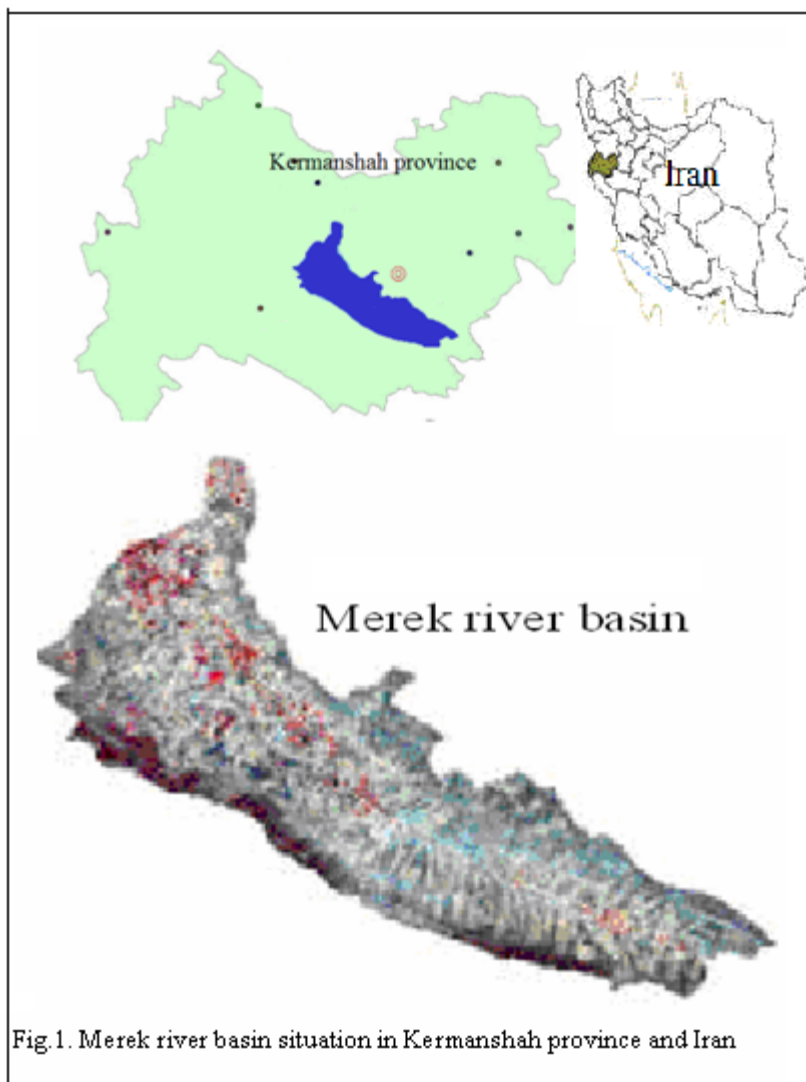


Fig.1. Merek river basin situation in Kermanshah province and Iran

2. Materials and methods

2.1. The study area

This study was conducted at the Merek river sub-basin, located in Kermanshah, Iran. It is the upper catchment of the Karkheh River Basin (KRB) within the Zagros Mountain Chains (western Iran) (Fig. 1). This watershed has an area of 149330 ha lies between 34° 00' 38" and 34° 09' 3" N and 47° 04' 25" and 47° 22' 18" E, comprising plains, hilly and mountainous areas with forest, rangeland and agricultural lands. The mean annual precipitation and temperature are 481 mm and 17.7 °C, respectively. The minimum and maximum altitude above the sea level is 1360 and 2774 m, respectively.

2.2. Main land use

Land use alteration during 1955-2002 was evaluated for main land use including forest, rangeland, rain-fed and irrigated agriculture. The maps of land use prepared for three periods of 1955, 1989 and 2002 using aerial photo (1955) and satellite image (TM 1989 and ETM 2002). The borders of each land use verified in the field and digitized using GIS (Arc.Gis 9.1) and change in area of them during these three periods were mapped (Figure2). Land use on satellite images was separated from each other using vegetation indexes (NDVI).

3. Results and Discussion

3.1. Change in the Forest Area

This investigation showed that the forest has been reduced from 13928.4 ha (1955) to 9384.40 ha (2002) which is annually 63 ha. The respective area of forest in 1955, 1989 and 2002 is 13923.5, 10135.2 and 9384.4 ha (Table 1). This deforestation was occurred mainly due to population growth, increase in agricultural machinery and ineffective official control as well as enhancing the land value.

3.2. Rangeland Changing

As shown in Table 1, the respective change in rangeland in 1955, 1989 and 2002, is 22031.0, 17685.0 and 13907.0 ha. However, this study revealed that rangelands were reduced annually 173 during 47 years (Table 1). Field survey showed that the some parts of rangeland which were converted to steep rain-fed agriculture were observed in vicinity of agricultural land with slope of 10-25 present. In this process, farmers change borders between their land and rangeland and convert some parts of rangelands to rain-fed areas annually through tillage practice. This area is subjected to unsuitable agricultural activities (mainly up-down the slope plowing) and consequently siltation phenomenon (Fig.1).

Table1. Change in land use area during three periods 1955, 1989 and 2002 in the Merek river basin

Land use	1955		1989		2002	
	(ha)	(%)	(ha)	(%)	(ha)	(%)
Forest	13928.4	9.3	10135.2	6.8	9384.4	6.3
Rangeland	22031.6	14.8	17685	11.8	13907	9.3
Rain-fed agriculture	94383.6	63.2	102081.2	68.4	97480.4	62.3
Irrigation agriculture	1520	1.0	1887.3	1.2	3383.9	2.3
Mix land use	17467.2	11.7	17542.1	11.8	25175.1	19.8
Sum	149330.8	100	149330.8	100	149330.8	100

3.3. Change in the Rain-fed Land

As shown in Table 1 and Fig.2, the respective change in rain-fed agriculture in 1955, 1989 and 2002, was 94383.6, 102081.2 and 97480.4 ha. However, the rate of change for rain-fed lands was 66 ha/yr since 1955 until 2002 (47 years). Field verification explored that the rangeland and forest area were converted to steep rain-fed agriculture which are characterized by steep slope, low soil quality, high soil erosion hazard and consequently low crop productivity potential. The area of rain-fed land has been increased from 94383 (1955) to 102081 (1989) and adversely faced a reduction during last period (1989-2002) due to development of irrigated area which has been occurred among rain-fed lands (Fig.2).

3.4. Change in the Irrigated land

The respective change in irrigated land in the 1955, 1989 and 2002, is 1520.0, 1887.3 and 3383.9 ha indicating 40 ha/yr increase in this land-use type (Table 1). Field survey showed that the rain-fed area was changed to irrigate lands in plain areas where slope is mainly less than 5 present due to groundwater extraction. It is carried out through

drilled wells and has been increased during recent years affecting reduction of aquifer water and chemical fertilizer application for irrigated crops such as corn and sugar beet.

3.5. Mix Land-use

In some area, the border of rangeland, forest and agriculture on the satellite image was mixed and separation their borders were difficult because of small areas. So these pieces were selected as the mix land-use. These lands occupy 25177.1 ha (19.8%) of the study area. This type of land-use has been increased from 17467.2 ha (1955) to 25175.1 ha (2002) (Table 1). Field survey showed that the mix land-use is more related to land degradation, especially deforestation over grazing and improper plowing. In addition, forest and rangeland in these areas are fragmented pieces and mainly are surrounded by arable lands.

5. Conclusions

The result of this study showed that converting the forest and rangeland to arable lands is the certain land use alteration within the Merek river basin. Periodic comparing the land use alteration during 1955-2002 indicates 5544 and 8124.6 ha reduction in forest and rangeland areas resulting in development of arable lands. During 1955-2002 13668.6 ha (9.1%) of natural resources was degraded trough forest clearance and rangeland destruction. In addition, forest and rangeland in vicinity of agricultural lands are more vulnerable to alteration and consequently as the critical areas for sustain environment due improper agricultural activities and soil erosion hazards. Furthermore, increase in irrigated areas through water well drilling is also related to land use change, especially rain-fed area. This land use change not only contribute to soil erosion and siltation problems, but negatively also cause plant biodiversity issue mainly destruction of some valuable vegetation species such as *Quercus sp*, *Agropirom sp* and *Festuca sp*.

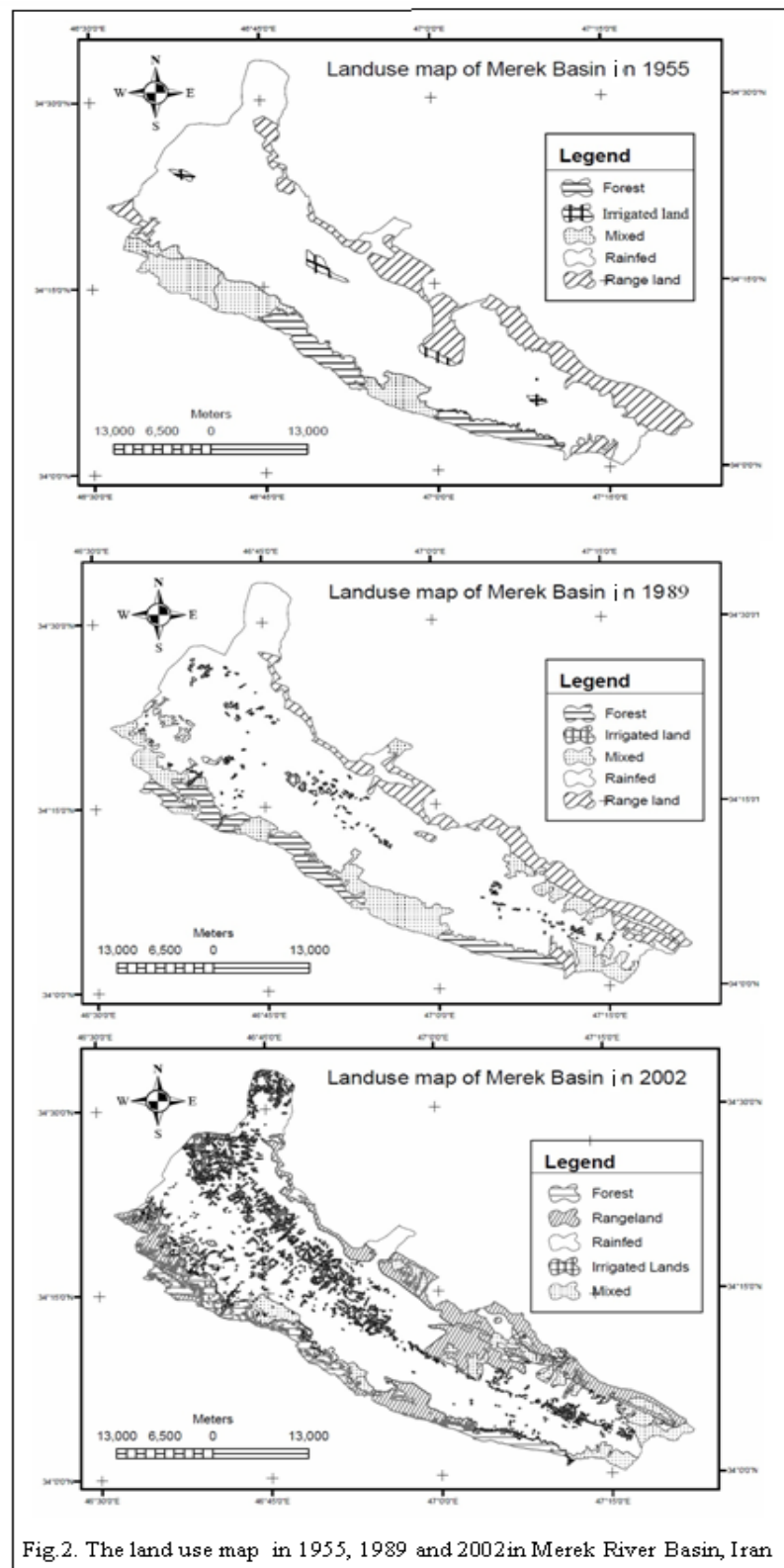


Fig.2. The land use map in 1955, 1989 and 2002 in Merek River Basin, Iran

Acknowledgements

The authors would like to acknowledge Soil conservation and Watershed Management Institute of Iran, Agricultural Research and Education Organization of Iran (AREO) and Department of Watershed Management, Agriculture and Natural Resources Research Center of Kermanshah, Iran for their financial and technical supports.

References

- [1] Barkhordari, J., Zarae Mehrjerdi, M., Khosroshahi, M., 2005. Trend monitoring of the landuse changes in protected area of Kabir Kouh with use of RS and GIS (Ilam Province-Case Study). Journal of water and soil conservation. N 2.,
- [2] Heshmati M and Gheitury M., 2001. Mapping erosion forms in Merek sub basin. Soil Conservation and Watershed Management Research Center.
- [3] Jafarian jeloudar, Z. , Garaei, P., Kelarestaghi, A., 2006.Landuse changes detection and spatial distribution with using GIS techniques, case study Lajim Rood Drainage Basin, Iran. Map Asia 2006 conference.
- [4] Thapa, R B and Murayama, Y., 2006. Land use change analysis using remote sensing and GIS: A case study of Kathmandu metropolitan, Nepal.pp22.
- [5] Srivastava,S.k and Gupta.D.2003. Monitoring of changes in land use/land cover using multi – sensor satellite data. Map India conference.

The comparison of phytoremediation and electrokinetic methods in remediation of petroleum hydrocarbons contaminated soil

Gholami Meade, Yousefi Kebria Daryoush
Babol noushivani technology university, Iran

ABSTRACT

Total petroleum hydrocarbons (TPHs) are toxic micro pollutants which are resistant to environmental degradation have adverse effect on human's health. Multiple methods that affect different aspects of contaminant removal can improve remediation of petroleum hydrocarbons from soils. Phytoremediation and electrokinetic are innovative methods for degradation different contaminant in soils. Phytoremediation is insitu method that use of plants and their associated microorganisms to degrade, contain or render harmless contaminants in soils or groundwater. Electrokinetic remediation is a technology that applies current electric field in soil to generate a voltage gradient drives soluble pollutants out of soil by electromigration, electroosmosis and electrophoresis. In this study, the ability of phytoremediation and electrokinetic methods in remediation of hydrocarbons contaminated soils was investigated. According to this study, plants with wide fiber roots, enhance degradation of petroleum contaminants, and are low-cost effective method, but need a lot of time, while electrokinetic is more effective method in degradation of petroleum contaminant in short time and more expensive method. In short sentence, combined electrokinetic and phytoremediation technology can uptake more contaminant, and electro-phytoremediation is the best technology for remediation of contaminated soils.

Keywords: Phytoremediation, Electrokinetic, Soils, Petroleum Hydrocarbons

1. INTRODUCTION

Over the past years, Rapid increase in population Increase fuel consumption, industrial chemicals, fertilizers and pesticides. Despite the use of these materials, part of these materials into the environment, and Actual and potential environmental hazards are created. One of the important issues that different communities are facing is Soil contamination in the environment. Soil is considered unique environment for life forms, especially plants. Soil is a natural purified, and These features are result in physical, chemical and biological properties, but it is long that oil and its derivatives in transport or storage are cause the soil contamination. Petroleum hydrocarbons are one of a variety of environmentally persistent organic pollutants, which are hazardous for living organisms. Sources of petroleum hydrocarbons in soil are crude oil extraction, transportation, refining and fuel. Soil remediation of petroleum hydrocarbons is very costly and time consuming. Improved purification methods, Elimination or reduction of total petroleum hydrocarbons in soil, may require mechanical ways to stimulate microbial activity. Expansion of soils contaminated with petroleum hydrocarbons, the effective and economic method is one of the environmental problems. There are various physical, chemical and biological methods to deal with oil pollution of soils in which many of them due to high cost and harmful side effects are used less. Among these methods, phytoremediation and electrokinetic to remove oil contaminants, are more economical and yet is harmless. According to the importance of soil contamination, in this study, phytoremediation and electrokinetic in refining

contaminated soils is introduced and Performance, advantages and disadvantages of each of the methods and results of various researchers in this field were compared.

2. Phytoremediation

Phytoremediation is a relatively new technology and economic purification of contaminated soils that use Suitable plants to remove or reduce the concentration of inorganic pollutants, radioactive and organic compounds, especially oil from the environment. This method the first time in 1983 has been used to remove metals and other pollutants in soil. Phytoremediation technology is based on combining its operations with plants and microbial community that analysis, transmission, and living off the pollutants compound of soil and groundwater[1]. In Phytoremediation technology, plant roots have stimulatory effect on microbial activity which causes suitable environmental conditions for growth and proliferation of the microbial population. The result is soil degradation and further reduces emissions oil from soil. Plants can also supply carbon, nutrients, and ... in the soil. Thus heterotrophic bacteria grow and decompose pollutants[2]. In general, plants provide to purify contaminated soils direct and indirect state. Direct refinement, plants through the absorption of pollutants and accumulation within their cells and then degradation and analyzed them, in result these pollutants are reduced or eliminated. As well as in indirect refining, Plants through their discharge stimulate microorganisms in the rhizosphere and increase microbial degradation of organic pollutants. Root discharge such as amino acids, carbohydrates, nucleic acids, growth factors, enzymes and other compounds with supply of energy resources, carbon and nitrogen requirements

of dominant microorganism in the soil, cause accelerate and intensify the destruction of these pollutants in soil[3].

2.1 Phytoremediation mechanism

Phytoremediation on the type of substance that are refined, (metals or chemicals) are classified 7 types of stem: phytoextraction, Phytovolatalization, Phytodegradation, Rhizodegradation, Rhizofiltration, Phytostabilization and Hydraulic control. phytoextraction is absorbed pollutants by roots and accumulation them in the shoot and then The plant biomass is harvested and destroyed[4]. Phytovolatalization is the plant uptake of pollutants and evaporation from the folia ge. Phytovolatalization is including pollution absorption by plants and then release the steam of pollutants out. The resulting product, the vapor should be less toxic than the original contaminants. Phytodegradation is performed by uptake and metabolism of contaminants in the roots, stems or leaves. This method is degradation Pollutants a process in which Including absorption, metabolism and analysis of contaminants in soil, Sediment, sludge, and groundwater or surface by produced and released enzymes by the plant[5]. Rhizodegradation is performed by root absorption of pollutants and no transfer take place to shoot. Rhizofiltration is extraction of pollutants by root from surface water, waste water or ground water by sedimentation on the root or absorbed into the roots. Phytostabilization is due to inactivity of Contaminant materials in the soil. Phytostabilization is the use of green plant for the cleanup of existing pollution in soil through improved physical, chemical and biological soil conditions. Hydraulic control is the use of green plant to impress the groundwater and soil water from the way of uptake and consumption of large volumes of water.

2.2 Factors in phytoremediation

In order to be successful and achieve the greatest reduction, in order to be successful and achieve the greatest reduction of these compounds concentrations in soil, various environmental factors are important. Type of soil and organic matter present in it, can be effective in the biological availability of petroleum product. Soil moisture is effective on plant grows and microbial activity of plants.

2.3 Advantages of Phytoremediation

A significant advantage of phytoremediation is that a variety of organic and inorganic compounds are amenable to the phytoremediation process. Phytoremediation can be used either as an *in situ* or *ex situ* application. Another advantage of phytoremediation is that it is a green technology and when properly implemented is both environmentally friendly and aesthetically pleasing to the public.

2.4 Disadvantages and Limitations of Phytoremediation

In contrast to its many positive aspects, phytoremediation does have a few disadvantages and limitations. It is restricted to the rooting depth of premeditative plants. Remediation with plants is a lengthy process, thus it may take several years or longer to clean up a hazardous waste site, and the contamination may still not be fully remediated.

2.5 Plant Selection Criteria

Plants should be selected according to the needs of the application, the contaminants of concern and their potential to thrive on contaminated soil. Design requirements should include the use of native plants to avoid introduction of invasive species. The main aim is to ensure that roots expand throughout the entire contaminated zone. Plant tolerance to high contaminant concentrations is also a very important factor to keep in mind. The phytotoxicity of petroleum hydrocarbons is a function of the specific contaminant composition, its concentration, and the plant species used[6].

3 ELECTROKINETICS

The term "electrokinetics" (EK) refers to the introduction of an electrical gradient (as opposed to a hydraulic or pressure gradient) in the soil to mobilize or promote the migration of water and/or various chemical species towards the preferred electrode. Electrokinetics as a soil remediation technology is relatively young, having become an alternative procedure for the removal of toxic chemical species in ionic form in the soil in the late 1980's[7]. Electrokinetics is a process that separates and extracts heavy metals, radionuclide and organic contaminants from saturated or unsaturated soils, sludge, and sediments. A low intensity direct current is applied across electrode pairs that have been implanted in the ground on each side of the contaminated soil mass. The electrical current causes electro osmosis and ion migration (electromigration) and electrophoresis, which move the aqueous phase contaminants in the subsurface from one electrode to the other. Contaminants in the aqueous phase or contaminants desorbed from the soil surface are transported towards respective electrodes depending on their charge. The contaminants may then be extracted to a recovery system or deposited at the electrode. Surfactants and complexing agents can be used to increase solubility and assist in the movement of the contaminant.

3.1 Process and mechanisms

When an electric field is created across a soil volume, it provides a driving force that may induce mass movement of particles, similar to the effect of other driving forces, such as pressure gradient, concentration gradient and thermal gradient. In particular, the application of an electric field causes the following main transport phenomena in soils: Electroosmosis, electro migration, electrophoresis. All these electrokinetic phenomena are highly influenced by the

surface charge densities of the soil particles, and therefore by the soil mineralogical Composition.

3.1.1 Electroosmosis

Electroosmosis is a bulk transport of water, which flows through the soil as a result of the applied electrical field. The fluid migration occurs mostly from the anode to the cathode, due to the predominance of a negative charge on the soil particle surfaces. In fact, the electroosmotic flow is caused by the fact that when an electric field is applied to a soil, the excess of cations close to soil particles surface (double layer) tend to move towards the cathode. The movement of these ions and of the water molecules associated with these species (hydration shells), imparts a net strain on the pore fluid surrounding the hydrations shell. This strain is transformed into a shear force because of the viscosity of the pore fluid. In sum, as there is usually an excess of cations close to soil particles, the electric fields leads to a net force towards the cathode which results in a pore fluid flux in this direction. Hence, the electric field causes the pore fluid to flow from the anode compartment to the cathode, producing a flux and forcing the water table to arise in the cathode compartment[8].

3.1.2 Electromigration

The second transport mechanism generated by the voltage gradient is electro migration, which is the Movement of ions in the pore solution under the influence of an electric field. Positive ions (cations) migrate towards the cathode while negative ions (anions) are transported towards the anode. Because of electro migration, ions tend to concentrate near the opposite charged electrode. The electro migration of cations and anions towards the electrode opposite in charge is proportional to the ion concentration in the pore water solution and to the electric field strength. The ionic mobility is a term used to describe the rate of migration of a specific ion species under a unit electric field. In soils, the rate of ionic migration can be better defined by the effective ionic mobility, which also accounts for soil porosity and tortuosity, which can significantly affect ion migration[9].

3.1.3 Electrophoresis

Electrophoresis consists of the movement of charged particles and colloids under the influence of an electrical field. When a direct current (DC) electric field is applied across a colloidal suspension, charged particles and colloids that are suspended in the pore fluid are electrostatically attracted to one of the electrodes and repelled from the other. Similarly to the electro migration process, positively charged particles tend to move towards the cathode and negatively charged particles tend to move towards the anode. For example, negatively charged clay particles tend to move towards anode. Usually, for environmental applications, electrophoresis is less important than electroosmosis and electromigration in terms of mass flux although in some cases electrophoresis may play a role in decontamination, e.g. if the migrating colloids have the contaminants adsorbed on them[9].

3.2 Factors affecting electrokinetic technology

Electromigration rates in the subsurface depend upon grain size, ionic mobility, contamination concentration, total ionic concentration, and significantly upon the soil pore water current density and pH. The direction and quantity of the contaminant movement is influenced by the contaminant Concentration (anions versus cations), soil type and structure, pH, interfacial chemistry, and current density of the soil pore water. The efficiency of extraction relies upon several factors Such as the type of species, their solubility in the specific soil, their electrical charge, their concentration relative to other species, their location and form in the soil, and availability of organic matter in the soil. Electrokinetics is applicable in zones of low hydraulic conductivity, particularly with high clay content.

4 CONCLUSIONS

Phytoremediation involves the use of living plants and their associated microorganisms to remove, degrade, or sequester inorganic and organic pollutants from soil, sediment, and groundwater. The main advantages of this method are low cost and ecological friendliness. However, this method is limited to shallow depths (limited by the root depth) slow plant growth, and also solubility and availability of the pollutant. Coupling electrokinetics with phytoremediation is aimed at increasing the availability of the contaminants and also facilitating their transport toward the root zone. The effects of electric field on soil pH, availability of nutrients, and so on may also help plant growth. Electrodes are placed strategically and a low direct current or voltage gradient is applied and the contaminants are transported by electromigration and/or electroosmosis processes toward the plant root zone. Electrode solutions of reduced toxicity toward plants can be used to enhance solubilization of the contaminants. Small - scale experiments showed that the plants are not affected by the exposed electric fields and that overall contaminant removal efficiency is controlled by different geochemical reactions. More research is needed to address organic contaminants and contaminant mixtures and possible effects on soil quality and biology[10].

5 REFERENCES

- [1] 1. Cunningham, S., et al. *Phytoremediation of contaminated water and soil*. 1997: ACS Publications.
- [2] 2. Günther, T., U. Dornberger, and W. Fritsche, *Effects of ryegrass on biodegradation of hydrocarbons in soil*. Chemosphere, 1996. **33**(2): p. 203-215.
- [3] 3. Minai-Tehrani, D., et al., *Effect of salinity on biodegradation of aliphatic fractions of crude oil in soil*. Pak. J. Biol. Sci, 2006. **9**: p. 1531-1535.
- [4] 4. Pivetz, B.E., *Ground water issue: phytoremediation of contaminated soil and ground water at hazardous waste sites*. 2001, DTIC Document.
- [5] 5. Sun, Y., et al., *Phytoremediation for co-contaminated soils of benzo [a] pyrene (B [a] P) and heavy metals using ornamental plant Tagetes patula*. Journal of Hazardous Materials, 2011.
- [6] 6. Gleba, D., et al., *Use of plant roots for phytoremediation and molecular farming*. Proceedings of the National Academy of Sciences, 1999. **96**(11): p. 5973.

- [7] 7. Reddy, K.R. and U.S. Parupudi, *Removal of chromium, nickel and cadmium from clays by in - situ electrokinetic remediation*. Soil and Sediment Contamination, 1997. **6**(4): p. 391-407.
- [8] 8. Lynch, R., et al., *Preliminary tests of an electrokinetic barrier to prevent heavy metal pollution of soils*. Electrochimica acta, 2007. **52**(10): p. 3432-3440.
- [9] 9. Kim, S.S., J.H. Kim, and S.J. Han, *Application of the electrokinetic-Fenton process for the remediation of kaolinite contaminated with phenanthrene*. Journal of Hazardous Materials, 2005. **118**(1): p. 121-131.
- [10] 10. Shenbagavalli, S. and S. Mahimairaja, *Electro kinetic remediation of contaminated habitats*. African Journal of Environmental Science and Technology, 2011. **4**(13): p. 930-935.
- [11]

USING METACOGNITIVE STRATEGIES ON LISTENING COMPREHENSION

On the Effect of Using Metacognitive Strategies on Listening Comprehension of Iranian
EFL Learners

Abstract

Listening skill in the procedure of second or foreign language learning has not carried the same attention as the other skills. Nevertheless, it's been apparently elucidated that as a receptive skill, listening plays a major role in enabling the language learners to acquire linguistic information. Relevant to this fact, the present study aimed at suggesting a way to facilitate the process of comprehending foreign/second language listening tasks; though so general, listening comprehension tasks in a foreign language class are perceived by the researcher so crucial and require special consideration and attention. Accordingly, conscious application of metacognitive strategies while doing the listening tasks is the major concern of this study, and is intended to be investigated in order to answer the question: "Do Metacognitive Strategies have any impact on the Listening Comprehension of Iranian Guidance school EFL learners?"

In this regard, two groups of first graders of guidance school were chosen as the control and experimental group. The experimental group went under two months treatment of discussing about and applying the introduced metacognitive strategies while doing English listening tasks whereas the control group did the same listening tasks without receiving any identical treatment. During the treatment phase, the participants got familiar with a number of listening metacognitive strategies and were asked to apply them in listening comprehension tasks while focusing on their difficulties. Meanwhile, they jotted down diaries regarding their perception towards using such strategies. The t-test obtained out of the listening comprehension pre-tests and post-tests revealed considerable improvement in the experimental group listening comprehension performance. The findings of this study could have implications for foreign/second

language learners and teachers as well as the designers of a foreign/second language course books.

Key Words: Learning Strategies; Metacognitive Strategies; Listening Comprehension

Introduction

Listening skill, despite its significant role in the process of foreign language learning, has not been often considered seriously in language teaching and learning. To this fact, it has been called “Cinderella skill” by Nunan (1997):

Listening is the Cinderella skill in second language learning. All too often, it has been overlooked by its elder sister: speaking. For most people, being able to claim knowledge of a second language means being able to speak and write in that language. (Para#1)

However, second/foreign language learners usually find listening comprehension task such a tough activity, and difficult to manage. Ur (1984) maintains that a large number of foreign language listeners feel anxious while involving in a listening comprehension task because of their false expectation that they have to understand every word they hear and puts the responsibility of alleviating this worry on the shoulders of the teachers.

In respect to language learning in general and listening skill in particular and the difficulties occur to the listeners, the concepts of cognition and metacognition in learning comes into one’s mind.

Based on Miller’s (1983) point of view, cognitive process orientation lead learners toward intellectual autonomy and its curriculum “aims to develop skills so that the individual can examine problems, consider alternative solutions, evaluate those alternatives, choose an alternative, then implement and evaluate the solution” (p.121).

Metacognition, on the other hand, implies the knowledge of this cognitive process that particularly used in the realm of learning, based on which learners are consciously got involved in the process of learning, to the purpose of being aware of their problematic areas and finding out appropriate ways to overcome such difficulties. (Richards & Schmidt 1985)

To this purpose, learners employ some specific strategies required for a particular situation to help them progress, known as “learning strategies”. Among the three types of learning strategies, metacognitive strategies are at the centre of emphasis in this study. Metacognitive strategies play a direct role on self-directed learning and learner’s autonomy (Danuwong 2006; Shannon 2008).

As the final point, a model of metacognitive strategy training developed by Vandergrift et al. (2006) is worth describing here, since it’s the primary instrument used in the present study as a means of familiarizing the participants with such strategies. *Metacognitive Awareness Listening Questionnaire (MALQ)* consists of 21 item questionnaire which is related to five metacognitive factors: problem-solving, planning and evaluation, mental translation, personal knowledge, and directed attention. This questionnaire helps learners raise their awareness of the process of listening comprehension as well as the strategies they intentionally benefit from to enhance comprehension. It can also be used for self-assessment purposes by the students or diagnostic purposes by the teacher.

This study has been run to the aim of boosting foreign language learners’ awareness towards their foreign language listening skill, and suggesting a way that could probably help them to tackle listening comprehension tasks. The researcher states her null hypothesis as, “There is no significant difference between the listening comprehension of Iranian EFL learners who use Metacognitive strategies for listening comprehension and that of those who do not.”

Method

Research Design

This study was conducted based on the quasi-experimental design in which two groups are involved, the experimental group and the control group. The independent variable refers to the application of a number of metacognitive strategies, and the dependant variable is the listening comprehension skill.

Participants

The intended participants of the study were 60 female students of an educational complex who were going to start their guidance school as first graders. They were generally about 11 or 12 years old.

Materials

A complete sample of KET was administered to determine the participants' English proficiency level and to make sure that they were homogeneous in this regard. The listening sections of two different samples of KET were employed as the pre-test and post-test with a time interval. A questionnaire including 21- item of metacognitive strategies called MALQ developed by Vandergrift et al. (2006) was applied as a written source of such strategies to be used by the participants. Besides, as a peripheral purpose, this questionnaire was used to demonstrate the frequency of the strategy used by the participants of the experimental group. A supplementary listening book, "Tactics of listening" in the basic level appropriate to their level, was also applied during the practice phase.

Procedure

First a standard proficiency test (KET) was administered to assure the homogeneity of the participants, as a result of which, they were divided into two groups.

Then, the two groups were taken a listening comprehension test (one of the samples of KET) as a pre-test. Besides, in order to raise their listening skill awareness, the experimental group participants were asked to jot down self reports regarding their

listening comprehension skill and their probable weaknesses. At this step, the students attempted to reflect on their proficiency in this skill, and many of whom came into several problematic areas while involving in a foreign language listening task. These reports collected by the researcher, were just considered as a warm up step without any statistics computed on them. (Although, the reports were so much in detail and could have been analyzed and ideally applied as the descriptive data, , the researcher just aimed at raising their sensitivity towards listening tasks through these reports.)

As the first step of the treatment, which was considered as the introduction phase, a number of metacognitive strategies driven from Vandergrift et al's (2006) "Metacognitive Strategy Awareness Listening Questionnaire" was introduced to the participants of the experimental group, and for half of a session, each item was explained, translated and supported by appropriate examples by the researcher; meanwhile the participants got involved and commented on each one.

Following this very first session, the practice phase started. During this step which lasted for about two months, four sessions a week, the strategies were regularly discussed and practiced during the tasks of listening comprehension. Following each sessions of metacognitive reflection and application while doing the listening tasks, the participants were asked to write a diary and include their perceptions towards the use and effect of the strategies. Simultaneously, the control group received the same listening tasks but in a traditional way of listening activities which includes listening to the recorded instruction and doing each section as they are required.

After this period of two months metacognitive strategy instruction and practice during the listening activities, the final phase began with reaching a reasonable conclusion driven from a listening comprehension test as a posttest.

Results and Discussions

The test given as a pre-test, listening section driven from a typical sample of KET led to the data shown in the following two tables:

Table 1: results of the paired sample statistics in the pre-test

	Mean	N	Std. Deviation	Std. Error Mean
Pair 1 E1	15.3333	30	3.63255	.66321
C1	15.7000	30	4.06965	.74301

*Note.*E1 stands for Experimental group and C1 for the control group before the treatment

Table 2: Results of the T-test before the treatment

	Paired Differences					t	df	Sig. (2-tailed)
	Mean	Std. Deviation	Std. Error Mean	95% Confidence Interval of the Difference				
				Lower	Upper			
Pair 1	-							
E1 - C1	.36667	5.77440	1.05426	-2.52286	1.78953	-.348	29	.731

As it is shown, the mean difference of the two groups in pre-test, with 95% confidence of interval, fell between the lower limit of -2.522 and the upper limit of 1.789, indicating that the obtained results were meaningful. There must be noted that despite of the fact that the mean difference indicated a correlation between the groups, the obtained significance exceeded 0.05, a raised issue that will be discussed later.

Having passed the period of treatment, the experimental group as well as the control group took a post-test which was a listening section of another sample of KET. Tables 3 and 4 demonstrate the obtained results:

Table 3: Results of Paired sample statistics in the post-test

		Mean	N	Std. Deviation	Std. Error Mean
Pair 1	E2	20.9333	30	2.67728	.48880
	C2	18.8667	30	3.29821	.60217

Table 4: Results of the T-test after the treatment

		Paired Differences					t	df	Sig. (2-tailed)
		Mean	Std. Deviation	Std. Error Mean	95% Confidence Interval of the Difference				
					Lower	Upper			
Pair 1	E2 - C2	2.06667	4.57077	.83450	.35991	3.77342	2.477	29	.019

Accordingly, it can be inferred that with the significance of $0.01 < 0.05$, the mean difference of the experimental and control group fell in the range of lower limit and upper limit of 95% confidence of interval: $0.3599 < m < 3.7734$. Thus, it can be safely claimed that the observed mean difference was meaningful and significant.

It must be notified that as it was promised before, the computed significance in the pre-test which exceeded 0.05 must be justified here. Based on the obtained mean difference in the pre-test and post-test, it could be concluded, as a by product, that lacking the knowledge of metacognitive strategies while performing listening comprehension tasks, could have a negative effect on decision making about their

homogeneity in this skill. Actually, even a standard test seems to be incapable in reaching a logical conclusion about the homogeneity of the students.

Consequently, the findings computed from the post-test revealed a meaningful difference between the listening comprehension of the two groups with the significance of 0.01, comparing to the pre-test, the null hypothesis of the study which maintained that “There is no significant difference between the listening comprehension of Iranian Guidance school EFL learners who use Metacognitive strategies for listening comprehension and that of those who do not”, could be rejected. This conclusion supports the previous related studies regarding the application of metacognitive strategies in facilitating and promoting listening comprehension of EFL learner.

The study’s implications and recommendations

The findings of the present study could lead to a variety of implications in different fields:

- It suggests *syllabus designers* to include different types of learning strategies particularly metacognitive strategies along with each skill exercises, to explicitly familiarize language learners with their required strategies and schedule several exercises to create opportunities to apply them.
- It recommends *language teachers* to regularly remind learners to take benefit from metacognitive strategies and encourage them to become autonomous learners, who are aware of their learning processes, as well as their strengths and weaknesses.
- Finally *language learners* are suggested to reflect on metacognitive strategies and their use while engaging in different language tasks, and seek for occasions to apply them.

Furthermore, the researcher states some recommendations for other related studies. Firstly, it would be more satisfying to run the same study within larger group of participants, so that generalization would be safely implemented. Secondly, the number and variety of the taught and practiced metacognitive strategies can be extended to the

whole 21-items stated in the “Metacognitive Awareness Listening Questionnaire”, obviously within more allocated time. Thirdly, this research will achieve its most reasonable and informative results if it could be done in both quantitative and qualitative ways of gathering data, since the learners’ individual perceptions and experiences while getting familiar with metacognitive strategies gained via self-reports or diaries would be as much valuable as their scores in the tests or the questionnaire, and both of which could lead to the more comprehensive conclusion.

Finally, the researcher suggests the test makers running a research to find out more about the idea that metacognitive strategy knowledge and use could influence a sensible result of learners’ homogeneity through standard tests.

References

- Danuwong, C. (2006). *The Role of Metacognitive Strategies in Promoting Learning English as a Foreign Language Independently*. Unpublished doctoral dissertation, Edith Cowan University-Thailand.
- Miller, J. P. (1983). *The Educational Spectrum*. New York: Longman.
- Nunan, D. (1997). *Listening in Language Learning*. Retrieved September 15, 1997, from <http://www.jalt-Publications.org/tlt/files/97/sep/nunan.html>
- Richards, J. C., & Schmidt, R. (1985). *Longman Dictionary of Language Teaching & Applied Linguistics*. London: Longman.
- Shannon, S. V. (2008). Using Metacognitive Strategies and Learning Styles to Create Self-directed Learners. *Institute for Learning Styles Journal*, 1, 14-28.
- Ur, P. (1996). *A Course in Language Teaching: Practice and theory*. New York: Cambridge University Press.
- Vandergrift, L. Goh, C. M., Mareschal, C. J. &

Tafaghodtari, M. H. (2006). The Metacognitive Awareness Listening Questionnaire: Development and validation. *Language learning research club*, 56, 431-462.

Evaluation of Run-Off Supply Projects in Hamadan Province (Iran)

N. Rostam Afshar¹, M. Abdoli²

¹Associate Professor, University Malaysia Sarawak, Civil Engineering Department
Email¹: anrostam@feng.unimas.my

²Project Manager, West Regional Water Company, Hamadan-Iran

Abstract

Water resources project is for the control or use of water. Where utilization is proposed, the first question is usually how much water is needed. This is probably the most difficult of all the design problems to answer accurately because it involves social and economical aspect as well as engineering.

In order to meet the various demands and of water requirements in Hamadan province which is situated in west of Iran, more than 28 projects were defined and studied, but only few of them were adopted.

This paper presents a criteria based on the ratio of reservoir capacity to volume of earthen dam named as feasibility factor (F) for exact evaluation of different alternatives to assure the designer, so that, to obtain sufficient quantity of water in a form which can be easily and cheaply made fit for various uses.

Keywords:

Water requirement, Reservoir capacity, volume of earthen dam, Evaluation of run-off supply, Economic analysis

1. Introduction

Hamadan province is located in the western part of Iran with an area of more than 19000 square kilometers. Hamadan is a beautiful highland covered with huge mountains and green slopes, farmlands, pastures, snowcapped peaks, anti fertile valleys under a blue sky.

Annual precipitation is 6822 million cubic meters and 4000 million cubic meters evaporate. Annual water consumption in Hamadan is 2900 million cubic meters in which ground water possess 81 percent of the demand and 19 percent is supplied through surface run-off. Reference [6] shows that, 93 percent of the total Water consumption is reserved for agricultural activities, 5 percent for urban use and 2 percent in industrial sector. It may be seen that there is severe shortages of water supply through-out the year. In the other words, it is necessary to provide

such a large volume of water scarcity specially in drought periods [4].

In the two recent decades, in order to overcome water shortages, 28 reservoir dam projects were proposed in Hamadan province. Two projects completed, four projects put under construction, 11 projects were in the feasibility studies and 11 projects rejected.

2. Objectives and scope

In order to meet various demands and water requirements in Hamadan province, more than 28 projects were proposed and studied, but few of them were adopted. There is always an essential question, whether these projects are economically feasible and could be able to provide water shortages or not? Therefore, the main objective of this research, is to present a criteria for selecting those projects so that

decision makers could be assure of water supply with maximum net benefits.

3. Methodology

In order to provide agricultural water requirements, few parameters such as water quantity, agricultural pattern, irrigation method, irrigation efficiency, water conveying systems and benefit cost ratio are to be considered. Usually, achievement of objective of water resources projects is ambiguous. In this research, economic evaluation based on the existing approaches such as supply cost and reservoir storage planning along with suggested criteria, “physical characteristics of the project”, have been used for estimating run-off supply projects in Hamadan Province. These methods could be used in screening phase to assure adequate supply and economic justification.

According to Rogers [5], the real value of water, depends upon the user view with respect to quantity and quality and water use to which it is put. The exact value, is the summation of intrinsic and economic value. In the other words, full cost of water use, includes investment costs, operational and maintenance costs, a water scarcity rent and the cost of negative externalities of water use [8].

For economic equilibrium, the value of water, should equal the full cost of water. However, in practice, the value of water in use is typically expected to be higher than the estimated full cost. This is often because of difficulties in estimating the externalities in the full cost calculations. More ever, in many cases, it may be lower than full cost, since political and social obligations override the economic issues. Full supply cost or average value per cubic meters of water which has been used in this research, includes the cost associated with the supply of water to consumer without consideration of externalities and alternate use of the water.

4. Analysis

4.1 Evaluation on the basis of physical characteristics of projects

Whenever, a water-resources project is planned, it must be ensured that the proposed proposal is the best, and any other possible alternative will not be better than purposed one. To obtain such a criteria for selecting optimum proposal, the ratio of reservoir capacity to volume of earth fill dam named as feasibility factor ($F=C/V$) was studied and noticed that whenever the actual ratio estimated, is equal or greater than F , the scheme is considered to be successful. The average value of F for existing large dams in Iran is “20” and “9” for Hamadan. This parameter could be used as a primary evaluation and project selection. The actual ratio for two proposed projects in Hamadan, namely “Yengjeh” and “Shirin sou” dams equaled to 8 and 30 respectively. From the above discussion, it is clear that, Shrin sou dam is only feasible in comparison with suggested criteria.

4.2 Evaluation on the basis of Primary investment

As already discussed earlier, the cost of one cubic meter of water is a function of investment costs, operational and maintenance costs. According to [1], average value (base value) per cubic meter of water estimated on the basis of 2001's tariff given by ministry of energy is equal to 520 Rials(0.065\$) and in accordance with shadow price in agricultural sector, is equal to 420 Rials(0.052\$) [2].

“Reference [3], [7] show that the cost of water per cubic meter with interest rate of 7 to 14 percent for Yengjeh and Shirin sou dams in Hamadan is estimated to be 650(0.082\$) to 1300 Rials(0.16\$) and 307(0.040\$) to 717 Rials(0.090\$) respectively. Comparison of the estimated water cost with the water base value, reveals that the average cost of water per cubic meter for Shirin sou dams equals the base value given by ministry of energy. Therefore, it may be concluded that on the basis of primary

investment, only Shirin sou dam is economically feasible.

4.3 Evaluation on the basis of reservoir storage planning

The storage, capacity of a reservoir is to be planned keeping in view the overall objective of the water resources development. The policies and guide lines of the government in a relation to water resources development of the region are to be adhered too. Therefore, the determination of storage capacity needs detailed and careful study as the same is depend on a number of factors. Some of the important factors are, inflow, desired annual demand and its distribution over time, operating policy and losses through evaporation and seepage. If the planned storage capacity is small, it may not serve the purpose for which it has been designed. On the other hand, over estimation of the storage capacity will result in considerably high cost of the project rendering the

project to be uneconomical. Hence, it is necessary to make a very judicious estimate of the storage capacity.

Reservoir storage planning for Shirin sou and Yengjeh dam have been worked out and the results for Yengjeh With a volume equal to 570 thousand cubic meter is shown in “tab.”1. It may be seen that during the months of April to October, inflow (108000 cubic meter) into the reservoir goes down but demand for irrigation (2232000 cubic meter) is high. In the other word, out flow decreases and cannot meet the demand. Moreover, water scarcity ranges from 26 to 100 percent throughout the year. During monsoon months (November to March), irrigation requirements is small, and reservoir volume rises to 248 thousand cubic meter which is only 43.50 percent of the designed capacity of the reservoir. It may be concluded that planned storage capacity of Yengje dam is small and can not meet the demand.

“Tab.” 1- Reservoir storage planning for Yengjeh dam
(Units in thousand cubic meters)

Month	Inflow	Demand	Outflow	Reservoir volume		Overflow	Water scarcity		Remarks
				Beginning	End		Volume	%	
September	1	120	1	0	0	0	119	99	Scarcity
October	16	24	16	0	0	0	8	8	Scarcity
November	39	0	0	0	39	0	0	0	Normal
December	50	0	0	39	89	0	0	0	Normal
January	61	0	0	89	150	0	0	0	Normal
February	98	0	0	150	248	0	0	0	Normal
March	145	168	168	248	225	0	0	0	Normal
April	78	408	303	225	0	0	105	26	Scarcity
May	12	672	12	0	0	0	660	98	Scarcity
June	1	480	1	0	0	0	479	99	Scarcity

July	0	288	0	0	0	0	288	100	Scarcity
August	0	240	0	0	0	0	240	100	Scarcity

5. Conclusions

This study has been mainly directed towards suggesting a suitable criteria for evaluation of run-off supply projects in Hamadan province and the data of Yengjeh and Shirin sou dams have been used to present the suggested approach. It may be noted that, the existing methods (primary investment and reservoir storage planning) take into account the various aspects which are required for economical evaluation of different alternatives.

As discussed earlier, the existing methods, envisage that, Shirin sou dams is only economically feasible. Furthermore, in this particular case, suggested criteria(physical characteristics of the project) proposes that, selection of Yengjeh dam is not a proper decision but, Shirin sou project is economically feasible as well as there is no water scarcity during the reservoir operation.

5. Acknowledgement

The authors wish to acknowledge the faculty of engineering university Malaysia Sarawak for their financial support, Head of water engineering department (Power and water University of Technology, Tehran) and Managing director of water affairs Hamadan who collaborated to develop this article.

References:

- [1] Abdollahi,M, Rostam Afshar, Nasser, “evaluation the effectiveness of runoff supply projects in Hamdean province”, Master thesis ,Power and Water University of Technology.
- [2] Jafari.E, Rezvani, M, “Evaluating methods to encounter crisis in Hamadan province”,2001. Hamedan programming and management organization.
- [3] Hamedan agricultural organization Jahad ,” Yengjeh reservoir dam designing report”,1996.
- [4] Rostam Afshar, Nasser., Fahmi, Hedayatollah, “Total predicted precipitation in Iran”,1995. water resource research organization.
- [5] Rogers, p,” Water as social and Economic good”, Global Water Partnership/Swedish international development cooperation, Sweden, 1998.
- [6] Water affairs of Hamadan, “proper situation of water in Hamedan”,2001.
- [7] Water affairs of Hamadan,” report of Shirin sou reservoir dam design”1996.
- [8] Water bureau of economic,” full supply cost of water”, Water management of Iran,2008.

Protective measures of the monumental pine in Rikuzen-Takada with soil-water-air-solved material coupled model

Y. Sugiyama, S. Nomura, K. Kawai and A. Iizuka
Kobe University, Japan

ABSTRACT

The coastal area of eastern Japan was hit by Tsunami due to the gigantic earthquake on March 11th 2011. Tsunami gave serious damage to Rikuzen-Takada and drowned out famous pine woods, called "Takadanomatsubara". But, only one pine tree of 70,000 had survived miraculously without falling down. People decided to preserve this pine tree as the monumental pine for the symbol of recovery. However, there are some problems, groundwater rise due to land sinking and salt concentrating from seawater. These factors could kill root system. In this study, the current situation around the monumental pine was simulated with soil/water/air coupled F. E. code applying the mass transport equation first. Next, alternative preservation methods, pumping water up and flashing, were examined. Consequently, it was found that pumping water up from deep inside of sheet pile is effective for inhibiting salt diffusion and flashing is effective for washing salt away from ground. This challenge will contribute to interactions between geotechnical engineering and agronomic science.

1. INTRODUCTION

March 11th 2011, the northeast part of Honshu Island, Japan, seriously suffered severe damage and terrible Tsunami disasters due to the gigantic earthquake of M9.0. At coastal area of Rikuzen-Takada, 70,000 pine trees were swept away by the tsunami and the famous pine forest disappeared. But, among them, only a pine tree survived and monumentally encouraged local people. It was decided to preserve this pine tree as a symbol of recovery (Fig.1).

However, the ground surface around the monumental pine sunk 80cm due to the earthquake and groundwater level rose near the ground surface. There occurred concerns that roots of the monumental pine are soaked in seawater and salt might accumulate around the roots resulting in letting the pine tree die. Then, the protection project of the monumental pine was operated. Namely, steel sheet piles (15m×15m) were driven to prevent infiltration of seawater and pumping up the water near the pine tree was operated to lower the ground water level around the pine tree. However, these efforts did not effectively work and it was not possible to stop that the pine tree was dying.



Fig.1 Takadanomatsubara before earthquake[1] and the monumental pine

In this study, such measures to preserve the monumental pine tree are discussed based on a series of numerical simulations using the soil/water/air coupled F. E. technique. And other possible measures are examined.

2. Governing equations for soil-water-air-solved material coupled problem[2]

In order to simulate environmental and mechanical response that the monumental pine tree experiences after the earthquake, soil/water/air 3 phase mixture coupled formulation considering advection-diffusion is employed as follows, for details, see Nomura et al.

$$\text{Equilibrium} \quad \dot{\sigma}_{ij,j} = 0, \dot{\sigma}_{ij} = \dot{\sigma}_{ji} \quad (1)$$

$$\text{Effective stress} \quad \dot{\sigma}'_{ij} = \dot{\sigma}_{ij}^N + \dot{p}_s \delta_{ij}, \dot{\sigma}_{ij}^N = \dot{\sigma}_{ji} - \dot{p}_a \delta_{ij} \quad (2)$$

$$\text{Constitutive equation} \quad \dot{\sigma}'_{ij} = D_{ijkl} \dot{\epsilon}_{kl} - c_{ij}^s \dot{S}_e \quad (3)$$

$$\text{Compatibility equation} \quad \dot{\epsilon}_{kl} = -\frac{1}{2}(\dot{u}_{l,j} + \dot{u}_{j,l}) \quad (4)$$

$$\text{Darcy's law (water)} \quad \tilde{v}_{w_i} = -K_{w_{ij}} h_{,j} = -k_{rw} k_{w_{ij}} h_{,j} \quad (5)$$

$$\text{Darcy's law (air)} \quad \tilde{v}_{a_i} = -K_{a_{ij}} h_{a,j} = -k_{ra} k_{a_{ij}} h_{a,j} \quad (6)$$

$$\text{Fick's law (solved material)} \quad J_i = -D_{ij} c_{,j} \quad (7)$$

$$\text{Continuity equation (water)} \quad \tilde{v}_{w,i} = \dot{\epsilon}_v S_r - n \dot{S}_r - n S_r \frac{\gamma}{1+\gamma c} \dot{c} \quad (8)$$

$$\text{Continuity equation (air)} \quad \tilde{v}_{a,i} = (1-S_r) \dot{\epsilon}_v + n \dot{S}_r - \frac{n(1-S_r) \dot{p}_a}{K_a} \quad (9)$$

$$\text{Advection-diffusion equation} \quad -S_r c \dot{\epsilon}_v + n \dot{S}_r c + n S_r \dot{c} + c \tilde{v}_{w,i} + n S_r J_{i,i} = 0 \quad (10)$$

Here, σ_{ij} is total stress tensor, σ'_{ij} is effective stress tensor, σ_{ij}^N is net stress tensor, p_s is suction stress, p_a is pore air pressure, D_{ijkl} is elastic-stiffness tensor, ϵ_{ij} is strain tensor,

c_{ij}^s is coefficient tensor, S_e is effective saturation, S_r is degree of saturation, u_i is displacement tensor, ε_v is volume strain, n is porosity, γ is saturated solubility, c is concentration, $K_{w_{ij}}$ is unsaturated permeability coefficient tensor, k_{rw} is specific permeability, $k_{w_{ij}}$ is saturated permeability coefficient tensor, m is Mualem's coefficient, K_a is compressibility of pore air, $K_{a_{ij}}$ is unsaturated extinction coefficient tensor, k_{ra} is permeability coefficient ratio, $k_{a_{ij}}$ is saturated extinction coefficient tensor, \tilde{v}_f and \tilde{v}_a are velocity of water flow and air flow, J_i is density flux, D_{ij} is coefficient of diffusion tensor, respectively, h is total water head, and p_a is atmospheric pressure.

3. Simulations of advective diffusion

3.1 Analysis condition

F.E. mesh and geometric boundary conditions employed in the computation are summarized in Fig.2. Analysis domain is assumed to be a half space because of geometric symmetry. The ground water level is set to be 1.0m deep from the ground surface as a water head boundary. Right hand side of domain is assumed to be permeable. Climate conditions such as precipitation and evaporation employed in the computation as input data are indicated in Fig.3. The amount of evaporation is estimated using Penman model[3]. But actual amount of evaporation from the ground surface varies depending on the degree of saturation of the surface layer. Sheet piles are installed 5.0m deep. And it is initially assumed that seawater under the bottom of the sheet piles contains salt of which initial concentration is $C=0.1$ but the ground water above the bottom of sheet piles is fresh water containing no salt. In order to account for bio-mechanical response of the pine tree such as transpiration, root elements[4] are employed to model

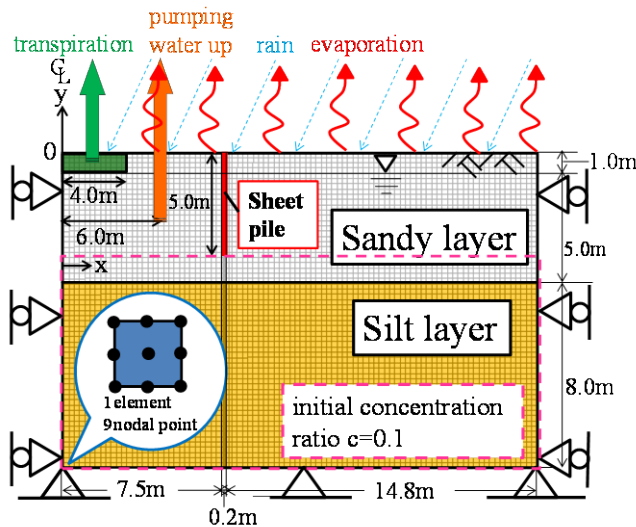


Fig.2 Analysis mesh and geometric boundary condition

the root system. Since the monumental pine is categorized to be Akamatsu, transpiration ability can be estimated to be $0.01\text{m}^3/\text{day}$ and the limit of salinity tolerance can be set to be $C=0.01$ [5].

The ground consists of sandy layer (0 to 6m deep) and silt layer (6 to 14.0m deep), according to field survey[6]. Coefficients of permeability for both layers are estimated using Creager method[7]. The moisture characteristic curves of both soil materials are assumed as in Fig.4. Input parameters used in the computation are tabulated in Table.1. Computed cases are summarized in Table.2. In CASE-1, influence of the weather condition and transpiration is examined. In CASE-2, the actual measure employed to protect the monumental pine by pumping up the water from 2.0m deep is simulated. In CASE-3 and CASE-4, differences of the depth from which water is pumped up, that is, 5.0m deep and 8.0m deep, are examined. In CASE-5, the effect of flashing on the ground surface is examined.

3.2 Influence of weather condition and transpiration (CASE-1)

Fig.5 shows the salt concentration distribution which was computed in CASE-1. The white color in Fig.5 indicates the limit value of salt tolerance of the pine. According to the computed results of CASE-1, the salt concentration rises upward to the ground surface gradually. The first six months were rich in rain comparing with evaporation but after the difference between precipitation and evaporation becomes smaller. The distribution of total water head is shown in Fig.6, in which total water heads under the roots of pine and outside of sheet pile are compared. Hydraulic gradient varies with seasons and pore water migrates in accordance with it. Also, since the total water head at the inside of the sheet pile is lower than that at the outside of the sheet pile due to the water absorption by the root of pine, the ground water migration occurs from the outside of the sheet pile resulting in supplying the saline water to the inside of the sheet pile. As to the influence of climate conditions such as precipitation and evaporation at this site, the precipitation is generally more dominant than the evaporation and it urges the downward flow of the ground water. However, it is not enough to prevent the migration of salt content to the area of roots of pine tree. According to the computed results, it is predicted that the salt concentration exceeds the limit value of salt tolerance of the pine tree at 6 months later and the pine tree

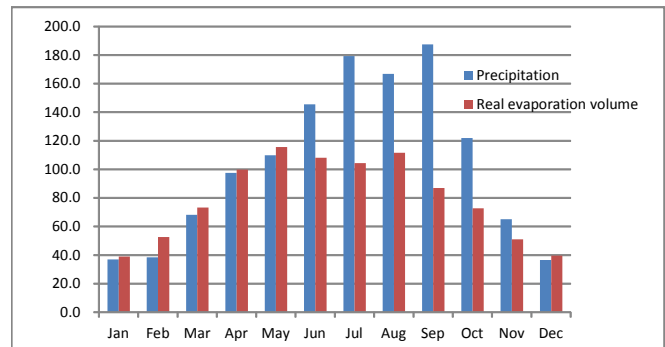


Fig.3 Climate conditions

Table. 1 Parameters for analysis

	λ	κ	M	ν	e_i
sand silt sheet -pile	0.30	0.06	1.38	0.30	1.0

	k_f (m/day)	k_a (m/day)	m	D (m ² /day)
sand	2.3×10^0	2.3×10^2	0.8	2.3×10^{-2}
silt	2.4×10^{-1}	2.4×10		2.4×10^{-3}
sheet -pile	1.0×10^{-10}	1.0×10^{-10}		1.0×10^{-10}

m : Mualem[9]

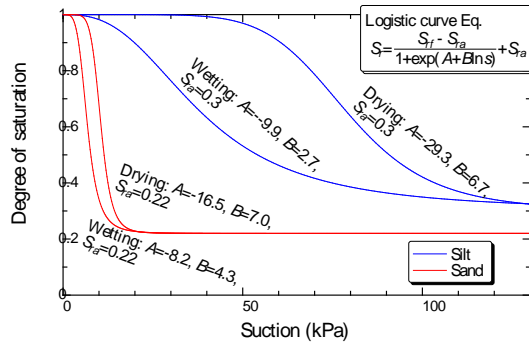


Fig.4 Moisture characteristic curves of the soil material

Table.2 CASES of analysis

	Weather condition (rain-evaporation)	transpiration	Depth of pumping water up(m)	flashing
CASE1	○	○	×	×
CASE2	○	○	2.0m	×
CASE3	○	○	5.0m	×
CASE4	○	○	8.0m	×
CASE5	○	○	8.0m	○

will die. It is found that the measure of sheet pile installation and pumping up water from the inside of the sheet pile is not sufficiently effective to protect the monumental pine tree. Furthermore the ground water level cannot be kept lower at the inside of the sheet pile as shown in Fig.7.

4. Simulation of pumping water up

In this section, it is examined how pumping up the ground water influences the migration of salt content in the ground.

4.1 Analysis condition

Two pumps were installed at the location of 1.5m inside from the sheet pile to take up water from 2.0m deep and operated for about 4 months from Jun 13th to Oct 12th, 2011. The ground water table at the inside of sheet pile had been lowered about 20.0cm during that period. Therefore, the amount of 5.0 m³ is roughly estimated to be pumped up a day. In the computation, it is assumed that pumping up is continuously operated after Oct 12th in order to examine its long term effectiveness. Also, their intake location in the ground is

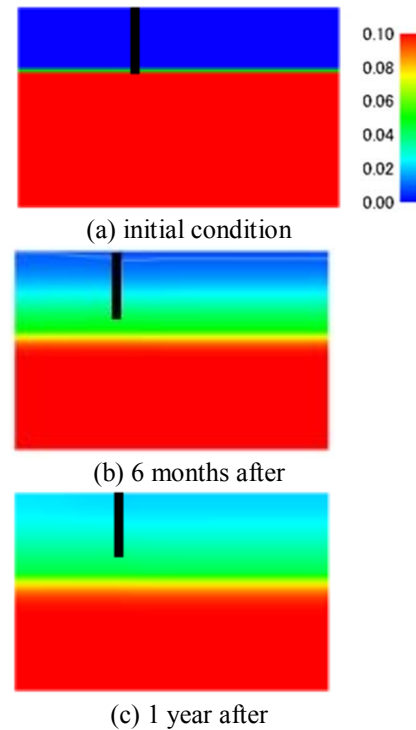


Fig.5 Salt concentration (CASE-1)

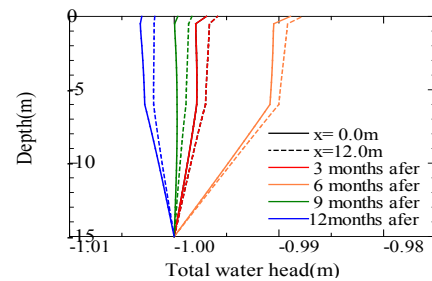


Fig.6 Distribution of total water head (CASE-1)



Fig.7 Distribution of degree of saturation around the pine's root system (CASE-1)

varied to be 2.0m deep (CASE-2), 5.0m deep (CASE-3) and 8.0m deep (CASE-4) in the computation.

4.2 Simulation results and discussion

4.2.1 Result of CASE-2

Actual effect of pumping up water is evaluated as shown in Fig.8, in which changes of salt concentration with time during pumping up water are depicted. When the computed results of CASE-1 where the operation of pumping up water is not considered, are compared with those of CASE-2, it is found that the operation of pumping up water urges worse salinity

development around the roots of pine tree. The saline sea water reaches the inlet of pump in a year. Fig.9 shows the total water head distribution. The operation of pumping up water develops the hydraulic gradient and draws the salinity into the area of root system of the monumental pine tree. However, it is recognized that the operation of pumping up water lowers the ground water table and prevents development of higher degree of saturation in the surface layer as shown in Fig.10. In this sense, it can be said that it is not effective enough to suppress root rot of the pine tree.

4.2.2 Result of CASE-3 and CASE-4

The imaginary cases that the inlet in the ground for pumping

up water is located at the 5.0m deep (CASE-3) and 8.0m deep (CASE-4) are considered. Fig.11 shows change of salt concentration (CASE-3). The location of inlet in the ground is the same depth with the bottom of sheet pile in this case. Similar to the results of CASE-2, it is found that salinity is gathered around the tip of sheet pile. Fig.12 indicates distribution of total water head. The hydraulic gradient generates downward flow of ground water near the ground surface but it does not much grow because of water absorption by the monumental pine. It is not effective enough to suppress the upward advection and diffusion of salinity. Also, it does not much contribute to lower the ground water table as shown in Fig.13. On the other hand, in CASE-4 that

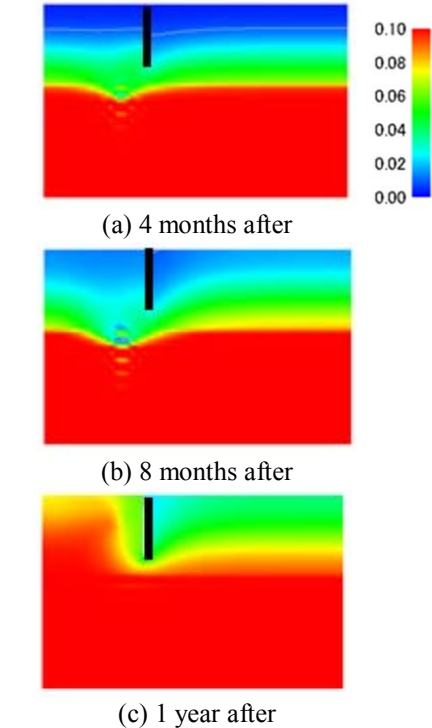


Fig.8 Salt concentration (CASE-2)

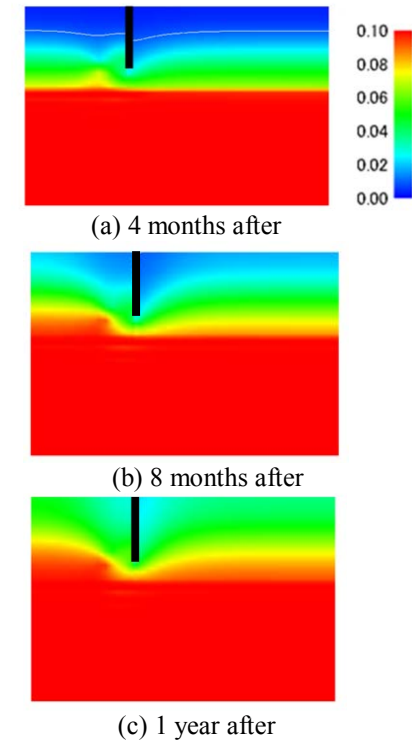


Fig.11 Salt concentration (CASE-3)

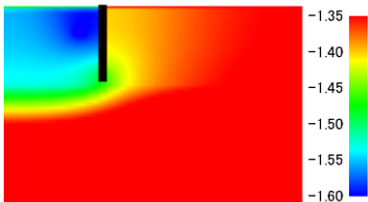


Fig.9 Distribution of Totl water head(CASE-2)

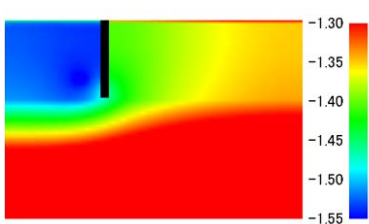


Fig.12 Distribution of Totl water head(CASE-3)



Fig.10 Distribution of degree of saturation around the pine's root system (CASE-2)

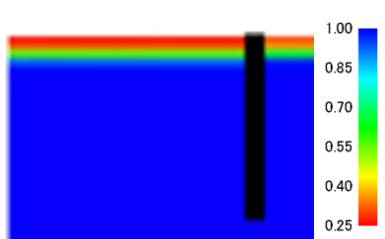


Fig.13 Distribution of degree of saturation around the pine's root system (CASE-3)

water is pumped up from 8.0m deep in the ground, the effect of suppressing rise of salt concentration is more remarkably recognized than others as shown in Fig.14 and Fig.15. However, it is not effective enough to lower the ground water table as seen in Fig.16.

5. Simulation of flashing (CASE-5)

In this section, it is examined how fresh water flashing effects dilution of salinity and protect the monumental pine tree.

5.1 Analysis condition

In the computation, fresh water is supplied into the ground surface as Neumann boundary condition. It is expected to

generate downward flow of the ground water and prevent rise of salinity. Simultaneously, pumping up water from 8.0m deep in the ground, $5.0\text{m}^3/\text{day}$, is also considered in the computation.

5.2 Simulation result and discussion

When amount of water for flashing was assumed to be $5.0\text{m}^3/\text{day}$, it was found that roots of the pine tree rotted out. It is because the ground around roots of the monumental pine tree is fully saturated. Then, the amount of water for flashing is assumed to be $0.01\text{m}^3/\text{day}$, which is the half of the amount of water pumped up. Fig.17 shows change of salt concentration. It is understood that rise of salinity

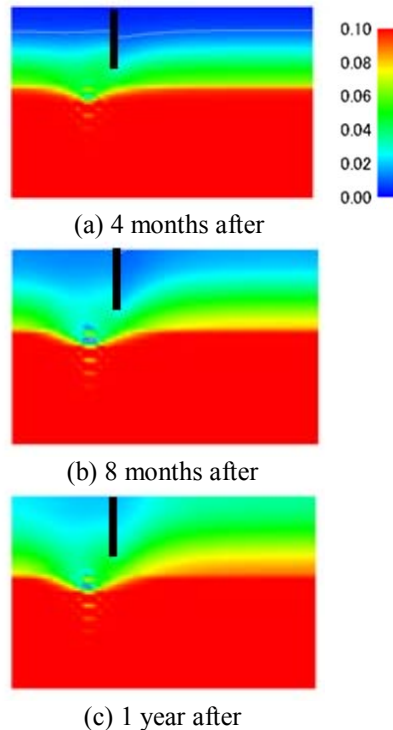


Fig.14 Salt concentration (CASE-4)

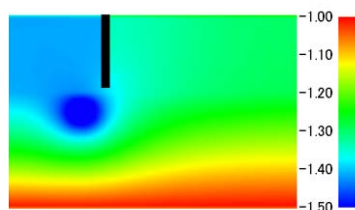


Fig.15 Distribution of Totl water head(CASE-4)

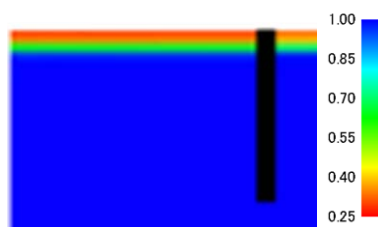


Fig.16 Distribution of degree of saturation around the pine's root system (CASE-4)

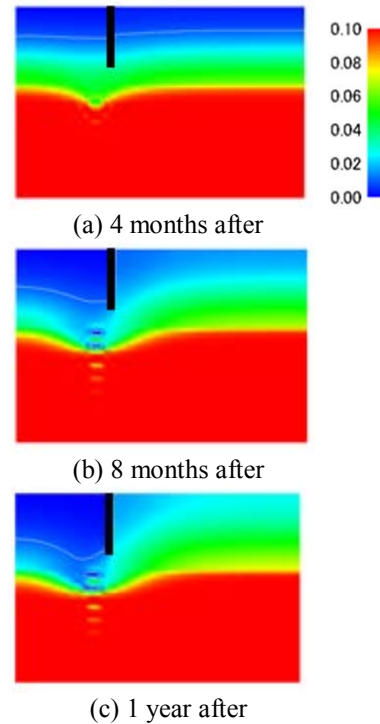


Fig.17 Salt concentration (CASE-5)

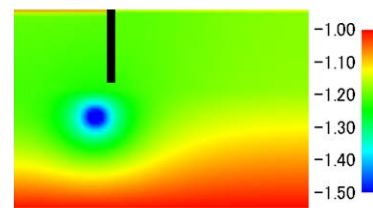


Fig.18 Distribution of Totl water head(CASE-5)

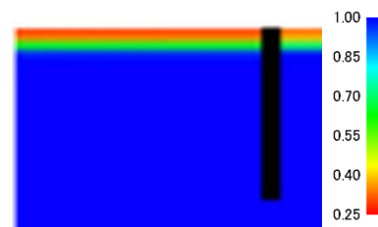


Fig.19 Distribution of degree of saturation around the pine's root system (CASE-5)

concentration around the roots of pine tree is well suppressed. The hydraulic gradient does not much developed as seen in Fig.18. Therefore, it can be said that the use of flashing and pumping up together is effective to save the monumental pine tree. In addition, it is found that the salt concentration does not exceed the limit value of salt tolerance of the pine tree. Fig.19 shows distribution of the degree of saturation. The ground around roots of the monumental pine tree does not reach fully saturation in a year. This implies that the root rot will be avoided. However, on the other hand, seamless operation of pumping up water and flashing at the same time would not be actually feasible from economical viewpoint.

6. Conclusions

In order to protect a monumental pine that survived from tsunami disaster in Rikuzen-Takada, possible measures were examined through a series of numerical simulations using soil/water/air coupled and advection-diffusion F.E. code, DACSAR. First, actual protective measure employed in the site was examined. And other possible measures were discussed. Concluding remarks are as follows.

1. The sheet pile of 5.0 m long is not sufficient to interrupt inflow of seawater into the area of roots of the pine tree. Some supplementary measures are required.
2. In the operation of pumping up the ground water, the location of inlet is important. In the case of relatively shallow location of inlet for pumping up water, it does not work so as to prevent migration of salinity into the area of roots of the pine tree. It urges rise of salinity instead. On the contrary, too deep location of it does not work to lower the ground water table. It possibly causes root rot of the pine tree because roots of the pine tree are immersed.
3. The use of fresh water flashing together with pumping water operation is effective. Continuous supply of fresh water into the ground surface prevent rise of salinity. And pumping water operation works so as to lower the ground water table. However, its feasibility is still questionable from economical viewpoint.

7. REFERENCES

- [1] <http://www.iwatetabi.jp/event/detail/03210/115.html>
- [2] Nomura, S. Mathematical model of soil/water/air coupled problem for unsaturated soils considering mass transfer within pore-water, *Proc. of the 5th Asia-Pacific Conference on Unsaturated Soils*, Vol.1, pp.287-292, 2011.
- [3] Penman, H.L. Natural evapotranspiration from open water, bare soil and grass, *Proc. Roy. Soc. London*, A193, pp.120-146, 1948
- [4] Kawai, K, Iizuka, A, Simonaga, K, Tachibana, S. The influence of uptake of vegetation on the ground, *Journal of Applied Mechanics JSCE*, Vol.10, pp.375-381, 2007.
- [5] Larchel, W. *Okophysiologie der Pflanzen*, Springer-Verlag Tokyo, p-350, 2004.
- [6] The business report of current situation survey of the ground and seawall in Rikuzen Takada, 1999.

- [7] Creager, W.P., J.D. Justin and J. Hind: Chap.16 soil tests and their utilization, *Engineering for dams, Vol.III:Earth,Rock-fill,Steel and Timber Dams*, John Wiley and Sons, pp.645-654, 1944.
- [8] Kawai, K, Wang, W, Iizuka, A. The expression of hysteresis appearing on water characteristic curves and change of stresses in unsaturated soils, *Journal of Applied Mechanics JSCE*, Vol.5, pp.777-784, 2002.
- [9] Mualem, Y. A new model for predicting the hydraulic conductivity of unsaturated porous media, *Water Resources Research*, 12(3), 514-522.1976.

Effects of Biosurfactants in Electrokinetic Remediation of contaminated soils

Bour Moslem¹ and Yousefi kebria Daryoush²
Babol Nushirvani University of Technology, Iran

ABSTRACT

One of the most important In-situ remediation methods of contaminated soils is electrokinetic remediation, that by using a direct electric field with various mechanisms (electromigration, electroosmosis, electrophoresis and electrolysis), the pollutants move in and exit from the soil. Electrokinetic remediation in soil has been limited due to low solubility of organic materials in water and their non-ionic nature. The use of surfactants (agent active surface) increases the remediation efficiency with increasing the solubility of insoluble liquid petroleum compounds in water and enhances their bioavailability. Biosurfactants are produced by microorganisms and contain a hydrophobic and hydrophilic moiety. They increase the water concentration of hydrophobic compounds and mass transfer rate by desorbing and emulsifying the adsorbed hydrocarbons to organic materials of soil. Therefore, they help that acceleration in biodegradation be occurred. Studies show that the extraction efficiency of oil compounds by using of synthetic surfactant could be increased 1.5 to 5 times in comparison with water, whereas the ability of Biosurfactant for removing of petroleum contaminants in the soil is 1.9 to 2.3 times more than synthetic surfactant.

Keywords: Electrokinetic, Remediation, Biosurfactants, Contaminated soil

1. INTRODUCTION

It's a long period of time that the oil materials and its derivative in transportation or storage develop pollution in soil. Oil pollution is an inevitable consequence of a rapid increase in population and industrialization processes that Soil contamination by substances that followed Hydrocarbonate and vast of oil exploration and refining facilities in around the broad and topical routes of transmission of this material is visible. In addition to direct emissions of these pollutants, dust from fuel emission with oil, over the years been able to add toxic and harmful substances in that soils. Biotechnology is one of the branches of the oil business and today the list of services offered by companies active in environmental issues is seen, is the Biological clear waters and soils contaminated with petroleum compounds. According to Iran's oil resources, production, Refining and distributing petroleum products, it is heavily exposed to oil contaminated soil. Based on this and due to the destructive environmental effects, cleanup oil contaminated areas has great importance. Mostly purifying the contaminated areas is done in two ways including inside and outside of place. The electrokinetic process is one of the most important ways in clean up the contaminated soils, faces with limitation because of low solubility of organics in water and their non-ionic nature. In order to enhance the biological availability of oil pollution and overcome to the hydrophobicity of their property, surfactants are used. The purpose of this study is to evaluate the impact of biosurfactants at the remediation of oil contaminated soils using electrokinetic method.

1.1 Soil, properties and contamination

Soil is one of the important resources and valuable nature which is produce human diet of about 95 percent. Without healthy soil, Life and living on earth would not be possible, therefore having planning for a healthy soil is essential for human survival. Soils are Mixture of mineral and organic which are formed of Degradation and destruction resulting from weathering of rocks, and generally are composed of two sections living and dead. Typical soil has 50% minerals and organic material and has 50% air and water that fills the empty spaces in the soil and keep living organisms in the soil. The type and combination of the soils in various regions is different depending on the district condition.

Soil pollution is the presence, distribution or mixing one or more foreign substances in the soil, while the amount and time that changes the quality of physical, chemical and biological of soil, so that it is dangerous for humans or other living creatures or plants or works and buildings. In other words Soil pollution is any changes in the characteristics of the soil forming components So that it is impossible for using. Most oil pollution of soil resources is seen around refineries. Much oil materials will penetrate deeper into the soil, more difficult to fix its pollution and its costs will be multiplied. The reason of Retention and stability of oil pollutants in soil properties returns due to the hydrophobicity of compound. An overall emission in the soil takes place in two stages; Initial phase that is short and quickly terminated then began the long phase and slowly goes away.

1.2 Soil decontamination methods

Nowadays the development of effective methods to soil remediation is allocated an important part of the research to the environment. Most remediation methods have been established and protection of human, animal and environmental liberation from exposure risks to toxic

substances. Many methods are used for the purification of contaminated soil, has resulted of research and experience in other sciences.

Broad range of technologies exists for purifying contaminated soils, but is generally divided into two categories:

1- *In-situ Remediation*: To do the process of clearing in contaminated site and

2- *Ex-situ Remediation*: The contaminated soil is transferred from contaminated area to another location for remediation.

2. Electrokinetic Remediation

Electrokinetic process consists of applying an electric field to the soil environment by placing two electrodes into the contaminated soil that flow directly between the electrodes is low and provide conditions that are different mechanisms of pollutants during pregnancy in the state will move toward the electrode with opposite charge. This process has widely used today to separate contaminants in soil and is classified as one of the methods of physical - chemical cleanup of contaminated soils [1]-[2]. Electrokinetic is a controlled method which is applicable in every area so that the cleanup of contaminated soils would be possible under buildings constructed without damage to the building [3]. This process was first developed by the Reuss then by Helmutz, Pallat and Smolochiwski the theory was presented. For soil and sludge samples were also used by Kasagrand [4]-[5]-[6]-[7].

2.1. Mechanisms of Electrokinetic process

Electrokinetic process has different mechanisms (showed in Fig 1) such as:

1- *Electrolysis*: Chemical reactions are performed in the electrolyte around the electrodes.

Establish the electric field with the following reactions occurs at the electrodes during electrolysis.

In Anode: $2\text{H}_2\text{O} - 4\text{e}^- \rightarrow \text{O}_2 + 4\text{H}^+$

In Cathode: $4\text{H}_2\text{O} + 4\text{e}^- \rightarrow 2\text{H}_2 + 4\text{OH}^-$

H^+ production at the anode is decreased causes reduction in pH. Acid front generated at the anode will migrate to the cathode during the process when water is electrolysed. Maybe PH at the anode decreases to less than 2 and at the cathode increases to more than 12. As a result, ion of H^+ will move toward cathode and ion of OH^- toward anode. Ion speed for Ion of H^+ at least is double Ion of OH^- that the flow Electroosmosis becomes more. If the buffering capacity of soil is not acidic side of the transmission delay Ion of H^+ transport within the sample dominates the acidic [8].

2- *Electromigration*: Motion of ions under the influence of an electrical gradient.

3- *Electrophoresis*: Motion of charged particles under the influence of colloidal and electrical gradient.

As for the similar mechanisms of ion migration and electrophoresis, generally, both as a general mechanism are considered. In general, charged particles including colloids and ions move toward the non-pole. Metal ions, Ammonium ions and positively charged organic compounds move

toward the cathode and anions and negatively charged organic compounds move toward the anode. After certain time, the pollutants accumulate in the Cathode and anode and with adequate measures isolation would be available [8].

4- *Electroosmosis*: Water transfer between soil cavities under the influence of an electrical gradient.

The effect of electric field applied along the soil mass, Positive charges towards the negative pole (cathode) and negative charges toward the positive pole (anode) are absorbed. A number of additional positive charges on the surface soil are pregnant. When this additional charges move toward the negative pole, Water due to friction force with the particle moves toward the negative pole. There is also a trend toward the positive pole, but because the water flow toward the cathode is generally smaller and is called electroosmosis [8].

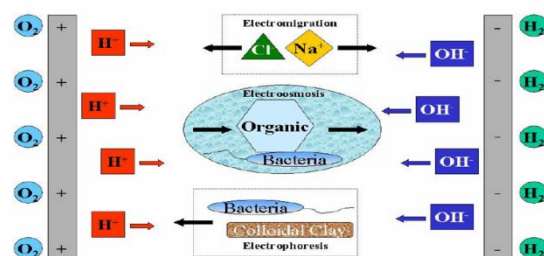


Fig.1 Mechanisms of electrokinetic process

2.2. Format Mechanisms for various pollutants

In Electrokinetic process any pollutants are removed from the soil to one of the following statements:

- Minerals by the mechanism of ionic migration in electric field move toward opposite poles and are removed from the soil.
- Polar organic compounds are removed from the soil by ionic migration.
- Non-polar organic compounds soluble in water due to solubility in water, by electroosmosis mechanism get sent the cathodes and are removed from bulk soil.
- Non-polar organic compounds insoluble in water due to the use of solvents and surfactants in the Andes as extraction materials they move from the anode to the cathode go to the cathode.

The main purpose of the application process to remove contaminants such as heavy metals Electrokinetic, anions and polar organic compounds in soil, sludge, mud, dredged sediments at sea etc. this method has better yields in soil with low permeability soils that soils are generally clay or is mixed silt and clay that like, Capabilities of pollutants will be better to move some of the mechanisms Electrokinetic. On the one hand, Heterogeneous soils with low permeability because of the limited movement of pollutants, Bacteria and nutrients, bacteria cannot decompose pollutants therefore the need for special arrangements is unavoidable. The problem

is removed with direct current electricity generated by a series of electrodes in the soil mass, because the flow is resulted in various phenomena such as: osmotic movement, ion migration and the particle motion. For removing organic contaminants by using the Electrokinetic method, Molecular size and tendency to accumulation or adsorption to the soil surface are the main factors controlling soil improvement. The high concentration of ionic particles in electrochemical reactions, Migration of electrolyte and water transfer between ions and water are friction factors. Obviously, Electrokinetic process efficiency depends on organic removal of solubility their being polar [1]-[8].

2.3. Advantages and disadvantages of Electrokinetic process

The main advantages of the Electrokinetic process application:

This method is very fast and relatively with high efficiency and easily prevents the spread of contamination.

As well as out of place in situ is applicable.

Unlike other in-situ recovery methods that are not effective in soils with low permeability or small seed, Electrokinetic method due to the negative surface charge of clay particles, has the highest efficiency in loam soil. So Electrokinetic is an effective method for moving water, and colloidal ions in soils with a small seed.

In addition to removing the decontamination, it has so much application such as: compassing the contamination, Inundation and concentrate dewatering sludge and extracting industrial metals in mineral and environmental sectors.

The most important problems in the Electrokinetic process are the Change in pH near the cathode and the sequestration of metals in this range. This phenomenon begins when large amount of ions OH^- Produced at the cathode and the surrounding medium is strongly alkaline. However, production H^+ around the anode, pH is greatly reduced. Usually in this case a sharp pH gradient is created between two electrodes. pH changes causes disruption in the transfer process, Biological activity of bacteria and adsorption and biodegradation of organic matter in the soil [8].

3. Surfactants

Surfactants are compounds of amphiphilic that free energy of the system by the replacement of large molecules with high energy in the medium reduces. They are using for soil washing because of the ability to move the pollutants. They have a slight hydrophobic environment with low interest bulk and hydrophilic groups which are willing to fly to the environment (showed in Fig 2).



Fig.2 Schematic of the Amphiphilic molecule of surfactants

Currently the use of surfactants has extensively developed in industry. In industrial applications, the ionic surfactants are often classified based on their charge which has at neutral pH when dissolving in water. These categories include anionic surfactants, cationic and neutral or Amphoters. Petrochemical are most traditional users of this material as a facilitator for oil removal from tannery wastewater. In this application, Petrochemical surfactants increase the solubility of compounds. This material also for floating materials are used in mining and the pharmaceutical industry and health [9].

Increasing the solubility of oil and liquid petroleum compounds which are water insoluble is the main uses of surfactants. Increasing the solubility by reducing the surface tension and interfacial tension in the layer between the water and oil is carried out with petroleum compounds. Surfactants in the intermediate level solid-liquid, liquid-liquid or vapour-liquid are gathered. There are two distinct phases between the interfaces hydrophobic component of water when hydrophilic component towards a solution, will accumulate on surface. The effect of surfactants is determined by their ability to reduce surface tension, criterion for the surface free energy per unit area for the bringing the bulk phase to the surface of the molecule [9]. Solubility of non-aqueous phase liquids by surfactants with reducing the surface tension between the joint surfaces to air-water and water-oil is increased. There is a correlation between surfactant concentration and surface tension. When the concentration increases the surface tension is reduced to a minimum value. Surfactant concentration at this point called as the critical micelle concentration (CMC). Surfactant properties including increased solubility, reducing surface tension and the low critical micelle concentration. One of the important characteristics is the critical concentration cleansing that depends on many of their physical properties such as emulsion formation, compounds dissolve oil and petroleum, Foaming, cleaning, the surface elasticity and between the surface elasticity. These properties are considered important criteria to determine the appropriate surfactants in soil washing process. Because of surfactant presence, less work is needed for moving the molecule to the surface and the surface tension decreases. Surface tension is related to concentration of surface activators until the concentration reaches to a critical micelle. Effective surfactants have with the less critical Micelle concentrations. CMC is defined as the minimum concentration required initiating the creation of micelle. Actually, CMC is the maximum monomer surfactant in water that influenced by pH, temperature and ionic strength. Rising temperature causes reduction in CMC and thus increases the efficiency of non-ion surfactants and also increases the solubility of ionic surfactants. Increasing the salt concentration in water can also reduce the amount of CMC for ionic surfactants but has no significant effect on their non-ionic types [9]. Surfactants in terms of production are divided into two categories: Synthetic surfactant, Biosurfactant.

3.1. Synthetic surfactants

Various types of cleansing which are produced using various chemical compounds are known as synthetic surfactants. Synthetic surfactants are produced in three types including anionic, non-ionic, Cations that all of which are used for soil washing. SDS, A synthetic anionic surfactant that cleans the soil in the field is the most common surfactant [10]. In addition, non-ionic surfactant due to their lower CMC than the anionic surfactant., Higher degree of surface tension reduction and relatively constant properties in the presence of salt have better performance and less need to use and consequently are used in improved cleaning process with surfactant assistance. One of the non-ionic synthetic surfactants can be named as Triton X100. Out of the cleaners Benefits in the industry, Use of surfactants in the environmental engineering can be count on the following:

- Make improvements in the toxins absorbed from the soil
- Improved desorption of organic contaminants in soil
- Desorption of organic contaminants from soil

Like many artefacts of human manufacture of synthetic surfactants significant negative have effects on biological activity Ecosystems and our environment. One of the major disadvantages is the effect that the use of this material is in the burning eyes and skin. Although different surfactants have effects, the negative effects and toxicity of these substances are found for living cells. All arrangements are the use of alternatives reason in addition to preventing their spread. One of the alternatives for these surfactants are synthetic surfactants that have similar properties as Biological surfactants And their negative impact is very low because they are one of the nature part [11]-[12].

3.2. Biosurfactants

Those surfactants that are obtained from natural compounds called biological surfactants. These surfactants besides the cleaning animals and plants, by microorganisms, yeast or bacteria to biological methods, of different nutrients, including sugar, oils, alkenes, and wastes are produced. Most Biosurfactants are a kind of non-ionic or anionic surfactant and include one or several parts of lipophilic and hydrophilic [1]-[13]-[14]. The Lipophilic part can be a protein or a lipid with a large number of sidelong hydrophobic chains. But often the hydrocarbon chain of a fatty acid with 10 to 18 carbon atoms is formed. The Water friend sector can be an Esther, A hydroxyl, or a phosphate or a carbohydrate group and or a Hydroxilit. Biosurfactant based on chemical structure and type of producing microorganism have different types and are classified In groups of glycolipid, phospholipids, lipid complexes – Poly saccharin, Lipoprotein – Lipopidieta Neutral lipids and fatty acids Hydroxilat [1]-[14].

3.3. Work of biosurfactants in removal in oil combination

When biosurfactants is added to the soil it collects to name of micelle is gathered that polar section toward out and hydrophobia tails toward in is stand. In this state the hydrophobic hydrocarbons located in the core of this micelle and in the form of a hydrophilic colloid in coming and are separated from the soil surface if higher concentrations of

surfactants, afar said colloids even are eventuated to solution[15]-[16]-[17]-[18]. This is exactly the same function as the soap is fat food. The fat particles in the soap micelle and with water from the soil surface are removed. Biosurfactant to remove petroleum compounds from soil by two main mechanisms are strengthened:

1- *Mobilization*: The motion of particles in the oil

2- *Solubilisation*: Solubility of oil components in water

Mechanism of stimulation usually occurs at concentrations below the critical concentration and micelle surfactants. Reduce surface tension and between the surfaces, reduction of capillary force, Moisture variability and increase the contact angle is. Surfactant monomers increase the contact angle of between hydrophobic pollutants in soil, the separation of contaminants develop from soil particles and ultimately are removed the oil out of the soil. In this mechanism, in concentrations below the CMC surfactants are reduce the surface tension between surface the phases of surface and air-water, oil-water and soil-water. Surfactants that are in contact with the surface between two phases of soil and oil, Contact angle increases and are decreases the tensile force between soil and oil levels. And therefore the main cause of stick to the soil and oil particles that the capillary force is reduced. The simulation mechanism depends on of ionic time surfactants; therefore, the metals in the soil to absorb anionic surfactants may reduce their effective concentration in the soil [18]-[19]. With the capture of surfactants for their effect on soil and soil stimulation may occur with the highest concentrations of surfactants. When the amount of surfactant is more than critical concentration, pollutants from soil to cores of micelle hydrophobic are removed by surfactant. Crude oil Solubility in water with production increase fields monomeric surfactants. Hydrophobic ends of surfactant molecules to form a cluster inside the building had accumulated micelle and love water ends them are located bottom exterior surface in contact with the aqueous phase structure if micelle, the internal part of a micelle as a medium suitable for hydrophobic molecules in the organic material comes and is capable oil particles to separating from the soil surface and into solution. This process is known as dissolution. Biological surfactant to facilitate the desorption of oil pollution of soil or by spreading oil particles attached to the soil surface droplets into the liquid phase so that microorganisms are easily available be modified to process and analyze biological compounds, petroleum contaminated soils will help. Given the existence of different types of hydrocarbon molecules complexity and extent of physical and chemical properties are very low solubility in crude oil and most of them and lack of access to the very low interfacial tension in the soil washing and effect of The mechanism of dissolution of crude oil in oil to remove

contaminants from soil, Is almost negligible to minor. The removal of crude oil composition of the soil would be related to the mechanism of stimulation [18]-[19].

3.4. Biosurfactants benefits of in comparison with synthetic surfactants

The tendency to Bio-surfactants in comparison with synthetic surfactants has increased day to day. This is partly because of better indicator of bio-surfactants in comparison with synthetic surfactants which can be listed as below: - Facilitate procurement of renewable natural resources

- Less toxicity and excellent surface activity than synthetic Surfactants
- Biodegradable
- Environmental sustainability of industrial effluent discharged into the environment of the soil washing process
- And ability to operate at high temperatures
- Ability to maintain the high pH, more than 12
- Ability to tolerate high concentration of salt dissolved in water
- Ability to remove oil contaminants from soil, 1.9 to 2.3 times more than synthetic surfactants [20]

4. CONCLUSION

- 1) Decisions about choosing the best method or methods normally, Shall be based on cost And cannot be said with certainty which method is more economical than other, because some of the technologies depending on the soil can be very costly.
- 2) Electrokinetic process due to the possibility of being implemented in the site and simplicity has widely used in recent years. Also, the above process is able to remove a wide range of pollutants from the soil.
- 3) Low solubility and non-ionic nature of the soil organic matter in the water causes electrokinetic process to be limited.
- 4) Using surfactant and increasing the solubility of liquid petroleum compounds insoluble in water and enhance the accessibility of their biological can increase the cleanup efficiency.
- 5) The main biological features of soil after clearing process remains unchanged.

5. REFERENCE

[1] O. Gozini, A. Palza, M. C. Lob, L. Di Palma, Electrokinetic remediation of gasoil contaminated soil enhanced by rhamnolipid, Springer Science+Business Media B.V. 40:1239–1248, 2010.

[2] Riser-Roberts E, Remediation of gasoil contaminated soils: biological, physical and chemical processes, Lewis Publisher, Boca Raton, 1998.

[3] Rosanne M., Paszkuta M., Adler P.M. (2006) Electrokinetic phenomena in saturated compact clays, Journal of Colloid and Interface Science. 297: 353-364.

[4] AEC, 1997. In – situ Electrokinetic Remediation for Metals Contaminated Soils FY96, Annual Report, No.SFIM-AEC-ET-CR-97013, pp.87-88.

[5] Chung, H.I., Kang, B.H., 1999. Lead removal from contaminated marine clay by Electrokinetic soil decontamination. Engineering Geology, 53: 139 – 150.

[6] DOE, Office of E.M., 1995. Electrokinetic Remediation of Heavy Metals and Radionuclides Technology Catalogue. second edition, EM-0235, 201-203.

[7] EPA, 1997. Recent Development For In-situ treatment of metal contaminated Soils.

[8] Virkutyt, J, Sillanpa, M, Latostenmaa, P., 2002, Electrokinetic soil remediation – critical overview, The science of the total Environmen, 289, 97 – 121.

[9] Rosen, M.J., Surfactants and Inter facial Phenomena, John Wiley, New York,1989.

[10] Giannis A, Gidarakos E, Skouta A, Application of sodium dodecyl sulphate and humic acid as surfactants on electrokinetic remediation of cadmium-contaminated soil, Desalination 211:249–260, 2007.

[11] Urum, K. and Pekdemir, T., Evaluation of biosurfactants for crude oil contaminated soil washing, Chemosphere, Vol.57,2004,pp.1139-50.

[12] Paria S, Surfactant-enhanced remediation of organic contaminated soil and water, Advances in Colloid and Interface Science,Vol.138, pp.2458, 2008.

[13] Catherine N.M, Environmental applications for biosurfactants, Environ. Pollut.133 183-198, 2005.

[14] Kosaric N, Biosurfactants and Their Application for Soil Bioremediation, Biosurfactants for Soil Bioremediation, Food Technol. Biotechnol. 39 (4): 295,304, 2001.

[15] Kuyukina M.S, Irena B. Ivshina, Sergey O. Makarov, Litvinenko L.V., Cunningham C.J., Philp J.C, Effect of biosurfactants on crude oil desorption and mobilization in a soil system, Environment International. 31, 155,161, 2005.

[16] Mulligan,C.N., F.,Eftekhari, Remediation with Surfactant Foam of PCP-Contaminated Soil, Engineering Geology, 70 (3-4):269-27, 2003.

[17] Mulligan, C.N., R.N.,Yong, B.F.,Gibbs, Surfactant Enhanced Remediation of Contaminated Soil: a review, Engineering Geology 60, pp. 371-382, 2001.

[18] Mulligan, C.N., Environment Application for Biosurfactants: Environmental Pollution, Vol. 133, pp. 183-19, 2005.

[19] Rahman,K.S.M., et al, Bioremediation of Gasoline Contaminated Soil by a Bacterial Consortium Amended with poultry litter, Litter Coir Pith Rhamnolipid Biosurfactant, Bioresource Technology, 81(1):25-32, 2002.

[20] Urum,K., Y.,Pekdemir, M.,Çopur, Optimum Conditions for Washing of Crude Oil Contaminated Soil with Biosurfactants Solutions,Trans IChemE, Vol. 81, 2003.

O2117 Change in structure of ground-beetle assemblage on river areas after construction of biotopes using the technique, “Nature oriented river works”

Michko Masuda¹, Takaaki Tsukada¹ and Fumitake Nishimura²

¹Department of Civil Engineering, Nagoya Institute of Technology, ²Department of Environmental Engineering, Kyoto University.

ABSTRACT

Nature oriented river works means the river is managed for maintenance and the creation of a native habitat of the living things that the river originally maintains and various river spectacles. The kind of river constructions has been tried by using the living things such as dragonflies, butterflies, birds and fishes. The assessment is dependent on an investigator's skill, and does not serve as quantitative data. Then we tried environment assessment using ground-beetle assemblage. There are many kinds of species in the ground-beetles. It is suitable for prediction of the influence of an artificial disturbance, and the index for evaluation. Some pit-fall trap were set up at some different vegetation in the two biotopes and the structure of ground-beetle assemblage was investigated over six months. As a result of the followings become clear, 1)ground-beetle assemblage had the same tendency as the natural river areas. 2)Ground-beetle assemblage on artificial area is reflection the characteristic of local environment and we can use it for environment assessment as an index.

Keywords: Environment assessment, River management, Biodiversity investigation, Environmental indicator

1. INTRODUCTION

The river law of Japan was revised in 1997. After then "Nature oriented river works" has been done as a stream management that considers the environment. "Nature oriented river works" means the river is managed for maintenance and the creation of a native habitat of the living thing that the river originally maintains and various river spectacles. Disturbance, destruction and reduction of the habitat of wildlife are take place by river improvement. In order to evaluate the influence by an artificial disturbance to biota, it is important to monitor change of the kind phase of an object living thing, and to compare disturbance order. Until now, the researches of environment assessments were carried out using aquatic insects, butterflies and dragonflies [1]-[9]. However there are some problems in using dragonflies and butterflies. Dragonflies seriously depend on the water quality, and butterflies flight area are very vast, then the quantitative investigation are not easy. It is not necessarily appropriate to consider it as the index living thing universally used for much environment [10].

The ground-beetles in Japan are which has very many numbers of species, and numbers of individuals and in which ecological research is also progressing [11]-[13]. The ground beetles are a general term for beetles which mainly walk along earth surface, carry out surroundings ingestion and are living, such as a ground beetle, carabid beetle, a burying beetle. Moreover, the ground-beetles forms the community structure according to a slight environmental change of each habitat, and reacts to an environmental change quickly very sensitively [11] [14]. Then, it is indicated that the characteristic of the ground-beetles is suitable for prediction

of the influence of an artificial disturbance and the index for evaluation [15] [16]. Research about the ground-beetles as the environmental indicator has been done centering on Europe from the 1960s [17]. In Japan, it is these days that research on the environmental indicator of the ground-beetles has been done [18][19].

However, there are few researches on the environment assessment using the ground-beetles in the new biotopes developed by "Nature oriented river works". So, in this research, it aimed at clarifying analysis of the community structure of the ground-beetles in an investigation place, environment assessment, and correlativity with a plant community by investigating quantitatively the number of the ground-beetles of the biotope circumference of Yadagawa, river and the Shonai river that flows through northern Nagoya, the center of Japan.

Furthermore, from a viewpoint of conservation of the ground-beetles, it advocates considering it as one index of the future production of the "Nature oriented river works".

2. Materials and Methods

2.1 Study site

The study was carried out on the two biotopes at left bank of Yada River at Joganji, Nagoya City (35° 21' 60"N, 136° 91' 70"E, altitude 9 m). and at left bank of Shonai River at Nishibiawajima, Kiyosu City (35° 19' 03"N, 136° 85' 80"E, altitude 3 m) in Fig.1. Yada river is a urban river in the Shonai River water system of the extension 23km and 115 km² in the valley area. Shonai river is a urban river water system of the extension 96km and 1010 km² in the valley area. Each point and environmental condition showed in Table 1.

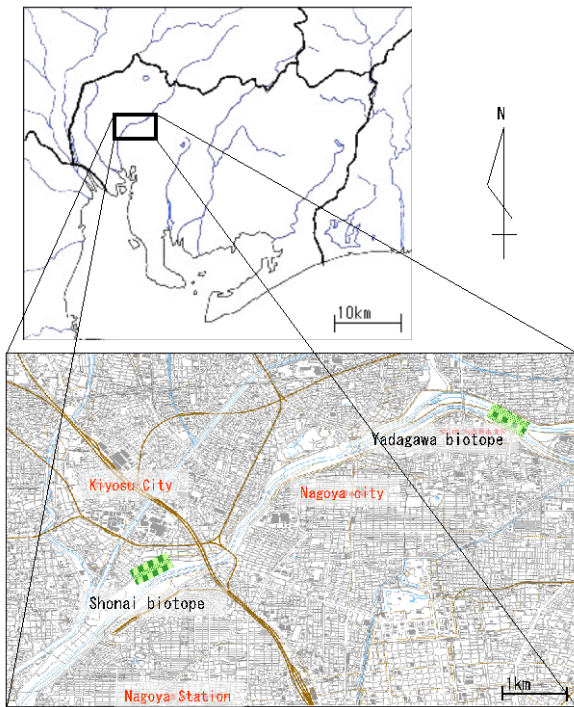


Fig. 1. The map of study site, Yadagawa biotope and Shonai biotope.

Table 1. The environmental condition of each study plots.

Biotope site	Vegetation type	Disturbance degree
Yadagawa	Grass land	high
	Floodplain forest	low
Shonai	Grass land	high
	Floodplain forest	low
	wetland	high

2.2 Field census

For the census of the ground-beetles, the pitfall trap method was set at every 5 plots. It is the method of collecting the insect by which buries the with 7 cm in diameter, a depth of 10 cm, and a capacity of 280 ml glass made from plastic materials with no bate on the ground (Fig. 2). 20 traps were set at every 2 m from each other in each plot, a total of 100 of a trap buried at a time. The pitfall trap was remained for 2 days at one census. The species and the numbers of collecting the ground-beetles was identified. The recorded beetles were removed from the traps. Census was carried out from August 10, 2010 to December 7, 2010 at every week, the total of 23 times census were done.



Fig. 2. The picture of a pitfall trap. .

2.3 Statistical analysis

In order to analysis of the census, five diversity index, an evenness index, two expected value and a disturbance index were used. Each index was calculated along the Table 2.

Table 2. The equations of each index

Statistical value	Equations
Diversity	Simpson index $\lambda = \sum \frac{n_i(n_i - 1)}{N(N - 1)}$ Shanon-Winner index $H' = - \sum \frac{n_i}{N} \log_2 \frac{n_i}{N}$
evenness	Pielou index $J' = N H'$
Expected	Chao species richness index $ES = S + \frac{a^2}{2b}$
Disturbance	Ishitani index $ID = \frac{\sum N_{ij} \cdot I_i}{\sum N_{ij}}$ niche breadth = $\frac{1}{I_i}$, $I_i = \sum \left(\frac{N_{ij}}{N_i} \right)^2$

n_i : the number of entities belonging to the i th type, N : the total number of entities, S : the total number of species, a : the number of species observed only one individual per species, b : the number of species observed more than one individual per species. I_i : Environmental index value of the i th type, N_{ij} : the number of the i th species in j th investigated plots.

Detrended correspondence analysis (DCA) was conducted to evaluate variations in the ground-beetles assemblages among different vegetation plots. DCA was conducted with a rearrangement at each plot, and scored.

3. Results

3.1 Field census

A total of 3707 ground-beetles, representing 82 sepecies, was collected in the census in Table 3. Only two species, *Colichus halensis* and *Harpalus niigataus*, were observed in all plots. Some species were collected only one plots. Especially in grassland in Shonai biotope 6 indegeous species were observed.

The Statistical analysis of the census was shown in Table 4. The value of diversity index was almost same in all plots. But the highest Shanon-Winner index was observed in grassland in Yadagawa biotope. The same result was shown about the evenness of Chao index. From the index of disturbance, Ishitani index, the forest plots in both biotopes were classified into forest area, and other plots into the flood plain in Fig. 3.

The result of DCA of the ground-beetles assemblages was shown in Fig. 4. It indicated that different vegetation plots placed along the first DCA axis increasingly, Shonai-grassland < Shonai-wetland < Yadagawa-grassland < Yadagawa-forest < Shonai-forest. It also indicated that different ecological characteristics placed along the first DCA axis increasingly, grassland-species < generalist < forest-species.

4. Discussion

It became clear that various the ground-beetles communities are maintained in two biotopes, Shonai and Yadagawa that have same river system, by this research. There were greater

differences in the temporal activity density and species richness of the ground-beetles among the vegetation types with disturbance frequency.

Table 3. The list of collected ground-beetles at each plots.

Family	Species	Number of individuals					Total
		Yadagawa		Shonai river			
		Grassland	Forest	grassland	wetland	forest	
Cerambycidae	<i>Myiodontia speculifera</i>	0	0	3	0	0	3
Scarabaeidae	<i>Campylota chinensis</i>	2	2	64	11	0	79
	<i>Cataglyphis arvensis</i>	8	1	0	0	0	9
	<i>Damaster blaptoides blaptoides</i>	23	4	0	0	0	27
	<i>Archips rosae</i>	31	10	1	0	0	42
	<i>Adelius chinensis</i>	0	0	0	3	1	4
	<i>Scaphisoma tricornis</i>	10	0	5	20	1	36
	<i>Leptocryptus</i>	1	5	3	2	0	11
	<i>Pterostichus nigriventris</i>	15	93	1	1	0	113
	<i>Pterostichus sumatrensis</i>	0	0	1	0	0	1
	<i>Pterostichus subcylindricus</i>	3	1	3	0	0	7
	<i>Pterostichus asagiri</i>	1	20	3	0	0	24
	<i>Pterostichus microcephalus</i>	0	0	1	0	0	1
	<i>Pterostichus subcylindricus</i>	3	1	0	0	1	5
	<i>Pterostichus longicollis</i>	0	2	0	0	0	2
	<i>Delidius delidius</i>	15	9	63	25	3	115
	<i>Prionoxystus</i>	3	1	1	0	0	5
	<i>Acacia chinensis</i>	0	0	1	0	0	1
	<i>Acacia stipularis</i>	2	0	2	0	0	4
	<i>Acacia gileadensis</i>	0	0	0	0	0	0
	<i>Acacia gileadensis</i>	2	0	2	0	0	4
	<i>Harporhinus</i>	3	10	0	0	1	14
	<i>Harporhinus</i>	2	9	4	6	0	15
	<i>Harporhinus</i>	1	5	0	0	0	6
	<i>Harporhinus</i>	5	5	7	0	1	18
	<i>Harporhinus</i>	97	11	97	30	2	242
	<i>Harporhinus</i>	0	1	1	1	0	3
	<i>Harporhinus</i>	25	0	80	32	0	137
	<i>Harporhinus</i>	3	0	3	3	0	9
	<i>Harporhinus</i>	76	0	10	0	0	86
	<i>Harporhinus</i>	10	1	16	0	0	27
	<i>Chalcidius</i>	10	0	3	2	0	15
	<i>Chalcidius</i>	23	3	23	0	0	49
	<i>Chalcidius</i>	33	16	20	0	0	69
	<i>Chalcidius</i>	14	1	3	2	0	20
	<i>Chalcidius</i>	22	26	2	0	0	50
	<i>Chalcidius</i>	0	1	0	1	0	2
	<i>Chalcidius</i>	1	5	3	3	0	12
	<i>Chalcidius</i>	0	0	0	0	1	1
	<i>Chalcidius</i>	0	1	0	0	0	1
	<i>Chalcidius</i>	0	1	0	0	0	1
	<i>Chalcidius</i>	0	0	2	0	0	2
Brachyidae	<i>Brachyidae</i>	291	51	2	11	0	355
Hydrophilidae	<i>Hydrophilidae</i>	0	0	0	0	1	1
	<i>Hydrophilidae</i>	0	0	0	1	0	1
Hydrophilidae	<i>Hydrophilidae</i>	0	0	0	1	0	1
Silphidae	<i>Silphidae</i>	25	22	0	0	25	72
	<i>Silphidae</i>	47	185	0	0	49	281
Scarabaeidae	<i>Scarabaeidae</i>	0	0	1	0	0	1
	<i>Scarabaeidae</i>	5	68	1	0	7	81
	<i>Scarabaeidae</i>	0	0	0	0	1	1
	<i>Scarabaeidae</i>	2	0	0	0	0	2
Scarabaeidae	<i>Scarabaeidae</i>	1	8	1	0	15	25
	<i>Scarabaeidae</i>	0	3	0	0	15	18
	<i>Scarabaeidae</i>	0	0	19	0	20	39
	<i>Scarabaeidae</i>	0	0	0	0	2	2
	<i>Scarabaeidae</i>	0	0	1	1	1	3
	<i>Scarabaeidae</i>	1	0	0	0	0	1
	<i>Scarabaeidae</i>	1	0	0	0	0	1
	<i>Scarabaeidae</i>	0	0	0	1	1	2
Elaphidae	<i>Elaphidae</i>	1	2	1	0	8	12
	<i>Elaphidae</i>	1	0	0	0	2	3
	<i>Elaphidae</i>	4	0	5	0	0	9
Curculionidae	<i>Curculionidae</i>	1	0	0	1	1	3
Curculionidae	<i>Curculionidae</i>	1	0	0	0	0	1
	<i>Curculionidae</i>	3	0	3	0	0	6
Curculionidae	<i>Curculionidae</i>	0	2	0	0	0	2
	<i>Curculionidae</i>	1	0	0	0	0	1
Curculionidae	<i>Curculionidae</i>	10	0	25	1	0	36
	<i>Curculionidae</i>	3	0	2	0	0	5
Elaphidae	<i>Elaphidae</i>	0	1	0	0	0	1
Elaphidae	<i>Elaphidae</i>	11	5	3	0	35	54
Elaphidae	<i>Elaphidae</i>	115	6	651	85	7	874
Elaphidae	<i>Elaphidae</i>	11	0	13	120	0	144
Elaphidae	<i>Elaphidae</i>	8	10	2	0	56	76
Elaphidae	<i>Elaphidae</i>	29	4	43	51	5	132
Elaphidae	<i>Elaphidae</i>	1	0	3	1	0	5
	<i>Elaphidae</i>	0	0	1	0	0	1
Elaphidae	<i>Elaphidae</i>	2	0	7	2	0	11
Elaphidae	<i>Elaphidae</i>	0	1	0	2	34	37
Elaphidae	<i>Elaphidae</i>	0	0	3	1	0	4
Elaphidae	<i>Elaphidae</i>	0	1	3	0	0	4
Elaphidae	<i>Elaphidae</i>	11	2	6	0	0	19
Elaphidae	<i>Elaphidae</i>	14	2	2	2	5	25
No. of individuals		1063	586	1227	102	146	3704
No. of Species		31	11	15	30	29	116

Table 4. The statistical values in each plots.

Statistical value	Biotope				
	Yadagawa		Shonai		
	grassland	forest	grassland	wetland	forest
No. of individuals	780	468	457	182	171
No. of species	35	32	41	20	18
Simpson index	1.208	1.115	1.146	1.122	1.215
Shannon-Wiener index	3.340	3.681	3.316	3.545	2.959
Pielou evenness index	0.651	0.737	0.669	0.820	0.710
Chao's species richness index	36.6	52.3	41.0	22.7	50.0
Ishitani disturbance index	1.94	1.40	1.77	1.82	1.38

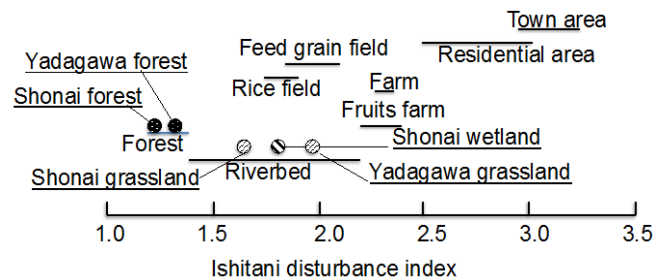


Fig. 3. The relationship between vegetation type and Ishitani disturbance index. The value of the index in each plot were shown in circles.

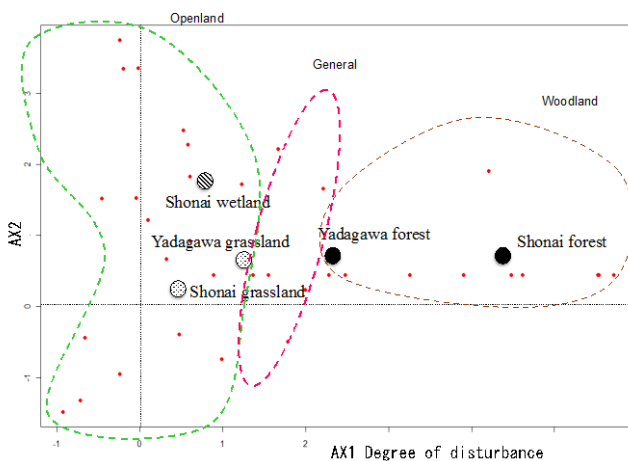


Fig. 4. DCA of the ground-beetles. • : each species of collected in all plots, circle: the average of each plots.

4.1 Characteristics of the ground-beetles in Biotopes

In this investigation, many *Harpalus sinicus*, *Harpalus niigatanus* of phytophagy, habitat generalist *Campylota chinensis*, were collected in the whole region. From this, it can be said that these kinds are representation kinds of the Shonai river system in Nagoya. The respectively characteristic species was collected in each biotope, *Pheropsophus jessoensis*, *Eusilpha japonica* and *Damaster blaptoides blaptoides* at Yadagawa biotope, *Dolichus halensis* and *Onthophagus tricornis* at Shonai biotope.

Campylota chinensis has flight capability, the capability to produce a large number of eggs and the resistance to

disturbance [20]. *Dolichus halensis* is carnivore with flight ability and is widely distributed over whole extent of Japan from mountain land to urban areas. *Harpalus* species has flight capability and eats grasses that distributed widely. This genus was observed in all the plots as a generalist.

Damaster blaptoides blaptoides is an endemic species of the area and their food is snails. The distribution of the species is widely from a forest to a grassland [21]. Although *Pheropsophus jessoensis* has flight capability and an imago is carnivorousness, the ecology of a larva is specialized, it is parasitic eggs on Gryllotalpidae. The habitat of the species is stable grassland. It is decreasing with reduction in Gryllotalpidae in recent years. *Eusilpha japonica* is a common species that has flight ability and is distributed over mountain land from the flatland. The habitat of the species is a little stable forest. It is thought that the area where these two species were collected is comparatively stable. The forest specialist who inhabits more stable mature forest was not collected. Most forest specialists are indicator species and rare species. As mentioned above, the ground beetles community of the Shonai river system is consist of the species that has flight capability, power of resistance to disturbance. Because of the Shonai biotope was constructed one years ago, the community structure of the Shonai biotope is consist of disturbance dependence species. On the other hands, it passed three years after the construction of Yadagawa biotope, the species of the community structure is consisted of the species that likes stable grassland.

Saprinusspl endens is a kind of Histeridae which likes stable environment[22]. In this research, only one species was collected in the Shonai river wetland. It did not breed and generate in the wetland one year after development, but it is thought that it came flying from other habitats. The same way, the species of *Nepa hoffmanni* can be considered the migration from another habitat.

Damaster blaptoides blaptoides, *Carabus arrowianus* and *Onthophaqus tricornis* are generalists, that live in the places where many kinds of vegetation is mixed. The species was collected all over the plots, then when disturbance happened, the species evacuates a surrounding grassland area or woodland area temporarily.

4.2 The cause of the biodiversity in biotopes

Through all the research periods, there were most the numbers of individuals and the species of the Yadagawa biotope grassland plot. It was shown that there was a twice as amount of biomass as this by simple calculation. However, there is no difference of diversity index among five plots. It is because the collected number of *Phropsophus jessoensis* loses the balance of the species composition of each investigation plot (291 individuals) of the Yadagawa grassland plot. If the dominant species collected over 40 individuals is removed, the other species are collected with sufficient balance, became a factor of high biodiversity and showed the characteristics of each community of the ground-beetles.

The result in which the classification result of the investigation plots, grassland, forest, wetland, by Ishitani's

disturbance index[17] reflected the feature of the investigation plots well was obtained. But only a few individuals of the species that reflect the wetland, such as *Archipatrobus flavipes*, *Scarites terricola pacificus*, *Drypta japonia*, *Chlaenius variicornis*, and *Pterostichus sulcitaris*, were collected in Shonai wetland plots. And also the species of Bembidiinae was not checked. On the other hands, forest species, such as *Haplochiaenius costiger* in Yadagawa forest and *Pterostichus noguchii* in Shonai forest plot, were collected. This is considered that the construction time of the habitat affected the community of each plot.

Some studies indicated the axis 1 of DCA is environmental fastidiousness [23]-[25], on the other hands the axis 2 of DCA showed nothing. The same result was shown in this study. Since the biotopes of this research was recently constructed, the litters layer has piled up only about 1 cm in depth. Then the biotopes are not evacuation habitat yet for the ground-beetles. It is thought that the biotopes became the collecting feeds area and laying eggs area. In Shonai biotope grassland plot the mowing is done completely, but the production of seeds by Gramineae was observed. There are a sufficient biomass to maintain the *Harpalus* community in Shonai biotope grassland plot. *Pheropsophus jessoensis* was collected in grassland plots and wetland plot in both biotopes. The species has a special feature that larva of the species lives on *Gryllotalpa orientalis*. But *G. orientalis* was not collected sufficiently in Yadagawa Biotope, then it is not showed that the reproduction of the species was occurred. The Adult of the species utilize as the feed area, and in the other plots they breed and laid eggs. In the Shonai biotope collection, sufficient number of *G. orientalis* was collected, the reproduction of *P. jessoensis* was occurred.

It was pointed out that *Chlaeniu micans* lives in forest and their larva feed the caterpillars on the vegetation [26][27]. In both biotopes *C. micans* was collected in early autumn. The reason is that a mowing in September was reduced the caterpillars, then there was no feeds in the biotopes.

4.3 The conservation of the biodiversity in biotopes

Many researchers have pointed out that the management method of vegetation has seriously influence on a biological community [27]-[31]. Forest specialists can invade the areas that maintaining the stable forest environment, accordingly succession degree be established gradually. It can be said that the succession degree affects influence on the ground beetles community also in the riverbed. From the data of Shonai biotope, completely mowing affects the biodiversity, then it is important by leaving without cutting down some willows to aim at recovery of the ground beetle community which makes that a habitation base. The immigrant from the habitat of the circumference of a biotope was suggested. It is important that stepping stones or corridor to which the import to a biotope is urged to form a habitat network.

5. CONCLUSION

We get two main conclusion.

1) Investigated the ground beetles community was the same tendency as the structure of the community of a general riverbed. Although the species that is characterized by the biotopes was not checked, the ground-beetle community of forest habitat was collected also in small-scale riverbed forest.

2) In the newly constructed biotopes, the ground beetles community was reflecting the characteristic of the area, and can use it for environment assessment as an index which shows maturity and disturbance degree.

Based on these conclusions, three proposals about the management method of a biotope are made.

1) In a part of low riverbed area, it refrains from felling, willows are grown up naturally, and small-scale riverbed forest is made.

2) Within the distance from which a grassland species can escape, mowing makes a mowing zone and a non-mowing zone like "tiger cutting", and various vegetations are arranged like a mosaic.

3) In the tall grassland and riverbed forest like a reed or willows, the conservation area leave the natural succession is set up.

6. ACKNOWLEDGMENT

We wish to thank the member of Ministry of Land, Infrastructure and Transport Shonai River Office for research support and permission to work in the river. We also thank the members of our laboratory for their assistance in the field works.

7. REFERENCES

- [1] Zelinka M, Marvan P, "Zur Praezisierung der biologischen Klassifikation der Reinheit fließender Gewässer," Arch. Hydrobiol, vol. 37, 1961, pp. 387-407.
- [2] Tsuda M, Biology of Freshwater. Hokuryukan: 1964, pp. 258.
- [3] Morishita M, "Measuring of interspecific association and similarity between communities" Men. Fac. Sci. Kyushu Univ. Ser. E. Biol, vol. 3, 1959, pp. 65-80.
- [4] Inaizumi M, Butterflies in Tochigi Prefecture. Insect fancier: 1975, pp. 148-160.
- [5] Tanaka B, "The one method of environment assessment by butterflies-The recent advances in butterfly mathematics," Lepidopterological Society of Japan special report, vol. 6, 1988, pp. 517-566.
- [6] Ishii M, *et al.*, "Diversity of the butterfly community in the city park in the Osaka Prefecture," Jap. J. of Environ. Ent. and Zool. vol. 3, 1991, pp. 183-195.
- [7] Sunose T, "The one method of butterfly community research," Ruin and Conservation of butterflies, vol. 2, 1993, pp. 83-90.
- [8] Sunose, T, "Environment assessment by line transect methods" Insect and Nature, vol. 31, 1993, pp. 9-12.
- [9] Nakamura H, "Methods of the analysis of the biotic community and the environmental assessment," J. of Facul. of Agri. Shinshu Univ., vol. 36, 2000, pp. 1-10.
- [10] Ishitani M, "Ecological research on the ground beetles as an environmental indicator," Hiwa Sci. Muse. Rep. Res., vol. 34, 1996, pp. 1-110.
- [11] Thiele HU, Carabid beetles in their environment. A study of habitat by selection adaptation in physiology and behavior. Springer-Verlag: 1977
- [12] Ishitani M, "The ecological research of the ground beetles: different vegetation area affects the community," Chugoku area Insect, vol. 17, 2004, pp. 13-18.
- [13] Hiramatsu S, "The community of the ground-beetles in the forest of the Hakusan," the Research report of Hakusan conservation center, vol. 31, 2004, pp. 55-65.
- [14] Niemela J, "Effect of changes in the habitat on carabid assemblages in a wooded meadow on the Åland Islands," Notulae Entomologicae. vol. 69, 1990, pp. 169-174
- [15] Lenski RE, "The impact of forest cutting on the diversity of ground beetles [Coleoptera: Carabidae] in the southern Appalachians," Ecol. Entomol., vol. 7, 1982, pp. 385-390.
- [16] Maleque MA *et al.*, "Arthropods as bioindicators of sustainable forest management, with a focus on plantation forests," Applied Ent. and Zool., vol. 44, 2009, pp. 1-11.
- [17] Ishitani M, "The wandering ground beetles as an environmental indicator," Insect and Nature, vol. 31, 1996, pp. 2-7.
- [18] Mano T, *et al.*, "Bait trap survey of insects in the central part of Toyota City (Aichi prefecture)," Res. of Yahagi river, vol. 10, 2006, pp. 15-42.
- [19] Lee C, *et al.*, "Change in structure of ground-beetle assemblage on levee of paddy field after the paddy reclamation in southern Osaka, central Japan," Insect and Nature, vol. 43, 2008, pp. 6-10.
- [20] Ishitani, M Yano K, "Species Composition and seasonal activities of ground beetles (Coleoptera) in a fig orchard. Jpn. J. Ent., vol. 62, 1994, pp. 201-210.
- [21] Ishitani M, "The biology of the ground beetle - things the start-," Insect and Nature, vol. 43, 2008, pp. 2-5.
- [22] Mochizuki S, "Studies on ecology of the bright blue hister beetle, *Saprinus speciosus* Erichson (Coleoptera: Histeridae)," Jpn. J. Appl. Ent. and Zool., vol. 29, 1985, pp. 21-25
- [23] Tanaka K, "The water assessing-environment method by biota," The agricultural environmental monitoring manual for water environmental preservation, second ed. National Institute for Agro-environmental Sciences: 2005, pp. 211-216.
- [24] Kagawa Y, "Studies on structure and conservation biocontrol use of ground beetle assemblages in agricultural landscape" in Kobe University repository thesis, 2005.
- [25] Seyffert A, "Diversity of ground beetles and saproxylic beetles (Coleoptera: Carabidae Div. Saproxylic) in East Mediterranean ecosystems (Israel): dispersal, habitat, activity and reproduction," Ine-book, urn:nbn:de:gbv:luen4-opus-141889 URL: <http://opus.uni-lueneburg.de/opus/volltexte/2010/14188/>
- [26] Tanaka B, *et al.*, "The insect fauna of between Heisei Memorial Bridge and Takahashi Bridge district, margins of

- Yahagigawa River,” Res. of Yahagi river, vol. 2, 1998, pp. 33-73.
- [27] Matsumoto K, “Management of the village-vicinity mountain, and the biodiversity,” Insect and Nature, vol. 43, 2008, pp. 20-26.
- [28] Suzaki T, Tanaka B, “Examination of mowing method which supports the inhabits of plants, insects and spiders on the embankment,” Res. of Yahagi river, vol. 8, 2004, pp. 149-169.
- [29] Tanaka B, “Insects in the researches along the riverside of the Yahagigawa in urban blocks of Toyota City from 1995 through 1999,” Res. of Yahagi river, vol. 5, 2001, pp. 47-67.
- [30] Den Boer PJ, “On the stabilization of animal numbers. Problems of testing,” Oecologia, vol. 83, 1990, pp. 38-46.

Dense granular-fluid mixture: the effects of the natural grains characteristics and the interstitial fluid viscosity

Anna Maria Pellegrino and Leonardo Schippa
University of Ferrara, Italy

ABSTRACT

An experimental study about the rheology of debris flow was carried out on debris flow soils and on natural sand using several rheometrical tools in order to investigate the rheological behaviour of the “fluid-like” material mixture. The results obtained on debris flow material mixtures suggest that, in the fluid-like regime, the typical rheological behaviour of this mixture is that of yield stress fluids and the rheology of the mixtures is strongly dependent on the grain concentration. The velocity profile obtained on natural sand-Newtonian fluid mixtures were analyzed in order to identify the shearing zone and to explain the dependence of the flow characteristics (i.e., transition from quasi-static regime to liquid regime) on viscosity and shear rate. The results suggest that, in that field, the interstitial fluid viscosity influence the shearing material layer and that no flow is possible for solid fraction higher than a maximum value.

Keywords: Dense granular suspensions, rheology, solid concentration, interstitial fluid viscosity, velocity profile

1. INTRODUCTION

In the last 50 years, the risk of landslides has increased enormously. The soil characteristics have already been explored, but there is still a lack of studies focused on the properties of the ‘post-failure’ material. Within the frame of a fluid mechanics treatment, the rheological characteristics of the flowing material would be useful for a better understanding of the flow characteristics of such events. In this paper, interesting informations in that field have been got by studying the rheological characteristics of a debris flow dry soil remixed with different amounts of water and a natural monogranular sand remixed with Newtonian fluids having different viscosity. These are materials that may behave like a yield stress fluid and their rheological parameters are strictly related to grain characteristics (i.e., size, shape, etc) and to interstitial fluid viscosity [1]-[2]-[3]-[4]-[5]-[10]-[11]-[13]. Because of the wide grain size distribution of the debris flow material (varying from clay to gravel), it has been prefer to refer as the solid volumetric concentration, which is a parameter that relates the solid amount to the total volume of the entire mixture. On one hand, with a conventional rheometer it is possible to analyze the rheological behaviour of the debris flow material considering a 70% of the whole grain size distribution and to study the changing of the rheological parameter with the variation of the solid fraction. On the other hand, with a large scale annular rheometer it is possible to analyze the rheological behaviour of a large particles mixtures (i.e., the monogranular-sand suspensions) and the influence of the grain size and of the interstitial fluid viscosity on different characteristic flowing parameters.

2. EXPERIMENTAL SETUP, PROCEDURES AND MATERIALS TESTED

A rotational rheometer CVOR (Bohlin Instruments) equipped with a vane rotor geometry system had been used, which consists of four thin blades arranged at equal angles around a small cylindrical shaft. The blade radius was $R_1=13$ mm, and the blade height was $L=48$ mm. The vane rotor was immersed in the sample (the sample volume was roughly 27 ml) contained in a cylindrical cup of radius $R_2 = 18.5$ mm. During the test, a part of the material is trapped in the blades so that as a first approximation the flow characteristics are similar to those between two solid coaxial cylinders, with the inner radius equal to that of the blade [12]. Under usual assumptions (no inertia effects, negligible normal stress differences) one can estimate the shear stress τ and the shear rate $\dot{\gamma}$ within the material from the following formulae:

$$\tau = T / 2\pi R_1^2 L \quad (1)$$

$$\dot{\gamma} = \Omega R_1 / R_2 - R_1 \quad (2)$$

It was possible to define the deformation undergone by the material from the initial time. At time t , the deformation γ is equal to:

$$\gamma = \int_0^t \dot{\gamma} dt \quad (3)$$

Creep tests were carried out, which consisted of imposing a constant stress and measuring the induced deformation of the material over time. The deformation is expressed in terms of

angle of rotation of the inner cylinder since the initial application of the stress. A complete test consists of imposing various values of stress, preparing each sample in the same initial state before each new stress value.

A large scale annular rheometer has also been used, which consists of two concentric horizontal aluminium circular disks assemblies mounted on a vertical shaft fixed on the basement of the apparatus. The lower disk assembly is mounted on the shaft with two roller bearings allowing rotation but no vertical motion. The lower disk is restrained from rotating by a torque arm connected to a load cell. This lower part has an annular trough 100 mm wide and 35 mm deep and has a mean radius of 200 mm; it is therefore called channel. The channel is closed above by a heavy rotating upper disk assembly mounted on the same vertical shaft through two roller bearings allowing both rotation and vertical movements. The surfaces of the upper (i.e. the ceiling of the channel) and of the lower disk (i.e. the bottom of the channel) were made rough with a glued sand paper sheet having a roughness of about 1.2 mm. The angular velocity is obtained by recording the pulse rate and, knowing the size of the gear and of the cogged wheel, the rotation speed of the upper plate of the shear cell is easily obtained. The vertical displacement of the upper disk is measured, with respect to the channel bottom, via a cable linear position transducer. Before starting a run, the shearing channel is filled with a known amount of granular material, carefully mixed with the liquid (special attention is paid to removing any trapped air). After a few rotations aiming to settle the material (the lower plate remaining at rest), the vertical position of the disk is measured. The counter weight strictly necessary to balance the disk weight is determined and, by unloading the counterweight, a fixed vertical pressure is caused. The disk is then let turn and a run is performed according to one of the two following procedures: one or more assigned velocities of the upper disk are reached, and the corresponding upper disk displacements are measured; the velocity is increased until a desired displacement of the rotating disk is reached; the velocity of the upper disk is increased step by step and subsequently decreased as well. During the test several desired velocities are reached. Torque, velocity and displacement are anyway monitored and a video record is taken.

The debris flow material has been tested with the rotational rheometer. It was sampled from the source area of a debris flows occurred in the Campania region (Nocera, Salerno, southern Italy, March 2005). The soil type, in a thickness of about a meter, depends on the most recent pyroclastic deposits deriving from the volcanic activity of Mount Somma/Vesuvius. The grain size distributions of the collected sample are reported in Fig. 2.1: the soil is a sandy silt with a small clay fraction. The bedrock underlying the soil is limestone, the specific gravity of soil particles is 2.61, the dry and total weight of soil per unit volume are respectively 9.08 and 11.35 kN/m³ and the porosity is 0.66. With the debris flow material, it was decided to perform tests on the

soil fraction with a particle diameter less than 0.5 mm, in order to respect at best the continuum assumption (it is necessary to have a material thickness much larger than the particle size in the material). Doing so retains about 50–70% of the whole grain size distribution, as shown in Fig. 2.1.

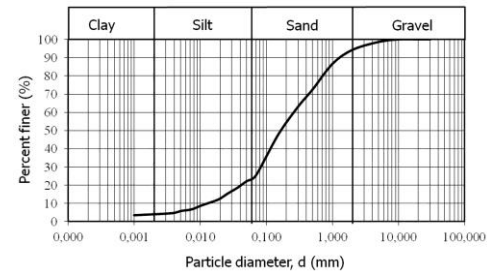


Fig. 2.1 Grain size distribution of the collected debris flow material.

All the experiments involving debris flow materials were carried out with mixtures of dry soils with different amounts of water. The solid concentration is described with the help of the solid volume fraction Φ , that is, the ratio of the volume of solids, V_s , to the total volume V_T (water plus solids) of the sample. In fact, according to the mixtures involving debris flow material and water, it is not possible to determine exactly how much of the dry material contributes to the formation of interstitial fluid (i.e., composed by water and smaller particles) and how much of the material set up the solid phase of the mixture (see Fig. 2.2). For each material tested, material mixtures of about 500 ml were prepared, mixing soils and distilled water with an electronic mixer (at about 30 rev/min) for 15 min. Then a sample volume of about 30 ml was used for each test at a constant temperature (23°C).



Fig. 2.2 Tested materials. a) debris flow material; b) natural sand.

The natural sand has been tested with the annular rheometer. The natural sand have uniform granulometric distribution ($d=1.4\text{--}1.68$ mm), the shape of the grains is irregular and the density is equal to 2670 Kg/m³. All experiments were carried out with mixtures of dry sand remixed with different fluids: clear water (low viscosity interstitial fluid, 0,001 Pa·s) and. Glycerine (high viscosity interstitial Newtonian fluid, 0,394 and 0,598 Pa·s). The combinations of fluid and grains lead to mixtures of fluid and irregular grains having solid-fluid density ratios ranging from 1 to 3. According to [13] the linear concentration λ , i.e. the ratio between particle diameter and their relative distance, related to the actual concentration Φ and to the maximum theoretical bulk concentration Φ_0 (i.e. the concentration at which all particles are in reciprocal contact) has been used. As reference concentration, the

maximum concentration $\Phi_m = 0.56$ has been used. The actual concentration has been derived from the displacement of the upper disk. The residual volume was measured and taking into account the residual volume and the corresponding displacement of the upper disk, the granular concentration of the shearing layer is then derived. It is important to note that in the case of the natural sand has been possible to accurately determine the maximum packing concentration (for the detailed procedure see [4]) while for the debris flow material it has been simply deduced.

3 EXPERIMENTAL RESULTS

3.1 Creep tests

Creep tests were carried out imposing a constant stress to the debris flow material mixtures and measuring the induced deformation over time. A complete test consists of imposing various values of stress, lower and larger than a critical stress, called static yield stress (i.e. the value of stress after that the mixture starts to flow like a fluid) [9]. The value of the static yield stress for each debris flow material mixtures analyzed was determined with some stress sweep tests carried out using the rotational rheometer. The stress sweep tests consist in measuring the apparent flow curves by applying an increasing shear stress ramp. The shear stress was continuously increased in a logarithmic way from 0.1 Pa to a large (maximum) value, and the corresponding shear rate was measured. The maximum stress value was specifically determined for each sample from independent (rheometrical) tests under similar technical conditions so as to get a rapid flow in the liquid regime without fluid expulsion out of the geometry (for the complete procedures and results see [11]). Before each creep test performed, the material was set up inside the geometry, immediately imposing a pre-shear at the maximum stress value above described for 30 s, and then starting the test in order to homogenize the sample. In Fig. 3.1 is showed the experimental results obtained with a creep test on debris flow material mixture at solid volumetric concentration Φ of 42%. It is observed that for stresses lower than critical stress the deformation's curve remains concave, with a slope continuously decreasing in time on a logarithmic scale, and exhibits an apparent horizontal asymptote. The deformation is limited, and the instantaneous shear rate decreases continuously to lower values, so that no steady state is reached. Finally, the material apparently stops moving and this should correspond to the solid regime of the material (the apparent shear rate $\dot{\gamma}$ is close to zero) [14]. For stress values higher than the critical value, the initial slope of the curve is similar to that under smaller stresses, but after some time there is an inflection point, and the curves gradually tend to reach an inclined straight line, with a slope equal to 1. In this case the deformation increases at a constant rate, which means that the apparent shear rate is constant, and a steady-state flow has been reached. These curves correspond to the liquid regime of the material [15]. However, the transition from the solid to the liquid regime is abrupt (see Fig. 3.1): for a stress just above the yield stress, the material rapidly reaches a shear rate level that is relatively high

(typically of the order of or larger than 1 s^{-1}). This suggests some viscosity bifurcation effect [9], again associated with a critical shear rate ($\dot{\gamma}_c$) below which no steady flow can be observed, as has already been observed from the results obtained in the sweep test on the same material mixtures. Note that the apparent critical shear rate may depend on the flow history, which can explain a slight difference between the value deduced from Fig. 3.1 and that found from the specific procedure used for sweep tests, showed in Fig.3.2. A recent work [8], focused on the behaviour of concentrated granular suspensions exhibiting similar characteristics, showed that this material exhibits a critical shear rate below which they cannot flow steadily. This could be an effect leading to shear-banding when an apparent shear rate is imposed below this value. The same trends occur here with the debris flow material mixtures analyzed: the static yield stress corresponds to the stress needed to unjam the locally settled structure, and then the dispersed suspension flows more easily. Consistent with this scheme, along the stress plateau associated with the static yield stress the material shear-bands and, increasing shear rate beyond the critical value, the material flows as a homogeneous fluid. (see Fig.3.2). As a consequence we have an unstable behaviour: when a stress is imposed while the mixtures are at rest they will not flow until the static yield stress has been reached, and just beyond this value suddenly flow at a shear rate larger than the critical shear rate. It has been noted that, in the absence of sedimentation and with very small particles, the material behaves like a Newtonian fluid up to a critical shear rate [6]-[7]-[8] - [9].

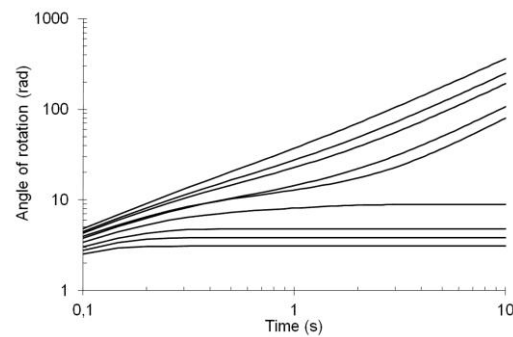


Fig. 3.1 Creep tests for debris flow material (42%). Deformation against time for different stress levels (from bottom to top): 90, 110, 120, 140, 142, 160, 170, 180, 200 Pa.

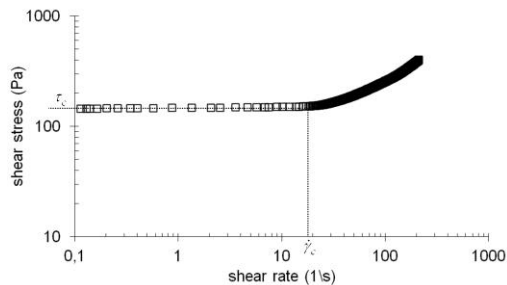


Fig. 3.2 Sweep tests with debris flow material 1 at 42% (Representative test).

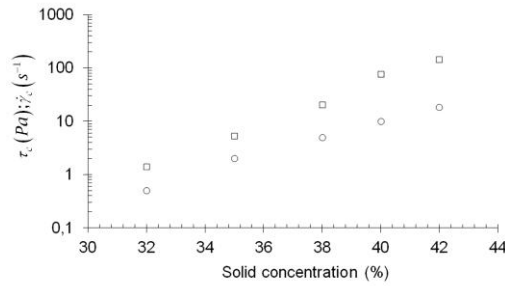


Fig. 3.3 Rheological characteristics of debris flow material as a function of solid fraction: static yield stress (empty squares symbols) and critical shear rate (empty circles symbols).

This behaviour is strictly related to the characteristics of these mixtures, i.e. particle type and interstitial fluid viscosity, which are strongly related to the solid volumetric concentration of the mixtures as showed in section 2. In fact it is especially interesting to look at the variations of the static yield stresses and the critical shear rate with the solid fraction (see Fig. 3.3). It can be seen that the yield stress and the critical shear rate increase in a similar way with solid fraction and they increase by two orders of magnitude over the very narrow range of concentration analyzed (less than 10%) in which the debris flow material mixtures tested behave as homogeneous fluids (for more details on the identification of the range of concentrations in which this type of material may be considered as fluids and thus can be characterized with the usual rheological tools see [11]). It is important to note that if the critical shear rate increases more or less like the yield stress when the solid fraction increases, then the material strength increases, and its apparent velocity when it starts to flow increases proportionally.

3.2 Velocity profiles

Measurements of velocity profiles were performed by Laser Doppler Anemometer equipment mounted on the large scale annular rheometer [4]. The used system is made up of a Flow Lite integrated laser-optics unit with a Flow Velocity Analyzer signal processor (FVA). The optic unit is mounted on a specific support, and it is driven manually in order to perform measurements at different point inside the shearing channel. Typical run was performed in analogy with the former procedure, i.e.: the channel is filled by a known amount of grains and fluid, by a counterweight a normal load is applied to the rotating upper disk, after few rotations the upper disk remains at rest aiming to settle the material and extrude any trapped air,. the vertical displacement of the upper disk is measured, the upper disk is set into rotation at the fixed velocities and measurements are then accomplished. In every run, the entire channel depth is visible through the window mounted on the external wall. Velocity measurements are performed inside the shearing gap along a vertical at different levels. The first set of measurements deals with a vertical just close to the wall. Afterwards, the measuring volume of LDA is moved inside the channel and a

new set of measurements is carried out along a different vertical. Measures along different verticals, located at different positions apart from the wall, were repeated as many times as possible depending on the optical characteristics of the mixture. The most remote measuring point was usually located 3-4 mm apart from the sidewall towards the core of the channel (about 2-3 grain diameter).

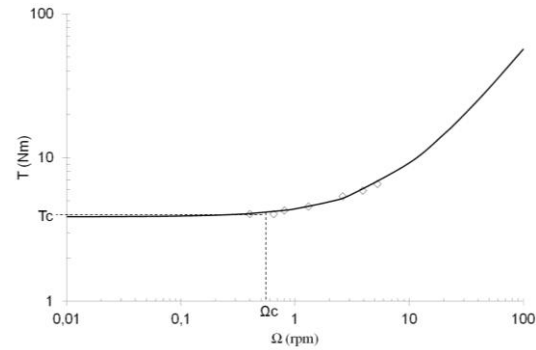


Fig. 3.4 Torque vs. the rotational velocity in the steady state of a 56% suspension. The line is a fit to a Bingham model: $T=T_c + \alpha\Omega$ with $T_c=3.86$ N m and $\alpha=0.53$ Pa·s.

In this way any boundary effect related to the presence of the wall (which was actually evident), could have been evaluated; both velocity profiles and actual shearing zone could have been extrapolated, as it is described in the following. Measurements were carried out during several runs, reproducing with strict approximation the experimental condition of the corresponding rheometer tests; velocity profiles were measured along few verticals from the external wall towards the centre of the channel. In Fig. 3.4, the torque vs. the rotational velocity for the steady flows of a 56% sand-water suspension has been reported. As observed in the experiments on debris flow materials (see previous section), it has been observed a quasi static regime (i.e., the solid regime of the material) followed by a viscous regime (i.e., the liquid regime of the material). It has been found a shear torque plateau at low velocities and a linear increase of torque with the velocity above a critical velocity Ω_c (Fig. 3.4). The data can be well fitted to a Bingham law $T=T_c + \alpha\Omega$ with $T_c=3.86$ N m and $\alpha=0.53$ Pa·s: this suspension seems to exhibit a yield stress and to behave macroscopically like yield stress fluids. In the following, the regime for which the torque increases linearly with the rotational velocity will be called the “macro-viscous” regime (as in [13]). A typical measured velocity profiles obtained are plotted in Fig 3.5: the dimensionless velocity profiles for the steady flows of a 56% sand-water suspension for various rotational velocities. As it is evident the measured velocity profiles are similar in shape. Measurements show that the velocity profiles are roughly exponential and that they occupy the whole gap for the considered rotation velocities. These velocity profiles show the mixture in the called macro-viscous regime [4]-[13], in which typically the applied shear rate is higher than the critical one. In fact, in this regime (i.e. at high rotation

velocities), the mixture inside the gap is all sheared. In the case, the whole sample is sheared, and all the reduced velocity $V(z_i)/V(z)$ profiles plotted vs. the radius fall along the same curve. It is noted that the critical velocity below which the shear flow is localized is as the same order of magnitude of the one associated with the torque plateau in Fig. 3.4. The velocity profiles obtained confirmed the Non Newtonian character of these mixtures: indeed the velocity profiles in the macro-viscous regime are very different from those expected for a Newtonian fluid; i.e. a quasi-linear velocity profile. In Fig. 3.6, it has been plotted the dimensionless velocity profiles of sand in a 56% suspension with different interstitial fluids at equal rotational velocity (20 rpm). This rotational velocity belongs to the macro-viscous regime of these three suspensions, in which the mixtures analyzed behaviour like a fluid and easily flow. In the case of the water-sand suspension, it has been seen that in the macro-viscous regime all the gap is sheared. In the case of glycerine-sand suspensions, it has been observed that the gap cannot be fully sheared: there still is a 1 mm region where the material is not sheared. In this case, when the rotational velocity increases, the thickness of the sheared layer does not increase anymore for $\Omega_i > \Omega_c$, and it remains smaller than the gap size. Analyzing velocity profiles and video records, it seems reasonable to assume an active shearing layer z_m , which extends from the ceiling of the channel to the level corresponding to 10% of the higher velocity (see Fig.3.7).

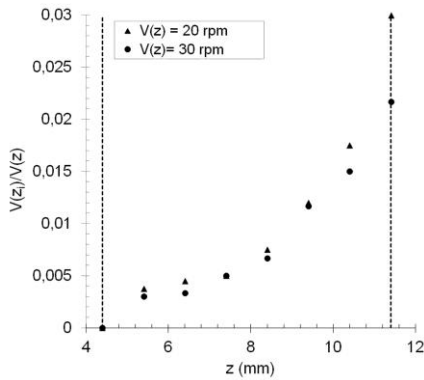


Fig. 3.5 Dimensionless velocity profiles in the steady state of a 56% water-sand suspension, at various rotational velocities.

Below this level we assumed that the quasi-locked lower layer z_s is at rest. It has been thus observed that the thickness of the sheared layer in the macro-viscous regime (i.e. for $\Omega_i > \Omega_c$), does not depend on the velocity and cannot exceed a maximum value z_m , which decreases when the suspension's viscosity increases. A value of 7.5 mm was found for the water-sand suspension, whereas 7 mm for the glycerine-sand suspensions. Actually, we observe that viscous flows at low velocities are not stable (i.e. for $\Omega_i > \Omega_c$ and $\dot{\gamma} > \dot{\gamma}_c$), and that the flow localizes. The mechanical origin of localization was evidenced by [7]: there is no steady flow for a shear rate below a critical shear rate $\dot{\gamma}_c$ that depends on the material's

properties. When the rotational velocity is lower than Ω_c , the apparent shear rate in the gap is lower than $\dot{\gamma}_c$. Therefore, the flow has to localize so as to ensure that in the flowing material $\dot{\gamma} > \dot{\gamma}_c$ and during localization, the shear stress increases while $\dot{\gamma}$ tends to $\dot{\gamma}_c$: the stationary shear stress at the walls is then approximately $\tau > \tau_c$. Shear localization thus leads to a shear stress plateau τ_c at low velocities (Fig. 3.4); however the flowing behaviour of the sand mixtures analyzed is always a purely viscous behaviour, even when the flow is localized, in the range of velocities studied. Finally, it has been noted that the mixtures behaviour dependences on the volume fraction: there may be no flow for Φ_m . The macro-viscous regime of dense suspensions then starts when the sheared region has reached a region where $\Phi = \Phi_m$: the thickness of the sheared layer cannot increase anymore, and now the torque has to increase linearly with the rotational velocity since the local shear rate now increases linearly with the velocity and since the flowing material behave like a purely viscous material. It is finally showed in Fig. 3.8 the comparison between the variations of the yield stresses with the solid fraction for every material mixtures tested in this study. It can be seen the same trend regardless the material: yield stress increase with solid fraction in exponential way and debris flow material mixtures and water sand suspensions increase in a similar way with solid fraction.

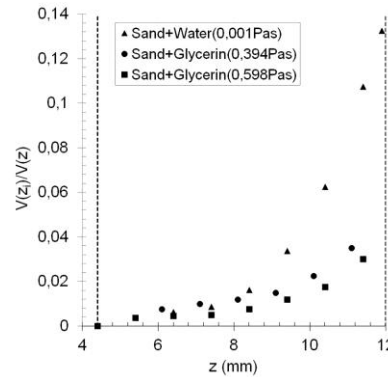


Fig. 3.6 Dimensionless velocity profiles in the steady state of sand in a 56% suspension with different interstitial fluids at equal rotational velocity (20 rpm).

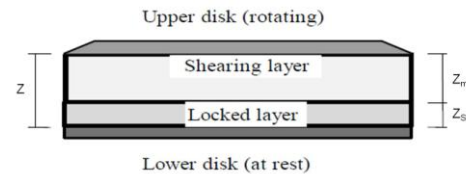


Fig. 3.7 Sketch of shearing and quasi-locked layer in the shearing gap.

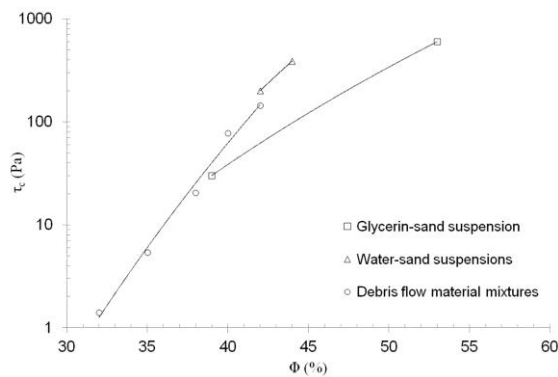


Fig. 3.8 Static yield stress as a function of solid fraction for all the material mixtures tested: comparison between debris flow material and monogranular sand.

4 CONCLUSION

In this paper it has been studied the flowing behaviour of debris flow material-water mixtures and natural sand water and glycerine suspensions by coupling local velocity and concentration measurements through large scale annular rheometer and macroscopic rheometrical experiments in a vane geometry. From rheometrical experiments performed and with the help of the velocity profile measurements, it has thus shown that the local material behaviour is a purely viscous behaviour. Creep tests and sweep tests have been shown that the typical rheological behaviour of these suspensions is that of a yield stress fluid exhibiting a static yield stress. The flow of such materials is usually unstable: they will start to flow beyond a critical stress, but just beyond this value will reach a high shear rate associated with a high flowing velocity. Then, the yield stresses and the critical shear rates are strongly influenced from solid fraction: if the solid fraction increases they increase in an exponential way. Analyzing velocity profile has been possible to identify and quantify the actual shearing layer and deriving the related parameters. Velocity measurements have been confirmed that these kind of mixtures are non Newtonian (they can flow only if a critical value of velocity has been reached, i.e., critical shear rate) and that the grain characteristics not appear to affect the macroscopic rheological behaviour of both mixtures. Moreover in the velocity profiles it has been clearly seen the influence of the interstitial fluid viscosity on the mixtures behaviour: the shared material layer decrease when the viscosity of the interstitial fluid increase and the relative velocity also decrease. These results suggest that, in the field, a small change in solid fraction will cause a slight decrease of the static yield stress, inducing a flow rapidly reaching a shear rate larger than the critical shear rate associated with a rapid flow. These results raise many questions: first, the physical mechanism associated with critical shear rate; second, the cause leading to the formation of two distinct layers within the material: the lower quasi-locked layer and the upper fully sheared layer; third, the characterization of the suspension at very low velocities in the quasi-static regime.

5 REFERENCES

- [1] Phillips CJ & Davies TRH. Determining rheological parameters of debris flow material. *Geomorphology* 4, No. 2, 1991, pp. 101–110.
- [2] Major JJ & Pierson TC. Debris flow rheology: experimental analysis of fine-grained slurries. *Water Resour. Res.* 28, No. 3, 1992, pp 841–857.
- [3] Coussot P & Piau JM. A large-scale field coaxial cylinder rheometer for the study of the rheology of natural coarse suspensions. *J. Rheol.* 39, No. 1, 1995, pp. 105–124.
- [4] Schippa L & Lamberti A. Experiments on the rheology of a dense granular flow. Final report of EC Research Programme DFR ENV4-CT96-0253. June 1999, pp. 1-34.
- [5] Schatzmann et al.. Rheometry for large-particulated fluids: analysis of the ball measuring system and comparison to debris flow rheometry. *Rheol. Acta* 48, No. 7, 2009, pp. 715–733.
- [6] Ancey C & Coussot P. Frictional-viscous transition for concentrated suspensions. *C.R. Acad. Sci., Paris* 327, 1999, pp. 515–522.
- [7] Huang et al.. Flow of wet granular materials. *Phys. Rev. Lett.* 94, No. 2, 2005.
- [8] Ovarlez G, Bertrand F & Rodts S. Local determination of the constitutive law of a dense suspension of noncolloidal particles through MRI. *J. Rheol.* 50, No. 3, 2006, pp. 259–292.
- [9] Fall et al.. Yield stress and shear-banding in granular suspensions. *Phys. Rev. Lett.* 103, No. 17, 2009.
- [10] Pellegrino et al.. Rheological behaviour of pyroclastic debris flow, 3rd Int. Conf. “Debris Flow III”, Milano, Italia, 24 - 26 May, 2010.
- [11] Scotto di Santolo et al. Rheological behaviour of reconstituted pyroclastic debris flow, *Geotechnique Journal*, Vol 62, Issue 1, 2011, pp. 19 –27.
- [12] Nguyen QD & Boger DV. Direct yield stress measurement with the vane method. *J. Rheol.* 29, No. 3, 1985, pp. 335–347.
- [13] Bagnold RA. Experiment on a gravity-free dispersion of large solid sphere in a Newtonian fluid under shear. *Proc. R. Soc. London Ser. A* 225, No. 1160, 1954, pp. 49–63.
- [14] Coussot P. Rheometry of pastes, suspensions and granular materials: Application in industry and environment. New York: John Wiley & Sons, 2005.
- [15] Coussot P. et al.. Aging and solid or liquid behavior in pastes. *J. Rheol.* 50, No. 6, 2006, pp. 975–994.

Back-analysis of Frictional Jacking Forces Based on Shear Box Testing of Excavated Spoils

Choo Chung Siung¹ and Dominic Ong E. L.²

^{1,2}Swinburne University of Technology (Sarawak Campus), Malaysia

ABSTRACT

Trenchless technology has become the preferred technique for installation of buried infrastructure due to advantages such as minimised ground surface disturbances as well as reduced social disruptions. These benefits have led to an increased demand for trenchless technologies such as the pipe-jacking method, with its application well-suited for urban environments. The construction of trunk sewers in Kuching, Sarawak has been carried out using the pipe-jacking method. Critical to this micro-tunnelling technique were the associated frictional forces anticipated during the jacking process. Excessive jacking forces could damage installed pipes. The Authors have studied the use of a few well-established empirical equations to validate frictional resistance during jacking supplemented by laboratory direct shear box tests carried out on spoils obtained from pipe-jacking drives. The tested spoils were by-products of the slurry transport system for spoil removal at the tunnel face. Shear box test results have been attempted for use to predict the pipe-jacking forces based on the well-established empirical equations. The predicted jacking forces for this study show fair agreement when benchmarked against actual, measured forces. However, it is the intention of the Authors to carry out more tests to further verify the reliability of this method for a wider variety of local rock types, especially in geologically 'young' weathered rock where competent rock cores are usually difficult to obtain.

Keywords: Pipe-jacking, direct shear, back-analysis

1. INTRODUCTION

There has been a growing need for trenchless technology for the construction of various pipelines. This trend has been evidenced by its implementation in the installation of trunk sewers in Kuching, Sarawak. Sewer lines comprising of concrete pipes were installed using micro-tunnelling by pipe-jacking. This method was elected over conventional open trench methods due to the minimised socio-economic disruption and pollution. However, the technicalities of such tunnelling works required specialist expertise. During the jacking process, various components were necessary for the works to proceed. The capacity of the microtunnel boring machine (MTBM), the application of lubrication, the capacity of main jacks, the use of intermediate jacking stations, and the design of jacking pipes are constituents of the synchronous system for successful pipe-jacking. A key factor affecting the above components is the frictional jacking load.

2. BACKGROUND

Studies have been carried out to investigate the behaviour of jacking loads during the pipe-jacking process. Pioneering studies on pipe-jacking were carried out by researchers at Oxford University, U.K. Norris & Milligan [1] detailed drives entailing instrumented concrete jacked pipes were carried out. Instrumented pipes were outfitted with pore pressure probes, contact stress transducers, extensometers, and other monitoring equipment. Data on variations of normal stresses and pore pressures on the instrumented pipes provided valuable early insight into the effects of lubrication on jacking

stresses [2, 3]. Pellet-Beaucour & Kastner [4] studied the influence of various parameters on the build-up of frictional forces for drives in varying soil conditions across France. The authors proposed two frictional force models in their analyses. Staheli [5] studied the behaviour of pipe-soil interface friction by conducting laboratory shear box tests. Sand specimens were applied normally on pipe crown segments of varying roughness. A similar test was carried out by Shou et al. [6], with the addition of lubrication. Interface frictional coefficients were derived from the shear box tests and verified using three-dimensional finite element modelling. The experiences and results reported by these researchers have been carefully reviewed and understood, so as to ensure that the methodologies reported in this paper are within acceptable conditions and practice.

3. SHEAR BOX TESTING OF EXCAVATED SPOILS

2.1 Direct shear test and geology

Due to the weathered nature of the 'young' sedimentary and metamorphic rock of the Tuang Formation in the Kuching City area, intact and competent rock cores ($\geq 100\text{mm}$ in length) are usually difficult to obtain during Soil Investigation works, thus making the strength parameters (c' and ϕ') for these weathered rocks rather elusive. Rock Quality Designation (RQD) may not be the best indication of rock strength as the values are usually zero or close to zero due to its friability. However, this observation does not necessarily represent the in-situ strength of the rock mass as a whole. Hence, performing direct shear tests where excavation spoils are reconstituted with appropriate confining stress

during testing may be a worthwhile and feasible method. Direct shear test was conducted using the GeoComp ShearTrac-II direct shear system (Figure 1). The ShearTrac II system enables full automation of shear box testing. Automation of the test ensures repeatability of testing regime.



Figure 1 ShearTrac II direct shear system

Control of the ShearTrac II system is achieved through the use of the SHEAR software. Users are given control over the shear box testing regime by inputting the desired consolidation stresses and shear strain rates. Results from tests are generated regularly in terms of horizontal and vertical displacements, as well as shear stresses along the shear band. The ability of the user to obtain results at a high-resolution allows for close scrutiny of tests. The ShearTrac II system is also able to maintain the consolidation and confining pressures throughout the test, from the consolidation stage through to the shearing stage.

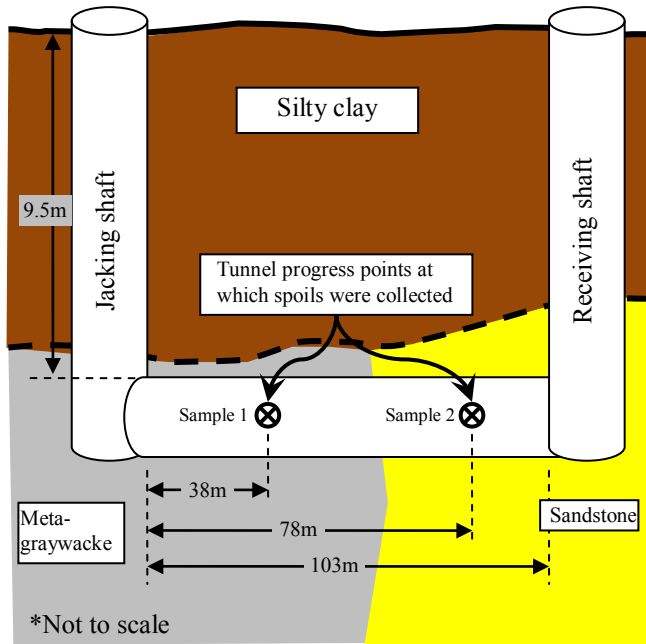


Figure 2 Estimated locations where Sample 1 (metagraywacke) and Sample 2 (sandstone) were collected as excavation spoils from slurry

2.2 Collection of excavated spoils

Excavated spoils were collected from the slurry separation plant (also known as desander). The excavated spoils were transported from the MTBM face through suspension in a pressurized slurry transport system and discharged in the desander. The desander recycles the slurry through filtration and segregates the spoils from the slurry. The slurry is then pumped back through the slurry supply line, back to the TBM face. Figure 2 shows approximate chainages at which excavated spoils were collected for testing.

2.3 Shearbox testing and results

Test samples were prepared according to AS1289.6.2.2-1998 [7]. Scalping of samples was carried out according to the allowances stated in the above-mentioned standard. The test samples consisted of grains passing the 2.36mm sieve, and retained by the 75 μ m sieve. Such scalping method has already been carried out by Bagherzadeh-Khalkhali & Mirghasemi [8]. Scalping was deemed necessary as preliminary shear box testing showed large fluctuations, particularly beyond the peak stress threshold. The consolidated drained shear box tests were conducted with samples placed in the reservoir filled with distilled water. Shearing was initially carried out at three confining pressures σ_1 , i.e. 170kPa, 180kPa, and 190kPa. These were approximate in-situ stresses acting on the pipe. Two further sets of tests were conducted at confining pressures of 100kPa and 250kPa, for better data distribution when measuring the respective strength characteristics.

Table 1 Results from shearbox testing on excavated spoils

Sample number	σ_1 (kPa)	Peak strength characteristics			Residual strength characteristics		
		τ_{peak} (kPa)	ϕ_{peak} (°)	c_{peak} (kPa)	τ_{res} (kPa)	ϕ_{res} (°)	c_{res} (kPa)
Sample 1	100	117	36	49	96	28	37
	170	179			128		
	180	171			128		
	190	186			134		
	250	227			178		
Sample 2	100	183	49	78	112	47	4
	170	282			201		
	180	282			203		
	190	282			204		
	250	360			275		

Table 1 above tabulates the results from shear box tests on the spoils. Generally, higher confining pressures, σ_1 resulted in larger shear strengths, τ_{peak} and τ_{res} . Strength characteristics were interpreted according to the Mohr-Coulomb failure criterion. Sample 2 showed higher strength characteristics than Sample 1 at both peak and residual strains. This is attributed to the particle shapes of the respective samples, with Sample 2 exhibiting generally angular particles as compared to the rounded particles of Sample 1 (Figure 3). As expected, peak strength parameters were generally higher than the residual counterparts for both samples. This is particularly evident for Sample 1. For Sample 2, the decrease in strength from peak to residual states was significantly due to a loss of cohesion. There was minimal observed decrease in friction angle of Sample 2. The residual strength of the

samples is thought to mimic the excavation process better as the in-situ rock mass is expected to be crushed till failure by the roller cutter bits found at the face of the MTBM. Besides, the continuous jacking process involved in the installation of pipes is also analogous of a shearing process in large-strain condition. The test results obtained were subsequently utilized for the prediction of frictional jacking forces.



Figure 3 (left) Sample 1 (spoils of metagraywacke); (right) Sample 2 (spoils of sandstone) used for direct shear tests

3. ANALYSIS OF FRICTIONAL JACKING FORCES

In the pipe-jacking process, jacking forces comprise of soil pressures acting on the face of the MTBM and normal stresses accumulating along the outer peripheral surface of the pipeline. The frictional component nominally forms the major portion of the jacking loads as the pipe-soil contact area increases with jacking progress.

3.1 Frictional jacking force equation

Frictional forces have been the subject of much research. The work carried out by Pellet-Beaucour & Kastner [4] employed the model shown in Eq.(1), which is expressed as a function of vertical soil stress on the pipe crown, σ_{EV} as in Eq. (2).

$$F = \mu L D_e \frac{\pi}{2} \left\{ \left(\sigma_{EV} + \frac{\gamma D_e}{2} \right) + K \left(\sigma_{EV} + \frac{\gamma D_e}{2} \right) \right\} \dots (1)$$

$$\sigma_{EV} = \frac{b(\gamma - \frac{2C}{b})}{2K \tan \delta} \left(1 - e^{-2K \frac{h}{b} \tan \delta} \right) \dots (2)$$

L is the length of the pipe string, D_e is the outer diameter of pipe, γ is the soil unit weight of ground cover, h is the height of cover at the pipe crown, K is the coefficient of lateral soil pressure, δ is the angle of wall friction in the shear plane, b is the influencing width of soil above the pipe. μ is the coefficient of soil-pipe friction, expressed as

$$\mu = \tan \delta \dots (3)$$

Pellet-Beaucour & Kastner [4] suggested upper limit values $\delta = \phi$, and lower limit values of $\delta = \phi/2$ or $\phi/3$ for soil-structure interaction calculations. They also reported values for b , δ and K by various organizations (Table 2).

Staheli [5] and Pellet-Beaucour & Kastner [4] further reported the use of some values of friction coefficient, μ . These values were obtained from Stein et al. [9].

Table 2 Summary of various parameters for use with frictional model by Pellet-Beaucour & Kastner [4]

b	δ	K
$D_e \left(1 + 2 \tan \left(\frac{\pi - \phi}{4} \right) \right)$	ϕ	1

Table 3 Friction coefficient values for various friction states from Stein (as summarized in Ref. [4])

	Static friction	Sliding friction	Fluid friction (lubrication)
Concrete on gravel or sand	0.5 – 0.6	0.3 – 0.4	0.1 – 0.3
Concrete on clay	0.3 – 0.4	0.2 – 0.3	
Asbestos or centrifuged concrete on gravel or sand	0.3 – 0.4	0.2 – 0.3	
Asbestos or centrifuged concrete on clay	0.2 – 0.3	0.1 – 0.2	

3.2 Case study for back-analysis

A case study was considered for a drive negotiating through the geology of the Kuching inner city area. The pipeline lies embedded in rock, with the crown at a level 9.5m below ground surface. The 103m alignment of 1.2m diameter concrete pipes traversed metagraywacke (metamorphic) and sandstone synonymous with the Tuang formation. As reported by Tan [10], the metagraywacke encountered in the Tuang formation is characterised as weathered, with occurrences of quartz veins. This was consistent with findings from soil investigation works. Metagraywacke in the Tuang formation is often found interbedded with moderately weathered phyllite.

The tunnel was excavated using an Iseki Unclemole Super TCS 1200. The closed-face MTBM had an outer diameter of 1.472m, creating a theoretical overcut annulus of 19mm around jacking pipes of outer diameter 1.434m. As mentioned earlier, the MBTM used the slurry transport system for maintaining a stable tunnel face, as well as for the transportation of excavated spoils. A shield embodied the machinery in the MTBM, with a succeeding sleeve attached. The cutter face was outfitted with four roller cutters arranged on the face, and three roller cutters at the peripheral for formation of the overcut.

Site data of measured jacking loads (Figure 4) from the earlier described site was used for benchmarking against predicted frictional forces. Site data could be generalised under two drive sections. The jacking forces within the initial drive portion (Section 1 – 0 to 60m) accumulated within a lower bound of 7kN/m and an upper bound of 12kN/m. The latter drive portion (Section 2 – 60m to 108m) exhibited gains in frictional loads of between 71kN/m (upper bound) and 41kN/m (lower bound). The positions where the samples were collected from are entailed in Figure 4 below, including the respective shear box test results.

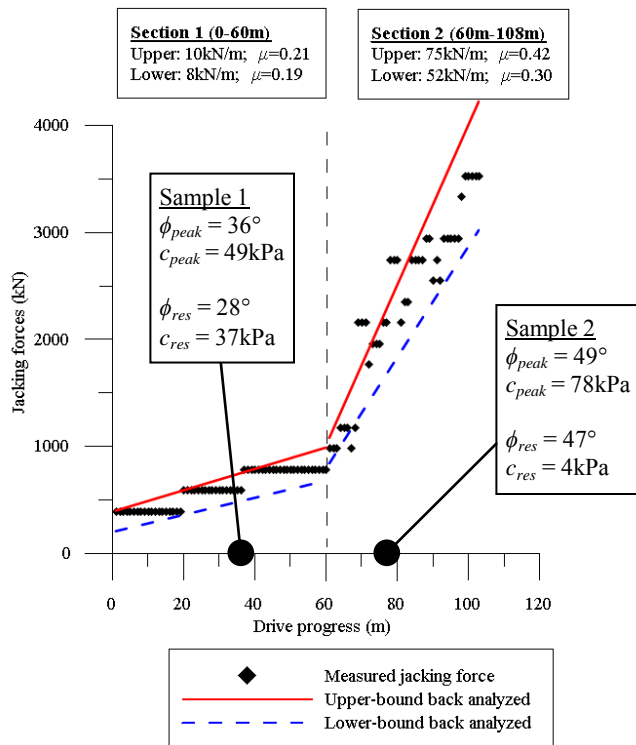


Figure 4 Back-analysed upper and lower bound jacking forces with respect to measured values including effect of stoppages in jacking in Section 2 only

Using Eqs. (1), (2) & (3) together with the residual strength properties of the excavated spoils, the required frictional coefficients for back-analysis were determined and presented in Figure 4.

The results were based on the Terzaghi set of parameters from Table 2. For the initial portion of the drive, the back-analysed frictional coefficients were 0.19 (lower-bound) and 0.21 (upper-bound), while those for the latter portion of the drive were 0.30 (lower-bound) and 0.42 (upper-bound). With reference to Table 3, the lower-bound coefficients of friction lie within the range of values reported for lubricated drives. The upper-bound frictional coefficient lies beyond the range of acceptable values for lubricated drives.

3.3 Effect of stoppage on jacking forces

In Section 2 of the drive, the disparity between upper and lower bounds for the coefficients could be explained by the stoppages in jacking works. Jacking forces in this latter section have been segregated as shown in Figure 5, thus Figure 5 shows jacking forces associated with only on-going jacking works. Frictional coefficients for the lubricated Section 2 are seen to have reduced to 0.32 (lower-bound) and 0.34 (upper-bound). These coefficient values were slightly above the upper limit of the corresponding values reported in Table 3 (under lubrication component). Figure 6 shows jacking forces, with forces attributed to stoppages presented for Section 2 of the drive. Frictional coefficients for Section 2 are 0.36 (lower-bound) and 0.42 (upper-bound), which are generally higher as re-start of jacking works after periods of stoppages are known to induce greater static frictional

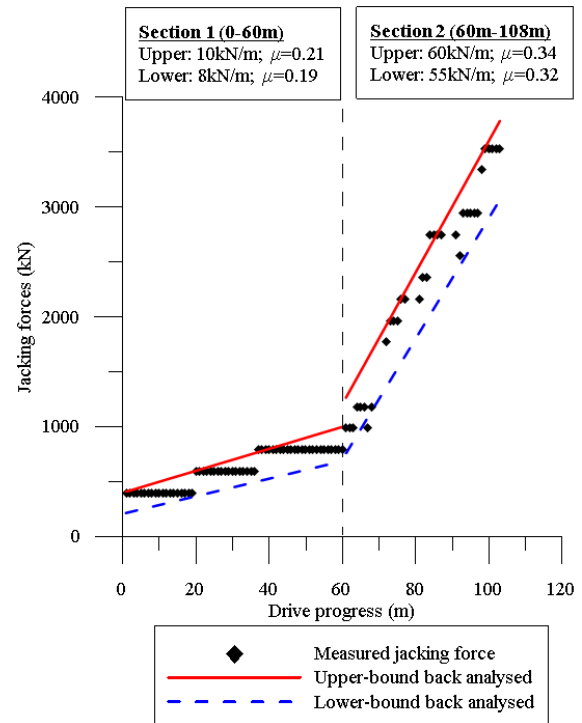


Figure 5 Back-analysed upper and lower bound jacking forces with respect to measured values, but with effect of stoppages excluded from Section 2 only

resistance and effects of lubrication are usually mitigated at this initial stage of work. This is confirmed by the back-analysed coefficients, which are comparable to those for unlubricated sliding friction for concrete on gravel or sand as per Table 3.

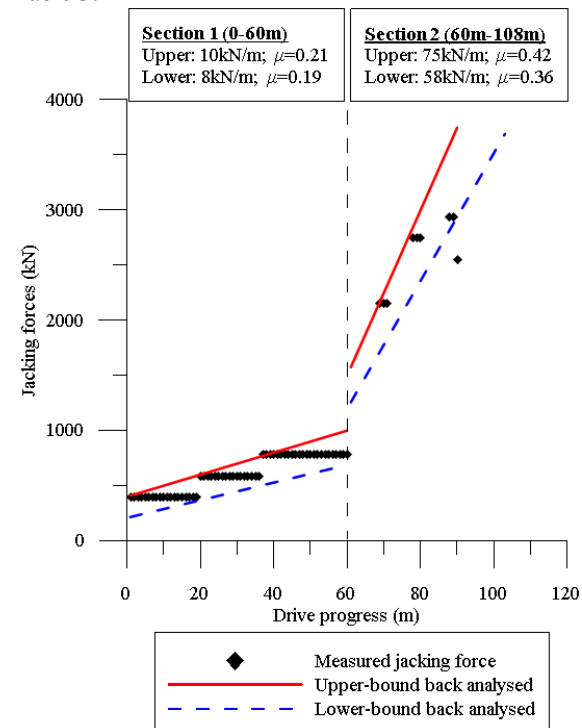


Figure 6 Back-analysed upper and lower bound jacking forces with respect to measured values, with only effect of stoppages in Section 2 only

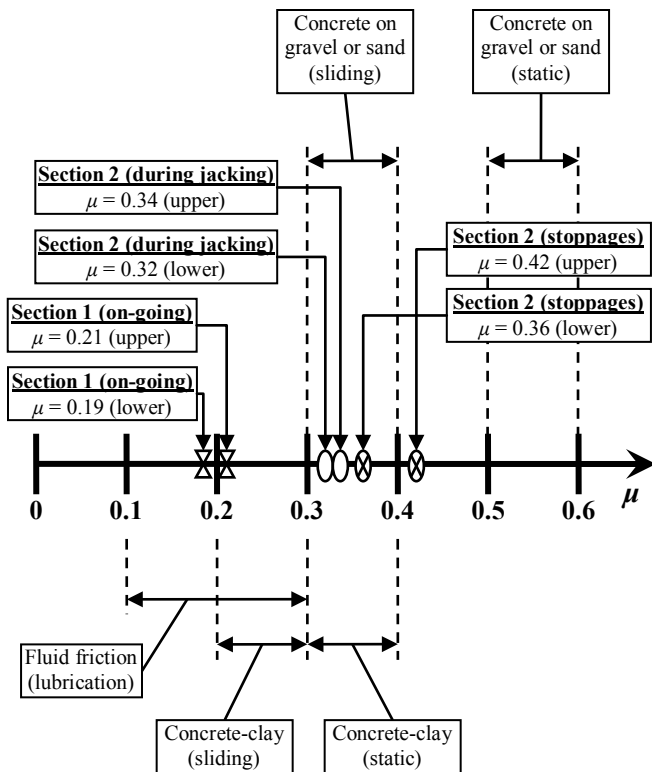


Figure 7 'Dynamic' behaviour of coefficient of friction during various stages of the pipe jacking process

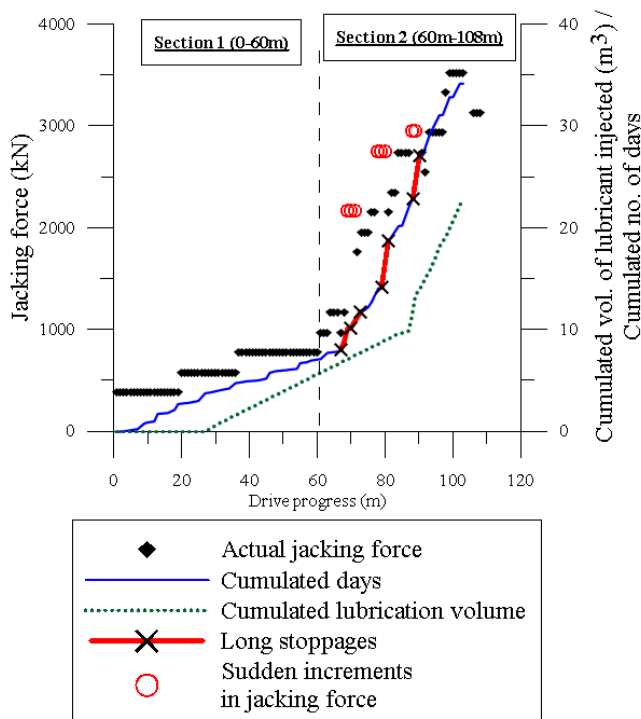


Figure 8 Development of jacking force and elapsed time in relation to stoppages and volume of lubricant injected into tunnel overcut

Figure 7 shows the 'dynamic' propagation of friction coefficients during different stages of work in the

pipe-jacking process as had been described in detail earlier and interpreted from Figures 4, 5 and 6.

Figure 8 illustrates the occurrences of extended stoppages, where sudden increments in jacking forces have been previously presented. These were not weekend stoppages as jacking was on-going through the weekends. Such stoppages in work could have been due to major maintenance works, possibly from the replacement of roller cutters. During such stoppages, lubricant injected into the overcut around the pipe peripheral could be lost through fissures in the surrounding geology as shown schematically in Figure 9.

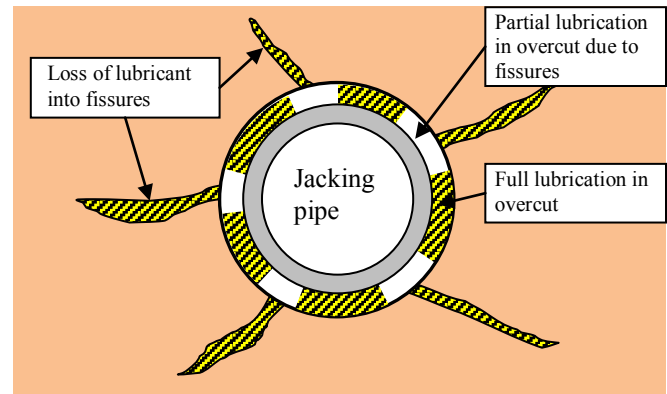


Figure 9 Schematic idealisation showing loss of lubrication through fissures in a rock mass

The pressure for lubricant injection would also be relieved, mitigating any buoyancy effect that may have reduced the frictional forces. The effect of loss of buoyancy supporting the weight of the pipe could result in higher pipe-soil contact area. There was an observed change of the lubricating regime in Section 2 of the drive, particularly upon the advent of the third major stoppage. This increase in the volume of lubricant (from 170 litres to 800 litres per metre run) was in reaction to the increased rate of frictional loads upon transition from Section 1 to Section 2 of the drive. However, this intensified effort had only been initiated after several spikes in the jacking load had been accrued.

4. CONCLUSIONS

This paper has highlighted the potential of using direct shear testing of excavation spoils to obtain residual strength values of geologically 'young' weathered rock to predict jacking forces. The main advantage of using reconstituted excavation spoils as specimens is the ability to obtain rock strength parameters which otherwise would be elusive as intact and competent rock cores ($\geq 100\text{mm}$ in length) are usually difficult to obtain in such weathered and friable conditions. One of the main factors affecting the accuracy of the back-analysis of the lower and upper bound jacking forces is the 'dynamic' or fluctuation nature of the coefficients of friction as the pipes penetrate into differing geology within a similar drive and also due to its construction activity (whether jacking is on-going or stopped for maintenance). The back-analysed coefficient of friction seems to be also affected by the fact that whether the drive is fully or partially

lubricated. Hence, soil-structure interaction is indeed an important consideration in any pipe-jacking work. Jacking forces have been observed to have increased during the re-start of jacking activities after periods of stoppages as more thrust is required to overcome static frictional resistance prior to the realisation of the positive benefits of lubrication. However, it is the intention of the Authors to carry out more tests to further verify the reliability of this method for a wider variety of local rock types, especially in geologically 'young' weathered rock.

5. ACKNOWLEDGMENTS

The authors would like to thank the generosity of Hock Seng Lee Bhd and Jurutera Jasa (Sarawak) Sdn Bhd for their support during this study. The authors are also thankful to the ground staff of Shaft & Tunnel Sdn Bhd for their assistance and patience during the study of the microtunnelling drive. The work described in this paper would not have been possible without the efforts of Leong Hsiao Yun and Lionel Foo Fang Ho.

6. REFERENCES

- [1] Norris, P. and G.W.E. Milligan, *Field instrumentation for monitoring the performance of jacked concrete pipes*, in *3rd International Symposium on Field Measurements in Geomechanics*, G. Sørum, Editor 1991, A.A. Balkema: Oslo, Norway.
- [2] Milligan, G.W.E. and M.A. Marshall. *The functions and effects of lubrication in pipe jacking*. in *World Tunnel Congress*. 1998. Sao Paulo, Brazil: Balkema.
- [3] Milligan, G.W.E. and M.A. Marshall. *The influence of lubrication on jacking loads from six monitored pipe jacks*. in *16th International ISTT No-Dig 1998*. 1998. Lausanne, Switzerland: ISTT.
- [4] Pellet-Beaucour, A.L. and R. Kastner, *Experimental and analytical study of friction forces during microtunneling operations*. Tunnelling and Underground Space Technology, 2002. **17**(1): p. 83-97.
- [5] Staheli, K., *Jacking force prediction an interface friction approach based on pipe surface roughness*, in *School of Civil and Environmental Engineering 2006*, Georgia Institute of Technology: Georgia. p. 385.
- [6] Shou, K., J. Yen, and M. Liu, *On the frictional property of lubricants and its impact on jacking force and soil-pipe interaction of pipe-jacking*. Tunnelling and Underground Space Technology, 2010. **25**(4): p. 469-477.
- [7] The Australian Standards, *AS1289.6.2.2-1998 Soil strength and consolidation tests - Determination of the shear strength of a soil - Direct shear test using a shear box*, 1998, Standards Australia: Australia.
- [8] Bagherzadeh-Khalkhali, A. and A.A. Mirghasemi, *Numerical and experimental direct shear tests for coarse-grained soils*. Particuology, 2009. **7**(1): p. 83-91.
- [9] Stein, D., K. Möllers, and R. Bielecki, *Microtunnelling : Installation and Renewal of Nonman-Size Supply and Sewage Lines by the Trenchless Construction Method*. 1989, Berlin, Germany: Ernst.
- [10] Tan, D.N.K., *Geology of the Kuching Area, West Sarawak, Malaysia*, 1993, Geological Survey of Malaysia: Kuching.

Jan Jaremski

Rzeszow University of Technology, Rzeszów, Poland, jjaremsk@prz.edu.pl

KEYWORDS: flysch eluvium, reservoir, rock eluvium, mud avalanches, swelling

ABSTRACT: The paper presents possibilities of construction of multi-functional reservoir in mountain regions, especially those with soft rocks. Construction of relatively small reservoir instead of big ones and taking the area configuration into account allows to eliminate expensive embankments and insists to construction of cofferdams. The cofferdam can be formed of the occurring rock eluvium. Such idea was analyzed for the south of Poland. At present we can observe the climate changes accompanied by increase of the weather dynamics and unusual intensity of extreme phenomena. Mineralogical composition of rocks or their eluvia occurring in the considered area is usually not taken into account while forecasting of such phenomena. The proposed tests on determination of the eluvium areas especially susceptible to formation of mud avalanches in the mountains sites.

1. INTRODUCTION

The climate variation has been observed recently. They are accompanied by increase of the weather dynamics and unusual intensity of extreme phenomena. Precipitations are very intense and they are accompanied by landslides and mud avalanches, or long-lasting droughts. A lack of suitable retention causes a fast flow of discharge water to the seas. Mineralogical composition of rocks or their eluvia occurring in the considered area is usually not taken into account while forecasting of such phenomena. Colloidal activity, a state of colloidal bonding and crystallization strongly influence formation of avalanches, strength of the mixtures and reversibility of their reactions with participation of clay minerals.

Polish water resources are rather poor in comparison with other European countries. 1600 m³ falls to one person in a typical year; in a dry year it is below 1450 m³ [1]. In Spain such number is twice higher, and for all Europe this number equals to 4500 m³. Retention ability of Polish reservoirs equals to 6% of the mean flow of the surface water per year. Moreover, it does not prevent against periodical excess of deficit of water. Our water resources vary at different seasons and their distribution is not uniform. The Podkarpacie region, especially its mountain part, belongs to the regions where the water resources are the most poor. Only 20% of all the underground water of that region occur in its mountain part. In this region there is a lack of rich aquiferous layers because of an unique

geological structure, i.e. the laminar Carpathian flysch. It is water-permeable (there are no faults and dislocations), so in this region there are very good conditions for small flood pools. Such conditions allow for high surface flows which can be significantly slowed down owing to renaturization of the flows and so-called "small retention". The program of "small retention" gives the best results in mountain and forest areas, for example the Bieszczady mountains in the south of Poland. "Small retention" satisfies most requirements connected with ecological methods of water economics, and if it is correctly realized, it can help in improvement of natural values of ecosystems [2]. The Podkarpacie region belongs to the mountains range of the Carpathian arc and the fall before the Carpathians. The region is very diversified considering its configurations and geological structure. Such diversification influences hydrography, climate, soils, flora and fauna etc.

Intense precipitations in the summer are very important for the idea of construction of flood pools. The mountain part of the region belongs to the Carpathian climate with thermal conditions varying depending on the site height.

Geological and hydrogeological conditions of the region in its mountain part are really suitable for the flood pools. The eastern Carpathians are built of flysch formations, weathered in their top layer. The eluvia usually occur as dust or dust clays. The external part of the massif contains flysch formations (Fig. 1), i.e. sandstone, mudstone, menillites, etc.[14].

Fig. 1. Outcrops of the Carpathian Flysch

The Bieszczady Mountains are the area where there are very good conditions for the considered reservoirs because of favourable tectonics and its effects. It appears from the tests realized in the Podkarpacie region it appears that the eluvia occurring under the surface are of a high volume, and from mineralogical tests it results that they are suitable for location of reservoirs because they guarantee the maximum tightness. Thus, construction of small earth dams or rock-fill dams probably will not require application of additional sealing elements. The eluvium of suitable parameters will play that role. The eluvia in the layers located just under the surface usually occur as dust or dust clays.

Generally speaking, in the flysch formations of the Podkarpacie region there are no advanced aquiferous layers. The minimum surface permeability is also an effect of mineralogical structure of the surface layers. Under moderate swelling, illite minerals seal the site surface and increase intensity of the surface flow. In a consequence, even relatively low precipitations cause a flood situation at many water-courses and rivers in the Podkarpacie region. Thus, construction of multi-functional pools of small retention on the limited areas protects the water-courses of the Podkarpacie region against the results of floods. The proposed idea increases pure water resources, influences beauty of the region. It also changes geotechnical conditions and improves stabilization of slopes, protects against landslides.

The proposed idea seems to be reasonable because in 1995 in Japan 360 such reservoirs were built in the mountains, and the country was protected against floods. At the same time, suitable amount of water was delivered for rice growing (Japan is an important exporter of rice at present).

Let us note that the considered pools are located in the mountains, and the cofferdams baffling the valleys are made of soil concrete because of a large amount of montmorillonite in the rock eluvia. In the past in Andalusia the Moor engineers built the reservoirs used for the purposes of agriculture, and this area of Spain developed very quickly. Let us remember that the proposed pools should be supplied by water flowing from the eastern Carpathians being an enclave of unique environmental conditions.

Water-bearing character of the flysch rocks is connected with their slots – it results from their low porosity,

i.e. from 0.02 to 0.1. The flow in the interporous spaces is difficult because of their small dimensions; moreover they are filled with the weathered illite fraction, susceptible to shrinkage and swelling, decreasing water absorbability of the flysch, sometimes to zero. Water absorbability gets worse as the depth of layer deposits rises. Resources of underground water is very low, there are no water-bearing layers. Water is stopped and occurs only in the cracked rocks. Under such conditions, precipitation waters can easily flow to the water-courses, and next to the fall before the Carpathians where they supply the reservoir of underground waters. From that reservoir they flow through the underground gutters to the basin of the Dniestr River. Minimal surface permeability is also an effect of mineralogical structure of surface layers, i.e. illite and smectite minerals. Because of swelling, these minerals seal the surface and increase intensity of the surface run-off. In a consequence, even relatively small amount of precipitations cause floods at many rivers and water-courses of the Podkarpacie region.

Climate variation causes serious rain-storms which are very dangerous for inhabitants of the Podkarpacie region. Such storm took place on the 26th July, 2005 near locality Zagórz. Some villages were flooded in a very short time. The mentioned above example of Japan also proves that the proposed solution seems to be reasonable.

2. THE PREDICTED KINDS OF FLOOD POOLS

Rational management of water resources in the Podkarpacie region requires minimization of their variation at time and space (periods of drought and flood). Thus, retention must be developed in the area of the basin. Construction of small multi-functional pools is recommended. In management of each pool one function here is usually dominating (flood protection, touristic, ecological or energy function and so on), and other tasks are assigned as that main function. In practice, there are pools satisfying two or three main economic tasks at the same time depending on local needs.

There is no one official classification of flood pools. So-called “small retention” includes all the microreservoirs, and small pools positively influencing the environment [10]. Small pools are usually of total volume to 0.1 of million m³ and the maximum swell height 5 m. They are built one by one, or in a cascade system [12]. All the cascade is usually used for energetic purposes. The systems of small retention pools are proposed instead of one big reservoir. In Bieszczady mountains there are many river valleys (Fig.2) which are good places for the proposed flood



pools. In the past many people lived in those valleys, at present they uninhabited.

According to the proposed concept, reservoirs – depending on their location – can be flood pools, equalizing tanks, they can also be auxiliary reservoirs near big flood pools [3]. Some reservoirs should play the role of flow reservoirs formed as a result of partition of water-courses. Dry reservoirs are also provided as anti-flood protection. They will be accumulate the flowing eluvium or organic products.



Fig. 2. An exemplary site for a reservoir in the Bieszczady mountains

In the considered region, the intense precipitations, of big slopes of the ground and the flysch substrate cause intense run-off of the weathered flysch layer, sometimes being like an avalanche. The rubble occurring in the reservoirs and flumes of water-courses causes that they become more and more shallow. Thus, construction of dry reservoirs is. In the considered area there are unusual conditions of flysch weathering, especially biological weathering. Such conditions are a result of rich afforestation. Generally speaking, in the considered region plan dry reservoirs it will be possible to plan dry reservoirs where will be accumulate the flowing weathered eluvia or organic products. Such places will be the programmed enclave of the intense development of flora and fauna and, we can also expect favourable humus processes.

3. APPLICATION OF FLYSCH ELUVIA FOR CONSTRUCTION OF COFFERDAMS

From the investigations on landslides in the Podkarpacie area it appears that the eluvia existing under the site surface are of a large thickness. From mineralogical tests it results that such eluvia are very good for location of reservoirs because they provide the maximum tightness. Thus, construction of small earth dams will not require additional sealing elements. This role should be played by a layer of eluvium of suitable parameters.

Experience obtained while investigations on marl eluvia as well as the elaborated test methods were applied for investigations of the Carpathian flysch and dust soils occurring in the river terraces, grounds of loess massif, illite clays and baidelite clays [4,5]. These grounds are susceptible to moisture changes accompanied by shrinkage and swelling as well as petrification. This property is strictly connected with presence of illite in mineralogical composition of the considered media. Even a very small amount of that mineral influences joints of the basic minerals.

The samples prepared of eluvium shales were tested and next the obtained results were compared with the results obtained for the samples from river valleys treated as the accumulated sediment of the flysch eluvium [5]. The test were carried out in order to estimate usability of flysch eluvia for construction of cofferdams by identification of clayey minerals. Differentiation of these minerals is important because the contents of smectite groups exerts an unfavourable influence on setting and hardening of ground concrete [11]. As for the considered ground media, their basic geotechnical parameters were tested and special attention was paid to swelling tests allowing to distinguish clayey minerals. Before the swelling tests, physical, chemical and strength tests as well as mineralogical tests of the considered media were carried out [4, 6]. Recognition of the grounds was based on chemical and mineralogical compositions by means of fluorescence, X-ray diffractometry and scanning microscopy. Moreover, derivatographic analysis was realized. Recognition of microstructure of the clays with so-called hidden swelling parameter were carried out by means of scanning microscopy. The mentioned tests of chemical composition (Fig.3) show the presence of potassium which occurs only in illite. It was proved by tests realized by means of the scanning electron microscope (SEM).

The tests of flysch swelling, swelling clay or the media with so-called hidden swelling parameter used the method described previously [8]. This

method allows for cheap tests of flysch eluvia and estimation of their usability. Identification of illite in the flysch eluvium allows to qualify it as a material for construction of cofferdams because of moderate shrinkage and swelling as well as favourable petrification and sealing properties. Moreover, the proposed tests could help in selection of places for reservoir location into taking a proper tightness of the ground account.

Presence of illite being an aluminosilicate responsible for eluvium petrification allows for application of flysch chips and flysch eluvia for construction of earth cofferdams according to the proposed construction of multi-functional pools in the Bieszczady mountains [3]. In Japan, the flood pools were located in the mountains and the cofferdams in the valleys

were the ground-concrete is made. The eluvia occurring in Japan contain montmorillonites, so formation of cofferdams is difficult, because it is necessary to add much cement to the eluvia. It is also necessary to take care of ground-concrete because of formation of scratches caused by shrinkage of montmorillonite [13].

Construction of cofferdams using flysch chips and flysch eluvia is considered for each reservoir in Bieszczady, depending on its geological structure. Of course, a suitable amount of clayey minerals for petrification and sealing is necessary. If there are not enough illite minerals in the eluvium, we must consider a solution using geotextiles and sealing foils for cofferdams, and materials offered by such firms as Tensar International Corporation, Ten Cate Geosynthetics and Geobrugg.

4. THE PROPOSED TESTS FOR DETERMINATION OF THE ELUVIUM AREAS ESPECIALLY SUSCEPTIBLE TO FORMATION OF MUD AVALANCHES IN THE MOUNTAINS SITES

Experience obtained in the while works on marl eluvia [2,4,7], and the elaborated test methods were used during tests of Carpathian flysch and dust soils occurring in river terraces generated as a result of the eluvia accumulation [5,11].

The samples prepared from the shale eluvia were tested and compared with the samples from the river valleys, treated as the accumulated sediment of the flysch eluvium. The basic geotechnical parameters of the considered ground media were tested. Special attention was paid to swelling tests allowing to identify clayey minerals. At present, the author is engaged in works connected with the causes of mud avalanches formation. In such cases, hydraulic conditions and influence of

mineralogical composition should be taken into account. Tests of susceptibility of the soft rocks for formation of the mud avalanches could be limited to drawing of eluvium samples occurring at the slope. The samples should be subjected to swelling tests by means of the method given in the some previous papers [4,8,11]. This simple method allows to identify clayey minerals responsible for swelling, occurring in the rocks. While tests we use the presence of endothermic maxima – the temperature points at which the heated sample loses contents of bound water. The author found that minerals from the groups of montmorillonite and illite (causing swelling) lost that water at the temperature up to 200 degrees, and kaolinite – at 600 degree. Thus, the comminuted eluvium sample prepared to the standard swelling test and free from water, subjected to the swelling test manifests swelling up to tens %. Under such conditions, the kaolinite sample swells up to some %. Let us remember that montmorillonites soak to 700%, while kaolinite soaks to 90%.

4.1 THE PROPOSED METHOD OF EXAMINATION OF CLAY MINERALS

Application of the method of swelling ability test, given in the author's earlier works [2,4,8] was proposed as method of determining the content of illite and smectite minerals. It has been proved so far that it is just these minerals that are responsible for moisture changes, extreme strength parameters and processes of petrification and maximum moisturizing.

Tests were carried out on the material taken from the deposit of different breakups, and samples were grouped in accordance with the diameter of sieve meshes. With the method of successive trials, it has been found that the most stable and real results are obtained by conducting the tests in the following way [11]:

1. the material undergoes a preliminary air-drying in the case of water content so that it can be sifted through the of $\varnothing=0.76$ mm
2. the material thus prepared is subjected to moisture content near to the plasticity limit (during the trial of roller bursts at the first or second instant) and is subjected to working (just like a typical "dough")
3. forming the material into the "cake" – like shape of 10 mm in height
4. then, samples with the diameter $\varnothing=50$ mm and 65 mm and the

- height of 10 mm and 20 mm are cut by means of a ring
5. the samples thus prepared are weighed and dried in a drier at a temperature of 200 C for the period from two hours until reaching constant weight
6. after drying and cooling process the samples are weighed to determine their water content
7. the samples are subjected for the examination of swelling minerals in the apparatus testing unbounded swelling
8. after swelling has been defined the final moisture is determined.

The considered test informs us about the amounts and kinds of swelling minerals in the point of sampling. Thus, we get also the data concerning ability of the tested rock medium to water stoppage and moisture degree, as well as the maximum moisture occurring under natural conditions.

Fig.3.Examples
of rocks samples after the investigation

After swelling, the sample moisture is the maximum moisture, under which we get the worst numerical values of the strength parameters. Under such conditions, landslides are possible. In our analysis, soft rocks are treated as mixtures containing much clayey minerals. In the case of occurrence of greater contents of montmorillonite, greater amount of moisture is present and it is accompanied by fluidization and formation of mud avalanches. Similarly, content of the swelling minerals in higher parts of mountains causes their collecting in the rock slots. Then, possibility of landslides and rock falls increases.

The swelling investigation were preceded by physical, chemical and strength tests of the considered media. Recognition of such soils were based on tests of chemical and mineralogical composition by means of fluorescence and X-ray diffraction method . Moreover, derivatographic analyses were performed. Tests of clay structure with so-called swelling parameter were realized by means of scanning microscopy(SEM)



utilization of SEM, derivatogram method, fluorescence, diffraction method,.

Simple analyses and tests according to the discussed swelling tests allow to identify sites which can be easily subjected to mud avalanches and rock falls. Such information are very useful for the site management.

6. CONCLUSIONS

- 6.1. Suitable geological (soft rocks) structure allows for cheap construction of reservoirs. Dislocations and fault fissures filled with weathering materials because of their mineralogical structure, i.e. swelling minerals cause self-sealing of the bottom. A lack of water-bearing layers eliminates uncontrolled outlet of water to the ground.
- 6.2. Distinct improvement of protection against floods is an advantage of the proposed solution (see the mentioned solution in Japan). At present, intense precipitations are transported to water-courses and rivers because they cannot percolate to the ground (it is favourable for reservoir structure).
- 6.3. Water supply for inhabitants of a given region and water collecting in reservoirs can be very important in the future. Large amount of water of high quality should be a valuable good. Water resources could influence future development of many regions.
- 6.4. Construction of the considered reservoirs is rather cheap because it is possible to introduce unified earth cofferdams using ground-concrete as a construction material.
- 6.5. Introduction of the considered reservoirs could help in generation of new places of employment (construction and service, tourists' service)
- 6.6. Some reservoirs could be used in energetics.

7. REFERENS

- [1] Bogacz – Rygas M : (2007) Aspekty ekologiczne stosowania nowych rozwiązań odprowadzania wód opadowych i ich zagospodarowanie(in polish),. Wavin Metalplast-Buk.Kielce.
- [2] Jaremski J.:(1994) Influence of physical and chemical processes occurring in eluvium of the Opole marls and their influence on the geotechnical parameters, Proceedings of the 7th International Congress IAEG, Lisboa , A.A Balkema, 859-868.
- [3] Jaremski J.:(2007) O niektórych aspektach budowy wielofunkcyjnych zbiorników retencyjnych w części górzystej województwa podkarpackiego. Cywilizacja i żywioły, (in polish), seria: Monografie Instytutu Meteorologii i Gospodarki Wodnej, Warszawa.
- [4] Jaremski J.:(1995) Proposal for a method determining value of the maximum swelling of soil by example of the Opole marls eluvium and illite clays. Proc. of 8th Int. Cong. on Rock Mechanics, Tokyo, A.A.Balkema.
- [5] Jaremski J.:(2004) The influence of changes of weathering water content on the formation of landslides in the Carpathian Flysch. Proc. of 9th Australia New Zealand Conference on Geomechanics, Auckland – February 2004, New Zealand Geotechnical Society Inc.
- [6] Jaremski J.:(2005), The influence of physical and chemical processes occurring in the weathered Opole marls on the geotechnical parameters, Publishing House of Rzeszów University of Technology, 2005,p. 98.
- [7] Jaremski J.(1991), Creep property of Opole marls weathering on the base of the model laboratory research and the research “ in situ” , Proceedings of the 7th International Congress on Rocks Mechanics, Aachen, A.A. Balkema, 1991, 269-273.
- [8] Jaremski J.:(1994) Proposal for method of stating the value of maximum swelling of the soil on the example of Opole marls eluvium. Proc. 3th Int. Conf. on Trop. Resid. Soils., Maseru , A.A.Balkema,
- [9] Jaremski J.:(1990) Analysis of swelling of marl eluvium of water infiltration. Proc. 6th Int. Cong. IAEG. Amsterdam, A.A. Balkema, Rotterdam .
- [10] Jaremski J.:(2010) Aspekty geotechniczne w ochronie zasobów wodnych województwa podkarpackiego. Inżynieria Morska i Geotechnika (in polish), nr. 1. Gdańsk 2010.
- [11] Jaremski J.:(2010), Influence of moisture changes on physico - chemical processes and geotechnical parameters in soft rocks , Studia Geotechnica et Mechanica, Vol. XXXII, No. 1, 2010
- [12] Mioduszewski W.:(2008) Mała retencja w lasach elementem kształtowania i ochrony zasobów wodnych. Studia i Materiały Centrum Edukacji Przyrodniczo-Leśnej R. 10. Zeszyt 2 (18) (in polish) .
- [13] WAKIZAKA Y.:(1994) Influence of montmorillonite group Bering aggregates on concrete. 7th International IAEG Congress, A.A. Balkema 1994, s. 3285-3294.
- [14] Zabuski L., Thiel K., Bober L.(1999), Landslides in Polish Carpathian Flysch, (in polish), IBWN PAN, Gdańsk, p. 172.

Estimation Method of Amount of Tsunami Disaster Wastes during the 2011 off the Pacific Coast of Tohoku Earthquake

Minoru YAMANAKA¹, Naoya TOYOTA², and Shuichi HASEGAWA³, Atsuko NONOMURA⁴

^{1,4} Associate professor, Kagawa University, Japan ² Graduate student, Kagawa University, Japan

³ Professor, Kagawa University, Japan

ABSTRACT

A huge amount of disaster wastes was accumulated along coastline areas of the Tohoku region by tsunami during the 2011 off the Pacific coast of Tohoku Earthquake. It is very important to estimate an amount of tsunami disaster wastes as for quick recover and revival of damaged areas. This paper describes a method of wastes amount estimation based on the officially announced data analyzed in GIS platform. It was found that there is a good relationship between the amount of the disaster wastes and land use, land cover and tsunami height. Therefore, it is necessary to subdivide the affected area according to land use and cover, the tsunami height and so on.

Keywords: disaster wastes, tsunami, earthquake, estimation

1. Introduction

A huge amount of disaster wastes was accumulated along coastline areas of the Tohoku region by tsunami during the 2011 off the Pacific coast of Tohoku Earthquake. The total amount of tsunami disaster wastes was estimated to be 26.7 million tons. It is 50 % of the total amount of the waste of Japan in 2009. The Tohoku earthquake caused widespread damage. Since the coastal line of Tohoku region is highly indented, it is difficult to find secure places for piling the wastes. Moreover, road is only a means of transportation of wastes to the waste disposal site. All port facilities were already damaged. This means Japan is in extremely difficult situation to dispose the disaster wastes.

Since magnitude or height of tsunami in Shikoku region due to predicted earthquakes such as the Tokai Earthquake and the Nankai Earthquake is comparable to the Tohoku Earthquake, anticipated amount of disaster wastes in Shikoku is also very high. It is very important to estimate an amount of tsunami disaster wastes for quick recover and revival of damaged areas.

This paper describes a method of wastes amount estimation based on the officially announced data analyzed in GIS platform.

2. Characteristic and amount of disaster wastes

2.1 Characteristics of the disaster wastes

The characteristics of earthquake, flood and tsunami disaster wastes are shown in Table.1. They are look alike occur suddenly and extensively. However in tsunami disaster wastes, it is necessary to secure large places for piling the wastes, since the huge amount of wastes contained large volume of debris mainly discharged by heavy machinery. Similarly, tsunami disaster wastes contain various kinds of materials, such as waste wood, metals, salt water. In case of earth and sand mixed with disaster wastes, unless the disaster wastes are not removed, the earth and sand are also dealt as disaster wastes. In order to decrease amount of the earth and sand in disaster wastes, it is aimed to utilize a technology for separating earth and

sand from the wastes. Wood waste can be recycled, but salinity, earth and sand, metals can possesses harmful effect while recycling or incineration of wood.

2.2 Amount of disaster wastes of main previous earthquake

The amount of disaster wastes and situation of damage due to earthquake is shown in Table.2, and the status in Rikuzentakata city damaged by the tsunami is shown in Fig.1 (a)-(b). The amount of disaster wastes of Great Hanshin Awaji Earthquake in 1995 was about 20 million tons^[2]. About 640 thousand houses were damaged in the earthquake and the amount of wastes was about eight times as much as an amount of wastes of Hyogo region on a year in 2006. Fortunately, most of them can be disposed in Phoenix Landfill Disposal Site near the damaged areas. The amount of disaster wastes of the Niigata Chuetsu Earthquake whose seismic centre is on the mountainous area in 2004 was about 500 thousand tons. About 120 thousand houses were damaged in the earthquake. 92 % of the disaster wastes were destruction wastes. Concrete debris (51 %) and waste wood (25 %) accounted for 76 % of the total^[2].

On the other hand, the amount of flood disaster wastes of Typhoon No.16 in 2004, which struck Takamatsu city, was 23,123 tons. It was twice as much as a month of wastes on Takamatsu city in 2003. Since the wastes contained salinity, a large amount of unusable household goods was abandoned. Therefore, it took long time to manage the disaster wastes^[3].

2.3 Unit amount of disaster wastes in published paper

Estimation of unit amount of disaster wastes also corresponds amount of past disaster wastes per household or per square kilometer.

Nakamichi estimates unit amount of the disaster wastes to be 0.571 t/km² on wooden constructions or 1.47 t/km² on RC buildings, and 1.27t/km² on steel constructions. He did this estimation from amount of the disaster wastes of Great

Hanshin Awaji Earthquake [4].

Shimaoka estimates unit amount of the disaster wastes to be 0.31 t/km² on wooden constructions or 1.09 t/km² on RC buildings, and 1.80 t/km² on steel constructions [2].

Hirayama estimates unit amount of the disaster wastes considering the extent of household's damage on flood disaster to be 12.9 tons per household on completely destroyed, 6.5 tons per household on a half destroyed, 2.5 tons per household on partially destroyed, 4.6 tons per household on inundation above floor level, 0.62 ton per household on inundation under floor level [5]. The unit of disaster wastes for estimating amount of the tsunami disaster wastes in Tohoku earthquake was 61.9 tons per

household or 113 tons per a building [6].

3. Amount of tsunami disaster wastes

The amount of disaster wastes in each municipal corporation, damaged by tsunami, are shown in Fig.2 (a) ~ (c). Fig.2 (a) illustrates the amount of disaster wastes is much in Ishinomaki and Higashimatsushima, Sendai, which are highly built-up areas. Fig.2 (b) shows the amount disaster waste per flooded areas is high in Kamaishi and Rikuzentakata where were damaged by more than 10 m of tsunami height. In Fig.2 (c), Yamamoto where flooded area is relatively small.

Table.1 Characteristic of the each disaster [1]

type	Earthquake disaster	Flood disaster	Tsunami disaster
occurrences	<ul style="list-style-type: none"> • Occur heavily and suddenly • Low earthquake-resisting capacity buildings were damaged • broken up by a crane 	<ul style="list-style-type: none"> • Occur heavily and suddenly • The lower – lying districts are damaged by the collapse of the embankment. • The proportion of household refuse is high. 	<ul style="list-style-type: none"> • Occur heavily and suddenly • It is necessary to secure large places for leaving the wastes.
Characteristics	<ul style="list-style-type: none"> • composed of household and debris of fallen houses • There are many recyclable, reusable things among the wastes. • It can be expected to separate wastes by demolition management. 	<ul style="list-style-type: none"> • household wastes by inundation above or under floor level. • It is difficult to separate on the site. • The wastes are perishable since it contains plenty of water and sand 	<ul style="list-style-type: none"> • The wastes contain various kinds of materials, such as waste wood, metals, salt water. • Salinity contained the wastes sometimes have a harmful effect while recycling or incineration.

Table.2 Amount of disaster wastes and situation of damage of main previous earthquake [2]

Name	Great Hanshin Awaji Earthquake	Niigata Chuetsu Earthquake	Noto Peninsula Earthquake	Niigataken Chuetsu-oki Earthquake
Date of occurring	Jan.17.1995	Oct.23.2004	Mar.25.2007	Jul.16.2007
Magnitude	7.3	6.8	6.9	6.8
Damaged areas	Kobe, Nishinomiya, Awaji-shima	Nagaoka, Yamakoshi, Ojiya	Wajima, Nanao, Siga	Kashiwazaki, Kariwa
Situation of damage	House: Completely destroyed 104,906 houses Half destroyed 144,274 houses Partially destroyed 390,506 houses	House: Completely destroyed 3,157 houses Half destroyed 13,808 houses Partially destroyed 103,854 houses	House: Completely destroyed 638 houses Half destroyed 1,563 houses Partially destroyed 13,553 houses	House: Completely destroyed 1,224 houses Half destroyed 5,241 houses Partially destroyed 34,277 houses
Amount of disaster wastes	About 20 million tons	About 0.49 million tons	About 0.43 million tons	About 0.36 million tons
Regions wastes in 2006	Hyogo Pref.: About 0.25 million tons	Niigata Pref.: About 1.12 million tons	Ishikawa Pref.: About 0.5 million tons	Niigata Pref.: About 1.12 million tons

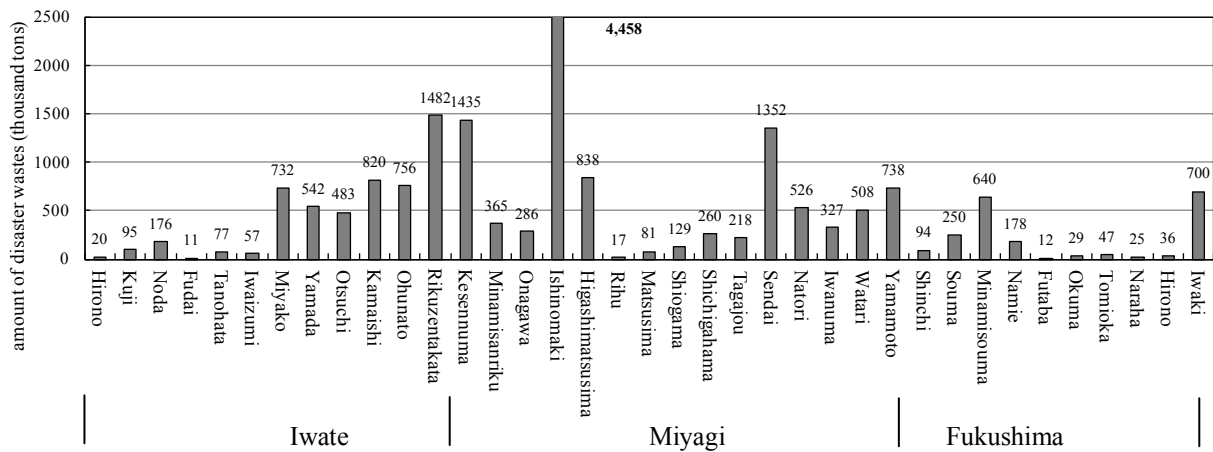


(a) photo on April 6, 2012 .

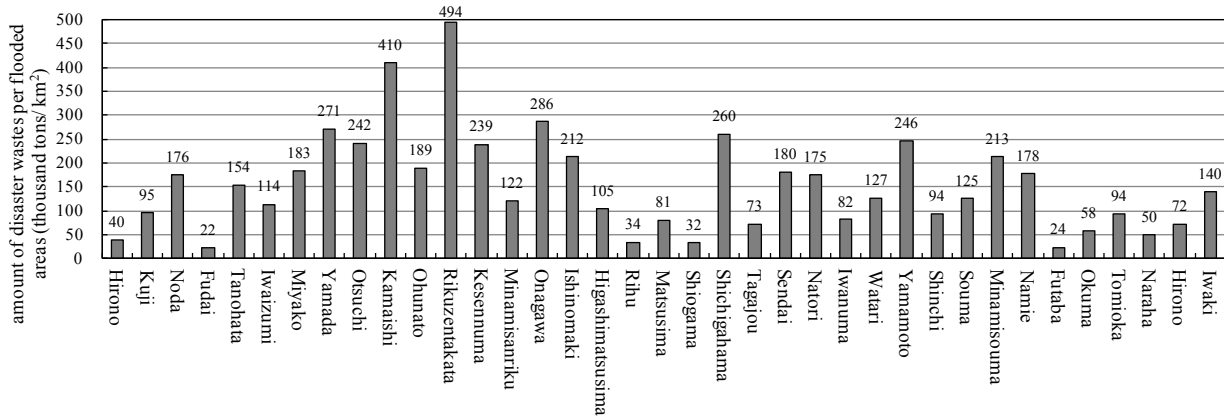


(b) photo on June 5, 2012.

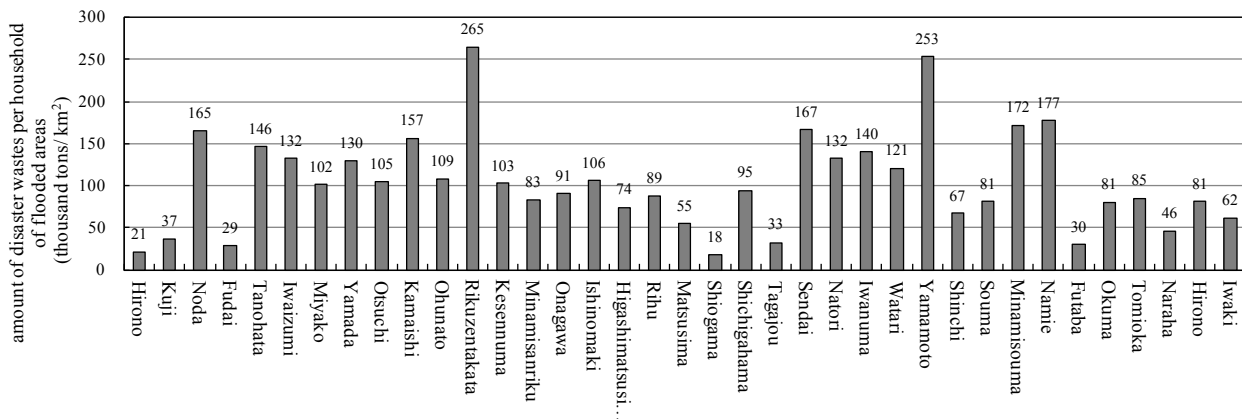
Fig.1 Disaster wastes in Rikuzentakata City



(a) Amount of disaster wastes

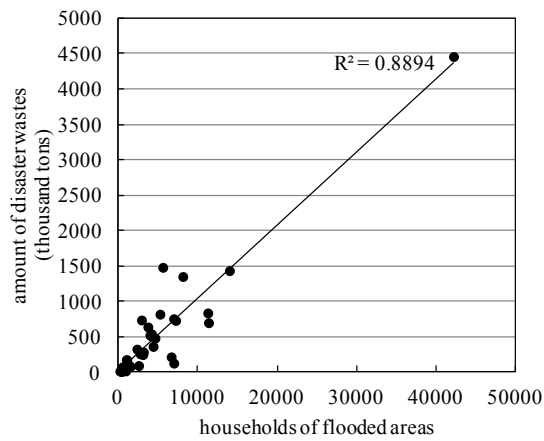


(b) Amount of disaster wastes per flooded areas

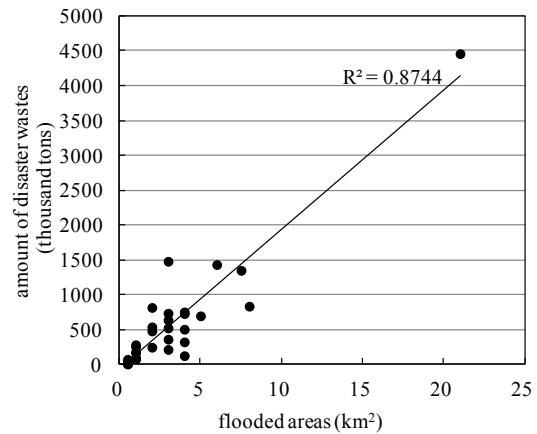


(c) Amount of disaster wastes per household of flooded areas

Fig.2 Difference of amount of disaster wastes by damaged municipal corporation in the Tohoku region



(a) Flooded area



(b) Number of household

Fig.3 Relationship between amount of disaster and each disaster data in Tohoku earth quake

Relationship between amount of disaster and each disaster data are shown in Fig.3 (a) and (b). Fig.3 (a) shows that relationship between the flooded area by the tsunami and the amount of the disaster wastes has a positive correlation. In addition, since it seems that the correlation is separated by the magnitude of the flood area, it is needed to separate the urban and agricultural land. And the correlation between the number of households in flooded area and the amount of tsunami disaster wastes was found to be high as shown in Fig.3 (b). From this, unit amount of disaster wastes as per household is estimated it 104 ton.

4. Height of tsunami and unit amount of disaster wastes

It is considered the amount of disaster wastes in flooded areas deals with the height of tsunami. The relationship between the height of tsunami in each municipal corporation and the amount of disaster wastes per flooded areas is shown in Fig.4. There are two lines on the relationship because there is probably the difference in proportion of residential area in flooded area. In this case, further consideration is needed.

5. Conclusion

In conclusion, it is found that there is a correlation between unit amount of tsunami disaster wastes and each disaster data. It is now possible to contribute in Tonankai or Nankai earthquake related possible disaster wastes. The following are main conclusion of this study;

- 1) We can estimate the necessary action for disaster waste disposal or recommend suitable places for deposit the waste.
- 2) We can estimate the scale of disposal site and the number of roads or harbors needed.
- 3) Now estimation of amount of recyclable disaster wastes is possible. Similarly, service plan for rebuilding and recovery is also possible.

Reference

- [1]YAMANAKA Minoru, HATIMURA Tomoaki, Problems about Disposal of Disaster Waste, Chishitsu to chousa, pp.34-39, 2011
- [2]SHIMAOKA Takayuki, "Abnormal Weather and Disaster Waste accompanied by Global Warming" Disaster Waste, Japan Society of Material Cycles and

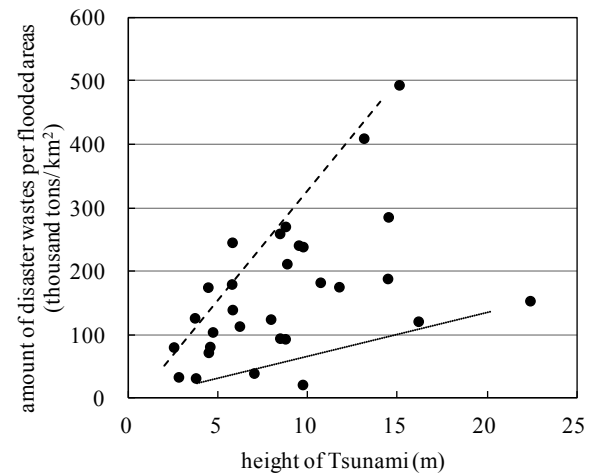


Fig.4 Relationship between the height of tsunami and the amount of disaster wastes per flooded areas

Waste Management Series, Chuohoki, 2009, pp.3-20.

- [3]Waste Management and Recycling Department: Measure Guideline of flood waste, Ministry of the Environment, 2005.9.1
- [4]NAKAMICHI Tamehiro, "Waste Disposal Act of Great Hanshin Awaji Earthquake" Disaster Waste, Japan Society of Material Cycles and Waste Management Series Vol.3, Chuohoki, 2009, pp.23-46.
- [5]HIRAYAMA Nagahisa, Estimation Procedure for Quantity of Disaster Waste from the Viewpoint of Emergency Responses of Public Authorities at Flood Disaster, J Environment system, Vpl.33, pp.29-36, 2005
- [6]National Institute for Environmental Studies, About Unit Amount of disaster waste Vol.1, Disaster Response Network 2011.6.28
- [7]Statistics Bureau, Statistical Data Pertaining to the Great East Japan Earthquake, Ministry of Internal Affairs and Communications, 2011.11
- [8]HARAGUCHI Tsuyoshi and IWAMATSU Akira, Detailed Maps of the Impacts of the 2011 Japan Tsunami Vol.1: Aomori, Iwate and Miyagi prefectures. Japan: Kokon-Shoin, 2011.
- [9]HARAGUCHI Tsuyoshi and IWAMATSU Akira, Detailed Maps of the Impacts of the 2011 Japan Tsunami Vol.2: Fukushima, Ibaraki and Chiba prefectures. Japan: Kokon-Shoin, 2011.

Assessment of Runoff in the High Humid Foot-hill Areas of Arunachal Himalayas Using Thornthwaite Equation

Md. Eahya Al Huda and Surendra Singh
Department of Geography, North-Eastern Hill University, Shillong-793022, India

ABSTRACT: Present paper examines daily runoff trend in Dikrong river catchment which is located in the lower foot-hills of Arunachal Himalayas. The river catchment is characterized by the monsoon dominated hydrologic regime. For the purpose, daily statistics of temperature, rainfall and discharge were collected from the various sources of state Government of Assam, Guwahati and Government of Arunachal Pradesh, Itanagar and used for testing the validity of Thornthwaite-Mather [T-M] method considering Dikrong river catchment of high humid conditions. It is found that this method does not give the significant result for the correct assessment of daily Potential Evapotranspiration [PET] as well as daily runoff [RO]. The fluctuation in predicted RO is found more than the observed one with it's over estimation during high rainfall intensity and under estimation in the period of low rainfall regime.

Keywords: Runoff, Potential Evapotranspiration, Thornthwaite-Mather method, Arunachal Himalayas, discharge rate

1. INTRODUCTION

There are numerous studies on the assessment of runoff in a river catchment using universally accepted Thornthwaite equation for the quick and correct prediction of runoff [1], [2], because this method is implicitly based on water balance equation and simple to use with universally available statistics of two hydro-meteorological parameters, namely, precipitation and temperature.

In India especially in the most-humid areas where 'saturation excess' processes of runoff generation are more prevalent rather than 'infiltration' processes in the monsoon dominated hydrologic regime [3], there is a need of testing the validity of Thornthwaite-Mather [T-M] procedure to assess the runoff in such high rainfall conditions. There are other methods than T-M procedure used for the assessment of reference ET not only in Indian conditions but across the world. In this regard, Indian references are important to compare the suitability of these methods. For example, Mishra, *et al.* [4] used T-M method for tropical regions of the country. Meshram, *et al.* [5] used other methods and found suitability of FAO Penman-Monteith method, while Lenka, *et al.* [6] tested the validity of different methods like Blaney-Criddle [7], Hamon method [8], Hargreaves and Samani [9], Papadakis [10], FAO Penman-Monteith [11] that have different bases of PET calculation for the prediction of reference ET. It is argued and found that T-M procedure of the assessment of PET is simpler than the other methods because it is water balance based equation that is more appropriate to analyze the hydrologic cycle while the other methods are based on atmospheric energy parameters. Such other methods may be useful for the study of meteorological phenomena rather than hydrological regime of a river catchment.

For the purpose, present paper examines the daily runoff trend and its associated factors and also evaluates the significance of the application of T-M procedure taking into account Dikrong river catchment of about 1,556 sq km area of

which more that 80% is under the hill topography with an average annual rainfall of 3,294mm.

1.1 Study Area

Dikrong river catchment is located in the foot-hills of Arunachal Himalayas between 26°55' to 27°22'N latitudes and 93°13'E to 94°0'E longitudes with its transitional characteristics of its location as it falls under Inter Tropical Convergence Zone [ITCZ] where climate is monsoonal in this part of Asian region [Fig.-1]. Being its location in the loop of Eastern Himalayas, it is more humid and has different hydrological characteristics than the other parts of North-East Region of the Country. The length of the main river is recorded 145 km with an average slope of 5-15% with the perimeter of 264 km. Topographically, hill slopes are steep covering a area of about 61.54% with its narrow flat valleys located in the upper parts of the river catchment. Such topography helps in accelerating the saturation processes and fast flow while the lower part is gentle plain accommodating about a quarter part of the catchment [27.01%] with sediment deposition [Fig.-2].

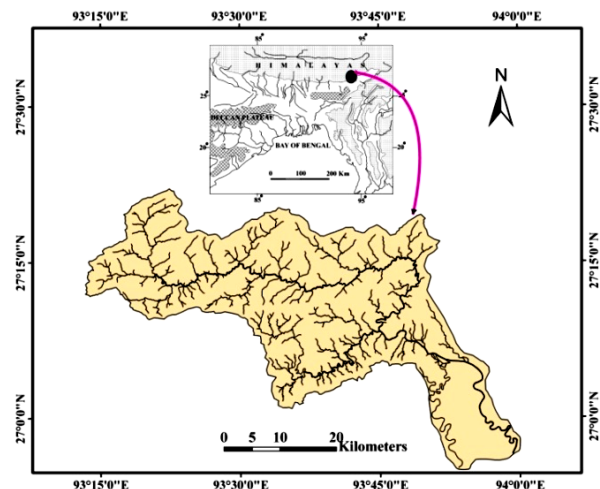
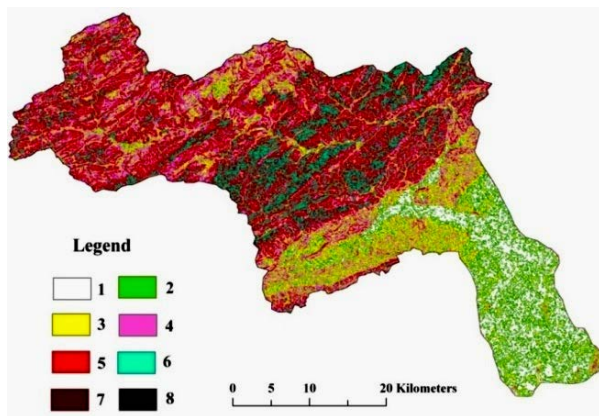


Fig.-1: Location of the Dikrong river catchment



Abbreviations: Slope in percent; 1= Very Gentle (2- 4), 2= Gentle (4-10), 3= Moderate (10-20), 4= Moderately Steep (20-35), 5= Steep (35-60), 6= Very Steep (60-100), 7= Most Steep (100-175), 8= Extremely Steep (above 175).

Fig-2: Slope Variations in the Dikrong River Catchment

Land use/ land cover pattern of Dikrong river catchment is dominated by forest [75% areas are under dense and open forests] in the upper parts and agricultural and abandoned land [12% of total area] in the lower parts of the catchment. In such land surface conditions, the runoff has peculiar trend to develop erratic floods in the lower parts of river catchment. Soils are fine loamy and coarse silty which have high fraction of sand helping in retaining more water to regulate runoff. As a result, runoff has also been recorded in the dry weather of winter seasons in spite of less rainfall and moderate PET conditions [Fig.-3].

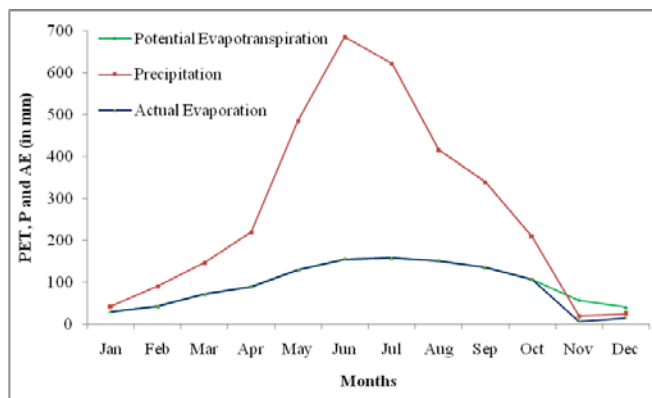


Fig-3: Normal water balance for Dikrong river catchment

2. METHODS AND MATERIALS

Of course, there are various methods of assessing the reference evapotranspiration $[ET_0]$ mainly classical method forwarded by Blaney-Criddle establishing relation of day time duration with temperature, Hamon method that is based on water vapor density in the environment, Hargreaves and Samani on radiation balance and temperature variation, and Papadakis method which is saturation deficit based [12], [13], [14]. Such methods are largely dependent on field observations used for different environmental conditions. The PET calculation by T-M procedure which is first introduced by Thornthwaite [15] and, later on, Thornthwaite and Mather

[16] with its notebook procedure has been used by many geographers [17], meteorologists and climatologists [18], and found its suitability especially for the monsoon based hydrologic regime. In this method, temperature- based heat index, i.e., $i = [T^{0c}/5]^{1.514}$ with a location specific correction factor of unadjusted PET is used for the assessment of soil moisture and runoff variability over time. In order to compare daily runoff with other parameters of water balance equation $[P = RO + PET + \Delta ST]$, where RO = Runoff, P = Precipitation, PET = Potential Evapotranspiration and ΔST = Changes in soil moisture], the T-M procedure is used. In order to make data standard, daily statistics of temperature and rainfall for three consecutive years [2004-2006], its average figures were used for Itanagar station [that is centrally located in the study area]. The concerned statistics were collected from the Rural Works Department, Government of Arunachal Pradesh, Itanagar. While daily discharge statistics of the same period of time were collected from the Water Resource Department, Government of Assam, Guwahati for Sisapather gauge station [that is at the mouth of river catchment]. Calculations of daily soil moisture availability and runoff were made to set the water holding capacity of 200 mm as specified by NBSS & LUP, Jorhat [19] with adopting standard procedure of water retention capacity analysis.

3. RESULTS AND DISCUSSION

Of course, rainfall-runoff relationship always becomes positive with its strong degree though with Curve Number $[CN]$ method was adopted by USDA [20] to evaluate the effect of land cover/land use and soil types on runoff. Similarly, this relationship is significantly strong $[r = 0.996]$ with its regression gradient of slightly lesser than unity $[1:1]$ relationship shows $CN = 100$ in the situation that there is no effect of land use and soil on runoff generation in the river catchment] as $b = 0.925$ [Fig.-4]. The rainfall-runoff ratio is therefore calculated 0.5624 for Dikrong river catchment. It means 56.24 % rainfall becomes runoff in this catchment and shows the effect of surface condition [slope, soil and land use] on runoff processes. Runoff regression equation shows interestingly that daily rainfall below 1.24 mm does not produce any runoff in this area as $[a = -1.242]$ that is indicative of the origin of runoff. Such runoff production level in the river catchment clearly shows that there is production of runoff during winter season varying from 4.80mm per day in November to 4.24mm in January [Fig.-5]. Runoff of about 4.47mm daily was observed in these days due to sub-surface flow, while its amount is influenced by soil and land use factors. Concentration period of two days to reach the runoff at mouth is also factor which shifts the runoff trend.

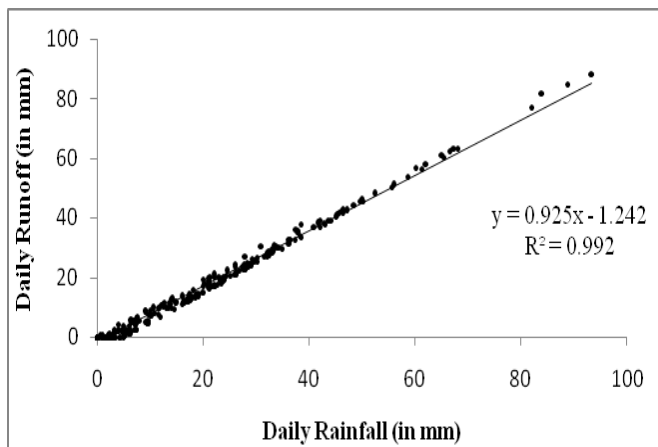


Fig.-4: The relationship between daily rainfall and daily RO

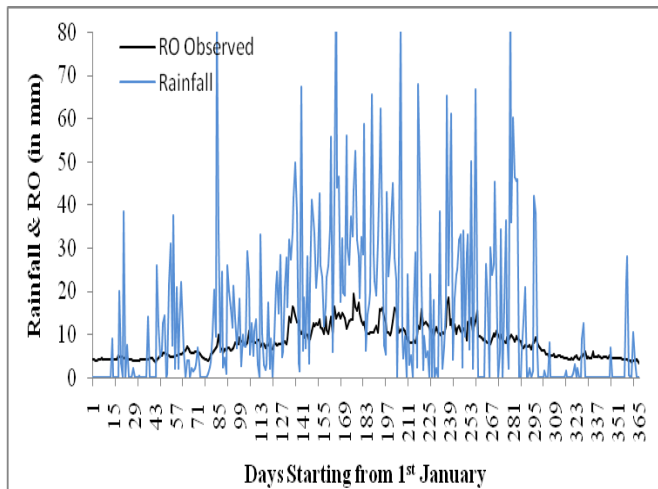


Fig.-5: Daily trends rainfall and observed RO

Rainfall does not correspond much to PET because PET is more associated with temperature variation. The relationship between them is too weak [$r=0.475$] to draw some conclusions. However, the degree of fluctuation of rainfall is observed much higher [CV=124.78%] than PET [CV=47.9 %] [Table-1].

Table-1: Daily Mean, Standard Deviation and Coefficient of Variation of Hydrologic Parameters

Parameters	Daily Mean	Standard Deviation	Coefficient of Variation (%)
Mean daily Temperature ($T^0 C$)	22.57	4.19	18.58
Rainfall (mm)	14.44	18.02	124.78
Heat Index (unit less)	9.92	2.72	27.38
PET (mm)	3.12	1.49	47.96
AE (mm)	2.33	1.98	84.85
Runoff (mm)	8.12	16.75	138.1
Runoff Ratio (%)	56.24	-	-

In the event of increasing rainfall-intensity with wet antecedent moisture conditions, the rainfall-runoff ratio becomes higher that produces more discharge in the month of late June to August. There are fast changes in soil moisture conditions during the dry winter season when rainfall is occasional that infiltrates its total amount and fluctuates soil moisture availability. The summer does not have much change in antecedent soil moisture conditions. They are fully saturated and generate more surface and subsurface runoff.

A total runoff is predicted 4,426mm annually with its rainfall-runoff ratio of .8398 that deviates 27.74 % from observed runoff. Comparing observed with predicted runoff over time, it is obvious to highlight that at the time of high rainfall intensity during the wet monsoon season, T-M Procedure made over estimation of runoff trend and it was under-estimated during the dry winters. On the whole, the annual prediction of RO is over estimated as it predicts higher rainfall-runoff ratio. However, the trend of observed runoff is found much smoother than predicted one [Fig.-6] as the main features of such trends are given below.

- Increasing rainfall increases fluctuation in runoff. For example, the month of July and August [peak monsoon season] has its very high fluctuation.
- On account of over estimation of runoff by T-M method, the error term in distribution becomes too high that reduces the significance level with low degree of determinant [$R^2=0.306$] [Fig.-7].
- There is fast fluctuation in the soil moisture availability during winter season when there is an occasional rain. But on the other hand, PET trend is quite smooth, increases gradually during pre-monsoon months [April-May], becomes flat during monsoon period and again fall down during the post-monsoon period. PET follows the temperature variation rather than rainfall trend [Fig.-8].
- The ratio of rainfall-runoff recorded very high during the monsoon period because of the fully saturated soil and its wet antecedent soil moisture conditions.

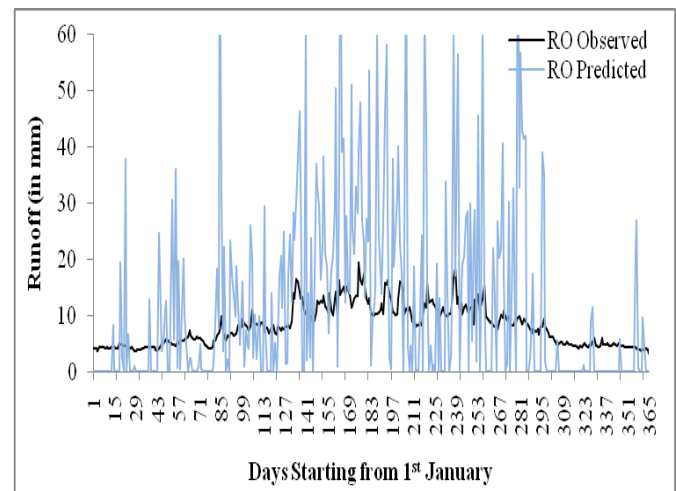


Fig.-6: Daily trends of observed and predicted runoff

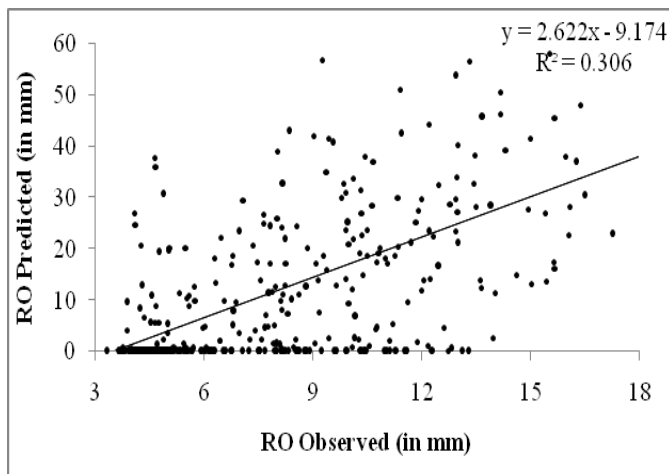


Fig.-7: The relationship between daily observed and predicted RO

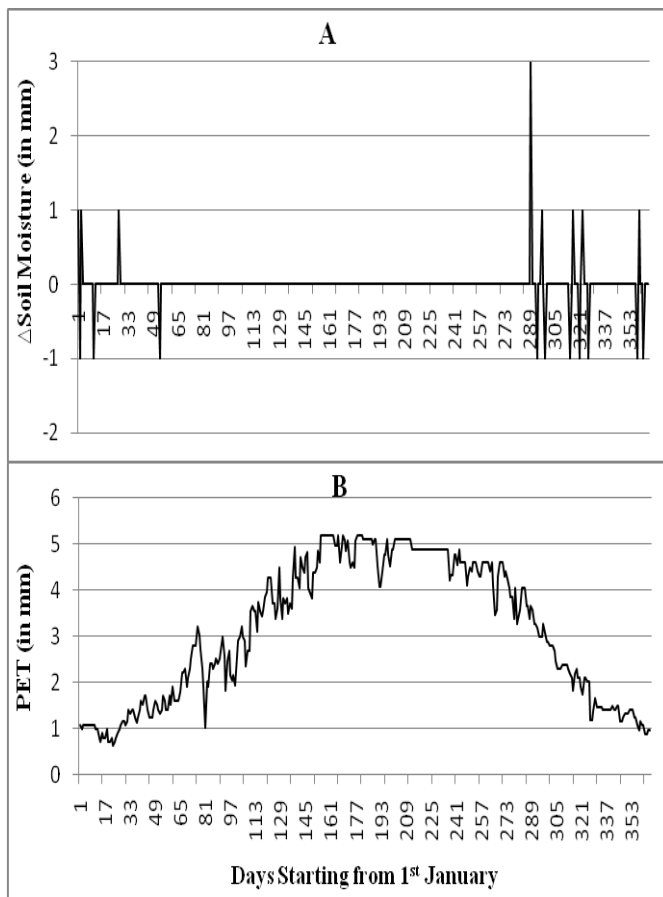


Fig.-8: Trends of daily A. Changes in Soil Moisture, B. Potential Evapotranspiration

4. CONCLUSION

In the specific high humid conditions of landforms in the foot-hills of Arunachal Himalayas, where temperature varies from 10⁰-35⁰C during the hydrologic regime of monsoon climate, there are some general conclusions regarding the

trend of daily RO. Daily RO is not so smooth in this region as it happens in the sub-tropical region of the world. Dry winters have one-third discharge conditions in the river catchments when rainfall was recorded very low. On the other hand, the amount of RO is concentrated during the monsoon season when more than 80% rain is precipitated. There are some specific findings inferred from the present analysis:

- No doubt, T-M procedure is simple to use with available parametric statistics of meteorological phenomena. However, it fails to predict correctly the PET as well as RO parameters for this region of high humidity.
- T-M procedure estimate more fluctuation in daily predicted RO phenomena than the observed one.
- It over estimate the RO at high rainfall intensity.

5. REFERENCES

- Tadesse N, "Surface Water Potential of the Hantebel Basin, Tigray, Northern Ethiopia," Agri. Engi. Int. CIGR Ejournal, Vol. 8, 2006, pp. 1-31.
- Strzepek KM, Yates DN and Quosy DENE, "Vulnerability assessment of water resources in Egypt to climatic changes in the Nile Basin," Climate Research, Vol. 6, 1996, pp. 89-95.
- Singh S and Syiemlieh HJ, "Prediction of runoff in the Um-U-Lah catchment of extremely humid area of Cherrapunji, India," Geographia Polonica, Vol. 82 No. 2, 2011, pp. 127-139.
- Mishra SK, SARKAR R, Dutta S and Panigrahy S, "A physically hydrological model for paddy agriculture dominated hill watershed in tropical region," Journal of Hydrology, Vol. 357, 2008. Pp. 389-404.
- Meshram DT, Mittal HK, Gorantiwar SD and Purohit RC, "Reference crop evapotranspiration of western part of Maharashtra, India," Indian J. Soil Cons., Vol. 38 No. 2, 2010, pp. 80-85.
- Lenka NK, Panda RK, Sudhishri S and Dass A, "Comparison of some empirical methods for estimating of ET₀ in high lands of Eastern Ghats of Orissa," Indian J. Soil Cons., Vol. 37 No. 1, 2009, pp. 22-25.
- Blaney HF and Criddle WD, "Evaporation from free water surface at high altitudes," Trans. ASCE., Vol. 123, 1962, pp. 243-265.
- Hamon WR, "Estimating potential evapotranspiration," Journal of Hydraulics Division, Proceedings of the American Society of Civil Engineers Vol. 871, 1961, pp. 107-120.
- Hargreaves GH, and Samani ZA, "Reference crop evapotranspiration from temperature," Trans. ASAE, Vol 1 No. 2, 1985, pp. 96-99.
- Papadakis J, "Climate of the World and their Potentialities," A. V. Cordoba 4564, Buenos Aires, Argentina, 1975, pp. 5-6.
- Beven K, "A sensitivity analysis of Penman-Monteith evapotranspiration estimates," Journal of Hydrology, Vol. 44, 1979, pp. 169-190.
- Xu, CY and Singh VP, (2001): "Evaluation and generalization of temperature-based methods for

- calculating evaporation,” *Hydrol. Process*, Vol. 15, 2001, pp. 305–319.
- [13] Loukas A, Vasiliades L and Mpastrogianis N, “Water balance model for the evaluation of surface water resources, in *Proc. 8th Int. Conf. on Environmental and Technology*, 2003, pp. 492-499.
- [14] Bautista F, Bautista D and Carranza CD, “Calibration of the equations of Hargreaves and Thornthwaite to estimate the potential evapotranspiration in semi-arid and subhumid tropical climates for regional applications,” *Atmósfera*, Vol. 22 No. 4, 2009, pp. 331-348.
- [15] Thornthwaite CW, “An approach towards a rational classification of Climate,” *Geogr. Rev.*, Vol. 38 No. 1, 1948, pp. 55-94.
- [16] Thornthwaite CW and Mather JR, “Instructions and Tables for Computing Potential Evapotranspiration and Water Balance,” *Publications in Climatology*, Vol. X No. 3, Drexel Institute of Technology, Centertown, New Jersey, 1957, pp. 185-204.
- [17] Soja R, Starkel L and Singh S, “Water Circulation and Availability of Water,” *Land Degradation and Ecorestoration in the Extremely Wet Monsoon Environment of Cherrapunji Area, India*, 1st ed., Singh S, Starkel L and Syiemlieh HJ Eds. Bookwell, New Delhi, 2010, pp. 30-50.
- [18] Subrahmanyam, VP, “Water balance approach to the study of aridity and droughts with special reference to India,” in *Proc. of the Hamburg Workshop*, 1983, pub. No. 148, pp. 125-135.
- [19] NBSS and LUP, “The Soils of Arunachal Pradesh,” at R.F. 1: 250,000, prepared for Government of Arunachal Pradesh, Itanagar by the National Bureau of Soil Survey and Land Use Mapping, Regional Centre, Jorhat, 1993.
- [20] USDA- Soil Conservation Service, *Hydrology: National Engineering Handbook*, Washington DC, 1972, Section 4.

Natural Radiation level in Groundwater from Katsina, a Semi Arid Region of Northern Nigeria

B.G. Muhammad¹ and M.S. Jaafar²

1. Department of Physics, Umaru Musa Yar'adua University, Katsina.

2. School of Physics, Universiti Sains, Malaysia.

e-mail: bashirgide@umyu.edu.ng

ABSTRACT

The World Health Organization's radiological water quality protocol was observed to screen samples of groundwater from Katsina, a semi-arid region part of northern Nigeria, for radiological safety. Initially, the gross alpha and gross beta activity concentrations as measured by an eight channel gas flow proportional counting system indicated some parts of the study area to have elevated alpha and beta activity concentrations when compared with the ICRP (1991) Maximum Acceptable Values (MAVs) of 500 Bqm⁻³ for alpha; 1,000 Bqm⁻³ for beta activity concentrations. This prompts the need for further screening. In this respect, gamma spectroscopy was employed to evaluate the natural radioactive materials responsible for the elevated alpha and beta activity concentration values. Subsequently, UNSCEAR dose conversion factors (DCF) were used to estimate the committed effective dose so as to ascertain the health risk level of using the water for drinking purposes.

Keywords: natural radioactivity, activity concentration, committed effective dose.

1. INTRODUCTION

NORM, an acronym for naturally occurring radioactive materials, refers to the long-lived radioactive elements such as uranium, thorium and potassium and their decay products, such as radium and radon that existed since the formation of the earth. These elements have always been present in the earth's crust and subsequently, in all environmental media (soil, air and water). Their presence makes them inevitably ingested into humans through food and drinking water [1-3]. Evidences from both human and animal studies also shows that radiation exposure at low to moderate doses such as those from drinking water may increase the long-term incidence of cancer [4-6]. Due to the possible adverse effect from ingestion of radionuclides, through drinking water, a standard need to be set in order to curb the unwanted radiation exposure to human. Many countries adopt the WHO recommendation of reference dose level [RDL] of committed effective dose of 0.1 mSv from one year's consumption of drinking water[7]. The RDL of 0.1 mSv is equal to 10% of the dose limit for members of the public, recommended by the ICRP (1991) and the International Basic Safety Standards (IAEA, 1996) and are acceptable to most WHO Member States [8].

In arid and semi-arid regions, such as the study area, evapo-transpiration rates are much high, recharge is less, flow paths longer and residence times much greater and hence much higher levels of natural mineralization. Thus the major ion contents and TDS are often high. In some desert regions, even if groundwater can be found it may be so salty (extremely high TDS) as to be undrinkable, and the difficulty of meeting even the most basic domestic requirements can have serious impacts on health and livelihood. This prompts the need to always screen domestic water supply from groundwater

sources that are often utilized in arid regions. The WHO radiological water quality protocol was followed to screen samples of groundwater from Katsina, a semi-arid region of northern Nigeria, for radiological safety. The result shows elevated gross alpha and gross beta values exceeding the WHO maximum contaminants levels of 500 and 1000 Bqm⁻³ respectively. The results of this segment of the work was earlier reported[9]. In the present work, gamma spectroscopy was employed to determine the natural radioactive materials responsible for the elevated alpha and beta activity concentration values. Subsequently, UNSCEAR dose conversion factors (DCF) were used to estimate the committed effective dose so as to ascertain the health risk level of using the water for drinking purposes.

Materials and Methods

Sampling

After using a GPS to measure the geographical coordinates of the sampling sites, clean polythene containers were used to collect groundwater from boreholes of the selected sites. The sites were chosen for their proximity to the neighboring Niger Republic that is known to have natural uranium deposits as depicted in the IAEA world's commercial uranium deposits map. The samples were then immediately brought to the laboratory for analysis. Guidelines provided by international organization for standardization on water quality sampling were strictly adhered to[10]. To prepare water samples for gamma spectroscopy, 500 ml of each sample was acidified with 10 ml of concentrated HNO₃ (analytical grade) [11] and then sealed in the polythene counting sample container and kept for a period of at least four weeks prior to counting.

Gamma spectroscopic system

Gamma spectroscopic measurements were carried out using a high efficiency 3''x 3'' Thallium doped, sodium iodide [NaI(Tl)] scintillation detector (Ortec, USA), with serial

number 101909H connected to a 3'' (B76D01W N 2034257) PMT photomultiplier tube. The set-up was coupled to a multi channel analyser (MCA). The detector was enclosed in a 10 cm lead shield to reduce background radiation in the counting environment. The set-up is illustrated in figure 1 below. The system has relative efficiency and resolution of about 50% and 7.2% respectively at energy of 0.662 MeV (^{137}Cs). These are considered adequate to distinguish the gamma ray energies of interest in this work. The spectral analysis and peak fitting were performed using Fitzpeak NaI(Tl) (low resolution) gamma calibration and analysis software developed by JF Scientific UK. This software is specially optimized to be used for low resolution gamma detector NaI(Tl). The energy calibration was carried out using IAEA certified standards of known energies such as ^{60}Co , for $E_\gamma = 1332.5$ and 1173.2 keV, and ^{137}Cs , for $E_\gamma = 661.6$ keV. The efficiency calibration was also performed by using IAEA certified ^{152}Eu standard[12] for $E_\gamma = 121.8, 224.7, 344.3, 778.9, 964.0, 1085.8, 1112.0$ and 1408.0 keV. A counting time of 86400 s was allowed for both background and sample due to the low emission nature of the samples. The activity concentrations of the radionuclides in the samples were determined from their respective gamma-ray lines or gamma-ray lines emitted from their decay products. The gamma line of 1460.8 keV was used directly to determine ^{40}K . The weighted mean activity concentrations from gamma lines of 911.1 keV (^{228}Ac) and 583.1 keV (^{212}Pb) were used to determine ^{232}Th . The gamma lines of 351.9 keV (^{214}Pb) and 609.3 keV (^{214}Bi) were used to determine ^{238}U and 186.1 keV (^{226}Ra) gives the activity concentration of ^{226}Ra as a natural source.

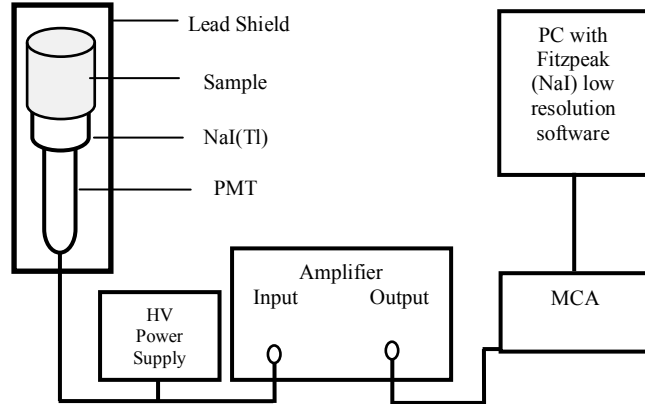


Fig. 1 The radio-elemental gamma spectroscopy set-up

Committed effective dose

Estimation of committed effective dose E_d (Sv y^{-1}) to an individual due to the consumption of the natural radionuclides present in the drinking water was done using equation 1 [1]. The WHO A_i values of 230, 330 and 730 litres for infants (1-2 years), children (>7-12 years) and adults (>17 years) respectively were used [7, 13].

$$E_d = A_c * A_i * C_f \quad (1)$$

where A_c is the radionuclide activity concentration (Bq l^{-1}), A_i is the annual intake of water (l y^{-1}) and C_f is the dose conversion factor for the radionuclide (Sv Bq^{-1}). The dose conversion coefficients provided by UNSCEAR 2000 report[14] were also used for the dose estimation. The total committed effective dose D (Sv y^{-1}) to an individual was established by summing up the contributions from all radionuclides present in the water samples as given by equation 2.

$$D = \sum A_c * A_i * C_f \quad (2)$$

Results and Discussion

The activity concentration of natural radionuclides in the groundwater from the study area is presented in table 1. Table 2 presents the estimated total committed effective dose resulting as a consequence of direct ingestion of dissolved radionuclides in the groundwater. Table 3 compares the results of the present study with those from other parts of the world.

The world annual natural radioactivity level, including external exposure, consumption of food and water containing natural radionuclides, and inhalation of radon with its daughter products, amounts on average to 2.4 mSv, with a range from 1 to 10 mSv[19]. The United Nations Scientific Committee on Effects of Atomic Radiation (UNSCEAR) report also indicated that the average worldwide exposure to natural sources in foods and drinking water is 0.29 mSv y^{-1} (about 0.17 mSv y^{-1} from ^{40}K and about 0.12 mSv y^{-1} from Uranium and Thorium)[19]. For prolonged exposure situations in case of all environmental radioactive sources, including natural and human-made sources, the International Commission on Radiological Protection (ICRP) recently recommended a generic intervention level of annual dose of 10 mSv as the level below which intervention is unjustified, taking into account radiological, economic and social factors[20]. The world health organization in its guidelines for drinking water quality, adopted the International commission on radiological protections' recommendation of reference dose level (RDL) of the committed effective dose, to be equal to 0.1 mSv from 1 year's consumption of drinking-water (from the possible total radioactive contamination of the annual drinking-water consumption).

Comparing the results of this study with other sources from other parts of the world, the mean measured activity concentration values of 0.43, 0.52 and 1.02 Bq l^{-1} for ^{232}Th , ^{40}K and ^{226}Ra respectively are well below the reported concentrations of 12, 12 and 29 Bq l^{-1} of (untreated) lake water from Biseni, Nigeria[17]. In water used for drinking and other domestic purposes, the mean measured activity concentration values on the other hand, are above the earlier reported values for bottled water from Pakistan as well as the tap water from Egypt, but the values (^{226}Ra and ^{40}K) from this area are still far below the earlier reported values for well drinking water from Akure Nigeria, where high level of radium was discovered. Consequently, the total committed

Table 1 Activity concentration of natural radionuclides in the groundwater sources

S/N	Location	Location		Activity Concentration (Bq l ⁻¹)			
		Geographical coordinates		²³⁸ U	²³² Th	⁴⁰ K	²²⁶ Ra
1.	Dutsin Safe Low-cost	N13° 00' 20.1"	E7° 35' 10.1"	0.48±0.035	0.39±0.021	0.79±0.042	0.29±0.012
2.	Dutsin Safe extension	N13° 00' 11.7"	E7° 35' 00.9"	0.49±0.028	0.54±0.033	0.78±0.067	0.28±0.021
3.	Fed. Medical Centre	N12° 59' 06.4"	E7° 34' 38.8"	0.22±0.011	1.30±0.023	0.91±0.072	1.09±0.073
4.	Sokoto Rima	N12° 58' 41.5"	E7° 35' 37.3"	0.29±0.021	0.17±0.011	1.16±0.091	1.39±0.077
5.	Abbatoir	N12° 58' 24.3"	E7° 35' 27.7"	0.22±0.012	0.04±0.003	0.91±0.082	1.09±0.081
6.	Central Market	N12° 58' 16.3"	E7° 36' 06.0"	0.34±0.021	0.23±0.012	1.32±0.088	1.68±0.093
7.	Sabuar Unguwa	N12° 58' 11.0"	E7° 36' 32.7"	0.31±0.017	0.27±0.023	1.20±0.076	1.54±0.082
8.	Bread	N12° 58' 23.1"	E7° 36' 50.4"	0.78±0.076	0.64±0.043	0.39±0.031	1.48±0.076
9.	Garama Quarters	N12° 59' 07.9"	E7° 36' 19.9"	0.81±0.065	0.66±0.017	4.07±0.089	1.55±0.088
10.	Sabon Layi	N12° 59' 13.0"	E7° 36' 19.1"	0.39±0.022	0.15±0.014	0.64±0.067	0.22±0.033
11.	Emir's Palace	N12° 59' 42.5"	E7° 36' 01.0"	0.50±0.031	0.49±0.051	0.89±0.073	0.32±0.023
12.	Farin Yaro	N12° 59' 48.3"	E7° 35' 30.5"	0.44±0.062	1.20±0.087	0.78±0.055	0.28±0.022
13.	Unguwar Yari	N12° 59' 28.9"	E7° 35' 36.0"	0.04±0.003	1.11±0.096	0.71±0.076	0.25±0.012
14.	'Yar adua	N12° 59' 38.7"	E7° 36' 18.7"	0.47±0.053	0.24±0.019	0.71±0.081	0.25±0.018
15.	Tudun Wada	N12° 59' 54.4"	E7° 36' 26.4"	0.43±0.033	0.12±0.023	0.70±0.073	0.25±0.021
16.	School of Nursing	N13° 00' 04.2"	E7° 36' 16.3"	0.43±0.043	0.14±0.012	0.68±0.056	0.25±0.014
17.	Filin Samji	N13° 00' 22.4"	E7° 36' 35.4"	0.46±0.036	0.33±0.023	0.78±0.055	0.28±0.022
18.	Dutsin Amare	N12° 59' 30.2"	E7° 36' 39.6"	0.42±0.021	0.21±0.018	0.73±0.047	0.27±0.017
19.	Kofar Marusa	N12° 59' 19.1"	E7° 36' 33.2"	0.04±0.032	0.02±0.003	0.60±0.044	0.22±0.011
20.	Shararrar Pipe	N12° 58' 38.1"	E7° 36' 23.5"	0.49±0.033	0.30±0.016	0.84±0.067	0.31±0.021
21.	Rafin Dadi	N12° 58' 57.0"	E7° 35' 40.5"	0.46±0.023	0.22±0.017	0.73±0.056	0.27±0.015
22.	Dan Marna	N12° 59' 06.2"	E7° 36' 05.6"	0.44±0.022	0.16±0.021	0.72±0.066	0.27±0.023
23.	Layout	N12° 58' 56.5"	E7° 36' 56.5"	0.46±0.034	0.20±0.022	0.77±0.043	0.28±0.023
24.	W.T.C.	N12° 58' 34.4"	E7° 37' 50.1"	0.06±0.027	0.05±0.002	0.73±0.052	0.27±0.011
25.	New Stadium	N12° 58' 17.0"	E7° 38' 34.5"	0.39±0.022	0.23±0.011	0.71±0.055	0.25±0.031
26.	C.B.N.	N12° 59' 24.1"	E7° 37' 47.2"	0.39±0.034	0.26±0.021	0.65±0.061	0.24±0.014
27.	High Court	N12° 59' 12.5"	E7° 38' 22.5"	0.39±0.055	0.27±0.015	0.62±0.034	0.22±0.017
28.	Motel	N13° 00' 01.8"	E7° 37' 53.5"	0.39±0.042	0.20±0.009	0.64±0.033	0.24±0.021
29.	G.R.A.	N12° 59' 59.8"	E7° 38' 28.6"	0.41±0.044	0.25±0.021	0.72±0.045	0.27±0.033
30.	Cutoms Barracks	N13° 00' 23.8"	E7° 37' 19.1"	0.85±0.058	0.07±0.004	1.32±0.086	0.48±0.034
31.	Goruba Housing Est.	N13° 00' 06.9"	E7° 37' 16.8"	0.18±0.014	0.20±0.021	3.00±0.098	1.05±0.088
32.	Nitel	N12° 59' 47.3"	E7° 37' 08.6"	0.85±0.043	0.97±0.055	1.56±0.077	0.53±0.045
33.	Kofar Durbi	N12° 59' 42.2"	E7° 36' 57.7"	0.77±0.062	0.89±0.037	1.32±0.087	0.46±0.033
34.	Social Development	N12° 59' 55.2"	E7° 36' 51.7"	0.85±0.066	0.89±0.054	1.32±0.078	0.45±0.034
35.	Area Council	N12° 59' 42.7"	E7° 36' 33.0"	0.73±0.056	0.83±0.076	1.32±0.088	0.45±0.025
36.	Unguwar Liman	N12° 59' 56.8"	E7° 35' 53.5"	0.60±0.034	0.67±0.044	0.95±0.065	0.35±0.026
37.	Kofar Kaura	N12° 59' 56.8"	E7° 36' 17.3"	0.77±0.055	0.70±0.034	1.32±0.073	0.46±0.044
38.	Canada Quarters	N12° 58' 16.1"	E7° 37' 07.3"	0.35±0.034	0.86±0.066	1.19±0.077	0.42±0.031
39.	Aishatu Memorial	N12° 58' 07.8"	E7° 37' 24.2"	0.46±0.035	0.33±0.044	0.78±0.045	0.28±0.013
40.	Danfodio Institute	N12° 58' 40.2"	E7° 37' 16.5"	0.42±0.051	0.21±0.031	0.73±0.052	0.27±0.016

Table 2 Estimated age dependent total committed effective dose (mSv y⁻¹) in groundwater due to natural radionuclides in the area

S/N	Location	Geographical coordinates		Infants (1-2 y)	Children (2-16 y)	Adults (>16 y)
1.	Dutsin Safe Lowcost	N13° 00' 20.1"	E7° 35' 10.1"	0.14	0.14	0.15
2.	Dutsin Safe extension	N13° 00' 11.7"	E7° 35' 00.9"	0.16	0.15	0.18
3.	Fed. Medical Centre	N12° 59' 06.4"	E7° 34' 38.8"	0.42	0.43	0.47
4.	Sokoto Rima	N12° 58' 41.5"	E7° 35' 37.3"	0.39	0.41	0.35
5.	Abbatoir	N12° 58' 24.3"	E7° 35' 27.7"	0.30	0.31	0.26
6.	Central Market	N12° 58' 16.3"	E7° 36' 06.0"	0.46	0.49	0.42
7.	Sabuar Unguwa	N12° 58' 11.0"	E7° 36' 32.7"	0.43	0.46	0.39
8.	Nakowa Bread	N12° 58' 23.1"	E7° 36' 50.4"	0.46	0.49	0.46
9.	Garama Quarters	N12° 59' 07.9"	E7° 36' 19.9"	0.51	0.52	0.49
10.	Sabon Layi	N12° 59' 13.0"	E7° 36' 19.1"	0.12	0.10	0.10

11.	Emir's Palace	N12° 59' 42.5"	E7° 36' 01.0"	0.18	0.16	0.19
12.	Farin Yaro	N12° 59' 48.3"	E7° 35' 30.5"	0.21	0.20	0.28
13.	Unguwar Yari	N12° 59' 28.9"	E7° 35' 36.0"	0.18	0.18	0.24
14.	'Yar adua	N12° 59' 38.7"	E7° 36' 18.7"	0.10	0.10	0.11
15.	Tudun Wada	N12° 59' 54.4"	E7° 36' 26.4"	0.10	0.10	0.10
16.	School of Nursing	N13° 00' 04.2"	E7° 36' 16.3"	0.10	0.10	0.10
17.	Filin Samji	N13° 00' 22.4"	E7° 36' 35.4"	0.12	0.12	0.14
18.	Dutsin Amare	N12° 59' 30.2"	E7° 36' 39.6"	0.11	0.11	0.11
19.	Kofar Marusa	N12° 59' 19.1"	E7° 36' 33.2"	0.08	0.07	0.06
20.	Shararrar Pipe	N12° 58' 38.1"	E7° 36' 23.5"	0.15	0.14	0.15
21.	Rafin Dadi	N12° 58' 57.0"	E7° 35' 40.5"	0.12	0.11	0.12
22.	Dan Marna	N12° 59' 06.2"	E7° 36' 05.6"	0.11	0.11	0.11
23.	Layout	N12° 58' 56.5"	E7° 36' 56.5"	0.12	0.11	0.12
24.	W.T.C.	N12° 58' 34.4"	E7° 37' 50.1"	0.07	0.08	0.07
25.	New Stadium	N12° 58' 17.0"	E7° 38' 34.5"	0.10	0.10	0.11
26.	C.B.N.	N12° 59' 24.1"	E7° 37' 47.2"	0.10	0.10	0.11
27.	High Court	N12° 59' 12.5"	E7° 38' 22.5"	0.10	0.10	0.11
28.	Motel	N13° 00' 01.8"	E7° 37' 53.5"	0.09	0.09	0.10
29.	G.R.A.	N12° 59' 59.8"	E7° 38' 28.6"	0.10	0.11	0.11
30.	Cutoms Barracks	N13° 00' 23.8"	E7° 37' 19.1"	0.15	0.16	0.14
31.	Goruba Housing Est.	N13° 00' 06.9"	E7° 37' 16.8"	0.29	0.31	0.27
32.	Nitel	N12° 59' 47.3"	E7° 37' 08.6"	0.26	0.26	0.31
33.	Kofar Durbi	N12° 59' 42.2"	E7° 36' 57.7"	0.23	0.23	0.28
34.	Social Development	N12° 59' 55.2"	E7° 36' 51.7"	0.24	0.23	0.28
35.	Area Council	N12° 59' 42.7"	E7° 36' 33.0"	0.22	0.22	0.26
36.	Unguwar Liman	N12° 59' 56.8"	E7° 35' 53.5"	0.18	0.18	0.21
37.	Kofar Kaura	N12° 59' 56.8"	E7° 36' 17.3"	0.22	0.21	0.25
38.	Canada Quarters	N12° 58' 16.1"	E7° 37' 07.3"	0.26	0.29	0.25
39.	Aishatu Memorial	N12° 58' 07.8"	E7° 37' 24.2"	0.12	0.12	0.14
40.	Danfodio Institute	N12° 58' 40.2"	E7° 37' 16.5"	0.11	0.11	0.11

Table 3 Natural radioactivity in water from other parts of the world

Area	Type of Source	Mean specific activity (Bq l ⁻¹)			
		²³² Th	²²⁶ Ra	⁴⁰ K	Reference
Egypt	Tap water	0.008	0.0157	0.152	[15]
Islamabad, Pakistan	Bottled water	0.0113	0.052	0.0409	[16]
Biseni, Nigeria	Lake water	12	12	29	[17]
Akure, Nigeria	Well water	NR	7.15	13.54	[18]
Chittagong, Bangladesh	Well and tap	0.19	0.043	4.16	[1]
Katsina, Nigeria	Groundwater	0.43	0.52	1.02	This work

NR- not reported

effective dose due to one year's direct ingestion of the groundwater from the study area was estimated to vary from 0.07 to 0.46, 0.08 to 0.49 and 0.06 to 0.49 for infants, children and adults respectively. This indicates that the value in most of the groundwater sources seems to exceed the reference dose values of 0.1 mSv y⁻¹ as recommended by the WHO. However, the total committed effective dose estimated in all the samples considered is below 1 mSv y⁻¹, which is the 10% of the level above which intervention is justified taking into account radiological, economic and social factors.

CONCLUSION

The results of this study provides a baseline data of the natural radioactivity levels in the groundwater resources abundantly utilised for drinking and other domestic purposes by inhabitants of Katsina, a semi arid region in northern Nigeria. Comparatively, the moderate natural activity

concentration values in groundwater from arid and semi arid regions such as the study area are attributable to the nature of the water sources, that is, less recharge and high residence time resulting in more dissolved solids accumulation in the water. Despite the fact that the concentrations of natural radioisotopes and subsequent committed effective doses in many samples were substantially higher than those in other populations, most still remained low when compared with generic intervention level. The magnitude of risk expected in our study is therefore small. Radionuclides screening as well as the use of best available technologies (BAT) such as ion exchange, reverse osmosis or lime softening (as recommended by USEPA) for areas where the natural radionuclides concentrations results in committed effective dose that exceeds RDL are recommended in order to safeguard the members of the public from radiation exposure above recommended limits.

REFERENCES

1. Alam, M.N.C., M.I. Kamal, M. Ghose, S. Islam, M.N. and Anwaruddin, M., *Radiological assessment of drinking water of the chittagong region of Bangladesh* Radiation Protection Dosimetry, 1999. **82**(3): p. 207-14.
2. Dalma, N., et al., *Gross alpha and beta activities in tap waters in Eastern Black Sea region of Turkey*. Chemosphere, 2006. **62**: p. 956-960.
3. Gruber, V., F.J. Maringer, and C. Landstetter, *Radon and other natural radionuclides in drinking water in Austria: measurement and assessment*. Appl Radiat Isot, 2009. **67**(5): p. 913-7.
4. Abo, M., et al., *Cytogenetic effects of radon inhalation*. Radiation Measurements, 2008. **43**: p. 1265 - 1269.
5. Collman, G.W., D.P. Loomis, and D.P. Sandler, *Childhood cancer mortality and radon concentration in drinking water in North Carolina*. Br J Cancer, 1991. **63**(4): p. 626-9.
6. Amrani, D. and D.E. Cherouati, *Health effects from radon-222 in drinking water in Algiers*. J Radiol Prot, 1999. **19**(3): p. 275-9.
7. WHO, *Guidelines for Drinking-water Quality*. World Health Organisation Publication, 1988. **1**: p. 197-209.
8. Bonotto, D.M. and T.O. Bueno, *The natural radioactivity in Guarani aquifer groundwater, Brazil*. Appl Radiat Isot, 2008. **66**(10): p. 1507-22.
9. Muhammad, B.G., M.S. Jaafar, and T.C. Akpa, *A survey of gross alpha and beta activity concentrations in groundwater from Katsina area of Northern Nigeria*. Radiat Prot Dosimetry, 2010. **141**(2): p. 127-33.
10. ISO, *Water quality - Sampling - Part 1: Guidance on the design of sampling programmes and sampling techniques* British Standard, 2006. **1**(5667): p. 1-31.
11. ISO, *Water quality - Sampling - Part 6: Guidance on sampling of rivers and streams* British Standard, 2005. **6**(5667): p. 1-16.
12. ISO, *Measurement of radioactivity in the environment*, in *Measurement of gammaemitting radionuclides*. 2007, ISO. p. 30.
13. Ajayi, O.S. and J. Achuka, *Radioactivity in drilled and dug well drinking water of Ogun state Southwestern Nigeria and consequent dose estimates*. Radiat Prot Dosimetry, 2009. **135**(1): p. 54-63.
14. UNSCEAR, *Dose assessment methodologies*, in *SOURCES AND EFFECTS OF IONIZING RADIATION*. 2000, UNSCEAR. p. 63.
15. Amin, R.M., F.A. Khalil, and M.A. El Fayoumi, *Natural radioactivity and chemical concentrations in Egyptian groundwater*. Environ Monit Assess, 2011. **173**(1-4): p. 29-35.
16. Fatima, I., et al., *Measurement of natural radioactivity in bottled drinking water in Pakistan and consequent dose estimates*. Radiat Prot Dosimetry, 2007. **123**(2): p. 234-40.
17. Agbalagba, E.O. and R.A. Onoja, *Evaluation of natural radioactivity in soil, sediment and water samples of Niger Delta (Biseni) flood plain lakes, Nigeria*. J Environ Radioact, 2011. **102**(7): p. 667-71.
18. Ajayi, O.S. and T.P. Owolabi, *Determination of natural radioactivity in drinking water in private dug wells in Akure, Southwestern Nigeria*. Radiat Prot Dosimetry, 2008. **128**(4): p. 477-84.
19. UNSCEAR, *Sources and effects of ionizing radiation*, UNSCEAR, Editor. 2000: New York.
20. Wrixon, A.D., *New ICRP recommendations*. Journal of Radiological Protection, 2008. **28**(161): p. 161-168.

Cost-Performance Studies of Abandoned Shell Husks (ASH) in Japan

Md. Toriqul Islam, Md. Zakaria Hossain, Masaaki Ishida, Md. Bellal Hossain and Md. Jamal Uddin
Graduate School of Bioresources, Mie University, Japan
Capital Development Authority (RAJUK), Bangladesh

ABSTRACT

This paper presents a comprehensive study on the cost analysis of abandoned shell husks (ASH) and its performance for soil reinforcement applications. Along with field visit at the shell husk abandoned area, data collected from the public city office and private company offices were analyzed. It was observed that the abandoned shell husks causing environmental pollution through spreading bad smell to the neighbor of the abandoned area. Analyses of the data showed that the shells were not only abandoned without any commercial value but huge amount of money was being spent for its disposal. In order to conserve natural resources and to mitigate the pollution and environmental problems, composite reinforcement using abandoned shell husks were prepared in the laboratory and soil-structure interaction tests were conducted for soil reinforcement applications. Overall response of the shear properties of composite reinforcement containing abandoned shell husk were demonstrated under varying surcharge such as different normal loading conditions. It was observed that the use of shell husk in composite reinforcement improved the shear performance significantly.

Keywords: Shell husk, Cost analysis, Environment pollution, Composite reinforcement, Slope protection

1. INTRODUCTION

A huge amount of abandoned shell husk is produced in Japan produced as a byproduct of shell production every year causing serious environmental problem through spreading bad smell to the surroundings. Some abandoned shell husk thrown in Tsu city, Mie Prefecture, Japan is shown in Fig.1. Along with environmental concern, a lot of money is being spent for the disposal of these shell husks in Mie and all over Japan. With the rapid increase in demand for balance between natural phenomena and ecology in bio-environment, there is a significant need for continuous development of new technologies that consume these abandoned shell husks [1,2]. This solves mainly two environmental and economic aspects, such as, (1) solving the waste storage problem and (2) protection of limited natural resources of aggregates [3,4]. Both the economic and environmental benefits can be achieved by using the abandoned shell husk as recycled aggregate in concrete or in cement-based composites. Some researches on concrete or cementitious composites with other recycled aggregate produced from building destruction can be found in the technical literature [5-8]. Light weight concrete masonry with recycled wood aggregate was studied by Stahl [9]. The latest researches on the assessment of the surface resistance and permeation properties of recycled aggregates concrete is also found [10,11]. In spite of the volume of available information in the technical literature, there is a no research work available on the use of abandoned shell husks in cementitious composites for soil reinforcement applications [12].

If abandoned shell husk properly applied for the surface treatment of composite reinforcement, shear resistance between the soil and the reinforcement may be significantly improved. However, this needs to be substantiating by evidence through laboratory experiment and if necessary by field applications. In view of the above distinct advantages for environmental conservation and protection of limited natural resources as well as soil-reinforcement applications; the present research work is undertaken to fulfill this basic need. It is expected that the outcomes of this research assist in possible utilization of abandoned shell husk as aggregate for producing cement-based composite reinforcements for prospective uses in the field such as; terrace lands, roads, canals, pavements, embankments, ridge between paddy fields and other agricultural and engineering structures in the form of earth slope protection. For effective utilization of cementitious composites containing abandoned shell husks in soil and geotechnical works, it is necessary to study various engineering properties such as soil-reinforcement interaction. Shear tests are commonly performed to study the behavior and shear resistance of cement based composite materials. Shear tests (soil-structure interaction) between soil and composite reinforcement containing abandoned mactridae shell husk under different surcharge such as normal loading conditions were demonstrated. A comparison of the test results with ordinary reinforcement is depicted.



Fig.1 Abandoned mactridae shell husks in Tsu city, Mie Prefecture, Japan

2. DETAILS ABOUT ABANDONED SHELL HUSK

The abandoned shell husks were collected from the sea coast near to Mie University, Tsu city, Mie Prefecture, Japan (Fig.1) are the Mactridae type shell husk. After collection, the shell husks were graded by performing sieve analysis. The fineness modulus and the maximum size of the abandoned shell husks were 4.35 and 4.76mm, respectively. The shell size distribution curve can be found elsewhere []. According to the Japanese Ministry of Forestry, Fisheries and Agriculture; Mactridae, also known as trough shells or duck clams, is a family of marine bivalve clams of the order Veneroida. The amount of shell production and disposal cost were given in Table 1 based on city, prefecture and country and depicted in the results and discussion section. Therefore, there are not repeated in this section.

3. PREPARATION OF SPECIMENS

Ordinary Portland cement and river sand passing through a No.8 (2.38mm) sieve, which has a fineness modulus of 2.33, were used for casting. For all the specimens, the water to cement ratio and cement to sand ratio both were 0.5 by weight. The requisite amount of sand and cement was dry-mixed in a pan, and then the requisite quantity of water was added

gradually while the mix was continuously stirred. Rectangular specimens were made in the wooden moulds with open tops. The moulds were made in such a way that the side walls and the base were detachable so that the mould could be easily separated from the specimens after its initial setting (Fig.2). The contact surfaces of the mould to the mortar were greased before casting the specimens to ease the demolding process. At first, thin layer (4 to 5 mm) of mortar was spread on the base of the mold and then the mesh made of small diameter (1mm) with c/c opening 10mm was placed on the mortar. After that the second layer of mortar was spread on the mesh covering by mortar again 4 to 5 mm. Therefore, the final thickness of the composite reinforcement was made of 10mm. The shell husks were spread on the mortar in such a way so that each shell was 50% inside the mortar with 50% above the mortar. The husks were spread randomly. Overall surface area that was covered by the shell was 20%. A hole at the center of the composite was made in order to drain pore water from the soil structure (Fig.3). This also provides additional shear resistance.

The specimens were air-dried for 24 hours for initial setting and then immersed in water for curing. The specimens were removed from water after 28 days and were air-dried for 2 days in room temperature of about 25°C and relative humidity of about 50%; then the tests were performed.



Fig. 2 Mold for cast composite reinforcement



Fig. 3 Completed composite reinforcement containing ASH

4. METHOD OF TESTING

The apparatus used in this study is shown in Fig. 4 which is capable of performing both pullout and direct shear tests. For convenience of the readers, the important components of the testing equipment are numbered numerically starting from top-left to right-down in the increasing way such as, the number from [1] to [8] where the number [1] is the normal load application plate for upper box, [2] is the shear stress measuring device, [3] is the upper box filled with soil, [4] is the ASH panel, [5] is the lower box, [6] is the electrically operated shear jack, [7] is the displacement measuring dial gauge and [8] is the device taking normal load which acted on the upper box.

The ASH panels were made to obtain rectangular pieces of 316 mm by 380 mm in size with 120-mm extended mesh. The specified length of the pieces was selected in order to facilitate clamping with the shear apparatus. The panels were clamped in the box in such a way that the embedded length of the panel is 380 mm in the loading direction and 316 mm in the transverse direction. After embedding the ASH panel on

the lower box, the upper part was set on the panel, and then the Toyoura sand was rained in the upper box with 80cm height. This provides nearly 90% compaction of the soil in the upper box. The tests were carried out in the way of pushing out the panel along with the lower box from the soil with constant selected speed by means of screw jack under electrically operated constant pressure. The shear force and the displacements were measured by using the linear variable differential transformers (LVDTs). All the tests were carried out under surcharges of 40, 80, 120, 160 kPa.

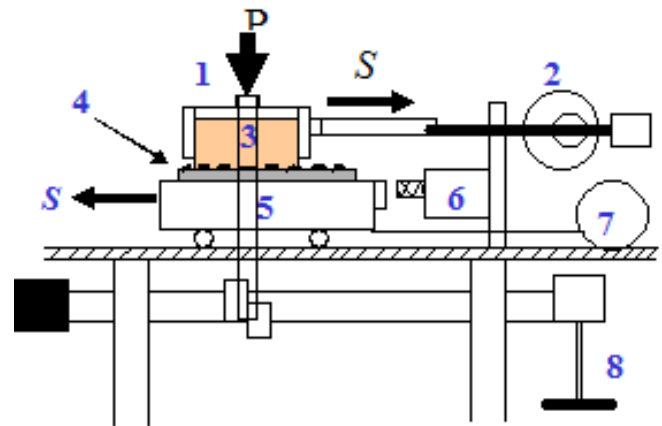


Fig. 4 Shear testing apparatus

5. RESULTS AND DISCUSSION

The amount of ASH production and required cost for its disposal in Japan are given in Table 1. As can be seen, the amount of the ASH is about 151000 tons per year according to the Japanese Ministry of Forestry, Fisheries and Agriculture. Among these, about 9627 tons/year are produced in Mie prefecture and 715 tons/year are produced in Tsu city along with 407 tons/year of *Macra Chinensis* (*Macridaes*) in Tsu city. According to the information of disposal site office in Tsu city, the cost for disposing the ASH is about 18 yen per kilogram which means that nearly 12.8 million yen is required for disposing ASH in Tsu city (nearly 7.3 million yen is required for *Macridaes*) only. In addition to this, nearly 2 million US\$ is required in Mie Prefecture and nearly 32 million US\$ is required in Japan. These ASHs which are not only thrown away without any commercial return and a lot of money is being spent for its disposal but also causing pollution and environmental problems.

Table 1 Amount of ASH and cost for its disposal in 2009

Place	Amount of shells production (tons))	Cost required to dispose shells (yen)
Japan	151,000	2718000000
Mie prefecture	9,627	173286000
Tsu City	715	12870000
Tsu City (mainly <i>Macra Chinensis</i>)	407	7326000

The shear behavior of ASH in terms of soil-ASH interaction is depicted in Fig. 5 with the surcharges in abscissa and ultimate shear strength in ordinate.

4 Conclusions

The possible utilization of abandoned shell husks in concrete construction is studied in this paper. Engineering properties such as compressive strength, Young's modulus, tensile strength, unit weight, water absorption capacity and coefficient of hydraulic conductivity results agree well with the ACI results. In designing light weight concrete structure such as partition wall, slope surface protection, ridge between paddy fields, roads and embankments slopes and sea-shore protection structures where strength does not a great factor but the water absorption properties are advantageous, concrete with shell aggregates may be used.

References

- [1] Wang, I., Takamura, S., Nakamura, M. and Tsukinaga, Y. A Study on the ratio and composition of the porous concrete containing shells, Transactions of Cement and Concrete, 2003, 57:572-577 (In Japanese)
- [1] Delwar M. et al. Use of reclaimed asphalt pavements as an aggregate in Portland cement concrete. ACI Material J, 1997; 94(3): 251-256.
- [2] Kansai, Y. Demolition and reuse of concrete masonry, Proceedings RILEM Symposium, Tokyo, Chapman and Hall, 1988, pp.774.
- [3] Hansen, T.C. Recycled aggregates and recycled-aggregates concrete, state-of-the-art report developments 1945-1985, RILEM Technical Committee 37-DRC, Material structures 1986, 19(111): 20-46.
- [4] Rim, K.A. et al. Influence of the proportion of wood on the thermal and mechanical performances of clay-cement-wood composites, cement and concrete composites, 1999; (21): 269-276.
- [5] Ajdukiewicz, A. et al. Influence of recycled aggregates on the mechanical properties of HS/HPC, cement and concrete composites, 2002; (24): 269-279.
- [6] Banthia, N. and Chan, C. Use of Recycled Aggregate in plain and Fiber Reinforced Shot Crete, Concrete International: design and Construction, American Concrete Institute, 2000; 22(6): 41-46.
- [7] Sagoe-crentsil, K.K. et al. Performance of Concrete made with Commercially Produced Coarse Recycled Concrete Aggregate, Cement and Concrete Research, 2001; 31(5): 707-712.
- [8] Hossain, M.Z. and Inoue, S. Finite Element Analysis of Thin Panels Reinforced with a Square Mesh, J. of Ferrocement, 2002; 32(2): 109-125.
- [9] Stahl [9]. D.C et al. Light weight concrete masonry with recycled wood aggregate , J. of Materials in Civil Engineering, 2002; 14 (2): 116-121.
- [10] Yamauchi, T. Sahara, H. and Kudo, K. On the Use of Hotate Shells as Concrete Aggregates, Proceedings of the 60th Technical Conference of Civil Engineering, 2005: 435-437 (In Japanese)
- [11] Frondistou-Yannas, S.T. Waste Concrete as aggregate for New Concrete, ACI Journal, 1977; 74(8): 373-376.
- [12] Hansen, T.C. and Boegh, E. Elasticity and Drying Shrinkage of Recycled Aggregate Concrete, ACI Journal, 1985; 82(5): 648-652.
- [1] Islam MR, "Conference proceedings," in Proc. 2nd Int. Conf. on GEOMAT, 2011, pp. 8-13.

Cyclones Path and Severities: Effect on Flood Height and Damages of Land and Embankments in Bangladesh

Musahaq Ali, Zakaria Hossain and Shigeko Haruyama
Graduate School of Bioresources, Mie University, Japan

ABSTRACT

The influence of tropical cyclones on flood height and damages of land and embankments in Bangladesh have been studied based on the field visits to cyclone site, collected data and information on damages of land and embankments during field visits. Review of technical literature on tropical cyclones obtained from recent publications was conducted for a comparative study of this research. An analysis of death of peoples, damages of lands, embankments and properties, flood surge heights, wind speed and radius of the severe storm were demonstrated. It is concluded that the south side of Bangladesh was not only the affected region but also the other parts of the country such as Sirajgonj district and Jamuna River were greatly affected due to the tropical cyclones in Bangladesh. The Bay of Bengal was particularly vulnerable to tropical cyclones where at least sixteen major cyclones including four severe cyclonic storms occurred that killed over 400 thousand people after the independence of Bangladesh..

Keywords: Tropical Cyclones, Severity, Agriculture, Land, Flood height, Wind speed, Death

1. INTRODUCTION

The tropical cyclones occurred in the year of 1970 (Bhola), 1991 (Tropical), 1999 (Orissa) and 2007 (Sidr) are four severe cyclones along with over 16 major cyclones occurred in Bangladesh (Hossain et al). The 1970 Bhola cyclone was a devastating cyclone that struck on November 12, 1970 (Islam, 2006). It was the deadliest tropical cyclone ever recorded, and one of the deadliest natural disasters in modern times. More than 250,000 people lost their lives in the storm, primarily as a result of the storm surge that flooded much of the low-lying islands of the Ganges Delta. This cyclone was the sixth cyclonic storm of the 1970 North Indian Ocean cyclone season, and was also the most powerful, reaching a strength equivalent to a Category 3 hurricane. This cyclone formed over the central Bay of Bengal on November 8 and traveled north, intensifying as it did so. It reached its peak with winds of 185 km/h (115 mph) on November 12, and made landfall on the coast of East Pakistan that night. The storm surge devastated many of the offshore islands, wiping out villages and destroying crops throughout the region. The city of Thana, Tazumuddin, was the most severely affected, with over 45% of the population of 167,000 killed by the storm (Paul and Rahman, 2006).

The cyclone which struck Bangladesh on the night of 29-30, April, 1991 was particularly severe causing widespread damage, killing 138,882 people (Bern, et al 1993). There has been massive damage to life line systems as well as private properties. Total loss has been estimated at US\$2.07 billion dollars for all sectors. Cyclone on 18th October, '99 hit on the eastern coast of India along the Bay of Bengal affecting the coastal districts of Ganjam, Puri, Jagatsinghpur, Khurda,

Gajapati and Balasore. Subsequently, the State was hit by a Super Cyclone on 29th October, '99 with winds of more than 250 km/h, tidal waves rising 20 feet high and torrential rains. The Super Cyclone and its aftermath caused "severe" damage in the districts of Jagatsinghpur, Balasore, Cuttack, Puri, Nayagarh, Jajpur Kendrapada, Bhadrak and Khurda and "moderate" damage in the districts of Mayurbhanj, Dhenkanal and Keonjhar (BWDB, 1998). In 2007, Bangladesh suffered a natural disaster like the cyclone Sidr of November 15, an unusually powerful storm that triggered giant waves up to 30ft (7m) high and killed more than 10,000 people in the south western coastal belt of Bangladesh covering the districts of Bagerhat, Barisal, Patuakhali, Pirozepur, Khulna and Satkhira. Even five days after the calamity, in village after village along the battered roads of the coastal districts, the survivors of the storm, their cheeks hollow and eyes sunken from hunger wait in vain for relief to come. True, natural disasters are a universal reality. But in modern times, it is the preparedness that counts. Damage can be minimized, rehabilitation can be effective, but only if a nation has an organized disaster management plan. Unhappily, Bangladesh does not. Accompanied by 260 km/h ravaging winds and sea surge as high as 30ft that swept about 20 km inland, a grade 5 hurricane, the highest level possible, devastated 23 districts in the south western part of Bangladesh at midnight on November 15, 2007 (EU, 1998). The country is yet to fully repair many of the damages done to her infrastructure due to devastating flood occurred in the same year just three months ago (Hossain and Sakai, 2008). Agricultural infrastructures such as farm structures, irrigation structures, dairy, poultry, fisheries, shelter, sanitation, drinking water, electricity supplies, transportation services including both land and water transports are in great danger in the region of Bay of Bengal where natural disasters occurred

frequently. Considering the above facts, the damages of agricultural land, flood heights and death of people along with other factor are focused in this paper.

2. PATH OF CYCLONES AND SEVERITIES

The path of the four severe cyclones along with the physical facts of Bangladesh is shown in Fig.2. It should be noted that Bangladesh extends between 21° and 27° North latitude and 88° and 92.5° East longitude. The Bay of Bengal is in the south side of the country. The total area is 144,000 sq km and size of population is around 15 million (2007). Per capita income is around US\$ 550, one of the lowest in the world. The coastal land of Bangladesh (710 km long) is of recent origin formed out of the process of sedimentation. Most parts of the area are, therefore, low lying which can be subject to inundation even under ordinary circumstances of tides. A tidal surge accompanied by a cyclone storm makes the situation alarming which is further exacerbated by the triangular shape of the Bay of Bengal (Fig.1).



Fig.1 Paths of 4 extremely severe cyclones

The wide shallow continental shelf is conducive to amplification of surges causing wide spread flooding. The country has been subjected to frequent natural disasters in many forms, particularly cyclonic storms and tidal surges. From 1970 to 2007, four major cyclone storms and tidal surges have been reported. These indicate that Bangladesh is prone to frequent destructive tropical cyclones associated with tidal surge. The low-lying coastal areas are particularly vulnerable, thus placing these population, infrastructure, agriculture, livestock and economic development in a high-risk situation. During the 1991 cyclone, the cyclonic storm was detected as a low pressure area over the Southeast

Bay and adjoining Andaman Sea on 23 April. Finally, the cyclone of hurricane intensity crossed the Chittagong coast a little north of Chittagong at 2 a. m. of 30 April, 1991 that killed some 143,000 people in Bangladesh. The aspects of the detection of the cyclone, its monitoring and prediction and weakness of warning and special weather bulletins have been reflected upon. Most of the worst affected thanas are either off-shore islands or coastal thanas. The less affected thanas are mostly located inside and further from the coast. The 2007 cyclone Sidr smashed into the country's southern coastline late on Thursday midnight of November 15 with 250 km/h (155 m/h) winds that whipped up a five meter tidal surge and swept about 20 km inland, a grade 5 hurricanes, the highest level possible, devastated 23 districts in the south western part of Bangladesh. Gigantic walls of water smashed into the coastline, washing away everything in their path. The backwash dragged hundreds of people into the sea, bodies were towards the shoreline -- twisted, bloated and broken -- washing up from the overflowing creeks and ponds around the villages. Death and its nauseating stench were everywhere.

3. EFFECT ON WIND, FLOOD AND LAND

In order to understand the severity of storm of the tropical cyclones in Bangladesh, a comparative study of the maximum wind speed and storm surge of major cyclones those struck in Bay of Bengal during the last four decades is depicted in Figs.2 and 3. The high power of the storm was mainly due to the higher wind speed which is apparent from Fig.2 for all the cases after 1970. In 1970 that is known as Bhola cyclone, though the wind speed was not as high as of the recent cyclones that can be found in 1991, 1998 and 2007, however, the number of casualties was severe at that time. The wind speed of Bhola cyclone was nearly 227 km/h whereas the others were over 230 km/h such as 257, 237 and 247 km/h for the cyclones occurred in the year of 1991, 1999 and 2007, respectively. The storm surge, on the other hand, was recorded as 7.8, 8.8, 8.1 and 8.4 m for the cyclones occurred in the year of 1991, 1999 and 2007, respectively, as shown in Fig.3. The radius of the major cyclones is shown in Fig.4.

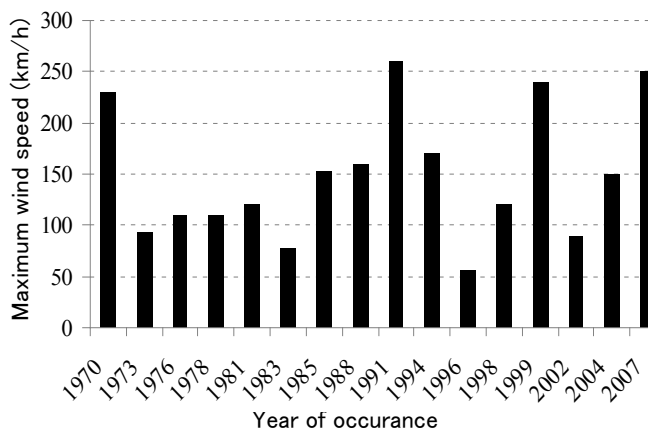


Fig.2 Wind Speed during the major cyclones in Bangladesh

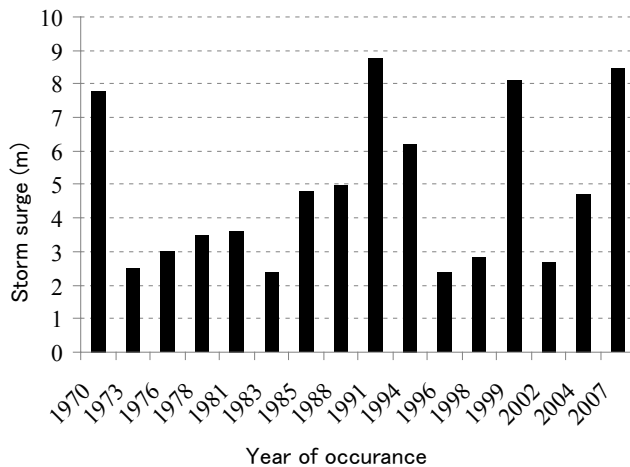


Fig.3 Flood surge height during the major cyclones in Bangladesh

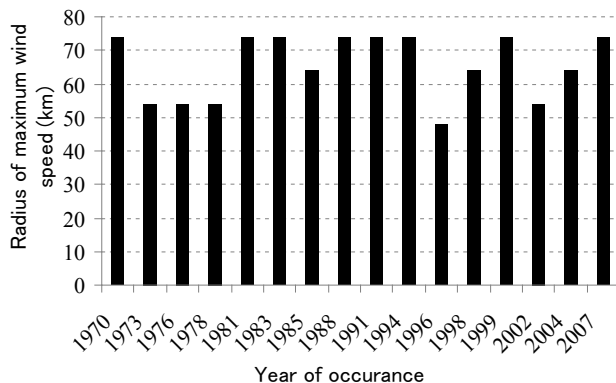


Fig.4 Maximum radius of major cyclones

4. EFFECT ON PEOPLE AND EMBANKMENT

The number of death of people and the damages due to major cyclones in Bangladesh are given in Fig.6 as the line graphs for the sake of clarification of the ferocious devastation brought to Bangladesh by the cyclones in just 37 years. Although the wind speed and tidal surge was lower for the 1970 Bhola cyclone, than the recent ones, the number of death of people was extremely higher at that time. It was estimated that more than 250000 people was died during the 1970 Bhola cyclone. It was saying that this was the deadliest one in the earth in its history. On the other hand, the 1991 cyclone was also other deadliest tropical cyclones on record that struck greater Chittagong with strong winds and storm surge, killing at least 140000 people and leaving as many as one crore people homeless and destroying 10 lakh homes. The damage of property was estimated at 1.8 billion US dollar in 1991.

The damage in 1999 and 2007 is noted as 4.2 and 5.3 billion US dollar. A large number of boats and smaller ships ran aground. Bangladesh Navy and Air Force were also heavily hit. BNS Isha Khan Naval Base was flooded, with heavy damage to the ships. Most of the fighter planes of the Air Force were also damaged. Comparison between the death of people and the damages in Fig.5 in terms of money in US\$ during the past four major cyclones notices that the number of death of people is getting to decrease although the damages of the properties increases in the recent years. This clearly indicates the awareness and preparedness of the people in the coastal region, improvement of weather broadcasting system and countermeasures taken by the government of the country. However, these measures could not be considered enough yet and more action need to be taken to minimize the death and damages of the peoples, their

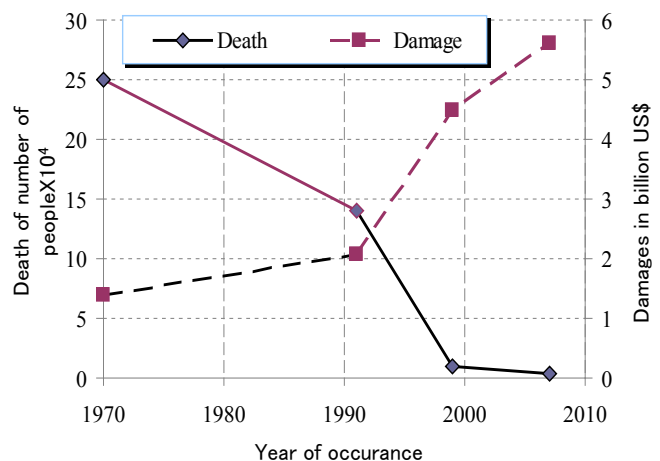


Fig.5 Number of death of people and damages of severe cyclonic storms in Bangladesh

homes, cattle, agriculture, forestry and fisheries, as well as its environment, bio-diversity, Sundarbans (world largest mangrove) and wildlife.

5. DISCUSSION

There was widespread damage to transport and communications networks. Rural roads, and many of the embankments protecting such roads, were extensively damaged. Most of the road damage was associated with the tidal surges in coastal areas. Large uprooted trees on roadsides also account for some of the damages, as trees were uprooted segments of tarmac or earthen roads became cracked or fragmented. Damage to transport infrastructure in coastal and inland waterways had occurred. Numerous ferries, and associated landing and loading areas damaged. In more than a few cases, the storm surge was so strong that medium to large sized ferries were actually lifted clear out of the water and beached on neighboring land.

6. CONCLUSIONS

Nineteen ninety one's cyclone killed at least 138,000 people, and the 1970 cyclone in Bhola, which left as many as above 250,000 people dead and is considered the deadliest cyclone, and one of the worst natural disasters, in human history. Sidr 2007 is another recent deadliest one causing thousands of people dead, millions of acres of cropland washed down by the sweeping ocean-surge, one third of Sundarban, a world natural heritage, utterly torn down, and substantial infrastructural damages have caused combined losses of assets and agricultural production. About 3,931 km long coastal embankment to protect coastal land from inundation by tidal waves and storm-surges, and drainage channels of total length of 4,774 km have so far been constructed, but lack of maintenance has rendered them almost ineffective. The results reported in this paper can be used as the preparatory information about flood height and scale of effect on land and people of Bangladesh.

7. REFERENCES

- [1] Hossain MZ, Islam MT, Sakai T and Ishida M. Impact of Tropical Cyclones on Rural Infrastructures in Bangladesh, *Agricultural Engineering International: the CIGR Ejournal*. Invited Overview No. 2, Vol. X. April, 2008
- [2] Islam, T. 2006. Integrated Approach to Cyclone Wind Analysis and disaster planning for the Benladesh coast, Ph.D. Dissertation, Texas Tech University, December.
- [3] Paul, A., and Rahman, M. 2006. Cyclone Mitigation Perspectives in the Islands of Bangladesh: A Case of Sandwip and Hatia Islands, *Coastal Management*, 34, Issue 2 April, pp.199-215.
- [4] Bern, C., Sniezek, J., Mathbor, G. M., Siddiqi, M. S., Ronsmans, C., Chowdhury, A. M., Choudhury, A. E., Islam, K., Bennish, M., and Noji, E. 1993. Risk factors for mortality in the Bangladesh cyclone of 1991, *Bulletin of the World Health Organization*, 71(1), pp.73-78.
- [5] BWDB. 1998. DHV, Meghna Estuary Study, Draft Master Plan, Volume 1, Main Report, for BWDB, Dhaka.
- [6] EU (European Community). 1998. Cyclone Shelter Preparatory Study (CPSP), Stage I, Feasibility Study, Draft Final Report, Vol. 3.
- [7] Hossain, M.Z. and Sakai, T. Extent and Severity of Flood Embankments in Bangladesh, *Agricultural Engineering International, the CIGR Ejournal*. Manuscript LW 08 004. Vol. X.
- [8] UN (United Nation), 2007. Cyclone Sidr United Nations Rapid Initial Assessment Report, With a Focus on 9 Worst Affected Districts, 22 November.

Authors Index

A

A. A. Mirghasemi, Iran
A. Abdul Rahman, India
A. Elahi, Iran
A. Ghalandarzadeh, Iran
A. Gholampour, Iran
A. Iizuka, Japan
A. M. Al-Mahbashi, Saudi Arabia
A. Rajendra Prasad, India
A. Rajendra Prasad, India
A. Tohidi, Iran
A. Abdul Rahman, India
A. Dhanalakshmi, India
A. Haghollahi, Iran
A. Iizuka, Japan
A. Kanazawa, Japan
A. Kumar, Australia
ASM Abdul Awal
Abbas Ghalandarzadeh, Iran
Abbasali Taghavi, Iran
Abdoullah Namdar, Malaysia
Afshin Asadi, Malaysia
Ahaiti Rehemani, Japan
Ahmad Fahimifar, Iran
Ahmed A. Mohamed, Egypt.
Ahmed H. Abdul Kareem, Iraq
Ahmed Hassan, Egypt
Ahmed M. Eltohamy, Egypt.
Ahmed Rusdy Towfek, Egypt.
Akhila Manne, India
Akihiro Hashimoto, Japan
Akira Kikuchi, Malaysia
Akram Y. Al-Sa'aty, Iraq
Al Serif M. Abd Alazez, Egypt.
Alain Le Kouby, France
Ali Ghazat, Iran

Ali Sobhanmanesh, Malaysia
Alireza sadeghabadi, Iran
Alkroosh, Nikraz, Australia
Aly Ahmed, Egypt
Amin Falamaki, Iran
Amin Naeimabadi, Iran
Aniruddha Senguptar, India
Anna Grzyb, France
Anna Maria Pellegrino, Italy
Antoine Guimond-Barrett, France
Ardalan Akbari Hamed, Iran
Arifin Abdu, Malaysia
Arvin Abdolmaleki, Iran
Asskar Janalizade Choobbasti, Iran
Atrchian mohammad reza, Iran
Atsuko Nonomura, Japan
Azlan Bin Adnan, Malaysia
Azza M. Elleboudy, Egypt

B

B. Gatmiri, Iran
B. Maher, Australia
B. Rafieey, IRAN
B.G. Muhammad, Malaysia
Bipul Hawlader, Canada
Bour Moslem, Iran
Bujang bin Kim Huat, Malaysia

C

C. Behnia, Iran
C. S. Chen, Malaysia
Carrillo-Acevedo, Peru
Carrillo-Gil, Peru
Chaminda Gallage, Australia
Charrismanagara Arry, Australia
Choo Chung Siung, Malaysia

D

D. Elmi, Iran
D. Wanatowski, United Kingdom
D.E.L. Ong, Malaysia
Daghigh younes, Iran
Dominic Ong E. L, Malaysia
Dygku Salma Awg Ismail, Malaysia

F

Fabien Szymkiewicz, France
Faisal Ali, Malaysia
Fakher Ali, Iran
Farshad Fayyaz Jahani, Iran
Farzad Allahyari, Iran
Fathi M. O. Mohamed, Canada
Ferry Fatnanta, Indonesia
Frederic Pellet, France
Fukawa, H. , Japan
Fumitake Nishimura, Japan

G

G.R. Reddy, India
Gauhar Sabih, Pakistan
Ghanbari namin hamed, Iran
Gholami Meade, Iran
Gholamreza Darvishi, Iran
Gholamreza Shoaie, Iran
Gi-Dae Oh, Korea
Gratchev Ivan, Australia

H

H. Elahi, Iran
H. S. Sagady, Sudan
Hakime Rabbani, Iran
Hamed A. Keykha, Malaysia
Hamed Bavanpouri, Iran
Hamidreza Saba, Kuwait

Hara, T., Japan

Hasan A. Kamal, Kuwait
Hasan Sharafi, Iran
Hassan J. Karam, Kuwait
Hayano, K.
Hijiri Hashimoto, Japan
Hirochika Hayashi, Japan
Hirochika Hayashi, Japan
Hiroo Shiojiri, Japan
Hiroshi Masuya, Japan
Hiroyasu Ohtsu, Japan
Hongyu Qin, Australia
Hooman Abadi, Malaysia
Hossein Moayedi, Iran
Hossein Tavallali, Iran
Hyun-Ku Park, Korea

I

Ideris Bin Zakaria, Malaysia
Iman Ashayeri, Iran

J

J. M. Kate, India
J. Rajaraman, India
J. Santhosh, India
J. Shamsuddin, Malaysia
Jahangir Khazaie, Iran
Jahangir Khazaie, Iran
Jan Jaremski, Poland
Janaka J. Kumara, Japan
Jia He, USA
Jian Chu, USA
Jitsangiam P., Australia
John N. Mukabi, Kenya
Jun Sugawara, Australia

K

K. Kawai, Japan

K. Kawai, Japan	M. P. Bhorkar, India
K. Oda, Japan	M. Shafieyzadeh, Iran
K. Yamamoto, Iran	M.S LEE, Japan
K.Thiruvenkatasamy, India	M.S. Jaafar, Malaysia
Kamran Akhtar, Pakistan	Mahdi Ali Bolandi, Iran
Kaoru Kobayashi, Japan	Mahdy Khari, Malaysia
Kazuhiro Oda, Japan	Mahmoud Dhaybi, France
Kazuo Fujita, Japan	Mahnoosh Biglari, Iran
Keizo Ugai, Egypt	Mahshid Mirzaaghaee, Iran
Kenichiro Nakarai, Japan	Majid Mirzaei, Malaysia
Kenji Hotta, Japan	Man-Kwon Choi, Japan
Khairul Anuar Bin Kassim, Malaysia	Masaaki Ishida, Japan
Khazaie Jahangir, Iran	Masaaki Kondo, Japan
Khosro Ebrahimkhani, Iran	Masahiko Katoh, Japan
Kiarash Ashtari, Iran	Md. Bellal Hossain, Japan
Kimitoshi Hayano, Japan	Md. Eahya Al Huda, India
Koichi Onohara, Japan	Md. Iftekharuzzaman, Canada
Kota Sasaki, Japan	Md. Toriqul Islam, Japan
Kyoichi Okamoto, Japan	Md. Zakaria Hossain, Japan
	Mehdi Arab Ameri, Iran
L	Mehdi Arab Ameri, Iran
L G Tham, Hong Kong	Mehdi Mokhberi, Australia
L.R. Stace, United Kingdom	Michko Masuda, Japan
Lee Min Lee, Malaysia	Minatour Yasser, Iran
Lee Sieng Kai, Malaysia	Minoru YAMANAKA, Japan
Leonardo Schippa, Italy	Minsun Lee, Japan
Lim Lion Yee, Malaysia	Mitsuhiro Inoue, Japan
	Mohamad Sharifipour, Iran
M	Mohamad T. Al-Layla, Iraq
M H. Sadagiani, Iran	Mohammad Ahmadi, Iran.
M. A. Dafalla, Saudi Arabia	Mohammad Arab Ameri, Iran
M. Abdoli, Iran	Mohammad Arab Ameri, Iran
M. Akiyama, Japan	Mohammad Gheitury, Iran.
M. Dianah, Malaysia	Mohammad Mahdi Roozbahani , Malaysia
M. Fathalikhani, Iran	Mohammad Moghadaripour, Iran
M. Hira, Japan	Mohammad Reza Atrchian Iran
M. Mirshekari, Iran	Mohammad Reza Atrechian, Iran
M. Moradi, Iran	Mohammad S. Pakbazy, IRAN

Mohammad Sharifipour, Iran
 Mohammed K. Fekheraldin, Iraq
 Mohd Raihan Taha, Malaysia
 Morikawa, Y. Japan
 Morteza Ala, Iran
 Mosayeb Heshmati, Iran
 Mosayeb Heshmati, Iran.
 Moshe Livneh, Israel
 Mosleh Al Shamrani l, Saudi Arabia
 Mostafa Yousefi Rad, Iran
 Muhamad Faiz, Malaysia
 Muhamad Ghaituri, Iran
 Musa Mutah, Malaysia
 Musahaq Ali, Japan
 Mu'azu Mohammed Abdullahi, Malaysia

N

N. Aramaki, Japan
 N. Rostam Afshar, Iran
 N.Z. Mohd Yunus, Malaysia
 Naoto Takashita, Japan
 Naoya Toyota, Japan
 Narges Janalizadeh, Malaysia
 Navid Khayat, Iran
 Navid Shahnazi, Iran
 Nazri Bin Ali, Malaysia
 Neelima Satyam, India
 Ng Wei Soon, Malaysia
 Nik Muhamad Majid, Malaysia
 Nikraz H., Australia
 Noam A. Livneh, Israel
 Nor Eman Ismail, Malaysia
 Noriyuki Yasufuku, Japan
 Nuri al-Mohamadi, Jordan
 Nurly Gofar, Malaysia
 Nurmunira Binti Muhammad, Malaysia

O

Omar Mustafa, Iraq
 Osama M. A. Daoud, Sudan
 Osama M. A. Daoud, Sudan

P

P. Egodawatta, Australia
 P. Sethu Raja, India
 Philippe Reiffsteck, France
 Poona Abadi, Malaysia
 Poona Abadi, Malaysia
 Purwana, Y.M., Australia

Q

Qutayba Nazar Al-Saffar, Iraq

R

R. Ziaie Moayed, Iran
 R.Sanjeev, India
 Raid R. Al-Omari, Iraq
 Ramin Doostmohammadi, Iran
 Ramli Nazir, Malaysia
 Reza Ziaie Moayed, Iran
 Rouzbeh Abadi, Malaysia
 Rouzbeh Abadi, Malaysia

S

S. Fakhretaha, Iran
 S. Jayakody, Australia
 S. Kawasaki, Japan
 S. Muhammad Jamil, Pakistan
 S. Nomura, Japan
 S. Ohno, Japan
 S. Raei, Iran
 S. Sakamoto, Japan
 S. Tsurumi, Japan
 S.M. Abdul Awal, Malaysia
 S.M. Binesh, Iran
 S.Nishiyama, Japan

S. Ohno, Japan	Sunil Kumar, India
S. Tsurumi, Japan	Surendra Singh, India
S. Usha, India	Syawal SATIBI, Indonesia
Sabzi Zahra, Iran	
Sai K. Vanapalli, Canada	T
Salam J. Bash Al-Maliky, Iraq	T. Negami, Japan
Salman Hanifi, Iran	T. Souliyavong, Australia
Salman hanifi, Iran	T. Y. Elkady, Saudi Arabia
Samaneh Kargar, Iran	T. Kikuchi, Japan
Satoru Kawasaki, Japan	T. Yano, Japan
Satoru Kawasaki, Japan	Taghizadeh Maryam, Iran
Satoshi MASAKI, Japan	Takaaki Tsukada, Japan
Satoshi Nishimoto, Japan	Takamitsu Kajisa, Japan
Satoshi Nishimoto, Japan	Takayuki Isoda, Japan
Satoshi Nishimoto, Japan	Takayuki Kawai, Japan
Sawada, K., Japan	Takehana, K.
Seok Yoon, Korea	Takeshi SATO, Japan
Seung-Rae Lee, Korea	Tam Sy HO, Japan
Seyed Ali Farjam, Australia	Tan Jui Siang, Malaysia
Seyed Ali Hashemi, Iran	Tanaka, S.
Seyed Salman Musavi, Iran	Taro Uchimura, Japan
Shaharin Ibrahim, Malaysia	Tetsuya Suzuki, Japan
Shahrbanoo Rezanejad Farahmand, Iran	Toshihiro Morii, Japan
Shigeeko Haruyama, Japan	Toshimitsu Komatsu, Japan
Shinsuke Matsumoto, Japan	Toshinori Sakai, Japan
Shinya Inazumi, Japan	Tschuschke W. , Poland
Shiran Jayakody, Australia	Tsuguhiro Nonaka, Japan
Shokouhi Ali, Australia	Tsuji, S., Japan
Shotaro Kitamura, Japan	
Shuichi HASEGAWA, Japan	V
Shushi Sato, Japan	V. Phommachanh, Japan
Siamak Pahlevanzadeh, Australia	V. Rashidian, Iran
Siavash Zamiran, Kuwait	Viktor Stabnikov, USA
Sina Kazemian, Iran	Vivi Anggraini, Malaysia
Siti Noor Linda Taib, Malaysia	Volodymyr Ivanov, USA
Soewignjo Agus Nugroho, Indonesia	
Sonia Fanelli, France	W
Srijit Bandyopadhyay, India	W.W. Ng, Hong Kong

Wei Dong Guo, Australia

Wierzbicki J. , Poland

X

Xu Kai, Hong Kong

Y

Y. Hayashi, Japan

Y. Sugiyama, Japan

Y. Takayama, Japan

Y.Takayama, Japan

Yasuo Tanaka, Malaysia

Yoshida, M., Japan

Yoshihiro Kimura, Japan

Yoshio Suematsu, Japan

Yousefi Kebria Daryoush, Iran

Yousefi Kebria Daryoush, Iran

Yousefi kebria Daryoush, Iran

Yousry M. Mowafe, Egypt.

Yuki Hasegawa, Japan

Yuki Yokoyama, Japan

Yuuki Shigekuni, Japan

Z

Zakaria Hossain, Japan

Zeinab Bakhshipour, Malaysia

Zieaoddin Shoaee, Iran

List of Countries

Australia

Canada

Egypt

France

Hong Kong

India

Indonesia

Iran

Iraq

Israel

Italy

Japan

Jordan

Kenya

Korea

Saudi Arabia

Kuwait

Malaysia

Nigeria

Pakistan

Peru

Poland

Singapore

Sudan

United Kingdom

United States of America